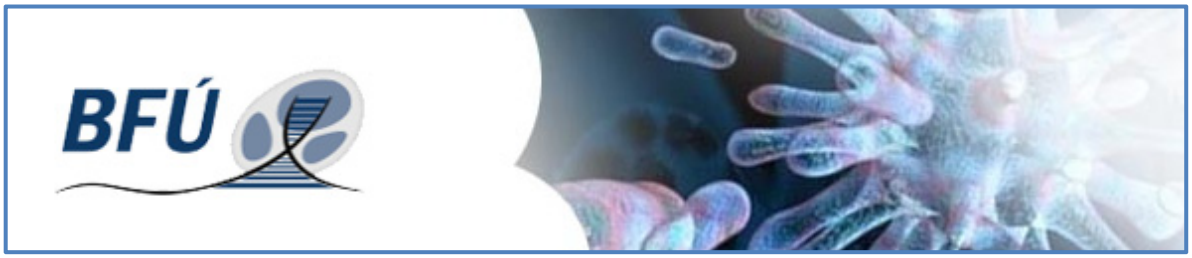

Institute of Biophysics of the Czech Academy of Sciences

Department of Cell Biology and Radiobiology

Habilitation Thesis

DNA Damage and Repair upon Cell Exposure to Different Types of Ionizing Radiation – the Importance of Chromatin Context and New Perspectives of Cancer Radiotherapy

Brno, 1st October 2019

RNDr. Martin Falk, Ph.D.

The most beautiful thing we can experience is the mysterious. It is the source of all true art and science

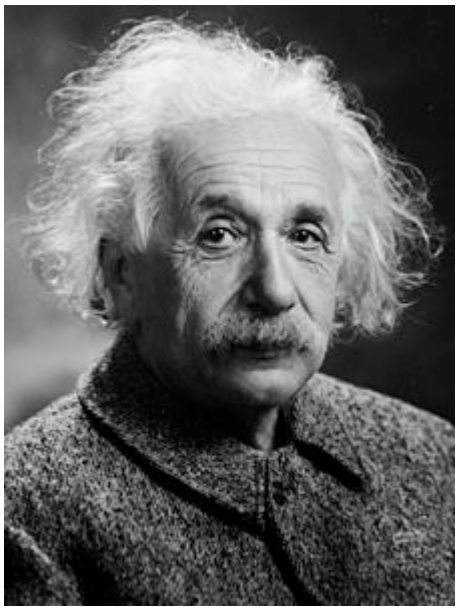

(Albert Einstein)

ACKNOWLEDGEMENT

Above all, my deepest gratitude belongs to my wife, RNDr. Iva Falková, Ph.D. my parents, Mgr. Venuše Falková and Mgr. František Falk, and my parents in law, Dana Kroupová and Ing. Otmar Kroupa, for extensively supporting me in all aspects of my life, especially during my childhood and studies. I am heartily thankful to my parents also for continuously developing my sense for the beauty and mystery of nature and my enthusiasm for exploration. I also have to mention Gary and Rory, our black Labradors, who always did their best to make my life as wonderful as possible and inspired me by their dog wisdom in many ways.

Many people contributed, directly or indirectly, to results included in the present habilitation thesis. This work would not have been possible unless the long-time helpfulness of Assoc. Prof. RNDr. Stanislav Kozubek, DrSc., the former director of the Institute of Biophysics of CAS, and Ing. Emilie Lukášová, Ph.D., who lead my first steps in science and supported my scientific career in many ways. In addition, I would like to thank Prof. RNDr. Jiří Fajkus, CSc., Mgr. Olga Kopečná, Ph.D., Mgr. Eva Pagáčová, Ph.D., Ing. Alena Bačíková, Ing. Lucie Ježková, Ph.D., Mgr. Lenka Štefančíková, Ph.D., and all my former and current colleagues who participated in the herein presented research, performed excellent experimental work, and provided me with stimulating discussions.

My deep thanks belong also to my national and international collaborators, who extensively contributed to the discoveries described herein and largely enriched our technological and methodological abilities. I am very grateful and proud that they also became my close friends. Prof. Dr. Rer. Nat. Michael Hausmann, Ph.D. (Kirchhoff Institute for Physics, Heidelberg, Germany) opened us

doors to an exciting nanocosmos of the cell by providing us with the opportunity to study cellular processes at the nanoscale with unique Single Molecule Localization Microscopy (SMLM). In addition, Michael shared with me his extensive expertise in biophysics and helped me in many ways whenever needed. Ing. Marie Davídková, Ph.D. (Nuclear Physics Institute of CAS, Prague, CR) and Accad. Prof. Evgeny Krasavin (Joint Institute for Nuclear Research in Dubna, Russia) assured our access to particle accelerators (proton and heavy ion irradiation). With their colleagues, they contributed to many parts of our radiobiological research. Assoc. Prof. Ing. Irena Kratochvílová, Ph.D. (Institute of Physics of CAS, Prague, CR) stood at the beginning of our cryobiological research and had a substantial role in its development. Prof. Dr. Rer. Nat. Bořivoj Klejdus, Ph.D. (Mendel University, Brno, CR) complemented our studies with important metabolic analyses. Assoc. Prof. Michal Masařík, Ph.D., MUDr. Jaromír Gumulec, Ph.D. (both from Masaryk University, Brno, CR) and MUDr. Zuzana Horáková, Ph.D. (Faculty Hospital, Olomouc, CR) shared with us an effort to better understand the radiosensitivity of tumor cells, developed special cell primocultures used in our studies, participated in associated transcriptomic studies and extensively assisted to Ing. Tomáš Vičar, Ph.D. (Brno Technical University, Brno, Czech Republic), with development of IRIF focus detection software. Prof. Pier Giuseppe Pelicci, M.D., Ph.D. (Director of the Department of Experimental Oncology, European Institute of Oncology [EIO], Milan, Italy), Assoc. Prof. Ivan Gaetano Dellino, Ph.D. (EIO, Milan, Italy), and Dr. Mario Faretta, Ph.D. (EIO, Milan, Italy) invited us to participate in an interesting research of APL leukemia research. Finally, cooperation with Prof. Sandrine Lacombe, Ph.D. (University Paris Sud, Paris, France) lead to surprising new results on nanoparticle-mediated tumor cell radiosensitization. Assoc. Prof. MUDr. Zdeněk Kleibl, Ph.D. and Mgr. Jan Ševčík, Ph.D. (Department of Oncology, First Faculty of Medicine, Charles University in Prague and General University Hospital in Prague), initiated our mutual research on DSB repair efficiency in cells containing alternative splicing variants of BRCA1. Together, we enjoyed uncountable never-ending discussions on many scientific and everyday life topics. This holds true also for Prof. MUDr. Zdeněk Lukáš, CSc., one of the last representatives of "old-school" Renaissance professors who unfortunately seem to undergo extinction. He inspired me as a man who lived for his work but still was capable of admiring the beauty of life.

Looking back to my beginnings, I owe my gratitude to RNDr. Marie Vojtíšková, CSc., my Diploma Thesis supervisor, Assoc. Prof. RNDr. Alena Španová, CSc., Assoc. Prof. Ing. Bohuslav Rittich, CSc., and to all lecturers from the Masaryk University Brno – Prof. RNDr. Stanislav Rosypal, DrSc., Prof. RNDr. Jiřina Relichová, CSc., Prof. RNDr. Jan Šmarda, CSc., and Prof. RNDr. Jiří Doškař, CSc., among others.

Finally, my thanks belong to all scientists that build up the current body of knowledge we can further develop.

I hereby declare that I wrote this thesis on my own and followed the literature involved. The herein presented papers were all written by the author or at least with his extensive contribution. The thesis is composed of new commenting texts and texts adapted from the indicated original papers of the author.

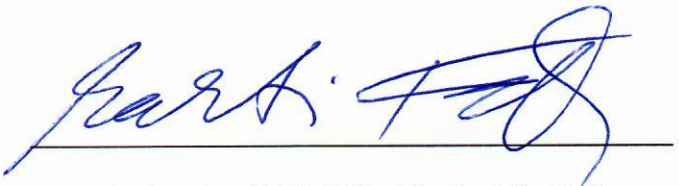

Brno, 1st October 2019, RNDr. Martin Falk, Ph.D.

CONTENT

LIST OF FIGURES (and their sources)

MPORTANT ABBREVIATIONS

AcetylH3K9	histone H3 acetylated at lysine 9
AcetylH4K5	histone H4 acetylated at lysine 5
AML	acute myeloid leukemia
AntiRIDGEs	counterpart sequences to RIDGEs
APL	acute promyelocytic leukemia
BER	base excision repair
CML	chronic myeloid leukemia
CT	chromosomal territory
CTX	chromosomal territory of chromosome X
CX	centromere of chromosome X
Cy3	cyanine dye (excitation [512], 550 nm; emission 570, [615] nm)
DAPI	4',6-Diamidino-2-phenylindole dihydrochloride (excitation 350 nm; emission 470 nm)
Dc	diffusion coefficient
DDR	DNA damage response
DNA-PKcs	DNA-PK catalytic subunit
DNMTs	DNA methyltransferases
DSB	DNA double-strand break
E1	exons 5-7 of *DMD* gene
E2	exons 46-47 of *DMD* gene
EC	euchromatin nuclear domain
EC-DSB	DSBs localized in euchromatin
FISH	fluorescence *in situ* hybridization
FITC	fluorescein isothiocyanate (excitation 494 nm; emission 521 nm)
FRAP	fluorescence recovery after photobleaching
FWC	fluorescence-weight center of chromosomal territory
GFP	green fluorescent protein
GFP-HP1β	HP1β tagged with green fluorescent protein
HC-DSB	DSBs localized in heterochromatin
HC	heterochromatin
HCD	heterochromatin nuclear domain
HDACs	Histone deacetylases
High-LET	ionizing radiation with high linear energy transfer
HL60	human promyelocytic leukemia cells
HMTs	histone methyltransferases
HOM	hyper-osmotic
HP1	Heterochromatin protein 1
HP1α (γ, β)	Heterochromatin protein 1 isoform α (γ, β)
HR	homologous recombination (DSB repair pathway)
HSA	human chromosome
HypoOM	hypo-osmotic
IBCT	ion-beams cancer therapy
ImmunoFISH	immunocytochemistry combined with FISH
IR	ionizing radiation
LET	linear energy transfer
Low-LET	ionizing radiation with low LET
Mb	megabase
mBanding	multicolor chromosome banding
MBD	methyl-CpG-binding domain
MCF-7	a breast cancer cell line isolated from a 69-year-old Caucasian woman (Michigan Cancer Foundation – 7)
MENT	myeloid and erythroid nuclear termination protein
MetH3K27	histone H3 methylated at lysine 9
mFISH	multicolor FISH
MMEJ	Microhomology-mediated end joining
MMR	mismatch repair
MRN complex	DSB repair complex composed from NBS1, MRE11 and RAD50
NBs	nuclear bodies (= PML bodies)
NER	nucleotide excision repair
NHEJ	non-homologous end-joining (DSBs repair pathway)
OMIM	Online Mendelian Inheritance in Man (database: www.ncbi.nlm.nih.gov/omim)
P[t(*a*;*d*)]	probability of translocation between DSB lesions (for example) *a* and *d*
PCR	polymerase chain reaction
PEV	position effect variegation
Ph-chromosome	Philadelphia chromosome, appearing due to the t(9;22)(q34;q11) translocation
PI	post-irradiation (*e.g.,* 5 min PI)
PML/RARa	PML/RARa fusion *oncogene*/oncoprotein arising from t(15;17)(q22;q12) chromosomal translocation
RA	*all-trans* retinoic acid
RARE	RARα response element
RARα	retinoic acid α-receptor
RIDGEs	Regions of Increased Gene Expressions
ROS	reactive oxygen species
SKY	spectral karyotyping
SMLM	Single Molecule Localization Microscopy
SSA	single-strand annealing
t(*a*;*b*)	translocation between loci (genes) *a* and *b*
TAF	tumor-associated fibroblasts
TOPRO-3	4-[3-(3-methyl-1,3-benzothiazol-2(3H)-ylidene)prop-1-en-1-yl]-1-[3-(trimethylammonio)propyl]quinolinium (excitation 642 nm; emission 661 nm)
Tri-metH3K79	histone H3 tri-methylated at lysine 79
TSA	trichostatin A
TSS	transcription starting site
TUNEL	terminal deoxynucleotidyl transferase dUTP nick end labeling
WCP	whole-chromosome painting probe
wt	wild-type
Xa	active homologue of chromosome X
Xi	inactive homologue of chromosome X
XL	larger homologue of chromosome X
XS	smaller homologue of chromosome X
Δd^2	mean squared displacement
γH2AX	histone H2AX phosphorylated at serine 139
γIR	gamma ionizing radiation (γ-rays)

% R	percent of nuclear radius
3D-FISH	fluorescence *in situ* hybridization on spatially fixed cells

KEYWORDS

TOPICS

Ionizing radiation (of different types)
γ-rays
Proton beams
High-LET radiation / accelerated ion beams
Space radiation
Biological effects of ionizing radiation
DNA damage and repair
DNA double strand breaks (DSBs)
Non-homologous end-joining (NHEJ)
Homologous recombination (HR)
Alternative BRCA1 splicing variants
DSB repair pathway selection
DSB repair pathway kinetics and efficiency
DSB repair focus micro- & nano-structure
γH2AX foci
53BP1 foci
Clustered / multiple DSBs
Particle track (streak) micro- & nano-structure
Microdosimetry
Replication fork collapse, replication stress
Higher-order chromatin structure
Euchromatin & heterochromatin
Chromosomal territories
Regions of increased gene expression
Epigenetic modifications and radiation
Chromatin dynamics
Spatio-temporal aspects of DSB repair
Chromosomal aberration formation
Breakage first theory
Position first theory
Cell-type specific radioresistance
Carcinogenesis
Cancer therapy
Radiotherapy (RT)
Tumor radioresistance
Genomic instability
Cell communication and radioresistance
Individual radiosensitivity
Cancer cell radiosensitization
Ion beam cancer therapy (IBCT)
Nanoparticle-mediated radio-sensitization
Pre-irradiation cell freezing
Normal cell radioprotection
Radioprotection by amifostine
Apoptosis

CELLS & CANCERS

Head and neck tumor cell primocultures
Breast cancer
Colon cancer
Acute myeloid leukemia (AML)
Chronic myeloid leukemia (CML)
Promyelocytic leukemia (AML)
U87 glioblastoma cell line
MCF7 breast cancer cell line
Detroit head and neck cancer cell line
FaDu head and neck cancer cell line
U937-PR9 promonocytic cell line
White blood cells (lymphocytes, granulocytes)
NHDF - normal human skin fibroblasts

METHODS

Particle irradiation / accelerators
Gamma-irradiation
High-resolution confocal microscopy
Single Molecule Localization Microscopy (SMLM)
Immunocytological staining
Fluorescence *in situ* hybridization (FISH)
3D-FISH
mFISH
ImmunoFISH
Live cell real time microscopy
FRAP
Western blotting

.

ABSTRACT

Ionizing radiation (IR) causes cancer and other serious health problems, but also kills tumor cells when applied therapeutically. These effects of IR have been known from the very beginning of the twentieth century, but only current technological and methodological progress has allowed for the study of cellular damage and response to irradiation at the molecular level. Diving into this field and obtaining more knowledge will open doors to more efficient cancer radiotherapy, aging deceleration, radiation protection and crisis planning, and interplanetary space exploration.

The present habilitation thesis summarizes the scientific results achieved by the author and his research team on the biological effects of different types of IR—γ-rays, protons of different energies, and various accelerated heavy ions—with the emphasis here placed on the still unexplored roles of the higher-order chromatin structure in the mechanisms of the induction and repair of DNA double-strand breaks (DSBs). DSBs are the focus because they represent the most deleterious type of DNA lesions and hence dominantly contribute to radiation-induced carcinogenesis and cell destruction. Extensively addressed in the present thesis are the mechanisms of cell-type-specific and individual radioresistance and potential new methods for tumor cell radiosensitization and normal cell radioprotection. This includes research on ion-beam irradiation, metal nanoparticle-mediated radiosensitization, preirradiation DNA damaging by cell freezing, and selective normal cell radioprotection offered by some chemical agents, such as amifostine.

Altogether, the results of the current dissertation show that chromatin is organized nonrandomly in the cell nucleus, and its higher-order structure participates in the regulation and mediation of vital processes, including DNA damage induction, repair, and misrepair. Based on the synthesis of the data, we propose a new model on the relationship between the physical properties of radiation, higher-order chromatin structure, chromatin dynamics, sensitivity of structurally and functionally distinct chromatin domains to radiation damaging, efficiency of DNA repair, and mechanisms of chromosomal aberration formation. Among other conclusions, the model shows that genetically inactive heterochromatin—because of its structure and composition—is better protected than active euchromatin against the indirect effect of sparse IR. On the other hand, for the same structural purposes, heterochromatin provides more targets per volume for densely ionizing particles (that mostly damage DNA directly) and is more difficult to repair because it requires chromatin decondensation to occur. This decondensation is followed by the protrusion of damaged chromatin into the nuclear areas with a low density of chromatin that seem to represent repair permissive subcompartments. This local chromatin mobilization has no features of directed DSB migration into putative “repair factories,” as predicted by some authors, but rather, it improves the accessibility of repair proteins to damaged DNA while at the same time increasing the risk of chromosomal aberration formation. The most threatening form of DSBs (multiple DSBs or DSB clusters) thus arise because of primary chromatin fragmentation by densely IR or, in the case of any radiation, secondarily as a byproduct of the repair processes, especially in heterochromatin. Consequently, although the probabilities of chromosomal translocations between

the particular genetic loci primarily depend on their spatial separation (global nuclear architecture), they can be dominantly altered by the preexisting higher-order chromatin structure (texture) at the sites of the DSBs, which changes during the repair process.

An exciting opportunity to obtain deeper insights into the structuro-functional organization of DSB damage and repair processes in space and time has been possible thanks to recently developed single molecule localization microscopy (SMLM), which we took advantage in our newest studies. With a resolution of 10–20 nm, SMLM revealed that DSB repair foci (IRIFs) have an internal nanostructure of numerous internal molecular clusters of γH2AX and clusters of individual DSB repair proteins (such as 53BP1). The number of these nano-clusters increases with the radiation linear energy transfer (LET), which is in agreement with their expected higher complexity. Nevertheless, whether this nanostructure corresponds to the numbers of DSBs present inside microscopically defined IRIFs remains a question.

Interestingly, the IRIF nanostructure and its postirradiation spatio-temporal dynamics differed for normal and tumor cells and for specific types of chromatin domains. This observation opens the possibility that IRIF assembly reflects the nanostructure of chromatin at the sites of DSB damage, which could explain how the features of DSBs themselves and of the surrounding chromatin can participate in the decision-making process for a specific repair mechanism at each individual DSB lesion site. Thus, the chromatin nanostructure-dependent IRIF nanostructure could also influence cell radiosensitivity. We continue with experiments to confirm these conclusions.

Several surprising findings followed from our exploration of tumor cell radiosensitization: All radiosensitizing approaches studied in the current work—the application of ion beams, metal nanoparticles, or freeze-thaw cycles—improved tumor cell killing by radiation; however, this did not always occur (metal nanoparticles) via increasing the nuclear/mitochondrial DNA damage and/or reducing the cell repair capacity. Targeting the cytoplasmic organelles, for instance, like lysosomes, emerged as a potentially efficient and safer strategy of radiation toxicity escalation in tumor cells that should be studied.

High-LET ions generated DSBs of a markedly higher complexity than photon gamma rays. The complexity of DSBs correlated with radiation LET and cell killing, as expected, but different ions with similar LET and energy caused differently complex DSBs that were repaired with different efficiency. Hence, parameters of radiation beyond LET and energy should be taken into consideration in treatment planning and predicting the biological effects of different energetic particles.

Instead of extensively fragmenting chromatin as proposed by many studies, preirradiation cell freezing altered the higher-order chromatin structure in the majority of cells and caused a collapse of replication forks in S-phase cells. Because tumor cells replicate faster than normal cells (and have defects in DSB repair pathways and cell cycle checkpoints), they could be more affected, as observed herein for MCF7 cells.

Finally, amifostine, the drug known for its selective radioprotective effect on normal cells, not only improved the survival of normal cells upon irradiation, but also decreased the viability of tumor cells by impairing their DSB repair.

To conclude, the present thesis answers the fundamental questions associated with the principles of higher-order chromatin organization and its role in the processes of DNA damage induction, repair, misrepair and carcinogenesis, and tumor cell radioresistance. However, even more questions emerged throughout the course of conducting this research. In addition to the scientific knowledge obtained, the practical benefits of the herein discussed research could be seen in the future mostly in cancer therapy and radiation protection (space exploration). Methodologically, SMLM has proven to be a very useful and novel method in both scientific research and clinical use.

SUMMARY

The collection of papers presented in the current habilitation thesis summarizes the contribution of the author and his team to the development of radiobiology. Specifically, the present thesis creates a better understanding of the biological effects of different types of IR, including γ-rays, protons, and various accelerated ions with a high LET. The included papers introduce step by step the team's contribution, leading from recognition of the principles of the higher-order chromatin organization in the cell nucleus to suggesting a new model that describes the relationship between the physical properties of IR, higher-order chromatin structure (or other cell-type-specific intracellular factors), and DNA damage induction, repair, and misrepair. Consequently, the impact of our findings on the (tumor) cell radioresistance and therapeutic possibilities of how it could be therapeutically manipulated or overcome is considered. The current thesis provides discussion on the published results, which are supplemented with explaining and summarizing comments, putting the findings in a broader context. Figures and pieces of text from the original papers are also enclosed in a modified form to provide the reader with a deeper understanding of the problems without asking the reader to go over the original works. The results are organized into three chapters: The first chapter (Chapter 2.1) explores the principles of the higher-order chromatin organization (nuclear architecture) and its role in fundamental physiological processes in normal cells and pathological processes in tumor cells, respectively. The second chapter (Chapter 2.2) then focuses on the question of how the higher-order chromatin structure participates in the mechanisms of radiation damage induction, repair, and formation of chromosomal aberrations. Finally, the third chapter (Chapter 2.3) addresses the causes of tumor cell radioresistance and possible methods for therapeutic lowering. The achieved results are briefly summarized below.

In Chapter 2.1, we propose the principles of the higher-order chromatin organization in the nuclei of normal cells[1–5] and point to their alterations in cancer cells.[6–9] Together with others[1] we showed—which contrasts the previous opinion of the biological community—that the cell nucleus is a highly organized organelle with nonrandom higher-order chromatin structure that, importantly, has functional aspects.[1–5]

In the interphase nucleus, chromosomes appear as so-called chromosomal domains (or territories), showing their internal structure and distribution in the cell nucleus that follows some rules, though of

a statistical character. In spherical human cells, for instance, lymphocytes, the territories of gene-dense chromosomes tend to occupy a more central space of the cell nucleus while the territories of gene poor chromosomes preferentially appear underneath the nuclear envelope. Each pair of homologous chromosomal territories thus preferentially occurs in a specific concentric shell of the cell nucleus with a defined mean distance from the nuclear center (further referred to as "radial distance"). This mean distance increases with the overall genetic activity of the particular chromosome, is characteristic for each pair of homologous chromosomes, and, to some extent, also depends on the cell type.[1,2] The same rule holds true also for the internal organization of subchromosomal chromatin domains within chromosomal territories and causes their structurally functional polarization.[1,2] The nuclear topology of chromosomal territories in flat cells, such as fibroblasts, follows similar organization principles, but their radial distribution is based on the size of chromosomal territories rather than gene density/activity. In contrast to the radial distribution, the mutual arrangement of chromosomes at the surface of imaginary concentric spheres is random.[1,2] Genetic activity influences and, in turn, is influenced by the level of chromatin condensation.[3] Genetically (transcriptionally) active chromosomal territories and their chromatin subdomains are less condensed and occupy bigger nuclear volumes compared with the genetically inactive counterparts of a comparable molecular size.[3] In some cases, genetically active chromatin even protrude outside of the territory's core area. Therefore, genetically active territories are more irregular than inactive ones and, to a larger extent, intermingle with their neighbors.

The higher-order chromatin structure is disturbed in different ways in tumor cells and actively contributes to disease development.[6–10] For instance, we discovered that an oncogenic protein may initiate cancer just by generating changes in the higher-order chromatin structure.[11] As another example, we revealed that there is incomplete chromatin maturation (composition and condensation) in the terminally differentiated granulocytes of acute and chronic myeloid leukemia (AML, CML) patients. Importantly, this immature status persists in patients' granulocytes even after a successful cancer treatment, leading to complete clinical and molecular remission with the disappearance of the Philadelphia chromosome. Importantly, this defect is of serious functional relevance because it prevents AML/CML granulocytes' immune functioning.[6] Defects in the higher-order chromatin organization appear even in the cells isolated from a morphologically normal tissue adjacent (e.g., 10 cm distant) to the colon tumor. These changes could thus be considered either as premalignant epigenetic defects or feedback chromatin alterations provoked by the tumor in the surrounding cells.[10]

Finally, the specific features of the higher-order chromatin structure could be the explanation for why both spontaneous and radiation-induced DNA breaks, which cause the chromosomal aberrations causative of myelodysplastic syndromes (MDSs), emerge at specific chromosomal loci. Nevertheless, these breakpoint loci are not as sharply defined as, for instance, in the case of leukemia, and only a few of them colocalize with chromosome fragile sites. This suggests that specific higher-order chromatin structures could be responsible for (or at least contribute to) the susceptibility of MDS breakpoints to DSB formation.[8,9] Indeed, our preliminary data show more frequent colocalization of the γH2AX foci (DSB marker) with some MDS breakpoints in cells exposed to γ-rays (Falk et al., manuscript in

preparation). Interestingly, in this context, MDSs frequently appear as the secondary cancer developed as a result of previous radiotherapy history. These results thus form the logical bridge to the next chapter dedicated to the relationship between the higher-order chromatin structure and effects of IR.

Chapter 1.9 demonstrated in detail the importance of the higher-order chromatin structure for fundamental cellular processes. Based on this, it is reasonable to hypothesize that the organization of chromatin into structurally and functionally distinct chromatin domains can influence the sensitivity of DNA to radiation-induced damaging,[12,13] the mechanisms of DSB repair,[14–18] and, in turn, the mechanisms for the formation of chromosomal aberrations.[14–18] These studies are the subject of the second chapter of results (Chapter 2.2); here, we focused on DNA double-strand breaks (DSBs) because they are the most deleterious type of DNA lesions generated by IR. It should be noted that IR is the most potent DSB inducer among other DNA-damaging agents. Even a single DSB can result in cancer or cell death if repaired improperly or left unrepaired, respectively.

We showed[13,14] that decondensed, genetically active (eu)chromatin is a more critical target for low-LET radiation than its condensed, genetically inactive counterpart (hetero)chromatin. This difference in the radiosensitivity between the "heterochromatin" and "euchromatin" domains may be because sparse IR types mostly attack DNA through the production of reactive oxygen species (ROS), and as we observed, heterochromatin is better shielded against ROS than euchromatin because of its abundant heterochromatin-binding proteins[12,13] (reviewed in [15,17,18]). Moreover, because ROS arise from water radiolysis and are very short lived (i.e., can only damage biomolecules in their immediate surroundings), heterochromatin is protected against ROS also by its lower hydration compared with euchromatin[12,13] (reviewed in [15,17,18]). On the other hand, heterochromatin, with its higher DNA density, provides more targets per volume for high-LET particles, which mostly attack chromatin directly, and thus without regard to chromatin structure.[16–18]

The higher-order chromatin structure has important consequences for the mechanism of DSB repair and the formation of chromosomal aberrations[14] (reviewed in [15,17,18]). The repair of heterochromatic DNA breaks is more complicated than the repair of euchromatic breaks and requires decondensation of the affected chromatin domains before the process can continue. This decondensation allows for better access of repair factors to the damaged chromatin, mediating the relocation of DSBs into nuclear areas with a low density of chromatin that probably represent more suitable subcompartments for repair than condensed chromatin. Indeed, our confocal microscopy experiments on live cells with condensed chromatin domains that were labeled with HP1β-GFP and damaged by UV laser micro-irradiation revealed that although small sensors of DSBs (NBS1-RFP) can freely penetrate into these dense chromatin structures, large proteins (53BP1-RFP) acting in the later phases of DSB repair can do it only after preceding decondensation of the domain.[16] Despite the spatial relocation of some of DSB repair foci during the postirradiation time, it should be noted that their movement has no features of the targeted migration of multiple DSBs into putative repair factories,[14,14,17,18] the existence of which has been proposed by several authors. In fact, most damaged chromatin sites remain rather stable and DSB clustering—observed only occasionally after low-LET exposure—represents an unavoidable side effect of repair.[12,13] Our results indicate that DSB clustering provoked by repair processes increases the

risk of broken DNA ends misrejoining, perhaps explaining how complex chromosomal translocations occasionally form even in cells that are irradiated with low-LET IR.[13] Thus, the scenario described above adopts some aspects of both the "breakage-first" and "position-first" hypotheses, originally postulated as the opposite views regarding the involvement of chromatin dynamics in the mechanism of the formation of chromosomal translocations (or aberrations in general). We can conclude that chromosomal translocations usually appear between broken chromosomal loci that have been located in mutual proximity in the cell nucleus before damage induction; however, in some cases, illegitimate rejoining can proceed also between originally distant DSBs if they are mobilized by repair processes.[12,13,15]

The higher-order chromatin structure (texture) influences the probability of chromosomal translocations between particular DSBs in an even more complex way—it determines the vectors (extent and direction) of damaged chromatin movements and thus the possibility of their mutual meeting in the cell nucleus.[13,15] For instance, a heterochromatic "barrier" separating two DSBs can prevent their association and chromatin exchange between the affected loci. This challenges the current hypothesis presupposing that the probability of a translocation event occurring between specific genomic loci is simply proportional to their spatial separation in the cell nucleus, an assumption taken because of the nuclear architecture.

The relationship between the higher-order chromatin structure and repair processes described above is relevant also for high-LET irradiation;[16–18,18,19] however, high-LET particles generate a large number of DNA fragments along their track, that is, in a very limited volume of the cell nucleus.[19] With this condition, the higher-order chromatin structure can be locally lost so that (complex) chromosomal translocations can easily form between numerous free DNA fragments randomly. Complex aberrations in cells exposed to high-LET IR thus mostly appear as the result of the microdosimetric character of radiation energy deposition.[19] Based on these described findings, we propose a new model for the complex relationship between the properties of IR, microscale higher-order chromatin structure, sensitivity of distinct chromatin domains to radiation damage, DSB repair processes, and mechanism of formation of chromosomal aberrations.[13,14,16–19]

Even deeper insights into the mechanisms of the functional architecture of the cell nucleus and processes of DNA damage induction and repair could be obtained with super-resolution microscopy, technology that emerged only recently because of tremendous progress and that represents a breakthrough in cell research. In the frame of the presented research, in cooperation with Prof. Michael Hausmann from the Kirchhoff Institute in Heidelberg, Germany, we have adapted single molecule localization microscopy (SMLM) with a resolution of 10–20 nm for detailed analyses of chromatin and DSB repair focus (IRIF) nanostructures.[18,20–22] The obtained nanoscale results are relevant for more chapters of the current thesis; nevertheless, to prevent redundancy, they are only discussed in Chapters 2.3.1 and 2.3.2 in the context of particular research topics.

The last chapter (Chapter 2.3) presents our research on the diversity and mechanisms of tumor cell radioresistance[23–25] and the development of new approaches to therapeutically overcome tumor cell

radioresistance.[19,20,22,25–32] Introduced are also the results of the opposite way to improve tumor radiotherapy, that is, normal cell radioprotection.[33–35] Thus, the results are also partially relevant for civil/military radiation protection.

One crucial factor with potentially strong influence on cell radioresistance is DSB repair, which from different points of view has been explored in the frame of the previous chapter. Therefore, we studied here how DSB repair efficiency varies between different normal and tumor cell types[22,25] and between the cells of the same type but that were obtained from different cancer patients[25] or that carried alterations in important repair proteins.[23,24]

Tumor cells are known to have various mutations in the genes that are involved in DNA repair, cell cycle control, and cell death pathways, which can modify their response to radiotherapy. However, cancer cells also carry genetic alterations of other types; the effect these alterations have on DSB repair and cell radioresistance is still unexplored. Here,[23,24] we focused on the relevance of the alternative splicing variants of the BRCA1 protein, which functions in the decision making for a particular repair mechanism (NHEJ, nonhomologous end-joining; HR, homologous recombination; or alternative backup pathways) at individual DSB lesions. We revealed that cancer-specific misregulation of the splicing process may lead to the formation of irregular alternative splicing variants (ASVs) of BRCA1, for instance, with BRCA1Δ14–15 and BRCA1Δ17–19 ASVs, which according to our observations, undermines NHEJ activity and delays the repair of ionizing radiation-induced DSB damage; BRCA1Δ17–19 also impairs HR. Our results suggest that the alternative splicing variants of BRCA1 (and thus ASVs in general) may negatively influence genome stability, thereby contributing to enhanced probability of cancer development in the affected individuals. This finding could have important implications for the prevention and treatment of breast cancer.

Concerning the cell-type-specific and individual (tumor) radioresistance, we are running a study with primocultures of different cell types isolated from tumors of head and neck cancer patients. Head and neck tumors (HNT) were selected because half of them responded to radiotherapy, while the remaining half was highly radioresistant. The reasons behind this different radiosensitivity are unknown, as are the clinically usable markers of radioresistance, which strongly impairs the current tendency in HNT oncology to shift from surgery to noninvasive (chemo)irradiation to improve patients“ posttreatment quality of life.

To shed more light on these issues, we prepared primocultures of $CD90^-$ (tumor) cells, $CD90^+$ (tumor-associated) fibroblasts (TAF), and their mixed ($CD90^-$ (+) $CD90^+$) cultures[25] (Vicar et al., manuscript in preparation; Falk et al., manuscript in preparation). Consequently, we compared the DSB repair efficiency and postirradiation cell survival between the primocultures of these different cell types that were isolated from a single tumor and between the primocultures of the same cell type isolated from different tumors. The preliminary results revealed that many tumor primocultures could repair DSBs, with the kinetics and efficiency comparable to normal cells (cultured fibroblasts and fibroblasts taken from morphologically normal tonsil tissue); nevertheless, the deviations in both directions—faster or slower repair—were detected and frequently correlated with a higher or lower tumor cell

radioresistance. In many cases, however, the DSB repair kinetics were found to remain unchanged, even if the cells exhibited increased or decreased radioresistance. This indicates that although DSB repair definitely represents a critical contributor to tumor cell radioresistance, the response of HNT cells to irradiation is in fact a very complex phenomenon. The search for other factors substantially influencing this response in addition to DSB repair is just beginning, taking advantage of RNA chips designed by the author (in collaboration with J. Gumulec, M. Raudenska, and M. Masařík) for more than 350 of the genes involved in different relevant aspects of cell life (DSB repair, cell cycle regulation, apoptosis initiation, etc.).

Importantly, tumor-associated fibroblasts (TAFs) often repaired DSBs with similar kinetics as tumor cells isolated from the same tumor, even when the tumor cells extensively diverged from normal repair velocity. This held true also for cells obtained from morphologically normal tissues spatially separated from the tumor by about 10 cm. Although these observations need to still be interpreted, at least three interesting possible explanations are possible and not unprecedented in cancer biology. First, premalignant changes may exist in the tumor-surrounding tissue although it still preserves normal morphological features. This idea has already been proposed in our earlier work on colon cancer.[10] Second, the functions of normal cells in tumor proximity could be altered by tumor cells. Finally, faster or slower DSB repair of TAF- and tumor cell primocultures (compared with the average for normal cells) could reflect the genetic background of individual patients, that is, appear independently of cancer.

In many patients, large numbers of DSBs appear in nonirradiated tumor cells. This points to their permanent genomic instability (of a still unknown origin but most likely related to replication stress or telomere damage), which seems to be a quite frequent factor leading to an initially positive response of HNT cells to irradiation but that leads to the development of potentially resistant clones in a long-term perspective.

A substantial body of the presented research concerns new approaches capable of improving current radiotherapy by decreasing tumor cell radioresistance and/or by selectively protecting normal cells against the deleterious effects of irradiation. First, we investigated DSB induction, DSB repair, and cell survival upon irradiation with protons of different energies and various accelerated ions.[19,22,26] An enhanced capability of ion beams to kill tumor cells (compared with γ-rays or X-rays) follows from the well-understood physics behind this phenomenon. However, the real biological effects remain to be determined in terms of both their mechanism and extent. Consequently, the curing protocols are built up on empirical knowledge rather than on a solid body of experimental data, which prevents maximal therapeutic benefit from the physical advantages of ion beams.

As expected, we observed that the complexity of DSB clusters correlates with radiation LET and significantly influences both the reparability of DSB lesions and the survival of cells upon irradiation. Surprisingly, the complexity and reparability of DSBs also varied for different accelerated particles that have a similar LET and energy. This could be explained by the slight but significant differences in the microdosimetric character of DNA damage induced by the studied particles. The diameter of the track core seems to be an interesting parameter in this respect.[19]

The relationship between the DSB structure and reparability was further studied at the nanoscale, here again taking advantage of SMLM. This attempt represents an important feature of the novelty of the present thesis. In cooperation with Prof. Michael Hausmann (KIP Heidelberg, Germany), we have adapted SMLM for analyses of the structuro-functional and spatio-temporal aspects of DSB damage induction and repair, producing a resolution of up to about 10–20 nm.[21,22]

Our motivation to study the nanostructure of DSB repair foci in the context of (tumor) cell radiosensitivity followed from earlier reports suggesting that different types of cells and DNA damage can activate nonhomologous end-joining (NHEJ) and homologous recombination (HR)—the two main DSB repair mechanisms in human cells—but with different preferences. Because NHEJ, HR, and possibly the backup repair pathways operate with incomparable kinetics and fidelity, it is of the utmost importance to find out how various cell types pick a particular repair mechanism at each single DSB site. Our observations and those of other groups suggest that the decision-making mechanism could be based, at least partially, on the structural characteristics of a damaged chromatin domain and the DSB itself. These characteristics may regulate the attraction and accessibility of individual repair proteins to DSB sites[16] and thus the assembly and structure of DSB repair complexes (DSB repair foci, IRIFs). The structure of DSB repair foci could be an important factor further driving the repair mechanism to NHEJ, HR, or the backup pathways. Nevertheless, other cell-type-specific factors, such as intracellular levels and/or mutations of repair proteins, can influence the composition of DSB repair foci and thus their (nano)structure; these factors could differ significantly among cells, especially between normal and different tumor cells. DSB repair-focused (nano)structures can be more or less directly related to the mechanism of repair and, consequently, to cell radioresistance.

In the study of Depeš et al. (2018),[21] we demonstrated the applicability of SMLM as one highly resolving method for analyses of dynamic repair protein distribution and repair-focused internal nanoarchitecture in intact cell nuclei. This study is the first report on SMLM visualization of γH2AX and 53BP1 repair foci induced by low-LET and high-LET radiation, respectively. Thanks to a "trick"—we irradiated the cell monolayer at a sharp angle (10°)—we were able to analyze the numbers and distributions of individual γH2AX and 53BP1 molecules inside microscopically defined foci and along the particle tracks. DSB repair foci generated by high-LET ions were considerably more complex than those appearing after γ-irradiation and showed an internal nanostructure. Although the research is just in its infancy, the preliminary results revealed that this focus nanostructure and its spatio-temporal dynamics could depend on the cell type, as we have demonstrated for normal human skin fibroblasts and highly radioresistant U87 tumor cells. Hence, DSB repair-focused nanostructures may be functionally relevant and correlate with cell-specific radiosensitivity.[22] Methodologically, the study proved SMLM as being a highly appropriate method for investigating spatio-temporal (DNA repair) protein distributions in cell nuclei and their subcompartments, such as DSB repair foci. We suppose that SMLM can provide deeper insights into how chromatin and DSB repair-focused structures influence the decision making for a particular repair pathway at a given DSB site.

As another approach that could improve both the efficiency and (tumor cell) specificity of radiation-based therapies and that can be combined both with standard radiotherapy and the ion-beam cancer

therapy introduced above, we studied the extent and mechanism of the radiosensitizing effect of metal nanoparticles (NPs).[20,27,28,36,37] The radiosensitization from NPs has been predicted based on their physical properties, specifically the ability to emit showers of secondary electrons upon irradiation and thus increase the absorbed dose at the microscale. Moreover, NPs are preferentially internalized by tumor cells, even passively because of the so-called *enhanced permeabilization and retention* (EPR) effects. The original hypothesis thus counts the DNA molecule as the primary target for NP-mediated radiosensitization and increased induction of DSBs as the mechanism of this effect.

Our results confirmed that various metal NPs can be used to radiosensitize even very radioresistant (e.g., U87) tumor cells, at least *in vitro*. The biological mechanisms of this radiosensitization and their dependence on DNA damage remain obscure. At the nanoscale, we recorded higher numbers of γH2AX molecule signals in the nuclei of cells irradiated in the presence of 10 nm gold NPs than in cells irradiated in their absence. On the other hand, neither the numbers of microscopically defined DSB repair foci (γH2AX + 53BP1) increased, nor did the DSB repair kinetics decrease, in cells incubated prior to irradiation with other NP types, even though the radiosensitizing effect was obvious. Therefore, we propose that more phenomena participate in the nanoparticle-mediated (tumor) cell radiosensitization, with the individual contributions depending on the nanoparticle, cell, and radiation properties. Because the nanoparticles in our experiments were mostly encapsulated in lysosomes and did not colocalize with mitochondria—the only cytoplasmic organelles containing DNA in human cells—we hypothesize that lysosomal damage could represent a new mechanism of NP-mediated radiosensitization. This is compatible with new findings highlighting the important role of lysosomes in intracellular signaling, which also includes the initiation of apoptosis. Hence, depending on the extent of lysosome disruption, the compounds released from these organelles into the cytoplasm may either alter cellular signaling and initiate apoptotic cell death or directly digest the cytoplasm and therein the dispersed organelles. Current opinions on metal nanoparticle-mediated radiosensitization are discussed in Pagáčová et al. (2019) and Falk et al. (2019).[28,37]

Freezing is known to kill unprotected cells, has been proven to be effective (cryoablation) in the treatment of several cancers, and is crucial in reproductive medicine (cryopreservation). However, uncertainty remains about its effects on chromatin. The majority of studies point to chromatin fragmentation in frozen/thawed cells because of extensive DSB formation, while other studies recognize DSBs only in cells with somehow defective chromatin already prior to freezing/thawing, with the few remaining studies reporting a failure to observe DSBs at all. Hence, we have analyzed how freezing/thawing influences chromatin condition[29–32] in the context of cell viability and have considered the potential of this approach for tumor cell radiosensitization.

To clarify the mechanism of chromatin cryo-damaging, we analyzed changes in the chromatin integrity and higher-order chromatin structure in normal and tumor cells frozen/thawed in the absence or presence of cryoprotectants of different types; we then correlated them to cell viability after defrosting. The results we obtained support the hypothesis that freezing/thawing causes DSBs only under specific conditions—as we discovered,[32] in cells just undergoing DNA replication. In these (S-phase) cells, dozens to hundreds of colocalized γH2AX and 53BP1 DSB repair foci can be seen because

of a collapse of replication forks, which is probably followed by their conversion into DSBs. Non-S-phase cells, on the other hand, lack DSBs, but together with S-phase cells, suffer from extensive alterations to the higher-order chromatin structure. In some cells, ruptures of the nuclear envelope even lead to chromatin leakage into the cytoplasm. Interestingly, although the extent of nuclear envelope and chromatin structure damage depends on the method of cryoprotection, the collapse of replication forks could not be reduced by the cryoprotectants studied. Taken together, our results on freezing/thawing show that it seriously damages chromatin; however, the induction of DSBs is restricted to S-phase cells that are mostly affected by freezing/thawing. Because tumors contain more S-phase cells in principle than normal tissues, this discovery could provide a mechanistic explanation for why cryoablation could efficiently eradicate tumor cell populations. In addition, we showed that chromatin condensation provoked by some cryoprotectants before freezing can efficiently reduce cell cryo-damage and improve post-thaw cell survival. Whether and how freezing/thawing influences the ability of irradiated cells to repair DSBs and it possibly sensitizes tumor cells to irradiation is under exploration.

The last approach studied in the present thesis—to enhance radiotherapy—follows the opposite strategy than those described above: it is based on selective radioprotection of normal cells. In our research, we focused on the biological effects of amifostine (WR-2721),[33] currently the only drug approved for clinical use that is capable of improving the survival of normal, not tumor, cells after irradiation. In normal cells, amifostine is converted to its active ROS scavenging metabolite WR-1065 by alkaline phosphatase (ALP), the levels of which are decreased in many cancers. Nevertheless, more mechanisms of amifostine action have been proposed that remain to be explored. Hence, we were interested in how amifostine influences DSB induction and repair in normal and tumor cells, respectively. Interestingly, although amifostine reduced the radiation damage to DNA only in normal cells, as expected, it also supported DSB repair in γ-irradiated normal cells and altered it at least in some (MCF7) tumor cell types. Thus, amifostine not only protected normal cells from the deleterious effects of radiation in multiple ways, but also disturbed DSB repair in tumor cells. Hence, we have confirmed that the selective functioning of amifostine in normal and tumor cells can be ascribed to the common differences between these cells in their ability to convert amifostine. Nevertheless, we propose new scenarios, named here the “good and bad,” “Jekyll and Hyde,” and “third player” hypothesis (Hofer et al. 2016),[33] theoretically interconnecting the networks of already known and newly discovered amifostine effects, ensuring its double-edged activities. Other possibilities of (combined) radioprotection are reviewed in papers (Hofer et al. 2017a, 2017b).[34,35]

LIST OF ADDRESSED AUTHOR'S PAPERS

The roles of higher-order chromatin structure in normal cell functioning and carcinogenesis (Chapter 2.1)

The principles of higher-order chromatin organization and its function in normal cells

1. Kozubek S, Lukásová E, Jirsová P, Koutná I, Kozubek M, Ganová A, Bártová E, Falk M, Paseková R. 3D Structure of the human genome: order in randomness. Chromosoma. 2002;111(5):321-31. doi: 10.1007/s00412-002-0210-8.

2. Lukásová E, Kozubek S, Kozubek M, Falk M, Amrichová J. The 3D structure of human chromosomes in cell nuclei. Chromosome Res. 2002;10(7):535-48.

3. Falk M, Lukásová E, Kozubek S, Kozubek M. Topography of genetic elements of X-chromosome relative to the cell nucleus and to the chromosome X territory determined for human lymphocytes. Gene. 2002;292(1-2):13-24.

4. Ondrej V, Lukásová E, Falk M, Kozubek S. The role of actin and microtubule networks in plasmid DNA intracellular trafficking. Acta Biochim Pol. 2007;54(3):657-63.

5. Ondrej V, Kozubek S, Lukásová E, Falk M, Matula P, Matula P, Kozubek M. Directional motion of foreign plasmid DNA to nuclear HP1 foci. Chromosome Res. 2006;14(5):505-14. doi: 10.1007/s10577-006-1058-1.

Changes of higher-order chromatin organization and function during carcinogenesis

6. Lukášová E, Kořistek Z, Klabusay M, Ondřej V, Grigoryev S, Bačíková A, Řezáčová M, Falk M, Vávrová J, Kohútová V, Kozubek S. Granulocyte maturation determines ability to release chromatin NETs and loss of DNA damage response; these properties are absent in immature AML granulocytes. Biochim Biophys Acta. 2013;1833(3):767-79. doi: 10.1016/j.bbamcr.2012.12.012.

7. Lukásová E, Koristek Z, Falk M, Kozubek S, Grigoryev S, Kozubek M, Ondrej V, Kroupová I. Methylation of histones in myeloid leukemias as a potential marker of granulocyte abnormalities. J Leukoc Biol. 2005;77(1):100-11. doi: 10.1189/jlb.0704388.

8. Lukásová E, Kozubek S, Falk M, Kozubek M, Zaloudík J, Vagunda V, Pavlovský Z. Topography of genetic loci in the nuclei of cells of colorectal carcinoma and adjacent tissue of colonic epithelium. Chromosoma. 2004;112(5):221-30. doi: 10.1007/s00412-003-0263-3.

9. Pagáčová E, Falk M, Falková I, Lukášová E, Michalová K, Oltová A, Raška I, Kozubek S. Frequent chromatin rearrangements in myelodysplastic syndromes--what stands behind? Folia Biol. 2014;60 Suppl 1:1-7.

10. Stepka K, Falk M. Image analysis of gene locus positions within chromosome territories in human lymphocytes. Lecture Notes in Computer Science (including subseries Lecture Notes in Artificial Intelligence and Lecture Notes in Bioinformatics). 2014; 8934:125-134. doi: 10.1007/978-3-319-14896-0_11.

11. Dellino I., Falk M., et al. New mechanism of Acute Promyelocytic Leukemia. Manuscript in preparation.

Roles of higher-order chromatin structure in DNA damage induction, repair and misrepair upon cell exposure to different kinds of ionizing radiation (Chapter 2.2)

12. Falk M, Lukásová E, Kozubek S. Chromatin structure influences the sensitivity of DNA to gamma-radiation. Biochim Biophys Acta. 2008;1783(12):2398-414. doi: 10.1016/j.bbamcr.2008.07.010.

13. Falk M, Lukasova E, Gabrielova B, Ondrej V, Kozubek S. Local changes of higher-order chromatin structure during DSB-repair. Journal of Physics: Conference Series. 2008;101(1):012018. doi: 10.1088/1742-6596/101/1/012018.

14. Falk M, Lukasova E, Gabrielova B, Ondrej V, Kozubek S. Chromatin dynamics during DSB repair. Biochim Biophys Acta. 2007;1773(10):1534-45. doi: 10.1016/j.bbamcr.2007.07.002.

15. Falk M, Lukášová E, Štefančíková L, Baranová E, Falková I, Ježková L, Davídková M, Bačíková A, Vachelová J, Michaelidesová A, Kozubek S. Heterochromatinization associated with cell differentiation as a model to study DNA double strand break induction and repair in the context of higher-order chromatin structure. Appl Radiat Isot. 2014;83 Pt B:177-85. doi: 10.1016/j.apradiso.2013.01.029.

16. Falk M, Lukasova E, Kozubek S. Higher-order chromatin structure in DSB induction, repair and misrepair. Mutat Res. 2010;704(1-3):88-100. doi: 10.1016/j.mrrev.2010.01.013.

17. Falk M, Hausmann M, Lukášová E, Biswas A, Hildenbrand G, Davídková M, Krasavin E, Kleibl Z, Falková I, Ježková L, Štefančíková L, Ševčík J, Hofer M, Bačíková A, Matula P, Boreyko A, Vachelová J, Michaelidesová A, Kozubek S. Determining Omics spatiotemporal dimensions using exciting new nanoscopy techniques to assess complex cell responses to DNA damage: part A--radiomics. Crit Rev Eukaryot Gene Expr. 2014;24(3):205-23.

18. Falk M, Hausmann M, Lukášová E, Biswas A, Hildenbrand G, Davídková M, Krasavin E, Kleibl Z, Falková I, Ježková L, Štefančíková L, Ševčík J, Hofer M, Bačíková A, Matula P, Boreyko A, Vachelová J, Michaelidisová A, Kozubek S. Determining Omics spatiotemporal dimensions using exciting new nanoscopy techniques to assess complex cell responses to DNA damage: part B--structuromics. Crit Rev Eukaryot Gene Expr. 2014;24(3):225-47.

Tumor cell radioresistance and potential therapeutic approaches of tumor cell radio-sensitization and normal cell radioprotection (Chapter 2.3)

Tumor cell radioresistance in the context of DSB repair and higher-order chromatin structure

19. Sevcik J, Falk M, Macurek L, Kleiblova P, Lhota F, Hojny J, Stefancikova L, Janatova M, Bartek J, Stribrna J, Hodny Z, Jezkova L, Pohlreich P, Kleibl Z. Expression of human BRCA1Δ17-19 alternative splicing variant with a truncated BRCT domain in MCF-7 cells results in impaired assembly of DNA repair complexes and aberrant DNA damage response. Cell Signal. 2013;25(5):1186-93. doi: 10.1016/j.cellsig.2013.02.008.

20. Sevcik J, Falk M, Kleiblova P, Lhota F, Stefancikova L, Janatova M, Weiterova L, Lukasova E, Kozubek S, Pohlreich P, Kleibl Z. The BRCA1 alternative splicing variant Δ14-15 with an in-frame deletion of part of the regulatory serine-containing domain (SCD) impairs the DNA repair capacity in MCF-7 cells. Cell Signal. 2012;24(5):1023-30. doi: 10.1016/j.cellsig.2011.12.023.

21. Falk M, Horakova Z, Svobodova M, Masarik M, Kopecna O, Gumulec J, Raudenska M, Depes D, Bacikova A, Falkova I, Binkova H. γH2AX/53BP1 foci as a potential pre-treatment marker of HNSCC tumors radiosensitivity – preliminary methodological study and discussion. European Physical Journal D. 2017; 71(9). doi: 10.1140/epjd/e2017-80073-2.

Hadron (proton and ion) radiotherapy

22. Ježková L, Falk M, Falková I, Davídková M, Bačíková A, Štefančíková L, Vachelová J, Michaelidesová A, Lukášová E, Boreyko A, Krasavin E, Kozubek S. Function of chromatin structure and dynamics in DNA damage, repair and misrepair: γ-rays and protons in action. Appl Radiat Isot. 2014;83 Pt B:128-36. doi: 10.1016/j.apradiso.2013.01.022.

23. Jezkova L, Zadneprianetc M, Kulikova E, Smirnova E, Bulanova T, Depes D, Falkova I, Boreyko A, Krasavin E, Davidkova M, Kozubek S, Valentova O, Falk M. Particles with similar LET values generate DNA breaks of different complexity and reparability: a high-resolution microscopy analysis of γH2AX/53BP1 foci. Nanoscale. 2018;10(3):1162-1179. doi: 10.1039/c7nr06829h.

24. Depes D, Lee J, Bobkova E, Jezkova L, Falkova I, Bestvater F, Pagacova E, Kopecna O, Zadneprianetc M, Bacikova A, Kulikova E, Smirnova E, Bulanova T, Boreyko A, Krasavin E, Hausmann M, Falk M. Single-molecule localization microscopy as a promising tool for γH2AX/53BP1 foci exploration. European Physical Journal D. 2018; 72(9). doi: 10.1140/epjd/e2018-90148-1.

25. Bobkova E, Depes D, Lee JH, Jezkova L, Falkova I, Pagacova E, Kopecna O, Zadneprianetc M, Bacikova A, Kulikova E, Smirnova E, Bulanova T, Boreyko A, Krasavin E, Wenz F, Bestvater F, Hildenbrand G, Hausmann M, Falk M. Recruitment of 53BP1 Proteins for DNA Repair and Persistence of Repair Clusters Differ for Cell Types as Detected by Single Molecule Localization Microscopy. Int J Mol Sci. 2018;19(12). doi: 10.3390/ijms19123713.

Metal nanoparticle-mediated tumor cell radiosensitization

26. Pagáčová E, Štefančíková L, Schmidt-Kaler F, Hildenbrand G, Vičar T, Depeš D, Lee JH, Bestvater F, Lacombe S, Porcel E, Roux S, Wenz F, Kopečná O, Falková I, Hausmann M, Falk M. Challenges and Contradictions of Metal Nano-Particle Applications for Radio-Sensitivity Enhancement in Cancer Therapy. Int J Mol Sci. 2019;20(3). doi: 10.3390/ijms20030588.

27. Falk M. Nanodiamonds and nanoparticles as tumor cell radiosensitizers-promising results but an obscure mechanism of action. Ann Transl Med. 2017;5(1):18. doi: 10.21037/atm.2016.12.62.

28. Štefančíková L, Lacombe S, Salado D, Porcel E, Pagáčová E, Tillement O, Lux F, Depeš D, Kozubek S, Falk M. Effect of gadolinium-based nanoparticles on nuclear DNA damage and repair in glioblastoma tumor cells. J Nanobiotechnology. 2016;14(1):63. doi: 10.1186/s12951-016-0215-8.

29. Falk M. Nanoscopy and Nanoparticles Hand-in-Hand to Fight Cancer: An Exciting Entrée into the Rising NANOworld. Biophys J. 2016;110(4):872-3. doi: 10.1016/j.bpj.2016.01.005.

30. Falk M., Wolinsky M., Veldwijk M.R., Hildenbrand G. and Hausmann M. Gold Nanoparticle Enhanced Radiosensitivity of Cells: Considerations and Contradictions from Model Systems and Basic Investigations of Cell Damaging for Radiation Therapy. In: Nanopharmaceuticals: Principles and Applications. Springer, in press

DNA damage potentiation by cell freezing

31. Kratochvílová I, Kopečná O, Bačíková A, Pagáčová E, Falková I, Follett SE, Elliott KW, Varga K, Golan M, Falk M. Changes in Cryopreserved Cell Nuclei Serve as Indicators of Processes during Freezing and Thawing. Langmuir. 2018; doi: 10.1021/acs.langmuir.8b02742.

32. Golan M, Pribyl J, Pesl M, Jelinkova S, Acimovic I, Jaros J, Rotrekl V, Falk M, Sefc L, Skladal P, Kratochvilova I. Cryopreserved Cells Regeneration Monitored by Atomic Force Microscopy and Correlated With State of Cytoskeleton and Nuclear Membrane. IEEE Trans Nanobioscience. 2018;17(4):485-497. doi: 10.1109/TNB.2018.2873425.

33. Falk M, Falková I, Kopečná O, Bačíková A, Pagáčová E, Šimek D, Golan M, Kozubek S, Pekarová M, Follett SE, Klejdus B, Elliott KW, Varga K, Teplá O, Kratochvílová I. Chromatin architecture changes and DNA replication fork collapse are critical features in cryopreserved cells that are differentially controlled by cryoprotectants. Sci Rep. 2018;8(1):14694. doi: 10.1038/s41598-018-32939-5.

34. Kratochvílová I, Golan M, Pomeisl K, Richter J, Sedláková S, Šebera J, Mičová J, Falk M, Falková I, Řeha D, Elliott KW, Varga K, Follett SE, Šimek D. Theoretical and experimental study of the antifreeze protein AFP752, trehalose and dimethyl sulfoxide cryoprotection mechanism: correlation with cryopreserved cell viability. RSC Adv. 2017;7(1):352-360. doi: 10.1039/C6RA25095E.

Mechanisms of selective normal cell radioprotection

35. Hofer M, Falk M, Komůrková D, Falková I, Bačíková A, Klejdus B, Pagáčová E, Štefančíková L, Weiterová L, Angelis KJ, Kozubek S, Dušek L, Galbavý Š. Two New Faces of Amifostine: Protector from DNA Damage in Normal Cells and Inhibitor of DNA Repair in Cancer Cells. J Med Chem. 2016;59(7):3003-17. doi: 10.1021/acs.jmedchem.5b01628.

36. Hofer M, Hoferová Z, Falk M. Pharmacological Modulation of Radiation Damage. Does It Exist a Chance for Other Substances than Hematopoietic Growth Factors and Cytokines? Int J Mol Sci. 2017;18(7). doi: 10.3390/ijms18071385.

37. Hofer M, Hoferová Z, Depeš D, Falk M. Combining Pharmacological Countermeasures to Attenuate the Acute Radiation Syndrome-A Concise Review. Molecules. 2017;22(5). doi: 10.3390/molecules22050834.

NATIONAL AND INTERNATIONAL COLLABORATION

Most of work presented in this thesis was done at the Institute of Biophysics of CAS, the Department of Cell Biology and Radiobiology, established and led by the author. However, the cooperation with other respected scientists and institutes must be disclosed and deeply appreciated:

Prof. Michael Hausmann, Ph.D. (Kirchhoff Institute for Physics, University of Heidelberg, Heidelberg, Germany) – developed SMLM microscopy and participated both theoretically and experimentally in nanoscale research presented in this thesis; this includes also critical discussions and paper preparation.

Dipl. Ing. Marie Davídková, Ph.D. (Nuclear Physics Institute CAS, Řež by Prague, Czech Republic) and **Acad. Prof. Evgeny Krasavin, Ph.D.** (Joint Institute for Nuclear Research, Dubna, Russia) – provided access to proton and high-LET particle accelerators, respectively. NPI and JINR teams also contributed by direct experimental support.

Assoc. Prof. RNDr. Irena Kratochvílová, Ph.D. (Institute of Physics CAS, Prague, Czech Republic) – initiated and extensively contributed to our research on chromatin cryo-damage, participated in manuscript preparation.

Assoc. Prof. Michal Masařík, Ph.D., MUDr. Gumulec, Ph.D., Martina Raudenská, Ph.D. (Masaryk University, Brno, Czech Republic) – co-designed our research projects on head and neck tumor radiosensitivity, extensively contributed theoretically and experimentally, prepared tumor cell primocultures, participated in transcriptomic and big data analyses and software development.

MUDr. Zuzana Horáková, Ph.D. (Faculty Hospital, Olomouc, Czech Republic) and **MUDr. Hana Binková, Ph.D.** (Military Hospital Brno, Brno, Czech Republic) – co-designed our research projects on head and neck tumor radiosensitivity, were responsible for the clinical part.

Prof. Michal Kozubek, Ph.D., Assoc. Prof. Pavel Matula, Ph.D., and Assoc. Prof. Petr Matula, Ph.D. (Centre for Biomedical Image Analysis, Faculty of Informatics, Masaryk University, Brno, Czech Republic) – developed software and hardware for acquisition and analysis of microscopic images.

Prof. Pier Giuseppe Pelicci, M.D., Ph.D., Assoc. Prof. Ivan Gaetano Dellino, Ph.D. and Mario Faretta, Ph.D. (European Institute of Oncology, Milan, Italy) – proposed the idea of an alternative mechanism of APL pathogenesis and performed genomic and mouse model analyses related to APL pathogenesis.

Prof. Sandrine Lacombe, Ph.D. (University Paris Sud, Paris, France) – cooperated on our research on metal nanoparticle-mediated radiosensitization, ensured nanoparticle synthesis.

Ing. Tomáš Vičar, Ph.D. (Brno Technical University, Brno, Czech Republic) – developed new software for DSB repair focus detection and analysis based on artificial neural networks/machine learning.

Prof. MUDr. Zdeněk Kleibl, Ph.D. and Jan Ševčík, Ph.D. (Department of Oncology, First Faculty of Medicine, Charles University in Prague and General University Hospital in Prague, Czech Republic) – constructed stable cell clones expressing alternative splicing variants of BRCA1 and dominantly participated in the associated research

Prof. RNDr. Bořivoj Klejdus, Ph.D. (Mendel University in Brno, Brno, Czech Republic) – designed and performed LC-MS, DART and DESI analyses

Prof. RNDr Karel Angelis, CSc. (Institute of Experimental Botany CAS, Prague, Czech Republic) – shared with us his expertise on DSB analysis by comet assay.

COOPERATION WITH JINR DUBNA – HIGH-LET IRRADIATION EXPERIMENTS

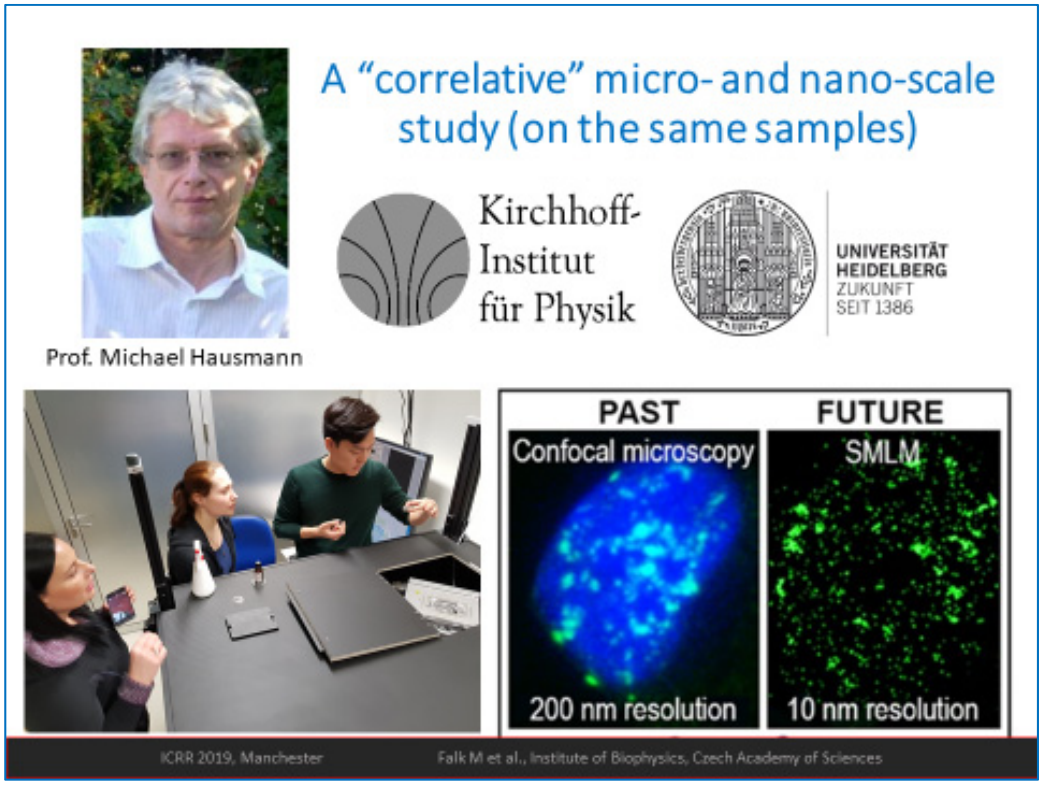

COOPERATION WITH KIP HEIDELBERG – SUPER-RESOLUTION MICROSCOPY

THESIS AIMS

At the most general level, the current thesis aimed to provide deeper microscale and nanoscale insights into the biological effects of different types of IR, including γ-rays, the protons of different energies, and various accelerated particles with high linear energy transfer (LET). The first emphasis was on the roles of the higher-order chromatin structure in DSB damage induction, repair, and misrepair. This attempt to better comprehend the principles of the higher-order chromatin organization in the nuclei of normal and tumor cells was followed by an effort to disclose the complex relationship between the properties of IR, exposition regimen, higher-order chromatin structure, other cell-type-specific factors, the extent of DNA DSB induction, micro- and nanodosimetric character of DSB lesions, the mechanisms of DSB repair, and the mechanism of chromosomal aberration formation. In the next step, we wanted to reveal how the individual factors mentioned above influence, either solely or in combination, the radioresistance of normal and tumor cells, and investigate how this multiparametrically determined phenomenon could be therapeutically manipulated or overcome (i.e., selectively decreased in tumor cells and strengthened in normal cells).

‘Any fool can know. The point is to understand.’
— Albert Einstein —

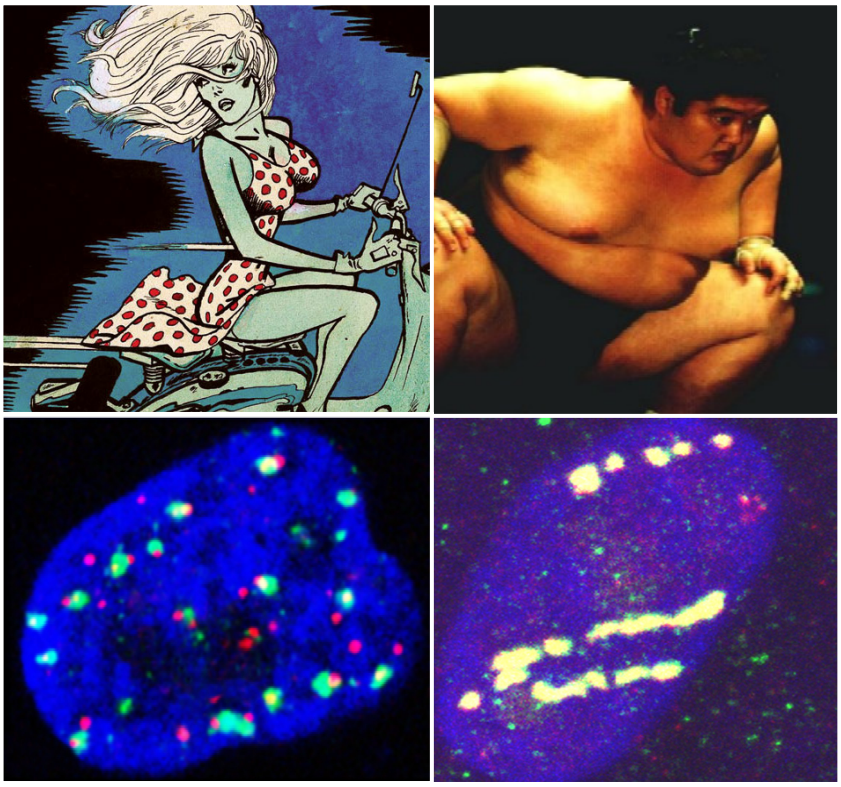

Figure 1. Micro- and nano-scale differences between low-LET and different high-LET radiation types are still explored only insufficiently. Top images: Kája Saudek (photo: Museum of Art Olomouc) (left) and free web-page source. Bottom images: data of the author.

1. INTRODUCTION – AUTHOR'S RESEARCH IN A BROADER CONTEXT

1.1 IR and Renaissance of Radiobiology

There are few phenomena that provoke as intensive and contradictory emotions among people as IR, simply spoken about as "radioactivity" in the general population. This is not surprising considering the fact that although IR cannot be sensed by humans, it may cause cancer and genetic birth defects at low doses and even death at high doses. Mixed feelings about IR are further potentiated by the double-edged history of its application. IR currently represents the most powerful and still irreplaceable source of energy and is one of the most efficient tools in industry and medicine. In the past few decades, we have witnessed enormous progress in the field of radiodiagnostics and radiotherapy that currently can save numerous patients otherwise sentenced to death. On the other hand, the atomic bombing of Japan and the Chernobyl and Fukushima nuclear accidents were such disastrous moments in the past that they can never be forgotten. Moreover, an ever-present threat of nuclear materials misuse by terrorists has recently emerged with renewed vigor.

The fear of radiation is further fed by persisting uncertainty about the biological effects of IR, especially after a low-dose exposure. This situation leaves room for rumors and is increasingly alarming in light of the dramatically growing number of radiodiagnostic examinations, including whole-body computed tomography (CT) scans. Another question that has arisen with new urgency concerns the interactions of biological systems with IR of different types. Many tumors remain resistant to photon radiotherapy despite the progress that has been reached in X-ray and γ-ray irradiation technology. Therefore, for physically advantageous behavior, proton and high-LET ion beams have been studied as promising novel radiotherapeutic approaches that could improve tumor targeting (protons) or even killing (high-LET ions).[38] Although numerous hadron therapy centers already operate all around the world, the irradiation regimens are based on empirical experience rather than a solid body of scientific knowledge. Deeper insights into the biological effects of protons and high-LET particles are also necessary in the context of planning manned interplanetary missions, during which astronauts will be exposed to mixed radiation fields.

The methods that can be used for solving the above-mentioned and other radiobiological questions have made a giant step from the cytological to molecular level. This holds true for optical microscopy, which is widely used in the present thesis, where several tricks of how to overcome Abbe's limit have been discovered, and various approaches offering resolution down to about 10 nm have been introduced. An urgent need for a better understanding of many radiobiological problems combined with concurrent improvement of modern technologies has started a new era of intensive radiobiological research that could be, without any exaggeration, regarded as the renaissance of radiation biology.

IR is named according to its ability to ionize atoms and molecules. In a water environment, this is characteristic of biological systems (the cytoplasm), and the minimum energy needed to eject an electron from an atom is 33 eV, which corresponds to a wavelength shorter than UV rays (about 40

nm). The interaction of IR with cells starts with the same physical processes (radiation energy transfer on atoms) and is driven by the same physical laws as its interaction with inanimate matter. The particularity of living organisms begins only with the biochemical and biological responses, some aspects of which are studied in the present thesis. From a biophysical point of view, it should be emphasized that the energy required to damage or even kill a cell is much lower for IR than other types of energy sources. For instance, the whole-body exposure of an 80-kg man to 10 Gy (10 $J.kg^{-1}$) of γ-rays leads to the absorption of only 800 J, but this still causes a fatal form of acute radiation syndrome (ARS). This could be surprising considering that we need about five times more energy (4184 J) just to raise 1 liter of water by 1 degree Celsius. The mentioned dose of 10 Gy of γ-rays then increases the human body's temperature only 0.002 °C. The biological effectiveness of IR thus cannot be simply explained in terms of its transmitted energy. A hypothesis was postulated that the deleterious effects of radiation on living beings appear because of the concentrated release of high-energy quanta inside a small volume of cells or, more precisely, in the proximity of DNA. This points to the fundamental importance of the microscale interactions between IR and chromatin. Because the character of energy deposition by different radiations significantly varies and chromatin forms different structures depending on its functional status (a topic broached later), the relationship between IR properties and chromatin structures, which is extensively addressed by the present research, appears to lie at the root of the biological effects of IR. This allows us to hypothesize that the chromatin and radiation parameters determine the character of DNA damage, and the character of DNA damage together with the chromatin structure of the damaged domain consequently participate in the decision making for the particular repair mechanism at each damaged site. IR damages all biomolecules, but DNA is the most important target of IR because of its unique functions and high susceptibility to radiation damage. IR can generate various DNA lesions (**Figure 2**), among which DNA DSBs represent the most deleterious and mutagenic type. Indeed, IR is the most efficient DSB inducer. Therefore, the present thesis is focused on the induction, repair, and misrepair of DSBs.

1.2 Ever-Present DNA Damage and Repair – The Prerequisites of Life

Adapted from Falk et al. (2012).[39] DNA is constituently damaged by intracellular "metabolism"[40–43] and environmental factors, especially mutagenic chemicals,[44–46] UV radiation, and IR [44,47–50] (reviewed in [51]). About as many as 2×10^4 to 1 million different DNA lesions (**Figure 2**) occur in every cell of the human body each day[51,52] (reviewed in [53]) because of these harmful attacks.[51,54] As could be easily calculated, this means about 800 DNA lesions are generated per cell per hour.[43] For instance, at least 5,000 single-strand breaks (SSBs) arise in DNA during a single cell cycle because of ROS production, and about 1% of these are converted to DSBs; thus, approximately 50 endogenous DSBs are generated in a single cell during one replication round.[40,55] Therefore, DNA repair, which continuously takes care of genome stability, belongs among the fundamental processes of life.

DSBs challenge DNA repair systems by simultaneously breaking both DNA chains; they represent the most serious threat to genome integrity and, consequently, human health. Even a single DSB can lead to cell death if left unrepaired, or more seriously, it can cause mutagenesis and cancer if repaired

improperly.[50,55–64] The importance of repair systems is evidenced also by the recognition that the accumulation of unrepaired or misrepaired DSBs is responsible for chronic inflammation,[65] aging, and some nonmalignant neurodegenerative diseases.[63,66,67] On the other hand, precisely regulated DSB induction mediates vital physiological processes such as immunoglobulin V(D)J rearrangements[68,69] and class switch[70] (reviewed in [71]) and may be the only chance to resolve stalled replication or transcription forks.[72–74] Allowing mitotic recombination[75,76] and introducing some degree of genetic variability because of an imprecise repair, DSBs drive molecular evolution and enable life adaptation (at the level of whole populations).[72,77] Importantly, DSB induction by radiotherapy or chemotherapy currently represents one of the most efficient strategies for tumor cell eradication. Therefore, the DSB repair mechanism has been of particular interest to (radio)biologists for half a century, but because of technical limitations, it has been studied only at the biochemical and cytological scale.

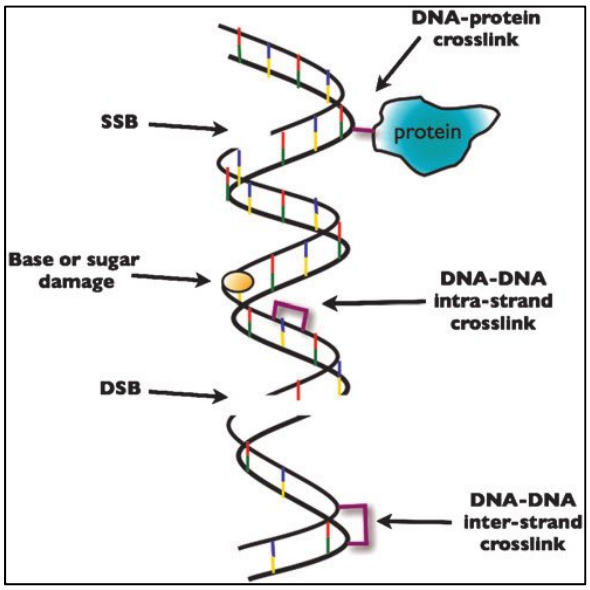

Figure 2. Different types of radiation-induced DNA lesions. From **Kavanagh et al. 2013**.[78]

1.3 DNA Damage Response and DNA Repair Pathways

When DNA damage occurs, cells activate a complex network of DNA damage responses (DDRs)[78] to decide whether to reversibly stop the cell cycle and repair the damage (reviewed in [63,79]) or stop it irreversibly and enter senescence[80] or programmed cell death (apoptosis) (review [81,82]). Alternatively, the cell may die immediately because of irreparable DNA damage (interphase death) or enter mitosis, even in the presence of unrepaired DSBs (reviewed in [83]). The latter scenario may end up in cell "adaptation" associated with a risk of a radioresistant clone development or mitotic catastrophe because of the inability of cells to separate genetic material into daughter cells (delayed, mitotic death). If the cell survives the first critical moments after irradiation, a complicated multistep process of DNA repair is being executed by precisely regulated sequences of spatio-temporally organized biochemical processes: DNA repair pathways (**Figure 3**). The whole cascade is initiated by DNA damage detection (still poorly understood in the case of DSBs) and is aimed at the processing of a specific type of DNA lesion. Several specific repair pathways interconnected in complicated networks thus participate in DNA repair[84] (reviewed in [78]). DSBs are repaired by nonhomologous end-joining (NHEJ), HR, or one of several alternative pathways that have been considered backup mechanisms but remain incompletely explored.[85,86] Other pathways, just mentioned here to draw a more complex picture, are the base-excision repair (BER), nucleotide-excision repair (NER), and mismatch repair (MMR). The BER pathway processes damages that are made to single DNA bases, NER recognizes distortions in the DNA helix (especially pyrimidine dimers and 6,4-photoproducts formed by UV-light),[87] and MMR detects

undamaged but mispaired regions in newly synthesized DNA strands that are the result of polymerase errors or slippage during replication or recombination.[88] NHEJ and HR are briefly described in the next chapter; for surveys of the remaining pathways, the reader is referred to a few particular literature reviews.[48,49,89–92]

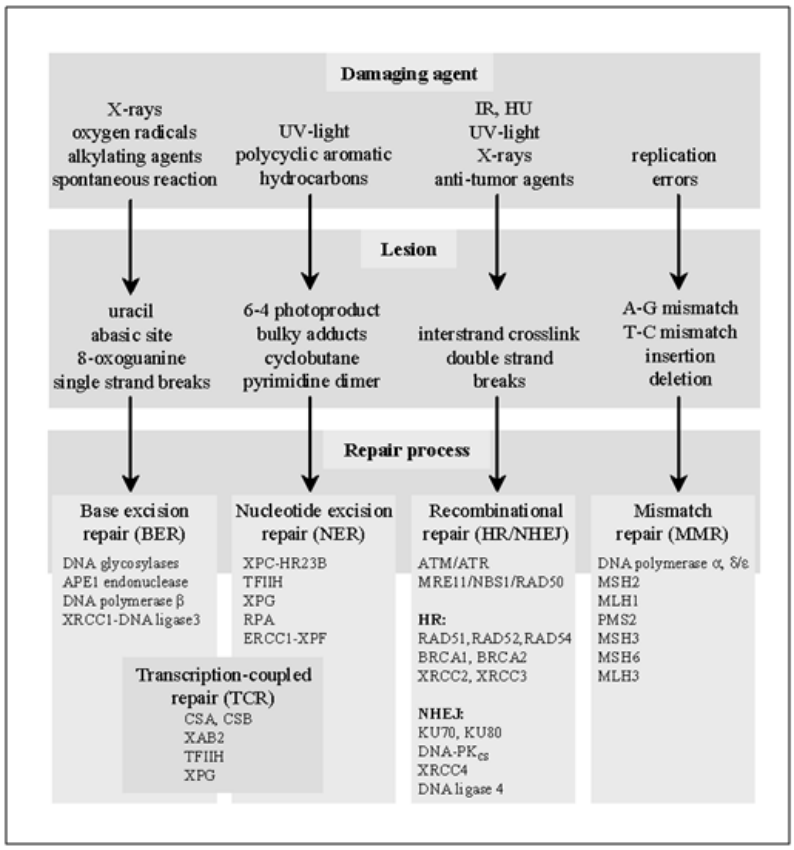

Figure 3. A complex network of DNA repair pathways operating in humans on different damage substrates. The essential genes involved in each DNA repair pathway are shown below the corresponding titles. HR, homologous recombination; NHEJ, non-homologous end joining. From **Allinen, 2002**.[93]

DSB repair pathways are hierarchically organized, and participating proteins can be illustratively divided according to their functions: "sensors" that specifically recognize the lesion, "effectors" that participate in processing the lesion, and "mediators" that interact with signaling proteins to connect these two steps and individual DDR pathways. This organization of DDR enables precise regulation and high flexibility in the cellular response, as well as amplification of very weak damage signals.[94] However, although it is useful for educational purposes, this categorization of DDR proteins is a considerable simplification because many of them have multiple activities in different repair steps. For example, the MRN complex (Mre11-Rad50-Nbs1) acts as one of the putative DSB sensors, a coactivator of DSB checkpoint signaling (e.g., by activating ATM) and as an effector protein both in the NHEJ and HR.[95–99] In addition, multiple regulatory feedback loops complicate our understanding of the temporal order of protein–protein and protein–DNA interactions involved in DDR. For instance, the identity of the first sensor necessary to recognize DSB lesions is still disputed.

DNA DSBs can be repaired by NHEJ, HR, or one of alternative (backup) repair mechanisms that are more or less dependent on DNA microhomologies (**Figs. 3, 4**). NHEJ represents a very efficient but possibly mutagenic pathway. In principle, DSBs can be repaired with the participation of only five "core" NHEJ proteins, including Ku heterodimer, DNA-PKcs, XRCC4, and DNA ligase 3.[100] The basic NHEJ pathway *per se* (absent cellular signaling) probably begins with the binding of Ku proteins to DSB ends, where it stabilizes damaged chromatin, prevents DNA ends resection, potentially recognizes the lesion,[101] and enables Ku70/80 interaction with the DNA-PK catalytic subunit (DNA-PKcs), a member of PIKK subfamily of PI-3 kinases,[94,102] and its activation.[94,103,104] Once active, DNA-PK holoenzyme phosphorylates several targets at the site of the DSB, including itself, which results in dissociation of DNA-PKcs subunits from DSBs[104] and their exchange for NHEJ or HR proteins. Thus, DNA-PK (and Ku) probably tethers free DNA ends together until DNA ligase and XRCC4 (LC complex) become bound to DSBs and rejoin them.[49,50,105,106]

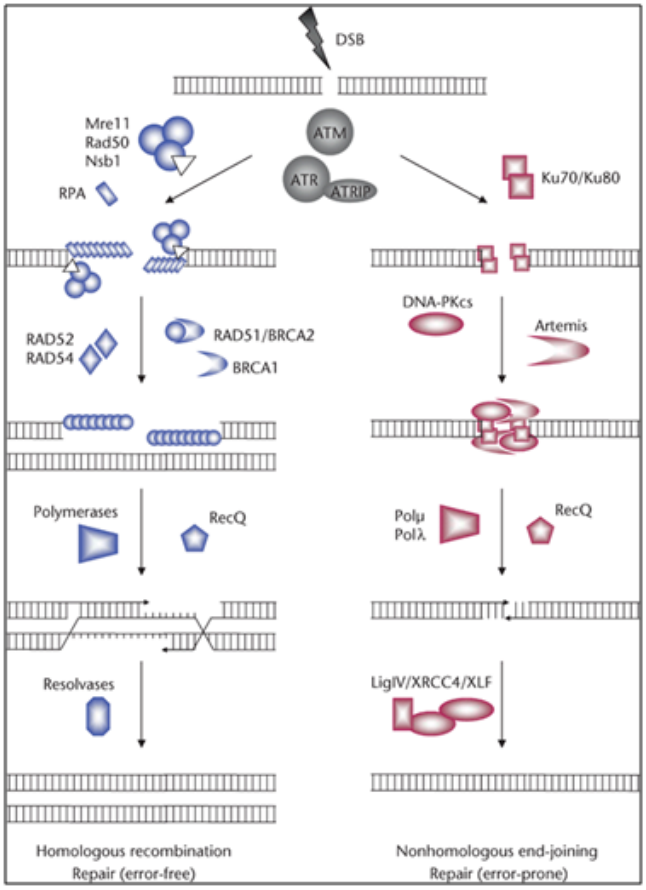

Figure 4. DNA double strand break (DSB) repair – the basic principle of two main repair pathways – homologous recombination (HR, left) and non-homologous end-joining (NHEJ, right) – is outlined. While HR requires long single-stranded DNA overhangs to be formed at the sites of DSBs that consequently invade homologous DNA template, NHEJ simply ligates free DNA ends. HR is therefore generally considered to be error-free, while NHEJ could be frequently error-prone. Image taken from **García-Muse and Aguilera 2011**.[114]

The simple scenario described above is only possible when euchromatic DSBs with undamaged DNA ends are being repaired.[107–112] In this case, DSBs are rejoined quickly, often without changes in genetic information. However, most DSBs induced by IR contain "dirty" ends with single-stranded overhangs

and damaged bases. Repair of these DSBs requires DNA-end processing before rejoining.[113] Additional steps that include modifications of chromatin structure are necessary to repair heterochromatic breaks.

The nuclease activities required to clear DNA ends have been recognized for the Mre11 component of the MRN complex[114–116] and are, with its affinity to DNA, stimulated by another MRN member, Rad50.[116] The third MRN member, Nbs1, mediates nuclear localization of the MRN complex (reviewed in [117,118]) and further stimulates its activities.[116,118,119] However, the physiological importance of the exonuclease function of MRN is uncertain because only 15% of DSBs induced by IR (that contain damaged DNA ends) require this protein for repair.[107,108,110–112] Therefore, other endonucleases, such as Artemis, probably clear DNA ends (reviewed in [112]), whereas the MRN complex serves as an activator of ATM signaling.[72,120–122] Because Artemis is activated by ATM, this interaction represents one of the contact points between NHEJ and ATM signaling, demonstrating the participation of both of these pathways in the repair of more complex DSBs or DSBs located in more complex (dense) chromatin.

Another important early step of DSB repair is ATM-mediated phosphorylation of the histone H2AX,[55,123,124] ending in the formation of γH2AX foci that cover megabase regions on either side of DSB[125] and creating a platform for binding of "noncore" repair proteins, such as MDC1,[126,127] 53BP1,[127,128] BRCA1,[129,130] SMC1, and others[130] to the site of damage. These proteins are also phosphorylated by ATM and, once activated, bind to γH2AX foci. Even though the activity of these "mediators" is dispensable for the initial binding of DSB sensors to the lesion sites[131] and for the repair of most DSBs,[107–112] they are necessary for a proper DDR response[127,129,132] and the repair of a subgroup of DSBs that are repaired only with difficulty[107,108,110–112] (discussed later). The main function of these mediators that exhibit pleiotropic functions with many partners is probably to serve as a scaffold for protein–protein interactions at the sites of DSBs.[129] The spectrum of "noncore" proteins recognized as operating in DSB repair is broad and continues to grow. Many of these proteins participate in the reorganization of chromatin structure at the sites of DSBs to allow for their repair.

Under still imprecisely defined conditions (discussed later), DSB repair can proceed via HR, which is more precise but also complicated compared with NHEJ. In brief, the exonuclease activity of the MRN (RAD50/MRE11/NBS1) complex first resects DNA ends in the 5' to 3' direction to provide long single-stranded DNA overhangs.[133] Consequently, these 3' single-stranded "tails" invade the DNA double helix of the intact sister chromatid, which is used as a template for DNA polymerase. Following branch migration and ligation, Holliday junctions are resolved by resolvases, yielding two intact DNA molecules.[50] For a detailed biochemical description of HR (and NHEJ), the reader is referred to comprehensive reviews.[134–136]

How NHEJ and HR (or the backup mechanisms) are selected at the particular DSB sites remains poorly understood. When possible, cells employ DNA repair processes (BER, NER, MMR, and HR) that use complementary DNA strands as an undamaged template for the precise synthesis of removed damaged fragments. Thus, lesions are usually processed quickly, without any persistent consequences for the genome. On the other hand, this is not the case with DSBs, where the simultaneous disruption of both DNA ends challenges the repair systems in two important aspects. First, if repair cannot proceed through HR, the original genetic information is usually lost on both complementary DNA strands; this

can happen because of the complex nature of a lesion (chromatin fragmentation) or because of required DNA ends resection before their ligation. Second, all DSBs destabilize chromatin so that "sticky" and free DNA ends can move and form chromosomal translocations or other aberrations because of illegitimate end-joining.

A possible way to solve the first problem repose in HR between the sister chromatids (**Figure 4**), which are, however, available only in the S- and G_2-phase of the cell cycle. Because homologous chromosomes[(see footnote 1)] are only rarely located close to each other in the cell nucleus, this almost precludes true HR in G_1.[137–141] Therefore, during this period, DSBs must be simply rejoined by NHEJ (**Figure 4**), without the "knowledge" of the original DNA sequence. Thus, DSB repair in G_1 usually brings an increased risk of small chromatin deletions or insertions, despite "clear" DSBs (not requiring DNA-end resection) to be precisely repaired.

How HR and NHEJ compete or cooperate in the G_2-phase for DSB targets is not fully understood, though there are persuading indications that the decision for the particular pathway in the case of a concrete lesion strongly depends on the structure of the DSB, higher-order structure of DSB-surrounding chromatin[(2)] (see later), and cell type.[145,146] For preferential use of NHEJ or HR, it is possible that evolution "follows" different strategies depending on the organism or, more precisely, the parameters of their genomes. For its fidelity, HR could appear as the best first choice. This scenario evidently holds true for organisms with small genomes (e.g., yeasts) but could not be efficient for organisms with large genomes known to "favor" NHEJ. As a rapid process,[147] NHEJ can repair numerous DSBs generated in large genomes fast enough to prevent the formation of extensive chromosomal aberrations that would cause cell death in mitosis, if left unrepaired. Although the rapidness of NHEJ comes at the price of the higher mutagenity of this mechanism compared with HR, "preferential" use of NHEJ is still advantageous because, for instance, in humans, only about 2% of DNA contain coding sequences, and an even smaller proportion represents critical targets for radiation carcinogenesis (protooncogenes and tumor suppressors). Hence, NHEJ enables cell survival upon massive DNA damage, coming with an acceptable risk of serious genetic consequences. HR may be then selectively focused on DSBs in actively transcribed genes or those that are otherwise problematic (e.g., complex or multiple) DSBs.[148,149] Nevertheless, it should be emphasized that HR can also be mutagenic like, for instance, in the case when repetitive sequences (providing homologies) are present in heterochromatin. This could be one of the reasons why damaged chromatin protrudes out of affected heterochromatin domains, as discussed later. Concluding this chapter, HR and NHEJ are the two dominant pathways conserved through evolution (described in yeasts, mammals, and other organisms, including prokaryotes; for reviews, see [135,136,140,150,151]), but interestingly, their contribution to DSB repair differs among species and cell types (e.g., stem cells vs. differentiated cells), probably according to the cell cycle and genome organization. Answering the question how NHEJ, HR, or backup mechanisms are selected at individual DSB sites remains an important task of current radiobiology. Importantly, in the of context of the

[1] also possibly providing more or less homologous sequences for HR

[2] By note, several alternative NHEJ mechanisms exist (sometimes designated as 'separated' repair pathways), like microhomology-mediated end-joining (MMEJ) or single-strand annealing (SSA) (reviewed in [85,142–144]); however, they are always mutagenic and their roles remain speculative.

present thesis, this decision making could be based on, at least partially, the structure of the damaged chromatin domain and DSB itself.

1.4 DSB Complexity and Repair Efficiency, Radiation LET

In contrast to simple DSBs induced by endonucleases and some chemicals (etoposide, H_2O_2), IR induces highly heterogeneous DSBs. Upon irradiation, in principle, the DSBs can be formed in two ways: directly by depositing radiation energy to DNA bases or sugars or indirectly via DNA interactions with ROS generated by water radiolysis.[152] The contribution of these mechanisms differs based on the radiation types,[153,154] with the indirect effect predominating for sparsely ionizing (low-LET) radiation and the direct effect for densely ionizing (high-LET) radiation. For instance, about 65% of DSBs are generated because of an indirect effect after the exposure of cells to γ-rays,[153,155] while this value reaches only ~32% for high-LET particles with LET values of 2,106 keV/μm.[156] In the latter work,[156] DSB complexity correlates with LET and the survival of irradiated cells. Multiple and complex DSBs thus form especially upon the action of high-LET IR, while most gamma radiation-induced DSBs are simple.[(3)] [21,21,22] Considering also the different charges, energies, and further characteristics of radiation (discussed in [19]), it is evident that radiation-induced DSBs and their biological effects are not equal.

Indeed, DSB repair has been shown to include rapid- and slow-kinetic components, where the latter is considered to represent the repair of complex DSBs that are processed only with difficulty[107,112] (for a review, see [15,39]). The contribution of the higher-order chromatin structures to this observation, as discussed in the next chapter, was initially undiscovered. Concerning the structurally and functionally distinct chromatin domains, DSBs were thought to arise homogeneously and be repaired by the same molecular mechanism and with the same efficiency. Recent results, however, show that both DSB induction and repair are markedly influenced by chromatin compaction and structure[12–15,107,108,110–112,157–166] (for a review, see [15]).

1.5 DNA Damage and Repair in the Context of Chromatin

1.5.1 Higher-order chromatin structure – a brief introduction

Between 1888 and 1915, Boveri, Sutton, and Morgan demonstrated that Mendelian genes are arranged linearly along chromosomes and in a specific order.[167–170] Thus, chromosomes were recognized as the material carriers of genetic information. About a hundred years later, the Human Genome Project started as an exhausting but exciting 13-year endeavor that brought us the "complete" knowledge of the human genomic DNA sequence. Technically accomplished in 2003, it became evident that decoding the DNA sequence and understanding protein functions is insufficient in explaining the regulation and maintenance of human genome functions. Therefore, the existence of a regulation mechanisms acting above the genetic code was postulated and later proven.[171,172] The nature and complexity of these mechanisms nominated them as a new biological code, named the epigenetic (epi = above) code. The

[3] Which mirrors the fact that most of damage caused by γ-rays results from the indirect effect mediated by ROS; in addition, local energy deposition of γ-photons is much lower compared to ion beams.

genetic code thus tells the cell how to read the genetic information while the epigenetic code tells them how to use it (i.e., what DNA parts, when, and with what intensity it should be read). The growing body of evidence then showed that epigenetic modifications of DNA and histones set up the higher-order chromatin structure that, in turn, participates in the regulation of chromatin functions. Hence, the Human Genome Project represents a fantastic but only first step on our way toward understanding the human genome.

Nowadays, it is evident that changes in the higher-order chromatin structure participate in the regulation of the fundamental processes associated with cell life, both in health and disease. During the last decade, the critical roles of the higher-order chromatin structure have also been recognized in DNA damage induction and repair and in carcinogenesis. Indeed, the higher-order chromatin structure influences numerous aspects of DNA damage and repair at the same time: the sensitivity of particular chromatin domains to radiation damage, repair mechanisms and their fidelity, mechanisms of formation of chromosomal aberrations, and probability of involvement of specific chromosomal loci in these aberrations. However, the relationship between the higher-order chromatin structure, organization in the cell nucleus (the cell nucleus architecture), and function in the above-mentioned processes remains to be understood. Therefore, the present thesis is largely dedicated to research on the chromatin structure–function relationship as the newly identified phenomenon in the cell response to irradiation.

1.5.2 Structural and spatio-temporal aspects of DSB repair

A considerable body of knowledge has been accumulated about the organization of proteins and their biochemical activities in DNA repair pathways. However, it becomes more and more evident that the chromatin structure regulates and, in turn, reflects the activity of processes in the cell nucleus (see Chapter 1.9). As a result, structurally and functionally distinct chromatin domains and—at a higher level of organization—the chromosomal territories form in the three-dimensional (3D) space of the cell nucleus (see Chapter 1.9). Nuclear processes—including DNA repair—must therefore operate in structurally and functionally distinct chromatin environments instead of in a homogeneous tangle of randomly floating chromatin fibers. It is necessary not only to understand the biochemical aspects of DSB repair, but also to reveal how it depends—in terms of the mechanism, efficiency, and fidelity—on chromatin structure and how it is organized in the time and space of the cell nucleus. In fact, we lack generally accepted answers even to very basic but critical questions, including the following:

- What is the mechanisms of DSB detection?
- What factors decide the repair mechanism at the sites of particular DSB lesions?
- Are DSBs induced with the same efficiency in decondensed chromatin with active genes as they are in condensed heterochromatin, which is genetically silent?
- Moreover, how is this influenced by the LET of IR, dose rate, presence of radical scavengers, and other conditions?

- Once DSBs are induced, are they repaired at their sites of origin, or do they migrate into nuclear subdomains that are more permissive for repair or perhaps to specialized "repair factories," where several DSBs are repaired simultaneously?
- Hence, do chromosomal translocations between the particular loci form because of their predetermined physical proximity in the nonrandom higher-order chromatin structure (nuclear architecture) or because of their mutual approach evoked by DSB repair processes?
- If the latter case is true, do these dynamics reflect chromatin damage, changes of local chromatin structure at the sites of DSB required to enable their repair, or directed movement of DSBs to repair competent subdomains of the cell nucleus?
- If they exist, can repair factories form *de novo* anywhere in the cell nucleus or only in special nuclear subcompartments?

Different answers to these questions can be found in the literature.[12–15,107,108,110,110–112,157–166,173–192] Indeed, chromatin structure might influence DSB repair in all its phases: DSB detection, DNA ends processing, ligation, and restoration of the original chromatin structure. Because DSB repair is mediated by large repair complexes, the chromatin structure regulates their accessibility to the lesion. It is tempting to speculate that molecular DSB sensors must be small molecules that can easily penetrate both euchromatin and heterochromatin[(4)] and permanently scrutinize DNA for damage. The primary signalers of DSB lesions have not been identified unequivocally, but the members of the MRN complex, Ku proteins, or perturbed chromatin structure *per se* are mostly disputed players in the field. In agreement, we have observed the penetration of nibrin (NBS1)—which participates in early DSB response[(5)]—into dense heterochromatin, while the 53BP1 protein, which is supposed to be engaged in later phases of the repair process, failed at invading these domains before their decondensation.[16] Chromatin decondensation is thus probably necessary to allow for the assembly of repair complexes and enable, or at least simplify, DSB processing (discussed later in the comments to the author's publications). On the other hand, chromatin condensation might be favorable for stabilizing free DNA ends, silencing transcription from damaged chromatin loci, and DSB ligation. Too extensive chromatin decondensation may also increase the probability of chromosomal translocations and complicate restoration of the original chromatin structure after the repair has been accomplished (discussed in [15,39,193]). Therefore, DSB repair deals with just opposite requirements of the chromatin structure in different phases of the process, indicating it must be precisely and dynamically regulated in space and time.

Two alternative chromatin structures known from the very beginning of chromatin exploration and that are important in the context of the present thesis are euchromatin (EU) and heterochromatin (HC). Although the EU is a decondensed (opened), gene-dense, and genetically active structure, HC is more condensed, transcriptionally silent, and associates with a large amount of heterochromatin-binding

[4] Nevertheless, in spite of this precondition, it is not sure whether DSBs located deeply inside the heterochromatic domains could not be less 'visible' for sensing as compared with euchromatic DSBs.
[5] NBS1 is a member of MRN-complex and one of the candidates for DSB sensor.

proteins (see Chapter 1.9). These differences show that the higher-order chromatin domains might behave differently when it comes to DSB induction, repair, and biological consequences of potential repair errors. Indeed, it was clearly shown that the repair of heterochromatic DSBs (HC-DSB) is more complicated, slower, and less efficient than DSBs in euchromatin.[13–15,107–111,193]

About 85% of DSBs introduced by sparsely IR do not require ATM activity for their repair;[107,112,194] surprisingly, DSBs that persist unrepaired are almost exclusively localized in condensed heterochromatin.[107,108,110,111,194] Therefore, it seems that different "NHEJ" mechanisms with different efficiencies and fidelities act on the open and condensed chromatin substrates. In this model, "euchromatic" DSBs are rapidly rejoined by the "core" NHEJ members, whereas more complicated processes associated with the ATM-signaling pathway are required for the repair of DSBs in dense heterochromatin.[107,108,110,111,194] This is in line with other results[13,15,195] that show DSB repair proceeds faster in EC than in HC. By contrast, the proportion of DSBs in euchromatin progressively increases up to about 60 min PI.[12,13] What may seem to be a paradox can, however, be easily explained by rapid chromatin decondensation around heterochromatic DSBs. This decondensation is necessary either to allow for a repair competent environment (increase the accessibility of large repair complexes to damaged DNA) at the original sites of DSB lesions or to enable the movement of DSBs into nuclear subcompartments that are more convenient locations for repair processes (as discussed in Falk et al., 2010[15]).

Both these hypotheses are not mutually exclusive and are not unprecedented in cellular biology: the potential movement into repair factories may be similar to the dynamic associations of genes in transcription factories. On the other hand, it is also generally accepted that the condensed nature of heterochromatin poses a barrier to enzymes and other proteins that operate on DNA (reviewed in [196]), and heterochromatin must relax to allow transcription and replication;[197–199] therefore, chromatin decondensation may also be expected at the sites of heterochromatic DSBs. Indeed, the epigenetic histone modifications that are typical for open euchromatin such as increased H4K5 acetylation, decreased H3K9 dimethylation, and other modifications were observed at the sites of the DSBs almost immediately after their induction.[160] As already discussed, ATM activates the repair proteins that mediate chromatin decondensation, such as KAP-1 (KRAB-associated protein 1, also known as TIF1b, TRIM28, or KRIP-1).[108,193,200] Importantly, this ATM activity is necessary only for the repair of heterochromatic DSBs. In support of this, the dissociation of heterochromatin protein 1 (HP1; reviewed in [201,202]) from the affected heterochromatin domains can be observed soon after irradiation.[(6)] [13,204–208] Moreover, in addition to local chromatin decondensation observed at the sites of lesions, global pan-nuclear decondensation initiated by DSB damage was described by Ziv et al.[200] Finally, ATM initiates a complex DDR that includes cell cycle arrest,[79] which provides additional time for repairing heterochromatic breaks that can only be processed slowly.

[6] Interestingly, some authors report HP1 binding to DSB sites after DNA breakage.[203] The simultaneous dissociation and recruitment of HP1 from/to DSB sites could be explained by local chromatin structure remodeling, where detachment of HP1 allows chromatin decondensation required for assembly of repair complexed and DSB repair while chromatin recruitment (through a different mechanism) allows silencing of damaged gene transcription to prevent dangerous collision between transcription and repair processes.

Therefore, the chromatin structure is an important determinant of the initiation phase of DSB repair. Because in addition to ATM many other proteins such as γH2AX, MDC1, 53BP1, RNF8, RNF168, and Artemis are specifically required only for the processing of DSBs in heterochromatin,[111,193] the above results can be interpreted as an adaptive modification of NHEJ to a problematic chromatin structure. Altogether, DSB repair in heterochromatin seems to be slower, less efficient, and is potentially associated with the increased formation of chromosomal translocations, as discussed in the next chapter.

The higher-order chromatin structure, however, also plays an important role in the terminal phase of DSB repair. Because gene transcription is regulated by a chromatin structure determined by an epigenetic code (Chapter 1.9.3), the original chromatin status must be somehow reconstructed along megabase-sized chromosome sequences that encompass DSBs to restore normal gene transcription. This process logically requires the removal of repair-specific histone modifications and *de novo* re-configuration of the original epigenetic code. The most striking reversion is the disappearance of γH2AX from DSBs after repair. This process is mediated either by γH2AX dephosphorylation or by replacement with nonphosphorylated histone H2AX.[209–211] Because reaccumulation of the HP1 protein at DSB sites was also reported at longer periods of time PI (about four hours),[12] γH2AX diffusion and HP1 binding may reflect recondensation of chromatin domains that had been relaxed during DSB repair.

The exact steps necessary to reconstitute chromatin after DNA ends have been rejoined are not understood. Nevertheless, it is reasonable to hypothesize that the unrestored chromatin structure is dangerous for the cell. Indeed, “epimutations” may affect chromatin structure in large, megabase-sized DNA regions and, on the other hand, do not affect DNA integrity, so cells can theoretically proceed through mitosis without any obstacles and transmit the altered expression patterns of genes to subsequent generations.

The chromatin structure thus significantly influences the mechanism, efficiency, and fidelity of DSB repair for all of its phases. Additional experiments are required to confirm the presented results; however, taken together, our findings suggest that the heterochromatin structure poses a serious obstacle to repair for several reasons. First, especially after exposure to densely IR, a higher density of heterochromatin provides more DNA targets in close mutual proximity when compared with euchromatin. Complex clustered lesions that are repaired only with difficulty can easily form. Second, the repair of heterochromatic DSBs requires extensive decondensation of chromatin at the sites of lesions to allow for the assembly of huge repair complexes and DNA processing. Third, the decondensed chromatin structure and epigenetic code must be returned to the original state that existed before damage. Therefore, the repair of heterochromatic DSBs includes additional steps (compared with euchromatin) that are mechanistically and topologically problematic. This not only complicates the repair, but also induces a chromatin “movement” that might simplify the formation of chromosomal translocations.

1.5.3 Mobility of DSBs and chromosomal translocations

The question of DSB mobility is one of the most disputed questions in radiobiology (reviewed, e.g., in Falk et al., 2010[15]). Active regions of the chromosome may protrude from their subdomains and even from CTs,[212,213] allowing some dynamic intermingling of chromatin, such as the spatial colocalization of several (coregulated) genes in transcription factories[214–217] or interactions between transcription enhancers and gene promoters.[218] On the other hand, the long-range pan-nuclear movement of undamaged chromatin has been rarely reported[219–221] but in principle can occur (Tom Misteli, personal communication). Therefore, the nucleus does not have either a random structure (formerly likened to a bowl of soup with randomly swimming DNA "noodles") or a rigid, deterministic organization; rather, it has a dynamic higher-order chromatin architecture necessary for executing nuclear functions. Important questions in the context of DSB repair then are of how chromatin organization and its dynamics can influence DSB damage induction, repair, and the formation of translocations between the particular chromosomal loci (reviewed in [15]). Consequently, it would be interesting to know how the nuclear environment modifies the transcriptional activity of the translocated chromosomal parts, for example, because of their heterochromatinization after translocation to heterochromatic nuclear domains.

Chromatin "movement" may directly follow from dynamic chromatin reorganization during DSB repair, for example, from the relaxation of free DNA ends caused by DSB induction, the already described chromatin decondensation at the sites of DSBs, the activities of huge repair complexes, the invasion of broken DNA chains into undamaged template (for HR), and, possibly, other repair activities. Indeed, after irradiating cells with densely ionizing α-particles, Aten et al. (2004)[157] observed clustering of γH2AX foci during the time PI, which was interpreted as the migration of DSBs into the "repair factories," where several DSBs are simultaneously repaired.[157,187,222–224] Markova et al. (2007)[225] arrived at similar conclusions when considering low-LET γ-rays. The mechanism proposed is not unprecedented in cellular biology. For example, the "migration" of several cotranscribed genes into common transcription factories is well-known, even for loci on different chromosomes (e.g.,[215,226]). Such compartmentalization of transcription processes provides many advantages for the cell, including easier accumulation of the proteins involved at transcription sites, better regulation, more intensive cellular signaling for weak initial stimuli, and lower energetic expenses, among others. Why can a similar mechanism not operate in DSB repair? One reason could be the increased risk of misrejoining if multiple free DNA ends were captured in such a "factory." Indeed, one of the two most widespread and disputed hypotheses to describe the mechanism of formation of chromosomal translocations, the "breakage-first theory," presupposes that the release of free DNA ends caused by DSBs extends the movement of damaged chromatin, consequently enabling chromosomal translocations between originally distant DNA loci[157,185,222,227–229] (reviewed in [15,105,230]).

However, the immunostaining of γH2AX foci in cells irradiated with low-LET radiation (γ, X) has shown relatively high spatial stability of DSBs during PI[14,192] (reviewed in [15]). In fact, the mobility of DSBs was equivalent to the Brownian movement of undamaged chromatin.[14,15,192,231–233] Similar results were also obtained for DSBs induced by other methods, such as UV-lasers[159] or even heavy charged-

particles.[189,234–236] Because individual DSBs colocalize with repair proteins already at their sites of origin in the first few minutes PI and later disappear without prior clustering with other lesions (marked as γH2AX foci), it is not probable that DSBs must migrate into repair factories to be processed.[14,15,192,231–233] DSBs are hence usually repaired individually at the sites of their origin. This is related to the second widespread and perhaps most accepted hypothesis for describing the mechanism of formation of chromosomal translocations: the "position-first theory." If this was true, translocations would form only between DNA loci proximate in the cell nucleus before DSB induction (reviewed in [15,39,183,185,228,231]). So why do some translocations appear much more frequently than others do? Is this because of the higher-order chromatin structure or DSB movement?[7] In the latter case, is there a higher chance that some loci will move to a particular nuclear domain and will mutually interact more frequently because of their higher-order structure? Or is a combination of both hypotheses required?

Because DSB movement has been observed when cells are irradiated with densely[157] but usually not sparsely[14,159] ionizing radiation, one explanation of the contradictory results regarding DSB mobility could be that high-LET IR fragments chromatin[231] because of high-energy deposition along the particle track. It is indeed hardly conceivable that in principle different mechanisms—one processing DSBs at the sites of origin and one that requires their directed movement into repair factories—would operate depending on the quality of damaging IR or kind of DSBs produced. In support of this, our experiments in which DSBs were induced by low-LET γ-rays and immuno-detected as γH2AX, NBS1, or 53BP1 foci revealed generally little movement of DSBs while showing that some foci had exceptionally high mobility[14] (reviewed in [15]). In agreement with the results of P. Jeggo's group[107,108,110–112] that showed a specific repair mechanism for heterochromatic DSBs (discussed earlier), mobile foci were initially almost exclusively located inside the condensed heterochromatin or at its border with decondensed euchromatin domains (called "chromatin holes" because of their low staining with DNA dyes in the interphase nuclei).[14] In addition, the seemingly chaotic movement of "mobile DSBs" was, in fact, directed from the condensed chromatin into chromatin holes, where it occasionally ended with the clustering of two or rarely more γH2AX foci[14] (reviewed in Falk et al., 2010).[15] Because heterochromatic DSBs largely colocalize (early after irradiation) with epigenetic markers, suggesting chromatin decondensation,[13,14] their movement probably reflects the opening of dense heterochromatin domains initiated by DSB repair. The "directed" nature of this movement, although unexpected if resulting from "random" decondensation, can also be simply explained. The protrusion of damaged chromatin into chromatin holes is frequently easier than decondensation of the whole affected chromatin domain, especially when it comes to the DSBs located close to the border of the chromatin hole[14] (reviewed in [15]). The local chromatin structure (texture) thus determines nonrandom vectors of damaged chromatin movements (see **Figure 34** in the Results section for illustration).

Importantly, the limited space within chromatin holes sometimes causes temporal or stable clustering of the repair foci that protrude into the same hole.[14] So what then represents these γH2AX clusters: complex multiple DSBs, repair factories, or the by-products of DSB repair with an increased risk of formation of chromosomal translocations? Because γH2AX clusters persist longer than single foci in cell

[7] Provoked either by DSB induction or repair.

nuclei, the last possibility seems to be the most probable. A model that illustrates the potential relationships between higher-order chromatin structure, DSB repair, and the formation of chromosomal translocations is described in detail in the review of Falk et al. (2010)[15] (see also **Fig. 34)**.

1.5.4 Sensitivity of structurally and functionally distinct chromatin domains to DSB induction

As described earlier, the chromatin structure determines the mechanism of DSB repair and markedly influences its efficiency. Therefore, it is reasonable to ask whether the higher-order chromatin structure and nuclear architecture also affect the sensitivity to DSB induction within structurally and functionally distinct chromatin domains, such as the euchromatin and heterochromatin (Chapter 1.9). This is an important question because DSBs in a gene-rich chromatin cluster can damage many important genes, including oncogenes and protooncogenes. Indeed, many experiments have shown preferential localization of γH2AX foci in decondensed euchromatin[12–14,107,108,110,111,161,161–163,194,234,236,237] both after cell exposure to low- and high-LET IR, but the explanation for this phenomenon is unknown[13,161] (reviewed in [238]). The same conclusions have been recently confirmed by the CRISPR-Cas9 technique[239] and SMLM,[240] which (similar to our confocal microscopy results)[14] showed localization of γH2AX (and other DSB repair foci) at the border of EC and HC (condensed and decondensed) chromatin domains.

Considering chromatin damage by different types of IR, a particle that transits through the cell nucleus accompanied by a very high-energy deposition along its path should theoretically damage chromatin without regard to the chromatin's structure. If this is true, a high-density chromatin provides more DNA targets for high-LET IR. This is in accordance with early studies on the potentially different radiosensitivity of euchromatin and heterochromatin revealing more chromosomal translocations in heterochromatin[242] (and the citations therein). However, other authors[243] provided conflicting results and found that most chromosomal aberrations occurred in euchromatin (reviewed in [60]). Indirect scoring of "DSBs" as the number of chromosomal translocations in EU- and heterochromatic bands of mitotic chromosomes, which were used in both studies, nevertheless considers not only the frequency of DSB induction, but also the processes of DSB repair and formation of chromosomal translocations, which also differ for these chromatin domains. Along with technological development, direct quantification of DSBs using pulse-field gel electrophoresis (PFGE) showed a higher radiosensitivity of euchromatin after exposure to both sparse[244] and dense[245] IR. Nevertheless, the results continue to be contradictory. For example, many authors reported equivalent sensitivities of different EU- and heterochromatin domains when using the same method,[246–249] or they readdressed this question by analyzing complex genome rearrangements by newly available multicolor fluorescence *in situ* hybridization (FISH).[250]

Because γH2AX foci were recognized as a specific marker of DSBs, their immunostaining in interphase nuclei[123–125,251–253] promised to end this dispute because the technique provides the highest sensitivity of DSB detection and working on intact cells eliminates problems with experiments on isolated chromatin. Using this method, γH2AX foci were found almost exclusively in decondensed

"euchromatin." Unfortunately, actively transcribed genes could be protected against γH2AX formation[241] and also heterochromatin is refractory to γH2AX foci formation,[254] which can be alternatively explained by immediate heterochromatin decondensation at the sites of DSB induction that transforms heterochromatic DSBs to "euchromatic."[13,14] The latter observation could explain the paradox where γH2AX foci are required only for the repair of heterochromatic DSBs[65,107–109,111,111,112] and how the heterochromatin structure precludes their formation.[254] A simple detection of γH2AX foci nevertheless does not allow for their scoring in the context of the original chromatin structure.

We have recently circumvented this obstacle[13] by employing the ImmunoFISH method[255] to simultaneously label γH2AX foci with specific chromosomal (sub)domains. Thus, by comparing the numbers of γH2AX foci introduced in individual chromosomal territories[(8)] or RIDGE and antiRIDGE gene clusters of equivalent molecular sizes,[13] it was possible to score DSBs independently of the changes in the original chromatin structure at DSBs (monitored, e.g., by DNA dyes).[13] In the case of DSBs formed in a condensed antiRIDGE domain, all lesions were correctly considered heterochromatic,[(9)] despite chromatin decondensation at the sites. For sparsely ionizing γ-radiation, these experiments showed that decondensed chromatin had a higher susceptibility to DSB damage.[13] Because most of the damage introduced with γ-rays is not caused by the photon *per se* but rather by the indirect effect of irradiation,[256] these results were interpreted to mean that the structural features[(10)] of heterochromatin[257] might protect DNA against free radicals[13,258–260] (reviewed in [261]) generated by water radiolysis.[262,263] Active DNA loci containing important genes therefore seem to be at a higher risk for radiation damage, coming with the previously described potential consequences for human health[13] (reviewed in Falk et al., 2010).[15] Overall, the chromatin structure can contribute to the different radiosensitivities seen in different cell types or in varying developmental stages. On the other hand, after exposure to dense IR, the number of DSBs generated could be a positive function of chromatin density because a higher locally deposited energy results in a different mechanism of DNA damage than γ-radiation (for high-LET particles characterized by a prevalence of the direct IR effect). Interestingly, many authors have shown that in this case, DSB distribution is also nonrandom, suggesting that the same principles of DSB repair (chromatin decondensation) operate in cells exposed to low-LET and high-LET IR, irrespectively of the different structural character of the initial DNA damage.[264,265]

To conclude, DSB induction in a particular higher-order chromatin domain (e.g., euchromatin and heterochromatin) may reflect not only the damaged domain structure *per se*, but also the way of how this "structure" interacts with a concrete form of the damaging agent. As discussed later in the comments on the author's publications,[12–15,18,19] heterochromatin might be more resistant to γ-rays but more "sensitive" to heavy ions (when compared with euchromatin). Heterochromatin is associated with a large amount of heterochromatin-binding proteins, so this phenomenon could be explained by a shielding effect that these proteins have against harmful ROS[13] (reviewed in [15,18,39]). On the other

[8] of similar molecular sizes or nuclear volumes

[9] and not misinterpreted as euchromatic

[10] but not simply its compactness

hand, heterochromatin—being much denser than euchromatin—provides more DNA targets for high-energy particles that can damage chromatin without any regard to its structure (discussed in [13,15]).

The introduction on the first part of the present thesis could be concluded as follows: The general principles of the higher-order chromatin organization in normal cell nuclei, together with their alterations in tumor cells or otherwise pathologically changed cells (described in detail in Chapter 1.9), represent an important aspect of cell (radio)biology that should be studied. Concerning the scope of the present thesis, particularly interesting is the relationship between the physical characteristics of IR, higher-order chromatin structure at DSB sites, extent of DSB damage, micro- and nanostructures of DSB damage, the mechanism and efficiency of DSB repair, the mechanism of formation of chromosomal aberrations, and cell survival.

1.6 Tumor Cell Radioresistance and Novel Ways of Radiotherapy Improvement

Cell types, even individual cells of the same population, differ considerably in their response to IR and survival. This is especially relevant for tumor cells known for their ability to develop numerous mechanisms to cope with DNA damage and the other otherwise deleterious effects of irradiation. Therefore, some cell clones can achieve high radioresistance. This is a serious problem in oncology, considering that >50% of cancer patients are treated with radiotherapy at some stage of the disease. Radioresistance may be an inherent feature of a tumor or develop secondarily because of radiotherapy. Despite tremendous innovations in the field of radiotherapy technology, radioresistance remains a substantial barrier to the successful therapy of many tumor types.[266,267] This fact and the enormous complexity of radioresistance mechanisms emphasize the importance of our better understanding of this phenomenon and its molecular mechanisms that include, but are not limited to, alterations in the regulation of DNA damage repair, cell cycle progression, apoptosis and senescence initiation, autophagy, oxygen level maintenance, energy metabolism, and immune checkpoint functions (**Figure 5**).[267–286] Recent findings have also pointed to the important roles of miRNAs and cancer stem cells (CSC) (**Figure 5**).[267,269,281,283,284] Radioresistance thus has molecular, cellular, and microenvironmental aspects that can accumulate during carcinogenesis and act in a synergic manner. For instance, the Epidermal growth factor receptor (EGFR) normally translocates to the cell nucleus, where it interacts with DNA-PKcs, a key kinase of the NHEJ pathway of DSB repair. Overexpression of EGFR, which has been detected in several cancer types, thus directly increases the repair capacity of tumor cells. At the same time, superabundant EGFR inhibits apoptosis through PI3K/AKT pathway activation, supporting tumor cell repopulation via stimulation of the Ras/Raf/MEK/ERK and STAT signaling.[283] In accordance, cetuximab (an anti-EGFR monoclonal antibody) decreases DNA repair in head and neck cancer cells because of the retention of EGFR in the cytoplasm and prevention of its interaction with DNA-PKcs.[283] Most frequently observed here is deregulation of the p53, EGFR, PI3K/AKT, ERK, Wnt/β-catenin, Nrf2/Keap1, and RAS pathways.[267–271,280–288] A detailed explanation of the individual mechanisms of tumor cell

radioresistance, however, goes above the scope of the current thesis. The reader is referred to the above-mentioned reviews and research articles for more information.

The causes of radioresistance can vary considerably between different tumor types and individual tumors of the same type (i.e., between patients). Hence, it is critical to identify clinically applicable markers for personalized cancer therapy and to design novel therapeutic strategies to reduce tumor cell radioresistance and/or protect normal cells that are also affected by radiotherapy. Research on this topic constitutes a substantial part of the current thesis. Specifically, we focused on the radioresistance mechanisms in HNTs,[25] which are of particular interest for their variable response to IR and have poor curability. In addition, we studied the effects of ASVs of the BRCA1 protein. BRCA1 plays a crucial role in DSB repair because it probably participates in switching between NHEJ and HR repair pathways. BRCA1 ASVs were detected in breast cancer patients, but their effect on DSB repair and clinical relevance were unknown.[23,24] In the final step, we focused on potential radiotherapy improvements (tumor cell radiosensitization); we researched the radiosensitizing effect of accelerated ion-beams[21,21,22] and metal (high-Z material) nanoparticles.[27,28,37] Also, we analyzed the "opposite" strategy regarding how to enhance effects of radiation therapy—the mechanisms of selective normal cell radioprotection through amifostine.

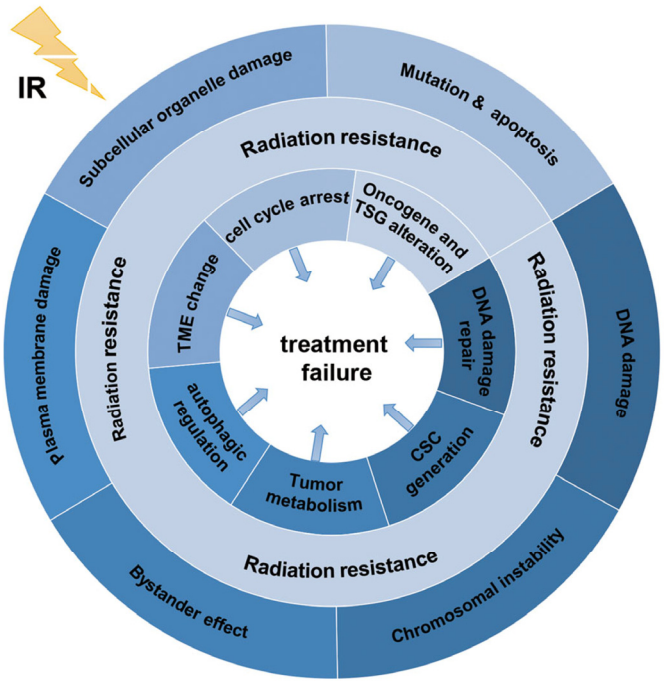

Figure 5. The complex nature of tumor cell radioresistance. The outer ring indicates the effects of irradiation in normal cells. Alterations of these processes are related to radioresistance development in tumor cells. The inner ring points to various mechanisms of radioresistance that then participate in the formation of the radioresistant phenotype of tumor cells and therapy failure. Taken from **Freneau et al. 2018**.[289]

1.6.1 Radioresistance of head and neck tumors

Head and neck tumors (HNT) are usually aggressive neoplasms with high recurrence rates and often have high resistance to (radio)therapy. Surgery could be efficient; however, surgery usually causes patient mutilation, significantly reducing patient quality of life. Moreover, tumor resection is often impossible because they are juxtaposed with vital organs. Nonsurgical (chemo-radiotherapy) approaches are therefore preferred over surgery, though ~50 % of HNTs are radioresistant (reviewed, e.g., [268]) for still poorly understood reasons. If (radio)therapy fails, salvage tumor surgery on the irradiated terrain provides only poor therapeutic outcomes.[289] Considering the absence of markers

capable of predicting individual tumor radioresistance before therapy initiation, it is evident that oncologists permanently face a serious dilemma when choosing the first-line therapy (reviewed in [25]).
The research on the causes of HNT radioresistance and the search for its markers has been only partially successful because of the (epi)genetic heterogeneity of HNTs and the complexity of the phenomena (described in the introduction to this chapter, page 47). In contrast to some other tumor types, no founder mutations associated with HNT pathogenesis and radioresistance have been identified (see [290] and the citations therein) although some genes (e.g., p53) are quite often mutated in these tumors.[290] Hence, different roots of radioresistance could reasonably be expected in individual HNTs. However, because DNA repair plays a central role in the cells' response to irradiation, we can reasonably hypothesize that important markers of tumor radiosensitivity/radioresistance might be associated with the DNA repair processes in tumor cells. Among various DNA lesions, we focused here on the repair of DSBs that are the most deleterious DNA damage type induced by IR and radiomimetic chemicals.[291] Nevertheless, defects in other fundamental processes[23,24,292–299] must also be considered as possibly contributing to or even dominantly determining the radioresistance of HNTs. These defects may include, but are surely not limited to, resistance to apoptosis,[292] inefficient cell cycle blockade,[293] the ability to survive with damaged genome (adaptation),[294] altered equilibrium in autophagy,[280,300–302] immune checkpoint manipulation,[273,303,304] competence to escape from senescence,[295–297] and the expansion of CSC.[305,306]
This situation complicates the use of permanent cancer cell lines or transgenic animals as model systems for radioresistance research, requiring instead direct studies with patient material. Moreover, each tumor is a highly heterogeneous and dynamic system composed of mutually interacting different cell types. This creates questions of how individual cell types inhabiting the tumor respond to irradiation and mutually influence each other in terms of radioresistance.[298,299] In the frame of the current thesis, we describe our exploration of some of the above-mentioned questions, taking advantage of cell primocultures prepared from different cell types (CD^{90-}, CD^{90+}, and their mixture) isolated from HNTs.

1.6.2 IBCT

The text updated from Ježková et al. (2018).[19] As already described, radiation cell killing is mostly based on DNA damage. A unique attribute of IR is its ability to deposit energy within nanometer volumes, thus inducing clustered/complex DNA damage containing various combinations of DSBs, SSBs, chemically modified or lost bases, DNA–DNA cross-links, DNA–protein cross-links, heat and alkali-labile sites, and other potential impairments (see **Figure 2**). The complexity of DNA damage depends on the radiation quality, and for radiobiological purposes, this quality is typically described in terms of LET.[307,308]

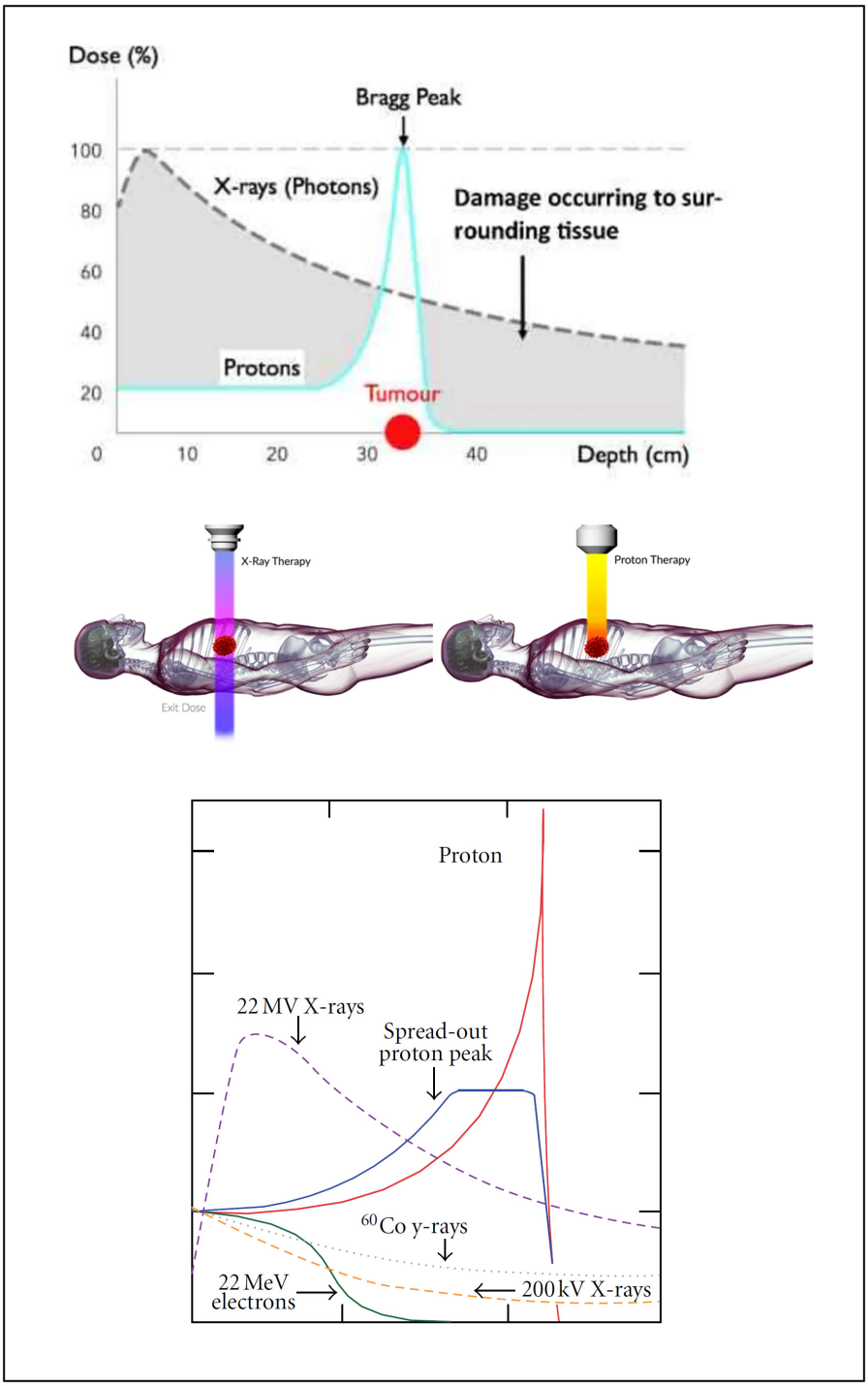

Figure 6. Ion Beam Cancer Therapy (IBCT) – the Bragg peak and its benefits for cancer therapy. From **Cianchetti and Amichetti 2012.**

Two main groups of radiation have been distinguished based on LET, their mechanism of action, and biological effects. Low-LET radiation sparsely and uniformly deposits energy within the whole volume of the cell nucleus. Hence, exposure to γ-rays or X-rays—two representatives of this category—typically leads to the formation of simple DNA lesions. In contrast, clustered or complex damage (multiple DSBs and other lesions within a few helical DNA turns) is the characteristic feature of high-LET irradiation.[307–310] Complex lesions pose a serious challenge for DNA repair systems because in many instances, this

damage is irreparable, may be repaired incorrectly, or may lead to the formation of even more serious DNA damage.[307,309,310] Being exposed to high-LET particles leads to the formation of complex chromosomal rearrangements at a high frequency.[311] Hence, clustered/complex DNA damage represents the main cause of cell death or mutagenesis upon irradiation and have been considered the key determinant of the radiobiological effectiveness of radiation. Therefore, it is generally believed that efficient cell killing by high-LET radiation depends on the physical ability of accelerated particles to generate complex DNA damage, which is largely mediated by LET.

For this physical property and a more advantageous profile of energy deposition (Bragg peak) compared with photon radiation, accelerated ions with high-LET promise significant improvements in cancer radiotherapy, especially in cases where the tumors are juxtaposed with vital organs and/or are resistant to photon irradiation.[312] The presence of the Bragg peak at the end of a particle trajectory (see **Figure 6** for an explanation) ensures that the destroying energy (of protons and high-LET ions) is more precisely targeted to the tumor volume than with what can be done with photon IR, improving tumor eradication and the preservation of surrounding normal tissues at the same time (**Figure 6**). This holds true also for protons although their relative biological effectiveness (RBE) is only slightly higher compared with gamma or X-ray photons.[313–317]

Nevertheless, in contrast to the solid physical rationale behind ion-beam cancer therapy (IBCT), the biological effects of protons of different energies and various high-LET ions remain largely unexplored.[312] This lack of knowledge prevents the optimal application and further development of proton therapy and IBCT although numerous proton and ion-beam therapy centers already operate all around the world, mostly based on empirical experience. The biological effects of protons and high-LET ions have hence received increasing attention, not only in the context of radiotherapy. The research on IBCT is of the utmost importance in space exploration, where exposure to mixed radiation fields represents one of the major obstacles complicating the realization of maned interplanetary missions.[318–323]

The phenomenon of clustered/multiple DNA damage is evoked by the nature of the energy transferred, and by definition, high-LET radiation densely releases energy along the track of the particle such that several types of damage form in a single localized spot volume. The spatial structure of high-LET particle tracks depends on the physical parameters of the particle and chromatin structure (reviewed in Falk et al. 2010).[15] The distribution of energy deposited by high-LET radiation along the particle track can be divided into two spatial components: the core and the penumbra, also known as the region of δ-rays.[324,325] The core is typically referred to as the central region of extremely dense energy deposition, where biomolecules are directly damaged by the particle itself and by contributions from low-energy knock-on electrons that do not escape from the core volume. Secondary electrons of higher energy (δ-rays) subsequently radiate out from the core and form the penumbra. Although a generally accepted definition of these track components is not yet available,[325] the microdosimetric characteristics of the track core and the penumbra together determine the initial complexity of DNA damage.[325,326] This notion is also true for the relationship between these spatial track/streak components and the RBE of radiation.

LET is frequently calculated to definitively determine the RBE of radiation; however, this parameter cannot precisely predict how particle tracks will appear and behave in space and time.[19] A considerable body of evidence has revealed the positive dependence of RBE on LET, where the biological endpoints of irradiation, such as cell killing,[327–330] the induction of mutations[331–333] (reviewed in [334]) and formation of chromosomal aberrations,[335–338] all increase as the LET value increases. However, a certain LET value (approximately 100 keV μm^{-1}) will correspond to the maximum peak RBE, and from this point, the RBE decreases only with increasing LET. Moreover, the most biologically damaging LET value largely fluctuates between 100 and 200 keV μm^{-1} for different particles, also depending on the cell type and endpoint studied.[326,339–341] Hence, a reasonable hypothesis is that the particles generate tracks with different spatio-temporal characteristics based on the specific sets of individual physical parameters (e.g., energy, charge, diameter, etc.), even if various combinations of these parameters show similar LET values.[19,326,342] However, experimental studies focusing on the microstructure of DNA damage observed following the action of different high-LET particles with similar LET values are rare. In addition to the initial (static) structure of DNA damage, changes in the DNA dynamics over time after irradiation may also principally influence the reparability of DNA damage and, therefore, the RBE of radiation types. Chromatin fragmentation occurring in response to high-LET irradiation and chromatin decondensation that occurs during DSB repair (in response to both high-LET and low-LET irradiation) locally mobilizes the damaged chromatin to some extent, generating clustered/complex DNA lesions.[15,157,159,235] The extent of chromatin fragmentation and the spatial density of DSBs depend on LET, and the spatio-temporal dynamics of DNA damage is also expected to rely on LET. Nevertheless, researchers have not determined whether and how chromatin dynamics vary for different particles with similar LET.

The importance of particle LET/energy becomes particularly relevant for low-dose/particle fluences—the conditions especially relevant for space exploration and addressed in the present study. The characterization of the particle tracks (DNA damage structure) in space and time thus emerges as a promising and needed new approach to explain many aspects of the radiobiological effects of physically different radiation types. Studies of the spatio-temporal aspects of DNA damage have become feasible with the discovery of the focal accumulation of DSB repair proteins at DSB lesions.[125] The microscopy of γH2AX/IRIF foci *in situ* and its advantages in the context of the present research were described earlier in the present thesis and in our previous works.[343–345] The relationship between the number of DSBs and γH2AX foci is approximately one to one for low-LET radiation;[124,125] however, high-LET radiation generates DSBs that are located so close to one another that these lesions cannot be further separated at the resolution of standard optical microscopy.[236,346] Various super-resolution (nanoscopy) techniques have been proposed and have more or less successfully been implemented into research practice to overcome this problem[347,348] (reviewed by Falk[20]); however, these methods still remain technically challenging and are typically applicable only to relatively small sample numbers. Two studies by Lorat et al.[349,350] took advantage of transmission electron microscopy to precisely quantify DSB complexity upon high-LET irradiation at a single molecule level. However, despite the superior resolution power and undisputable advantages of this approach, it suffers from serious limitations that primarily result from the complicated sample preparation requirements and the inability to

quantitatively analyze DSB damage in the entire (3D) volume of the cell nucleus.[351] Hence, a method for the precise, reliable, high throughput, and complex (i.e., in 3D volumes) analysis of DSBs under physiological conditions is not currently available. Therefore, many fundamental questions remain open. For example, the above discussed super-resolution study[349] revealed up to approximately 500 DSBs per 1 μm^3 volume of the carbon ion track (LET = 190 keV μm^{-1}, energy E = 9.5 MeV per n). This result is surprising and prompts questions of how a single DSB is defined at the molecular level and what level of complexity DSBs generated by different radiation types are present. Our nanoscale studies with SMLM included in the current thesis[21,22] represent two from several first attempts in this direction.

1.6.3 Nanoparticles

The text updated from Štefančíková et al. (2016).[27] Most common treatments based on highly penetrating MeV photons (X-rays and γ-rays) have the advantage of being non-invasive and applicable on inoperable tumors, as already introduced in Chapter 1.6.1. However, though the current technology enables highly precise irradiation, the photon radiotherapy in principle suffers from a serious disadvantage—it lacks tumor specificity. Tumor targeting can be improved when protons or high-LET ions are used instead of gamma or X-ray photons (Chapter 1.6.2). Nevertheless, all types of radiation still induce more or less extensive damage and inflicting severe side effects in the healthy tissue. The opposite problem is that some tumors are resistant to currently common treatment with high-energy photons. Therefore, a simultaneous enhancement of the tumor selectivity and biological effectiveness of IR is a long-lasting objective of cancer radiotherapy. In addition to earlier introduced IBCT (Chapter 1.6.2), a potential strategy to reach this aim (that can be possibly combined with IBCT) studied in the present thesis is based on the selective radiosensitization of tumor cells by metal nanoparticles (further referred to as "nanoparticles" or NPs). The rationale for the idea to use NPs composed of high-Z atoms as new nanodrugs to enhance radiotherapy came from the observation that lymphocytes of patients undergoing diagnostic imaging with NPs contained increased numbers of chromosomal aberrations. The results consequently obtained for various NPs showed that they can increase radiation killing of tumor cells,[352–355] moreover in a selective manner since they are preferentially sequestered by tumors. This happens even passively due to *the enhanced permeability and retention effect* (EPR).[356,357] Among metal-based NPs, gold NPs have been probably most widely used for diagnostics as contrast agents, and for therapy as nano-enhancers of radiation effects[358–362] for their good biocompatibility. Several studies demonstrated that gold NPs potentiate the effects of different photon beams, both *in vivo* and *in vitro.*[352–355,361,363,364] More recently, we have found[27,365] that also platinum NPs enhance the effects of both low-LET and high-LET radiation types, including γ-rays and accelerated medical ions. Numerous types of metal oxide nanoparticles are currently evaluated in oncology clinical trials as compounds for tumor diagnostic and cancer treatment.[366,367] An important step forward has been the development of gadolinium-based nanoparticles (GdNPs), studied in the present thesis, which can act as multimodal agents and improve not only the therapeutic index of the treatment but also MRI performance (theranostics) (see Štefančíková et al., 2016).[27] Due to its atomic mass (Z = 64), gadolinium is a good electron emitter, which is the physical property required to enhance the biological radiation effects.

When applied in combination with both low and high energy X-rays, γ-rays,[368,369] or accelerated ions,[370] GdNPs significantly amplified radiation-induced cell killing, even in the case of U87 glioblastoma cells derived from a highly aggressive and radio-resistant human tumor.[27,371] When combined with several types of radiation of different energies (≥keV), GdNPs exerted strong radiosensitizing effect on tumors.[369–372] Concomitantly, GdNPs served as good contrast agents[373] while they were rapidly eliminated from the organism by the kidneys, with no evidence of significant toxicity.[371,374–377]

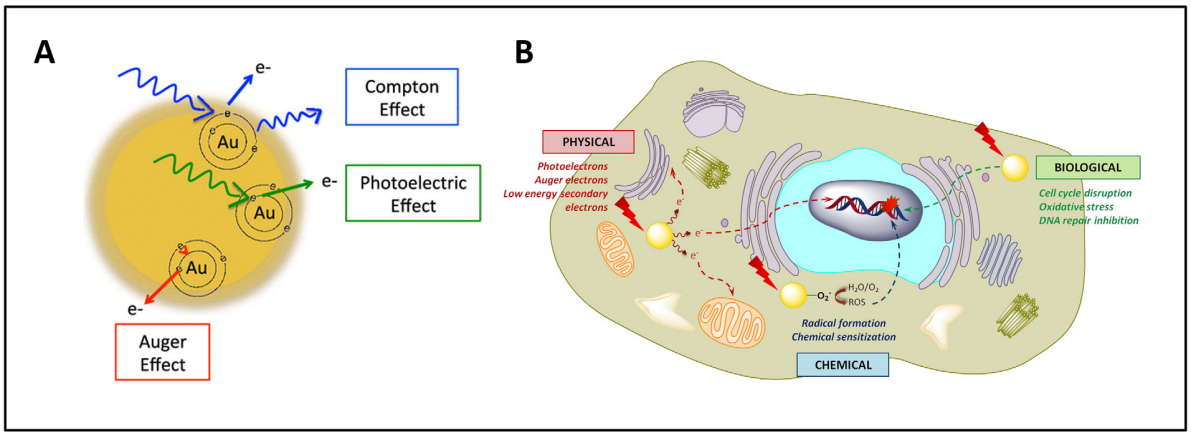

Figure 7. Variability and versatility of nanoparticles in medicine and research applications. Taken from **Her et al. 2017**.[378]

For γ-rays, used in our studies with NPs, the radiosensitization appears due to prominent physical processes, namely the photoelectric and Compton effects, in dependence of the photon beam energy. The cascade of GdNPs-mediated processes resulting to cell radiosensitization starts with the emission of electron showers by irradiated NPs and continues with water radiolysis producing free reactive oxygen radicals (ROS).[379] As these ROS are concentrated in nano-clusters, they are expected to induce complex nanosized bio-damages that are lethal for the cells.[380,381] NPs thus increase the ionizing density (and damage) at the nanoscale, without influencing the macroscopic dose deposition.[380,382–384] In accordance with this hypothesis, Burger and co-workers[385] found that high focal concentration of NPs is required to ensure an increased cellular inactivation by irradiated NPs. This prerequisite was confirmed also by the local effect model (LEM) simulations that suggested that the nanosized character of dose amplification is the key aspect of the "nanosensitization."[383,384]

Though the radio-enhancing effect of different NPs has been clearly proved and explained in terms of physics, the structures and processes targeted by nanoparticles in cells remain a subject of controversy. The nuclear DNA is logically the first suspect: it represents a critical cell structure and its damage by DSBs is commonly considered as the cause of radiation-induced cell death.[386,387] Hence, it has been proposed that NPs radiosensitize cells through amplifying the DSB damage. However, numerous *in vitro* studies, including those involved in the present thesis, demonstrated[363,370,388–391] that the radiosensitizers (metal complexes or NPs) are located in the cell cytoplasm. As discussed below, this opens the question whether secondary electrons only produced in close vicinity of cytoplasmically localized NPs may reach and damage the cell nucleus to a sufficient extent or whether NPs can amplify cell killing without entering the nucleus and enhancing DNA damage. Is it possible that the cytoplasmic

structures in closer proximity to NPs represent another, or even a more important target for NP-mediated radiosensitization?[27,28]

Jones et al.[392] showed that also the dose enhancement by NPs can spread as far as several micrometers. Leung et al.[393] reported that electrons can travel up to 3 µm or even 1 mm when activated by a 50 kVp and 6 MV source, respectively; this flying range is sufficient to reach the nuclear DNA. Thus, at least some electrons from electron showers emitted by NPs might directly damage the nuclear DNA.[385] Whether this is sufficient to enhance cell killing remains a question.

Important evidence that the cytoplasmic damage may strongly influence the cell nucleus emerged from recent microbeam experiments. The group of Kevin Prise demonstrated that also cytoplasmically micro-irradiated cells develop 53BP1 protein foci—the markers of DNA DSBs—dispersed in the nucleus.[394] Moreover, these experiments revealed that the radiation damage to the cytoplasm can elicit 53BP1 foci formation both in directly exposed and bystander cells, independently of the dose and number of cells targeted. Hence, we can conclude that the cytoplasmic injury might also be followed by DNA damage with a corresponding biological response, though its kinetics for the pan-cellular and cytoplasmic irradiations differs. The expansion of radiation damage from the cytoplasm to the nucleus is thus probably mediated by ROS.[395]

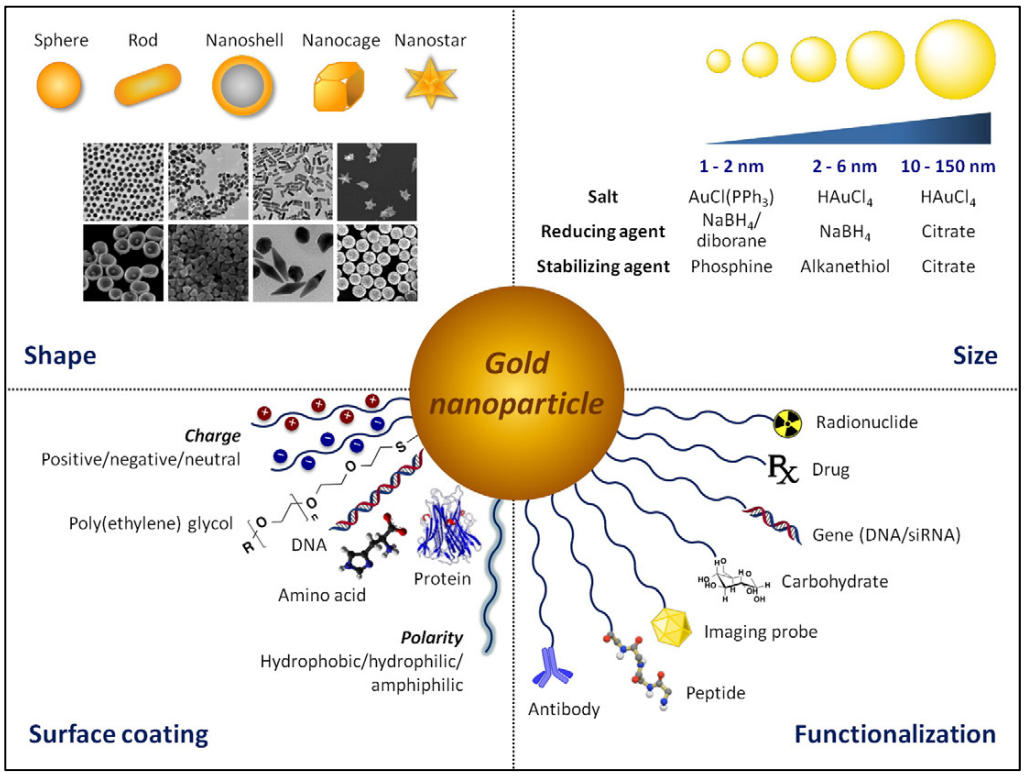

Figure 8. Physical processes in irradiated nanoparticles potentially leading to cell radiosensitization. Potential biological mechanisms leading to cell radiosensitization. Currently, it is not known whether electrons emitted by irradiated nanoparticles in the cytoplasm may damage the nuclear DNA extent to a sufficient extent to ensure radiosensitization. Alternative mechanisms based on the cytoplasmic damage have therefore been proposed. A, taken from **Rosa et al. 2017**;[396] B, taken from **Her et al. 2017**.[378]

In accordance, we can hypothesize that NPs might enhance the nuclear DNA damage by amplifying ROS production in the cytoplasm. In addition, disruption to protein transport and synthesis in the cytoplasm

upon high radiation doses may slow down or even preclude DNA repair and further contribute to the cell killing by irradiated NPs. However, the information on the damage exerted by NPs to the nuclear DNA remains very limited and conflicting as comparison of the available studies faces huge heterogeneity precluding the combination of results. This situation calls for further comprehensive analyses comparing the impact of physico-biological properties of various NPs and different treatment protocols on the radiosensitization processes. Interestingly, problematically comparable results followed also from our microscale and nanoscale observations, as it is reviewed in Pagáčová et al.[28]

To summarize, not all NPs exert the radiosensitizing effect on cells according to clonogenic survival and the mechanism of this radiosensitization remains obscure.[37] On the other hand, it should be emphasized that NPs represent potentially very useful and versatile tool in medicine since they can be prepared from various materials, in different shapes and sizes, and differently coated and functionalized.[397] For instance, NPs can be tagged with oligonucleotides to support their nuclear localization and ensure damage of specific genomic regions.[385,398,399] Alternatively, NPs can be modified to target cytoplasmic organelles,[400–403] used as vesicles for (anti-cancer) therapeutic compounds,[399,402–406] or applied in other ways to enhance cancer treatment. Nevertheless, in order to allow rational design of advanced (e.g. multi-modal) anti-cancer nanoparticles, the mechanism of their action must be better understood. Nanoscopy techniques, as also used in the present thesis, will represent an important tool in this respect.

1.6.4 Freezing thawing

Updated from Falk et al. (2018).[32] Freezing and thawing cycles are known to damage cells in the absence of an efficient cryoprotectant.[29–32] As extensive literature describes chromatin fragmentation upon freezing/thawing, we have hypothesized that cell freezing could be used as a relatively safe approach to augment DNA damage and tumor cell killing by radiation therapy (see Falk et al.[32]). Indeed, the combination of cryoablation with immunotherapy has already been described in clinical practice.[407] Even the development in the field of cryosurgery itself have the promise of positive therapeutic outcomes with few side effects in the treatment of certain cancers (e.g., skin, breast, prostate, kidney and liver).[408–417] However, regarding the sensitivity of different cancer cell types to low temperatures,[418] there is a lack of deep understanding of the mechanisms underlying this phenomenon as only few studies have sought to compare the responses of normal somatic cells and cancer cells to freezing and thawing. Nevertheless, even normal (non-transformed) cells are known to differ in their resistance to freezing and thawing.[419] The conditions of the cell nucleus and chromatin are critical for the cell survival and functioning as well as for the preservation of original genetic information. Therefore, varying sensitivities of chromatin to cryodamage may be an important factor as to why different cells respond differently to the freeze-thaw process. The effects of freezing/thawing (in combination with IR) on chromatin integrity and higher-order structure are therefore addressed in the present thesis as the third strategy of tumor cell radiosensitization.

1.6.5 Amifostine – normal cell radioprotection

Updated from Hofer et al. (2016).[33] The last strategy how to improve radiotherapy that is addressed by the present thesis is based on the opposite approach than in previous chapters—selective normal cell radioprotection by radioprotective drugs. Radioprotectants are studied also in the context of civil radiation protection and military applications for their ability to lower deleterious health effects of accidental radiation expositions. For general overview of the current possibilities of radioprotection, the reader is referred to our recent reviews (attached, Hofer et al.[34,35]). In the context of this thesis, we focused on radioprotectants that have the ability to selectively protect normal but not tumor cells. In fact, the only radioprotectant of this kind approved for clinical use is amifostine (ethanethiol, 2-[(3-aminopropyl)amino]dihydrogen phosphate), also known as WR-2721. Amifostine is an organic thiophosphate agent that it is rapidly dephosphorylated by alkaline phosphatase (ALP) at the cell surface of healthy tissues, giving rise to its clinically active metabolite, WR-1065.[420–422] When activated, amifostine protects cells from radiation- and chemotherapy-induced DNA damage, mostly by competing with oxygens and preventing their interactions with DNA radicals and donating hydrogen to repair the already existing DNA damage.[235,423]

Concerning the practical application of amifostine in human medicine, a key role has been ascribed to its differential effect on cancer and normal cells, respectively: Whereas in normal cells or tissues amifostine clearly acts as a radio- and chemoprotective agent, this property of the drug is lost in cancer cells.[424–429] This cell type-specific behavior of amifostine has been largely attributed to low levels of ALP in (some) cancer cell types as compared with normal cells;[430] however, the situation is still not that clear because a variety of human cancers ectopically express high levels of ALP, thus leading some scientists to the (opposite) suggestion that ALP might be critically involved in tumor development.[431–433] Indeed, a comprehensive comparison of ALP mRNA and protein expression and activity in cancer cells in the literature is missing. This uncertainty points to the caution with which each model of disease (e.g., different cell types) should be tested. In addition, it is still not obvious how the four main classes of ALP (tissue nonspecific TNAP, intestinal IAP, placental PLAP, and placental-like GCAP) participate in amifostine conversion in various normal and especially cancer cells where expression of ALP isoenzymes may be altered.[434] ALP genes are also highly inducible by many agents.[432] Finally, though covalently anchored to the outer surface of the plasma membrane,[433] ALP can be released into the serum (or extracellular medium) by the GPI-dependent phospholipase D under stress and some medical conditions, such as cancer. While previous reports showed that the membrane-bound ALP has different enzymatic kinetics and molecular properties as compared to the soluble enzyme,[433,435] the question remains how this finding is reflected in amifostine metabolism in normal and cancer tissues.

Importantly in the context of this thesis, amifostine has been shown to modulate induction of DSBs[436,437] that represent the most serious DNA lesions induced by IR (as it has been already mentioned earlier) and therefore the most relevant type of DNA lesions concerning the cell radioprotection and radiosensitization. The mechanism of this activity is supposed to be based on sequestration of ROS by amifostine, more precisely its active metabolite WR-1065. Conversion of amifostine to WR-1065 is mediated by alkaline phosphatase (ALP) that is only low abundant in many tumors. Decreased ALP levels in tumor cells have therefore been considered as the molecular cause of selective

radioprotection of normal cells by amifostine. Moreover, some reports described amifostine effects also on DSB repair, the mechanisms of which are not sufficiently understood. How amifostine selectively protects normal cells against radiation thus remains unsure. Therefore, we decided to compare DSB induction and repair in normal and tumor cells irradiated in presence and absence of amifostine, respectively. Surprisingly, we found that amifostine not only decreased DSB damage in normal cells, it also improved DSB repair in normal cells and altered it in tumor cells. Hence, in this thesis, we discuss on possible mechanisms of these complex amifostine effects and offer three new hypotheses (Chapter 2.3.2.4).

1.7 Conclusions and Perspectives

It is now generally accepted that the spatio-temporal organization of chromatin plays an important role in the cell's response to irradiation—it influences the sensitivity of structurally and functionally distinct chromatin domains to DSB induction, the mechanism of DSB repair, and the mechanism of formation of chromosomal translocations. More specifically, recent results have shown that the higher-order chromatin structure codetermines the extent and complexity of DSBs produced, the speed, efficiency, and fidelity of DSB repair, the risk of formation of chromosomal translocations between particular loci, and, potentially, other aspects of complex cellular response to DNA damage. Therefore, it is evident that the impact of the higher-order chromatin structure on "DSB repair" is quite complex.

The processes associated with DSB induction and repair, the formation of chromosomal translocations, and, finally, the clinical manifestation of DNA damage, encompass a broad range of time and spatial dimensions. Very promising is the recent development in the field of microscopy and molecular biology methods that has facilitated experiments previously unimaginable, even recently. Super-resolution microscopy approaches, also used in the present research, currently offer resolutions of about 10 nm. The combination of live cell microscopy and high-throughput methods such as flow-cytometry and various omic techniques allows for continuous monitoring of DSB repair in individual cells in real-time, and, at the same time, multiparameter pan-omic studies on large populations. A significant improvement of our understanding of radiation-mediated DNA damage and repair could be expected in the next few years, which can allow further enhancements in the field of radiotherapeutic technologies (e.g., IBCT) and the rational design of more advanced agents capable of modifying the cellular response to irradiation (e.g., functionalized metal nanoparticles). Nevertheless, multidisciplinary cooperation is necessary; for example, IBCT could not be safely and fully introduced without additional coordinated physical, chemical, biological, medical, and technological research. Many other benefits that can be anticipated are discussed in the "Conclusion Remarks" portion of this work.

1.8 Methodology

Numerous molecular biology, biophysical, and biochemical methods were used in the current thesis (particle irradiation at the particle accelerators, micro-irradiation with a UV laser, advanced microscopy and DNA/protein staining techniques, *in vivo* protein labeling and cell observation, etc.) (**FIGURES 9 –**

12), the complete descriptions of which can be found in the original papers attached. Nevertheless, SMLM and the variants of FISH, including immunoFISH, will be briefly introduced below because of their importance for the presented research.

It should also be noted that several important methodological results were achieved in the frame of the present thesis:

- Application of SMLM super-resolution microscopy (nanoscopy) for the analysis of DNA damage induced by accelerated heavy ions
- Development of advanced software based on machine learning/artificial neural networks for the detection and evaluation of different DSB repair foci (IRIFs) and their colocalization
- Development of RNA chips to study the expression of >350 genes involved in the different aspects of cell response to irradiation/DNA damage

1.8.1 FISH

The basic principle of FISH is explained in **Figure 9**. Advanced FISH applications, which are also used in the present thesis, include 3D-FISH, multicolor FISH (mFISH, or its variant spectral karyotyping, SKY), multicolor chromosome banding (mBanding), combinatorial oligonucleotide FISH (COMBO-FISH),[442–446] and ImmunoFISH. **3D-FISH** preserves spatial architecture of the interphase nuclei and thus enables quantitative exploration of the higher-order chromatin structure.[1] **mFISH/SKY** (**Figure 11A,B**) allows simultaneous visualization of all chromosomes in the cell nucleus and is therefore irreplaceable for analyses of the genome architecture, complex karyotype rearrangements, and the mechanisms of their formation. **mBanding** (**Figure 11C**) is a variant of mFISH where the probes are designed to label specific loci alongside a particular chromosome and detect even negligible intrachromosomal rearrangements in mitosis or internal arrangement of interphase chromosome territories. **COMBO-FISH** represents a next-generation method that, combined with newly developed SMLM microscopy (**Figure 12**), makes possible the visualization of specific loci at the nanoscale, with a resolution of ~10 nm.[447–451] COMBO-FISH[442,443,445,446,448] takes advantage of a set of short oligonucleotides (15–30 nts), which better preserve the native chromatin structure compared with standard FISH. Moreover, the probes can be designed to bind DNA via Hoogsteen pairing, that is, without the necessity of its harmful denaturation. The method can potentially be carried out under *in vivo* conditions when the disturbance of the chromatin structure is *de facto* eliminated. Finally, **ImmunoFISH (Figure 11D)** combines classic immunocytological and FISH techniques, allowing for simultaneous detection of selected nuclear proteins together with the genetic elements of interest (e.g., chromosomal territories, genes, telomeres, centromeres, or RIDGEs/antiRIDGEs). This makes mechanistic studies on nuclear processes possible, though other methods are necessary to confirm the observed protein-DNA interactions. Immunostaining, 3D-FISH and ImmunoFISH are the most commonly used labeling methods in the present work.

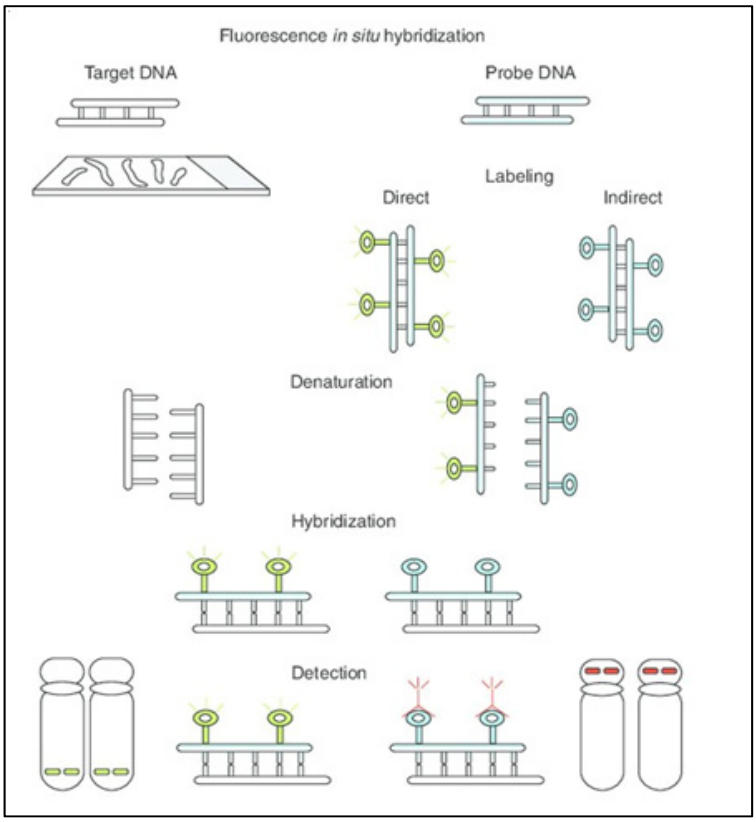

Figure 9. The principle of FISH. FISH represents a powerful technique for visualizing specific DNA or RNA sequences *in situ*. Fluorescently labeled (DNA) probes have a sequence complementary to the chromosomal loci of interest (genes, telomeres, centromeres, chromosome arms, or whole chromosomes). After cell fixation and permeabilization, the DNA probe penetrates into the nucleus. The probe(s) and nuclear DNA are then denatured and mutually hybridized based on their mutual sequence complementarity (in the case of RNA-FISH, denaturation is also used to eliminate the secondary and higher-order structures of RNA molecule). After about ten hours of hybridization in a humified chamber, selected targets can be visualized *in situ* by various microscope approaches. The picture was taken from **Dorritie et al. (2004)**.[792]

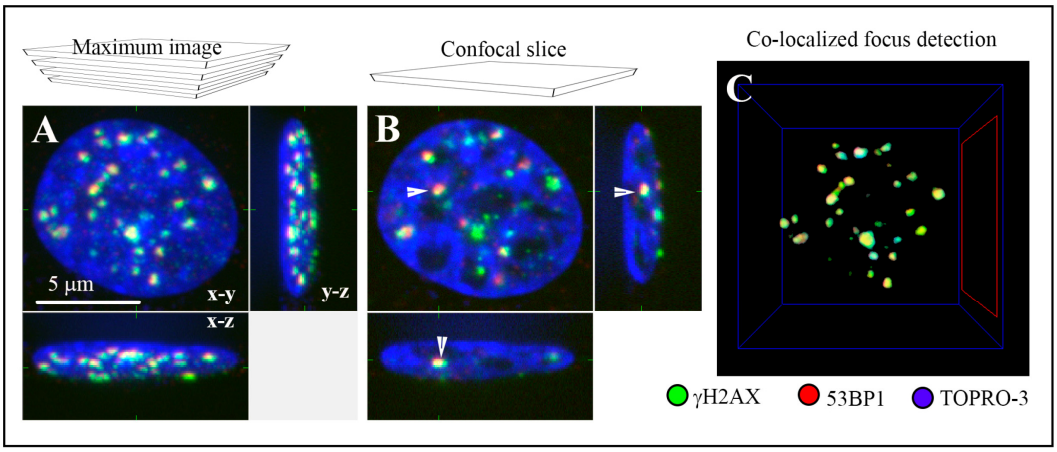

Figure 10. The ability of immunofluorescence confocal microscopy to quantify DSBs in irradiated cells. DSBs were quantified by means of immunofluorescence detection of colocalized H2AX (green) and 53BP1 (red) repair foci, the DSB markers. The nucleus of an illustrative U87 cell exposed to 2 Gy of γ-rays and spatially (three-dimensional = 3D) fixed at 2 h postirradiation (PI) is shown as: **(A)** a maximum intensity projection of 40 confocal slices (0.3 m thick; "maximum image") or **(B)** a single confocal slice (0.3 m thick) intersecting the indicated (white arrow) H2AX/53BP1 focus. Images are displayed in all three (in the x-y, x-z, and y-z) planes, and the chromatin is counterstained with TO-PRO-3 (artificially blue). **(C)** An example of computational detection of colocalized (yellow), H2AX (green), and 53BP1 (red) repair foci in 3D space (Aquarium Software). Taken from **Pagáčová et al. (2019)**.[28]

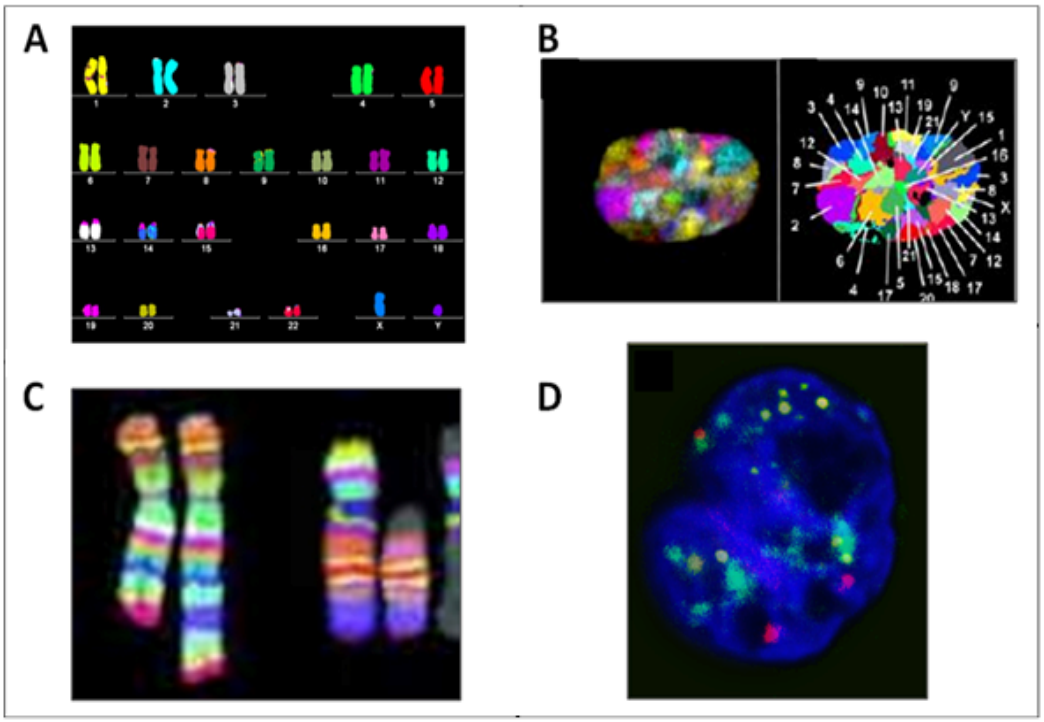

Figure 11. The examples of the results of current sophisticated FISH methods. **A**. Visualization of complete karyotype (mitotic chromosomes) with complex rearrangements by multicolor FISH (mFISH). Each chromosome can be identified by using a combination labeling scheme in which each chromosome is labeled with a different set of fluorochromes **B**. Multicolor FISH performed on interphase nuclei to determine the mutual nuclear positions of chromosomal territories. All chromosome territories, each in a different color, can be visualized simultaneously in intact interphase nuclei. **C**. Multicolor chromosome banding (mBanding) for detailed studies of chromosomal rearrangements. **D**. An interphase nucleus of U937 PR9 cells with territories of chromosome 17, its centromere and PML bodies simultaneously visualized by the ImmunoFISH technique. Images were taken from A: **Catalina et al. (2007)**[438]; B: **Bolzer et al. (2005)**; **Bolzer et al. (2005);**[439,440] C: illustrative photo: MetaSystems. D: a result of the author.[441]

1.8.2 Single Molecule Localization Microscopy (SMLM)

The breakthrough principle of SMLM[(11)] should also be briefly mentioned. The "trick" of this super-resolution optical microscopy technique with a resolution of about 10 nanometers is in using reversibly bleached states of conventional fluorochromes (such as Alexa dyes), which allows for optical isolation of individual fluorochrome molecules and an accurate position determination far below Abbe's limit.[21,444,449–451] The principle of SMLM is explained and illustrated in **Figure 12**. The fundamental advantage of SMLM is that it keeps all of the advantages of optical microscopy over electron microscopy but offers a resolution that is about one order better (compared with standard confocal microscopy). Moreover, SMLM generates a matrix of 3D coordinates and other parameters of individual fluorochrome molecules that can be directly submitted to various mathematical analyses without necessity of image processing.[(12)] SMLM can be combined with advanced labeling techniques such as COMBO-FISH (see the previous chapter). The combination of SMLM with COMBO-FISH is a real dream of cell biologists that is just coming true and accessible for our laboratory in the frame of cooperation with Prof. Michael Hausmann (Kirchhoff Institute for Physics, Heidelberg, Germany).

[11] SMLM is sometimes named also as Spectral Precision Distance Determination Microscopy or Spatial Position Determination Microscopy (SPDM)

[12] For this feature, SMLM could be called as "microscopy without images".

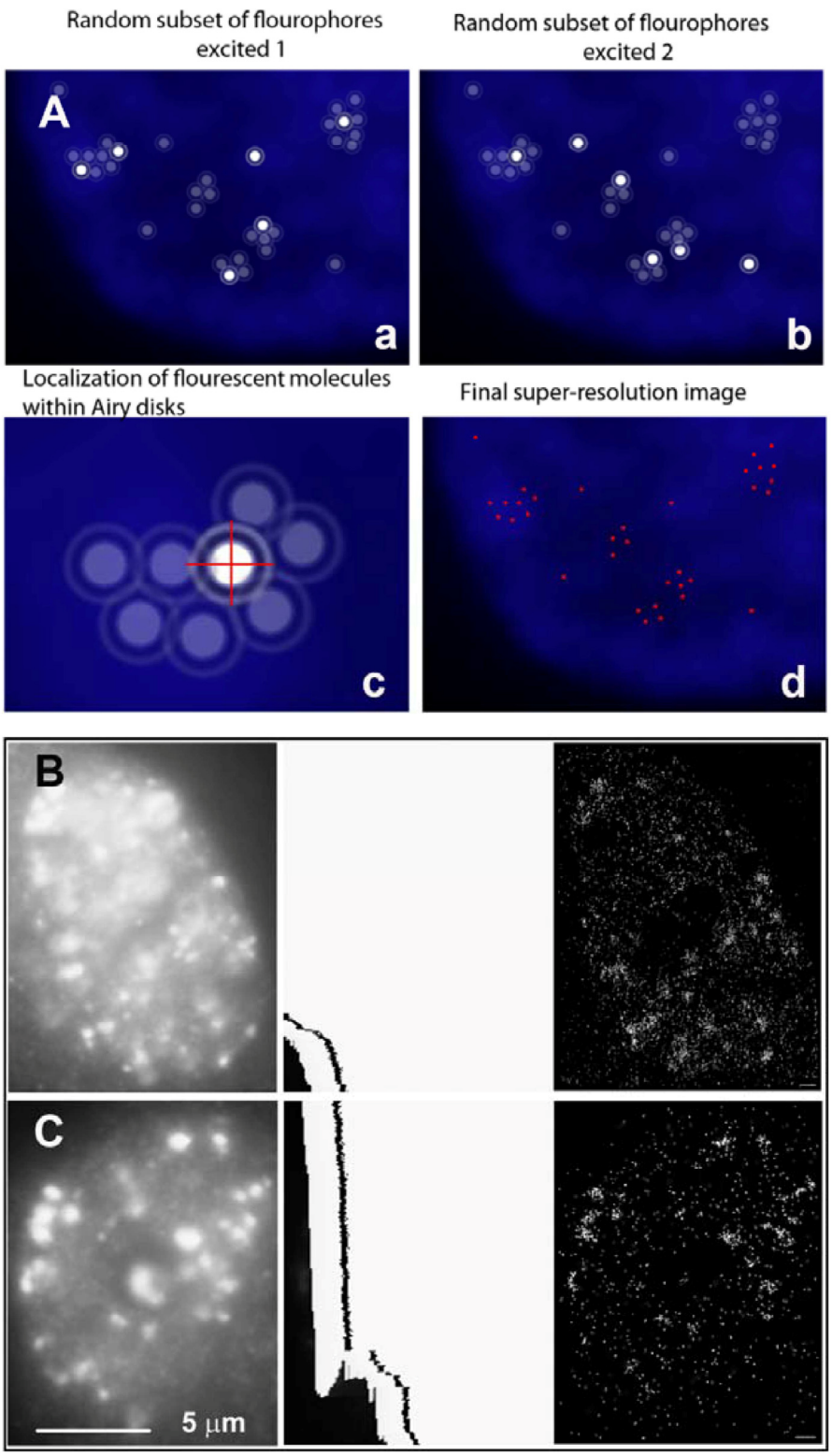

Figure 12. The principle of single-molecule localization microscopy (SMLM). **(A)** Fluorochrome blinks are recorded during time after sample photobleaching (a + b). Precise positions (= position of the intensity barycenter) and their errors are then calculated for all fluorochrome molecules (c). As a result, a super-resolved pointillist image is artificially generated by further mathematical processing (d). **(B)** Compares the standard wide field microscopy image of H2AX foci (left) and the corresponding SMLM image (right) taken after reversible photobleaching of the same cell nucleus (middle). **(C)** The same as B, but 53BP1 foci are visualized. U87 glioblastoma cells exposed to 4 Gy of 15N ions (see Tab. 1 for the radiation characteristics) are shown. From **Depeš et al., 2018.**[21]

1.9 Detailed Explanation on the Principles of Higher-Order Chromatin Organization in Cell Nuclei of Normal and Cancer Cells

1.9.1 Chromatin and its structure – historical and current perspectives

In the eukaryotic cell nucleus, DNA does not appear "naked" but forms complexes with histones, non-histone proteins, and RNAs, termed *chromatin*. Chromatin, discovered by Walther Flemming at the end of the 19th century,[452] is hierarchically organized into chromosomes, with the maximum level of compaction reached in mitosis (**Figure 13**). After the introduction of the Boveri–Sutton *Theory of Chromosomal Inheritance*—that recognized chromosomes as stable *genophores* transmitting the genetic information from generation to generation[168,169,453] (reviewed in [454])—chromatin and chromosomes moved to the center of biological research.

Emil Heitz, who studied chromosomes between the years 1928 and 1935, revealed that they are longitudinally composed of euchromatin and heterochromatin, the two components that are differently stained by chromatin dyes.[455,456] With Giemsa solution,[13] the intensive (G-dark) and weak (G-light) bands can be seen to periodically change along the mitotic chromosomes. Later analyses showed that G-light bands (euchromatin) contain more G-C base pairs[457] and the majority of all genes, including permanently active housekeeping genes.[458] On the other hand, G-dark bands (heterochromatin) represent compact chromosomal regions with prevalence of A-T base pairs and only few, mainly tissue-specific genes.[14] [37,458,459] Further differences between euchromatin and heterochromatin include the replication timing and recombination frequency during mitosis, as it is summarized in **Figure 14**. Based on the structure and character of genetic information obtained, two types of heterochromatin can be distinguished:[460] Constitutive HC represents the permanent heterochromatic structure that is stable during the cell cycle, differentiation, and in all cell types. It forms centromeres and predominantly contains satellite DNA consisting of large numbers of short tandem repeats[460] (α-satellite DNA, DNA satellite I, II and III). On the other hand, facultative heterochromatin contains DNA loci that were originally active but inactivated during the cell differentiation. The distribution of facultative heterochromatin along chromosomes is thus cell-type specific. The best-known example of facultative heterochromatin is the inactivated chromosome X that could be detected in female somatic cells as the so-called Barr body or sex chromatin.[461] Since cytological staining reflects different features of chromosomal bands,[15] the discovery of heterochromatin and euchromatin can be considered as the first proof of nonhomogeneous organization of genetic information along the linear (2D) sequence of chromosomes.

The first step (and a giant leap) on our way towards the understanding of spatial (3D) chromatin structure was made by James Watson and Francis Crick in 1953, and in parallel by Maurice Wilkins and Rosalinda Franklin,[462–464] who discovered the DNA double helix. The next decades then brought about

[13] DNA stain composed from basic aminophenothiazine dyes, *i.e.* azure A, azure B, azure C, thionin, and methylene blue, and the acidic dye eosin

[14] Heterochromatin location enables their silencing with cell type differentiation.

[15] This 'bar-code', since unique to each chromosome, can serve for their unequivocal identification and studies of their structural and numerical aberrations.

knowledge on the hierarchical levels of chromatin fiber organization. Experiments showed that (eukaryotic) DNA first wraps around the histone octamers—composed of two H2A-H2B dimers and one $(H3)_2$-$(H4)_2$ tetramer—forming thus the nucleohistone fiber with 146 base pairs of DNA per nucleosome and 10 nm in diameter.[465–467] For its electron-microscopy visage, this fiber is usually named as the *beads on the string* (right panel, second line from the top) (**Figure 13**). In a higher ionic strength, this fiber associates with "linker" histones H1 (or H5) that initiate its condensation into the 30-nm solenoid[468] (reviewed in [469]) with a compaction rate of about 40:1.[470] In this structure, nucleosomes are supposed to follow a helical path, with adjacent nucleosomes placed side by side, six nucleosomes per one turn. The 30-nm solenoid is then further spiralized into higher organization levels (*e.g.* as described by Manuelidis[459]) leading to the maximum compaction of 1 : 10,000 to 1 : 20,000 in mitotic chromosomes.[470] However, the organization levels above the 30-nm solenoid (**Figure 13**), referred to as the ***"higher-order chromatin structure***," are unknown and disputable.[(16)] [466,467,469] In fact, even well explored basic levels of chromatin organization described above (**Figure 13A**) have recently been challenged by newly emerging results, leading to postulation of alternative models, as for instance the Dynamic and Fractal Chromatin Folding Model[466,471] (**Figure 13B**).

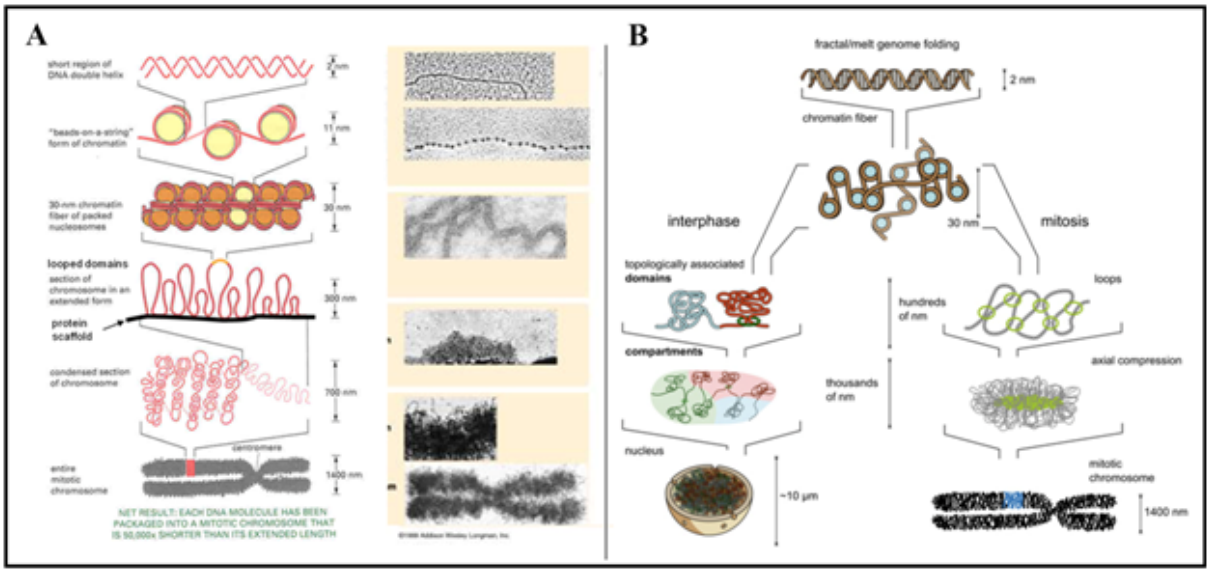

Figure 13. Chromatin folding according to the 'standard' (**A**) and newly (**B**) proposed Dynamic and Fractal Folding Model. The levels of spiralization above the 30-nm solenoid, termed as '*higher-order chromatin structure*' are still poorly understood (figure adapted from **Alberts 2002**[792] and **Moraru and Schalch, 2019**.[466]

[16] Actually, neither the structure of the 30-nm chromatin fibre is definitively clear. An alternative model to the solenoid structure counts with a zigzag formation, where the nucleosomes follow a zigzag path along the chromatin fibre so that adjacent nucleosomes are opposite each other. Some researchers also presuppose that the structure consists of both the solenoid and the zigzag formation that are in dynamic balance with each other (reviewed in Li a Reinberg, 2011).[469]

Structurally distinct chromatin domains in the interphase nucleus and their functional means

Heterochromatin (HC) and euchromatin (EU) (**Figure 14**) described in the previous paragraphs are the most easily and strikingly distinguishable types of chromosomal structures discovered with cytological staining of mitotic chromosomes already in 1928.[455] Importantly, Heitz recognized that heterochromatin remains condensed and therefore stainable also in the interphase when chromosomes (euchromatin) experience extensive decondensation and become no more visible after the accomplished mitosis.[455] This finding could be thus considered as the first indication pointing to the existence of structurally and functionally distinct 3D chromatin domains in interphase nuclei (**Figure 15**). Importantly, it also shows that euchromatic domains adopt more "open" chromatin structure in interphase compared to heterochromatic domains. Considering the differences between heterochromatin and euchromatin in their gene content, it is reasonable to hypothesize about the (functional) relationship between the genetic activity and higher-order chromatin structure of a particular type of an interphase chromatin domain or even individual domain. However, the mechanisms behind this relationship and its nature are still not clear, as are not the details about the arrangement of interphase chromatin. The topic is discussed in the following text.

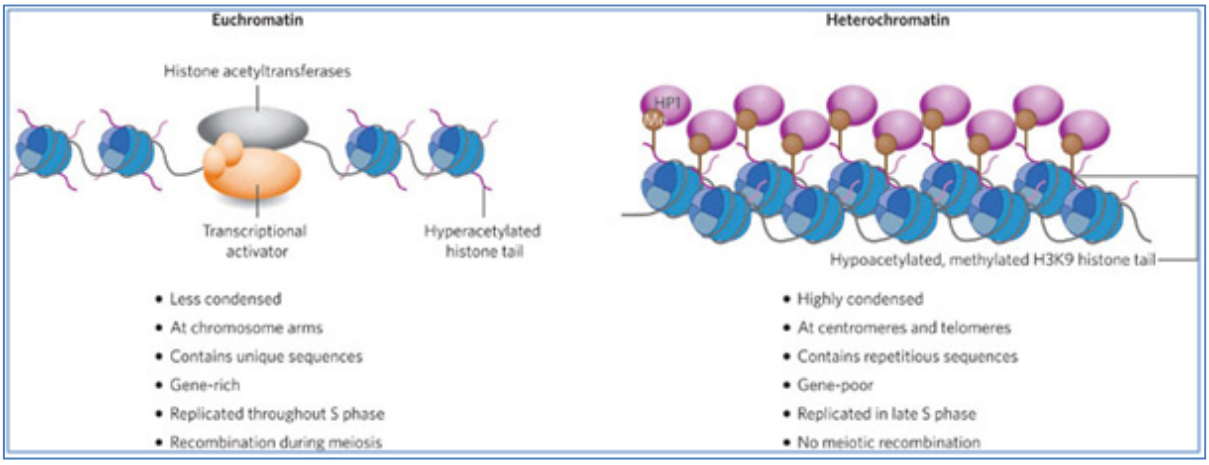

Figure 14. Euchromatin and heterochromatin - The basic characteristics of euchromatin and heterochromatin are compared at the image. Taken from **Grewal a Elgin, 2007**.[472]

The most obvious function of extensive chromatin condensation (higher-order chromatin structure) is obvious if we consider that about 2 m of human DNA must be somehow packed into the cell nucleus of about 10 nm in diameter. Another easily imaginable function then resides in mediating chromosome segregation during the cell division. However, mitotic chromosomes largely decondense during the interphase, which suggests that the maximal compaction of mitotic chromosomes prevents genetic activities of chromatin. This demonstrates that DNA transcription, replication, repair and other nuclear processes cannot proceed in tightly condensed chromatin and/or that interphase chromatin has to adopt some specific nuclear landscape setup, compatible with ongoing processes.[13–15,469,473,474]
Experiments showed that a link between the chromatin condensation and its genetic activity can be of functional relevance, since condensed chromatin structure helps reduce transcription in heterochromatin.[3,469,475–477] The open structure, on the other hand, allows better access of regulation and effector factors to euchromatin, assembly of huge protein complexes and intensive transcription,

replication or repair. Nevertheless, open (eu)chromatin structure may not only represent the prerequisite of indicated nuclear processes; it may also appear in consequence of chromatin decondensation secondarily provoked by protein activity in chromatin, such as intensive transcription. The dynamic chromatin structure changes thus serve as the control mechanism but also integrate the effects of ongoing processes in chromatin.[478–480]

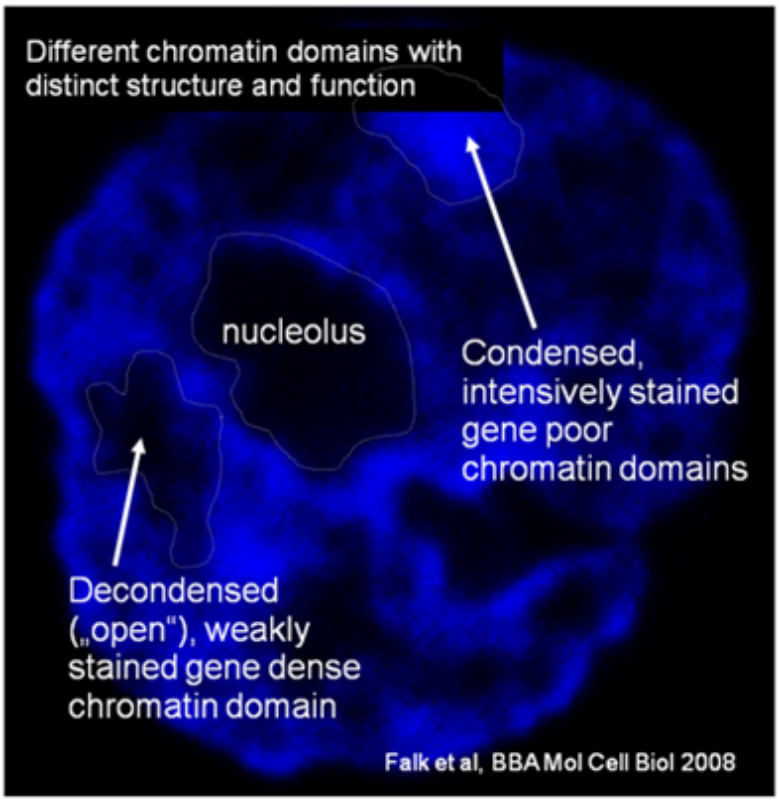

Figure 15. Preservation of euchromatic and heterochromatic loci in 3D space of the cell nucleus - The euchromatic and heterochromatic nuclear subdomains visualized by TOPRO-3 are demarcated. Human skin fibroblast, 0.2 μm thick optical slice in the central plane of the nucleus (data of the author).

The fundamental role of the higher-order chromatin structure in regulation of nuclear processes can be illustrated on the phenomenon known as the Position Effect Variegation (PEV).[481,482] PEV refers to variable silencing of an active gene in consequence of its relocation to a heterochromatic nuclear domain, for instance due to a chromosomal translocation. The effect is mediated by the transmission of transcriptionally non-permissive chromatin structure of heterochromatin on the juxtaposed gene. We have discovered that similar effect can represent a new mechanism in the pathogenesis of acute promyelocytic leukemia (APL), as it is extensively discussed in the corresponding chapter (2.1.2).[11] Since heterochromatin usually appears at the nuclear periphery and around nucleoli, PEV also points to the importance of the chromatin nuclear topology (nuclear architecture) as introduced in the next chapter (**Figure 16**). Chromatin structure-mediated regulation of vital nuclear processes could be well exemplified also by the series of chromatin structure reorganizations that appear during DSB repair and are in detail examined in our papers associated to the present thesis.[14,15,18]

The previous paragraphs could leave the impression that chromatin is a rigid structure that regulates nuclear processes simply by allowing or restricting the access of necessary protein factors to the DNA.

However, even though the number, shape and nuclear localization of heterochromatic domains do not markedly change through the cell cycle,[483] heterochromatin is far from being a rigid inaccessible complex. A breakthrough in this context was brought about by fluorescence recovery after photobleaching (FRAP) measurements showing that HP1 protein—an important constituent of heterochromatin structure—binds and leaves chromatin with rapid binding kinetics. Heterochromatin is thus highly dynamic in nature with continuous exchange of proteins.[483–485] Hence, heterochromatin is accessible at least to some proteins that constituently compete for their binding sites and, doing so, dynamically set up the structure and epigenetic modifications of the particular HC domain.[483,485] This conclusion is supported also by the results obtained in the frame of this thesis showing that while heterochromatin is inaccessible for large proteins involved in DNA double strand break repair, such as 53BP1, small proteins acting as DSB sensors (NBS1) can penetrate its condensed domains.[16] Regulation of nuclear processes through higher-order chromatin structure is therefore evidently based on a complex and dynamic "landscape" code that interconnects structuro-epigenetic features of each particular chromatin domain instead of a simply setting its rigid accessibility for specific proteins.[486]

Since the epigenetically determined heterochromatic status can be hereditary transmitted to the cell progeny, HC is responsible for setting up and stabilization of cellular transcriptional patterns during the cell differentiation and development. Hence, even if not mentioning here many other functions of heterochromatin, it is evident that it is far from being a useless or even "parasitic" component of the genome. Indeed, disruption of the balance between euchromatin and heterochromatin can dramatically deregulate normal cell functioning, potentially leading to genome instability, unrestricted cell growth and development of cancer. This can happen, for instance, due to silencing of tumor suppressor genes in consequence of the inactivation of the boundary elements that prevent spreading of HC along the chromosome (reviewed in [487,488]).

1.9.2 Nuclear architecture, chromosomal territories and subchromosomal chromatin organization

As it follows from the previous chapters, chromatin structure significantly influences nuclear processes. Nevertheless, in the early era of cytogenetics, only the mitotic chromosomes were detectable with light microscopy and classical chromatin staining; this prevented studies of their structure during the interphase. Therefore, chromosomes were thought to be only randomly folded temporary structures perpetually forming *de novo* in each mitosis (**Figure 16A**) and the interphase nucleus was regarded as a structureless organelle containing an amorphous nucleoplasm. This point of view did not change until the beginning of the 19th century, when Rabl, Strasbourger and Boveri[489–491] started to speculate about some order in chromatin organization.

Boveri[491] proposed that interphase chromosomes decondense only partially and maintain their spatial integrity so that they form so called chromosomal territories (CTs) occupying only a limited volume of the nucleus and only partially intermingling one with another. Together with Mendel's laws, this discovery provided the basis for the *Sutton-Boveri Theory of Chromosomal Inheritance* (reviewed in [87]) that recognized chromosomes as stable "*genophores*" transmitting genetic information from generation to generation. However, electron-microscopy search for chromosomal territories mostly

failed (positive results were rather exceptional (*e.g.* Wischnitzer[492]) leaving the majority of scientific world doubting.[493–495]

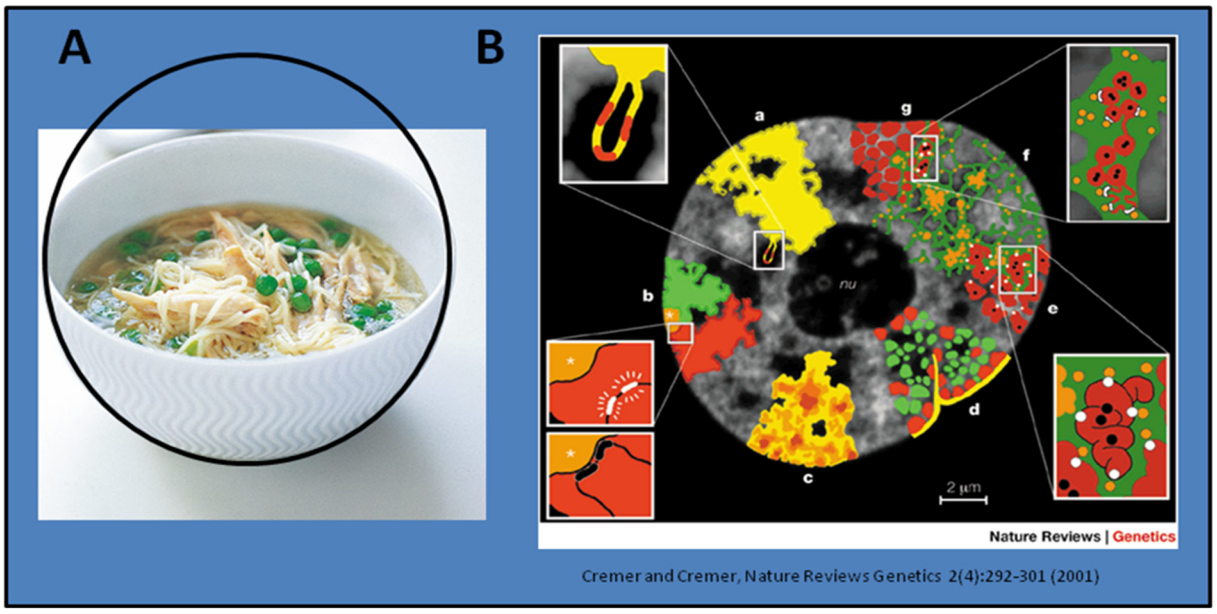

Figure 16. Comparison of old **(A)** and current **(B)** views on the cell nucleus. A demonstrates a cell nucleus with random distribution of chromatin, frequently resembled to a dish of soup with randomly swimming (chromatin) noodles. **B** explains one of the currently mostly disputed models of nonrandom chromatin organization in the cell nucleus. **a:** demonstrates that also decondensed interphase chromosomes encompass only a limited spaces of the cell nucleus, termed as chromosomal territories (CTs). CTs have complex folded surfaces and only very partially intermingle with each other. Enlarged area indicates that highly expressed genes are usually located at the surface (or even outside) of the CTs or "subchromosomal" chromatin domains, whereas inactive genes appear inside these structures – here, a giant chromatin loop with several active genes (red) expands from the CT surface into the "interchromatin" space. **b:** Interphase CTs preserve their separation of p- and q-arms, which are spatially distinct in the nucleus (centromeric domain is also preserved and marked by asterisks). Top insert: actively transcribed genes (white) are located on a chromatin loop that has no spatial contact with centromeric heterochromatin. On the other hand (bottom insert), recruitment of the same genes (black) to heterochromatic domains leads to silencing of their activity. **c:** Neither subchromosomal chromatin distribution is random. The image demonstrates variable chromatin density inside the CT (dark brown, dense chromatin; light yellow, low density chromatin). Decondensed chromatin loops from low-density domains protrude into "interchromatin" space. **d:** Early-replicating chromatin domains (green) and mid-to-late-replicating chromatin domains (red) of CT are shown. Gene-poor chromatin (late-replicating, red) appears preferentially on the nuclear periphery (nuclear lamina, yellow), whereas gene-rich chromatin (green) is more in the nuclear center. **e:** the extension of image *a* that explains topological view of gene regulation: active genes (white dots) are located at the surface of chromatin domains, silenced genes (black dots) may be located towards the interior. **f, g:** According to the CT–IC model[496] large nucleoprotein complexes (orange dots), like transcription factories, splicing sites, DNA replication and repair conglomerates, are located in interchromatin space. Taken from **Cremer a Cremer, 2001**.[496]

"A point of no return" was crossed in 1982 by elegant experiments of Thomas Cremer.[497,498] Cremer micro-irradiated restricted areas of interphase nuclei with UV-laser and, taking advantage of replicative synthesis, visualized them with labeled thymidine. In the consecutive mitosis, the signal appeared only in several chromosomes, with the probability reflecting their molecular size. By this "trick", Cremer proved the existence of chromosomal territories (CTs)[(17)] [497,498] though direct visualization of CTs was performed several years later, with radioactive in situ hybridization (RISH).[499,500] The improvement of this technique by using fluorescently labeled probes (FISH, fluorescence *in situ* hybridization)[501–504] enabled sensitive visualization of interphase chromosomes or even their specific parts, representing

[17] The terms 'chromosomal territories' and 'chromosomal domains' are equivalent, both referring to interphase chromosomal territories, and are used depending on individual authors. In this work, we prefer the term 'chromosomal territory'. The term 'domains' is being used here for chromatin domains at the subchromosomal level.

thus a milestone in chromatin research (**Figure 9**, **11**). With the whole-chromosome painting probes (WCP), centromeric probes, telomeric probes and gene specific probes, it was step-by-step demonstrated that nothing is farther away from the truth than the original vision of the nucleus as a dish of soup with randomly swimming chromatin noodles (**Figure 16A**). The principle of basic and advanced FISH applications is explained in Chapter 1.8.1.

By the means of FISH techniques combined with high-resolution confocal microscopy, several groups, including us, described that chromosomal territories (CTs) are in several aspects nonrandomly distributed in the cell nucleus.[1] For example, CTs with a high density of genes and intensive overall transcription preferentially locate to nuclear interior, whereas gene poor, genetically "inactive" chromosomes tend to occupy more peripheral nuclear space.[1,2,439,439,505–511] Interestingly, this rule holds also for chromatin organization inside the CTs, which causes their structural and functional polarization, with active genes and telomeres heading to (in human cells) the nuclear center and inactive chromatin (including the centromere) directed towards the periphery.[2,512] In addition, active chromosomal territories (e.g. human chromosome 19; HSA19) and their highly transcribed subdomains (such as so called RIDGEs, Regions of Increased Gene Expressions)[237,513] occupy much bigger nuclear volumes compared to genetically rather silent territories (HSA18, the inactive HSAX) or subdomains (antiRIDGEs)[237,513] of similar molecular size. Chromatin decondensation at the scale of chromosomal territories therefore correlates with their overall genetic activity and sets up a nonhomogeneous internal structure of these territories (e.g. Kozubek et al.[1]).

Interestingly, large chromatin loops protruding out of the maternal chromosomal territory and carrying highly active genes were observed. For example, Volpi et al.[212] describes this phenomenon for the Major Histocompatibility Complex (MHC) after stimulating the cells with interleukin (an activator of MHC transcription). Extraterritorial loops thus probably form when a cluster of coregulated genes is activated, since, similar to MHC, chromatin looping was demonstrated for the chromosomal locus 1q21 that contains functionally associated genes of the epidermal differentiation complex.[(18)] [213] In accordance with this hypothesis, extraterritorial looping appeared in keratinocytes, where the epidermal differentiation complex is highly active, but not in other cell types (*e.g.* lymphocytes).[213] However, the results remain controversial—some authors detected the loops only in case of ongoing transcription[197] while the others even in the presence of transcription inhibitors.[198,514] Francastel et al.[515] observed an "open" chromatin structure in transcription "committed" genes, which means prior to initiation of transcription. In line, α-globin locus remained constitutively opened and transcriptionally permissive in several cell types, although its transcription takes place only in the erythroid cells.[516,517] Similarly, β-globin and *c-MYC* genes showed sensitivity to nucleases and histone H4 acetylation in hematopoietic stem cells where they are not transcribed.[518,519] Therefore, the second activation step resting in binding of specific transcription factors to gene promoters is necessarily required to fire the transcription, as it was discussed earlier.[515] The results thus mostly indicate that changes in the higher-order chromatin structure precede the transcription *per se* and therefore

[18] Participating in keratinocyte differentiation.

represent a regulation mechanism, rather than the consequence of transcription processes[220,469,520–525] (older results reviewed in Falk[441]); the opposite conclusion is presented *e.g.* by Müller and Leutz.[197] Summarizing the previous text, three "topographical" changes may contribute to gene activation: 1) chromatin decondensation, potentially resulting in 2) looping out of the locus from a condensed chromatin domain or even maternal chromosomal territory and 3) prolongation of the gene's 3D-distance from the peripheral heterochromatin. The question remains whether chromosomal territories or specific genetic loci with similar radial distances occupy nonrandom nuclear positions relative to one another (i.e., in the space of the particular concentric radial "shell"). In support of this idea, some coregulated genes were reproducibly shown to colocalize in transcription factories[214,217,521,526–529] (see Falk[441] for references). In addition, reproducible mutual distribution of chromosomal territories, to some extent specific for a particular cell type, was described,[530–533] as for instance pairing of homologous chromosomes in *Diptera* and some other organisms (e.g. [534,535]; reviewed in Falk[441]). Moreover, some older reports demonstrated "heritably" preserved topological distribution of chromosomal territories in the daughter cells.[555–558]

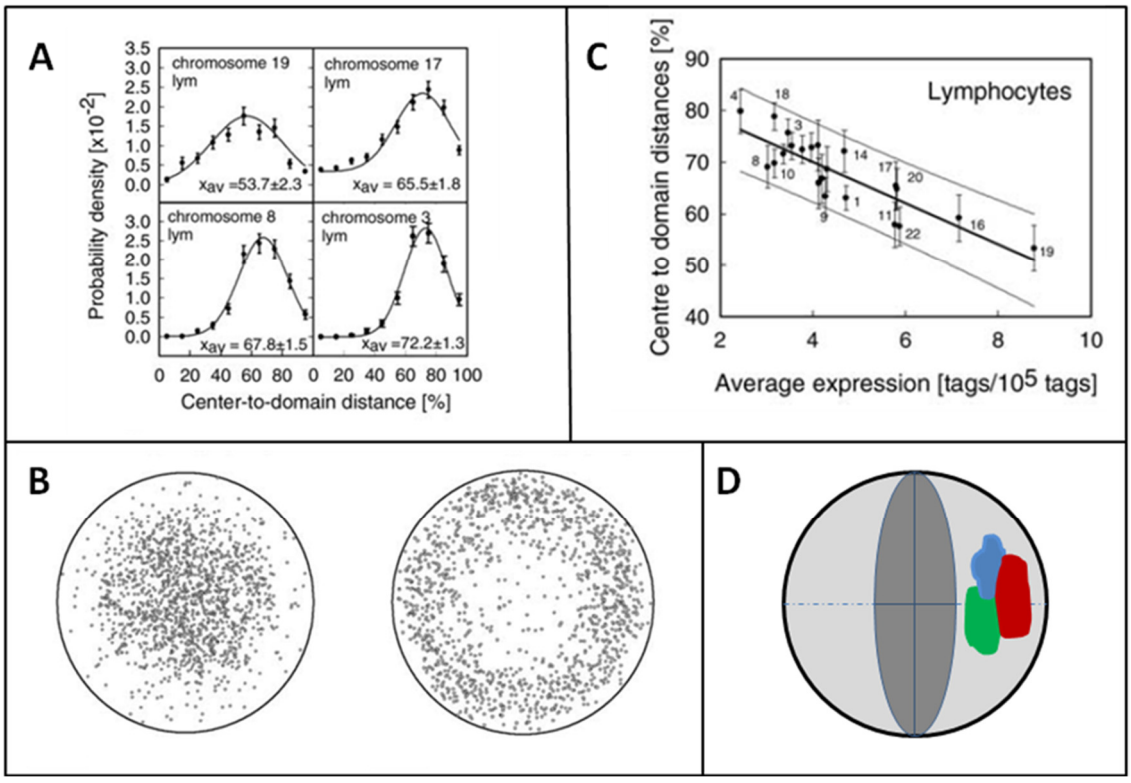

Figure 17. Distribution of chromosomal territories in the cell nucleus. **A:** Chromosomal territories occupy nonrandom concentric nuclear 'shells' (defined by a specific mean radial distance between the chromosome territory weighted center and center of the nucleus) typical for every particular chromosome. The radial distributions of chromosomes 19, 17, 8 and 3 in human G_0-lymphocytes are displayed, together with the mean radial distances for the particular chromosome (in percentage of the cell radius ± SD). **B:** A graphic interpretation of concentric radial shells: the signals represent positions of chromosomal territories determined in thousands of nuclei – the probability densities of the territory location are compared for a highly expressed (left) and genetically silent (right) chromosome. **C:** The relationship between the mean radial distances of chromosomal territories and average level of gene expression of the particular chromosome measured in human G_0-lymphocytes. The experimental values (points) are shown with 95 % confidence interval, the results of linear regression are presented with 95% prediction intervals; the correlation coefficient is 0.73 ($P<0.01$); see Kozubek et al. (2002),[1] for a more details). **D:** A schema of mutual distribution of individual chromosomal territories on the concentric nuclear shells – are there some rules beyond this organization? Adapted from **Kozubek et al. 2002**.[1]

Nonrandom mutual distribution of some specific genes followed also form irradiation experiments, where translocations between these genes appeared more frequently than could be expected for randomness.[531,536–545] Interestingly, this was frequently the case of genes forming oncogenic fusion proteins causing leukemia or lymphomas.[546–549,537,538,541–545] This observation was typical for exposures to high-LET IR that produces DSBs concentrated along the particle track; translocations thus preferentially form between genetic loci of one single chromosome or neighboring chromosomes (see Chapters 2.2.1, 2.2.2 and associated figures).

However, nonrandom mutual positioning was only rarely confirmed for other genetic elements than the above-mentioned leukemogenic loci and chromosomes involved in nucleolar assembly.[441,550–553] The majority of researches therefore believe that most chromosomes are localized randomly with respect to one another and randomly redistributed after each mitosis (*e.g.* Walter et al.[554]). Nevertheless, this does not exclude functional associations of genetic loci in the cell nucleus based on coregulated activity of involved genes. Well-documented transcription factories (and theoretically also the repair factories that were, however, not confirmed at microscale) can serve as an example of this behavior.

Altogether, we can conclude that chromosomal territories occupy characteristic "shells" of the cell nucleus, defined by the mean radial distance[(19)] and width[(20)] of the shell (**Figure 17**). For instance, when dividing the nucleus into 10 concentric radial shells according to 10 % R, chromosomes with similar overall transcription activity will often share the same shell while the shells of differently transcribed chromosomes will overlay less frequently (**Figure 17**).[1,473,559–561] Whether there are some rules determining mutual distribution of chromosomal territories in the frame of these shells remains unsure (**Figure 17D**).

During the mitosis, chromosomes migrate towards the newly forming daughter cells. This provides some window for chromatin reorganization. However, how stable or dynamic the higher-order chromatin structure is in the remaining period of the cell cycle remains disputed. While proteins may "freely" diffuse through the cell nucleus, chromatin was considered as being much less mobile.[15,192,562–565] On the other hand, an experiment with fluorescence recovery after photobleaching (FRAP) revealed a highly dynamic binding of HP1 protein to chromatin, clearly showing that even condensed heterochromatin is not a rigid structure.[566,567] FRAP and similar methods showed that chromatin mobility in human cells does not exceed 1 to 2 μm in the course of several hours.[554,563–565,567–569] This movement limitation probably reflects spatial restrictions following from the volume ratio of chromosomal territories to the cell nucleus and/or chromatin attachment to nuclear matrix and envelope (nuclear skeleton).[569,570] In contrast to this insignificant (Brownian) short-term movement, chromosomal domains show distinct movements in the longer-time perspective of the cell cycle, especially between the end of the mitosis and early G1-phase and in the S-phase.[552,554,564,571] It is tempting to speculate that in the early G1-phase, chromosomal territories are still not completely

[19] I.e. the distance between the nucleus center and chromosome FWC (fluorescence weight center), usually expressed in percent of the nuclear radius [%R]

[20] Given by the difference between the maximal and minimal radial distance measured for the particular chromosome in the cell population.

bound to the nuclear skeleton and undergo reorganization processes, as described sooner. Later, in the S-phase, chromosomes are submitted to replication, which may also increase the chromatin mobility. Supportive evidence to this hypothesis comes from the nuclear topology of chromosomal territories that varies between cycling, quiescent and senescent cells.[459,572] Importantly, chromosomal misplacement was found in several pathologies, for example in focal epilepsy where a centripetal shift of chromosome X centromeres from the peripheral heterochromatin was observed.[573] In the DNA molecule, the X-centromeres are located in the proximity to the synapsin gene[574] probably playing a role in chronic epileptic attacks. Together, it seems that extensive changes in global transcription activity and replication timing may provoke chromosomal relocalization, while smaller changes probably have only a local effect influencing only the affected chromatin subdomains. More experiments are, however, needed to confirm these conclusions, especially concerning the scale, the cause and the mechanisms of directed chromatin movements.[221,567,575–577]

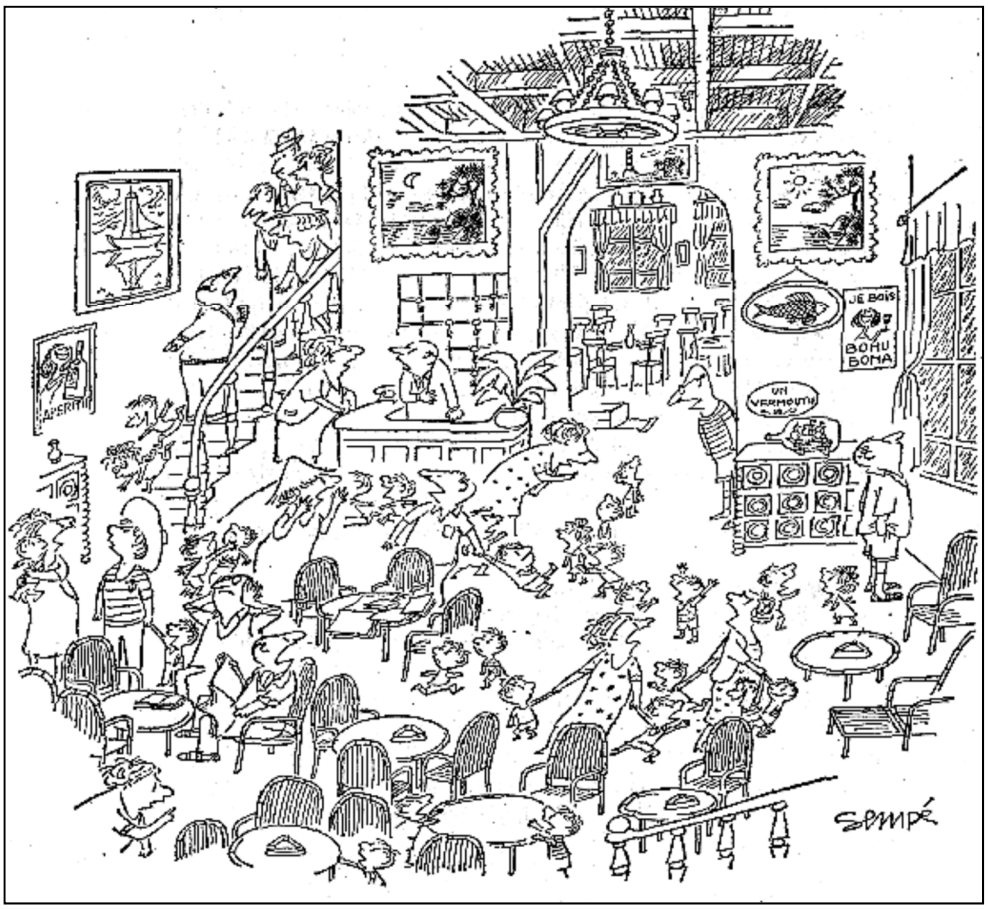

Figure 18. 'Order in Randomness'. The total noise in a party room, composed from interfering individual dialogues, is 'chaotic'. However, the individual dialogues surly have a precise meaning. The illustration of Jean-Jacques Sempé (taken from the Dissertation Thesis of the author, originally published in Goscinny, Sempé, Little Nicholas, BB art, 1997.[792]

Finally, to emphasize the importance of the higher-order chromatin structure, it should be noted that the same principles of chromatin organization were confirmed for many different biological species, as for instance higher primates and birds in addition to humans.[578,579] Although some cell types in some species show other style of chromatin organization than described here (e.g. the Rabl's

configuration),[580,581] these cases usually represent only functionally specialized cells. On the other hand, the preservation of the same principle of chromatin organization between birds and humans—separated by more than 300–350 million years of evolution and having markedly diverged genomes—strongly supports the functional relevance of higher-order chromatin structure.[578,579] In fact, the same principles of (radial) chromatin organization can be traced much farther back in evolution, even up to the simplest eukaryotic organisms – yeasts.

Taking into consideration the variability of the results from previous chapters, it is not surprising that many models of the nuclear architecture have been proposed, depicting different aspects of the higher-order chromatin organization[220,469,582] and its impact on transcription, replication, DNA repair, nuclear trafficking and other nuclear functions (extensively discussed in Falk[441]). Refusing any functional role of chromatin organization on one side (e.g. the Giant Loop/Random Walk Model, the Fractal Globule Model)[583–585] and emphasizing its irreplaceable position in regulation of *de facto* all nuclear processes on the other side (the Radial-Loop Model; the Interchromosomal/Interchromatin Domain Compartment Model, the 3D multi-loop aggregate/rosette chromatin architecture model, *etc.*),[561,582,586–588] these models cover the whole spectrum of ideas between the two extremes. Thus, it is evident that our knowledge of the structural and functional organization of the cell nucleus remains incomplete, mostly due to extremely high complexity of biological systems organization and technological limitations. In addition, the nuclear architecture is of statistical (probabilistic) character, which requires studies of hundreds to thousands of cells in order to obtain conclusive results. On the other hand, individual cells in the cell population differ in their immediate physiological state. Different mutually interfering nuclear processes thus take place in individual cells so that the averaging of results for the cell population may overshadow various aspects of nuclear organization and "mimic" the random chromatin folding. The only solution of how to progress with our understanding of the functional architecture of the cell nucleus is to combine high-throughput analyses with studies of individual live cells, which is unfortunately not always methodologically possible. Our position therefore resembles the situation when—in an overcrowded room full of party guests—we want to distinguish the dialogues between people from a chaotic background noise (**Figure 18**). The higher-order chromatin structure may be therefore aptly characterized as "the order in randomness."[1]

Figure 18 also demonstrates how important is a sufficient resolution for recognizing individual ongoing processes. Deeper insights into the higher-order chromatin organization and nuclear architecture are therefore expected from super-resolution microscopy approaches, only recently developed.[348,447,448,478,479,589–594] Single Molecule Localization Microscopy (SMLM), as one of these "nanoscopic" techniques, was used in the present thesis to study chromatin (nano)structure and its changes upon irradiation, as introduced in Chapter 1.8.2 and discussed latter in the context of the corresponding results.[20–22]

1.9.3 Histone code and regulation of gene transcription via dynamic changes of higher-order chromatin structure

By the definition, the epigenetics refers to all heritable determinants of gene expression that are not coded by the DNA sequence itself[595] (reviewed in [596,597]). As such, it links together the effects of long-term physiological regulations (despite potentially reversible),[598,599] and random, accidental, but stably inherited changes of the genome expression pattern. Epigenetic chromatin modifications may therefore explain how "non-genetic" factors such as the alimentary diet and environmental components permanently or in long-term perspective influence the cell expression pattern. However, it should be noted that the epigenetic landscape of the cell nucleus is dependent on the activity of enzymes participating in epigenetic modifications, and their potential mutations; therefore, the epigenetic regulation is not totally independent of genetic factors.

The epigenetic code is mechanistically translated into genome functions via reorganizing the higher-order chromatin structure.[469] These modifications can be long-lasting and transmitted from the parental cell to its progeny, in accordance with the original definition of epigenetics, but also dynamic (only temporary). Therefore, for simplification and to better follow the purposes of this work, we use the term "epigenetic changes" to address all changes in chromatin structure and function, both of transient and heritable nature, that are independent of DNA sequence mutations.

Many factors participate in the determination of chromatin structure and genetic activity, including reorientation and reposition of nucleosomes along the DNA by macromolecular protein complexes that utilize energy from ATP hydrolysis, RNA-mediated gene silencing, DNA methylation, posttranslational histone modifications,[171,172,190,600] exchange of histone variants[601,602] and binding of non-histone architectural proteins to chromatin.[603] Moreover, these processes are mutually closely interconnected and precisely coordinated. Despite the principles of higher-order chromatin organization are only poorly understand, chromatin is definitely dynamic structure.

There is more than 80 % of DNA associated with nucleosomes in the human genome[604] that protect DNA from nuclease degradation and enable sensitive regulation of chromatin structure.[605] All histones in nucleosomes are assembled so that their C-ends form compact hydrophobic domains responsible for mutual interactions between histones and between histones and DNA, whereas positively charged N-terminal parts of histone molecules protrude out of the nucleosome core as free "tails", accessible to covalent posttranslational modifications – methylation, acetylation, phosphorylation, ubiquitination, citrullination, and ADP-rybosilation at specific amino acid residues (reviewed in [606–608]). There are two consequences of these modifications – direct influencing of electrostatic interactions between the histone molecules and DNA, and setting of a histone code with a specific signaling function. For example, acetylation of specific lysines, usually associated with gene activation, decreases a positive charge of histone tails, which in turn reduces their electrostatic attraction with negatively charged DNA molecule. In addition, repulsion between individual DNA phosphate groups increases because of less efficient neutralization of a negative charge of DNA phosphates. As a result, chromatin decondenses and opens its structure for binding of *e.g.* transcription factors. Not surprisingly, many of transcription factors itself exert histone acetyltransferase (or transacetylase) activity. On the other

hand, methylation increases a positive charge of histones and thus intensifies histone-DNA interactions, which is followed by chromatin condensation and, for example, transcription silencing.

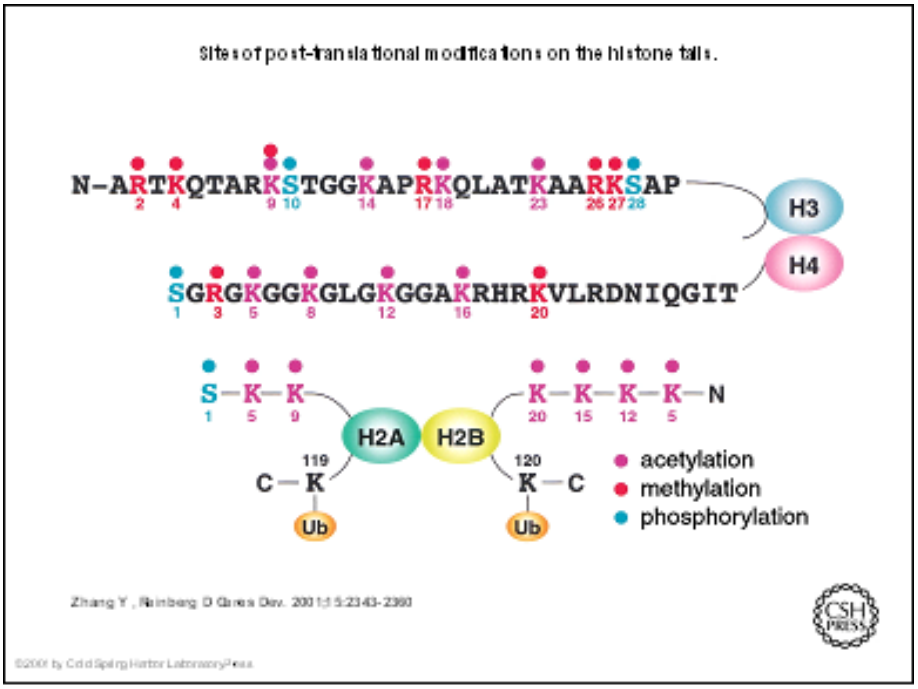

Figure 19. Histone code – the complexity of histone modifications. The possible sites of post-translational modifications on the histone tails [acetylation (purple), methylation (red), phosphorylation (green), and ubiquitination (orange)]. Taken from **Zhang and Reinberg 2001**.[609]

In parallel, acetylation of histone tails in combination with other modifications set up a specific "histone code" (*e.g.* [171,172,608,609]) that poses a signal for binding of additional structural or effector proteins to chromatin. These proteins consequently actively reorganize chromatin structure in order to enable a desired function. For example, in accordance with the electrostatic changes introduced to histones, acetylation of the lysine 9 at histone H3 (acetylH3K9) represents an activation mark for transcription.[285] Similarly, acetylH3K14 is found in actively transcribed promoters.[285] On the other hand, methylation of H3 at K27 (metH3K27) is associated with facultatively repressed genes[610] and trimethylation of H3 at K9 (trimetH3K9) with genes repressed constitutively.[610] However, the situation is not that simple: For example, trimethylation at H3K4 is found in actively transcribed promoters, particularly just after the transcription start site (TSS), while its demethylation correlates with silencing of the particular genomic region.[285] As well, di- and tri-methylation of H3K36 is linked to transcriptional activation and not silencing,[(21)] [612] as it could be deduced from expected reduced electrostatic repulsion between DNA and histones.[613] Moreover, while mono-methylation of H3K9 and H3K27 corresponds to gene activation,[610] dimethylation of H3K9 and dimethylation or trimethylation of H3K27 to gene silencing.[610,614,615] However, in case of H3K79, all methylation "levels", mono-methylation, di-methylation and tri-methylation represents activating signals[616] (the opposite results for tri-metH3K79 were established by Barski et al.[610] Histone code therefore functions rather on the basis of specific signaling to chromatin

[21] despite the conclusions on the function of H3K36 methylation are still disputed ([611])

structure modifiers and the role of the particular "code" is difficult to predict. Considering that all the histones undergo modifications at many different amino acid residues (**Figure 19**), that modifications act in mutual combinations, and that every single histone of the genome can be differently modified, it is easy to imagine a complexity of this "Histone Code" (e.g. [171,172,608,609]). For this purpose, the reader is referred to mentioned articles for a comprehensive overview on individual histone modifications (**Figure 19)**.

Though complete cracking of the histone code will take many years, it is already clear that histone modifications dynamically influence local chromatin structure via attracting specific chromatin binding proteins. Although our knowledge of how the histone code is translated into higher-order chromatin structures is only superficial, the situation can be roughly illustrated on the process of heterochromatinization (**Figure 20**): Acetylated active chromatin is first deacetylated by histone deacetylases (HDACs) and consequently methylated at lysine 9 of histone H3 (H3K9) by histone methyltransferases (HMTs, like Suv39h1). These changes in histone modifications result in recruitment of the heterochromatin protein 1 (HP1), which serves as an adaptor molecule that enables interactions responsible for setting of the heterochromatic structure. HP1 also binds (via different protein cascades) HMTs, HDACs and DNA methyltransferases (DNMTs), which constitutes a positive feedback loop that, together with methylation of CpG islands in DNA molecule, accomplishes heterochromatin formation and enables its spreading to the surrounding chromatin (**Figs. 20**, **21**). The methylation of DNA by the DNMT, in turn, permits binding of methyl-CpG-binding domain (MBD) proteins to DNA. Since MBDs can recruit HDAC complexes and H3K9 methyltransferases (H3K9 HMTs), the cycle of heterochromatinization where silencing histone modifications potentiate DNA methylation and *vice versa* is getting closed. DNA methylation thus closely cooperates with histone modifications, however,

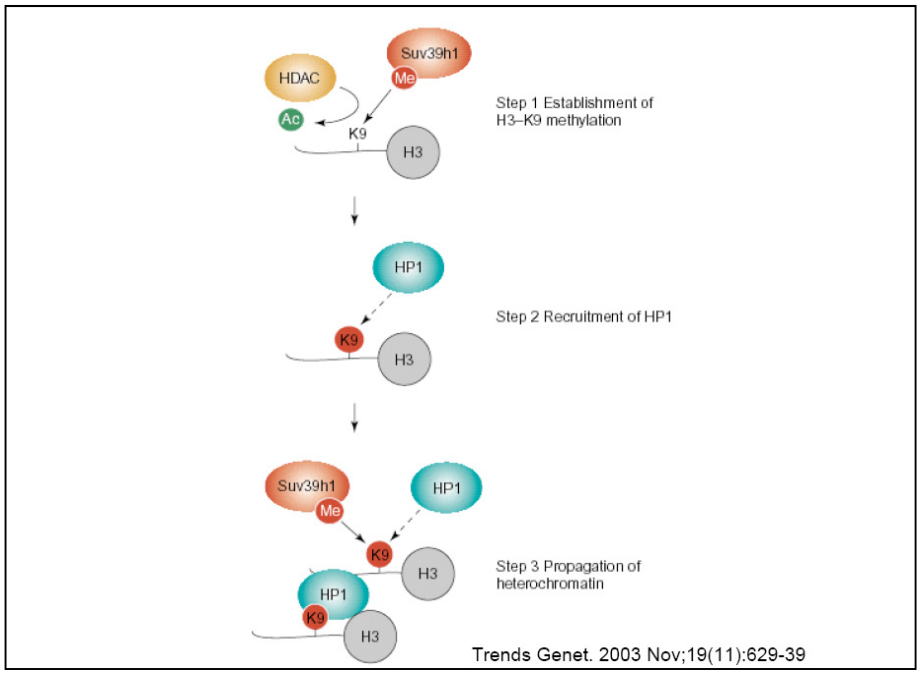

Figure 20. A possible mechanism of heterochromatin formation. See the text for a more detailed description. From **Zhang and Reinberg 2001**.[616]

which one of these processes initiates heterochromatin formation and how heterochromatin exerts its

silencing function is not clear. For example, in developmentally silenced chromatin where DNA is methylated at CpGs, HMTs and consequently the rest of the silencing machinery described above are attracted to chromatin.

On the other hand, in case of active genes to be silenced, silencers that specifically bind downregulated genes (e.g. KRAB-domain containing zinc-finger repressor proteins) attract transcriptional co-repressors, like protein KAP1/TIF1β (KRAB associated protein 1). KAP1/TIF1β directly tethered to DNA is sufficient to repress transcription (e.g. Agata et al.[617]), however, it also exhibits molecular scaffold properties that ensure formation of heterochromatin higher-order structures via binding of further chromatin remodelers. Among others, the interactions with NuRD histone deacetylase complex, H3K9 selective methyltransferase SETDB1, and heterochromatin protein 1 (HP1) should be emphasized (reviewed in Sripathy et al. [618]). Importantly, as it follows form experiments of Cammas et al.,[619] HP1 relocates the silenced loci to cytologically defined nuclear heterochromatic domains. Nevertheless, as discussed earlier, it seems that heterochromatin domains do not silence transcription by simply preventing access to transcription factors. In addition, HP1β and even more so HP1γ – two of the three human HP1 proteins (α, β and γ)[620,621] – bring their regulatory functions also to euchromatin.[620] Heterochromatic and euchromatic activities of HP1 are regulated by the chromoshadow domain and chromodomain, which differentially contribute to HP1 binding in euchromatin and heterochromatin (e.g. Fanti a Pimpinelli[620]). Importantly, the kinetics of HP1 exchange is quite fast supporting thus a dynamic competition model, where transcription silencers and activators compete for their binding sites. Hence, heterochromatin probably regulates transcription by dynamic modifications of a binding platform for regulatory proteins, pushing so the events either to silencing or activation[483] (**Figure 21**).

Furthermore, recent experiments suggest that not only histone modifications but also the replacement of "canonical" histones and their substitution for specific histone variants participate on regulation of chromatin structure and nuclear processes.[601,602] Unstable and dynamic interactions with chromatin are most prominent for the linker histone H1, with its different variants exerting different levels of chromatin condensation.[622] Though the core histones also seem to be replaced, the extent of this process, its cooperation with the histone code and whether it takes place also out of the replication must be further studied. However, an important role of (core) histone exchanges simply follows from existence of their variants, slightly differing in amino acid composition, structure and specific functions. For example, gene transcription is supported by the substitution of the histone H3 for its variant H3.3,[601] which then induces covalent histone modifications required for transcription initiation. This example therefore illustrates also the link between histone variant exchanges and the histone code. Finally, it should be mentioned that not only the histone composition but also their orientation and distribution (e.g. spacing) along the chromatin fiber predetermine gene activation. Therefore, disassembly and reassembly of nucleosomes may be required for "nucleosome sliding" and proper positioning. This chromatin remodeling is accomplished by ATPase containing complexes, referred to as the SWI/SNF family; the process is therefore active and energy dependent. Four subfamilies of

remodeling complexes can be distinguished based upon their associated ATPase,[(22)] so it allows specific and precise control of chromatin remodeling (Shipra et al.[623] and citations therein).

Together, these observations clearly show that chromatin architecture is hierarchical structure, with the higher-order levels of organization dependent on the lower ones. In a simplified way, all the mechanisms of chromatin modification described in previous chapters determine the structure of chromatin fiber and interactions with chromatin binding proteins, which in turn results in formation of specific higher-order chromatin domains, like euchromatin and heterochromatin; the characteristics of these structurally distinct chromatin domains then influence their distribution and functioning in the cell nucleus. Since epigenetic chromatin modifications may persist through the cell divisions, they represent a way how to transmit adjusted chromatin structure and gene expression profiles during the cell differentiation and preserve them *e.g.* after DNA damage.[624]

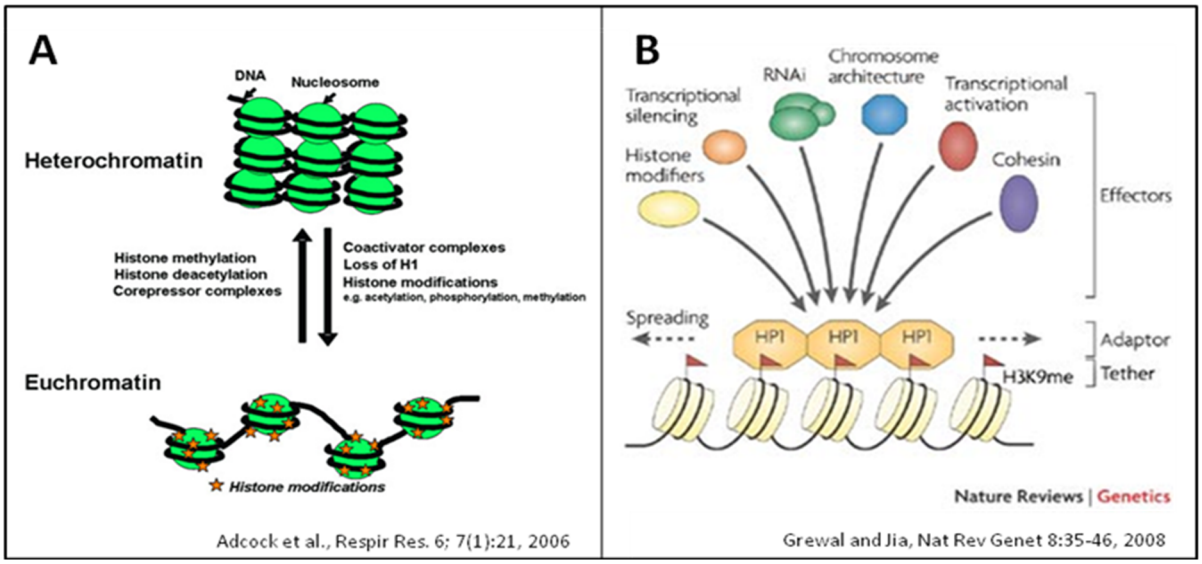

Figure 21. Heterochromatin structure and HP1 protein. **A:** A schematic illustration of the structure transitions between euchromatin and heterochromatin. In euchromatin, histone lysines are acetylated and chromatin fiber is largely decondensed. Therefore, transcription activators can bind to gene promoters. Reversely, loss of histone H1, histone lysine deacetylation, methylation of histone H3 at K9 (and other specific sites) and consequent binding of HP1 and other corepressor complexes causes chromatin condensation; this helps to set up transcriptionally repressive chromatin status, despite it probably does not simply follow from inaccessibility of heterochromatin to regulatory proteins – see the text. The image taken from **Adcock et al. 2006**.[596] **B:** HP1-regulated activities are mediated by its interactions with a plethora of partners, such as factors involved in chromosome segregation (cohesin), gene silencing (RNAi and histone deacetylases) transcriptional activation, chromatin structure forming, histone modifications etc. The image taken from **Grewal and Jia 2007**.[476]

[22] SWI2/SNF2 [mammalian Brm (SNF2α) and Brg1 (SNF2β)], imitation switch (ISWI), Mi-2 (CHD1) and INO80. The ISWI complexes are divided into the nucleosome remodeling factor (NURF), chromatin accessibility complex (CHRAC), and ATP-dependent chromatin and remodeling factor (ACF) complexes.

2. SPECIFIC DISCUSSION ON PRESENTED RESULT COLLECTION (AUTHOR'S PUBLICATIONS)

2.1 The Principles of Higher-Order Chromatin Organization in Normal Cells and Their Alterations During Carcinogenesis

2.1.1 The principles of higher-order chromatin organization and its function in normal cells

In this chapter, the publications that mainly deal with the higher-order chromatin structure in normal cells and its relationship with the genetic activity of chromatin are provided. Because this topic has already been extensively described and discussed in the introduction part of this work, we focus here only on the questions being addressed in the presented papers.

The cell nucleus is probably the best known but least understood cell organelle. In particular, there is a lack of clarity regarding the generally acceptable conclusions on nuclear architecture and chromatin organization in relation to nucleus functioning. One of the most fundamental questions of molecular biology that can have significant outputs in the medical field is the mechanisms of genome expression regulation. To exert its functions, the cell must precisely regulate and coordinate all nuclear and cellular processes in space and time. For example, gene transcription must only be initiated from the correct loci at exact periods of the cell cycle, and the intensity must be well balanced with other genes. A transcription pattern depends on the cell type, level of cell differentiation, phase of the cell cycle, actual cellular levels of individual proteins and RNAs, and many other factors. Even subtle changes to gene expression may cause serious diseases, including cancer.

Currently, we have quite detailed imaginations about the mechanisms of transcription regulation at a biochemical scale. This knowledge usually concerns individual genes, but how the transcription is regulated at the pan-genomic scale in the frame of the cell cycle or cell differentiation remains much less understood. Nevertheless, it is evident that "simple" interactions of gene promoters with transcription factors cannot explain all the complexity of gene expression regulation, for example, the dependence of transcription activity of an inserted transgene on its genomic and nuclear location. Another interesting phenomenon is impersonated by the inactivation of one of the two chromosome X homologues in mammalian female somatic cell, which is associated with marked structural changes of the affected chromosomal territory. Inspired by these and similar results, we have studied the principles of higher-order chromatin organization in the cell nucleus and the relationship of higher-order chromatin structures with nuclear functions. The results obtained are discussed in the following listed articles (full extenso papers are attached) and briefly in the next chapters.

Relevant publications discussed:

1. Kozubek S, Lukásová E, Jirsová P, Koutná I, Kozubek M, Ganová A, Bártová E, Falk M, Paseková R. 3D Structure of the human genome: order in randomness. Chromosoma. 2002;111(5):321-31. doi: 10.1007/s00412-002-0210-8.
2. Lukásová E, Kozubek S, Kozubek M, Falk M, Amrichová J. The 3D structure of human chromosomes in cell nuclei. Chromosome Res. 2002;10(7):535-48.
3. Falk M, Lukásová E, Kozubek S, Kozubek M. Topography of genetic elements of X-chromosome relative to the cell nucleus and to the chromosome X territory determined for human lymphocytes. Gene. 2002;292(1-2):13-24.
4. Ondrej V, Lukásová E, Falk M, Kozubek S. The role of actin and microtubule networks in plasmid DNA intracellular trafficking. Acta Biochim Pol. 2007;54(3):657-63.
5. Ondrej V, Kozubek S, Lukásová E, Falk M, Matula P, Matula P, Kozubek M. Directional motion of foreign plasmid DNA to nuclear HP1 foci. Chromosome Res. 2006;14(5):505-14. doi: 10.1007/s10577-006-1058-1.

Discussion on Kozubek et al. (2002)[1]

The work of Kozubek et al. (2002)[1] represents a comprehensive study on the higher-order chromatin structure and the principles of chromatin organization in the cell nucleus. Various parameters of spatial arrangement of chromosomal territories and specific genetic elements (genes, centromeres and telomeres) were studied taking advantage of fluorescence *in situ* hybridization on spatially fixed cells (3D-FISH) in combination with high-throughput high-resolution confocal microscopy enabling evaluation of hundreds of cells. By this approach, we were able to show in 3D space that the radial positioning[(23)] of chromosomal territories and genetic elements in the cell nucleus[(24)] is nonrandom. The radial distributions of genetic elements correlated with distributions of their maternal territories, demonstrating that the territories behave to some extent as the solid bodies. This is in accordance with previous findings of Cremer at al.[625] revealing a territorial organization of the interphase chromosomes with only limited mutual intermingling. Nevertheless, radial positions of genetic elements were markedly influenced by specific characteristics of these loci. Importantly, we showed that the mean radial distances of both chromosomal territory fluorescence weight centers (FWCs) and genetic elements correlate with transcription activity – with average transcription of the whole chromosomes and particular genetic loci, respectively. Intensively transcribed territories tended to be localized closer to the nuclear interior while the inactive ones preferentially occupied the periphery. Correspondingly, with respect to internal organization of chromosomal territories, inactive genes concentrated in their peripheral (i.e. facing the nuclear envelope) subdomains while active genes protruded towards their centripetal (i.e. facing the nuclear center) parts. The centromeres of all chromosomes were peripheral,

[23] The distributions of radial distances between the genetic element and center of the nucleus.

[24] It means distributions of distances between the territory fluorescence weight centers (FWCs) or signals of genetic elements and the nuclear center.

in accordance with their heterochromatic status. This principle of higher-order chromatin structure thus ensures spatial and functional "polarization" of the cell nucleus and chromosomal territories as well.

Specifically, we determined radial positions of 22 chromosomes in human G_0-lymphocytes and some other cell types. Among the chromosomes studied, chromosomes 16, 19 and 22 were the most central and chromosomes 3, 4, 8, and 18 the most peripheral. For G_0-lymphocytes, the average radial distances [% R] of the chromosomes studied are compared in **Figure 17C**, where they are plotted against the mean values of total chromosome transcription. For the results on specific genetic elements, the reader is referred to the original manuscript (attached).

In contrast to radial distributions, mutual angular positioning[(25)] of both homologous and heterologous genetic elements[(26)] was recognized to be random, with some important exceptions. For example, angular distributions were shifted to lower values than expected for randomness for BCR-BCR and EWS-EWS homologous gene pairs, indicating close mutual proximity of these loci in a substantial faction of cell nuclei. Among heterologous gene pairs, significantly nonrandom angular distances were measured *e.g.* for ABL-BCR and BCR-PML pairs. These short mutual distances can be explained, in some cases (*e.g.* BCR-BCR, BCR-PML), by the location of interacting partners on the acrocentric chromosomes; however, the reason for non-random distribution of other loci must be studied. Obviously, this nonrandom proximity often "affected" gene pairs that are involved in frequent leukemogenic chromosomal translocations.

In about 10 % – 25 % of G_0-lymphocytes isolated from 5 healthy donors, the minimal distance[27] between the ABL and BCR genes was less than 1 μm.[28] Interestingly, this distribution shift to lower distances was significant in $CD34^+$ progenitors but not stimulated lymphocytes and HL-60 cells. This indicates that higher-order chromatin structure follows the same rules of organization in different cell types (discussed in the next paragraph) but, at the same time, reflects specific functional differences between the cells.

In addition, since leukemia (including CML in this case) are supposed to arise from the early blood progenitors, we can conclude that the close proximity of ABL and BCR genes observed in these cells supports formation of the Philadelphia chromosome.[29] [626] The short distances between specific genes that follow from higher-order chromatin structure (nuclear architecture) may be thus, at least partially, more generally responsible for creation of frequently appearing types of (oncogenic) chromosomal rearrangements. Together with equivalent conclusions reported for some other gene pairs (*e.g.* by Nikiforova et al.,[627] for RET and H4), these results confirm in 3D space our previous findings obtained in 2D-fixed cells.[542,628]

---

[25] By measuring the angular distributions and distance distributions of gene pairs, their mutual positioning and space separation could be determined (see Kozubek et al. 2002 for more detailed explanation).

[26] Distributions of angles between the two copies a genetic element on homologous chromosomes and the center of the nucleus (for homologous genetic elements), or angles between two genetic elements and the center of the nucleus (for heterologous genetic elements).

[27] the minimal distances of four possible distances between heterologous elements in each nucleus

[28] no translocation between these genes was found in mitotic chromosomes (in stimulated lymphocytes) for the donors

[29] representing the molecular cause of chronic myeloid leukemia (CML)

The non-randomness of higher-order chromatin structure and a more general link between the leukemogenic translocations and nuclear position of involved loci followed also from irradiation experiments. We and other groups have demonstrated that chromosomal translocations that are frequently detected in leukemia and lymphoma patients widely emerge upon cell irradiation with fast neutrons.[628] Because neutrons generate DSBs concentrated along the particle track (i.e. in a very restricted volume of the cell nucleus), we can conclude that loci often participating in translocations are separated by only small nuclear distances in a substantial fraction of cells. This confirms that at least several genetic loci from different chromosomes share somehow predefined nuclear subcompartments (*e.g.* in specific radial concentric nuclear spheres, discussed earlier) though their mutual positioning is based on statistical roots. One explanation for spatial proximity of specific genes may be for instance colocalization of coregulated genes in transcription factories; however, the reasons for gene "associations" in individual cases remain to be studied.

The principles of higher-order chromatin structure described in the previous text were followed in different cell types with surprisingly similar distributions of the genetic elements (despite the differences discussed). This is in accordance with the finding that clusters of highly expressed genes (RIDGEs)[513] in different cell types/cell differentiation stages contain mostly housekeeping genes and are thus situated at the same positions along chromosomes (DNA molecules) in these cells. Hence, it seems that chromosomal distribution of housekeeping genes but not tissue-specific genes determines the nuclear distribution of chromosomal territories and chromatin domains. Nevertheless, transcription activation or silencing of a (tissue-specific) gene may potentially cause local chromatin reorganization and, for instance, protrusion of the affected locus out of the "maternal" chromatin domain or even chromosomal territory; this behavior is typical for large loci of coregulated genes.[212]

In summarization, the work of Kozubek et al. (2002)[1] supports a view that the cell nucleus is a highly organized organelle, where higher-order chromatin structure plays an important role in mediating nuclear functions. However, the high variability in nuclear positions of genetic elements in individual nuclei of the same cell type clearly shows that the principles of chromatin organization are manifested through statistical regularities.

Discussion on Lukasova et al. (2002) and Falk et al. (2002)[2,3]

The next papers discussed, Lukasova et al. (2002) and Falk et al. (2002),[2,3] further develop the research on the principles of chromatin organization in the cell nucleus but are more focused on the internal structure of chromosomal territories. Both works study the relationship between the transcription status of particular chromosomal loci and their 3D arrangement inside chromosomal territories. In Falk et al.,[3] we addressed structural differences between active chromosome X territories and their homologous counterparts that became inactivated (**Figure 22**); the paper of Lukasova et al.[2] then compares internal structure of interphase chromosomes either containing or containing not the large clusters of highly expressed genes (RIDGEs) (**Figure 23**).

It is well known that in mammalian female somatic cells one of the chromosome X homologues undergoes genetic inactivation as a result of gene dosage compensation.[629–631] Since the inactive chromosome X can be in some types of interphase cells visualized by routine chromatin staining as the Barr body,[493] it was reasonable to hypothesize that the inactivation process is mediated or at least associated with extensive structural changes of the chromosomal territory. Experts in the field usually believed that the inactive homologue X (further referred to as Xi) becomes tightly condensed and re-locates towards the nuclear envelope[632] as the consequence of inactivation, while the active homologue remains decondensed and localized closer to the nuclear interior.[1,633–636] Chromosome X therefore provides an excellent model to study the impacts of extensive transcription intensity changes on the structure of (inactivated) chromosomal territory and its nuclear position. Moreover, the dystrophin (*DMD*) gene—one of the largest in the human genome—can be found on chromosome X. The *DMD* gene is located to Xp21.1-3 and contains 79 exons spanning 2.7 Mbp of DNA.[637] Its structural reorganizations and/or repositioning due to inactivation can be thus studied by the means of fluorescence *in situ* hybridization (FISH). Hence, by combining FISH on spatially fixed cells (3D-FISH) with high-resolution confocal microscopy, we analyzed nuclear topography of whole chromosome X territories (CTX), centromeres X (CX), and two different parts of the DMD gene. These parts corresponded to the proximal part of the gene, covering exons 5 – 7 (labeled as E1 in Falk et al. 2002)[3] and a more distant part, encompassing exons 46 – 47 (labeled as E2).

Smaller (XS) and larger (XL) territories from each nucleus, supposed to represent the inactive and active chromosomes X, respectively, were separated into two datasets and analyzed separately. The results were quite surprising. XL and XS territories differed much less in their size than was expected on the basis of cytogenetic staining (the ratio of mean XL/XS volumes equaled to 1.67) and also the radial distributions of chromosome territory fluorescence weight centers were statistically undistinguishable for XL and XS. The latter held true also for all genetic elements located in XL and XS territories, respectively. Moreover, the radial distributions measured separately for XL and XS chromosomes/genetic elements in female cells resembled that for the only X chromosome in male cells. Nevertheless, mutual distances between genetic elements (E1, E2 and CX) were about two times longer in XL, with the most prominent increase of distances measured for E1-CX and E2-CX. In addition, the surface of XL territories was more irregular (indented) compared to XS. Stimulation of G0-lymphocytes with phytohemaglutinin did not resulted in changes of any parameter (**Figure 22**).

Based on these results, we had to reconsider previous opinions about chromosome X inactivation and about the influence of transcription on chromatin structure of higher-order and nuclear topology. Chromosome X silencing results to chromatin contraction and approaching of genes to the centromere. This is in accordance with a suppressive effect of the centromeric heterochromatin on gene transcription and thus probably helps keep the inactive status of Xi chromosomes in a long-term perspective. Simultaneous chromatin contraction and decrease of the territory volume suggestively indicate that smaller X territories are equal to inactive chromosomes. The less prominent decrease of territory volume relative to the level of chromatin contraction probably reflects the persistence of interchromatin domains[625,638] in chromosome X territories upon inactivation. From the opposite point of view, the tendency of DMD loci to keep their distance from the centromere in XL territories supports

the idea of transcription activation as a two-step process, where chromatin decondensation and separation from heterochromatin represents the first step. However, nuclear repositioning of the whole chromosome X territory is not necessary either for initiation and maintenance of chromosome X silencing or for its activation after lymphocyte stimulation. This observation is contrary to the previous hypothesis[639] and might be potentially explained by relatively low total expression of chromosome X.

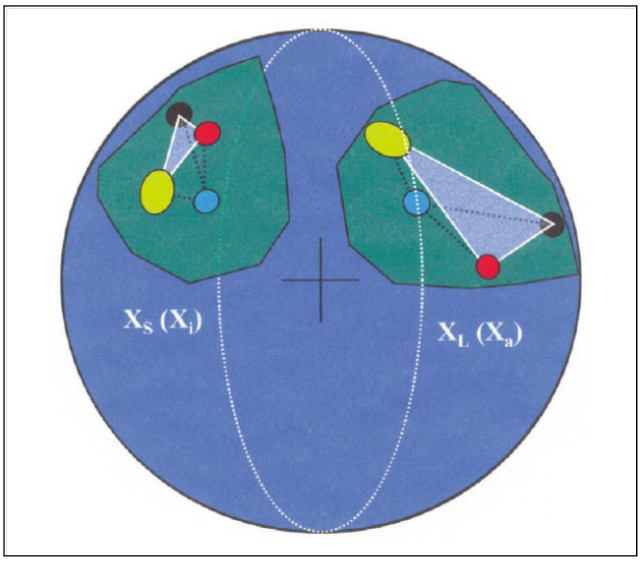

Figure 22. Chromosomal territories of active and inactive chromosome X homologue. Schematic drawing of mutual arrangement of investigated genetic elements – dystrophin exons E1 (black circle), E2 (red circle), CX-centromeres (green ellipse), and of respective fluorescence weight centers (FWC, blue circle) of the XL and XS chromosome. Chromosome territories are displayed as the green areas. Dark dashed and white lines demonstrate links between genetic elements drawn to demonstrate their spatial (tetrahedral) arrangement and mutual distances. The violet triangles demonstrate the area hold by the arms of the E1–CX–E2 angle and show the elongation of mutual distances. The E1–CX–E2 angles between genetic elements located on the XL comparing to the XS chromosome are similar. In addition, potentially flatter shape of XL chromosome territory is shown. The radial distances of drawn genetic elements are not proportional to real radial distances. Image taken from **Falk et al. (2002)**.[3]

In Lukasova et al. (2002),[2] we have compared structural organization of chromosomal territories either containing (HSA 9, HSA 17) or containing not (HSA 8, HSA 13) large clusters of highly expressed genes (RIDGEs). We found that RIDGE chromatin domains occupy that part of the territory that is oriented towards the nuclear center (as summarized in Kozubek et al. 2002)[1] while non-transcribed "antiRIDGE" domains preferentially appeared in its part facing the nuclear envelope (**Figure 23**). In territories of chromosomes without RIDGEs and with only low total expression, chromosomal loci studied were homogeneously distributed all over the territory. Chromosomal territories thus undoubtedly have internal structure with non-random, though statistically defined positioning of genetic loci (**Figure 23**). Importantly, the principles of intra-territorial chromatin organization seem to correspond with those relevant for the organization of chromosomal territories in the cell nucleus (see Kozubek et al. 2002).[1]

Discussion on Lukasova et al. (2002) and Falk et al. (2002)[2,3]

The manuscripts of Ondřej et al. (2006)[4] and Ondřej et al. (2007)[5] extend our previous works for dynamic aspects—chromatin mobility and nuclear trafficking. A GFP-HP1β–expressing construct labeled with Cy3 was transfected in MCF7 cells. Since GFP-HP1β expression was neither dependent on genomic insertion of the vector nor disrupted by its Cy3 labeling, the motion of the transgenic construct could be quantified and followed, for instance relative to nuclear heterochromatic (HP1β-labeled) domains. After transfection, random Brownian movement was observed in short time intervals (D_c = 7 x 10^{-3} $\mu m^2/s$). However, in a longer time perspective of several days, also a non-random aspect of the

transgene path was revealed, usually directing the vector to the nearest HP1 domain. In addition, the transgene track seemed to be limited only to specific nuclear subcompartments. When reaching the HP1 domain, the expression of transgene has been silenced and its movement restricted to the extent of heterochromatin. Tracking of the HP1β domains shown limited movement of heterochromatin with the diffusion coefficient $D_c = 7 \times 10^{-3}$ μm^2/s. Interestingly, the transgene plasmid seemed to employ cytoplasmic actin and microtubule networks when transpassing the cytoplasm from the site of its cellular internalization towards the nucleus. Interruptions of this cytoplasmic cytoskeleton by chemical drugs precluded the plasmid transport.

The works of Ondřej et al.[4,5] thus provide important information on chromatin mobility and functional relevance of higher-order chromatin structure. It is evident for example, that heterochromatin is in general only slightly mobile and helps to organize nuclear chromatin due to its structure and, probably, attachment to the nuclear matrix. This confirms the existence of global nuclear architecture, though dynamic in nature. Another important function of heterochromatin then probably poses in sequestration of active transgenes entering the cell. Potentially dangerous transgenes are transported to heterochromatin, where they are heterochromatinized and silenced. Finally, the non-random plasmid travelling through the nucleus, where its track crosses only specific areas, clearly demonstrates nuclear compartmentalization into structurally and functionally distinct chromatin domains.

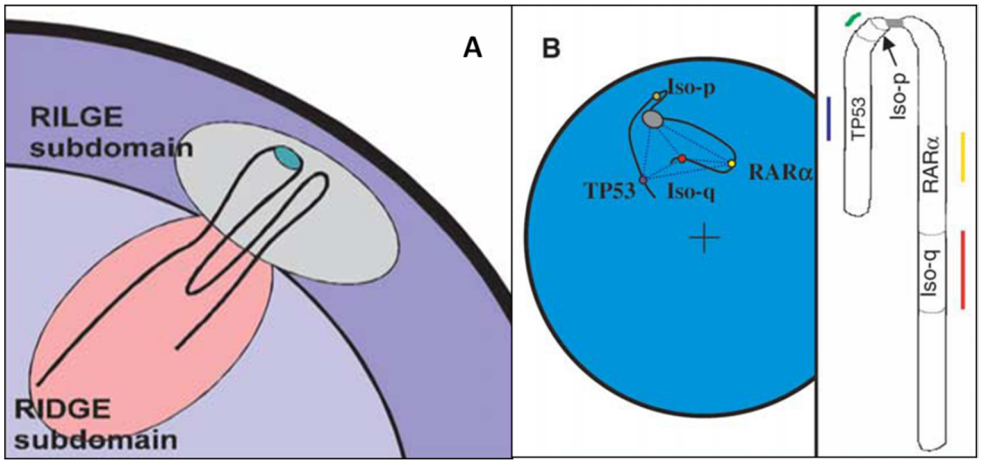

Figure 23. Internal structure of chromosomal territories. **A**. A model of an interphase chromosome. The chromosome territory is divided into a RIDGE subdomain oriented to the nuclear center (pink) and a RILGE subdomain facing the nuclear membrane (grey) and involving the centromere (green spot). The central backbone of the chromosome (black curve) thus bends from the RILGE to RIDGE subdomain and *vice versa*. Colored areas (pink and gray) represent chromatin loops attached to the backbone. Individual chromatin subdomains then associate in RIDGE or RILGE according to their function (and structure) distinct subdomains. **B:** Localization of five genetic elements of HSA 17 in the cell nucleus and the spatial arrangement of the chromosome backbone (traced through these loci). The distances between the genetic elements and their nuclear positions indicate that they do not occur in the same plane of the nucleus. The inserted schema shows location the genetic elements at the metaphase chromosome. Images taken from **Lukášová et al. 2002**.[2]

Together, our works discussed in this section show a non-random organization of the cell nucleus and substantially extend the previous knowledge of this organelle. We provide proofs of the relationship between the chromatin structure and function, and propose fundamental rules based on which the nuclear architecture is established. For example, we demonstrate that changes of the higher-order chromatin structure represent the first step in activation or silencing of gene transcription. Importantly

not only local chromatin structure but also nuclear positioning of chromosomes and genes contributes to regulation of genetic activity. As the character of the higher-order chromatin structure is probabilistic in nature, we can consider the nuclear organization as "the order in randomness."[1]

The publications presented here represent a cornerstone and springboard for our radiobiological studies presented later. Concerning the biological effects of ionizing radiation, an important finding is that chromatin domains differ in their structure and function, so that it is reasonable to hypothesize that they exert different sensitivity to DNA damage by ionizing radiation and potentially different efficiency of DNA repair. Since chromatin structure is related to its function, the processes executed by sensitive domains (for instance transcription) could be preferentially damaged by irradiation while functions of more resistant domains may remain unaffected. Moreover, the existence of nonrandom genome topology and only limited chromatin mobility indicate that some (oncogenic) chromosomal translocation may arise with a higher frequency than other ones. For the same purpose, some individuals might be in a higher-risk of radiation-induced cancer. The higher-order chromatin structure could be therefore relevant also in the context of the mechanism of formation of chromosomal aberrations upon irradiation and cell radioresistance/radiosensitivity.

2.1.2 Changes of higher-order chromatin organization and function during carcinogenesis

Fundamental nuclear process, replication and transcription, must be precisely regulated in order to enable and preserve physiological functions of the cell. Overexpression of protooncogenes and, on the other hand, silencing of tumor suppressors are well-known mechanisms of cancer development. Recently, it was revealed that chromatin structure changes participate in these processes. However, while the biochemical aspect of transcription regulation (transcription factor binding to gene promoters) has been studied for many years, the relationship between the higher-order chromatin structure and genetic activity of genes is much less explored.

It seems that chromatin structure may induce pathological gene expression via different mechanisms, directly or indirectly. For example, it is evident that altered chromatin conformation (*e.g.* due to errors in histone modifications) may influence binding of transcription activators and silencers to gene promoters, respectively. At higher levels of chromatin organization, de-repression of heterochromatin structure may prevent gene silencing during the cell differentiation and thus contribute to cancer development. On the other hand, the relocalization of tumor suppressors in the proximity of a heterochromatic domain may suppress their function with the same consequences. Chromatin decondensation may also point to gene amplification, a phenomenon common in cancers.

Indeed, cancer cells have been demonstrated to show significant changes in genome expression patterns that are associated with extensive disturbance of the higher-order chromatin structure. It is probable that changes of chromatin higher-order structure can accompany but also precede (i.e. cause) gene expression defects, as for instance in consequence of chromosomal aberrations, erroneous epigenetic modifications and potentially other mechanisms controlling the chromatin structure.

Importantly, chromosomal aberrations might influence not only the expression of directly participating genes, but also of large chromosomal loci encompassing the rearranged chromatin. Studies on the relationship between the structural and functional aspects of the higher-order chromatin structure are therefore important to disclose basic principles of regulation of genetic information at both the scale of individual genes and the whole genome, both in normal and cancer cells. Indeed, even some non-malignant diseases may be related to altered chromatin structure. In the radiobiological context, the presented research is important to better comprehend the late genetic effects of radiation – for instance the mechanisms how radiation-induced chromatin rearrangements are formed in the context of the higher-order chromatin structure and the health consequences of these rearrangements.

Relevant publications discussed:

1. Lukášová E, Kořistek Z, Klabusay M, Ondřej V, Grigoryev S, Bačíková A, Řezáčová M, Falk M, Vávrová J, Kohútová V, Kozubek S. Granulocyte maturation determines ability to release chromatin NETs and loss of DNA damage response; these properties are absent in immature AML granulocytes. Biochim Biophys Acta. 2013;1833(3):767-79. doi: 10.1016/j.bbamcr.2012.12.012.
2. Lukásová E, Koristek Z, Falk M, Kozubek S, Grigoryev S, Kozubek M, Ondrej V, Kroupová I. Methylation of histones in myeloid leukemias as a potential marker of granulocyte abnormalities. J Leukoc Biol. 2005;77(1):100-11. doi: 10.1189/jlb.0704388.
3. Lukásová E, Kozubek S, Falk M, Kozubek M, Zaloudík J, Vagunda V, Pavlovský Z. Topography of genetic loci in the nuclei of cells of colorectal carcinoma and adjacent tissue of colonic epithelium. Chromosoma. 2004;112(5):221-30. doi: 10.1007/s00412-003-0263-3.
4. Pagáčová E, Falk M, Falková I, Lukášová E, Michalová K, Oltová A, Raška I, Kozubek S. Frequent chromatin rearrangements in myelodysplastic syndromes--what stands behind? Folia Biol. 2014;60 Suppl 1:1-7.
5. Stepka K, Falk M. Image analysis of gene locus positions within chromosome territories in human lymphocytes. Lecture Notes in Computer Science (including subseries Lecture Notes in Artificial Intelligence and Lecture Notes in Bioinformatics). 2014; 8934:125-134. doi: 10.1007/978-3-319-14896-0_11.
6. Dellino I., Falk M., et al. New mechanism of Acute Promyelocytic Leukemia. Manuscript in preparation.

Discussion on Lukasova et al. (2005) and Lukasova et al. (2013)[6,7]

In Lukasova et al. (2005, 2013)[6,7] we have studied changes of higher-order chromatin structure in blood cells of patients suffering from chronic (CML) and acute (AML) myeloid leukemia. In blood cells, the extent of chromatin condensation increases with differentiation. This is the consequence of gene inactivation and their heterochromatinization. Therefore, the maximal level of compaction is reached in terminally differentiated cells, like granulocytes. Interestingly, heterochromatin structure in terminally differentiated cells differs from that in cycling cells, especially, it is not accompanied with binding of heterochromatin protein 1 (HP1) to heterochromatin.[640,641] In addition, HP1 is not associated

with formation of facultative heterochromatin during the chromosome X inactivation.[642] Therefore, it seems that different heterochromatin structures differ in cycling and differentiated cells. It was demonstrated[640,643] that in terminally differentiated avian blood cells (mainly granulocytes), HP1 protein becomes replaced by the nuclear myeloid and erythroid nuclear termination protein (MENT). Hence, we were interested whether heterochromatin condensation and composition differ between differentiated white blood cells possessing a certain level of proliferation capacity (lymphocytes and monocytes) and totally differentiated cells (granulocytes) also in humans. Up to this end, we studied nuclear levels and distributions of histone H3 mono-methylated, di-methylated or tri-methylated at lysine 9 (mono-metH3K9, di-metH3K9 and tri-metH3K9) and colocalization of these histone signals with HP1 protein variants α, β and γ. As expected, all types of H3K9 methylation and HP1 variants were detected in human CD34+ blood progenitor cells, differentiated lymphocytes and monocytes. Surprisingly, the mentioned signals were absent in neutrophil granulocytes and to large extent in eosinophils. In striking contrast, both the methylated H3K9 and HP1 proteins were found in HL60 and U937 cell lines differentiated with the *all-trans* retinoic acid (RA). It is not surprising in the latter case, since U937 cells differentiate into monocytes/macrophages. On the other hand, HL60 cells terminally differentiate into granulocytes. Therefore, it is obvious that chromatin structure in artificially differentiated immortalized cancer cell lines is not equivalent to normal cells and may remain "immature."

Therefore, we focused on H3K9 methylation and the presence of HP1 in different developmental stages of the blood cells isolated from patients suffering from chronic (CML) and acute (AML) myeloid

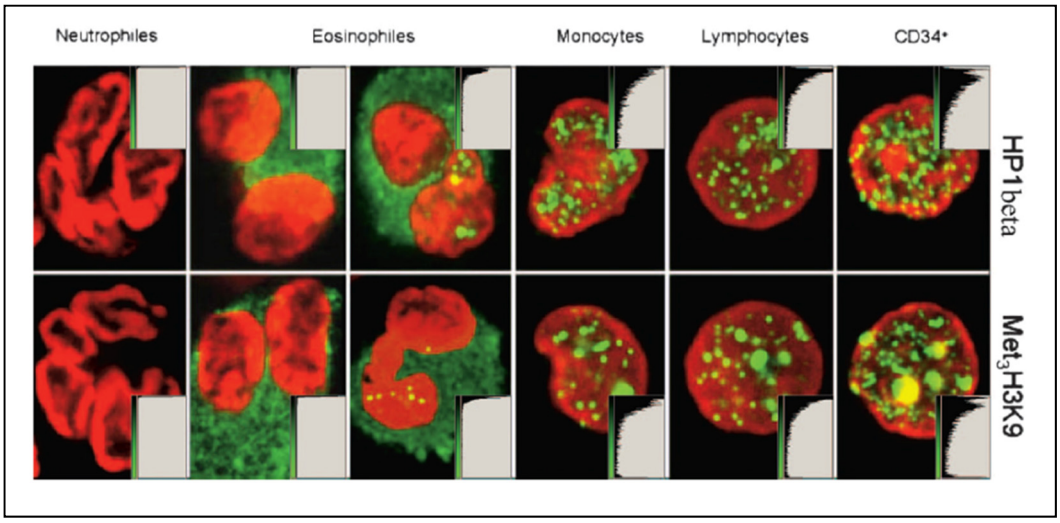

Figure 24. Higher-order chromatin structure (and composition) in different human blood cells. Distribution of HP1β and tri-metH3K9 in human peripheral blood cells (lymphocytes, monocytes, eosinophils, and neutrophils) and in human blood progenitor $CD34^+$ cells. HP1β (green, upper line) and tri-metH3K9 (green, bottom line) were found in $CD34^+$ cells, lymphocytes, and monocytes but not in neutrophils and some eosinophils. Chromatin was counterstained with TOPRO3 (artificially red). The images represent confocal slices in the x-y plane. Taken from **Lukasova et al. 2005**.[6]

leukemia, respectively. Mono-metH3K9 and di-metH3K9 signals were present to variable degrees in CML granulocytes, without being accompanied by HP1. Moreover, in CML patients in the acute phase of the disease and in AML, even stronger H3K9 methylation was detected together with HP1 protein. These findings indicate incomplete formation of terminally differentiated heterochromatin that

sustains its immature features typical for cycling cells. Therefore, gene silencing might be less efficient in cells obtained from CML and AML patients as compared to healthy donors, in accordance with higher proliferation of cancer cells. Importantly, these markers remain preserved even in successfully cured patients characterized by complete clinical and molecular remission with the absence of Philadelphia chromosome [t(9;22)(q34;q11)]. This suggests that the current treatments do not completely recover the physiological chromatin structure, which might contribute to disease relapse. Based on this observation, it is tempting to speculate whether the disruption of higher-order chromatin structure may precede formation of the Ph-chromosome and contribute to its formation.

In CML, the level of H3K9 methylation did not strongly correlate with disease progression. Nevertheless, chromatin structure changes have evidently physiological consequences. In Lukasova et al. (2013),[7] we demonstrated that granulocyte maturation determines the ability of these cells to release chromatin NETs that are necessary to inactivate bacteria and other hostile agents. This property is absent in immature AML granulocytes. In addition, it remains to be studied whether the alterations of higher-order chromatin structure may predict the patients' susceptibility to the development of pre-cancerous CML/AML stages. This work thus brings important findings concerning the changes of chromatin structure during cell differentiation and in pathogenesis of myeloid type leukemia. It undoubtedly demonstrates an important role of the higher-order chromatin structure in carcinogenesis. Some observations are directly relevant also in the context of radiobiological research. First, the changes in chromatin structure that appear during differentiation of some white blood cell types—i.e. chromatin condensation and protein recomposition—lead to the loss of ability of these cells to respond to DSB damage, as it is also described in our later presented works (Falk et al.[16]). This is unimportant from the physiological point of view in normal cells, since granulocytes are only short living, do not proliferate, and their function in the immune response is independent of the genome integrity. However, DSB repair becomes reactivated in AML granulocytes with immature chromatin structure. Whether this could be somehow important for radiotherapy remains to be studied. In any case, our results clearly demonstrate fundamental importance of the higher-order chromatin structure in DSB repair processes, as it is extensively discussed later in this thesis. In addition, we can reasonably speculate that the epigenetic status of chromatin (and its function) can be changed at sites of radiation-induced DNA damage, even if the primary lesion (e.g. a DNA double strand break, DSB) has been successfully repaired.

Discussion on Dellino et al. (in preparation)[11]

In previous paragraphs, we showed that changes of higher-order chromatin structure, provoked by altered cellular processes or irradiation, could potentially initiate cancer genesis or at least contribute to this process. The same conclusions follow also from other papers presented in this chapter. Nevertheless, since the relationship between the higher-order chromatin structure and cancer is, by itself, not the main scope of the present thesis, only a brief discussion will be provided. The manuscript of Dellino et al. (in preparation)[11] continues with our research on the roles of higher-order chromatin

structure in the mechanisms of cancer pathogenesis, but it turns our attention to acute promyelocytic leukemia (APL). APL originates from the reciprocal translocation between PML and RARα genes, t(15;17)(q22;q12).[644,645] PML is a tumor suppressor protein[646] while RARα (retinoic acid receptor α)[647] is a ligand-inducible transcription factor essential for terminal differentiation of promyelocytes.[648,649] The pathogenesis of APL has been described in detail, though many important issues remain controversial. Currently, the mechanism of APL seems to be based on different abilities of RARα and PML/RARα to respond to retinoic acid (RA) stimuli, as it is explained in **Figure 25** and the literature.[650,651,651–654,655] Binding of PML/RARα chimera to the promoters of RA-responding genes and disintegration of PML bodies (NBs) result in altered transcription of downstream regulated loci.[646] The loss of proapoptotic and tumor suppressive activities of PML then contributes to a very complex pathophysiology of APL.[646,656,657] Since stable binding of PML/RARα to the RARE elements inside the promoters of RA-responding genes prevents epigenetic activation of these genes, APL could be considered as a biochemically or genetically initiated epigenetic disease.[658–660,661,662–664]

The reason for our research[11] was grounded in our finding (EIO Milan) that, among 1150 genes identified to be down-regulated in APL cells, only ~20 % contain RAREs in their promoters. Since the

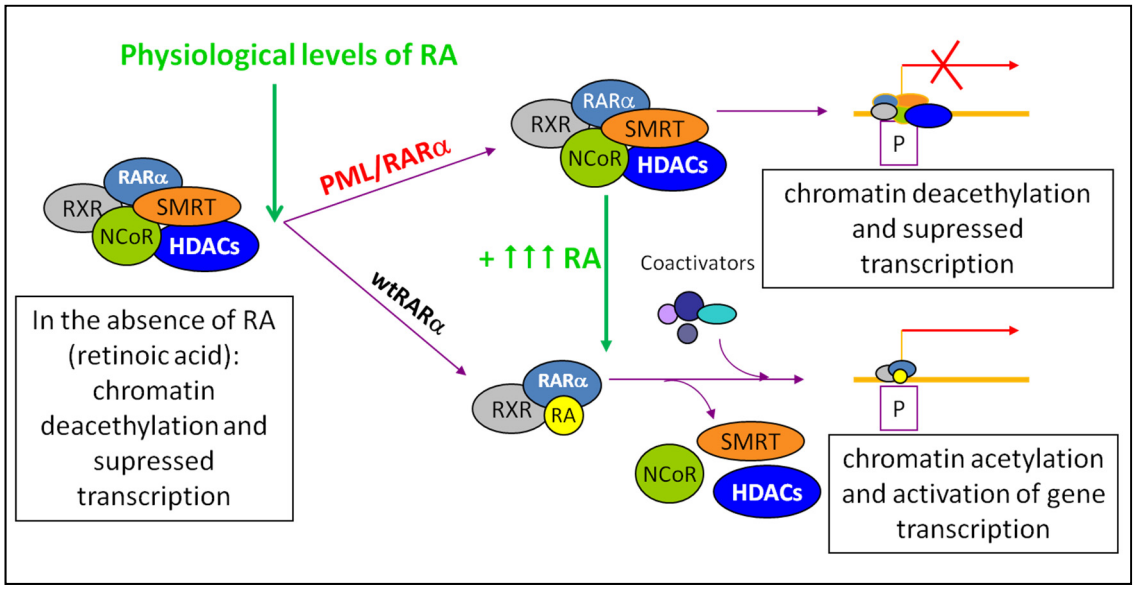

Figure 25. Currently accepted mechanism of PML/RAR induced gene down-regulation in acute promyelocytic leukemia (APL). In the absence of all-trans retinoic acid (RA), RAR binds to its target genes, attracts transcription-repression complexes to their TSS and silences them (left). When RA signal appears, repression complexes disassemble, which allows activation of genes (bottom). However, PML/RAR forms more stable repression complexes as compared with *wt*RAR (upper image) and only high therapeutic concentrations of RA enable their dissociation from the silenced promoters (bottom).

RARE elements are necessary for specific binding of RAR (and PML/RARα), it was tempting to speculate that PML/RAR might repress transcription through still unknown epigenetic mechanisms. Indeed, after more than 15 years of research, we revealed that changes in the higher-order chromatin organization are the early events in APL pathogenesis. PML/RARα expression provokes formation of giant chromatin loops that directly disseminate this oncogenic protein to RARE-free genes known to show affected expression in APL (**Figure 26**). In conclusion, this work describes a new mechanism of PML/RAR induced oncogenesis, which works via extensive changes of higher-order chromatin structure. The message for

radiobiological research is that an oncogenic protein may, by itself, alter chromatin structure, which could be reflected for instance by tumor cell radiosensitivity/radioresistance and/or DSB repair capacity. Histone deacetylases (HDAC) inhibitors were shown to both revert APL phenotype and influence DNA damage induction and repair.

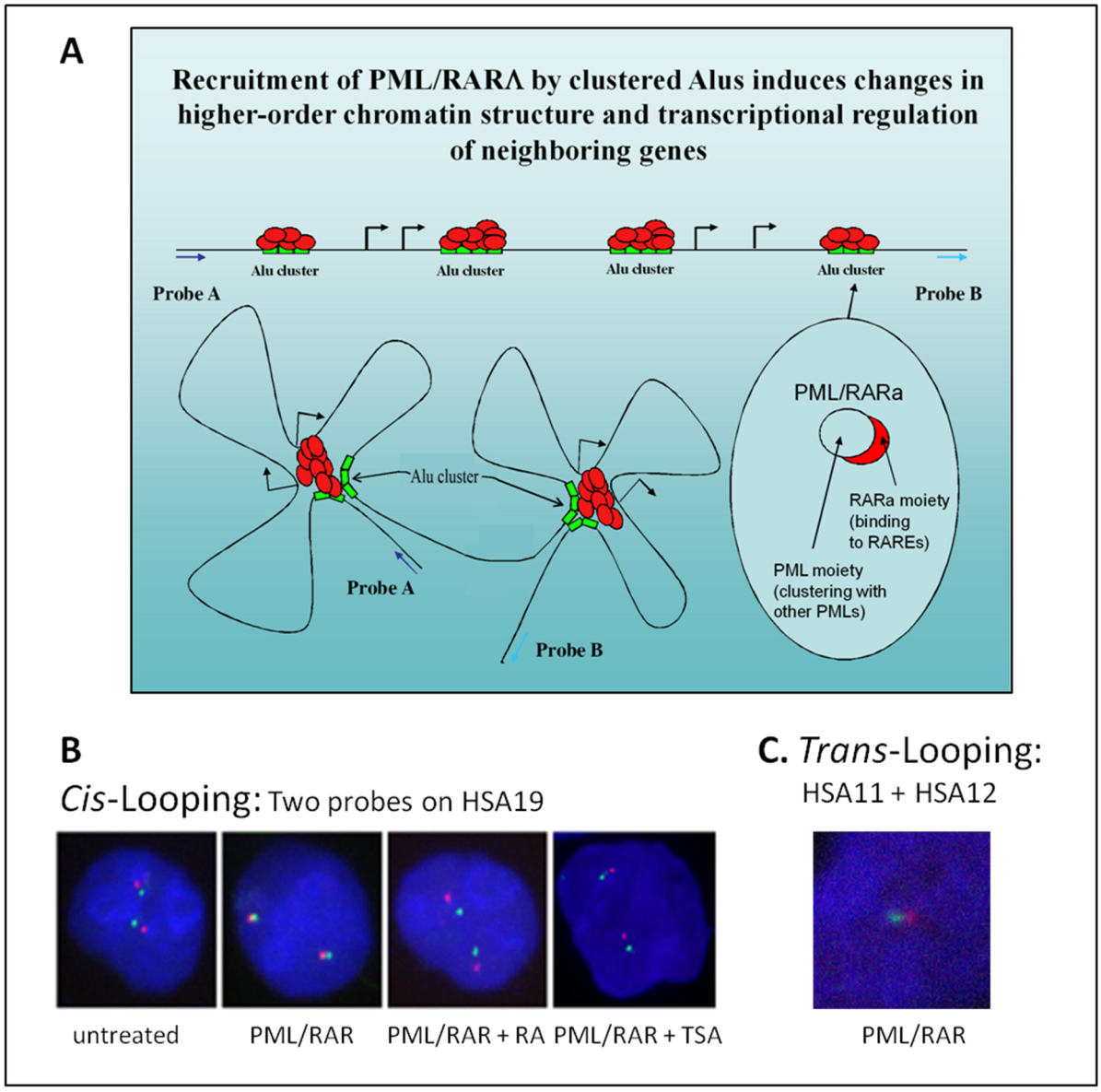

Figure 26. The proposed mechanism of APL pathogenesis. **Panel A:** A schematic illustration of the new mechanism of APL pathogenesis (proposed in [11]). The current model of APL pathogenesis presupposes that PML/RAR binds to the retinoic acid responsive elements (RAREs) of target genes where it induces their silencing by loading transcription suppressor complexes (that contain histone deacetylases, HDACs) and, in turn, setting up transcriptionally non-permissive chromatin structure. However, a vast majority of genes downregulated in APL do not contain RARE elements. Here, we show that PML/RAR red) also binds to non-canonical RARE elements of the Alu-Ya5 subfamily ("Alu-RAREs", green). Since Alu-RARE repeats form huge clusters, PML/RARa accumulates there to high amounts and, as the consequence, induces distortions of the higher-order chromatin structure (chromatin looping; the bottom image). Most probably, based on the chromatin structure and/or epigenetic modifications of target genes, multiple chromatin loops specifically and reproducibly interact with selected, genetically active genes that are mostly organized in clusters along the DNA molecule. Doing this, PML/RAR is transferred to the transcription start sites (TSS, black arrows) of the affected genes where it induces their silencing by the same way as it is suggested by currently accepted model of APL pathogenesis. **Panels A and B** show chromatin looping in the frame of one chromosome (*cis*-looping) but interacting genetic elements can be located also in different chromosomes (*trans*-looping) **(Panel C)**. Chromatin looping was revealed by the chromatin conformation capture (3C) in isolated chromatin (not shown) and confirmed in intact, spatially fixed cells by using *in situ* fluorescence hybridization (FISH) in combination with a high-resolution

confocal microscopy **(Panel B, C)**. FISH measurements of 3D nuclear distances between two paired DNA probes (represented by light blue and dark blue arrows at Panel A and red and green signals at Panels B and C) separated by several megabases of DNA and hybridizing with genomic sequences in Alu-RARE clusters and clusters of downregulated genes, respectively, revealed the distance shortening in PML/RAR expressing cells (marked as "PML/RAR"). This was in contrast to controls (expressing *wt*RAR and *wt* PML, marked as "untreated") (Panel B, C). Nuclear distances between the paired probes are shorter in PML/RAR expressing cells treated with all-trans retinoid acid (PML/RAR + RA) and TSA (PML/RAR + TSA), respectively, demonstrating diminishing of chromatin loops after applying these therapeutic agents and thus the fact that chromatin looping arises due to PML/RAR expression.

Discussion on Lukasova et al. (2004)[10]

The manuscript of Lukasova et al. (2004)[10] is important especially for one finding – it shows that while the higher-order chromatin structure could be altered in cancer cells for various purposes, the basic principles of chromatin organization in the cell nucleus remain preserved. It is well known that, in tumor cells, genes frequently undergo amplifications, which could result to their increased expression. Therefore, we were interested whether the nuclear topography and higher-order chromatin structure of amplified and/or highly expressed genes undergo changes during cancer development. We focused on genetic loci that were suggested to have an increased expression in all types of colorectal carcinoma: 7p22.3-7p21.3; 7q35-7q36.3; 11p15.5-11p15.4; 20p13; 20p12.2; 20q11.21 and 20q12. For a comparison, adjacent tissue of morphologically normal colonic epithelium was studied.

The nuclear distances between genetic elements located inside the above-mentioned chromosomal regions were in some cases larger in tumor cells as compared with normal epithelial cells. This result was characteristic for loci showing only a low degree of gene amplification. It is in agreement with our previous works showing opening of chromatin structure with increasing transcription. Perhaps surprisingly, the distances between genetic loci inside an amplified locus in tumor cells decreased with increasing amplification of the particular locus. Our findings might therefore point to a tendency of cancer cells, in spite of their malignant status, to down-regulate the expression of amplified loci. A significant variability was however noticed for individual loci as well as individual patients.

On the other hand, the global higher-order chromatin structure did not significantly differ for cancer and normal cells. For short genomic separations, the mean nuclear distances increased linearly with increasing separation between the BAC clones on the DNA molecule. However, some loci felt outside this general correlation curve, suggesting that individual loci may sometimes adopt specific chromatin folding. The linear increase of nuclear distances with their molecular separation stopped at the separation of about 4.5 Mb. This indicates existence of two levels of chromatin organization as predicted by the random-walk giant-loop model.[583,584,585] Nevertheless, in contrary to this model and in agreement with our previous works,[2,512] we observed non-random looping of the chromosome "backbone" even for very large genomic separations (*e.g.* those between genetic elements situated on the opposite arms of the chromosome). Among other consequences, this suggests that the higher-order chromatin organization influences the probability of (radiation-induced) chromosomal translocations between specific loci and that genetic loci separated by a long molecular distance can in some cases be closer to each other in space of the cell nucleus than loci separated by a shorter molecular distance.

Discussion on Pagáčová et al. (2014)[8] and Štěpka et al. (2014)[9]

The last manuscripts presented in this chapter – Pagáčová et al. (2014)[8] and Štěpka et al. (2014)[9] – address the question whether the higher-order chromatin structure can contribute to the susceptibility of some chromosomal loci to DSB induction. It is well known that spontaneous DNA breaks that give rise to chromosomal deletions and translocations in myelodysplastic syndromes (MDSs) preferentially appear in specific chromosomal bands. However, in contrast to leukemogenic translocations that arise from precisely defined breakpoints, the breakpoint loci in MDS are not as sharply defined. Interestingly, only few MDS breakpoint loci colocalize with chromosome fragile sites. This suggests that the higher-order chromatin structure could, for still unknown reason, support formation of DSBs in the affected loci and influence the probability of formation of particular chromosomal aberrations detected in MDS. Indeed, our preliminary data revealed that the loci frequently broken in "MDS cells", that were studied in the present work, contain more DSBs (detected as γH2AX foci) in γ-irradiated lymphocytes as compared to loci unaffected by DNA breaks in MDS cells (Falk et al., manuscript in preparation). Hence, it seems that the same factor makes MDS breakpoint loci susceptible to spontaneous and radiation-induced DSB formation. In support of this observation, MDSs frequently appear as the secondary cancers after previous radiation therapy or chemotherapy. Though the cause of increased DSB formation in MDS breakpoint loci remains to be identified, it has become obvious that frequent formation of some MDS-associated deletions can be explained, at least partially, by specific chromatin looping (i.e. the higher-order chromatin organization).

Chapter conclusions

To conclude this chapter, the publications presented provide a meaningful body of evidence proving that the higher-order chromatin structure not only regulates fundamental physiological processes in the cell nucleus, but also substantially contributes to carcinogenesis. Importantly, the existence of the higher-order chromatin structure has serious implications for biological effects of ionizing radiation, since DNA damage induction, repair, and misrepair all seem to be in multiple aspects influenced by chromatin structure and nuclear organization. The results achieved thus represent the necessary roots for our radiobiological research described in the following chapters.

2.2 The Roles of Higher-Order Chromatin Structure in DNA Damage Induction, Repair and Misrepair Upon Cell Exposure to Different Kinds of IR

The publications on the biological effects of different types of IR are central to the current thesis. In Chapters 2.2.1 and 2.2.2, the main concern is the relationship between the higher-order chromatin structure and DNA damage induction, repair, and misrepair. The presented collection of papers further develops our research on chromatin structure and nuclear organization (Chapter 2.1) but focuses on the structuro-functional aspects of the cell response to DNA DSB generated by IR of different types.

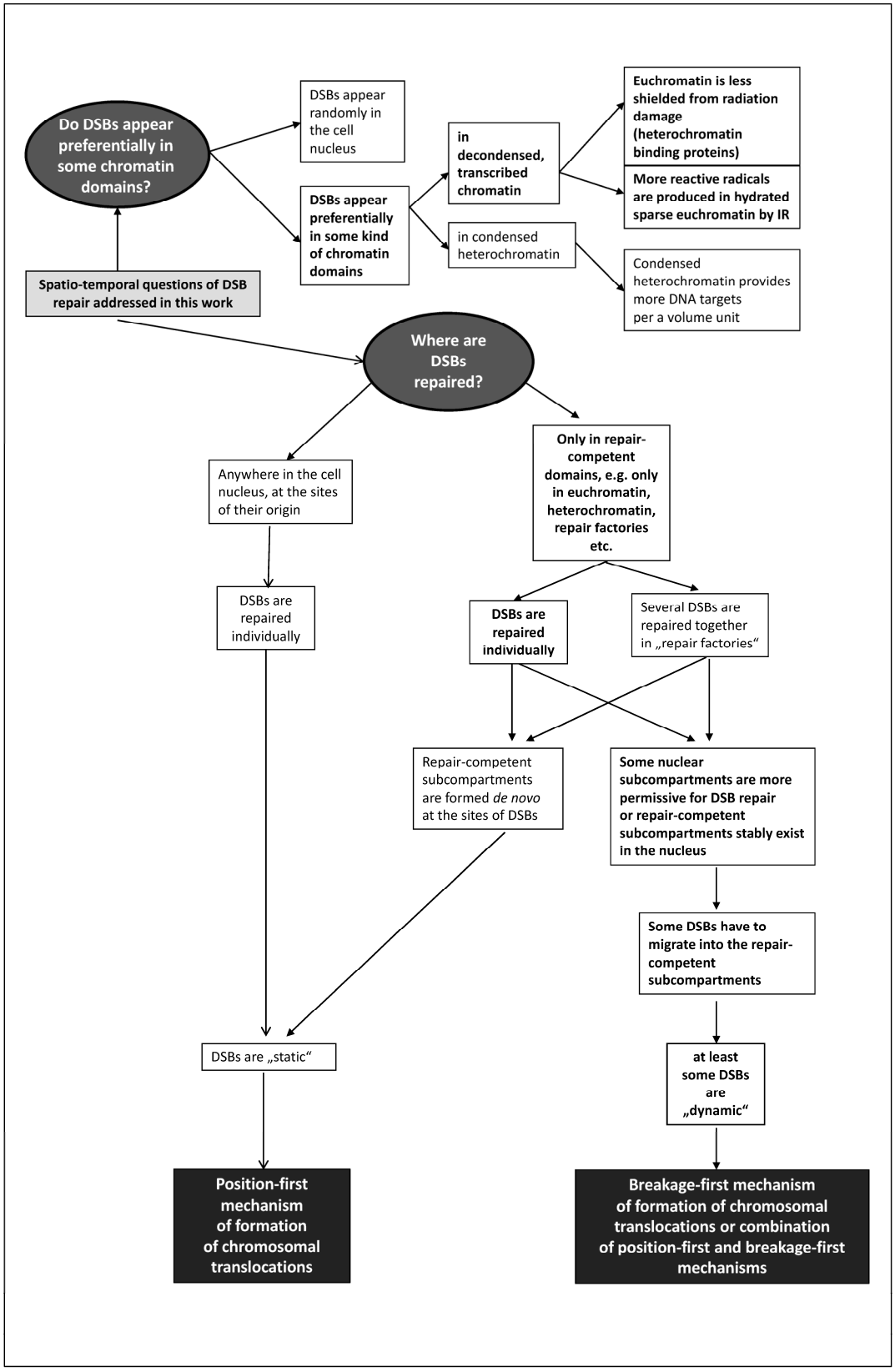

Figure 27. Spatio-temporal questions associated with DSB induction, repair, and the formation of chromosomal translocations addressed in this work. The possible relationships between the higher-order chromatin structure and these processes are displayed. The more probable alternatives according to our results (Falk et al. 2007, 2008)[13,664] are printed in bold. From **Falk et al. (2012)**.[665]

Among all DNA lesion types, DSBs have been seen as the most deleterious type of DNA lesions that can be repaired but with difficulty. As such, DSBs and IR, which is the most efficient DSB inducer, are a double-edged sword when it comes to cancer. On the one side, DSBs introduced by IR, other factors ever-present in the environment or processes naturally occurring in cells can lead to chromosomal aberrations or other mutations, potentially causing cancer. On the other hand, DSB induction by means of radiotherapy or chemotherapy currently represents the most efficient way of tumor cell killing. It should be emphasized that cancer poses a growing problem within the field of medicine despite the dramatic progress achieved in the field of anticancer (radio)therapy. Many tumors remain resistant even to improved approaches, and the number of cancer patients is progressively growing in developed countries.

In Chapter 2.3, novel approaches, for instance, IBCT, are intensively investigated as potentially more efficient alternatives to already well-established radiation therapies with high-energy (X- or gamma) photons. Nevertheless, although well mastered technically, IBCT application still relies on the physics and more or less empirical experience because the biological effects of proton and ion beams are still insufficiently explored. For instance, there is a consensus among scientists that the high radiobiological effectiveness (RBE) of high-LET ions can be ascribed to their ability to generate complex and/or multiple DSBs; however, therapeutic irradiation protocols only count with the number of DSBs induced per dose of the particular radiation, not with the complexity of the generated lesions. The same lack of knowledge, especially on the biological effects of various heavy ions, complicates the current planning of long-term manned interplanetary missions, during which astronauts will be exposed to a mixed field of cosmic radiation. Finally, new data on DNA damage and repair are critically needed in civil radiation protection, where contradictory models are discussed on the relationship between the radiation dose and biological effects.

Despite decades of intensive research on DSB damage induction and repair, many questions remain. Completely underexplored are, for instance, the dependence of DSB repair on higher-order chromatin structures and the spatio-temporal organization of DSB repair, the aspects of DDR that remained hidden in the “Pandora’s box” of the cell nucleus for a long time. The two reasons for this were the absence of the necessary technologies and a multidisciplinary character of radiobiological research. DNA damage and repair include physical, chemical, and biological processes dispersed over an extremely broad time (ranging from 10^{-22} s to decades) and wide spatial scale (picometers to meters). Research of DNA damage and repair hence requires close cooperation between many research disciplines and depends on advanced (e.g., particle accelerators) or still unavailable experimental technologies. Hence, the current boom in the development of molecular biology and biophysical methods involving a dramatic increase in computational power, various omics techniques, super-resolution optical microscopy (as, for instance, SMLM used in our research), and many other breakthrough experimental and theoretical improvements opens the door to a new era of nanoscale (molecular) radiobiology. Emphasizing the topicality of the herein presented research, we can say that radiobiology is just experiencing its renaissance.

The higher-order chromatin structure may influence the extent and character of DNA damage, efficiency and fidelity of DNA repair processes, and, finally, the genetic consequences of irradiation (**Figure 27**).[15,665] Because structurally and functionally distinct chromatin domains exist in the cell nucleus, the radiation damage to DNA may be distributed nonrandomly in the genome and have characteristics dependent on the local chromatin structure.[13,15] The relationship between the chromatin structure and radiation DNA damage micro- and nanostructure is discussed in the next chapter.

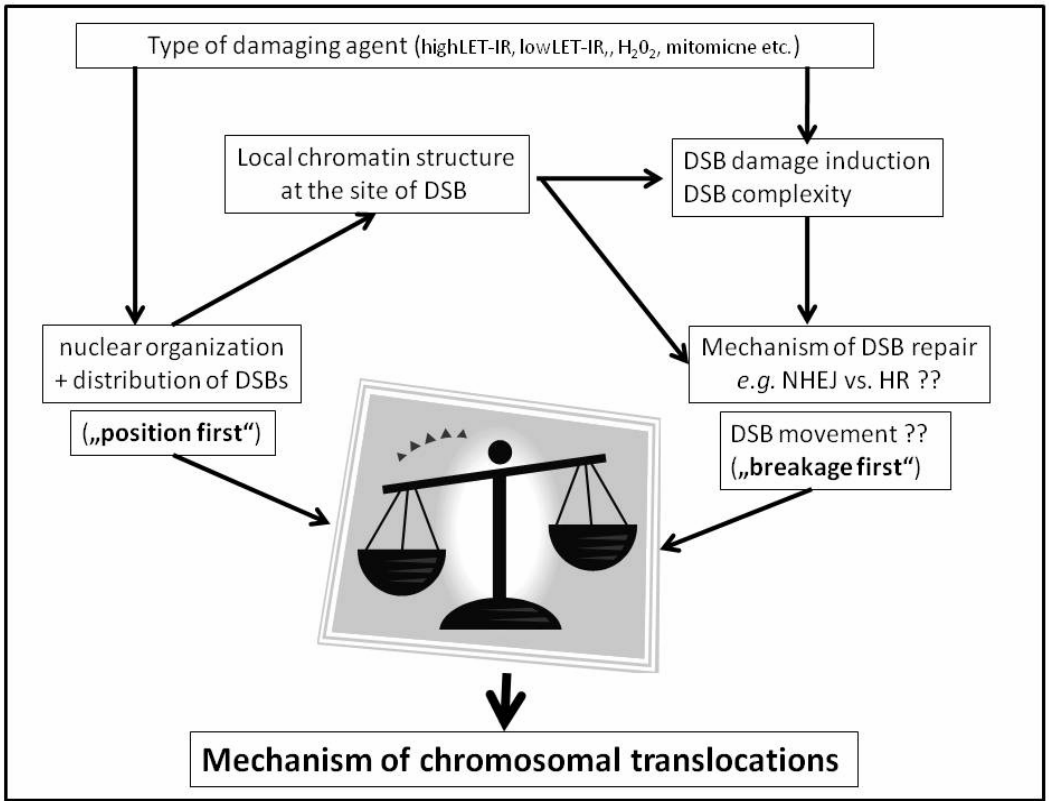

Figure 28. A potential network of parameters influencing DNA repair and formation of chromosomal translocations. The possible interconnection of nuclear organization and higher-order chromatin structure in this network is depicted. Different combinations of parameters might shift the mechanism of formation of chromosomal translocations closer to the "position first" hypothesis or "breakage first" hypothesis. From **Falk et al. (2012)**.[665]

After DNA damage induction, the character of DSB and the structuro-functional properties of the surrounding chromatin are thought to determine many aspects of the repair processes at all their stages—from the repair mechanism to its kinetics, efficiency, and fidelity. We have hypothesized that the complexity of a DSB lesion (strongly dependent on radiation LET) in combination with the micro- and/or nanostructure of the affected domain may dominantly participate in the decision-making process for a particular repair mechanism (pathway) at each individual DSB site. Because DSB induction, repair, and misrepair are mutually interdependent, the chromatin structure would play a central role in the mechanism of formation of chromosomal aberrations[15,665] and other mutations. Moreover, because some genes can be juxtaposed to others in a non-negligible proportion of cell nuclei and, at

the same time, IR deposits its energy in locally restricted nuclear volumes (depending on its LET),[(30)] the higher-order chromatin structure may be the cause for the more frequent formation of specific types of chromosomal aberrations, as, for instance, with the translocations associated with leukemia. Taken together, we can reasonably expect that the higher-order chromatin structure actively participates in a plethora of processes related both to the radiation damaging of DNA and the cell response to DNA damage (DDR) (**Figure 27**).[15,39] In our previous works,[12,13,15,39,665,666] we have fist focused on two seemingly simple structuro-topological questions: 1) whether low-LET radiation (γ-rays) induces DSBs randomly or nonrandomly in the cell nucleus and 2) where the DSBs are repaired **(Figure 27**, **28)**. In other words, we asked whether there are some chromatin subdomains more sensitive/resistant to DSB induction by radiation (discussed separately in the next chapter) and whether DSBs are immobile (i.e., repaired at the sites of their origin) or mobile and perhaps migrate toward some nuclear subcompartments, that are more permissive, or may even be specialized for DSB repair. If the latter proves to be true, are DSBs repaired individually or several in common in so-called *repair factories*? In addition, how does the mobility of DSBs depend on the structure of the affected chromatin domain and the type of radiation the cells were exposed to?[(31)] Finally, we wanted to know how the positional stability of structurally and functionally distinct chromatin domains—or, on the other hand, their mobility upon damage—contributes to the mechanism of formation of chromosomal translocations. Despite being seemingly simple, the answers to all these questions remain disputed, even years after our first results were published (Falk et al., 2010, 2012).[15,39]

It should be emphasized that the effects of irradiation on DNA are not limited to changes in its sequence (genetic and genomic mutations). DSBs not only disintegrate the DNA molecule, but also seriously damage the local epigenetic code. Moreover, DSB repair processes *per se* are associated with extensive epigenetic reprogramming at DSB sites. How efficient are the cells in removing these repair-related epigenetic modifications and recovering the original epigenetic status is unknown. Hence, we hypothesize that the exposure to radiation, especially high-LET radiation, can lead to “epimutations” (**Figure 27**). The consequences of epimutations for the genome condition are still unexplored. The following texts are adapted from Falk, M., *Book of Proceedings by the American Institute of Physics* [AIP].[666] For a description of DSB repair pathways, see Chapter 1.3.

Relevant publications discussed

1. Falk M, Lukásová E, Kozubek S. Chromatin structure influences the sensitivity of DNA to gamma-radiation. Biochim Biophys Acta. 2008;1783(12):2398-414. doi: 10.1016/j.bbamcr.2008.07.010.

2. Falk M, Lukasova E, Gabrielova B, Ondrej V, Kozubek S. Local changes of higher-order chromatin structure during DSB-repair. Journal of Physics: Conference Series. 2008 February; 101(1):012018. doi: 10.1088/1742-6596/101/1/012018.

[30] dependent on the type and energy of ionizing radiation

[31] High-LET radiation locally fragments chromatin and generates DSB of high complexity. The mobility of chromatin fragments after exposure to high-LET IR could be therefore much higher compared to free DNA ends of a simple DSB produced by low-LET IR.

3. Falk M, Lukasova E, Gabrielova B, Ondrej V, Kozubek S. Chromatin dynamics during DSB repair. Biochim Biophys Acta. 2007 Oct;1773(10):1534-45. doi: 10.1016/j.bbamcr.2007.07.002.

4. Falk M, Lukášová E, Štefančíková L, et al. Heterochromatinization associated with cell differentiation as a model to study DNA double strand break induction and repair in the context of higher-order chromatin structure. Appl Radiat Isot. 2014 Jan;83 Pt B:177-85. doi: 10.1016/j.apradiso.2013.01.029.

5. Falk M, Lukasova E, Kozubek S. Higher-order chromatin structure in DSB induction, repair and misrepair. Mutat Res. 2010;704(1-3):88-100. doi: 10.1016/j.mrrev.2010.01.013.

6. Falk M, Hausmann M, Lukášová E, et al. Determining Omics spatiotemporal dimensions using exciting new nanoscopy techniques to assess complex cell responses to DNA damage: part B--structuromics. Crit Rev Eukaryot Gene Expr. 2014;24(3):225-47.

7. Falk M, Hausmann M, Lukášová E, et al. Determining Omics spatiotemporal dimensions using exciting new nanoscopy techniques to assess complex cell responses to DNA damage: part A--radiomics. Crit Rev Eukaryot Gene Expr. 2014;24(3):205-23.

2.2.1 *Distribution of DSBs in the cell nucleus and sensitivity of chromatin domains to DSB*

Comments on Falk et al. (2008)[13]

To reveal how DSBs are distributed in the cell nucleus is particularly interesting as it can tell us whether some chromatin domains are more sensitive to low-LET IR[(32)] and/or radiomimetics than the others are. For instance, could be decondensed euchromatin rich for active genes more sensitive than condensed, genetically silent heterochromatin? And if so, may heterochromatin protect important genetic loci (housekeeping genes, protooncogenes, tumor suppressors *etc.*) for instance by preferentially sequestering free radicals?[578] A question also remains, how the initial damage is later reflected in formation and persistence of chromosomal rearrangements and DNA mutations. In other words, if the sensitivity to DNA damage induction of a particular chromatin domain type correlates with repair efficiency and fidelity.

Susceptibility to radiation damaging has been in many studies compared for euchromatin (EC) and heterochromatin (HC), as these domains represent the oldest functionally distinct chromatin structures. Better understanding of this issue would shed new light on the mechanism of DNA damaging by radiation and is important also from a medical point of view since EC contains the majority of genes, including tumor suppressors and protooncogenes. In spite of seeming simplicity of this problem, the results remained contradictory for a long time, since methods for sensitive direct measurement of DSBs in the context of chromatin did not exist. DNA damage in HC and EC was therefore only estimated, for instance based on chromosomal translocation formation. In addition, the

[32] Due to the characteristics of high-LET IR, most of DSBs are induced by high energy particles *per se* (the direct effect of IR) – these particles have energy enough to make DSBs without respect to chromatin structure; therefore we suppose the probability of DSB induction just simply correlates with chromatin density (*i.e.* the density of DNA targets).

employment of different radiation types (low-LET and high-LET IR) and experimental systems generated results that can be mutually compared only with difficulty.

Recently, it was discovered that histone H2AX becomes quickly phosphorylated at DSB sites by ATM, ATR or DNA-PKcs kinases. γH2AX signal appears in minutes after DSB induction and spreads over about 2 Mbp of the affected chromatin domain.[123,125] This phosphorylated form of H2AX, generally referred to as γH2AX, can be quantified by flow cytometry or directly visualized *in situ* by immunofluorescence microscopy as so called γH2AX foci (also known as IRIFs, Ionizing Radiation Induced Foci).[667] The latter approach currently represents the most sensitive and reliable method to quantify DSB damage; moreover, it allows to study DSBs in the context of the cell nucleus and chromatin. Therefore, we decided to compare DSB induction in heterochromatin and euchromatin by the means of high-resolution immunofluorescence confocal microscopy of γH2AX foci in spatially (3D) preserved cells fixed by paraformaldehyde. Taking advantage of this approach, we first determined the proportions of γH2AX foci in chromatin domains densely and weakly stained with DNA dyes, respectively.[13,14] To maximize the accuracy of our analysis, we used low doses of low-LET γ-rays leading to formation of simple, non-clustered DSB lesions with about 1:1 ratio to γH2AX foci. These conditions not only improve DSB quantification but also prevent local chromatin fragmentation that is characteristic for expositions to high-LET radiation and may affect chromatin mobility, i.e. complicate studies of spatio-temporal aspects of DSB repair. To further increase the precision of our measurements, and to distinguish between different γH2AX focus states (early, actively repairing, and late), we immunostained γH2AX foci together with one of DSB repair proteins (like NBS1, MRE11 and 53BP1) that are attracted by γH2AX to DSB sites.

At the first glimpse, γH2AX foci seemed to be randomly dispersed over cell nuclei. However, when we inspected individual confocal slices instead of "maximum images" (i.e. images composed of superimposed projections of individual confocal slices)[(33)] it become evident that the distribution of γH2AX foci is nonrandom, with a majority of foci (70 – 80 %) located in decondensed chromatin weakly stained with DNA dyes (further referred to as *chromatin holes*). This result could have been interpreted as a higher sensitivity to DSB induction by low-LET γ-rays of decondensed EC compared to condensed HC, if other phenomena had not potentially contributed to this observation. However, we could not exclude the possibility that DSBs persist longer time in EC than HC (because of more efficient repair in heterochromatin, *e.g.* due to better stabilization of free DNA ends), that γH2AX is less efficiently phosphorylated in HC, or that HC-DSBs migrate, for some purpose, out of dense chromatin domains. Such a movement of γH2AX foci either may appear passively in consequence of repair processes or may reflect purposeful reorganization of chromatin structure necessary to allow DSB processing. Not mutually exclusive to the latter alternative, DSBs may also migrate into nuclear subcompartments more suitable for repair (reviewed in Falk et al., 2010[15]). In addition, some authors reported that HC is refractory to γH2AX formation and/or could be "inaccessible" for γH2AX antibody. Both these phenomena may thus result to underestimation of HC-DSBs. However, our TUNEL[(34)] labeling of free

[33] Typically, the maximum image consisted of 40 superimposed optical confocal slices taken with a z-step of 0.2 μm.

[34] Terminal Transferase dUTP Nick End Labeling Assay (TUNEL) is mostly used for detection of apoptosis via chromatin fragmentation.

DNA ends that is independent of H2AX phosphorylation efficiency (γH2AX focus formation) and chromatin permeability for antibodies at DSB sites confirmed the significant predominance of EC-DSBs over HC-DSBs, with a similar ratio of EC-DSBs to HC-DSBs as estimated with antibodies. Furthermore, HC domains could successfully be stained with HP1α antibody, demonstrating that HC is in principle accessible for antibodies. Therefore, it does not seem probable that we detected more DSBs in EC because of underestimating HC-DSBs. In support of this statement, more recent works suggest that γH2AX foci can also form in dense HC domains.[669,670]

Importantly, even more γH2AX foci appeared in decondensed chromatin when we scored only the foci colocalizing with repair proteins and their fraction was progressively increasing with the time PI (up to about 1 h PI). This suggests that either chromatin must decondense around DSB lesions or DSBs must migrate into repair-competent (or even specialized) nuclear subdomains in order to complete the repair. Alternatively repair of HC-DSBs could proceed without formation of γH2AX foci, which is not much probable since repair in HC was shown to be slower and is more complicated.[109–111,671]

To find the reason for almost exclusive location of DSBs in sparse chromatin ("euchromatin"), we took advantage of ImmunoFISH method[255] that allowed us to compare DSB induction in precisely defined regions of increased gene expression (RIDGEs)[513] and their structuro-functional counterparts, antiRIDGEs. The advantage of ImmunoFISH is that it enables simultaneous visualization of γH2AX foci (or other IRIFs) on the background of labeled chromatin domains of known functional and structural characteristics. Importantly, as it follows from the principle of the method,[255] chromatin domains studied are visualized regardless of their possible decondensation during DNA repair processes, although sparse chromatin is stained with a lower intensity. This prevents underestimation of HC-DSBs as it may happen if HC is simply stained with DNA dyes (DAPI, TOPRO3).[13]

An interesting model to study the sensitivity of structurally and functionally distinct chromatin domains to DSB induction was offered by RIDGE and antiRIDGE clusters.[513] These chromatin domains show mutually opposite functional and structural characteristics, are functionally and structurally very homogeneous, and RIDGEs of comparable molecular size to antiRIDGEs can be found in the genome. Hence, we compared DSB induction and efficiency of repair in one RIDGE and one antiRIDGE cluster, both encompassing very similar length (~11 Mb) of chromosome 11. In this analysis, a higher dose of γ-rays (8 Gy) was used to generate statistically comparable numbers of γH2AX foci in relatively small RIDGE and antiRIDGE domains.

The experiments with RIDGEs and RIDGEs confirmed our conclusions earlier obtained for total nuclear euchromatin and heterochromatin, with even more striking predominance of γH2AX foci in the RIDGE compared to antiRIDGE domain (8 vs. 2 γH2AX foci per territory, respectively). Since the numbers of γH2AX foci sharply decreased in the RIDGE but not antiRIDGE domain at 4 h post-irradiation, we can suppose that the predominance of γH2AX foci in decondensed (eu)chromatin reflects its higher sensitivity to DSB induction rather than more efficient repair in heterochromatin (compared to euchromatin), proceeding without the necessity of IRIF formation.

However, because of relatively small volume of our RIDGE and antiRIDGE domains and relatively late post-irradiation time of the first measurements (15 min PI), we still could not exclude the possibility that some HC-DSBs escaped detection because of very fast and extensive domain decondensation,

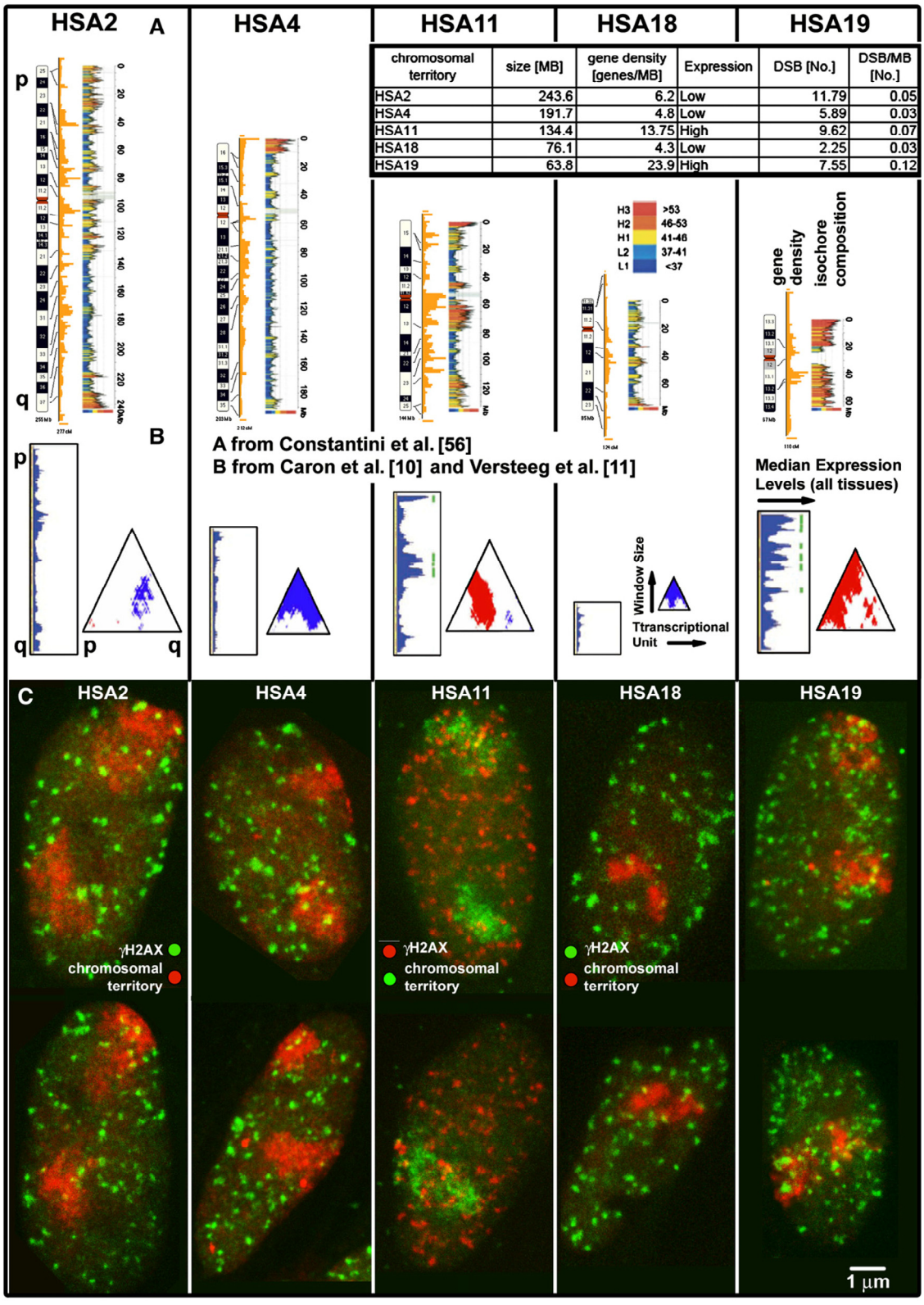

chromosomal territory	size [MB]	gene density [genes/MB]	Expression	DSB [No.]	DSB/MB [No.]
HSA2	243.6	6.2	Low	11.79	0.05
HSA4	191.7	4.8	Low	5.89	0.03
HSA11	134.4	13.75	High	9.62	0.07
HSA18	76.1	4.3	Low	2.25	0.03
HSA19	63.8	23.9	High	7.55	0.12

Figure 29. Sensitivity of chromosomal territories with different levels of overall transcription level to DSB induction by γ-rays. Characteristics **(A, B)** of the five chromosomes (HSA2, HSA4, HSA11, HSA18 and HSA19) used for quantification of the chromatin density effect on the induction of DSBs by γ-radiation (dose of 3 Gy). **(A)** Gene density according to Ensemble database (orange) and isochore distributions for individual chromosomes from Costantini et al. 2006[668] (GC content is expressed by different colors) **(B)** transcriptome maps (blue) and 'RIDGEograms' (triangles) are from Caron et al. 2001[513] and Versteeg et al. 2003,[237] respectively (see Fig. 1 in Falk et al. 2008[13] for more detailed explanation of panels A and B. **(C)** Images of fibroblast nuclei with simultaneously visualized (ImmunoFISH) territories of specific chromosomes (red; green for HSA11) and induced γH2AX foci (green; red for HSA11) detected 15 min PI. Taken from **Falk et al. (2008)**.[13]

leading to relocalization of DSBs out of antiRIDGE territory (small extraterritorial chromatin protrusions are hardly detectable by ImmunoFISH). Moreover, due to the different genetic activity and consequently chromatin structure, antiRIDGE territories occupy smaller nuclear volume as compared with RIDGEs of the same molecular size; this can also contribute to some underestimation of HC-DSBs. To preclude the above-mentioned obstacles, we performed the same ImmunoFISH experiments as described earlier for RIDGE and antiRIDGE clusters but with the whole chromosomal territories differing in total gene expression (**Figure 29**). First, we have compared DSB induction in territories of human chromosome 4 (HSA4) and chromosome 18 (HSA18). These chromosomes are of similar gene density but significantly differ in their molecular size.[237,513] As expected, the number of γH2AX per territory in this case reflected the size (volume) of chromosomes, with very similar values of DSBs generated per DNA length unit (i.e. in a similar molecular density). Next, we have compared chromosomes 18 and 19 (HSA19) of the equivalent molecular size but largely different gene density and transcription activity.[(35)] [237,513] For this combination, the number of γH2AX foci significantly differed between the chromosomes, with a much higher DSB density observed for HSA19. This was in agreement with our observations for RIDGE and antiRIDGE clusters. However, because of its low genetic activity and thus highly condensed status, the nuclear volume of HSA18 is little smaller than that of HSA19. To eliminate this complication, we finally compared chromosomes 4 and 19, where chromosome 19 is much smaller than HSA4 in terms of its molecular size and nuclear volume but is much more intensively expressed. This time, the number of γH2AX foci per territory was very similar for both chromosomes, clearly demonstrating a higher DSB density (number of DSBs per Mb of DNA) for HSA19. Concerning the large volume of chromosomal territories, we feel improbable (but could not definitely exclude) that a significant number of DSBs can leave maternal territory as a consequence of chromatin decondensation during DSB repair and thus escape detection. Highly expressed decondensed chromatin thus seems to be more sensitive to DSB induction (**Figure 29**).

To further study the mechanism behind the higher sensitivity of decondensed and transcriptionally active chromatin to DSB induction by low-LET IR, we have analyzed formation of γH2AX foci in cells with artificially hypercondensed and hypocondensed chromatin, respectively. The cells were incubated for 10 min either in hypertonic (HOM, 570 mOsm) or hypotonic (HypoOM, 140 mOsm) medium, irradiated, and transferred for 10 min to normal (isotonic) conditions to allow development of γH2AX foci.[(36)] γH2AX foci were consequently scored inside the whole nuclei with surprising results: whereas the HypoOM treatment significantly increased the number of γH2AX foci, an expected decrease under the HOM conditions was not observed.

Therefore, we analyzed the structure of newly formed hypercondensed chromatin patches and found that they colocalize neither with heterochromatin markers (like dimetH3K9 or trimetH3K9) nor with heterochromatin binding proteins (HP1α, HP1β) that participate on heterochromatin formation under physiological conditions.[12,13] Together with the fact that low-LET IR induces DSBs mostly indirectly via production of highly reactive free radicals (ROS), it seems that chromatin decondensation, potentially

[35] HSA19 is the mostly expressed chromosome in the human genome, whereas HSA18 is gene poor.

[36] that is reversibly inhibited in HOM

followed by dissociation of proteins from the chromatin fiber (in both hypotonic-induced and physiological conditions), sensitizes chromatin to harmful activities of ROS. On the other hand, chromatin condensation *per se* does not protect DNA from DSB damage. It seems, therefore, that a large amount of heterochromatin binding proteins, which associate with heterochromatin under physiological conditions, probably partially shields DNA from harmful ROS (**Figure 30**). In addition, since ROS mostly come from the water radiolysis and are only extremely short living, more hydrated and decondensed euchromatin could face to more radical attacks than heterochromatin, if the situation upon cell exposure to low-LET radiation is concerned (**Figure 30**). Moreover, the discrepancy between the proportions of heterochromatic DSBs determined by simple DNA (TOPRO3) staining and FISH staining points to extensive decondensation of damaged HC domains. This could be followed by the relocalization of damaged HC-DSBs, possibly into repair-competent nuclear subdomains during DSB repair, as it is discussed below in comments on Falk et al., 2007.[14]

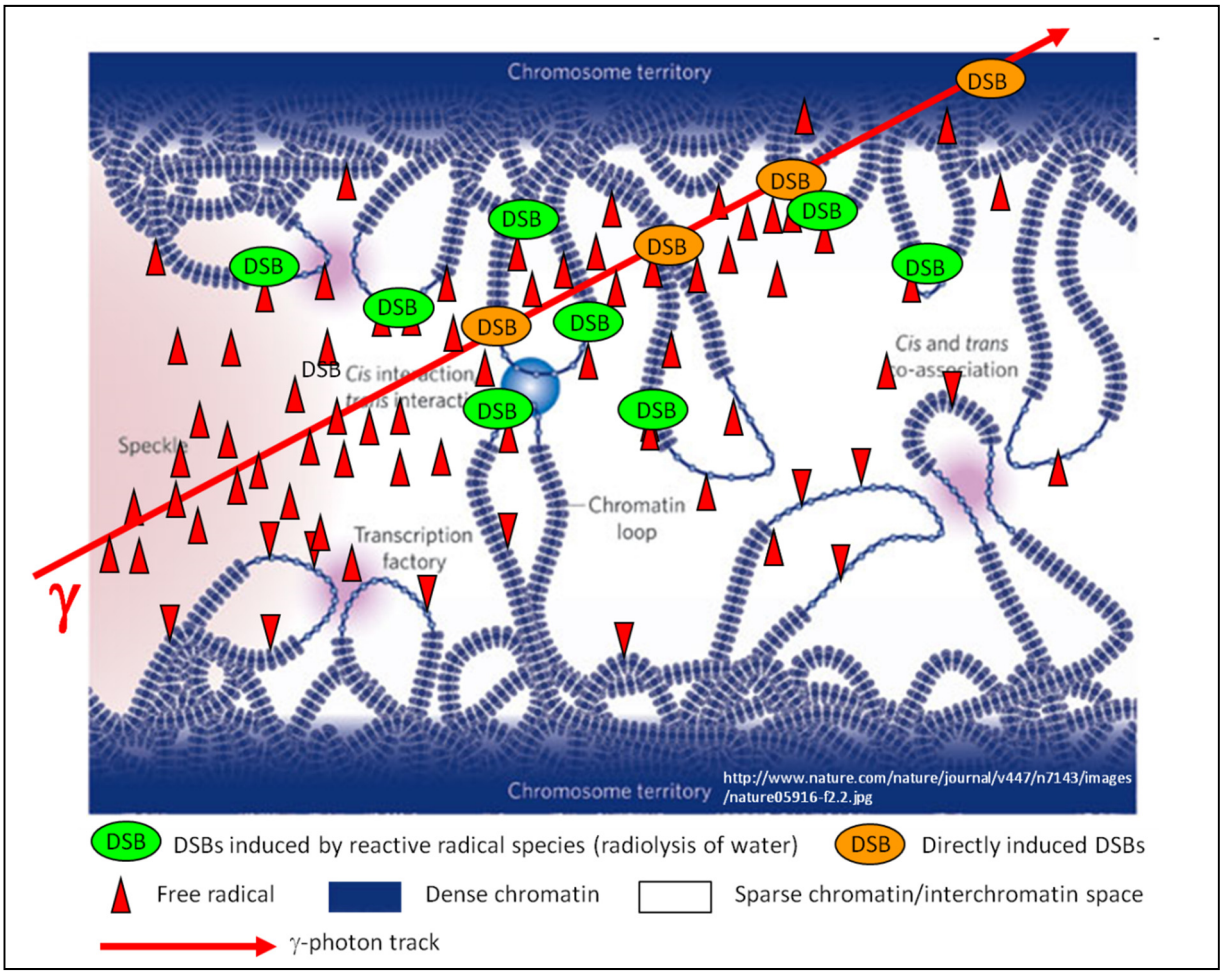

Figure 30. The proposed mechanism of DSB induction in relation to the chromatin density. Heterochromatin is dense and associated with a large amount of heterochromatin binding proteins (like HP1 *etc.*), while euchromatin is decondensed, less associated with proteins and hydrated. After irradiating the cells with γ-rays, some DSBs are induced directly by the crossing photon; however, most of DSBs are caused by reactive free radicals produced by water radiolysis. Since free radicals are extremely short living and sparse (eu)chromatin is more hydrated, more DSBs appear in this chromatin domain (despite more DSBs may be induced by the photon itself in condensed heterochromatin, because of it provides more DNA targets per volume unit). In addition, heterochromatin is better protected from free radicals by bounded proteins. According to **Falk et al. (2014)**[16], the background image (chromatin) is taken from **Fraser and Bickmore 2007.**[528]

2.2.2 *Mechanisms of DSB repair and formation of chromosomal translocations: Position-first or breakage-first scenario?*

Comments on Falk et al. (2007)[665]

In the present work, spatio-temporal aspects of DSB repair and their consequences for formation of chromosomal translocations were studied. Since results in the literature were contradictory, we were interested how DSB insertion influences the mobility of damaged chromatin. Moreover, we wanted to know how this mobility depends on the higher-order structure of the affected chromatin domain. In spatially fixed fibroblasts irradiated with relatively low doses of low-LET γ-rays (1 – 4 Gy), we observed that about 41 % of γH2AX foci colocalize with repair proteins (NBS1, MRE11) already 5 min PI (or even earlier), which means at the original sites of DSB induction. Later on, the number of γH2AX foci per nucleus increases up to about 30 or 60 min PI without any signs of marked focus clustering. These observations suggest that DSBs are in principle repaired individually, at or close to the nuclear sites of their formation. On the other hand, the fraction of γH2AX foci in decondensed (eu)chromatin progressively increased with PI time and HC-DSBs usually did not colocalize with microscopically detectable foci of repair proteins. In addition, in our above described experiments with chromosomal territories (Falk et al.[13]) γH2AX foci were detected almost exclusively in their decondensed parts, even in the case of otherwise condensed territories of gene poor chromosomes. These data point to a "movement" of at least some foci. Therefore, we directly measured the mean squared displacement (Δd^2)[(37)] of NBS1 and 53BP1 foci in living cells. If averaged for all possible pairs of all foci, the Δd^2 of NBS1 and 53BP1 corresponded with that measured for HP1β protein (that binds to heterochromatin). Our results thus suggested that the "average" mobility of DSBs is comparable to undamaged chromatin. However, when we traced individual NBS1 or 53BP1 foci, the mobility was sometimes much higher than the measured average mean squared displacement. Importantly, as the size of highly mobile and stable foci was similar, it is improbable that the mobile foci represent free (unbound to chromatin) protein aggregates. Therefore, we further analyzed the character of NBS1 and 53BP1 focus movement. While it corresponded to the Brownian movement in general, the highly mobile foci frequently experienced targeted relocation from dense to sparse chromatin domains (**Figure 31**). The consequent experiments proved extensive chromatin decondensation at the sites of DSB lesions;[(38)] we could, therefore, reasonably suppose that the decondensation associated with chromatin domain damage and DSB repair forces DSBs out into the closest interchromatin (or low-density chromatin) space (**Figure 31**). The consequences of this phenomenon are discussed in the following paragraphs and reviewed in our previous works.[15,18,26,39] The necessity of chromatin decondensation for DSB repair was confirmed in

---

[37] $\Delta d^2 = \left(d_t - d_{t+\Delta t}\right)^2$, where t-intervals were 20 – 500 ms and ***d*** was calculated as $d=\sqrt{(x_1-x_n)^2 + (y_1-y_n)^2}$ in 2D space or $d=\sqrt{(x_1-x_n)^2 + (y_1-y_n)^2 + (z_1-z_n)^2}$ in 3D. x_1, y_1 and z_1 (x_n, y_n and z_n) were coordinates for the first measurement and the n[th] measurement of the same object. The *mean* d^2 was calculated from individual d_i^2 values of all possible signal pairs at the particular time point. The mean difference of d^2 ($mean\ \Delta d^2$) was calculated at each time point (t) as $\Delta d^2 = (d_t - d_{t+\Delta t})^2$, where Δt was the time interval between measurements (see Falk et al. 2007 [14] for a more detailed explanation).

[38] demonstrated by a local decrease of TOPRO3 and H2B-GFP staining at the site of DSB, followed by colocalization of γH2AX with acetylH4K5, acetylH4K12 and Tip60, with the peak values at 20 min PI

live cell experiments. They revealed that nibrin, being a small protein probably serving as one of the DSB sensors, can penetrate into dense heterochromatin domains, while 53BP1, as a larger protein acting later in repair, could do it only if the domain had decondensed (F**igure 32**).[16]

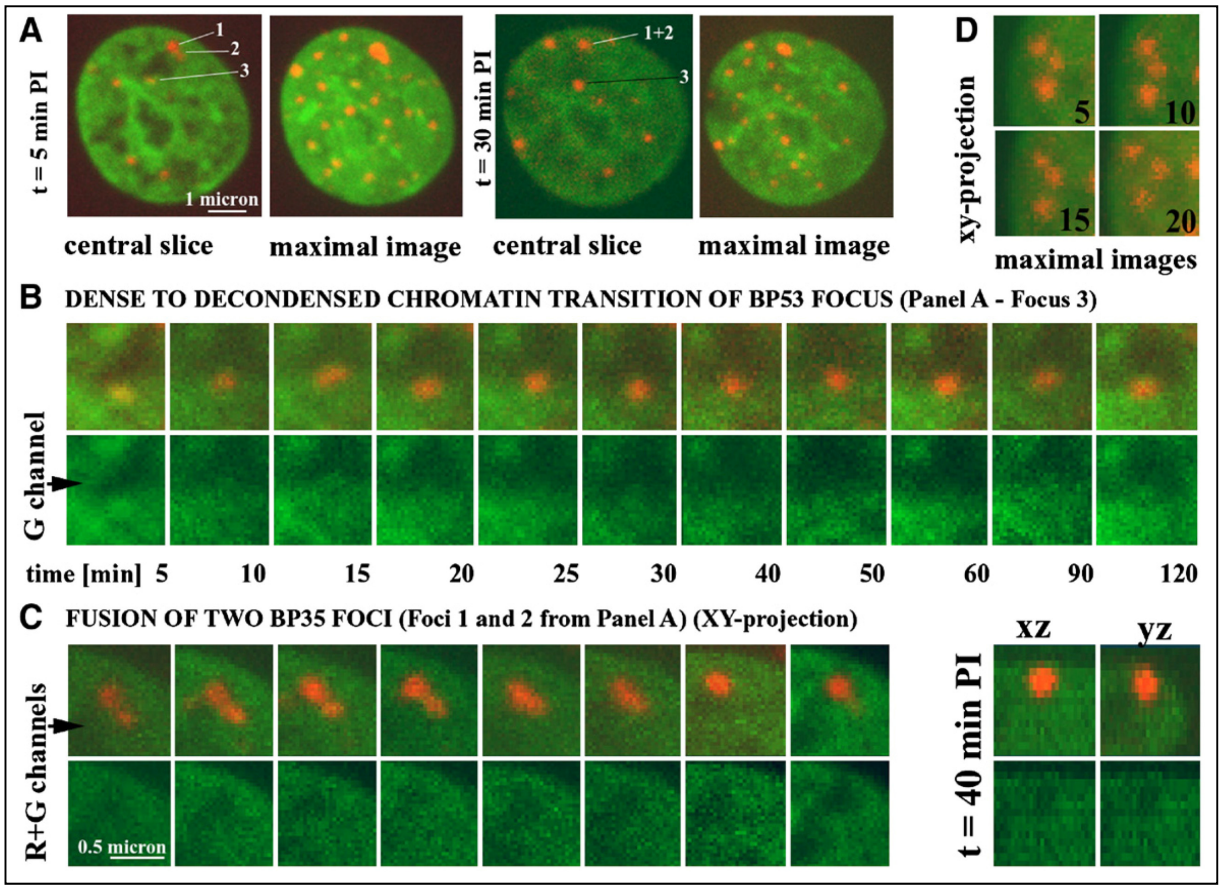

Figure 31. Changes of chromatin density observed in vivo at the sites of DSBs (presented as 53BP1-RFP foci) and their displacements after γ-radiation of MCF7 cells. (A) Central slices (0.4 μm) and maximal images in x–y plane of human MCF7 cells double-transfected with 53BP1-RFP and H2B-GFP proteins, irradiated with a dose of 1 Gy of γ-rays are displayed at 5 min (left panel) and 30 min PI (right panel). Localization of three 53BP1 foci (red) is shown relative to chromatin density (H2B-GFP, green). **(B)** Displacement of the *focus 3* from dense (intensively green) to sparse (faintly stained) chromatin is shown in detail during the PI time (from 5 to 120 min PI). **(C)** Fusion of the *foci 1* and *2* during the PI time (5–50 min PI) in x–y plane; for 40 min PI also the x–z and y–z slices are displayed to demonstrate the fusion in the 3D-space. The *focus 2* first relocates from dense chromatin (intensively green) to H2B-GFP faintly stained domain where it fuses together with the *focus 1*. **(D)** Short-distance movement of another three 53BP1 foci (red) monitored from 5 to 20 min PI, in 5-min intervals. Taken from **Falk et al. 2007**.[14]

Due to the decondensation of damaged domains, γH2AX foci protrude from heterochromatin into interchromatin/low-density chromatin space of the cell nucleus (referred to as “chromatin holes” for its weak staining with chromatin dyes), where there is sometimes too little room. Two or possibly more DSBs may therefore occasionally form clusters (**Figure 31** and **Figure 33**). Clustering of DSB repair foci was observed also *in vivo*, in MCF7 cells co-transfected with 53BP1-RFP and H2B-GFP fusion proteins to monitor the movement of 53BP1 foci in the context of the higher-order chromatin structure. The recorded interactions of 53BP1 foci clusters were usually of a temporary nature, but some of them persisted in nuclei until the end of the experiment (>40 min PI). The clusters did form between foci that had been already present in the particular hole and foci protruding into this hole from surrounding

heterochromatin domains. On the contrary, we did not recorded formation of focus clusters in heterochromatin or between foci pertaining to different chromatin holes and thus mutually separated by a heterochromatin "barrier" (**Figure 33**). This observation supports our previous conclusions that the mobility of HC-DSBs follows from the decondensation of heterochromatin domains. Since stable focus clusters occurred relatively rarely and, once formed, persisted in nuclei for longer periods of time than non-clustered foci, it is improbable they could be repair factories, where clustering of most foci could be expected. DSB repair focus clusters thus most probably represent by-products of DSB repair – complex lesions with an increased risk of chromosomal translocation (**Figure 34** and **Figure 35**).

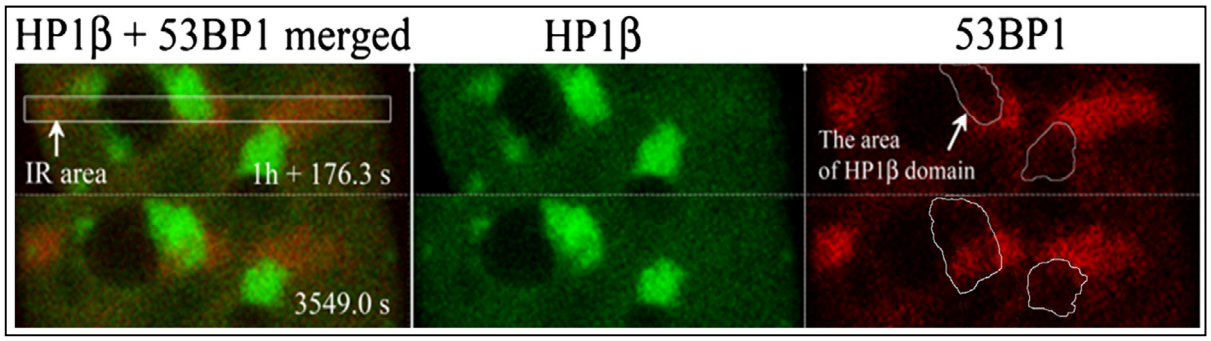

Figure 32. The accessibility of HC and EU for 53BP1 at different time points PI. The top line images show the distribution of 53BP1 (red) in the irradiated area relative to HC (HP1b, intensively green) and EU (faintly green background), in 1 h PI (1 h + 176.3 s). The bottom line corresponds with the situation about 1 h later (1h + 3549 s). A confocal slice (0.3 μm thick) in the x–y plane intersecting the irradiated domains is displayed for MCF7 cells co-transfected with 53BP1-RFP (red) and HP1β–GFP (green). DSBs were introduced in selected subcompartments (ROI, white rectangle) of the cell nucleus (top left image, IR area) by the UV lase micro-irradiation (see Section 2). ROIs were designed to intersect heterochromatic (HC) and euchromatic (EU) domains at the same time. At 1 h PI (top line), intensive accumulation of 53BP1 can be seen in the irradiated (DSB-containing) EU while penetration into the irradiated HC (HP1β) domain is not detectable. The colocalization of HP1β and 53BP1 remains incomplete until the end of the observation, indicating only slow and limited penetration of 53BP1 into the condensed heterochromatin. Taken from **Falk et al. 2014.**[16]

Based on these results, we have postulated novel model of formation of chromosomal translocations that has some aspects of both "Position-first hypothesis" and "Breakage-first hypothesis" [(39)] (**Figure 35**). Briefly, the higher-order chromatin structure at the pan-nuclear scale (nuclear architecture) determines the probability map of all possible mutual interactions between the particular genomic loci. Our earlier results[542,628] as well as the results of other research groups[626,627,672,673] clearly showed that the closer the foci are in the space of the cell nucleus, the higher is the probability of possible chromatin translocation ("Position-first" hypothesis). However, the "probability map" could be dominantly changed by the local higher-order chromatin structure, especially by mutual distribution of heterochromatin and euchromatin domains. The situation is explained in **Figure 33**: Let's consider the probability of mutual translocations between the loci *a*, *b*, *c* and *d*, distributed in the cell nucleus as shown. The spatial distance is the shortest between *a*-*c*, larger between *a*-*b* and *b*-*c*, and the longest between *a*-*d*, *b*-*d* and *c*-*d*. The probabilities of translocations (P[t]) based on the nuclear distances between genetic loci (Position-first theory) would therefore decrease from P[t(a;c)] to P[t(a;b)] or P[t(b;c)], to P[t(a;d)] or P[t(c;d)], and finally to P[t(b;d)]. However, the closest partners – *a* and *c* – are in our case separated by a heterochromatic "barrier" that precludes their mutual interaction.

[39] these two hypotheses are usually being considered as mutually contradictory

On the other hand, as it follows from the local higher-order chromatin structure, *a* and *b* will protrude into the same chromatin hole. Hence, originally too distant though, lesions *a* and *b* may approach each other and form a translocation, in contrast to *a* and *c*. Our model thus introduces important new aspects to the mechanisms of DSB repair and formation of chromosomal translocations. Especially, we show that the mobility of DSBs depends on the character of affected chromatin domain, and the vectors of chromatin movement, and thus also the probabilities of mutual interactions between specific chromosomal loci, are dominantly influenced by the local higher-order chromatin structure ("texture").

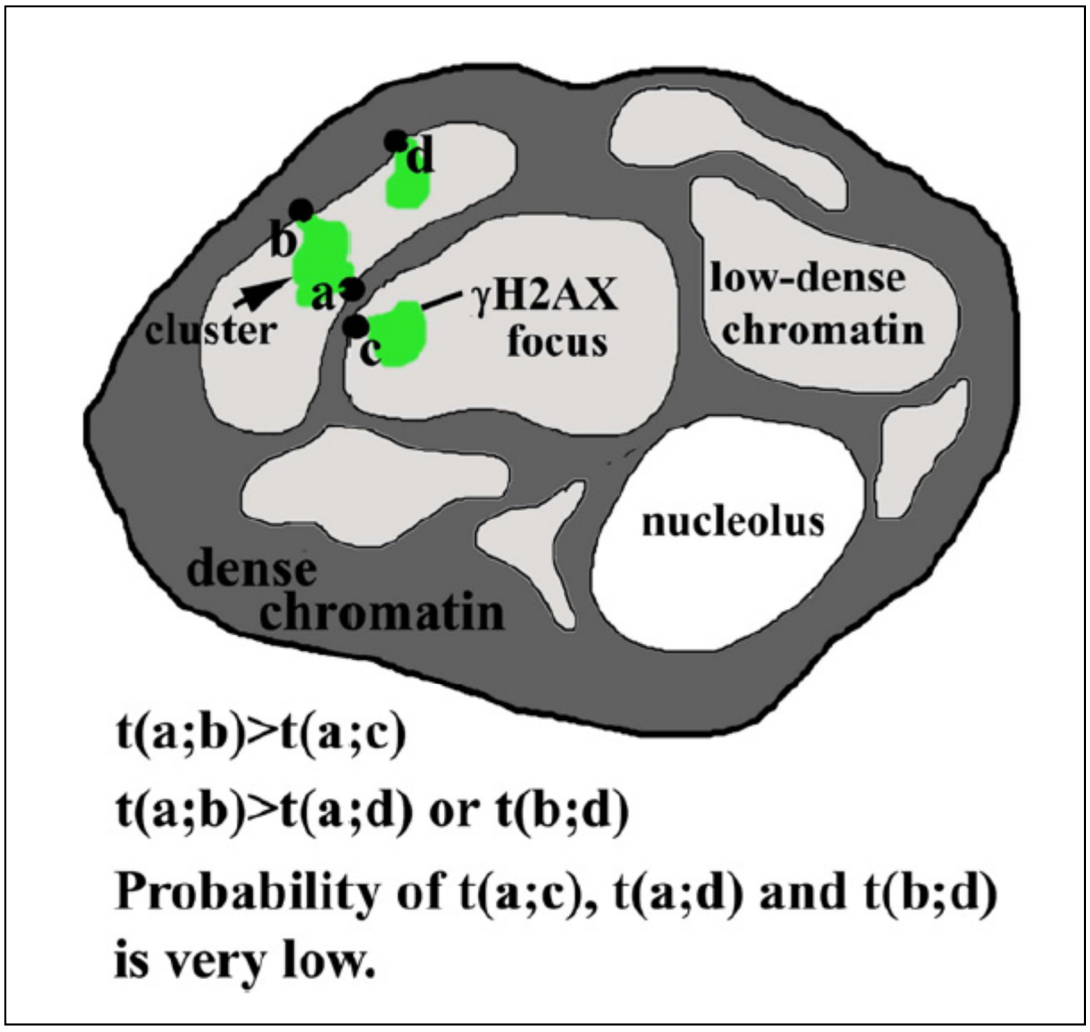

Figure 33. The proposed model of the mechanism of formation of chromosomal translocations. Schematic drawing shows the protrusion of γH2AX (DSB) (green) from the dense chromatin into the low-density chromatin 'holes'. Accumulation of more DSBs in the same hole results sometimes in their clustering (*a* and *b*), especially after higher radiation doses. *t(a;b)* indicates the probability of the translocation (t) between damaged loci (breaks) *a* and *b*; *t(a;b)* between loci *a* and *c etc.* According to the currently accepted hypothesis, the probability of translocation is the highest for loci *a* and *c*. However, it can happen that the closes DSBs (*a* and *c*) protrude into different chromatin 'holes', which seems to minimize the chance of chromatin exchange between these two lesions. The lesion *d* protrudes to the same ‚hole' as *a* and *b* but is too distant from these lesions; so the probability of *t(a;d)* and *t(b;d)* is very low (though in some cases possible). The highest probability of translocation is therefore between lesions a and b, which is determined both by 'preset' nuclear architecture (Position-first aspect) and chromatin dynamics (Breakage-first aspect) restricted by local chromatin structure. See the text above for more detailed explanation of the mechanism. Taken from **Falk et al. 2007**.[14]

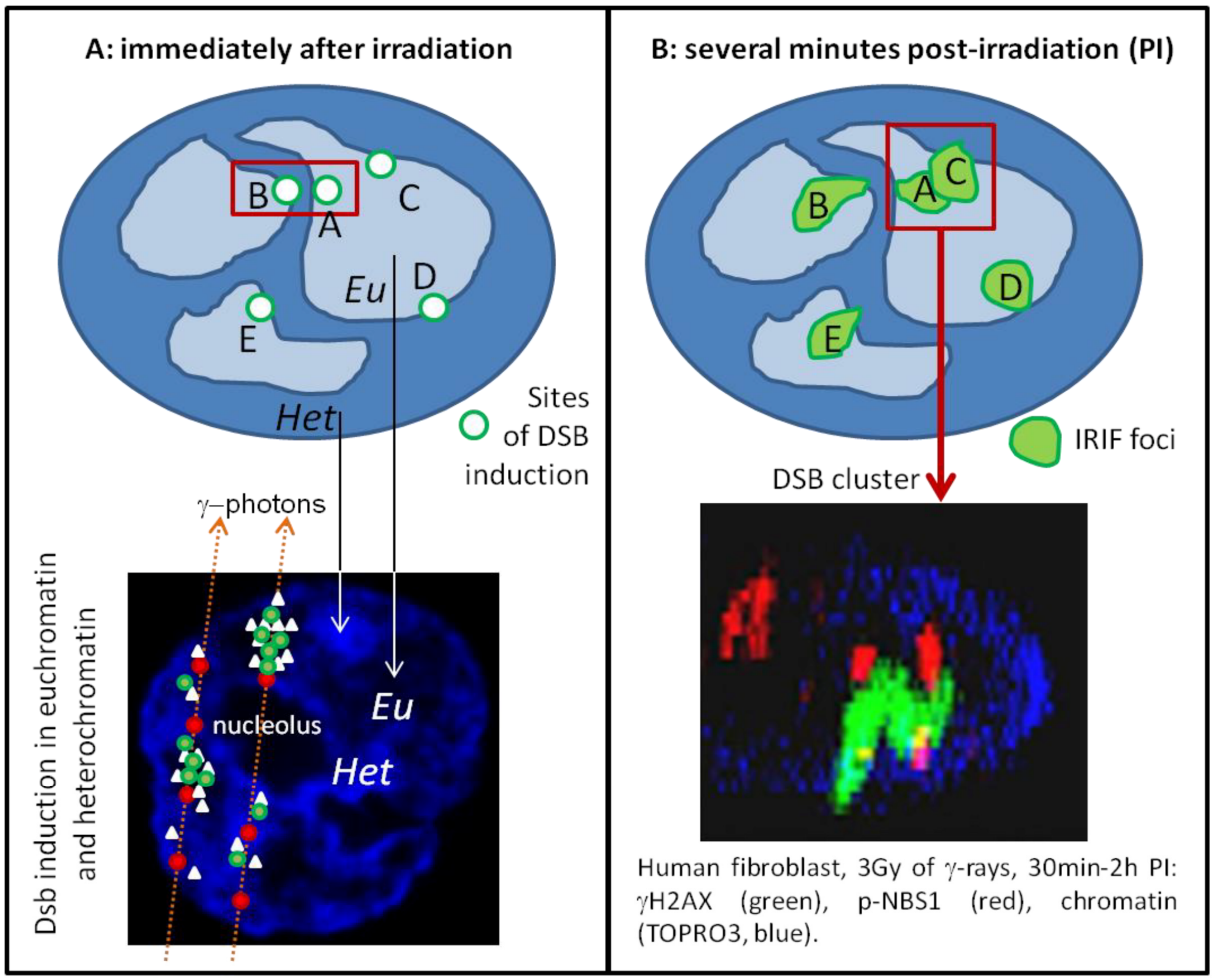

Figure 34. The summarization of the relationship between the higher order chromatin structure, sensitivity of chromatin to DSB induction by γ-rays, DSB repair, and the mechanism of chromosomal translocations formation. Bottom-left image: Some DSBs are generated directly by transversing γ-photons (red circles) but most DSBs (green circles) are generated by reactive oxygen species (white triangles). ROS-generated DSBs preferentially form in hydrated euchromatin (black areas) that is also less protected against ROS by proteins compared to less-hydrated heterochromatin (blue areas) abundant for heterochromatin binding proteins, such as HP1. Top-left image: Topography of induced DSBs is schematically shown together with higher-order chromatin structure (texture); chromatin of high density (heterochromatin) – dark blue; chromatin of low density (euchromatin) – light blue. Without the influence of the higher-order chromatin structure (i.e. according to the current hypothesis), the highest risk of translocation can be expected between lesions A and B, because they are the closest to each other. Top-right image: When the mechanism of DSB repair (chromatin decondensation at heterochromatic DSB sites) and the effect of the higher-order chromatin structure on the vectors of damaged chromatin protrusion is concerned, the probabilities of translocations between the particular lesions will be modified. The highest risk now appears for lesions A and C (instead for A and B). While A and B are separated by a heterochromatin barrier forcing them to protrude into different chromatin "holes", A and C protrude into the same chromatin "hole", and are still close enough to mutually interact. Lesions E and D are too distant from A (and, E is also separated by heterochromatin) to approach each other with a reasonable probability, though infrequent translocations were also observed between originally (before DSB induction) very distant loci[230,232]. Bottom-right image: A detail of a DSB cluster in 3D; confocal microscopy image, blue – chromatin stained with TOPRO3, green – γH2AX, red – NBS1. Taken from: **Falk M, COST Nano-IBCT Newsletter 2, 2011**.

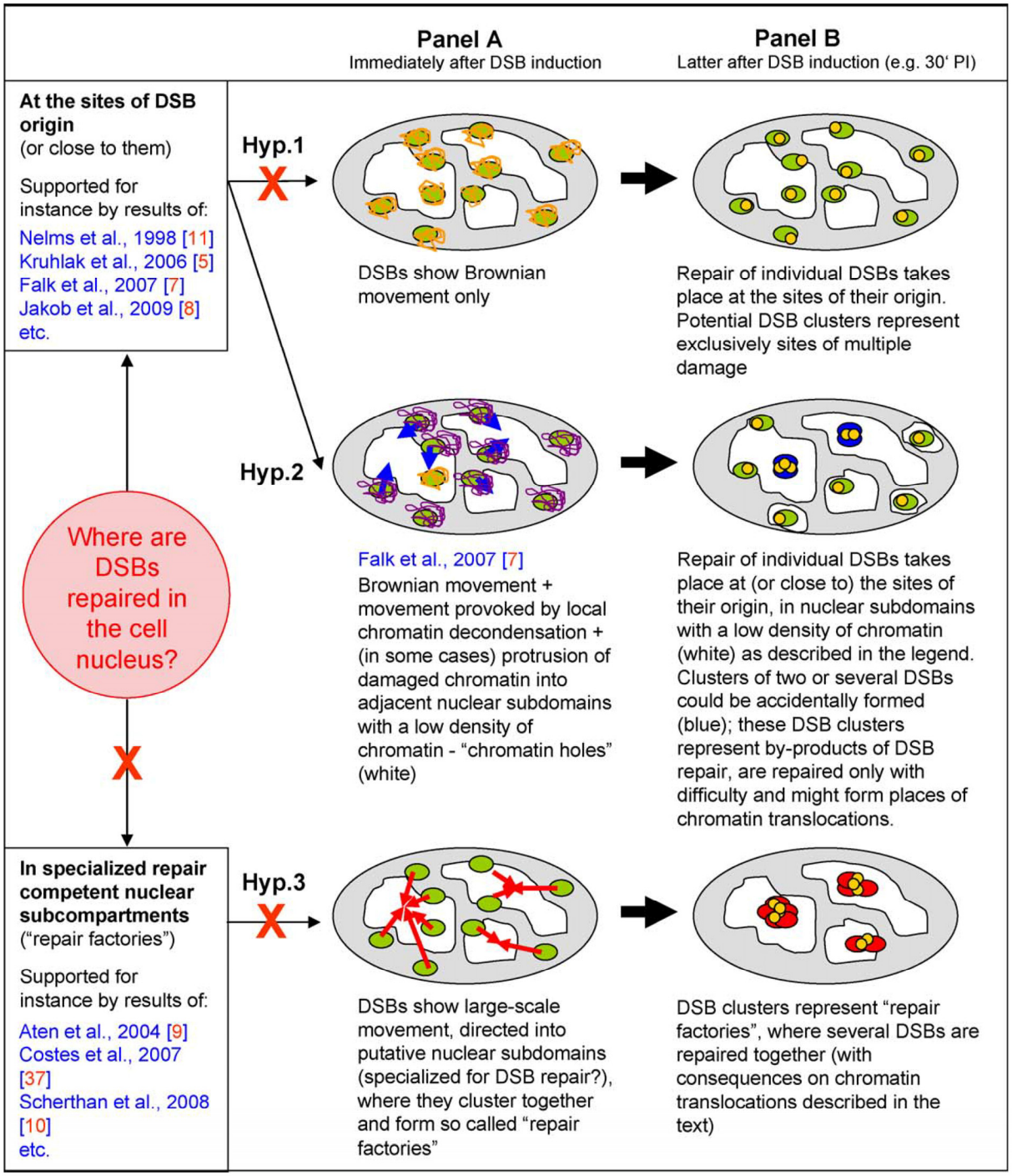

Figure 35. Highly disputed questions on spatio-temporal organization of DSB repair and mechanism of formation of chromosomal translocations. What is the sense of γH2AX foci clustering? Are the clusters only "byproducts" of the repair mechanism and thus the sites of an increased risk of chromatin translocations or do they reflect accumulation of DSBs in repair competent nuclear subcompartments or even "repair factories"? Intensively disputed questions on spatio-temporal organization of DSB repair in the cell nucleus are provided with potential alternative answers and supporting references. Briefly: The first hypothesis presupposes repair of DSB lesions (green spots) at the sites of their origin. "Movement" of DSBs is equivalent only to that of undamaged chromatin (Brownian movement, **Panel A**, orange trajectories). DSBs colocalize with DSB repair proteins (**Panel B**, yellow circles) at the sites of their origin, where they are also repaired. The second hypothesis[14] extends the previous one about the movement of DSBs that is induced by chromatin decondensation, provoked by DSB repair process. **Panel** A: Dense chromatin domains (gray) that contain DSB (green spots) are first decondensed to allow progression of DSB repair. This decondensation might led to a random short-range movement of DSBs (purple trajectories), in addition to Brownian movement (orange trajectories), or to their protrusion (blue arrows) into nuclear subdomains with a low density of chromatin (white). Movement of "euchromatic" DSBs is usually equivalent to the Brownian movement (orange trajectories). **Panel B**: In general, DSBs (green spots) colocalize with DSB repair proteins (yellow circles) at the sites of their origin, where

they are also repaired. In case of some DSBs (usually "heterochromatic", (gray)), chromatin decondensation accompanied by protrusion of DSB into low-dense chromatin subdomains might led to clustering of two or more DSBs, due to a limited space of these chromatin domains (white). These clustered DSBs (blue) are reparable only with difficulty and probably represent sites of an increased risk of chromatin translocations. The third hypothesis presupposes highly-dynamic DSBs (green) that migrate in a large-scale manner (Panel A, red arrows) into putative nuclear subdomains (specialized for DSB repair?), where they cluster together and form so called "repair factories" (Panel B, red clusters). Therein, several DSBs are repaired together, with the consequences for chromatin translocations described in the text. Conclusions supported and not supported by our results are indicated by arrows and crossed arrows respectively. Taken from **Falk et al. 2010.**[15]

2.3 Tumor Cell Radioresistance and Potential Therapeutic Approaches to Radio-sensitize Tumor Cells and Protect Normal Cells

More than 50 % of cancer patients are nowadays treated with ionizing radiation at some stage of disease. The insensitivity of tumor cells to radiotherapy (which is frequently associated with resistance also to other means of cancer therapy) is thus a serious problem. Since tumors are very heterogeneous systems and the radioresistance can be based on many mutually interconnected factors, fighting against this phenomenon is very difficult both theoretically and practically. In this chapter, the author discusses, based on his papers, on the role of DSB repair in the radiosensitivity/radioresistance of breast tumors, head and neck tumors, and glioblastoma tumors that were selected as interesting models. Consequently, novel approaches to overcome tumor cell radioresistance are tested and their mechanisms studied.

2.3.1 The roles of DSB repair in different tumor cell radioresistance

Relevant publications discussed

1. Sevcik J, Falk M, Macurek L, Kleiblova P, Lhota F, Hojny J, Stefancikova L, Janatova M, Bartek J, Stribrna J, Hodny Z, Jezkova L, Pohlreich P, Kleibl Z. Expression of human BRCA1Δ17-19 alternative splicing variant with a truncated BRCT domain in MCF-7 cells results in impaired assembly of DNA repair complexes and aberrant DNA damage response. Cell Signal. 2013;25(5):1186-93. doi: 10.1016/j.cellsig.2013.02.008.
2. Sevcik J, Falk M, Kleiblova P, Lhota F, Stefancikova L, Janatova M, Weiterova L, Lukasova E, Kozubek S, Pohlreich P, Kleibl Z. The BRCA1 alternative splicing variant Δ14-15 with an in-frame deletion of part of the regulatory serine-containing domain (SCD) impairs the DNA repair capacity in MCF-7 cells. Cell Signal. 2012;24(5):1023-30. doi: 10.1016/j.cellsig.2011.12.023.
3. Falk M, Horakova Z, Svobodova M, Masarik M, Kopecna O, Gumulec J, Raudenska M, Depes D, Bacikova A, Falkova I, Binkova H. γH2AX/53BP1 foci as a potential pre-treatment marker of HNSCC tumors radiosensitivity – preliminary methodological study and discussion. European Physical Journal D. 2017;71(9). doi: 10.1140/epjd/e2017-80073-2.

Discussion on Ševčík et al. 2012[23], Ševčík et al. 2013[24]

Modified according to Ševčík et al. 2012 and 2013.[23,24] In the present papers of Ševčík et al.,[23,24] we summarize our research on the influence of alternative splicing variants (ASVs) of BRACA1 protein on

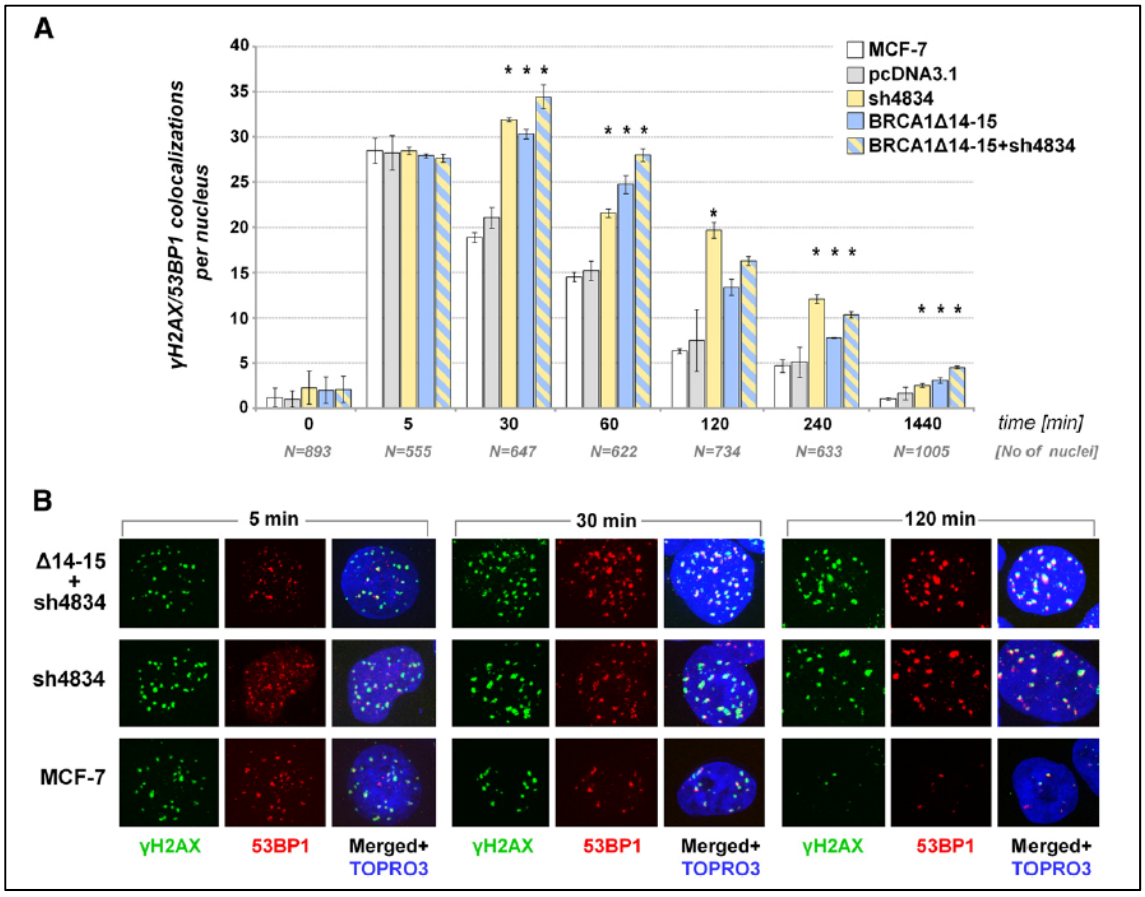

Figure 36. The kinetics of IRIF formation/dissociation in MCF7 cells expressing BRCA1 Δ14-15 alternative splicing variant. The kinetics of IRIF formation/dissociation (A) were determined by counting the number of the colocalizations of γH2AX (green) and 53BP1 (red) proteins characterizing an early response to DSB in spatiotemporal manner in times of 5, 30, 60, 120, 240, and 1440 min PI using high-resolution fluorescent confocal microscopy (B). Maximal images composed from 40 confocal optical slices taken with a z-step of 0.2 μm are shown. Total nuclear chromatin was counterstained by TOPRO-3 (artificially blue). Data are mean ± S.D., N=total number of analyzed nuclei in group. *pb0.05 (Wilcoxon test). From **Ševčík et al. 2012.**[23]

DSB repair capacity of (mammary cancer) cells and consequently their clinical relevance. BRCA1 is a large multifunctional protein that plays a central role in DSB repair and the maintenance of genomic stability. Defects in BRCA1 and BRCA2 functions have been related to pathogenesis of breast cancer (BC) that is the most common malignancy among women worldwide. Inactivating alterations of BRCA1 (MIM# 113705) and BRCA2 (MIM# 600185) cause ~3–5 % of all BC cases and strongly predispose their holders for BC development.[674] Functionally, BRCA1 is a large platform protein that participates in assembly of DSB repair complexes[675–677] and decision-making process between homologous recombination (HR)[678] and non-homologous end joining (NHEJ).[679] BRCA1 protein can be phosphorylated by various protein kinases, including ATM, ATR, Chk2, Cdk2, Akt, and AURKA.[680] Depending on the particular stimuli, these kinases phosphorylate specific serine residues of BRCA1, predominantly localized in its serine-containing domain (SCD).[681,682] These specific post-translational modification then regulate BRCA1 functions, including its targeting to DSB sites and participation in DSB repair pathways, by defining its protein-protein interaction capabilities and intracellular localization.[683,684,685] The surprisingly high number of upstream kinases directly regulating BRCA1 affirms its central position in DNA-repair pathway selection, which was recently confirmed also by

super-resolution microscopy techniques.[686–688] The exact molecular function of BRCA1 in DSB repair and associated processes remains to be understood though.

Similar to γH2AX, BRCA1 and its complexes could be visualized as DSB repair foci (also referred to as IRIFs).[689] A proper assembly of BRCA1 complexes at DSB sites and, in turn, efficient DSB damage signaling and repair strictly depend on BRCA1 structure.[690,691] Besides clearly pathogenic BRCA1 gene mutations and structural alterations, a large group of sequence variants of uncertain clinical significance has been identified. At present, a growing interest is focused on unbalanced or aberrant BRCA1 pre-mRNA splicing, while the generation, molecular effects, and clinical significance of naturally occurring alternative BRCA1 pre-mRNA splicing variants (ASVs) remain obscure. Indeed, many ASVs have been identified in various healthy or pathological tissues and cell lines with unknown tissue specificity and biological activities.[692] The alternative splicing is a mechanism able to produce protein isoforms with markedly different biological properties from a single primary pre-mRNA transcript and thus it is responsible for great genetic diversity.[693,694] We can therefore reasonably hypothesize that the overall biological activity of a certain gene's product is determined by the actual pool of its particular protein isoforms generated by the alternative (or aberrant) pre-mRNA splicing. BRCA1 has several common alternative splicing variants occurring frequently together with the main full-length transcripts.[692] The concentrations of the particular mRNAs are, at least partially, dependent on the cell cycle phase suggesting their natural regulatory function within the global BRCA1 expression profile.[695]

The relevance of the BRCA1 splicing variants on the cellular processes has been demonstrated in studies of the BRCA1 variant lacking exon 11, which showed that BRCA1Δ11 failed to deliver Rad51 recombinase to the sites of DSB, resulting in severe impairment of HR and genome instability.[696,697] It seems that the occurrence of the BRCA1 alternative splicing variants is frequent rather than rare, though the exact tissue specificity and quantity of particular alternative splicing variants is not known yet. More than twenty BRCA1 ASVs have been described so far,[692,698] with the majority of them being classified as variants of unknown clinical significance. Altogether, these facts and the result of our current work imply the importance of further functional analyses of BRCA1 ASVs.

The majority of interaction events between BRCA1 and its binding partners are realized via the N-terminally localized RING finger domain and a tandem of two BRCA1 C-terminal (BRCT) domains.[699] Besides BRCA1 aberrant splicing variants described during the last decades,[692,698] Pohlreich et al.[700–702] identified numerous BRCA1 ASVs in high-risk breast and/or ovarian cancer families. Among them, several in-frame ASVs leading to the loss of the critical BRCA1 functional domains were observed, including the variant BRCA1Δ14-15, lacking the C-terminal part of its SCD, and BRCA1Δ17-19 ASV, which misses a portion of its BRCT domain. Hence, in the frame of herein discussed studies, we attempted to characterize the influence of the two mentioned BRCA1 ASVs on the DSB repair kinetics and efficiency in irradiated (mammary carcinoma) cells. For this purpose, we constructed the MCF-7-derived clones stably expressing the indicated ASVs. At the same time, the cells either expressed the wild type (wt) BRCA1 or its endogenous expression was downregulated with shRNA. To obtain the information on how the DSB repair efficiency and kinetics depend on the ratio between the *wt* BRCA1 protein and its BRCA1Δ14-15 or BRCA1Δ17-19 ASV in the established clones, we irradiated the cells with 1.5 Gy of γ-

radiation and quantified the formation/disappearance of γH2AX/53BP1 foci during the post-irradiation (PI) time.[13,665]

The γH2AX and 53BP1 proteins (used in the present studies as the DSB markers) participate in both HR and NHEJ pathways. The time course of their co-localization after the γ-IR-induced DNA damage in our model system suggests that a downregulation of endogenous *wt* BRCA1 or an overexpression of BRCA1Δ14-15 negatively influences the initial rapid phase of DSB repair (**Figure 36**). The results of our study thus showed that a relatively subtle change in the BRCA1Δ14-15 mRNA structure can lead to the production of a BRCA1 protein isoform that alters the initial kinetics of DSB repair in a dominant negative-manner. At the same time, the MCF-7 clones with a downregulated expression of endogenous *wt* BRCA1 were hypersensitive to the DNA cross-linking agent, mitomycin C, which is in accordance with the position of BRCA1 protein in the HR pathway. Surprisingly, the cells expressing the BRCA1Δ14-15 ASV displayed no difference in sensitivity to mitomycin C compared with the non-transfected MCF-7 controls. This suggests that the presence of the BRCA1Δ14-15 protein isoform does not corrupt the activity of HR. Contrary to that, the results of a direct *in vitro* NHEJ assay proved that the activity of NHEJ was lower both in clones with depleted wt BRCA1 and in clones expressing the BRCA1Δ14-15 ASV. Taking together, wt BRCA1 downregulation impairs both the HR and NHEJ pathways, as it has been already documented,[697] while the BRCA1Δ14-15 alternative splicing variant only disturbs NHEJ (**Figure 36**). This indicates that the SCD plays a role in regulation of the BRCA1 activity in the NHEJ pathway.

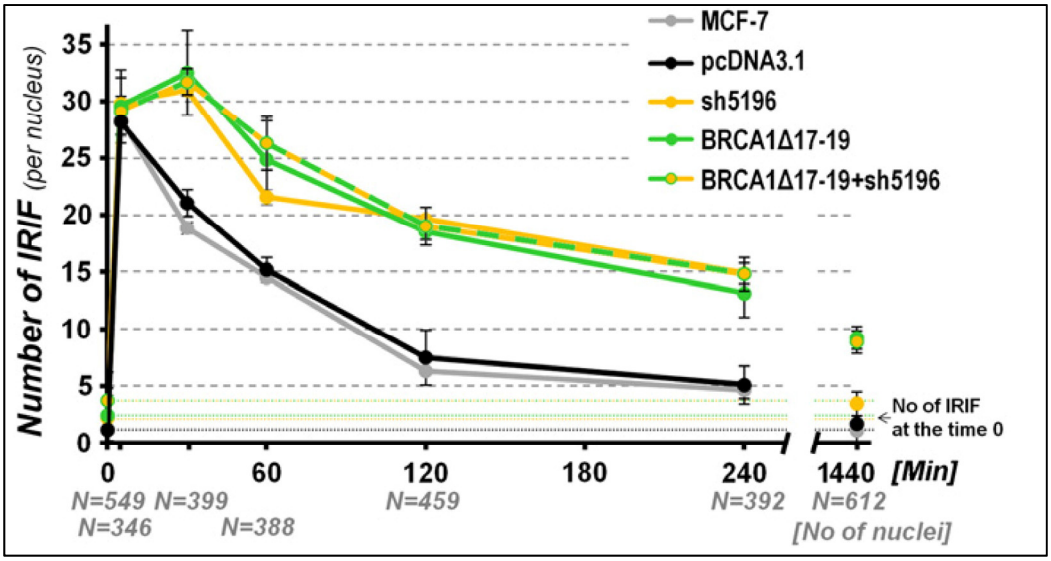

Figure 37. The kinetics of IRIF formation/dissociation in MCF7 cells expressing BRCA1 D17-19 alternative splicing variant. The kinetics of IRIF formation and persistence in diverse clones of MCF-7 cells. The kinetics of DDSB signaling/repair were assessed by counting the γH2AX/53BP1 colocalizations per nucleus at the indicated time points (0, 5, 30, 60, 120, 240 and 1440 min, respectively) after ionizing irradiation (1.5 Gy) using confocal immunofluorescence microscopy. The endogenous level of DDSBs in the indicated clones is represented here as the number of IRIF per nucleus in non-irradiated cells (time 0; depicted by dotted lines). Data are mean ± S.D. From **Ševčík et al. 2013**.[24]

On the other hand, overexpression of BRCA1Δ17–19 ASV with an in-frame deletion affecting a substantial part of the BRCT domain impaired DSB repair executed by both NHEJ and HR pathway, as it delayed the initial dynamics of the IR-induced DSB repair (γH2AX and 53BP1) focus formation/disappearance (**Figure 37**) and sensitized cells to mitomycin C. Based on our observations,

we suppose that the ectopically expressed BRCA1Δ17–19 protein is unable to interact with Abraxas and CtIP while it retains its BARD1-binding capacity. This defect probably causes the observed hypersensitivity to mitomycin C and the reduced activity of IR-induced DSB repair in MCF-7 cells. The presence of the BRCA1Δ17–19 variant also alters the assembly of DSB repair complexes (γH2AX and 53BP1 foci) during the early PI period, and impairs thus the NHEJ activity.

The majority of protein-protein interactions in the processes of DNA repair take place in a phosphorylation- or ubiquitin-dependent manner. The exons 14 and 15 deleted in the analyzed BRCA1Δ14-15 variant contain six serine residues known to be the targets of ATM kinase activated upon DNA damage. Altered phosphorylation of BRCA1 thus probably changes balance in the formation of specific BRCA1-containing complexes.[683,685] The BRCA1-CtIP (BRCA1-C) complex together with additional nucleases and helicases promote during the S- and G2-phases a strand resection generating long ssDNA regions indispensable for the HR.[703] Contrary to that, the assembly of the BRCA1-RAP80 complex that is facilitated by ubiquitin-modified chromatin near the break site prevents the strand resection and hence HR by blocking of CtIP activity.[704] Thus, the phosphorylation-directed formation of the BRCA1-containing complexes critically involves BRCA1 function in the DNA repair. In concordance with that, and as indicated by our results, the BRCA1Δ14-15 variant (lacking the substantial part of SCD) results in formation of protein isoform with impaired sensitivity to the DNA damage up-stream signaling resulting in impaired DSB repair. We assume, that an overexpression of the BRCA1Δ14-15 variant (originally described as an alternative pre-mRNA splicing variant in PBMCs obtained from the BRCA1 mutation-negative BC patient) in MCF-7 cells results in the expression of BRCA1 isoform corrupting the NHEJ pathway and in turn leading to preferential use of HR DSB repair.

HR is dependent on the formation of long 3′ ssDNA overhangs of the free DNA ends at DSB sites.[705] These overhangs are dominantly generated by the activity of CtIP exonuclease, which activity increases as CtIP is bound to BRCA1 within the BRCA1 C-complex. On the other hand, the resection by unbound CtIP molecules is inhibited by their association with the DNA repair modulator 53BP1.[706,707] Limited resection of DNA ends is insufficient for further HR, and therefore the integration of CtIP into the BRCA1 C-complex overcomes the inhibitory activity of 53BP1 and enables the formation of long 3′ DNA overhangs.[708] Hence, the impaired resection caused by the inability of the BRCA1Δ17–19 isoform to bind CtIP can cause the delay in DSB repair observed in the present study. Defective assembly of the BRCA1 C-complex in MCF-7 cell clones expressing the BRCA1Δ17–19 isoform as well as in those with downregulated *wt* BRCA1 expression can explain their similar behavior in terms of increased sensitivity to mitomycin C and delayed early phase of DNA repair.

Our observations have important consequences for the radiosensitivity and susceptibility to tumorigenesis of cells harboring BRCA1 ASVs. The BRCA1 protein was initially identified as a mediator of the apical signal in HR. Later it was reported that BRCA1 may also participate in the NHEJ pathway.[709] We may therefore assume that inactivating mutations in the *BRCA1* gene affect both DNA repair pathways. However, specific analyses of the BRCA1's role in the DNA repair pathways brought several seemingly contradictory results. While Jasin et al.[710] showed that *BRCA1*-deficient cells have a heavily impaired HR, an instable genome, and increased sensitivity to mitomycin C compared with wt BRCA1-expressing cells, Dever et al.[711] documented that a mutation in the BRCA1 BRCT domain leads to a

hyper-recombination. Further, Jasin et al.[697] observed that the BRCA1−/− cell line has reduced HR, while NHEJ is slightly elevated at the same time as a compensatory mechanism for the decreased DNA repair capacity. On the other hand, Wang et al. proved that a BRCA1 knock-down compromises the NHEJ accuracy.[709] Nevertheless, in spite of these contradictions, we can propose that the differential expression of BRCA1 ASVs, regulated by currently uncharacterized mechanisms, may represent a system altering the selection of particular molecular pathways of DSB repair. This may negatively affect genome integrity by undermining the overall capacity or precision of DNA repair, and possibly promoting hyperactivity of HR. Even a shift towards NHEJ or HR can influence sensitivity of cells. The precise involvement of HR and NHEJ in human cells and the hierarchy of activation of these pathways are still discussed. The HR pathway is a precise mechanism of DSB repair; however, it probably plays only a limited role in eukaryotic cells compared to a relatively error-prone NHEJ. Though excision-based mechanisms operate also in G1, most authors agree that HR (in its precise definition) can be most effectively used during the S- and G2-phases of a cell cycle, when sister chromatids are available for a homologous exchange.[(40)] NHEJ takes place faster than HR and is the prevailing DNA repair mechanism within a period of the first four hours after a genotoxic DNA insult.[712] On the other hand, HR is probably restricted to specific chromatin regions and proceeds much slower. IRIF foci of a homology-directed DNA repair thus typically occur with a delay and persist for a longer time period after irradiation.[110] In addition, still incompletely characterized alternative (or backup) repair pathways operate in cells.[85,86] Activation of these, usually mutagenic repair pathways must also be considered in consequence of BRCA1 ASV expression. An unreasoned preference for one of the repair mechanisms due to the presence of BRCA1 ASVs may therefore influence both susceptibility of normal cells to mutagenesis and sensitivity of cancer cell to radiotherapy.

In addition, HR must be inhibited once DSBs are repaired in order to prevent hype-recombination and formation of undesirable DNA crossovers (referred to as hyper-HR).[710] Taking into account the results of comet assays showing that the majority of DSBs are repaired within 120 min PI and colocalization studies showing increased persistence of DSB repair foci beyond this time, it could be suggested that the presence of the BRCA1Δ17–19 variant interferes with processing of the slowly-repaired DSBs localized in the highly complex chromatin regions[26] or disturbs the termination of HR by blocking the DSB repair focus removal. Dever et al.[711] showed that BRCA1 mutation in its BRCT domain causes increased recombination leading to genomic instability. These results indicate that the BRCA1 A-complex is a negative regulator of ubiquitination-dependent DNA repair pathways. The inability of the BRCA1Δ17–19 ASV to bind Abraxas, a central protein of the BRCA1 A-complex, might contribute to the

[40] The most recent results, as presented at the ICRR 2019 congress (Manchester, Great Britain), show that HR can operate also in G1 phase of the cell cycle where it uses nascent mRNAs as repair templates. It means that HR in G1 mostly proceeds in actively transcribed sequences that should be repaired with the highest possible fidelity. Alternatively, the homologous chromosome can also be used as a repair template in G1, though with a lower efficiency. HR could be thus the first repair pathway the cells try to activate after DSB damage and HR is replaced by NHEJ only if unable to proceed further or somehow inhibited. The most important genomic sequences are thus repaired by HR throughout the cell cycle while NHEJ is used to repair less important sequences. NHEJ thus allows fast repair of numerous DSBs in large eukaryotic genomes, which is necessary to prevent formation of chromosomal aberrations usually leading to cell death in the next mitosis. On the other hand, formation of `small` mutations inside genetically inactive genomic sequences represents an acceptable cost of cell survival. However, the cooperation or competition between HR and NHEJ remains only poorly understood.

observed prolonged persistence of DSB repair foci. Moreover, the BRCA1 mutation p.I26A affecting the RING domain was shown to reverse the increased recombination rate in cells expressing the BRCA1 BRCT mutant p.K1702M.[711] This is consistent with our observation that persistence of DSB repair foci was prolonged in cell ectopic expression BRCA1Δ17–19 (which maintains the RING domain-mediated BARD1 binding) but not in cells with downregulated *wt* BRCA1

Several ASVs were shown to negatively influence the BRCA1-mediated cell cycle control and DNA repair activity.[23,713] This indicates that BRCA1 ASVs generated in a tissue-specific manner by misregulated pre-mRNA splicing can also contribute to tumorigenesis. It has been observed that the formation of BRCA1 aberrant splicing variants can promote malignant transformation.[714–716] On the other hand, the involvement of regulated alternative splicing in cancer development is virtually unknown.[694] For numerous gene products, including BRCA1, it has been shown that the formation of specific ASVs can be determined by a cell cycle phase,[695] or by the DNA damage response.[717,718] This suggests that alternative splicing is an important post-transcriptional regulatory event responding to specific signals. Thus, alternative splicing misregulation can lead to formation of an alternative protein product with potentially aberrant function or uncoupled from upstream regulation. The resulting appearance of ASVs that should normally be created under different cellular conditions and/or in a different amount can markedly alter the downstream processes that depend on the protein subjected to AS, with potential implications for human diseases including cancer. To conclude, various BRCA1 ASVs can on the one hand predispose cells to cancer development, and on the other hand, sensitize tumor cells to radiotherapy and treatments based on DSB repair inhibition.[63]

Discussion on Falk et al. 2017

Modified according to Falk et al., 2017.[25] In this work, we focused on several important questions related to radiosensitivity of head and neck squamous-cell carcinomas (HNSCC; herein referred to as HNT, head and neck tumors). Especially, we attempted to find out how DSB repair efficiency and survival upon γ-irradiation vary for the cells of the same type isolated from HNTs of different patients and, on the other hand, different cell types inhabiting the same tumor. We were also interested in whether these phenomena may be influenced by the communication between cell types inside the tumor and whether tumors can modify DNA damage response of normal cells localized in the tumor surroundings. Considering our earlier studies,[10] we also researched on the possibility of whether the cells of morphologically normal tissue taken at distance from the tumor can possibly show similar DSB repair defects as do the tumor cells. Since permanent tumor cell lines cannot be used for the described purposes, we prepared the primocultures of epithelial $CD90^-$ ("tumor") and $CD90^+$ (tumor-associated fibroblasts, TAFs) cells from head and neck tumors.

In the present work, we describe our first results on DSB repair kinetics and efficiency in $CD90^-$ and $CD90^+$ cell primocultures isolated from HNT that were clinically considered either as radiosensitive or radioresistant. We demonstrate here our ability to prepare $CD90^-$ and $CD90^+$ primocultures and follow DSB repair in these cells *in vitro* with the highest possible sensitivity and precision. While the only radioresistant tumor among the tumors involved into the published results showed characteristics of

DSB repair similar to (radioresistant) normal human skin fibroblasts, the radiosensitive tumors suffered from genetic instability and markedly delayed repair kinetics with increased persistence of unrepaired DSBs even at long periods post-irradiation. Nevertheless, whether these results are more generally valid, and whether the monitoring of DSB repair *in vitro* can be used to predict the response of individual tumors to radiotherapy, is just being studied. The project is currently in the stage of result evaluation, so the conclusions postulated here must be understand as preliminary. The head and neck tumors were selected for two purposes. First, they represent an interesting experimental model for radioresistance studies (explained later), and, second, there is an urgent call from the clinical oncologists for identification of markers of HN tumor radioresistance.

HNT can be either surgically removed or eradicated by radiotherapy that is usually combined with chemotherapy. (Chemo)-radiotherapy is often preferred over operation as HNTs are frequently juxtaposed with vital organs. The surgery is thus often seriously mutilating or impossible. The problem is that only ~50 % of HNT respond to irradiation. [25] Since markers of HNT radiosensitivity are not known, radiotherapy is being applied more or less "blind." HNT to be treated by radiotherapy are selected based on their clinical parameters, response to neoadjuvant chemotherapy, and patients' preferences. However, our clinical experience from past 15 years (180 – 220 newly diagnosed patients/year) shows that the chemosensitivity of HNT (with the highest share of laryngeal, oropharyngeal and hypopharyngeal locality, mostly in advanced stage) does not sufficiently correlate with the radiosensitivity. Searching for reliable markers of HNT radiosensitivity/radioresistance thus still represents an important task of radiobiological research. Though many other processes may also contribute to HNT radioresistance, the discrepancy between the outputs of chemotherapy (for HNT usually based on cisplatin-mediated formation of DNA crosslinks repaired by the base excision pathway) and radiotherapy (based on induction of DSBs that are repaired by the NHEJ/HR repair pathways) suggests that DSB repair could play an important role. DSBs are most efficiently introduced by IR and represent the most lethal type of DNA damage.

In this work, therefore, we tested whether DSB repair significantly differs among HNTs and analyzed the possibility whether evaluation of DSB repair in tumor cell primocultures irradiated *in vitro* might open new way to predict response of individual tumors to radiotherapy.[719] We have successfully introduced the methods for preparing the primocultures of different cell types from HNTs and employed currently the most sensitive method – immunofluorescence confocal microscopy of γH2AX/53BP1 repair foci[33] – to monitor DSB induction and repair in these primocultures prior to and upon irradiation. We have already demonstrated that the results of γH2AX/53BP1 immunofluorescence microscopy well correlate with the results of comet assay, representing the gold standard method in radiobiology to directly quantify DSBs.[33] Taking advantage of the described approach, we compared various parameters of DSB repair for $CD90^-$, $CD90^+$ and mixed $CD90^-$ (+) $CD90^+$ tumor cell primocultures derived from about 70 – 100 HN tumors. In the cohort addressed by the discussed paper, one tumor was clinically radioresistant, two tumors were radiosensitive and remaining tumors were of unknown status. The enhanced dataset that is just being analyzed includes dozens of tumors of both types. The reason for separating cells according to the CD90 surface antigen positivity was as follows: though there are some uncertainties in the literature about interpretation of CD90

expression, we can reasonably suppose that CD90⁻ cells in our study represent epithelial tumor cells while CD90⁺ cells contain a predominant fraction of tumor-associated fibroblasts (TAFs). Important roles of TAFs in influencing malignant potential and treatment response of tumors have repeatedly been described (e.g. in Raudenska et al., 2015[720] and citations therein). The mixed CD90⁻ (+) CD90⁺ primoculture allowed us to follow a potential influence of CD90⁻ and CD90⁺ cell interactions on DSB repair. Cultured human skin fibroblast (NHDF) provided us DSB repair characteristics for normal, non-malignant cells and served thus as the patient-independent DSB repair standard. Comparisons of

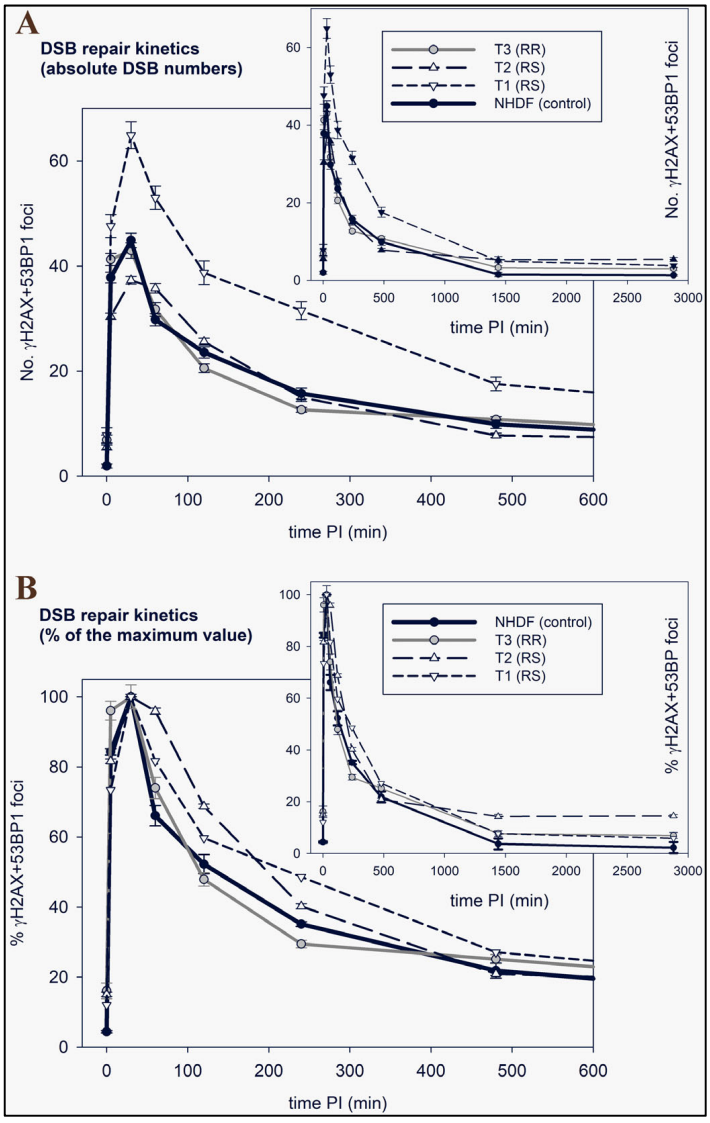

Figure 38. γH2AX/53BP1 foci formation, disappearance and persistence (DSB repair kinetics and efficiency) compared for normal human skin fibroblasts (NHDF) and CD90+ tumor cells primocultures derived from clinically radiosensitive (T1 and T2) and radioresistant (T3) tumors, respectively. See Table 1 for the tumors' characteristics. **A:** The mean numbers of γH2AX/53BP1 foci per nucleus during the time post-irradiation with 2 Gy of γ-rays. The values obtained by immunofluorescence confocal microscopy in spatially (3D) fixed cells are shown. Error bars represent standard deviations (T1, T2 and T3) or standard errors of means (NHDF) calculated for two independent experiments. **B:** As A but the percentage of γH2AX/53BP1 foci per nucleus is shown (100% correspond to the maximum value detected for all samples at 30 min PI). From **Falk et al., 2017**.[25]

results to normal mucosa cells extracted from histologically normal HN tissues (e.g. tonsils) of corresponding HNT patients were impossible for present tumors; however, we hope to obtain such data at least for some tumors in future. This information will allow for determining the patient-specific DSB repair efficiency ratio between normal and tumor cells, while comparison with NHDF cell line may reveal potential defects of DSB repair or even pre-malignant alterations in histologically normal patients' tissues sampled far distant from the tumor.[7,10] After accomplishing all the analyses, the results would contribute to our better understanding of HNT development as well as to better therapy planning in future. A brief discussion on this issue, based on recently obtained samples is provided at the end of this text.

Concerning the published results, we first analyzed the presence of DSBs in non-irradiated NHDF cells and all types of tumor primocultures **(Figure 38**, **39**). The results revealed that even non-irradiated CD90⁻, CD90⁺, and mixed CD90⁻ (+) CD90⁺ primocultures derived from the radioresistant tumor T3 show markedly higher average numbers of γH2AX/53BP1 foci per nucleus than NHDF cells. Since the

increased numbers of γH2AX/53BP1 repair foci appeared in the majority of cells, we suppose this observation points to increased genomic instability in all three primocultures of tumor T3. Interestingly, non-irradiated primocultures isolated from numerous other tumors, including the radiosensitive tumors T1 and T2, also contained increased DSB repair focus numbers, higher than NHDF cells. Though more tumors must be analyzed, it seems that the presence of DSB repair foci in non-irradiated tumor cells, indicative of genomic instability, is quite common phenomena in HNT biology. Whether the permanent presence of DSB damage can be interpreted as an increased sensitivity of affected tumors to radiation due to inefficient genome maintenance, or rather as their radioresistance following from the cell adaptation to permanent DNA damage, is currently analyzed. In any case, tumors with a higher level of DNA damage may more easily accumulate genetic changes, which, in turn, allows faster development of cell clones. Some of these clones might exhibit radioresistant features.

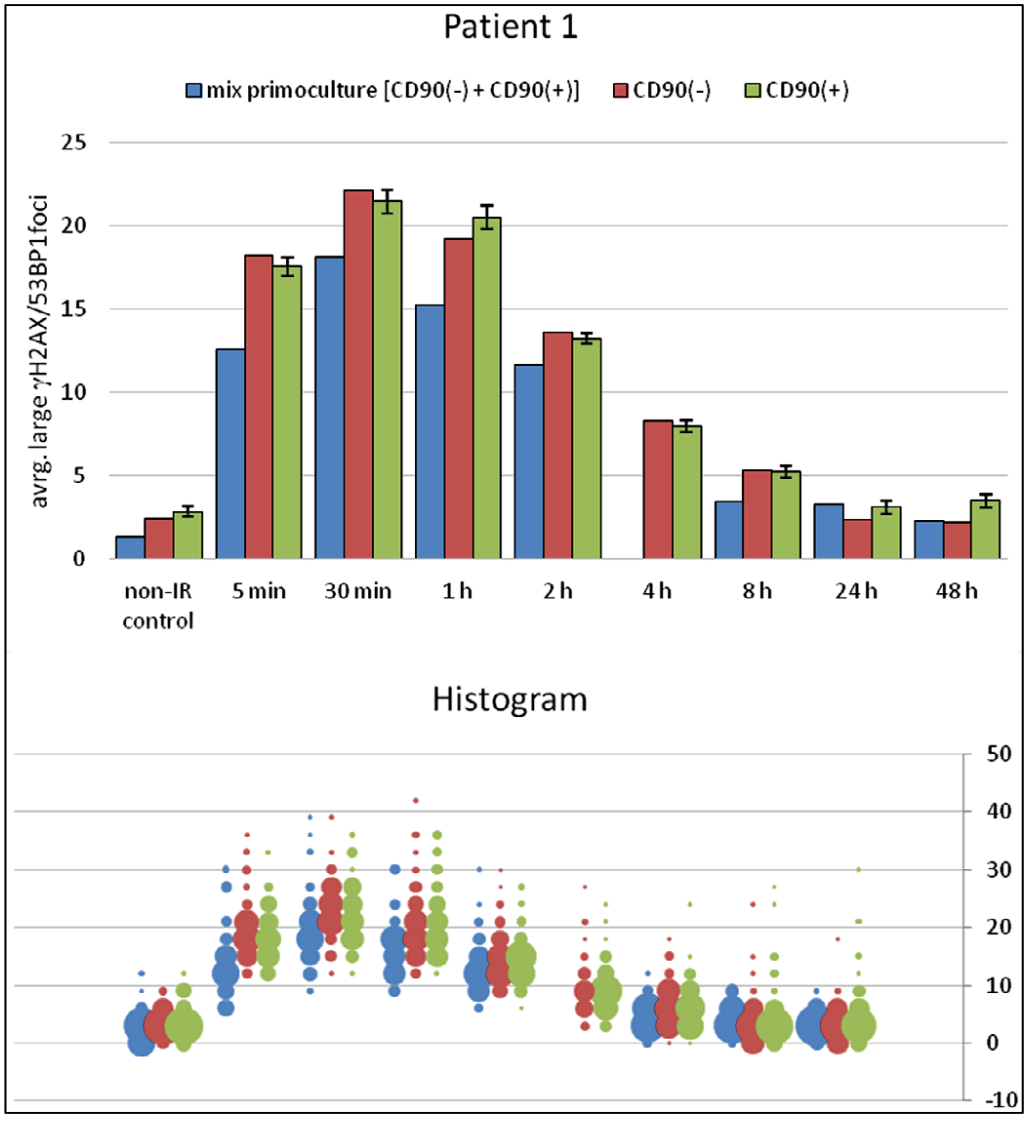

Figure 39. DSB induction and repair compared for CD90− and CD90+ cells and for their mixed culture (CD90− + CD90+); all primocultures were derived from the radiosensitive tumor T1. Mean values of large γH2AX/53BP1 foci per nucleus are shown with standard errors. From **Falk et al., 2017**.[25]

However, the genomic instability observed may primarily point to cell radiosensitivity due to DSB repair dysfunction. Hence, we compared the DSB repair capacity (kinetics and efficiency) of individual tumor cell primocultures and NHDF fibroblasts after irradiation with a single dose of 2 Gy (1 Gy/min) of γ-rays (**Figure 38**). While the maximum average numbers of DSBs per nucleus induced by irradiation in $CD90^-$, $CD90^+$, and mixed $CD90^-$ (+) $CD90^+$ primocultures varied with tumors, DSB repair kinetics was quite similar to (or even faster than in) NHDF fibroblasts for the (only one) radioresistant tumor analyzed. On the other hand, the primocultures derived from the radiosensitive tumors showed significantly delayed DSB repair relative to NHDF fibroblasts, with a substantial fraction of DSBs persisting in cells for a long period of time (48 h) after irradiation (**Figure 38**). Hence, though general validity of the described results and their relationship to the tumors' radioresistance remain to be determined at the molecular level, it seems that radiosensitive tumors exhibit defects or dysregulation of DSB repair, and, at the same time, do not tolerate persistent DSBs. On the other hand, radioresistant tumors can probably tolerate unrepaired DSBs to some extent and benefit from them in terms of tumors' future evolution.[721–724] Unrepaired DSBs may increase genetic "dynamics" of radioresistant tumors and their adaptability to radiation-induced damaging and/or other types of cell stress.

The defects in repair processes might be of epigenetic origin since otherwise the same genetic mutations would appear both in $CD90^-$ and $CD90^+$ cells of the tumor. However, even this "mutation" alternative is not unprecedented in cancer biology. For instance, we revealed for colon cancer that genetic changes may appear even in cells of histologically normal tissue taken (10 cm) far from the tumor.[10]

$CD90^-$ and $CD90^+$ primocultures from the same tumor showed similar DSB repair characteristics, even if these characteristics differed from normal NHDF fibroblasts. In accordance with this observation, we also revealed that expression of some important genes in $CD90^+$ primocultures (tumor associated fibroblasts) more resembles that in $CD90^-$ cells ("tumor" cells) than that in $CD90^+$ fibroblasts taken from histologically normal HN tissue. Surprisingly, lower numbers of radiation-induced γH2AX/53BP1 repair foci could be found in mixed $CD90^-$ (+) $CD90^+$ cultures when compared to $CD90^-$ or $CD90^+$ cells derived from some tumor and cultured separately. γH2AX/53BP1 foci also disappeared slightly faster in $CD90^-$ (+) $CD90^+$ primocultures than in separated primocultures of these cells; nevertheless, the numbers of foci persisting in nuclei at long (>24 h) periods of time post-irradiation were similar for all three primoculture types (**Figure 39**). The more efficient repair in $CD90^-$ (+) $CD90^+$ primocultures might thus point to mutually supportive interactions between $CD90^-$ and $CD90^+$ cells that stimulate DSB repair, though the measured differences observed were only faint. Similar conclusions followed from measurements of post-IR cell viability.

Finally, we succeeded with obtaining several paired samples of tumor and "normal" cells isolated each pair from one particular patient. Interestingly, the samples that had already been analyzed revealed that DSB repair characteristics and post-IR cell viability might be similar for tumor cells and cells considered as normal based on the sample tissue morphology and distance from the tumor. For instance, "normal" cell primocultures of several patients showed similar repair delay as corresponding "tumor" cell primocultures (prepared from the same patient) as compared to normal NHDF fibroblasts. This result can be interpreted in two opposite ways. It is possible that tumor cells influence DSB repair

in surrounding normal cells. Alternatively, but not mutually exclusive, precarcinogenic changes may exist already in the cells of morphologically normal tissue from which part the tumor finally developed. Indeed, both alternatives are not unprecedented in cancer biology.

Discussion on Bobkova et al. 2018 [22]

The article of Bobkova et al. (2018)[22] focuses on nano-structure and nano-composition of DSB repair foci induced by high-LET radiation (**Table 1**, page 124) and is therefore in a more detail discussed in the next chapter dedicated to ion-beam cancer therapy (IBCR). However, it is worth mentioning here that we observed a significant difference in several nanoscale parameters of 53BP1 DSB repair foci between normal human skin fibroblasts (NHDF) and radioresistant U87 glioblastoma cells (**Figs 40, 41**).

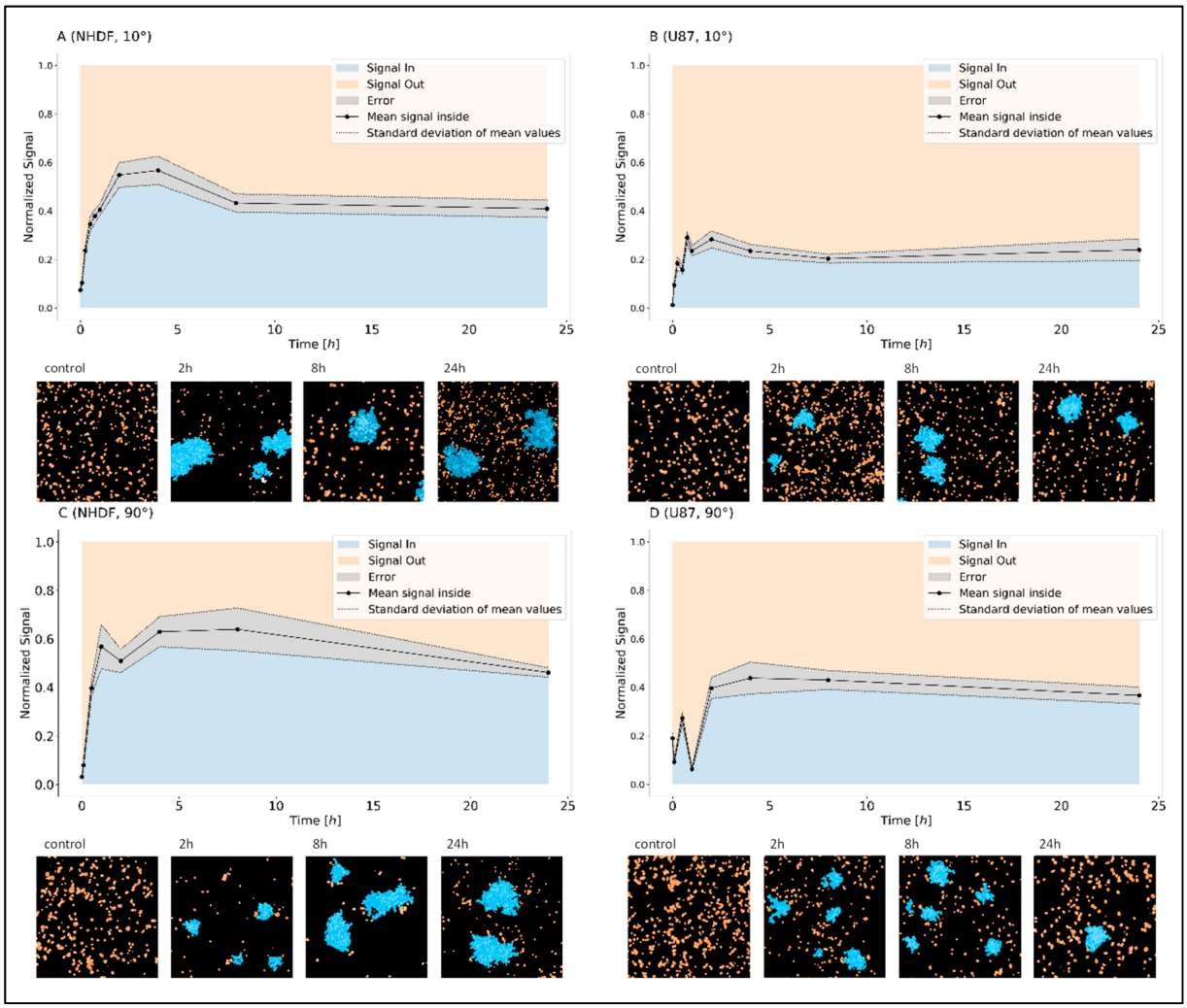

Figure 40. Relative amounts of 53BP1 signals detected within (blue) and outside (orange) repair clusters as defined for SMLM. Graphs: Mean values and margins given by the standard deviation are depicted in gray. The values are always normalized to the mean number of signals detected at a given time point. The data are presented for NHDF fibroblasts **(A, C)** and U87 cells **(B, D)** after 1.3 Gy tangential ^{15}N-irradiation **(A, B)** (10° angle between the ion beam and the cell layer), and 4 Gy perpendicular ^{15}N-irradiation **(C, D)** (90° angle between the ion beam and the cell layer). Images: The pointillist images represent examples of sections of cell nuclei with labeling points inside (blue) and outside (orange) clusters at the given time points. The samples were taken as aliquots of the same culture at different time points (from 5 min to 24 h) after irradiation. 24 h) after irradiation. For comparison, examples of non-irradiated control cells are presented (= 0 min). From **Bobkova et al., 2018**.[22]

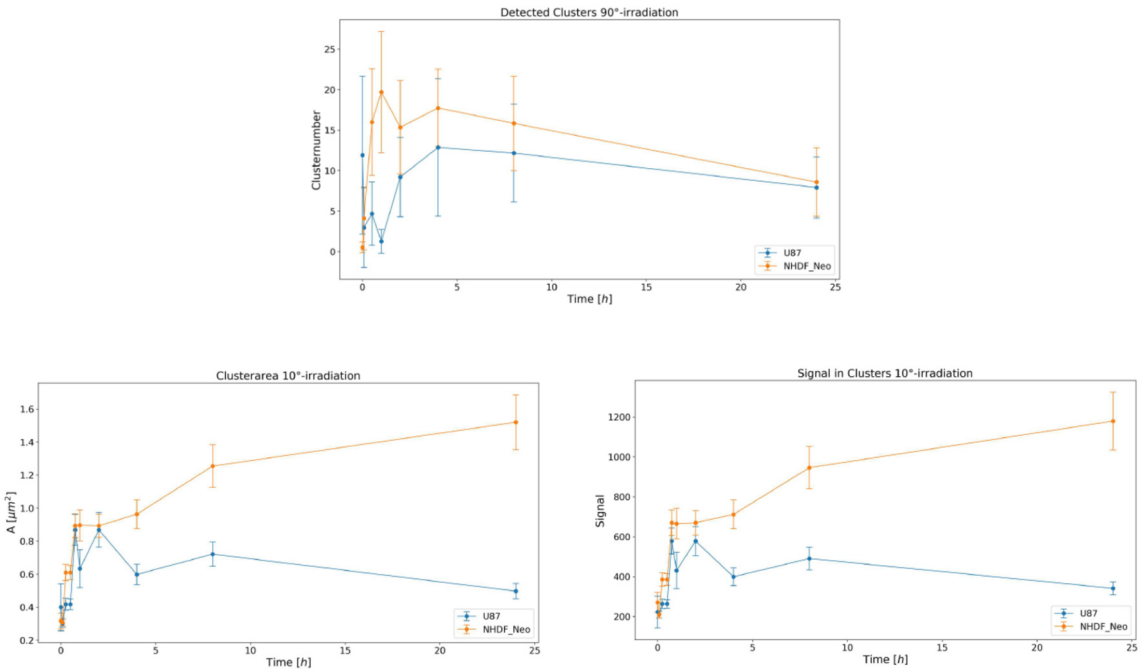

Figure 41. Average number (top) of 53BP1 signal clusters determined by SMLM in different periods of time post-irradiation in normal human skin fibroblasts (NHDF, orange line) and U87 glioblastoma cells (blue line). Bottom left: the average area and, bottom right, the average number of 53BP1 signals inside the 53BP1 cluster. The cells were irradiated with 4 Gy of ^{20}Ne ions in 90°-geometry (top image) or 10°-geometry (bottom images). Error bars – standard deviations of mean values. Taken from **Bobkova et al., 2018 (Bachelor thesis).**

Specifically, we found out that normal fibroblasts sequester a higher proportion of nuclear 53BP1 protein into DSB repair foci as compared with U87 cells exposed to the same radiation dose and analyzed at the same period post-irradiation. Whether it means that normal cells form 53BP1 repair foci more efficiently or whether U87 cells express more 53BP1 remained to be analyzed (below). The second alternative could mean that elevated levels of 53BP1 in U87 cells (at least in our clone) could promote NHEJ more efficiently than normal fibroblasts, in accordance with the high radioresistance of these tumor cells.

Importantly, the 53BP1 cluster size – defined in terms of both the number of signals inside the cluster and cluster area – was larger in normal fibroblasts compared to U87 tumor cells 30 min post-irradiation. Later on, the 53BP1 cluster size progressively increased with time in normal fibroblasts but decreased in U87 tumor cells (**Figure 41**). Hence, we can suppose that the highly radioresistant U87 tumor cells are more efficient in repairing (or at least rejoining) clustered DSB damage than normal fibroblasts. Though still preliminary, the results suggest that nano-structure of DSB repair foci may provide new mechanistic insights into the cell type-specific differences in DSB repair mechanism and consequently the cell radioresistance.

2.3.2 Tumor cell radiosensitization and normal cell radioprotection

In this chapter, a collection of the author's papers that concern new approaches of tumor cell radiosensitization and normal cell radioprotection is presented. These approaches include a) IBCT, b) tumor cell radiosensitization by metal nanoparticles or c) freezing, and d) selective radioprotection of normal cells with amifostine. All these strategies provided promising results in terms of the augmentation of radiation cell killing and brought about several interesting discoveries of more general relevance. Specifically, we found the following:

a) Different high-LET ions of mutually similar LET can generate DSBs of different complexities and microdosimetric parameters. Because the complexity of the generated lesions correlates with the efficiency of their repair, we propose that more parameters of high-LET particles, not only their LET, may be relevant when searching for biologically more efficient radiation types or when trying to explain their effects.[19]
b) Various metal nanoparticles can radiosensitize tumor cells to radiation; however, this effect is not always dependent on DNA damage augmentation and/or DNA repair alteration. Instead, the cytoplasmic damage independent of DNA (nuclear, mitochondrial) damage can play a role. Apoptotic signaling by damaged lysosomes might by one of these mechanisms.[27]
c) Freezing and thawing dramatically damages chromatin and nucleus envelope structures in non-cryo-protected cells. However, the nature of this damage is not based on chromatin fragmentation (DSB induction), as has been often proposed. The exception could be just replicating (S-phase) cells, where freezing/thawing damages replication forks and causes their collapse with still unknown consequences. Fast-replicating tumor cells may hence be particularly sensitive to "cryoablation."[32]
d) Amifostine, the only radioprotectant approved for clinical use, not only selectively protects normal cells from DNA damage induction, but it also alters DSB repair in (some) tumor cells.[33]
e) Nanoscale analyses of DSB repair foci using SMLM revealed their internal nanostructure may differ for various cell types, as shown for normal fibroblasts and radioresistant U87 glioblastoma cells.[22]

2.3.2.1 Hadron (proton and high-LET ion) radiotherapy

Compared with photon irradiation, cancer therapy with high-LET ions may improve tumor cell killing because of the higher RBE of high-LET particles and their better targeting of the tumor (Bragg peak). The latter advantage is also the basis of therapy with protons that have an RBE comparable to photon radiation. A general discussion of the principles and benefits of IBCT has already been provided in the introduction part of the current thesis (page 48). Here, we describe and more specifically discuss our results on the relationship between the high-LET radiation parameters, microscale and nanoscale structure of DNA damage, reparability of this damage, and cell survival upon irradiation. The results are compared for high-LET ions and γ-rays and for normal and tumor cells. Importantly, for the first time in the present papers (Depeš et al., 2018[21] and Bobkova et al., 2018[22]), we describe the application of SMLM (e.g., [21,444,592]) for the structure analysis of DSB repair foci and their clusters along high-LET particle (**Table 1**) tracks, importantly in the context of the chromatin environment. With a resolution

of about 10 nm, SMLM allowed us to shift our microscopy studies toward nano-dimensions and obtain a completely new sort of data on radiation DNA damage and its repair. The presented articles belong within the first nanoscale studies on the assembly and disassembly of radiation-induced DSB repair foci during the postirradiation time. The obtained data can thus reveal new aspects of the relationship between the radiation quality, DNA repair mechanism (efficiency and fidelity), formation of chromosomal aberrations, and cell survival, which could contribute to improving (IBCT) radiotherapy in the future.

Relevant publications discussed

4. Ježková L, Falk M, Falková I, Davídková M, Bačíková A, Štefančíková L, Vachelová J, Michaelidesová A, Lukášová E, Boreyko A, Krasavin E, Kozubek S. Function of chromatin structure and dynamics in DNA damage, repair and misrepair: γ-rays and protons in action. Appl Radiat Isot. 2014;83 Pt B:128-36. doi: 10.1016/j.apradiso.2013.01.022.

5. Jezkova L, Zadneprianetc M, Kulikova E, Smirnova E, Bulanova T, Depes D, Falkova I, Boreyko A, Krasavin E, Davidkova M, Kozubek S, Valentova O, Falk M. Particles with similar LET values generate DNA breaks of different complexity and reparability: a high-resolution microscopy analysis of γH2AX/53BP1 foci. Nanoscale. 2018;10(3):1162-1179. doi: 10.1039/c7nr06829h.

6. Depes D, Lee J, Bobkova E, Jezkova L, Falkova I, Bestvater F, Pagacova E, Kopecna O, Zadneprianetc M, Bacikova A, Kulikova E, Smirnova E, Bulanova T, Boreyko A, Krasavin E, Hausmann M, Falk M. Single-molecule localization microscopy as a promising tool for γH2AX/53BP1 foci exploration. European Physical Journal D. 2018; 72(9). doi: 10.1140/epjd/e2018-90148-1.

7. Bobkova E, Depes D, Lee JH, Jezkova L, Falkova I, Pagacova E, Kopecna O, Zadneprianetc M, Bacikova A, Kulikova E, Smirnova E, Bulanova T, Boreyko A, Krasavin E, Wenz F, Bestvater F, Hildenbrand G, Hausmann M, Falk M. Recruitment of 53BP1 Proteins for DNA Repair and Persistence of Repair Clusters Differ for Cell Types as Detected by Single Molecule Localization Microscopy. Int J Mol Sci. 2018;19(12). doi: 10.3390/ijms19123713.

Discussion on Ježková et al. 2014 and 2018

Adapted from Ježková et al. 2018.[19] To our knowledge, this study is the first to address the spatiotemporal aspects of DNA damage and repair after cell exposure to different low energy high-LET ions of mutually similar LET. The previous literature usually compares radiation types with largely different energies and/or LET values. These differences are frequently in the orders of magnitude.[325,343,725] Although this experimental design enables useful analyses aiming to correlate the DNA damage (or other biological endpoints) to LET and radiation energy, large differences in these parameters mask possible effects of other radiation qualities. In radiobiological studies, LET is usually considered as a single value; however, the final character of energy deposition jointly reflects various physical components (energy, charge, particle size etc.), the combination of which is unique for the particular radiation. The mechanism by which different high-LET particles affect the DNA molecule under conditions of similar LET and energy values thus remains poorly understood. In addition, experimental research on biological effects of high-LET radiation has primarily focused on ions with high energies (≥100 MeV per n) while results for low-energy (<50 MeV per n) ions are still rare. Better

understanding of physical values that contribute to character of the DNA damage would be important for further development of IBCT and space exploration.

The paper of Ježková et al. (2018)[19] addresses the above-described gap in our knowledge. We evaluated the extent, spatiotemporal behavior, and repair of DSBs in normal human fibroblasts (NHDF) irradiated with boron and neon ions, respectively, that had been accelerated to similar low energies and similar LET values (see **Table 1**). Gamma rays were included into the study as representative of low-LET radiation. It is known that the RBE increases with the LET for many biological endpoints. However, the maximum RBE can be reached at different LET values, oscillating between 100 – 200 keV μm^{-1} for different radiations, cell types, and biological endpoint studied.[339–341,726] This suggest that the LET may not always be accepted as the only determinant of the RBE. As discussed below, the explanation could rest in the possibility that radiation types of similar LET generate DNA damage of different complexity and spatiotemporal behavior. Hence, micro-morphological analyses of DNA damage, as performed herein, could be expected to significantly contribute to our better understanding of still mysterious mechanisms by which low-LET and various high-LET radiations, respectively, kill the cells with different efficiency (RBE).

Table 1 Irradiation schemes and radiation parameters.

Particle	*Z*	Geometry°	Energy, MeV per n	LET, keV μm^{-1}	Fluence*, 1 cm^{-2}	Particles per nucleus#
^{11}B	5	90	8.1	138.1	4.52×10^6	8.4
^{11}B	5	10	7.5	148.3	4.21×10^6	3.3
^{20}Ne	10	90	46.6	132.1	4.73×10^6	8.8
^{20}Ne	10	10	33.9	170.9	3.65×10^6	2.7

Z – charge, ○ – geometry of irradiation (the angle between the ion beam and the plane of the cell monolayer), * – fluence per 1 Gy absorbed in water, # – the number of particles per 1 Gy traversing a nucleus with an average area. The LET of Ne particles increased with increasing distance traversed along the glass at 10° irradiation, for which it was difficult to compensate. We cannot exclude minor influences on the results, but we consider this effect rather insignificant. Notably, identical conclusions to those drawn using 10° irradiation were obtained (though with lower precision) using 90° irradiation, where the LET values for B and Ne ions are much more similar.

As discussed later, optical microscopy offers several important advantages over electron microscopy for DNA damage analyses but without super-resolution upgrades suffers from relatively low resolution. Super-resolution microscopy then provides resolution down to single molecules, though only a limited number of samples can be analyzed at the current level of technological development. Considering these limitations, we decided for dual-immunofluorescence high-resolution confocal microscopy[33] as the optimal method for our pilot studies. Nevertheless, we used several "tricks" to maximize the resolution of our approach: First, we analyzed spatially (3D) preserved nuclei. In contrast with reports of Costes et al.[727] or Antonelli et al.[728] 3D analyses in our hands improved the detection of γH2AX/53BP1 (sub)foci by approximately 40 % compared with a simple 2D analysis. Second, as previously reported by Jakob et al.[346] we irradiated the cells at a sharp angle, which allowed us to image DSB repair foci and their clusters accumulated along particle tracks in the x-y observation plane. This set up reduced limitations arising from the insufficient resolution power of confocal microscopy in the vertical (z)-direction, and also from the flatness of cells (including herein studied fibroblast) growing attached to surfaces.[729] Third, to identify individual foci within clusters, we combined information on cluster morphology, fluorescence heat maps, and fluorescence intensity profiles along the paths

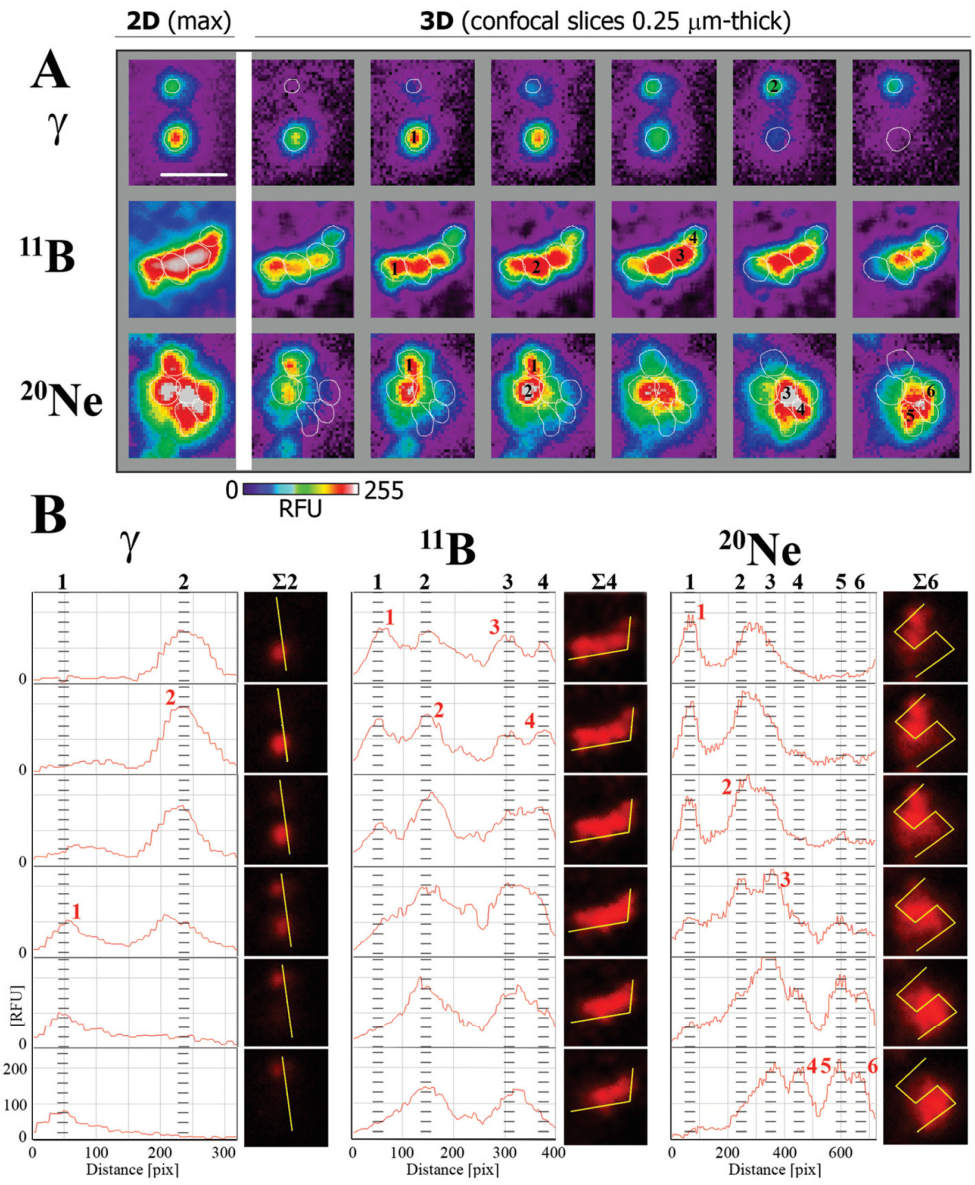

Figure 42. Identification and demarcation of individual γH2AX/53BP1 foci within a cluster, for clusters induced by γ-rays, boron ions and neon ions. The boundaries of individual γH2AX/53BP1 foci within the cluster and the complexity of 3D foci in the cluster (number of clustered foci) were semi-computationally determined by combining information obtained from **(A)** fluorescence intensity heat maps computed for cluster images for each individual confocal slice of the z-stack (examples from the second left image to the right) as well as for the maximum images (left) composed of superimposed confocal slices; **(B – left panels)** red channel fluorescence intensity profiles (R-profiles) measured for each individual confocal slice of the image z-stack along the path (yellow line) drawn to identify eventual fluorescence maxima and minima between putative foci (since signals of 53BP1 precisely corresponded to γH2AX signals but showed better mutual separation in clusters, we used the 53BP1 red channel for image analyses); **and (B – right panels)** cluster morphology (shape/size) characterized for each individual 0.25 μm-thick confocal slice of the image z-stack. **A.** For γ-rays, the heat maps (relative fluorescence intensity units; RFU, 0–255) revealed 2 fluorescence maxima (with red and green intensity levels, respectively), corresponding to 2 morphologically regular and spatially separated foci; no cluster is present. In the case of boron ions, 1 cluster contained 4 maxima of red intensity. The cluster induced by neon ions exhibited 6 fluorescence maxima of red or even white intensity. The lines demarcating the area of each focus in the cluster (white circles) were manually drawn according to the focus heat map signal using the confocal slice showing the strongest fluorescence maximum or on the maximum image. Typically, the signal at two levels above the heat map background (green signal) was used for this purpose. Individual foci are indicated by (black) numbers at the slice of their maximal fluorescence intensity. Scale bar (white) = 400 nm. **B.** Relative fluorescence intensity (vertical axis, 0–255 [RFU]) profiles for the red (53BP1) channel measured along the path (yellow) shown in the corresponding right panels, where the path is plotted over the analyzed clusters of foci. The profiles of consecutive confocal slices are sorted from top to bottom (left column – γ-rays; middle column – ^{11}B ions; right column – ^{20}Ne ions). Individual foci

are indicated by red numbers at the confocal slice and the position along the yellow path (horizontal axis [pixels]) where they showed the maximum fluorescence intensity. Summarized numbers of foci for all confocal slices are indicated by the black numbers above the top image. As shown in these images, the numbers of foci determined according to R-channel line profiles were well correlated with the results based on the heat maps (A) and cluster morphology analyses (B, right panels). Foci forming a spatial unit and connected by at least the "green" fluorescence level (heat maps) were considered to occupy one cluster. The morphology of the clusters was studied in 3D with Acquiarium software, and R-profiles and heat maps were prepared with ImageJ and CellProfiler software, respectively. From **Ježková et al. 2019**.[19]

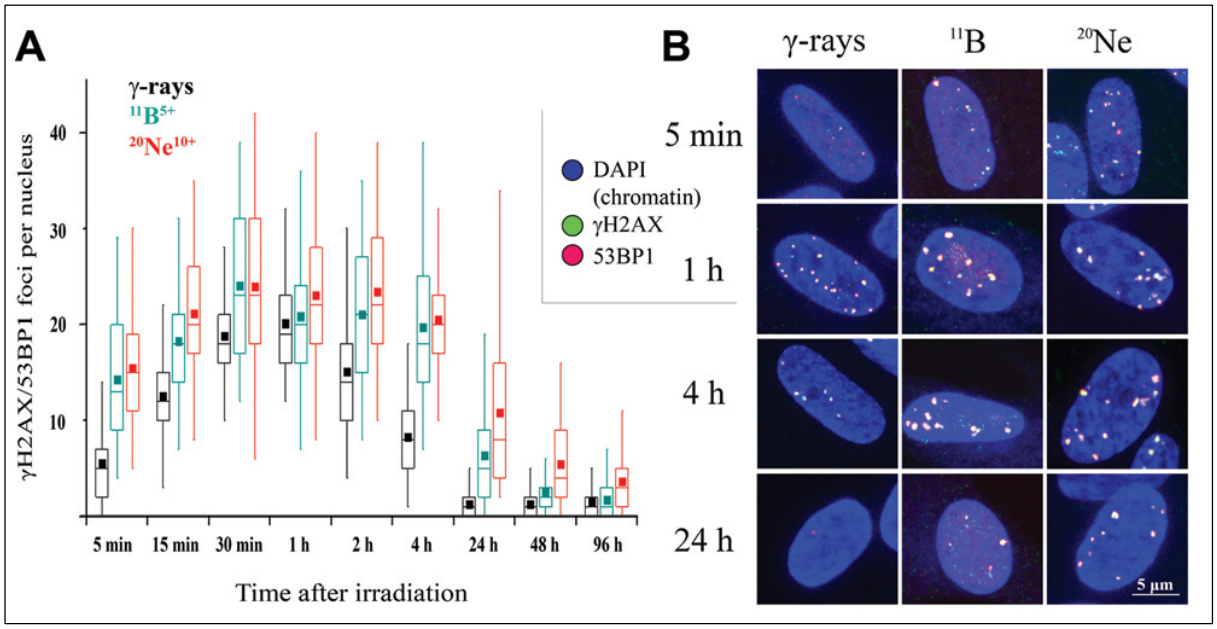

Figure 43. γH2AX/53BP1 foci formation and loss (DSB repair dynamics) upon exposure to radiation of different qualities. NHDF-Neo cells were irradiated in the perpendicular (90°) geometry with 1 Gy of γ-rays, ^{20}Ne ions (LET = 132.1 keV µm−1, E = 46.6 MeV per n) or ^{11}B ions (LET = 138.1 keV µm−1, E = 8.1 MeV per n) and fixed at different times PI, as indicated. **(A)** Quantification of the number of γH2AX/53BP1 foci in 3D images. Sham-irradiated cells contained (not shown) 0.1 foci per nucleus on average. The box-and-whisker plot indicates the mean (black square), median (median line inside the box), 25th and 75th percentiles (the top and bottom of box, respectively), and minimum and maximum (whiskers) of the pooled data from two experiments (approximately 100 counted cells). **(B)** Representative maximum intensity images of the corresponding cell nuclei. γH2AX (green), 53BP1 (red), chromatin (DAPI). From **Ježková et al. 2019.**[19]

intersecting putative foci in non-overexposed parts of the cluster (**Figure 42**). Forth, selective scoring of colocalized γH2AX and 53BP1 foci allowed us to improve the precision of focus identification and increased the probability of observing still unrepaired DSBs, especially in later periods of time PI. Nevertheless, it should be noted that also analyses of non-colocalized γH2AX and 53BP1 foci can be of biological relevance, since their different roles were described as for instance in the context of cell radioresistance monitoring.[730] However, non-colocalized foci could appear in consequence of inhomogeneous cell immunostaining and were therefore ignored (rare cases only) in the present study.[731–733] Finally, mostly G1 cells were involved into the study, which reduced heterogeneity of results.

Based on these improvements, we successfully visualized a detailed substructure of colocalized γH2AX and 53BP1 focus clusters and their streaks along ^{11}B and ^{20}Ne particle tracks *in situ* and in large datasets. Although high precision of the spatiotemporal analysis was achieved, low resolution power of confocal microscopy, leading to a certain amount of artificial overlap in complex arrangements of foci due to diffraction (technical restrictions; reviewed in Waters, 2009)[729] as well as spreading of H2AX

phosphorylation over 1–2 Mb chromatin domains and overlapping signals (biological reality) prevented the discrimination of individual DSBs in multiple lesions (≥2 DSBs within 1–2 helical turns). The complexity of DSBs was thus only estimated.

Taking advantage of the above-described approach, we found that the microdosimetric complexity of γH2AX/53BP1 (DSB) repair foci differs not only for cells irradiated with low-LET γ-rays and high-LET radiation types, respectively, but also for cells irradiated with boron ions and neon ions, which have very similar LET and low-energy values. Mathematical modelling/simulations and novel ultrasensitive immunogold-labelling transmission electron microscopy (TEM) provides clear evidence that high-LET radiation causes complex DSBs, and in contrast to low-LET radiation, the majority of γH2AX foci contain more than one DSB.[344,349,350] As recently reviewed by Goodhead et al.,[326] approximately 20 % (γ-rays) and 70 % (high-LET ions) of DSB damage sites contain at least three DNA-chain breaks, according to simulations.[326] Based on our direct measurements (1 h PI), approximately 16 %, 42 %, and 56 % of γH2AX/53BP1 foci generated from γ-rays, boron ions, and neon ions, respectively, exist in clusters with additional foci (**Figure 45**). Nevertheless, these numbers were not able to be directly compared with other studies that typically quantify the proportion of simple foci to DSB clusters. In any case, consistent with previous findings,[349,351,734] our 3D analysis revealed highly clustered (>3) γH2AX/53BP1 foci only after exposure to high-LET particles, whereas clusters observed after γ-irradiation comprised a maximum of two or occasionally (2 %) three foci.

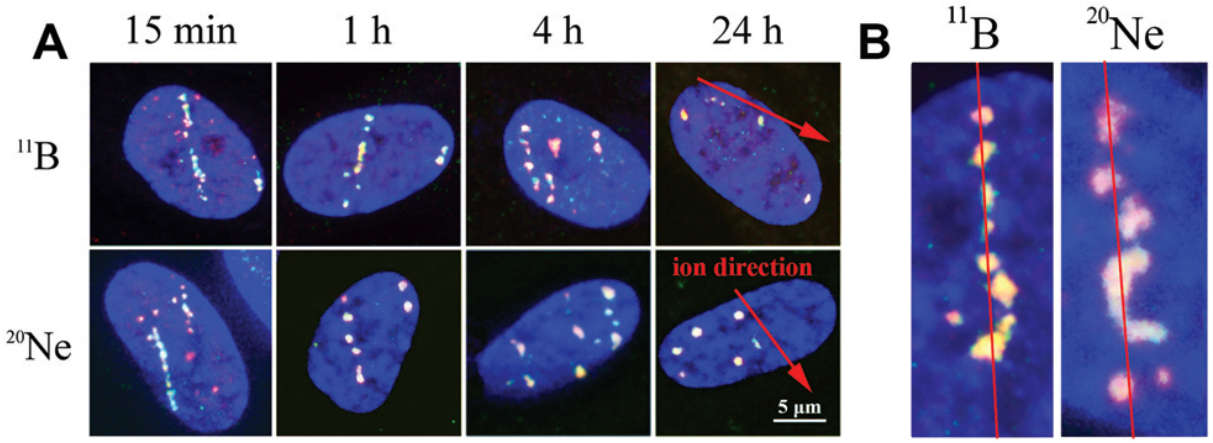

Figure 44. Structures of γH2AX/53BP1 focus streaks and their dynamic changes with time PI. NHDF-neo cell nuclei were exposed to an average of three ^{20}Ne or ^{11}B ions (i.e., 1.2 and 1.0 Gy, respectively) emitted at a sharp angle to the cell monolayer. Cells were spatially (3D) fixed at the indicated periods of time PI, and immunostaining for γH2AX (green) and 53BP1 (red) repair foci is presented. **(A)** Comparisons of γH2AX/53BP1 focus streaks induced by boron and neon at the indicated periods PI. **(B)** Detailed structures and deflections of foci from a linear particle track observed at 2 h after radiation exposure. Maximum images comprising ~25 superimposed 0.25 µm-thick confocal slices are shown in the x–y plane in both A and B. Chromatin was counterstained with DAPI (blue). From **Ježková et al. 2019**.[19]

The difference between DSB complexity following the exposure of cells to γ-rays and high-LET ions (boron or neon) was expected and primarily explained by the different characters of energy deposition (ionization density and distribution) by these radiation types. However, based on the present and previous results,[13,15,17] we propose that not only the character of energy deposition *per se* but also the character of energy deposition in the context of higher-order chromatin structure[1] (see **Figure 50**) significantly contributes to the increased complexity of DNA damage and RBE following exposure to

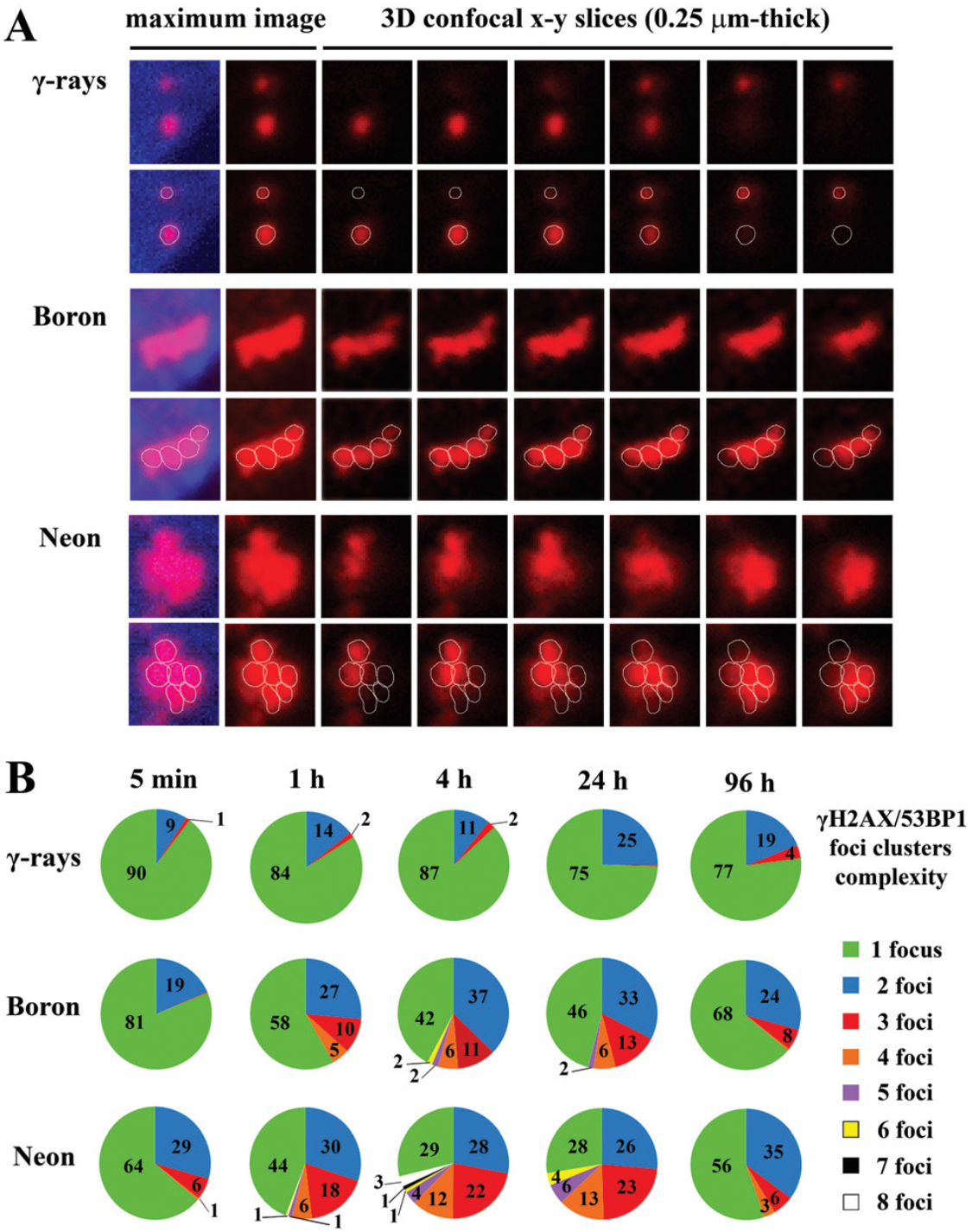

Figure 45. Comparison of the complexity of γH2AX/53BP1 focus clusters in spatially (3D) fixed NHDF-Neo fibroblasts irradiated with γ-rays, 20Ne ions, or 11B ions. The dose was 1.0 Gy for γ-rays, 1.0 Gy for boron ions, and 1.2 Gy for neon ions to ensure that an average of 3 particles traversed the nucleus in both high-LET radiation cases. Cells were irradiated in the sharp-angle (10°) geometry. **(A)** Representative γH2AX/53BP1 foci/focus clusters at the time period of their maximum complexity (4 h PI). The maximum (2D) images, shown on the left, comprise ~25 confocal slices obtained with a z-step of 0.25 μm. Individual consecutive confocal slices through the γH2AX/53BP1 focus clusters (right columns) presented here subsequently show the composition of individual foci in the cluster and the ability to precisely describe their complexity. Only the 53BP1 signal is shown because this signal enables better discrimination of individual foci than the γH2AX signal. See ([19] for details of the foci discrimination procedure. **(B)** The γH2AX/53BP1 foci complexity was quantitatively compared for the radiation types studied. For different periods of time PI, the percentages of γH2AX/53BP1 foci presented in clusters of a given complexity level are indicated. The mean values are calculated for pooled data from two experiments (>200 foci). From **Ježková et al. 2019**.[19]

high-LET radiation types. Specifically, high-LET radiation types attack condensed (hetero)chromatin, which contains a much higher density of potential DNA targets than decondensed (eu)chromatin, more efficiently than low-LET radiation types[13] (reviewed in [15,17]). However, γ-rays preferentially damage low-density chromatin, since, in condensed (hetero)chromatin, more abundant (hetero)chromatin-binding proteins better shield the DNA from free radicals largely mediating the harmful effects of low-LET radiation (**Figure 30**). Therefore, it is important not only how, but also where the radiation energy is released in the cell nucleus (see **Figure 50**).

The complexity of DSBs was inversely correlated with the disappearance of γH2AX/53BP1 foci from the cell nuclei, i.e., the kinetics and efficiency of DSB repair, and cell survival (**Figure 43**, **44**). Consistent with some earlier reports,[1,13,18,345,665,728,734] simple and on principle frequently euchromatic[13] γH2AX/53BP1 foci generated by γ-rays were largely eliminated within the first (4 h) hours PI in the present study (**Figure 43**). Similar findings of the rapid repair and disappearance of non-clustered (smaller) individual γH2AX/53BP1 foci were observed in cells irradiated with high-LET ions (^{11}B and ^{20}Ne). However, large γH2AX/53BP1 foci, and particularly clusters of these foci, were repaired with difficulty irrespective of their origin in euchromatin (EC) or heterochromatin (HC), and they persisted in the cell nuclei for much longer periods of 1 day (^{11}B) or more (^{20}Ne) after irradiation (**Figure 43**).

For ^{20}Ne ions that produced the most complex DSB lesions in this study, approximately ¾ of DSB foci persisting at 24 h PI formed clusters (**Figure 45**). These results precisely correspond to an interesting study by Jakob et al.,[670] who observed the slower repair of DSBs generated by carbon ions than of DSBs produced by γ-rays, and this delayed repair was even higher for HC-associated damage. Based on the evidence obtained in this and previous studies, we conclude that both DSB complexity and the chromatin environment surrounding DSBs significantly influence the repair of initially formed lesions (appearing as the consequence of energy deposition), which at least partially explains the higher RBE of high-LET ions (see **Figure 50**).

The average complexity of clusters and number of clusters per cell gradually increased with time PI and started to decrease only after 24 h PI (**Figure 45**). This scenario suggests the gradual processing of less complex and individual DSBs within the clusters[734] and highlights the long-term persistence of complex DSB clusters. An alternative, but not mutually exclusive possibility is that these repair kinetics may reflect the formation of DSB focus clusters over a longer time post-irradiation, due to chromatin movement provoked by DSB repair processes, as described below. The cells with unrepeatable DSB clusters (of either origin) are expected to die or undergo mutagenesis at later periods of time PI. Indeed, a much higher proportion of cells underwent apoptosis following irradiation with boron ions (almost 50 % of cells exposed to a 4 Gy dose) compared with γ-rays (less than 20 % of cells exposed to a 4 Gy dose), indicating that a) DSBs produced by high-LET ions are repaired but only with difficulty and b) the proportions of cells with complex γH2AX/53BP1 foci and the complexity of persistent DSBs at >24 h PI may be even greater than reported here (because the seriously damaged cells died, detached from the microscopic slides and escaped detection). Moreover, concerning the long period of time examined post-irradiation (up to 96 h PI), a proportion of cells may also die due to mitotic catastrophe, since as was only recently shown,[734,735] even cells with relatively high numbers (e.g., 10–15) of DSBs can enter mitosis under some circumstances. These conclusions are consistent with the combined results of

previous studies of carbon and ferrous ions.[350,734,736] Finally, we cannot exclude the possibility that previously repaired cells may overpopulate cells still harboring damage and, thus, further decrease the average number of foci per nucleus observed in later time periods PI. Since the critical level of DSBs (<10–20)[735] allowing cells to enter mitosis is reached more rapidly (within approximately 4 h PI) using γ-rays than using both high-LET ions (>24 h PI), this effect may possibly lead to underestimation of DSBs, especially in γ-irradiated cells. However, any significant effect of cell division on DSB repair kinetics and differences in such effects between the different types of radiation studied are unlikely since a) only a small fractions of fibroblasts were dividing; b) only background DSB numbers were detected in γ-irradiated cells at 24 h PI (and this number plateaued at later times); and c) the most prominent differences in DSB repair kinetics were observed at PI times <4 h. We also calculated the average numbers of γH2AX/53BP1 foci per nucleus specifically in γH2AX/53BP1-positive cells (not shown), which resulted in the same trends/conclusions obtained from analyses performed for whole cell populations (γH2AX-positive + γH2AX-negative cells). Moreover, most cells exposed to γ-rays contained <20 DSB (mean = approximately 10 DSBs) foci per nucleus at 4 h PI, and damaged cells could therefore theoretically also undergo mitosis, similar to undamaged cells.

An additional level of DSB complexity that negatively influences DSB repair may paradoxically appear as a side effect of repair processes *per se*. First, the processing of complex (even non-DSB) lesions directly generates secondary DSBs.[737,738] Second, the HC structure has consistently been reported to represent a barrier to DNA repair and thus DSBs in condensed HC are repaired but only with difficulty, with slower kinetics and lower efficiency than DSBs in euchromatin.[13,26,349–351,670]

The repair of HC-DSBs requires extensive (hetero)chromatin decondensation, which in turn locally mobilizes damaged chromatin domains to some extent.[16,159,200,665] This increased mobility of HC-DSBs can result in collisions of two or more DSBs (**Figs. 31– 34**) and the formation of secondary DSB clusters (the term “secondary” distinguishes these clusters from the “primary" clusters discussed above, which are directly formed by high-LET particles due to localized energy deposition) (**Figure 49**). Although this phenomenon occurs occasionally upon irradiation with γ-rays, its importance has dramatically increased for cells exposed to high-LET radiation types, in which the local chromatin structure is highly fragmented and DSBs are concentrated along a relatively thin particle path, i.e., located in close proximity to one another. Indeed, the secondary DSB clusters observed after high-LET irradiation are in fact frequently higher order clusters comprising primary DSB clusters.[17,26]

Consistent with this scenario, we observed deflections of some foci from otherwise linear particle tracks and these mobile foci mostly occurred at the border between condensed (hetero)chromatin and decondensed (eu)chromatin domains. The protrusion of HC-DSBs into decondensed (eu)chromatin has also been reported in other studies upon high-LET[189,235,670] and low-LET (see **Figure 31**) irradiation[26,665,669] (reviewed by [15,191]). Moreover, the highest numbers of clusters were detected between 4 and 24 h, i.e., when the DSB repair of non-complex lesions is mostly complete. During this PI period, the clusters also showed the greatest irregularity and complexity, with 2 to 5 smaller foci per cluster observed in boron-irradiated cells and up to 8 foci observed in neon-irradiated cells. Together, these results highlight the problematic spatiotemporal stabilization of complex γH2AX/53BP1 focus clusters, particularly in the initial phase and most active period of DSB repair. Conceivably, after high-

LET irradiation, simultaneous chromatin fragmentation and dispersion supported by chromatin decondensation occurring in the frame of repair processes locally mobilize chromatin to a much greater extent than in cells exposed to low-LET γ-rays. This phenomenon dramatically increases the complexity of DSB lesions and the risk of repair errors or failure. Finally, these observations demonstrate that two phenomena – energy deposition, leading to primary chromatin fragmentation, and DNA repair, provoking secondary chromatin decondensation – contribute to (restricted) chromatin movement and formation of (complex/multiple) DSB clusters and chromosomal aberrations in cells exposed to high-LET ions (**Figure 50**).

The greater complexity and delayed repair of DSB lesions induced by ^{20}Ne ions compared with that induced by ^{11}B ions, which was observed in our morphological and kinetic studies, is harder to explain than the differences between high-LET and low-LET types of radiation. For low radiation energies, the δ-electrons emitted by the transversing particle are expected to significantly damage DNA inside or close to the track core since they do not have sufficient energy to escape. Consistently, for both boron and neon ions, we observed only occasional γH2AX/53BP1 foci (more frequent for neon ions) that were attributed to the activity of δ-electrons at sites located outside of γH2AX/53BP1 focus streaks. In the proximity of the track core, some large γH2AX/53BP1 foci diverged from the linearity of the streaks, in addition to small γH2AX/53BP1 foci produced by δ-electrons (**Figure 44**); these objects likely correspond to complex foci relocated from the track core or increased energy deposition at the ends of δ-electron tracks.[739–741] Whether δ-electron ends can generate DSBs with a sufficient density to form multiple DSBs is unclear;[739–741] in any case, such DSB clusters would be less complex than clusters inside the track core. Hence, based on the relatively large size of observed out-of-line foci and the gradually decreasing linearity of the particle tracks with the PI period, we consider the first scenario to be more likely/important.

The track core therefore probably plays a crucial role in influencing the characteristics of DSB damage under the conditions of the present study, although long-range δ-electrons may also influence characteristics such as the complexity of chromosomal aberrations (see **Figure 46**). Therefore, we complemented our experiments with theoretical calculations on the track core (as described by Chatterjee[742]) to determine potential factors that may explain why neon ions induce DNA damage of greater complexity than boron ions. The results revealed a core radius of only 13 Å for ^{11}B ions but 30 Å for ^{20}Ne ions. An approximately two-times wider track "core" for ^{20}Ne ions was also observed in RITRACKS simulations (**Figure 46**). Based on these results, we propose that ^{20}Ne ions generate a wider particle track core that is better able to cause complex DNA (DSB) lesions than the thinner track core of ^{11}B ions. This conclusion is not in disagreement with the findings of Saha et al.[343] who associated a thinner track of low-energy ions (more concentrated energy deposition) with more efficient DNA damage induction than was associated with a wider track of high-energy ions – the tracks of the ^{11}B and ^{20}Ne ions used here are both much thinner than the tracks of high-energy ions.

The proposed relationships between the particle track structures of ^{11}B and ^{20}Ne ions, the higher-order chromatin architecture and the formation of (complex) DSBs and chromosomal aberrations (discussed here as the endpoint of irradiation most directly related to DSB induction) are illustrated in **Figure 46**.

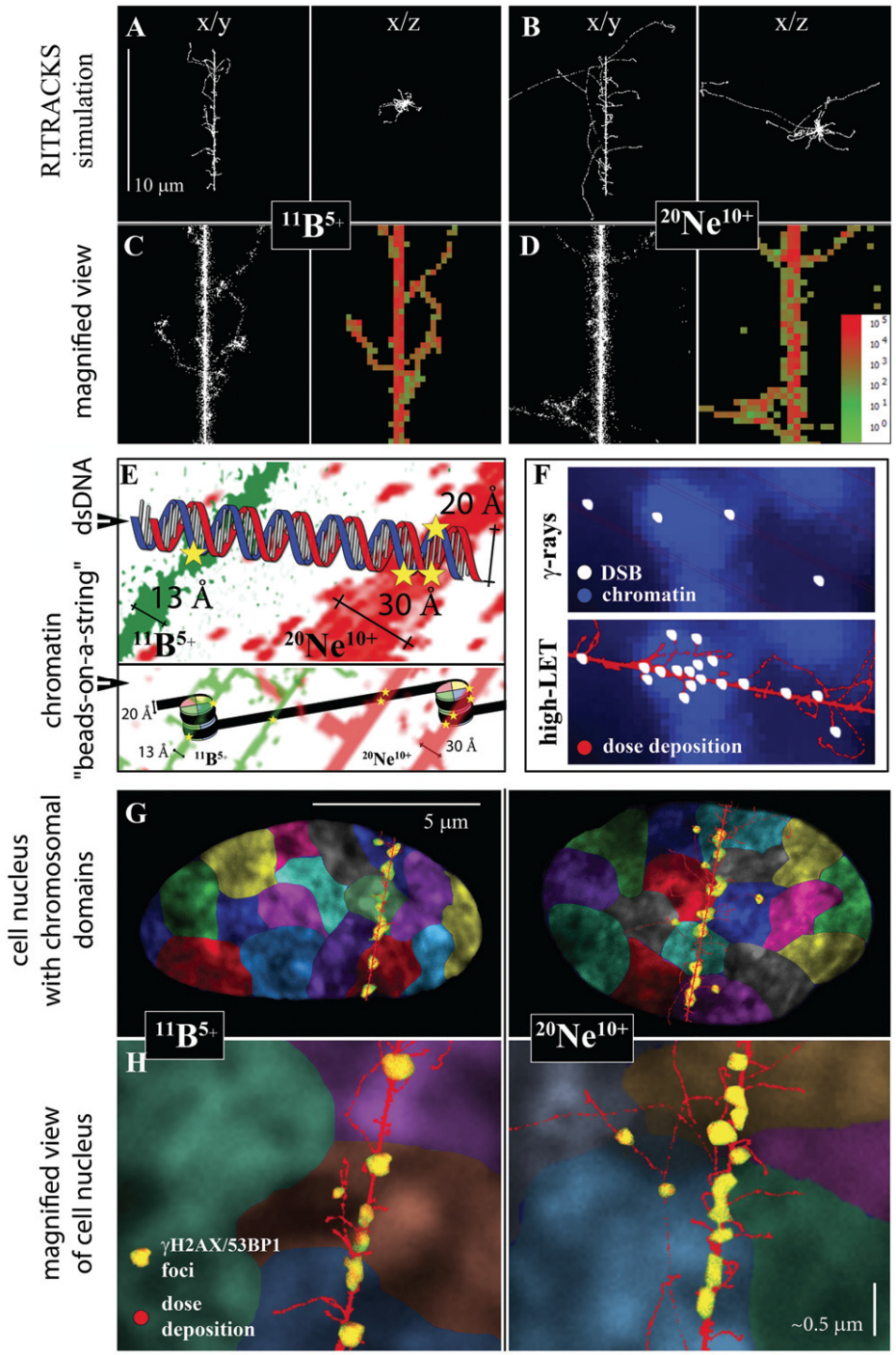

Figure 46. Relationships between radiation energy deposition, higher-order chromatin structure and DNA double-strand break induction for γ-rays and ^{11}B and ^{20}Ne ions (see **Table 1** for radiation parameters). **A, B.** Simulations of 10 µm-long track structures for ^{11}B and ^{20}Ne ions using RITRACS software; the range and distribution of δ-electrons relative to the track core can be observed in x/y and x/z projections. **C, D.** Detailed views along the tracks, with emphasis on the core structure. Free radical tracks (left panel) are shown together with dose deposition tracks (right panels). Dose deposition decreases from red to green, as indicated. The simulations show that δ-electrons penetrate deeper with neon ions, while they are more concentrated along the track core with boron ions. Nevertheless, the combined action of the neon particle itself plus low-energy electrons (that do not escape from the track core) generates a thick track core, approximately twice as thick as the boron ion. **E.** Compared with 11B ions, a wider track core of 20Ne ions (which is still highly concentrated compared, for example, to particles of high energy) directly damages both strands of the DNA molecule with a higher probability/frequency. Moreover, 20Ne ions can more easily attack both DNA turns around the nucleosome at the same time (bottom image). Chromatin is shown at the organization level of "beads-on-a-string" for simplification. **F.** Relationships between dose deposition, higher-order chromatin structure and DSB induction. γ-rays (top image) induce DSBs randomly across the cell nucleus, with euchromatin being more sensitive than heterochromatin to free radicals (which largely mediate harmful effects

of low-LET radiation), since heterochromatin is better protected by larger amounts of (hetero)chromatin-binding proteins.24,64,79 In contrast, high-LET radiation (bottom image) deposits energy in a concentrated manner along the particle track, which causes DNA damage that cannot be prevented by the chromatin structure. Condensed (hetero) chromatin provides more DNA targets per volume unit and is therefore more seriously damaged (fragmented) by high-LET particles.[18] **G, H.** Relationships between the character of energy deposition, higher-order chromatin structure, and induction of chromosomal aberrations. The dose deposition (red) simulated for ^{11}B and ^{20}Ne ions by the RITRACKS code is overlaid onto the cell nucleus, with schematically illustrated chromosomal territories (various colors) and γH2AX/53BP1 foci (yellow). A slightly greater complexity of γH2AX/53BP1 foci in cells irradiated with ^{20}Ne ions (compared with ^{11}B ions) is indicated by their larger size. The higher-order chromatin structure is shown via DAPI staining (condensed chromatin is intensively stained). Both ions and kick-off electrons of low energy generate extensive damage along the particle path and thus complex chromosomal aberrations. In addition, ^{20}Ne ions emit longer-range δ-electrons than ^{11}B ions (panel A vs. B). These electrons radiate to sufficient distances from the track core to cause DSBs in the neighboring chromosomal territories; nevertheless, these DSBs may still be sufficiently close to interact with DSBs along the particle core, particularly if we consider the chromatin fragmentation and decondensation caused by irradiation and the associated, though limited, chromatin movement. Typically, damaged chromatin (labelled with 53BP1-GFP in living cells) is displaced at a distance of approximately 1 µm in cells irradiated with accelerated ions, but the displacement of <2% foci occasionally exceeds 5 µm in the 12 h interval after Ni irradiation.[235] Therefore, we propose that chromosomal aberrations formed with 20Ne ions may involve more chromosomes than those that appear with ^{11}B ions, and their complexity in terms of the number of DNA breaks can be higher, as shown in the present study. Consider that human skin fibroblasts are flat cells (as shown on the image), and even more chromosomal territories may participate in chromosomal aberrations in spherical cells. Panel H: Section of panel G magnified approximately 10 times. Scale bar, approximately 0.5 µm (schematic illustration). From **Ježková et al. 2019**.[19]

Briefly, both high-LET ions (^{11}B and ^{20}Ne) and kick-off electrons of low energy generate extensive damage along the particle track core, which leads to complex chromosomal aberrations that may involve chromosomes whose (interphase) territories are intersected by the particle. A wider but still highly focused (dense energy deposition) track core of ^{20}Ne ions can more efficiently induce DSBs than too narrow track core of ^{11}B ions. In addition, ^{20}Ne ions emit longer-range δ-electrons than ^{11}B ions. These electrons radiate to sufficient distances from the track core and may cause numerous DSBs, mostly at the end of their tracks, i.e., in neighboring (more distant) chromosomal territories.

Nevertheless, these DSBs may be still sufficiently close to interact with DSBs along the particle core, particularly if we consider the chromatin fragmentation and decondensation caused by irradiation and the associated, though limited, chromatin movement. Typically, damaged chromatin (labelled with 53BP1-GFP in living cells) may be displaced by a distance of approximately 1 µm in cells irradiated with accelerated ions, although relocation occasionally (<2 % foci) exceeds 5 µm during the 12 h interval after high-LET nickel ion exposure.[235] Therefore, we propose that chromosomal aberrations formed with ^{20}Ne ions may involve more chromosomes than appear in association with ^{11}B ions, and their complexity in terms of the number of DNA breaks can be higher, as shown in the present study (**Figure 46G** and **H**; note that even more chromosomal territories may participate in chromosomal aberrations in spherical cells than in flat fibroblasts).[335,743,744] Nevertheless, this hypothesis remains to be experimentally confirmed. Moreover, the radiation types used in the present study differed in particle charge (^{20}Ne = 10+, ^{11}B = 5+), which was not considered in our calculations. Because the higher charge of Ne ions is reasonably expected to influence the microdosimetric distribution of ionization and thus significantly contribute to the track (core) structure,[745,746] we can hypothesize that it also increases DNA damage complexity under conditions of similar LET and energy values for different radiation types. However, the physical quality of the particle, which primarily determines the characteristics of DNA damage under conditions of similar LET and energy values for the radiation types, should be further investigated.

The γH2AX/53BP1 foci/focus clusters generated by boron and neon ions and γ-rays differed not only in complexity but also in structural parameters and spatiotemporal behaviors. Neon ions provoked the most rapid formation of γH2AX/53BP1 foci in irradiated cells and neon ions also induced the largest and most irregular foci (the lowest circularity). The results for ^{11}B ions were generally more similar to ^{20}Ne ions than to γ-rays. Faster formation of DSB foci in cells irradiated with high-LET ions compared with low-LET γ-rays is not unprecedented in radiobiology,[189,235,236] but negative observations[727,747] leave the question open. We postulate that chromatin fragmentation by high-LET radiation types opens damaged chromatin sites for DSB sensors and repair factors, which is manifested in rapid focus formation, occurring faster and to greater extent than fragmentation induced by γ-rays. Alternatively, but not mutually exclusively, clustered DSBs (together with factors such as high local concentrations of radicals), which represent a serious threat to genome integrity, may induce a more severe shock to the cells than a comparable, or even higher, level of spatially separated DSBs, and the repair systems are therefore activated faster or at a higher level. Finally, reflecting the character of energy deposition (highly localized vs. dispersed, with high-LET and low-LET radiation, respectively), primary DSB clusters generated by high-LET ions appear in cells immediately following irradiation, whereas the formation of occasional secondary clusters induced by γ-rays requires additional time. As previously discussed, primary clusters originate from physico-chemical processes occurring immediately after irradiation, while secondary clusters form later, as a consequence of restricted chromatin movement provoked by DNA repair (**Figure 50**) [13,159,189,235] (reviewed in Falk et al. 2014).[748] Based on the results from the present study, the complexity of DNA damage influences the speed of DSB recognition or γH2AX/53BP1 foci formation.

In summary, different particles with similar LET and energy values induce DSB damage with different microdosimetric (spatiotemporal) characteristics that are correlated with the efficiency of DSB repair and cell survival. We propose that the extent and character of DSBs induced by radiation types with similar LET and energy values critically depend on the particle track core diameter. However, the physical quality of the particle that primarily dictates this diameter requires further study. Hence, not only the physical characteristics of radiation types but also the spatiotemporal features and behaviors of induced DNA damage (**Figure 50**) should be considered in future radiotherapy studies and investigations of the effects/risks of space missions.

The present study brought about also several methodological conclusions. Optical microscopy in our hands offered many advantages over electron microscopy. Electron microscopy dispose with a superior resolution power that enables the precise quantification of DSB complexity;[349,350,350,351,736] however, the necessity of sample sectioning makes analyses of entire particle tracks in space and time difficult. Moreover, experimental artefacts might appear, reflecting (harmful) sample fixation steps, such as dehydration or freezing (reviewed by Winey et al., 2014).[749] Nevertheless, detailed studying of DSB focus structure and composition by the means of optical microscopy remains challenging for its low resolution. This forced us to apply some “tricks” to improve the situation, so that we were able to estimate the complexity even for highly complex foci generated by high-LET radiation types.[18] On the other hand, Costes et al.,[727] attempting to study DSB damage in cells irradiated with nitrogen ions (19.5 MeV per n, LET = 132 keV μm^{-1}), or Antonelli et al.[728] performing a similar exploration with α particles

(0.75 MeV per n, LET = 125 keV μm^{-1}), failed to distinguish any substructure of γH2AX focus clusters with confocal microscopy, although they analyzed cell nuclei in the 3D space (similarly to the present study). Hence, we have to admit that the precise boundaries and, thus, the numbers of very closely spaced DSB foci cannot be determined by standard optical microscopy. The biological nature of the complex γH2AX/53BP1 focus clusters observed in the present study and the precise numbers of DSBs present in γH2AX/53BP1 foci/focus clusters (in general) therefore remain uncertain. At the same time, various super-resolution microscopy approaches have been developed only recently and shifted the resolution of optical microscopy down to about 10 nm.[17,348,748] Altogether, this motivated us to perform nanoscopic DSB focus analysis in our next studies,[21,22] as discussed below.

Discussion on Bobkova et al. 2018, Depeš et al. 2018 and Falk et al. 2014

Several recent reports[447,589,750,751] demonstrated that various super-resolution localization optical microscopy approaches offer an exciting but still challenging means of analyzing the same biological specimens (and sample labeling) in parallel with confocal microscopy, but with much more detailed data. In the papers presented in this chapter, we took advantage of this strategy to obtain more precise answers to questions on the relationship between the quality of ionizing radiation, higher-order chromatin structure, character of generated DSB damage, mechanism and efficiency of DSB repair, and cell survival, already addressed earlier in this thesis, as well as on new questions emerging along with new abilities of nanoscopy approaches. The current studies thus represent an important step on our way from microscopic dimensions towards the cell "nanocosmos." By using Single Molecule Localization Microscopy (SMLM),[348,589] we made possible to detect individual fluorochrome molecules of labeled proteins and DNA loci of interest, respectively, and study cellular processes at the nanoscale (or molecular) level. The principle of SMLM[(41)] and the trick of how to overcome Abbe's limit of optical resolution have already been described in Chapter 182. The studies of Depeš et al.[21] and Bobkova et al. 2018[22] thus in numerous aspects further develop the story started by the previous paper of Ježková et al.[19]

As the studies taking advantage of optical super-resolution methods still remain rare and technically demanding,[347,734,752] and their results are new in nature, the interpretation of SMLM and other super-resolution data remains challenging.[22] Hence, we decided to combine SMLM "nanoscopy" with high-resolution confocal immunofluorescence microscopy already introduced in the previous chapters, in order to obtain mutually correlated data on the same studied phenomena. This strategy allowed us to a) better understand the character of nanoscale data and b) put the nanoscale details into the context of cellular processes already recognized at the microscale. We thus obtained multi-parameter multi-scale structuro-mechanistic data on DSB damage and repair, providing deeper and more complex insights into the mechanisms of these processes.

[41] earlier also referred to as SPDM – Spectral Precision Distance Microscopy

The paper of Depeš et al. (2018)[21] represents the first report on the application of SMLM for a detailed analysis of DSB (γH2AX + 53BP1) repair focus nanostructure and composition in cells irradiated with high-LET ions (**Figure 48)**. The combination of 53BP1 and γH2AX[(42)] used in these experiments opens the possibility to correlate 53BP1 repair focus nanostructure with the nanostructure of damaged chromatin domains, in the time course of repair processes (**Figure 47**, **48**).[18]

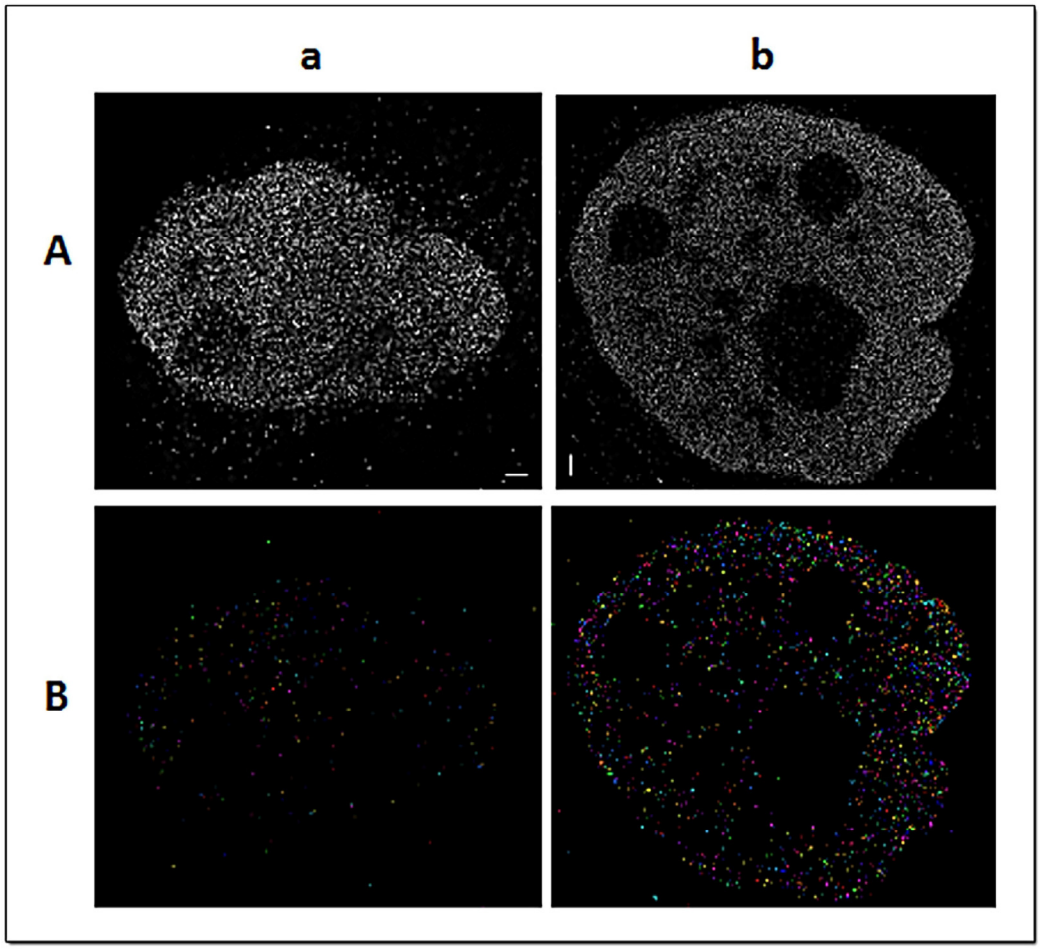

Figure 47. Nanoscopy in radiobiological research. Image sections through cell nuclei with nucleosomes labelled by H2A-green fluorescent protein after evaluation of time stacks of spectral precision distance/position determination localization nanoscopic images: example of a cell nucleus before radiation exposure **(a)**; example of irradiated cell nucleus during DNA repair **(b)**. A: Both images show several tens of thousands of individual nucleosomes (white spots) detected with a localization precision in the range of 20–30 nm. B: The same nuclei are shown but include only those nucleosomes that were involved in cluster formation (color spots). The increase of nucleosomes forming clusters is obvious. From **Falk et al., 2014**.[18]

In the paper of Bobkova et al. 2018[22] (**Figure 49**), we compared the nanostructure of 53BP1 repair foci in normal and tumor cells irradiated with γ-rays and high-LET ^{20}Ne ions (**Table 1**), respectively, with 10–20 nm resolution. Importantly, we revealed that various nano-structural parameters and composition of these foci, and the development of these parameters during the post-irradiation time, may depend on the cell type (see **Figs. 40** and **41**). This observation suggests that the nanostructure of DSB repair foci could influence the capacity and fidelity of DSB repair, and thus the radiosensitivity/

[42] (or other chromatin structure markers, e.g. H3K9-met)

radioresistance of particular cells. In this context, the results have been already discussed on page 120. Below, we go through further consequences of our findings, e.g. for the mechanisms of DSB damage and repair.

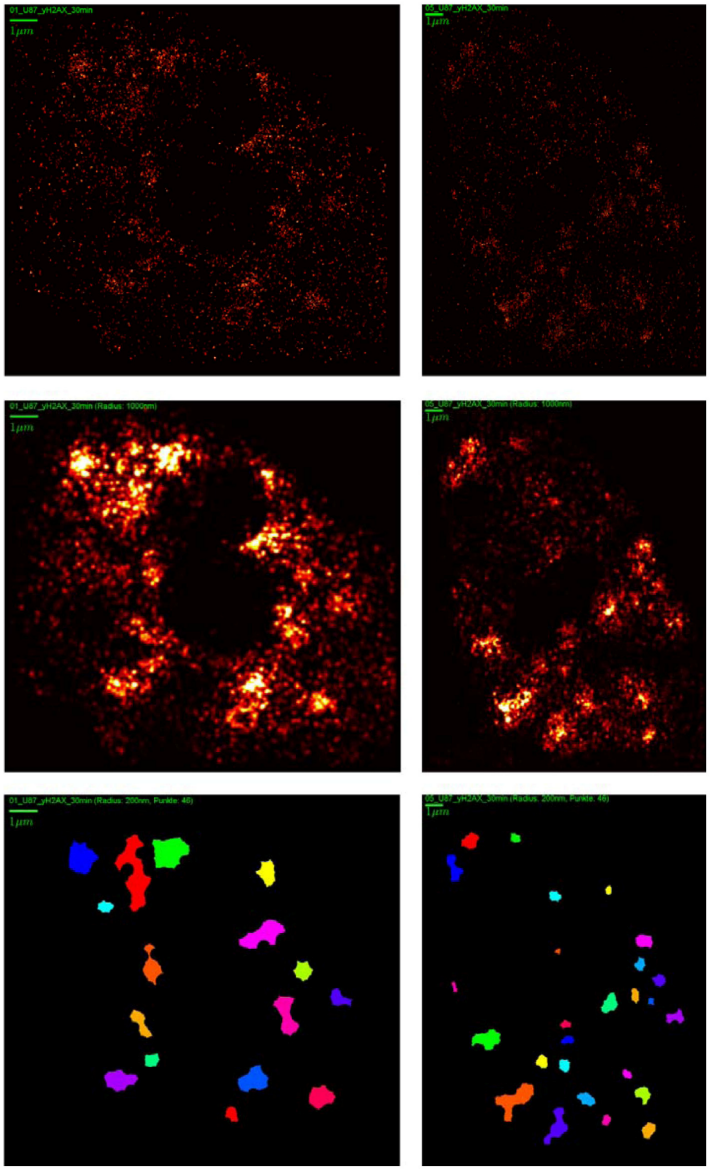

Figure 48. SMLM microscopy used to detect H2AX foci in U87 cells irradiated with 4 Gy of nitrogen ions (see **Table 1**) for the radiation characteristics) and fixed 30 min post-irradiation. Two illustrative nuclei are shown. **Top images:** super-resolved pointillist SMLM images (unprocessed). **Middle images:** pointillist images of the signals artificially spread by the localization precision and encoded so that the point brightness corresponds to the number of neighbors in a given surrounding (nearest-neighbor images). **Bottom images:** H2AX clusters detected computationally according to estimated parameters (i.e., a given minimum of neighbor signals separated by a maximal allowed radius, etc.). Different clusters are shown in different colors, which has no further meaning. See the main text for a discussion on the nature and relevance of these foci. From **Depeš et al., 2018**.[21]

Adapted from Bobkova et al. (2018).[22] DNA damage repair is a process controlled by multiple parameters.[17,19] Especially complex damages and multiple DSBs, as could occur after high-LET irradiation, require a diversity of proteins attaching the damaged site in a manner dependent on the repair pathway applied, e.g., HR, canonical NHEJ or alternative repair mechanisms.[753–755] The involved proteins have to address broken ends of the DNA and join them appropriately. Therefore, it seems to

be reasonable that the recruitment of repair proteins forms certain subunits (here called clusters) around the broken ends.[21,239,240,349,350,756,757] In the case of photon irradiation, several of such clusters, only detectable at nanoscale, contribute to microscopically visible foci.[239,240] They show a typical spatial structure or topology[758] and were found to differ in their repair activity and repair pathway choice,[239] indicating the importance of repair focus nano-architecture for the repair mechanisms occurring in a given chromatin environment. An important new question therefore arises about whether the nano-composition of foci influences repair strategy and efficiency at a given DSB site. Indeed, not only the spatial nano-arrangement and nano-topology of H2AX phosphorylation sites (i.e. damaged chromatin structure) but also of repair proteins recruited to the damaged sites may determine the repair process. Moreover, in the case of high-LET radiation, multiple foci cluster along the particle track and participate in formation of repair units, which may differ for different ionizing radiation and cell types. This may explain different RBE of various high-LET ions and why the number of foci detected by confocal microscopy in cells irradiated with these ions more or less underestimates the real number of DSBs.[21,752,757,759] However, it still remains to be answered whether the number of nano-clusters defined by SMLM or rather the number of foci visually separated by confocal microscopy corresponds better to the real number of DSBs. The present paper thus joins our research on the principles of DSB repair and cell-type specific radioresistance (described earlier) with the research on new approaches capable of more efficient tumor cell killing (Ion Beam Cancer Therapy).

To better understand the mechanisms behind the DNA damage and repair-induced protein cluster formation and relaxation, we followed the composition of 53BP1 protein clusters/foci during a long post-irradiation period at the nanoscale. By using SMLM super-resolution microscopy,[444,760,761] we studied the clusters in two differently radio-sensitive cell types – normal human skin fibroblasts (NHDF) and U87 glioblastoma cells – exposed to different doses of accelerated ^{15}N ions delivered in two different geometries (10°- and 90°-irradiation). SMLM offered the advantage of the nano-resolution, which was achieved with standard immunofluorescence methods and therefore cells maintaining their natural 3D-shape.[447] Since 53BP1 is one of the early recruited repair proteins participating in both NHEJ and HR,[762,763] it represents an appropriate candidate to study the architecture and dynamics of repair clusters as defined by SMLM and foci composed of several clusters in relation to their importance for DSB repair. Moreover, 53BP1 protein seems to be one of the decision-makers that directs the repair mechanism at a given DSB site to either NHEJ or HR. In contrast to H2AX phosphorylation, an epigenetic histone modification marking damaged chromatin sites almost immediately after DSB induction, 53BP1 is an early indicator of a starting activity of NHEJ/HR repair machinery. Hence, it is reasonable to investigate the behavior of 53BP1 during the repair independently. This has been supported by our recent investigation[21] indicating that γH2AX clusters and 53BP1 clusters differ in shape and do not always mutually co-localize. In the context of the repair pathway chosen by the irradiated cells, the question comes up in which cell cycle phase the cells have been irradiated. Non-synchronized cells were used in this study to better mimic the situation in patients' tissues during radiotherapy. However, it has been shown[19] that a vast majority of cells was irradiated in a G1 phase of the cell cycle using the experimental conditions described here[19]. The majority of DSBs can therefore be expected to be repaired by NHEJ or the alternative/backup NHEJ pathways. Moreover, recent reports suggest that

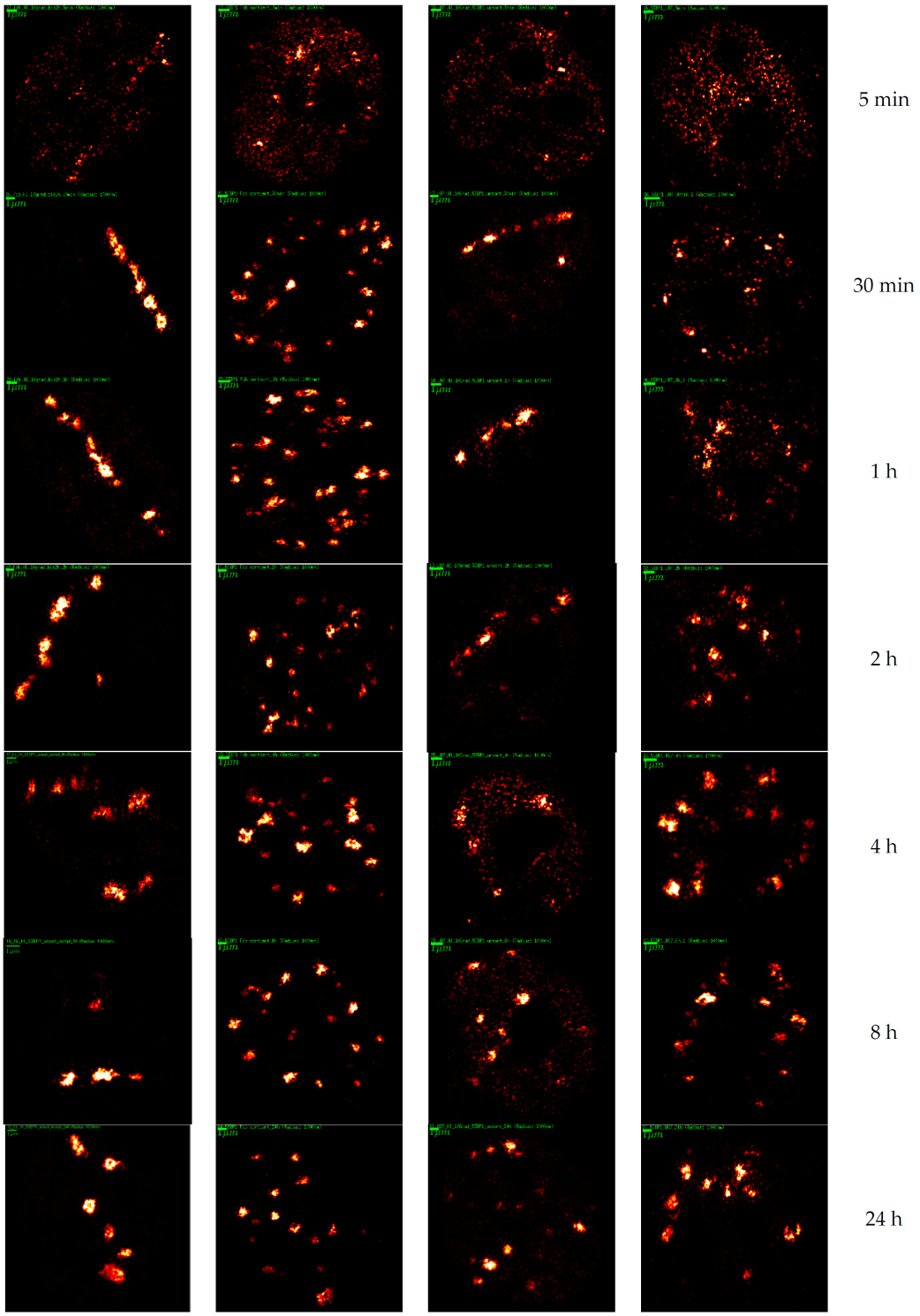

Figure 49. 2D density SMLM images of 53BP1 repair proteins. Typical examples are shown for fluorescently-labeled 53BP1 proteins in NHDF cells **(A,B)** and U87 cells **(C,D)** after 1.3 Gy tangential ^{15}N-irradiation **(A,C)** (10° angle between the ion beam and the cell layer) and 4 Gy perpendicular ^{15}N-irradiation **(B,D)** (90° angle between the ion beam and the cell layer). Along this time line, the samples were taken as aliquots of the same culture and fixed at different time points (5 min, 30 min, 1 h, 4 h, 8 h and 24 h) after irradiation. For comparison, examples of non-irradiated control cells are presented. The density images do not show all signal points detected but instead encode the number of neighbors of each signal within a circle of 1 μm radius by the point intensity—the number of signals in the given surroundings around one signal grows as the color of the point changes from red to white. The green bars equal to 1 μm. From **Depeš et al., 2018**.[22]

cells can recover from the cell cycle arrest even in presence of some persisting DSBs. This can happen as soon as the number of DSBs per nucleus decreases to 10–20.[735] In cell cultures irradiated with low-LET γ-rays, the cells are arrested for relatively short periods, i.e., about 4 h. For high LET radiation, the arrest is significantly longer than for γ-rays, i.e., about 48 h and more[764,765] or even permanent,[766] depending on the LET of the ion radiation. Thus, for the LET of ^{15}N as used in the experiments presented here, a checkpoint arrest release can be expected if about 10–15 DSBs remain unrepaired.[734] Thus, the mechanism of repair may be expected to depend more on the location and number of DSBs and the chromatin architecture at the particular damage site than on the cell cycle progress.

By means of SMLM, we explored the time course of 53BP1 cluster formation, relaxation, persistence and focus composition on the single molecule level. We found that the accumulation of the labeled protein inside as well as outside the clusters depends on the cell type (**Figure 40)**. This principle behavior seemed to be less influenced by radiation dose or perspective of the particle track (irradiation geometry). For the radio-resistant U87 cancer cell type,[767] the relative number of signals in clusters was always considerably lower than the relative amount outside the clusters. This relation does not reflect the absolute number of 53BP1 proteins available but gives information about the "just-in-availability. High nucleoplasmic levels of freely floating 53BP1 proteins may point to a permanent repair activity also in non-irradiated cells. This is well compatible with genetically unstable status of cancer cells and presence of an increased (compared to NHDF fibroblasts) average number of γH2AX/53BP1 foci observed here also in cells prior to irradiation. The kinetics seems to indicate rather the recruitment of the existing proteins floating through the cell nucleus than a *de novo* production and directed recruitment to the damaged site. In contrast to U87 cells, normal non-transformed NHDF fibroblasts showed no or very little repair activity in non-irradiated cells and recruit the repair proteins just-in-time for the repair cluster formation. Nuclear levels and distribution of repair proteins prior to DNA damage induction could therefore be potentially causatively linked to the cell-type specific radio-resistance, at least partially and/or in some cell types. Our results also support the idea that different cell types may vary in the preferred mechanism of DSB repair and, thus, requirements for particular repair proteins including 53BP1.

A lower co-localization of γH2AX and 53BP1 proteins and longer-time persistence of γH2AX/53BP1 repair foci in cell nuclei have previously been associated with a radiosensitive phenotype of radiotherapy-experiencing patients, i.e., with compromised DSB repair due to suboptimal cooperation of repair factors.[768] This explanation can be reasonably acceptable in general but is hardly compatible with a radio-resistant character of U87 cells.[767] On the other hand, although the relevance to the results described here remains to be elucidated, Ochs et al. 2016[763] revealed that silencing 53BP1 or altering its ability to bind damaged chromatin shifts limited DSB resection towards hyper-resection and, consequently, error-free gene conversion towards mutagenic single-strand annealing (SSA).[769] 53BP1 may thus foster the fidelity rather than final efficiency of DSB repair, which could indeed be expected in aggressive tumor cells. In accordance, although we observed more γH2AX/53BP1 repair foci in U87 cells at 24 h post-irradiation, the same holds true also for non-irradiated cells. In both cell types, a considerable fraction of repair foci and clusters persisted in cell nuclei also after 24 h of repair. Since it has been shown that heavily damaged cell nuclei can maintain repair activity over several

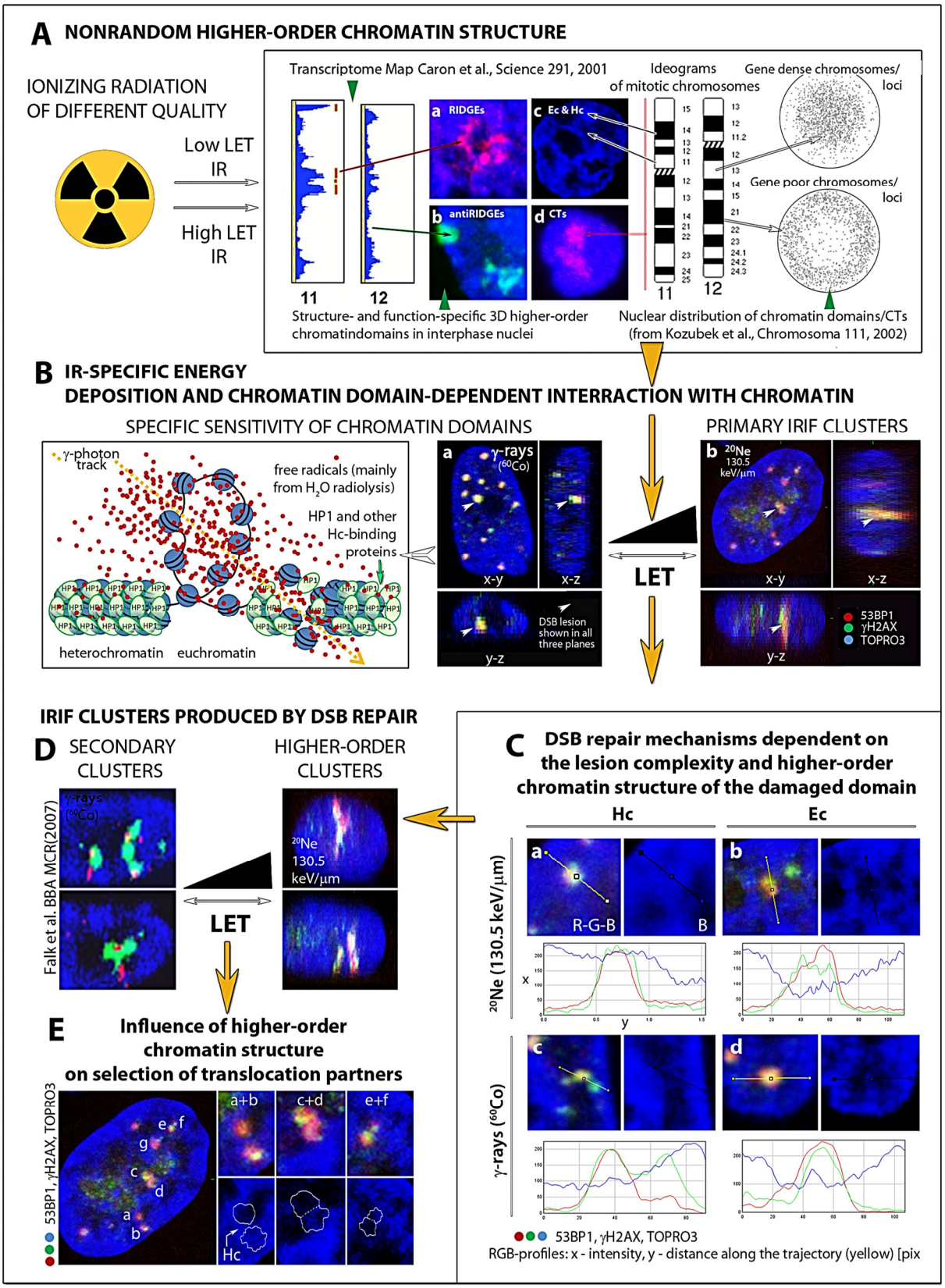

Figure 50. The nonrandom architecture and higher-order chromatin structure of the cell nucleus in DSB repair and mechanism of chromosomal translocations. **A:** The transcriptome maps (left panels, according to Caron et al., 2001,[513] demonstrate clustering of highly expressed and unexpressed genes along chromosomes 11 and 12 (horizontal axis: transcription intensity; vertical axis: path along the chromosome). Clusters of highly expressed genes (RIDGEs) are marked by vertical red lines. Middle panels (a–d) show functionally and structurally specific chromatin domains in the interphase cell nucleus: RIDGE domains (red,

a); anti-RIDGE domains (green, b); euchromatin (Ec, faintly blue) and heterochromatin (Hc, intensively blue) domains (c); and chromosomal territories (CTs, red, d). The arrows link the interphase RIDGE/anti-RIDGE and Ec/Hc domains to mitotic chromosomes (right, schematic drawing). Note that highly expressed RIDGEs are more decondensed and indented relative to unexpressed antiRIDGEs. Domains at a, b, and d were visualized by fluorescence in situ hybridization (FISH) on spatially fixed nuclei (3-dimensional FISH)[2]; chromatin counterstaining (including Hc domains in c) with TOPRO3 (artificially blue). Maximal images composed from several confocal slices 0.2 µm thick are shown. Right panel: Gene density-dependent, nonrandom nuclear distribution of structurally and functionally distinct chromatin domains (images modified according to Kozubek et al., 2002).[1] While gene-dense chromosomes or loci are preferentially located closer to the nuclear center (upper image), those that are gene-poor usually appear closer to the nuclear membrane (lower image). **B:** Different kinds of radiation specifically interact with nonrandom higher-order chromatin structure. Hc contains large amounts of Hc-binding proteins (such as HP1 [green]) and is less hydrated compared with Ec. γ Rays represent a low linear energy transfer (LET) radiation that mostly damages DNA via its indirect effect (i.e., production of harmful free radicals mostly coming from water radiolysis). a, left scheme: Ec is more sensitive to DSB induction with γ-rays since DNA in Hc is better shielded from these radicals (red) by the domain's structure and composition (left panel is modified according to Falk et al. 2014).[16] b. Another specific appears for high-LET ionizing radiation (IR), represented here by ^{20}Ne (LET = 130.5 keV/µm). The high-energy particle massively loses its energy along the short path, so clustered DSBs (multiple DSBs, "primary clusters") frequently form. Hypothetically, DNA damage can be more serious in Hc because the density of chromatin per volume is higher compared to Ec. IRIFs were immunodetected in spatially fixed normal human skin fibroblasts, exposed to 1 Gy of the particular IR (1 Gy/minutes), with antibodies against phosphorylated 53BP1 (red) and γH2AX (green) 5 minutes after irradiation and chromatin counterstaining with TOPRO3. Maximal images composed from several confocal slices 0.2 µm thick are shown. **C:** Because of specific chromatin structure, and probably the different characteristics of Ec and Hc lesions, the mechanism of DSB repair differs for Ec and Hc. To proceed, DSB repair requires extensive modifications of the higher-order chromatin structure, namely chromatin decondensation at the sites of Hc-DSBs. Figures a and b show colocalization of γH2AX foci with p53BP1 protein in Hc (left images) and Ec (right images) after irradiating cells with ^{20}Ne (LET = 130.5 keV/µm,1 Gy, 1 Gy/min). Figures c and d illustrate the same situation but for cells exposed to the same dose of γ-rays. Images and intensity profiles in the red, green, and blue channels (RGB profiles) show that p53BP1 colocalizes with γH2AX foci at the resolution power of confocal microscopy in all cases except the combination of γ-rays with Hc. Therefore, p53BP1 probably binds to chromatin at broken DNA ends only after the decondensation of the Hc domain; in the case of ^{20}Ne, the domain is seriously fragmented, which probably allows p53BP1 to enter Hc immediately. In terms of its mechanism, kinetics, and fidelity, DSB repair depends on the combination of IR quality and higher-order chromatin structure. RGB-profiles: x-axis, the path through the nucleus along the yellow line; y-axis, the pixel intensity in R-G-B [the range of 0 to 255]. Description of images is the same as that in Fig. A. **D:** Chromatin decondensation at the sites of Hc-DSBs may lead to IRIF protrusion into the nuclear domains with low-density chromatin and formation of IRIF (DSB) clusters. To distinguish these DSB clusters produced by the activity of DSB repair from those formed by the energy deposition (primary clusters), we call these "secondary clusters" (left images). For high-LET IR, similar interactions and clustering may also appear between the IRIF tracks along the particle path that are comprised from multiple IRIFs; these are the higher-order clusters (right images). Since the secondary/higher-order clusters are quite rare, usually temporary, and their number increases with time after irradiation, they probably represent sites with an increased risk of chromatin exchanges rather than putative repair factories. Description of the images is the same as in B and C, but the cells were fixed between 30 minutes and 2 hours after irradiation. Images for γ-rays are modified according to Falk et al., 2007.[665] **E:** The proposed model of the relationship between the higher-order chromatin structure, DSB repair, and the mechanism of chromosomal translocations formation Falk et al., 2007.[665] Since DSBs are spatially quite stable, the global higher-order chromatin structure determines the (dynamic) nuclear positions of loci a, b, c, d, e, f, and g, and thus their nuclear separation and the elementary probability of mutual chromosomal translocations (t). For instance, the probability (pt) is high for lesions a + b, c + d, and e + f, but negligible for a + d and c + g. However, the local higher-order chromatin structure may significantly modify pt determined on the mutual distances of interacting partners since it can influence the protrusion of IRIFs into the nuclear subdomains with low-density chromatin. Lesions a + b appear at the opposite sides of an Hc domain; therefore, they will protrude into different nuclear subcompartments of the low-density chromatin. This precludes their mutual interaction despite that the lesions are located in very close mutual proximity; pt(a+b) will therefore only be low. On the other hand, lesions c + d appear close to each other in a limited space of the same Ec (i.e., low-density chromatin) domain, so they can easily interact, and pt(c+d) will be inconsiderable. Similarly, lesions e + f arise from different Hc domains that are located facing one another at the opposite "banks" of the same low-density chromatin nuclear subdomain. Therefore, there is a high chance that both of these lesions will protrude to the same nuclear subdomain, where they can consequently produce chromosomal translocations. Since usually only limited "movements" of Hc-DSBs were observed, translocations between largely separated lesions (a + d, c + g, etc.) seem to remain insignificant despite chromatin decondensation. The description of the image is the same as for D. From Falk et al., 2014.[18]

days,[751,770] this observation may suggest that the cells are still actively processing complex damage introduced into DNA by relatively high doses (1.3 or 4 Gy) of high-LET (about 180-138.1 keV.µm^{-1}) ^{15}N-radiation. Indeed, in accordance with some other reports (e.g., Asaithamby and Chen[771]) we have shown for other types of heavy ions, boron and neon (^{11}B: LET = 138.1 keV.µm^{-1}, E = 8.1 MeV per n;

^{20}Ne: LET = 132.1 keV.μm^{-1}, E = 46.6 MeV per n), that the average number of γH2AX/53BP1 foci per nucleus can (^{11}B) or cannot (^{20}Ne) return back to the baseline in irradiated (2 Gy) NHDF fibroblasts after a longer period post-irradiation (96 h PI).[19] Alternatively, in accordance with what has been proposed[19,772], such a long persistence of DSBs, together with their high complexity revealed, could indicate that the repair remains incomplete and the cells are going to die, unless they manage their survival by some other processes. A high radio-resistance of U87 cells could therefore also be ascribed to their adaptation for survival with unrepaired DNA. This may be a result of loss of function in some aspects of DNA repair which is supported by slower repair of glioma cells and the persistence of high levels of Rad51 and DNA-PK in U87 cells throughout the cell cycle.[773] Only cluster formation and relaxation were investigated in this study. Whether the clusters of 53BP1 (and other repair proteins) differ in their topology,[758] for instance as a consequence of different damage complexity, structure or type of damaged chromatin (e.g., heterochromatin vs. euchromatin), and repair mechanism initiated (NHEJ, and HR), remains to be elucidated. This will be a subject of future investigations aimed at better understanding how the cluster topology and chromatin architecture contribute to the cell decision for a certain repair pathway at a given damaged chromatin site. Nevertheless, it is evident already from the present results on 53BP1 focus nano-structure (**Figure 41**) that U87 dispose with markedly better ability than normal fibroblasts to repair the clustered DSBs, i.e. the most dangerous DNA damage. This finding thus probably points to the most important factor causing the high radioresistance of U87 cells, though all described phenomena may mutually cooperate.

Future systematic investigations of spatial organization of γH2AX foci and focus sub-units and their topology in relation to chromatin environment, followed by detailed structure measurements of repair protein arrangements at given repair loci, may lead to conclusive description on why certain repair proteins are recruited to a given damage site and how the repair pathway choice at this site is determined. This may considerably affect the understanding of repair mechanisms and individual radio-sensitivity, as it is a matter of fact in radiation tumor treatment.

2.3.2.2 Metal nanoparticle-mediated tumor cell radiosensitization

Nanoparticles (NPs) of various materials offer extensive application not only in medicine. Metal nanoparticles are then studied as novel nanodrugs especially in the context of tumor cell radiosensitization and theranostics. This usage is reasoned by their ability to emit electron showers after irradiation. Hence, on physical basis, metal (high-Z) NPs are able to amplify radiation dose at microscale. As NPs are also preferentially internalized and cumulated by tumors (*e.g.* due to so called EPR effect), radiotherapy in presence of NPs could selectively increase DNA damage in tumor cells and thus ensure better tumor cell killing and preservation of normal tumor-surrounding tissue at the same time. At least, these are the physical presuppositions. However, both biological systems (cells, tissues) and nanoparticles are very variable, which may lead to very unique mutual interactions and interactions with IR. Therefore, it is easy to imagine that the biological effects of irradiated nanoparticles are still unexplored and sometimes surprising compared to that what was expected.

The main “problem” with the mechanism of nanoparticle-mediated radiosensitization resides in a well-documented fact that NPs, including those of very fine dimensions, e.g. of 2 nm in diameter, do not

penetrate into the cell nucleus. This was confirmed by various approaches, including confocal microscopy (**Figure 51A**), fluorescence spectroscopy (**Figure 51B**), and SMLM nanoscopy (**Figure 52**). Considering mostly short range of secondary electrons emitted by irradiated NPs, a question emerges of whether these electrons released in the cytoplasm may reach the nucleus and cause damage to DNA that would be sufficient for radiosensitization. In the cytoplasm, NPs may occupy different compartments depending on their features. Containing DNA as the only cytoplasmic organelles (in human cells), mitochondria represent the first cytoplasmic target for NP-mediated radiosensitization. However, we did not observed colocalization of gadolinium NPs (2 – 3 nm gadolinium) with mitochondria (**Figure 53**). Surprisingly, different NP types have been most frequently reported to colocalize with endosomes and lysosomes, as was also observed in our experiments (**Figure 53**). These observations point to a very interesting possibility that NP-mediated radiosensitization is, at least in some cases, independent of DNA damage augmentation. Indeed, for various NPs (Pt, Au, and Gd) involved in our experiments, we saw only insignificant differences in DSB induction between cells γ-irradiated in presence of NPs and those irradiated with the same dose in absence of NPs (**Figs. 54– 57**). This result was independent of the incubation time with nanoparticles prior to irradiation, as studied up to 24 h-long period. Interestingly, for larger (10 nm) gold nanoparticles, an increased number of γH2AX molecule signals were measured by SMLM for cells exposed to higher (>2 Gy) but not lower radiation doses in presence of NPs (**Figure 58**). Altogether, our results show that, despite of intensive experimental effort, the mechanism of metal nanoparticle-mediated tumor cell radiosensitization remains obscure and is perhaps dependent on the nanoparticle and/or cell type.[27,28,37] Moreover, not all NPs exert radiosensitizing effect as measured by clonogenic assay that represents the gold standard method in radiobiology for evaluating cell survival upon irradiation.[37]

Relevant publications discussed

8. Pagáčová E, Štefančíková L, Schmidt-Kaler F, Hildenbrand G, Vičar T, Depeš D, Lee JH, Bestvater F, Lacombe S, Porcel E, Roux S, Wenz F, Kopečná O, Falková I, Hausmann M, Falk M. Challenges and Contradictions of Metal Nano-Particle Applications for Radio-Sensitivity Enhancement in Cancer Therapy. Int J Mol Sci. 2019;20(3). doi: 10.3390/ijms20030588.

9. Falk M. Nanodiamonds and nanoparticles as tumor cell radiosensitizers-promising results but an obscure mechanism of action. Ann Transl Med. 2017;5(1):18. doi: 10.21037/atm.2016.12.62.

10. Štefančíková L, Lacombe S, Salado D, Porcel E, Pagáčová E, Tillement O, Lux F, Depeš D, Kozubek S, Falk M. Effect of gadolinium-based nanoparticles on nuclear DNA damage and repair in glioblastoma tumor cells. J Nanobiotechnology. 2016;14(1):63. doi: 10.1186/s12951-016-0215-8.

11. Falk M. Nanoscopy and Nanoparticles Hand-in-Hand to Fight Cancer: An Exciting Entrée into the Rising NANOworld. Biophys J. 2016 Feb 23;110(4):872-3. doi: 10.1016/j.bpj.2016.01.005.

12. Falk M., Wolinsky M., Veldwijk M.R., Hildenbrand G. and Hausmann M. Gold Nanoparticle Enhanced Radiosensitivity of Cells: Considerations and Contradictions from Model Systems and Basic Investigations of Cell Damaging for Radiation Therapy. In: Nanopharmaceuticals: Principles and Applications. Springer, in press

Discussion on Štefančíková et al. 2016, Pagáčová et al. 2019, and Falk et al. 2019

In the following text, potential mechanisms of nanoparticle-mediated radiosensitization are discussed in a more detail, based on the text adapted from Pagáčová et al. (2019).[28] Our data suggest that there are at least some nanoparticles that increase cell killing upon irradiation[27,385] while they have none or a negligible effect on numbers of nuclear DNA double strand breaks visualized by the γH2AX/53BP1 markers. This confirms our intuition on the cytoplasmic action mode of the radiosensitizing nanoparticles. In other experiments, we observed great increase in the life span of animals bearing tumor (9L cell gliosarcoma in brain) or the inhibition of tumor growth (A375sc melanoma in flank) when the animals were treated by radiotherapy after intravenous (9L gliosarcoma) or intratumoral (melanoma) injection whereas the majority of the nanoparticles in the tumor were suspected to be outside the cells (unpublished results discussed in Pagáčová et al. 2019).[28] Moreover, we also observed in many experiments that the number of γH2AX/53BP1 foci is not influenced by the incubation of cells with radiosensitizing NPs prior to irradiation. Hence, these NPs seem to sensitize cells to radiation through cytoplasmic effects that are independent of DNA damage and/or repair. While our findings do not exclude the possibility that some NP types support radiation cell killing through the "classic" DNA damage-based mechanism, they open the doors to exiting research of new mechanisms that could be dominant under some circumstances. For instance, accumulation of nanoparticles in endosomes and lysosomes as revealed in our earlier reports[27,774] could result in damage of these structures with important consequences. While lysosomes were originally thought only as cellular dustbins, recent studies involve lysosomes in important cell signaling pathways, possibly initiating apoptosis (see Falk et al., 2014[17] and citations therein). In addition, even simple disruption of a larger amount of lysosomes due to their membrane damage by locally amplified radiation effects, mediated by intra-lysosomal nanoparticle accumulations, may result in massive leakage of lytic enzymes from these "suicide bags" [775,776] and extensive cytoplasmic damage. This can also initiate cell death. Indeed, the destabilization of lysosomes via lysosomal membrane permeabilization (LMP), leading to release of their aggressive content into the cytoplasm, is currently intensively studied as a potentially efficient way of therapeutic cell death triggering.[777]

Cytoplasmically located nanoparticles may also influence organelles or structures that they do not co-localize with. For instance, increased production of ROS has been frequently reported in the literature as a main cause of nanoparticles' cytotoxicity. Therefore, ROS generated by nanoparticles in extensive amounts upon irradiation may damage organelles located in close proximity to nanoparticle location sites, for instance mitochondria. Among other cytoplasmic targets, mitochondria are especially attractive since they are critical for cell survival (energy metabolism) and represent the only extra-nuclear structures having their own DNA. Therefore, nanoparticle-mediated fragmentation of mitochondrial DNA may represent an elegant modification of the "classic" DNA damage-based hypothesis on cell radiosensitization by nanoparticles, returning this idea into the game. It should also be noted that ROS are effective signaling molecules with a strong potential to directly influence biochemical cellular pathways.

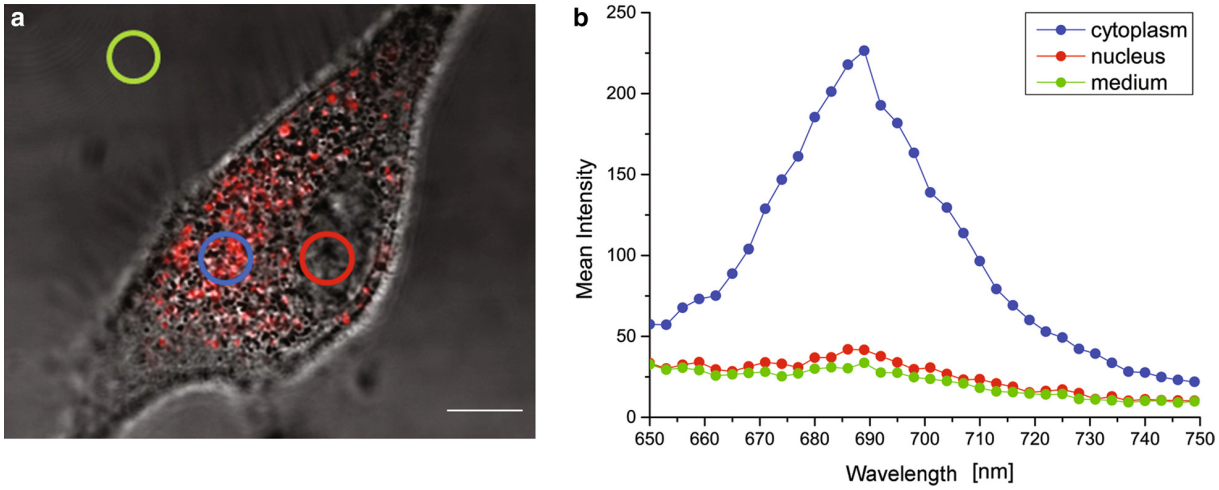

Figure 51. Localization of GdBNs-Cy5.5 nanoparticles in U87 cell. **A:** Correlative fluorescence confocal image and transmission light image of U87 cell with internalized GdBNs-Cy5.5 (red) at the end of 16 h-long observation. The scale bar equals to 10 µm. The circles represent the regions of fluorescence spectroscopy measurements, cytoplasm (blue), nucleus (red), and plain medium (green). **B:** Fluorescence emission spectra of the three regions. From **Štefančíková et al., 2016**.[27]

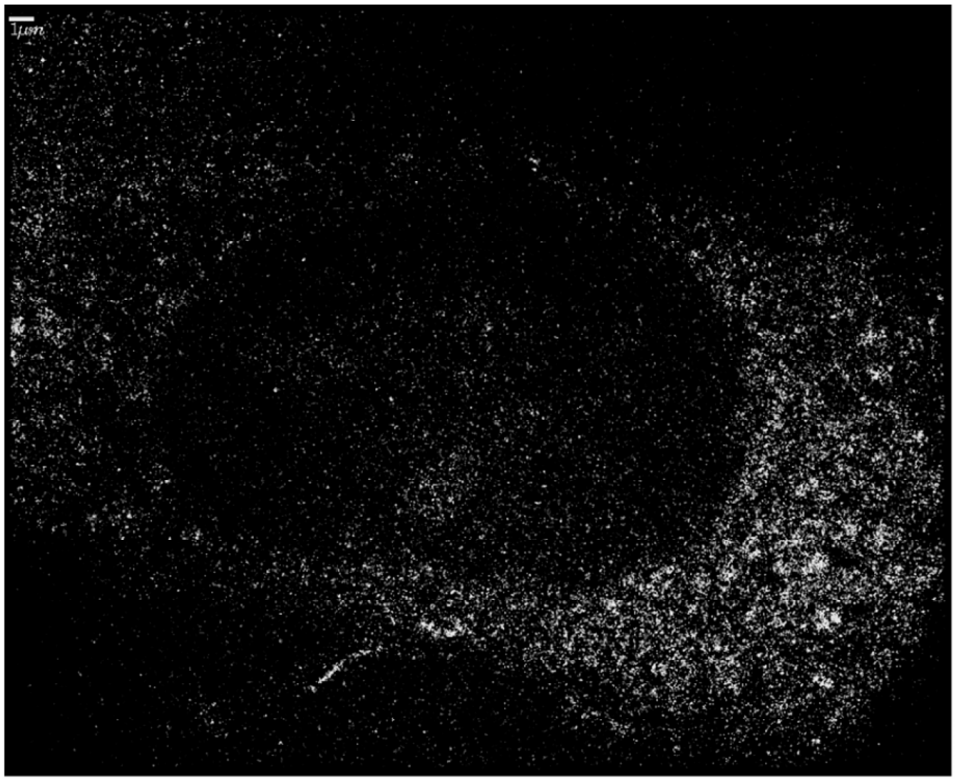

Figure 52. An illustrative Single Molecule Localization Microscopy (SMLM) image of an SkBr3 cell after uptake of 10 nm Au-NPs in the cytosol. The Au-NPs show a fluorescent blinking after laser illumination at 594 nm. Each point thus represents a single Au nanoparticle. Whereas the cytosol seems to be full of nanoparticles, the nucleus is empty. The points of low intensity seemingly covering the nucleus in the image either are the background or belong to out-of-focus image planes above or below the nucleus. Scale bar 1 µm. From **Pagáčová et al., 2019**.[28]

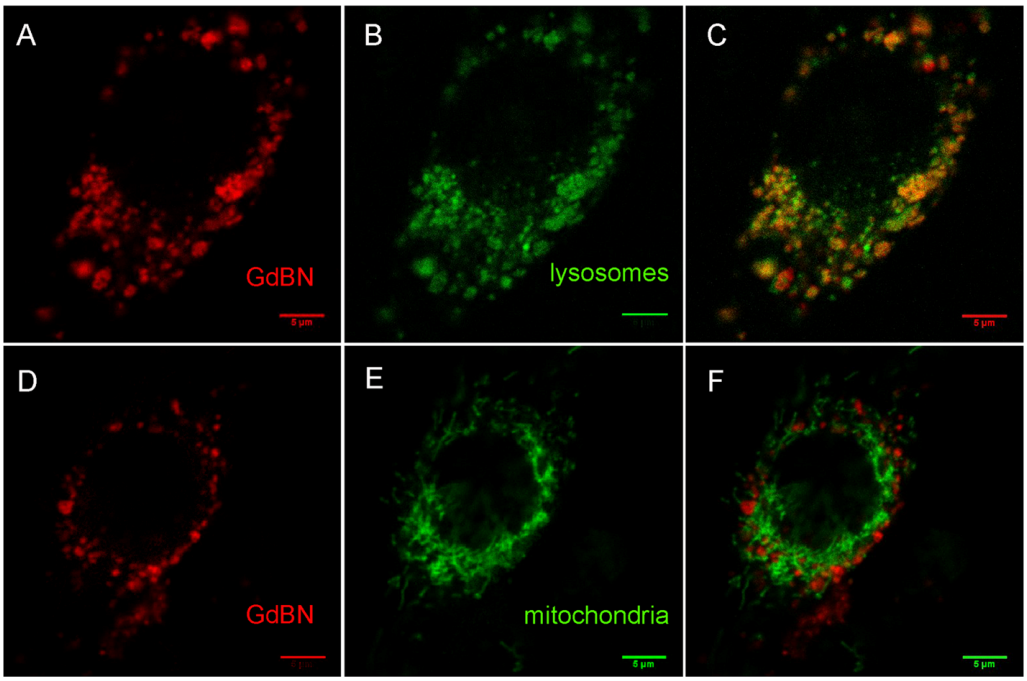

Figure 53. Colocalization of gadolinium nanoparticles with lysosomes but not mitochondria. Fluorescence images obtained by confocal microscopy of U87 loaded with GdBN-Cy5.5 1 mM (red) (A, D, C and F) in the presence of Lysotracker-green (green) (B and C) or Mitotracker green (green) (E and F). (C) Merged image of (A) and (B). (F) Merged image of (D) and (E). From **Štefančíková et al. 2014**.[774]

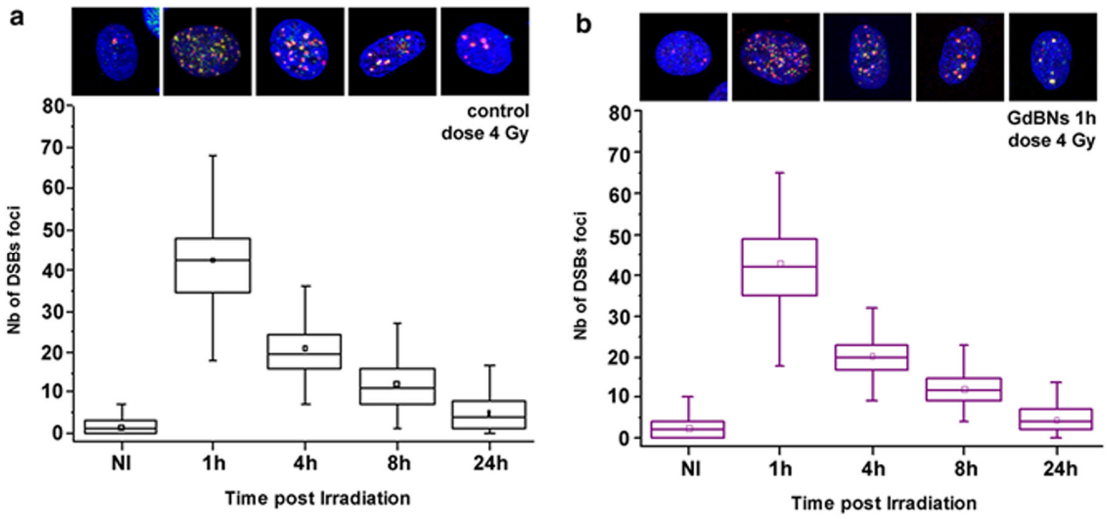

Figure 54. Effect of GdBNs on DSBs formation and repair in irradiated (4 Gy) U87 cells. Distribution of DSBs foci in U87 cells never incubated with GdBNs (a) and incubated with 1 mM GdBNs for 1 h (b). Non-irradiated controls (NI) are also compared. The respective maximum images of representative nuclei for each period of time PI are shown above: γH2AX—green, 53BP1—red, chromatin—artificially blue. From **Štefančíková et al., 2016.**[27]

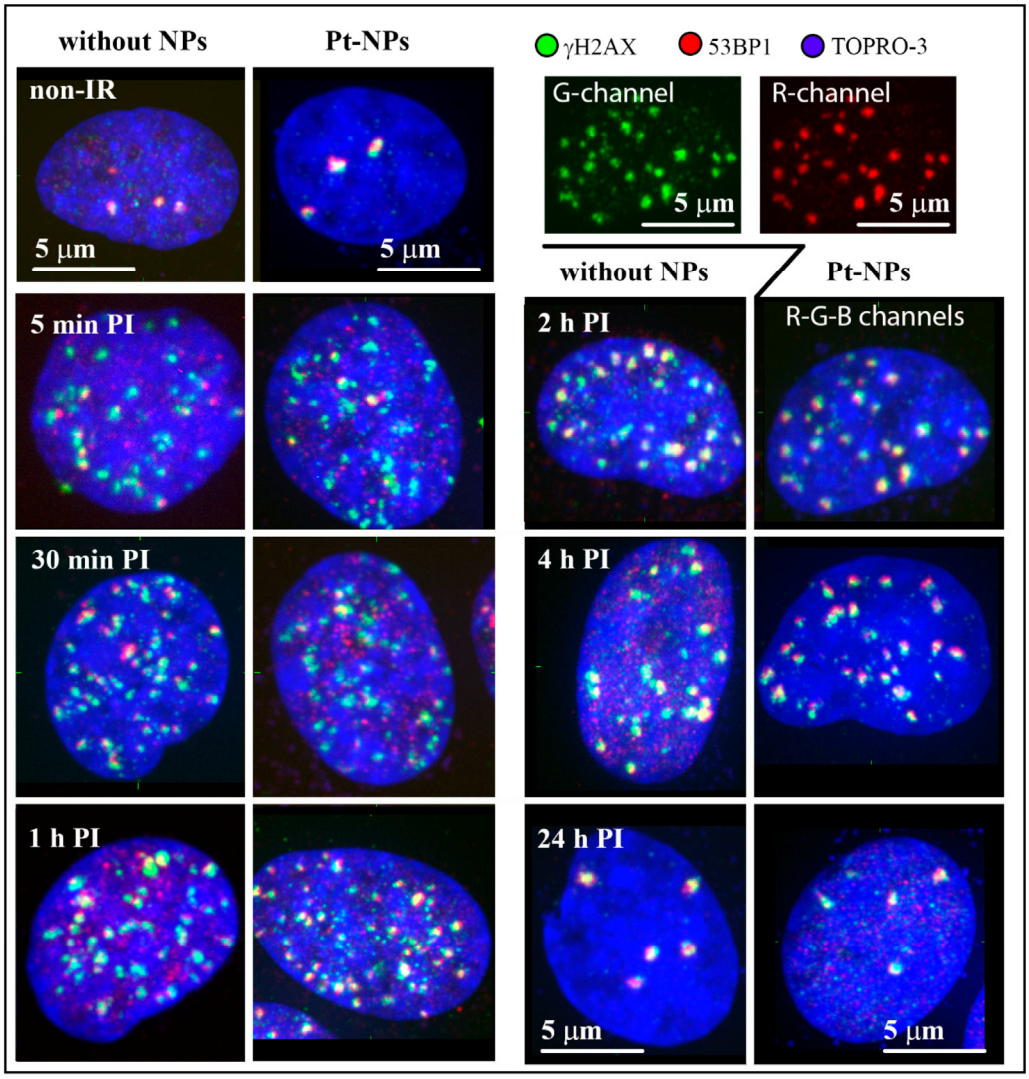

Figure 55. γH2AX/53BP1 foci (DSB) formation and repair kinetics in U87 cells incubated or not incubated with 2.6 nm platinum nanoparticles (Pt-NPs; 0.5 mM for 6 h) and consequently irradiated with 4 Gy of γ-rays. Maximum images are displayed for representative nuclei of cells that were spatially (3D) fixed in the indicated periods of time PI. For the nucleus fixed at 2 h PI, γH2AX foci (inserted G-channel panel) and 53BP1 foci (inserted R-channel panel) are also shown separately to demonstrate their mutual co-localization. γH2AX (green), 53BP1 (red), and chromatin counterstained with TO-PRO-3 (artificially blue). None-IR figures correspond to non-irradiated cells. From **Pagáčová et al. 2019**.[28]

The Endoplasmic Reticulum (ER) may represent another target for nanoparticle effects. While the efficient functioning of the ER is essential for most cellular activities and survival, it may be under some modifications also invaded by nanoparticles.[778] Moreover, ER plays an important role in the response to oxidative stress-induced damage and is quite sensitive to ROS.[779] Hence, irradiated nanoparticles may exert cytotoxic effects on cells by modulating ER stress.[779] For instance, Ag-NPs resulted in cytotoxicity and cell death by apoptotic, which was associated with (secondary) DNA fragmentation.[779] This observation not only explains how nanoparticles may initiate cell death through disturbing functions of ER, but also stresses the importance of time when interpreting the nanoparticle-mediated DNA effects. In this light, it is possible that in some studies the nanoparticle-mediated effects on DNA can rather reflect this secondary apoptotic DNA fragmentation than primary enhancement of DSB induction by radiation. The mechanism, how ER stress can lead to apoptosis, has been described by

Szegezdi et al.[780] A disruption of ER function leads to accumulation and aggregation of unfolded proteins accompanied with stress signaling. The stress signals are detected by transmembrane receptors, which in turn initiate the unfolded protein response (UPR) trying to restore normal ER functions. However, if the stress persists too long, apoptotic cell death ensues.[780]

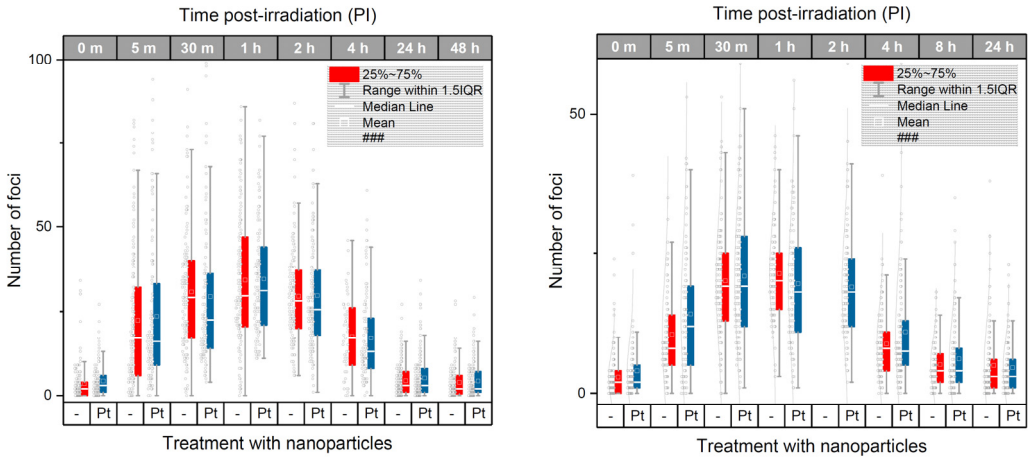

Figure 56. Software analysis of the extent of γH2AX+53BP1 focus (DSB) induction and repair kinetics in U87 glioblastoma cells irradiated with 4 Gy (**a**) or 2 Gy (**b**) of γ-rays compared with cells treated (0.5 mM for 6 h) or not treated prior to irradiation with 2.6 nm platinum nanoparticles (Pt-NPs). The average and median numbers of co-localized γH2AX + 53BP1 repair foci (i.e., DSBs) per nucleus are shown for different periods of time PI, together with the focus number distributions in each cell population. The boxes include 50% of the values (25th to 75th percentile) centered on the median (the horizontal line through the box). The mean values are represented by the squares within the boxes. The outliers were identified according to the 1.5*IQR method (IQR = interquartile range). Pt—samples treated with platinum nanoparticles, m—the period of time after irradiation in minutes, 0 m—non-irradiated samples. From **Pagáčová et al., 2019**.[28]

Altogether, we show that the radiosensitizing effect of at least some metal nanoparticles may rely on cytoplasmic processes rather than DNA damaging events. Based on the available literature, we also outline the way of how damage of the most relevant cytoplasmic structures may initiate cell death. Though we did not observe different responses to nanoparticles *per se* or irradiation in presence of nanoparticles for the two studied cell types (U87, and HeLa), we emphasize the necessity to analyze in detail each particular combination of nanoparticles and the cell type planned to be therapeutically targeted. This imperative follows from extensive controversies that are still present in the literature on the nanoparticle-mediated irradiation effects. For instance, Au-NPs induced apoptosis in MCF-7 and U87 cancer cell lines by disrupting lysosomes and mitochondria, but this effect did not appear in normal Chinese hamster ovary (CHO) and 293T cell lines. This observation further supports our conclusion that nanoparticle-mediated cell killing enhancement may be located in the cytoplasm, but, more importantly, gives a perspective of selective nanoparticle toxicity for tumor cells.[781,782] Interestingly, from the opposite point of view, some radio-protective chemicals (amifostine) protect normal cells from radiation effects but delay DSB repair in tumor cells.[783]

The final question remains whether it is in principle a good or bad massage finding that nanoparticles damage the cells without affecting DNA. On the one hand, it could be beneficial since nanoparticles located outside the tumor will not increase the risk of genome damage and secondary malignancies induction in normal tissues surrounding the tumor. On the other hand, the radiosensitizing mechanism operating through DNA damage could be more efficient.

A solution of this dilemma could be based on selective targeting of nanoparticles to specific genome sequences, like oncogenes, using appropriately designed oligo-nucleotides as being available for radio-emitters.[398] With techniques of COMBO-FISH[446,447] and PNA probe combinations,[443] NPs may be transferred to cell nuclei and specifically addressed to given chromatin targets. This could be achieved by adding a nuclear localization signal (NLS) peptide motif and a specific PNA oligonucleotide probe to the surface of nanoparticles.[784] Using such sophisticated approaches of specific targeting of genome aberrations like multiple gene copies would open new aspects in tumor therapy.

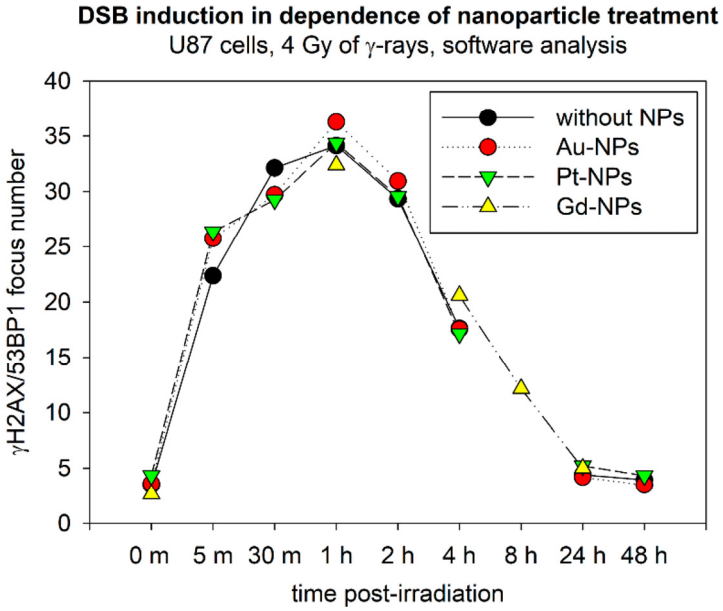

Figure 57. Comparison of γH2AX/53BP1 focus (DSB) formation and repair in U87 cells irradiated with 4 Gy of γ-rays in absence or presence of 2.6 nm Pt-NPs, 2.4 nm Au-NPs or 2.0 nm Gd-NPs. The results of an automated software analysis are shown as mean numbers of foci per nucleus measured at the indicated periods of time PI. Black circles—without NPs, green triangles—Pt-NPs (0.5 mM, 6 h incubation), and red circles—Au-NPs (0.5 mM, 6 h-incubation; preliminary results). The data are also compared to our earlier results[27] for Gd-NPs (1 mM for 1 h, ^{60}Co-irradiation, 4 Gy) (yellow triangles). X-axis: m = minutes, h = hours; 0 min = non-irradiated samples. From **Pagáčová et al., 2019**.[28]

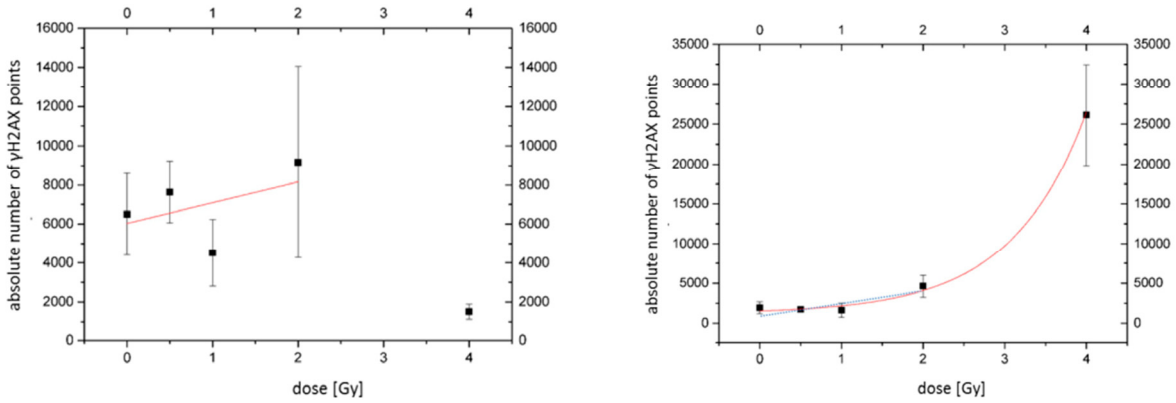

Figure 58. Dose–efficiency curves – the number of γH2AX labelling tags counted by SMLM vs. dose for cells incubated or not incubated with gold nanoparticles and irradiated). For the irradiated SkBr3 cell nuclei without Au-NP incorporation (left graph, a linear increase (red fit curve) can be observed at doses between 0 and 2 Gy. This was compatible to the blue linear fitting curve for irradiated SkBr3 cell nuclei with Au-NP incorporation (right graph). For the higher dose values, an exponential growth (red fit curve) or quadratic increase could be fitted to the values (black square: mean value; error bar: standard deviation). From **Pagáčová et al., 2019**.[28]

2.3.2.3 DNA damage potentiation by cell freezing

Relevant publications discussed

13. Kratochvílová I, Kopečná O, Bačíková A, Pagáčová E, Falková I, Follett SE, Elliott KW, Varga K, Golan M, Falk M. Changes in Cryopreserved Cell Nuclei Serve as Indicators of Processes during Freezing and Thawing. Langmuir. 2018; doi: 10.1021/acs.langmuir.8b02742.

14. Golan M, Pribyl J, Pesl M, Jelinkova S, Acimovic I, Jaros J, Rotrekl V, Falk M, Sefc L, Skladal P, Kratochvilova I. Cryopreserved Cells Regeneration Monitored by Atomic Force Microscopy and Correlated With State of Cytoskeleton and Nuclear Membrane. IEEE Trans Nanobioscience. 2018;17(4):485-497. doi: 10.1109/TNB.2018.2873425.

15. Falk M, Falková I, Kopečná O, Bačíková A, Pagáčová E, Šimek D, Golan M, Kozubek S, Pekarová M, Follett SE, Klejdus B, Elliott KW, Varga K, Teplá O, Kratochvílová I. Chromatin architecture changes and DNA replication fork collapse are critical features in cryopreserved cells that are differentially controlled by cryoprotectants. Sci Rep. 2018;8(1):14694. doi: 10.1038/s41598-018-32939-5.

16. Kratochvílová I, Golan M, Pomeisl K, Richter J, Sedláková S, Šebera J, Mičová J, Falk M, Falková I, Řeha D, Elliott KW, Varga K, Follett SE, Šimek D. Theoretical and experimental study of the antifreeze protein AFP752, trehalose and dimethyl sulfoxide cryoprotection mechanism: correlation with cryopreserved cell viability. RSC Adv. 2017;7(1):352-360. doi: 10.1039/C6RA25095E.

Discussion on Falk et al. (2018), Kratochvílová et al. (2018) and Kratochvílová et al. (2017)

Freezing and thawing of cells has been studied as a potential way haw to increase cell response to radiotherapy. Cryoablation is successfully used to eradicate or control many types of tumors (see Introduction) so we hypothesized it could be advantageously combined with irradiation. Freezing/thawing has been repeatedly described to fragment chromatin (i.e. induce DSBs into DNA); however, the results are contradictory with some reports recognizing chromatin fragmentation only in specific cases (e.g. defective cells) or completely failing to observe this type of damage. Therefore, we were interested how freezing/thawing damages chromatin of normal and tumor cells, respectively, and how it influences capability of these cells to repair DSBs.

We revealed that freezing/thawing does not induce DSBs in the majority of cells. Most of cells frozen/thawed in absence of cryoprotectants had extensively altered the higher-order chromatin structure (**Figure 59**) and sometimes also disrupted nuclear envelops. Nevertheless, we identified a small subset of cells that suffered from dozens to hundreds of DSBs (**Figs. 59, 60**). These cells were consequently identified as just replicating (S-phase) cells (**Figs. 61**, **62**). Therefore, DSBs in these cells most probably represent collapsed replication forks, eventually converted into DSBs (**Figure 61**). While we were able to reduce the damage to chromatin structure by cryoprotectants, replication forks were affected independently of cryoprotection. Hence, based on the comparison for normal skin fibroblasts and MCF7 tumor cells, we hypothesize that mitotically active tumor cells may be particularly sensitive to freezing/thawing. We also suppose that freezing/thawing could be thus efficiently used as a cell pre-

sensitizing procedure for radiotherapy, though effects on the DSB repair capacity of cells are still being analyzed. The published results were considered interesting also by the Czech media (see the Appendix).

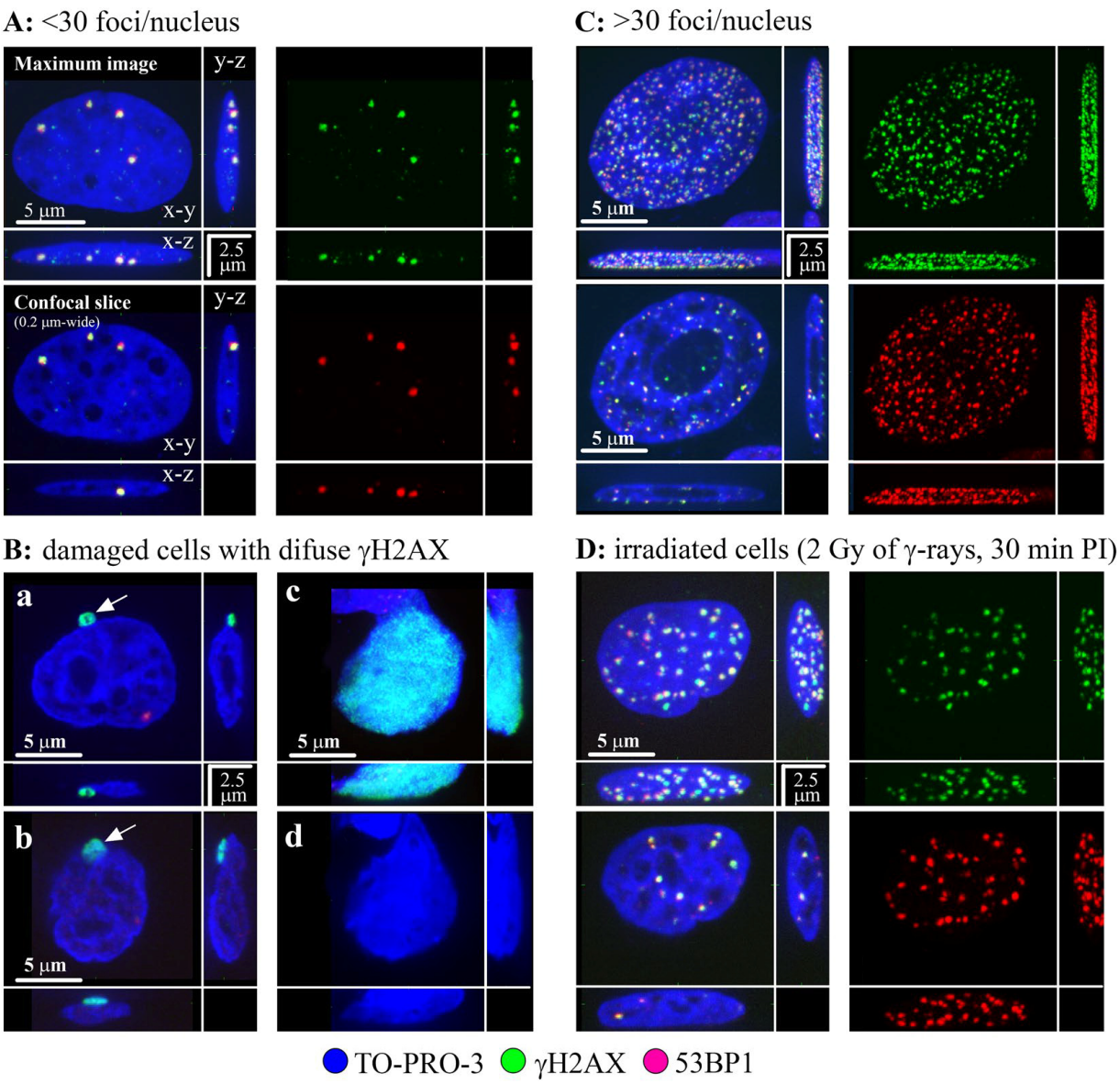

Figure 59. Three main categories (A–C) of MCF7 cells according to their γH2AX signal upon freezing/thawing. **(A)** The majority of cells remained unaffected by freezing/thawing in terms of DSB induction (category A, <30 γH2AX/53BP1 foci); the cells of this category were typical for DMSO-treated samples since in unprotected ones or those incubated with trehalose, a majority/substantial proportion of cells had damaged nuclei **(B)**. In category (B) nuclei were stained with diffuse, localized (a,b) or pan-nuclear (c) γH2AX signals that did not colocalize with 53BP1. Cells with localized intense γH2AX signals largely preserved chromatin structure but with localized structure less chromatin protrusion(s) from the cell nucleus (white arrow). The chromatin structure of cells with pan-nuclear γH2AX was frequently altered (d), typically decondensed with complete loss of structure (panel d only shows chromatin staining). **(C)** A fraction of cells showed, for all cryoprotectant treatments, extremely high numbers of tiny γH2AX foci (green) that colocalized with 53BP1 protein foci (red) (category C, >30 γH2AX/53BP1 foci). The overall chromatin structure of these cells remained preserved, especially in cryopreserved samples. Preservation of higher-order chromatin structure for cells A and C is demonstrated in 3D confocal (0.3 μm-thick) images. **(D)** Formation of γH2AX/53BP1 foci at sites of DNA double strand breaks (DSBs) in MCF7 cells irradiated with 2 Gy of γ-rays (60Co, 1 Gy/min) and visualized 30 min post-irradiation. γH2AX – green, 53BP1 – red, TO-PRO-3 (chromatin) – blue. From **Falk et al. 2018**.[32]

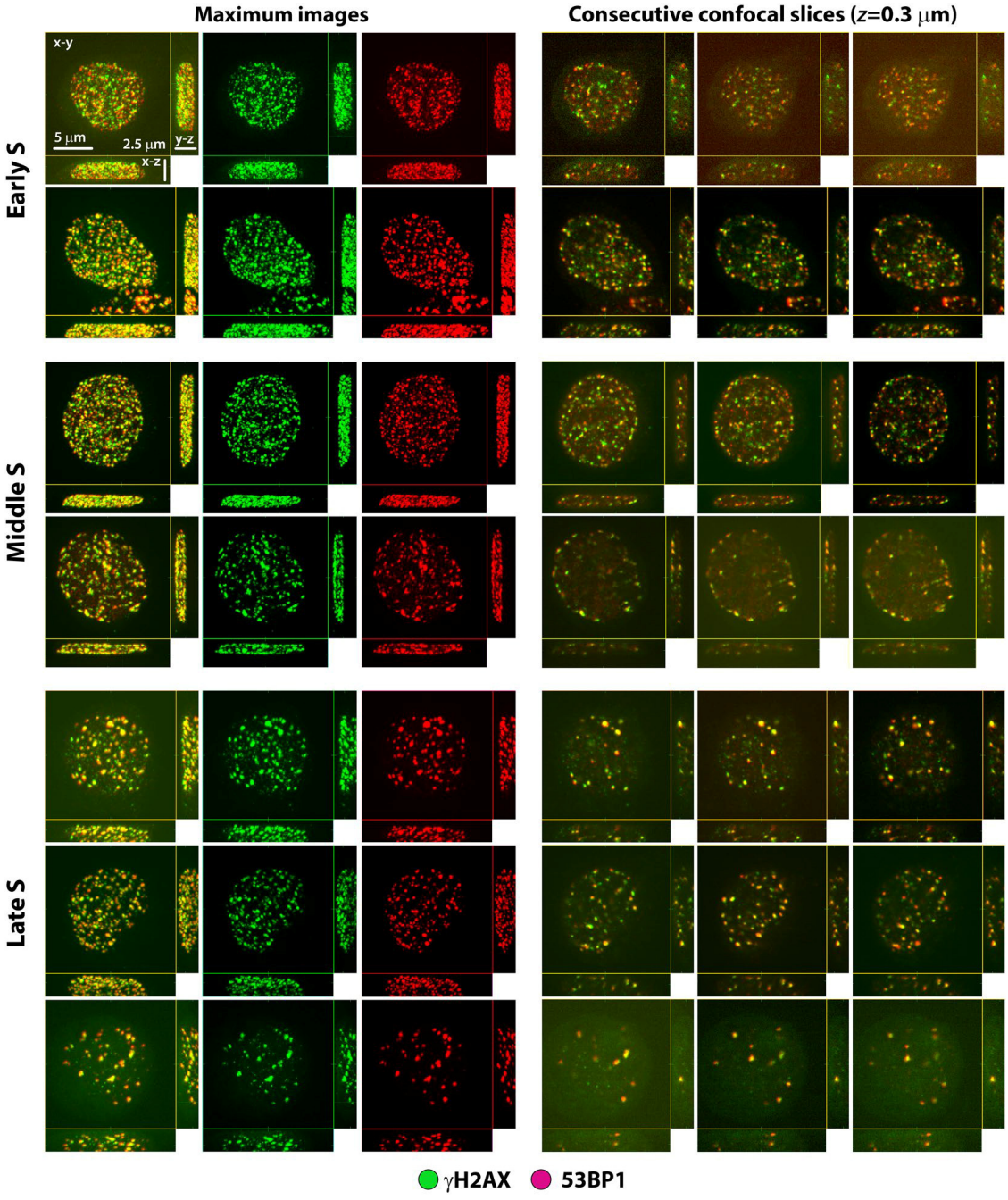

Figure 60. Three subcategories of MCF7 cells with increased numbers of γH2AX/53BP1 foci/nucleus after freezing/thawing, as determined using immunofluorescence confocal microscopy. Category 1 (top): nuclei with about >100 small γH2AX/53BP1 foci dispersed throughout the nucleus. Category 2 (middle): nuclei with >100 small γH2AX/53BP1 foci but distributed largely along the nuclear rim. Category 3 (bottom): nuclei with approximately 30 to 100 both small and large γH2AX/53BP1 foci distributed along the nucleolus and irregularly throughout the rest of the nucleus. There is evident similarity between the described γH2AX patterns (numbers and distribution) and the patterns of early (top), mid (middle), and late (bottom) S-phase replication (left captions). γH2AX foci (cells of category 1–3) thus seem to represent replication forks in S-phase cells collapsed upon freeze/thaw. 3D projections (x-y, x-z and y-z) of representative nuclei are shown for the composed of 40 confocal slices, each 0.3 μm thick (left column) and three consecutive single confocal slices, 0.3 μm thick (remaining columns). For maximum images, γH2AX (green) and 53BP1 (red) signals are also shown separately to demonstrate their mutual colocalization. Chromatin staining suppressed to improve the visibility of γH2AX/53BP1 foci. From **Falk et al. 2018**.[32]

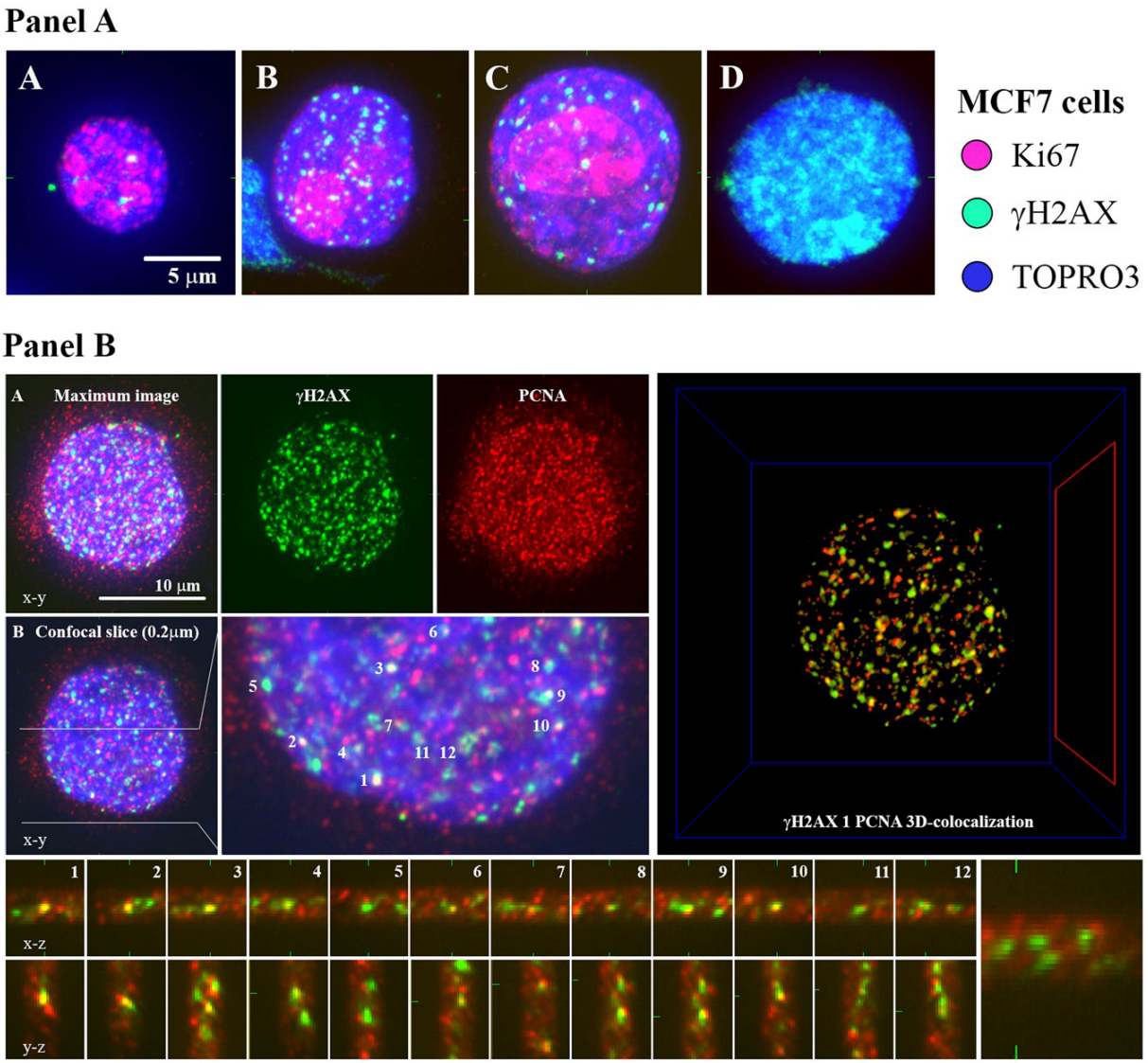

Figure 61. Cells with >30 γH2AX/53BP1 foci are S-phase cells with collapsed replication forks. **Panel (A)** Immunofluorescence microscopy of freeze-thawed MCF7 cells, stained with anti-γH2AX (green) and anti-Ki67 (red) antibodies, demonstrates the S-phase status of the cells with >30 γH2AX foci. (A) Cell nuclei with <30 γH2AX foci mostly showed jaguar-like patterns of Ki67 distribution typical of G1-phase or nucleolar staining with nucleoplasmic staining typical of G2-phase. (B,C) Cell nuclei with >30 γH2AX foci predominantly showed intense nucleolar Ki67-staining as typical for S-phase cells. (D) Most nuclei with pan-nuclear γH2AX staining (apoptotic or disintegrated nuclei) showed no Ki67 signal. Maximum projection images composed of approximately 40 confocal slices, each 0.3 µm thick, are displayed. Chromatin was counterstained with TO-PRO-3 (artificially colored blue). **Panel (B)** Immunofluorescence microscopy of frozen/thaw MCF7 cells, stained with anti-γH2AX (green) and PCNA (red) antibodies, demonstrates the colocalization of γH2AX foci with replication forks (PCNA) in cells containing >30 γH2AX foci. (A) Maximum projection images (composed of approximately 40 confocal slices, each 0.3 µm thick), showing patterns for anti-γH2AX and anti- PCNA antibodies, merged and separately. (B) Same as (A) but only showing the central confocal slice. The right panel displays an enlarged view of the colocalization of γH2AX and PCNA signals in the x-y plane. Detailed 3D colocalization for twelve γH2AX foci indicated in (panel B, bottom). Software-generated 3D-colocalization for all γH2AX and PCNA foci (panel B, right; Acquiarium software). Chromatin was counterstained (where relevant) with TO-PRO-3 (artificially colored blue). From **Falk et al. 2018**.[32]

2.3.2.4 Mechanisms of selective normal cell radioprotection

Relevant publications discussed

1. Hofer M, Falk M, Komůrková D, Falková I, Bačíková A, Klejdus B, Pagáčová E, Štefančíková L, Weiterová L, Angelis KJ, Kozubek S, Dušek L, Galbavý Š. Two New Faces of Amifostine: Protector from DNA Damage in Normal Cells and Inhibitor of DNA Repair in Cancer Cells. J Med Chem. 2016;59(7):3003-17. doi: 10.1021/acs.jmedchem.5b01628.
2. Hofer M, Hoferová Z, Falk M. Pharmacological Modulation of Radiation Damage. Does It Exist a Chance for Other Substances than Hematopoietic Growth Factors and Cytokines? Int J Mol Sci. 2017;18(7). doi: 10.3390/ijms18071385.
3. Hofer M, Hoferová Z, Depeš D, Falk M. Combining Pharmacological Countermeasures to Attenuate the Acute Radiation Syndrome-A Concise Review. Molecules. 2017;22(5). doi: 10.3390/molecules22050834.

Discussion on Hofer et al. (2016)[783]

Adapted from Hofer et al., 2016.[783] The last approach addressed in the present thesis with the aim to improve radiotherapy is the selective radioprotection of normal cells that are also always affected by irradiation. Radiotherapy is based on the therapeutic window given by the difference between the radiosensitivity of normal cells and tumor cells, i.e. normal cells must better repair DSB damage compared to tumor cells. The reduction of normal cell damage or improvement of their DNA repair capacity could thus allow for radiation dose escalation and better killing/controlling of tumors otherwise resistant to lower doses. Currently the only compound capable to selectively protect normal cells, also approved for clinical use, is amifostine. Amifostine (ethanethiol, 2-[(3-aminopropyl)amino]dihydrogen phosphate), also known as WR-2721, is an organic thiophosphate agent; it is rapidly dephosphorylated by alkaline phosphatase (ALP) at the cell surface of healthy tissues, giving rise to its clinically active metabolite, WR-1065.[420–422] WR-1065 then scavenges free oxygen radicals that emerge during water radiolysis and potentially protects cells also by some other ways (below). The cell type-specificity of radioprotection by amifostine has been usually attributed to low levels of ALP in cancer cells as compared with normal cells;[422] however, the situation is still not that clear because a variety of human cancers ectopically express high levels of ALP.[431–433]

We showed that amifostine protects normal cells from DNA damage induction by IR or chemotherapeutics, as expected. However, we also revealed that instead of remaining uninfluenced, tumor cells surprisingly suffer from a decreased DSB repair capacity, as it follows from the results of comet assay and currently the most sensitive method of DSB quantification based on γH2AX/53BP1 immunofluorescence microscopy (**Figure 62** and **Figure 63**). Amifostine treatment thus seem to support DSB repair in γ-irradiated normal NHDF fibroblasts but alter it in MCF7 carcinoma cells. These effects can be attributed to the significantly lower activity of alkaline phosphatase measured in MCF7 cells and their supernatants as compared with NHDF fibroblasts. Liquid chromatography–mass spectrometry confirmed that the amifostine conversion to WR-1065 was significantly more intensive in normal NHDF

fibroblasts than in tumor MCF cells. In conclusion, due to common differences between normal and cancer cells in their abilities to convert amifostine to its active metabolite WR-1065, amifostine may not only protect in multiple ways normal cells from radiation-induced DNA damage but also make cancer cells suffer from DSB repair alteration. Based on the achieved data, we propose new hypotheses on amifostine activity in normal and tumor cells, respectively. **"The Good and the Bad" hypothesis** is based on the toxicity of amifostine and protective behavior of its metabolite WR-1065. While amifostine was considered as biologically inactive in previous works, some authors[785,786] and our current results show that this prodrug *per se* is rather toxic, with direct and/or indirect negative effects on DSB repair and cell survival. As it is illustrated in **Figure 64**, amifostine is almost not converted to WR-1065 in cancer cells because of low levels of ALP and acidic pH and behaves as "Bad." On the other hand, amifostine in normal cells is converted to WR-1065, its "Good" active metabolite, that ensures protection of normal cells against immediate cytoplasmic and DNA radiation-induced damage by scavenging free radicals (ROS).

However, as also shown here, it supports the repair of DSBs too, directly by (physicochemical) interactions with damaged DNA and/or indirectly by modifying gene expression and biochemical cell regulatory pathways (see the attached original paper for more detailed discussion). The alternative **"Jekyll and Hyde" hypothesis** (Panel C) is partially similar to the "The Good and The Bad" hypothesis (Panel B) but the negative effect on cancer cells is exerted by WR-1065 (instead of amifostine). Low

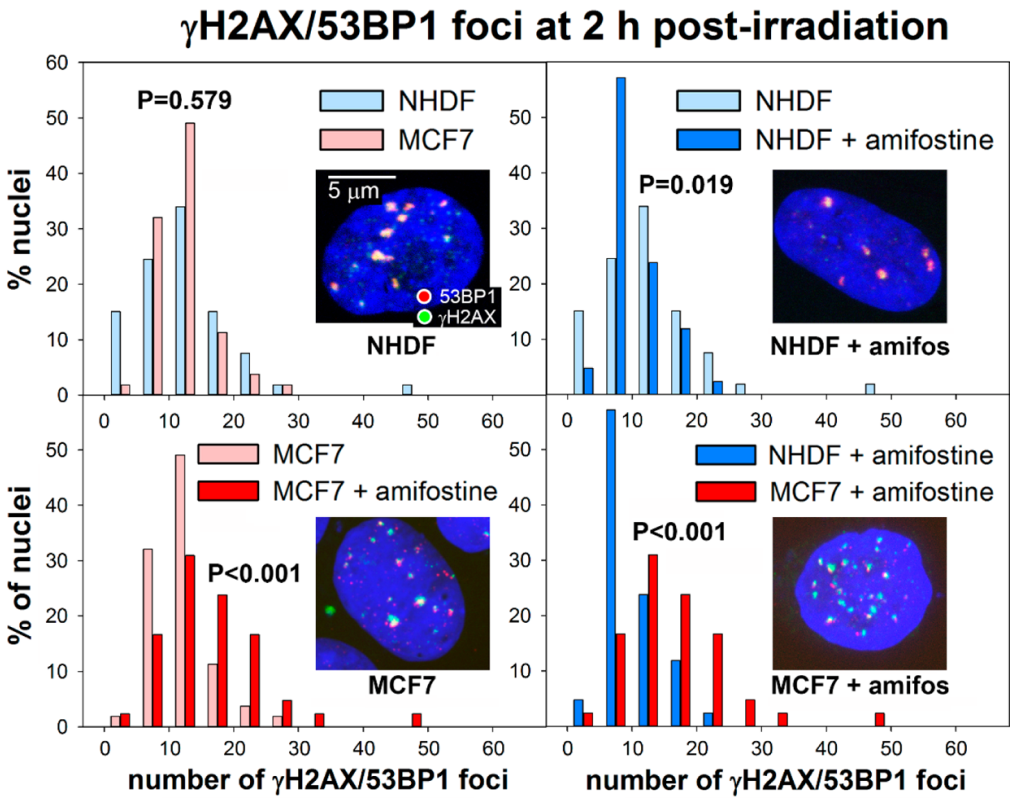

Figure 62. Influence of amifostine on DSB repair in normal NHDF and tumor MCF7 cells, exposed to 1 Gy of γ-rays – Distributions of the numbers of ionizing radiation-induced repair foci (γH2AX and 53BP1) persisting 2 h post-irradiation in nuclei of these cells. Illustrative images of nuclei are inserted. Chromatin counterstaining with TO-PRO-3. P-values indicate the results of the Mann–Whitney U test. From **Hofer et al. Med Chem. 2016**.[783]

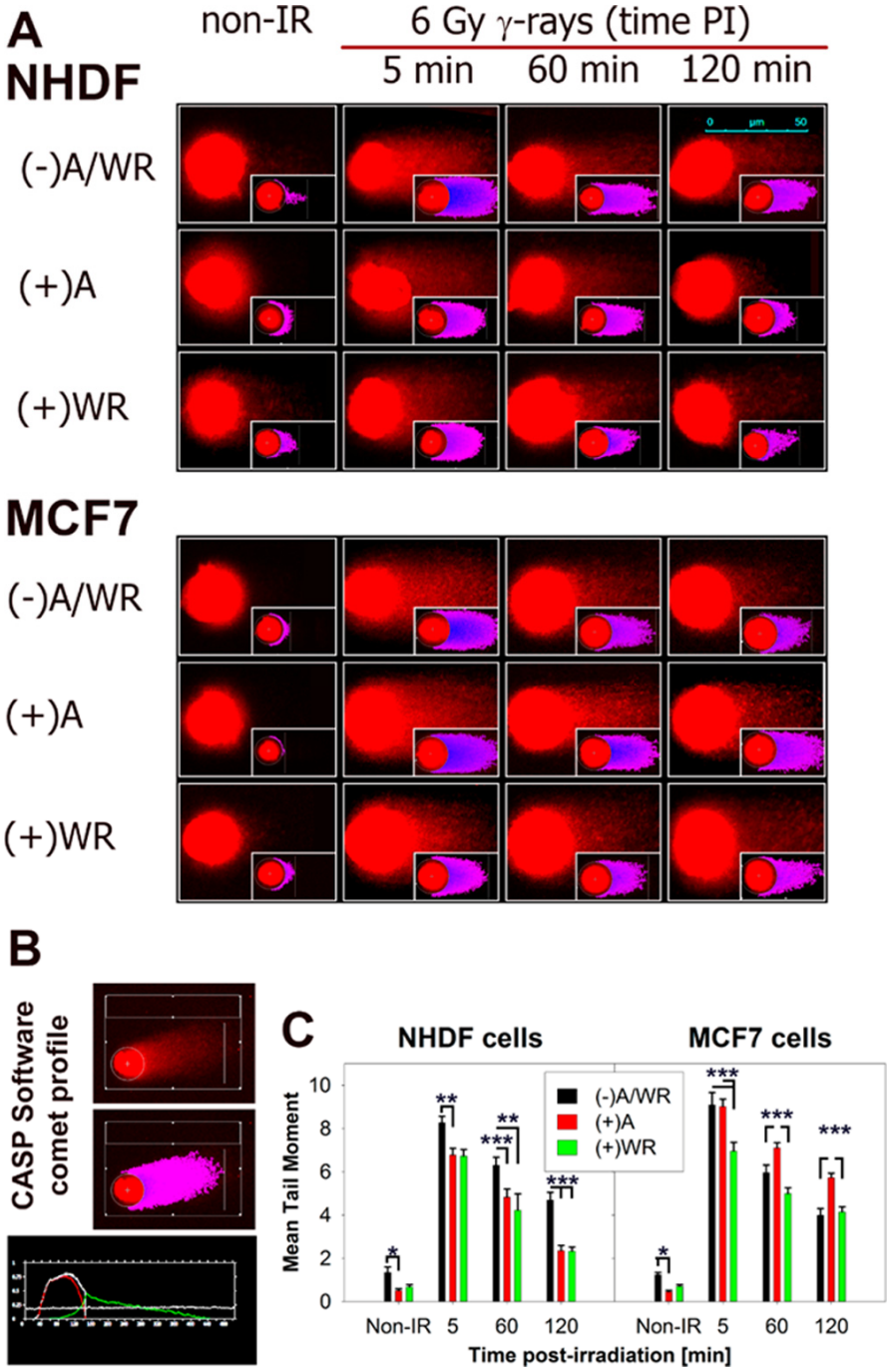

Figure 63. Influence of amifostine on DSB repair in normal NHDF and tumor MCF7 cells, exposed to 1 Gy of γ-rays – DSB induction and repair quantified by the neutral comet assay. A. Illustrative DNA comets of NHDF and MCF7 cells treated or not treated for 15 min with 4 mM amifostine or WR-1065 prior to irradiation with 6 Gy of γ-rays (1 Gy/min). Detailed DNA comets at 5, 60, and 120 min PI are shown as the maximum images obtained by superimposition of 30–50 individual confocal slices taken with a z-step of 0.3 µm using the 63× oil-immersion lens. Inserted comet images show the comet tails and amounts of DNA in these tails (the purple to blue gradient reflects increasing DNA staining) as detected by the CASP Lab Software (see Experimental Section). B. Comet analysis by the CASP Lab Software. Top image: an example of DNA comet stained with Gel Red and obtained by superimposition of a confocal 3D z-stack (described in A). Middle image: the comet head and tail as detected by the CASP software. Bottom image: red fluorescence (606–708 nm) profiles quantifying DNA amounts in the comet head (red line) and tail (green line); white line indicates the cell nucleus. C. Average comet tail moments with standard errors calculated for particular cells and cell treatments (described in A); statistical significance of differences between the samples was determined by the Mann–Whitney U test (*, $P < 0.05$; **, $P < 0.01$; ***, $P < 0.001$). From **Hofer et al. Med Chem. 2016.**[783]

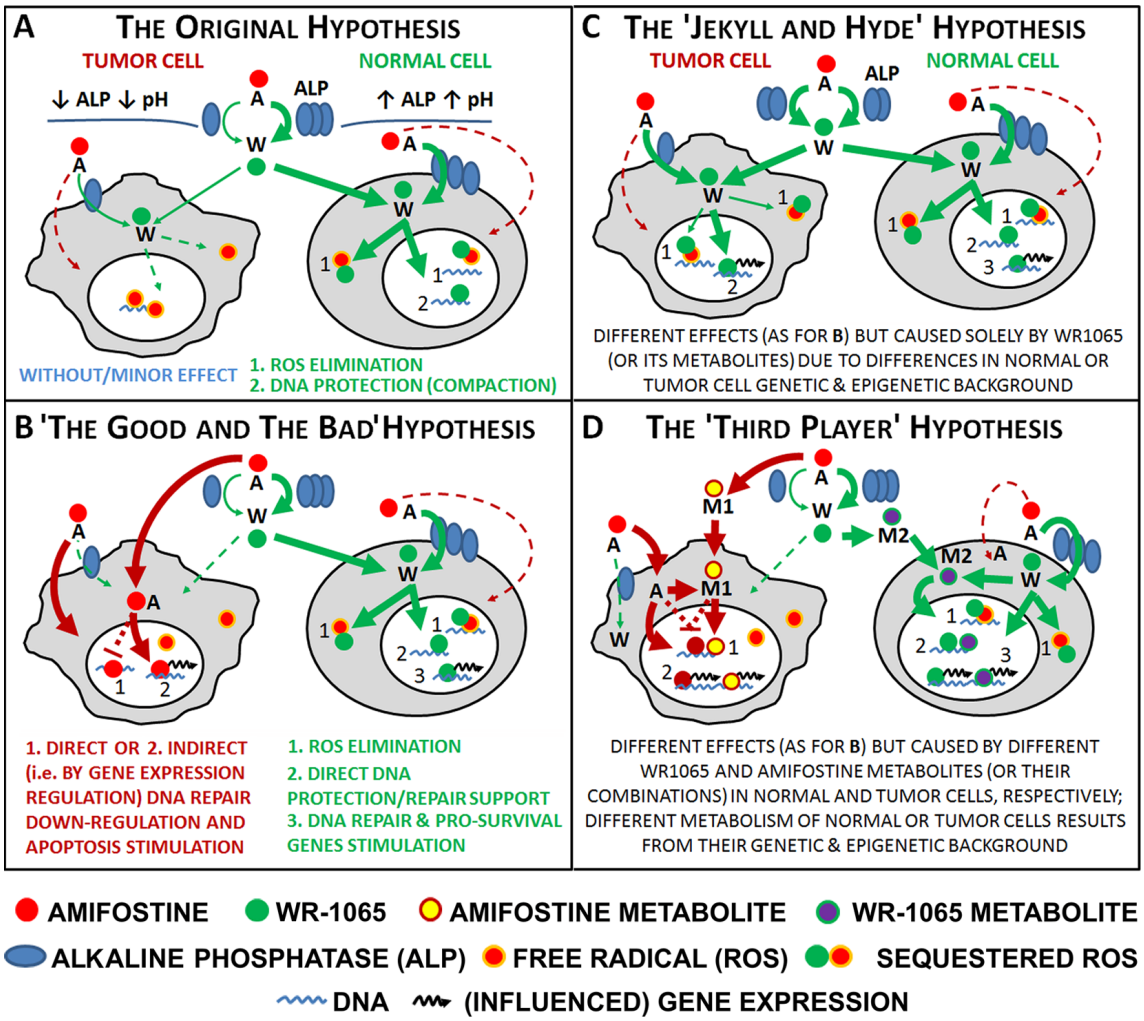

Figure 64. The proposed mechanisms of selective normal cell radioprotection and tumor cell radiosensitization exerted by amifostine – The original hypothesis **(A)** and the current 'Good and Bad' **(B)**, 'Jekyll and Hyde' **(C)**, and 'Third Player' **(D)** hypotheses. **B:** In cancer cells, amifostine is almost not converted to WR-1065 (because of low levels of ALP and acidic pH) and behaves as 'Bad'. While amifostine was considered as biologically inactive in previous works (panel A), some authors55,86 show that this prodrug per se is rather toxic, with direct and/or indirect negative effects on DSB repair and cell survival. On the other hand, amifostine in normal cells is converted to WR-1065, its 'Good' active metabolite. WR-1065 primarily ensures protection of normal cells against immediate cytoplasmic and DNA radiation-induced damage by scavenging free radicals (ROS). However, as also shown here, it supports the repair of DSBs too, directly by (physicochemical) interactions with damaged DNA and/or indirectly by modifying gene expression and biochemical cell regulatory pathways (see main text for more detailed discussion). **C:** As for (B) but the negative effect on cancer cells is exerted by WR-1065 (instead of amifostine). Low amounts of WR-1065 in cancer cells cannot protect these cells from DSB induction but are sufficient to negatively influence their DSB repair (and potentially other functions). The opposite effects of WR-1065 on DSB repair in normal and cancer cells follow from different WR-1065 levels and/or genetic backgrounds of these cells. WR-1065 thus only shows its 'Mr. Hyde' face in cancer cells but 'Mr. Jekyll' face in normal cells. **D:** As for B and C but varying mixtures of amifostine, WR-1065 and their metabolites are produced in normal and cancer cells, respectively; these mixtures interact with processes in normal and cancer cells in specific ways. From: **Hofer et al. Med Chem. 2016**.[783]

amounts of WR-1065 in cancer cells cannot protect these cells from DSB induction but are sufficient to negatively influence their DSB repair (and potentially other functions). The opposite effects of WR-1065 on DSB repair in normal and cancer cells may follow from different WR-1065 levels and/or genetic backgrounds of these cells. WR-1065 thus only shows its "Mr. Hyde" face in cancer cells but "Mr. Jekyll" face in normal cells. The last, so called "**Third Player" hypothesis** (Panel D) follows a more complex scenario, where varying mixtures of amifostine, WR-1065 and their downstream metabolites are

produced in normal and cancer cells, respectively; these mixtures interact with processes in normal and cancer cells in specific ways.

Currently, it is difficult to judge what mechanism of amifostine action is the most probable. Nevertheless, in any case, our results put amifostine in an entirely new light. In the treatment of some malignancies, this drug can not only selectively protect normal tissues but can also act as a radiosensitizer which in parallel improves the killing of the cancer cells by disrupting DNA DSB repair. This finding highlights separated effects of amifostine on DSB induction and repair. Nevertheless, the complexity of cellular processes potentially specifically influenced by amifostine and its metabolites in various normal and cancer cells prevents a simple extension of our results to normal and cancer cells in general. Hence, the action of amifostine and other radio-modifiers should be studied carefully for each particular cell type. Fortunately, the rapidly growing repertoire of new molecular-genetic, proteomic, and other "omic" methods[17,748] now opens new dimensions of further research on radio-modifying drugs and the mechanisms of their action.

2.3.3 Concluding remarks and discussion on the chapter

Our results identified the higher-order chromatin structure as an important player for DSB repair. The structure definitely influences both the chromatin sensitivity to DSB induction and, consequently, DSB repair in all its aspects, including its mechanism, efficiency, kinetics, and fidelity. Therefore, it is evident that the higher-order chromatin structure has a general impact on cell radioresistance and the formation of chromosomal aberrations. We showed that DSB repair proceeds more easily in decondensed (eu)chromatin because extensive chromatin decondensation and remodeling are required at the sites of heterochromatic DSB lesions, which complicates the repair process. Although most DSBs are repaired individually at sites of their origin, chromatin decondensation introduces a dynamic aspect to the mechanism of DSB repair and formation of chromatin exchanges. The decondensation around heterochromatic DSBs, also reported by Durante et al.,[669,670] causes protrusion of damaged chromatin into low-density chromatin domains (referred to as "chromatin holes" in our original paper[665]), where usually two or three DSBs (upon γ-ray IR) can mutually interact and form temporary or, more rarely, stable DSB clusters. These foci persist in cell nuclei longer than the simple lesions, so it is reasonable to suppose that they are repaired only with difficulty and represent sites with an increased risk of chromatin translocation (or aberration formation in general). The probability of chromatin translocation between particular chromosome loci follows from global chromatin organization in the cell nucleus; however, this probability could be in a dominant manner affected by chromatin movement provoked by the described chromatin decondensation. Furthermore, the local higher-order chromatin structure determines the vectors of the DSB movements by defining the "accessible" and "nonaccessible" channels and nuclear subcompartments. The higher-order chromatin structure hence influences not only the general susceptibility of chromatin domains to the formation of chromosomal translocations (aberrations), but also the probability with what the particular genetic loci could be involved. In combination with the structure of DNA and chromatin at the lower levels

(responsible, e.g., for chromatin fragility), this could explain why some specific translocations usually associated with leukemia and lymphomas can be observed so frequently.

The model of chromosomal translocation formation we proposed makes a bridge between the "position-first" and "breakage-first" hypotheses previously proposed to explain this phenomenon. It reveals how some of otherwise "immobile" DSBs can be mobilized, which seems to be the necessary prerequisite for the formation of translocations between chromosomal loci originally distant in the cell nucleus and for the formation of complex chromosomal translocations.[43] [743,744] On the other hand, our results do not support the idea of targeted migration of microscale-sized DSB foci into putative repair factories, which has been proposed by some authors as the nuclear repair centers.[157] Our conclusions are also in a good agreement with the breakthrough results of Jeggo et al.[107–112,194,671,712,787–790] showing that euchromatic and heterochromatic DSBs require repair mechanisms of different complexity. Nevertheless, it should be noted that it still remains to be determined how the mobility of particular DSBs differs in the G_1 and G_2 phases of the cell cycle[791] because our experiments describing the clustering of DSB foci were mainly performed with G_1 cells.

The crucial questions to be answered are how NHEJ, HR, or alternative repair pathways become activated at individual DSB sites, especially how their selection depends on DSB complexity and a higher-order chromatin structure. In the G_2-phase of the cell cycle, DSBs can be repaired by either NHEJ or HR. We can suppose that more factors—the higher-order chromatin micro- and nanostructure and genetic activity of the affected domain, the nanostructure and complexity of the DSB itself, the cell-type-specific presence of repair proteins, and potentially other still unknown factors—contribute to the decision-making process for HR, NHEJ, or alternative (backup) repair pathways. The situation is seemingly less complicated in the G_1 phase, where both euchromatic and heterochromatic DSBs have been theorized to be repaired by NHEJ. However, even in this phase of the cell cycle, the repair of heterochromatic DSBs is substantially slower and requires the activity of additional "noncore" NHEJ repair proteins, such as 53BP1 and ATM. Moreover, a growing body of evidence suggests that HR can proceed, though in a limited extent, in G_1 as well,[44] and the activity of alternative repair pathways based on DNA resection should also be considered. The same factors deciding on NHEJ or HR activation in the G_2 phase, as described above, may therefore also be relevant in the G_1 phase. Further experiments are needed to shed more light on this crucial issue of DSB repair.

Altogether, despite the extensive progress in the field of radiobiology in recent years, the results on the spatio-temporal organization of DSB repair are still intensively disputed. Therefore, the Pandora's box of spatio-temporal organization of DSB repair still waits to be opened. In this respect, we expect a lot from our SMLM studies and from new rapidly developing multiomic approaches (**Figure 65**), the combination of which could cover all the tremendous variability of biological systems and complexity of radiobiological problems (**Figure 66**). Indeed, our first SMLM results reveal that there is an internal nanostructure of DSB repair foci. Numerous nano-clusters of γH2AX and other DSB repair protein

[43] At least upon low-LET irradiation.

[44] As presented at ICRR 2019 (Manchester, Great Britain), actively transcribed genes can be repaired by HR also in G1 phase of the cell cycle, using nascent RNA chain as the template for repair.

molecules were observed inside γH2AX clusters that were detected at the microscale. Whether these nano-clusters correspond to DSBs (and microscale γH2AX foci thus represent some sort of "repair factories") has to be further studied but it seems more probable that the nature of these nano-clusters is different and perhaps random. Nevertheless, we showed that the nanostructure and nano-composition of DSB repair foci dynamically change with postirradiation time and also markedly differ for (normal and cancer) cell types and even for structurally and functionally distinct chromatin domains. Therefore, we can reasonably hypothesize that the nanostructure of damaged chromatin at the DSB site, the character of the DSB, and the availability of repair proteins in the cell influence the "accessibility" of damaged chromatin for individual repair proteins, their binding to DSB, and, finally, the assembly of repair complexes at each particular DSB lesion. The nanostructure (nano-topology) of DSB repair foci can thus directly participate in the decision-making processes for the particular repair mechanism at each individual DSB site, in turn contributing to a determination of the cell-type-specific radiosensitivity. Our nanoscale observations thus confirm the conclusions earlier made based on microscale data about the crucial relevance of the structure in the regulation of DNA repair processes. Most importantly, nanoscale observations from SMLM (and other super-resolution methods) open the doors to an exciting cell nanocosmos.[20]

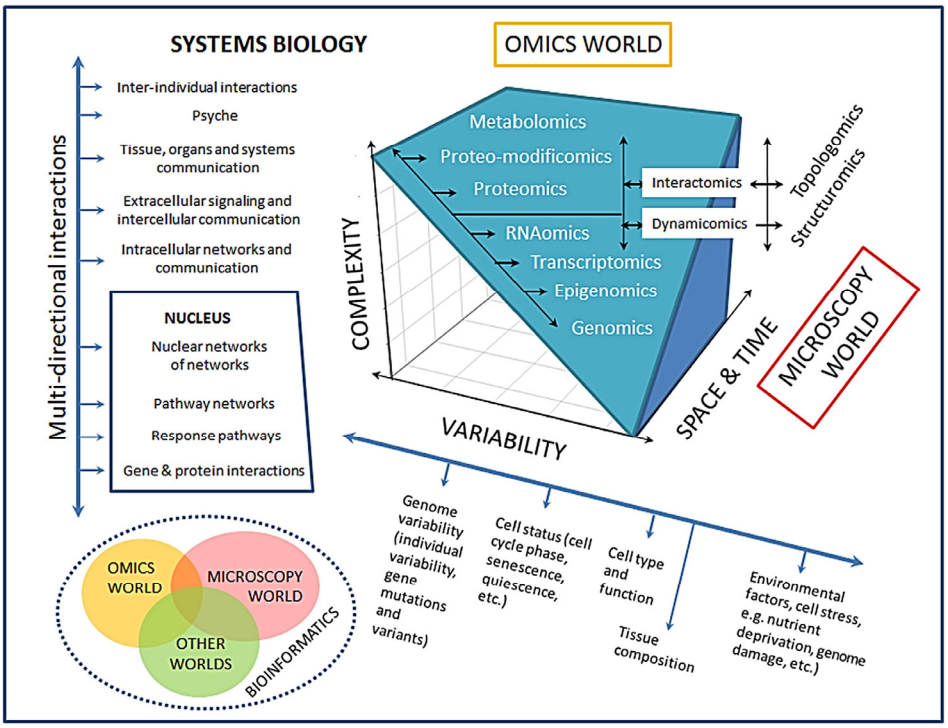

Figure 65. Complementary and irreplaceable roles of Omics and microscopy approaches in (radio)biological research. Extensive complex (left vertical axis) and variable (horizontal axis) functional biological networks, continuously changing in space and time (right horizontal axis), can be studied nowadays in a more holistic way by means of various omics (e.g., genomics, transcriptomics, proteomics; white lettering). However, the omic assays cannot provide information on the spatiotemporal organization and spatiotemporal dynamics of interactions between individual players of a particular omics system (e.g., protein–protein interactions) and between distinct omics (e.g., gene–protein interactions) (black lettering in white boxes). On the other hand, Structuromics and topologomics data (the graph, right side) can be studied with (real-time, living-cell) microscopy and nanoscopy (super-resolution microscopy). Micro-/nanoscopy thus allows Omics data to be put into the context of time and space of nonrandom architecture of the cell and cell nucleus. Both Omics and micro-/nanoscopy worlds could not exist without an extensive support from bioinformatics (bottom left diagram). From: **Falk et al. Crit Res Rev. 2014**.[18]

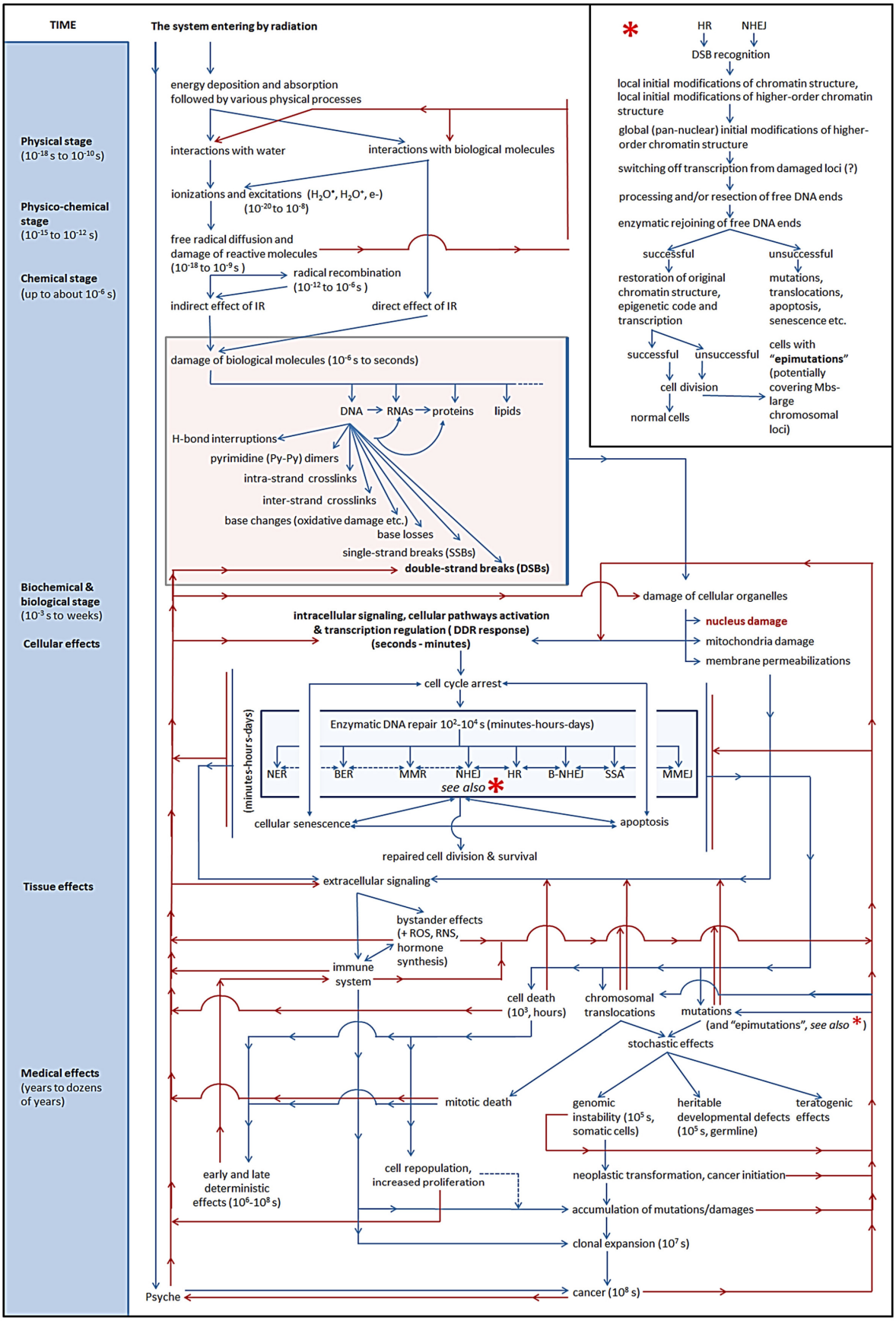

Figure 66. The spatiotemporal complexity and multidisciplinary nature of radiomics. The processes that take place after the irradiation of a biological system start with physical energy deposition in a time scale of about 10^{-18} s after irradiation). Then the processes continue with physicochemical and chemical reactions. Finally, biological responses continue for weeks after irradiation. Deleterious health effects possibly arising from a few misrepaired DNA lesions in one cell can appear at the level

of an organism even dozens of years after irradiation. Uninterrupted blue arrows show the interconnections between individual processes. The time axis also roughly correlates with the complexity of post-irradiation processes. Red dashed arrows indicate how processes at higher-hierarchical levels (or that appear later after irradiation) can, in turn, influence the upstream processes; complex regulatory and executing circuits and networks are thus formed. The red asterisk in the DNA repair box refers to the upper-left panel, disclosing the main processes associated with nonhomologous end-joining (NHEJ) and homologous recombination (HR), which are the main cellular pathways to repair the most serious DNA lesions, DNA double-strand breaks (DSBs). This panel also emphasizes the possibility that DSBs can lead to serious damage to the genome even if they are successfully rejoined, but the higher-order chromatin structure of the damaged chromatin domain is not restored to the original status. These "epimutations" can encompass MBs (large regions of DNA) and therefore might represent a serious threat to human health. Base Excision Repair (BER); Backup NHEJ (B-NEHEJ) - alternative to DNA-PK dependent NHEJ; DNA Damage Response (DDR); Microhomology-Mediated Joining (MMEJ); DNA Mismatch Repair (MMR); Nucleotide Excision Repair (NER); ROS, reactive oxygen species; RNS, reactive nitrogen species; Single Strand Annealing (SSA). From: **Falk et al. Crit Res Rev. 2014**.[17]

Cancer represents one of the most common causes of death in developed countries, and IR is still one of the most effective tools for treating this disease. Despite dramatic progress in irradiation technology, the radioresistance of tumor cells still represents a serious treatment complication, frequently leading to therapy failure. We have explored several new possibilities for tumor cell radiosensitization and normal cell radioprotection: ion-beam irradiation, metal nanoparticle-based radiosensitization, cell cryo-damaging, and selective normal cell radioprotection. Although these improvements are to some extent already used in clinical practice or at least subjected to (pre)clinical studies, the biological mechanisms of their functioning are largely unknown, preventing their optimal use and further development. Although we have confirmed radiosensitizing/radioprotecting (as applicable) effects of all these approaches, we achieved some surprising results that could possibly lead to paradigm shifts in radiobiology. This especially concerns a) the mechanism of metal nanoparticle-mediated radiosensitization and the role of cytoplasmic damage in initiating cell death upon irradiation. Furthermore, attention must be paid to the relationship between the properties of IR and character of DNA damage, where, for radiation types with similar LET, the effect of radiation on DNA cannot be attributed only to LET as a single value, but rather, numerous individual particle parameters contributing to the character of energy deposition must be considered. Finally, we discovered new mechanisms of radioprotection using amifostine.

3. POINT SUMMARIZATION OF THE MOST IMPORTANT RESULTS ACHIEVED IN THE FRAME OF PRESENTED PUBLICATIONS

The Principles of Higher-Order Chromatin Organization in Normal Cells

1. The cell nucleus is a highly organized organelle with a nonrandom higher-order chromatin structure; this is in a striking contrast to the previous imagination of the nucleus as a bowl with randomly swimming chromatin noodles.[1]

2. Importantly, the higher-order chromatin structure is of functional relevance.[1]

3. The higher-order chromatin structure is of statistical character and could be aptly characterized as "order in randomness."[1]

4. The mutual positions of chromosomal territories are usually random, while their radial distances from the nuclear center (or nuclear envelope) depend on the gene density and transcriptional activity.[1]

5. The principles of the higher-order chromatin organization hold true for different cell types; however, this organization is dynamic in nature, and its various aspects may reflect the current status of the cell or pathological processes.[1]

6. The principles of the higher-order chromatin structure described above are also relevant for chromatin organization inside the chromosomal territories; therefore, the territories of transcriptionally active chromosomes are polarized into active subdomains facing the nuclear center and inactive (heterochromatin) subdomains oriented toward the nuclear envelope.[2,3]

7. Gene-dense, transcriptionally active chromosomes or genetic loci are more decondensed and occupy a larger nuclear volume compared with their inactive counterparts of similar molecular size.[3]

The Changes of Higher-Order Chromatin Organization in Cancer Cells

8. The principles of higher-order chromatin organization are also preserved in cancer cells; however, marked disturbances of the chromatin structure may be observed, sometimes even in precancerous cells; the higher-order chromatin structure may also more or less directly participate in cancer initiation or development (next points).[10]

9. The higher-order chromatin structure in terminally differentiated blood cells (granulocytes) of leukemia patients in some cases resembles the structure of normal cycling cells more than the structure of normal terminally differentiated cells.[7]

10. Leukemia-associated changes of the higher-order chromatin structure may persist in patients' blood cells, even after successful treatment associated with the clinical and molecular remission with the complete disappearance of the Philadelphia chromosome.[7]

11. Premalignant (?) changes in the higher-order chromatin structure can be detected even in morphologically normal tissue that is distant from the tumor.[10]

12. A new mechanism of acute promyelocytic leukemia (APL) pathogenesis was revealed and involves changes in the higher-order chromatin structure that are provoked by PML/RARa oncoprotein and that are associated with gene downregulation.[11]

DSB Repair and Misrepair in the Context of Chromatin Structure

13. The higher-order chromatin structure influences the sensitivity of DNA to the induction of DSBs by (low-LET) IR. Heterochromatin is better protected from the indirect effect of IR than euchromatin because large amounts of proteins are specifically bound to heterochromatin and shield the heterochromatic domains against free radicals. Moreover, compared with heterochromatin, euchromatin is more hydrated and thus attacked by more radicals, which come from water radiolysis and live only very briefly.[13]

14. On the other hand, the repair of DSBs is more complicated and less efficient in heterochromatin. The affected heterochromatic domain must first decondense to allow processing of the lesion, which slows down the repair and, at the same time, increases the mobility of damaged chromatin. Therefore, despite DSBs being generally spatially stable and repaired at the sites of their origin, chromatin decondensation makes possible the interactions between originally distant DSBs. This interaction (DSB repair focus clustering) is an artifact of DSB repair and clustered DSBs, representing complex lesions that are repaired only with difficulty, thus pose an increased risk of chromatin translocation formation instead of being repaired in repair factories where several DSBs migrate to be repaired.[665]

15. Based on these results, we propose a new model of formation of chromosomal translocations that has aspects of both “position-first” and “breakage-first” hypotheses, originally postulated as mutually exclusive alternatives to explain this phenomenon. The most important point of our model is that although nuclear distances between loci, which are determined by the global chromatin organization, negatively correlate with the probability of translocation between the loci, as predicted by the “position-first” hypothesis, this probability may be dominantly influenced by the movement of some heterochromatic DSBs because of the affected chromatin domain decondensation (the “breakage-first” aspect). Moreover, the local higher-order chromatin structure determines the vectors of the damaged chromatin movement and thus supports or prevents mutual interactions of particular DSBs.[665]

16. Different high-LET ions of similar LET and energy can generate DNA damage of different microdosimetric parameters and DSBs of different complexities. The complexity of DSB damage correlates with DSB repair efficiency, showing that other parameters of the particle than only its LET may be relevant when searching for biologically more efficient radiation types or trying to explain their effects.[19]

17. The first application of SMLM for the research of DSB damage induction upon high-LET particle irradiation and repair of these lesions has brought about completely new sort of data that provided new insights into the mechanisms of these processes. SMLM has been proven as a breakthrough method for current and future (radio)biological research.[21,22]

18. SMLM shows that DSB repair foci have their internal nanostructures. Although the exact nature of this nanostructure remains to be revealed, the growing body of nanoscale data suggests that the nanostructure of DSB repair foci and damaged chromatin domain plays an important role in the decision-making process for the particular DSB repair mechanism at the site of each DSB lesion. The nanostructure of DSB repair foci and damaged chromatin domains could be directly related to the efficiency and fidelity of the repair processes and the radioresistance of the cell.[21,22]

19. The nanostructure/nano-composition of DSB repair foci may differ for different (normal and tumor) cell types. The nano-parameters of DSB repair foci and surrounding chromatin domain may contribute to the efficiency of DSB repair and, in turn, the cell-type-specific radiosensitivity.[22]

Novel Approaches to Radiosensitize Tumor Cells

20. DNA DSBs induced by high-LET particles are repaired only with difficulty, which correlates with the higher RBE of these radiation types when compared with γ-rays. Proton beams (15 MeV and 30 MeV) at the plateau of the Bragg curve generated DSBs repaired with only slightly slower kinetics than DSBs formed after γ-irradiation.[19]

21. Various metal nanoparticles can radiosensitize tumor cells to IR; however, this effect is evidently not always based on DNA damage augmentation and/or DNA repair alteration. Instead, the cytoplasmic events, which are probably independent of mitochondrial DNA damage according to our results, seem to play a role here. The digestion of cytoplasmic organelles by aggressive enzymes released from disrupted lysosomes or apoptotic signaling by these organelles after damage might be the relevant mechanisms.[27]

22. The freeze/thaw cycle dramatically alters the nuclear envelope integrity and chromatin structure in cells frozen/thawed in the absence of efficient cryoprotectants. However, the chromatin is not disintegrated by DBSs in most cells. The exception is just replicating (S-phase) cells, where freezing/thawing causes a collapse of replication forks, which is potentially followed by their conversion into DSBs. Fast-replicating cells, including tumor cells, may therefore be susceptible to preirradiation "cryoablation." Tumor cells could be particularly sensitive because they also suffer from defects in the DSB repair pathways.[32]

23. Amifostine, currently the only radioprotectant approved for clinical use, selectively protects normal cells from DNA damage induction but alters DSB repair in (at least) some tumor cell types too.[33]

4. CONCLUDING REMARKS AND FUTURE PERSPECTIVES

In the frame of the current thesis, the author presents a collection of his papers that, from several points of view, focus the biological effects of different types of IR. Emphasized is the role of a new phenomenon in DNA damage induction and repair: the higher-order chromatin structure. Extensively addressed are also new possibilities of radiotherapy development (IBCT, tumor cell radiosensitization, and normal cell radioprotection).

Some interesting discoveries have been achieved in the frame of the presented research, and these were well accepted by the scientific community; however, they should be seen as the first stars emerging in the evening sky. This is especially true for our nanoscopic studies, which brought about data of a completely new sort that remain to be fully understood. Also, our knowledge about the higher-order chromatin structure and its role in DNA repair is still fuzzy despite several decades of intensive research. Nevertheless, the window to the "structuromics" and cell nanocosmos has been opened, and the described shift toward nano-resolution (with optical microscopy!) represents the long-

awaited breakthrough in the field. Moreover, in combination with technological and methodological development in "omic" technologies, the current progress allows us to think about connecting individual research stories into dynamic and complex networks of cellular functions (**Figs. 65**, **66**). This methodological transition could be generally characterized as the beginning of the "nano-omic" era, which attempts to unify the results of super-resolution microscopy (structuromics), genomics, proteomics, metabolomics, and so forth. More complex, important discoveries can thus be expected in the near future.

The advantage of the micro- and nanoscopic techniques used in the present thesis is that they make it possible to observe individual cells in large numbers and under physiological (or even *in vivo*) conditions. This reduces the danger that some critical processes may remain hidden in the background noise that generally occurs because of averaging the differences between individual cells.[(45)] Therefore, we could follow and directly visualize the spatio-temporal aspects of DNA damage and repair in individual cells, even at individual DSB sites, which previously escaped detection and were ignored for a long time. Our results help us understand the processes in the cell nucleus in a broader and more complex extent than the results of earlier studies.

Nowadays, it is becoming apparent that especially in cancers, the molecular processes contributing to pathogenesis and clinical manifestation of the "same" disease dramatically differ from patient to patient. With expanding knowledge of these differences, there is a growing need for personalized biomedicine, where the treatment would be targeted against specific cellular processes that are deregulated in a particular patient. We have found that the higher-order chromatin structure and the structure of DSB repair complexes are altered in many cancers. Therefore, therapeutic modification of the chromatin structure and the influence of DSB repair may represent efficient and relatively new tools in the treatment of cancer and other diseases. This is, for example, the case of APL (as discussed in Chapter 2.1.2), where eliminating chromatin looping through retinoic acid or Trichostatin A causes remission of clinical symptoms despite causative translocation t(15;17) still persisting in cells. On the other hand, changes in the higher-order chromatin structure may indicate commencing pathological processes and could be of important diagnostic meaning. This is exemplified, for example, in our results showing altered higher-order chromatin structure in healthy head and neck or colon tissue sampled away from the tumor. Therefore, the higher-order chromatin structure might, at least in some cases, reveal neoplastic cell conversion in its premalignant phase. We also observed an altered chromatin structure in the blood cells of patients suffering from AML and CML, respectively, even if these patients reached clinical and molecular remission characterized by the absence of the Philadelphia chromosome after a successful treatment. Hence, it is possible that changes in the chromatin structure precede or even promote the formation of carcinogenic translocations.

Modifications of the higher-order chromatin structure could be advantageously used in combination with the "standard" therapy, where they may increase its efficiency. Nowadays, this approach is mostly

[45] importantly, these methods enable analyses of hundreds to thousands of individual cells, which is in a striking difference to methods working on 'averaged' material isolated from many cells

studied in the context of cancer radiotherapy and chemotherapy. Because radiotherapy—and frequently chemotherapy as well—kills tumor cells by inducing DSBs in the DNA molecule, chromatin structure modifications may sensitize chromatin to radiation damaging. Therefore, lower doses of IR or chemical drugs could be applied in the presence of chromatin-structure-modifying agents, which would enhance tumor cell killing and protect the normal tissue in the tumor surroundings against the acute and delayed (secondary cancers) radiation damage. Alternatively, chromatin structure modifiers may improve the killing of (radioresistant) tumors if the dose is kept unchanged.

For the same purposes, IBCT is being developed to replace the currently used γ-rays in the treatment of some tumor types. Although IBCT seems to be very promising, the application of ion beams is mostly based on empirical knowledge rather than a solid body of scientific data. Research on DSB induction by different kinds of IR and the repair of generated lesions is hence necessary to enable further progress in the field. Therefore, in the present thesis, we tried to better comprehend the complex relationship between the physical parameters of IR, chromatin structure at the site of damage, character of DNA damage, cell content of repair factors, decision-making mechanism for the particular repair process, mechanism and efficiency of DNA repair, and, finally, the overall radiosensitivity of the cell and possibilities of its therapeutic manipulation. In the future, we plan to compare DSB damage and repair for different medically relevant ion beams and low-LET photon rays (γ, X) in parallel at the micro-, meso-, and nanoscales. A better understanding of molecular processes at DSB sites may possibly disclose new mechanisms of tumor cell radioresistance (in cases where the radioresistance is based on DSB repair), identifying clinically applicable markers of cell radiosensitivity that are critically missed by oncologists. The obtained knowledge may also pave the way for efficiently inhibiting the repair process in tumor cells in a personalized way. A promising approach of tumor radiosensitization currently studied in the author's lab is immuno-radiotherapy. Irradiation may potentially unmask the tumor for an immune system response, and immune treatment may stimulate radiation-mediated killing of tumor cells.

An urgent call for a deeper comprehension of DNA damage and repair and the cell's response to DNA damage in a broader context sounds also from different fields. This is especially true for civil protection (in light of the Fukushima disaster and a threat of terrorist attacks with radioactive materials) and space exploration, where exposure to mixed fields of IR represents one of the most serious obstacles in planning manned long-term interplanetary missions. The importance of radiobiological research is also evident in the existence of the numerous European networks that have been established (with the author's lab's participation) to speed up progress in the field. In addition to the already mentioned radiotherapy, of the utmost importance are the biological effects of low radiation doses, which can still be experimentally studied but with difficulty.

Altogether, the current work points to the importance of the micro- and nanostructure for the cell nucleus and chromatin functioning. We describe how IR of different types interacts with structurally and functionally distinct chromatin domains, with consequences for DNA damaging, repair, and possibly misrepair, especially in the spatio-temporal orchestration of these processes. Finally, we proved efficient IBCT and some novel approaches of tumor cell radiosensitization and normal cell radioprotection, revealing surprising mechanisms behind these phenomena.

Perhaps, I shall conclude with my personal opinion. The ongoing technological boom in super-resolution microscopy and molecular biology methods, together with an already described urgent need for much deeper "radiobiological" knowledge, currently is pushing radiobiology into a new era. Hence, it is not an overestimation to say that radiobiology nowadays is experiencing its renaissance. Exciting discoveries could be expected in the near future, potentially leading to changes in some important paradigms.

REFERENCES

1 S. Kozubek, E. Lukásová, P. Jirsová, I. Koutná, M. Kozubek, A. Ganová, E. Bártová, M. Falk and R. Paseková, *Chromosoma*, 2002, **111**, 321–331.

2 E. Lukásová, S. Kozubek, M. Kozubek, M. Falk and J. Amrichová, *Chromosome Res. Int. J. Mol. Supramol. Evol. Asp. Chromosome Biol.*, 2002, **10**, 535–548.

3 M. Falk, E. Lukásová, S. Kozubek and M. Kozubek, *Gene*, 2002, **292**, 13–24.

4 V. Ondrej, S. Kozubek, E. Lukásová, M. Falk, P. Matula, P. Matula and M. Kozubek, *Chromosome Res. Int. J. Mol. Supramol. Evol. Asp. Chromosome Biol.*, 2006, **14**, 505–514.

5 V. Ondrej, E. Lukásová, M. Falk and S. Kozubek, *Acta Biochim. Pol.*, 2007, **54**, 657–663.

6 E. Lukasova, Z. Koristek, M. Falk, S. Kozubek, S. Grigoryev, M. Kozubek, V. Ondrej and I. Kroupová, *J. Leukoc. Biol.*, 2005, **77**, 100–111.

7 E. Lukášová, Z. Kořistek, M. Klabusay, V. Ondřej, S. Grigoryev, A. Bačíková, M. Řezáčová, M. Falk, J. Vávrová, V. Kohútová and S. Kozubek, *Biochim. Biophys. Acta*, 2013, **1833**, 767–779.

8 E. Pagáčová, M. Falk, I. Falková, E. Lukášová, K. Michalová, A. Oltová, I. Raška and S. Kozubek, *Folia Biol. (Praha)*, 2014, **60 Suppl 1**, 1–7.

9 Karel Štěpka and Martin Falk, in *mage Analysis of Gene Locus Position within Chromosome Territories in Human Lymphocytes. Lecture notes in Computer Science (LNCS)*, Springer International Publishing, 2014, pp. 125–134.

10 E. Lukasova, S. Kozubek, M. Falk, M. Kozubek, J. Zaloudík, V. Vagunda and Z. Pavlovský, *Chromosoma*, 2004, **112**, 221–230.

11 I. Dellino, M. Falk, P. G. Pelicci, M. Faretta and E. Lukasova, .

12 M. Falk, E. Lukasova, B. Gabrielova, V. Ondrej and S. Kozubek, *J. Phys. Conf. Ser.*, , DOI:10.1088/1742-6596/101/1/012018.

13 M. Falk, E. Lukásová and S. Kozubek, *Biochim. Biophys. Acta*, 2008, **1783**, 2398–2414.

14 M. Falk, E. Lukasova, B. Gabrielova, V. Ondrej and S. Kozubek, *Biochim. Biophys. Acta BBA - Mol. Cell Res.*, 2007, **1773**, 1534–1545.

15 M. Falk, E. Lukasova and S. Kozubek, *Mutat. Res.*, 2010, **704**, 88–100.

16 M. Falk, E. Lukášová, L. Štefančíková, E. Baranová, I. Falková, L. Ježková, M. Davídková, A. Bačíková, J. Vachelová, A. Michaelidesová and S. Kozubek, *Appl. Radiat. Isot. Data Instrum. Methods Use Agric. Ind. Med.*, 2014, **83 Pt B**, 177–185.

17 M. Falk, M. Hausmann, E. Lukášová, A. Biswas, G. Hildenbrand, M. Davídková, E. Krasavin, Z. Kleibl, I. Falková, L. Ježková, L. Štefančíková, J. Ševčík, M. Hofer, A. Bačíková, P. Matula, A. Boreyko, J. Vachelová, A. Michaelidesová and S. Kozubek, *Crit. Rev. Eukaryot. Gene Expr.*, 2014, **24**, 205–223.

18 M. Falk, M. Hausmann, E. Lukášová, A. Biswas, G. Hildenbrand, M. Davídková, E. Krasavin, Z. Kleibl, I. Falková, L. Ježková, L. Štefančíková, J. Ševčík, M. Hofer, A. Bačíková, P. Matula, A. Boreyko, J. Vachelová, A. Michaelidisová and S. Kozubek, *Crit. Rev. Eukaryot. Gene Expr.*, 2014, **24**, 225–247.

19 L. Jezkova, M. Zadneprianetc, E. Kulikova, E. Smirnova, T. Bulanova, D. Depes, I. Falkova, A. Boreyko, E. Krasavin, M. Davidkova, S. Kozubek, O. Valentova and M. Falk, *Nanoscale*, 2018, **10**, 1162–1179.

20 M. Falk, *Biophys. J.*, 2016, **110**, 872–873.

21 D. Depes, J.-H. Lee, E. Bobkova, L. Jezkova, I. Falkova, F. Bestvater, E. Pagacova, O. Kopecna, M. Zadneprianetc, A. Bacikova, E. Kulikova, E. Smirnova, T. Bulanova, A. Boreyko, E. Krasavin, M. Hausmann and M. Falk, *Eur. Phys. J. D*, , DOI:10.1140/epjd/e2018-90148-1.

22 E. Bobkova, D. Depes, J.-H. Lee, L. Jezkova, I. Falkova, E. Pagacova, O. Kopecna, M. Zadneprianetc, A. Bacikova, E. Kulikova, E. Smirnova, T. Bulanova, A. Boreyko, E. Krasavin, F. Wenz, F. Bestvater, G. Hildenbrand, M. Hausmann and M. Falk, *Int. J. Mol. Sci.*, , DOI:10.3390/ijms19123713.

23 J. Sevcik, M. Falk, P. Kleiblova, F. Lhota, L. Stefancikova, M. Janatova, L. Weiterova, E. Lukasova, S. Kozubek, P. Pohlreich and Z. Kleibl, *Cell. Signal.*, 2012, **24**, 1023–1030.

24 J. Sevcik, M. Falk, L. Macurek, P. Kleiblova, F. Lhota, J. Hojny, L. Stefancikova, M. Janatova, J. Bartek, J. Stribrna, Z. Hodny, L. Jezkova, P. Pohlreich and Z. Kleibl, *Cell. Signal.*, 2013, **25**, 1186–1193.

25 M. Falk, Z. Horakova, M. Svobodova, M. Masarik, O. Kopecna, J. Gumulec, M. Raudenka, D. Depes, A. Bacikova, I. Falkova and H. Binkova, *Eur. Phys. J. D*, 2017, 241.

26 L. Ježková, M. Falk, I. Falková, M. Davídková, A. Bačíková, L. Štefančíková, J. Vachelová, A. Michaelidesová, E. Lukášová, A. Boreyko, E. Krasavin and S. Kozubek, *Appl. Radiat. Isot. Data Instrum. Methods Use Agric. Ind. Med.*, 2014, **83 Pt B**, 128–136.

27 L. Štefančíková, S. Lacombe, D. Salado, E. Porcel, E. Pagáčová, O. Tillement, F. Lux, D. Depeš, S. Kozubek and M. Falk, *J. Nanobiotechnology*, 2016, **14**, 63.

28 E. Pagáčová, L. Štefančíková, F. Schmidt-Kaler, G. Hildenbrand, T. Vičar, D. Depeš, J.-H. Lee, F. Bestvater, S. Lacombe, E. Porcel, S. Roux, F. Wenz, O. Kopečná, I. Falková, M. Hausmann and M. Falk, *Int. J. Mol. Sci.*, , DOI:10.3390/ijms20030588.

29 I. Kratochvílová, M. Golan, K. Pomeisl, J. Richter, S. Sedláková, J. Šebera, J. Mičová, M. Falk, I. Falková, D. Řeha, K. W. Elliott, K. Varga, S. E. Follett and D. Šimek, *RSC Adv.*, 2017, **7**, 352–360.

30 M. Golan, J. Pribyl, M. Pesl, S. Jelinkova, I. Acimovic, J. Jaros, V. Rotrekl, M. Falk, L. Sefc, P. Skladal and I. Kratochvilova, *IEEE Trans. Nanobioscience*, 2018, **17**, 485–497.

31 I. Kratochvílová, O. Kopečná, A. Bačíková, E. Pagáčová, I. Falková, S. E. Follett, K. W. Elliott, K. Varga, M. Golan and M. Falk, *Langmuir ACS J. Surf. Colloids*, 2019, **35**, 7496–7508.

32 M. Falk, I. Falková, O. Kopečná, A. Bačíková, E. Pagáčová, D. Šimek, M. Golan, S. Kozubek, M. Pekarová, S. E. Follett, B.

Klejdus, K. W. Elliott, K. Varga, O. Teplá and I. Kratochvílová, *Sci. Rep.*, 2018, **8**, 14694.
33 M. Hofer, M. Falk, D. Komůrková, I. Falková, A. Bačíková, B. Klejdus, E. Pagáčová, L. Štefančíková, L. Weiterová, K. J. Angelis, S. Kozubek, L. Dušek and Š. Galbavý, *J. Med. Chem.*, 2016, **59**, 3003–3017.
34 M. Hofer, Z. Hoferová and M. Falk, *Int. J. Mol. Sci.*, , DOI:10.3390/ijms18071385.
35 M. Hofer, Z. Hoferová, D. Depeš and M. Falk, *Mol. Basel Switz.*, , DOI:10.3390/molecules22050834.
36 M. Falk, *Ann. Transl. Med.*, 2017, **5**, 18.
37 M. Falk, M. Wolinsky, M. Veldwijk, G. Hildenbrand and M. Hausmann, in *Nanopharmaceuticals: Principles and Applications*, Springer International Publishing, 2019.
38 O. I. Obolensky, E. Surdutovich, I. Pshenichnov, I. Mishustin, A. V. Solov'yov and W. Greiner, *Nucl. Instrum. Methods Phys. Res. Sect. B Beam Interact. Mater. At.*, 2008, **266**, 1623–1628.
39 M. Falk, E. Lukasova and S. Kozubek, in *Radiation Damage in Biomolecular Systems*, eds. G. García Gómez-Tejedor and M. C. Fuss, Springer Netherlands, Dordrecht, 2012, pp. 329–357.
40 A. Tubbs and A. Nussenzweig, *Cell*, 2017, **168**, 644–656.
41 M. M. Vilenchik and A. G. Knudson, *Proc. Natl. Acad. Sci.*, 2003, **100**, 12871–12876.
42 G. Slupphaug, *Mutat. Res. Mol. Mech. Mutagen.*, 2003, **531**, 231–251.
43 M. M. Vilenchik and A. G. Knudson, *Proc. Natl. Acad. Sci.*, 2000, **97**, 5381–5386.
44 J. V. Harper, J. A. Anderson and P. O'Neill, *DNA Repair*, 2010, **9**, 907–913.
45 L. F. Povirk and M. J. Austin, *Mutat. Res.*, 1991, **257**, 127–143.
46 P. Heisig, *Mutagenesis*, 2009, **24**, 465–469.
47 P. A. Jeggo, *Adv. Genet.*, 1998, **38**, 185–218.
48 J. H. Hoeijmakers, *Nature*, 2001, **411**, 366–374.
49 J. H. Hoeijmakers, *Maturitas*, 2001, **38**, 17–22; discussion 22-23.
50 K. K. Khanna and S. P. Jackson, *Nat. Genet.*, 2001, **27**, 247–254.
51 M. E. Lomax, L. K. Folkes and P. O'Neill, *Clin. Oncol. R. Coll. Radiol. G. B.*, 2013, **25**, 578–585.
52 H. F. Lodish, Ed., *Molecular cell biology*, W.H. Freeman, New York, 6th ed., 2008.
53 R.-S. Mani and A. M. Chinnaiyan, *Nat. Rev. Genet.*, 2010, **11**, 819–829.
54 W. L. Santivasi and F. Xia, *Antioxid. Redox Signal.*, 2014, **21**, 251–259.
55 M. Podhorecka, A. Skladanowski and P. Bozko, *J. Nucleic Acids*, , DOI:10.4061/2010/920161.
56 A. Noda, *J. Radiat. Res. (Tokyo)*, 2018, **59**, ii114–ii120.
57 A. L. Winship, J. M. Stringer, S. H. Liew and K. J. Hutt, *Hum. Reprod. Update*, 2018, **24**, 119–134.
58 A. García-Rodríguez, J. Gosálvez, A. Agarwal, R. Roy and S. Johnston, *Int. J. Mol. Sci.*, , DOI:10.3390/ijms20010031.
59 E. Werner, Y. Wang and P. W. Doetsch, *Radiat. Res.*, 2017, **188**, 373–380.
60 W. J. Cannan and D. S. Pederson, *J. Cell. Physiol.*, 2016, **231**, 3–14.
61 P. A. Jeggo and M. Lobrich, *Biochem. J.*, 2015, **471**, 1–11.
62 J. H. J. Hoeijmakers, *N. Engl. J. Med.*, 2009, **361**, 1475–1485.
63 S. P. Jackson and J. Bartek, *Nature*, 2009, **461**, 1071–1078.
64 G. Obe, C. Johannes and D. Schulte-Frohlinde, *Mutagenesis*, 1992, **7**, 3–12.
65 T. Morio and H. Kim, *Int. J. Biochem. Cell Biol.*, 2008, **40**, 598–603.
66 K. W. Caldecott, V. A. Bohr and P. J. McKinnon, *Mech. Ageing Dev.*, 2011, **132**, 353–354.
67 A. Nijnik, L. Woodbine, C. Marchetti, S. Dawson, T. Lambe, C. Liu, N. P. Rodrigues, T. L. Crockford, E. Cabuy, A. Vindigni, T. Enver, J. I. Bell, P. Slijepcevic, C. C. Goodnow, P. A. Jeggo and R. J. Cornall, *Nature*, 2007, **447**, 686–690.
68 D. Jung and F. W. Alt, *Cell*, 2004, **116**, 299–311.
69 D. Jung, C. Giallourakis, R. Mostoslavsky and F. W. Alt, *Annu. Rev. Immunol.*, 2006, **24**, 541–570.
70 S. Franco, M. M. Murphy, G. Li, T. Borjeson, C. Boboila and F. W. Alt, *J. Exp. Med.*, 2008, **205**, 557–564.
71 J. Chaudhuri, U. Basu, A. Zarrin, C. Yan, S. Franco, T. Perlot, B. Vuong, J. Wang, R. T. Phan, A. Datta, J. Manis and F. W. Alt, *Adv. Immunol.*, 2007, **94**, 157–214.
72 M. Shrivastav, L. P. De Haro and J. A. Nickoloff, *Cell Res.*, 2008, **18**, 134–147.
73 C. L. Limoli, R. Laposa and J. E. Cleaver, *Mutat. Res.*, 2002, **510**, 121–129.
74 R. Rothstein, B. Michel and S. Gangloff, *Genes Dev.*, 2000, **14**, 1–10.
75 S. L. Andersen and J. Sekelsky, *BioEssays*, 2010, **32**, 1058–1066.
76 S. Keeney and M. J. Neale, *Biochem. Soc. Trans.*, 2006, **34**, 523–525.
77 B. Maresca and J. H. Schwartz, *Anat. Rec. B. New Anat.*, 2006, **289**, 38–46.
78 J. W. Harper and S. J. Elledge, *Mol. Cell*, 2007, **28**, 739–745.
79 J. van den Berg, A. G. Manjón, K. Kielbassa, F. M. Feringa, R. Freire and R. H. Medema, *Nucleic Acids Res.*, 2018, **46**, 10132–10144.
80 T. Van Nguyen, N. Puebla-Osorio, H. Pang, M. E. Dujka and C. Zhu, *J. Exp. Med.*, 2007, **204**, 1453–1461.
81 S. Nowsheen and E. S. Yang, *Exp. Oncol.*, 2012, **34**, 243–254.
82 W. P. Roos and B. Kaina, *Trends Mol. Med.*, 2006, **12**, 440–450.
83 J. Bartek and J. Lukas, *Curr. Opin. Cell Biol.*, 2007, **19**, 238–245.
84 D. B. Pontier and M. Tijsterman, *Curr. Biol.*, 2009, **19**, 1384–1388.
85 G. Iliakis, *Radiother. Oncol. J. Eur. Soc. Ther. Radiol. Oncol.*, 2009, **92**, 310–315.
86 G. Iliakis, T. Murmann and A. Soni, *Mutat. Res. - Genet. Toxicol. Environ. Mutagen.*, 2015, **793**, 166–175.
87 A. J. F. Griffiths, Ed., *An introduction to genetic analysis*, W.H. Freeman, New York, 7th ed., 2000.
88 P. Bertrand, D. X. Tishkoff, N. Filosi, R. Dasgupta and R. D. Kolodner, *Proc. Natl. Acad. Sci. U. S. A.*, 1998, **95**, 14278–14283.
89 T. M. Neher and J. J. Turchi, *Antioxid. Redox Signal.*, 2011, **14**, 2461–2464.
90 M. Spry, T. Scott, H. Pierce and J. A. D'Orazio, *Front. Biosci. J. Virtual Libr.*, 2007, **12**, 4191–4207.
91 C. L. Peterson and J. Côté, *Genes Dev.*, 2004, **18**, 602–616.
92 O. Fleck, *J. Cell Sci.*, 2004, **117**, 515–517.
93 M. Allinen, University of Oulu, 2002.
94 A. N. Blackford and S. P. Jackson, *Mol. Cell*, 2017, **66**, 801–817.
95 C. Bruhn, Z.-W. Zhou, H. Ai and Z.-Q. Wang, *Cell Rep.*, 2014, **6**, 182–195.
96 B. J. Lamarche, N. I. Orazio and M. D. Weitzman, *FEBS Lett.*, 2010, **584**, 3682–3695.
97 R. S. Williams, J. S. Williams and J. A. Tainer, *Biochem. Cell Biol. Biochim. Biol. Cell.*, 2007, **85**, 509–520.
98 B. Sochanowicz and I. Szumiel, *NUKLEONIKA*, 2005, 129−138.
99 K. K. Khanna, M. F. Lavin, S. P. Jackson and T. D. Mulhern, *Cell Death Differ.*, 2001, **8**, 1052–1065.
100 P. A. Jeggo, *Radiat. Res.*, 1998, **150**, S80-91.
101 N. Tomimatsu, B. Mukherjee, K. Deland, A. Kurimasa, E. Bolderson, K. K. Khanna and S. Burma, *DNA Repair*, 2012, **11**, 441–448.
102 S. P. Jackson, *Biochem. Soc. Trans.*, 2009, **37**, 483–494.
103 K. S. Pawelczak, S. M. Bennett and J. J. Turchi, *Antioxid. Redox Signal.*, 2011, **14**, 2531–2543.
104 N. Jette and S. P. Lees-Miller, *Prog. Biophys. Mol. Biol.*, 2015, **117**, 194–205.
105 Y. Zhang, *Chromosome translocation*, 2018.
106 Y. Li, P. Reynolds, P. O'Neill and F. A. Cucinotta, *PLoS ONE*, 2014, **9**, e85816.

107 E. Riballo, M. Kühne, N. Rief, A. Doherty, G. C. M. Smith, M.-J. Recio, C. Reis, K. Dahm, A. Fricke, A. Krempler, A. R. Parker, S. P. Jackson, A. Gennery, P. A. Jeggo and M. Löbrich, *Mol. Cell*, 2004, **16**, 715–724.
108 A. A. Goodarzi, A. T. Noon, D. Deckbar, Y. Ziv, Y. Shiloh, M. Löbrich and P. A. Jeggo, *Mol. Cell*, 2008, **31**, 167–177.
109 A. A. Goodarzi, A. T. Noon and P. A. Jeggo, *Biochem. Soc. Trans.*, 2009, **37**, 569–576.
110 A. A. Goodarzi, P. Jeggo and M. Lobrich, *DNA Repair*, 2010, **9**, 1273–1282.
111 A. T. Noon, A. Shibata, N. Rief, M. Löbrich, G. S. Stewart, P. A. Jeggo and A. A. Goodarzi, *Nat. Cell Biol.*, 2010, **12**, 177–184.
112 M. Löbrich and P. A. Jeggo, *Radiother. Oncol. J. Eur. Soc. Ther. Radiol. Oncol.*, 2005, **76**, 112–118.
113 K. M. Prise, M. Pinto, H. C. Newman and B. D. Michael, *Radiat. Res.*, 2001, **156**, 572–576.
114 R. A. Deshpande, J.-H. Lee, S. Arora and T. T. Paull, *Mol. Cell*, 2016, **64**, 593–606.
115 A. Shibata, D. Moiani, A. S. Arvai, J. Perry, S. M. Harding, M.-M. Genois, R. Maity, S. van Rossum-Fikkert, A. Kertokalio, F. Romoli, A. Ismail, E. Ismalaj, E. Petricci, M. J. Neale, R. G. Bristow, J.-Y. Masson, C. Wyman, P. A. Jeggo and J. A. Tainer, *Mol. Cell*, 2014, **53**, 7–18.
116 T. T. Paull and M. Gellert, *Genes Dev.*, 1999, **13**, 1276–1288.
117 K. Hiyama, Ed., *Telomeres and telomerase in cancer*, Springer, New York, 2009.
118 M. van den Bosch, R. T. Bree and N. F. Lowndes, *EMBO Rep.*, 2003, **4**, 844–849.
119 A. Desai-Mehta, K. M. Cerosaletti and P. Concannon, *Mol. Cell. Biol.*, 2001, **21**, 2184–2191.
120 T. T. Paull, *Annu. Rev. Biochem.*, 2015, **84**, 711–738.
121 M. Lavin, S. Kozlov, M. Gatei and A. Kijas, *Biomolecules*, 2015, **5**, 2877–2902.
122 T. Uziel, *EMBO J.*, 2003, **22**, 5612–5621.
123 E. P. Rogakou, D. R. Pilch, A. H. Orr, V. S. Ivanova and W. M. Bonner, *J. Biol. Chem.*, 1998, **273**, 5858–5868.
124 O. A. Sedelnikova, D. R. Pilch, C. Redon and W. M. Bonner, *Cancer Biol. Ther.*, 2003, **2**, 233–235.
125 E. P. Rogakou, C. Boon, C. Redon and W. M. Bonner, *J. Cell Biol.*, 1999, **146**, 905–916.
126 M. Stucki and S. P. Jackson, *DNA Repair*, 2006, **5**, 534–543.
127 K. Minter-Dykhouse, I. Ward, M. S. Y. Huen, J. Chen and Z. Lou, *J. Cell Biol.*, 2008, **181**, 727–735.
128 L. Anderson, C. Henderson and Y. Adachi, *Mol. Cell. Biol.*, 2001, **21**, 1719–1729.
129 N. F. Lowndes, *DNA Repair*, 2010, **9**, 1112–1116.
130 Z. Lou, C. C. S. Chini, K. Minter-Dykhouse and J. Chen, *J. Biol. Chem.*, 2003, **278**, 13599–13602.
131 A. Celeste, S. Difilippantonio, M. J. Difilippantonio, O. Fernandez-Capetillo, D. R. Pilch, O. A. Sedelnikova, M. Eckhaus, T. Ried, W. M. Bonner and A. Nussenzweig, *Cell*, 2003, **114**, 371–383.
132 I. M. Ward, K. Minn, K. G. Jorda and J. Chen, *J. Biol. Chem.*, 2003, **278**, 19579–19582.
133 A. Syed and J. A. Tainer, *Annu. Rev. Biochem.*, 2018, **87**, 263–294.
134 R. D. Jachimowicz, J. Goergens and H. C. Reinhardt, *Cell Cycle*, 2019, **18**, 1423–1434.
135 R. Ceccaldi, B. Rondinelli and A. D. D'Andrea, *Trends Cell Biol.*, 2016, **26**, 52–64.
136 J. Her and S. F. Bunting, *J. Biol. Chem.*, 2018, **293**, 10502–10511.
137 M. Löbrich and P. Jeggo, *Trends Biochem. Sci.*, 2017, **42**, 690–701.
138 J. Saha, S.-Y. Wang and A. J. Davis, in *Methods in Enzymology*, Elsevier, 2017, vol. 591, pp. 97–118.
139 D. Branzei and M. Foiani, *Nat. Rev. Mol. Cell Biol.*, 2010, **11**, 208–219.
140 Z. Mao, M. Bozzella, A. Seluanov and V. Gorbunova, *Cell Cycle Georget. Tex*, 2008, **7**, 2902–2906.
141 M. Lisby, J. H. Barlow, R. C. Burgess and R. Rothstein, *Cell*, 2004, **118**, 699–713.
142 A. Sallmyr and A. E. Tomkinson, *J. Biol. Chem.*, 2018, **293**, 10536–10546.
143 A. Porro, *Grappling with the Multifaceted World of the DNA Damage Response*, Frontiers Media SA, Place of publication not identified, 2017.
144 M. McVey and S. E. Lee, *Trends Genet. TIG*, 2008, **24**, 529–538.
145 A. Kohutova, J. Raška, M. Kruta, M. Seneklova, T. Barta, P. Fojtik, T. Jurakova, C. A. Walter, A. Hampl, P. Dvorak and V. Rotrekl, *FASEB J.*, 2019, **33**, 6778–6788.
146 E. D. Tichy, R. Pillai, L. Deng, L. Liang, J. Tischfield, S. J. Schwemberger, G. F. Babcock and P. J. Stambrook, *Stem Cells Dev.*, 2010, **19**, 1699–1711.
147 Z. Mao, M. Bozzella, A. Seluanov and V. Gorbunova, *DNA Repair*, 2008, **7**, 1765–1771.
148 E. Zlotorynski, *Nat. Rev. Mol. Cell Biol.*, 2018, **19**, 675–675.
149 A. Marnef, S. Cohen and G. Legube, *J. Mol. Biol.*, 2017, **429**, 1277–1288.
150 I. Brandsma and D. C. Gent, *Genome Integr.*, 2012, **3**, 9.
151 E. Sonoda, H. Hochegger, A. Saberi, Y. Taniguchi and S. Takeda, *DNA Repair*, 2006, **5**, 1021–1029.
152 I. G. Draganić and Z. D. Draganić, *The radiation chemistry of water*, Academic Press, New York, 1971.
153 O. Desouky, N. Ding and G. Zhou, *J. Radiat. Res. Appl. Sci.*, 2015, **8**, 247–254.
154 T. E. Schmid, G. Dollinger, W. Beisker, V. Hable, C. Greubel, S. Auer, A. Mittag, A. Tarnok, A. A. Friedl, M. Molls and B. Röper, *Int. J. Radiat. Biol.*, 2010, **86**, 682–691.
155 G. B. Saha, *Physics and radiobiology of nuclear medicine*, Springer, New York, Fourth edition., 2013.
156 R. Hirayama, A. Ito, M. Tomita, T. Tsukada, F. Yatagai, M. Noguchi, Y. Matsumoto, Y. Kase, K. Ando, R. Okayasu and Y. Furusawa, *Radiat. Res.*, 2009, **171**, 212–218.
157 J. A. Aten, J. Stap, P. M. Krawczyk, C. H. van Oven, R. A. Hoebe, J. Essers and R. Kanaar, *Science*, 2004, **303**, 92–95.
158 C. Lukas, J. Bartek and J. Lukas, *Chromosoma*, 2005, **114**, 146–154.
159 M. J. Kruhlak, A. Celeste and A. Nussenzweig, *Cell Cycle Georget. Tex*, 2006, **5**, 1910–1912.
160 J. I. Loizou, R. Murr, M. G. Finkbeiner, C. Sawan, Z.-Q. Wang and Z. Herceg, *Cell Cycle Georget. Tex*, 2006, **5**, 696–701.
161 I. G. Cowell, N. J. Sunter, P. B. Singh, C. A. Austin, B. W. Durkacz and M. J. Tilby, *PloS One*, 2007, **2**, e1057.
162 T. C. Karagiannis, K. N. Harikrishnan, H. Kn and A. El-Osta, *Oncogene*, 2007, **26**, 3963–3971.
163 A. Kinner, W. Wu, C. Staudt and G. Iliakis, *Nucleic Acids Res.*, 2008, **36**, 5678–5694.
164 C. Orlowski, L.-J. Mah, R. S. Vasireddy, A. El-Osta and T. C. Karagiannis, *Chromosoma*, 2011, **120**, 129–149.
165 R. S. Vasireddy, T. C. Karagiannis and A. El-Osta, *Cell. Mol. Life Sci. CMLS*, 2010, **67**, 291–294.
166 R. S. Vasireddy, M. M. Tang, L.-J. Mah, G. T. Georgiadis, A. El-Osta and T. C. Karagiannis, *J. Vis. Exp.*, , DOI:10.3791/2203.
167 T. H. Boveri, *Z. Med. Phys. J. Med. Phys.*, 1888, 685–882.
168 W. S. Sutton, *Biol. Bull.*, 1902, 24–39.
169 W. S. Sutton, *Biol. Bull.*, 1903, 231–251.
170 T. H. Morgan, A. H. Sturtevant and H. J. Muller, *The Mechanism Of Mendelian Heredity (1915)*, Kessinger Publishing, LLCKessinger Publishing, LLC, 2008.
171 B. D. Strahl and C. D. Allis, *Nature*, 2000, **403**, 41–45.
172 T. Jenuwein and C. D. Allis, *Science*, 2001, **293**, 1074–1080.
173 C. Zimmer and E. Fabre, *Curr. Genet.*, 2019, **65**, 1–9.
174 J. Lou, L. Scipioni, B. K. Wright, T. K. Bartolec, J. Zhang, V. P. Masamsetti, K. Gaus, E. Gratton, A. J. Cesare and E. Hinde, *Proc. Natl. Acad. Sci.*, 2019, **116**, 7323–7332.
175 K. Mekhail, *Front. Genet.*, , DOI:10.3389/fgene.2018.00095.
176 E. Fabre and C. Zimmer, *Nucleus*, 2018, **9**, 161–170.
177 S. Espinoza-Corona, M. L. Bazán-Tejeda, U. O. García-Lepe and R. M. Bermúdez-Cruz, in *Ubiquitination Governing DNA*

Repair - Implications in Health and Disease, eds. E. Boutou and H.-W. Stürzbecher, InTech, 2018.
178 M. H. Hauer and S. M. Gasser, *Genes Dev.*, 2017, **31**, 2204–2221.
179 S. Herbert, A. Brion, J. Arbona, M. Lelek, A. Veillet, B. Lelandais, J. Parmar, F. G. Fernández, E. Almayrac, Y. Khalil, E. Birgy, E. Fabre and C. Zimmer, *EMBO J.*, 2017, **36**, 2595–2608.
180 P. C. Caridi, L. Delabaere, G. Zapotoczny and I. Chiolo, *Philos. Trans. R. Soc. B Biol. Sci.*, 2017, **372**, 20160291.
181 F. Lottersberger, R. A. Karssemeijer, N. Dimitrova and T. de Lange, *Cell*, 2015, **163**, 880–893.
182 J. Miné-Hattab, V. Recamier, I. Izeddin, R. Rothstein and X. Darzacq, *bioRxiv*, , DOI:10.1101/042051.
183 C. Lemaître and E. Soutoglou, *J. Mol. Biol.*, 2015, **427**, 652–658.
184 A. Becker, M. Durante, G. Taucher-Scholz and B. Jakob, *PloS One*, 2014, **9**, e92640.
185 O. V. Iarovaia, M. Rubtsov, E. Ioudinkova, T. Tsfasman, S. V. Razin and Y. S. Vassetzky, *Mol. Cancer*, 2014, **13**, 249.
186 V. Roukos, T. C. Voss, C. K. Schmidt, S. Lee, D. Wangsa and T. Misteli, *Science*, 2013, **341**, 660–664.
187 P. M. Krawczyk, T. Borovski, J. Stap, T. Cijsouw, R. t. Cate, J. P. Medema, R. Kanaar, N. A. P. Franken and J. A. Aten, *J. Cell Sci.*, 2012, **125**, 2127–2133.
188 T. Misteli and E. Soutoglou, *Nat. Rev. Mol. Cell Biol.*, 2009, **10**, 243–254.
189 B. Jakob, J. Splinter and G. Taucher-Scholz, *Radiat. Res.*, 2009, **171**, 405–418.
190 A. Göndör, University Library Universitetsbiblioteket, 2007.
191 I. Chiolo, J. Tang, W. Georgescu and S. V. Costes, *Mutat. Res.*, 2013, **750**, 56–66.
192 E. Soutoglou and T. Misteli, *Curr. Opin. Genet. Dev.*, 2007, **17**, 435–442.
193 K. L. Cann and G. Dellaire, *Biochem. Cell Biol. Biochim. Biol. Cell.*, 2011, **89**, 45–60.
194 P. A. Jeggo and M. Löbrich, *Cell Cycle Georget. Tex*, 2005, **4**, 359–362.
195 J. Surrallés, S. Sebastian and A. T. Natarajan, *Mutagenesis*, 1997, **12**, 437–442.
196 M. A. Osley, T. Tsukuda and J. A. Nickoloff, *Mutat. Res.*, 2007, **618**, 65–80.
197 C. Müller and A. Leutz, *Curr. Opin. Genet. Dev.*, 2001, **11**, 167–174.
198 A. C. Nye, R. R. Rajendran, D. L. Stenoien, M. A. Mancini, B. S. Katzenellenbogen and A. S. Belmont, *Mol. Cell. Biol.*, 2002, **22**, 3437–3449.
199 A. E. Carpenter, S. Memedula, M. J. Plutz and A. S. Belmont, *Mol. Cell. Biol.*, 2005, **25**, 958–968.
200 Y. Ziv, D. Bielopolski, Y. Galanty, C. Lukas, Y. Taya, D. C. Schultz, J. Lukas, S. Bekker-Jensen, J. Bartek and Y. Shiloh, *Nat. Cell Biol.*, 2006, **8**, 870–876.
201 A. Shimada and Y. Murakami, *Epigenetics*, 2010, **5**, 30–33.
202 W. Zeng, A. R. Ball and K. Yokomori, *Epigenetics*, 2010, **5**, 287–292.
203 M. S. Luijsterburg, C. Dinant, H. Lans, J. Stap, E. Wiernasz, S. Lagerwerf, D. O. Warmerdam, M. Lindh, M. C. Brink, J. W. Dobrucki, J. A. Aten, M. I. Fousteri, G. Jansen, N. P. Dantuma, W. Vermeulen, L. H. F. Mullenders, A. B. Houtsmuller, P. J. Verschure and R. van Driel, *J. Cell Biol.*, 2009, **185**, 577–586.
204 N. Ayoub, A. D. Jeyasekharan and A. R. Venkitaraman, *Cell Cycle Georget. Tex*, 2009, **8**, 2945–2950.
205 N. Ayoub, A. D. Jeyasekharan, J. A. Bernal and A. R. Venkitaraman, *Cell Cycle Georget. Tex*, 2009, **8**, 1494–1500.
206 N. Ayoub, A. D. Jeyasekharan, J. A. Bernal and A. R. Venkitaraman, *Nature*, 2008, **453**, 682–686.
207 A. R. Ball and K. Yokomori, *J. Cell Biol.*, 2009, **185**, 573–575.
208 C. Dinant and M. S. Luijsterburg, *Mol. Cell. Biol.*, 2009, **29**, 6335–6340.
209 M.-C. Keogh, J.-A. Kim, M. Downey, J. Fillingham, D. Chowdhury, J. C. Harrison, M. Onishi, N. Datta, S. Galicia, A. Emili, J. Lieberman, X. Shen, S. Buratowski, J. E. Haber, D. Durocher, J. F. Greenblatt and N. J. Krogan, *Nature*, 2006, **439**, 497–501.
210 T. Ikura, S. Tashiro, A. Kakino, H. Shima, N. Jacob, R. Amunugama, K. Yoder, S. Izumi, I. Kuraoka, K. Tanaka, H. Kimura, M. Ikura, S. Nishikubo, T. Ito, A. Muto, K. Miyagawa, S. Takeda, R. Fishel, K. Igarashi and K. Kamiya, *Mol. Cell. Biol.*, 2007, **27**, 7028–7040.
211 H. van Attikum and S. M. Gasser, *Trends Cell Biol.*, 2009, **19**, 207–217.
212 E. V. Volpi, E. Chevret, T. Jones, R. Vatcheva, J. Williamson, S. Beck, R. D. Campbell, M. Goldsworthy, S. H. Powis, J. Ragoussis, J. Trowsdale and D. Sheer, *J. Cell Sci.*, 2000, **113 (Pt 9)**, 1565–1576.
213 R. R. E. Williams, S. Broad, D. Sheer and J. Ragoussis, *Exp. Cell Res.*, 2002, **272**, 163–175.
214 J. Dorier and A. Stasiak, *Nucleic Acids Res.*, 2010, **38**, 7410–7421.
215 H. Sutherland and W. A. Bickmore, *Nat. Rev. Genet.*, 2009, **10**, 457–466.
216 C. G. Spilianakis, M. D. Lalioti, T. Town, G. R. Lee and R. A. Flavell, *Nature*, 2005, **435**, 637–645.
217 C. S. Osborne, L. Chakalova, K. E. Brown, D. Carter, A. Horton, E. Debrand, B. Goyenechea, J. A. Mitchell, S. Lopes, W. Reik and P. Fraser, *Nat. Genet.*, 2004, **36**, 1065–1071.
218 I. K. Nolis, D. J. McKay, E. Mantouvalou, S. Lomvardas, M. Merika and D. Thanos, *Proc. Natl. Acad. Sci. U. S. A.*, 2009, **106**, 20222–20227.
219 J. R. Chubb, S. Boyle, P. Perry and W. A. Bickmore, *Curr. Biol. CB*, 2002, **12**, 439–445.
220 C. L. Woodcock and R. P. Ghosh, *Cold Spring Harb. Perspect. Biol.*, 2010, **2**, a000596–a000596.
221 J. M. Bridger and I. S. Mehta, in *Advances in Nuclear Architecture*, eds. N. M. Adams and P. S. Freemont, Springer Netherlands, Dordrecht, 2011, pp. 149–172.
222 B. R. Schrank, T. Aparicio, Y. Li, W. Chang, B. T. Chait, G. G. Gundersen, M. E. Gottesman and J. Gautier, *Nature*, 2018, **559**, 61–66.
223 P. M. Krawczyk, J. Stap, C. van Oven, R. Hoebe and J. A. Aten, *Radiat. Prot. Dosimetry*, 2006, **122**, 150–153.
224 M. Lisby, U. H. Mortensen and R. Rothstein, *Nat. Cell Biol.*, 2003, **5**, 572–577.
225 E. Marková, N. Schultz and I. Y. Belyaev, *Int. J. Radiat. Biol.*, 2007, **83**, 319–329.
226 N. Simonis, D. Gonze, C. Orsi, J. van Helden and S. J. Wodak, *J. Mol. Biol.*, 2006, **363**, 589–610.
227 A. Amitai, O. Shukron, A. Seeber and D. Holcman, *Local decondensation at double-stranded DNA breaks modifies chromatin at long distances and reduces encounter times during homology search*, Genetics, 2018.
228 A. T. Natarajan, *Mutat. Res.*, 2002, **504**, 3–16.
229 B. E. Nelms, R. S. Maser, J. F. MacKay, M. G. Lagally and J. H. Petrini, *Science*, 1998, **280**, 590–592.
230 V. Roukos and T. Misteli, *Nat. Cell Biol.*, 2014, **16**, 293–300.
231 F. Tobias, M. Durante, G. Taucher-Scholz and B. Jakob, *Mutat. Res.*, 2010, **704**, 54–60.
232 K. J. Meaburn, T. Misteli and E. Soutoglou, *Semin. Cancer Biol.*, 2007, **17**, 80–90.
233 E. Soutoglou, J. F. Dorn, K. Sengupta, M. Jasin, A. Nussenzweig, T. Ried, G. Danuser and T. Misteli, *Nat. Cell Biol.*, 2007, **9**, 675–682.
234 B. Jakob, J. H. Rudolph, N. Gueven, M. F. Lavin and G. Taucher-Scholz, *Radiat. Res.*, 2005, **163**, 681–690.
235 B. Jakob, J. Splinter, M. Durante and G. Taucher-Scholz, *Proc. Natl. Acad. Sci. U. S. A.*, 2009, **106**, 3172–3177.
236 S. V. Costes, A. Ponomarev, J. L. Chen, D. Nguyen, F. A. Cucinotta and M. H. Barcellos-Hoff, *PLoS Comput. Biol.*, 2007, **3**, e155.
237 R. Versteeg, *Genome Res.*, 2003, **13**, 1998–2004.
238 D. V. Firsanov, L. V. Solovjeva and M. P. Svetlova, *Clin. Epigenetics*, 2011, **2**, 283–297.

239 F. Natale, A. Rapp, W. Yu, A. Maiser, H. Harz, A. Scholl, S. Grulich, T. Anton, D. Hörl, W. Chen, M. Durante, G. Taucher-Scholz, H. Leonhardt and M. C. Cardoso, *Nat. Commun.*, , DOI:10.1038/ncomms15760.

240 M. Hausmann, E. Wagner, J.-H. Lee, G. Schrock, W. Schaufler, M. Krufczik, F. Papenfuß, M. Port, F. Bestvater and H. Scherthan, *Nanoscale*, 2018, **10**, 4320–4331.

241 J. S. Iacovoni, P. Caron, I. Lassadi, E. Nicolas, L. Massip, D. Trouche and G. Legube, *EMBO J.*, 2010, **29**, 1446–1457.

242 A. T. Natarajan and G. Ahnstrom, *Chromosoma*, 1969, **28**, 48–61.

243 G. A. Folle, W. Martínez-López, E. Boccardo and G. Obe, *Mutat. Res.*, 1998, **404**, 17–26.

244 M. C. Elia and M. O. Bradley, *Cancer Res.*, 1992, **52**, 1580–1586.

245 M. Löbrich, P. K. Cooper and B. Rydberg, *Int. J. Radiat. Biol.*, 1996, **70**, 493–503.

246 A. Sak, M. Stuschke, N. Stapper and C. Streffer, *Int. J. Radiat. Biol.*, 1996, **69**, 679–685.

247 K. Rothkamm and M. Löbrich, *Mutat. Res.*, 1999, **433**, 193–205.

248 B. Fouladi, L. Sabatier, D. Miller, G. Pottier and J. P. Murnane, *Neoplasia N. Y. N*, 2000, **2**, 540–554.

249 M. Löbrich, M. Kühne, J. Wetzel and K. Rothkamm, *Genes. Chromosomes Cancer*, 2000, **27**, 59–68.

250 S. Puerto, M. J. Ramírez, R. Marcos, A. Creus and J. Surrallés, *Mutagenesis*, 2001, **16**, 291–296.

251 O. A. Sedelnikova, E. P. Rogakou, I. G. Panyutin and W. M. Bonner, *Radiat. Res.*, 2002, **158**, 486–492.

252 K. Rothkamm and M. Löbrich, *Proc. Natl. Acad. Sci. U. S. A.*, 2003, **100**, 5057–5062.

253 M. Löbrich, A. Shibata, A. Beucher, A. Fisher, M. Ensminger, A. A. Goodarzi, O. Barton and P. A. Jeggo, *Cell Cycle Georget. Tex*, 2010, **9**, 662–669.

254 J.-A. Kim, M. Kruhlak, F. Dotiwala, A. Nussenzweig and J. E. Haber, *J. Cell Biol.*, 2007, **178**, 209–218.

255 A. Pombo, P. Cuello, W. Schul, J. B. Yoon, R. G. Roeder, P. R. Cook and S. Murphy, *EMBO J.*, 1998, **17**, 1768–1778.

256 N. Degani and D. Pickholz, *Radiat. Bot.*, 1973, **13**, 381–383.

257 S. Dietzel, K. Zolghadr, C. Hepperger and A. S. Belmont, *J. Cell Sci.*, 2004, **117**, 4603–4614.

258 R. L. Warters and B. W. Lyons, *Radiat. Res.*, 1992, **130**, 309–318.

259 M. Běgusová, N. Gillard, D. Sy, B. Castaing, M. Charlier and M. Spotheim-Maurizot, *Radiat. Phys. Chem.*, 2005, **72**, 265–270.

260 V. Štísová, S. Goffinont, M. Spotheim-Maurizot and M. Davídková, *Radiat. Prot. Dosimetry*, 2006, **122**, 106–109.

261 C. von Sonntag, *Free-radical-induced DNA damage and its repair a chemical perspective*, Springer, Berlin; New York, 2006.

262 W. G. Burns, *Nature*, 1989, **339**, 515–516.

263 K. Haygarth and D. M. Bartels, *J. Phys. Chem. A*, 2010, **114**, 7479–7484.

264 H. C. Newman, K. M. Prise and B. D. Michael, *Int. J. Radiat. Biol.*, 2000, **76**, 1085–1093.

265 I. Radulescu, K. Elmroth and B. Stenerlöw, *Radiat. Res.*, 2004, **161**, 1–8.

266 J. T. Leith, S. A. Mousa, A. Hercbergs, H.-Y. Lin and P. J. Davis, *Oncotarget*, , DOI:10.18632/oncotarget.26434.

267 P. Ahmad, J. Sana, M. Slavik, P. Slampa, P. Smilek and O. Slaby, *Dis. Markers*, 2017, **2017**, 1–8.

268 M. Gérard, A. Corroyer-Dulmont, P. Lesueur, S. Collet, M. Chérel, M. Bourgeois, D. Stefan, E. J. Limkin, C. Perrio, J.-S. Guillamo, B. Dubray, M. Bernaudin, J. Thariat and S. Valable, *Front. Med.*, , DOI:10.3389/fmed.2019.00117.

269 A. Schulz, F. Meyer, A. Dubrovska and K. Borgmann, *Cancers*, 2019, **11**, 862.

270 M. Jarosz-Biej, R. Smolarczyk, T. Cichoń and N. Kułach, *Int. J. Mol. Sci.*, , DOI:10.3390/ijms20133212.

271 Z. Chen, K. Cao, Y. Xia, Y. Li, Y. Hou, L. Wang, L. Li, L. Chang and W. Li, *Oncol. Rep.*, , DOI:10.3892/or.2019.7209.

272 L. Long, X. Zhang, J. Bai, Y. Li, X. Wang and Y. Zhou, *Cancer Manag. Res.*, 2019, **Volume 11**, 4413–4424.

273 J. Boustani, M. Grapin, P.-A. Laurent, L. Apetoh and C. Mirjolet, *Cancers*, , DOI:10.3390/cancers11060860.

274 A. Nagao, M. Kobayashi, S. Koyasu, C. C. T. Chow and H. Harada, *Int. J. Mol. Sci.*, 2019, **20**, 238.

275 T. Hide, I. Shibahara and T. Kumabe, *Brain Tumor Pathol.*, 2019, **36**, 63–73.

276 W.-T. Wang, C. Han, Y.-M. Sun, T.-Q. Chen and Y.-Q. Chen, *J. Hematol. Oncol.J Hematol Oncol*, , DOI:10.1186/s13045-019-0748-z.

277 H. Wang, H. Jiang, M. Van De Gucht and M. De Ridder, *Cancers*, , DOI:10.3390/cancers11010112.

278 N. Albadari, S. Deng and W. Li, *Expert Opin. Drug Discov.*, 2019, **14**, 667–682.

279 F. Eckert, K. Zwirner, S. Boeke, D. Thorwarth, D. Zips and S. M. Huber, *Front. Immunol.*, , DOI:10.3389/fimmu.2019.00407.

280 L. Tang, F. Wei, Y. Wu, Y. He, L. Shi, F. Xiong, Z. Gong, C. Guo, X. Li, H. Deng, K. Cao, M. Zhou, B. Xiang, X. Li, Y. Li, G. Li, W. Xiong and Z. Zeng, *J. Exp. Clin. Cancer Res.*, , DOI:10.1186/s13046-018-0758-7.

281 L. Chaiswing, H. L. Weiss, R. D. Jayswal, D. K. St. Clair and N. Kyprianou, *Crit. Rev. Oncog.*, 2018, **23**, 39–67.

282 M. Krause, A. Dubrovska, A. Linge and M. Baumann, *Adv. Drug Deliv. Rev.*, 2017, **109**, 63–73.

283 P. Seshacharyulu, M. J. Baine, J. J. Souchek, M. Menning, S. Kaur, Y. Yan, M. M. Ouellette, M. Jain, C. Lin and S. K. Batra, *Biochim. Biophys. Acta BBA - Rev. Cancer*, 2017, **1868**, 69–92.

284 G.-Z. Chen, H.-C. Zhu, W.-S. Dai, X.-N. Zeng, J.-H. Luo and X.-C. Sun, *J. Thorac. Dis.*, 2017, **9**, 849–859.

285 C. M. Koch, R. M. Andrews, P. Flicek, S. C. Dillon, U. Karaöz, G. K. Clelland, S. Wilcox, D. M. Beare, J. C. Fowler, P. Couttet, K. D. James, G. C. Lefebvre, A. W. Bruce, O. M. Dovey, P. D. Ellis, P. Dhami, C. F. Langford, Z. Weng, E. Birney, N. P. Carter, D. Vetrie and I. Dunham, *Genome Res.*, 2007, **17**, 691–707.

286 H. S. Park, G. E. You, K. H. Yang, J. Y. Kim, S. An, J.-Y. Song, S.-J. Lee, Y.-K. Lim and S. Y. Nam, *Eur. J. Cell Biol.*, 2015, **94**, 653–660.

287 Y. Yang, H. Zhou, G. Zhang and X. Xue, *J. Cancer Res. Ther.*, 2019, **15**, 272–277.

288 S. Wu, H. Lu and Y. Bai, *Cancer Med.*, 2019, **8**, 2252–2267.

289 M. Hamoir, E. Holvoet, J. Ambroise, B. Lengelé and S. Schmitz, *Oral Oncol.*, 2017, **67**, 1–9.

290 G. Mountzios, T. Rampias and A. Psyrri, *Ann. Oncol.*, 2014, **25**, 1889–1900.

291 W. Han, *Advances in genetics research.*, Nova Science, Place of publication not identified, 2015.

292 T. Ettl, S. Viale-Bouroncle, M. G. Hautmann, M. Gosau, O. Kölbl, T. E. Reichert and C. Morsczeck, *Oral Oncol.*, 2015, **51**, 158–163.

293 G. Peng, R.-B. Cao, Y.-H. Li, Z.-W. Zou, J. Huang and Q. Ding, *Mol. Med. Rep.*, 2014, **10**, 1709–1716.

294 M. Maalouf, G. Alphonse, A. Colliaux, M. Beuve, S. Trajkovic-Bodennec, P. Battiston-Montagne, I. Testard, O. Chapet, M. Bajard, G. Taucher-Scholz, C. Fournier and C. Rodriguez-Lafrasse, *Int. J. Radiat. Oncol.*, 2009, **74**, 200–209.

295 Q. Wang, P. C. Wu, R. S. Roberson, B. V. Luk, I. Ivanova, E. Chu and D. Y. Wu, *Int. J. Cancer*, 2011, **128**, 1546–1558.

296 T. Kuilman, C. Michaloglou, W. J. Mooi and D. S. Peeper, *Genes Dev.*, 2010, **24**, 2463–2479.

297 A. Lujambio, *BioEssays*, 2016, **38**, S56–S64.

298 A. Affolter, I. Schmidtmann, W. J. Mann and J. Brieger, *Oncol. Rep.*, 2013, **29**, 785–790.

299 X. Ji, J. Ji, F. Shan, Y. Zhang, Y. Chen and X. Lu, *Int. J. Clin. Exp. Med.*, 2015, **8**, 7002–7008.

300 D. Digomann, A. Linge and A. Dubrovska, *Autophagy*, 2019, 1–2.

301 M. W. Han, J. C. Lee, J.-Y. Choi, G. C. Kim, H. W. Chang, H. Y. Nam, S. W. Kim and S. Y. Kim, *Anticancer Res.*, 2014, **34**, 1449–1455.

302 H. Chaachouay, P. Ohneseit, M. Toulany, R. Kehlbach, G. Multhoff and H. P. Rodemann, *Radiother. Oncol.*, 2011, **99**, 287–292.
303 S. D. Karam and D. Raben, *Lancet Oncol.*, 2019, **20**, e404–e416.
304 A. Al-Samadi, B. Poor, K. Tuomainen, V. Liu, A. Hyytiäinen, I. Sulymanova, K. Mesimaki, T. Wilkman, A. Mäkitie, P. Saavalainen and T. Salo, *Exp. Cell Res.*, 2019, 111508.
305 P. Reid, P. Wilson, Y. Li, L. G. Marcu, A. H. Staudacher, M. P. Brown and E. Bezak, *PLOS ONE*, 2017, **12**, e0186186.
306 H. O. Kaseb, H. Fohrer-Ting, D. W. Lewis, E. Lagasse and S. M. Gollin, *Exp. Cell Res.*, 2016, **348**, 75–86.
307 E. Sage and N. Shikazono, *Free Radic. Biol. Med.*, 2017, **107**, 125–135.
308 R. Okayasu, *Int. J. Cancer*, 2012, **130**, 991–1000.
309 Z. Nikitaki, V. Nikolov, I. V. Mavragani, E. Mladenov, A. Mangelis, D. A. Laskaratou, G. I. Fragkoulis, C. E. Hellweg, O. A. Martin, D. Emfietzoglou, V. I. Hatzi, G. I. Terzoudi, G. Iliakis and A. G. Georgakilas, *Free Radic. Res.*, 2016, **50**, S64–S78.
310 S. Moore, F. K. T. Stanley and A. A. Goodarzi, *DNA Repair*, 2014, **17**, 64–73.
311 R. M. Anderson, *Clin. Oncol.*, 2019, **31**, 311–318.
312 E. T. Vitti and J. L. Parsons, *Cancers*, 2019, **11**, 946.
313 M. Newpower, D. Patel, L. Bronk, F. Guan, P. Chaudhary, S. J. McMahon, K. M. Prise, G. Schettino, D. R. Grosshans and R. Mohan, *Int. J. Radiat. Oncol. Biol. Phys.*, 2019, **104**, 316–324.
314 E. R. Szabó, M. Brand, S. Hans, K. Hideghéty, L. Karsch, E. Lessmann, J. Pawelke, M. Schürer and E. Beyreuther, *PLOS ONE*, 2018, **13**, e0206879.
315 F. Guan, C. Geng, D. Ma, L. Bronk, M. Kerr, Y. Li, D. Gates, B. Kroger, N. Sahoo, U. Titt, D. Grosshans and R. Mohan, *Int. J. Part. Ther.*, 2018, **5**, 160–171.
316 A. Michaelidesová, J. Vachelová, M. Puchalska, K. P. Brabcová, V. Vondráček, L. Sihver and M. Davídková, *Australas. Phys. Eng. Sci. Med.*, 2017, **40**, 359–368.
317 T. I. Marshall, P. Chaudhary, A. Michaelidesová, J. Vachelová, M. Davídková, V. Vondráček, G. Schettino and K. M. Prise, *Int. J. Radiat. Oncol.*, 2016, **95**, 70–77.
318 J. D. Boice, *Int. J. Radiat. Biol.*, 2019, 1–9.
319 F. Kiffer, M. Boerma and A. Allen, *Life Sci. Space Res.*, 2019, **21**, 1–21.
320 A. Mitchell, D. Pimenta, J. Gill, H. Ahmad and R. Bogle, *Eur. J. Prev. Cardiol.*, 2019, 204748731983149.
321 V. S. Kokhan, E. V. Shakhbazian and N. A. Markova, *Behav. Brain Res.*, 2019, **362**, 311–318.
322 F. A. Cucinotta, E. Cacao, M.-H. Y. Kim and P. B. Saganti, *Radiat. Prot. Dosimetry*, 2019, **183**, 213–218.
323 I. Shuryak and D. J. Brenner, *Radiat. Prot. Dosimetry*, 2019, **183**, 203–212.
324 F. A. Cucinotta, H. Nikjoo and D. T. Goodhead, *Radiat. Res.*, 2000, **153**, 459–468.
325 D. M. Sridharan, L. J. Chappell, M. K. Whalen, F. A. Cucinotta and J. M. Pluth, *Radiat. Res.*, 2015, **184**, 105–119.
326 D. T. Goodhead, *Radiat. Prot. Dosimetry*, 2015, **166**, 276–281.
327 M. Suzuki, C. Tsuruoka, T. Kanai, T. Kato, F. Yatagai and M. Watanabe, *Uchu Seibutsu Kagaku*, 2003, **17**, 302–306.
328 C. Tsuruoka, M. Suzuki and K. Fujitaka, *Uchu Seibutsu Kagaku*, 2004, **18**, 188–189.
329 T. Takatsuji, I. Yoshikawa and M. S. Sasaki, *J. Radiat. Res. (Tokyo)*, 1999, **40**, 59–69.
330 M. Niemantsverdriet, M.-J. van Goethem, R. Bron, W. Hogewerf, S. Brandenburg, J. A. Langendijk, P. van Luijk and R. P. Coppes, *Int. J. Radiat. Oncol.*, 2012, **83**, 1291–1297.
331 H. Tauchi, S. Endo, K. Eguchi-Kasai, Y. Furusawa, M. Suzuki, S. Matsuura, K. Ando, N. Nakamura, S. Sawada and K. Komatsu, *J. Radiat. Res. (Tokyo)*, 1999, **40 Suppl**, 45–52.
332 Y. Kazama, K. Ishii, T. Hirano, T. Wakana, M. Yamada, S. Ohbu and T. Abe, *Plant J.*, 2017, **92**, 1020–1030.
333 P. Bláha, N. A. Koshlan, I. V. Koshlan, D. V. Petrova, Y. V. Bogdanova, R. D. Govorun, V. Múčka and E. A. Krasavin, *Mutat. Res. Mol. Mech. Mutagen.*, 2017, **803–805**, 35–41.
334 F. Yatagai, *Uchu Seibutsu Kagaku*, 2004, **18**, 224–234.
335 H. A. Foster, G. Estrada-Girona, M. Themis, E. Garimberti, M. A. Hill, J. M. Bridger and R. M. Anderson, *Mutat. Res. Toxicol. Environ. Mutagen.*, 2013, **756**, 66–77.
336 R. M. Anderson, D. L. Stevens, N. D. Sumption, K. M. S. Townsend, D. T. Goodhead and M. A. Hill, *Radiat. Res.*, 2007, **167**, 541–550.
337 S. Ritter, E. Nasonova and E. Gudowska-Novak, *Int. J. Radiat. Biol.*, 2002, **78**, 191–202.
338 I. Testard, B. Dutrillaux and L. Sabatier, *Int. J. Radiat. Biol.*, 1997, **72**, 423–433.
339 M. Joiner and A. van der Kogel, Eds., *Basic clinical radiobiology*, Hodder Arnold, London, 4th ed., 2009.
340 J. Kiefer, P. Schmidt and S. Koch, *Radiat. Res.*, 2001, **156**, 607–611.
341 M. Suzuki, Y. Kase, H. Yamaguchi, T. Kanai and K. Ando, *Int. J. Radiat. Oncol. Biol. Phys.*, 2000, **48**, 241–250.
342 R. Grün, T. Friedrich, E. Traneus and M. Scholz, *Med. Phys.*, 2019, **46**, 1064–1074.
343 J. Saha, P. Wilson, P. Thieberger, D. Lowenstein, M. Wang and F. A. Cucinotta, *Radiat. Res.*, 2014, **182**, 282.
344 G. Du, G. A. Drexler, W. Friedland, C. Greubel, V. Hable, R. Krücken, A. Kugler, L. Tonelli, A. A. Friedl and G. Dollinger, *Radiat. Res.*, 2011, **176**, 706–715.
345 A. Asaithamby, N. Uematsu, A. Chatterjee, M. D. Story, S. Burma and D. J. Chen, *Radiat. Res.*, 2008, **169**, 437–446.
346 B. Jakob, M. Scholz and G. Taucher-Scholz, *Radiat. Res.*, 2003, **159**, 676–684.
347 R. Lopez Perez, G. Best, N. H. Nicolay, C. Greubel, S. Rossberger, J. Reindl, G. Dollinger, K.-J. Weber, C. Cremer and P. E. Huber, *FASEB J. Off. Publ. Fed. Am. Soc. Exp. Biol.*, 2016, **30**, 2767–2776.
348 Y. Zhang, G. Máté, P. Müller, S. Hillebrandt, M. Krufczik, M. Bach, R. Kaufmann, M. Hausmann and D. W. Heermann, *PloS One*, 2015, **10**, e0128555.
349 Y. Lorat, C. U. Brunner, S. Schanz, B. Jakob, G. Taucher-Scholz and C. E. Rübe, *DNA Repair*, 2015, **28**, 93–106.
350 Y. Lorat, S. Timm, B. Jakob, G. Taucher-Scholz and C. E. Rübe, *Radiother. Oncol.*, 2016, **121**, 154–161.
351 C. E. Rübe, Y. Lorat, N. Schuler, S. Schanz, G. Wennemuth and C. Rübe, *DNA Repair*, 2011, **10**, 427–437.
352 J. F. Hainfeld, D. N. Slatkin and H. M. Smilowitz, *Phys. Med. Biol.*, 2004, **49**, N309-315.
353 S. Jain, J. A. Coulter, A. R. Hounsell, K. T. Butterworth, S. J. McMahon, W. B. Hyland, M. F. Muir, G. R. Dickson, K. M. Prise, F. J. Currell, J. M. O'Sullivan and D. G. Hirst, *Int. J. Radiat. Oncol.*, 2011, **79**, 531–539.
354 D. B. Chithrani, *Recent Pat. Nanotechnol.*, 2010, **4**, 171–180.
355 J. F. Hainfeld, F. A. Dilmanian, D. N. Slatkin and H. M. Smilowitz, *J. Pharm. Pharmacol.*, 2008, **60**, 977–985.
356 Y. Matsumura and H. Maeda, *Cancer Res.*, 1986, **46**, 6387–6392.
357 Y. Noguchi, J. Wu, R. Duncan, J. Strohalm, K. Ulbrich, T. Akaike and H. Maeda, *Jpn. J. Cancer Res. Gann*, 1998, **89**, 307–314.
358 A. C. Powell, G. F. Paciotti and S. K. Libutti, *Methods Mol. Biol. Clifton NJ*, 2010, **624**, 375–384.
359 Z.-Z. J. Lim, J.-E. J. Li, C.-T. Ng, L.-Y. L. Yung and B.-H. Bay, *Acta Pharmacol. Sin.*, 2011, **32**, 983–990.
360 J. F. Hainfeld, D. N. Slatkin, T. M. Focella and H. M. Smilowitz, *Br. J. Radiol.*, 2006, **79**, 248–253.
361 N. Chattopadhyay, Z. Cai, Y. L. Kwon, E. Lechtman, J.-P. Pignol and R. M. Reilly, *Breast Cancer Res. Treat.*, 2013, **137**, 81–91.
362 A. J. Mieszawska, W. J. M. Mulder, Z. A. Fayad and D. P. Cormode, *Mol. Pharm.*, 2013, **10**, 831–847.
363 X. Zhang, J. Z. Xing, J. Chen, L. Ko, J. Amanie, S. Gulavita, N. Pervez, D. Yee, R. Moore and W. Roa, *Clin. Investig. Med. Med. Clin. Exp.*, 2008, **31**, E160-167.
364 Y. Zheng, D. J. Hunting, P. Ayotte and L. Sanche, *Radiat. Res.*, 2008, **169**, 19–27.

365 E. Porcel, K. Kobayashi, N. Usami, H. Remita, C. Le Sech and S. Lacombe, *J Phys Conf Ser*, , DOI:10.1088/1742-6596/261/1/012004.
366 K. Maier-Hauff, F. Ulrich, D. Nestler, H. Niehoff, P. Wust, B. Thiesen, H. Orawa, V. Budach and A. Jordan, *J. Neurooncol.*, 2011, **103**, 317–324.
367 M. S. Bradbury, E. Phillips, P. H. Montero, S. M. Cheal, H. Stambuk, J. C. Durack, C. T. Sofocleous, R. J. C. Meester, U. Wiesner and S. Patel, *Integr. Biol. Quant. Biosci. Nano Macro*, 2013, **5**, 74–86.
368 G. Le Duc, I. Miladi, C. Alric, P. Mowat, E. Bräuer-Krisch, A. Bouchet, E. Khalil, C. Billotey, M. Janier, F. Lux, T. Epicier, P. Perriat, S. Roux and O. Tillement, *ACS Nano*, 2011, **5**, 9566–9574.
369 P. Mowat, A. Mignot, W. Rima, F. Lux, O. Tillement, C. Roulin, M. Dutreix, D. Bechet, S. Huger, L. Humbert, M. Barberi-Heyob, M. T. Aloy, E. Armandy, C. Rodriguez-Lafrasse, G. Le Duc, S. Roux and P. Perriat, *J. Nanosci. Nanotechnol.*, 2011, **11**, 7833–7839.
370 E. Porcel, O. Tillement, F. Lux, P. Mowat, N. Usami, K. Kobayashi, Y. Furusawa, C. Le Sech, S. Li and S. Lacombe, *Nanomedicine Nanotechnol. Biol. Med.*, 2014, **10**, 1601–1608.
371 L. Sancey, F. Lux, S. Kotb, S. Roux, S. Dufort, A. Bianchi, Y. Crémillieux, P. Fries, J.-L. Coll, C. Rodriguez-Lafrasse, M. Janier, M. Dutreix, M. Barberi-Heyob, F. Boschetti, F. Denat, C. Louis, E. Porcel, S. Lacombe, G. Le Duc, E. Deutsch, J.-L. Perfettini, A. Detappe, C. Verry, R. Berbeco, K. T. Butterworth, S. J. McMahon, K. M. Prise, P. Perriat and O. Tillement, *Br. J. Radiol.*, 2014, **87**, 20140134.
372 I. Miladi, M.-T. Aloy, E. Armandy, P. Mowat, D. Kryza, N. Magné, O. Tillement, F. Lux, C. Billotey, M. Janier and C. Rodriguez-Lafrasse, *Nanomedicine Nanotechnol. Biol. Med.*, 2015, **11**, 247–257.
373 J.-L. Bridot, A.-C. Faure, S. Laurent, C. Rivière, C. Billotey, B. Hiba, M. Janier, V. Josserand, J.-L. Coll, L. V. Elst, R. Muller, S. Roux, P. Perriat and O. Tillement, *J. Am. Chem. Soc.*, 2007, **129**, 5076–5084.
374 A. Mignot, C. Truillet, F. Lux, L. Sancey, C. Louis, F. Denat, F. Boschetti, L. Bocher, A. Gloter, O. Stéphan, R. Antoine, P. Dugourd, D. Luneau, G. Novitchi, L. C. Figueiredo, P. C. de Morais, L. Bonneviot, B. Albela, F. Ribot, L. Van Lokeren, I. Déchamps-Olivier, F. Chuburu, G. Lemercier, C. Villiers, P. N. Marche, G. Le Duc, S. Roux, O. Tillement and P. Perriat, *Chem. Weinh. Bergstr. Ger.*, 2013, **19**, 6122–6136.
375 A. Bianchi, S. Dufort, F. Lux, A. Courtois, O. Tillement, J.-L. Coll and Y. Crémillieux, *Magma N. Y. N*, 2014, **27**, 303–316.
376 F. Lux, A. Mignot, P. Mowat, C. Louis, S. Dufort, C. Bernhard, F. Denat, F. Boschetti, C. Brunet, R. Antoine, P. Dugourd, S. Laurent, L. Vander Elst, R. Muller, L. Sancey, V. Josserand, J.-L. Coll, V. Stupar, E. Barbier, C. Rémy, A. Broisat, C. Ghezzi, G. Le Duc, S. Roux, P. Perriat and O. Tillement, *Angew. Chem. Int. Ed Engl.*, 2011, **50**, 12299–12303.
377 S. Roux, O. Tillement, C. Billotey, J. L. Coll, G. L. Duc, C. A. Marquette and P. Perriat, *Int. J. Nanotechnol.*, 2010, **7**, 781.
378 S. Her, D. A. Jaffray and C. Allen, *Adv. Drug Deliv. Rev.*, 2017, **109**, 84–101.
379 M. Misawa and J. Takahashi, *Nanomedicine Nanotechnol. Biol. Med.*, 2011, **7**, 604–614.
380 E. Porcel, S. Liehn, H. Remita, N. Usami, K. Kobayashi, Y. Furusawa, C. Le Sech and S. Lacombe, *Nanotechnology*, 2010, **21**, 85103.
381 Z. Krpetić, P. Nativo, V. Sée, I. A. Prior, M. Brust and M. Volk, *Nano Lett.*, 2010, **10**, 4549–4554.
382 E. Lechtman, S. Mashouf, N. Chattopadhyay, B. M. Keller, P. Lai, Z. Cai, R. M. Reilly and J.-P. Pignol, *Phys. Med. Biol.*, 2013, **58**, 3075–3087.
383 S. J. McMahon, W. B. Hyland, M. F. Muir, J. A. Coulter, S. Jain, K. T. Butterworth, G. Schettino, G. R. Dickson, A. R. Hounsell, J. M. O'Sullivan, K. M. Prise, D. G. Hirst and F. J. Currell, *Radiother. Oncol.*, 2011, **100**, 412–416.
384 S. J. McMahon, W. B. Hyland, M. F. Muir, J. A. Coulter, S. Jain, K. T. Butterworth, G. Schettino, G. R. Dickson, A. R. Hounsell, J. M. O'Sullivan, K. M. Prise, D. G. Hirst and F. J. Currell, *Sci. Rep.*, 2011, **1**, 18.
385 N. Burger, A. Biswas, D. Barzan, A. Kirchner, H. Hosser, M. Hausmann, G. Hildenbrand, C. Herskind, F. Wenz and M. R. Veldwijk, *Nanomedicine Nanotechnol. Biol. Med.*, 2014, **10**, 1365–1373.
386 A. I. Kassis and S. J. Adelstein, *J. Nucl. Med. Off. Publ. Soc. Nucl. Med.*, 2005, **46 Suppl 1**, 4S-12S.
387 M. Belli, O. Sapora and M. A. Tabocchini, *J. Radiat. Res. (Tokyo)*, 2002, **43 Suppl**, S13-19.
388 M.-Y. Chang, A.-L. Shiau, Y.-H. Chen, C.-J. Chang, H. H.-W. Chen and C.-L. Wu, *Cancer Sci.*, 2008, **99**, 1479–1484.
389 W. Rima, L. Sancey, M.-T. Aloy, E. Armandy, G. B. Alcantara, T. Epicier, A. Malchère, L. Joly-Pottuz, P. Mowat, F. Lux, O. Tillement, B. Burdin, A. Rivoire, C. Boulé, I. Anselme-Bertrand, J. Pourchez, M. Cottier, S. Roux, C. Rodriguez-Lafrasse and P. Perriat, *Biomaterials*, 2013, **34**, 181–195.
390 N. Usami, Y. Furusawa, K. Kobayashi, S. Lacombe, A. Reynaud-Angelin, E. Sage, T.-D. Wu, A. Croisy, J.-L. Guerquin-Kern and C. Le Sech, *Int. J. Radiat. Biol.*, 2008, **84**, 603–611.
391 T. Kong, J. Zeng, X. Wang, X. Yang, J. Yang, S. McQuarrie, A. McEwan, W. Roa, J. Chen and J. Z. Xing, *Small Weinh. Bergstr. Ger.*, 2008, **4**, 1537–1543.
392 B. L. Jones, S. Krishnan and S. H. Cho, *Med. Phys.*, 2010, **37**, 3809–3816.
393 M. K. K. Leung, J. C. L. Chow, B. D. Chithrani, M. J. G. Lee, B. Oms and D. A. Jaffray, *Med. Phys.*, 2011, **38**, 624–631.
394 L. Tartier, S. Gilchrist, S. Burdak-Rothkamm, M. Folkard and K. M. Prise, *Cancer Res.*, 2007, **67**, 5872–5879.
395 L.-J. Wu, G. Randers-Pehrson, A. Xu, C. A. Waldren, C. R. Geard, Z. Yu and T. K. Hei, *Proc. Natl. Acad. Sci.*, 1999, **96**, 4959–4964.
396 S. Rosa, C. Connolly, G. Schettino, K. T. Butterworth and K. M. Prise, *Cancer Nanotechnol.*, , DOI:10.1186/s12645-017-0026-0.
397 A. O. Maslova and I. M. Hsing, *Nanoscale Adv.*, 2019, **1**, 430–435.
398 V. Dahmen and R. Kriehuber, *Int. J. Radiat. Biol.*, 2012, **88**, 972–979.
399 E. Fattal and G. Barratt, *Br. J. Pharmacol.*, 2009, **157**, 179–194.
400 F. Lin, Y.-W. Bao and F.-G. Wu, *Molecules*, 2018, **23**, 3016.
401 A. Parodi, C. Corbo, A. Cevenini, R. Molinaro, R. Palomba, L. Pandolfi, M. Agostini, F. Salvatore and E. Tasciotti, *Nanomed.*, 2015, **10**, 1923–1940.
402 C. S. O. Paulo, R. Pires das Neves and L. S. Ferreira, *Nanotechnology*, 2011, **22**, 494002.
403 H. Padh and Niraj Sakhrani, *Drug Des. Devel. Ther.*, 2013, 585.
404 L. A. Dykman and N. Khlebtsov, *Gold nanoparticles in biomedical applications*, 2018.
405 D. M. Klinman, T. Sato and T. Shimosato, *Wiley Interdiscip. Rev. Nanomed. Nanobiotechnol.*, 2016, **8**, 631–637.
406 I. Pilipenko, V. Korzhikov-Vlakh, V. Sharoyko, N. Zhang, M. Schäfer-Korting, E. Rühl, C. Zoschke and T. Tennikova, *Pharmaceutics*, 2019, **11**, 317.
407 B. M. Aarts, E. G. Klompenhouwer, S. L. Rice, F. Imani, T. Baetens, A. Bex, S. Horenblas, M. Kok, J. B. A. G. Haanen, R. G. H. Beets-Tan and F. M. Gómez, *Insights Imaging*, , DOI:10.1186/s13244-019-0727-5.
408 D. J. Lomas, D. A. Woodrum, R. H. McLaren, K. R. Gorny, J. P. Felmlee, C. Favazza, A. Lu and L. A. Mynderse, *Abdom. Radiol.*, , DOI:10.1007/s00261-019-02147-4.
409 M. Oishi, I. S. Gill, A. Tafuri, A. Shakir, G. E. Cacciamani, T. Iwata, A. Iwata, A. Ashrafi, D. Park, J. Cai, M. Desai, O. Ukimura, D. K. Bahn and A. L. Abreu, *J. Urol.*, , DOI:10.1097/JU.0000000000000456.
410 A. Rühle, N. Andratschke, S. Siva and M. Guckenberger, *Clin. Transl. Radiat. Oncol.*, 2019, **18**, 104–112.

411 B. Surtees, S. Young, Y. Hu, G. Wang, E. McChesney, G. Kuroki, P. Acree, S. Thomas, T. Blair, S. Rastogi, D. L. Kraitchman, C. Weiss, S. Sukumar, S. C. Harvey and N. J. Durr, *PLOS ONE*, 2019, **14**, e0207107.
412 R. Tarkowski and M. Rzaca, *Gland Surg.*, 2014, **3**, 88–93.
413 V. M. Zemskov, K. N. Pronko, D. A. Ionkin, A. V. Chzhao, M. N. Kozlova, A. A. Barsukov, N. S. Shishkina, V. S. Demidova, A. M. Zemskov and A. Sh. Revishvili, *Med. Sci.*, 2019, **7**, 73.
414 J. Wu, J. Chang, H. X. Bai, C. Su, P. J. Zhang, G. Karakousis, S. Reddy, S. Hunt, M. C. Soulen, S. W. Stavropoulos and Z. Zhang, *J. Vasc. Interv. Radiol. JVIR*, 2019, **30**, 1027-1033.e3.
415 R. C. Ward, A. P. Lourenco and M. B. Mainiero, *Am. J. Roentgenol.*, 2019, 1–7.
416 K. Redifer Tremblay, W. B. Lea, J. C. Neilson, D. M. King and S. M. Tutton, *J. Surg. Oncol.*, 2019, **120**, 366–375.
417 L. Ratanaprasatporn, N. Sainani, J. B. Duda, A. Aghayev, S. Tatli, S. G. Silverman and P. B. Shyn, *Abdom. Radiol.*, 2019, **44**, 2602–2626.
418 D. Theodorescu, *Rev. Urol.*, 2004, **6 Suppl 4**, S9–S19.
419 J. Konc, K. Kanyó, R. Kriston, B. Somoskői and S. Cseh, *BioMed Res. Int.*, 2014, **2014**, 307268.
420 P. M. Calabro-Jones, R. C. Fahey, G. D. Smoluk and J. F. Ward, *Int. J. Radiat. Biol. Relat. Stud. Phys. Chem. Med.*, 1985, **47**, 23–27.
421 P. M. Calabro-Jones, J. A. Aguilera, J. F. Ward, G. D. Smoluk and R. C. Fahey, *Cancer Res.*, 1988, **48**, 3634–3640.
422 M. Levi, J. A. Knol, W. D. Ensminger, S. J. DeRemer, C. Dou, S. M. Lunte, H. S. Bonner, L. M. Shaw and D. E. Smith, *Drug Metab. Dispos. Biol. Fate Chem.*, 2002, **30**, 1425–1430.
423 H. I. Tahsildar, J. E. Biaglow, M. M. Kligerman and M. E. Varnes, *Radiat. Res.*, 1988, **113**, 243–251.
424 C. W. Taylor, L. M. Wang, A. F. List, D. Fernandes, G. D. Paine-Murrieta, C. S. Johnson and R. L. Capizzi, *Eur. J. Cancer Oxf. Engl. 1990*, 1997, **33**, 1693–1698.
425 C. M. Kurbacher and P. K. Mallmann, *Anticancer Res.*, 1998, **18**, 2203–2210.
426 M. Orditura, F. De Vita, A. Roscigno, S. Infusino, A. Auriemma, P. Iodice, F. Ciaramella, G. Abbate and G. Catalano, *Oncol. Rep.*, 1999, **6**, 1357–1362.
427 A. Buschini, C. Alessandrini, A. Martino, L. Pasini, V. Rizzoli, C. Carlo-Stella, P. Poli and C. Rossi, *Biochem. Pharmacol.*, 2002, **63**, 967–975.
428 I. Majsterek, E. Gloc, J. Blasiak and R. J. Reiter, *J. Pineal Res.*, 2005, **38**, 254–263.
429 B. S. Margulies, T. A. Damron and M. J. Allen, *J. Orthop. Res. Off. Publ. Orthop. Res. Soc.*, 2008, **26**, 1512–1519.
430 A. Eisbruch, *J. Clin. Oncol. Off. J. Am. Soc. Clin. Oncol.*, 2011, **29**, 119–121.
431 B. Brenner, L. Wasserman, E. Beery, J. Nordenberg, J. Schechter, H. Gutman and E. Fenig, *Oncol. Rep.*, 2003, **10**, 1609–1613.
432 L. C. Tsai, M. W. Hung, Y. H. Chen, W. C. Su, G. G. Chang and T. C. Chang, *Eur. J. Biochem.*, 2000, **267**, 1330–1339.
433 A. Sadeghirizi and R. Yazdanparast, *Acta Biochim. Pol.*, 2007, **54**, 323–329.
434 T. C. Chang, J. K. Wang, M. W. Hung, C. H. Chiao, L. C. Tsai and G. G. Chang, *Biochem. J.*, 1994, **303 (Pt 1)**, 199–205.
435 J. R. Chan and R. A. Stinson, *J. Biol. Chem.*, 1986, **261**, 7635–7639.
436 E. Almeida, J. L. Fuentes, E. Cuetara, E. Prieto and M. Llagostera, *Environ. Toxicol.*, 2010, **25**, 130–136.
437 A. C. Muller, S. U. Pigorsch and J. Dunst, *Strahlenther Onkol*, 2003, 657–657.
438 P. Catalina, F. Cobo, J. L. Cortés, A. I. Nieto, C. Cabrera, R. Montes, Á. Concha and P. Menendez, *Cell Biol. Int.*, 2007, **31**, 861–869.
439 A. Bolzer, G. Kreth, I. Solovei, D. Koehler, K. Saracoglu, C. Fauth, S. Müller, R. Eils, C. Cremer, M. R. Speicher and T. Cremer, *PLoS Biol.*, 2005, **3**, e157.
440 M. R. Speicher and N. P. Carter, *Nat. Rev. Genet.*, 2005, **6**, 782–792.
441 M. Falk, Disertation Thesis, Faculty of Sciences, Masaryk University, Brno, Czech Republic, 2004.
442 J.-H. Lee, Kirchhoff-Institute for Physics, University of Heidelberg, Im Neuenheimer Feld 227, 69120 Heidelberg, Germany, F. B. estvater, German Cancer Research Center (DKFZ), Im Neuenheimer Feld 280, 69120 Heidelberg, Germany, M. Hausmann and Kirchhoff-Institute for Physics, University of Heidelberg, Im Neuenheimer Feld 227, 69120 Heidelberg, Germany, *OBM Genet.*, 2018, **3**, 1–1.
443 P. Müller, E. Schmitt, A. Jacob, J. Hoheisel, R. Kaufmann, C. Cremer and M. Hausmann, *Int. J. Mol. Sci.*, 2010, **11**, 4094–4105.
444 P. Lemmer, M. Gunkel, D. Baddeley, R. Kaufmann, A. Urich, Y. Weiland, J. Reymann, P. Müller, M. Hausmann and C. Cremer, *Appl. Phys. B*, 2008, **93**, 1–12.
445 J. Schwarzfinsterle, S. Stein, C. Grosmann, E. Schmitt, H. Schneider, L. Trakhtenbrot, G. Rechavi, N. Amariglio, C. Cremer and M. Hausmann, *Cell Biol. Int.*, 2005, **29**, 1038–1046.
446 M. Hausmann, R. Winkler, G. Hildenbrand, J. Finsterle, A. Weisel, A. Rapp, E. Schmitt, S. Janz and C. Cremer, *BioTechniques*, 2003, **35**, 564–577.
447 M. Krufczik, A. Sievers, A. Hausmann, J.-H. Lee, G. Hildenbrand, W. Schaufler and M. Hausmann, *Int. J. Mol. Sci.*, , DOI:10.3390/ijms18051005.
448 M. Stuhlmüller, J. Schwarz-Finsterle, E. Fey, J. Lux, M. Bach, C. Cremer, K. Hinderhofer, M. Hausmann and G. Hildenbrand, *Nanoscale*, 2015, **7**, 17938–17946.
449 R. Kaufmann, P. Müller, M. Hausmann and C. Cremer, *Micron Oxf. Engl. 1993*, 2011, **42**, 348–352.
450 M. Bohn, P. Diesinger, R. Kaufmann, Y. Weiland, P. Müller, M. Gunkel, A. von Ketteler, P. Lemmer, M. Hausmann, D. W. Heermann and C. Cremer, *Biophys. J.*, 2010, **99**, 1358–1367.
451 M. Gunkel, F. Erdel, K. Rippe, P. Lemmer, R. Kaufmann, C. Hörmann, R. Amberger and C. Cremer, *Biotechnol. J.*, 2009, **4**, 927–938.
452 W. Flemming, *Arch. Für Mikrosk. Anat.*, 1879, **16**, 302–436.
453 T. H. Boveri, *Fish. Jena*.
454 T. Cremer and H. Schipperges, *Von der Zellenlehre zur Chromosomentheorie*, Springer Berlin Heidelberg, Berlin, Heidelberg, 1985.
455 E. Heitz, *Jahrb Wiss Bot*, 1928, 762–818.
456 E. Heitz, *Ber Bot. Ges*, 1929, 274–284.
457 G. Holmquist, M. Gray, T. Porter and J. Jordan, *Cell*, 1982, **31**, 121–129.
458 C. Carvalho, H. M. Pereira, J. Ferreira, C. Pina, D. Mendonça, A. C. Rosa and M. Carmo-Fonseca, *Mol. Biol. Cell*, 2001, **12**, 3563–3572.
459 L. Manuelidis, *Science*, 1990, **250**, 1533–1540.
460 P. Oberdoerffer and D. A. Sinclair, *Nat. Rev. Mol. Cell Biol.*, 2007, **8**, 692–702.
461 M. F. Lyon, *Am. J. Hum. Genet.*, 1962, **14**, 135–148.
462 J. D. Watson and F. H. C. Crick, *Nature*, 1953, **171**, 737–738.
463 M. H. F. Wilkins, A. R. Stokes and H. R. Wilson, *Nature*, 1953, **171**, 738–740.
464 R. E. Franklin and R. G. Gosling, *Nature*, 1953, **171**, 740–741.
465 P. J. Horn and C. L. Peterson, *Science*, 2002, **297**, 1824–1827.
466 M. Moraru and T. Schalch, *Essays Biochem.*, 2019, **63**, 123–132.
467 A. Chicano and J.-R. Daban, *FEBS Lett.*, 2019, **593**, 810–819.
468 D. Pruss, J. J. Hayes and A. P. Wolffe, *BioEssays News Rev. Mol. Cell. Dev. Biol.*, 1995, **17**, 161–170.
469 G. Li and D. Reinberg, *Curr. Opin. Genet. Dev.*, 2011, **21**, 175–186.
470 A. S. Belmont, *Proc. Natl. Acad. Sci. U. S. A.*, 2002, **99**, 15855–15857.
471 K. Maeshima, S. Ide and M. Babokhov, *Curr. Opin. Cell Biol.*, 2019, **58**, 95–104.
472 S. I. S. Grewal and S. C. R. Elgin, *Nature*, 2007, **447**, 399–406.
473 H. Strickfaden, A. Zunhammer, S. van Koningsbruggen, D. Köhler and T. Cremer, *Nucl. Austin Tex*, 2010, **1**, 284–297.

474 D. M. MacAlpine and G. Almouzni, *Cold Spring Harb. Perspect. Biol.*, 2013, **5**, a010207–a010207.
475 J. R. Girton and K. M. Johansen, *Adv. Genet.*, 2008, **61**, 1–43.
476 S. I. S. Grewal and S. Jia, *Nat. Rev. Genet.*, 2007, **8**, 35–46.
477 D. Maya-Miles, E. Andújar, M. Pérez-Alegre, M. Murillo-Pineda, M. Barrientos-Moreno, M. J. Cabello-Lobato, E. Gómez-Marín, M. Morillo-Huesca and F. Prado, *Epigenetics Chromatin*, 2019, **12**, 47.
478 U. J. Birk, *Genes*, , DOI:10.3390/genes10070493.
479 N. Gilbert, *Curr. Opin. Genet. Dev.*, 2019, **55**, 66–75.
480 C. Bonifer and P. N. Cockerill, Eds., *Transcriptional and epigenetic mechanisms regulating normal and aberrant blood cell development*, Springer, Heidelberg, 2014.
481 A. S. Shatskikh, O. M. Olenkina, A. A. Solodovnikov and S. A. Lavrov, *Biochem. Biokhimiia*, 2018, **83**, 542–551.
482 A. S. Shatskikh, Y. A. Abramov and S. A. Lavrov, *Fly (Austin)*, 2017, **11**, 96–103.
483 T. Cheutin, A. J. McNairn, T. Jenuwein, D. M. Gilbert, P. B. Singh and T. Misteli, *Science*, 2003, **299**, 721–725.
484 L. C. Bryan, D. R. Weilandt, A. L. Bachmann, S. Kilic, C. C. Lechner, P. D. Odermatt, G. E. Fantner, S. Georgeon, O. Hantschel, V. Hatzimanikatis and B. Fierz, *Nucleic Acids Res.*, 2017, **45**, 10504–10517.
485 D. Kumar and S. Antonarakis, *Medical and Health Genomics*, 2016.
486 P. W. L. Tai, S. K. Zaidi, H. Wu, R. A. Grandy, M. Montecino, A. J. van Wijnen, J. B. Lian, G. S. Stein and J. L. Stein, *J. Cell. Physiol.*, 2014, **229**, 711–727.
487 L. Verrier, F. Taglini, R. R. Barrales, S. Webb, T. Urano, S. Braun and E. H. Bayne, *Open Biol.*, 2015, **5**, 150045.
488 J. Yang and V. G. Corces, in *Advances in Cancer Research*, Elsevier, 2011, vol. 110, pp. 43–76.
489 C. Rabl, *Jahrbuch*, 1885, 214–330.
490 E. Strasburger, *Die stofflichen Grundlagen der Vererbung im organischen Reich.*, Gustav. Fischer, Jena, Germany., 1905.
491 T. H. Boveri, *Arch. Zellforsch.*, 1909, 181–268.
492 S. Wischnitzer, *Int. Rev. Cytol.*, 1973, **34**, 1–48.
493 D. E. Comings, *Am. J. Hum. Genet.*, 1968, **20**, 440–460.
494 F. Vogel and T. M. Schroeder, *Humangenetik*, 1974, **25**, 265–297.
495 D. E. Comings, *Adv. Hum. Genet.*, 1972, **3**, 237–431.
496 T. Cremer and C. Cremer, *Nat. Rev. Genet.*, 2001, **2**, 292–301.
497 T. Cremer, C. Cremer, T. Schneider, H. Baumann, L. Hens and M. Kirsch-Volders, *Hum. Genet.*, 1982, **62**, 201–209.
498 T. Cremer, C. Cremer, H. Baumann, E. K. Luedtke, K. Sperling, V. Teuber and C. Zorn, *Hum. Genet.*, 1982, **60**, 46–56.
499 L. Manuelidis, *Proc. Natl. Acad. Sci. U. S. A.*, 1984, **81**, 3123–3127.
500 M. Schardin, T. Cremer, H. D. Hager and M. Lang, *Hum. Genet.*, 1985, **71**, 281–287.
501 D. Pinkel, T. Straume and J. W. Gray, *Proc. Natl. Acad. Sci. U. S. A.*, 1986, **83**, 2934–2938.
502 T. Cremer, P. Lichter, J. Borden, D. C. Ward and L. Manuelidis, *Hum. Genet.*, 1988, **80**, 235–246.
503 J. B. Lawrence, C. A. Villnave and R. H. Singer, *Cell*, 1988, **52**, 51–61.
504 P. Lichter, T. Cremer, J. Borden, L. Manuelidis and D. C. Ward, *Hum. Genet.*, 1988, **80**, 224–234.
505 K. Torabi, D. Wangsa, I. Ponsa, M. Brown, A. Bosch, M. Vila-Casadesús, T. S. Karpova, M. Calvo, A. Castells, R. Miró, T. Ried and J. Camps, *Chromosoma*, 2017, **126**, 655–667.
506 M. Orsztynowicz, D. Lechniak, P. Pawlak, B. Kociucka, S. Kubickova, H. Cernohorska and Z. E. Madeja, *PLOS ONE*, 2017, **12**, e0182398.
507 K. W. Jeon, *International review of cell and molecular biology.*, 2015.
508 S. Goetze, J. Mateos-Langerak, H. J. Gierman, W. de Leeuw, O. Giromus, M. H. G. Indemans, J. Koster, V. Ondrej, R. Versteeg and R. van Driel, *Mol. Cell. Biol.*, 2007, **27**, 4475–4487.
509 M. Cremer, K. Küpper, B. Wagler, L. Wizelman, J. von Hase, Y. Weiland, L. Kreja, J. Diebold, M. R. Speicher and T. Cremer, *J. Cell Biol.*, 2003, **162**, 809–820.
510 P. J. Verschure, I. van Der Kraan, E. M. Manders and R. van Driel, *J. Cell Biol.*, 1999, **147**, 13–24.
511 S. N. Fatakia, I. S. Mehta and B. J. Rao, *Sci. Rep.*, 2016, **6**, 36819.
512 J. Amrichová, E. Lukásová, S. Kozubek and M. Kozubek, *Exp. Cell Res.*, 2003, **289**, 11–26.
513 H. Caron, B. van Schaik, M. van der Mee, F. Baas, G. Riggins, P. van Sluis, M. C. Hermus, R. van Asperen, K. Boon, P. A. Voûte, S. Heisterkamp, A. van Kampen and R. Versteeg, *Science*, 2001, **291**, 1289–1292.
514 T. Tumbar, G. Sudlow and A. S. Belmont, *J. Cell Biol.*, 1999, **145**, 1341–1354.
515 C. Francastel, D. Schübeler, D. I. Martin and M. Groudine, *Nat. Rev. Mol. Cell Biol.*, 2000, **1**, 137–143.
516 Z. Hua-bing, L. De-Pei and L. Chih-Chuan, *Int. J. Hematol.*, 2002, **76**, 420–426.
517 S. V. Ulianov, A. A. Galitsyna, I. M. Flyamer, A. K. Golov, E. E. Khrameeva, M. V. Imakaev, N. A. Abdennur, M. S. Gelfand, A. A. Gavrilov and S. V. Razin, *Epigenetics Chromatin*, 2017, **10**, 35.
518 L. P. O'Neill and B. M. Turner, *EMBO J.*, 1995, **14**, 3946–3957.
519 D. Schübeler, D. M. MacAlpine, D. Scalzo, C. Wirbelauer, C. Kooperberg, F. van Leeuwen, D. E. Gottschling, L. P. O'Neill, B. M. Turner, J. Delrow, S. P. Bell and M. Groudine, *Genes Dev.*, 2004, **18**, 1263–1271.
520 J.-W. Xu, S. Ling and J. Liu, *Mediators Inflamm.*, 2017, **2017**, 1–6.
521 M. Ruiz-Velasco and J. B. Zaugg, *Curr. Opin. Syst. Biol.*, 2017, **1**, 129–136.
522 S. Venkatesh and J. L. Workman, *Nat. Rev. Mol. Cell Biol.*, 2015, **16**, 178.
523 P. Chen and G. Li, *Protein Cell*, 2010, **1**, 967–971.
524 B. Li, M. Carey and J. L. Workman, *Cell*, 2007, **128**, 707–719.
525 A. Németh and G. Längst, *Brief. Funct. Genomic. Proteomic.*, 2004, **2**, 334–343.
526 Z. Dai, *Cells*, 2019, **8**, 754.
527 Z. Dai and X. Dai, *Nucleic Acids Res.*, 2012, **40**, 27–36.
528 S. V. Razin, A. A. Gavrilov, A. Pichugin, M. Lipinski, O. V. Iarovaia and Y. S. Vassetzky, *Nucleic Acids Res.*, 2011, **39**, 9085–9092.
529 P. Fraser and W. Bickmore, *Nature*, 2007, **447**, 413–417.
530 M. Olszewska, E. Wiland, N. Huleyuk, M. Fraczek, A. T. Midro, D. Zastavna and M. Kurpisz, *BMC Med. Genomics*, 2019, **12**, 30.
531 A. J. Fritz, N. Sehgal, A. Pliss, J. Xu and R. Berezney, *Genes. Chromosomes Cancer*, 2019, **58**, 407–426.
532 A. Pliss, A. J. Fritz, B. Stojkovic, H. Ding, L. Mukherjee, S. Bhattacharya, J. Xu and R. Berezney, *J. Cell. Physiol.*, 2015, **230**, 427–439.
533 L. Manuelidis and J. Borden, *Chromosoma*, 1988, **96**, 397–410.
534 M. Y. Walker and R. S. Hawley, *Chromosoma*, 2000, **109**, 3–9.
535 J. Vazquez, A. S. Belmont and J. W. Sedat, *Curr. Biol. CB*, 2002, **12**, 1473–1483.
536 P. P. Rocha, M. Micsinai, J. R. Kim, S. L. Hewitt, P. P. Souza, T. Trimarchi, F. Strino, F. Parisi, Y. Kluger and J. A. Skok, *Mol. Cell*, 2012, **47**, 873–885.
537 S. Kozubek, E. Lukásová, L. Rýznar, M. Kozubek, A. Lisková, R. D. Govorun, E. A. Krasavin and G. Horneck, *Blood*, 1997, **89**, 4537–4545.
538 E. Lukásová, S. Kozubek, M. Kozubek, J. Kjeronská, L. Rýznar, J. Horáková, E. Krahulcová and G. Horneck, *Hum. Genet.*, 1997, **100**, 525–535.
539 M. Skalníková, S. Kozubek, E. Lukásová, E. Bártová, P. Jirsová, A. Cafourková, I. Koutná and M. Kozubek, *Chromosome Res. Int. J. Mol. Supramol. Evol. Asp. Chromosome Biol.*, 2000, **8**, 487–499.

540 A. Cafourková, E. Luká ová, S. Kozubek, M. Kozubek, R. D. Govorun, I. Koutná, E. Bártová, M. Skalníková, P. Jirsová, R. Paseková and E. A. Krasavin, *Int. J. Radiat. Biol.*, 2001, **77**, 419–429.
541 R. K. Sachs, A. M. Chen and D. J. Brenner, *Int. J. Radiat. Biol.*, 1997, **71**, 1–19.
542 S. Kozubek, E. Lukásová, A. Marecková, M. Skalníková, M. Kozubek, E. Bártová, V. Kroha, E. Krahulcová and J. Slotová, *Chromosoma*, 1999, **108**, 426–435.
543 L. Parada and T. Misteli, *Trends Cell Biol.*, 2002, **12**, 425–432.
544 L. A. Parada, P. G. McQueen, P. J. Munson and T. Misteli, *Curr. Biol. CB*, 2002, **12**, 1692–1697.
545 I. Alcobia, A. S. Quina, H. Neves, N. Clode and L. Parreira, *Exp. Cell Res.*, 2003, **290**, 358–369.
546 A. B. Glassman, *Clin. Lab. Med.*, 2000, **20**, 39–48.
547 T. Burmeister and E. Thiel, *J. Cancer Res. Clin. Oncol.*, 2001, **127**, 80–90.
548 M. Feuring-Buske, W. Hiddemann and C. Buske, *Internist*, 2002, **43**, 1179–1189.
549 M. F. Colby-Graham and C. Chordas, *J. Pediatr. Nurs.*, 2003, **18**, 87–95.
550 P. Emmerich, P. Loos, A. Jauch, A. H. Hopman, J. Wiegant, M. J. Higgins, B. N. White, M. van der Ploeg, C. Cremer and T. Cremer, *Exp. Cell Res.*, 1989, **181**, 126–140.
551 S. Popp, H. P. Scholl, P. Loos, A. Jauch, E. Stelzer, C. Cremer and T. Cremer, *Exp. Cell Res.*, 1990, **189**, 1–12.
552 M. Ferguson and D. C. Ward, *Chromosoma*, 1992, **101**, 557–565.
553 A. C. Chandley, R. M. Speed and A. R. Leitch, *J. Cell Sci.*, 1996, **109 (Pt 4)**, 773–776.
554 J. Walter, L. Schermelleh, M. Cremer, S. Tashiro and T. Cremer, *J. Cell Biol.*, 2003, **160**, 685–697.
555 H. Nagase, N. Ogawa, T. Endo, M. Shiro, H. Ueda and M. Sakurai, *J. Phys. Chem. B*, 2008, **112**, 9105–9111.
556 H. B. Sun and H. Yokota, *Chromosome Res. Int. J. Mol. Supramol. Evol. Asp. Chromosome Biol.*, 1999, **7**, 603–610.
557 D. Gerlich and J. Ellenberg, *Curr. Opin. Cell Biol.*, 2003, **15**, 664–671.
558 D. Gerlich, J. Beaudouin, B. Kalbfuss, N. Daigle, R. Eils and J. Ellenberg, *Cell*, 2003, **112**, 751–764.
559 S. Maharana, K. V. Iyer, N. Jain, M. Nagarajan, Y. Wang and G. V. Shivashankar, *Nucleic Acids Res.*, 2016, **44**, 5148–5160.
560 K. J. Meaburn and T. Misteli, *Nature*, 2007, **445**, 379–381.
561 T. Cremer and M. Cremer, *Cold Spring Harb. Perspect. Biol.*, 2010, **2**, a003889–a003889.
562 D. B. Whitefield, S. T. Spagnol, T. J. Armiger, L. Lan and K. N. Dahl, *Sci. Rep.*, 2018, **8**, 18084.
563 V. Dion and S. M. Gasser, *Cell*, 2013, **152**, 1355–1364.
564 D. Zink and T. Cremer, *Curr. Biol. CB*, 1998, **8**, R321-324.
565 R. D. Shelby, K. M. Hahn and K. F. Sullivan, *J. Cell Biol.*, 1996, **135**, 545–557.
566 X. Bi, *IUBMB Life*, 2014, **66**, 657–666.
567 J. R. Abney, B. Cutler, M. L. Fillbach, D. Axelrod and B. A. Scalettar, *J. Cell Biol.*, 1997, **137**, 1459–1468.
568 D. Ranade, R. Pradhan, M. Jayakrishnan, S. Hegde and K. Sengupta, *BMC Mol. Cell Biol.*, 2019, **20**, 11.
569 K. Wiesmeijer, I. M. Krouwels, H. J. Tanke and R. W. Dirks, *Differentiation*, 2008, **76**, 83–90.
570 C.-H. Chuang and A. S. Belmont, *Semin. Cell Dev. Biol.*, 2007, **18**, 698–706.
571 G. Li, G. Sudlow and A. S. Belmont, *J. Cell Biol.*, 1998, **140**, 975–989.
572 J. M. Bridger, S. Boyle, I. R. Kill and W. A. Bickmore, *Curr. Biol. CB*, 2000, **10**, 149–152.
573 J. Borden and L. Manuelidis, *Science*, 1988, **242**, 1687–1691.
574 T. L. Yang-Feng, L. J. DeGennaro and U. Francke, *Proc. Natl. Acad. Sci.*, 1986, **83**, 8679–8683.
575 P.-Y. Hsu, H.-K. Hsu, T.-H. Hsiao, Z. Ye, E. Wang, A. L. Profit, I. Jatoi, Y. Chen, N. B. Kirma, V. X. Jin, Z. D. Sharp and T. H.-M. Huang, *Oncogene*, 2016, **35**, 2379–2389.
576 E. M. Manders, H. Kimura and P. R. Cook, *J. Cell Biol.*, 1999, **144**, 813–821.
577 P. Heun, A. Taddei and S. M. Gasser, *Trends Cell Biol.*, 2001, **11**, 519–525.
578 H. Tanabe, F. A. Habermann, I. Solovei, M. Cremer and T. Cremer, *Mutat. Res. Mol. Mech. Mutagen.*, 2002, **504**, 37–45.
579 F. A. Habermann, M. Cremer, J. Walter, G. Kreth, J. von Hase, K. Bauer, J. Wienberg, C. Cremer, T. Cremer and I. Solovei, *Chromosome Res. Int. J. Mol. Supramol. Evol. Asp. Chromosome Biol.*, 2001, **9**, 569–584.
580 C.-L. Tiang, Y. He and W. P. Pawlowski, *Plant Physiol.*, 2012, **158**, 26–34.
581 A. P. Santos and P. Shaw, *J. Microsc.*, 2004, **214**, 201–206.
582 T. Cremer, M. Cremer, B. Hübner, H. Strickfaden, D. Smeets, J. Popken, M. Sterr, Y. Markaki, K. Rippe and C. Cremer, *FEBS Lett.*, 2015, **589**, 2931–2943.
583 L. A. Mirny, *Chromosome Res.*, 2011, **19**, 37–51.
584 H. Yokota, G. van den Engh, J. E. Hearst, R. K. Sachs and B. J. Trask, *J. Cell Biol.*, 1995, **130**, 1239–1249.
585 R. K. Sachs, G. van den Engh, B. Trask, H. Yokota and J. E. Hearst, *Proc. Natl. Acad. Sci.*, 1995, **92**, 2710–2714.
586 T. A. Knoch, M. Wachsmuth, N. Kepper, M. Lesnussa, A. Abuseiris, A. M. Ali Imam, P. Kolovos, J. Zuin, C. E. M. Kockx, R. W. W. Brouwer, H. J. G. van de Werken, W. F. J. van IJcken, K. S. Wendt and F. G. Grosveld, *Epigenetics Chromatin*, , DOI:10.1186/s13072-016-0089-x.
587 S. V. Razin and I. I. Gromova, *BioEssays*, 1995, **17**, 443–450.
588 L. Manuelidis and T. L. Chen, *Cytometry*, 1990, **11**, 8–25.
589 M. Hausmann, N. Ilić, G. Pilarczyk, J.-H. Lee, A. Logeswaran, A. Borroni, M. Krufczik, F. Theda, N. Waltrich, F. Bestvater, G. Hildenbrand, C. Cremer and M. Blank, *Int. J. Mol. Sci.*, 2017, **18**, 2066.
590 A. Szczurek, U. Birk, H. Knecht, J. Dobrucki, S. Mai and C. Cremer, *Nucl. Austin Tex*, 2018, **9**, 182–189.
591 A. Szczurek, L. Klewes, J. Xing, A. Gourram, U. Birk, H. Knecht, J. W. Dobrucki, S. Mai and C. Cremer, *Nucleic Acids Res.*, 2017, **45**, e56.
592 A. Szczurek, J. Xing, U. J. Birk and C. Cremer, *Front. Genet.*, 2016, **7**, 114.
593 D. J. Wynne and H. Funabiki, *Mol. Biol. Cell*, 2016, **27**, 3395–3404.
594 B. Dong, L. M. Almassalha, Y. Stypula-Cyrus, B. E. Urban, J. E. Chandler, T.-Q. Nguyen, C. Sun, H. F. Zhang and V. Backman, *Proc. Natl. Acad. Sci. U. S. A.*, 2016, **113**, 9716–9721.
595 P. Cheung and P. Lau, *Mol. Endocrinol. Baltim. Md*, 2005, **19**, 563–573.
596 I. M. Adcock, P. Ford, K. Ito and P. J. Barnes, *Respir. Res.*, 2006, **7**, 21.
597 N. M. Al Aboud, B. Simpson and I. Jialal, in *StatPearls*, StatPearls Publishing, Treasure Island (FL), 2019.
598 S. J. Bultman, *Trends Endocrinol. Metab. TEM*, 2018, **29**, 529–531.
599 I. Lacal and R. Ventura, *Front. Mol. Neurosci.*, 2018, **11**, 292.
600 R. Margueron and D. Reinberg, *Nat. Rev. Genet.*, 2010, **11**, 285–296.
601 K. Ahmad and S. Henikoff, *Cell*, 2002, **111**, 281–284.
602 M. G. Goll and T. H. Bestor, *Genes Dev.*, 2002, **16**, 1739–1742.
603 G. Egger, G. Liang, A. Aparicio and P. A. Jones, *Nature*, 2004, **429**, 457–463.
604 A. Stein, T. E. Takasuka and C. K. Collings, *Nucleic Acids Res.*, 2010, **38**, 709–719.
605 H. A. Cole, F. Cui, J. Ocampo, T. L. Burke, T. Nikitina, V. Nagarajavel, N. Kotomura, V. B. Zhurkin and D. J. Clark, *Nucleic Acids Res.*, 2016, **44**, 573–581.
606 M. Fardi, S. Solali and M. Farshdousti Hagh, *Genes Dis.*, 2018, **5**, 304–311.
607 Z. Chen, S. Li, S. Subramaniam, J. Y.-J. Shyy and S. Chien, *Annu. Rev. Biomed. Eng.*, 2017, **19**, 195–219.
608 A. J. Bannister and T. Kouzarides, *Cell Res.*, 2011, **21**, 381–395.
609 Z. Shahid, B. Simpson and G. Singh, in *StatPearls*, StatPearls Publishing, Treasure Island (FL), 2019.

610 A. Barski, S. Cuddapah, K. Cui, T.-Y. Roh, D. E. Schones, Z. Wang, G. Wei, I. Chepelev and K. Zhao, *Cell*, 2007, **129**, 823–837.
611 E. J. Wagner and P. B. Carpenter, *Nat. Rev. Mol. Cell Biol.*, 2012, **13**, 115–126.
612 W. Yuan, M. Xu, C. Huang, N. Liu, S. Chen and B. Zhu, *J. Biol. Chem.*, 2011, **286**, 7983–7989.
613 M. Ransom, B. K. Dennehey and J. K. Tyler, *Cell*, 2010, **140**, 183–195.
614 J. A. Rosenfeld, Z. Wang, D. E. Schones, K. Zhao, R. DeSalle and M. Q. Zhang, *BMC Genomics*, 2009, **10**, 143.
615 G. Wei, L. Wei, J. Zhu, C. Zang, J. Hu-Li, Z. Yao, K. Cui, Y. Kanno, T.-Y. Roh, W. T. Watford, D. E. Schones, W. Peng, H. Sun, W. E. Paul, J. J. O'Shea and K. Zhao, *Immunity*, 2009, **30**, 155–167.
616 D. J. Steger, M. I. Lefterova, L. Ying, A. J. Stonestrom, M. Schupp, D. Zhuo, A. L. Vakoc, J.-E. Kim, J. Chen, M. A. Lazar, G. A. Blobel and C. R. Vakoc, *Mol. Cell. Biol.*, 2008, **28**, 2825–2839.
617 Y. Agata, E. Matsuda and A. Shimizu, *J. Biol. Chem.*, 1999, **274**, 16412–16422.
618 S. P. Sripathy, J. Stevens and D. C. Schultz, *Mol. Cell. Biol.*, 2006, **26**, 8623–8638.
619 F. Cammas, M. Oulad-Abdelghani, J.-L. Vonesch, Y. Huss-Garcia, P. Chambon and R. Losson, *J. Cell Sci.*, 2002, **115**, 3439–3448.
620 L. Fanti and S. Pimpinelli, *Curr. Opin. Genet. Dev.*, 2008, **18**, 169–174.
621 G. Lomberk, L. Wallrath and R. Urrutia, *Genome Biol.*, 2006, **7**, 228.
622 S. W. Harshman, N. L. Young, M. R. Parthun and M. A. Freitas, *Nucleic Acids Res.*, 2013, **41**, 9593–9609.
623 A. Shipra, K. Chetan and M. R. S. Rao, *Bioinforma. Oxf. Engl.*, 2006, **22**, 2940–2944.
624 D. Rossetto, A. W. Truman, S. J. Kron and J. Cote, *Clin. Cancer Res.*, 2010, **16**, 4543–4552.
625 T. Cremer, A. Kurz, R. Zirbel, S. Dietzel, B. Rinke, E. Schrock, M. R. Speicher, U. Mathieu, A. Jauch, P. Emmerich, H. Scherthan, T. Ried, C. Cremer and P. Lichter, *Role Chromosome Territ. Funct. Compart. Cell Nucl. Cold Spring Harb. Symp. Quant. Biol. LVIII 777-792*.
626 T. H. Rabbitts, *Nature*, 1994, **372**, 143–149.
627 M. N. Nikiforova, J. R. Stringer, R. Blough, M. Medvedovic, J. A. Fagin and Y. E. Nikiforov, *Science*, 2000, **290**, 138–141.
628 E. Lukášová, S. Kozubek, M. Kozubek, V. Kroha, A. Marečková, M. Skalníková, E. Bártová and J. Šlotová, *Radiat. Res.*, 1999, **151**, 375–384.
629 M. F. Lyon, *Nature*, 1961, **190**, 372–373.
630 S. M. Gartler and M. A. Goldman, *Dev. Genet.*, 1994, **15**, 504–514.
631 E. Heard, P. Clerc and P. Avner, *X-chromosome inactivation in mammals*, 1997, vol. 31.
632 C. L. Walker, C. B. Cargile, K. M. Floy, M. Delannoy and B. R. Migeon, *Proc. Natl. Acad. Sci. U. S. A.*, 1991, **88**, 6191–6195.
633 A. Bischoff, J. Albers, I. Kharboush, E. Stelzer, T. Cremer and C. Cremer, *Microsc. Res. Tech.*, 1993, **25**, 68–77.
634 R. M. Zirbel, U. R. Mathieu, A. Kurz, T. Cremer and P. Lichter, *Chromosome Res.*, 1993, **1**, 93–106.
635 R. Eils, S. Dietzel, E. Bertin, E. Schröck, M. R. Speicher, T. Ried, M. Robert-Nicoud, C. Cremer and T. Cremer, *J. Cell Biol.*, 1996, **135**, 1427–1440.
636 J. A. Croft, J. M. Bridger, S. Boyle, P. Perry, P. Teague and W. A. Bickmore, *J. Cell Biol.*, 1999, **145**, 1119–1131.
637 C. Cinti, L. Stuppia and N. M. Maraldi, *Am. J. Med. Genet.*, 2002, **107**, 115–118.
638 T. Cremer, G. Kreth, H. Koester, R. H. A. Fink, R. Heintzmann, M. Cremer, I. Solovei, D. Zink and C. Cremer, *Crit. Rev. Eukaryot. Gene Expr.*, 2000, **10**, 179–212.
639 K. A. Dyer, T. K. Canlfield and S. M. Gartler, *Cytogenet. Genome Res.*, 1989, **50**, 116–120.
640 S. A. Grigoryev, J. Bednar and C. L. Woodcock, *J. Biol. Chem.*, 1999, **274**, 5626–5636.
641 N. Gilbert, S. Boyle, H. Sutherland, J. d. Las Heras, J. Allan, T. Jenuwein and W. A. Bickmore, *EMBO J.*, 2003, **22**, 5540–5550.
642 A. H. F. M. Peters, J. E. Mermoud, D. O'carroll, M. Pagani, D. Schweizer, N. Brockdorff and T. Jenuwein, *Nat. Genet.*, 2002, **30**, 77–80.
643 S. A. Grigoryev and C. L. Woodcock, *J. Biol. Chem.*, 1998, **273**, 3082–3089.
644 J. D. Rowley, H. M. Golomb, J. Vardiman, S. Fukuhara, C. Dougherty and D. Potter, *Int. J. Cancer*, 1977, **20**, 869–872.
645 A. Zelent, F. Guidez, A. Melnick, S. Waxman and J. D. Licht, *Oncogene*, 2001, **20**, 7186–7203.
646 K.-S. Hsu and H.-Y. Kao, *Cell Biosci.*, 2018, **8**, 5.
647 A. P. Reddy, J. Y. Chen, T. Zacharewski, H. Gronemeyer, J. J. Voorhees and G. J. Fisher, *Biochem. J.*, 1992, **287 (Pt 3)**, 833–840.
648 A. Parrado, C. Chomienne and R. A. Padua, *Leuk. Lymphoma*, 2000, **39**, 271–282.
649 B. Cassinat and C. Chomienne, *Oncogene*, 2001, **20**, 7154–7160.
650 J. D. Chen and R. M. Evans, *Nature*, 1995, **377**, 454–457.
651 L. Alland, R. Muhle, H. Hou, J. Potes, L. Chin, N. Schreiber-Agus and R. A. DePinho, *Nature*, 1997, **387**, 49–55.
652 K. Noack, N. Mahendrarajah, D. Hennig, L. Schmidt, F. Grebien, D. Hildebrand, M. Christmann, B. Kaina, A. Sellmer, S. Mahboobi, K. Kubatzky, T. Heinzel and O. H. Krämer, *Arch. Toxicol.*, 2017, **91**, 2191–2208.
653 P. Kastner and S. Chan, *Oncogene*, 2001, **20**, 7178–7185.
654 P. Kastner, H. J. Lawrence, C. Waltzinger, N. B. Ghyselinck, P. Chambon and S. Chan, *Blood*, 2001, **97**, 1314–1320.
655 A. Baniahmad, X. Leng, T. P. Burris, S. Y. Tsai, M. J. Tsai and B. W. O'Malley, *Mol. Cell. Biol.*, 1995, **15**, 76–86.
656 M. Morimoto and C. F. Boerkoel, *Biology*, 2013, **2**, 976–1033.
657 V. Lallemand-Breitenbach and H. de The, *Cold Spring Harb. Perspect. Biol.*, 2010, **2**, a000661–a000661.
658 G.-B. Zhou, W.-L. Zhao, Z.-Y. Wang, S.-J. Chen and Z. Chen, *PLoS Med.*, 2005, **2**, e12.
659 H. Zhou, R. Miki, M. Eeva, F. M. Fike, D. Seligson, L. Yang, A. Yoshimura, M. A. Teitell, C. A. M. Jamieson and N. A. Cacalano, *Clin. Cancer Res.*, 2007, **13**, 2344–2353.
660 F. Mandelli, D. Diverio, G. Avvisati, A. Luciano, T. Barbui, C. Bernasconi, G. Broccia, R. Cerri, M. Falda, G. Fioritoni, F. Leoni, V. Liso, M. C. Petti, F. Rodeghiero, G. Saglio, M. L. Vegna, G. Visani, U. Jehn, R. Willemze, P. Muus, P. G. Pelicci, A. Biondi and F. Lo Coco, *Blood*, 1997, **90**, 1014–1021.
661 A. Eberharter and P. B. Becker, *EMBO Rep.*, 2002, **3**, 224–229.
662 C. K. Govind, D. Ginsburg and A. G. Hinnebusch, *Methods Mol. Biol. Clifton NJ*, 2012, **833**, 15–27.
663 C. Das and J. K. Tyler, *Biochim. Biophys. Acta*, 2013, **1819**, 332–342.
664 H. van Bakel, K. Tsui, M. Gebbia, S. Mnaimneh, T. R. Hughes and C. Nislow, *PLoS Genet.*, 2013, **9**, e1003479.
665 M. Falk, E. Lukasova, B. Gabrielova, V. Ondrej and S. Kozubek, *Biochim. Biophys. Acta*, 2007, **1773**, 1534–1545.
666 M. Falk, E. Lukásová, L. Štefančíková, L. Weiterova, A. Bačíková and S. Kozubek, *Book Proc. Am. Inst. Phys. AIP*.
667 J. Seo, S. C. Kim, H.-S. Lee, J. K. Kim, H. J. Shon, N. L. M. Salleh, K. V. Desai, J. H. Lee, E.-S. Kang, J. S. Kim and J. K. Choi, *Nucleic Acids Res.*, 2012, **40**, 5965–5974.
668 M. Costantini, O. Clay, F. Auletta and G. Bernardi, *Genome Res.*, 2006, **16**, 536–541.
669 I. Chiolo, A. Minoda, S. U. Colmenares, A. Polyzos, S. V. Costes and G. H. Karpen, *Cell*, 2011, **144**, 732–744.
670 B. Jakob, J. Splinter, S. Conrad, K.-O. Voss, D. Zink, M. Durante, M. Löbrich and G. Taucher-Scholz, *Nucleic Acids Res.*, 2011, **39**, 6489–6499.
671 A. A. Goodarzi and P. A. Jeggo, *Int. J. Mol. Sci.*, 2012, **13**, 11844–11860.
672 J. J. Roix, P. G. McQueen, P. J. Munson, L. A. Parada and T. Misteli, *Nat. Genet.*, 2003, **34**, 287–291.

673 T. Misteli, *Cold Spring Harb. Perspect. Biol.*, 2010, **2**, a000794.
674 M. Mateju, J. Stribrna, M. Zikan, Z. Kleibl, M. Janatova, S. Kormunda, J. Novotny, P. Soucek, L. Petruzelka and P. Pohlreich, *Neoplasma*, 2010, **57**, 280–285.
675 J. Yan, X.-P. Yang, Y.-S. Kim and A. M. Jetten, *Cancer Res.*, 2008, **68**, 4269–4276.
676 R. A. Greenberg, B. Sobhian, S. Pathania, S. B. Cantor, Y. Nakatani and D. M. Livingston, *Genes Dev.*, 2006, **20**, 34–46.
677 B. Sobhian, G. Shao, D. R. Lilli, A. C. Culhane, L. A. Moreau, B. Xia, D. M. Livingston and R. A. Greenberg, *Science*, 2007, **316**, 1198–1202.
678 Y. Hu, R. Scully, B. Sobhian, A. Xie, E. Shestakova and D. M. Livingston, *Genes Dev.*, 2011, **25**, 685–700.
679 L. Wei, L. Lan, Z. Hong, A. Yasui, C. Ishioka and N. Chiba, *Mol. Cell. Biol.*, 2008, **28**, 7380–7393.
680 T. Ouchi, *Cancer Biol. Ther.*, 2006, **5**, 470–475.
681 B. Xu, A. H. O'Donnell, S.-T. Kim and M. B. Kastan, *Cancer Res.*, 2002, **62**, 4588–4591.
682 D. Cortez, Y. Wang, J. Qin and S. J. Elledge, *Science*, 1999, **286**, 1162–1166.
683 S. Okada and T. Ouchi, *J. Biol. Chem.*, 2003, **278**, 2015–2020.
684 R. Scully, J. Chen, R. L. Ochs, K. Keegan, M. Hoekstra, J. Feunteun and D. M. Livingston, *Cell*, 1997, **90**, 425–435.
685 J. N. M. Glover, R. S. Williams and M. S. Lee, *Trends Biochem. Sci.*, 2004, **29**, 579–585.
686 M. Spies and A. Malkova, *Mechanisms of DNA Recombination and Genome Rearrangements.*, Elsevier Science & Technology, San Diego, 2018.
687 K. Bermudez-Hernandez, S. Keegan, D. R. Whelan, D. A. Reid, J. Zagelbaum, Y. Yin, S. Ma, E. Rothenberg and D. Fenyö, *Sci. Rep.*, 2017, **7**, 14882.
688 J. R. Chapman, A. J. Sossick, S. J. Boulton and S. P. Jackson, *J. Cell Sci.*, 2012, **125**, 3529–3534.
689 T. T. Paull, E. P. Rogakou, V. Yamazaki, C. U. Kirchgessner, M. Gellert and W. M. Bonner, *Curr. Biol.*, 2000, **10**, 886–895.
690 B. Xu, S.-T. Kim and M. B. Kastan, *Mol. Cell. Biol.*, 2001, **21**, 3445–3450.
691 R. A. Greenberg, *Chromosoma*, 2008, **117**, 305–317.
692 T. I. Orban and E. Olah, *J. Clin. Pathol. - Mol. Pathol.*, 2003, **56**, 191–197.
693 C. Y. Li, J. Y. Chu, J. K. Yu, X. Q. Huang, X. J. Liu, L. Shi, Y. C. Che and J. Y. Xie, *Cell Res.*, 2004, **14**, 473–479.
694 E. Scholzová, R. Malík, J. Ševčík and Z. Kleibl, *Cancer Lett.*, 2007, **246**, 12–23.
695 T. I. Orban and E. Olah, *Biochem. Biophys. Res. Commun.*, 2001, **280**, 32–38.
696 L. J. Huber, T. W. Yang, C. J. Sarkisian, S. R. Master, C.-X. Deng and L. A. Chodosh, *Mol. Cell. Biol.*, 2001, **21**, 4005–4015.
697 M. E. Moynahan, J. W. Chiu, B. H. Koller and M. Jasint, *Mol. Cell*, 1999, **4**, 511–518.
698 C. A. Pettigrew, J. D. French, J. M. Saunus, S. L. Edwards, A. V. Sauer, C. E. Smart, T. Lundström, C. Wiesner, A. B. Spurdle, J. A. Rothnagel and M. A. Brown, *Breast Cancer Res. Treat.*, 2010, **119**, 239–247.
699 Y. Nominé, M. V. Botuyan, Z. Bajzer, W. G. Owen, A. J. Caride, E. Wasielewski and G. Mer, *Biochemistry*, 2008, **47**, 9866–9879.
700 P. Pohlreich, J. Stříbrná, Z. Kleibl, M. Zikán, R. Kalbáčová, L. Petruželka and B. Konopásek, *Med. Princ. Pract.*, 2003, **12**, 23–29.
701 P. Pohlreich, M. Zikan, J. Stribrna, Z. Kleibl, M. Janatova, J. Kotlas, J. Zidovska, J. Novotny, L. Petruzelka, C. Szabo and B. Matous, *Breast Cancer Res.*, , DOI:10.1186/bcr1282.
702 P. Pohlreich, J. Stribrna, M. Zikan and J. Novotny, *19th Meet. Eur. Assoc. Cancer Res. ProgramProcceedings Bp. June 1-4 2006*, 2006, 260.
703 J. Lukas, C. Lukas and J. Bartek, *Nat. Cell Biol.*, 2011, **13**, 1161–1169.
704 K. A. Coleman and R. A. Greenberg, *J. Biol. Chem.*, 2011, **286**, 13669–13680.
705 A. A. Sartori, C. Lukas, J. Coates, M. Mistrik, S. Fu, J. Bartek, R. Baer, J. Lukas and S. P. Jackson, *Nature*, 2007, **450**, 509–514.
706 A. Bothmer, D. Robbiani, M. Di Virgilio, S. Bunting, I. Klein, N. Feldhahn, J. Barlow, H.-T. Chen, D. Bosque, E. Callen, A. Nussenzweig and M. Nussenzweig, *Mol. Cell*, 2011, **42**, 319–329.
707 L. Chen, C. J. Nievera, A. Y.-L. Lee and X. Wu, *J. Biol. Chem.*, 2008, **283**, 7713–7720.
708 S. F. Bunting, E. Callén, N. Wong, H.-T. Chen, F. Polato, A. Gunn, A. Bothmer, N. Feldhahn, O. Fernandez-Capetillo, L. Cao, X. Xu, C.-X. Deng, T. Finkel, M. Nussenzweig, J. M. Stark and A. Nussenzweig, *Cell*, 2010, **141**, 243–254.
709 H.-C. Wang, W.-C. Chou, S.-Y. Shieh and C.-Y. Shen, *Cancer Res.*, 2006, **66**, 1391–1400.
710 M. Jasin, *Oncogene*, 2002, **21**, 8981–8993.
711 S. M. Dever, S. E. Golding, E. Rosenberg, B. R. Adams, M. O. Idowu, J. M. Quillin, N. Valerie, B. Xu, L. F. Povirk and K. Valerie, *Aging*, 2011, **3**, 515–532.
712 P. A. Jeggo, V. Geuting and M. Löbrich, *Radiother. Oncol.*, 2011, **101**, 7–12.
713 K. Chock, J. M. S. Allison and W. M. Elshamy, *Oncogene*, 2010, **29**, 5274–5285.
714 R. D. Brandão, K. E. P. Van Roozendaal, D. Tserpelis, B. Caanen, E. G. García and M. J. Blok, *Breast Cancer Res. Treat.*, 2012, **131**, 723–725.
715 L. Zhang, L. Chen, R. Bacares, J. M. Ruggeri, J. Somar, Y. Kemel, Z. K. Stadler and K. Offit, *Breast Cancer Res. Treat.*, 2011, **130**, 1051–1056.
716 M. Thomassen, A. Blanco, M. Montagna, T. V. O. Hansen, I. S. Pedersen, S. Gutiérrez-Enríquez, M. Menéndez, L. Fachal, M. Santamariña, A. Y. Steffensen, L. Jønson, S. Agata, P. Whiley, S. Tognazzo, E. Tornero, U. B. Jensen, J. Balmaña, T. A. Kruse, D. E. Goldgar, C. Lázaro, O. Diez, A. B. Spurdle and A. Vega, *Breast Cancer Res. Treat.*, 2012, **132**, 1009–1023.
717 D. S. Chandler, R. K. Singh, L. C. Caldwell, J. L. Bitler and G. Lozano, *Cancer Res.*, 2006, **66**, 9502–9508.
718 M. J. Muñoz, M. S. P. Santangelo, M. P. Paronetto, M. de la Mata, F. Pelisch, S. Boireau, K. Glover-Cutter, C. Ben-Dov, M. Blaustein, J. J. Lozano, G. Bird, D. Bentley, E. Bertrand and A. R. Kornblihtt, *Cell*, 2009, **137**, 708–720.
719 G. T. Wolf, *Ear. Nose. Throat J.*, 2001, **80**, 897–901.
720 M. Raudenska, M. Sztalmachova, J. Gumulec, M. Fojtu, H. Polanska, J. Balvan, M. Feith, H. Binkova, Z. Horakova, R. Kostrica, R. Kizek and M. Masarik, *Tumor Biol.*, 2015, **36**, 9929–9939.
721 K. Salmina, A. Huna, M. Kalejs, D. Pjanova, H. Scherthan, M. S. Cragg and J. Erenpreisa, *Genes*, , DOI:10.3390/genes10020083.
722 J. Erenpreisa, K. Salmina, A. Huna, T. R. Jackson, A. Vazquez-Martin and M. S. Cragg, *Oncoscience*, 2015, **2**, 3–14.
723 J. Erenpreisa and M. S. Cragg, *Cancer Cell Int.*, 2013, **13**, 92.
724 G. Mosieniak and E. Sikora, *Curr. Pharm. Des.*, 2010, **16**, 734–740.
725 D. M. Sridharan, A. Asaithamby, S. M. Bailey, S. V. Costes, P. W. Doetsch, W. S. Dynan, A. Kronenberg, K. N. Rithidech, J. Saha, A. M. Snijders, E. Werner, C. Wiese, F. A. Cucinotta and J. M. Pluth, *Radiat. Res.*, 2015, **183**, 1–26.
726 D. T. Goodhead, *J. Radiat. Res. (Tokyo)*, 1999, **40**, 1–13.
727 S. V. Costes, A. Boissière, S. Ravani, R. Romano, B. Parvin and M. H. Barcellos-Hoff, *Radiat. Res.*, 2006, **165**, 505–515.
728 F. Antonelli, A. Campa, G. Esposito, P. Giardullo, M. Belli, V. Dini, S. Meschini, G. Simone, E. Sorrentino, S. Gerardi, G. A. P. Cirrone and M. A. Tabocchini, *Radiat. Res.*, 2015, **183**, 417–431.
729 J. C. Waters, *J. Cell Biol.*, 2009, **185**, 1135–1148.
730 E. Markova, S. Vasilyev and I. Belyaev, *Neoplasma*, 2015, **62**, 770–776.
731 J. M. Daley and P. Sung, *Mol. Cell. Biol.*, 2014, **34**, 1380–1388.
732 S. Pellegrino, J. Michelena, F. Teloni, R. Imhof and M. Altmeyer, *Cell Rep.*, 2017, **19**, 1819–1831.

733 A. J. Nakamura, V. A. Rao, Y. Pommier and W. M. Bonner, *Cell Cycle*, 2010, **9**, 389–397.
734 N. I. Nakajima, H. Brunton, R. Watanabe, A. Shrikhande, R. Hirayama, N. Matsufuji, A. Fujimori, T. Murakami, R. Okayasu, P. Jeggo and A. Shibata, *PLoS ONE*, , DOI:10.1371/journal.pone.0070107.
735 D. Deckbar, P. A. Jeggo and M. Löbrich, *Crit. Rev. Biochem. Mol. Biol.*, 2011, **46**, 271–283.
736 Y. Lorat, S. Schanz, N. Schuler, G. Wennemuth, C. Rübe and C. E. Rübe, *PLoS ONE*, , DOI:10.1371/journal.pone.0038165.
737 N. Shikazono, M. Noguchi, K. Fujii, A. Urushibara and A. Yokoya, *J. Radiat. Res. (Tokyo)*, 2009, **50**, 27–36.
738 S. K. Singh, M. Wang, C. Staudt and G. Iliakis, *Nucleic Acids Res.*, 2011, **39**, 8416–8429.
739 W. Friedland, P. Jacob, H. G. Paretzke and T. Stork, *Radiat. Res.*, 1998, **150**, 170–182.
740 W. Friedland, P. Jacob, H. G. Paretzke, A. Ottolenghi, F. Ballarini and M. Liotta, *Radiat. Prot. Dosimetry*, 2006, **122**, 116–120.
741 B. Boudaïffa, P. Cloutier, D. Hunting, M. A. Huels and L. Sanche, *Science*, 2000, **287**, 1658–1660.
742 A. Chatterjee and W. R. Holley, *Adv. Radiat. Biol.*, 1993, **17**, 181–226.
743 R. M. Anderson, D. G. Papworth, D. L. Stevens, N. D. Sumption and D. T. Goodhead, *Cytogenet. Genome Res.*, 2006, **112**, 35–44.
744 M. Durante, D. Pignalosa, J. A. Jansen, X. F. Walboomers and S. Ritter, *Radiat. Res.*, 2010, **174**, 20–26.
745 V. Conte, P. Colautti, B. Grosswendt, D. Moro and L. De Nardo, *New J. Phys.*, , DOI:10.1088/1367-2630/14/9/093010.
746 G. Kraft, M. Krämer and M. Scholz, *Radiat. Environ. Biophys.*, 1992, **31**, 161–180.
747 T. Neumaier, J. Swenson, C. Pham, A. Polyzos, A. T. Lo, P. Yang, J. Dyball, A. Asaithamby, D. J. Chen, M. J. Bissell, S. Thalhammer and S. V. Costes, *Proc. Natl. Acad. Sci. U. S. A.*, 2012, **109**, 443–448.
748 M. Falk, M. Hausmann, E. Lukášová, A. Biswas, G. Hildenbrand, M. Davídková, E. Krasavin, Z. Kleibl, I. Falková, L. Ježková, L. Štefančíková, J. Ševčík, M. Hofer, A. Bačíková, P. Matula, A. Boreyko, J. Vachelová, A. Michaelidisová and S. Kozubek, *Crit. Rev. Eukaryot. Gene Expr.*, 2014, **24**, 225–247.
749 M. Winey, J. B. Meehl, E. T. O'Toole and T. H. Giddings Jr., *Mol. Biol. Cell*, 2014, **25**, 319–323.
750 J. P. Eberle, A. Rapp, M. Krufczik, M. Eryilmaz, M. Gunkel, H. Erfle and M. Hausmann, *Super-resolution microscopy techniques and their potential for applications in radiation biophysics*, Humana Press Inc., 2017, vol. 1663.
751 M. Bach, C. Savini, M. Krufczik, C. Cremer, F. Rösl and M. Hausmann, *Int. J. Mol. Sci.*, , DOI:10.3390/ijms18081726.
752 J. Reindl, G. A. Drexler, S. Girst, C. Greubel, C. Siebenwirth, S. E. Drexler, G. Dollinger and A. A. Friedl, *Phys. Biol.*, , DOI:10.1088/1478-3975/12/6/066005.
753 A. Schipler and G. Iliakis, *Nucleic Acids Res.*, 2013, **41**, 7589–7605.
754 R. Dueva and G. Iliakis, *Transl. Cancer Res.*, 2013, **2**, 163–177.
755 G. Iliakis, *Sustain. Risk Manag.*, 2018, 149–158.
756 M. Eryilmaz, E. Schmitt, M. Krufczik, F. Theda, J.-H. Lee, C. Cremer, F. Bestvater, W. Schaufler, M. Hausmann and G. Hildenbrand, *Cancers*, , DOI:10.3390/cancers10010025.
757 J. Reindl, S. Girst, D. W. M. Walsh, C. Greubel, B. Schwarz, C. Siebenwirth, G. A. Drexler, A. A. Friedl and G. Dollinger, *Sci. Rep.*, 2017, **7**, 40616.
758 A. Hofmann, M. Krufczik, D. W. Heermann and M. Hausmann, *Int. J. Mol. Sci.*, , DOI:10.3390/ijms19082263.
759 U. Eberlein, M. Peper, M. Fernández, M. Lassmann and H. Scherthan, *PLoS ONE*, , DOI:10.1371/journal.pone.0123174.
760 P. Lemmer, M. Gunkel, Y. Weiland, P. Müller, D. Baddeley, R. Kaufmann, A. Urich, H. Eipel, R. Amberger, M. Hausmann and C. Cremer, *J. Microsc.*, 2009, **235**, 163–171.
761 C. Cremer, R. Kaufmann, M. Gunkel, S. Pres, Y. Weiland, P. Müller, T. Ruckelshausen, P. Lemmer, F. Geiger, S. Degenhard, C. Wege, N. A. W. Lemmermann, R. Holtappels, H. Strickfaden and M. Hausmann, *Biotechnol. J.*, 2011, **6**, 1037–1051.
762 A. Kakarougkas, A. Ismail, K. Klement, A. A. Goodarzi, S. Conrad, R. Freire, A. Shibata, M. Lobrich and P. A. Jeggo, *Nucleic Acids Res.*, 2013, **41**, 9719–9731.
763 F. Ochs, K. Somyajit, M. Altmeyer, M.-B. Rask, J. Lukas and C. Lukas, *Nat. Struct. Mol. Biol.*, 2016, **23**, 714–721.
764 M. Scholz, W. Kraft-Weyrather, S. Ritter and G. Kraft, *Int. J. Radiat. Biol.*, 1994, **66**, 59–75.
765 S. Sora, N. Hamada, T. Hara, T. Funayama, T. Sakashita, Y. Yokota, T. Nakano and Y. Kobayashi, *Biol Sci Space*, 2008, **22**, 54–58.
766 K. Tsuboi, T. Moritake, Y. Tsuchida, K. Tokuuye, A. Matsumura and K. Ando, *J. Radiat. Res. (Tokyo)*, 2007, **48**, 317–325.
767 J. R. Williams, D. S. Gridley and J. M. Slater, *Radiobiol. Radioresistant Glioblastoma*, 2011, 3–22.
768 P. Lobachevsky, T. Leong, P. Daly, J. Smith, N. Best, J. Tomaszewski, E. R. Thompson, N. Li, I. G. Campbell, R. F. Martin and O. A. Martin, *Cancer Lett.*, 2016, **383**, 212–219.
769 S. J. DiBiase, Z.-C. Zeng, R. Chen, T. Hyslop, W. J. Curran Jr. and G. Iliakis, *Cancer Res.*, 2000, **60**, 1245–1253.
770 J. Schwarz-Finsterle, H. Scherthan, A. Huna, P. González, P. Mueller, E. Schmitt, J. Erenpreisa and M. Hausmann, *Mutat. Res. - Genet. Toxicol. Environ. Mutagen.*, 2013, **756**, 56–65.
771 A. Asaithamby and D. J. Chen, *Mutat. Res. - Fundam. Mol. Mech. Mutagen.*, 2011, **711**, 87–99.
772 D. Tsao, P. Kalogerinis, I. Tabrizi, M. Dingfelder, R. D. Stewart and A. G. Georgakilas, *Radiat. Res.*, 2007, **168**, 87–97.
773 S. C. Short, C. Martindale, S. Bourne, G. Brand, M. Woodcock and P. Johnston, *Neuro-Oncol.*, 2007, **9**, 404–411.
774 L. Štefančíková, E. Porcel, P. Eustache, S. Li, D. Salado, S. Marco, J.-L. Guerquin-Kern, M. Réfrégiers, O. Tillement, F. Lux and S. Lacombe, *Cancer Nanotechnol.*, , DOI:10.1186/s12645-014-0006-6.
775 C. Duve, *Eur. J. Biochem.*, 1983, **137**, 391–397.
776 R. Wattiaux, S. W.-D. Coninck, M. Jadot, I. Hamer, V. Bielande and V. Beauloye, in *Endocytosis*, ed. P. J. Courtoy, Springer Berlin Heidelberg, Berlin, Heidelberg, 1992, pp. 433–437.
777 B. Yameen, W. I. Choi, C. Vilos, A. Swami, J. Shi and O. C. Farokhzad, *J. Control. Release Off. J. Control. Release Soc.*, 2014, **190**, 485–499.
778 G. Hildenbrand, P. Metzler, G. Pilarczyk, V. Bobu, W. Kriz, H. Hosser, J. Fleckenstein, M. Krufczik, F. Bestvater, F. Wenz and M. Hausmann, *PLoS ONE*, , DOI:10.1371/journal.pone.0190183.
779 R. Zhang, M. J. Piao, K. C. Kim, A. D. Kim, J.-Y. Choi, J. Choi and J. W. Hyun, *Int. J. Biochem. Cell Biol.*, 2012, **44**, 224–232.
780 E. Szegezdi, S. E. Logue, A. M. Gorman and A. Samali, *EMBO Rep.*, 2006, **7**, 880–885.
781 H. Sun, J. Jia, C. Jiang and S. Zhai, *Int. J. Mol. Sci.*, 2018, **19**, 754.
782 F. Zhang, X. Zhu, J. Gong, Y. Sun, D. Chen, J. Wang, Y. Wang, M. Guo and W. Li, *Nanomed.*, 2016, **11**, 1993–2006.
783 M. Hofer, M. Falk, D. Komůrková, I. Falková, A. Bačíková, B. Klejdus, E. Pagáčová, L. Štefančíková, L. Weiterová, K. J. Angelis, S. Kozubek, L. Dušek and S. Galbavý, *J. Med. Chem.*, 2016, **59**, 3003–3017.
784 M. A. Zanta, P. Belguise-Valladier and J. P. Behr, *Proc. Natl. Acad. Sci. U. S. A.*, 1999, **96**, 91–96.
785 Y. Xu, K. Parmar, F. Du, B. D. Price and Y. Sun, *Int. J. Biochem. Mol. Biol.*, 2011, **2**, 295–302.
786 E. Gloc, M. Warszawski, W. Młynarski, M. Stolarska, G. Hoser, T. Skorski and J. Błasiak, *Acta Biochim. Pol.*, 2002, **49**, 121–128.
787 R. A. Baldock, M. Day, O. J. Wilkinson, R. Cloney, P. A. Jeggo, A. W. Oliver, F. Z. Watts and L. H. Pearl, *Cell Rep.*, 2015, **13**, 2081–2089.
788 H. Yajima, H. Fujisawa, N. I. Nakajima, H. Hirakawa, P. A. Jeggo, R. Okayasu and A. Fujimori, *DNA Repair*, 2013, **12**, 936–946.

789 J. M. Murray, T. Stiff and P. A. Jeggo, *Biochem. Soc. Trans.*, 2012, **40**, 173–178.
790 A. A. Goodarzi, T. Kurka and P. A. Jeggo, *Nat. Struct. Mol. Biol.*, 2011, **18**, 831–839.
791 A. Beucher, J. Birraux, L. Tchouandong, O. Barton, A. Shibata, S. Conrad, A. A. Goodarzi, A. Krempler, P. A. Jeggo and M. Löbrich, *EMBO J.*, 2009, **28**, 3413–3427.

APPENDIX

3.1 Awards from the scientific community

- 2019: M. Falk – **Editorial Board of Scientific Reports (Nature)**
- 2018: 1st Prize for poster presentation given by The Society for Low Temperature Biology (SLTB) at the SLTB Meeting, 6th September 2018, Prague, Czech Republic (Contribution: Falk M. et al.. Complex description of cryopreserved cell nuclei defects by immunofluorescence microscopy: DNA lesions, chromatin decondensation, nuclear membrane ruptures).
- 2015: Young Investigators Travel Award, 15th International Congress of Radiation Research (ICRR 2015), Kyoto, Japan.
- **2009: The Premium of Otto Wichterle for outstanding young scientists, devoted by the Academy of Sciences of CR.**
- 2008: Second place (not administrated) in the competition for the New England Biolabs Poster Prize, Biochemical Society Annual Symposium – DNA Damage: From Causes to Cures, December 15-17, 2008, Cambridge, Great Britain, for presented results: Direct visualization of DSB induction and repair in gene dense (RIDGE) and gene poor (anti-RIDGE) chromatin domains.
- 2008: The Prize of Deutsche Gesellchaft für DNA-Reparaturforschung (DGDR), 10th Biennial Meeting of the DGDR, Berlin, Germany: Devoted for results obtained at the field of DNA repair: 'Different sensitivity and response of functionally distinct chromatin domains to DSB induction'
- 2004: The Prize of Institute of Biophysics of ASCR for excellent young scientists.

3.2 ACHIEVED RESULTS IN THE CZECH MEDIA

- **Radio Broadcast** – The Czech Radio (Český rozhlas / Radiožurnál), interview with Martin Falk + Irena Kratochvílová on the topic "Freezing of Tumor Cells Could Improve Cancer Therapy", Author: Vojtěch Koval, Prague 18:36 28th January 2018; http://prehravac.rozhlas.cz/audio/3974981; iRadio (text comments): short link: http://irozhl.as/347 ; full link: https://www.irozhlas.cz/zivotni-styl/zdravi/rakovina-bunky-zmrazovani-vedci_1801281836_pj
- **Radio Broadcast** – The Czech Radio 2 (Český rozhlas 2) – Coffee at 4 o'clock (Káva o čtvrté) on the topic "Cell Aging – Is There an Elixir of Youth?" Interview (40 min) with Martin Falk (conductor: Tomáš Voženílek). Archive record (mp3): https://dvojka.rozhlas.cz/starnuti-bunek-aneb-existuje-elixir-mladi-7624981

3.3 LECTURES AND CONFERENCE CONTRIBUTIONS (where the results of the theses were presented)

3.3.1 Invited Lectures

1. Falk M., Lukášová E., Kozubek M. and Kozubek S. Model of chromosome structure in interphase nuclei of human lymphocytes. *Conference on New Models and Nuclear Methods in Biophysics and Biochemistry*, 24-25 January 2002, Joint Institute for Nuclear Research, Russian Academy of Sciences, **Dubna, Russia** (in English),

2. Falk M. Application of confocal microscopy in research of higher-order chromatin structure dynamics. *Workshop on Confocal microscopy*, 15 March 2005, **Brno, Czech Republic**.

3. Falk M., Lukášová E., Gabrielová B., Ondřej V., Kozubek M., Kroupová I. 2006. Nuclear organization and dynamics of the DSB-repair. *COST P9 Action 'Radiation Damage to Biomolecules', Working Group 5 Meeting RISC-RAD Work Package 5 Meeting, Workshop on Challenges for Modelling of Radiation Damage in Biological Systems*. 17 - 19 October 2006, **Physik-Zentrum Bad Honnef, Germany**

4. Pelicci P.G. (results of Falk M., Lukášová E. and Kozubek S. included): PML-RAR – A Model to Cure Leukemia. Salk Institute, Nature and Foundation *IPSEN Conference on Biological Complexity: Diseases of Transcription*. January 11-14, 2007, Salk Institute, **La Jolla, CA, USA**.

5. Falk M., Lukasova E., Kozubek S.: The role of higher-order chromatin structure and nuclear topography in DSB induction, repair and chromatin translocation. *ESF-EMBO Symposium: Spatio-Temporal Radiation Biology: Transdisciplinary Advances for Biomedical Applications*, 16-21 May 2009, Hotel Eden Roc, **Sant Feliu de Guixols (Costa Brava), Spain**

6. Falk M., Lukasova E., Bacikova A., Kozubek S.: The role of chromatin structure in DNA damage and its monitoring. ERR09 – Prague, 37th Annual Meeting of the European Radiation Research Society, 26-29th August 2009, **Prague, Czech Republic**.

7. Falk M., Lukasova E., Kozubek S., Bacikova A.: Induction and repair of DNA double-strand breaks in the context of higher-order chromatin structure. *7th International Conference on Radiation Damage in Biomolecular Systems (RADAM 2010)*, 30 June – 4 July 2010, **Madrid, Spain**.

8. Falk M., Lukášová E., Kozubek S., Štefančíková L. Higher-order chromatin structure in DNA double-strand break induction, repair and formation of chromosomal translocations. Brunel University (Invited by Dr. Rhona Anderson), June 29 - July 1, 2011, **London, Great Britain**.

9. Falk M., Lukášová E., Kozubek S., Štefančíková L. Higher-order chromatin structure in DNA double-strand break induction, repair and formation of chromosomal translocations. *The ARR & UKEMS Joint Annual Meeting*, June 29 - July 1, 2011, Nottingham University, Jubilee Campus, **Nottingham, Great Britain**.

10. Falk M., Lukášová E., Kozubek S., Štefančíková L. Function of chromatin structure and dynamics in DNA damage, repair and misrepair. *Sixth International Summer Student School on Nuclear Physics Methods and Accelerators in Biology and Medicine*, 2 - 12th July 2011, **Dubna, Russia**.

11. Falk M., Vojtíšková M., Lukáš Z., Falková I., Štefančíková L., Kozubek S. Current detection possibilities of unstable alleles in the myotonic dystrophy and Huntington's disease loci. *EPS Montreal Occupational Safety and Health Forum*, 15th – 16th August 2011, **Montreal, Canada**.

12. Falk M., Lukášová E., Kozubek S., Štefančíková L., Weiterová L. Induction, repair and misrepair of DNA double-strand breaks (DSBs) in the context of higher-order chromatin structure. *The 14th International Congress of Radiation Research*, 28.08 - 01.09.2011, **Warsaw, Poland**.

13. Falk M., Lukasova E., Kozubek S., Stefancikova L., Weiterova L. Spatio-Temporal Aspects of DNA Double-Strand Break Repair and Formation of Chromosomal Translocations. *The 1st Nano-IBCT Conference (in the framework of the COST Action MP1002 (Nano-scale Insights into Ion Beam Cancer Therapy)*, October 2nd to October 6th, 2011, **Caen, France**.

14. Falk M., Falková I., Ježková L., Davídková M., Bačíková A., Lukášová E., Štefančíková L., Vachelová J., Michaelidisová A., Kozubek S. γH2AX/53BP1 foci formation and DSB repair in cells irradiated with γ-rays and protons of different energy – influence of higher-order chromatin structure. *Quantum Scattering Codes and Monte Carlo Simulations to Model Dynamical Processes in Biosystems, Nano-IBCT Workshop*, 7. – 9. November 2012, **Madrid, Spain**.

15. Falková I., Ježková L., Baranová E., Štefančíková L., Lukášová E., Kozubek S., Boreyko A., Krasavin E., and Falk M. γH2AX/53BP1 foci formation and DSB repair in cycling cells and differentiated cells irradiated with γ-rays. *Quantum Scattering Codes and Monte Carlo Simulations to Model Dynamical Processes in Biosystems, Nano-IBCT Workshop*, 7. – 9. November 2012, **Madrid, Spain**.

16. Falk M. et al. Repair of DNA double strand breaks in the context of chromatin and nuclear structure. 15th. November, 2012, Palacky Univerzity, **Olomouc, Czech Republic**.

17. Lacombe S., Porcel E., Le Sech C., Tillement O., Mowat P., Usami N., Kobayashi K., Stefancikova L., Falk M., Kozubek S., Schlatholter T. Hadrontherapy: nanoparticles in action. *Radiation Damage in Biomolecular Systems: Nanoscale Insights into Ion-Beam Cancer Therapy, 2nd NANO-IBCT Conference 2013*, 20-24 May 2013, Gdansk University of Technology, **Sopot, Poland**.

18. Falk M., Falková I., Davídková M., L. Ježková L., Bačíková A., Štefančíková L., Vachelová J., Michaelidesová A., Kozubek S. Influences of radiation quality and higher-order chromatin structure on DSB induction and repair – comparison of gamma and proton irradiation. R*adiation Damage in Biomolecular Systems: Nanoscale Insights into Ion-Beam Cancer Therapy, 2nd NANO-IBCT Conference 2013*, 20-24 May 2013, Gdansk University of Technology, **Sopot, Poland**.

19. Falk M. et al. Heterochromatin – Dr Jekyll and Mr Hyde of the DNA Damage Repair. *3rd World Congress on Molecular Biology*, June 14-16, 2013, **Suzhou, China**.

20. Falk M. From genomics to spatio-temporal organization of cellular processes: What can confocal microscopy tell us about the mechanism of DNA repair and formation of chromosomal translocations? *Genomics 2013*, November 12-14, 2013, DoubleTree by Hilton Hotel Chicago-North Shore, **Chicago, IL, USA**.

21. Štefančíková L., Porcel E., Eustache P., Li S., Salado-Leza D., Réfrégier M., Kozubek S., Falk M. and Lacombe S. Nanoparticle cellular localization, uptake and effect on DNA damage response upon irradiation. Nano-IBCT meeting, 8th November 2013, **Belfast, Ireland.**

22. Falk M. Indukce chromosomálních aberací ionizujícím zářením různých kvalit. XXIII. konference rehabilitační, fyzikální a balneo medicíny, 7. – 8.2.2014, **Jáchymov, Czech Republic**

23. Falk M. Epigenetics and higher-order chromatin structure in regulation of fundamental nuclear processes including DNA repair (Invited Lectute). International Workshop on Nuclear Architecture. Istitutio Superiore di Sanitá (Italian NIH, Prof. Alessandro Giuliani), April 22 – 28, 2014, **Roma, Italy**

24. Lukášová E., Kořistek Z., Klabusay M., Ondřej V., Grigoryev S., Bačíková A., Řezáčová M., Vávrová J., Kohútová V., (presented by) Falk M., Kozubek S. DNA damage and repair in the context of chromatin structure and function - the influence of cell differentiation and quality of ionizing radiation. *13th International Workshop on Radiation Damage to DNA*, June 14-18, 2014, Massachusetts Institute of Technology (M.I.T.), **Cambridge, MA, USA**.

25. Falk M., Ježková L., Falková I., Lukášová E., Bačíková A., Davídková M., Zadneprianetc M., Pagáčová E., Vachelová J., Michaelidesová M., Boreyko A., Krasavin E., Kozubek S. CHARACTERISTICS OF IONIZING RADIATION, CHROMATIN STRUCTURE, AND DNA DOUBLE STRAND BREAK (MIS)REPAIR. 3rd International Conference 'Radiation damage in Biomolecular Systems: Nanoscale insights into Ion Beam Cancer Therapy', Nano-IBCT 2014 Conference, 27th – 31th October 2014, **Boppard am Rhein, Germany.**

26. Falk M. et al. New trends in radiotherapy from a biologist's point of view – from photons to accelerated ions and combined radio-sensitizing therapy, current and future possibilities of tumor cell radio-sensitization. XXIV. Conference of rehabilitation and physical- and balneo-medicine, February 6 – 7, 2015, **Jáchymov, Czech Rep**.

27. Falk M. Higher-order chromatin structure in induction and repair of DNA double strand breaks upon the action of ionizing radiation of different quality. Functional Organization of the Cell Nucleus Symposium. October 19, 2015, **Prague, Czech Rep**.

28. Falk M. 'Ionizing radiation – a double-edged sword in biology and medicine' (Ionizující záření – dvousečný meč v biologii a medicíně), 60th Student Conference (60. Studentská vědecká konference). 25th May, 2016, Masaryk University, Medical Faculty, **Brno, Czech Republic. (Plenary Lecture, invited)**

29. Falk M., Falková I., Ježková L., Bačíková A., Pagáčová E., Lukášová E., Štefančíková L., Davídková M., Boreyko A., Krasavin E., Kozubek S. Účinky různých druhů ionizujícího záření na buňku a možnosti jejich cílené modifikace. Conference on '30 let od havárie Jaderné elektrárny v Černobylu', 6th May 2016, **Prague, Czech Republic. (Invited lecture)**

30. Štefančíková L., Lacombe S., Salado D., Porcel E., Pagáčová E., Tillement O., Lux F., Depeš D., Falková I., Bačíková A., Kozubek S., and Falk M (presenting author). The mechanism of metal nanoparticle-mediated radiosensitization of tumor cells may be independent of DNA damage amplification and DNA repair inhibition. 7th World Nano Conference, June 20-21, 2016, **Cape Town, South Africa. (Falk M presenting author, Invited)**

31. Falk M. Towards a complex view on DNA damage and repair – epigenetic and spatio-temporal aspects. 2nd International Conference on Systems and Synthetic Biology, August 18-20, 2016 **London, UK. (Plenary Lecture, invited)**

32. Falk M. DNA Repair in Head and Neck Cancers and their Radiosensitivity. 6th International Conference on Genomics & Pharmacogenomics September 12-14, 2016 **Berlin, Germany. (Invited)**

33. Falk M. Chromatin structure and chromosomal rearrangements in CD34+ cells and lymphocytes from Myelodysplastic syndromes (MDS) patients. 6th International Conference on Genomics & Pharmacogenomics September 12-14, 2016, **Berlin, Germany. (Keynote lecture)**

34. Svobodova M., Gumulec J., Raudenska M., Polanská H., Balvan J., Fojtu M., Binkova H., Horakova H., Kostrica R., Babula P., Falk M., Falková I., Kopečná O., Bačíková A., and Masarik M. Study and characterization of primary tumour cell lines of head and neck carcinoma and their malignant potential. Conference on Cell Biology and Radiobiology – Satellite Symposium of the '6th International Conference on Genomics and Pharmacogenomics' held in Berlin, 9th-10th September 2016, **Brno, Czech Republic. (New & Notable, Invited)**

35. Horáková Z., Depeš D., Masařík M., Falk M., Falková I., Kopečná O., Bačíková A., Kozubek S., Binková H., Svobodova M., Gumulec J., Raudenska M., Polanská H, Balvan J., Fojtu M., Kostrica R., Babula P., and Masarik M. A step towards personalized therapy in head & neck cancers: How different cell types isolated from H & N tumors respond to irradiation? Conference on Cell Biology and Radiobiology – Satellite Symposium of the '6th International Conference on Genomics and Pharmacogenomics' held in Berlin, 9th-10th September 2016, **Brno, Czech Republic. (Invited)**

36. Michaelidesová A., Vachelová J, Konířová J., Havránek V., Štursa J, Zach V., Davídková M, Falková I., Falk M. Cell response of normal human fibroblasts to irradiation by protons and alpha particles. Conference on Cell Biology and Radiobiology – Satellite Symposium of the '6th International Conference on Genomics and Pharmacogenomics' held in Berlin, 9th-10th September 2016, **Brno, Czech Republic. (Invited)**

37. Falk M. The biological mechanism of metal nanoparticle-mediated radiosensitization. International Conference 'Dynamics of Systems on the Nanoscale' (DySoN 2016), 3rd -7th October, **Bad Ems, Germany (invited)**.

38. Falk M. Detection of DSB repair foci as a potent tool in biodosimetry and cancer research. Future Forces Forum, Medical Workshop, October 20, 2016, **Prague, Czech Republic** (invited).

39. Falk M et al. Tumor cell radiosensitization-ion beams and metal nanoparticles. 3rd International Conference on Systems and Synthetic Biology, July 20-21, 2017, **Munich, Germany**

40. Falk M et al. Metal nanoparticles in tumor cell radiosensitization. INTERNATIONAL CONFERENCE ON FUNCTIONAL NANOMATERIALS AND NANODEVICES, 24-27 September 2017, **Budapest, Hungary**

41. Falk M. Sensitive monitoring of DNA damage and repair in biodosimetry and cancer research. The Research Institute of Nuclear Engineering, University of Fukui, 15-23 March 2017, **Tsuruga, Japan**.

42. Falkova I. DNA Repair in Head & Neck Cancers and their Radiosensitivity. The Research Institute of Nuclear Engineering, University of Fukui, 15-23 March 2017, **Tsuruga, Japan**.

43. Falk M. et al., Confocal Microscopy in research on DNA damage and repair: implications on cancer, Advanced Techniques Days - New possibilities in high-speed spinning disk confocal microscopy; 9. 01. 2017, Charles University, Faculty of Science**, Prague, Czech Republic**, Invited speaker.

44. Falk M. Renaissance of Radiobiology in the New Millennium. 2-h lecture for National Radiation Protection Institute (SURO) and Nuclear Physics Institute of the Czech Academy of Sciences, 12th April 2017, **Prague, Czech Republic**.

45. Falk M. Spatio-temporal aspects of DNA damage and repair upon action of ionizing radiations of different types (**60 min Educational Lecture**). World Congress on Medical Physics & Biomedical Engineering. June 3-8, 2018, **Prague, Czech Republic**

46. DNA damage and repair in normal and tumor cells upon cell exposure to ionizing radiation of different quality. BIT's 8th Annual World Congress of Molecular & Cell Biology-2018, October 16-18, 2018, **Fukuoka, Japan.**

47. Falk M. Multiple mechanisms of metal nanoparticle-mediated radiosensitization of tumor cells? NANOSCIENCE MEET 2018: Annual conference on Nanoscience, Nanotechnology and Advanced materials. November 26-28, 2018, **Bali, Indonesia. Invited** lecture.

48. Hausmann M., Lee J.-H., Maus E., Brieger E., Muhtadi R., Wagner E., Bobkova E., Bestvater F., Schumann S., Falkova I., Falk M., Pilarczyk G., Hildenbrand G., Scherthan H. A Pointillist View on Particle Tracks and DNA-Repair in 3D-Conserved Cell Nuclei by means of Super-Resolution Localization Microscopy. 1st International Collaboration Meeting, 20-22 May 2019, **GSI Darmstadt, Germany**.

49. Pagáčová E et al. (Falk M. presenting and corresponding author). The promises and contradictions of nanoparticle-mediated tumor cell radiosensitization. Chromatin Architecture in Carcinogenesis and (Particle Enhanced) Radiation Treatment. September 21st 2019, **KIP Heidelberg, University of Heidelberg, Heidelberg, Germany**.

50. Falková I. Relevance of DNA double strand break repair in head and neck tumor cell radioresistance. Chromatin Architecture in Carcinogenesis and (Particle Enhanced) Radiation Treatment. September 21st 2019, **KIP Heidelberg, University of Heidelberg, Heidelberg, Germany**.

3.3.2 Other Lectures – International conferences

>150 lectures

Falk M., Gaillyová R. and Vojtíšková M. Use of New Modified PCR-based Methods for Rapid Differential Diagnostics of Myotonic Dystrophy. 10th International Congress of Human Genetics, Vienna, **Austria**, May 15-19, 2001

Falk M., Lukášová E., Kozubek S., Kozubek M. Topography of genetic elements of X-chromosome relative to the cell nucleus and to the chromosome X territory determined for human lymphocytes. 2nd Elmau Conference on Nuclear Organization, Gene Regulation and Nuclear Structure, Schloss Elmau, **Germany** (in English), October 6-9, 2002.

Vojtíšková M., Froster U., Enzmann G., Falk M., Šilhánová E. Determination of CTG repeats: Unstable alleles in Myotonic Dystrophy locus. 13th Annual Meeting of German Society of Human Genetics, Leipzig, **Germany**, September 29th – October 2nd, 2002.

Španová A., Rittich B., Falk M. Degradation of plasmid and high-molecular weight DNAs by lanthanide ions. 22nd International Symposium on the Separation of Proteins, Peptides and Polynucleotides. Heidelberg, **Germany**: Dechema, 2002.

Rittich B., Španová A., Falk M., Beneš M., Hrubý M. Cleavage of double stranded plasmid DNA by lanthanide complexes. In 3rd International Symposium on Separations in BioSciences SBS 2003, 100 Years of Chromatography. Russian Academy of Sciences, Moscow, **Russia**, 2003.

Falk M., Vojtíšková M., Froster U. Methodological possibilities for the determination of the number of CTG/CAG repeats in triplet repeat units of the human genome. International Conference on Applied Genomics, 9th ESACP/ 16th ISDQP Meeting, Amsterdam, **The Netherlands**, October 1-4, 2003.

Falk M., Lukasova E., Kozubek S., Pellici G.I., Faretta M., Kozubek M., Rocchi M. Changes in gene expression induced by PML/RARa fusion protein correlate with the degree of chromatin compaction. International Conference on Applied Genomics, 9th ESACP/ 16th ISDQP Meeting, Amsterdam, **The Netherlands**, October 1-4, 2003.

Kozubek S., Bartova E., Lukasova E., Kozubek M., Amrichova J., Taslerova R., Falk M., Ondrej V. Large-scale organization of human genome and chromosomal territories in the nucleus of normal and cancer cells and its functional implications. International Conference on Applied Genomics, 9th ESACP/ 16th ISDQP Meeting, Amsterdam, **The Netherlands**, October 1-4, 2003.

Kozubek S., Lukášová E., Bártová E., Kozubek M., Amrichová J., Falk M., Ondřej V. Detailed studies of the 3D structure of chromosome territories. European Cytogenetics Conference, Bologna, **Italy**, 2003.

Lukáš Z., Falk M., Kroupová I et al. Imunohistochemiical and molecular biology methods in diagnostics of muscular dystrophies. 12. Sjezd Slovenské a České společnosti patologů s mezinárodní účastí, Bratislava, **Slovak Republic**, 8 - 10.9.2004.

Kozubek S., Bártová E., Lukášová E., Falk M., Ondřej V., Kozubek M, Kroupová J., Matula P and Matula Pe. High-Resolution cytometry represents the main technology used in the laboratory of molecular cytology and cytometry. Cytomics Emerging from Cytometry 16th Annual Meeting of the German Society for Cytometry, Leipziger Kubus, Leipzig, **Germany**, 18 – 21st October, 2006.

Falk M., Lukášová E., Gabrielová B., Ondřej V., Kozubek S. Local changes of higher-order chromatin structure during DSB-repair. RADAM Conference 2007 – Radiation Damage in Biomolecules Conference, Dublin, **Ireland**, June 19-22, 2007.

Falk M., Lukášová E., Gabrielová B, Kroupová I. and Kozubek S. Nuclear Organization and Dynamics of the DSB-repair − Direct Visualization of Double Strand Breaks in Functionally Different Chromatin Domains. Salk Institute, Nature and Fondation IPSEN Conference on Biological Complexity: Diseases of Transcription, Salk Institute, La Jolla, **CA**, **USA**, January 11-14, 2007.

Falk M., Lukášová E., Gabrielová B., Ondřej V., Kozubek S, Kroupova I. DSB-repair requires specific sequence of higher-order chromatin structure changes - Direct visualization of double strand breaks in functionally different chromatin domains. Symposium on Radiation Effects of Biomedical Interest, Madrid, **Spain,** February, 22-25, 2007.

Lukáš Z., Falková-Kroupová I., Falk M., Valášková I., Fajkusová L., Sedláčková J. RNA fluorescence in situ hybridization analysis of fetal tissues from a family affected by myotonic dystrophy – A case report. 12th International Congress of the World Muscle Society, Giardini Naxos – Taormina, **Sicily**, **Italy**, 17-20 October, 2007.

Falk M., Lukášová E., Kozubek S. Different sensitivity and response of functionally distinct chromatin domains to DSB induction. 10th Biennial Meeting of the DGDR (German Society for Research on DNA Repair, Berlin, **Germany**, 2-5 September 2008

Falk M., Lukášová E., Kozubek S. Direct visualization of DSB induction and repair in gene dense (RIDGE) and gene poor (anti-RIDGE) chromatin domains. Biochemical Society Annual Symposium – DNA Damage: From Causes to Cures, Cambridge, **United Kingdom**, December 15-17, 2008.

Lukáš Z., Falková I., Falk M., Zaorálková J., Hrabálková R. In situ hybridization analysis of mRNA in differentiated tissues of adult patients with myotonic dystrophy 1 and 2. 14th International Congress of the World Muscle Society, Uni-Mail, Geneva, **Switzerland**, September 9-12, 2009.

Falk M., Lukasova E., Bacikova A., Kozubek S. DSB damage in structurally and functionally distinct higher-order chromatin domains – relationship between nuclear architecture, DSB induction and repair. ABCAM conference on Maintenance of Genome Stability 2010, **Antigua**, March 8-11, 2010.

Lukáš Z., Falk I., Falk M., Hrabalkova R., Zaoralkova J. Colocalization of DMPK and ZNF9 transcripts with MBNL1 protein in differentiated tissues from patients with myotonic dystrophy. XII International Congress on Neuromuscular Diseases, Naples, **Italy**, 17-22 July 2010.

Falk M., Lukáš Z., Falková I., Hrabalkova R., Zaoralkova J. Ribonuclear foci in differentiated tissues of patients with DM2. 15th International Congress of the World Muscle Society, Kumamoto, **Japan**, October 12-16, 2010.

Sevcik J., Falk M., Kleiblova P., Lhota F., Pohlreich P., Kleibl Z. In vitro analysis of population specific BRCA1 splicing variants. 21st Meeting of the European Association for Cancer Research, Oslo, **Norway**, 26 - 29 June 2010.

Falk M, Lukášová E, Kozubek S, Štefančíková L. Spatio-temporal questions of DNA double-strand break repair and formation of chromosomal translocations. International Symposium for Radiation Research and Medical Physics, Shanghai, **China**, May 30 - June 2, 2011.

Lukas Z., Vohanka S., Feit J., Falk M., Falkova I., Hrabalkova R., Zaoralkova J. Sequestration of MBNL1 protein by mutant ZNF9 RNA in lymphocytes of patients with myotonic dystrophy type. 16th International Congress of the World Muscle Society, Almancil, Algarve, **Portugal**, 18-22 October 2011

Lukáš Z., Voháňka S., Falková I., Falk M., Feit J., Hrabálková R., Zaorálková J. Exprese RNA a proteinu ZNF9 v lymfocytech pacientů s DM2 – možnosti diagnostiky z periferní krve. IV. Neuromuskulární kongres, 22. neuromuskulární symposium, XII. konferencia o neuromuskulárných ochoreniach. Bratislava, **Slovak Republic**, 5.-6. máj 2011.

Falkova I, Falk M., Lukas Z., Stefancikova L., Hrabalkova R., Zoaralkova J., Feit J. Insulin receptor splicing in human adipose tissue of patients with DM2. 16th International Congress of the World Muscle Society, Almancil, Algarve, **Portugal**, 18-22 October 2011

Falkova I., Stefancikova L., Baranova E., Lukasova E., Jezkova L., Bacikova A., Kozubek S., Davidkova M., and Falk M. Heterochromatin structure prevents DSB repair but not formation of repair foci and protrusion of DSBs into the low-dense chromatin. Heavy Ion in Therapy and Space Radiation Symposium 2013 (HITSRS2013), Chiba, **Japan**, May 15-18, 2013.

Falk M., Falkova I., Davidkova M., Bacikova A., Stefancikova L., Lukasova E., Jezkova L., Vachelova J., Michaelidesova A., Kozubek S. 'Secondary' clustering of DSB repair foci and repair kinetics compared for γ-rays and protons of different energies. Heavy Ion in Therapy and Space Radiation Symposium 2013 (HITSRS2013), Chiba, **Japan**, May 15-18, 2013.

Michaelidesová A.,. Vachelová J., Havránek V., Štursa J., Zach V., Falk M., Falková I., Ježková L., Vondráček V., Davídková M. Response of human normal fibroblasts to proton irradiation. 11th Microbeam Workshop, Microbeam Probes of Cellular Radiation Response. Bordeaux, **France**, October 3rd & 4th, 2013.

Michaelidesova A., Vachelova J., Falk M., Falkova I., Litvinchuk A., Havránek V., Štursa J., Zach V., Vondráček V., Davídková M. Response of normal skin fibroblasts to proton irradiation. 16th International Symposium on Microdosimetry, Treviso, **Italy**, October 20 - 25.2013.

Štefančíková L., Porcel E., Eustache P., Kozubek S., Falk M. and Lacombe S. Localization and radiosensitizing effect of Gd nanoparticles in cancer cells. SPRING 13 U: Design of multifunctional nano-objects for biomedical applications. Strasbourg, **France**, May 27 - 31, 2013.

Falk M., Falková I., Ježková L., Davídková M., Bačíková A., Zadneprianetc M., Pagáčová E., Štefančíková L., Vachelová J., Michaelidesová A., Lukášová E., Boreyko A., Krasavin E.A., Kozubek S. DSB Repair and Primary and Secondary (DSB repair-induced) IRIF Clusters upon the Action of High-LET and Low-LET Radiations. *13th International Workshop on Radiation Damage to DNA*, June 14-18, 2014, Massachusetts Institute of Technology (M.I.T.), **Cambridge, MA, USA**.

Pagáčová E., Falk M., Falková I., Štěpka K., Lukášová E., Michalová K., Zemanová Z., Matula P., Kozubek S. Chromosomal rearrangements of the chromosome 5 in myelodysplastic syndrome. Advanced Workshop on Interdisciplinary Views on Chromosome Structure and Function. 15 - 19 September 2014, **Trieste, Italy**

Ježková L., Boreyko A., Bulanova T., Falk M., Falkova I., Davidkova M., Kozubek S., Krasavin E., Kruglyakova E., Valentova E., Zadneprianetc M. Induction and repair of clustered DNA double strand breaks in human fibroblasts after irradiation with Boron ions and g-rays. 60th Annual International Meeting of Radiation Research Society. September 21-24, 2014, **Las Vegas, Nevada, USA**.

Falková I., Ježková L., Lukášová E., Bačíková A., Davídková M., Zadneprianetc M., Pagáčová E., Vachelová J., Michaelidesová A., Boreyko A., Krasavin E., Kozubek S., and Falk M. PRIMARY AND SECONDARY gH2AX FOCI CLUSTERS UPON IRRADIATING CELLS WITH DIFFERENT RADIATIONS AND THEIR ROLES IN FORMATION OF CHROMOSOMAL TRANSLOCATIONS. 3rd International Conference 'Radiation damage in Biomolecular Systems: Nanoscale insights into Ion Beam Cancer Therapy', Nano-IBCT 2014 Conference, 27th – 31th October 2014, **Boppard am Rhein, Germany.**

Pagáčová E., Falk M., Falková I., Štěpka K., Lukášová E., Michalová K., Zemanová Z., Matula P., Kozubek S. Relationship between chromatin structure and chromosomal rearrangements in myelodysplastic syndromes. International Conference on Chromosomal Genetics and Evolution (ICCGE 2015), February 16-17 2015, **London**, **United Kingdom**

Zadneprianetc M., Boreyko A., Bulanova T., Falk M., Falkova I., Davídková M., Ježková L., Kozubek S., Krasavin E., Kruglyakova E., Valentová O. IRIF cluster formation and structure in human fibroblasts after irradiation with boron ions and γ-rays. RAD 2014, Second International Conference on Radiation and Dosimetry in Various Fields of Research. May 27 – 30, 2014. **Niš, Serbia**.

Falk M., Lukášová E., Štefančíková L., Falková I., Kozubek S. Amifostine, a redioprotective drug acting as radical scavenger, preferentially protects active genes in decondensed chromatin. ICRR 2015 – 15th International Congress of Radiation Research. May 25 – 29, 2015, **Kyoto, Japan**.

Falk M., Falková I., Ježková L., Davídková M., Bačíková A., Zadneprianetc M., Pagáčová E., Vachelová J., Michaelidesová A., Lukášová E., Boreyko A., Krasavin E.A., Kozubek S. DSB repair in normal and radioresistant tumor cells exposed to γ-rays, protons of different energies, and high-LET ions. ICRR 2015 – 15th International Congress of Radiation Research. May 25 – 29, 2015, **Kyoto, Japan**.

Ježková L., Boreyko A., Bulanova T., Falk M., Falkova I., Davídková M., Kozubek S., Krasavin E., Kruglyakova E., Valenova O., Zadneprianetc. Analysis of DSB repair and structure of IRIF clusters induced by high- and low-LET radiations. ICRR 2015 – 15th International Congress of Radiation Research. May 25 – 29, 2015, **Kyoto, Japan**.

Štefančíková L., Salado D., Porcel E., Maury P., Pagáčová E., Bolsa M., Ivošev V., Sanchez G.J., Roux S., Tillement O., Lux F., Falk M. and Lacombe S. Metal- and lanthanide-based nanoparticles improve the performances of radiotherapies. Nanoparticles. Advances in nanopraticulate carriers: Applications in diseases and infections. October 19th-21st, 2015, Institut Pasteur, **Paris, France.**

Falk M., Falková I., Pagáčová E., Bačíková A., Golan M., Šimek D., Ignácová S.S., Mičová J., Šebera J., Richter J., Řeha D., Follett S.E., Elliott K.W., Varga K., Kratochvílová I. Viability of cryopreserved cells, state of their nuclei and properties of cryoprotectants. CRYO2016: The 53rd Annual Meeting of the Society for Cryobiology, July 24-27, 2016, **Ottawa, Canada.**

Ježková L., Borezko A., Bulanova T., Falk M., Falkova I., Davidkova M., Koyubek S., Krasavin E., Kruglzakova E., Valentova O., Smirnova E., Yadneprianetc M. Time and dose response of γH2AX and 53BP1 foci in human fibroblasts exposed to radiation of different qualities. Conference on Radiation & Health titled 'Public Health Impact of Current Sources of Radiation Exposure: New Data and Insights from Biology, Epidemiology, and Statistics', October 15-17, 2016, **Waikoloa Village, Hawaii**.

Falk M, Štefančíková L, Lacombe S, Salado D, Porcel E, Pagáčová E, Tillement O, Lux L, Depeš D, Falková I, Bačíková A, Kozubek S, Horáková Z, Falková I. 10–14 September 2017; **Jerusalem, Israel;** https://2017.febscongress.org

Falková I, Falk M, Pagáčová E, Štěpka K, Michalová K, Zemanová Z, Matula P. Relationship between chromatin structure and chromosomal rearrangements in myelodysplastic syndromes. 10–14 September 2017; **Jerusalem, Israel;** https://2017.febscongress.org

Falková I, Pagáčová E, Falk M*, Štěpka M, Lukášová E, Michalová K, Zemanová Z, Matula P, Kozubek S. Chromosomal rearrangements in myelodysplastic syndromes. October 2-6, 2017, **Varadero, Cuba**.

Ježková L, Zadneprianetc M, Kruglyakova E, Bulanova T, Smirnova E, Boreyko A, Krasavin E, Falková I, Valentová O, Davídková M, Kozubek S, Depeš D, and Falk M.* Particles with similar LET values generate DNA breaks of different complexity and reparability: a high-resolution microscopy analysis of γH2AX/53BP1 foci. October 2-6, 2017, **Varadero, Cuba**.

Kopečná O., Masařík M., Horáková Z., Falk M., Falková I., Bačíková A., Depeš D., Hoferová Z., Pagáčová E., Kozubek S. Study of radiosensitivity and DNA repair in different cell lines isolated from head and neck tumors. 6th EU-US Conference on Repair of Endogenous DNA Damage, September 24-28, 2017, University of Udine, **Udine, Italy.**

Falková I., Relationship between chromatin structure and chromosomal rearrangements in myelodysplastic syndromes. 3rd International Conference on Systems and Synthetic Biology, July 20-21, 2017, **Munich, Germany.**

Falk M., Dellino I., Faretta M., Hausmann M., Falková I., Kopečná O., Pagáčová E., Bobková E., Bačíková A., Lukášová E., Kozubek S., Pelicci PG. Higher-order chromatin structure in pathogenesis of the acute promyeloctic leukemia. COST Action CA15214 Workshop: Nuclear Lamins, Nuclear Organization And Transcription. 4-5th July 2018, **Riga, Latvia.**

Falková I., Pagáčová E., Michalová K., Zemnová Z., Štěpka K., Matula P., Kozubek S. and Falk M.. Chromosomal rearrangements in myelodysplastic syndromes. COST Action CA15214 Workshop: Nuclear Lamins, Nuclear Organization And Transcription. 4-5th July 2018, **Riga, Latvia.**

Falková I., et al. Study of radiosensitivity and DNA repair in different cell lines isolated from head and neck tumors. COST Action CA15214 Workshop: Nuclear Lamins, Nuclear Organization And Transcription. 4-5th July 2018, **Riga, Latvia.**

Přibyl J., Kratochvílová I., Golan M., Pešl M., Jelínková Š., Acimovic I., Jaroš J., Rotrekl V., .Skládal P., Falk M. Cryopreserved cells regeneration monitored by AFM and correlated with state of cytoskeleton and nuclear membrane. CRYO2018: Scientific Challenges of Cryobiology. 10-13 July, **Madrid, Spain**

Golan M., Falk M., Falková I., Pagáčová E., Bačíková A., Kopečná O., Šimek D., Klejdus B., Varga K., Teplá O., Kratochvílová I. Critical defects in cryopreserved cell nuclei: DNA structure changes CRYO2018: Scientific Challenges of Cryobiology. 10-13 July, **Madrid, Spain**

Falk M., Falková I., Pagáčová E., Kopečná O., Bačíková A., Varga K., Golan M, Kratochvílová I. Complex description of cryopreserved cell nuclei defects by immunofluorescence microscopy: DNA lesions, chromatin decondensation, nuclear membrane ruptures.The Society for Low Temperature Biology (SLTB) Meeting, 6th September 2018, **Prague, Czech Republic** (**1st Prize for poster presentation**).

Falková I. et al. Are Myelodysplastic Syndromes (MDS) a Chromatin Structure Disease. BIT's 8th Annual World Congress of Molecular & Cell Biology-2018, October 16-18, 2018, **Fukuoka, Japan.**

Pagáčová E., Falk M., Falková I., Kopečná O., Michalová K., Kozubek S. Chromosomal instability of the chromosome 5 in myelodysplastic syndrome. Genetic Conference of The Gregor Mendel Genetic Society, 12-14th September 2018, **Bratislava, Slovakia**.

Falková I. et al. Radio-sensitization of resistant head and neck tumor cells by metal nanoparticles. NANOSCIENCE MEET 2018: Annual conference on Nanoscience, Nanotechnology and Advanced materials. November 26-28, 2018, **Bali**, **Indonesia**. Invited lecture.

Falk M. et al. Influence of freezing and thawing process on cryopreserved cells nuclei. Functions and physico-chemical properties of cryoprotectants. CRYO2019: 56th Annual Meeting of the Society for Cryobiology. 22 - 25 July 2019, **San Diego, USA**.

Hausmann M., Lee J.-H., Maus E., Hofmann A, Pilarczyk G., Heermann D.W., Falkova I., Falk M., Hildenbrand G., Scherthan H. Analysis of the nano-topology of repair clusters by localization microscopy: Towards understanding of topological impact on repair pathway decision. 16th International Congress of Radiation Research (ICRR 2019), 25th-29th August 2019, **Manchester, England**. (selected for oral presentation)

Falkova I., Pagáčová E., Kopečná O., Gumulec J., Raudenská M., Vičar T., Bačíková A., Horáková Z., Binková H., Kozubek S., Masařík M., Falk M. (corresp. au.). Inter-individual and cell type-specific differences in response to radiation-induced DNA damage of different cell types isolated from patients' head-and-neck tumors. 16th International Congress of Radiation Research (ICRR 2019), 25th-29th August 2019**, Manchester, England**. (poster presentation)

Falk M., Ježková L., Hausmann M., Lee J.-H., Kopečná O., Pagáčová E., Falková I., Bobkova E., Bačíková A., Smirnova E., Zadneprianetc M., Kulikova E., Bulanova T., Boreyko A., Krasavin E., Davidkova M., Kozubek S. Micro-scale and nano-scale complexity of DNA double-strand break repair foci induced by accelerated ions of similar LET. 16th International Congress of Radiation Research (ICRR 2019), 25th-29th August 2019**, Manchester, England**. (selected for oral presentation)

Vojtíšková M., Falk M., Lukáš Z., Ravčuková B., Gaillyová R. Utility of PCR methods for characterization of pathological alleles associated with myotonic dystrophy. International conference on medical genetics, 15.-17. September 1999, **Olomouc, Czech Rep.**

Falk M., Lukáš Z., Gaillyová R., Vojtíšková M. Rapid detection of CTG repeat expansions by PCR: Application for postnatal diagnostics of myotonic dystrophy. International conference on DNA conformation, modification and recognition in biomedicine, July 1.-6., 2000. **Brno, CR.**

Falk M., Šilhánová E., Grochová I. and Vojtíšková M. Stable and unstable trinucleotide CTG repeat alleles in myotonic dystrophy locus. Mendel – Brno 2000, Conference on DNA structure and interactions, July 19-23 2000, **Brno, CR.**

Falk M., Vojtíšková M., Gaillyová R. Methodological Possibilities for detection of expanded trinucleotide repeats in myotonic dystrophy locus. IV. Workshop of Biochemists on Molecular Biologists, 9 February 2000, **Brno, Czech Republic.**

Falk M. New trends in diagnostics of myotonic dystrophy. Čs. biological society meeting, 4 November 2000, **Brno, Czech Republic.**

Vojtíšková M., Falk M. PCR methods for detection of large trinucleotide repeat expansions. 8. International Fair of Medical Technology and Pharmacy – MEFA 2000 Congress on progress in medicine and pharmacy, section of genetics and physiology, 7.-10.11.2000, **Brno, Czech Republic**. (in English)

Falk M., Vojtíšková M. Detection of trinucleotide repeat expansions at the myotonic dystrophy locus. 4. National conference on DNA diagnostics with international participation, 13.-14. December. 2000, **Prague, Czech Republic.** (in English)

Falk M., Gaillyová R. and Vojtíšková M. Use of new modified PCR-based methods for rapid differential diagnostics of myotonic dystrophy. V. Workshop of Biochemists and Molecular Biologists, 14 February 2001, **Brno, Czech Republic**. (in English)

Falk M., Vojtíšková M. An application of modern diagnostics methods in studies of etiology of severe neuromuscular inherited diseases. Symposium of ČLS JEP Society for prevention of genetic diseases – News in clinical genetics, 29 April 2001, **Průhonice, Czech Republic.**

Vojtíšková M, Falk M. Possibilities of LIF in prenatal diagnosis. Symposium of ČLS JEP Society for prevention of genetic diseases – News in clinical genetics, 29 April 2001, **Průhonice, Czech Republic**

Vojtíšková M., Kadlecová J., Ravčuková B., Falk M., Valášková I., Gaillyová R. Molecular diagnostics of serious hereditary neurological diseases. The report about complex diagnostic program results (Lederer foundation), 11 April 2000, **Brno, Czech Republic.**

Vojtíšková M., Falk M., Oltová A., Žáková J., Vodinská M., Ventruba M. 2001. Application of fluorescent quantitative PCR methods in prenatal diagnostic. XVI. Days of Biology, 5.-7. September 2001, **Olomouc, Czech Republic.**

Falk M., Lukášová E., Kozubek S., Kozubek M. Topography of dystrophin exons relative to the cell nucleus and to the active and inactive chromosome X territory determined for human lymphocytes. Conference on Biophysics of the Genome and Its Interactions, October 15 – 17, 2001, **Hlohovec, Czech Republic** (in English)

Falk M, Španová A., Rittich B. Interactions of metal ions with immobilized DNase I. In VI. Workshop of Biochemists and Molecular Biologists. 7. 2, 2002, **Brno, Czech Republic.**

Falk M., Lukášová E., Faretta M., Dellino I., Kozubek S., Pelicci G.I., Kozubek M., Rocchi M. Colocalization of PML bodies and PML/RARα microspeckles with up- and down-regulated loci and changes of chromatin structure in APL leukemia cells. Third Workshop on Biophysics of the Genome, 12-13 October 2003, **Brno, Czech Republic.**

Lukášová E., Falk M., Kořistek Z., Kozubek S., Grigoryev S., Kozubek M., Ondřej V., Kroupová I. Methylation of histone H3K9 on lysine 9 distinguishes granulocytes of healthy individuals and patients with myeloid leukemia. Third Workshop on Biophysics of the Genome, 12-13 October 2003, **Brno, Czech Republic.**

Lukasova E., Kozubek S., Falk M., Kozubek M., Žaloudík J., Vagunda V., Rocchi M., Pavlovský Z. Organization of selected loci of chromosomes 7,11, and 20 in cells colorectal carcinoma and adjacent colonic tissue. Conference on Biophysics of the Genome, 2003, **Hlohovec, Czech Republic.**

Falk M., Kroupová I., Vojtíšková M., Lukáš Z. 2005 New trends in molecular diagnostics and pathogenesis of myotonic dystrophy. XVI. Neuromuscular Sympisium, 22-23 April 2005, **Rožnov pod Radhoštěm, Czech Republic.**

Falk M., Lukášová E., Faretta M., Dellino I., Kozubek S., Pelicci G.I., Kozubek M., Rocchi M. 2005. Changes of nuclear architecture and chromatin structure induced by PML/RARa fusion protein in APL leukemic cells. 3rd Conference on Analytic Cytometry, 21. - 25. June 2005, **Červenohorské sedlo, Czech Republic.**

Dellino I.G., Falk M., Lukášová E., Faretta M., Pelicci P.G., Kozubek S. PML/RARa fusion oncoprotein, new mechanisms of gene downregulation in leukemia and aimed therapy. Analytical Cytometry IV, July 23-26, 2007, **Brno, CR.**

Lukáš Z., Kroupová I., Valášková I., Falk M., Fajkusová L., Sedláčková J. FISH analýza tkání fetu postiženého kongenitální myotonickou dystrofií. XVIII. Neuromuscular symposium, 11. - 12. May 2007, **Brno, CR.**

Pala J., Krist P., Falk M. Konfokální fluorescenční mikroskopie v histologické laboratoři. Principy, praktická diagnostika a praktická ukázka. 15. sjezd českých a slovenských patologů, 29. -31. srpna 20007, **Rožnov pod Radhoštěm, CR.**

Lukáš, Z., Kroupová, I., Falk, M. In situ hybridization analysis of mRNA in tissues of adult patients with myotonic dystrophy. 15. sjezd českých a slovenských patologů, 29.-31. srpna 20007, **Rožnov pod Radhoštěm, CR.**

Lukáš Z., Falková I., Falk M. In situ hybridization analysis of DMPK mRNA in differentiated tissues of the myotonic dystrophy patients. Neuromuskulární kongres – 19. neuromuskulární sympózium, 23-24 May 2008, **Brno, CR.**

Falková I., Lukáš Z., Falk M., Valášková I., Fajkusová L., Sedláčková J. RNA fluorescence in situ hybriddization analysis of fetal tissues from a family affected by myotonic dystrophy. 35. Sjezd českých patologů, 18.-19. června 2008, **Brno, CR.**

Ševčík J, Lhota F, Kleiblová P, Hojný J, Falk M, Štefančíková L, Měšťák O, Pavlišta D, Pohlreich P, Kleibl Z. Alternative splicing of BRCA1 - desired tool for DNA repair regulation or 'messy garbage' of splicing events? Genes, Genetics & Genomics 2012 (G3 2012), May 10th-11th, 2012, the First Faculty of Medicine, Charles University, **Prague, Czech Republic**

Falk M., Lukášová E., Štefančíková L., Bačíková A., and Kozubek S. Nuclear architecture and DSB repair. International Workshop on Radiation Damage to DNA, June 2nd – 6th, 2012, **Prague, Czech Republic**

Baranova E., Štefančíková L., Falková I., Kozubek S., Boreyko A., Krasavin E., and Falk M. Comparison of DNA γH2AX/53BP1 foci formation, nuclear distribution and DNA double strand break repair compared for skin fibroblasts and lymphocytes either irradiated with gamma-rays or incubated with hydrogen peroxide. International Workshop on Radiation Damage to DNA, June 2nd – 6th, 2012, **Prague, Czech Republic**

Lukášová E., Falk M., Štefančíková L., Bačíková A., and Kozubek S. Chromatin changes during DSB repair in euchromatin and heterochromatin. International Workshop on Radiation Damage to DNA, June 2nd – 6th, 2012, **Prague, Czech Republic**

Falk M., Lukášová E., Štefančíková L., Falková I., Ježková L., Bačíková A., Davídková M., Vachelová J., Michaelidisová A., Kozubek S. DNA damage and repair in the context of chromatin structure. Advanced Confocal Microscopy and Living Cell Studies, 15 – 19 October, 2012, **Brno, Czech Republic**

Štefančíková L., Porcel E., Lacombe S., Falk M., Kozubek S. Localization of nanoparticles in cancer cells. Advanced Confocal Microscopy and Living Cell Studies, 15 – 19 October, 2012, **Brno, Czech Republic**

Falk M., Lukáš Z., Falková I., Janoušová E., Fajkusová L., Štefančíková L., Zaorálková J., Hrabálková R., Feit J. A multilevel pathogenesis of myotonic dystrophy - dynamic DNA expansions, RNA expansions, and protein interactions come into play. High-Resolution Microscopy in the Biology of the Cell Nucleus, November 18 - 22, 2013, **Hustopeče, Czech Rep.**

Štefančíková L., Porcel E., Eustache P., Li S., Salado-Leza D., Kozubek S., Lacombe S. and Falk M. Nanoparticles cellular localization, uptake and effect on DNA damage response upon irradiation. High-Resolution Microscopy in the Biology of the Cell Nucleus, November 18 - 22, 2013, **Hustopeče, Czech Rep.**

Depeš D., Falk M., Masařík M., Falková I., Gumulec J., Bačíková A., Horáková Z., Pagáčová E., Binková H. Analýza možností využití detekce γH2AX/53BP1 ohnisek a monitorování reparace dvouřetězcových zlomů DNA pro pre-terapeutické stanovení radiosensitivity nádorů hlavy a krku. XXXVII. DNY RADIAČNÍ OCHRANY. November 09 – 13, 2015, **Mikulov, Czech Rep.**

Depeš D., Falk M. Automatické počítání reparačních ohnisek DSB v buněčných jádrech pomocí programu FociCounter 1.0. XXXVII. DNY RADIAČNÍ OCHRANY. November 09 – 13, 2015, **Mikulov, Czech Rep.**

Michaelides A., Vachelová J., Pachnerová-Brabcová K., Sýkorová P., Depeš D., Falk M., Falková I., Vondráček V., Davídková M. Vliv dávkového příkonu na odezvu buněčných kultur. XXXVII. DNY RADIAČNÍ OCHRANY. November 09 – 13, 2015, **Mikulov, Czech Rep.**

Falk M. Induction of DNA double strand breaks (as a double-edge sword) in cancer development and treatment. Seminář 'Molekulární genetika nádorových onemocnění' pořádaný v rámci výzkumného programu QUALITAS Strategie AV21. 3. prosince 2015, **Prague, Czech Republic.**

Falk M (Chair). AWHP Aspects of work of helping professions (Aspekty práce pomáhajících profesí): Imigrace – bezpečnostní a zdravotní rizika. 2. 10. 2015., **Prague, Czech Rep.**

Horáková Z., Binková H., Falk M., Masařík M., Falková I., Depeš D., Gumulec J., Bačíková A., Pagáčová E., Kostřica R. In vitro stanovení radiosenzitivity nádorů hlavy a krku. XL. Brněnské onkologické dny a XXX. konference pro nelékařské zdravotnické pracovníky, 27.–29. April, 2016, **Brno, Czech Republic.** Abstract in: Klinická onkologie 29/Suppl2, 2016.

Falk M., Štefančíková L., Ježková L., Lacombe S., Pagáčová E., Depeš D., Davídková M., Falková I., Bačíková A., Zadneprianetc M., Daniela Salado., Porcel E., Tillement O., Lux F., Vachelová J., Michaelides A., Boreyko A., Krasavin E., Lukášová E., Kozubek S. Response of normal and tumor cells to ionizing radiations of different qualities. Strategy 21, 8th June 2016, **Brno, Czech Republic.**

Štefančíková L., Lacombe S., Salado D., Porcel E., Pagáčová E., Tillement O., Lux F., Depeš D., Kozubek S., and Falk M. The mechanism of metal nanoparticle-mediated tumor cells radiosensitization – is nuclear DNA damage necessary? Conference on Cell Biology and Radiobiology – Satellite Symposium of the '6th International Conference on Genomics and Pharmacogenomics' held in Berlin, 9th-10th September 2016, **Brno, Czech Republic.**

Falková I., Pagáčová E., Bačíková A., Michalová K., Zemanová Z., Štěpka K., Matula Pa., and Falk M. Relationship between chromatin structure and chromosomal rearrangements in myelodysplastic syndromes. Conference on Cell Biology and Radiobiology – Satellite Symposium of the '6th International Conference on Genomics and Pharmacogenomics' held in Berlin, 9th-10th September 2016, **Brno, Czech Republic.**

Golan M et al. Viability of cryopreserved cells, state of their nuclei and cryoprotectants' properties. Conference on Cell Biology and Radiobiology – Satellite Symposium of the '6th International Conference on Genomics and Pharmacogenomics' held in Berlin, 9th-10th September 2016, **Brno, Czech Republic.**

Michaelidesová A., Vachelová J., Konířová J., Vondráček V., Davídková M., Falková I., Falk M. When proton meets a cell. Conference on Cell Biology and Radiobiology – Satellite Symposium of the '6th International Conference on Genomics and Pharmacogenomics' held in Berlin, 9th-10th September 2016, **Brno, Czech Republic.**

Štefančíková L., Pagáčová E., Lacombe S., Depeš D., Salado D., Porcel E., Tillement O., Lux F., Kozubek S. and Falk M. Nanoparticles to improve tumor radiotherapy. Functional Organization of the Cell Nucleus Symposium, 3rd November 2016, **Prague, Czech Republic.**

Kopečná O. et al. Krok kupředu ke kombinované personalizované terapii: Jak odpovídají různé typy buněk izolované z nádorů hlavy a krku na ozáření? XXXVIII. DNY RADIAČNÍ OCHRANY, 7. – 11. 11. 2016, Zámek **Mikulov, Czech Republic.**

Štefančíková L., Falk M., Lacombe S., Depeš D., Porcel E., Pagáčová E., Salado D., Tillement O., Lux F., Kozubek S. Nový pohled na radiosenzitizační efekt kovových nanočástic. XXXVIII. Dny radiační ochrany (DRO), 7. – 11. 11. 2016, Zámek **Mikulov, Czech Republic.**

Falk M., Hofer M., Komůrková D., Falková I., Bačíková A., Klejdus B., Pagáčová E., Štefančíková L., Weiterová L., Angelis K., Kozubek S., Dušek L., Galbavý Š. XXXVIII. DNY RADIAČNÍ OCHRANY, 7. – 11. 11. 2016, Zámek **Mikulov, Czech Republic.**

Horáková Z., Falk M., Falková I., Kopečná O., Bačíková A., Kozubek S., Depeš D., Binková D., Gál B., Svobodová M., Gumulec J., Raudenská M., Polanská H., Masařík M. Předléčebné stanovení radiosensitivity nádorů hlavy a krku, cesta k individualizované terapii? XXXVIII. Dny radiační ochrany (DRO), 7. – 11. 11. 2016, Zámek **Mikulov, Czech Republic.**

Bačíková A. et al. Single Molecule Localization Microscopy as a promissing tool for gH2AX/53BP1 foci exploration. XL. Dny radiační ochrany (DRO2018), 5. – 9. 11. 2018, Zámek **Mikulov, Czech Republic.**

Pagáčová E. Tumor Cell Radiosensitivity and Nanoparticles. XL. Dny radiační ochrany (DRO2018), 5. – 9. 11. 2018, Zámek **Mikulov, Czech Republic.**

Lee J.-H. et al. Mechanisms and Challenges for Understanding Radiation Induced Changes in Chromatin Nanoarchitecture. XL. Dny radiační ochrany (DRO2018), 5. – 9. 11. 2018, Zámek **Mikulov, Czech Republic.**

Horáková Z. DNA damage and its mechanism in cell cultures of head and neck tumor cells upon experimental irradiation. XL. Dny radiační ochrany (DRO2018), 5. – 9. 11. 2018, Zámek **Mikulov, Czech Republic.**

Kopečná O. et al. Applicability of gH2AX/53BP1 foci detection as potential predictive markers of head and neck tumor radioresistance. XL. Dny radiační ochrany (DRO2018), 5. – 9. 11. 2018, Zámek **Mikulov, Czech Republic.**

Falk M. et al. Critical damage in frozen and thawed cells. Symposium on Cell Biology and Pathology, 28-29th May 2019, **Brno, Czech Republic**

Gumulec J. et al.. Image analysis of microscopic image data using machine learning approaches. Symposium on Cell Biology and Pathology, 28-29th May 2019, **Brno, Czech Republic**

Perečko T. et al. Neutrophils: Freinds or Foes. Symposium on Cell Biology and Pathology, 28-29th May 2019, **Brno, Czech Republic**

Lee J-H. et al., Single Molecule Localization Microscopy of Nanoprobes to Study Chromatin Architecture, Function and Dynamics. Symposium on Cell Biology and Pathology, 28-29th May 2019, **Brno, Czech Republic**

Dobešová L. et al. Radiosensitizing effect of metal nanoparticles. Symposium on Cell Biology and Pathology, 28-29th May 2019, **Brno, Czech Republic**

3.3.3 National Conferences

Falk M., Štefančíková L., Lukášová E., Bačíková A., Falková I., Kozubek S. Funkce, poškození a reparace chromatinu – představení činnosti skupiny; vliv uspořádání chromatinu v jádře na vznik jednoduchých a komplexních přestaveb chromosomů. Dynamics and Organization of Chromosomes in the Cell Cycle and during Differentiation under Normal and Pathological Condition. Project Excellence 302/12/G157 Workshop No. 1. 29 – 30 March 2012, **Brno, Czech Republic**

Lukášová E., Bačíková A., Štefančíková L., Falk M., Kozubek S., Trbušek M., Šebejová L. Zvýšená fosforylace H2AX, změny chromatinové struktury a buněčná smrt po zablokování replikace a Chk1 kinázy v leukemických buňkách. Dynamics and Organization of Chromosomes in the Cell Cycle and during Differentiation under Normal and Pathological Condition. Project Excellence 302/12/G157 Workshop No. 1. 29 – 30 March 2012, **Brno, Czech Republic**

Štefančíková L., Falk M., Lukášová E., Bačíková A., Kozubek S. Senzitizace nádorových buněk k záření pomocí nanočástic. Dynamics and Organization of Chromosomes in the Cell Cycle and during Differentiation under Normal and Pathological Condition. Project Excellence 302/12/G157 Workshop No. 1. 29 – 30 March 2012, **Brno, Czech Republic**

Vachelová J., Michaelidesová A., Pachnerová Brabcová K., Falk M., Falková I., Ježková L., Davídková M. Pilotní studie radiačního poškození fibroblastů' XXXIV. Dny radiační ochrany, 5. - 9. 11. 2012, **Třeboň, CR**

Falk M., Štefančíková L., Lukášová E., Bačíková A., Falková I., Kozubek S. Reparace DNA a vliv uspořádání chromatinu v jádře na vznik jednoduchých a komplexních přestaveb chromosomů. Advanced Confocal Microscopy and Living Cell Studies, enclosed Meeting of GACR Project, Center of Excellence No.: P302/12/G157, 15 – 19 October, 2012, **Brno, Czech Republic**

Lukášová E., Bačíková A., Štefančíková L., Falk M., Kozubek S., Trbušek M., Šebejová L. Zvýšená fosforylace H2AX, změny chromatinové struktury a buněčná smrt po zablokování replikace a Chk1 kinázy v leukemických buňkách – pokroky ve výzkumu. Advanced Confocal Microscopy and Living Cell Studies, enclosed Meeting of GACR Project, Center of Excellence No.: P302/12/G157, 15 – 19 October, 2012, **Brno, Czech Republic**

Štefančíková L., Falk M., Lukášová E., Bačíková A., Kozubek S. Senzitizace nádorových buněk k záření pomocí nanočástic – pokroky ve výzkumu. dvanced Confocal Microscopy and Living Cell Studies, enclosed Meeting of GACR Project, Center of Excellence No.: P302/12/G157, 15 – 19 October, 2012, **Brno, Czech Republic**

Michaelidesová A., Vachelová J., Litvinchuk A., Falk M., Falková I., Havránek V., Štursa J., Vondráček V., Davídková M. Response of cell cultures of normal human skin fibroblasts to proton irradiation. XXXV. Dny radiační ochrany, November 11 - 15, 2013. **Třeboň, Czech Republic.**

Falk M. et al. 'Micro-scale DNA damage and double-strand break repair compared for high-LET ions of similar LET and low energy. Project Excellence Workshop, 2017, **Brno, CR.**

Falk M et al. Radiobiology and Cancer Treatment – Current Research Topics. Interactions of Ionizing Radiation with Live Organisms – Seminar of The Society for Radiobiology and Crisis Planning of the Czech Medical Association of Jan Evangelista Purkyne (SRKP ČLS JEP) and University of Defence, 11th November 2018, **Hradec Kralove, Czech Republic**.

Falk M. Current possibilities to monitor DNA damage and repair. Meeting on Biodosimetry. National Radiation Protection Institute (SURO), 23rd May 2019, **Prague, Czech Republic**.

3.4 Research Projects Associated with the Thesis

- 2017-2021 **COST Action CA16113 – CliniMARK**: 'good biomarker practice' to increase the number of clinically validated biomarkers.
- 2016-2019 **AZV (MZCR) 16-29835A** – Molecular-genetic markers for prediction of radiotherapy response in head and neck cancer.
- 2012-2014 **MEYS COST LD12039** – Influence of higher-order chromatin structure on the mechanism of DNA double-strand break (DSB) repair and formation of chromosomal translocations in cells irradiated with gamma rays and medically potentially relevant ion beams.
- 2008-2011 **GAAV IAA500040802** – New mechanisms of oncoprotein action in genesis of promyelocytic leukemia (in cooperation with European Institute of Oncology, Prof. P. G. Pelicci, Assoc. Prof. I. G. Dellino) (Accomplished without objections).
- 2006-2009 **Czech Science Foundation (GAČR) 204/06/P349** – Dynamic structure a function of the cell nucleus associated with DNA breaks (Accomplished as 'Excellent results with international importance').
- **2017-2019 Czech Science Foundation Project GACR 17-08066Y (JUNIOR)** – Complex view on the role of nitrated fatty acids in regulation of cell functions and processes (Komplexní pohled na roli nitrovaných mastných kyselin v regulaci buněčných).
- **2016-2018 Czech Science Foundation (GAČR) 16-12454S** – Characterizing & modifying complex response of head & neck tumor cells to different radiations - a step forward to combined personalized radiotherapy.
- **MEYS LC535: The Project of Excellence** – Dynamics and Organization of Chromosomes in the Cell Cycle and during Differentiation under Normal and Pathological Conditions (2012-2018).
- **OPVK CZ.1.07** : – Development of human resources in the field of cell biology (2012-2015).
- **GAČR: P302/10/1022** – Chromatin dynamics during DNA repair (2010-2015).
- **MEYS: LC535** – Dynamics and organization of chromosomes during cell cycle in norm and pathology (2005-2009).
- **1QS500040508** – Histone H3 methylation in granulocytes as a prognostic marker of chronic myeloid leukemia remission (2005-2009).
- **GAAV CR: IAA5004306** – The structure of the human genome (2003-2007).
- **Czech Science Foundation (GAČR) GA202/04/0907** – Live cell high-resolution microscopy (2004-2006).
- **Czech Science Foundation (GAČR) GA202/02/0804** – Estimation of the radiation risk for chronic myeloid leukemia development based on the distance measuring between ABL and BCR genes in hematopoietic cells (2002-2004).

- **IGA MZ: NC6987** – Epigenetically controlled changes of gene expression in tumor diseases (2002-2004).
- **GAAV CR: IBS5004010** – Development of new diagnostic tools for oncology (2000-2004).
- 2010-2014 **COST EU: Nano-scale insights in ion beam cancer therapy (Nano-IBCT)**, COST action MP1002.
- 2005-2007 **COST 405 (MŠMT 1P05OC084):** Dynamic structure and function of the cell nucleus after irradiation. Accomplished as excellent (excellent results with international importance).
- 2004-2006 **LSHG-CT-2003-503441, 6th EU Frame program:** 3D Genome structure and function (principal investigator Prof. Roel van Driel, Uni Amsterdam).

- 2019-2021 **The 3-Plus-3 Project:** Ionizing radiations of different quality and cell manipulations tools to eradicate radioresistant tumors. Project is included in Topical Plan for Research and International Cooperation in JINR in the frame of the theme number 04-9-1077-2019/2020 'Ionizing radiations of different quality and cell manipulations as tool to eradicate radioresistant tumors' (Principal investigators: A.E. Krasavin and M. Falk)
- 2019 **The Grant of Czech plenipotentiary:** Effect of LET on DNA damage and complex response of normal and tumor cells to ionizing radiation - New insights into the mechanisms of radiation-induced repair foci (IRIF) formation at microscale and nanoscale. Project is included in Topical Plan for Research and International Cooperation in JINR in the frame of the theme number 04-9-1077-2015/2020 'Investigations of Induction and Repair Mechanisms After Action of Ionizing Radiation of Different Qualities' (Principal investigators: A.E. Krasavin and M. Falk)
- 2016-2018 **The 3-Plus-3 Project:** Ionizing radiations of different quality and cell manipulations tools to eradicate radioresistant tumors. Project is included in Topical Plan for Research and International Cooperation in JINR in the frame of the theme number 04-9-1077-2015/2017 'Investigations of Induction and Repair Mechanisms After Action of Ionizing Radiation of Different Qualities' (Principal investigators: A.E. Krasavin and M. Falk)
- 2018 **The Grant of Czech plenipotentiary:** Effect of RBE on DNA damage and complex cellular response to ionizing radiation - New insights into the mechanisms of formation of chromosomal translocations. Project is included in Topical Plan for Research and International Cooperation in JINR in the frame of the theme number 04-9-1077-2015/2017 'Investigations of Induction and Repair Mechanisms After Action of Ionizing Radiation of Different Qualities' (Principal investigators: A.E. Krasavin and M. Falk)
- 2017 **The Grant of Czech plenipotentiary:** Effect of RBE on DNA damage and complex cellular response to ionizing radiation - New insights into the mechanisms of formation of chromosomal translocations. Project is included in Topical Plan for Research and International Cooperation in JINR in the frame of the theme number 04-9-1077-2015/2017 'Investigations of Induction and Repair Mechanisms After Action of Ionizing Radiation of Different Qualities' (Principal investigators: A.E. Krasavin and M. Falk)
- 2016 **The Grant of Czech plenipotentiary:** Effect of RBE on DNA damage and complex cellular response to ionizing radiation - New insights into the mechanisms of formation of chromosomal translocations. Project is included in Topical Plan for Research and International Cooperation in JINR in the frame of the theme number 04-9-1077-2015/2017 'Investigations of Induction and Repair Mechanisms After Action of Ionizing Radiation of Different Qualities' (Principal investigators: A.E. Krasavin and M. Falk)
- 2015 **The 3-Plus-3 Project:** Effect of RBE on DNA damage and complex cellular response to ionizing radiation - New insights into the mechanisms of formation of chromosomal translocations. Project

is included in Topical Plan for Research and International Cooperation in JINR in the frame of the theme number 04-9-1077-2015/2017 'Investigations of Induction and Repair Mechanisms After Action of Ionizing Radiation of Different Qualities' (Principal investigators: A.E. Krasavin and M. Falk)

- 2015 **The Grant of Czech plenipotentiary:** Chromatin structure modification and DNA repair pathways inhibition as tools to therapeutically increase or decrease cell survival upon the action of ionizing radiation of different quality. Project is included in Topical Plan for Research and International Cooperation in JINR in the frame of the theme number 04-9-1077-2015/2017 'Investigations of Induction and Repair Mechanisms After Action of Ionizing Radiation of Different Qualities' (Principal investigators: A.E. Krasavin and M. Falk)
- 2014 **The 3-Plus-3 Project:** DNA double-strand break (DSB) repair and formation of chromosomal translocations in the context of higher-order chromatin structure and upon action of ionizing radiation of different quality. Project is included in Topical Plan for Research and International Cooperation in JINR in the frame of the theme number 04-9-1077-2012/2014 'Investigations of Induction and Repair Mechanisms After Action of Ionizing Radiation of Different Qualities' (Principal investigators: A.E. Krasavin and M. Falk)
- 2014 **The Grant of Czech plenipotentiary:** Grant of the Government Plenipotentiary of CR, Chromatin structure modification and DNA repair pathways inhibition as tools to therapeutically increase or decrease cell survival upon the action of ionizing radiation of different quality (in the frame of the cooperation with JINR, theme number 04-9-1077-2012/2014 (Principal investigators: A.E. Krasavin and M. Falk)
- 2013 **The 3-Plus-3 Project:** Effect of RBE on DNA damage and complex cellular response to ionizing radiation - New insights into the mechanisms of formation of chromosomal translocations. Project is included in Topical Plan for Research and International Cooperation in JINR in the frame of the theme number 04-9-1077-2012/2014 'Investigations of Induction and Repair Mechanisms After Action of Ionizing Radiation of Different Qualities' (Principal investigators: A.E. Krasavin and M. Falk)
- 2013 **The Grant of Czech plenipotentiary:** Grant of the Government Plenipotentiary of CR, Chromatin structure modification and DNA repair pathways inhibition as tools to therapeutically increase or decrease cell survival upon the action of ionizing radiation of different quality (in the frame of the cooperation with JINR, theme number 04-9-1077-2012/2014 (Principal investigators: A.E. Krasavin and M. Falk)
- 2012 **The 3-Plus-3 Project:** Effect of RBE on DNA damage and complex cellular response to ionizing radiation - New insights into the mechanisms of formation of chromosomal translocations. Project is included in Topical Plan for Research and International Cooperation in JINR in the frame of the theme number 04-9-1077-2012/2014 'Investigations of Induction and Repair Mechanisms After Action of Ionizing Radiation of Different Qualities' (Principal investigators: A.E. Krasavin and M. Falk)
- 2012 **The Grant of Czech plenipotentiary:** Grant of the Government Plenipotentiary of CR, Chromatin structure modification and DNA repair pathways inhibition as tools to therapeutically increase or decrease cell survival upon the action of ionizing radiation of different quality (in the frame of the cooperation with JINR, theme number 04-9-1077-2012/2014 (Principal investigators: A.E. Krasavin and M. Falk)

DNA Damage and Repair upon Cell Exposure to Different Types of Ionizing Radiation – the Importance of Chromatin Context and New Perspectives of Cancer Radiotherapy

ATTACHMENT TO HABILITATION THESIS

RNDr. Martin Falk, Ph.D.

Brno, 1st October 2019

Chromosoma (2002) 111:321–331
DOI 10.1007/s00412-002-0210-8

ORIGINAL ARTICLE

**Stanislav Kozubek · Emilie Lukásová · Pavla Jirsová
Irena Koutná · Michal Kozubek · Alena Ganová
Eva Bártová · Martin Falk · Renata Paseková**

3D Structure of the human genome: order in randomness

Received: 19 February 2002 / Revised: 22 May 2002 / Accepted: 1 July 2002 / Published online: 18 September 2002

Abstract A complex study of the spatial arrangement of different genetic elements (genes, centromeres and chromosomal domains) in the cell nucleus is presented and the principles of this arrangement are discussed. We show that the radial location of genetic elements in the three-dimensional (3D) space between the center of the nucleus and the nuclear membrane is element specific and dependent on the position of the element on the chromosome. In contrast, mutual angular positioning of both homologous and heterologous genetic elements is, in the majority of cases, random. In several cases, tethering of heterologous genetic elements was observed. This close proximity of specific loci may be responsible for their mutual rearrangement and the development of cancer. Comparison of our results with transcriptome maps shows that the nuclear location of chromosomal domains with highly expressed genes is more central when compared with chromosomes with low expression. The higher-order chromatin structure is strikingly similar in various human cell types, which correlates with the fact that the profiles of gene expression are also similar.

Introduction

The cell nucleus is one of the best known but least understood of cellular organelles. Since the first visualization of chromosomes by fluorescence in situ hybridization (FISH) in mammalian and plant cells (Cremer et al. 1988; Lichter et al. 1988; Pinkel et al. 1988), the structure of the cell nucleus has been intensively investigated. However, in spite of rapid developments in visualization techniques, image acquisition and analysis tools, the location of genetic elements in the cell nucleus, as well as the internal structure of chromosomal territories, the organization of the interphase nucleus as a whole and the functional aspects of nuclear organization, are still poorly understood.

The compaction of DNA is achieved by its hierarchical folding involving interactions with a variety of proteins, maintaining the integrity of chromosomes and facilitating their condensation/decondensation during the cell cycle and activation of transcription (Cook et al. 1975; Paulson and Laemmli 1977; Vogelstein et al. 1980). Several models of genomic packaging into large-scale chromatin structures, based on chromatin loops, have been proposed (Manuelidis and Chen 1990; Belmont and Bruce 1994; Li et al. 1998; Sachs et al. 1995; Yokota et al. 1995; Munkel et al. 1999). It is believed that higher order clusters of loops may represent distinct functional units of chromatin in the nucleus.

Individual chromosomes have been shown to maintain their identity during the entire cell cycle, occupying discrete regions of the nuclear volume (Schardin et al. 1985). The relationship between chromosomal structure and genomic function is most clearly illustrated in the experiments of Volpi et al. (2000). These authors have demonstrated that the active transcription of genes in the major histocompatibility complex leads to the decondensation of this large gene cluster, observable on an external chromatin loop emerging from the chromosomal territory.

Investigation of the higher order compartmentalization of chromatin according to its replication timing demonstrates a polar orientation of early and late replicating subregions of chromosomes (Ferreira et al. 1997; Sadoni et al. 1999), with transcription-competent and active chromatin located within the nuclear interior. In accordance with this observation, some individual genes have been reported in the interior of the nucleus

Edited by: U. Scheer

S. Kozubek (✉) · E. Lukásová · P. Jirsová · A. Ganová
E. Bártová · M. Falk
Laboratory of Molecular Cytology and Cytometry,
Institute of Biophysics,
Academy of Sciences of the Czech Republic,
Královopolská 135, 612 65 Brno, Czech Republic
e-mail: kozubek@ibp.cz

I. Koutná · M. Kozubek · R. Paseková
Laboratory of Optical Microscopy, Faculty of Informatics,
Masaryk University, Botanická 68a, Brno, Czech Republic

(Kozubek S et al. 1997; Parreira et al. 1997; Skalníková et al. 2000) as well as gene-rich chromosomes (Croft et al. 1999; Kozubek S et al. 1999; Boyle et al. 2001). Chromosomal territories are structurally complex and irregularly shaped objects (Visser and Aten 1999; Volpi et al. 2000). A recent study of the boundary areas of individual chromosomes during interphase showed penetration of extensions of one chromosome into another (Visser and Aten 1999), indicating surface interaction of adjacent chromosomes. The close proximity of the *ABL* and *BCR* genes in a large number of human lymphocytes might allow such functional interaction (Kozubek S et al. 1999). Surface interactions between adjacent chromosomes have been implicated in aberration formation after irradiation of human lymphocytes with ionizing radiation (Lukásová et al. 1999).

The data currently available support the view that the nucleus is far from being a randomly arranged bag of molecules, but functions rather as an integrated and highly ordered machine (Lamond and Earnshaw 1998). On the other hand, the high degree of variability observed among nuclei with stained genetic elements leads to the conclusion that order in nuclear organization might be manifested through statistical regularities.

Using FISH of interphase nuclei and high-resolution three-dimensional (3D) cytometry (Kozubek M et al. 1999, 2001), we have performed a large number of measurements and determined basic statistical regularities governing the location of genetic elements in cell nuclei. We show that genetic elements and whole chromosomes are located nonrandomly between the center of the nucleus and the nuclear membrane, although the angular positioning is in the majority of cases random. On the other hand, the close proximity of specific loci (pertaining to the same chromosome or to different chromosomal domains) was observed. These tethered states may be responsible for mutual rearrangement and development of cancer. The nuclear positioning of individual genetic elements is determined by their chromosomal position. Genetic elements located in regions of increased gene expression occur in the nuclear interior; those located in regions of low gene expression are close to the nuclear membrane.

Materials and methods

Cell cultures

The human leukemic promyelocytic cell lines HL-60 and ML-1 were obtained from the American Type Culture Collection (Manassas, Va.), and the promonocytic cell line U-937, colon carcinoma HT-29, Ewing sarcoma RDES1 cells, and human diploid fibroblasts IMR-90 were obtained from the European Collection of Cell Cultures (Porton Down, UK). Lymphocytes, promyelocytic and promonocytic cell lines were maintained in RPMI 1640 medium supplemented with 10% fetal calf serum (FCS; Pan Systems, Germany), at 37°C in a humidified atmosphere containing 5% CO_2. HT-29 cells, Ewing sarcoma RDES1 cells and diploid fibroblasts were cultured in Dulbecco's modified Eagle's medium (DMEM) (Pan, Germany) with 10% FCS and 2 mM glutamine.

Isolation of human lymphocytes

Human lymphocytes were isolated from heparinized blood (20–30 U/ml) from healthy donors by Ficoll-Hypaque (Pharmacia Biotech, Uppsala, Sweden) density-gradient centrifugation as previously described (Kozubek S et al. 1999).

Estimation of the average level of expression of individual chromosomes

The level of expression was estimated using the results of Caron et al. (2001). The expression profiles of individual chromosomes were integrated and the area under each profile (total chromosomal expression) was determined. The average expression level of a chromosome was calculated by dividing the area by the number of expressed sequences per chromosome.

The transcriptome map published by Caron et al. (2001) shows gene expression profiles for human chromosomes in 12 normal and pathological tissue types. These results show a general feature of the human genome consisting in the arrangement of highly expressed genes into clusters located at specific chromosomal regions that are similar in all investigated cell types. Therefore, we also used the expression levels of genes revealed in Caron's transcriptome map for G_0 lymphocytes.

Cell fixation

Dehydration of the nuclei was avoided to preserve the native 3D structure. One hundred microliters of dense cell suspension in PBS buffer was spread on a poly-L-lysinated microscope slide. The cells attached to the surface of the slide (in about 5 min without drying), were fixed in 3.7% paraformaldehyde with 0.5% Triton X-100 and HEPEM (65 mmol/L PIPES, 30 mmol/L HEPES, 10 mmol/L EGTA, 2 mmol/L $MgCl_2$, pH 6.9) (Neves et al. 1999) for 12–15 min (depending on cell type) at room temperature and thoroughly washed in PBS (3 times for 5 min). Fixed cells were either stored for 3 days at +4°C or immediately permeabilized for hybridization. The resulting shape of the cell nuclei was very near to spherical. It followed from the observation of x-z and y-z projections as well as from the dispersion of signal positions in the z-direction, which was very similar to the dispersion in the lateral direction.

Cell permeabilization

Permeabilization of cells was performed in 0.7% Triton X-100, 0.1 N HCl, PBS pre-cooled to +4°C for 10–12 min (depending on cell type) on ice. Subsequently, cells were incubated with 0.1 mg/mL RNase A in 2×SSC for 30 min at 37°C, then washed 3 times in PBS, denatured in 50% formamide, 2×SSC for 20 min at 75°C and immediately hybridized. (1×SSC is 0.15 M NaCl, 0.015 M sodium citrate.)

DNA probes and FISH

Fluorescence in situ hybridization was performed using unique sequence probes: M-*BCR-ABL* translocation probe (Vysis, USA) (spectrum green-*BCR* 22q11, spectrum orange-*ABL* 9q34), digoxigenated c-*MYC* (8q24), *TP53* (17p13.1) and *RB* (13q14.2) were purchased from Oncor. *IGH* (14q32) and *BCL1* (11q13) PAC clones were kindly provided by Dr. M. Dyer (Institute of Cancer Research, Sutton, UK); cosmid clones G9 and F7 located proximally and distally from the breakpoint region of the *EWS* gene (22q12) and 1p3 and 1d1 cosmids of the *FLI1* gene (11q24) were kindly provided by Dr. A. Aurias (Laboratory of Tumor Genetics at the Curie Institute, Paris, France). DNA probes of different exons of the dystrophin gene were kindly provided by Prof. J. den Dunnen (Leiden University, The Netherlands). The PAC and cos-

mid clones were amplified and DNA was isolated using a Qiagen kit. All DNA probes were labeled by spectrum green and spectrum orange using a nick translation kit (Vysis, USA). Alpha-satellite DNA sequences of the centromeric region of chromosomes 1, 6, 9, 19 (digoxigenated), and 3, 8, 17, and 18 (biotinylated) were purchased from Oncor; total chromosomal DNA probes of chromosomes 3, 8, 9, 14, 17, and 18 used for 3D analysis were fluorescein isothiocyanate labeled (Oncor, USA); all other total chromosomal probes were Cy3 labeled (Cambio, UK). Ten microliters of a single probe or a mixture of two probes with different chemical modification was applied on a microscope slide. Probe denaturation, hybridization and a post-hybridization wash were performed according to protocols very similar to those recommended by the probe manufacturers.

Briefly, we usually used a mixture of a painting probe with a centromeric probe of the same chromosome in the same hybridization. Each probe was prepared and denatured separately and mixed just before application onto the slide. For example, 10 µl of a painting probe for chromosome 9 from Oncor was denatured at 72°C for 10 min, centrifuged briefly and incubated at 37°C for 30 min to preanneal. Then 0.5 µl of a centromeric probe from Oncor was mixed with 9.5 µl of Hybrisol VI, denatured 10 min at 72°C and immediately cooled on ice, where the probe was kept until ready to use. Just before application on a slide, the painting probe was mixed with the centromeric probe. The unique sequences mixed together were the probes prepared in our laboratory (*BCL1* and *IGH*, *BCL1* and *FLI1*, *EWS* and *FLI1*) and the probes purchased from Oncor (c-*MYC* and *RB*). Two microliters (containing about 20 ng of DNA) of each of our own probes was mixed with 8 µl Hybrisol VI. The probes were denatured and preannealed separately under the same conditions as given above for painting probes and mixed just before application onto a slide. The probes for unique sequences of c-*MYC* and *RB* were not denatured and preannealed. Ten microliter aliquots of each probe were taken and mixed together just before their application on a slide as recommended by the manufacturer. The translocation DNA probes for M-*BCR*/*ABL* and *PML*/*RARA* (Oncor) are bicolor and were not combined with other probes. The probes were denatured for 5 min at 72°C and applied onto a slide. Applied probes were covered with a glass coverslip, sealed with rubber cement and incubated overnight in a humidified chamber. The post-hybridization wash was identical for all probes. 50% formamide, 2×SSC, pH 7 at 43°C for 15 min was followed with 3 washes in 0.1×SSC, 0.1% Triton X-100 at 43°C for 5 min. After detection of the signal with rhodamine-labeled anti-digoxigenin and fluorescein-labeled avidin (for probes that were not directly labeled), the slides were rinsed 3 times in 4×SSC with Igepal CA-630 for 4 min before application of counterstain 4′,6-diamidino-2-phenylindole (0.2 µg/ml) in Vectashield.

Repeated hybridization

Coverslips from the first hybridization were removed by the immersion of slides in 4×SSC, 0.1% Triton X-100. The slides were then washed in three changes of the same solution, once in 2×SSC (for 4 min each) and immediately denatured under the same conditions as during the first hybridization. Repeated hybridization was used for the visualization of the *ABL*/*BCR* genes and *PML*/*RARα* genes in the same nuclei.

Using repeated hybridization to the same genetic elements, it can be easily demonstrated that their positions in cell nuclei are not influenced by repeated denaturation (e.g. between the first and second hybridization). Images and the topographic parameters of signals obtained from the first and second hybridization are compared in the paper by Falk et al. (2002). In repeated hybridizations, the images are superimposed according to the positions of the weight centers of all nuclei in the image. Therefore, in spite of the fact that the positions of individual nuclei can be shifted up to 5 µm after re-hybridization and re-allocation, the superposition of images is calculated much more precisely (better than ±0.2 µm) (Kozubek M et al. 2001).

Confocal cytometry

High-resolution cytometry was performed as previously described (Kozubek M et al. 1999, 2001). A high-resolution cytometer based on an inverted completely automated Zeiss Axiovert 100 (Jena, Germany) fluorescence microscope equipped with a Carv confocal unit (Atto Instruments, USA) was used. Images were captured in confocal mode using a fully programmable Micromax digital CCD camera (Princeton Instruments, USA). The whole system was controlled by a personal computer equipped with two Intel Pentium III processors (Intel Corporation, San Francisco, Calif.). The acquisition of images with FISH-stained interphase nuclei was automated, as was the on-line analysis of image quality, finding cell nuclei and compression of images. The recording level of the intensity was set at the beginning of image acquisition using the acquisition time and the selection of a window in the dynamic range of the camera as parameters. In most cases, the intensity was stable enough to enable overnight runs of the cytometer. It was possible repeatedly to acquire hybridized nuclei. For each hybridization, the same cells were re-allocated, re-acquired and re-analyzed. The results of analyses from different hybridizations were then superimposed in the computer memory. This allowed an increase in the number of simultaneously observed genetic loci within the same nucleus. The number of nuclei recorded per hour depended on the acquisition time (intensity of light), the number of fluorochromes used, and the density of nuclei per image. Typical values for the number of nuclei per hour were 30–120.

Off-line analysis was performed using FISH 2.0 software (Kozubek M et al. 1999, 2001) that, in addition to other functions, allows correction for chromatic aberrations. The remaining errors related to chromatic aberrations were about 10–20 nm laterally and 10–60 nm axially (Kozubek M and Matula 2000). Orthogonal views (xy, xz, and yz) of 3D data were used to check the results of analysis. In repeated hybridizations, user-defined attributes were set for the identified signals to distinguish elements pertaining to a particular chromosomal homolog. Information about the signals was saved into text files and further analyzed using the Sigma Plot statistical package (Jandel Scientific, Calif.). Typical values of precision were 10–30 nm laterally and 20–100 nm axially. Typical values for resolution were 250–350 nm laterally and 700–900 nm axially as measured using 0.2 µm beads. The precision is defined as the standard deviation in the determination of the weight center of a signal; the resolution is the width of a small signal such as a 0.2 µm bead or a visualized short DNA sequence (i.e. the minimal distance at which two small signals of the same color can be distinguished) (Kozubek M 2001).

Evaluation of the results

Fluorescence weight centers of cell nuclei (FWC), chromosomal territories (FWT), genes and centromeres were determined (Kozubek M et al. 1999, 2001) and used for further calculations. The FWCs were used as the origins of the coordinate systems for the calculation of the topographic parameters of genes, centromeres and chromosomal territories. Radial distances were determined as the differences between the signal positions and FWCs. The radial distances were normalized to local radii (FWC to membrane distances determined in the directions of the given FISH signals in 3D space). The distances between homologous or heterologous elements were normalized to the average of the corresponding two local radii. The local radius was determined in the plane perpendicular to the x-y plane passing through the nuclear weight center and the signal investigated. The image in this plane was calculated and segmented using local thresholding (Kozubek M et al. 2001).

Cell nucleus sizes may differ slightly even in the same cell population (e.g. lymphocytes from the same donor); in these cases normalized parameters are well preserved for cells with different radii. Normalization should also reduce the effects of small deformation of cell nuclei: the absolute values of distances are much more influenced by deformation than the relative values. Cell nuclei of dividing cells were classified according to doublets, i.e., signals on both chromatids after DNA duplication. The proportion

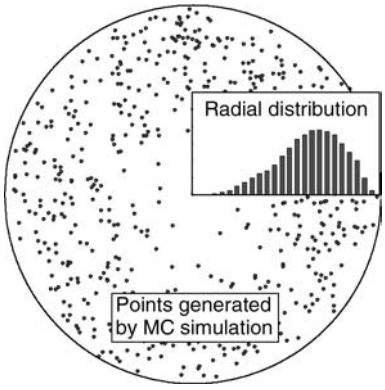

Fig. 1 Two-dimensional (2D) projections of spatial positions of points representing genetic elements in a sphere. The positions were calculated using a modulated random number generator in which the radial probability is modulated by experimental radial distributions (*insert*). (*MC* Monte-Carlo)

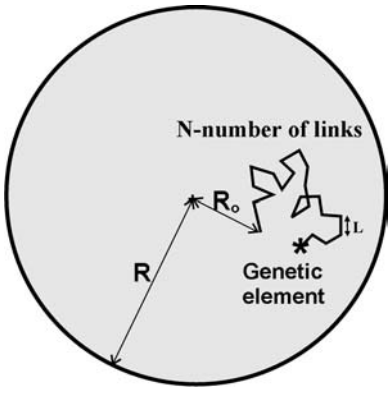

Fig. 2 Scheme of the random walk simulation. A genetic element (*asterisk*) is attached to a linear polymer with N links of length L. The polymer is anchored to the mean radial position of the element (R_0). Monte-Carlo simulation of the positions of N polymer links of length L was done step by step using the random number generator

of cells in G_1 represents the largest subpopulation of dividing cells. We excluded from the analysis cell nuclei with at least one double signal in order to reduce further the fraction of cells in the S- and G_2-phases of the cell cycle. Therefore, our results predominantly concern the G_1-stage of the cell cycle in dividing cells.

Average values for topographic parameters were determined from at least 3 independent experiments in which 500–2000 nuclei per experiment were analyzed. Comparison of different data sets was performed using the Student's *t*-test option in SigmaPlot (Jandel Scientific, Calif.).

The distribution of locus-to-locus distances of both homologous and heterologous genetic loci was compared with the theoretical expectation calculated according to the RS model (Kozubek S et al. 1997, 1999). In brief, positions in 3D space inside a sphere were generated using Monte-Carlo simulation precisely according to the measured radial distributions of the given genetic element(s) on the assumption of random angular distributions. First, the direction in 3D space of the position of an element was generated using 3 random numbers placed into a sphere as x, y, and z components of the direction vector. Second, the radial distance of an element was set by a modulated random number generator (i.e. a generator giving different probabilities at different radial distances; see Fig. 1). Experimental radial distributions were used as the amplitude of the generator modulation. In the next step, the distances between positions representing homologous (heterologous) elements were calculated for each generation. After 10^5 repeats, the distributions of the locus-to-locus distances were determined.

Random-walk function for a genetic element in a sphere

A very simple model is used to show that the radial distributions are probably produced as a consequence of the influence of a random factor: the radial positions of an element in different nuclei can be predicted as the result of a random walk of a polymer with an attached genetic element around some mean radial location. The radial distributions are, therefore, random (or Gaussian) distributions.

In order to calculate the model functions for radial distributions of genetic elements, we assumed that an element is attached to a linear polymer with N links of length L (Fig. 2). The polymer is anchored to the mean radial position of the element (R_0); its angular position is arbitrary. The positions of N polymer links with length L were determined step by step using a random number generator (see also Sachs et al. 1995). Monte Carlo simulation started from the medium position of an element at distance R_0 from the center of a sphere with radius R. The position of each next link was calculated using 3 random numbers (relative x, y, z coordinates) that determined the direction; the length was constant (L). Possible positions of the polymer links were limited by the spherical volume. The position of each link was tested and the calculation repeated if the position of the link happened to be outside the sphere. After N steps, the final position of the element was identified and its distance from the center of the sphere determined. The entire distribution was derived by repeating the calculation 30,000 times. The standard deviation of the element position (σ_e) was calculated using the number of links of the polymer (N) and the length of one link (L): $\sigma_e = L \times \sqrt{N}$. The mean positions, as well as the standard deviations, were fitted to experimental data.

The radius R was set to 20 for L=1 (the units and ratio are arbitrary but L << R). For different elements we obtained good agreement between experimental points and theoretical line if N was taken between 30–150 giving different standard deviations of the element positions. However, standard deviation is equal to $L \times \sqrt{N}$ and consequently the same results would be obtained for longer L if a smaller number of N is taken and vice versa. Therefore, L cannot be identified with a particular length of polymer (Kuhn length).

The biological mechanism of the creation of the radial distributions is not known and different mechanisms can be seen that will produce random (Gaussian) or nearly random radial distributions (for example random expansion of a chromosome during its decondensation in late telophase). The most straightforward idea is that random positioning around some mean location is due to random fluctuations of a polymer anchored to the mean position. This idea can also be easily modeled. This is the reason why the model described above was introduced.

Results

Owing to the large number of genetic elements and cell types investigated, results are shown only for selected genetic elements that cover the range of variability of topographic distributions. The other results (similar to some of those shown in the figures) are mentioned in the text.

Radial distributions of genes and centromeres in cell nuclei are locus specific and largely preserved in different cell types

The distances between the center of the nucleus and a genetic element were determined in nuclei of several

cell types and normalized to the local radii (the radius in the direction of a given element). The distributions of center-to-element distances, called "radial distributions", were investigated. In addition, the probability density of the genetic element occurrence per volume unit was calculated and distributions of these probabilities are presented. The significance of these distributions is illustrated in Fig. 3.

In Fig. 3, the positions of the *EWS* (Fig. 3A) and c-*MYC* (Fig. 3B) genes in the central section of the nucleus (width 1 μm) derived from 3D confocal measurements are shown. The point density represents the probability density per volume unit of the occurrence of the genetic element at a given position. For the *EWS* gene (Fig. 3A), the probability density is maximal at the center of the nucleus and very low at the nuclear periphery. The probability density of the occurrence of the c-*MYC* gene in the nuclear center is low (Fig. 3B), increasing to a maximum value at about 66% of the nuclear radius and decreasing again at the nuclear periphery.

The radial distributions of genetic elements depend on the volume accessible in the nucleus, which increases with the distance from the nuclear center (r) as r^2; the radial distributions of all genetic elements are, therefore, zero in the nuclear center (Fig. 3C, D). The results are shown only for the *EWS*, *IGH* and c-*MYC* genes (Fig. 3C), which represent roughly the range of variability of radial distributions of genes. The most central position was found for the *ABL* and *BCR* genes in G_0 lymphocytes (x_{av}≈50% of the local radius); slightly higher values for these genes (up to x_{av}=60%) were obtained for stimulated lymphocytes, HL-60, ML-1, U-937, HT-29 cells, and skin fibroblasts. Average center-to-gene distances of x_{av}=50%–60% were also demonstrated for the *EWS* gene in G_0 lymphocytes, HL-60 and Ewing sarcoma cells; for *TP53*, *PML*, and *BCL-1* genes in G_0 lymphocytes and ML-1 cells, for the *RARα* gene in G_0 lymphocytes, and for *APC* in HT-29 cells. A substantially more peripheral location, similar to c-*MYC* in G_0 lymphocytes or HL-60 cells (x_{av}≈75%), was observed for the *RB* gene in G_0 lymphocytes and HL-60 cells and for *FLI-1* in G_0 lymphocytes. c-*MYC* was also found at the nuclear periphery in skin fibroblasts.

Centromeres (C3, C6, C8, C9, C17, C18, and CX) in G_0 lymphocytes and HL-60 cells are usually located near the nuclear periphery (x_{av}≈70%–85%), although a more central location was observed for the C1 centromere (x_{av}≈60%). The results are shown only for C1, C9, and CX (Fig. 3D). Consistent results for genes and centromeres were previously found using either 2D or 3D analysis of cell nuclei of several other cell types including human colon tissue sections and bone marrow cells (Koutná et al. 2000; Skalníková et al. 2000).

In general, individual genetic elements exhibit characteristic distributions. On the other hand, similar values for the average location of individual genetic elements have been obtained in various cell lines, even for those obtained from tissue sections (colon tissue).

In Fig. 3E, F the probability density of genetic element occurrence per volume unit versus the nuclear radius is shown. This density should be constant (represented by a horizontal straight line) for homogeneously (i.e. randomly) distributed loci. The plots in Fig. 3E, F show the non-random positioning in cell nuclei of the same genetic loci as in Fig. 3C, D. In all cases, substantial deviations from random distributions were observed. Some genetic elements located in the nuclear interior (*EWS*, *ABL*, *IGH*, *BCR*, *TP53*, etc.) have an average location at a distance of about 50% from the nuclear center (in Fig. 3C shown for *EWS* and *IGH*). However, the density of the occurrence of these genes per unit volume is higher at shorter distances from the nuclear center (Fig. 3E). The same tendency is also observed for elements located near the nuclear membrane. This difference between the two plots is related to the increasing available space at larger distances from the nuclear center.

The curves in Fig. 3C, D were calculated according to the random-walk function for a genetic element in a sphere (see Materials and methods). Mean radial values (R_0) of the theoretical distributions of center-to-element distances range from 40% to 50% of the local radius for *ABL*, *BCR*, *EWS*, *TP53*; R_0=50%–60% for *IGH*, *RARα*, and 60%–70% for c-*MYC*, *FLI-1*, and *RB*. For centromeres, values of R_0=50%–60% for C1 and R_0=65%–75% for C6, C8, C9, C17, and C18 were obtained. The standard deviation values (σ_r) range from 15% to 25 % for different genetic elements. The functions derived theoretically describe the experimental distributions well, as seen in Fig. 3C, D.

Angular distributions of genetic elements in cell nuclei are random

One of the easily measurable topographic nuclear parameters is the distance between homologous genetic loci. Interpretation of the distributions of these distances is, however, quite difficult. The situation becomes much more straightforward if the coordinates of the center of the nucleus are known and the locus-center-locus angle is investigated. We refer to the distribution of these angles as "angular distribution".

When plotting a pair of genetic elements in the cell nucleus with the origin of the coordinate system in its center (FWC), one element can be positioned on the x-axis and the second rotated around the x-axis to reach the x-y plane. Then the locus-center-locus angle is visualized in 2D. These angles are shown for the *ABL* and c-*MYC* genes in G_0 lymphocytes in Fig. 4A, B. As shown, the angles are more frequent around 90° and less frequent at 0° and 180°.

The reason for such a distribution becomes clear if we imagine that the genetic elements are located on the surface of a sphere (at the same radial distance for the sake of simplicity) and one of the homologous loci is placed on the x-axis (Fig. 4C). Random positioning of

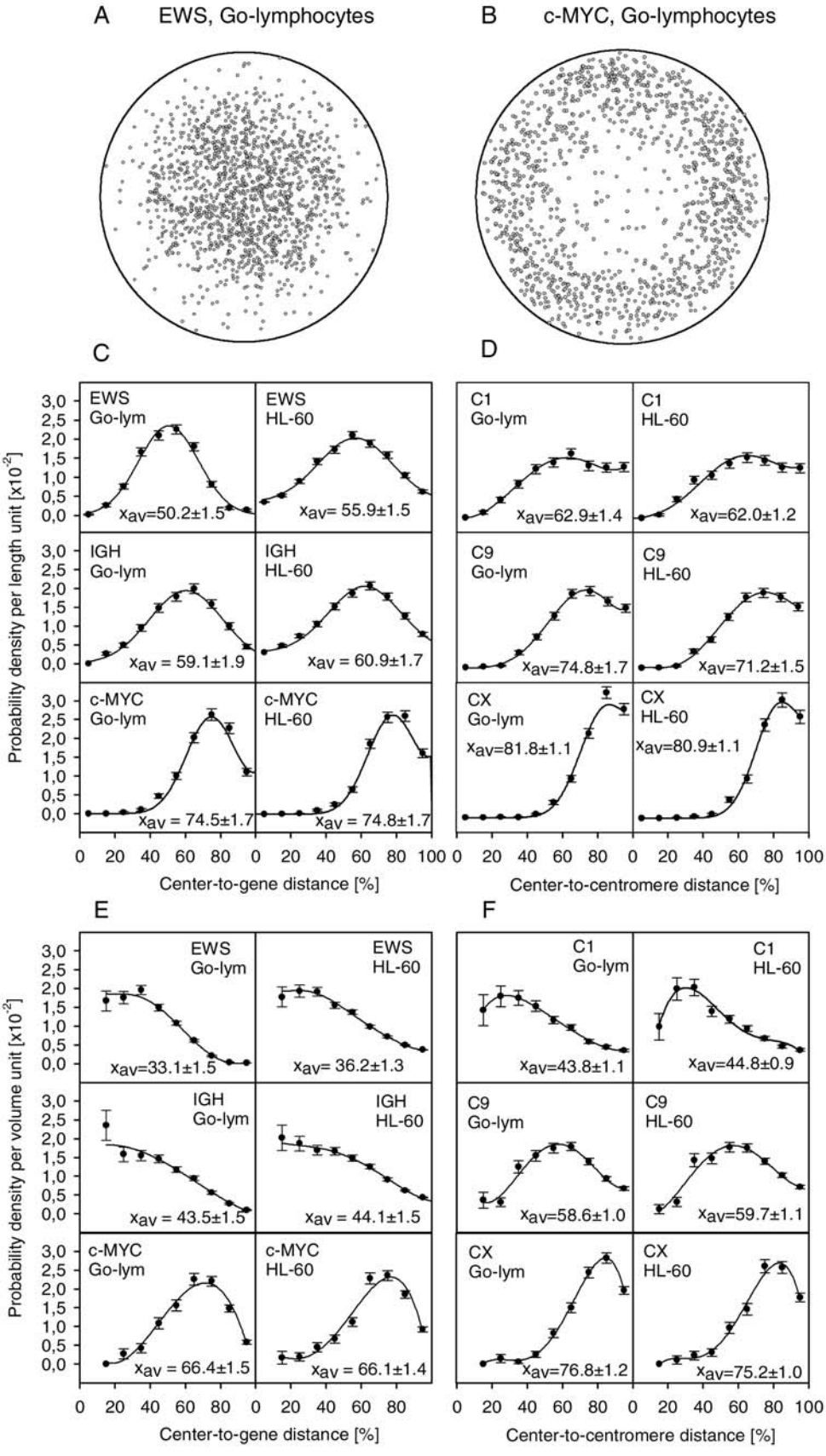

Fig. 3A–F Radial distributions of genetic loci in human cell nuclei. **A, B** The central section of a cell nucleus (1 μm thick) with x-y positions of the *EWS* (**A**) and c-*MYC* (**B**) genes from approximately 2000 nuclei with similar radii. The distributions are nonrandom and different for various genetic elements. **C, D** Radial 3D distributions for the *EWS*, *IGH,* and c-*MYC* genes (**C**) and chromosomes 1, 9, and X centromeres (**D**) are shown for G_0 lymphocytes and HL-60 cells. Experimental points are shown with standard errors. Mean values of the distributions (x_{av}) and their standard errors are given in each panel. Theoretical curves were calculated using the random-walk model. **E, F** Distributions of the probability density of occurrence of an element versus the center-to-element distances for the same genetic elements and cell types as in **C** and **D**. Experimental points are shown with standard errors

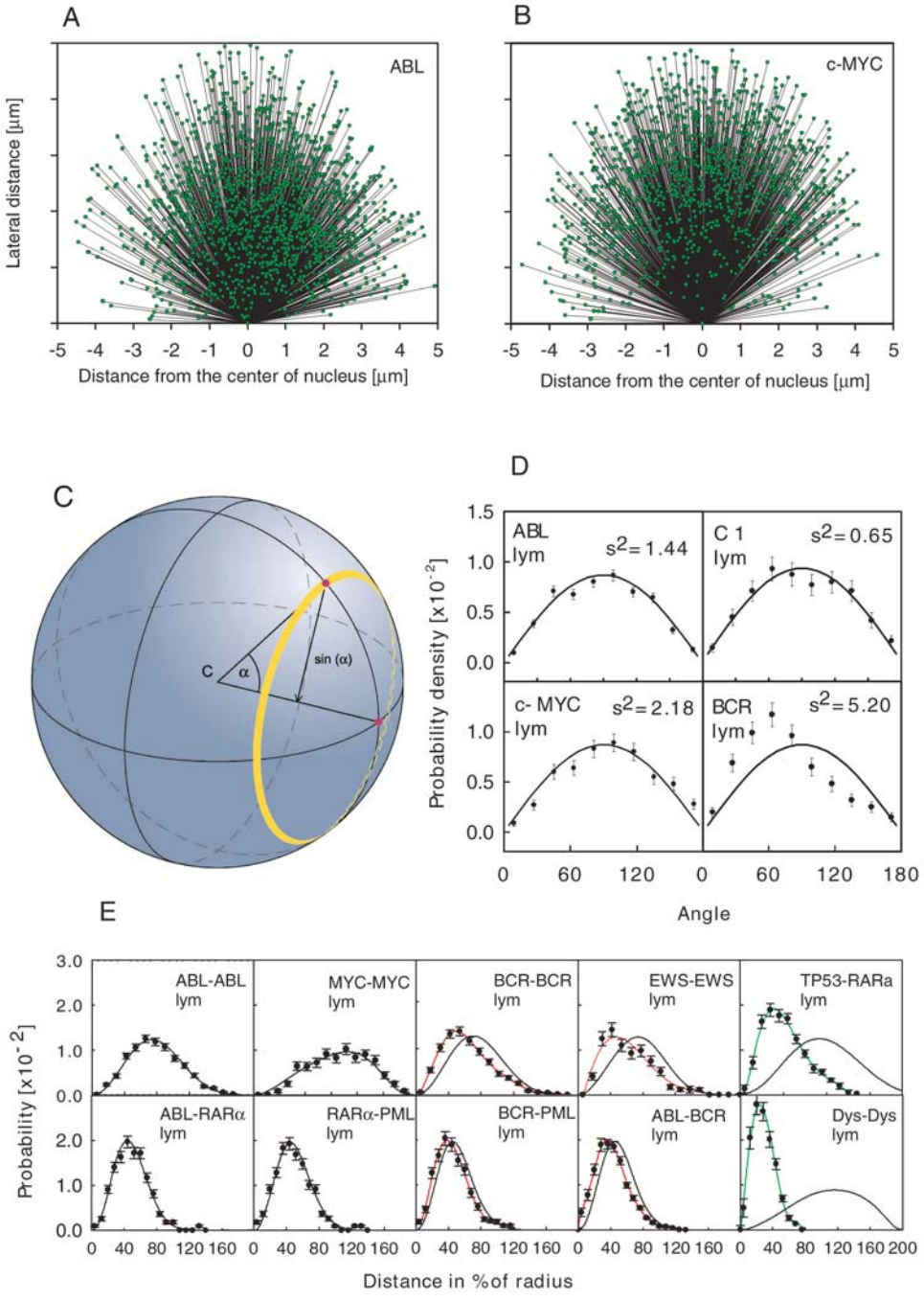

Fig. 4A–E Angular and distance distributions of homologous and heterologous genetic loci in human cell nuclei. **A, B** Gene-center-gene angles are shown for the *ABL* (**A**) and c-*MYC* (**B**) genes. One of the homologous genes was positioned on the x-axis, the second was positioned in the x-y plane by rotating around the axis. **C** Scheme showing a model situation in which the loci are placed on the surface of a sphere, one of them on the x-axis. The *yellow sector* shows part of a spherical surface corresponding to the locus-center-locus angle α. The area of the sector is proportional to sin(α). **D** The angular distributions for the *ABL*, c-*MYC*, *C1*, and *BCR* genetic elements are shown. In order to test the randomness of the angular distribution, the sum of squares of differences between experimental and theoretical values was calculated and normalized to standard deviation and to degree of freedom (number of experimental points). This quantity has χ^2 distribution and its value should be near to 1. The sum of squares per degree of freedom (s^2) shows good agreement of the distributions with the sine function for *ABL*, c-*MYC*, and *C1*. The same distributions for the *BCR* (*lower right panel*) and *EWS* (not shown) genes show substantial deviations from the sine function with maximum occurrence of an angle of 60°. The sum of squares per degree of freedom is s^2=5.20 for *BCR* and 4.20 for *EWS*, which rules out random angular distributions of the *BCR* or *EWS* genes. Experimental points are shown with standard errors. **E** Gene-to-gene distance distributions for several homologous and heterologous genes. Experimental distributions (*points*) are compared with theoretical calculations using the RS model (*black curves*), which is based on the assumption of random positioning of genetic loci inside spherical layers (shells). Good agreement was achieved in the vast majority of cases; for the purposes of illustration, the *four panels on the left* show *ABL-ABL*, *MYC-MYC*, *ABL-RARα*, and *RARα-PML*. The gene-to-gene distance distributions are shifted to shorter values for genetic elements of chromosomes participating in the formation of nucleoli (*BCR* and *EWS* homologous loci, *BCR* and *PML*) and also for *ABL* and *BCR* genes in G_0 lymphocytes (*red curves*). This shift reflects some kind of tethering between chromosomes. As expected, a shift to lower values of the mutual distances was also found for genes pertaining to the same chromosome (dystrophin exons, *TP53*, and *RARα*) (*green curves*). Experimental points are shown with standard errors

the second element on the surface of the sphere then corresponds to the random angular distribution. All elements having the same angle are located in a fraction of the spherical surface (see the yellow sector in Fig. 4C). Consequently, the frequency of the occurrence of a given angle should be proportional to the fraction of the corresponding spherical surface. Random angular distribution is, therefore, described by the sine function of the locus-center-locus angle. Owing to the small surface areas corresponding to the sine function of 0° and 180°, the number of elements occurring under these angles is low. The largest surface area corresponds to an angle of 90° and, therefore, the highest probability of the occurrence of an element is at this angle.

We have tested the randomness of angular distributions for a large number of homologous pairs of genetic loci, and comparison of the distributions with the sine function shows extremely good agreement. Examples of the angular distributions for the *ABL*, c-*MYC*, and C1 loci in nuclei of human lymphocytes are shown in Fig. 4D. Very similar results without significant deviations from the sine function were also obtained for all the genetic elements and cell types mentioned in the previous section (not shown). There are, however, several exceptions to this rule. The occurrence of homologous *BCR* and *EWS* genes under an angle of about 60° was significantly higher than the value predicted by the sine function (see Fig. 4D, panel for the *BCR* gene).

The distributions of distances between homologous genetic loci obtained experimentally can be theoretically predicted using Monte-Carlo simulation (see Materials and methods) based on the assumption of random angular positioning of genetic loci. Good agreement was achieved between experiment and theory in a large number of measurements. In Fig. 4E, the distance distributions between homologous genes are shown for *ABL* and c-*MYC*. Similar agreement between experimental and theoretical distance distributions of homologous regions was also observed for *RARα*, *BCL-1*, *PML*, *IGH*, *FLI-1*, and *RB* genes, and for centromeres C1, C3, C6, C8, C9, C17, and C18 (not shown). Two exceptions were found in the distance distributions of homologous genes; distances *BCR-BCR* and *EWS-EWS* (Fig. 4E) were significantly shifted to lower values compared with the predicted distributions. Both of these genes are located on chromosome 22.

By investigating the angular distributions and distance distributions of homologous pairs, it can be demonstrated that genetic loci of the same chromosome are mutually interrelated and, therefore, their mutual spatial positioning is not random. For example, the distance distribution between two chromosome X regions represented by exons 5–7 and 46–47 of the dystrophin gene separated by a molecular distance of 0.97 Mb (Fig. 4E) is quite different from the theoretically predicted random distribution (Fig. 4E, lower right panel). A similar difference was also observed for the distributions of distances between *TP53* (17p13.1) and *RARα* (17q21) genes pertaining to chromosome 17, which are, however, separated by a larger molecular distance than the exons of dystrophin (Fig. 4E, upper right panel).

If genetic elements on different chromosomes are independent of one another, then they should exhibit random mutual distributions (for both angles and distances). One sensitive test of possible non-randomness is a comparison of an experimentally measured distribution of the minimal of four possible distances between heterologous elements for each nucleus, with this distance distribution predicted by Monte-Carlo simulation using the RS model (see Materials and methods). Examples of distributions of minimal distances between different genetic elements stained in dual-color hybridization are shown in Fig. 4E for the *ABL-RARα*, *RARα-PML*, *BCR-PML*, and *ABL-BCR* genes in G_0 lymphocytes. The distributions for the *ABL-RARα* and *RARα-PML* genes agree with theoretical prediction. Similar agreement was observed for the *BCR-RARα*, *EWS-FLI-1*, *ABL-MYC*, and *BCR-MYC* genes (not shown). However, the experimental distributions of minimal distances between *ABL-BCR* and *BCR-PML* in human lymphocytes exhibit differences from theoretical predictions (Fig. 4E); the distribution of these distances is shifted to lower values. In about 10%–25% of G_0 lymphocytes from five different healthy individuals, the minimal distance between *ABL* and *BCR* genes was less than 1 μm. No translocation between these genes was found in metaphases of stimulated lymphocytes from these individuals. The shift of distance distributions for the *ABL* and *BCR* genes was not observed for stimulated lymphocytes and HL-60 cells; however, tethering was observed in preliminary experiments for $CD34^+$ progenitor cells (not shown).

Mean radial position of chromosomal territories correlates with the average level of their gene expression

Radial distributions of the fluorescence weight centers of chromosomal territories (FWT) measured in 3D for cell nuclei of human G_0 lymphocytes were determined for 22 chromosomes (Fig. 5 A). The most central location was found for chromosomes 16, 19, and 22; the most peripheral for chromosomes 3, 4, 8, and 18 (Fig. 5B). In Fig. 5B, the average 3D positions of the FWTs are presented for human G_0 lymphocytes versus the level of gene expression of individual chromosomes derived from the transcriptome map (see Materials and methods).

As seen in Fig. 5B, the center-to-chromosome mean distance is approximately proportional to the average level of gene expression for G_0 lymphocytes. The radial distributions of chromosomal positions in cell nuclei are rather broad, which means that there is a great variability of radial positions of chromosomal territories. This variability may be in part due to non-homogeneous staining of condensed and decondensed parts of chromosomes using painting probes.

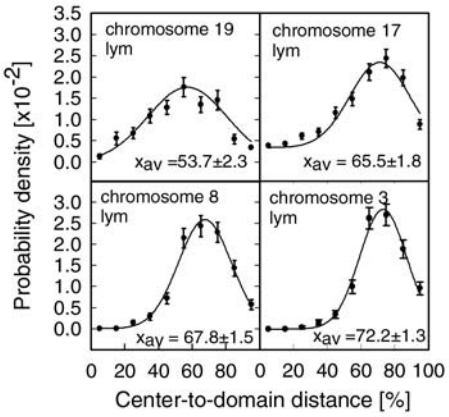

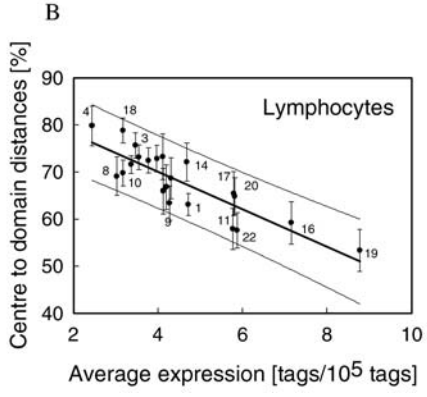

Fig. 5A, B Location of chromosomal domains in human cell nuclei. **A** Radial 3D distributions of chromosomal domains in cell nuclei of human G_0 lymphocytes are shown for four chromosomes. The mean values of the distributions and their standard errors are given in each panel. **B** The dependence of the mean 3D distances between the nuclear center (FWC) and the chromosomal fluorescence center (FWT) on the average level of gene expression of an individual chromosome. Experimental points are shown with 95% confidence intervals. The results of linear regression are presented with 95% prediction intervals; the correlation coefficient is 0.73 (P<0.01). For groups of chromosomes that are not marked in the figure: chromosomes 21, 15, and 6 are located above chromosome 9; chromosomes 2, 5, 7, and 13 are located below chromosome 3

Discussion

In this paper we have presented a comprehensive study of the spatial organization of various genetic elements (genes, centromeres and chromosomal territories) in the cell nucleus based on a large number of 3D measurements. An integrated view of the structure of the interphase cell nucleus is presented and an attempt is made to discover the principles of the 3D arrangement in relation to its function.

We have shown for many genetic elements that their locations form a non-random radial distribution between the center of the nucleus and the membrane. In addition, our results show that the average center of nucleus-to-element distances are element specific and largely maintained in different cell types. However, the mutual positions of the majority of investigated homologous elements at a given radial distance are random. Consequently, their angular distributions are also random; this has been verified for a large number of homologous and heterologous pairs of loci. This type of randomness in the location of genetic elements might be largely responsible for the variability of cell nuclei.

It should be noted that the compatibility of experimental distributions with "random models" might be due to the effect of the overlay of many nuclear structures, each of them being nonrandom but following a complex rule. Therefore, it cannot be excluded that there are subtle rules of nuclear organization that lead or allow different arrangements in various nuclei that are observed as random.

Earlier observations by various authors have shown either nonrandom or random arrangement of specific genetic elements in nuclei of various eukaryotic cells. Marshall et al. (1996) demonstrated specific radial positioning, together with lateral positioning relative to the nuclear axis, of chromosomal loci in *Drosophila*. On the other hand, the relative arrangement of chromosomal homologs to each other did not appear to be spatially defined or regulated in mouse lymphocytes (Vourc'h et al. 1993). Recent observations of living yeast show that early firing origins of DNA replication are randomly localized within the nucleus through the cell cycle, while the position of late firing origins is highly dynamic due to the specific modification of chromatin structure in this region (Heun et al. 2001). Contrary to this observation, studies of living human cells suggest that chromosomal regions are relatively immobile during interphase (Shelby et al. 1996; Zink et al. 1998). A nonrandom radial arrangement of some small and large chromosomal territories in spherical and ellipsoid human cell nuclei was observed by Cremer et al. (2001).

In our experiments, a nonrandom angular distribution of homologous and heterologous elements was found in some cases. Shorter distances than predicted by random distribution were found between *BCR*/*BCR* genes located on homologous acrocentric chromosomes or between *BCR*/*PML* belonging to heterologous acrocentric chromosomes. Acrocentric chromosomes participate in the formation of the nucleolus and it is possible that this common function influences their nuclear location and leads in some cases to mutual proximity.

The reasons for the close proximity (tethered state) of specific regions are not known. One explanation could be that it is due to some functional dependence between these regions (Savage 2000) or a consequence of the association with particular proteins maintaining special genomic regions or whole individual chromosomes in mutual proximity. The nonrandom organization of some chromosomes in prometaphase rosettes, consisting in the frequent adjacency of specific chromosomes, has been shown by Nagele et al. (1995). The proximity of specific chromosomal regions can lead to their mutual rearrangement under some conditions, as was shown for RET/H4 (Nikiforova et al. 2000). Our results obtained in 2D (Kozubek S et al. 1999) or 3D (this paper) show very

close proximity of *ABL*/*BCR* genes (<1 μm) in about 15%–20% of G_0 lymphocytes. The proximity of these regions might be one of the reasons for their interchanges and the formation of the Philadelphia chromosome typical of chronic myeloid leukemia (Rabbitts 1994). The high frequency of interchanges induced by fast neutrons between chromosomes involved in translocations leading to most frequent hematologic malignancies also indicates the nonrandom arrangement of some chromosomes in cell nuclei (Lukásová et al. 1999).

It follows from the results presented that the location of chromosomes in the cell nucleus correlates well with the average level of expression of genes on the chromosomes. The domains of chromosomes with a very high level of expression (19, 22, 16 and 17) are located in the nuclear interior (Fig. 5B). The dependence of the chromosomal location on gene density in 2D has been studied earlier for lymphoblasts (Boyle et al. 2001). The degree of correlation for both gene density and average gene expression is similar. Croft et al. (1999) found that gene-rich chromosome 19 is located near the nuclear center, while gene-poor chromosome 18 occurs near the nuclear periphery. We have previously reported that gene-rich chromosomes 9 and 22 are found in the nuclear interior, while gene-poor chromosome 8 is found at the nuclear periphery (Kozubek S et al. 1999). The results presented here show several small differences (<5.5%) between the positions measured and those expected from their expression.

The location of genes belonging to highly expressed gene regions (e.g. *ABL*, *BCR*, *BCL-1*) as well as the location of chromosomal territories rich in highly expressed genes (19, 16, 22, 17) in the nuclear interior, strongly suggest that the highly expressed gene regions themselves are located in the nuclear interior. In addition, we have demonstrated that the nuclear location of chromosomal regions is preserved in different cell types, which correlates very well with the recent finding that clusters of highly expressed genes (RIDGEs) reside at the same chromosomal location in various cell types (Caron et al. 2001). These results indicate that the mechanism through which functional nuclear organization of chromatin is established and maintained consists in the arrangement of highly expressed genes to clusters located in specific regions of individual chromosomes that are predominantly localized in the nuclear interior. Thus, two principal compartments composed of regions with high gene expression (RIDGEs) and regions with low gene expression (RILGEs), to which multiple regions of individual chromosomes contribute, are established in cell nuclei. This interphase compartmentalization is probably established during the late telophase and early G_1, and does not depend upon activation of gene expression at the time of compartment formation (see Ferreira et al. 1997). Tissue-specific genes do not seem to influence the basic location of a chromosome; however, induced transcription of some gene(s) can lead to changes to the structure of the locus and its nuclear location particularly for large loci. This has been shown by Volpi et al. (2000) for the MHC region involving about 3 Mb.

Acknowledgements We thank H. Krivánková and V. Fucíková for their technical assistance. This work was supported by the Academy of Sciences (Z5004920, S5004010), Ministry of Education (MSM 143300002), Ministry of Health (NC5955), and Grant Agency of the Czech Republic (202/01/0197 and 301/01/0186).

References

Belmont AS, Bruce K (1994) Visualization of G_1 chromosomes: a folded, twisted, supercoiled chromonema model of interphase chromatid structure. J Cell Biol 127:287–302

Boyle S, Gilchrist S, Bridger JM, Mahy NL, Ellis JA, Bickmore WA (2001) The spatial organisation of human chromosomes within the nuclei of normal and emerin-mutant cells. Hum Mol Genet 10:211–219

Caron H, Van Schaik B, Van der Mee M, Baas F, Riggins G, Van Sluis P, Hermus MC, Van Asperen R, Boon K, Voute PA, Heisterkamp S, Van Kampen A, Versteeg R (2001) The human transcriptome map: clustering of highly expressed genes in chromosomal domains. Science 291:1289–1292

Cook PR, Brazell IA, Jost E (1975) Characterization of nuclear structures containing superhelical DNA. J Cell Sci 22:303–324

Cremer M, Hase J, Volm T, Brero A, Kreth G, Walter J, Fischer C, Solovei I, Cremer C, Cremer T (2001) Non-random radial higher-order chromatin arrangements in nuclei of diploid human cells. Chromosome Res 9:541–567

Cremer T, Lichter P, Borden J, Ward DC, Manuelidis L (1988) Detection of chromosomal aberrations in metaphase and interphase tumor cells by in situ hybridization using chromosome specific library probes. Hum Genet 80:235–246

Croft JA, Bridger JM, Boyle S, Perry P, Teague P, Bickmore WA (1999) Differences in the localization and morphology of chromosomes in the human nucleus. J Cell Biol 145:1119–1131

Falk M, Lukásová E, Kozubek S, Kozubek M (2002) Topography of genetic elements of X-chromosome in the cell nucleus and relatively to the chromosome X territory in human lymphocytes. Gene 292:13–24

Ferreira J, Paolella G, Ramos C, Lamond AL (1997) Spatial organization of large-scale chromatin domains in the nucleus: a magnified view of single chromosome territories. J Cell Biol 139:1597–1610

Heun P, Laroche T, Raghuraman MK, Gasser SM (2001) The positioning and dynamics of origins of replication in the budding yeast nucleus. J Cell Biol 152:385–400

Koutná I, Kozubek S, Zaloudík J, Kozubek M, Lukásová E, Matula P, Bártová E, Skalníková M, Cafourková A, Jirsová P (2000) Topography of genetic loci in tissue samples: towards new diagnostic tool using interphase FISH and high-resolution image analysis techniques. Anal Cell Pathol 20:173–185

Kozubek M (2001) Theoretical versus experimental resolution in optical microscopy. Microsc Res Tech 53:157–166

Kozubek M, Matula P (2000) An efficient algorithm for measurement and correction of chromatic aberrations in fluorescence microscopy. J Microsc 200:206–217

Kozubek M, Kozubek S, Lukásová E, Marecková A, Bártová E, Skalníková M, Jergová A (1999) High-resolution cytometry of FISH dots in interphase cell nuclei. Cytometry 36:279–293

Kozubek M, Kozubek S, Lukásová E, Bártová E, Skalníková M, Matula Pa, Matula Pe, Jirsová P, Cafourková A, Koutná I (2001) Combined confocal and wide-field high-resolution cytometry of FISH stained cells. Cytometry 45:1–12

Kozubek S, Lukásová E, Rýznar L, Kozubek M, Lisková A, Govorun RD, Krasavin EA, Horneck G (1997) Distribution of ABL and BCR genes in cell nuclei of normal and irradiated lymphocytes. Blood 89:4537–4545

Kozubek S, Lukásová E, Marecková A, Skalníková M, Kozubek M, Bártová E, Kroha V, Krahulcová E, Slotová J (1999) The topological organization of chromosomes 9 and 22 in cell nuclei has a determinative role in the induction of t(9,22) translocations and in the pathogenesis of t(9,22) leukemias. Chromosoma 108:426–435

Lamond AI, Earnshaw WC (1998) Structure and function in the nucleus. Science 280:547–553

Li G, Sudlow G, Belmont AS (1998) Interphase cell cycle dynamics of late replicating, heterochromatic homogenously staining regions: precise choreography of condensation/decondensation and intracellular positioning. J Cell Biol 140:975-989

Lichter P, Cremer T, Borden J, Manuelidis L, Ward DC (1988) Delineation of individual human chromosomes in metaphase and interphase cells by in situ suppression hybridization using recombinant DNA libraries. Hum Genet 80:224–234

Lukásová E, Kozubek S, Kozubek M, Kroha V, Marecková A, Skalníková M, Bártová E, Slotová J (1999) Chromosomes participating in translocations typical of malignant hemoblastoses are also involved in exchange aberrations induced by fast neutrons. Radiat Res 151:375–384

Manuelidis L, Chen TL (1990) A unified model of eucaryotic chromosomes. Cytometry 11:8–25

Marshall WF, Dernburg AF, Harmon B, Agard DA, Sedat JW (1996) Specific interactions of chromatin with the nuclear envelope – positional determination within the nucleus in *Drosophila melanogaster*. Mol Biol Cell 7:825–842

Münkel C, Eils R, Dietzel S, Zink D, Mehring C, Wedemann G, Cremer T, Langowski J (1999) Compartmentalization of interphase chromosomes observed in simulation and experiment. J Mol Biol 285:1053–1065

Nagele R, Freeman T, McMorrow L, Lee H (1995) Precise spatial positioning of chromosomes during prometaphase: evidence for chromosome order in human cells. Science 270:1831–1835

Neves H, Ramos C, Gomez da Silva M, Parreira A, Parreira L (1999) The nuclear topography of ABL, BCR, PML and RARα genes: evidence for gene proximity in specific phases of the cell cycle and stages of hematopoietic differentiation. Blood 93:1197–1207

Nikiforova MN, Stringer JR, Blough R, Medvedovic M, Fagin JA, Nikiforov YE (2000) Proximity of chromosomal loci that participate in radiation-induced rearrangements in human cells. Science 290:138–142

Parreira L, Telhada M, Ramos C, Hernandez R, Neves H, Carmo-Fonseca M (1997) The spatial distribution of human immunoglobulin genes within the nucleus: evidence for gene topography independent of cell type and transcriptional activity. Hum Genet 100:588–594

Paulson JR, Laemmli UK (1977) The structure of histone-depleted metaphase chromosomes. Cell 12:817–828

Pinkel D, Landegent J, Collins C, Fuscoe J, Segraves R, Lucas J, Gray JW (1988) Fluorescence in situ hybridization with human chromosome-specific libraries: detection of trisomy 21 and translocations of chromosomes 4. Proc Natl Acad Sci USA 85:9138–9142

Rabbitts TH (1994) Chromosomal translocations in human cancer. Nature 372:143–149

Sachs RK, van den Engh G, Trask B, Yokota H, Hearst JE (1995) A random-walk/giant-loop model for interphase chromosomes. Proc Natl Acad Sci U S A 92:2710-2714

Sadoni N, Langer S, Fauth C, Bernardi G, Cremer T, Turner BM, Zink D (1999) Nuclear organization of mammalian genomes: polar chromosome territories build up functionally distinct higher order compartments. J Cell Biol 146:1211–1226

Savage JK (2000) Proximity matters. Science 290:62–63

Schardin MT, Cremer T, Hager HD, Lang M (1985) Specific staining of human chromosome position in chinese hamster x man hybrid cell lines demonstrates interphase chromosome territories. Hum Genet 71:281–287

Shelby RD, Hahn KM, Sullivan KF (1996) Dynamic elastic behaviour of α-satellite DNA domains visualized in situ in living human cells. J Cell Biol 135:545-557

Skalníková M, Kozubek S, Lukásová E, Bártová E, Jirsová P, Cafourková A, Koutná I, Kozubek M (2000) Spatial arrangement of genes, centromeres and chromosomes in human blood cell nuclei and its changes during the cell cycle, differentiation and after irradiation. Chromosome Res 8:487–499

Visser AE, Aten JA (1999) Chromosomes as well as chromosomal subdomains constitute distinct units in interphase nuclei. J Cell Sci 112:3353–3360

Vogelstein B, Pardoll DM, Coffey DS (1980) Supercoiled loops and euchromatic DNA replication. Cell 22:79–85

Volpi EV, Chevret E, Jones T, Vatcheva R, Williamson J, Beck S, Campbell RD, Goldsworthy M, Powis SH, Ragoussis J, Trowsdale J, Sheer D (2000) Large-scale chromatin organization of the major histocompatibility complex and other regions of human chromosome 6 and its response to interferon in interphase nuclei. J Cell Sci 113:1565–1576

Vourc'h C, Taruscio D, Boyle AL, Ward DC (1993) Cell cycle-dependent distribution of telomeres, centromeres, and chromosome-specific subsatellite domains in the interphase nucleus of mouse lymphocytes. Exp Cell Res 205:142–151

Yokota H, van den Engh G, Hearst JE, Sachs RK, Trask BJ (1995) Evidence for the organization of chromatin in megabase pair-sized loops arranged along a random walk path in human G_0/G_1 interphase nucleus. J Cell Biol 130:1239–1249

Zink D, Cremer T, Saffrich R, Fischer R, Trendelenburg MF, Ansorge W, Stelzer EHK (1998) Structure and dynamics of human interphase chromosome territories in vivo. Hum Genet 102:241–251

Chromosome Research **10**: 535–548, 2002.

The 3D structure of human chromosomes in cell nuclei

E. Lukášová[1], S. Kozubek[1]*, M. Kozubek[2], M. Falk[1] & J. Amrichová[2]
[1]*Laboratory of Molecular Cytology and Cytometry, Institute of Biophysics, Academy of Sciences of the Czech Republic, Královopolská 135, 612 65 Brno, Czech Republic; Tel: (+420 5) 4151 7139; Fax: (+420 5) 41240498; E-mail: kozubek@ibp.cz;* [2]*Laboratory of Optical Microscopy, Faculty of Informatics, Masaryk University, Botanická 68a, Brno, Czech Republic*
**Correspondence*

Received 3 June 2002. Received in revised form and accepted for publication by Adrian Sumner 14 August 2002

Key words: chromosome structure, confocal microscopy, mathematical models, nuclear architecture

Abstract

The spatial arrangement of some genetic elements relative to chromosome territories and in parallel with the cell nucleus was investigated in human lymphocytes. The structure of the chromosome territories was studied in chromosomes containing regions (clusters) of highly expressed genes (HSA 9, 17) and those without such clusters (HSA 8, 13). In chromosomes containing highly expressed regions, the elements pertaining to these regions were found close to the centre of the nucleus on the inner sides of chromosome territories; those pertaining to regions with low expression were localized close to the nuclear membrane on the opposite sides of the territories. In chromosomes with generally low expression (HSA 8, 13), the elements investigated were found symmetrically distributed over the territories. Based on the investigations of the chromosome structure, the following conclusions are suggested: (1) Chromosome territories have a non-random internal 3D structure with defined average mutual positions between elements. For example, RARα, TP53 and Iso-q of HSA 17 are nearer to each other than they are to the HSA 17 centromere. (2) The structure of a chromosome territory reflects the number and chromosome location of clusters of highly expressed genes. (3) Chromosome territories behave to some extent as solid bodies: if the territory is found closer to the nuclear centre, the individual genetic elements of this chromosome are also found, on average, closer the centre of the nucleus. (4) The positions of centromeres are, on average, nearer to the fluorescence weight centre of the territory (FWCT) than to genes. (5) Active genes are not found near the centromeres of their own territory. A simple model of the structure of chromosome territory is proposed.

Introduction

The arrangement of interphase chromosomes into separate territories provides a framework for the investigation of the relationship between the higher-order chromatin structure and function (Cremer *et al*. 1988, Lichter *et al*. 1988, Pinkel *et al*. 1988). A basic question is whether gene expression

is determined, at least in part, by the structure of chromosome territory. The studies trying to resolve this issue are aimed at determining whether particular genomic sequences occupy special positions within chromosome territories, whether these positions differ according to the transcriptional activity of the sequences and whether genomic regions or whole individual chromosomes occupy particular compartments within the cell nucleus (Belmont & Bruce 1994, Nagele *et al*. 1995, Ferreira *et al*. 1997, Lamond & Ernshaw 1998, Belmont *et al*. 1999, Cockel & Gasser 1999, Croft *et al*. 1999, Sadoni *et al*. 1999, Verschure *et al*. 1999, Nagele *et al*. 2000, Volpi *et al*. 2000, Chevret *et al*. 2000, Cremer *et al*. 2000, Cremer & Cremer 2001, Sadoni *et al*. 2001).

Several studies lend support to the hypothesis that genes are not randomly positioned within chromosome territories and that the transcriptional status of certain genes is affected by their nuclear topography. Kurz *et al*. (1996) noted that several active and inactive genes were preferentially located on the periphery of chromosome territories; Volpi *et al*. (2000) described the three-dimensional large-scale chromatin organisation of the major histocompatibility complex locus on human chromosome 6. These authors observed large chromatin loops containing several Mb of DNA extending outwards from the chromosome territory. Transcriptional upregulation led to an increase in the frequency with which active genes (but not inactive control genes) were found on an external chromatin loop.

Dynamic repositioning of certain genes in mouse lymphocytes and during differentiation of HL-60 cells depending on their transcriptional status was observed (Brown *et al*. 1997, 1999, Bártová *et al*. 2002). The transcriptionally inactive genes were localized at centromeric heterochromatin clusters in contrast to transcriptionally active genes which were positioned away from them. In spite of evidence that the proximity of genetic loci to the centromeric heterochromatin leads to inactivation of their transcription activity, very little is known about the mechanisms controlling the spatial and functional distribution of chromatin within the nucleus.

The relationship between the nuclear localization of chromosomes and their gene content was shown for the first time by Jenny Croft *et al*. (1999) for HSA 19 and 18. The authors showed that gene-rich HSA 19 is located in the centre of the nucleus, while similarly sized HSA 18 poorly populated with genes adopt a more peripheral position in the cell nucleus. Further results from our laboratory (Bártová *et al*. 2001, Kozubek S. *et al*. 2002) and Bickmore's laboratory (Boyle *et al*. 2001) show that other chromosomes containing more actively transcribed genes also adopt a more internal position in the cell nucleus contrary to gene-poor chromosomes.

With the progress of genome-sequencing projects, a genetic map has been developed showing the chromosomal positions of about 24 thousand genes. In addition to this, the expression profiles for any chromosomal regions in several normal and pathological tissue types were also detected. These expression profiles reveal clustering of highly expressed genes into specific chromosomal regions that are largely conserved in different tissues, indicating that this arrangement may be reflected in the higher order structure of the genome (Caron *et al*. 2001).

In this study we have tried to determine whether the arrangement of highly expressed genes into clusters on individual chromosomes is actually translated into the structure of chromosome territories in the cell nucleus. The structure of the chromosome territories was studied in chromosomes containing clusters of highly expressed genes (HSA 9, 17) and those without such clusters (HSA 8, 13). In HSA 17, the relative positions of 5 genetic loci (from telomere p to telomere q: TP53, Iso-p, centromere, RARα, Iso-q) were investigated. The expression of genes is rather high throughout the whole HSA 17, with the exception of a small region close to the centromere where Iso-p is located (Caron *et al*. 2001).

Materials and methods

Isolation of human lymphocytes

Human lymphocytes were isolated from heparinized blood (20–30 U/ml) from healthy donors by Ficoll-Hypaque (Pharmacia Biotech., Uppsala, Sweden) density-gradient centrifugation as previously described (Kozubek S. *et al*. 1999).

Cell fixation

Dehydration of the nuclei was avoided to preserve the native 3D structure. Dense cell suspension in PBS buffer (100 µl) was spread on a poly-L-lysinated microscope slide. The cells attached to the surface of the slide (in about 5 min without drying) were fixed in 3.7% paraformaldehyde with 0.5% Triton X-100 and HEPEM (65 mmol/L PIPES, 30 mmol/L HEPES, 10 mmol/L EGTA, 2 mmol/L $MgCl_2$, pH 6.9) (Neves *et al*. 1999) for 12 min at room temperature and thoroughly washed in PBS (3 times for 5 min). The fixed cells were either stored for 3 days at $+4\,^{\circ}C$ or immediately permeabilized for hybridization.

Cell permeabilization

Permeabilization of cells was performed in 0.7% Triton X-100/0.1 N HCl/PBS precooled to $+4\,^{\circ}C$ for 10 min on ice (Neves *et al*. 1999). Subsequently, cells were incubated with 0.1 mg/mL RNAse A in $2 \times$ SSC for 30 min at 37 °C, then washed 3 times in PBS, denatured in 50% formamide/$2 \times$ SSC for 20 min at 75 °C and immediately hybridized.

DNA probes, fluorescence in-situ *hybridization*

FISH was performed using unique sequence probes: MBCR-ABL translocation probe (Vysis, USA) (spectrum green-BCR 22q11, spectrum orange-ABL 9q34), digoxigenated c-MYC (8q24), TP53 (17p13.1) and RB (13q14.2); t(15,17) translocation probe identifying the retinoic acid receptor alpha (RARα) gene (digoxigenated) (17q21) and PML gene (biotinylated) (15q22); probe for identification of isochromosome 17 consisting of Iso-p (17q11.2) (bitinylated) and Iso-q (17q21.3-q23) (digoxigenated), all purchased from Oncor, USA). Alpha-satellite DNA sequences of the centromeric region of HSA 9, 19 (digoxigenated), 8, 17 (biotinylated) were from Oncor; total chromosome DNA probes of HSA 8, 9, 17 were FITC labelled (Oncor, USA), that for HSA 13 was Cy3 labelled (Cambio, UK). Human telomere DNA probes for HSA 8, 9, 19 p arm (digoxigenated) and q arm (biotinylated) were purchased from Cambio, UK. Ten microlitres of a single probe or a mixture of two probes with different chemical modification was applied onto a microscopic slide. Probe denaturation, hybridization and a post-hybridisation wash were performed according to the instructions of the probe manufacturers.

Repeated hybridization

Cover slips from the first hybridization were removed by the immersion of slides in $4 \times$ SSC/0.1% Triton X-100. The slides were then washed in three changes of the same solution, once in $2 \times$ SSC (for 4 min each) and immediately denatured under the same conditions as before the first hybridization. Using repeated hybridization to the same genetic elements, it can be easily demonstrated that their positions in the cell nuclei are not influenced by repeated denaturation.

Confocal cytometry

High-resolution cytometry was performed as previously described (Kozubek M. *et al*. 1999, 2001). A high-resolution cytometer based on an inverted completely automated Zeiss Axiovert 100 (Jena, Germany) fluorescence microscope equipped with confocal unit CARV (Atto Instruments, USA) was used. Images were captured in confocal mode using a fully programmable Micromax digital CCD camera (Princeton Instruments, USA). The whole system was controlled by a personal computer equipped with two Intel Pentium® III processors (Intel Corporation, San Francisco, CA). The acquisition of images with FISH-stained interphase nuclei was automated, as was the on-line analysis of image quality, finding cell nuclei and compression of images. It was possible to repeatedly acquire hybridized nuclei. For each hybridization, the same cells were re-allocated, re-acquired and re-analysed. The results of analyses from different hybridizations were then superimposed in the computer memory. This allowed an increase in the number of simultaneously observed genetic loci within the same nucleus.

Off-line analysis was performed using FISH 2.0 software (Kozubek M. *et al*. 1999, 2001) that, in addition to other functions, allows correction for chromatic aberrations. Orthogonal views (xy, xz and yz) of 3D data were used to check the results of analysis. In repeated hybridization, user-defined attributes were set for the identified signals to distinguish elements pertaining to a particular

chromosome homologue. Information about the signals was entered into text files and further analysed using the statistical package Sigma Plot (Jandel Scientific, CA). Typical values of precision are 20–30 nm laterally and 20–100 nm axially. Typical values for resolution are 250–350 nm laterally and 700–900 nm axially.

Evaluation of the results

The fluorescence weight centres of cell nuclei were determined (Kozubek M. *et al*. 1999, 2001) and used for the calculation of the topographic parameters of genes, centromeres and chromosome fluorescence signals (territories). The fluorescence weight centres of the territories (FWCT) were used to determine their positions. The radial distances of all genetic elements were normalized to the local radius (radius determined in the direction of the given FISH signal in 3D space). The distances between homologous or heterologous elements were normalized to the average of the corresponding two local radii. The local radius was determined in the plane perpendicular to the x–y plane passing through the signal investigated. The image in this plane was calculated and segmented using local thresholding (Kozubek M. *et al*. 2001). Cell nucleus sizes may slightly differ even in the same cell population (e.g. lymphocytes from the same donor); in these cases normalized parameters are well conserved for cells with different radii.

Average values for topographic parameters were determined from at least 3 independent experiments in which 500–2000 nuclei per experiment were analysed. Comparison of different data sets was performed using the Student's *t*-test option in SigmaPlot (Jandel Scientific, Ltd., CA).

The distribution of locus-to-locus distances of both homologous and heterologous genetic loci was compared with theoretical expectation calculated according to the RS model (Kozubek S. *et al*. 1997, 1999). In brief, positions in the 3D space inside a sphere were generated using Monte-Carlo simulation precisely according to the measured radial distributions of the given genetic element(s) on the assumption of random angular distributions. In the next step, the distances between positions representing homologous (heterologous) elements were calculated for each generation. After 10^5 repeats, the distributions of the locus-to-locus distances were determined.

Random-walk function for a genetic element in a sphere

In order to calculate model functions for radial distributions of genetic elements, Monte Carlo simulation of positions of N polymer links with length L were determined step by step using a random number generator (see Sachs *et al*. 1995). MC simulation started from the mean position at distance R_o from the centre of a sphere with radius R. Possible positions of the polymer links were restricted by the spherical volume. The position of each link was tested and the calculation repeated if the position of the link happened to be outside the sphere. After N steps, the final position of the element was identified and its distance from the centre of the sphere was determined. For $R = 20$, we used $N = 30–150$ links with $L = 1$; the entire distribution was derived by repeating the calculation 30 000 times. The standard deviation of the element position (σ_e) was calculated using the number of links of the polymer (N) and the length of one link (L): $\sigma_e = L^*\sqrt{N}$. The mean positions, as well as the standard deviations, were fitted to the experimental data.

Results

Chromosome structure of 'euchromatic' and 'heterochromatic' territories

The internal structure of the chromosome territories and their topology in the cell nucleus were investigated in detail for two 'euchromatic' chromosomes (HSA 9 and 17) containing a large number of expressed genes (according to Caron *et al*. 2001), and for two 'heterochromatic' chromosomes (HSA 8 and 13) using repeated dual-colour hybridization, as well as reallocation and reacquisition of a large number ($\sim$500) of 3D images for each chromosome. The positions of the fluorescence weight centre of the chromosome territories (FWCT) were visualized in parallel with centromeres and genes (c-MYC, ABL, RB, TP53 and RARα). The results for 'euchromatic' chromosomes 17 and 9 are shown in Figure 1A, B;

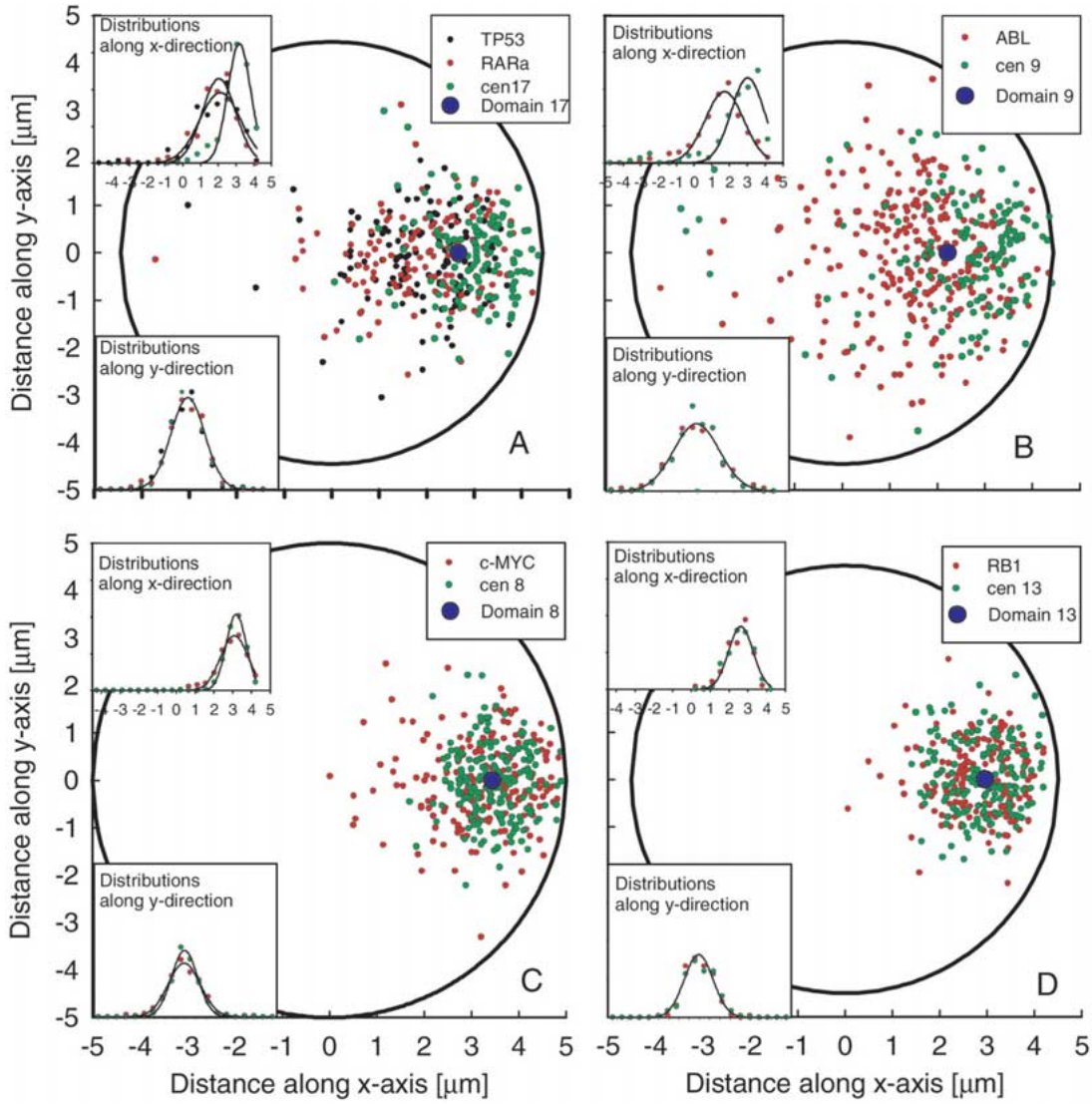

Figure 1. Structure of a chromosome in the cell nucleus. (**A**) HSA 17, (**B**) HSA 9, (**C**) HSA 8, and (**D**) HSA 13. The x-axis was set to the FWCT by the rotation of the cell nucleus and a thin section (1 µm) was cut in the central plane. The whole chromosome was then shifted to the mean position of the territory along the x-axis. The figures show the positioning of genes (red and black circles) and centromeres (green circles) relative to the FWCT (blue circle) in the nucleus. The degree of variation in the x direction for the genes and centromeres is presented (upper left panel), as well as the degree of variation in the y direction (lower left panel).

those obtained for 'heterochromatic' chromosomes 8 and 13 are shown in Figure 1C, D. In Figure 1A–D, the FWCT was positioned by 3D rotation to the x-axis and the whole chromosome was shifted along the x-axis to the FWCT mean position. In this way, the fluctuations of spatial positions of the chromosome as a whole were removed. In order to show the real values of mutual distances between genetic elements, the x–y positions of genes and centromeres are shown only for such nuclei where z co-ordinates were near the central plane. The points, therefore, represent the genetic elements in a narrow slice through the central plane of the nucleus after its rotation. In this case, genes, as well as centromeres, form distributions (inserted plots in the left panels of

Table 1. Mean 3D distances between genetic elements with standard errors and mean centre of nucleus-to-element distances (CE) with standard errors for HSA 17 expressed in % of nuclear radius.

Genetic element	C17 (%)	Iso-p (%)	Iso-q (%)	RARα (%)	CE (%)
C17					74.9 ± 2.7
Iso-p	38.8 ± 3.8				77.3 ± 2.7
Iso-q	55.4 ± 2.8	46.9 ± 2.3			58.2 ± 2.5
RARα	65.6 ± 3.3	64.3 ± 3.4	53.2 ± 3.1		55.4 ± 2.3
TP53	55.5 ± 1.4	63.8 ± 2.0	49.8 ± 2.1	46.3 ± 1.9	50.4 ± 1.8

Figure 1A–D) that are narrower when compared with the radial nuclear distributions, owing to the fact that the fluctuations of the chromosome territory relative to the cell nucleus were removed. For the centromeres of HSA 9 and 17 the distance distributions in the x-direction are narrower and shifted towards the nuclear membrane as compared with the corresponding genes (upper left panels).

The mean positions of some investigated genetic loci (radial location) of 'euchromatic' chromosomes (ABL 9q34; TP53 17p13.1; RARα 17q21; Iso-q 17q21.3-q23) are closer to the centre of the nucleus as compared to the FWCT; on the other hand, Iso-p 17p11.2 and centromeres of these chromosomes are located near the nuclear periphery (Table 1, Figure 1A, B). The differences between the radial locations of genes and centromeres are much smaller for HSA 8 and 13 (Figure 1C, D).

The nuclear location of genetic elements of HSA 17 was investigated using repeated hybridization (Figure 2A, Table 1). It was found that TP53, RARα and Iso-q are located close to the nuclear centre (at a mean distance of 50, 55 and 58% of the radius from the nuclear centre, respectively). Centromeres and Iso-p were found close to the nuclear periphery (at a mean distance of 75 and 77%).

Nuclear distances between couples of genes located on different arms of HSA 17 (RARα and TP53; Iso-q and TP53) are shorter than the distances between these genes and centromere 17 in spite of the larger molecular distances between these genes as compared to gene-to-centromere distances (Figure 2B, Table 1). For example, the mean distances between C17 and the TP53 and RARα genes are 55.5 ± 1.4 and 65.6 ± 3.3% of the nuclear radius, respectively, while the mean distance between both these genes is only 46.3 ± 1.9%. A similar phenomenon was observed for Iso-q and TP53 (Figure 2B, Table 1). In addition, the distances between both telomeres of the HSA 8, 9 and 19 were also shorter than the distances of telomeres to centromere (unpublished observation). The mean distances of telomere q and p from the centromere of the HSA 9 were 45.12 ± 1.60 and 49.17 ± 1.59% of the nuclear radius, respectively. The mean distance between both telomeres of HSA 9 was only 34.6 ± 1.56%. For the HSA 8 these values are 35.96 ± 1.51% and 45.55 ± 1.56% for the distances between the centromere and telomere p and q, respectively. The mean distance between both telomeres of this chromosome is 32.99 ± 1.52%. Telomeres p and q are extremely close to each other in HSA 19. In about 40% of cells, they are associated with a distance shorter than 10% of the nuclear radius ($\approx 0.5\,\mu m$).

The investigated genetic loci of HSA 17 are not located in close proximity to the centromere in the cell nucleus (Figure 2C, Table 1). An exception is the Iso-p locus, which is very close to the centromere (Figure 2A, Table 1) and its mean position is closer to the nuclear membrane than is the position of the centromere. The mean distances of the centromeres of HSA 17, 9 and 8 from the FWCT of these chromosomes are shorter than the distances of genes of these chromosomes from the FWCT (Figure 2D). The greatest difference between the distance of the centromere and the gene from the FWCT was found for HSA 9.

In order to show the correlation between the nuclear location of the TP53 gene and the HSA 17 territory, the nuclei were divided into two groups according to the distance of the HSA 17 FWCT to the nuclear centre (chromosome-to-centre distance). The first group contained nuclei where the

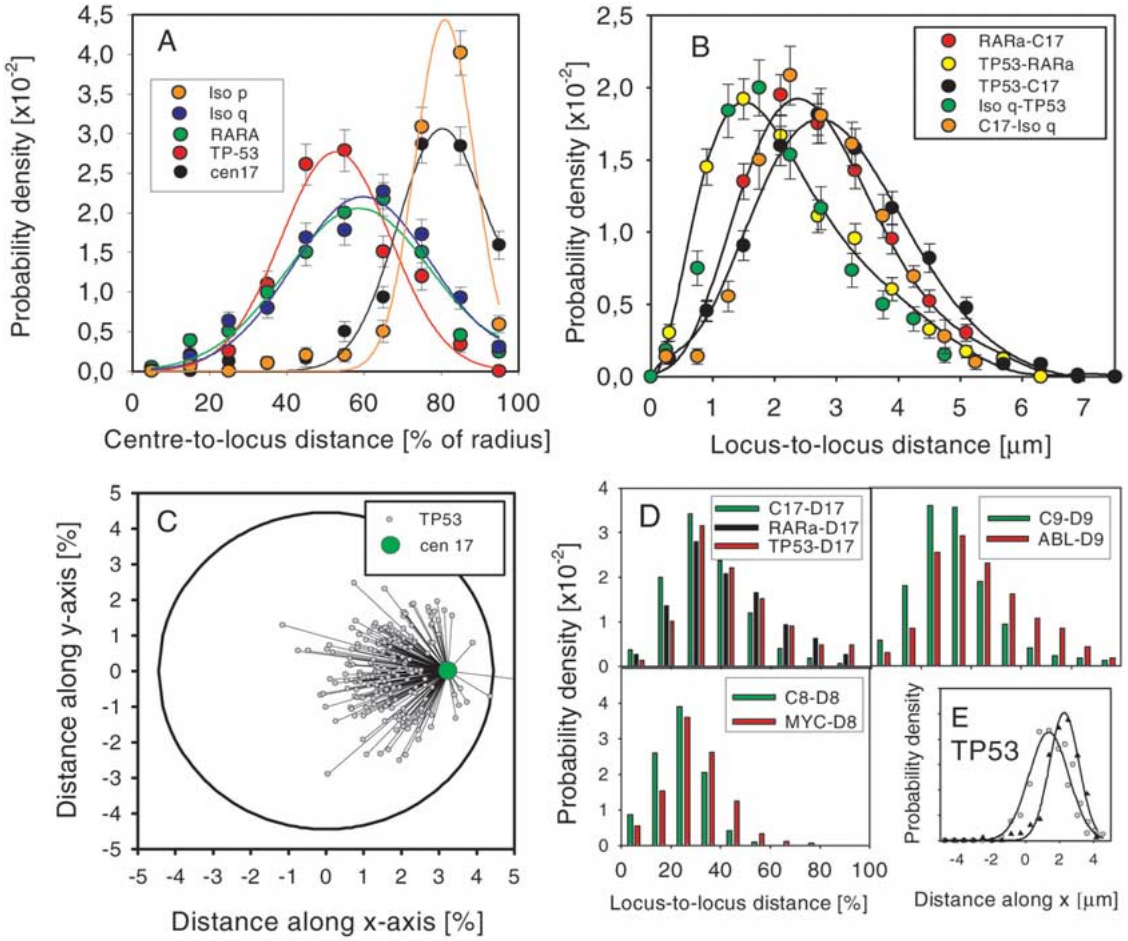

Figure 2. (**A**) Centre-to-locus distances for genetic elements of HSA 17. The most central location was found for the TP53 gene, further for the Iso-q locus, and for the RARα gene. The centromere, as well as the Iso-p locus, was found near the nuclear periphery. (**B**) The locus-to-locus distances for genetic elements of HSA 17. The centromere-to-TP53 (black circles), centromere-to-RARα (red circles), and centromere-to-Iso-q (orange circles) distances are, on average, longer than TP53-to-RARα, TP53-to-Iso-q distances (yellow and green circles). (**C**) The positioning of TP53 relative to the centromere of HSA 17 shown in a narrow slice (1 µm) through a central plane of cell nuclei. The centromere was put onto x-axis by rotation of the whole nucleus and shifted to its mean position by shifting the whole territory. The investigated genes do not approach the corresponding centromeres. A similar phenomenon was also observed for the mutual positions of the ABL genes relative to centromere 9. (**D**) The distributions of distances between genetic elements and the FWCT (denoted as D) for HSA 17, 9, and 8. (**E**) The distribution of TP53 in the nuclei of human lymphocytes selected according to the distance of FWCT from the centre of the nucleus. Open circles – the nuclei with FWCT < $FWCT_{mean}$; closed triangles – the nuclei with FWCT > $FWCT_{mean}$; $FWCT_{mean}$ = 56.6% of the nuclear radius. The quantity on the y-axis, probability density, is the probability normalized to unit of some quantity. For example, if we determine the probability for a genetic element to occur at different distances from the centre of the cell nucleus, we divide the whole interval into smaller intervals (e.g. 0–10%, 10–20% . . . 90–100% of the radius). In these smaller intervals we determine the probability of the occurrence using the number of positive events (genes at a given interval) and normalization to the total number of events. The resulting ratio is the probability density, i.e. probability per 10% of the radius.

chromosome-to-centre distance was shorter than 56.6% of the local radius (the mean value). Nuclei in which this distance was larger were placed into the second group. We found that the location of the TP53 gene is to some extent correlated with the location of the chromosome territory. The distribution of genes pertaining to chromosomes located closer to the nuclear centre was also shifted in the same direction (Figure 2E) and its standard deviation was larger.

Spatial relationships of genetic elements of chromosome 17 territory

To determine the spatial arrangement of different loci of HSA 17, the centromere was placed into the origin of the co-ordinate system and the chromosome territory was rotated to bring the RARα genes to the x-axis (Figure 3A); further rotation of the territory around the x-axis placed the Iso-q to the same plane with the centromere and RARα loci. In this arrangement it is evident that the Iso-p is located close to the centromere (as in metaphase chromosome). The Iso-q, positioned more distally from the centromere than RARα on the same arm of the methaphase chromosome (Figure 3B, inserted schema), is located apart from the RARα locus in the space of the nucleus; the angle between RARα–centromere and Iso-q–centromere is greater than 90°. The spatial arrangement of these loci can also be deduced from their mutual distances and their positioning in the nucleus (Table 1). Taking into account these parameters, it proved possible to draw up a schema of the arrangement of a part of the chromosome (Figure 3B, Table 1). TP53, RARα and Iso-q are localized close to the nuclear centre (their mean distances range from 50% to 58% of the nuclear radius from the nuclear centre). The distance of TP53 and Iso-q from the centromere is the same (about 55% of the radius); this distance for RARα is longer (65%). The distances, Iso-q–RARα, Iso-q–TP53 TP53–RARα, Iso-q–centromere and TP53–centromere, are very similar, indicating that all these regions cannot be in the same plane of the nucleus. If TP53, centromere and RARα are in the same plane, then Iso-q should be outside this plane. It is drawn on the top of a tetrahedron, the base of which is determined by TP53, RARα and the centromere. Neither Iso-p is located in this plane. The distance of this locus from TP53 is longer than is the distance of the TP53 from the centromere, even if the molecular distance between TP53 and Iso-p on metaphase chromosome is shorter (see Figure 3, inserted schema). The nuclear distance of Iso-p from Iso-q is significantly shorter than the distance of Iso-q from the centromere. Iso-p is at about the same distance from RARα as is the distance of RARα from the centromere. Iso-p cannot, therefore, be in the same plane as TP53, Iso-q and the centromere, nor in the plane determined by Iso-q, RARα and the centromere, as has already been shown by the rotation of nuclei.

A simple model of chromosome nuclear structure

A simple model of chromosome territory that reflects the basic features of chromosome structure is proposed (Figure 4A). In this model, two subdomains of chromosome territory are assumed (RIDGE and RILGE subdomains) with chromosome backbone looping according to the level of gene expression. Simulation of the 3D structure of HSA 9 in the nucleus was performed using the MC method (Figure 4B). Let us assume (in agreement with Caron *et al*. 2001) that approximately half of the genes of this chromosome are highly expressed. In the frame of the model, the actual positions of the territory with two equal subdomains are subject to random fluctuations around mean positions (R_o for the territory; R_{01} and R_{02} for the subdomains, $R_o = (R_{01} + R_{02})/2$), either independent of each other or correlated, i.e. with constant distance between subdomains (corresponding to fluctuations of the territory as a whole). These fluctuations were represented by Gaussian distributions of the positions of the territory and subdomains. At the beginning of the calculation, the positions of the territory and subdomains in the cell nucleus were attributed by a random-number generator. The calculation continued with generation of two random-walk polymers simulating the random positioning of genes (centromeres) in a sphere starting at the positions of subdomains. The radial distributions of genetic elements (ABL, C9, HSA 9 territory), the interelement distributions, and the centre-to-ABL vs. centre-to-C9 dependence were calculated (Figure 4B). The parameters of the model for the HSA 9 territory are as follows: $R_{01} = 46\%$ for the subdomain consisting of regions with increased gene expression (RIDGE), $R_{02} = 68\%$ for the subdomain consisting of regions with low gene expression (RILGE), $R_o = (R_{01}+R_{02})/2 = 57\%$ for the mean position of the territory, with the variation of this position being $\sigma_d = 7\%$. The independent variation of the subdomains is about $\sigma_s = 11\%$ and the variations of the elements are approximately $\sigma_e = 17\%$ for ABL and C9. The results of these model calculations correspond well to the experimental data (Figure 4B).

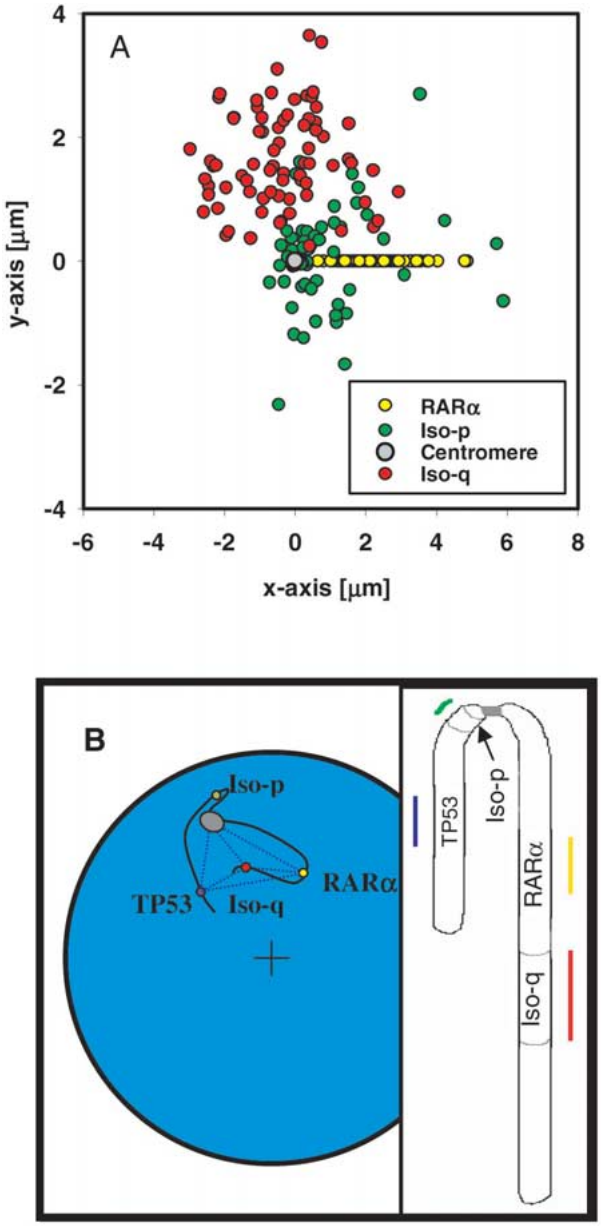

Figure 3. 3D structure of HSA 17 territory. (**A**) Mutual positions of 4 genetic elements of HSA 17. The centromere is placed in the origin of the coordinate system and the territory is rotated to bring the RARα locus onto the x-axis. Further rotation of the territory around the x-axis places the Iso-q locus onto the x−y plane. Thus, the centromere and RARα and Iso-q are in the same plane. Iso-p is outside this plane. (**B**) Localization of five loci of HSA 17 in the cell nucleus and the spatial arrangement of chromosome backbone traced through the loci. The distances between the loci and their nuclear positions indicate that they do not occur in the same plane of the nucleus. The inserted schema indicates the genetic element locations in metaphase HSA 17.

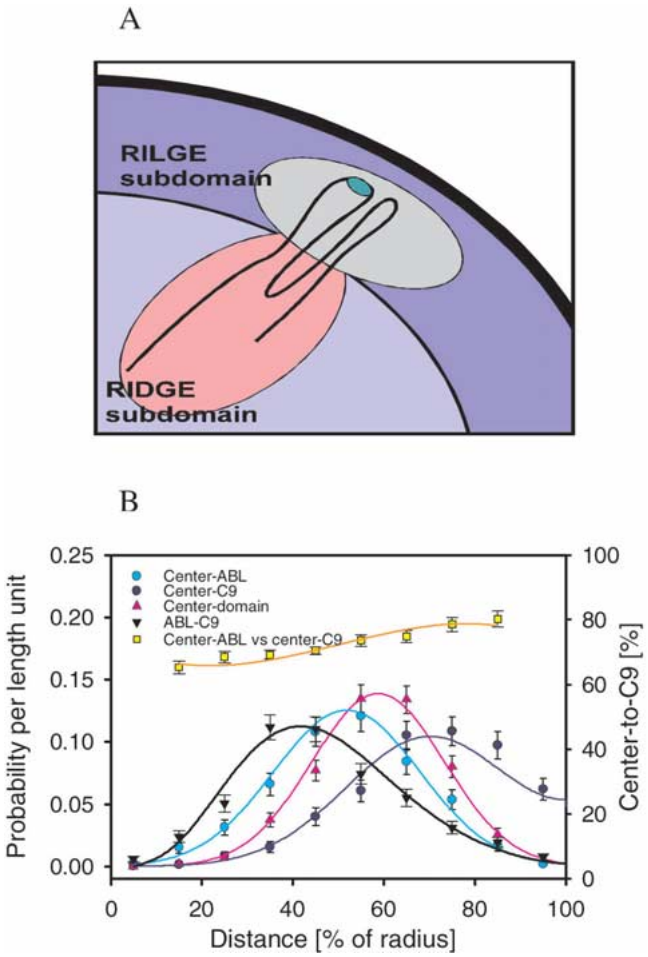

Figure 4. A model of an interphase chromosome. (**A**) The chromosome territory is divided into a RIDGE subdomain located more centrally (pink) and a RILGE subdomain located more peripherally (grey) involving centromere (green spot). The central backbone of the chromosome (black curve) protrudes from the RILGE to the RIDGE subdomain and *vice versa*. Coloured areas represent chromatin loops attached to the backbone. The subdomains can be formed by different parts of the chromosome according to the level of gene expression, which requires bending of the chromosome backbone. (**B**) The results of Monte-Carlo simulation of HSA 9 structure (solid lines). Radial distributions of the *ABL* gene and *C9* centromere (blue and black circles), the territory of HSA 9 (red triangles) and the distribution of mutual distances between *ABL* and *C9* (inverse black triangles) are appropriately described by the model. In addition, the correlation between *ABL* and *C9* radial positions is also fitted (yellow squares).

Discussion

In this study, we show that the radial position of a given element in the cell nucleus depends on the radial position of the corresponding chromosome territory and on the location of the element relative to the territory. The chromosome territory and all its regions behave to some extent as a solid body: if the territory is shifted closer to the nuclear centre, the gene or the centromere pertaining to this chromosome is also shifted to the centre as is shown for TP53 (Figure 2E). Simultaneously, it was observed that the territory of the same chromosome located closer to the nuclear centre is more decondensed than the territory located closer to the membrane. The spatial fluctuations of genetic elements of the more decondensed territory are higher, indicating that decondensed chromatin is more flexible.

The distribution of gene expression in the human genome for many different tissue types has been shown by transcriptome maps (Caron *et al.* 2001).

These maps reveal that genes that are highly expressed in different cell types (housekeeping genes) are not dispersed homogenously through chromosomes, but are grouped into clusters (RIDGEs). Some chromosomes are rich in these clusters (HSA 19, 17, 16, 20); others do not contain such clusters at all (HSA 4, 8, 13, 18). Territories of the former chromosomes are located close to the nuclear center; they are irregular and more diffuse (e.g. HSA 9, 17). The latter are more condensed and adopt a more peripheral position (e.g. HSA 8, 13; Kozubek S. *et al.* 2002). In the majority of chromosomes, RIDGEs alternate with regions poorly expressed (RILGEs). The territories of these chromosomes have a distinctly polar character, are irregular and stretched from the periphery to the nuclear centre.

An important factor influencing the nuclear location of a genetic element seems to be the concentration of highly expressed genes in the element environment on the chromosome. Each genetic element can be positioned on the transcriptome map and the density of highly expressed genes in the environment can be established according to Caron *et al*. (2001). If the genetic element is located in the region rich in highly expressed genes, its nuclear location is close to the nuclear centre (e.g. ABL, TP 53, RARα, Iso-q). If it is in the region poorly populated with expressed genes, its nuclear position is more peripheral (RB, Iso-p, c-MYC). The observation of Carvalho *et al*. (2001), implying that each individual chromosome constitutes a particular microenvironment in the interphase nucleus, which imposes specific positioning of centromeric heterochromatin in the cell nucleus, is in agreement with our results. These authors found that this microenvironment consists of tight correlation between the nuclear location of centromeric α-satellite DNA and the presence of G-dark bands in the vicinity of the centromere.

As follows from the presented results, the polar character of chromosome territories is determined by RIDGEs that protrude from the more condensed parts of the chromosome located in the proximity of the nuclear membrane to the nuclear centre (e.g. HSA 9). The ABL gene is located in the RIDGE occurring close to the telomere (9q34.1). The spatial fluctuations of this gene are rather broad in the central part of the nucleus, far from the centromere and the FWCT of the chromosome territory (Figure 1B). The higher fluctuation of the positions of genetic elements occurring in the regions of clusters of highly expressed genes may be associated with the higher flexibility of the decondensed chromatin that is characteristic for regions with highly expressed genes. A higher degree of intermingling between chromosomes can be expected in the central region of the cell nucleus. On the other hand, c-MYC, located in the chromosomal region with low expression of genes close to the telomere (8q24), is distributed in a relatively narrow spatial volume (together with the centromere of HSA 8) around the FWCT of HSA 8 that is located more peripherally in the cell nucleus than FWCT of HSA 17 and 9 (Figure 1C). Distribution similar to the c-MYC gene was also observed for the RB gene (13q14) (Figure 1 D). Both HSA 8 and 13 are free of RIDGEs, their territories are relatively condensed and close to the nuclear membrane. Bartova *et al*. (2002) observed that, after differentiation of promyelocytes to granulocytes, the ABL gene is significantly shifted to the nuclear membrane in contrast to the c-MYC and RB genes. This phenomenon seems to be related to the different content of highly expressed genes that determine the degree of decondensation in corresponding chromosomes. A gene pertaining to the most decondensed region of a chromosome is exposed to the most pronounced changes in nuclear localization after cell differentiation and chromosome condensation. These results confirm our suggestions that the nuclear location of a genetic element is determined by the occurrence of clusters of highly expressed genes in the environment of its chromosome location.

Distances shorter than expected from the molecular location were observed between genes located on the p- and q-arms of HSA 17 (TP53/RARα, TP53/Iso-q). A similar phenomenon was also observed by Nikiforova *et al*. (2000) for RET and H4 genes located on the q- and p-arms of HSA 10, respectively. This phenomenon may be related to the hairpin-like structure of chromosomes. Such a structure of chromosomes has already been proposed by Ferguson & Ward (1992) and also follows from our further results showing that the centromeres of HSA 9 and 8 are relatively close to the nuclear membrane and both telomeres are oriented to the nuclear centre in human lymphocytes. In addition to this, the

nuclear distances between telomeres of both chromosomes are shorter than the distances of the corresponding telomere and the centromere. In accordance with these results Nogami *et al*. (2000) observed the mutual proximity of telomeres and their orientation towards the nuclear centre for HSA 12.

Based on the presented findings, a simple mathematical model was developed describing several distinct features of interphase chromosome structure. In the model, RIDGE and RILGE subdomains of a chromosome are distinguished (Figure 4A). The results herein show that the actual position of a chromosome territory in individual nuclei fluctuates around a mean value. The subdomains may follow the fluctuations of the territory or may behave relatively independently. In general, a partial correlation between fluctuations of a territory and subdomains can be expected. The actual positions of genetic elements belonging to a particular subdomain acquire the fluctuations of the territory (σ_d) and the subdomain (σ_s), and show additional fluctuations (σ_e) that depend on the length of the chromatin loops where they are located. These fluctuations concern differences between cell nuclei that may appear during their formation at the end of telophase (Ferreira *et al.* 1997) and/or as a consequence of a slow motion of genetic elements during interphase (Zink *et al.* 1998).

The 3D structure of the HSA 17 territory was reconstructed based on the 3D positions of 5 genetic elements. The complex 3D structure of this chromosome territory obviously results from the distribution of highly expressed genes along the chromosome. It follows from the presented results, showing the nuclear location of 5 different loci of HSA 17, that the structure of this chromosome is not a simple hairpin, rather that the chromosome backbone may be bent several times (Figure 3). The flexion of the chromosome backbone seems to be required for the spatial arrangement of the chromosome territory. It should allow the regions of highly expressed genes to approach the nuclear centre and the regions of low gene expression interspersed between them to reach the nuclear membrane. Thus, two chromosome subdomains are created to which multiple regions of RIDGEs and RILGEs contribute. The chromosome positions of RIDGEs and their separation by RILGEs are obviously responsible for the flexion of the chromosome and for the structure of the chromosome territory. Therefore, two genetic elements of a particular subdomain may exist closer to each other than the elements located in different subdomains, depending on the chromosomal positions of RIDGEs and RILGEs. Indeed, we have demonstrated that the RARα and TP53 genes, as well as TP53 and Iso-q, are located closer to each other in comparison to their distances from centromere 17, despite the greater molecular distance between the genes located on the opposite arms of the chromosome. These conclusions are in contradiction to some previous reports showing that physical distances between two DNA loci of the same chromosome are related to their molecular distances (Trask *et al.* 1991, Yokota *et al.* 1995). Our results show that, in general, there is no proportionality between the physical and molecular distance of two genetic elements of the same chromosome in the cell nucleus.

In reality, the 3D structure of the chromosome territory is probably more complex than would follow only from the radial flexion of the chromosome backbone (see Figure 3). The arrangement of chromatin into loops of various hierarchy, their spatial orientation in the territory and in the cell nucleus, the folding and condensation of these loops together with binding of the territory to the nuclear membrane and/or matrix, intrachromosomal and interchromosome tethering (Kozubek S. *et al.* 1999, Nikiforova *et al.* 2000, Kozubek S. *et al*. 2002) can play an important role in the spatial structure of chromosome territories and localization of individual genetic elements in the frame of the territory and in the cell nucleus.

Our study was performed on human non-stimulated lymphocytes to exclude the possible influence of different stages of the cell cycle on the structure of chromosome territory and its location in the cell nucleus. These cells can be considered representative for other cells of spherical shape, as shown by Skalníková *et al*. (2000). Our previous results show that the nuclear location of different genetic elements in cells of colorectal epithelium and in HT 29 cells of oval shape (Koutná et al. 2001) is similar to that of spherical blood cells. However, the validity of our findings for cells of other types should be further verified.

Acknowledgements

We would like to thank H. Křivánková and V. Fučíková for their technical help. This work was supported by the Academy of Sciences (Z5004920, S5004010, A1065203), the Ministry of Education (MSM 143300002), the Ministry of Health (NC5955) and the Grant Agency of the Czech Republic (GA202/01/0197 and GA301/01/0186).

References

Bártová E, Kozubek S, Jirsová P *et al*. (2001) Higher-order chromatin structure of human granulocytes. *Chromosoma* **110**: 360–370.

Bártová E, Kozubek S, Jirsová P *et al*. (2002) Nuclear structure and gene activity in human differentiated cells. *J Struct Biol* (in press).

Belmont AS, Bruce K (1994) Visualization of G_1 chromosomes, A folded, twisted, supercoiled chromonema model of interphase chromatide structure. *J Cell Biol* **127**: 287–302.

Belmont AS, Dietzel S, Nye AC, Strukov YG, Tumbar T (1999) Large scale chromatin structure and function. *Curr Opin Cell Biol* **11**: 307–311.

Boyle S, Gilchrist S, Bridger JM, Mahy NL, Ellis JA, Bickmore WA (2001) The spatial organization of human chromosomes within the nuclei of normal and emerin-mutant cells. *Hum Mol Genet* **10**: 211–219.

Brown KE, Guest SS, Smale ST, Hahm K, Merkenschlager M, Fisher AG (1997) Association of transcriptionally silent genes with Ikaros complexes at centromeric heterochromatin. *Cell* **91**: 845–854.

Brown KE, Baxter J, Graf D, Merkenschlager M, Fisher AG (1999) Dynamic repositioning of genes in the nucleus of lymphocytes preparing for cell division. *Mol Cell* **3**: 207–217.

Caron H, Van Schaik B, Van der Mee M *et al*. (2001) The human transcriptom map, Clustering of highly expressed genes in chromosomal domains. *Science* **291**: 1289–1292.

Carvalho C, Pereira HM, Ferreira J *et al*. (2001) Chromosomal G-dark bands determine the spatial organization of centromeric heterochromatin in the nucleus. *Mol Biol Cell* **12**: 3563–3572.

Chevret E, Volpi EV, Sheer D (2000) Mini review: Form and function in the human interphase chromosome. *Cytogenet Cell Genet* **90**: 13–21.

Cockel M, Gasser, S (1999) Nuclear compartments and gene regulation. *Curr Opin Genet Dev* **9**: 199–205.

Cremer T, Cremer C (2001) Chromosome territories nuclear architecture and gene regulation in mammalian cells. *Nature Rev Genet* **2**: 292–301.

Cremer T, Lichter P, Borden J, Ward DC, Manuelidis L (1988) Detection of chromosome aberrations in metaphase and interphase tumor cells by *in situ* hybridization using chromosome specific library probes. *Hum Genet* **80**: 235–246.

Cremer T, Kreth G, Koester H *et al*. (2000) Chromosome territories, interchromatin domain compartment and nuclear matrix. An integrated view of the functional nuclear architecture. *Crit Rev Eucar Gene Expres* **10**: 179–212.

Croft JA, Bridger JM, Boyle S, Perry P, Teague P, Bickmore WA (1999) Differences in the localization and morphology of chromosomes in the human nucleus. *J Cell Biol* **145**: 1119–1131.

Ferguson M, Ward DC (1992) Cell cycle dependent chromosomal movement in premitotic human T-lymphocyte nuclei. *Chromosoma* **101**: 557–565.

Ferreira J, Paolella G, Ramos C, Lamond AL (1997) Spatial organization of large-scale chromatin domains in the nucleus A magnified view of single chromosome territories. *J Cell Biol* **139**: 1597–1610.

Koutná I, Kozubek S, Žaloudík J *et al*. (2000) Topography of genetic loci in tissue samples: towards new diagnostic tool using interphase FISH and high-resolution image analysis techniques. *Anal Cell Pathol* **20**: 173–185.

Kozubek M, Kozubek S, Lukášová E *et al*. (1999) High-resolution cytometry of FISH dots in interphase cell nuclei. *Cytometry* **36**: 279–293.

Kozubek M, Kozubek S, Lukášová E *et al*. (2001) Combined confocal and wide-field high-resolution cytometry of FISH stained cells. *Cytometry* **45**: 1–12.

Kozubek S, Lukášová E, Rýznar L *et al*. (1997) Distribution of ABL and BCR genes in cell nuclei of normal and irradiated lymphocytes. *Blood* **89**: 4537–4545.

Kozubek S, Lukášová E, Marečková A *et al*. (1999) The topological organization of chromosomes 9 and 22 in cell nuclei has a determinative role in the induction of t(9,22) translocations and in the pathogenesis of t(9,22) leukemias. *Chromosoma* **108**: 426–435.

Kozubek S, Lukášová E, Jirsová P *et al*. (2002) 3D structure of the human genome: Order in randomness. *Chromosoma* (in press).

Kurz A, Lampel S, Nickolenko JE *et al*. (1996) Active and inactive genes localize preferentially in the periphery of chromosome territories. *J Cell Biol* **135**: 1195–1205.

Lamond AI, Earnshaw WC (1998) Structure and function in the nucleus. *Science* **280**: 547–553.

Lichter P, Cremer T, Borden J, Manuelidis L, Ward DC (1988) Delineation of individual human chromosomes in metaphase and interphase cells by *in situ* suppression hybridization using recombinant DNA libraries. *Hum Genet* **80**: 224–234.

Nagele R, Freeman T, McMorrow L, Lee H (1995) Precise spatial positioning of chromosomes during metaphase: evidence for chromosomal order. *Science* **270**: 1831–1835.

Nagele RG, Valesco AQ, Anderson WJ *et al*. (2000) Telomere associations in interphase nuclei: possible role in maintenance of interphase chromosome topology. *J Cell Sci* **114**: 377–388.

Neves H, Ramos C, Gomez da Silva M, Parreira A, Parreira L (1999) The nuclear topography of ABL, BCR, PML and RARα genes: Evidence for gene proximity in specific phases of the cell cycle and stages of hematopoietic differentiation. *Blood* **93**: 1197–1207.

Nikiforova MN, Stringer JR, Blough R, Medvedovic M, Fagin JA, Nikiforov YE (2000) Proximity of chromosomal loci that participate in radiation-induced rearrangements in human cells. *Science* **290**: 138–142.

Nogami M, Nogami O, Kagotani K *et al*. (2000) Intranuclear arrangement of human chromosome 12 correlates to large-scale replication domains. *Chromosoma* **108**: 514–522.

Pinkel D, Landegent J, Collins C *et al*. (1988) Fluorescence *in situ* hybridization with human chromosome-specific libraries: detection of trisomy 21 and translocations of chromosomes 4. *Proc Natl Acad Sci USA* **85**: 9138–9142.

Sachs RK, van den Engh G, Trask B, Yokota H, Hearst JE (1995) A random-walk/giant-loop model for interphase chromosomes. *Proc Natl Acad Sci USA* **92**: 2710–2714.

Sadoni N, Langer S, Fauth C *et al*. (1999) Nuclear organization of mammalian genomes: polar chromosome territories build up functionally distinct higher order compartments. *J Cell Biol* **146**: 1211–1226.

Sadoni N, Sullivan KF, Weinzierl P, Stelzer EHK, Zink D (2001) Large-scale chromatin fibres of living cells display a discontinuous functional organization. *Chromosoma* **110**: 39–51.

Skalníková M, Kozubek S, Lukášová E *et al*. (2000) Spatial arrangement of genes, centromeres and chromosomes in human blood cell nuclei and its changes during the cell cycle, differentiation and after irradiation. *Chromosome Res* **8**: 487–499.

Trask BJ, Massa H, Kenwrick S, Gitschier J (1991) Mapping of human chromosome Xq28 by two-color fluorescence *in situ* hybridization of DNA sequences to interphase cell nuclei. *Am J Hum Genet* **48**: 1–15.

Verschure PJ, van der Kraan I, Manders EMM, van Driel R (1999) Spatial relationship between transcription sites and chromosome domains. *J Cell Biol* **147**: 13–24.

Volpi EV, Chevret E, Jones T *et al*. (2000) Large-scale chromatin organization of the major histocompatibility complex and other regions of human chromosome 6 and its response to interferon in interphase nuclei. *J Cell Sci* **113**: 1565–1576.

Yokota, H, van den Engh G, Hearst JE, Sachs RK, Trask BJ (1995) Evidence for the organization of chromatin in megabase pair-sized loops arranged along a random walk path in human G_0/G_1 interphase nucleus. *J Cell Biol* **130**: 1239–1249.

Zink D, Cremer T, Saffrich R *et al*. (1998) Structure and dynamics of human interphase chromosome territories in vivo. *Hum Genet* **102**: 241–251.

ELSEVIER

Gene 292 (2002) 13–24

GENE
AN INTERNATIONAL JOURNAL ON GENES AND GENOMES

www.elsevier.com/locate/gene

Topography of genetic elements of X-chromosome relative to the cell nucleus and to the chromosome X territory determined for human lymphocytes

Martin Falk[a], Emilie Lukášová[a], Stanislav Kozubek[a,*], Michal Kozubek[b]

[a]*Laboratory of Molecular Cytology and Cytometry, Institute of Biophysics, Academy of Sciences of the Czech Republic, Královopolská 135, 612 65 Brno, Czech Republic*

[b]*Laboratory of Optical Microscopy, Faculty of Informatics, Masaryk University, Botanická 68a, 602 00, Brno, Czech Republic*

Received 18 March 2002; received in revised form 19 April 2002; accepted 30 April 2002
Received by V. Paces

Abstract

Topography of three genetic elements – dystrophin (*dmd*) exons 5–7 (E_1), 46–47 (E_2), and centromere of chromosome X (N_X) were studied relative to cell nuclei and to chromosome X territories of spatially fixed human lymphocytes. Repeated three-dimensional (3D) dual color fluorescence in situ hybridization combined with high-resolution cytometry was used. In addition, the nuclear location of fluorescence weight centers (FWC), spatial volume, and maximal area per one section of chromosome-X territories were investigated. The larger (X_L) and smaller (X_S) homologous X-chromosomes were distinguished for each nucleus according to the 3D volume of their territories. The distributions of the [center of nucleus]-to-[genetic element] distances (radial distributions) of *dmd* exons E_1, E_2, centromere N_X and FWC were very similar for both homologous X-chromosomes of female lymphocytes as well as for the chromosome X of the human male. On the other hand, larger average mutual distances between all pairs of signals (E_1, E_2, N_X, FWC) and larger average maximal area were observed for the larger chromosome (X_L) in comparison with the smaller one (X_S). The territory of the larger homologue showed also more irregular surface. The most significant differences between homologous X-chromosomes were found for N_X–E_1, N_X–E_2 and E_1–E_2 distances that were in average about twice longer for X_L as compared with X_S. These parameters correlate to each other and can be used for the reliable determination of more (de)condensed X-chromosome territory. The longer E_1–E_2 distances for X_L indicate more open chromatin structure of the dystrophin gene on this chromosome in contrary to closed structure on X_S. Substantially shorter distances of the dystrophin exons from the centromeric heterochromatin in X_S as compared to X_L can be explained by silencing effect of centromeres as described in Nature 1 (2000) 137.

Keywords: Nuclear architecture; Chromosome X inactivation; Three dimensional fluorescence in situ hybridization; Confocal microscopy; Chromatin condensation

1. Introduction

The higher-order chromatin structure of interphase cell nuclei and their functional organization are the subject of intensive investigations. Some results demonstrate a non-random organization of chromosomes and their genetic elements in the cell nucleus (Cremer et al., 1993; Kozubek et al., 1997, 1999b; Croft et al., 1999; Verschure et al., 1999; Nogami et al., 2000; Boyle et al., 2001); however, the principles of this arrangement and its functional manifestations are still unknown.

Results of several recent studies indicate that chromatin structure represents an epigenetic factor influencing gene expression. Francastel et al. (2000) suggested two stages of gene activation in which open chromatin structure is formed in the first stage. Furthermore, it was found that active transcription is associated with chromatin decondensation (Volpi et al., 2000). Experiments on living cells demonstrated that the degree of chromatin decondensation is correlated with the level of transcription (Müller et al., 2001). Other lines of evidence suggested that transcriptional

Abbreviations: C, center of nucleus; 3D-FISH, three dimensional fluorescence in situ hybridization; *dmd*, dystrophin gene; E_1, 5–7 exon of *dmd* gene; E_2, 46–47 exon of *dmd* gene; E_1–E_2, distance between elements E_1 and E_2; FWC, fluorescence weight center of chromosome territory; N_X, centromere X; R, nuclear radius; X_a, active chromosome X; X_i, inactive chromosome X; X_L, chromosome X with larger volume of the territory; X_S, chromosome X with smaller volume of the territory

* Corresponding author. Tel.: +420-5-4151-7139; fax: +420-5-4124-0498.
E-mail address: kozubek@ibp.cz (S. Kozubek).

0378-1119/02/$ - see front matter
PII: S0378-1119(02)00667-4

repression is associated with condensed chromatin. Highly condensed heterochromatin is usually transcriptionally silent (Hennig, 1999).

The relationship between the gene activity and its position inside the chromosome territory is not yet resolved. It has been suggested that both the condensation state and the shape of chromosome territory are correlated with chromosome transcriptional activity (Bischoff et al., 1993; Cremer et al., 1993; Eils et al., 1996; Croft et al., 1999). In addition, the hypothesis that the expressed genetic elements are localized on the surface of chromosome territories (Cremer et al., 1993) was confirmed by several authors (Kurz et al., 1996; Dietzel et al., 1999; Tajbakhsh et al., 2000; Volpi et al., 2000). Verschure et al. (1999) using incorporation of BrUTP into newly transcribed RNA has demonstrated that transcription takes place at the surfaces of chromatin-rich sub-domains throughout chromosome territories.

Genes located on X-chromosome in female cell nuclei provide an excellent object for the studies of the influence of transcription on the structure and nuclear position of the chromosome territory and its genetic elements, showing distinctly different transcriptional activity. During early developmental stages in female mammalian somatic cells one of homologous X-chromosomes (X_i) is genetically largely inactivated as a result of gene dosage compensation while the other one (X_a) remains transcriptionally active (Lyon, 1961; Gartler and Goldman, 1994; Heard et al., 1997). The total transcriptional level of inactive chromosome X is many times lower in comparison with the active homologue since only a small proportion of genes escape the inactivation. In some interphase cell types the X_i chromosome can be clearly visualized by routine staining as sex chromatin forming the Barr body (Comings, 1968). The Barr body was suggested to be randomly attached or situated adjacent to the nuclear membrane (Walker et al., 1991).

In this paper, the topography of X-chromosome genetic elements was studied relative to cell nuclei and to chromosome territories in spatially fixed human lymphocytes. Exons 5–7 (E_1) and 46–47 (E_2) of the largest human gene, dystrophin (*dmd*), together with centromere (N_X) and fluorescence weight center (FWC) of chromosome X were visualized by means of repeated three-dimensional (3D) dual color fluorescence in situ hybridization (FISH). The *dmd* gene is located on the short arm of chromosome X (Xp21.2–3) and is expressed mainly in muscular cells (Chelly et al., 1988). In lymphoblastoid cells the expression level is very low (Chelly et al., 1988). The *dmd* gene contains 79 exons spanning 2.7 Mbp of genomic DNA (Cinti et al., 2002). That's why the *dmd* gene is an appropriate model for studies of the nuclear topography and of the large scale chromatin structure in relation to chromosome X inactivation, taking the advantage of uniform expression level in the frame of one transcription unit.

To test the structural differences between homologous X-chromosomes, the larger (X_L) and smaller (X_S) chromosomes were investigated separately. In the case of the X_L, mutual distances between genetic elements inside territories were significantly elongated. Specific topographic parameters are suggested for the identification of the (de)condensed X-chromosome territory.

2. Materials and methods

2.1. Cell culture and isolation of lymphocytes

T-lymphocytes were isolated from heparinized human blood (20–30 U/ml) by Ficoll-Hepaque density gradient centrifugation (Pharmacia Biotech, Uppsala, Sweden) as described in Kozubek et al. (1999b). The blood samples were obtained from healthy donors without any signs of muscular or other disorder.

G_0-lymphocytes were cultured in RPMI-1640 medium supplemented with 10% fetal calf serum (PAN SYSTEMS GmbH, Germany) under 5% CO_2 humified atmosphere at 37°C. To induce G_0–G_1 transition, G_0-lymphocytes were stimulated by phytohemaglutinin HA 15 (Murex, UK) and maintained in the same conditions as described above for 18–20 h.

2.2. Cell fixation

In all experiments cells were fixed in buffered paraformaldehyde and air drying was carefully avoided to preserve the 3D structure of nuclei. Dense cell suspension in phosphate-buffered saline (PBS) (100 μl) was applied on poly-L-lysinated slides. After the cell adhesion (approximately 5 min, drying meticulously avoided) the slides were immersed in 3.7% paraformaldehyde with 0.5% Triton X-100 and 1 × HEPEM (65 mM PIPES, 30 mM HEPES, 10 mM EGTA, 2 mM $MgCl_2$, pH 6.9) (Neves et al., 1999) for 15 min at room temperature. Consecutively, the cells were washed three times in fresh PBS (3 × 5 min). Usually, fixation was immediately followed by permeabilization. In some cases, fixed cells were stored in refrigerator at 4°C for maximally 3 days then permeabilized and hybridized.

2.3. Cell permeabilization and denaturation

Cells were permeabilized in ice-pre-cooled PBS solution containing 0.7% Triton X-100 and 0.1 N HCl for 12 min under continuous cooling on ice, then washed in PBS 3 × 5 min. RNA was degraded by RNase A treatment (0.1 mg/ml in 2 × 0.15 M NaCl/0.015 M Na_3 citrate pH 7.6, SSC) for 30 min at 37°C followed by washing slides in PBS (3 × 5 min) and denaturation in 50% formamide/2 × SSC solution for 18 min at 75°C. Denatured and preannealed probes were immediately applied to the pretreated cells.

2.4. The probes

Gene specific probes (cosmid cAW40 encompassing dystrophin exons 5–7 (E_1) and cyD4.54 for exons 46–47 (E_2)), chromosome X alphasatellite centromeric repeat

probe (N_X) and whole chromosome X painting probe were used. Dystrophin exons probes, kindly provided by Prof. J den Dunnen (Leiden University, The Netherlands), were directly labeled by spectrum orange (exons E_2) or spectrum green (exons E_1) using nick translation procedure (Vysis, USA). The other probes were labeled either by digoxigenin or biotin. The E_1 and E_2 probes were mixed in Hybrisol VI (Oncor, USA), denatured at 75°C for 10 min, and then incubated for 30–45 min at 37°C before applying on slides. Other probes were treated according to manufacturer's instructions.

2.5. Fluorescence in situ hybridization

Hybridization was carried out in humidified chamber heated up to 37°C for 14 h. Digoxigenated and biotinilated probes were immunodetected by a single layer of anti-digoxigenin-rhodamine or avidin-FITC conjugate respectively. Slides were mounted in the antifade solution (Vectashield, Vector Laboratories, CA) and mixed with 4,6-diamino-2-phenylindole (10 μl, 0.1 μg/ml).

Repeated hybridization was accomplished at the same conditions given for the first hybridization. Before rehybridization the coverslips were carefully cleaned by ethanol and left to fall away in 0.1% Triton X-100/4 × SSC, then washed in the same solution 3 × 4 min and in 2 × SSC (1 × 4 min), denatured and hybridized.

We use the repeated hybridization to detect the topographic parameters of more genetic elements in the same nuclei. To find out the extent of structural changes brought about by the repeated denaturation (preceding each hybridization), we performed the analysis of topographic parameters of the same genetic elements (subtelomeric sequences of *p* a *q* arms of chromosome 11) after the first and second hybridization. Our experiments have demonstrated that the positions of signals after repeated FISH that involves second denaturation are visually very similar (Fig. 1). The same conclusions were done by other authors who stained cells before denaturation using antibodies against centromeric proteins conjugated with fluorochromes and after denaturation using FISH (Cremer et al., 1993; Verschure et al., 1999). These results strongly suggest that the repeated denaturation of cell nuclei fixed by paraformaldehyde does not induce major changes in the nuclear topography.

After repeated hybridization, the 3D coordinates (relative to the center of cell nucleus) of the same signal are determined by computer analyses with precision of about ±0.2

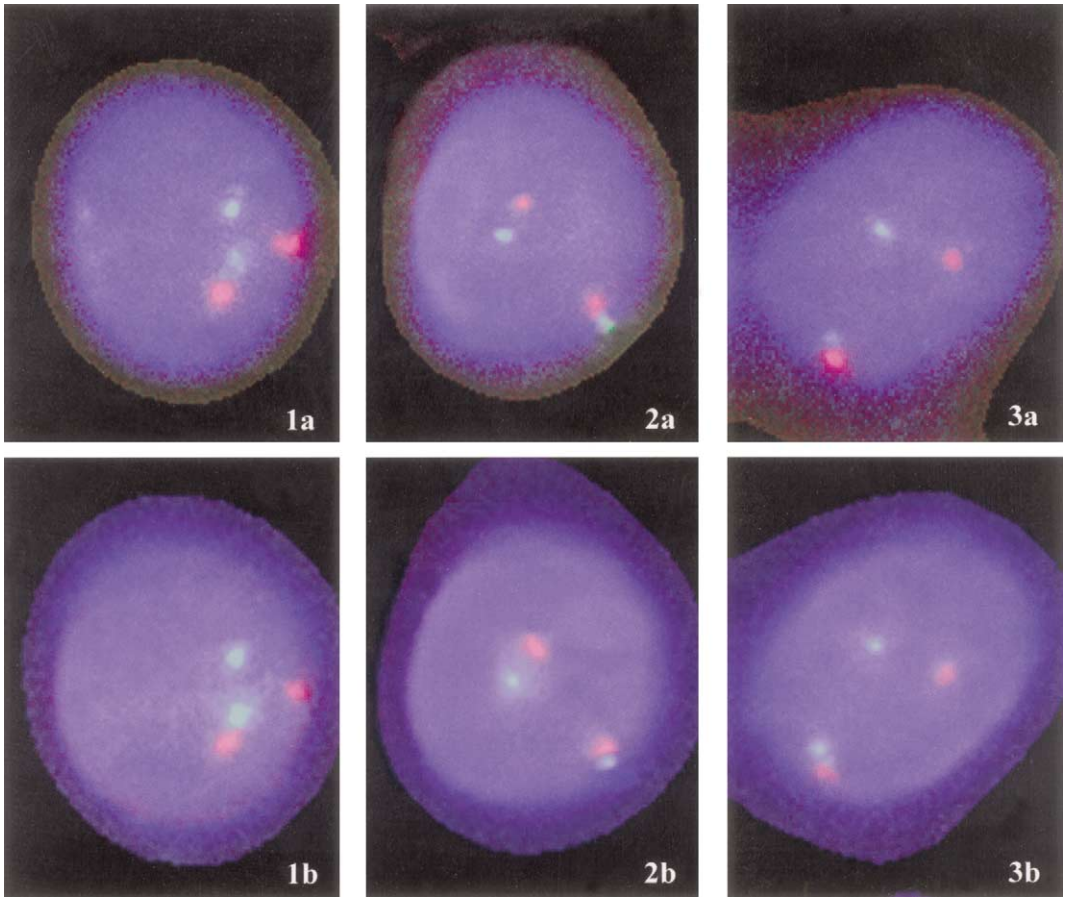

Fig. 1. Comparison of the 1st (a); and 2nd (b) hybridization of cell nuclei (nucleus no. 1–3) with the same dual-color DNA probe of subtelomeric sequences of *q* (red) and *p* (green) arms of HSA 11.

μm. The differences are, however, mostly due to the randomly shifted center of the nucleus. Therefore, the mutual distances are determined more precisely. The radial and mutual distributions determined for the first and second hybridizations are also very similar with nearly identical mean values, standard deviations and standard errors (Table 1). Small reduction of the total nuclear volume that is sometimes observed in the second hybridization can be corrected and does not influence substantially the topographic parameters.

2.6. Image acquisition and microscopy

The Leica DM RXA fluorescence microscope equipped with automated Micromax CCD camera (Princeton Instruments, USA) driven by personal computer (the two Pentium III® processors) was used for image acquisition (Kozubek et al., 1999a, 2001). Automated exposition, image quality control and the other procedures were performed under the FISH 2.0 software (Kozubek et al., 1999a, 2001). Approximately 150 positions per slide, providing sufficient number of correctly hybridized nuclei, were selected and saved in computer memory. To reconstruct 3D structure of the nuclei, 40 optical serial sections in 0.2 μm interval (along the z-axis) were captured for each position. Image acquisition of rehybridized slides was realized employing the positions from the first hybridization recalled from computer memory.

2.7. Analysis of experimental data

For the analysis, only completely hybridized nuclei with highly preserved nuclear architecture after both hybridizations were selected using the x–y, x–z and y–z projections enabling observation of the nuclear sections in three planes. Nuclei with the roundness factor overlapping the value of 1.5, with wrong number of dots or with correct number of signals but of unclear etiology, were excluded from the analysis. In single experiment, 65 up to 1047 nuclei were undergone to measurements as further specified. The roundness factor is defined as $1/(4\pi)*O^2/A$, where O is the nuclear perimeter and A is the nuclear area. The factor is equal to 1 for the circle and increases with growing irregularity of objects.

The first hybridization was performed with probes specific for two *dmd* gene regions (exons E_1 and E_2). In the second hybridization the centromeric (N_X) and painting probe for chromosome X were used. The data from both hybridizations were computationally merged (FISH 2.0) and analyzed in Sigma Plot statistical package (Jandel Scientific, CA). To test the influence of genetic activity on the nuclear topography and chromatin structure, the data obtained for all chromosomes X were analyzed together, as well as separately for X_L and X_S.

Local thresholding segmentation or alternatively manual demarcation was used to determine the nuclear and chromosome territory boundaries. The signals of individual elements from both hybridizations were visually affiliated to their chromosome territory and marked by numeric parameters 1 or 2 to allow further computational evaluation. Radial positions ([nuclear center]-to-[genetic element] distances), mutual distances ([genetic element]-to-[genetic element]) and angular distribution of homologous elements (e.g. [N_X(X_L chromosome)]-[nuclear center]-[N_X(X_S chromosome)]) were determined for *dmd* exons E_1, E_2, centromeres N_X and chromosome territories. Location of chromosome territory was represented by the position of its fluorescence weight center (FWC). Coordinates of FWC were obtained after smoothing the territory signal applying the 5×5 Gauss filter, followed by spatial analysis. For chromosomes, the number of sections containing chromosome signal, the maximal area on optical serial sections and volume of their territories were also calculated. The real volume of chromosome territory is very problematic to be accurately determined. We have used the equivalent value resulting from the addition of areas encompassed by chromosome territory in all individual serial sections containing the territory signal. The same threshold determined from the maximum image was used for all sections.

In all cases, the measured distances were normalized to the nuclear radius to allow accurate length comparison and are presented in percents of nuclear radius [% of R] or in microns, where [radial distance in μm] = [radial distance in % of R]/100*R/9.3. For the volume of chromosome territory

Table 1
Comparison of 3D topographic parameters (with standard deviations and standard errors) obtained from the 1st and the 2nd hybridization of about 60 nuclei of G_0 human lymphocytes

Topographic parameter (distance)[a]	1st Hybridization			2nd Hybridization		
	Mean (% of R)	Stddev	Stderr	Mean (% of R)	Stddev	Stderr
(Red-Red)/R	80.9	34.8	4.5	80.9	36.5	4.7
(Green-Green)/R	107.5	35.5	4.6	106.6	33.2	4.3
(C-Red)/R	60.9	18.8	2.5	59.1	18.5	2.2
(C-Green)/R	70.8	21.1	3.3	69.0	17.2	2.3

[a] Topographic parameters: (Red-Red)/R – distance between red signals normalized to nuclear radius; (Green-Green)/R – distance between green signals normalized to nuclear radius; (C-Red)/R – nuclear centre to red signal distance normalized to nuclear radius; and (C-Green)/R – nuclear centre to green signal distance normalized to nuclear radius.

and its maximal area on serial sections, voxels ([1 voxel] = [1 pixel]*0.2) or μm^3 ([1 μm^3] = [1 pixel]/9.3*0.2) and pixels ([1 pixel] = 0.011 μm^2) were used, respectively.

2.8. Theoretical interpretation of some experimental distributions

In most cases, the angular distributions are random, which means they are well described by a sine function. The reason for such distribution becomes clear if we imagine that the genetic elements are located on the surface of a sphere (at the same radial distance for the sake of simplicity) and one of the homologous genetic elements is placed on the x-axis. Random positioning of the second element on the surface of the sphere then corresponds to the random angular distribution. All elements having the same angle (α) are located in an infinitely small fraction of the spherical surface (ΔS), which is equal to $2\pi\sin(\alpha)\Delta$, where Δ is the width of the circular band. The frequency of the occurrence of a given angle should be proportional to ΔS and, consequently, to $\sin(\alpha)$. Random angular distribution is, therefore, described by the sine function of the [genetic element]-center-[genetic element] angle. Owing to the small surface areas ΔS corresponding to the sine function of 0° and 180°, the number of elements occurring under these angles is low. The largest surface area ΔS corresponds to the angle of 90° and, therefore, the highest probability of an element's occurrence is at this angle.

The distribution of [genetic element]-to-[genetic element] distances of homologous genetic elements was compared with theoretical expectation calculated according to the RS model (Kozubek et al., 1997, 1999b). In brief, positions in 3D space inside a sphere were generated using modulated random number generator in such a way that the measured radial distributions of the given genetic element(s) were reproduced. The angular distributions were kept random. In the next step, the distances between positions representing homologous elements were calculated for each cycle. After 10^5 repeats, the distributions of the [genetic element]-to-[genetic element] distances were determined.

3. Results

3.1. Nuclear topography of the investigated genetic elements

In our experiments, DNA probes for exon 5–7 (E_1) and exon 46–47 (E_2) of *dmd* gene, X-centromere (N_X) and whole territory painting probe for the detection of the FWC were used. The [center of nucleus]-to-[genetic element] distance distributions (radial nuclear distributions) as well as the distributions of mutual distances between genetic elements were determined using image acquisition and analysis. Both *dmd* gene specific probes (E_1 and E_2) were found to be located markedly peripherally in the cell nucleus, very close to the nuclear envelope. In different experiments, the mean values of the radial distances for both E_1 and E_2 oscillated between 77 and 81% of nuclear radius [% of R], which corresponds to statistical standard errors of about 2%. The histograms of radial distributions show increasing occurrence of both *dmd* signals in the direction from the nuclear center to the envelope. The maximum occurrence was found in the concentric layer at 80–90% of R (Figs. 2A,B). There was no significant difference in radial distributions of E_1 and E_2 *dmd* regions.

In order to determine the spatial arrangement of *dmd* gene exons in the concentric nuclear layer, the distributions of exon-[center of nucleus]-exon angles (angular distribution) for the E_1 and E_2 exons were investigated. In addition, the distributions of distances between signals of homologous exons (E_1-to-E_1 and E_2-to-E_2 distances) were also measured. As it follows from the angular distributions of homologous *dmd* exons (Fig. 2C) the spatial localization of these exons in the respective concentric layer is random for both E_1 and E_2. The distributions of mutual distances between the exons (E_1-to-E_1 and E_2-to-E_2) also correspond to theoretical prediction based on the assumption of random positioning of the exons in the concentric layer (Fig. 2D). The mean values of these distributions for E_1 and E_2 are similar (118.7 ± 2.1 and 119.7 ± 2.5% of R).

The mean radial position of the N_X-centromere was also peripheral (the most frequent location is in the interval 80–90% of R from the nuclear center) but with the tendency to be located slightly more centrally (the mean value 73.7 ± 1.7%) in comparison with *dmd* exons (Fig. 2E). As in the case of the exons, the angular distribution of homologous centromeres corresponds to the assumption of random positioning in their nuclear concentric layer (theoretical curve calculated according to a sine function is shown by the solid line) (Fig. 2F).

Localization of the FWC of X-chromosome was the most central of all tested genetic elements (the mean distance from the nuclear center is 65.0 ± 1.0% of R), with the maximum occurrence between 60 and 80% of R. The radial distances are summarized in Table 2.

3.2. Mutual distances between genetic elements

After computational merging and superposition of the data from the first and second hybridization, the signals of both *dmd* exons were visually linked to the relevant signal of N_X-centromere and FWC of X-chromosome. The distributions of mutual distances and their mean values were calculated for all pairs of genetic elements (*dmd* E_1 and E_2 exons, N_X-centromeres and FWCs). In agreement with short molecular distance between the E_1 and E_2 exons (approximately 0.8 Mbp), their spatial distance was also the shortest one with the mean value 0.91 ± 0.04 μm. The distance between the N_X-centromere and FWC was in average 1.12 ± 0.04 μm. Substantially larger distances were found between

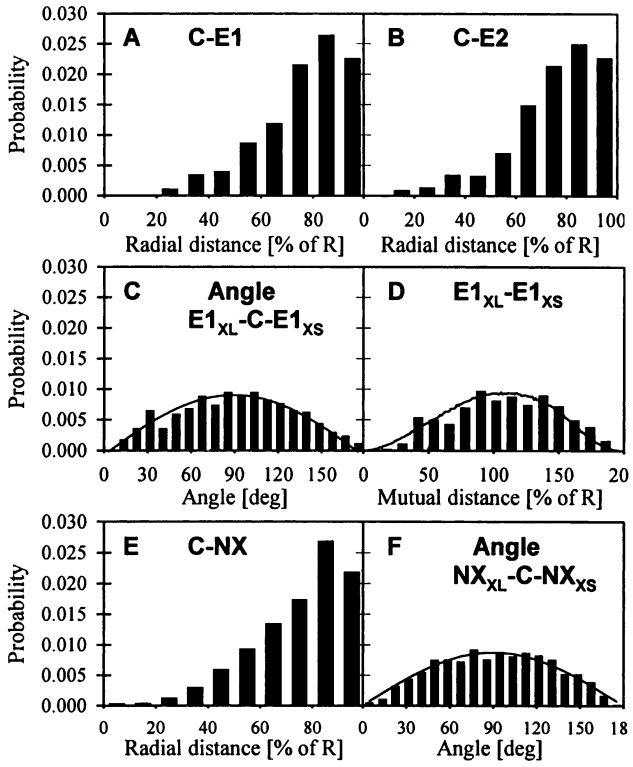

Fig. 2. Nuclear topography of X-chromosome genetic elements. (A, B) Distributions of radial distances of dystrophin exons E_1 and E_2; (C) angular distribution of exon E_1 (distribution of $E_1(X_L)$-[nuclear center]-$E_1(X_S)$ angles); (D) distribution of mutual distances between E_1 exons (E_1–E_1); (E) distribution of radial distances of N_X-centromeres; and (F) their angular distribution ($N_X(X_L)$-[nuclear center]-$N_X(X_S)$) are shown. The theoretical curves calculated for (C) and (F) representing sine functions and the curve for distribution of mutual distances (D), computed using M-C simulation, correspond with experimental data.

FWC or centromere and both *dmd* gene exons (in average 1.7 ± 0.1 μm). All mean mutual distances are shown in Table 2. The radial and mutual distances distributions of the investigated genetic elements indicate specific higher-order chromatin organization in the cell nucleus as well as in the chromosome X territory.

Table 2
Mean radial and mutual distances of genetic elements investigated (with standard deviations)

	Mean (% of R)	Stddev	Mean (μm)	Stddev
Radial distance				
$(E_2\text{-}C)/R$	78.0 ± 2.1	21.4	2.8 ± 0.1	0.8
$(E_1\text{-}C)/R$	77.0 ± 2.0	19.5	2.7 ± 0.1	0.7
$(N_X\text{-}C)/R$	73.7 ± 1.7	18.8	2.6 ± 0.1	0.7
(FWC-C)/R	65.5 ± 0.7	15.7	2.34 ± 0.03	0.56
Mutual distance				
FWC–N_X	31.3 ± 1.2	20.0	1.12 ± 0.04	0.72
FWC–E_2	48.6 ± 1.6	26.3	1.7 ± 0.1	0.9
FWC–E_1	48.5 ± 1.5	25.0	1.7 ± 0.1	0.9
$N_X\text{-}E_2$	49.0 ± 1.7	28.8	1.7 ± 0.1	1.0
$N_X\text{-}E_1$	47.1 ± 1.6	26.7	1.7 ± 0.1	1.0
E_1–E_2	25.4 ± 1.2	19.4	0.91 ± 0.04	0.69

3.3. Volume and shape of chromosome X territories

The volume of chromosome X territories oscillated from approximately 200–2000 voxels (0.46–4.6 μm^3) for both larger (X_L) and smaller (X_S) chromosomes with the mean value 929 voxels = 2.14 μm^3 (Fig. 3A). However, certain shift to lower values of chromosome volume was observed for X_S. The mean values were 706 ± 26 voxels for X_S and 1090 ± 62 voxels for X_L territories. The most frequent values were around 800 and 1000 voxels for X_S and X_L chromosomes, respectively (Fig. 3A). The X_L/X_S volume ratio fluctuated between 1.0 and 2.5; the mean volume ratio was 1.67 ± 0.06. The comparison of maximal areas per section through both chromosome territories shows similar results as the comparison of chromosome volumes

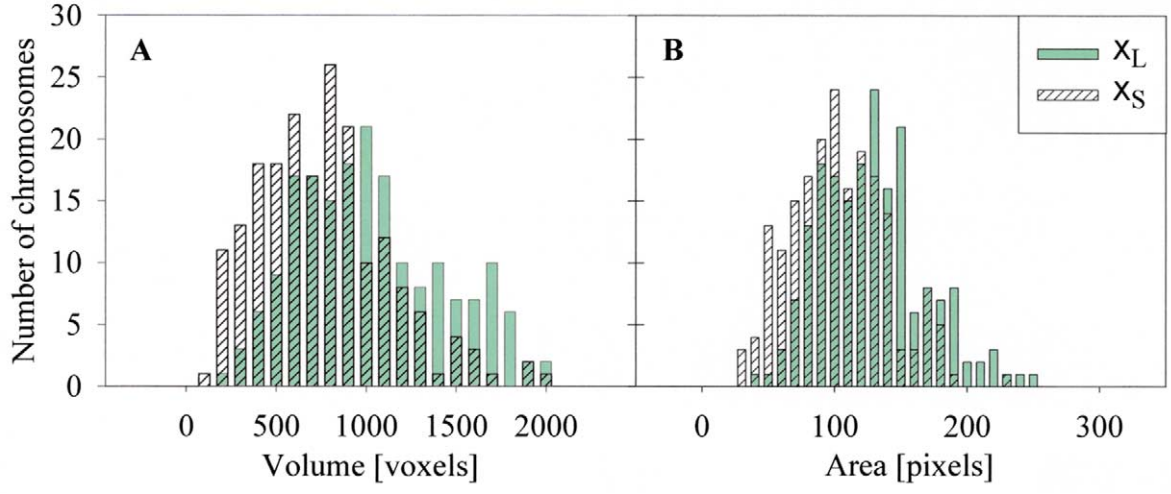

Fig. 3. Volume and maximal section area of the larger X_L (green bars) and smaller X_S (dashed bars) chromosomes. (A) Comparison of the volume distributions of the X_L and X_S; and (B) distributions of the maximal section area for the X_L and X_S chromosomes are presented.

Table 3
Mean radial distances and standard deviations for genetic elements investigated, determined separately for the larger (X_L) and smaller (X_S) chromosome X

Radial distance	X_S			
	Mean (% of R)	Stddev	Mean (μm)	Stddev
(E_2-C)/R	75.8 ± 3.9	26.8	2.7 ± 0.1	1.0
(E_1-C)/R	78.0 ± 3.4	23.5	2.8 ± 0.1	0.8
(N_X-C)/R	70.9 ± 2.5	19.0	2.5 ± 0.1	0.7
(FWC-C)/R	65.1 ± 1.0	16.3	2.32 ± 0.04	0.68
Radial distance	X_L			
	Mean (% of R)	Stddev	Mean (μm)	Stddev
(E_2-C)/R	77.7 ± 3.7	23.2	2.8 ± 0.1	0.8
(E_1-C)/R	77.0 ± 3.1	21.4	2.7 ± 0.1	0.8
(N_X-C)/R	67.6 ± 3.1	21.0	2.4 ± 0.1	0.7
(FWC-C)/R	65.9 ± 1.0	15.1	2.35 ± 0.03	0.54
Radial distance	$\Delta = X_L - X_S$		Δ/X_S*100 shift of X_s to center (%)	Δ/X_L*100 shift of X_s to center (%)
	Mean (% of R)	Mean (μm)		
(E_2-C)/R	1.9	0.1	2.5	2.4
(E_1-C)/R	−1.2	−0.1	−1.5	−1.6
(N_X-C)/R	−3.4	−0.1	−4.8	−4.8
(FWC-C)/R	0.8	0.03	1.2	1.2

(Fig. 3B). The maximal areas were distributed in the interval from approximately 25 to 250 pixels with the mean values 125 ± 3 pixels for X_L and 99 ± 3 pixels for X_S. The mean value of ratios of maximal chromosome areas per section through X_L and X_S (calculated for individual nuclei) was 1.38 ± 0.05. The number of optical sections containing signal of the chromosome territory was a little higher for the X_L, with the most frequent value 12.6 ± 0.2 (ranging from 7 to 19) and 10.8 ± 0.2 for X_S. The total number of optical sections was 40 with the step 0.2 μm. The territory of larger chromosome X seemed to occupy slightly more open structure in comparison with rather compact smaller chromosome. In some nuclei, the borders of the X_L territories on optical sections were more intended comparing to X_S territories.

3.4. Structure of the larger and smaller chromosome X territory

To test the possible influence of genetic activity on the architecture of chromosome X territory, the volume of individual chromosomes was determined and separate analyses of larger (X_L) and smaller (X_S) territory were performed. The internal structure of chromosome X homologous territories was compared in selected nuclei where the volume ratio of X_L/X_S was higher than 1.4.

The radial positions of all genetic elements independently of their location on X_L or X_S chromosome were very similar in female lymphocytes (Table 3; Figs. 4A–D). Experiments with chromosome X of human male showed similar radial distributions for the E_1 and E_2 exons as well as for N_X-centromeres (not shown).

In contrast, the measurement of mutual distances revealed significant elongation of all distances between genetic elements pertaining to X_L (Table 4; Figs. 4F–K). The difference in the degree of condensation between homologous X-chromosomes was expressed as a difference between mutual distances of two genetic elements on X_L and X_S (e.g.

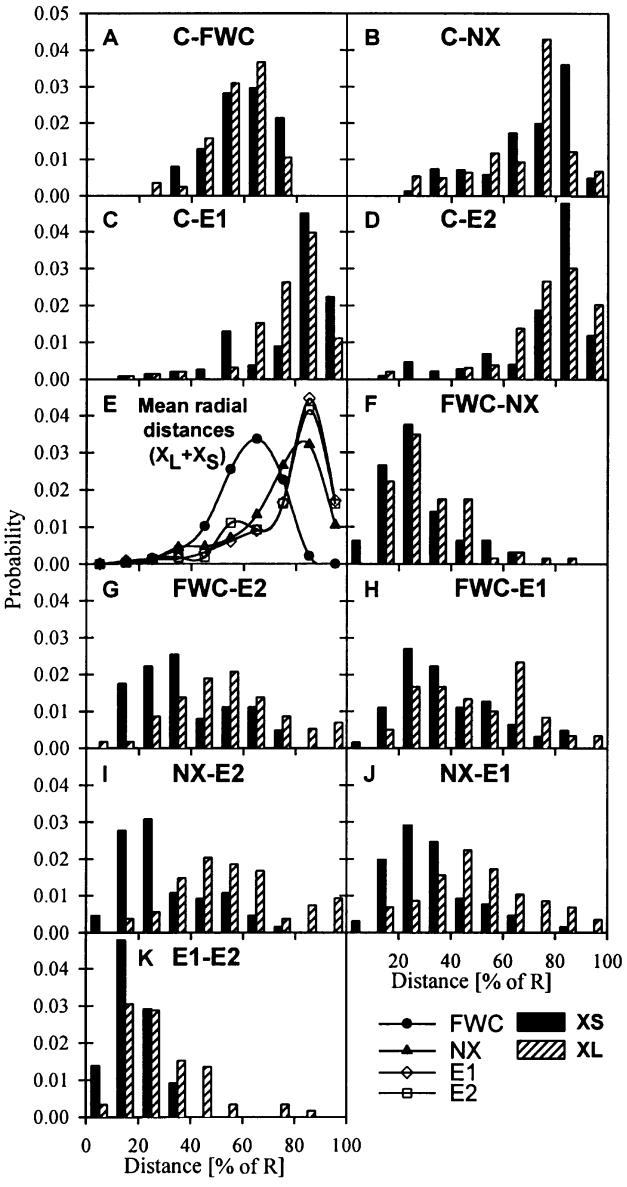

Fig. 4. Comparison of radial (A–E); and mutual (F–K) distance distributions of individual genetic elements (dystrophin exons E_1, E_2 and centromere N_X) and of the X-chromosome territory fluorescence weight center (FWC), located on the X_L (dashed bars) or X_S (black bars) chromosomes. The radial distance distributions of the investigated elements are averaged for the X_L and X_S in (E).

$\Delta = (E_1–E_2)_{XL} - (E_1–E_2)_{XS}$) normalized to one of these distances ($\Delta/(E_1–E_2)_{XL}$*100% or $\Delta/(E_1–E_2)_{XS}$*100%) (Table 4). The most significant differences between X_L and X_S were observed for mean *dmd* exon-to-exon ($E_1–E_2$) and centromere-to-exon distances ($N_X–E_1$ and $N_X–E_2$) (Table 4; Figs. 4I–K). Conversely, the lowest difference of distances was recorded between the centromere and FWC of the homologues (Table 4; Fig. 4F).

Chromosome structure can be investigated without respect to the cell nucleus by comparison of the mutual positions of genetic elements pertaining to individual chromosome territory. In such a way the fluctuations of the positions of genetic elements attributable to variable chromosome positioning and to orientation in the cell nucleus can be removed. In Figs. 5A,B, the N_X-centromere together with both exons investigated is placed to the plane of the figure for a number of chromosomes. The centromeres are placed in the origin of the coordinates, E_2 is placed on the x-axis and, after another rotation, E_1 is lowered to the plane of the figure. Shorter distances between the elements for X_S as compared with X_L are evident. The distributions of the E_1-centromere-E_2 angles are shown in upper panels of Figs. 5A,B. These distributions were similar for the X_L and X_S territories suggesting proportional extension (contraction) of the structure during decondensation (condensation). However, the larger of the chromosome territories exhibits more pronounced dispersion of the positions of genetic elements.

3.5. Positions of genetic elements relative to chromosome X territories in cell nuclei

The difference in chromatin condensation of X_L and X_S chromosome territories can be deduced also from the distributions of genetic elements relative to chromosome territory (territorial distributions). The territorial distributions can be obtained if FWCs of chromosomes from different nuclei are positioned to a single point. For example, FWC (together with other genetic elements) can be placed to the x-axis by 3D rotation of the cell nucleus and shifted along this axis to the FWC mean radial location. Thus, the fluctuations of territory positions in the cell nucleus are removed and the territorial distributions of centromeres and exons are shown (Figs. 6A,B). In order to demonstrate the real values of mutual distances between genetic elements, the x–y positions are shown only for such nuclei where the z-coordinates of genetic elements were near to zero. The points, therefore, represent genetic elements in a narrow x–y slice through the

Table 4
Mean mutual distances and standard deviations for genetic elements investigated, determined separately for the larger (X_L) and smaller (X_S) chromosome X

Mutual distance	X_S			
	Mean (% of R)	Stddev	Mean (μm)	Stddev
FWC–N_X	28.4 ± 2.1	17.3	1.0 ± 0.1	0.6
FWC–E_2	40.4 ± 3.0	24.0	1.4 ± 0.1	0.9
FWC–E_1	41.5 ± 3.1	25.2	1.5 ± 0.1	0.9
N_X–E_2	30.1 ± 2.0	16.4	1.1 ± 0.1	0.6
N_X–E_1	32.0 ± 1.9	15.4	1.1 ± 0.1	0.5
E_1–E_2	18.2 ± 0.9	7.6	0.68 ± 0.03	0.27
Angle E_1–FWC–E_2	29.6 ± 3.1	25.2	–	–
Mutual distance	X_L			
	Mean (% of R)	Stddev	Mean (μm)	Stddev
FWC–N_X	34.1 ± 2.9	23.4	1.2 ± 0.1	0.8
FWC–E_2	61.2 ± 3.8	31.0	2.2 ± 0.1	1.1
FWC–E_1	54.8 ± 3.4	27.8	2.0 ± 0.1	1.0
N_X–E_2	68.1 ± 4.4	35.8	2.4 ± 0.2	1.3
N_X–E_1	59.7 ± 3.9	31.0	2.1 ± 0.1	1.1
E_1–E_2	37.3 ± 3.9	31.3	1.3 ± 0.1	1.1
Angle E_4–FWC–E_2	37.7 ± 4.5	36.3	–	–
Mutual distance	$\Delta = X_L–X_S$		Δ/X_S*100 decond. (%)	Δ/X_L*l00 cond. (%)
	Mean (% of R)	Mean (μm)		
FWC–N_X	5.7	0.2	20.2	16.8
FWC–E_2	20.8	0.8	51.4	33.9
FWC–E_1	13.3	0.5	31.9	24.2
N_X–E_2	38.1	1.3	126.7	55.9
N_X–E_1	27.7	1.0	86.7	46.4
E_1–E_2	19.1	0.7	104.9	51.2
Angle E_1–FWC–E_2	8.1	–	–	–

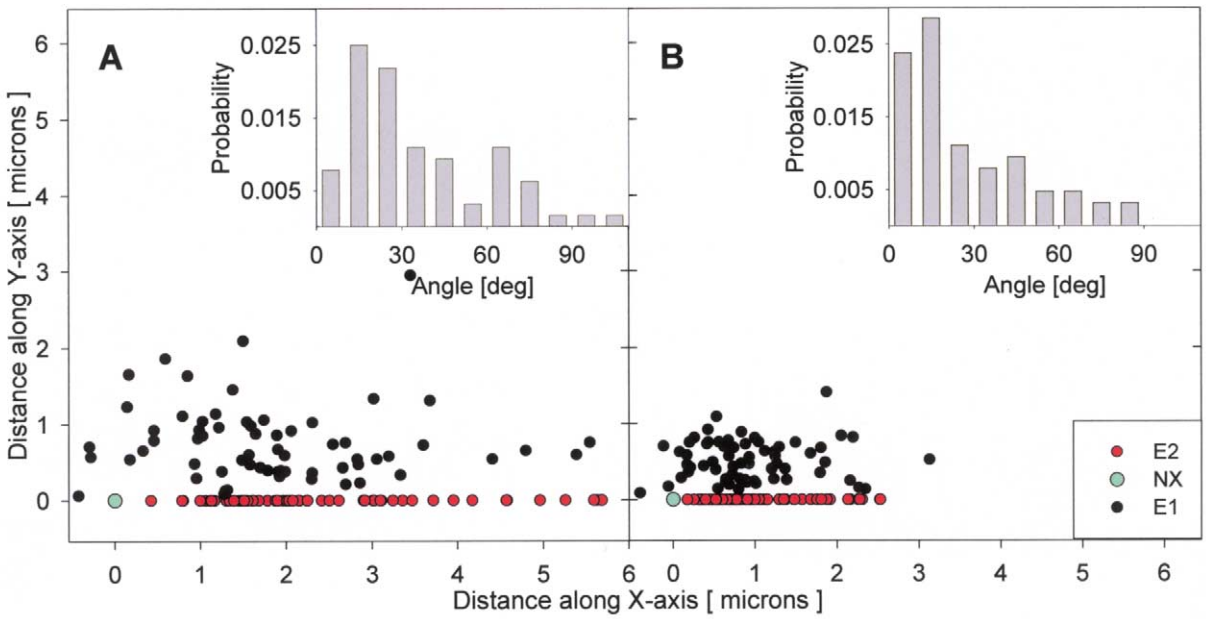

Fig. 5. Chromosome territory structure of the X_L (A); and X_S (B). In the main figures, the genetic elements of the X-chromosome territories X_L (A); and X_S (B) are shown using the following symbols: green circle – N_X-centromere, black circle – E_1 and red circle – E_2. The centromere was placed in the origin, the E_2 exon was placed to the x-axis and the E_1 exon was lowered to the plane of the figure. Longer distances between genetic elements and slightly larger E_1–N_X–E_2 angles are clearly visible in the case of X_L (A). The distributions of the E_1–N_X–E_2 angles are shown in the top-right panels. For other depiction of the E_1–N_X–E_2 angle see also Fig. 7.

central plane of the nucleus (and the territory) after its rotation. In this case, it can be seen that the fluctuations of genetic elements (*dmd* exons and N_X-centromeres) relative to the territory are more pronounced for X_L comparing to X_S (Figs. 6A,B).

If the centromere is positioned by 3D rotation to the x-axis in the way similar to that described for FWC, the fluctuations of genetic elements (*dmd* exons) relative to the centromere are also more pronounced for X_L (Figs. 6C,D). As seen, the exon-to-centromere distances are much longer for X_L as compared to X_S.

4. Discussion

Recent papers show that the active (X_a) and inactive (X_i) X-chromosome territories differ in their size, although to smaller extent than earlier expected (Bischoff et al., 1993; Rinke et al., 1995; Eils et al., 1996). Bischoff et al. (1993) suggested that X_L represents X_a, while X_S represents X_i in most cases (see also Clemson et al., 1996; Eils et al., 1996). Therefore, in our approach, X-chromosome territories with larger and smaller volume were distinguished and further analyzed. The mean ratio of the sizes of the homologous territories was $\rho = 1.67 \pm 0.06$ in agreement with findings of other authors (Bischoff et al., 1993; Rinke et al., 1995; Eils et al., 1996). In order to ensure that X_L represent X_a and X_S represent X_i, the nuclei with clearly separated territories and with the ratio of territory volumes above $\rho = 1.4$ were selected for further analyses. The larger and smaller territories were analyzed separately in order to find differences between them that would be indicative for active and inactive state of chromosome territories.

One of the questions is, whether inactivation of a chromosome X has any influence on the nuclear position of the whole chromosome territory or of its parts. Our results obtained on human lymphocytes do not show any difference between X_L and X_S in the radial distributions of territories represented by FWC or of their elements. Moreover, the same radial distributions of the corresponding genetic elements were obtained for the male chromosome X in human lymphocytes. This finding is in contrast to earlier observations of very peripheral location of the Barr body and more central position of the other territory and does not support the requirement for specific nuclear location of the inactive X-territory (X_i) in order to maintain its inactive state (Dyer et al., 1989). As presented by (Bridger et al., 2000), the nuclear arrangement may be different in quiescent, senescent and cycling cells. In G_0-lymphocytes the transcription level of the X_a could be suppressed to the level similar to the X_i, situating thus both chromosomes to the same radial position (Table 3). The N_X-centromeres, E_1 and E_2 exons were found near the nuclear periphery, with the mean radial distances 74–78% of the nuclear radius. This finding corresponds to earlier studies showing peripheral position of centromeres (Skalníková et al., 2000) as well as of some genes such as c-myc or rb in human blood cells (Bartova et al., 2002). These genes, similarly

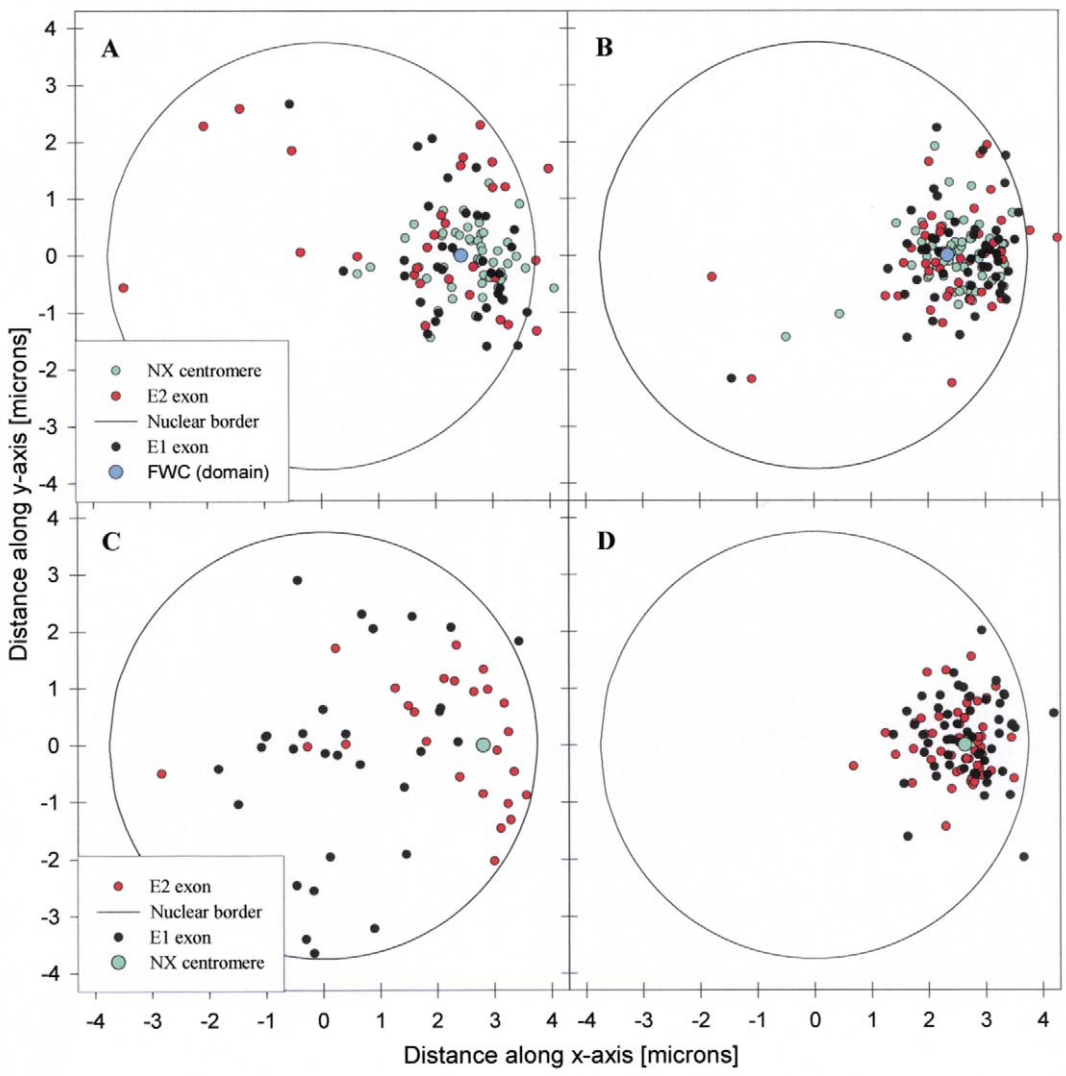

Fig. 6. Distribution of genetic elements in corresponding chromosome territory with respect to their nuclear positions. (A, B) Distribution of dystrophin exons E_1 (black circles), E_2 (red circles) and N_X-centromere (green circles) around the mean fluorescence weight center (FWC, large blue circle) of X_L (A); and X_S (B) chromosome in the central section of the nucleus (width 1 μm) derived from 3D confocal measurements is shown. Owing to the positioning of FWCs of individual chromosomes to their mean position on the x-axis, the fluctuations in the nuclear positions of chromosome territories are removed. The point density in the figure represents the probability density per volume unit of the genetic element occurrence at a given position. (C, D) The distribution of dystrophin exons E_1 and E_2 around the $N_X(X_L)$ (C); and $N_X(X_S)$ (D) centromere after similar transformation described for figures A and B (N_X-centromeres placed to their mean position on the x-axis, large green circle). The other symbols are the same as in (A) and (B).

as dmd exons, are located near G-bands in metaphase chromosomes and their expression is restricted only to some cell types. In our experiments, no differences between G_0 and G_1 lymphocytes in positions of dmd exons were observed.

The angular distributions obtained for homologous exons or centromeres are well described by a sine function (see Section 2.7), which suggests random positioning of the elements and consequently also of the whole chromosome territories in concentric spherical nuclear shells. This finding is also in good agreement with earlier results obtained for some genes and centromeres (Skalníková et al., 2000).

Contrary to the radial distances, significantly larger mutual distances were found between all pairs of genetic elements on the X_L as compared with X_S (Table 4). Increased mutual distances between *ant2* (Xq24–q25) and *ant3* (Xp22.3) genes of X_L as compared with X_S were observed by Dietzel et al. (1999) for amniotic fluid cell nuclei. The differences found correspond to our results for FWC-to-[other genetic element] distances. Substantially more pronounced differences between X_L and X_S were observed in the structure of the *dmd* gene (E_1–E_2 distance) and in its distance to N_X-centromere. This finding is in agreement with conclusions of Francastel et al. (2000) on more open chromatin structure of expressed genes that are located more distantly from nearest centromeres. In spite of relatively low level of expression of the *dmd* gene, increased

E_1–E_2 distance and consequently more open structure of this gene was observed. The striking shift of E_1 and E_2 away from centromere N_X and, in the same time, much smaller changes in the chromosome territory linear dimension ($\sqrt[3]{1.7} = 1.2$ times) following chromosome X inactivation may be related to an important role of centromeric heterochromatin in gene silencing (Francastel et al., 1999; Bartova et al., 2002). Our observation of elongated distances between genetic elements of X_L that are correlated with greater volume of chromosome X territory strongly suggests that the X_L is identical to the active X_a chromosome. Owing to its sensitivity, the distance of the *dmd* gene (E_1 or E_2) to the N_X-centromere can be suggested as an appropriate topographic parameter for the identification of the active/inactive X-chromosome.

Significant differences of some distances investigated, together with similar sizes of X_L and X_S, may indicate the presence of small interchromatin areas, containing little or no DNA, inside the chromosome territory (Cremer et al., 1993; Zirbel et al., 1993). Reticular organization of chromosome territories only partially filled by DNA has been described by Verschure et al. (1999). Alternative explanation of similar sizes of X_L and X_S is the formation of protrusions of chromatin extended outside from chromosome territories (see Volpi et al., 2000) that are not detected by standard FISH. The existence of the protrusions would explain substantial extension of some mutual distances between genetic elements. The presumptive structure of the X_L and X_S territories and of *dmd* gene is schematically presented on Fig. 7. The *dmd* exons E_1 and E_2 as well as N_X-centromere are localized on the nuclear periphery while the FWC is localized more centrally. The distances between genetic elements (*dmd* exons, N_X-centromere and FWC) and their nuclear location indicate that these signals are not located in the same plane. Therefore, they are displayed on apexes of a tetrahedron. Inactivation of an X-chromosome results in the shortening of distances between genetic elements leading to a more compact territory of X_S. In our experiments, more prominent contraction of mutual distances in lateral direction (perpendicular to radial axis intersecting the nuclear center and relevant FWC) compared to radial changes was observed (see Fig. 7). It may indicate flatter shape of the larger chromosome X comparing to the smaller one as described by Eils et al. (1996).

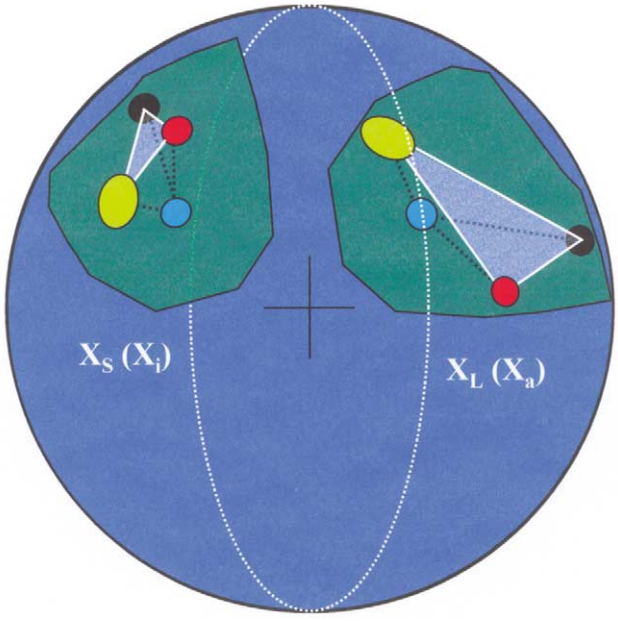

Fig. 7. Schematic drawing of mutual arrangement of investigated genetic elements – dystrophin exons E_1 (black circle), E_2 (red circle), N_X-centromeres (green ellipse), and of respective fluorescence weight centers (FWC, blue circle) of the X_L and X_S chromosome. Chromosome territories are displayed as the green areas. Dark dashed and white lines demonstrate links between genetic elements and are drawn in order to demonstrate their spatial (tetrahedral) arrangement and mutual distances. The violet triangles demonstrate the area hold by the arms of the E_1–N_X–E_2 angle (see also Fig. 5) and show the elongation of mutual distances. The E_1–N_X–E_2 angles between genetic elements located on the X_L comparing to the X_S chromosome are similar. In addition, potentially flatter shape of X_L chromosome territory is shown. The radial distances of drawn genetic elements are not proportional to real radial distances.

Acknowledgements

We thank Iva Kroupová for technical assistance. This work was supported by the Academy of Sciences (S5004010), Ministry of Health (NC5955), and Grant Agency of the Czech Republic (202/01/0197 and 301/01/0186).

References

Bartova, E., Kozubek, S., Jirsova, P., Kozubek, M., Gajova, H., Lukasova, E., Skalnikova, M., Ganova, A., Koutna, I., Hausmann, M., 2002. Nuclear structure and gene activity in human differentiated cells. J. Struct. Biol. in press.

Bischoff, A., Albers, J., Kharboush, I., Stelzer, E., Cremer, T., Cremer, C., 1993. Differences of size and shape of active and inactive X-chromosome domains in human amniotic fluid cell nuclei. J. Microsc. Res. Tech. 25, 68–77.

Boyle, S., Gilchrist, S., Bridger, J.M., Mahy, N.L., Ellis, J.A., Bickmore, W.A., 2001. The spatial organization of human chromosomes within the nuclei of normal and emerin-mutant cells. Hum. Mol. Genet. 10, 211–219.

Bridger, J.M., Boyle, S., Kill, I.R., Bickmore, W.A., 2000. Re-modelling of nuclear architecture in quiescent and senescent human fibroblasts. Curr. Biol. 10, 149–152.

Chelly, J., Kaplan, J.-C., Maire, P., Gautron, S., Kahn, A., 1988. Transcription of the dystrophin gene in human muscle and non-muscle tissues. Nature 333, 858–860.

Cinti, C., Stuppia, L., Maraldi, N.M., 2002. Combined use of PRINS and FISH in the study of the dystrophin gene. Am. J. Med. Genet. 107, 115–118.

Clemson, C.M., McNeil, J.A., Willard, H.F., Lawrence, J.B., 1996. XIST RNA paints the inactive X chromosome at interphase: evidence for a novel RNA involved in nuclear/chromosome structure. J. Cell. Biol. 132, 259–275.

Comings, D.E., 1968. The rationale for an ordered arrangement of chromatin in the interphase nucleus. Am. J. Hum. Genet. 20, 440–460.

Cremer, T., Kurz, A., Zirbel, R., Dietzel, S., Rinke, B., Schrock, E., Speicher, M.R., Mathieu, U., Jauch, A., Emmerich, P., Scherthan, H., Ried, T., Cremer, C., Lichter, P., 1993. Role of Chromosome Territories in the Functional Compartmentalization of the Cell Nucleus. Cold Spring Harbor Symposia on Quantitative Biology LVIII: 777–792, Cold Spring Harbor Laboratory Press, Cold Spring Harbor, NY.

Croft, J.A., Bridger, J.M., Boyle, S., Perry, P., Teague, P., Bickmore, W.A., 1999. Differences in the localization and morphology of chromosomes in the human nucleus. J. Cell. Biol. 145, 1119–1131.

Dietzel, S., Schiebel, K., Little, G., Edelmann, P., Rappold, G.A., Eils, R., Cremer, C., Cremer, T., 1999. The 3D positioning of ANT2 and ANT3 genes within female X chromosome territories correlates with gene activity. Exp. Cell. Res. 252, 363–375.

Dyer, K.A., Canfield, T.K., Gartler, S.M., 1989. Molecular cytological differentiation of active from inactive X domains in interphase: implications for X chromosome inactivation. Cytogenet. Cell. Genet. 50, 116–120.

Eils, R., Dietzel, S., Bertin, E., Schröck, E., Speicher, M.R., Ried, T., Robert-Nicoud, M., Cremer, C., Cremer, T., 1996. Three-dimensional reconstruction of painted human interphase chromosomes: active and inactive X chromosome territories have similar volumes but differ in shape and surface structure. J. Cell. Biol. 135, 1427–1440.

Francastel, C., Walters, M.C., Groudine, M., Martin, D.I., 1999. A functional enhancer suppresses silencing of a transgene and prevents its localization close to centrometric heterochromatin. Cell 99, 259–269.

Francastel, C., Schübeler, D., Martin, D.I.K., Groudine, M., 2000. Nuclear compartmentalization and gene activity. Nature 1, 137–143.

Gartler, S.M., Goldman, M.A., 1994. Reactivation of inactive X-linked genes. Dev. Genet. 15, 504–514.

Heard, E., Clerc, P., Avner, P., 1997. X-chromosome inactivation in mammals. Annu. Rev. Genet. 31, 571–610.

Hennig, W., 1999. Heterochromatin. Chromosoma 108, 1–9.

Kozubek, S., Lukášová, E., Rúznar, L., Kozubek, M., Lišková, A., Govorun, R.D., Krasavin, E.A., Horneck, G., 1997. Distribution of ABL and BCR genes in cell nuclei of normal and irradiated lymphocytes. Blood 89, 4537–4545.

Kozubek, M., Kozubek, S., Lukášová, E., Marečková, A., Bártová, E., Skalníková, M., Jergová, A., 1999a. High-resolution cytometry of FISH dots in interphase cell nuclei. Cytometry 36, 279–293.

Kozubek, S., Lukášová, E., Marečková, A., Skalníková, M., Kozubek, M., Bártová, E., Kroha, V., Krahulcová, E., Šlotová, J., 1999b. The topological organizations of chromosomes 9 and 22 in cell nuclei has a determinative role in the induction of t(9,22) translocations and in the pathogenesis of t(9,22) leukemias. Chromosoma 108, 426–435.

Kozubek, M., Kozubek, S., Lukasova, E., Bartova, E., Skalnikova, M., Matula, P., Matula, P., Jirsova, P., Cafourkova, A., Koutna, I., 2001. Combined confocal and wide-field high-resolution cytometry of fluorescent in situ hybridization-stained cells. Cytometry 45, 1–12.

Kurz, A., Lampel, S., Nickolenko, J.E., Bradl, J., Benner, A., Zirbel, R.M., Cremer, T., Lichter, P., 1996. Active and inactive genes localize preferentially in the periphery of chromosome territories. J. Cell. Biol. 135, 1195–1205.

Lyon, M.F., 1961. Gene action in the X-chromosome of the mouse (*Mus musculus* L.). Nature 190, 372–373.

Müller, W.G., Walker, D., Hager, G.L., McNally, J.G., 2001. Large-scale chromatin decondensation and recondensation regulated by transcription from a natural promoter. J. Cell. Biol. 154, 33–48.

Neves, H., Ramos, C., da Silva, M.G., Parreira, A., Parreira, L., 1999. The nuclear topography of ABL, BCR, PML, and RARalpha genes: evidence for gene proximity in specific phases of the cell cycle and stages of hematopoietic differentiation. Blood 93, 1197–1207.

Nogami, M., Nogami, O., Kagotani, K., Okumura, M., Taguchi, H., Ikemura, T., Okumura, K., 2000. Intranuclear arrangement of human chromosome 12 correlates to large-scale replication domains. Chromosoma 108, 514–522.

Rinke, B., Bischoff, A., Meffert, M.-C., Scharschmidt, R., Hausmann, M., Stelzer, E.H.K., Cremer, T., Cremer, C., 1995. Volume ratios of painted chromosome territories 5, 7 and X in female human cell nuclei studied with confocal laser microscopy and Cavalieri estimator. Bioimaging 3, 1–11.

Skalníková, M., Kozubek, S., Lukášová, E., Bártová, E., Jirsová, P., Cafourková, A., Koutná, I., Kozubek, M., 2000. Spatial arrangement of genes, centromeres and chromosomes in human blood cell nuclei and its changes during the cell cycle, differentiation and after irradiation. Chromosome Res. 8, 487–499.

Tajbakhsh, J., Luz, H., Bornfleth, H., Lampel, S., Cremer, C., Lichter, P., 2000. Spatial distribution of GC- and AT-rich DNA sequences within human chromosome teritoriem. Exp. Cell. Res. 255, 229–237.

Verschure, P.J., van der Kraan, I., Manders, E.M.M., van Driel, R., 1999. Spatial relationship between transcription sites and chromosome territories. J. Cell. Biol. 147, 13–24.

Volpi, E.V., Chevret, E., Jones, T., Vatcheva, R., Williamson, J., Beck, S., Campbell, R.D., Goldsworthy, M., Powis, S.H., Ragoussis, J., Trwsdale, J., Sheer, D., 2000. Large-scale chromatin organization of the major histocompatibility complex and other regions of human chromosome 6 and its response to interferon in interphase nuclei. J. Cell. Sci. 113, 1565–1576.

Walker, L.Ch., Cargile, C.B., Floy, K.M., Delannoy, M., Migeon, B.R., 1991. The Barr body is a looped X chromosome formed by telomere association. Proc. Natl. Acad. Sci. USA 88, 6191–6195.

Zirbel, R.M., Mathieu, U.R., Kurz, A., Cremer, T., Lichter, P., 1993. Evidence for a nuclear compartment of transcription and splicing located at chromosome domain boundaries. Chromosome Res. 1, 93–106.

Acta Biochimica Polonica

Vol. 54 No. 3/2007, 657–663

on-line at: www.actabp.pl

Communication

The role of actin and microtubule networks in plasmid DNA intracellular trafficking

Vladan Ondřej✉, Emilie Lukášová, Martin Falk and Stanislav Kozubek

Laboratory of Molecular Cytology and Cytometry, Institute of Biophysics, Academy of Sciences of the Czech Republic, Brno, Czech Republic

Received: 23 May, 2007; revised: 04 July, 2007; accepted: 01 August, 2007
available on-line: 23 August, 2007

This work is focused on the function of the microtubule and actin networks in plasmid DNA transport during liposomal transfection. We observed strong binding of plasmid DNA–lipid complexes (lipoplexes) to both networks and directional long-range motion of these lipoplexes along the microtubules. Disruption of either of these networks led to the cessation of plasmid transport to the nucleus, a decreased mobility of plasmids, and accumulation of plasmid DNA in large aggregates at the cell periphery. Our findings show an indispensable but different role of both types of cytoskeleton, actin and microtubular, in the processes of gene delivery.

Keywords: plasmid DNA–lipid complexes, cytoplasmic trafficking, actin filaments, microtubules

INTRODUCTION

The intracellular transport of plasmid DNA, in the context of gene delivery by transfection using non-viral vectors, is still poorly explored. Relatively little is known about the kinetics and fate of the transfected DNA, such as its intracellular transfer and localization. A variety of intracellular barriers must be overcome to deliver exogenous DNA into the cell nucleus of the host cell to allow its expression. Vectors must cross the plasma membrane, move through the cytoplasm, enter the nucleus, and then locate to a specific site suitable for vector integration and DNA transcription. The intracellular movement of plasmid DNA complexes affecting gene delivery may represent one of the major barriers, and remains to be explored (Zhou *et al.*, 2004). Many authors found that plasmid DNA entered the cells within 1 h after transfection, and that this DNA accumulated in the perinuclear region (Zabner *et al.*, 1995; Coonrod *et al.*, 1997; Johnson & Jurcisek, 1999). It has also been shown by Lukacs *et al.* (2000) that molecules of DNA larger than 2000 bp are unable to diffuse freely in the cytoplasm. However, it is known that despite this apparent inability of plasmids to diffuse through the cytoplasm, transfections do result in expression. Thus, plasmids must be able to cross the cytoplasm by other means than diffusion.

Trafficking of viral DNA has been studied more intensively. Like plasmids, viruses enter their hosts and traverse the cytoplasm to enter the cell nucleus for replication. Recent studies have pointed to the use by viruses of the cytoskeleton to facilitate transport towards the nucleus (van Loo *et al.*, 2001; McDonald *et al.*, 2002; Lee *et al.*, 2006). Viruses such as herpes simplex virus type 1 and adenovirus move to the nucleus by latching on to dynein motor proteins and moving along the microtubules (reviewed in Campbell & Hope, 2005). Recent data indicate that HIV-1 also uses dynein motors and the microtubules for its movement (reviewed in Anderson & Hope, 2005). Although microtubules appear to be the dominant highways for viruses, they are by no means the exclusive route. Van Loo *et al.* (2001) showed that baculovirus uses the actin cytoskeletal network to move towards the nucleus, using myosin V motors. Also, some mRNAs are actively translo-

✉**Corresponding author**: Vladan Ondřej, Laboratory of Molecular Cytology and Cytometry, Institute of Biophysics, Academy of Sciences of the Czech Republic, v.v.i., Královopolská 135, Brno 612 65, Czech Republic; tel.: (420) 541 517 165, fax: (420) 541 211 293, e-mail: ondrej@ibp.cz

cated from nuclear pores on cytoskeletal filaments, and ultimately localize at specific regions of the cell (Shav-Tal & Singer, 2005).

Like that of viruses, the transport of plasmids to the cell nucleus could also be facilitated by the cytoskeletal network. A recent contribution of Vaughan and Dean (2006) showed that disruption of microtubules or dynein inhibition decreased expression of microinjected plasmids. Taken together, these results led to the idea that plasmids probably become attached to cytoskeletal motors, much like viruses do, and move along the microtubules to the cell nucleus. Here, we report experiments with fluorescently labeled plasmid DNA transfected by means of liposomes to find and distinguish the roles of two cytoskeletal networks, actin and microtubules, in plasmid DNA trafficking throughout the cytoplasm. Labelled plasmids, together with networks visualized by means of fluorescent fusion proteins or live staining, enable us to track plasmid DNA *in vivo* and to assign dynamic parameters to it. We also followed cytoplasmic transport of plasmid DNA after network disruption using different drug treatments. Based on a series of *in vivo* cell measurements and observations of fixed cells, we conclude that the microtubule network is utilized by plasmid DNA–lipid complexes (lipoplexes) for long-range movement. Unlike complexes attached to the microtubule network, complexes attached to the actin network are highly immobile. Interestingly, disruption of either network stopped the transport of plasmid DNA and resulted in accumulation of lipoplexes at the cytoplasmic periphery.

MATERIALS AND METHODS

Cell culture and cell transfection. Fibroblasts (04-147), originated from Academic Medical Center University of Amsterdam (The Netherlands), were grown in DMEM medium, supplemented with 10% fetal calf serum (FCS), penicillin (100 U/ml) and streptomycin (100 μg/ml), in humidified air with 5% CO_2 at 37°C. Transfection was performed using Lipofectamine 2000 (Invitrogen) in OPTIMEM medium (Gibco), according to the manufacturer's protocol, in six-well multidishes or in special chambers for *in vivo* observations. After 5 h of cell transfection in the presence of Lipofectamine 2000, the medium was replaced with DMEM containing 10% FCS without antibiotics, and cells were incubated for 24 h. Before fixation, the DMEM medium was replaced with OPTIMEM to which green Lumio reagent was added to produce the recommended concentration of 2.5 μM. The cells were incubated for 30 min and then fixed or used for *in vivo* observation. To visualize microtubules *in vivo* in transfected cells, the fibroblasts were incubated with OPTIMEM medium supplemented with an appropriate volume of TubulinTracker Green (Invitrogen) for 20 min, according to the manufacturer's protocol. After that, the medium was supplemented with 200 μM trolox (Sigma-Aldrich), and the cells were ready for observation *in vivo*.

Vectors used and DNA labelling. The Lumio technology (Invitrogen) and the HORF clone of the β-actin gene (IOH3654, Invitrogen) were used for fusion protein preparation, where the fluorescent tag is a Lumio tetracysteine sequence.

The plasmid DNA, composed of the pENTR 221 vector containing β-actin cDNA, the gene for kanamycin resistance, the Kozak consensus sequence and the pUC origin, was labelled before transfection with Label IT Tracker reagent Cy5 (Mirus Co.), at the Cy5:DNA ratio recommended by the manufacturer, at 37°C for 1 h. The unbound Cy5 reagent was removed through DNA precipitation.

Drug treatment. Fibroblast cultures were treated with two different inhibitors of actin polymerization, latrunculin B (20 μM) or cytochalasin D (4 μM) (both from Sigma-Aldrich), or twice with nocodazole (20 μM) (Sigma-Aldrich) to inhibit tubulin polymerization. The first treatment was carried out 2 h after transfection, and the second one just before cell fixation. Inhibition of actin polymerization lasted 1 h, and inhibition of tubulin polymerization 2 h.

Cell fixation and immunostaining. Cells were fixed in 4% paraformaldehyde and permeabilized. The primary antibody used was mouse anti-tubulin α (Santa Cruz Biotechnology, Inc.), diluted in 7% FCS + 2% BSA/PBS. The secondary antibody was affinity-purified donkey anti-mouse-FITC-conjugated from Jackson ImmunoResearch (West Grove, PA, USA). Actin filaments were stained with rhodamine-phalloidin (Invitrogen) after tubulin detection. After brief washing in 2 × SSC, Vectashield medium (Vector Laboratories) was used for final mounting of samples. Nuclei were stained with TOPRO-3 (Molecular Probes).

Image acquisition and analysis of experimental data. For image acquisition we used an automated Leica DM RXA fluorescence microscope equipped with a CSU10a Nipkow disc (Yokogawa, Japan) for confocal imaging, a CoolSnap HQ CCD-camera (Photometrix) or alternatively an iXon DV 887ECS-BV (Andor) for *in vivo* observation, and an Ar/Kr laser (Inova 70C, Coherent), driven by a personal computer. Automated exposure, image quality control and other procedures were performed using FISH 2.0 software (Kozubek *et al.*, 2001), and the Acquiarium software was used for live cell imaging. An oil immersion Plan Fluotar objective (100×/NA 1.3) was used. Fourty optical sections (15 for live cells) at 0.3 μm steps along the z-axis were acquired for each

nucleus at a constant temperature of 26°C (37°C for live cells), and stored in the computer memory.

Changes in positions of the fluorescence signals (object tracking) were determined using the FISH 2.0 and 3D viewer software (Kozubek *et al.*, 2004), which allowed us to assign 3D coordinates to the fluorescence signals. The coordinates were taken at the centre of gravity of the visualized objects. The subsequent images of lipoplexes were captured every 30 s for 1 min. The lipoplexes were traced in the time-lapse series on the basis of matching algorithms (Kozubek *et al.*, 2004). In 3D, the length of the lipoplex trajectory was calculated using the equation: $d = \sqrt{(x_1-x_n)^2 + (y_1-y_n)^2 + (z_1-z_n)^2}$, where x_1, y_1 and z_1 (x_n, y_n and z_n) were coordinates for the first measurement and the n-th measurement of the same object. The mean square of differences in the length of the trajectory (Δd^2) at each time point (t) was calculated as $\Delta d^2 = (d_t - d_{t+\Delta t})^2$, where Δt was the time interval between measurements. The diffusion coefficient (D) was calculated as $D = \Delta d^2/t$. Evaluation of data, distance calculation and statistical analyses were performed using the Sigma Plot statistical package (Jandel Scientific).

RESULTS

Cytoplasmic trafficking of plasmid DNA

To investigate the role of the actin network in plasmid DNA trafficking, human fibroblasts were firstly transfected with a β-actin-Lumio construct, and plasmid DNA was then labelled with Cy5. The prepared construct bears the gene for human non-muscle β-actin protein fused with the tetracysteine Lumio tag, allowing visualisation of the fusion protein using the green Lumio reagent. Twenty-four hours after transfection, β-actin-Lumio proteins formed cytoplasmic filaments, a perinuclear actin layer, and intranuclear structures (Fig. 1). The proper formation of cytoplasmic filaments by the actin-lumio protein was verified using phalloidin staining on fixed specimens (Fig. 1C). The microtubule network was labelled by taxol conjugated with green fluorescent dye for *in vivo* experiments.

The *in vivo* observations showed that plasmid DNA–lipid complexes were frequently bound to microtubules and actin filaments (Fig. 2). During a one-minute interval, three images were acquired and movements of the plasmid signals were analysed. Lipoplexes attached to actin filaments were highly restricted in their motion ($D = 1.42 \times 10^{-3}$ $\mu m^2/s$, number of measured lipoplexes was 17, std. error = 5.09×10^{-4}). The average velocity (v) of the lipoplexes bound to the actin network was calculated as $v = 0.292$ μm/min (number of measured lipoplexes = 17, std. error = 4.5×10^{-2}), which is at the lower limit of CCD camera resolution. On the other hand, lipoplexes attached to the microtubule network displayed directional motion mostly toward the cell nucleus along the microtubules, as demonstrated in representative time-lapse images (Fig. 2, bottom row of images). The average velocity along the microtubules was $v = 1.119$ μm/min (number of measured lipoplexes = 30, std. error = 8.8×10^{-2}).

Immunostaining of microtubules and phalloidin staining of actin filaments in fixed cells transfected with labelled plasmid DNA were used to determine the location of plasmid DNA signals inside the cytoplasm in relation to both networks visualized simultaneously in the same cells. Plasmids in lipoplexes clearly bound to both networks (Fig. 3A). In many cases, plasmid signals co-localized simultaneously with the actin filament and with microtubules (Fig. 3A). The lipoplexes entered the cytoplasm by endocytosis and bound to the peripheral actin filaments. At these sites, they subsequently formed small lipoplexes, as observed in live cells (Fig. 3B). These lipoplexes were bound to both actin filaments and to microtubules (Fig. 3A). Plasmids accumulated around the nucleus, co-localized with the perinuclear actin shell, and entered the nucleus (Fig. 3C).

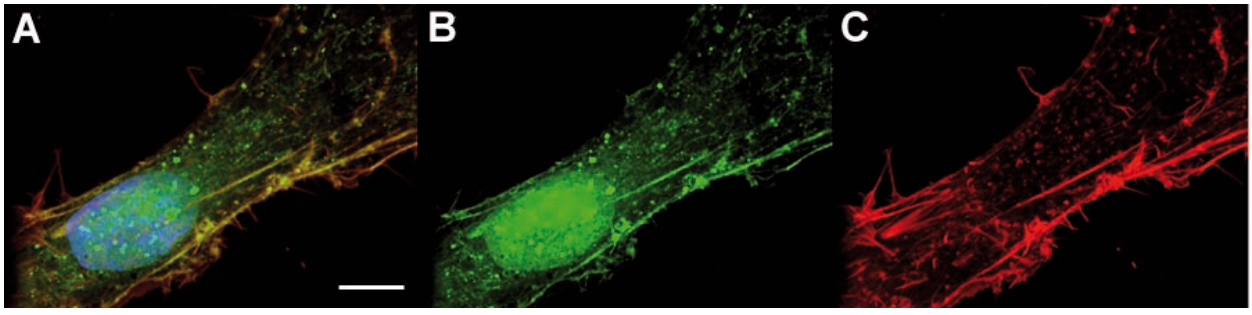

Figure 1. The actin-Lumio fusion protein expression and visualization in fibroblasts.
A fibroblast transfected with the vector bearing gene coding for the actin-Lumio fusion protein (A). The actin-Lumio protein formed cytoplasmic actin filaments visualized in green (B), which strongly co-localized with phalloidin, stained red (C). The cell nucleus visualized with TOPRO-3 (A), coincides with the distribution of nuclear actin (B). Scale bar 5 μm.

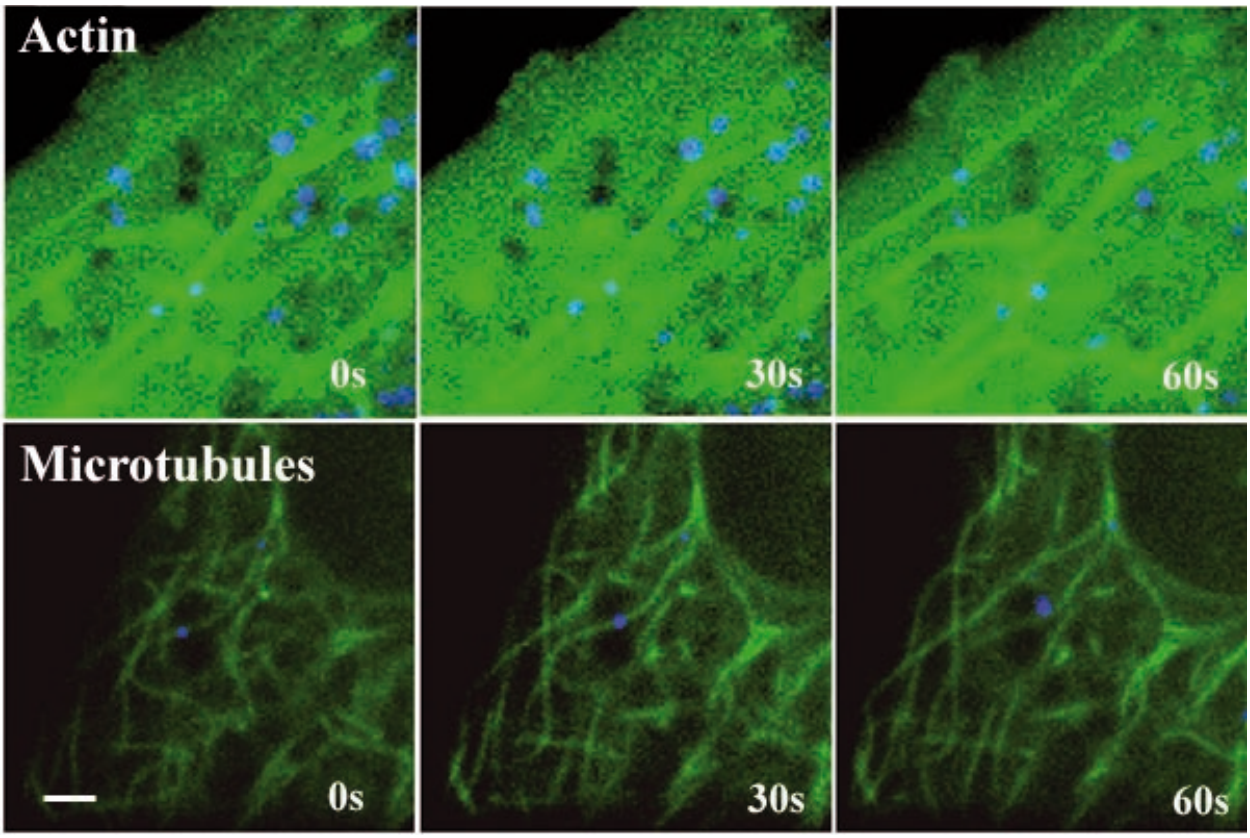

Figure 2. Movement of plasmid DNA lipoplexes in live cells visualized simultaneously with cytoskeletal networks. The upper row of images taken at successive time points shows the highly constrained motion of lipoplexes (blue) bound to actin filaments (green), visualized by means of the actin-Lumio fusion protein. The bottom row of images demonstrates the directional movement of two lipoplexes (blue) along a microtubule towards the cell nucleus during 1 min. Scale bar 1 μm.

The role of disruption of the cytoplasmic networks in plasmid trafficking

To elucidate the role of the cytoskeleton in the trafficking of plasmids to the cell nucleus, inhibitors of polymerization of actin or microtubule networks were used (Fig. 4). Nocodazole treatment changed the shape of cells (Fig. 4A) and disrupted the microtubule network as visualized by tubulin immunostaining (Fig. 4E). The plasmid DNA lipoplexes changed their cytoplasmic location. Unlike in untreated control cells (Fig. 4H), lipoplexes accumulated in large aggregates at the cytoplasmic periphery (Fig. 4E). The lipoplexes also changed their mobility. Directional movement was not detectable, and the diffusion coefficient was similar to the value measured for the dynamics of plasmids bound to actin filaments in untreated cells (1.36×10^{-3} $\mu m^2/s$; number of measured lipoplexes = 20, std. error = 2.9×10^{-4}). The nocodazole treatment also halted plasmid transport into the cell nucleus. As Fig. 5 shows, the number of plasmid signals inside the nucleus decreased significantly compared with the number of plasmid signals in nuclei of untreated cells. Although the microtubule network in nocodazole-treated cells was disrupted, the actin filaments were still visible (Fig. 4E). But this single network did not allow plasmid DNA transport.

The actin network was disrupted using treatment of cells with latrunculin B or cytochalasin D. Both drugs reversibly inhibited polymerization of actin filaments. The inhibitors disorganized the actin cytoskeleton and changed the shape of cells and nuclei (Figs. 4B, C). The inhibition of actin polymerization also changed the distribution of lipoplexes in the cytoplasm, and their mobility decreased to 3.8×10^{-4} $\mu m^2/s$ (number of measured lipoplexes = 10, std. error = 1.4×10^{-4}). The plasmid DNA accumulated in large aggregates at the cytoplasmic periphery, and plasmid transport to the cell nucleus was stopped as in the case of nocodazole treatment (Figs. 4F, G). Although the microtubule network was not substantially affected by inhibitors of actin polymerization, and microtubules were visible using immunostaining of tubulin (Figs. 4F, G), there was no transport along microtubules. Disruption of plasmid transport after the treatment of cells with both types of inhibitors was also reflected in the low number of plasmid

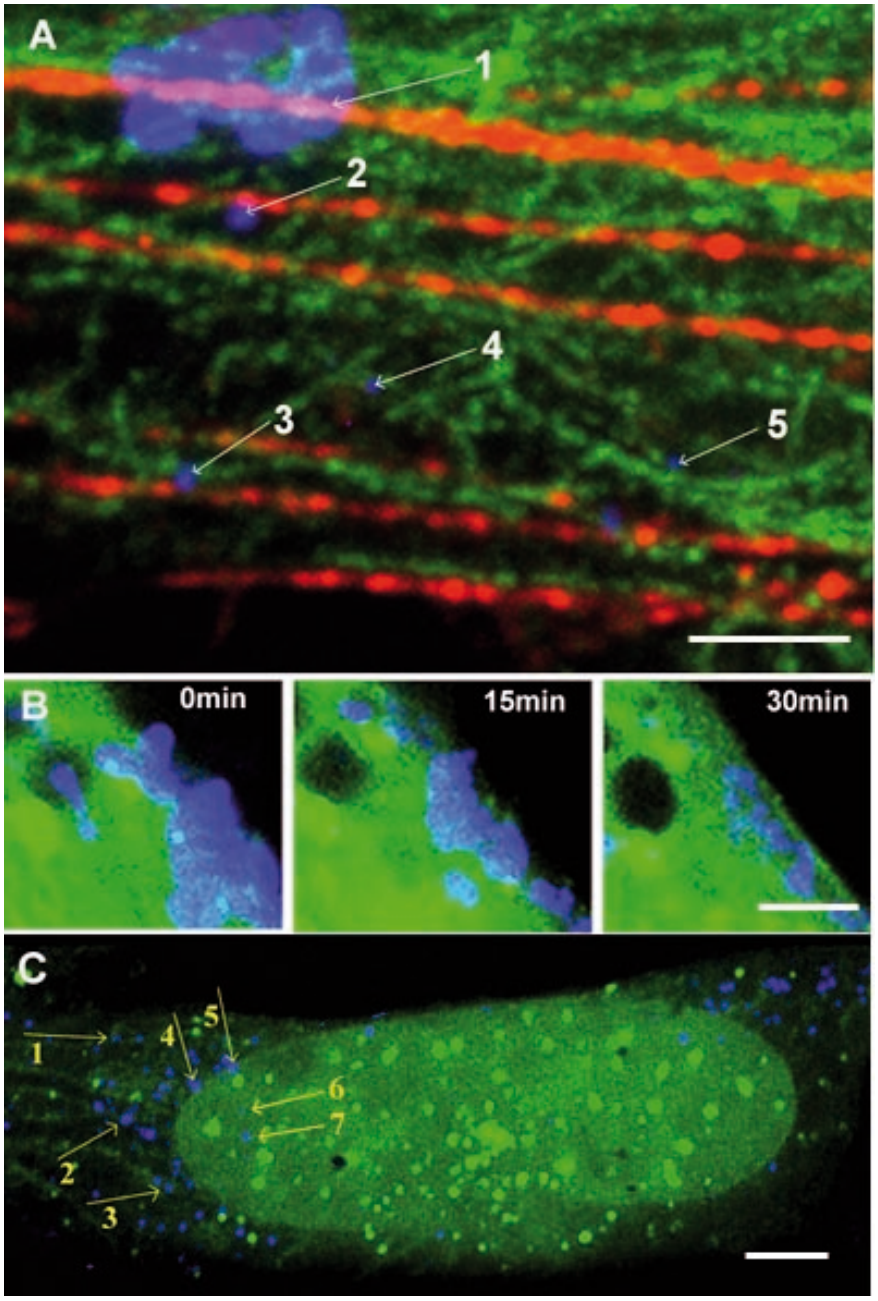

Figure 3. Distribution of lipoplexes throughout the cell cytoplasm and their binding to cytoskeletal networks.
Panel A of the image demonstrates the co-localization of signals of plasmid DNA lipoplexes (blue) with the networks inside the cytoplasm. Arrow 1 indicates a large mass of lipoplexes bound to a peripheral actin filament (red). Arrow 2 shows lipoplexes attached to the actin network (red). Arrow 3 indicates lipoplexes bound to both a microtubule (green) and an actin filament (red); arrows 4 and 5 show lipoplexes bound to microtubules only. The decomposition of the large mass of lipoplexes to the smaller ones at the periphery of the live cell is shown in panels B. The distribution of plasmid DNA lipoplexes in a whole fibroblast expressing actin-Lumio fusion protein (green) is demonstrated in panel C. The actin-Lumio proteins visualize actin filaments and the cell nucleus. Plasmid DNA is concentrated near the nucleus (yellow arrows 1–3), at the actin perinuclear shell (yellow arrows 4 and 5) and within the nucleus (yellow arrows 6 and 7). Scale bars 2 μm.

particles entering the nucleus (Fig. 4I). The results show that plasmids require both networks to be unaffected for transport towards the cell nucleus.

DISCUSSION

The purpose of this study was to analyse the roles of the cytoplasmic actin and microtubule networks in plasmid DNA trafficking. Labelled plasmid DNA was transfected into fibroblasts that expressed the fluorescent fusion protein actin-Lumio, or into fibroblasts stained with a fluorescent dye that bound to the microtubules. Using this approach, we were able to track plasmid DNA simultaneously with the cytoskeleton *in vivo*, and study the mobility of the plasmid DNA–lipid complexes in relation to the networks and its binding to them.

When plasmids enter the cell (in this work by means of liposome transfection), they need to travel long distances through the cytoplasm to reach the cell nucleus. On the other hand, Lukacs *et al.* (2000) and Dauty and Verkman (2005) have shown that DNA fragments cannot move *via* diffusion through the cytoplasm. Since diffusion through the dense meshwork of the cytoplasm is not likely, other mechanisms must exist by which plasmids can move towards the cell nucleus. Recently, it became clear that the cytoskeleton does not constitute a barrier for successful gene delivery, but on the contrary, some

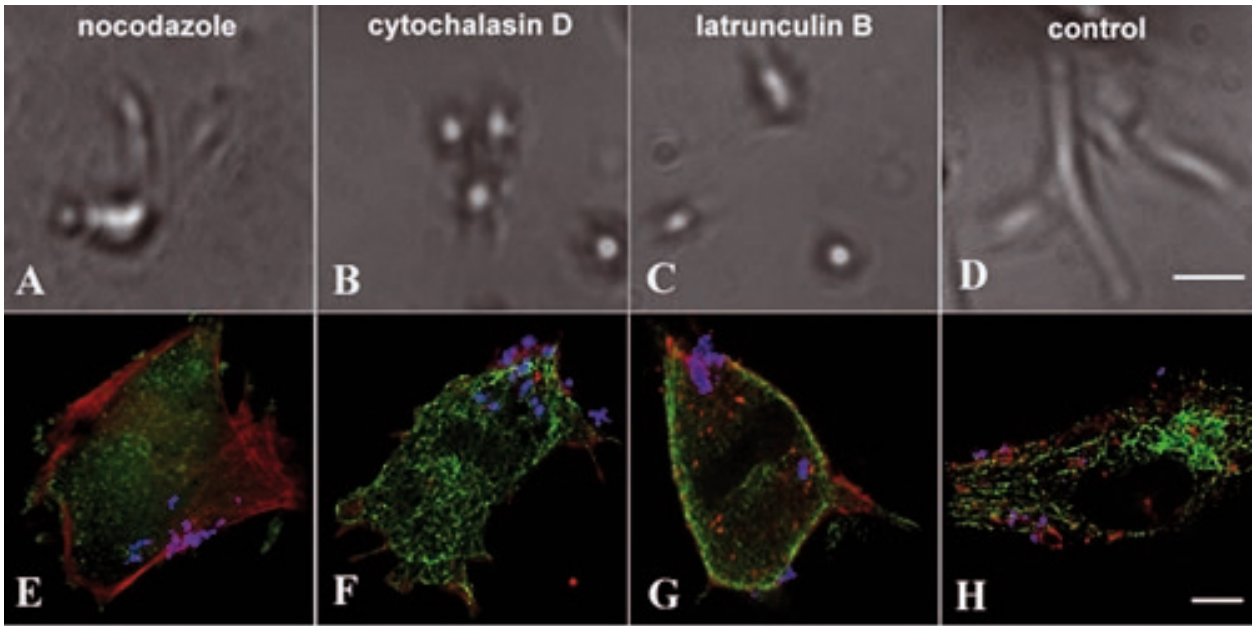

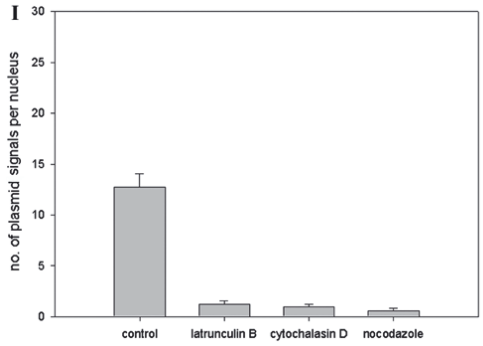

Figure 4. Disruption of cytoskeletal networks influenced the transport of lipoplexes throughout the cell cytoplasm.
Images of fibroblasts after inhibition of tubulin polymerization by nocodazole (A, E), or inhibition of actin polymerization using cytochalasin D (B, F) or latrunculin B (C, G). Nocodazole disrupted the microtubular network (green), but did not affect the actin network. Cytochalasin D and latrunculin B disrupted the actin network (red). Both types of inhibitors changed the shape of the cells, and caused accumulation of plasmid DNA lipoplexes (blue) as huge aggregates at the periphery of the cytoplasm, unlike in control cells (D, H), where signals of small lipoplexes were bound to the cytoskeleton. Scale bars 20 μm (A–D) and 5 μm (E–H). The bar graph (I) shows the decreased number of plasmid DNA signals per nucleus after treatment with the actin polymerization inhibitors, latrunculin B and cytochalasin D, or with the tubulin polymerization inhibitor nocodazole, 24 h after cell transfection.

components of cytoplasmic networks actively contribute to transport of plasmids in complexes, just as they do for viruses (Zhou *et al.*, 2004; Vaughan & Dean, 2006). As already published (McDonald *et al.*, 2002; Lee *et al.*, 2006), viruses utilize dynein motors to move along the microtubules. Some viruses, such as baculovirus (Van Loo *et al.*, 2001), also utilize actin filaments. Moreover, pathogens like the *Listeria* bacterium and Vaccinia virus stimulate actin filament polymerisation for their movement in the cell (Gruenheid & Finlay, 2003). In this study, it was demonstrated that plasmid DNA–lipid complexes bind to microtubules and show directional movement along the microtubule network, similar to viruses (Fig. 2). This agrees with the findings of Vaughan and Dean (2006), who showed an important role for microtubules in plasmid transport, because of the decrease in expression of microinjected plasmids after the inhibition of dynein motors or disruption of microtubules. On the other hand, our results show that actin filaments immobilized the bound plasmid DNA lipoplexes. They displayed highly restricted diffusive motion, with corresponding slow randomly-oriented movement (average velocity 0.292 μm/min).

Considering these results, it was rather surprising that disruption of either of the networks investigated led to a complete stoppage of plasmid transport. Nocodazole treatment disintegrated microtubules, which inhibited plasmid trafficking, as also observed by Vaughan and Dean (2006). In our experiments, untreated cells showed accumulation of small clumps of lipoplexes at the perinuclear region, similar to the studies of Zabner *et al.* (1995) and Coonrod *et al.* (1997). After the nocodazole treatment, lipoplexes formed large aggregates at the cell periphery. This shows that plasmid transport was interrupted after the lipoplexes entered the cell, and their inability to move toward the nucleus led to their accumulation. A similar disruption of plasmid transport was achieved using inhibitors of actin polymerization, although the microtubules were not

disorganized. Although actin filaments restricted the movement of lipoplexes, it is evident that they must play some important role in plasmid trafficking. A large number of lipoplexes were localized on actin filaments and microtubules together. These results indicate that the plasmids in the complex with lipids that entered the cytoplasm first encounter the peripheral actin cytoskeleton. They become immobilized and their aggregates form smaller ones, which are probably moved to nearby microtubules and uploaded on to them as cargo. After that, the lipoplexes move towards the cell nucleus. Similarly, the actin cytoskeleton may act as a barrier to incoming retroviral vectors at the plasma membrane. However, some studies indicate that the actin network may also play a positive role in early retroviral trafficking (reviewed in Anderson & Hope, 2005; Campbell & Hope, 2005). Interestingly, the diffusion coefficient and velocity of plasmid DNA lipoplexes bound to actin filaments in the cytoplasm are similar to the parameters of the intranuclear movement of nuclear bodies like Cajal and PML (polymyelocytic leukemia) bodies (Platani *et al.*, 2002; Gőrich *et al.*, 2004), and also to the intranuclear dynamics of plasmid DNA localized inside the cell nucleus (Ondrej *et al.*, 2006). Because of the similar dynamic parameters of plasmids in both cytoplasm and nucleoplasm, the directional movement of plasmids inside the nucleus (Ondrej *et al.*, 2006), and the presence of nuclear actin in forms ranging from monomers to polymers (McDonald *et al.*, 2006), we suggest that the nuclear plasmids are also attached to actin polymers and could move along them for short distances.

Acknowledgements

This work was supported by the Grant Agency of the Czech Republic GA202/02/0804, 202/04/0907, the Academy of Sciences of the Czech Republic IQS50040508 and Ministry of Education LC535.

We thank M. Kozubek (Faculty of Informatics, Masaryk University, Brno), who kindly provided the software for image acquisition and analysis.

REFERENCES

Anderson JL, Hope TJ (2005) *Gene Ther* **12**: 1667–1678.
Campbell EM, Hope TJ (2005) *Gene Ther* **12**: 1353–1359.
Coonrod A, Li FQ, Horwitz M (1997) *Gene Ther* **4**: 1313–1321.
Dauty E, Verkman AS (2005) *J Biol Chem* **280**: 7823–7828.
Gőrisch SM, Wachsmuth M, Ittrich C, Bacher CP, Rippe K, Lichter P (2004) *Proc Natl Acad Sci USA* **101**: 13221–13226.
Gruenheid S, Finlay BB (2003) *Nature* **422**: 775–781.
Johnson AL, Jurcisek JA (1999) *AAPS Pharmsci* 1, e6.
Kozubek M, Kozubek S, Lukášová E, Bártová E, Skalníková M, Matula P, Matula P, Jirsová P, Cafourková A, Koutná I (2001) *Cytometry* **45**: 1–12.
Kozubek M, Matula P, Matula P, Kozubek S (2004) *Microsc Res Tech* **64**: 164–175.
Lee GE, Murray JW, Wolkoff AW, Wilson DW (2006) *J Virol* **80**: 4264–4275.
Lukacs GL, Haggie P, Seksek O, Lecherdeur D, Freedman N, Verkman AS (2000) *J Biol Chem* **275**: 1625–1629.
McDonald D, Vodicka MA, Lucero G, Svitkina TM, Borisy GG, Emerman M, Hope TJ (2002) *J Cell Biol* **159**: 441–452.
McDonald D, Carrero G, Andrin Ch, de Vries G, Hendzel MJ (2006) *J Cell Biol* **172**: 541–552.
Ondrej V, Kozubek S, Lukasova E, Falk M, Matula Pa, Matula P, Kozubek M (2006) *Chrom Res* **14**: 505–514.
Platani M, Goldberg I, Lamond AI, Swedlow JR (2002) *Nat Cell Biol* **4**: 502–508.
Shav-Tal Y, Singer RH (2005) *J Cell Sci* **118**: 4077–4081.
Van Loo ND, Fortunati E, Ehlert E, Rabelink M, Grosveld F, Scholte BJ (2001) *J Virol* **75**: 961–970.
Vaughan EE, Dean DA (2006) *Mol Ther* **13**: 422–428.
Zabner J, Fasbender AJ, Moninger T, Poellinger KA, Welsh MJ (1995) *J Biol Chem* **270**: 18997–19007.
Zhou R, Geiger Ch, Dean DA (2004) *Expert Opin Drug Deliv* **1**: 127–140.

Chromosome Research (2006) 14:505–514
DOI: 10.1007/s10577-006-1058-1

Directional motion of foreign plasmid DNA to nuclear HP1 foci

Vladan Ondřej[1]*, Stanislav Kozubek[1], Emílie Lukášová[1], Martin Falk[1], Pavel Matula[2], Petr Matula[2] & Michal Kozubek[2]
[1]*Laboratory of Molecular Cytology and Cytometry, Institute of Biophysics AS CR, Kralovopolska 135, Brno, 612 65, Czech Republic; Tel: +42-0541-517165; Fax: +42-0541-211293; E-mail: ondrej@ibp.cz;* [2]*Laboratory of Optical Microscopy, Faculty of Informatics, Masaryk University, Botanicka 68a, Brno, 602 00, Czech Republic*
* *Correspondence*

Received 2 March 2006. Received in revised form and accepted for publication by Pat Heslop-Harrison 12 April 2006

Key words: heterochromatin, HP1 protein, nuclear compartments, plasmid, transfection

Abstract

Movement of labelled plasmid DNA relative to heterochromatin foci in nuclei, visualized with HP1-GFP, was studied using live-cell imaging and object tracking. In addition to Brownian motion of plasmid DNA we found a pronounced, non-random movement of plasmid DNA towards the nearest HP1 focus, while time-lapse microscopy showed that HP1 foci are relatively immobile and positionally stable. The movement of plasmid DNA was much faster than that of the HP1 foci. Contact of transgene DNA with an HP1 focus usually resulted in cessation of the directional motion. Moreover, the motion of plasmid DNA inside the heterochromatin compartment was more restricted (limited to 0.25 μm) than when the plasmid DNA was outside heterochromatin (R = 0.7 μm). Three days after transfection most of the foreign labelled DNA colocalized with centromeric heterochromatin.

Introduction

Transfection of plasmid DNA into mammalian cells has become a routine procedure in cellular and molecular biology experiments, but the mechanism by which the plasmid DNA reaches its nuclear destination remains poorly understood. Small circular DNA molecules invade the nucleus of eukaryotic cells during viral infection, gene therapy, or experimental transfections (Kashihara *et al*. 1998). The most commonly used method, liposome-mediated gene transfer, involves endocytotic uptake, release from endosomes, dissociation of DNA from lipid, diffusion through the cytoplasm, transport across nuclear pores, and diffusion to nuclear target sites (Xu & Szoka 1996, Friend *et al*. 1996). Despite these common events and experiments, little is known about the fate and mobility of incorporated DNA molecules in the nuclei of living cells.

Recent studies (Johnson & Jurcisek 1999, Lukacs *et al*. 2000, Verkman 2002, Mearini *et al*. 2004) have provided some information about the diffusion of incoming DNA fragments and small or macromolecule-sized solutes in the cytoplasm and nucleus. It was found that, in the nucleus, the diffusion of DNA fragments of different sizes was more severely restricted than in cytoplasm (Lukacs *et al*. 2000). In contrast, similar-sized dextrans diffused freely in the nucleus. At present it is not known which components are responsible for the observed immobilization of DNA fragments and plasmids inside the nucleus. It has been suggested that there is an involvement of the nuclear matrix and scaffold, binding to nuclear components such as positively

charged histones, or formation of DNA–protein complexes (Lukacs *et al*. 2000, Mearini *et al*. 2004). Therefore, our study focused on the movement and the destination of foreign DNA in cell nuclei immediately after transfection. We transfected MCF-7 cells with Cy3-labelled plasmid DNA bearing a gene coding for the HP1-GFP fusion protein. Labelling of the constructs did not disrupt their function, which could be seen as light emission from HP1 foci corresponding to GFP excitation and emission wavelengths. This allowed simultaneous visualization of the transgene DNA and the heterochromatin, the latter represented by HP1 proteins.

Heterochromatin, in contrast to euchromatin, is very compact and dense. The main component of heterochromatin is HP1 protein which is recruited to this compartment by histone H3 methylation on the lysine 9 (Howe *et al*. 1995, Berger 2001, Jenuwein & Allis 2001, Dillon & Festenstein 2002). It is transcriptionally silent and contains tandemly repeated (satellite) sequences (Gilbert & Allan 2001). HP1 is a conserved component of heterochromatin, and plays a key role in heterochromatin formation and maintenance (Aagaard *et al*. 1999, Bannister *et al*. 2001, Cheutin *et al*. 2003, Festenstein *et al*. 2003, Verschure *et al*. 2005). In humans, three subtypes of HP1 (HP1α, β, γ) have been identified, with different preferences in their heterochromatin location during the cell cycle. For example, HP1β is closely connected with centromeric heterochromatin during interphase as Hayakawa *et al*. (2003) described. Heterochromatin has different functional properties from euchromatin, and often causes silencing of active genes in its proximity (Brown *et al*. 1997, Francastel *et al*. 2000, Bártová *et al*. 2002).

In this study we investigated the mobility of the plasmid DNA, which is transiently active in transcription without requiring prior integration into the genome, in two physically and functionally different compartments of nucleus. We found that, as well as random motion of plasmid DNA, there was a distinct directional motion towards a single heterochromatin focus, usually the nearest one. This was followed by restriction of movement of the plasmid DNA. Three days after transfection, most of the foreign labelled DNA colocalized with centromeric heterochromatin.

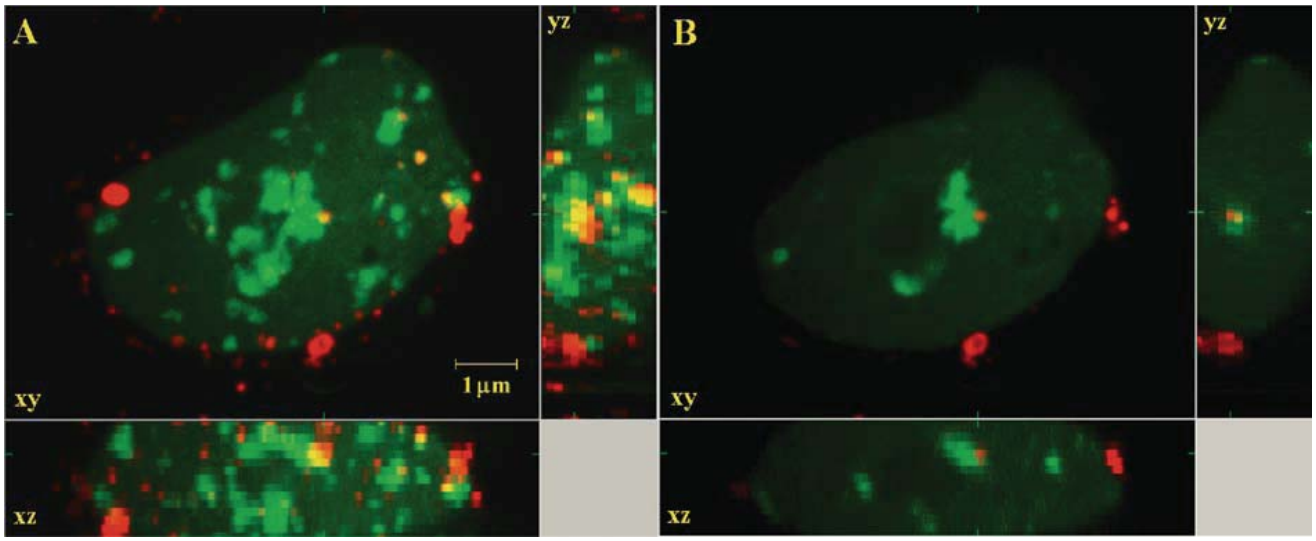

Figure 1. The monitoring of labelled plasmid DNA (red) and heterochromatin foci represented by expressed HP1-GFP (green) in the cell nucleus after transfection. Maximum image computed from 3D images in XY, XZ and YZ planes through the nucleus is shown with DNA signals in an MCF7 cell. (**A**) Much of the labelled DNA was observed in the cytoplasm, as well as accumulated against the nuclear membrane. Most nuclear signals are localized close to or in the centromeric heterochromatin, defined by expressed HP1β-GFP fusion protein, and a minority of signals are remote from heterochromatin in cells with transgene expression. In (**B**), the single cut, 2D images in the XY, XZ and YZ planes demonstrate the position of a single foreign DNA signal inside the cell nucleus localized on the surface of a heterochromatic region.

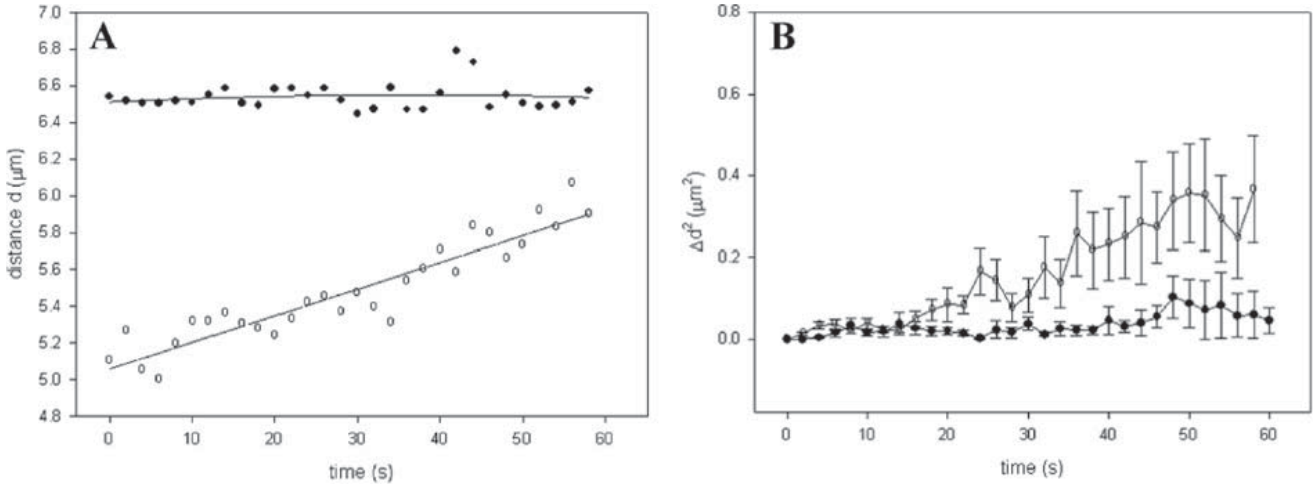

Figure 2. The dynamics of plasmid DNA in the living cell nucleus within a 1-min period. (**A**) Changes in the distances between two DNA signals are shown in relation to time up to 60 s. DNA signals close to an HP1 focus (closed circles) and outside heterochromatin (open circles) are shown. (**B**) The Δd^2 vs time plot for plasmid DNA remote from heterochromatin (open circles) and that associated with HP1 foci (closed circles).

Materials and methods

Cell culture, cell transfection and DNA construct labelling

A human MCF7 mammary carcinoma cell line was grown in DMEM medium supplemented with 10% fetal calf serum (FCS), penicillin (100 U/ml) and streptomycin (100 μg/ml) in humidified air with 5% CO_2, at 37°C.

One day before transfection, 0.8–1 $\times$ 10^6 cells were plated in 2 ml of growth medium without antibiotics in a 35 mm diameter Petri dish so as to be 90–95% confluent at the time of the transfection. For measurements of heterochromatin motion the cells were transfected with expression vector containing

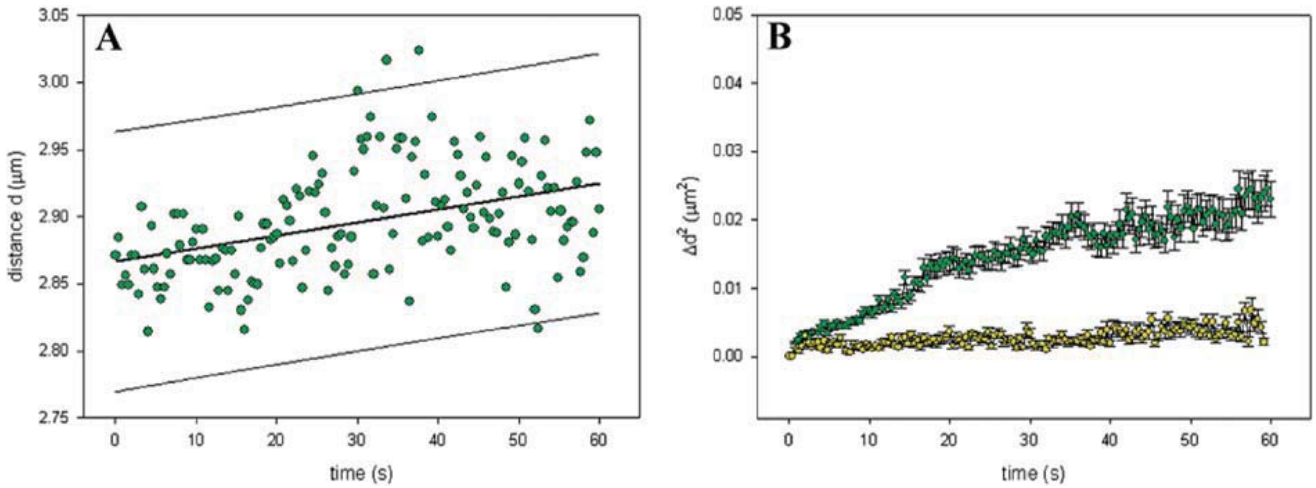

Figure 3. Short-term movement of the HP1β foci in the nuclei of MCF7 cells: (**A**) scatter plot of distances between two foci (d) in relation to time in a living cell. The intervals between individual measurements were 400 ms; the total observation time was 60 s. The deviations of the distances between subsequent measurements were about 0.04 μm; the mean distance between the two foci increased from 2.85 to 2.90 μm. (**B**) The relationship of Δd^2 to time for living (green) and fixed cells (yellow) averaged from 10 cell nuclei. In each cell nucleus approximately five to-10 foci were analysed using the object tracking algorithm, and distances between all pairs were used for calculations.

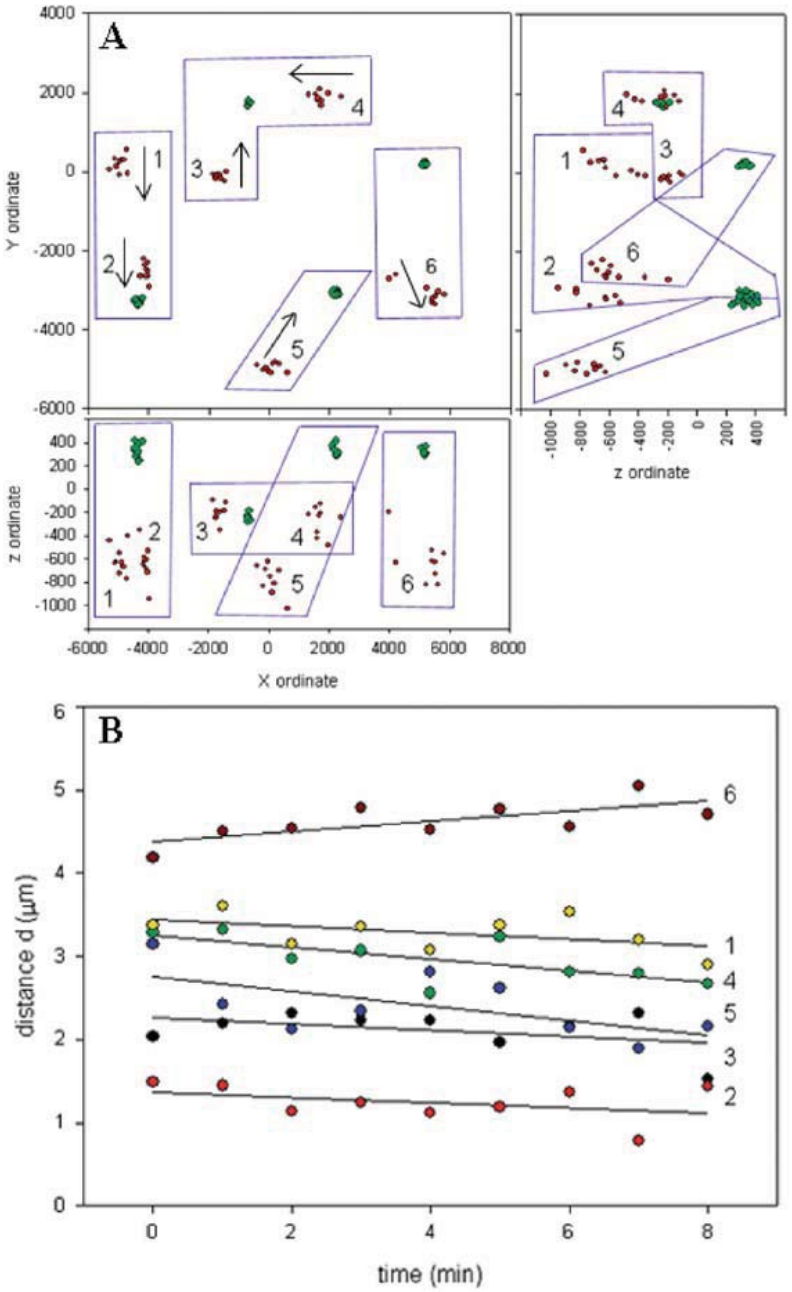

Figure 4. Medium-term observation of transgene loci in relation to the HP1 foci. Schematic illustration of the movement of the signals of foreign DNA (red circles) in 3D space of the cell nucleus during medium-term observation. The plasmid DNA moved directionally (see arrows) in most cases to the nearest HP1 focus (green circles). The nuclear spatiofunctional compartments corresponding to the HP1 foci (transgene loci) are shown by blue lines. XY, YZ and XZ projections are shown (**A**). Distances between individual DNA signals (each colour indicates a different signal) and the nearest HP1 foci in the cell nucleus decreased with time in most cases during observation (**B**).

GFP-tagged HP1β. The transfection was performed using Lipofectamine 2000 (Invitrogen) in OPTIMEM medium according to the manufacturer's protocol. After 5 h of cell transfection in the presence of Lipofectamine 2000, the medium was replaced with DMEM containing 10% FCS without antibiotics, and the cells were incubated for 48 h before imaging.

The vector bearing the HP1β-GFP gene was labelled before transfection with Label IT Tracker reagent Cy3 (Mirus Co.), at the ratio of Cy3:DNA

recommended by the manufacturer, at 37°C for 1 h. The unbound Cy3 reagent was separated by DNA precipitation. The Cy3-labelled DNA of the transgene enabled us to observe simultaneously the localization of the transgene (red) and the expressed protein tagged with GFP. Green fluorescence of HP1 protein in the cell nucleus indicates expression of the transgene.

Cell fixation and immunolabelling

The transfected cells were grown on glass coverslips for 72 h. The cells were washed for 2 × 3 min with PBS (37°C), fixed for 10 min with 4% paraformaldehyde/PBS, washed for 3 × 5 min with PBS, permeabilized in 0.2% Triton X-100 in PBS, washed for 3 × 5 min in PBS, and sequentially incubated with the primary and secondary antibodies. The primary antibody against CENP-A was from UPSTATE (Lake Placid, NY), diluted 1000-fold. The secondary anti-rabbit FITC-conjugated antibody (dilution 50×) was from Jackson ImmunoResearch (West Grove, PA, USA). The chromatin was counterstained with a freshly prepared 1 μM solution of TOPRO-3 (Molecular Probes) in 2 × SSC for 5 min. After brief washing in 2 × SSC, the antifade mounting medium Vectashield (Vector Laboratories) was placed on the labelled area and covered with a coverslip.

Living cell observation and time-lapse microscopy

Twenty-four hours before image acquisition the cells were trypsinized and resuspended in fresh DMEM medium without phenol red, supplemented with 10% FCS and 200 μM Trolox (Sigma), and put into a special chamber for microscope imaging. The images were obtained by means of a high-resolution confocal cytometer (Kozubek *et al*. 2004). The cytometer is based on a completely automated Leica DM RXA fluorescence microscope equipped with a confocal unit CSU-10a (Yokogawa, Japan), a CoolSnap HQ CCD camera (Photometrix) or alternatively an iXon DV 887ECS-BV (Andor), and an Ar/Kr laser Inova 70C (Coherent). Three types of *in-vivo* observations were performed: short-, medium- and long-term. For the short-term observations 2D transgene images were acquired every 2 s for a period of 1 min. For medium-term observations 3D images were acquired from 15 optical sections taken at 0.6 μm z-steps. Intervals of 2 min were allowed between each series of 15 sections, and observations were continued for a total of 18 min. For the long-term observations 3D images were acquired as for the medium-term observations, but with longer intervals (40 min) between each series of 15 sections. Except for measurement of DNA mobility, we also measured movement of HP1 foci for comparison. The light exposure was kept as low as possible to avoid phototoxic effects.

Analysis of motion of loci and calculation of diffusion constants

The changes in the positions of the fluorescence signals (object tracking) were determined using the FISH 2.0 software and a 3D viewer (Kozubek *et al*. 2004), which allowed us to assign 2D or 3D coordinates to the fluorescence signals. The coordinates were taken at the centre of gravity of the visualized objects, and corrected for the rotation of the cell nucleus and drift of the images acquired during the longer time-lapse observations. The objects were traced in the time-lapse series on the basis of matching algorithms. In 2D the distances between two transgene loci or HP1 foci, and between the DNA signal and an HP1 focus, were calculated using the equation: $d = \sqrt{[(x_1-x_n)^2 + (y_1-y_n)^2]}$; or in 3D: $d = \sqrt{[(x_1-x_n)^2 + (y_1-y_n)^2 + (z_1-z_n)^2]}$, where x_1, y_1 and z_1 (x_n, y_n and z_n) were coordinates for the first measurement and the nth measurement of the same object. The mean square of differences in the distance (Δd^2) between two objects at each time point (t) was calculated as $\Delta d^2 = (d_t - d_{t+\Delta t})^2$, where Δt was the time interval between measurements. The diffusion coefficient (D_c) in 2D was calculated as $D_c = \Delta d^2/(4 \times \Delta t)$.

Results

To monitor movements of foreign DNA in living cells we transfected MCF-7 cells with Cy3-labelled plasmid DNA bearing the gene for the fusion protein HP1β-GFP. Three-dimensional observations of fixed cells showed two to 12 transgene DNA signals per nucleus (n = 50). A large amount of labelled DNA

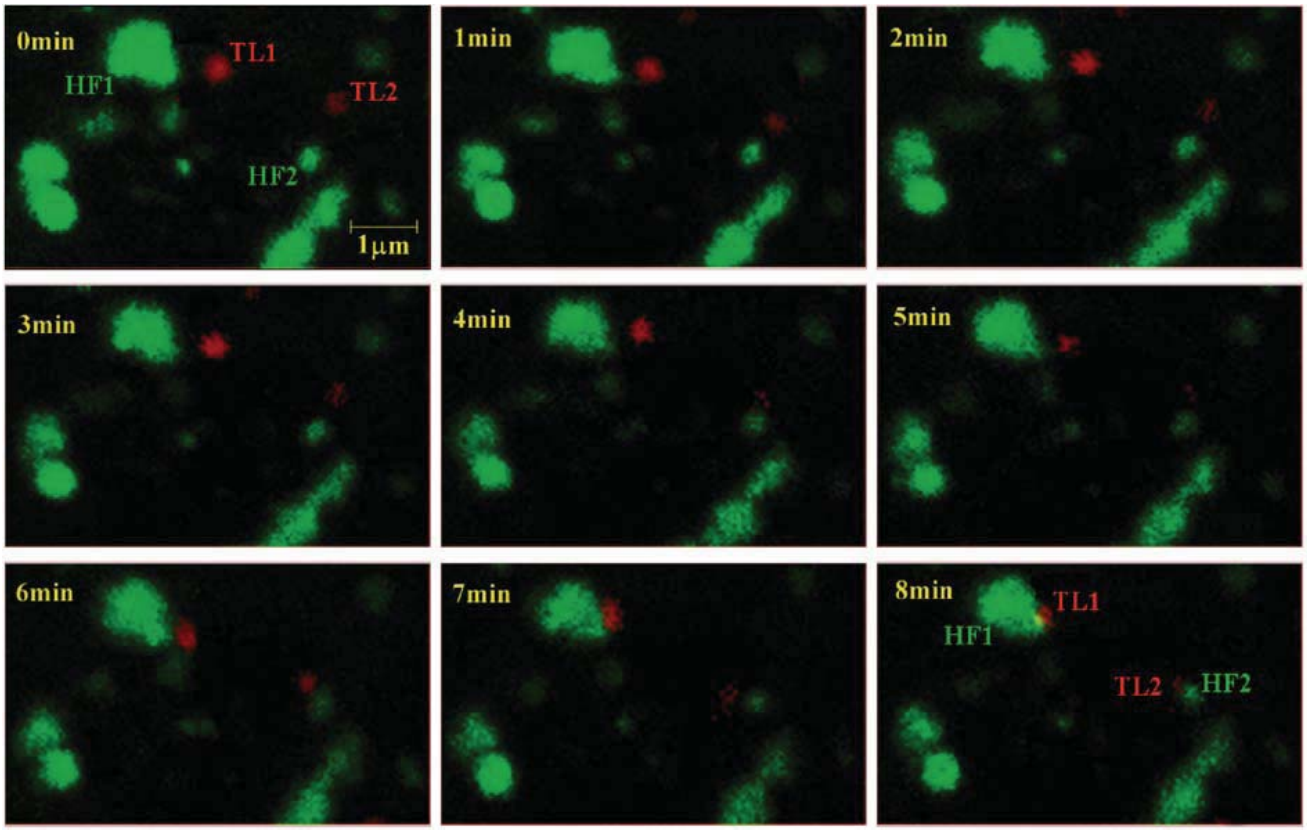

Figure 5. Four-dimensional tracking of the plasmid DNA (red) and the HP1 foci (green) in the cell nucleus. A 3D time-lapse image series (nine frames in 8 min) displays the movement of the plasmid DNA, marked as TL1 and TL2, towards the nearest HP1 foci (HF1, HF2) in a dynamic and directional manner.

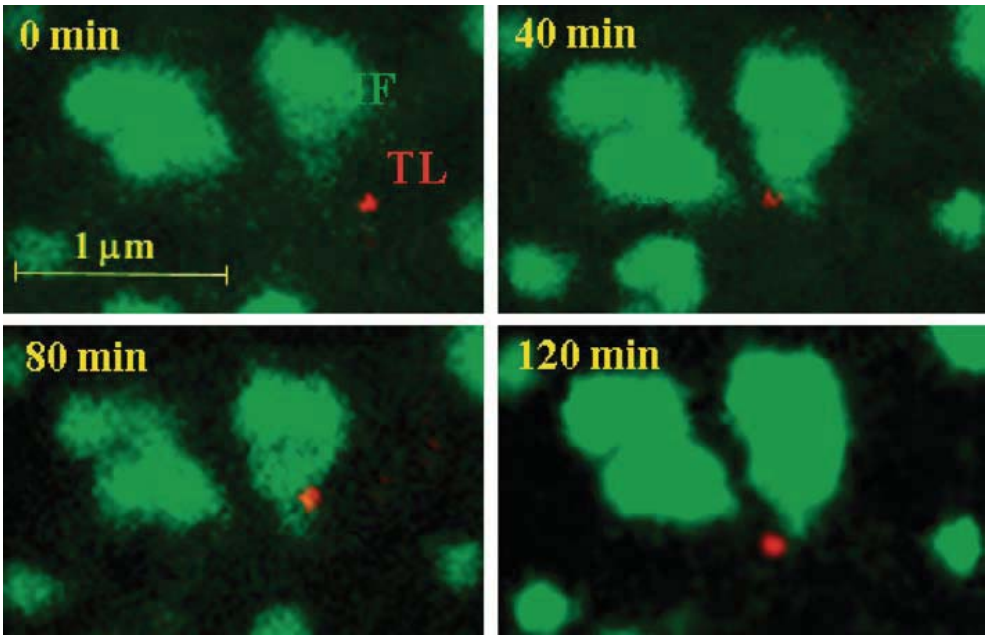

Figure 6. *In-vivo* images from long-term observations of plasmid DNA. Changes in the labelled DNA (red) in the cell nucleus and the HP1-GFP foci (green) are shown for a period of observation of 120 min. The labelled plasmid DNA (TL) became associated with the nearest HP1 focus (HF) within the first 40 min; after that the plasmid DNA movement was restricted only for compartment of relevant HP1 focus.

was observed in the cytoplasm, as well as accumulated against the nuclear membrane. The majority of signals in the nucleus were localized in or close to the centromeric heterochromatin, defined by expressed HP1β-GFP fusion protein; a minority of signals were distant from the heterochromatin in cells with transgene expression (Figure 1). The cells were observed *in vivo*, 48 h after transfection, when transient expression usually peaks (around 60% transfected cells showed GFP signals) similarly as described by Johnson & Jurcisek (1999); after that transient expression decreases.

The movement of individual plasmid signals in human cells is restricted, but there are differences in the level of restriction. The shortest time interval for plasmid DNA image acquisition was 2 s and therefore we were able to collect 30 2D frames in 1 min. The occurrence of several plasmid DNA structures in the cell nucleus allowed calculation of two-dimensional distances between them. As shown in Figure 2, the movement of plasmid DNA outside the heterochromatin (up to 1 μm/min, with an average $D_c = 7 \times 10^{-3}$ μm^2/s) was significantly faster than the movement of plasmid DNA inside the heterochromatin compartments ($D_c = 1.5 \times 10^{-3}$ μm^2/s); the speed of movement was very variable. As expected, the plot of Δd^2 values against time showed that transgenes had a significantly higher rate of diffusion than the HP1β foci, which were also measured at 1 min intervals using a 400 ms time-lapse series (Figures 2 and 3). The average value of Δd^2 for 60 s was estimated to be 0.35 μm^2, i.e. 15 times higher than the value for the HP1β foci. For plasmid DNA inside the heterochromatin compartment the average value of Δd^2 was around 0.06 μm^2, which is just three times higher than the value for the HP1β foci.

To check the correctness of the distance measurements in living cells, the distances between HP1β foci were measured in paraformaldehyde-fixed cells under identical conditions. The distances measured in fixed cells thus quantify the apparent motion attrib-

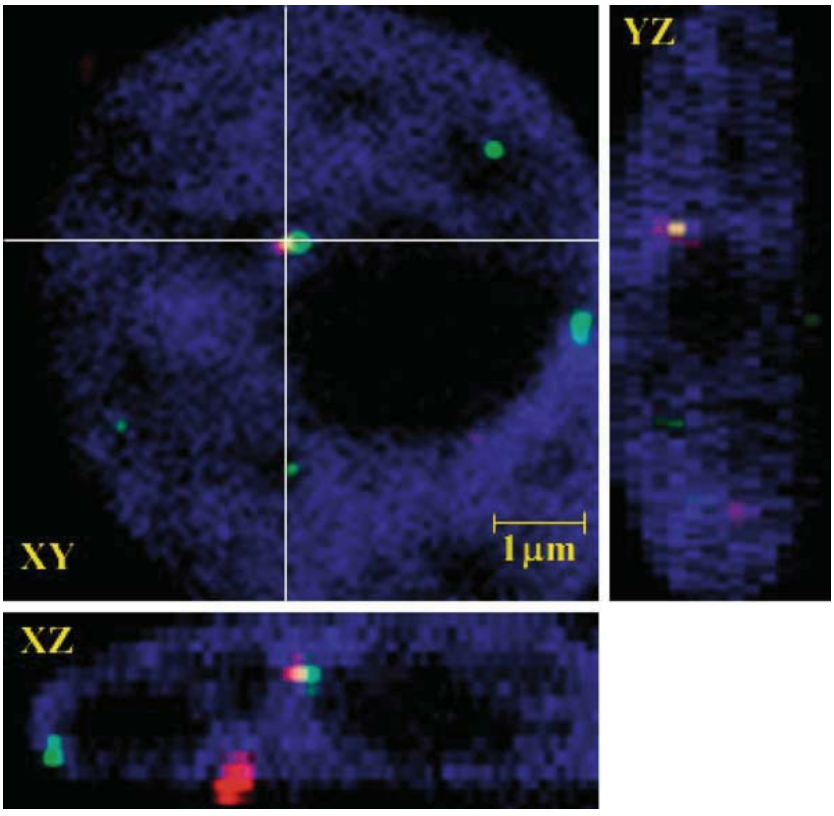

Figure 7. The image shows a cell nucleus fixed 3 days after transfection with the plasmid DNA (red) localized near centromeric regions (green). Green signals correspond to the centromeric protein CENP-A visualized using antibodies. Chromatin was stained with TO-PRO. XY, XZ and YZ sections through the transgene; because of the sectioning, only a relatively small number of centromeres can be seen.

utable to measurement errors resulting from external influences. A comparison of the dependence of Δd^2 on time for HP1 foci in living and fixed cells is shown in Figure 3b. Displacement of HP1 foci in living cells is relatively small, but significantly different from that observed in fixed nuclei.

Simultaneous observation of HP1 foci and transgene loci revealed several important aspects of transgene DNA mobility and HP1 focus function. For any one transgene and its closest HP1 focus, the distance between them usually decreased with time (Figures 4 and 5). Although the movement was predominantly in one direction, the paths of the transgenes were neither straight nor the shortest possible. These results led us to the hypothesis that the cell nucleus can be divided into several compartments, as shown in the simple sketch in Figure 4.

During long-term observation we found that transgene DNA movement is still located and restricted within space of relevant HP1 focus. A typical example is shown in Figure 6, where the transgene locus moved to the heterochromatin and surrounded it for a period of 120 min. Expression of transgenes in the cell population was dramatically reduced by 3 days after cell transfection (nearly 10% of cells showed GFP signals at different levels), although the presence of plasmid DNA in the cell population could be detected. At this time, colocalization of the plasmid DNA with centromeres (Figure 7) could be detected using antibodies in cell nuclei without expression of the fusion protein.

Discussion

Plasmid DNA bearing a transgene for an HP1-GFP fusion protein was labelled to visualize the process of silencing. Labelling of the constructs did not disrupt their function, which could be seen as light emission from HP1 foci. Thus transgene expression was monitored by the light emission in parallel with spatial positioning of the transgenes and the HP1 foci. The transgenes were expressed shortly after cell transfection and penetration into the cell nucleus (see Figure 1). However, after some time (3 days after transfection) the transient expression of fusion protein was silenced. At that time point the plasmid DNA signals colocalized with centromeric protein CENP-A, which was visualized using antibodies.

Before associating with heterochromatin the plasmid DNA in the cell nucleus moved along complex pathways. Fast diffusive motion, observed in the course of the first minute for free transgenes ($D_c = 7 \times 10^{-3}$ μm^2/s), was superimposed on a systematic directional movement towards the nearest HP1 focus during medium-term observations (Figures 2 and 4). The motion of plasmid DNA outside the heterochromatic region corresponds to the dynamic parameters for small circular DNA in the mammalian nucleus (Mearini *et al*. 2004). After the capture of the plasmid DNA by an HP1 focus, its motion became restricted (R = 0.25 μm) with parameters similar to the values published by Chubb *et al*. (2002) for lacO array loci integrated in the nuclear periphery or nucleolar neighbourhood (R = 0.3 μm).

In this study we compared the motion of plasmid DNA bearing an HP1-GFP transgene with that of large heterochromatin foci visualized by the HP1-GFP protein. Analysis of the movement of HP1 foci in the cell nucleus during short-term observation (Figure 3) demonstrates a very limited diffusion of these large heterochromatin structures. Our time-lapse measurements revealed that the rate of diffusion of HP1 foci as measured by their diffusion coefficient ($D_c = 1.1 \times 10^{-4}$ μm^2/s) was similar to that for Cajal bodies–$D_c = 1.1 \times 10^{-4}$ μm^2/s, PML bodies–$D_c = 1.2 \times 10^{-4}$ μm^2/s (Görisch *et al*. 2004), or nucleoplasmic chromatin with integrated *lacO* arrays–$D_c = 1.3 \times 10^{-4}$ μm^2/s (Chubb *et al*. 2002). Our results concerning HP1 foci correspond to experiments of Cheutin *et al*. (2003), in which the authors estimated similar relative displacement of heterochromatin domains (0.14 μm/min), but calculated over a longer time interval. The random motion of HP1 foci was limited to approximately R = 0.13 μm. In agreement with the findings of these authors, our results show that HP1 foci are among the structures with the most restricted motion in the cell nucleus. This suggests a structural role of HP1 foci as anchoring elements in the chromatin.

HP1 protein is known to contribute to the formation of heterochromatin, which plays an important functional role in silencing of genes or transgenes (Howe *et al*. 1995, Jenuwein & Allis 2001, Verschure *et al*. 2005). In this study heterochromatin not only affected the mobility of plasmid DNA because of its physically dense structure, but probably changed the expression level of transgenes because of its

functional character. Many authors (Dobie *et al*. 1996, Francastel *et al*. 1999, Cryderman *et al*. 1999, Porteus *et al*. 2003) have observed the colocalization of silent integrated transgene loci with centromeres or centromeric heterochromatin and their neighbourhood and, moreover, that transgenes integrated into such sites are usually strongly silenced (Dobie *et al*. 1996, Francastel *et al*. 1999, Mutskov & Felsenfeld 2004). As we have demonstrated, transgene DNA finished its journey in the centromeric regions. It is not known if this foreign DNA integrated into these nuclear sites or not.

The foreign DNA was subject to directional movement to the nearest HP1 focus. These movements were restricted to some spatiotemporal compartments of the cell nucleus (Figure 4). The driving force behind this directional movement to the nearest heterochromatin and to the transcriptionally silent regions is not yet known. It is likely that an extended network exists in the nucleus which provides a platform for the organization of nuclear subdomains and for supporting their functionality. This leads us to hypothesize that plasmid DNA could bind to the network of nuclear matrix and scaffold which is dynamic and maintained nuclear architecture (Ma *et al*. 1999). The studies of nuclear actin (reviewed in Pederson 2000) remind us that filament-forming protein families are present in cells. We can also hypothesize that plasmid DNA might tether to short nuclear actin filaments where actin is partly a component of nuclear matrix, plays a direct part in the nuclear export of retroviral RNA and cellular proteins and is necessary for transcription by RNA polymerase II (Clubb & Locke 1998, Kimura *et al*. 2000, Hofmann *et al*. 2004). Moreover, we can speculate that the plasmid DNA movement to the transcriptionally silent regions represents some kind of cell defence mechanism against alien genetic information. To our best knowledge this kind of movement in the cell nucleus has not been described before.

Acknowledgments

We thank T. Misteli, who kindly provided the backbone vector for HP1β-GFP expression. This work was supported by the Grant Agency of the Czech Republic GA202/02/0804 and the Academy of Sciences of the Czech Republic A1065203.

References

Aagaard L, Laible G, Selenko P *et al*. (1999) Functional mammalian homologues of the *Drosophila* PEV-modifier Su(var)3–9 encode centromere-associated proteins which complex with the heterochromatin component M31. *EMBO J* **18**: 1923–1938.

Bannister AJ, Zegerman P, Partridge JF *et al*. (2001) Selective recognition of methylated lysine 9 on histone H3 by the HP1 chromo domain. *Nature* **410**: 120–124.

Bártová E, Kozubek S, Jirsová P *et al*. (2002) Nuclear structure and gene activity in human differentiated cells. *J Struct Biol* **139**: 76–89.

Berger SL (2001) An embarrassment of niches: the many covalent modifications of histones in transcriptional regulation. *Oncogene* **20**: 3007–3013.

Brown KE, Guest SS, Smale ST, Hahm K, Merkenschlager M, Fisher AG (1997) Association of transcriptionally silent genes with Ikaros complexes at centromeric heterochromatin. *Cell* **91**: 845–854.

Cheutin T, McNairn AJ, Jenuwein T, Gilbert DM, Singh PB, Misteli T (2003) Maintenance of stable heterochromatin domains by dynamic HP1 binding. *Science* **299**: 721–725.

Chubb JR, Boyle S, Perry P, Bickmore WA (2002) Chromatin motion is constrained by association with nuclear compartments in human cells. *Curr Biol* **12**: 439–445.

Clubb BH, Locke M (1998) Peripheral nuclear matrix actin forms perinuclear shells. *J Cell Biochem* **70**: 240–251.

Cryderman DE, Morfia EJ, Biessmann H, Elgin SC, Wallrath LL (1999) Silencing at *Drosophila* telomeres: nuclear organization and chromatin structure play critical roles. *EMBO J* **18**: 3724–3735.

Dillon N, Festenstein R (2002) Unravelling heterochromatin: competition between positive and negative factors regulates accessibility. *Trends Genet* **18**: 252–258.

Dobie KW, Lee M, Fantes JA *et al*. (1996) Variegated transgene expression in mouse mammary gland is determinated by the transgene integration locus. *Proc Natl Acad Sci USA* **93**: 6659–6664.

Festenstein R, Pagakis SN, Hiragami K *et al*. (2003) Modulation of heterochromatin protein 1 dynamics in primary mammalian cells. *Science* **269**: 1429–1431.

Francastel C, Walter MC, Groundine M, Martin DIK (1999) A functional enhancer suppresses silencing of a transgene and prevents its localization close to centromeric heterochromatin. *Cell* **99**: 259–269.

Francastel C, Schubeler D, Martin DI, Groudine M (2000) Nuclear compartmentalization and gene activity. *Nat Rev Mol Cell Biol* **1**: 137–143.

Friend DS, Papahadjopoulos D, Debs RJ (1996) Endocytosis and intracellularprocessing accompaning transfection mediated by cationic liposomes. *Biochim Biophys Acta* **1278**: 41–50.

Gilbert N, Allan J (2001) Distinctive higher-order chromatin structure at mammalian centromeres. *Proc Natl Acad Sci USA* **98**: 11949–11954.

Görisch SM, Wachsmuth M, Ittrich C, Bacher CP, Rippe K, Lichter P (2004) Nuclear body movement is determined by chromatin accessibility and dynamics. *Proc Natl Acad Sci USA* **101**: 13221–13226.

Hayakawa T, Haraguchi T, Masumoto H, Horaoka Y (2003) Cell cycle behavior of human HP1 subtypes: distinct molecular domains of HP1 are required for thein centromeric localization dutiny interphase and metaphase. *J Cell Sci* **116**: 3327–3338.

Hofmann W, Stojiljkovic L, Fuchsova B *et al*. (2004) Actin is part of pre-initiation complexes and is necessary for transcription by RNA polymerase II. *Nat Cell Biol* **6**: 1094–1101.

Howe M, Dimitri P, Berloco M, Wakimoto BT (1995) *Cis*-effects of heterochromatin on heterochromatic and euchromatic gene activity in *Drosophila melanogaster*. *Genetics* **140**: 1033–1045.

Jenuwein T, Allis CD (2001) Translating the histone code. *Science* **293**: 1074–1080.

Johnson L, Jurcisek JA (1999) A method to monitor DNA transfer during transfection. *AAPS Pharmsci* **1**(3): 1–7.

Kashihara N, Maeshima Y, Makino H (1998) Antisense oligonucleotides. *Exp Nephrol* **6**: 84–88.

Kimura T, Hashimoto I, Yamamoto A, Nishikawa M, Fujisawa JI (2000) Rev-dependent association of the intron-containing HIV-1 *gag* mRNA with the nuclear actin bundles and the inhibition of its nucleocytoplasmic transport by latrunculin-B. *Genes Cells* **5**: 289–307.

Kozubek M, Matula Pe, Matula Pa, Kozubek S (2004) Automated acquisition and processing of multidimensional image data in confocal in vivo microscopy. *Microsci Res Tech* **64**: 164–175.

Lukacs GL, Haggie P, Seksek O, Lecherdeur D, Freedman N, Verkman AS (2000) Size-dependent DNA mobility in cytoplasm and nucleus. *J Biol Chem* **275**: 1625–1629.

Ma H, Siegel AJ, Berezney R (1999) Association of chromosome territories with nuclear matrix: disruption of human chromosome territories correlates with the release of subset of nuclear matrix proteins. *J Cell Biol* **146**: 531–541.

Mearini G, Nielsen PE, Fackelmayer FO (2004) Localization and dynamics of small circular DNA in live mammalian nuclei. *Nucleic Acids Res* **32**: 2642–2651.

Mutskov V, Felsenfeld G (2004) Silencing of transgene transcription precedes methylation of promoter DNA and histone H3 lysine 9. *EMBO J* **23**: 138–149.

Pederson T (2000) Half a century of 'the nuclear matrix'. *Mol Biol Cell* **11**: 799–805.

Porteus MH, Canthomen T, Weitzman MD, Baltimore D (2003) Efficient gene targeting mediated by adeno-associated virus and DNA double-strand breaks. *Mol Cell Biol* **23**: 3558–3565.

Verkman AS (2002) Solute and macromolecule diffusion in cellular aqueous compartments. *Trends Biochem Sci* **27**: 27–33.

Verschure PJ, van der Kraan I, de Leeuw W *et al*. (2005) *In vivo* HP1 targeting causes large-scale chromatin condensation and enhanced histone lysine methylation. *Mol Cell Biol* **25**: 4552–4564.

Xu Y, Szoka FC (1996) Mechanism of DNA release in cationic liposomemediated gene transfection. *Biochemistry* **35**: 5616–5623.

Biochimica et Biophysica Acta 1833 (2013) 767–779

Contents lists available at SciVerse ScienceDirect

Biochimica et Biophysica Acta

journal homepage: www.elsevier.com/locate/bbamcr

Granulocyte maturation determines ability to release chromatin NETs and loss of DNA damage response; these properties are absent in immature AML granulocytes

Emilie Lukášová [a,*], Zdeněk Kořistek [b], Martin Klabusay [b], Vladan Ondřej [a], Sergei Grigoryev [c], Alena Bačíková [a], Martina Řezáčová [d], Martin Falk [a], Jiřina Vávrová [e], Viera Kohútová [b], Stanislav Kozubek [a]

[a] The Institute of Biophysics, Academy of Sciences of the Czech Republic, Královopolská 135, 612 65 Brno, Czech Republic
[b] Department of Internal Medicine — Hematooncology, University Hospital Brno, Jihlavská 20, 625 00 Brno, Czech Republic
[c] Penn State University College of Medicine, Department of Biochemistry & Molecular Biology, H171, Milton S. Hershey Medical Center, P.O. Box 850, 500 University Drive, Hershey, PA, 17033
[d] Department of Medical Biochemistry, Faculty of Medicine in Hradec Králové, Charles University in Prague, Šimkova 870, 500 01 Hradec Králové, Czech Republic
[e] Department of Radiobiology, Faculty of Military Health Sciences, Hradec Králové, University of Defense Brno, Třebešská 1575, 500 01 Hradec Králové, Czech Republic

ARTICLE INFO

Article history:
Received 2 August 2012
Received in revised form 10 December 2012
Accepted 12 December 2012
Available online 23 December 2012

Keywords:
In vivo and *ex vivo* blood stem cells differentiation
Immature AML neutrophil
Higher-order chromatin remodeling
Neutrophil extracellular trap (NET)
HP1 protein
DNA double-strand break repair

ABSTRACT

Terminally-differentiated cells cease to proliferate and acquire specific sets of expressed genes and functions distinguishing them from less differentiated and cancer cells. Mature granulocytes show lobular structure of cell nuclei with highly condensed chromatin in which HP1 proteins are replaced by MNEI. These structural features of chromatin correspond to low level of gene expression and the loss of some important functions as DNA damage repair, shown in this work and, on the other hand, acquisition of a new specific function consisting in the release of chromatin extracellular traps in response to infection by pathogenic microbes. Granulocytic differentiation is incomplete in myeloid leukemia and is manifested by persistence of lower levels of HP1γ and HP1β isoforms. This immaturity is accompanied by acquisition of DDR capacity allowing to these incompletely differentiated multi-lobed neutrophils of AML patients to respond to induction of DSB by γ-irradiation. Immature granulocytes persist frequently in blood of treated AML patients in remission. These granulocytes contrary to mature ones do not release chromatin for NETs after activation with phorbol myristate-12 acetate-13 and do not exert the neutrophil function in immune defence. We suggest therefore the detection of HP1 expression in granulocytes of AML patients as a very sensitive indicator of their maturation and functionality after the treatment. Our results show that the changes in chromatin structure underlie a major transition in functioning of the genome in immature granulocytes. They show further that leukemia stem cells can differentiate *ex vivo* to mature granulocytes despite carrying the translocation BCR/ABL.

1. Introduction

To understand development of leukemia, it is important to know how changes of chromatin structure are orchestrated during the $CD34^+$ stem cells differentiation and how they correlate with chromatin functions in normal differentiated cells and leukemia conditions. New blood cells of different cell lineages are formed from bone marrow hematopoietic stem cells (HSCs), which provide a constant supply of blood cells throughout life. HSCs show considerable plasticity and can reprogram their gene expression in response to signals produced by a combination of cytokines giving rise to different clones of blood cells with specific functions. For example, granulocytic colony stimulating factor (G-CSF) is used to mobilize HSCs to peripheral blood for using peripheral blood stem cells (PBSC) in transplantation regimes [1] and also to stimulate granulocytic differentiation of HSCs in vitro. HSCs express several specific antigens on the surface (particularly $CD34^+$) and do not express lineage antigens of differentiated cells (Lin^- cells) [2].

Terminal cell differentiation involves a large-scale chromatin remodeling that turns most of the open euchromatin into condensed heterochromatin [3]. During this process, most genes that are required for cell "housekeeping" functions acquire heterochromatin organization and become repressed [4,5]. Heterochromatin is associated with certain types of histone lysine methylation (e.g. at histone H3 lysines 9 and 27 and histone H4 lysine 20), which have a role in preserving heterochromatin structure and rendering histones less susceptible to activatory modifications [6]. The preservation and spreading of heterochromatin is mediated through the direct interaction of dimethylated histone H3 at lysine 9 (H3K9me2) with heterochromatin protein 1 (HP1) [6–8]. However, recent data show that the HP1 is dramatically reduced in mature erythrocytes, lymphocytes and especially granulocytes [9–13]. On

* Corresponding author at: Institute of Biophysics, Academy of Sciences of the Czech Republic, Královopolská 135, 612 65 Brno, Czech Republic. Tel.: +420 541517165; fax: +420 541240498.
E-mail address: lukasova@ibp.cz (E. Lukášová).

0167-4889/$ – see front matter © 2013 Elsevier B.V. All rights reserved.
http://dx.doi.org/10.1016/j.bbamcr.2012.12.012

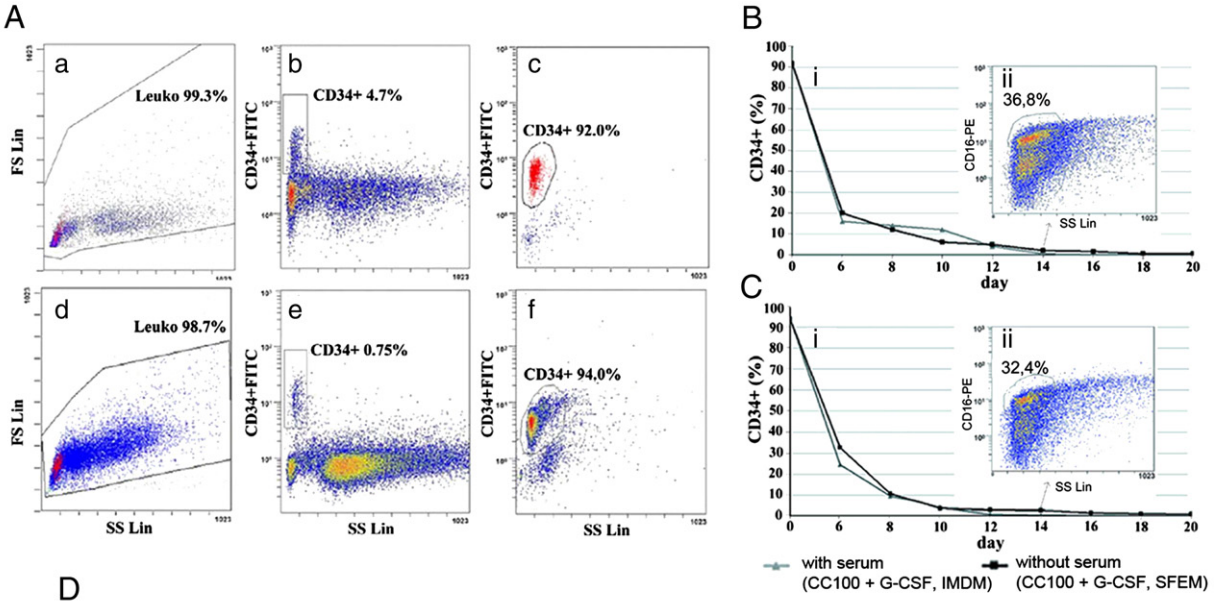
A
a
Leuko 99.3%
FS Lin
b
CD34+ 4.7%
CD34+FITC
c
CD34+ 92.0%
CD34+FITC
d
Leuko 98.7%
FS Lin
SS Lin
e
CD34+ 0.75%
CD34+FITC
SS Lin
f
CD34+ 94,0%
CD34+FITC
SS Lin
B
i
CD34+ (%)
day
ii
36,8%
CD16-PE
SS Lin
C
i
CD34+ (%)
day
ii
32,4%
CD16-PE
SS Lin
with serum
(CC100 + G-CSF, IMDM)
without serum
(CC100 + G-CSF, SFEM)

D

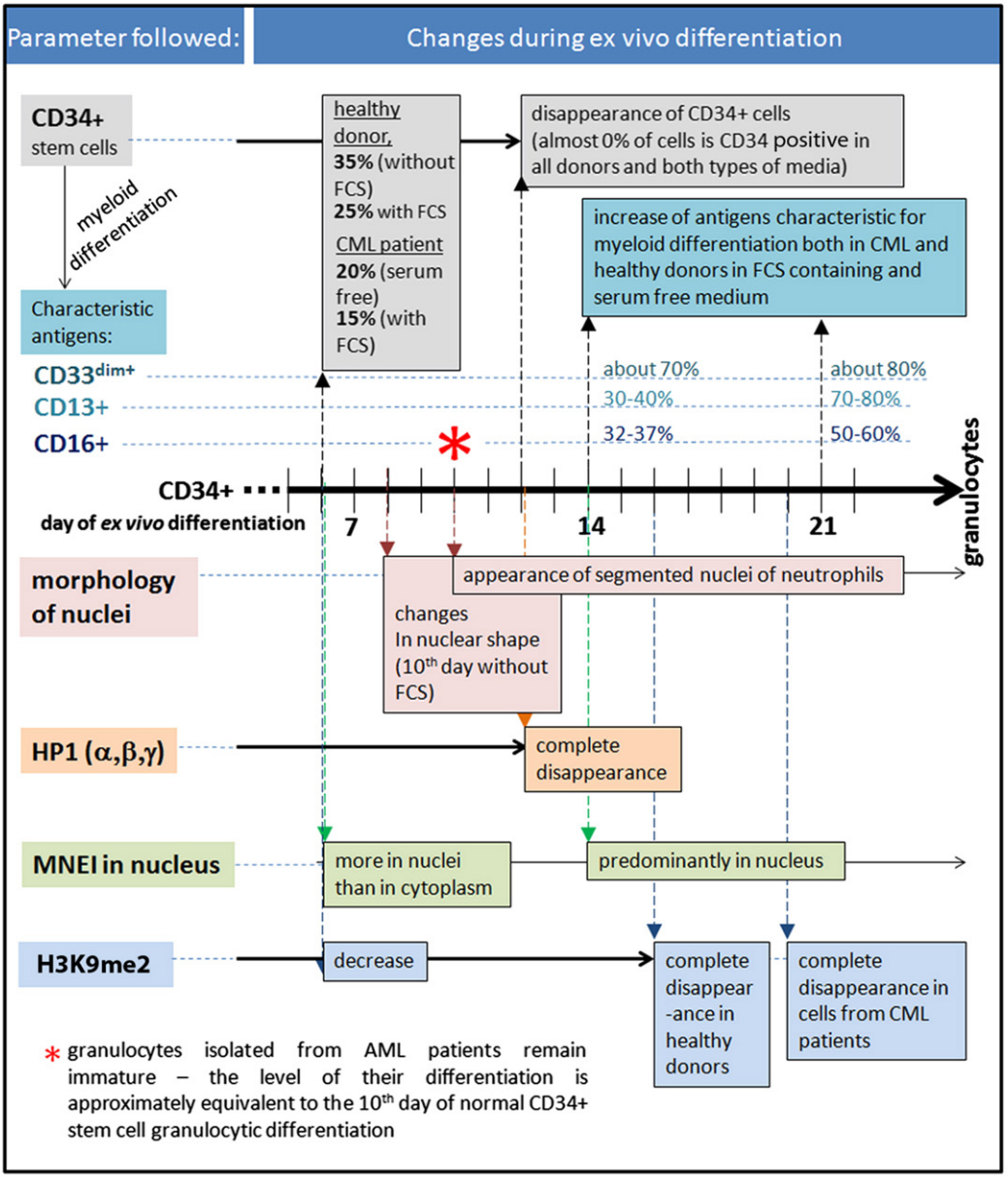
Parameter followed:
Changes during ex vivo differentiation
CD34+
stem cells
myeloid differentiation
Characteristic antigens:
CD33dim+
CD13+
CD16+
CD34+
day of ex vivo differentiation
healthy donor,
35% (without FCS)
25% with FCS
CML patient
20% (serum free)
15% (with FCS)
disappearance of CD34+ cells
(almost 0% of cells is CD34 positive in all donors and both types of media)
increase of antigens characteristic for myeloid differentiation both in CML and healthy donors in FCS containing and serum free medium
about 70%
30-40%
32-37%
about 80%
70-80%
50-60%
7
14
21
granulocytes
morphology of nuclei
appearance of segmented nuclei of neutrophils
changes
In nuclear shape
(10th day without FCS)
HP1 (α,β,γ)
complete disappearance
MNEI in nucleus
more in nuclei than in cytoplasm
predominantly in nucleus
H3K9me2
decrease
complete disappear-ance in healthy donors
complete disappearance in cells from CML patients
* granulocytes isolated from AML patients remain immature – the level of their differentiation is approximately equivalent to the 10th day of normal CD34+ stem cell granulocytic differentiation

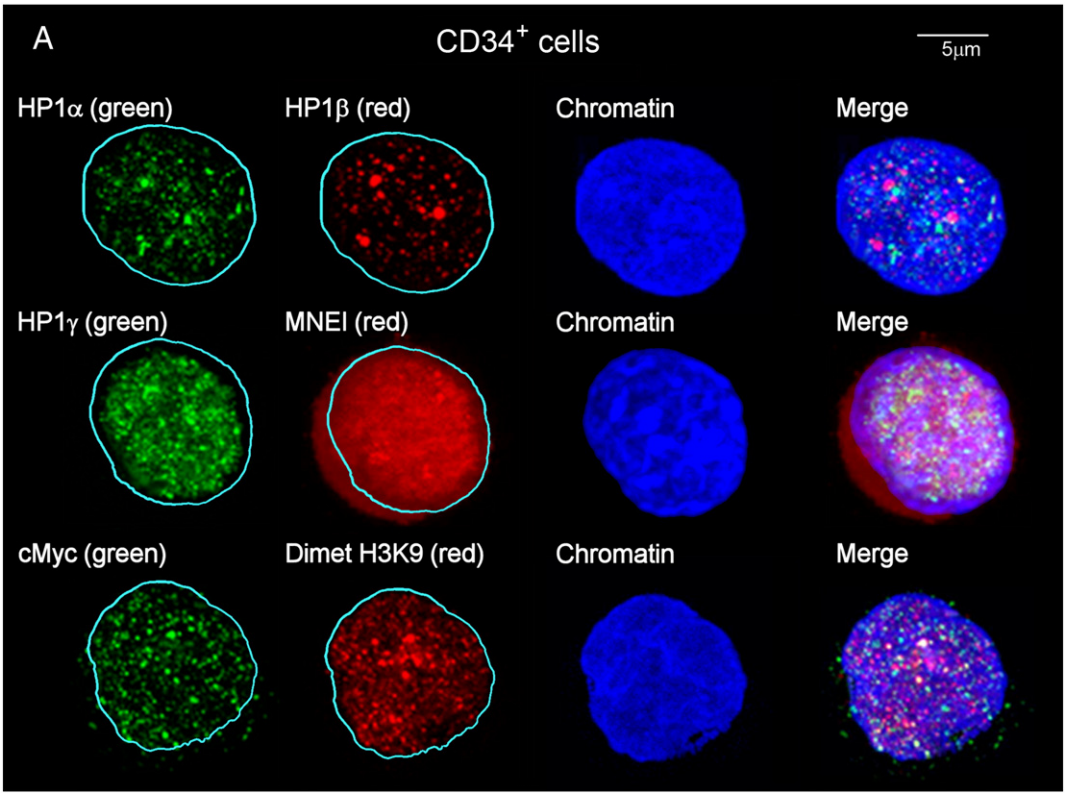

Fig. 2. CD34$^+$ cells isolated from the bone marrow of a CML patient. Cells were fixed by paraformaldehyde and submitted to co-immunodetection with antibodies derived from a rabbit and a mouse to HPlα and HP1β; HP1γ, and MNEI; cMYC and H3K9me2. Total images of nuclei (composed from 40 slices of 0.2 μm thin) were obtained by the confocal microscope Leica DM RXA.

the other hand, it was shown that the level of H3K9me2 in mature granulocytes is high [14] despite this epitope being immunochemically undetectable [13] due to its weak exposure in the tightly condensed chromatin. Nevertheless, a distinct level of H3K9me2 was detected by immunofluorescence in neutrophils of patients in the chronic phase of chronic myeloid leukemia (CML) without detectable HP1 proteins. Dimethylated histone became more easily detected in granulocytes of CML patients in blast crisis and in acute myeloid leukemia (AML) [13,14] where it was also accompanied by high levels of HP1 proteins. The accessibility of the histone H3K9 for immunodetection indicates an incomplete chromatin condensation of AML neutrophils, also frequent in patients in remission.

The leukocytes of healthy donors, chronic CML and AML patients express a nucleo-cytoplasmic serpin MNEI (monocyte neutrophil elastase inhibitor) that was proposed to replace HP1 during the terminal myeloid differentiation [14] similar to the closely related serpin MENT (myeloid and erythroid nuclear termination stage-specific protein) expressed in terminally differentiated avian granulocytes [15,16]. MNEI accumulates in the nuclei of neutrophils at one of the late stage of their maturation [17]. The presence of HP1 proteins in multi-lobed nuclei of neutrophils of leukemic individuals and decreased MNEI thus indicate that chromatin of these cells is not completely condensed and that these cells are immature.

To determine whether elimination of HP1 proteins, increase of nuclear MNEI and chromatin condensation occur coordinately during granulopoiesis of normal and leukemic stem cells or possibly reflect the presence of genetic translocation between BCR-ABL genes in these last cells, we followed *ex vivo* differentiation of CD34$^+$ cells isolated from the bone marrow of patients with chronic-phase CML with complete hematological response to imatinib mesylate (Glivec), the PBSCs of healthy donors and from patients with non-Hodgkin's lymphoma (NHL). In patients with NHL, the differentiation into granulocytic lineage should not be affected, thus these samples served as an additional control for comparison with the CML sample.

Next to changes in chromatin structure, we focused on functional differences between terminally differentiated granulocytes from healthy donors and incompletely differentiated blood cells taken from AML patients. Due to the stable repression of many genes accompanied by profound changes in chromatin structure, differentiated cells dramatically change their metabolic activity and responsiveness to many signals; however, they mostly preserve the ability to maintain the genome integrity including the detection, signaling and repair of DNA damage. Here we studied differentiation-dependent changes in the DNA damage response (DDR) induced by one of the most profound damages to the genome the interruption of both DNA strands called double-strand break

Fig. 1. CD34$^+$ cells isolation and *ex vivo* differentiation. (A) Flow cytometric data of CD34$^+$ cell fractions from bone marrow of a CML patient and PBSC of a healthy donor before and after immunomagnetic separation: (A-a, A-b) flow cytometric analysis of bone marrow of a CML patient before immunomagnetic selection of CD34$^+$ cells. (A-a) Forward scatter vs. side scatter, (A-b) CD34$^+$ labeled with FITC vs. side scatter. (A-c) Flow cytometric analysis of CD34$^+$ purity (92%) after immunomagnetic selection. (A-d, A-e) flow cytometric analysis of PBSC from a healthy donor before immunomagnetic selection. (A-d) Forward scatter vs. side scatter, (A-e) CD34$^+$ labeled with FITC vs. side scatter. (A-f) Flow cytometric analysis of CD34$^+$ purity (94%) after immunomagnetic selection. (B, C) Progress of HSC differentiation (measured as decrease in CD34 expression) during culture of the enriched fraction of CD34$^+$ mononuclear cells in serum-free (black line, squares) and serum-supplemented (blue line, triangles) medium: (B) Cells from the bone marrow of a CML patient; (C) cells from PBSC of a healthy donor. Insets (Bii, Cii): CD16 expression after 14-day culture in serum-free medium. (D) A scheme showing the timing of the changes in the antigens expression, nuclear morphology and epigenetic markers of chromatin structure during *ex vivo* differentiation of CD34$^+$ cells to granulocytes. The arrows emanating from the time-axis indicate the appearance of the particular changes (described in the boxes).

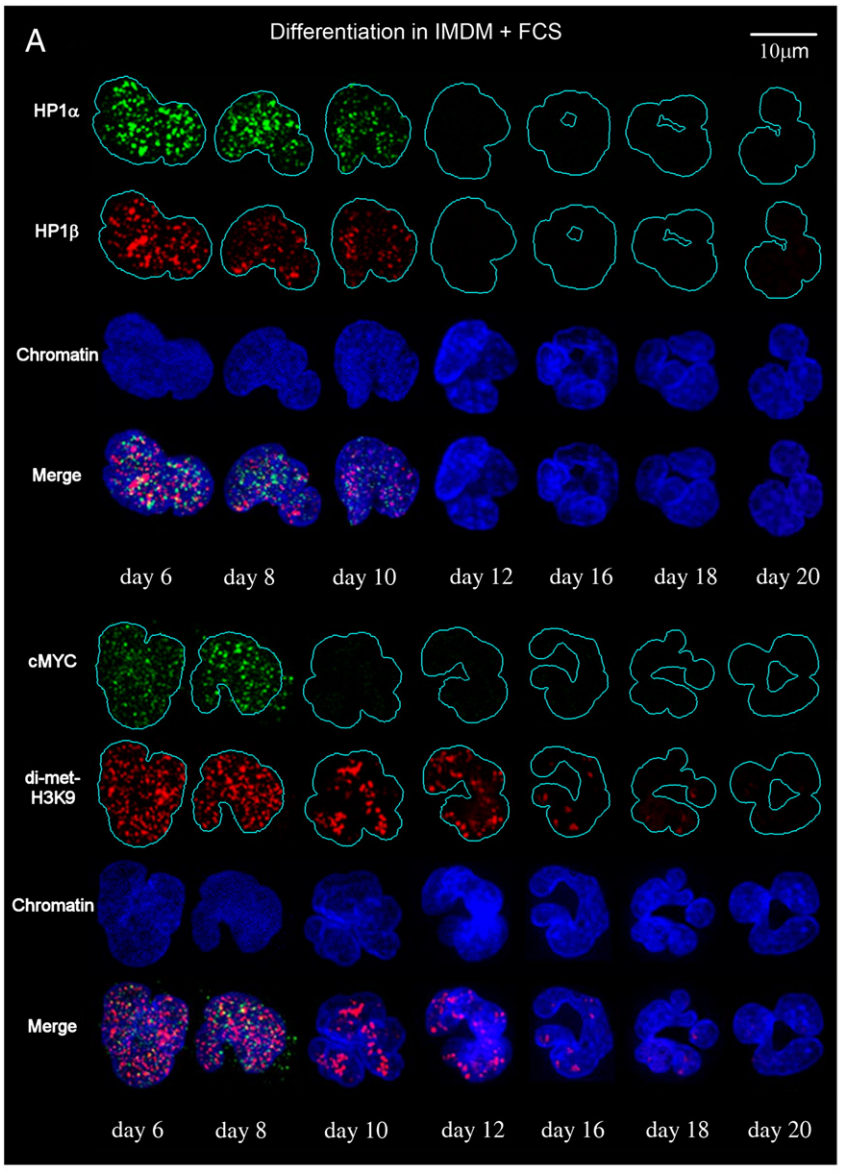
A
Differentiation in IMDM + FCS
10μm
HP1α
HP1β
Chromatin
Merge
day 6
day 8
day 10
day 12
day 16
day 18
day 20
cMYC
di-met-H3K9
Chromatin
Merge
day 6
day 8
day 10
day 12
day 16
day 18
day 20

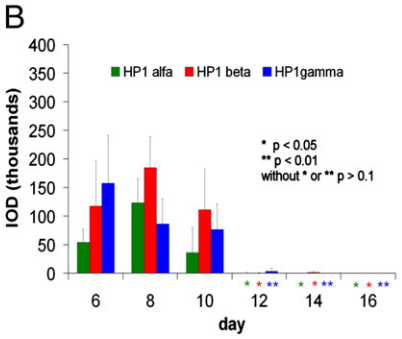
B
HP1 alfa
HP1 beta
HP1gamma
* p < 0.05
** p < 0.01
without * or ** p > 0.1
IOD (thousands)
day

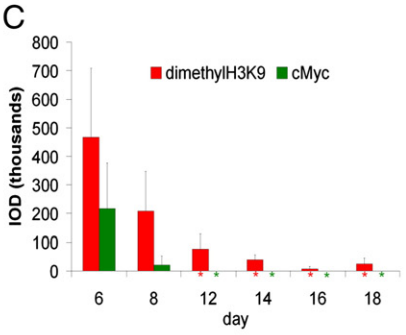
C
dimethylH3K9
cMyc
IOD (thousands)
day

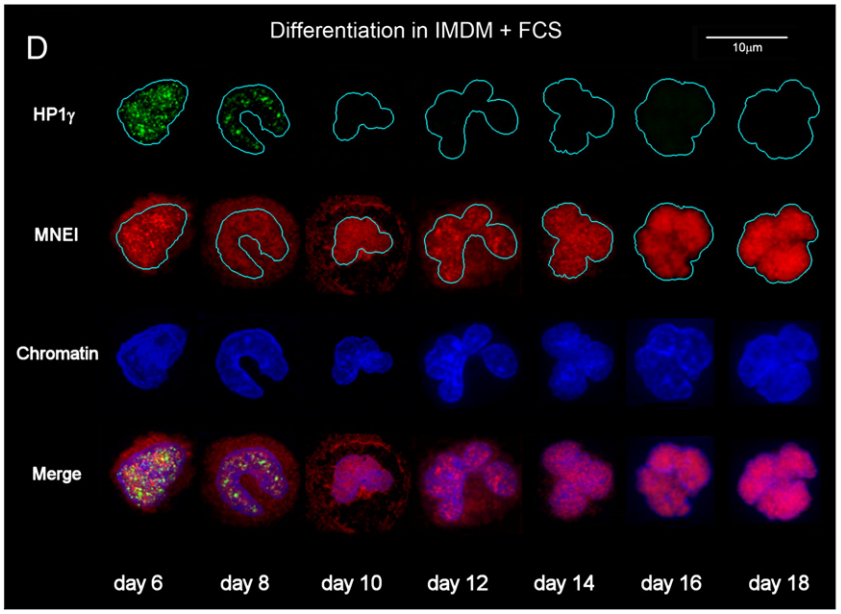
D
Differentiation in IMDM + FCS
10μm
HP1γ
MNEI
Chromatin
Merge
day 6
day 8
day 10
day 12
day 14
day 16
day 18

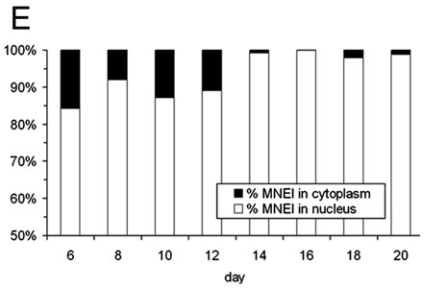
E
% MNEI in cytoplasm
% MNEI in nucleus
day

(DSB). Within several minutes after irradiation, the nucleosomal histone H2AX is phosphorylated on serine 139 (γH2AX) by ATM kinase in the proximity of DSBs. This phosphorylation spreads up to the distance of about 2Mbp of DSB flanking chromatin forming thus foci known as IRIFs [18–20]. These foci are generally used for the detection of DSBs. Many repair proteins including sensors, transducers and effectors are rapidly attached to γH2AX to repair this damage. MDC1, NBS1, MRE11, RAD50, ATM kinase, 53BP1 colocalize with γH2AX as the first and their presence in IRIF indicates the ongoing process of DSB repair [20]. Global chromatin condensation was shown to inhibit DDR [21] while HP1 proteins may play a positive role in DDR [22].

We examined whether the DDR induced by ionizing radiation is preserved in terminally differentiated mature granulocytes that have condensed chromatin, a short life span, are capable to unravel neutrophil extracellular traps (NETs) to capture and kill microbes [23], but lack HP1 [13]. This ability was examined also in the immature granulocytes and incompletely differentiated precursors emerging in peripheral blood of leukemic individuals before the disease treatment as well as in remission. In addition, we investigated whether the ability of mature neutrophils to release chromatin NETs after activation [23–28] is also preserved by immature neutrophils of AML patients expressing HP1γ.

We show that CML stem cells can differentiate *ex vivo* to mature granulocytes despite the presence of the BCR/ABL translocation and that mature granulocytes from healthy donors neither express DNA repair proteins nor undergo proper DDR contrary to immature leukemia granulocytes. Immature neutrophils of AML patients are not able to release chromatin into neutrophil extracellular traps (NETs) after activation with phorbol 12-myristate 13-acetate (PMA) and thus execute the principal function of neutrophils. Taken together, a tight correlation between chromatin structure and cell function has been observed giving an interesting picture of mechanisms governing granulocytic differentiation.

2. Material and methods

2.1. Cells

Mature granulocytes and mononuclear cells (lymphocytes and monocytes) were isolated from peripheral blood as described earlier [13]. The resulting cell population contained more than 95% of mature neutrophils as assessed by microscopy analysis. Immature neutrophils were isolated by the same procedure from the peripheral blood of patients with acute myeloid leukemia (AML). The informed consent of all blood donors was obtained.

2.2. Patients

The peripheral blood was obtained from ten AML patients from the Hemato-Oncology Clinic of Faculty Hospital in Brno–Bohunice and three patients from the Hemato Oncology Clinic of Faculty Hospital in Olomouc. The causal mutations of the disease were different at these patients. Patients were divided into 2 groups according to presence or absence of HP1 proteins in their neutrophils isolated from the peripheral blood without respect to genetic changes.

2.3. Cell irradiation

Cells were irradiated with 3 Gy of γ-rays (^{60}Co, 1 Gy/min) in RPMI medium with 10% fetal calf serum (FCS) immediately after isolation and maintained in this medium for next 30 min before fixation or RNA and protein isolation.

2.4. Hemopoietic stem cells (HSCs) isolation, enrichment and separation of the CD34$^+$ cell population

CD34$^+$ cells for *ex vivo* differentiation were enriched from bone marrow (BM) of a patient with CML and, for comparison, also from PBSCs of two patients with lymphoma undergoing autologous transplantation and from two healthy donors. HSCs of lymphoma patients and of healthy donors were taken from the leukapheresis product of peripheral blood (PBSC graft) after recombinant granulocyte-colony stimulating factor (rhG-CSF) (Filgrastim; Inc., Amgen, USA) administration. Approximately 50 ml of bone marrow were obtained from a patient with CML in complete hematological remission during the collection of the back-up graft. Leukapheresis products were enriched for CD34$^+$ cells as described in the Supplement.

2.5. Stem cells expansion and differentiation

Two different systems were used for the expansion of CD34$^+$ cells. The first expansion system consisted of Iscove's modified Dulbecco's medium (IMDM; Sigma-Aldrich, USA) completed with 10% FCS (Sigma-Aldrich, USA). The second system contained serum-free expansion medium (SFEM) (StemCell Technologies, Inc., Vancouver, Canada) without FCS. Both types of media were completed with 100 ng/ml of rhG-CSF (Filgrastim, Inc., USA) and a mixture of recombinant human cytokines (CC100; StemCell Technologies, Inc., Canada) containing 100 ng/ml of stem cell factor (SCF), 20 ng/ml of interleukin-3 (IL-3), 20 ng/ml of interleukin 6 (IL-6) and 100 ng/ml of stem cell tyrosine kinase-1 ligand (Flt-3-L). The initial concentration of CD34$^+$ cells was 2×10^4/ml in both types of systems. Cells were cultured for 21 days and counted in two-day intervals using an automatic cell counter (Abbott, USA) to determine the absolute leukocyte count in the samples. The culture medium was half exchanged every two days, and its volume was adjusted to keep the cell concentration below 1×10^6/ml in order to prevent cell overgrowth. A constant concentration of cytokines was maintained. Samples of 2×10^5 cells were taken in two-day intervals from the 6th day for the immunodetection of chromatin structure markers and DSB repair proteins. The vitality of growing cells was assessed regularly by a LIVE/DEAD® Viability/Cytotoxicity Kit (Molecular Probes, Eugene,USA).

2.6. Flow cytometry

The phenotype of growing cells was analyzed after 14 and 21 days of culture, and the expression of CD34 antigen was followed every 2 days on a Cytomics FC500 cytometer (Beckman-Coulter, USA). Number of cells taken for these measurements was 1×10^6 in all samples. The myeloid lineage specific antigens CD33, CD14 and CD16 were detected

Fig. 3. Changes in the presence of HP1α, β, cMYC, dimethylated H3K9 (A, B, C), HP1γ and MNEI (D, E) detected by immunofluorescence during *ex vivo* differentiation of CD34$^+$ cells of a CML patient in IMDM completed with FCS. (A, D) Images of DNA inside the cell nuclei (blue, TOPRO3) represent the most progressive fraction of cells at the given time of the process. (A) The levels of HP1α and β decreased on day 10 and disappeared from the nuclei by day 12. cMYC expression was stopped from day 10. Dimethylated histone was detectable until day 18 of the process in neutrophils originated from CD34$^+$ cells of the CML donor; but its level decreased considerably from day 12. (B, C) Histograms of the integrated optical density (IOD) express levels of specific proteins during differentiation of CD34$^+$ cells through granulocytes. IOD was measured as described in Section 2.8 for 80–130 nuclei per specific time. Attached cells preserved their natural shape and were not deformed. All values are expressed as mean standard deviation (s.d.) of (n) number nuclei in specific time of observation and given in IOD. High s.d. show differences in IOD of individual nuclei present on slides for specific times of differentiation. These differences are likely connected with different stages of cells differentiation on the slide. A statistically significant difference of results relative to the values obtained for day 6 was calculated using the Student's *t*-test: $^*P<0.05$, $^{**}P<0.01$. (D) The level of MNEI in cells at given times of the differentiation process. The histograms (E) present relation between the content of MNEI in the nucleus and cytoplasm expressed as % of the mean value of IOD measured in the central slice (0.2 μm thin) through the cells; the mean was calculated from about 100 cells in each time. The proportion of the IOD in the nucleus and the cytoplasm was calculated from the total cellular value for each cell separately. The level of MNEI in the cytoplasm was significantly lower ($P<0.05$) than in the nucleus from day 6 and decreased to a negligible value from day 14. RGB channels were nonlinearly increased by the Photoshop curves function in order to allow the figure printing.

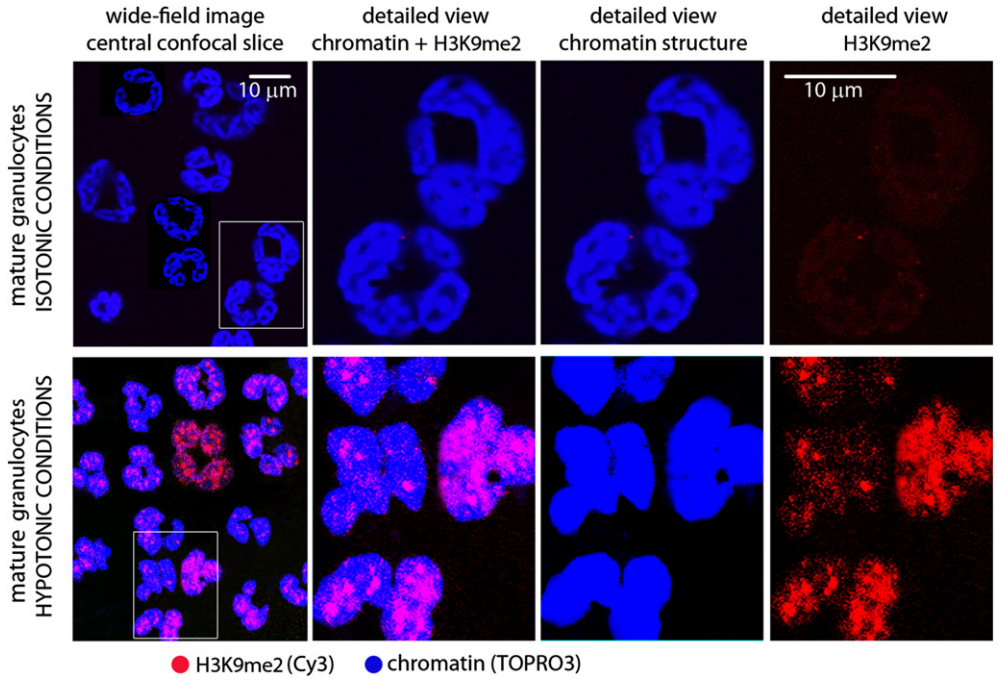

Fig. 4. Changes in chromatin structure of mature neutrophils after short exposure to hypotonic treatment. Freshly isolated mature neutrophils of a healthy donor were incubated in 0.5× PBS for 10 min and then immediately submerged to 4% paraformaldehyde for fixation. Chromatin relaxation in neutrophils obtained by this treatment enabled positive immunodetection of histone H3K9me2 (lower range of images). In neutrophils that were immediately fixed after isolation, the immunodetection of this antigen was negative (upper range of images).

with the monoclonal antibodies directly labeled with FITC, R-PE or PE-Cy5 (Becton-Dickinson, USA; Caltag Lab, USA).

2.7. Cell fixation and immunostaining

Cells harvested at different time intervals from the growing culture and freshly isolated granulocytes from the peripheral blood were processed as described earlier [13] and in the Supplement.

2.8. Fluorescence microscopy

Images were obtained with a high-resolution Leica DM RXA confocal cytometer (Leica, Wetzlar, Germany) described in [29,30], equipped with a CSU-10a confocal unit (Yokogawa, Japan), a CoolSnap HQ charged-coupled device camera (Photometrix, Melbourne, Australia) and an Ar-Kr laser Inova 70C Spectrum (Coherent, Hilton SA, Australia). The oil immersion Plan Fluotar objective (100×/NA 1.3) was used. Forty optical sections at 0.2 μm steps were acquired for each nucleus using the software FISH 2.0 [29,30] at the constant temperature of 26 °C. The exposition time and dynamic range of the camera in the red, green and blue channels were adjusted to the same values for all slides to obtain quantitatively comparable images. Integrated optical density (IOD) in red or green color channels was measured using the image analysis software Image-Pro Plus, version 5.1.2.59 (Media Cybernetics, Inc., MA, USA). IOD registers average intensity per measured object. It was measured in the central, i.e., 20th slice (0.2 μm thick), through the cell nucleus. At least 50 nuclei were scored for the measurements of specific antibodies IOD. The statistical significance (P) of the values obtained during the differentiation relative to the values on day 6 was determined according to the normal distribution by the Student t-test.

2.9. RT-PCR

The total RNA was isolated from granulocytes and mononuclear cells by High Pure RNA Isolation Kit (Roche). 10^6 cells of each type were used. cDNA synthesis was performed using Transcriptor High Fidelity cDNA Synthesis Kit with oligo $(dT)_{18}$ as a primer (Roche). PCR amplification was carried out using HotStarTaq Master Mix Kit (Qiagen) with specific primers listed in the Supplement.

2.10. Protein extraction, gel electrophoresis and western blotting

Protein extraction, gel electrophoresis and western blotting were done according to the standard procedures, as described in the Supplement.

2.11. Activation of neutrophils by phorbol 12-myristate 13-acetate to generate neutrophil extracellular traps

Brinkmann et al. [23] disclosed the capacity of mature neutrophils to release chromatin and proteins from cytoplasmic granules to form extracellular fibers (NETs) that capture and kill microorganisms. This capacity of neutrophils can be stimulated not only by pathogenic microorganisms but also by alternative stimuli [26,28], the most potent of which is phorbol 12-myristate 13-acetate (PMA). We used PMA to detect the capability of NETs formation by AML neutrophils that are not completely mature, express HP1γ protein and have immunodetectable H3K9me2. Granulocytes were isolated from the peripheral blood of 2 healthy donors and 5 AML patients after elimination of erythrocytes using Ficoll-Hypacque centrifugation gradient. Freshly isolated neutrophils were resuspended in RPM1 medium containing 2% of FCS to 1×10^6 cells/ml. 200 μl of this cell suspension was seeded to a positively charged microscopic slide and incubated for 1 h in CO_2 incubator at 37°C. Then, 4 ml of 21 nM PMA or 10,5 nM PMA in RPMI with 2% FCS were added to cells attached to the slides to obtain the final 20 nM or 10 nM concentration of PMA. Cells were incubated in these media for 150 min and 240 min in a CO_2 incubator at 37^0C before fixation in 4% paraformaldehyde for 10 min. Cells were then washed 3 times in PBS, permeabilized in PBS containing 0.2% Triton X-100 and immunostained with anti-histone H2B antibody from Millipore as described in Supplement.

2.12. Hypotonic treatment of granulocytes

Granulocytes isolated from peripheral blood of 2 healthy donors were resuspended in PBS to 1×10^6 cell/ml. 200 μl of this cell suspension were seeded to a microscopic slide and incubated for 30 min in a CO_2 incubator at 37 °C. Next, 4 ml of 0.525× PBS were added and cells were incubated in this low-salt (150 mOsm) medium (0.5× PBS) for 10 min, fixed in 4% paraformaldehyde for 10 min, permeabilized and immunostained with anti-histone H3K9me2 antibody (Upstate). (Normal culture medium or 1× PBS have the osmolarity of 300 mOsm).

3. Results

3.1. Purity of the CD34$^+$ cells

To analyze changes in chromatin structure during the CD34$^+$ cells differentiation into granulocytes and the ability of CD34$^+$ cells isolated from CML patients to differentiate (in the presence of the BCR/ABL translocation), CD34$^+$ cells were isolated, differentiated *ex vivo*, and immunologically analyzed for the expression of specific surface antigens and chromatin structure determining proteins. The purity of CD34$^+$ cells from bone marrow is usually lower than the purity of cells obtained from a PBSC graft after single-step separation. Therefore, the bone marrow cells were purified in a two-step procedure. The average purity of the enriched CD34$^+$ cell fraction from PBSC grafts was 94% and that of BM of a CML patient was 92% (Fig. 1A). The PCR analysis in combination with FISH method confirmed the presence of BCR/ABL translocation in 70% of enriched CD34$^+$ cells of a CML patient.

3.2. Ex vivo cell expansion and differentiation of healthy and CML blood stem cells

Cells from all samples expanded much more efficiently in the SFEM medium without than with FCS in IMDM (Figure S1). Cells of a CML patient expanded approximately 876× in serum free medium and only 96× in a medium supplemented with FCS. Cells from PBSC graft of a healthy donor expanded 39× in serum free medium and 7× in the medium supplemented with FCS. Massive expansion of leukemia cells from a CML patient in SFEM medium was about 20 times higher than the expansion of cells from a healthy PBSC in this medium and about 13 times higher in the medium completed with FCS.

The lower expansion of both cell types in IMDM medium containing 10% FCS could be, probably due to a more rapid cell differentiation, indicating that there are some, not yet known cytokines in FCS that are favorable for terminal granulocyte differentiation and maturation and were not added into the system. Very similar results were obtained with stem cells of different donors in repeated experiments. More rapid differentiation of stem cells in IMDM medium completed with FCS was manifested by more rapid loss of CD34 antigen (Fig. 1 Bi, Ci) at both types of donors and also by earlier disappearance of HP1γ protein and later accumulation of MNEI in cell nuclei of stem cells of a CML patient during ex vivo differentiation (Fig. 3D, Figure S2).

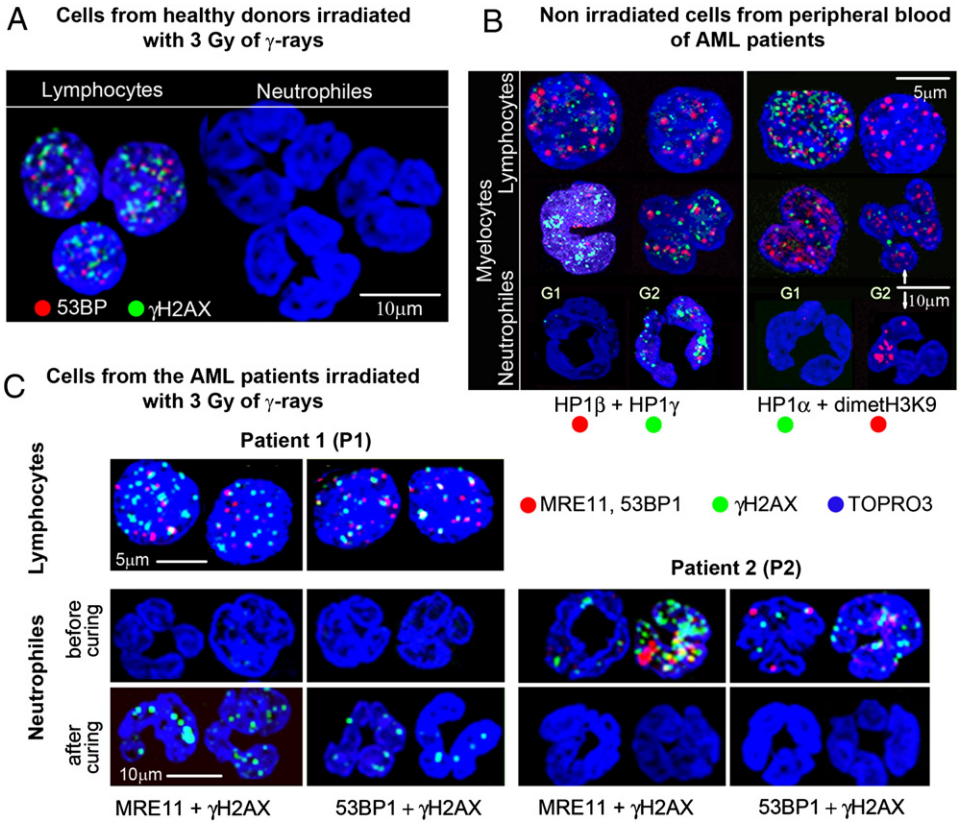

Fig. 5. Presence of chromatin structure markers and DSB repair proteins in nuclei of blood cells isolated from healthy donors and AML patients. (A) The comparison of the expression of γH2AX and repair proteins in human lymphocytes and neutrophil granulocytes isolated from the blood of healthy donors and irradiated with the dose of 3 Gy of γ-rays. There are neither repair proteins nor γH2AX in irradiated mature neutrophils contrary to irradiated lymphocytes. (B) HP1α, β, γ and H3K9me2 immunodetected in lymphocytes, myelocytes and neutrophils of peripheral blood of AML patients at the time of the disease diagnosis. HP1 proteins and H3K9me2 are present in lymphocytes however they are not in neutrophils of the G1 group of AML patients contrary to those of the G2 group. (C) Immunodetection of γH2AX and repair proteins in γ-irradiated lymphocytes and neutrophils isolated from the blood of AML patients P1 (group1) and P2 (group2) before and after the leukemia treatment. The cells were irradiated with 3 Gy of γ-rays and fixed 30 min PI. While all detected proteins were found in lymphocytes, they were not found in neutrophils of the group 1 patients, represented by P1, before the treatment and in neutrophils of the group 2 represented by P2 after the treatment. Chromatin was counterstained with TOPRO-3. RGB channels were nonlinearly increased by the Photoshop curves function in order to allow the figure printing.

The rate of differentiation characterized by the loss of CD34 antigen was higher for stem cells from the CML donor (Fig. 1 Bi) compared to that for PBSC (Fig. 1 Ci) of healthy donors in both types of media. A "timetable" summarizing the changes in antigen expression during the cell differentiation is displayed and compared with changes in chromatin structure and cell morphology on Fig. 1D. CD34 antigen almost disappear from cells of PBSC cultured in serum-free and serum-supplemented media at day 12 and the day 14 from cells of a CML donor (Fig. 1 Bi, Ci, D) and the disappearance of CD34 antigen is accompanied by the increase of cells expressing antigens characteristic of myeloid differentiation ($CD33^{dim+}$, $CD13^{+}$ and $CD16^{+}$). The number of cells expressing these antigens increased, and, on day 21, some 80% of cells from the BM of a CML patients and the PBSC of a healthy donor were expressing $CD33^{dim+}$, 70%–80% expressed $CD13^{+}$ and 50%–60% expressed $CD16^{+}$ in both culture systems (Fig. 1 Bii, Cii, D). Vitality of cells in all systems was above 90% from the beginning to the end of the culture process.

3.3. Changes of HP1, MNEI and H3K9me2 during stem cell differentiation

Stem cells express CD34 antigen, all HP1 proteins, cMYC and H3K9me2 (Fig. 2). These proteins were successively eliminated during ex vivo differentiation that was accompanied also by changes in the shape of cell nuclei. The rate of differentiation was not the same for all cells in the culture, as shown by differences in the nuclear shape and different levels of detected proteins at the appropriate time of cell examination (Fig. 3A, B, C, D). The homogeneity of cells increased with the time of differentiation and was higher in the presence of FCS. Many banded cells were already present by the 8th day of the process (Fig. 1D). The changes in the shape of the nuclei were accompanied by a decrease in the level of HPl proteins and H3K9me2 signal on the one hand (Fig. 1D, 3A, B, C) and by an increased nuclear relocation of MNEI on the other (Fig. 1D, 3D, E). Cells expressing HP1α and HP1β proteins disappeared completely by the 12th day, cells with HP1γ by the 10th day of the differentiation and the level of MNEI in the nucleus was higher than in the cytoplasm from the 6th day (Fig. 1D, 3D, E); from the 14th day and later, this protein was observed predominantly in the nucleus (Fig. 1D, 3D, E). The disappearance of HP1 proteins was correlated with the appearance of higher number segmented nuclei of neutrophils (Fig. 1D). Importantly, the differentiation process was not significantly influenced by the origin of $CD34^{+}$ cells (healthy donor, BCR/ABL translocation or NHL patient), despite the H3K9me2 signal persisted in neutrophils coming from the $CD34^{+}$ cells of the CML patient some days longer (from 16th to 18th day) than in the healthy and NHL cells. To show that inaccessibility of H3K9me2 for immunodetection is caused by a tighter chromatin condensation during the differentiation of $CD34^{+}$ cells to granulocytes, we exposed the granulocytes isolated from peripheral blood of healthy donors to a short (10 min) incubation in a hypotonic solution of 0.5× PBS before fixation. Chromatin structure of granulocytes exposed to this lower-salt solution became more relaxed enabling H3K9me2 detection (Fig. 4).

It thus appears that there are coordinated consecutive changes of heterochromatin factors during the granulocyte differentiation process that include cessation of protein expression (HP1), cytoplasm-nuclear relocation (MNEI) and protection of antigenic epitopes due to chromatin condensation (H3K9me2).

3.4. Capacity of white blood cells for DDR induced by γ-rays

Next, we analyzed how changes in chromatin structure established in terminally differentiated granulocytes are reflected in their functions, and whether there are some differences between mature terminally differentiated granulocytes obtained from healthy donors and immature granulocytes of AML patients. Since DNA repair was reported to be active in majority of cell types, we followed the DDR induced by DSBs that are the most serious DNA lesions. Granulocytes and mononuclear cells (lymphocytes and monocytes) isolated from the peripheral blood of healthy donors were irradiated with 3 Gy of γ-rays and formation of IRIF foci at the sites of DSBs was followed by immunodetection 30 min post-irradiation (PI). While in lymphocytes and monocytes (Fig. 5A) as well as in stem cells (not shown), the IRIFs appeared very soon after DSB induction and their colocalization with different repair proteins was observed, neither the IRIFs nor the repair proteins were detected in mature neutrophils of healthy donors (Fig. 5A). These

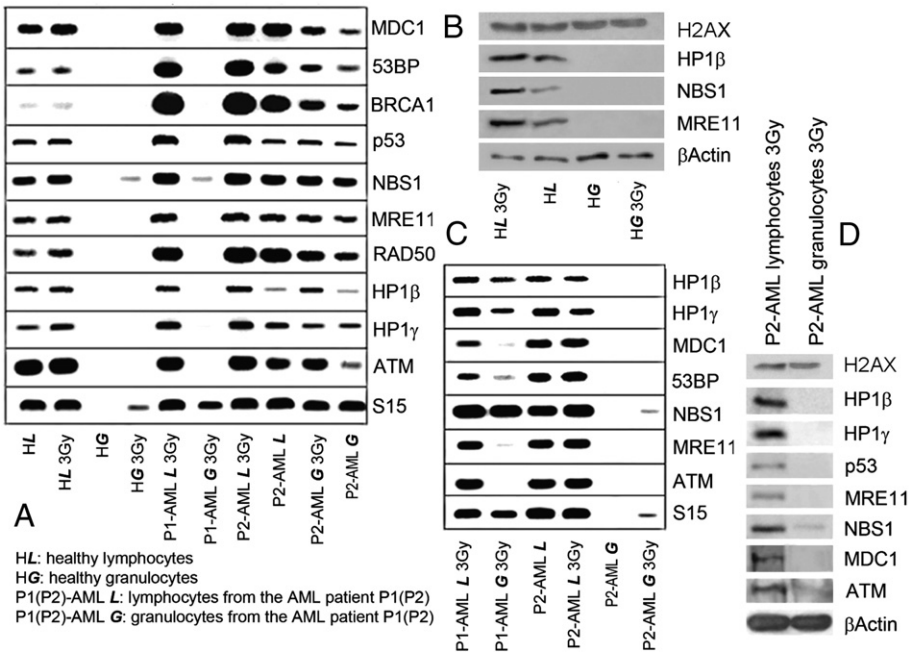

Fig. 6. Transcription activity (RT-PCR) of HP1β, HP1γ and selected DSB repair genes in lymphocytes and granulocytes of a healthy donor, AML patients P1 and P2 (representing the group 1 and 2). (A, C) Transcription activity before and after the treatment, respectively. (B, D) Levels (WB) of HP1β and HP1γ and some repair proteins before (B) and after (D) the treatment.

neutrophils did not express any of HP1 proteins (not shown) contrary to mononuclear cells and myelocytes isolated from the peripheral blood of AML patients before the treatment and incompletely differentiated AML neutrophils (Fig. 5B, C). The presence of HP1 proteins in neutrophils of some AML patients made us to divide them into groups for further analyses: While the neutrophils of the group 1 (G1) AML patients did not present any HP1 proteins similarly as the healthy mature neutrophils, those of the group 2 (G2) expressed small amount of HP1 proteins even if they had multi-lobed nuclei, typical for mature neutrophils (Fig. 5B). The cells of G2 patients expressed also repair proteins and phosphorylated H2AX after γ-irradiation; however the colocalization of γH2AX with repair proteins was rare 30 min post-irradiation (PI) (Fig. 5C). The expression of HP1γ, HP1β as well as repair proteins after irradiation thus represent marks of incompletely mature granulocytes. The absence of the repair proteins in the nuclei of terminally differentiated neutrophils (from healthy donors and G1-patients) was consistent with missing of the corresponding gene transcription detected by RT-PCR and western blotting (Fig. 6 A, B). The exception was the expression of small amount of Nibrin (NBS1) in irradiated terminally differentiated granulocytes of healthy donors and G1 patients.

The level of granulocytic maturation in the peripheral blood was followed in detail at 1 patient (P1) of the group 1 and one of the group 2 (P2) again 10 month after the beginning of leukemia treatment. At this time, the amount of WBC of P1 was almost normal, (3.41×10^9/L), however with only 1.33×10^9/L of neutrophils (presenting 39% of WBC). The level of P2 WBC was completely normal (8.8 x 10^9/L with 62.8% of neutrophils). The neutrophils of the latter patient were entirely mature; they expressed none of HP1 proteins, did not form γH2AX foci and expressed none of repair proteins after γ-radiation. (Fig. 5C, 6C). On the other hand, about 50% of neutrophils of the P1 were not mature. Many of them were in the stage of band cells. Both, the band and segmented cells expressed HP1 proteins, detected in the nuclei by specific antibodies (not shown). The activity of genes coding for HP1 isoforms and repair proteins detected by RT-PCR in extracts from granulocytes significantly contrasted for P1 and P2 after the treatment (Fig. 6C). RT-PCR showed active mRNA expression of HP1β and HP1γ and low expression of genes for DNA repair proteins in case of P1, however none of these genes were expressed in P2 granulocytes. In spite of low expression of several repair protein genes (MDC1, 53BP,

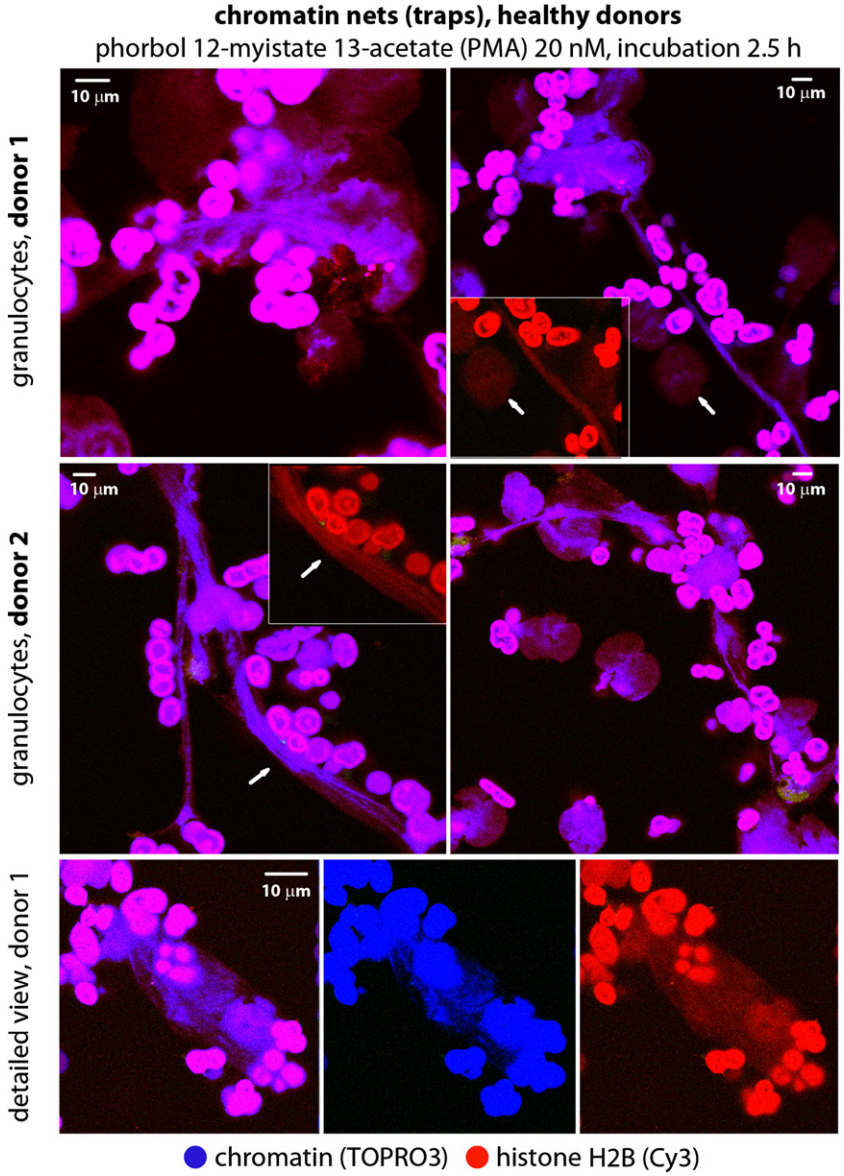

Fig. 7. Mature neutrophils isolated from healthy donors release extracellular traps (NETs) after activation with phorbol 12-myristate 13-acetate (PMA). Freshly isolated mature neutrophils were incubated in PMA (20 nM) for 2.5 h at 37 °C before fixation in paraformaldehyde and immunodetection of histone H2B.

MRE11) in P1 granulocytes, the proteins encoded by these genes were not found by immunodetection on cell nuclei (Fig. 5C, 6D); however, γH2AX foci marking regions of DSB were detected in the P1 nuclei after irradiation (Fig. 5C). Their number was smaller as compared with the lymphocytes irradiated with the same dose.

In some cases when the treatment of leukemia at patients of the group 2 lead to the attainment of normal mature granulocytes, this situation was not stable and the patients had to undergo further consolidation treatments. Therefore, we conclude that only the treatment of AML that removes the cells with causal mutations and simultaneously leads to persistent granulocyte maturation could effectively prevent AML relapse. The state of granulocyte maturation was followed for patients of the G1 and G2 groups for additional 10 to 19 months by immunological detection of HP1β and HP1γ expression. All five patients of the G2 had normal number of white blood cells and neutrophils did not show the marks of immature cells. Two patients of this group were observed after the stem cells allogenic transplantation. All three patients of the group 1 underwent at least one additional consolidation treatment during this time, however even though they have a normal number of white blood cells at present, their neutrophils contain HP1 proteins indicating an incomplete differentiation.

3.5. The incomplete maturation of AML neutrophils negatively affects the function of these cells to form neutrophil extracellular traps (NETs)

The ability to release chromatin NETs upon incubation with PMA was detected with granulocytes from 2 healthy donors (Fig. 7) and 5 AML patients (Fig. 8). Neutrophils of two of them expressed HP1γ in about 43% cells; one patient had HP1γ in about 70% of neutrophils, and two other expressed it in 90% and 94% neutrophils. The neutrophils of the last two patients did not respond to activation with PMA used at two different concentrations (10 nM and 20 nM) for 2.5 h and 4 h. The NETs were not found in any neutrophils among about 2×10^5 cells fixed on the microscopic slide and expressing HP1γ protein in about 90% of cells. The similar results were also obtained with neutrophils expressing HP1γ protein in about 70% cells. Nuclei of majority of these cells preserved the shape and structure of chromatin, (Fig. 8C), while at mature neutrophils exposed to 20 nM PMA for 4 h., the majority of nuclei lost their lobular shape, expanded and released chromatin NETs into the extracellular space (Fig. 8A).

The ability to release NETs and corresponding changes of chromatin structure were also observed in neutrophils, where the expression of HP1γ was found in about 40–43% of the cells (Fig. 8B). These results suggest that remodeling of chromatin structure during neutrophil differentiation enable these cells to rapidly react to pathogenic microbes in a body by releasing chromatin to extracellular space and forming NETs for capture and killing these microbes and thus exert the basic function of granulocytes in fighting bacterial infections. However, when the process of differentiation is not completed and neutrophils continue to express HP1 proteins, their capability to release chromatin NETs is precluded.

4. Discussion

In this work, the consequent changes of chromatin structure during differentiation of normal and leukemia blood progenitors to granulocytes were followed and the capability of differentiated cells to repair DNA DSB was analyzed. We show that heterochromatin epigenetic markers change substantially during the *ex vivo* differentiation of $CD34^+$ cells. These changes consist of the progressive disappearing of HP1 proteins from differentiating neutrophils, inaccessibility of H3K9me2 for immunodetection, and nuclear accumulation of a nucleocytoplasmic serpin MNEI (Figs. 1, 3D, E). The complete absence of all three heterochromatin proteins HP1 isoforms from differentiated HSCs $CD34^+$ is in excellent agreement with our previous study showing that the loss of these epigenetic markers distinguishes mature granulocytes from other human differentiated cells [13].

In order to determine the differences in the behavior of normal and leukemic cells during the differentiation process, dynamic changes of chromatin structure were followed for $CD34^+$ cells isolated from the peripheral blood of healthy and NHL donors and from bone marrow of a CML patient in chronic phase and after treatment with Glivec (while still preserving BCR/ABL translocation in the majority of cells). Changes of chromatin markers during cell differentiation were followed by *in situ* immunodetection as it is more favorable than "averaging" methods working with cell lysates for several reasons: It is applicable for a low number of cells (very important in case of stem cells) and as already mentioned, provides reliable information about the expression of antigens in individual cells during their differentiation and thus precludes "averaging" of results typical for western blotting and RT-PCR. It is really very important in this case due to the differences in the progress of differentiation between individual cells. By maintaining the same conditions in all experiments, we observed that the changes of studied markers during differentiation were not influenced by the origin of the $CD34^+$ cells and that $CD34^+$ cells can differentiate in mature granulocytes *ex vivo*, even in the presence of BCR/ABL translocation (Fig. 3). It means that the negative influence of the translocated BCR/ABL tyrosine kinase can be overcome by specific cytokines *ex vivo*.

In parallel with altering expression of surface antigens and changing morphology of the nuclei during differentiation, we observed several changes of higher-order chromatin structure. Soon after stopping proliferation, HP1 proteins disappear, followed by almost complete relocation of MNEI from the cytoplasm to the nucleus (Fig. 3D). Simultaneously, the accessibility of H3K9me2 for immunodetection decreases (Fig. 3A). Association of MNEI with condensed nuclear chromatin after the elimination of HP1 indicates that this protein could replace HP1 in chromatin condensation, similar to the homologous serpin MENT in chicken granulocytes [9,15,31].

It was shown recently that nuclear MNEI plays a role in maintaining heterochromatin compactness in neutrophils preventing premature formation of NETs [17]. Our results showing that the mature granulocytes accumulating nuclear MNEI have inhibited DDR further suggest that replacing HP1 with MNEI might be associated with DDR inhibition.

The mechanistic link between the HP1 disappearance from chromatin during terminal differentiation of human neutrophils, its possible replacement by MNEI and chromatin condensation remains to be examined. Nevertheless, our results indicate that the timing and extent of HP1 loss, nuclear accumulation of MNEI, and inaccessibility of H3Kme2 reflect the level of chromatin compaction and, likely, differentiation. It follows from these results that there is a coordinated temporal order of changes in chromatin proteins and structure and that these changes are intimately linked with one of the basic functions of neutrophils, the formation of extracellular NETs, in which chromatin serves as the principal tool.

It thus appears that the purpose of the above mentioned changes in chromatin structure during differentiation is to enable the unique function of neutrophils in immune defence. The tightly condensed chromatin and gene repression in terminally differentiated neutrophils must be rapidly reversed upon their activation by microbial infection to allow increased changes in gene expression [32–34] and chromatin relaxation into extracellular fibers NETs to kill bacteria [23]. The rapid and extensive changes in gene expression and chromatin relaxation in neutrophils are unique phenomena among the terminally differentiated cells. We show in this work, that the chromatin condensation in mature neutrophils in absence of HP1 is tighter than in its presence as indicted by the low accessibility of H3K9me2 for immunodetection. The fact that a short exposure of the neutrophils to hypotonic conditions makes the N-tails of histone H3 accessible to immunodetection (Fig. 4) shows that the level of H3K9me2 remains high in these cells and that this high chromatin

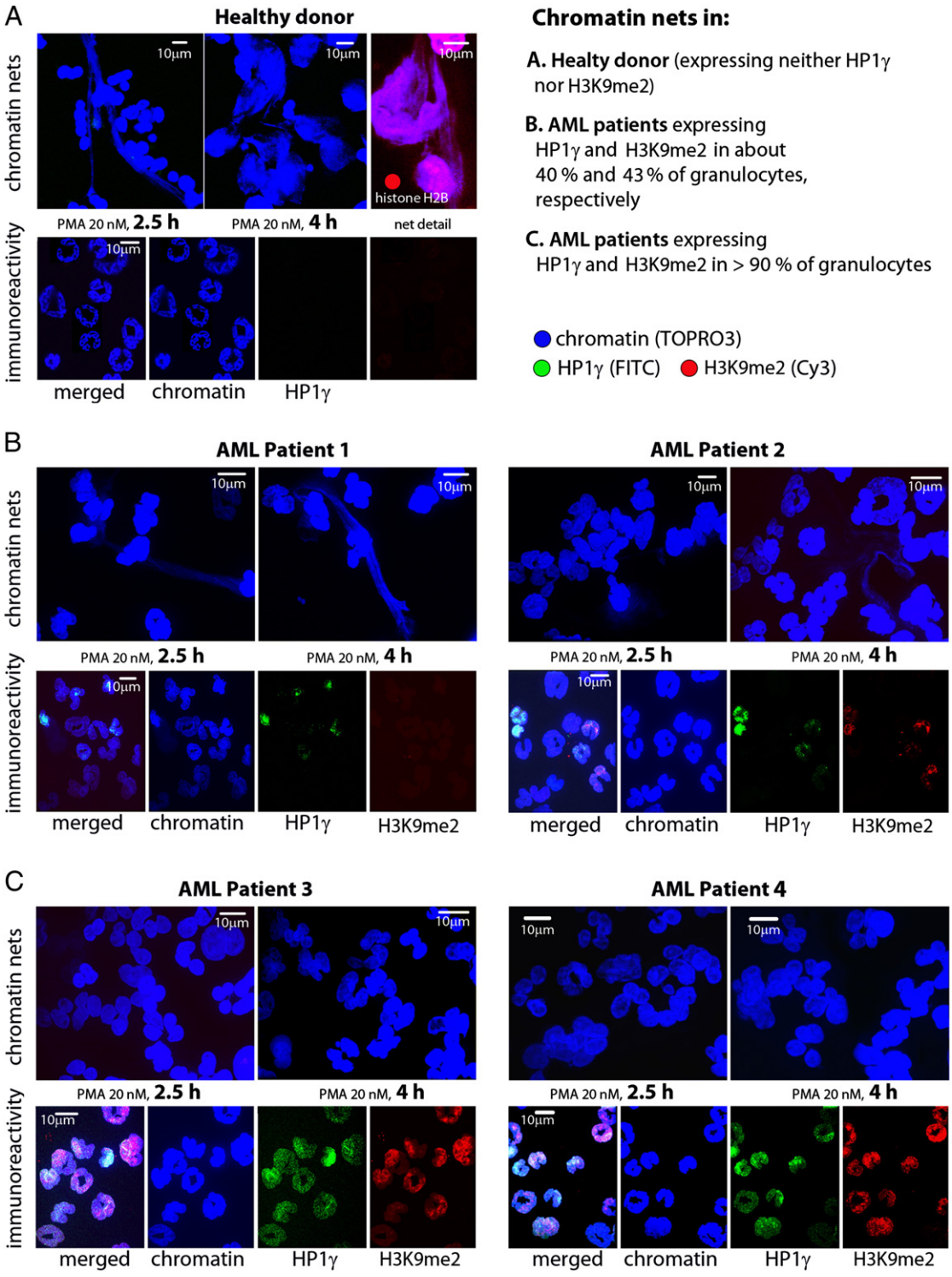

Fig. 8. Immature neutrophils expressing HP1γ do not form NETs after activation with PMA. Formation of nets was observed in peripheral neutrophils of the AML patients 1 and 2 expressing HP1γ in about 43% of these cells. No NETs were released by neutrophils of the AML patients 3 and 4, that expressed HP1γ in 90% and 93% of cells.

condensation rather than histone H3K9 demethylation is responsible for protection of H3K9me2 in mature granulocytes.

This tight chromatin condensation can be abruptly reversed by concerted action of peptidylarginine deaminase catalyzing histone citrullination and unfolding of chromatin higher-order structure [35] and by specific proteases (such as neutrophil elastase) translocating into the nuclei after their release from granules and causing large-scale digestion of histones [36]. MNEI which is a specific inhibitor of neutrophil elastase [37] may fulfill its function in protecting chromatin from decondensation by promoting chromatin higher-order folding and simultaneously inhibiting the proteases leaking into the nucleus prior to massive NET activation.

The short lifespan of neutrophils and specific role of their chromatin in forming NETs seem to be the reasons for silencing of genes participating in DNA double-strand break repair in mature neutrophils as we show in this work (Fig. 6). Obviously, the conformational transition of chromatin during NET formation does not require the integrity of genome and therefore DSBs need not to be repaired. Importantly,

granulocytic differentiation is incomplete in myeloid leukemia triggered by mutations in some genes and we show in this work that these immature cells do not have the ability to release chromatin into extracellular space and form the NETs. This may have a direct impact on the ability of AML patients in remission to fight bacterial infection. Bacterial and fungal infections are an important cause of mortality during AML therapy [38,39]. Different genetic changes inducing AML have apparently a crucial influence on progress and curability of the disease. At present, not all genetic mutations leading to AML (and their impact on granulocytic differentiation) are known. Some patients have mutation in one or more genes that occur frequently in AML (for ex. FLT3, c-KIT, RAS, NPM1, translocation AML1/ETO); nevertheless, the sequencing of AML genome showed that leukemia cells also contained acquired mutations in several genes that had not previously been associated with the disease [40]. Therefore the relationship between the clinical parameters of successful treatment (normal level of white blood cells, etc.), markers of complete maturation of granulocytes suggested in this work (including the ability to express HP1 and form chromatin NETs) and specific genetic changes should be studied in complex to disclose the cause of incomplete granulocytic maturation during the treatment. We believe that successful elucidation of the important issue why consolidation therapy does in some cases lead to attainment of mature granulocytes and in other cases does not, could make the leukemia treatment more efficient.

5. Conclusions

We show in this work that proteins expressed in human blood stem cells (e.g. CD34, all HP1, cMYC) are successively eliminated during ex vivo differentiation that is accompanied by changes in the shape of cell nuclei, chromatin condensation, and accumulation of the MNEI protein in the nuclei. Terminally differentiated granulocytes loss their ability to recognize and repair DNA damage but acquire another function — creation of chromatin extracellular traps (NETs) as a response to infection. The incompletely differentiated granulocytes of AML patients expressing HP1 proteins behave differently from the mature ones. When irradiated with ionizing radiation, they activate the DDR. The presence of the DDR markers in nuclei of immature neutrophils shows that these cells are not equivalent to mature cells. One of the most important consequences of the incomplete maturation of these cells is the loss of their natural function to release NETs to capture and kill infecting microbes. Importantly, AML treatment does not always lead to complete maturation of granulocytes, even if it restores the level of total blood cells including granulocytes to the normal values. We suggest detection of HP1 proteins in peripheral granulocytes of AML patients as a very sensitive indicator of their successful maturation as well as functionality after the treatment.

Supplementary data to this article can be found online at http://dx.doi.org/10.1016/j.bbamcr.2012.12.012.

Acknowledgements

The work was supported by grants from the Grant Agency of the Czech Republic (P302/10/1022 and P302/12/G157) and the Ministry of Education of the Czech Republic (LD12039) and OPVK CZ.1.07/2.3.00/30.0030) and from the Czech contribution to JINR Dubna (the Grant of Government Plenipotentiary, 2012 and the Grant 3+3, 2012).

References

[1] M.L. Lozano, F. Ortuno, F. de Arriba, Effect of rh-G-CSF on the mobilization of CD38 and HLA-DR subfractions of $CD34^+$ peripheral blood progenitor cells, Ann. Hematol. 71 (1995) 105–110.
[2] W.H. Levering, D. Sutherland, M. Keeneye, Hematopietic stem and progenitor cells: enumeration, phenotypic characterisation, and clinical applications, Transfus. Med. Hemother. 31 (2004) 341–352.
[3] S.A. Grigoryev, Y.A. Bulynko, E.Y. Popova, The end adjusts the means: heterochromatin remodeling during terminal cell differentiation, Chromosome Res. 14 (2006) 53–69.
[4] B. Hoffman, A. Amanullah, M. Shafarenko, D.A. Liebermann, The protooncogene c-myc in hematopoietic development and leukemogenesis, Oncogene 21 (2002) 3414–3421.
[5] S.T. Kosak, M. Groudine, Form follows function: the genomic organization of cellular differentiation, Genes Dev. 18 (2004) 1371–1384.
[6] A.J. Bannister, P. Zegerman, J.F. Partridge, E.A. Miska, J.O. Thomas, R.C. Allshire, T. Kouzarides, Selective recognition of methylated lysine 9 on histone H3 by the HP1 chromo domain, Nature 410 (2001) 120–124.
[7] M. Lachner, D. O´Carroll, S. Rea, K. Mechtler, T. Jenuwein, Methylation of histone H3 lysine 9 creates a binding site for HP1 proteins, Nature 410 (2001) 116–120.
[8] S. Khorasanizadeh, The nucleosome: from genomic organization to genomic regulation, Cell 116 (2004) 259–272.
[9] N.E. Istomina, S.S. Shushanov, E.M. Springhetti, V.L. Karpov, I.A. Krasheninnikov, K. Stevens, K.S. Zaret, P.B. Singh, S.A. Grigoryev, Insulation of the chicken β-globin chromosomal domain from a chromatin-condensing protein MENT, Mol. Cell. Biol. 23 (2003) 6455–6468.
[10] N. Gilbert, S. Boyle, H. Sutherland, J. de Las Heras, J. Allan, T. Jenuwein, W.A. Bickmore, Formation of facultative heterochromatin in the absence of HP1, EMBO J. 22 (2003) 5540–5550.
[11] S.A. Grigoryev, Keeping fingers crossed: heterochromatin spreading through interdigitation of nucleosome arrays, FEBS Lett. 564 (2004) 4–8.
[12] J. Baxter, S. Sauer, A. Peters, R. John, R. Williams, M.L. Capparos, K. Arney, A. Otte, T Jenuwein, Histone hypomethylation is an indicator of epigenetic plasticity in quiescent lymphocytes, EMBO J. 23 (2004) 4462–4472.
[13] E. Lukášová, Z. Kořistek, M. Falk, S. Kozubek, S. Grigoryev, M. Kozubek, V. Ondřej, I. Kroupová, Methylation of histones in myeloid leukemias as a potential marker of granulocyte abnormalities, J. Leukoc. Biol. 77 (2005) 100–111.
[14] E.Y. Popova, D.F. Claxton, E. Lukášová, P.I. Bird, S.A. Grigoryev, Epigenetic heterochromatin markers distinguish terminally differentiated leucocytes from incompletely differentiated leukemia cells in human blood cells, Exp. Hematol. 34 (2006) 453–462.
[15] S.A. Grigoryev, C.L. Woodcock, Chromatin structure in granulocytes. A link between tight compaction and accumulation of a heterochromatin-associated protein (MENT), J. Biol. Chem. 273 (1998) 3082–3089.
[16] S.A. Grigoryev, J. Bednar, C.L. Woodcock, MENT, a heterochromatin protein that mediates higher order chromatin folding, is a new serpin family member, J. Biol. Chem. 274 (1999) 5626–5636.
[17] K. Farley, J.M. Stolley, P. Zhao, J. Cooley, E. Remold-O Donnell, A serpinB1 regulatory mechanism is essential for restricting neutrophil extracellular trap generation, J. Immunol. 189 (2012) 4574–4581.
[18] O. Fernandez-Capetillo, A. Lee, M. Nussenzweig, A. Nessenzweig, H2AX: the histone guardian of the genome, DNA Repair 3 (2004) 959–967.
[19] M.J. Kruhlak, A. Celeste, G. Dellaire, O. Fernandez-Capetillo, W.G. Muller, J.G. McNally, D.P. Bazett-Jones, A. Nussenzweig, Changes in chromatin structure and mobility in living cells at sites of DNA double-strand breaks, J. Cell Biol. 172 (2001) 823–834.
[20] N. Mailand, S. Bekker-Jensen, H. Faustrup, F. Melander, J. Bartek, C. Lukas, J. Lukas, RNF8 ubiquitylates histones at DNA double-strand breaks and promotes assembly of repair proteins, Cell 131 (2007) 887–900.
[21] M. Murga, I. Jaco, Y. Fan, R. Soria, B. Martinez-Pastor, M. Cuadrado, S.M. Yang, M.A. Blasco, A.I. Skoultchi, O. Fernandez-Capetillo, Global chromatin compaction limits the strength of the DNA damage response, J. Cell Biol. 178 (2007) 1101–1108.
[22] G. Soria, S.E. Polo, G. Almouzni, Prime, repair, restore: the active role of chromatin in the DNA damage response, Mol. Cell 46 (2012) 722–734.
[23] V. Brinkmann, U. Reichard, C. Goosmann, B. Fauler, Y. Uhlemann, D.S. Weiss, Y. Weirauch, A. Zychlinsky, Neutrophile extracellular traps kill bacteria, Science 303 (2004) 1532–1535.
[24] V. Brinkmann, A. Zichlinsky, Neutrophil extracellular traps: Ia immunity the second function of chromatin? J. Cell Biol. 198 (2012) 773–783.
[25] V. Brinkmann, A. Zychlinsky, Beneficial suicide: why neutrophils die to make NETs, Nat. Rev. Microbiol. 5 (2007) 577–582.
[26] V. Brinkmann, B. Laube, U.A. Abed, C. Goosmann, A. Zychlinsky, Neutrophil extracellular traps: how to generate and visualize them, J. Vis. Exp. 36 (2010), http://dx.doi.org/10.3791/1724.
[27] C.F. Urban, S. Lourido, A. Zychlinsky, How do microbes evade neutrophil killing? Cell. Microbiol. 8 (2006) 1687–1696.
[28] T.A. Fuchs, U. Abed, C. Goosmann, R. Hurwitz, I. Schulze, V. Wahn, Y. Weinreich, V. Brinkmann, A. Zychlinsky, Novel cell death program leads to neutrophil extracellular traps, J. Cell Biol. 176 (2007) 231–241.
[29] M. Kozubek, S. Kozubek, E. Lukášová, E. Bártová, M. Skalníková, Pe. Matula, Pa. Matula, High resolution cytometry of FISH dots in interphase cell nuclei, Cytometry 36 (1999) 279–293.
[30] M. Kozubek, S. Kozubek, E. Lukášová, A. Marečková, E. Bártová, M. Skalníková, A. Jergová, Combined confocal and wide-field high resolution cytometry of fluorescent in situ hybridization-stained cells, Cytometry 45 (2001) 1–12.
[31] S.A. Grigoryev, T. Nikitina, J.R. Pehrson, P.B. Singh, C.L. Woodcock, Dynamic relocation of epigenetic chromatin markers reveals an active role of constitutive heterochromatin in the transition from proliferation to quiescence, J. Cell Sci. 117 (2004) 6153–6162.
[32] P.E. Newburger, Y.V. Subrahmanyam, S.M. Weissman, Global analysis of neutrophil gene expression, Curr. Opin. Hematol. 7 (2000) 16–20.
[33] Y.V. Subrahmanyam, S. Yamaga, Y. Prashar, H.H. Lee, N.P. Hoe, Y. Kluger, M. Gertein, J.D. Goguen, P.E. Newburger, S.M. Weisman, RNA expression patterns change dramatically in human neutrophils exposed to bacteria, Blood 97 (2001) 2457–2468.

[34] Y. Tsukahara, Z. Lian, X. Zhang, C. Whitney, Y. Kluger, D. Tuck, S. Yamaga, Y. Nakayama, S.M. Weissman, P.E. Newburger, Gene expression in human neutrophils during activation and priming by bacterial lipopolysaccharide, J. Cell. Biochem. 89 (2003) 848–861.
[35] Y. Wang, M. Li, S. Stadler, S. Correll, P. Li, D. Wang, R. Hayama, L. Leonelli, H. Han, S.A. Grigoryev, C.D. Allis, S.A. Coonrad, Histone hypercitrullination mediates chromatin decondensation and neutrophil extracellular trap formation, J. Cell Biol. 184 (2009) 202–213.
[36] C. Benarafa, J. Cooley, W. Zeng, P.I. Bird, E. Remold-O'Donnell, Characterization of four murine homologs of the human ov-serpin monocyte neutrophil elastase inhibitor MNEI (SERPINB1), J. Biol. Chem. 277 (2002) 42028–42033.
[37] J. Cooly, T.K. Takayama, S.D. Shapiro, N.M. Schechter, E. Remold-O´Donnell, The serpin MNEI inhibits elastase like and chymotrypsin-like serine proteases through efficient reactions at two active sites, Biochemistry 40 (2001) 15762–15770.
[38] L. Sung, B.J. Lange, R.B. Gerbing, T.A. Alonzo, J. Feusner, Microbiologically documented infections and infection-related mortality in children with acute myeloid leukemia, Blood 110 (2007) 3532–3539.
[39] K. Leventakos, R.E. Lewis, D.P. Kontoyiannis, Fungal infections in leukemia patients: how do we prevent and treat them? Clin. Infect. Dis. 50 (2010) 405–415.
[40] M.C. Wendl, R.K. Wilson, Aspect of coverage in medical DNA sequencing, BMC Bioinforma. 9 (2008) 239–251.

Methylation of histones in myeloid leukemias as a potential marker of granulocyte abnormalities

Emilie Lukášová,* Zdeněk Kořistek,† Martin Falk,* Stanislav Kozubek,*,[1] Sergei Grigoryev,‡ Michal Kozubek,§ Vladan Ondřej,* and Iva Kroupová¶

*Institute of Biophysics, Academy of Sciences of the Czech Republic, Brno; †Department of Internal Haematooncology and ¶Institute of Pathology, Masaryk University Hospital, and §Faculty of Informatics, Masaryk University, Brno Czech Republic; and ‡Department of Biochemistry and Molecular Biology, Pennsylvania State University College of Medicine, Hershey

Abstract: We show that common heterochromatin antigenic protein markers [HP1α, -β, -γ and mono-, di-, and trimethylated histone H3 lysine 9 (H3K9)], although present in human blood progenitor CD34$^+$ cells, differentiated lymphocytes, and monocytes, are absent in neutrophil granulocytes and to large extent, in eosinophils. Monomethylated and in particular, dimethylated H3K9 are present to variable degrees in the granulocytes of chronic myeloid leukemia (CML) patients, without being accompanied by HP1 proteins. In patients with an acute phase of CML and in acute myeloid leukemia patients, strong methylation of H3K9 and all isoforms of HP1 are detected. In chronic forms of CML, no strong correlations among the level of histone methylation, disease progression, and modality of treatment were observed. Histone methylation was found even in "cured" patients without Philadelphia chromosome (Ph) resulting from +(9;22)(q34;q11) BCR/ABL translocation, suggesting an incomplete process of developmentally regulated chromatin remodeling in the granulocytes of these patients. Similarly, reprogramming of leukemia HL-60 cells to terminal differentiation by retinoic acid does not eliminate H3K9 methylation and the presence of HP1 isoforms from differentiated granulocytes. Thus, our study shows for the first time that histone H3 methylation may be changed dramatically during normal cell differentiation. The residual histone H3 methylation in myeloid leukemia cells suggests an incomplete chromatin condensation that may be linked to the leukemia cell proliferation and may be important for the prognosis of disease treatment and relapse. *J. Leukoc. Biol.* 77: 100–111; 2005.

Key Words: *human granulocytes differentiation · chromatin condensation · heterochromatin · HP1 proteins*

INTRODUCTION

It is generally accepted that there are two distinct structural states of chromatin in eukaryotic cell nuclei: euchromatin and heterochromatin [1]. In contrast to euchromatin, heterochromatin is highly condensed and transcriptionally silent. Heterochromatin proteins are associated with DNA repeats, which surround centromeres and are required for proper sister-chromatid cohesion and chromosome segregation [1–5]. Heterochromatin also stabilizes repetitive DNA elsewhere in the genome by inhibiting recombination between homologous repeats [6, 7]. In addition to its role in the maintenance of genome stability, heterochromatin plays a central role in the regulation of gene expression during development and cell differentiation [8].

Chromatin-associated markers, distinguishing heterochromatin from euchromatin in eukaryotic chromosomes, include DNA methylation, specific histone methylation at histone H3 lysine 9 (H3K9), the absence of histone H3K9 acetylation, and the presence of heterochromatin protein 1 (HP1). Although the molecular details of the euchromatin and heterochromatin structure in proliferating cells are not fully understood, HP1, a major component of heterochromatin, is thought to establish and maintain the transcriptionally repressive heterochromatin structure [8]. HP1 binds to histone H3 if the lysine at position 9 (K9) is methylated [8, 9]. This amino acid may be methylated to a varying degree, but the functional significance of mono-, di-, and trimethylation of lysine residues remains unclear. The results produced by Rice et al. [10] show that mono- and dimethylated H3K9 localize specifically to silent domains within euchromatin; in contrast to this, trimethylated H3K9 is enriched at pericentric heterochromatin. These authors further show that enzymes known to methylate H3K9 display different enzymatic properties in vivo. In mammals, G9a was found to be responsible for all detectable H3K9 dimethylation and a significant amount of monomethylation, and Suv39h1 and Suv39h2 directed trimethylation of H3K9 at pericentric heterochromatin.

The results produced by Cheutin et al. [11] and Festenstein et al. [12] show that HP1 is a highly mobile molecule. Given the rapid exchange of HP1 in heterochromatic foci, any other

[1]Correspondence: Department of Molecular Cytology and Cytometry, Institute of Biophysics, Academy of Sciences of the Czech Republic, Královopolská 135, 612 65 Brno, Czech Republic. E-mail: kozubek@ibp.cz

Received July 8, 2004; revised September 7, 2004; accepted October 5, 2004; doi: 10.1189/jlb.0704388.

soluble nuclear proteins, such as transcription factors, should be able to gain access, compete with silencing factors, and potentially activate genes located within heterochromatin. These results, in contrast to previous models, indicate that interphase heterochromatin is a dynamic structure.

In blood cells, the extent of chromatin condensation increases during cell differentiation, reaching a maximum in terminally differentiated cells [13]. Recent results [14, 15] show that condensation of chromatin in differentiated avian granulocytes and nucleated erythrocytes is not accompanied by the presence of the HP1 protein. In addition to this, HP1 is not involved in the facultative heterochromatin formation of inactivated X chromosomes in mammals [16]. This finding indicates that HP1 proteins are not essential for all types of heterochromatin.

As chromatin condensation and a general decrease of transcription in mature vertebrate tissues are often correlated with the appearance and accumulation of tissue-specific histone H1 subtypes, these proteins have long been considered the key factors in differentiation stage-specific chromatin condensation and gene repression [17, 18]. However, gene regulation studies in cells, overexpressing or lacking certain types of histone H1, have shown that the accumulation of linker histones is not per se sufficient to cause major chromatin remodeling or a general inhibition of transcription [19–22].

Grigoryev et al. [14, 23] found a high level of expression of the nuclear protein myeloid and erythroid nuclear termination (MENT) stage-specific protein in terminally differentiated avian blood cells, particularly in granulocytes, where it becomes the predominant nuclear nonhistone protein concentrated in peripheral heterochromatin. This developmentally regulated protein brings about condensation of the chromatin higher-order structure [23] in terminally differentiated avian cells. These results indicate some similarity between the HP1 and MENT proteins in their binding to methylated histone H3K9. The MENT distribution profile correlates with that of histone H3 dimethylated at lysine 9 [24]; HP1 also binds to methylated histone H3, although the degree of H3K9 methylation necessary for its binding is not as yet well known [25, 26]. Although MENT brings about chromatin condensation and terminal differentiation in chicken granulocytes and erythrocytes [14], HP1 assists in maintaining constitutive and facultative heterochromatin and gene silencing in the interphase chromatin of proliferating cells [8, 9, 16, 27]. None of these chromatin-condensation factors were found in enucleated mouse erythrocytes with abundant heterochromatin [15]. It is, therefore, conceivable that in these cells, chromatin condensation must be accomplished by other mechanisms without the participation of these chromatin-condensing proteins. It is interesting that the absence of HP1 proteins in avian and mouse granulocytes and erythrocytes is not accompanied by the concomitant disappearance of methylated histone H3K9 [15, 24], suggesting that this type of histone modification may be the primary heterochromatin marker underlying chromatin condensation and silencing.

The differentiation of human blood cells provides a convenient system for investigating the regulation of chromatin condensation. During this process, malignant cells can arise at any stage, leading to many different types of leukemia, whose cells may retain some characteristics of the stage of differentiation at which the cells become cancerous. To determine the differences in the degree of chromatin condensation between human differentiated white blood cells possessing a certain limited proliferation capacity (lymphocytes, monocytes) and those that have completely lost this capacity (granulocytes), we studied the level and distribution of all types of histone H3 methylation at the lysine K9 (metH3K9) and the presence of HP1β, -γ, -α in white cells isolated from human peripheral blood and in $CD34^+$ progenitor blood cells. Our studies also focused on the detection of these proteins in patients suffering from chronic myeloid leukemia (CML) and acute myeloid leukemia (AML).

Certain myeloid cell lines can be induced to differentiate to mature cells and therefore provide a useful experimental model to study histone methylation processes and "differentiation therapy" of leukemia [28]. The HL-60 cell line is particularly interesting, as it undergoes granulocyte differentiation following treatment with retinoic acid (RA) [29, 30]. The monoblastic U-937 cells are arrested at a more advanced stage of differentiation than the HL-60 cells, and therefore, treatment of these cells with RA carries their differentiation into monocytes/macrophages [31]. Our goal was to find a correlation between the degree of differentiation of these two cell lines, the methylation status of histone H3K9, and the distribution of HP1 proteins and to compare the results with findings for the granulocytes of CML and AML patients.

It follows from the results presented that HP1 and metH3K9 histone are not involved in chromatin condensation during terminal differentiation of human neutrophil granulocytes and that there is a unique mechanism regulating chromatin condensation during granulocyte differentiation. This mechanism is apparently impaired during the development of myeloid leukemia and is not restored during treatment of the disease by enforced differentiation and other currently used therapies.

MATERIALS AND METHODS

Separation of mononuclear cells and granulocytes from human peripheral blood

Erythrocytes were eliminated from the peripheral blood of five healthy donors by means of dextran T 500 (Amersham, Piscataway, NJ)–Telebrix N 350 (Leciva, Prague, Czech Republic) solution (density 1.095 g/ml). Separation of white cells from the remaining plasma was performed according to the methods described in *Current Protocols in Immunology* [32] by means of Ficoll-Hypaque gradient centrifugation.

Ficoll-Hypaque gradient centrifugation allows the separation of granulocytes from mononuclear cells (lymphocytes and monocytes). Monocytes, depleted from lymphocytes, by taking advantage of their capacity to adhere to plastic, were contaminated with ~5% of lymphocytes and vice versa. These two cell types can be well distinguished on the microscopic slide by the morphology of their nuclei: The nuclei of lymphocytes are spherical, and those of monocytes resemble kidneys in shape. Granulocytes have the characteristic multilobular nucleus clearly distinguishable from the nuclei of other cells. Erythrocytes, slightly contaminating granulocytes, are not observable on the microscope slide after nuclei contra-staining with TOPRO-3, as they do not contain chromatin. Owing to the characteristic morphology of the nuclei of the investigated cell types, none of the contaminating nuclei were included in the

analysis of any particular cell type. Immunochemical detection of heterochromatic proteins and histone methylation was performed on sets of individual nuclei fixed on microscopic slides, enabling consideration of nuclei of a single cell type during analysis and accurate calculation of the percentage of cells manifesting a particular antigen.

A proportion of the isolated lymphocytes was stimulated to divide with phytohemagglutinin (PHA). The cells were resuspended in a complete RPMI medium containing 10% fetal calf serum (FCS; 10^6/ml) and incubated with 20 μl/ml PHA H15 (Murex, UK) at 37°C for 36 h.

$CD34^+$ hematopoietic progenitor cells were isolated from concentrated mononuclear cells separated from the mobilized blood of two patients with a lymphoma. The cells were labeled with anti-$CD34^+$ magnetic microbeads (Miltenyi Biotec, Auburn, CA) and separated in the magnetic field of the MiniMacs using a positive selection column. Granulocytes of 20 CML and three AML patients were isolated from 1.7 ml peripheral blood after erythrocyte elimination. The informed consent of all blood donors was obtained.

Cell culture and differentiation

A human HL-60 promyelocytic leukemia cell line and a U-937 monoblastic cell line were grown in RPMI-1640 medium supplemented with 10% FCS, penicillin (100 U/ml), and streptomycin (100 μg/ml) in humidified air with 5% CO_2 at 37°C.

Twelve hours before the induction of differentiation, cells were harvested and resuspended in fresh medium at 2×10^5 cells/ml. Both cell types were induced to differentiate for 6–8 days with 1 μM all-trans RA (ATRA; Sigma Chemical Co., St. Louis, MO) with no change of media.

Flow cytometric detection of cell differentiation

The differentiation of HL-60 cells into granulocytes was determined after 6 days of incubation with 1 μM RA by the expression of CD11b-fluorescein isothiocyanate (FITC) and CD14-phycoerythrin (PE) surface antigen. The cells were washed two times with phosphate-buffered saline (PBS) containing 0.1% NaN_3 and 1% bovine serum albumin (BSA) at 4°C. CD11b-FITC (2 μl) and 2 μl CD14-PE monoclonal antibodies (Coulter Company, Immunotech, France) were added to 50 μl cell suspension (10^6 of living cells/ml) in PBS containing 1% BSA and 0.1% NaN_3. The cell suspension was incubated for 40 min at 4°C. The expression of CD11b and CD14 antigens was measured by a FACSCalibur flow cytometer (Becton Dickinson, San Jose, CA). The same procedure was used for the detection of differentiation of U937 cells with 1 μM RA. Isotypic controls were used for result correction.

Cell fixation and immunolabeling

A dense suspension of cells in PBS (100 μl) was dropped onto positively charged microscopic slides. After attachment to the slide (~5 min), cells were fixed with 4% paraformaldehyde in PBS for 10 min, washed 4×5 min in PBS, permeabilized in 0.2% Triton X-100/PBS, washed 2×5 min, blocked with 7% normal goat serum/PBS for 30 min, and sequentially incubated with the primary and secondary antibodies. The following antibodies were used: anti-HP1β (rabbit polyclonal), HP1γ (fusion protein, mouse), HP1α (fusion protein, mouse), trimethyl H3K9 (rabbit polyclonal), dimethyl H3K9 (mouse monoclonal), monomethyl H3K9 (synthetic peptide, rabbit), acetyl H3K9 (rabbit polyclonal), histone H1 (mouse monoclonal), histone H1°/H5 (mouse monoclonal), anticentromere protein A (anti-CENP-A; rabbit, immunoaffinity-purified), all from Upstate Biotechnology (Lake Placid, NY). Antibodies were diluted 1:1000. Secondary antibodies—goat anti-rabbit-FITC and goat anti-mouse-FITC (Jackson Laboratory, Bar Harbor, ME)—were diluted 1:50. Counterstaining was performed by 1 μM TOPRO-3 (Molecular Probes, Eugene, OR) in $2 \times$ saline sodium citrate prepared fresh from the stock solution. The percentage of cells expressing the particular antigen was calculated from 300 to 500 cells.

Fluorescence microscopy

Images were obtained by a high-resolution confocal cytometer [33, 34] based on a completely automated Leica DM RXA fluorescence microscope equipped with a CSU-10a confocal unit (Yokogawa, Japan) and a CoolSnap HQ charged-coupled device camera (Photometrix, Melbourne, Australia). Forty optical sections at a 0.3-μm step were acquired for each nucleus and stored in the computer memory. The XY, XZ, YZ projections shown in **Figure 1** demonstrate the three-dimensional preservation of the nuclei. The exposition time and dynamic range of the camera in the red, green, and blue channels were adjusted to the same values for all slides to obtain quantitatively comparable images. The antibody signal intensity was measured as the mean value of the green channel histogram in the dynamic range from 0 to 255 using Adobe Photoshop 5.5 software.

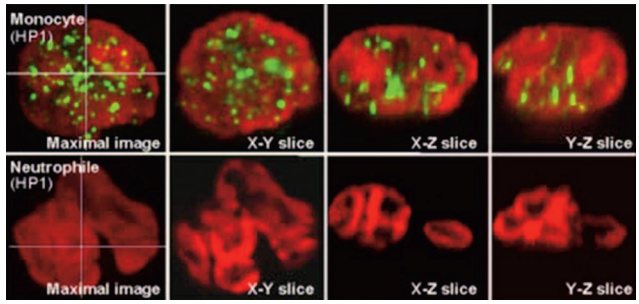

Fig. 1. Maximal XY image, XY, XZ, and YZ sections through the monocyte and neutrophil granulocyte nuclei after immunodetection of HP1β. XY sections show one of the 40 slices through the nucleus; XZ section shows a cut along the horizontal white line through the nucleus; YZ section shows a cut along the vertical white line. Only the foci that cross the given cut are visible. Immunodetection was performed using FITC-labeled secondary antibodies. DNA was counterstained with TOPRO-3.

Isolation of nuclear proteins and chromatin for Western blotting

The suspensions of lymphocytes and granulocytes separated by Ficoll-Hypaque density gradient centrifugation were washed two times with PBS, centrifuged for 3 min at 1000 *g*, cooled on ice to 2°C, and resuspended in lysis buffer (50 mM Tris-HCl, pH 7.5, 120 mM NaCl, 0.5% Nonidet P-40, and 1 mM phenylmethylsulfonyl fluoride) by vigorous vortexing for 1 min and left on ice for 30 min with intermittent homogenization with a plastic pestle, briefly (10 s) sonicated and spun down (14,000 rpm for 15 min). The supernatant was transferred into a new tube and kept on ice.

Protein electrophoresis, detection, and quantification

Proteins were separated in 15% polyacrylamide gels. Samples containing proteins and chromatin were diluted to the same value of A260 absorbance, boiled in sodium dodecyl sulfate loading buffer, and loaded on the gel. After electrophoresis, the gels were stained with Coomassie blue R-250 (Sigma Chemical Co.) or electrotransferred in Tris-glycine buffer containing 10% methanol to a nitrocellulose membrane. The membranes were blocked, treated with antidimethyl H3K9 (dilution 1:150) or with anti-HP1γ, HP1α antibodies (Upstate Biotechnology; dilution 1:500), and then treated with secondary peroxidase-conjugated anti-mouse antibodies and detected with an ehanced chemiluminescence (ECL) detection system (Amersham Corp., Little Chalfont, UK). The intensity of the protein bands was compared after ECL detection using the Vilber Lourmat photodocumentation and imaging system.

RESULTS

Different levels of methylated histone H3K9 and HP1 immunofluorescence in the white blood cells of healthy donors

The levels and nuclear distributions of HP1β and tri-metH3K9 in human progenitor $CD34^+$ cells, lymphocytes, monocytes, and terminally differentiated granulocytes (neutrophils and eosinophils) are shown in **Table 1** and **Figure 2**. The majority

TABLE 1. The Mean Values of Antibody Signal Intensity in Different Cell Types from Peripheral Blood and Different Cell Lines

	HP1α	HP1β	HP1γ	Monomethyl H3K9	Dimethyl H3K9	Trimethyl H3K9	Acetyl H3K9	H1	H1°	CENP-A
CD34*	–	75.10	–	–	–	81.88	–	–	–	–
Lymphocytes	5.72	49.10	26.50	65.84	0.79*/53.67	48.11	124.95	66.56	0.78*/37.17	18.73
Monocytes	16.70	67.29	36.44	82.45	39.54	54.97	111.56	79.04	0.25**/68.11	36.79
Eosinophils	0.26	0.15**/10.39	0.32	0.46	0.33	0.49**/4.84	10.66#/	99.89	0.58	12.81
Neutrophils		1.47				0.52	/51.05			
HL-60	–	55.50	79.58	–	50.07	34.84	–	–	–	–
HL-60 + ATRA	–	40.59	61.15	–	58.77	64.38	–	–	–	–
U937	–	112.20	90.77	–	47.01	36.12	–	–	–	–
U937 + ATRA	–	107.61	64.75	–	43.86	35.90	–	–	–	–
AML granulocytes	2.12	120.83	10.52	163.25	73.81	78.51	122.52	163.70	–	13.72

The amount of particular antigen was measured for a single nuclei as the mean value of antibody-signal intensity histogram (in the dynamic scale 0–255 of the green channel). The displayed numbers represent the mean values calculated for several nuclei. About 100% of neutrophils from healthy donors did not show any methylation of H3K9 histone and expression of any of the isoforms of HP1 protein contrary to other white blood cells, where the expression of these proteins was found in 98–100% of cells. An exception represents G0 lymphocytes (not expressing the Ki67 antigen), which did not show the di-metH3K9 signal, whereas all stimulated lymphocytes did. –, Not measured; * value for G0-lymphocytes (the Ki67 not expressed); ** value for monocytes and eosinophils not expressing particular antigen; # value for granulocytes (eosinophils and neutrophils) with low expression of a particular antigen.

of HP1β foci are distributed through the cell nucleus with a low density of chromatin in lymphocytes and monocytes (Figs. 1 and 2). A smaller number of foci of this protein were found in chromatin characterized by an increased intensity of TOPRO-3 fluorescence (probably heterochromatin). The foci of HP1β were also detected in peripheral heterochromatic regions in $CD34^+$ cells (Fig. 2). In contrast to lymphocytes and monocytes, there was only a low signal of HP1β in eosinophil granulocytes. HP1β was not detected in the majority of these cells; in some eosinophils, HP1β foci, similar to those in lymphocytes or monocytes, were present in one or both lobes (Fig. 2). The green color of the eosinophil cytoplasm is caused by nonspecific fluorescence of the secondary antibody. The HP1β signal was completely absent in neutrophil granulocytes (Fig. 2). The level of tri-metH3K9 in blood cells resembled that of HP1β (Table 1, Fig. 2). Not only was the tri-metH3K9 distributed in the center of nuclei with a low density of chromatin, but some foci were also found in high-density chromatin on the nuclear periphery. In contrast, the tri-metH3K9 signal, as was the case for HP1β, was completely lost from neutrophils and to large extent, from eosinophils. Experiments were carefully repeated, and similar results were obtained for all types of cells separated from the peripheral blood of five healthy donors.

The absence of trimethylated H3K9 and HP1β in granulocytes also prompted us to investigate the distribution of di- and monomethylated H3K9 as well as HP1α and -γ isoforms in various blood cells. None of these proteins were detected in neutrophil granulocytes by immunodetection (**Fig. 3A**); however, a low number of di-metH3K9 and HP1γ foci were observed in eosinophils in which mono-metH3K9 was more frequent. The results obtained for lymphocytes, monocytes, and granulocytes were confirmed by Western blotting (**Fig. 4**). Conversely, di-, mono-metH3K9 and HP1γ and -α isoforms were present in lymphocytes (nonstimulated and stimulated) and monocytes (Figs. 3, B and C, and 4). In contrast to the two isoforms of HP1 (γ, α), preferentially located in the central part of the nucleus, the foci of di-metH3K9 and mono-metH3K9 were distributed throughout the entire nuclear volume, similarly as for trimethylated histones. This modification of histone H3K9 was not observed in the nuclei of G0 lymphocytes (detected according to Ki67 expression), although it was present in the majority of stimulated lymphocytes. Although HP1β and -γ occurred in a large number of foci (those of γ were larger than those of β), HP1α presented only several foci per nucleus of lymphocytes and monocytes. The levels of methylated histone H3K9 and HP1 proteins detected quantitatively using the intensity of green fluorescence on the cell nuclei are shown in Table 1. The results show that in lymphocytes and monocytes, HP1β is the most abundant, and HP1α is less abundant. Mono-metH3K9 is the most frequent and tri-metH3K9 the least frequent methylation of histone H3.

Approximately 100% of neutrophils from healthy donors did not show any methylation of the H3K9 histone and expression of any of the isoforms of HP1 protein, contrary to other white blood cells, where the expression of these proteins was found in 98–100% of cells. An exception to this is represented by G0 lymphocytes (not expressing the Ki67 antigen), which did not show the di-metH3K9 signal, whereas all stimulated lymphocytes did.

In lymphocytes and monocytes, histone H1 was present in a large number of foci of a similar size as that for HP1γ or centromeric protein CENP-A, although it showed a much larger number of much smaller dots in granulocytes covering the entire area of chromatin (Fig. 3). H1 was the most prominent of all the studied protein markers in granulocytes. In addition to the H1 histone, granulocytes also displayed acetylated H3K9. This protein marker was non-homogenously distributed through the lobes of chromatin and occurred mostly in the inner part of the nucleus. A significantly higher level of acetylated H3K9 was present in lymphocytes and monocytes than in granulocytes (Table 1). In contrast to granulocytes, some nuclei of lymphocytes and monocytes (18–20%) contained a larger amount of the histone H1° subtype (Fig. 3, B and C).

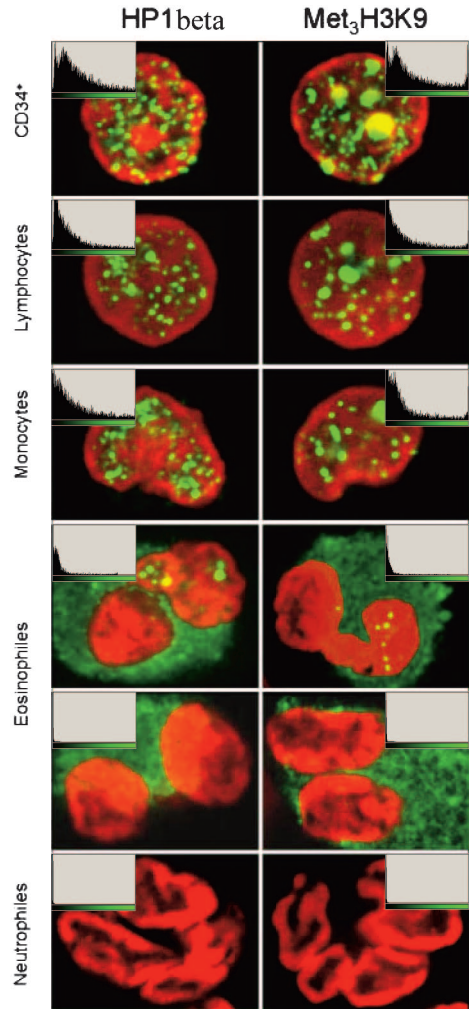

Fig. 2. Distribution of HP1β and tri-metH3K9 in human peripheral blood cells (lymphocytes, monocytes, eosinophils, and neutrophils) and in human blood progenitor $CD34^+$ cells. HP1β and tri-metH3K9 were found in $CD34^+$ cells, lymphocytes, and monocytes but not in neutrophils and some eosinophils. The images represent the central XY cuts through the nuclei. Immunodetection was performed using FITC-labeled secondary antibodies. DNA was counterstained with TOPRO-3. Inserted histograms represent the level of antibody signals measured as the mean value of green channel intensity in the dynamic range from 0 to 255 using Adobe Photoshop 5.5 software.

Changes in the methylation status of H3K9 and the levels of HP1 proteins in the granulocytes of patients with CML and AML

The methylation profiles of histone H3 at lysine K9 and the presence of HP1 proteins in the granulocytes of patients suffering from myeloid leukemia are changed relative to those in the granulocytes of healthy individuals. Strong signals from tri-, di-, and monomethylated H3K9, as well as γ and β isoforms of HP1, were detected in all the investigated patients with AML. Histone H3K9 acetylation was also prominent (**Fig. 5**), and some cells showed a higher level than others. Granulocytes of AML patients also exhibited a strong signal of histone H1, as well as several foci of its subtype H1°. HP1α gave lower intensity signals comparable with those in the lymphocytes and monocytes of healthy individuals.

In the granulocytes of CML patients, the methylation status of histone H3K9 and the levels of HP1 protein staining were changed (compared with healthy granulocytes), although to a lower degree as compared with AML patients. Significant variations among individual patients were observed (**Table 2**). HP1β was found in the granulocytes of only two of 20 investigated CML patients. These patients also showed a very high degree of H3K9 methylation. In CML patients, the only changes compared with healthy individuals were found in the levels of mono- and di-metH3K9. Mono-metH3K9 was found in rather high amounts for all patients, and di-metH3K9 varied. The patients were classified into six groups according to the amount of di-metH3K9 (Table 2). The tri-metH3K9 was detected in samples from only several patients from all groups; all patients in blast or accelerated phase showed increased levels of this type of methylation.

Three patients had only a small number of di-metH3K9 foci in their granulocytes (the first group; the mean level of green channel intensity 0–1). The patients in this group also had a small amount of mono-metH3K9 in their granulocytes (**Fig. 6**). One of these patients had no tri-metH3K9 at all, one had tri-metH3K9 concentrated in two to five small islets in the nuclei of only some cells (~5%), and the third had several dots in most of the nuclei; this patient was in the accelerated phase.

In the second group (four patients; mean level of green channel intensity 1–5), the di-metH3K9 was distributed in small foci mostly in the inner part of the nuclei, where the concentration of chromatin (manifested by intense TOPRO-3 staining) is lower than in the periphery of the nucleus (Table 2, Fig. 6). Two patients in this group contained a small amount of tri-metH3K9 concentrated in three to five islets per nucleus. All these patients manifested a complete cytogenetic response to the treatment with a lowering of the amount of the Ph chromosome (<1%). These patients have mono-metH3K9 in an amount similar to the patients in the first group.

The patients in the third group had an increased level (the mean level of green channel intensity 5–20) of di-metH3K9 in their granulocytes compared with the previous group (Fig. 6). One of these patients was in the blast phase, and the others were in the chronic phase. Two of these patients showed a small amount of tri-metH3K9 in the form of islets or free foci. The foci of di-metH3K9 were small, concentrated in larger aggregates similarly as for those of tri-metH3K9.

Patients characterized by a rather high amount of di-metH3K9 (the mean level of green channel intensity 20–50) in their granulocytes were placed in the fourth group. These patients also had a large amount of mono-metH3K9, and two also had a small amount of tri-metH3K9. One patient without tri-metH3K9 is in the second chronic phase; the other is in the first chronic phase. The patient with the highest amount of tri-metH3K9 manifested complete cytogenetic response to the treatment (Ph chromosome <1%; Table 2).

Patients placed in the fifth group showed an extremely large amount of di-metH3K9 (the mean level of green channel intensity 50–100). Although not all of them contained tri-metH3K9, one patient had an extremely large amount of tri-metH3K9. Nonetheless, complete cytogenetic response to the treatment was observed. These patients are in the chronic phase. The data for two patients were lost from the register and are therefore incomplete in Table 2. There was a high proportion of cells not manifesting well-developed nuclear lobulation;

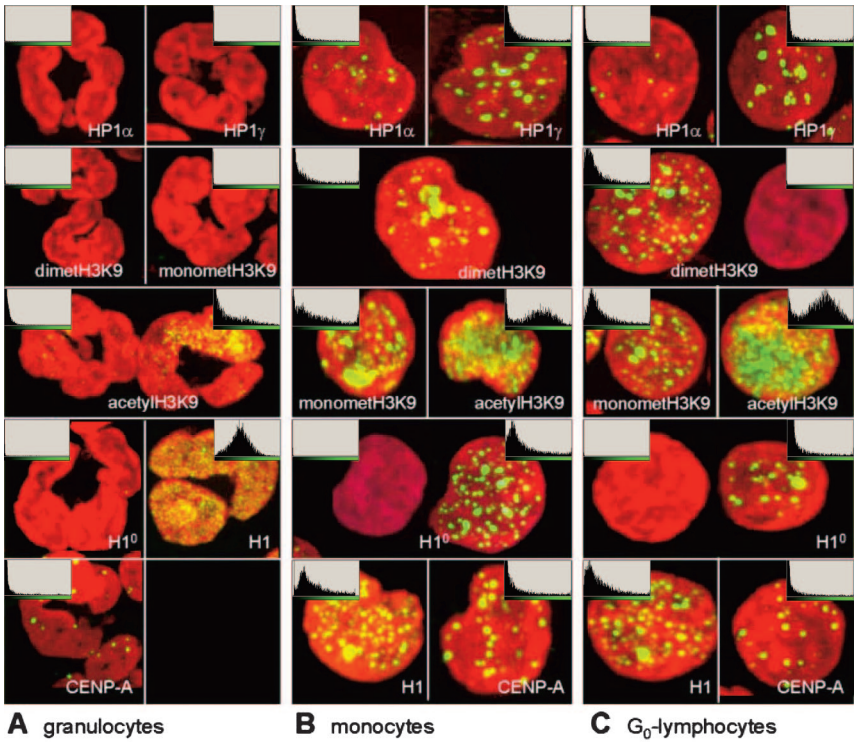

Fig. 3. Distribution of HP1α and -γ isoforms, differently modified histone H3K9, and linker histones in human neutrophil granulocytes (A), monocytes (B), and lymphocytes (C) isolated from peripheral blood. Neither methylated H3K9 nor HP1 proteins were detected in healthy human neutrophil granulocytes. Some differences in H3K9 methylation and in the presence of HP1 were observed between neutrophils and eosinophils. H1 and CENP-A proteins are present in contrary to H1°. Similar patterns of HP1 proteins, methylated, acetylated histone H3K9, linker histone H1, its variant H1°, and CENP-A were observed in monocytes and G0-lymphocytes. H1° was present only in a part of the cell population of both cell types. Immunodetection was performed using FITC-labeled secondary antibodies. DNA was counterstained with TOPRO-3. Inserted histograms represent the level of antibody signals measured as the mean value of green channel intensity in the dynamic range from 0 to 255 using Adobe Photoshop 5.5 software.

a lot of small, poorly differentiated forms containing a large amount of di- and mono-metH3K9 were also observed. Moreover, even the morphologically, well-differentiated granulocytes of this group contained a large amount of mono- and di-metH3K9. A small amount of HP1β was detected in one patient, whose granulocytes were not morphologically well-differentiated and contained a large amount of tri-metH3K9.

One patient was placed in the sixth group (the mean level of green channel intensity >100 for di-metH3K9), as his granulocytes were poorly differentiated and contained an extremely

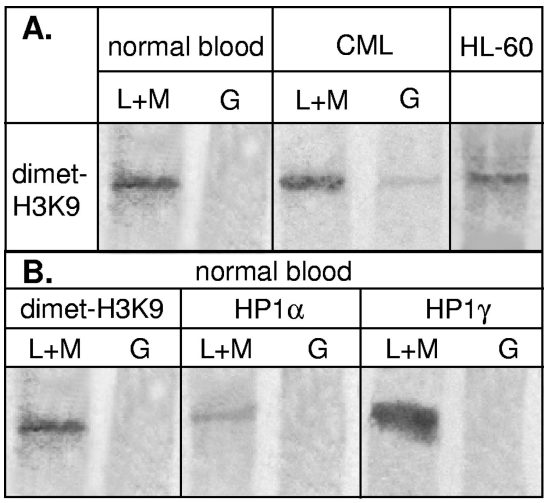

Fig. 4. Western blot of proteins from lymphocytes (L), moncytes (M), and granulocytes (G) isolated from human peripheral blood of a healthy individual, a patient with chronic myeloid leukemia (CML), and HL-60 cells using antibodies detecting dimethyl H3K9, HP1α, and HP1γ. The level of di-metH3K9 in granulocytes of CML patients determined by Western blotting is ~10 times lower than the level of this protein in lymphocytes and monocytes of healthy donors. These values are in accordance with mean relative values of the immunofluorescence measured on individual nuclei using Adobe Photoshop software in the dynamic range of green channel intensity from 0 to 255. The mean level of green channel intensity of di-metH3K9 in healthy donor lymphocytes was found ~54, that of di-metH3K9 in granulocytes of the CML patient 5.3, and the value 50 was found in HL-60 cells.

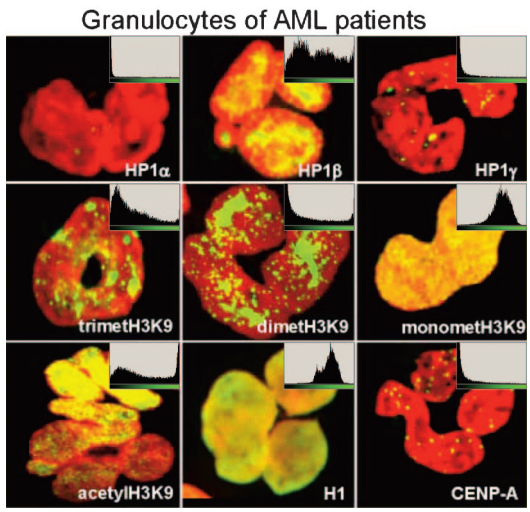

Fig. 5. Distribution of HP1 isoforms, differently modified histone H3K9, and linker histones in granulocytes isolated from peripheral blood of AML patients. In granulocytes of AML patients, all isoforms of HP1 were detected (in different intensities) as well as tri-metH3K9, di-metH3K9, and monometH3K9. In contrary to linker histone H1, which is present in large amounts in small foci, its variant H1° was present only in several points (not shown). A usual pattern of centromeric protein CENP-A was observed. Immunodetection was performed using FITC-labeled secondary antibodies. DNA was counterstained with TOPRO-3. Inserted histograms represent the level of antibody signals measured as the mean value of green channel intensity in the dynamic range from 0 to 255 using Adobe Photoshop 5.5 software.

TABLE 2. Clinical Characteristics of CML Patients, the Level of Di-, Tri-metH3K9, and HP1β in Their Granulocytes

UPN	Age	Date of diag.	Current disease stage	Current response	Current therapy	Leukocyte count (x10e9/l)	Dimethyl H3K9	Trimethyl H3K9	HP1β	History of the disease and therapy
59702	36	1/2004	CP	CHR	STI	4.3	1 (0.78)	0	0	Cytoreduction with H, STI from 2/04
59703	44	8/2000	CP	CHR	STI	7.4	1 (1.00)	2	0	H, I + A from 1/01, 4/04 CCR, 12/2003 PCR, 2/04 progression and STI (Ph^+ 32%)
59704	56	11/2003	AP	–	STI	21.0	1 (0.34)	2	0	Diagnosis in AP, from 11/03 H, STI from 1/04 (no effect)
59705	61	5/2002	CP	CCR	I + A	5.5	2 (1.54)	1	0	H, I + A from 7/02, CCR 7/2003 (1/04 BCR/ABL 0.8%)
59707	62	5/2000	CP	MiCR	STI	5.7	2 (3.16)	0	0	H, I + A from 8/00, I + H from 10/00, only CP, STI from 5/02, 12/02 CHR (Ph+ 50%)
59709	57	8/2002	CP	CHR	STI	4.7	2 (5.00)	0	0	I + A from 10/02, from 2/03 only I, 5/03 CHR, from 2/04 STI for no cytogenetic response
59710	64	1/2002	CP	CCR	I + A	3.1	2 (2.90)	1	0	I + A from 3/02, 7/02 CHR, 4/03 CCR (3/04 BCR/ABL 0.2%)
59701	67	3/1994	BP	–	H	44.0	3 (5.23)	2	0	H, three attempts to use I, but intolerance, 3/03 AP, STI from 7/03, 12/03 2.CP, 1/04 BP
59708	60	8/2001	CP	MiCR	STI	4.7	3 (6.83)	0	0	I + H from 10/01, 2/02 CHR, 11/02 I + A, for progression from 3/03 STI, 7/03 CHR (Ph+ 50%)
59706	47	9/1993	CP	CCR	STI	4.7	3 (12.02)	1	0	H, I + H from 12/93, 3/96 CCR, 11/96 progression, STI from 7/01, 11/02 CCR (2/04 BCR/ABL 10%)
59711	56	5/1997	CP	MiCR	STI	3.3	3 (13.49)	0	0	H, 11/98 ICE, 1/99 aTx, I from 4/99, CHR from 8/99, 11/01 again progression and H, 3/02 STI, 7/02 CHR (2/04 Ph+ 47%)
59712	41	3/1998	CP2	CCR	STI	4.2	4 (35.69)	0	0	H, 9/98 CHR, 10/98 ICE, 1/99 aTx, I from 5/99 CHR, 9/00 molecule remission, 6/03 progression, from 12/03 STI for AP, 2/04 CCR
59715	66	3/2000	CP	CCR	STI	5.7	4 (50.56)	2	0	H, 6/00 CHR, I + A from 7/00, 2/02 Ph+ 3.6%, from 1/03 slow progression, STI from 9/03 (Ph+ 76%), CCR 12/03 (BCR/ALB 0.5%)
59713	65	5/1999	CP	MaCR	STI	4.9	4 (47.82)	0	0	H, 8/99 CHR, I-H from 9/99, 7/02 from progression A + I, STI from 2/03, CHR 8/03 (11/03 Ph+ 20%)
59716	59	6/2003	CP	MaCR	STI	4.9	4 (44.28)	1	0	H, I + H from 7/03, 12/03 CHR, from 2/04 STI for intolerance of I
59714	47	3/2003	CP	CCR	STI	5.0	5 (62.32)	1	0	I, CCR 10/03 (Ph+ 16%), from 11/03 STI for intolerance of I, 1/04 CCR (BCR/ABL 10%)
59717	51	9/2000	CP	CCR	STI	3.0	5 (64.12)	3	1	H, 1-3/01 ICE and aTx, 6/01 CCR, I from 8/01 (Ph+ varied between 0 and 28%), last CCR 11/03, STI from 1/04 for intolerance of I
59719							5 (79.87)			Clinical data not complete
59720							5 (59.17)			Clinical data not complete
59718	63	5/1993	AP	–	H	82.0	6 (113.32)	3	3	H, I form 8/94, progression 1/96, 2/98 AP, 5/98 CP2, 9/00 AP, 12/00 CP3, 10/01 STI, 7/02 CHR, 5/03 AP and H for STI resistance

Patients were classified into six categories according to the amount of dimethyl H3K9 measured as the mean value of antibody-signal intensity at dynamic scale of the green channel ranging from 0 to 255 (see Materials and Methods). Category 1 (0–1); category 2 (1–5); category 3 (5–20); category 4 (20–50); category 5 (50–100); category 6 (>100). CP, Chronic phase; AP, accelerated phase; BP, blast phase; CCR, complete cytogenetic response; MaCR, major cytogenetic response (<33% Ph+ cells); MiCR, minor cytogenetic response (<66% Ph+ cells); CHR, complete hematological response; H, hydroxyurea; I, interferon; A, cytosinarabinoside; STI, imatinib mesylate; ICE, idarubicin + cytosinarabinoside + VP16; aTx, autologous peripheral-blood stem-cell transplantation. UPN, Unique patient number; PCR, polymerase chain reaction; Ph, Philadelphia chromosome; BCR/ABL, +(9;22)(q34;q11) between BCR and ABL genes.

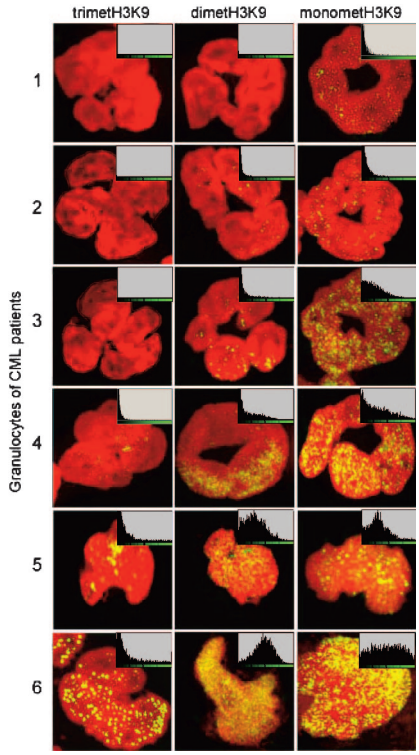

Fig. 6. Distribution of methylated H3K9 in granulocytes isolated from peripheral blood of selected CML patients. Selected patients represent six groups classified according to the degree of the di-metH3K9 (Table 1). In CML patients, tri-metH3K9 was also observed, particularly for the nuclei with a high amount of di-metH3K9. Mono-metH3K9 was observed even in patients without the other types of H3K9 methylation. Patient's UPN number: 1, 59702; 2, 59709; 3, 59708; 4, 59715; 5, 59717; 6, 59718. Immunodetection was performed using FITC-labeled secondary antibodies. DNA was counterstained with TOPRO-3. Inserted histograms represent the level of antibody signals measured as the mean value of green channel intensity in the dynamic range from 0 to 255 using Adobe Photoshop 5.5 software.

large amount of mono-, di-, and tri-metH3K9 and in addition, a rather large amount of HP1β. This patient reached the acute phase because of resistance to the treatment (Table 2, Fig. 6). The methylation of histone H3K9 in the granulocytes of this patient resembled that of AML patients (Fig. 5).

Methylation of histone H3K9 and the status of HP1 proteins in differentiated HL-60 and U-937 cells

Promyelocytic HL-60 and monoblastic U937 cells were induced to differentiate with 1 μM RA. The cell proliferation of both of these cell lines was strongly reduced on the third day of cell incubation with this agent. HL-60 cells acquired granulocyte morphology with chromatin condensed into characteristic lobes and the loss of nucleoli. The results of flow cytometric measurements of the expression of surface antigens CD11b and CD14 by HL-60 and U937 cells incubated in the presence of RA for 6 days are presented in **Figure 7**. HL-60 cells show an increase in the expression of the CD11b antigen, indicating their differentiation into granulocytes. The expression of this antigen is only slightly changed in monocytes on the sixth day of incubation with RA; in contrast, there is an increase of CD14 antigen expression indicating the differentiation of these cells into macrophages. The viability of control HL-60 and U937 cells was 83% and 92%, respectively, for those treated with RA 68% and 77% on the sixth day of incubation.

The RA treatment resulted in the induction of U937 cell differentiation toward a more mature state with major characteristics of monocytes/macrophages: large cytoplasm with vacuolization, chromatin not condensed, and persistence of nucleoli. In contrast to HL-60 cells, the chromatin of U937 was not morphologically changed as compared with the original cells. Both types of differentiated cells retained this characteristic morphology during incubation with RA (8 days).

Even if the morphology of differentiated HL-60 cells displayed the characteristic lobulation, the methylation status of H3K9 of these cells was quite different from that of mature granulocytes isolated from the healthy peripheral blood (**Figs.** 3 and **8**). The granulocytic forms of HL-60 differentiated by RA (distinguished on the slide by the characteristic lobulation) contained a large amount of tri-, di-, and mono-metH3K9, similar to the control HL-60 cells incubated in the absence of RA. They also contained a highly similar pattern of all three forms of the HP1 protein (high signals of β and γ and low signal of α) to the original, nondifferentiated cells (Table 1).

The occurrence of mono-, di-, and trimethylated histone H3K9 and HP1 isoforms in monocytes/macrophages differentiated from U937 cells by 8-day RA treatment was also highly similar to that in control cells not induced to differentiation (Table 1).

DISCUSSION

Our results show an absence of immunofluorescence of all three isoforms of HP1 (α, β, γ) and the absence of any type of histone H3K9 methylation in human neutrophil granulocytes isolated from the peripheral blood of healthy donors. The absence of HP1 proteins and histone H3K9 methylation in

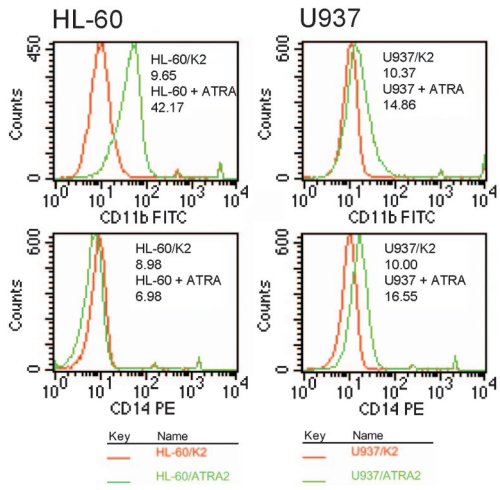

Fig. 7. Expression of CD11b and CD14 antigens in HL-60 and U937 cells before and after incubation of cells with RA for 6 days. HL-60/K2 and U937/K2—control cells, HL-60 + ATRA, and U937 + ATRA—cells treated with RA. Modal values are shown for all cell populations.

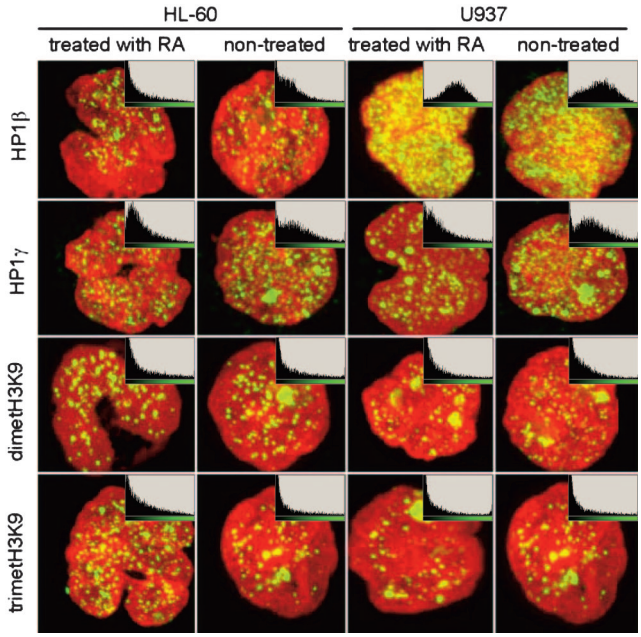

Fig. 8. Distribution of HP1α and -β isoforms, tri- and dimethylated H3K9 in HL-60, and U937 cells, treated and nontreated with 1 μM RA for 8 days. Immunodetection was performed using FITC-labeled secondary antibodies. DNA was counterstained with TOPRO-3. HL-60 cells show lobular morphological changes after the treatment with RA; however, the exposure of methylation and HP1 remains conserved. Inserted histograms represent the level of antibody signals measured as the mean value of the green channel intensity in the dynamic range from 0 to 255 using Adobe Photoshop 5.5 software.

healthy granulocytes was also proved by Western blotting. Only a limited amount of these proteins was found in eosinophils. In contrast to granulocytes, two other types of white blood cells, lymphocytes and monocytes, contained high levels of all these protein markers with the exception of HP1α, which is present in much lower amounts than the two other HP1 isomers. These results indicate a difference between the structure of the chromatin of human granulocytes on one hand and lymphocytes and monocytes on the other. This difference is manifested during manipulation with these cells: Neutrophil granulocytes fixed with 4% formaldehyde for 10 min are much less stable (the chromatin swells, expands to an enormous size, and loses its original shape) compared with lymphocytes, monocytes, and even eosinophils and must be subjected to immunostaining and microscopic observation immediately.

HP1 is thought to play a central role in creating a stable heterochromatic network by interacting with several other proteins, in particular, with methylated histone H3K9 [8, 34, 35, 36]. This histone modification and the presence of HP1 are considered to be important signs of inactive chromatin regions. In addition to human granulocytes, a sharp decline in HP1 levels has also been observed in other terminally differentiated cells with highly condensed chromatin, such as chicken lymphocytes and erythrocytes from other vertebrate species [14, 23]. The absence of HP1 in the heterochromatin of these terminally differentiated cells indicates that its function is not necessary for maintaining chromatin condensation, centromere function, and regulation of gene expression in these terminally differentiated blood cells in contrast to proliferating cells, even those with limited proliferating capacity (lymphocytes and monocytes). The proliferative ability of lymphocytes is well known, as is the limited proliferation of monocytes induced by a macrophage colony-stimulating factor in vitro [37]. In chicken granulocytes and erythrocytes, histone H3 methylation at lysine 9 (di-metH3K9) regulates chromatin condensation directly by recruitment of a serpin-like protein mature erythrocyte nuclear termination (MENT) [24]. In contrast to chicken granulocytes, where HP1 is replaced by MENT, and methylation of H3K9 is preserved, HP1 proteins and methylated H3K9 are not detectable in human granulocytes, as is shown in this work.

We considered the possibility of methylated histone H3 replacement by its variant CENP-A, owing to its participation in the formation of condensed centromeric heterochromatin [25, 38] and its ability to replace H3 in octameric complexes with H4, H2A, and H2B and to form reconstituted nucleosomes in experiments in vitro [39]. However, our results show that in human granulocytes, the amount of CENP-A protein is not higher than that in lymphocytes and monocytes and that this protein is normally integrated into centromeric heterochromatin foci (Fig. 3A). We did not detect the presence of the H1° variant of the linker histone H1 in human granulocytes, although a small amount of H1° was present in some lymphocytes and monocytes. The H1° variant was preferentially found in nondividing cells [40]; however, the relationship between the function of histone H1° in proliferation and differentiation has not yet been established. Variant H1°/H5 was shown by Gilbert et al. [15] to be increased in chicken erythrocytes during development, paralleling decreased levels in HP1s, and the authors speculate about the role of this protein in chromatin compaction in place of HP1. Nevertheless, it has been shown earlier that the accumulation of the linker histone per se is not sufficient to cause a major chromatin remodeling [17, 18]. Thus, it remains an open question as to which chromosomal protein(s) controls chromatin condensation in differentiated granulocytes.

Models of heterochromatin higher-order folding in terminally differentiated cells, where only a small part of the genes remain active, have recently been revised by Grigoryev [41] to include an extremely compact, longitudinal folding of a 30-nm fiber or extensive lateral self-association and intercalation of nucleosome arrays [42] and folding of the chromatin 30-nm fiber back onto itself. Progressing chromatin folding may result in the global chromatin condensation observed in terminally differentiated cells, leaving behind only the genes protected by boundary elements [43] or by nuclear matrix association [44], separating the active chromatin from the mass of spreading heterochromatin. The histone H3 N-terminal domains are involved in nucleosome linker folding within the zig-zag nucleosome arrays [45]. Nucleosome linkers, along with histone H3 N-termini, should become highly inaccessible within a compact 30-nm fiber or extensively intercalated zig-zags [41]. Conversely, the positive detection of acetylated H3K9 (as well as CENP-A and H1) indicates that chromatin condensation in granulocytes does not prevent the penetration of antibodies. Therefore, the negative detection of the signal of mono-, di-, and tri-metH3K9 indicates rather the absence of this lysine residue methylation. This conclusion is also supported by

Western blot analysis (Fig. 4), which also failed to detect H3K9 methylation.

Our results further show that monomethylated and in particular, dimethylated H3K9 appears to a variable degree in the granulocytes of CML patients, without being accompanied by HP1 proteins. It follows from the results presented that the variable methylation of histone H3 in CML granulocytes could be an extremely important phenomenon in tumor development and progression. It is well known that CML is a hematopoietic stem cell disorder associated with the chromosomal translocation t(9;22), which progresses from a relatively benign chronic phase to a terminal blastic phase. The mechanism of the transformation of the disease from the chronic to the acute phase is not yet fully understood, although it seems that factors other than BCR/ABL are responsible for the progression of CML and evolution into an acute leukemia. In this connection, the question arises as to whether the t(9;22) translocation is the primary event or whether it occurs in an already defective stem cell. Fialkow et al. [46] and Raskind et al. [47] have studied individuals with CML, heterozygous for glucose-6-phosphate dehydrogenase (G6PD) isoenzyme expression, and their results indicate that there are patients with Ph-negative B cells expressing the same G6PD isoenzyme as their Ph-positive myeloid cells. This observation supports the idea that defective hematopoiesis could precede the t(9;22) translocation, at least in some cases.

The data published here show that strong methylation of H3K9 can be found even in patients with a very low number, if any, of BCR/ABL-positive cells. We can speculate that the impaired methylation profile is a possible manifestation of the defective hematopoiesis and therefore, can be seen even in granulocytes from CML patients without BCR/ABL translocation. On the basis of the results put forward, we can assume that the primary, structural defects are to be found in the local chromatin decondensation. This structural disorder might lead to genetic instability and to the development of further genetic rearrangement(s). The reason for the variability of the degree of methylation in CML patients is not known. The treatment of CML is focused on the elimination of the clone containing BCR/ABL translocation and does not eliminate cells with primary structural changes that may be individually variable.

The chromatin of AML granulocytes, possessing a larger proliferating capacity and accordingly higher amount of actively transcribed genes, should be much more decondensed than the chromatin of CML granulocytes. The presence of all isoforms of HP1 indicates that chromatin condensation of AML granulocytes is not as complete as in healthy granulocytes and that the mechanisms controlling chromatin condensation in AML granulocytes are rather similar to those in lymphocytes and monocytes.

The changes in the chromatin structure manifested by H3K9 methylation of granulocytes in CML and AML patients indicate that the process of differentiation in these cells has become incomplete, where incomplete differentiation was also observed in HL-60 cells induced to differentiation by RA. In spite of prolonged exposure of cells to RA (8 days), methylated forms of histone H3K9 and all isoforms of the HP1 protein remained at approximately the same level as in control cells not exposed to RA, indicating that the chromatin structure in differentiated HL-60 cells is not the same as in normal peripheral blood granulocytes. Little condensed chromatin in granulocytes differentiated by RA from HL-60 cells, as compared with normal peripheral blood granulocytes, has been revealed earlier by Olins et al. [29, 30]. The authors show that granulocyte chromatin looks quite different from that of the other differentiated cell types: It has highly reduced nuclear lamina, although an increased number of lamina binding receptors (LBR). The amount of LBR increases significantly after RA treatment of HL-60 cells [30]. Evidence has been presented showing that LBR interacts with HP1α, which might stabilize linkage between the nuclear envelope and the peripheral heterochromatin of granulocytes [48]. Further evidence that HL-60 and other leukemic cell lines fail to differentiate fully toward mature granulocytes, if induced by RA, is their inability to synthesize secondary granules [49]. This secondary granule deficiency is an abnormality closely associated with aberrantly differentiated leukemic blasts. Aberrant differentiation of HL-60 cells to granulocytes induced by RA has also been shown in this work. This is demonstrated by the presence of mono-, di-, and tri-metH3K9 and HP1 proteins in the chromatin of induced granulocytic forms, which are absent in healthy human granulocytes isolated from the peripheral blood.

Similarly as in granulocytes differentiated by RA from HL-60 cells, the level of H3K9 methylation and the presence of HP1 were also preserved in macrophages differentiated from U937 cells. However, contrary to granulocytes, the chromatin of macrophages is not condensed, and its structure, including the presence of nucleoli, resembles that of monocytes. Similar levels of H3K9 methylation and the presence of HP1 isoforms in differentiated cells, as compared with original U937 cells, are therefore not surprising. Condensation of chromatin in these cells is apparently directed by other mechanisms than in human granulocytes.

It follows from the results presented that the absence of the methylated H3K9 marker in human granulocytes distinguishes these cells from other differentiated human blood cells. It has recently been shown [50] that during activation, neutrophils release chromatin and granule proteins, which assemble into extracellular fibers [neutrophil extracellular traps (NETs)], serving to bind and kill bacteria and degrade virulence factors. The specific structure of the chromatin of neutrophils may facilitate the release of DNA (a major structural component of NETs) and histones to generate these fibers.

RA is often used to stimulate some tumor cells to differentiate and undergo terminal cell division and loss of tumorigenicity. However, our results suggest that even if some leukemia cells (and presumably, some cells of other tumors that are genetically abnormal) can be reprogrammed to a nonmalignant phenotype by inducing differentiation, their chromatin structure need not be restored completely. The presence of methylated histone H3K9 in apparently mature human granulocytes derived from leukemia indicates an absence of completely condensed chromatin, implying a certain degree of instability and risk of leukemia relapse.

ACKNOWLEDGMENTS

This work was supported by the Ministry of Health of the Czech Republic (NC6987-3), the Academy of Sciences of the Czech Republic (A1065203, KSK 5052113, Z5004920, S5004010), the Grant Agency of the Czech Republic (GA202/02/0804), and the Ministry of Education (ME565). We thank L. Stixová, Laboratory of Cytokinetics, Institute of Biophysics, AS CR, Brno, for flow cytometric measurements.

REFERENCES

1. Frenster, J. H., Allfrey, V. G., Mirsky, A. E. (1963) Repressed and active chromatin isolated from interphase lymphocytes. *Proc. Natl. Acad. Sci. USA* **50,** 1026–1032.
2. Bernard, P., Maure, J. F., Partridge, J. F., Genier, S., Javerzat, J. P., Allshire, R. C. (2001) Requirement of heterochromatin for cohesion at centromeres. *Science.* **294,** 2539–2542.
3. Peters, A. H., O'Carroll, D., Scherthan, H., Mechtler, K., Sauer, S., Schofer, C., Weipoltshammer, K., Pagani, M., Lachner, M., Kohlmaier, A., Opravil, S., Doyle, M., Sibilia, M., Jenuwein, T. (2001) Loss of the Suv39h histone methyltransferases impairs mammalian heterochromatin and genome stability. *Cell* **107,** 323–337.
4. Nonaka, N., Kitajima, T., Yokobayashi, S., Xiao, G. P., Yamamoto, M., Grewal, S. I., Watanabe, Y. (2002) Recruitment of cohesin to heterochromatic regions by Swi6/HP1 in fission yeast. *Nat. Cell Biol.* **4,** 89–93.
5. Hall, I. M., Nom, K., Grew, S. I. (2003) RNA interference machinery regulates chromosome dynamics during mitosis and meiosis in fission yeast. *Proc. Natl. Acad. Sci. USA* **100,** 193–198.
6. Grewal, S. I., Klar, A. (1997) A recombinationally repressed region between mat2 and mat3 loci shares homology to centromeric repeats and regulates directionality of mating-type switching in fusion yeast. *Genetics* **146,** 1221–1238.
7. Guarente, L. (2000) Sir2 links chromatin silencing, metabolism, and aging. *Genes Dev.* **14,** 1021–1026.
8. Lachner, M., O'Carroll, D., Rea, S., Mechtler, K., Jenuwein, T. (2001) Methylation of histone H3 lysine 9 creates a binding site for HP1 proteins. *Nature* **410,** 116–120.
9. Bannister, A. J., Zegerman, P., Partridge, J. F., Miska, E. A., Thomas, J. O., Allshire, R. C., Kouzarides, T. (2001) Selective recognition of methylated lysine 9 on histone H3 by the HP1 chromodomain. *Nature* **410,** 120–124.
10. Rice, J. C., Brrigs, S. D., Ueberheide, B., Barber, C. M., Shabanowitz, J., Hunt, D. F., Shinkai, Y., Allis, C. D. (2003) Histone methyltransferases direct different degrees of methylation to define distinct chromatin domains. *Mol. Cell* **12,** 1591–1598.
11. Cheutin, T., McNairin, A. J., Jenuwein, T., Gilbert, D. M., Singh, P., Misteli, T. (2003) Maintenance of stable heterochromatin domains by dynamic HP1 binding. *Science* **299,** 721–725.
12. Festenstein, R., Pagaki, S. N., Hiragami, K., Lyon, D., Verreaul, A., Sekkai, B., Kioussis, D. (2003) Modulation of heterochromatin protein 1 dynamics in primary mammalian cells. *Science* **299,** 719–721.
13. Francastel, C., Schbeler, D., Martin, D. I., Groudine, M. (2000) Nuclear compartmentalization and gene activity. *Nat. Rev. Mol. Cell Biol.* **1,** 137–143.
14. Grigoryev, S. A., Bednar, J., Woodcock, C. L. (1999) MENT, a heterochromatin protein that mediates higher order chromatin folding, is a new serpin family member. *J. Biol. Chem.* **274,** 5626–5636.
15. Gilbert, N., Boyle, S., Shuterland, H., de Las Heras, J., Allan, J., Jenuwein, T., Bickmore, W. A. (2003) Formation of facultative heterochromatin in the absence of HP1. *EMBO J.* **22,** 5540–5550.
16. Peters, A. H., Mermoud, J. E., O'Carroll, D., Pagani, M., Schweizer, D., Brockdorff, N., Jenuwein, T. (2002) Histone H3 lysine 9 methylation is an epigenetic imprint of facultative heterochromatin. *Nat. Genet.* **30,** 77–80.
17. Weintraub, H. (1985) Assembly and propagation of repressed and depressed chromosomal states. *Cell* **42,** 705–711.
18. Zlatanova, J., van Holde, K. (1992) Histone H1 and transcription: still an enigma? *J. Cell Sci.* **103,** 889–895.
19. Sun, J. M., Wiaderkiewicz, R., Ruiz-Carrillo, A. (1989) Histone H5 in the control of DNA synthesis and cell proliferation. *Science* **245,** 68–71.
20. Sirotkin, A. M., Edelmann, W., Cheng, G., Klein-Szanto, A., Kucherlapati, R., Skoultchi, A. I. (1995) Mice develop normally without the H1(0) linker histone. *Proc. Natl. Acad. Sci. USA* **92,** 6434–6438.
21. Shen, X., Yu, L., Weir, J. W., Gorowsky, M. A. (1995) Linker histones are not essential and affect chromatin condensation in vivo. *Cell* **82,** 47–56.
22. Shen, X., Gorowsky, M. A. (1996) Linker histone H1 regulates specific gene expression but not global transcription in vivo. *Cell* **86,** 475–483.
23. Grigoryev, S. A., Woodcock, C. L. (1998) Chromatin structure in granulocytes. A link between tight compaction and accumulation of a heterochromatin-associated protein (MENT). *J. Biol. Chem.* **273,** 3082–3089.
24. Istomina, N. A., Shushanov, S. S., Springhetti, E. M., Karpov, V. L., Krasheninnikov, I. A., Stevens, K., Zaret, K. S., Singh, P. B., Grigoryev, S. A. (2003) Insulation of the chicken β-globin chromosomal domain from a chromatin-condensing protein, MENT. *Mol. Cell. Biol.* **23,** 6455–6468.
25. Gilbert, N., Allan, J. (2001) Distinctive higher-order chromatin structure at mammalian centromeres. *Proc. Natl. Acad. Sci. USA* **98,** 11949–11954.
26. Cowell, I. G., Aucott, R., Mahadevaiah, S. K., Burgoyne, P. S., Huskisson, N., Bongiorni, S., Prantera, G., Fanti, L., Pimpinelli, S., Wu, R., Gilbert, D. M., Shi, W., Fundele, R., Morrison, H., Jeppesen, P., Singh, P. B. (2002) Heterochromatin, HP1 and methylation at lysine 9 of histone H3 in animals. *Chromosoma* **111,** 22–36.
27. Jenuwein, T. (2001) Re-SET-ing heterochromatin by histone methyltransferases. *Trends Cell Biol.* **11,** 266–273.
28. Sachs, L. (1996) The control of hematopoiesis and leukemia: from basic biology to the clinic. *Proc. Natl. Acad. Sci. USA* **93,** 4742–4749.
29. Olins, A. L., Buendia, B., Herrmann, H., Lichter, P., Olins, D. E. (1998) Retinoic acid induction of nuclear envelope-limited chromatin sheets in HL-60. *Exp. Cell Res.* **245,** 91–104.
30. Olins, A. L., Herrmann, H., Lichter, P., Kratzmeier, M., Doenecke, D., Olins, D. E. (2001) Nuclear envelope and chromatin compositional differences comparing undifferentiated and retinoic acid- and phorbol ester-treated HL-60 cells. *Exp. Cell Res.* **268,** 115–128.
31. Grolleau, A., Sonenberg, N., Wietzerbin, J., Beretta, L. (1999) Differential regulation of 4E-BP1 and 4E-BP2, two repressors of translation initiation, during human myeloid cell differentiation. *J. Immunol.* **162,** 3491–3497.
32. Coligan, J. E., Kruisbeek, A. M., Margulies, D. H., Shevach, E. M., Strober, W., eds. (1991) *Current Protocols in Immunology*, New York, NY, John Wiley and Sons.
33. Kozubek, M., Kozubek, S., Lukášová, E., Marečková, A., Bártová, E., Skalníková, M., Jergová, A. (1999) High resolution cytometry of FISH dots in interphase cell nuclei. *Cytometry* **36,** 279–293.
34. Kozubek, M., Kozubek, S., Lukášová, E., Bártová, E., Skalníková, M., Matula, P., Matula, P., Jirsová, P., Cafourková, A., Koutná, I. (2001) Combined confocal and wide-field high resolution cytometry of fluorescent in situ hybridization-stained cells. *Cytometry* **45,** 1–12.
35. Bannister, A. J., Zegerman, P., Partridge, J. F., Miska, E. A., Thomas, J. O., Allshire, R. C., Kourazides, T. (2001) Selective recognition of methylated lysine 9 on histone H3 by the HP1 chromo domain. *Nature* **410,** 120–124.
36. Nielsen, P. R., Nietlispach, D., Mott, H. R., Callaghan, J., Bannister, A., Kouzarides, T., Murzin, A. G., Murzina, N. V., Laue, E. D. (2002) Structure of HP1 chromodomain bound to histone H3 methylated at lysine 9. *Nature* **416,** 103–107.
37. Antonov, A. S., Munn, D. H., Kolodgie, F. D., Virmani, R., Gerrity, R. G. (1997) Aortic endothelial cells regulate proliferation of human monocytes in vitro via a mechanism synergistic with macrophage colony-stimulating factor. Convergence at the cyclin E/p27(Kip1) regulatory checkpoint. *J. Clin. Invest.* **99,** 2867–2876.
38. Blower, M. D., Sullivan, B. A., Karpen, G. H. (2002) Conserved organization of centromeric chromatin in flies and humans. *Dev. Cell* **2,** 319–330.
39. Yoda, K., Ando, S., Morishita, S., Houmura, K., Hashimoto, K., Takeyasu, K., Okazaki, T. (2000) Human centromere protein A (CENP-A) can replace histone H3 in nucleosome reconstitution in vitro. *Proc. Natl. Acad. Sci. USA* **97,** 7266–7271.
40. Zlatanova, J., Doenecke, D. (1994) Histone H1 zero: a major player in cell differentiation? *FASEB J.* **8,** 1260–1268.
41. Grigoryev, S. A. (2004) Keeping fingers crossed: heterochromatin spreading through interdigitation of nucleosome arrays. *FEBS Lett.* **564,** 4–8.
42. Woodcock, C. L., Horowitz, R. A. (1995) Chromatin organization reviewed. *Trends Cell Biol.* **5,** 272–277.
43. Ishii, K., Laemmli, U. K. (2003) Structural and dynamic functions establish chromatin domains. *Mol. Cell* **11,** 237–248.
44. Cai, S., Han, H. J., Kohwi-Shigematsu, T. (2003) Tissue-specific nuclear architecture and gene expression regulated by SATB1. *Nat. Genet.* **34,** 42–51.
45. Zlatanov, J., Leuba, S. H., van Holde, K. (1998) Chromatin fiber structure: morphology, molecular determinants, structural transitions. *Biophys. J.* **74,** 2554–2566.
46. Fialkow, P. J., Martin, P. J., Najfeld, V., Penfold, G. F., Jacobson, R. J., Hansen, J. A. (1981) Evidence for a multistep pathogenesis of chronic myelogenous leukemia. *Blood* **58,** 158–163.

47. Raskind, W. H., Ferraris, A. M., Najfeld, V., Jacobson, R. H., Moohr, J. W., Fialkov, P. J. (1993) Further evidence for the existence of a clonal Ph-negative stage in some cases of Ph-positive chronic myelocytic leukemia. *Leukemia* **7,** 1163–1167.
48. Ye, Q., Barton, R. M., Worman, H. J. (1998) Nuclear lamin-bibding proteins. In *Subcellular Biochemistry*, vol. 31 (H. Hermann and J. R. Harris, eds.), New York, NY, Plenum, 587–610.
49. Miyauchi, J., Ohyashiki, K., Inatomi, Y., Toyama, K. (1997) Neutrophil secondary-granule deficiency as a hallmark of all-trans retinoic acid—induced differentiation of acute promyelocytic leukemia cells. *Blood* **90,** 803–813.
50. Brinkmann, V., Reichard, U., Goosmann, C., Fauler, B., Uhlemann, Y., Weiss, D. S., Weinrauch, Y., Zychlinsky, A. (2004) Neutrophil extracellular traps kill bacteria. *Science* **303,** 1532–1535.

Chromosoma (2004) 112:221–230
DOI 10.1007/s00412-003-0263-3

RESEARCH ARTICLE

Emilie Lukášová · Stanislav Kozubek · Martin Falk · Michal Kozubek · Jan Žaloudík · Václav Vagunda · Zdeněk Pavlovský

Topography of genetic loci in the nuclei of cells of colorectal carcinoma and adjacent tissue of colonic epithelium

Received: 19 February 2002 / Revised: 25 August 2003 / Accepted: 2 October 2003 / Published online: 13 January 2004

Abstract To determine the influence of increased gene expression and amplification in colorectal carcinoma on chromatin structure, the nuclear distances between pairs of bacterial artificial chromosome (BAC) clones with genomic separation from 800 to 29,000 kb were measured and compared between the tumor and parallel epithelial cells of six patients. The nuclear distances were measured between the loci in chromosomal bands 7p22.3–7p21.3; 7q35–7q36.3; 11p15.5–11p15.4; 20p13; 20p12.2; 20q11.21 and 20q12 where increased expression had been found in all types of colorectal carcinoma. The loci were visualized by three-dimensional fluorescence in situ hybridization using 22 BAC clones. Our results show that for short genomic separations, mean nuclear distance increases linearly with increased genomic separation. The results for some pairs of loci fell outside this linear slope, indicating the existence of different levels of chromatin folding. For the same genomic separations the nuclear distances were frequently shorter for tumor as compared with epithelial cells. Above the initial growing phase of the nuclear distances, a plateau phase was observed in both cell types where the increase in genomic separation was not accompanied by an increase in nuclear distance. The ratio of the mean nuclear distances between the corresponding loci in tumor and epithelium cells decreases with increasing amplification of loci. Our results further show that the large-scale chromatin folding might differ for specific regions of chromosomes and that it is basically preserved in tumor cells in spite of the amplification of many loci.

Communicated by T. Hassold

E. Lukášová · S. Kozubek (✉) · M. Falk
Institute of Biophysics,
Czech Academy of Sciences,
Královopolská 135, 612 65 Brno, Czech Republic
e-mail: kozubek@ibp.cz

M. Kozubek
Faculty of Informatics,
Masaryk University,
Botanická 68a, 602 00 Brno, Czech Republic

J. Žaloudík · V. Vagunda · Z. Pavlovský
Masaryk Memorial Cancer Institute,
Žlutý kopec 7, 656 53 Brno, Czech Republic

Introduction

The organization of eukaryotic chromatin has a major impact on all nuclear processes, especially DNA replication and gene expression. Gene expression is affected by the positioning of individual nucleosomes relative to regulatory sequence elements (Jenuwein and Allis 2001), by the folding of the nucleosomal fiber into higher-order structures and by the compartmentalization of functional domains within the nucleus. The spatial arrangement of chromatin may play an important role in the regulation of gene expression and other nuclear processes (Van Driel et al. 1995; Spector 1996; Bridger and Bickmore 1998; Lamond and Ernshaw 1998; Schul et al. 1998). Confocal laser scanning microscopy (CLSM) studies have suggested a specific three-dimensional (3D) arrangement of chromosome territories, visualized by fluorescence in situ hybridization (FISH), and their relationships with other nuclear components and processes (Ferreira et al. 1997; Visser et al. 1998; Sadoni et al. 1999; Zink et al. 1999; Kozubek et al. 2002).

However, not enough is known about changes in higher-order chromatin structure and related functional relationships brought about by genetic abnormalities accumulated in the process of carcinogenesis. These abnormalities are of genetic or epigenetic origin. Epigenetically mediated changes in gene structure and function are being increasingly recognised (Baylin and Herman 2000; Rountree et al. 2001; Brown and Strathedee 2002; Eberharter and Becker 2002; Horn and Peterson 2002; Suzuki et al. 2002). Extensive diversity is often observed in neoplastic tissue. Mammalian cells possess effective control mechanisms for maintaining genomic integrity that are abrogated during tumor development (Di Leonardo et al. 1993; Tlsty et al. 1993). The genetic instability that tumorigenic cells often demonstrate is manifested in

chromosomal rearrangements: translocations, insertions, amplifications, loss of heterozygosity and deletions. Gene amplification is observed through the genome (Kallioniemi et al. 1992) and it is the major mechanism for overexpression of oncogenes, cell surface receptors, cell cycle regulators and intracellular signal transduction molecules that occur in many human tumors (Schwab 1990; Di Leonardo et al. 1993). It was found that the ability of genes to be amplified occurs early in cell progression toward neoplastic transformation and it is increased in a sporadic fashion as a cell population proceeds to malignant transformation (Jonzyk et al. 1993; Tlsty et al. 1993).

Colorectal carcinoma is one of the most frequent cancers in the Western world. Cytogenetic studies have revealed few recurrent tumor-characteristic chromosome aberrations in colorectal tumors (Fearon and Vogelstein 1990). Sequencing in coding regions of tumor DNA from 470 genes shows that sporadic colorectal cancers do not display a mutator phenotype at the nucleotide level (Wang et al. 2002). Colorectal carcinomas mostly show highly complex karyotypes and rearrangements (Melcher et al. 2000; Bomme et al. 2001), aneuploidy and gene amplification (Fearon et al. 1987; Jen et al. 1994). Balanced structural rearrangements are rarely seen and the more complex karyotypes are dominated by various chromosomal imbalances, frequently including loss of chromosomal arms 8p, 17p 18p, 8q and gains of 6q, 7p, 7q, 8q, 11p, 13q, 20 p and 20q (Aust et al. 2000; Nakao et al. 2001).

Using 3D FISH, we have observed significant intratumor variations in chromosome copy number and in the degree of amplification of different loci in cells of colorectal carcinoma (unpublished). Amplification of both shorter and longer genetic loci, frequently in many copies, was observed. Heterogeneity in the number of these copies inside the cell population of the same tumor as well as among tumors was found. The nuclear topography of amplified loci was variable: they were either randomly distributed in the nucleus in the form of individual loci, or formed chains or clusters or more complex aggregates. The majority of these amplifications were located inside the territories of their chromosomes.

In this work, the nuclear distances (NDs) between the loci in chromosomal bands 7p22.3–7p21.3; 7q35–7q36.3; 11p15.5–11p15.4; 20p13; 20p12.2; 20q11.21 and 20q12 were measured using 3D FISH and 22 bacterial artificial chromosome (BAC) clones in the tumor and adjacent epithelial tissue of six patients. In these regions increased expression was found in all types of colorectal carcinoma (Birkenkamp-Demtroder et al. 2002; http://bioinfo.amc.uva.nl/HTM/). The NDs between two BAC clones with genomic separation (GS) ranging from 800 to 29,000 kb were measured and compared between the tumor and epithelial cells. The results show that the NDs between the loci are influenced by the degree of their amplification in tumor cells. They show further differences in local chromatin folding in both types of tissues.

Materials and methods

Tumor specimens

The material consisted of fresh tumor specimens of surgically removed primary colorectal carcinoma and parallel healthy colonic epithelium cut at a distance of about 10–15 cm from the tumor of six patients who underwent surgery at the Masaryk Memorial Cancer Institute in Brno (Table 1). All tumors were sporadic because none of the patients belonged to families with heritable colorectal carcinoma. No patient had a metastatic focus in the liver. Tumors were extensively histopathologically examined and staged according to the TNM classification (Sobin and Wittekind 2002). The Grade of tumor differentiation was evaluated in terms of good, moderate or poor (I, II or III). The fresh specimens of tissues were immediately frozen in liquid nitrogen where they were stored until analysis. A control parallel tissue section was always taken for histopathological assessment in order to determine the percentage of tumor cells in each sample. Informed consent was obtained from patients to use their specimens for research purposes.

Tumor imprint preparation for FISH

At the time of tumor imprint preparation, the tumor tissue was thawed and blotted on filter paper before touching onto silanized microscope slides. The preparation was left to attach for about 3 min and then fixed by paraformaldehyde for the study of nuclear arrangement of different genetic elements or by methanol:acetic acid for detection of deletions and abnormal number of chromosomes.

Paraformaldehyde fixation and permeabilization

Slides were immersed in a 3.7% solution of paraformaldehyde with 0.5% Triton X-100 and HEPEM buffer (65 mM PIPES, 30 mM HEPES, 10 mM EGTA, 2 mM $MgCl_2$, pH 6.9) (Neves et al. 1999) and fixed for 15 min at room temperature, washed three times for 5 min in PBS and permeabilized in 0.1 N HCl with 0.7% Triton X-100 and PBS for 12 min on ice. Then, the slides were washed (three times for 5 min) in PBS, digested with 0.002% pepsin in 0.9%

Table 1 Clinicopathological features and polyploidy of the investigated chromosomes in colorectal carcinoma

Patient	TNM pT	Grade	TNM pN	Tumor location	Age	Gender	Copy number of chromosome		
							7	11	20
1	2	II	0	Right colon	69	F	3–4	3–4	3–5
2	3	I	0	Right colon	61	F	3 in 10%	2	2
3	3	III	1	Transverse colon	35	F	3 in 20%	2–3	3–5
4	2	I	0	Right colon	72	F	3–5	3–5	2–5
5	3	II	2	Sigmoid colon	28	M	3	3 in 15%	2
6	3	I	1	Left colon	67	F	3	3–5	2

Table 2 Probes prepared from PAC/BAC clones and used for fluorescent in situ hybridization (FISH)

Clone	Sequence	Map position	Sequence position (kb) [a]	Probe marking	Pairs of probes used in one FISH	Molecular distance between probes (kb)
RP11–449P15	AC073957	7p22.3	562	7A	7C green + 7D red	1,632
RP11–425P5	AC009412	7p22.1	5,911	7B	7C green + 7B red	2,286
RP4–696N1	AC004457	7p21.3	8,197	7C	7H green + 7G red	4,776
RP4–755G17	AC004879	7p21.3	9,829	7D	7A green + 7E red	11,315
RP11–507C1	AC007321	7p21.3	11,877	7E	7F green + 7I red	13,399
RP11–374N8	AC074384	7q35	142,759	7F		
RP11–428D5	AC013273	7q36.1	147,589	7G		
RP11–422E4	AC024730	7q36.2	152,365	7H		
RP11–518I12	AC093856	7q36.3	156,158	7I		
RP11–401C19	AC131933	11p15.5	364	11C	11B green +11C red	1,323
vRP11–295K3	AC068580	11p15.5	1,687	11B	11E green + 11A red	4,654
RP11–534I22	AC051649	11p15.5	1,911	11A	11C green+11D red	6,111
RP11–645I8	AC021935	11p15.4	6,475	11D		
RP11–290F24	AC022762	11p15.4	6,565	11E		
RP5–1103G7	AL034548	20p13	173	20A	20C–20D	820
RP5–1187M17	AL121891	20p13	3,013	20B	20E–20F	1,426
RP5–1119D9	AL031652	20p12.2	9,335	20C	20G–20H	1,480
RP5–1068F16	AL023913	20p12.2	10,155	20D	20A–20B	2,840
RP5–836N17	AL049539	20q11.21	30,411	20E	20E–F green + 20A–B red	28,824
RP5–1137F22	AL034421	20111.21	31,837	20F	20G–H green + 20C–D red	29,811
RP5–892M9	AL121828	20q12	38,486	20G		
RP5–1167E19	AL133229	20q12	39,966	20H		

[a] The order of the clones on the chromosome sequence map is based on the UCSC database (http://genome.ucsc.edu), November 2002 release

NaCl, pH 1.5, for 4 min, washed in PBS (three times for 5 min each), and postfixed for 5 min in 0.1% paraformaldehyde in PBS followed by a wash (three times for 5 min each). The slides were then immersed in 50% formamide in 2×SSC, pH 7 where they were stored at 4°C until used.

DNA probes used for FISH

The DNA probes used for investigation of nuclear arrangement of selected regions of chromosomes 7, 11 and 20 with increased gene expression in colorectal carcinoma were prepared from BAC and P1 bacterial artificial chromosome (PAC) clones from RP5 or RP11 P. de Jong libraries, kindly provided by Mariano Rocchi, University of Bari, Italy. The list of probes, their mapping on the chromosome and position on the chromosome working draft sequence map derived from the UCSC database (November 2002 release) are presented in Table 2. Five probes were used for 7p22.3–7p21.3, four probes for 7q35–7q36.3, five for 11p15.5–11.15.4, two for 20p13, two for 20p12.2 and four probes for 20q11.21–20q12. Indirectly labeled centromere-specific alpha-satellite repeat probes purchased from Appligene-Oncor (Strasbourg, France) were used for enumeration of chromosomes 7, 11 and 20. The probes from BAC and PAC clones were isolated by the standard anion-exchange procedure using Qiagen (Hilden, Germany) columns and labeled by nick translation with spectrum green- and spectrum orange-11-dUTP using the Vysis (USA) kit. Before removing the unincorporated nucleotide by ethanol precipitation, Cot1-DNA (Roche, Mannheim, Germany) was added in 50-fold concentration of the DNA probe and labeled DNA was resuspended in a TE buffer to a concentration of 100 ng/μl.

Hybridization

Tumor imprints fixed by paraformaldehyde were denatured for 5 min in 70% formamide with 2×SSC at 73°C then placed for 7 min into a formamide solution of the same composition pre-cooled to −20°C followed by probe application.

The mixture of two differently labeled probes was used for each hybridization. Probe combinations are presented in Table 2. About 200 ng (2 μl) of the mixture of two or more probes isolated from BAC/PAC clones and directly labeled by spectrum orange or spectrum green were mixed with 13 μl Hybrisol VI (Oncor) (65% formamide, 10% dextran sulfate, 2×SSC), denatured at 75°C for 5 min and allowed to preanneal at 37°C for 30–60 min. The denatured probes were applied to the slide immediately after nuclear DNA denaturation, covered with coverslip, sealed with rubber cement and allowed to hybridize for 2 days at 37°C. The centromeric probe, denaturation and pretreatment were performed according to the instructions of the manufacturer. Tumor imprints fixed by methanol:acetic acid were pretreated in 2×SSC, pH 7 with 0.1% Triton X-100 at 37°C for 30 min, digested with RNase A, 1 mg/ml (Sigma) in 2×SSC for 30 min, washed with 2×SSC (three times for 5 min each) at 37°C and dehydrated in 70%, 80% and 96% ethanol for 2 min each. After drying in air, the slides were denatured in 70% formamide with 2×SSC, pH 7 at 72°C for 3 min and dehydrated in 70%, 80% and 96% ethanol precooled to −20°C for 2 min. Probes were applied to dry slides. Their mixtures were prepared in the same way as for the imprints fixed by paraformaldehyde. Hybridization was done overnight. Post-hybridization washings were described earlier (Kozubek et al. 2002).

Repeated hybridization with painting and centromeric probes

Coverslips from the first hybridization were removed by immersion of slides in 4×SSC, 0.1% Triton X-100. The slides were then washed in three changes of the same solution, once in 2×SSC (for 4 min each) and immersed in 50% formamide 2×SSC, pH 7 at 5°C overnight. Denaturation was performed as in the first hybridization. Our previous results show (Falk et al. 2002) that the positions of genetic elements are not influenced by repeated hybridization. The repeated hybridization was performed using the mix of painting and centromeric probes on the same slides hybridized in the first hybridization with two differently labeled probes of the corresponding chromosome to find the number and structure of chromosome territories and the location of amplified loci in tumor cells.

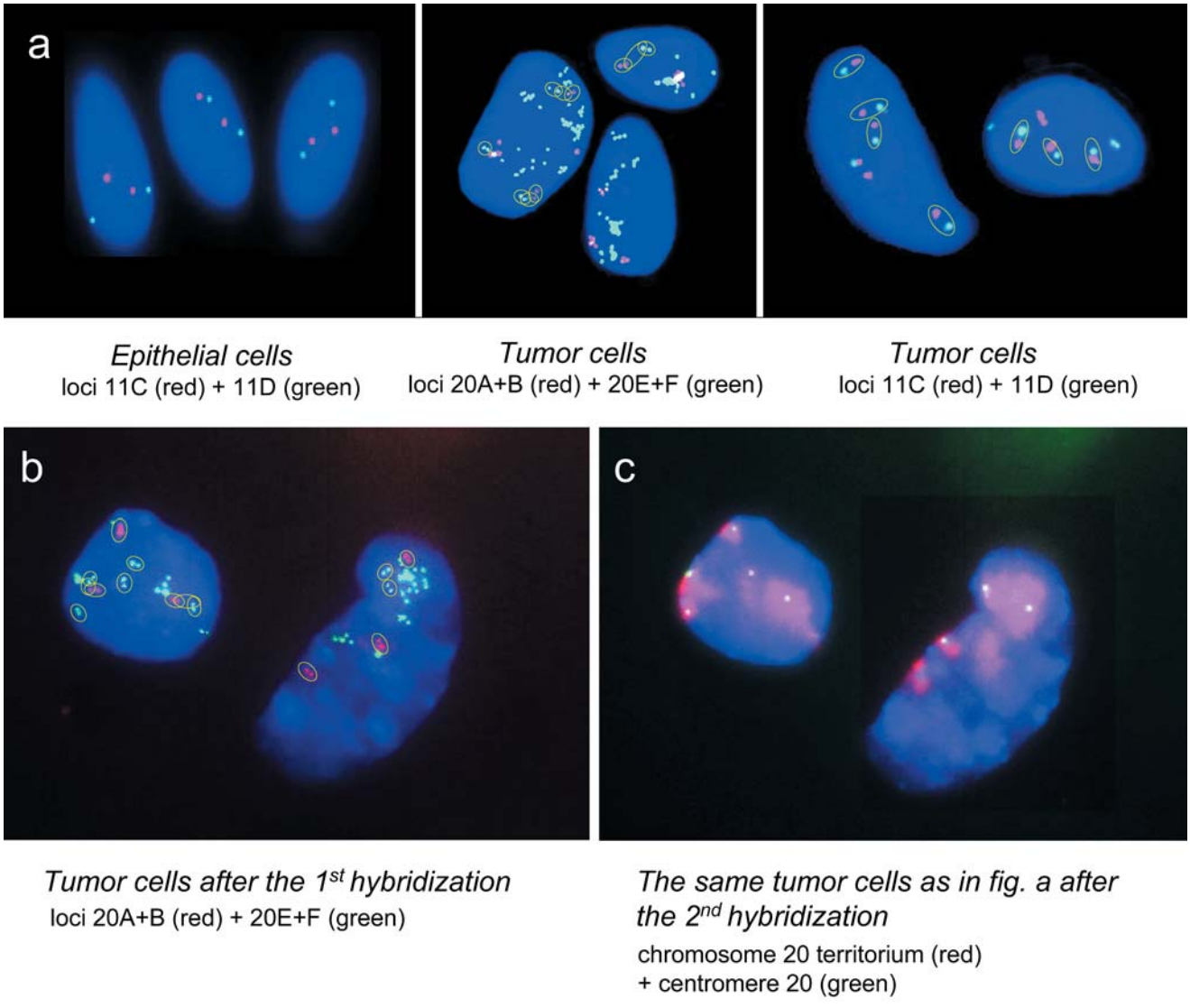

Fig. 1 **a** Examples of cells of colonic epithelium and colorectal carcinoma. The loci (*red* and *green*) of chromosome 11 (11C+11D) or 20 (A+B) and (E+F) (Table 2) were visualized by three-dimensional (3D) fluorescence in situ hybridization (FISH). The pairs of loci taken for nuclear distance (ND) measurements in tumor cells are *circled*. **b, c** Examples of nuclei after repeated hybridization. In the first hybridization (**b**), the loci 20A+B (*red*) and 20E+F (*green*) were detected; in the second hybridization (**c**) the chromosome 20 territories (*red*) and centromeric sequences (*green*) were visualized. The pairs of signals used for distance measurements are shown in *circles*. It can be seen that some territories of chromosome 20 are much enlarged

Cytometry

High resolution cytometry was performed as previously described (Kozubek M et al. 1999, 2001). The high-resolution cytometer is based on a completely automated Leica DM RXA fluorescence microscope equipped with a Nipcow disc (Yokogawa, Japan) creating a confocal effect and a CCD camera (Princeton Instruments, USA). The whole system is controlled by a personal computer equipped with two Intel Pentium III processors (Intel Corporation, San Francisco, Calif.), enabling automated acquisition of images.

Distance measurements

Distances were measured between two loci (labeled by different fluorochromes and in chromosome 20 also between two loci of the same fluorochrome) of known position on a chromosome sequence map pertaining to the same or neighboring chromosomal bands (Table 2) by means of the FISH 2.0 software (Kozubek M 1999, 2001). Two probes used for the same hybridization were intentionally selected to form pairs in the mutual proximity in a nucleus, allowing the distinguishing of those pertaining to the same chromosomal region in tumor nuclei where amplification of whole chromosomes as well as longer or shorter chromosomal sequences is frequent. The probes formed two pairs of signals in epithelial cells. In tumor cells, two or more pairs of these signals were found owing to the different degree of amplification. Owing to short distances between the pairs of probes (0.5–1 μm) in comparison with the nuclear dimensions (10 μm), randomly scattered pairs of amplified loci could be clearly distinguished in most cases. In addition, the chromosomes as well as centromeres were painted using repeated hybridization to make sure that the probes of a pair pertain to the same chromosome territory (Fig. 1). In a similar way the pairs of probes were distinguished in cases where only one of the probes was amplified forming many individual signals. In

tumor nuclei, distances were measured between clearly distinguishable pairs of signals. They were not measured in cases where another green or red signal was in the proximity of a pair of signals. Several regions with increased expression in colorectal carcinoma were found in chromosome 20 (http://bioinfo.amc.uva.nl/HTM/, Birkenkamp-Demtroder et al. 2002). To detect the topography in higher numbers of these regions, four probes were used together in one hybridization. Owing to the short distances between the pairs of probes used for chromosome 20 (approx. 0.5 μm), it was possible to stain the pair with the same color and distinguish the isolated amplified pairs from each other. The signals of both pairs of probes were separated in most cases and distances between them could easily be measured. Two of them located in the p-arm were red and another two in the q-arm were green. All selected regions of this chromosome, especially those in the q-arm were strongly amplified, forming aggregates in several tumors, which very often precluded being able to distinguish pairs of corresponding signals. However, in most nuclei some isolated pairs of signals were clearly identified for all probe combinations in all tumors.

The distances measured in individual nuclei were normalized to the mean nuclear radius. The mean distances (expressed as a percentage of the nuclear radius) were calculated from about 200 nuclei in both types of tissues for all six patients.

Results

Amplification of genetic loci inside the tumor tissue

Amplification of the loci investigated was found in all tumors; however, the degree of amplification of individual loci differed in cells within the tumor and among tumors. The amplification heterogeneity of six loci on chromosomes 7, 11 and 20 is shown in Fig. 2 for three different tumors. Nuclei with a different number of signals of the individual genetic loci were observed in all tumors. The heterogeneity can be characterized by the standard deviations (SD) of the distributions. The cell population of T1 was the most heterogeneous in the amplification of locus 20E+F (SD=1.0), and 20A+B (SD=0.8); meanwhile the amplification of other loci was less heterogeneous (SD=0.3–0.5). In some tumors, larger fractions of cells existed that had the same number of amplified loci. For example, about 47% of cells had three copies of 11C in T1; 38.5% and 52.1% of cells, respectively, contained four copies of this locus in T3 and T4. Similar fractions of cells of these latter tumors also contained three and four copies of 11D. These results show low heterogeneity of amplified loci 11C and 11D in T3 and T4 (SD=0.3 for T3 and 0.4 for T4).

Nuclear 3D distances between chromosomal loci of different GS in interphase nuclei of epithelial and tumor cells

Chromosome 7 p- and q-arms

The 1,632 kb GS between the pair of loci (7C–7D) of chromosome 7p was the shortest. The mean ND between these loci (measured in cells of T1 and E1) was roughly the same as the value of ND between the loci 7B–7C (ND 7B–7C) with a slightly longer GS (2,286 kb), which was

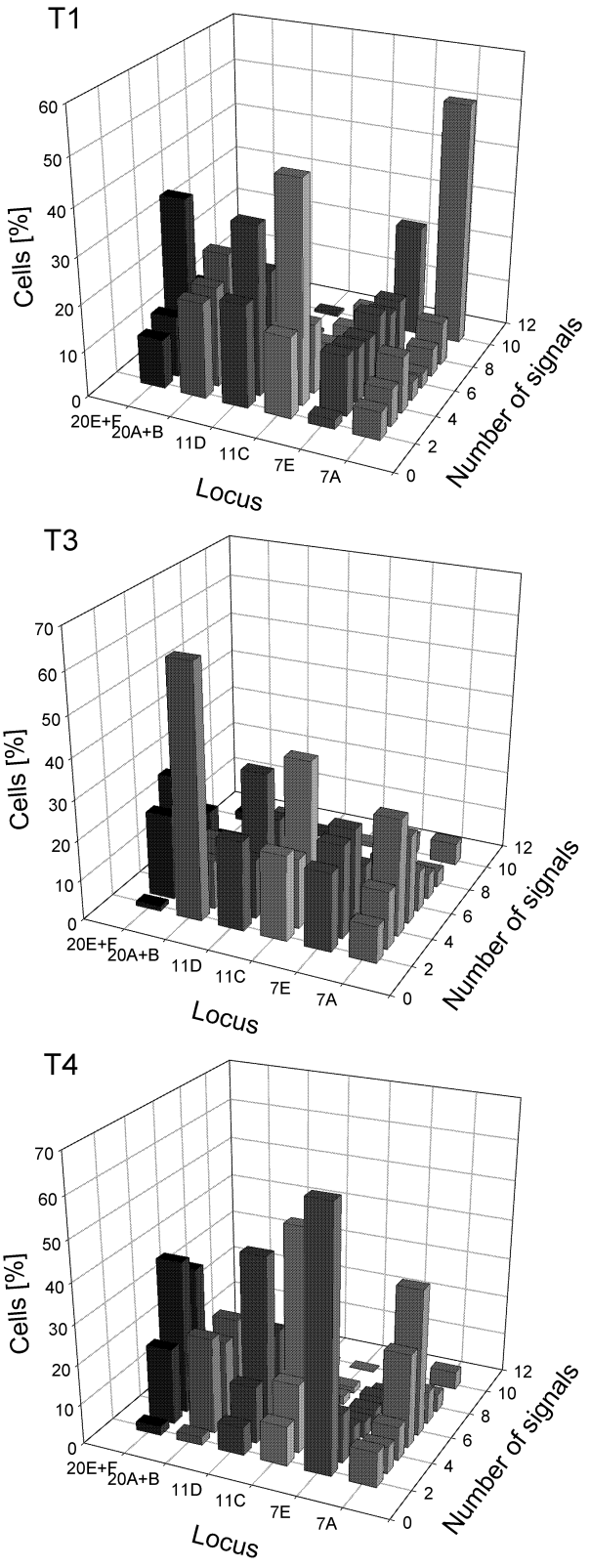

Fig. 2 Heterogeneity of amplification of selected loci in cells of three tumors (*T1*, *T3* and *T4*). Loci 7A and 7E mapped to 7p22.3 and 7p21.3, respectively; 11C and 11D mapped to 11p15.5 and 11p15.4, respectively; 20A+B and 20E+F mapped to 20p13 and 20q11.21, respectively

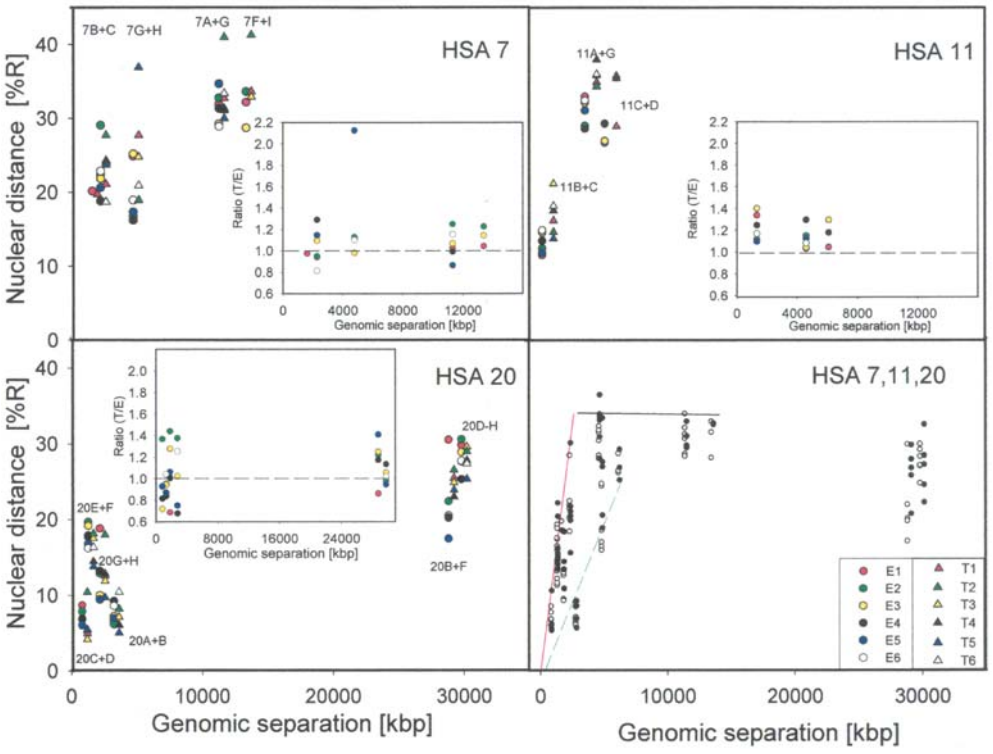

Fig. 3 The dependence of the mean nuclear distance (ND) between the pairs of loci on their genomic separation (GS) in colonic epithelium (*circles*) and tumor cells (*triangles*) of different patients. This relationship is shown separately for chromosomes (HSA)7, HSA11 and HSA20. ND(GS) for loci of all chromosomes is presented in panel HSA7, 11, 20 for tumor (*solid circles*) and epithelial cells (*open circles*). *[%R]* percentage of nuclear radius. *Insert*: Ratio of mean NDs between the loci in tumor (*T*) and epithelial cells (*E*)

measured in all patients. In T2 and E2 the 7B–7C ND was significantly larger than in the other patients (Fig. 3, HSA7). However, the 7G–7H ND with a GS of 4,776 kb was a little lower than that of 7B–7C with the exception of E1, E3, T1, T3 and T5. In the last tumor, the ND for 7G–7H was much higher than in other epithelial and tumor cells. Approximately the same values of ND were found for the loci 7A–7E (GS=11,315 kb) and 7F–7I (GS=13,399 kb) in the nuclei of all epithelial and tumor cells despite the 2,000 kb GS difference. However, in the majority of tumors the ND values were a little less than in corresponding epithelial cells as indicated by the ratio between ND in tumor and epithelial cells ($R=ND_t/ND_e$) (Fig. 3, HSA7, insert). The NDs of both pairs of loci were significantly larger in T2. The ratio ND_t/ND_e was higher than 1 in T2 for three pairs of loci (7G–7H, 7A–7E and 7F–7I), in T3 for loci 7F–7I, in T6 for 7A–7E and in T5 for 7G–7H (Fig. 3, HSA7, insert). Particularly high was the value of R for 7G–7H in patient 5.

Chromosome 11 p-arm

In chromosome 11, the NDs were measured between three pairs of loci (Table 2). The largest GS (6,110 kb) was between loci 11C–11D; the GSs of 11B–11C and 11A–11E were 1,323 kb and 4,654 kb, respectively. In most cases, the largest value of ND was found for 11A–11E even if the GS of these loci was lower than that for 11C–11D (Fig. 3, HSA11). In tumor cells the mean values of ND (ND_t) were higher than in corresponding epithelial cells, especially in loci 11B–11C with the exception of T6. The ND_t were larger than ND_e also for loci 11A–11E in T2 and T4. In other tumors the ND_ts were the same or lower than ND_e as shown in Fig. 3 (HSA11, insert).

Chromosome 20 p- and q-arms

Nuclear distances were measured between six pairs of loci with known GSs (Table 2). Two pairs of loci (20A–20B and 20C–20D) were allocated at 20p, and their GSs were 2,840 kb and 820 kb, respectively; two other pairs (20E–20F and 20G–20H) allocated at 20q had GS=1,426 kb and 1,480 kb, respectively. The distances were measured also between loci 20B (20p) and 20F (20q) with GS=28,824 kb and between loci 20D (20p) and 20H (20q) with GS=29,811 kb. Two pairs of loci, both located at 20q, had the same GS; however, their NDs differed. In epithelial cells, the ND of 20E–20F was significantly larger than the ND of 20G–20H (Fig. 3, HSA20) with the exception of E1. In addition, the ND values for 20E–20F were significantly larger than those of 20A–20B even if the GS of 20A–20B was two times larger. The ND values of 20A–20B were the same as those of ND 20C–20D. However, the GS of the latter locus was more than three times less than the former one (Table 2). The largest ND were found between loci 20D–20H, located at different arms of chromosome 20. On the other hand, the ND of 20B–20F with a similar GS to 20D–20H, was significantly lower in epithelial than in tumor cells with the exception of E1.

In the majority of tumor cells, the ND between the loci in chromosome 20 was shorter than in epithelial cells with

the exception of T2 in all loci, and T3 and T5 in loci 20G–20H. Higher ND_ts in comparison with ND_es were also observed between loci 20B–20F, representing different arms of chromosome 20, in all tumors with the exception of T2 (Fig. 3, HSA20, insert).

Functional relationship between ND and GS

The relationship between the mean ND and the GS of the loci of three investigated chromosomes in colonic epithelium and in tumor cells showed a linear initial phase in the region up to about 2 Mb determined by a large number of experimental points (Fig. 3, HSA7, 11, 20). However, the NDs of two pairs of loci (20A–20B, 7G–7H) clearly fell outside this linear relationship. The line with a steep slope encompasses the loci 20C–20D, 11B–11C, 20E–20F, 20G–20H and 7B–7C. Interestingly, two pairs of loci with very similar GS (2,840 kb between 20A–20B and 2,228 kb between 7B–7C) show very different NDs in all epithelial and tumor cells. Also, another two pairs (7G–7H and 11A–11E) of similar GS (4,700 kb and 4,560 kb, respectively) exhibit significantly different NDs (Fig. 3, HSA7, HSA11). A shorter ND was found also in loci 11C–11D with a longer GS (6,111 kb) compared with loci 11A–11E with a GS of 4,560 kb. At the larger GSs of loci representing the same arm of chromosome, the relationship between the molecular and NDs forms a plateau (Fig. 3, HSA7, 11, 20). Nuclear distances in both tissue types decrease at large molecular distances between loci representing different arms of the same chromosome.

The relationship between the ratio of NDs in tumor and epithelial cells and the average degree of amplification of the loci

The degree of amplification of individual loci was distinct inside the same tumor and among investigated tumors. A high degree of amplification was observed especially at the loci of chromosome 20, but also in some loci of chromosomes 7 and 11. The mean number of amplified pairs of loci per cell was calculated and the dependence of the ratio of the NDs between loci in tumor and epithelial cells [R(T/E)] on this number was plotted (Fig. 4). In the majority of tumor cells, the mean distances between the loci were the same or shorter than in the corresponding epithelial cells. The ratio of mean distances between the loci in tumor and epithelial cells (T/E) were variable; however, on average decreasing with a growing number of amplifications. In T2, where only rare amplifications were found, the greatest differences in the distances between the loci in epithelial and tumor cells were observed. The most amplified loci in this tumor were 20E–20F. Amplifications were found in about 40% of cells (the mean number of this pair of loci per cell was 2.9). In contrast to the non-amplified loci of this tumor, the distances between the moderately amplified loci 20E–20F in the tumor were approximately the same as in epithelial cells (R=T/E=0.95). A high value of R was observed also in some tumors for loci with a low degree of amplification (T1 and T3 in loci 11B–11C and T3 in loci 20G–20H). However, in more cases the value of R was lower than the average value expressed by the linear relationship in Fig. 4. On average, the value of R seems to depend on the degree of amplification of loci.

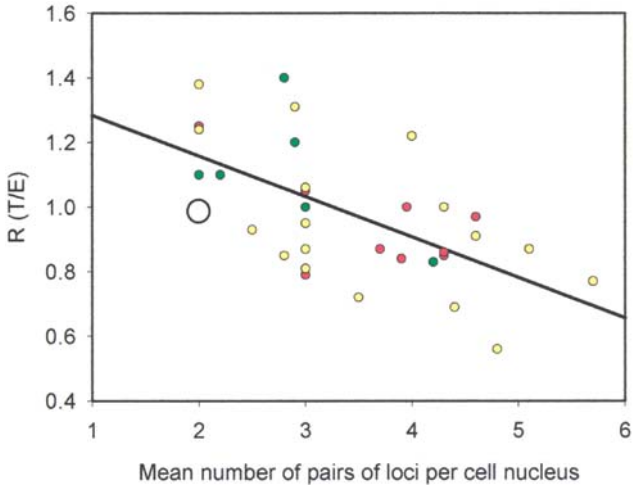

Fig. 4 The relationship between the ratio of nuclear distances (NDs) of the pairs of loci in tumor (*T*) and epithelial cells (*E*) and the mean degree of amplification of the loci per cell nucleus. *Solid circles* represent the T/E ratio for the pairs of loci in chromosomes 7 (*red*), 11 (*green*) and 20 (*yellow*) for different patients versus the mean degree of amplification of the loci. The *open circle* represents the supposed position of the point when the NDs between two loci in tumour and epithelial cells are the same (T/E=1) and both compared loci are in two copies per cell

Discussion

Changes in the chromosome structure in tumor cell nuclei compared with normal epithelial tissue are very complex. Heterogeneity was found in amplifications of shorter and longer regions of chromosomes, in a number of amplified regions per cell of the same tumor and in the arrangement of amplified loci in the cell. Owing to amplification of loci and their nuclear arrangement we were able to distinguish: the loci amplified individually and distributed randomly in the whole space of the nucleus; neighboring loci of the same chromosomal band amplified together and distributed as in the previous case; loci forming chains or clumps in two or more regions of the nucleus; and, finally, aggregates of many chains or clumps of amplified loci. Centromeres of all investigated chromosomes were frequently present in a higher number of copies, indicating the gain of the whole or a part of chromosome. Frequently, the degree of amplification of individual loci was substantially higher than the number of corresponding centromeres, showing an extra amplification of the locus that might indicate an important role of these loci in the carcinogenesis of colonic epithelium.

Territories of some chromosomes were often considerably enlarged, probably due to the massive amplification of different regions (Fig. 1).

In this paper we present data relating NDs between pairs of loci to their GSs in healthy epithelial cells of colonic epithelium and parallel tumor cells of six patients to find differences in spatial conformation of studied chromosomal regions. Seven regions of chromosomes 7, 11 and 20 containing a relatively high density of genes with increased expression in colorectal carcinoma were selected (http://bioinfo.amc.uva.nl/HTM/, Birkenkamp-Demtroder et al. 2002). We wished to find out whether increased transcription in tumor cells influences the structure of chromatin in these regions. The structure of chromatin was studied by measurements of NDs between pairs of loci with known position on the chromosome sequence map visualized by 3D FISH. All loci investigated showed amplification to a different degree and a distinct nuclear arrangement in tumor cells. Our results show that the relationship between the mean ND and GS of the loci is linear up to about 2 Mb with the same slope for both tissue types (Fig. 3, HSA 7, 11, 20). Two pairs of loci (20A+20B, 7G+7H) fell outside this linear slope, indicating the existence of two levels of chromatin folding. The pairs of loci 7B–7C and 20A-20B have a very similar GS (2.3 and 2.8 Mb); however, the ND of 7B–7C is significantly longer in both tissue types than the ND of 20A–20B (Fig. 3). Both these pairs of loci are located in R bands and are amplified in all tumors; contrary to 7B+7C the amplification of loci 20A+20B is much more pronounced. In tumor cells, the ND of 7B–7C is longer than in epithelial tissue in contrast to the ND of 20A–20B where the ND is shorter in most tumors. An opening of local chromatin structure and an increase in the distances between genetic loci was observed for regions with increased transcription induced by PML/RARα fusion protein and vice versa (Falk et al. unpublished). These results suggest that the increase in ND in some loci of tumor cells compared with epithelium is related to increased transcription. On the other hand, highly amplified loci showed decreased ND and, consequently, we hypothesize that the rate of transcription per locus is lower. These results are in agreement with the recent findings of Platzer et al. (2002) showing that chromosomal amplifications do not result in global induction of gene expression. The authors found that genes demonstrating significantly increased expression in association with chromosomal amplification are few in number and are not clustered together. These results support the conclusion that only genes of high relevance for carcinogenesis are both overexpressed and amplified.

Pairs of loci with similar GS (7B–7C with 2,286 kb GS and 20A–20B with 2,840 kb as well as 7G–7H with 4,776 kb and 11A–11E with 4,564 kb) differ in ND not only in tumor but also in epithelial cells, indicating a difference in chromatin compaction of these pairs in both cell types. The loci with similar GS but shorter ND do not fit into the linear relationship ND(GS) (Fig. 3) and seem to contain more condensed chromatin in both epithelium and tumor cells in contrast to the loci with longer ND and the same GS. In tumor cells, ND can be either longer or shorter (in highly amplified loci) than in epithelial cells, which explains the fact that the slope of the ND(GS) dependence is the same in both tissue types (Fig. 3, HSA7, 11, 20). Comparison of the NDs between loci with the same GS in different regions of chromosomes can provide information about local chromatin condensation. It follows from our results that large-scale chromatin structure is specific for specific regions and that it is preserved in tumor cells despite the amplification and higher expression of the regions.

For loci of larger GS (above 4.5 Mb), the ND did not increase in either epithelial or tumor cells (Fig. 3, HSA7, 11, 20), which can be explained by the existence of two levels of chromatin organization similar to those proposed by Yokota et al. (1995). Contrary to the random-walk giant-loop model (Sachs et al. 1995; Yokota et al. 1995, 1997), in which a random walk of the chromosome backbone leads to increasing ND in the range up to 100 Mb, our results showed a non-random looping of the chromosome backbone leading to relatively short distances between loci with high GS (e.g. lying on opposite arms of chromosomes) (Lukášová et al. 2002; Amrichová et al. 2003). Shorter ND of loci with high GS (around 30 Mb) in comparison to ND with lower GS (12 Mb) were observed in this work for loci pertaining to different arms of chromosome 20 (20B–20F and 20D–20H). This effect can be related to the flexion of the chromosome backbone in the centromeric region as shown earlier (Lukášová et al. 2002; Amrichová et al. 2003).

The relationship between the ratio of mean ND in tumor (T) and epithelial cells (E) and the mean degree of amplification in both loci is shown in Fig. 4. It follows from this figure that the T/E ratio decreases with an increase of amplification of the loci. On average, the T/E ratio for loci with low degree of amplification is greater than 1, indicating a more open chromatin structure in the loci of tumor cells. T/E is decreased for more amplified loci, which can be explained by the presence of a mechanism controlling the global level of expression of these loci by increasing chromatin condensation. The fluctuation of the T/E ratio at the same average level of amplification can be related to a different degree of amplification of individual loci, length of amplified regions or a higher-order chromatin structure in the loci connected with their position in the regions with different density of genes and different degree of expression of these genes.

General nuclear positions of genetic loci in tumor cells were investigated in our earlier papers (Koutna et al. 2000; Kozubek S et al. 2002). We found similar radial distributions of genetic loci investigated in epithelium as well as in tumor HT-29 cells, which is in contrast to the pronounced changes of chromosome structure, rearrangements and heterogeneity of amplification described here. It suggests that the mechanisms of formation of rearrangements conform to some general principles of nuclear order.

Acknowledgements The authors thank M. Rocchi for the generous supply of BAC clones. The work was supported by the Ministry of Health of the Czech Republic (NC6987-3), Ministry of Education (ME565), the Academy of Sciences of the Czech Republic (A1065203, A5004306) and the Grant Agency of the Czech Republic (GA202/02/0804, GA202/01/0197).

References

Amrichová J, Lukášová E, Kozubek S, Kozubek M (2003) Nuclear and territorial topography of chromosome telomeres in human lymphocytes. Exp Cell Res 289:11–26

Aust DE, Willenbucher RF, Terdiman JP, Ferrell LD, Chang CG, Moore DH, Molinard J, Clark A, Baretton GB, Loehrs U, Waldman FM (2000) Chromosomal alterations in ulcerative colitis-related and sporadic colorectal cancers by comparative genomic hybridization. Hum Pathol 31:109–114

Baylin SB, Herman JG (2000) DNA hypermethylation in tumorigenesis: epigenetics joins genetics. Trends Genet 16:168–174

Birkenkamp-Demtroder K, Christensen LL, Olesen SH, Frederiksen CM, Laiho P, Aaltonen LA, Laurberg S, Sorensen FB, Hagemann R, Orntoft TF (2002) Gene expression in colorectal cancer. Cancer Res 62:4352–4363

Bomme L, Lothe RA, Bardi G, Fenger C, Kronborg O, Heim S (2001) Assessment of clonal composition of colorectal adenomas by FISH analysis of chromosomes 1, 7, 13, and 20. Int J Cancer 92:816–823

Bridger JM, Bickmore WA (1998) Putting the genome on the map. Trends Genet 14:403–409

Brown R, Strathedee G (2002) Epigenomics and epigenetic therapy of cancer. Trends Mol Med 8:S43–48

Di Leonardo A, Linke SP, Yin Y, Wahl GM (1993) Cell cycle regulation of gene amplification. Cold Spring Harbor Symp Quant Biol LVIII: 655–667

Eberharter A, Becker PB (2002) Histone acetylation: a switch between repressive and permissive chromatin. Second in review series on chromatin dynamics. EMBO Rep 3:224–229

Falk M, Lukášová E, Kozubek S, Kozubek M (2002) Topography of genetic elements of X-chromosome relative to the cell nucleus and to the chromosome X territory determined for human lymphocytes. Gene 292:13–24

Fearon ER, Vogelstein B (1990) A genetic model for colorectal tumorigenesis. Cell 61:759–767

Fearon ER, Hamilton SR, Vogelstein B (1987) Clonal analysis of human colorectal tumors. Science 238:193–197

Ferreira J, Paollela G, Ramos C, Lamond AI (1997) Spatial organization of large-scale chromatin domains in the nucleus: a magnified view of single chromosome territories. J Cell Biol 139:1597–1610

Horn PJ, Peterson CL (2002) Molecular biology. Chromatin higher order folding-wrapping up transcription. Science 297:1824–1827

Jen J, Powell SM, Papadopoulos N, Smith KJ, Hamilton SR, Vogelstein B, Kinyler KW (1994) Molecular determinants of dysplasia in colorectal lesions. Cancer Res 54:5523–5526

Jenuwein T, Allis CD (2001) Translating the histone code. Science 293:1074–1080

Jonczyk P, White A, Lum K, Barrett JC, Tlsty TD (1993) Amplification potential in preneoplastic and neoplastic Syrian Hamster embryo fibroblasts transformed by various carcinogenes. Cancer Res 53:3098–3102

Kallioniemi A, Kallioniemi OP, Sudar D, Rutovitz D, Gray JW, Waldman F, Pinkel D (1992) Comparative genomic hybridization for molecular cytogenetic analysis of solid tumors. Science 258:818–821

Koutná I, Kozubek S, Žaloudík J, Kozubek M, Lukášová E, Matula Pa, Bártová E, Skalníková M, Cafourková A, Jirsová P (2000) Topography of genetic loci in tissue samples: towards new diagnostic tool using interphase FISH and high-resolution image analysis techniques. Anal Cell Pathol 20:173–185

Kozubek M, Kozubek S, Lukášová E, Marečková A, Bártová E, Skalníková M, Jergová A (1999) High-resolution cytometry of FISH dots in interphase nuclei. Cytometry 36:279–293

Kozubek M, Kozubek S, Lukášová E, Bártová E, Skalníková M, Matula P, Matula P, Jirsová P, Cafourková A, Koutná I (2001) Combined confocal and wide-field high-resolution cytometry of fluorescence in situ hybridization-stained cells. Cytometry 45:1-12

Kozubek S, Lukášová E, Jirsová P, Koutná I, Kozubek M, Gaňová A, Bártová E, Falk M, Paseková R (2002) 3D structure of the human genome: order in randomness. Chromosoma 111:321–331

Lamond AI, Earnshaw WC (1998) Structure and function in the nucleus. Science 280:547–553

Lukášová E, Kozubek S, Kozubek M, Falk M, Amrichová J (2002) The 3D structure of human chromosomes in cell nuclei. Chromosome Res 10:535–548

Melcher R, Steinlein C, Feichtinger W, Muller CR, Menzel T, Luhrs H, Scheppach W, Schmid M (2000) Spectral karyotyping of the human colon cancer cell lines SW480 and SW620. Cytogenet Cell Genet 88:145–152

Nakao K, Shibusawa M, Ishihara A, Yoshizawa H, Tsunoda A, Kusano M, Kurose A, Makita T, Sasaki K (2001) Genetic changes in colorectal carcinoma tumors with liver metastases analyzed by comparative genomic hybridization and DNA ploidy. Cancer 91:721–726

Neves H, Ramos C, Gomez da Silva M, Parreira A, Parreira L (1999) The nuclear topography of ABL, BCR, PML and RARα genes: evidence for gene proximity in specific phases of the cell cycle and stages of hematopoietic differentiation. Blood 93:1197–1207

Platzer P, Upender MB, Wilson K, Willis J, Luttenbaugh J, Nosrati A, Willson JK, Mack D, Ried T, Markowitz S (2002) Silence of chromosomal amplifications in colon cancer. Cancer Res 62:1134–1138

Rountree MR, Bachman KE, Herman JG, Baylin SB (2001) DNA methylation, chromatin inheritance, and cancer. Oncogene 28:3156–3165

Sachs RK, van den Engh G, Trask BJ, Yokota H, Hearst JE (1995) A random-walk/giant-loop model for interphase chromosomes. Proc Natl Acad Sci U S A 92:2710–2714

Sadoni N, Langer S, Fauth C, Bernardi G, Cremer T, Turner BM, Zink D (1999) Nuclear organization of mammalian genomes: polar chromosome territories build up functionally distinct higher order compartments. J Cell Biol 146:1211–1226

Schul W, de Jong L, van Driel R (1998) Nuclear neighbors: the spatial and functional organization of genes and nuclear domains. J Cell Biochem 70:159–171

Schwab M (1990) Oncogene amplification in neoplastic development and progression of human cancers. Crit Rev Oncogen 2:35–45

Sobin LH, Wittekind Ch (eds) (2002) TNM classification of malignant tumours (6 th edition). New York, Wiley-Liss

Spector DL (1996) Nuclear organization and gene expression. Exp Cell Res 229:189–197

Suzuki H, Gabrielson E, Chen W, Anbazhagan R, van Engeland M, Weijenberg MP, Herman JG, Baylin SB (2002) A genomic screen for genes upregulated by demethylation and histone deacetylase inhibition in human colorectal cancer. Nat Genet 31:141–149

Tlsty TD, Jonczyk P, White A, Sage M, Hall I, Schaefer D, Briot A, Livanos E, Roelofs H, Poulose B, Sanchez J (1993) Loss of chromosomal integrity in neoplasia. Cold Spring Harbor Quant Biol LVIII:645–654

Van Driel R, Wansink DG, Van Steensel B, Grande MA, Schul W, De Jong L (1995) Nuclear domains and the nuclear matrix. Int Rev Cytol 162A:151–189

Visser AE, Eils R, Jauch A, Little G, Bakker, PJM, Cremer T, Aten JA (1998) Spatial distributions of early and late replicating chromatin in interphase chromosome territories. Exp Cell Res 243:398–407

Wang T-L, Rago C, Silliman N, Ptak J, Markowitz S, Willson JKV, Parmigiani G, Kinzler KW, Vogelstein B, Valculescu VE (2002) Prevalence of somatic alterations in colorectal cancer cell genome. Proc Natl Acad Sci U S A 99:3076–3080

Yokota H, van den Engh G, Hearst JE, Sachs RK, Trask BJ (1995) Evidence for the organization of chromatin in megabase pair-sized loops arranged along a random walk path in the human G0/G1 interphase nucleus. J Cell Biol 130:1239–1249

Yokota H, Singer MJ, van den Engh GJ, Trask BJ (1997) Regional differences in the compaction of chromatin in human G0/G1 interphase nuclei. Chromosome Res 5:157–166

Zink D, Bornfleth H, Visser AE, Cremer C, Cremer T (1999) Organization of early and late replicating DNA in human chromosome territories. Exp Cell Res 247:176–188

Review Article

Frequent Chromatin Rearrangements in Myelodysplastic Syndromes – What Stands Behind?

(myelodysplastic syndromes / chromosomal rearrangements / chromosome 5 deletions / chromatin structure / architecture of the cell nucleus / chromothripsis)

E. PAGÁČOVÁ[1], M. FALK[1], I. FALKOVÁ[1,2,3], E. LUKÁŠOVÁ[1], K. MICHALOVÁ[4], A. OLTOVÁ[3], I. RAŠKA[5], S. KOZUBEK[1]

[1]Institute of Biophysics, Academy of Sciences of the Czech Republic, v. v. i., Brno, Czech Republic
[2]Department of Medical Technology, St. Elisabeth University of Health and Social Sciences, Bratislava, Slovak Republic, Signatory of Magnae Chartae Universitatum Bologna, European Union
[3]Department of Internal Medicine – Haematology and Oncology, University Hospital Brno and Faculty of Medicine, Masaryk University, Brno, Czech Republic
[4]Centre of Oncocytogenetics, General University Hospital in Prague, Prague, Czech Republic, and The Institute of Haematology and Blood Transfusion (IHBT), Prague, Czech Republic
[5]Institute of Cellular Biology and Pathology, First Faculty of Medicine, Charles University in Prague, Prague, Czech Republic

Abstract. Myelodysplastic syndromes (MDS) represent a clinically and genetically heterogeneous group of clonal haematopoietic diseases characterized by a short survival and high rate of transformation to acute myeloid leukaemia (AML). In spite of this variability, MDS is associated with typical recurrent non-random cytogenetic defects. Chromosomal abnormalities are detected in the malignant bone-marrow cells of approximately 40–80 % of patients with primary or secondary MDS. The most frequent chromosomal rearrangements involve chromosomes 5, 7 and 8. MDS often shows presence of unbalanced chromosomal changes, especially large deletions [del(5), del(7q), del(12p), del(18q), del(20q)] or losses of whole chromosomes (7 and Y). The most typical cytogenetic abnormality is a partial or complete deletion of 5q- that occurs in roughly 30 % of all MDS cases either as the sole abnormality or in combination with other aberrations as a part of frequently complex karyotypes. The mechanisms responsible for the formation of MDS-associated recurrent translocations and complex karyotypes are unknown. Since some of the mentioned aberrations are characteristic for several haematological malignancies, more general cellular conditions could be expected to play a role. In this article, we introduce the most common rearrangements linked to MDS and discuss the potential role of the non-random higher-order chromatin structure in their formation. A contribution of the chromothripsis – a catastrophic event discovered only recently – is considered to explain how complex karyotypes may occur (during a single event).

Received June 27, 2014. Accepted July 21, 2014.

This work was supported by: the OPVK CZ.1.07/2.3.00/30.0030 and COST-LD12039 projects of the Ministry of Education, Youth and Sports of the Czech Republic, the Project of Excellence P302/12/G157 of the Grant Agency of the Czech Republic, and the Czech Republic contribution to JINR Dubna in 2014.

Corresponding author: Martin Falk, Institute of Biophysics, Academy of Sciences of CR, v. v. i., Královopolská 135, 612 65 Brno, Czech Republic. Phones: (+420) 541515116/165; (mobile) (+420) 728084060; e-mails: mfalk@seznam.cz, falk@ibp.cz

Abbreviations: AML – acute myeloid leukaemia, CA – chromosomal aberrations, C-CA – complex chromosomal aberrations, CDR – commonly/critical deleted region, DSB – DNA double-strand break, MDS – myelodysplastic syndrome, RIDGE – regions of increased gene expression, RS – replication stress.

I. Myelodysplastic syndromes – a brief introduction

Myelodysplastic syndromes (MDS) represent a diverse group of heterogeneous clonal bone marrow diseases (Vardiman et al., 2009; Ades et al., 2014) that are associated with ineffective haematopoiesis, peripheral blood cytopoenias and increased risk of progression to acute myeloid leukaemia (AML) (Lindsley and Ebert, 2013). Typical morphologic features of MDS involve, among others, defects in maturation in the myeloid series and rising amounts of blasts or ringed sideroblasts (Nimer, 2006). The annual incidence of MDS is about four cases per 100,000 people (Ades et al., 2014).

Although MDS may also appear in childhood as a consequence of various inherited predispositions, such

as Fanconi anaemia (Liew and Owen, 2011; Ades et al., 2014; West et al., 2014), most cases burst sporadically and patients are diagnosed in their late 60s or early 70s, with a median age at diagnosis being 65–70 years; less than 10 % of patients are younger than 50 years. This might indicate that MDS originates from accumulation of unrepaired DNA defects caused by normal physiological cellular processes (Kryston et al., 2011; Ghosal and Chen, 2013; Behrens et al., 2014). The life style, history of various diseases, and exposures to stress are therefore expected to contribute to MDS initiation. On the other hand, chromothripsis – a still mysterious process of chromosome "explosion" (Stephens et al., 2011; Forment et al., 2012) – has recently been discovered as a single-step alternative to this multi-step development of complex cancer karyotypes and cancer disease.

II. Recurrent chromosomal abnormalities in MDS

At the molecular level, MDS syndromes arise due to various types of genetic aberrations (Table 1) (Fernandez-Mercado et al., 2013; Huret et al., 2013); hence, different subtypes of MDS can be distinguished with a different molecular pathogenesis and various propensity for development of acute myeloid leukaemia (AML). On average, AML occurs in 10–15 % of MDS patients (reviewed e.g. in Ades et al., 2014; Visconte et al., 2014).

The most frequent initiating aberration in MDS is a large, unbalanced chromosomal deletion that can include even whole chromosome arms (Fig. 1) (Zemanova et al., 2008). This fact seriously complicates identification of genes that are critically involved in MDS pathogenesis. The deletions typically include long arms of chromosome 5 (Fig. 1), 7, and 20 but can affect different parts of other chromosomes as well, such as chromosomes 3q, 12p, 13q, 16q, 17p, 18q, and 20q (Haase et al., 2007). Except deletions, trisomies (8, less frequently 11 and 21) monosomies (21 and 10), and other unbalanced chromosomal changes (Haase et al., 2007) were reported. Chromosomes 5, 7, and 17 also frequently participate in rearrangements that involve more chromosomes (Zemanova et al., 2008, 2014). Simple chromosomal aberrations (CA) are typical of primary MDS (Fig. 1), while secondary MDS are frequently characterized by very complex genomic rearrangements (C-CA) (similar to an AML karyotype in Fig. 2).

Table 1: Cytogenetic abnormalities in myelodysplastic syndrome (Greenberg et al., 1997; Bernasconi et al., 2006; Olney and Le Beau, 2007)

Recurring cytogenetic abnormalities	
Abnormality	**Incidence**
De novo MDS	
- 5/del (5q)	6-20%
- 7/del (7q)	1-10%
Trisomy 8	5-10%
Y	1-10%
del(20q)	2-5%
del(17q)	< 1-7%
Complex (≥ 3 abnormalities)	10-20%
Treatment-related MDS	
- 5/del (5q)	40%
- 7/del (7q)	40%

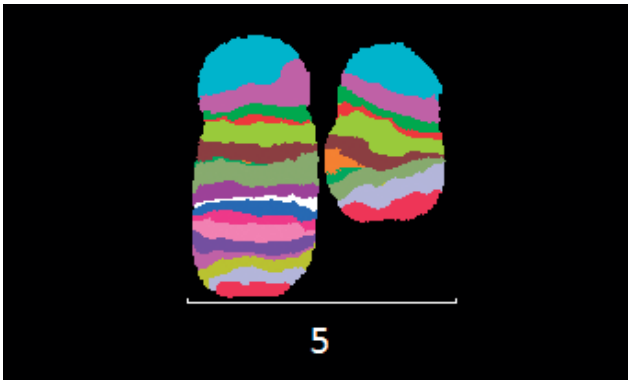

Fig. 1. An illustrative example of large recurrent deletions of the long arm of chromosome 5 in MDS. Figure shows the deletion del(5)(q13.3q33.3) detected by multicolour banding (m-band) in the karyotype of a patient suffering from MDS.

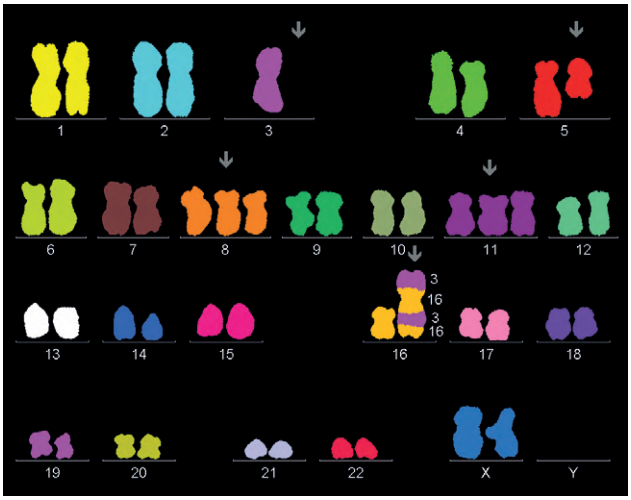

Fig. 2. An illustrative example of complex karyotypes associated with MDS/AML. Figure shows the karyotype 47,XX,-3,del(5)(q13q33),+8,+11,der(16)ins(16;3)(q22;?)t(3;16)(?;p13) that was discovered in an AML patient by multicolour fluorescence *in situ* hybridization (m-FISH). Each chromosome is identified by a specific colour.

II.1. Chromosome 5

Interstitial deletions of 5q (Fig. 1) represent one of the most frequent cytogenetic aberrations in myeloid malignancies and can be found in the majority of all *de novo* MDS cases (about 10–20 %) – either as an isolated abnormality (in 14 % of patients with clonal abnormalities) (Fig. 1), together with one other abnormality (5 %), or as a part of a more complex karyotype (11 %) (Bernasconi et al., 2005; Haase et al., 2007; Fernandez-Mercado et al., 2013). Patients carrying the interstitial deletion of 5q as a single defect are classified as a distinct MDS subcategory (5q- syndrome). Interstitial de-

letions of 5q also appear with a similar frequency in acute myeloid leukaemia (AML) (Fig. 2). Interestingly, no differences in the breakpoints were noticed for these different diseases, which suggests the same origin of the rearrangements (Giagounidis et al., 2004). However, the mechanisms responsible for this specific impairment of the bone marrow in MDS and AML patients are still largely unknown, as discussed later.

The position and size of 5q deletions depend on the study, methods used, and patients involved, but two commonly deleted regions (CDR) were identified: CDR1, which includes chromosomal bands 5q32-5q33.2 (8.5 Mb), and CDR2, which encompasses bands 5q31.2--5q31.3 (1.92 Mb). While deletions of 5q32-q33 were mostly linked with the milder form of MDS (5q- syndrome), the region 5q31 was absent in many MDS patients with a high risk of progression into AML (Le Beau et al., 1993). Boultwood et al. (2010) demonstrated that the majority of all reported interstitial deletions of chromosome 5 fall into one of the three following types: del(5)(q13q31), del(5)(q13q33), and del(5)(q22q35). In most cases, the deletions include all the three or two of these regions.

For the description of other frequent rearrangements and CDR on the remaining chromosomes, the reader is referred to the following original works: chromosome 7 (Stephenson et al., 1995; Le Beau et al., 1996; Bernasconi et al., 2006; Olney and Le Beau, 2007; Haase, 2008; Adema et al., 2013) chromosome 20 (Dewald et al., 1993; Bench et al., 2000; Bernasconi et al., 2006; Douet-Guilbert et al., 2008; Huh et al., 2010; Okada et al., 2012; Bacher et al., 2014); and chromosome 8 (Greenberg et al., 1997; Mishima et al., 1998; Paulsson and Johansson, 2007).

III. Speculations on the mechanism responsible for formation of recurrent and complex chromosomal rearrangements in MDS

If we could better understand MDS at the molecular level, we could more efficiently develop the disease treatment and diagnostics. Nowadays, researchers can scrutinize genomes by modern methods of molecular cytogenetics. Although this methodological progress helped us to reveal some genes and functions of their products involved in MDS pathogenesis (Visconte et al., 2014), we still poorly comprehend how the most frequent aberrations form in MDS, and what is the relationship between single and complex rearrangements.

The existence of recurrent chromosomal aberrations in MDS points to important roles of the affected regions in the disease pathogenesis, which is probably associated with clonal selection of these particular aberrations. In addition, this may also indicate that some chromosomes and their loci are more prone to chromatin damage and rearrangements. As described, deletions of the q-arms of chromosomes 5 (Fig. 1), 7, and 20 markedly predominate in MDS. In addition to deletions, the same chromosomes can often also be affected by other types of aberrations, such as translocations. Multiple rearrangements of these chromosomes are detected in almost all patients with complex genotype changes. On the other hand, some other chromosomes or their parts, e.g. the short arms of chromosome 10, do not participate in MDS-associated chromatin rearrangements at all. Importantly, the most frequent chromosomal abnormalities described above are characteristic not only for MDS, but also for some other blood malignancies (Fig. 2).

These facts suggest that both the formation and clonal selection of recurrent aberrations might be driven by more general cell conditions that are not limited to MDS. Concerning the formation of chromosomal lesions and rearrangements, we propose that a cell type-specific or even individual cell-specific chromatin structure could play a role, potentially in combination with some other still unspecified/unknown factors.

For instance, a chromatin structure that allows fragile sites to appear at specific chromosomal loci may simplify "directed" chromatin damage and result in preferential formation of *sui generis* aberrations that may be consequently selected during clonal evolution of the cancer genome (Wang et al., 2008; Burrow, et al., 2009; Dillon et al., 2010; Monyarch et al., 2013). Indeed, the FRA5C and FRA5G fragile sites were discovered at q31 and q35 loci of chromosome 5, respectively, and put into context with cancer development (Calin et al., 2004; Monyarch et al., 2013).

However, the size and breakpoints of interstitial deletions at chromosome 5, chromosome 7, and chromosome 20 largely vary among patients, although some common chromosomal regions (CDR) are deleted in most cases. Hence, the locus-specific chromatin structure at higher levels of organization, together with global nuclear chromatin architecture, could also be reasonably suspected to participate in the formation of some typical chromosomal aberrations in MDS. Likely, various hierarchical levels of chromatin organization might contribute to an additive or even synergistic effect.

Contrary to the older hypothesis, the cell nucleus is now considered as a highly organized organelle (reviewed in Manuelidis and Chen, 1990; Münkel et al., 1999; Kozubek et al., 2002; Cremer and Cremer, 2010). Many researchers confirmed that genes are distributed non-homogeneously along the genome (Caron et al., 2001) and that the dynamic chromatin structure regulates its function (Kozubek et al., 2002; Goetze et al., 2007). Historically distinguished chromatin domains are euchromatin and heterochromatin, which can be stained with Giemsa on metaphase chromosomes and recognized as the G-light and dark bands, respectively. While heterochromatic G-dark bands contain only about 9.3 genes per megabase (Mb) of DNA and are tightly condensed, gene-rich G-bands (G-light) and very gene-rich sub-telomeric T-bands (in humans) are largely decondensed and estimated to include 20 and 78 genes/Mb, respectively (Bernardi, 1993). Genetically active chromatin and inactive chromatin also differ in their

protein composition. We have recently shown that inactive condensed chromatin, abundant in heterochromatin-binding proteins, is better protected by these proteins from induction of DNA double-strand breaks (DSB) by free radicals coming from water radiolysis (Falk et al., 2008, 2010, 2014). On the other hand, repair of DSB in heterochromatin is more difficult and slower, and requires extensive chromatin decondensation to proceed (Kruhlak et al., 2006; Falk et al., 2007, 2008). This decondensation may locally increase chromatin mobility at the sites of heterochromatic DSB, which is followed by protrusion of these lesions into the nuclear subcompartments of low chromatin density or interchromatin space (Falk et al., 2007). This behaviour may increase the probability of chromatin translocations between originally more distant partner loci (reviewed in Falk et al., 2010).

Genetically active chromosomal regions locate preferentially closer to the nuclear centre, while the inactive ones mostly appear around the nucleolus and nuclear envelope (Cremer and Cremer, 2010). Importantly, the same rules also apply to chromatin organization inside chromosomal territories (Falk et al., 2002; Kozubek et al., 2002; Lukasova et al., 2002) where the centromere and heterochromatic loci usually occupy the envelope-oriented part of the territory, while telomeres and active chromatin "protrude" to its inner part facing the nuclear centre (Falk et al., 2002; Kozubek et al., 2002; Lukasova et al., 2002). This causes functional and structural polarization of genetically active chromosomal territories, such as in chromosomes 17 and 19 (Kozubek et al., 2002; Lukasova et al., 2002), which can potentially introduce some tension in specific chromatin loci.

The polarization is less prominent or absent in territories with only low overall expression, like chromosomes 18 and X (Falk et al., 2002; Kozubek et al., 2002). Therefore, chromosome-specific polarization forces may create chromatin loops that could perhaps contribute to preferential deletions of large chromatin blocks that contain specific CDR regions but arise at variable breakpoints; in contrast, more precise breakage hotspots may be expected if MDS deletions appear due to a simple presence of chromatin fragile sites.

Highly expressed loci, e.g. those containing clusters of co-regulated genes or so called Regions of Increased Gene Expression (RIDGE; Caron et al., 2001), may even protrude outside of their maternal territory, into the interchromatin space (Pombo et al., 1998; Volpi et al., 2000; Branco and Pombo, 2006). Evidently, this phenomenon in general might simplify formation of chromosome breaks at specific loci as well.

The radial distribution of the whole chromosomal territories in interphase nuclei also reflects their overall transcription levels; the active territories preferentially inhabit central concentric shells of the nucleus and *vice versa* (Kozubek et al., 2002; Cremer and Cremer, 2010). The width of radial shells occupied by particular chromosomes is chromosome-specific (Kozubek et al., 2002). The higher-order chromatin structure therefore also determines the probability of mutual chromatin interactions and potentially chromosomal translocations between individual chromosomes (Kozubek et al., 1997; Lukasova et al., 1999; Neves et al., 1999; Falk et al., 2010; Kenter et al., 2013).

The chance that particular loci would be involved in a translocation may further increase with their localization in the outer zone of the territory, characterized by more or less extensive intermingling between chromatin of neighbouring chromosomes (Branco and Pombo, 2006). Although the nuclear positions of specific loci are in general dictated by the location of their maternal chromosome territories, some chromatin loops can protrude even outside the territory, as already discussed. Whether and to what extent the described observations can explain formation of frequent chromosomal aberrations in MDS is under investigation (Falk et al., unpublished).

Advanced MDS are accompanied by very complex chromosomal rearrangements. For instance, Zemanova et al. (2013, 2014) discovered that the true monosomy of chromosome 5, frequently reported in MDS, *de facto* does not exist. Rather, chromosome 5 seems to undergo extensive pulverization followed by translocation of the generated chromatin fragments to the "surrounding" chromosomes (Zemanova et al., 2013, 2014). What triggers such chromosome "explosion" and why it affects only specific chromosomes or chromosomal loci represents an exciting subject of current research. Zemanova et al. (2014) suggest that initial deletion at the long arm of chromosome 5 destabilizes the chromosome, which is consequently easily prone to further damage. However, chromosome fragmentation by chromothripsis has recently been described as a new and probably more common phenomenon in carcinogenesis (Stephens et al., 2011; Forment et al., 2012). Contrary to the currently accepted theory of the multi-step tumour development (Righolt and Mai, 2012; Burrell et al., 2013; Korbel and Campbell, 2013; Pihan, 2013; Zhang et al., 2013), chromothripsis presupposes sudden multiple chromosome rearrangements that can result in complex karyotypes in a single step. What fraction of cancers can be initiated by chromothripsis is under investigation; nevertheless, it is already evident that the mechanism of chromothripsis must also be applicable to other cancer types, not always associated with large deletions. Hence, although chromosomal deletions might decrease the chromosome stability, chromothripsis is probably initiated by a more general process in cancer cells.

A frequent and early event during the tumour genesis is replication stress (RS). RS is a dynamic chain of events that starts from acutely arrested replication forks with fully assembled replisomes. If RS persists, stalled forks are converted into collapsed forks (Lambert and Carr, 2005), specific nucleases cleave problematic DNA, and finally transform collapsed forks into DSBs (Fekairi et al., 2009; Forment et al., 2012). Recently, Toledo et al. (2013) suggested that long-lasting RS causes a replication catastrophe and cell death due to exhaustion of RPA proteins. RPA bind to ssDNA in replication forks and protect them from DNA breakage. Hence, the lack

of these proteins initiates massive and synchronized fragmentation of chromatin loops that are associated in the affected replication factory/factories and may originate from one or more chromosomes. The authors propose that this chromosome destruction mostly brings about complete disintegration of the nucleus, but may also represent a precursor of cancer-related genomic abnormalities. This may happen when DNA, previously "pulverized" by chromothripsis, is erratically reassembled (Stephens et al., 2011; Forment et al., 2012). Nevertheless, various mechanisms of chromothripsis have been put forward, so that further research is necessary to shed more light on the processes by which complex MDS karyotypes are formed.

IV. Conclusion

MDS is associated with various chromosomal aberrations among which interstitial deletions of the q arms of several chromosomes are the most prevalent. The same chromosomes also participate in other types of rearrangements that frequently form very complex MDS karyotypes. Some chromosomal abnormalities typical of MDS are also recurrent in other haematological malignancies. The cause of preferential selection or formation of these specific aberrations is not yet known. We propose that the higher-order chromatin structure, cell type-specific or even individual cell-specific, might represent one of important cellular factors that influence formation of MDS-associated deletions, translocations, and other genomic lesions. Complex MDS karyotypes may potentially arise as a consequence of chromothripsis, which allows formation of complicated multiple rearrangements in a "single" step. However, more experiments are needed to support the above-presented theoretical speculations.

References

Adema, V., Hernandez, J. M., Abaigar, M., Lumbreras, E., Such, E., Calull, A., Dominguez, E., Arenillas, L., Mallo, M., Cervera, J., Marugan, I., Tormo, M., Garcia, F., Gonzalez, T., Luño, E., Sanzo, C., Martin, M. L., Fernandez, M., Costa, D., Blazquez, B., Barreña, B., Marco, F., Batlle, A., Buño, I., Laperche, C. M., Noriega, V., Collado, R., Ivars, D., Carbonell, F., Vallcorba, I., Melero, J., Delgado, E., Vargas, M. T., Grau, J., Salido, M., Espinet, B., Melero, C., Florensa, L., Pedro, C., Sole, F. (2013) Application of FISH 7q in MDS patients without monosomy 7 or 7q deletion by conventional G-banding cytogenetics: does -7/7q- detection by FISH have prognostic value? *Leuk. Res.* **37**, 416-421.

Ades, L., Itzykson, R., Fenaux, P. (2014) Myelodysplastic syndromes. *Lancet* **383**, 2239-2252.

Bacher, U., Haferlach, T., Schnittger, S., Zenger, M., Meggendorfer, M., Jeromin, S., Roller, A., Grossmann, V., Krauth, M., T., Alpermann, T., Kern. W., Haferlach, C. (2014) Investigation of 305 patients with myelodysplastic syndromes and 20q deletion for associated cytogenetic and molecular genetic lesions and their prognostic impact. *Br. J. Haematol.* **164**, 822-833.

Behrens, A., van Deursen, J. M., Rudolph, K. L., Schumacher, B. (2014) Impact of genomic damage and ageing on stem cell function. *Nat. Cell Biol.* **16**, 201-207.

Bench, A. J., Nacheva, E. P., Hood, T. L., Holden, J. L., French, L., Swanton, S., Champion K. M, Li, J., Whittaker, P., Stavrides, G., Hunt, A. R., Huntly, B. J., Campbell, L. J., Bentley, D. R., Deloukas, P., Green, A. R. (2000) Chromosome 20 deletions in myeloid malignancies: reduction of the common deleted region, generation of a PAC/BAC contig and identification of candidate genes. UK Cancer Cytogenetics Group (UKCCG). *Oncogene* **19**, 3902-3913.

Bernardi, G. (1993) The vertebrate genome: isochores and evolution. *Mol. Biol. Evol.* **10,** 186-204.

Bernasconi, P., Klersy, C., Boni, M., Cavigliano, P. M., Calatroni, S., Giardini, I., Rocca, B., Zappatore, R., Caresana, M., Quarna, J., Lazzarino, M., Bernasconi, C. (2005) Incidence and prognostic significance of karyotype abnormalities in de novo primary myelodysplastic syndromes: a study on 331 patients from a single institution. *Leukemia* **19**, 1424-1431.

Bernasconi, P., Boni, M., Cavigliano, P. M., Calatroni, S., Giardini, I., Rocca, B., Zappatore, R., Dambruoso, I., Caresana, M. (2006) Clinical relevance of cytogenetics in myelodysplastic syndromes. *Ann. N. Y. Acad. Sci.* **1089**, 395-410.

Boultwood, J., Pellagatti, A., McKenzie, A. N. J., Wainscoat, J. S. (2010) Advances in the 5q- syndrome. *Blood* **116**, 5803-5811.

Branco, M. R., Pombo, A. (2006) Intermingling of chromosome territories in interphase suggests role in translocations and transcription-dependent associations. *PLoS Biol.* **4**, e138.

Burrell, R. A., McGranahan, N., Bartek, J., Swanton, C. (2013) The causes and consequences of genetic heterogeneity in cancer evolution. *Nature* **501**, 338-345.

Burrow, A. A., Williams, L. E., Pierce, L. C., Wang, Y. H. (2009) Over half of breakpoints in gene pairs involved in cancer-specific recurrent translocations are mapped to human chromosomal fragile sites. *BMC Genomics* **10**, 59.

Calin, G. A., Sevignani, C., Dumitru, C. D., Hyslop, T., Noch, E., Yendamuri, S., Shimizu, M., Rattan, S., Bullrich, F., Negrini, M., Croce, C. M. (2004) Human microRNA genes are frequently located at fragile sites and genomic regions involved in cancers. *Proc. Natl. Acad. Sci. USA* **101**, 2999-3004.

Caron, H., van Schaik, B., van der Mee, M., Baas, F., Riggins, G., van Sluis, P., Hermus, M. C., van Asperen, R., Boon, K., Voûte, P. A., Heisterkamp, S., van Kampen, A., Versteeg, R. (2001) The human transcriptome map: clustering of highly expressed genes in chromosomal domains. *Science* **291**, 1289-1292.

Cremer, T., Cremer, M. (2010) Chromosome territories. In: *CSH Perspectives in Biology 2*. Cold Spring Harbor Laboratory Press, New York.

Dewald, G. W., Schad, C. R., Lilla, V. C., Jalal, S. M. (1993) Frequency and photographs of HGM11 chromosome anomalies in bone marrow samples from 3,996 patients with malignant hematologic neoplasms. *Cancer Genet. Cytogenet.* **68**, 60-69.

Dillon, L. W., Burrow, A. A., Wang, Y. H. (2010) DNA instability at chromosomal fragile sites in cancer. *Curr. Genomics* **11**, 326-337.

Douet-Guilbert, N., Basinko, A., Morel, F., Le Bris, M. J., Ugo, V., Morice, P., Berthou, C., De Braekeleer, M. (2008) Chro-

mosome 20 deletions in myelodysplastic syndromes and Philadelphia-chromosome-negative myeloproliferative disorders: characterization by molecular cytogenetics of commonly deleted and retained regions. *Ann. Hematol.* **87**, 537-544.

Falk, M., Lukasova E., Kozubek, S., Kozubek, M. (2002) Topography of genetic elements of X-chromosome relative to the cell nucleus and to the chromosome X territory determined for human lymphocytes. *Gene* **292**, 13-24.

Falk, M., Lukasova, E., Gabrielova, B., Ondrej, V., Kozubek, S. (2007) Chromatin dynamics during DSB repair. *Biochim. Biophys. Acta* **1773**, 1534-1545.

Falk, M., Lukasova, E., Kozubek, S. (2008) Chromatin structure influences the sensitivity of DNA to γ-radiation. *Biochim. Biophys. Acta* **1783**, 2398-2414.

Falk, M., Lukasova, E., Kozubek, S. (2010) Higher-order chromatin structure in DSB induction, repair and misrepair. *Mutat. Res.* **704**, 88-100.

Falk, M., Lukasova, E., Falkova, I., Stefancikova, L., Jezkova, L., Bacikova, A., Davidkova, M, Boryeko, A., Krasavin, E. A., Kozubek, S. (2014) Chromatin differentiation of white blood cells decreases DSB damage induction, prevents functional assembly of repair foci, but has no influence on protrusion of heterochromatic DSBs into the low-dense chromatin. *J. Rad. Res.* **55**, i81-i82.

Fekairi, S., Scaglione, S., Chahwan, C., Taylor, E. R., Tissier, A., Coulon, S., Dong, M. Q., Ruse, C., Yates, J. R., Russell, P., Fuchs, R. P., McGowan, C. H., Gaillard, P. H. L. (2009) Human SLX4 is a Holliday junction resolvase subunit that binds multiple DNA repair/recombination endonucleases. *Cell* **138**, 78-89.

Fernandez-Mercado, M., Burns, A., Pellagatti, A., Giagounidis, A., Germing, U., Agirre, X., Prosper, F., Aul, C., Killick, S., Wainscoat, J. S., Schuh, A., Boultwood, J. (2013) Targeted re-sequencing analysis of 25 genes commonly mutated in myeloid disorders in del(5q) myelodysplastic syndromes. *Haematologica* **98**, 1856-1864.

Forment, J. V., Kaidi, A., Jackson, S. P. (2012) Chromothripsis and cancer: causes and consequences of chromosome shattering. Nature reviews. *Cancer* **12**, 663-670.

Ghosal, G., Chen, J. (2013) DNA damage tolerance: a double-edged sword guarding the genome. *Transl. Cancer Res.* **2**, 107-129.

Giagounidis, A. A. N., Germing, U., Haase, S., Hildebrandt, B., Schlegelberger, B., Schoch, C., Hildebrandt, B., Schlegelberger, B., Schoch, C., Wilkens, L., Heinsch, M., Willems, H., Aivado, M., Aul, C. (2004) Clinical, morphological, cytogenetic, and prognostic features of patients with myelodysplastic syndromes and del(5q) including band q31. *Leukemia* **18**, 113-119.

Goetze, S., Mateos-Langerak, J., van Driel, R. (2007) Three-dimensional genome organization in interphase and its relation to genome function. *Semin. Cell. Dev. Biol.* **18**, 707-714.

Greenberg, P., Cox, C., LeBeau, M. M., Fenaux, P., Morel, P., Sanz, G., Vallespi, T., Hamblin, T., Oscier, D., Ohyashiki, K., Toyama, K., Aul, C., Mufti, G., Bennett, J. (1997) International scoring system for evaluating prognosis in myelodysplastic syndromes. *Blood* **89**, 2079-2088.

Haase, D., Germing, U., Schanz, J., Pfeilstöcker, M., Nösslinger, T., Hildebrandt, B., Kundgen, A., Lübbert, M., Kunzmann, R., Giagounidis, A. A., Aul, C., Trümper, L., Krieger, O., Stauder, R., Müller, T. H., Wimazal, F., Valent, P., Fonatsch, C., Steidl, C. (2007) New insights into the prognostic impact of the karyotype in MDS and correlation with subtypes: evidence from a core dataset of 2124 patients. *Blood* **110**, 4385-4395.

Haase, D. (2008) Cytogenetic features in myelodysplastic syndromes. *Ann. Hematol.* **87**, 515-526.

Huh, J., Tiu, R. V., Gondek, L. P., O'Keefe, C. L., Jasek, M., Makishima, H., Jankowska, A. M., Jiang, Y., Verma, A., Theil, K. S., McDevitt, M. A., Maciejewski, J. P. (2010) Characterization of chromosome arm 20q abnormalities in myeloid malignancies using genome-wide single nucleotide polymorphism array analysis. *Genes Chromosomes Cancer* **49**, 390-399.

Huret, J. L., Ahmad, M., Arsaban, M., Bernheim, A. (2013) Atlas of genetics and cytogenetics in oncology and haematology in 2013. *Nucleic Acids Res.* **41**, D920-D924.

Kenter, A. L., Wuerffel, R., Kumar, S., Grigera, F. (2013) Genomic architecture may influence recurrent chromosomal translocation frequency in the Igh locus. *Front. Immunol.* **4**, 500.

Korbel, J. O., Campbell, P. J. (2013) Criteria for inference of chromothripsis in cancer genomes. *Cell* **152**, 1226-1236.

Kozubek, S., Lukasova, E., Ryznar, L., Kozubek, M., Liskova, A., Govorun, R. D., Krasavin, E. A. Horneck, G. (1997) Distribution of ABL and BCR genes in cell nuclei of normal and irradiated lymphocytes. *Blood* **89**, 4537-4545.

Kozubek, S., Lukasova, E., Jirsova, P., Koutna, I., Kozubek, M., Ganova, A., Bartova, E., Falk, Pasekova, R. (2002) 3D Structure of the human genome: order in randomness. *Chromosoma* **111**, 321-331.

Kryston, T. B., Georgiev, A. B., Pissis, P., Georgakilas, A. G. (2011) Role of oxidative stress and DNA damage in human carcinogenesis. *Mutat. Res.* **711**, 193-201.

Kruhlak, M. J., Celeste, A., Nussenzweig, A. (2006) Spatiotemporal dynamics of chromatin containing DNA breaks. *Cell Cycle* **5**, 1910-1912.

Lambert, S., Carr, A. M. (2005) Checkpoint responses to replication fork barriers. *Biochimie* **87**, 591-602.

Le Beau, M. M., Espinosa, R., 3rd, Neuman, W. L., Stock, W., Roulston, D., Larson, R. A., Keinanen, M., Westbrook, C. A. (1993) Cytogenetic and molecular delineation of the smallest commonly deleted region of chromosome 5 in malignant myeloid diseases. *Proc. Natl. Acad. Sci. USA* **90**, 5484-5488.

Le Beau, M. M., Espinosa, R., 3rd, Davis, E. M., Eisenbart, J. D., Larson, R. A., Green, E. D. (1996) Cytogenetic and molecular delineation of a region of chromosome 7 commonly deleted in malignant myeloid diseases. *Blood* **88**, 1930-1935.

Liew, E., Owen, C. (2011) Familial myelodysplastic syndromes: a review of the literature. *Haematologica* **96**, 1536-1542.

Lindsley, R. C., Ebert, B. L. (2013) Molecular pathophysiology of myelodysplastic syndromes. *Annu. Rev. Pathol.* **8**, 21-47

Lukasova, E., Kozubek, S., Kozubek, M., Kroha, V., Mareckova, A., Skalnikova, M., Bartova, E., Slotova, J. (1999) Chromosomes participating in translocations typical of malignant hemoblastoses are also involved in exchange aberrations induced by fast neutrons. *Radiat. Res.* **151**, 375-384.

Lukasova, E., Kozubek, S., Kozubek, M., Falk, M., Amrichova, J. (2002) The 3D structure of human chromosomes in cell nuclei. *Chromosome Res.* **10**, 535-548.

Manuelidis, L., Chen, T. L. (1990) A unified model of eukaryotic chromosomes. *Cytometry* **11**, 8-25.

Mishima, A., Aoba, M., Yamaji, S., Taguchi, J., Kanamori, H., Motomura, S., Mohri, H., Okubo, T. (1998) Progression of a myelodysplastic syndrome with trisomy 8 to acute lymphoblastic leukemia. *Am. J. Hematol.* **58**, 342.

Monyarch, G., de Castro Reis, F., Zock, J. P., Giraldo, J., Pozo-Rodriguez, F., Espinosa, A., Castano-Vinyals, G., Gomez, F. P., Anto, J. M., Coll, M. D., Barbera, J. A., Fuster, C. (2013) Chromosomal bands affected by acute oil exposure and DNA repair errors. *PLoS One* **8,** e81276. doi: 10.1371/journal.pone.0081276.

Münkel, C., Eils, R., Dietzel, S., Zink, D., Mehring, C., Wedemann, G., Cremer, T., Langowski, J. (1999) Compartmentalization of interphase chromosomes observed in simulation and experiment. *J. Mol. Biol.* **285**, 1053-1065.

Neves, H., Ramos, C., da Silva, M. G., Parreira, A., Parreira, L. (1999) The nuclear topography of ABL, BCR, PML, and RARα genes: evidence for gene proximity in specific phases of the cell cycle and stages of hematopoietic differentiation. *Blood* **93**, 1197-1207.

Nimer, S. D. (2006) Clinical management of myelodysplastic syndromes with interstitial deletion of chromosome 5q. *J. Clin. Oncol.* **24**, 2576-2582.

Okada, M., Suto, Y., Hirai, M., Shiseki, M., Usami, A., Okajima, K., Teramura, M., Mori, N. Motoji, T. (2012) Microarray CGH analyses of chromosomal 20q deletions in patients with hematopoietic malignancies. *Cancer Genet.* **205**, 18-24.

Olney, H. J., Le Beau, M. M. (2007) Evaluation of recurring cytogenetic abnormalities in the treatment of myelodysplastic syndromes. *Leuk. Res.* **31**, 427-434.

Paulsson, K., Johansson, B. (2007) Trisomy 8 as the sole chromosomal aberration in acute myeloid leukemia and myelodysplastic syndromes. *Pathol. Biol.* **55**, 37-48.

Pihan, G. A. (2013) Centrosome dysfunction contributes to chromosome instability, chromoanagenesis, and genome reprograming in cancer. *Front. Oncol.* **3**, 277.

Pombo, A., Cuello, P., Schul, W., Yoon, J. B., Roeder, R. G., Cook, P. R., Murphy, S. (1998) Regional and temporal specialization in the nucleus: a transcriptionally-active nuclear domain rich in PTF, Oct1 and PIKA antigens associates with specific chromosomes early in the cell cycle. *EMBO J.* **17**, 1768-1778.

Righolt, C., Mai, S. (2012) Shattered and stitched chromosomes-chromothripsis and chromoanasynthesis-manifestations of a new chromosome crisis? *Genes Chromosomes Cancer* **51**, 975-981.

Stephens, P. J., Greenman, C. D., Fu, B., Yang, F., Bignell, G. R., Mudie, L. J., Pleasance, E. D., Lau, K. W., Beare, D., Stebbings, L. A., McLaren, S., Lin, M. L., McBride, D. J., Varela, I., Nik-Zainal, S., Leroy, C., Jia, M., Menzies, A., Butler, A. P., Teague, J. W., Quail, M. A., Burton, J, Swerdlow, H., Carter, N. P., Morsberger, L. A., Iacobuzio-Donahue, C., Follows, G. A., Green, A. R., Flanagan, A. M., Stratton, M. R., Futreal, P. A., Campbell, P. J. (2011) Massive genomic rearrangement acquired in a single catastrophic event during cancer development. *Cell* **144**, 27-40.

Stephenson, J., Lizhen, H., Mufti, G. J. (1995) Possible coexistence of RAS activation and monosomy 7 in the leukaemic transformation of myelodysplastic syndromes. *Leuk. Res.* **19**, 741-748.

Toledo, L. I., Altmeyer, M., Rask, M. B., Lukas, C., Larsen, D. H., Povlsen, L. K., Bekker-Jensen, S., Mailand, N., Bartek, J., Lukas, J. (2013) ATR prohibits replication catastrophe by preventing global exhaustion of RPA. *Cell* **155**, 1088-1103.

Vardiman, J. W., Thiele, J., Arber, D. A., Brunning, R. D., Borowitz, M. J., Porwit, A., Harris, N. L., Le Beau, M. M., Hellström-Lindberg, E., Tefferi, A., Bloomfield, C. D. (2009) The 2008 revision of the World Health Organization (WHO) classification of myeloid neoplasms and acute leukemia: rationale and important changes. *Blood* **114**, 937-951.

Visconte, V., Selleri, C., Maciejewski, J. P., Tiu, R. V. (2014) Molecular pathogenesis of myelodysplastic syndromes. *Transl. Med. UniSa* **8**, 19-30.

Volpi, E. V., Chevret, E., Jones, T., Vatcheva, R., Williamson, J., Beck, S., Campbell, R. D., Goldsworthy, M., Powis, S. H., Ragoussis, J., Trowsdale, J., Sheer, D. (2000) Large-scale chromatin organization of the major histocompatibility complex and other regions of human chromosome 6 and its response to interferon in interphase nuclei. *J. Cell Sci.* **113(Pt 9),** 1565-1576.

Wang, L., Fidler, C., Nadig, N., Giagounidis, A., Della Porta, M. G., Malcovati, L., Killick, S., Gattermann, N., Aul, C., Boultwood, J., Wainscoat, J. S. (2008) Genome-wide analysis of copy number changes and loss of heterozygosity in myelodysplastic syndrome with del(5q) using high-density single nucleotide polymorphism arrays. *Haematologica* **93**, 994-1000.

West, A. H., Godley, L. A., Churpek, J. E. (2014) Familial myelodysplastic syndrome/acute leukemia syndromes: a review and utility for translational investigations. *Ann. N. Y. Acad. Sci* **1310**, 111-118.

Zemanova, Z., Michalova, K., Brezinova, J., Lizcova, L., Izakova, S., Siskova, M., Cerna, O., Cermak, J. (2008) Molecular cytogenetic studies of complex karyotypes in myelodysplastic syndromes (MDS): conventional cytogenetics, FISH and multiplex FISH (mFISH/mBAND). *ASH Annual Meeting Abstracts* **112**, 5075.

Zemanova, Z., Michalova, K., Buryova, H., Brezinova, J., Lizcova, L., Kostylkova, K., Sarova, I., Izakova, S., Ransdorfova, S., Krejcik, Z., Dostalova Merkerova, M., Siskova, M., Jonasova, A.T., Neuwirtova, R., Cermak, J. (2013) Putative monosomy 5 in myelodysplastic syndromes (MDS) is probably resulting from chromothripsis. *Blood* **122**, 21.

Zemanova, Z., Michalova, K., Buryova, H., Brezinova, J., Kostylkova, K., Bystricka, D., Novakova, M., Sarova, I., Izakova, S., Lizcova, L, Ransdorfova, S., Krejcik, Z., Merkerova, M. D., Dohnalova, A., Siskova, M., Jonasova, A., Neuwirtova, R., Cermak, J. (2014) Involvement of deleted chromosome 5 in complex chromosomal aberrations in newly diagnosed myelodysplastic syndromes (MDS) is correlated with extremely adverse prognosis. *Leuk. Res.* **38**, 537-544.

Zhang, C. Z., Leibowitz, M. L., Pellman, D. (2013) Chromothripsis and beyond: rapid genome evolution from complex chromosomal rearrangements. *Genes Dev.* **27**, 2513-2530.

Image Analysis of Gene Locus Positions within Chromosome Territories in Human Lymphocytes

Karel Štěpka[1] and Martin Falk[2]

[1] Centre for Biomedical Image Analysis,
Faculty of Informatics, Masaryk University,
Brno, Czech Republic
172454@mail.muni.cz
[2] Department of Cell Biology and Radiobiology,
Institute of Biophysics of ASCR,
Brno, Czech Republic
falk@ibp.cz

Abstract. One of the important areas of current cellular research with substantial impacts on medicine is analyzing the spatial organization of genetic material within the cell nuclei. Higher-order chromatin structure has been shown to play essential roles in regulating fundamental cellular processes, like DNA transcription, replication, and repair. In this paper, we present an image analysis method for the localization of gene loci with regard to chromosomal territories they occupy in 3D confocal microscopy images. We show that the segmentation of the territories to obtain a precise position of the gene relative to a hard territory boundary may lead to undesirable bias in the results; instead, we propose an approach based on the evaluation of the relative chromatin density at the site of the gene loci. This method yields softer, fuzzier "boundaries", characterized by progressively decreasing chromatin density. The method therefore focuses on the extent to which the signals are located inside the territories, rather than a hard yes/no classification.

1 Introduction

The study of the spatial organisation of the genetic material within the nuclei of eukaryotic cells is one of the most important avenues of current intracellular research. ToDo: mention what can be studied

Three-dimensional images of the genetic material can be acquired using confocal fluorescence microscopy. The objects of interest (e.g. the whole nucleus, individual chromosomes, their parts or individual gene loci) are fluorescently stained, so that they appear as bright areas or spots in the acquired images. The fluorescent staining can be performed using fluorscent proteins or antibodies attached to proteins, or, in the case of individual gene loci, using bacterial artificial chromosomes (BAC). These DNA fragments are first prepared to match the target DNA, fluorescently tagged, and then hybridized with the target in a process called fluorescence *in situ* hybridization (FISH). [1]

Human chromosome 5 (HSA5) is one of the human autosomes. Conditions related to the chromosomal aberrations of HSA5 include the cri du chat syndrome, familial adenomatous polyposis, myelodysplastic syndromes, or Crohn's disease [2], [3], [4], [5]. Understanding of the spatial arrangement of the chromosome and the ways it can interact with other chromosomes is therefore of high interest.

2 Image Data

ToDo: describe the cells we have

The chromosomes are actually tangled and looped strands of chromatin, i.e., DNA and proteins. In some places, mostly at the center of the territory occupied by the chromosome, these loops are densely packed. In other places, chromatin may be more decondensed, and the chromatin strand may be arranged more loosely.

However, due to the fact that the width of the strand is below the diffraction limit for optical microscopes, we cannot examine (or even reliably detect) the individual loops of the strand – when passing through the optical system, the light gets distorted by the point spread function (PSF) of the system, and the resulting image does not contain areas thinly or thickly populated by the loops of the chromatin, but only areas of low or high total fluorescence. The image areas with higher total fluorescence intensity correspond to the regions containing more chromatin loops, more densely packed.

The 3D images of a sample cell can be seen in Fig. 1. The three images show the individual channels: the cell nucleus, the two HSA5 territories, and the two gene loci, one per each chromosome territory. All three channels were aligned. We can see that the nucleus is partially visible even in the channels reserved for the territories and the loci, as a result of fluorescence bleed-through (also referred to as crosstalk or crossover), a common problem in fluorescence microscopy. We can also note that while the cell nucleus has a relatively well-defined boundary, and the gene loci appear as point-like particles that can be sufficiently represented by their center of mass, the chromosome territories are of more irregular shapes, and do not have a definite boundary that would allow for a clear segmentation.

There have been methods introduced specifically to segment chromosome territories, such as [6] or [7]. However, as noted in [8], when used to help determine the relative positions of gene loci within the territories, these methods suffer from the bias introduced by arbitrarily selecting the threshold value for the hard territory boundary.

It has been shown that genes positioned more peripherally within the territory are more active than those closer to the center [8], [9]. Therefore, to avoid the bias caused by a binary "inside boundary/outside boundary" classification of genes that are of such high interest, we propose an approach in which the gene loci are related to the spatial density of the chromatin loops, with higher density usually located at the territory center, and lower density at the periphery. This will remove the arbitrary thresholds between the loci deep inside the chromo-

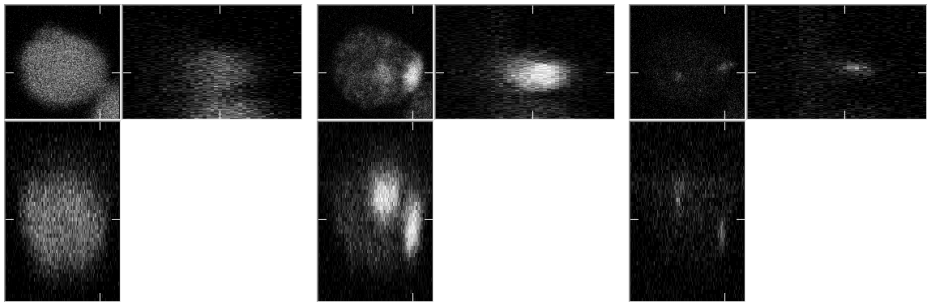

Fig. 1. The individual channels of the acquired images. From left to right: cell nucleus, chromosome territories, gene loci. (*xy*-, *xz*-, and *yz*-planes; the ticks at the image borders indicate the position of the cutting planes)

some territories, the loci in the areas of lesser density chromatin, and the loci which seem to be completely outside the territories (in such cases, it is assumed that the gene locus is on a chromatin strand that extends relatively far from the center of the territory, and whose fluorescence is not high enough for the strand to be detectable on its own).

3 Analysis Method

3.1 Nucleus Segmentation

As the basis for the further analysis, in each image, the cell nucleus was segmented. The cell nuclei in the data set were counterstained with DAPI, and they were approximately spherical and relatively regular, with very few to none non-convex areas. Segmenting cell nuclei is a common task in biomedical image analysis, and most of the common approaches are reliable when used on regularly shaped cells with enough contrast.

For our study, we selected the method described by Gué et al. in [10]. This approach first median-filters the image to suppress noise, then determines an intensity threshold using the ISODATA algorithm [11]. Finally, the nucleus mask is smoothed using a 3D mathematical morphologic closing, followed by opening.

3.2 Gene Loci Detection

To detect small, point-like particles in fluorescent images, several methods have been proposed, whose properties and performance have been discussed in comparison studies such as [12].

From these methods, we selected the one proposed by Matula et al. in [13], based on the 3D morphological extended maxima (EMax) transform. After suppressing the noise with a 3D Gaussian filter, a morphological HMax transform is computed; this transform identifies those local intensity maxima whose height

exceeds a specified threshold. The EMax image is then defined as the regional maxima of the result. After the computation of the EMax transform, the components whose size does not fall within the range allowed for fluorescence spots can be discarded.

An advantage of this method is the straightforward relationship between its result and its HMax height parameter. Since the number of fluorescent spots present in each nucleus in our data set is expected to be equal to 2, the height threshold can be automatically adjusted for each image, so that the spots are detected even in those images whose contrast deviates from the average contrast of the data set. This helps with non-supervised processing of large data sets, in which the images acquired later during the session may be affected by photobleaching.

3.3 Chromosome Territory Processing

ToDo:

In order to process the chromosome territories, it is necessary to suppress the bleed-through from the nucleus channel, i.e., the part of the signal emitted not by the marked chromosomes, but by the whole counterstained nucleus.

To do this, we first take that part of the territory channel which corresponds to the areas masked by the nucleus segmentation, as obtained in section 3.1. Within this region, we compute an intensity threshold using the Otsu algorithm [14]. This value is then subtracted from the territory channel, clamping the lowest intensities at 0. This removes the background fluorescence caused by the bleed-through. Following this, the territory image intensities were normalized to $\langle 0; 1 \rangle$.

For noise suppression, we used Gaussian blurring with $\sigma = 1$ voxel. Apart from suppressing the noise, this also smoothed the territories proper, replacing the need for averaging the intensity values around the gene loci positions detected in section 3.2. The influence of any possible imprecisions in the localization of the loci has also been reduced.

For each gene locus, the normalized territory intensity at its position was obtained. Being already normalized, this value would represent the location of the gene locus in respect to the chromosome territory – a value of 0 would mean the locus is completely "outside", on an otherwise invisible chromatin strand extending from the the territory; conversely, a value of 1 would correspond to the locus being situated in the area of the highest fluorescence, and, consecutively, the highest chromatin density (which may sometimes, but not always, correspond to the center of a hard segmentation of the territory).

However, in some of the images, the maximum intensities of the two chromosome territories differed significantly, and relating both gene loci to the same maximum intensity might not have revealed all important information. Therefore, for each locus, we also calculated the ratio of the territory intensity at its location to the maximum intensity of the territory to which this particular locus belonged.

To determine which locus belonged to which territory, we computed rough segmentations of the territories by searching for the lowest intensity threshold yielding two connected components. These hard masks did not necessarily represent the ideal segmentations that would be comparable across all images. However, within a single image (and therefore coming from the same thresholding operation), they made it possible to determine whether a gene locus was closer to one territory or the other. To do this, we calculated the Euclidean distance transform (DT) of the rough territory mask. In the DT image, every voxel value either corresponded to its distance from the territory mask (for voxels outside the mask), or had the value of 0 (for voxels inside the mask). From the DT images, it was then possible to determine which locus was closer to which terrritory.

We can see an example of these results in Fig. 2. The line running from top to bottom is the boundary between the influence zones of the two territories, whose rough segmentations are also shown. The cross marks correspond to the positions of the two gene loci; note that the left locus appears to be positioned just at the border of the territory mask. If the threshold for the hard segmentation changed, the position of the locus might change from "inside" to "outside" or vice versa. Because of this, the hard classification is prone to bias related to the threshold value.

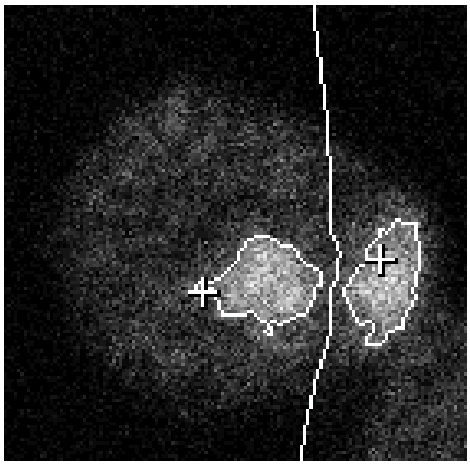

Fig. 2. The boundary between the influence zones of the two chromosome territories, overlaid over the original territory channel. The small closed curves around the territories show the rough boundaries, from which the DT was computed. The crosses mark the positions of the gene loci; the loci themselves are not visible in this channel. Note the left locus lying just at the border of the hard segmentation. (xy-plane)

However, the assignment of the loci to the territories is not negatively influenced by the fact that the segmentation may not be precise. This is illustrated in

Fig. 3. The figure shows that with different thresholds (all of them yielding two chromosome territories), the influence zones undergo changes much less rapid than the territory masks themselves, thus still allowing reliable assignment.

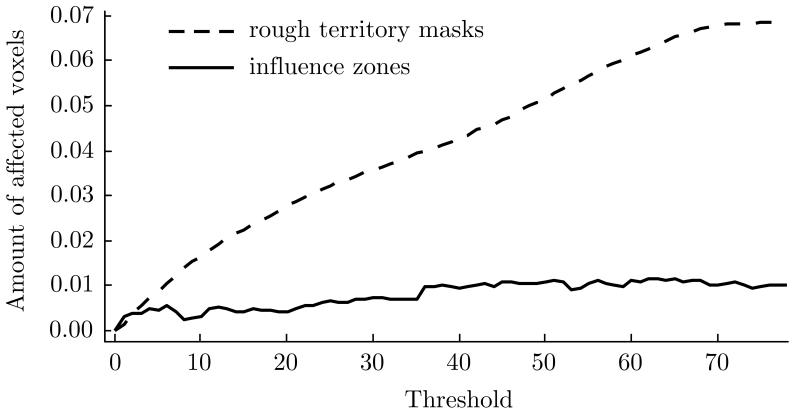

Fig. 3. Stability of the influence zones. X-axis: different intensity thresholds yielding two territories. Y-axis: the amount of voxels which are different when compared to using the first threshold, as percentage of the whole image. We can see that even though the difference between the masks taken at higher thresholds grows, as the masks shrink, the difference between the influence zones is much more stable, keeping the assignment of the loci to the territories largely independent of the exact territory segmentation

4 Results

The results measured can be seen in Fig. 4. The figure shows the histograms of the chromatin intensities at the gene loci, relative to the maximum intensity of the territories assigned to each locus. In each nucleus, a pair of gene loci was present, one locus per each of the chromosome territories. The grey bars show the data for the less intensive loci of each pair, the black bars show the data for the more intensive loci.

We can clearly see that the two populations are different, suggesting than in each nucleus, one of the two copies of the gene tends to be located more centrally, while the other is located more peripherally, possibly allowing the gene more interaction with its surrounding.

To investigate the relationship between the chromatin intensities at the gene loci, and the distances of the loci from the rough segmentation boundaries of the chromosome territories, we calculated the Pearson's coefficient according to

$$\rho_{X,Y} = \frac{\mathrm{cov}(X,Y)}{\sigma_X \sigma_Y} \,, \tag{1}$$

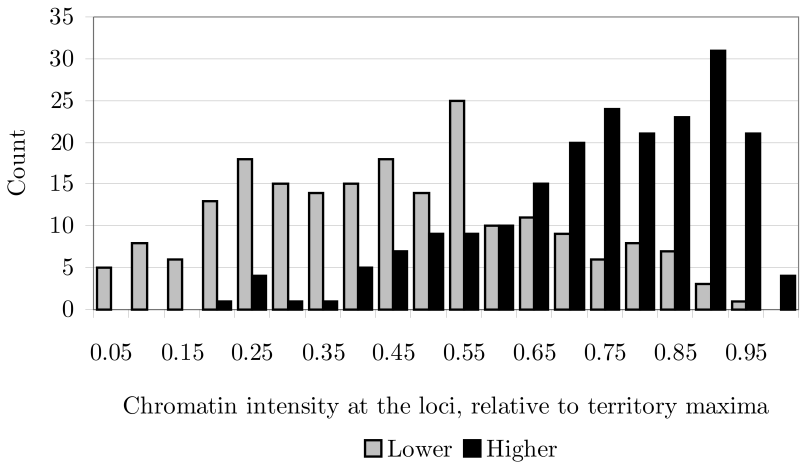

Fig. 4. Histogram of the chromatin intensities at the gene loci, relative to the maximum intensity of the assigned chromosome territory. The grey bars represent the less intensive loci of each pair, the black bars represent the more intensive ones

where cov is the covariance, and σ_X is the standard deviation of X. The value of the correlation coefficient was below 0.39, which suggests that there is indeed a positive relationship between the values, but the distance from the hard segmentation boundary does not capture all details of the chromatin structure inside the territory (such as in the cases when the territory contains interior areas with lower chromatin density).

5 Conclusion

We have studied ToDo: some cells, chromosomes and genes, which were fluorescently stained somehow.

After a relatively straightforward segmentation of the cell nuclei and the detection of the gene loci, we focused on the analysis of the locus positions in relation to their chromosome territories.

As noted in the literature, segmentation of chromosome territories is difficult, mainly because of the fact that they have no definite, hard boundary. To avoid the bias caused by the arbitrary selection of such boundary, we analyzed the gene loci not in relation to the territory segmentation, but rather to the fluorescence intensity, corresponding to the density of the chromatin at the specified location. As an additional benefit of this, we were able to take into account the variations of the chromatin density in the areas that would otherwise fall inside the hard segmentation boundary. These areas would then be counted as being "hidden" in the deep interior, while in reality, the chromatin strands may be more decondensed there, allowing for more interaction with their surrounding.

Our approach enabled us to determine the intensities at the gene loci and observe that in each nucleus, one gene locus of the pair tends to be located in an area of high fluorescence, while the other locus of the pair is located more peripherally. From the medicine and biology point of view, this is related to the amount of interaction with the neighboring chromosomes that is possible for such locus, and may be of high interest to further studies focusing e.g. on chromosomal breakpoints.

References

1. Tanke, H. J., Florijn, R. J., Wiegant, J., Raap, A. K., Vrolijk, J.: CCD microscopy and image analysis of cells and chromosomes stained by fluorescence in situ hybridization. The Histochemical Journal (1995), vol. 27, no. 1, 4–14.
2. Van den Berghe, H., Cassiman, J.-J., David, G., Fryns, J.-P., Michaux, J.-L., Sokal, G.: Distinct Haematological Disorder with Deletion of Long Arm of No. 5 Chromosome. Nature (1974), vol. 251, no. 5474, 437–438.
3. Carlock, L. R., Wasmuth, K. J.: Molecular Approach to Analyzing the Human 5p Deletion Syndrome, Cri du Chat. Somatic Cell and Molecular Genetics (1985), vol. 11, no. 3, 267–276.
4. Siddiqi, R., Gilbert, F.: Disease Genes and Chromosomes: Disease Maps of the Human Genome, Chromosome 5. Genetic Testing (2003), vol. 7, no. 2, 169–87.
5. Huff, C. D., Witherspoon, D. J., Zhang, Y., Gatenbee, C., Denson, L. A., Kugathasan, S., Hakonarson, H., Whiting, A., Davis, C. T., Wu, W., Xing, J., Watkins, W. S., Bamshad, M. J., Bradfield, J. P., Bulayeva, K., Simonson, T. S., Jorde, L. B., Guthery, S. L.: Crohns Disease and Genetic Hitchhiking at IBD5. Molecular Biology and Evolution (2012), vol. 29, no. 1, 101–111.
6. Rinke, B., Bischoff, A., Meffert, M.-C., Scharschmidt, R., Hausmann, M., Stelzer, E. H. K., Cremer, T., Cremer, C.: Volume Ratios of Painted Chromosome Territories 5, 7 and X in Female Human Cell Nuclei Studied with Confocal Laser Microscopy and the Cavalieri Estimator. Bioimaging (1995), vol. 3, no. 1, 1–11.
7. Eils, R., Dietzel, S., Bertin, E., Schröck, E., Speicher, M. R., Ried, T., Robert-Nicoud, M., Cremer, C., Cremer, T.: Three-Dimensional Reconstruction of Painted Human Interphase Chromosomes: Active and Inactive X-chromosome Territories Have Similar Volumes but Differ in Shape and Surface Structure. Journal of Cell Biology (1996), vol. 135, 1427–1440.
8. Dietzel, S., Schiebel, K., Little, G., Edelmann, P., Rappold, G. A., Eils, R., Cremer, C., Cremer, T.: The 3D Positioning of ANT2 and ANT3 Genes within Female X Chromosome Territories Correlates with Gene Activity. Experimental Cell Research (1999), vol. 252, 363–375.
9. Kurz, A., Lampel, S., Nickolenko, J. E., Bradl, J., Benner, A., Zirbel, R. M., Cremer, T., Lichter, P.: Active and Inactive Genes Localize Preferentially in the Periphery of Chromosome Territories. Journal of Cell Biology (1996), vol. 135, no. 5, 1195–1205.
10. Gué, M., Messaoudi, C., Sheng Sun, J., Boudier, T.: Smart 3D-FISH: Automation of Distance Analysis in Nuclei of Interphase Cells by Image Processing. Cytometry Part A (2005), vol. 36, no. 4, 279–293.
11. Ridler, T., Calvard, S.: Picture Thresholding Using an Iterative Selection Method. IEEE Transactions on Systems, Man, and Cybernetics (1978), vol. 8, no. 8, 630–632.

12. Smal, I., Loog, M., Niessen, W., Meijering, E.: Quantitative Comparison of Spot Detection Methods in Fluorescence Microscopy. IEEE Transactions on Medical Imaging (2010), vol. 29, no. 2, 282–301
13. Matula, P., Verissimo, F., Wörz, S., Eils, R., Pepperkok, R., Rohr, K.: Quantification of Fluorescent Spots in Time Series of 3-D Confocal Microscopy Images of Endoplasmic Reticulum Exit Sites Based on the HMAX Transform. In: Molthen, R. C., Weaver, J. B. (eds.): Medical Imaging 2010: Biomedical Applications in Molecular, Structural, and Functional Imaging, vol. 7626. Society of Photo-Optical Instrumentation Engineers, San Diego (2010).
14. Otsu, N.: A Threshold Selection Method from Gray-Level Histograms. IEEE Transactions on Systems, Man, and Cybernetics (1979), vol. 9, no. 1, 62–66.

Higher-order chromatin changes induced by an oncogenic transcription factor

Gaetano Ivan Dellino[1], Martin Falk[3], Mario Faretta[1,2], Gabriele Bucci[1], Francesca De Santis[1], Matteo Cesaroni[1,2], Lucilla Luzi[2], Emilie Lukasova[3], Simona Segalla[1], Myriam Alcalay[1,2], Saverio Minucci[1,5], Stanislav Kozubek[3] and Pier Giuseppe Pelicci[1,2,4]

[1] Department of Experimental Oncology, European Institute of Oncology, 20141 Milan, Italy.

[2] IFOM-FIRC Institute of Molecular Oncology, 20139 Milan, Italy.

[3] Institute of Biophysics, Academy of Sciences, Kralovopolska 135, 612 65 Brno, Czech Republic

[4] Dipartimento di Medicina, Chirurgia e Odontoiatria, University of Milano, Milan, Italy

[5] Department of Biomolecular sciences and biotechnologies, University of Milan, Milan Italy

Gross modifications in chromatin texture and global changes of gene expression are constant features of cancer cells[1,2,3]. The underlying mechanisms, however, as well as their mechanistic links remain largely unknown. We report here the effects of the PML-RAR oncogenic transcription factor[4] on higher-order chromatin structure[5] and their consequences on gene expression. We found that 30% of the >1000 transcriptional targets of PML-RAR are distributed in the genome as gene clusters, do not possess PML-RAR - specific DNA-recognition elements (RAREs) within their promoters, and are flanked by one or more clusters of 30-40 Alu repeats each containing one RARE (Alu-RAREs). Chromatin analysis revealed that PML-RAR is first recruited at clusters of Alu-RAREs, where it accumulates at high density, and then at the transcription start sites (TSSs) of adjacent genes, through the formation of multiple DNA loops. High-resolution *in vivo* imaging showed co-localization of PML-RAR with clusters of co-regulated genes and long-range chromatin changes of the corresponding chromosomal regions. Treatment with drugs that target PML-RAR and induce tumor regression (RA and TSA) reverted higher-order chromatin changes and transcriptional repression of clustered genes. These findings demonstrate that higher-order chromatin changes are early events following PML-RAR oncogene expression and that they cause global changes of gene expression. Since also wild-type RARs bind Alu-RAREs[6,7] and Alu repeats contain DNA-recognition elements for different transcription factors[8], specific recruitment to transposable elements and induction of higher-order chromatin changes might function as a general mechanism of transcriptional regulation.

The PML-RAR fusion protein functions as a transcriptional repressor of retinoic acid (RA) target genes. Critical to this activity is its ability to complex with several chromatin modifying enzymes, including histone deacetylases (HDACs)[9], histone- and DNA-methyltransferases[10,11]. PML-RAR recognizes DNA specifically, through interaction of the DNA-binding domain of its RAR moiety with specific DNA sequences at target promoters (RA-responsive elements; RAREs), consisting of two direct repeats (DRs) of the (A/G)G(G/T)TCA consensus, variably spaced[12,13]. Upon DNA binding, PML-RAR induces local modifications of chromatin (histone deacetylation/methylation and DNA methylation)[9,10,11], which lead to heterochromatin formation and transcriptional repression. In the RARβ promoter, one of the best-

studied PML-RAR targets, the RARE is located only 35 base pairs 5' to the TSS, suggesting that local chromatin changes induced by the fusion protein might affect transcription directly[11].

Gene profiling analysis of early transcriptional events following PML-RAR induction in PR9 (hematopoietic precursors carrying the PML-RAR cDNA under a zinc-inducible promoter) vs control (MT) cells identified 1150 down-regulated genes[14]. However, only about 20% contain putative RAREs in their promoter[15], suggesting that PML-RAR might repress transcription through other mechanisms. Physical mapping of the down-regulated genes in the human genome revealed that 312 (~30%) are distributed within clusters, each containing 3-10 regulated genes (Fig. 1 and Supplementary Table S1). We initially focused on chromosome 19 Cluster #1, that contains 25 genes, of which 5 are down-regulated by PML-RAR, as predicted by gene-chip analysis. However, analysis of 18 genes, by qRT-PCR, revealed no expression of 4 and down-regulation of 12 of the remaining 14 (Fig. 2a,b).

To investigate mechanisms of PML-RAR-dependent regulation, we searched for putative RAREs in the Cluster #1 gene promoters (±2 Kb from TSSs), using the canonical (A/G)G(G/T)TCA consensus repeat with spacings of 2-10 nucleotides (DR2-10). Only one gene (HA-1) showed two identical DR8-RAREs at -1.1 and +1.1 Kb from the TSS. Quantitative chromatin immunoprecipitation (qChIP) analysis revealed PML-RAR binding to the 3' DR8-RARE of HA-1 and, to a lesser extent, around its TSS region (Fig. 2c). Binding of PML-RAR to the HA-1 TSS region was comparable to that observed for RARβ, under identical experimental conditions, and correlated with decreased Polymerase II (Pol II) recruitment and histone H3-acetylation (Fig. 2c,d).

We then extended the search for canonical RAREs to the entire Cluster #1 region and identified 66 matches, of which 43 are DR2-RAREs with identical sequence (AGGTCAnnAGTTCA), each contained within the promoter region of one Alu repeat (Supplementary Fig. S1). The existence of Alu repeats containing functional DR2-RAREs has been already reported[6,7]. Since recruitment of wild-type RAR to Alu repeats might also occur through non-canonical DR2-RAREs[6], we re-analysed the entire Cluster #1 region using the degenerate DR2-RARE consensus AGGTCAnnAGWTCR (Supplementary Fig. S1) and identified 157 matches, all contained within promoters of Alu repeats and mainly distributed as clusters within relatively gene-free regions (A1 and A2 clusters; Fig. 3a). QChIP analysis revealed

binding of PML-RAR to individual Alu repeats, to an extent comparable to that of Cluster #1 promoters, both in PR9 (Fig. 2d,e) and in leukemic patient (Supplementary Fig. S2) cells.

We then investigated whether the genomic clusters of PML-RAR regulated genes are all flanked by Alu repeats containing functional RAREs. 99.6% of our degenerate DR2-RARE consensus sequences (~302,000 in total) are within Alu repeats, with maximal frequency in the still actively transposing members of the youngest Alu Ya5 subfamily[16] (Fig. 3b). PML-RAR binds to the Ya5 subfamily, but not to a sub-population of AluJ and AluS repeats (Supplementary Fig. S3). The relative abundance of the four permutations of the DR2-RARE consensus (Supplementary Fig. S3) and the distribution of DR2-RAREs within the different Alu subfamilies is the same in the chromosome 19 Cluster #1 as in the whole human genome (Fig. 3b). Strikingly, the Alu repeats containing functional DR2-RAREs (from now on denominated Alu-RAREs) are distributed as clusters in the human genome, in close proximity to the clusters of PML-RAR regulated genes (Fig. 1), suggesting that Alu-RARE clusters are platforms of PML-RAR recruitment, which might be involved in the regulation of neighboring genes.

Despite their genomic proximity, however, the Alu-RARE clusters are still at considerable distance from the regulated genes (325 Kb between the A1 cluster and the farthest gene analysed – ELA2 – in Gene Cluster #1). We thus investigated whether PML-RAR induces physical proximity between Alu-RAREs and regulated genes, using the Chromosome Conformation Capture (3C) assay[17]. Cross-linked chromatin was digested with the *Hind*III enzyme, re-ligated and analysed by PCR using primers from specific *Hind*III fragments (Fig. 3a,c). PML-RAR induced juxtaposition of the fragments containing the A1 Alu-RARE Cluster and the regulated genes (the entire ELA2 locus or the 5' half of HA-1) (Fig. 3c). Identical results were obtained using chromatin from leukemia patient cells (Supplementary Fig. S2). Notably, physical interaction was also observed between DNA fragments containing two consecutive Alu clusters (A1 and A2), but not between: i) the 3' end of HA-1 and the A1 Alu-RARE Cluster, ii) the ELA2 and the HA-1 genes, iii) the ELA2 (or HA-1) gene and the A2 Alu-RARE cluster (Fig. 3a,c), thus indicating that formation of multiple chromatin loops after PML-RAR expression follows precise rules, leading to the juxtaposition of the A1 Alu-RARE cluster with the 5' end of the neighboring

regulated genes and with the A2 Alu-RARE cluster. Similar results were obtained after 3C analysis of chromosome 12 Cluster #4 (Fig. 3d). Together, these data demonstrate that PML-RAR triggers the formation of multiple chromatin loops, which bring together Alu-RARE clusters and the 5' end of regulated genes.

Thus, we investigated whether PML-RAR is recruited to the promoter regions of Cluster #1 genes. QChIP analysis showed PML-RAR binding to 8/8 active gene promoters tested (Fig. 2c,d), but not to the PRTN3 gene, which is not expressed in PR9 cells (Fig. 2d). Notably, binding of PML-RAR peaked around the TSS region (Fig. 2c; AZU1 and ELA2) and was maximal for the down-regulated genes: HA-1, MIDN, ELA2, STK11 and AZU1 (Fig. 2d). Similar results were obtained using patient-derived leukemic cells (Supplementary Fig. S2). It appears, therefore, that PML-RAR is recruited at the TSS region of the Cluster #1 regulated genes.

We then analysed the temporal order of PML-RAR recruitment: qChIP revealed optimal PML-RAR binding first at Alu repeats and then at the regulated genes (Fig. 2e and not shown). Since each Alu-RARE cluster contains 30 DR2-RAREs on average, these findings suggest that high local concentrations of PML-RAR form at the Alu-RARE clusters that then trigger binding to promoters of clustered genes and DNA loop formation.

Chromatin modifications at gene-regulatory regions function as specificity determinants for the binding of transcription factors[18]. To investigate the mechanism of PML-RAR recruitment to the regulated promoters, we analysed local histone modifications prior to PML-RAR binding. Levels of H3-K4me3 and H3-acetylation were high around the TSSs of HA-1, AZU1 and ELA2 genes, while became very low or undetectable at their 5' or 3' flanking regions, following a pattern that is comparable to that of PML-RAR binding to the same promoters (Fig. 2c). Levels of H3K27me1 and H3K9me3 around the TSSs were instead uniformly lower than in their flanking regions (not shown). ChIP-on-chip analysis using tiled arrays of the repeat-masked chromosome 19 revealed binding of PML-RAR only to promoters showing peaks of H3K4me3 (Figs. 2c and Supplementary S4) and H3-acetylation (not shown). It appears, therefore, that binding of PML-RAR to the TSSs of regulated genes is dictated by pre-existing epigenetic features typical of open chromatin[18,19].

We then used high-resolution imaging techniques to investigate whether the observed effects of PML-RAR on purified chromatin correlate with chromosomal changes in

intact cells. To this end we measured, by 3D-FISH[20], the mutual distance between locus-specific DNA probes (1.4-2.9 Mb apart) flanking either the analysed clusters of co-regulated genes (on chromosomes 19 and 12) or, as control, genes which are not regulated by PML-RAR (on 13q22.3) (Fig. 1). Strikingly, PML-RAR induced marked shortening of the distance between paired probes of chromosomes 19 and 12 (15% and 26%, respectively), while it had no effect on the distance between probes of chromosome 13 (Figs. 4a and Supplementary S5; Table S2), thus confirming that PML-RAR induces higher-order chromatin changes in chromosome regions containing clusters of regulated genes and Alu-RAREs. Finally, we analysed the physical relationship between PML-RAR and clusters of regulated genes in intact cells. The pattern of PML-RAR nuclear localization consists of 100-200 microspeckles of <0,1μm in diameter[21]. We observed co-localization of PML-RAR microspeckles with DNA probes from the analysed clusters of regulated genes on chromosomes 19 and 12, but not with a DNA probe from the chromosome 13 control region (Figs. 4b and Supplementary S6), thus confirming that high local concentration of PML-RAR forms in the proximity of clusters of regulated genes.

The leukemogenetic potential of PML-RAR is reverted by treatment with RA or HDAC inhibitors, like TSA, which induce leukemia remission in patients or mouse models[22,23]. Both drugs reverted the chromosome contraction induced by PML-RAR (Figs. 4a and Supplementary S5). Also the repressive effect of PML-RAR on transcription of Cluster #1 target genes was alleviated by treatment with RA (not shown) or TSA (as revealed by increased acetylation and PolII binding at their TSSs, even if compared to their basal levels; Supplementary Fig. S7), thus indicating that higher-order chromatin changes and transcriptional repression induced by PML-RAR are reversible and suggesting that they are mechanistically linked.

To investigate the mechanisms of the RA and TSA effects on higher-order chromatin structure, we analysed the nuclear localization pattern of PML-RAR. RA induced degradation of PML-RAR (not shown) and the disappearance of the PML-RAR microspeckles (Supplementary Fig. S6). TSA did not alter the morphology and distribution of the PML-RAR microspeckles, nor abrogated their co-localization with clusters of co-regulated genes at chromosome 19 or 12 (Figs. 4b and Supplementary S6). QChIP analysis of PML-RAR binding after TSA treatment revealed persistence of the fusion protein at the Alu-RAREs, and marked decrease at the TSSs of Cluster #1 regulated genes (Figs. 4c and Supplementary S7). Together, these findings indicate

that recruitment of PML-RAR at the Alu-RAREs clusters is not sufficient to trigger long-range chromatin interactions and transcriptional repression, which instead depend on further binding of the fusion protein to the TSSs of regulated genes.

In conclusion, we demonstrated that PML-RAR induces higher-order chromatin changes that result into global changes of gene expression. Mechanistically, we showed that PML-RAR is first recruited at clusters of Alu-RAREs and then at the TSSs of adjacent genes, through formation of multiple chromatin loops. The first event is mediated by recognition of specific DNA sequences, while the second is facilitated by pre-existing epigenetic marks (high H3-K4 methylation and H3 acetylation). Other events may contribute to the formation and/or stability of these topological domains, including PML-RAR homodimerization[24] or binding of its two moieties, PML and RAR, to the matrix attachment region-binding protein SATB1[25], or to the TFIIH component of the basal transcription complex[26], respectively. Since H3K4 tri-methylation and H3-acetylation are generally associated with active genes, these epigenetic marks might specify target selection by PML-RAR. Notably, PML-RAR exerts the dual effect of repressing transcriptionally active genes and preventing gene activation by other transcription factors[9,27]. Furthermore, unscheduled accumulation of topological DNA loops might affect replication-fork dynamics and lead to genomic rearrangements[28], thus further contributing to the leukemogenic potential of PML-RAR.

Analyses of complete genomes and whole-genome expression patterns suggest that the order of genes along chromosomes is not random and that genes with coordinated expression are often clustered[29]. Though the underlying molecular mechanisms are unknown, emerging evidence suggests that chromosomal domains of expression are imposed by higher-order chromatin structure[30]. The described effect of PML-RAR might reflect de-regulation, by the fusion protein, of a physiological mechanism mediated by wild-type RAR. Endogenous RARs bind to Alu repeats containing the DR2-(A/G)G(G/T)TCA motif[7], a subclass of the Alu-RAREs described here, and to promoters and individual Alu repeats of Cluster #1 (Supplementary Fig. S8). Moreover, in the absence of PML-RAR expression, a modest, yet detectable, interaction occurs between Alu repeats and regulated genes (Fig. 3d), while RA-treatment induces changes of the chromosomal regions containing clustered genes (Fig. 4a), as well as up-regulation of Cluster #1 gene expression (unpublished results). It appears, therefore, that also wild-type RAR regulates expression of clustered target

genes through Alu-RARE binding and induction of higher-order chromatin changes. Notably, gene Cluster #1 on human chromosome 19 is conserved in mouse (locus 10QC1), is flanked by clusters of SINE-B2 repeats containing non-canonical DR2-RAREs and is also down-regulated by PML-RAR (unpublished data), suggesting that this mechanism might be conserved across species.

Methods

Cell culture, qChIP and Q-PCR analyses. PR9, MT, NB4 and Phoenix cells were grown and processed for qChIP analysis as described[31], using the following antibodies: anti-Pml (H-238; Santa Cruz, CA); anti-RAR (C-20; Santa Cruz), anti-Pol II (N-20; Santa Cruz); anti-H3pan-ac (06-599; Upstate); anti-H3K4me3 (ab8580; AbCam, UK); anti-H3K9me3 and -H3K27me1 (provided by T. Jenuwein; Institute of Molecular Pathology, Wien, Austria)[32]. Immunoprecipitated DNA from 1 X 10^7 cell equivalents was resuspended in 300 µl of 10 mM Tris at pH 8.0. Real-time PCR was performed with 6 µl of DNA per reaction and 200 nM primers, diluted in a final volume of 20 µl in SYBR Green PCR Master Mix (Applied Biosystems). Total RNA was reverse-transcribed and specific mRNA sequences were quantified by real-time PCR with TaqMan Gene expression assays (Applied Biosystems - https://myscience.appliedbiosystems.com).

3C assay. The 3C assay was performed as described[33]. 1 X 10^6 nuclei were digested overnight with 200 U of *Hind*III. Digested chromatin (2 ug) was ligated 6 hours with 1,000 U of T4 DNA ligase in a final volume of 1 ml. 300 ng DNA was used as template in PCR reactions (35 cycles). Control PCR products were obtained by mixing equimolar amounts of multiple PCR products spanning the *Hind*III sites of interest. The mixture was digested with *Hind*III and re-ligated to generate a library of randomly ligated control fragments. The specificity of the 3C primers was tested by PCR using 1 ng of the randomly ligated control fragment mixture with 200 ng of genomic DNA as template (Control). All the PCR products were sequenced. 3C primer sequences are available upon request.

3D-FISH. BAC clones (RP11) used are: chromosome 19: 75H6 and 333F10; chromosome 12: 680A11 and 426E10; chromosome 13: 138N13 and 188A23. Isolated DNA was labeled with spectrum green or spectrum orange using the nick-

translation kit from Vysis (Downers Grove, IL). 3D cell fixation, permeabilization and denaturation were performed as described[34].

Immuno-FISH. Immuno-FISH was performed for the simultaneous visualization of proteins and specific *DNA* loci, as described[35], using the mouse monoclonal anti-PML PGM3 antibody (Santa Cruz, mAb PGM3) and specific BAC clones (see text).

Fluorescence microscopy. Images were obtained using a high-resolution confocal cytometer[20], equipped with a CSU 10a Nipkow disc (Yokogawa, Japan) for confocal imaging. Forty optical sections (z-step 0.3 μm) in all R-G-B channels were acquired at the constant temperature of 26 °C using the FISH 2.0 software[20]. More details are available on request. Off line analysis of colocalizations and nuclear distances between signals of differently labeled paired probes were performed using FISH 2.0[20] and SigmaPlot 8.0 (Jandel Scientific,CA) software.

References

1. Cremer, M. et al. Inheritance of gene density-related higher order chromatin arrangements in normal and tumor cell nuclei. J Cell Biol 162, 809-20 (2003).
2. Guasconi, V., Souidi, M. & Ait-Si-Ali, S. Nuclear positioning, gene activity and cancer. Cancer Biol Ther 4, 134-8 (2005).
3. Chung, C. H., Bernard, P. S. & Perou, C. M. Molecular portraits and the family tree of cancer. Nat Genet 32 Suppl, 533-40 (2002).
4. Alcalay, M. et al. Common themes in the pathogenesis of acute myeloid leukemia. Oncogene 20, 5680-94 (2001).
5. Misteli, T. Beyond the sequence: cellular organization of genome function. Cell 128, 787-800 (2007).
6. Vansant, G. & Reynolds, W. F. The consensus sequence of a major Alu subfamily contains a functional retinoic acid response element. Proc Natl Acad Sci U S A 92, 8229-33 (1995).
7. Laperriere, D., Wang, T. T., White, J. H. & Mader, S. Widespread Alu repeat-driven expansion of consensus DR2 retinoic acid response elements during primate evolution. BMC Genomics 8, 23 (2007).
8. Polak, P. & Domany, E. Alu elements contain many binding sites for transcription factors and may play a role in regulation of developmental processes. BMC Genomics 7, 133 (2006).
9. Grignani, F. et al. Fusion proteins of the retinoic acid receptor-alpha recruit histone deacetylase in promyelocytic leukaemia. Nature 391, 815-8 (1998).
10. Carbone, R. et al. Recruitment of the histone methyltransferase SUV39H1 and its role in the oncogenic properties of the leukemia-associated PML-retinoic acid receptor fusion protein. Mol Cell Biol 26, 1288-96 (2006).
11. Di Croce, L. et al. Methyltransferase recruitment and DNA hypermethylation of target promoters by an oncogenic transcription factor. Science 295, 1079-82 (2002).

12. Perez, A. et al. PMLRAR homodimers: distinct DNA binding properties and heteromeric interactions with RXR. Embo J 12, 3171-82 (1993).
13. Kamashev, D., Vitoux, D. & De The, H. PML-RARA-RXR oligomers mediate retinoid and rexinoid/cAMP cross-talk in acute promyelocytic leukemia cell differentiation. J Exp Med 199, 1163-74 (2004).
14. Alcalay, M. et al. Acute myeloid leukemia fusion proteins deregulate genes involved in stem cell maintenance and DNA repair. J Clin Invest 112, 1751-61 (2003).
15. Meani, N. et al. Molecular signature of retinoic acid treatment in acute promyelocytic leukemia. Oncogene 24, 3358-68 (2005).
16. Mills, R. E., Bennett, E. A., Iskow, R. C. & Devine, S. E. Which transposable elements are active in the human genome? Trends Genet (2007).
17. Dekker, J., Rippe, K., Dekker, M. & Kleckner, N. Capturing chromosome conformation. Science 295, 1306-11 (2002).
18. Guccione, E. et al. Myc-binding-site recognition in the human genome is determined by chromatin context. Nat Cell Biol 8, 764-70 (2006).
19. Bernstein, B. E., Meissner, A. & Lander, E. S. The mammalian epigenome. Cell 128, 669-81 (2007).
20. Kozubek, M. et al. Combined confocal and wide-field high-resolution cytometry of fluorescent in situ hybridization-stained cells. Cytometry 45, 1-12 (2001).
21. Weis, K. et al. Retinoic acid regulates aberrant nuclear localization of PML-RAR alpha in acute promyelocytic leukemia cells. Cell 76, 345-56 (1994).
22. Warrell, R. P., Jr. et al. Differentiation therapy of acute promyelocytic leukemia with tretinoin (all-trans-retinoic acid). N Engl J Med 324, 1385-93 (1991).
23. Minucci, S. & Pelicci, P. G. Histone deacetylase inhibitors and the promise of epigenetic (and more) treatments for cancer. Nat Rev Cancer 6, 38-51 (2006).
24. Minucci, S. et al. Oligomerization of RAR and AML1 transcription factors as a novel mechanism of oncogenic activation. Mol Cell 5, 811-20 (2000).
25. Rochette-Egly, C., Adam, S., Rossignol, M., Egly, J. M. & Chambon, P. Stimulation of RAR alpha activation function AF-1 through binding to the general transcription factor TFIIH and phosphorylation by CDK7. Cell 90, 97-107 (1997).
26. Kumar, P. P. et al. Functional interaction between PML and SATB1 regulates chromatin-loop architecture and transcription of the MHC class I locus. Nat Cell Biol 9, 45-56 (2007).
27. Kastner, P. et al. Structure, localization and transcriptional properties of two classes of retinoic acid receptor alpha fusion proteins in acute promyelocytic leukemia (APL): structural similarities with a new family of oncoproteins. Embo J 11, 629-42 (1992).
28. Heller, R. C. & Marians, K. J. Replisome assembly and the direct restart of stalled replication forks. Nat Rev Mol Cell Biol 7, 932-43 (2006).
29. Sproul, D., Gilbert, N. & Bickmore, W. A. The role of chromatin structure in regulating the expression of clustered genes. Nat Rev Genet 6, 775-81 (2005).
30. Tolhuis, B., Palstra, R. J., Splinter, E., Grosveld, F. & de Laat, W. Looping and interaction between hypersensitive sites in the active beta-globin locus. Mol Cell 10, 1453-65 (2002).
31. Frank, S. R., Schroeder, M., Fernandez, P., Taubert, S. & Amati, B. Binding of c-Myc to chromatin mediates mitogen-induced acetylation of histone H4

and gene activation. Genes Dev 15, 2069-82 (2001).
32. Martens, J. H. et al. The profile of repeat-associated histone lysine methylation states in the mouse epigenome. Embo J 24, 800-12 (2005).
33. Osborne, C. S. et al. Active genes dynamically colocalize to shared sites of ongoing transcription. Nat Genet 36, 1065-71 (2004).
34. Neves, H., Ramos, C., da Silva, M. G., Parreira, A. & Parreira, L. The nuclear topography of ABL, BCR, PML, and RARalpha genes: evidence for gene proximity in specific phases of the cell cycle and stages of hematopoietic differentiation. Blood 93, 1197-207 (1999).
35. Pombo, A. et al. Regional and temporal specialization in the nucleus: a transcriptionally-active nuclear domain rich in PTF, Oct1 and PIKA antigens associates with specific chromosomes early in the cell cycle. Embo J 17, 1768-78 (1998).

Supplementary Information is linked to the online version of the paper at www.nature.com/nature.

Aknowledgments We thank B. Amati, M. Foiani and V. Pirrotta for helpful discussion and critical reading of this manuscript, T. Jenuwein for providing antibodies against different histone marks, Laura Tizzoni and Loris Bernard (IFOM-IEO Campus Real-Time PCR Facility) for assistance. This work was supported by AIRC and EC grants to PGP and SM and by ASCR to SK.

Author Contributions M.Fal. performed image and data analysis of Figs. 4a,b, S5 and S6; E.L. performed 3D-FISH and immuno-FISH experiments; S.K. set up high-resolution cytometer and generated Suppl. Table S2; M.Far. optimized confocal analysis; G.B. generated Figs. 3b and S3a; F.D.S. performed ChIP assays for Figs. 2, S2a, S3b, S7 and S8; M.C. and L.L. performed statistical analysis of Fig.1 and Table S1; S.S. performed ChIP assay for Fig. S4; M.A. provided expression profile data; G.I.D. generated all the remaining Figs., contributed to experimental design and wrote the manuscript; S.M. and P.G.P. planned the project and discussed the results.

Author Information The authors declare no competing financial interests. Correspondence and requests for materials should be addressed to P.G.P. (piergiuseppe.pelicci@ifom-ieo-campus.it) or G.I.D (gaetano.dellino@ifom-ieo-campus.it).

Figure Legends

Figure 1. Distribution of PML-RAR down-regulated genes and Alu-RAREs along representative human chromosomes. Top: chromosome ideogram; middle: Gene Clusters; bottom: Alu-RARE Clusters. Gene or Alu-RARE clusters were identified, respectively, by plotting the probability (-Log p-value) of gene or Alu-RARE clustering over gene density or Alu random distribution, using sliding windows of 500 Kb or 50 Kb (see Supplementary Notes). The Gene Clusters analysed in this study are indicated in green. Red bars indicate the DNA probes used in the 3D-FISH experiments, stars those also used for immuno-FISH.

Figure 2. Binding, transcriptional effects and chromatin modifications induced by PML-RAR on Gene Cluster #1. ***a***. Map of Gene Cluster #1. Numbers below indicate its position along chromosome 19. Boxes indicate gene loci. Black: down-regulated by PML-RAR; empty: not regulated; gray: not expressed; hatched: not tested. ***b***. QRT-PCR analysis of the effect of PML-RAR on expression of the indicated genes (normalized with 18S rDNA). Results are expressed as ratio of values obtained from zinc-treated (8 hrs) and untreated PR9 cells. **c**. QChIP analysis of PML-RAR (α-PML) and PolII (α-PolII) binding, levels of histone-H3 acetylation (α-H3PanAc) and K4 tri-methylation (α-H3K4me3), at the promoter region of the indicated genes. Analysed regions are indicated below (arrow: TSS; boxed number: distance, in Kb, from the TSS). DR8-RAREs of HA-1 gene and dashed lines showing reference ChIP values for the same antibody are also indicated. Results are expressed as percent of immunoprecipitated DNA with respect to input DNA. Gray and black bars represent values obtained prior and 8 hours after PML-RAR expression, respectively. ***d***. QChIP analysis of PML-RAR binding to the TSS of the indicated genes, Alu1, Alu2 and RARβ. Results are expressed as in *c*. ***e***. QChIP analysis of PML-RAR binding at the TSSs of ELA2 and AZU1 genes and at the Alu1 repeat, performed prior (white bars) and after 5 (gray bars) or 8 (black bars) hours of PML-RAR expression, as indicated. Results are expressed as in *c*.

Figure 3. **Physical proximity between clustered gene promoters and Alu repeats.** ***a***. Map of Gene Cluster #1, as in Fig. 2a, with A1 and A2 Alu-RARE clusters (drawn in scale). Individual Alu-RAREs are shown in the magnification below the map. The double-arrowed lines above are described in panel *c*. ***b***. Percent distribution of Alu-RAREs (gray bars) in the J, S Y and Ya5 Alu sub-families in Cluster #1, chromosome 19 and the whole genome, as indicated. ***c.*** 3C analysis of physical proximity between genes and Alu-RAREs within chromosome 19 Cluster #1. Chromatin from PR9 cells prior to (-PML-RAR) or 8 hrs after (+PML-RAR) PML-RAR expression was digested with the *Hind*III restriction enzyme; the position of the relevant e, h5, h3, a1 and a2 *Hind*III fragments (frgm) is indicated below the Cluster #1 map in panel *a*. Orientation and position of the PCR primers is indicated by arrows in panel *a*. The DNA interval between the different 3C primers is shown at the top of panel *a* by a double-arrowed line, interrupted by a number indicating its length (in Kb). Results of the 3C assay are shown in the 2% agarose gels, with the 3C primer combinations indicated in the diagram below. The PCR reactions showing positive or negative interaction between different *Hind*III fragments are indicated as 3C+ or 3C- in panel *a*. DNA molecular weight markers (MW) are a 100 bp ladder (top band= 500 bp). Control ligation/PCR products are described in Methods. ***d***. 3C analysis of physical proximity between genes and Alu-RAREs within chromosome 12 Cluster #4 (same conditions as in *a*). Left: Map of Gene Cluster #4 and the A3 Alu-RARE cluster. PCR primers and *Hind*III fragments are indicated below the map. The DNA interval between two 3C primers is indicated with double-arrowed lines as in *a*. Right: Results of the 3C assay are shown by the 2% agarose gels (MW as in *c*, top band= 300 bp).

Figure 4. **Chromosome distances across clusters of co-regulated genes and colocalization between PML-RAR and Gene Clusters.** ***a***. Top: Relative elongation or shortening of the indicated chromosomal regions (average size of 1.4-2.9 Mb), as determined by 3D-FISH measurement of the mutual distance between two locus-specific DNA probes flanking each region. For each analysed cell, distance was calculated as % of nuclear radius, to account for variations in nuclear size. For each treatment, average distance was compared with that obtained from untreated MT or PR9 cells (reference line) and expressed as percent of elongation or shortening. Error bars indicate s.e.m. (n≥255). The various treatments (Zinc, RA, TSA, Zinc+RA,

Zinc+TSA) are indicated with a color code. Bottom: Representative FISH-images of PR9 cells: untreated, 8hrs after Zinc treatment alone (+PML-RAR) or followed by 4hrs with 10uM RA (+PML-RAR+RA) or 100 nM TSA (+PML-RAR+TSA). ***b***. Immuno-FISH co-localization experiments using an αPML antibody and genomic BAC clones (see Methods). The αPML antibody recognizes PML-bodies in untreated cells or PML/RAR microspeckles in cells expressing PML-RAR. Results are expressed as average percent of cells showing colocalization with αPML signals of none (yellow), one (green) or both (red) of the two BAC signals found in each cell. Error bars indicate s.d. (n=2), >200 nuclei analysed). ***c***. QChIP analysis of PML-RAR (α-PML) binding at the TSS region of the indicated Cluster #1 genes, RARβ and Alu1, in cells expressing PML-RAR (8 hrs of Zinc treatment) and further treated (+Zn+TSA) or not (+Zn) with TSA for 4 hrs. Results are expressed as fold variations with respect to PML-RAR binding to Alu1 (=1). Actual PML-RAR binding values are shown in Supplementary Fig. S7.

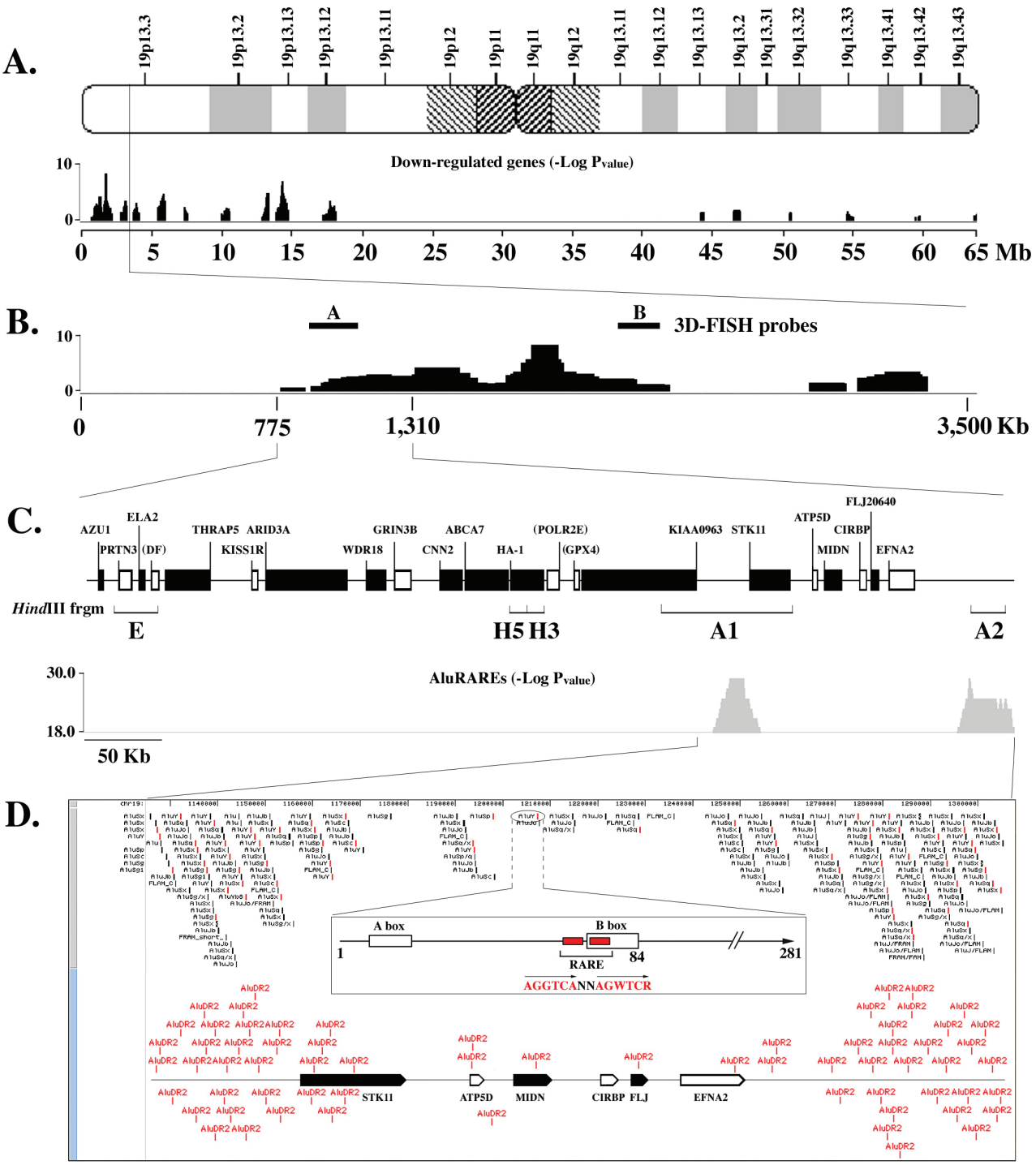
A.
19p13.3
19p13.2
19p13.13
19p13.12
19p13.11
19p12
19p11
19q11
19q12
19q13.11
19q13.12
19q13.13
19q13.2
19q13.31
19q13.32
19q13.33
19q13.41
19q13.42
19q13.43
Down-regulated genes (-Log Pvalue)
10
0
0 5 10 15 20 25 30 35 40 45 50 55 60 65 Mb
B.
A
B
3D-FISH probes
10
0
0 775 1,310 3,500 Kb
C.
AZU1
ELA2
PRTN3
(DF)
THRAP5
ARID3A
KISS1R
GRIN3B
WDR18
ABCA7
CNN2
HA-1
(POLR2E)
(GPX4)
KIAA0963
STK11
ATP5D
CIRBP
FLJ20640
MIDN
EFNA2
HindIII frgm
E
H5 H3
A1
A2
30.0
18.0
AluRAREs (-Log Pvalue)
50 Kb
D.
A box
B box
1
84
281
RARE
AGGTCANNAGWTCR
AluDR2
STK11
ATP5D
MIDN
CIRBP
FLJ
EFNA2

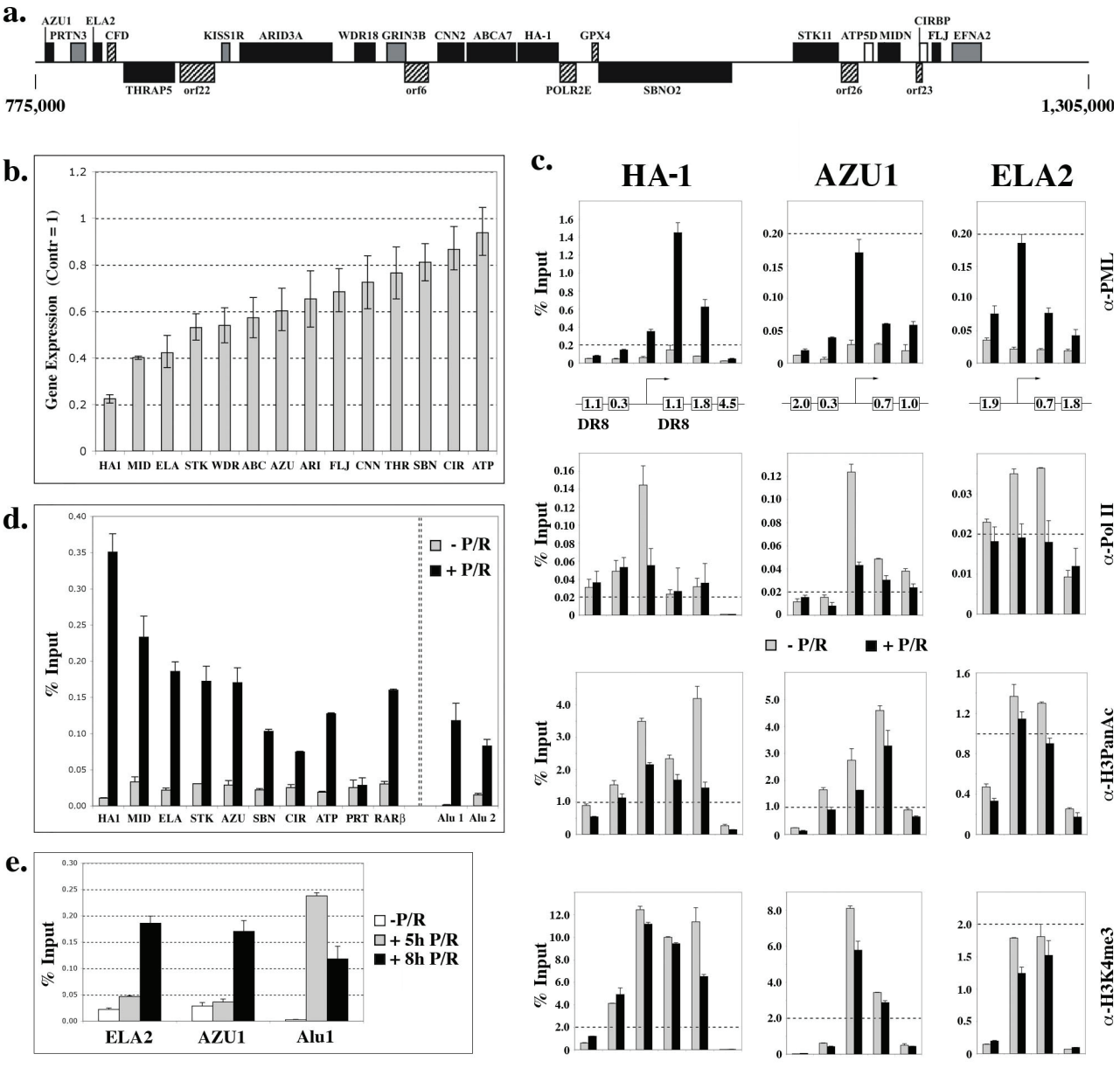

Pelicci Fig.2

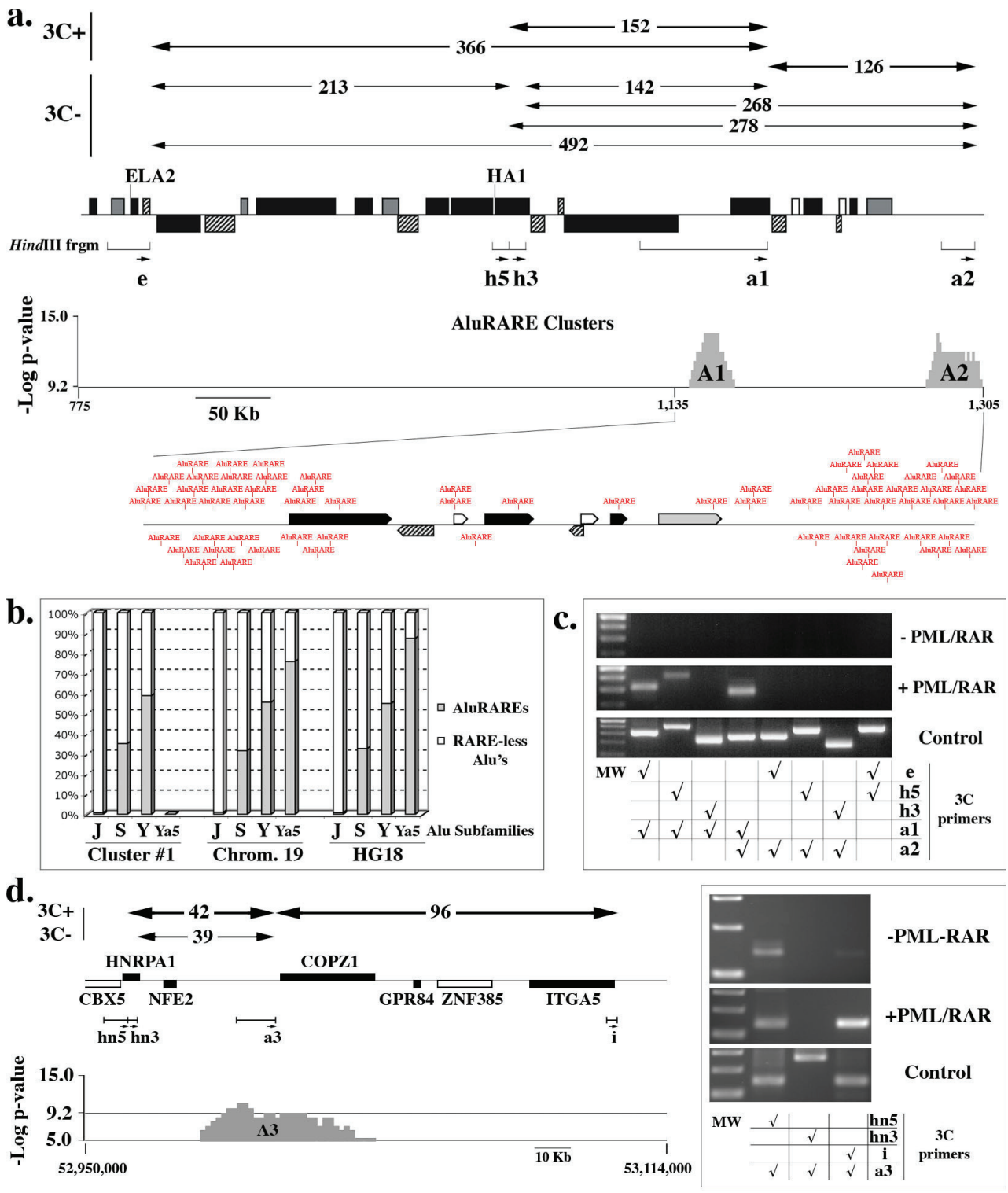

Pelicci Fig.3

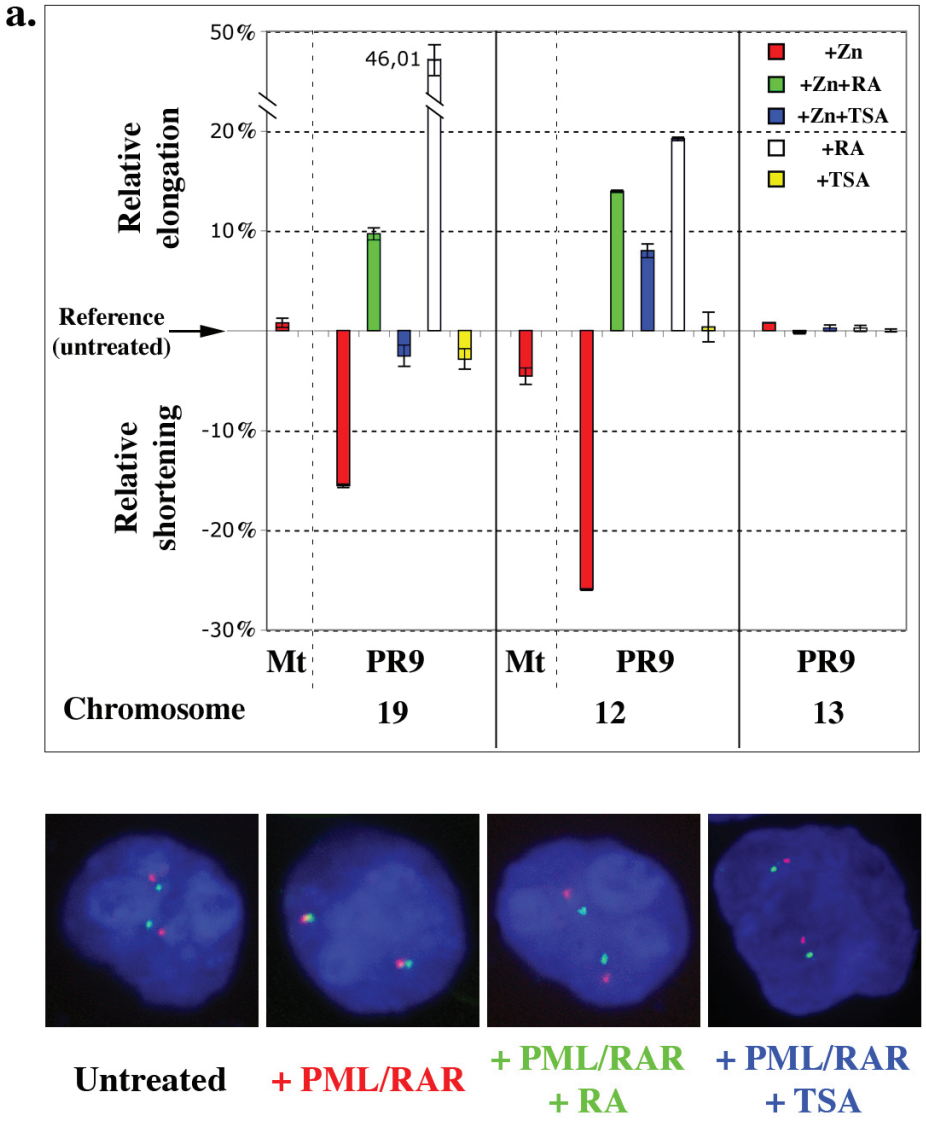
a.
50%
20%
10%
-10%
-20%
-30%
46,01
Relative elongation
Relative shortening
Reference (untreated)
+Zn
+Zn+RA
+Zn+TSA
+RA
+TSA
Mt
PR9
Mt
PR9
PR9
Chromosome
19
12
13

Untreated
+ PML/RAR
+ PML/RAR + RA
+ PML/RAR + TSA

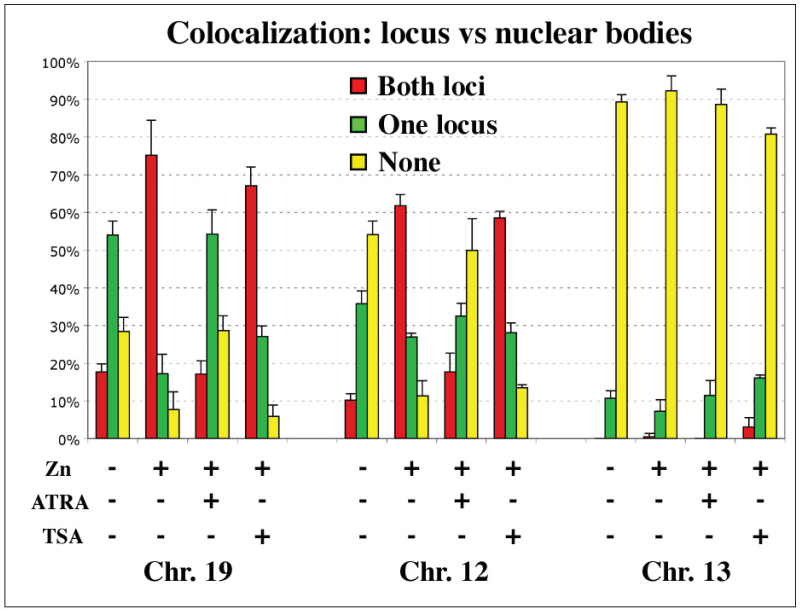
b.
Colocalization: locus vs nuclear bodies
100%
90%
80%
70%
60%
50%
40%
30%
20%
10%
0%
Both loci
One locus
None
Zn
ATRA
TSA
Chr. 19
Chr. 12
Chr. 13

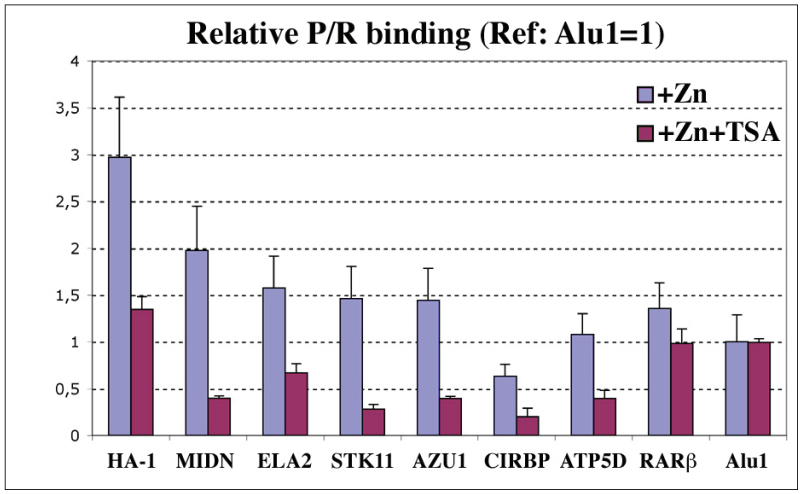
c.
Relative P/R binding (Ref: Alu1=1)
4
3,5
3
2,5
2
1,5
1
0,5
0
+Zn
+Zn+TSA
HA-1
MIDN
ELA2
STK11
AZU1
CIRBP
ATP5D
RARβ
Alu1

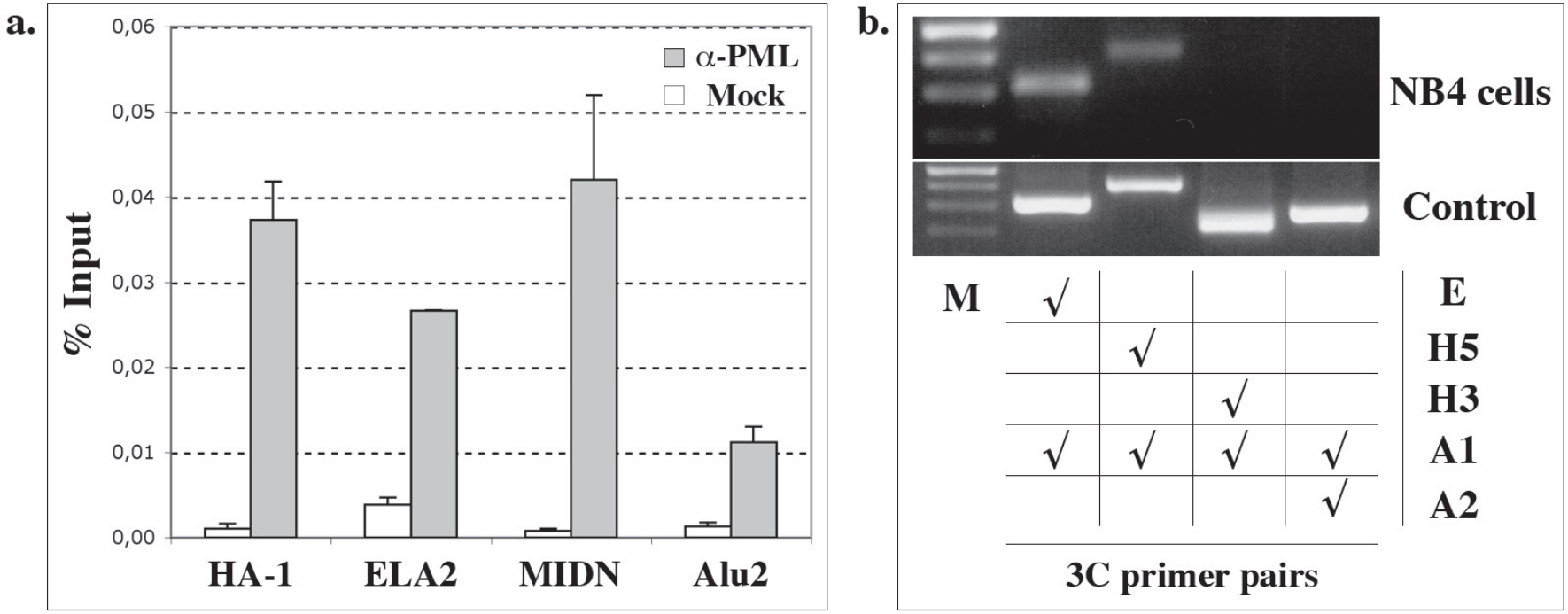
a.
0,06
0,05
0,04
0,03
0,02
0,01
0,00
% Input
α-PML
Mock
HA-1
ELA2
MIDN
Alu2
b.
NB4 cells
Control
M
E
H5
H3
A1
A2
3C primer pairs

a.

DR type	Nr. of RAREs	
DR2	49	43:AGGTCA-AGTTCA 2:GGGTCA-AGGTCA 1:GGGTCA-GGTTCA 1:AGGTCA-GGTTCA 1:AGGTCA-GGGTCA 1:AGGTCA-AGGTCA
DR3	0	
DR4	4	2:GGGTCA-AGGTCA 2:AGGTCA-AGGTCA
DR5	1	GGTTCA-GGGTCA
DR6	2	1:GGGTCA-GGTTCA 1:GGGTCA-GGGTCA
DR7	1	GGGTCA-GGGTCA
DR8	7	3:GGGTCA-GGGTCA 2:GGGTCA-AGGTCA 1:AGTTCA-AGGTCA 1:AGGTCA-GGGTCA
DR9	0	
DR10	2	1:GGGTCA-AGTTCA 1:GGGTCA-GGGTCA
	66	

b. Alu-RARE

DR2-Alu

DR2-Cluster#1	AGGTCANNAGTTCA
DR2-K18	AGGTCANNAGATCG
DR2-Alu Consensus	AGGTCAnnAGWTCR

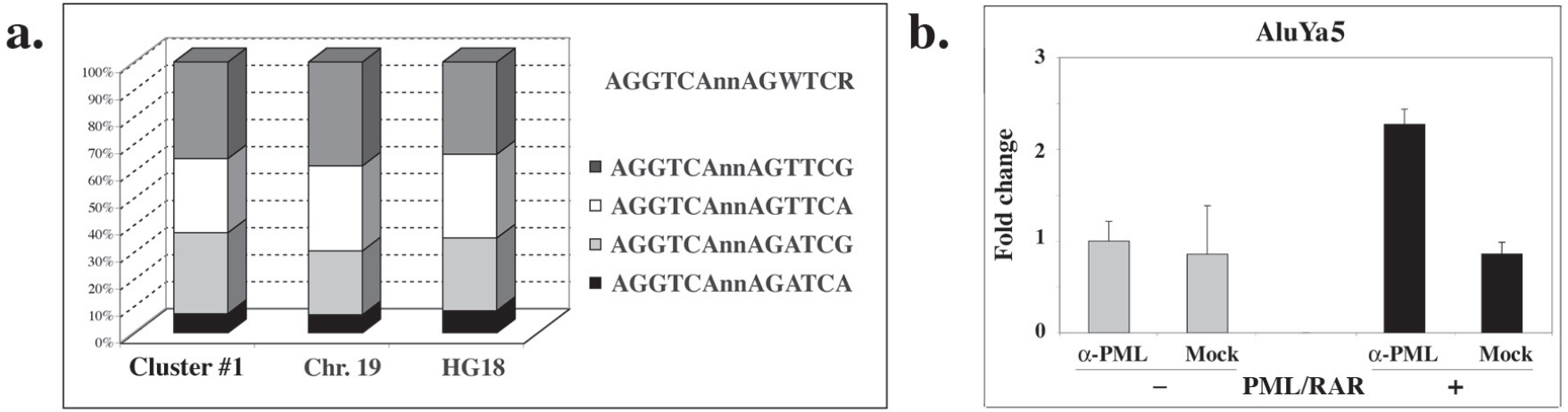
a.
100%
90%
80%
70%
60%
50%
40%
30%
20%
10%
0%
Cluster #1
Chr. 19
HG18
AGGTCAnnAGWTCR
AGGTCAnnAGTTCG
AGGTCAnnAGTTCA
AGGTCAnnAGATCG
AGGTCAnnAGATCA
b.
AluYa5
Fold change
3
2
1
0
α-PML
Mock
α-PML
Mock
–
PML/RAR
+
c.
AluS
AluY
1,052,500
Alu1
AluS
AluS
1,135,700
Alu2
100 bp

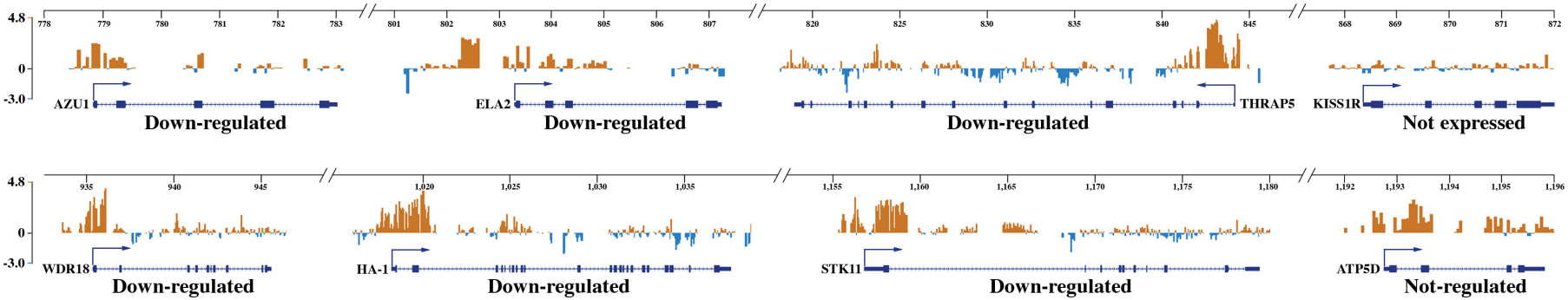
4.8
0
-3.0
778
779
780
781
782
783
801
802
803
804
805
806
807
820
825
830
835
840
845
868
869
870
871
872
AZU1
ELA2
THRAP5
KISS1R
Down-regulated
Down-regulated
Down-regulated
Not expressed
4.8
0
-3.0
935
940
945
1,020
1,025
1,030
1,035
1,155
1,160
1,165
1,170
1,175
1,180
1,192
1,193
1,194
1,195
1,196
WDR18
HA-1
STK11
ATP5D
Down-regulated
Down-regulated
Down-regulated
Not-regulated

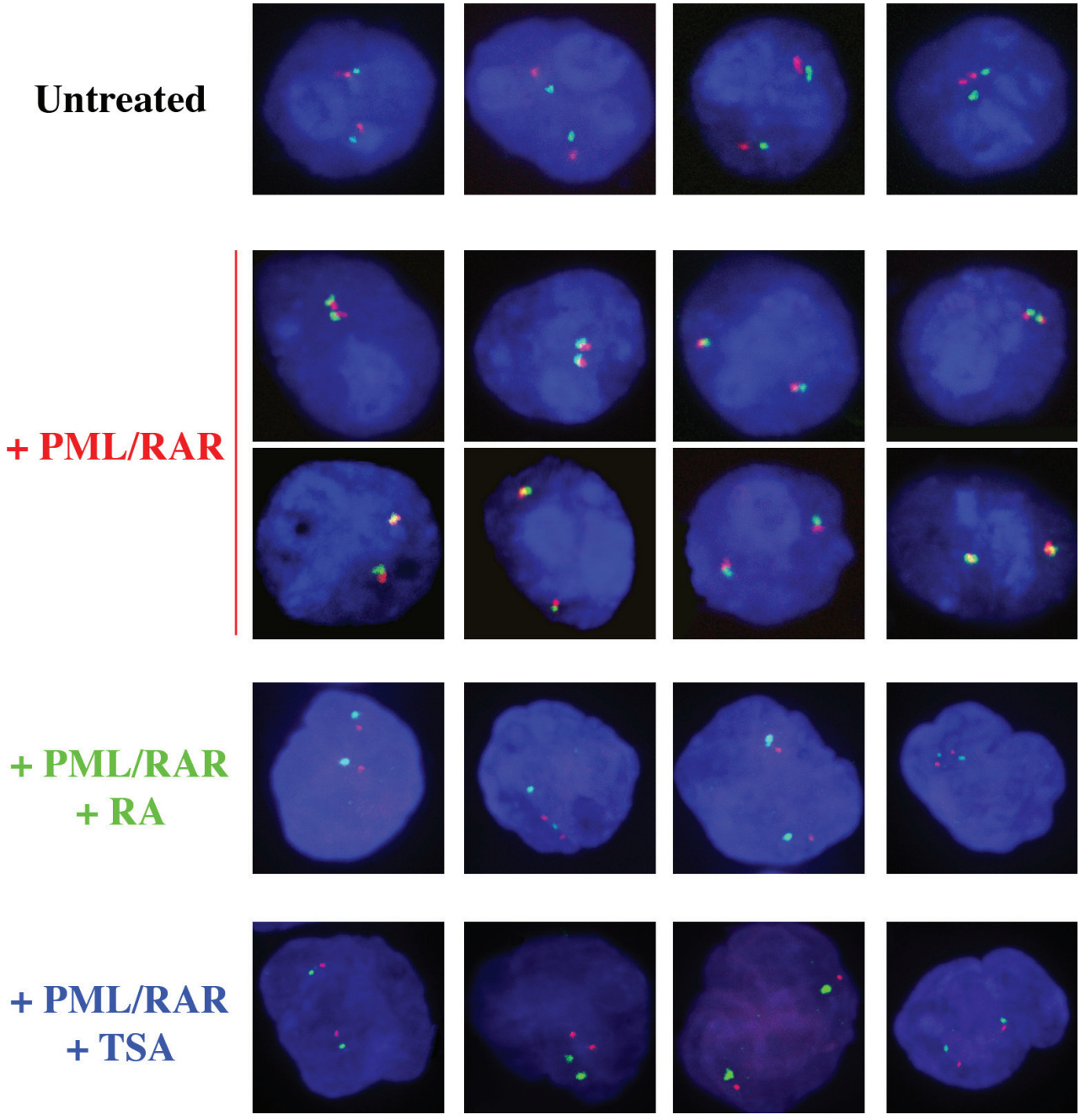
Untreated
+ PML/RAR
+ PML/RAR
+ RA
+ PML/RAR
+ TSA

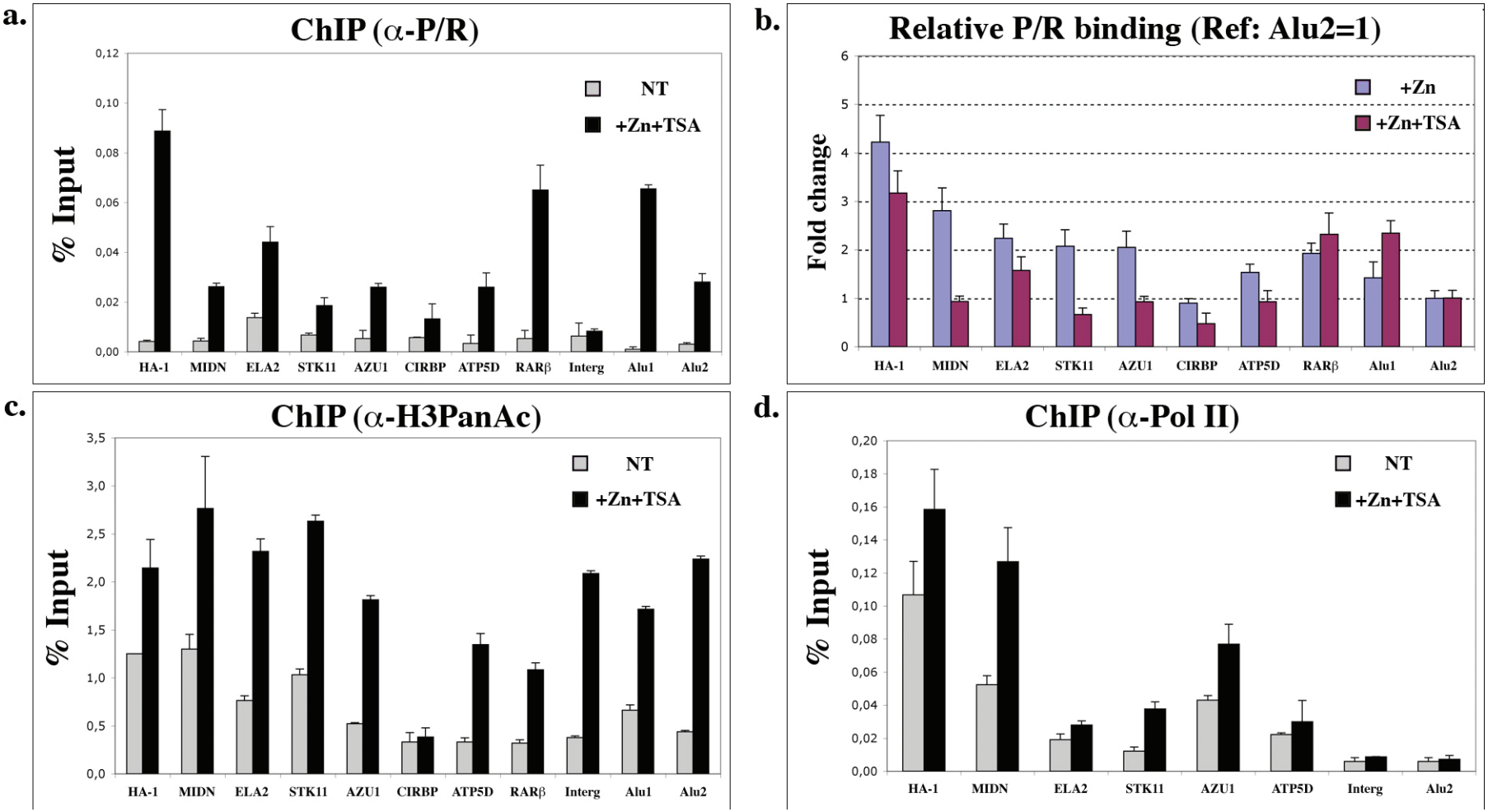
a.
ChIP (α-P/R)
% Input
0,12
0,10
0,08
0,06
0,04
0,02
0,00
NT
+Zn+TSA
HA-1
MIDN
ELA2
STK11
AZU1
CIRBP
ATP5D
RARβ
Interg
Alu1
Alu2
b.
Relative P/R binding (Ref: Alu2=1)
Fold change
6
5
4
3
2
1
0
+Zn
+Zn+TSA
HA-1
MIDN
ELA2
STK11
AZU1
CIRBP
ATP5D
RARβ
Alu1
Alu2
c.
ChIP (α-H3PanAc)
% Input
3,5
3,0
2,5
2,0
1,5
1,0
0,5
0,0
NT
+Zn+TSA
HA-1
MIDN
ELA2
STK11
AZU1
CIRBP
ATP5D
RARβ
Interg
Alu1
Alu2
d.
ChIP (α-Pol II)
% Input
0,20
0,18
0,16
0,14
0,12
0,10
0,08
0,06
0,04
0,02
0,00
NT
+Zn+TSA
HA-1
MIDN
ELA2
STK11
AZU1
ATP5D
Interg
Alu2

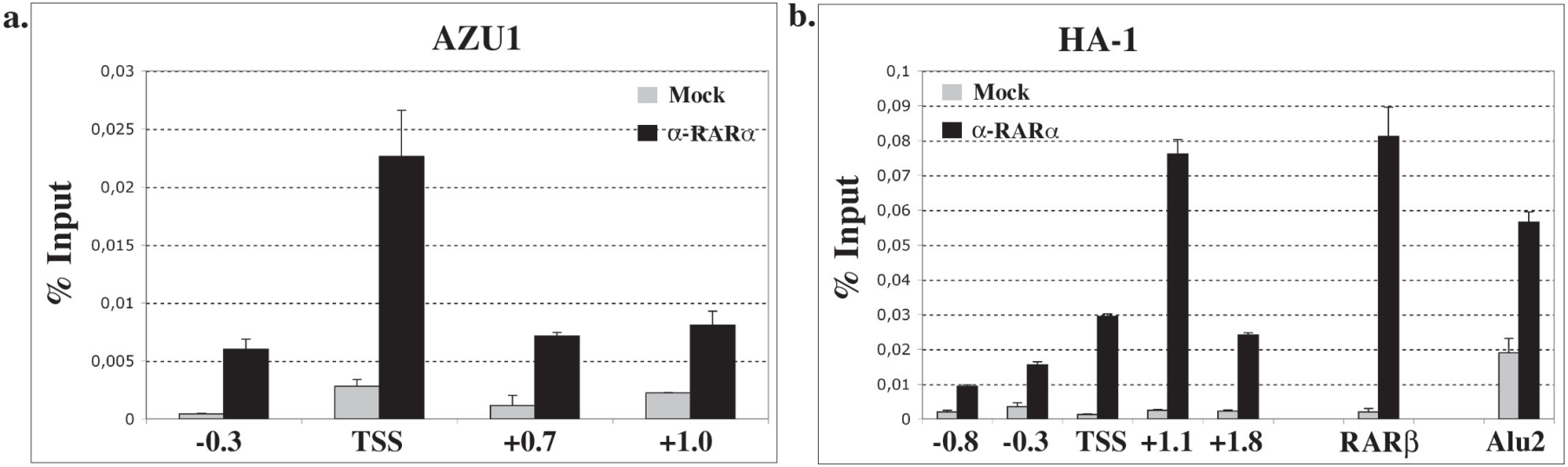
a.
AZU1
% Input
Mock
α-RARα
0,03
0,025
0,02
0,015
0,01
0,005
0
-0.3
TSS
+0.7
+1.0
b.
HA-1
% Input
Mock
α-RARα
0,1
0,09
0,08
0,07
0,06
0,05
0,04
0,03
0,02
0,01
0
-0.8
-0.3
TSS
+1.1
+1.8
RARβ
Alu2

Chrom.	Nr. of clusters	Nr. of genes	
1	10	36	
2	1	4	
3	1	3	
4	0	0	
5	3	11	
6	4	12	
7	2	9	
8	2	6	
9	0	0	
10	3	9	
11	7	30	
12	8	39	
13	1	3	
14	3	10	
15	2	6	
16	5	18	
17	10	37	
18	0	0	
19	15	56	
20	2	6	
21	2	6	
22	3	11	
Y	0	0	
X	0	0	
	84	312	**Total**

b.

compared treatments **Chromosome 19**	Nr. of chromosomes exp1	Nr. of chromosomes exp2	Degrees of Freedom	P-value	T-value
PR9-C vs PR9+Zn (8h)	1094	3366	4458	0,0000	6,5190
PR9-C vs PR9+Zn+ATRA (8+4h)	1094	2437	3529	0,0002	3,6857
PR9-C vs PR9+Zn+TSA (8+4h)	1094	335	1427	0,4228	0,8018
PR9-C vs PR9-C+ATRA (4h)	1094	527	1619	0,0000	11,2832
PR9-C vs PR9-C+TSA (4h)	1094	497	1589	0,9985	0,0018
PR9+Zn (8h) vs PR9+Zn+ATRA (8+4h)	3366	2437	5801	0,0000	13,2284
PR9+Zn (8h) vs PR9+Zn+TSA (8+4h)	3366	335	3699	0,0017	3,1371
PR9-C+ATRA (4h) vs PR9+Zn+ATRA (8+4h)	527	2437	2962	0,0000	9,4462
PR9-C+TSA (4h) vs PR9+Zn+TSA (8+4h)	497	335	830	0,4535	0,7500
PR9+Zn+ATRA (8+4h) vs PR9+Zn+TSA (8+4h)	2437	335	2770	0,0029	2,9816
PR9-C+ATRA (4h) vs PR9+C+TSA (4h)	527	497	1022	0,0000	8,9183

compared treatments **Chromosome 19**	Nr of chromosomes exp 1	Nr of chromosomes exp 2	Degrees of Freedom	P-value	T-value
BULK-C vs BULK+Zn (8h)	673	1128	1799	0,8992	0,1267

compared treatments **Chromosome 12**	Nr of chromosomes exp1	Nr of chromosomes exp2	Degrees of Freedom	P-value	T-value
PR9-C vs PR9+Zn (8h)	337	435	770	0,0000	8,9601
PR9-C vs PR9+Zn+ATRA (8+4h)	337	354	689	0,0003	3,6457
PR9-C vs PR9+Zn+TSA (8+4h)	337	329	664	0,0515	1,9505
PR9-C vs PR9-C+ATRA (4h)	337	535	870	0,0000	4,8647
PR9-C vs PR9-C+TSA (4h)	337	265	600	0,9344	0,0823
PR9+Zn (8h) vs PR9+Zn+ATRA (8+4h)	435	354	787	0,0000	12,3399
PR9+Zn (8h) vs PR9+Zn+TSA (8+4h)	435	329	762	0,0000	9,7491
PR9-C+ATRA (4h) vs PR9+Zn+ATRA (8+4h)	535	354	887	0,2009	1,2798
PR9-C+TSA (4h) vs PR9+Zn+TSA (8+4h)	265	329	592	0,1341	1,5002
PR9+Zn+ATRA (8+4h) vs PR9+Zn+TSA (8+4h)	354	329	681	0,1784	1,3472
PR9-C+ATRA (4h) vs PR9+C+TSA (4h)	535	265	798	0,0001	3,9623

compared treatments **Chromosome 12**	Nr of chromosomes exp 1	Nr of chromosomes exp 2	Degrees of Freedom	P-value	T-value
BULK-C vs BULK+Zn	394	255	647	0,2735	1,0959

compared treatments **Chromosome 13**	Nr of chromosomes exp2	Nr of chromosomes exp2	Degrees of Freedom	P-value	T-value
PR9-C vs PR9+Zn (8h)	491	432	921	0,8236	0,2229
PR9-C vs PR9+Zn+ATRA (8+4h)	491	515	1.004	0,9556	0,0557
PR9-C vs PR9+Zn+TSA (8+4h)	491	279	768	0,9427	0,0719
PR9-C vs PR9-C+ATRA (4h)	491	541	1.030	0,9416	0,0732
PR9-C vs PR9-C+TSA (4h)	491	396	885	0,9931	0,0087
PR9+Zn (8h) vs PR9+Zn+ATRA (8+4h)	432	515	945	0,7749	0,2860
PR9+Zn (8h) vs PR9+Zn+TSA (8+4h)	432	279	709	0,8946	0,1326
PR9-C+ATRA (4h) vs PR9+Zn+ATRA (8+4h)	541	515	1.054	0,8927	0,1350
PR9-C+TSA (4h) vs PR9+Zn+TSA (8+4h)	396	279	673	0,9489	0,0641
PR9+Zn+ATRA (8+4h) vs PR9+Zn+TSA (8+4h)	515	279	792	0,9008	0,1247
PR9-C+ATRA (4h) vs PR9+C+TSA (4h)	541	396	935	0,9507	0,0619

Biochimica et Biophysica Acta 1783 (2008) 2398–2414

Contents lists available at ScienceDirect

Biochimica et Biophysica Acta

journal homepage: www.elsevier.com/locate/bbamcr

Chromatin structure influences the sensitivity of DNA to γ-radiation

Martin Falk, Emilie Lukášová *, Stanislav Kozubek

Institute of Biophysics, Academy of Sciences of the Czech Republic, Kralovopolska 135, 61265 Brno, Czech Republic

ARTICLE INFO

Article history:
Received 22 May 2008
Received in revised form 11 July 2008
Accepted 11 July 2008
Available online 25 July 2008

Keywords:
Chromatin structure
DNA damage
Double-strand break (DSB)
DNA repair
Experimentally changed radiosensitivity
Apoptosis

ABSTRACT

For the first time, DNA double-strand breaks (DSBs) were directly visualized in functionally and structurally different chromatin domains of human cells. The results show that genetically inactive condensed chromatin is much less susceptible to DSB induction by γ-rays than expressed, decondensed domains. Higher sensitivity of open chromatin for DNA damage was accompanied by more efficient DSB repair. These findings follow from comparing DSB induction and repair in two 11 Mbp-long chromatin regions, one with clusters of highly expressed genes and the other, gene-poor, containing mainly genes having only low transcriptional activity. The same conclusions result from experiments with whole chromosome territories, differing in gene density and consequently in chromatin condensation. It follows from our further results that this lower sensitivity of DNA to the damage by ionizing radiation in heterochromatin is not caused by the simple chromatin condensation but very probably by the presence of a higher amount of proteins compared to genetically active and decondensed chromatin. In addition, our results show that some agents potentially used for cell killing in cancer therapy (TSA, hypotonic and hypertonic) influence cell survival of irradiated cells via changes in chromatin structure and efficiency of DSB repair in different ways.

1. Introduction

Chromosomes are organized in territories which are non-randomly distributed in cell nuclei. In many human cell types, chromosome territories (CTs) have a radial organization [1–3]; however, the basic principles of chromatin folding in CTs are not yet clearly understood. A large body of evidence shows that the higher-order folding of chromatin fibres in CTs is closely related to genome function, in particular, transcription and replication [[4] and citations herein]. Recent experiments show that dynamic changes in chromatin structure in the vicinity of DSBs are required for their repair [5,6]. These changes reflect local chromatin decondensation connected with post-translational modifications of histones, and assembly of diverse proteins at the sites of chromosomal lesions [6,7].

Double-strand breaks (DSBs) in DNA occur frequently in the genome through the action of DNA-damaging agents or during genome replication [8]. They are hazardous for the cell because improper repair of them may lead to tumorigenic translocations [9]. The most dangerous translocations are those affecting proto-oncogenes, oncogenes, regulatory DNA sequences and genes. Since most coding genes occur in open chromatin [10,11], it is important to know whether this chromatin has greater sensitivity to DNA-damaging agents than condensed chromatin, which contains a low density of genes characterized by a low level of transcriptional activity. In other words, we wish to know how DNA damage is affected by chromatin structure and the architecture of the interphase nucleus. The influence of chromatin structure on the susceptibility of DNA to damage, and the efficiency of its repair in human lymphocytes, were indirectly deduced from the different yields of aberrations observed for individual chromosomes in mitosis [12,13]. There were more exchange aberrations in chromosomes that contained a higher density of genes. Although the results clearly show a higher risk of chromosomal translocations in gene-dense chromatin, they do not provide evidence of higher sensitivity of this open chromatin to the initial DNA damage, since not all DSBs give rise to exchange aberrations; indeed, most breaks are repaired correctly soon (several minutes) after their induction [14,15]. Therefore, the results described above, as well as other recent results, do not deal either with the induction or kinetics of DSB repair in different chromatin structures. Moreover, gene density and the expression of particular loci may differ according to the cell type studied, which requires further studies of the relationship between these factors.

The radial distribution of chromosomes in human interphase nuclei is correlated with gene density. The most gene-rich chromosomes are localized in the central part of the nucleus, whereas the gene-poor chromosomes occupy more peripheral positions close to the nuclear membrane [1,3]. This arrangement of chromosomes evidently has functional importance, because it correlates with gene expression [16]. Besides, it has been suggested that the radial organization could have a protective role for the genome [17]. Heterochromatic chromosomes located at the nuclear periphery might absorb mutagens as they enter the nucleus, and hence protect DNA in the central part of the nucleus from damage. This arrangement

* Corresponding author. Tel.: +420 541517165; fax: +420 541240498.
E-mail address: lukasova@ibp.cz (E. Lukášová).

0167-4889/$ – see front matter © 2008 Elsevier B.V. All rights reserved.
doi:10.1016/j.bbamcr.2008.07.010

would ensure the preferential protection of many coding sequences, since the most gene-rich chromosomes are located in the centre of the nucleus [17]. However, a protective effect of the radial arrangement of chromosomes against the oxidative effect of UV-C radiation was not found; indeed, more damage was induced in the nuclear centre than at the periphery [18]. On the basis of these findings, the authors suggested that the sequences located in the centre of the nucleus are more susceptible to damage. Again, these results do not show directly the influence of chromatin structure on sensitivity to DNA-damaging agents, but do show unequivocally that there are factors responsible for the non-homogeneous distribution of DSBs in the cell nucleus. Nowadays, the above mentioned questions can be addressed more directly and more precisely due to progress in microscopical and immunological techniques. The most convenient method for detection and nuclear localization of DSBs (the most dangerous DNA damage) immediately after their induction is the direct observation of phosphorylated H2AX (γH2AX), which accumulates specifically at sites of DSBs [19,20] and which can be visualized by specific antibody. By monitoring assemblage of repair proteins at DSB sites, this method allows the study of DSB repair during the period after damage induction, and quantification of the repair progress. In combination with fluorescence in situ hybridization (FISH), this method (Immuno-FISH, [21]) permits direct detection of DSBs and/or proteins participating in DSB repair, together with specific DNA sequences, and thus the time course of damage induction and repair can be studied.

To analyse the relationship between the susceptibility of DNA to DSBs and chromatin structure, we irradiated cells with γ-rays (used as a source of low linear energy transfer radiation), and followed DSB induction in two regions of the human genome that differed in their density of highly expressed genes. Clustering of the most highly transcribed genes into several domains called "RIDGEs" (regions of increased gene expression) was found in all tissues studied on the basis of expression profiles of chromosomal genes [10,11]. The genomic regions that are gene-poor and contain mainly genes that, if expressed, have only low transcriptional activity, were also identified and called "anti-RIDGEs". One RIDGE and one anti-RIDGE

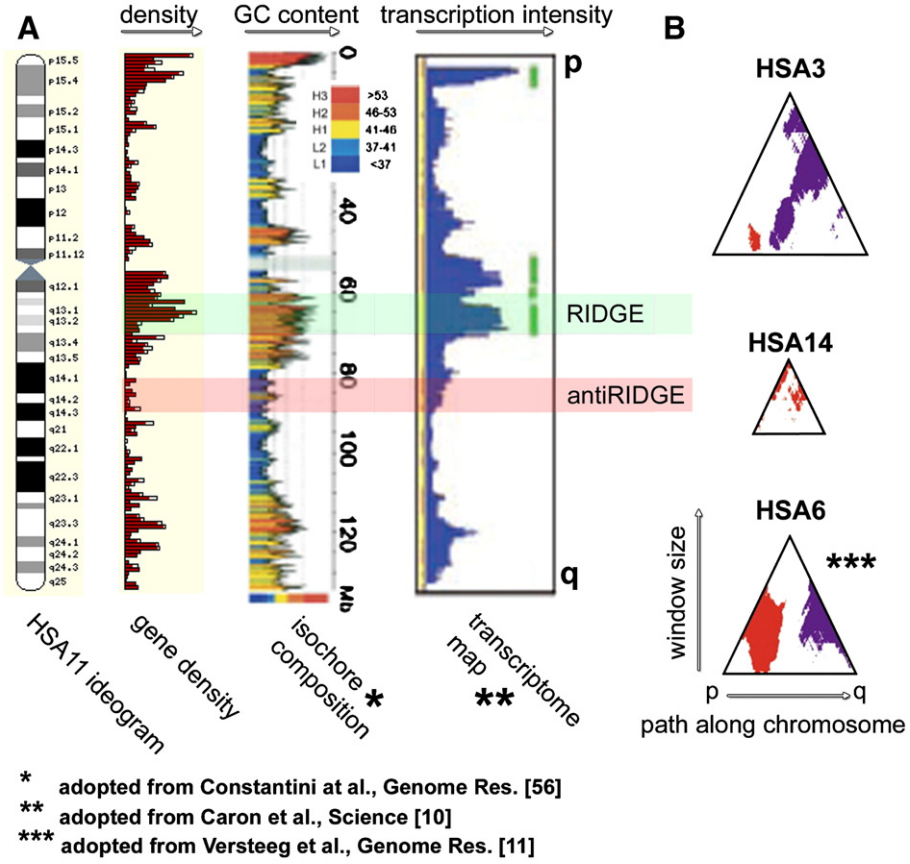

Fig. 1. The parameters used for characterization of chromosomes and specific chromosomal regions (RIDGE, anti-RIDGE) in this work. Efficiency of DSB repair and sensitivity to their induction were studied for chromosomes and specific chromosomal regions differing in their gene density (according to Ensembl database, released Mar 2008, http://www.ensembl.org/Homo_sapiens/mapview), isochore composition (according to Costantini et al., Genome Res. [56]) and gene transcription (adopted from Caron et al., Science [10] and Versteeg et al., Genome Res. [11]). Chromosome 11 containing both types of chromatin studied in this work – the clusters of highly expressed genes (RIDGEs, highlighted in green) and chromatin domains with very low expression (anti-RIDGEs, highlighted in red) – is used as an example (A). The overall gene density and transcription intensity follow from the graphs (in panel A). The vertical axis shows the path along the chromosome from p- to q-telomere (the position of genes/transcription units and isochore composition on the chromosome, respectively), the horizontal axis (from left to right) indicates increasing gene density, GC content and transcription intensity respectively. Most intensively expressed RIDGEs are labeled by the green bars (vertical), the RIDGE and anti-RIDGE clusters analysed in this work are highlighted in green and red respectively. The isochore composition of the whole chromosome and RIDGE and anti-RIDGE clusters follows from the middle graph: isochore L1 (ultramarine blue, GC-poorest), L2 (blue, GC=37–41%), H1 (yellow, GC=41–46%), H2 (orange, GC=46–53%), H3 (red, GC>53%). (B) "Ridgeograms" identifying chromosomal regions of significant extremes in gene expression and their clustering along DNA sequence (adopted from Rogier Versteeg et al., Genome Res. [11]). Transcription intensity was measured along the chromosome (horizontal axis, left: p-telomere, right: q-telomere) as the function of the window size (horizontal axis, starting with a window size 19 genes, at the base of the triangle, until the maximum possible window size for each chromosome at the top apex of the triangle). The ridgeograms show a tendency of highly (RED) and weakly (BLUE) expressed transcription units to form clusters along the DNA sequence, thus forming RIDGE (regions of increased gene expression) and anti-RIDGE clusters respectively (red and blue "spots" in ridgeograms respectively). Three types of RIDGE clusters can be distinguished on the ridgeograms: the RIDGEs consisting of a limited number of genes with very intensive expression (the upper triangle, e.g. HSA3), RIDGEs containing a large number of moderately expressed genes (the middle triangle, e.g. HSA14) and RIDGEs characterized by both very high expression level and a high number of genes (the bottom triangle, e.g. HSA6). For more details see [10, 11].

region of the same length (11 Mbp), both localized on 11q, were analysed in this work. DSB induction and repair in these regions were compared with those in selected nuclear territories of interphase chromosomes differing in their gene density (and content of RIDGEs) and consequently in chromatin condensation. To analyse whether simple changes in chromatin compaction alone (without participation of chromatin binding proteins) can influence DSB induction and repair efficiency, these processes were also studied after experimentally induced transient chromatin hyper- or hypocondensation by short (<10 min) incubation of cells in media with different osmolarities. The short exposure to high osmolarity leads to the immediate restoration of chromatin structure and cell functions and do not increase the annexin positivity of cells after their transfer to the normal (isotonic) medium. Hypertonic treatment of cells was described earlier as a method of reversibly modifying chromatin structure [22,23], sensitizing cells to chromosomal damage and killing by ionizing radiation [24]. Moreover, it was shown that injection of 7.2% saline into a carcinoma inhibited tumor growth [25]. High salt injections have also been used clinically for a wide variety of lesions including renal cysts, hemangioma and lumbar vertebral disks [25]. It is therefore of utmost importance to deeply analyse mechanisms by which higher osmolarity influences DNA sensitivity to DSB induction and repair. The influence of another promising enhancer of radiation therapy [26,27], histone deacetylase (HDAC) inhibitor trichostatin A (TSA), on DSB induction and repair was also investigated. While hyper/hypotonic treatment influences folding of the total nuclear chromatin, HDAC inhibitors, globally increase acetylation of histones, leading to reversible decondensation of dense chromatin regions [28].

2. Materials and methods

2.1. Cell culture, synchronization and irradiation

Human skin BJ fibroblasts, obtained from the American Type Culture Collection (Manassas, VA, USA), were grown in DMEM medium supplemented with 10% fetal calf serum (FCS), penicillin (100 I.E.) and streptomycin (100 μg/ml) at 37 °C with 5% CO_2. Synchronization of cells in the G_0 phase of the cell cycle was achieved by incubation of confluent culture without serum for 4 days. After trypsinization, cells were plated on microscope slides and incubated in the medium with 10% serum for 12 h before irradiation. During this period, more than 95% of cells were in the G_1 phase of the cell cycle [6]. Cells were irradiated with γ-rays from ^{60}Co with different doses: 1.0, 1.5, 3.0, 5.0 and 7 Gy (1 Gy/min). To explore the role of chromatin structure in radiosensitivity of cells, the osmolarity of the medium was changed 5 min before irradiation of cells, and maintained in this medium after irradiation 5–120 min before fixation. In another experiment, the irradiated cells, incubated for different periods of time in hyper- or hypoosmotic medium, were transferred to normal physiological medium, in which they were incubated for 10 min to 24 h before fixation.

2.2. Formation of medium with different osmolarities

The osmolarity of standard culture medium is 290 mOsm [23]. To obtain hypercondensed chromatin (HCC), the cells were incubated in a hyperosmotic medium (HOM) with an osmolarity of 570 mOsm. This medium was prepared by addition of 1 ml 20 × PBS (2.8 M NaCl, 54 mM KCl, 130 mM Na_2PO_4, 30 mM KH_2PO_4, pH 7.4) to 19 ml DMEM containing 10% FCS [23]. To reverse the effect, the cells were transferred directly to the standard physiological medium (290 mOsm); up to about 10–15 min the hyperosmotic (and also hypoosmotic) treatment has no effect on cell viability and all changes in chromatin structure and cellular processes were reversible. Hypocondensed chromatin in cells was obtained by cell incubation in hypoosmotic (HypoOM) medium. Hypoosmotic medium of about 140 mOsm was prepared by diluting standard culture medium with an equal quantity of sterile ddH_2O. Since chromatin condensation and decondensation started within seconds, washing in physiological salt solution before cell fixation was strictly avoided. The influence of HDAC inhibition on chromatin structure and cell radiosensitivity was studied by the addition of 1 μM or 0.2 μM trichostatin A (TSA) (Sigma-Aldrich, UK) to standard medium 12 h before irradiation, and keeping the cells in this medium for different periods of time after irradiation, prior to cell fixation.

2.3. Annexin positivity

An apoptosis detection kit (Sigma-Aldrich, UK) was used to detect the early stages of apoptosis in cells exposed to the hyperosmotic medium (570 mOsm). The principal component of this kit is annexin V-Cy3 that binds to phosphatidyl-serine (PS) if this is transposed to the external side of the plasma membrane. This transposition occurs at the onset of apoptosis, and thus makes the PS available for binding to annexin V. Binding was observed as red fluorescence. The procedure was performed on cells growing on microscope slides according to the manufacturer's recommendations. Living cells were stained green, due to their capacity to hydrolyse 6-carboxyfluorescein diacetate, which is the part of the kit.

2.4. Cell fixation and immunofluorescence staining of proteins

Cells were fixed with 4% formaldehyde in 1 × PBS for 10 min at room temperature (RT), washed several times in 1 × PBS, permeabilized with 0.2% Triton X 100/PBS for 15 min, and washed three times for 5 min in 1 × PBS. Before incubation with primary antibody (overnight at 4 °C), the cells were blocked with 7% inactivated FCS+2% bovine serum albumin/PBS for 30 min at RT. Antibodies from two different hosts (rabbit and mouse) were used to detect two different proteins in the same nuclei: anti-phospho-H2AX (serine 139), anti-phospho-ATM (1981), anti-HP1β, anti-acetyl-histone H4 lysine 5, and anti-dimethyl-histone H3 lysine 9 were from Upstate Biotechnology (Lake Placid, NY). Anti-phospho-NBS1 (serine 343) and anti-53BP were from Cell Signaling, anti-DNA-PK from Santa Cruz Biotechnology (CA, USA), and anti BRCA1, clone M4C7, from Millipore (MA, USA). Secondary antibodies were affinity purified FITC-conjugated donkey anti-mouse and Cy3-conjugated donkey anti-rabbit from Jackson Laboratory (West Grove, PA). The mixture of both antibodies was applied to each slide (after their pre-incubation with 5.5% donkey serum/PBS for 30 min at RT) and incubated for 1 h in the dark at RT. This was followed by washing (three times for 5 min each) in PBS. Cells were counterstained with 1 μM TOPRO-3 (Molecular Probes, Eugene, USA) in 2 × saline sodium citrate (SSC) prepared fresh from a stock solution. After brief washing in 2 × SSC, Vectashield medium (Vector Laboratories, Burlingame, CA, USA) was used for the final mounting of slides.

2.5. ImmunoFISH

ImmunoFISH was used to analyse the amount and localization of double-strand breaks (visualized as γ-H2AX foci) in the territories of human chromosomes HSA2, HSA4, HSA11, HSA18 and HSA19.

Fig. 2. Characteristics (A, B) of the five chromosomes (HSA2, HSA4, HSA11, HSA18 and HSA19) used for quantification of the chromatin density effect on the induction of DSBs by γ-radiation (dose of 3 Gy). (A) Gene density according to Ensemble database (orange) and isochore distributions for individual chromosomes from Costantini et al. [56] (GC content is expressed by different colors) (B) transcriptome maps (blue) and "ridgeograms" (triangles) are from Caron et al. [10] and Versteeg et al. [11] respectively (see Fig. 1 for more detailed explanation of these panels (A and B). (C) Images of fibroblast nuclei with simultaneously visualized (ImmunoFISH) territories of specific chromosomes (red; green for HSA11) and induced γH2AX foci (green; red for HSA11) detected 15 min PI.

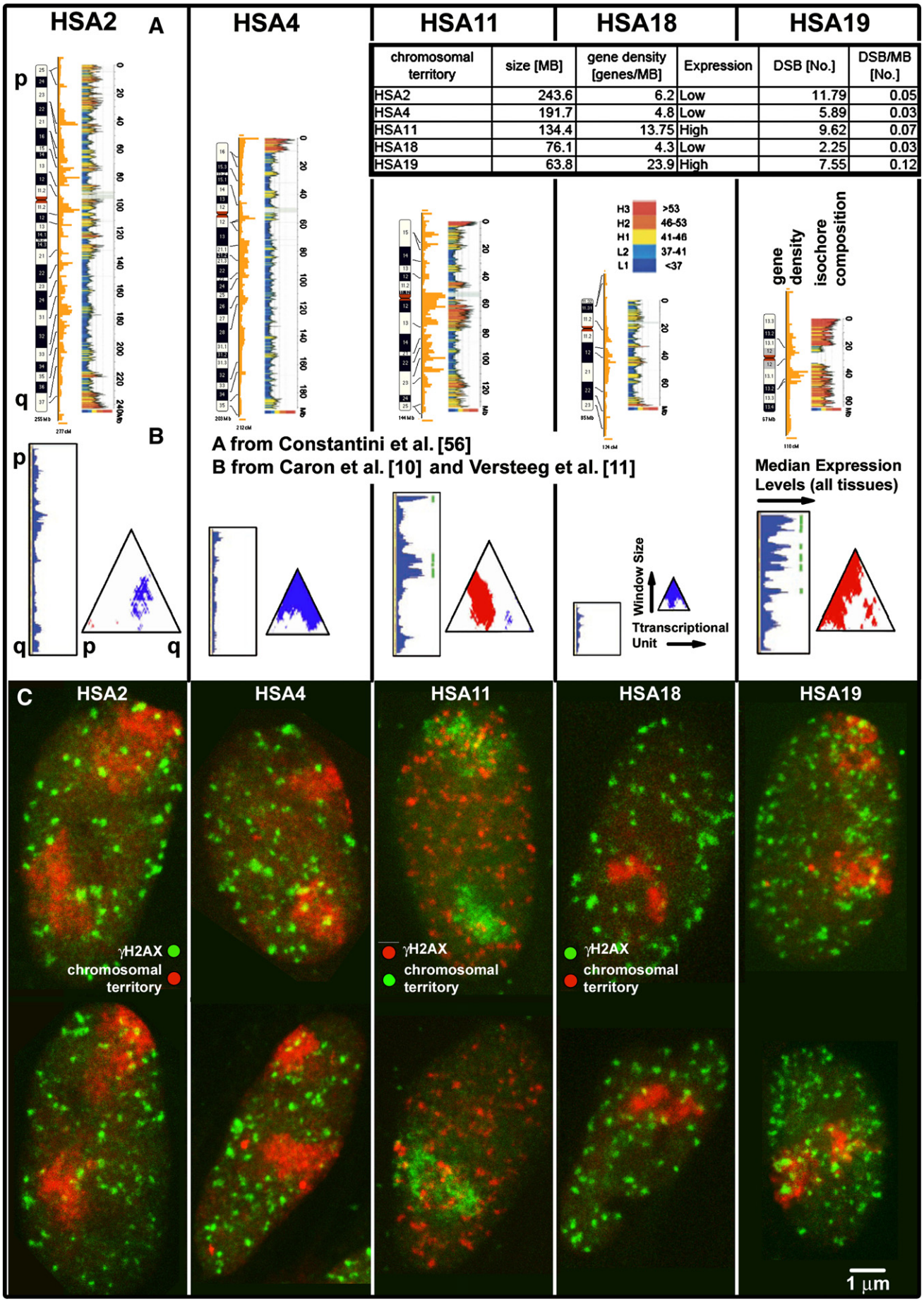

chromosomal territory	size [MB]	gene density [genes/MB]	Expression	DSB [No.]	DSB/MB [No.]
HSA2	243.6	6.2	Low	11.79	0.05
HSA4	191.7	4.8	Low	5.89	0.03
HSA11	134.4	13.75	High	9.62	0.07
HSA18	76.1	4.3	Low	2.25	0.03
HSA19	63.8	23.9	High	7.55	0.12

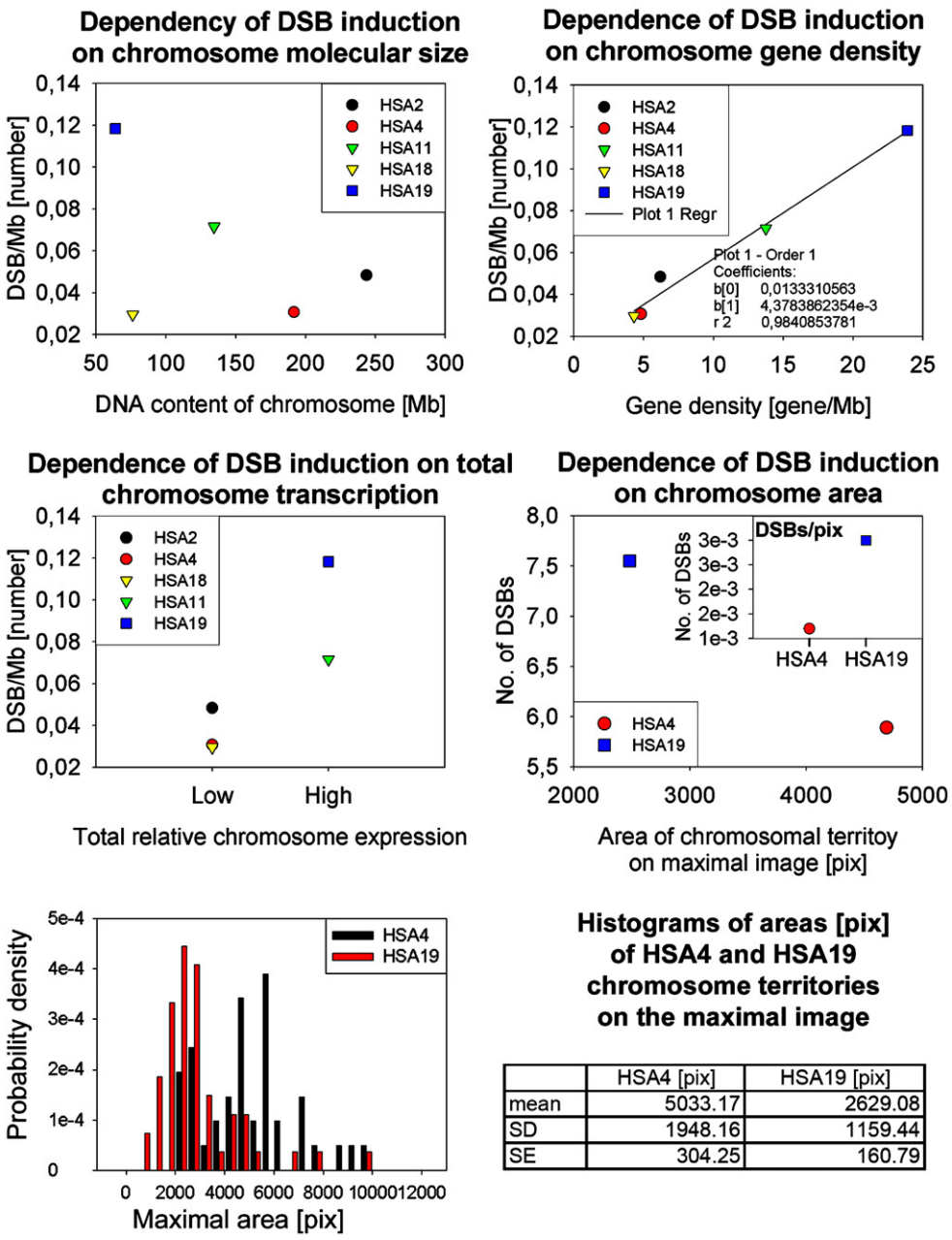

	HSA4 [pix]	HSA19 [pix]
mean	5033.17	2629.08
SD	1948.16	1159.44
SE	304.25	160.79

Fig. 3. Influence of different chromosomal parameters on the induction of DSBs by γ-radiation.

Chromosomes 19 and 18 (HSA19 and HSA18) were selected because of their contrasting characteristics and similar molecular size: HSA19 is genetically the most active chromosome in the human genome (human transcriptome map, [10]) with a decondensed, open chromatin structure; on the other hand, HSA18 is characterized by a very low transcription level and very compact chromatin. HSA2 is a chromosome with intermediate parameters, whereas HSA11 and HSA4 are further examples of active/decondensed and inactive/condensed chromosomes respectively. The level of DSB damage was also studied in two genomic regions with a known density of highly expressed genes and with well defined chromatin structure [4]. The RIDGE region (R) contains a large number of highly expressed genes and markedly decondensed chromatin, in contrast to the gene-poor and condensed anti-RIDGE (AR) region. Chromatin in this region is about 40% more condensed than in a RIDGE ([4] and our unpublished results). The size of both regions is 11 Mbp, both are located at 11q and separated by 12 Mbp.

Fig. 4. Comparison of chromatin texture in the territories of HSA19, containing a high density of highly expressed genes, and HSA4, with a low density of genes having generally low expression. (A) Upper: nuclei show the location of HSA4 and HSA19 territories (red) in nuclei of human fibroblasts irradiated with a dose of 3 Gy and subjected to immunoFISH 15 min PI. γH2AX foci are green. Lower: series of enlarged images of the HSA4 and HSA19 territories showing nuclear chromatin condensation as the intensity of TOPRO-3 (blue); or grey; merged images of chromosomal territories (CTs) and nuclear chromatin (red); and chromosomal territories alone (red). Different intensities of red show chromatin compaction in the chromosome territory. Green foci indicate the location of DSBs. It can be seen that these foci are predominantly located in regions of low chromatin density (faintly labeled by TOPRO-3, or red color of CTs). (B) Comparison of γH2AX foci location after immunodetection without denaturation of chromatin (Immuno) and after immunoFISH including chromatin denaturation (ImmunoFISH). Merging the two upper images shows that the location of γH2AX foci is almost unchanged after immunoFISH. (C) Optical slices through the territory of HSA4 (red) in *z*-steps of 0.2 μm, showing the location of γH2AX foci (green) in the region of low chromatin density (faintly red).

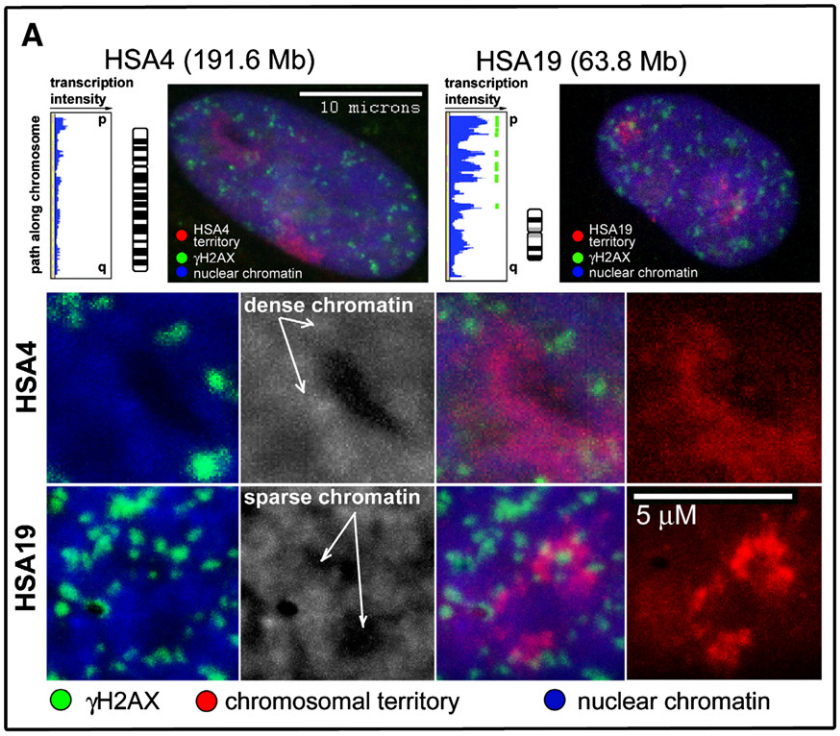
A
HSA4 (191.6 Mb)
HSA19 (63.8 Mb)
transcription intensity
path along chromosome
p
q
10 microns
HSA4 territory
γH2AX
nuclear chromatin
HSA19 territory
dense chromatin
sparse chromatin
5 μM
HSA4
HSA19
γH2AX
chromosomal territory
nuclear chromatin

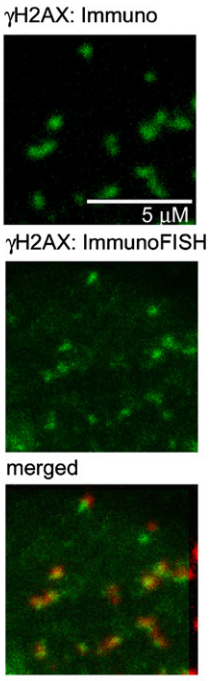
B
γH2AX: Immuno
5 μM
γH2AX: ImmunoFISH
merged

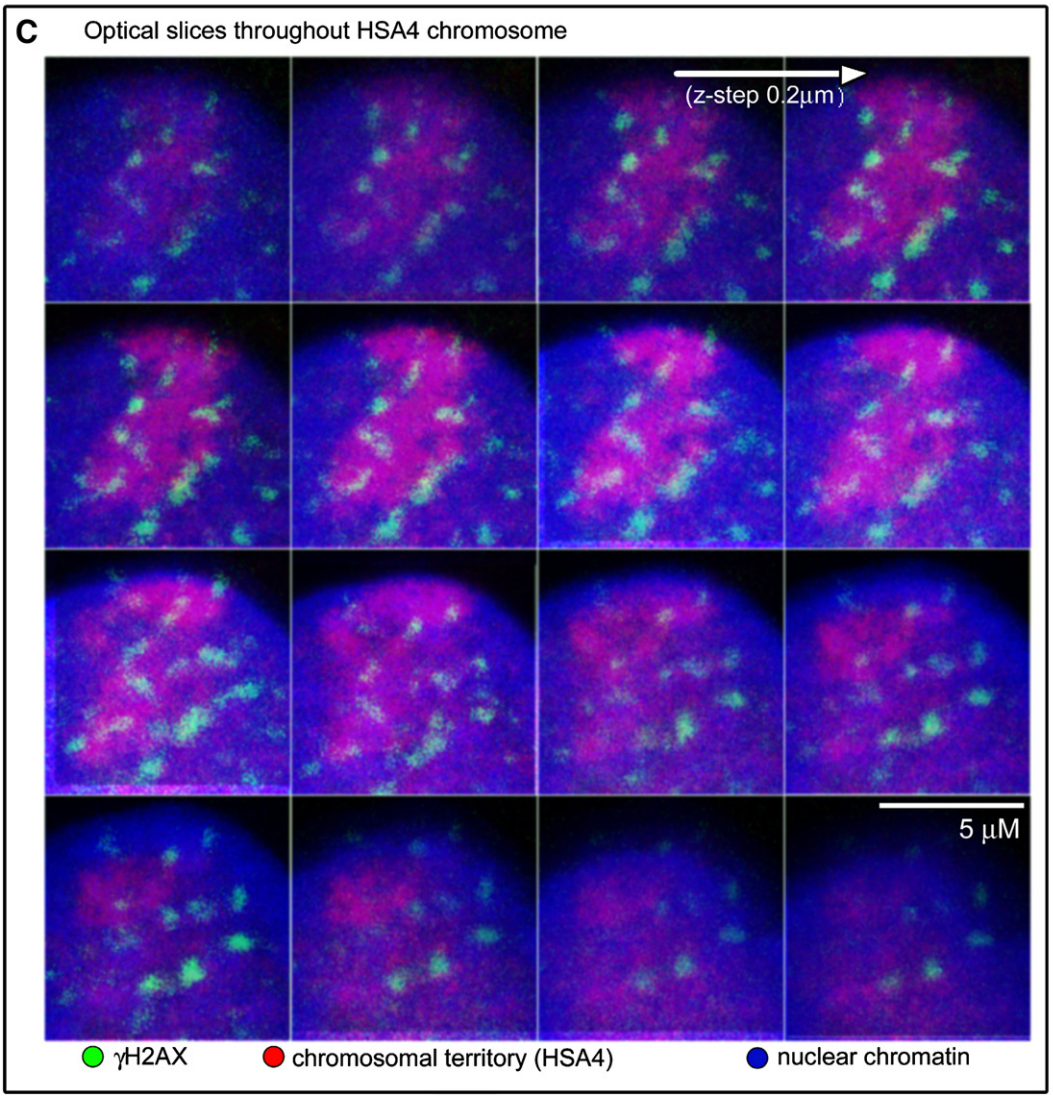
C
Optical slices throughout HSA4 chromosome
(z-step 0.2μm)
5 μM
γH2AX
chromosomal territory (HSA4)
nuclear chromatin

Directly labeled painting probes (Appligene-Oncor, Illkirch, France) for visualization of whole chromosomal territories were treated before hybridization according to the manufacturer's instructions. The probes for RIDGE and anti-RIDGE regions, conjugated with digoxigenin and biotin respectively, were obtained from S. Goetze (Swammerdam Institute of Live Sciences, University of Amsterdam). The immunoFISH protocol was adopted from [21] with slight modifications. In brief, the cells, on slides, were fixed in 4% formaldehyde/0.1% Triton X 100 for 30 min at 4 °C, followed by inactivation of aldehyde groups in 100 mM glycine/PBS for 20 min. Cells were permeabilized in 0.5% Triton X 100/0.5% saponin in PBS for 1 h and washed (3×5 min) in PBS. Before incubation overnight at 4 °C with antibody for γH2AX, the cells were blocked with 5% FCS/PBS for 30 min. Washing (3×5 min) in PBS preceded blocking with 5% donkey serum/PBS for 30 min and incubation with secondary antibody for 1 h, followed by washing in PBS (3×5 min). To fix the antibody before cell denaturation, the slides were immersed in 4% formaldehyde/0.1% Triton X 100 for 30 min at 4 °C, followed by inactivation of aldehyde groups in 100 mM glycine/PBS for 20 min. Cells were permeabilized in 0.5% Triton X 100/0.5% saponin in PBS for 35 min, washed in PBS (3×5 min), treated with 0.1 M HCl for 18 min, washed (3×5 min), and incubated in 20% glycerol for 15 min, and then in 2 × SSC for 10 min. Denaturation was performed in 70% formamide/2 × SSC (pH 7) for 3 min, followed by 50% formamide/2 × SSC for 1 min, both at 74 °C. The probes were denatured separately at 75 °C for 10 min, preannealed for 30 min at 37 °C and applied to denatured cells on slides. After hybridization overnight, slides were washed, and chromatin was stained with TOPRO-3 and mounted in Vectashield (Vector Laboratories, Burlingame, CA, USA). The slides labeled with RIDGE or anti-RIDGE probes conjugated with digoxigenin or biotin were blocked with 7% FCS/2% BSA for 30 min before detection with anti-digoxigenin-Cy3 and streptavidin-FITC, respectively, for 1 h at RT, followed by washing in 4 × SSC/0.1% Tween 20 at 37 °C (3×5 min), chromatin labeling, and mounting in Vectashield.

2.6. Image acquisition and confocal microscopy

An automated Leica DM RXA fluorescence microscope, equipped with a CSU10a Nipkow disc (Yokogawa, Japan) for confocal imaging, a CoolSnap HQ CCD-camera (Photometrix, Tucson, AZ, USA) and an Ar/Kr-laser (Innova 70C, Coherent, Palo Alto, CA) and an oil immersion Plan Fluotar objective (100×/NA1.3) was used for image acquisition [29,30]. Automated exposure, image quality control and other procedures were performed using FISH 2.0 software [29,30]. The exposure time and dynamic range of the camera in the red, green and blue channels were adjusted to the same values for all slides to obtain quantitatively comparable images. Forty serial optical sections were captured at 0.2 μm intervals along the z-axis at a constant temperature of 26 °C.

3. Results

3.1. DSB induction in chromatin containing different amounts of highly expressed genes

3.1.1. The dependence of DSB induction on chromosome gene density

The sensitivity of DNA to DSB induction was compared for five chromosomes, differing in their molecular size (DNA content, [Mbp]), isochore composition, gene density, the number of highly transcribed genes, the overall level of transcription and consequently their chromatin structure; these parameters are explained in Fig. 1 and the characteristics of all the chromosomes studied are summarized in Fig. 2A, B. DSB induction and the consequent repair process were studied by means of immunoFISH, enabling direct visualization of γH2AX foci, the markers of DSB, together with individual interphase chromosomal territories (Fig. 2C).

In correlation with the highest gene density (23.9 genes/Mbp), overall expression activity and number of intensely expressed genes of HSA19 (Fig. 2A, B), irradiation of cells with γ-rays induced the largest number of DSBs per megabase pair of all the chromosomes analysed within the territory of this chromosome (0.12 DSB/Mbp) (Figs. 2C and 3). The gene density of HSA11 is still high, but nevertheless about half that of HSA19 (13.75 genes/Mbp); on the other hand, its molecular size, 134.4 Mbp, is about twice that of HSA19 (63.8 Mbp) (table in Fig. 2A). Interestingly, the mean number of DSBs induced under the same conditions inside the territory of HSA11 was about half (0.07 DSB/Mbp) that of HSA19 (Figs. 2C and 3).

HSA18 has a very low density of genes (4.3 genes/Mbp, Fig. 2A) and does not contain highly expressed genes at all (Fig. 2B). Despite being about the same molecular size as HSA19 (76.1 Mbp), the mean number of DSBs induced inside the territory of this chromosome was a quarter of that for HSA19 (0.03 DSB/Mbp) (Fig. 3). The molecular size of HSA4 is about three times larger (191.7 Mbp) than that of HSA18, but its gene density is almost the same (4.8 genes/Mbp) (Fig. 2A). Reflecting the latter parameter, the mean number of DSBs induced inside the territory of HSA4, normalized to one megabase of DNA, was the same (0.03 DSB/Mbp) as in HSA18 (Fig. 3).

The largest chromosome analysed in this study was HSA2 (243.6 Mbp). Its gene density is rather low (6.2 genes/Mbp), but still about a third higher than that of HSA4 and HSA18 (Fig. 2A, B). In accordance with the gene density of chromosomes analysed, the mean number of DSBs induced in the territory of HSA2 was higher (0.05 DSB/Mbp) than that in HSA18 and HSA4, but significantly lower than that in HSA11 and HSA19 (Fig. 3).

Taken together, these results show unequivocally that the mean number of DSBs induced inside the chromosome territory correlates predominantly with the gene density of the chromosome, but not with the molecular size (DNA content) or nuclear size (the volume of chromosome territory in an interphase nucleus) (Fig. 3).

3.1.2. DSB induction in RIDGE and anti-RIDGE regions of HSA11

When total nuclear chromatin was counterstained with TOPRO-3, DSBs immunodetected as γH2AX foci appeared more frequently (about 70%) in faintly labeled nuclear areas, representing decondensed chromatin domains or nuclear space with a low chromatin concentration (Fig. 4).

To confirm the results for five different chromosomes described above, we studied the level of DSB damage in two genomic regions, a RIDGE and an anti-RIDGE, with known densities of highly expressed genes and with well defined chromatin structure (Fig. 5A, our unpublished results). In these experiments, the cells were irradiated with higher doses (7 Gy) of γ-rays to produce a number of DSBs sufficient for statistical comparison in each 11 Mbp region analysed. Even after this higher dose, a large fraction of surviving and normally repairing cells remained, as verified by annexin labeling (not shown) and monitoring of DSB repair during the post-irradiation (PI) period (Fig. 5B, left panel). The mean number of DSBs induced, counted 15 min PI was 7.93±0.32 in the RIDGE and a quarter of this (1.90±0.02 DSBs) in the anti-RIDGE (Fig. 5B). This result clearly shows that γ-radiation preferentially damages DNA in regions of open, decondensed chromatin.

3.2. Influence of chromatin structure on DSB repair

The influence of chromatin structure on the efficiency of DSB repair was studied by monitoring the decrease in DSB number 4 h PI. During this period, 80.6% of DSBs induced in the RIDGE, but only 52% of those in the anti-RIDGE, were repaired (Fig. 5B, left panel), indicating that the efficiency of DSB repair is also dependent on chromatin structure. A higher rate of DSB repair was also observed in gene-dense chromosomes (HSA19, HSA11) than in those with a low number of genes (HSA18, HSA4) (Fig. 6A, B). Similar to the

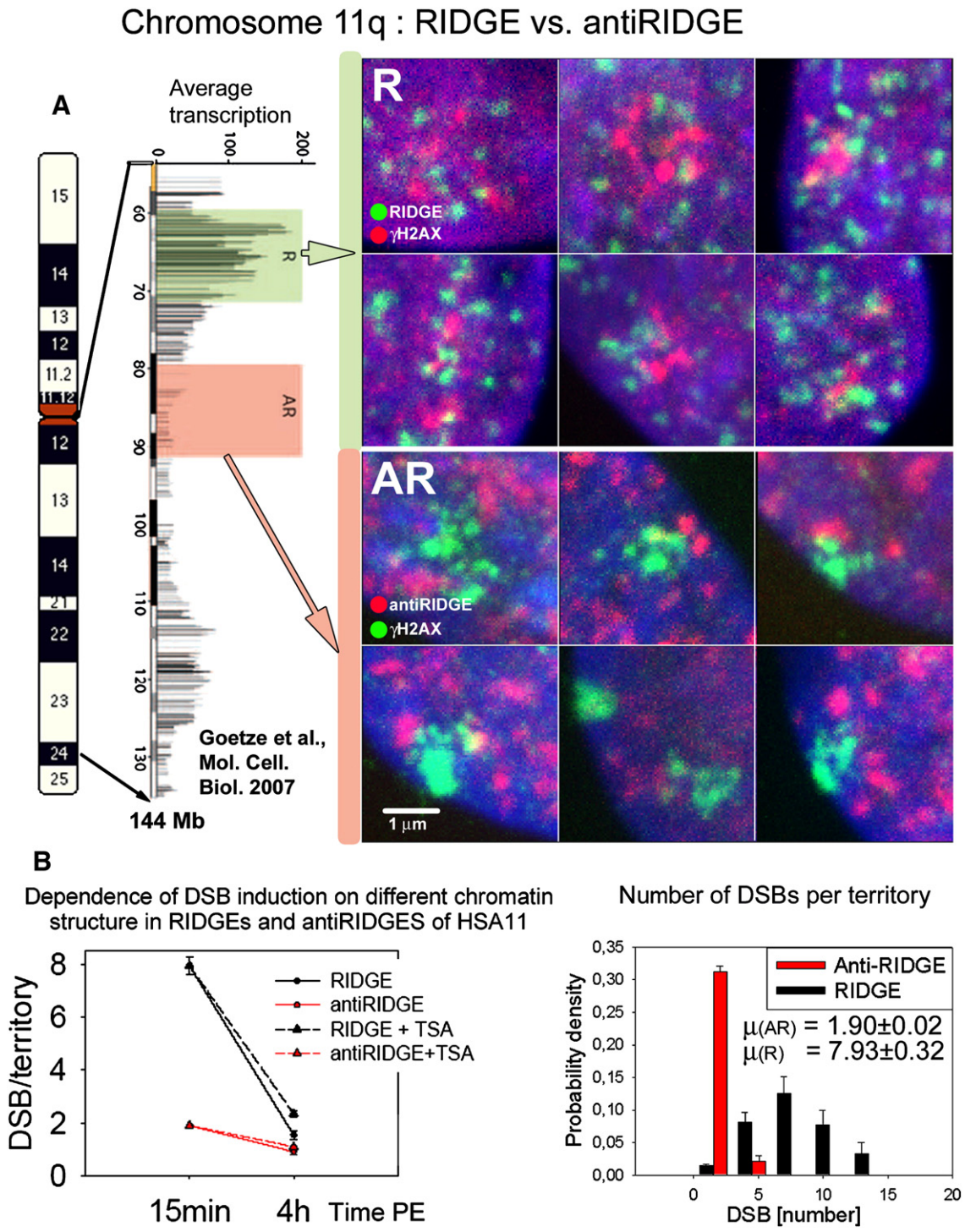

Fig. 5. DSBs induction and efficiency of repair in RIDGE and anti-RIDGE (both located in 11q) in human fibroblasts irradiated with a dose of 7 Gy of γ-rays. (A) Left: chromosome 11 ideogram and human transcriptome map of HSA11 (from Goetze et al. [4]) showing localization and transcriptional activity of the RIDGE and anti-RIDGE regions studied. Right: images R display the location and number of γH2AX foci (green) in RIDGE territories (red) of six nuclei, visualized together by immunoFISH. Images AR display the same for γH2AX foci (red) in relation to anti-RIDGE regions (green). (B) Graph: differences in DSB induction and repair during 4 h PI between the RIDGE and anti-RIDGE regions in cells incubated in ISO medium (full lines) and in the presence of 1 μm TSA 12 h before irradiation (dashed line). The histogram shows the distribution of DSBs per territory of RIDGE and anti-RIDGE, 15 min PI; μ indicates the mean values ± standard error.

values measured for the RIDGE, about 78% of DSBs were already repaired in HSA19 at 4 h after irradiation of the cells with 3 Gy (Fig. 6B). In other chromosomes, these values were 77% in HSA11, 69% in HSA2, 65% in HSA4, and 60% in HSA18 (Fig. 6B, C). It is obvious, therefore, that the rapidity of DSB repair in different chromosomes is correlated with their gene density, and consequently their chromatin structure.

3.2.1. Effect of HDAC inhibition with TSA on the induction and repair of DSBs in chromatin of different gene density

Incubation of cells with 1 μM trichostatin (TSA) before (12 h) and during γ-irradiation did not affect the mean number of DSBs induced, either in chromosomes with a high density of genes (HSA19, HSA11) or in the RIDGE (Figs. 6A and 5B respectively); the

same number of DSBs was also induced in the anti-RIDGE in treated and control cells (Fig. 5B) On the other hand, TSA treatment surprisingly increased the mean number of DSBs induced in chromosome territories containing a low density of genes (Fig. 6A). The efficiency of DSB repair was nevertheless slowed down by TSA in all chromosomes, as well as in the RIDGE and anti-RIDGE

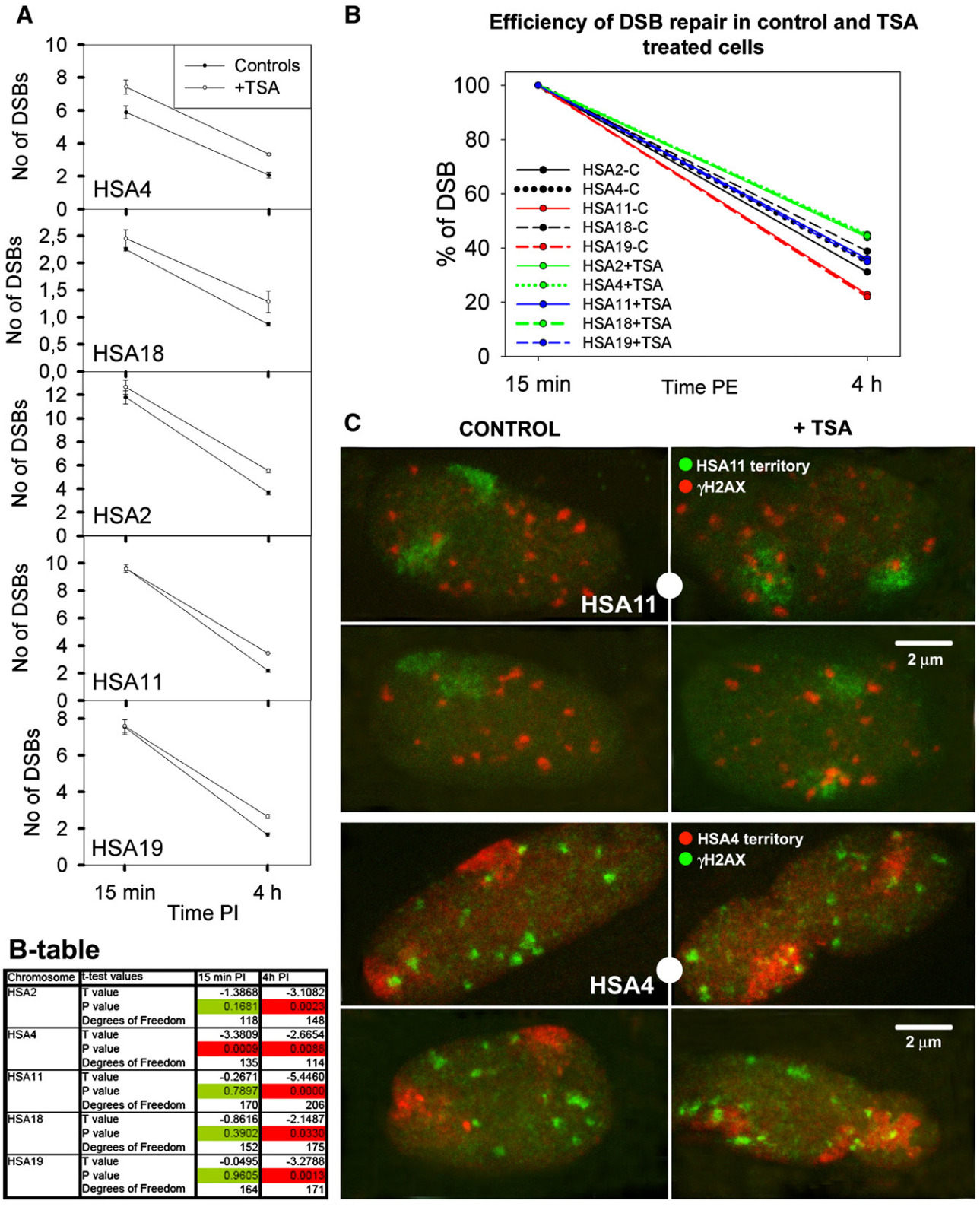

B-table

Chromosome	t-test values	15 min PI	4h PI
HSA2	T value	-1.3868	-3.1082
	P value	0.1681	0.0023
	Degrees of Freedom	118	148
HSA4	T value	-3.3809	-2.6654
	P value	0.0009	0.0088
	Degrees of Freedom	135	114
HSA11	T value	-0.2671	-5.4460
	P value	0.7897	0.0000
	Degrees of Freedom	170	206
HSA18	T value	-0.8616	-2.1487
	P value	0.3902	0.0330
	Degrees of Freedom	152	175
HSA19	T value	-0.0495	-3.2788
	P value	0.9605	0.0013
	Degrees of Freedom	164	171

Fig. 6. Influence of 1 μm TSA on DSB induction and repair in five chromosomes with different gene densities. (A) Induction and decrease of the mean number of DSB per chromosome territory during 4 h of cell incubation in isotonic medium post-irradiation, and in the medium supplemented with 1 μm TSA for 12 h before irradiation and 4 h PI. (B) Efficiency of DSB repair in five chromosomes with different gene density during cell incubation in isotonic medium for 4 h PI, and in cells treated with 1 μm TSA for 12 h before irradiation and 4 h PI. Table: statistical significance of the differences in DSB induction (15 min PI) and repair (4 h PI) between the cells growing in normal medium and that exposed to 1 μm TSA; green: $P > 10^{-2}$, red: $P < 10^{-2}$. (C) Images of HSA11 (green) and HSA4 (red) territories with the localization of γH2AX (red or green, respectively) in these territories.

regions (Figs. 6A, B, C and 5B respectively). Moreover, the efficiency of repair decreased more markedly in the RIDGE region (from 80.6% to 70.5%) than in the anti-RIDGE (from 52% to 45%) (Fig. 5B) and similar, but not so striking, results were also obtained for chromosomes with high and low concentrations of expressed genes (Fig. 6). The efficiency of repair decreased from 77.83% to 67.83% in HSA19, from 77.8% to 64% in HSA11, from 69% to 54% in HSA2, and from about 65% to 56% in HSA4 and HSA18, respectively. It seems therefore, that the sensitizing effect of TSA on DSB induction predominates in condensed, genetically silenced regions of the human genome, whereas its effect on inhibition of DSB repair takes place throughout the nucleus, but mainly in highly expressed chromatin domains.

3.3. DSB induction and repair in nuclei with experimentally changed chromatin condensation

3.3.1. Chromatin condensation

Hyperosmotic treatment is known to condense chromatin, inhibit tumor growth and sensitize cells to radiation. To determine whether these effects are functionally related, we have studied the influence of hyperosmotic-forced chromatin compaction on induction of DSBs by ionizing radiation and their repair post-irradiation (PI). We have addressed also another important question, whether the simple chromatin condensation provoked by hyperosmotic conditions without participation of additional proteins corresponds with our results obtained for functionally and structurally different chromatin domains in situ under physiological conditions. We studied the formation of γH2AX foci in human fibroblasts with experimentally changed chromatin condensation, using an approach first described by [31,32]. It allows the transient induction of hypercondensed chromatin (HCC) in living cells by increasing the osmolarity of the culture medium (290 mOsm). Our results show that, contrary to prolonged treatments, the short-time incubation (about 10 min) of cells in HOM does not influence the cell viability (Fig. 7A, B).

The hyperosmotic (HOM) treatment of cells for 10 min (HOM-cells$_{10\ min}$) resulted in marked changes in chromatin texture in the whole nucleus, manifested as branched bundles of hypercondensed chromatin (HCC) surrounded by extensive interchromatin space (as seen in Fig. 7C, middle nucleus). If HOM-cells were γ-irradiated with 1.0 or 3.0 Gy in HOM and left to repair their DNA under these conditions for 10 min, only small dots of γH2AX and repair proteins such 53BP (Fig. 7C, middle nucleus), NBS1, MDC1, ATM, BRCA1 etc. (not shown) were seen, dispersed through the nucleus, instead of the larger foci observed in normal isotonic (ISO) medium (Fig. 7, the first nucleus). The transfer of irradiated HOM-cells$_{10\ min}$ into isotonic medium for the next 10 min (HOM-ISO-cells$_{10+10\ min}$) led to complete restoration of chromatin structure, as well as the formation of γH2AX foci, showing phosphorylation of H2AX histones and assembly of repair proteins at these sites of damage (see Fig. 7C, right nucleus, for 53BP, not shown for NBS1, ATM, BRCA1 etc.), and thus reversibility of the structural and physiological changes induced by HOM (Fig. 7C, compare the left and right nucleus). Surprisingly, the sensitivity of hypercondensed chromatin to DSB induction by γ-radiation did not differ from chromatin in normal cells (P=0.68, Fig. 7D, compare also the left and right nucleus at Fig. 7C). Cells incubated for 10 min in HOM, irradiated during this time with 1.5 Gy and left to repair for the next 10 min in normal medium, had about the same number of DSBs (26.20±2.30) as in controls (26.35±1.35, Fig. 7D); equivalent results were obtained for irradiation of cells with 3 Gy (7D, histogram). Also, quantification of the disappearance of γH2AX foci in HOM-cells$_{10\ min}$ at different periods of time after their transfer to normal medium (Fig. 7E) revealed a very similar rate of DSB repair to control cells.

On the other hand, prolonged incubation of irradiated cells in HOM (15–60 min) was reflected in the formation of new γH2AX foci, the size and number of which progressively increased with time of incubation (Figs. 7A and 8A, B). γH2AX foci were formed even in non-irradiated cells during a prolonged incubation in HOM, indicating induction of DSB under these conditions (Fig. 9A) However, the formation of γH2AX foci was not followed by assembly of repair complexes and colocalization of foci with repair proteins in HOM (Figs. 8A and 9A for 53BP, not shown for NBS1, BRCA1, ATM etc.). In addition, the number of cells positively labeled for annexin increased concomitantly with the time of incubation in HOM, indicating a growing fraction of cells at the beginning of apoptosis (as already shown at Fig. 7A). The loss of vitality of cells exposed to HOM for long time is manifested also by their inability to restore the chromatin structure when transferred to normal medium (Fig. 9A).

These results show that short incubation (<10 min) of cells in HOM during and after irradiation induces reversible changes of chromatin structure and stalling of DSB repair; however, cells treated in this medium for longer were unable to repair DSB damage, and were forced into apoptosis even when transferred to isotonic medium.

3.3.2. Chromatin decondensation

The influence of chromatin decondensation on DSB induction and repair was studied in hypoosmotic medium (HypoOM, 140 mOsm). Surprisingly, HypoOM-treated cells for 10 min developed a chromatin texture similar to that induced by HOM: bundles of intensely labeled condensed chromatin distributed through the nucleus. However, these bundles were wider (swollen), and the nuclear space encompassing these bundles was largely filled with chromatin of low density (Fig. 8C), in contrast to the wide interchromatin space formed in HOM. Moreover, unlike to the rapid restoration of chromatin structure in cells incubated for 10 min in HOM, the similar chromatin texture that developed in cells treated with HypoOM only slowly returned to the normal state after their transfer into normal medium (Fig. 8C).

The mean number of DSBs induced per cell irradiated with a dose of 1.5 or 3 Gy and incubated in HypoOM for 10 min (irradiation during the fifth minute of incubation) was significantly higher (31 and 45.4 respectively, P=3.50e^{-5} for 1.5 Gy) than that induced in cells incubated in normal isotonic medium (26.5 and 38.7 respectively) (Fig. 7D). Moreover, DSB repair in HypoOM-cells$_{10\ min}$ was evidently slower than in control cells (Fig. 7E). While the mean number of DSBs per nucleus fell to 7.86 in controls (irradiated with 1.5 Gy) at 4 h PI, in cells incubated for 10 min in HypoOM prior to their transfer to normal medium for 4 h this value only dropped to 10.41 DSBs/nucleus. Compared with cells not exposed to HypoOM, 10 min incubation in this medium before replacing cells in normal medium resulted in a higher fraction of cells containing breaks (usually 1 or 2) even at 24 h PI (Fig. 8D). These results indicate higher sensitivity of chromatin decondensed by HypoOM to DSB induction, and a reduction of DSB repair long after the initial short incubation in HypoOM. However, despite these observations, and contrary to HOM-cells$_{10\ min}$, the majority of γH2AX foci colocalized with repair proteins even in HypoOM medium (Fig. 8C).

3.3.3. DSB induction and repair in the presence of trichostatin A

If human fibroblasts were cultured for 12 h before and 10 min after irradiation (1.50 or 3.0 Gy) in normal medium containing 0.2 μM or 1 μM TSA, the mean number of DSBs counted was slightly higher than in control cells (29.6±1.1 and 29.0±1.0 respectively, Fig. 7D). Surprisingly, while this number of DSBs differed significantly from that in normal medium only in the case of 1 μM TSA (P=0.19 and 0.05 for 0.2 μM and 1.0 μM TSA, respectively, in contrast to P=3.50e^{-5} after the HypoOM treatment), the repair of DSB damage was reduced considerably at both drug concentrations (Fig. 7E). Even 24 h after the cell irradiation (1.5 Gy), a large fraction of cells remained (88.5%, s.d.=4.4%) that contained two or more unrepaired DSBs in TSA-treated (1 μM) cells, whereas only 34.8% (s.d.=8.7%) of nuclei were DSB-positive (containing 1 to 2 breaks) in controls (Fig. 8D). Moreover, if repair proceeded in the absence of TSA following incubation with this drug (1 μM) for 12 h before and 10 min after irradiation, the fraction of DSB-positive cells was reduced to 58.8%

(s.d.=8.0%) (Fig. 8D), which is still significantly above the control level and is about the same as in cells irradiated and incubated in HypoOM for 10 min PI before their transfer to normal medium. Colocalization of γH2AX foci with repair proteins was not disrupted in TSA-treated cells and started early after irradiation, similarly to the HypoOM-treated cells and contrary to the HOM-treated cells. Together, these results show that short incubation of cells in TSA hinders the repair of DSBs, similarly to HypoOM, but does not markedly influence the number of radiation-induced DSB lesions (Fig. 7D, E). Moreover, contrary to HypoOM, TSA treatment induced less distinct changes in chromatin structure. Chromatin texture visualized by TOPRO-3 staining (Fig. 8C) consisted of a more

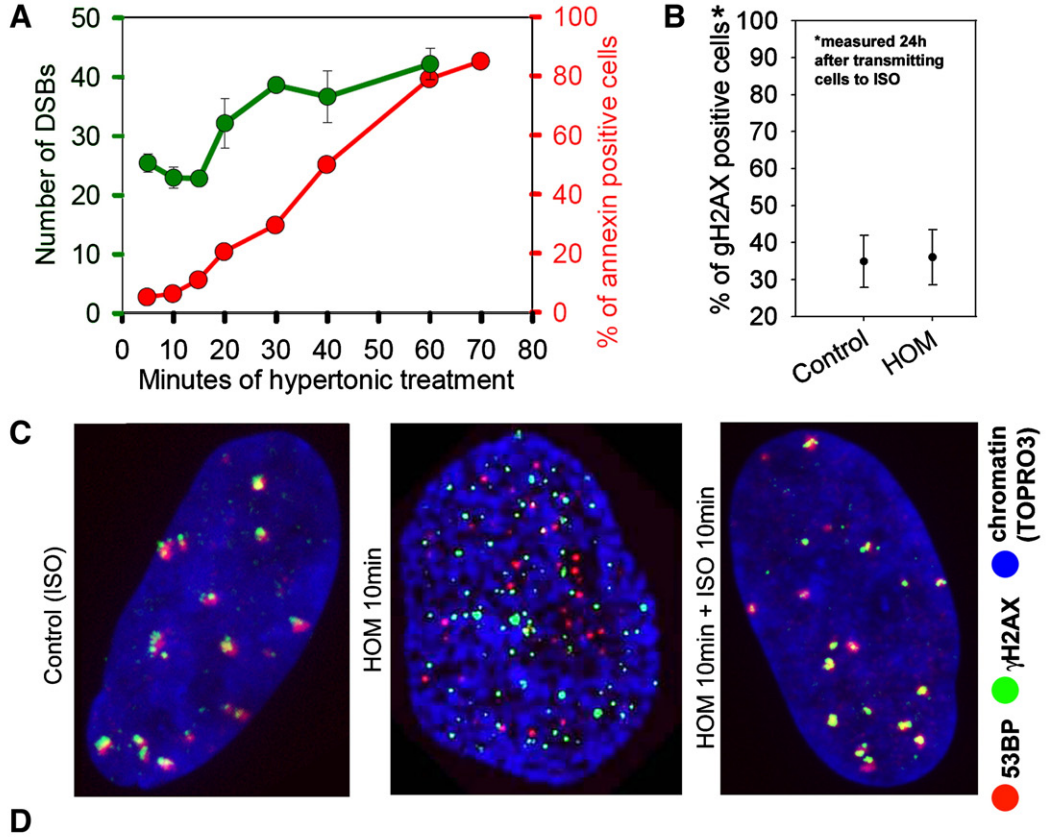

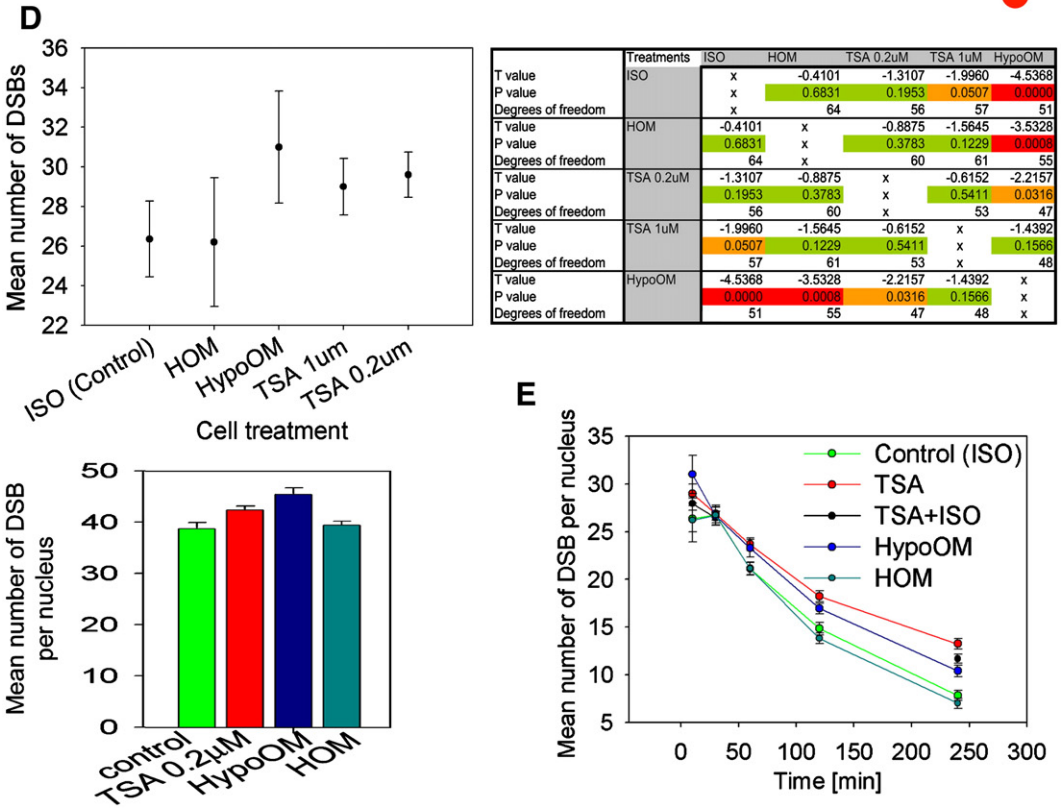

	Treatments	ISO	HOM	TSA 0.2uM	TSA 1uM	HypoOM
T value	ISO	x	-0.4101	-1.3107	-1.9960	-4.5368
P value		x	0.6831	0.1953	0.0507	0.0000
Degrees of freedom		x	64	56	57	51
T value	HOM	-0.4101	x	-0.8875	-1.5645	-3.5328
P value		0.6831	x	0.3783	0.1229	0.0008
Degrees of freedom		64	x	60	61	55
T value	TSA 0.2uM	-1.3107	-0.8875	x	-0.6152	-2.2157
P value		0.1953	0.3783	x	0.5411	0.0316
Degrees of freedom		56	60	x	53	47
T value	TSA 1uM	-1.9960	-1.5645	-0.6152	x	-1.4392
P value		0.0507	0.1229	0.5411	x	0.1566
Degrees of freedom		57	61	53	x	48
T value	HypoOM	-4.5368	-3.5328	-2.2157	-1.4392	x
P value		0.0000	0.0008	0.0316	0.1566	x
Degrees of freedom		51	55	47	48	x

homogeneous distribution of chromatin than in control cell nuclei. The changes in DSB induction and repair induced by HOM, HypoOM and TSA treatments are summarized in Table 1.

4. Discussion

It is generally believed that open chromatin containing active genes is more sensitive to radiation damage than compact chromatin, however direct proofs are still absent. For the first time, using immunoFISH method, we have directly visualized double-strand breaks (marked by γH2AX) together with functionally and structurally distinct genetic loci and also whole chromosome territories in situ under physiological conditions. Our results on chromatin sensitivity obtained by comparison of functionally and structurally different chromatin domains show (Fig. 5) that condensed chromatin in the anti-RIDGE region (low density of expressed genes) [10] is much less susceptible to DSB induction by γ-rays than decondensed chromatin in the RIDGE, characterized by an extremely high density of highly expressed genes. Chromatin condensation in the anti-RIDGE is 40% higher [4, our unpublished results] than that of the RIDGE (of the same length), and the number of DSBs induced in the anti-RIDGE region was 76% lower than in the RIDGE, despite both regions being the same length. A difference in sensitivity to radiation damage was also observed for chromosomes containing high (HSA19 and HSA11) and low densities of genes (HSA4, HSA18 and HSA2). This difference was, however, not so great (about 50%), probably because neither group of chromosomes contains only condensed or decondensed chromatin, unlike the RIDGE and anti-RIDGE. These results show that chromatin structure is one of the most important factors that determine DNA susceptibility to γ-radiation damage, with decondensed, open, genetically active chromatin being more sensitive. The same conclusions also follow from studies of DSB distribution inside the cell nucleus, as well as in individual chromosomal territories (CTs) (Fig. 4A, C). Simultaneous visualization of γH2AX foci and individual chromosome territories of HSA2, HSA4, HSA11, HSA18 and HSA19 by immunoFISH (Fig. 2C) also revealed that DSB lesions arise preferentially in weakly stained subdomains of the CTs, independently of the average characteristics of the whole chromosome, such as gene density.

We were interested whether, apart from higher amount of proteins in heterochromatin, the only higher chromatin condensation *per se* also contributes to a lower sensitivity of heterochromatin for DSB induction and efficiency of their repair. Therefore, we followed radiation sensitivity of hypercondensed chromatin induced by hyperosmotic conditions without participation of additional proteins. Hyperosmotic treatment is known to condense chromatin [23,24] and, in addition, it inhibits growth of tumor [25] and sensitize cells to radiation [24]. It is therefore important to determine, whether these effects are functionally related, in other words, whether therapeutically induced cell killing is caused by changes of chromatin structure, sensitivity to DSB induction and efficiency of their repair.

Our results show, that short-time exposure of cells to hyperosmotic (HOM) medium induced chromatin hypercondensation (HCC) into a network of bundles separated by a contiguous network of large interchromatin channels (ICC) (Fig. 7C) that was rapidly restored to normal chromatin structure after cell transfer to normal medium as already described by [23]. We expected that HCC would protect DNA against damage from γ-radiation. Contrary to our expectation, the sensitivity of HCC, determined as the total number of γH2AX foci per nucleus, remained the same as that of chromatin in cells irradiated in normal medium (ISO).

Together, these results show that condensed chromatin (functionally usually equivalent to heterochromatin) in the cell nucleus protects DNA against damage by γ-radiation, contrary to hypercondensation induced by HOM. The explanation for these different protective effects of these two types of condensed chromatin could reside in their dissimilar way of compaction, and consequently their distinct structure. Physiological heterochromatin is formed with the assistance of chromatin binding proteins (e.g. HP1) [33,34] and is characterized by specific epigenetic modifications (DNA and histone tail methylation, and absence of histone acetylation, reviewed in [35]); the higher density of linker histone H1 in heterochromatin could also contribute to the observed differences [36,37]. Chromatin binding proteins form the principal protective barrier against ionizing radiation (diminishing the accessibility of radicals to the DNA, and themselves reacting with these radicals) [38,39]. The concentration of DNA-binding proteins is lower in open decondensed chromatin, as it is also the density of chromatin per volume unit [40]. Since these proteins require specific histone modifications to bind to DNA, it is very improbable that their amount per unit of chromatin is increased by chromatin hypercondensation in HOM, and therefore the sensitivity of this HCC remains unchanged. Immunochemical detections of the principal epigenetic markers of constitutive heterochromatin (trimethylated histone H3K9, HP1α and β proteins) as well as those (dimethylated H3K9 and HP1 proteins) determining silenced euchromatin (facultative heterochromatin) show that there are hypercondensed chromatin domains in the HOM-treated nuclei that are intensively labeled by TOPRO-3 (chromatin dye) but not with antibodies against mentioned heterochromatic markers (Fig. 9B). The mechanism of hypercondensation is not yet understood, but a high concentration of cations and the resulting decrease in the negative charge of the DNA backbone may play an essential role [41,42]. HCC is probably formed by the contraction of relaxed chromatin, due to the decrease in the negative charge of the DNA in the high concentration of salts, without the participation of additional proteins. This chromatin is not, therefore, protected against damage, and its sensitivity to ionizing radiation remains the same as that in cells with a normal distribution of hetero- and euchromatin.

Fig. 7. Impact on cell viability, DSB repair, chromatin structure, formation of γH2AX foci and their colocalization with 53BP, of short and prolonged incubation of irradiated cells (1.5 Gy) in media with different osmolarities. (A) Green line: increase in the mean number of DSBs per cell in the dependence on incubation time in HOM. After incubation in HOM, the cells were transferred to isotonic medium for 10 min before fixation to allow development of countable γH2AX foci. Red line: the dependence of annexin positivity (beginning stage of apoptosis) on the period of incubation in HOM. (B) Mean fractions of cells containing unrepaired DSBs after 24 h incubation PI in normal (isotonic) medium. Before transfer to isotonic medium, the cells were incubated in HOM for 10 min, (including irradiation with 1.5 Gy). Control cells were not exposed to HOM. (C) Examples of nuclei irradiated with a dose of 1 Gy, and incubated in media with different osmolarities, showing the formation of γH2AX (green) and its colocalization with 53BP (red) at the sites of DSBs. The first nucleus was irradiated in normal isotonic medium, and incubated in this medium for 10 min PI; the second nucleus was irradiated in HOM and incubated in HOM for 10 min after irradiation; γH2AX (green) and 53BP (red) are dispersed as very small dots with non-overlapping distribution. Only about 4.4% of γH2AX colocalize with 53BP. The third nucleus was incubated in HOM for 10 min before irradiation, irradiated in HOM, and transferred to isotonic medium for the next 10 min PI. Foci of γH2AX (green) colocalizing with 53BP (red) are formed, and the chromatin structure resembles that of a normal nucleus. (D) The mean number of DSBs induced by doses of 1.5 Gy (graph) and 3 Gy (histogram) in human fibroblasts incubated in media with different osmolarities 10 min before irradiation, transferred to isotonic immediately after irradiation for further 10 min and fixed. Evaluation was effected in about 60 nuclei. ISO: isotonic medium; HOM: hyperosmotic medium (570 mOsm); HypoOM: hypoosmotic medium (140 mOsm); TSA: incubation for 12 h before irradiation and for 10 min PI. Histogram: control isotonic (green), TSA 0.2 μM (red), HypoOM (dark blue), HOM (blue). Table: Statistical parameters (unpaired t-test) comparing differences in DSB repair between control cells and cells exposed to media with different osmolarities or to TSA (green: $P > 0.05$, orange: $P \leq 0.05$, red: $P \leq 10^{-3}$). (E) The decrease in the number of DSBs (γH2AX) during 4 h PI. The cells were irradiated with a dose of 1.5 Gy in media of different osmolarities, and at 10 min PI transferred to the isotonic medium for different periods of time. Control: normal isotonic medium (290 mOsm); Hyper: hyperosmotic medium (570 mOsm); Hypo: hypoosmotic medium (140 mOsm); TSA: trichostatin A (1 μM) for 12 h before irradiation and after irradiation until cell fixation; TSA-ISO: trichostatin A (0.2 μM) for 12 h before irradiation and transfer to isotonic medium 10 min PI.

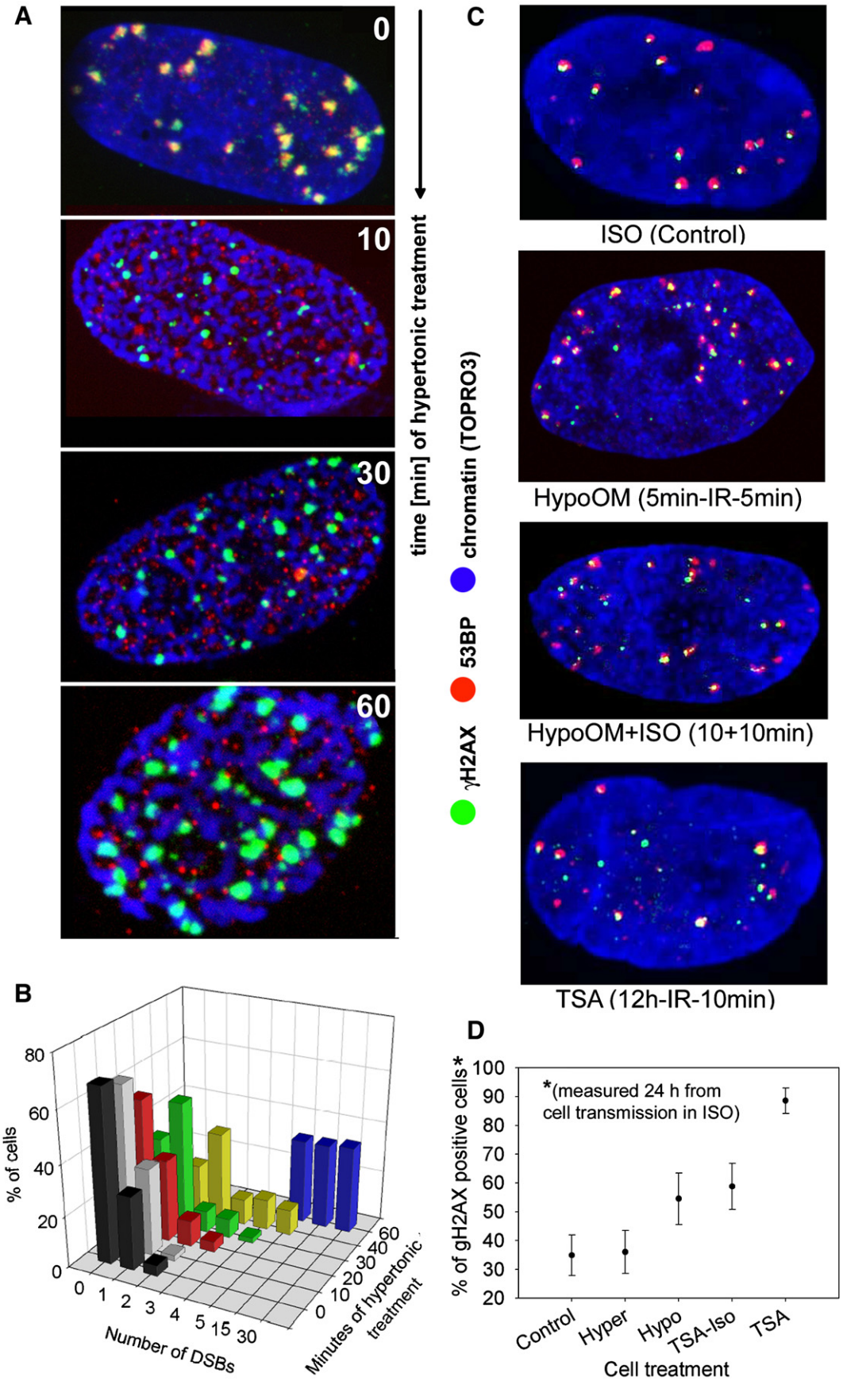
A
0
10
30
60
time [min] of hypertonic treatment
chromatin (TOPRO3)
53BP
γH2AX
C
ISO (Control)
HypoOM (5min-IR-5min)
HypoOM+ISO (10+10min)
TSA (12h-IR-10min)
B
% of cells
Number of DSBs
Minutes of hypertonic treatment
D
% of gH2AX positive cells*
*(measured 24 h from cell transmission in ISO)
Control
Hyper
Hypo
TSA-Iso
TSA
Cell treatment

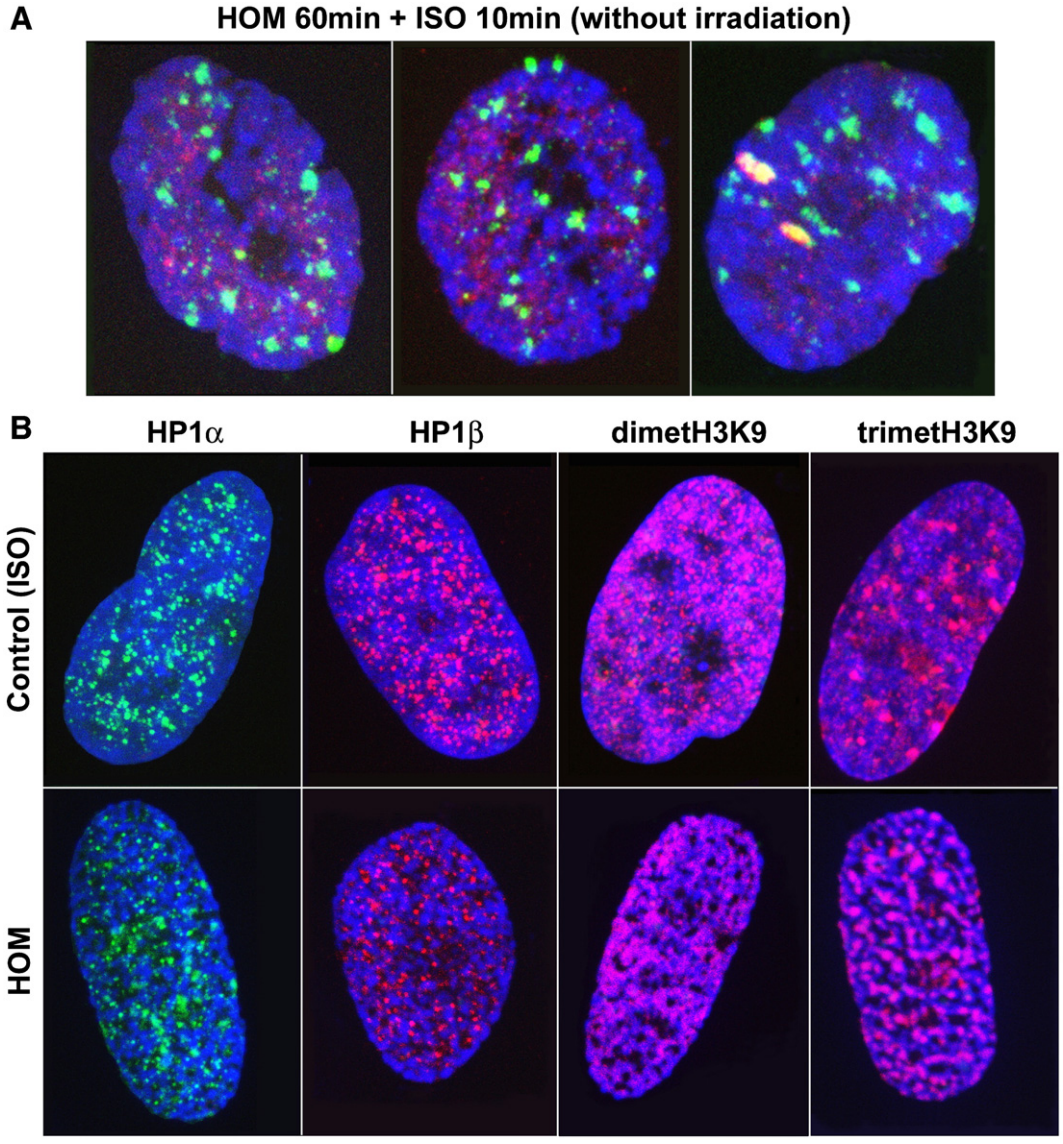

Fig. 9. Induction of γH2AX foci in nuclei of non-irradiated human fibroblasts exposed to HOM for 60 min and nuclear distribution of epigenetic markers of constitutive and facultative heterochromatin compared for HOM-treated (10 min) and control cells. (A) Examples of three nuclei exposed to HOM for 60 min followed by 10 min incubation in normal medium before cell fixation. Green foci of γH2AX indicate induced DSBs, small red dots represent 53BP. The colocalization of two of these foci is seen in the third nucleus, indicating that the nucleus is still surviving, contrary to the first two nuclei. However, neither the third nucleus is completely recovered from the long HOM-treatment as reflected in the incompletely restored chromatin texture. The chromatin of the first two nuclei still remains completely hypercondensed, indication initiation of apoptosis. (B) Immunochemical detection of epigenetic markers of condensed chromatin in control and hypercondensed nuclei (incubated for 10 min in HOM before fixation). Chromatin is labeled by TOPRO-3 (blue), HP1 α (green), HP1β, dimethylated histone H3K9 and trimethylated H3K9 are red. It can be seen that there are hypercondensed chromatin domains also in the HOM-treated nuclei that are intensively labeled by TOPRO-3 (chromatin dye) but not by the antibodies against to the mentioned heterochromatic proteins. This indicates that HOM-induced hypercondensed chromatin is formed without participation of heterochromatic proteins, contrary to physiological heterochromatin.

Exposure of cells to HOM for 10 min, unlike prolonged exposure, did not influence either DSB induction or DSB repair after their transfer to ISO (Fig. 7). However HOM prevented DSB repair and colocalization of repair proteins with γH2AX foci (Fig. 7). The results of Albiez et al. [23] show stalling of other physiological processes such as transcription and replication in HOM, probably as a result of an inhibitory effect of the increased ionic concentration. A high concentration of ions can probably inhibit the activity of many enzymes; it could also alter mutual interactions among proteins, between proteins and DNA, and reduce protein movements [43],

Fig. 8. DSB induction and repair in γ-irradiated (1.5 Gy) human skin fibroblasts relative to the time of these cells exposure to the media with different osmolarities and in the presence of TSA. (A) Examples of irradiated nuclei incubated for different periods of time in HOM, showing the formation of γH2AX (green) foci that do not colocalize with 53BP (red). Emerging colocalization seems to be accidental because of a large amount of red foci and the increasing size of green foci. 4.4%, 14% and 12.6% of green foci colocalize with red foci after 10, 30 and 60 min of cells exposure to HOM, respectively. The first nucleus (control) was incubated for 10 min PI in isotonic medium (0 min in HOM). (B) Distribution of cells with various numbers of DSBs induced by exposure to HOM for different times (0–60 min) and than transferred to isotonic medium for 24 h before evaluation. (C) Changes of chromatin structure, formation of γH2AX foci and their colocalization with DSB-repair proteins in media with different osmolarities: ISO (control): incubation in isotonic medium for 10 min; HypoOM (5 min – IR – 5 min): incubation for 5 min in hypoosmotic medium before, during and after irradiation; HypoOM + ISO (10 + 10 min): incubation 10 min before and during irradiation in hypoosmotic medium, followed by 10 min incubation PI in isotonic medium; TSA (12 h – IR – 10 min): incubation with 1 μm TSA 12 h before irradiation and 10 min PI, including irradiation. (D) Mean fractions of cells containing unrepaired DSBs after 24 h incubation PI in normal (isotonic) medium. Before transfer to isotonic medium, the cells were incubated for 10 min, including irradiation in media of different osmolarities. Incubation with 1 μm TSA was for 12 h before and 24 h after irradiation (TSA), or for 12 h before and only 10 min after irradiation (TSA-Iso), followed by transfer to isotonic medium for 24 h.

Table 1
Comparison of changes of chromatin structure, DSB induction and efficiency of DSB repair induced by hypertonic (HOM), hypotonic (HypoOM) and trichostatin (TSA) treatments

Treatment of cells before and during irradiation (1.5 Gy)	No. of DSBs		Chromatin structure	γH2AX foci	Colocalization of γH2AX foci with repair proteins	Reversibility of changes induced in chromatin structure after transmission to isotonic	The rate of DSB repair after transmission to isotonic
Isotonic (control)	26.4	100%	Normal	+	+		
HOM	26.2	99.24%	Changed[a]	− (early PI) + (20min PI[b])	−	Rapid	Rapid (as in control)
HypoOM	31.0	117.42%	Changed[c]	+	+	Very slow	Very slow
TSA (0.2 μM)	29.0	109.85%	Slightly changed[d]	+	+	Slow	Very slow
TSA (1.0 μM)	29.6	112.12%	Slightly changed[d]	+	+	Slow	Very slow

[a] Condensed bundles encompassed by wide channels of interchromatin space, unstained by chromatin dyes.
[b] Foci started to appear approximately 20 min PI and their size continually increased to values slightly larger than in control cells.
[c] Swelled bundles of condensed chromatin encompassed by thinner channels filled with decondensed chromatin.
[d] Chromatin more diffused and locally more decondensed.

which could result in interruption of physiological functions, including DSB repair. In accordance with this supposition is our observation that well developed foci of γH2AX colocalizing with 53BP in irradiated cells incubated for 20 min in ISO medium disappear, and are replaced by many small dots of both proteins, which do not colocalize with each other after transferring cells into HOM for 10 min (not shown).

We observed that longer (>10 min) exposure of irradiated and also of unirradiated cells to HOM results in an increase in the number of DSBs and annexin positivity (Figs. 7A and 8A, B). This indicates that HOM poses a stress for the cells that could be intensified by the presence of unrepaired DSBs. If these conditions persist for a longer time than can be tolerated by the cell, it is forced into apoptosis. Additional DSBs detected in cells exposed to HOM could probably be induced by nucleases, activated in the early stages of apoptosis [44,45], but also by the loss of water and changes in chromatin conformation. The above described effects of hypertonic, especially inhibition of DSB repair and secondary damage of chromatin, thus could explain recently described successful therapy of VX2 liver carcinoma in rabbits, by injection of hypertonic solution [25]. Summarizing these results, we propose that the increased radiosensitivity of cells exposed to HOM [24] is brought about by inhibition of DSB repair, leading to apoptosis and not by the increased induction of DSBs by radiation. It is necessary to note that results obtained for hypertonic treatment exceeding about 15 min brings new important information concerning the synergic killing of irradiated cells but are not convenient for the study of physiological processes (e.g. DSB repair).

Irradiation of cells in hypoOM followed by short (10 min) exposure to this medium led to a significant increase in DSB induction, as well as reduced rate of repair after the transfer of cells to ISO ($P = 10e^{-3}$) (Fig. 7D, E). The chromatin structure of cells incubated in hypoOM was noticeably changed, forming swollen bundles of condensed chromatin, branched throughout the nucleus in the similar way as bundles of hypercondensed chromatin in cells exposed to HOM (Fig. 8C). The similarity of branched condensed chromatin structure in hypoOM to the hypercondensed bundles induced in HOM supports the concept of a global 3D chromatin network, established in early G_1, as proposed by Gerlich et al. [46] and Walter et al. [47], and also supported by the findings of Albiez et al. [23], who showed the stability of chromatin bundles during repeated NCC-HCC-NCC cycles (NCC, normally condensed chromatin). Contrary to HCC induced during the short-time (<10 min) incubation in HOM, which is completely reversible after transfer of the cells to ISO, chromatin changes developed in hypoOM return to normal (Fig. 8C) only very slowly (2 h PI or more). The explanation for this slow reversibility could reside in the more profound changes of chromatin structure: The decrease of cation concentration probably results in destabilization of nucleosome structure, especially in decondensed chromatin. It has been shown that nucleosome conformation is strongly dependent on ionic strength [48]. A low concentration of ions thus could influence the structure of DNA, via modified interactions of its phosphate groups with basic amino-acid residues of the histone octamer [49]. Such a disturbance of physiological chromatin structure that persists even when the hypoOM conditions were removed could be responsible for the low efficiency of DSB repair.

As HDAC inhibitors are currently used in clinical trials, because of their promising anticancer effects [50], and are used as additives, or synergistic with conventional cancer therapies such as radiotherapy [51], we used one of these inhibitors, TSA, to evaluate DSB induction and repair efficiency in human fibroblasts. The effect of TSA was evaluated for whole chromatin, and separately for condensed and decondensed chromatin of selected chromosomes, RIDGE and anti-RIDGE regions (Figs. 5 and 6). Surprisingly, we observed only a small non-significant increase of DSB induction in whole nuclei of cells exposed to TSA for 12 h before irradiation (with doses of 1.5 Gy and 3 Gy of γ-rays) and in chromosomes with more condensed chromatin (HSA4, HSA18 and HSA2), while the number of DSBs was the same as in untreated control cells in chromosomes with a high level of decondensed chromatin. The increased number of DSBs induced in condensed chromatin of cells treated with TSA before irradiation could be related to globally increased acetylation of histones, leading to reversible decondensation of dense chromatin regions, as found by Tóth et al. [28]. Our observation of a more homogenous distribution of chromatin in nuclei exposed to TSA (Fig. 8C) and a slightly higher induction of DSBs in heterochromatic chromosomes (Fig. 6), is consistent with the observed TSA-induced relaxation of condensed chromatin domains containing several megabase pairs of DNA [28].

The significant decrease of DSB-repair efficiency in cells treated with TSA, especially in the decondensed chromatin of the RIDGE, contrasts with the observation of only small changes in DSB induction. In this region, the number of DSBs was reduced 5.2 times after 4 h of repair (relative to the values immediately PI) in untreated cells, but was only reduced 2.9 times in cells treated with 1 μM TSA. Similarly, for chromosomes containing a high density of genes, and therefore a higher level of decondensed chromatin (HSA19 and HSA11), this reduction was 4.6 times in untreated cells, and only 2.7 times in TSA-treated cells. For chromosomes with a low gene density and more condensed chromatin, the difference in repair efficiency between the untreated and treated cells was lower 3 times for HSA2 and 2.3 times for HSA18 and HSA4. The small difference between the TSA-treated and untreated cells was found also for the anti-RIDGE (2.1 times and 1.7 times, respectively). These results show a significant dependence of the repair efficiency on chromatin structure in untreated cells, and a decrease of this efficiency, especially in open chromatin, in TSA-treated cells.

Numerous studies have already shown that HDAC inhibitors can enhance radiosensitivity of various cancer cell lines [51,52], but the mechanism by which HDAC inhibitors enhance this sensitivity in human cells remains unclear. The long-lasting acetylation of histones, creating open chromatin, could be the main reason for the slowdown of DSB repair in cells exposed to TSA. Our earlier results [6] showed

that increased acetylation in the region of γH2AX foci (developed immediately after DSB induction) was soon replaced by histone modification typical for condensed chromatin (decreased acetylation of H4K5 and increased methylation of H3K9). These relatively rapid changes in epigenetic modification of both histones in the proximity of DSBs indicate the necessity for conversion from less to more condensed chromatin during repair. This condensation is probably not possible in the presence of HDAC inhibitor, and could lead to decreases in repair efficiency. In addition, repair efficiency could also be influenced by more indirect effects of increased histone acetylation, including recruitment of chromatin-remodeling complexes [53,54] and other chromosomal proteins [55] that modify higher-order chromatin conformation.

Acknowledgements

We thank Sandra Goetze for kindly providing us the probes for RIDGE and anti-RIDGE regions. This work was supported by the Grant Agency of the Czech Republic (204/06/P349), the GAAV of the Czech Republic (IAA500040802, 1QS500040508), the Academy of Sciences of the Czech Republic (AV0Z50040507, AV0Z50040702), and the Ministry of Education of the Czech Republic (LC535).

References

[1] S. Boyle, S. Gilchrist, J.M. Bridger, U.L. Mahy, J.A. Ellis, W.A. Bickmore, The spatial organization of human chromosomes within the nuclei of normal and emerin-mutant cells, Hum. Mol. Genet. 10 (2001) 211–219.
[2] M. Cremer, J. von Haase, T. Volm, A. Brero, G. Kreth, J. Walter, C. Fisher, I. Solovei, C. Cremer, T. Cremer, Non-random radial higher-order chromatin arrangements in nuclei of diploid human cells, Chromosome Res. 9 (2001) 541–567.
[3] S. Kozubek, E. Lukášová, P. Jirsová, I. Koutná, M. Kozubek, A. Gaňová, E. Bártová, M. Falk, R. Paseková, 3D structure of human genome: order in randomness, Chromosoma 111 (2002) 321–331.
[4] S. Goetze, J. Mateos-Langerak, H. Gierman, W. de Leeuw, O. Giromus, M.H.G. Indemans, J. Koster, V. Ondřej, R. Versteeg, R. van Driel, The three-dimensional structure of human interphase chromosomes is related to the transcriptome map, Mol. Cell. Biol. 27 (2007) 4475–4487.
[5] Y. Ziv, D. Bielopolski, Y. Galanty, C. Lukas, Y. Taya, D.C. Schultz, J. Lukas, S. Bekker-Jensen, J. Bartek, Y. Shiloh, Chromatin relaxation in response to DNA double-strand breaks is modulated by a novel ATM- and KAP-1 dependent pathway, Nature Cell Biol. 8 (2006) 870–876.
[6] M. Falk, E. Lukasova, B. Gabrielova, V. Ondřej, S. Kozubek, Chromatin dynamics during DSB repair, Biochim. Biophys. Acta 1773 (2007) 1534–1545.
[7] O. Fernandez-Capetillo, A. Lee, M. Nussenzweig, A. Nussenzweig, H2AX: the histone guardian of the genome, DNA Repair 3 (2004) 959–967.
[8] R. Kanaar, J.H. Hoeijmakers, D.C. van Gent, Molecular mechanisms of DNA double strand breaks repair, Trends Cell Biol. 8 (1998) 483–489.
[9] B. Eliot, M. Jasin, Double-strand breaks and translocations in cancer, Cell. Mol. Life Sci. 59 (2002) 373–385.
[10] H. Caron, B. van Schaik, M. van der Mee, F. Baas, G. Riggins, P. van Sluis, M.C. Hermus, R. van Asperen, K. Boon, P.A. Voute, R. Versteeg, et al., The human transcriptome map: clustering of highly expressed genes in chromosomal domains, Science 291 (2001) 1289–1292.
[11] R. Versteeg, B.D.C. van Schaik, M.F. van Batenburg, M. Roos, R. Monajemi, H. Caron, H.J. Bussemaker, A.H.C. van Kampen, The human transcriptome map reveals extremes in gene density, intron length, GC content and repeat pattern for domains of highly and weakly expressed genes, Genome Res. 13 (2003) 1998–2004.
[12] J. Surrallés, S. Sebastian, A.T. Natarajan, Chromosomes with high gene density are preferentially repaired in human cells, Mutagenesis 12 (1997) 437–442.
[13] F. Daroudi, J. Fomina, M. Meijers, A.T. Natarajan, Kinetics of the formation of chromosome aberrations in X-irradiated human lymphocytes using PCC and FISH, Mutat. Res. 404 (1998) 55–65.
[14] G. Iliakis, G.E. Pantelias, R. Seaner, Effect of arabinofuranosyladenine on radiation induced chromosome damage in plateau-phase CHO cells measured by premature chromosome condensation: implication for repair and fixation of alpha-PLD, Radiat. Res. 114 (1988) 361–378.
[15] L. Metzger, G. Iliakis, Kinetics of DNA double-strand break repair through the cell cycle as assayed by pulsed field gel electrophoresis in CHO cells, Int. J. Rad. Biol. 59 (1991) 1325–1339.
[16] D. Sproul, N. Gilbert, W.A. Bickmore, The role of chromatin structure in regulating the expression of clustered genes, Nat. Rev. Genet. 6 (2005) 775–781.
[17] H. Tanabe, F.A. Habermann, I. Solovei, M. Cremer, T. Cremer, Non-random radial arrangement of interphase chromosome territories: evolutionary considerations and functional implications, Mutat. Res. 504 (2002) 37–45.
[18] E. Gazave, P. Gautier, S. Gilchrist, W.A. Bickmore, Does radial nuclear organisation influence DNA damage? Chromosome Res. 13 (2005) 377–388.
[19] E.P. Rogakou, D.R. Pilch, A.H. Orr, V.S. Ivanova, W.M. Bonner, DNA double strand breaks induce histone H2AX phosphorylation on serine 139, J. Biol. Chem. 273 (1998) 5858–5868.
[20] C.J. Bakkenist, M.B. Kastan, DNA damage activates ATM through intermolecular autophosphorylation and dimmer association, Nature 421 (2003) 499–506.
[21] A. Pombo, P. Cuello, W. Schul, J.B. Yoon, R.G. Roeder, P.R. Cook, S. Murphy, Regional and temporal specialization in the nucleus: a transcriptionally-active nuclear domain rich in PTF, Oct1 and PIKA antigens associated with specific chromosomes early in the cell cycle, EMBO J. 17 (1998) 1768–1778.
[22] T. Reitsema, D. Klokov, J.P. Banáth, P.L. Olive, DNA-PK is responsible for enhanced phosphorylation of histone H2AX under hypertonic conditions, DNA Repair 4 (2005) 1172–1181.
[23] H. Albiez, M. Cremer, C. Tiberi, L. Vecchio, L. Schermelleh, S. Dittrich, K. Kupper, B. Joffe, T. Thormeyer, J. von Hase, S. Yang, K. Rohr, H. Leonhardt, I. Solovei, C. Cremer, S. Facan, T. Cremer, Chromatin domains and the interchromatin compartments from structurally defined and functionally interacting nuclear networks, Chromosome Res. 14 (2006) 707–733.
[24] C.M. Dettor, W.C. Dewey, L.F. Winans, J.S. Noel, Enhancement of X-ray damage in synchronous Chinese hamster cells by hypertonic treatments, Radiat. Res. 52 (1972) 352–372.
[25] Y.C. Lin, J.H. Chen, K.W. Han, W.C. Shen, Ablation of liver tumor by injection of hypertonic saline, AJR Am. J. Roentgenol. 184 (2005) 212–219.
[26] D. Cerna, K. Camphausen, P.J. Tofilon, Histone deacetylation as a target for radiosensitization, Curr. Top Dev. Biol. 73 (2006) 243–251.
[27] K. Camphausen, P.J. Tofilon, Inhibition of histone deacetylation: a strategy for tumor radiosensitization, J. Clin. Oncol. 25 (2007) 4051–4056.
[28] K.F. Tóth, T.A. Knoch, M. Wachsmuth, M. Frank-Stöhr, M. Stöhr, C.P. Bacher, G. Müller, K. Rippe, Trichostatin A-induced histone acetylation causes decondensation of interphase chromatin, J. Cell Sci. 117 (2004) 4277–4287.
[29] M. Kozubek, S. Kozubek, E. Lukasova, A. Mareckova, E. Bartova, M. Skalnikova, A. Jergova, High-resolution cytometry of FISH dots in interphase cell nuclei, Cytometry 36 (1999) 279–293.
[30] M. Kozubek, S. Kozubek, E. Lukasova, E. Bartova, M. Skalnikova, P. Matula, P. Matula, P. Jirsova, A. Cafourkova, I. Koutna, Combined confocal and wide-field high-resolution cytometry of fluorescent in situ hybridization-stained cells, Cytometry 45 (2001) 1–12.
[31] Y. Kuwada, T. Sakamura, A contribution to the colloidchemical and morphological study of chromosomes, Protoplasna 1 (1927) 239–254.
[32] O. Bank, Abhaenigigkeit der Kernstruktur von der Ionenkonzentration, Protoplasma 32 (1939) 20–30.
[33] A.J. Banister, P. Zegerman, J.F. Partridge, E.A. Miska, J.O. Thomas, R.C. Allshire, T. Kouzarides, Selective recognition of methylated lysine 9 on histone H3 by the HP1 chromo domain, Nature 410 (2001) 120–124.
[34] M. Lachner, D. O, Carroll, S. Rea, K. Mechtler, T. Jenuwein, Methylation of histone H3 lysine 9 creates a binding site for HP1 protein, Nature 410 (2001) 116–120.
[35] E.J. Richards, S.C. Elgin, Epigenetics codes for heterochromatin formation and silencing: rounding up the usual suspects, Cell 108 (2002) 489–500.
[36] J. Tazi, A. Bird, Alternative chromatin structure at CpG islands, Cell 60 (1990) 909–920.
[37] J. Zlatanova, P. Caiafa, K. van Holde, Linker histone binding and displacement: versatile mechanism for transcriptional regulation, FASEB J. 14 (2000) 1697–1704.
[38] M. Bĕgusova, N. Gillard, D. Sy, B. Castaing, M. Charlier, M. Spotheim-Maurizo, Radiolysis of DNA–protein complexes, Radiat. Phys. Chem. 72 (2005) 265–270.
[39] M. Davídková, V. Štisová, S. Goffinont, N. Gillard, B. Castaing, M. Spotheim-Maurizot, Modification of DNA radiolysis by DNA-binding proteins: structural aspects, Rad. Protect. Dosim. 10 (2006) 1–6.
[40] S. Dietzel, K. Zolghadr, C. Hepperger, A.S. Belmont, Differential large-scale chromatin compaction and intranuclear positioning of transcribed versus non-transcribed transgene arrays containing beta-globin regulatory sequences, J. Cell Sci. 117 (2004) 4603–4614.
[41] J.C. Hansen, Conformational dynamics of the chromatin fibre in solution: determinants, mechanisms and functions, Annu. Rev. Biophys. Biomol. Struct. 31 (2002) 361–392.
[42] P.J. Horn, C.L. Peterson, Molecular biology. Chromatin higher order folding-wrapping up transcription, Science 297 (2002) 1824–1827.
[43] M. Lund, B. Jönsson, A mesoscopic model for protein–protein interactions in solutions, Biophys. J. 85 (2003) 2940–2947.
[44] J.Z. Parrish, D. Xue, Cuts can kill: the roles of apoptic nucleases in cell death and animal development, Chromosoma 115 (2006) 89–97.
[45] K. Samejima, W.C. Ernshaw, Trashing the genome: the role of nucleases during apoptosis, Nat. Rev. Mol. Cell. Biol. 6 (2005) 677–688.
[46] D. Gerlich, J. Beaudouin, B. Kalbfess, N. Daigle, R. Eils, J. Ellenberg, Global chromosome positions are transmitted through mitosis in mammalian cells, Cell 112 (2003) 751–764.
[47] J. Walter, L. Schermelleh, M. Cremer, S. Tashiro, T. Cremer, Chromosome order in HeLa cells during mitosis and early G1, but is stably maintained during subsequent interphase stages, J. Cell Biol. 160 (2003) 685–697.
[48] T.J. Richmond, C.A. Davey, The structure of DNA in the nucleosome core, Nature 423 (2003) 145–150.
[49] G.S. Manning, Is a small number of charge neutralizations sufficient to bend nucleosome core DNA onto its superhelical ramp? J. Am. Chem. Soc. 125 (2003) 15087–15092.
[50] R.L. Piekarz, R.W. Robey, Z. Zhan, G. Kayastha, A. Sayah, A.H. Abdeldaim, T-cell lymphoma as a model for the use of histone deacetylase inhibitors in cancer therapy: impact of depsipeptide on molecular markers, therapeutic targets, and mechanisms of resistance, Blood 103 (2004) 4636–4643.

[51] K. Camphausen, W. Burgan, M. Cerra, K.A. Oswald, J.B. Trepel, M.J. Lee, Enhanced radiation-induced cell killing and prolongation of gammaH2AX foci expression by the histone deacetylase inhibitor MS-275, Cancer Res. 64 (2004) 316–321.
[52] T.C. Karagiannis, H. Kn, A. El-Osta, Disparity of histone deacetylase inhibition on repair of radiation-induced DNA damage on euchromatin and constitutive heterochromatin, Oncogene 25 (2007) 3963–3971.
[53] P.T. Georgel, T. Tsukiyama, C. Wu, Role histone tails in nucleosome remodelling by Drosophila NURF, EMBO J. 16 (1997) 4717–4726.
[54] C. Logie, C. Tse, J.C. Hansen, C.L. Peterson, The core histone N-terminal domains are required for multiple rounds of catalytic chromatin remodelling by SWI/SNF and RSC complexes, Biochemistry 38 (1999) 2514–2522.
[55] C. Maison, D. Bailly, A.H. Peters, J.P. Quivy, D. Roche, A. Taddei, M. Lachner, T. Jenuvein, G. Almouzni, Higher-order structure in pericentric heterochromatin involves a distinct pattern of histone modification and RNA component, Nat. Genet. 30 (2002) 329–334.
[56] M. Costantini, O. Clay, F. Auletta, G. Bernardi, An isochore map of human chromosomes, Genome Res. 16 (2006) 536–541.

Local changes of higher-order chromatin structure during DSB-repair

2008 J. Phys.: Conf. Ser. 101 012018

(http://iopscience.iop.org/1742-6596/101/1/012018)

Journal of Physics: Conference Series **101** (2008) 012018 doi:10.1088/1742-6596/101/1/012018

Local changes of higher-order chromatin structure during DSB-repair

M Falk, E Lukasova, B Gabrielova, V Ondrej and S Kozubek

Institute of Biophysics, Academy of Sciences of Czech Republic, Kralovopolska 135, 612 65 Brno, Czech Republic

mfalk@seznam.cz

Abstract. We show that double-strand breaks (DSBs) induced in DNA of human cells by γ-radiation arise mainly in active, gene-rich, decondensed chromatin. We demonstrate that DSBs show limited movement in living cells, occasionally resulting in their permanent clustering, which poses a risk of incorrect DNA rejoining. In addition, some DSBs remain unrepaired for several days after irradiation, forming lesions repairable only with difficulty which are hazardous for genome stability. These "late" DSBs colocalize with heterochromatin markers (dimethylated histone H3 at lysine 9, HP1 and CENP-A proteins), despite the low density of the surrounding chromatin. This indicates that there is epigenetic silencing of loci close to unrepaired DSBs and/or stabilization of damaged decondensed chromatin loops during repair and post-repair reconstitution of chromatin structure.

1. Introduction

Genome integrity is continuously impaired by endogenous and exogenous factors. The most serious threat is represented by double-strand breaks (DSBs), which interrupt both strands of the DNA molecule and can give rise to chromosomal exchange aberrations. If unrepaired, DSBs lead to cell death or, rarely but more importantly, the cell can survive with an unstable genome, posing a serious risk of tumorigenesis. Despite the introduction of new experimental approaches, there have been limited advances in understanding exchange aberration formation, and there remains little information on the spatiotemporal organization of DSB repair (reviewed in [1]).

The involvement of chromatin translocations in many human cancers, especially lymphomas and leukemias, was discovered many years ago, but their mechanisms of formation are still poorly understood. It is therefore crucial to broaden our understanding of double-strand break generation and repair. Our recent results [2] as well as earlier results of other authors [1, 3; 4] show that chromatin structure and dynamics must play an important role in regulation and facilitation of DNA repair.

There are contradictory data on the role of DSB mobility in formation of chromatin translocations, probably due to the different LET-characteristics of the radiation used to generate DNA lesions. With low-LET soft X-rays, stable nuclear positions of DSBs were observed [5] and only breaks generated close to one another were thought to be liable to DNA misjoining. On the other hand, movement and temporary clustering of individual DSBs was found when using high-LET α-particles [6] or lasers [3], sources which often generate clustered DNA lesions [7, 8, 9, 10]. Lisby et al [9] and Aten et al [6] interpreted the association of DSBs as relocation into special nuclear compartments or "repair factories"; however, this aggregation allows misjoining of DNA ends of previously distant DSBs. Concentration of nuclear processes into specialized nuclear subcompartments is not unprecedented, and occurs, for example, with co-regulated genes during transcription [reviewed in 11, 12, 13].

Indirect support for the dynamic nature of DSBs is also provided by the temporary centripetal shift of centromeres minutes to hours after irradiation or application of radiomimetic drugs (H_2O_2) [14, 15, 16]. However, data for DSB dynamics after the physiologically most relevant γ-irradiation (resulting in isolated, non-clustered DSB-breaks) remain poor and inconclusive.

Both major repair pathways that developed during evolution – homologous recombination (HR) and non-homologous end joining (NHEJ) [for review see 17] – process DSBs using large multiprotein complexes. Since DNA in eukaryotes is packed into compact, highly organized chromatin, the question arises of how the repair machinery gains access to free DNA ends; in particular, whether the assembly of huge repair complexes takes place at decondensed original DSB sites [5], or whether relocation of DSBs into appropriate nuclear compartments is required [9, 6]. Loizou et al [4] reviewed that chromatin remodelling enzymes colocalize with DSBs as well as DSB repair enzymes, facilitating changes in chromatin structure during DSB processing. Rapid phosphorylation of histone H2AX (an H2A variant) at sites of DSBs is an example [reviewed in 18], although the exact role in this has yet to be quantified. Theoretically, two alternative chromatin conformations may be required for DSB processing: an "open" structure, allowing access of proteins to damaged DNA and assembly of repair complexes, or a "condensed" structure stabilizing free DNA ends and preventing transcription from damaged sites [19]. In support of both possibilities, enzymes participating both in chromatin condensation and decondensation (e.g. histone acetylases and deacetylases respectively) were detected at DSB sites [discussed e.g. in 20]. Antagonistically acting enzymes thus could function sequentially and/or simultaneously [20, 21, etc.].

As well as their role in the repair process and/or transcriptional silencing of damaged loci, chromatin modifiers may also influence the formation of translocations directly by regulating the ability of free DNA ends to fuse. In *Drosophila*, chromosomal ends are protected from end-to-end fusions by heterochromatin protein 1 (HP1) even when all telomere-associated sequences have been deleted [22]. Accordingly, frequent chromosomal fusions were observed in cells lacking ATM (Ataxia Telangiectasia Mutated kinase) or HP1 [22]. In mammals and other organisms that use sequence-specific binding proteins such as TRF2 to protect telomeric ends, the ATM and HP1 pathway plays a minor role in stabilization of normal chromosomal DNA ends, but may be critical in the case of telomeres that are too short to bind telomere-sequence specific TRF2 [22]. This situation could be similar to DSB repair and, not surprisingly, ATM and TRF2 were the first proteins to colocalize with newly formed DSBs [23, 24].

In this work we analyzed the movement of DSB-breaks induced by γ-rays producing isolated lesions. We show limited movement of DSBs, probably associated with decondensation and their relocation into low-density chromatin. Sometimes, clusters of DSB-foci can be seen, which may persist for several days after irradiation, and may represent sites of formation of exchange aberrations. These late lesions, which are probably difficult to repair, colocalized with dimetH3K9 and HP1, despite their location in sparse chromatin. We suggest that these proteins play an important role in transcriptional silencing of damaged loci and/or in recondensation of decondensed chromatin domains after repair. We also show that DSBs are induced preferentially in low density chromatin.

2. Materials and Methods

2.1. Cell culture and transfection

Human MCF7 mammary carcinoma cell line and human skin fibroblasts 04-147 were grown in DMEM medium supplemented with 10% fetal calf serum (FCS) and antibiotics. Cells were transfected with GFP-tagged NBS1 [25], HP1β [26] and PML using Lipofectamine 2000 (Invitrogen) according to the manufacturer's instructions.

2.2. Cell irradiation, fixation, permeabilization and immunostaining

Cells grown on microscope slides were irradiated with ^{60}Co γ-rays 24 hr after plating, and either fixed immediately or incubated for various periods of time before fixation. Doses of 1.5, 4.5 and 7 Gy (1 Gy/min) were used.

To fix the cells, the slides were immersed in 4% paraformaldehyde/2 × SSC at room temperature (RT) for 10 min, washed three times in fresh PBS (1x Phosphate buffered saline), permeabilized with 0.2% Triton X-100 in PBS for 18 min, washed 3 × 5 min in PBS, and then immunolabelled.

Primary antibodies from two different hosts (rabbit and mouse) were used to detect two different antigens in the same nucleus; incubation was overnight, followed by washing. Labelling was detected by incubation for 1 hr at RT with FITC-conjugated donkey anti-mouse, and Cy3-conjugated donkey anti-rabbit antibodies (Jackson Laboratory). Nuclei were counterstained with 1 μM TOPRO-3 (Molecular Probes).

2.3. Image acquisition and microscopy

An automated Leica DM RXA fluorescence microscope, equipped with a CSU10a Nipkow disc (Yokogawa, Japan) for confocal imaging, a CoolSnap HQ CCD-camera (Photometrix) and an Ar/Kr-laser (Inova 70C, Coherent), was used for image acquisition [27, 28]. Automated exposure, image quality control and other procedures were performed using FISH 2.0 software [27, 28]. The exposure time and dynamic range of the camera in the red, green and blue channels were adjusted to the same values for all slides to obtain quantitatively comparable images. Forty serial optical sections were captured at 0.3 μm intervals (along the z-axis). For observation of living cells, an iXon DV 887ECS-BV (Andor) camera was used together with the 3D viewer [29].

2.4. Living cell observation and time-lapse microscopy

Two types of *in vivo* observations were performed: short and medium-term. For short-term experiments, "2D" images consisting of a few (3–5) confocal slices with a z-step of 0.3-0.5 μm were acquired in a millisecond (20-500 ms) interval for a period of approximately 1.5 min. For medium-term observations, 40 optical sections were captured (3D-images) with a 0.2-0.3 μm z-step. Intervals of 50 s were allowed between individual stacks of 40 sections, and observations were continued for a total of 20 min. The light exposure was kept as low as possible to avoid phototoxic effects.

2.5. Analysis of experimental data and motion of loci

The analysis method used was described in [2]. Briefly, the off-line image analysis and tracking (2D, 3D) of fluorescence signals were done with the FISH 2.0 software and a 3D image viewer [28, 29]. Coordinates were taken at the centre of gravity of the visualized objects, and corrected for rotation of the cell nucleus and drift of the images during longer time-lapse observations. The objects were traced in the time-lapse series on the basis of matching algorithms. In 2D, the distances between two signals were calculated using the equation: $d = \sqrt{(x_1-x_n)^2 + (y_1-y_n)^2}$; or in 3D: $d = \sqrt{(x_1-x_n)^2 + (y_1-y_n)^2 + (z_1-z_n)^2}$, where x_1, y_1 and z_1 (x_n, y_n and z_n) were coordinates for the first measurement and the n-th measurement of the same object. The mean d^2 was calculated from individual d_i^2 values of all possible signal pairs at the particular time point. The mean difference of d^2 (mean Δd^2) was calculated at each time point (t) as $\Delta d^2 = (d_t - d_{t+\Delta t})^2$, where Δt was the time interval between measurements.

Evaluation of data and statistical analyses were performed using the Sigma Plot statistical package (Jandel Scientific). When required, measured distances were normalized to the nuclear radius [% of R] to allow comparison between nuclei. Intensity profiles of R-G-B channels were obtained using Andor iQ 1.2.0 Software (Andor Technology).

2.6. SDS-PAGE and Western analysis

Cell suspensions were washed twice with PBS, centrifuged for 3 min at 1000 × g, cooled on ice to 2ºC and resuspended in lysis buffer (50 mM TrisHCl pH 7.5, 120 mM NaCl, 0.5% Nonidet P40 and 1 mM phenylmethylsulfonyl fluoride (PMSF)) by vigorous vortexing for 1 min, and left on ice for 30 min

with intermittent homogenization with a plastic pestle, briefly (10 sec) sonicated, and spun down (14,000 rpm for 15 min). The supernatant was transferred into a new tube and kept on ice. Samples containing proteins and chromatin were diluted to the same value of A_{260} absorbance, boiled in SDS loading buffer, and loaded on the gel. Proteins were separated in 15% polyacrylamide gels. After electrophoresis, the gels were either stained with Coomassie blue R-250 (Sigma) or electrotransferred to a nitrocellulose membrane in Tris-glycine buffer containing 10% methanol. The membranes were blocked, incubated with anti-HP1β (Upstate) (dilution 1:100) and anti-PML (Santa Cruz) (dilution 1:10) antibodies, and then treated with peroxidase-conjugated anti-mouse antibodies and detected with an ECL detection system (Amersham Corp.). The intensity of the protein bands was compared after ECL detection using the Vilber Lourmat Photodocumentation and Imaging System.

3. Results

3.1. Nuclear distribution of DSBs induced by γ-rays relative to functionally different chromatin domains

We analyzed the nuclear distribution of double-strand breaks (DSBs) immediately (2 min) post irradiation (PI). DSBs induced by a single exposure to 1.5, 4.5 or 7 Gy of γ-rays were immunocytochemically visualized *in situ* in spatially fixed human fibroblasts, using antibody against the DSB-specific marker histone H2AX phosphorylated at serine 139 (γH2AX). Except in S-phase nuclei, γH2AX foci were found in only a small proportion of non-irradiated cells (the mean was about 0.4 γH2AX foci per non S-phase nucleus). On average, 38 DSBs per nucleus per Gy appeared rapidly (2-5 min) after exposure to 1.5 and 4.5 Gy; after 7 Gy a large number of DSBs was produced which were difficult to count. In all experiments, most breaks (about 70%) were formed in low-density chromatin, identified as weak TOPRO-3 staining ("chromatin holes") (Fig. 1A). It is important to note that rest of the breaks were in medium or intensely stained nuclear areas (Fig. 1A). In this figure, the localization of two representative DSBs in sparse (left) and dense chromatin (right) is clearly shown by the intensity profiles of the R-G-B channels.

Regions of chromatin not stained by TOPRO-3 ("holes") were distinguished from nucleoli by anti-fibrillarin antibody. Although nucleoli are free of DSBs, holes of sparse chromatin contain many breaks (Fig. 1B). DSBs did not directly colocalize with histone H4 acetylated at lysine 12 (acetylH4K12), the characteristic marker of active chromatin, but were close to it (Fig. 2A, B). Acetylated histone H4K12 usually formed a linker between the γH2AX and denser chromatin stained by TOPRO-3 (Fig. 2B). In the case of DSBs located in dense chromatin, acetylH4K12 signals were usually absent (Fig. 2A, bottom RGB profile). Changes of histone modifications (acetylH4K12, acetylH4K5) at sites of DSB during the PI time and colocalization of DSBs with Tip60 histone acetylase were described in [2] and showed progressive chromatin decondensation up to 20min PI.

3.2. Nuclear dynamics of DSBs during the post-irradiation period

At later post-irradiation (PI) times (30 min, 120 min and 240 min), rapid phosphorylation of H2AX led to the progressive growth of γH2AX foci and their protrusion into the TOPRO-3 "holes" (Fig. 2B). Unlike early breaks located either in sparse or dense (Fig. 1A, 3A), later DSBs associated with the MRN-complex, marked here by phosphorylated NBS protein (NBSp), were located almost exclusively in TOPRO-3 "holes" (Fig. 3B). Moreover, accumulation of γH2AX + NBSp foci in the restricted space of the chromatin "holes" occasionally resulted in clustering of two or more foci (Fig. 3C). The number of these clusters increased with the PI time and correlated with the increasing percentage of γH2AX foci localized in sparse chromatin.

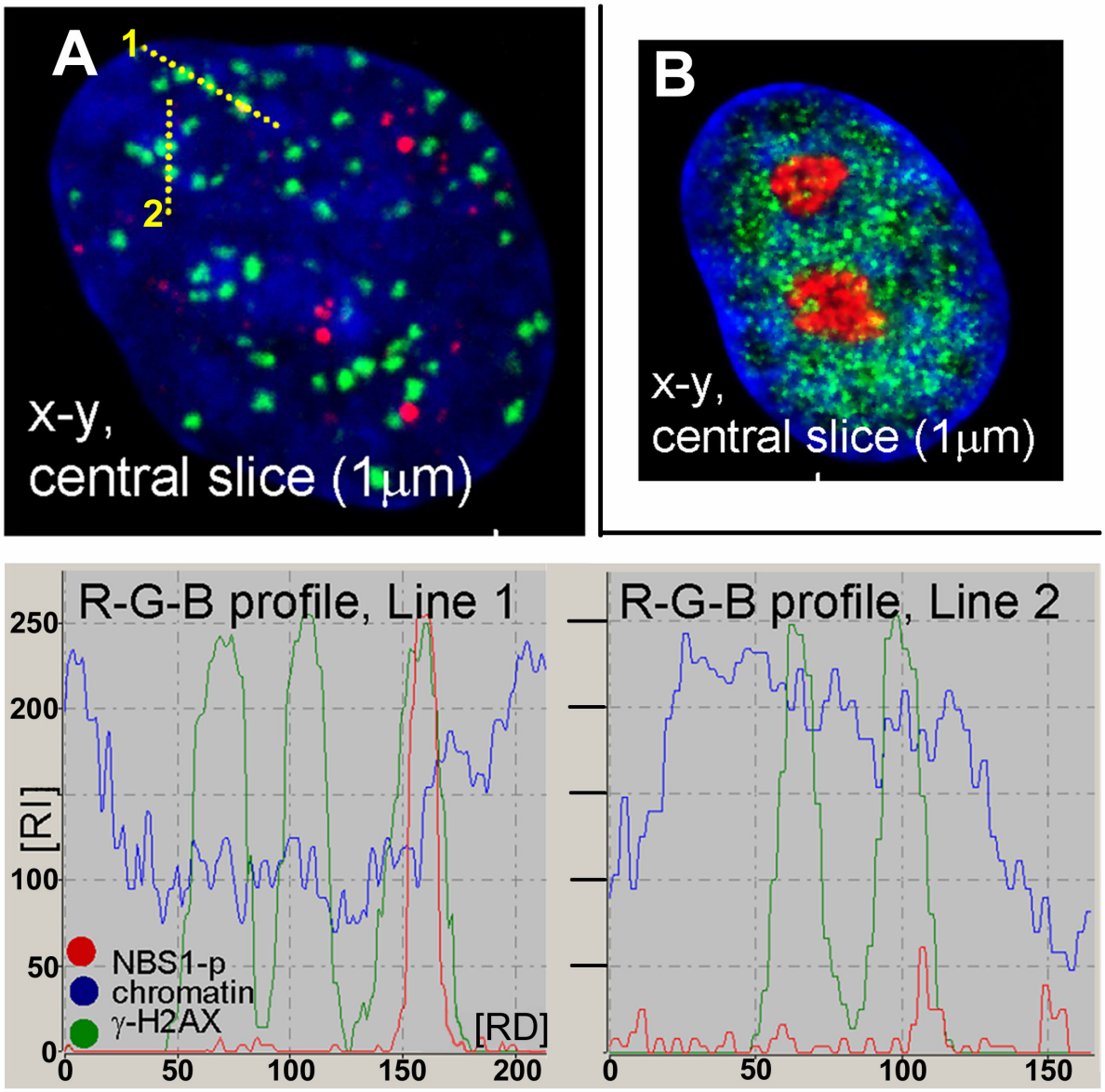

Figure 1. Localization of DSBs in functionally different chromatin domains. A: Localization of early DSBs (5 min PI) in weakly stained sparse chromatin and intensely stained dense chromatin (γH2AX foci intersected by yellow lines 1 and 2 respectively) is demonstrated on the central slice (1 μm thick) through the nucleus of a γ-irradiated (1.5 Gy) human fibroblast and by the intensity profiles of RGB channels (R = red, NBSp; G = green, γH2AX foci; B = blue, TOPRO-3 stained chromatin) along the yellow lines (x-axis: relative fluorescence, y-axis: relative distance along the indicated path). B: DSBs are absent from nucleoli (red: antifibrillarin antibody; green: HP1β; blue: TOPRO-3) but were detected in most TOPRO-3 unstained chromatin "holes" (Fig. A).

To exclude the possibility that the clustering and changes in the higher-order chromatin structure are only due to growth of γH2AX foci, we analysed nuclear dynamics of DSBs in living human cells after irradiation with 3.0 Gy. Expression of GFP-tagged NBS protein was observed both in transiently

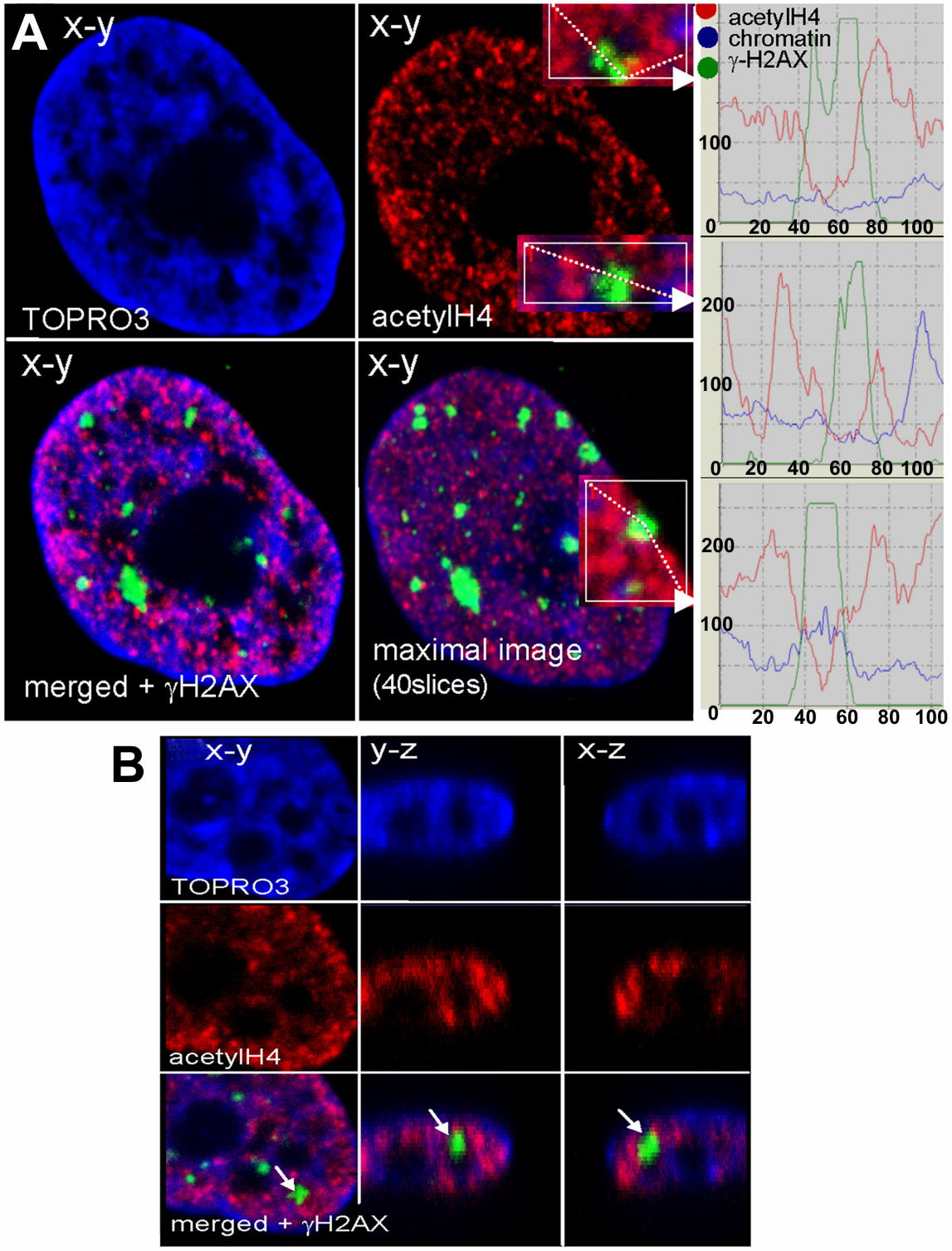

Figure 2. Mutually exclusive localizations of DSBs (γH2AX foci, green) and an active chromatin marker (histone H4 acetylated at lysine 12, acetylH4K12, red). Maximal images together with RGB profiles intersecting three randomly selected γH2AX foci are shown at Fig. A (x-axis: relative fluorescence, y-axis: relative distance along the indicated path), the x-y, y-z and x-z slices throughout indicated (arrow) γH2AX focus at Fig. B.

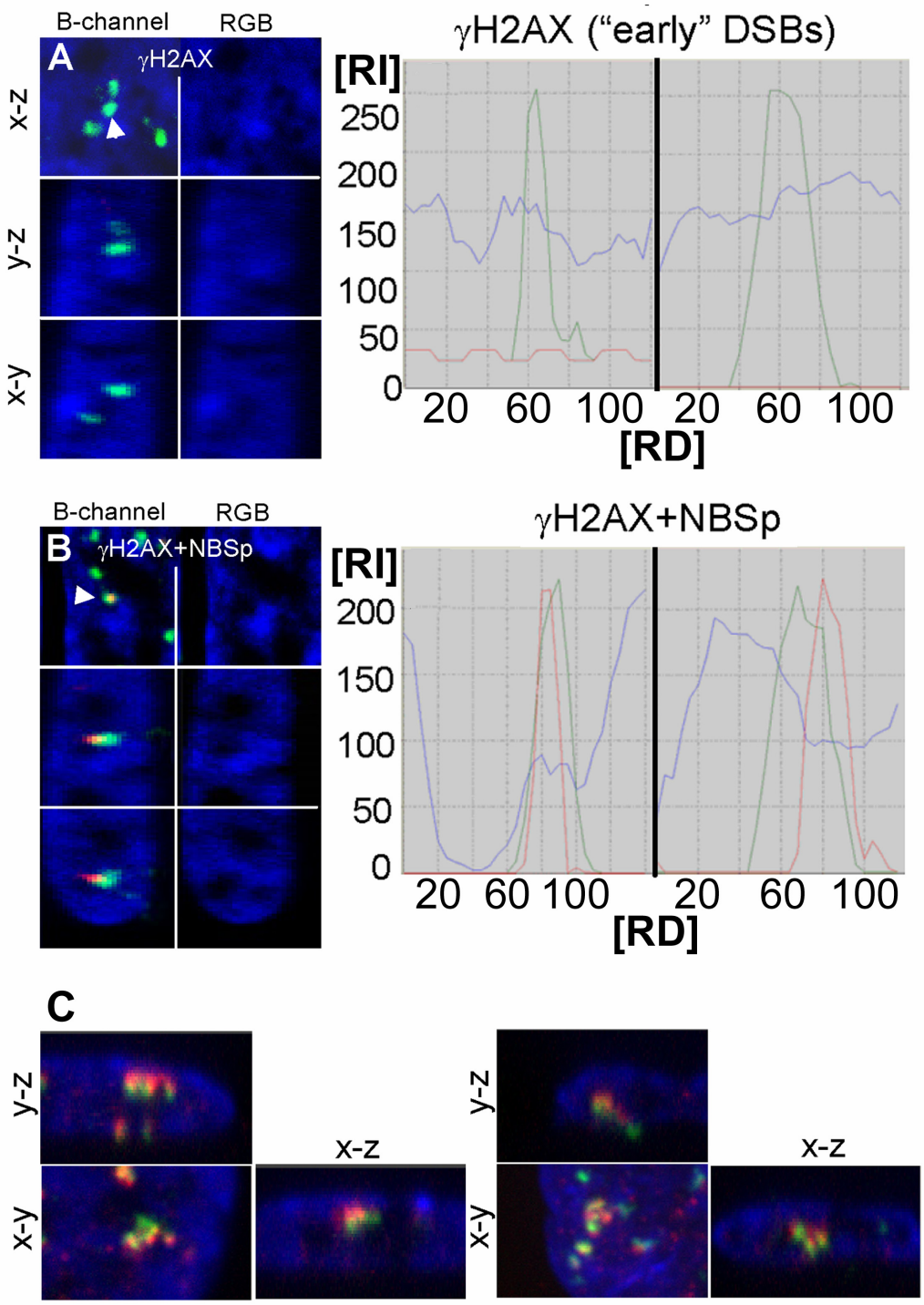

Figure 3. Nuclear movement and clustering of DSBs. A and B compares nuclear localization of γH2AX (green) and γH2AX + NBSp (green + red) foci in 3D-fixed human fibroblasts γ-irradiated with 1.5Gy. Right panels: intensity profiles of RGB channels (R: NBSp; G: γH2AX: B: TOPRO-3; x-axis: relative fluorescence, y-axis: relative distance along the nuclear path) for the indicated DSBs (arrows at left panels). C: Clustering of actively repaired DSBs 10-20 min PI in the same cells (3D projections with optical slices 0.3 μm, γH2AX foci -green, NBSp - red, chromatin counterstaining with TOPRO-3 - blue).

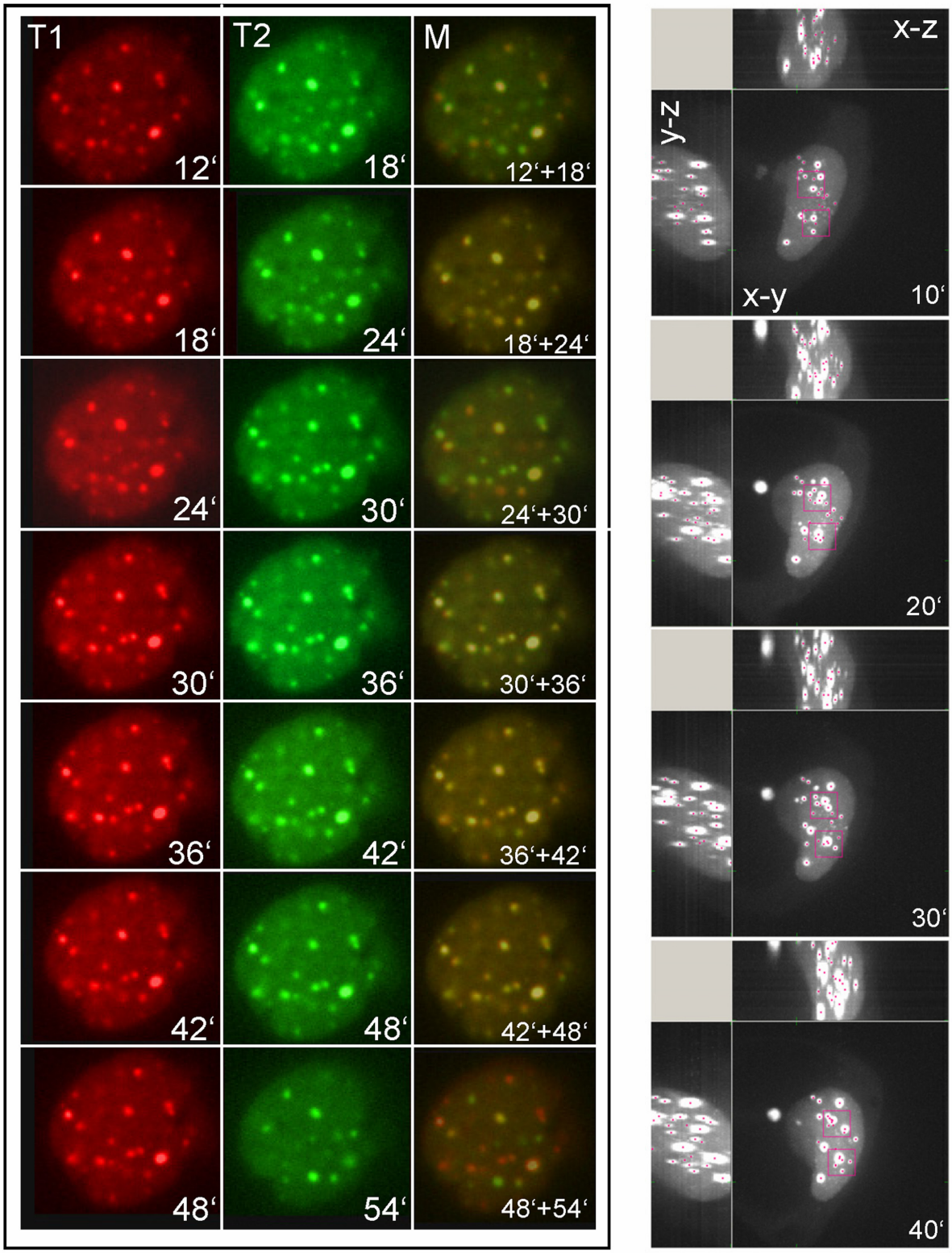

Figure 4. Left panel: Nuclear positions of GFP-NBS foci in irradiated (γ, 1.5 Gy) MCF7 cells during the PI time. The “M” column shows superimposed images from the “T1” and “T2” columns. Right panel: An example of DSB cluster formation from spatially distinct DSBs (GFP-NBS foci) monitored in 3D + time in living MCF-7 cells during a 40 min interval PI.

transfected MCF7 control and irradiated cells, but larger NBS foci appeared in the latter as well as small signals. NBS foci in irradiated cells were also more frequent than in the controls.

Measurements of DSB (NBS) movement were therefore derived from changes in the distances between all possible pairs of large NBS foci and were described in [2]. A very short period of 20-500 ms between slices was used to eliminate "shivering" of the whole nucleus. The mean Δd2 calculated revealed similar mobility of NBS (0.025 μm2/min) as for chromatin [2] (Fig. 4). However, for a small proportion of individual NBS foci, noticeable movement sometimes resulting in stable or temporal fusion of signals was observed (Fig. 4, right). Using CENP-A immunostaining, some extent of movement was observed also for centromeres, which showed a centripetal shift 30 min after exposure to 1.5 Gy. Histograms of DSBs radial-distance distributions ([locus]-to-[nuclear centre] distances) in control (87.534 ± 0.466%R) and irradiated (83.276 ± 0.487%R) fibroblasts are compared in Fig. 5.

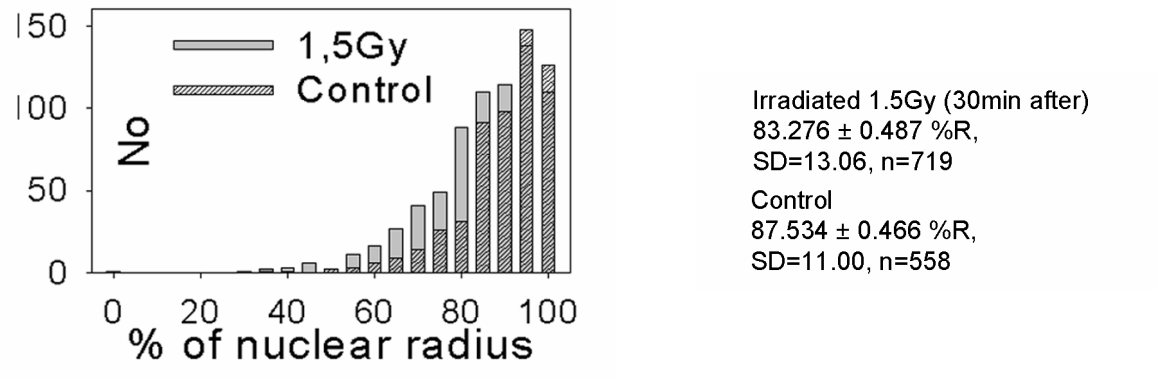

Figure 5. Radial distributions ([locus]-to-[nuclear centre] distances normalized to the nuclear radius [R], expressed as [%R]) of centromeres (CENP-A protein) in control (dashed bars, n = 558) and γ-irradiated (1.5 Gy) (grey bars, n = 719) human fibroblasts.

Double-labelling experiments immunostaining simultaneously γH2AX and NBS or Mre11 proteins, both representing members of the MRN complex, revealed that localization of DSBs (γH2AX foci) in sparse chromatin (chromatin holes) increases with continually growing colocalization of this foci with mentioned repair proteins (Fig. 6). In other words, DSBs located in decondensed sparse chromatin already colocalized with MRN complex, whereas DSBs in dense chromatins domain either colocalized or not. Only 41% and 24% of γH2AX foci colocalized on average with NBSp and Mre11, respectively, immediately (2 min) PI. During the PI period the size and frequency of colocalizing γH2AX foci increased up to 2 h (76% for NBSp and 73% for Mre11) [2] and than started to decrease; Large γH2AX foci however still persisted in a subgroup of nuclei, colocalizing with NBSp and MRE11 (Fig. 6). Increasing localization of γH2AX foci in low-density chromatin was associated with a higher probability of clustering (Fig. 3C, 6). Clustered DSB lesions started to appear within minutes PI (Fig. 3C, 6) and their number increased slightly with time.

3.3. Late DSBs and clustered lesions

Long-time persisting foci frequently corresponded with clustered lesions. These complex lesions usually colocalized with the MRN-complex but without being repaired, indicating a lower repair efficiency of clustered γH2AX. Despite the presence of unrepaired DSBs, some cells have divided, as shown by the presence of adjacent micronuclei, sometimes containing double-minute DSB lesions

(see [2]). Chromatin containing DSBs was either deleted from the genome and excluded in micronuclei, or persisted unrepaired in the next cell generation.

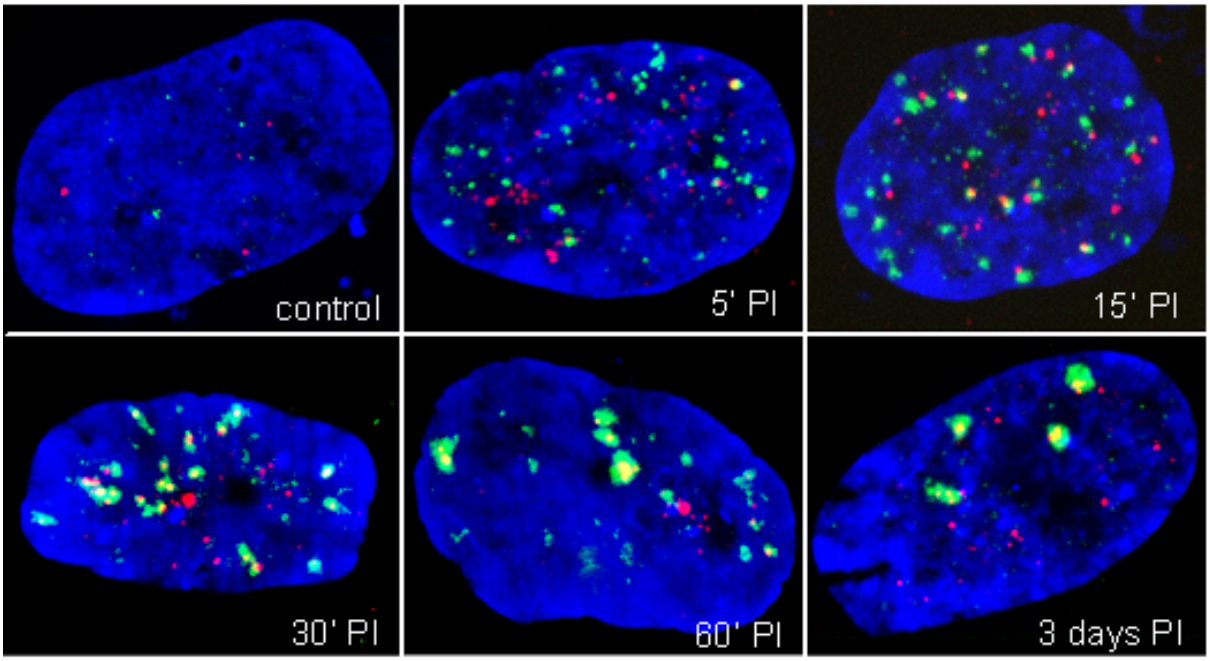

Figure 6. DSB repair and late DSBs. Development of γH2AX foci (green) and their colocalization with MRN-complex participants (NBSp protein, red) during a long PI period (5 min to 3 days). Human fibroblasts irradiated with 1.5 Gy, chromatin counterstaining by TOPRO-3 (blue).

3.4. Late DSBs show many features of transcriptionally silenced heterochromatin

As described above, DSBs were located preferentially in decondensed chromatin, adjacent to, but not colocalizing with, acetylH4K12, with a peak 30 min PI (Fig. 7A). On the other hand, late γH2AX foci colocalized with heterochromatin markers: dimethylated histone H3 at lysine 9 (dimetH3K9) [2], HP1β protein, and in some cases centromeric heterochromatin (CENP-A protein) (Fig. 7B). The frequency of colocalization with dimetH3K9 and HP1β increased significantly with PI time, and late DSBs in particular showed almost complete colocalization with HP1β (Fig. 8A) despite the constant nuclear level of this protein, which was not affected by irradiation as determined by Western blotting (Fig. 9). A similar tendency was shown for large γH2AX foci and centromeres (Fig. 8A), but when all γH2AX foci were included in the analysis, colocalization started to decrease slightly 2 h PI (Fig. 8A). Simultaneous visualization of γH2AX, NBSp and HP1β revealed that 50% (at 2 h PI) of the γH2AX foci colocalize with both the proteins during repair (in other words, about 77% of γH2AX foci colocalizing with NBSp colocalized with HP1β). From 2 to 4 h PI, the number of [γH2AX+NBSp+HP1β] foci decreased slightly, in accordance with the decreasing and stable number of [γH2AX+NBSp] and [γH2AX+HP1β] foci respectively (Fig. 8B). A positive correlation between the proportion of γH2AX colocalizing with HP1β and the PI time was confirmed in living MCF7 cells transfected with NBS protein, γ-irradiated with 1.5 Gy, and subsequently immunoassayed with HP1β antibody (Fig. 10A, B).

We also studied the colocalization of γH2AX foci with two other human HP1 isoforms (α, γ). Stably high colocalization (about 80%) of both proteins was observed independently of PI time, unlike the gradually increasing colocalization with HP1β and dimetH3K9 (Fig. 11A). However, minor

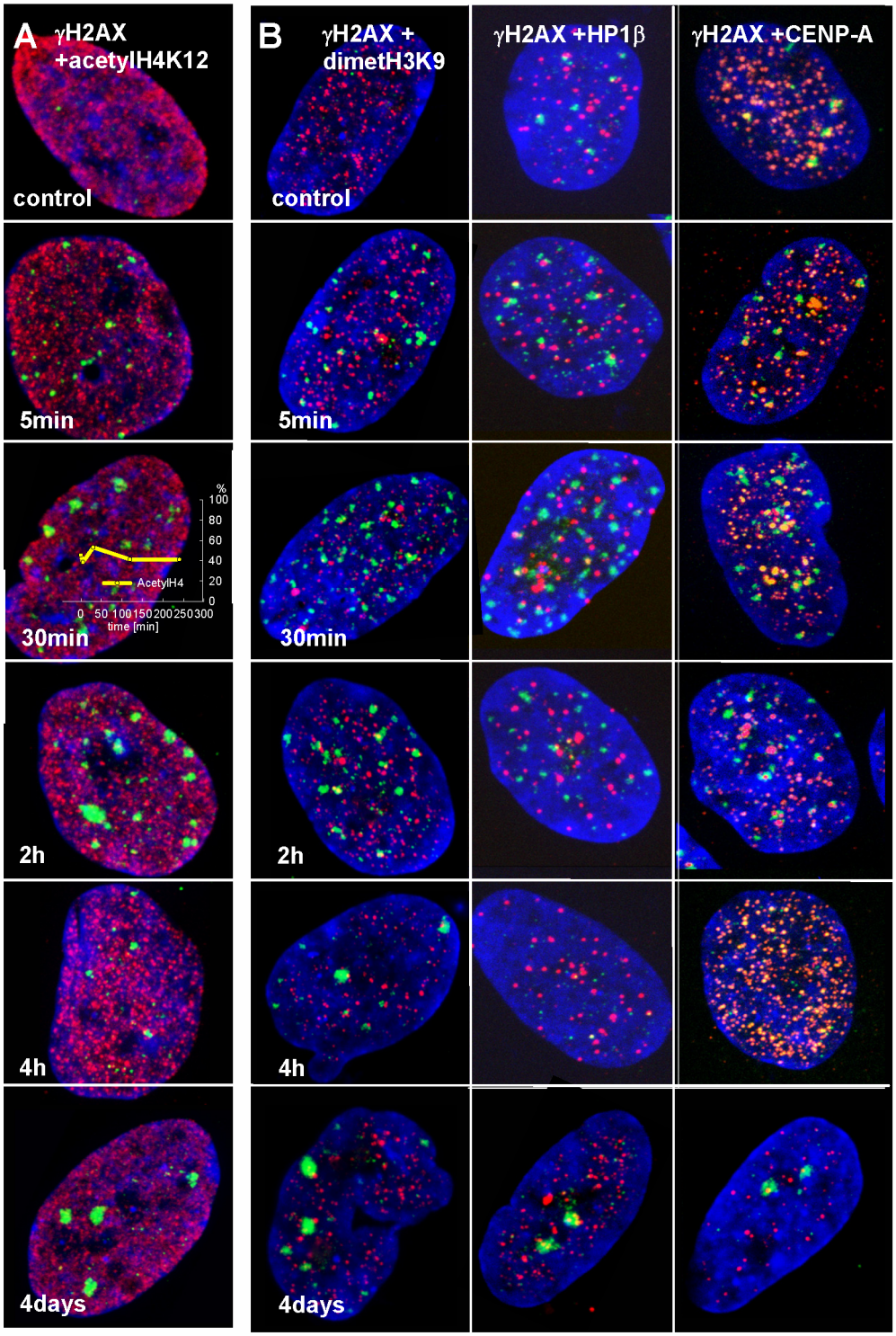

Figure 7. Colocalization of DSBs with heterochromatin markers. A: Localization of γH2AX foci (green) exclusively to transcriptionally active domains characterized by H4 histone acetylated at lysine 12 (acetylH4K12, red) during the PI period. Human fibroblasts, central sections (0.3 μm); chromatin counterstained with TOPRO-3 (for all images of Fig. 4). Inserted graph shows the proportion of γH2AX foci colocalizing with acetylH4K12 against PI time. B: Colocalization of γH2AX (green) with dimetH3K9, HP1β and CENP-A proteins respectively (all red) during the PI period. Human fibroblasts, central sections (0.9 μm).

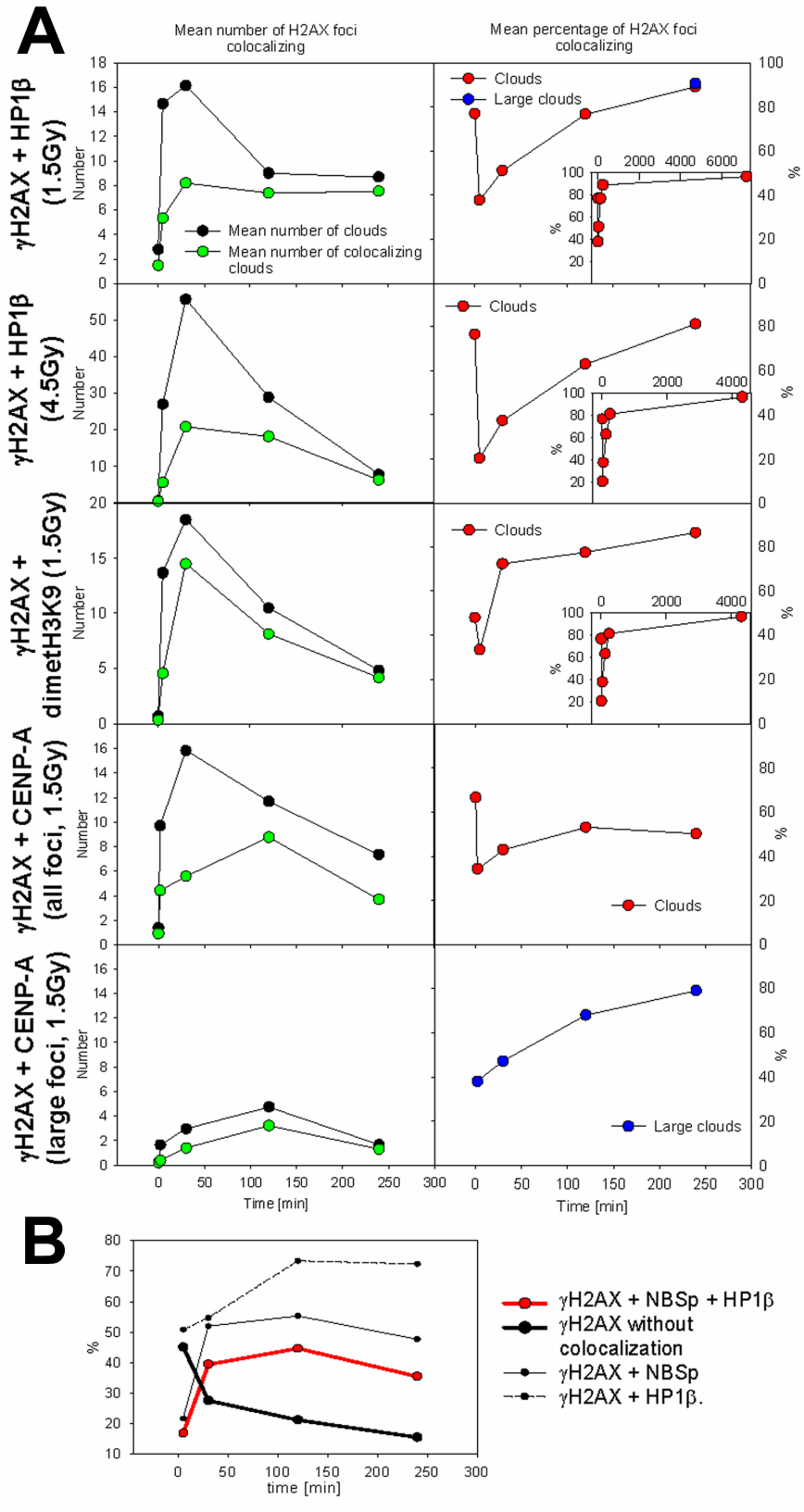

Figure 8.
A. Proportion of γH2AX foci colocalizing with hetero-chromatin markers HP1β, dimet-H3K9 and CENP-A in relation to PI time (human fibroblasts expo-sed to 1.5 or 4.5 Gy γ-rays, as indicated). Left: number of γH2AX foci (black circles) observed at the PI time indicated, and the number of γH2AX foci colocalizing with the heterochromatin mar-ker (green circles). Right: percentage of colocalized γH2AX foci. Inserted graphs show the same distributions when only large γH2AX foci were scored. B. Colocalization of γH2AX, NBSp and HP1β proteins during the PI period. Human fibroblasts γ-irradiated with 1.5 Gy; red circles: colocalization of all three proteins, black circles: γH2AX without any colo-calization; small black circles: γH2AX + NBSp; dashed line: γH2AX + HP1β.

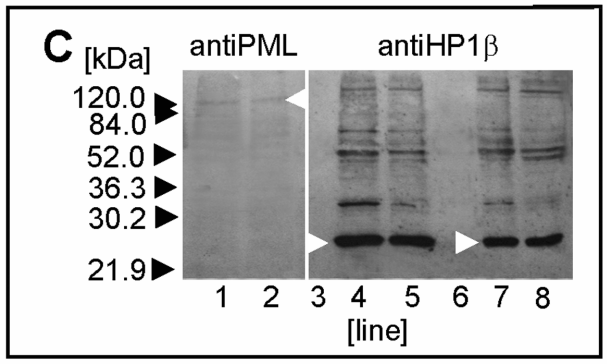

gel loading	cell population	Band volume	Peak height	Peak area	MW
1	control	75158	76	1865	27.767
	1h after 1.5Gy	69030	76	1742	27.767
0.5	control	57322	90	1396	27.413
	1h after 1.5Gy	62149	92	1667	27.413

Figure 9. Western blot comparison of the amount of HP1β in control (lane 4) and γ-irradiated (1.5 Gy, 1 h PI) (lane 5) human fibroblasts. Half sample concentrations (relative to lanes 4, 5) were independently loa--ded in lanes 7, 8 for more precise evaluation. Quantification of PML protein (lane 1: non-irradiated; lane 2: irradiated cells) was used as a control with unchanged expression (previously confirmed for PI times up to 1 h, see also [30]. Results of densitometric and software analysis of the protein bands are summarized in the associated table.

(20-30%) and "moderate" (40-50%) colocalization was detected for HP1α and γ respectively only when HP1 signals significantly protruding into γH2AX foci were scored (Fig. 11A, inserted graph, 11B), except the higher values (about 45 and 65% respectively) measured 3 days PI. Unlike HP1γ and especially HP1β and dimetH3K9 signals, which were usually located inside the γH2AX territories, colocalizing signals of HP1α formed often bridges between γH2AX foci and the TOPRO-3 stained rim of chromatin "holes" (Fig. 11C-J). Optical slices intersecting the γH2AX foci in two planes (x-z, y-z) clearly demonstrate colocalization of HP1β and dimetH3K9 with γH2AX and the absence of those proteins in the vicinity of γH2AX (Fig. 11G, I), proving that the gradual increase of colocalization with PI time is not simply due to a simultaneously growing volume of γH2AX foci. Moreover, the increase of γH2AX colocalization with HP1β and dimetH3K9 (Fig. 11A, B) does not correspond to the increase of the mean γH2AX volume during the PI period (Fig. 11B, inserted graph).

4. Discussion

In our contribution we show that DSB repair is accompanied by specific sequence of epigenetic changes of chromatin structure, starting with decondensation that enables assembly of huge repair complexes and following with condensation that mediates silencing of loci close to unrepaired DSBs and/or stabilization of decondensed chromatin loops during repair and post-repair reconstitution of chromatin structure. In addition, we have observed and quantified [2] limited nuclear movement of DSBs (γH2AX foci), similar to that described by Kruhlak et al [3]. Unlike Aten et al [6], we have demonstrated that most DSBs do not move over longer distances and are repaired individually where they form. However, we identified a subpopulation of DSBs with significantly higher mobility than average. We also found that early DSBs (γH2AX foci) generated by γ-radiation appear both in weak- and dense chromatin, but that later DSBs (2 h–4 days PI), represented by γH2AX foci colocalizing with the MRN-complex marked by NBSp, were mostly located in low-density chromatin. What causes changes in chromatin density in the region of DSBs persisting beyond 30 min PI? Does it reflect de-condensation of damaged heterochromatin, or looping-out of heterochromatic DSBs to less condensed areas where large repair complexes can assemble? To discriminate between these two models is extremely difficult. Chromatin decondensation is supported by continuous spreading of histone H2AX phosphorylation throughout the damaged region during the PI period and increased histone H4 acetylation in the vicinity of DSBs until about 20-30 min PI. On the other hand, occasional movement and clustering of some DSBs were also observed in living and 3D-fixed cells during the PI period, presenting the risk of chromatin exchange during the repair process. The frequency of clusters

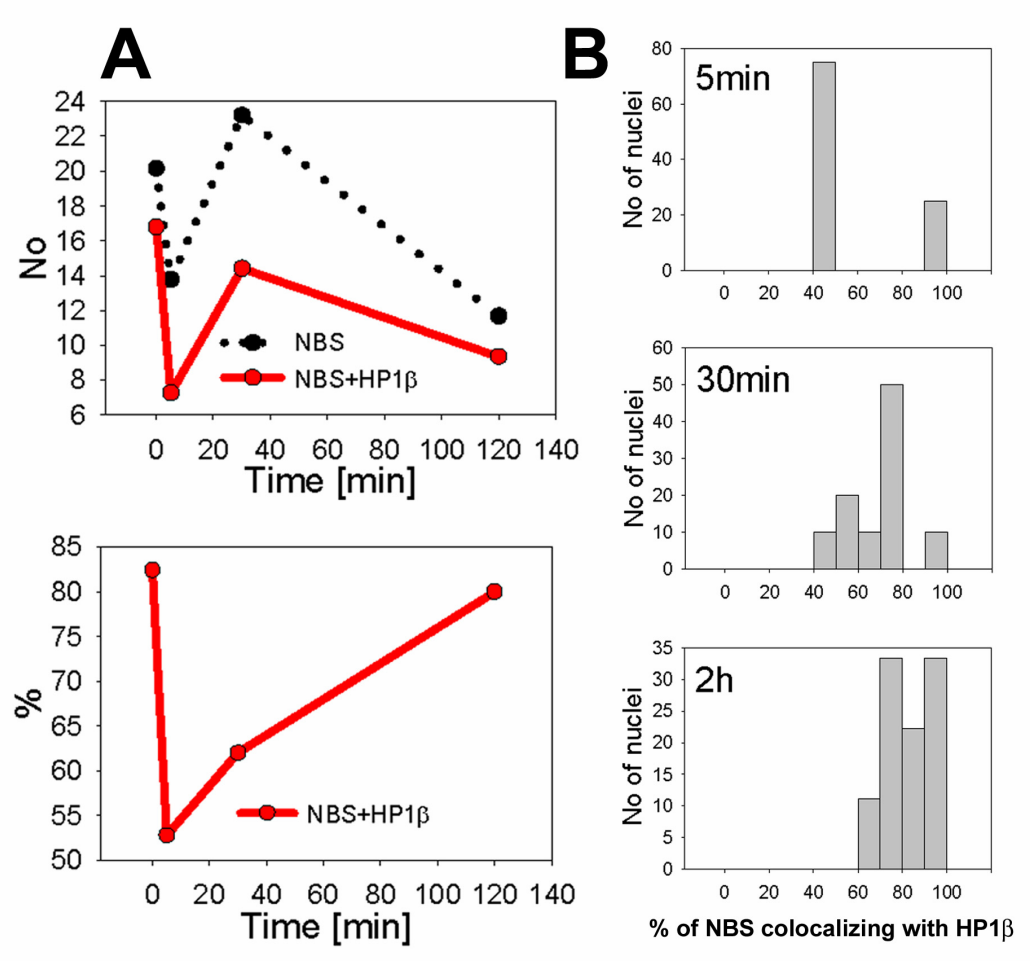

Figure 10. A Confirmation of the relation between the proportion of γH2AX colocalizing with HP1β and PI time, in living human MCF-7 cells γ-irradiated with 1.5 Gy. Upper graph: total numbers of γH2AX foci (black dashed line) observed at the PI time indicated, and the number of γH2AX foci colocalizing with HP1β (red line). Bottom graph: percentage of colocalized γH2AX foci. B: Distributions of nuclei showing percentage of γH2AX foci colocalizing with HP1β protein, measured in living MCF-7 cells 5, 30 or 120 min after exposure; x-axis: % of colocalizing γH2AX foci; y-axis: number of nuclei.

increased with the absorbed dose, correlating with a higher number and density of DSBs rendering a growing probability of association of adjacent DSBs. Clustering may also appear to result from over--lapping of enlarging γH2AX foci during the PI period. However, DSBs are already clustered several minutes PI, when γH2AX foci are still very small. Moreover, unlike the temporarily formed clusters described by Kruhlak et al [3], at least some of the clusters in living cells were stable. Some DSB clusters observed in low-density chromatin remained unrepaired even several days after irradiation, indicating that these lesions were difficult to repair and could represent an increased risk of chromatin exchange. The fraction of late-foci-positive cells and the average number of foci per nucleus increased significantly with the γ-dose absorbed. In some cases, cells probably divided despite containing late DSBs (not only DSB clusters) that persisted in the divided cells. Some of these divided cells were accompanied by micronuclei that sometimes also contained lesions.

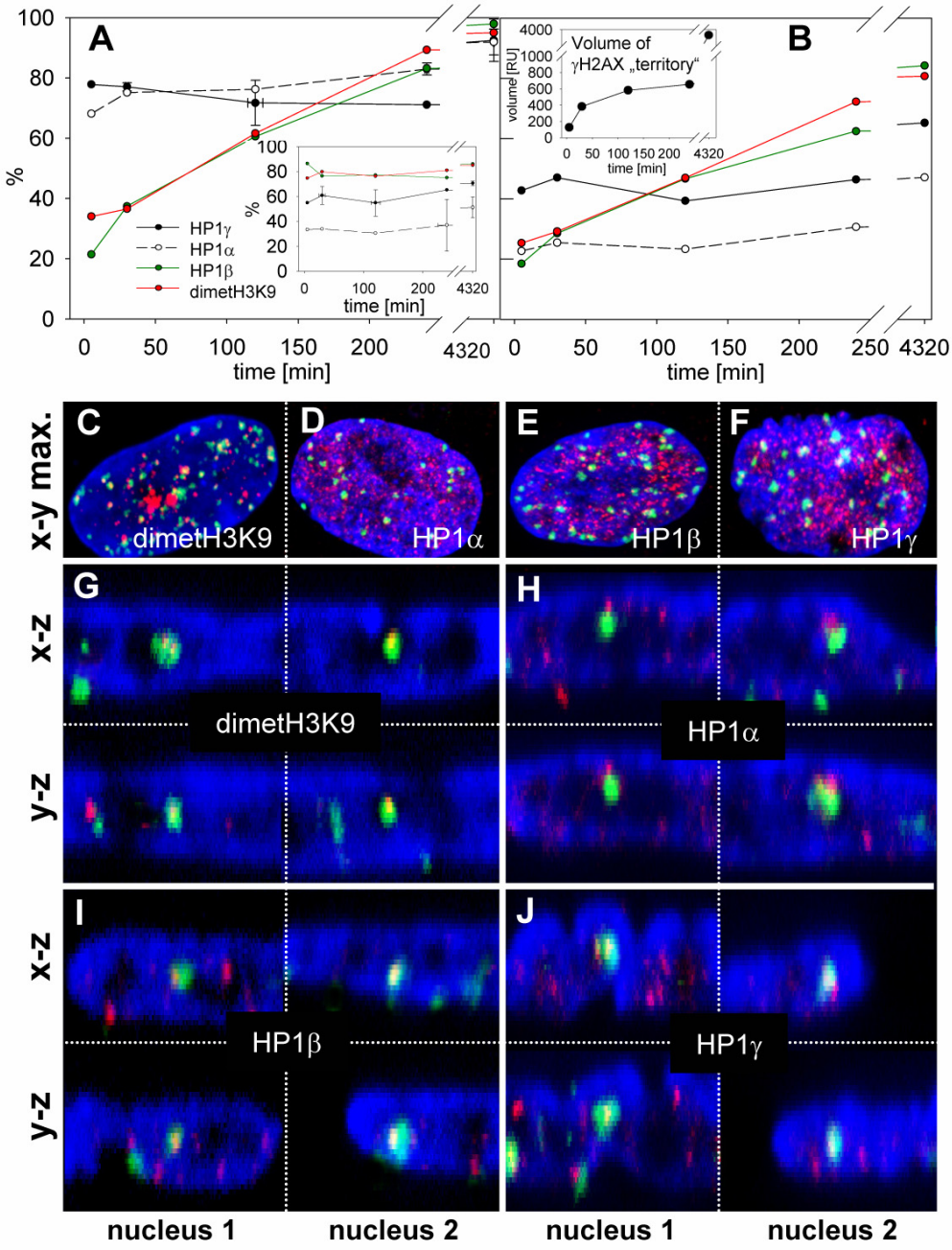

Figure 11. Colocalization of γH2AX with different isoforms of HP1 protein. A: Proportion of γH2AX foci adjacent to HP1α (dashed black line), HP1β (green line), HP1γ (black line), and dimetH3K9 (red line), against PI time (human fibroblasts exposed to 1.5 Gy of γ-rays). Inserted graph (A) shows the percentage from colocalizing signals that "touched" or protruded significantly into γH2AX foci. B: as A, but only signals at least partially overlapping γH2AX foci were scored. Inserted graph (B) shows the increase in the mean γH2AX volume with PI time. C-F: Maximal images of γH2AX foci (green) colocalizing with (red) dimetH3K9 (C), HP1α (D), HP1β (E) and HP1γ (F) respectively, and G-J: x-z and y-z sections (0.3 μm) through γH2AX foci (green) colocalizing with indicated proteins (human fibroblasts γ-irradiated with 1.5 Gy).

Our results show the immediate appearance of γH2AX foci in irradiated nuclei and their colocalization with MRN-complex several minutes PI, and thus indicate that the most prominent changes in chromatin structure and nuclear topology (associated with the recognition and processing of DSBs) take place very early after DNA damage. Opposite conclusions about the mobility of DSBs (suggesting highly mobile and completely immobile DSBs, respectively) have been proposed [3, 5, 6, and others], most probably for two reasons: (1) observation of changes at different PI times, and (2) use of different kinds of radiation to induce DSBs. Petrini and Stracker [31] postulated that late DSB foci (observed hours PI) analyzed in most studies represent sites of unsuccessful repair rather than normally repaired breaks. Further, high-LET particles [6] or microlasers [3], most frequently used for DSB generation, produce clustered DNA breaks [10]; such concentrated fragmentation of chromatin may lead to lesions that are difficult to repair and that may behave differently from the single DSBs usually generated in cells under physiological conditions. Indeed, high mobility of DSBs and their clustering was described after exposure of cells to α-particles [6]. On the other hand, irradiation with ultra-soft RTG rays resulted in immobile lesions [5]. To minimize the problems described above, we used γ-radiation to generate isolated DSB-breaks instead of tracks or foci of clustered DSBs, and monitored changes in higher-order chromatin structure from minutes up to several days PI. Our results "unify" the "breakage-first" [5] and "position-first" [6] theories, that explain the probable genesis of chromatin exchange aberrations: chromatin exchange may arise either between two "stable" DSBs when they are formed sufficiently close to one another, or between two or more DSBs that become clustered by chance.

Another important question associated with exchange aberrations concerns the sensitivity of specific chromatin domains to DNA damage. In accordance with previous studies [32 and others], we found, on average, 38 DSBs per Gy per nucleus with 2–5 min PI. The nuclear distribution of DSB was non-homogenous; most were induced in low-density chromatin (usually containing active genes, [19, 33, 34]). These observations support the view that most DNA lesions induced by γ-radiation are produced by indirect effects of the products of water radiolysis that are more abundant in low-density chromatin. DNA of dense chromatin may also be better shielded from free radicals by its compact structure and bound proteins [35].

Actively repaired DSBs (γH2AX + NBSp foci) specifically colocalize with dimetH3K9 and HP1β, despite being located almost exclusively in low-density euchromatin, as shown by TOPRO-3 staining. Although apparently contradictory, these results probably provide an explanation of how the cell solves the conflicting requirements for chromatin structure in DSB repair. Low-density chromatin in which DSBs occur (due to decondensation of damaged chromatin or looping out of heterochromatic DSBs into euchromatin holes) would permit interactions with repair proteins. Nevertheless, γH2AX foci, representing unrepaired DSBs, did not colocalize directly with acetylH4K12, characteristic of active and open chromatin, but instead were adjacent, indicating exclusion of damaged loci from transcribed domains. Temporarily increased colocalization of γH2AX with acetylH4K12 (and acetylH4K5 + Tip60 histone acetylase, [2]) observed up to 20-30 min PI is in accordance with published results [36, 37] and is probably associated with chromatin decondensation in early stages of repair. DSBs also colocalize with HP1γ and especially HP1β as well as with dimetH3K9. Since dimetH3K9 represents the histone code for binding HP1 proteins [38], responsible for heterochromatinization and gene silencing. It seems that a specific part of the damaged domains, despite being undetectable by TOPRO-3 staining due to its small size, has a condensed, inactive conformation. HP1 proteins may therefore stabilize free DNA ends in the surrounding medium and/or temporarily protect free DNA ends against fusion, as already described for telomeres [22, 39]. Alternatively, due to the progressively increasing frequency of colocalization of dimetH3K9 and HP1β during the PI period, HP1 proteins may be involved in transcriptional silencing [40, 41] of breaks that are difficult to repair or are only repaired slowly, or in re-condensation of decondensed chromatin domains after repair. Reduced colocalization of HP1α compared with β and γ probably

corresponds to different "playgrounds" of these isoforms [42] but more experiments are required to clarify this question.

5. Acknowledgement

The work was supported by the Grant Agency of the Czech Republic No. 204/06/P349 and IQS500040508, the Grant Agency of the Academy of Sciences of the Czech Republic No. IAA1065203 and the Ministry of Education of the Czech Republic No. ME 1P05OC084.
We thank Jiri and Claudia Lukas for their critical reading of the manuscript, J. Lukas, T. Misteli and M. Fareta for GFP-NBS, GFP-HP1β and GFP-PML plasmids.

References

[1] Lukas C, Bartek J, Lukas J 2005 *Chromosoma* **114** 146
[2] Falk M, Lukasova E, Gabrielova B, Ondrej V, Kozubek S 2007 *Biochim. Biophys. Acta* **1773** 1534
[3] Kruhlak MJ, Celeste A, Dellaire G, Fernandez-Capetillo O, Muller WG, McNally JG, Bazett-Jones DP, Nussenzweig A 2006 *J. Cell. Biol.* **172** 823
[4] Loizou JI, Murr R, Finkbeiner MG, Sawan C, Wang ZQ, Herceg Z 2006 *Cell Cycle* **5** 696
[5] Nelms BE, Maser RS, MacKay JF, Lagally MG, Petrini JH 1998 *Science* **280** 590
[6] Aten JA, Stap J, Krawczyk PM, van Oven CH, Hoebe RA, Essers J, Kanaar R 2004 *Science* **303** 92
[7] Prise KM et al 1998 *Int. J. Radiat. Biol.* **74** 173
[8] Tashiro S, Walter J, Shinohara A, Kamada N, Cremer T 2000 *J. Cell. Biol.* **150** 283
[9] Lisby M, Mortensen UH, Rothstein R 2003 *Nat. Cell. Biol.* **5** 572
[10] Kim MS, Baek JH, Chakravarty D, Sidransky D, Carrier F 2005 *Exp. Cell. Res.* **306** 102
[11] Pombo A, Jones E, Iborra FJ, Kimura H, Sugaya K, Cook PR, Jackson DA 2000 *Crit. Rev. Eukaryot. Gene Expr.* **10** 21
[12] Osborne CS, Chakalova L, Brown KE, Carter D, Horton A, Debrand E, Goyenechea B, Mitchell JA, Lopes S, Reik W, Fraser P 2004 *Nat. Genet.* **36** 1065
[13] Chuang CH, Belmont AS 2005 *Genome. Biol.* **6** 237
[14] Dolling JA, Boreham DR, Brown DL, Raaphorst GP, Mitchel RE 1997 *Int. J. Radiat. Biol.* **72** 303
[15] Jirsova P, Kozubek S, Bartova E, Kozubek M, Lukasova E, Ganova A, Koutna I, Skalnikova M 2001 *Radiation Research* **155** 311
[16] Monajembashi S, Rapp A, Schmitt E, Dittmar H, Greulich KO, Hausmann M 2005 *Biophys. J.* **88** 2309
[17] Lieber MR, Ma Y, Pannicke U, Schwarz K 2003 *Nat. Rev. Mol. Cell. Biol.* **4** 712
[18] Moore JD, Krebs JE 2004 *Biochem. Cell. Biol.* **82** 446
[19] Francastel C, Schubeler D, Martin DI, Groudine M 2000 *Nat. Rev. Mol. Cell. Biol.* **1** 137
[20] Fernandez-Capetillo O, Nussenzweig A 2004 *Proc. Natl. Acad. Sci. U S A* **101** 1427
[21] Jenuwein T, Allis CD 2001 *Science* **293** 1074
[22] Oikemus SR, McGinnis N, Queiroz-Machado J, Tukachinsky H, Takada S, Sunkel CE, Brodsky MH 2004 *Genes Dev.* **18** 1850
[23] Andegeko Y, Moyal L, Mittelman L, Tsarfaty I, Shiloh Y, Rotman G 2001 *J. Biol. Chem.* **276** 38224
[24] Bradshaw PS, Stavropoulos DJ, Meyn MS 2005 *Nat. Genet.* **37** 193
[25] Lukas C, Melander F, Stucki M, Falck J, Bekker-Jensen S, Goldberg M, Lerenthal Y, Jackson SP, Bartek J, Lukas J 2004 *EMBO J.* **23** 2674

[26] Cheutin T, McNairn AJ, Jenuwein T, Gilbert DM, Singh PB, Misteli T 2003 *Science* **299** 721
[27] Kozubek M, Kozubek S, Lukasova E, Mareckova A, Bartova E, Skalnikova M, Jergova A 1999 *Cytometry* **36** 279
[28] Kozubek M, Kozubek S, Lukasova E, Bartova E, Skalnikova M, Matula P, Matula P, Jirsova P, Cafourkova A, Koutna I 2001 *Cytometry* **45** 1
[29] Kozubek M, Matula P, Matula P, Kozubek S 2004 *Microsc. Res. Tech.* **64** 164
[30] Xu ZX, Timanova-Atanasova A, Zhao RX, Chang KS 2003 *Mol. Cell. Biol.* **23** 4247
[31] Petrini JH, Stracker TH 2003 *Trends Cell. Biol.* **13** 458
[32] Rothkamm K, Lobrich M 2003 *Proc. Natl. Acad. Sci. U S A* **100** 5057
[33] Verschure PJ, van Der Kraan I, Manders EM, van Driel R 1999 *J. Cell. Biol.* **147** 13
[34] Volpi EV et al 2000 *J. Cell. Sci.* **113** 1565
[35] Begusova M, Sy D, Charlier M, Spotheim-Maurizot M 2000 *Int. J. Radiat. Biol.* **76** 1063
[36] Martin SG, Laroche T, Suka N, Grunstein M, Gasser SM 1999 *Cell* **97** 621
[37] Murr R, Loizou JI, Yang YG, Cuenin C, Li H, Wang ZQ, Herceg Z 2006 *Nat. Cell. Biol.* **8** 91
[38] Lachner M, O'Carroll D, Rea S, Mechtler K, Jenuwein T 2001 *Nature* **410** 116
[39] Cenci G, Siriaco G, Raffa GD, Kellum R, Gatti M 2003 *Nat. Cell. Biol.* **5** 82
[40] Hwang KK, Eissenberg JC, Worman HJ 2001 *Proc. Natl. Acad. Sci.* **98** 11423.
[41] Janicki SM et al 2004 *Cell* **116** 683
[42] Smothers JF, Henikoff S 2001 *Mol. Cell. Biol.* **21** 2555

Available online at www.sciencedirect.com
ScienceDirect
Biochimica et Biophysica Acta 1773 (2007) 1534–1545
Biochimica et Biophysica Acta BBA
www.elsevier.com/locate/bbamcr

Chromatin dynamics during DSB repair

Martin Falk, Emilie Lukasova *, Barbora Gabrielova, Vladan Ondrej, Stanislav Kozubek

Institute of Biophysics, Academy of Sciences of the Czech Republic, Kralovopolska 135, 612 65 Brno, Czech Republic

Received 19 February 2007; received in revised form 4 July 2007; accepted 9 July 2007
Available online 18 July 2007

Abstract

We show that double strand breaks (DSBs) induced in chromatin of low as well as high density by exposure of human cells to γ-rays are repaired in low-density chromatin. Extensive chromatin decondensation manifested in the vicinity of DSBs by decreased intensity of chromatin labelling, increased H4K5 acetylation, and decreased H3K9 dimethylation was observed already 15 min after irradiation. Only slight movement of sporadic DSB loci for short distances was noticed in living cells associated with chromatin decondensation around DSBs. This frequently resulted in their protrusion into the low-density chromatin domains. In these regions, the clustering (contact or fusion) of DSB foci was seen *in vivo*, and *in situ* after cell fixation. The majority of these clustered foci were repaired within 240 min, but some of them persisted in the nucleus for several days after irradiation, indicating damage that is not easily repaired. We propose that the repair of DSB in clustered foci might lead to misjoining of ends and, consequently, to exchange aberrations. On the other hand, the foci that persist for several days without being repaired could lead instead to cell death.

Keywords: Chromatin structure; DNA damage; Double-strand breaks (DSB); DNA repair; Exchange aberration; Genomic instability

1. Introduction

Cells have developed sophisticated ways to deal with exposure to toxic agents in our environment. In particular, cells must be able to respond appropriately when their DNA has been damaged, either by natural processes or by exposure to chemicals or ionizing radiation. The most serious damage induced in DNA is interruption of its integrity resulting in double-strand breaks (DSBs). Improper repair of DSBs can lead to the development of cancer. Once a cancer has developed, radiation and chemotherapy are used to damage DNA so as to kill the tumour cells. Thus, recognition of how cells respond to DNA damage is critical for understanding both the development of cancer and its therapy. The first molecular events that happen in cells after DNA breakage following exposure to ionizing radiation have been identified [1,2]. Immediately after DSB induction, histone H2AX, a variant of H2A, is phosphorylated at its C-terminal serines (Ser136 and Ser139) by ATM and other phosphatidylinositol 3-kinases [1] at the site of the DSB. ATM activated by DSB formation phosphorylates a multitude of proteins that take part in a damage response pathway [3,4]. Phosphorylated H2AX (γH2AX) can be detected within minutes after the induction of DSBs, and is involved in recruitment to the sites of DSBs of other known proteins of the DNA repair signalling pathway, including NBS1/MRE11/Rad50, Brca1 and 53BP1 [5–9]. Phosphorylated H2AX does not just localize at the sites of DNA breakage, but quickly spreads to the surrounding megabase region. It is likely that this build up of γH2AX around the DSB is the signal that leads to the retention of DNA damage-response factors [5,10,11]. γH2AX may serve as a docking site for these proteins [5] or alternatively, modulate chromatin structure and thus indirectly facilitate their accumulation [12]. Chromatin structure and dynamics are strongly suspected of playing an important role in the regulation and facilitation of DNA repair [13–15]. Since genomic DNA is packed into highly organized, more or less condensed chromatin, it is conceivable that this structure must be relaxed to allow access to damaged DNA of an array of repair protein complexes [16–18]. Decondensation to allow assembly and function of huge multi-protein complexes is not unprecedented in molecular biology; it has been extensively documented, for example, at sites of gene transcription [19–21]. An

* Corresponding author. Tel.: +420 541517165; fax: +420 541240498.
E-mail address: lukasova@ibp.cz (E. Lukasova).

0167-4889/$ - see front matter © 2007 Elsevier B.V. All rights reserved.
doi:10.1016/j.bbamcr.2007.07.002

enduring question is whether chromatin also undergoes decondensation in regions of induced DSBs. Evidence suggests that such process is indeed induced by DNA damage, including DSBs [16–18]. Recently, local chromatin relaxation in the vicinity of DSBs has been demonstrated in yeast [22], and a similar process, independent of ATM, has been shown in mammalian cells [14,23]. The results of Ziv et al. [18] show that DSBs induce an ATM-dependent wave of chromatin relaxation, starting in the vicinity of DSBs and quickly extending into the entire genome as a result of the action of the ATM-phosphorylated protein KAP-1. The authors propose [18] that this global, ATM- and KAP-1-dependent chromatin relaxation that follows the local ATM-independent relaxation [14] may create the chromatin configuration that is essential for a fully efficient repair process.

Experimental evidence of chromatin decondensation induced by DSBs has been obtained by several laboratories; however, it does not provide unequivocal information about the possible regional movement of damaged DNA during this decondensation. Results of experiments dealing with this movement are contradictory [14,24–26]. The data available on DSB mobility were obtained after irradiation of cells with radiation of different quality high LET α-radiation (^{241}Am, LET > 20 keV/μm, in [24]), low energetic X-rays (synchrotron-generated ultrasoft X-rays, <5 keV in [25]) and local laser beams (e.g. argon ion UV laser, 364-nm emission line, in [14]; UV-A pulse nitrogen laser, 337 nm emission line in [26]) resulting in different local concentration of DSBs (clustered or single DSBs) [14,24–26]. Local release of high energy by high LET α-particles induces large numbers of DSBs in close proximity to each other, which could produce DNA fragmentation, unlike low LET X-rays and γ-rays that induce isolated DSBs. Bekker-Jensen et al. [8] showed that DSB yields per a nuclear volume obtained with UV-A (λ = 337 nm) laser were equivalent to about 10 Gy of ionizing radiation (delivered by X-ray generator, 150 kV; 15 mA; dose rate 2.18 Gy/min).

In this work, we contribute to the elucidation of chromatin structure and dynamics in the vicinity of DSBs induced by sparsely ionizing γ-rays of ^{60}Co (1.1 MeV, 1 Gy/min), in human fibroblasts and MCF7 mammary carcinoma cells. Our results show chromatin decondensation manifested by a decrease of intensity of chromatin labelling, increase of H4K5 acetylation and decrease of H3K9 dimethylation at sites of DSBs. A limited "movement" associated with chromatin decondensation and protrusion of DSBs into the low-density chromatin can be seen *in vivo* and *in situ* after cell fixation. Some of clustered foci persisted in the nucleus for several days after irradiation, indicating damage that was only reparable with difficulty.

2. Materials and methods

2.1. Cell culture and transfection

Human MCF7 mammary carcinoma cells and human lung fibroblasts 04-147 were grown in DMEM medium supplemented with 10% fetal calf serum (FCS) and standard antibiotics. To get transient expression of NBS1-GFP (a gift from J. Lukas), HP1β-GFP (a gift from T. Misteli), PML-GFP (a gift from M. Faretta), the cells were transfected with the GFP constructs using Lipofectamine 2000 (Invitrogene) according to the manufacturer's instructions and used for observation of protein movement 12 h after transfection, and within 30 min after irradiation. Changes in chromatin structure in regions of DSBs and breaks displacement were studied in cells co-transfected with H2B-GFP (Clontech) and pm53BP1-RFP (a gift from J. Lukas), using Fugene HD (Roche). The cells were irradiated with the dose of 1 Gy of ^{60}Co γ-rays, 35 h after transfection and immediately observed.

2.2. Cell synchronization, irradiation, fixation, permeabilization and immunostaining

Cells used for irradiation were in the G1 phase of the cell cycle (Fig. 1). Synchronization of cells in the G0 phase of the cell cycle was achieved by incubation of confluent culture of human fibroblasts without serum for 4 days. The cells were trypsinized and plated on microscope slides where they were cultured in the presence of 10% FCS. After 12 h of incubation, the cells were irradiated with γ-rays from ^{60}Co and either fixed immediately or incubated for various periods of time before fixation. The doses of γ-rays were 1.0, 1.5, 4.5 and 7 Gy (1 Gy/min).

Cells harvested at different time intervals after irradiation (5, 30, 120, or 240 min and 3 or 5 days) were washed twice for 3 min each in PBS (140 mM NaCl, 2.7 mM KCl, 1.5 mM KH_2PO_4, 6.5 mM Na_2HPO_4; pH 7.2), fixed with 4% freshly prepared paraformaldehyde in PBS for 10 min at 21 °C, rinsed quickly in PBS, then washed three times for 5 min each in PBS, permeabilized in 0.2% Triton X-100/PBS for 15 min at room temperature (RT), rinsed in PBS and washed twice for 5 min each. Before incubation with primary antibodies (overnight at 4 °C), the cells were blocked with 7% inactivated FCS + 2% bovine serum albumin/PBS for 30 min at RT. Antibodies from two different hosts (rabbit and mouse) were used on each slide to detect two different antigens in the same nuclei. Anti-H2AX phosphorylated at serine 139 (mouse) was from Upstate; anti-NBS1 phosphorylated at serine 343 (rabbit) from Cell Signaling; anti-acetyl histone H4 at lysine 12 (mouse) and Mre11 (rabbit) were from Upstate. Secondary antibodies were affinity purified donkey anti-mouse-FITC-conjugated, and affinity purified donkey anti-rabbit-Cy3-conjugated, from Jackson Laboratory (West Grove, PA). The mixture of both antibodies was applied to each slide (after their pre-incubation with 5.5% of donkey serum/PBS for 30 min at RT) and incubated for 1 h in the dark at RT. This was followed by washing (three times for 5 min each) in PBS. Cells were counterstained with 1 μM TOPRO-3 (Molecular Probes, Eugene, USA) in 2× saline sodium citrate (SSC) prepared fresh from a stock solution. After brief washing in 2× SSC, Vectashield medium (Vector Laboratories, Burlingame, CA) was used for the final mounting of samples.

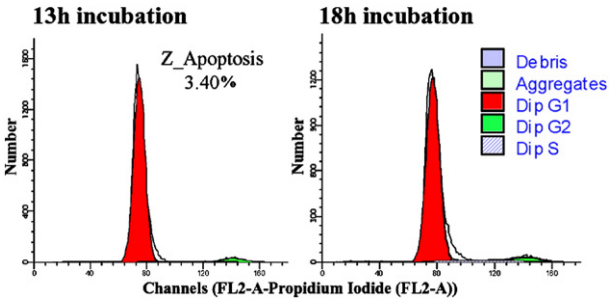

Time	G1 [%]	S [%]	G2 [%]
4h	88.81	2.61	8.59
9h	94.66	0.83	4.51
13h	95.4	0.63	3.97
18h	90.38	5.2	4.42
24h	85.43	12.96	1.6
27h	78.99	12.36	8.65

Fig. 1. Flow-cytometric monitoring of the cell cycle of human fibroblasts cultured for different periods of time (in DMEM containing 10% FCS) after their synchronization by starvation in confluence.

2.3. Cell cycle analysis

After starvation, cells were trypsinized, plated in 2×10^5 per a dish containing 5 ml of DMEM with 10% FCS and grown at 37 °C. In different time intervals, the cells were trypsinized, resuspended in the medium with 10% FCS and sedimented by centrifugation (200×*g*, 5 min, 4 °C). Cell suspension was washed in two volumes of PBS, centrifuged, resuspended in about 0.5 ml of PBS, fixed after addition of 4 ml of 70% ethanol at 4 °C for 30 min (and

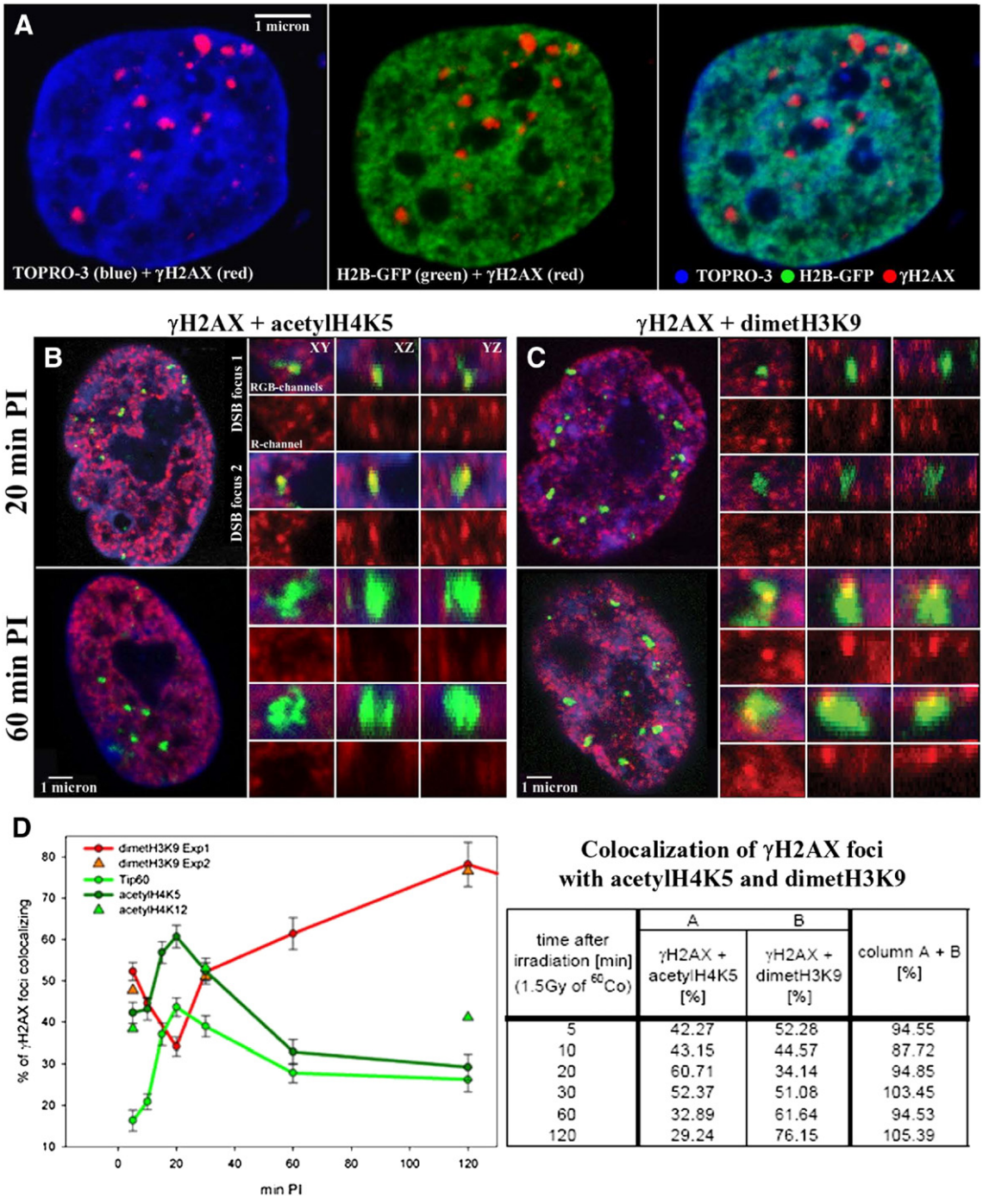

Colocalization of γH2AX foci with acetylH4K5 and dimetH3K9

time after irradiation [min] (1.5Gy of ^{60}Co)	A γH2AX + acetylH4K5 [%]	B γH2AX + dimetH3K9 [%]	column A + B [%]
5	42.27	52.28	94.55
10	43.15	44.57	87.72
20	60.71	34.14	94.85
30	52.37	51.08	103.45
60	32.89	61.64	94.53
120	29.24	76.15	105.39

Fig. 2. Location of γH2AX foci relative to low- and high-density chromatin and dynamics of epigenetic modification of histones at sites of DSBs (induced with 1.5 Gy of γ-rays) during repair. (A) Cell nucleus transfected with H2B-GFP, 3D fixed 10 min PI and immunostained with anti-γH2AX (red). The nucleus was also labelled with TOPRO-3 to compare the distribution of chromatin density detected by this labelling with that of H2B-GFP. The central x–y slices through MCF7 cells are displayed to show the location of foci γH2AX relative to dense and sparse chromatin domains. (B) Central slices (0.2 μm thick) through the cell nuclei of human fibroblasts showing colocalization of γH2AX foci (green) with acetylH4K5 (red) at different times after irradiation (PI). Nuclei were fixed at 20 or 60 min PI (upper and bottom panel, respectively), immunostained with anti-γH2AX and anti-acetylH4K5 and counterstained with TOPRO-3 (blue). Right: x–y, x–z and y–z slices (0.2 μm thick) through two γH2AX foci to show their colocalization with acetylH4K5 in all three planes. Density of acetylH4K5 at sites of γH2AX foci can be seen separately in the red channel. (C) The same figure as B but for nuclei immunostained by anti-dimethylH3K9 antibody (red) in addition to γH2AX (green). Other description is the same as in B. (D) Dynamic changes of H4K5 acetylation and H3K9 dimethylation at sites of γH2AX foci during the time after cell irradiation.

maintained at this temperature until the cells of all time intervals were fixed), then centrifuged (200×*g*, 5 min, 4 °C) and washed with PBS. DNA was labelled with propidium iodide in 0.5 ml of Vindel solution (1 ml 1 M Tris, pH 8.0, +1 mg RNAsa (Sigma R-5503) +100 µl NP-40+60 mg NaCl+5 mg propidium iodide, completed to 100 ml H_2O) for 30 min at 37 °C. The cells were fractionated according to the DNA content by flow-cytometry using the FACSCalibur device (Becton Dickinson, San Jose, California, USA) with argon laser, the excitation maximum 488 nm. In each sample, 2×10^4 of cells were analysed. Fractions of cells in different phases of the cell cycle were estimated using the ModFit 3.0 software (Verity Software House, Topsham, California, USA). The results are shown for different periods of time after synchronization in Fig. 1. It can be seen that 13 h after starvation, 95.4% of cells are still in the G1 phase.

2.4. Image acquisition and microscopy

An automated Leica DM RXA fluorescence microscope (Leica, Wetzlar, Germany), equipped with an oil immersion Plan Fluotar objective (100×/NA 1.3), a CSU 10a Nipkow disc (Yokogawa, Japan) for confocal imaging, a CoolSnap HQ CCD-camera (Photometrix, Tuscon, AZ, USA) and an Ar/Kr-laser (Innova 70C Spectrum, Coherent, Santa Clara, CA, USA), were used for image acquisition [27,28]. Automated exposure, image quality control and other procedures were performed using FISH 2.0 software [27,28]. The exposure time and dynamic range of the camera in the red, green and blue channels were adjusted to the same values for all slides to obtain quantitatively comparable images. Forty serial optical sections were captured at 0.2-µm intervals (along the *z*-axis). For observation of living cells, an iXon DV 887ECS-BV (Andor) camera was used together with the 3D viewer software [29].

2.5. Living cell observation and time-lapse microscopy

Two types of *in vivo* observations were performed: short and medium-term. For short-term experiments, "2D" images consisting of a few (3–5) confocal slices with a z-step of 0.3–0.5 µm were acquired in extremely short intervals (20–500 ms) for a period of approximately 1.5 min. For medium-term observations, 40 optical sections were captured (3D images) with a 0.2–0.3 µm z-step. Intervals of 50 s were allowed between individual stacks of 40 sections, and observations were continued for a total of 20 min. The light exposure was kept as low as possible to avoid phototoxic effects. Double transfected cells with H2B-GFP and pm53BP1-RFP were observed in 5 min intervals until 30 min PI, followed by 10 min intervals until 60–120 min PI. In each interval, 15 slices with a z-step of 0.4 µm were taken. The temperature (37 °C) of medium and the 5% concentration of CO_2 in the atmosphere were kept constant during observation.

2.6. Analysis of experimental data and motion of loci

The off-line image analysis and tracking (2D, 3D) of fluorescence signals were done with the FISH 2.0 software and a 3D image viewer [27–29]. Coordinates were taken at the centre of gravity of the visualized objects, and corrected for rotation of the cell nucleus and drift of the images during longer time-lapse observations. The objects were traced in the time-lapse series on the basis of matching algorithms. In 2D, the distances between two signals were calculated using the equation: $d=\sqrt{(x_1-x_n)^2+(y_1-y_n)^2}$; or in 3D: $d=\sqrt{(x_1-x_n)^2+(y_1-y_n)^2+(z_1-z_n)^2}$, where x_1, y_1 and z_1 (x_n, y_n and z_n) were coordinates for the first measurement and the nth measurement of the same object. The mean d^2 was calculated from individual d_i^2 values of all

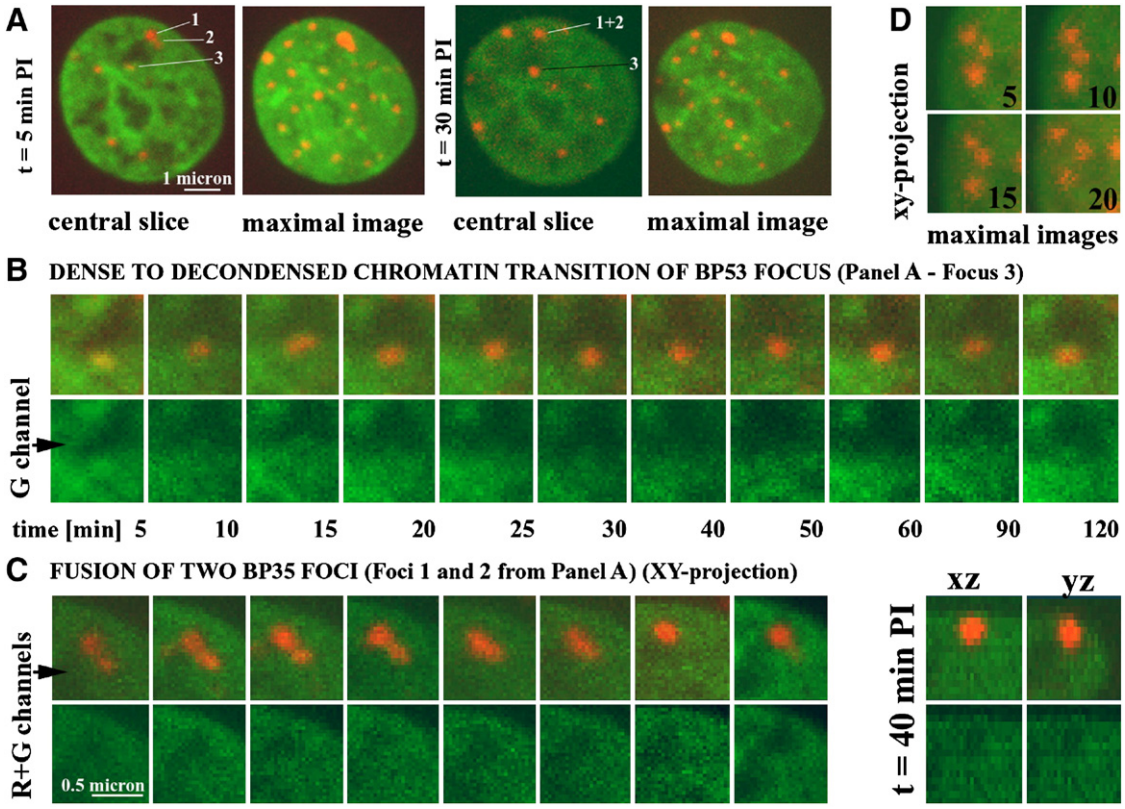

Fig. 3. Changes of chromatin density observed *in vivo* at the sites of DSBs (presented as 53BP1-RFP foci) and their displacements after γ-irradiation of MCF7 cells. (A) Central slices (0.4 µm) and maximal images in x–y plane of human MCF7 cells double-transfected with 53BP1-RFP and H2B-GFP proteins, irradiated with a dose of 1 Gy of γ-rays are displayed at 5 min (left panel) and 30 min PI (right panel). Localization of three 53BP1 foci (red) is shown relative to chromatin density (H2B-GFP, green). (B) Displacement of the focus 3 from dense (intensively green) to sparse (faintly stained) chromatin is shown in detail during the PI time (from 5 to 120 min PI). (C) Fusion of the foci 1 and 2 during the PI time (5–50 min PI) in x–y plane; for 40 min PI also the x–z and y–z slices are displayed to demonstrate the fusion in the 3D-space. The focus 2 first relocates from dense chromatin (intensively green) to H2B-GFP faintly stained domain where it fuses together with the locus 1. (D) Short-distance movement of another three 53BP1 foci (red) monitored from 5 to 20 min PI, in 5-min intervals.

Table 1
Dynamics of DSB foci (RFP-53BP1) location relative to chromatin density detected as GFP-H2B fluorescence intensity, during PI time after irradiation of MCF 7 cells with the dose of 1 Gy of γ-rays

Time PI [min]	No of foci in chromatin of different density			
	Low-density chromatin	Dense chromatin	Border of low-density and dense chromatin	Total number of foci
5	14	12	7	33
10	16	10	7	33
15	17	6	8	31
20	15	6	6	27
30	14	5	6	25
40	13	3	4	20
50	10	2	5	19
60	9	2	6	17

Dynamics of DSB foci (RFP-53BP1) location relative to low- and high-density chromatin detected as GFP-H2B fluorescence intensity, during PI time after irradiation of MCF 7 cells with the dose of 1 Gy of γ-rays.

possible signal pairs at the particular time point. The mean difference of d^2 (mean Δd^2) was calculated at each time point (t) as $\Delta d^2=(d_t-d_{t+\Delta t})^2$, where Δt was the time interval between measurements.

Evaluation of data and statistical analyses was performed using the Sigma Plot statistical package (Jandel Scientific). When required, measured distances were normalized to the nuclear radius [% of R] so as to be comparable between nuclei.

3. Results

3.1. Chromatin dynamics and epigenetic modifications in the proximity of DSBs during the post-irradiation period

DSBs induced by a dose of 1.5 Gy of ^{60}Co γ-rays were detected in fixed cells by an antibody against γH2AX as soon as 5 min post-irradiation (PI). At this time, the small γH2AX foci were dispersed throughout the nucleus with the majority of these lesions (about 70%) in weakly stained (low-density) and borderline chromatin. However, in cells fixed later after irradiation (PI=30, 120 or 240 min), the γH2AX foci were progressively extending, and protruded from the chromatin intensely labelled by TOPRO-3 or H2B-GFP (Fig. 2A) into the weakly stained chromatin "holes". This observation indicates decondensation of higher-order chromatin structure around the DSBs or DSB movement. To discriminate between changes of higher-order chromatin structure driven by chromatin decondensation or real movement of DSB foci, we analysed epigenetic modifications and nuclear dynamics of DSBs *in situ* and *in vivo*.

Chromatin decondensation in proximity of DSBs was confirmed by a sharp increase of histone H4 acetylation at lysine 5 (H4K5) and colocalization of γH2AX with Tip60 histone acetylase (HAT) between 10 and 30 min after irradiation, with the maximum at 20 min PI (about 60% of γH2AX colocalized with acetylH4K5 at this time, Fig. 2B, D,

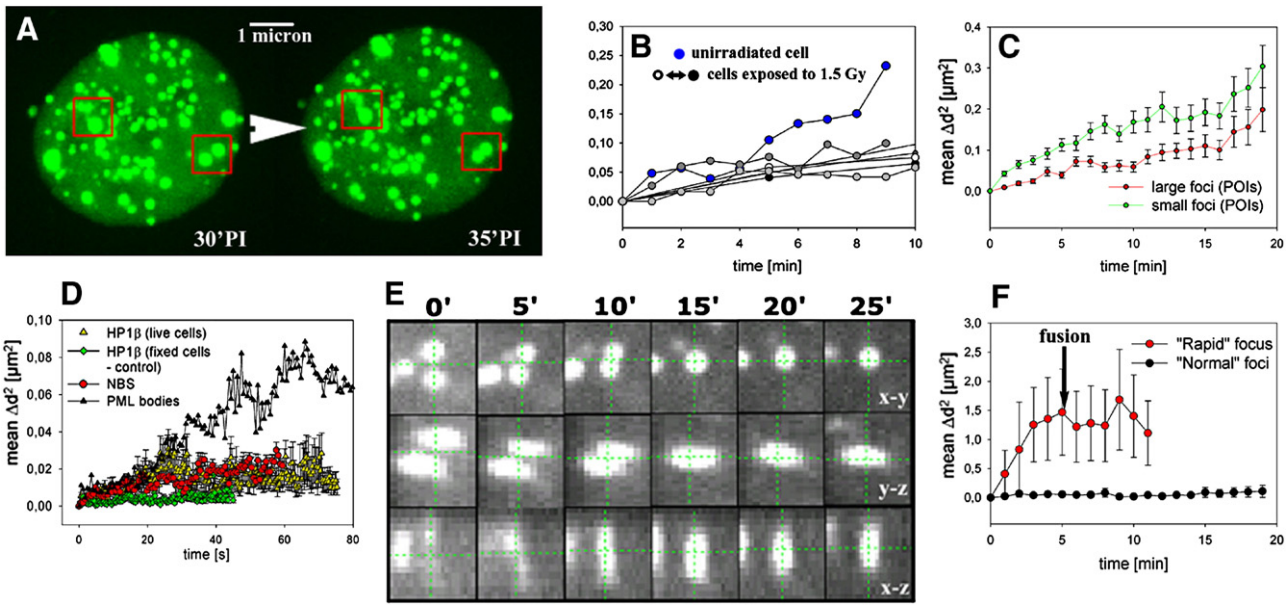

Fig. 4. Nuclear movement and fusions of DSB foci measured *in vivo* in human MCF-7 cells irradiated with 3 Gy of γ-rays. (A) Larger NBS1-GFP foci (green) framed in red, marking sites of DSBs, were tracked from 30 min (left nucleus) to 35 min (right nucleus) after exposure of cells to γ-rays. (B) The mean squared displacement (mean Δd^2) of NBS1-GFP focus before irradiation (blue) and the decreased mobility of foci after irradiation (0.03 μm^2/min vs. 0.01 μm^2/min) measured 10 min PI in several samples (grey). (C) Comparison of the mean squared displacement (mean Δd^2) of large (red) and small (green) NBS1-GFP foci in living irradiated cells. (D) Mean squared displacement (mean Δd^2) of NBS1-GFP foci (red) in γ-irradiated living cells measured for 60 s with a 0.5-s interval, 30 min PI. Mean Δd^2 values are also shown for HP1β in non-irradiated 3D-fixed cells (green diamonds), and in living cells (yellow triangles), representing background movement and mobility of heterochromatin, respectively, and for PML bodies (black triangles) showing the movement of a non-chromatin protein complex. (E) An example of cluster formation from spatially distinct NBS1-GFP foci (DSBs) monitored in 4D during a 25-min interval, starting 20 min PI. The cluster was formed after 15 min of monitoring and remained stable for at least next 10 min. (F) Comparison of the mean squared displacement (mean Δd^2) for normally visible (black circles) and highly mobile (red circles) NBS1-GFP foci in γ-irradiated living cells. The arrow indicates fusion of the tracked highly mobile focus with another one, and the consequent decrease of the mobility of the cluster.

and 40% colocalized with Tip60, Fig. 2D). A high level of histone H4 acetylation at lysine 12 (acetylH4K12) was also detected (about 55% of γH2AX presented the signal of acetylH4K12 at 30 min after irradiation, Fig. 2D). The sharp increase of acetylH4K5 and Tip60 localization at sites of DSBs was followed by a decrease of these signals after reaching the maximum at 20 min PI. Signals of acetylH4K5 and acetylH4K12 did not usually cover whole foci of γH2AX, but colocalized only with the edge of them, as if forming a link between the focus and denser chromatin, stained by TOPRO-3 (Fig. 2B). On the other hand, Tip60 was localized rather in the centre of H2AX foci (not shown). The rapid increase of histone

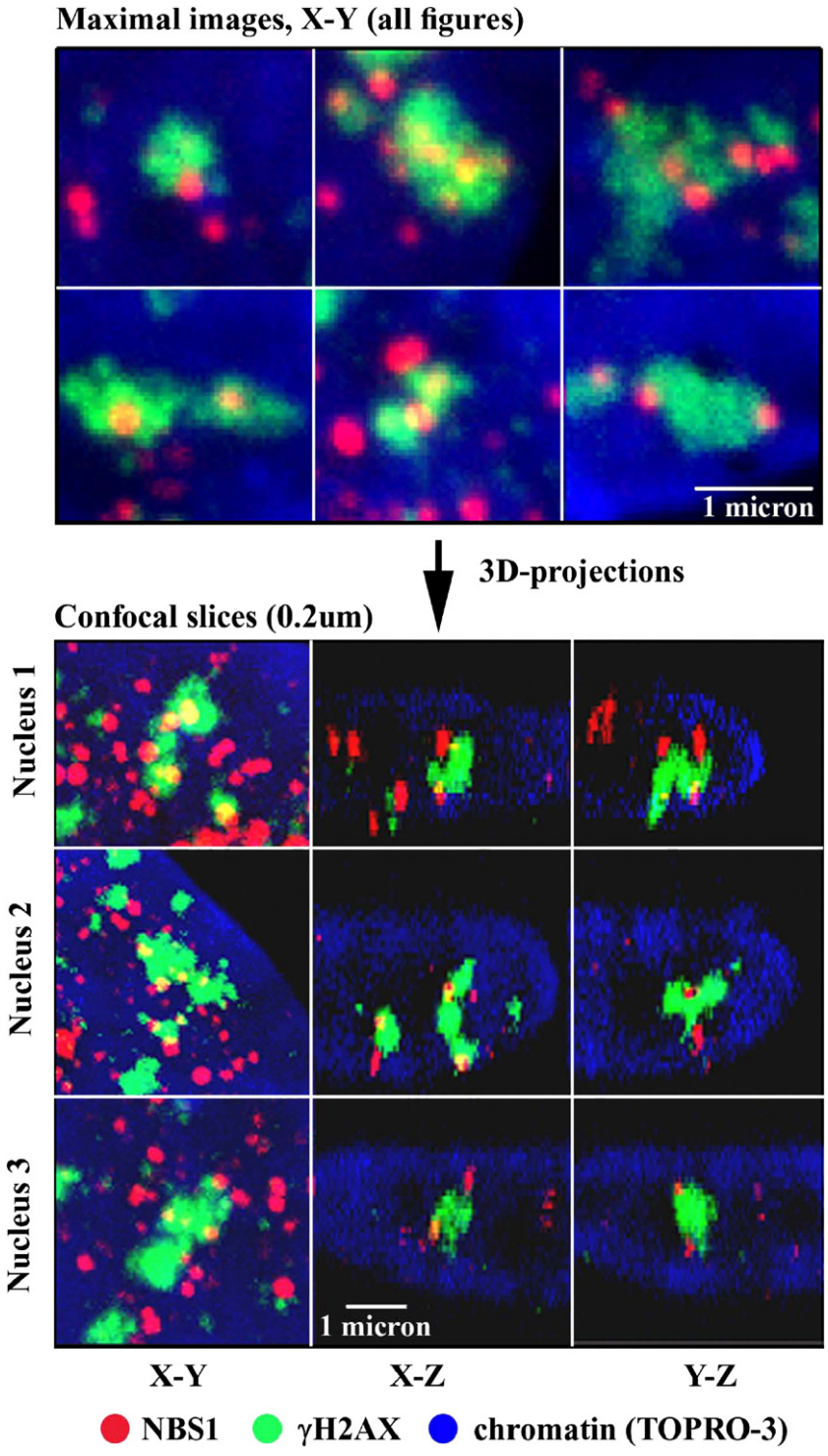

Fig. 5. γH2AX foci clustering in spatially fixed human fibroblasts irradiated with 3 Gy of γ-rays. Top: maximal images (x–y plane, 40 slices) showing clustering of γH2AX foci (green) observed between 30 min and 2 h PI; NBS1 (red), chromatin stained with TOPRO-3 (blue). Bottom: verification of clustering of γH2AX foci in 3D space: optical slices (0.2 μm) through three γH2AX clusters in x–y, y–z and x–z planes.

H4K5 acetylation was accompanied by a corresponding decrease of dimethylH3K9 in γH2AX foci (Fig. 2B–D), and inversely, the decrease of acetylH4K5 was followed by an increase of dimethylH3K9, later PI (Fig. 2B–D). Observed changes in epigenetic modifications of histones H4 and H3 seemed to complement each other and took place in a relatively short interval of time after DSB induction. The number of γH2AX foci containing a signal of dimethylH3K9 progressively increased up to about 76% at 120 min PI, when the number of foci with acetylated H4K5 was about 29% (Fig. 2D). Interestingly, while the increase of histone H4K5 acetylation accompanied by the decrease of histone H3K9 dimethylation were followed by a visible chromatin decondensation, manifested by spreading of chromatin regions with low intensity of H2B-GFP at sites of DSBs (Fig. 3A, B), the decrease of H4K5 acetylation and increase of H3K9 methylation were not followed by detectable changes of chromatin density (Figs. 2D, 3A, B).

3.2. Displacement and fusion of DSBs in living cells

To track the displacement of DSB foci, we observed living cells double-transfected with H2B-GFP and 53BP1-RFP at 5 min intervals during the PI time. Fig. 3 show that signals of 53BP1-RFP (foci 3 and 2 in 3B and 3C respectively), first located in dense chromatin (represented by an intense fluorescence of H2B-GFP), gradually protrudes into chromatin of low density (in about 15–25 min PI), where it persists to 90 min PI. This displacement was accompanied by slight changes of chromatin structure in the proximity of the signal (Fig. 3B, C; bottom rows). Relocation of all 53BP1-RFP foci relative to chromatin density, followed in 2 nuclei at 5-min intervals from 5 to 60 min PI, is evaluated in Table 1. At five minutes PI, there were about 14 and 12 foci in decondensed and dense chromatin, respectively, and 7 in the boundary area of both chromatin domains. The number of foci in decondensed chromatin increased to 16 at the expense of condensed one in 10 min PI. The most marked changes in foci location were observed at 15 min PI, when the number of foci in condensed chromatin decreased to 6; on the other hand, it increased in decondensed and "borderline" chromatin domains. In 60 min PI, the number of foci in condensed chromatin decreased to 2; however, it decreased also in decondensed and borderline chromatin, probably as the result of DSB repair. According to visual inspection, the changes of higher-order chromatin structure observed at DSB sites consisted in protrusion of 53BP1 foci into decondensed chromatin domains rather than in their real longer-distance displacement. In general, the movement of foci was rare; nevertheless, we identified also some foci with a higher mobility. The slight movement of three 53BP1-RFP foci during 15 min (5–20 min PI) can be seen in Fig. 3D.

In order to quantify the DSB mobility exactly and confirm these observations also for other repair proteins, we tracked computationally foci of GFP-tagged NBS1 protein in both transiently transfected control and γ-irradiated MCF7 cells (dose of 3 Gy); larger NBS1 foci appeared only in irradiated cells (Fig. 4A). The mean squared displacement (mean Δd^2) of NBS1-GFP also revealed a decrease in mobility of NBS1-GFP foci after irradiation (0.03 μm^2/min vs. 0.01 μm^2/min) measured 10 and 20 min PI respectively (Fig. 4B), with a greater effect for larger NBS1 foci (0.02 μm^2/min vs. 0.008 μm^2/min) (Fig. 4C). This indicates that larger NBS1 foci become attached to DSB sites and can be therefore used to determine their mobility. Short-term measurements of the movement of NBS1 foci were performed with a very short period of 20–500 ms to eliminate "shivering" of the whole nucleus. The mean Δd^2 calculated from changes of distances between all possible pairs of large NBS1 foci revealed similar mobility of NBS1 (0.025 μm^2/min) and HP1β protein (0.020 μm^2/min), characteristic of proteins bound to "immobile" heterochromatin (Fig. 4D). This value was significantly higher than the total background movement determined with NBS1 in spatially fixed cells (0.005 μm^2/min), but lower than that of PML bodies (0.070 μm^2/min) in living cells, which represent an example of a non-chromatin-bound and therefore more mobile nuclear protein complexes (Fig. 4D). However, tracking of individual NBS1 signals instead of measurement of mean Δd^2 revealed noticeable movement of a small proportion of foci (Fig. 4A, E). The mobility of such a highly-mobile NBS1 focus is quantified in Fig. 4F (about 0.37 μm^2/min in the initial phase of movement).

In some (relatively rare) cases, two or more NBS1 foci (DSBs) fused together and formed larger, more stable clusters, later dissociating into individual foci or persisting in nuclei (Fig. 4A, E interval, 2.5–12 min). To exclude that this observation reflects a tendency of over-expressed protein to form GFP-aggregates, the experiment was performed also with cells expressing very low levels of 53BP1-RFP protein. The number of foci in double transfected (53BP1-RFP+H2B-GFP) living cells corresponded to the number of γH2AX foci immuno-detected in fixed cells irradiated with the same dose (1 Gy) of γ-rays; it indicates that 53BP1-RFP is not highly expressed and that its foci really represent DSBs. Similarly, as in living cells where DSBs were represented by NBS-GFP foci, a rare clustering was also observed among foci of 53BP1-RFP. A fusion of two 53BP1-RFP foci located close to each other is shown in Fig. 3A, C. One of these foci (focus 1, Fig. 3A, C) was located in decondensed and one (focus 2, Fig. 3A, C) in condensed chromatin at the beginning of the observation (5 min PI); during the continuing PI time, the latter one displaced progressively to the other (located in decondensed chromatin) until their fusion at 25–40 min PI.

Consequently, large populations of fixed cells were studied to quantify clustering of DSB foci. Also in the fixed cells, accumulation of γH2AX+NBS1 foci in the restricted space of the chromatin "holes" was observed that occasionally resulted in clustering of two or more foci (Fig. 5). The number of these clusters increased with the PI time (3 clusters was the mean per nucleus 120 min PI) when an increasing percentage of γH2AX foci localized in decondensed chromatin.

To monitor DSB movement and clustering relative to the ongoing repair process, we analysed the dependence on PI time of the interaction of NBS1 and Mre11 proteins (both members of the MRN complex) with DSBs (γH2AX signals), and of the nuclear localization of DSBs in functionally different chromatin domains (condensed and decondensed chromatin) (Fig. 6A, B). In nuclei

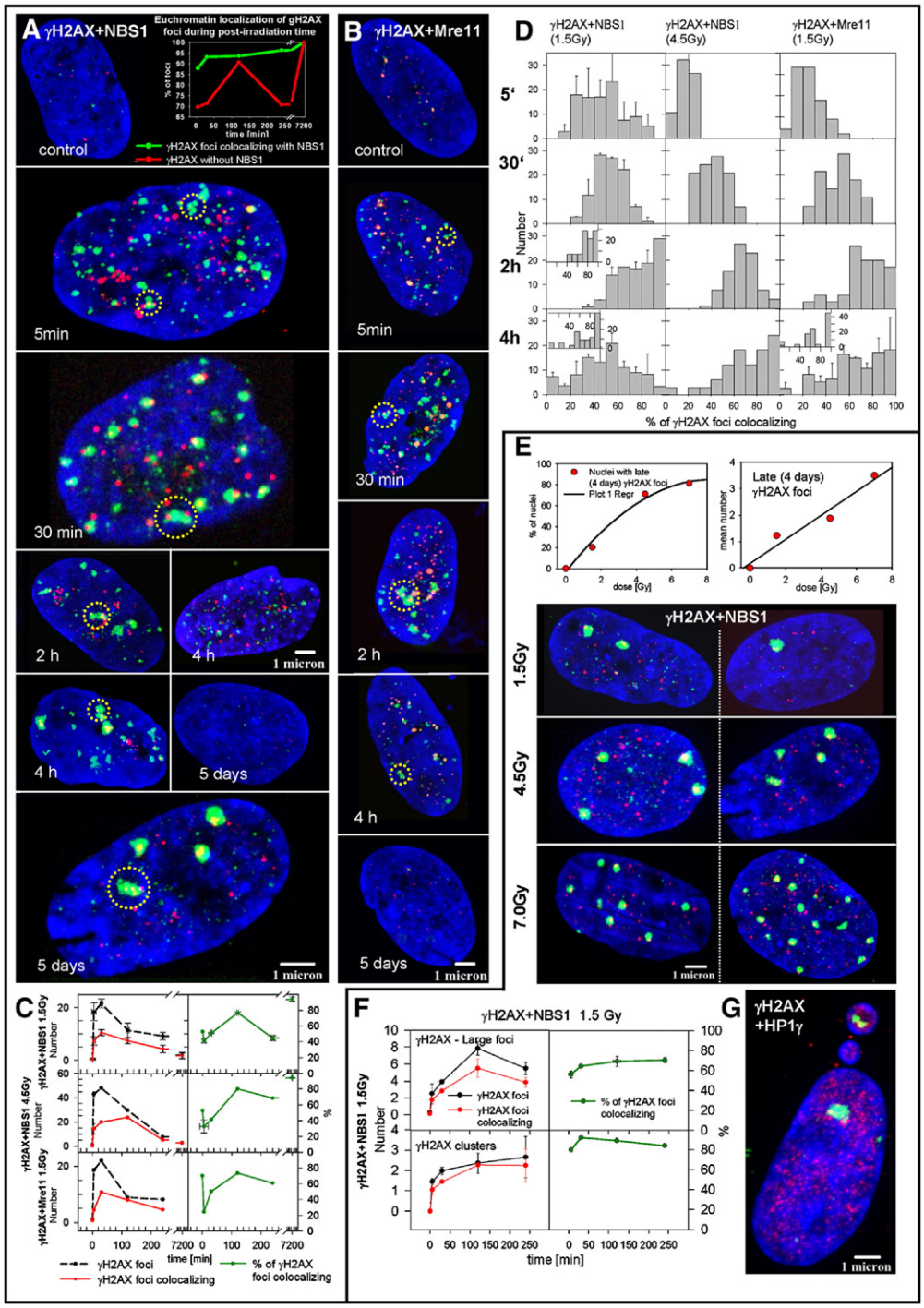

Fig. 6. The development of γH2AX foci, their colocalization with NBS1 and Mre11, and their dependence on time after irradiation. γH2AX foci (green) and their colocalization with MRN-complex components (A) NBS1 (red), and (B) Mre11 (red) during a long PI period (5 min to 5 days). The inset graph in (A) compares the dependence on PI time of the location in sparse chromatin (weak TOPRO-3 staining) of γH2AX foci that do not (red line) or do (green line) colocalize with NBS1 Yellow circles mark clustered γH2AX foci. (C) Time-dependent colocalization of γH2AX foci (clouds) with NBS1 and Mre11 from 5 min to 5 days PI in human fibroblasts irradiated with 1.5 or 4.5 Gy of γ-rays. Left: number of γH2AX foci (black circles, dashed line) observed at a particular PI time, and the number of γH2AX foci colocalizing with NBS1 or Mre11 protein (red circles, continuous line). Right: percentage of γH2AX clusters. Vertical and horizontal error bars represent SD and SE respectively. (D) Distributions of nuclei according to the percentage of γH2AX foci colocalizing with NBS1 or Mre11 proteins at different PI times. Inserted graphs show the same distributions when only large γH2AX foci were scored. (E) Left: percentage of irradiated human fibroblasts containing γH2AX foci 4 days PI plotted against the absorbed γ-ray dose [Gy]. Right: linear relation between the mean number of γH2AX foci persisting in nuclei 4 days PI, and the absorbed dose [Gy] (only nuclei containing γH2AX foci were scored). Maximal images of nuclei containing γH2AX foci (green) 4 days PI for doses of 1.5, 4.5 and 7.0 Gy. The increase in the number of γH2AX foci per nucleus with the absorbed dose, and an almost complete colocalization of γH2AX foci (green) with NBS1 (red), are clearly visible. (F) Lower repair efficiency of large, and especially clustered, γH2AX foci (clouds) compared with the "usual" DSB population (see Fig. 4C for comparison) is demonstrated by their long persistence G: Maximal image of the nucleus of a human fibroblast accompanied by micronuclei, one containing a double-minute (green). The cells were irradiated with 4.5 Gy of γ-rays and fixed 4 days PI.

fixed by paraformaldehyde, γH2AX foci detected 5 min after irradiation did not yet colocalize with NBS1 in all cases; at that time, on average only 41% and 24% of γH2AX foci visually colocalized with NBS1 and Mre11 respectively, even if there were enough of free foci of these proteins, especially at short PI time. (These foci could represent, likely, free proteins not yet coupled with the MRN complexes or the MRN complexes not bound to DSBs; but, in some cases, small dots might represent a background signal). During the PI period, the size and frequency of colocalizing γH2AX foci increased up to 2 h (76% for NBS1 and 73% for Mre11) and the number of free NBS1 and Mre11 foci decreased (Fig. 6A–C). Four hours PI, colocalization of both proteins with γH2AX foci decreased to 44–60% (Fig. 6C) as the proportion of nuclei with repaired DSBs increased (decaying γH2AX foci have low colocalization with NBS1, Fig. 6A); large γH2AX foci, however, still persisted in a subgroup of nuclei, colocalizing with NBS1 and Mre11 (Fig. 6A, D–G).

The percentage of γH2AX foci located in low-density chromatin increased from a few minutes up to 2 h PI, and decreased again at 4 h (Fig. 6A, inset graph), corresponding to the curve of γH2AX colocalization with the MRN-complex (Fig. 6C). The frequency of DSBs associated with large repair complexes (γH2AX+NBS1 foci) was very high (about 90%) at all PI times in low-density chromatin, with a slight tendency to increase gradually (Fig. 6A, inset graph).

Thus, from 30 min to about 2 h PI, almost all foci colocalized with NBS1 and Mre11 proteins, indicating that the repair process is going on (Fig. 6A, B) (NBS1 represents here the MRN complex, which also contains Mre11 and Rad50). These actively repaired DSBs prevailing in the nucleus were almost all located in low-density chromatin, unlike the breaks detected early (2–5 min) after irradiation (Figs. 2A, 3, 6A). Moreover, increasing localization of γH2AX foci in low-density chromatin was associated with a higher probability of clustering; clustered DSB lesions started to appear within minutes after irradiation (Fig. 6A, B yellow circles) and their number increased slightly with PI time (data not shown). Clustering appeared between DSBs protruding into the same chromatin "hole" (lesions A and B at Fig. 7), even when another lesion (lesion C at Fig. 7) closer to one of the clustered breaks was present but separated by condensed chromatin and protruding into another chromatin "hole".

3.3. DSBs persisting for several days after irradiation

Very large and intense γH2AX foci persisted in a fraction of nuclei even 5 days PI; the fraction of nuclei containing such foci was quadratically dependent on the dose absorbed (from 18% with 1.5 Gy to >80% with 7 Gy) (Fig. 6E, left graph). The average number of late foci per nucleus depended linearly on the absorbed γ-ray dose (from 1 with 1.5 Gy to 3.5 with 7 Gy) (Fig. 6E, right graph) and almost all of them colocalized with NBS1 (Fig. 6A, C, nuclei at Fig. 6E). Some of the late foci were clearly clustered lesions, persisting for a long time without being repaired (colocalizing with the MRN-complex). Lower repair efficiency of large and especially clustered γH2AX foci was shown by a significantly slower decrease in their number

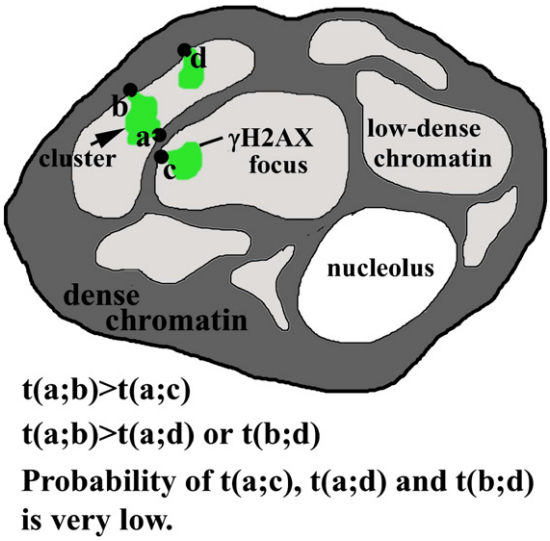

Fig. 7. Schematic drawing of a cell nucleus showing the protrusion of γH2AX (DSB) (green) from the dense chromatin into the low-density chromatin "holes". Accumulation of more DSBs in the same hole results sometimes in their clustering (a and b), especially after higher radiation doses. *t*(*a*;*b*) indicates probability of a translocation (*t*) between fragments of chromosomes corresponding to loci (breaks) *a* and *b*. Sometimes DSBs induced in close proximity (a and c) protrude into different chromatin "holes", which probably lowers the chance of chromatin exchange between them.

with PI time (long time persistence) compared with the rest of the DSB population (Fig. 6F). Sometimes, a micronucleus, sporadically having a γH2AX focus, was observed adjacent to a cell still containing unrepaired foci. It is not clear, however, when these micronuclei arise; whether it is before or after the cell irradiation, and whether or not cell division is required for their formation (Fig. 6G).

4. Discussion

In this work we bring new insights into the crucial question of the mobility of DSBs induced by irradiation of cells with γ-rays. Evidence of DSB mobility is extremely important, especially in connection with recognition of the possible mechanism of formation of exchange aberrations. Despite intensive research, we still do not know enough about the topology of DSBs and chromatin structure at the site of this DNA damage.

It is obvious that all nuclear processes that use DNA as a template require accessibility for specific protein machineries, which could be gained by chromatin relaxation. It is well known that histone acetylases (HAT) are important chromatin modifiers that play a central role in chromatin relaxation [30]. Recent results showed that binding of HAT Tip60 to the chromatin surrounding sites of DSBs was accompanied by chromatin acetylation [23] allowing accumulation of repair proteins and DSB repair by homologous recombination. These processes were prevented if HAT function was inhibited, indicating the necessity of chromatin acetylation for DSB repair. We show that the frequency of HAT colocalization with γH2AX foci increases rapidly immediately after irradiation and decreases after reaching the maximum at 20 min PI (Fig.

2). The increase and decrease of the enzyme colocalization was accompanied by corresponding changes of H4K5 acetylation at γH2AX foci. It can be seen that neither acetylH4K5 nor acetylH4K12 cover the whole foci of phosphorylated H2AX but colocalize only with their parts. We can only speculate about the reason for this phenomenon. Phosphorylation of H2AX in the DSB region may be sufficient to relax chromatin in the close vicinity of a break and that acetylation is needed to open the more distant chromatin. It is also possible that phosphorylation of H2AX hampers acetylation in this region. The increased acetylation of H4K5 in regions of DSB foci was accompanied by the decreased dimethylation of H3K9. These epigenetic modifications of H4 and H3 histones, characteristic for decondensed chromatin, were soon (40 min PI) replaced by histone modifications typical of condensed chromatin (decreased acetylation of H4K5 and increased methylation of H3K9 [31–33]). Relatively rapid changes of epigenetic modifications of both histones in the proximity of DSBs indicate a necessity of chromatin conversion to less condensed state during the repair. The increased H4K5 acetylation accompanied by decreased H3K9 methylation was reflected in decrease of fluorescence intensity of H2B-GFP and TOPRO-3 in regions of DSBs; however, opposite epigenetic modifications characteristic for condensed chromatin were not associated with a visible chromatin re-condensation (Fig. 2B, C, 3A, B). Instead, low intensity of chromatin labelling at sites of γH2AX foci progressively extended with the time after irradiation, up to 60 min PI in living as well as in fixed cells. These observations are difficult to explain for the time being. It is possible, that increased methylation of H3K9 in γH2AX foci could lead only to local chromatin condensation, preventing access of transcription complexes to these regions until termination of DSB repair; alternatively, it could present a signal for later chromatin condensation, after dissociation of repair proteins and/or γH2AX dephosphorylation.

We were able to visualize changes in chromatin compaction around DSBs by the decrease of H2B-GFP and TOPRO-3 fluorescence intensity within the time after irradiation, and show that chromatin structure in the vicinity of DSBs changes very soon after their induction. While at 5 min PI, DSBs were located in both condensed and decondensed chromatin (Table 1, Fig. 2A), 25 min later the majority of DSBs were observed in low-density chromatin, but usually in contact with dense chromatin at one side (Figs. 2B, C and 3B, C). This arrangement gave an impression of DSBs protruding into the chromatin "hole". The space around the DSBs appeared as a hole because of the very faint chromatin staining by H2B-GFP and TOPRO-3 in the region. Use of TOPRO-3 to determine chromatin density provides even more stringent conditions for distinguishing chromatin density than DAPI, since TOPRO-3 stains DNA, and to a lesser extent RNA. Equivalent results to those with TOPRO-3 were obtained when H2B-GFP was used to visualize chromatin (Figs. 2A, 3A, B), indicating that TOPRO-3 could legitimately be used to estimate chromatin density. Decondensation of chromatin in the proximity of DSBs induced with a dose of 10 Gy of γ-rays or with 364-nm UV laser in the presence of Hoechst 33342 (the dose equivalent to about 2.5 Gy of γ-rays) in mouse embryonic stem cells was also observed using a different approach by Kruhlak et al. [14].

What causes changes in chromatin density in the vicinity of DSBs 15 min after irradiation and later? Does it reflect the simple chromatin decondensation or active movement of DSBs from dense to less condensed areas? We tried to get the answer to this question by observing double-transfected living cells (H2B-GFP and 53BP1-RFP) in 5 min intervals during the PI time, starting 5 min PI. It follows from this observation (Fig. 3B) that the density of H2B-GFP progressively decreases in regions of 53BP1-RFP foci (DSBs), and the space of faintly labelled chromatin extends. We followed the density of chromatin labelling at sites of all 53BP1-RFP foci in two living nuclei (Table 1) and found a progressive chromatin decondensation in the vicinity of those originally located in dense chromatin; only 2 from 12 foci remained in condensed chromatin 60 min PI. In the majority of cases, foci of 53BP1-RFP (in living cells) as well as γH2AX (in fixed cells) located in the low-density chromatin were in touch with intensely labelled (condensed) chromatin (Figs. 2B, 3B) and not isolated in faintly labelled chromatin "holes". Thus, it rather indicates local chromatin decondensation than DSB movement to specific nuclear domains. The majority of foci stayed at sites of their origin and does not noticeably move. Only in rare cases, the slight movement was observed that occasionally resulted in clustering of 53BP1-RFP and NBS1-GFP foci occurring in mutual proximity (Figs. 3A, 4A). In the case of NBS1-GFP, we could not exclude that "mobile" NBS1 foci (>2%) might represent NBS1 protein already detached from chromatin instead of highly mobile DSB ends. These results show that there is no significant movement of DSBs in the irradiated cell nucleus, and that their repair proceeds at the sites of their origin, after chromatin decondensation. Our observations indicate that there is a low probability of DSB repair in condensed chromatin, in accordance with results of Ziv et al. [18] that show global chromatin decondensation starting in DSBs early after their induction.

Sometimes, several γH2AX foci appeared in the same "hole" of decondensed chromatin. Two or more of these foci were often in contact, and formed clusters 15 min and later after irradiation. This clustering may develop during decondensation of a chromatin region with two or more DSBs in mutual proximity; alternatively, it might arise from the coalescence of two proximal γH2AX foci during their movement, as it was rarely observed in living cells (Figs. 3A, E, 4). Clusters of γH2AX loci are rare early (5 min) after DSB induction, comprising about 5% of all foci (in average 1 cluster per 20 foci); nevertheless, they can be a risk factor for chromatin exchange during repair. Later after irradiation, the number of clusters increases significantly (in average 2.5 clusters per 8 foci, about 31% in 2 h PI) indicating that DSB clusters are difficult to repair.

The frequency of clusters increased with the absorbed dose, correlating with a higher number and density of DSBs, which in turn leads to an increasing probability of association of adjacent DSBs. An appearance of clustering might also result from non-functional overlapping of γH2AX foci as they enlarge during the PI period. However, some DSBs were already clustered several minutes PI, when γH2AX foci were still very small. Moreover, unlike the temporary clusters described by Kruhlak

et al. [14], at least some of the clusters we observed in living cells were stable and obviously not easily reparable, since they persisted in nuclei for hours or even days PI.

Contradictory results concerning mobility of DSBs (suggesting highly mobile and completely immobile DSBs, respectively) have been published [14,24,25]. There are most probably two reasons for this: (1) observation of changes at different PI times and phases of the cell cycle; (2) use of different kinds of radiation to induce DSBs. Petrini and Stracker [34] postulated that the late DSB foci (observed hours PI) analysed in most studies represent sites of unsuccessful repair rather than normally repaired breaks. Further, high-LET particles [24] and also microlasers [14], frequently used for DSB generation, produce a high density of DNA breaks at the site of energy deposition [35]. Such a high density of breaks (clustered breaks) may lead to chromatin fragmentation, resulting in repair difficulties. Moreover, short DNA fragments may be released, which are more mobile than the chromatin at the site of DSBs. Indeed, high mobility of DSBs and their clustering was described after exposure of cells to α-particles [24]. On the other hand, irradiation with ultra-soft X-rays resulted in immobile lesions [25]. We used γ-radiation to generate isolated DSB-breaks and monitored changes in higher-order chromatin structure from minutes up to several days PI.

As stated above, some γH2AX foci, especially clustered ones but also single foci remained in low-density chromatin even several (3–5) days after irradiation, indicating that these lesions were difficult to repair. It is not clear whether all long-lasting γH2AX foci represent not yet repaired DSBs. We observed a decrease of the number of 53BP1 foci (another marker of DSBs) to about 78% in 30 min PI and 51% in 1 h PI in living cells. In fixed cells, the number of γH2AX foci reached the maximum at 30 min PI, and then decreased to about 50% in 2 h PI. These observations are in agreement with findings of the Tomilin group [36], showing that dephosphorylation of γH2AX foci does not follow immediately after DSB rejoining, and that γH2AX persists at the sites of already repaired break for some time. How γH2AX is removed from chromatin remains unknown.

Late DSBs that persist in nuclei for 24 h and longer do not seem to be only resolved γH2AX foci, inefficiently dephosphorylated after finished repair, but rather not yet repaired lesions. Our opinion is based on the observation that two kinds of persisting γH2AX foci could be distinguished from about 4 h after irradiation. The first type is represented by fuzzy γH2AX foci, with frequency and colocalization with repair proteins progressively decreasing during PI time. These foci are supposed to be already resolved breaks. On the other hand, the foci dominating in nuclei long time PI, are intensively labelled, gradually growing, and almost all of them still colocalize with repair proteins. The evidence for a long-time persistence of DSBs in human cells exposed to very low doses of X-rays presented also Rothkamm and Löbrich [37].

The fraction of cells with the late foci and the average number of foci per nucleus, increased significantly with the absorbed dose of γ-radiation. It is possible that in some cases, cells might divide despite containing late DSBs, and DSBs appeared in parental cells as well as in their progeny. This presupposition is based on the observation that some cells were accompanied by micronuclei, some of which also contained DSBs; some authors suppose that micronuclei appear during cell division [38,39]. Division of cells containing broken DNA cannot be frequent, since it is prevented by the S-phase checkpoint that stops replication. However, there is the evidence that some specialized polymerases can sometimes bypass the broken DNA, and continue DNA replication without completing DSB repair [40]. Nevertheless, the cell cannot tolerate broken DNA for a long time, and is usually forced into apoptosis (our preliminary results).

Acknowledgments

We thank Mario Faretta (The European Institute of Oncology, Milan), Jiri Lukas (The Danish Cancer Research Centre, Copenhagen) and Tom Misteli (NIH, Bethesda, Maryland) for their gifts of plasmids and to Karel Soucek (The Institute of Biophysics ASCR, Brno) for flow-cytometric analysis.

The work was supported by the Grant Agency of the Czech Republic No. 204/06/P349 and IQS500040508, the Grant Agency of the Academy of Sciences of the Czech Republic No. IAA1065203 and the Ministry of Education of the Czech Republic No. ME 1P05OC084.

References

[1] E.P. Rogakou, D.R. Pilch, A.H. Orr, V.S. Ivanova, W.M. Bonner, DNA double strand breaks induce histone H2AX phosphorylation on serine 139, J. Biol. Chem. 273 (1998) 5858–5868.
[2] C.J. Bakkenist, M.B. Kastan, DNA damage activates ATM through intermolecular autophosphorylation and dimmer association, Nature 421 (2003) 499–506.
[3] Y. Shiloh, The ATM-mediated DNA-damage response: taking shape, Trends Biochem. Sci. 31 (2006) 402–410.
[4] C.J. Bakkenist, M.B. Kastan, Initiating cellular stress responses, Cell 118 (2004) 9–17.
[5] A. Celeste, O. Fernandez-Capetillo, M.J. Kruhlak, D.R. Pilch, D.W. Staudt, A. Lee, R.F. Bonner, W.M. Bonner, A. Nussenzweig, Histone H2AX phosphorylation is dispensable for the initial recognition of DNA breaks, Nat. Cell Biol. 5 (2003) 675–679.
[6] C. Lukas, J. Falck, J. Bartkova, J. Bartek, J. Lukas, Distinct spatiotemporal dynamics of mammalian checkpoint regulators induced by DNA damage, Nat. Cell Biol. 5 (2003) 255–260.
[7] O.A. Sedelnikova, D.R. Pilch, C. Redon, W.M. Bonner, Histone H2AX in DNA damage and repair, Cancer Biol. Ther. 2 (2003) 233–235.
[8] S. Bekker-Jensen, C. Lukas, R. Kitagawa, F. Melander, M.B. Kastan, J. Bartek, J. Lukas, Spatial organization of mammalian genome surveillance machinery in response to DNA strand breaks, J. Cell Biol. 173 (2006) 195–206.
[9] I.M. Ward, K. Minn, K.G. Jorda, J. Chen, Accumulation of checkpoint protein 53BP1 at DNA breaks involves its binding to phosphorylated histone H2AX, J. Biol. Chem. 278 (2003) 19579–19582.
[10] C.H. Bassing, W. Swat, F.W. Alt, The mechanism and regulation of chromosomal V(D)J recombination, Cell 109 (2002) S45–S55.
[11] A. Celeste, S. Petersen, P.J. Romanienko, O. Fernandez-Capetillo, H.T. Chen, O.A. Sedelnikova, B. Reina-San-Martin, V. Coppola, E. Meffre, M.J. Difilippantonio, C. Redon, D.R. Pilch, A. Olaru, et al., Genomic instability in mice lacking histone H2AX, Science 296 (2002) 922–927.
[12] O. Fernandez-Capetillo, S.K. Mahadevaiah, A. Celeste, P.J. Romanienko, R.D. Camerini-Otero, W.M. Bonner, K. Manova, P. Burgoyne, A. Nussenzweig,

H2AX is required for chromatin remodelling and inactivation of sex chromosomes in male mouse meiosis, Dev. Cell 4 (2003) 497–508.
[13] C. Lukas, J. Bartek, J. Lukas, Imaging of protein movement induced by chromosomal breakage: tiny 'local' lesions pose great 'global' challenges, Chromosoma 114 (2005) 146–154.
[14] M.J. Kruhlak, A. Celeste, G. Dellaire, O. Fernandez-Capetillo, W.G. Muller, J.G. McNally, D.P. Bazett-Jones, A. Nussenzweig, Changes in chromatin structure and mobility in living cells at sites of DNA double-strand breaks, J. Cell Biol. 172 (2006) 823–834.
[15] J.I. Loizou, R. Murr, M.G. Finkbeiner, C. Sawan, Z.Q. Wang, Z. Herceg, Epigenetic information in chromatin: the code of entry for DNA repair, Cell Cycle 5 (2006) 696–701.
[16] A.M. Gontijo, C.M. Green, G. Almouzni, Repairing DNA damage in chromatin, Biochemie 85 (2003) 1134–1147.
[17] A. Verger, M. Crossley, Chromatin modifiers in transcription and DNA repair, Cell. Mol. Life Sci. 61 (2004) 2154–2162.
[18] Y. Ziv, D. Bielopolski, Y. Galanty, C. Lukas, Y. Taya, D.C. Schultz, J. Lukas, S. Bekker-Jensen, J. Bartek, Y. Shiloh, Chromatin relaxation in response to DNA double-strand breaks is modulated by a novel ATM- and KAP-1 dependent pathway, Nat. Cell Biol. 8 (2006) 870–876.
[19] W.G. Muller, D. Walker, G.L. Hager, J.G. McNally, Large-scale chromatin decondensation resulted by transcription from a natural promoter, J. Cell Biol. 154 (2001) 33–48.
[20] A.C. Nye, R.R. Rajendran, D.L. Stenoien, M.A. Mancini, B.S. Katzenellenbogen, A.S. Belmont, Alteration of large-scale chromatin structure by estrogen receptor, Mol. Cell Biol. 22 (2002) 3437–3449.
[21] A.E. Carpenter, S. Memedula, M.J. Plutz, A.S. Belmont, Common effect of acidic activators on large-scale chromatin structure and transcription, Mol. Cell Biol. 25 (2005) 958–968.
[22] T. Tsukuda, A.B. Fleming, J.A. Nickoloff, M.A. Osley, Chromatin remodelling of a DNA double-strand break site in *Saccharomyces cerevisiae*, Nature 438 (2005) 379–383.
[23] R. Murr, J.I. Loizou, Y.G. Yang, C. Cuenin, H. Li, Z.Q. Wang, Z. Herceg, Histone acetylation by Trrap-Tip60 modulated loading of repair proteins and repair of DNA double-strand breaks, Nat. Cell Biol. 8 (2006) 91–99.
[24] J.A. Aten, J. Stap, P.M. Krawczyk, C.H. van Oven, R.A. Hoebe, J. Essers, R. Kanaar, Dynamics of DNA double-strand breaks revealed by clustering of damaged chromosome domains, Science 303 (2004) 92–95.
[25] B.E. Nelms, R.S. Maser, J.F. MacKay, M.G. Lagally, J.H. Petrini, In situ visualization of DNA double-strand break repair in human fibroblasts, Science 280 (1998) 590–592.
[26] C. Lukas, F. Melander, M. Stucki, J. Falck, S. Bekker-Jensen, M. Goldberg, Y. Lerenthal, S.P. Jackson, J. Bartek, J. Lukas, Mdc1 couples DNA double-strand break recognition by Nbs1 with its H2AX-dependent chromatin retention, EMBO J. 23 (2004) 2674–2683.
[27] M. Kozubek, S. Kozubek, E. Lukasova, A. Mareckova, E. Bartova, M. Skalnikova, A. Jergova, High-resolution cytometry of FISH dots in interphase cell nuclei, Cytometry 36 (1999) 279–293.
[28] M. Kozubek, S. Kozubek, E. Lukasova, E. Bartova, M. Skalnikova, P. Matula, P. Matula, P. Jirsova, A. Cafourkova, I. Koutna, Combined confocal and wide-field high-resolution cytometry of fluorescent in situ hybridization-stained cells, Cytometry 45 (2001) 1–12.
[29] M. Kozubek, P. Matula, P. Matula, S. Kozubek, Automated acquisition and processing of multidimensional image data in confocal in vivo microscopy, Microsc. Res. Tech. 64 (2004) 164–175.
[30] T. Kouzaridez, Histone acetylases and deacetylases in cell proliferation, Curr. Opin. Genet. Dev. 9 (1999) 40–48.
[31] A.J. Bannister, P. Zergman, J.F. Partridge, E.A. Miska, J.O. Thomas, R.C. Allshire, T. Kouzarides, Selective recognition of methylated lysine 9 on histone H3 by the HP1 chromo domain, Nature 410 (2001) 120–124.
[32] W.H. Lachner, D. O'Carroll, S. Rea, K. Mechtler, T. Jenuwein, Methylation of histone H3 Lysine 9 creates a binding site for HP1 proteins, Nature 410 (2001) 116–120.
[33] S. Khorasanizadeh, The nucleosome: from genomic organization to genomic regulation, Cell 116 (2004) 259–272.
[34] J.H. Petrini, T.H. Stracker, The cellular response to DNA double-strand breaks: defining the sensors and mediators, Trends Cell Biol. 13 (2003) 458–462.
[35] R.K. Sachs, A.M. Chen, D.J. Brenner, Proximity effects in the production of chromosome aberrations by ionizing radiation, Int. J. Radiat. Biol. 71 (1997) 1–19.
[36] I.B. Nazarov, A.N. Smirnova, R.I. Krutilina, M.P. Svetlova, L.V. Solovjeva, A.A. Nikiforov, S.L. Oei, I.A. Zalenskaya, P.M. Yau, E.M. Bradbury, N.V. Tomilin, Dephosphorylation of histone gamma-H2AX during repair of DNA double-strand breaks in mammalian cells and its inhibition by calyculin A, Radiat. Res. 160 (2003) 309–317.
[37] K. Rothkamm, M. Löbrich, Evidence for a lack of DNA double-strand break repair in human cells exposed to very low X-ray doses, Proc. Natl. Acad. Sci. U. S. A. 100 (2003) 5057–5062.
[38] N.N. Bhat, B.S. Rao, Dose rate effect on micronuclei induction in cytokinesis blocked human peripheral blood lymphocytes, Radiat. Prot. Dosim. 106 (2003) 45–52.
[39] Vijayalaxmi, K.S. Bisht, W.F. Pickard, M.L. Meltz, J.L. Roti Roti, E.G. Moros, Chromosome damage and micronucleus formation in human blood lymphocytes exposed in vitro to radiofrequency radiation at a cellular telephone frequency (847.74 MHz, CDMA), Radiat. Res. 156 (2001) 430–432.
[40] R.T. Abraham, Cell cycle checkpoint signalling through the ATM and ATR kinases, Genes Dev. 15 (2001) 2177–2196.

Applied Radiation and Isotopes 83 (2014) 177–185

Contents lists available at ScienceDirect

Applied Radiation and Isotopes

journal homepage: www.elsevier.com/locate/apradiso

Heterochromatinization associated with cell differentiation as a model to study DNA double strand break induction and repair in the context of higher-order chromatin structure

Martin Falk [a,*], Emilie Lukášová [a], Lenka Štefančíková [a], Elena Baranová [b], Iva Falková [a,c], Lucie Ježková [a,b,d], Marie Davídková [e], Alena Bačíková [a], Jana Vachelová [e], Anna Michaelidesová [e], Stanislav Kozubek [a]

[a] Institute of Biophysics Brno, Czech Academy of Sciences, Brno 61265, Czech Republic
[b] Joint Institute for Nuclear Research, Dubna, Moscow Region, Russia
[c] Clinic of Internal Medicine—Hematology and Oncology, Faculty Hospital Brno, Czech Republic
[d] Institute of Chemical Technology Prague, Faculty of Food and Biochemical Technology, Prague, Czech Republic
[e] Nuclear Physics Institute, Academy of Sciences of the Czech Republic, Řež, Czech Republic

HIGHLIGHTS

- DSB repair is absent in mature granulocytes with condensed chromatin.
- Repair proteins and γH2AX appear in immature stages but rarely colocalize.
- γH2AX persist long times in these cells and DSB repair is inefficient.
- Even though, γH2AX foci "move" out of the dense chromatin.
- 53BP1 enters HP1β domains only after their decondensation.

ARTICLE INFO

Available online 29 January 2013

Keywords:
DNA double strand break (DSB) repair
Immature and terminally differentiated granulocytes
γH2AX/53BP1 repair foci
Higher-order chromatin structure
Chromatin sensitivity to DSB induction
Heterochromatin

ABSTRACT

Cell differentiation is associated with extensive gene silencing, heterochromatinization and potentially decreasing need for repairing DNA double-strand breaks (DSBs). Differentiation stages of blood cells thus represent an excellent model to study DSB induction, repair and misrepair in the context of changing higher-order chromatin structure. We show that immature granulocytes form γH2AX and 53BP1 foci, contrary to the mature cells; however, these foci colocalize only rarely and DSB repair is inefficient. Moreover, specific chromatin structure of granulocytes probably influences DSB induction.

1. Introduction

About 2×10^4 to one million DNA lesions appear in every cell of the human body each day (Lodish et al., 2004; Mani and Chinnaiyan, 2010), which means about 800 different DNA damages per cell per hour (Vilenchik and Knudson, 2003). Importantly, though the environmental factors like UV-light, ionizing radiation and (radiomimetic) chemicals are potent inducers of DNA lesions, fundamental intracellular processes like DNA replication, transcription, energetic metabolism and recombination (Isbir et al., 2011) also contribute substantially. At least 5000 DNA single-strand breaks (SSB) can be detected in the cell during one division as the consequence of free radicals (ROS) production (reviewed in Podhorecka et al. (2010)). About 1% of these lesions are converted into DNA double strand breaks (DSBs), giving rise to approximately 50 DSBs produced endogenously per cell per one replication cycle (Podhorecka et al., 2010). Thus, there is no escape for the cell to DNA assaults with the DNA double strand breaks (DSBs) representing the most serious threat to the genome integrity (because of cutting the DNA molecule) (West et al., 2002). To face this continuous DNA damage, cells have evolved sophisticated repair pathways (or rather networks). Since individual cell types differ in their level of proliferation, differentiation and genome expression, they show variable radiosensitivity. The higher-order chromatin structure – recently discovered (Boyle et al., 2001; Cremer et al., 2001, 2006; Kozubek et al., 2002;

* Corresponding author. Tel.: +420 541 517165; fax: +420 728 084060.
E-mail addresses: mfalk@seznam.cz, falk@ibp.cz (M. Falk).

0969-8043/$ - see front matter © 2013 Elsevier Ltd. All rights reserved.
http://dx.doi.org/10.1016/j.apradiso.2013.01.029

Tanabe et al., 2002; Goetze et al., 2007 etc.) – changes and is changed by these processes, so it is reasonable to hypothesize that it participates in the determination of the cell sensitivity to DSB induction and influences the repair efficiency of DSB lesions. Hence, the answer, how cells repair DSB damage in the context of the nuclear architecture and higher-order chromatin structure, represents an important goal of current radiobiology.

In past decades, chromatin was thought to be randomly "dispersed" in the cell nucleus, resembling for instance noodles in a soup. Hence, DSB repair has been simply approached as a biochemical process, without placing it into the context of nuclear architecture. The situation has changed dramatically after the discovery of the higher-order chromatin structure (Boyle et al., 2001; Cremer et al., 2001, 2006; Kozubek et al., 2002; Tanabe et al., 2002; Goetze et al., 2007 etc). However, the question how the higher-order chromatin structure influences DSB induction and repair in functionally and structurally distinct chromatin domains remains open due to the complexity of the problematics (Nelms et al., 1998; Nikiforova et al., 2000; Aten et al., 2004; Kruhlak et al., 2006; Loizou et al., 2006; Falk et al., 2007, 2008a, 2008b; Ayoub et al., 2008; Goodarzi et al., 2008; Scherthan et al., 2008; Goodarzi, Jeggo, (2009); Goodarzi, Jeggo, 2009; Falk et al., 2010; Noon et al., 2010; Chiolo et al., 2011; Jakob et al., 2011; Rübe et al., 2011).

In order to place about 2 m of human DNA into the cell nucleus of about 10 μm in the diameter, DNA associates with histones and non-histone proteins to form hierarchically organized chromatin (Perez-Ortin et al., 1988). The maximum level of chromatin compaction is reached in mitotic chromosomes (Vagnarelli, 2012) and enables their transmission to the daughter cells. However, the condensed status of chromatin precludes physiological functions of the genome. Therefore, in the interphase, chromatin decondenses to a variable extent specific to particular genetic loci; this reflects the non-homogeneous distribution of genes and other functional sequences along the DNA molecule. The dynamic "adjustment" of chromatin structure is mediated by interactions of the DNA molecule with chromatin proteins. Variable proteins bind to specific chromosomal loci in different amounts, which is dependent on the DNA sequence, local chromatin structure and further phenomena. In addition, DNA, histones and associated proteins are being posttranslationally modified to regulate the expression of the genetic information. As a result, functionally and structurally distinct chromatin domains form along the DNA and, consequently, in the 3D space of the interphase nucleus.

The heterochromatin (HC) and euchromatin (EU) (Frenster, 1965) are the most general examples of such domains with an "opposite" structure and function: EU represents the domain that is gene rich, intensively transcribed, early-replicating and decondensed. Euchromatin thus impersonates the nuclear subcompartment responsible for exerting the genetic information, especially gene transcription. On the other hand, HC contains only few genes, is transcriptionally silent, late replicating, highly condensed and associated with a large amount of heterochromatin-binding proteins (e.g., HP1, Tamaru, 2010). Although the function of HC in the interphase is less clear than that of EU, it is legitimate to suppose that one of its functions is to stabilize the higher-order chromatin structure (reviewed in Dillon (2004)).

Contrary to the previous opinion, interphase chromosomes occupy only confined space of the cell nucleus with a limited mutual intermingling (Visser et al., 2000; Cremer et al., 2006). These "chromosomal territories" differ in the overall gene density and expression, and consequently in chromatin structure and nuclear distribution (Caron et al., 2001; Cremer et al., 2006). Because of their genetic homogeneity, the structural and functional differences are even more pronounced for specific sub-chromosomal chromatin domains like RIDGEs (regions of increased gene density) and their counterparts antiRIDGEs (Caron et al., 2001; Versteeg et al., 2003). While RIDGEs are composed of large clusters of highly expressed genes, antiRIDGEs represent gene-poor DNA loci of very low expression (Caron et al., 2001; Versteeg et al., 2003); surprisingly, antiRIDGEs do not always correspond with heterochromatin.

Considering local variations in the chromatin "texture" (global higher-order chromatin structure) and specific properties of different types of ionizing radiation and radiomimetics, it might be possible that the sensitivity to DSB induction and efficiency of DSB repair differ for distinct chromatin domains (Falk et al., 2008a, 2008b; reviewed in Falk et al. (2010)). Though gamma photons or irradiating particles can pass through the cell nucleus without regard to the chromatin structure and protein composition, interactions of DNA with the free radicals (ROS) (Kuna, 2006) might be influenced (Falk et al., 2008b, 2010). The higher-order chromatin structure may potentially modify also the exposition of damaged DNA to the repair proteins. Many aspects of DSB repair including the tendency to form chromosomal aberrations might thus relate with the higher-order chromatin structure (Nelms et al., 1998; Nikiforova et al., 2000; Aten et al., 2004; Kruhlak et al., 2006; Loizou et al., 2006; Falk et al., 2007, 2008a, 2008b, 2010; Ayoub et al., 2008; Goodarzi et al., 2008; Scherthan et al., 2008; Goodarzi and Jeggo, 2009; Noon et al., 2010; Chiolo et al., 2011; Jakob et al., 2011; Rübe et al., 2011). The sensitivity of EU and HC to the radiation damage has been studied for a long time, since they represent the oldest chromatin domains discovered. However, despite this fact and the apparent simplicity of the problem, the results are still contradictory and were frequently obtained only by indirect methods, like counting of chromosomal translocations.

Importantly, extensive changes of the higher-order chromatin structure take place during the cell differentiation—the process that is followed by large gene inactivation and chromatin heterochromatinization. Terminally differentiated cells leave the cell cycle and exert specific cell functions. Mature granulocytes, for example, serve to combat against infectious agents. When activated, they "fire" chromatin nets to trap and inactivate the pathogen (Brinkmann et al., 2004). Theoretically, the genome integrity is necessary neither for this function of granulocytes nor their short-term survival. In addition, heterochromatin was shown to pose a barrier to DSB repair (Goodarzi et al., 2009). We can thus hypothesize that DNA repair activity varies in different cell types. Indeed, the absence of DSB repair in terminally differentiated granulocytes was described in our recent work (Lukášová et al., 2013); these cells neither formed DSB repair foci nor expressed essential repair proteins. Other reports suggest that only the active genes undergo repair in immature cell stages (Bill et al., 1992; Nouspikel, 2007; Asaithamby et al., 2011; Rezáčová et al., 2011). Taken together, different differentiation stages of (white blood) cells provide an interesting model to study how the DSB repair activity depends on the cell function, proliferation capacity and chromatin structure. For example, concerning the differentiated cells, is there a difference between short-living granulocytes and e.g., neuronal cell lines with a long lifespan? From the point of view of radiotherapy, it should be studied whether pan-cellular chromatin composition influences complex cellular response to radiation damage and, consequently, whether chromatin structure modifying agents and/or different kinds of radiation may influence this response.

Cancer development is being intensively studied in the context of radiation exposure. Nevertheless, organs and tissues can also be affected by the nonmalignant damage (Jackson and Bartek, 2009; Nijnik et al., 2007; Crowe et al., 2011). Dysfunctions of specific tissues were reported not only after high IR doses (Chen

et al., 2007; Rask et al., 2008; Baleriola et al., 2010; Jeggo, 2010). This might point to a cumulative (non-repaired) damage, e.g., in differentiated and/or aging cells. As an example, slowly-dividing long-living neurons were found to be highly sensitive to DSB induction (reviewed in Jackson and Bartek (2009), Baleriola et al. (2010)). On the other hand, tumor cell lines, like the glioblastoma U87, can be extremely radio-resistant (Naidu et al., 2010). The relationship between the radioresistance, cell differentiation and chromatin structure is not yet fully understood. Contrary to the granulocyte differentiation, the DSB repair activity was shown to be up-regulated during the early adipogenesis, due to an up-regulation of DNA-PK expression (Meulle et al., 2008) Thus, recent reports suggest ambiguous and bidirectional dependence between the DSB repair and differentiation (Sherman et al., 2011). Though heterochromatinization associated with cell differentiation can be suspected of complicating or even precluding DSB repair (as discussed in "Results and Discussion", and in our earlier works, Falk et al., 2007, 2010; Lukasova et al., 2013), the situation with mature granulocytes might be exceptional because of their unique function closely connected with the specific chromatin structure.

In this work, we report on the changing sensitivity to DSB induction and repair activity during the differentiation (and heterochromatinization) of the human granulocytes. The results are discussed in the context of our earlier findings (Falk et al., 2007; Falk et al., 2008a,b) describing the relationship between the higher-order chromatin structure, DSB induction and DSB repair in human skin fibroblasts irradiated with γ-rays. To analyze the mechanism of DSB repair in heterochromatin, we compare the results for the same cells upon the action of γ-rays and protons, where the energy is deposited randomly through the cell nucleus and "concentrated" along the particle path, respectively. In addition, repair of DSBs induced in structurally and functionally distinct chromatin domains by laser micro-irradiation was studied in living cells.

2. Methods

2.1. Separation of mononuclear cells and granulocytes from human peripheral blood

Erythrocytes were eliminated from the peripheral blood of healthy donors by the sedimentation through the Dextran T 500 (Amersham, USA)–Telebrix N 350 solution (density 1.095 g/ml, Leciva, Prague, CR). Separation of the mature granulocytes from mononuclear blood cells (lymphocytes, monocytes, immature granulocytes) was performed as described earlier (Lukásová et al., 2005) by means of Ficoll–Hypaque gradient centrifugation. Immature granulocytes and monocytes were consequently depleted from lymphocytes by taking advantage of their capacity to adhere to plastic/glass surfaces (Wahl et al., 2006). The fraction of immature granulocytes was contaminated with monocytes and approximately 5% of lymphocytes; however, these cells are easily distinguishable on microscopic slides by the morphology of their nuclei: the nuclei of lymphocytes are spherical, while those of monocytes resemble kidneys in shape; immature granulocytes, depending on the level of their maturation, have band or even segmented nucleus and nuclear chromatin also changes from a smooth, "dispersed" pattern to more coarse and clumped distribution. Mature granulocytes have the characteristic multilobular nucleus clearly distinguishable from the nuclei of other cells. Erythrocytes, slightly contaminating granulocytes, are not observable on the microscope slide after nuclei counterstaining with TOPRO-3 because they do not contain chromatin. Owing to the characteristic morphology of the nuclei of the investigated cell types, none of the contaminating nuclei were included in the analysis of any particular cell type.

2.2. Cell culture

Human foreskin fibroblasts and MCF7 cells were cultivated in the DMEM medium supplemented with 10% fetal calf serum (FCS) and standard antibiotics (penicillin, streptomycin) at 37 °C and 5% CO_2 atmosphere.

2.3. Cell transfection

To get transient expression of NBS1-GFP (a gift from J. Lukas), HP1β-GFP (a gift from T. Misteli), H2B-GFP (Clontech) and pm53BP1-RFP (a gift from J. Lukas), the MCF7 cells were transfected with the GFP constructs using Lipofectamine 2000 (Invitrogene) or Fugene HD (Roche) according to the manufacturer's instructions and used for observation of protein (re)localization 12 h after transfection, and at different times after irradiation. DSB repair in heterochromatic and euchromatic regions was studied in cells co-transfected with H2B-GFP and pm53BP1-RFP or NBS1-RFP.

2.4. Cell fixation and immunolabeling

Cells were irradiated (as described in the particular paragraph) and taken for immunolabeling at different times post-irradiation (PI). Dense suspensions in PBS (100 μl) of isolated cells (granulocytes/monocytes) were dropped onto positively charged microscope slides (Superfrost, Thermo Scientific, Germany). After attachment to the slide (about 5 min; human skin fibroblasts were cultured directly on cover slips, see Chapter 2.6), cells were fixed with 4% paraformaldehyde in PBS for 10 min/21 °C, washed 3 × 5 min in PBS, permeabilized in 0.2% Triton X-100/PBS for 15 min (room temperature, RT), washed 3 × 5 min, blocked with 7% inactivated FCS+2% bovine serum albumin in PBS for 30 min at RT and co-immunostained (10 min/RT+4 °C overnight) with two primary antibodies from different hosts: the mouse monoclonal antibody against H2AX phosphorylated at serine 139 (γH2AX, Upstate) together with rabbit polyclonal antibody against NBS1 phosphorylated at serine 343 (Cell Signaling) or 53BP1 (Upstate). γH2AX is generally accepted quantitative marker of DNA double-strand breaks (DSBs) (Rogakou et al., 1998), applicable even for very low doses of ionizing radiation (IR). NBS1 and 53BP1 represent DSB repair proteins of different molecular size and function (both in non-homologous end-joining, NHEJ, and homologous recombination, HR). Secondary antibodies–the FITC-conjugated donkey anti-mouse and Cy3-conjugated donkey anti-rabbit (Jackson Laboratory, West Grove, PA) – were applied for 1 h/RT after their pre-incubation with 5.5% of donkey serum in PBS (30 min at RT). Total nuclear chromatin was counterstained with 1 μM TOPRO-3 (Molecular Probes) in 2x SSC prepared fresh from the stock solution.

2.5. Combined fluorescence in situ hybridization and immunolabeling (ImmunoFISH)

The ImmunoFISH method was used to visualize DNA double strand breaks (γH2AX foci) inside the selected chromosomal territories (CHT), RIDGE domains and antiRIDGE domains (Caron et al., 2001; Versteeg et al., 2003), respectively. The protocol of A pombo (Pombo et al. 1998) was used with the modifications described in Falk et al. (2008a). Directly labelled painting probes (Appligene-Oncor, Illkirch, France) treated before the hybridization according to the manufacturer's instructions were used to visualize whole CHTs. The probes for RIDGE and anti-RIDGE domains (the kind gift of Sandra Goetze, Swammerdam Institute of Live Sciences, University of Amsterdam) were conjugated with digoxigenin and biotin, respectively. The antibody for γH2AX was the same as for simple immunostaining.

2.6. DNA double strand break induction

Gamma irradiation with ^{60}Co was described in our previous works (Falk et al., 2007; Falk et al., 2008a, b).

Proton irradiation enabled us to compare DSB damage induction and repair upon the action of radiation with a different pattern of the energy deposition (as compared with γ-rays): Irradiations were performed with an isochronic cyclotron U—120 M (Nuclear Physics Institute, Řež) that accelerates protons up to about 32 MeV. Confluent cells cultured in cultivation flasks (Nunc, culture area 25 cm^2) were trypsinized and re-seeded onto the Glass Bottom Petri Dishes (MatTek Corporation, 35 mm in diameter, 1 mm thick glass) 20 h before irradiation. Immediately prior to the irradiation, Petri dishes with grooving cells (in a monolayer) were completely filled with preheated DMEM medium (37 °C) to prevent drying during the procedure (irradiation proceeds in vertical position). Cells were irradiated with 1 and 4 Gy (4 Gy/min) of 15 and 30 MeV protons, respectively. The homogeneity of the proton irradiated field (10 × 10 cm) was ± 10% as determined by the gafchromic film. After irradiation, cells were fixed (see the particular paragraph) in different time points ranging from 2 min post-irradiation (PI) to 4 days PI (2, 5, 15, 30, 60, 120 and 240 min PI, and 1, 2, 3 and 4 days PI).

The treatment of cells with H_2O_2 was used to mimic DSB induction by the indirect effect of ionizing radiation. Cells were cultured for 30 min in the culturing medium supplemented with H_2O_2 to the final concentration of 1.5%.

Local micro-induction of DSBs at the subnuclear level was performed with the Leica SP5 microscopy system in order to study DSB repair separately in structurally and functionally distinct chromatin domains. The cells pre-sensitized to DSB induction by the incubation with BrdU (10 μM, 24 h) were consequently irradiated with the 355 nm UV-laser (luminous power at laser output < 500 mW, luminous power in focal plane < 10 mW). Regions of interest (ROIs) selected for irradiation were demarcated by the Leica LAS AF software; also all other operations were driven by LAS AF. The (minimum) energy required to induce DSBs at the extent roughly approximate to 4 Gy of γ-rays (^{60}Co) was used in order to keep conditions of the cell as physiological as possible but induce sufficient damage inside the ROI. The spherical ROIs were demarcated to include either euchromatic (EU) or heterochromatic (HC) subdomains (in latter case visualized ether by H2B-GFP (Clontech) or HP1β-GFP (a gift from T. Misteli)). The rectangular ROIs of different sizes were designed to intersect both EU and HC domains at the same time. The induction of DSBs in ROIs was confirmed by the immunostaining of UV-irradiated cells (transfected with pm53BP1-RFP and RFP/NBS1-RFP, respectively) with γH2AX antibody (mouse monoclonal, FITC-conjugated) after their spatial fixation with 4% paraformaldehyde (as described in the particular paragraph); as expected, the signals of artificially expressed repair proteins colocalized with γH2AX foci.

2.7. Image acquisition and microscopy

An automated Leica DM RXA fluorescence microscope (Leica, Wetzlar, Germany), equipped with an oil immersion Plan Fluotar objective (100 × /NA 1.3), a CSU10a Nipkow disc (Yokogawa, Japan) for confocal imaging, a CoolSnap HQ CCD-camera (Photometrix) or an iXon DV 887ECS-BV camera (Andor, for living cell observation) and an Ar/Kr-laser (Inova 70 C, Coherent, Santa Clara, CA, USA), was used for image acquisition (Kozubek et al., 1999, 2001). Alternatively, the Leica SP5 confocal microscopy system equipped with the white laser for multiple fluorochrome excitation, heated box for living cell observations (with regulated continuous influx of CO_2) and sensitive hybrid detectors (Leica) was used. Automated exposure, image quality control and other procedures were performed using the software FISH 2.0, Aquarium and Leica AS (Kozubek et al., 2001, 2004; Matula et al., 2010). The exposure time and dynamic range of the camera (gain of the detectors) in the red, green and blue channels were adjusted to the same values for all slides to obtain quantitatively comparable images. Twenty to 40 serial optical sections were captured at 0.2–0.5-μm step along the *z*-axis. Living cell observation of double transfected cells (see the particular paragraph) was performed at the constant temperature of 37 °C and 5% concentration of CO_2 in the atmosphere.

3. Results and discussion

3.1. Sensitivity of structurally and functionally distinct chromatin domains to DSB induction

In the context of DSB repair, the strand-break induction is the first step that might partially depend on the higher-order chromatin structure. The complexity and distribution of DSBs may consequently influence repair processes. We have approached this question by analyzing the nuclear distribution of γH2AX foci–the most sensitive DSB markers (Rogakou et al., 1998) – in cells with spatially (3D) preserved chromatin structure and protein distribution (fixed by paraformaldehyde). For γ-rays, the comparison of γH2AX fractions in condensed and decondensed chromatin domains (densely and weakly stained with DNA dyes, respectively) revealed the majority of foci in the latter nuclear subcompartment. Since γH2AX foci were detected in the low-dense chromatin very early (5 min) post-irradiation (PI), we could presuppose that decondensed, transcriptionally active chromatin is more sensitive to radiation damage. The reason is probably the better protection of heterochromatin against the indirect effect of radiation (Falk et al., 2008b; reviewed in Falk et al. (2010)).

Employing the ImmunoFISH method (Pombo et al., 1998), a significantly higher appearance of DSBs (again marked as γH2AX foci) was observed in chromosomal territories (CHTs) of gene dense, actively transcribed chromosomes (Falk et al., 2008b). For instance, chromosomes 4 and 8 are of similar gene density but significantly differ in their molecular size (Caron et al., 2001; Versteeg et al., 2003). The number of γH2AX foci normalized to one megabase of DNA ("DSB density") did not significantly differ for these chromosomes, in accordance with corresponding values of the first parameter. Next, we have analyzed chromosomes 18 and 19 of equivalent molecular size but largely different by their gene density and transcription activity. HSA19 is the most expressed chromosome in the human genome, whereas HSA18 is very gene poor (Caron et al., 2001; Versteeg et al., 2003). In this case, the number of γH2AX foci significantly differed between the chromosomes with a much higher DSB density observed for HSA19. However, because of its low genetic activity and thus highly condensed status, the nuclear volume of HSA18 is smaller than that of HSA19. To eliminate this variable, we have compared chromosome 19 with chromosome 4, where chromosome 4 is again much less expressed but markedly bigger than HSA19 (even when considering its nuclear volume). Importantly, the number of γH2AX foci per territory was very similar for both chromosomes, clearly demonstrating the higher DSB density in the case of HSA19 (see Falk et al. (2008b) for details).

By the same approach, the level of DSB damage was also studied (Falk et al., 2008b) in the regions of increased gene expression (RIDGEs) and their genomic counterparts, antiRIDGEs (Caron et al., 2001; Versteeg et al., 2003). One RIDGE and one antiRIDGE cluster, which were selected to be localized at the same chromosome (HSA11), have the same molecular size (11 Mbp) but differ in their chromatin condensation (about 40% more condensed in antiRIDGE, Goetze et al., 2007). In accordance

with the previous results on chromosomal territories, γH2AX foci significantly predominated in the RIDGE territories. Indeed, the difference between the RIDGE and antiRIDGE domains was even more pronounced than between the chromosomal territories. This observation can be easily explained by the structural and functional homogeneity of the RIDGE/antiRIDGE domains (relative to heterogeneous chromosomal territories) and confirms higher sensitivity of decondensed active chromatin to the harmful effect of reactive free radicals (Fig. 1; the reader is referred to Falk et al. (2008b) and (2010) for the description of experiments explaining the mechanism of this phenomenon).

3.2. DSB repair in condensed (hetero)chromatin

Upon the irradiation with γ-rays, the fraction of γH2AX foci in decondensed chromatin was growing with the time PI and only a low fraction of γH2AX foci colocalized with 53BP1 repair protein in heterochromatin (at the resolving power of confocal microscopy). The same phenomenon was observed with protons (30 MeV, 4 Gy/min), where the condensed (hetero)chromatin may reasonably be expected to contain many DSBs (due to ionizations concentrated along the particle tracks). Nevertheless, independently of the radiation used, γH2AX foci predominated in low-density chromatin already 2 min PI and this fraction increased with time (not shown). This suggests that chromatin must either decondense around DSB lesions or DSBs must migrate into the repair-competent nuclear subdomains in order to complete the repair (Falk et al., 2007, 2008a); reviewed in Falk et al (2010)). Alternatively, the repair of DSBs located in the condensed chromatin (further referred as to "heterochromatic" DSBs for simplicity; hcDSBs) can proceed without formation of γH2AX foci and participation of 53BP1. The latter explanation is not probable since it has been shown recently that γH2AX and 53BP1 are only necessary for the repair of hcDSBs (Goodarzi et al., 2008; Scherthan et al., 2008; Goodarzi and Jeggo, 2009; Goodarzi et al., 2009; Noon et al., 2010 etc.). Moreover, our direct real-time observations made in living cells – discussed in the next chapter – strongly argue for the first hypothesis.

3.3. Accessibility of heterochromatin for repair proteins in living cells

Earlier, we have studied chromatin decondensation at the sites of DSBs (marked as repair foci) and the mobility of DSB lesions in γ-irradiated cells co-transfected with H2B-GFP and 53BP1-RFP proteins. These experiments enabled us to follow movements of DSB lesions in the context of higher-order chromatin structure. Even though the overall mobility of DSB lesions (visualized as repair foci) was equivalent to that of the undamaged chromatin, hcDSBs progressively protruded into the low-density chromatin subdomains (see also Falk et al., 2007, 2008a).

Therefore, we have further addressed the requirement for the chromatin decondensation at the sites of DSBs in cells presentsized with BrdU, where DSBs were introduced separately in condensed and decondensed chromatin domains with the UV-laser. We have analyzed the penetration of NBS1-RFP and 53BP1-RFP repair proteins, respectively, into the condensed chromatin domains labeled either by H2B or HP1β proteins tagged with GFP. Whereas NBS1 is a small (85–95 kDa) repair protein potentially acting as one of the DSB sensors, 53BP1 is a much bigger (~220 kDa) adaptor protein providing an interaction platform for the assembly of other downstream players.

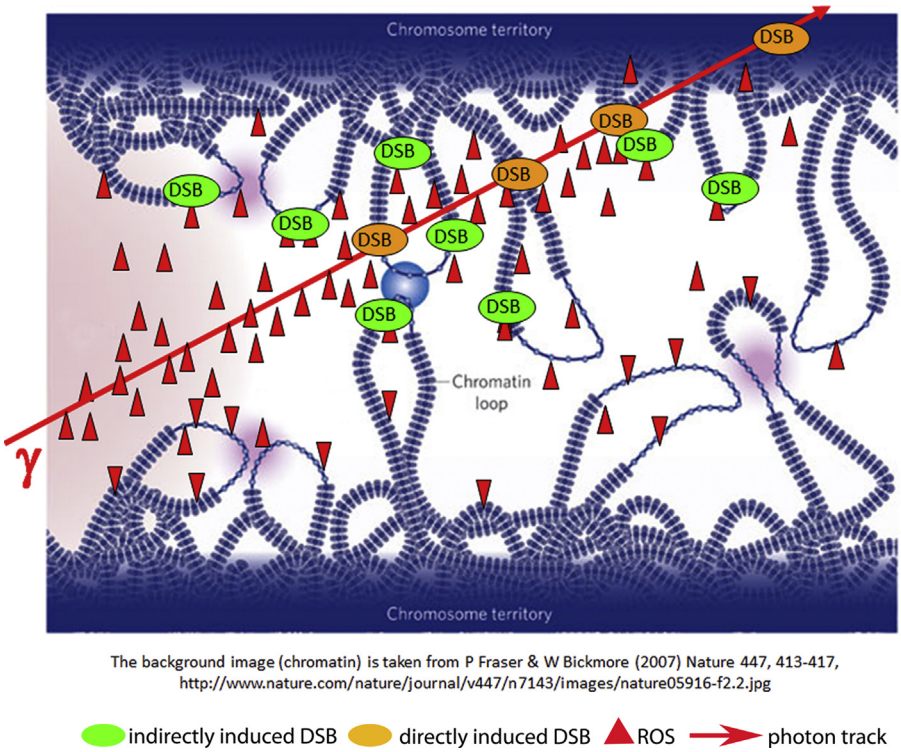

Fig. 1. A possible explanation of the higher sensitivity of the decondensed (eu)chromatin to the DSB induction by low-LET γ-rays. About 20% of DSBs along the photon path (red arrow) are introduced by the direct effect of ionizing radiation (orange ellipses). The vast majority of DSBs is however caused by the indirect effect (green ellipses) mediated by reactive free radicals (red triangles) produced especially by the water radiolysis. More radicals are produced in decondensed chromatin due to its high hydratation. Since the radicals are only shortly living, they damage DNA close to the sites of their induction. In addition, DNA in dense heterochromatin is better shielded against the harmful radicals due to heterochromatin protein composition (a larger amount of proteins, that can scavenge the radicals, binds specifically to heterochromatin). See Falk et al. (2008b) for further details. (For interpretation of the references to color in this figure legend, the reader is referred to the web version of this article.)

Interestingly, our preliminary results indicate that while NBS1 penetrates into all chromatin domains almost immediately without constrictions, 53BP1 invades HP1β domains only partially and slowly, not before the domain decondensation and/or restructuralization accompanied by a release of histones from chromatin (this problematics is just being investigated) (Fig. 2). These preliminary results confirm extensive chromatin decondensation at the sites of DSBs and indicate that some (larger) repair proteins can only bind DSBs in decondensed chromatin. The protrusion of hcDSBs into low-density chromatin domains is a very fast process that takes place from the first minutes post-irradiation (mainly in the time interval of about 2–30 min PI), as evidenced also by immunodetection of the γH2AX/53BP1 repair foci at different time points PI in human skin fibroblasts irradiated with γ-rays or 30 MeV protons and 3D-fixed by paraformaldehyde.

3.4. *Disrupted DSB repair in immature human granulocytes and the mechanism of γH2AX protrusion*

Up to date, no proteins specifically responsible for γH2AX protrusion out of the condensed (hetero)chromatin were identified, despite the described roles of TIP60, KAP1 and HP1 in the maintenance and restriction of heterochromatin (reviewed in Cann and Dellaire (2011)). Hence, to further study the mechanism, we have followed DSB repair in immature human granulocytes. Recently, we have shown (Lukášová et al., 2013) that chromatin undergoes extensive changes in the structure and composition during the granulocyte maturation. The majority of genes are silenced, which is followed by chromatin heterochromatinization and, importantly, the loss of DSB repair capacity. As the consequence, neither DSB repair proteins are expressed nor the repair foci form in terminally differentiated mature granulocytes.

In immature granulocytes, DSB repair pathways remain partially active. This was evidenced by γH2AX foci formation and 53BP1 repair protein expression in these cells (Fig. 3). Nevertheless, as compared with fibroblasts at the same time points PI, γH2AX foci colocalized only very rarely and imprecisely with 53BP1 (Fig. 3(A) and (B)). In addition, the level of colocalization seemed to decrease or stagnate from 30 min PI, which is just the opposite behavior to the fibroblasts, where colocalization reaches almost 100% early PI and then persists so high until the end of the repair (Fig. 3B). Moreover, γH2AX foci were small and 53BP1 usually only appeared as tiny protein aggregates. Together with the preliminary observation that most of DSBs remain unrepaired at least during the first hour post-irradiation (PI) (Fig. 3C), these results suggest that the chromatin structure regulates the silencing of repair proteins and prevents foci formation.

Interestingly, in spite of interrupted repair processes and a large proportion of heterochromatin (relative to euchromatin) in immature granulocytes, γH2AX foci were largely localized to the low-density chromatin domains (Fig. 3A). γH2AX foci colocalized with 53BP1 only rarely (Fig. 3A) and almost never in heterochromatin. This is in agreement with our results obtained in living MCF7 cells (Fig. 2) and suggests that some repair proteins probably could not accumulate into a detectable extent at the sites of hcDSB. This probably prevents DSB repair in granulocytes. Concerning the mechanism of γH2AX foci protrusion, it is possible that some proteins upstream of 53BP1 regulate this process, or it simply follows the physical forces without the requirements for indispensable enzymatic activity (Jakob et al., 2011). For instance, the interruption of DNA chains might relax the higher-order structure of a heterochromatic domain. As suggested by Jakob et al. (2011), such a situation could create significant alterations in the balance of physical forces inside the affected domain, which is consequently manifested in protrusion of hcDSBs to its surface. Since chromatin decondensation appears only locally, it is possible that boundary elements (Labrador and Corces, 2002) prevent its spreading out of the damaged domain. The reader is referred to the works of Jakob et al. (2011) and Bleicher et al. (2012) for a more detailed discussion on this topic. In the next steps, 53BP1 may modify chromatin structure in DSB surroundings or help to "dismantle" damaged heterochromatic domains from outside. This explanation could be in accordance with relatively rapid protrusion of hcDSBs into the low-density chromatin and, at the same time, slow repair of these lesions. Our results indicate that the protrusion mostly appears in the time period of about 2 to 30 min PI whereas the interior of HP1β domains could not colocalize with 53BP1 even hours PI. Lorat et al. (2012) suggested that the essential function of 53BP1 is to promote the retention of activated ATM at hcDSBs, concentrate there the phosphorylated KAP-1, and thereby modulate chromatin structures encompassing the DSB site (also discussed in Goodarzi et al. (2009)). The contribution of 53BP1 to the early phase of chromatin decondensation is therefore questionable and additional experiments are required to shed more light on this phenomenon.

DSB induction by γ-rays was markedly lower in monocytes/immature granulocytes as compared with skin fibroblasts (not shown). This could be expected if heterochromatin was less sensitive to an indirect effect of γ-rays as it has been discussed earlier. Even though it is practically difficult to correlate the decrease in DSB induction with the increasing level of chromatin heterochromatinization, the difference between the cell types was evident. About 13% of DSBs were located in heterochromatin in fibroblasts after γ-irradiation; this fraction was lower in H_2O_2-treated fibroblasts but much higher in the mono/granulocytes

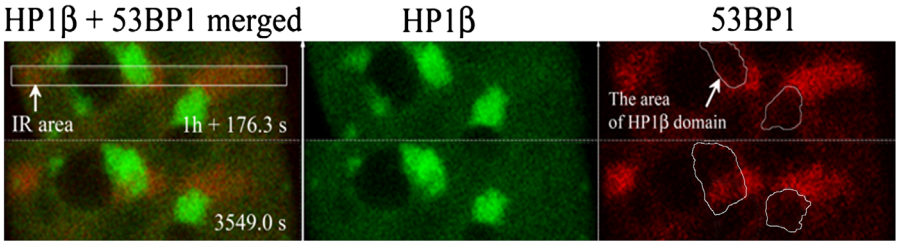

Fig. 2. Accessibility of HC and EU for 53BP1 at different time points PI. The top line images show the distribution of 53BP1 (red) in the irradiated area relative to HC (HP1β, intensively green) and EU (faintly green background), in 1 h PI (1 h+176.3 s). The bottom line corresponds with the situation about 1 h later (1 h+3549 s). A confocal slice (0.3 μm thick) in the *x*–*y* plane intersecting the irradiated domains is displayed for MCF7 cells co-transfected with 53BP1-RFP (red) and HP1β–GFP (green). DSBs were introduced in selected subcompartments (ROI, white rectangle) of the cell nucleus (top left image, IR area) by the UV laser micro-irradiation (see Section 2). ROIs were designed to intersect heterochromatic (HC) and euchromatic (EU) domains at the same time. At 1 h PI (top line), intensive accumulation of 53BP1 can be seen in the irradiated (DSB-containing) EU while penetration into the irradiated HC (HP1β) domain is not detectable. The colocalization of HP1β and 53BP1 remains incomplete until the end of the observation, indicating only slow and limited penetration of 53BP1 into the condensed heterochromatin. (For interpretation of the references to color in this figure legend, the reader is referred to the web version of this article.)

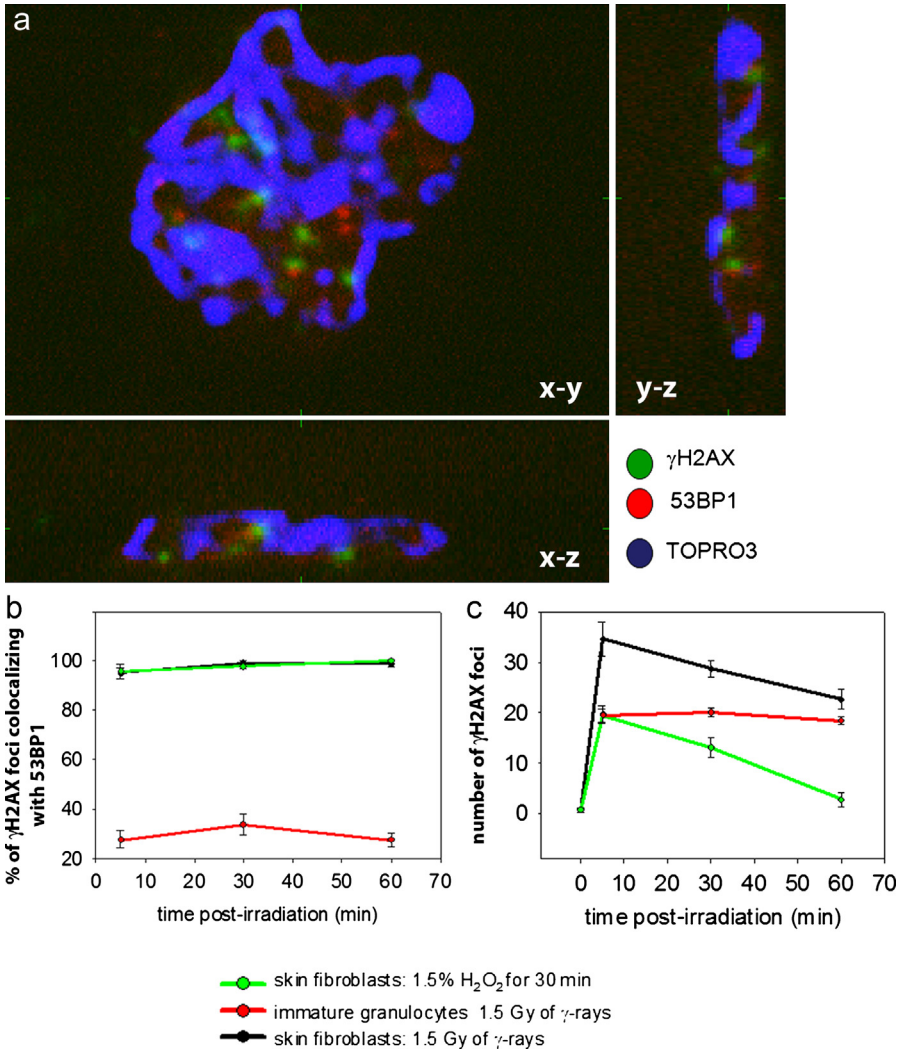

Fig. 3. Disrupted DSB repair in immature human granulocytes. Contrary to the mature cells, γH2AX foci (green) still form in immature stages but they colocalize with 53BP1 repair protein (red) only rarely (A) and (B). Together with the long persistence of γH2AX foci in nuclei after irradiation (C), this indicates that DSBs are repaired only inefficiently in incompletely differentiated granulocytes. Despite that, γH2AX foci extensively protrude from the condensed chromatin (intensively blue) into the nuclear subcompartments with only a low density of chromatin (dark spaces). A: A confocal slice 0.3 μM thick is displayed in all three planes; chromatin counterstaining with TOPRO-3 (artificially blue), condensed (hetero)chromatin corresponds to intensively blue domains. (For interpretation of the references to color in this figure legend, the reader is referred to the web version of this article.)

irradiated with γ-rays (40–50%, preliminary results). The observation in fibroblasts nicely agrees with the data generally published for the γ-rays (about 15–20% of DSBs in Hc) and the lower number of heterochromatic DSBs detected in H_2O_2-treated cells then corresponds with the mechanism of H_2O_2-induced DSB damage. On the other hand, much higher fraction of heterochromatic DSBs revealed upon γ-irradiation in the mono/granulocytes probably reflects almost "complete" heterochromatinization of these cells, which also explains why the total number of DSBs induced is lower than that in fibroblasts (due to the higher protection of HC against free radicals discussed earlier).

4. Conclusions

As time passes from the discovery of the higher-order chromatin structure and nuclear architecture, more and more functions in fundamental cellular processes are being attributed to these phenomena. Together with other research groups we have clearly demonstrated that DNA repair is not the exception. It was shown in this contribution that the higher-order chromatin structure (in a broad sense) influences the sensitivity of chromatin domains to DSB induction and repair of DSB lesions. DSB repair is being switched off during the granulocyte differentiation. It is in accordance both with their short life and specific physiological function carried out by chromatin (Lukášová et al., 2013). Since also less γH2AX foci per dose per nucleus appear in immature granulocytes as compared with some other cell types, it seems that the higher-order chromatin structure substantially contributes to the cell function, radiosensitivity and also DSB repair silencing. Potential implications of these findings for radiotherapy are however uncertain since the relationship between the activity of DSB repair and cell differentiation seem to vary in different cell types. We have showed earlier that the gene-dense and transcriptionally active chromatin is more sensitive to the indirect effect of radiation because of better protection of heterochromatin against ROS (by the heterochromatin-binding proteins). Here, we provide additional evidence that DSB repair is complicated in heterochromatin, so DSBs must protrude into the low-dense chromatin subcompartments in order to be repaired. This process appears already in minutes post-irradiation (mostly in the interval of about 2–30 min PI in our conditions) and, at least in its

initiation phase, probably proceeds without the participation of proteins downstream of 53BP1. In addition, the re-localization of DSBs takes place also in cells (immature granulocytes) with inefficient DSB repair, where 53BP1 do not colocalize with γH2AX foci (even in the decondensed chromatin). Therefore, either the proteins upstream of 53BP1 participate in DSB protrusion or it simply follows the physical forces (as discussed in the previous chapter).

Acknowledgements

The work was supported by the COST LD12039 project of The Czech Ministry of Education, Youth and Sports.

References

Asaithamby, A., Hu, B., Delgado, O., Ding, L.H., Story, M.D., Minna, J.D., Shay, J.W., Chen, D.J., 2011. Irreparable complex DNA double-strand breaks induce chromosome breakage in organotypic three-dimensional human lung epithelial cell culture. Nucleic Acids Res. 39 (13), 5474–5488.

Aten, J.A., Stap, J., Krawczyk, P.M., van Oven, C.H., Hoebe, R.A., Essers, J., Kanaar, R., 2004. Dynamics of DNA double-strand breaks revealed by clustering of damaged chromosome domains. Science 303 (5654), 92–95.

Ayoub, N., Jeyasekharan, A.D., Bernal, J.A., Venkitaraman, A.R., 2008. HP1-beta mobilization promotes chromatin changes that initiate the DNA damage response. Nature 453 (7195), 682–686.

Baleriola, J., Suárez, T., de la Rosa, E.J., 2010. DNA-PK promotes the survival of young neurons in the embryonic mouse retina. Cell Death Differ. 17 (11), 1697–1706.

Bill, C.A., Grochan, B.M., Vrdoljak, E., Mendoza, E.A., Tofilon, P.J., 1992. Decreased repair of radiation-induced DNA double-strand breaks with cellular differentiation. Radiat. Res. 132 (2), 254–258.

Bleicher, M., Burigo, L., Durante, M., Herrlitz, M., Krämer, M., Mishustin, I., Müller, I., Natale, F., Pshenichnov, I., Schramm, S., Taucher-Scholz, G., Wälzlein, C., 2012. Nanolesions induced by heavy ions in human tissues: experimental and theoretical studies. Beilstein J. Nanotechnol. 3, 556–563.

Boyle, S., Gilchrist, S., Bridger, J.M., Mahy, U.L., Ellis, J.A., Bickmore, W.A., 2001. The spatial organization of human chromosomes within the nuclei of normal and emerinmutant cells. Hum. Mol. Genet. 10, 211–219.

Brinkmann, V., Reichard, U., Goosmann, C., Fauler, B., Uhlemann, Y., Weiss, D.S., Weinrauch, Y., Zychlinsky, A., 2004. Neutrophil extracellular traps kill bacteria. Science 303 (5663), 1532–1535.

Cann, K.L., Dellaire, G., 2011. Heterochromatin and the DNA damage response: the need to relax. Biochem. Cell Biol. 89 (1), 45–60.

Caron, H., van Schaik, B., van der Mee, M., Baas, F., Riggins, G., van Sluis, P., Hermus, M.C., van Asperen, R., Boon, K., Voûte, P.A., Heisterkamp, S., van Kampen, A., Versteeg, R., 2001. The human transcriptome map: clustering of highly expressed genes in chromosomal domains. Science 291 (5507), 1289–1292.

Chen, J.H., Hales, C.N., Ozanne, S.E., 2007. DNA damage, cellular senescence and organismal ageing: causal or correlative? Nucleic Acids Res. 35 (22), 7417–7428.

Chiolo, I., Minoda, A., Colmenares, S.U., Polyzos, A., Costes, S.V., Karpen, G.H., 2011. Double-strand breaks in heterochromatin move outside of a dynamic HP1a domain to complete recombinational repair. Cell 144 (5), 732–744.

Cremer, M., von Haase, J., Volm, T., Brero, A., Kreth, G., Walter, J., Fisher, C., Solovei, I., Cremer, C., Cremer, T., 2001. Non-random radial higher-order chromatin arrangements in nuclei of diploid human cells. Chromosome Res. 9, 541–567.

Cremer, T., Cremer, M., Dietzel, S., Müller, S., Solovei, I., Fakan, S., 2006. Chromosome territories—a functional nuclear landscape. Curr. Opin. Cell Biol. 18 (3), 307–316.

Crowe, S.L., Tsukerman, S., Gale, K., Jorgensen, TJ., Kondratyev, A.D., 2011. Phosphorylation of histone H2A.X as an early marker of neuronal endangerment following seizures in the adult rat brain. J. Neurosci. 31 (21), 7648–7656.

Dillon, N., 2004. Heterochromatin structure and function. Biol. Cell 96 (8), 631–637.

Falk, M., Lukasova, E., Gabrielova, B., Ondrej, V., Kozubek, S., 2007. Chromatin dynamics during DSB repair. Biochim. Biophys. Acta 1773 (10), 1534–1545.

Falk, M., Lukasova, E., Gabrielova, B., Ondrej, V., Kozubek, S., 2008a. Local changes of higher-order chromatin structure during DSB-repair. J. Phys. Conf. Ser. 101, 012018.

Falk, M., Lukasova, E., Kozubek, S., 2008b. Chromatin structure influences the sensitivity of DNA to gamma-radiation. Biochim. Biophys. Acta 1783 (12), 2398–2414.

Falk, M., Lukasova, E., Kozubek, S., 2010. Higher-order chromatin structure in DSB induction, repair and misrepair. Mutat. Res. 704 (1–3), 88–100.

Frenster, J.H., 1965. Ultrastructural continuity between active and repressed chromatin. Nature 205, 1341–1342.

Goetze, S., Mateos-Langerak, J., Gierman, H.J., de Leeuw, W., Giromus, O., Indemans, M.H., Koster, J., Ondrej, V., Versteeg, R., van Driel, R., 2007. The three-dimensional structure of human interphase chromosomes is related to the transcriptome map. Mol. Cell. Biol. 27 (12), 4475–4487.

Goodarzi, A.A., Jeggo, P.A., 2009. A mover and a shaker: 53BP1 allows DNA doublestrand breaks a chance to dance and unite. F1000 Biol. Rep. 1, 21.

Goodarzi, A.A., Noon, A.T., Deckbar, D., Ziv, Y., Shiloh, Y., Löbrich, M., Jeggo, P.A., 2008. ATM signaling facilitates repair of DNA double-strand breaks associated with heterochromatin. Mol. Cell 31 (2), 167–177.

Goodarzi, A.A., Noon, A.T., Jeggo, P.A., 2009. The impact of heterochromatin on DSB repair. Biochem. Soc. Trans. 37 (Pt 3), 569–576.

Isbir, T., Demircan, B., Kirac, D., Dalan, B., Gormus, U., 2011. DNA Repair, Cancer and Cancer Therapy—The Current State of Art, DNA Repair and Human Health. In: Dr. Sonya Vengrova (Ed.), InTech, ISBN:978-953-307-612-6.

Jackson, S.P., Bartek, J., 2009. The DNA-damage response in human biology and disease. Nature 461 (7267), 1071–1078.

Jakob, B., Splinter, J., Conrad, S., Voss, K.O., Zink, D., Durante, M., Löbrich, M., Taucher-Scholz, G., 2011. DNA double-strand breaks in heterochromatin elicit fast repair protein recruitment, histone H2AX phosphorylation and relocation to euchromatin. Nucleic Acids Res. 39 (15), 6489–6499.

Jeggo, P., 2010. The role of the DNA damage response mechanisms after low-dose radiation exposure and a consideration of potentially sensitive individuals. Radiat. Res. 174 (6), 825–832.

Kozubek, M., Kozubek, S., Lukásová, E., Bártová, E., Skalníková, M., Matula, P., Matula, P., Jirsová, P., Cafourková, A., Koutná, I., 2001. Combined confocal and wide-field high-resolution cytometry of fluorescent in situ hybridization-stained cells. Cytometry 45 (1), 1–12.

Kozubek, M., Kozubek, S., Lukásová, E., Marecková, A., Bártová, E., Skalníková, M., Jergová, A., 1999. High-resolution cytometry of FISH dots in interphase cell nuclei. Cytometry 36 (4), 279–293.

Kozubek, M., Matula, P., Matula, P., Kozubek, S., 2004. Automated acquisition and processing of multidimensional image data in confocal in vivo microscopy. Microsc. Res. Tech. 64 (2), 164–175.

Kozubek, S., Lukásová, E., Jirsová, P., Koutná, I., Kozubek, M., Ganová, A., Bártová, E., Falk, M., Paseková, R., 2002. 3D structure of the human genome: order in randomness. Chromosoma 111 (5), 321–331.

Kruhlak, M.J., Celeste, A., Dellaire, G., Fernandez-Capetillo, O., Müller, W.G., McNally, J.G., Bazett-Jones, D.P., Nussenzweig, A., 2006. Changes in chromatin structure and mobility in living cells at sites of DNA double-strand breaks. J. Cell Biol. 172 (6), 823–834.

Kuna, P., 2006. Chemical radioprotective substances: the past, the present and the future. Biomedicína 8, 112–122.

Labrador, M., Corces, V.G., 2002. Setting the boundaries of chromatin domains and nuclear organization. Cell 111 (2), 151–154.

Lodish, H., Berk, A., Matsudaira, P., Kaiser, C.A., Krieger, M., Scott, M.P., Zipursky, S.L., Darnell, J., 2004. Molecular Biology of the Cell, fifth ed. WH Freeman, New York.

Loizou, J.I., Murr, R., Finkbeiner, M.G., Sawan, C., Wang, Z.Q., Herceg, Z., 2006. Epigenetic information in chromatin: the code of entry for DNA repair. Cell Cycle 5 (7), 696–701.

Lorat, Y., Schanz, S., Schuler, N., Wennemuth, G., Rübe, C., Rübe, C.E., 2012. Beyond repair foci: DNA double-strand break repair in euchromatic and heterochromatic compartments analyzed by transmission electron microscopy. PLoS One 7 (5), e38165.

Lukásová, E., Koristek, Z., Falk, M., Kozubek, S., Grigoryev, S., Kozubek, M., Ondrej, V., Kroupová, I., 2005. Methylation of histones in myeloid leukemias as a potential marker of granulocyte abnormalities. J. Leukocyte Biol. 77 (1), 100–111.

Lukášová, E., Kořistek, Z., Klabusay, M., Ondřej, V., Grigoryev, S., Bačíková, A., Řezáčová, M., Falk, M., Vávrová, J., Kohútová, V., Kozubek, S., 2013. Granulocyte maturation determines ability to release chromatin NETs and loss of DNA damage response; these properties are absent in immature AML granulocytes. BBA Mol. Cell Res. 1833, 767–779.

Mani, R.S., Chinnaiyan, A.M., 2010. Triggers for genomic rearrangements: insights into genomic, cellular and environmental influences. Nat. Rev. Genet. 11 (12), 819–829.

Matula, Pa., Danek, O., Maska, M., Vinkler, M., Kozubek, M., 2010. Acquiarium: free software for image acquisition and image analysis in cytometry. Mikroskopie, 2010.

Meulle, A., Salles, B., Daviaud, D., Valet, P., Muller, C., 2008. Positive regulation of DNA double strand break repair activity during differentiation of long life span cells: the example of adipogenesis. PLoS One 3 (10), e3345.

Naidu, M.D., Mason, J.M., Pica, R.V., Fung, H., Peña, L.A., 2010. Radiation resistance in glioma cells determined by DNA damage repair activity of Ape1/Ref-1. J. Radiat. Res. 51 (4), 393–404.

Nelms, B.E., Maser, R.S., MacKay, J.F., Lagally, M.G., Petrini, J.H., 1998. In situ visualization of DNA double-strand break repair in human fibroblasts. Science 280 (5363), 590–592.

Nijnik, A., Woodbine, L., Marchetti, C., Dawson, S., Lambe, T., Liu, C., Rodrigues, N.P., Crockford, T.L., Cabuy, E., Vindigni, A., Enver, T., Bell, J.I., Slijepcevic, P., Goodnow, C.C., Jeggo, P.A., Cornall, R.J., 2007. DNA repair is limiting for haematopoietic stem cells during ageing. Nature 447 (7145), 686–690.

Nikiforova, M.N., Stringer, J.R., Blough, R., Medvedovic, M., Fagin, J.A., Nikiforov, Y.E., 2000. Proximity of chromosomal loci that participate in radiation-induced rearrangements in human cells. Science 290 (5489), 138–141.

Noon, A.T., Shibata, A., Rief, N., Löbrich, M., Stewart, G.S., Jeggo, P.A., Goodarzi, A.A., 2010. 53BP1-dependent robust localized KAP-1 phosphorylation is essential for heterochromatic DNA double-strand break repair. Nat. Cell Biol. 12 (2), 177–184.

Nouspikel, T., 2007. DNA repair in differentiated cells: some new answers to old questions. Neuroscience 145 (4), 1213–1221.

Perez-Ortin, J., Matallana, E., Tordera, V., 1988. Analysis of chromatin structure and composition. Biochem. Educ. 16, 45–47.
Podhorecka, M., Skladanowski, A., Bozko, P., 2010. H2AX phosphorylation: its role in DNA damage response and cancer therapy. J. Nucleic Acids 3, 2010.
Pombo, A., Cuello, P., Schul, W., Yoon, J.B., Roeder, R.G., Cook, P.R., Murphy, S., 1998. Regional and temporal specialization in the nucleus: a transcriptionally-active nuclear domain rich in PTF, Oct1 and PIKA antigens associated with specific chromosomes early in the cell cycle. EMBO J. 17, 1768–1778.
Rask, J., Vercoutere, W., Navarro, B.J., Krause, A., 2008. National Aeronautic and Space Administration. Space faring. The radiation challenge. An Interdisciplinary Guide on Radiation and Human Space Flight.
Rezáčová, M., Rudolfová, G., Tichý, A., Bačíková, A., Mutná, D., Havelek, R., Vávrová, J., Odrážka, K., Lukášová, E., Kozubek, S., 2011. Accumulation of DNA damage and cell death after fractionated irradiation. Radiat. Res. 175 (6), 708–718.
Rogakou, E.P., Pilch, D.R., Orr, A.H., Ivanova, V.S., Bonner, W.M., 1998. DNA double-stranded breaks induce histone H2AX phosphorylation on serine 139. J. Biol. Chem. 273 (10), 5858–5868.
Rübe, C.E., Lorat, Y., Schuler, N., Schanz, S., Wennemuth, G., Rübe, C., 2011. DNA repair in the context of chromatin: new molecular insights by the nanoscale detection of DNA repair complexes using transmission electron microscopy. DNA Repair (Amst.) 10 (4), 427–437.
Sherman, M.H., Bassing, C.H., Teitell, M.A., 2011. Regulation of cell differentiation by the DNA damage response. Trends Cell Biol. 21 (5), 312–319.
Scherthan, H., Hieber, L., Braselmann, H., Meineke, V., Zitzelsberger, H., 2008. Accumulation of DSBs in gamma-H2AX domains fuel chromosomal aberrations. Biochem. Biophys. Res. Commun. 371 (4), 694–697.
Tamaru, H., 2010. Confining euchromatin/heterochromatin territory: jumonji crosses the line. Genes Dev. 24 (14), 1465–1478.
Tanabe, H., Habermann, F.A., Solovei, I., Cremer, M., Cremer, T., 2002. Non-random radial arrangements of interphase chromosome territories: evolutionary considerations and functional implications. Mutat. Res. 504 (1-2), 37–45.
Vagnarelli, P., 2012. Mitotic chromosome condensation in vertebrates. Exp. Cell. Res. 318 (12), 1435–1441.
Versteeg, R., van Schaik, B.D., van Batenburg, M.F., Roos, M., Monajemi, R., Caron, H., Bussemaker, H.J., van Kampen, A.H., 2003. The human transcriptome map reveals extremes in gene density, intron length, GC content, and repeat pattern for domains of highly and weakly expressed genes. Genome Res. 13 (9), 1998–2004.
Vilenchik, M.M., Knudson, A.G., 2003. Endogenous DNA double-strand breaks: production, fidelity of repair, and induction of cancer. Proc. Nat. Acad. Sci. USA. 100 (22), 12871–12876.
Visser, A.E., Jaunin, F., Fakan, S., Aten, J.A., 2000. High resolution analysis of interphase chromosome domains. J. Cell Sci. 113 (Pt 14), 2585–2593.
Wahl, L.M., Wahl, S.M., Smythies, L.E., Smith, P.D., 2006. Isolation of human monocyte populations. Curr. Protoc. Immunol., 70:7.6A.1–7.6A.10.
West, C.E., Waterworth, W.M., Story, G.W., Sunderland, P.A., Jiang, Q., Bray, C.M., 2002. Disruption of the Arabidopsis AtKu80 gene demonstrates an essential role for AtKu80 protein in efficient repair of DNA double-strand breaks in vivo. Plant J. 31 (4), 517–528.

Mutation Research 704 (2010) 88–100

Contents lists available at ScienceDirect

Mutation Research/Reviews in Mutation Research

journal homepage: www.elsevier.com/locate/reviewsmr
Community address: www.elsevier.com/locate/mutres

Review

Higher-order chromatin structure in DSB induction, repair and misrepair

Martin Falk, Emilie Lukasova *, Stanislav Kozubek

Institute of Biophysics, Academy of Sciences of the Czech Republic, Kralovopolska 135, 612 65 Brno, Czech Republic

ARTICLE INFO

Article history:
Accepted 21 January 2010
Available online 6 February 2010

Keywords:
DNA double strand breaks
DSB repair
Higher-order chromatin structure
Nuclear organization
Radiosensitivity

ABSTRACT

Double-strand breaks (DSBs), continuously introduced into DNA by cell metabolism, ionizing radiation and some chemicals, are the biologically most deleterious type of genome damage, and must be accurately repaired to protect genomic integrity, ensure cell survival, and prevent carcinogenesis. Although a huge amount of information has been published on the molecular basis and biological significance of DSB repair, our understanding of DSB repair and its spatiotemporal arrangement is still incomplete. In particular, the role of higher-order chromatin structure in DSB induction and repair, movement of DSBs and the mechanism giving rise to chromatin exchanges, and many other currently disputed questions are discussed in this review. Finally, a model explaining the formation of chromosome translocations is proposed.

Contents

Abbreviations: DSB, DNA double-strand break; γH2AX, histone H2AX phosphorylated on serine 139; PFGE, pulse-field gel electrophoreses; PI, post-irradiation; IR, ionizing radiation; IRIF, ionizing radiation-induced foci; RIDGE, regions of increased gene expression; antiRIDGE, opposite sequences to RIDGE; HSA, *Homo sapiens* chromosome.

* Corresponding author. Tel.: +420 541517165; fax: +420 541212179.
E-mail address: lukasova@ibp.cz (E. Lukasova).

1383-5742/$ – see front matter © 2010 Elsevier B.V. All rights reserved.
doi:10.1016/j.mrrev.2010.01.013

1. Introduction – simple question on hard problems

In this review, we will focus on repair of DNA double-strand breaks (DSBs), the most deleterious lesions of DNA ([1] and citations therein). DSBs represent simultaneous interruption of both DNA chains and thus cause severe disruption to genetic information, local chromatin structure and nuclear architecture. Importantly, even a single DSB may result in cell death or carcinogenesis if unrepaired or repaired improperly ([2], reviewed in [3]). On the other hand, much anti-cancer therapeutics, including radiotherapy, is based on killing tumour cells by DSB induction. Recognition of how cells repair DSB damage is therefore critical for our understanding of both development and therapy of cancer. Unfortunately, we are still far from having a complete picture of this fundamental process. To progress, we must understand not only the biochemical standpoints of DSB repair, but also its organization in time and space in the cell nucleus [4–7]. At present, a lot is known about biochemical aspects of DSB repair, but very little about how chromatin structure influences this process and the sensitivity of DNA to DSB induction. We lack the answers even to very basic questions, like (Figs. 1 and 2): Are DSBs induced equally in functionally and structurally distinct chromatin domains? Where and how are DSBs actually repaired: individually at their sites of origin, or together in specialized, repair-competent nuclear subcompartments [5,7,8]. Are DSBs spatially stable or do they migrate into "repair factories" [9]. And what are the DSB clusters observed by several authors [e.g. 5, 7, 9]: sites of multiple DNA damage, repair factories [e.g. 9], or by-products of DSB repair that potentially increase the risk of chromatin mis-rejoining [7,10]? Consequently, which is the more important factor that underlies chromosomal translocations – predetermined nuclear proximity of DSBs ("position first" hypothesis, [11,12]) in a range of Brownian movement of chromatin (about 0.5 μm, [13–16]), or their more extensive, potentially directed movement during the repair process that brings them close to each other ("breakage first" hypothesis, [9])? Further, does sensitivity to DSB induction and consequently the efficiency and fidelity of DSB repair differ for structurally and functionally distinct chromatin domains, such as active genes characterized by an "open" chromatin structure, and genetically "inactive", condensed heterochromatic domains, containing only few genes? In this article, rather than reviewing the whole field, we want to provide some different points of view on highly disputed fundamental questions concerning DSB induction, repair and mis-repair, to stimulate further interdisciplinary approaches to their solution. This article is largely inspired by the ESF-EMBO Symposium on Spatio-Temporal Radiation Biology held in Spain on 16-21st May 2009 [17].

2. Actual problems with monitoring DSB induction and repair

2.1. γH2AX foci – specific markers of DSBs?

One of the most daunting problems is detection of DSBs. Modern imaging techniques like fluorescence confocal microscopy, which contributed fundamentally to uncovering the mechanism of DSB repair in recent years, are based on detection of phosphorylated histone H2AX (γH2AX) as a specific marker of DSBs [18–23]. At present, immunostaining of γH2AX foci allows the most sensitive monitoring of DSB induction (with ionizing radiation doses in the order of cGy or even mGy) and repair [reviewed in 19, 24, 25]. Until recently, it was widely accepted that, in general, each DSB forms a γH2AX focus, each γH2AX focus contains just one DSB [19–23] and the disappearance of γH2AX foci reflects DSB rejoining [reviewed in 19, 20]. However, some doubts about the nature of γH2AX foci have emerged, challenging their usefulness as DSB markers.

2.2. Are all DSBs detected by immunostaining of γH2AX foci?

Earlier work demonstrated an approximately 1:1 correspondence between DSBs detected by physical methods (pulse-field gel electrophoresis, PFGE), and immunodetection of γH2AX foci [19–23, 26–28, reviewed in 29]. This correlation is usually relevant also for the kinetics of DSB repair, when dealing with normal human

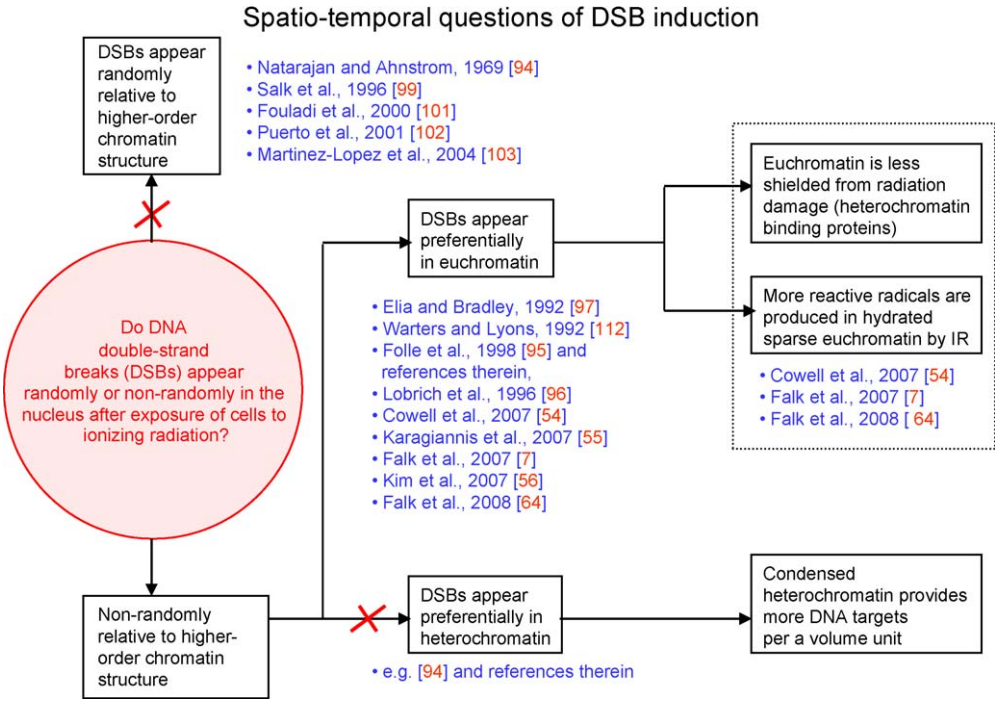

Fig. 1. Current spatio-temporal questions of DSB induction. Currently disputed questions concerning induction of DSBs relative to higher-order chromatin structure are displayed together with alternative answers and references supporting each particular hypothesis. Conclusions supported and not supported by our results are indicated by arrows and crossed arrows respectively.

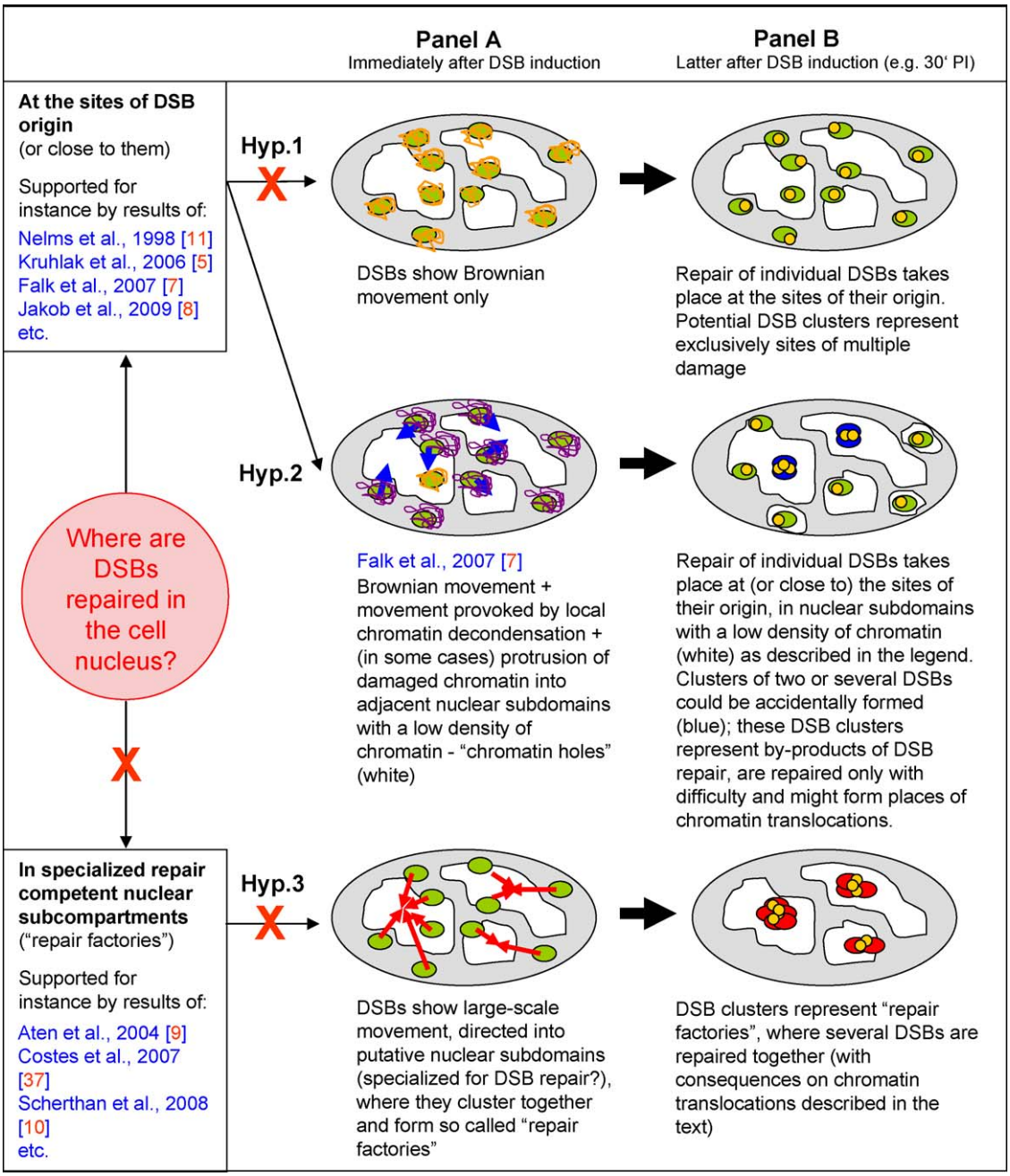

Fig. 2. Highly disputed questions on spatio-temporal organization of DSB repair. Intensively disputed questions on spatio-temporal organization of DSB repair in the cell nucleus are provided with potential alternative answers and supporting references. Briefly: The first hypothesis presupposes repair of DSB lesions (green spots) at the sites of their origin. "Movement" of DSBs is equivalent only to that of undamaged chromatin (Brownian movement, Panel A, orange trajectories). DSBs colocalize with DSB repair proteins (Panel B, yellow circles) at the sites of their origin, where they are also repaired. The second hypothesis (Falk et al. [7]) extends the previous one about the movement of DSBs that is induced by chromatin decondensation, provoked by DSB repair process. Panel A: Dense chromatin domains (gray) that contain DSB (green spots) are first decondensed to allow progression of DSB repair. This decondensation might led to a random short-range movement of DSBs (purple trajectories), in addition to Brownian movement (orange trajectories), or to their protrusion (blue arrows) into nuclear subdomains with a low density of chromatin (white). Movement of "euchromatic" DSBs is usually equivalent to the Brownian movement (orange trajectories). Panel B: In general, DSBs (green spots) colocalize with DSB repair proteins (yellow circles) at the sites of their origin, where they are also repaired. In case of some DSBs (usually "heterochromatic", (gray)), chromatin decondensation accompanied by protrusion of DSB into low-dense chromatin subdomains might led to clustering of two or more DSBs, due to a limited space of these chromatin domains (white). These clustered DSBs (blue) are reparable only with difficulty and probably represent sites of an increased risk of chromatin translocations. The third hypothesis presupposes highly-dynamic DSBs (green) that migrate in a large-scale manner (Panel A, red arrows) into putative nuclear subdomains (specialised for DSB repair?), where they cluster together and form so called "repair factories" (Panel B, red clusters). Therein, several DSBs are repaired together, with the consequences for chromatin translocations described in the text. Conclusions supported and not supported by our results are indicated by arrows and crossed arrows respectively.

diploid cells irradiated with low LET radiation (γ, X), where DSB repair half-time is usually about 50 min–1 h; such results were reported for example for human skin fibroblasts (GM5758) irradiated with X- or γ-rays (^{137}Cs and ^{60}Co) [30–32] and reviewed e.g. in Foray et al. [33,34] (γ/α-rays, normal human HF19 fibroblasts, AT5BI fibroblasts derived from an AT patient and human 149BR fibroblasts). However, it is very complicated to compare the results from different authors, since foci appearance, numbers and DSB repair kinetics depend strongly on the protocols used – protocol itself, radiation type, animal species, cell type, etc.

Moreover, also the combinations of these factors may provide diametrically different results. For example, irradiation of normal human fibroblasts with 30 Gy of γ-rays with a dose rate of 0.1 Gy/min only results to moderately slower DSB repair as compared to irradiation with the same dose but a dose rate of 1 Gy/min; this delay in DSB repair for cells irradiated with the lower dose rate is however very prominent in untransformed AT5BI human fibroblasts derived from an AT patient [33]. Finally, it must be said here, that there is a great variety of choices made by authors for considering the "zero" time for repair measurements. For example, some authors consider only 10 min PI as the moment where all DSBs are already recognizable and few γH2AX foci disappear during this time, whereas the others deliberately choose 20 or 30 min PI, although there is already evidence of a DSB repair during this period. In addition, two different types of DSB repair operate in the cells: non-homologous end-joining (NHEJ) [35] and homologous recombination (HR) [36]. Whereas NHEJ is able to fix broken ends in a fast and cell-cycle-independent manner, HR requires the presence of a sister chromatid to accurately repair DSBs with much slower kinetics. Since the choice of DSB repair pathway might depend also on the complexity of the DSB, cell type and many other factors and, at the same time, kinetics of γH2AX foci formation/disappearance could differ at DSB sites repaired by NHEJ or HR respectively, conclusions on the relation between DSBs and γH2AX foci might be significantly influenced by combinations of these variables. An influence of the cell type, genotype, radiation type and chromatin condensation to the DSB repair kinetics is compared e.g. in Foray et al. [33,34]. These parameters must be borne in mind when making any comparisons.

Interestingly, a number of recent results, obtained frequently with tumour cells, show fewer γH2AX foci (about 60–70%) than mathematically predicted or detected DSBs by PFGE [e.g. 32, 37] (normal human mammary epithelial cells HMEC-184, 1Gy of ^{137}Cs γ-rays, 1 GeV/amu Fe ions, HeLa cells, 160-kV X-ray source). Curious from this point of view is the observation that whereas up to about 50% of DSBs are repaired during about the first 15 min post irradiation (PI) (reported for example for following combinations of cells and types of ionizing radiation: carcinomic human alveolar basal epithelial cells A549, X-rays [29], CHO cells, X-rays [38], mouse CB-17 cells, γ-rays [39], Large Cell U-1810 Lung Carcinoma Cell Line, X-rays [40], human G_1-lymphocytes, X-rays [41]), other observations show that the maximal number of γH2AX foci appears at about 30 min PI [7,11,27,37,42,43].

In line with these results, it was hypothesized that early DSB rejoining can proceed without foci formation, since H2AX-deficient cells can repair DSBs induced by ionizing radiation (IR) and activate cell-cycle checkpoints [44–46]. However, increased radiosensitivity and frequency of chromosomal aberrations in these cells revealed [44–48] that γH2AX foci are required to retain repair proteins at the sites of damage and amplify the repair signal at later times [46]. Formation of foci may thus be necessary for efficient repair of longer-persisting, probably more complex DSB lesions.

Importantly, only about 15% of DSBs were found to require the activity of ATM and additional proteins of the ATM signalling cascade, including γH2AX and 53BP1, for completing non-homologous end-joining (NHEJ) repair [26,49–51], although these proteins do in general colocalize with γH2AX foci. Remarkably, these ATM- and 53BP1-dependent DSB lesions were located in heterochromatin. However, it is also known that DNA DSBs caused by ionizing radiation or chemicals result in rapid ATM autophosphorylation, leading to checkpoint activation and phosphorylation of substrates that regulate cell-cycle progression, DNA repair (e.g. H2AX in the site of DSBs, NBS1, MDC1, repair cofactor XRCC4, Tip60 acetyl kinase), transcription and cell death [52]. ATM lacking cells are thus unable to impede the progress of the cell cycle [53], which is not discussed here. These results show some ambiguity about the role of ATM on DSB repair in dense and sparse chromatin. It might be thus possible that euchromatic DSBs could potentially be repaired without formation of foci.

Paradoxically, heterochromatin was refractory to γH2AX modification, after both heavy charged-particle [42] and X/γ-ray irradiation [5,37,54–56]. The reason is probably its dense structure, since "opening" of heterochromatin by ongoing DNA replication also permitted phosphorylation of H2AX in these regions [54] (see Section 3.2 for additional discussion). Therefore, the absence of γH2AX foci at sites of heterochromatic DSBs might explain the discrepancy between PFGE and immunostaining data. However, the extensive chromatin decondensation at sites of DSBs, repeatedly reported [5,7,57–63], suggests that heterochromatic DSBs are also "open" for γH2AX phosphorylation. Nevertheless, formation of foci at sites of heterochromatic DSBs proceeds with slower kinetics than in open chromatin domains [26,49–51,64]. An increase in the number of fully developed γH2AX foci (unequivocally distinguishable from the background) during the first 30 min after DSB induction by X-rays in G_1-human lymphocytes [41] and by γ-rays in normal human diploid fibroblasts [7,64–65] may thus explain a lower number of microscopically distinguishable γH2AX foci relative to the number of "physical" DSBs, detected in the first few minutes PI. Interestingly, we found an increase of about 20% in the number of γH2AX foci during this period, corresponding to the proportion of DSBs (about 20%) found in heterochromatin [7,64–65]. Eventually, complex DSBs might induce ionizing radiation-induced foci (IRIF) formation more rapidly (within 5 min PI) than single DSBs [37]. In fact, a number of small γH2AX foci is detected in nuclei 5 min PI, but they could not be distinguished from the background noise [7,65] due to their small size and lack of colocalization with repair proteins. (In this review the term "colocalization" is used for colocalization observed at the resolving power of confocal microscopy; limitations of optical colocalization, e.g. bleed-through phenomenon, tendency of some labelled proteins to cluster, etc., must be therefore kept on mind when interpreting the data). It should be also noticed that the mentioned increase in a number of γH2AX foci during the period of about 30 min after irradiation was reported mainly for tumour cells and cells with a high exonuclease activity, for example, whereas with normal non-transformed human cells continuous decrease of foci was also observed by some authors [e.g. 66].

The lower number of γH2AX foci relative to DSBs is also frequently explained as the consequence of DSB clustering during repair (discussed in Sections 4.3, 4.4, 5 and 6). Meanwhile, it is still believed that the number of γH2AX foci at the time of their maximal appearance (about 30 min PI) corresponds with the initial DSB damage. However, it should be borne in mind that not all DSBs may be detected by γH2AX visualization at early time points after their induction.

2.3. Do all γH2AX foci represent DSBs, and do late γH2AX foci represent still unrepaired DSBs?

Questioning the nature of "late" γH2AX foci, Markova et al. [25] observed similar kinetics of DSB joining by PFGE among several cell lines, but different kinetics of disappearance of γH2AX foci; usually, the foci persisted longer than DSBs [25,67–68]. If these results do not reflect a low sensitivity of PFGE for residual DSBs, what do "late" γH2AX foci represent if not unrejoined DSBs: are they relics of repair complexes or sites of ongoing repair, but with already rejoined DNA ends? Since the maxima of H2AX foci and their colocalization with repair proteins appear at about 30 min PI [7, 25, 68, etc.] and the size of foci grow actively until they disappear [7,65], the latter seems more probable. Besides, the disappearing foci could be morphologically diffuse, not

colocalizing with repair proteins. In additional support of the "active" nature of "late" foci, cells in irradiated populations analyzed hours to days PI contain either discrete γH2AX foci colocalizing with repair proteins, or do not contain these foci at all. Persistent γH2AX foci may be thus required for reconstituting the original chromatin structure at the site of damage and/or cellular signalling, even though the DNA ends have already rejoined. This could be very important, for example in heterochromatic lesions, the repair of which is associated with extensive chromatin rearrangements and proceeds with slower kinetics (Section 2.2) [26,49–51]. This is also supported by increased colocalization of "late" γH2AX foci with heterochromatin protein 1 (HP1β) [7,69]. Contrary results, however, follow from experiments with normal and DNA-PKcs-deficient mouse cells [70]. Although cells deficient for the DNA-PK catalytic subunit show gross defects in DSB repair, contrary to normal cells, the kinetics of γH2AX disappearance were very similar in both cell lines. Further experiments are therefore required to shed more light on this issue because, especially at later times PI, γH2AX foci may also represent complex, still unrepaired lesions that are repaired only with difficulty (Sections 4.4, 5 and 6) [7,64,65].

Elucidation of the true nature of "late" γH2AX foci is extremely important, since physical methods directly detecting DSBs fail to detect residual DSB damage and many fundamental conclusions, particularly about cancer initiation and development, are thus based just on the detection of "late" γH2AX foci. For instance, Sandel and Zakian [71] in *Saccharomyces cerevisiae*, Yoo et al. [72] in *Xenopus* extracts, and Syljuasen at al [73] with others [74,75] in human cells observed so-called cellular "adaptation" to DSB damage when, despite the persistence of DSBs, cells unblock G_2-arrest of the cell cycle and enter mitosis [reviewed in 74]. For the time being, the immunostaining of γH2AX foci is the only efficient method of detecting DSBs persisting in the cell long after "completing" the repair process; however we have to examine what they really represent. At the end of this paragraph, it should be noted that γH2AX foci probably do not "cover" the complete response of a cell to radiation damage, as follows for example from continuing disputations on a very complex problem of cellular radiosensitivity [20,76,77].

3. Higher-order chromatin structure and induction of DNA double-strand breaks

Higher-order chromatin structure plays an important role in regulation of nuclear processes [78–82, see 83–89 and citations therein for the review]. So how does chromatin structure influence cell radiosensitivity and DNA repair i.e., how do structurally and functionally distinct chromatin domains differ in their sensitivity to DSB induction, mechanism and efficiency of DSB repair, and susceptibility to formation of chromosomal translocations? Genes are not homogenously distributed in the human genome, and gene density determines some aspects of higher-order chromatin structure. Highly expressed genes are clustered in specific regions of chromosomes called RIDGEs (Regions of Increased Gene Expression) [90–91], in which chromatin structure is more open [92, our unpublished results] than in the regions containing low numbers of genes, mostly with low expression (antiRIDGEs). Chromatin in antiRIDGE regions is condensed, contains large amount of chromatin-bound proteins, and is more peripherally located in the nucleus [79,83,92,93] than the decondensed chromatin of RIDGES; these rules hold also for chromosome territories [79,83]. Of special interest, therefore, is the question whether these gene-dense higher-order chromatin domains that contain widely expressed housekeeping genes, and also genes critical for cell proliferation such as protooncogenes and tumour suppressor genes, are more susceptible to radiation-induced DSB damage than condensed, genetically silent genome regions.

3.1. Do frequencies of chromosomal aberrations and nuclear distribution of γH2AX foci reflect chromatin sensitivity to radiation damage?

In the sixties, suitable methods for distinguishing condensed and decondensed chromatin in interphase nuclei were not available, and the question of chromatin sensitivity to ionizing radiation was assessed from the occurrence of chromosomal aberrations on mitotic chromosomes, with conflicting results. Earlier work indicated that there were more chromosome breakpoints in heterochromatin [94 and citations therein], but with methodological progress the opinion was shifted rather to a higher occurrence of translocations in euchromatin [95 and citations therein]. In parallel, a higher sensitivity to densely [96] and sparsely [97] ionizing radiation of euchromatin was confirmed by directly quantifying DSBs using PFGE. By the same method, however, an equal content of DSBs was observed for Giemsa-light (Xq26) and Giemsa-dark (21q21) chromosomal bands, that contain active housekeeping genes and mostly inactive tissue-specific genes respectively [98, similar conclusions 99–101]. More recently, several authors readdressed this question taking advantage of newly available multicolour-FISH. Detecting chromosomal aberrations in γ-irradiated cells, Puerto et al. [102] observed no difference between the large heterochromatic and euchromatic blocks (1cen-1q12 vs. 17cen-p53) in the frequency of chromosome breakpoints. Similarly, irradiating CHO9 cells with X-rays, Martinez-Lopez et al. [103] found a corresponding frequency of chromosomal aberrations in the euchromatic short arm and heterochromatic long arm of the X chromosome, even though the latter contained more translocations after etoposide treatment.

It is, in principle, difficult to assess whether the number of chromosomal aberrations in a particular chromatin domain reflects its sensitivity to initial DSB induction, or instead, the efficiency or fidelity of DSB repair in that domain. Indeed, despite observing a higher translocation frequency in heterochromatin, Natarajan and Ahnström already in 1969 [94] assumed the same frequency of initial damage in euchromatic and heterochromatic regions. The suitability of chromosomal translocations for quantifying initial DSB damage is therefore questionable.

The most convenient and direct method today for comparing the sensitivity of distinct chromatin domains to radiation-induced DSBs is immunocytological visualization of γH2AX foci *in situ* in interphase cell nuclei [19–23]. In combination with a high-resolution confocal microscopy, this method allows "direct" visualization of DSBs as γH2AX foci against the background of nuclear chromatin. However, many authors found heterochromatin refractory to formation of IRIFs, including γH2AX [5,7,8,37,54–56,64,65], and demonstrated mostly their "euchromatic" localization (see Sections 2.1 and 2.2 for deeper discussion). In any case, these results [64] are contrary to the supposed correlation between chromatin density and DSB induction [discussed e.g. in 37, 54], as well as to chromatin radiosensitivity quantified by counting chromosomal translocations in eu- and heterochromatin respectively (works cited above). Thus neither the localization of γH2AX foci relative to chromatin density reflects the original positions of DSBs. Indeed, Kim et al. [56] observed both in yeast and mammalian cells inefficient phosphorylation of H2AX histones at DSB induced at the specific site in heterochromatin by endonuclease cleavage. Accordingly, the preferential localization of γH2AX foci in "chromatin holes" could reflect inaccessibility of heterochromatin to γH2AX modification [5,7,8,37,54–56,64] and also rapid decondensation of chromatin at the sites of DSBs during their repair [5,7,64] (discussed later in Sections 4.1 and 4.2), rather

than only a higher sensitivity of decondensed euchromatin to DSB induction. This conclusion is supported also by preferential localization of γH2AX foci in "chromatin holes" observed along the nuclear tracks of heavy charged particles [8,37,42] where, unlike low-LET photons, random or preferentially heterochromatic distribution of foci along the track could theoretically be expected (see Section 3.3). So at present, neither measurement of chromosomal aberration frequencies nor localization of γH2AX foci relative to euchromatin or heterochromatin can provide conclusive data on radiosensitivity of structurally and functionally different chromatin domains.

3.2. Do structurally and functionally distinct chromatin domains differ in their sensitivity to radiation-induced DSB damage?

To overcome the above problems of estimating chromatin sensitivity to radiation-induced DSBs, we compared γH2AX frequencies in selected chromosomal territories of similar size but largely differing in overall transcriptional activity and thus in chromatin structure [64]. Using ImmunoFISH [104], we could simultaneously visualize γH2AX foci and genomic loci of interest. Since both condensed and decondensed subdomains of chromosome territories are more or less painted by the FISH probe, potential chromatin decondensation at sites of DSBs or their movement into decondensed chromatin domains (during DSB repair) do not influence the numbers of γH2AX foci counted in a particular territory. This eliminates the potential underestimation of heterochromatic DSBs due to the refractory nature of heterochromatin to foci formation. Moreover, since we compare DNA molecules of known molecular size, normalization of γH2AX numbers to DNA content is much easier than when comparing radiosensitivity of hetero- and euchromatin. It is, in fact, very difficult to make this normalisation in the later case, because of the smooth gradation between dense and sparse chromatin domains and supposed changes in chromatin condensation at the sites of DSBs. Nevertheless, by showing more γH2AX foci in territories of genetically active chromosomes with "open" chromatin structure, we have reached similar conclusions to those obtained when comparing heterochromatin with euchromatin.

Human chromosomes 18 and 19 (HSA18, HSA19), of similar size (62.8 Mb and 76.1 Mb respectively) but opposite functional and structural characteristics, serve as an example. In correlation with the highest gene density (23.9 genes/Mbp), overall expression activity and number of intensely expressed genes among the human chromosomes [90], γ-rays induced 0.12 DSB per megabase pair in HSA19, the highest frequency of DSBs of all the chromosomes analysed. On the other hand, in HSA18, which has a very low density of genes (4.3 genes/Mbp) and does not contain any highly expressed genes [90], there was only a quarter of the number of DSBs found in HSA19 (0.03 DSB/Mbp in mean) [64], despite its slightly larger molecular size.

A similar preponderance of γH2AX foci was observed, by the same method, in the RIDGE of HSA11 when compared to the antiRIDGE region [64] of the same size (11 Mbp) and chromosomal localization (11q), but with about 40% higher chromatin condensation [92, our unpublished results]. The mean number of DSBs induced, 15 min PI, was about 8 in the RIDGE and 2 in the antiRIDGE. The advantage of these experiments with RIDGEs and antiRIDGEs is that they compare chromatin domains of very homogeneous but opposite structural and functional characteristics. Altogether, these results suggest that sparsely ionizing γ-radiation preferentially harms DNA in regions of open decondensed chromatin [64]. It remains to be determined whether and why, contrary to these results, most translocations occur in heterochromatic loci. A possible explanation is discussed in Section 5.

3.3. What is the cause of the higher sensitivity of decondensed chromatin to DSB induction by sparsely ionizing radiation?

The next step is to find the reason for the higher resistance of heterochromatin to DSB induction by sparsely ionizing radiation. Densely ionizing radiation induces DSBs predominantly by the direct interaction of high energy particles with chromatin; DNA damage should therefore correlate with chromatin concentration along the particle track. The lower energy of γ- or X-ray photons can also directly damage chromatin regardless of its structure, but less intensively than densely ionizing radiation; in fact, most damage induced by this radiation is mediated indirectly by reactive radicals arising from radiolysis of water. According to Mee and Adelstein [105], 56% of γ-radiation-induced DSBs can be attributed to the action of hydroxyl radicals. The different sensitivity of distinct chromatin domains to DSB induction by sparsely ionizing radiation must therefore reside in their response to the indirect effect of radiation. With their extremely short lifespan (10^{-10} to 10^{-5} s), free radicals can harm DNA only within a radius on the nanometre scale [1 and citations therein, 106, 107]. More decondensed, and thus more hydrated, euchromatin may therefore be more seriously affected by sparsely ionizing radiation. Moreover, the ability of proteins to sequester free radicals and modify radiation damage to DNA is well documented [1,105–108]. For instance, histones and inhibition of Fenton oxidation in anoxic nuclear conditions were shown to quench the oxidative damage about 50-fold [97,107]; heterochromatin thus may be doubly protected from a harmful effect of sparsely ionizing radiation – by a lower amount of water and a higher abundance of shielding proteins, since more chromatin binding proteins, like HP1, are specific for heterochromatin [109–111]. Indeed, higher sensitivity of cells depleted of HP1 orthologs in *C. elegans* has been reported [69].

To test these alternatives (Fig. 1), we have subjected cell nuclei to hyper- or hypotonic treatment, and followed changes in induction of γH2AX foci. Together, changes in epigenetic modifications at the sites of newly formed chromatin domains and their association with chromatin-binding proteins were followed [64]. Surprisingly, artificial chromatin hypercondensation reversibly inhibited the repair process but did not decrease chromatin sensitivity to γH2AX induction. Importantly, artificially hypercondensed chromatin domains, newly formed after hypertonic treatment from previously decondensed chromatin, colocalized neither with epigenetic markers of heterochromatin nor heterochromatin-binding protein 1 (HP1) [64]. On the other hand, hypotonically induced chromatin hypocondensation increased induction of γH2AX foci compared with untreated nuclei. A higher sensitivity of hypotonic-decondensed chromatin was confirmed also using gel electrophoresis [112].

Together, it seems that chromatin-binding proteins, highly abundant in heterochromatin, protect DNA from radiation damage caused by reactive metabolites of water radiolysis, since simple chromatin condensation *per se* is not sufficient to do so. This is supported by the findings of Karagiannis et al. [55], who showed that induction of γH2AX in heterochromatin remains significantly lower than in euchromatin even when the cells were treated with TSA, an inhibitor of histone deacetylases. Hypotonic-induced chromatin decondensation is therefore probably associated with dissociation of some proteins from chromatin, which increases its sensitivity to DSB induction. On the other hand, our results suggest that the hypertonic-induced cell sensitization to chromosomal damage and killing described by Dettor et al. [113] could be attributed instead to apoptosis, activated by inhibition of nuclear processes provoked by irreversible changes of chromatin structure after more prolonged hypertonic treatment (>10–15 min), rather than to increased sensitivity to radiation-induced DNA damage of this altered chromatin structure. Thus, mechanisms of cell sensitization to IR seem to differ for TSA and hypo- and hypertonic

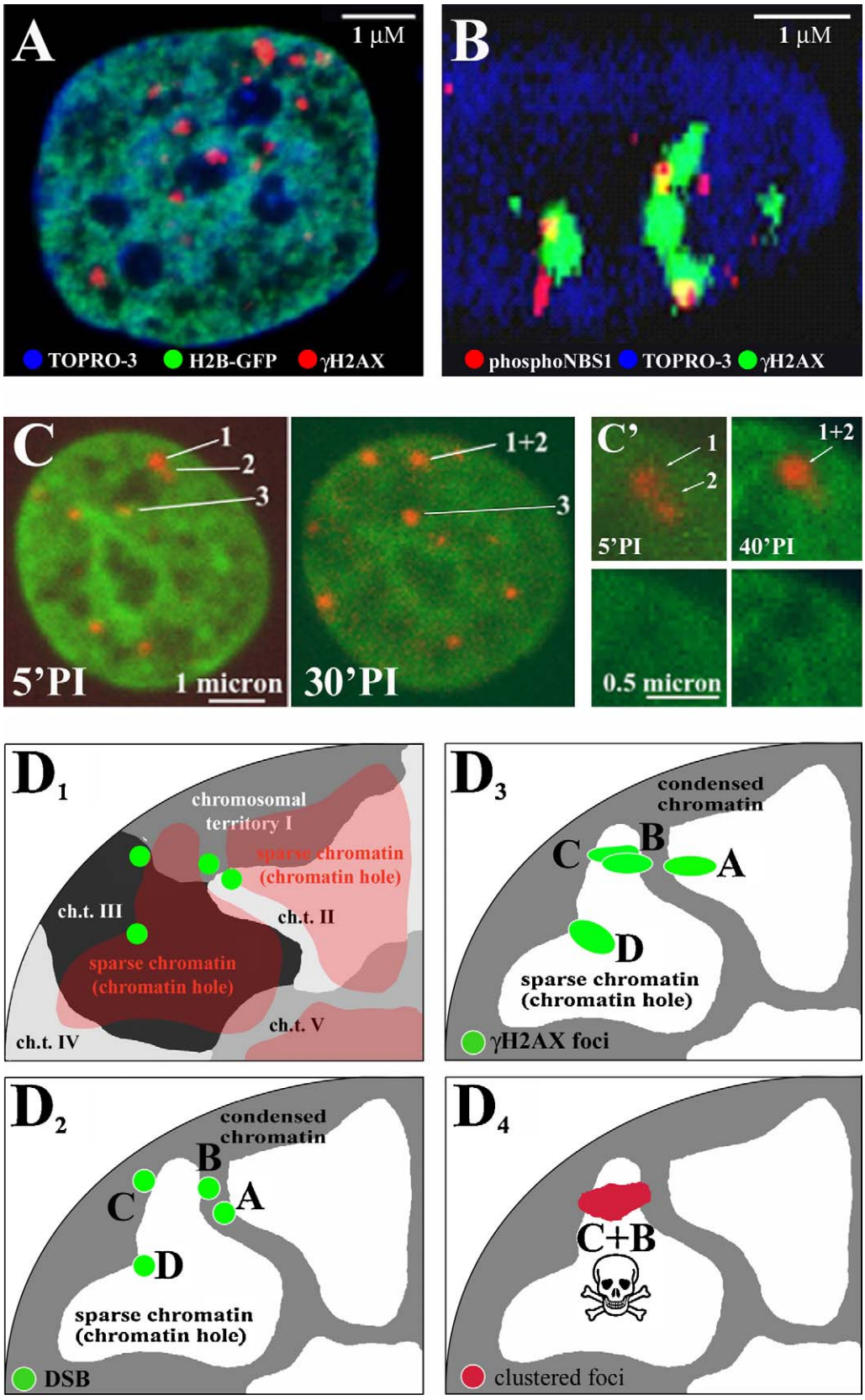

Fig. 3. A model showing the relationships between higher-order chromatin structure, DSB repair and formation of chromosomal translocations. (A) *x–y* central slice through a spatially fixed MCF7 cell nucleus shows the location of γH2AX foci (red), induced with 1.5 Gy of γ-rays, relative to dense and sparse chromatin domains, 10 min PI. Chromatin density is reflected by the intensity of H2B-GFP (green) and TOPRO-3 (blue) staining. Dark areas represent nucleoli and "chromatin holes". (B) Clustering of γH2AX foci shown in 3D space (x-z plane) in spatially fixed normal human fibroblasts irradiated with 3 Gy of γ-rays. γH2AX foci (green) observed 2 h PI; NBS1 (red), chromatin (TOPRO-3, blue). (C) Central slices (0.4 μm in *x–y* plane) of human MCF7 cells double-transfected with 53BP1-RFP and H2B-GFP proteins, irradiated with a dose of 1.5 Gy of γ-rays, displayed at 5 min and 30 min PI, show re-localization of 53BP1 foci 2 and 3 (red) from dense to sparse chromatin. After this relocalization, focus 2 formed a cluster with focus 1; this cluster persisted until the end of observation (40 min PI, enlarged detail at panel C′). Chromatin density, green (H2B-GFP). (D) Proposed model of the relationship between

treatment. Since modifiers of chromatin structure, recognised as promising agents in cancer therapy, are frequently used in combination with radiotherapy, deeper understanding of the relationship between chromatin structure and its sensitivity to radiation damage is of the utmost importance.

4. Higher-order chromatin structure and DSB repair

4.1. How does DSB repair contribute to the non-random distribution of γH2AX foci?

As described above, IRIFs are non-randomly distributed in the cell nucleus relative to higher-order chromatin structure, at least partly due to a higher sensitivity of decondensed chromatin to DSB induction (Fig. 1). However, the mechanism of DSB repair probably also contributes significantly; this is supported by experiments of many authors [9, 37, 114, etc.] showing that the non-randomness of the distribution of γH2AX foci increases within an hour following irradiation (Fig. 2). Since DSB repair was shown to proceed faster in euchromatin than in heterochromatin [49–51,64,115], the progressively increasing euchromatic localization of γH2AX foci [7] may indicate, instead of slower repair in euchromatin, that some additional steps are required for DSB repair in heterochromatin, which include chromatin decondensation in the vicinity of DSB sites, or movement to repair-competent subcompartments in open chromatin before histone H2AX can be phosphorylated. This would not be surprising, since the condensed nature of heterochromatin poses a barrier to enzymes and regulation factors that process DNA [e.g. 116] and heterochromatin must be relaxed to allow nuclear processes like transcription and replication [117–119]. Also, a concentration in several specialized nuclear centres is well documented for transcription [86, 120, 121, see 122–124 and citations therein for review]. Both possibilities, "decondensation" and "migration", are thus not unprecedented in cellular biology, and are discussed below. In contrast, as could be deduced from other recent works [26, 49–51, etc.], we feel it improbable that repair of heterochromatic DSBs could proceed with less extensive chromatin modifications (i.e. without foci formation) than the repair of DSBs in the less condensed euchromatin (see also the Section 2.2). Strong evidence against this comes from work of Goodarzi et al. [49], who showed that knockdown of KAP-1, HP1 or HDAC1/2 proteins can alleviate the requirement for ATM and revert increased radiosensitivity of ATM-deficient cells. For the same reason, chromatin decondensation at the sites of DSBs is apparently not only a "passive" consequence of repair activity. In addition, it is unlikely that heterochromatin-bound proteins can compensate for the functions of ATM, γH2AX and other "foci-forming" proteins.

4.2. Does chromatin decondensation at sites of DSBs reflect formation of repair-competent nuclear conditions at the sites of DSB origin or migration of DSBs into repair subcompartments?

Chromatin decondensation in the vicinity of DSBs, initiated immediately after their induction, has often been reported in the past few years both for yeast and mammalian cells [5,7,57–63]. Chromatin relaxation takes place independently of ATM activity [5,62], so probably precedes and enables formation of foci. In addition, a wave of chromatin relaxation throughout the nucleus, starting at DSB sites and spreading through the entire chromatin, was discovered by Ziv et al. [63], as a result of KAP-1 phosphorylation by ATM kinase. This demonstrates that DSB repair requires competent chromatin structure. Thus, in addition to the factors described in Section 3.3, the preferential localization of γH2AX foci in highly decondensed chromatin probably reflects chromatin reorganization connected with the formation of repair-competent nuclear conditions at DSB sites. Taking together, it seems that more DSBs are induced in decondensed euchromatin due to its higher radiosensitivity (Fig. 1) and, at the same time, heterochromatic DSBs are decondensed during their repair (Fig. 2). However, it is still argued whether chromatin decondensation forms repair-competent "subcompartments" at the sites of DSB origin, or whether it only releases "DSBs" from a tight chromatin structure so that they can migrate into specific DSB repair domains [5,7,9,11,37,68].

4.3. Are DSBs mobile or immobile?

Experiments in which DSBs were induced by sparsely ionizing X or γ-radiation that produce isolated DSBs dispersed throughout the nucleus showed similar mobility of IRIF foci to undamaged chromatin [7, 11, reviewed in 125]; the same conclusions were also obtained for DSBs generated by some other approaches, e.g. by argon ion UV laser (364 nm emission line) [5]. On the other hand, DSBs induced by densely ionizing radiation were shown to change their positions and often cluster during the post-irradiation period [9,126,127]. This was interpreted as directed movement of DSBs into so-called "repair factories", where several DSBs are repaired together [9,127–129]. These contradictory results could be hardly explained by the existence of two different repair mechanisms (Fig. 2), where one repairs individual DSBs induced by sparsely ionizing radiation at the sites of their induction, and the other repairs several DSBs induced by densely ionizing radiation together in repair factories, since the same repair machinery is used in both cases. It is more probable that particles of densely ionizing radiation release high energy along their tracks, which induces multiple DSBs close to each other, leading to chromatin fragmentation, movement of these fragments, and clustering of adjacent DSBs [37,43,114,130,131]. DSB mobility may therefore to some extent correspond with the linear energy transfer (LET) of the damage inducing radiation, which nevertheless reflects the chromatin fragmentation and not the mechanism of DSB repair.

Spatio-temporal DSB mobility is therefore more complicated, and could not be simplified to the relationship between DSBs mobility and radiation quality. For instance, Markova et al. [25] quantified the area of γH2AX/53BP1 foci induced by γ-radiation during the post-irradiation period, and surprisingly found that a progressive decrease in the number of γH2AX/53BP1 foci was not followed by an equivalent decrease in overall area of foci; instead, it remained unchanged up to 4 h PI. The authors interpreted this observation as clustering of foci or transposition of γH2AX/53BP1 proteins from disappearing to persistent foci. On the other hand, consistent with most results for sparsely ionizing radiation, Jakob et al. [8,132] observed no significant movement of DSB foci in cells irradiated with heavy charged-particles. In line with this conclusion are our results [7,65] that demonstrate that most γH2AX foci induced by γ-radiation are spatially stable, but some "breaks" show significantly higher mobility [7,65] (Fig. 2). When mobility was quantified as the mean change of the distances between all possible DSB pairs (53BP1 or NBS1 foci) in time, the mobility of

higher-order chromatin structure, DSB repair and formation of chromosomal translocations. (D_1) Schematic location of chromosomal territories that could be subject to chromatin exchange during DSB repair. (D_2) The higher-order chromatin structure and Brownian movement of chromatin determine the original radius of mutual DSB (γH2AX foci, green) interactions. Heterochromatin between A and B prevents their mutual interaction. (D_3) chromatin decondensation at sites of DSBs induced at the boundary of eu- and heterochromatin can significantly increase (foci B and C) or decrease (foci A and B) the original probability of interactions between DSBs. (D_4) Foci B and C are at the highest risk of chromatin exchanges despite the shortest nuclear distance being between foci A and B. See Section 6 for a detailed explanation of figure D.Figures A, B and C are adopted from Falk et al. [7].

damaged chromatin was equivalent to that of undamaged. However, when tracking individual foci, we identified a subgroup with significantly increased mobility.

To explain this, we double-transfected MCF7 cells with the protein 53BP1 and histone H2B fused with GFP and RFP respectively, so that we could follow the movement of 53BP1 foci relative to chromatin density. Interestingly, the foci showing increased (but restricted) movement frequently corresponded with heterochromatic DSBs. This movement, although seemingly random when studied at the pan-nuclear level, was from high-density chromatin at the sites of DSB origin to immediately adjacent domains of sparse chromatin [7,65] (Fig. 2).

In addition, epigenetic modifications at the original sites of DSBs showed local chromatin decondensation manifested by increased H4K5 acetylation, decreased H3K9 dimethylation, and obviously decreased chromatin staining with DNA dyes [7,65]. This chromatin decondensation presumably allows access of large repair complexes to sites of damaged DNA and results in short-range chromatin movement. Therefore, we monitored the colocalization of γH2AX foci with several repair proteins (p-NBS1, 53BP1, MDC1, MRE11, etc.) in spatially fixed cells up to several hours post-irradiation. Almost immediately after DSB induction, γH2AX foci started to colocalize with these repair proteins, still at the sites of DSBs, which shows ongoing DSB repair of individual DSBs at their sites of origin, and militates against the hypothesis of DSB migration into specialized repair centres (Fig. 2). In the case of heterochromatic DSBs adjacent to decondensed chromatin, however, heterochromatin decondensation results in a protrusion of the chromatin surrounding the DSBs into the adjacent low-density chromatin domain ("chromatin hole"), which is apparently an easier and more efficient way to create repair-competent conditions than extensive relaxation of the whole condensed chromatin domain around a DSB (Fig. 2). In the case of euchromatic DSBs, however, extensive relaxation is either not required or has a less obvious effect on chromatin structure; chromatin decondensation and mobility at the sites of euchromatic DSBs is therefore usually not so marked (Fig. 2). These results were obtained for sparsely ionizing γ-rays and non-homologous end joining (NHEJ) in G1 cells, so results for other types of radiation and/or homologous recombination (HR) in S/G2 phase of the cell cycle might differ.

4.4. Does the clustering of IRIF foci reflect repair factories, clustered damage, or by-products of DSB repair?

Ionizing radiation is known to induce clustered DSB damage, as a consequence of local deposition of large energy; these clusters appear at the original sites of DNA damage. Several authors however described additional "dynamic" clustering of γH2AX (IRIF) foci upon DSB induction that is observed during the repair process [5,7,9,25,126–129]. In this case, DSB clusters are formed at sites that differ from the original positions of DSB lesions. At first, it was thought that the presence of these clusters confirmed the existence of the "repair factories" already described above [9,127–129] (Fig. 2). However, contrary to the frequent clustering of foci in cells irradiated with high-LET radiation [9,126,127], only a few clusters per cell, each containing usually only 2 or 3 γH2AX foci, appear after a dose of 1 Gy (1 Gy/min) of γ-rays [7,65]. It means that no more than 5–8 γH2AX foci out of about 35 DSBs induced per cell on average after this dose usually form clusters, and that most foci have not entered clusters even several hours after γ-irradiation [7,65]. These results do not support the hypothesis of "repair factories", and the clustering of γH2AX foci after α-irradiation [9] apparently reflects only random "movement" of DNA fragments, induced by locally concentrated energy deposition resulting in complex DNA damage (Section 4.3) [132, 133 reviewed in 134, 135]. To find out whether this is also the case with the relatively rare γH2AX clusters induced by γ-irradiation, we have studied *in vivo* when IRIFs start to appear in the cell nuclei, and whether the occasional movement of 53BP1 or NBS1 foci could lead to cluster formation. Indeed, both 53BP1 and NBS1 foci occasionally clustered; some clusters were only temporary, in agreement with Kruhlak et al. [5], but others persisted in cell nuclei at least until the end of the live-cell observations [7,65]. Soon after irradiation (5 min PI), the frequency of clustered foci was low, but increased with time PI. Most γ-induced foci we observed therefore seem to appear as a consequence of the repair process and not multiple damage, since otherwise more DSB clusters would be expected in dense heterochromatin (with more concentrated DNA "targets"). However, in reality, clustering took place preferentially in "chromatin holes", originally with very low chromatin concentration. These clustered foci thus apparently represent by-products of DSB repair where chromatin decondensation at the sites of DSB results in protrusion of IRIF foci into the limited space of "chromatin holes" (Fig. 2). In addition, multiple DNA damages very close to each other, caused by radiation *per se,* are probably hardly distinguishable at the resolution power of confocal microscopy from single DSBs.

5. Higher-order chromatin structure, DSB repair, and chromosomal translocations – are clustered DSBs sites with increased risk of chromatin exchange?

IRIF foci clustered during the DSB repair are a by-product of this process rather than "repair factories" [5,7,65], but does this clustering reflect only spatial "interactions" or does it have also some functional significance? Supporting the latter idea, the number of isolated foci swiftly decreased during the time PI, whereas γH2AX clusters were resistant to repair, and some persisted in the nucleus even several days after irradiation [7]. We believe these clusters represent unrepaired DSBs, since they still colocalized with other repair proteins (MRE11, NBS1, 53BP1) at a resolution power of confocal microscopy. It indicates that IRIF clusters could be repaired only with difficulty, and it is therefore tempting to speculate that they represent sites with an increased risk of chromosomal aberrations (Fig. 2). Indeed, Scherthan et al. [10] recently reported results that strongly support this hypothesis. Comparing the numbers of γH2AX foci induced by different doses of X-rays with corresponding frequencies of chromosomal aberrations detected by spectral karyotyping (SKY), they showed that more DSBs accumulate in a single γH2AX focus after a higher dose of IR, which correlates with an increased risk of DNA misrejoining and the formation of complex aberrations.

In addition, it seems that clustered foci also contribute to the process of cell adaptation to ionizing radiation described by the Bartek and Lukas group [136, 137, reviewed in 138]. This process enhances the risk of fixing chromosomal aberrations, because it allows the cell to enter mitosis with unrepaired DSB damage. Although most cells die due to their inability to complete mitosis, some may survive with an altered genotype. Indeed, we observed [7] that sporadic cells probably divided with DSB damage, as demonstrated by the presence of micronuclei (which apparently appear only during cell division [139,140]) adjacent to a nucleus still containing unrepaired foci.

6. A possible model of the relationship between higher-order chromatin structure, DSB repair, and formation of chromosomal translocations

6.1. "Breakage First" or "Position First" theories of chromosomal translocation origin – which one is true? And are they mutually exclusive?

There is a wide gap between the "Position First" and "Breakage First" theories of DSB mobility and formation of chromosomal

translocations. Whereas the first assumes that chromatin exchanges can form only between genetic loci that are in close mutual proximity before irradiation [11, 12, 140–149], the second gives priority to DSB movement and supposes that chromatin translocations take place as a consequence of DSB mixing in putative "repair factories" [9,30]. Therefore, these hypotheses are widely regarded as mutually exclusive. However, our data suggest that both these hypotheses, although greatly modified in the latter case, could help to explain formation of translocations, as illustrated in Fig. 3 [7,65].

As discussed earlier, DSB repair takes place, in principle, at the site of its induction (Fig. 3A–C). Spatial organization of the genome thus predetermines the initial nuclear positions and limits the "movement" of individual damaged loci (Fig. 3A, C, D_1) as well as probabilities of their mutual interactions (Fig. 3, C, D_2), since there is no consistent evidence for long-distance nuclear movement of IRIF foci [5, 7, 8, 11, 12, 150–152 reviewed in 125]. Up to this point, the mechanism of chromosomal translocation corresponds to the well established "Position First" theory.

However, after irradiation, chromatin at the sites of DSBs largely decondenses as a consequence of DSB repair, and some DSBs protrude into "chromatin holes" where they could potentially cluster (Fig. 3B, C, D_3) and form complex lesions that are repaired only with difficulty and pose an increased risk of chromosomal translocations (Fig. 3C, D_4). An important difference of this model from the "position-first" theory is that ongoing DSB repair dependent on local higher-order chromatin structure may significantly change (Fig. 3D_2–D_4) the probabilities of (short-range) DSB interactions, simply derived from nuclear distances of damaged loci (Fig. 3D_1-D_2).

As an example, four DSBs are illustrated in Fig. 3D_2 and labelled A, B, C, D. If these DSBs interacted purely according to the "Position First" hypothesis, the probability of chromosomal translocations would be the highest between A and B, since they are closest to each other, whereas mutual interactions between other lesions would be very improbable because of their large nuclear separation (Fig. 3D_1–D_2). In fact, however, the highest frequency of interactions was observed between lesions B and C, for following reasons: Lesions A and B are located on the opposite sites of a heterochromatin block that forms a "barrier" between them and "forces" the lesions A and B to protrude into different "chromatin holes", preventing their interactions despite their minimal nuclear separation (Fig. 3D_3). On the other hand, higher-order chromatin structure determines that extensive chromatin decondensation at the sites of B and C results in protrusion of lesions into the same "chromatin hole" and their clustering (Fig. 3D_3), which provides a "substrate" for potential chromatin translocations (Fig. 3D_4). This "mobile" aspect, added to the "Position First" theory, markedly simplifies the explanation of the origin of complex translocations, in accordance with data of Anderson et al. [114].

7. Prospective conclusion

In this review we recapitulate current knowledge about the influence of higher-order chromatin structure on DSB induction, repair and misrepair. It is evident that despite of great progress in this field during the last decade there are many questions to which the responses were not yet found or are not univocal. A considerable body of knowledge have been already obtained at the field of radiation physics and biochemical response of a cell to DSB damage. The results show the important role of chromatin structure in the cell response, however the conclusions about this role are not yet definitive The promising way how to better comprehend the respective roles of chromatin structure in sensitivity to DSB induction, repair and DSB mobility could come from more extensive comparison of γH2AX foci behaviour in cells derived from genetic diseases associated with defects in chromatin decondensation but not in DSB repair and conversely diseases with defects in DSB repair but not in chromatin decondensation. The results of this study could elucidate whether some changes in higher-order chromatin structure could predispose the cell to the higher risk of cancer due to imperfect DSB repair. Especially, more extensive studies in living cells could contribute to better understanding of the repair processes in dense and sparse chromatin in real time.

Conflict of interest statement

The authors declare that there are no conflicts of interest.

Acknowledgements

We thank Dr. Adrian T. Sumner for improving the English of this article. The work was supported by the following grants: GAAV IAA500040802, 1QS500040508, LC535, ME919, 1AV0Z50040507 and AV0Z50040702.

References

[1] Board on Radiation Effects Research (BRER) Committee to Assess Health Risks from Exposure to Low Levels of Ionizing Radiation, National Research Council, Health Risks from Exposure to Low Levels of Ionizing Radiation: BEIR VII Phase 2, National Academies Press, Washington, DC, 2006.
[2] B. Elliott, M. Jasin, Double-strand breaks and translocations in cancer, Cell Mol. Life Sci. 59 (2002) 373–385.
[3] K.D. Mills, D.O. Ferguson, F.W. Alt, The role of DNA breaks in genomic instability and tumorigenesis, Immunol. Rev. 194 (2003) 77–95.
[4] C. Lukas, J. Bartek, J. Lukas, Imaging of protein movement induced by chromosomal breakage: tiny 'local' lesions pose great 'global' challenges, Chromosoma 114 (2005) 146–154.
[5] M.J. Kruhlak, A. Celeste, G. Dellaire, O. Fernandez-Capetillo, W.G. Muller, J.G. McNally, D.P. Bazett-Jones, A. Nussenzweig, Changes in chromatin structure andmobility in living cells at sites of DNA double-strand breaks, J. Cell Biol. 172 (2006) 823–834.
[6] J.I. Loizou, R. Murr, M.G. Finkbeiner, C. Sawan, Z.Q. Wang, Z. Herceg, Epigenetic information in chromatin: the code of entry for DNA repair, Cell Cycle 5 (2006) 696–701.
[7] M. Falk, E. Lukasova, B. Gabrielova, V. Ondrej, S. Kozubek, Chromatin dynamics during DSB repair, BBA – Mol. Cell Res. 1773 (10) (2007) 1534–1545.
[8] B. Jakob, J. Splinter, M. Durante, G. Taucher-Scholz, Live cell microscopy analysis of radiation-induced DNA double-strand break motion, PNAS 106 (9) (2009) 3172–3177.
[9] J.A. Aten, J. Stap, P.M. Krawczyk, C.H. van Oven, R.A. Hoebe, J. Essers, R. Kanaar, Dynamics of DNA double-strand breaks revealed by clustering of damaged chromosome domains, Science 303 (2004) 92–95.
[10] H. Scherthan, L. Hieber, H. Braselmann, V. Meineke, H. Zitzelsberger, Accumulation of DSBs in γ-H2AX domains fuel chromosomal aberrations, Biochem. Biophys. Res. Commun. 371 (4) (2008) 694–697.
[11] B.E. Nelms, R.S. Maser, J.F. MacKay, M.G. Lagally, J.H. Petrini, In situ visualization of DNA double-strand break repair in human fibroblasts, Science 280 (1998) 590–592.
[12] M.N. Nikiforova, J.R. Stringer, R. Blough, M. Medvedovic, J.A. Fagin, Y.E. Nikiforov, Proximity of chromosomal loci that participate in radiation-induced rearrangements in human cells, Science 290 (5489) (2000) 138–141.
[13] J. Vazquez, A.S. Belmont, J.W. Sedat, Multiple regimes of constrained chromosome motion are regulated in the interphase Drosophila nucleus, Curr Biol. 11 (2001) 1227–1239.
[14] T. Tumbar, A.S. Belmont, Interphase movements of a DNA chromosome region modulated by VP16 transcriptional activator, Nat. Cell Biol. 3 (2001) 134–139.
[15] P. Heun, T. Laroche, K. Shimada, P. Furrer, S.M. Gasser, Chromosome dynamics in the yeast interphase nucleus, Science 294 (2001) 2181–2186.
[16] J.R. Chubb, S. Boyle, P. Perry, W.A. Bickmore, Chromatin motion is constrained by association with nuclear compartments in human cells, Curr Biol. 12 (2002) 439–445.
[17] The ESF-EMBO Symposium on Spatio-Temporal Radiation Biology: Transdisciplinary Advances for Biomedical Applications, 16–21st May 2009, Sant Feliu de Guixols (Costa Brava), Spain.
[18] M. Modesti, R. Kanaar, DNA repair: spot(light)s on chromatin, Curr. Biol. 11 (2001) R229–R232.
[19] K. Rothkamm, M. Löbrich, Misrepair of radiation-induced DNA double-strand breaks and its relevance for tumorigenesis and cancer treatment, Int. J. Oncol. 21 (2) (2002) 433–440.
[20] K. Rothkamm, M. Löbrich, Evidence for a lack of DNA double-strand break repair in human cells exposed to very low X-ray doses, PNAS 100 (2003) 5057–5062.

[21] E.P. Rogakou, D.R. Pilch, A.H. Orr, V.S. Ivanova, W.M. Bonner, DNA double strand breaks induce histone H2AX phosphorylation on serine 139, J. Biol. Chem. 273 (1998) 5858–5868.
[22] E.P. Rogakou, C. Boon, C. Redon, W.M. Bonner, Megabase chromatin domains involved in DNA double-strand breaks in vivo, JCB 146 (5) (1999) 905–916.
[23] O.A. Sedelnikova, E.P. Rogakou, I.G. Panyutin, W.M. Bonner, Quantitative detection of (125)IdU-induced DNA double-strand breaks with gamma-H2AX antibody, Radiat. Res. 158 (4) (2002) 486–492.
[24] T.T. Paull, E.P. Rogakou, V. Yamazaki, C.U. Kirchgessner, M. Gellert, W.M. Bonner, A critical role for histone H2AX in recruitment of repair factors to nuclear foci after DNA damage, Curr. Biol. 10 (2000) 886–895.
[25] E. Markova, N. Schultz, I.Y. Belyaev, Kinetics and dose-response of residual 53BP1/gamma-H2AX foci: co-localization, relationship with DSB repair and clonogenic survival, Int, J. Radiat. Biol. 83 (5) (2007) 319–329.
[26] E. Riballo, M. Kühne, N. Rief, A. Doherty, G.C.M. Smith, M.-J. Recio, C. Reis, K. Dahm, A. Fricke, A. Krempler, et al., A pathway of double-strand break rejoining dependent upon ATM, artemis, and proteins locating to γ-H2AX foci, Mol. Cell 16 (2004) 715–724.
[27] F. Antonelli, M. Belli, G. Cuttone, V. Dini, G. Esposito, G. Simone, E. Sorrentino, M.A. Tabocchini, Induction and repair of DNA double-strand breaks in human cells: dephosphorylation of histone H2AX and its inhibition by calyculin A, Radiat. Res. 164 (2005) 514–517.
[28] E.L. Leatherbarrow, J.V. Harper, F.A. Cucinotta, P. O'Neill, Induction and quantification of γ-H2AX foci following low and high LET-irradiation, Int. J. Radiat. Biol. 82 (2006) 111–118.
[29] A. Kinner, W. Wu, Ch. Staudt, G. Iliakis, γ-H2AX in recognition and signaling of DNA double-strand breaks in the context of chromatin, NAR 36 (17) (2008) 5678–5694.
[30] N. Foray, C. Badie, G. Alsbeih, B. Fertil, E.P. Malaise, A new model describing the curves for repair of both DNA double-strand breaks and chromosome damage, Radiat. Res. 146 (1) (1996) 53–60.
[31] B. Stenerlöw, K.H. Karlsson, B. Cooper, B. Rydberg, Measurement of prompt DNA double-strand breaks in mammalian cells without including heat-labile sites: results for cells deficient in nonhomologous end joining, Radiat. Res. 159 (4) (2003) 502–510.
[32] F.A. Cucinotta, J.M. Pluth, J.A. Anderson, J.V. Harper, P. O'Neill, Biochemical kinetics model of DSB repair and induction of gamma-H2AX foci by nonhomologous end joining, Radiat. Res. 169 (2) (2008) 214–222.
[33] N. Foray, C. Monroco, B. Marples, J.H. Hendry, B. Fertil, D.T. Goodhead, C.F. Arlett, E.P. Malaise, Repair of radiation-induced DNA double-strand breaks in human fibroblasts is consistent with a continuous spectrum of repair probability, Int. J. Radiat. Biol. 74 (5) (1998) 551–560.
[34] N. Foray, A.M. Charvet, D. Duchemin, V. Favaudon, D. Lavalette, The repair rate of radiation-induced DNA damage: a stochastic interpretation based on the gamma function, J. Theor. Biol. 236 (4) (2005) 448–458.
[35] M.R. Lieber, The mechanism of human nonhomologous DNA end joining, J. Biol. Chem. 283 (2008) 1–5.
[36] L.H. Thompson, D. Schild, Homologous recombinational repair of DNA ensures mammalian chromosome stability, Mutat. Res. 477 (2001) 131–153.
[37] S.V. Costes, A. Ponomarev, J.L. Chen, D. Nguyen, F.R. Cucinotta, M.H. Barcellos-Hoff, Image-based modeling reveals dynamic redistribution of DNA damage into nuclear sub-domains, PLOS Computat. Biol. 3 (8) (2007) 1477–1488.
[38] L. Metzger, G. Iliakis, Kinetics of DNA double-strand break repair throughout the cell cycle as assayed by pulsed field gel electrophoresis in CHO cells, Int. J. Radiat. Biol. 59 (6) (1991) 1325–1339.
[39] C. Chang, K.A. Biedermann, M. Mezzina, J.M. Brown, Characterization of the DNA double strand break repair defect in scid mice, Cancer. Res. 53 (6) (1993) 1244–1248.
[40] B. Cedervall, F. Sirzea, O. Brodin, R. Lewensohn, Less Initial rejoining of X-ray-induced DNA double-strand breaks in cells of a small cell (U-1285) compared to a large cell (U-1810) lung carcinoma cell line, Radiat. Res. 139 (1) (1994) 34–39.
[41] I. Gradzka, T. Iwaneńko, A non-radioactive, PFGE-based assay for low levels of DNA double-strand breaks in mammalian cells, DNA Repair 4 (10) (2005) 1129–1139.
[42] B. Jakob, M. Scholz, G. Taucher-Scholz, Biological imaging of heavy charged-particle tracks, Radiat. Res. 159 (2003) 676–684.
[43] K.H. Karlsson, B. Stenerlow, Focus formation of DNA repair proteins in normal and repair-deficient cells irradiated with high-LET ions, Radiat. Res. 161 (2004) 517–527.
[44] C.H. Bassing, K.F. Chua, J. Sekiguchi, H. Suh, S.R. Whitlow, J.C. Fleming, B.C. Monroe, D.N. Ciccone, C. Yan, K. Vlasakova, et al., Increased ionizing radiation sensitivity and genomic instability in the absence of histone H2AX, PNAS 99 (2002) 8173–8178.
[45] A. Celeste, S. Petersen, P.J. Romanienko, O. Fernandez-Capetillo, H.T. Chen, O.A. Sedelnikova, B. Reina-San-Martin, V. Coppola, E. Meffre, M.J. Difilippantonio, C. Redon, D.R. Pilch, A. Olaru, M. Eckhaus, R.D. Camerini-Otero, L. Tessarollo, F. Livak, K. Manova, W.M. Bonner, M.C. Nussenzweig, A. Nussenzweig, Genomic instability in mice lacking histone H2AX, Science 296 (5569) (2002) 922–927.
[46] A. Celeste, O. Fernandez-Capetillo, M.J. Kruhlak, D.R. Pilch, D.W. Staudt, A. Lee, R.F. Bonner, W.M. Bonner, A. Nussenzweig, Histone H2AX phosphorylation is dispensable for the initial recognition of DNA breaks, Nat. Cell Biol. 5 (2003) 675–679.
[47] D.R. Pilch, O.A. Sedelnikova, C. Redon, A. Celeste, A. Nussenzweig, W.M. Bonner, Characteristics of γ-H2AX foci at DNA double-strand breaks sites, Biochem. Cell Biol. 81 (3) (2003) 123–129.
[48] A. Celeste, S. Difilippantonio, M.J. Difilippantonio, O. Fernandez-Capetillo, D.R. Pilch, O.A. Sedelnikova, M. Eckhaus, T. Ried, W.M. Bonner, A. Nussenzweig, H2AX haploinsufficiency modifies genomic stability and tumor susceptibility, Cell 114 (2003) 371–383.
[49] A.A. Goodarzi, A.T. Noon, D. Deckbar, Y. Ziv, Y. Shiloh, M. Löbrich, P.A. Jeggo, ATM signaling facilitates repair of DNA double-strand breaks associated with heterochromatin, Mol. Cell 31 (2008) 167–177.
[50] A.A. Goodarzi, P.A. Jeggo, 'A mover and a shaker': 53BP1 allows DNA double-strand breaks a chance to dance and unite, F1000 Biol Rep 1 (2009) 21.
[51] A.A. Goodarzi, A.T. Noon, P.A. Jeggo, The impact of heterochromatin on DSB repair, Biochem. Soc. Trans. 37 (2009) 569–576.
[52] Y. Zhondsheng, J.M. Bailis, S.A. Johnson, S.M. Dilworth, T. Hunter, Rapid activation of ATM on DNA flanking double-strand breaks, Nat. Cell Biol. 9 (2008) 1311–1318.
[53] A.A. Goodarzi, A.T. Noon, P.A. Jeggo, Heterochromatic DNA double strand break repair, Acta Med. Nagasaki 53 (2009) 13–17.
[54] I.G. Cowell, N.J. Sunter, P.B. Singh, C.A. Austin, B.W. Durkacz, M.J. Tilby, γH2AX foci form preferentially in euchromatin after ionising-radiation, PLoS ONE 2 (10) (2007) e1057, doi:10.1371/journal. pone.0001057.
[55] T.C. Karagiannis, H. Kn, A. El-Osta, Disparity of histone deacetylase inhibition on repair of radiation-induced DNA damage on euchromatin and constitutive heterochromatin, Oncogene 25 (2007) 3963–3971.
[56] J.A. Kim, M. Kruhlak, F. Dotiwala, A. Nussenzweig, J.E. Haber, Heterochromatin is refractory to g-H2AX modification in yeast and mammals, J. Cell. Biol. 178 (2007) 209–218.
[57] C.J. Bakkenist, M.B. Kastan, DNA damage activates ATM through intermolecular autophosphorylation and dimmer association, Nature 421 (2003) 499–506.
[58] A.M. Gontijo, C.M. Green, G. Almouzni, Repairing DNA damage in chromatin, Biochemie 85 (2003) 1134–1147.
[59] O. Fernandez-Capetillo, A. Lee, M. Nussenzweig, A. Nussenzweig, H2AX: The histone guardian of the genome, DNA Repair 3 (8–9) (2004) 959–967.
[60] A. Verger, M. Crossley, Chromatin modifiers in transcription and DNA repair, Cell. Mol. Life Sci. 61 (2004) 2154–2162.
[61] T. Tsukuda, A.B. Fleming, J.A. Nickoloff, M.A. Osley, Chromatin remodelling of a DNAdouble-strand break site in *Saccharomyces cerevisiae*, Nature 438 (2005) 379–383.
[62] R. Murr, J.I. Loizou, Y.G. Yang, C. Cuenin, H. Li, Z.Q. Wang, Z. Herceg, Histone acetylation by Trrap-Tip60 modulated loading of repair proteins and repair of DNA double-strand breaks, Nat. Cell Biol. 8 (2006) 91–99.
[63] Y. Ziv, D. Bielopolski, Y. Galanty, C. Lukas, Y. Taya, D.C. Schultz, J. Lukas, S. Bekker-Jensen, J. Bartek, Y. Shiloh, Chromatin relaxation in response to DNA double-strand breaks is modulated by a novel ATM- and KAP-1 dependent pathway, Nat. Cell Biol. 8 (2006) 870–876.
[64] M. Falk, E. Lukasova, S. Kozubek, Chromatin structure influences the sensitivity of DNA to γ-radiation, BBA – Mol. Cell Res. 1783 (12) (2008) 2398–2414.
[65] M. Falk, E. Lukasova, B. Gabrielova, V. Ondrej, S. Kozubek, Local changes of higher-order chromatin structure during DSB-repair, J. Phys. 101 (2008) 012018, doi:10.1088/1742-6596/101/1/012018.
[66] E.L. Leatherbarrow, J.V. Harper, F.A. Cucinotta, P. O'Neill, Induction and quantification of g -H2AX foci following low and high LET-irradiation, Int. J. Radiat. Biol. 82 (2) (2006) 111–118.
[67] B. Nevaldine, J.A. Longo, M. Vilenchik, G.A. King, P.J. Hahn, Induction and repair of DNA double-strand breaks in the same dose range as the shoulder of the survival curve, Radiat. Res. 140 (2) (1994) 161–165.
[68] L.B. Schultz, N.H. Chehab, A. Malikzay, T.D. Halazonetis, p53 binding protein 1 (53BP1) is an early participant in the cellular response to DNA double-strand breaks, JCB 151 (7) (2000) 1381–1390.
[69] M.S. Luijsterburg, C. Dinant, H. Lans, J. Stap, E. Wiernasz, S. Lagerwerf, D.O. Warmerdam, M. Lindh, M.C. Brink, J.W. Dobrucki, et al., Heterochromatin protein 1 is recruited to various types of DNA damage, JCB 185 (2009) 577–586.
[70] S. Burma, B.P. Chen, M. Murphy, A. Kurimasa, D.J. Chen, ATM phosphorylates histone H2AX in response to DNA double-strand breaks, J. Biol. Chem. 276 (45) (2001) 42462–42467.
[71] L.L. Sandell, V.A. Zakian, Loss of a yeast telomere: arrest, recovery, and chromosome loss, Cell 75 (4) (1993) 729–739.
[72] H.Y. Yoo, A. Kumagai, A. Shevchenko, W.G. Dunphy, Adaptation of a DNA replication checkpoint response depends upon inactivation of Claspin by the Polo-like kinase, Cell 117 (2004) 575–588.
[73] R.G. Syljuasen, S. Jensen, J. Bartek, J. Lukas, Adaptation to the ionizing radiation-induced G2 checkpoint occurs in human cells and depends on checkpoint kinase 1 and Polo-like kinase 1 kinases, Cancer Res. 66 (2006) 10253–10257.
[74] J. Bartek, J. Lukas, DNA damage checkpoints: from initiation to recovery or adaptation, Cur. Opin. Cell Biol. 19 (2007) 238–245.
[75] S.P. Jackson, J. Bartek, The DNA-damage response in human biology and disease, Nature 461 (2009) 1071–1078.
[76] A. Joubert, K.M. Zimmerman, Z. Bencokova, J. Gastaldo, N. Chavaudra, V. Favaudon, C.F. Arlett, N. Foray, DNA double-strand break repair defects in syndromes associated with acute radiation response: at least two different assays to predict intrinsic radiosensitivity? Int. J. Radiat. Biol. 84 (2) (2008) 107–125.
[77] I. Szumiel, Intrinsic radiation sensitivity: cellular signaling is the key, Radiat. Res. 169 (3) (2008) 249–258.
[78] E. Bartova, S. Kozubek, P. Jirsova, M. Kozubek, H. Gajova, E. Lukasova, M. Skalnikova, A. Gannova, I. Koutna, M. Hausmann, Nuclear structure and gene activity in human differentiated cells, J. Struct. Biol. 139 (2) (2002) 76–89.
[79] S. Kozubek, E. Lukasova, P. Jirsová, I. Koutna, M. Kozubek, A. Ganova, E. Bartova, M. Falk, R. Pasekova, 3D structure of the human genome: order in randomness, Chromosoma 111 (5) (2002) 321–331.

[80] N.L. Mahy, P.E. Perry, S. Gilchrist, R.A. Baldock, W.A. Bickmore, Spatial organization of active and inactive genes and noncoding DNA within chromosome territories, JCB 157 (4) (2002) 579–589.
[81] M. Neusser, V. Schubel, A. Koch, T. Cremer, S. Müller, Evolutionarily conserved, cell type and species-specific higher order chromatin arrangements in interphase nuclei of primates, Chromosoma 116 (3) (2007) 307–320.
[82] M.S. Gandhi, J.R. Stringer, M.N. Nikiforova, M. Medvedovic, Y.E. Nikiforov, Gene position within chromosome territories correlates with their involvement in distinct rearrangement types in thyroid cancer cells, Genes Chrom. Cancer 48 (3) (2009) 222–228.
[83] T. Cremer, M. Cremer, S. Dietzel, S. Müller, I. Solovei, S. Fakan, Chromosome territories – a functional nuclear landscape, Curr. Opin. Cell Biol. 18 (3) (2006) 307–316.
[84] E. Bártová, S. Kozubek, Nuclear architecture in the light of gene expression and cell differentiation studies, Biol. Cell. 98 (6) (2006) 323–336.
[85] M.R. Branco, A. Pombo, Intermingling of chromosome territories in interphase suggests role in translocations and transcription-dependent associations, PLoS Biol. 4 (5) (2006) 780–788.
[86] P. Fraser, W. Bickmore, Nuclear organization of the genome and the potential for gene regulation, Nature 447 (7143) (2007) 413–417.
[87] T. Sexton, H. Schober, P. Fraser, S.M. Gasser, Gene regulation through nuclear organization, Nat. Struct. Mol. Biol. 14 (11) (2007) 1049–1055.
[88] T. Misteli, Cell biology: nuclear order out of chaos, Nature 456 (7220) (2008) 333–334.
[89] O.J. Rando, H.Y. Chang, Genome-wide views of chromatin structure, Annu. Rev. Biochem. 78 (2009) 245–271.
[90] H. Caron, B. van Schaik, M. van der Mee, F. Baas, G. Riggins, P. van Sluis, M.C. Hermus, R. van Asperen, K. Boon, P.A. Voute, et al., The human transcriptome map: clustering of highly expressed genes in chromosomal domains, Science 291 (2001) 1289–1292.
[91] R. Versteeg, B.D.C. van Schaik, M.F. van Batenburg, M. Roos, R. Monajemi, H. Caron, H.J. Bussemaker, A.H.C. van Kampen, The human transcriptome map reveals extremes in gene density, intron length, GC content, and repeat pattern for domains of highly and weakly expressed genes, Genome Res. 13 (9) (2003) 1998–2004.
[92] S. Goetze, J. Mateos-Langerak, H. Gierman, W. de Leeuw, O. Giromus, M.H.G. Indemans, J. Koster, V. Ondřej, R. Versteeg, R. van Driel, The three-dimensional structure of human interphase chromosomes is related to the transcriptome map, Mol. Cell. Biol. 27 (2007) 4475–4487.
[93] E. Lukášová, S. Kozubek, M. Kozubek, M. Falk, J. Amrichová, The 3D structure of human chromosomes in cell nuclei, Chrom. Res. 10 (2002) 535–548.
[94] A.T. Natarajan, G. Ahnström, Heterochromatin and chromosome aberrations, Chromosoma 28 (1969) 48–61.
[95] G.A. Folle, W. Martínez-López, E. Boccardo, G. Obe, Localization of chromosome breakpoints: implication of the chromatin structure and nuclear architecture, Mutat. Res. 404 (1–2) (1998) 17–26.
[96] M. Löbrich, P.K. Cooper, B. Rydberg, Non-random distribution of DNA double-strand breaks induced by particle irradiation, Int. J. Radiat. Biol. 70 (1996) 493–503.
[97] M.C. Elia, M.O. Bradley, Influence of chromatin structure on the induction of DNA double strand breaks by ionizing radiation, Cancer Res. 52 (1992) 1580–1586.
[98] K. Rothkamm, M. Löbrich, Misrejoining of DNA double-strand breaks in primary and transformed human and rodent cells: A comparison between the HPRT region and other genomic locations, Mutat. Res. 433 (1999) 193–205.
[99] A. Sak, M. Stuschke, N. Stapper, C. Streffer, Induction of DNA double-strand breaks by ionizing radiation at the c-myc locus compared with the whole genome: a study using pulsed-field gel electrophoresis and gene probing, Int. J. Radiat. Biol. 69 (6) (1996) 679–685.
[100] M. Löbrich, M. Kühne, J. Wetzel, K. Rothkamm, Joining of correct and incorrect DNA double-strand break ends in normal human and ataxia telangiectasia fibroblasts, Genes Chrom. Cancer. 27 (1) (2000) 59–68.
[101] B. Fouladi, Ch.A. Waldren, B. Rydberg, P.K. Cooper, Comparison of repair of DNA double-strand breaks in identical sequences in primary human fibroblast and immortal hamster–human hybrid cells harboring a single copy of human Chromosome 11, Radiat. Res. 153 (6) (2000) 795–804.
[102] S. Puerto, M.J. Ramirez, R. Marcos, A. Creus, J. Surralles, Radiation-induced chromosome aberrations in human euchromatic (17cen-p53) and heterochromatic (1cen–1q12) regions, Mutagenesis 16 (2001) 291–296.
[103] W. Martinez-Lopez, G.A. Folle, G. Cassina, L. Mendez-Acuna, M.V. Di-Tomase, et al., Distribution of breakpoints induced by etoposide and X-rays along the CHO X chromosome, Cytogenet. Genome Res. 104 (2004) 182–187.
[104] A. Pombo, P. Cuello, W. Schul, J.B. Yoon, R.G. Roeder, P.R. Cook, S. Murphy, Regional and temporal specialization in the nucleus: a transcriptionally-active nuclear domain rich in PTF, Oct1 and PIKA antigens associated with specific chromosomes early in the cell cycle, EMBO J. 17 (1998) 1768–1778.
[105] L.K. Mee, S.J. Adelstein, Radiation damage to histone H2A by the primary aqueous radicals, Rad. Res. 110 (1987) 155–160.
[106] J.F. Ward, W.F. Blakely, E.I. Joner, Mammalian cells are not killed by DNA single-strand breaks caused by hydroxyl radicals from hydrogen peroxide, Radiat. Res. 1113 (1985) 383–392.
[107] H. Joenje, Genetic toxicologz of oxygen, Mutat. Res. 219 (1989) 193–208.
[108] V. Stepán, M. Davídková, Theoretical modelling of radiolytic damage of free DNA bases and within DNA macromolecule, Radiat. Prot. Dosimetry 122 (2006) 110–112.
[109] A.J. Bannister, P. Zergman, J.F. Partridge, E.A. Miska, J.O. Thomas, R.C. Allshire, T. Kouzarides, Selective recognition of methylated lysine 9 on histone H3 by the HP1 chromo domain, Nature 410 (2001) 120–124.
[110] W.H. Lachner, D. O'Carroll, S. Rea, K. Mechtler, T. Jenuwein, Methylation of histone H3 Lysine 9 creates a binding site for HP1 proteins, Nature 410 (2001) 116–120.
[111] I.G. Cowell, R. Aucott, S.K. Mahadevaiah, P.S. Burgoyne, N. Huskisson, et al., Heterochromatin, HP1 and methylation at lysine 9 of histone H3 in animals, Chromosoma 111 (2002) 22–36.
[112] R.L. Warters, B.W. Lyons, Variation in radiation-induced formation of DNA double-strand breaks as a function of chromatin structure, Radiat. Res. 130 (1992) 309–318.
[113] C.M. Dettor, W.C. Dewey, L.F. Winans, J.S. Noel, Enhancement of X-ray damage in synchronous Chinese hamster cells by hypertonic treatment, Radiat. Res. 52 (1972) 352–373.
[114] R.M. Anderson, D.L. Stevens, D.T. Goodhead, M-FISH analysis shows that complex chromosome aberrations induced by alpha-particle tracks are cumulative products of localized rearrangements, PNAS 99 (2002) 12167–12172.
[115] J. Surrallés, F. Darroudi, A.T. Natarajan, Low level of DNA repair in human chromosome 1 heterochromatin, Genes Chromosom. Cancer 20 (1997) 173–184.
[116] M.A. Osley, T. Tsukuda, J.A. Nickoloff, ATP-dependent chromatin remodeling factors and DNA damage repair, Mutat. Res. 618 (2007) 65–80.
[117] W.G. Muller, D. Walker, G.L. Hager, J.G. McNally, Large-scale chromatin decondensation resulted by transcription from a natural promoter, J. Cell Biol. 154 (2001) 33–48.
[118] A.C. Nye, R.R. Rajendran, D.L. Stenoien, M.A. Mancini, B.S. Katzenellenbogen, A.S. Belmont, Alteration of large-scale chromatin structure by estrogen receptor, Mol. Cell Biol. 22 (2002) 3437–3449.
[119] A.E. Carpenter, S. Memedula, M.J. Plutz, A.S. Belmont, Common effect of acidic activators on large-scale chromatin structure and transcription, Mol. Cell Biol. 25 (2005) 958–968.
[120] C.S. Osborne, L. Chakalova, K.E. Brown, D. Carter, A. Horton, E. Debrand, B. Goyenechea, J.A. Mitchell, S. Lopes, W. Reik, et al., Active genes dynamically colocalize to shared sites of ongoing transcription, Nat. Genet. 36 (2004) 1065–1071.
[121] M. Simonis, P. Klous, E. Splinter, Y. Moshkin, R. Willemsen, E. de Wit, B. van Steensel, W. de Laat, Nuclear organization of active and inactive chromatin domains uncovered by chromosome conformation capture-on-chip (4C), Nat. Genet. 38 (2006) 1348–1354.
[122] A. Dean, Jackson, The amazing complexity of transcription factories, Brief. Funct. Genom. Proteom. 4 (2) (2005) 143–157.
[123] T. Sexton, D. Umlauf, S. Kurukuti, P. Fraser, The role of transcription factories in large-scale structure and dynamics of interphase chromatin, Semin. Cell Dev. Biol. 18 (5) (2007) 691–697.
[124] H. Sutherland, W.A. Bickmore, Transcription factories: gene expression in unions? Nat. Rev. Genet. 10 (2009) 457–466.
[125] E. Soutoglou, T. Misteli, Mobility and immobility of chromatin in transcription and genome stability, Curr. Opin. Genet. Dev. 17 (5) (2007) 435–442.
[126] N. Desai, E. Davis, P. O'Neill, M. Durante, F.A. Cucinotta, H. Wu, Immunofluorescence detection of clustered γ-H2AX foci induced by HZE-particle radiation, Radat. Res. 164 (4) (2005) 518–522.
[127] P.M. Krawczyk, J. Stap, C. van Oven, R. Hoebe and J.A. Aten, Clustering of double strand break-containing chromosome domains is not inhibited by inactivation of major repair proteins, Radiat. Prot. Dosim. 2006 122 (1–4) 150–153; doi:10.1093/rpd/ncl479.
[128] M. Lisby, U.H. Mortensen, R. Rothstein, Colocalization of multiple DNA double-strand breaks at a single Rad52 repair centre, Nat. Cell Biol. 5 (2003) 72–577.
[129] M. Lisby, J.H. Barlow, R.C. Burgess, R. Rothstein, Choreography of the DNA damage response: spatiotemporal relationships among checkpoint and repair proteins, Cell 118 (2004) 699–713.
[130] S. Brons, K. Psonka, M. Heiß, E. Gudowska-Nowak, G. Taucher-Scholz, R. Neumann, Direct visualisation of heavy ion induced DNA fragmentation using Atomic Force Microscopy, Radiother. Oncol. 73 (2) (2004) S112–S114.
[131] B. Stenerlöw, E. Höglund, J. Carlsson, DNA fragmentation by charged particle tracks, Adv. Space Res. 30 (4) (2002) 859–863.
[132] B. Rydberg, Clusters of DNA damage induced by ionizing radiation: formation of short DNA fragments. II. Experimental detection, Radiat. Res. 145 (1996) 200–209.
[133] H. Nikjoo, P. O'Neill, W.E. Wilson, D.T. Goodhead, Computational approach for etermining the spectrum of DNA damage induced by ionizing radiation, Radiat. Res. 156 (2001) 577–583.
[134] K.M. Prise, G. Ahnstrom, M. Belli, J. Carlsson, D. Frankenberg, J. Kiefer, M. Lobrich, B.D. Michael, J. Nygren, G. Simone, B. Sternerlow, A review of dsb induction data for varying quality radiations, Int. J. Radiat. Biol. 74 (1998) 173–184.
[135] K.M. Prise, M. Pinto, H.C. Newman, B.D. Michael, A review of studies of ionizing radiation-induced double-strand break clustering, Radiat. Res. 156 (2001) 572–576.
[136] R.G. Syljuåsen, S. Jensen, J. Bartek, J. Lukas, Adaptation to the ionizing radiation-induced G2 checkpoint occurs in human cells and depends on Chk1 and Plk1 kinases, Cancer Res. 66 (2006) 10253–10257.
[137] R.G. Syljuåsen, Checkpoint adaptation in human cells, Oncogene 26 (2007) 5833–5839.
[138] J. Bartek, J. Lukas, DNA damage checkpoints: from initiation to recovery or adaptation, Curr. Opin. Cell Biol. 19 (2) (2007) 238–245.

[139] K.S. Vijayalaxmi, W.F. Bisht, M.L. Pickard, J.L. Meltz, E.G. Roti Roti, Moros, Chromosome damage and micronucleus formation in human blood lymphocytes exposed in vitro to radiofrequency radiation at a cellular telephone frequency (847.74 MHz, CDMA), Radiat. Res. 156 (2001) 430–432.
[140] N.N. Bhat, B.S. Rao, Dose rate effect on micronuclei induction in cytokinesis blocked human peripheral blood lymphocytes, Radiat. Prot. Dosim. 106 (2003) 45–52.
[141] S. Kozubek, E. Lukasova, L. Ryznar, M. Kozubek, A. Liskova, R.D. Govorun, E.A. Krasavin, G. Horneck, Distribution of ABL and BCR genes in cell nuclei of normal and irradiated lymphocytes, Blood 89 (12) (1997) 4537–4545.
[142] E. Lukasova, S. Kozubek, M. Kozubek, J. Kjeronska, L. Ryznar, J. Horakova, E. Krahulcova, G. Horneck, Localisation and distance between ABL and BCR genes in interphase nuclei of bone marrow cells of control donors and patients with chronic myeloid leukaemia, Hum. Genet. 100 (5–6) (1997) 525–535.
[143] A. Cafourkova, E. Lukasova, S. Kozubek, M. Kozubek, R.D. Govorun, I. Koutna, E. Bartova, M. Skalnikova, P. Jirsova, R. Pasekova, E.A. Krasavin, Exchange aberrations among 11 chromosomes of human lymphocytes induced by gamma-rays, Int. J. Radiat. Biol. 77 (4) (2001) 419–429.
[144] J.J. Roix, P.G. McQueen, P.J. Munson, L.A. Parada, T. Misteli, Spatial proximity of translocation-prone gene loci in human lymphomas, Nat. Genet. 34 (3) (2003) 287–291.
[145] E. Roccato, P. Bressan, G. Sabatella, C. Rumio, L. Vizzotto, M.A. Pierotti, A. Greco, Proximity of TPR and NTRK1 rearranging loci in human thyrocytes, Cancer Res. 65 (7) (2005) 2572–2576.
[146] B. Jakob, J. Splinter, G. Taucher-Scholz, Positional Stability of damaged chromatin domains along radiation tracks in mammalian cells, Radiat. Res. 171 (4) (2009) 405–418.
[147] E. Soutoglou, T. Misteli, On the contribution of spatial genome organization to cancerous chromosome translocations, J. Natl. Cancer. Inst. Monogr. 39 (2008) 16–19.
[148] E. Soutoglou, J.F. Dorn, K. Sengupta, M. Jasin, A. Nussenzweig, T. Ried, G. Danuser, T. Misteli, Positional stability of single double-strand breaks in mammalian cells, Nat. Cell. Biol. 9 (2007) 675–682.

Critical Reviews™ in Eukaryotic Gene Expression, 24(3):205-223 (2014)

Determining Omics Spatiotemporal Dimensions Using Exciting New Nanoscopy Techniques to Assess Complex Cell Responses to DNA Damage: PART A—Radiomics

Martin Falk,[1,*] Michael Hausmann,[2] Emílie Lukášová,[1] Abin Biswas,[2,3] Georg Hildenbrand,[2,3] Marie Davídková,[4] Evgeny Krasavin,[5] Zdeněk Kleibl,[6] Iva Falková,[1] Lucie Ježková,[1,5,7] Lenka Štefančíková,[1] Jan Ševčík,[6] Michal Hofer,[1] Alena Bačíková,[1] Pavel Matula,[1,8] Alla Boreyko,[5] Jana Vachelová,[4] Anna Michaelidesová,[4,9] & Stanislav Kozubek[1]

[1]Institute of Biophysics, Academy of Sciences of the Czech Republic, Brno, Czech Republic; [2]Kirchhoff Institute for Physics, University of Heidelberg, Heidelberg, Germany; [3]Department of Radiation Oncology, University Medical Center Mannheim, University of Heidelberg, Heidelberg, Germany; [4]Nuclear Physics Institute, Academy of Sciences of the Czech Republic, Řež, Czech Republic; [5]Joint Institute for Nuclear Research, Dubna, Moscow, Russia; [6]Institute of Biochemistry and Experimental Oncology, First Faculty of Medicine, Charles University, Prague, Czech Republic; [7]Institute of Chemical Technology Prague, Prague, Czech Republic; [8]Centre for Biomedical Image Analysis, Faculty of Informatics, Masaryk University, Brno, Czech Republic; [9]Proton Therapy Center, Prague, Czech Republic

*** Address all correspondence to:** Martin Falk, PhD, Department of Chromatin Function, Damage and Repair Institute of Biophysics, Academy of Sciences of the Czech Republic, Královopolská 135 612 65 Brno, Czech Republic; Tel.: +420-541517165; falk@ibp.cz, mfalk@seznam.cz.

ABSTRACT: Recent ground-breaking developments in Omics have generated new hope for overcoming the complexity and variability of biological systems while simultaneously shedding more light on fundamental radiobiological questions that have remained unanswered for decades. In the era of Omics, our knowledge of how genes and proteins interact in the frame of complex networks to preserve genome integrity has been rapidly expanding. Nevertheless, these functional networks must be observed with strong correspondence to the cell nucleus, which is the main target of ionizing radiation. Nuclear architecture and nuclear processes, including DNA damage responses, are precisely organized in space and time. Information regarding these intricate processes cannot be achieved using high-throughput Omics approaches alone, but requires sophisticated structural probing and imaging. Based on the results obtained from studying the relationship between higher-order chromatin structure, DNA double-strand break induction and repair, and the formation of chromosomal translocations, we show the development of Omics solutions especially for radiation research (radiomics) (discussed in this article) and how confocal microscopy as well as novel approaches of molecular localization nanoscopy fill the gaps to successfully place the Omics data in the context of space and time (discussed in our other article in this issue, "Determining Omics Spatiotemporal Dimensions Using Exciting New Nanoscopy Techniques to Assess Complex Cell Responses to DNA Damage: Part B—Structuromics"). Finally, we introduce a novel method of specific chromatin nanotargeting and speculate future perspectives, which may combine nanoprobing and structural nanoscopy to observe structure–function correlations in living cells in real time. Thus, the Omics networks obtained from function analyses may be enriched by real-time visualization of Structuromics.

KEY WORDS: Omics, ionizing radiation, low-dose dilemma, biological complexity and variability, higher-order chromatin structure, DNA damage response, formation of chromosomal translocations, confocal microscopy, localization nanoscopy

ABBREVIATIONS: γH2AX, histone **H2AX** phosphorylated on serine 139; **2D,** 2-dimensional; **3D,** 3-dimen sional; **ASV,** alternative splicing variant; **DSB,** double-strand breaks; **HUGO,** Human Genome Project; **IR,** ionizing radiation; **IRIF,** ionizing radiation–induced repair foci; **LET,** linear energy transfer; **LNT,** linear nonthreshold.

I. INTRODUCTION

A. Radiation Research on the Way from Dosimetry to Functional Radiation Response Mechanisms (Radiomics)

In this review we describe developments in radiation research that began in the late 60s, early 70s, when "physical" and later "biological" dosimetry were in focus. We show how functional understanding of Omics procedures leads to new perspectives in investigating radiation effects and opens an avenue for understanding mechanisms of biological radiation response beyond just purely counting the effects via dosimetry.

B. Deciphering God's Programming of Life, Our Transition to the Era of "Omics," and Optical Microscopy

In 1990, the Human Genome Project (HUGO)[1] was started with the primary goal of revealing the complete nucleotide sequence of the human genome. This international endeavor lasted for the next 13 years and undoubtedly represents one of the most important human projects in terms of its challenges, costs, and scientific benefits; it can be roughly compared with the cosmic Apollo project (see Ref. 2 and the citations therein). While the Apollo missions allowed mankind to venture out from mother Earth's embrace and journey to other celestial bodies for the first time, HUGO exposed humans to their "virtual essence" and transferred us from the era of genetics to genomics. However, by accomplishing the sequencing of the human genome and disclosing its nucleotide composition, we have only discovered a Pandora's box. To successfully decipher "God's programming of life," we must also identify genes and determine their respective protein counterparts and the diverse regulatory elements of the genome at different levels of interactions. This scientifically challenging process is still going on.

In addition, in the post-genome era, we face challenges that are much more ambitious than HUGO. What remains to be disclosed (after linking linear DNA sequences with individual functional units of the genome and proteome) are the mechanisms of how genomic instructions are translated to complex networks of precisely regulated life processes. To fully understand the problem, linguistically speaking, we must also comprehend the grammar, single words, sentences, paragraphs, chapters, stylistic elements, and finally the book in all its complexity. This attempt—feasible only because of the unbelievable progress made in bioinformatics and many fields of technology—resulted in the birth to the world of "Omics": transcriptomics (RNAomics), proteomics, metabolomics, epigenomics, interactomics, pharmacogenomics, pharmacoproteomics, and a plethora of other possible Omics disciplines. The suffix *-omics* is used to emphasize that the research deals with "holistic" systems, for instance, in the case of proteomics, with all proteins of an organelle, cell, organ, tissue, or organism. Individual fields of Omics thus study the composition, expression, and regulation of the genome at different parallel and hierarchical levels. Only integrated data from various Omics can, therefore, disclose the more complex image of the interplay between individual actors (single genes, micro RNAs, messenger RNAs, proteins, epigenetic markers, etc.) in the playground of interconnected signaling and "executive" pathways, their networks, and finally the networks of these networks. This "pan-omics" holistic approach is now referred as systems biology (e.g., see Refs. 3–6; see Ref. 7 for definitions). Although we are on the right path, tackling a challenge of this size will require (yet-)uninvented scientific techniques and devices that are capable of producing, analyzing, and storing extremely large amounts of data.

II. WAITING FOR THE OMICS: RADIOBIOLOGY ON THE ROAD TO COMPLEXITY

Radiobiological issues, which are focused on in this review, are an excellent example of a field of research where not only systems biology but also interdisciplinary cooperation between the natural sciences is of utmost importance. Radiation damage to biomolecular systems begins with the depo-

sition of physical energy, continues with chemical and biological processes, and potentially/ultimately ends up with medical consequences. This scenario can last from 10^{-18} seconds to several decades and encompasses spatial dimensions from molecules to whole organisms and their populations (reviewed by Foffa et al.,[8] Solov'yov et al.,[9] and Surdutovich et al.[10]) (Fig. 1). Even if we consider only biological response, radiation exposure simultaneously alters networks of interconnected regulatory and executive networks at different levels of hierarchy, which further induce positive as well as negative regulatory circuits (Fig. 1). Because of the extreme complexity (further discussed in the section "Complexity: Networks of Biological Networks"), some fundamental questions have remained unanswered since the beginning of radiobiological research.

A. The Low-Dose Dilemma

For instance, the persisting uncertainty regarding the biological effects of low radiation doses (<200 mSv) (Fig. 2) after decades of research is aggravating. In lieu of increasing exposures to ionizing radiation (IR) arising from medical radiodiagnostics, radiotherapy, and cosmic research, coupled with potential threats of "nuclear" terrorist attacks and industrial accidents, this topic currently emerges with a new urgency. Since the beginning of life, molecular and cellular systems have always been exposed to more or less sparse levels of IR. The issue of the noxiousness or profitability of radiation is an intriguing subject through which to study the development of mankind.

Because conclusions made from associated questions would possibly have extensive consequences on the philosophy and strategy of social development, extensive efforts have long been exerted to obtain epidemiological data on the risks of low doses of IR for human health. Many experiments also have been performed on animals and cells in culture to understand the mechanisms of radiobiological response (reviewed by Morgan and Bair[11]). However, instead of clarifying the situation, a knot of (contradictory) data from different experimental systems and conditions currently warrants the representation of more general conclusions.

Epidemiological data collected from highly exposed survivors of the Hiroshima, Nagasaki, and Chernobyl disasters revealed a linear dependence between detrimental health effects of IR exposure and the dose absorbed (the linear nonthreshold [LNT] model; Fig. 2, line a).[12–15] Such behavior is compatible with the idea of cell death that predominantly depends on DNA damage induced in proportion to the dose delivered. Low doses of IR are insufficient to cause deterministic end points but might initiate carcinogenesis and other stochastic (probabilistic) effects that have been proposed to arise from DNA damage with a linear relationship. Health risk estimates for low exposures, therefore, work on the assumption that the dose–response curve constructed for higher doses can also be extrapolated for doses that are much lower.[16,17] Accordingly, biological effects are believed to occur after any low level of exposure, without the threshold dose (Fig. 2, line a).[12,13]

A growing body of evidence, however, suggests that the dose–response relationship is no more linear for low IR doses (<200 mSv). Detailed biological experiments using various cell types along with different approaches to study double-strand break (DSB) repair at varying cellular end points of exposures to low doses of IR provide inconclusive results concerning the shape of the dose–response curve and frequently challenge the currently accepted LNT model (Fig. 2) (e.g., see Refs. 18–29; reviewed in Refs. 11 and 30–34; also see the citations therein). Many of these experiments point to considerable negative effects than would be expected from LNT predictions[35] (Fig. 2, curve b) (reviewed in Refs. 11 and 30–33; see also the citations therein). For instance, using a gel microdrop/flow cytometry assay to monitor single cell proliferation, Enns et al.[35] revealed a marked cell type–specific hypersensitivity of human A549 lung carcinoma cells and T98G glioma cells, but not MCF7 mammary carcinoma cells, to γ-radiation doses <50 cGy. In comparable studies, following cell survival as the end point, higher cell killing was usually observed for doses less than several

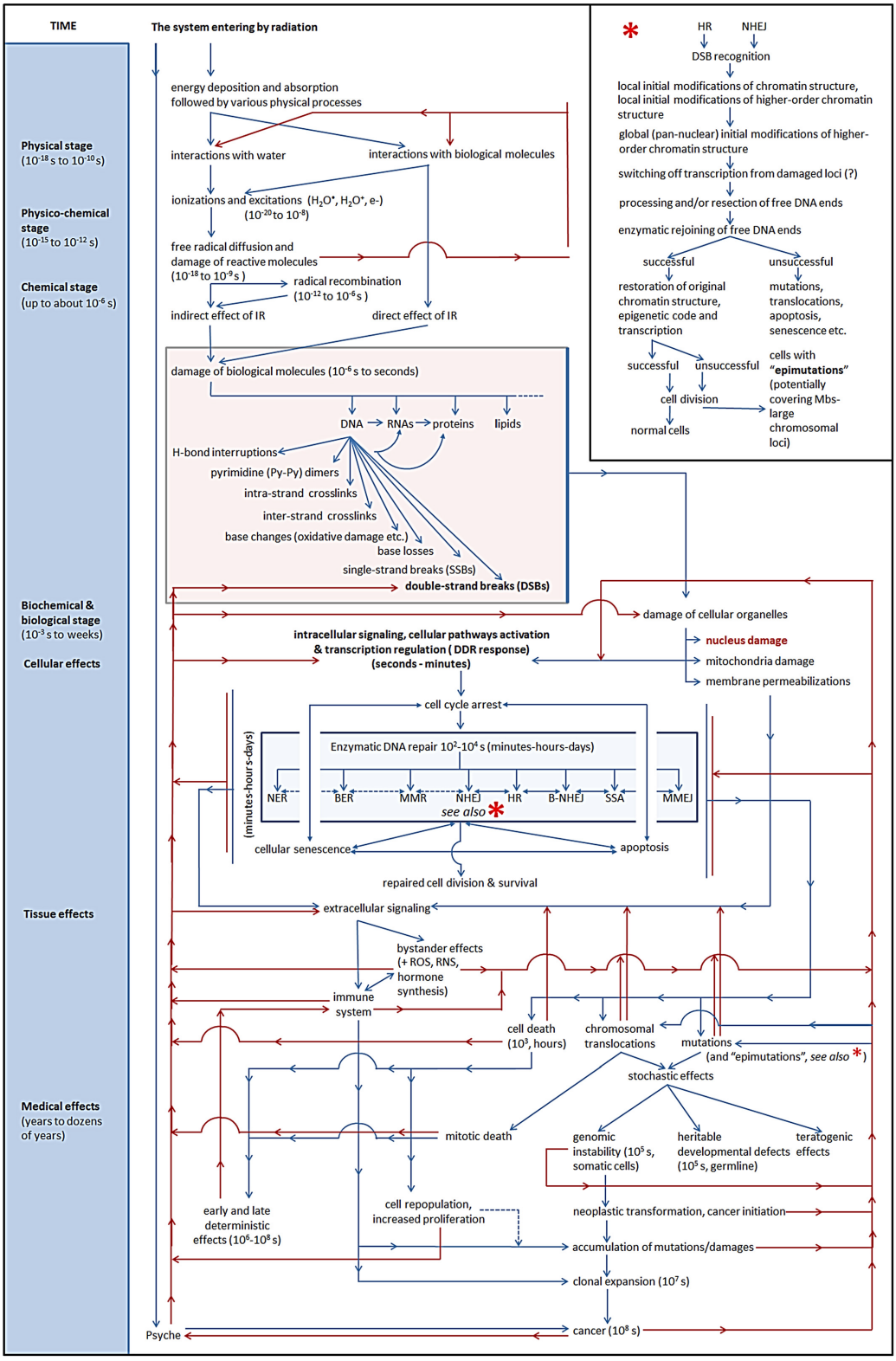
TIME
The system entering by radiation
Physical stage
(10-18 s to 10-10 s)
Physico-chemical stage
(10-15 to 10-12 s)
Chemical stage
(up to about 10-6 s)
Biochemical & biological stage
(10-3 s to weeks)
Cellular effects
Tissue effects
Medical effects
(years to dozens of years)
energy deposition and absorption followed by various physical processes
interactions with water
interactions with biological molecules
ionizations and excitations (H2O*, H2O+, e-) (10-20 to 10-8)
free radical diffusion and damage of reactive molecules (10-18 to 10-9 s)
radical recombination (10-12 to 10-6 s)
indirect effect of IR
direct effect of IR
damage of biological molecules (10-6 s to seconds)
DNA
RNAs
proteins
lipids
H-bond interruptions
pyrimidine (Py-Py) dimers
intra-strand crosslinks
inter-strand crosslinks
base changes (oxidative damage etc.)
base losses
single-strand breaks (SSBs)
double-strand breaks (DSBs)
damage of cellular organelles
nucleus damage
mitochondria damage
membrane permeabilizations
intracellular signaling, cellular pathways activation & transcription regulation (DDR response) (seconds - minutes)
cell cycle arrest
Enzymatic DNA repair 10²-10⁴ s (minutes-hours-days)
(minutes-hours-days)
NER
BER
MMR
NHEJ
HR
B-NHEJ
SSA
MMEJ
see also *
cellular senescence
apoptosis
repaired cell division & survival
extracellular signaling
bystander effects (+ ROS, RNS, hormone synthesis)
immune system
cell death (10³, hours)
chromosomal translocations
mutations (and "epimutations", see also *)
stochastic effects
mitotic death
genomic instability (10⁵ s, somatic cells)
heritable developmental defects (10⁵ s, germline)
teratogenic effects
early and late deterministic effects (10⁶-10⁸ s)
cell repopulation, increased proliferation
neoplastic transformation, cancer initiation
accumulation of mutations/damages
clonal expansion (10⁷ s)
cancer (10⁸ s)
Psyche
*
HR
NHEJ
DSB recognition
local initial modifications of chromatin structure, local initial modifications of higher-order chromatin structure
global (pan-nuclear) initial modifications of higher-order chromatin structure
switching off transcription from damaged loci (?)
processing and/or resection of free DNA ends
enzymatic rejoining of free DNA ends
successful
unsuccessful
restoration of original chromatin structure, epigenetic code and transcription
mutations, translocations, apoptosis, senescence etc.
successful
unsuccessful
cell division
normal cells
cells with "epimutations" (potentially covering Mbs-large chromosomal loci)

FIG. 1: The spatiotemporal complexity and multidisciplinary nature of radiomics. The processes that take place after the irradiation of a biological system start with physical energy deposition in a time scale of about 10^{-18} s after irradiation). Then the processes continue with physicochemical and chemical reactions. Finally, biological responses continue for weeks after irradiation. Deleterious health effects possibly arising from a few misrepaired DNA lesions in one cell can appear at the level of an organism even dozens of years after irradiation. The interconnections between individual processes are shown by uninterrupted blue arrows. The time axis also roughly correlates with the complexity of postirradiation processes. Red dashed arrows indicate how processes at higher-hierarchical levels (or that appear later after irradiation) can, in turn, influence the upstream processes; complex regulatory and executing circuits and networks are thus formed. The red asterisk in the DNA repair box refers to the upper-left panel, disclosing the main processes associated with nonhomologous end-joining (NHEJ) and homologous recombination (HR), which are the main cellular pathways to repair the most serious DNA lesions, DNA double-strand breaks (DSBs). This panel also emphasizes the possibility that DSBs can lead to serious damage to the genome even if they are successfully rejoined, but the higher-order chromatin structure of the damaged chromatin domain is not restored to the original status. These "epimutations" can encompass MBs (large regions of DNA) and therefore might represent a serious threat to human health. Base Excision Repair (BER); Backup NHEJ (B-NEHEJ) - alternative to DNA-PK dependent NHEJ; DNA Damage Response (DDR); Microhomology-Mediated Joining (MMEJ); DNA Mismatch Repair (MMR); Nucleotide Excision Repair (NER); ROS, reactive oxygen species; RNS, reactive nitrogen species; Single Strand Annealing (SSA),

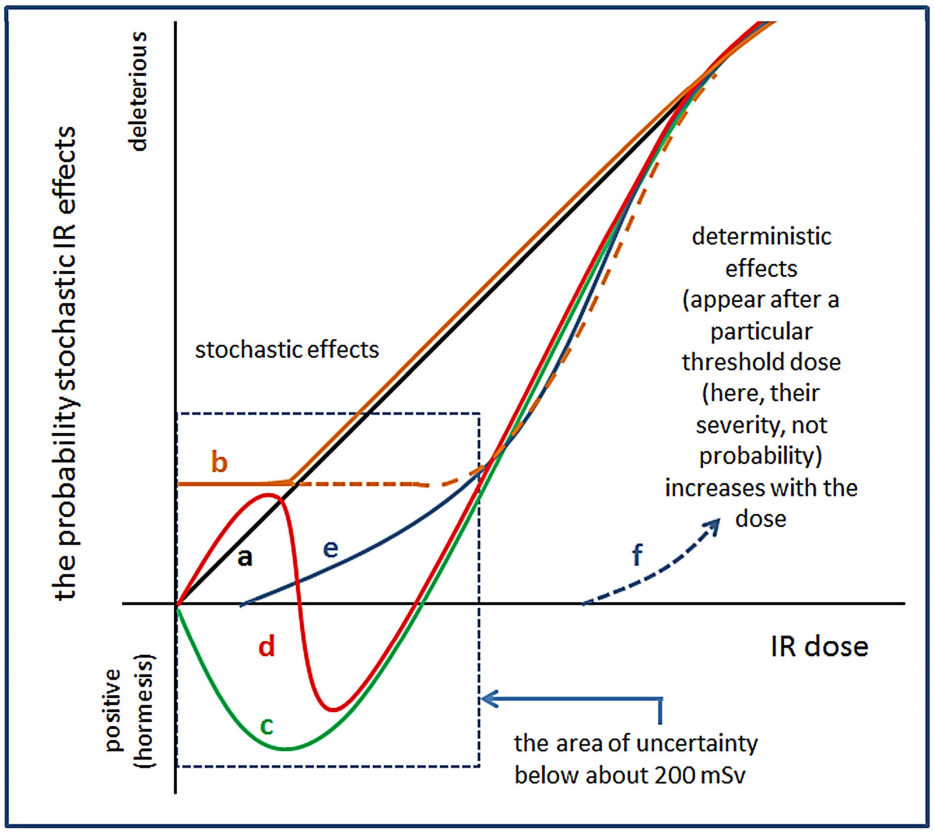

FIG. 2: The possible shapes of the dose-response curve in the range of low doses of irradiation (IR): linear non-threshold dependence (**a**); the low-dose hypersensitivity (**b**); the hormesis effect (the low-dose hyposensitivity) (**c**); a more complex dependence (here composed from hypersensitive and hyposensitive regions) (**d**); a threshold low-dose dependence (**e**); deterministic effects appearing after higher IR doses (i.e., always after some threshold dose) in addition to stochastic effects (**f**).

dozen millisieverts (reviewed by Joiner et al.[36]). Also, increased risk of chromosomal breakage occurred among a range of low doses and ascribed the existence of a threshold below which low-dose DNA damage fails to activate cell cycle arrest.[34] A similar conclusion was observed from the immune detection of γH2AX (histone H2AX phosphorylated on serine 139) foci,[37–39] currently one of the most sensitive methods for detecting DNA DSBs.[40]

Acquiring data at the epidemiological level in support of the above-mentioned observations is extremely complicated since (stochastic) clinical effects induced by low doses of IR interfere with those attributable to other environmental factors.[41,42] In the case of cancer, for instance, no markers—clinical, biological, or others—were found to be specific for any disease initiated by IR.[13] In spite of this difficulty, reports and meta-analyses demonstrate an excessive lifelong risk of developing specific cancers even for people exposed to IR doses as low as a few dozen millisieverts.[20–29] This risk was especially significant for those exposed in utero or during early childhood.[43–46] Both cellular hypersensitivity and increased neoplastic transformation can be reasonably explained by the same mechanism: very subtle DNA damage introduced by low doses of IR is insufficient to trigger full cellular recovery processes.[34,40] As a consequence, some lesions might remain unrepaired, and the cells are killed by apoptosis, die during mitosis, or survive with an altered genome.[35,40] Even small initial DNA damage can cause cancer. It happens if important genes (from the point of cancer development) are affected (by these small changes), these changes are consequently genetically fixed (e.g. stably transmitted to next cell generations) and therefore can accumulate with time. Accumulating (initially small) damage in a growing number of fundamental genes finally may result in cancer.

On the other hand, many authors recently showed that chronic low-dose irradiation boosts the repair of both endogenous and exogenous DSBs (Fig. 2, line c) (reviewed, e.g., by Joiner et al.[36]). For instance, Osipov et al.[19] recently examined DSB repair in murine blood leukocytes and splenocytes during long-term, chronic, low-dose γ-irradiation (80 days of exposure; corresponding to a total dose of 288 mGy with a dose rate of 0.15 mGy/hour). They showed that the number of DSBs decreased even below the level of nonirradiated controls. The cells also were less sensitive to DSB induction after applying an acute dose of 4Gy. Shorter expositions (40 days) had only minor or no effects on DSB repair and radiosensitivity.[18,19] Low-dose irradiation also was shown to increase the activity of mitochondrial enzymes capable of scavenging free radicals, demonstrating that adaptive responses are not limited to the cell nucleus (see Ref. 47 and the citations therein). In support of the hormesis effect, Feinendegen et al.[48] pointed toward the fact that adaptive protection, preventing only about 2–3% of endogenous lifetime cancer risk, would fully balance an estimated induced cancer risk at about 100 mSv. On the basis of these results, chronic exposure to low-dose IR might be expected to rather stimulate DSB repair and other adaptive processes (it is discussed later in the section "Complexity: Networks of Biological Networks") than cause cellular hypersensitivity.[18,48]

Adaptive protection was usually maximal after single absorbed doses around 100–200 mSv.[48] Hence, as an alternative to simple hypersensitivity or simple hyposensitivity, the cellular response could be more complicated in a range of low doses. For instance, it might be hypersensitive for dozens of millisieverts, show a hormesis effect above this threshold, and be linear from about 200 mSv (Fig. 2, line c).[19] However, contrary to Osipov et al.[19] others[31,49] demonstrated that the frequency of neoplastic transformation could be decreased by doses as low as 10 cGy or even 1 mGy (in the work of Azzam et al.,[49] irradiation was delivered at a dose rate of 2.4 mGy min^{-1}). The characteristics of cellular response in the low-dose interval—whether linear, hypersensitive, hyposensitive, or complex—is, therefore, still intensely disputed.

The above overview is far from being a comprehensive discussion of the topic. For further information, refer to devoted reviews cited in the sections above. The aim of the next few sections is to introduce examples of some of the most serious problems in current radiobiology, such as the

complexity of biological objects and the variability of experimental models, designs, and methodologies used.

B. Complexity: Networks of Biological Networks

As outlined earlier, biological systems include multiple levels of hierarchical organization that are interconnected both horizontally and vertically, forming dynamic multidirectional regulatory circuits (Fig. 1; see also Fig. 1 in our other article in this issue, "Determining Omics Spatiotemporal Dimensions Using Exciting New Nanoscopy Techniques to Assess Complex Cell Responses to DNA Damage: Part B—Structuromics" [referred to hereafter as "Part B"). Such an arrangement enables the amplification of weak signals (e.g., coming from only a few DSBs), along with dynamic and sensitive regulation, variable modulation, and multilevel backup of cellular responses. From several studies mentioned above it is evident that IR miscellaneously damages different cellular targets (DNA bases, DNA backbone, chromatin epigenetic signals, chromatin structure at different hierarchical levels, membranes, etc.) and functions (coding of genetic information, chromosomal segregation, epigenetic signaling, gene transcription and replication, cell cycle progression, protein synthesis, membrane permeability, energy production in mitochondria, etc.). Depending on the extent and type of damage from irradiation, particular response networks are initiated in which many biochemical pathways that specialize in repair of various DNA lesions, elimination of free radicals, cell cycle checkpoint signaling, apoptosis, differentiation, senescence, and other functions interdependently cooperate with each other (Fig. 1). As a result of these integrated activities, a spectrum of phenomena at the cellular level was recognized; it substantially influences the shape of the dose–response curve in a range of low doses of IR (Fig. 2). Together, genomic instability, hypersensitivity, adaptive responses, inverse dose rate, induced DNA repair, and bystander effects that occur with low doses can augment or counteract effects of DNA damage in an interconnected manner (reviewed in Refs. 30, 40, and 50–54).

Bystander effects can illustratively exemplify the complexity of IR-induced cellular damage and the subsequent response[55–57] (Fig. 1; see also Fig. 1 in Part B). Although the cell nucleus with DNA is undoubtedly the most significant target for IR, distinct cellular responses can be initiated even in the absence of direct DNA damage, as recently shown with microbeams capable of precisely delivering a dose to small subcellular compartments.[58] Tartier et al.[59] revealed that 53BP1 IR-induced repair foci (IRIF) form in nuclei although only the cytoplasmic regions of cells were irradiated. Moreover, even unirradiated cells can respond to IR in a way similar to their directly irradiated neighbors.[60] Further studies extend the bystander effects of a variety of IR damage end points, including micronuclei induction, cell lethality, gene expression, and oncogenic transformation in human and rodent cell lines (reviewed by Zhou et al.[58]). Importantly, the bystander responses in unirradiated cells or cells with irradiated cytoplasms were usually phenotypically similar to those of cells directly exposed to irradiation but occurred independent of the dose and with markedly different kinetics (discussed by Zhou et al.).

Bystander effects thus stress the importance of both intra- and intercellular interactions. In addition, cell cooperation occurs above the network of processes (co)operating inside a particular tissue. For instance, irreparable irradiated cells can frequently undergo senescence instead of apoptosis.[61] Whether these cells will be reactivated and destined for cancer initiation depends on the status of the organism at many levels. Alternatively, less efficient DNA repair after low doses of IR might be balanced by the activity of the stimulated immune system that effectively eliminates damaged cells along with those that appear simultaneously, thus substantially decreasing the incidence of cancer.[40] Interestingly, Rothkamm and Löbrich[40] observed the slowdown and low efficiency of DSB repair after low-dose IR expositions in cultured cells. However, in their later work, Löbrich et al.[62] did not observe these phenomena in cells isolated at differ-

ent time points after irradiation from patients examined with computed tomography. In accordance with this, while hereditary defects have been recognized as a serious consequence of IR exposure in experiments with cells, they occurred less than expected in the first two generations of progeny of nuclear bombing survivors (reviewed by Köteles[32,33]). Hence, not all biological responses to IR recognized in cultured cells necessarily account for detrimental consequences in the organism (reviewed by Brooks[63]). These examples clearly demonstrate that to understand the biological responses to IR in a more holistic fashion, we must proceed to Omics experiments on 3-dimensional (3D) artificial cellular networks, mimicking the intercellular signaling and other features of real tissues.

Pilot experiments have already been reported. In cells organized in "tissues," DSB repair proceeded with kinetics different than those in cells cultured in the monolayer.[64,65] For example, Lin et al.[66] and Sowa et al.[64] observed a higher rate of cell survival against X-rays in 3D cultures, although their results are inconclusive. As mentioned, Löbrich et al.[62] recognized compromised DSB repair kinetics in cells exposed to low doses of IR in vitro in cell cultures[40] but not in cells from donors undergoing computed tomography examinations. While the contradiction between the results of Lin et al. and Sowa et al. might be explained by unspecified differences in cell models and experimental conditions used (which again highlights the necessity of Omics approaches), the reason for diverse repair turnovers measured in 2-dimensional (2D) and 3D cell "monocultures" remains to be uncovered. One possible explanation is differences in the chromatin structure, controlled by the tissue architecture, cell shape, and extracellular signaling,[67] when comparing cells grown in 2D and 3D cultures. Specifically, an increase in the chromatin condensation in 3D cultured cells might account for their increased radioresistance.[68] This is in accordance with our observations[69–73] indicating that heterochromatin structure/composition protects DNA against the indirect effect of sparsely ionizing radiation. On the other hand, heterochromatin structure might cause further complications in the repair of DNA DSBs[71–74] (as discussed in Part B).

Interestingly, cellular pathways involved in the maintenance of chromatin/cell structures and DSB repair pathways seem to be directly interconnected. PAR3, a tight junction protein involved in the process of apical polarization, was shown to regulate DSB repair by interacting with the Ku70–Ku80 heterodimer in the cell nucleus.[75] In addition, a number of other apical polarity complex proteins were found to influence chromatin organization (reviewed by Lelièvre[67]). It should be noted that although parallel information on the efficiency of DSB repair is usually absent, altered chromatin structure is a characteristic feature of transformed cells. For example, even though general principles of the chromatin organization were preserved in different colon tumors and normal epithelial cells separated from the tumor by about 10 cm, local higher-order chromatin structure was altered in numerous amplified loci.[76]

To complete the image of radiobiological complexity, biological and clinical effects of IR exposure strongly depend on the radiation type (as discussed in Section I of Part B) and, in the case of low doses, strongly interfere with contributions from environmental factors[42] (see Fig. 1 in Part B). In humans, the stress arising from being aware of irradiation, though at the doses that are significantly lower than those people are exposed to (e.g. per a year) from naturally occurring sources like the Rn-background, cosmic and Sun radiation etc. (i.e. "natural background"). Paradoxically, the psyche might cause, albeit indirectly, the most serious consequences of low-dose irradiation. Although difficult to prove, the anxiety from the radioactive fallout that spread after the Chernobyl disaster among practically unexposed women possibly resulted in the unnecessary termination of many pregnancies.

C. Variability

Functional roles of individual cell types are associated with different, dynamically changing epigenetic, transcriptomic, proteomic, and cycling profiles. Hence, it is not surprising that cells respond variably to IR. For instance, even subtle differences in

cell cycle distribution were reported to markedly influence the low-dose radiosensitivity, with higher fractions of hypersensitive cells occupying the G_2/M phases.[77] Covering this topic is, however, beyond the scope of this article. Nevertheless, a brief discussion of the relationship between cellular differentiation, changes in higher-order chromatin structure, and DSB repair capacity is provided in Part B in the section "DSB Repair in the Context of Higher-Order Chromatin Structure" (see Refs. 72, 78, and 79 for details).

The second source of the tremendous variability that (radio)biological research must face is the diversity of genomes. Even the same kind of cells, which possess equivalent functional, biochemical, and environmental conditions, deal differently with identical radiation damage, depending on the genetic background. If we consider the number of human genes and their potential physiological and pathological variants, there emerges a frightful plethora of gene sets and interactions that can influence the cellular response to radiation and eventually individual cell-specific radiosensitivity. We also are confronted with an extensive and still unknown variability if we take into account only single genes with major direct effects on DNA damage repair and signaling, as is illustrated below for the *BRCA1* gene.

Several nonsense and missense mutations that disrupt or modify the activity of *BRCA1* and highly predispose its carriers to breast and ovarian cancers at very early ages have been detected. For breast cancer, the related risk estimates for the age of 70 years—irrespective of differences between particular mutations—are as high as about 65%.[80] During the screening of families with a high risk of breast cancer, we ascertained numerous endogenously expressed alternative splicing variants (ASVs), in addition to classic mutations that occurred in various tissues.[81] The biological and clinical significance of *BRCA1* ASVs are unknown. Since *BRCA1* plays multiple roles in DSB repair, we studied the effects of the DSB processing of 2 ASVs, *BRCA1Δ14–15* and *BRCA1Δ17–19*, with an in-frame deletion affecting the regulatory serine-containing domain and a portion of the BRCA1 C terminus domain, respectively.[81,82] Using a comet assay, in vitro non-homologous end-joining (NHEJ) assay, mitomycin C sensitivity assay, and γH2AX + 53BP1 dual IRIF immunolabeling in combination with high-resolution confocal microscopy, we showed that the stable expression of the *BRCA1Δ14–15* variant delays DSB repair, alters the kinetics of IRIF formation/decomposition, and reduces the NHEJ capacity in human MCF-7 mammary cancer cells irradiated with 1.5 Gy of γ-rays (0.58–1.0 Gy/min).[81] The *BRCA1Δ17–19* also impairs homologous recombination repair.[82] Among its many functions, *BRCA1* forms a platform to mediate interactions between numerous proteins involved in DNA damage repair and signaling. Hence, *BRCA1* ASVs can easily deregulate specific combinations of multiple cellular pathways and networks and modify individual sensitivity to IR exposition. Though *BRCA1* is probably an extreme example because of its multifunctionality, the above paragraph illustrates how important it is to have the Omics knowledge of genomic background when comparing results from different experimental models.

Importantly, not only mutations of genes directly involved in DNA damage response and regulation of nuclear processes modify the cellular response to low IR expositions. For example, alterations in redox mitochondrial processes may play a crucial role in the response to low-dose IR.[47,83] Mutations in the *SDHC* gene coding for the mitochondrial electron transport chain protein (succinate dehydrogenase subunit C) have been shown to markedly increase the steady-state levels of hydrogen peroxide and $O_2^{\bullet-}$, consequently increasing clonogenic cell killing after low-dose/low linear energy transfer radiation (5–50 cGy).[47]

III. RADIOBIOLOGY: A LARGE PLAYGROUND FOR OMICS APPLICATIONS AND BENEFITS

A. Points of Intersection to Understand Complex (Radio)biological Responses

The complexity and variability of (radio)biological systems described earlier (Fig. 1; see also Fig. 1 in Part B) could not be grasped in the era before

Omics, so currently available results usually describe only isolated pieces of the puzzle, without knowing the relationship with other cellular and above-cellular (functional) processes. Radiation-induced carcinogenesis—the most serious end point of the exposure to low IR doses—can serve as an illustrative example. Exposures to IR and/or different chemicals (coming from alimentary diet, environmental pollutants, medical therapies, etc.); genetic background; stress; the immune system; the psyche; and other factors participate in the process of tumor development (Fig. 1; see also Fig. 1 in Part B). To understand the phenomenon in a more holistic context, together with associated mechanisms, we need points of intersection that allow us to link the data from different contributing processes, experimental models, and settings. Providing these cross-points is the main goal of current procedures summarized by Omics.

Until recently, obtaining the information on the function of a single gene or protein would last for years. Thanks to high-throughput methods and a tremendous increase in computer performance and robotics technology, it is currently possible to simultaneously acquire large-scale meta-Omics data that integrate genomics, epigenomics, transcriptomics, miRNAomics, proteomics, interactomics, and other Omics results on DSB repair, apoptosis, cell cycle signaling, epigenetic signaling/chromatin modification, transcription, mitochondrial activity, and other molecular processes that occur during and after exposure to IR (Fig. 1; see also Fig. 1 in Part B). Storage of Omics data in currently available open databases[84,85] allow for their synthesis, computational meta-analysis, interpretation in the context of genomic background (with possible mutations), and consequently step-by-step construction of multidimensional matrices that intricately describe the radiation response at the cellular level. These matrices will then serve as dynamic platforms to organize more detailed results from specialized experiments and, in turn, replenish and improve themselves.

For reasons described earlier, future experiments should extend current efforts to analyze repair processes of chromatin and other responses to IR in individual cells and cellular systems organized in complex tissues. Although, in principle, this is possible from the Omics point of view, a step forward is necessary in 2D and finally 3D tissue engineering[86] to understand cellular response in the natural context of the organism.

B. Radiations of Different Quality, Ion Beam Cancer Therapy, and Cosmic Research

Nowadays, holistic Omics research is required to compare the biological effects of exposure to IR of different qualities (see, e.g., George et al.[87]). Some decades ago, IR was mostly associated with high-energy photon (X-ray, γ-ray) radiation obtained by natural or medical radiation sources. Presently, the increased possibility of generating high-energy particle beams, such as proton or heavy-ion beams, has extended radiation research and allowed for the inclusion of different kinds and qualities of radiation sources and beams. The results from these new radiation sources are impatiently awaited in, for example, the field of cosmic research. Although radiation effects on astronauts and cosmonauts were not seriously considered and investigated in great detail in the early space programs of the 1950s and 1960s, the altered response of society to different kinds of radiation consequences nowadays has triggered huge efforts to elucidate radiation exposure in space and its long-term effects on the human organism. International radiation research programs are conducted actively on the International Space Station.[88] Furthermore, in planned extraorbital missions (e.g., manned mission to Mars), astronauts will be exposed to variable doses of mixed radiation for lengthy durations, with changing dose rates and limited possibilities for protection.[89–95] Artificially produced particle beams such as proton or carbon heavy-ion beams also have many applications in medical therapy, as seen in the case of brain tumors, which so far have been difficult to treat using conventional radiation therapy. This is mainly because of the highly advantageous deposition of a precise dose in the tumor, without serious side effects on the

surrounding nontumor tissue (reviewed by Combs and Debus[96] and Loeffler and Durante.[97]). Nevertheless, successful translation of particle beams in medical applications requires extensive experimental data on molecular and regular biological effects of therapeutic ion beams. Ion beam cancer therapy is undergoing significant development these days, but irradiation protocols still mostly depend on empirical knowledge.[9,98,99]

C. Biomarkers of Individual Exposure and Radiosensitivity

In addition to providing deeper views into the mechanisms of cellular response to IR, the pan-Omic approach also has the potential to reveal biological markers of individual radiosensitivity and absorbed IR dose. Genomic screens in radiosensitive patients and consequent data meta-analysis could identify new genes and their variants as well as single nucleotide polymorphisms engaged in complex cellular radiation response.[100–102] In turn, since recent results show that genomic individuality is closely correlated to single nucleotide polymorphisms, this would allow rapid pretherapeutic characterization of patients in terms of their radiosensitivity, as well as a better understanding of the functions of particular genes and their networks.[102] Also, the reverse approach is possible using, for example, inhibitory RNA microarrays to follow the consequences of abrogated gene activity in the Omic context.[103–105]

Proof-of-concept experiments showing changes in proteomic profiles after very low doses of γ and α radiation (10 mGy applied in low-dose rates of 5 mGy/hour) have been published (discussed, e.g., by Tapio et al.[106]). Accordingly, even subtle doses of different radiations can leave proteomic fingerprints that are specific to both dose and type of radiation. In the study by Bajinskis et al.,[107] the levels of proteins involved in proliferation and cell cycle regulation were altered after exposure to 30 mGy. More important is that radiosensitive and radioresistant cells provide distinct proteomic profiles[107] (further reports of this are found in Refs. 108–111). Since extensive epigenetic modifications, along with reorganization of the higher-order chromatin structure, take place during DNA damage repair, potential biomarkers could also be based on these changes (and not only stay proteomic). Indeed, persistent changes in protein expression and altered differentiation, as observed by Bajinskis et al., are indicative of an epigenetic rather than a cytotoxic mechanism.

By providing information on individual genome constellations, metaomics opens the door to personalized medicine. For instance, the risks and benefits of mammographic examinations for a carrier of a concrete *BRCA1/2* gene mutation would be better weighted if we knew about the complex effects of the particular *BRCA1/2* mutation along with information on the presence of other mutated genes in the genome involved in the response to IR (reviewed by Heyes et al.[112]). This knowledge would also allow more precise radiotherapy planning and posttherapeutic treatment. The benefit of quantitative biomarkers is evident in radiation accidents where information on the absorbed dose is lacking. Finding qualitative biomarkers sensitive to radiation features (e.g., high LET vs. low LET) is, then, extremely useful and will allow us to analyze the risks associated with cosmic research and to comprehend the mechanisms of damage from different radiations. Currently known IR biomarkers usually include only specific chromosomal aberrations; however, the spectrum of the Omics markers could be much wider, as it is clear from the above discussion.

D. Pharmaco-omics, Radiosensitizers, and Radioprotectors

Pharmaco-omics can improve radiotherapy by extending the search for both drugs that sensitize cells to (different kinds of) IR and usable chemotherapeutics. Radiation protection will, on the other hand, benefit from compounds that deliver an opposite effect. The importance of Omics becomes especially apparent when analyzing complex effects evoked by combinations of drugs with different mechanisms of action.

Despite the identification of numerous ef-

fective low-mass chemicals that stimulate IR response, the only drug currently approved for clinical use as a radioprotective agent is amifostine[113–115] (reviewed by Kouvaris et al.[116]). The mechanism of action of amifostine is still mostly unknown, although it evidently acts as a radical scavenger that protects DNA against initial damage.[117,118] In addition, amifostine seems to trigger DNA repair and other prosurvival processes by yet-unknown methods. Another interesting phenomenon of amifostine action has been described: Reports (e.g., Margulies et al[119]; reviewed by Kouvaris et al. and Orditura et al.[120]) and our results (Hofer et al., submitted for publication) show that amifostine significantly reduces initial damage to normal cells but it fails to do so in tumor cells. Surprisingly, amifostine also disturbed DSB repair in cancer (MCF7) cells to some degree in our experiments (Hofer et al., submitted for publication). The opposite influence of amifostine on DSB induction could be explained, at least in part, by a different extent of activation by alkaline phosphatase (whose concentrations differ in normal and cancer cells) (see Ref. 121 and the citations therein). However, the reason why amifostine exerts diverse effects on DSB repair is unknown.

On the other hand, several different approaches to increase cell death after IR are being tested. An obvious possibility is the inhibition of transcription or activity of genes or proteins, respectively, involved in DNA repair pathways.[122–127] Although the effects of this strategy have been scrutinized for many years, the results are still disappointing, probably because of multiple backups of gene functions. For instance, ATM, ATR, and DNA-dependent protein kinase[128-130] - can phosphorylate in an overlapping manner many DSB repair proteins; therefore, inhibition of one of a single gene (in this example either for ATM, ATR, or DNA-PK) is insufficient to "knock-out" DSB repair. DSBs in the case of primary pathway alteration have been described[131,132] (reviewed by Iliakis[133]). On the other hand, one single protein (like CtBP-interacting protein or ataxia telangiectasia mutated protein) can regulate the activity of numerous pathways, so its inhibition might cause multiple and unexpected outcomes.[134] Chromatin structure modifications (e.g., with histone deacetylase inhibitors) are another way how to sway the cellular response to IR[135–138] (reviewed by Cerna et al.[139]), which again leads to Omics consequences (e.g., influencing the transcription of many genes).

As a final example, nanoparticles composed of high-Z materials (such as gadolinium [Gd], platinum, and gold [Au]) were shown to stimulate substantial IR-induced cell death[140–146] (reviewed by Kwatra et al.[147] and Dorsey et al.[148]). Veldwijk et al.[149] recently showed a significant reduction in cell survival after radiation after gold nanoparticles were incorporated into the cytoplasm by transfection. The same phenomenon has been observed after incubating cells with platinum, Au, and Gd nanoparticles in the medium before irradiation (Štefančíková et al., manuscript in preparation). Although an increase of repair foci in the cell nucleus has been reported after, for example, treatment with titanium dioxide,[150] silver,[151–153] and Au nanoparticles,[154] our results (Štefančíková et al., manuscript in preparation) suggest that neither DNA nor mitochondrial damage is increased by the admission of Gd or Au nanoparticles. Such contradictory results are supported by cell type–specific survival after irradiation and the incorporation of Au[154] or chromatin damage after incorporating Au nanoparticles into the cytoplasm and microirradiation of the cytoplasm.[155] Preliminary results of changes in chromatin conformation indicate a different radiation response by cells loaded with Au nanoparticles compared to those without (Al Saroori et al., manuscript in preparation). Distinct and cell-specific effects of different nanoparticles (composition, size, etc.) thus point to the need for extensive Omics research to determine the mechanisms of nanoparticle-mediated cell sensitization (especially in the cases where no effect on nuclear or mitochondrial DNA integrity could be observed). Although many other relevant examples could be discussed, it clearly follows from the above paragraphs that Omics approaches are necessary to understand (modified) IR response in its entirety.

IV. CONCLUSION

Dedicated to the importance of Omics in radiobiology, it should be noted that a growing number of projects focusing on interdisciplinary collaboration in the field have been launched in the past ten years. In Europe these include the RADAM (Radiation Damage in Biomolecular Systems, COST Action P9); Nano-IBCT (Nanoscale insights into Ion Beam Cancer Therapy, COST Action MP1002); European Network of Excellence DoReMi (Low-Dose Research Towards Multidisciplinary Integration); MELODI (Multidisciplinary European Low Dose Initiative) studies and others. Therefore, it seems that the time for Omics has come, and it is expected that many interesting results regarding functional mechanisms, regulatory networks, and network interactions will be obtained in the near future, allowing further resolution of old but nevertheless still fascinating questions of response of living systems to low-dose IR and the multiple processes used by them to escape the catastrophe of cell death.

ACKNOWLEDGMENT

The work was supported by GACR Center Excellence P302/12/G157 and P302/10/1022, MEYS of the Czech Republic (COST-LD12039, LD12008, OPVK-CZ.1.07/2.3.00/30.0030), and a Czech contribution to JINR Dubna in 2013. Furthermore, the financial support of the German Federal Ministry for the Environment, Nature Conservation and Nuclear Safety (SR/StSch/INT 3610S30015 to FKZ) is gratefully acknowledged. The authors also thank Christoph Cremer and his group (Institute for Molecular Biology, Mainz) for their continuous collaboration in all fields of superresolution microscopy, as well as Frederik Wenz (University Medical Center, Mannheim) for providing access to several source of medical radiation.

REFERENCES

1. All about the Human Genome Project [webpage on the Internet]. Bethesda (MD): National Human Genome Research Institute; 2014 [updated 18 Mar 2014; cited 10 Apr 2014]. Available from: http://www.genome.gov/10001772.
2. Apollo program [article on the Internet]. Wikimedia Foundation Inc. [modified 7 Apr 2014; cited 10 Apr 2014]. Available from: http://en.wikipedia.org/wiki/Apollo_program.
3. Chuang HY, Hofree M, Ideker T. A decade of systems biology. Annu Rev Cell Dev Biol. 2010;26:721–44.
4. Casci T. Gene networks go global. Nat Rev Genet. 2004;5:84.
5. Flintoft L. Rewiring the network. Nat Rev Genet. 2004;5:808.
6. Wilson N. A powerful combination. Nat Rev Mol Cell Biol. 2004;5:257.
7. Leroy Hood [article on the Internet]. Wikimedia Foundation Inc. [modified 8 Apr 2014; cited 10 Apr 2014]. Available from: http://en.wikipedia.org/wiki/Leroy_Hood.
8. Foffa I, Cresci M, Andreassi MG. Health risk and biological effects of cardiac ionising imaging: from epidemiology to genes. Int J Environ Res Public Health. 2009;6:1882–93.
9. Solov'yov AV, Surdutovich E, Scifoni E, Mishustin I, Greiner W. Physics of ion beam cancer therapy: a multiscale approach. Phys Rev E Stat Nonlin Soft Matter Phys. 2009;79:011909.
10. Surdutovich E, Scifoni E, Solov'yov AV. Ion-beam cancer therapy: news about a multiscale approach to radiation damage. Mutat Res. 2010;704:206–12.
11. Morgan WF, Bair WJ. Issues in low dose radiation biology: the controversy continues. A perspective. Radiat Res. 2013;179:501–10.
12. Ozasa K, Shimizu Y, Suyama A, Kasagi F, Soda M, Grant EJ, Sakata R, Sugiyama H, Kodama K. Studies of the mortality of atomic bomb survivors, Report 14, 1950-2003: an overview of cancer and noncancer diseases. Radiat Res. 2012;177:229–43.
13. Wakeford R. Cancer risk modelling and radiological protection. J Radiol Prot. 2012;32:N89–93.
14. UNSCEAR 2000 published. United Nations Scientific Committee on the Effects of Atomic Radiation. Health Phys. 2001;80(3):291.
15. 1990 Recommendations of the International Commission on Radiological Protection. Ann ICRP. 1991;21(1–3):1–201.
16. de González BA, Darby S. Risk of cancer from diagnostic X-rays: estimates for the UK and 14 other countries. Lancet. 2004;363:345–51.
17. Brenner DJ, Elliston CD. Estimated radiation risks potentially associated with full-body CT screening. Radiology. 2004;232:735–8.
18. Mitchel RE, Burchart P, Wyatt H. A lower dose threshold for the in vivo protective adaptive response to radiation.

Tumorigenesis in chronically exposed normal and Trp53 heterozygous C57BL/6 mice. Radiat Res. 2008;170:765–75.
19. Osipov AN, Buleeva G, Arkhangelskaya E, Klokov D. In vivo γ-irradiation low dose threshold for suppression of DNA double strand breaks below the spontaneous level in mouse blood and spleen cells. Mutat Res. 2013; 30;756(1–2):141–5.
20. Stevens W, Thomas DC, Lyon JL, Till JE, Kerber RA, Simon SL, Lloyd RD, Elghany NA, Preston-Martin S. Leukemia in Utah and radioactive fallout from the Nevada test site. A case-control study. JAMA. 1990;264:585–91.
21. Doody MM, Lonstein JE, Stovall M, Hacker DG, Luckyanov N, Land CE. Breast cancer mortality after diagnostic radiography: findings from the US Scoliosis Cohort Study. Spine. 2000;25:2052–63.
22. Tubiana M, Feinendegen LE, Yang C, Kaminski JM. The linear no-threshold relationship is inconsistent with radiation biologic and experimental data. Radiolobilogy. 2009;251:13–22.
23. Noshchenko AG, Moysich KB, Bondar A, Zamostyan PV, Drosdova VD, Michalek AM. Patterns of acute leukaemia occurrence among children in the Chernobyl region. Int J Epidemiol. 2001;30:125–9.
24. Sont WN, Zielinski JM, Ashmore JP, Jiang H, Krewski D, Fair ME, Band PR, Létourneau EG. First analysis of cancer incidence and occupational radiation exposure based on the National Dose Registry of Canada. Am J Epidemiol. 2001;153:309–18.
25. Preston DL, Shimizu Y, Pierce DA, Suyama A, Mabuchi K. Studies of mortality of atomic bomb survivors. Report 13: solid cancer and noncancer disease mortality: 1950-1997. Radiat Res. 2003;160:381–407.
26. Cardis E, Vrijheid M, Blettner M, Gilbert E, Hakama M, Hill C, Howe G, Kaldor J, Muirhead CR, Schubauer-Berigan M, Yoshimura T, Bermann F, Cowper G, Fix J, Hacker C, Heinmiller B, Marshall M, Thierry-Chef I, Utterback D, Ahn YO, Amoros E, Ashmore P, Auvinen A, Bae JM, Solano JB, Biau A, Combalot E, Deboodt P, Diez Sacristan A, Eklof M, Engels H, Engholm G, Gulis G, Habib R, Holan K, Hyvonen H, Kerekes A, Kurtinaitis J, Malker H, Martuzzi M, Mastauskas A, Monnet A, Moser M, Pearce MS, Richardson DB, Rodriguez-Artalejo F, Rogel A, Tardy H, Telle-Lamberton M, Turai I, Usel M, Veress K. Risk of cancer after low doses of ionising radiation: retrospective cohort study in 15 countries. BMJ. 2005;331(7508):77.
27. Darby S, Hill D, Auvinen A, Barros-Dios JM, Baysson H, Bochicchio F, Deo H, Falk R, Forastiere F, Hakama M, Heid I, Kreienbrock L, Kreuzer M, Lagarde F, Mäkeläinen I, Muirhead C, Oberaigner W, Pershagen G, Ruano-Ravina A, Ruosteenoja E, Rosario AS, Tirmarche M, Tomásek L, Whitley E, Wichmann HE, Doll R. Radon in homes and risk of lung cancer: collaborative analysis of individual data from 13 European case-control studies. BMJ. 2005;330(7485):223.
28. Ron E, Schneider AB. Thyroid cancer. In: Schottenfeld D. and Fraumeni J, editors. Cancer epidemiology and prevention. 3rd ed. New York: Oxford University Press; 2006. p. 975–94.
29. Zablotska LB, Bazyka D, Lubin JH, Gudzenko N, Little MP, Hatch M, Finch S, Dyagil I, Reiss RF, Chumak VV, Bouville A, Drozdovitch V, Kryuchkov VP, Golovanov I, Bakhanova E, Babkina N, Lubarets T, Bebeshko V, Romanenko A, Mabuchi K. Radiation and the risk of chronic lymphocytic and other leukemias among Chornobyl cleanup workers. Environ Health Perspect. 2013;121:59–65.
30. Buzatu S. Cellular low-dose effects of ionizing radiation. Riv Biol. 2008;101:279–98.
31. Redpath JL. Nonlinear response for neoplastic transformation following low doses of low let radiation. Nonlinearity Biol Toxicol Med. 2005;3:113–24.
32. Köteles GJ. The low dose dilemma. Centr Eur J Occup Environm Med. 1998;4:103–13.
33. Köteles GJ. Biological responses in low-dose range. Int J Low Radiation. 2006;2:97–110.
34. Mullenders L, Atkinson M, Paretzke H, Sabatier L, Bouffler S. Assessing cancer risks of low-dose radiation. Nat Rev Cancer. 2009;9:596–604.
35. Enns L, Bogen KT, Wizniak J, Murtha AD, Weinfeld M. Low-dose radiation hypersensitivity is associated with p53-dependent apoptosis. Mol Cancer Res. 2004;2:557–66.
36. Joiner MC, Marples B, Lambin P, Short SC, Turesson I. Low-dose hypersensitivity: current status and possible mechanisms. Int J Radiat Oncol Biol Phys. 2001;49:379–89.
37. Rogakou EP, Pilch DR, Orr AH, Ivanova VS, Bonner WM. DNA double-stranded breaks induce histone H2AX phosphorylation on serine 139. J Biol Chem. 1998;273:5858–68.
38. Rogakou EP, Boon C, Redon C, Bonner WM. Megabase chromatin domains involved in DNA double-strand breaks in vivo. J Cell Biol. 1999;146:905–16.
39. Sharma A, Singh K, Almasan A. Histone H2AX phosphorylation: a marker for DNA damage. Methods Mol Biol. 2012;920:613–26.
40. Rothkamm K, Löbrich M. Evidence for a lack of DNA double-strand break repair in human cells exposed to very low x-ray doses. Proc Natl Acad Sci U S A. 2003;100:5057–62.
41. Land CE. Estimating cancer risks from low doses of ionizing radiation. Science. 1980;209:1197–203.
42. Dauer LT, Brooks AL, Hoel DG, Morgan WF, Stram D, Tran P. Review and evaluation of updated research on the health effects associated with low-dose ionising radiation. Radiat Prot Dosimetry. 2010;140:103–36.

43. Clarke RH. The threshold controversy. Didcot, UK: National Radiological Protection Board; 1996.
44. Sobolev B, Heidenreich WF, Kairo I, Jacob P, Goulko G, Likhtarev I. Thyroid cancer incidence in the Ukraine after the Chernobyl accident: comparison with spontaneous incidences. Radiat Environ Biophys. 1997;36:195–9.
45. Miller RW, Boice JD Jr. Cancer after intrauterine exposure to the atomic bomb. Radiat Res. 1997;147:396–7.
46. Delongchamp RR, Mabuchi K, Yoshimoto Y, Preston DL. Cancer mortality among atomic bomb survivors exposed in utero or as young children, October 1950–May 1992. Radiat Res. 1997;147:385–95.
47. Aykin-Burns N, Slane BG, Liu AT, Owens KM, O'Malley MS, Smith BJ, Domann FE, Spitz DR. Sensitivity to low-dose/low-LET ionizing radiation in mammalian cells harboring mutations in succinate dehydrogenase subunit C is governed by mitochondria-derived reactive oxygen species. Radiat Res. 2011;175:150–8.
48. Feinendegen LE, Pollycove M, Neumann RD. Low-dose cancer risk modeling must recognize up-regulation of protection. Dose Response. 2009;8:227–52.
49. Azzam EI, De Toledo SM, Raaphorst GP, Mitchel R. Low dose ionizing radiation decreases the frequency of neoplastic transformation to a level below the spontaneous rate in C3H10T1/2 cells. Radiat Res. 1996;146:369–73.
50. Feinendegen LE, Pollycove M, Sondhaus CA. Responses to low doses of ionizing radiation in biological systems. Nonlinearity Biol Toxicol Med. 2004;2(3):143–71.
51. Feinendegen LE, Neumann RD. The issue of risk in complex adaptive systems: the case of low-dose radiation induced cancer. Hum Exp Toxicol. 2006;25:11–7.
52. Feinendegen LE, Pollycove M, Neumann RD. Whole-body responses to low-level radiation exposure: new concepts in mammalian radiobiology. Exp Hematol. 2007;35:37–46.
53. Brenner DJ, Sachs RK. Do low dose-rate bystander effects influence domestic radon risks? Int J Radiat Biol. 2002;78:593–604.
54. Little JB. Radiation carcinogenesis. Carcinogenesis. 2000;21:397–404.
55. Gow MD, Seymour CB, Ryan LA, Mothersill CE. Induction of bystander response in human glioma cells using high-energy electrons: a role for TGF-beta1. Radiat Res. 2010;173:769–78.
56. Chapman KL, Kelly JW, Lee R, Goodwin EH, Kadhim MA. Tracking genomic instability within irradiated and bystander populations. J Pharm Pharmacol. 2008;60:959–68.
57. Kaznacheev VP, Mikhaĭlova LP, Kartashova NB. Distant intercellular electromagnetic interactions between two tissue cultures. Bull Exp Biol Med. 1980;89:345–8.
58. Zhou H, Hong M, Chai Y, Hei TK. Consequences of cytoplasmic irradiation: studies from microbeam. J Radiat Res. 2009;50(Suppl A):A59–65.
59. Tartier L, Gilchrist S, Burdak-Rothkamm S, Folkard M, Prise KM. Cytoplasmic irradiation induces mitochondrial-dependent 53BP1 protein relocalization in irradiated and bystander cells. Cancer Res. 2007;67:5872–9.
60. Mothersill C, Seymour CB. Radiation-induced bystander effects—implications for cancer. Nat Rev Cancer. 2004;4:158–64.
61. Rezáčová M, Rudolfová G, Tichý A, Bačíková A, Mutná D, Havelek R, Vávrová J, Odrážka K, Lukášová E, Kozubek S. Accumulation of DNA damage and cell death after fractionated irradiation. Radiat Res. 2011;175:708–18.
62. Löbrich M, Rief N, Kühne M, Heckmann M, Fleckenstein J, Rübe C, Uder M. In vivo formation and repair of DNA double-strand breaks after computed tomography examinations. Proc Natl Acad Sci U S A. 2005;102:8984–9.
63. Brooks AL. Evidence for "bystander effects" in vivo. Hum Exp Toxicol. 2004;23:67–70.
64. Sowa MB, Chrisler WB, Zens KD, Ashjian EJ, Opresko LK. Three-dimensional culture conditions lead to decreased radiation induced cytotoxicity in human mammary epithelial cells. Mutat Res. 2010;687:78–83.
65. Vidi PA, Chandramouly G, Gray M, Wang L, Liu E, Kim JJ, Roukos V, Bissell MJ, Moghe PV, Lelièvre SA. Interconnected contribution of tissue morphogenesis and the nuclear protein NuMA to the DNA damage response. J Cell Sci. 2012;125:350–61.
66. Lin YF, Nagasawa H, Peng Y, Chuang EY. Bedford JS. Comparison of several radiation effects in human MCF10A mammary epithelial cells cultured as 2D monolayers or 3D acinar structures in matrigel. Radiat Res. 2009;171:708–15.
67. Lelièvre SA. Tissue polarity-dependent control of mammary epithelial homeostasis and cancer development: an epigenetic perspective. J Mammary Gland Biol Neoplasia. 2010;15(1):49–63.
68. Storch K, Eke I, Borgmann K, Krause M, Richter C, Becker K, Schröck E, Cordes N. Three-dimensional cell growth confers radioresistance by chromatin density modification. Cancer Res. 2010;70:3925–34.
69. Falk M, Lukasova E, Kozubek S. Chromatin structure influences the sensitivity of DNA to γ-radiation. Biochim Biophys Acta. 2008;1783:2398–414.
70. Falk M, Lukasova E, Gabrielova B, Ondrej V, Kozubek S. Local changes of higher-order chromatin structure during double strand break repair. J Phys Conf Ser. 2008;101:012018.
71. Falk M, Lukasova E, Kozubek S. Higher order chromatin structure in DSB induction, repair and misrepair. Mutat Res. 2010;704:88–100.
72. Falk M, Lukášová E, Stefančíková L, Baranová E, Falková I, Ježková L, Davídková M, Bačíková A, Vachelová J, Michaelidesová A, Kozubek S. Heterochromatinization associated with cell differentiation as a model to study DNA double strand break induction and repair in

the context of higher-order chromatin structure. Appl Radiat Isot. 2014;83(Pt B):177–85.
73. Ježková L, Falk M, Falková I, Davídková M., Bačíková A, Štefančíková L, Vachelová J, Michaelidesová A, Lukášová E, Boreyko A, Krasavin E, Kozubek S. Function of chromatin structure and dynamics in DNA damage, repair and misrepair: γ-rays and protons in action. Appl Radiat Isot. 2014;83(Pt B):128–36.
74. Falk M, Lukasova E, Gabrielova B, Ondrej V, Kozubek S. Chromatin dynamics during DSB repair. Biochim Biophys Acta. 2007;1773:1534–45.
75. Fang L, Wang Y, Du D, Yang G, Tak Kwok T, Kai Kong S, Chen B, Chen DJ, Chen Z. Cell polarity protein Par3 complexes with DNA-PK via Ku70 and regulates DNA double-strand break repair. Cell Res. 2007;17:100–16.
76. Lukásová E, Kozubek S, Falk M, Kozubek M, Zaloudík J, Vagunda V, Pavlovský Z. Topography of genetic loci in the nuclei of cells of colorectal carcinoma and adjacent tissue of colonic epithelium. Chromosoma. 2004;112:221–30.
77. Krueger SA, Wilson GD, Piasentin E, Joiner MC, Marples B. The effects of G2-phase enrichment and checkpoint abrogation on low-dose hyper-radiosensitivity. Int J Radiat Oncol Biol Phys. 2010; 77:1509–17.
78. Lukásová E, Koristek Z, Falk M, Kozubek S, Grigoryev S, Kozubek M, Ondrej V, Kroupová I. Methylation of histones in myeloid leukemias as a potential marker of granulocyte abnormalities. J Leukoc Biol. 2005;77:100–11.
79. Lukášová E, Kořistek Z, Klabusay M, Ondřej V, Grigoryev S, Bačíková A, Řezáčová M, Falk M, Vávrová J, Kohútová V, Kozubek S. Granulocyte maturation determines ability to release chromatin NETs and loss of DNA damage response; these properties are absent in immature AML granulocytes. Biochim Biophys Acta. 2013;1833:767–79.
80. Petrucelli N, Daly MB, Feldman GL. BRCA1 and BRCA2 hereditary breast and ovarian cancer. In: Pagon RA, Adam MP, Bird TD, et al., editors. Gene reviews [serial online]. Seattle: University of Washington; 1998 [updated 26 Sept 2013; cited 10 Apr 2014]. Available from: http://www.ncbi.nlm.nih.gov/books/NBK1247/.
81. Sevcik J, Falk M, Kleiblova P, Lhota F, Stefancikova L, Janatova M, Weiterova L, Lukasova E, Kozubek S, Pohlreich P, Kleibl Z. The BRCA1 alternative splicing variant Δ14-15 with an in-frame deletion of part of the regulatory serine-containing domain (SCD) impairs the DNA repair capacity in MCF-7 cells. Cell Signal. 2012;24:1023–30.
82. Sevcik J, Falk M, Macurek L, Kleiblova P, Lhota F, Hojny J, Stefancikova L, Janatova M, Bartek J, Stribrna J, Hodny Z, Jezkova L, Pohlreich P, Kleibl Z. Expression of human BRCA1Δ17-19 alternative splicing variant with a truncated BRCT domain in MCF-7 cells results in impaired assembly of DNA repair complexes and aberrant DNA damage response. Cell Signal. 2013;25:1186–93.
83. Pandey BN, Gordon DM, De Toledo SM, Pain D, Azzam EI. Normal human fibroblasts exposed to high- or low-dose ionizing radiation: differential effects on mitochondrial protein import and membrane potential. Antioxid Redox Signal. 2006;8:1253–61.
84. Schofield PN, Tapio S, Grosche B. Archiving lessons from radiobiology. Nature. 2010;468(7324):634.
85. Birschwilks M, Gruenberger M, Adelmann C, Tapio S, Gerber G, Schofield PN, Grosche B. The European radiobiological archives: online access to data from radiobiological experiments. Radiat Res. 2011;175:526–31.
86. Naderi H, Matin MM, Bahrami AR. Review paper: critical issues in tissue engineering: biomaterials, cell sources, angiogenesis, and drug delivery systems. J Biomater App. 2011;26:383–417.
87. George KA, Hada M, Chappell L, Cucinotta FA. Biological effectiveness of accelerated particles for the induction of chromosome damage: track structure effects. Radiat Res. 2013;180:25–33.
88. Berger T, Meier M, Reitz G, Schridde, M. Long-term dose measurements applying a human anthropomorphic phantom onboard an aircraft. Radiat Meas. 2008;43:580–4.
89. Cucinotta FA, Manuel FK, Jones J, Iszard G, Murrey J, Djojonegro B, Wear M. Space radiation and cataracts in astronauts. Rad Res. 2001;156:460–6.
90. Cucinotta FA, Durante M. Cancer risk from exposure to galactic cosmic rays: implications for space exploration by human beings. Lancet Oncol. 2006;7:431–5.
91. Blakely EA, Chang PY. A review of ground-based heavy ion radiobiology relevant to space radiation risk assessment: cataracts and CNS effects. Adv Space Res. 2007;40:1307–19.
92. Sihver L. Physics and biophysics experiments needed for improved risk assessment in space. Acta Astronaut. 2008;63:886–98.
93. Seed T (2011) Acute effects [article on the Internet]. The Health Effects of Extraterrestrial Environments, Universities Space Research Association, Division of Space Life Sciences; 2011 [cited 10 Apr 2014]. Available from: http://three.usra.edu/articles/SeedAcuteEffects.pdf.
94. Kerr RA. Planetary exploration. Radiation will make astronauts' trip to Mars even riskier. Science. 2013;340(6136):1031.
95. Zeitlin C, Hassler DM, Cucinotta FA, Ehresmann B, Wimmer-Schweingruber RF, Brinza DE, Kang S, Weigle G, Böttcher S, Böhm E, Burmeister S, Guo J, Köhler J, Martin C, Posner A, Rafkin S, Reitz G. Measurements of energetic particle radiation in transit to Mars on the Mars Science Laboratory. Science. 2013;340:1080–4.
96. Combs SE, Debus J. Treatment with heavy charged particles: systematic review of clinical data and current clinical (comparative) trials. Acta Oncol. 2013;52:1272–86.

97. Loeffler JS, Durante M. Charged particle therapy-optimization, challenges and future directions. Nat Rev Clin Oncol. 2013;10:411–24.
98. Obolensky OI, Surdutovich E, Pshenichnov I, Mishustin I, Solov'yov AV, Greiner W. Ion beam cancer therapy: fundamental aspects of the problem. Nucl Instrum Methods Phys Res B. 2008;266(8):1623–8.
99. Falk M, Lukasova E, Kozubek S. Repair mechanisms of DNA double-strand breaks–biochemical and spatio-temporal aspects. In: García G, Fuss M, editors. Radiation damage in biomolecular systems. New York: Springer Science+Business Media; 2012. p. 329–359.
100. Zschenker O, Raabe A, Boeckelmann IK, Borstelmann S, Szymczak S, Wellek S, Rades D, Hoeller U, Ziegler A, Dikomey E, Borgmann K. Association of single nucleotide polymorphisms in ATM, GSTP1, SOD2, TGFB1, XPD and XRCC1 with clinical and cellular radiosensitivity. Radiother Oncol. 2010;97:26–32.
101. Michikawa Y, Suga T, Ishikawa A, Hayashi H, Oka A, Inoko H, Iwakawa M, Imai T. Genome wide screen identifies microsatellite markers associated with acute adverse effects following radiotherapy in cancer patients. BMC Med Genet. 2010;11:123.
102. Kim HS, Kim SC, Kim SJ, Park CH, Jeung HC, Kim YB, Ahn JB, Chung HC, Rha SY. Identification of a radiosensitivity signature using integrative metaanalysis of published microarray data for NCI-60 cancer cells. BMC Genomics. 2012;13:348.
103. Mousses S, Caplen NJ, Cornelison R, Weaver D, Basik M, Hautaniemi S, Elkahloun AG, Lotufo RA, Choudary A, Dougherty ER, Suh E, Kallioniemi O. RNAi microarray analysis in cultured mammalian cells. Genome Res. 2003;13:2341–7.
104. Silva JM, Mizuno H, Brady A, Lucito R, Hannon GJ. RNA interference microarrays: high-throughput loss-of-function genetics in mammalian cells. Proc Natl Acad Sci U S A. 2004;101:6548–52.
105. Rantala JK, Mäkelä R, Aaltola AR, Laasola P, Mpindi JP, Nees M, Saviranta P, Kallioniemi O. A cell spot microarray method for production of high density siRNA transfection microarrays. BMC Genomics. 2001;12:162.
106. Tapio S, Hornhardt S, Gomolka M, Leszczynski D, Posch A, Thalhammer S, Atkinson MJ. Use of proteomics in radiobiological research: current state of the art. Radiat Environ Biophys. 2010;49:1–4.
107. Bajinskis A, Lindegren H, Johansson L, Harms-Ringdahl M, Forsby A. Low-dose/dose-rate γ radiation depresses neural differentiation and alters protein expression profiles in neuroblastoma SH-SY5Y cells and C17.2 neural stem cells. Radiat Res. 2011;175:185–92.
108. Feng XP, Yi H, Li MY, Li XH, Yi B, Zhang PF, Li C, Peng F, Tang CE, Li JL, Chen ZC, Xiao ZQ. Identification of biomarkers for predicting nasopharyngeal carcinoma response to radiotherapy by proteomics. Cancer Res. 2010;70:3450–62.
109. Wu P, Zhang H, Qi L, Tang Q, Tang Y, Xie Z, Lv Y, Zhao S, Jiang W. Identification of ERp29 as a biomarker for predicting nasopharyngeal carcinoma response to radiotherapy. Oncol Rep. 2012;27:987–94.
110. Skvortsova I, Skvortsov S, Stasyk T, Raju U, Popper BA, Schiestl B, von Guggenberg E, Neher A, Bonn GK, Huber LA, Lukas P. Intracellular signaling pathways regulating radioresistance of human prostate carcinoma cells. Proteomics. 2008;8:4521–33.
111. Smith L, Qutob O, Watson MB, Beavis AW, Potts D, Welham KJ, Garimella V, Lind MJ, Drew PJ, Cawkwell L. Proteomic identification of putative biomarkers of radiotherapy resistance: a possible role for the 26S proteasome? Neoplasia. 2009;11:1194–207.
112. Heyes GJ, Mill AJ, Charles MW. Mammography-oncogenecity at low doses. J Radiol Prot. 2009;29:A123–32.
113. Calabro-Jones PM, Fahey RC, Smoluk GD, Ward JF. Alkaline phosphatase promotes radioprotection and accumulation of WR-1065 in V79-171 cells incubated in medium containing WR-2721. Int J Radiat Biol. 1985;47:23–7.
114. Calabro-Jones PM, Aguilera JA, Ward JF, Smoluk GD, Fahey RC. Uptake of of WR-2721 derivatives by cells in culture: identification of the transported form of the drug. Cancer Res. 1988;48:3634–40.
115. Nicolatou-Galitis O, Sarri T, Bowen J, Di Palma M, Kouloulias VE, Niscola P, Riesenbeck D, Stokman M, Tissing W, Yeoh E, Elad S, Lalla RV; Mucositis Study Group of the Multinational Association of Supportive Care in Cancer/International Society of Oral Oncology (MASCC/ISOO). Systematic review of amifostine for the management of oral mucositis in cancer patients. Support Care Cancer. 2013;21(1):357–64.
116. Kouvaris JR, Kouloulias VE, Vlahos LJ. Amifostine: the first selective-target and broad-spectrum radioprotector. Oncologist. 2007;12:738–47.
117. Tahsildar HI, Biaglow JE, Kligerman MM, Varnes ME. Factors influencing the oxidation of radioprotector WR-1065. Radiat Res. 1988;113:243–51.
118. Durand RE, Olive PL. Radiosensitisation and radioprotection by BSO and WR-2721: the role of oxygenation. Br J Cancer. 1989;60:517–22.
119. Margulies BS, Damron TA, Allen MJ. The differential effects of the radioprotectant drugs amifostine and sodium selenite treatment in combination with radiation therapy on constituent bone cells, Ewing's sarcoma or bone tumor cells, and rhabdomyosarcoma tumor cells in vitro. J Otrhopaed Res. 2008;26:1912–9.
120. Orditura M, de Vita F, Roscigno A, Infusino S, Auriemma A, Iodice P, Ciaramella F, Abbate G, Catalano G. Amifostine: a selective cytoprotective agent of normal tissues from chemo-radiotherapy induced toxicity (Review). Oncol Rep. 1999;6(6):1357–62.

121. Levi M, Knol JA, Ensminger WD, DeRemer SJ, Dou C, Lunte SM, Bonner HS, Shaw LM, Smith DE. Regional pharmacokinetics of amifostine in anesthetized dogs: role of the liver, gastrointestinal tract, lungs, and kidneys. Drug Metab Dispos. 2002;30:1425–30.
122. Son JCH, Kang DW, Yang KM, Choi KY, Son TG, Min do S. Phospholipase D inhibitor enhances radiosensitivity of breast cancer cells. Exp Mol Med. 2013;45:e38.
123. Raghavan P, Tumati V, Yu L, Chan N, Tomimatsu N, Burma S, Bristow RG, Saha D. AZD5438, an inhibitor of Cdk1, 2, and 9, enhances the radiosensitivity of non-small cell lung carcinoma cells. Int J Radiat Oncol Biol Phys. 2012;84:e507–14.
124. Lowery MA, Vanoli F, Yu KH, Jasin M, O'Reilly EM, Mary Ellen Moynahan ME. Inhibition of poly (ADP-ribose) polymerase-1 (PARP-1) to increase radiosensitivity of human pancreatic cancer (PAC) cell lines proficient in homology-directed repair (HDR). J Clin Oncol. 2012;30(Suppl 4):204.
125. Wang M, Morsbach F, Sander D, Gheorghiu L, Nanda A, Benes C, Kriegs M, Krause M, Dikomey E, Baumann M, Dahm-Daphi J, Settleman J, Willers H. EGFR receptor inhibition radiosensitizes NSCLC cells by inducing senescence in cells sustaining DNA double-strand breaks. Cancer Res. 2011;71:6261–9.
126. Kriegs M, Kasten-Pisula U, Rieckmann T, Holst K, Saker J, Dahm-Daphi J, Dikomey E. The epidermal growth factor receptor modulates DNA double-strand break repair by regulating non-homologous end-joining. DNA Repair (Amst). 2010;9:889–97.
127. Toulany M, Kasten-Pisula U, Brammer I, Wang S, Chen J, Dittmann K, Baumann M, Dikomey E, Rodemann HP. Blockage of epidermal growth factor receptor-phosphatidylinositol 3-kinase-AKT signaling increases radiosensitivity of K-RAS mutated human tumor cells in vitro by affecting DNA repair. Clin Cancer Res. 2006;12:4119–26.
128. Liu S, Opiyo SO, Manthey K, Glanzer JG, Ashley AK, Amerin C, Troksa K, Shrivastav M, Nickoloff JA, Oakley GG. Distinct roles for DNA-PK, ATM and ATR in RPA phosphorylation and checkpoint activation in response to replication stress. Nucleic Acids Res. 2012;40:10780–94.
129. Wang H, Wang M, Wang H, Böcker W, Iliakis G. Complex H2AX phosphorylation patterns by multiple kinases including ATM and DNA-PK in human cells exposed to ionizing radiation and treated with kinase inhibitors. J Cell Physiol. 2005;202:492–502.
130. Stiff T, O'Driscoll M, Rief N, Iwabuchi K, Löbrich M, Jeggo PA. ATM and DNA-PK function redundantly to phosphorylate H2AX after exposure to ionizing radiation. Cancer Res. 2004;64:2390–6.
131. Manova V, Singh SK, Iliakis G. Processing of DNA double strand breaks by alternative non-homologous end-joining in hyperacetylated chromatin. Genome Integr. 2012;3:4.
132. Singh SK, Bednar T, Zhang L, Wu W, Mladenov E, Iliakis G. Inhibition of B-NHEJ in plateau-phase cells is not a direct consequence of suppressed growth factor signaling. Int J Radiat Oncol Biol Phys. 2012;84:e237–43.
133. Iliakis G. Backup pathways of NHEJ in cells of higher eukaryotes: cell cycle dependence. Radiother Oncol. 2009;92:310–5.
134. Geuting V, Reul C, Löbrich M. ATM release at resected double-strand breaks provides heterochromatin reconstitution to facilitate homologous recombination. PLoS Genet. 2013;9:e1003667.
135. Purrucker JC, Fricke A, Ong MF, Rübe C, Rübe CE, Mahlknecht U. HDAC inhibition radiosensitizes human normal tissue cells and reduces DNA double-strand break repair capacity. Oncol Rep. 2010;23:263–9.
136. Yu J, Mi J, Wang Y, Wang A, Tian X. Regulation of radiosensitivity by HDAC inhibitor trichostatin A in the human cervical carcinoma cell line Hela. Eur J Gynaecol Oncol. 2012;33:285–90.
137. Rajendran P, Ho E, Williams DE, Dashwood RH. Dietary phytochemicals, HDAC inhibition, and DNA damage/repair defects in cancer cells. Clin Epigenetics. 2011;3:4.
138. Koprinarova M, Botev P, Russev G. Histone deacetylase inhibitor sodium butyrate enhances cellular radiosensitivity by inhibiting both DNA nonhomologous end joining and homologous recombination. DNA Repair (Amst). 2011;10:970–7.
139. Cerna D, Camphausen K, Tofilon PJ. Histone deacetylation as a target for radiosensitization. Curr Top Dev Biol. 2006;73:173–204.
140. Le Sech C, Kobayashi K, Usami N, Furusawa Y, Porcel E, Lacombe S. Comment on 'Therapeutic application of metallic nanoparticles combined with particle-induced x-ray emission effect'. Nanotechnology. 2012;23:078001.
141. Ma J, Xu R, Sun J, Zhao D, Tong J, Sun X. Nanoparticle surface and nanocore properties determine the effect on radiosensitivity of cancer cells upon ionizing radiation treatment. J Nanosci Nanotechnol. 2013;13:1472–5.
142. Joh DY, Sun L, Stangl M, Al Zaki A, Murty S, Santoiemma PP, Davis JJ, Baumann BC, Alonso-Basanta M, Bhang D, Kao GD, Tsourkas A, Dorsey JF. Selective targeting of brain tumors with gold nanoparticle-induced radiosensitization. PLoS One. 2013;8:e62425.
143. Rezaei-Tavirani M, Dolat E, Hasanzadeh H, Seyyedi SS, Semnani V, Sobhi S. TiO2 Nanoparticle as a sensitizer drug in radiotherapy: in vitro study. Iran J Cancer Prev. 2013;6:37–44.
144. Porcel E, Kobayashi K, Usami N, Remita H, Le Sech , Lacombe S. Photosensitization of plasmid-DNA loaded with platinum nano-particles and irradiated by low energy X-rays. J Phys Conf Ser. 2011;261:012004.
145. Roa W, Zhang X, Guo L, Shaw A, Hu X, Xiong Y, Gulavita S, Patel S, Sun X, Chen J,Moore R, Xing JZ. Gold

nanoparticle sensitize radiotherapy of prostate cancer cells by regulation of the cell cycle. Nanotechnology. 2009;20:375101.
146. Zhang X, Xing JZ, Chen J, Ko L, Amanie J, Gulavita S, Pervez N, Yee D, Moore R, Roa W. Enhanced radiation sensitivity in prostate cancer by gold-nanoparticles. Clin Invest Med. 2008;31:E160–7.
147. Kwatra D, Venugopal A, Anant S. Nanoparticles in radiation therapy: a summary of various approaches to enhance radiosensitization in cancer. Transl Cancer Res. 2013;2:330–42.
148. Dorsey JF, Sun L, Joh DY, Witztum A, Al Zaki A, Kao GD, Alonso-Basanta M, Avery S, Tsourkas A, Hahn SM. Gold nanoparticles in radiation research: potential applications for imaging and radiosensitization. Transl Cancer Res. 2013;2:280–91.
149. Veldwijk M, Burger N, Kirchner A, Wenz F, Herskind C. Efficient DNA-mediated transfer of small gold nanoparticles for the radiosensitization of cells. In: Book of Abstracts from GBS Jahrestagung 2013, 25–27 Sept 2013, Darmstadt, Germany. p. 143.
150. Trouiller B, Reliene R, Westbrook A, Solaimani P, Schiestl RH. Titanium dioxide nanoparticles induce DNA damage and genetic instability in vivo in mice. Cancer Res. 2009;69:8784–9.
151. Asharani PV, Hande MP, Valiyaveettil S. Anti-proliferative activity of silver nanoparticles. BMC Cell Biol. 2009;10:65.
152. Asharani PV, Low Kah Mun G, Hande MP, and Valiyaveettil S. Cytotoxicity and genotoxicity of silver nanoparticles in human cells. ACS Nano. 2009;3:279–90.
153. Ahamed M, Karns M, Goodson M, Rowe J, Hussain SM, Schlager JJ, Hong Y. DNA damage response to different surface chemistry of silver nanoparticles in mammalian cells. Toxicol Appl Pharmacol. 2008;233:404–10.
154. Jain S, Coulter JA, Hounsell AR, Butterworth KT, McMahon SJ, Hyland WB, Muir MF, Dickson GR, Prise KM, Currell FJ, O'Sullivan JM, Hirst DG. Cell-specific radiosensitization by gold nanoparticles at megavoltage radiation energies. Int J Radiat Oncol Biol Phys. 2011;79:531–9.
155. Taggart L, McMahon SJ, Ghita M, Butterworth K, Prise KM, Currell F, Schettino G. The characterisation of radiosensitising effect of gold nanoparticales. In: Proc 40th Annual Meeting of the ERR, 1–5 Sept 2013, Dublin, Ireland p. W-31.

Critical Reviews™ *in Eukaryotic Gene Expression,* 24(3):225-247 (2014)

Determining Omics Spatiotemporal Dimensions Using Exciting New Nanoscopy Techniques to Assess Complex Cell Responses to DNA Damage: Part B—Structuromics

Martin Falk,[1,*] Michael Hausmann,[2] Emílie Lukášová,[1] Abin Biswas,[2,3] Georg Hildenbrand,[2,3] Marie Davídková,[4] Evgeny Krasavin,[5] Zdeněk Kleibl,[6] Iva Falková,[1] Lucie Ježková,[1,5,7] Lenka Štefančíková,[1] Jan Ševčík,[6] Michal Hofer,[1] Alena Bačíková,[1] Pavel Matula,[1,8] Alla Boreyko,[5] Jana Vachelová,[4] Anna Michaelidisová,[4,9] & Stanislav Kozubek[1]

[1]Institute of Biophysics, Academy of Sciences of the Czech Republic, Brno, Czech Republic; [2]Kirchhoff Institute for Physics, University of Heidelberg, Heidelberg, Germany; [3]Department of Radiation Oncology, University Medical Center Mannheim, University of Heidelberg, Heidelberg, Germany; [4]Nuclear Physics Institute, Academy of Sciences of the Czech Republic, Řež, Czech Republic; [5]Joint Institute for Nuclear Research, Dubna, Moscow, Russia; [6]Institute of Biochemistry and Experimental Oncology, First Faculty of Medicine, Charles University, Prague, Czech Republic; [7]Institute of Chemical Technology Prague, Prague, Czech Republic; [8]Centre for Biomedical Image Analysis, Faculty of Informatics, Masaryk University, Brno, Czech Republic; [9]Proton Therapy Center, Prague, Czech Republic

*** Address all correspondence to:** Martin Falk, PhD, Department of Chromatin Function, Damage and Repair; Institute of Biophysics, Academy of Sciences of the Czech Republic, Královopolská 135; 612 65 Brno, Czech Republic; , Tel. (office): +420-541517165; Tel. (mobile): +420-728084060; falk@ibp.cz, mfalk@seznam.cz.

ABSTRACT: Recent groundbreaking developments in Omics and bioinformatics have generated new hope for overcoming the complexity and variability of (radio)biological systems while simultaneously shedding more light on fundamental radiobiological questions that have remained unanswered for decades. In the era of Omics, our knowledge of how genes and dozens of proteins interact in the frame of complex signaling and repair pathways (or, rather, networks) to preserve the integrity of the genome has been rapidly expanding. Nevertheless, these functional networks must be observed with strong correspondence to the cell nucleus, which is the main target of ionizing radiation. Information regarding these intricate processes cannot be achieved using high-throughput Omics approaches alone; it requires sophisticated structural probing and imaging. In the first part of this review, the article "Giving Omics Spatiotemporal Dimensions Using Exciting New Nanoscopy Techniques to Assess Complex Cell Responses to DNA Damage: Part A—Radiomics," we showed the development of different Omics solutions and how they are contributing to a better understanding of cellular radiation response. In this Part B we show how high-resolution confocal microscopy as well as novel approaches of molecular localization nanoscopy fill the gaps to successfully place Omics data in the context of space and time. The dynamics of double-strand breaks during repair processes and chromosomal rearrangements at the microscale correlated to aberration induction are explained. For the first time we visualize pan-nuclear nucleosomal rearrangements and clustering at the nanoscale during repair processes. Finally, we introduce a novel method of specific chromatin nanotargeting based on a computer database search of uniquely binding oligonucleotide combinations (COMBO-FISH). With these challenging techniques on hand, we speculate future perspectives that may combine specific COMBO-FISH nanoprobing and structural nanoscopy to observe structure–function correlations in living cells in real-time. Thus, the Omics networks obtained from function analyses may be enriched by real-time visualization of Structuromics.

KEY WORDS: Omics, ionizing radiation, low-dose dilemma, biological complexity and variability, higher-order chromatin structure, DNA damage response, formation of chromosomal translocations, confocal microscopy, localization nanoscopy

ABBREVIATIONS: γH2AX, histone H2AX phosphorylated on serine 139; **3D,** 3-dimensional; **CHT,** chromosomal territory; **COMBO-FISH**, combinatorial oligo–fluorescence in situ hybridization; **CTR,** chromosomal/chromatin

translocation; **DSB,** double-strand break; **Ec**, euchromatin; **FISH,** fluorescence in situ hybridization; **FTL,** frequently translocated locus; **GFP,** green fluorescent protein; **Hc,** heterochromatin; **HR,** homologous recombination; **IR**, ionizing radiation; **IRIFs,** ionizing radiation–induced repair foci; **LET,** linear energy transfer; **NHEJ,** nonhomologous end-joining; **RIDGEs**, regions of increased gene expression; **SPDM,** spectral precision distance/position determination microscopy; **TEM,** transmission electron microscopy.

I. FROM OMICS TO NUCLEAR ARCHITECTURE: ON THE AVENUE TO STRUCTUROMICS

The complexity and variability of biological systems (Fig. 1) calls for high-throughput techniques and enormous computing power (along with large amounts of the input material) to attempt and find solutions to (radio)biological problems in their entirety (see Fig. 1 in our other article in this issue, "Determing Omics Spatiotemporal Dimensions Using Exciting New Nanoscopy Techniques to Assess Complex Cell Responses to DNA Damage: Part A—Radiomics," hereafter referred to as Part A). The Omics approaches based on high-throughput methods, however, in principle suffer from 2 serious limitations as the sample material is isolated from cells and studied in vitro: (1) the information about the structure, dynamics, and spatiotemporal organization of the genome, proteome, metabolome, etc., is lost; and (2) only average results for the particular (in many aspects heterogeneous) cell population can be achieved.

Although microscopy is primarily not a high-throughput method, it exceeds the true Omics assays described in Part A by its capability to directly visualize cellular processes in situ or even in vivo. Microscopic techniques thus represent unique, irreplaceable research tools that can place Omics data into the context of the cell architecture and provide structural, mechanistic, and spatiotemporal real-time views on the mechanisms of cellular processes (Figs. 1 and 2). Here, this approach is called "Structuromics." Such knowledge is especially significant in the light of revolutionary findings recognizing the cell nucleus as a hierarchically organized organelle with a nonrandom (chromatin) architecture[1–25] (Fig. 2A) (reviewed in Refs. 26–33). In addition, microscopy can provide information on the situation in single cells isolated from cell populations, contrary to methods working with "averaged" amounts of material. The influence of averaging could lead to a lost of significant or specific information when studying. This becomes immense when studying heterogeneous cell populations or tissues such as tumors.

With the discovery of new technological concepts to allow us to break Abbe's limit[34–37] (Fig. 3), fluorescently label DNA, RNA, to proteins in living cells,[38,39] and acquire 3-dimensional images of thousands of cells in acceptable times,[21,40–43] optical microscopy undoubtedly belongs to the most rapidly developing fields of modern systems biology and radiation research.

After providing several examples of fundamental but still unresolved radiobiological issues to demonstrate the complexity and variability of (radio)biological systems and thus the irreplaceability of "pan-Omics" (or "meta-omics") and cross-disciplinary approaches to grasp the problems in a more holistic way (see Part A), we illustrate here our own results that show how optical fluorescence microscopy can contribute to research on the DNA damage response and overcome some of the above-mentioned limitations. We focus on microscopic studies of DNA double-strand breaks (DSBs) that are the most dangerous among a plethora of different DNA lesions introduced in DNA by ionizing radiation (IR); we also concretely discuss the relationship between the higher-order chromatin structure, chromatin sensitivity to DSBs, DSB repair mechanisms and efficiency, and chromosomal translocations. The importance of higher-order chromatin structure in regulating and performing fundamental vital processes in the cell nucleus has been overlooked for years.

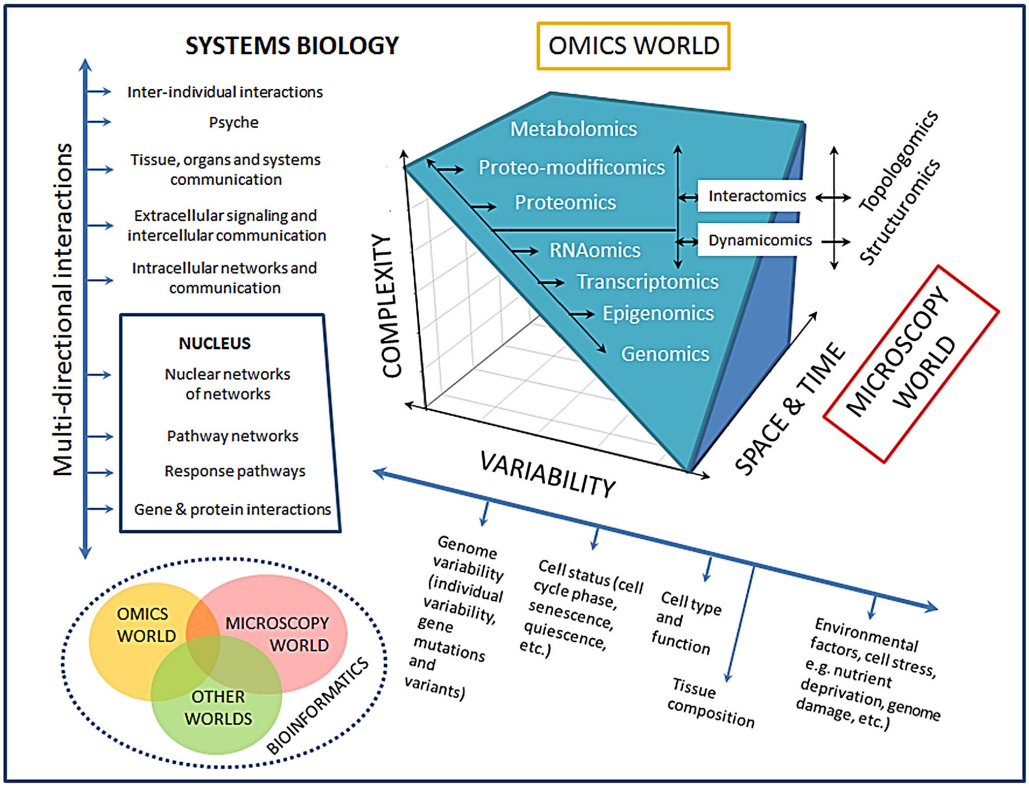

FIG. 1: Complementary and irreplaceable roles of Omics and microscopy approaches in (radio)biological research. Extensive complex (left vertical axis) and variable (horizontal axis) functional biological networks, continuously changing in space and time (right horizontal axis), can be studied nowadays in a more holistic way by means of various omics (e.g., genomics, transcriptomics, proteomics; white lettering). However, the omic assays cannot provide information on the spatiotemporal organization and spatiotemporal dynamics of interactions between individual players of a particular omics system (e.g., protein–protein interactions) and between distinct omics (e.g., gene–protein interactions) (black lettering in white boxes). On the other hand, Structuromics and topologomics data (the graph, right side) can be studied with (real-time, living-cell) microscopy and nanoscopy (superresolution microscopy). Micro-/nanoscopy thus allows Omics data to be put into the context of time and space of nonrandom architecture of the cell and cell nucleus. Both Omics and micro-/nanoscopy worlds could not exist without an extensive support from bioinformatics (bottom left diagram).

Last, we introduce some breakthrough ideas in the field of optical high-resolution localization nanoscopy that attempt to overcome current technological limitations and can push us far beyond the horizons of our current understanding of (radio) biological problems. These approaches may give us new insights about the mechanisms of and response to irradiation, which, when integrated with reports of Omics functions, could lead to a novel and complete understanding of the repertoire of the cellular survival program after exposure to natural and/or artificial radiation (Fig. 1).

A. DNA DSBs and DSB Repair

DSBs can arise from the action of IR, radiomimetic chemicals, and endogenous cellular processes such as energetic metabolism, replication,

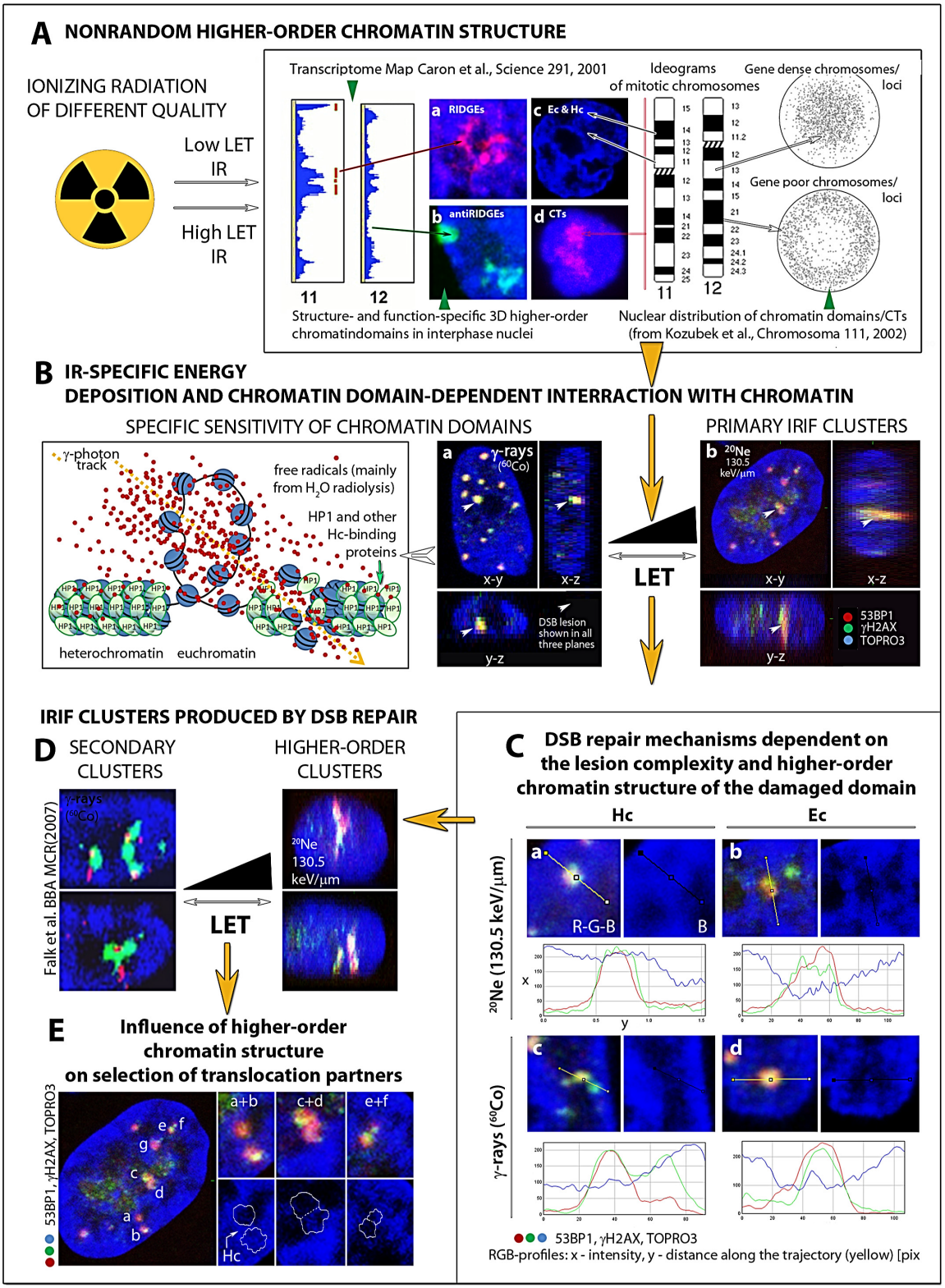
A NONRANDOM HIGHER-ORDER CHROMATIN STRUCTURE
IONIZING RADIATION OF DIFFERENT QUALITY
Low LET IR
High LET IR
Transcriptome Map Caron et al., Science 291, 2001
Ideograms of mitotic chromosomes
Gene dense chromosomes/ loci
Gene poor chromosomes/ loci
a RIDGEs
b antiRIDGEs
c Ec & Hc
d CTs
11
12
Structure- and function-specific 3D higher-order chromatindomains in interphase nuclei
Nuclear distribution of chromatin domains/CTs (from Kozubek et al., Chromosoma 111, 2002)
B IR-SPECIFIC ENERGY DEPOSITION AND CHROMATIN DOMAIN-DEPENDENT INTERRACTION WITH CHROMATIN
SPECIFIC SENSITIVITY OF CHROMATIN DOMAINS
PRIMARY IRIF CLUSTERS
γ-photon track
free radicals (mainly from H2O radiolysis)
HP1 and other Hc-binding proteins
heterochromatin
euchromatin
γ-rays (60Co)
20Ne 130.5 keV/µm
x-y
x-z
y-z
DSB lesion shown in all three planes
LET
53BP1
γH2AX
TOPRO3
IRIF CLUSTERS PRODUCED BY DSB REPAIR
D SECONDARY CLUSTERS
HIGHER-ORDER CLUSTERS
Falk et al. BBA MCR(2007)
E Influence of higher-order chromatin structure on selection of translocation partners
53BP1, γH2AX, TOPRO3
a+b
c+d
e+f
Hc
C DSB repair mechanisms dependent on the lesion complexity and higher-order chromatin structure of the damaged domain
Hc
Ec
R-G-B
B
20Ne (130.5 keV/µm)
γ-rays (60Co)
53BP1, γH2AX, TOPRO3
RGB-profiles: x - intensity, y - distance along the trajectory (yellow) [pix

FIG. 2: A: The nonrandom architecture and higher-order chromatin structure of the cell nucleus. The transcriptome maps (left panels, according to Caron et al.[79]) demonstrate clustering of highly expressed and unexpressed genes along chromosomes 11 and 12 (horizontal axis: transcription intensity; vertical axis: path along the chromosome). Clusters of highly expressed genes (RIDGEs) are marked by vertical red lines. Middle panels (*a*–*d*) show functionally and structurally specific chromatin domains in the interphase cell nucleus: RIDGE domains (red, *a*); anti-RIDGE domains (green, *b*); euchromatin (Ec, faintly blue) and heterochromatin (Hc, intensively blue) domains (*c*); and chromosomal territories (CTs, red, *d*). The arrows link the interphase RIDGE/anti-RIDGE and Ec/Hc domains to mitotic chromosomes (right, schematic drawing). Note that highly expressed RIDGEs are more decondensed and indented relative to unexpressed antiRIDGEs. Domains at a, b, and d were visualized by fluorescence in situ hybridization (FISH) on spatially fixed nuclei (3-dimensional FISH) (according to Lukásová et al.[20]); chromatin counterstaining (including Hc domains in *c*) with TOPRO3 (artificially blue). Maximal images composed from several confocal slices 0.2 µm thick are shown. Right panel: Gene density-dependent, nonrandom nuclear distribution of structurally and functionally distinct chromatin domains (images modified according to Kozubek et al. [21]). While gene-dense chromosomes or loci are preferentially located closer to the nuclear center (upper image), those that are gene-poor usually appear closer to the nuclear membrane (lower image). **B:** Different kinds of radiation specifically interact with nonrandom higher-order chromatin structure. Hc contains large amounts of Hc-binding proteins (such as HP1 [green]) and is less hydrated compared with Ec. γ Rays represent a low linear energy transfer (LET) radiation that mostly damages DNA via its indirect effect (i.e., production of harmful free radicals mostly coming from water radiolysis). *a, left scheme*: Ec is more sensitive to DSB induction with γ-rays since DNA in Hc is better shielded from these radicals (red) by the domain's structure and composition (left panel is modified according to Falk et al.,[138] ARI 2014). *b.* Another specific appears for high-LET ionizing radiation (IR), represented here by ^{20}Ne (LET = 130.5 keV/µm). The high-energy particle massively loses its energy along the short path, so clustered DSBs (multiple DSBs, "primary clusters") frequently form. Hypothetically, DNA damage can be more serious in Hc because the density of chromatin per volume is higher compared to Ec. IRIFs were immunodetected in spatially fixed normal human skin fibroblasts, exposed to 1 Gy of the particular IR (1 Gy/minutes), with antibodies against phosphorylated 53BP1 (red) and γH2AX (green) 5 minutes after irradiation and chromatin counterstaining with TOPRO3. Maximal images composed from several confocal slices 0.2 µm thick are shown. **C.** Because of specific chromatin structure, and probably the different characteristics of Ec and Hc lesions, the mechanism of DSB repair differs for Ec and Hc. To proceed, DSB repair requires extensive modifications of the higher-order chromatin structure, namely chromatin decondensation at the sites of Hc-DSBs. Figures *a* and *b* show colocalization of γH2AX foci with p53BP1 protein in Hc (left images) and Ec (right images) after irradiating cells with ^{20}Ne (LET = 130.5 keV/γm,1 Gy, 1 Gy/minute). Figures *c* and *d* illustrate the same situation but for cells exposed to the same dose of γ-rays. Images and intensity profiles in the red, green, and blue channels (RGB profiles) show that p53BP1 colocalizes with γH2AX foci at the resolution power of confocal microscopy in all cases except the combination of γ-rays with Hc. Therefore, p53BP1 probably binds to chromatin at broken DNA ends only after the decondensation of the Hc domain; in the case of ^{20}Ne, the domain is seriously fragmented, which probably allows p53BP1 to enter Hc immediately. In terms of its mechanism, kinetics, and fidelity, DSB repair depends on the combination of IR quality and higher-order chromatin structure. RGB-profiles: *x*-axis, the path through the nucleus along the yellow line; *y*-axis, the pixel intensity in R-G-B [the range of 0 to 255]. Description of images is the same as that in Fig. A. **D.** Chromatin decondensation at the sites of Hc-DSBs may lead to IRIF protrusion into the nuclear domains with low-density chromatin and formation of IRIF (DSB) clusters. To distinguish these DSB clusters produced by the activity of DSB repair from those formed by the energy deposition (primary clusters), we call these "secondary clusters" (left images). For high-LET IR, similar interactions and clustering may also appear between the IRIF tracks along the particle path that are comprised from multiple IRIFs; these are the higher-order clusters (right images). Since the secondary/higher-order clusters are quite rare, usually temporary, and their number increases with time after irradiation, they probably represent sites with an increased risk of chromatin exchanges rather than putative repair factories. Description of the images is the same as in **B** and **C**, but the cells were fixed between 30 minutes and 2 hours after irradiation. Images for γ-rays are modified according to Falk et al.,[104] BBA MCR 1773. **E.** The proposed model of the relationship between the higher-order chromatin structure, DSB repair, and the mechanism of chromosomal translocations formation (Falk et al.[28,104,138]). Since DSBs are spatially quite stable, the global higher-order chromatin structure determines the (dynamic) nuclear positions of loci *a*, *b*, *c*, *d*, *e*, *f*, and *g*, and thus their nuclear separation and the elementary probability of mutual chromosomal translocations (t). For instance, the probability (p_t) is high for lesions a + b, c + d, and e + f, but negligible for a + d and c + g. However, the local higher-order chromatin structure may significantly modify p_t determined on the mutual distances of interacting partners since it can influence the protrusion of IRIFs into the nuclear subdomains with low-density

chromatin. Lesions a + b appear at the opposite sides of an Hc domain; therefore, they will protrude into different nuclear subcompartments of the low-density chromatin. This precludes their mutual interaction despite that the lesions are located in very close mutual proximity; $p_t(a+b)$ will therefore only be low. On the other hand, lesions c + d appear close to each other in a limited space of the same Ec (i.e., low-density chromatin) domain, so they can easily interact, and $p_t(c+d)$ will be inconsiderable. Similarly, lesions e + f arise from different Hc domains that are located facing one another at the opposite "banks" of the same low-density chromatin nuclear subdomain. Therefore, there is a high chance that both of these lesions will protrude to the same nuclear subdomain, where they can consequently produce chromosomal translocations. Since usually only limited "movements" of Hc-DSBs were observed, translocations between largely separated lesions (a + d, c + g, etc.) seem to remain insignificant despite chromatin decondensation. The description of the image is the same as for **D**.

transcription, and DNA repair[44–51] (reviewed by Gospodinov and Herceg[52]); therefore, genomes are continuously exposed to DSB formation. Even single lesions can cause mutations, chromosome aberrations, or cancerogenic development when the DNA is repaired incorrectly. Only a few DSBs are sufficient to initiate cell death if they remain unrepaired.[53] The accumulation of segregated or misrepaired DSBs also largely contributes to the development of chronic inflammation,[54] aging, and some nonmalignant neurodegenerative degenerations (reviewed in Refs. 20, 55, and 56). Because of this threat, sophisticated repair pathways—or, rather, networks—have evolved to guard the genome while its integrity is under the pressure of continuous damage.[57]

Nonhomologous end joining (NHEJ) and homologous recombination (HR) are recognized as 2 major mechanisms responsible for DSB removal[58,59] (reviewed by Helleday[60] and Valerie and Povirk[61]). By identifying mutated genes in radiosensitive patients (reviewed in Refs. 62–64) and, reversely, by analyzing abrogated functions in manipulated cultured cells (e.g., Refs. 65–67), dozens of proteins operating in NHEJ and HR were identified and characterized in terms of their structure, function, and mutual interactions. Many of these proteins were revealed to be of central importance for the repair pathway that is considered to be applied, and they exert various multiple functions and thus interconnect NHEJ, HR, and regulatory pathways engaged in controlling the cell cycle, differentiation, apoptosis, senescence, immune response, and so on.[68–74] (reviewed by Falk et al.[28] and Shrivastav et al.[75]]) (see also Fig. 1 in Part A). Though a holistic view of DSB repair could not be achieved in the pre-Omics era, we already have quite a detailed imaginary about the biochemistry of participating pathways and networks. What we largely miss, however, is knowledge of the spatiotemporal orchestration of these processes and their placement in the context of the higher-order chromatin structure (reviewed by Falk et al.[28]) (Fig. 1). The nonrandom higher-order chromatin structure has been recognized only recently (overviewed in section I.B, below) mostly because of technical limitations. Of note, the breakthrough discovery of interphase chromosomal territories (Fig. 2A) that opened the door to research of higher-order chromatin structure and spatiotemporal organization of nuclear processes was achieved by the far-sighted application of molecular-genetic methods in combination with optical microscopy (reviewed by Cremer and Cremer[76]).

B. The Function in Structure: The New Level of Complexity in (Radio)biology

In eukaryotes, DNA does not appear "naked" but in a complex with histones and nonhistone proteins called chromatin (reviewed by Woodcock et al.[77]). To allow about 2 m of human DNA to be compacted into a cell nucleus with an approximate diameter of 10 μm, chromatin is hierarchically wrapped into higher-order chromatin structures, and a maximal level of condensation is reached in mitotic chromosomes[77] (Fig. 2A). Although the separation of genetic information in daughter cells is possible during cell division, such a compaction

precludes physiological functioning of the genome. Therefore, in interphase cells, chromatin must variably decondense in a process that is precisely regulated and correlated with the function of a particular genetic locus.[78] Functionally similar DNA sequences are not homogeneously distributed along the chromosomes; rather, they form specified clusters[79] (Fig. 2A, transcriptome map [left panels]). As a consequence, structurally and functionally distinct chromatin domains are established within the 3D space of the cell nucleus (Fig. 2A, panels a–d). Some principles responsible for the nonrandom nuclear distribution of these domains have been recently discovered[21,29,80] (Fig. 2A, right panels), revealing the cell nucleus as a highly organized organelle in both space and time. This is in striking contrast with the previously accepted hypothesis of random chromatin folding, where the nucleoplasm was frequently compared to a soup with randomly swimming chromatin "noodles." Heterochromatin (Hc) and euchromatin (Ec), regions of increased gene expression (RIDGEs) and their counterpart, anti-RIDGEs,[79] and chromosomal territories (CHTs) (Fig. 2A, panels a–d), which are divided into chromosomal subdomains such as centromeres, teleomeres, or band domains, are well-known higher-order chromatin domains. All these domains are characterized by particular functions and a corresponding unique structure. Ec is a gene-dense, highly transcribed domain with an "open" chromatin structure, whereas Hc is gene poor, genetically mostly silent, associated with heterochromatin-binding proteins, and largely condensed.[55]. (Nevertheless, Hc definitely has its important functions in, e.g., nuclear chromatin organization and possibly the generation of electric forces responsible for many nuclear processes.[81]) These characteristics are even more prominent for RIDGEs and anti-RIDGEs[82] (see our Lukasova Emilie, Gabrielova Barbora, Ondrej Vladan, Falk Martin, Kozubek Stanislav) since they are formed by huge homogeneous clusters; RIDGEs contain highly expressed (usually housekeeping) genes, whereas anti-RIDGEs are condensed, unexpressed clusters (Fig. 2A, the Transcriptome map and panels a and b), albeit ones that do not always correspond with Hc. CHTs (Fig. 2A, panel d) are heterogeneous, higher-order domains that mutually intermingle to only a limited extent[54,83]; they are composed of the above-mentioned "subdomains." Overall, therefore, the gene expression, chromatin structure, and nuclear location of CHTs largely differ. Despite mutual positions, CHTs seem to be mostly random.[21] Their radial distributions correlate with mean transcription levels of chromosomes; highly expressed territories are located preferentially in the nuclear interior and vice versa[21] (Fig. 2A, right panels). Similar rules of organization also hold for the various chromosomal subdomains (such as those already mentioned: Hc, Ec, RIDGEs, anti-RIDGEs, centromeres, telomeres, and genes), which are responsible for the structural and functional polarization of CHTs.[20,21] There currently exists convincing evidence that higher-order chromatin structure and nuclear architecture play essential roles in fundamental nuclear processes such as transcription and replication.[21,84–87] Like other researchers[88–95] (reviewed in Refs. 28, 52, and 96–103), we demonstrated that this is also true for the DNA damage response[104–107] (reviewed by Falk et al.[28]); this is discussed below.

C. The Mechanism of Chromosomal Translocation: The Most Illustrative Example of the Importance of Chromatin Structure

1. The State of Art

The research on DSB repair and the mechanism of chromosomal/chromatin translocation (CTR) formation is perhaps the most illustrative example demonstrating the irreplaceability of optical microscopy in the Omics era. CTRs seem to be an initiating event in the development of leukemia and lymphomas, so they represent a severe threat to hu-

man health. Secondary translocations also arise as a result of the genomic instability associated both with blood cancers and solid tumors.

However, the mechanism of how CTRs are formed remains to be disclosed. Two principal alternative hypotheses of the mechanism of CTR—the "position first" hypothesis and the "breakage first" hypothesis—have been postulated and are still subject to intense discussions (reviewed by Falk et al.[28], and the citations therein). Briefly, the first hypothesis presupposes that CTRs can form only between loci that were located close to each other before the induction of a DNA DSB. (For simplicity, the opinion that the repair of one DSB may result in DNA breakage and the formation of a second DSB in close proximity is not discussed here.) The breakage first hypothesis, on the other hand, presuppose an increased movement of free DNA ends (that occur as a consequence of DSB), which introduces more freedom in the selection of translocating partners. Chromatin exchanges between initially distant loci are not excluded, although recent results indicate a subdiffusive motion of free ends, reducing the probability that ends separated by more than 0.5 μm will misjoin[108] (reviewed by Zidovska et al.[109]).

Despite the importance of the topic for (not only) human health and the endeavor to disclose this mystery, the results of CTR formation are still contradictory. Moreover, it seems that the abovementioned hypotheses, originally postulated as being mutually exclusive, highlight only a specific aspect of the CTR mechanism and that the real situation is even more complicated (discussed Falk et al.[28] and "Mechanism of Chromosomal Translocations"). In addition, the radiation used to induce DSBs largely influences the character of initial DNA damage, for example, its complexity and distribution[110–114] (reviewed by Georgakilas et al.[115]), with extensive consequences on subsequent repair processes.

So, what does this data tell us about chromosomal translocations? Given the limited extent of chromatin movement and the mutual intermingling of chromosomal territories, along with their nonrandom radial distributions, some chromosomal translocations can evidently be expected to form with a markedly higher probability than others. In addition, local chromatin structure might influence the sensitivity of a particular locus (or chromatin domain) to spontaneous DNA damage or the induction of DSBs[105] ("Sensitivity of Higher-Order Chromatin Domains to Radiation Damage"). Indeed, only a limited spectrum of translocations was frequently recognized to cause leukemias (reviewed by Gauwerky and Croce[116]). Although this phenomenon could also be explained by the different pathogenicity of individual translocations, a close nuclear separation was shown for some partners that often appear in oncogenic chromosomal rearrangements[27,56,117–123] (reviewed by Roukos et al.[124] and the citations therein). This is in agreement with the position first hypothesis and demonstrates how the global higher-order chromatin structure influences the probability of the formation of particular translocations (Fig. 2). For instance, a closer proximity of *BCR-ABL* genes was measured in a fraction of healthy donors in our later work,[56,117,118] and it could be speculated that small, individual-specific deviations in the higher-order chromatin structure (those that possibly are heritable or caused by other cofactors) may predispose some people to the development of chronic myeloid leukemia (CML). In addition, *BCR-ABL* and some other translocations were frequently shown to appear after exposing cells to fast neutrons.[125] Because high linear energy transfer (LET) radiation (including neutrons) frequently induces complex DSBs (multiple DSBs within very close proximity) (Fig. 2B, right panels), this observation was interpreted as a consequence of nuclear localization of the genes before irradiation. This agrees with the finding that the frequency of translocations between particular chromosomes correlates with the extent of their mutual intermingling.[54] In addition, specific local chromatin structure and compaction might predispose *ABL* and *BCR* genes to DNA breakage,[126–128] which may further support IR-induced or spontaneous formation of the *BCR-ABL* translocation. From the opposite point of view, these data show us how important

the character and distribution of the initial DNA damage (and thus the mechanism of action of the damaging agent) is for the mechanism of CTR formation (Fig. 2B; see the section "Sensitivity of Higher-Order Chromatin Domains to Radiation Damage").

On the other hand, mathematical simulations and some experiments show that the complex translocations observed in some patients with leukemia and other cancers probably could not form without some extent of chromatin dynamics.[126,129–133] In line with this opinion are results demonstrating the increased mobility of damaged chromatin after DSB induction, accompanied by clustering of several ionizing radiation–induced repair foci (IRIFs)[126,129,130] or DSBs.[89,134] Therefore, some authors concluded that chromatin dynamics mostly contributes to chromatin exchanges and rearrangements of nuclear architecture.[127,129–133] Moreover, DSB clusters were interpreted to be "repair factories" where several DSBs are repaired together (see Falk et al.[28] for illustrations). The processing of DSBs in repair factories would provide numerous advantages (e.g., energetic savings, more efficient catalysis of multistep biochemical processes) but, at the same time, seriously increase the risk of intermingling between free DNA ends. Despite existing serious doubts of this interpretation of DSB clusters (reviewed by Falk et al.[28] and in the sections "DSB Repair in the Context of Higher-Order Chromatin Structure" and "Mechanism of Chromosomal Translocations"), the results imperatively suggest that spatiotemporal organization of DSB repair must be studied in detail to deepen our understanding of CTR. DSB induction and repair processes seem to be markedly influenced by the higher-order chromatin structure of damaged chromatin domains and their nuclear surroundings, as discussed in detail in our previous work[28,104] and briefly summarized in the next sections.

2. Sensitivity of Higher-Order Chromatin Domains to Radiation Damage

In brief, we found that Hc is better protected against the indirect effects of γ-rays as compared to Ec.[105] Using dual immunostaining of IRIFs (γH2AX and 53BP1, MRE11, NBS1, or other DSB repair proteins that bind to IRIFs) in combination with high-resolution confocal microscopy in spatially fixed cells, we found that the vast majority of DSBs occur immediately after irradiation (within 2–5 minutes) in chromatin domains only weakly stained with DNA dyes (DAPI, TOPRO3). Similar results were obtained in living cells transiently transfected with 53BP1-RFP and histone H2B–green fluorescent protein to visualize IRIFs in the frame of chromatin architecture.[104] In all cases, however, the recruitment of repair proteins described by the time delay and an increase of protein appearance seems to depend on the type of protein and the quality of radiation.[135]

Nevertheless, our experiments also revealed rapid binding of TIP60 to γH2AX foci, which was accompanied by a steep increase in H4K12 acetylation and a decrease of H3K9 demethylation in DSB surroundings.[104] Maximal changes were seen between 20 and 30 minutes after irradiation. These results suggest that the chromatin domains containing DSBs undergo rapid local decondensation soon after the break occurs. On the contrary, only late γH2AX foci colocalized with the resolution power of confocal microscopy with Hc markers (such as dimethylated histone H3K9 and HP1β protein[106]); this perhaps indicates the effort to restore the original epigenetic and higher-order chromatin structure at sites of already rejoined DSBs. In this context, localization of IRIFs in weakly stained (euchromatic) nuclear domains reflects the decondensation of damaged domains rather than the higher radiosensitivity of Ec.

To shed more light on this phenomenon, we visualized the γH2AX/53BP1 repair foci,[136] together with interphase territories of chromosomes that significantly differ in their chromatin composition and transcription activity, using immuno–fluorescence in situ hybridization (FISH). We were able to quantify IRIF formation independent of chromatin decondensation, although the staining intensity still differs between condensed and decondensed territories. Most of the IRIFs appeared inside

the territories of highly transcribed decondensed chromosomes.[105] Even more striking results were achieved by similar experiments using the bacterial artificial chromosome (BAC) clones to label structurally and functionally homogeneous RIDGE and anti-RIDGE clusters instead of CHTs.[105] The higher radiosensitivity of Ec also was supported by measurements evaluating IRIF formation in nuclei incubated for varying periods of time in hypotonic and hypertonic media before, during, and after irradiation. Surprisingly, while hypotonic (trichostatin A) treatment significantly increased the amount of IRIFs, the results with hypertonic treatment were comparable to those of isotonic controls, despite marked chromatin condensation in the former. Therefore, chromatin condensation per se does not seem to influence chromatin sensitivity to DSB induction.[106] Nonetheless, the hypertonic-induced heterochromatin patches colocalized neither with the HP1 proteins(α and β) nor H3K9 di- and trimethylation,[105] contrary to physiologically assembled Hc. Hence, it is probable that abundant heterochromatin-binding proteins better protect Hc domains against the indirect effect of IR, whereas "naked" and decondensed Ec remains exposed to harmful free radicals (Fig. 2B). The prevalence of γH2AX/53BP1 foci in the weakly stained chromatin existed for γ-rays and proton beams of different energies (15 and 30 MeV[107]); instead, accelerated ^{20}Ne particles (energy = 47.51 MeV; LET = 130.5 keV/μm) seem to introduce severe damage in both sparse and condensed domains, although the γH2AX/53BP1 particle track is evidently influenced by the higher-order chromatin structure (Fig. 2D, preliminary data). Together, these results show the following: (1) γH2AX foci can also appear in condensed chromatin (in accordance with data from the study by Jakob et al.[137]). Thus, our discussed observations do not reflect the refractory nature of Hc to H2AX phosphorylation or inaccessibility of γH2AX epitopes for antibodies. (2) More extensive damage might be caused by heavy particles in Hc because of the higher chromatin density per volume in this domain. (3) Genomic DNA damage patterns could, therefore, be different for low-LET and high-LET radiation.

3. DSB Repair in the Context of Higher-Order Chromatin Structure

On the other hand, DSB repair in Hc seems to be compromised or, at least, more complicated and less efficient compared to Ec.[104,138,139] In our most recent work[138,139] we compared DSB repair capacity and kinetics in variably differentiated human white blood cells: lymphocytes, monocytes, immature granulocytes, and fully developed granulocytes. While lymphocytes, monocytes, and mature granulocytes appear during different functions in blood from healthy donors, the blood from leukemia patients also contains incompletely differentiated granulocyte stages. Using confocal microscopy together with immunostaining of proteins involved in chromatin maintenance (e.g., HP1 isoforms), we revealed that chromatin structure and composition are altered in these immature cells.[18,139,140] Importantly, while DSB repair protein (53BP1, NBS1, MRE11, etc.) expression and IRIF formation took place in lymphocytes, both these processes were absent in mature granulocytes.[139] In immature granulocyte stages, some repair proteins were detected and γH2AX foci did appear after γ-irradiation. However, these foci do not colocalize with the above-mentioned repair proteins, indicating that DSB repair processes are disturbed.[139] Similar results were obtained for monocytes, where lower numbers of γH2AX foci than in lymphocytes were detected; their colocalization with 53BP1 repair proteins was, again, very low (especially in highly condensed chromatin subdomains), and foci persisted (unrepaired) in cells for a long time after irradiation. The low colocalization of γH2AX foci with 53BP1 in immature granulocytes and monocytes corresponds with our finding in normal human skin fibroblasts and MCF7 mammary carcinoma cells, revealing that 53BP1 starts to accumulate in repair foci only after damaged Hc domain decondense and/or chromatin protrudes into the low-density chromatin nuclear subcompartments[104,106] (Fig. 2C). Together, these findings correspond with greater resistance of Hc to the indirect effects of IR (as discussed in "Sensitivity of Higher-Order Chromatin Domains to

Radiation Damage") and also support the idea that Hc must first decondense in order to enable the repair.[104,141–143]

Real-time microscopic monitoring of 53BP1 foci formation in living MCF7 cells confirmed that red fluorescent protein–labelled 53BP1 can penetrate in sufficient amounts to dense Hc, visualized with HP1**α**-GFP, only after the domain decondensation.[138] Interestingly, in the case of damage produced by heavy ions (preliminary results) such as ^{20}Ne, 53BP1 seems to follow **γ**H2AX particle paths through the heterochromatic regions (visualized with TOPRO3). Nevertheless, highly dense Hc again "bends" the **γ**H2AX/53BP1 tracks so that both proteins protrude from the Hc domain, similar to the situation with **γ**-rays. Rapid dynamic exclusion of **γ**H2AX foci from Hc in first 20 minutes after irradiation was most illustratively demonstrated in living cells by Jakob et al.,[137] who precisely targeted chromocenters in mouse cells with single energetic particles, along with continuous microscopic monitoring. Collectively, it seems that extensive chromatin fragmentation caused by heavy ions may open damaged chromatin for 53BP1 entering/binding but, in principle, decondensation of Hc domains is necessary to allow the interaction of 53BP1 with chromatin at DSB ends and continuity of DSB repair. To support this idea, transmission electron microscopy (TEM) of localized 53BP1 labelled with golden nanoparticles almost exclusively to the decondensed periphery of Hc domains and measurements of DSB repair kinetics revealed slower recognition and processing of Hc-DSBs, probably because of the already suggested need for chromatin decondensation.[89] This can explain why additional protein players and even signaling pathways participate in the rejoining of heterochromatic Hc-DSBs.[141–144]

The exact mechanism of γH2AX protrusion and the role of 53BP1 in this process are still unknown. While Ataxia telangiectasia mutated (kinase) (Ataxia telangiectasia mutated = ATM) TM-mediated phosphorylation of KAP1 and its consequent interaction with HP1 protein were reported to participate on chromatin decondensation at sites of Hc-DSBs,[93,94,145–147] no proteins specifically responsible for damaged chromatin protrusion have yet been revealed. Hence, initial chromatin relaxation/protrusion upon the damage might proceed without need for enzymatic activity and is just driven by physical forces that occur when DSB releases topological constrictions of the DNA molecule and whole, damaged higher-order chromatin domains. Refer to the work of Jakob et al.,[137] Bleicher et al.,[148] and Falk et al.[138] for a more detailed discussion on this topic.

Kanev et al.[83] also have recently proposed an exciting idea: the consortium of authors, including experts both in biology and physics, recognized chromosomes as electrically active entities that can resemble, both structurally and functionally, a combination of the classic and Tesla transformer. Since positive and negative electric charges exist in DNA on a nanoscale, defects in chromatin architecture may result in electrostatic interactions that can eventually cause chromosomal breakages, translocations, and other phenomena.[83] It could, therefore, be hypothesized that electrostatic forces (mainly) contribute to chromatin behavior after DSB damage.

53BP1 was shown to amplify Mre11–NBS1 accumulation at Hc-DSBs, concentrating active ATM and enabling localized phosphorylation of KAP-1.[145] Without the recruitment of 53BP1, foci of phosphorylated KAP1 cannot form. In the light of results discussed in the above text, 53BP1 may, therefore, help to "dismantle" damaged Hc domains from outside while proteins upstream of 53BP1 participate in initial decondensation steps.[138] The most recent findings of Kakarougkas et al.[149] show that 53BP1 restricts the resection of broken DNA ends and thus homologous recombination inhibits HR. In that article, the authors propose a model where *BRCA1* promotes HR by repositioning 53BP1 to the IRIF periphery in later phases of DSB repair (see also Chapman et al.[150]). Nevertheless, we did not observe the penetration of 53BP1 into the centeral of HP1 domains in the first few minutes and hours after irradiation. Since we have studied the mentioned (specific) Hc domains, it is possible that we and Kakarougkas et al. describe 2 distinct phenomena concerning the

behavior of 53BP1 that are, however, not mutually exclusive.

Nevertheless, many controversies regarding 53BP1 must be explained. For example, although TEM provided strong evidence for Hc decondensation at DSB sites and localization of 53BP1 in these decondensed Hc areas, the method surprisingly "failed" to detect 53BP1 in Ec.[89] This is in contrary to currently available results obtained with the high-resolution confocal microscopy both in spatially fixed and living cells (discussed earlier in the text). The explanation, although unknown, does not seem to reflect the inefficient detection of 53BP1 in Ec by TEM.[89]

4. Mechanism of Chromosomal Translocations

Following the introduction of this chapter we described there are several methods by which free DNA ends can appear in mutual proximity, which allows sufficient chromatin interchanges. This distance is estimated to be up to 2 μm[134,151] (reviewed by Sachs et al.[152]). "Primary clusters" may appear as a consequence of the introduction of multiple DSBs due to localized high energy deposition (Fig. 2B). Primary clusters are, therefore, characteristic (but not limited) to high-LET IR (Fig. 2B, panel b) (e.g., Nakajima et al.[153]). Genes located in close mutual proximity, as determined by the global higher-order chromatin structure (Fig. 2A), will, therefore, preferentially participate in CTRs (Fig. 2E).

We recently showed that another kind of cluster appears as a consequence of chromatin decondensation in the frame or repair processes[104] (Fig. 2D). We refer to these as "secondary clusters." Upon decondensation, Hc-DSBs frequently protrude into the nuclear subcompartments with low-density chromatin, where some of them mutually cluster[104] (Fig. 2D). Probably repaired with difficulty, these clusters increase in number after irradiation (see below, which describes the visualization of cluster formation that can be obtained by localization nanoscopy) and seem to be by-products of DSB repair rather than repair factories.[28,104] Nevertheless, the idea of repair factories at the nano-scale has been recently revived.[134] Neumaier and colleagues[134] observed that the number of IRIFs does not increase in proportional to the dose and that there is a saturating number of IRIFs that does not increase further with the dose or LET. However, the number of DSBs per IRIF were increased by higher doses/LET. Since the mobility of IRIF foci was repeatedly reported to be rather low, Neumaier et al.[134] concluded that DSBs migrate into IRIFs before their assembly, and individual IRIFs thus represent "repair factories" of different complexity (depending on the dose and type of IR). If confirmed to be correct, our secondary clusters would represent collisions of these repair factories with numerous DSBs. The term *secondary* would then point to not only the mechanism of how these foci arise but also their higher hierarchy. In any case, it is tempting to speculate that secondary clusters represent sites of an increased risk of CTR. How severe this risk can be follows from our observations showing that extensive collisions also appear between γH2AX/53BP1 tracks, which remain after high-LET particle transitions (Fig. 2D). These clusters may be called "tertiary clusters since they associate several secondary clusters (Fig. 2D).

Importantly, we have shown that local higher-order chromatin structure dominantly influences mutual interactions between individual IRIFs and thus the formation of secondary DSB clusters (see Fig. 2E for an illustration and a more detailed explanation). For example, an Hc domain (despite being only a thin spatial barrier) between 2 close DSBs may preclude their mutual interaction. On the other hand, the probability of chromosomal translocations between more distant DSBs may be higher if they protrude into the same low-density chromatin nuclear subcompartments ("chromatin hole"). However, nuclear positions of the majority of IRIFs were found to be quite stable,[108] and formation of clusters was not observed between lesions located far away from each other.

Therefore, global and local higher-order chromatin structure "cooperate" based on the mechanisms of chromatin exchanges that seem to have aspects similar to both the position first and breakage first hypotheses. The real situation is thus more

complicated than previously thought, and CTRs might form at multiple levels. Factors considered earlier to be mutually exclusive in fact probably cooperate under the influence of a previously overlooked higher-order chromatin structure.

II. NOVEL APPROACHES AND FUTURE PERSPECTIVES

During the past decade fluorescence light microscopy has circumvented the diffraction limit of resolution, which was thought to be the ultimate limit of resolution in light microscopy for more than a hundred years. The different embodiments of super-resolution microscopy can be divided in focus-engineered systems such as 4Pi, stimulated emission depletion, spatially modulated illumination microscopy and localization-based systems like photoactivated localization microscopy, fluorescence photoactivated localization microscopy, stochastic optical reconstruction microscopy (STORM), and spectral precision distance microscopy (SPDM). Depending on the type and quality of the specimen, these methods resolve structures on the nanoscale, that is, in a resolution range of single molecules in their natural 3D cellular environment. Since a complete overview of the different variants of nanoscopy available nowadays and their pros and cons exceeds the scope of this article, we refer to the review articles by Cremer et al.[37,154] and the citations therein.

It is evident from the previous sections that the nuclear distribution of frequently translocated loci (FTLs), as well as their mutual localization and localization relative to functionally and structurally distinct higher-order chromatin domains, should be studied in detail, together with DSB repair processes. Moreover, the nanostructure of FTLs and the surrounding chromatin have to be disclosed; the same holds for the composition of IRIFs. All the super-resolution techniques mentioned above have strong potential to give new insights into the nanostructure organization of cells and cell nuclei. The application of these techniques in radiation research is still in its infancy. To successfully apply these techniques, specimen preparation and treatment must be modified with consideration of super-resolution conditions. Novel procedures to handle and evaluate the huge amounts of image data are being developed (Grunzke R, Hesser J, Starek J, Kepper N, Gesing S, Hardt M, Hartmann V, Kindermann S, Potthoff J, Hausmann M, Müller-Pfefferkorn R, Jäkel R (2014) Device-driven metadate management solution for scientific big data use cases. 22nd Euromicro Int. Conf. Parallel, Distributed, and Network-Based Processing (PDP 2014), February 2014, Turin, Italy. IEEE Comp. Soc. Proc. PDP 2014: 317 – 321 (doi: 10.1109/PDP.2014. 119)) or have to be developed in the near future to obtain tools to implement the so far unvisualized dimensions of nanostructures and molecular arrangements. In the following section we show for the first time how SPDM localization nanoscopy can contribute to the study of the chromatin response to radiation treatment during repair, and we give an outlook of how available nanoprobing technologies may be extended to live cells to elucidate nanostructural dynamics in vivo using super-resolution microscopy.

A. Entering the Nanocosmos of Nucleosomes

SPDM has become one of the established localization microscopic techniques[155,156] that enables effective optical resolution in the nanometer range, even in 3D conserved cell nuclei.[157] It is based on the application of fluorophores that can be switched between 2 different spectral states to achieve a temporal isolation ("blinking") and thus a spatial separation of the signals. After acquiring a time series of up to 2000 images of the same section, subsequent computational calculations of dye molecule "blinking" events allows the precise positions of the individual fluorophores, as well as the measurement of their spatial distances (even if they are below the conventional optical resolution), to be determined. In contrast to many other super-resolution techniques, SPDM works with standard specimen preparation methods and many conventional dyes used, for instance, in confocal microscopy. Although 3D-SPDM modifications

are far from being routinely used, the first results are very promising.[158]

Using SPDM for radiation research, the nuclear nanostructure and arrangements of Ec and Hc in irradiated and nonirradiated HeLa cells was investigated after nucleosome labeling via fluorescent proteins (H2A-GFP or H2B-yellow fluorescent protein) and specific antibodies against Ec or Hc, respectively. In nonirradiated cell nuclei, theoretical approaches of chromatin modeling and statistical analyses revealed a nonrandom organization of nucleosomes at a scale of <100 nm.[157] Beyond precise molecular localization, measuring distances between the labeling molecules, and estimating cluster formation, the images were evaluated by means of statistical physics and graph theory. Pair correlation functions as well as edge length distributions were calculated, and mean coordination numbers for graphs were obtained by triangulations of the marker positions. When compared to nonirradiated specimens subjected to the same preparation conditions, the nucleosomal patterns indicate typical conformational changes after irradiation and during repair time, depending on the radiation treatment parameters, which varied during the experiments. Hc and Ec regions show different behavior just after irradiation and during the repair processes, which can be interpreted by relaxation processes and repair-induced chromatin remodelling (Máté et al, manuscript submitted). Thus, image information obtained by SPDM measurements may offer new insights into the understanding of conformational dynamics and repair mechanisms and may support new types of dose-efficiency correlations.

Chromatin damage caused by IR and subsequent DNA repair processes are accompanied by complex changes of the chromatin nanoarchitecture and nucleosomal arrangement within the treated cell nuclei, resulting in the formation of nucleosomal clusters (see also "Mechanism of Chromosomal Translocations"). To investigate local chromatin remodeling and structural changes as a function of dose, dose rate, radiation energy, radiation cofactors, and different repair times, the HeLa cell systems were subjected to different treatment conditions, and the formation of clusters (obtained by searching for a minimum number of detected points within a given radius around a starting point) was calculated in comparison to the nontreated control specimen.

After repair activation, an increase of nucleosomes involved in cluster formation and of the cluster density (per micrometer squared) of a nuclear section were observed. Such an increase was always observed after irradiation indicating pan-nuclear chromatin rearrangements independent from radiation-induced damage loci (Biswas et al., Krufczik et al, manuscript in preparation): Fig. 3A shows typical examples of image sections obtained from time stacks acquired by SPDM localization nanoscopy. Several tens of thousands of nucleosomes are detected in each image section. Figure 3a shows a nontreated cell nucleus with only a small percentage of nucleosomes involved in cluster formation. Figure 3b shows a nucleus after exposure to radiation. As visualized in Fig. 3B, the number of nucleosomes involved in cluster formation is significantly increased upon IR. Systematic analysis of such images revealed the treatment-specific development of clusters with repair time. For instance, for irradiation with a 6-MeV photon-generating linear accelerator at a dose of 3.5 Gy, an increase in the percentage of cluster-forming nucleosomes (from 11% to 25%) was found during 48 hours of repair. These values differ from the values obtained after assuming a random distribution of the same amount of nucleosomes as detected in the images. Whether cluster formation decreases at later time points is presently under investigation. Moreover, it seems that changing only the photon energy and neither the dose nor the dose rate has an influence on the formation of clusters during repair. Further details will be published elsewhere (Biswas et al., manuscript in preparation).

B. Combinatorial Oligo–FISH Nanoprobing and Localization Nanoscopy: From Static to Dynamic

It is evident from the previous section that the nano architecture—not only of the entire chromatin ar-

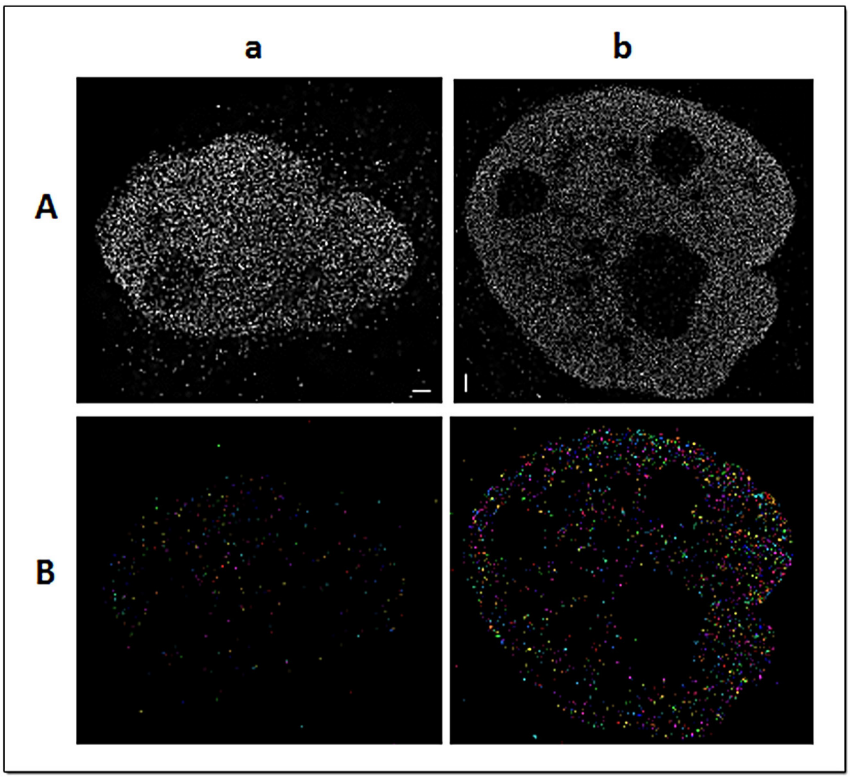

FIG. 3: Nanoscopy in radiobiological research. Image sections through cell nuclei with nucleosomes labelled by H2A-green fluorescent protein after evaluation of time stacks of spectral precision distance/position determination localization nanoscopic images: example of a cell nucleus before radiation exposure (**a**); example of irradiated cell nucleus during DNA repair (**b**). **A:** Both images show several tens of thousands of individual nucleosomes (white spots) detected with a localization precision in the range of 20–30 nm. **B:** The same nuclei are shown but include only those nucleosomes that were involved in cluster formation (color spots). The increase of nucleosomes forming clusters is obvious.

rangement but also of FTLs—should be studied in detail together with DSB repair processes to better understand the mechanisms behind clustering and the different radiation response of Hc and Ec. This has not yet been done mainly because of serious technical and methodological limitations. Problems are associated not only with microscopy but also with molecular-biological methods for visualizing particular proteins and genetic loci, especially under physiological conditions (or even in living cells) and in the required nanoscale resolution.

Despite that, the problem with labeling was more or less precluded for proteins by tagging them with GFP spectral variants. A similar method for particular genes or chromatin domains remains a dream of the future. However, the first steps in this direction have been taken.[155,156,159,160] Until recently, DNA could be labeled only in fixed cells using the FISH.[161] Although fixation methods compatible with FISH that are able to preserve the 3D higher-order chromatin structure have been developed, the method still suffers from serious artifacts; harmful denaturation of DNA[162,163] is required along with the use of long DNA probes that interfere with the chromatin structure of the target. To eliminate these complications, the so-called combinatorial oligo (COMBO)–FISH method was introduced.[159,160,164] In comparison to classic FISH,

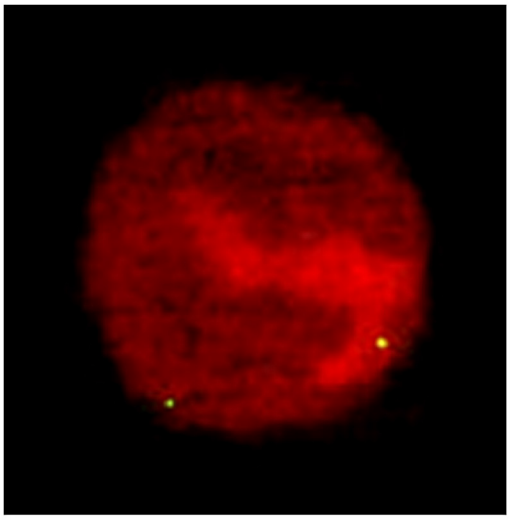

FIG. 4: An example of a cell nucleus after COMBO-fluorescence in situ hybridization labelling of an α-methylacyl-CoA racemase–associated region (green) on chromosome 5 targeting a chromatin region of about 25 kb by 29 colocalizing oligonucleotides.

a set of about 20–30 very short oligonucleotides (15–30 nts) with differing sequences is used to specifically label the DNA target (Fig. 4). This improvement of specifically targeting extremely small regions in a focused manner was enabled by accomplishments such as the sequencing of the human genome and a marked development in the field of computing technology; a bioinformatics search through the genome databases is used to determine the oligonucleotide sequences and their combinations in such a way that they uniquely colocalize at the given target region.[165] Computational modeling is consequently used to test binding properties of selected oligos. Importantly, the probes can be designed in different ways to allow either strand–strand association (Watson-Crick pairing of the bases) or Hoogsteen pairing with duplex DNA strands so that the denaturation step can be omitted, which is a serious advantage compared to standard FISH techniques. Since denaturation is no longer necessary, the method can potentially be carried out under in vivo conditions,[39] and de facto disturbance of chromatin structure is eliminated.

The development of COMBO-FISH for use in routine labeling under in vivo conditions would be extremely useful for understanding DSB misrepair and the formation of chromosomal translocations in the context of chromatin conformation changes. Thus, the combination of improved COMBO-FISH and SPDM localization nanoscopy will be a great challenge for the future. However, the prerequisites are prepared and the tools for these developments are clear so that the dream is coming close to reality. DSBs could then be artificially introduced, for instance, by an oligonucleotide carrying an Auger electron emitter,[166] into specific structurally and functionally distinct chromatin domains. These could be labeled by a fluorescence point pattern of specific oligonucleotides and their behavior during repair could be followed in real time with living cells with the help of high-tech, live-cell, 3D multicolor nanoscopy.

III. CONCLUSIONS

Omic disciplines, microscopy/nanoscopy, and bioinformatics are rapidly developing. While Omics approaches provide views on the functioning of complex biological networks, microscopy enables the placement of this knowledge into the context of cell structure, space, and time. In Part A of this discussion, we compared the HUGO project to the cosmic project Apollo. Let us, therefore, conclude with another cosmic simile. In astronomy, the order-of-magnitude improvements in the accuracy of Galileo's telescope enabled him to make several breakthrough discoveries in about 3 years (the map of the moon, the four moons of Jupiter, the phases of Venus, sun spots and its rotation, and the composition of the Milky Way from many weakly shining stars).[167] We currently have a similar opportunity with microscopy. It is, therefore, extremely exciting to follow what will emerge from the synergic connection of Omics disciplines, microscopy, and bioinformatics in the next few years. This progress would ultimately lead to a comprehensive model of the hierarchy, function, and interactions of structures. The synergy of a broad spectrum of Omics and high-resolution visualization on the

micro- and nanoscale ("Structuromics") will open novel insights into the "trickster" cellular response to irradiation and the survival strategies of life.

ACKNOWLEDGMENTS

The work was supported by the GACR Center of Excellence (P302/12/G157 and P302/10/1022); MEYS of CR (COST-LD12039, LD12008, OPVK-CZ.1.07/2.3.00/30.0030); and a Czech contribution to JINR Dubna for 2013. Furthermore, the financial support of the German Federal Ministry for the Environment, Nature Conservation, Building, and Nuclear Safety (FKZ: SR/StSch/INT 3610S30015) is gratefully acknowledged. The authors thank Christoph Cremer and his group (Institute for Molecular Biology, Mainz) for the continuous collaboration in all fields of superresolution microscopy, as well as Frederik Wenz (University Medical Center, Mannheim) for access to several kinds of medical radiation sources. This work also has been supported by the Helmholtz Portfolio Extension Large Scale Data Management and Analysis with contributions from the Data Life Cycle Lab Key Technologies and the Data Services Integration Team.

REFERENCES

1. Barbieri M, Chotalia M, Fraser J, Lavitas LM, Dostie J, Pombo A, Nicodemi M. A model of the large-scale organization of chromatin. Biochem Soc Trans. 2013;41(2):508–12.
2. Gasser SM. Open questions: epigenetics and the role of heterochromatin in development. BMC Biol. 2013 Mar 4;11:21.
3. Rozwadowska N, Kolanowski T, Wiland E, Siatkowski M, Pawlak P, Malcher A, Mietkiewski T, Olszewska M, Kurpisz M. Characterisation of nuclear architectural alterations during in vitro differentiation of human stem cells of myogenic origin. PLoS One. 2013;8(9):e73231.
4. Wei Z, Huang D, Gao F, Chang WH, An W, Coetzee GA, Wang K, Lu W. Biological implications and regulatory mechanisms of long-range chromosomal interactions. J Biol Chem. 2013;288(31):22369–77.
5. Kölbl AC, Weigl D, Mulaw M, Thormeyer T, Bohlander SK, Cremer T, Dietzel S. The radial nuclear positioning of genes correlates with features of megabase-sized chromatin domains. Chromosome Res. 2012;20(6):735–52.
6. Markaki Y, Smeets D, Fiedler S, Schmid VJ, Schermelleh L, Cremer T, Cremer M. The potential of 3D-FISH and super-resolution structured illumination microscopy for studies of 3D nuclear architecture: 3D structured illumination microscopy of defined chromosomal structures visualized by 3D (immuno)-FISH opens new perspectives for studies of nuclear architecture. Bioessays. 2012;34(5):412–26.
7. Pombo A, Starr DA. Nuclear cell biology. Mol Biol Cell. 2011;22(6):722.
8. Cremer T, Zakhartchenko V. Nuclear architecture in developmental biology and cell specialisation. Reprod Fertil Dev. 2011;23(1):94–106.
9. Mehta IS, Amira M, Harvey AJ, Bridger JM. Rapid chromosome territory relocation by nuclear motor activity in response to serum removal in primary human fibroblasts. Genome Biol. 2010;11(1):R5.
10. Rouquette J, Cremer C, Cremer T, Fakan S. Functional nuclear architecture studied by microscopy: present and future. Int Rev Cell Mol Biol. 2010;282:1–90.
11. Jefferson A, Colella S, Moralli D, Wilson N, Yusuf M, Gimelli G, Ragoussis J, Volpi EV. Altered intra-nuclear organisation of heterochromatin and genes in ICF syndrome. PLoS One. 2010;5(6):e11364.
12. Postberg J, Lipps HJ, Cremer T. Evolutionary origin of the cell nucleus and its functional architecture. Essays Biochem. 2010;48(1):1–24.
13. Pombo A, Gilbert DM. Nucleus and gene expression: the structure and function conundrum. Curr Opin Cell Biol. 2010;22(3):269–70.
14. Morris KJ, Chotalia M, Pombo A. Nuclear architecture in stem cells. Adv Exp Med Biol. 2010;695:14–25.
15. Szczerbal I, Foster HA, Bridger JM. The spatial repositioning of adipogenesis genes is correlated with their expression status in a porcine mesenchymal stem cell adipogenesis model system. Chromosoma. 2009;118(5):647–63.
16. Ondrej V, Lukásová E, Falk M, Kozubek S. The role of actin and microtubule networks in plasmid DNA intracellular trafficking. Acta Biochim Pol. 2007;54(3):657–63.
17. Ondrej V, Kozubek S, Lukásová E, Falk M, Matula P, Matula P, Kozubek M. Directional motion of foreign plasmid DNA to nuclear HP1 foci. Chromosome Res. 2006;14(5):505–14.
18. Lukásová E, Koristek Z, Falk M, Kozubek S, Grigoryev S, Kozubek M, Ondrej V, Kroupová I. Methylation of histones in myeloid leukemias as a potential marker of granulocyte abnormalities. J Leukoc Biol. 2005;77(1):100–11.
19. Lukásová E, Kozubek S, Falk M, Kozubek M, Zaloudík J, Vagunda V, Pavlovský Z. Topography of genetic loci in the nuclei of cells of colorectal carcinoma and adjacent tissue of colonic epithelium. Chromosoma. 2004;112(5):221–30.

20. Lukásová E, Kozubek S, Kozubek M, Falk M, Amrichová J. The 3D structure of human chromosomes in cell nuclei. Chromosome Res. 2002;10(7):535–48.
21. Kozubek S, Lukásová E, Jirsová P, Koutná I, Kozubek M, Ganová A, Bártová E, Falk M, Paseková R. 3D Structure of the human genome: order in randomness. Chromosoma. 2002;111(5):321–31.
22. Misteli T. Higher-order genome organization in human disease. Cold Spring Harb Perspect Biol. 2010;2(8):a000794.
23. Falk M, Lukášová E, Kozubek S, Kozubek M. Topography of genetic elements of X-chromosome relative to the cell nucleus and to the chromosome X territory determined for human lymphocytes. Gene. 2002;292(1–2):13–24.
24. Volpi EV, Chevret E, Jones T, Vatcheva R, Williamson J, Beck S, Campbell RD, Goldsworthy M, Powis SH, Ragoussis J, Trowsdale J, Sheer D. Large-scale chromatin organization of the major histocompatibility complex and other regions of human chromosome 6 and its response to interferon in interphase nuclei. J Cell Sci. 2000;113 (Pt 9):1565–76.
25. Zorn C, Cremer T, Cremer C, Zimmer J. Laser UV microirradiation of interphase nuclei and post-treatment with caffeine. A new approach to establish the arrangement of interphase chromosomes. Hum Genet. 1976;35(1):83–9.
26. Cavalli G, Misteli T. Functional implications of genome topology. Nat Struct Mol Biol. 2013;20(3):290–9.
27. Misteli T. Higher-order genome organization in human disease. Cold Spring Harb Perspect Biol. 2010;2(8):a000794.
28. Falk M, Lukasova E, Kozubek S. Higher order chromatin structure in DSB induction, repair and misrepair. Mutat Res. 2010;704(1–3):88–100.
29. Cremer T, Cremer M. Chromosome territories. Cold Spring Harb Perspect Biol. 2010 March; 2(3): a003889.
30. Mehta IS, Elcock LS, Amira M, Kill IR, Bridger JM. Nuclear motors and nuclear structures containing A-type lamins and emerin: is there a functional link? Biochem Soc Trans. 2008;36(Pt 6):1384–8.
31. Bridger JM, Foeger N, Kill IR, Herrmann H. The nuclear lamina. Both a structural framework and a platform for genome organization. FEBS J. 2007;274(6):1354–61.
32. Taddei A, Hediger F, Neumann FR, Gasser SM. The function of nuclear architecture: a genetic approach. Annu Rev Genet. 2004;38:305–45.
33. Chevret E, Volpi EV, Sheer D. Mini review: form and function in the human interphase chromosome. Cytogenet Cell Genet. 2000;90(1–2):13–21.
34. ZanacchiC F, Lavagnino Z, Faretta M, Furia L, Diaspro A. Light-sheet confined super-resolution using two-photon photoactivation. PLoS One. 2013;8(7):e67667.
35. Müller P, Weiland Y, Kaufmann R, Gunkel M, Hillebrandt S, Cremer C, Hausmann M. Analysis of fluorescent nanostructures in biological systems by means of spectral position determination microscopy (SPDM). In: Méndez-Vilas A, editor. Current microscopy contributions to advances in science and technology. Vol. 1. Badajoz, Spain: Formatex Research Center; 2012. p. 3–12.
36. Sapienza R, Coenen T, Renger J, Kuttge M, van Hulst NF, Polman A. Deep-subwavelength imaging of the modal dispersion of light. Nat Mater. 2012;11(9):781–7.
37. Cremer C, Kaufmann R, Gunkel M, Pres S, Weiland Y, Müller P, Ruckelshausen T, Lemmer P, Geiger F, Degenhard S, Wege C, Lemmermann NA, Holtappels R, Strickfaden H, Hausmann M. Superresolution imaging of biological nanostructures by spectral precision distance microscopy. Biotechnol J. 2011;6(9):1037–51.
38. Hausmann M, Müller P, Kaufmann R, Cremer C. Entering the nano-cosmos of the cell by means of spatial position determination microscopy (SPDM): Implications for medical diagnostics and radiation research. IFMBE Proc. 2013;38:93–95.
39. Nolte O, Müller M, Häfner B, Knemeyer J-P, Stöhr K, Wolfrum J, Hakenbeck R, Denapaite D, Schwarz-Finsterle J, Stein S, Schmitt E, Cremer C, Herten D, Hausmann M, Sauer M. Novel singly labelled probes for identification of microorganisms, detection of antibiotic resistance genes and mutations, and tumor diagnosis (SMART PROBES). In: Popp J, Strehle M, editors. Biophotonics: visions for better health care. Weinheim: Wiley-VCH; 2006. p. 167–230.
40. Furia L, Pelicci PG, Faretta M. A computational platform for robotized fluorescence microscopy (I): high-content image-based cell-cycle analysis. Cytometry A. 2013;83(4):333–43.
41. Furia L, Pelicci PG, Faretta M. A computational platform for robotized fluorescence microscopy (II): DNA damage, replication, checkpoint activation, and cell cycle progression by high-content high-resolution multiparameter image-cytometry. Cytometry A. 2013;83(4):344–55.
42. Kozubek M, Kozubek S, Lukásová E, Bártová E, Skalníková M, Matula P, Matula P, Jirsová P, Cafourková A, Koutná I. Combined confocal and wide-field high-resolution cytometry of fluorescent in situ hybridization-stained cells. Cytometry. 2001;45(1):1–12.
43. Koutná I, Kozubek S, Zaloudík J, Kozubek M, Lukásová E, Matula P, Bártová E, Skalníková M, Cafourková A, Jirsová P. Topography of genetic loci in tissue samples: towards new diagnostic tool using interphase FISH and high-resolution image analysis techniques. Anal Cell Pathol. 2000;20(4):173–85.
44. Suberbielle E, Sanchez PE, Kravitz AV, Wang X, Ho K, Eilertson K, Devidze N, Kreitzer AC, Mucke L. Physiologic brain activity causes DNA double-strand breaks in neurons, with exacerbation by amyloid-β. Nat Neurosci. 2013;16(5):613–21.

45. Falk M, Lukasova E, Kozubek S. Repair mechanisms of DNA double-strand breaks: biochemical and spatiotemporal aspects. In: Gómez-Tejedor GG, Fuss MC, editors. Radiation damage in biomolecular systems. Heidelberg: Springer Science + Business Media; 2012. p. 329–57.
46. Harper JV, Anderson JA, O'Neill P. Radiation induced DNA DSBs: contribution from stalled replication forks? DNA Repair (Amst). 2010;9(8):907–13.
47. Magnander K, Hultborn R, Claesson K, Elmroth K. Clustered DNA damage in irradiated human diploid fibroblasts: influence of chromatin organization. Radiat Res. 2010;173(3):272–82.
48. Rakiman I, Chinnadurai M, Baraneedharan U, Paul SFD, Venkatachalam P. γ-H2AX assay: a technique to quantify DNA double strand breaks. Adv Biotech. 2008;39–41.
49. Jackson SP. Sensing and repairing DNA double-strand breaks. Carcinogenesis. 2002;23(5):687–96.
50. Arnaudeau C, Lundin C, Helleday T. DNA double-strand breaks associated with replication forks are predominantly repaired by homologous recombination involving an exchange mechanism in mammalian cells. J Mol Biol. 2001;307(5):1235–45.
51. Chu G. Double strand break repair J Biol Chem. 1997;272(39):24097–100.
52. Gospodinov A, Herceg Z. Chromatin structure in double strand break repair. DNA Repair (Amst). 2013;12(10):800–10.
53. Dynan W, Takeda Y, Roth D, Bao G. Understanding and re-engineeringnucleoprotein machines to cure human disease. Nanomedicine (Lond). 2008;3(1):93–105.
54. Branco MR, Pombo A. Intermingling of chromosome territories in interphase suggests role in translocations and transcription-dependent associations. PLoS Biol. 2006;4(5):e138.
55. Sharma RP, Gavin DP, Chase KA. Heterochromatin as an incubator for pathology and treatment non-response: implication for neuropsychiatric illness. Pharmacogenomics J. 2012;12(5):361–7.
56. Lukásová E, Kozubek S, Kozubek M, Kjeronská J, Rýznar L, Horáková J, Krahulcová E, Horneck G. Localisation and distance between ABL and BCR genes in interphase nuclei of bone marrow cells of control donors and patients with chronic myeloid leukaemia. Hum Genet. 1997;100(5–6):525–35.
57. Ciccia A, Elledge SJ. The DNA damage response: making it safe to play with knives. Mol Cell. 2010;40(2):179–204.
58. Mao Z, Bozzella M, Seluanov A, Gorbunova V. Comparison of nonhomologous end joining and homologous recombination in human cells. DNA Repair (Amst). 2008;7(10):1765–71.
59. Derbyshire MK, Epstein LH, Young CS, Munz PL, Fishel R. Nonhomologous recombination in human cells. Mol Cell Biol. 1994;14(1):156–69.
60. Helleday T. Pathways for mitotic homologous recombination in mammalian cells. Mutat Res. 2003;532(1–2):103–15.
61. Valerie K, Povirk LF. Regulation and mechanisms of mammalian double-strand break repair. Oncogene. 2003;22(37):5792–812.
62. Blundred RM, Stewart GS. DNA double-strand break repair, immunodeficiency and the RIDDLE syndrome. Expert Rev Clin Immunol. 2011;7(2):169–85.
63. McKinnon PJ. DNA repair deficiency and neurological disease. Nat Rev Neurosci. 2009;10(2):100–12.
64. Schnerch D, Wäsch R. Chromosomal instability and cancer. In: Gloscow EJ, editor. New research on genomic instability. Hauppauge (NY): Nova Publishers; 2013. p. 47–76.
65. Wijnhoven SW, van Steeg H. Transgenic and knockout mice for DNA repair functions in carcinogenesis and mutagenesis. Toxicology. 2003;193(1–2):171–87.
66. Barnes DE, Stamp G, Rosewell I, Denzel A, Lindahl T. Targeted disruption of the gene encoding DNA ligase IV leads to lethality in embryonic mice. Curr Biol. 1998;8(25):1395–8.
67. Barlow C, Hirotsune S, Paylor R, Liyanage M, Eckhaus M, Collins F, Shiloh Y, Crawley JN, Ried T, Tagle D, Wynshaw-Boris A. Atm-deficient mice: a paradigm of ataxia telangiectasia. Cell. 1996;86(1):159–71.
68. Deriano L, Roth DB. Modernizing the nonhomologous end-joining repertoire: alternative and classical NHEJ share the stage. Annu Rev Genet. 2013;47:433–55.
69. Geuting V, Reul C, Löbrich M. ATM release at resected double-strand breaks provides heterochromatin reconstitution to facilitate homologous recombination. PLoS Genet. 2013;9(8):e1003667.
70. Yuan SS, Hou MF, Hsieh YC, Huang CY, Lee YC, Chen YJ, Lo S. Role of MRE11 in cell proliferation, tumor invasion, and DNA repair in breast cancer. J Natl Cancer Inst. 2012;104(19):1485–502.
71. Sevcik J, Falk M, Kleiblova P, Lhota F, Stefancikova L, Janatova M, Weiterova L, Lukasova E, Kozubek S, Pohlreich P, Kleibl Z. The BRCA1 alternative splicing variant Δ14-15 with an in-frame deletion of part of the regulatory serine-containing domain (SCD) impairs the DNA repair capacity in MCF-7 cells. Cell Signal. 2012;24(5):1023–30.
72. Sevcik J, Falk M, Macurek L, Kleiblova P, Lhota F, Hojny J, Stefancikova L, Janatova M, Bartek J, Stribrna J, Hodny Z, Jezkova L, Pohlreich P, Kleibl Z. Expression of human BRCA1Δ17-19 alternative splicing variant with a truncated BRCT domain in MCF-7 cells results in impaired assembly of DNA repair complexes and aberrant DNA damage response. Cell Signal. 2013;25(5):1186–93.
73. Peng G, Lin SY. Exploiting the homologous recombi-

nation DNA repair network for targeted cancer therapy. World J Clin Oncol. 2011;2(2):73–9.
74. Wei L, Lan L, Hong Z, Yasui A, Ishioka C, Chiba N. Rapid recruitment of BRCA1 to DNA double-strand breaks is dependent on its association with Ku80. Mol Cell Biol. 2008;28(24):7380–93.
75. Shrivastav M, De Haro LP, Nickoloff JA. Regulation of DNA double-strand break repair pathway choice. Cell Res. 2008;18(1):134–47.
76. Cremer T, Cremer C. Chromosome territories, nuclear architecture and gene regulation in mammalian cells. Nat Rev Genet. 2001;2(4):292–301.
77. Woodcock CL, Dimitrov S. Higher-order structure of chromatin and chromosomes. Curr Opin Genet Dev. 2001;11(2):130–5.
78. Morey C, Da Silva NR, Perry P, Bickmore WA. Nuclear reorganisation and chromatin decondensation are conserved, but distinct, mechanisms linked to Hox gene activation. Development. 2007;134(5):909–19.
79. Caron H, van Schaik B, van der Mee M, Baas F, Riggins G, van Sluis P, Hermus MC, van Asperen R, Boon K, Voûte PA, Heisterkamp S, van Kampen A, Versteeg R. The human transcriptome map: clustering of highly expressed genes in chromosomal domains. Science. 2001;291(5507):1289–92.
80. Markaki Y, Gunkel M, Schermelleh L, Beichmanis S, Neumann J, Heidemann M, Leonhardt H, Eick D, Cremer C, Cremer T. Functional nuclear organization of transcription and DNA replication: a topographical marriage between chromatin domains and the interchromatin compartment. Cold Spring Harb Symp Quant Biol. 2010;75:475–92.
81. Kanev I, Mei W, Mizuno A, Dehaai K, Sanmann J, Hess M, Starr L, Grove J, Dave B, Sanger W. Searching for electrical properties, phenomena and mechanisms in the construction and function of chromosomes. Comput Struct Biotechnol J. 2013;6 e201303007.
82. Goetze S, Mateos-Langerak J, Gierman HJ, de Leeuw W, Giromus O, Giromus O, Indemans MH, Koster J, Ondrej V, Versteeg R, van Driel R. The three-dimensional structure of human interphase chromosomes is related to the transcriptome map. Mol Cell Biol. 2007;27(12):4475–87.
83. Aten JA, Kanaar R. Chromosomal organization: mingling with the neighbors. PLoS Biol. 2006;4(5):e155.
84. Gilbert N, Bickmore WA. The relationship between higher-order chromatin structure and transcription. Biochem Soc Symp. 2006;(73):59–66.
85. Chambers EV, Bickmore WA, Semple CA. Divergence of mammalian higher order chromatin structure is associated with developmental loci. PLoS Comput Biol. 2013;9(4):e1003017.
86. Tabancay AP Jr, Forsburg SL. Eukaryotic DNA replication in a chromatin context. Curr Top Dev Biol. 2006;76:129–84.
87. Weinreich M, Palacios DeBeer MA, Fox CA. The activities of eukaryotic replication origins in chromatin. Biochim Biophys Acta. 2004;1677(1–3):142–57.
88. Britton S, Coates J, Jackson SP. A new method for high-resolution imaging of Ku foci to decipher mechanisms of DNA double-strand break repair. J Cell Biol. 2013;202(3):579–95.
89. Lorat Y, Schanz S, Schuler N, Wennemuth G, Rübe C, Rübe CE. Beyond repair foci: DNA double-strand break repair in euchromatic and heterochromatin compartments analyzed by transmission electron microscopy. PLoS One. 2012;7(5):e38165.
90. Jakob B, Splinter J, Durante M, Taucher-Scholz G. Live cell microscopy analysis of radiation-induced DNA double-strand break motion. Proc Natl Acad Sci U S A. 2009;106(9):3172–7.
91. Jakob B, Splinter J, Taucher-Scholz G. Positional stability of damaged chromatin domains along radiation tracks in mammalian cells. Radiat Res. 2009;171(4):405–18.
92. Kruhlak MJ, Celeste A, Dellaire G, Fernandez-Capetillo O, Muller WG, McNally JG, Bazett-Jones DP, Nussenzweig A. Changes in chromatin structure andmobility in living cells at sites of DNA double-strand breaks. J Cell Biol. 2006;172(6):823–34.
93. Goodarzi AA, Noon AT, Jeggo PA. The impact of heterochromatin on DSB repair. Biochem Soc Trans. 2009;37(Pt 3):569–76.
94. Ziv Y, Bielopolski D, Galanty Y, Lukas C, Taya Y, Schultz DC, Lukas J, Bekker-Jensen S, Bartek J, Shiloh Y. Chromatin relaxation in response to DNA double-strand breaks is modulated by a novel ATM- and KAP-1 dependent pathway. Nat Cell Biol. 2006;8(8):870–6.
95. Lukas C, Falck J, Bartkova J, Bartek J, Lukas J. Distinct spatiotemporal dynamics of mammalian checkpoint regulators induced by DNA damage. Nat Cell Biol. 2003;5(3):255–60.
96. Goodarzi AA, Jeggo PA. The repair and signaling responses to DNA double-strand breaks. Adv Genet. 2013;82:1–45.
97. Hunt CR, Ramnarain D, Horikoshi N, Iyengar P, Pandita RK, Shay JW, Pandita TK. Histone modifications and DNA double-strand break repair after exposure to ionizing radiations. Radiat Res. 2013;179(4):383–92.
98. Price BD, D'Andrea AD. Chromatin remodeling at DNA double-strand breaks. Cell. 2013;152(6):1344–54.
99. Costes SV, Chiolo I, Pluth JM, Barcellos-Hoff MH, Jakob B. Spatiotemporal characterization of ionizing radiation induced DNA damage foci and their relation to chromatin organization. Mutat Res. 2010;704(1–3):78–87.
100. Misteli T. Cell biology: nuclear order out of chaos. Nature. 2008;456(7220):333–4.
101. Downs JA, Nussenzweig MC, Nussenzweig A. Chromatin dynamics and the preservation of genetic information. Nature. 2007;447(7147):951–8.

102. Taucher-Scholz G, Jakob B. Ion irradiation as a tool to reveal the spatiotemporal dynamics of DNA damage response processes In: Lankenau D-H, editor. Genome integrity, genom dynamics and stability. New York: Springer-Verlag; 2006. p. 453–78.
103. Lukas J, Lukas C, Bartek J. Mammalian cell cycle checkpoints: signalling pathways and their organization in space and time. DNA Repair (Amst). 2004;3(8–9):997–1007.
104. Falk M, Lukasova E, Gabrielova B, Ondrej V, Kozubek S. Chromatin dynamics during DSB repair. Biochim Biophys Acta. 2007;1773(10):1534–45.
105. Falk M, Lukasova E, Kozubek S. Chromatin structure influences the sensitivity of DNA to γ-radiation. Biochim Biophys Acta. 2008;1783(12):2398–414.
106. Falk M, Lukasova E, Gabrielova B, Ondrej V, Kozubek S. Local changes of higher-order chromatin structure during double strand break repair. J Phys Conf Ser. 2008;101(1):012018.
107. Ježková L, Falk M, Falková I, Davídková M., Bačíková A, Štefančíková L, Vachelová J, Michaelidesová A, Lukášová E, Boreyko A, Krasavin E, Kozubek S. Function of chromatin structure and dynamics in DNA damage, repair and misrepair: γ-rays and protons in action. Appl Radiat Isot. 2014;83(Pt B):128–36.
108. Girst S, Hable V, Drexler GA, Greubel C, Siebenwirth C, Haum M, Friedl AA, Dollinger G. Subdiffusion supports joining of correct ends during repair of DNA double-strand breaks. Sci Rep. 2013;3:2511.
109. Zidovska A, Weitz DA, Mitchison TJ. Micron-scale coherence in interphase chromatin dynamics. Proc Natl Acad Sci U S A. 2013;110(39):15555–60.
110. Michalik V. Estimation of double-strand break quality based on track-structure calculations. Radiat Environ Biophys 1993;32(3):251–8.
111. Prise KM, Folkard M, Newman HC, Michael BD. Effect of radiation quality on lesion complexity in cellular DNA. Int J Radiat Biol. 1994;66(5):537–42.
112. Pastwa E, Neumann RD, Mezhevaya K, Winters TA. Repair of radiation-induced DNA double-strand breaks is dependent upon radiation quality and the structural complexity of double-strand breaks. Radiat Res. 2003;159(2):251–61.
113. Jakob B, Taucher-Scholz G. Interaction of heavy ions with nuclear chromatin: spatiotemporal investigations of biological responses in a cellular environment. Nucl Instr and Meth in Phys Res. 2006;245(1):292–7.
114. Loucas BD, Cornforth MN. The LET dependence of unrepaired chromosome damage in human cells: a break too far? Radiat Res. 2013 Feb 22. [Epub ahead of print]
115. Georgakilas AG, O'Neill P, Stewart RD. Induction and repair of clustered DNA lesions: what do we know so far? Radiat Res. 2013;180(1):100–9.
116. Gauwerky CE, Croce CM. Chromosomal translocations in leukaemia. Semin Cancer Biol. 1993;4(6):333–40.
117. Kozubek S, Lukásová E, Rýznar L, Kozubek M, Lisková A, Govorun RD, Krasavin EA, Horneck G. Distribution of ABL and BCR genes in cell nuclei of normal and irradiated lymphocytes. Blood. 1997;89(12):4537–45.
118. Radivoyevitch T, Kozubek S, Sachs RK. Biologically based risk estimation for radiation-induced CML. Inferences from BCR and ABL geometric distributions. Radiat Environ Biophys. 2001;40(1):1–9.
119. Neves H, Ramos C, da Silva MG, Parreira A, Parreira L. The nuclear topography of ABL, BCR, PML, and RARalpha genes: evidence for gene proximity in specific phases of the cell cycle and stages of hematopoietic differentiation. Blood. 1999;93(4):1197–207.
120. Parada LA, McQueen PG, Munson PJ, Misteli T. Conservation of relative chromosome positioning in normal and cancer cells. Curr Biol. 2002;12(19):1692–7.
121. Bickmore WA, Teague P. Influences of chromosome size, gene density and nuclear position on the frequency of constitutional translocations in the human population. Chromosome Res. 2002;10(8):707–15.
122. Roix JJ, McQueen PG, Munson PJ, Parada LA, Misteli T. Spatial proximity of translocation-prone gene loci in human lymphomas. Nat Genet. 2003;34(3):287–91.
123. Foster HA, Estrada-Girona G, Themis M, Garimberti E, Hill MA, Bridger JM, Anderson RM. Relative proximity of chromosome territories influences chromosome exchange partners in radiation-induced chromosome rearrangements in primary human bronchial epithelial cells. Mutat Res. 2013;756(1–2):66–77.
124. Roukos V, Burman B, Misteli T. The cellular etiology of chromosome translocations. Curr Opin Cell Biol. 2013;25(3):357–64.
125. Kozubek S, Lukásová E, Marecková A, Skalníková M, Kozubek M, Bártová E, Kroha V, Krahulcová E, Slotová J. The topological organization of chromosomes 9 and 22 in cell nuclei has a determinative role in the induction of t(9,22) translocations and in the pathogenesis of t(9,22) leukemias. Chromosoma. 1999;108(7):426–35.
126. Grossmann C, Schwarz-Finsterle J, Schmitt E, Birk U, Hildenbrand G, Cremer C, Trakhtenbrot L and Hausmann M. Variations of the spatial fluorescence distribution in ABL gene chromatin domains measured in blood cell nuclei by SMI microscopy after COMBO–FISH labelling. In: Microscopy: science, technology, applications and education. Badajoz, Spain: Formatex Research Center; 2010. p. 688–95.
127. Esa A, Edelmann P, Kreth G, Trakhtenbrot L, Amariglio N, Rechavi G, Hausmann M, Cremer C. Three-dimensional spectral precision distance microscopy of chromatin nano-structures after triple-colour DNA labelling: a study of the BCR region on chromosome 22 and the Philadelphia chromosome. J Microsc. 2000;199(Pt 2):96–105.

128. Arlt MF, Durkin SG, Ragland RL, Glover TW. Common fragile sites as targets for chromosome rearrangements. DNA Repair (Amst). 2006;5(9–10):1126–35.
129. Hausmann M, Esa A, Edelmann P, Trakhtenbrot L, Amariglio N, Rechavi G, Cremer C. Einblicke in die dreidimensionale Architektur des Zellkerns. In: Heinemann G, Müller W-U, editors. Strahlenbiologie und Strahlenschutz–Individuelle Strahlenempfindlichkeit und ihre Bedeutung für den Strahlenschutz. Köln: TÜV-Verlag Rheinland; 2000. p. 87–104.
130. Aten JA, Stap J, Krawczyk PM, van Oven CH, Hoebe RA, Essers J, Kanaar R. Dynamics of DNA double-strand breaks revealed by clustering of damaged chromosome domains. Science. 2004;303(5654):92–5.
131. Krawczyk PM, Borovski T, Stap J, Cijsouw T, ten Cate R, Medema JP, Kanaar R, Franken NA, Aten JA. Chromatin mobility is increased at sites of DNA double-strand breaks. J Cell Sci. 2012;125(Pt 9):2127–33.
132. Krawczyk PM, Stap J, Hoebe RA, van Oven CH, Kanaar R, Aten JA. Analysis of the mobility of DNA double-strand break-containing chromosome domains in living mammalian cells. Methods Mol Biol. 2008;463:309–20.
133. Schwarz-Finsterle J, Scherthan H, Huna A, González P, Müller P, Schmitt E, Erenpreisa J, Hausmann M. Volume increase and spatial shifts of chromosome territories in nuclei of radiation-induced ployploidizing tumour cells. Mutat Res. 2013;756(1–2):56–65.
134. Neumaier T, Swenson J, Pham C, Polyzos A, Lo AT, Yang P, Dyball J, Asaithamby A, Chen DJ, Bissell MJ, Thalhammer S, Costes SV. Evidence for formation of DNA repair centers and dose-response nonlinearity in human cells. Proc Natl Acad Sci U S A. 2012;109(2):443–8.
135. Hable V, Drexler GA, Brüning T, Burgdorf C, Greubel C, Derer A, Seel J, Strickfaden H, Cremer T, Friedl AA, Dollinger G. Recruitment kinetics of DNA repair proteins Mdc1 and Rad52 but not 53BP1 depend on damage complexity. PLoS One. 2012;7(7):e41943.
136. Pombo AP, Cuello W, Schul JB, Yoon RG, Roeder PR, Cook PR, Murphy S. Regional and temporal specialization in the nucleus: a transcriptionally-active nuclear domain rich in PTF, Oct1 and PIKA antigens associated with specific chromosomes early in the cell cycle. EMBO J. 1998;17(6):1768–78.
137. Jakob B, Splinter J, Conrad S, Voss KO, Zink D, Durante M, Löbrich M, Taucher-Scholz G. DNA double-strand breaks in heterochromatin elicit fast repair protein recruitment, histone H2AX phosphorylation and relocation to euchromatin. Nucleic Acids Res. 2011;39(15):6489–99.
138. Falk M, Lukášová E, Stefančíková L, Baranová E, Falková I, Ježková L, Davídková M, Bačíková A, Vachelová J, Michaelidesová A, Kozubek S. Heterochromatinization associated with cell differentiation as a model to study DNA double strand break induction and repair in the context of higher-order chromatin structure. Appl Appl Radiat Isot. 2014;83(Pt B):177–85.
139. Lukášová E, Kořistek Z, Klabusay M, Ondřej V, Grigoryev S, Bačíková A, Řezáčová M, Falk M, Vávrová J, Kohútová V, Kozubek S. Granulocyte maturation determines ability to release chromatin NETs and loss of DNA damage response; these properties are absent in immature AML granulocytes. Biochim Biophys Acta. 2013;1833(3):767–79.
140. Popova EY, Claxton DF, Lukasova E, Bird PI, Grigoryev SA. Epigenetic heterochromatin markers distinguish terminally differentiated leukocytes from incompletely differentiated leukemia cells in human blood. Exp Hematol. 2006;34(4):453–62.
141. Anderson RM, Stevens DL, Goodhead DT. M-FISH analysis shows that complex chromosome aberrations induced by alpha -particle tracks are cumulative products of localized rearrangements. Proc Natl Acad Sci U S A. 2002;99:12167–72.
142. Anderson RM, Papworth DG, Stevens DL, Sumption ND, Goodhead DT. Increased complexity of radiation-induced chromosome aberrations consistent with a mechanism of sequential formation. Cytogenet Genome Res. 2006;112:35–44.
143. Goodarzi AA, Jeggo P, Lobrich M. The influence of heterochromatin on DNA double strand break repair: Getting the strong, silent type to relax. DNA Repair (Amst). 2010;9(12):1273–82.
144. Goodarzi AA, Jeggo PA. The heterochromatic barrier to DNA double strand break repair: how to get the entry visa. Int J Mol Sci. 2012;13(9):11844–60.
145. Noon AT, Shibata A, Rief N, Löbrich M, Stewart GS, Jeggo PA, Goodarzi AA. 53BP1-dependent robust localized KAP-1 phosphorylation is essential for heterochromatic DNA double-strand break repair. Nat Cell Biol. 2010;12(2):177–84.
146. Bolderson E, Savage KI, Mahen R, Pisupati V, Graham ME, Richard DJ, Robinson PJ, Venkitaraman AR, Khanna KK. Kruppel-associated Box (KRAB)-associated co-repressor (KAP-1) Ser-473 phosphorylation regulates heterochromatin protein 1β (HP1-β) mobilization and DNA repair in heterochromatin. J Biol Chem. 2012;287(33):28122–31.
147. White D, Rafalska-Metcalf IU, Ivanov AV, Corsinotti A, Peng H, Lee SC, Trono D, Janicki SM, Rauscher FJ 3rd. The ATM substrate KAP1 controls DNA repair in heterochromatin: regulation by HP1 proteins and serine 473/824 phosphorylation. Mol Cancer Res. 2012;10(3):401–14.
148. Bleicher M, Burigo L, Durante M, Herrlitz M, Krämer M. Nanolesions induced by heavy ions in human tissues: experimental and theoretical studies. Beilstein J Nanotechnol. 2012;3:556–63.
149. Kakarougkas A, Ismail A, Klement K, Goodarzi AA, Conrad S, Freire R, Shibata A, Lobrich M, Jeggo PA.

Opposing roles for 53BP1 during homologous recombination. Nucleic Acids Res. 2013;41(21):9719–31.
150. Chapman JR, Sossick AJ, Boulton SJ, Jackson SP. BRCA1-associated exclusion of 53BP1 from DNA damage sites underlies temporal control of DNA repair. J Cell Sci. 2012;125(Pt 15):3529–34.
151. Sachs RK, Chen AM, Simpson PJ, Hlatky LR, Hahnfeldt P, Savage JR. Clustering of radiation-produced breaks along chromosomes: modelling the effects on chromosome aberrations. Int J Radiat Biol. 1999;75(6):657–72.
152. Sachs RK, Chen AM, Brenner DJ. Review: proximity effects in the production of chromosome aberrations by ionizing radiation. Int J Radiat Biol. 1997;71(1):1–19.
153. Nakajima NI, Brunton H, Watanabe R, Shrikhande A, Hirayama R, Matsufuji N, Fujimori A, Murakami T, Okayasu R, Jeggo P, Shibata A. Visualisation of γH2AX foci caused by heavy ion particle traversal; distinction between core track versus non-track damage. PLoS One. 2013;8(8):e70107.
154. Cremer C. Optics far beyond the diffraction limit: from focused nanoscopy to spectrally assigned localization microscopy. In: Träger F, editor. Springer handbook of lasers and optics. Berlin, Heidelberg: Springer; 2012. p. 1359–97.
155. Lemmer P, Gunkel M, Baddeley D, Kaufmann R, Urich A, Weiland Y, Reymann J, Müller P, Hausmann M, Cremer C. SPDM: light microscopy with single-molecule resolution at the nanoscale. Appl Phys B. 2008;93(1):1–12.
156. Lemmer P, Gunkel M, Weiland Y, Muller P, Baddeley D, Kaufmann R, Urich A, Eipel H, Amberger R, Hausmann M, Cremer C. Using conventional fluorescent markers for far-field fluorescence localization nanoscopy allows resolution in the 10-nm range. J Microsc. 2009;235(2):163–71.
157. Bohn M, Diesinger P, Kaufmann R, Weiland Y, Muller P, Gunkel M, von Ketteler A, Lemmer P, Hausmann M, Heermann DW, Cremer C. Localization microscopy reveals expression-dependent parameters of chromatin nanostructure. Biophys J. 2010;99(5):1358–67.
158. Kaufmann R, Müller P, Hildenbrand G, Hausmann M, Cremer C. Analysis of Her2/neu membrane protein clusters in different types of breast cancer cells using localization microscopy. J Microsc. 2011;242(1):46–54.
159. Zeller D, Kepper N, Hausmann M, Schmitt E. Sequential and structural biophysical aspects of combinatorial oligo FISH in Her2/neu breast cancer diagnostics. IFMBE Proc. 2013;38:82–5.
160. Hausmann M, Winkler R, Hildenbrand G, Finsterle J, Weisel A, Rapp A, Schmitt E, Janz S, Cremer C. COMBO-FISH: specific labeling of nondenatured chromatin targets by computer-selected DNA oligonucleotide probe combinations. Biotechniques. 2003;35(3):564–70, 572–7.
161. Bridger JM, Volpi E. Fluorescence in situ hybridization (FISH): protocols and applications. New York: Humana Press; 2010.
162. Rauch J, Wolf D, Hausmann M, Cremer C. The influence of formamide on thermal denaturation profiles of DNA and metaphase chromosomes in suspensions. Z Naturforsch C. 2000;55(9–10):737–46.
163. Winkler R, Perner B, Rapp A, Durm M, Cremer C, Greulich KO, Hausmann M. Labelling quality and chromosome morphology after low temperature FISH analysed by scanning far-field and scanning near-field optical microscopy. J Microsc. 2003;209(Pt 1):23–33.
164. Müller P, Schmitt E, Jacob A, Hoheisel J, Kaufmann R, Cremer C, Hausmann M. COMBO-FISH enables high precision localization microscopy as a prerequisite for nanostructure analysis of genome loci. Int J Mol Sci. 2010;11(10):4094–105.
165. Schmitt E, Wagner J, Hausmann M. Combinatorial selection of short triplex forming oligonucleotides for fluorescence in situ hybridisation COMBO-FISH. J Comput Sci. 2012;3(5):328–34.
166. Dahmen V, Kriehuber R. Cytotoxic effects and specific gene expression alterations induced by I-125-labeled triplex-forming oligonucleotides. Int J Radiat Biol. 2012;88(12):972–9.
167. Grygar J. Úloha přesnosti při astronomických objevech (The role of accuracy in astronomical discoveries). Pokroky matematiky, fyziky a astronomie. 1998;43(3):177–83.

Cellular Signalling 25 (2013) 1186–1193

Contents lists available at SciVerse ScienceDirect

Cellular Signalling

journal homepage: www.elsevier.com/locate/cellsig

Expression of human BRCA1Δ17–19 alternative splicing variant with a truncated BRCT domain in MCF-7 cells results in impaired assembly of DNA repair complexes and aberrant DNA damage response

Jan Sevcik [a,e,*], Martin Falk [b], Libor Macurek [c,d], Petra Kleiblova [a], Filip Lhota [a], Jan Hojny [a], Lenka Stefancikova [b], Marketa Janatova [a], Jiri Bartek [c,f,g], Jana Stribrna [a], Zdenek Hodny [c], Lucie Jezkova [b,h], Petr Pohlreich [a], Zdenek Kleibl [a,**]

[a] Institute of Biochemistry and Experimental Oncology, First Faculty of Medicine, Charles University in Prague, U Nemocnice 5, CZ-128 53 Prague 2, Czech Republic
[b] Institute of Biophysics, The Academy of Sciences of the Czech Republic, Kralovopolska 135, CZ-61265 Brno, Czech Republic
[c] Laboratory of Genome Integrity, Institute of Molecular Genetics, v.v.i., The Academy of Sciences of the Czech Republic, Videnska 1083, CZ-14220 Prague, Czech Republic
[d] Laboratory of Cancer Cell Biology, Institute of Molecular Genetics, v.v.i., The Academy of Sciences of the Czech Republic, Videnska 1083, CZ-14220 Prague, Czech Republic
[e] Prague Burn Centre, Charles University, Third Faculty of Medicine and Teaching Hospital Kralovske Vinohrady, Srobarova 50, CZ-10034 Prague 10, Czech Republic
[f] Institute of Molecular and Translational Medicine, Faculty of Medicine and Dentistry, Palacky University Olomouc, Hnevotinska 5, CZ-779 00, Czech Republic
[g] Danish Cancer Society Research Center, Strandboulevarden 49, DK-2100 Copenhagen, Denmark
[h] Institute of Chemical Technology Prague, Faculty of Food and Biochemical Technology, Technicka 5, CZ-166 28 Prague 6, Czech Republic

ARTICLE INFO

Article history:
Received 14 January 2013
Accepted 8 February 2013
Available online 14 February 2013

Keywords:
BRCA1
Alternative splicing
Breast cancer
DNA damage
Homologous recombination (HR)
Non-homologous end joining (NHEJ)
BRCA1 C-terminal (BRCT) domain
BRCA1 containing complexes
Ionizing radiation-induced foci (IRIF)
Abraxas
CtIP
BARD1

ABSTRACT

Alternative pre-mRNA splicing is a fundamental post-transcriptional regulatory mechanism. Cancer-specific misregulation of the splicing process may lead to formation of irregular alternative splicing variants (ASVs) with a potentially negative impact on cellular homeostasis. Alternative splicing of BRCA1 pre-mRNA can give rise to BRCA1 protein isoforms that possess dramatically altered biological activities compared with full-length wild-type BRCA1. During the screening of high-risk breast cancer (BC) families we ascertained numerous BRCA1 ASVs, however, their clinical significance for BC development is largely unknown. In this study, we examined the influence of the BRCA1Δ17–19 ASV, which lacks a portion of the BRCT domain, on DNA repair capacity using human MCF-7 BC cell clones with stably modified BRCA1 expression. Our results show that overexpression of BRCA1Δ17–19 impairs homologous recombination repair (sensitizes cells to mitomycin C), delays repair of ionizing radiation-induced DNA damage and dynamics of the ionizing radiation-induced foci (IRIF) formation, and undermines also the non-homologous end joining repair (NHEJ) activity. Mechanistically, BRCA1Δ17–19 cannot interact with the partner proteins Abraxas and CtIP, thus preventing interactions known to be critical for processing of DNA lesions. We propose that the observed inability of BRCA1Δ17–19 to functionally replace wtBRCA1 in repair of DNA double-strand breaks (DDSB) reflects impaired capacity to form the BRCA1-A and -C repair complexes. Our findings indicate that expression of BRCA1Δ17–19 may negatively influence genome stability by reducing the DDSB repair velocity, thereby contributing to enhanced probability of cancer development in the affected families.

1. Introduction

BRCA1 (MIM# 113705) is a multifunctional protein and established tumor suppressor participating in the regulation of several distinct cellular processes. Its main activity involves mediating the DNA damage response [1,2]. BRCA1 participates in non-homologous end joining (NHEJ) and homologous recombination (HR) of DNA double-strand breaks (DDSB), where it acts as a protein–protein interaction platform [3,4]. Specific differential activities of BRCA1 within the DDSB repair process are determined by assembly of discrete multiprotein complexes, through association of various interacting proteins with the BRCA1 C-terminal BRCT domain and the N-terminal RING finger motif [5]. While the participation of BRCA1 in NHEJ is not mechanistically

Abbreviations: AS, alternative splicing; ASV, alternative splicing variant; B2M, β-2-microglobulin; BARD1, BRCA1-associated RING domain 1; BC, breast cancer; BRCA1/2, breast cancer-associated gene 1/2; BRCT, BRCA1 C-terminal domain; BRCC36, BRCA1/BRCA2-containing complex subunit 36; BRIP1, BRCA1-interacting protein 1; CtIP, C-terminal interaction protein; DDR, DNA damage response; DDSB, DNA double strand break; HR, homologous recombination; IRIF, ionizing radiation-induced foci; NHEJ, non-homologous end joining; PBGD, porphobilinogen deaminase; PE, plating efficiency; PI, post-irradiation; RING, Really interesting new gene (domain); RPA, replication protein A; RTCA, real-time cell analyzer; SCD, serine-containing domain; SF, surviving fraction; shRNA, short-hairpin RNA; ssDNA, single-stranded DNA; 53BP1, p53 binding protein 1.

* Correspondence to: J. Sevcik, Institute of Biochemistry and Experimental Oncology, First Faculty of Medicine, Charles University in Prague, U Nemocnice 5, CZ-128 53, Prague 2, Czech Republic. Tel.: +420 22496 5745; fax: +420 22496 5732.
** Corresponding author. Tel.: +420 22496 5745; fax: +420 22496 5732.
E-mail addresses: jsevc@lf1.cuni.cz (J. Sevcik), zdekleje@lf1.cuni.cz (Z. Kleibl).

0898-6568/$ – see front matter © 2013 Elsevier Inc. All rights reserved.
http://dx.doi.org/10.1016/j.cellsig.2013.02.008

understood, it is known that at least three distinct BRCA1-containing complexes (BRCA1 A, BRCA1 B and BRCA1 C, respectively) orchestrate HR. The core of the BRCA1 A-complex consists of the Abraxas (CCDC98) adaptor protein bound to BRCA1's BRCT domain. This complex possesses both ubiquitin ligase (provided by BRCA1/BARD1) and deubiquitinase (provided by BRCC36) activities [6]. It has been proposed that the ubiquitination of proteins acting in DDSB repair sustains a subtle balance in the rate of DNA resection at the DDSB site [7]. The BRCA1 B-complex is formed by binding BRIP1 (alias BACH1) helicase to BRCA1 and it is important for the extension of ssDNA regions and RPA loading during the resolution of stalled replication forks [8]. The BRCA1 C-complex contains CtIP exonuclease linked with BRCA1, and it represents the main enzyme to carry out 5′-to-3′ resection of free DNA ends at the DDSB site [9].

The step-wise formation and regulation of the BRCA1 complexes are not fully known yet, but these processes likely determine the precise timing and nature of BRCA1's activities in the DNA damage response [10]. The assembly of BRCA1 complexes can be limited by the spatio-temporal availability and binding capacity of BRCA1 and its binding partners. The nuclear targeting of BRCA1 itself is regulated by its nuclear localization and export signals, while its binding capacity is regulated by phosphorylation of the BRCA1 protein, particularly on its serine-containing domain (SCD) [11]. Changes in the BRCA1 protein structure especially in conservative domains broadly impair BRCA1's binding capacity and hence its ability to form functionally active complexes. Alterations in exons coding for conservative BRCA1 motifs frequently represent pathogenic mutations predisposing to breast, ovarian and other BRCA1-associated cancers in their carriers [12]. The structure of the BRCA1 protein could also be affected by altered pre-mRNA splicing (AS). Besides BRCA1 aberrant splicing (arising from alterations in conservative *cis*-regulatory splicing sequences), a number of BRCA1 alternative splicing variants (ASVs) have been reported [13,14]. While the functional and clinical significance of BRCA1 ASVs is mostly unknown, some variants show an obvious alteration in BRCA1 activities [15]. In general, pre-mRNA AS is considered as a means to increase genetic diversity by formation of protein isoforms with changed biological activities on the post-transcriptional level. Despite growing evidence of AS relevance for malignant transformation, there is a lack of knowledge about cancer-specific (de)regulation of AS and little mechanistic insight into malfunction of the various cancer-specific ASVs [16,17].

This work follows our previous study focused on the functional *in vitro* characterization of the BRCA1Δ14–15 ASV lacking a part of phosphorylation-targeted SCD. Here we report the functional characterization of the BRCA1Δ17–19 ASV, identified during the screening of high-risk breast cancer (BC) patients in the Czech Republic [18]. In particular, we describe the impact of the BRCA1Δ17–19 ASV on γ-radiation-induced DDSB repair complexes and repair capacity, using human MCF-7 BC cells as a model.

2. Material and methods

2.1. Construction of expression vectors

A pcDNA3.1-HA-wtBRCA1 construct was generously provided by Dr. Paul D. Harkin [19]. A pcDNA3.1-HA-BRCA1Δ17–19 expression construct (with in-frame deletion of exons 17–19 that code for a substantial portion of the first BRCT domain) was prepared by a PCR splicing approach using pcDNA3.1-HA-wtBRCA1 as a template, as described previously [15].

A pSUPER.retro.puro (Oligoengine) vector system was used for a short hairpin RNA (shRNA)-mediated downregulation of an endogenous wtBRCA1 expression. Particular pSUPER.retro.puro shRNA plasmids were constructed as described previously [20]. To assess only the biological activity of the BRCA1Δ17–19 ASV, the interfering RNAs were targeted to the BRCA1 exon 17 (shRNA 5196: 5′-GATCCCC**GTACAAGTTTGCCAGAAAA**TTCAAGAGATTTTCTGGCAAACTTGTACTTTTTGGAAC-3′) and 18 (shRNA 5331: 5′-GATCCCC**GAAAATGGGTAGTTAGCTA**TTCAAGAGATAGCTAACTACCCATTTTCTTTTTGGAAC-3′), respectively. Critical experiments were performed with both shRNAs to rule out an off-target effect of the used shRNA (Supplementary Fig. 1).

2.2. Cell culture and transfection

The MCF-7 cell line was used for functional analysis of the BRCA1Δ17–19 ASV, and the 293T cell line was used for an analysis of BRCA1 complexes with the BRCA1Δ17–19 ASV. Both cell lines were grown in DMEM (Gibco) medium supplemented with 10% fetal calf serum (Gibco), at 37 °C in a humidified atmosphere of 5% CO_2. The MCF-7 clones with stably modified expression of BRCA1 were selected as described previously [15,20]. Transient transfectants of 293T cells were prepared by polyethylenimine transfection as described [21].

2.3. Irradiation of cells

Non-synchronized cells grown on Petri dishes were irradiated with a single dose of 1.5 Gy of ionizing radiation using ^{60}Co (0.58 Gy/min) as described previously [15].

2.4. Comet assay

The MCF-7 clones grown in triplicates under standard conditions were γ-irradiated as described above. Non-irradiated cells (0 min) and cells at the particular times after irradiation (15, 30, 60, and 120 min) were assayed according to the manufacturer's instructions using a neutral CometAssay (Trevigen). The results were analyzed using the CometScore v1.5 (TriTec) software.

2.5. Mitomycin C sensitivity assay

An xCELLigence real-time cell analyzer (RTCA; Roche) was used for testing the sensitivity of clones to mitomycin C, as described previously [15]. The RTCA software ver. 1.2 (Roche) was used to analyze cell proliferation and dose response curves.

2.6. Immunofluorescence and high-resolution confocal microscopy

The MCF-7 clones grown under standard conditions were treated with γ-radiation as described above. Non-irradiated cells (0 min) and cells at the particular times (5, 30, 60, 120, 240 and 1440 min) after irradiation were fixed (4% paraformaldehyde, 10 min RT), permeabilized (0.2% Triton X100/PBS for 14 min RT) and immunoassayed for γH2AX/53BP1 colocalization as described previously, using the following antibodies: anti-phospho-H2AX (Upstate Biotechnology), rabbit anti-53BP1 (Cell Signaling), FITC-conjugated donkey anti-mouse and Cy3-conjugated donkey anti-rabbit antibodies (Jackson Laboratory), and TOPRO-3 (Molecular Probes) [15,22–24]. These IRIF markers – a phosphorylated form of the H2AX histone (γH2AX) and the DDSB mediator protein 53BP1 – co-localize at the site of DNA damage [11]. While γH2AX foci formation is generally accepted as a sufficient quantitative marker of DDSBs [25], the used double-labeling with 53BP1 enables a more precise quantification of DDSBs. The exposure time and dynamic range of the camera in the red, green and blue channels were adjusted to the same values for all slides to obtain quantitatively comparable images. Forty serial optical sections were captured at 0.2–0.3 μm steps along the z-axis, using the automated DM RXA confocal fluorescence microscope (Leica).

2.7. In vitro NHEJ assay

The overall capacity and precision of NHEJ was determined by a luciferase vector-based *in vitro* assay, as described previously [15]. Briefly, the DDSB was simulated by an enzymatic cleavage of a reporter pGL (Promega) vector at two different sites prior to transfection. Expression

of active luciferase from an EcoRI-linearized pGL vector in the luciferase coding sequence is ensured only after a precise ligation, and hence it reflects the precise NHEJ activity, while expression of active luciferase from a HindIII-linearized pGL vector in the luciferase promoter sequence requires any arbitrary ligation and thus reflects the overall NHEJ capacity. The luciferase activity was measured by a Dual Luciferase reporter assay (Promega) 48 h after transfection. The activity of pGL luciferase was normalized to a control circular pRL-tk vector.

2.8. Immunoprecipitation

The 293T cells were co-transfected with a pcDNA3.1-HA-wtBRCA or pcDNA3.1-HA-BRCA1Δ17–19 construct (8 μg) together with a pOZ-N-FLAG-Abraxas [26], pcDNA3.1-FLAG-CtIP or pcDNA3.1-FLAG-BARD1 construct (each 2 μg) using polyethylenimine and grown for 48 h. Subsequently the cells were extracted by an ice-cold EBC buffer (50 mM Tris pH 7.5, 150 mM NaCl, 0.5% NP-40, 1 mM EGTA) supplemented with 1 mM NaF and protease inhibitor cocktail (Roche), sonicated (3×10 s, amplitude 7, 100 W) and spun down (20,000 g, 10 min, 4 °C). Normalized cell extracts were incubated with an anti-FLAG M2 affinity gel (Sigma) for 3 h at 4 °C. Beads with immunoprecipitated proteins were extensively washed with an EBC buffer and then eluted with a sample buffer. Proteins were electrophoretically separated using 3–8% Tris-Acetate precast gradient gels (Invitrogen). The immunoblotted samples were then probed with anti-HA conjugated with HRP (Roche) or with anti-FLAG antibodies.

2.9. Statistical analysis

A statistical analysis was performed using the non-parametric ANOVA (Wilcoxon two sample test) test and an Excel spreadsheet. P values <0.05 were considered statistically significant. All data are presented as mean ± standard deviation (S.D.).

3. Results

3.1. BRCA1Δ17–19 sensitizes MCF-7 cells to mitomycin C

The MCF-7-based clones with a stably modified BRCA1 expression were selected and characterized following double-transfection with an expression construct containing the analyzed BRCA1 ASV and shRNA targeting wtBRCA1, using a procedure described previously [15]. For details see Supplementary Fig. 2.

BRCA1 is a key regulator of homology-directed DNA repair pathway(s) responsible for the DNA interstrand cross-link repair. Hence, depletion of BRCA1 sensitizes cells to DNA cross-linking agents such as mitomycin C, and the observed sensitivity of cells to mitomycin C reflects HR capacity, a major DNA repair mechanism operating in S/G2 cell-cycle phases of proliferating cells [1]. Considering this, we first examined the proliferation rate of the MCF-7 clones with a modified expression of BRCA1 treated by different concentrations of mitomycin C. Cell growth was continually monitored by an RTCA. The sensitivities of particular clones to mitomycin C were assessed by an estimate of the EC-50 concentration (Table 1) and evaluation of growth curves (Fig. 1). The MCF-7 clone with downregulated expression of endogenous BRCA1 (sh5196) was the one most sensitive to mitomycin C, responding rapidly to the addition of an active substance by slowing its growth rate. Both types of clones expressing the BRCA1Δ17–19 ASV [either (Δ17–19 + sh5196) alone or together with wtBRCA1 (Δ17–19)] also showed significantly increased sensitivity to mitomycin C compared to controls (MCF-7 and pcDNA3.1^{empty}). These results indicate that ectopically expressed BRCA1Δ17–19 overrides the capacity of homology-directed DNA repair in MCF-7 cells.

Table 1
The effective concentration (EC-50) of mitomycin C for MCF-7 clones with modified expression of BRCA1. The EC-50 was calculated at a time point of 64 h from the seeding of cells onto the plate as a cell index at a time point *versus* concentration. Data represent means from triplicates ± S.D.

Mitomycin C EC-50	MCF-7	Clone			
		pcDNA3.1	shRNA5196	Δ17–19	Δ17–19 + sh5196
[μg/ml] ± S.D.	6.18 ±0.18	6.06 ±0.23	2.89 ±0.27	4.02 ±0.71	3.60 ±0.2

3.2. BRCA1Δ17–19 slows down repair of ionizing radiation-induced DNA damage

Next, we directly measured the extent of DNA damage and DNA repair kinetics by a neutral comet assay in MCF-7 clones expressing the BRCA1Δ17–19 ASV following γ-irradiation (Fig. 2).

There were no detectable differences in DNA repair between the clone with downregulated wtBRCA1 expression (sh5196) and clones expressing the BRCA1Δ17–19 ASV. Notably however, the DNA repair velocity in cells with downregulated endogenous wtBRCA1 expression and cells expressing BRCA1Δ17–19 was slower compared to controls. The greatest difference in the degree of DNA damage between clones with modified expression of BRCA1 and controls was registered at 15 min post irradiation (PI). From that time on, the DNA damage rate progressively decreased, but at 120 min PI it was still significantly higher in clones with a modified BRCA1 expression.

These results show that both downregulation of wtBRCA1 and ectopic expression of the BRCA1Δ17–19 ASV slow down DDSB repairs in MCF-7 cells. Surprisingly, the expression of Δ17–19 negatively affected the DDSB repair capacity of MCF-7 cells similar to downregulation of endogenous wtBRCA1. The observed delay of the DDSB repair early after irradiation indicates that the BRCT protein interaction motif that is missing in the BRCA1Δ17–19 ASV is required primarily in the initial phase of DDSB repair, though it is not indispensable for the completion of the DNA repair process.

3.3. BRCA1Δ17–19 negatively impacts IRIF dynamics

The BRCA1 protein accumulates, along with many other DDR signaling and repair proteins, at DDSB-flanking regions of dynamically modified chromatin that are microscopically visible, commonly referred to as ionizing radiation-induced foci (IRIF), and eventually mediate repair of the DDSB lesions [27]. BRCA1 serves as a protein interaction modulator mediating the association of specific protein factors important for all phases of DNA repair. Thus, we further examined if the presence of the BRCA1Δ17–19 ASV that lacks a substantial part of the BRCA1 protein-interaction motif (in the first BRCT domain) can influence the kinetics of IRIF assembly and disassembly in response to ionizing radiation-induced DNA damage. For this purpose, we assessed the kinetics of γH2AX and 53BP1 co-localizations (well-established surrogate markers for IRIF) in fixed cells using immunofluorescence confocal microscopy after a single dose of 1.5 Gy of γ-radiation. Given that all analyzed clones originated from the MCF-7 cell line, and were exposed to the same radiation dose, it could be expected that identical initial average numbers of DDSBs occur in these settings.

The maximum number of IRIF in irradiated control MCF-7 cells was already detected at 5 min PI (Fig. 3). IRIF dissociation was apparent from that time on: over 75% of IRIF were dismantled within the first 2 h PI and the remaining IRIF subsequently disappeared reaching basal levels by 24 h PI, consistent with the expected kinetics of DNA repair. In MCF-7 clones with shRNA-mediated knock-down of endogenous wtBRCA1 (sh5196), and in clones expressing the BRCA1Δ17–19 ASV (Δ17–19 and Δ17–19 + sh5196, respectively), the number of IRIF further increased beyond the time of 5 min PI, reaching peak values at 30 min PI. The kinetics of the subsequent decline of the formed IRIF

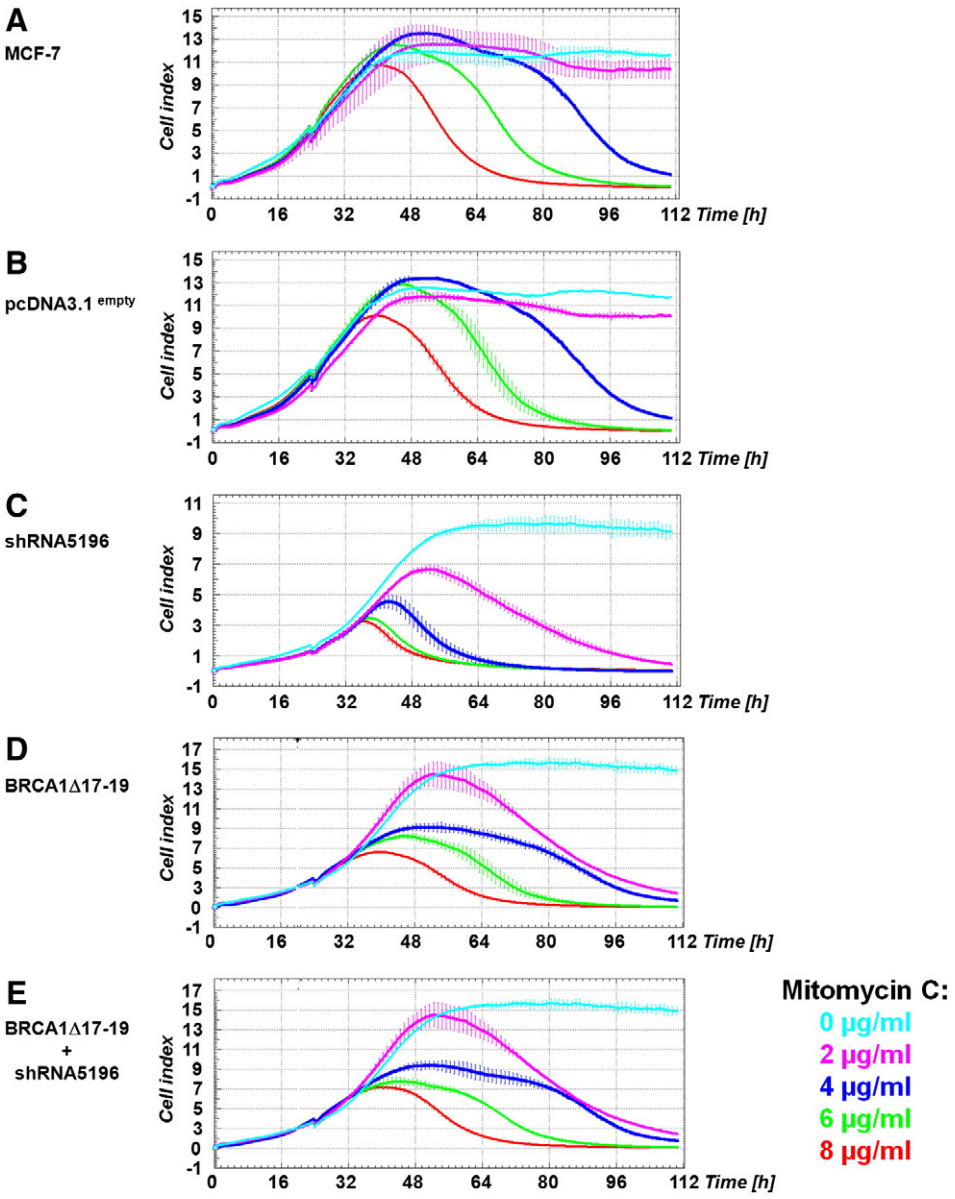

Fig. 1. Sensitivity of MCF-7 clones with modified expression of BRCA1 to mitomycin C. Cells were cultured for 5 days in a medium with different concentrations of mitomycin C (0, 2, 4, 6, and 8 µg/ml), under continual measurement of proliferation activity expressed here as a cell index (CI) using the xCELLigence RTCA analyzer. The CI was normalized to the time of addition of mitomycin C. Data are mean ± S.D.

were comparable to controls, but only 40% of IRIF (compared to 75% in control cells) were repaired by 2 h PI, likely reflecting the initial delay in IRIF formation and persistence. Interestingly, after 24 h PI the number of IRIF in MCF-7 clones with downregulated wtBRCA1 (sh5196) decreased to the basal pre-irradiation level, while in clones expressing BRCA1Δ17–19 IRIF numbers were still more than twice above the initial basal level (Fig. 3).

These findings are consistent with the results of comet assays and show that both downregulations of wtBRCA1 and ectopic expressions of the BRCA1Δ17–19 variant impair DDSB repair and the kinetics of IRIF formation. Surprisingly, downregulation of endogenous wtBRCA1 negatively influenced the assembly of IRIF while the decomposing phase of IRIF dynamics was unaffected. On the other hand, ectopic expression of the BRCA1Δ17–19 ASV impaired both phases of IRIF dynamics. Moreover, the negative impact on IRIF formation in the latter cells was apparently independent of the presence of wtBRCA1.

3.4. BRCA1Δ17–19 reduces NHEJ activity

BRCA1 is involved in both major DDSB repair pathways (HR and NHEJ) and negative effects of BRCA1 inactivation on NHEJ capacity [28] and fidelity [29] have been described. To find out whether ectopic expression of the BRCA1Δ17–19 ASV influences NHEJ activity and precision in MCF-7 cells, we performed an *in vitro* NHEJ repair assay. As can be seen from the data presented in Fig. 4, both the overall activity and the precision of NHEJ were significantly lower in all examined clones with altered BRCA1 expression, including clones with downregulated expression of wtBRCA1, and those expressing the ectopic BRCA1Δ17–19 variant. Notably, while the decrease in the overall NHEJ activity was similar in cells with knocked-down wtBRCA1 (to 34% ± 6.2 of the control values) and those expressing BRCA1Δ17–19 (a drop to 34% ± 3.8), the precision aspect of NHEJ was more dramatically affected in the latter clones: being decreased to 22% ± 3.2, as compared to a decline to 52% ± 3.4 seen upon shRNA-mediated knock-down of endogenous BRCA1 (Fig. 4).

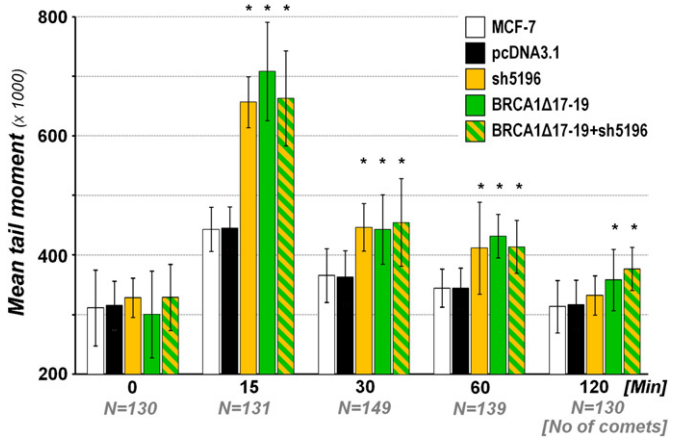

Fig. 2. DNA damage time-course in clones with modified BRCA1 expression after γ-irradiation. A neutral comet assay was used to determine the DNA damage level. At least 30 comets were analyzed for each clone using fluorescence microscopy at times 0, 15, 30, 60, and 120 min PI. For a DDSB repair time course quantification, the comet mean tail moment was calculated using the CometScore ver. 1.5 software (AutoComet). Non-irradiated samples are represented as time 0. Data are mean ± S.D. $^{*}p<0.01$ for MCF-7, (Wilcoxon test).

These results show that downregulation of wtBRCA1 as well as ectopic expression of the BRCA1Δ17–19 ASV negatively influence both the overall activity and fidelity of NHEJ in MCF-7 cells.

3.5. BRCA1Δ17–19 fails to interact with a subset of BRCA1 binding partners

Skipping exons 17–19 of BRCA1 leads to the production of a protein isoform missing a substantial part of the BRCT phosphoprotein-interaction module (aa 1664–1732). It can be expected that the protein-binding capacity of this BRCA1 isoform will be impaired. The inability to interact with specific binding partners could explain the results of previous experiments which showed an altered IRIF kinetics in MCF-7 clones expressing the BRCA1Δ17–19 ASV. To test the protein–protein interaction ability of the variant BRCA1 protein, we next analyzed the interactions between BRCA1Δ17–19 and two proteins, Abraxas and CtIP, that constitute a core of BRCA1-containing complex BRCA1-A and BRCA1-C, respectively. Both Abraxas and CtIP interact with BRCA1 *via* the BRCT domain and actively participate in DNA repair. Our results showed that in non-irradiated 293T cells, the BRCA1Δ17–19 isoform fails to co-precipitate with either Abraxas or CtIP, respectively, contrary to proficient interactions with either partner in case of wtBRCA1 (Fig. 5). To prove that the inability of BRCA1Δ17–19 to interact with Abraxas and CtIP is attributable to the truncation in the C-terminal BRCT domain, we further immunoprecipitated BRCA1Δ17–19 with BARD1 that binds to BRCA1 exclusively *via* the N-terminal RING domain. In this case, both the wtBRCA1 and the BRCA1Δ17–19 variant proteins co-precipitated with BARD1.

These results show that the BRCA1Δ17–19 ASV is unable to form stable protein complexes with important BRCA1 binding partners such as Abraxas and CtIP. This finding complements the above functional assays of IRIF kinetics and repair, and implies that the BRCA1Δ17–19 ASV protein is unable to execute the role of a protein-interaction modulator, normally provided by the wild-type BRCA1 protein, due to an impaired binding capacity of the C-terminal BRCT domain.

4. Discussion

In this study, we characterized the impact of the BRCA1Δ17–19 ASV on cell proliferation, sensitivity to DNA-damaging insults and capacity for DDSB repair. We identified this in-frame ASV previously in two *BRCA1* mutation-negative BC individuals during genetic screens of high-risk families [18]. Interestingly, intragenic *BRCA1* deletions affecting region coding for exons 17–19 that result in expression of identical BRCA1 protein isoform were reported in high-risk BC patients of the Western European descent [30,31]. As discussed below, this work extends our previous report indicating the importance of BRCA1 ASVs for the maintenance of genome integrity [15], and provides novel insights into the biological impact and mechanistic basis for malfunction of the so far uncharacterized variant BRCA1Δ17–19 of the BRCA1 tumor suppressor protein.

Timely and error-free repair of a DDSB in eukaryotic cells is secured by a cooperative action of NHEJ and HR pathways [32]. NHEJ is the prominent repair mechanism during the G1 and early S phase, and throughout the cell cycle when DDSBs occur in easily accessible euchromatin [33]. Due to low demands for the modification of free DNA ends at the breakage site, NHEJ is a relatively simple mechanism and represents a fast component of the global DDSB repair that ensures prompt elimination of such highly deleterious DNA lesion [34]. The exact participation of BRCA1 in NHEJ is not understood yet, and the results concerning BRCA1's importance for NHEJ are contradictory [35,36]. The *in vivo* regulation of NHEJ relies on extensive chromatin modifications (methylation, ubiquitination) that are unlikely to be faithfully recapitulated in ectopically expressed constructs used as reporters for cell culture analyses [37]. Hence, the results of such reporter-based NHEJ assay may not exactly reflect the activity of NHEJ *in vivo*. Such concerns notwithstanding, our results indicate that downregulation of endogenous wtBRCA1 or ectopic expression of the BRCA1Δ17–19 variant has a negative impact on the capacity of NHEJ *in vitro*. This is consistent with the observed delay of DNA repair in the period shortly after DDSB induction.

Homology-directed DNA repair represents a slow but precise component of DDSB repair ensuring fidelity in elimination of a highly deleterious DNA lesion. Our present confocal immunofluorescence microscopy analysis showed that the formation of γH2AX/53BP1 IRIF was significantly retarded within 30 min PI and further persistence of IRIF was markedly prolonged in MCF-7 cells pretreated by either shRNA-mediated knockdown of wtBRCA1 or ectopic expression of BRCA1Δ17–19 ASV. These results, together with increased sensitivity to mitomycin C, document a negative impact of the analyzed variant BRCA1 protein expression on HR.

The BRCA1 protein participates in several protein complexes that ensure discrete successive steps of HR [4]. The inability of BRCA1 to interact with its binding partners results in delayed and/or erroneous spatio-temporal regulation and function at the sites of DNA damage which, in turn, deregulate the highly orchestrated DDSB repair process. Indeed, a delay of a single rate-limiting step can delay the entire repair process, and a total blockage in one of the HR steps may cause a

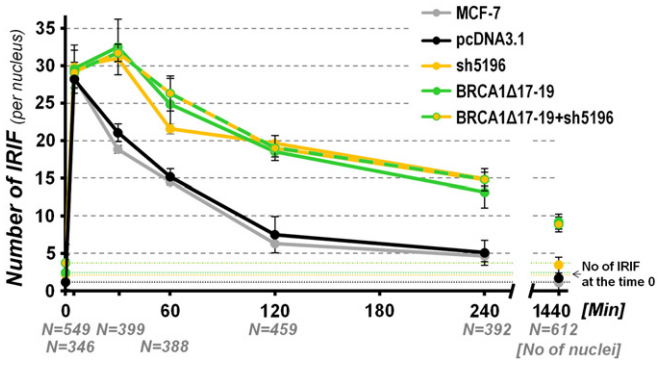

Fig. 3. The kinetics of IRIF formation and persistence in diverse clones of MCF-7 cells. The kinetics of DDSB signaling/repair were assessed by counting the γH2AX/53BP1 colocalizations per nucleus at the indicated time points (0, 5, 30, 60, 120, 240 and 1440 min, respectively) after ionizing irradiation (1.5 Gy) using confocal immunofluorescence microscopy. The endogenous level of DDSBs in the indicated clones is represented here as the number of IRIF per nucleus in non-irradiated cells (time 0; depicted by dotted lines). Data are mean ± S.D.

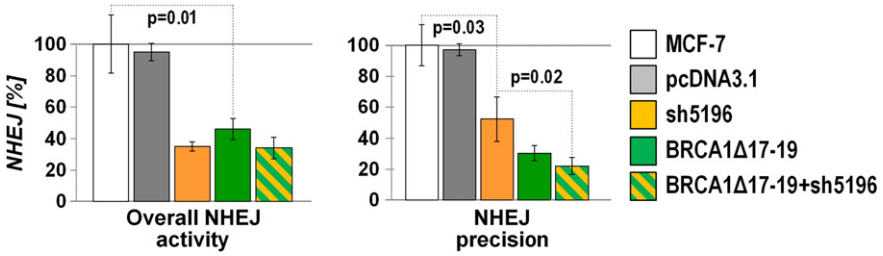

Fig. 4. The *in vitro* NHEJ assay. The particular clones and relevant controls were co-transfected by a linearized pGL-control vector and a circular pRL-tk vector. The rescued activity of luciferase was measured using the dual luciferase assay kit and normalized to the activity of control pRL-tk luciferase. The luciferase activity rescued from the HindIII-linearized pGL-control vector reflects the overall NHEJ activity, while that from the EcoRI-linearized pGL-control vector reflects the NHEJ precision [15]. The experiment was repeated three times, data are mean ± S.D., significant p-values are indicated.

time-consuming functional switch redirecting the DDSB repair from HR to another repair pathway [38].

The formation of long 3′ ssDNA overhangs of the free DNA ends at the DDSB site enables a successful strand exchange for a homology-directed DNA repair [9]. These overhangs are dominantly generated by the activity of CtIP exonuclease. The rate of the CtIP-mediated DNA end resection increases as CtIP is bound to BRCA1 within the BRCA1 C-complex, while the activity of unbound CtIP molecules is inhibited by their association with the DNA repair modulator 53BP1 at the DDSB site [39,40]. Limited resection of DNA ends is insufficient for further HR, and therefore the integration of CtIP into the BRCA1 C-complex overcomes the inhibitory activity of 53BP1 and enables the formation of long 3′ DNA overhangs [41]. Impaired resection caused by the inability of the BRCA1Δ17–19 isoform to bind CtIP can cause the observed delay in DDSB repair. Defective assembly of the BRCA1 C-complex in MCF-7 cell clones expressing the BRCA1Δ17–19 isoform as well as in those with downregulated wtBRCA1 expression can explain their similar behavior in terms of increased sensitivity to mitomycin C and delayed early phase of DNA repair.

Once the DDSBs are fully repaired, HR must be resolved by dismantling the active IRIFs to prevent a potential undesirable DNA crossover (referred to as hyper-HR) [2]. Taking into account the results of comet assays showing that the majority of DDSBs are repaired within 120 min PI and colocalization studies showing increased persistence of IRIFs beyond this time, it could be suggested that the presence of the BRCA1Δ17–19 variant interferes with processing of the slowly-repaired DDSBs localized in the highly complex chromatin regions [42] or disturbs the termination of HR by blocking the IRIF removal.

The consecutive association of protein factors that form the active IRIF at the DDSB site is regulated by covalent protein modifications. Besides phosphorylation, the importance of ubiquitination is indicated by recent findings showing that ubiquitination and deubiquitination of histones are critical for genome stability maintenance [27,43]. The BRCA1 ubiquitin ligase activity, enhanced by heterodimerization with BARD1 *via* the RING domain-mediated interaction, targets several proteins directly involved in the DNA repair process [44,45]. Alongside the E3 activity of BRCA1, the BRCA1 A-complex anchoring to the DDSB site binds BRCC36 deubiquitinylase [46]. Though the exact mechanism of the IRIF disassembly is currently unknown, Hu et al. reported that downregulation of non-BRCA1 members of the BRCA1 A-complex causes hyper-HR [47]. Furthermore, Dever et al. showed that BRCA1 mutation in its BRCT domain causes increased recombination leading to genomic instability [48]. These results indicate that the BRCA1 A-complex is a negative regulator of ubiquitination-dependent DNA repair pathways. The inability of the BRCA1Δ17–19 ASV to bind Abraxas, a central protein of the BRCA1 A-complex, might contribute to the observed prolonged persistence of IRIF. Moreover, the BRCA1 mutation p.I26A affecting the RING domain was shown to reverse the increased recombination rate in cells expressing the BRCA1 BRCT mutant p.K1702M [48]. This is consistent with our observation that persistence of IRIF was prolonged in cell ectopic expression BRCA1Δ17–19 (which maintains the RING domain-mediated BARD1 binding) but not in cells with downregulated wtBRCA1.

More than twenty BRCA1 ASVs have been described so far [13,14]. The majority of them are classified as variants of unknown clinical significance. However, several of these ASVs were shown to negatively

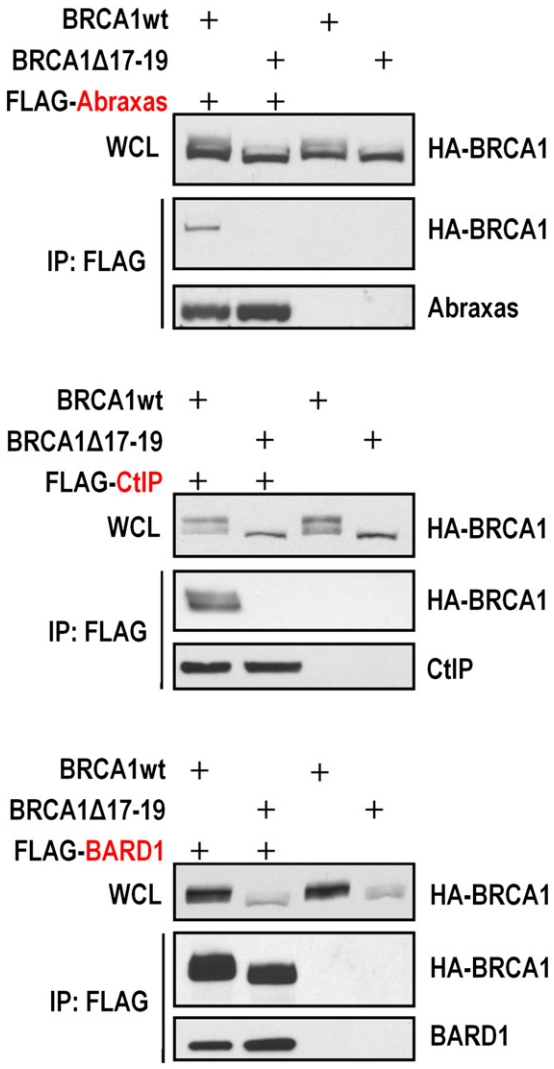

Fig. 5. Immunoprecipitation (IP) of the BRCA1Δ17–19 ASV with Abraxas, CtIP, and BARD1, respectively. 293T cells were transiently co-transfected with an expression vector containing HA-tagged full-length BRCA1 or HA-tagged BRCA1Δ17–19 variant together with vectors containing FLAG-tagged BARD1, Abraxas or CtIP, respectively. The expression levels of the individual proteins were validated by western blotting (WB) in whole-cell lysates (WCL). Co-immunoprecipitation was performed in non-irradiated cells. The results show that the Δ17–19 isoform with the deletion of a substantial part of the BRCT domain is unable to interact with the natural BRCA1 C-terminal binding partners Abraxas and CtIP, while the intact N-terminal RING domain-mediated binding to BARD1 is preserved.

influence the BRCA1-mediated cell cycle control and DNA repair activity [49,15]. This indicates that BRCA1 ASVs generated in a tissue-specific manner by misregulated pre-mRNA splicing can also contribute to tumorigenesis. It has been observed that the formation of BRCA1 aberrant splicing variants can promote malignant transformation [50–52]. On the other hand, the involvement of regulated AS in cancer development is virtually unknown [53]. For numerous gene products, including BRCA1, it has been shown that the formation of specific ASVs can be determined by a cell cycle phase [54], or by the DNA damage response [55,56]. This suggests that AS is an important post-transcriptional regulatory event responding to specific signals. Thus AS misregulation can lead to formation of an alternative protein product with potentially aberrant function or uncoupled from upstream regulation. The resulting appearance of ASVs that should normally be created under different cellular conditions and/or in a different amount can markedly alter the downstream processes that depend on the protein subjected to AS, with potential implications for human diseases including cancer.

In our previous study we showed that ectopic expression of the BRCA1Δ14–15 ASV that lacks a part of the phosphorylation-regulated SCD does not change the sensitivity of MCF-7 cells to mitomycin C but impairs the DDSB repair capacity by decreasing the NHEJ activity [15]. Our current results show a distinct, genome-destabilizing phenotype, in that ectopic expression of the BRCA1Δ17–19 ASV in MCF-7 cells significantly increases their sensitivity to mitomycin C. This indicates a negative effect of the BRCA1Δ17–19 ASV on DDSB repairs with a broader impact on the HR pathway, with potential implications for tumorigenesis and sensitivity to emerging new treatments such as PARP inhibitors, that selectively target cancer cells with functionally impaired homologous recombination [57].

5. Conclusions

Based on the present results we conclude that the ectopically expressed BRCA1Δ17–19 ASV protein with an in-frame deletion affecting a substantial part of the BRCT domain is unable to interact with Abraxas and CtIP while it retains the BARD1-binding capacity. This defect probably causes the observed hypersensitivity to mitomycin C and the reduced activity of ionizing radiation-induced DDSB repair in MCF-7 cells. The presence of the BRCA1Δ17–19 variant decelerates DNA repair and the assembly of IRIF during early PI periods, and impairs the NHEJ activity. Similar phenotypes were observed in cells with downregulated expression of endogenous wtBRCA1, indicating that the Δ17–19 ASV is unable to functionally substitute full-length BRCA1 in DNA repair. Moreover, expression of the BRCA1Δ17–19 isoform significantly prolongs the persistence of IRIF regardless of the actual DNA damage level. In a broader context, our results suggest that expression of in-frame ASVs of BRCA1 mRNA that selectively lack portions of critical structural domains may negatively affect genome integrity by undermining the overall capacity or precision of DNA repair, and possibly promoting hyperactivity of HR.

Supplementary data to this article can be found online at http://dx.doi.org/10.1016/j.cellsig.2013.02.008.

Acknowledgment

We thank all members of our laboratories and Jan Flemr for proofreading. This study was supported by grants from the Grant Agency of the Czech Republic (No. P301/12/1850 and P301/10/1525), the Internal Grant Agency of the Ministry of Health (No. NT12280 and NT11065), the European Commission (projects DDResponse and Biomedreg), the Charles University Grant Agency (No. 428711), MEYS COST LD12039, GACR Center Excellence (302/12/G157), and the Charles University in Prague (project PRVOUK-P27/LF1/1).

References

[1] M.E. Moynahan, T.Y. Cui, M. Jasin, Cancer Research 61 (2001) 4842–4850.
[2] M. Jasin, Oncogene 21 (2002) 8981–8993.
[3] S.M. Sy, M.S. Huen, J. Chen, Proceedings of the National Academy of Sciences of the United States of America 106 (2009) 7155–7160.
[4] B. Wang, Cell & Bioscience 2 (2012) 6–12.
[5] R.A. Greenberg, B. Sobhian, S. Pathania, S.B. Cantor, Y. Nakatani, D.M. Livingston, Genes & Development 20 (2006) 34–46.
[6] L. Feng, J. Wang, J. Chen, Journal of Biological Chemistry 285 (2010) 30982–30988.
[7] S. Panier, D. Durocher, DNA Repair (Amst) 8 (2009) 436–443.
[8] L. Dohrn, D. Salles, S.Y. Siehler, J. Kaufmann, L. Wiesmuller, Biochemical Journal 441 (2012) 919–926.
[9] A.A. Sartori, C. Lukas, J. Coates, M. Mistrik, S. Fu, J. Bartek, R. Baer, J. Lukas, S.P. Jackson, Nature 450 (2007) 509–514.
[10] M.T. Mok, B.R. Henderson, Traffic 13 (2012) 800–814.
[11] B.R. Henderson, Bioessays 27 (2005) 884–893.
[12] W.D. Foulkes, S.A. Narod, Clinical and Investigative Medicine 18 (1995) 473–483.
[13] T.I. Orban, E. Olah, Molecular Pathology 56 (2003) 191–197.
[14] C.A. Pettigrew, J.D. French, J.M. Saunus, S.L. Edwards, A.V. Sauer, C.E. Smart, T. Lundstrom, C. Wiesner, A.B. Spurdle, J.A. Rothnagel, M.A. Brown, Breast Cancer Research and Treatment 119 (2010) 239–247.
[15] J. Sevcik, M. Falk, P. Kleiblova, F. Lhota, L. Stefancikova, M. Janatova, L. Weiterova, E. Lukasova, S. Kozubek, P. Pohlreich, Z. Kleibl, Cellular Signalling 24 (2012) 1023–1030.
[16] M. Takahashi, Y. Furukawa, H. Shimodaira, M. Sakayori, T. Moriya, Y. Moriya, Y. Nakamura, C. Ishioka, Familial Cancer 11 (2012) 559–564.
[17] L. Schwarzova, J. Stekrova, M. Florianova, A. Novotny, M. Schneiderova, P. Lnenicka, V. Kebrdlova, J. Kotlas, K. Vesela, M. Kohoutova, Familial Cancer (2012), http://dx.doi.org/10.1007/s10689-012-9569-8.
[18] P. Pohlreich, J. Stribrna, Z. Kleibl, M. Zikan, R. Kalbacova, L. Petruzelka, B. Konopasek, Medical Principles and Practice 12 (2003) 23–29.
[19] J.E. Quinn, R.D. Kennedy, P.B. Mullan, P.M. Gilmore, M. Carty, P.G. Johnston, D.P. Harkin, Cancer Research 63 (2003) 6221–6228.
[20] E. Vondruskova, R. Malik, J. Sevcik, P. Kleiblova, Z. Kleibl, Neoplasma 55 (2008) 130–137.
[21] C. Ehrhardt, M. Schmolke, A. Matzke, A. Knoblauch, C. Will, V. Wixler, S. Ludwig, Signal Transduction 6 (2006) 179–184.
[22] M. Falk, E. Lukasova, S. Kozubek, Biochimica et Biophysica Acta 1783 (2008) 2398–2414.
[23] M. Falk, E. Lukasova, B. Gabrielova, V. Ondrej, S. Kozubek, Biochimica et Biophysica Acta 1773 (2007) 1534–1545.
[24] M. Kozubek, S. Kozubek, E. Lukasova, E. Bartova, M. Skalnikova, P. Matula, P. Matula, P. Jirsova, A. Cafourkova, I. Koutna, Cytometry 45 (2001) 1–12.
[25] A. Sharma, K. Singh, A. Almasan, Methods in Molecular Biology 920 (2012) 613–626, http://dx.doi.org/10.1007/978-1-61779-998-3_40, (613-626).
[26] J. Patterson-Fortin, G. Shao, H. Bretscher, T.E. Messick, R.A. Greenberg, Journal of Biological Chemistry 285 (2010) 30971–30981.
[27] J. Lukas, C. Lukas, J. Bartek, Nature Cell Biology 13 (2011) 1161–1169.
[28] Q. Zhong, T.G. Boyer, P.L. Chen, W.H. Lee, Cancer Research 62 (2002) 3966–3970.
[29] E.G. Thompson, H. Fares, K. Dixon, Environmental and Molecular Mutagenesis 53 (2012) 32–43.
[30] M.A. Unger, K.L. Nathanson, K. Calzone, D. Antin-Ozerkis, H.A. Shih, A.M. Martin, G.M. Lenoir, S. Mazoyer, B.L. Weber, American Journal of Human Genetics 67 (2000) 841–850.
[31] T.V.O. Hansen, L. Jønson, A. Albrechtsen, M.K. Andersen, B. Ejlertsen, F.C. Nielsen, Breast Cancer Research and Treatment 115 (2009) 315–323.
[32] E.M. Kass, M. Jasin, FEBS Letters 584 (2010) 3703–3708.
[33] A.A. Goodarzi, P. Jeggo, M. Lobrich, DNA Repair (Amst) 9 (2010) 1273–1282.
[34] Y. Lorat, S. Schanz, N. Schuler, G. Wennemuth, C. Rube, C.E. Rube, PLoS One 7 (2012) e38165.
[35] M.E. Moynahan, J.W. Chiu, B.H. Koller, M. Jasin, Molecular Cell 4 (1999) 511–518.
[36] H.C. Wang, W.C. Chou, S.Y. Shieh, C.Y. Shen, Cancer Research 66 (2006) 1391–1400.
[37] A.T. Noon, A.A. Goodarzi, DNA Repair (Amst) 10 (2011) 1071–1076.
[38] A. Bothmer, D.F. Robbiani, M. Di Virgilio, S.F. Bunting, I.A. Klein, N. Feldhahn, J. Barlow, H.T. Chen, D. Bosque, E. Callen, A. Nussenzweig, M.C. Nussenzweig, Molecular Cell 42 (2011) 319–329.
[39] B. Sobhian, G. Shao, D.R. Lilli, A.C. Culhane, L.A. Moreau, B. Xia, D.M. Livingston, R.A. Greenberg, Science 316 (2007) 1198–1202.
[40] L. Chen, C.J. Nievera, A.Y. Lee, X. Wu, Journal of Biological Chemistry 283 (2008) 7713–7720.
[41] S.F. Bunting, E. Callen, N. Wong, H.T. Chen, F. Polato, A. Gunn, A. Bothmer, N. Feldhahn, O. Fernandez-Capetillo, L. Cao, X. Xu, C.X. Deng, T. Finkel, M. Nussenzweig, J.M. Stark, A. Nussenzweig, Cell 141 (2010) 243–254.
[42] L. Ježková, M. Falk, I. Falková, M. Davídková, A. Bačíková, L. Stefančíková, J. Vachelová, A. Michaelidesová, E. Lukášová, A. Boreyko, E. Krasavin, S. Kozubek, Applied Radiation and Isotopes (in press), http://dx.doi.org/10.1016/j.apradiso.2013.01.022.
[43] G. Shao, D.R. Lilli, J. Patterson-Fortin, K.A. Coleman, D.E. Morrissey, R.A. Greenberg, Proceedings of the National Academy of Sciences of the United States of America 106 (2009) 3166–3171.
[44] R. Scully, J. Chen, R.L. Ochs, K. Keegan, M. Hoekstra, J. Feunteun, D.M. Livingston, Cell 90 (1997) 425–435.
[45] G.T. Lok, S.M. Sy, S.S. Dong, Y.P. Ching, S.W. Tsao, T.M. Thomson, M.S. Huen, Nucleic Acids Research 40 (2012) 196–205.

[46] Y. Dong, M.A. Hakimi, X. Chen, E. Kumaraswamy, N.S. Cooch, A.K. Godwin, R. Shiekhattar, Molecular Cell 12 (2003) 1087–1099.
[47] Y. Hu, R. Scully, B. Sobhian, A. Xie, E. Shestakova, D.M. Livingston, Genes & Development 25 (2011) 685–700.
[48] S.M. Dever, S.E. Golding, E. Rosenberg, B.R. Adams, M.O. Idowu, J.M. Quillin, N. Valerie, B. Xu, L.F. Povirk, K. Valerie, Aging (Albany, NY) 3 (2011) 515–532.
[49] K. Chock, J.M. Allison, W.M. Elshamy, Oncogene 29 (2010) 5274–5285.
[50] R.D. Brandao, K.E. van Roozendaal, D. Tserpelis, B. Caanen, G.E. Gomez, M.J. Blok, Breast Cancer Research and Treatment 131 (2012) 723–725.
[51] L. Zhang, L. Chen, R. Bacares, J.M. Ruggeri, J. Somar, Y. Kemel, Z.K. Stadler, K. Offit, Breast Cancer Research and Treatment 130 (2011) 1051–1056.
[52] M. Thomassen, A. Blanco, M. Montagna, T.V. Hansen, I.S. Pedersen, S. Gutierrez-Enriquez, M. Menendez, L. Fachal, M. Santamarina, A.Y. Steffensen, L. Jonson, S. Agata, P. Whiley, S. Tognazzo, E. Tornero, U.B. Jensen, J. Balmana, T.A. Kruse, D.E. Goldgar, C. Lazaro, O. Diez, A.B. Spurdle, A. Vega, Breast Cancer Research and Treatment 132 (2012) 1009–1023.
[53] E. Scholzova, R. Malik, J. Sevcik, Z. Kleibl, Cancer Letters 246 (2007) 12–23.
[54] T.I. Orban, E. Olah, Biochemical and Biophysical Research Communications 280 (2001) 32–38.
[55] M.J. Munoz, M.S. Perez Santangelo, M.P. Paronetto, M. de la Mata, F. Pelisch, S. Boireau, K. Glover-Cutter, C. Ben-Dov, M. Blaustein, J.J. Lozano, G. Bird, D. Bentley, E. Bertrand, A.R. Kornblihtt, Cell 137 (2009) 708–720.
[56] D.S. Chandler, R.K. Singh, L.C. Caldwell, J.L. Bitler, G. Lozano, Cancer Research 66 (2006) 9502–9508.
[57] S.P. Jackson, J. Bartek, Nature 461 (2009) 1071–1078.

Supplementary figure 1:

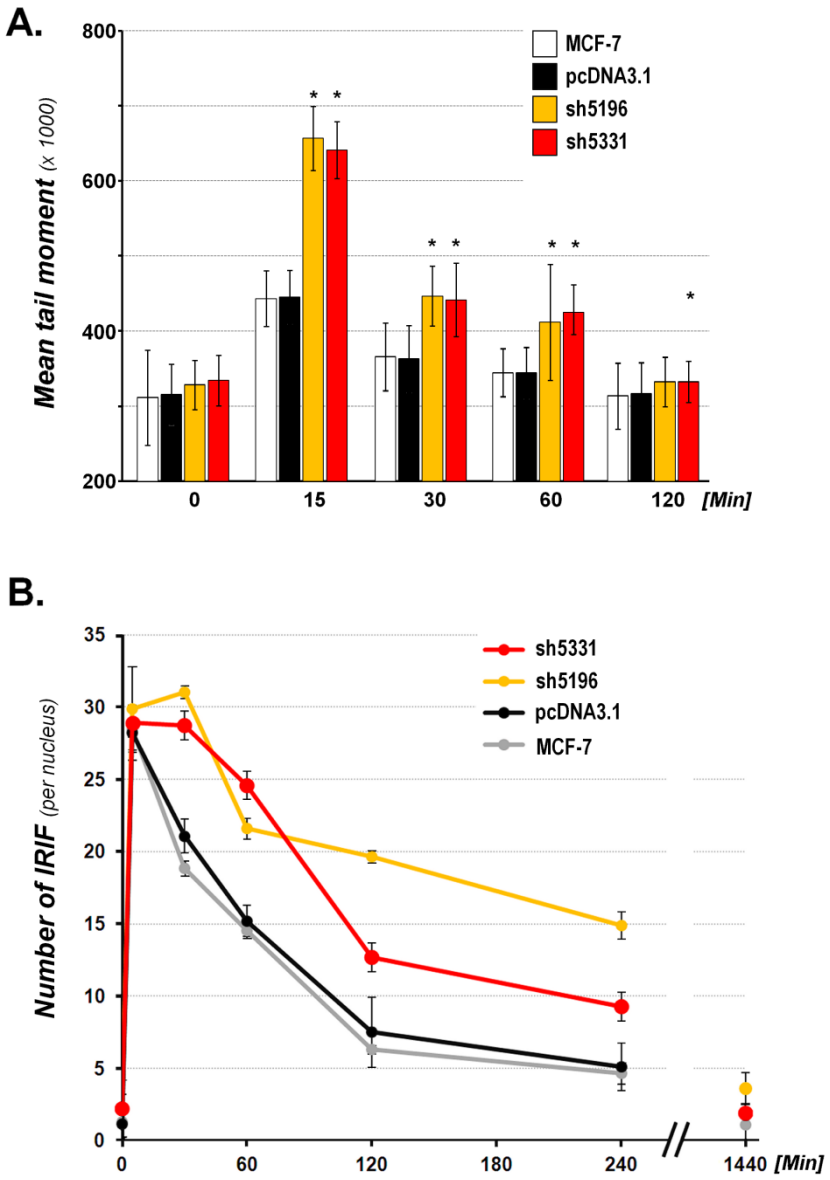

Supplementary figure 1. Comet assays (A) and high-resolution confocal microscopy (B) experiments were performed with two sets of clones expressing shRNAs [sh5196 (targeting BRCA1 exon 17) and sh5331 (targeting BRCA1 exon 18)] to rule out the off-target effect of the designed shRNAs. Data represent means from analyses of two clones (each in triplicate) ± S.D. Both shRNAs show similar effects. Less apparent impairment of sh5331 on IRIF disassembly is probably attributable to the weaker downregulation of wtBRCA1 reached by this shRNA (Supplementary Fig. 2B)

Supplementary figure 2:

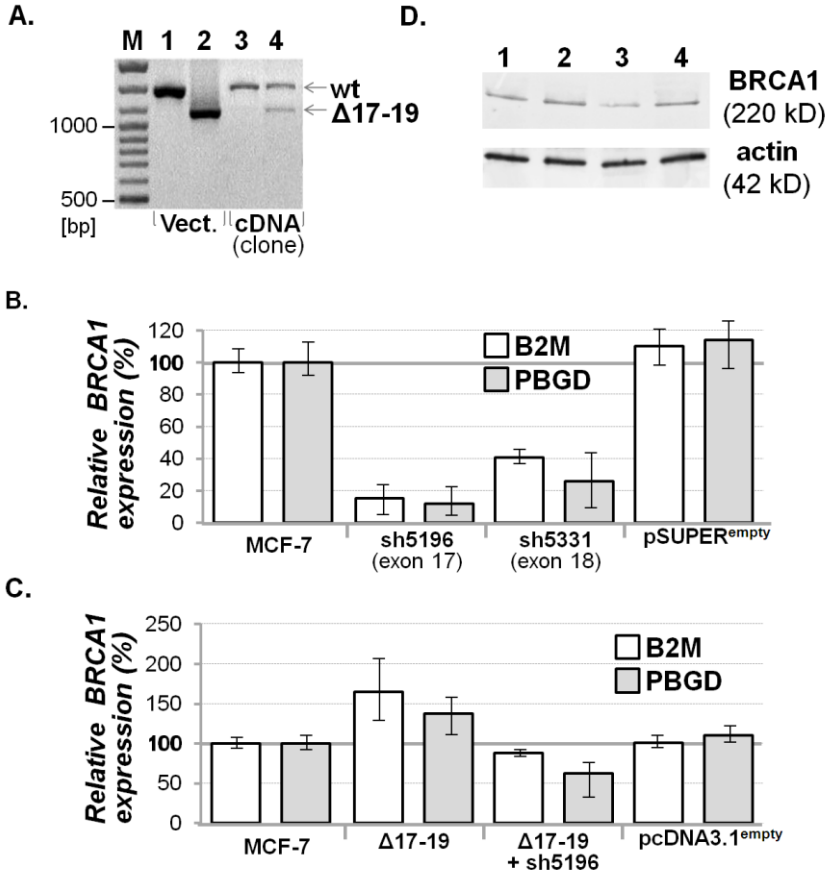

Supplementary figure 2. The pcDNA3.1 BRCA1Δ17-19 expression construct was prepared by a PCR splicing approach. The shRNA sequences were designed according to generally accepted rules for a functional interfering RNA. The indicated shRNAs were targeted to the DNA regions missing in Δ17-19: sh5196 (exon 17) and sh5331 (exon 18), respectively. Stable MCF-7-derived clones were prepared by calcium-phosphate transfection followed by selection with hygromycin B and puromycin.

The functionality of the expression system was proved by RT-PCR (**A**; M – marker; 1 – pcDNA3.1 wtBRCA1 vector; 2 – pcDNA3.1 BRCA1Δ17-19 vector; 3 – cDNA prepared from non-transfected MCF-7 cells; 4 – cDNA prepared from MCF-7 cells transfected by a pcDNA3.1 BRCA1Δ17-19) and qPCR [**B, C** – relative expression of BRCA1 was normalized using β- 2 microglobulin (B2M) and (PBGD) as housekeeping] on the mRNA level and by western blotting (**D**; 1 . MCF-7 non-transfected; 2 – pcDNA3.1.^{empty}; 3 - sh5196, 4 - Δ17-19 + sh5196) on the protein level.

Cellular Signalling xxx (2012) xxx–xxx

Contents lists available at SciVerse ScienceDirect

Cellular Signalling

journal homepage: www.elsevier.com/locate/cellsig

The BRCA1 alternative splicing variant Δ14-15 with an in-frame deletion of part of the regulatory serine-containing domain (SCD) impairs the DNA repair capacity in MCF-7 cells

Jan Sevcik [a,b,*], Martin Falk [c], Petra Kleiblova [a], Filip Lhota [a], Lenka Stefancikova [c], Marketa Janatova [a], Lenka Weiterova [c], Emilie Lukasova [c], Stanislav Kozubek [c], Petr Pohlreich [a], Zdenek Kleibl [a,*]

[a] Institute of Biochemistry and Experimental Oncology, First Faculty of Medicine, Charles University in Prague, U Nemocnice 5, 128 53 Prague 2, Czech Republic
[b] Prague Burn Centre, Charles University, Third Faculty of Medicine and Teaching Hospital Kralovske Vinohrady, Srobarova 50, 10034 Prague 10, Czech Republic
[c] Institute of Biophysics, Academy of Sciences of the Czech Republic, Kralovopolska 135, 61265 Brno, Czech Republic

ARTICLE INFO

Article history:
Received 12 December 2011
Accepted 28 December 2011
Available online xxxx

Keywords:
BRCA1
Alternative splicing
Breast cancer
DNA damage
Homologous recombination
Non-homologous end joining
BRCA1-serine-containing domain (SCD)

ABSTRACT

The *BRCA1* gene codes for a protein involved in the DNA double strand break (DDSB) repair. Alongside the dominant full-length splicing form of BRCA1, numerous endogenously expressed alternative splicing variants of unknown significance have been described in various tissues. Some of them retain the original BRCA1 reading frame but lack several critical BRCA1 structural domains, suggesting an altered function of the resulting protein in the BRCA1-regulated processes.

To characterize the effect of the BRCA1Δ14-15 splicing variant (with an in-frame deletion affecting the regulatory serine-containing domain) on the DDSB repair, we constructed the MCF-7 clones stably expressing the analyzed variant with/without a shRNA-mediated downregulation of the endogenous full-length wild-type BRCA1 expression.

Our results show that the expression of the BRCA1Δ14-15 variant delays the γ-radiation-induced DDSB repair, alters the kinetics of irradiation-induced foci formation/decomposition and reduces the non-homologous end-joining capacity in MCF-7 cells. Therefore, the BRCA1Δ14-15 is not able to functionally replace the full-length wt BRCA1 in the DDSB repair.

Our findings indicate that the endogenously expressed BRCA1 alternative splicing variants may negatively influence genome stability and support the growing evidence of the pathological potential of the sequence variants generated by an altered or misregulated alternative splicing in the process of mammary malignant transformation.

1. Introduction

Breast cancer (BC) is the most common malignancy among women worldwide [1]. Inactivating alterations in the tumor suppressor genes *BRCA1* (MIM# 113705) and *BRCA2* (MIM# 600185) represent major genetic BC-predisposition factors [2]. Mutations in these genes account for 3–5% of all BC cases. The proportion between mutations in *BRCA1* and *BRCA2* varies in different populations. The Czech Republic, together with other Central European countries, belongs to regions with a prevailing incidence of mutations in *BRCA1* [3]. Besides clearly pathogenic *BRCA1* gene alterations, a large group of sequence variants of uncertain clinical significance (VUS) has been identified. At present, a growing interest is focused on VUS that generate unbalanced or aberrant BRCA1 pre-mRNA splicing, while the effects and generation of naturally-occurring alternative BRCA1 pre-mRNA splicing variants remain largely neglected. The most frequent BRCA1 transcription variant (NM_007294) contains 23 exons coding for a protein consisting of 1863 amino acids (220 kDa); however, many other alternative BRCA1 mRNA splicing variants have been identified in various healthy or pathological tissues and cell lines, but their significance, tissue specificity, and biological activities are almost unknown [4].

Abbreviations: ATM, ataxia telangiectasia mutated; ATR, ataxia telangiectasia and Rad3-related; AURKA, Aurora kinase A; BC, breast cancer; BRCA1/2, breast cancer-associated gene 1/2; BRCT, BRCA1 C-terminal domain; B2M, beta-2-microglobulin; Cdk2, cyclin-dependent kinase 2; Chk2, check-point kinase 2; CtIP, CTBP-interacting protein; DDSB, DNA double-strand break; GAPDH, glyceraldehyde-3-phosphate dehydrogenase; HR, homologous recombination; IRIF, ionizing radiation-induced foci; NHEJ, non-homologous end joining; NLS, nuclear localization signal; PARP, poly(ADP-ribose)polymerase; PBMCs, peripheral blood mononuclear cells; PI, post-irradiation; RNAi, RNA interference; RPA, replication protein A; SCD, serine-containing domain; shRNA, short-hairpin RNA; VUS, variants of uncertain significance.

* Corresponding authors at: Institute of Biochemistry and Experimental Oncology, First Faculty of Medicine, Charles University in Prague, U Nemocnice 5, 128 53, Prague 2, Czech Republic. Tel.: +420 22496 5745; fax: +420 22496 5732.
E-mail addresses: jsevc@lf1.cuni.cz (J. Sevcik), zdekleje@lf1.cuni.cz (Z. Kleibl).

0898-6568/$ – see front matter © 2011 Elsevier Inc. All rights reserved.
doi:10.1016/j.cellsig.2011.12.023

BRCA1 is a large multifunctional nuclear protein involved in the maintenance of genomic stability. The BRCA1 protein directly participates in DNA double strand break repair where BRCA1 contributes to the regulation of both homologous recombination (HR) [5] and non-homologous end joining (NHEJ) [6] pathways. Although the exact molecular function of BRCA1 in these processes is not fully understood, it has been suggested that BRCA1 serves as a protein-protein interaction modulator participating in the formation of DNA repair protein super-complexes [7–9], which could be visualized at the DDSB sites as so-called ionizing radiation-induced foci (IRIF) [10]. A proper assembly of IRIF at DDSB sites ensures an efficient DNA repair and a mediation of initial DNA damage signaling [11,12]. Although the exact function and composition of IRIF remain to be fully understood [13], the quantification of their formation and decomposition in time provides a reliable tool for monitoring DDSB repair kinetics [14,15]. Both the protein-protein interaction capacity and the intracellular/intranuclear localization of BRCA1 influence its activities in DDSB repair pathways [16,17]. The majority of interaction events between BRCA1 and its binding partners are realized via the N-terminally localized RING finger domain and a tandem of two BRCA1 C-terminal (BRCT) domains [18]. BRCA1 molecules are rapidly redistributed in intracellular and intranuclear compartments following the DNA damage [16,19]. The intranuclear targeting to the site of action is governed in a phosphorylation-dependent manner to some degree [20]. The BRCA1 protein is the target of various protein kinases (Fig. 1), including ATM, ATR, Chk2, Cdk2, Akt, and AURKA [21]. Following distinct stimuli, these kinases phosphorylate specific BRCA1 serine residues predominantly localized in a BRCA1 serine-containing domain (SCD) [22,23]. The unusually high number of upstream kinases directly regulating the BRCA1 protein affirms its central position in DNA-repair pathways.

During the past decade, we have performed a mutation analysis of the *BRCA1* gene in high-risk breast and/or ovarian cancer families [24–26]. Alongside the identification of mutations, we have also detected numerous alternative splicing variants of BRCA1 in the analyzed RNA samples from peripheral blood mononuclear cells (PBMCs) [27]. Among them, several in-frame alternative splicing variants leading to the loss of the critical BRCA1 functional domains were observed (Fig. 1), including the variant BRCA1Δ14-15 lacking the C-terminal part of the SCD. The aim of this study was to characterize the influence of the in-frame BRCA1 alternative splicing variant BRCA1Δ14-15 on the DNA repair capacity *in vitro*. We constructed the MCF-7-derived clones stably expressing the BRCA1Δ14-15 variant with/without a coincidently shRNA-downregulated expression of the endogenous wild-type (wt) BRCA1, and analyzed the DNA repair capacity in the established clones following γ-radiation-induced DNA damage.

2. Materials and methods

2.1. Construction of expression vectors

A pcDNA3.1 Hygro (Invitrogen) expression construct of the BRCA1 splicing variant BRCA1Δ14-15 was prepared by the PCR-splicing approach [28] using pcDNA3.1-BRCA1wt as a template (the method is described in detail in Supplementary Fig. 1).

A pSUPER.retro.puro (Oligoengine) vector system was used for a shRNA-mediated downregulation of the endogenous wt BRCA1 expression. Particular pSUPER.retro.puro shRNA plasmids were constructed as described previously [29], using generally accepted conventions for an effective interfering RNAs design [30,31]. Interfering RNAs were targeted to exonic sequences missing in the BRCA1Δ14-15 splicing variant (Table 1). To ensure the specificity of the shRNA-mediated wt BRCA1 downregulation effect, two different shRNAs were designed and further used for the experiments.

2.2. Cell culture and transfection

The MCF-7 cells were cultivated in DMEM (Gibco), supplemented with 10% fetal calf serum (Gibco), at 37 °C in a humidified atmosphere of 5% CO_2.

The calcium-phosphate protocol was used for cell transfection as described previously [32]. The cells were first transfected by the expression construct pcDNA3.1-BRCA1Δ14-15 or an empty pcDNA3.1 vector as a control. Single-cell colony clones were obtained by a hygromycin B (200 μg/ml; Invitrogen) selection. Stable clones selected after the first transfection were subsequently transfected by an empty pSUPER vector, by a pSUPER vector containing the relevant anti-wt BRCA1 shRNA, and by a control pSUPER vector containing an irrelevant shRNA targeted to the mouse CCAAT/Enhancer Binding Protein γ (C/EBPγ) [29]. Single cell colony clones were obtained by a puromycin (2 ng/ml; Invitrogen) selection. The integration of the expression construct into the host's chromosomal DNA was checked by PCR using the gDNA template. The PCRs were performed with primers complementary to the corresponding sequence of pcDNA3.1 or pSUPER vectors (5′-GTGTTGGAGGTCGCTGAGTAG-3′ or 5′-TGAACCTCCTCGTTCGACCC-3′, respectively) and sequences of *BRCA1* or interfering RNA (5′-GTGTTGGAGGTCGCTGAGTAG-3′ or 5′-GCATGTCGCTATGTGTTCTG-3′, respectively). For the 20 μl PCR reaction, 2 μg of gDNA, 0.5 mM of each primer and 0.5 U of TaKaRa La Taq polymerase were used. The PCR was performed in 30 cycles (98 °C for 10s; 56 °C for 10s; 68 °C for 7.5 min) with initial denaturation at 94 °C for 1 min and terminal elongation at 72 °C for 10 min. The efficiency of the BRCA1 expression modulation was scored by qPCR and western blotting.

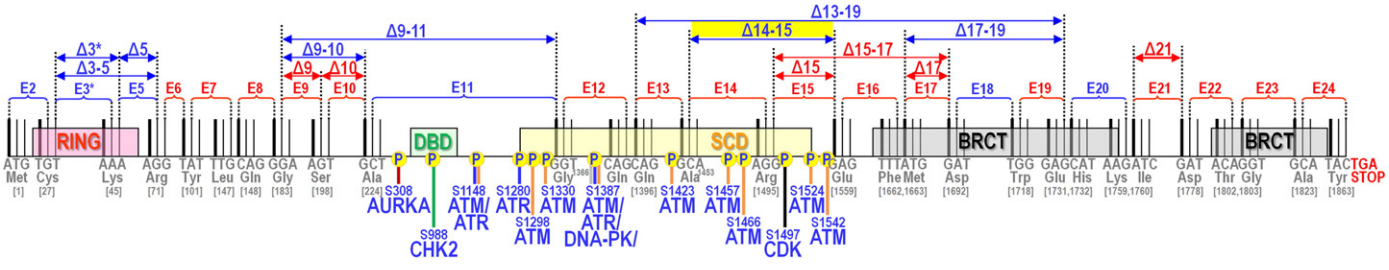

Fig. 1. The schematic organization of BRCA1 functional domains and important phosphorylation sites with appropriate protein kinases, within the BRCA1 coding sequence (RING finger domain — RING; DNA binding domain — DBD; serine containing domain — SCD; BRCA1 C terminal domain — BRCT). BRCA1 splicing variants detected during the screening program of high-risk Czech families are represented as arrows depicting a particular missing region. Splicing events retaining the original reading frame are depicted as blue arrows, splicing events affecting the original reading frame are depicted as red arrows. (* skipping of exon 3 produces termination codon TGA) The analyzed BRCA1 splicing variant BRCA1Δ14-15 (highlighted in yellow) retains the original reading frame and has affected the BRCA1 structurally conservative protein motif. The BRCA1Δ14-15 variant lacks exons E14 and E15, resulting in the expression of protein shortened for 106 amino acids in the C-terminal portion of SCD. (For interpretation of the color references in this figure, the reader is referred to the online version.)

Please cite this article as: J. Sevcik, et al., Cell. Signal. (2012), doi:10.1016/j.cellsig.2011.12.023

Table 1
A list of used oligonucleotides for the engineering of pSUPER-based anti-BRCA1 shRNA vectors. The shRNA sequence complementary to the target are highlighted in bold.

shRNA designation (localization in BRCA1 mRNA)	Sequences of the pSUPER vector insert
shRNA 4834 (exon 15)	5′–GATCCCCCACGATTTGACGGAAACATTTCAAG AGA**ATGTTTCCGTCAAATCGTG**TTTTTGGAAC–3′
shRNA 4836 (exon 15)	5′–GATCCCCCGATTTGACGGAAACATCTTTCAAG AGA**AGATGTTTCCGTCAAATCG**TTTTTGGAAC–3′

2.3. RNA isolation and quantitative real-time PCR (qPCR)

Total RNA was isolated by the RNeasy isolation kit (Qiagen). Reverse transcription was performed using SuperScript III Reverse Transcriptase (Invitrogen) according to the manufacturer's instructions. The qPCR analysis of BRCA1 expression was performed using the Light Cycler Fast Start DNA Master SYBR Green I kit (Roche) and its relative quantification as regards the expression of glyceraldehyde-3-phosphate dehydrogenase (GAPDH) and β-2 microglobulin (B2M) was performed using the REST-2005 software as described previously [29].

2.4. Western blotting

Cells were rinsed once with ice-cold PBS and lysed directly on a culture dish by a RIPA buffer containing a protease inhibitor cocktail (Roche) for 15 min on ice. Protein concentration was measured using the BCA Protein Assay (Bio-Rad). For each sample, 30 μg of total protein per well was loaded onto 6% polyacrylamide gel, separated and transferred onto a nitrocellulose membrane (Amersham). The membranes were blocked in 5% non-fat milk, incubated with primary antibody anti-BRCA1 (mAbMS110; Calbiochem mouse); anti β-actin (A300-491A; Bethyl rabbit polyclonal), then with horse-radish peroxidase-conjugated secondary antibody [Anti-mouse IgG-HRP (Sigma; A-0168) and Anti-rabbit IgG-HRP (Sigma; A-545)] and visualized using the Super Signal West Pico chemiluminiscent substrate (Pierce). After developing, UN-SCAN-IT gel ver. 6.1 (SilkScientific) was used for a relative quantification of BRCA1 bands using β-actin as a protein loading control.

2.5. Comet assay

Cells were grown in triplicates under the standard cultivation conditions and then treated with a single dose of 1.5 Gy of γ-radiation using ^{60}Co (0.6 Gy/min). Non-irradiated cells (marked here as 0 min) and irradiated cells collected in the particular times (15, 30, 60, and 120 min) post-irradiation (PI) were rinsed once with ice-cold PBS, diluted to the final concentration of 1×10^5 cells/ml in ice-cold PBS and proceeded according to the manufacturer's instructions using a neutral CometAssay (Trevigen). The slides were analyzed using BX41 fluorescent microscope (Olympus) and NIS-Elements software (Laboratory Imaging). The CometScore ver. 1.5 software (AutoComet) was used for the analysis.

2.6. Fluorescence immunohistochemistry and confocal microscopy of IRIF

Non-irradiated cells (0 min) and cells in particular times (5, 30, 60, 120, 240, and 1440 min) PI with 1.5 Gy of γ-radiation using ^{60}Co (1.0 Gy/min) were spatially fixed (4% paraformaldehyde, 10 min, RT), permeabilized (0.2% Triton X100/PBS for 14 min, RT) and immunoassayed as described in [14,15]. The primary mouse anti-phospho-H2AX (serine 139; Upstate Biotechnology) and rabbit anti-53BP1 (Cell Signaling) antibodies were used simultaneously to detect the IRIF. The bound antibodies were visualized with the secondary FITC-conjugated donkey anti-mouse and Cy3-conjugated donkey anti-rabbit antibodies (both Jackson Laboratory); nuclear chromatin was counterstained with 1 μM TOPRO-3 (Molecular Probes).

An automated DM RXA confocal fluorescence microscope (Leica), equipped with a CSU10a Nipkow disc (Yokogawa) and an oil immersion Plan Fluotar objective (100×/NA1.3), was used for image acquisition. Forty serial optical sections were captured at 0.2 μm intervals along the z-axis to reconstruct 3D-images of the nuclei, at a constant temperature of 26 °C. The maximal images represent computational superimpositions of individual confocal slices.

2.7. A mitomycin C sensitivity test

Cells were seeded onto the E plate 96 (Roche) in a density of 3×10^4 cells per well in triplicates and grown for 24 hours under standard cultivation conditions. Subsequently, mitomycin C (Sigma-Aldrich) was added to the final concentration of 2; 4; 6 and 8 μg/ml and cells were grown for an additional 5 days with continual measuring of the cell index (CI; derived as a relative change in measured electrical impedance to represent cell status, for details see: https://www.roche-applied-science.com/sis/xcelligence/index.jsp?) using an xCELLigence RTCA analyzer (Roche).

2.8. In vitro NHEJ assay

The NHEJ capacity was assayed by measuring the recovery of lucipherase activity in the cells co-transfected by the pGL-control (Promega) vector linearized by either HindIII (overall NHEJ) or EcoRI (precise NHEJ), and by the circular pRL-tk vector as an internal control [33]. The cells were grown in triplicate under the standard cultivation conditions and co-transfected by 0.5 μg of a pure linearized pGL-control vector together with 0.05 μg of a pRL-tk vector using Lipofectamine 2000 (Invitrogen). The lucipherase activity was scored by the Dual lucipherase reporter assay (Promega) 48 hours post transfection according to the manufacturer's instructions. Cells treated with 2 mmol benzamide (Roche) as a potent PARP-1 inhibitor for 48 hours prior to the transfection were used as a control of assay functionality (Supplementary Fig. 2).

2.9. Statistical analyses

A statistical analysis was done using the non-parametric ANOVA (Wilcoxon two sample test). $P<0.05$ was considered statistically significant. All data are presented as mean ± standard deviation.

3. Results

3.1. Establishment of a model system for a functional analysis of BRCA1 splicing variants

A stable human breast adenocarcinoma-derived cell line MCF-7 was used as an *in vitro* model system. In the established clones the studied BRCA1 splicing variant BRCA1Δ14-15 was co-expressed together with the endogenous wt BRCA1 (Fig. 2A). To assess solely the effects of the studied BRCA1 splicing variant, we prepared MCF-7 clones combining an overexpression of the analyzed BRCA1 splicing constructs together with a shRNA-mediated downregulation of endogenous wt BRCA1. To rule out the unspecific effect of transfection procedure and the construct's integration into the host genome, three stable MCF-7 clones of each engineered expression construct were further examined. The results represent highly similar phenotype observed in all three analyzed clones of the particular expression construct. As controls for analyses, we used stable MCF-7 clones expressing the BRCA1-targeted shRNAs only, irrelevant shRNAs (targeted to mouse CEBPγ), empty pSUPER and pcDNA3.1 vectors, and non-transfected MCF-7 cells.

Please cite this article as: J. Sevcik, et al., Cell. Signal. (2012), doi:10.1016/j.cellsig.2011.12.023

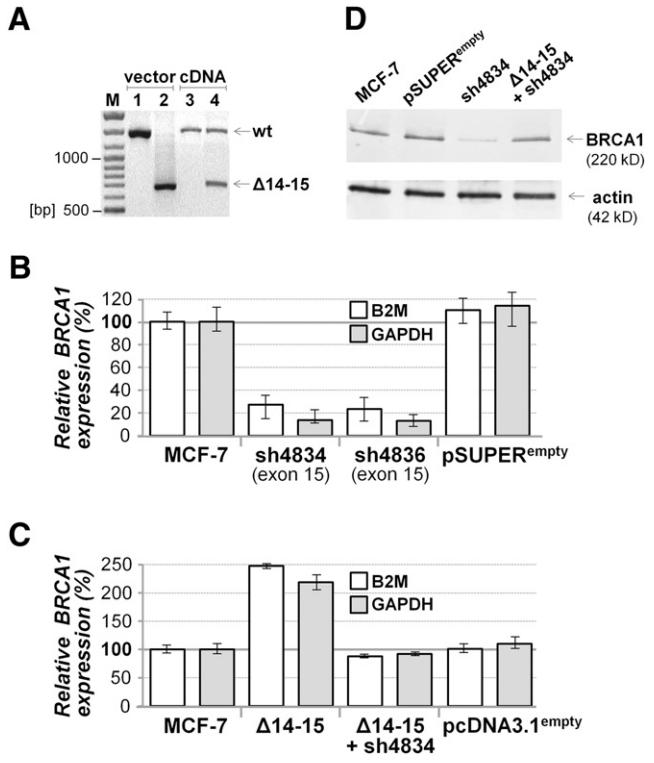

Fig. 2. Modulation of a BRCA1 expression in the model MCF-7 clones. Using a two-step transfection and selection of single cell colonies, a set of stable MCF-7 clones with a modified expression of BRCA1 was prepared. (A) The upregulated expression of the BRCA1Δ14-15 alternative splicing variant alongside the endogenous wt BRCA1 was proved by RT-PCR on the RNA level [lanes: pcDNA3.1 vector carrying full-length BRCA1 insert (1) and the BRCA1Δ14-15 variant (2), cDNA prepared from non-transfected MCF-7 cells (3) and stable clone expressing the BRCA1Δ14-15 variant (4)]. (B,C) A long-term modulation of the BRCA1 expression was checked by qPCR using cDNA templates prepared from mRNAs isolated from particular clones in two different passages. The expression of BRCA1 on the mRNA level was quantified by qPCR using GAPDH and B2M as house keepings. (B) The endogenous wt BRCA1 was specifically downregulated by shRNAs (sh4834 and sh4836) up to <10% relative to control cells [pSUPER vector]. (C) Upregulation of the BRCA1Δ14-15 variant expressed in stable MCF-7 clones without (Δ14-15) and with (Δ14-15 + sh4834) coincidentally downregulated wt BRCA1 in comparison to non-transfected MCF-7 (= 100%) and MCF-7 transfected by an empty pcDNA3.1 vector. (D) A modulation of the BRCA1 expression in untransfected MCF-7 cells and stable MCF-7 clones on the protein level scored by WB.

The results of RT-PCR (Fig. 2A), qPCR (Fig. 2B, C) and WB analyses (Fig. 2D) in the stable clones in two consecutive passages proved the functionality and stability of the model system. The small difference in molecular weight between full-length BRCA1 and BRCA1Δ14-15 (207.7 kDa vs.195.9 kDa[1]) did not enable the distinguishing of endogenous wt BRCA1 and the expressed splicing variant on the protein level.

3.2. The BRCA1 splicing variant BRCA1Δ14-15 slows down the DDSB repair

With regard to the importance of BRCA1 in the DNA damage repair pathways, we first examined whether the expression of the BRCA1Δ14-15 splicing variant influences the DNA repair capacity. The time course of the DNA damage level was directly scored by a comet assay after a single dose of 1.5 Gy of γ-radiation (Fig. 3). Due to the time-consuming sample preparation, the first analyzed time was 15 min PI followed by 30, 60, and 120 min PI, respectively. The peak DNA damage was detected at the time of 15 min PI with significant differences in the rate of DNA damage between controls and clones with modified BRCA1 expression (Fig. 3). The differences in

[1] Theoretical molecular weight calculated using Sequence Manipulation Suite (http://www.bioinformatics.org/sms2/).

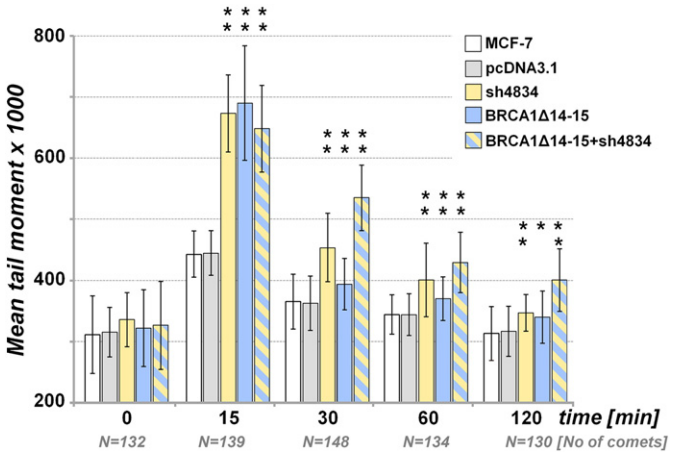

Fig. 3. DNA damage rate of MCF-7 clones with a modified expression of BRCA1 and relevant controls. A DDSB repair time course is illustrated by a comet mean tail moment in the particular time after a single dose of 1.5 Gy γ-radiation. Non-irradiated samples are represented as time 0. Data are mean ± S.D. $^{*}p<0.05$, $^{**}p<0.001$ (Wilcoxon test).

the degree of DNA damage between controls and clones with modified BRCA1 expression decreased with time; however, the DNA damage rate was still significantly higher in all other clones with modified BRCA1 expression until the time of 120 min PI. These results show that either a downregulation of wt BRCA1 or an overexpression of the BRCA1Δ14-15 splicing variant slow down the DDSB repair in the initial phase following DNA damage. Moreover, the presence of the BRCA1Δ14-15 alternative splicing variant interferes with the activity of wt BRCA1 in a dominant-negative fashion.

3.3. Overexpression of BRCA1Δ14-15 increases the rate of endogenous DNA damage and influences the kinetics of IRIF formation

Considering the proposed role of BRCA1 as a protein interaction modulator in the orchestration of the DNA damage response, we next analyzed whether the BRCA1Δ14-15 splicing variant influences the kinetics of IRIF formation. For this purpose, we scored the co-localization of γH2AX with 53BP1 (Fig. 4) using the fluorescence confocal microscopy [13,34]. Immediately after the DNA damage, histone H2AX is phosphorylated at serine 139 in about 2-Mbp region around the DDSBs, forming so-called γH2AX foci that are generally accepted as a specific and most sensitive marker of this type of DNA lesion. The 53BP1 protein was used for IRIF visualization because of its unequivocal co-localization with γH2AX foci within a few minutes PI [14], irrespective of a further DDSB repair pathway. Moreover, in comparison with BRCA1, the 53BP1 foci are more precisely distinguishable from the background. Therefore, a co-localization of γH2AX and 53BP1 foci was used in this work to quantify unrepaired DDSBs. Compared to the neutral comet assay, this DNA damage assessment is more sensitive and allows us to determine the level of endogenous DNA damage. The number of γH2AX/53BP1 foci was determined in different times after the same single dose of 1.5 Gy of γ-radiation as in the previous experiment and in non-irradiated clones. As all analyzed clones originated in an identical MCF-7 line, it could be assumed that γ-irradiation induced an identical initial number of DDSBs.

The rate of endogenous DDSB damage was significantly higher in clones with a downregulated expression of wt BRCA1 (sh4834) and in clones expressing BRCA1Δ14-15 (Δ14-15 and Δ14-15 + sh4834) (Fig. 5A, B). This suggests that a low expression of full-length BRCA1 as well as an overexpression of BRCA1Δ14-15 reduce the overall DDSB repair capacity and could contribute to genome instability in the MCF-7 clones.

In γ-irradiated control cells, the maximum number of γH2AX/53BP1 foci was detected at the time of 5 min PI. A continuous

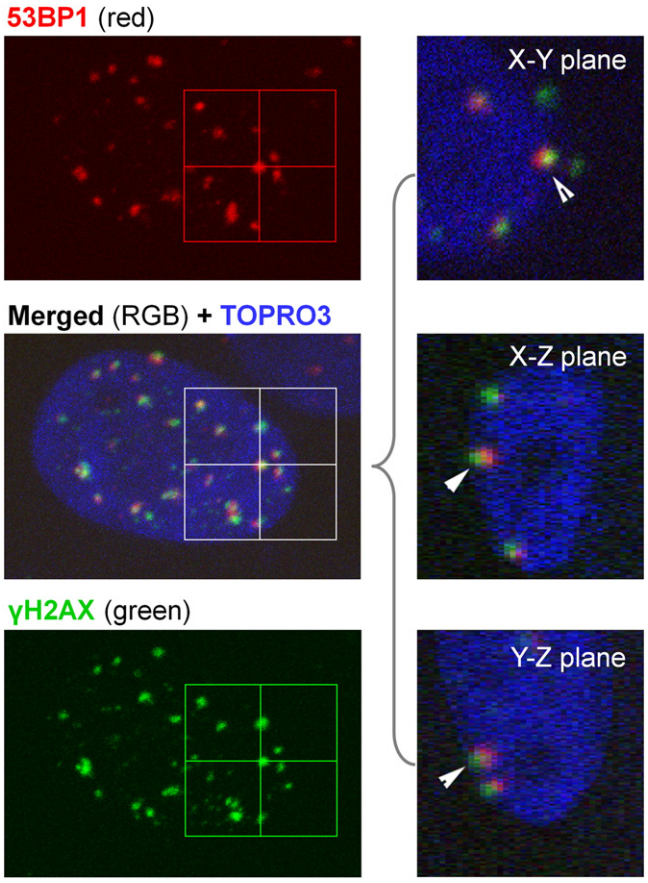

Fig. 4. A preservation of the 3D structure of nuclei analyzed after the spatial fixation of cells with 4% paraformaldehyde and an analysis by a high-resolution fluorescence confocal microscopy. Intranuclear localization of γH2AX (green) and 53BP1 (red) signals and their mutual colocalization in all three planes is demonstrated in maximal images (composed from 40 confocal slices taken with a z-step 0.2 μm; left panels) as well as individual confocal slices in all three planes (x–y, x–z and y–z; right panels). The positions of the planes are indicated in the maximal images by a white cross; the γH2AX/53BP1 focus located in the intersection of x–y, x–z and y–z planes is marked by an arrow at confocal slices (right panels). Nuclear chromatin was counterstained by TOPRO-3 (artificially blue). (For interpretation of the color references in this figure, the reader is referred to the online version.)

dissociation of γH2AX/53BP1 foci was apparent since that time as the number of IRIF progressively decreased over the whole analyzed time period (Fig. 5).

In γ-irradiated clones with a downregulated expression of wt BRCA1 (sh4834), and with an overexpression of BRCA1Δ14-15 (BRCA1Δ14-15 and BRCA1Δ14-15 + sh4834), the number of IRIF further increased at times beyond 5 min PI, reaching the peak values at 30 min PI (Fig. 5A).

In clones expressing the BRCA1Δ14-15 splicing variant, the number of IRIF further decreased in a rather similar manner compared to controls since the time of 30 min PI; however, the initial delay was sustained throughout the overall period of observation.

In clones with a downregulated expression of endogenous wt BRCA1 (sh4834), a disassembly of IRIF was decelerated since the time of 60 min PI and was the slowest throughout the whole analyzed time period compared to controls and clones expressing the BRCA1Δ14-15 splicing variant (BRCA1Δ14-15 and BRCA1Δ14-15 + sh4834).

These results show that an overexpression of the BRCA1Δ14-15 splicing variant increases the formation of IRIF in MCF-7 cells during the first 30 min PI and decreases the speed of their disappearance during the initial rapid phase of DDSB repair. This indicates that this splicing variant is not able to functionally substitute wt BRCA1 in the process of a precise formation of γH2AX/53BP1-containing DNA repair protein complexes in MCF-7 cells.

3.4. The BRCA1Δ14-15 splicing variant does not change the sensitivity of cells to mitomycin C

Mitomycin C causes DNA interstrand covalent cross-links which can be repaired exclusively by HR. Thus the sensitivity of cells to mitomycin C treatment indirectly reflects the HR capacity. With respect to the previous results, we further examined the response of MCF-7 clones with a modified expression of BRCA1 to the different concentrations of mitomycin C on the proliferation level.

Clones with a downregulated expression of wt BRCA1 were the most sensitive to mitomycin C as the lowest used concentration of mitomycin C (2 μg/ml) was lethal for them (Fig. 6). The sensitivities of clones expressing the BRCA1Δ14-15 splicing variants alone or together with wt BRCA1 were comparable with the controls (Fig. 6).

These results are consistent with previously published findings that a downregulation of wt BRCA1 impairs the HR pathway and causes hypersensitivity to the DNA cross-linking agents. On the other hand, the BRCA1Δ14-15 splicing variant did not influence the sensitivity of the cells to mitomycin C. This suggests that unlike the depletion of wt BRCA1, an overexpression of the BRCA1Δ14-15 alternative splicing variant does not substantially impair the HR.

3.5. The activity of NHEJ is reduced in clones with a modified expression of BRCA1

The negative effect of BRCA1 inactivation on the capacity and fidelity of the DDSB repair has been described in both HR and NHEJ pathways. We further examined the activity of NHEJ using an indirect *in vitro* assay based on the measurement of recovery of the lucipherase activity from the pGL-control expression vector. To distinguish between overall and precise NHEJ, the pGL-control vector was linearized before transfection to the model clones by either HindIII or EcoRI recognizing unique restriction sites located within the lucipherase promoter (HindIII) or the lucipherase coding sequence (EcoRI), respectively. A relatively error-prone joining of the free DNA ends represented by the overall NHEJ activity was sufficient for lucipherase expression in the experiment with the HindIII-linearized vector. Contrary to that, only a precise joining of EcoRI-linearized vector ensures the expression of fully functional lucipherase in the assay examining the precise NHEJ activity.

In all examined clones with a downregulated expression of wt BRCA1 and an expression of the BRCA1Δ14-15 splicing variant, the activities of both overall and precise NHEJ were significantly lower than in controls (Fig. 7).

These results indicate that an expression of the BRCA1Δ14-15 alternative splicing variant has a dominant-negative effect on the activity and fidelity of NHEJ comparable to the shRNA-mediated downregulation of wt BRCA1.

4. Discussion

The HR pathway is a precise mechanism of DDSB repair; however, it plays only a limited role in eukaryotic cells compared to a relatively error-prone NHEJ. Moreover, HR can only be effectively used during the S- and G2-phases of a cell cycle, when sister chromatids are available for a homologous exchange. The decision-making element governing the selection of either form of these two DNA repair mechanisms has not been fully understood yet. It has been proposed that these two pathways at least to some degree compete with each other and that the strand resection is one of the main factors governing the usage of these two possible repair mechanisms [35]. While classic NHEJ does not require additional processing of free DNA ends in the break site, long RPA-coated ssDNA regions are necessary for the HR [36].

Various experiments with silencing the expression of particular members of HR and NHEJ pathways have shown that NHEJ takes place

Please cite this article as: J. Sevcik, et al., Cell. Signal. (2012), doi:10.1016/j.cellsig.2011.12.023

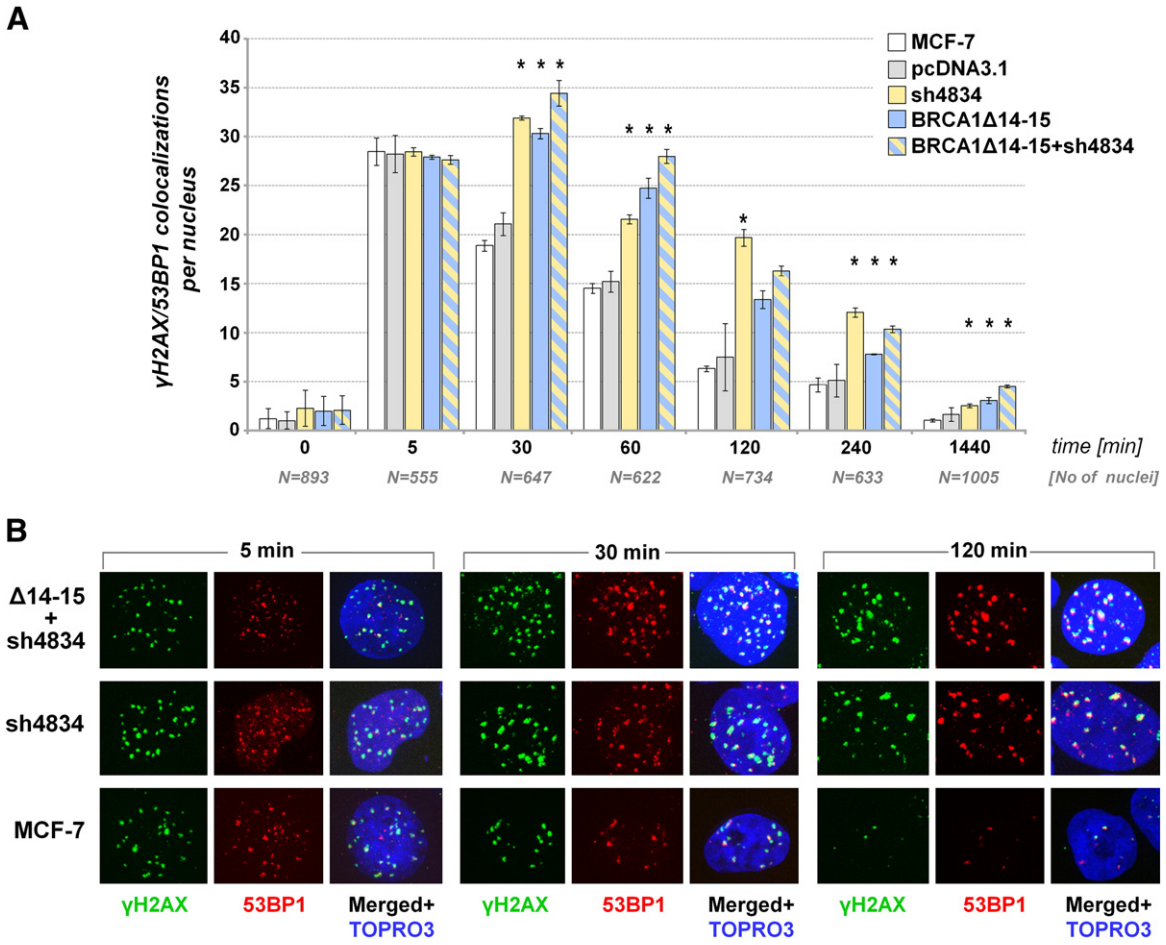

Fig. 5. The kinetics of IRIF formation/dissociation (A) were determined by counting the number of the colocalizations of γH2AX (green) and 53BP1 (red) proteins characterizing an early response to DSB in spatiotemporal manner in times of 5, 30, 60, 120, 240, and 1440 min PI using high-resolution fluorescent confocal microscopy (B). Maximal images composed from 40 confocal optical slices taken with a z-step of 0.2 m are shown. Total nuclear chromatin was counterstained by TOPRO-3 (artificially blue).Data are mean ± S.D., N = total number of analyzed nuclei in group. *p<0.05 (Wilcoxon test). (For interpretation of the color references in this figure, the reader is referred to the online version.)

faster than HR and is the prevailing DNA repair mechanism within a period of the first four hours after a genotoxic DNA insult [37]. On the other hand, HR is used for a DDSB repair in specific chromatin regions, and the IRIF of a homology-directed DNA repair typically occur with a delay and persist for a longer time period [38]. The γH2AX and 53BP1 proteins are involved in both HR and NHEJ pathways. The time course of their co-localization after the γ-radiation-induced DNA damage in our model system suggests that a downregulation of endogenous wt BRCA1 or an overexpression of BRCA1Δ14-15 negatively influences the initial rapid phase of DDSB repair.

It has been documented that the depletion of the BRCA1 protein has a detrimental effect on the DNA repair [39]. The BRCA1 protein was initially identified as a mediator of the apical signal in HR. Later it was proposed that BRCA1 may also participate in the NHEJ pathway [33]. We may therefore assume that inactivating mutations in the *BRCA1* gene affect both DNA repair pathways. However, specific analyses of the BRCA1's role in the DNA repair pathways brought several seemingly contradictory results. While Jasin et al. showed that *BRCA1*-deficient cells have a heavily impaired HR, an instable genome, and increased sensitivity to mitomycin C compared with wt BRCA1-expressing cells [40], Dever et al. documented that a mutation in the BRCA1 BRCT domain leads to a hyperrecombination [41]. Further, Jasin et al. observed that the BRCA1$^{-/-}$ cell line has reduced HR, while NHEJ is slightly elevated at the same time as a compensatory mechanism for the decreased DNA repair capacity [39]. On the other hand, Wang et al. proved that a *BRCA1* knock-down compromises the NHEJ accuracy [33].

The results of our study showed that a relatively subtle change in the BRCA1Δ14-15 mRNA structure leads to the production of a BRCA1 protein isoform which decreases the initial rapidity of a DDSB repair in a dominant negative-manner in MCF-7 cells. In accordance with the position of the BRCA1 protein in the HR pathway, the MCF-7 clones with a downregulated expression of endogenous wt BRCA1 were hypersensitive to the DNA cross-linking agent, mitomycin C. Surprisingly, the cells expressing the BRCA1Δ14-15 alternative splicing variant displayed no difference in sensitivity to mitomycin C compared with the non-transfected MCF-7 controls. This suggests that the presence of the BRCA1Δ14-15 protein isoform does not corrupt the activity of HR. Contrary to that, the results of a direct *in vitro* NHEJ assay proved that the activity of NHEJ was lower both in clones with depleted wt BRCA1 and in clones expressing the BRCA1Δ14-15 alternative splicing variant. Taking together, wt BRCA1 downregulation impairs both the HR and NHEJ pathways, while the BRCA1Δ14-15 alternative splicing variant only disturbs the NHEJ. This indicates that the SCD plays a role in a regulation of the BRCA1 activity in the NHEJ.

The majority of protein-protein interactions in the processes of a DNA repair take place in a phosphorylation- or ubiquitin-dependent manner. The exons 14 and 15 deleted in the analyzed BRCA1Δ14-15 variant contain six serine residues known to be the targets of ATM kinase activated upon DNA damage (Fig. 1). The phosphorylation status of BRCA1 appeared to be an important factor influencing its intracellular localization and trafficking [20]. Following a DNA damage, specific BRCA1 serine residues are phosphorylated by upstream kinases,

Please cite this article as: J. Sevcik, et al., Cell. Signal. (2012), doi:10.1016/j.cellsig.2011.12.023

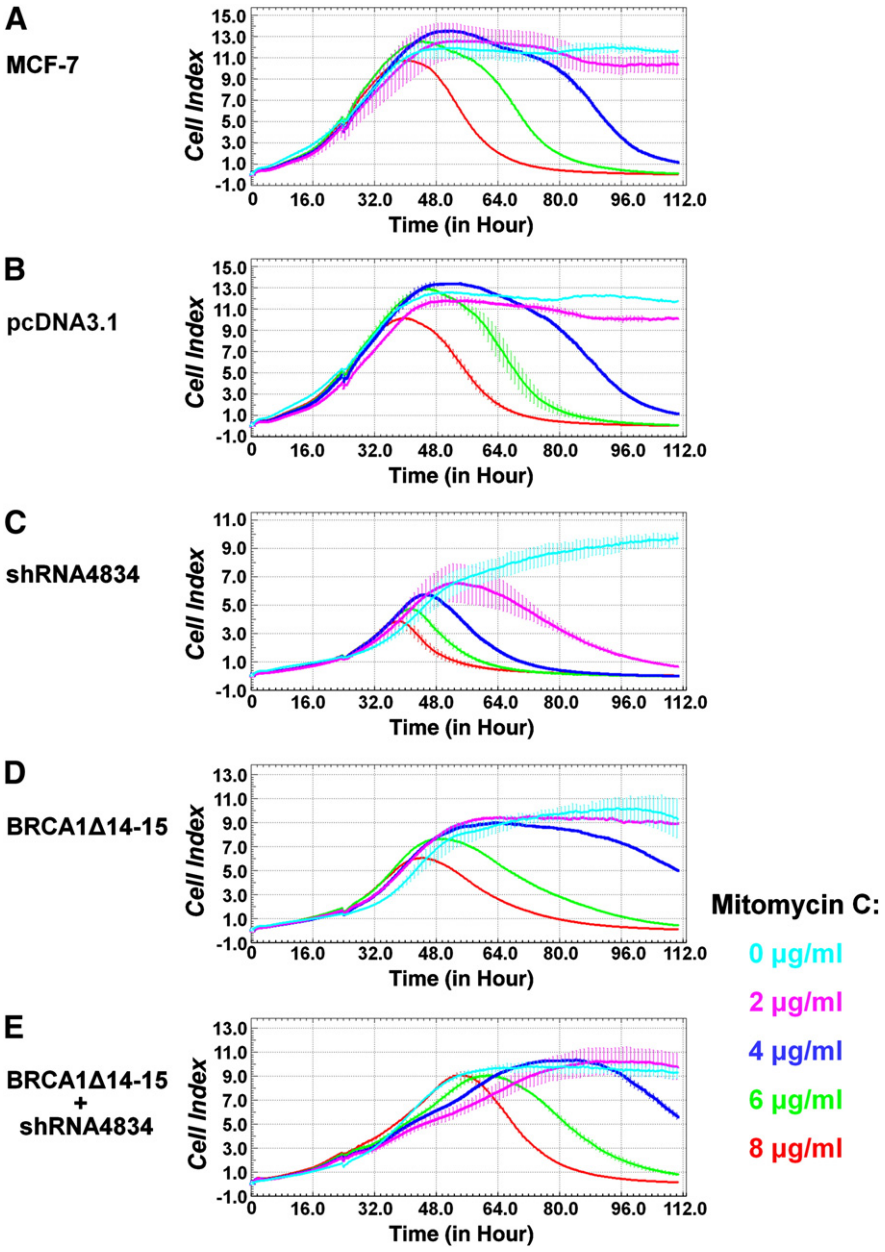

Fig. 6. The sensitivity of MCF-7 clones with a modified expression of BRCA1 to mitomycin C. Cells were cultivated for 5 days in a medium with different concentrations of mitomycin C (0, 2, 4, 6 and 8 μg/ml, respectively) with a continual measurement of proliferation activity using an xCELLigence RTCA analyzer. Clones with a shRNA-mediated downregulation displayed a hyper-sensitivity to mitomycin C, while the sensitivity of cells expressing the BRCA1Δ14-15 alternative splicing variants was comparable to non-transfected MCF-7 and control cells transfected with an empty expression vector. Data are mean ± S.D. (For interpretation of the color figure, the reader is referred to the online version.)

which could regulate the BRCA1 binding specificity [17] and can thus influence the formation of specific BRCA1-containing complexes. The BRCA1-CtIP (BRCA1-C) complex together with additional nucleases and helicases promote during the S- and G2-phases a strand resection generating long ssDNA regions indispensable for the HR [42]. Contrary to that, the assembly of the BRCA1-RAP80 complex that is facilitated by ubiquitin-modified chromatin near the break site prevents the strand resection and hence HR by blocking of CtIP activity [43]. Thus,

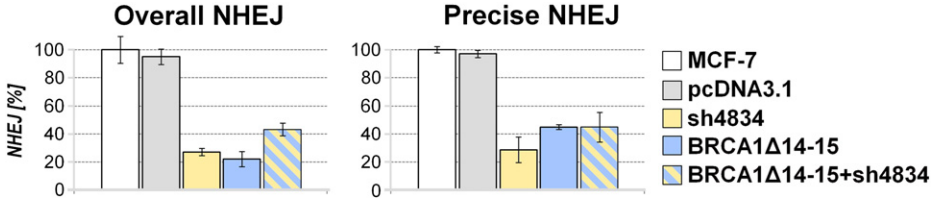

Fig. 7. NHEJ activity in clones with a modified expression of BRCA1. The particular clones and relevant controls were co-transfected by a linearized pGL-control vector and a circular pRL-tk vector. Forty-eight hours after transfection, the rescued activity of glow worm (pGL) lucipherase was measured in triplicates using the dual lucipherase assay kit. The pGL lucipherase activity was normalized to the activity of control pRL-tk lucipherase. The lucipherase activity rescued from the EcoRI linearized pGL-control vector reflects the precise NHEJ, while that from the HindIII linearized pGL-control vector reflects the overall NHEJ. The experiment was repeated three times. Data are mean ± S.D.

Please cite this article as: J. Sevcik, et al., Cell. Signal. (2012), doi:10.1016/j.cellsig.2011.12.023

the phosphorylation-directed formation of the BRCA1-containing complexes critically involves BRCA1 function in the DNA repairs. In concordance with that, and as indicated by our results, the BRCA1Δ14-15 variant (lacking the substantial part of SCD) results in formation of protein isoform with impaired sensitivity to the DNA damage up-stream signaling resulting in impaired DDSB repair. We assume, that an overexpression of the BRCA1Δ14-15 variant (originally described as an alternative pre-mRNA splicing variant in PBMCs obtained from the BRCA1 mutation-negative BC patient) in MCF-7 cells results in the expression of BRCA1 isoform corrupting the NHEJ pathway and in turn leading to preferential use of HR DDSB repair.

The alternative splicing is a mechanism able to produce protein isoforms with markedly different biological properties from a single primary pre-mRNA transcript and thus it is responsible for great genetic diversity [44,45]. We hypothesize that the overall biological activity of a certain gene's product is determined by the actual pool of its particular protein isoforms generated by the alternative (or aberrant) pre-mRNA splicing. BRCA1 has several common alternative splicing variants occurring frequently together with the main full-length product [4]. Their mRNA concentrations are at least partially dependent on the cell cycle phase suggesting their natural regulatory function within the global BRCA1 expression profile [46]. The relevance of the BRCA1 splicing variants on the cellular processes has been demonstrated in studies of the BRCA1 variant lacking exon 11, which showed that BRCA1Δ11 failed to deliver the Rad51 recombinase to the site of DDSBs, resulting in severe impairement of HR and genome instability [47,39]. It seems that the occurrence of the BRCA1 alternative splicing variants is frequent rather than rare, though the exact tissue specificity and quantity of particular alternative splicing variants is not known yet. This fact together with the result of our current work implies the importance of a further functional analysis of the BRCA1 alternative splicing variants.

5. Conclusions

In this study we characterized the effect of the BRCA1Δ14-15 alternative splicing variant lacking a part of BRCA1 SCD on the capacity of a γ-radiation-induced DDSB repair in MCF-7 cells. An overexpression of BRCA1Δ14-15 decelerated the DNA repair after DNA damage, slowed down the initial formation of IRIF, and prolonged their persistence similarly to an shRNA-mediated downregulation of wt BRCA1. Contrary to a wt BRCA1 downregulation affecting both HR and NHEJ repair processes, the BRCA1Δ14-15 alternative splicing variant expression showed a broader impact on NHEJ, indicating that the presence of SCD and its phosphorylation status could alter the subtle balance between a BRCA1-mediated activation of HR and NHEJ in MCF-7 cells, respectively. In a broader context, we assume that the differential expression of BRCA1 alternative splicing variants, regulated by currently uncharacterized mechanisms, may represent a system influencing the selection of particular molecular pathways of the DDSB repair. Although these conclusions are consistently supported by our results obtained on model MCF-7 cells, their generalization should be considered with caution, and further experiments are required.

Supplementary materials related to this article can be found online at doi:10.1016/j.cellsig.2011.12.023.

Acknowledgment

We thank all members of our lab, Dr. Libor Macurek for a valuable discussion and Jan Flemr for proofreading. This study was supported by the grants of the Internal Grant Agency of the Ministry of Health No. NT12280; the Charles University Grant Agency No. 428711, the Grant SVV-2011-262513, the Grant of the Czech Science Foundation No. P302/10/1022, and the Grant Agency of the Academy of Sciences of the Czech Republic No. IAA500040802.

References

[1] The International Agency for Research on Cancer (IARC), http://globocan.iarc.fr/factsheets/populations/factsheet.asp?uno=900(accessed October 15, 2011).
[2] W.D. Foulkes, S.A. Narod, Clinical and Investigative Medicine 18 (1995) 473–483.
[3] M. Mateju, J. Stribrna, M. Zikan, Z. Kleibl, M. Janatova, S. Kormunda, J. Novotny, P. Soucek, L. Petruzelka, P. Pohlreich, Neoplasma 57 (2010) 280–285.
[4] T.I. Orban, E. Olah, Molecular Pathology 56 (2003) 191–197.
[5] Y. Hu, R. Scully, B. Sobhian, A. Xie, E. Shestakova, D.M. Livingston, Genes & Development 25 (2011) 685–700.
[6] L. Wei, L. Lan, Z. Hong, A. Yasui, C. Ishioka, N. Chiba, Molecular and Cellular Biology 28 (2008) 7380–7393.
[7] J. Yan, X.P. Yang, Y.S. Kim, A.M. Jetten, Cancer Research 68 (2008) 4269–4276.
[8] R.A. Greenberg, B. Sobhian, S. Pathania, S.B. Cantor, Y. Nakatani, D.M. Livingston, Genes & Development 20 (2006) 34–46.
[9] B. Sobhian, G. Shao, D.R. Lilli, A.C. Culhane, L.A. Moreau, B. Xia, D.M. Livingston, R.A. Greenberg, Science 316 (2007) 1198–1202.
[10] T.T. Paull, E.P. Rogakou, V. Yamazaki, C.U. Kirchgessner, M. Gellert, W.M. Bonner, Current Biology 10 (2000) 886–895.
[11] B. Xu, S. Kim, M.B. Kastan, Molecular and Cellular Biology 21 (2001) 3445–3450.
[12] R.A. Greenberg, Chromosoma 117 (2008) 305–317.
[13] M. Falk, E. Lukasova, S. Kozubek, Mutation Research 704 (2010) 88–100.
[14] M. Falk, E. Lukasova, B. Gabrielova, V. Ondrej, S. Kozubek, Biochimica et Biophysica Acta 1773 (2007) 1534–1545.
[15] M. Falk, E. Lukasova, S. Kozubek, Biochimica et Biophysica Acta 1783 (2008) 2398–2414.
[16] R. Scully, J. Chen, R.L. Ochs, K. Keegan, M. Hoekstra, J. Feunteun, D.M. Livingston, Cell 90 (1997) 425–435.
[17] J.N. Glover, R.S. Williams, M.S. Lee, Trends in Biochemical Sciences 29 (2004) 579–585.
[18] Y. Nomine, M.V. Botuyan, Z. Bajzer, W.G. Owen, A.J. Caride, E. Wasielewski, G. Mer, Biochemistry 47 (2008) 9866–9879.
[19] K.M. Brodie, B.R. Henderson, Cellular Signalling 22 (2010) 291–302.
[20] S. Okada, T. Ouchi, Journal of Biological Chemistry 278 (2003) 2015–2020.
[21] T. Ouchi, Cancer Biology & Therapy 5 (2006) 470–475.
[22] B. Xu, A.H. O'Donnell, S.T. Kim, M.B. Kastan, Cancer Research 62 (2002) 4588–4591.
[23] D. Cortez, Y. Wang, J. Qin, S.J. Elledge, Science 286 (1999) 1162–1166.
[24] P. Pohlreich, J. Stribrna, Z. Kleibl, M. Zikan, R. Kalbacova, L. Petruzelka, B. Konopasek, Medical Principles and Practice 12 (2003) 23–29.
[25] P. Pohlreich, M. Zikan, J. Stribrna, Z. Kleibl, M. Janatova, J. Kotlas, J. Zidovska, J. Novotny, L. Petruzelka, C. Szabo, B. Matous, Breast Cancer Research 7 (2005) R728–R736.
[26] I. Ticha, Z. Kleibl, J. Stribrna, J. Kotlas, M. Zimovjanova, M. Mateju, M. Zikan, P. Pohlreich, Breast Cancer Research and Treatment 124 (2010) 337–347.
[27] P. Pohlreich, J. Stribrna, M. Zikan, J. Novotny, 19th Meeting of European Association for Cancer Research Program/Procceedings, Budapest June 1–4, 2006, 2006, p. 260.
[28] A. Gratchev, http://www.methods.info/Tips/mutagenesis/PCR_splicing.html(accessed June 5, 2011).
[29] E. Vondruskova, R. Malik, J. Sevcik, P. Kleiblova, Z. Kleibl, Neoplasma 55 (2008) 130–137.
[30] M. Amarzguioui, H. Prydz, Biochemical and Biophysical Research Communications 316 (2004) 1050–1058.
[31] K. Ui-Tei, Y. Naito, F. Takahashi, T. Haraguchi, H. Ohki-Hamazaki, A. Juni, R. Ueda, K. Saigo, Nucleic Acids Research 32 (2004) 936–948.
[32] E. Flemington, http://www.flemingtonlab.com/Protocols/CalciumPhosphateTransf.pdf(accessed July 10, 2010).
[33] H.C. Wang, W.C. Chou, S.Y. Shieh, C.Y. Shen, Cancer Research 66 (2006) 1391–1400.
[34] I.Y. Belyaev, Mutation Research 704 (2010) 132–141.
[35] E.M. Kass, M. Jasin, FEBS Letters 584 (2010) 3703–3708.
[36] P. Huertas, Nature Structural and Molecular Biology 17 (2010) 11–16.
[37] P.A. Jeggo, V. Geuting, M. Lobrich, Radiotherapy and Oncology 101 (2011) 7–12.
[38] A.A. Goodarzi, P. Jeggo, M. Lobrich, DNA Repair (Amst) 9 (2010) 1273–1282.
[39] M.E. Moynahan, J.W. Chiu, B.H. Koller, M. Jasin, Molecular Cell 4 (1999) 511–518.
[40] M.E. Moynahan, T.Y. Cui, M. Jasin, Cancer Research 61 (2001) 4842–4850.
[41] S.M. Dever, S.E. Golding, E. Rosenberg, B.R. Adams, M.O. Idowu, J.M. Quillin, N. Valerie, B. Xu, L.F. Povirk, K. Valerie, Aging (Albany, NY) 3 (2011) 515–532.
[42] J. Lukas, C. Lukas, J. Bartek, Nature Cell Biology 13 (2011) 1161–1169.
[43] K.A. Coleman, R.A. Greenberg, Journal of Biological Chemistry 286 (2011) 13669–13680.
[44] C.Y. Li, J.Y. Chu, J.K. Yu, X.Q. Huang, X.J. Liu, L. Shi, Y.C. Che, J.Y. Xie, Cell Research 14 (2004) 473–479.
[45] E. Scholzova, R. Malik, J. Sevcik, Z. Kleibl, Cancer Letters 246 (2007) 12–23.
[46] T.I. Orban, E. Olah, Biochemical and Biophysical Research Communications 280 (2001) 32–38.
[47] L.J. Huber, T.W. Yang, C.J. Sarkisian, S.R. Master, C.X. Deng, L.A. Chodosh, Molecular and Cellular Biology 21 (2001) 4005–4015.
[48] J.E. Quinn, R.D. Kennedy, P.B. Mullan, P.M. Gilmore, M. Carty, P.G. Johnston, D.P. Harkin, Cancer Research 63 (2003) 6221–6228.

Eur. Phys. J. D (2017) 71: 241
DOI: 10.1140/epjd/e2017-80073-2

THE EUROPEAN PHYSICAL JOURNAL D

Regular Article

γH2AX/53BP1 foci as a potential pre-treatment marker of HNSCC tumors radiosensitivity – preliminary methodological study and discussion*

Martin Falk[1,a], Zuzana Horakova[2], Marketa Svobodova[3,4], Michal Masarik[3,4], Olga Kopecna[1], Jaromir Gumulec[3,4], Martina Raudenska[3,4], Daniel Depes[1], Alena Bacikova[1], Iva Falkova[1], and Hana Binkova[2]

[1] Department of Cell Biology and Radiobiology, Institute of Biophysics of CAS, 61265 Brno, Czech Republic
[2] Department of Otorhinolaryngology and Head and Neck Surgery, St. Anne's University Hospital and Faculty of Medicine, Masaryk University, 65691 Brno, Czech Republic
[3] Department of Pathological Physiology, Faculty of Medicine, Masaryk University, 62500 Brno, Czech Republic
[4] Department of Physiology, Faculty of Medicine, Masaryk University, 62500 Brno, Czech Republic

Received 31 January 2017 / Received in final form 10 July 2017
Published online 19 September 2017 –

Abstract. In order to improve patients' post-treatment quality of life, a shift from surgery to non-surgical (chemo)radio-treatment is recognized in head and neck oncology. However, about half of HNSCC tumors are resistant to irradiation and an efficient marker of individual tumor radiosensitivity is still missing. We analyzed whether various parameters of DNA double strand break (DSB) repair determined in vitro can predict, prior to clinical treatment initiation, the radiosensitivity of tumors. We compared formation and decrease of γH2AX/53BP1 foci in 48 h after irradiating tumor cell primocultures with 2 Gy of γ-rays. To better understand complex tumor behavior, three different cell type primocultures – $CD90^-$, $CD90^+$, and a mixed culture of these cells – were isolated from 1 clinically radioresistant, 2 radiosensitive, and 4 undetermined HPV–HNSCC tumors and followed separately. While DSB repair was delayed and the number of persisting DSBs increased in the radiosensitive tumors, the results for the radioresistant tumor were similar to cultured normal human skin fibroblasts. Hence, DSB repair kinetics/efficiency may correlate with clinical response to radiotherapy for a subset of HNSCC tumors but the size (and therefore practical relevance) of this subset remains to be determined. The same is true for contribution of different cell type primocultures to tumor radioresistance.

1 Introduction

Head and neck squamous cell cancer (HNSCC; shortened here as HN) are usually aggressive neoplasms with high recurrence rate and poor prognosis. Due to their proximity to vital structures, efficient radical surgery results in patients' mutilation with impaired quality of life. Non-surgical (chemo-radiotherapy) approaches are therefore preferred but bear the risk of radioresistance resulting in the tumor persistence or even progression after treatment, which cannot always be salvaged by surgery. Indeed, about 52% of HN tumors resist to irradiation and results of the salvage surgery are in principle incomparable to those of primary surgery, with protracted healing and risk of unrecognizable tumor growth in the irradiated terrain [1,2]. Oncologists thus permanently face to a serious dilemma of the optimal first-line therapy for a particular patient (reviewed in [3]).

Unfortunately, the radioresistance markers allowing tumor radiosensitivity estimation prior to therapy are still unknown. Their discovery is largely complicated by genetic and functional heterogeneity of tumors that seems to be particularly high in HN. Unlike some other cancer types, HN tumors can be considered neither radiosensitive nor radioresistant, since these tumors occupy both extremes of the radiosensitivity spectrum (reviewed e.g. in [4]). Though some genes have been repeatedly found to be mutated in HN, there are not common 'founder' mutations associated with these malignancies ([5] and citations therein) and their radiosensitivity.

The radiosensitivity/radioresistance markers might be logically associated with complex cell response to DNA damage. Most relevant in this sense is probably repair of DNA double strand breaks (DSBs) since DSBs represent the most serious lesions being extensively introduced into the DNA molecule by ionizing radiation and some kinds of chemotherapy [6]. However, also genetic or epigenetic defects affecting other processes [7–16] such as resistance to apoptosis [7], defects in cell cycle regulation [8], ability

* Contribution to the Topical Issue "Dynamics of Systems at the Nanoscale", edited by Andrey Solov'yov and Andrei Korol.

[a] e-mail: falk@ibp.cz

to divide with damaged genome [9] or competency to re-enter cell cycling from senescence [10] (reviewed in [11,12]) can significantly contribute to final cell radioresistance. Eventually, those mechanisms might even play a major role.

Hence, it would not be surprising to discover that the basis of radioresistance differs among individual tumors. This expectation then almost precludes usage of model systems, such as permanent cell lines or transgenic mice, to study HN tumor biology and behavior. Moreover, even single tumors are highly heterogeneous and dynamic systems. Still undetermined source of radioresistance heterogeneity thus also comes from characteristics and proportion of different cell types, their specific clones, and mutual interactions among all these cells [17–19].

In this study, by using immunofluorescence confocal microscopy for sensitively quantifying γH2AX/53BP1 foci formation and decrease in post-irradiation (PI) time, we attempt to find out how individual HN tumors vary in DNA double-strand break (DSB) repair kinetics and efficiency, whether these characteristics correlate with tumor cells' radiosensitivity, and whether in vitro monitoring of DSB repair could be predictive of tumors' clinical response to radiotherapy. To address these questions and in a need to deeper explore biological determinants of HN tumors' radioresistance, we prepared from patients' tumors three different cell primocultures – the primoculture of epithelial tumor cells characterized by absence of CD90 surface antigen ($CD90^-$ cells), the primoculture of remaining cells that were CD90 positive ($CD90^+$ cells), and a mixed culture of both these cell types. CD90 cluster of definition is expressed in several cell types, including a fraction of fibroblasts; $CD90^+$ cells used in our experiments thus contain a significant fraction of tumor-associated fibroblasts (TAFs) that are, in addition to $CD90^-$ tumor cells, expected to influence tumors' biology and characteristics [17–19]. We describe here our first results comparing DSB repair between tumors for each specific cell primoculture and between the primocultures for each particular tumor.

2 Methods

2.1 HN tumor biopsy extraction

HN tumor biopsy extraction was performed in the Department of Otorhinolaryngology and Head and Neck Surgery, St. Anne's University Hospital and Faculty of Medicine, Masaryk University, Brno, Czech Republic. Patients were completely examined clinically and the tumor staging was determined using radiodiagnostic approaches (CT, MRI, PET). Only newly diagnosed patients with none previous therapeutic history and with HN squamous-cell carcinoma (HNSCC) confirmed histopathologically were included in the study, after signing the informed consent. Biopsy cell samples were obtained by endoscopy under local or total anesthesia.

2.2 Tumor cells primocultures

Tumor cells primocultures were prepared in the Department of Pathological Physiology, Faculty of Medicine, Masaryk University, Brno, Czech Republic. The tumor tissue material obtained at surgery (see Sect. 2.1) was placed into culture medium (RPMI 1640, Biochrom, USA) with an addition of 1% antibiotic-antimycotic solution (Santa Cruz Biotechnology, Texas), 10 $\mu g\,ml^{-1}$ gentamicin sulphate (Santa Cruz Biotechnology, Texas) and 10 $\mu g\,ml^{-1}$ ciprofloxacin (Santa Cruz Biotechnology, Texas) to prevent bacteria, fungi and yeast contamination. Within sterile environment and after rinsing the sample by 70% EtOH (Sigma-Aldrich, Germany), the most viable tissue was selected while any necrotic tissue was discarded. Leavings of EtOH were removed by PBS (Invitrogen, USA) washing. Tissue was mechanically dissociated into small pieces and Trypsin (PAA Laboratories GmbH, Austria for proteolysis were used) was used according to Protocol 1 (below) to separate the cells.

Protocol 1. The small tissue fragments were added and stirred into sterile PBS (Invitrogen, USA) and centrifuged at 4 °C, 2700 rpm for 7 min. The cell pellet was re-suspended into 0.25% trypsin in RPMI 1640 medium and left overnight at 4 °C. Then medium was removed and tissue was incubated at 37 °C for 30 min. The cell pellet was re-suspended into medium with an addition of antibiotic-antimycotic solution, gentamicin sulphate, ciprofloxacin and 10% FBS. Primary cell lines were cultivated at 37 °C and 5% CO_2 in humidified atmosphere up to 50% confluence. As soon as the cells were seen attaching to the flask surface, medium was changed. Tumor cells were no longer affected by the use of antibiotic-antimycotic solution, gentamicin sulphate, or ciprofloxacin that were added to the early culture. At this time, cells were grown only in Pen/Strep antibiotic solution (PAA Laboratories GmbH, Austria) in the complete medium (penicillin 100 U ml^{-1} and streptomycin 0.1 mg ml^{-1}; RPMI-1640 medium with 10% FBS (Biochrom, USA)).

For separation of subpopulation derived from primary cell line magnetic particles-MiniMACS^{TM} Starting Kit (CD90 MicroBeads-human, MS Columns; Miltenyi Biotec, Germany) was used. Cells that adhered to the flask were grown in complete medium (RPMI-1640 medium with 10% FBS, penicillin 100 U ml^{-1} and streptomycin 0.1 mg ml^{-1}) until they reach 70% confluency; they were then passaged. For each tumor, we prepared separated primocultures for $CD90^-$, $CD90^+$, and their mixed co-culture serving to study possible interactions between the cell types. The whole procedure is described in Svobodova et al. (2017) (Oncotarget; DOI:10.18632/oncotarget.19914).

2.3 Irradiation with γ-rays

The cells were irradiated at the Institute of Biophysics, Czech Academy of Sciences, Brno, Czech Republic. In our first experiments, presented here, we irradiated the cell lines with a single dose of 2 Gy ($D = 1$ Gy/min) of γ-rays

Table 1. Tumors characteristics.

Patient	Sex	Age [y]	Tumor	Locality	Stage	Grade	Therapy	RT response	Current status, other characteristics
T1	m	60	SCC	OP	IV T4 N2b	G3	RT + BT	S	UT BT: cetuximab
T2	m	70	SCC	HL	T3 N1	G3	S + RT	S	REM (6 month) total laryngectomy + adjuv. RT
T3	m	66	SCC	L	II T2N0	G2	RT	R	UT tripl CA (mammary + renal + HN)
T4	m	77	SCC	OP	IV T4b N3	G2	None	?	†
T5	m	70	SCC	LHP	IV T3N1	G3	S + RT	?	REM (4 month) total laryngectomy + adjuv. RT
T6	f	90	SCC	OHP	IV T4N2	G3	None	?	†
T7	m							?	

Legend: m: male, f: female, OP: oropharynx, L: Larynx, HL: hypolarynx, LHP: laryngohypopharynx, OHP: orohypopharynx, RT: radiotherapy, S: surgery, BT: biological treatment, R: radioresistant (none/poor response), S: radiosensitive (good response), †: died, UT: under treatment, REM: remission.

(^{60}Co, Chisostat, Chirana, CR). Cells were irradiated in RPMI 1640 medium (37 °C, normal atmosphere) [20].

2.4 Evaluation of DNA double strand break (DSB) induction and repair in tumor cell primocultures

The evaluation of DSB induction and repair was performed at the Institute of Biophysics, Czech Academy of Sciences, Brno, Czech Republic. DSBs were quantified in different periods of time post-irradiation (5 min–48 h PI) by means of γH2AX and 53BP1 foci immunodetection combined with high-resolution 3D confocal microscopy. For more detailed description of visualization of γH2AX and 53BP1 in spatially (3D) fixed cells see [21].

2.5 3D high-resolution confocal microscopy

The microscopy of samples was performed at the Institute of Biophysics, Czech Academy of Sciences, Brno, Czech Republic. Leica DM RXA microscope [22] (equipped with DMSTC motorized stage, Piezzo z-movement, MicroMax CCD camera, CSU-10 confocal unit and 488, 562, and 714 nm laser diodes with AOTF) was used for acquiring detailed cell images (100× oil immersion Plan Fluotar lens, NA 1.3). The equipment was controlled by the Acquarium software developed in collaboration with Masaryk University [23]. Modern Leica SP5 microscopy system, equipped with white laser for multicolor microscopy, allowed "high-throughput" cell imaging [21]. Images were reconstructed and analysed in Acquarium (FI MU, Brno), LAS AF (Leica), Adobe Photoshop CS5 (Adobe), and ImageJ software. DSB repair foci were scored also manually by two experienced examiners. Though absolute numbers of foci were lower for software analyses, the trends for manual and software scoring were the same. SigmaPlot Scientific Software (SPSS, Systat Software, Inc.) was used for statistical evaluation of data.

3 Results

3.1 Patients/tumors characteristics

HNSCC tumor biopsies were taken from 5 patients' primary tumors after confirming SCC by conventional histopathology and signing the informed consent. Patients were completely examined clinically and basic tumor characteristics were determined (Tab. 1). Radiodiagnostic approaches (CT, MRI, PET) were employed to determine tumors' staging. Only patients with newly diagnosed HPV–HNSCC with none therapeutic history and recommended for non surgical treatment were included into the study; the purpose for this decision was to minimize unwanted biological/experimental variability and allow later comparison of results obtained in vitro to histopathological characteristics of tumors and their response to radiotherapy in vivo. From 7 tumors currently included into the study, 1 tumor (T3) was radioresistant, 2 tumors (T1 and T2) were radiosensitive, and the status of remaining tumors was unsure (patients died without treatment, etc.).

Regarding oncologic prognosis and quality of life, our collected therapeutic results from last 15 years show that the optimal treatment strategy for an individual patient can be still determined only with difficulty and low fidelity if it is only based on clinical data and/or tumors' response to chemotherapy [1,2]. Identification of marker(s) allowing radiosensitivity estimation prior to the therapy initiation therefore still remains of utmost importance.

3.2 Methodological strategy and results

3.2.1 Preparation and characterization of CD90$^-$ and CD90$^+$ cell primocultures

In order to deeper comprehend the phenomenon of tumor radiosensitivity, we decided to compare DSB repair

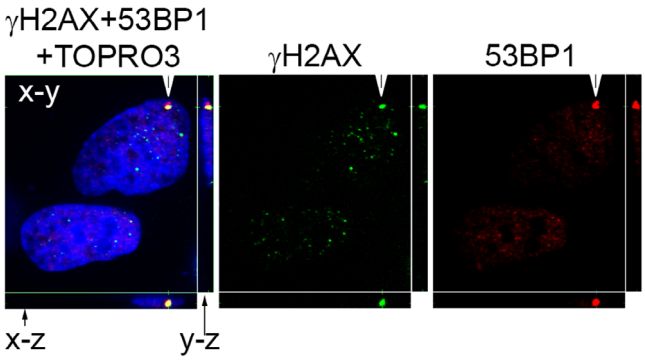

Fig. 1. Sensitive detection of DSBs by means of immunofluorescence confocal microscopy. Two DSB markers – γH2AX (green) and 53BP1 (red) – are detected simultaneously in spatially (3D) fixed cells. A single DSB detected in one of displayed non-irradiated human normal skin fibroblasts (top one) is indicated by colocalizing green and red signals (white arrow). This approach currently brings the maximum sensitivity and precision in DSB quantification. A single confocal slice (0.3 μm thick) through the cell nuclei in the plane of detected DSB is shown. Chromatin counterstaining by TOPRO3 (artificially blue); magnification 100×.

for two important cell types inhabiting the tumors – CD90$^-$ and CD90$^+$ cells – and for their mixed culture (CD90$^-$ + CD90$^+$). For this purpose, we developed and optimized [24] a protocol for immunoseparation of CD90$^-$ and CD90$^+$ from tumors according to their CD90 cluster of definition (surface CD antigens [25]). Using the procedure described in Section 2, the two cell types were successfully separated and their primocultures prepared and basically characterized in terms of gene expression. Interestingly, expression of some important genes, such as EGFR, MMP2 and MT2 in CD90$^+$ cells isolated from tumors resembled more tumor CD90$^-$ cells than normal CD90$^+$ fibroblasts (not shown).

3.2.2 Introduction of immunofluorescence confocal microscopy for DSB repair monitoring in CD90$^-$ and CD90$^+$ cell primocultures

Immunofluorescence confocal microscopy of γH2AX foci currently represents the most sensitive method to quantify DSBs [26]. This is demonstrated also by present results (Fig. 1) successfully revealing even occasional DSBs occurring in non-irradiated nonmalignant human skin fibroblasts (NHDF cells). Therefore, in this work, we tested applicability of γH2AX foci immunodetection as a tool to predict tumors' radiosensitivity/radioresistance in vitro and to study complex response of tumor cells to irradiation. To further maximize sensitivity and fidelity of the method, we decided to analyze two independent DSB markers – γH2AX and 53BP1 foci – in spatially (3D) fixed cells simultaneously (Fig. 1) [20,27]. Successful application of γH2AX/53BP1 foci immunofluorescence confocal microscopy to monitor DSB repair kinetics and efficiency in tumor cell primocultures is illustrated in Figure 2.

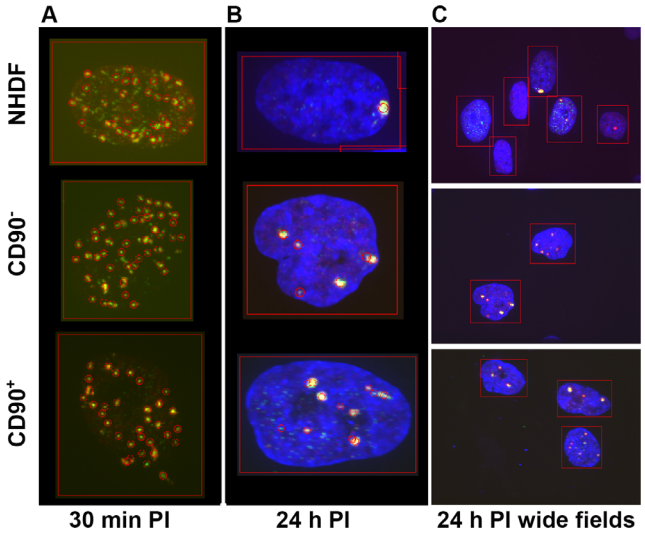

Fig. 2. γH2AX (green) and 53BP1 (red) repair foci co-detected by immunofluorescence confocal microscopy in irradiated (2 Gy of γ-rays; D = 1 Gy/min) normal human skin fibroblasts (NHDF) and CD90$^-$ and CD90$^+$ cell primocultures obtained from the radioresistant tumor T3 (see Tab. 1 for the tumor characteristics). The cells were spatially (3D) fixed and immunoassayed at 30 min (A) and 24 h (B, C) post-irradiation, respectively. Panel C shows wide-field images with more cells. Maximum images composed of 30 confocal slices 0.3 μm wide are shown. In B and C, chromatin is counterstained with TOPRO3 (artificially blue) while this staining is absent in A in order to make γH2AX (green) + 53BP1 (red) foci better visible. Foci detected by automatic software analyses are indicated by red circles (A, B, C). Magnification 100×.

3.3 DSB repair in CD90$^-$ and CD90$^+$ cell primocultures

Figure 2 shows illustrative microscopy images for normal human skin fibroblasts (NHDF) and CD90$^-$ and CD90$^+$ cells isolated from the radioresistant tumor T3 (see Tab. 1 for characteristics); mutually colocalizing γH2AX and 53BP1 foci were immunodetected at 30 min and 24 h after irradiation of the cells with 2 Gy (1 Gy/min) of γ-rays. While formation of γH2AX/53BP1 foci at 30 min PI (maximum DSB induction) was similar for all three cell types, an increased presence of foci at 24 h PI (persistence of unrepaired DSBs), relative to normal NHDF, could be seen in CD90$^-$ and CD90$^+$ radioresistant tumor primocultures. Figure 3 then provides detailed quantitative comparisons on DSB repair kinetics and efficiency for normal cultured fibroblasts and the mixed CD90$^-$ + CD90$^+$ primocultures isolated from radiosensitive (T1 and T2) and radioresistant (T3) tumors, respectively. Data for tumors T4–T7 are not displayed for their unknown clinical radiosensitivity and to allow better readability of the graphs. For all tumors, irrespective of their radiosensitivity status, the maximum DSB induction appeared at 30 min PI; however, the kinetics of γH2AX/53BP1 foci disappearance varied with samples: While DSB repair kinetics for the radioresistant tumor T3 closely resembled that of normal cultured fibroblasts, a significant delay of this process

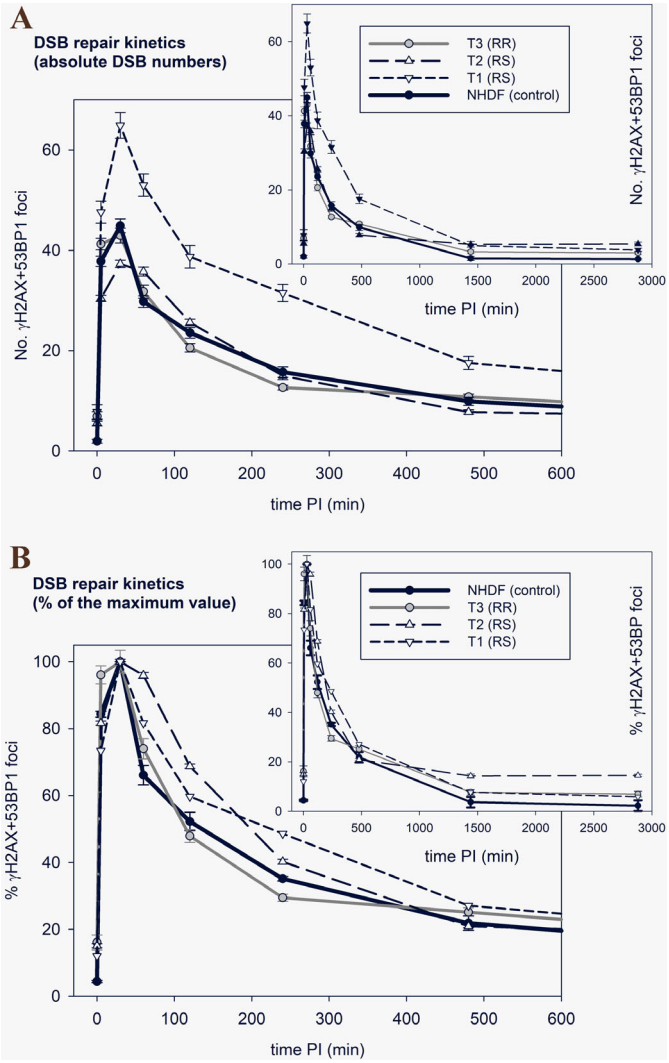

Fig. 3. γH2AX/53BP1 foci formation, disappearance and persistence (DSB repair kinetics and efficiency) compared for normal human skin fibroblasts (NHDF) and CD90$^+$ tumor cells primocultures derived from clinically radiosensitive (T1 and T2) and radioresistant (T3) tumors, respectively. See Table 1 for the tumors' characteristics. A: The mean numbers of γH2AX/53BP1 foci per nucleus during the time post-irradiation with 2 Gy of γ-rays. The values obtained by immunofluorescence confocal microscopy in spatially (3D) fixed cells are shown. Error bars represent standard deviations (T1, T2 and T3) or standard errors of means (NHDF) calculated for two independent experiments. B: As A but the percentage of γH2AX/53BP1 foci per nucleus is shown (100% correspond to the maximum value detected for all samples at 30 min PI).

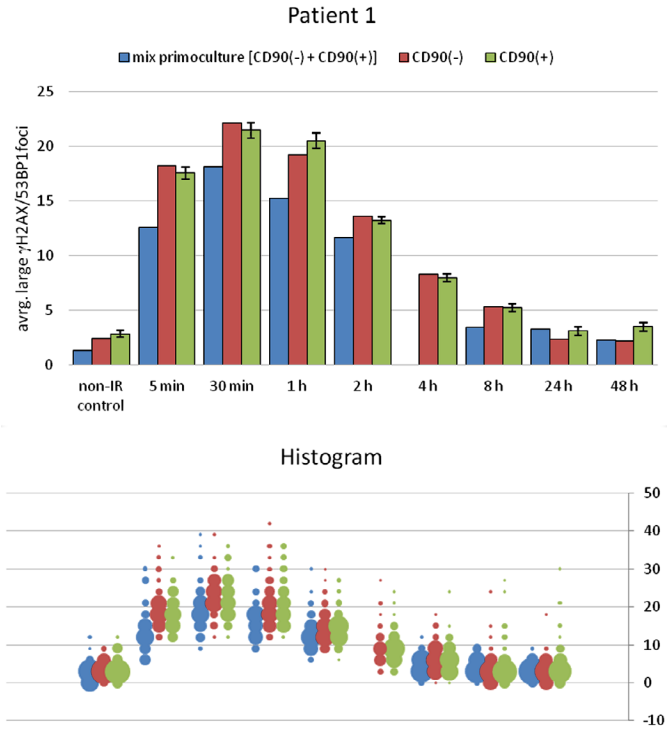

Fig. 4. DSB induction and repair compared for CD90$^-$ and CD90$^+$ cells and for their mixed culture (CD90$^-$ + CD90$^+$); all primocultures were derived from the radiosensitive tumor T1. Mean values of large γH2AX/53BP1 foci per nucleus are shown with standard errors.

appeared in the case of both radiosensitive tumors, T1 and T2 (Fig. 3). Nevertheless, the reason for this repair delay differed: In T1, the average number of DSBs per nucleus induced by 2 Gy of γ-rays dramatically exceeded that in NHDF fibroblasts and also all other tumors. This situation followed from an enormous size of T1 cells and extremely slowed the removal of DSBs (Fig. 3A), though the repair efficiency seemed to be unaffected (Fig. 3B). In contrast, both the average maximum number of γH2AX/53BP1 foci per nucleus and DSB repair efficiency were low in tumor T2 (Figs. 3A and 3B).

Moreover, the amount of γH2AX/53BP1 foci detected in non-irradiated cells (genomic instability) and the amount of foci persisting in cells long periods of time post-irradiation (48 h PI; DSB repair inefficiency/DSB tolerance) were increased (as compared to NHDF) in all tumors but especially in both radiosensitive tumors (Fig. 3). For the radiosensitive tumors T1 and T2 the numbers of persisting foci exceeded the average value measured for NHDF significantly (Fig. 3).

Experiments with separated CD90$^-$ and CD90$^+$ cell primocultures provided the results that were mutually comparable and roughly resembled those described above for the mixed CD90$^-$ + CD90$^+$ cultures; however, in several cases, the mixed CD90$^-$ + CD90$^+$ cultures showed lower formation and faster disappearance of γH2AX/53BP1 foci than we observed for both CD90$^-$ and CD90$^+$ cells. The results for tumor T1 are provided as an example in Figure 4.

4 Discussion

While only about 50% of HN tumors respond to irradiation [1,2], radiotherapy is being applied more or less "randomly" since any effective and reliable method to identify radiosensitive tumors has not been implemented yet. HN tumors to be treated by radiotherapy are therefore

only selected on the basis of their clinical parameters and/or response to neoadjuvant chemotherapy. However, our clinical experience from past 15 years (180–220 newly diagnosed patients/year) shows that the chemosensitivity of HN tumors (with the highest share of laryngeal, oropharyngeal and hypofaryngeal locality, mostly in advanced stage) does not sufficiently correlate with the radiosensitivity. Searching for a more direct and reliable HN tumor radiosensitivity/radioresistance marker thus still represents an important task of radiobiological research.

Though many other processes may also contribute, the repair of DSBs could be suspected of substantially determining the tumors' radiosensitivity/resistance. This is because DSBs represent the most lethal DNA damage being introduced into DNA of affected cells by radiotherapy and some kinds of chemotherapy. In this work, therefore, we tested this hypothesis for HN tumors and analyzed the possibility whether evaluation of DSB repair in tumor cell primocultures irradiated in vitro might open new way to predict an individual-specific response to radiotherapy [28].

We succeeded with introducing methods for preparing separate primocultures of different cell types from HN tumors and employed currently the most sensitive method – immunofluorescence confocal microscopy of γH2AX/53BP1 repair foci [27] – to monitor DSB induction and repair in these primocultures prior to and upon irradiation. We have demonstrated already earlier that results of γH2AX/53BP1 immunofluorescence microscopy well correlate with comet assay, the gold standard method in radiobiology to directly quantify DSBs [27]. Taking advantage of the described approach, we compared various parameters of DSB repair for $CD90^-$, $CD90^+$ and $CD90^-$ + $CD90^+$ tumor cell primocultures derived from 7 HN tumors, where 1 tumor was clinically radioresistant, 2 tumors were radiosensitive and remaining tumors were of unknown status. The reason for separating cells according to the CD90 surface antigen positivity is as follows: though there are some uncertainties in the literature about interpretation of CD90 expression, we can reasonably suppose that $CD90^-$ cells in our study represent epithelial tumor cells while $CD90^+$ cells contain a predominant fraction of tumor-associated fibroblasts (TAFs). Important roles of TAFs in influencing malignant potential and treatment response of tumors have repeatedly been described (e.g. [29] and citations therein). The mixed $CD90^-$+$CD90^+$ primoculture allowed us to reveal potential influence of $CD90^-$ and $CD90^+$ cell interactions on DSB repair.

Cultured human skin fibroblast (NHDF) provided us DSB repair characteristics for normal, non-malignant cells and served thus as the patient-independent DSB repair standard. Comparisons of results to normal mucosa cells extracted from histologically normal HN tissues (e.g. tonsils) of corresponding HN cancer patients were impossible for present tumors; however, we hope to obtain such data at least for some tumors in future. This information will allow for determining the patient-specific DSB repair efficiency-ratio between normal and tumor cells, while comparison with NHDF cell line may reveal potential functional (DSB repair) or even pre-malignant alterations in histologically normal patients' tissues far distant from the tumor [30,31]. The results may contribute to our better understanding of tumor development as well as to better therapy planning in future.

We first analyzed presence of DSBs in non-irradiated NHDF cells and tumor primocultures (see Fig. 3). The results revealed that even non-irradiated $CD90^-$, $CD90^+$, and $CD90^-$ + $CD90^+$ primocultures derived from the radioresistant tumor T3 show markedly higher average numbers of γH2AX/53BP1 foci per nucleus than NHDF cells. Since increased numbers of γH2AX/53BP1 repair foci appeared in the majority of cells, we suppose this observation reveals increased genomic instability in all three tumor T3 primocultures, rather than their higher mitotic activity. Though, both these possibilities might be not mutually exclusive and further experiments are necessary to shed more light on this phenomenon. Interestingly, non-irradiated primocultures isolated from radiosensitive tumors T1 and T2 also obtained increased foci numbers, higher than NHDF cells. Hence, more tumors must be analyzed to find out whether the genomic instability may point more generally to a higher tumor radioresistance. One explanation could consist in the fact that tumors with a higher level of genetic heterogeneity contain increased frequencies of cell clones, where some of them might exhibit radioresistant features. However, the genomic instability may also point to the cell radiosensitivity arising due to a dysfunction of DSB repair.

Consequently, we followed DSB repair kinetics and efficiency in NHDF fibroblasts and tumor cell primocultures after irradiation with a single dose of 2 Gy (1 Gy/min) of γ-rays. While the maximum average numbers of DSBs per nucleus induced by irradiation in $CD90^-$, $CD90^+$, and $CD90^-$ + $CD90^+$ primocultures varied with tumors, DSB repair kinetics was quite similar to (or even faster than in) NHDF fibroblasts for the radioresistant tumor analyzed (see Fig. 3).

On the other hand, the primocultures derived from the radiosensitive tumors (T1 and T3, Tab. 1) showed, relative to NHDF, significantly delayed DSB repair with a substantial fraction of DSBs persisting in cells for a long period of time (48 h) after irradiation. Hence, though general validity of described results and their connection to tumors' radioresistance at molecular level remain to be determined, it seems that radiosensitive tumors may exhibit defects or deregulation of DSB repair and at the same time do not tolerate persistent DSBs. On the other hand, it seems that radioresistant tumors can tolerate unrepaired DSBs and benefit from them. Unrepaired DSBs may increase genetic "dynamics" of radioresistant tumors and their adaptability (not only) to radiation-induced stress.

The defects in repair processes might be of epigenetic origin since otherwise the same genetic mutations would appear both in $CD90^-$ and $CD90^+$ cells of the tumor. However, even the "mutation" alternative does not seem to be unprecedented. For instance, in colon cancer, we revealed genetic changes even in cells of histologically normal tissue taken 10 cm far from the tumor [30].

Finally, $CD90^-$ and $CD90^+$ primocultures did not show striking differences in DSB repair characteristics.

However, for several tumors, lower numbers of γH2AX/53BP1 repair foci appeared upon irradiation in mixed $CD90^-$ + $CD90^+$ co-cultures than in $CD90^-$ or $CD90^+$ cells cultured separately (see Fig. 4); and existing foci also disappeared sooner from the former cells. In accordance with these results, we revealed that expression of some important genes in $CD90^+$ primocultures resembles more the situation in $CD90^-$ cells than in $CD90^+$ cells taken from histologically normal HN tissue. More efficient repair in $CD90^-$ + $CD90^+$ co-cultures may point to interactions between $CD90^-$ and $CD90^+$ cells that stimulate DSB repair.

5 Conclusions

In this work, we described our first results on DSB repair kinetics and efficiency in $CD90^-$ and $CD90^+$ cell primocultures isolated from radiosensitive and radioresistant HNSCC tumors, respectively. We demonstrated our ability to prepare $CD90^-$ and $CD90^+$ primocultures and follow DSB repair in these cells in vitro with highest possible sensitivity and precision. While the only radioresistant tumor in our study showed characteristics of DSB repair similar to normal human skin fibroblasts, both radiosensitive tumors exerted genetic instability and markedly delayed repair kinetics and increased persistence of unrepaired DSBs. Nevertheless, whether these results are more generally valid and monitoring of DSB repair can be used to predict the response of individual tumors to radiotherapy must be further studied.

This work was supported by the Czech Science Foundation (16-12454S).

Author contribution statement

Martin Falk and Michal Masarik designed the project, supervised the experiments and analyzed/interpreted the data. M.F. prepared the manuscript; Zuzana Horakova and Hana Binkova were responsible for clinical part of all works (patients diagnostics and follow up, tumors biopsies); Z.H. prepared clinical part of the manuscript; Jaromir Gumulec, Marketa Svobodova and Martina Raudenska isolated cells from patients tumors and prepared $CD90^-$ and $CD90^+$ cell primocultures; they also basically characterized gene expression of the primocultures; Olga Kopecna, Iva Falkova and Alena Bacikova participated in cell culturing, irradiated cells, and performed all immunofluorescence experiments on detection of γH2AX/53BP1 repair foci; O.K. also contributed to image analyses; Daniel Depes acquired microscopy images of γH2AX/53BP1 repair foci and analyzed the image data.

References

1. H. Binková, Otorinologie a foniatrie **59**, 114 (2010)
2. Z. Horáková, Otorinologie a foniatrie **59**, 107 (2010)
3. I. Falkova, Zdravotníctvo a Sociálna práca **11**, 19 (2016)
4. F. Perri, Head Neck **37**, 763 (2015)
5. G. Mountzios, Ann. Oncol. **25**, 1889 (2014)
6. W. Han, in *Advances in Genetics Research*, edited by K.V. Urbano (Nova Science, 2010)
7. T. Ettl, Oral Oncol. **51**, 158 (2015)
8. G. Peng, Mol. Med. Rep. **10**, 1709 (2014)
9. M. Maalouf, Int. J. Radiat. Oncol. Biol. Phys. **74**, 200 (2009)
10. Q. Wang, Int. J. Cancer **128**, 1546 (2011)
11. T. Kuilman, Genes Dev. **24**, 2463 (2010)
12. A. Lujambio, Bioessays **38**, S56 (2016)
13. L. Ježková, Appl. Radiat. Isot. **83(Pt B)**, 128 (2014)
14. M. Falk, Crit. Rev. Eukaryot. Gene Expr. **24**, 225 (2014)
15. J. Sevcik, Cell Signal. **24**, 1023 (2012)
16. J. Sevcik, Cell Signal. **25**, 1186 (2013)
17. A. Affolter, Oncol. Rep. **29**, 785 (2013)
18. X. Ji, Int. J. Clin. Exp. Med. **8**, 7002 (2015)
19. V. Salvatore, Oncotarget 1 (2016)
20. M. Falk, Appl. Radiat. Isot. **83**, 177 (2014)
21. M. Falk, Biochim. Biophys. Acta **1773**, 1534 (2007)
22. M. Kozubek, Cytometry **45**, 1 (2001)
23. P. Matula, in IEEE International Symposium on Biomedical Imaging: from Nano to Macro 2009 ISBI 09 (2009), p. 1138
24. M. Svobodova, Oncotarget, 2017, https://doi.org/10.18632/oncotarget.19914
25. B. Joshua, Head Neck **34**, 42 (2012)
26. M. Falk, Mutat. Res. **704**, 88 (2010)
27. M. Hofer, J. Med. Chem. **59**, 3003 (2016)
28. G. Wolf, Ear Nose Throat J. **80**, 897 (2001)
29. M. Raudenska, Tumour Biol. **36**, 9929 (2015)
30. E. Lukásová, Chromosoma **112**, 221 (2004)
31. E. Lukášová, Biochim. Biophys. Acta **1833**, 767 (2013)

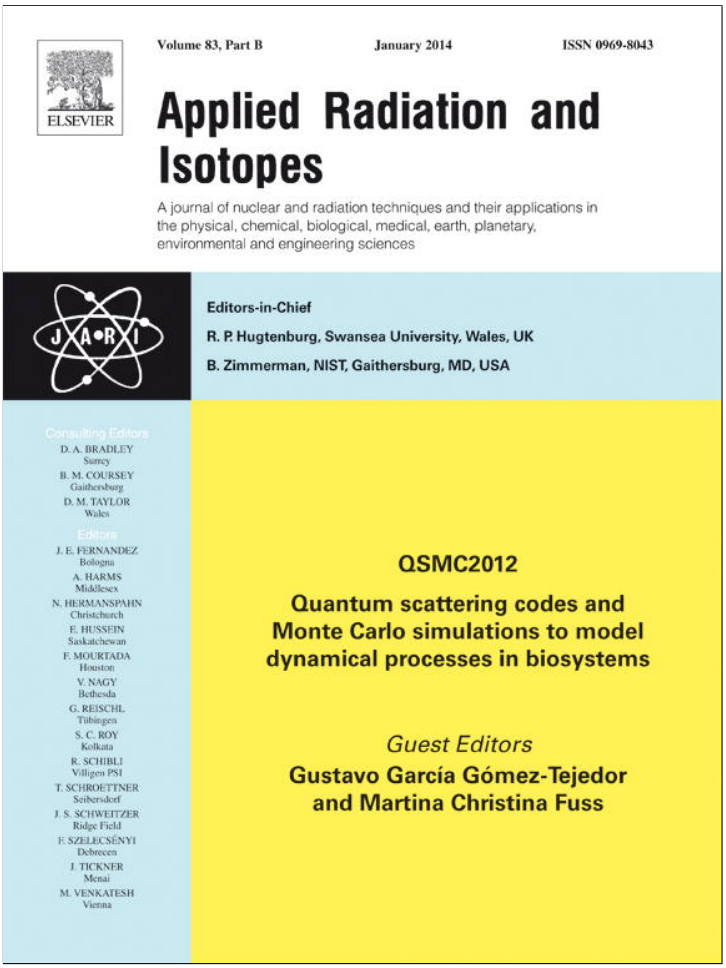

Applied Radiation and Isotopes 83 (2014) 128–136

Contents lists available at ScienceDirect

Applied Radiation and Isotopes

journal homepage: www.elsevier.com/locate/apradiso

Function of chromatin structure and dynamics in DNA damage, repair and misrepair: γ-rays and protons in action

Lucie Ježková [a,b,c], Martin Falk [a,*], Iva Falková [a,d], Marie Davídková [e], Alena Bačíková [a], Lenka Štefančíková [a], Jana Vachelová [e], Anna Michaelidesová [e], Emilie Lukášová [a], Alla Boreyko [b], Evgeny Krasavin [b], Stanislav Kozubek [a]

[a] Institute of Biophysics Brno, Academy of Sciences of the Czech Republic, Brno, Czech Republic
[b] Joint Institute for Nuclear Research, Dubna, Moscow Region, Russia
[c] Institute of Chemical Technology Prague, Prague, Czech Republic
[d] Clinic of Internal Medicine—Hematology and Oncology, Faculty Hospital Brno, Czech Republic
[e] Nuclear Physics Institute, Academy of Sciences of the Czech Republic, Řež, Czech Republic

HIGHLIGHTS

- The majority of DSBs are repaired individually close to the sites of their origin.
- Decondensation of damaged chromatin domains can potentiate clustering of lesions.
- DSB clustering might increase the risk of chromatin translocation.
- Distances of lesions and higher-order chromatin structure influence DSB clustering.
- The conclusions seem to hold both for DSB damage caused by γ-radiation and protons.

ARTICLE INFO

Available online 20 January 2013

Keywords:
DNA double-strand breaks (DSBs)
Higher-order chromatin structure and DSB repair
Formation of chromosomal translocations
Gamma rays and proton beams
γH2AX foci

ABSTRACT

According to their physical characteristics, protons and ion beams promise a revolution in cancer radiotherapy. Curing protocols however reflect rather the empirical knowledge than experimental data on DNA repair. This especially holds for the spatio-temporal organization of repair processes in the context of higher-order chromatin structure—the problematics addressed in this work. The consequences for the mechanism of chromosomal translocations are compared for gamma rays and proton beams.

1. Introduction

DNA double-strand breaks (DSBs) are the most deleterious lesions for human health that pose a real challenge for repair mechanisms (Board on Radiation Effects Research (BRER) Committee to Assess Health Risks from Exposure to Low Levels of Ionizing Radiation, National Research Council, 2006). They are continuously introduced into the human genome both by exogenous and endogenous factors like energetic metabolism, DNA replication, recombination and V(D)J rearrangement (essential for B and T cell maturation, Goetze et al., 2007). Ionizing radiation (IR) and radiomimetic drugs are the most potent environmental DSB inducers. Even a single DSB can lead to the cell death or cancer development if left unrepaired or repaired improperly (Mills et al., 2003, reviewed in Lukas et al., 2005). On the other hand, DSB induction currently enables the most efficient killing of tumor cells. Radiotherapy therefore represents one of the major curing modalities for many cancers. In present, new hopes are put into the development of the ion-beam cancer therapy that – from physical point of view – promises a much precise and efficient eradication of tumors with much lower damage delivered to normal surrounding cells at the same time (Durante et al., 2010). This broadens the applicability of the radiotherapy even to radio-resistant cells and tumors localized deep in a patient's body or in close proximity to important tissues and organs (e.g. tumors localized in brain, eye, prostate etc.). Although physical characteristics and calculations made for the protons and different ion beams seem to be very promising, the data on the cell

* Correspondence to: Laboratory of Chromatin Function, Damage and Repair, Department of Molecular Cytology and Cytometry, Institute of Biophysics, Academy of Sciences of CR Kralovopolska 135, 61265 Brno, Czech Republic. Tel.: +420 541517165; +420 728 084060 (mobile).
E-mail addresses: mfalk@seznam.cz, falk@ibp.cz (M. Falk).

0969-8043/$ - see front matter © 2013 Elsevier Ltd. All rights reserved.
http://dx.doi.org/10.1016/j.apradiso.2013.01.022

response at the "biological level" are still insufficient. Indeed, current irradiation protocols are dependent on empirical experience rather than a solid body of scientific data. The recognition of how cells repair the DSB damage is therefore of utmost importance for our understanding of both the development and therapy of cancer.

Since higher-order chromatin structure and nuclear organization have not been discovered until recently (Kozubek et al., 2002; Cremer et al., 2006), it was thought that chromatin is randomly distributed in the cell nucleus, resembling for example noodles in a soup. Therefore (and later because of technical limitations), only "biochemical aspects" of DSB repair were studied. However, how this process is organized in time and space of the cell nucleus remains unclear (Nelms et al., 1998; Nikiforova et al., 2000; Aten et al., 2004; Kruhlak et al., 2006; Loizou et al., 2006; Falk et al., 2007; Ayoub et al., 2008; Falk et al., 2008; Goodarzi et al., 2008; Scherthan et al., 2008; Goodarzi and Jeggo, 2009; Goodarzi et al., 2009; Falk et al., 2010; Noon et al., 2010; Chiolo et al., 2011; Jakob et al., 2011; Rübe et al., 2011).

Importantly, in eukaryotes, DNA does not appear "naked" but in the form of chromatin, where it associates with histones and different non histone proteins (Perez-Ortin et al., 1988; Vagnarelli, 2012). Since DNA is a very non-homogeneous molecule with respect to the distribution of genes and other functional sequences, different proteins in different amounts interact with particular DNA loci—this results in the formation of functionally and structurally distinct chromatin domains that are preserved also in the 3D space of interphase nuclei. The best known chromatin domains, discovered already at the beginning of the era of cytogenetics, are heterochromatin (HC) and euchromatin (EU) (Frenster, 1965). While EU is gene rich, highly transcribed, early-replicating and decondensed, HC contains repetitive sequences, only few genes, is transcriptionally silent, late replicating and highly condensed (Tamaru, 2010). Chromosomal territories and RIDGE/antiRIDGE clusters can serve as other examples of higher-order chromatin domains (Caron et al., 2001; Versteeg et al., 2003). Chromosomal territories differ in the content of genes, level of overall expression, chromatin structure and nuclear localization; RIDGEs represent large clusters of highly expressed (usually housekeeping) genes while antiRIDGEs are unexpressed clusters (Caron et al., 2001; Versteeg et al., 2003). It was found in recent years that such nonrandom "higher-order" chromatin structure and organization in the cell nucleus influences and, in turn, is influenced by fundamental nuclear processes like transcription and replication. Therefore, it is reasonable to suppose that DSB repair is not the exception.

Theoretically, many aspects of DSB repair might be tightly dependent on chromatin structure (Downs et al., 2007, reviewed in Falk et al. 2010) (Fig. 1). First, a DSB completely disintegrates the DNA molecule and seriously disrupts local chromatin structure with consequences for all processes of DNA "metabolism". The sensitivity to DSB induction might be influenced by local chromatin structure, at least for low-LET ionizing radiation (IR) (Falk et al., 2008) and chemical compounds, where DSB damage is mostly mediated indirectly by reactive free radicals and preferential binding to specific DNA sequences, respectively. Chromatin structure might also influence DSB recognition, commitment for repair, and the repair process per se in terms of their mechanism, efficiency, kinetics and fidelity (Nelms et al., 1998; Nikiforova et al., 2000; Aten et al., 2004; Kruhlak et al., 2006; Loizou et al., 2006; Falk et al., 2007; Ayoub et al., 2008; Falk et al., 2008; Goodarzi et al., 2008; Scherthan et al., 2008; Goodarzi and Jeggo, 2009; Goodarzi et al., 2009; Falk et al., 2010; Noon et al., 2010; Chiolo et al., 2011; Jakob et al., 2011; Rübe et al., 2011). Finally, nuclear architecture and chromatin structure might play an important role in the formation of potentially cancerogeneous genetic mutations, including chromosomal translocations (Falk et al., 2007; Falk et al., 2008). "Epimutations" then represent probably the most illustrative example (Fig. 1): even if DSBs were successfully rejoined, chromatin structure need not be necessarily successfully reverted to the original status. Although an extensive research at the field is still necessary, ionizing radiation-induced repair foci (IRIFs) that persist in cells days after the irradiation might indicate such "lesions" (in addition to DSBs repaired only with difficulty etc.) (Falk et al., 2010; Ševčík et al., 2012). The impact of epimutations on the expression and stability of the genome is unknown yet; however, it should be emphasized that megabase-long regions of chromatin can be affected. Since DSB induction, repair and misrepair are mutually interdependent, it seems that higher-order chromatin structure influences a plethora of DSB damage-associated nuclear processes that then interact in the frame of extensive DSB-responsive networks (Nelms et al., 1998; Nikiforova et al., 2000; Aten et al., 2004; Kruhlak et al., 2006; Loizou et al., 2006; Falk et al., 2007; Ayoub et al., 2008; Falk et al., 2008; Goodarzi et al., 2008; Scherthan et al., 2008; Goodarzi and Jeggo, 2009; Goodarzi et al., 2009; Falk et al., 2010; Noon et al., 2010; Chiolo et al., 2011; Jakob et al., 2011; Rübe et al., 2011).

In this work, we have focused on the question of whether DSBs are repaired at the sites of their origin or have to migrate into the repair-competent nuclear subcompartments in order to be repaired. And, if they exist, do these "repair domains" continually persist in cell nuclei or are they operatively assembled *de novo* around the associated damaged loci? Simply said, are DSBs spatially stable or mobile? In the latter case, are DSBs repaired individually or several in common, for example in putative repair factories (Nelms et al., 1998; Aten et al., 2004; Kruhlak et al., 2006)? Importantly, how are the answers on these questions reflected in the mechanism of formation of chromosomal translocations (Nelms et al., 1998; Aten et al., 2004; Kruhlak et al., 2006)? Despite seemingly simple, answers to all these questions are still intensively disputed (Nelms et al., 1998; Nikiforova et al., 2000; Aten et al., 2004; Kruhlak et al., 2006; Loizou et al., 2006; Falk et al., 2007; Ayoub et al., 2008; Falk et al., 2008; Goodarzi et al., 2008; Scherthan et al., 2008; Goodarzi and Jeggo, 2009; Goodarzi et al., 2009; Falk et al., 2010; Noon et al., 2010; Chiolo et al., 2011; Jakob et al., 2011; Rübe et al., 2011). In the context of ion-beam cancer therapy, it is of the utmost interest to find out how the results will differ for DSB damage introduced by ionizing radiation of different quality. Another important task in disclosing the mechanism of chromosomal translocations is to discriminate between the early effects caused by the photon/particle energy deposition and the later phenomena that can be ascribed to the repair processes (Fig. 2). For instance, DSB clusters potentially leading to translocations may appear either as the consequence of a condensed damage ("primary clusters") or due to chromatin decondensation in the frame of DSB repair ("secondary clusters") (discussed later). A different contribution of primary and secondary DSB clusters to formation of chromosomal translocations (and other aberrations) for ionizing radiation of different quality can be expected (Fig. 2).

2. Methods

2.1. Cell culture and transfection

Human foreskin fibroblasts and MCF7 mammary carcinoma cells were cultivated in the DMEM medium supplemented with 10% fetal calf serum (FCS) and standard antibiotics (penicillin, streptomycin). To get transient expression of NBS1-GFP (a gift

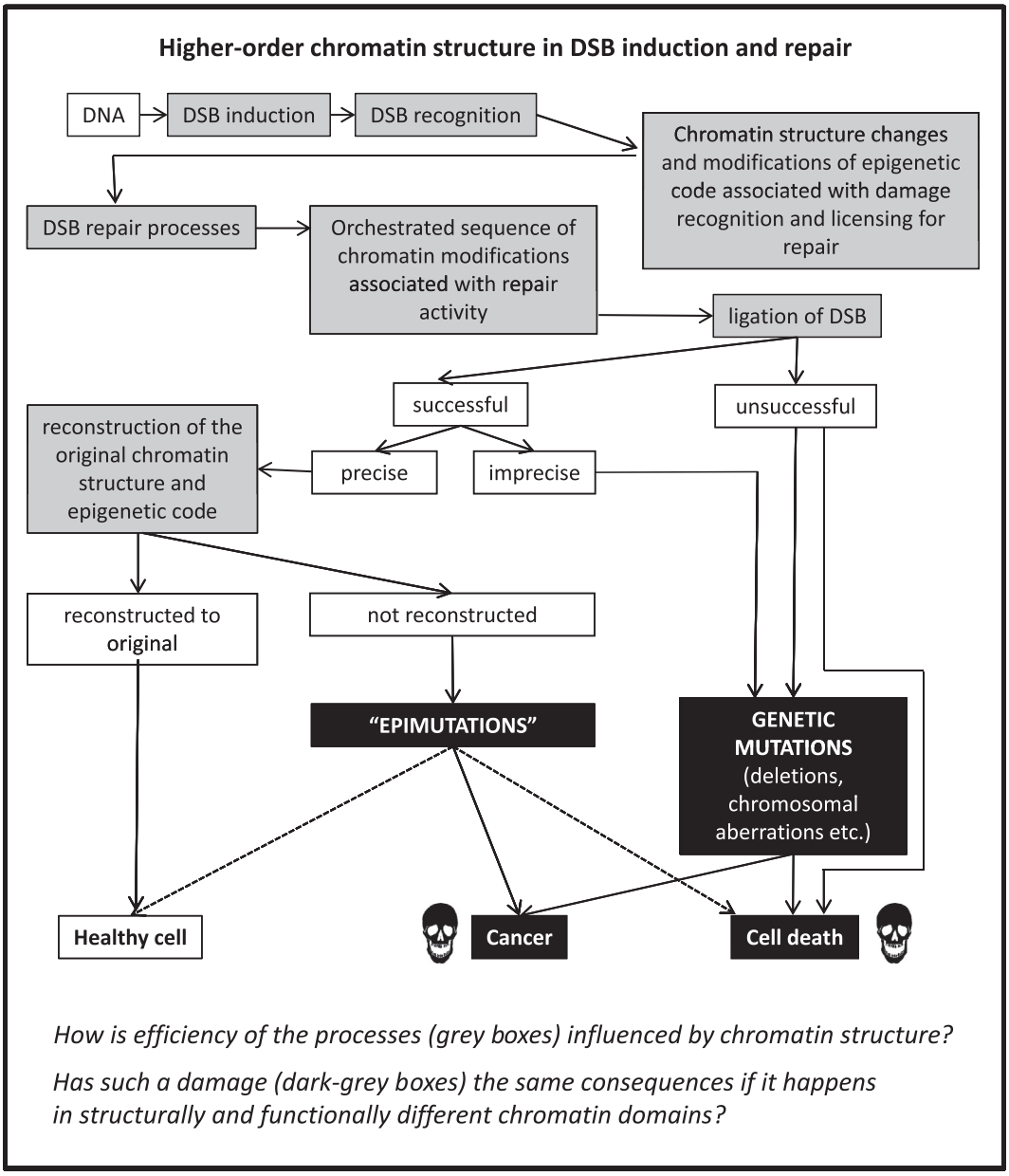

Fig. 1. The steps of the DSB repair (gray boxes) that might be influenced by the higher-order chromatin structure. The pathway from DSB induction to formation of genetic mutations and "epimutations" is displayed. The black boxes show possible negative endpoints of the DSB repair: the genetic mutations and "epimutations" – both these phenomena and their impact on human health are rationally supposed to depend on higher-order chromatin structure. Possible interconnections of nuclear organization and higher-order chromatin structure with the repair network are depicted. Different combinations of parameters also might probably shift the mechanism of formation of chromosomal translocations closer to the "Position First" hypothesis or "Breakage First" hypothesis. The role of higher-order chromatin structure on the individual steps of DSB repair might differ upon the action of ionizing radiation of different quality—this is the important question in the development of the ion-beam cancer therapy.

from J. Lukas), HP1β–GFP (a gift from T. Misteli), PML-GFP (a gift from M. Faretta), H2B-GFP (Clontech) and pm53BP1-RFP (a gift from J. Lukas), the cells were transfected with the GFP constructs using Lipofectamine 2000 (Invitrogene) or Fugene HD (Roche) according to the manufacturer's instructions and used for observation of protein movement 12 h after transfection, and within 30 min after irradiation. Changes in chromatin structure in regions of DSBs and breaks displacement were studied in cells co-transfected with H2B-GFP and pm53BP1-RFP.

2.2. Cell synchronization

For irradiation, either unsynchronized cell populations or cells synchronized in the G1 phase were used. Synchronization of cells in the G0 phase was achieved by incubation of confluent culture of human fibroblasts without serum for 4 days. After that, the cells were trypsinized and plated on microscope slides where they were cultured in the presence of 10% FCS. After 12 h of incubation, the cells were irradiated as described below.

2.3. Cell irradiation

Gamma rays: Cells were irradiated with 1 Gy or 4 Gy of γ-rays (Chizostat, Chirana, ^{60}Co, 4 Gy/min) at 37 °C. Proton irradiation: irradiations were performed with isochronic cyclotron U – 120 M (Nuclear Physics Institute, Řež) that accelerates protons up to about 32 MeV. Confluent cells cultured in cultivation flasks (Nunc, culture area 25 cm^2) were trypsinized and re-seeded onto the Glass Bottom Petri Dishes (MatTek Corporation, 35 mm in diameter, 1 mm thick glass) 20 h before irradiation. Immediately

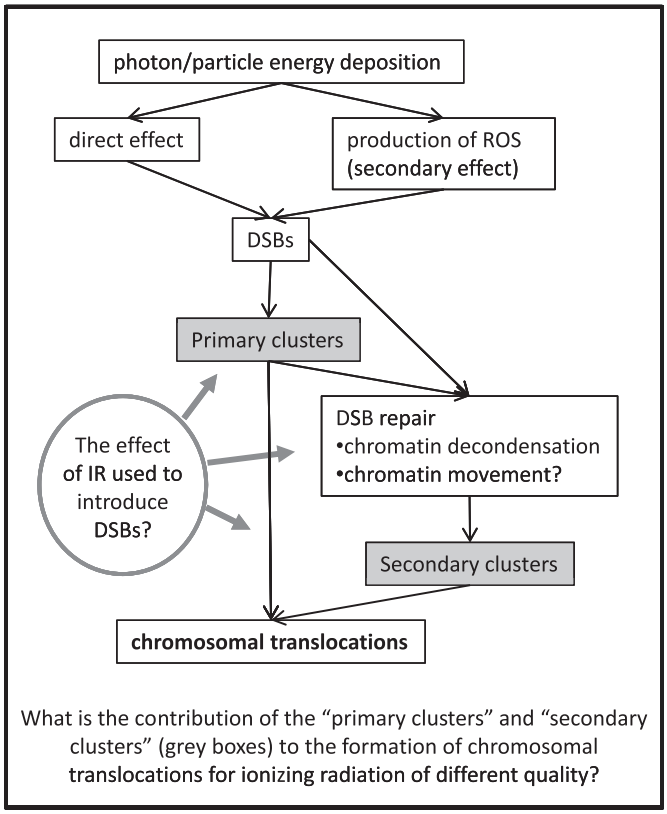

Fig. 2. The role of the "primary" and "secondary" DSB clusters in formation of chromosomal translocations. The "primary" clusters are formed due to high local energy deposition; the "secondary" clusters appear as the result of the repair processes. The contribution of the "primary" and "secondary" clusters to the mechanism of chromosomal translocation formation is unknown, however, it is supposed to depend both on the higher-order chromatin structure and the characteristics of ionizing radiation used to introduce DSBs.

prior to the irradiation, Petri dishes with grooving cells (in a monolayer) were completely filled with preheated DMEM medium (37 °C) to prevent drying during the procedure (cells are in vertical position during the irradiation) and mounted into the irradiation adapter. Cells were irradiated with 1 Gy and 4 Gy (4 Gy/min) of 15 MeV and 30 MeV protons, respectively. The homogeneity of the proton irradiated field (10 × 10 cm) was ± 10% as determined using gafchromic film. After irradiation, cells were fixed (see the particular paragraph) in different time points ranging from 2 min post-irradiation (PI) to 4 days PI (2 min, 5 min, 15 min, 30 min, 60 min, 120 min, 240 min, 1 day, 2 days, 3 days and 4 days PI).

2.4. Cell fixation, permeabilization and immunostaining

Cells harvested at different time intervals after irradiation (see the above paragraph) were washed twice for 2 min each in PBS, fixed with 4% freshly prepared paraformaldehyde (pFA) in PBS for 10 min at 21 °C, rinsed quickly in PBS, then washed three times for 5 min each in PBS, permeabilized in 0.2% Triton X-100/PBS for 15 min at room temperature (RT), rinsed in PBS and washed twice for 5 min each. Before incubation with primary antibodies (overnight at 4 °C), the cells were blocked with 7% inactivated FCS + 2% bovine serum albumin/PBS for 30 min at RT. Antibodies from two different hosts (rabbit and mouse) were used on each slide to detect two different antigens in the same nuclei. Mouse monoclonal antibody against H2AX phosphorylated at serine 139 (γH2AX, Upstate) and rabbit polyclonal antibody against NBS1 phosphorylated at serine 343 (Cell Signaling), Mre11 and 53BP1 repair proteins (both from Upstate) were used to visualize ionizing radiation-induced repair foci (IRIF). Although γH2AX is generally accepted as sufficiently quantitative marker of DNA double-strand breaks (DSBs), applicable even for very low doses of ionizing radiation (IR), this double-labeling enables the most precise quantification of DSBs and indicates DSBs that are actively repaired. Anti-acetyl histone H4 at lysine 12 (mouse) was from Upstate, Secondary antibodies were affinity purified donkey anti-mouse-FITC-conjugated, and affinity purified donkey anti-rabbit-Cy3-conjugated, from Jackson Laboratory (West Grove, PA). The mixture of both antibodies was applied to each slide (after their pre-incubation with 5.5% of donkey serum/PBS for 30 min at RT) and incubated for 1 h in the dark at RT. This was followed by washing (three times for 5 min each) in PBS. Cells were counterstained with 1.5 μM TOPRO-3 (Molecular Probes, Eugene, USA) freshly prepared in 2 × SSC. After brief washing in 2 × SSC (2 min) and 4 × SSC + 0.1% Igepal (2 s), the samples were mounted in Vectashield medium (Vector Laboratories, Burlingame, CA).

2.5. Cell cycle analysis

After starvation, cells were trypsinized, plated in 2×10^5 per a dish containing 5 ml of DMEM with 10% FCS and grown at 37 °C. In different time intervals, the cells were trypsinized, resuspended in the medium with 10% FCS and sedimented by centrifugation (200*g*, 5 min, 4 °C). Cell suspension was washed in two volumes of PBS, centrifuged, resuspended in about 0.5 ml of PBS, fixed after addition of 4 ml of 70% ethanol at 4 °C for 30 min and maintained at this temperature until the cells of all time intervals were fixed, then centrifuged (200*g*, 5 min, 4 °C) and washed with PBS. DNA was labeled with propidium iodide in 0.5 ml of Vindel solution (1 ml 1 M Tris, pH 8.0, 1 mg RNAsa (Sigma R-5503), 100 μl NP − 40 + 60 mg NaCl, 5 mg propidium iodide, completed to 100 ml H_2O) for 30 min at 37 °C. The cells were fractionated according to the DNA content by flow-cytometry using the FACS Calibur device (Becton Dickinson, San Jose, California, USA) with argon laser, the excitation maximum 488 nm. In each sample, 2×10^4 cells were analyzed. Fractions of cells in different phases of the cell cycle were estimated using the ModFit 3.0 software (Verity Software House, Topsham, California, USA).

2.6. Image acquisition and microscopy

An automated Leica DM RXA fluorescence microscope (Leica, Wetzlar, Germany), equipped with an oil immersion Plan Fluotar objective (100 × /NA 1.3), a CSU 10a Nipkow disc (Yokogawa, Japan) for confocal imaging, a CoolSnap HQ CCD-camera (Photometrix, Tuscon, AZ, USA) and an Ar/Krlaser (Innova 70C Spectrum, Coherent, Santa Clara, CA, USA), were used for image acquisition (Kozubek et al., 2001, 2004). Alternatively, the Leica SP5 confocal microscopy system equipped with the white laser for multiple fluorochrome excitation, heated box for living cell observations (with regulated continuous influx of CO_2) and sensitive hybrid detectors (Leica) was used. Automated exposure, image quality control and other procedures were performed using the software FISH 2.0, Aquarium and Leica AS (Kozubek et al., 2001, 2004; Matula et al., 2010). The exposure time and dynamic range of the camera (gain of the detectors) in the red, green and blue channels were adjusted to the same values for all slides to obtain quantitatively comparable images. Twenty to 40 serial optical sections were captured at 0.2–0.5-μm step along the *z*-axis.

2.7. Living cell observation and time-lapse microscopy

Two types of in vivo observations were performed: short and medium-term. For short-term experiments, "2D" images consisting of a few (3–5) confocal slices with a z-step of 0.3–0.5 μm were

acquired in extremely short intervals (20–500 ms) for a period of approximately 1.5 min. For medium-term observations, 40 optical sections were captured (3D images) with a 0.2–0.3 μm z-step. Intervals of 50 s were allowed between individual stacks of 40 sections, and observations were continued for a total of 20 min. The light exposure was kept as low as possible to avoid phototoxic effects. Double transfected cells with H2B-GFP and pm53BP1-RFP were observed in 5 min intervals until 30 min PI, followed by 10 min intervals until 60–120 min PI. In each interval, 15 slices with a z-step of 0.4 μm were taken. The temperature (37 °C) of medium and the 5% concentration of CO_2 in the atmosphere were kept constant during observation.

2.8. Analysis of experimental data and motion of loci

The off-line image analysis and tracking (2D, 3D) of fluorescence signals were done with the FISH 2.0 software, Aquarium software and a 3D image viewer (Matula et al., 2010) as described in Falk et al., 2007. In brief, the objects were traced in the time-lapse series on the basis of matching algorithms, eliminating movements of the whole nucleus. In 2D, the distances between two signals were calculated using the equation: $d=\sqrt{(x_1-x_n)^2+(y_1-y_n)^2}$; or in 3D: $d=\sqrt{(x_1-x_n)^2+(y_1-y_n)^2+(z_1-z_n)^2}$, where x_1, y_1 and z_1 (x_n, y_n and z_n) were coordinates for the first measurement and the nth measurement of the same object. The mean d^2 was calculated from individual values of all possible signal pairs at the particular time point. The mean difference of d^2 (mean Δd^2) was calculated at each time point (t) as $\Delta d^2=(d_t-d_{t+\Delta t})^2$, where Δt was the time interval between measurements. Evaluation of data and statistical analyses were performed using the Sigma Plot statistical package (Jandel Scientific).

3. Results and discussion

3.1. Distribution of DSBs in cell nuclei immediately after irradiation

Higher-order chromatin domains differ in their structure and function, so their sensitivity to DSB damage introduced by the indirect effect of ionizing radiation might also differ. Alternatively (but not necessarily mutually exclusively), DSB detection and repair might operate with different efficiency in distinct chromatin/nuclear subcompartments. Therefore, we were first interested in how DSBs – marked by γH2AX/53BP1 ionizing radiation-induced repair foci (IRIFs) – are distributed in the cell nuclei immediately (2 min) after the irradiation with ionizing radiations of different qualities (gamma photons, 30 MeV protons and 15 MeV protons).

To address this question, we have directly visualized DSB induction by immunostaining of γH2AX/53BP1 foci in spatially fixed (4% paraformaldehyde) human foreskin fibroblast, and compared the fractions in chromatin domains densely and weakly stained with DNA dye (TOPRO-3), respectively (Fig. 3A and B). In minutes post-irradiation (PI), histone H2AX becomes quickly phosphorylated by ATM and other kinases at megabase-pair regions around the DSB lesions (Rogakou et al., 1998). This phosphorylated form of H2AX (called γH2AX) can be therefore visualized as nuclear foci that are believed to specifically form at the sites of DSB (Rogakou et al., 1998, reviewed in Darzynkiewicz,

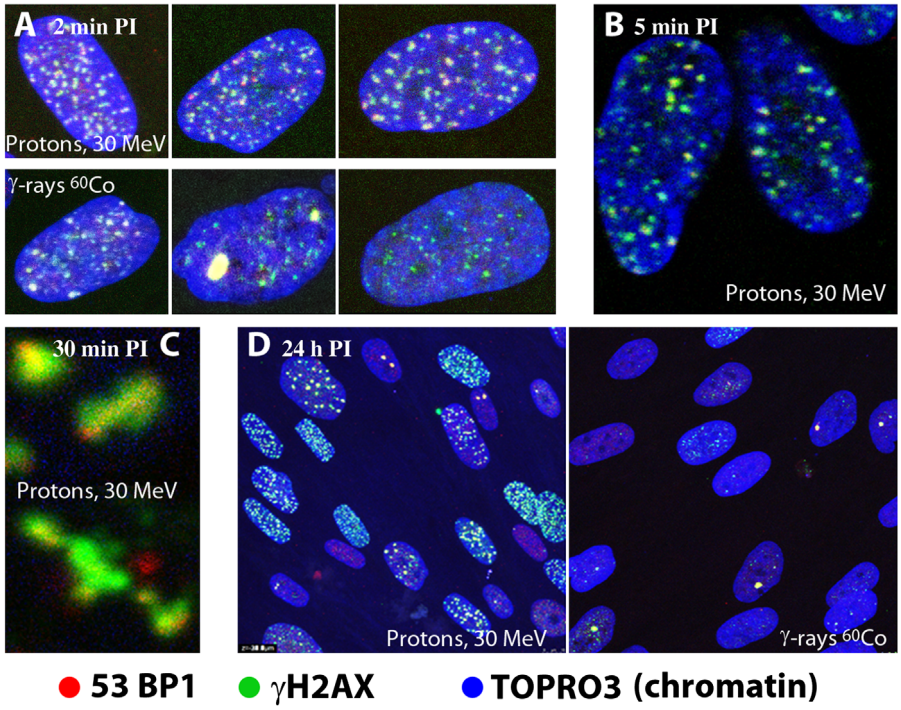

Fig. 3. (**A**) The DSB induction in human fibroblasts immediately (2 min) post-irradiation (PI) quantified by γH2AX (green) and 53BP1 (red) repair foci immunostaining. The situation is compared for cells irradiated with 1 Gy of 30 MeV protons (4 Gy/min, upper line) and γ-rays from ^{60}Co (4 Gy/min, bottom line). Images are composed from 25–35 confocal slices with the z-step of 0.3 μm, chromatin staining with TOPRO-3 (all images). (**B**) The localization of γH2AX/53BP1 foci relative to condensed "heterochromatin" and decondensed "euchromatin" in human fibroblasts irradiated with 30 MeV protons, detected at 5 min PI. The majority of the foci are clearly localized in decondensed chromatin domains (less intensively stained with TOPRO-3); the confocal slice is 0.4 μm. (**C**) The examples of γH2AX/53BP1 foci clusters detected in human fibroblasts 30 min after the irradiation with 30 MeV protons. What is the role of these clusters in the formation of chromosomal translocations? (For the clusters formed after the γ-irradiation the reader is referred to Falk et al., 2007). (**D**) The efficiency of DSB repair compared for 30 MeV protons (left panel) and γ-rays (right panel); the dose of 1.0 Gy (4 Gy/min) in both cases. The number of γH2AX/53BP1 foci persisting in cells (human skin fibroblasts) 24 h PI is displayed; the wide-field maximal images are composed of 35 confocal slices 0.3 μm thick.

2011; see Methods). The γH2AX foci then "attract" a plethora of repair proteins and enable assembly of particular repair complexes. Therefore, to distinguish between different stages of foci (early, actively repairing, and late) we have co-immunostained nuclei with γH2AX and repair proteins (like NBS1, MRE11 and 53BP1, Fig. 3). At maximal images (composed from 25 to 35 confocal optical slices captured with the z-step of 0.3 μm) the distribution of γH2AX was seemingly random (Fig. 3A); however, when we inspected individual confocal slices (0.4 μm) (Fig. 3B), γH2AX foci were distributed nonrandomly, with the majority located in decondensed chromatin weakly stained with DNA dyes (further referred as "chromatin holes"). Though this result was partially explained by the higher sensitivity of decondensed (eu)chromatin to DSB induction mediated by the indirect effect of low-LET γ-rays (Falk et al., 2008; Falk et al., 2010), other phenomena associated with DSB repair seem to contribute to this observation. Theoretically, for example, DSBs might persist longer times in "euchromatin" because of a more efficient repair in "heterochromatin" (e.g. due to better stabilization of free DNA ends). Alternatively, the "heterochromatic" DSBs (hcDSBs) might migrate out of the condensed chromatin, e.g. in order to relocate into the nuclear subcompartments more suitable for their repair (Falk et al., 2007; reviewed in Falk et al., 2010). In addition, some authors reported that heterochromatin could be refractory to γH2AX phosphorylation and foci formation, which might cause underestimation of hcDSBs. However, the similar proportion of heterochromatic and euchromatic DSBs to that obtained with γH2AX staining followed from labeling of free DNA ends by the TUNEL method (Terminal Transferase dUTP Nick End Labeling Assay, the method independent on the γH2AX phosphorylation). In addition, heterochromatic domains were also successfully visualized with HP1a antibody, demonstrating HC is generally accessible for antibodies/despite we could not exclude the possibility that some epitopes can be masked in dense chromatin). Together, it does not seem that more DSBs were attributed to euchromatin because of underestimation of hcDSBs. In support to this statement, more recent works suggest that γH2AX foci form also in dense HC domains (Chiolo et al., 2011; Jakob et al., 2011).

Interestingly, the fraction of γH2AX foci in decondensed chromatin was even bigger when scoring only the foci colocalizing with repair proteins. Moreover, the fraction of "euchromatic" DSBs progressively increased with the time PI (with the plateau phase reached in about 30 min PI); this suggests that chromatin must either decondense around DSB lesions or DSBs must migrate into repair-competent nuclear subdomains in order to complete the repair. Alternatively repair of hcDSBs could proceed without formation of γH2AX foci and participation of NBS1, MRE11 and 53BP1 repair proteins; however, it has been shown recently that γH2AX and 53BP1 are only necessary just for the repair of hcDSBs. Since the analysis of the DSB repair in RIDGE and antiRIDGE chromatin domains (Regions of Increased Gene Expression and their counterparts, respectively) (Falk et al., 2008) revealed slower kinetics in the latter case, it is evident that DSB repair processes include some dynamic aspect (chromatin reorganization).

3.2. *Formation of chromosomal translocations in the context of DSB repair and higher-order chromatin structure—the mobility of DSBs*

In normal human fibroblasts irradiated with different relatively low doses of low-LET γ-rays (1–4 Gy) the number of γH2AX foci detected per nucleus was increasing up to about 30 min PI, without any signs of extensive clustering (Falk et al., 2007). In addition, about 41% of γH2AX foci colocalized with repair proteins (NBS1, MRE11, 53BP1) at the sites of their origin already 5 min PI (Falk et al., 2007). Both in the case of 30 MeV protons and 15 MeV

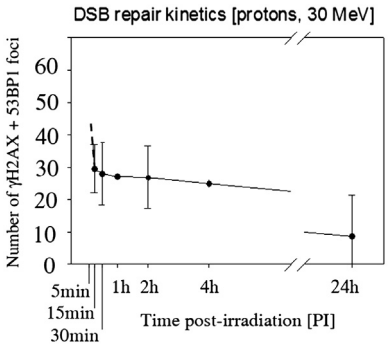

Fig. 4. The DSB repair kinetics in the human skin fibroblasts irradiated with 1.0 Gy of 30 MeV protons (4 Gy/min). Only preliminary data are shown; n=15–30 nuclei (the number of nuclei analyzed for the time point).

protons the number of γH2AX foci started to decrease immediately from 5 min PI (Fig. 4, preliminary results). The difference between γH2AX disappearance after the gamma and proton irradiation can be most probably explained by slightly different behavior of the lung fibroblasts, used in our previous experiments, and the foreskin fibroblasts being used now (the repair kinetics in the foreskin fibroblasts irradiated with 1 Gy and 4 Gy of γ-radiation is under analysis). Alternatively, if the difference was confirmed, the character of DSBs induced with γ-rays and protons (producing "overhanging" and "blunt" DSB ends, respectively) can be responsible for slightly slower initiation phase of DSB repair in the first case (because of the requirement of more extensive DNA-ends processing). However, extensive colocalization of γH2AX foci with NBS1/53BP1 was observed 5 min PI also for protons, without the necessity to form repair centers (at the level of γH2AX foci clustering) prior to the repair protein binding (Fig. 3A). Therefore, we can conclude that both the DSBs introduced by γ-rays and protons are in principle repaired individually, at the sites of their origin.

On the other hand, the fraction of γH2AX foci in decondensed euchromatin increased with the time PI and heterochromatically localized DSBs usually did not colocalize with larger foci of repair proteins. In addition, γH2AX foci were detected almost exclusively in decondensed parts of chromosomal territories, even in the case of condensed, gene poor chromosomes (Falk et al., 2008). All together, the data obtained indicate some "movement" of at least a part of foci. Therefore, we have measured the mean squared displacement (Δd^2) of NBS1 (see Methods and Falk et al., 2007).

If averaged for all possible pairs of all foci, the Δd^2 of NBS1 and 53BP1 corresponded with that measured for HP1β protein (dynamically attached to chromatin). Therefore, our results suggest that the mobility of DSBs, in general, resembles the one of undamaged chromatin (Falk et al., 2007). However, when we traced individual NBS1 or 53BP1 foci, the mobility was sometimes much higher than the average mean squared displacement measured. Importantly, due to the similar size of these "highly mobile" and "immobile" foci, it does not seem this observation can be attributed to unbound (free) protein aggregates. Therefore, we have further analyzed this movement and found that, in principle, it is identifiable with the Brownian movement as expected. However in many cases of highly mobile foci, the movement evidently proceeded from the dense chromatin domain into the nuclear subcompartment of low chromatin density. Consequent experiments revealed extensive chromatin decondensation at the sites of DSB lesions (demonstrated by a local decrease of TOPRO3 or H2B-GFP staining followed by colocalization of γH2AX with acetylH4K5, acetylH4K12 and Tip60, peaking at 20 min PI), so it is reasonable to suppose that in the case of DSBs located close to the

border of heterochromatin domain, chromatin decondensation associated with DSB repair could result in the protrusion of damaged chromatin into the closest low-density chromatin domain. The consequences of this phenomenon are discussed in the following paragraphs and our earlier works (Falk et al., 2007, reviewed in Falk et al., 2010).

3.3. Late γH2AX foci and DSB clusters—dangerous sites for the genome?

Protrusion of γH2AX foci into low-density chromatin domains and their accumulation in a limited space of these "chromatin holes", observed in spatially fixed human fibroblasts, occasionally resulted in mutual clustering of two or three lesions (Fig. 3C). These results were confirmed also in vivo in MCF7 cells cotransfected with 53BP1-RFP and H2B-GFP in order to enable tracking of 53BP1 foci in the relationship with higher-order chromatin structure. In these cells, 53BP1 foci clusters were usually temporary, but some of them persisted in nuclei till the end of the experiment (> 40 min PI). Importantly, the clusters formed inside the "chromatin holes" and included the foci already present in holes or protruding there from encompassing heterochromatin domains (Figs. 3C and 5). This observation was similar for cells irradiated with γ-rays and protons (of both the energies), and confirms our conclusions about the movement of hcDSBs in the consequence of damaged heterochromatin domain decondensation. Since stably clustered foci occur relatively rarely and, once formed, persist in nuclei for longer times than the simple foci, it is improbable they could impersonate repair factories. Rather, they might represent the "by-products" of DSB repair with an increased risk of chromosomal translocations (Fig. 5).

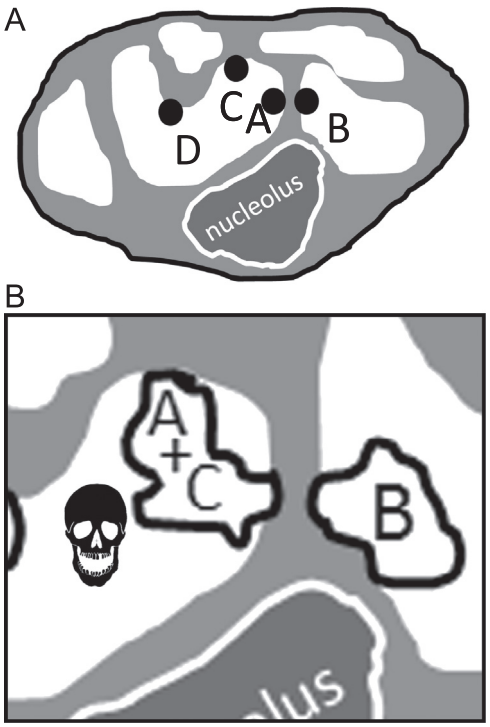

Fig. 5. The proposed working model of formation of chromosomal translocations disclosing the role of higher-order chromatin structure in the mechanism. See the particular chapter for a detailed description. (**A**) The irradiated cell immediately after the exposition—the sites of DSBs are indicated by the black circles; dense chromatin is gray, nuclear subcompartments with a low dense chromatin ("chromatin holes") are white. (**B**) As irradiation-induced repair foci (IRIF) starts to develop in slightly later times post-irradiation (2–30 min PI), the IRIFs protrude from dense chromatin domains into the "chromatin holes" where some of them make timely stable clusters. The probability of clustering between two particular IRIFs depends on their original mutual distance (at the time of their induction) and higher-order chromatin structure. For instance, "heterochromatin barrier" between the foci A and B significantly reduces the probability of their clustering. See the text for more detailed explanation. A, B, C, D=γH2AX or IRIF foci (DSBs). Modified according to Falk et al. BBA MCR, 2007.

Currently, we try to precisely quantify the formation of γH2AX foci clusters in cells irradiated with different doses of γ-rays and protons (of different energies). It is especially important to discriminate between the "primary" clusters produced by localized deposition of high energy immediately after the irradiation and "secondary" clusters that appear as byproducts of DSB repair. Although γ-rays and protons have similar radiobiological effects (RBE), the initial DNA damage seems to be markedly more serious upon the action of 30 MeV and 15 MeV protons (Fig. 3A). Importantly, DSB damage induced by protons remains unrepaired even several days after the irradiation, while DSBs produced by γ-rays are mostly repaired before 24 h PI (Fig. 3D). Concerning the biological endpoints, this indicates that DSBs produced by γ-rays and protons, differ in their complexity and thus in their reparability. However, the question still remains of what the main cause of these repair difficulties is — the "primary" clusters, "secondary" clusters, or even other phenomena? Importantly, it should be also determined how formation of γH2AX clusters corresponds to the cell death and formation of chromosomal translocations (Spectral Karyotyping, SKY, is in progress). These answers will be important for further development of proton therapy, mainly our understanding of the initiation of secondary malignancies. Concerning the efficiency of proton therapy, our preliminary results revealed more extensive DNA damage as compared with γ-rays (with the same dose delivered) and production of lesions that are repaired only with difficulty.

3.4. Working model disclosing the relationship between formation of chromosomal translocations, DSB repair and higher-order chromatin structure

Based on the results summarized above, we have postulated a working model (Fig. 5) of how chromosomal translocations form in the context of higher-order chromatin structure. Surprisingly, it "combines" aspects of two seemingly contradictory hypotheses – the "Position-first" theory and "Breakage-first" theory. Higher-order chromatin structure at the nuclear scale (nuclear architecture) determines the probability map of possible mutual translocation interactions between the particular loci. The closer the foci are in the space of the cell nucleus, the higher is the probability of possible chromatin translocation ("Position-first" hypothesis). However, at a local scale, the probability map could be dominantly changed by the local higher-order chromatin structure (especially by the mutual geometry of damaged functionally and structurally distinct chromatin domains). This is explained in Fig. 5 (modified according to Falk et al., 2007): Providing the lesions A, B C and D with the shortest nuclear distance between A and B, larger between A and C or B and C and the largest between A and D or B and D, the probability of translocations (P[t]) should be P[t(A;B)] > P[t(A;C)] or P[t(B;C)] > P[t(A;D)] or P[t(B;D)] > P[t(C;D)] according to the "Position-first" theory. However, the A and B are separated by a heterochromatic "barrier" that precludes their mutual interaction. The A and C are originally too distant to interact; however, chromatin decondensation around these hcDSB lesions causes their approaching, "driven" by the local higher-order chromatin structure that forces both these lesions to protrude into the same "chromatin hole". Since the lesion D is too far away at the nuclear level (it could not reach the lesion B in any circumstances), the highest probability of the translocation is between the lesions A and C (the combination

of "Position-first" hypothesis and "Breakage-first" hypothesis, with a contribution of local higher-order chromatin structure).

4. Conclusions

Our results identified higher-order chromatin structure as an important player at the DSB repair playground. It is evident that chromatin structure influences DSB repair in terms of its mechanism, efficiency, kinetics and probably also fidelity. In turn, all these phenomena determine the mechanism of the formation of chromosomal translocations. We show that DSB repair proceeds more easily in decondensed euchromatin, because extensive chromatin decondensation at the sites of heterochromatic lesions is required to allow completion of hcDSB processing. Although most DSBs are repaired individually at the sites of their origin, this decondensation introduces a mobile aspect to DSB repair and chromatin exchanges. Our mechanism is therefore also capable to easily explain the formation of complex chromosomal aberrations. Decondensation around hcDSBs may result in their protrusion into low-density chromatin domains ("chromatin holes"), where usually 2 or more DSBs can mutually interact and form temporary or, more rarely, stable foci. These foci persist in cell nuclei longer than simple lesions, so it is reasonable to suppose they are repaired only with difficulty and represent the sites with an increased risk of chromatin translocation. The approaching of previously distant DSB lesions, provoked by the chromatin decondensation and directed by the higher-order chromatin structure, may dominantly change the probability of translocation that was determined on the basis of the original nuclear distances between participating loci. Our model of formation of chromosomal translocations has therefore aspects of both seemingly contradictory "Position-First" and "Breakage-First" hypotheses. Importantly, it can also provide a source of movement that is necessary for the formation of complex chromosomal translocations (Tanabe et al., 2002; Anderson et al., 2006), since putative migration of DSBs into repair factories (thought to be responsible for this movement) has not been confirmed. These results are also in a good agreement with conclusions of P. Jeggo's group (Goodarzi et al., 2008; Goodarzi and Jeggo, 2009; Goodarzi et al., 2009; Noon et al., 2010) showing slower repair of hcDSBs associated with local chromatin decondensation and requirement for extra repair proteins as compared with euchromatic DSBs. The protrusion of hcDSBs outside of dense heterochromatin domain was recently nicely documented also by the group of M. Durante and other authors (Chiolo et al., 2011; Jakob et al., 2011). Since our experiments describing clustering of DSB lesions were performed mainly on the G_1 cells, it remains to be determined, what actually takes place in the G_2 phase of the cell cycle, where most recent findings suggest hcDSBs to be repaired exclusively by the homologous recombination (that operates in G_2 only) (Beucher et al., 2009). Finally, it should be noted that, despite an extensive progress on the field reached in recent years, the results on the spatio-temporal organization of DSB repair are still intensively disputed. Hence, the Pandora's Box still waits to be open!

Our results for the protons of 30 MeV and 15 MeV need to be further analyzed. However, they indicate that the rules described above hold both for the γ-rays and particle irradiation. Nevertheless, the damage introduced to cells by the proton beams is more serious as compared with the same doses of γ-rays and is repaired only with difficulty. Importantly, the contribution of "primary" and "secondary" DSB clusters to the induction of the cell death and formation of chromosomal translocations, or the role of DSB clusters in general, seems to differ for γ-rays and protons of different energies (and will surely differ for heavy ions). Therefore, especially in the context of the future development of the proton(ion)-beam cancer therapy, the relationship between the higher-order chromatin structure, DSB repair and misrepair upon the action of ionizing radiation of different quality must be studied.

Acknowledgments

The work was supported by the following projects: OPVK CZ.1.07/2.3.00/30.0030, GAČR Center of Excellence P302/12/G157, GAČR Nos. P302/10/1022 and P108/12/G108, COST LD12039 and LD12008 (MŠMT), EU COST MP1002 Nano-IBCT and from the Czech Republic contribution to JINR Dubna (the Grant of the Government Plenipotentiary, 2012 and the Grant 3+3, 2012).

References

Anderson, R.M., Papworth, D.G., Stevens, D.L., Sumption, N.D., Goodhead, D.T., 2006. Increased complexity of radiation-induced chromosome aberrations consistent with a mechanism of sequential formation. Cytogenet. Genome Res. 112 (1–2), 35–44.

Aten, J.A., Stap, J., Krawczyk, P.M., van Oven, C.H., Hoebe, R.A., Essers, J., Kanaar, R., 2004. Dynamics of DNA double-strand breaks revealed by clustering of damaged chromosome domains. Science 303 (5654), 92–95.

Ayoub, N., Jeyasekharan, A.D., Bernal, J.A., Venkitaraman, A.R., 2008. HP1-beta mobilization promotes chromatin changes that initiate the DNA damage response. Nature 453 (7195), 682–686.

Beucher, A., Birraux, J., Tchouandong, L., Barton, O., Shibata, A., Conrad, S., Goodarzi, A.A., Krempler, A., Jeggo, P.A., Löbrich, M., 2009. ATM and Artemis promote homologous recombination of radiation-induced DNA double-strand breaks in G2. EMBO J. 28 (21), 3413–3427.

Board on Radiation Effects Research (BRER) Committee to Assess Health Risks from Exposure to Low Levels of Ionizing Radiation, National Research Council, 2006. Health Risks from Exposure to Low Levels of Ionizing Radiation: BEIR VII Phase 2. National Academies Press, Washington, DC.

Caron, H., van Schaik, B., van der Mee, M., Baas, F., Riggins, G., van Sluis, P., Hermus, M.C., van Asperen, R., Boon, K., Voûte, P.A., Heisterkamp, S., van Kampen, A., Versteeg, R., 2001. The human transcriptome map: clustering of highly expressed genes in chromosomal domains. Science 291 (5507), 1289–1292.

Cremer, T., Cremer, M., Dietzel, S., Müller, S., Solovei, I., Fakan, S., 2006. Chromosome territories–a functional nuclear landscape. Curr. Opin. Cell Biol 18 (3), 307–316.

Darzynkiewicz, Z., 2011. Recent Advances in Cytometry, Part B, Fifth Edition Advances in Applications (Methods in Cell Biology), Volume 103. Academic Press.

Downs, J.A., Nussenzweig, M.C., Nussenzweig, A., 2007. Chromatin dynamics and the preservation of genetic information. Nature 447 (7147), 951–95821.

Durante, M., Pignalosa, D., Jansen, J.A., Walboomers, X.F., Ritter, S., 2010. Influence of nuclear geometry on the formation of genetic rearrangements in human cells. Radiat. Res. 174 (1), 20–26.

Falk, M., Lukasova, E., Gabrielova, B., Ondrej, V., Kozubek, S., 2007. Chromatin dynamics during DSB repair. Biochim. Biophys. Acta 1773 (10), 1534–1545.

Falk, M., Lukásová, E., Kozubek, S., 2008. Chromatin structure influences the sensitivity of DNA to gamma-radiation. Biochim. Biophys. Acta 1783 (12), 2398–2414.

Falk, M., Lukasova, E., Kozubek, S., 2010. Higher-order chromatin structure in DSB induction, repair and misrepair. Mutat. Res. 704 (1–3), 88–100.

Frenster, J.H., 1965. Ultrastructural continuity between active and repressed chromatin. Nature 205, 1341–1342.

Goetze, S., Mateos-Langerak, J., Gierman, H.J., de Leeuw, W., Giromus, O., Indemans, M.H., Koster, J., Ondrej, V., Versteeg, R., van Driel, R., 2007. The three-dimensional structure of human interphase chromosomes is related to the transcriptome map. Mol. Cell Biol. 27 (12), 4475–4487.

Goodarzi, A.A., Jeggo, P.A., 2009. 'A mover and a shaker': 53BP1 allows DNA doublestrand breaks a chance to dance and unite. F1000 Biol. Rep. 1, 21.

Goodarzi, A.A., Noon, A.T., Deckbar, D., Ziv, Y., Shiloh, Y., Löbrich, M., Jeggo, P.A., 2008. ATM signaling facilitates repair of DNA double-strand breaks associated with heterochromatin. Mol. Cell 31 (2), 167–177.

Goodarzi, A.A., Noon, A.T., Jeggo, P.A., 2009. The impact of heterochromatin on DSB repair. Biochem. Soc. Trans. 37 (3), 569–576.

Chiolo, I., Minoda, A., Colmenares, S.U., Polyzos, A., Costes, S.V., Karpen, G.H., 2011. Double-strand breaks in heterochromatin move outside of a dynamic HP1a domain to complete recombinational repair. Cell 144 (5), 732–744.

Jakob, B., Splinter, J., Conrad, S., Voss, K.O., Zink, D., Durante, M., Löbrich, M., Taucher-Scholz, G., 2011. DNA double-strand breaks in heterochromatin elicit fast repair protein recruitment, histone H2AX phosphorylation and relocation to euchromatin. Nucleic Acids Res. 39 (15), 6489–6499.

Kozubek, M., Kozubek, S., Lukásová, E., Bártová, E., Skalníková, M., Matula, P., Matula, P., Jirsová, P., Cafourková, A., Koutná, I., 2001. Combined confocal and wide-field high-resolution cytometry of fluorescent in situ hybridization-stained cells. Cytometry 45 (1), 1–12.

Kozubek, M., Matula, P., Matula, P., Kozubek, S., 2004. Automated acquisition and processing of multidimensional image data in confocal in vivo microscopy. Microsc. Res. Tech. 64 (2), 164–175.

Kozubek, S., Lukásová, E., Jirsová, P., Koutná, I., Kozubek, M., Ganová, A., Bártová, E., Falk, M., 2002. Paseková R. 3D Structure of the human genome: order in randomness. Chromosoma 111 (5), 321–331.

Kruhlak, M.J., Celeste, A., Dellaire, G., Fernandez-Capetillo, O., Müller, W.G., McNally, J.G., Bazett-Jones, D.P., Nussenzweig, A., 2006. Changes in chromatin structure and mobility in living cells at sites of DNA double-strand breaks. J. Cell. Biol. 172 (6), 823–834.

Loizou, J.I., Murr, R., Finkbeiner, M.G., Sawan, C., Wang, Z.Q., Herceg, Z., 2006. Epigenetic information in chromatin: the code of entry for DNA repair. Cell Cycle 5 (7), 696–701.

Lukas, C., Bartek, J., Lukas, J., 2005. Imaging of protein movement induced by chromosomal breakage: tiny 'local' lesions pose great 'global' challenges. Chromosoma 114 (3), 146–154.

Matula, Pa., Danek, O., Maska, M., Vinkler, M., Kozubek, M., 2010. Acquiarium: free software for image acquisition and image analysis in cytometry. Mikroskopie, 2010.

Mills, K.D., Ferguson, D.O., Alt, F.W., 2003. The role of DNA breaks in genomic instability and tumorigenesis. Immunol. Rev. 194, 77–95.

Nelms, B.E., Maser, R.S., MacKay, J.F., Lagally, M.G., 1998. Petrini JH. In situ visualization of DNA double-strand break repair in human fibroblasts. Science 280 (5363), 590–592.

Nikiforova, M.N., Stringer, J.R., Blough, R., Medvedovic, M., Fagin, J.A., Nikiforov, Y.E., 2000. Proximity of chromosomal loci that participate in radiation-induced rearrangements in human cells. Science 290 (5489), 138–141.

Noon, A.T., Shibata, A., Rief, N., Löbrich, M., Stewart, G.S., Jeggo, P.A., Goodarzi, A.A., 2010. 53BP1-dependent robust localized KAP-1 phosphorylation is essential for heterochromatic DNA double-strand break repair. Nat. Cell. Biol. 12 (2), 177–184.

Perez-Ortin, J., Matallana, E., Tordera, V., 1988. Analysis of chromatin structure and composition. Biochem. Educ. 16, 45–47.

Rogakou, E.P., Pilch, D.R., Orr, A.H., Ivanova, V.S., Bonner, W.M., 1998. DNA double-stranded breaks induce histone H2AX phosphorylation on serine 139. J. Biol. Chem. 273 (10), 5858–5868.

Rübe, C.E., Lorat, Y., Schuler, N., Schanz, S., Wennemuth, G., Rübe, C., 2011. DNA repair in the context of chromatin: new molecular insights by the nanoscale detection of DNA repair complexes using transmission electron microscopy. DNA Repair (Amst) 10 (4), 427–437.

Scherthan, H., Hieber, L., Braselmann, H., Meineke, V., Zitzelsberger, H., 2008. Accumulation of DSBs in gamma-H2AX domains fuel chromosomal aberrations. Biochem. Biophys. Res. Commun. 371 (4), 694–697.

Sevcik, J., Falk, M., Kleiblova, P., Lhota, F., Stefancikova, L., Janatova, M., Weiterova, L., Lukasova, E., Kozubek, S., Pohlreich, P., Kleibl, Z., 2012. The BRCA1 alternative splicing variant Δ14-15 with an in-frame deletion of part of the regulatory serine-containing domain (SCD) impairs the DNA repair capacity in MCF-7 cells. Cell. Signal 24 (5), 1023–1030.

Tamaru, H., 2010. Confining euchromatin/heterochromatin territory: jumonji crosses the line. Genes Dev. 24 (14), 1465–1478.

Tanabe, H., Habermann, F.A., Solovei, I., Cremer, M., Cremer, T., 2002. Non-random radial arrangements of interphase chromosome territories: evolutionary considerations and functional implications. Mutat. Res. 504 (1–2), 37–45.

Vagnarelli, P., 2012. Mitotic chromosome condensation in vertebrates. Exp. Cell Res. 318 (12), 1435–1441.

Versteeg, R., van Schaik, B.D., van Batenburg, M.F., Roos, M., Monajemi, R., Caron, H., Bussemaker, H.J., van Kampen, A.H., 2003. The human transcriptome map reveals extremes in gene density, intron length, GC content, and repeat pattern for domains of highly and weakly expressed genes. Genome Res. 13 (9), 1998–2004.

Nanoscale

PAPER

Cite this: *Nanoscale*, 2018, **10**, 1162

Particles with similar LET values generate DNA breaks of different complexity and reparability: a high-resolution microscopy analysis of γH2AX/53BP1 foci

Lucie Jezkova,[a,b] Mariia Zadneprianetc,[a,c] Elena Kulikova,[a,c] Elena Smirnova,[a] Tatiana Bulanova,[a,c] Daniel Depes,[d] Iva Falkova,[d] Alla Boreyko,[a,c] Evgeny Krasavin,[a,c] Marie Davidkova,[e] Stanislav Kozubek,[d] Olga Valentova[b] and Martin Falk *[d]

Biological effects of high-LET (linear energy transfer) radiation have received increasing attention, particularly in the context of more efficient radiotherapy and space exploration. Efficient cell killing by high-LET radiation depends on the physical ability of accelerated particles to generate complex DNA damage, which is largely mediated by LET. However, the characteristics of DNA damage and repair upon exposure to different particles with similar LET parameters remain unexplored. We employed high-resolution confocal microscopy to examine phosphorylated histone H2AX (γH2AX)/p53-binding protein 1 (53BP1) focus streaks at the microscale level, focusing on the complexity, spatiotemporal behaviour and repair of DNA double-strand breaks generated by boron and neon ions accelerated at similar LET values (~135 keV μm^{-1}) and low energies (8 and 47 MeV per n, respectively). Cells were irradiated using sharp-angle geometry and were spatially (3D) fixed to maximize the resolution of these analyses. Both high-LET radiation types generated highly complex γH2AX/53BP1 focus clusters with a larger size, increased irregularity and slower elimination than low-LET γ-rays. Surprisingly, neon ions produced even more complex γH2AX/53BP1 focus clusters than boron ions, consistent with DSB repair kinetics. Although the exposure of cells to γ-rays and boron ions eliminated a vast majority of foci (94% and 74%, respectively) within 24 h, 45% of the foci persisted in cells irradiated with neon. Our calculations suggest that the complexity of DSB damage critically depends on (increases with) the particle track core diameter. Thus, different particles with similar LET and energy may generate different types of DNA damage, which should be considered in future research.

Received 13th September 2017,
Accepted 8th December 2017

DOI: 10.1039/c7nr06829h

rsc.li/nanoscale

1 Introduction

Ionizing radiation (IR) is one of the most effective cytotoxic agents. Due to its ability to ionize atoms or molecules, IR induces several types of DNA damage. Among these lesions, DNA double-strand breaks (DSBs) are the most critical. Cells have evolved sophisticated DNA damage repair systems capable of efficiently removing a vast majority of lesions to maintain genome integrity, which is permanently threatened by various exogenous and endogenous factors.[1,2]

However, a unique attribute of IR is its ability to deposit energy within nanometre volumes and thus induce clustered/complex DNA damage containing various combinations of DSBs, single-strand breaks (SSBs), chemically modified or lost bases, DNA–DNA cross-links, DNA–protein cross-links, heat- and alkali-labile sites, and other potential impairments. These lesions pose a serious challenge for DNA repair systems, as in many instances, this damage is irreparable, may be repaired incorrectly or may lead to the formation of even more serious DNA damage.[1–3] Hence, because clustered/complex DNA damage represents the main cause of cell death or mutagenesis upon irradiation, these types of damage have been considered key determinants of the radiobiological effectiveness of radiation.

The complexity of DNA damage depends on the radiation quality, and for radiobiological purposes, this quality is typically described in terms of linear energy transfer (LET).[2,4] Two main groups of radiation have been distinguished based on

[a]*Joint Institute for Nuclear Research, Dubna, Russia*
[b]*University of Chemistry and Technology Prague, Prague, Czech Republic*
[c]*Dubna State University, Dubna, Russia*
[d]*Czech Academy of Sciences, Institute of Biophysics, Brno, Czech Republic. E-mail: falk@ibp.cz; Tel: +420-541517116, +420-728084060*
[e]*Czech Academy of Sciences, Nuclear Physics Institute, Prague, Czech Republic*

LET and their mechanism of action and biological effects. Low-LET radiation sparsely and uniformly deposits energy within the whole volume of the cell nucleus. Hence, exposure to γ-rays or X-rays, two representatives of this category, typically leads to the formation of simple DNA lesions. In contrast, clustered or complex damage (multiple DSBs and other lesions within a few helical DNA turns) is the characteristic feature of high-LET irradiation.[1–4] The phenomenon of clustered/multiple DNA damage is evoked by the nature of the energy transferred, and by definition, high-LET radiation densely releases energy along the track of the particle such that several types of damage form in a single localized spot volume.

The spatial structure of high-LET particle tracks depends on the physical parameters of the particle and chromatin structure. The distribution of energy deposited by high-LET radiation along the particle track is divided into two spatial components: the core and the penumbra, also known as the region of δ-rays.[5,6] The core is typically referred as to the central region of extremely dense energy deposition, where biomolecules are directly damaged by the particle itself along with contributions from low-energy knock-on electrons that do not escape from the core volume. Secondary electrons of higher energy (δ-rays) subsequently radiate out from the core and form the penumbra. Although a generally accepted definition of these track components is not yet available,[6] the microdosimetric characteristics of the track core and the penumbra together determine the initial complexity of DNA damage.[6,7] This notion is also true for the relationship between these spatial track/streak components and relative biological effectiveness (RBE) of radiation.

LET is frequently calculated to definitively determine the RBE of radiation; however, this parameter cannot precisely predict how particle tracks will appear and behave in space and time. A considerable body of evidence has revealed the positive dependence of RBE on LET, where the biological endpoints of irradiation, such as cell killing,[8–11] induction of mutations[12–14] (reviewed in Yatagai *et al.*[15]), and formation of chromosomal aberrations,[16–19] increase as the LET value increases. However, a certain LET value (approximately 100 keV μm^{-1}) will correspond to the maximum peak RBE, and from this point, RBE decreases only with increasing LET. Moreover, the most biologically damaging LET value largely fluctuates between 100 and 200 keV μm^{-1} for different particles, depending on the cell type and endpoint studied.[7,20–22] Hence, a reasonable hypothesis is that the particle generates tracks with different spatiotemporal characteristics according to specific sets of individual physical parameters (*e.g.*, energy, charge, diameter, *etc.*), even if various combinations of these parameters show similar LET values.[7] However, experimental studies focusing on the microstructure of DNA damage observed following the action of different high-LET particles with similar LET values are rare.

In addition to initial (static) structure of DNA damage, changes in the DNA dynamics over time after irradiation may also principally influence the reparability of DNA damage and therefore the RBE of radiation types. Chromatin fragmentation occurring in response to high-LET irradiation and chromatin decondensation that occurs during DSB repair (in response to both high-LET and low-LET irradiation) locally mobilizes damaged chromatin to some extent, generating clustered/complex DNA lesions.[23–26] The extent of chromatin fragmentation and spatial density of DSBs depend on LET, and the spatiotemporal dynamics of DNA damage is also expected to rely on LET. Nevertheless, researchers have not determined whether and how chromatin dynamics vary for different particles with similar LET. The importance of particle LET/energy becomes particularly relevant for low-dose/particle fluences – the conditions addressed in the present study. The characterization of the particle tracks (DNA damage structure) in space and time thus emerges as a promising and necessary new approach to explain many aspects of the radiobiological effects of physically different radiation types.

Studies of spatiotemporal aspects of DNA damage have become feasible with the discovery of the focal accumulation of DSB repair proteins at DSB lesions.[27] One of the first cell responses to DSB formation is the phosphorylation of histone H2AX on Ser-139, followed by the attraction of numerous downstream repair proteins to sites of DSB. Phosphorylated H2AX (referred as to γH2AX) rapidly spreads over 2 Mbps of damaged chromatin and becomes microscopically detectable as discrete nuclear (γH2AX) foci within minutes after irradiation.[27–29] Subsequently, numerous repair factors, including p53-binding protein 1 (53BP1), accumulate at γH2AX foci in a time-dependent manner, resulting in the formation of discrete nuclear domains, which are generally referred to as IR-induced foci (IRIF).[23,30]

Importantly, the structural parameters and assembly and disassembly kinetics of γH2AX/IRIF foci reflect the physical characteristics of the damaging agent, chromatin structure, and overall (genetic and physiological) cell status. Microscopy of γH2AX/IRIF foci *in situ* enables complex studies on spatiotemporal aspects of DSB damage induction, repair, and misrepair in the context of intact or even living cells. Moreover, this method offers unprecedented sensitivity and the possibility of simultaneous visualization of multiple DSB repair proteins.[30–32]

The relationship between the number of DSBs and γH2AX foci is approximately 1 : 1 for low-LET radiation.[28,33] However, high-LET radiation generates DSBs that are located so close to one another that these lesions cannot be further separated at the resolution of standard optical microscopy.[29,34] Various super-resolution (nanoscopy) techniques have been proposed and more or less successfully implemented into research practice to overcome this problem[35,36] (reviewed by Falk[37]); however, still these methods remain technically challenging and are typically applicable only to relatively small sample numbers. Two studies by Lorat and co-workers[38,39] took advantage of transmission electron microscopy to precisely quantify DSB complexity upon high-LET irradiation at a single molecule level. However, despite the superior resolution power and undisputable advantages of this approach, it suffers from serious limitations that primarily result from the complicated sample preparation requirements and the inability to quanti-

tatively analyse DSB damage in the entire (3D) volume of the cell nucleus.[40] Hence, a method for the precise, reliable, high-throughput and complex (*i.e.*, in 3D volumes) analysis of DSBs under physiological conditions is not currently available. Many fundamental questions therefore remain open. For example, the above discussed super-resolution study[38] revealed up to approximately 500 DSBs per 1 μm^3 volume of the carbon ion track (LET = 190 keV μm^{-1}, energy E = 9.5 MeV per n). This result is surprising and prompts questions of how a single DSB is defined at the molecular level and what level of complexity do DSBs generated by different radiation types present.

To our knowledge, the current study represents the first experimental research on the spatiotemporal aspects of DNA damage upon exposure to high-LET radiation with a similar LET and (low) energy. We used high-resolution immunofluorescence confocal microscopy to perform a detailed examination of the DNA damage generated by neon ions, which show potential to improve hadron therapy,[41,42] and boron ions, which are common secondary particles produced by nuclear interactions between high-energy neutrons and protons.[43] Surprisingly, only a few experimental[6,30,44] or theoretical[45,46] studies (reviewed in Hamada[47]) have more or less directly addressed the induction and distribution of DSBs in cell nuclei irradiated with different particles of similar (high) LET. In contrast to these studies, we modified the parameters of the accelerated ions to exhibit similar LET values close to the maximum RBE as well as similar low energies. We focused on lower-energy particles that although they are rarely studied, are attractive for several purposes: they may arise during radiation shielding or affect normal tissue in hadron therapy at the end of the Bragg peak. Moreover, low-energy ions induce more complex and persistent DNA damage than high-energy particles.[6,30,48]

^{20}Ne ions generate DSBs of higher complexity and lower reparability than ^{11}B ions, despite the similar LET values of both ions and slightly higher energy of neon. Besides other hypotheses, this result may be explained by the morphology and spatiotemporal dynamics of γH2AX/53BP1 focus streaks that also obviously differed for the two radiation types. Our detailed analysis of these streaks suggests that the particle track structure is the crucial determinant of the RBE of radiation, which roughly depends on LET and energy but might be largely modified by other particle parameters under conditions of similar LET/energy.

2 Materials and methods

2.1 Cell culture

Primary normal human neonatal dermal fibroblasts, NHDF-Neo (Lonza, CC-2509), were grown in Iscove's Modified Dulbecco's Medium (IMDM) supplemented with 10% foetal calf serum (FCS) and a 1% gentamicin–glutamine solution (all reagents from Sigma-Aldrich). Cells were maintained in T-25 cell flasks at 37 °C in a humidified atmosphere with 5% CO_2. All experiments were performed using cells at passages 6–9.

Prior to irradiation (16–18 h), cells were re-seeded on 14 mm glass coverslips (glued to the outer side of a 35 mm Petri dish with a microwell, MatTek Corporation, P35G-0.170-14-C) and cultivated to form an 80% confluent monolayer. For irradiation, dishes were aseptically closed and sealed with Parafilm M (Sigma-Aldrich) to prevent spillage and cell infection. All samples were irradiated at room temperature and immediately returned to the incubator (37 °C).

2.2 Low-LET and high-LET irradiation

Non-synchronized cell populations with >80% of cells in G1-phase (Fig. 1) were irradiated with accelerated ions using a U-400 M isochronous cyclotron in the Flerov Laboratory of Nuclear Reaction at the Joint Institute for Nuclear Research (JINR, Dubna), and the Genome-M facility was used for the automatic fast irradiation of biological samples.[49] According to the experiment, cells on glass coverslips (glued to a Petri dish as described above) were irradiated either at a perpendicular (90°) or sharp-angle (10°) geometry, *i.e.*, with 90° or 10° angle between the ion beam and the plane of the cell monolayer. The coverslips were oriented towards the ion beam so that the cells were hit by the particles before the beam continued into the culture medium in the Petri dish. Samples that were irradiated in the perpendicular geometry were used to evaluate the kinetics of DSB repair and cell death (apoptosis) upon exposure to radiation. Cells irradiated in the sharp-angle geometry enabled detailed analyses of the morphology of γH2AX/53BP1 foci and structures of particle tracks (streaks) in space and time. In these experiments, cells were exposed to an average of three particles per nucleus, which corresponds to a dose of 1 Gy for ^{11}B ions and 1.2 Gy for ^{20}Ne ions (calculated as described by Jakob *et al.*[29] for the average nuclear area of 186 μm^2). The non-homogeneity within the irradiation field of 14 mm in diameter was less than 5%, as monitored using five identical flow-type ionization chambers; the central chamber served as the monitor of the radiation dose.[49]

Fibroblasts were exposed to boron or neon beams with a dose rate of approximately 2 Gy min^{-1}. The initial energy of ^{11}B ions generated by the accelerator was 33 MeV per n. Due to the presence of different absorbers in the path of the ions in route to the sample (*e.g.*, 1.842 mm-thick aluminium foil, 0.170 mm-thick borosilicate glass, *etc.*), this energy decreased

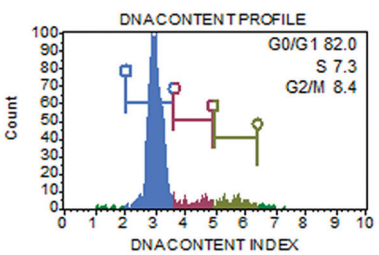

Fig. 1 Illustrative flow cytogram showing the distribution of human skin fibroblasts across the cell cycle at the time of irradiation. The Muse® Cell Analyser (Merck Millipore) and Muse® Cell Cycle Assay Kit (MCH100106) were used according to the manufacturer's instructions.

to the final value of 8.1 MeV per n at the plane of the cell monolayer irradiated in the 90° setup, corresponding to a LET value of 138.1 keV μm^{-1}. For the sharp-angle (10°) irradiation geometry, the energy of boron ions was further reduced to 7.5 MeV per n (the thickness of the glass at 10° was 0.979 mm) using an additional 1.006 mm-thick aluminium absorber, resulting in a LET value of 148.3 keV μm^{-1} (Table 1).

A beam of ^{20}Ne ions accelerated to 50.0 MeV per n was used as the second type of high-LET radiation. The energy at the cell monolayer was 46.6 MeV per n in the 90° geometry and 33.9 MeV per n in the sharp-angle (10°) setup; the corresponding LET values were 132.1 keV μm^{-1} and 170.9 keV μm^{-1}, respectively. For neon radiation, no additional absorbers (with the exception of mandatory absorbers, *e.g.*, separating foils, electrodes, air, and glass coverslips) were used. The energy and corresponding LET values of ions at the plane of the cell monolayer were calculated using LISE++ software.[50] The irradiation schemes and radiation characteristics are summarized in Table 1.

Gamma rays from a ^{60}Co source were used as a low-LET radiation. The samples were irradiated at the Rokus-M facility in Dzhelepov Laboratory of Nuclear Problems (JINR, Dubna) with 1 Gy of γ-rays at a dose rate of 1 Gy min^{-1}. Mock-irradiated cells were used as controls in all experiments.

2.3 Immunofluorescence assay

Irradiated cells were spatially (3D) fixed at different periods of time post-irradiation (PI), ranging from 5 min PI to 4 days PI, with 4% paraformaldehyde/PBS (10 min, room temperature (RT)) after a brief (2 × 2 min) wash with PBS (phosphate-buffered saline, 37 °C). Fixed cells were quickly rinsed (PBS), washed 3 × 5 min with PBS, and permeabilized with 0.2% Triton-X100/PBS (15 min at RT). After rinsing and washing (3 × 5 min) with PBS, cells were treated with the blocking solution I (5% inactivated FCS/2% bovine serum albumin/PBS) for 30 min at RT. The primary antibodies – mouse anti-γH2AX (ab22551, Abcam) and rabbit anti-53BP1 (ab21083, Abcam) – were diluted in the blocking solution I (1 : 700 and 1 : 600, respectively) and applied to the cells for 10 min at RT and subsequently overnight at 4 °C. Cells were rinsed with PBS, washed 3 × 5 min (RT) with PBS, and blocked (30 min) with blocking solution 2 (5% inactivated goat serum/PBS) to inhibit nonspecific binding. The secondary antibodies – Texas Red-conjugated goat anti-rabbit (ab6719, Abcam) and FITC-conjugated goat anti-mouse (ab97239, Abcam) – were diluted in blocking solution 2 (1 : 400 and 1 : 200, respectively) and applied to the cells for 30 min (RT, in the dark). This step was followed by washes with PBS (a brief rinse + 3 × 5 min at RT), 2× saline sodium citrate (SSC) (2 min) and 4× SSC + 0.1% Igepal. The chromatin was counterstained with 600 nM 4′,6-diamidino-2-phenylindole dihydrochloride (DAPI, Sigma-Aldrich) in Vectashield antifade mounting medium (Vector Laboratories).

2.4 Image acquisition and experimental data analysis

Images of the immunofluorescence staining were captured using an automated high-resolution Leica SP5 confocal laser-scanning fluorescence microscopy system equipped with a white laser for the excitation of multiple fluorochromes and sensitive hybrid detectors (Leica). Confocal slices of cells were obtained with a HCX PL APO lambda blue 63.0× 1.40 OIL UV immersion objective with 0.25 μm z-step increments across the nuclei, which were 2.7–3.4 μm-thick on average. Images were analysed using Acquiarium software,[51] which enabled the three-dimensional reconstruction of images and inspection of individual γH2AX and 53BP1 foci in 3D space. For all analyses, only colocalized γH2AX/53BP1 foci were considered. There were 3 reasons for scoring only the colocalized signals: (1) to increase the precision of DSB detection in the early stages post-irradiation; (2) to increase the probability that unrepaired DSBs are still observed in later and very late periods of time PI; and (3) to partially increase the homogeneity of cells (*i.e.*, the proportion of G1 cells) involved in the analyses. Notably, in early time periods post-irradiation, the γH2AX signal represents a mixture of small but more developed γH2AX foci (that colocalize with 53BP1) and similarly small or smaller γH2AX foci in very early stages, which could sometimes be difficult to distinguish from the background signal. In later periods of time PI, the persistence of the 53BP1 signal at γH2AX foci allowed us to legitimately presuppose that γH2AX/53BP1 foci present in nuclei still represent unrepaired DSBs and are not simply "relics" of previously repaired lesions. Finally, 53BP1 dissociates from γH2AX foci during late S-phase,[52,53] G2-phase[54] and mitosis;[54] thus, the evaluation of colocalizing γH2AX foci alone may also increase the predominance of G1 cells in the present analyses.

Table 1 Irradiation schemes and radiation parameters

Particle	*Z*	Geometry°	Energy, MeV per n	LET, keV μm^{-1}	Fluence*, 1 cm^{-2}	Particles per nucleus#
^{11}B	5	90	8.1	138.1	4.52×10^6	8.4
^{11}B	5	10	7.5	148.3	4.21×10^6	3.3
^{20}Ne	10	90	46.6	132.1	4.73×10^6	8.8
^{20}Ne	10	10	33.9	170.9	3.65×10^6	2.7

Z – charge, ○ – geometry of irradiation (the angle between the ion beam and the plane of the cell monolayer), * – fluence per 1 Gy absorbed in water, # – the number of particles per 1 Gy traversing a nucleus with an average area. The LET of Ne particles increased with increasing distance traversed along the glass at 10° irradiation, for which it was difficult to compensate. We cannot exclude minor influences on the results, but we consider this effect rather insignificant. Notably, identical conclusions to those drawn using 10° irradiation were obtained (though with lower precision) using 90° irradiation, where the LET values for B and Ne ions are much more similar.

The foci were manually counted by eye (2 independent experienced evaluators) in three-dimensional images of approximately 100 nuclei per each experimental condition. In the 10° irradiation experiments, the software analyses described below supported this estimation. The mean numbers with the standard errors per group were calculated for pooled data from two independent experiments (additional experiments were not possible because of the limited beam time awarded to users and the specific settings required). The area and circularity of γH2AX/53BP1 foci and complexity of γH2AX/53BP1 focus clusters were measured in nuclei irradiated in the sharp-angle (10°) geometry, which ensured a sufficiently high microscopic resolution of individual foci. The area and circularity were measured on maximum images composed of all superimposed confocal slices using Adobe Photoshop CS6 Extended software; at least 200 γH2AX/53BP1 foci were scored per group to calculate the mean values with standard errors. The boundaries of individual γH2AX/53BP1 foci within the cluster and the complexity of 3D foci in the cluster (number of clustered foci) (Fig. 2) were semi-computationally determined by combining information obtained from (a) the cluster morphology (shape/size) characterized for each individual 0.25 μm-thick confocal slice of the image *z*-stack; (b) cluster fluorescence intensity heat maps computed for each individual confocal slice of the *z*-stack as well as for the maximum images composed of superimposed confocal slices; and (c) cluster red-channel fluorescence intensity profiles (R-profiles) measured for each individual confocal slice of the image *z*-stack along the path drawn to identify eventual fluorescence maxima and minima between foci in overexposed cluster areas. Since the 53BP1 signals precisely corresponded to γH2AX signals but presented better mutual separation in clusters, we used the 53BP1 (red) channel for image analyses. First (with the exception of morphologically clearly distinguishable foci), we determined the local fluorescence maxima (fluorescence foci centres; heat maps) of the clusters and compared their numbers per cluster and positions relative to the number and positions of putative foci defined according to cluster morphology. When all parameters were correlated, the number of foci per cluster was counted as the number of fluorescence centres. When two or more foci were identified according to cluster morphology but the number of fluoresce centres was lower (*e.g.*, one large inseparable maximum existed for two putative foci), a fluorescence profile in the red channel (53BP1) was measured along the path intersecting putative foci in more peripheral areas, where the fluorescence signal was not overexposed. Decisions regarding the number of foci were made based on the number of local fluorescence maxima along the path. Alternatively (seemingly one focus contains two fluorescence centres), two foci were only scored under the following conditions: (a) both maxima were intensive, and (b) the focus was large and (c) sufficiently irregular to provide a legitimate impression of the existence of two foci (*e.g.*, large elliptic focus with two intensive eccentrically located fluorescence maxima). The morphology of the clusters was studied in 3D with Acquiarium software, and R-profiles and heat maps were prepared with ImageJ[55] and CellProfiler[56] software, respectively. The line demarcating the area of each focus in the cluster (white circles in Fig. 2A) was manually drawn according to the focus heat map signal in the confocal slice showing the strongest fluorescence maximum. Typically, the signal of two levels above the heat map background (green signal in Fig. 2A) was used for this purpose. The described procedures were repeatedly performed for all individual confocal slices in the image *z*-stack, and the data were combined to obtain the final results. The procedure is demonstrated for illustrative foci (later introduced in Fig. 8, Results) generated by γ-rays, boron ions and neon ions in Fig. 2. Foci forming a spatial unit and connected at least by the "green" fluorescence level (heat maps) were considered to occupy one cluster. Statistical analyses were performed with the Sigma Plot statistical package.

2.5 Quantification of apoptosis by flow cytometry

The percentage of apoptotic cells after γ-ray or boron ion irradiation was determined *via* flow cytometry staining of Annexin V/7-amino actinomycin (7-AAD)-positive cells (Muse™ Annexin-V & Dead Cell Assay kit). Cells that had been irradiated with 1 or 4 Gy were assayed at 24 h and again at 48 h PI on the Muse™ Cell Analyzer, according to the manufacturer's instructions. Briefly, adherent cells and cells floating in the culture medium were collected, diluted to the required concentration (1×10^5 to 5×10^5 cells per ml) and consecutively incubated with the Muse Cell Dispersal Reagent (20 min at RT to prevent the formation of aggregates and clumps) and the Muse™ Annexin-V & Dead Cell Assay kit (20 min at RT in the dark). All reagents and the cell analyser were obtained from EMD Millipore Bioscience. Each sample was measured in triplicate, and the mean values with standard errors were calculated. Six thousand cells were acquired and analysed per sample. The proportions of apoptotic cells were determined using the Muse Cell Analyzer software.

2.6 Core radius calculation

The radius r_c of the particle track core was calculated based on the model reported by Chatterjee and Holley[57] using the following formulas:

$$r_c = \frac{\beta \times c}{\Omega_p}, \quad (1)$$

$$\Omega_p = \left(\frac{4\pi n e^2}{m}\right)^{1/2}, \quad (2)$$

where β is the velocity of the particle in units of the velocity of light (c), Ω_p is the plasma oscillation frequency, n is the number density of electrons in water (3×10^{23} electrons per cm^3) and e and m are the charge and mass of the electron, respectively. In water, $\Omega_p = 3.09 \times 10^{18}$ s^{-1}.

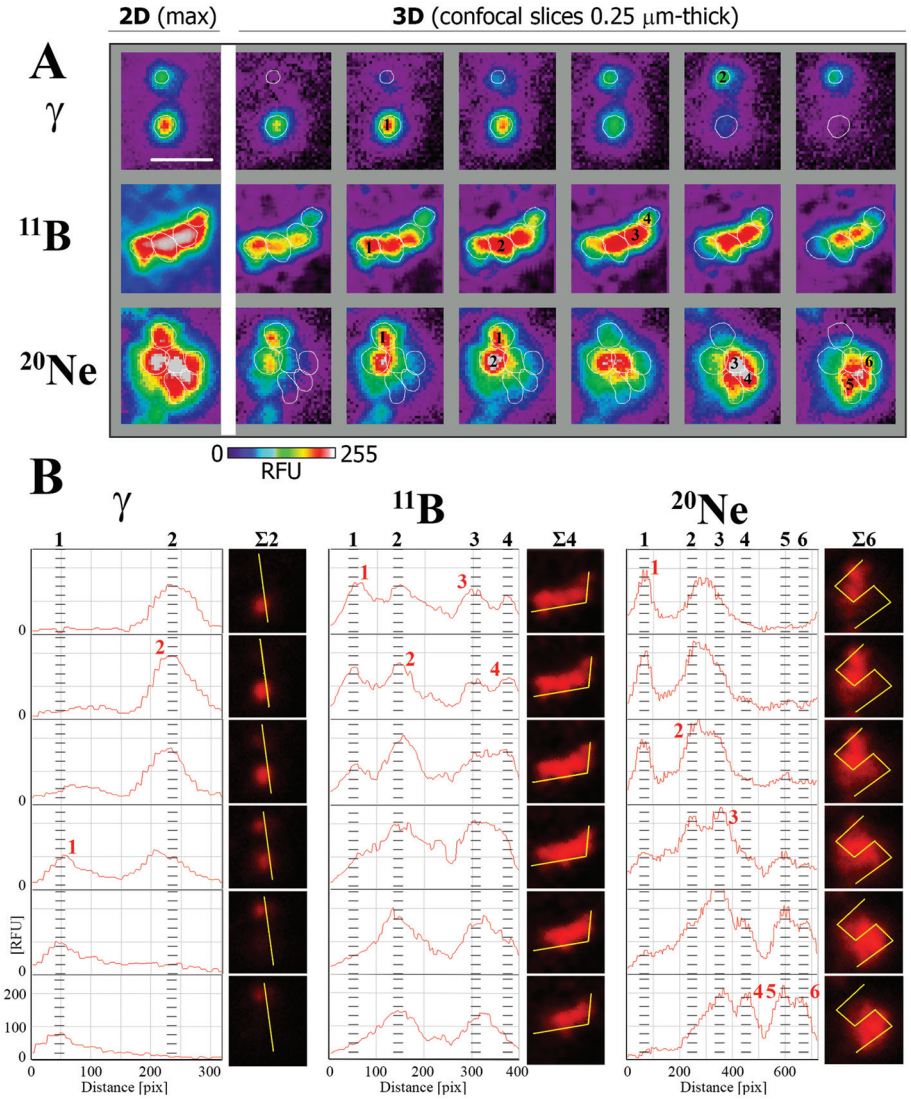

R chanel profiles: RFU (vertical axis) vs pixels along the (yellow; right) trajectory path (horizontal axis)

Fig. 2 Identification and demarcation of individual γH2AX/53BP1 foci within a cluster, for clusters induced by γ-rays, boron ions and neon ions. The boundaries of individual γH2AX/53BP1 foci within the cluster and the complexity of 3D foci in the cluster (number of clustered foci) were semi-computationally determined by combining information obtained from (A) fluorescence intensity heat maps computed for cluster images for each individual confocal slice of the *z*-stack (examples from the second left image to the right) as well as for the maximum images (left) composed of superimposed confocal slices; (B – left panels) red channel fluorescence intensity profiles (R-profiles) measured for each individual confocal slice of the image *z*-stack along the path (yellow line) drawn to identify eventual fluorescence maxima and minima between putative foci (since signals of 53BP1 precisely corresponded to γH2AX signals but showed better mutual separation in clusters, we used the 53BP1 red channel for image analyses); and (B – right panels) cluster morphology (shape/size) characterized for each individual 0.25 μm-thick confocal slice of the image *z*-stack. A. For γ-rays, the heat maps (relative fluorescence intensity units; RFU, 0–255) revealed 2 fluorescence maxima (with red and green intensity levels, respectively), corresponding to 2 morphologically regular and spatially separated foci; no cluster is present. In the case of boron ions, 1 cluster contained 4 maxima of red intensity. The cluster induced by neon ions exhibited 6 fluorescence maxima of red or even white intensity. The lines demarcating the area of each focus in the cluster (white circles) were manually drawn according to the focus heat map signal using the confocal slice showing the strongest fluorescence maximum or on the maximum image. Typically, the signal at two levels above the heat map background (green signal) was used for this purpose. Individual foci are indicated by (black) numbers at the slice of their maximal fluorescence intensity. Scale bar (white) = 400 nm. B. Relative fluorescence intensity (vertical axis, 0–255 [RFU]) profiles for the red (53BP1) channel measured along the path (yellow) shown in the corresponding right panels, where the path is plotted over the analysed clusters of foci. The profiles of consecutive confocal slices are sorted from top to bottom (left column – γ-rays; middle column – ^{11}B ions; right column – ^{20}Ne ions). Individual foci are indicated by red numbers at the confocal slice and the position along the yellow path (horizontal axis [pixels]) where they showed the maximum fluorescence intensity. Summarized numbers of foci for all confocal slices are indicated by the black numbers above the top image. As shown in these images, the numbers of foci determined according to R-channel line profiles were well correlated with the results based on the heat maps (A) and cluster morphology analyses (B, right panels). Foci forming a spatial unit and connected by at least the "green" fluorescence level (heat maps) were considered to occupy one cluster. The morphology of the clusters was studied in 3D with Acquiarium software, and R-profiles and heat maps were prepared with ImageJ and CellProfiler software, respectively.

3 Results

3.1 DSB repair kinetics compared for low-LET γ-rays and two high-LET particles with similar LET values

We examined the kinetics of γH2AX/53BP1 foci formation and characterized their decrease with time PI in normal human neonatal dermal fibroblasts (NHDF-Neo) exposed to three different types of radiation (section 2.2) to determine how radiation quality affects the induction of double-strand breaks (DSBs) in DNA molecules and assess the ability of human cells to repair this damage. Gamma rays from ^{60}Co, representing low-LET radiation, are used in the present study as the standard for comparisons. However, the boron (^{11}B) and neon (^{20}Ne) ions facilitated an examination of the effects of two high-LET particles with comparable LET values (similar to the maximum relative biological efficiency, RBE) and only slightly different energies (Table 1). For kinetics studies, we irradiated cell monolayers with 1 Gy of a particular radiation in the perpendicular (90°) geometry to the beam axis. Consequently, we visualized DSBs using high-resolution immunofluorescence confocal microscopy of colocalization of γH2AX and 53BP1 foci, the markers of DSBs,[58] in spatially (3D) fixed cells (Fig. 3). This approach currently provides the maximum sensitivity and fidelity for DSB detection[59] and, upon reconstructing 3D images of cell nuclei (Fig. 3), also enables efficient discrimination between individual γH2AX or 53BP1 foci (Fig. 3 and 4). The human skin fibroblasts used in the present study (representing a widely accepted model for studying normal tissue radiosensitivity)[60] are naturally flat cells with a height of approximately 2.8 μm.[61] We measured highly similar thicknesses of the nuclei of the cells (2.7–3.4 μm) (Fig. 3), which excluded their significant flattening during 3D fixation. At least 3 closely spaced γH2AX/53BP1 foci could be distinguished in the *z*-direction in cells irradiated with ^{11}B or ^{20}Ne ions. Hence, we were able to precisely examine the qualitative and quantitative characteristics of chromatin damage and DSB repair following exposure to different radiation types. The enhancement of DSB resolution in the 3D analysis compared with the 2D analysis is quantified in Fig. 4.

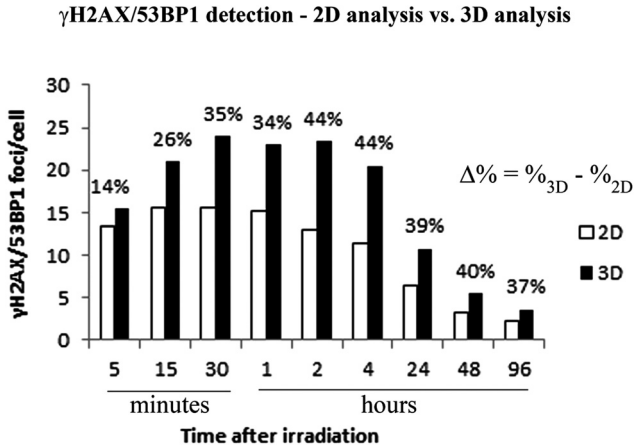

Fig. 4 Differences between the 2D (white columns) and detailed 3D (black columns) quantification of γH2AX/53BP1foci in NHDF-Neo fibroblasts irradiated with ^{20}Ne ions (LET = 132.1 keV μm^{-1}, *E* = 46.6 MeV per n) and spatially (3D) fixed with paraformaldehyde in both cases. The maximum images superimposed from individual confocal slices (through the complete volume of the nucleus) were used in 2D analyses, whereas these slices were individually inspected in 3D analyses. The means (left axis) ± standard errors for pooled data from two experiments (100 counted cells) and the percentage underestimation of the number of foci in the 2D analysis (numbers above the pairs of bars) are indicated.

We quantified the colocalization of γH2AX and 53BP1 foci at numerous times PI, ranging from 5 min PI to 96 h PI, to evaluate the kinetics of DSB repair. The maximum number of individual radiation-induced γH2AX/53BP1 foci per cell was observed between 30 min PI and 1 h PI, and the value was higher for samples exposed to both types of accelerated ions (^{11}B: 24.0 ± 1.1, ^{20}Ne: 23.9 ± 1.3) than for samples exposed to γ-rays (20.1 ± 0.5) (Fig. 5).

Additionally, the dynamics of foci formation and elimination differed with the radiation type. The fastest production

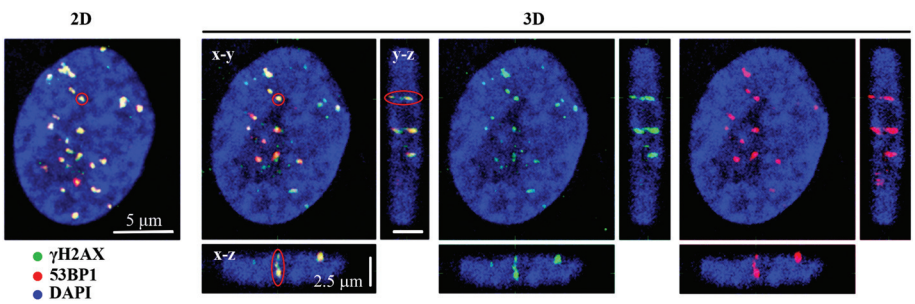

Fig. 3 Two- and three-dimensional visualization of γH2AX (green) and 53BP1 (red) DSB repair foci in spatially (3D) fixed NHDF-Neo fibroblasts irradiated with 1 Gy of accelerated ^{11}B ions (LET = 138.1 keV μm^{-1}, *E* = 8.1 MeV per n) in the perpendicular (90°) geometry. The cell shown here was fixed with paraformaldehyde 1 h after irradiation, followed by immunostaining for γH2AX and 53BP1 and counterstaining (chromatin) with DAPI (blue). The 2D maximum image (left) comprised ~25 confocal slices (including slices above and below the cell nuclei) obtained with a z-step of 0.25 μm. A single 3D confocal slice (right) reveals the increased ability of this technique to distinguish γH2AX/53BP1 foci in 3D space; an example of 3 foci that overlapped in the 2D image but were well separated in the 3D image is indicated by the red circle. Scale bars: *x*–*y*, 5 μm; and *x*–*z* and *y*–*z*, 2.5 μm.

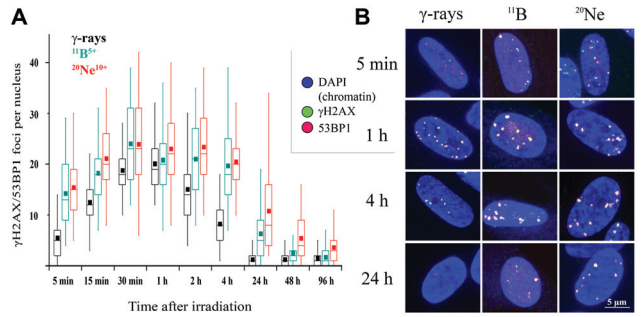

Fig. 5 γH2AX/53BP1 foci formation and loss (DSB repair dynamics) upon exposure to radiation of different qualities. NHDF-Neo cells were irradiated in the perpendicular (90°) geometry with 1 Gy of γ-rays, ^{20}Ne ions (LET = 132.1 keV μm^{-1}, E = 46.6 MeV per n) or ^{11}B ions (LET = 138.1 keV μm^{-1}, E = 8.1 MeV per n) and fixed at different times PI, as indicated. (A) Quantification of the number of γH2AX/53BP1 foci in 3D images. Sham-irradiated cells contained (not shown) 0.1 foci per nucleus on average. The box-and-whisker plot indicates the mean (black square), median (median line inside the box), 25th and 75th percentiles (the top and bottom of box, respectively), and minimum and maximum (whiskers) of the pooled data from two experiments (approximately 100 counted cells). (B) Representative maximum intensity images of the corresponding cell nuclei. γH2AX (green), 53BP1 (red), chromatin (DAPI).

of γH2AX/53BP1 foci upon irradiation was observed in cells irradiated with ^{20}Ne, whereas the slowest production was observed in cells subjected to γ-rays. The opposite situation emerged for foci elimination. For cells exposed to both types of high-LET ions, the foci disappeared more slowly than in cells subjected to γ-rays. Four hours after irradiating the cells with ^{20}Ne or ^{11}B ions, approximately 85% of the maximum numbers of γH2AX/53BP1 foci persisted in the cells, whereas this fraction was only 41% for cells irradiated with γ-rays (Table 2). Moreover, although the γH2AX/53BP1 foci per cell decreased to approximately 1 focus (6% of the maximum) at 24 h PI in γ-irradiated cells, approximately 6 (26%) and 11 (45%) foci remained in cells damaged by ^{11}B and ^{20}Ne ions, respectively (Fig. 5 and Table 2). Consistent with this observation, preliminary data for cells exposed to another accelerated charged particle, ^{12}C (LET = 9.8 keV μm^{-1}, E = 500 MeV per n, D = 0.3 Gy), revealed a similar delay in DSB repair; only a small number of foci disappeared from cells within the first

Table 2 Percentage of remaining γH2AX/53BP1 foci after irradiation with the same dose of different radiation types

	Time after irradiation				
Radiation type	2 h	4 h	24 h	48 h	96 h
γ-Rays (^{60}Co)	75.2	41.1	6.3	6.2	6.3
^{11}B	87.7	84.7	26.4	10.6	7.1
^{20}Ne	97.9	85.7	45.1	22.8	15.1

Mean percent values of pooled data from two experiments (approximately 100 counted cells) are shown. The data were normalized to the peak numbers for each radiation type, *i.e.*, the maximum number of foci scored for the particular radiation type, irrespective of the time PI.

4 h PI, and 16% of these foci persisted in cells at 24 h PI (data not shown).

Interestingly, despite the similar LET values for ^{11}B and ^{20}Ne ions and similar maximum numbers of γH2AX/53BP1 foci induced by these radiation types, both the elimination kinetics of γH2AX/53BP1 foci and their residual amounts measured at long periods of time (96 h) PI differed for these two radiation types. The number of γH2AX/53BP1 foci persisting at this period of time in cells irradiated with boron ions (1.7 foci per nucleus) decreased to values typical for γ-irradiated cells (1.3 foci per nucleus), but approximately 4 foci per nucleus persisted in cells exposed to ^{20}Ne ions (Fig. 5). These values were significantly higher than sham-irradiated (control) cells, with 0.1 foci per nucleus on average. These results demonstrate that the irradiation of NHDF cells with both ^{20}Ne and ^{11}B high-LET ions (as well as ^{12}C) delays the repair kinetics of DSBs compared with γ-rays, based on the persistence of γH2AX/53BP1 foci in cells during PI periods. Although this finding was expected according to current theoretical knowledge (see Discussion), the surprising observation is that neon ions caused significantly more severe damage than boron ions with a very similar LET value. Therefore, we characterized the DNA damage resulting from boron and neon in more detail (next sections).

3.2 γH2AX/53BP1 focus streaks induced by high-LET ions with similar LET values and their changes with time post-irradiation

In contrast to individual DSBs dispersed throughout the whole volumes of nuclei upon γ-ray irradiation, the exposure of cells to high-LET ions produced γH2AX/53BP1 foci that were concentrated along the particle path (γH2AX/53BP1 focus streaks). We studied the morphology and dynamics of these streaks in cells irradiated at a sharp (10°) angle to the particle beam to maximize the resolution of separate foci using confocal microscopy. Doses of 1.0 and 1.2 Gy were used for ^{11}B and ^{20}Ne ions, respectively, to ensure that an average of 3 particles traversed the nucleus in both cases. As early as 5 min PI, the streaks of γH2AX and 53BP1 foci were detectable in cells and were mutually colocalized. At least three γH2AX/53BP1 foci were required to appear in a straight line parallel with the (known) direction of irradiating particles to be considered a streak. Streaks of both ions exhibited a grainy substructure and comprised closely spaced γH2AX/53BP1 foci with non-stained "gaps" (Fig. 6). Within 1 h PI, streaks exhibited fully developed structures and the particle trajectories across the cell nuclei were clearly identified. As expected, most cells contained 3 γH2AX/53BP1 focus streaks.

Although the particles passed the nuclei along a linear path, some foci slightly deflected from this linear trajectory, particularly at longer periods of time PI (>2 h PI) (Fig. 6B). Beginning at 2 h PI, individual γH2AX/53BP1 foci in the streaks also began to disappear, indicating the on-going repair of some DSBs. However, 22 h later (24 h PI), approximately 40% and 30% of the nuclei that had been irradiated with neon and boron ions still contained focus streaks, with typically one

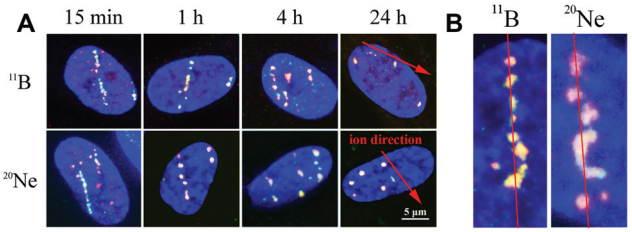

Fig. 6 Structures of γH2AX/53BP1 focus streaks and their dynamic changes with time PI. NHDF-neo cell nuclei were exposed to an average of three ^{20}Ne or ^{11}B ions (*i.e.*, 1.2 and 1.0 Gy, respectively) emitted at a sharp angle to the cell monolayer. Cells were spatially (3D) fixed at the indicated periods of time PI, and immunostaining for γH2AX (green) and 53BP1 (red) repair foci is presented. (A) Comparisons of γH2AX/53BP1 focus streaks induced by boron and neon at the indicated periods PI. (B) Detailed structures and deflections of foci from a linear particle track observed at 2 h after radiation exposure. Maximum images comprising ~25 superimposed 0.25 μm-thick confocal slices are shown in the *x*–*y* plane in both A and B. Chromatin was counterstained with DAPI (blue).

streak in the nucleus (Fig. 6A). Within the next two days (96 h PI), all streaks had dissolved and only individual foci persisted in the nuclei. This observation highlights the successful repair of most DSBs and the existence of residual DNA damage. We also expect that seriously damaged cells died (see section 3.4), detached from the microscopic slides, and thus were undetectable in the confocal microscopy analyses.

3.3 Morphology of γH2AX/53BP1 foci as a function of radiation quality (evaluation of foci structure)

The γH2AX/53BP1 foci and focus streaks induced by high-LET boron and neon ions differed in morphology, specifically their sizes and shapes. Moreover, as described above, we recognized that some larger γH2AX/53BP1 foci (later referred as to the γH2AX/53BP1 clusters) comprised several smaller, closely spaced foci.

Therefore, we also analysed γH2AX/53BP1 streaks in cells irradiated in the sharp-angle (10°) geometry prior to their spatial (3D) fixation in different periods of time PI to obtain more detailed insights (with better resolution power) into the morphology of γH2AX/53BP1 foci and compare the structure and complexity of their clusters following exposure to the radiation types studied here. We focused on the following parameters: (a) the size of γH2AX/53BP1 foci in the maximum images, (b) the circularity of γH2AX/53BP1 foci in the maximum images [4π*(area/perimeter^2)], and (c) the complexity of γH2AX/53BP1 foci. All measurements were performed exactly as in the previous experiments with samples collected at 15 min and 1, 4, 24 and 96 h after irradiating cells with an average of 3 high-LET particles (1 Gy ^{11}B and 1.2 Gy of ^{20}Ne ions, respectively). Low-LET γ-rays administered at a dose of 1 Gy were used for comparison.

For all radiation types, the foci size rapidly increased beginning at 15 min PI, when the foci had not yet completely formed (Fig. 7A). The mean areas of γH2AX/53BP1 foci induced by boron ions and γ-rays subsequently rapidly increased to maximum levels at 4 h PI. Afterwards, the mean areas of foci, which were larger for boron ions and smaller for γ-rays, plateaued at the maximum (γ-rays) or slightly decreased (boron ions) by the end of the experiment (96 h PI). Interestingly, γH2AX/53BP1 foci induced by neon ions behaved differently, increasing to values markedly exceeding the maximum sizes measured for γ-rays or boron ions until 24 h (Fig. 7A). Afterwards, the size of ^{20}Ne-induced foci also decreased slightly, reaching values comparable to the values measured for boron ions or γ-rays at the end of the experiment (96 h PI). Despite the differences in the growth dynamics and final area of the foci induced by ^{11}B and ^{20}Ne, we concluded that both high-LET ions evoked (a) the formation of DSB foci on a much more rapid timescale than low-LET γ-rays, and (b) these foci were also larger.

The second measured parameter, the circularity of γH2AX/53BP1 foci, also revealed significant quantitative differences between radiation types, reflecting their quality (Fig. 7B). Although the foci induced by γ-rays were mostly regular, with only small deviations from circularity, the foci showed marked

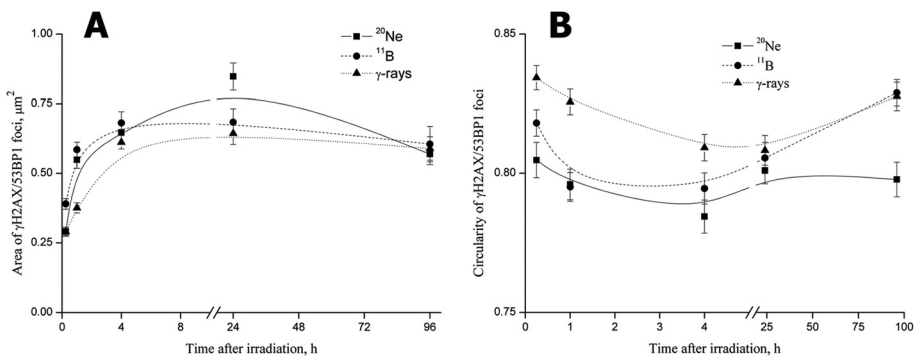

Fig. 7 Area (A) and circularity (B) of γH2AX/53BP1 foci measured at various periods of time after the exposure of NHDF-Neo fibroblasts to γ-rays (1.0 Gy), boron ions (1.0 Gy) or neon ions (1.2 Gy). The slightly different doses applied for boron and neon ions ensured that an average of 3 particles traversed the nucleus in both cases. The measurements were performed in spatially (3D) fixed cells irradiated in the sharp-angle (10°) geometry to maximize the resolution power. The data are presented as the means ± standard errors calculated for pooled data from two experiments (>200 foci). B-spline curves were fitted using the least squares method in Origin 8 software.

irregularities in shape after neon and boron irradiation, leading to lower circularity values. Interestingly, the circularity of γH2AX/53BP1 foci changed over time PI, with the most prominent foci irregularity (deviation from the circularity) detected at 4 h PI for all radiation types. Specifically, we recognized three different profiles of changes in the circularity of the three radiation types studied (Fig. 7B). For γ-rays, the highest circularity was detected immediately after irradiation, after which it subsequently decreased and eventually returned to approximately the original values at the late (96 h PI) period PI. A similar profile was observed for neon ions, but both the initial (15 min PI) and the final (96 h PI) circularities were much lower than for γ-rays (and boron ions). Finally, for boron ions, the profile started with an intermediate initial circularity (lying between the values for neon ions and γ-rays) that decreased in the first hour PI, stagnated at lower values until 4 h PI, and subsequently started to increase, returning to the initial value at 24 h PI. However, in contrast to γ-rays and neon ions, the circularity of boron-induced foci increased compared with the initial value (measured upon irradiation) until it reached the value characteristic for γ-rays at 96 h PI.

The above-described analyses performed on the maximum images (2D superimpositions of individual confocal slices) clearly revealed the relationship between the radiation quality and morphology of γH2AX/53BP1 foci. Therefore, in the next step, we thoroughly analysed the spatiotemporal changes in foci morphology in the 3D space using individual consecutive confocal slices (0.25 μm-thick) from all 3D image stacks (25 slices per stack).

At all monitored periods of time PI (15 min to 96 h), fractions of foci comprising several smaller foci appeared for all radiation types studied (representative images are shown in Fig. 8A). The yields and complexity of these clusters of foci largely depended on the radiation quality and the period of time PI (Fig. 8B). As expected, clusters of γH2AX/53BP1 foci were rare upon exposure to low-LET γ-rays and these clusters exhibited low complexity: approximately 13% of foci appeared in clusters containing 2 (11%) or occasionally 3 foci (<2%). In contrast, one-half or almost three-quarters of all γH2AX/53BP1 foci formed clusters in cells irradiated with boron and neon ions, respectively. In both cases, the complexity and fraction of focus clusters increased with time; both parameters were elevated until 4 h PI and subsequently decreased. Within 15 min PI, only 19% and 36% of foci occurred in clusters after boron and neon irradiation, respectively, whereas these fractions reached 58% and 71%, respectively, at 4 h PI. At this time point, the focus clusters typically contained 2, 3 and 4 smaller foci; however, clusters comprising 5 to 8 foci were also detected, particularly in cells exposed to neon ions. Only insignificant changes in the focus cluster composition were observed between 4 and 24 h PI, followed by a marked reduction in both parameters, the foci complexity and proportion of focus clusters with a higher level of complexity, at 96 h PI. However, approximately 32% (boron ions) and 44% (neon ions) of foci were still located in clusters at that time point. In summary, neon ions induced the greatest incidence

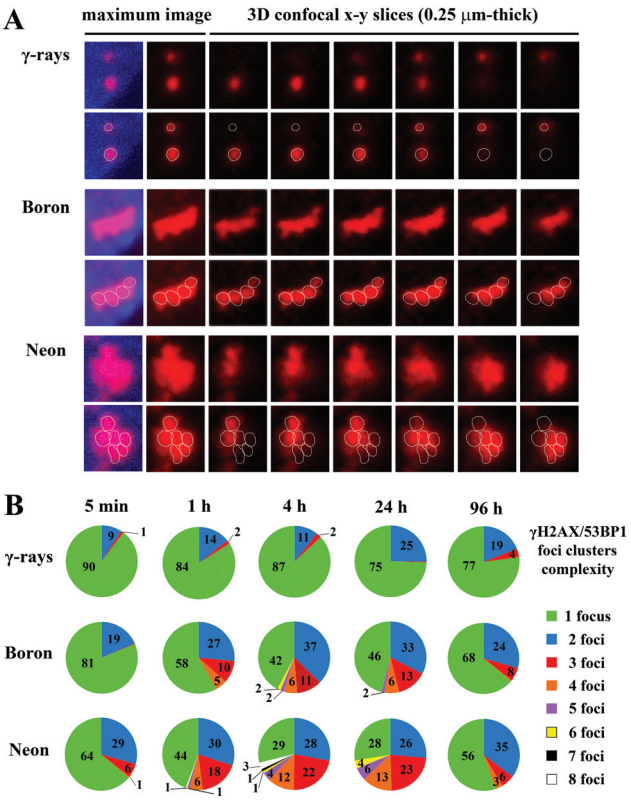

Fig. 8 Comparison of the complexity of γH2AX/53BP1 focus clusters in spatially (3D) fixed NHDF-Neo fibroblasts irradiated with γ-rays, ^{20}Ne ions, or ^{11}B ions. The dose was 1.0 Gy for γ-rays, 1.0 Gy for boron ions, and 1.2 Gy for neon ions to ensure that an average of 3 particles traversed the nucleus in both high-LET radiation cases. Cells were irradiated in the sharp-angle (10°) geometry. (A) Representative γH2AX/53BP1 foci/focus clusters at the time period of their maximum complexity (4 h PI). The maximum (2D) images, shown on the left, comprise ~25 confocal slices obtained with a z-step of 0.25 μm. Individual consecutive confocal slices through the γH2AX/53BP1 focus clusters (right columns) presented here subsequently show the composition of individual foci in the cluster and the ability to precisely describe their complexity. Only the 53BP1 signal is shown because this signal enables better discrimination of individual foci than the γH2AX signal. See Methods (chpt. 2.4) and Fig. 2 for details of the foci discrimination procedure. (B) The γH2AX/53BP1 foci complexity was quantitatively compared for the radiation types studied. For different periods of time PI, the percentages of γH2AX/53BP1 foci presented in clusters of a given complexity level are indicated. The mean values are calculated for pooled data from two experiments (>200 foci).

of the most complex clusters of foci. Compared with low-LET γ-rays and high-LET boron ions, a significantly greater proportion of γH2AX/53BP1 focus clusters persisted in the nuclei of cells exposed to high-LET neon ions, even at 96 h after irradiation (Fig. 8).

3.4 Apoptosis induction after irradiation with γ-rays and boron particles

Based on the obtained results, the kinetics of γH2AX/53BP1 foci elimination were markedly slower and the complexity of foci was greater in cells irradiated with high-LET radiation

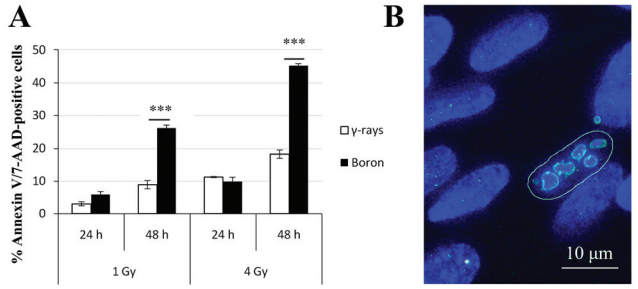

Fig. 9 Radiation-induced apoptosis of NHDF-Neo fibroblasts after exposure to γ-rays and ^{11}B ions. (A) The induction of apoptosis was detected by flow cytometry (Muse™ Annexin-V & Dead Cell Assay kit). Each bar represents the mean proportion of apoptotic cells after irradiation. The values were normalized to the "background" in the non-irradiated cells. *P* values were calculated using the two-tailed *t* test and are denoted by "***" ($P \leq 0.001$). Error bars represent standard errors from three independent measurements of 5000 cells. (B) Representative image of a late apoptotic cell (48 h PI), characterized by nuclear fragmentation and γH2AX (green) staining, after irradiation with 1 Gy of ^{11}B ions. Chromatin was stained with DAPI (blue).

types than in cells irradiated with γ-rays. Hence, we simultaneously quantified Annexin V- and 7-amino-actinomycin-positive irradiated cells using flow cytometry to determine whether these findings were also correlated with increased cell death. Because of limited beam time availability, only cells irradiated with boron ions and γ-rays were studied. The results for the two radiation types applied in two doses (1 Gy and 4 Gy) and scored at two different periods of time (24 h and 48 h) after irradiation are presented in Fig. 9. The values are expressed as the percentages of Annexin V-positive plus 7-AAD-positive or negative cells normalized to the background level in non-irradiated cells. For both the 1 and 4 Gy doses, similar apoptosis rates occurred for γ-rays and boron ions at 24 h PI, regardless of the different LET values for these radiation types. This finding strikingly contrasts with the situation observed at 48 h PI, when boron ions induced approximately 3-fold higher numbers of positive cells than γ-rays. This difference was particularly prominent for the higher dose of 4 Gy. For both radiation types, the number of apoptotic cells clearly depended on the dose.

4 Discussion

To our knowledge, this study is the first to address the spatiotemporal aspects of DNA damage and repair after cells are exposed to different high-LET radiation types with similar low-energy and LET values. Previous experimental research on the biological effects of high-LET radiation types have primarily focused on ions with high energies (≥100 MeV per n), but results for low-energy (<50 MeV per n) ions are still rare. Moreover, the mutually compared radiation types (in the literature) have typically largely differed in energy or LET values, frequently by orders of magnitude.[6,30,62] Although this experimental design enables useful analyses of DNA damage (or other biological endpoints) related to LET or radiation energy, large differences in these parameters mask possible effects of other radiation qualities. The mechanism by which different high-LET particles affect the DNA molecule under conditions of similar LET and energy values thus remains poorly understood. We evaluated the extent, spatiotemporal behaviour and repair of DSB damage in normal human neonatal dermal fibroblasts irradiated with either boron or neon ions that had been accelerated to similar lower energies and similar LET values (see Table 1) or γ-rays, a representative low-LET radiation, to address this current gap in knowledge.

For many biological endpoints, the RBE increases with LET. However, for different radiation types, LET values oscillating between 100 and 200 keV μm^{-1} may correspond to the maximum RBE, depending on the physical parameters of the particle, cell type and biological endpoint studied.[20–22,63] Alternatively, as shown in the present study, radiation types with similar LET values produce DNA damage with different complexities and spatiotemporal behaviours. Because increased DNA damage complexity was found to be correlated with slower DSB repair and increased cell death, our results confirm the hypothesis that the spatiotemporal characteristics of energy deposition and DNA damage, which cannot be simply described by LET, play a crucial role in determining the RBE of different radiation types.

Hence, micro-morphological analyses of DNA damage, as performed in the present study, significantly contribute to the current understanding of the mechanisms by which low-LET and high-LET radiation types kill cells and consequently the mystery of radiation RBE. To date, the knowledge in these areas is incomplete and optical microscopy approaches enabling detailed analyses of DSB damage under physiological conditions remain challenging.[64] For example, recent works attempting to study DSB damage in cells exposed (90° geometry) to nitrogen ions (19.5 MeV per n, LET = 132 keV μm^{-1})[65] or α particles (0.75 MeV per n, LET = 125 keV μm^{-1})[66] using classical confocal microscopy failed to distinguish a substructure of γH2AX focus clusters, although they analysed cell nuclei in the 3D space. Therefore, various super-resolution 'nanoscopy' methods that increase the resolution power of optical microscopy up to several nanometres have high expectations.[36,64,67] Unfortunately, studies taking advantage of optical super-resolution techniques remain rare and are extremely technically demanding (depending on the method); hence, studies have typically been limited to analyses of relatively small datasets.[35,61,68] Electron microscopy offers a superior resolution power that enables the precise quantification of DSB complexity;[38–40,69,70] however, the necessity of sample sectioning makes analyses of entire particle tracks in space and time difficult. Moreover, experimental artefacts might appear, reflecting (harmful) sample fixation steps, such as dehydration or freezing (reviewed by Winey *et al.*[71]).

Therefore, in the present study, we used dual-immunofluorescence high-resolution confocal microscopy on spatially (3D) fixed cells irradiated at a sharp angle.[59] Based on this approach, we successfully visualized a detailed substructure of

colocalized γH2AX and 53BP1 focus streaks along ^{11}B and ^{20}Ne particle tracks *in situ* and in large datasets. Selective scoring of colocalized γH2AX and 53BP1 foci improved the precision of these analyses and increased the probability of observing unrepaired DSBs, especially in later periods of time PI (see Methods, chapter 2.4 for explanation). The exclusion of cells with non-colocalizing signals (rare cases) also reduced the numbers of inefficiently immunostained cells and non-G1-cells[52–54] included in the analyses (we studied non-synchronized cell populations to better reflect the situation in irradiated tissues; the cultures contained >80% G1 cells at the time of irradiation).

In contrast with the results reported by Costes *et al.*[65] or Antonelli *et al.*,[66] 3D analyses of confocal image stacks performed in this study improved the detection of γH2AX/53BP1 (sub)foci by approximately 40% compared with a simple 2D analysis (see Fig. 4). Nevertheless, some potential and real limitations of the present study should be considered. First, cell fixation may influence chromatin structure. Therefore, we confronted the morphology of the cell nuclei (thickness and the maximal length *vs.* thickness ratio) of the fibroblasts (as a widely accepted model for exploring normal tissue radiosensitivity)[60] after 3D fixation with the results of other studies.[61,72,73] The measurements (nucleus thickness of approximately 2.7–3.4 μm) confirmed that the complexity of γH2AX/53BP1 focus clusters predominantly reflects the deposition of radiation energy, without a significant contribution of cell flattening. Indeed, closer approach of very tightly spaced γH2AX/53BP1 foci in the focus streaks of high-LET ions, potentially provoked by fixation-mediated cell flattening, would lead to overlapping foci and underestimation of focus cluster complexity, rather than to a dramatic increase in this parameter (*e.g.*, because of fusions between foci located inside of and more distant from the main particle track). In any case, relative comparisons should be unaffected, as the same potential effect was detected for all cells.

Second, as previously reported by Jakob *et al.*,[29] sharp-angle cell irradiation allowed us to substantially increase the resolution power; this strategy reduced limitations arising from fibroblast flatness and the insufficient resolution power of confocal microscopy in the vertical (*z*)-direction.[74] To identify individual foci within clusters, we combined information on cluster morphology, fluorescence heat maps, and fluorescence intensity profiles along the paths intersecting putative foci in non-overexposed parts of the cluster (see Methods, Fig. 2). Although high precision of the spatiotemporal analysis was achieved, serious technical restrictions (low resolution power of confocal microscopy, leading to a certain amount of artificial overlap in complex arrangements of foci due to diffraction; reviewed in Waters[74]) as well as biological reality (spreading of H2AX phosphorylation over 1–2 Mb chromatin domains and overlapping signals) prevented the discrimination of individual DSBs in multiple lesions (≥2 DSBs within 1–2 helical turns). Hence, the precise boundaries and, thus, the numbers of very closely spaced DSB foci were only estimated. The biological nature of the complex γH2AX/53BP1 focus clusters observed in the present study and the precise numbers of DSBs present in γH2AX/53BP1 foci/focus clusters (in general) therefore remain uncertain and must be further studied. Several recent reports[75–78] have suggested that super-resolution localization light microscopy offers an exciting but still challenging means of analysing the same biological specimens in parallel with confocal microscopy, but with much more detailed data. This strategy could be used to obtain answers to many questions discussed in this chapter in the near future.

Taking advantage of current approach, the microdosimetric complexity of γH2AX/53BP1 (DSB) repair foci differs not only for cells irradiated with low-LET γ-rays and high-LET radiation types, as expected, but also for cells irradiated with boron ions and neon ions, which have very similar LET and low-energy values. Mathematical modelling/simulations and novel ultrasensitive immunogold-labelling transmission electron microscopy (TEM) provides clear evidence that high-LET radiation causes complex DSBs, and in contrast to low-LET radiation, the majority of γH2AX foci contain more than one DSB.[32,38,39] As recently reviewed by Goodhead *et al.* (2015), approximately 20% (γ-rays) and 70% (high-LET ions) of DSB damage sites contain at least three DNA-chain breaks, according to simulations.[7] Based on our direct measurements (1 h PI), approximately 16%, 42%, and 56% of γH2AX/53BP1 foci generated from γ-rays, boron ions, and neon ions, respectively, exist in clusters with additional foci. Nevertheless, these numbers were not able to be directly compared with other studies that typically quantify the proportion of simple foci to DSB clusters. In any case, consistent with previous findings,[38,40,61] our 3D analysis revealed highly clustered (>3) γH2AX/53BP1 foci only after exposure to high-LET particles, whereas clusters observed after γ-irradiation comprised a maximum of two or occasionally (2%) three foci.

The difference between DSB complexity following the exposure of cells to γ-rays and high-LET ions (boron or neon) was primarily explained by the different characters of energy deposition (ionization density and distribution) by these radiation types. However, based on the present and previous results,[24,67,79] we propose that not only the character of energy deposition *per se* but also the character of energy deposition in the context of higher-order chromatin structure[80] (see Fig. 10F) significantly contributes to the increased complexity of DNA damage and RBE following exposure to high-LET radiation types. Specifically, high-LET radiation types attack condensed (hetero)chromatin, which contains a much higher density of potential DNA targets than decondensed (eu)chromatin, more efficiently than low-LET radiation types[79] (reviewed in ref. 24 and 67). However, γ-rays preferentially damage low-density chromatin, since, in condensed (hetero)chromatin, more abundant (hetero)chromatin-binding proteins better shield the DNA from free radicals largely mediating the harmful effects of low-LET radiation. Therefore, it is important not only how, but also where the radiation energy is released in the cell nucleus (also see Fig. 10F).

The complexity of DSBs was inversely correlated with the disappearance of γH2AX/53BP1 foci from the cell nuclei, *i.e.*,

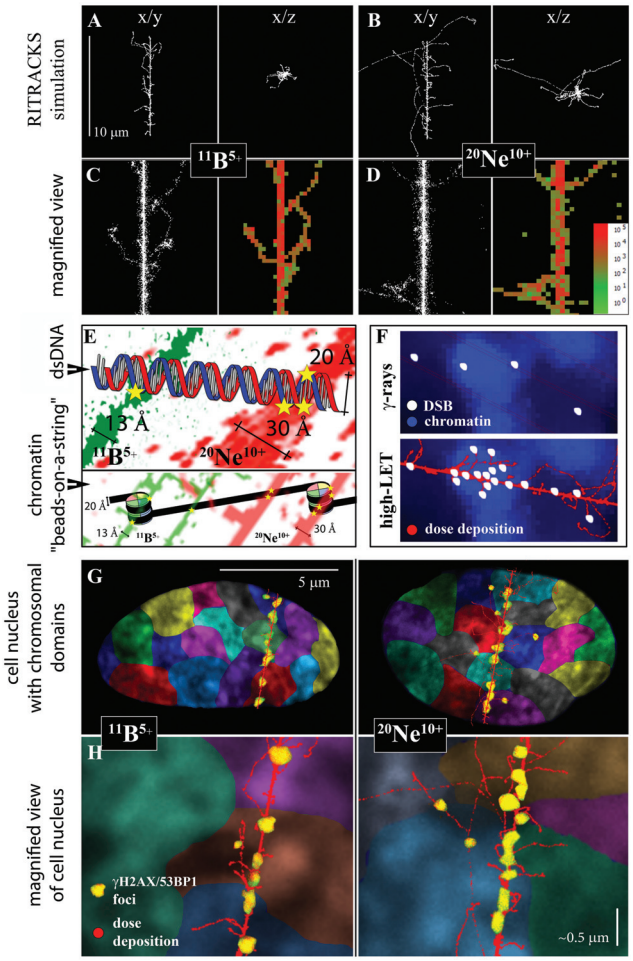

Fig. 10 Relationships between radiation energy deposition, higher-order chromatin structure and DNA double-strand break induction for γ-rays and ^{11}B and ^{20}Ne ions (see Table 1 for radiation parameters). A, B. Simulations of 10 μm-long track structures for ^{11}B and ^{20}Ne ions using RITRACS software; the range and distribution of δ-electrons relative to the track core can be observed in *x*/*y* and *x*/*z* projections. C, D. Detailed views along the tracks, with emphasis on the core structure. Free radical tracks (left panel) are shown together with dose deposition tracks (right panels). Dose deposition decreases from red to green, as indicated. The simulations show that δ-electrons penetrate deeper with neon ions, while they are more concentrated along the track core with boron ions. Nevertheless, the combined action of the neon particle itself plus low-energy electrons (that do not escape from the track core) generates a thick track core, approximately twice as thick as the boron ion. E. Compared with ^{11}B ions, a wider track core of ^{20}Ne ions (which is still highly concentrated compared, for example, to particles of high energy) directly damages both strands of the DNA molecule with a higher probability/frequency. Moreover, ^{20}Ne ions can more easily attack both DNA turns around the nucleosome at the same time (bottom image). Chromatin is shown at the organization level of "beads-on-a-string" for simplification. F. Relationships between dose deposition, higher-order chromatin structure and DSB induction. γ-rays (top image) induce DSBs randomly across the cell nucleus, with euchromatin being more sensitive than heterochromatin to free radicals (which largely mediate harmful effects of low-LET radiation), since heterochromatin is better protected by larger amounts of (hetero)chromatin-binding proteins.[24,64,79] In contrast, high-LET radiation (bottom image) deposits energy in a concentrated manner along the particle track, which causes DNA damage that cannot be prevented by the chromatin structure. Condensed (hetero) chromatin provides more DNA targets per volume unit and is therefore more seriously damaged (fragmented) by high-LET particles.[64] G, H. Relationships between the character of energy deposition, higher-order chromatin structure, and induction of chromosomal aberrations. The dose deposition (red) simulated for ^{11}B and ^{20}Ne ions by the RITRACKS code is overlaid onto the cell nucleus, with schematically illustrated chromosomal territories (various colours) and γH2AX/53BP1 foci (yellow). A slightly greater complexity of γH2AX/53BP1 foci in cells irradiated with ^{20}Ne ions (compared with ^{11}B ions) is indicated by their larger size. The higher-order chromatin structure is shown *via* DAPI staining (condensed chromatin is intensively stained). Both ions and kick-off electrons of low energy generate extensive damage along the particle path and thus complex chromosomal aberrations. In addition, ^{20}Ne ions emit longer-range δ-electrons than ^{11}B ions (panel A *vs.* B). These electrons radiate to sufficient distances from the track core to cause DSBs in the neighbouring chromosomal territories; nevertheless, these DSBs may still be sufficiently close to interact with DSBs along the particle core, particularly if we consider the chromatin fragmentation and decondensation caused by irradiation and the associated, though limited, chromatin movement. Typically, damaged chromatin (labelled with 53BP1-GFP in living cells) is displaced at a distance of approximately 1 μm in cells irradiated with accelerated ions, but the displacement of <2% foci occasionally exceeds 5 μm in the 12 h interval after Ni irradiation.[93] Therefore, we propose that chromosomal aberrations formed with ^{20}Ne ions may involve more chromosomes than those that appear with ^{11}B ions, and their complexity in terms of the number of DNA breaks can be higher, as shown in the present study. Consider that human skin fibroblasts are flat cells (as shown on the image), and even more chromosomal territories may participate in chromosomal aberrations in spherical cells.[17,94,95] Panel H: Section of panel G magnified approximately 10 times. Scale bar, approximately 0.5 μm (schematic illustration).

the kinetics and efficiency of DSB repair, and cell survival. Consistent with some earlier reports,[31,61,64,66,79–81] simple (and on principle frequently euchromatic[79]) γH2AX/53BP1 foci generated by γ-rays were largely eliminated within the first (4 h) hours PI in the present study. Similar findings of the rapid repair and disappearance of non-clustered (smaller) individual γH2AX/53BP1 foci were observed in cells irradiated with high-LET ions (^{11}B and ^{20}Ne). However, large γH2AX/53BP1 foci, and particularly clusters of these foci, were repaired with difficulty irrespective of their origin in euchromatin or heterochromatin, and they persisted in the cell nuclei for much longer periods of 1 day (^{11}B) or more (^{20}Ne) after irradiation. For ^{20}Ne ions that produced the most complex DSB lesions in this study, approximately 3/4 of DSB foci persisting at 24 h PI formed clusters. These results precisely correspond to an interesting study by Jakob *et al.*,[48] who observed the slower repair of DSBs generated by carbon ions than of DSBs produced by γ-rays, and this delayed repair was even higher for heterochromatin-associated damage. Based on the evidence obtained in this and previous studies, we conclude that both DSB complexity and the chromatin environment surrounding DSBs significantly influence the repair of initially formed lesions (appearing as a consequence of energy deposition), which at least partially explains the higher RBE of high-LET ions.

The average complexity of clusters and number of clusters per cell gradually increased with time PI and started to decrease only after 24 h PI. This scenario suggests the gradual processing of less complex and individual DSBs within the clusters[61] and highlights the long-term persistence of complex DSB clusters. An alternative, but not mutually exclusive possibility is that these repair kinetics may reflect the formation of DSB focus clusters over a longer time post-irradiation, due to chromatin movement provoked by DSB repair processes, as described below. The cells with unrepeatable DSB clusters (of either origin) are expected to die or undergo mutagenesis at later periods of time PI. Indeed, a much higher proportion of cells underwent apoptosis following irradiation with boron ions (almost 50% of cells exposed to a 4 Gy dose) compared with γ-rays (less than 20% of cells exposed to a 4 Gy dose), indicating that (a) DSBs produced by high-LET ions are repaired but only with difficulty and (b) the proportions of cells with complex γH2AX/53BP1 foci and the complexity of persistent DSBs at >24 h PI may be even greater than reported here (because the seriously damaged cells died, detached from the microscopic slides and escaped detection).

Moreover, concerning the long period of time examined post-irradiation (up to 96 h PI), a proportion of cells may also die due to mitotic catastrophe, since as was only recently shown,[61,82] even cells with relatively high numbers (*e.g.*, 10–15) of DSBs can enter mitosis under some circumstances. These conclusions are consistent with the combined results of previous studies of carbon and ferrous ions.[38,39,61]

Finally, we cannot exclude the possibility that previously repaired cells may overpopulate cells still harbouring damage and, thus, further decrease the average number of foci per nucleus observed in later time periods PI. Since the critical level of DSBs (<10–20)[82] allowing cells to enter mitosis is reached more rapidly (within approximately 4 h PI) using γ-rays than using both high-LET ions (>24 h PI), this effect may eventually lead to underestimation of DSBs, especially in γ-irradiated cells. However, any significant effect of cell division on DSB repair kinetics and differences in such effects between the different types of radiation studied are unlikely since (a) only a small fraction of fibroblasts were dividing; (b) only background DSB numbers were detected in γ-irradiated cells at 24 h PI (and this number plateaued at later times); and (c) the most prominent differences in DSB repair kinetics were observed at PI times <4 h. We also calculated the average numbers of γH2AX/53BP1 foci per nucleus specifically in γH2AX/53BP1-positive cells (not shown), which resulted in the same trends/conclusions obtained from analyses performed for whole cell populations (γH2AX-positive + γH2AX-negative cells). Moreover, most cells exposed to γ-rays contained <20 DSB (mean = approximately 10 DSBs) foci per nucleus at 4 h PI, and damaged cells could therefore theoretically also undergo mitosis, similar to undamaged cells.

An additional level of DSB complexity that negatively influences DSB repair may paradoxically appear as a side effect of repair processes *per se*. First, the processing of complex (even non-DSB) lesions directly generates secondary DSBs.[83,84] Second, the heterochromatin structure has consistently been reported to represent a barrier to DNA repair and thus DSBs in condensed heterochromatin are repaired but only with difficulty, with slower kinetics and lower efficiency than DSBs in euchromatin.[38–40,48,79,85] The repair of heterochromatic DSBs requires extensive (hetero)chromatin decondensation, which in turn locally mobilizes damaged chromatin domains to some extent.[25,81,86,87] This increased mobility of heterochromatic DSBs can result in collisions of two or more DSBs and the formation of secondary DSB clusters (the term 'secondary' distinguishes these clusters from the 'primary' clusters discussed above, which are directly formed by high-LET particles due to localized energy deposition). Although this phenomenon occurs occasionally upon irradiation with γ-rays, its importance has dramatically increased for cells exposed to high-LET radiation types, in which the local chromatin structure is highly fragmented and DSBs are concentrated along a relatively thin particle path, *i.e.*, located in close proximity to one another. Indeed, the secondary DSB clusters observed after high-LET irradiation are in fact frequently higher order clusters comprising primary DSB clusters.[67,85]

Consistent with this scenario, we observed deflections of some foci from otherwise linear particle tracks and these 'mobile' foci mostly occurred at the border between condensed (hetero)chromatin and decondensed (eu)chromatin domains. The protrusion of heterochromatic DSBs into decondensed (eu)chromatin has also been reported in other studies upon high-LET[26,48] and low-LET[81,86,88] irradiation (reviewed by Falk *et al.*;[24] Chiolo *et al.*[89]). Moreover, the highest numbers of clusters were detected between 4 and 24 h, *i.e.*, when the DSB repair of non-complex lesions is mostly complete. During this PI period, the clusters also showed the greatest irregularity and

complexity, with 2 to 5 smaller foci per cluster observed in boron-irradiated cells and up to 8 foci observed in neon-irradiated cells. Together, these results highlight the problematic spatiotemporal stabilization of complex γH2AX/53BP1 focus clusters, particularly in the initial phase and most active period of DSB repair. Conceivably, after high-LET irradiation, simultaneous chromatin fragmentation and dispersion supported by chromatin decondensation occurring in the frame of repair processes locally mobilize chromatin to a much greater extent than in cells exposed to low-LET γ-rays. This phenomenon dramatically increases the complexity of DSB lesions and the risk of repair errors or failure. Finally, these observations demonstrate that two phenomena – energy deposition, leading to primary chromatin fragmentation, and DNA repair, provoking secondary chromatin decondensation – contribute to (restricted) chromatin movement and formation of (complex/multiple) DSB clusters and chromosomal aberrations in cells exposed to high-LET ions.

The greater complexity and delayed repair of DSB lesions induced by neon ions compared with that induced by boron ions, which was observed in our morphological and kinetic studies, is harder to explain than the differences between high-LET and low-LET types of radiation. For low radiation energies, the δ-electrons emitted by the transversing particle are expected to significantly damage DNA inside or close to the track core since they do not have sufficient energy to escape. Consistently, for both boron and neon ions, we observed only occasional γH2AX/53BP1 foci (more frequent for neon ions) that were attributed to the activity of δ-electrons at sites located outside of γH2AX/53BP1 focus streaks. In the proximity of the track core, some large γH2AX/53BP1 foci diverged from the linearity of the streaks, in addition to small γH2AX/53BP1 foci produced by δ-electrons (see Fig. 6); these objects likely correspond to complex foci relocated from the track core or increased energy deposition at the ends of δ-electron tracks.[90–92] Whether δ-electron ends can generate DSBs with a sufficient density to form multiple DSBs is unclear;[90–92] in any case, such DSB clusters would be less complex than clusters inside the track core. Hence, based on the relatively large size of observed out-of-line foci and the gradually decreasing linearity of the particle tracks with the PI period, we consider the first scenario to be more likely/important. The track core therefore probably plays a crucial role in influencing the characteristics of DSB damage under the conditions of the present study, although long-range δ-electrons may also influence characteristics such as the complexity of chromosomal aberrations (see Fig. 10).

Therefore, we complemented our experiments with theoretical calculations on the track core (as described by Chatterjee, 1993,[57] see the Methods) to determine potential factors that may explain why neon ions induce DNA damage of greater complexity than boron ions. The results revealed a core radius of only 13 Å for boron ions but 30 Å for neon ions. An approximately two-times wider track "core" for ^{20}Ne ions was also observed in RITRACKS simulations (Fig. 10). Based on these results, we propose that neon ions generate a wider particle track core that is better able to cause complex DNA (DSB) lesions than the thinner track core of boron ions. This conclusion is not in disagreement with the findings of Saha *et al.* (2014),[30] who associated a thinner track of low-energy ions (more concentrated energy deposition) with more efficient DNA damage induction than was associated with a wider track of high-energy ions – the tracks of the ^{11}B and ^{20}Ne ions used here are both much thinner than the tracks of high-energy ions.

The proposed relationships between the particle track structures of ^{11}B and ^{20}Ne ions, the higher-order chromatin architecture and the formation of (complex) DSBs and chromosomal aberrations (discussed here as the endpoint of irradiation most directly related to DSB induction) are illustrated in Fig. 10. Briefly, both high-LET ions (^{11}B and ^{20}Ne) and kick-off electrons of low energy generate extensive damage along the particle track core, which leads to complex chromosomal aberrations that may involve chromosomes whose (interphase) territories are intersected by the particle. A wider but still highly focused (dense energy deposition) track core of ^{20}Ne ions can more efficiently induce DSBs than too narrow track core of ^{11}B ions. In addition, ^{20}Ne ions emit longer-range δ-electrons than ^{11}B ions. These electrons radiate to sufficient distances from the track core and may cause numerous DSBs, mostly at the end of their tracks, *i.e.*, in neighbouring (more distant) chromosomal territories. Nevertheless, these DSBs may be still sufficiently close to interact with DSBs along the particle core, particularly if we consider the chromatin fragmentation and decondensation caused by irradiation and the associated, though limited, chromatin movement. Typically, damaged chromatin (labelled with 53BP1-GFP in living cells) may be displaced by a distance of approximately 1 μm in cells irradiated with accelerated ions, although relocation occasionally (<2% foci) exceeds 5 μm during the 12 h interval after high-LET nickel ion exposure.[93] Therefore, we propose that chromosomal aberrations formed with ^{20}Ne ions may involve more chromosomes than appear in association with ^{11}B ions, and their complexity in terms of the number of DNA breaks can be higher, as shown in the present study (Fig. 10G and H; note that more chromosomal territories may participate in chromosomal aberrations in spherical cells than in flat fibroblasts).[17,94,95] Nevertheless, this hypothesis remains to be experimentally confirmed.

Moreover, the radiation types used in the present study differed in particle charge (^{20}Ne = 10+, ^{11}B = 5+), which was not considered in our calculations. Because the higher charge of Ne ions is reasonably expected to influence the microdosimetric distribution of ionization and thus significantly contribute to the track (core) structure,[96,97] we can hypothesize that it also increases DNA damage complexity under conditions of similar LET and energy values for different radiation types. However, the physical quality of the particle, which primarily determines the characteristics of DNA damage under conditions of similar LET and energy values for the radiation types, should be further investigated.

The γH2AX/53BP1 foci/focus clusters generated by boron and neon ions and γ-rays differed not only in complexity but

also in structural parameters and spatiotemporal behaviours. Neon ions provoked the most rapid formation of γH2AX/53BP1 foci in irradiated cells and neon ions also induced the largest and most irregular foci (the lowest circularity). The results for boron ions were generally more similar to neon ions than to γ-rays. Faster formation of DSB foci in cells irradiated with high-LET ions compared with low-LET γ-rays is not unprecedented in radiobiology,[34,93] but negative observations[65,98] leave the question open. We postulate that chromatin fragmentation by high-LET radiation types opens damaged chromatin sites for DSB sensors and repair factors, which is manifested in rapid focus formation, occurring faster and to greater extent than fragmentation induced by γ-rays. Alternatively, but not mutually exclusively, clustered DSBs (together with factors such as high local concentrations of radicals), which represent a serious threat to genome integrity, may induce a more severe shock to the cells than a comparable, or even higher, level of spatially separated DSBs, and the repair systems are therefore activated faster or at a higher level. Finally, reflecting the character of energy deposition (highly localized *vs.* dispersed, with high-LET and low-LET radiation, respectively), primary DSB clusters generated by high-LET ions appear in cells immediately following irradiation, whereas the formation of occasional secondary clusters induced by γ-rays requires additional time. As previously discussed, primary clusters originate from physico-chemical processes occurring immediately after irradiation, while secondary clusters form later, as a consequence of restricted chromatin movement provoked by DNA repair;[25,26,79] reviewed in Falk *et al.* (2014).[64] Based on the results from the present study, the complexity of DNA damage influences the speed of DSB recognition or γH2AX/53BP1 foci formation.

In summary, different particles with similar LET and energy values induce DSB damage with different microdosimetric (spatiotemporal) characteristics that are correlated with the efficiency of DSB repair and cell survival. We propose that the extent and character of DSBs induced by radiation types with similar LET and energy values critically depend on the particle track core diameter. However, the physical quality of the particle that primarily dictates this diameter requires further study. Hence, not only the physical characteristics of radiation types but also the spatiotemporal features and behaviours of induced DNA damage should be considered in future radiotherapy studies and investigations of the effects/risks of space missions.

Conflicts of interest

The authors have no conflicts of interest to declare.

Acknowledgements

The authors thank Y. G. Teterev and A. A. Bezbakh from the Flerov Laboratory of Nuclear Reactions (JINR) and G. N. Timoshenko and V. A. Krylov from the Laboratory of Radiation Biology (JINR) for exposing the cells to radiation with accelerated heavy ions using the U400M cyclotron and V. N. Gaevskiy from the Dzhelepov Laboratory of Nuclear Problems (JINR) for performing the gamma irradiation using the Rokus-M unit.

The work was supported by grants from the Czech Republic to the Joint Institute for Nuclear Research, Dubna (Projects of the Czech Plenipotentiary and the 3 + 3 Projects), the Czech Science Foundation (project 16-12454S), and the Ministry of Health of the Czech Republic (AZV grant no. 16-29835A, all rights reserved).

References

1 S. Moore, F. K. T. Stanley and A. A. Goodarzi, *DNA Repair*, 2014, **17**, 64–73.
2 E. Sage and N. Shikazono, *Free Radicals Biol. Med.*, 2016, **107**, 125–135.
3 Z. Nikitaki, V. Nikolov, I. V. Mavragani, E. Mladenov, A. Mangelis, D. A. Laskaratou, G. I. Fragkoulis, C. E. Hellweg, O. A. Martin, D. Emfietzoglou, V. I. Hatzi, G. I. Terzoudi, G. Iliakis and A. G. Georgakilas, *Free Radical Res.*, 2016, **50**, S64–S78.
4 R. Okayasu, *Int. J. Cancer*, 2012, **130**, 991–1000.
5 F. A. Cucinotta, H. Nikjoo and D. T. Goodhead, *Radiat. Res.*, 2000, **153**, 459–468.
6 D. M. Sridharan, L. J. Chappell, M. K. Whalen, F. A. Cucinotta and J. M. Pluth, *Radiat. Res.*, 2015, **184**, 105–119.
7 D. T. Goodhead, *Radiat. Prot. Dosim.*, 2015, **166**, 276–281.
8 M. Suzuki, C. Tsuruoka, T. Kanai, T. Kato, F. Yatagai and M. Watanabe, *Biol. Sci. Space.*, 2003, **17**, 302–306.
9 C. Tsuruoka, M. Suzuki and K. Fujitaka, *Biol. Sci. Space*, 2004, **18**, 188–189.
10 T. Takatsuji, I. Yoshikawa and M. S. Sasaki, *J. Radiat. Res.*, 1999, **40**, 59–69.
11 M. Niemantsverdriet, M.-J. van Goethem, R. Bron, W. Hogewerf, S. Brandenburg, J. A. Langendijk, P. van Luijk and R. P. Coppes, *Int. J. Radiat. Oncol., Biol., Phys.*, 2012, **83**, 1291–1297.
12 H. Tauchi, S. Endo, K. Eguchi-Kasai, Y. Furusawa, M. Suzuki, S. Matsuura, K. Ando, N. Nakamura, S. Sawada and K. Komatsu, *J. Radiat. Res.*, 1999, **40 Suppl**, 45–52.
13 Y. Kazama, K. Ishii, T. Hirano, T. Wakana, M. Yamada, S. Ohbu and T. Abe, *Plant J.*, 2017, **38**, 42–49.
14 P. Bláha, N. A. Koshlan, I. V. Koshlan, D. V. Petrova, Y. V. Bogdanova, R. D. Govorun, V. Múčka and E. A. Krasavin, *Mutat. Res., Fundam. Mol. Mech. Mutagen.*, 2017, **803–805**, 35–41.
15 F. Yatagai, *Biol. Sci. Space*, 2004, **18**, 224–234.
16 R. M. Anderson, D. L. Stevens, N. D. Sumption, K. M. S. Townsend, D. T. Goodhead and M. A. Hill, *Radiat. Res.*, 2007, **167**, 541–550.

17 H. A. Foster, G. Estrada-Girona, M. Themis, E. Garimberti, M. A. Hill, J. M. Bridger and R. M. Anderson, *Mutat. Res., Genet. Toxicol. Environ. Mutagen.*, 2013, **756**, 66–77.
18 S. Ritter, E. Nasonova and E. Gudowska-Novak, *Int. J. Radiat. Biol.*, 2002, **78**, 191–202.
19 I. Testard, B. D. X. Utrillau and L. Sabatier, *Int. J. Radiat. Biol.*, 1997, **72**, 423–433.
20 K. A. M. Suzuki, Y. Kase, H. Yamaguchi and T. Kanai, *Int. J. Radiat. Oncol., Biol., Phys.*, 2000, **48**, 241–250.
21 J. Kiefer, P. Schmidt and S. Koch, *Radiat. Res.*, 2001, **156**, 607–611.
22 M. C. Joiner, in *Basic Clinical Radiobiology*, ed. M. Joiner and A. van der Kogel, Hodder Arnold, 338 Euston Road, London, NW1 3BH, Great Britain, 4th edn, 2009, pp. 68–77.
23 J. A. Aten, J. Stap, P. M. Krawczyk, C. H. van Oven, R. A. Hoebe, J. Essers and R. Kanaar, *Science*, 2004, **303**, 92–95.
24 M. Falk, E. Lukasova and S. Kozubek, *Mutat. Res.*, 2010, **704**, 88–100.
25 M. J. Kruhlak, A. Celeste, G. Dellaire, O. Fernandez-Capetillo, W. G. Müller, J. G. McNally, D. P. Bazett-Jones and A. Nussenzweig, *J. Cell Biol.*, 2006, **172**, 823–834.
26 B. Jakob, J. Splinter and G. Taucher-Scholz, *Radiat. Res.*, 2009, **171**, 405–418.
27 E. P. Rogakou, D. R. Pilch, A. H. Orr, V. S. Ivanova and W. M. Bonner, *J. Biol. Chem.*, 1998, **273**, 5858–5868.
28 E. P. Rogakou, C. Boon, C. Redon and W. M. Bonner, *J. Cell Biol.*, 1999, **146**, 905–916.
29 B. Jakob, M. Scholz and G. Taucher-Scholz, *Radiat. Res.*, 2003, **159**, 676–684.
30 J. Saha, P. Wilson, P. Thieberger, D. Lowenstein, M. Wang and F. A. Cucinotta, *Radiat. Res.*, 2014, **182**, 282–291.
31 A. Asaithamby, N. Uematsu, A. Chatterjee, M. D. Story, S. Burma and D. J. Chen, *Radiat. Res.*, 2008, **169**, 437–446.
32 G. Du, G. A. Drexler, W. Friedland, C. Greubel, V. Hable, R. Krücken, A. Kugler, L. Tonelli, A. A. Friedl and G. Dollinger, *Radiat. Res.*, 2011, **176**, 706–715.
33 O. A. Sedelnikova, D. R. Pilch, C. Redon and W. M. Bonner, *Cancer Biol. Ther.*, 2003, **2**, 233–235.
34 S. V. Costes, A. Ponomarev, J. L. Chen, D. Nguyen, F. A. Cucinotta and M. H. Barcellos-Hoff, *PLoS Comput. Biol.*, 2007, **3**, e155.
35 R. Lopez Perez, G. Best, N. H. Nicolay, C. Greubel, S. Rossberger, J. Reindl, G. Dollinger, K.-J. Weber, C. Cremer and P. E. Huber, *FASEB J.*, 2016, **30**, 2767–2776.
36 Y. Zhang, G. Máté, P. Müller, S. Hillebrandt, M. Krufczik, M. Bach, R. Kaufmann, M. Hausmann and D. W. Heermann, *PLoS One*, 2015, **10**, e0128555.
37 M. Falk, *Biophys. J.*, 2016, **110**, 872–873.
38 Y. Lorat, C. U. Brunner, S. Schanz, B. Jakob, G. Taucher-Scholz and C. E. Rübe, *DNA Repair*, 2015, **28**, 93–106.
39 Y. Lorat, S. Timm, B. Jakob, G. Taucher-Scholz and C. E. Rübe, *Radiother. Oncol.*, 2016, **121**, 154–161.
40 C. E. Rübe, Y. Lorat, N. Schuler, S. Schanz, G. Wennemuth and C. Rübe, *DNA Repair*, 2011, **10**, 427–437.
41 F. Tommasino, E. Scifoni and M. Durante, *Int. J. Part. Ther.*, 2015, **2**, 428–438.
42 E. C. Halperin, *Lancet Oncol.*, 2006, **7**, 676–685.
43 M. Wang, J. Saha and F. A. Cucinotta, *Mutat. Res., Genet. Toxicol. Environ. Mutagen.*, 2013, **756**, 108–114.
44 A. L. Ponomarev and F. A. Cucinotta, *Radiat. Meas.*, 2006, **41**, 1075–1079.
45 W. Friedland, E. Schmitt, P. Kundrát, M. Dingfelder, G. Baiocco, S. Barbieri and A. Ottolenghi, *Sci. Rep.*, 2017, **7**, 45161.
46 W. E. Wilson and T. L. Criswell, *Adv. Space Res.*, 1986, **6**, 75–81.
47 N. Hamada, *J. Radiat. Res.*, 2009, **50**, 1–9.
48 B. Jakob, J. Splinter, S. Conrad, K.-O. Voss, D. Zink, M. Durante, M. Lobrich and G. Taucher-Scholz, *Nucleic Acids Res.*, 2011, **39**, 6489–6499.
49 A. A. Bezbakh, V. B. Zager, G. Kaminski, A. I. Krylov, V. A. Krylov, Y. G. Teterev and G. N. Timoshenko, *Phys. Part. Nucl. Lett.*, 2013, **10**, 175–178.
50 O. B. Tarasov and D. Bazin, *Nucl. Instrum. Methods Phys. Res., Sect. B*, 2016, **376**, 185–187.
51 P. Matula, M. Maška, O. Daněk, P. Matula and M. Kozubek, in *IEEE International Symposium on Biomedical Imaging*, IEEE, 2009, pp. 1138–1141.
52 J. M. Daley and P. Sung, *Mol. Cell. Biol.*, 2014, **34**, 1380–1388.
53 S. Pellegrino, J. Michelena, F. Teloni, R. Imhof and M. Altmeyer, *Cell Rep.*, 2017, **19**, 1819–1831.
54 A. J. Nakamura, V. A. Rao, Y. Pommier and W. M. Bonner, *Cell Cycle*, 2010, **9**, 389–397.
55 W. S. Rasband, *ImageJ*, U. S. National Institutes of Health, Bethesda, Maryland, USA, 1997–2016, https://imagej.nih.gov/ij/.
56 T. R. Jones, I. Kang, D. B. Wheeler, R. A. Lindquist, A. Papallo, D. M. Sabatini, P. Golland and A. E. Carpenter, *BMC Bioinf.*, 2008, **9**, 482.
57 A. Chatterjee and W. R. Holley, *Adv. Radiat. Biol.*, 1993, **17**, 181–226.
58 A. Asaithamby and D. J. Chen, *Mutat. Res., Fundam. Mol. Mech. Mutagen.*, 2011, **711**, 87–99.
59 M. Hofer, M. Falk, D. Komůrková, I. Falková, A. Bačíková, B. Klejdus, E. Pagáčová, L. Štefančíková, L. Weiterová, K. J. Angelis, S. Kozubek, L. Dušek and Š. Galbavý, *J. Med. Chem.*, 2016, **59**, 3003–3017.
60 S. Tenhumberg, E. Gudowska-Nowak, E. Nasonova and S. Ritter, *Int. J. Radiat. Biol.*, 2007, **83**, 501–513.
61 N. I. Nakajima, H. Brunton, R. Watanabe, A. Shrikhande, R. Hirayama, N. Matsufuji, A. Fujimori, T. Murakami, R. Okayasu, P. Jeggo and A. Shibata, *PLoS One*, 2013, **8**, e70107.
62 D. M. Sridharan, A. Asaithamby, S. M. Bailey, S. V. Costes, P. W. Doetsch, W. S. Dynan, A. Kronenberg, K. N. Rithidech, J. Saha, a. M. Snijders, E. Werner, C. Wiese, F. A. Cucinotta and J. M. Pluth, *Radiat. Res.*, 2015, **183**, 1–26.
63 D. T. Goodhead, *J. Radiat. Res.*, 1999, **40**(Suppl), 1–13.
64 M. Falk, M. Hausmann, E. Lukasova, A. Biswas, G. Hildenbrand, M. Davidkova, E. Krasavin, Z. Kleibl,

I. Falkova, L. Jezkova, L. Stefancikova, J. Sevcik, M. Hofer, A. Bacikova, P. Matula, A. Boreyko, J. Vachelova, A. Michaelidesova and S. Kozubek, *Crit. Rev. Eukaryotic Gene Expression*, 2014, **24**, 225–247.
65 S. V. Costes, A. Boissière, S. Ravani, R. Romano, B. Parvin and M. H. Barcellos-Hoff, *Radiat. Res.*, 2006, **165**, 505–515.
66 F. Antonelli, A. Campa, G. Esposito, P. Giardullo, M. Belli, V. Dini, S. Meschini, G. Simone, E. Sorrentino, S. Gerardi, G. A. P. Cirrone and M. A. Tabocchini, *Radiat. Res.*, 2015, **183**, 417–431.
67 M. Falk, M. Hausmann, E. Lukasova, A. Biswas, G. Hildenbrand, M. Davidkova, E. Krasavin, Z. Kleibl, I. Falkova, L. Jezkova, L. Stefancikova, J. Sevcik, M. Hofer, A. Bacikova, P. Matula, A. Boreyko, J. Vachelova, A. Michaelidesova and S. Kozubek, *Crit. Rev. Eukaryotic Gene Expression*, 2014, **24**, 205–223.
68 J. Reindl, G. A. Drexler, S. Girst, C. Greubel, C. Siebenwirth, S. E. Drexler, G. Dollinger and A. A. Friedl, *Phys. Biol.*, 2015, **12**, 66005.
69 Y. Lorat, S. Schanz, N. Schuler, G. Wennemuth, C. Rübe and C. E. Rübe, *PLoS One*, 2012, **7**, e38165.
70 Y. Lorat, S. Schanz and C. E. Rübe, *Clin. Cancer Res.*, 2016, **22**, 5300–5311.
71 M. Winey, J. B. Meehl, E. T. O'Toole and T. H. Giddings, *Mol. Biol. Cell*, 2014, **25**, 319–323.
72 A. Bolzer, G. Kreth, I. Solovei, D. Koehler, K. Saracoglu, C. Fauth, S. Müller, R. Eils, C. Cremer, M. R. Speicher and T. Cremer, *PLoS Biol.*, 2005, **3**, e157.
73 D.-H. Kim, B. Li, F. Si, J. M. Phillip, D. Wirtz and S. X. Sun, *J. Cell Sci.*, 2016, **129**, 457–457.
74 J. C. Waters, *J. Cell Biol.*, 2009, **185**, 1135–1148.
75 M. Hausmann, N. Ilić, G. Pilarczyk, J.-H. Lee, A. Logeswaran, A. Borroni, M. Krufczik, F. Theda, N. Waltrich, F. Bestvater, G. Hildenbrand, C. Cremer and M. Blank, *Int. J. Mol. Sci.*, 2017, **18**, 2066.
76 M. Krufczik, A. Sievers, A. Hausmann, J.-H. Lee, G. Hildenbrand, W. Schaufler and M. Hausmann, *Int. J. Mol. Sci.*, 2017, **18**, 1005.
77 J. P. Eberle, A. Rapp, M. Krufczik, M. Eryilmaz, M. Gunkel, H. Erfle and M. Hausmann, *Methods Mol. Biol.*, 2017, **1663**, 1–13.
78 M. Bach, C. Savini, M. Krufczik, C. Cremer, F. Rösl and M. Hausmann, *Int. J. Mol. Sci.*, 2017, **18**, 1726.
79 M. Falk, E. Lukášová and S. Kozubek, *Biochim. Biophys. Acta, Mol. Cell Res.*, 2008, **1783**, 2398–2414.
80 S. Kozubek, E. Lukásová, P. Jirsová, I. Koutná, M. Kozubek, A. Ganová, E. Bártová, M. Falk and R. Paseková, *Chromosoma*, 2002, **111**, 321–331.
81 M. Falk, E. Lukasova, B. Gabrielova, V. Ondrej and S. Kozubek, *Biochim. Biophys. Acta, Mol. Cell Res.*, 2007, **1773**, 1534–1545.
82 D. Deckbar, P. A. Jeggo and M. Löbrich, *Crit. Rev. Biochem. Mol. Biol.*, 2011, **46**, 271–283.
83 N. Shikazono, M. Noguchi, K. Fujii, A. Urushibara and A. Yokoya, *J. Radiat. Res.*, 2009, **50**, 27–36.
84 S. K. Singh, M. Wang, C. Staudt and G. Iliakis, *Nucleic Acids Res.*, 2011, **39**, 8416–8429.
85 L. Ježková, M. Falk, I. Falková, M. Davídková, A. Bačíková, L. Štefančíková, J. Vachelová, A. Michaelidesová, E. Lukášová, A. Boreyko, E. Krasavin and S. Kozubek, *Appl. Radiat. Isot.*, 2014, **83**, 128–136.
86 M. Falk, E. Lukášová, L. Štefančíková, E. Baranová, I. Falková, L. Ježková, M. Davídková, A. Bačíková, J. Vachelová, A. Michaelidesová and S. Kozubek, *Appl. Radiat. Isot.*, 2014, **83**, 177–185.
87 Y. Ziv, D. Bielopolski, Y. Galanty, C. Lukas, Y. Taya, D. C. Schultz, J. Lukas, S. Bekker-Jensen, J. Bartek and Y. Shiloh, *Nat. Cell Biol.*, 2006, **8**, 870–876.
88 I. Chiolo, A. Minoda, S. U. Colmenares, A. Polyzos, S. V. Costes and G. H. Karpen, *Cell*, 2011, **144**, 732–744.
89 I. Chiolo, J. Tang, W. Georgescu and S. V. Costes, *Mutat. Res., Fundam. Mol. Mech. Mutagen.*, 2013, **750**, 56–66.
90 W. Friedland, P. Jacob, H. G. Paretzke and T. Stork, *Radiat. Res.*, 1998, **150**, 170.
91 W. Friedland, P. Jacob, H. G. Paretzke, A. Ottolenghi, F. Ballarini and M. Liotta, *Radiat. Prot. Dosimetry*, 2006, **122**, 116–120.
92 B. Boudaïffa, P. Cloutier, D. Hunting, M. A. Huels and L. Sanche, *Science*, 2000, **287**, 1658–1660.
93 B. Jakob, J. Splinter, M. Durante and G. Taucher-Scholz, *Proc. Natl. Acad. Sci. U. S. A.*, 2009, **106**, 3172–3177.
94 R. M. Anderson, D. G. Papworth, D. L. Stevens, N. D. Sumption and D. T. Goodhead, *Cytogenet. Genome Res.*, 2006, **112**, 35–44.
95 M. Durante, D. Pignalosa, J. A. Jansen, X. F. Walboomers and S. Ritter, *Radiat. Res.*, 2010, **174**, 20–26.
96 G. Kraft, M. Kramer and M. Scholz, *Radiat. Environ. Biophys.*, 1992, **31**, 161–180.
97 V. Conte, P. Colautti, B. Grosswendt, D. Moro and L. De Nardo, *New J. Phys.*, 2012, **14**, 93010.
98 T. Neumaier, J. Swenson, C. Pham, A. Polyzos, A. T. Lo, P. Yang, J. Dyball, A. Asaithamby, D. J. Chen, M. J. Bissell, S. Thalhammer and S. V. Costes, *Proc. Natl. Acad. Sci. U. S. A.*, 2012, **109**, 443–448.

EPJ D

Recognized by European Physical Society

Atomic, Molecular, Optical and Plasma Physics

Eur. Phys. J. D (2018) 72: 158 DOI: 10.1140/epjd/e2018-90148-1

Single-molecule localization microscopy as a promising tool for γH2AX/53BP1 foci exploration

Daniel Depes, Jin-Ho Lee, Elizaveta Bobkova, Lucie Jezkova, Iva Falkova, Felix Bestvater, Eva Pagacova, Olga Kopecna, Mariia Zadneprianetc, Alena Bacikova, Elena Kulikova, Elena Smirnova, Tatiana Bulanova, Alla Boreyko, Evgeny Krasavin, Michael Hausmann, and Martin Falk

edp sciences

Società Italiana di Fisica

Springer

Eur. Phys. J. D (2018) 72: 158
https://doi.org/10.1140/epjd/e2018-90148-1

THE EUROPEAN PHYSICAL JOURNAL D

Regular Article

Single-molecule localization microscopy as a promising tool for γH2AX/53BP1 foci exploration*

Daniel Depes[1,2], Jin-Ho Lee[3], Elizaveta Bobkova[3], Lucie Jezkova[4], Iva Falkova[1], Felix Bestvater[5], Eva Pagacova[1], Olga Kopecna[1], Mariia Zadneprianetc[4], Alena Bacikova[1], Elena Kulikova[4], Elena Smirnova[4], Tatiana Bulanova[4], Alla Boreyko[4], Evgeny Krasavin[4], Michael Hausmann[3,a], and Martin Falk[1,b]

[1] Czech Academy of Sciences, Institute of Biophysics, v.v.i. Kralovopolska 135, 61265 Brno, Czech Republic
[2] Masaryk University, Faculty of Sciences, Brno, Czech Republic
[3] Kirchhoff-Institute for Physics, University of Heidelberg, Im Neuenheimer Feld 227, 69120 Heidelberg, Germany
[4] Joint Institute for Nuclear Research, Dubna, Russia
[5] German Cancer Research Center (DKFZ), Heidelberg, Germany

Received 31 March 2018 / Received in final form 2 June 2018
Published online 18 September 2018

Abstract. Quantification and structural studies of DNA double strand breaks (DSBs) are an essential part of radiobiology because DSBs represent the most serious damage introduced to the DNA molecule by ionizing radiation. Although standard immunofluorescence confocal microscopy has demonstrated its usefulness in a large number of research studies, it lacks the resolution required to separate individual, closely associated DSBs, which appear after cell exposure to high linear energy transfer (high-LET) radiation and can be visualized as clusters or streaks of radiation-induced repair foci (IRIFs). This prevents our deeper understanding of DSB induction and repair. Recent breakthroughs in super-resolution light microscopy, such as the development of single-molecule localization microscopy (SMLM), offer an optical resolution of approximately an order of magnitude better than that of standard confocal microscopy and open new horizons in radiobiological research. Unlike electron microscopy, SMLM (also referred to as "nanoscopy") preserves the natural structure of biological samples and is not limited to very thin sample slices. Importantly, SMLM not only offers a resolution on the order of approximately 10 nm, but it also provides entirely new information on the biochemistry and spatio-temporal organization of DSBs and DSB repair at the molecular level. Nevertheless, it is still challenging to correctly interpret these often surprising nanoscopy results. In the present article, we describe our first attempts to use SMLM to explore γH2AX and 53BP1 repair foci induced with ^{15}N high-LET particles.

1 Introduction

Ionizing radiation (IR) is defined by its ability to liberate electrons from atoms and molecules. This has a destructive effect on DNA molecules, which become affected through modified bases, crosslinks, and even strand breaks [1]. The most serious damage occurs when both strands of the DNA molecule are broken, creating a double strand break (DSB). DSBs challenge the repair mechanisms of cells and, if left unrepaired or repaired incorrectly, can lead to cell death or mutagenesis. The severity and extent of DSB induction depends on several factors, such as the dose and type of radiation, cell cycle phase, chromatin condensation, and cell type [2–4] reviewed in [5,6].

Multiple (or complex) DSB lesions, i.e., DSBs generated in very close mutual proximity and eventually combined with other type(s) of DNA damage, are the most critical. This sort of DSB appears especially after exposure to IR with high linear energy transfer (LET), which, compared to low-LET radiation, such as γ-rays or X-rays, generates DSBs of higher complexity. Complex DSBs can be repaired only with difficulty and have been recognized as the main factor responsible for increased mutagenesis and/or cell killing by high-LET particles [7], reviewed in [8]. Thus, high-LET radiation currently represents one of the most potent tools to treat cancer, and intensive effort is being exerted to investigate the biological effects of various energetic particles [9,10]. Nevertheless, a better understanding of DNA damage is important not only in the context of cancer treatment. DNA is permanently attacked by environmental factors,

* Contribution to the Topical Issue "Atomic Cluster Collisions", edited by Alexey Verkhovtsev, Andrey V. Solov'yov, Germán Rojas-Lorenzo, and Jesús Rubayo Soneira.

[a] e-mail: hausmann@kip.uni-heidelberg.de
[b] e-mail: falk@ibp.cz

such as background radiation or chemicals, and intracellular factors, which include energy metabolism, DNA replication and antibody production [11,12]. DNA damage and repair are therefore fundamental biological processes directly related to genome stability, evolution, immune system function, ageing, and both development and treatment of malignant as well as non-malignant (e.g., neurodegenerative) diseases. DNA damage is also of utmost interest in the context of planned long-term space missions, where exposure of astronauts to mixed fields of IR represents the most serious complication [13].

The need for a better understanding of the relationship between the physical characteristics of ionizing radiation and the consequent physical, chemical, and biological processes in (living) matter, including medical effects, initiated an extensive research effort on this topic. Several European network projects, such as COST NanoIBCT (Nanoscale Insights into Ion Beam Cancer Therapy [14,15]), have been launched to overcome the complexity and multidisciplinary character of associated research. As one of the important results, a procedure allowing prediction of the biological effects of IR on the basis of the physical parameters of the radiation has been introduced by Andrey Solov'yov's group [14–17]. The procedure allows theoretical estimations of irradiated cell survival without the necessity of performing time-consuming biological experiments [14–17]. Nevertheless, many questions about the complex biological effects of IR still remain to be answered. For instance, referencing the importance of further research, our recent report [18] suggests that the biological effects of high-LET ions are determined in a more complex way than simply by LET.

An important task, in addition to the already mentioned evaluation of the extent and character of DSB damage after irradiation, is to understand the repair of these lesions. A network of interconnected biochemical pathways has evolved to counteract DSBs. The two main pathways are non-homologous end joining (NHEJ) and homologous recombination (HR), which are activated [19,20] by DNA damage depending on the phase of the cell cycle, chromatin structure at the site of damage, character (e.g., complexity) of the DSB and potentially some other factors reviewed in [4]. Importantly, repair pathways are often deregulated in cancer cells [21], making tumors defective in DSB repair, and inhibition of the remaining functional pathway is a potentially promising therapeutic approach that can be combined with radiotherapy. On the other hand, some tumour cells are highly radioresistant [22].

As presented at the 8th International Symposium on Atomic Cluster Collisions (ISACC 2017 http://www.isacc-cuba.org [23]), immunofluorescence confocal (IC) microscopy is an advantageous method to study DNA damage and repair [3–6,24–27], since it allows direct observation of DSBs and DSB repair processes in the context of space and time, in individual cells, and under maximally physiological conditions or even in living cells. However, it offers only a limited resolution to resolve closely associated DSBs, which appear upon irradiation with accelerated heavy ions [18]. Higher resolution is also required to study DSB repair processes. Recent developments of super-resolution optical microscopy (or nanoscopy) thus represent a breakthrough (not only) in research on the biological effects of IR. In the present study, we illustrate the benefits of SMLM (reviewed in [28–34]), a variant of super-resolution microscopy, to study the composition, complexity, spatio-temporal dynamics, mutual colocalization, and final dissolution of γH2AX and 53BP1 repair foci generated by exposure of human U87 glioblastoma cells to ^{15}N high-LET ions. SMLM offers resolution on the order of approximately 10 nm and thus dramatically improves the microscopic information compared to that provided by IC microscopy. However, it may still be challenging to interpret the new type of data obtained by this method. Confocal microscopy can therefore serve to calibrate SMLM results with already known facts and estimate the best realistic parameters for consequent SMLM analyses.

2 Results and discussion

2.1 Immunofluorescence confocal microscopy

Radiobiologists are familiar with the fact that radiation with LET values ranging from 100 to 200 keV/μm exert maximal relative biological efficiency (RBE) [18]. In the present study, we used accelerated nitrogen (^{15}N) particles with LET = 182.9 keV/μm, which could be expected to generate highly complex DSBs. To ensure a sufficient number of particles to traverse each nucleus, human U87 glioblastoma cells were exposed to 4 Gy of this high-LET radiation.

Irradiated cells were spatially (3D) fixed in different periods of time post-irradiation (PI) (5 min to 24 h PI) and immunostained with antibodies against γHA2X and 53BP1 proteins. First, γHA2X and 53BP1 repair foci were visualized by standard confocal microscopy (Fig. 1). Compared to other methods, such as PFGE or comet assay, IC microscopy provides the most complex information on DSB damage – it covers the aspects of DSB complexity, spatiotemporal dynamics, and DSB repair and misrepair [3,4,24–27], reviewed in [5,6]. Moreover, all of these phenomena can be studied in single cells. Until recently, IC microscopy has been considered the most sensitive method to detect and analyse DSBs [5,6].

IC microscopy is based on immunological detection of protein complexes that accumulate at sites of DSB and are known as radiation-induced repair foci (IRIFs) [35]. The most-used DSB markers, also used in the present study, are γH2AX foci. At DSB sites, the histone H2AX becomes phosphorylated at serine 139 immediately after irradiation [36]. This modification, known as γH2AX, affects up to 2 Mb of DNA, making breaks visible for immunofluorescence microscopy as γH2AX foci [37]. Since γH2AX foci correlate with the number of DSBs following exposure to low-LET radiation, they are widely accepted as a quantitative indicator of these lesions [38]. DNA damage as low as a few DSBs generated by 1 mGy of radiation can be detected by immunofluorescence microscopy [39]. If required, DSBs can also be detected by TUNEL assay

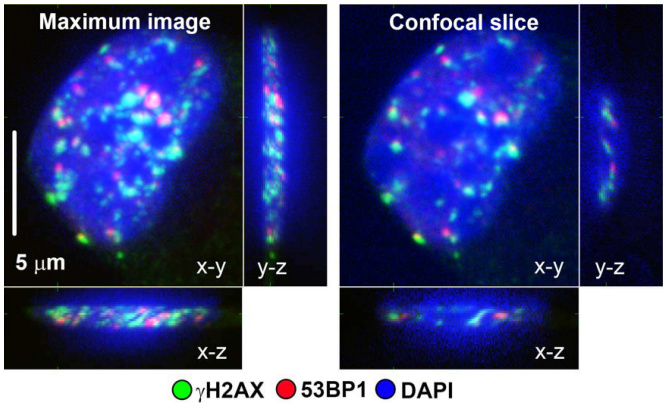

Fig. 1. Immunofluorescence confocal (IC) microscopy image of the nucleus (DAPI, blue) of a U87 glioblastoma cell irradiated with 4 Gy of ^{15}N ions accelerated to 13 MeV/n (182.9 keV/μm; Tab. 1). Cells were irradiated in a 90° geometry and stained for γH2AX (green) and 53BP1 (red) 5 min post-irradiation. The left panel shows the maximum intensity projection image composed of superimposed individual confocal slices (0.25 μm thick), while the right panel shows a single confocal slice. Both mutually colocalizing and non-colocalizing γH2AX and 53BP1 IRIF signals were visible at this period of time post-irradiation.

[40], which is independent of IRIF formation but preserves the advantages of IC microscopy. Moreover, immunostained (or TUNEL-labelled) DSBs can be quantified by flow cytometry, allowing large numbers of cells to be statistically analysed. There are many proteins of DSB repair machinery that bind to γH2AX foci and can be used as DSB markers in addition to γH2AX [41], such as MRE11, RAD50, and 53BP1. IC microscopy thus provides very useful and complex information on DSB damage induction and repair; however, as demonstrated in Figure 1, the complexity of γH2AX and 53BP1 foci clusters can only be roughly estimated because of signal intermingling and the limited resolution of IC microscopy. For the same reason, the internal structure of DSB repair foci remains hidden in IC images.

2.2 Single-molecule localization microscopy – the first attempt to understand γH2AX and 53BP1 foci structure at the nanoscale

To overcome the abovementioned limits of confocal microscopy, we analysed the morphology and composition of γH2AX/53BP1 foci/focus clusters by single-molecule localization microscopy (SMLM), which is a variant of super-resolution microscopy. The resolution restriction of fluorescence confocal microscopy is given by Abbe's diffraction limit (1) and is independent of the lens quality.

$$d_{\min} = \frac{\lambda}{2n\ \sin\alpha} = \frac{\lambda}{2NA}, \qquad (1)$$

$d_{\min}$ is the minimum distance between two points that can be still resolved, λ the wavelength of emission light, n the index of refraction, α the half angle of the cone of light that can enter the lens, and NA is the numerical aperture. Since light with a shorter than visible wavelength, such as UV or X-rays, emitted by the sample (i.e., fluorochromes tagged by antibodies used to detect proteins of interest in the case of ICM) is not suitable for immunofluorescence microscopy, the maximal resolution reachable with this method is approximately 200 nm (theoretically 167 nm for green light of 500 nm and an optical aperture $NA = 1.5$ under ideal optical specimen conditions). This means that small cellular structures located close to one another at the micro-scale, such as DSB foci generated by high-LET ions, become difficult or impossible to distinguish (Eq. (1)). On the other hand, electron microscopy (EM) provides superior resolution over optical microscopy and has been essential for the revelation of many cellular nanostructures (theoretically, the resolution can be roughly estimated to the order of 1 nm by (1) using the relevant DeBroglie wavelength of electrons). However, at the same time, EM suffers from several serious disadvantages, such as harsh preparation of the sample (i.e., fixation, freezing, or sectioning) and observation limited to very thin mechanically cut sample slices [42]. The discovery of super-resolution microscopy methods, such as SMLM, therefore represents a milestone in (radio)biological research [11,43,44]. While in principle, the same experimental procedures and conditions as those used with classic confocal microscopy were used in the present study, the real resolution power of SMLM was approximately 10 nm in the $x-y$ plane (i.e., one order of magnitude better than that of ICM). Advantageously, many routinely applied fluorochromes, such as AlexaFluor 488 and AlexaFluor 594 [28] used in the present work, or fluorescent proteins or nanoparticles [45] work with SMLM. SMLM thus offers an exceptional resolution power compared to classic confocal microscopy but preserves the benefits of that method (including very good preservation of the sample structure by structure-conserving fixation methods).

The principle of SMLM is explained in Figure 2. The cells are spatially (3D) fixed and immunostained with standard fluorochrome-labelled antibodies in the same way as in confocal microscopy (see methods). The only requirement is that fluorochromes able of blinking after photobleaching (e.g., Alexa Fluor) must be used. First, a standard-resolution widefield (non-confocal) image of a selected cell is acquired (Figs. 2B and 2C, left panels) to obtain a complete overview of the sample in its whole thickness. All fluorochrome molecules (Figs. 2A-a + b, grey and white dots) are permanently shining (all at the same time), which results in interference of their overlapped signals and low resolution (Figs. 2B and 2C, left panels). Consequently, to generate super-resolution confocal images, the sample is illuminated by a powerful laser (kW/cm^2 range) (Figs. 2B and 2C, middle panels) so that the fluorochrome molecules are switched off to a reversibly bleached state. After that, individual fluorochrome molecules recover from the bleached state to a temporarily fluorescent state in a spontaneous and stochastic manner (Fig. 2A-a + b, white dots). This means that individual fluorochrome molecules

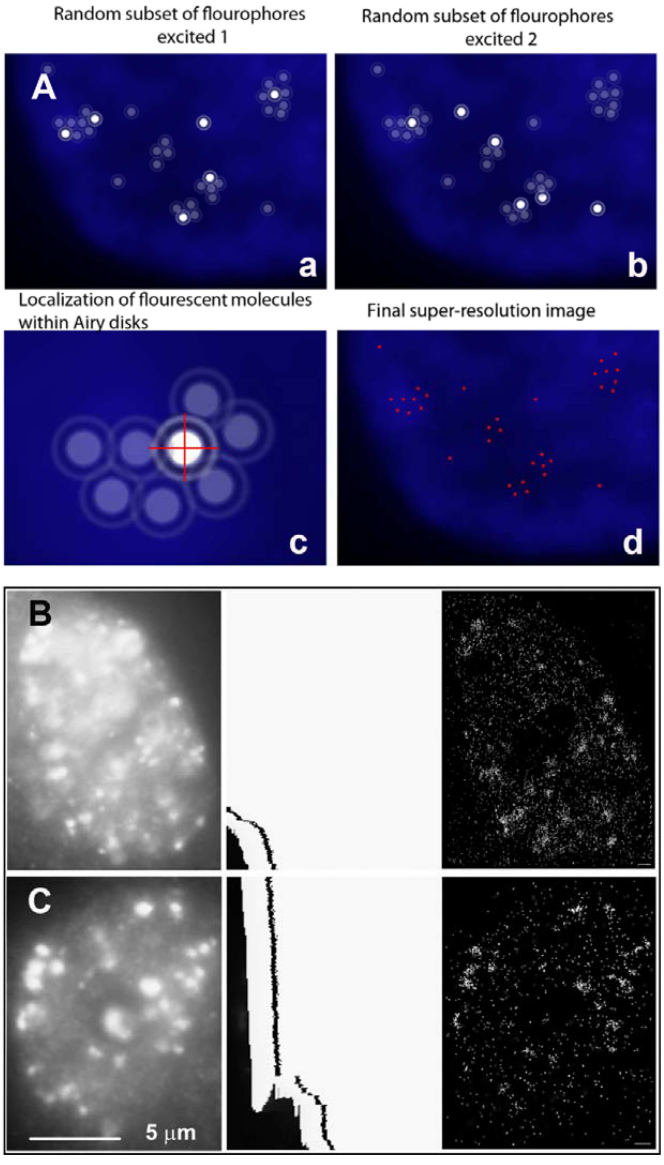

Fig. 2. The principle of single-molecule localization microscopy (SMLM). (A) Fluorochrome blinks are recorded during time after sample photobleaching (a + b). Precise positions (= position of the intensity barycentre) and their errors are then calculated for all fluorochrome molecules (c). As a result, a super-resolved pointillist image is artificially generated by further mathematical processing (d). (B) Compares the standard widefield microscopy image of γH2AX foci (left) and the corresponding SMLM image (right) taken after reversible photobleaching of the same cell nucleus (middle). (C) The same as B, but 53BP1 foci are visualized. U87 glioblastoma cells exposed to 4 Gy of ^{15}N ions (see Tab. 1 for the radiation characteristics) are shown.

are blinking, and different sets of only a few shining molecules (Fig. 2A-a vs. b) are registered at each particular moment of observation. The bleaching and blinking step thus allows spatio-temporal separation of single fluorochrome signals. This is the trick on which SMLM is based and how it can overcome Abbe's limit. Since only a few fluorochrome molecules are switched on at

Table 1. Radiation characteristics.

Particle	Z	Geometry° (degrees)	Energy, MeV/n	LET keV/μm	Fluence*, 1/cm^2 (1 Gy)	Particles/ nucleus# (1 Gy)
^{15}N	7	90	13	182.9	3.41×10^6	25.4

Z – charge, o – geometry of irradiation (the angle between the ion beam and the plane of the cell monolayer), * – fluence per 1 Gy absorbed in water, # – the number of particles per 1 Gy traversing a nucleus with an average area.

a particular period of time, the acquisition of a large series of images (2000 images/colour channel with an integration time of 100 ms in the present study) allows cumulative registration of individual flashes over time and extremely precise localization of the intensity barycentres of single fluorochrome molecules (Fig. 2A-c) – individual light flashes are uninfluenced by the interfering light of surrounding fluorochromes. The individual localization precision is obtained by the full width at half maximum of a Gaussian function fitted over each signal point represented by the Airy disk of a single molecule fluorescence signal. The intensity barycentre of the point can be calculated from the measured intensities of camera pixels around the maximum. As a result, a matrix of registered signal spatial coordinates (with measurement errors and other parameters) is obtained, and a super-resolved pointillist image can be artificially generated (Fig. 2A-d; Figs. 2B and 2C, right panels). Most importantly, the matrix can be used for further mathematical analyses without preparing an image. It should be noted that not all fluorochromes blink after bleaching.

Recently, we have successfully introduced SMLM to visualize γH2AX and MRE11 proteins at the nanoscale in cells irradiated with γ-rays [29,30]. In the present study, for the first time, we extended SMLM application to super-resolution analyses of γH2AX and 53BP1 foci in U87 glioblastoma cells irradiated with 4 Gy of high-LET nitrogen (^{15}N) ions (Tab. 1, 90° geometry) (Figs. 2B, 2C, 3, and 4). We selected U87 cells because they represent highly radioresistant tumour cells, and thus, differences in DSB induction/repair could be expected to exist compared to normal human skin fibroblasts (NHDF) studied in parallel (data not shown). Figures 2B and 2C display γH2AX foci and 53BP1 foci, respectively, detected by widefield fluorescence microscopy (left) and SMLM nanoscopy (right) in the same cell. While the widefield fluorescence images (left) show the foci as more or less homogeneous signals, with SMLM (right images), we can distinguish the signals of single molecules and thus the internal focus nanostructure.

Possible methods of super-resolved image processing are proposed in Figures 3 and 4, respectively. In these figures, 53BP1 (Fig. 3) and γH2AX (Fig. 4) signals were detected in U87 cells irradiated with nitrogen ions in a 90° geometry and fixed 30 min PI. The top images show "raw" pointillist images as calculated from the signal coordinates of individual fluorochromes detected by SMLM. Each point represents the position of one fluorochrome molecule. Images in the middle were modified so that the intensity of each signal reflects the number of

close-neighbour signals within a given radius. In addition, the size of each point was adjusted to correspond to its position estimation error (localization precision). Finally, 53BP1 and γH2AX foci were illustratively discriminated according to given parameters in the bottom images. The number of foci depends on the requested number of neighbouring signals with a maximal allowed value of spatial separation. Though the parameters were equilibrated to best fit the average number of foci on the immunofluorescence confocal microscopy slice of the corresponding thickness, the number of foci detected by SMLM reflects the internal structure of foci rather than their overall size or fluorescence intensity usually scored with immunofluorescence confocal microscopy. For both γH2AX and 53BP1 foci, the images show that individual foci have an internal structure, i.e., they are composed of several subfoci. How these subfoci correspond to the subfoci detected with high-resolution confocal microscopy [18] or DSBs are under investigation.

Comparison of Figures 3 and 4 reveals that there were more γH2AX foci than 53BP1 foci at 30 min PI, indicating that colocalization of these foci was still incomplete. This dislocation of γH2AX and 53BP1 has also been reported in literature [46]. Though this phenomenon depends on individual cells and must be further quantified, more extensive colocalization is typically seen at this period of time with classic confocal microscopy (Fig. 1). This observation could mean, for instance, that while H2AX is being continuously phosphorylated upon irradiation, pre-existing levels of 53BP1 have been already exhausted at higher radiation doses [47]. However, it is also possible that the parameters used for foci registration in the present work are still not fully optimized. With confocal microscopy, the complexity of γH2AX/53BP1 foci can be estimated in 3D images, as described in our previous work [18]. Briefly, individual foci were defined as compositions of several "subfoci" by their morphology and γH2AX/53BP1 fluorescence intensity heatmaps. The centres (and numbers) of subfoci forming a focus were identified by the fluorescence heatmap maxima. Foci pertaining to a single focus were then "glued" by a fluorescence signal lower than the fluorescence maxima but significantly higher than the background fluorescence, i.e., these subfoci could be separated on the basis of γH2AX/53BP1 fluorescence topology maps but still formed a morphologically integrated area in the cell nucleus characterized by increased fluorescence above the background. In the case of SMLM, this approach is not possible since individual signals are precisely separated from one another (the images represent pointillist maps of signals, and although this kind of representation could be less usual for man, it is much closer to the reality than the standard (spread) images obtained by confocal microscopy). Hence, with SMLM, γH2AX/53BP1 clusters were determined by cluster analysis using the parameters best corresponding, in terms of the number of γH2AX/53BP1 foci, to the results of confocal microscopy. Alternatively, the lower number of registered 53BP1 foci relative to γH2AX foci could be explained by less efficient fluorochrome blinking in the 53BP1 channel compared to the γH2AX channel. Moreover, it has also been shown that γH2AX subfoci could also lack other repair proteins [48]. All these possibilities show the challenging character of SMLM technology and of interpretation of the entirely new sort of results obtained. They also demonstrate how import it is to perform parallel studies with classic confocal microscopy – despite its relatively low resolution power, classic confocal microscopy can be an important tool to set up the most suitable parameters for SMLM image analyses and verify labelling efficiency.

The most challenging goal only possible with nanoscopy is to "decode" the internal nanostructure of γH2AX and other DSB repair protein foci participating in IRIF formation. It is evident that individual fluorochrome molecules form regions of different densities within both γH2AX and 53BP1 foci. This is suggestive of the existence of smaller γH2AX/53BP1 foci associated into larger clusters. Whether these "subfoci" correspond to individual DSBs or even fainter nanostructures within a single DSB focus is currently being studied in cells irradiated in 10° geometry (better resolution of individual foci forming the streaks [18]). Only a few reports on the IRIF nanostructure have been published [29,49]. For instance, Lorat et al. [48,50] used transmission electron microscopy to precisely quantify the DSB complexity upon high-LET carbon irradiation (LET = 190 keV μm^{-1}, energy E = 9.5 MeV per n) at the single-molecule level.

The authors revealed up to approximately 500 DSBs per 1 μm^3 volume of the carbon ion track. Although the precise relationship between the LET and the number of γH2AX foci induced by a particular radiation remains an important question of radiobiology to be solved, our confocal microscopy analyses (not shown) and some literature [51,52] suggest that the increase in the γH2AX focus number with LET is probably not dramatic. For instance, [51] a previous study showed that the relative radiobiological effectiveness (RBE) for the mean number of γH2AX foci/cell/Gy using MRC-5 cells was approximately 1 for α-radiation relative to low-LET radiation. According to current knowledge from earlier results of PFGE, comet assays, and IC microscopy, there are approximately 20–40 DSBs or γH2AX foci per 1 Gy and nucleus on average reviewed in [5,6,53]. Given a typical cell nucleus as a sphere of approximately 10 μm in diameter, its volume $(4/3\pi r^3)$ is about 4000 μm^3. Therefore, even if the particle only damages 1 μm^3 of the cell nucleus, and we consider that it generates 80 DSBs/Gy/nucleus (2 times more than the maximum typically reported for γ-rays), with each microscopically detected γH2AX focus being composed of not less than 5 "subfoci" [18], the result (400 DSBs/μm^3) still only roughly approaches 500 DSBs per 1 μm^3 volume reported by Lorat et al. [48,50]. This prompts the questions of how a single DSB is defined at the molecular (nanosopy) level and what level of complexity DSBs generated by different radiation types present. As low-LET γ-rays mostly generate simple DSBs, we propose that comparison of the γH2AX/53BP1 foci induced by high-LET particles and γ-rays, respectively, could provide new insight into the nature of internal IRIF substructures. The ongoing quantification of our results is

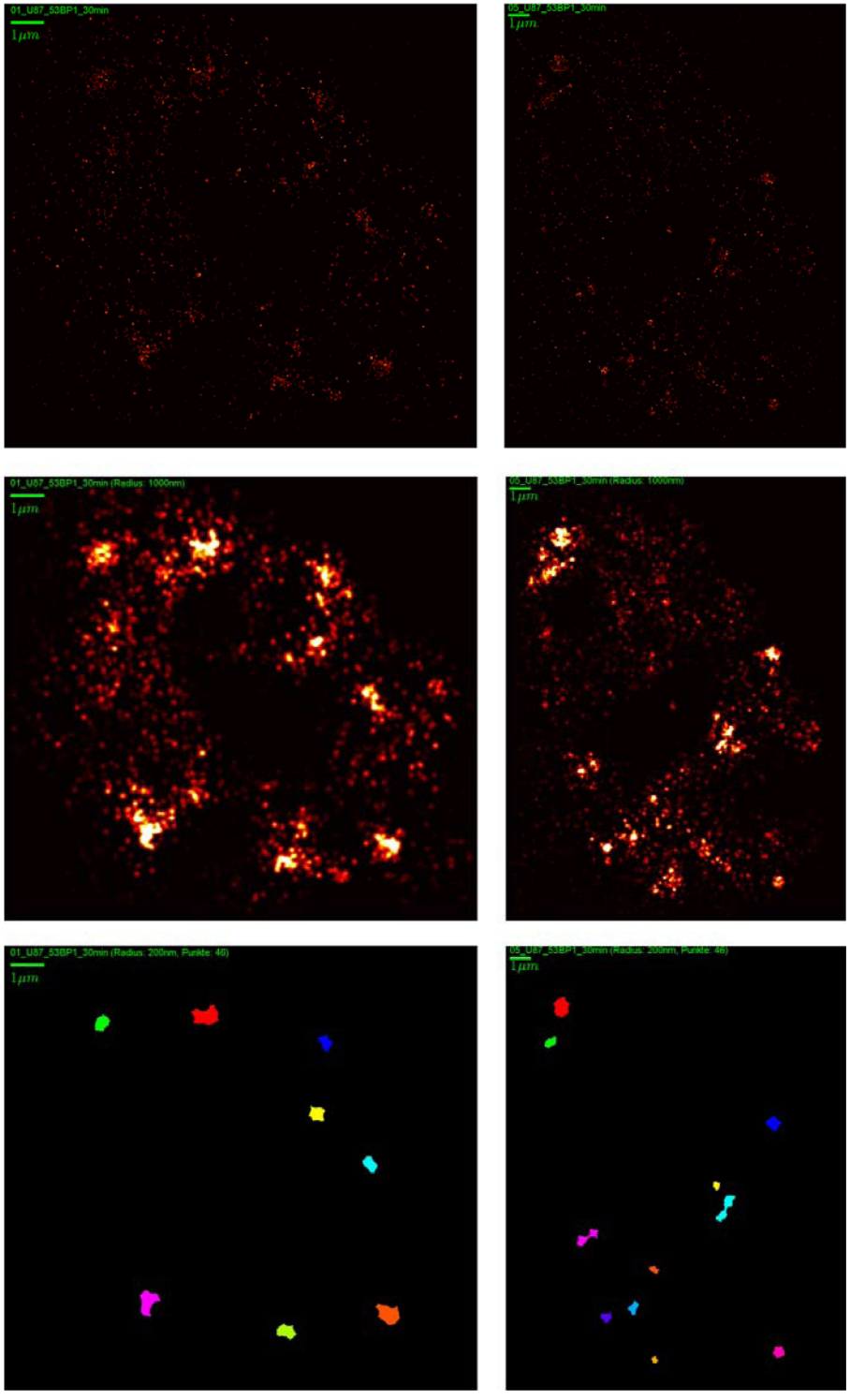

Fig. 3. SMLM microscopy used to detect 53BP1 foci in U87 cells irradiated with 4 Gy of nitrogen ions (see Tab. 1 for the radiation characteristics) and fixed 30 min post-irradiation. Two illustrative nuclei are shown. Top images: Super-resolved pointillist SMLM images (unprocessed). Middle images: Pointillist images of the signals artificially spread by the localization precision and encoded so that the point brightness corresponds to the number of neighbours in a given surrounding (nearest-neighbour images). Bottom images: 53BP1 clusters detected computationally according to estimated parameters (i.e., a given minimum of neighbour signals separated by a maximal allowed radius, etc.). Different clusters are shown in different colours, which has no further meaning. See the main text for a discussion on the nature and relevance of these foci.

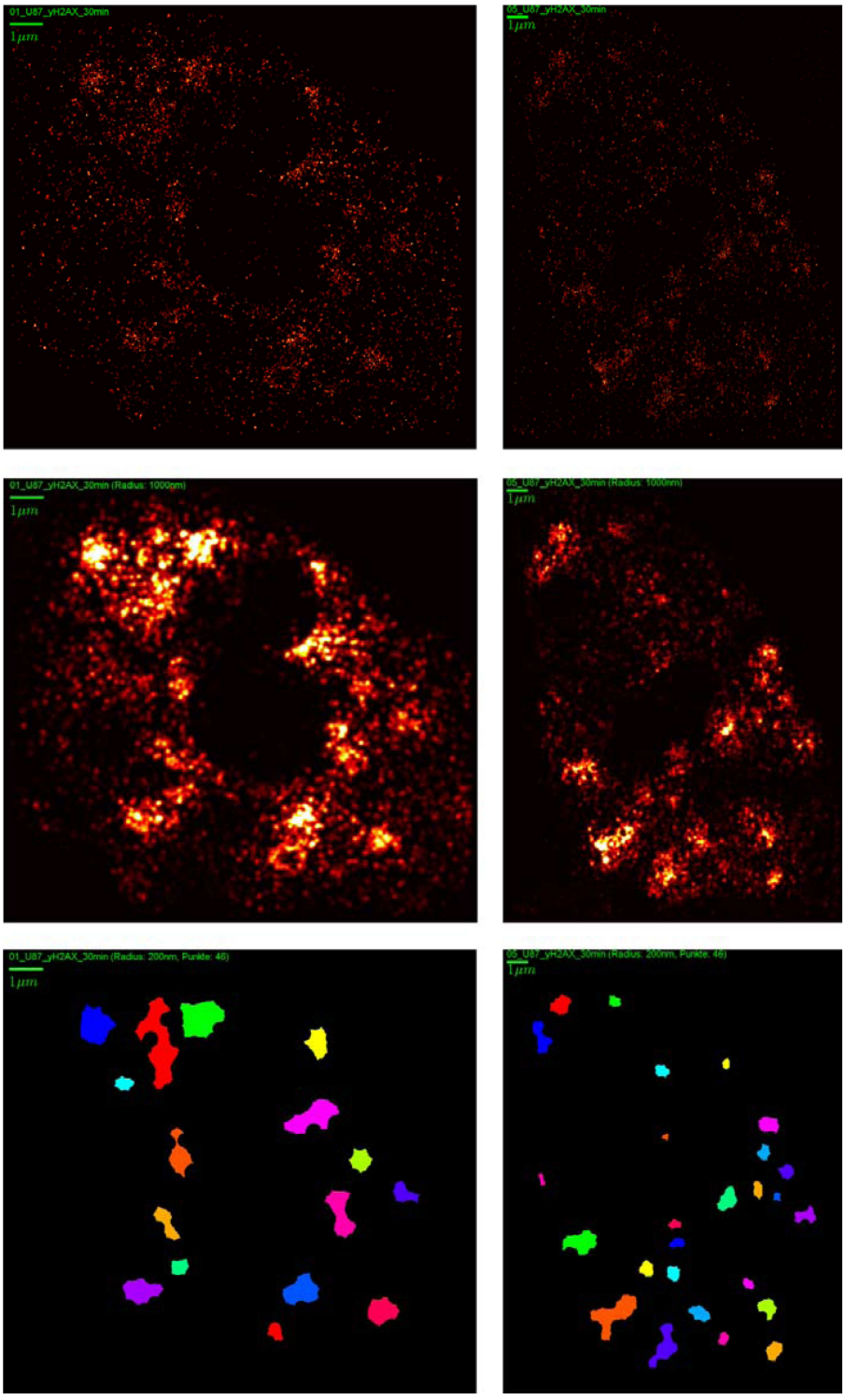

Fig. 4. SMLM microscopy used to detect γH2AX foci in U87 cells irradiated with 4 Gy of nitrogen ions (see Tab. 1 for the radiation characteristics) and fixed 30 min post-irradiation. Two illustrative nuclei are shown. Top images: super-resolved pointillist SMLM images (unprocessed). Middle images: pointillist images of the signals artificially spread by the localization precision and encoded so that the point brightness corresponds to the number of neighbours in a given surrounding (nearest-neighbour images). Bottom images: γH2AX clusters detected computationally according to estimated parameters (i.e., a given minimum of neighbour signals separated by a maximal allowed radius, etc.). Different clusters are shown in different colours, which has no further meaning. See the main text for a discussion on the nature and relevance of these foci.

expected to improve our understanding of DSB damage and repair in normal and tumour cells upon the action of ionizing radiation of different kinds.

3 Materials and methods

3.1 Cell culture

Primary normal human neonatal dermal fibroblasts (NHDF) (Lonza, CC-2509; passages 6–9) and human U87 glioblastoma cells were cultured in Dulbecco's modified Eagle medium (DMEM) supplemented with 10 % foetal calf serum (FCS) and a 1% gentamicin-glutamine solution (all reagents from Sigma-Aldrich). Cells were maintained in T-25 cell flasks at 37 °C in a humidified atmosphere with 5% CO_2. Prior to irradiation (16–18 h), cells were re-seeded on the glass bottom of a Petri dish (MatTek Corporation, P35G-0.170-14-C) and cultivated to form an 80% confluent monolayer. For irradiation, the dishes were aseptically closed and sealed with Parafilm M (Sigma–Aldrich) to prevent spillage and cell infection. All samples were irradiated at room temperature and immediately returned to the incubator (37 °C).

3.2 Accelerated-ion irradiation

Nitrogen (^{15}N) ions were accelerated to 13 MeV/n (LET = 182.9 keV/μm; fluence = 25.4 particles/nucleus; Tab. 1) using a U-400M isochronous cyclotron in the Flerov Laboratory of Nuclear Reaction at the Joint Institute for Nuclear Research (JINR, Dubna, Russia) [54]. Cells were irradiated on glass coverslips (at Petri dish bottoms) perpendicularly (90°), i.e., with a 90° angle between the ion beam and the plane of the cell monolayer. The side of the coverslips covered with cells was oriented towards the ion beam so that the cells were hit by the particles before the beam continued into the culture medium in the Petri dish. Non-synchronized cell populations with prevalent (>80%) G1 cells were irradiated in the culture medium with a dose of 4 Gy (dose rate of approximately 4 Gy/min) at 37 °C. During irradiation, the cells were kept in a thermostable box, ensuring a constant temperature and prevention from infection during the whole procedure. After irradiation, the cells were immediately placed back into the incubator (37 °C/5% CO_2) until fixation. The energy and corresponding LET values of ions in the plane of the cell monolayer were calculated using LISE++ software [55].

3.3 Immunofluorescence assay for SMLM (nanoscopy)

The cells were washed two times for 5 min in 1× PBS, permeabilized for 6 min in 0.2% Triton X-100 at RT, washed again three times for 5 min at room temperature (RT) in 1× PBS, and incubated in 2% bovine serum albumin (BSA) for 60 min at RT. Consequently, the same primary antibodies as those used for confocal immunofluorescence microscopy – mouse anti-γH2AX (ab22551, Abcam) and rabbit anti-53BP1 (ab21083, Abcam) – were added to the cells under the same conditions as described for the method. Next, the cells were rinsed with 0.2% Triton X-100 and washed three times with 1× PBS for 5 min at RT. The secondary antibodies for SMLM (nanoscopy) were AlexaFluor 594-conjugated goat anti-rabbit (Johnson Laboratories) and AlexaFluor 488-conjugated goat anti-mouse (Johnson Laboratories). The antibodies were diluted in blocking solution 2 (1:400 and 1:200, respectively) and applied to the cells for 30 min (RT, in the dark). After incubation, the cells were washed three times in 1× PBS for 5 min. The cell nuclei were stained with DAPI (5 min at RT) at a dilution of 1:20.000. Afterwards, the slides with cells were washed three times in 1× PBS for 5 min each. Finally, the cover slips were air dried, and the cells were embedded in ProLong Gold® (ThermoFisher Scientific). The Prolong Gold was left to polymerize for 24 hours in the dark at RT. After complete polymerization, the slides were sealed with nail polish and stored in the dark/4 °C.

3.4 Image acquisition and experimental data analysis – confocal microscopy

Confocal microscopy images of the immunofluorescence staining were captured using an automated high-resolution Leica DM RXA microscope (Leica, Wetzlar, Germany) equipped as follows: a Plan Fluotar oil-immersion objective (100×/NA1.3); a CSU 10a Nipkow disc (Yokogawa, Japan); a CoolSnap HQ CCD-camera (Photometrix, Tuscon, AZ, USA); and an Ar/Kr-laser (Innova 70C Spectrum, Coherent, Santa Clara, CA, USA). Automated image acquisition using Acquiarium software was described previously [56]. Forty serial optical sections were captured at 0.25-μm intervals along the z-axis. See [18,27] for detailed procedure descriptions.

3.5 Image acquisition and experimental data analysis – SMLM single-molecule localization microscopy (nanoscopy)

SMLM was performed as described previously [30] using a specially manufactured localization microscope (built by Wladimir Schaufler, DKFZ) with enhanced thermomechanical stability [29]. By indoor climate regulation and separate cooling of the optical elements, the instrumental temperature was maintained in the range of ±10 mK. During the course of the 2-min image acquisition time, the mechanical drift of the specimen was less than 10 nm.

The illumination light path was equipped with a LightHub laser combiner (Omicron Laserprodukte GmbH, Rodgau-Dudenhofen, Germany) assembled with four laser lines (405, 491, 561 and 642 nm), a polychromatic AOTF (Acousto Optical Tunable Filter; AA Opto Electronic, Orsay CEDEX, France), a variable beam expander 10BE03-2-8 (Standa Ltd., Vilnius, Lithuania), and a Flat-Top-Profile forming optics PiShaper (AdlOptica GmbH, Berlin, Germany). The circular Flat-Top laser beam profile was projected (downscaled) into the object plane using an achromatic focusing lens (f = 250 mm) and a 100/NA 1.46 oil plan apochromatic objective lens (Carl Zeiss Microscopy, Göttingen, Germany). For the AlexaFluor

488 dye and AlexaFluor 594 dye used here, illumination wavelengths of 491 nm and 561 nm, respectively, were used, resulting in approximately 1 kW/cm^2 power density in the object plane. The fluorescence light in the detection path was separated from the illumination light using two quadband interference filter glasses F73-410 and F72-866 (AHF analysentechnik AG, Tübingen, Germany) and was projected (magnified) by the objective – tube lens pair (Carl Zeiss Microscopy, Göttingen, Germany) and an additional twofold expander on the Andor Ultra EMCCD (Andor Technology, Belfast, Northern Ireland). All images were acquired after a 2-h start-up phase for thermal stabilization. For each cell nucleus, a time stack of 2000 image frames with an integration time of 100 ms each was registered and saved in 16-bit grey-scale TIFF image stack format. For each cell line and period of time PI, at least 20 cell nuclei were recorded and evaluated.

For determination of the local positions of the detected dye molecules from the blinking events, an algorithm described previously [57] was applied, which was based on subtraction of the brightness values of two successive frames. This method enables differentiation of the blinking events from the background. For each detected blinking point, the program defines a two-dimensional Gaussian distribution depending on the signal position and localization precision. A so-called "Orte-Matrix" was produced, which contained information about the signal amplitude, the lateral x- and y-coordinates, the standard deviations in the x and y directions, position errors, etc. [34,58]. From this matrix, pointillist images of the signals artificially spread by the localization precision can be produced. It is also possible to encode the point brightness by the number of neighbours in a given surrounding. This is called a nearest-neighbour image. For identification of clusters [59], appropriate parameters are currently being searched to correlate the cluster sizes to foci sizes obtained by confocal immunofluorescence microscopy.

4 Conclusions

High-resolution IC microscopy and SMLM (nanoscopy) were compared in the present work with respect to their ability to analyse the complexity of DSBs in U87 glioblastoma cancer cells exposed to ^{15}N high-LET particles. By confocal microscopy in combination with 3D cell fixation and 3D image analysis, we were able to roughly estimate the complexity of γH2AX and 53BP1 foci. The usefulness of confocal microscopy in this respect has also been demonstrated in our earlier report [18]. However, the precision in that study was limited by the insufficient resolution of confocal microscopy. To overcome this restriction, we introduced SMLM (nanoscopy) [29,31], which consequently proved its ability to precisely determine the complexity and internal nanostructure of IRIF foci/focus clusters. Though SMLM results remain to be analysed in a more complex manner, it is already evident now that SMLM can provide an entirely new sort of information regarding IRIF composition and biochemistry. Importantly, as with IC microscopy, samples for SMLM can be fixed at different periods of time PI, opening the possibility of time-dependent studies on DSB repair [29,30,33]. DSB repair kinetics, changes in DSB complexity with time PI and, for instance, the persistence of foci of different complexities can thus be studied with unprecedented precision.

Interpretation of SMLM results might be challenging [31]; therefore, confocal microscopy can be advantageously used to estimate the most suitable parameters for super-resolved SMLM image analyses. In addition, only a single confocal slice per cell can currently be analysed by SMLM. Standard fluorochromes keep blinking for minutes after triggering by high laser power, and this is sufficient to acquire a series of only approximately 2000 images in two or three colour channels in one focal plane. Hence, we propose a strategy wherein SMLM is combined with 3D-confocal microscopy to complement the SMLM information for spatial aspects, though with lower resolution. In the future, fluorochromes or nanoparticles with longer blinking periods will allow SMLM in 3D. Some approaches in this respect, for instance, antibody labelling with gold nanoparticles, are ready to be tested [45].

The authors thank Y.G. Teterev and A.A. Bezbakh from the Flerov Laboratory of Nuclear Reactions (JINR) and G.N. Timoshenko and V.A. Krylov from the Laboratory of Radiation Biology (JINR) for irradiating the cells with accelerated heavy ions using the U400M cyclotron. The work was supported by the Czech Science Foundation (project 16-12454S), the Ministry of Health of the Czech Republic (AZV Grant no. 16-29835A), by mobility action for international exchange of the Heidelberg University within the excellence initiative II of the Deutsche Forschungsgemeinschaft (DFG) to Michael Hausmann and from the grants from the Czech Republic to the Joint Institute for Nuclear Research, Dubna (Projects of the Czech Plenipotentiary and the 3 + 3 Projects, 2016–2018).

Author contribution statement

Daniel Depes: performed immunological detection of DSB repair proteins for confocal microscopy, performed high-resolution confocal microscopy at the Institute of Biophysics in Brno and largely participated in the manuscript and figure preparation. Jin-Ho Lee: arranged and performed single-molecule localization microscopy (SMLM) at the Kirchhoff Institute for Physics in Heidelberg, participated in figure and manuscript preparation. Elizaveta Bobkova: intensively worked at single-molecule localization microscopy (SMLM) at Kirchhoff Institute for Physics in Heidelberg, participated in figure and manuscript preparation. Lucie Jezkova: organized and performed heavy ion irradiation at the Joint Institute for Nuclear Research in Dubna, prepared immunofluorescence samples for SMLM. Iva Falkova: participated in immunological detection of DSB repair proteins for confocal microscopy, high-resolution confocal microscopy at the Institute of Biophysics in Brno, and SMLM microscopy at KIP Heidelberg. Felix Bestvater: set up SMLM microscope and participated in SMLM microscopy. Eva Pagacova: participated in immunological detection of DSB repair

proteins for confocal microscopy and high-resolution confocal microscopy at the Institute of Biophysics in Brno. Olga Kopecna: participated in immunological detection of DSB repair proteins for confocal microscopy and high-resolution confocal microscopy at the Institute of Biophysics in Brno. Mariia Zadneprianetc: participated in heavy ion irradiation at the Joint Institute for Nuclear Research in Dubna, prepared immunofluorescence samples for SMLM. Alena Bacikova: participated in immunological detection of DSB repair proteins for confocal microscopy and high-resolution confocal microscopy at the Institute of Biophysics in Brno. Elena Kulikova: participated in heavy ion irradiation at the Joint Institute for Nuclear Research in Dubna, prepared immunofluorescence samples for SMLM. Elena Smirnova: Participated in heavy ion irradiation at the Joint Institute for Nuclear Research in Dubna, prepared immunofluorescence samples for SMLM. Tatiana Bulanova: participated in heavy ion irradiation at the Joint Institute for Nuclear Research in Dubna, prepared immunofluorescence samples for SMLM. Alla Boreyko: Organized heavy ion irradiation at the Joint Institute for Nuclear Research in Dubna, contributed to data interpretation. Evgeny Krasavin: Organized heavy ion irradiation at the Joint Institute for Nuclear Research in Dubna, contributed to data interpretation. Michael Hausmann: invented SMLM microscope with Christoph Cremer, participated in its development, interpreted the results, participated in SMLM microscopy and contributed to manuscript preparation; supervises J.-H. Lee and E. Bobkova. Martin Falk: Together with Michael Hausmann, M.F. came up with the idea of research included in the manuscript. M.F. designed irradiation experiments and all other experiments, participated in high-resolution confocal microscopy at the Institute of Biophysics in Brno, SMLM microscopy at KIP Heidelberg, and data analysis. M.F. extensively contributed to the manuscript and figure preparation; supervises D. Depeš.

References

1. F.V. Rassool, Cancer Lett. **193**, 1 (2003)
2. E. Sage, N. Shikazono, Free Radic. Biol. Med. **107**, 125 (2017)
3. M. Falk, E. Lukasova, S. Kozubek, Biochim. Biophys. Acta **1783**, 2398 (2008)
4. M. Falk, E. Lukasova, L. Stefancikova, E. Baranova, I. Falkova, L. Jezkova, M. Davidkova, A. Bacikova, J. Vachelova, A. Michaelidesova, S. Kozubek, Appl. Radiat. Isot. **83**, 177 (2014)
5. M. Falk, E. Lukasova, S. Kozubek, Mutat. Res. **704**, 88 (2010)
6. M. Falk, M. Hausmann, E. Lukasova, A. Biswas, G. Hildenbrand, M. Davidkova, E. Krasavin, Z. Kleibl, I. Falkova, L. Jezkova, L. Stefancikova, J. Sevcik, M. Hofer, A. Bacikova, P. Matula, A. Boreyko, J. Vachelova, A. Michaelidisova, S. Kozubek, Crit. Rev. Eukaryot. Gene Expr. **24**, 225 (2014)
7. Z. Nikitaki, V. Nikolov, I.V. Mavragani, E. Mladenov, A. Mangelis, D.A. Laskaratou, G.I. Fragkoulis, C.E. Hellweg, O.A. Martin, D. Emfietzoglou, V.I. Hatzi, G.I. Terzoudi, G. Iliakis, A.G. Georgakilas, Free Radic. Res. **50**, S64 (2016)
8. M. Hada, A.G. Georgakilas, J. Radiat. Res. **49**, 203 (2008)
9. E. Surdutovich, G. Garcia, N. Mason, A.V. Solov'yov, Eur. Phys. J. D **70**, 86 (2016)
10. M.A. Smialek, P. Limao-Vieira, N.J. Mason, A.V. Solov'yov, Eur. Phys. J. D **68**, 312 (2014)
11. A. Takahashi, T. Ohnishi, Cancer Lett. **229**, 171 (2005)
12. M.M. Vilenchik, A.G. Knudson, Proc. Natl. Acad. Sci. U.S.A **100**, 12871 (2003)
13. M. Moreno-Villanueva, M. Wong, T. Lu, Y. Zhang, H.L. Wu, Npj Microgravity **3**, 14 (2017)
14. A.V. Solov'yov (Ed.), *Nanoscale Insights into Ion-Beam Cancer Therapy* (Springer Berlin Heidelberg, New York, NY, 2016)
15. http://www.cost.eu/COST_Actions/mpns/nano-ibct/
16. A. Verkhovtsev, E. Surdutovich, A.V. Solov'yov, Sci. Rep. **6**, 27654 (2016)
17. E. Surdutovich, A.V. Solov'yov, Eur. Phys. J. D **68**, 353 (2014)
18. L. Jezkova, M. Zadneprianetc, E. Kulikova, E. Smirnova, T. Bulanova, D. Depes, I. Falkova, A. Boreyko, E. Krasavin, M. Davidkova, S. Kozubek, O. Valentova, M. Falk, Nanoscale **10**, 1162 (2018)
19. E. Weterings, D.J. Chen, Cell Res. **18**, 114 (2008)
20. P.A. Jeggo, M. Lobrich, Biochem. J. **471**, 1 (2015)
21. M. Majidinia, B. Yousefi, DNA Repair **54**, 22 (2017)
22. J. Sakata, A. Hirosue, R. Yoshida, Y. Matsuoka, K. Kawahara, T. Yamamoto, H. Arita, H. Nakashima, S. Gohara, S. Kawaguchi, Y. Nagao, K. Yamana, H. Nakayama, Cancer Sci. **109**, 324 (2018)
23. 8th International Symposium "Atomic Cluster Collisions" - ISACC (2017) http://www.isacc-cuba.org
24. M. Falk, E. Lukasova, B. Gabrielova, V. Ondrej, S. Kozubek, Biochim. Biophys. Acta **1773**, 1534 (2007)
25. M. Falk, E. Lukasova, B. Gabrielova, V. Ondrej, S. Kozubek, J. Phys. Conf. Ser. **101**, 012018 (2008)
26. L. Jezkova, M. Falk, I. Falkova, M. Davidkova, A. Bacikova, L. Stefancikova, J. Vachelova, A. Michaelidesova, E. Lukasova, A. Boreyko, E. Krasavin, S. Kozubek, Appl. Radiat. Isot. **83**, 128 (2014)
27. M. Hofer, M. Falk, D. Komurkova, I. Falkova, A. Bacikova, B. Klejdus, E. Pagacova, L. Stefancikova, L. Weiterova, K.J. Angelis, S. Kozubek, L. Dusek, S. Galbavy, J. Med. Chem. **59**, 3003 (2016)
28. C. Cremer, R. Kaufmann, M. Gunkel, S. Pres, Y. Weiland, P. Muller, T. Ruckelshausen, P. Lemmer, F. Geiger, S. Degenhard, C. Wege, N. A. W. Lemmermann, R. Holtappels, H. Strickfaden, M. Hausmann, Biotechnol. J. **6**, 1037 (2011)
29. M. Hausmann, E. Wagner, J.H. Lee, G. Schrock, W. Schaufler, M. Krufczik, F. Papenfuss, M. Port, F. Bestvater, H. Scherthan, Nanoscale **10**, 4320 (2018)
30. M. Eryilmaz, E. Schmitt, M. Krufczik, F. Theda, J.H. Lee, C. Cremer, F. Bestvater, W. Schaufler, M. Hausmann, G. Hildenbrand, Cancers (Basel) **10**, 25 (2018)
31. M. Hausmann, N. Ilic, G. Pilarczyk, J.H. Lee, A. Logeswaran, A.P. Borroni, M. Krufczik, F. Theda, N. Waltrich, F. Bestvater, G. Hildenbrand, C. Cremer, M. Blank, Int. J. Mol. Sci. **18**, 2066 (2017)
32. J.P. Eberle, A. Rapp, M. Krufczik, M. Eryilmaz, M. Gunkel, H. Erfle, M. Hausmann, Methods Mol. Biol. **1663**, 1 (2017)

33. M. Bach, C. Savini, M. Krufczik, C. Cremer, F. Rosl, M. Hausmann, Int. J. Mol. Sci. **18**, 1726 (2017)
34. M. Krufczik, A. Sievers, A. Hausmann, J.H. Lee, G. Hildenbrand, W. Schaufler, M. Hausmann, Int. J. Mol. Sci. **18**, 1005 (2017)
35. A. Kinner, W.Q. Wu, C. Staudt, G. Iliakis, Nucleic Acids Res. **36**, 5678 (2008)
36. E.P. Rogakou, D.R. Pilch, A.H. Orr, V.S. Ivanova, W.M. Bonner, J. Biol. Chem. **273**, 5858 (1998)
37. J. Seo, S.C. Kim, H.S. Lee, J.K. Kim, H.J. Shon, N.L.M. Salleh, K.V. Desai, J.H. Lee, E.S. Kang, J.S. Kim, J.K. Choi, Nucleic Acids Res. **40**, 5965 (2012)
38. E.L. Leatherbarrow, J.V. Harper, F.A. Cucinotta, P. O'Neill, Int. J. Radiat. Biol. **82**, 111 (2006)
39. K. Rothkamm, M. Lobrich, Proc. Natl. Acad. Sci. U.S.A. **100**, 5057 (2003)
40. G. Alsbeih, W.A. Brock, N. Terry, M.D. Story, Radiat. Environ. Biophys. **42**, 107 (2003)
41. J. Yuan, J. Chen, J. Biol. Chem. **285**, 1097 (2010)
42. N.F. Cheville, J. Stasko, Vet. Pathol. **51**, 28 (2014)
43. C. Cremer, A. Szczurek, F. Schock, A. Gourram, U. Birk, Methods **123**, 11 (2017)
44. A. Esa, P. Edelmann, G. Kreth, L. Trakhtenbrot, N. Amariglio, G. Rechavi, M. Hausmann, C. Cremer, J. Microsc. **199**, 96 (2000)
45. F. Moser, G. Hildenbrand, P. Müller, A. AI Saroori, A. Biswas, M. Bach, F. Wenz, C. Cremer, N. Burger, N. Veldwijk, M.R. Veldwijk, M. Hausmann, Biophys. J. **110**, 947 (2016)
46. J. Reindl, S. Girst, D.W.M. Walsh, C. Greubel, B. Schwarz, C. Siebenwirth, G.A. Drexler, A.A. Friedl, G. Dollinger, Sci. Rep. **7**, 40616 (2017)
47. S. Barnard, S. Bouffler, K. Rothkamm, Genome Integr. **4**, 1 (2013)
48. Y. Lorat, C.U. Brunner, S. Schanz, B. Jakob, G. Taucher-Scholz, C.E. Rube, DNA Repair (Amst) **28**, 93 (2015)
49. F. Natale et al., Nat. Commun. **8**, 15760 (2017)
50. Y. Lorat, S. Timm, B. Jakob, G. Taucher-Scholz, C.E. Rube, Radiother. Oncol. **121**, 154 (2016)
51. E. Riballo et al., Mol. Cell **16**, 715 (2004)
52. E.L. Leatherbarrow, J.V. Harper, F.A. Cucinotta, P. O'Neill, Int. J. Radiat. Biol. **82**, 111 (2006)
53. M. Falk, M. Hausmann, A. Biswas, G. Hildenbrand, M. Davidkova, E. Krasavin, Z. Kleibl, I. Falkova , L. Jezkova, L. Stefancikova, J. Sevcik, M. Hofer, A. Bacikova, P. Matula, A. Boreyko, J. Vachelova, A. Michaelidesova, S. Kozubek, Crit. Rev. Eukaryot. Gene Expr. **24**, 205 (2014)
54. A.A. Bezbakh, V.B. Zager, G. Kaminski, A.I. Krylov, Y.G. Teterev, G.N. Timoshenko, Phys. Part. Nucl. Lett. **10**, 175 (2013)
55. O.B. Tarasov, D. Bazin, Nucl. Instrum. Meth. B **376**, 185 (2016)
56. P. Matula, M. Maska, O. Danek, P. Matula, M. Kozubek, in *IEEE International Symposium on Biomedical Imaging: From Nano to Macro* (2009), Vols. 1 and 2, p. 1138
57. F. Grull, M. Kirchgessner, R. Kaufmann, M. Hausmann, U. Kebschull, in *21st International Conference on Field Programmable Logic and Applications* (2011), p. 1
58. M. Stuhlmuller, J. Schwarz-Finsterle, E. Fey, J. Lux, M. Bach, C. Cremer, K. Hinderhofer, M. Hausmann, G. Hildenbrand, Nanoscale **7**, 17938 (2015)
59. P.S. Boyd, N. Struve, M. Bach, J.P. Eberle, M. Gote, F. Schock, C. Cremer, M. Kriegs, M. Hausmann, Nanoscale **8**, 20037 (2016)

International Journal of
Molecular Sciences

MDPI

Article

Recruitment of 53BP1 Proteins for DNA Repair and Persistence of Repair Clusters Differ for Cell Types as Detected by Single Molecule Localization Microscopy

Elizaveta Bobkova [1], Daniel Depes [2], Jin-Ho Lee [1], Lucie Jezkova [3], Iva Falkova [2], Eva Pagacova [2], Olga Kopecna [2], Mariia Zadneprianetc [3], Alena Bacikova [2], Elena Kulikova [3], Elena Smirnova [3], Tatiana Bulanova [3], Alla Boreyko [3], Evgeny Krasavin [3], Frederik Wenz [4], Felix Bestvater [5], Georg Hildenbrand [1,4], Michael Hausmann [1,*] and Martin Falk [2,*]

1 Kirchhoff-Institute for Physics, University of Heidelberg, Im Neuenheimer Feld 227, 69120 Heidelberg, Germany; elizaveta.bobkova@outlook.de (E.B.); Jin-Ho.Lee@kip.uni-heidelberg.de (J.-H.L.); hilden@kip.uni-heidelberg.de (G.H.)

2 Czech Academy of Sciences, Institute of Biophysics, v.v.i., Kralovopolska 135, 612 65 Brno, Czech Republic; depesd26@gmail.com (D.D.); ivafalk@ibp.cz (I.F.); evien@centrum.cz (E.P.); olga.kop@centrum.cz (O.K.); bacikovaalena@seznam.cz (A.B.)

3 Joint Institute for Nuclear Research, Joliot-Curie 6, 141980 Dubna, Russia; jezkova.luc@gmail.com (L.J.); marysaveleva@mail.ru (M.Z.); kruglyakovaea@bk.ru (E.Ku.); b-elva@mail.ru (E.S.); bulanova@jinr.ru (T.B.); albor@jinr.ru (A.B.); krasavin@jinr.ru (E.Kr.)

4 Department Radiation Oncology, Universitätsmedizin Mannheim, University of Heidelberg, Theodor- Kutzer-Ufer 3-5, 68159 Mannheim, Germany; Frederik.Wenz@medma.uni-heidelberg.de

5 German Cancer Research Center (DKFZ), Im Neuenheimer Feld 280, 69120 Heidelberg, Germany; f.bestvater@dkfz.de

* Correspondence: hausmann@kip.uni-heidelberg.de (M.H.); falk@ibp.cz or mfalk@seznam.cz (M.F.); Tel.: +49-6221-549824 (M.H.); Tel.: +420-541517116 (M.F.)

Received: 7 November 2018; Accepted: 20 November 2018; Published: 22 November 2018

Abstract: DNA double stranded breaks (DSBs) are the most serious type of lesions introduced into chromatin by ionizing radiation. During DSB repair, cells recruit different proteins to the damaged sites in a manner dependent on local chromatin structure, DSB location in the nucleus, and the repair pathway entered. 53BP1 is one of the important players participating in repair pathway decision of the cell. Although many molecular biology details have been investigated, the architecture of 53BP1 repair foci and its development during the post-irradiation time, especially the period of protein recruitment, remains to be elucidated. Super-resolution light microscopy is a powerful new tool to approach such studies in 3D-conserved cell nuclei. Recently, we demonstrated the applicability of single molecule localization microscopy (SMLM) as one of these highly resolving methods for analyses of dynamic repair protein distribution and repair focus internal nano-architecture in intact cell nuclei. In the present study, we focused our investigation on 53BP1 foci in differently radio-resistant cell types, moderately radio-resistant neonatal human dermal fibroblasts (NHDF) and highly radio-resistant U87 glioblastoma cells, exposed to high-LET ^{15}N-ion radiation. At given time points up to 24 h post irradiation with doses of 1.3 Gy and 4.0 Gy, the coordinates and spatial distribution of fluorescently tagged 53BP1 molecules was quantitatively evaluated at the resolution of 10–20 nm. Clusters of these tags were determined as sub-units of repair foci according to SMLM parameters. The formation and relaxation of such clusters was studied. The higher dose generated sufficient numbers of DNA breaks to compare the post-irradiation dynamics of 53BP1 during DSB processing for the cell types studied. A perpendicular (90°) irradiation scheme was used with the 4.0 Gy dose to achieve better separation of a relatively high number of particle tracks typically crossing each nucleus. For analyses along ion-tracks, the dose was reduced to 1.3 Gy and applied in combination with a sharp angle irradiation (10° relative to the cell plane). The results reveal a higher ratio of 53BP1 proteins recruited into SMLM defined clusters in fibroblasts as compared to U87 cells. Moreover, the speed of foci and thus cluster

formation and relaxation also differed for the cell types. In both NHDF and U87 cells, a certain number of the detected and functionally relevant clusters remained persistent even 24 h post irradiation; however, the number of these clusters again varied for the cell types. Altogether, our findings indicate that repair cluster formation as determined by SMLM and the relaxation (i.e., the remaining 53BP1 tags no longer fulfill the cluster definition) is cell type dependent and may be functionally explained and correlated to cell specific radio-sensitivity. The present study demonstrates that SMLM is a highly appropriate method for investigations of spatiotemporal protein organization in cell nuclei and how it influences the cell decision for a particular repair pathway at a given DSB site.

Keywords: repair foci nano-architecture; ^{15}N ion irradiation; single molecule localization microscopy (SMLM); repair cluster formation; repair cluster persistence

1. Introduction

Ionizing radiation (IR) causes different DNA damages depending on the radiation dose, dose rate, linear energy transfer (LET), photon or particle type, cell radio-sensitivity, DNA repair capacity, etc. [1–3]. The most serious damages occur upon high-LET irradiation or high-dose irradiation with low-LET rays, in both cases creating complex double-stranded breaks (DSBs) of the DNA molecule [4]. Such multiple or complex lesions (i.e., DSBs generated in close mutual proximity and often combined with other types of DNA damages) are the most critical for the cell [5] as they highly challenge its repair mechanisms [6–8]. Multiple and/or complex DSBs often remain unrepaired and can efficiently cause cell death as successfully used in radiation cancer treatment. On the other hand, in parallel to mediating a high radiobiological efficiency (RBE) of high-LET radiation, the complexity of lesions also increases the risk of mutagenesis, a serious problem, which radiation treatment schemes try to strictly avoid [9–11]. These completely diverging aims of radiation therapy highlight the need for research allowing to unequivocally understand the mechanisms of DNA damage and repair.

High-LET, heavy ion radiation, currently represents one of the most potent tools to treat cancer since, in addition to its high RBE, the radiation effectiveness (i.e., the 3D spatial position of the Bragg-peak) can precisely be targeted to the tumor by precise radiation planning and application schemes [12]. Nevertheless, the understanding of DNA damage-inducing mechanisms is important, not only in the context of the treatment and development of diseases, malignant as well as non-malignant (e.g., neurodegenerative). DNA is constantly attacked by environmental factors and repair processes are therefore fundamental biological processes directly related to genome stability, evolution, immune system functioning, and aging. DNA damage is of utmost interest in the field of planned long-term space missions, where exposure of astronauts to mixed fields of ionizing radiation occurring through galactic cosmic rays represents the most serious complication [13].

Generation of DSBs in certain regions of the genome leads to specific phosphorylation of histone H2AX in the damage surrounding chromatin, which is manifested as formation of so-called γH2AX foci [14]. Inside these foci, a network of interconnected biochemical pathways, evolved by the cells to counteract permanent DSB injury, operates to remove the lesions and recover DNA integrity. The main pathways are the canonic non-homologous end-joining (NHEJ) [15], the alternative NHEJ [16] and the homologous recombination (HR) [17], which become selectively activated by DNA damage depending on the phase of the cell cycle, chromatin structure at the site of damage, character (e.g., complexity) of DSB and potentially some other factors (reviewed in [18]). Importantly, repair pathways are often deregulated in cancer cells [19], making them defective in DSB repair. Inhibition of the remaining functional pathway is therefore intensively studied as a potentially promising therapeutic approach. On the other hand, despite these defects, some cancer cells remain highly radio-resistant [20].

Counting of γH2AX foci as well as foci formed by other repair proteins, e.g., MRE11, 53BP1, RAD51, etc., has become a method well established for intra-cellular dosimetry [21–24]. For low-LET

radiation, a direct correlation between the numbers of DSBs and γH2AX foci has been demonstrated [25]. Nevertheless, it is still under debate how many DSBs are represented by one focus, since staining efficiency, optical resolution of the microscopic instrument used and image segmentation have to be considered and calibrated. On the other hand, upon high-LET irradiation, it becomes obvious that fewer foci can be observed compared to the predicted number of DSBs but the focus sizes are growing with LET [26,27]. This phenomenon can be explained by agglomeration of individual foci. Unexplored internal architecture and complexity of repair foci may therefore largely depend on radiation LET (and local chromatin structure at a given DSB site). In addition, our recent report [1] has suggested that biological effects of radiation largely depend on LET but are determined in a more complex way than simply by this value. During the joint annual congress of the European Radiation Research Society (ERRS) and the German Society of Biological Radiation Research (GBS) in 2017, questions on the extent of the special structure and topology of foci were intensively discussed. Altogether, our observations and the open scientific questions call for an extensive research on the repair focus nano-structure and its relationship with characteristics of the damaging agents, chromatin architecture, and mechanisms and efficiency of DNA repair.

Current investigations using super-resolution light or electron microscopy revealed that γH2AX foci may be composed of several sub-units either called sub-foci or clusters [28–33]. Analyzing the spatial arrangement of γH2AX labeling tags after photon irradiation, the data revealed about four separated sub-units according to our measurements [29]. Among these sub-units, some did not contain other DSB related repair proteins [28]. On the other hand, the formation of sub-units was found also for foci of other repair proteins [34–36]. The number of repair-focused sub-units seems to correlate with the damage complexity and their topology may potentially influence the cells' decision-making for a specific repair mechanism at a given DSB site [5,37,38]. Moreover, the structure of foci and sub-units (often called clusters) determined by super-resolution microscopy parameters shows time-dependent re-organization during repair [28,29,34].

Beyond the internal γH2AX foci composition and topology, it has become obvious that the structure and topology of the follow-up recruited repair proteins is of central importance to understand the potential of their spatial organization in repair processes. This has reasoned that 53BP1 foci were analyzed in more detail. 53BP1 is not only involved in NHEJ but also acts as a stabilizing factor during HR [35,39]. Our study [40] as well as the studies of others [35,41] using super-resolution microscopy techniques reveal that 53BP1 foci also showed a diversification into sub-units. The individual γH2AX clusters as determined according to fixed parameters of super-resolution localization microscopy do not always co-localize with corresponding clusters of 53BP1 [40]. γH2AX foci are 1–2 megabase pair structures consisting of phosphorylated histones that are formed around sites of DSB damage. In contrast, 53BP1 is a repair protein that binds to methylated regions of histones where it interacts with other proteins, for instance to promote NHEJ. During such interactions, 53BP1 could be displaced from the primary damaged sites [35,42,43], opening them for instance for access of BRCA1 or CtIP [42]. This different behavior of γH2AX and 53BP1 foci, as shown in [35,40], led us to study 53BP1 foci, their sub-unit formation and their time dependent development after high-LET irradiation and during the following repair time independently of γH2AX.

In the present study, we continued to apply Single Molecule Localization Microscopy (SMLM) as described in detail in several recent studies [34,40,44–47]. SMLM has been successfully applied to analyze DNA repair and cluster formation of γH2AX molecules, i.e., their labeling molecules, respectively, during a long-term cell culture under folate deficiency [48], time course of γH2AX and MRE11 clusters determined by SMLM during DNA repair after low-LET irradiation [29,34] and also heavy ion irradiation as it follows from our proof-of-principle study [40]. These investigations have shown that foci sub-units are formed in a dose and treatment type specific way and first hints are indicating that the chromatin loci of the damages are correlated by similarities [38].

SMLM [49] makes use of the advantage to precisely, i.e., in the order of 10–20 nm, localize each labeled molecule in a coordinate matrix. This means a precision in the order of a single nucleosome.

Distance and structure calculations based on these image-free datasets can additionally be encoded in image values and thus dramatically improve the microscopic information. However, it might still be challenging to interpret the new sort of data brought about by this method, since it is based on mathematical analyses of signal coordinate matrices of single molecules instead of traditional imaging and computational image analysis. In continuation of our thus far established view on the nano-architecture of chromatin damage and repair loci, we present results of the analysis of 53BP1 foci and sub-units and show the damage response of two cell types with different radio-resistance.

2. Results

By combined means of standard immunofluorescence confocal microscopy and super-resolution SMLM microscopy, we investigated 53BP1 foci formation, persistence, and structural changes during the post-irradiation (PI) period in differently radio-resistant cell types exposed to high-LET ^{15}N ions. Neonatal human dermal fibroblasts (NHDF) were used as a model for lower radio-resistance and U87 glioblastoma cells as a model for higher resistance [50]. The selection of these cell types was driven by fact that even small differences would become detectable between extreme cases, if the repair capabilities and thus the 53BP1 recruitment would correlate to radio-sensitivity. The ability of cells to assemble repair foci may be one of the crucial factors influencing the repair efficiency. Since 53BP1 is recruited to γH2AX foci within the first minutes after irradiation, we initially concentrated our research on the early period PI (starting with 5 min PI), during which faster and more prominent structural changes of foci can be expected. Later time points up to 24 h PI were included to get insights into the kinetics of foci relaxation and removal.

Whereas γH2AX foci describe the shape and size of a chromatin locus with damaged DNA, 53BP1 foci provide information on the formation of foci during the recruitment of proteins for repair. In some cell types, these proteins seem to be abundantly available during the whole cell cycle. In others, they are processed immediately after chromatin damaging and transported to the damaged site. Despite similar labeling and microscopy parameters, 53BP1 foci could be better separated one from another than γH2AX foci (for comparison see [1]).

Firstly, we evaluated the extent and kinetics of 53BP1 focus formation in the cell types studied. As in recent experiments [40], the cells were exposed to 4 Gy of ^{15}N ions in a 90°-geometry (i.e., in the perpendicular direction to the cell monolayer) and the 53BP1 foci were qualitatively analyzed by confocal laser scanning microscopy after specific antibody labeling of the repair proteins. These experimental conditions were used for the following purposes: A higher dose of 4 Gy challenges DSB repair systems so that differences in repair capacity of NHDF and U87 cells could be expected to become more apparent. Because a clear discrimination of a large number of individual particle tracks crossing the nucleus is difficult upon this dose applied in 10°-angle, especially at later time points when the clusters determined by SMLM parameters show some diffusional movement by themselves, we coupled the 4 Gy-experiments with a perpendicular irradiation (90°-geometry).

In Figure 1, typical examples of 2D maximum intensity projection images obtained from about 25 confocal slices each are shown for the two cell lines during a time course of up to 24 h PI. Individual images were obtained for aliquots of the same irradiated cell culture fixed at the given time points after irradiation. The series were verified independently by different cell cultures. However, to always start from the same irradiation experiment, each irradiated cell culture was cultivated over more than 24 h and an aliquot was taken and fixed at each time point of repair. In both NHDF and U87 cells, high proportions of 53BP1 foci are visible and the repair proceeded much slower than in samples irradiated with low-LET γ-rays. For further details of foci analysis after heavy ion irradiation in comparison to γ-irradiation, we refer to our recent publication [1]. In NHDF cells showing no or very few 53BP1 signals in non-irradiated samples, compact foci became visible at 5 min PI. The number of foci increased within the first 30 min PI, which was followed by a continuous decrease during the later repair period. However, the foci were still visible at 24 h PI, indicating a persistent repair activity. In contrast to NHDF fibroblasts, U87 cells contained 53BP1 foci also prior to irradiation. In these

cells, the recruitment of 53BP1 for DSB repair seemed to be delayed since, up to 30 min PI, the foci appeared less compact and more dispersed than in NHDF cells. The maximum foci formation in U87 occurred at 60 min PI and the number of foci persisting at 24 h PI was significantly higher than that in NHDF fibroblasts.

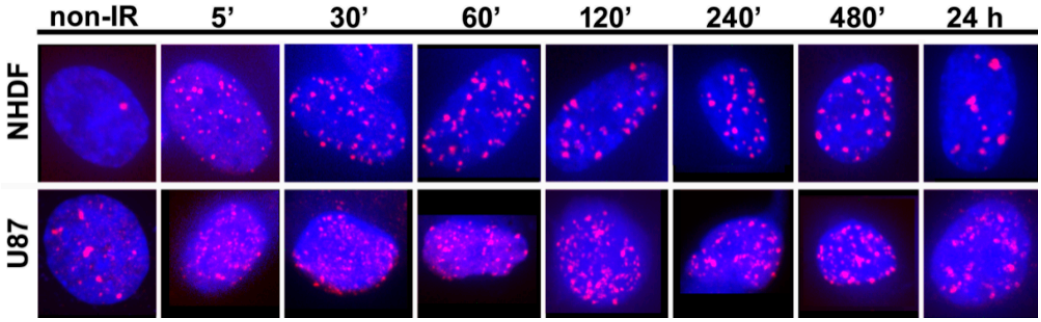

Figure 1. 2D maximum intensity projection images of confocal image stacks. Typical examples are shown for fluorescently-labeled 53BP1 foci in NHDF cells and U87 cells after 4 Gy ^{15}N-irradiation in 90°-geometry. Along the given time line, samples were taken as aliquots of the same culture at different time points (5 min, 30 min, 60 min, 2 h, 4 h, 8 h and 24 h) after irradiation. All timelines were repeated with independent cultures. For comparison, examples of non-irradiated cells are also presented.

Since the formation of sub-units (represented by clusters of labeling points defined by SMLM parameters) within the foci has been described as a topological finding of central importance, the evolution of these sub-units along the particle tracks and their persistence/behavior during the follow-up repair time course was studied by means of SMLM. For these analyses, the cells were irradiated in a sharp (10°) angle to generate the tracks running parallel to the xy-plane of microscopic observation and to achieve the maximum possible resolution and localization precision of labeled molecules in SMLM (10–20 nm). For the same purpose, we also reduced the radiation dose to 1.3 Gy. With this dose, 2–3 particles on average traversed the nucleus, producing well separated 53BP1 protein streaks. Nevertheless, for the reasons already mentioned above, and to obtain SMLM data directly comparable to immunofluorescence confocal microscopy, we also performed quantitative analyses of the formation and relaxation of dense sub-units (clusters) during DSB repair in parallel with the 4 Gy and 90°-irradiation.

In Figure 2, examples of 53BP1 density images are shown for the two cell lines and two radiation schemes inspected at different periods after irradiation. The cell nuclei were obtained from aliquots taken and fixed at different times PI from the same irradiated culture. The density images do not show all signal points detected but instead encode the number of neighbors of each signal within a circle of 1 µm radius by the point intensity. For 10° irradiation scheme, specimens of both cell lines showed characteristic tracks along which the labeling tags were arranged. In the beginning of the DNA repair, individual 53BP1 sub-units of foci lining the track occurred in very close mutual proximity so that their separation by eye was not possible. At later periods PI, the tracks partly dissolved into compact, well distinguished and separately visible protein units. In NHDF fibroblasts but not U87 cells, this separation was accompanied with progressive growth of the focus areas.

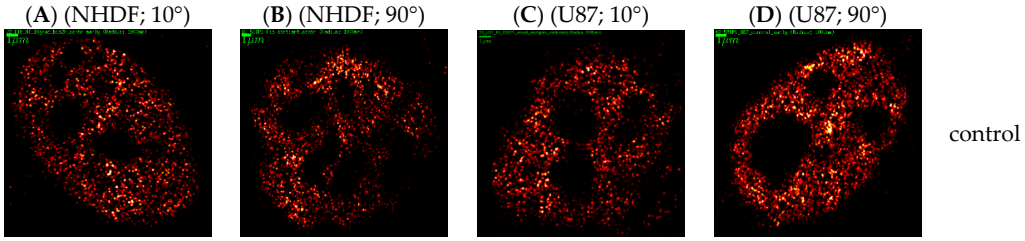

Figure 2. *Cont.*

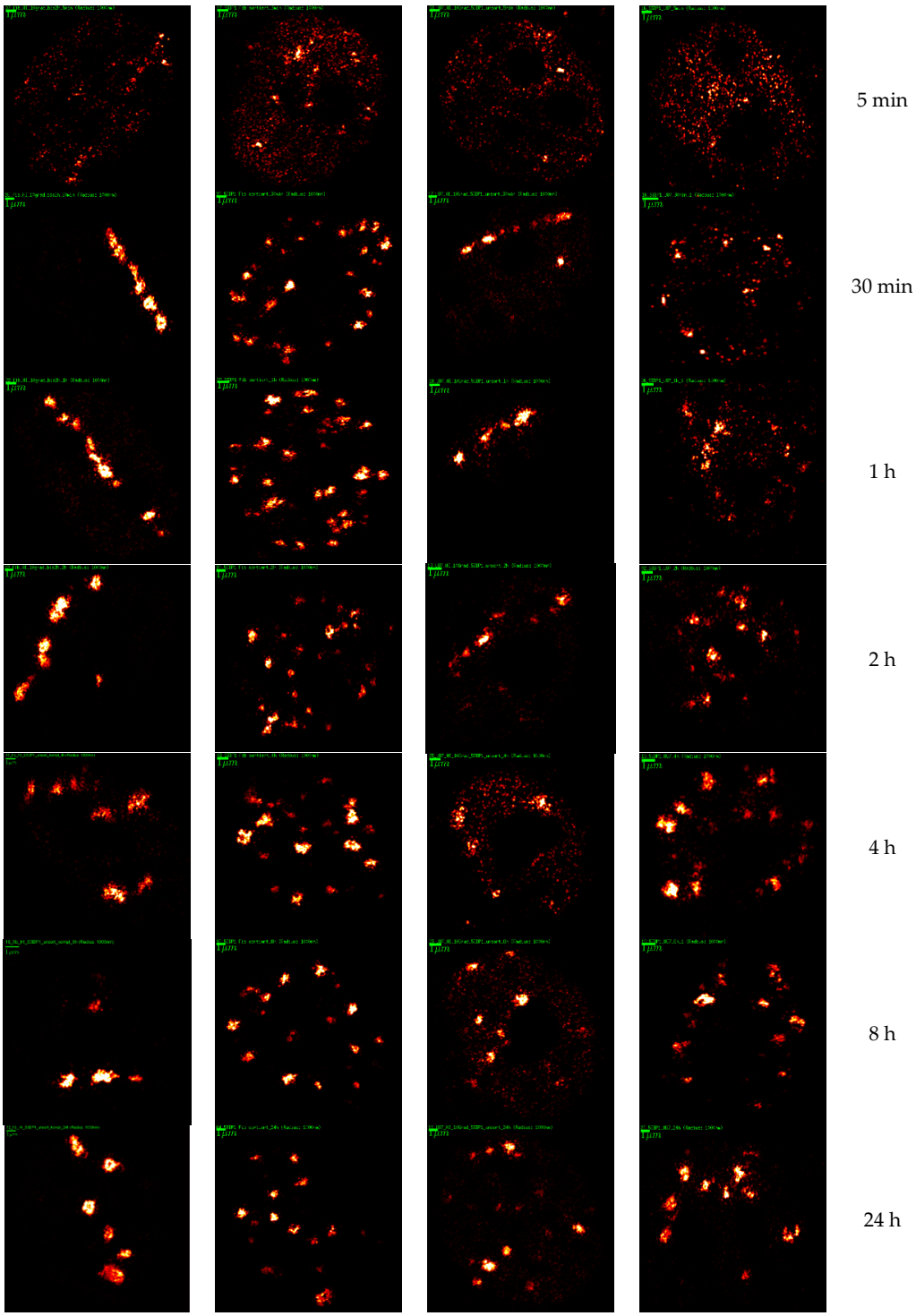

Figure 2. 2D density SMLM images of 53BP1 repair proteins. Typical examples are shown for fluorescently-labeled 53BP1 proteins in NHDF cells (**A**,**B**) and U87 cells (**C**,**D**) after 1.3 Gy tangential ^{15}N-irradiation (**A**,**C**) (10° angle between the ion beam and the cell layer) and 4 Gy perpendicular ^{15}N-irradiation (**B**,**D**) (90° angle between the ion beam and the cell layer). Along this time line, the samples were taken as aliquots of the same culture and fixed at different time points (5 min, 30 min, 1 h, 4 h, 8 h and 24 h) after irradiation. For comparison, examples of non-irradiated control cells are presented. The density images do not show all signal points detected but instead encode the number of neighbors of each signal within a circle of 1 μm radius by the point intensity—the number of signals in the given surroundings around one signal grows as the color of the point changes from red to white. The green bars equal to 1 μm.

According to the results coming from the 90°-irradiation scheme (4 Gy), the number of foci increased until 1 h (NHDF fibroblasts) or even 4 h PI (U87 cells) and afterwards started to decrease continuously, which was, again, as in the 10°-irradiation experiments, associated with growth of the focus areas. The numbers of 53BP1 molecule signals in control (non-irradiated) U87 cells were always higher than in corresponding NHDF samples. On the contrary, during the repair, we always recorded more signals in NHDF cells (up to about 15,000) than in U87 cells (up to about 10,000).

To further investigate the dynamics of 53BP1 molecules, the cluster formation of tagged 53BP1 molecules and their relaxation was studied. Thereby, the definition of clusters (see Section 4.6) followed strict rules of SMLM evaluation, i.e., a minimum number of labeling tags within a given radius. These rules were fixed interactively, as shown for instance in Figure 5. The relative amounts of 53BP1 signal points inside and outside the defined clusters were determined. Let us emphasize that the term "cluster" refers to 53BP1 protein sub-units of microscopically visible foci. Thus, each repair focus is composed of sub-units and these sub-units are quantified as clusters by SMLM parameters. In this context, cluster relaxation refers to a point ensample that no longer follows the limits for clustering.

The clustering dynamics varied for the two cell lines analyzed (Figure 3) but followed the same general tendency for the different doses and irradiation schemes. In NHDF fibroblasts, the average signal number (i.e., number of 53BP1 tags) within clusters rose to more than 60% during the first hour, remained constant until 8 h, and then dropped down slightly at 24 h PI. In U87 cells, the accumulation of signal points in clusters was delayed and not as efficient, although, in non-irradiated cells, a higher basis level of foci existed. An accrual of signals inside clusters occurred not earlier than between 1 and 8 h PI and the average proportion of signals forming the cluster was always considerably lower (up to about 45%) than in NHDF fibroblasts, thereby the more dispersed foci shape was considered by a lower minimum number of neighboring points within a cluster. Based on summarized data obtained for 10°- and 90°-irradiation, we can therefore conclude that normal (non-transformed) NHDF fibroblasts sequester higher proportions of 53BP1 labeling tags within the repair clusters than cancerous and relatively more radio-resistant U87 cells, which leave more than half the amount of 53BP1 outside the foci.

Comparing the 10°- and 90°-irradiation schemes for both cell types reveals a nearly constant mean value of points inside clusters between 8 and 24 h PI for the 10°-geometry, whereas a continuous drop down is observed for 90°-geometry. This may be interpreted by either a cluster relaxation starting from the track border or as a consequence of the different doses. At the higher dose, a couple of clusters may relax after a short time interval since the damage is repaired. Nevertheless, in both cases, a serious number of damages remain unrepaired at 24 h. The latter would stimulate future experiments with longer time intervals PI.

A long-time persistence of repair foci has often been correlated with the efficiency of DSB repair. Our findings suggest that 24 h after irradiation with 1.3 Gy or 4.0 Gy of ^{15}N-ions, the repair processes are still active in both NHDF and U87 cell types. At this period PI, about 14,000–20,000 53BP1 signal points were detected in total in NHDF cells, from which about 40% remained within the defined clusters. However, compared to U87 cells, the relative number of signals in clusters decreased from about 60% to about 40%. Thus, the shape of the curves suggests a rapid repair up-regulation followed by a continuous down-regulation. In contrast for highly radio-resistant U87 cells, about 25% (10°-irradiation scheme) or 35% (90°-irradiation scheme), i.e., 10,000–11,000 signal points, formed these clusters which seem to remain.

In conclusion, the data reveal a long-standing repair activity of 53BP1 protein in both cell types exposed to ^{15}N high-LET ions but a different kinetics along the repair period. DSBs generated in the present study by accelerated ^{15}N ions are considerably complex but are generated upon a different starting situation. From the foci counting, as in Figure 1, a higher basic level of damaged sites is expected. This is shown by a higher number of 53BP1 foci. Looking on the cluster formation in Figure 3 and assuming that the formation of clusters indicates repair activity, highly radio-resistant U87 cancer

cells seem to repair these complex DSBs in a similar way as other damages not induced by radiation, thereby recruiting fewer 53BP1 proteins in clusters than NHDF fibroblasts.

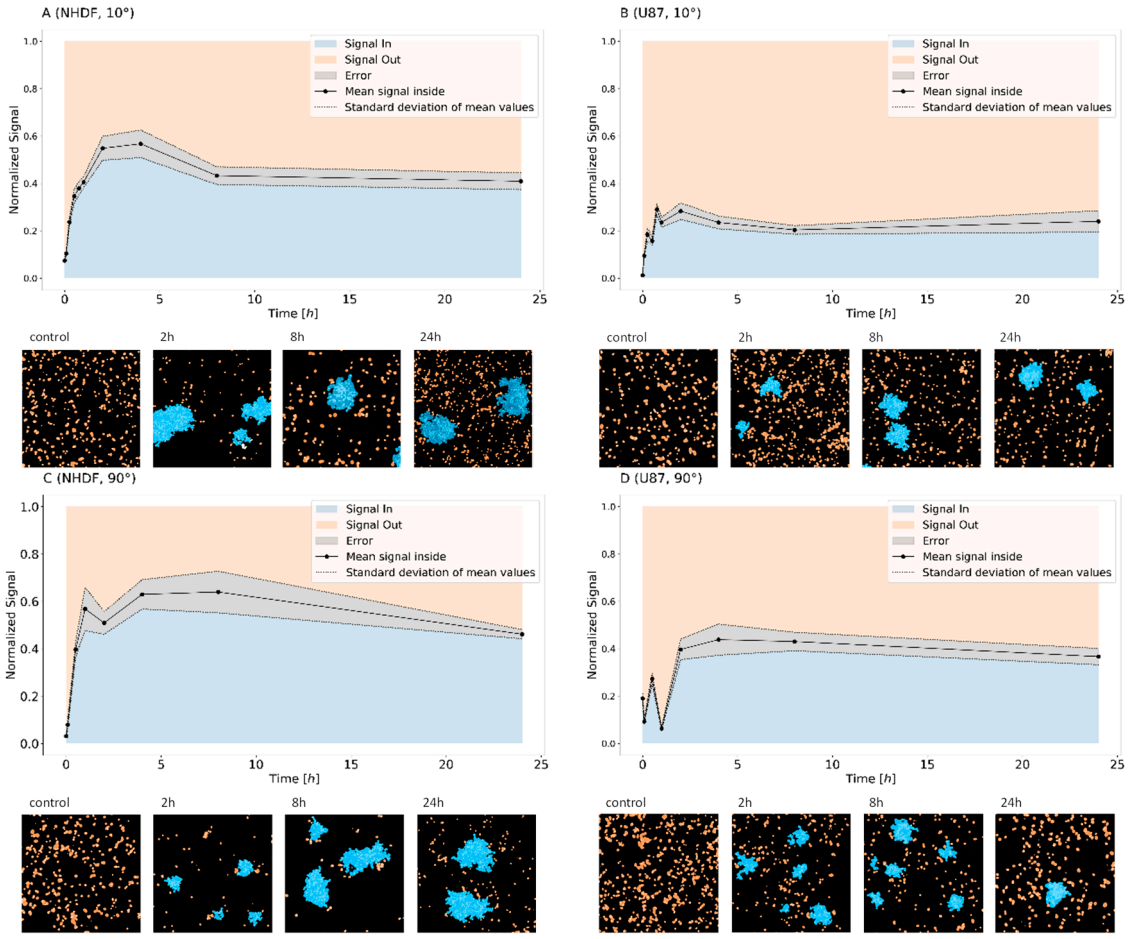

Figure 3. Relative amounts of 53BP1 signals detected within (blue) and outside (orange) repair clusters as defined for SMLM (see Section 4.6). Graphs: Mean values and margins given by the standard deviation are depicted in gray. The values are always normalized to the mean number of signals detected at a given time point. The data are presented for NHDF fibroblasts (**A**,**C**) and U87 cells (**B**,**D**) after 1.3 Gy tangential ^{15}N-irradiation (**A**,**B**) (10° angle between the ion beam and the cell layer), and 4 Gy perpendicular ^{15}N-irradiation (**C**,**D**) (90° angle between the ion beam and the cell layer). Images: The pointillist images represent examples of sections of cell nuclei with labeling points inside (blue) and outside (orange) clusters at the given time points. The samples were taken as aliquots of the same culture at different time points (from 5 min to 24 h) after irradiation. For comparison, examples of non-irradiated control cells are presented (=0 min).

3. Discussion

DNA damage repair is a process controlled by multiple parameters [1,2]. Especially complex damages and DSBs, as could occur after high-LET irradiation, require a diversity of proteins attaching the damaged site in a manner dependent on the repair pathway applied, e.g., HR, canonical NHEJ or alternative NHEJ [5,8,37]. The involved proteins have to address broken ends of the DNA and join them appropriately. Therefore, it seems to be reasonable that the recruitment of repair proteins forms certain sub-units (here called clusters) around the broken ends [28–31,34,35,40]. In the case of photon-irradiation, several of such clusters, only detectable at nanoscale, contribute to microscopically visible foci [28,29]. They show a typical spatial structure or topology [38] and were found to differ in their repair activity and repair pathway choice [28] indicating the importance of repair foci

nano-architecture for the repair mechanisms occurring at given chromatin environments. Important new questions therefore arise about whether the number of these nano-clusters defined by SMLM or rather the number of foci visually separated by confocal microscopy corresponds better to the number of DSBs, and whether the nano-composition of foci influences repair strategy and efficiency at a given DSB site. Not only the spatial arrangement and topology of γH2AX phosphorylation sites may determine the repair process but also the repair proteins recruited to the damaged site appeared in a cluster arrangement, which occurs in an even larger extent after exposure of cells to accelerated particles. In this case, not only components of a single focus but also multiple foci appear to participate in sub-unit or cluster formation, respectively, along the particle track. This explains why the number of foci detected in cells irradiated with different types of high-LET radiation more or less underestimates the real number of DSBs [25,35,40,43].

To better understand the mechanisms behind the DNA damage and repair-induced protein cluster formation and relaxation, we followed the composition of 53BP1 protein clusters/foci during a long post-irradiation period at the nanoscale. By using SMLM super-resolution microscopy [46,47,49], we studied the clusters in two differently radio-sensitive cell types (NHDF and U87) exposed to different doses of accelerated ^{15}N ions delivered in two different geometries (10°- and 90°-irradiation). SMLM offered the advantage of the nano-resolution, which was achieved with cells prepared with standard immunofluorescence methods and therefore maintaining their natural 3D-shape [51].

Since 53BP1 is one of the early recruited repair proteins participating in both NHEJ and HR [39,41], it represents an appropriate candidate to study the architecture and dynamics of repair clusters as defined by SMLM and foci composed of several clusters in relation to their importance for DSB repair. Moreover, 53BP1 protein seems to be one of the decision-makers that directs the repair mechanism at a given DSB site either to NHEJ or HR. In contrast to γH2AX, an epigenetic histone modification marking damaged chromatin sites almost immediately after DSB induction, 53BP1 is an early indicator of a starting activity of NHEJ/HR repair machinery. Hence, it is reasonable to investigate the behaviour of 53BP1 during the repair independently. This has been supported by our recent investigation [40] indicating that γH2AX clusters and 53BP1 clusters differ in shape and do not always mutually co-localize.

In the context of the repair pathway chosen by the irradiated cells, the question comes up in which cell cycle phase the cells have been irradiated. Non-synchronized cells were used in this study to better mimic the situation in patients' tissues during radiotherapy. However, it has been shown [1] that a vast majority of cells was irradiated in a G1 phase of the cell cycle using the experimental conditions described here. The majority of DSBs can therefore be expected to be repaired by NHEJ or the alternative/backup NHEJ pathways. Moreover, recent reports suggest that cells can recover from the cell cycle arrest even in presence of some persisting DSBs. This can happen as soon as the number of DSBs per nucleus decreases to 10–20 [52]. In cell cultures irradiated with low-LET γ-rays, the cells are arrested for relatively short periods, i.e., about 4 h. For high LET radiation, the arrest is significantly longer than for γ-rays, i.e., about 48 h and more [53,54] or even permanent [55], depending on the LET of the ion-radiation. Thus, for the LET of ^{15}N as used in the experiments presented here, a checkpoint arrest release can be expected if about 10–15 DSBs remain unrepaired [56]. Thus, the mechanism of repair may be expected to depend more on the location and number of DSBs and the chromatin architecture at the particular damage site than on the cell cycle progress.

In the present study, by means of SMLM, we explored the time course of 53BP1 cluster formation, relaxation, persistence and focus composition on the single molecule level. We found that the accumulation of the labeled protein inside as well as outside the clusters depends on the cell type. This principle behavior seemed to be less influenced by radiation dose or perspective of the particle track (irradiation geometry). For the radio-resistant U87 cancer cell type [50], the relative number of signals in clusters was always considerably lower than the relative amount outside the clusters. This relation does not reflect the absolute number of 53BP1 proteins available but gives information about the "just-in-time" availability. High nucleoplasmic levels of freely floating 53BP1 proteins may point

to a permanent repair activity also in non-irradiated cells. This is well compatible with genetically unstable status of cancer cells and presence of an increased (compared to NHDF fibroblasts) average number of γH2AX/53BP1 foci observed here also in cells prior to irradiation. The kinetics seems to indicate rather the recruitment of the existing proteins floating through the cell nucleus than a de novo production and directed recruitment to the damaged site. In contrast to U87 cells, normal non-transformed NHDF fibroblasts showed no or very little repair activity in non-irradiated cells and recruit the repair proteins just-in-time for the repair cluster formation. Nuclear levels and distribution of repair proteins prior to DNA damage induction could therefore be potentially causatively linked to the cell-type specific radio-resistance, at least partially and/or in some cell types. Our results also support the idea that different cell types may vary in the preferred mechanism of DSB repair and, thus, requirements for particular repair proteins including 53BP1.

A lower co-localization of γH2AX and 53BP1 proteins and longer-time persistence of γH2AX/53BP1 repair foci in cell nuclei have previously been associated with a radiosensitive phenotype of radiotherapy-experiencing patients, i.e., with compromised DSB repair due to suboptimal cooperation of repair factors [57]. This explanation can be reasonably acceptable in general but is hardly compatible with a radio-resistant character of U87 cells [50]. On the other hand, although the relevance to the results described here remains to be elucidated, Ochs et al. [41] revealed that silencing 53BP1 or altering its ability to bind damaged chromatin shifts limited DSB resection towards hyper-resection and, consequently, error-free gene conversion towards mutagenic single-strand annealing (SSA [58]). 53BP1 may thus foster the fidelity rather than final efficiency of DSB repair, which could indeed be expected in aggressive tumor cells. In accordance, although we observed more γH2AX/53BP1 repair foci in U87 cells at 24 h post-irradiation, the same holds true also for non-irradiated cells.

In both cell types, a considerable fraction of repair foci and clusters persisted in cell nuclei also after 24 h of repair. Since it has been shown that heavily damaged cell nuclei can maintain repair activity over several days [48,59], this observation may suggest that the cells are still actively processing complex damage introduced into DNA by relatively high doses (1.3 or 4 Gy) of high-LET (about 180 keV μm^{-1}) ^{15}N-radiation. Indeed, in accordance with some other reports (e.g., [58]), we have shown for other types of heavy ions, boron and neon (^{11}B: LET = 138.1 keV μm^{-1}, E = 8.1 MeV per n; ^{20}Ne: LET = 132.1 keV μm^{-1}, E = 46.6 MeV per n), that the average number of γH2AX/53BP1 foci per nucleus can (^{11}B) or cannot (^{20}Ne) return back to the baseline in irradiated (2 Gy) NHDF fibroblasts after a longer period post-irradiation (96 h PI) [1]. Alternatively, in accordance with what has been proposed in [1,60], such a long persistence of DSBs, together with their high complexity revealed, could indicate that the repair remains incomplete and the cells are going to die, unless they manage their survival by some other processes. A high radio-resistance of U87 cells could therefore also be ascribed to their adaptation for survival with unrepaired DNA. This may be a result of loss of function in some aspects of DNA repair which is supported by slower repair of glioma cells and the persistence of high levels of Rad51 and DNA-PK in U87 cells throughout the cell cycle [61].

Only cluster formation and relaxation were investigated in this study. Whether the clusters of 53BP1 (and other repair proteins) differ in their topology [38], for instance as a consequence of different damage complexity, structure or type of damaged chromatin (e.g., heterochromatin vs. euchromatin), and repair mechanism initiated (NHEJ, and HR), remains to be elucidated. This will be a subject of future investigations aimed at better understanding how the cluster topology and chromatin architecture contribute to the cell decision for a certain repair pathway at a given damaged chromatin site. Systematic investigations of spatial organization of γH2AX foci and sub-units, their topology in relation to chromatin environment followed by detailed structure measurements of repair protein arrangements at given repair loci may lead to a conclusive description on why certain repair proteins are recruited to a given damage site and how the repair pathway choice of a cell is determined. This may considerably impact the understanding of repair mechanisms and individual radio-sensitivity, as it is a matter of fact in radiation tumor treatment.

4. Materials and Methods

4.1. Cell Culture

As described in [40], primary neonatal human dermal fibroblasts (NHDF) and human U87 glioblastoma cells were cultured in Dulbecco's modified Eagle medium (DMEM) supplemented with 10% fetal calf serum (FCS) and a 1% gentamicin–glutamine solution (all reagents from Sigma-Aldrich). These two cell types were used because of their high difference in radio-resistance which has been verified using the Annexin V/Propidium Iodide assay and quantification of relative cell death by flow cytometry before and after exposure to 4 Gy γ-irradiation (Figure 4).

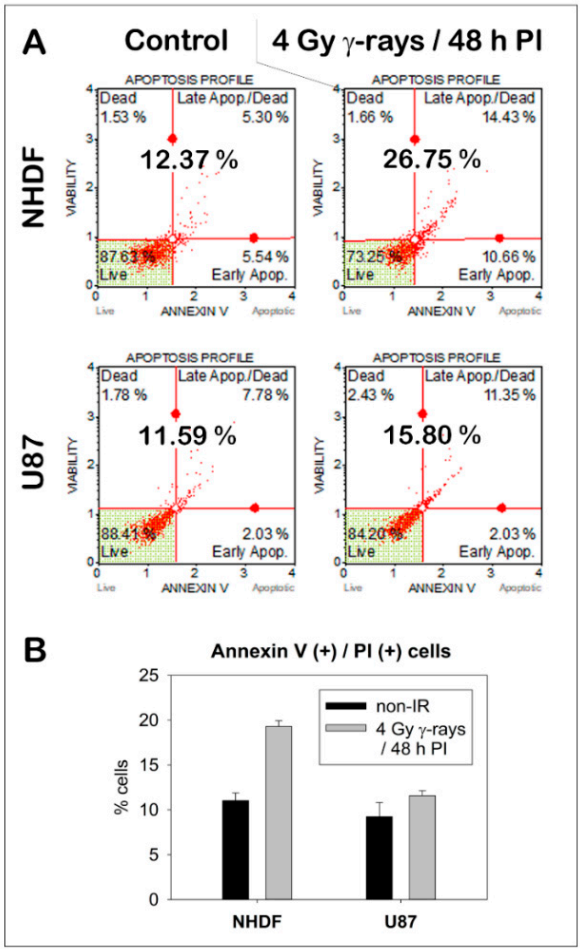

Figure 4. Cell death upon γ-irradiation compared for NHDF fibroblasts and U87 glioblastoma cells as quantified by flow cytometry 48 h post-irradiation (PI). (**A**) Illustrative flow-cytograms for NHDF and U87 cells prior to (left, control) and 48 h after irradiation with 4 Gy of γ-rays. x-axis: Annexin V positivity (a.u.); y-axis: propidium iodide (viability) positivity (a.u.); lower-left quarter (Annexin V (−)/Propidium Iodide (−)) = viable cells; lower right quarter (Annexin V (+)/Propidium Iodide (−)) = early apoptosis; upper left quarter (Annexin V (−)/Propidium Iodide (+)) = dead cells; upper right quarter (Annexin V (+)/Propidium Iodide (+)) = dead cells or late apoptosis shortly before dying. The total proportion of cells in the different quarters is given in percent of all cells measured. (**B**) Mean proportions (± standard deviation) of cells positive for Annexin V, Propidium Iodide (PI), or both these markers (white quarters in (**A**)) before (black columns) and 48 h after (grey columns) exposure of cells to 4 Gy of γ-rays.

For the ion-radiation experiments described in Section 2, the cells were maintained in T 25 cell flasks at 37 °C in a humidified atmosphere with 5% CO_2. Sixteen to eighteen hours before radiation treatment,

cells were seeded on the glass bottoms of Petri dishes and further cultivated until 80% confluence. For irradiation, the dishes were aseptically closed and sealed with Parafilm M (Sigma-Aldrich, Prague, Czech Republic). Irradiation took place at room temperature. After irradiation, the samples were further cultivated at 37 °C. At certain time points (5 min, 15 min only for 10°, 30 min, 45 min only for 10°, 1 h, 2 h, 4 h, 8 h, and 24 h) after irradiation aliquots of the same culture were taken and fixed with 4% formaldehyde/PBS (phosphate-buffered saline) for further labeling and SMLM analysis. This had the advantage that the cells used for the different repair periods and analyses were obtained from the same cell culture. This procedure was repeated independently with another cell culture.

4.2. Ion Irradiation

As recently described in [1], Nitrogen (^{15}N) ions were accelerated (for details see Table 1) using a U 400 M isochronous cyclotron in the Flerov Laboratory of Nuclear Reaction at the Joint Institute for Nuclear Research (JINR, Dubna) [62]. Cells were irradiated on glass coverslips (on Petri dish bottoms) tangentially, i.e., with a 10° angle between the ion beam and the cell layer, or perpendicularly, i.e., with a 90° angle between the ion beam and the cell layer. The side of the coverslips covered with cells was oriented towards the ion beam so that the cells were hit by the particles before the beam continued into the culture medium in the Petri dish.

Table 1. Irradiation Parameters for Different Irradiation Geometries.

Irradiation angle	Energy (MeV/n)	LET (keV/µm)	Fluence (10^6/cm) Per 1 Gy	Mean Number of Particles/Nucleus
10°	13.1	181.4	3.40	2.1
90°	13.0	182.9	3.41	25.4

Non-synchronized cell populations with prevalent (>80%) G1 cells were irradiated in the culture medium with a dose of 1.3 Gy (tangential irradiation scheme; 10°) and 4 Gy (perpendicular irradiation scheme; 90°) at 37 °C. During irradiation, the cells were kept in a thermostable box, ensuring a constant temperature and prevention from infection during the whole procedure. After irradiation, the cells were immediately placed back into the incubator (37 °C/5% CO_2) until fixation. The energy and corresponding LET values of ions in the plane of the cell monolayer were calculated using LISE++ software [63].

4.3. Immunofluorescence Staining

At the given time points (see Section 4.1), the cells were fixed in 4% formaldehyde/PBS (prepared freshly from paraformaldehyde) for 10 min and washed two times for 5 min in 1× PBS, permeabilized for 6 min in 0.2% Triton X-100 at RT, washed again three times for 5 min at room temperature (RT) in 1× PBS, and incubated in 2% bovine serum albumin (BSA) for 60 min at RT. Rabbit anti-53BP1 (ab21083, Abcam, Berlin, Germany) antibodies were diluted in the blocking solution I (1:600) and applied to the cells for 10 min at RT and subsequently overnight at 4 °C. The cells were then rinsed with 0.2% Triton X-100 and washed three times with 1× PBS for 5 min at RT. The secondary antibodies were AlexaFluor 594-conjugated goat anti-rabbit (Johnson Laboratories, New Brunswick, NJ, USA) antibodies. The antibodies were diluted in blocking solution II (1:400) and applied to the cells for 30 min (RT, in the dark). After incubation, the cells were washed three times in 1× PBS for 5 min. The cell nuclei were counter-stained with DAPI for 5 min at RT at a dilution of 1:20.000. After washing three times in 1× PBS for 5 min each, the cover slips were air dried, and the specimens were embedded in ProLong Gold® (Thermo Fisher Scientific, Waltham, MA, USA), which was left to polymerize for 24 h in the dark at RT. Finally, the slides were sealed and stored in the dark at 4 °C.

4.4. Confocal Microscopy

Confocal microscopy images were acquired using an automated high-resolution Leica DM RXA microscope (Leica, Wetzlar, Germany) equipped with a Plan Fluotar oil-immersion objective (100×/NA1.3), a CSU 10a Nipkow disc (Yokogawa, Japan), a CoolSnap HQ CCD-camera (Photometrix, Tuscon, AZ, USA), and an Ar/Kr-laser (Innova 70C Spectrum, Coherent, Santa Clara, CA, USA). Automated image acquisition using Acquiarium software was described previously [1]. Forty serial optical sections were recorded at 0.25 µm step size along the z-axis.

4.5. Single Molecule Localization Microscopy (SMLM)

For data acquisition, the localization microscope from the light microscopy facility of the German Cancer Research Centre (DKFZ) was used. A detailed description of the instrument has recently been published elsewhere [29,34,51]. The microscope has an oil-objective (100×/NA 1.46) and four lasers: 405, 491, 561, and 642 nm with maximal laser powers of 120, 200, 200, and 140 mW, respectively. An in-built electron multiplier (EM-gain) enhances signals detected by the EmCCD camera (80 nm/px). To minimize drifts, the microscope was installed on a Smart-Table, compensating for vibrations, and provided with a water-cooling system, to keep constant temperature. Lasers were controlled using the "Omicron Control Center" program and image acquisition was carried out using "Live Acquisition v. 2.6.0.14" software.

Criteria for the selection of cells were size (not larger than a G2 nucleus), form (no twisted or broken nuclei taken) and visibility of the track (for 10°-irradiation). Searching was performed with minimal laser powers (4–12% maximum intensity). After an appropriate cell was found, a region of interest (ROI) was chipped to the size of the nucleus and the focal plane was adjusted to the repair foci or the track of repair.

A protocol for automatized localization image acquisition was used [45,51]. In brief, an initial excitation (3 s at maximum laser power) switches most fluorophores into the reversibly bleached state, and then 2000 single images are taken at maximum laser power and exposure of 100 ms per image. Measurements were done with the 561 nm wavelength laser. Wide-field images were always taken before localization image acquisition. For each time point, a minimum of 23 cells were imaged. The data stacks were stored as *.tif stacks and subjected to further computational analysis as described in Section 4.6.

4.6. Data Analysis for Single Molecule Localization Microscopy

Super-resolution signal coordinates were calculated using in-house Matlab-based software, as described in [44,45,51,64]. Background levels were multiplied by threshold factors (th = 4 for U87 and th = 5 for NHDF) for more rigorous background subtraction. Additionally, the first 500 frames of each data stack were discarded to further reduce background. Each remaining signal was then fitted with a 2D Gaussian curve. The intensity maximum determined the x-, y-coordinates of a signal point with a certain localization error which was about 11 nm for the measurements done here. The resulting localization data were saved in a data matrix containing the signal coordinates along with additional data (Table 2).

Density images were created, which mimic the visual impressions of conventional fluorescence microscopy: For each nucleus, the intensity values for each pixel (pixel size 10 × 10 nm^2) were calculated according to the density of surrounding signals inside a radius of 1000 nm. The resulting intensities are normalized and blurred with a 50 nm sized Gaussian filter. The resulting image has a lower resolution than provided by the original data, but better visualizes the signal density and allows comparison with images obtained via conventional light microscopy.

For quantitative super-resolution data analyses, the total number of signal points and all-to-all point distances between signal points were calculated. Resulting single-cell data were summarized

for each experimental setup for further statistical analysis of DNA damage repair dynamics and nano-spatial analysis of repair proteins.

Table 2. Structure of the Localization Data Matrix.

Column-Number	Type of Data
1	Signal-amplitude in photoelectrons
2	Lateral y-coordinates in nm
3	Lateral x-coordinates in nm
4	Lateral y-coordinates error in nm
5	Lateral x-coordinates error in nm
6	Standard-deviation σ_y in nm
7	Standard-deviation σ_x in nm
8	Number of photoelectrons in the signal
9	Number of the picture where the signal was detected

Cluster analysis was performed according to interactively determined parameters (Figure 5): Pixel size = 10 nm, radius = 20 pixels, maximum distance for all distances = 200 nm, and maximum distance for next neighbors = 200 nm. The minimal neighbor value (N) was determined for each cell line separately. For 90°-irradiated cells, the optimal neighbor values were N = 55 for U87 and N = 84 for NHDF cells. For the 10°-irradiated slides, N = 65 was chosen for both cell lines. Mean number of clusters per cell, number of signals in clusters and cluster areas were calculated.

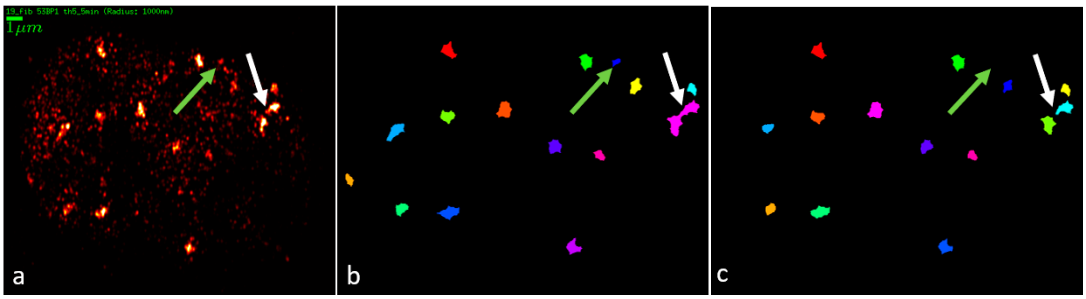

Figure 5. Exemplary images for a NHDF cell (90° irradiation) for cluster parameter comparison: (**a**) density-weighted image produced; (**b**) cluster image with minimum N = 63 neighbors; and (**c**) cluster image with minimum N = 84 neighbors. The white arrows show a separated cluster group in (**c**) and the green arrow a background signal wrongly counted as a cluster in (**b**). The different colors of the clusters are randomly chosen for better separation.

5. Conclusions

A better understanding of the mechanisms behind repair protein foci formation and separation in sub-units (clustering) after complex DNA damaging through high-LET particle radiation could shed new light on nuclear organization of DNA repair processes and their activation upon specific conditions. In the present study, we revealed a cell type-dependent behavior of repair clusters as defined by SMLM parameters at the nanoscale. We assume that the differences in 53BP1 protein recruitment and dynamics of such clusters in formation and relaxation may be correlated to different radiation sensitivity of the cell types studied as well as different demands on 53BP1 by ongoing repair mechanisms. Technically, we show that SMLM opens door for new investigations providing much deeper (nanoscale) insights into the organization of repair foci and repair processes. By means of suitable procedures of quantitative analyses, the dynamics of functionally relevant sub-units of foci, i.e., appropriately defined clusters, could be validated also for ion-irradiation and hypotheses about long-time persistence were verified. Such ultra-resolution measurements of repair foci architectures offer new perspectives to comprehend the factors responsible for the cell's decision for a particular repair pathway at a given damaged chromatin site, and, thus, repair efficiency and fidelity.

Author Contributions: Conceptualization, M.H. and M.F.; Methodology, M.H.; Validation, E.B., D.D., J.-H.L., I.F. and M.F.; Formal Analysis, E.B., J.-H.L., G.H., and M.F.; Investigation, E.B., D.D., J.-H.L., L.J., I.F., E.P., O.K., M.Z., A.B. (Alena Bacikova), E.K. (Elena Kulikova), E.S. and T.B.; Resources, A.B. (Alla Boreyko), E.K. (Evgeny Krasavin) and F.B.; Data Curation, E.B., D.D., J.-H.L., and M.F.; Writing—Original Draft Preparation, M.H. and M.F.; Writing—Review and Editing, M.H. and M.F.; Visualization, E.B. and M.F.; Supervision, E.K., F.W., G.H., M.H. and M.F.; Project Administration, M.H. and M.F.; and Funding Acquisition, F.B., M.H. and M.F.

Funding: The work was supported by the Czech Science Foundation (project 16-12454S), the Ministry of Health of the Czech Republic (AZV grant No. 16-29835A), by the Heidelberg University Mobility Grant for International Research Cooperation within the excellence initiative II of the Deutsche Forschungsgemeinschaft (DFG) to M.H., and from the grants from the Czech Republic to the Joint Institute for Nuclear Research, Dubna (Projects of the Czech Plenipotentiary and the 3 + 3 Projects). The financial support by Deutsche Forschungsgemeinschaft and Ruprecht-Karls-Universität Heidelberg within the funding program Open Access Publishing is gratefully acknowledged.

Acknowledgments: The authors acknowledge the constant encouragement by Magnus Foerßer-Mohr, Jin-Hau Ewwer, and Ina Dischen, Institute of Research Rating and Enhancement (IRRE), Altenburschla, Germany, to enrich our manuscript by further aspects.

Conflicts of Interest: The authors declare no conflict of interest. The funders had no role in the design of the study; in the collection, analyses, or interpretation of data; in the writing of the manuscript, and in the decision to publish the results.

References

1. Jezkova, L.; Zadneprianetc, M.; Kulikova, E.; Smirnova, E.; Bulanova, T.; Depes, D.; Falkova, I.; Boreyko, A.; Krasavin, E.; Davidkova, M.; et al. Particles with similar LET values generate DNA breaks of different complexity and reparability: A high-resolution microscopy analysis of γH2AX/53BP1 foci. *Nanoscale* **2018**, *10*, 1162–1179. [CrossRef] [PubMed]
2. Falk, M.; Hausmann, M.; Lukášová, E.; Biswas, A.; Hildenbrand, G.; Davídková, M.; Krasavin, E.; Kleibl, Z.; Falková, I.; Ježková, L.; et al. Determining OMICS spatiotemporal dimensions using exciting new nanoscopy techniques to asses complex cell responses to DNA damage—PART A (Radiomics). *Crit. Rev. Eukaryot. Gene Exp.* **2014**, *24*, 205–223. [CrossRef]
3. Falk, M.; Hausmann, M.; Lukášová, E.; Biswas, A.; Hildenbrand, G.; Davídková, M.; Krasavin, E.; Kleibl, Z.; Falková, I.; Ježková, L.; et al. Determining OMICS spatiotemporal dimensions using exciting new nanoscopy techniques to asses complex cell responses to DNA damage—PART B (Structuromics). *Crit. Rev. Eukaryot. Gene Exp.* **2014**, *24*, 225–247. [CrossRef]
4. Nikitaki, Z.; Nikolov, V.; Mavragani, I.V.; Mladenov, E.; Mangelis, A.; Laskaratou, D.A.; Fragkoulis, G.I.; Hellweg, C.E.; Martin, O.A.; Emfietzoglou, D.; et al. Measurement of complex DNA damage induction and repair in human cellular systems after exposure to ionizing radiations of varying linear energy transfer (LET). *Free Radic. Res.* **2016**, *50*, S64–S78. [CrossRef] [PubMed]
5. Schipler, A.; Iliakis, G. DNA double-strand–break complexity levels and their possible contributions to the probability for error-prone processing and repair pathway choice. *Nucleic Acids Res.* **2013**, *41*, 7589–7605. [CrossRef] [PubMed]
6. Mladenov, E.; Magin, S.; Soni, A.; Iliakis, G. DNA double-strand-break repair in higher eukaryotes and its role in genomic instability and cancer: Cell cycle and proliferation-dependent regulation. *Semin. Cancer Biol.* **2016**, *37–38*, 51–64. [CrossRef] [PubMed]
7. Ceccaldi, R.; Rondinelli, B.; Andrea, A.D.D. Repair pathway choices and consequences at the double-strand break. *Trends Biol.* **2016**, *26*, 52–64. [CrossRef] [PubMed]
8. Dueva, R.; Iliakis, G. Alternative pathways of non-homologous end joining (NHEJ) in genomic instability and cancer. *Transl. Cancer Res.* **2013**, *2*, 163–177.
9. Mladenov, E.; Magin, S.; Soni, A.; Iliakis, G. DNA double-strand break repair as determinant of cellular radiosensitivity to killing and target in radiation therapy. *Front. Oncol.* **2013**, *3*, 113. [CrossRef] [PubMed]
10. Bhattacharjee, S.; Nandi, S. Synthetic lethality in DNA repair network: A novel avenue in targeted cancer therapy and combination therapeutics. *IUBMB Life* **2017**, *69*, 929–937. [CrossRef] [PubMed]
11. Jeggo, P.A.; Loebrich, M. How cancer cells hijack DNA double-strand break repair pathways to gain genomic instability. *Biochem. J.* **2015**, *471*, 1–11. [CrossRef] [PubMed]
12. Durante, M.; Orecchia, R.; Loeffler, J.S. Charged-particle therapy in cancer: Clinical uses and future perspectives. *Nat. Rev. Clin. Oncol.* **2017**, *14*, 483–495. [CrossRef] [PubMed]

13. Kennedy, A.R. A Review: Biological effects of space radiation and developments of effective countermeasures. *Life Sci. Space Res.* **2014**, *1*, 10–43. [CrossRef] [PubMed]
14. Rogakou, E.P.; Pilch, D.R.; Orr, A.H.; Ivanova, V.S.; Bonner, W.M. DNA double-starnd breaks induce histone H2AX phosphorylation on serine 139. *J. Biol. Chem.* **1998**, *273*, 5858–5868. [CrossRef] [PubMed]
15. Chang, H.H.Y.; Pannunzio, N.R.; Adachi, N.; Lieber, M.R. Non-homologous DNA end joining and alternative pathways to double-strand break repair. *Nat. Rev. Mol. Cell Biol.* **2017**, *18*, 495–506. [CrossRef] [PubMed]
16. Iliakis, G.; Murmann, T.; Soni, A. Alternative end-joining repair pathways are the ultimate backup for abrogated classical non-homologous end-joining and homologous recombination repair: Implications for the formation of chromosome translocations. *Mutat. Res. Genet. Toxicol. Environ. Mutagen.* **2015**, *793*, 166–175. [CrossRef] [PubMed]
17. Jasin, M.; Rothstein, R. Repair of strand breaks by homologous recombination. *Cold Spring Harb. Perspect. Biol.* **2013**, *5*, a012740. [CrossRef] [PubMed]
18. Falk, M.; Lukasova, E.; Stefancikova, L.; Baranova, E.; Falkova, I.; Jezkova, L.; Davidkova, M.; Bacikova, A.; Vachelova, J.; Michaelidesova, A.; et al. Heterochromatinization associated with cell differentiation as a model to study DNA double strand break induction and repair in the context of higher-order chromatin structure. *Appl. Radiat. Isotopes* **2014**, *83*, 177–185. [CrossRef] [PubMed]
19. Majidinia, M.; Yousefi, B. DNA repair and damage pathways in breast cancer development and therapy. *DNA Repair* **2017**, *54*, 22–29. [CrossRef] [PubMed]
20. Tang, L.; Wei, F.; Wu, Y.; He, Y.; Shi, L.; Xiong, F.; Gong, Z.; Guo, C.; Li, X.; Deng, H.; et al. Role of metabolism in cancer cell radioresistance and radiosensitization methods. *J. Exp. Clin. Cancer Res.* **2018**, *37*, 87. [CrossRef] [PubMed]
21. Antonelli, F.; Campa, A.; Esposito, G.; Giardullo, P.; Belli, M.; Dini, V.; Meschini, S.; Simone, G.; Sorrentino, E.; Gerardi, S.; et al. Induction and repair of DNA DSB as revealed by H2AX phosphorylation foci in human fibroblasts exposed to low- and high-LET radiation: Relationship with early and delayed reproductive cell death. *Radiat. Res.* **2015**, *183*, 417–431. [CrossRef] [PubMed]
22. Hildenbrand, G.; Metzler, P.; Pilarczyk, G.; Bobu, V.; Kriz, W.; Hosser, H.; Fleckenstein, J.; Krufczik, M.; Bestvater, F.; Wenz, F.; et al. Dose enhancement effects of gold nanoparticles specifically targeting RNA in breast cancer cells. *PLoS ONE* **2018**, *13*, e0190183. [CrossRef] [PubMed]
23. Rothkamm, K.; Barnard, S.; Moquet, J.; Ellender, M.; Rana, Z.; Burdak-Rothkamm, S. DNA damage foci: Meaning and significance. *Environ. Mol. Mutagen.* **2015**, *56*, 491–504. [CrossRef] [PubMed]
24. Van Veelen, L.R.; Cervelli, T.; van de Rakt, M.W.; Theil, A.F.; Essers, J.; Kanaar, R. Analysis of ionizing radiation-induced foci of DNA damage repair proteins. *Mutat. Res.* **2005**, *574*, 22–33. [CrossRef] [PubMed]
25. Eberlein, U.; Peper, M.; Fernandez, M.; Lassmann, M.; Scherthan, H. Calibration of the γ-H2AX DNA double strand break focus assay for internal radiation exposure of blood lymphocytes. *PLoS ONE* **2015**, *10*, e0123174. [CrossRef] [PubMed]
26. Hauptner, A.; Friedland, W.; Dietzel, S.; Drexler, G.A.; Greubel, C.; Hable, V.; Strickfaden, H.; Cremer, T.; Friedl, A.A.; Krücken, R.; et al. Spatial distribution of DNA double-strand breaks from ion tracks. In *Ion Beam Science: Solved and Unsolved Problems*; Royal Danish Academy of Sciences and Letters: Copenhagen, Denmark, 2006; pp. 59–85.
27. Costes, S.V.; Boissière, A.; Ravani, S.; Romano, R.; Parvin, B.; Barcellos-Hoff, M.H. Imaging features that discriminate between foci induced by high- and low-LET radiation in human fibroblasts. *Radiat. Res.* **2006**, *165*, 505–515. [CrossRef] [PubMed]
28. Natale, F.; Rapp, A.; Yu, W.; Maiser, A.; Harz, H.; Schall, A.; Grulich, S.; Anton, T.; Hörl, D.; Chen, W.; et al. Identification of the elementary structural units of the DNA damage response. *Nat. Commun.* **2017**, *8*, 15760. [CrossRef] [PubMed]
29. Hausmann, M.; Wagner, E.; Lee, J.-H.; Schrock, G.; Schaufler, W.; Krufczik, M.; Papenfuß, F.; Port, M.; Bestvater, F.; Scherthan, H. Super-resolution microscopy of radiation-induced histone H2AX phosphorylation in relation to H3K9-trimethylation in HeLa cells. *Nanoscale* **2018**, *10*, 4320–4331. [CrossRef] [PubMed]
30. Lorat, Y.; Bunner, C.U.; Schanz, S.; Jacob, B.; Taucher-Scholz, G.; Rübe, C.E. Nanoscale analysis of clustered DNA damage after high-LET irradiation by quantitative electron microscopy—The heavy burden to repair. *DNA Repair* **2015**, *28*, 93–106. [CrossRef] [PubMed]

31. Lorat, Y.; Timm, S.; Jacob, B.; Taucher-Scholz, G.; Rübe, C.E. Clustered double-strand breaks in heterochromatin perturb DNA repair after high linear energy transfer irradiation. *Radiother. Oncol.* **2016**, *121*, 427–437. [CrossRef] [PubMed]
32. Lopez Perez, R.; Best, G.; Nicolay, N.H.; Greubel, C.; Rossberger, S.; Reindl, J.; Dollinger, G.; Weber, K.-J.; Cremer, C.; Huber, P.E. Superresolution light microscopy shows nanostructure of carbon ion radiation-induced DNA double-strand break repair foci. *FASEB J.* **2016**, *30*, 2767–2776. [CrossRef] [PubMed]
33. Sisario, D.; Memmel, S.; Doose, S.; Neubauer, J.; Zimmermann, H.; Flentje, M.; Djuzenova, C.S.; Sauer, M.; Sukhorukov, V.L. Nanostructure of DNA repair foci revealed by superresolution microscopy. *FASEB J.* **2018**, *12*, fj201701435. [CrossRef] [PubMed]
34. Eryilmaz, M.; Schmitt, E.; Krufczik, M.; Theda, F.; Lee, J.-H.; Cremer, C.; Bestvater, F.; Schaufler, W.; Hausmann, M.; Hildenbrand, G. Localization microscopy analyses of MRE11 clusters in 3D-conserved cell nuclei of different cell lines. *Cancers* **2018**, *10*, 25. [CrossRef] [PubMed]
35. Reindl, J.S.; Girst, S.; Walsh, D.W.M.; Geubel, C.; Schwarz, B.; Siebenwirth, C.; Drexler, G.A.; Friedl, A.A.; Dollinger, G. Chromatin organization revealed by nanostructure of irradiation induced γH2AX, 53BP1 and Rad51 foci. *Sci. Rep.* **2017**, *7*, 40616. [CrossRef] [PubMed]
36. Hable, V.; Drexler, G.A.; Brüning, T.; Burgdorf, C.; Greubel, C.; Derer, A.; Seel, J.; Strickfaden, H.; Cremer, T.; Friedl, A.A.; et al. Recruitment kinetics of DNA repair proteins Mdc1 and Rad52 but not 53BP1 depend on damage complexity. *PLoS ONE* **2012**, *7*, e41943. [CrossRef] [PubMed]
37. Iliakis, G. The Biological Foundations of Risks from Ionizing Radiation Exposures: How an Understanding of Associated Effects Will Help Their Quantification and Mitigation. In *Sustainable Risk Management*; Springer: Berlin, Germany, 2018; pp. 149–158.
38. Hofmann, A.; Krufczik, M.; Heermann, D.W.; Hausmann, M. Using persistent homology as a new approach for super-resolution localization microscopy data analysis and classification of γH2AX foci/clusters. *Int. J. Mol. Sci.* **2018**, *19*, 2263. [CrossRef] [PubMed]
39. Kakarougkas, A.; Ismail, A.; Klement, K.; Goodarzi, A.A.; Conrad, S.; Freire, R.; Shibata, A.; Löbrich, M.; Jeggo, P.A. Opposing roles for 53BP1 during homologous recombination. *Nucleic Acids Res.* **2013**, *41*, 9719–9731. [CrossRef] [PubMed]
40. Depes, D.; Lee, J.-H.; Bobkova, E.; Jezkova, L.; Falkova, I.; Bestvater, F.; Pagacova, E.; Kopecna, O.; Zadneprianetc, M.; Bacikova, A.; et al. Single molecule localization microscopy as a promising tool for γH2AX/53BP1 foci exploration. *Eur. Phys. J. D* **2018**, *72*, 158. [CrossRef]
41. Ochs, F.; Somyajit, K.; Altmeyer, M.; Rask, M.B.; Lukas, J.; Lukas, C. 53BP1 fosters fidelity of homology-directed DNA repair. *Nat. Struct. Mol. Biol.* **2016**, *23*, 714–721. [CrossRef] [PubMed]
42. Chapman, J.R.; Sossick, A.J.; Boulton, S.J.; Jackson, S.P. BRCA1-associated exclusion of 53BP1 from DNA damage sites underlies temporal control of DNA repair. *J. Cell Sci.* **2012**, *125*, 3529–3534. [CrossRef] [PubMed]
43. Reindl, J.; Drexler, G.A.; Girst, S.; Greubel, C.; Siebenwirth, C.; Drexler, S.E.; Dollinger, G.; Friedl, A.A. Nanoscopic exclusion between Rad51 and 53BP1 after ion irradiation in human HeLa cells. *Phys. Biol.* **2015**, *12*, 066005. [CrossRef] [PubMed]
44. Pilarczyk, G.; Nesnidal, I.; Gunkel, M.; Bach, M.; Bestvater, F.; Hausmann, M. Localisation microscopy of breast epithelial ErbB-2 receptors and gap junctions: Trafficking after gamma-irradiation, Neuregulin-1b and Herceptin application. *Int. J. Mol. Sci.* **2017**, *18*, 362. [CrossRef] [PubMed]
45. Hausmann, M.; Ilić, N.; Pilarczyk, G.; Lee, J.-H.; Logeswaran, A.; Borroni, A.P.; Krufczik, M.; Theda, F.; Waltrich, N.; Bestvater, F.; et al. Challenges for super-resolution localization microscopy and biomolecular fluorescent nano-probing in cancer research. *Int. J. Mol. Sci.* **2017**, *18*, 2066. [CrossRef] [PubMed]
46. Lemmer, P.; Gunkel, M.; Baddeley, D.; Kaufmann, R.; Urich, A.; Weiland, Y.; Reymann, J.; Müller, P.; Hausmann, M.; Cremer, C. SPDM—Light microscopy with single molecule resolution at the nanoscale. *Appl. Phys. B* **2018**, *93*, 1–12. [CrossRef]
47. Lemmer, P.; Gunkel, M.; Weiland, Y.; Müller, P.; Baddeley, D.; Kaufmann, R.; Urich, A.; Eipel, H.; Amberger, R.; Hausmann, M.; et al. Using conventional fluorescent markers for far-field fluorescence localization nanoscopy allows resolution in the 10 nm range. *J. Microsc.* **2009**, *235*, 163–171. [CrossRef] [PubMed]
48. Bach, M.; Savini, C.; Krufczik, M.; Cremer, C.; Rösl, F.; Hausmann, M. Super-resolution localization microscopy of γ-H2AX and heterochromatin after folate deficiency. *Int. J. Mol. Sci.* **2017**, *18*, 1726. [CrossRef] [PubMed]

49. Cremer, C.; Kaufmann, R.; Gunkel, M.; Pres, S.; Weiland, Y.; Müller, P.; Ruckelshausen, T.; Lemmer, P.; Geiger, F.; Degenhard, M.; et al. Superresolution imaging of biological nanostructures by Spectral Precision Distance Microscopy (SPDM). *Biotechnol. J.* **2011**, *6*, 1037–1051. [CrossRef] [PubMed]
50. Williams, J.R.; Gridley, D.S.; Slater, J.M. Advances in the Biology, Imaging and Therapies for Glioblastoma. In *Radiobiology of Radioresistant Glioblastoma*; Cheng, C., Ed.; IntechOPEN: London, UK, 2011; pp. 3–22.
51. Krufczik, M.; Sievers, A.; Hausmann, A.; Lee, J.-H.; Hildenbrand, G.; Schaufler, W.; Hausmann, M. Combining low temperature fluorescence DNA-hybridization, immunostaining, and super-resolution localization microscopy for nano-structure analysis of ALU elements and their influence on chromatin structure. *Int. J. Mol. Sci.* **2017**, *18*, 1005. [CrossRef] [PubMed]
52. Deckbar, D.; Jeggo, P.A.; Löbrich, M. Understanding the limitations of radiation-induced cell cycle checkpoints. *Crit. Rev. Biochem. Mol. Biol.* **2011**, *46*, 271–283. [CrossRef] [PubMed]
53. Scholz, M.; Kraft-Weyrather, W.; Ritter, S.; Kraft, G. Cell cycle delays induced by heavy ion irradiation of synchronous mammalian cells. *Int. J. Radiat. Biol.* **1994**, *66*, 59–75. [CrossRef] [PubMed]
54. Sora, S.; Hamada, N.; Hara, T.; Funayama, T.; Sakashita, T.; Yokota, Y.; Nakano, T.; Kobayashi, Y. Exposure of normal human fibroblasts to heavy-ion radiation promotes their morphological differentiation. *Biol. Sci. Space* **2008**, *22*, 54–58. [CrossRef]
55. Tsuboi, K.; Moritake, T.; Tsuchida, Y.; Tokuuye, K.; Matsumura, A.; Ando, K. Cell cycle checkpoint and apoptosis induction in glioblastoma cells and fibroblasts irradiated with carbon beam. *J. Radiat. Res.* **2007**, *48*, 317–325. [CrossRef] [PubMed]
56. Nakajima, N.I.; Brunton, H.; Watanabe, R.; Shrikhande, A.; Hirayama, R.; Matsufuji, N.; Fujimori, A.; Murakami, T.; Okayasu, R.; Jeggo, P.; et al. Visualisation of γH2AX foci caused by heavy ion particle traversal; distinction between core track versus non-track damage. *PLoS ONE* **2013**, *8*, e70107. [CrossRef] [PubMed]
57. Lobachevsky, P.; Leong, T.; Daly, P.; Smith, J.; Best, N.; Tomaszewski, J.; Thompson, E.R.; Li, N.; Campbell, I.G.; Martin, R.F.; et al. Compromized DNA repair as a basis for identification of cancer radiotherapy patients with extreme radiosensitivity. *Cancer Lett.* **2016**, *383*, 212–219. [CrossRef] [PubMed]
58. DiBiase, S.J.; Zeng, Z.C.; Chen, R.; Hyslop, T.; Curran, W.J., Jr.; Iliakis, G. DNA-dependent protein kinase stimulates an independently active, nonhomologous, end-joining apparatus. *Cancer Res.* **2000**, *60*, 1245–1253. [PubMed]
59. Schwarz-Finsterle, J.; Scherthan, H.; Huna, A.; González, P.; Müller, P.; Schmitt, E.; Erenpreisa, J.; Hausmann, M. Volume increase and spatial shifts of chromosome territories in nuclei of radiation-induced polyploidizing tumour cells. *Mutat. Res.* **2013**, *756*, 56–65. [CrossRef] [PubMed]
60. Tsao, D.; Kalogerinis, P.; Tabrizi, I.; Dingfelder, M.; Stewart, R.D.; Georgakilas, A.G. Induction and processing of oxidative clustered DNA lesions in 56Fe-ion-irradiated human monocytes. *Radiat. Res.* **2007**, *168*, 87–97. [CrossRef] [PubMed]
61. Short, S.C.; Martindale, C.; Bourne, S.; Brand, G.; Woodcock, M.; Johnston, P. DNA repair after irradiation in glioma cells and normal human astrocytes. *Neuro Oncol.* **2007**, *9*, 404–411. [CrossRef] [PubMed]
62. Bezbakh, A.A.; Zager, V.B.; Kaminski, G.; Krylov, A.I.; Krylov, V.A.; Teterev, Y.G.; Timoshenko, G.N. Upgrading the genome facility for radiobiological experiments with heavy-ion beams. *Phys. Part. Nuclei Lett.* **2013**, *10*, 175–178. [CrossRef]
63. Tarasov, O.B.; Bazin, D. LISE++: Radioactive beam production with in-flight separators. *Nucl. Instrum. Meth. B* **2008**, *266*, 4657–4666. [CrossRef]
64. Stuhlmüller, M.; Schwarz-Finsterle, J.; Fey, E.; Lux, J.; Bach, M.; Cremer, C.; Hinderhofer, K.; Hausmann, M.; Hildenbrand, G. In situ optical sequencing and nano-structure analysis of a trinucleotide expansion region by localization microscopy after specific COMBO-FISH labelling. *Nanoscale* **2015**, *7*, 17938–17946. [CrossRef] [PubMed]

International Journal of
Molecular Sciences

MDPI

Article

Challenges and Contradictions of Metal Nano-Particle Applications for Radio-Sensitivity Enhancement in Cancer Therapy

Eva Pagáčová [1], Lenka Štefančíková [1,2], Franz Schmidt-Kaler [3], Georg Hildenbrand [3,4], Tomáš Vičar [5], Daniel Depeš [1], Jin-Ho Lee [3], Felix Bestvater [6], Sandrine Lacombe [2], Erika Porcel [2], Stéphane Roux [7], Frederik Wenz [4], Olga Kopečná [1], Iva Falková [1], Michael Hausmann [3,*] and Martin Falk [1,*]

1 Czech Academy of Sciences, Institute of Biophysics, v.v.i., Kralovopolska 135, 612 65 Brno, Czech Republic; pagacova@ibp.cz (E.P.); StefancikovaL@seznam.cz (L.S.); depesd26@gmail.com (D.D.); kopecna@ibp.cz (O.K.); ivafalk@ibp.cz (I.F.)
2 Institute des Sciences Moléculaires d'Orsay (ISMO), Université Paris Saclay, Université Paris Sud, CNRS, 91405 Orsay Cedex, France; sandrine.lacombe@u-psud.fr (S.L.); erika.porcel@u-psud.fr (E.P.)
3 Kirchhoff-Institute for Physics, University of Heidelberg, Im Neuenheimer Feld 227, 69120 Heidelberg, Germany; franzschmidtkaler@web.de (F.S.-K.); hilden@kip.uni-heidelberg.de (G.H.); jin-ho.lee@kip.uni-heidelberg.de (J.-H.L.)
4 Department of Radiation Oncology, Universitätsmedizin Mannheim, Medical Faculty Mannheim, Heidelberg University, 68159 Mannheim, Germany; Frederik.Wenz@medma.uni-heidelberg.de
5 Brno University of Technology, Department of Biomedical Engineering, Technická 3082/12, 61600 Brno, Czech Republic; tomasvicar@gmail.com
6 German Cancer Research Center (DKFZ), Im Neuenheimer Feld 280, 69120 Heidelberg, Germany; f.bestvater@dkfz.de
7 Institute UTINAM, UMR CNRS 6213-Université de Bourgogne Franche-Comté, 25020 Besançon Cedex, France; stephane.roux@univ-fcomte.fr
* Correspondence: hausmann@kip.uni-heidelberg.de (M.H.); falk@ibp.cz (M.F.); Tel.: +49-6221-549824 (M.H.); +420-541517116 (M.F.)

Received: 17 January 2019; Accepted: 24 January 2019; Published: 30 January 2019

Abstract: From the very beginnings of radiotherapy, a crucial question persists with how to target the radiation effectiveness into the tumor while preserving surrounding tissues as undamaged as possible. One promising approach is to selectively pre-sensitize tumor cells by metallic nanoparticles. However, though the "physics" behind nanoparticle-mediated radio-interaction has been well elaborated, practical applications in medicine remain challenging and often disappointing because of limited knowledge on biological mechanisms leading to cell damage enhancement and eventually cell death. In the present study, we analyzed the influence of different nanoparticle materials (platinum (Pt), and gold (Au)), cancer cell types (HeLa, U87, and SKBr3), and doses (up to 4 Gy) of low-Linear Energy Transfer (LET) ionizing radiation (γ- and X-rays) on the extent, complexity and reparability of radiation-induced γH2AX + 53BP1 foci, the markers of double stand breaks (DSBs). Firstly, we sensitively compared the focus presence in nuclei during a long period of time post-irradiation (24 h) in spatially (three-dimensionally, 3D) fixed cells incubated and non-incubated with Pt nanoparticles by means of high-resolution immunofluorescence confocal microscopy. The data were compared with our preliminary results obtained for Au nanoparticles and recently published results for gadolinium (Gd) nanoparticles of approximately the same size (2–3 nm). Next, we introduced a novel super-resolution approach—single molecule localization microscopy (SMLM)—to study the internal structure of the repair foci. In these experiments, 10 nm Au nanoparticles were used that could be also visualized by SMLM. Altogether, the data show that different nanoparticles may or may not enhance radiation damage to DNA, so multi-parameter effects have to be considered to better interpret the radiosensitization. Based on these findings, we discussed on conclusions and

contradictions related to the effectiveness and presumptive mechanisms of the cell radiosensitization by nanoparticles. We also demonstrate that SMLM offers new perspectives to study internal structures of repair foci with the goal to better evaluate potential differences in DNA damage patterns.

Keywords: metal nanoparticles; cancer radiotherapy; tumor cell radiosensitization; DNA damage; DNA repair; DNA double strand breaks (DSBs); super-resolution microscopy; single-molecule localization microscopy (SMLM); DNA repair foci; damage to lysosomes

1. Introduction

More than a half of all cancer patients are currently treated with radiotherapy [1] that, together with chemotherapy, still represents the most efficient curative approach for many cancer types. The therapeutic window of radiotherapy (and chemotherapy) [2] is based on different capacities of normal and cancer cells to repair DNA damage. Because of defects in cell cycle checkpoints and/or repair pathways [3], cancer cells more or less suffer from genomic instability and are more susceptible than normal cells to DNA-damaging agents. Some tumors are highly radioresistant though, making them difficult to eradicate while preserving the surrounding normal tissues undestroyed [4–6]. A crucial part of cancer treatment development therefore concerns a question of how to deliver the radiation effectiveness into the tumor while preserving the normal surrounding tissues as much as possible. This issue becomes of fundamental importance for radioresistant tumors and/or tumors located in close proximity of vital organs or structures. An illustrative example could be the most aggressive and radioresistant tumor [7] starting in the brain—glioblastoma—leading us to select U87 glioblastoma cells as a model in the present study. HeLa cells, an often used model in bio-medical research, were included in the present study as a different cancer cell type for their lower radioresistance and different origin. SkBr3 cells [8] were involved as a model for breast cancer with Her2/neu up-regulation, on which the radiation effects are studied in combination with antibody and/or chemo-treatment [9].

Several promising strategies are continuously being developed to improve radiotherapy. For instance, spatial dose fractionation, time dose fractionation, micro/mini-beam irradiation, heavy-ion irradiation [10–17], and application of normal cell radio-protectants [18,19] and/or tumor cell radiosensitizers [20] could already be used in practice and eventually combined. One of the radiosensitizing approaches proposed is to selectively potentiate radiation toxicity for tumor cells by metal nanoparticles [21–28]. Due to their high electron content and photoelectric absorption cross-section, metal (high atomic number = high-Z material) nanoparticles emit showers of secondary electrons upon irradiation [29,30]. Launched electrons then generate clouds of high ionization densities, capable of enhancing radiation-induced cell damage and death rates [31].

The cell nucleus and DNA located therein are sensitive to many stressors [32–36] and can be highly damaged with relatively low doses of ionizing radiation [37,38]. As deleterious effects of ionizing radiation on (cancer) cells are mostly mediated through fragmentation of nuclear chromatin by inserting double strand breaks (DSBs) into the DNA molecule [39], nanoparticle radiosensitizing effects have primarily been ascribed to an increased number and/or complexity of DSBs generated by radiation in presence of nanoparticles [23]. Clustered (complex) DSBs can only be repaired with difficulty [16,40,41] and were recognized as the main factor responsible for the superior radiobiological efficiency (RBE) of densely ionizing radiations. Hence, according to this hypothesis, at a given absorbed dose and irradiation parameters, nanoparticles boost cell killing by locally amplifying the dose [42] and, in turn, DNA damage. Indeed, increased numbers relative to untreated samples of single-stranded breaks (SSBs) and DSBs were measured in DNA irradiated in the solution with various metal nanoparticles [43]. Since nanoparticles are preferentially internalized and accumulated by cancer cells, even passively due to mechanisms collectively known as the so-called Enhanced Permeability

and Retention (EPR) effect, these enhancement effects of radiotherapy could be selectively targeted to tumors [44–50]. Moreover, some nanoparticles exert dual multiple benefits in cancer treatment at the same time—they can be used as contrast agents in theranostics [51] and/or vehicles for delivery of various chemotherapeutics or biological treatment compounds to the tumor. Nanoparticles can be also functionalized (surface material modification, attached antibodies, size, shape, etc.) to better identify and infiltrate the tumor [23,48]. Moreover, nanoparticles can be used as imaging tags especially where photo-bleaching has to be avoided [52,53].

Aforementioned physical predictions on the mechanism of nanoparticle-mediated radiosensitization were confirmed experimentally [51]. As already noticed, isolated DNA showed increased fragmentation after being irradiated in presence of various nanoparticles [43]. In other experiments, nanoparticles also increased cell dying when being added to cell cultures prior to irradiation [21,43,54]. Nevertheless, it is in fact not so easy to explain the nanoparticle-mediated cell radiosensitization, despite seemingly ideal correspondence between the theoretical predications and experimental results. The Achilles' heel of the current "mainstream" hypothesis followed from in situ/in vivo experiments showing that nanoparticles, even those of very small dimensions (e.g., of 2–3 nm in diameter, as used in this work), penetrate the cells but not the cell nucleus [21,23,53,55] unless they are specifically modified for this purpose [42]. Nanoparticles of different materials and sizes, entering the cells by pinocytosis (reviewed in [56]), thus remain retained inside the cytoplasm, where they accumulate especially in endoplasmic vesicles (endosomes) and lysosomes [21,55,57]. Under some circumstances, nanoparticles may co-localize preferentially with the endoplasmic reticulum (ER) [23,58] and Golgi apparatus (reviewed in [56]). Interestingly, mitochondria, the only cytoplasmic organelles in human cells that contain their own DNA, do not represent a primary target for nanoparticles, though some nanoparticles can also be targeted to these structures (reviewed in [56]). These findings put into play a plethora of various cellular processes potentially participating in nanoparticle-mediated tumor cell radiosensitization. It is therefore possible that different nanoparticles do not share a common mode of action, both in terms of the type of cell damage and its underlying mechanism (reviewed in [59]).

In the present work, we analyzed for different metal nanoparticles, whether their extra-nuclear [21–23,55] presence in cells can, by itself or upon cell irradiation, enhance damage of the nuclear DNA. In addition, we followed in detail nanoparticle effects on the kinetics and efficiency of DNA repair in cells exposed to low-Linear Energy Transfer (LET) ionizing radiation (γ- and X-rays). We used high-resolution immunofluorescence confocal microscopy (ICM) and single molecule localization microscopy (SMLM) [38,60] to quantify γH2AX/53BP1 DSB repair foci formation [61] and disassembly during a long period of time post-irradiation (PI) in cells exposed to different doses of γ/X-rays after being or being not incubated with platinum nanoparticles (Pt-NPs). On the basis of these data, preliminary data for gold nanoparticles (Au-NPs), and our earlier data for gadolinium nanoparticles (Gd-NPs) [21], we discussed here on what is known about metal nanoparticle effects on cells and potential mechanisms of nanoparticle-mediated radiosensitization.

In general, the aim of the following study was to verify whether cell radiosensitization by metal nanoparticles is correlated with escalation of DNA damage and/or affection of DNA damage repair capacity. The results should contribute to a better understanding of the mechanism by which various nanoparticles (different materials and sizes) radiosensitize cells with future attempt to rationally design therapeutically more efficient nanoparticles.

2. Results

2.1. Experimental Conditions and Approaches

We explored how platinum (Pt) and gold (Au) nanoparticles influence DNA DSB induction and repair in three different cancer cell types, U87 glioblastoma cells, HeLa cervix cancer cells and SkBr3 breast cancer cells, exposed to γ-(^{137}Cs) or X-radiation. U87 glioblastoma cells were selected for their high resistance to radiotherapy. HeLa cells, showing relatively lower resistance to radiation,

were then involved into the study to explore how tumor cell types of different radiosensitivities and origins respond to nanoparticle uptake and nanoparticle uptake followed by irradiation. The SkBr3 model is known to be more radioresistant in comparison to HeLa cells and was especially taken for super-resolution localization microscopy. The mechanism and kinetics of nanoparticle internalization were in detail evaluated in our previous studies with Gd-NPs (3 ± 1 nm) [21,55] and Au-NPs (10 nm) [53] of a comparable size to Pt-NPs (2.6 nm) and Au-NPs (2.4 nm) used in the present study. We showed that these ultrafine Gd-NPs as well as the larger Au-NPs efficiently penetrate into the cell cytoplasm but remain restricted from the cell nucleus. Even short (2 h) incubation with nanoparticles was proved to be sufficient to ensure their internalization and cell radiosensitization upon irradiation with γ/X-rays [53]. Therefore, we used the compatible conditions also here, though lower concentration and longer incubation period (0.5 mM/6 h) were preferred to ensure sufficient cell accumulation but minimize the potential cytotoxicity.

Modern, top-tech microscopy approaches were used in the present study to analyze DNA damage and repair with high precision. ICM allowed for quantification of DSBs during a long PI time period [16] (Figure 1). When co-localized γH2AX and 53BP1 repair foci are used as DSB markers, the sensitivity of the method is clearly superior over other modern methods, including fluorescence COMET assay (single cell gel electrophoresis) on single cells [20]. Newly developed SMLM, used here for super-resolution ultra-structural analyses of repair foci [61], offers even better resolution (up to 10–20 nm) and sensitivity than ICM. Nevertheless, since higher numbers of cells can be currently analyzed by ICM, we took advantage of this method to determine the extent of DSB induction and DSB repair kinetics in statistically relevant numbers of spatially (three-dimensionally = 3D) fixed cells, still with a very high credibility and fidelity of analysis. To further increase the credibility of our study, we scored the repair foci both manually and automatically. This also allowed us to compare the positives and negatives of both approaches and to determine the influence of γH2AX/53BP1 focus scoring method on the results.

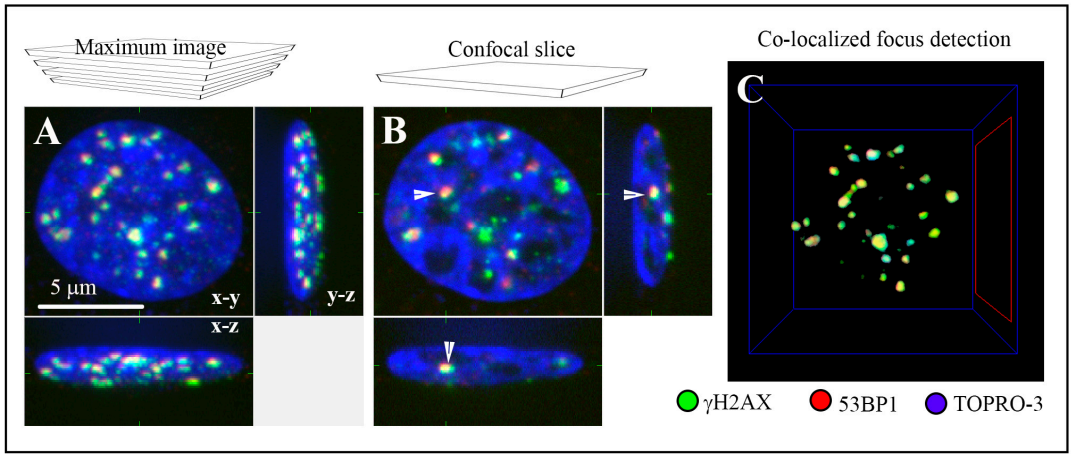

Figure 1. The ability of immunofluorescence confocal microscopy to quantify DSBs (Double Strand Breaks) in cells incubated with nanoparticles or incubated with nanoparticles and consecutively irradiated. DSBs were quantified by the means of immunofluorescence detection of co-localized γH2AX (green) and 53BP1 (red) repair foci, the DSB markers. The nucleus of an illustrative U87 cell exposed to 2 Gy of γ-rays and spatially (three-dimensionally = 3D) fixed at 2 h post-irradiation (PI) is shown as: (**A**) a maximum intensity projection of 40 confocal slices (0.3 µm thick; "maximum image") or (**B**) a single confocal slice (0.3 µm thick) intersecting the indicated (white arrow) γH2AX/53BP1 focus. Images are displayed in all three (in the x-y, x-z and y-z) planes, and chromatin is counterstained with TO-PRO-3 (artificially blue). (**C**) An example of computational detection of co-localized (yellow) γH2AX (green) and 53BP1 (red) repair foci in 3D space (Aquarium Software).

2.2. Pt-NP and Au-NP Short-Term Genotoxicity—the Effect on Nuclear DNA in Non-Irradiated Cells

Firstly, we analyzed potential negative influence of 2.6 nm Pt-NPs and 2.4 nm Au-NPs on the nuclear DNA of U87 and HeLa cells before irradiation. Cells were cultured with Pt-NPs or Au-NPs in the concentration of 0.5 mM for 6 h and potential induction of γH2AX/53BP1 (DSB) foci was studied as an indicator of nanoparticle-mediated genotoxicity. The repair foci have been present in both U87 and HeLa cell types already prior to incubation with nanoparticles and γH2AX foci mostly co-localized with 53BP1 protein. This observation points to a permanent existence of DSBs in U87 and HeLa cells, which is in accordance with their tumorous nature associated with genomic instability (Figure 2). U87 cells carried higher numbers of the foci than HeLa cells, with the mean values of 3.47 and 2.03, respectively. Figures 3–5 (0 min post irradiation (PI) in all graphs) show that the average/median numbers of the foci per nucleus were almost identical (manual analysis, Figure 3) or increased slightly (automatic analysis, Figures 4 and 5) after incubation of cells with Pt-NPs. The mean numbers of co-localized γH2AX/53BP1 foci per nucleus, provided by the automatic analyses, were 4.34 for U87 (Figure 3) and 3.88 HeLa cells (Figure 5). Such a differences, statistically significant though (U87: $p = 0.010$; HeLa: $p = 0.003$), are not supportive of biologically more relevant genotoxicity of the nanoparticles studied (2.6 nm Pt-NPs, and 2.4 nm Au-NPs; Figure 6), at least in terms of increased DNA fragmentation, consequently leading to genome rearrangements. Nevertheless, our studies limited to DSB induction cannot exclude a "milder" effect of nanoparticles on the DNA molecule, manifested for instance as oxidative base modifications. This kind of DNA damage may appear due to nanoparticle-mediated production of reactive oxygen species (ROS), which was frequently reported in the literature as the main cause of nanoparticle cytotoxicity. Moreover, especially in the context of what will follow, a negative potential of cytoplasmically localized nanoparticles may be preferentially or even exclusively targeted to the cytoplasmic structures. To summarize, our observations did not reveal more prominent genotoxicity of 2.6 nm platinum nanoparticles after short-term (6 h) incubation with U87 and HeLa cells, but more experiments are needed to comprehend potential cytotoxic effects of these nanoparticles in a more comprehensive way. Preliminary results seem to confirm this conclusion also for 2.4 nm Au-NPs.

2.3. DSB Induction and Repair in U87 Cancer Cells Treated or Not-Treated with Metal Nanoparticles Prior to Irradiation

After excluding the possibility that the studied 2.6 nm Pt-NPs and 2.4 nm Au-NPs markedly increase γH2AX/53BP1 focus (DSB) formation even by themselves, i.e., already in non-irradiated cells, we analyzed whether these nanoparticles can enhance DSB induction or affect DSB repair capacity of U87 and HeLa cells upon irradiation. The situation was compared for two γ-ray doses, 2 Gy and 4 Gy. We decided for a 2 Gy dose since this exposure is frequently used in clinical practice as a single fraction dose delivered to patients during a fractionated therapy. The higher dose of 4 Gy was applied in order to generate larger numbers of DSBs and explore differences between samples with better sensitivity (since the differences in DSB numbers per nucleus may be only small for low doses and therefore distinguishable from natural variability only with difficulty).

Figure 2 compares the γH2AX/53BP1 focus (DSB) formation and repair kinetics for U87 cells treated or not-treated with 2.6 nm Pt-NPs prior to irradiation with 4 Gy of γ-rays. Representative cell nuclei of both cell populations are displayed for different periods of time PI up to 48 h PI. Independently of the nanoparticle treatment, it is evident from Figure 2 that γH2AX foci are only incompletely formed in U87 cells early after irradiation (5–30 min PI) and also their co-localization with 53BP1 repair protein is very low. Correspondingly, the background signals (i.e., the proportions of γH2AX and especially 53BP1 molecules outside foci) are often high. A similar "picture" has also been reported for U87 cells exposed to heavy ions [62,63]. With ongoing time after irradiation, γH2AX and 53BP1 foci grow both in number and size and their mutual co-localization increases too. For both cell types (U87, and HeLa) and radiation doses (4 Gy, and 2 Gy), the number of co-localized γH2AX and 53BP1 foci reached the maximum between 30 min and 1 h PI. Later on, the number of foci started to decrease,

while the size of foci gradually increased and the extent of co-localization between γH2AX and 53BP1 remained very high. Importantly (as quantified later), we did not observe any visual difference between nanoparticle-treated cells and their untreated counterparts with regard to the extent of DSB induction and repair kinetics.

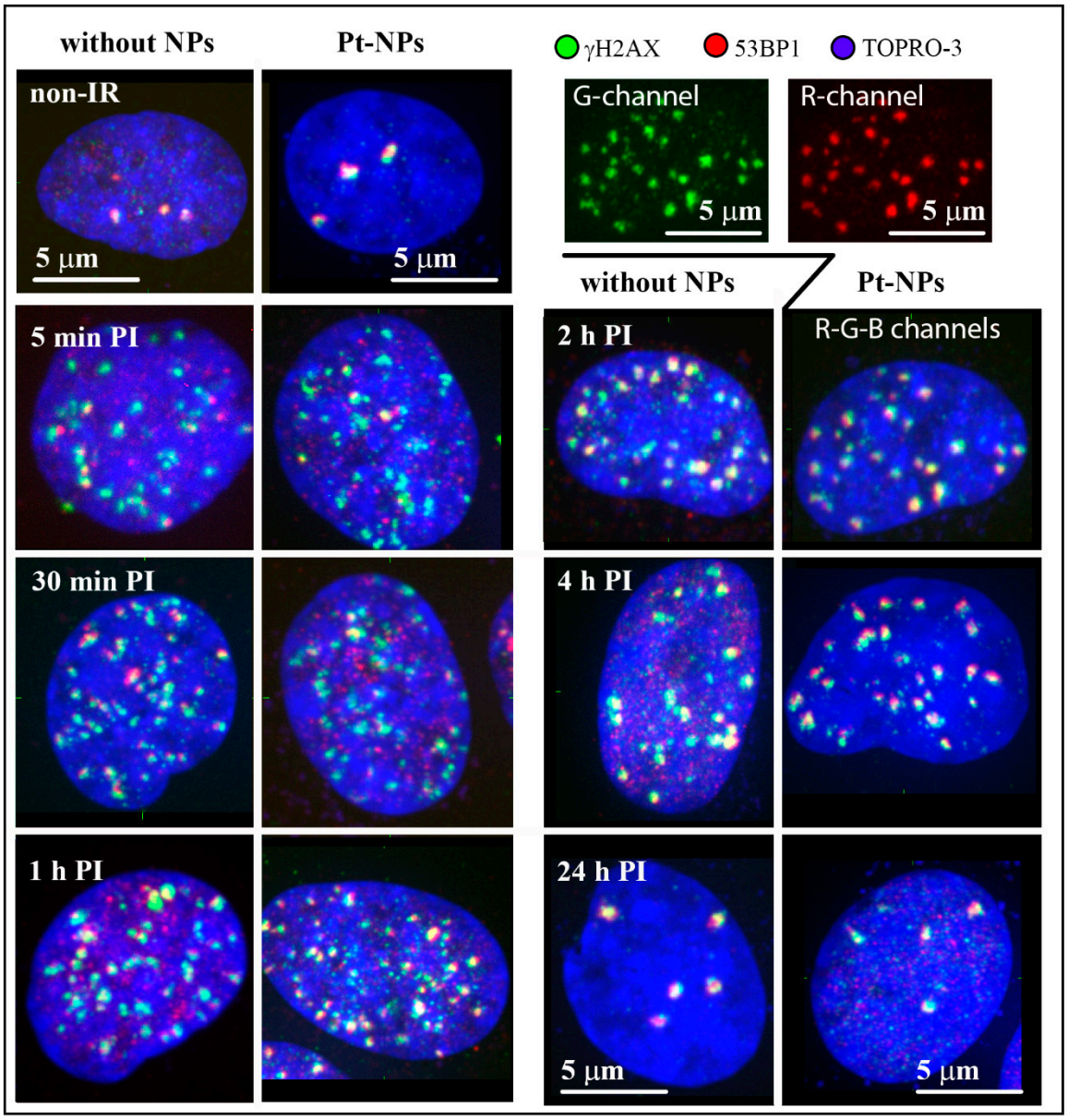

Figure 2. γH2AX/53BP1 foci (DSB) formation and repair kinetics in U87 cells incubated or not incubated with 2.6 nm platinum nanoparticles (Pt-NPs; 0.5 mM for 6 h) and consequently irradiated with 4 Gy of γ-rays. Maximum images (see Figure 1) are displayed for representative nuclei of cells that were spatially (3D) fixed in the indicated periods of time PI. For the nucleus fixed at 2 h PI, γH2AX foci (inserted G-channel panel) and 53BP1 foci (inserted R-channel panel) are also shown separately to demonstrate their mutual co-localization. γH2AX (green), 53BP1 (red), and chromatin counterstained with TO-PRO-3 (artificially blue). None-IR figures correspond to non-irradiated cells.

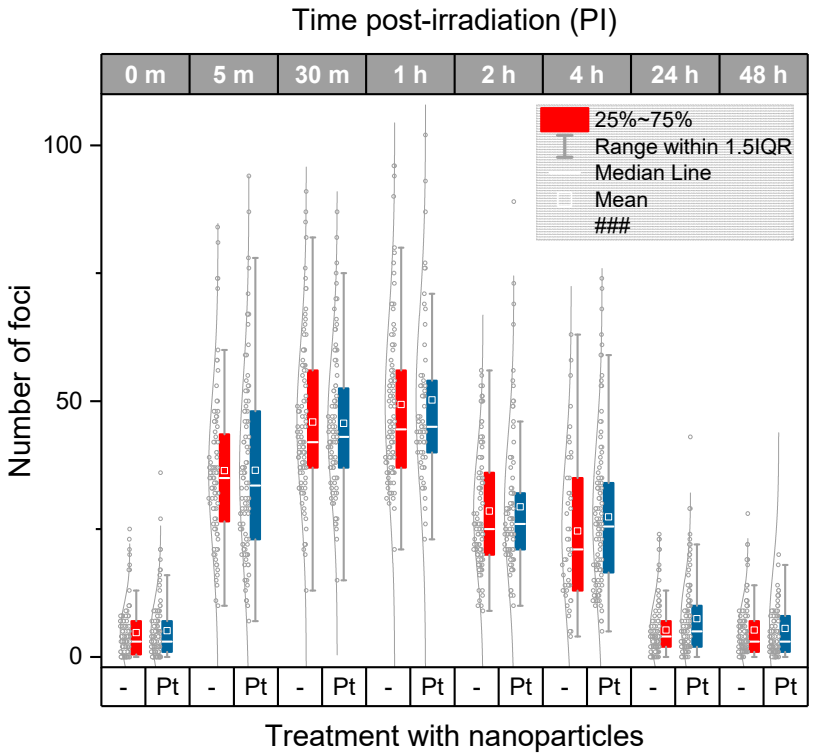

Figure 3. Manual analysis of the extent of γH2AX+53BP1 focus (DSB) induction and repair kinetics in U87 glioblastoma cells irradiated with 4 Gy of γ-rays compared with cells treated (0.5 mM for 6 h) and not treated prior to irradiation with 2.6 nm platinum nanoparticles (Pt-NPs). The average and median numbers of co-localized γH2AX + 53BP1 repair foci (i.e., DSBs) per nucleus are shown for different periods of time PI, together with the focus number distributions in each cell population. The boxes include 50% of the values (25th to 75th percentile) centered on the median (the horizontal line through the box). The mean values are represented by the squares within the boxes. The outliers were identified according to the 1.5*IQR method (IQR = interquartile range). Pt—samples treated with platinum nanoparticles, m—the period of time after irradiation in minutes, 0 m—non-irradiated samples.

The quantitative results obtained for different ways of analysis (i.e., manual and automated) and two radiation doses (4 Gy and 2 Gy) are summarized in Figures 3–5. Figure 3 compares the average/median numbers of γH2AX/53BP1 foci per nucleus together with the focus number distributions as gained by manual analysis for U87 cells exposed to 4 Gy of γ-rays in presence and absence of Pt-NPs, respectively. Except for two late time points PI (4 h and 24 h PI), all statistical characteristics (means, medians, and distributions) are almost identical for nanoparticle-treated and untreated cells.

The automated image analysis (Figure 4a) of the same cells that were previously evaluated manually provided much lower numbers of γH2AX/53BP1 foci compared to that in the manual analysis, especially at the early periods of time PI (up to 1 h PI). The maximum numbers of foci per nucleus were detected at 1 h PI in all samples, irrespective of the nanoparticle treatment and the way of analysis. During this period of time, about 50 foci per nucleus were counted manually while this value decreased to about 35 with the automated analysis. Taking into account previous reports showing that 1 Gy of γ-rays generates ~9–35 γH2AX foci per nucleus on average, depending on the cell type, the results of the manual analysis (mean = 12.5 foci/nucleus/Gy) can be considered as more realistic in terms of absolute numbers. A lower sensitivity of automatic analysis follows from the fact that computational parameters of focus scoring were set very strictly, just to detect only well-developed foci with an extensive overlap between γH2AX and 53BP1. The reason for this setting was to eliminate potential uncertainty with identification of small and/or immature foci since these foci could not be often easily separated from the background signal. Consistently, more prominent differences

between the manual and automated analysis appeared at the shorter time points PI (up to 1 h PI), i.e., during the period of time when the representation of immature foci was high, especially in U87 cells. Under such conditions, automatic software analysis is still extremely difficult and manual analysis promises more precise results, especially in terms of counting the absolute focus numbers. On the other hand, computational analysis ensures detection of only precisely specified foci and therefore high reproducibility and objectivity of results, independently of the observer experience.

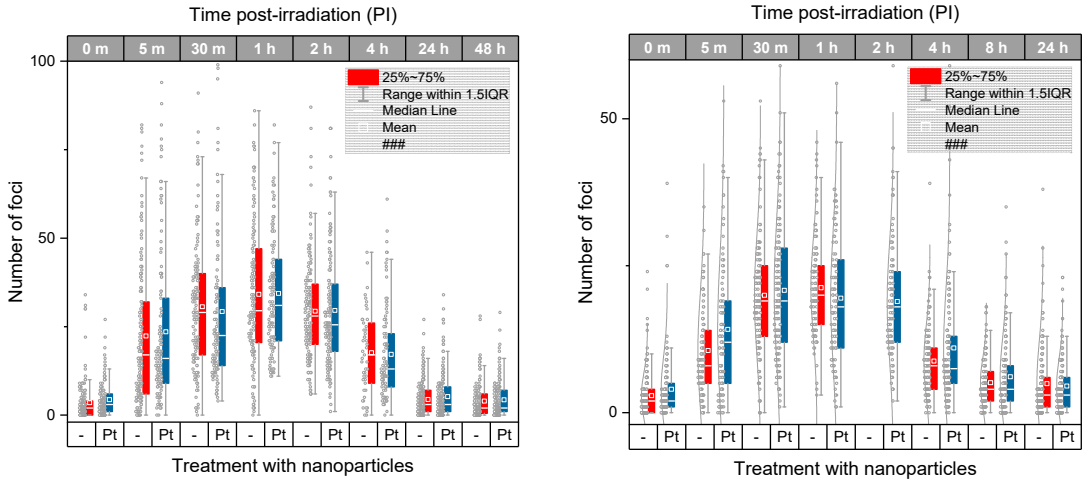

Figure 4. Software analysis of the extent of γH2AX+53BP1 focus (DSB) induction and repair kinetics in U87 glioblastoma cells irradiated with 4 Gy (**a**) or 2 Gy (**b**) of γ-rays compared with cells treated (0.5 mM for 6 h) or not treated prior to irradiation with 2.6 nm platinum nanoparticles (Pt-NPs). The average and median numbers of co-localized γH2AX + 53BP1 repair foci (i.e., DSBs) per nucleus are shown for different periods of time PI, together with the focus number distributions in each cell population. The boxes include 50% of the values (25th to 75th percentile) centered on the median (the horizontal line through the box). The mean values are represented by the squares within the boxes. The outliers were identified according to the 1.5*IQR method (IQR = interquartile range). Pt—samples treated with platinum nanoparticles, m—the period of time after irradiation in minutes, 0 m—non-irradiated samples.

Another motivation to restrict the automated analysis selectively on well-developed foci followed from the question whether nanoparticles in irradiated cells may differently influence generation or repair of small and large γH2AX foci (the smaller foci were scored as DSBs by the manual analysis but not automated analysis). Except as described, both approaches provided very similar results despite of the different characters of manual and automated focus counting. Importantly, as for the manual analysis, the average numbers, medians, and distributions of γH2AX/53BP1 foci varied only inappreciably between U87 cells irradiated (4 Gy) with Pt-NPs present or absent. Very similar results for nanoparticle-treated and untreated samples were found also at 4 h PI and 24 h PI (Figure 4a), making the differences obtained for these time points by the manual analysis rather a deviation from otherwise tightly "overlapping" γH2AX/53BP1 focus profiles in time PI than a biologically relevant result.

For the lower radiation dose of 2 Gy of γ-rays (equivalent to a common single daily dose in fractionated radiotherapy), the same results as for the higher dose of 4 Gy were acquired (Figure 4b). Again, very similar numbers of γH2AX+53BP1 foci per nucleus were counted in irradiated U87 cells, irrespective of their incubation with Pt-NPs. Slightly higher mean numbers of γH2AX foci per nucleus were recognized in nanoparticle-treated cells compared to those in untreated ones only at 8 h and 24 h PI; however, comparable medians of the compared samples do not support existence of significant differences between Pt-NP-containing cells and controls even at these periods of time.

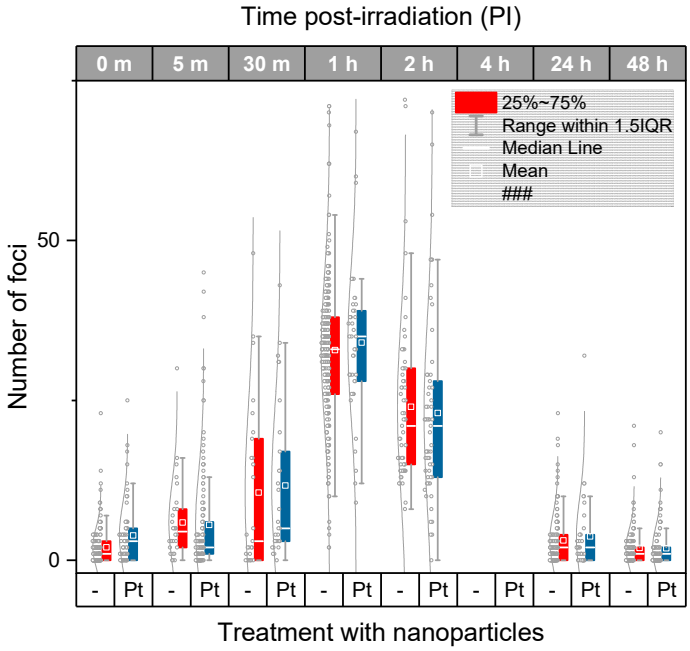

Figure 5. Automated analysis of the extent of γH2AX + 53BP1 focus (DSB) induction and repair kinetics compared for HeLa cells irradiated with 4 Gy of γ-rays in presence (0.5 mM for 6 h) or absence of 2.6 nm Pt-NPs. The average and median numbers of co-localized γH2AX+53BP1 foci (i.e., DSBs) per nucleus are shown for different periods of time PI, together with the focus number distributions in each cell population. The boxes include 50% of the values (25th to 75th percentile) centered on the median (the horizontal line through the box). The mean values are represented by the squares within the boxes. The outliers were identified according to the 1.5*IQR method (IQR = interquartile range). Pt—samples treated with platinum nanoparticles, m—the period of time after irradiation in minutes, 0 m—non-irradiated samples.

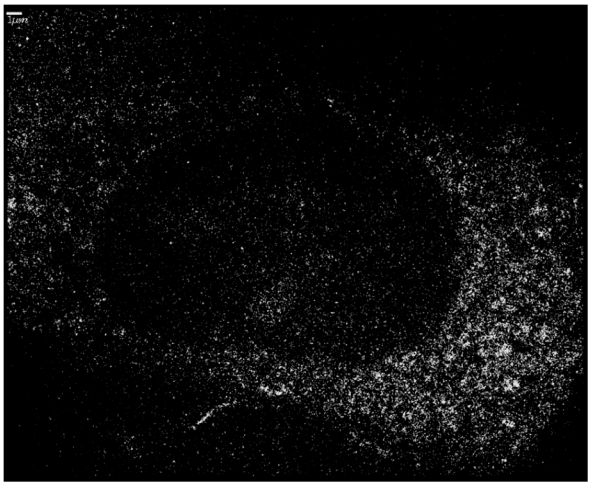

Figure 6. An illustrative Single Molecule Localization Microscopy (SMLM) image of an SkBr3 cell after uptake of 10 nm Au-NPs in the cytosol. The Au-NPs show a fluorescent blinking after laser illumination at 594 nm. Each point thus represents a single Au nanoparticle. Whereas the cytosol seems to be full of nanoparticles, the nucleus is empty. The points of low intensity seemingly covering the nucleus in the image either are the background or belong to out-of-focus image planes above or below the nucleus. Scale bar 1 μm.

2.4. DSB Induction and Repair in HeLa Cancer Cells Treated or not-Treated with Metal Nanoparticles Prior to Irradiation

In the next step, we performed the same experiments as described in the previous chapter for U87 cells also with HeLa cervix carcinoma cells that differ from U87 cell by their origin and relatively lower radioresistance. Involvement of the two cell types into the study is important since the same nanoparticles may behave unequally in dependence of specific cell characteristics. Results for HeLa cells irradiated with 4 Gy of γ-rays in presence or absence of 2.6 nm Pt-NPs are compared in Figure 5. Though some differences in the extent of γH2AX/53BP1 foci formation and kinetics of their disappearance appeared between U87 and HeLa cells, 2.6 nm Pt-NPs added to HeLa cells cultures prior to irradiation (0.5 mM, 6 h-incubation) had no effect on DNA damage and repair, confirming thus our findings for U87 cells. Cell-type-specific extent of γH2AX/53BP1 foci induction and repair capacity might be attributed to different radiosensitivities of U87 and HeLa cells. In the present study, however, different levels of radioresistance and other characteristics of U87 and HeLa cells did not influence the processes initiated by nanoparticles in both non-irradiated and irradiated cells. Similarly, as described above for non-irradiated U87 cells incubated with 2.6 nm PT-NPs, addition of Pt-NPs by itself slightly increased γH2AX/53BP1 focus numbers per nucleus also in HeLa cells (i.e., without irradiation). This can be considered as a sign of potential genotoxicity of Pt-NPs, but biological relevance of this finding does not seem to be high.

2.5. SkBr3 Cancer Cells Treated or Not-Treated with Gold Nanoparticles Prior to Irradiation—Studying γH2AX Arrangement and Focus Formation by Single Molecule Localization Microscopy

In the next step, we studied internal molecule arrangements and focus formation of γH2AX repair foci at the nanoscale by using SMLM [61]. These experiments can provide important new insights into the character of DSB damage generated by ionizing radiation in cells incubated or not incubated with metal nanoparticles. For these data, we assumed that the antibody tags against the H2AX phosphorylation sites represent the spatial topology of the foci. In the first approach, we therefore measured distance frequencies between labelling points and verified dose–efficiency curves on the point numbers in comparison to our recent approach [61].

SkBr3 cells were irradiated with 6 MeV X-rays at doses of 0, 0.5, 1, 2, or 4 Gy. For each dose, a specimen with and without 10 nm Au-NPs was irradiated. In order to ensure a maximum uptake and incorporation of these larger Au-NPs, incubation of cells was hold for 16 h prior to irradiation (Figure 6). Forty-five minutes after irradiation, the specimens were fixed and subjected to SMLM followed by software analysis of the H2AX labelling tags and their mutual distances. In Figure 7, typical next-neighbor density images are shown. In contrast to raw SMLM images showing just the positioning of fluorochromes with high precision (10–20 nm), these images encode the density of next neighbors in a 1000 nm environment by intensity. At a first glimpse, it seems that the cells with incorporated Au-NPs form more intensive foci, i.e., foci with more point signals than the cells that were irradiated with the same dose but without Au-NPs. In the case of the non-irradiated control, a random distribution may be supported by the visual impression, which contrasts with signal clustering in all irradiated cells.

A more quantitative analysis based on Ripley's K- and L-values [38] revealed a non-random distance distribution in all irradiated cell samples as it is shown for a case after 500 mGy radiation exposure without Au-NPs (Figure 8). This result indicates that, in all cases, clustering of γH2AX labelling tags can be expected. Therefore, we further studied the distance frequencies in order to find out whether the general γH2AX pattern is differing for the radiation doses and/or nanoparticle treatment conditions (Figure 9). In all irradiated cells, the average distance between γH2AX points was between 20 and 25 nm. Importantly, this γH2AX pattern did not change in specimens treated with Au-NPs.

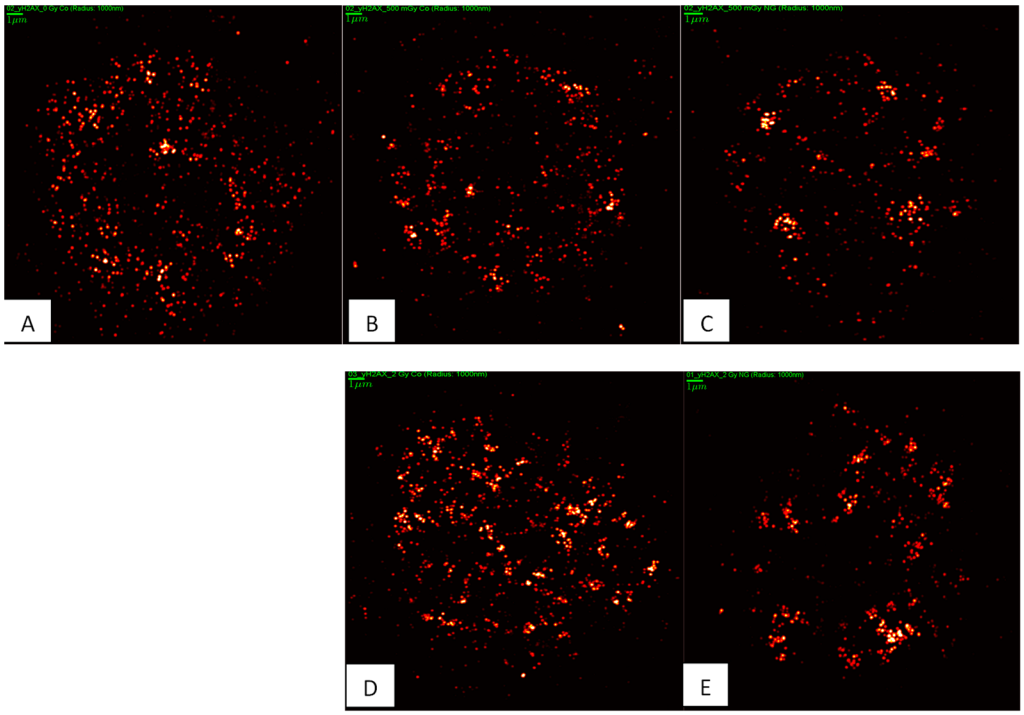

Figure 7. Illustrative SMLM next-neighbor density images comparing γH2AX labelling tag numbers and distributions in SkBr3 cells after irradiation (**B**,**D**) without particle incubation and after irradiation preceded by uptake of 10 nm Au-NPs into the cytosol (**C**,**E**). The intensity of the points represents the number of next neighbors in a 1000 nm radius environment. The control without any treatment (no NP-incubation, and no irradiation) is shown in (**A**), indicating some repair activity also in untreated cells. Images of irradiated cell were taken at 45 min PI. Scale bar: 1 μm.

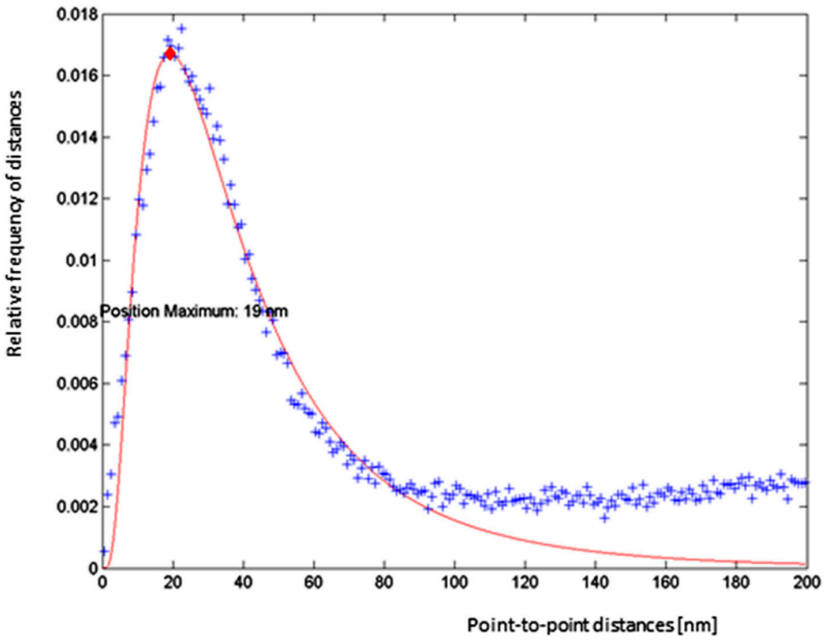

Figure 8. Example of a distance frequency distribution obtained for γH2AX labelling tags in an SkBr3 cell nucleus of the control (no NPs) specimen exposed to 0.5 Gy of X-rays. In all cases independent of the treatment, compatible distributions were obtained, indicating a characteristic non-random distance distribution. (blue crosses: number of measured distances; red diamond: peak maximum; red curve: fit curve)

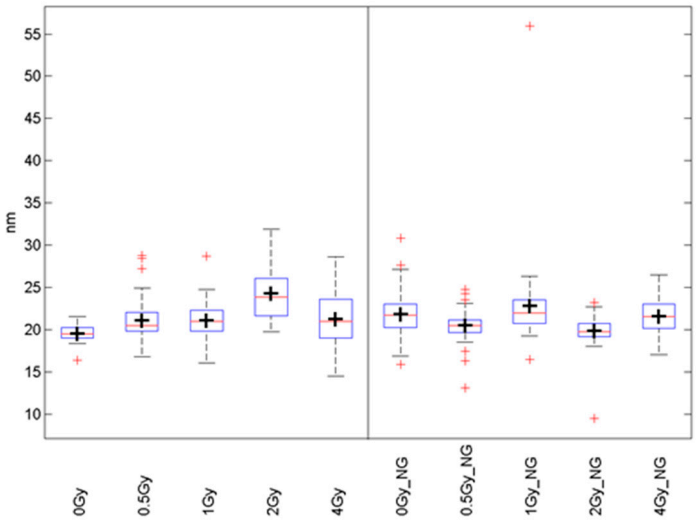

Figure 9. Boxplots of distance frequencies between γH2AX labelling tags in SkBr3 cell nuclei of irradiated specimens (left) and Au-NP-incorporated and irradiated specimens (NG, right). (black cross: mean value; red line: median value; red cross: outliner; blue box: first quartile; dashed line: standard deviation)

The numbers of γH2AX labelling tags can be used to determine the dependence of DNA damage extent on radiation dose and presence of nanoparticles [61]. Hence, we constructed preliminary dose–efficiency curves for X-ray doses up to 4 Gy and compared the numbers of γH2AX signal points in cells incubated or not incubated with Au-NPs (Figure 10). A slight linear increase in the number of γH2AX points was registered up to 2 Gy. In this dose interval, the curves were comparable for cells with and without Au-NP incorporation. Interestingly, a steep increase of the curve appeared between 2 Gy and 4 Gy after Au-NP incorporation, which was not observed in the control. In addition, the SMLM data indicate that the dose enhancement effects, as indicated by γH2AX signals, may be small, especially in dose ranges up to 2 Gy, which supports the data obtained above by ICM and foci counting. However, further experiments with other cell lines seem to be necessary for making the final conclusions.

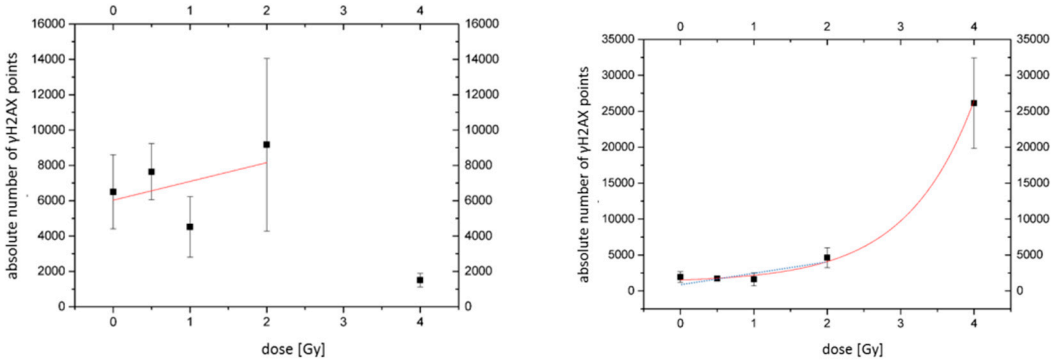

Figure 10. Dose–efficiency curves (number of γH2AX labelling tags vs. dose counted by SMLM). For the irradiated SkBr3 cell nuclei without Au-NP incorporation (left graph, a linear increase (red fit curve) can be observed at doses between 0 and 2 Gy. This was compatible to the blue linear fitting curve for irradiated SkBr3 cell nuclei with Au-NP incorporation (right graph. For the higher dose values, an exponential growth (red fit curve) or quadratic increase could be fitted to the values. (black square: mean value; error bar: standard deviation)

In any case, we show here that the microscopic tools for nano-architecture analysis are available and adaptable to the challenges of NP-modified radiation treatment. The techniques of nano-probing and localization microscopy can be further improved by topological analyses of other repair foci (e.g.,

53BP1 or Mre11) or analyses of chromatin conformation changes that may be induced by additional NP treatment.

2.6. Compared Effects of Pt, Au and Gd Nanoparticles—Preliminary Results

Finally, despite a preliminary character of the Au-NP data, we attempted here to compare DNA effects for three types of ultrafine (2–3 nm) metal nanoparticles composed of platinum, gold, and gadolinium, respectively. The size and incubation parameters were kept as similar as possible for all experiments to isolate only the effect of the nanoparticle material. The values for gadolinium(III) containing nanoparticles presented in Figure 11 were taken from our previous study performed with the same cells (U87) and under comparable experimental conditions [21]. As it is evident from Figure 11, the differences in DNA damage and repair between U87 cells exposed to 4 Gy of γ-rays after being or being not incubated with nanoparticles are quite small for all nanoparticles—platinum, gold, and gadolinium—studied. This means that 2.6 nm Pt, 2.4 nm Au and 2.0 nm Gd nanoparticles of given composition neither intensify DSB induction by ionizing radiation nor affect consequent repair of these lesions.

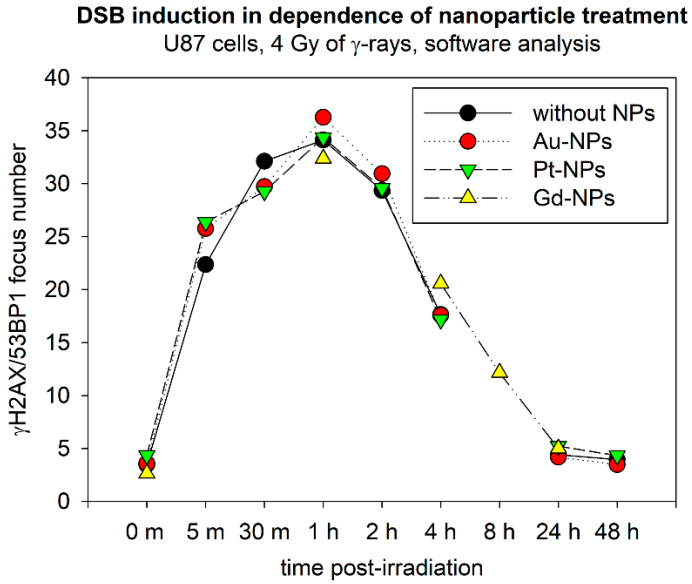

Figure 11. Comparison of γH2AX/53BP1 focus (DSB) formation and repair in U87 cells irradiated with 4 Gy of γ-rays in absence or presence of 2.6 nm Pt-NPs, 2.4 nm Au-NPs or 2.0 nm Gd-NPs. The results of an automated software analysis are shown as mean numbers of foci per nucleus measured at the indicated periods of time PI. Black circles—without NPs, green triangles—Pt-NPs (0.5 mM, 6 h-incubation), and red circles—Au-NPs (0.5 mM, 6 h-incubation; preliminary results). The data are also compared to our earlier results [21] for Gd-NPs (1 mM for 1 h, ^{60}Co-irradiation, 4 Gy) (yellow triangles). X-axis: m = minutes, h = hours; 0 min = non-irradiated samples.

Nevertheless, some indications can be recognized in our summarized data, eventually pointing to a delay in DSB repair, though the overall repair capacity of U87 cells has remained uninfluenced. Such a delay could be theoretically explained by a higher complexity of DSBs generated in presence of NPs. Therefore, as a rough estimation of DSB complexity, we quantified by Immune Fluorescence Microscopy) IFM the γH2AX focus areas for U87 cells irradiated (4 Gy) in presence or absence of Pt-NP nanoparticles. The results are presented in Figure 12. The curves for nanoparticle-treated cells and untreated controls seem to diverge starting with 4 h PI, indicating increased volumes of γH2AX foci in cells incubated with 2.6 nm Pt-NPs. Though these data are rather preliminary and experiments are needed for more nanoparticle types, well compatible results came also from SMLM nano-analyses, showing, compared to irradiated but untreated cells, more intensive γH2AX foci composed of more γH2AX signals in cells irradiated in presence of 10 nm Au-NPs. However, it remains difficult to explain

why the complexity but not the extent of DSB damage increased in presence of NPs. Alternatively, cytoplasmically located NPs may enhance radiation damage to the cytoplasm. Consequent suboptimal condition of cells may indirectly decrease DSB repair. This could be supported by the observation that potential indications of a slower repair in nanoparticle-treated cells appeared only in later periods of time PI. However, it should be emphasized that, as a whole, our results rather support the no-difference scenario for nanoparticle-treated and untreated irradiated cells.

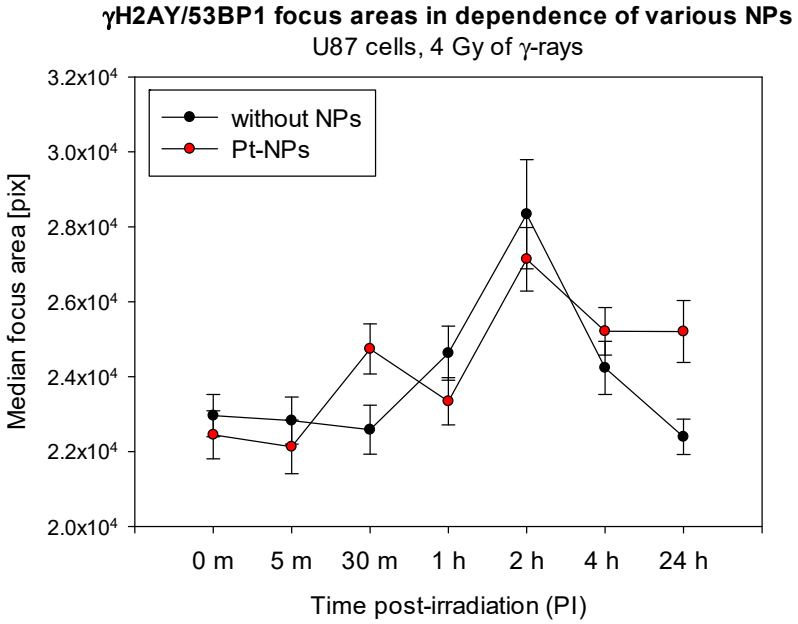

Figure 12. Comparison of γH2AX/53BP1 focus areas at different periods of time PI compared for U87 cells irradiated with 4 Gy of γ-rays in absence or presence of Pt-NPs. The results of an automated software analysis are shown as mean numbers of pixels per focus. Black circles—without NPs, and red circles—Pt-NPs (0.5 mM, 6 h-incubation; preliminary results). Error bars = standard error, m = minutes, pix = pixels, 0 m = non-irradiated samples.

3. Discussion

The radiosensitizing effect of metal nanoparticles on tumor cells has been widely reported in the literature [22]. However, the mechanism or even multiple mechanisms of this potential radiotherapy improvement remains unknown. From the potential of physics [31], nanoparticles would have multiple benefits in cancer diagnosis and radiation treatment. They have been used as contrast agents [51] and locally for tumor damaging [24,64]. Functionalized nanoparticles can be used as vehicles for bio-molecules and drugs to infiltrate a tumor [23,48]. According to the cell-killing mechanism of ionizing radiation, which is based on DNA fragmentation through DSB induction, and the capability of metal nanoparticles to locally amplify the absorbed radiation dose at the microscale, a hypothesis on nanoparticle-mediated cell radiosensitization has been proposed and increased cell dying confirmed by colony-forming assays [42]. It has been well documented that irradiated nanoparticles, preferentially sequestered by tumor cells due to the so-called EPR effect and other effects, emit showers of secondary electrons that consequently increase water radiolysis around the sites of nanoparticle accumulations and damage important biomolecules, mainly the nuclear DNA. The Achilles' heel of this otherwise very logical idea poses in a well-proved fact that while DNA is located in the cell nucleus, the nucleus is inaccessible even for nanoparticles of ultrafine dimensions (~2.5–10 nm) as used in the present study [53]. At the same time, the action radius of most secondary electrons kicked-off from cytoplasmically located nanoparticles is quite short [31]. Since some amounts of nanoparticles become concentrated around the cell nucleus or are specifically directed to the endoplasmic vesicles and reticulum, some secondary electrons may surely reach

and damage the chromatin [23]. However, to what extent these rather rare acts of damage could contribute (increase) to cell killing remains a subject of debates. Moreover, the research on this topic is largely complicated by tremendous variability in the nanoparticle design (material, composition, size, shape, surface functionalization, etc.), cell-type-specific behavior and experimental conditions (type of radiation, radiation doses, nanoparticle concentrations and incubation times, etc.). Based on this situation, the aim of this article was to show by improved techniques of light microscopy whether cell radiosensitization by metal nanoparticles is correlated with an escalation of DNA damage expressed by the number of repair foci and/or affection of DNA damage repair capacity expressed by the maintenance of repair foci.

In the present work, we analyzed effects on DNA DSB induction and repair exerted by ultrafine nanoparticles composed of three different materials—2.6 nm Pt-NPs, 2.4 nm Au-NPs, 10 nm Au-NPs and 2.0 Gd-NPs—with an emphasis on result precision. All experiments were performed under the comparable conditions and in three different cancer cell lines (U87, HeLa and SkBr3) exposed to different doses (up to 4 Gy) of γ-rays or X-rays to reduce a potential bias of specific experimental conditions. U87 cells show very high radioresistance, which makes them an ideal candidate for a potential nanoparticle-enhanced radiotherapy. HeLa cells, on the other hand, are more radiosensitive and SkBr3 cells lie between HeLa cells and U87 cells. To monitor DSB induction and repair in a more comprehensive way, we quantified DSB numbers per nucleus at several time points PI, up to 24 h PI. This allowed us to compare the samples, not only the initial extent of DSB induction but also the kinetics and final efficiency of DSB repair. In addition, we were able to eliminate false differences between samples that could possibly appear if only one or two periods of time were followed. We used currently the most sensitive and accurate approach for DSB quantification—ICM of γH2AX and 53 BP1 repair foci in spatially (3D) fixed cells. γH2AX foci and 53 BP1 foci were evaluated in parallel and only co-localized foci of both DSB markers were considered as DSBs to further improve the quality and relevance of results. For the same reason, and to study small and larger γH2AX/53BP1 foci separately, we scored the foci both manually and automatically, by using novel software that is based on machine learning and has been purposefully developed and calibrated in our laboratory for the present analyses.

Taken all the ICM results together, we cannot confirm a significant effect of any nanoparticle studied (Pt, Au, and Gd) on the introduced number or repair efficiency of DSBs in irradiated cells. This conclusion holds true for both cell types (U87, and HeLa), radiation doses (4 Gy, and 2 Gy), and means of analysis used in the present study. Moreover, nano-scale SMLM studies on SkBr3 breast cancer cells with incorporated 10 nm Au-NPs also indicated that the spatial organization of γH2AX labelling tags seems not to be influenced by the presence of NPs in cells irradiated with different doses (0.5–4 Gy) of X-rays. The exception from this conclusion could be a slight delay of DSB repair in cells treated with 2.6 nm Pt and 2.4 nm Au nanoparticles in later (>4 h PI) time points PI. This difference in repair kinetics might be related to a larger size/higher intensity of γH2AX foci in nanoparticle-treated cells as observed for 2.6 nm Pt-NPs by ICM and for 10 nm Au-NPs by SMLM. However, it should be noted that the reported differences between nanoparticle-treated and untreated irradiated cells were only minor and non-systematic. We can therefore reasonably conclude that while nanoparticle-mediated radiosensitization has often been related to escalated DNA damage, the results presented here for ultrafine Pt and Au nanoparticles and also our earlier data for Gd nanoparticles [21] do not support this idea as a general mechanism responsible for the radiosensitizing phenomenon. Only for 10 nm Au-NPs and doses of 2 Gy or higher, some increase of γH2AX focus number was observed by SMLM, especially after nanoparticle modification for specific targeting to the ER [23], whereby this has only been observed for one cell line.

Our data suggest that there are at least some nanoparticles that increase cell killing upon irradiation [21,42] while they have none or a negligible effect on nuclear DNA break regions highlighted by H2AX phosphorylation sites. This confirms our intuition on the action mode of the radiosensitizing nanoparticles we developed. In other experiments (unpublished), we observed a great increase in the

life span of animals bearing tumor (9L cell gliosarcoma in brain) or the inhibition of tumor growth (A375sc melanoma in flank) when the animals were treated by radiotherapy after intravenous (9L gliosarcoma) or intratumoral (melanoma) injection whereas the majority of the nanoparticles in the tumor were suspected to be outside the cells. Moreover, we also observed in preliminary experiments that the number of γH2AX is almost the same when irradiation is performed in presence or in absence of the radiosensitizing nanoparticles (unpublished results). Hence, these nanoparticles seem to sensitize cells to radiation through cytoplasmic effects that are independent of DNA damage and/or repair. While our findings do not exclude the possibility that some types of nanoparticles support radiation cell killing through the "classic" DNA damage-based mechanism, they open the door to exiting research of new mechanisms that could be dominant under some circumstances, as for instance chromatin topology-related effects and re-arrangements of compaction forms. Furthermore, accumulation of nanoparticles in endosomes and lysosomes as revealed in our earlier reports [21,55] could result in damage of these structures with important consequences. While lysosomes were originally thought only as cellular dustbins, recent studies involve lysosomes in important cell signaling pathways, eventually initiating apoptosis (see [32] and citations therein). In addition, even simple disruption of a larger amount of lysosomes due to their membrane damage by locally amplified radiation effects, mediated by intra-lysosomal nanoparticle accumulations, may result in massive leakage of lytic enzymes from these "suicide bags" [65,66] and extensive cytoplasmic damage. This can also initiate cell death. Indeed, the destabilization of lysosomes via lysosomal membrane permeabilization (LMP), leading to release of their aggressive content into the cytoplasm, is currently intensively studied as a potentially efficient way of therapeutic cell death triggering [56].

Cytoplasmically located nanoparticles may also influence organelles or structures which they do not co-localize with. For instance, increased production of ROS has been frequently reported in the literature as a main cause of nanoparticles' cytotoxicity. Therefore, ROS generated by nanoparticles in extensive amounts upon irradiation may damage organelles located in close proximity to nanoparticle location sites, for instance mitochondria. Among other cytoplasmic targets, mitochondria are especially attractive since they are critical for cell survival (energy metabolism) and represent the only extracellular structures having their own DNA. Therefore, nanoparticle-mediated fragmentation of mitochondrial DNA may represent an elegant modification of the "classic" DNA damage-based hypothesis on cell radiosensitization by nanoparticles, returning this idea into the game. It should also be noted that ROS are effective signaling molecules with a strong potential to directly influence biochemical cellular pathways.

The Endoplasmic Reticulum (ER) may represent another target for nanoparticle effects. While the efficient functioning of the ER is essential for most cellular activities and survival, it may be under some modifications also invaded by nanoparticles [23]. Moreover, ER plays an important role in the response to oxidative stress-induced damage and is quite sensitive to ROS [67]. Hence, irradiated nanoparticles may exert cytotoxic effects on cells by modulating ER stress [67]. For instance, Ag-NPs resulted in cytotoxicity and cell death by apoptotic, which was associated with (secondary) DNA fragmentation [67]. This observation not only explains how nanoparticles may initiate cell death through disturbing functions of ER, but also stresses the importance of time when interpreting the nanoparticle-mediated DNA effects. In this light, it is possible that in some studies the nanoparticle-mediated effects on DNA can rather reflect this secondary apoptotic DNA fragmentation than primary enhancement of DSB induction by radiation. The mechanism, how ER stress can lead to apoptosis, has been described by [68]. A disruption of ER function leads to accumulation and aggregation of unfolded proteins accompanied with stress signaling. The stress signals are detected by transmembrane receptors, which in turn initiate the unfolded protein response (UPR) trying to restore normal ER functions. However, if the stress persists too long, apoptotic cell death ensues [68].

Altogether, we show that the radiosensitizing effect of at least some metal nanoparticles may rely on cytoplasmic processes rather than DNA damaging events. Based on the available literature, we also outline the way of how damage of the most relevant cytoplasmic structures may initiate cell

death. Though we did not observe different responses to nanoparticles or irradiation in presence of nanoparticles for the two studied cell types (U87, and HeLa), we emphasize the necessity to analyze in detail each particular combination of nanoparticles and the cell type planned to be therapeutically targeted. This imperative follows from extensive controversies that are still present in the literature on the nanoparticle-mediated irradiation effects. For instance, Au-NPs induced apoptosis in MCF-7 and N87 cancer cell lines by disrupting lysosomes and mitochondria, but this effect did not appear in normal Chinese hamster ovary (CHO) and 293T cell lines. This observation further supports our conclusion that nanoparticle-mediated cell killing enhancement may be located in the cytoplasm, but more importantly gives a perspective of selective nanoparticle toxicity for tumor cells [64,69]. Interestingly, from the opposite point of view, some radio-protective chemicals (amifostine) protect normal cells from radiation effects but delay DSB repair in tumor cells [20].

The final question remains whether it is in principle a good or bad massage finding that nanoparticles damage the cells without affecting DNA. On the one hand, it could be beneficial since nanoparticles located outside the tumor will not increase the risk of genome damage and secondary malignancies induction in normal tissues surrounding the tumor. On the other hand, the radiosensitizing mechanism operating through DNA damage could be more efficient. A solution of this dilemma could be based on selective targeting of nanoparticles to specific genome sequences, like oncogenes, using appropriately designed oligo-nucleotides as being available for radio-emitters [70]. With techniques of COMBO-FISH [71,72] and PNA probe combinations [73], NPs may be transferred to cell nuclei and specifically addressed to given chromatin targets. This could be achieved by adding a nuclear localization signal (NLS) peptide motif and a specific PNA oligonucleotide probe to the surface of nanoparticles [74]. Using such sophisticated approaches of specific targeting of genome aberrations like multiple gene copies would open new aspects in tumor therapy.

4. Materials and Methods

4.1. Cells and Cell Culturing

Three cancer cell types were studied in the present study: highly radioresistant U87 glioblastoma cancer cells, radioresistant SkBr3 breast cancer cells and relatively less radioresistant HeLa cervix cancer cells. U87 and HeLa cells were obtained from ATCC (American Type Culture Collection, Manassas, VA, USA). SkBr3 was commercially available and used for several SMLM studies in our laboratory. U87 and HeLa cells were grown in Dulbecco's modified essential medium (Thermo Fisher Scientific, Waltham, MA, USA) supplemented with 10% heat-inactivated fetal calf serum (Thermo Fisher Scientific, Waltham, MA, USA), 100 U/mL penicillin (PAA), 100 µg/mL streptomycin (PAA), and 1% NEAA (Thermo Fisher Scientific, Waltham, MA, USA). Cell cultures were kept in T-25 cell flasks at 37 °C in a humidified atmosphere with 5% CO_2.

For the experiments with SMLM, SkBr3 cells were prepared as described in detail elsewhere [72]. SkBr3 cells were grown in McCoy's 5A cell medium, containing 10% fetal bovine serum (FBS) and 1% penicillin/streptomycin. Cells were cultivated and maintained at 37 °C in a humidified atmosphere at 95% air/5% CO_2. Then, the cells were trypsinized and transferred to coverslips, put into six-well plates and further cultivated (about three passages, i.e., about 38 h) until 80% confluence.

4.2. Nanoparticles and Incubation of Cells with Nanoparticles

Platinum nanoparticles (Pt-PEG-17, referred to as Pt-NPs) were prepared as explained in the recently submitted French patent (FR 1900008). Briefly: Pt-NPs were synthetized by γ-ray water radiolysis of Pt containing salt and embedded with polyethylene glycol (PEG) to increase their biocompatibility. Pt-NPs were mainly spherical with an average platinum core diameter of 2.6 nm. Preliminary results were obtained also for gold nanoparticles (Au-NPs) which are composed of a Au core of 2.4 nm encapsulated by the dithiolated polyaminocarboxylate (DTDTPA) shell. For SkBr3

Au-NPs incorporation, 8 µL of 10 nm-sized gold particles (Aurion, Wageningen, The Netherlands) were added to the medium in each well 16 h prior to irradiation in order to obtain a maximum uptake in the cell cytoplasm via diffusion (Figure 6) [53,75]. In other experiments 2.6 nm Pt-NPs or 2.4 nm Au-NPs were added to the medium 6 h before irradiation at 0.5 mM concentration.

4.3. Cell Irradiation

Cells were irradiated in 6-well culture plates containing a culture medium and 2.0×10^4–2.0×10^5 cells per well. Consecutively, cells were exposed to 2 or 4 Gy of γ-rays (1 Gy/min), delivered by a ^{137}Cs irradiator at room temperature (RT). During irradiation, the samples were kept in thermo-isolating boxes to prevent sample infection and temperature changes, and then immediately returned to the incubator (37 °C, 5% CO_2) until taken for the experiment. For SMLM experiments, 10 nm Au-NPs were incubated 16 h before irradiation. Then, the cells were simultaneously exposed with and without Au-NPs using a 6 MeV Linac radiation source (Artiste, Siemens, Erlangen, Germany). The exposure doses of 0.5, 1, 2 and 4 Gy were obtained by changing the irradiation time at the same dose rate.

4.4. Immunodetection of γH2AX/53BP1 Foci and Double Strand Break Quantification

DNA DSBs were quantified in spatially (three-dimensionally = 3D) fixed cells by the means of high-resolution ICM detection of co-localized γH2AX and 53BP1 repair foci as described earlier [16,20]. Briefly, cells were fixed with 4% paraformaldehyde (10 min, at room temperature RT) prior to irradiation (0 min PI, non-irradiated controls) and in several time points PI covering a long (48 h) PI period (5 min, 30 min, 1 h, 2 h, 4 h, 8 h, 24 h and 48 h PI). Cells were permeabilized in 0.2% Triton X-100/PBS (15 min, RT) and immunoassayed with mouse antiphospho-H2AX (serine 139) (Merck, Darmstadt, Germany, cat. no.: 05-636) and rabbit anti-53BP1 (Cell Signaling Technology, Danvers, MA, USA, cat. no.: 4937) primary antibodies to simultaneously detect the γH2AX and 53BP1. Antiphospho-H2AX antibody was visualized with the secondary FITC-conjugated donkey anti-mouse antibody and anti-53BP1 antibody with Cy3-conjugated donkey anti-rabbit antibody (both Jackson Laboratory, West Grove, PA, USA, cat. no.: 715-095-150 and 711-165-152). Chromatin was counterstained with 1 µM TO-PRO-3 (Molecular Probes, Eugene, OR, USA) prepared in 2× saline sodium citrate (SSC). After brief washing in 2× SSC, Vectashield medium (Vector Laboratories, Burlington, Ontario, Canada) was used for sample mounting.

4.5. Fixation and Immunostaining of γH2AX for Single Molecule Localization Microscopy

45 min after irradiation, the cells were fixed in order to obtain an early response of the biological system to damage. The cells were washed in 1× Phosphate-Buffered Saline (PBS) with $MgCl_2$ (0.901 mM)/$CaCl_2$ (0.493 mM) and fixed in 3.7% formaldehyde (in 1× PBS + Mg/Ca; freshly prepared from paraformaldehyde) for 20 min at RT. After washing twice with 1× PBS + Mg/Ca, the cells were stored in 3.7% formaldehyde (in 1× PBS + Mg/Ca) at 4 °C. After 4-weeks storage, the formaldehyde was replaced by 1× PBS (+ 0.1% sodium azide). After removing the sodium azide from the coverslips, the cell membranes were permeabilized by 0.2% Triton-X100 three times for 5 min. After washing three times in 1× PBS (+ Mg/Ca), the cells were blocked in 2% bovine serum albumin (BSA) for half an hour and incubated in 100 µL of the primary antibody solution (mouse anti-phospho-histone H2A.X (Ser139) antibody; Merck Chemicals, Darmstadt, Germany; dilution: 1:500) at 37 °C for 18 h in a humidified chamber. Thereafter the coverslips with the cells were washed three times for 5 min with 1× PBS (+ Mg/Ca) to remove the remaining, unbound primary antibodies. Afterwards the secondary AlexaFluor 647 goat anti-mouse antibody was incubated in a humidified chamber at 37 °C for 30 min. Then, the cells were fixed in 2% formaldehyde (in 1× PBS (+ Mg/Ca) at 37 °C for 10 min. Finally, the cells were counterstained with 4′19,6-diamidin-2-phenylindol (DAPI; Sigma Aldrich, now Merck, Darmstadt, Germany) for 5 min in darkness and were, after washing twice with 1× PBS (+ Mg/Ca) for 5 min each, embedded in 20 µL ProLong Gold embedding medium (ThermoFisher Scientific, Waltham,

MA, USA, ProLong Gold Antifade Mountant, P36930). The specimen was sealed and stored at 4 °C in complete darkness until SMLM application.

4.6. Confocal Microscopy

An automated high-resolution confocal fluorescence microscopic system Leica DM RXA [76–78], equipped with a CSU10a Nipkow disc (Yokogawa, Tokyo, Japan), an oil immersion Plan Fluotar objective (100×/NA1.3), a CoolSnap HQ CCD camera (Photometrix, Tucson, AZ, USA), and an Ar/Kr laser (Innova 70C Spectrum, Coherent, Santa Clara, CA, USA), was used for image acquisition [79,80]. About 40 individual confocal slices with 0.3 µm z-step increments across the nuclei were captured for each cell. Obtained images were analyzed using Acquiarium software [80] which enabled the three-dimensional reconstruction of images and inspection of individual γH2AX and 53BP1 foci in 3D space. Co-localized γH2AX/53BP1 foci were considered as DSBs to increase the precision of DSB detection, especially in the early-stage PI (with a higher background of signals) and also the probability that only unrepaired DSBs are still evaluated in later and very late periods of time PI.

4.7. Single Molecule Localization Microscopy

As described in detail elsewhere [61,81], the localization microscope used was equipped with four lasers to excite different fluorophores. The wavelength and the intensity of illumination were chosen by an acousto–optical tunable filter (AOTF). For our experiments, the 642 nm laser with 140 mW output power was used to stimulate the dye molecules to blink. A 100x/NA 1.46 oil immersion objective was used. The fluorescence of the specimen was separated from the illumination light by two quadband interference filters and was recorded by an EMCCD camera (Andor iXon Ultra 897, Belfast, UK). The EMCCD camera was operated at a gain of 100 and a series of 2000 up to 6000 image frames was recorded for each cell nucleus. Prior to the SMLM measurement, a widefield image was taken in the DAPI channel and the γH2AX channel with 10% laser intensity. Thereafter, the γH2AX image stack was recorded at 70% illumination intensity. Cells were chosen to have consistent size and form, a distinctive edge, a good staining signal-to-background ratio and a certain minimal distance to the next cell. The acquired data stacks were evaluated as described in detail in [61]. γH2AX labelling molecules were counted and distances between each point were determined.

Data displayed in box graphs (Figure 9) show the frequency distributions of distances of γH2AX-labelling molecules. The boxes include 50% of the values (25th to 75th percentile) centered on the median (the horizontal line through the box). The mean values are represented by the squares within the boxes. The vertical lines begin at the 5th percentile and end at the 95th percentile.

4.8. Data Analysis and Statistical Evaluation after Confocal Microscopy

The SigmaPlot 14.0 (Systat Software Inc., San Jose, CA 95131 USA) and Origin 2018b (OriginLab Corporation, Northampton, MA 01060, USA) were used for data analysis and processing. The Mann–Whitney rank sum test was employed to compare γH2AX/53BP1 focus (DSB) numbers in untreated and nanoparticle-treated cells at all the particular periods of time PI. The results were considered as statistically significant at $p < 0.05$. The foci numbers were quantified both manually and automatically. In manual analysis, around 100 nuclei in each single experiment were blind-inspected (no information about the sample treatment) by eye by an experienced evaluator. For computational analysis, between 100 and 250 nuclei were scored. Because there is not a suitable tool fulfilling our demands on automatic γH2AX/53BP1 foci counting with our specific data, a custom program for fast and accurate foci counting, calibrated to our data, has been developed. The program works in a semi-automatic manner, where it allows for a visual inspection with the possibility to make quick manual adjustments and corrections, if necessary. The algorithm is composed of 3 steps—nucleus segmentation, foci segmentation and final foci classification, in order to eliminate false detections. Convolution Neural Network (with SegNet topology) was trained for robust nuclei segmentation, followed by splitting of touching nuclei with watershed transform applied on the distance transform

of the segmented binary image. Inside a bounding box of each nucleus, the foci are segmented with a maximally stable extremal region detector, which is fast and invariant to image intensity values. The detector is set to high recall in order to obtain all possible foci for the classifier. Classification of true foci is done with Support Vector Machine classifiers on some extracted features (e.g., foci mean intensity and foci size). The program allows user to adjust the classifier bias value (to set classifier sensitivity), because the properties of foci are very heterogeneous between different samples and measurements. Besides the count of foci, it also allows exporting some other features for following analysis (cell size, foci sizes, foci intensities, etc.) (the full description of the software will be published separately). In Figures 3–5, the data are displayed as box graphs also showing the distributions of DSBs foci per nucleus. The boxes include 50% of the values (25th to 75th percentile) centered on the median (the horizontal line through the box). The mean values are represented by the squares within the boxes. The vertical lines begin at the 5th percentile and end at the 95th percentile.

5. Conclusions

In the present study, we demonstrate that ultrafine (2–10 nm) platinum and gold nanoparticles do not escalate DNA damage or compromise DSB repair in irradiated tumor cells of different types. This confirms our recent findings for 2.0 nm gadolinium nanoparticles [21]. However, 10 nm Au-NPs may potentially influence the character of DNA damage at the nanoscale, as it was discovered by using SMLM [61,72,81]. Some indications in this sense have been obtained also by ICM for 2 nm Pt-NPs. While these findings are difficult to be interpreted in terms of biological relevance, contradictions still persist in the literature on the enhancement of nuclear DNA damage in cells irradiated in presence of metal nanoparticles. At the current stage of knowledge, it is reasonable to conclude that different mechanisms, involving an enhancement of DNA damage on the one side and cytoplasmic effects on the other side, participate in radiosensitization exerted by metal nanoparticles. More mechanisms probably contribute to the final radiosensitizing effect, involvement of which depends on the nanoparticle characteristics (material, size, composition, and surface functionalization), cell type and experimental conditions. Therefore, many questions on nanoparticle-mediated radiosensitization remain open, emphasizing the importance of more systematic future research. Methodologically, we demonstrate current possibilities and usefulness of the newly developed super-resolution microscopy technique (SMLM) that together with appropriate nano-probing technologies has a potential to shift our studies on DNA damage and repair to nanoscale dimensions. Mutual comparison of micro- and nano-scale results may provide a clue on many important processes taking part in cells and their molecular mechanisms.

Author Contributions: Research conceptualization, M.F., M.H., G.H., L.S. and S.L; methodology development, M.F., M.H., S.L., L.S. and S.R.; experiment performance, E.P. (Eva Pagáčová), L.S., O.K., I.F., F.S.-K., J.-H.L. and S.R.; software development, T.V.; validation, D.D., E.P. (Eva Pagáčová), J.-H.L., G.H., M.H. and M.F.; formal analysis, D.D, E.P. (Eva Pagáčová), I.F., M.H., M.F.; investigation, E.P. (Eva Pagáčová), S.L., M.H. and M.F.; resources, F.B., F.W., M.H. and M.F.; data curation, M.F., D.D., E.P. (Eva Pagáčová), T.V.; writing of the original draft preparation, F.S.-K., M.F. and M.H.; writing of review and editing, G.H., S.L., M.F. and M.H.; visualization, E.P. (Eva Pagáčová), F.S.-K., D.D., I.F., O.K.; supervision, E.P. (Erika Porcel), S.L., M.H. and M.F.; project administration, M.F. and M.H.; funding acquisition, M.H. and M.F.

Funding: The work was supported by the Ministry of Health of the Czech Republic (AZV grant no. 16-29835A), the Czech Science Foundation (project 16-12454S), the Heidelberg University Mobility Grant for International Research Cooperation within the excellence initiative II of the Deutsche Forschungsgemeinschaft (DFG) to M.H., and from the grants from the Czech Republic to the Joint Institute for Nuclear Research, Dubna (Projects of the Czech Plenipotentiary and the 3 + 3 Projects). The financial support by Deutsche Forschungsgemeinschaft and Ruprecht-Karls-Universität Heidelberg within the funding program Open Access Publishing is gratefully acknowledged. The research leading to these results has also received funding from the People Programme (Marie Curie Actions) of the European Union's Seventh Framework Programme (FP7/2007–2013) under REA Grant Agreement No [624370].

Acknowledgments: The authors thank Emanuel Maus (Kirchhoff-Institute for Physics) for providing an SMLM image. The authors acknowledge Daniela Salado (Institute des Sciences Moléculaires d'Orsay, Université Paris Sud 11, Orsay Cedex, France) and Hynd Remita (Laboratoire de Chimie Physique, Orsay, France) for synthesizing platinum and 2.4 nm gold nanoparticles. Furthermore, we thank Jin-Hau Ewwer, Institute of Research Rating and Enhancement (IRRE), Altenburschla, Germany, and Paul I. M. Prinz Zippl, University of Vienna, Austria, for always finding the right way of haziness in constructive discussions.

Conflicts of Interest: The authors declare no conflicts of interest. The funders had no role in the design of the study; in the collection, analyses, or interpretation of data; in the writing of the manuscript, and in the decision to publish the results.

Abbreviations

DSB	double strand break
SMLM	single molecule localization microscopy
ICM	immunofluorescence confocal microscopy
Pt-NPs	platinum nanoparticles
Au-NPs	gold nanoparticles
PI	post-irradiation
EPR	enhanced permeability and retention

References

1. Atun, R.; Jaffray, D.A.; Barton, M.B.; Bray, F.; Baumann, M.; Vikram, B.; Hanna, T.P.; Knaul, F.M.; Lievens, Y.; Lui, T.Y.M.; et al. Expanding global access to radiotherapy. *Lancet Oncol.* **2015**, *16*, 1153–1186. [CrossRef]
2. Wenz, F.; Tiefenbacher, U.; Willeke, F.; Weber, K.-J. Auf der Suche nach der *Therapeutischen breite* in der Radioonkologie. *Oncol. Res. Treat.* **2001**, *24*, 51–55. [CrossRef] [PubMed]
3. Löffler, H.; Bochtler, T.; Fritz, B.; Tews, B.; Ho, A.D.; Lukas, J.; Bartek, J.; Krämer, A. DNA Damage-Induced Accumulation of Centrosomal Chk1 Contributes to its Checkpoint Function. *Cell Cycle* **2007**, *6*, 2541–2548. [CrossRef] [PubMed]
4. Tomita, K.; Kuwahara, Y.; Takashi, Y.; Igarashi, K.; Nagasawa, T.; Nabika, H.; Kurimasa, A.; Fukumoto, M.; Nishitani, Y.; Sato, T. Clinically relevant radioresistant cells exhibit resistance to H_2O_2 by decreasing internal H_2O_2 and lipid peroxidation. *Tumour Biol.* **2018**, *40*. [CrossRef]
5. Lam, W.W.; Oakden, W.; Murray, L.; Klein, J.; Iorio, C.; Screaton, R.A.; Koletar, M.M.; Chu, W.; Liu, S.K.; Stanisz, G.J. Differentiation of Normal and Radioresistant Prostate Cancer Xenografts Using Magnetization Transfer-Prepared MRI. *Sci. Rep.* **2018**, *8*, 10447. [CrossRef]
6. Gu, H.; Huang, T.; Shen, Y.; Liu, Y.; Zhou, F.; Jin, Y.; Sattar, H.; Wei, Y. Reactive Oxygen Species-Mediated Tumor Microenvironment Transformation: The Mechanism of Radioresistant Gastric Cancer. *Oxid. Med. Cell. Longev.* **2018**, *2018*, 5801209. [CrossRef]
7. Zhou, H.; Miki, R.; Eeva, M.; Fike, F.M.; Seligson, D.; Yang, L.; Yoshimura, A.; Teitell, M.A.; Jamieson, C.A.M.; Cacalano, N.A. Reciprocal Regulation of SOCS1 and SOCS3 Enhances Resistance to Ionizing Radiation in Glioblastoma Multiforme. *Clin. Cancer Res.* **2007**, *13*, 2344–2353. [CrossRef]
8. Engel, L.W.; Young, N.A. Human breast carcinoma cells in continuous culture: A review. *Cancer Res.* **1978**, *38*, 4327–4339.
9. Lacroix, M.; Leclercq, G. Relevance of breast cancer cell lines as models for breast tumours: An update. *Breast Cancer Res. Treat.* **2004**, *83*, 249–289. [CrossRef]
10. Durante, M.; Orecchia, R.; Loeffler, J.S. Charged-particle therapy in cancer: Clinical uses and future perspectives. *Nat. Rev. Clin. Oncol.* **2017**, *14*, 483–495. [CrossRef]
11. González, W.; Prezado, Y. Spatial fractionation of the dose in heavy ions therapy: An optimization study. *Med. Phys.* **2018**, *45*, 2620–2627. [CrossRef] [PubMed]
12. Jánváry, L.Z.; Ferenczi, Ö.; Takácsi-Nagy, Z.; Bajcsay, A.; Polgár, C. Application of CyberKnife stereotactic radiosurgery in the treatment of head and neck cancer. *Magy. Onkol.* **2018**, *62*, 180–185. [PubMed]
13. Zhang, H.; Wan, C.; Huang, J.; Yang, C.; Qin, Y.; Lu, Y.; Ma, J.; Wu, B.; Xu, S.; Wu, G.; et al. In Vitro Radiobiological Advantages of Hypofractionation Compared with Conventional Fractionation: Early-Passage NSCLC Cells are Less Aggressive after Hypofractionation. *Radiat. Res.* **2018**. [CrossRef] [PubMed]

14. Sammer, M.; Greubel, C.; Girst, S.; Dollinger, G. Optimization of beam arrangements in proton minibeam radiotherapy by cell survival simulations. *Med. Phys.* **2017**, *44*, 6096–6104. [CrossRef] [PubMed]
15. Prezado, Y.; Renier, M.; Bravin, A. A new method of creating minibeam patterns for synchrotron radiation therapy: A feasibility study. *J. Synchrotron Radiat.* **2009**, *16*, 582–586. [CrossRef] [PubMed]
16. Jezkova, L.; Zadneprianetc, M.; Kulikova, E.; Smirnova, E.; Bulanova, T.; Depes, D.; Falkova, I.; Boreyko, A.; Krasavin, E.; Davidkova, M.; et al. Particles with similar LET values generate DNA breaks of different complexity and reparability: A high-resolution microscopy analysis of γH2AX/53BP1 foci. *Nanoscale* **2018**, *10*, 1162–1179. [CrossRef]
17. Girst, S.; Greubel, C.; Reindl, J.; Siebenwirth, C.; Zlobinskaya, O.; Walsh, D.W.M.; Ilicic, K.; Aichler, M.; Walch, A.; Wilkens, J.J.; et al. Proton Minibeam Radiation Therapy Reduces Side Effects in an In Vivo Mouse Ear Model. *Int. J. Radiat. Oncol.* **2016**, *95*, 234–241. [CrossRef]
18. Hofer, M.; Hoferová, Z.; Depeš, D.; Falk, M. Combining Pharmacological Countermeasures to Attenuate the Acute Radiation Syndrome-A Concise Review. *Molecules* **2017**, *22*, 834. [CrossRef]
19. Hofer, M.; Hoferová, Z.; Falk, M. Pharmacological Modulation of Radiation Damage. Does It Exist a Chance for Other Substances than Hematopoietic Growth Factors and Cytokines? *Int. J. Mol. Sci.* **2017**, *18*, 1385. [CrossRef]
20. Hofer, M.; Falk, M.; Komůrková, D.; Falková, I.; Bačíková, A.; Klejdus, B.; Pagáčová, E.; Štefančíková, L.; Weiterová, L.; Angelis, K.J.; et al. Two New Faces of Amifostine: Protector from DNA Damage in Normal Cells and Inhibitor of DNA Repair in Cancer Cells. *J. Med. Chem.* **2016**, *59*, 3003–3017. [CrossRef]
21. Štefančíková, L.; Lacombe, S.; Salado, D.; Porcel, E.; Pagáčová, E.; Tillement, O.; Lux, F.; Depeš, D.; Kozubek, S.; Falk, M. Effect of gadolinium-based nanoparticles on nuclear DNA damage and repair in glioblastoma tumor cells. *J. Nanobiotechnol.* **2016**, *14*, 63. [CrossRef] [PubMed]
22. Ngwa, W.; Boateng, F.; Kumar, R.; Irvine, D.J.; Formenti, S.; Ngoma, T.; Herskind, C.; Veldwijk, M.R.; Hildenbrand, G.L.; Hausmann, M.; et al. Smart Radiation Therapy Biomaterials. *Int. J. Radiat. Oncol. Biol. Phys.* **2017**, *97*, 624–637. [CrossRef] [PubMed]
23. Hildenbrand, G.; Metzler, P.; Pilarczyk, G.; Bobu, V.; Kriz, W.; Hosser, H.; Fleckenstein, J.; Krufczik, M.; Bestvater, F.; Wenz, F.; et al. Dose enhancement effects of gold nanoparticles specifically targeting RNA in breast cancer cells. *PLoS ONE* **2018**, *13*, e0190183. [CrossRef] [PubMed]
24. Ngwa, W.; Kumar, R.; Sridhar, S.; Korideck, H.; Zygmanski, P.; Cormack, R.A.; Berbeco, R.; Makrigiorgos, G.M. Targeted radiotherapy with gold nanoparticles: Current status and future perspectives. *Nanomedicine* **2014**, *9*, 1063–1082. [CrossRef] [PubMed]
25. Lux, F.; Tran, V.L.; Thomas, E.; Dufort, S.; Rossetti, F.; Martini, M.; Truillet, C.; Doussineau, T.; Bort, G.; Denat, F.; et al. AGuIX® from bench to bedside-Transfer of an ultrasmall theranostic gadolinium-based nanoparticle to clinical medicine. *Br. J. Radiol.* **2018**. [CrossRef]
26. Kuncic, Z.; Lacombe, S. Nanoparticle radio-enhancement: Principles, progress and application to cancer treatment. *Phys. Med. Biol.* **2018**, *63*, 02TR01. [CrossRef] [PubMed]
27. Li, S.; Porcel, E.; Remita, H.; Marco, S.; Réfrégiers, M.; Dutertre, M.; Confalonieri, F.; Lacombe, S. Platinum nanoparticles: An exquisite tool to overcome radioresistance. *Cancer Nanotechnol.* **2017**, *8*, 4. [CrossRef] [PubMed]
28. Sancey, L.; Lux, F.; Kotb, S.; Roux, S.; Dufort, S.; Bianchi, A.; Crémillieux, Y.; Fries, P.; Coll, J.-L.; Rodriguez-Lafrasse, C.; et al. The use of theranostic gadolinium-based nanoprobes to improve radiotherapy efficacy. *Br. J. Radiol.* **2014**, *87*. [CrossRef] [PubMed]
29. Nikjoo, H.; Uehara, S.; Emfietzoglou, D.; Brahme, A. Heavy charged particles in radiation biology and biophysics. *New J. Phys.* **2008**, *10*, 075006. [CrossRef]
30. Hossain, M.; Su, M. Nanoparticle location and material dependent dose enhancement in X-ray radiation therapy. *J. Phys. Chem. C Nanomater. Interfaces* **2012**, *116*, 23047–23052. [CrossRef]
31. Zygmanski, P.; Liu, B.; Tsiamas, P.; Cifter, F.; Petersheim, M.; Hesser, J.; Sajo, E. Dependence of Monte Carlo microdosimetric computations on the simulation geometry of gold nanoparticles. *Phys. Med. Biol.* **2013**, *58*, 7961–7977. [CrossRef] [PubMed]
32. Falk, M.; Hausmann, M.; Lukášová, E.; Biswas, A.; Hildenbrand, G.; Davídková, M.; Krasavin, E.; Kleibl, Z.; Falková, I.; Ježková, L.; et al. Determining Omics spatiotemporal dimensions using exciting new nanoscopy techniques to assess complex cell responses to DNA damage: Part A—Radiomics. *Crit. Rev. Eukaryot. Gene Expr.* **2014**, *24*, 205–223. [CrossRef] [PubMed]

33. Falk, M.; Hausmann, M.; Lukášová, E.; Biswas, A.; Hildenbrand, G.; Davídková, M.; Krasavin, E.; Kleibl, Z.; Falková, I.; Ježková, L.; et al. Determining Omics spatiotemporal dimensions using exciting new nanoscopy techniques to assess complex cell responses to DNA damage: Part B—Structuromics. *Crit. Rev. Eukaryot. Gene Expr.* **2014**, *24*, 225–247. [CrossRef] [PubMed]
34. Rittich, B.; Spanová, A.; Falk, M.; Benes, M.J.; Hrubý, M. Cleavage of double stranded plasmid DNA by lanthanide complexes. *J. Chromatogr. B Analyt. Technol. Biomed. Life Sci.* **2004**, *800*, 169–173. [CrossRef] [PubMed]
35. Kratochvílová, I.; Golan, M.; Pomeisl, K.; Richter, J.; Sedláková, S.; Šebera, J.; Mičová, J.; Falk, M.; Falková, I.; Řeha, D.; et al. Theoretical and experimental study of the antifreeze protein AFP752, trehalose and dimethyl sulfoxide cryoprotection mechanism: Correlation with cryopreserved cell viability. *RSC Adv.* **2017**, *7*, 352–360. [CrossRef] [PubMed]
36. Freneau, A.; Dos Santos, M.; Voisin, P.; Tang, N.; Bueno Vizcarra, M.; Villagrasa, C.; Roy, L.; Vaurijoux, A.; Gruel, G. Relation between DNA double-strand breaks and energy spectra of secondary electrons produced by different X-ray energies. *Int. J. Radiat. Biol.* **2018**, 1–10. [CrossRef] [PubMed]
37. Falk, M.; Lukasova, E.; Kozubek, S. Higher-order chromatin structure in DSB induction, repair and misrepair. *Mutat. Res.* **2010**, *704*, 88–100. [CrossRef]
38. Hausmann, M.; Ilić, N.; Pilarczyk, G.; Lee, J.-H.; Logeswaran, A.; Borroni, A.; Krufczik, M.; Theda, F.; Waltrich, N.; Bestvater, F.; et al. Challenges for Super-Resolution Localization Microscopy and Biomolecular Fluorescent Nano-Probing in Cancer Research. *Int. J. Mol. Sci.* **2017**, *18*, 2066. [CrossRef]
39. Schipler, A.; Iliakis, G. DNA double-strand-break complexity levels and their possible contributions to the probability for error-prone processing and repair pathway choice. *Nucleic Acids Res.* **2013**, *41*, 7589–7605. [CrossRef]
40. Mladenov, E.; Magin, S.; Soni, A.; Iliakis, G. DNA double-strand-break repair in higher eukaryotes and its role in genomic instability and cancer: Cell cycle and proliferation-dependent regulation. *Semin. Cancer Biol.* **2016**, *37–38*, 51–64. [CrossRef]
41. Mladenov, E.; Magin, S.; Soni, A.; Iliakis, G. DNA double-strand break repair as determinant of cellular radiosensitivity to killing and target in radiation therapy. *Front. Oncol.* **2013**, *3*, 113. [CrossRef] [PubMed]
42. Burger, N.; Biswas, A.; Barzan, D.; Kirchner, A.; Hosser, H.; Hausmann, M.; Hildenbrand, G.; Herskind, C.; Wenz, F.; Veldwijk, M.R. A method for the efficient cellular uptake and retention of small modified gold nanoparticles for the radiosensitization of cells. *Nanomed. Nanotechnol. Biol. Med.* **2014**, *10*, 1365–1373. [CrossRef] [PubMed]
43. Porcel, E.; Liehn, S.; Remita, H.; Usami, N.; Kobayashi, K.; Furusawa, Y.; Le Sech, C.; Lacombe, S. Platinum nanoparticles: A promising material for future cancer therapy? *Nanotechnology* **2010**, *21*, 85103. [CrossRef] [PubMed]
44. Maeda, H. Tumor-selective delivery of macromolecular drugs via the EPR effect: Background and future prospects. *Bioconjug. Chem.* **2010**, *21*, 797–802. [CrossRef]
45. Maeda, H.; Matsumura, Y. EPR effect based drug design and clinical outlook for enhanced cancer chemotherapy. *Adv. Drug Deliv. Rev.* **2011**, *63*, 129–130. [CrossRef]
46. Fang, J.; Nakamura, H.; Maeda, H. The EPR effect: Unique features of tumor blood vessels for drug delivery, factors involved, and limitations and augmentation of the effect. *Adv. Drug Deliv. Rev.* **2011**, *63*, 136–151. [CrossRef]
47. Prabhakar, U.; Maeda, H.; Jain, R.K.; Sevick-Muraca, E.M.; Zamboni, W.; Farokhzad, O.C.; Barry, S.T.; Gabizon, A.; Grodzinski, P.; Blakey, D.C. Challenges and key considerations of the enhanced permeability and retention effect for nanomedicine drug delivery in oncology. *Cancer Res.* **2013**, *73*, 2412–2417. [CrossRef] [PubMed]
48. Bertrand, N.; Wu, J.; Xu, X.; Kamaly, N.; Farokhzad, O.C. Cancer nanotechnology: The impact of passive and active targeting in the era of modern cancer biology. *Adv. Drug Deliv. Rev.* **2014**, *66*, 2–25. [CrossRef]
49. Chithrani, D.B. Nanoparticles for improved therapeutics and imaging in cancer therapy. *Recent Pat. Nanotechnol.* **2010**, *4*, 171–180. [CrossRef]
50. Chithrani, D.B.; Jelveh, S.; Jalali, F.; van Prooijen, M.; Allen, C.; Bristow, R.G.; Hill, R.P.; Jaffray, D.A. Gold nanoparticles as radiation sensitizers in cancer therapy. *Radiat. Res.* **2010**, *173*, 719–728. [CrossRef]
51. Hainfeld, J.F.; Smilowitz, H.M.; O'Connor, M.J.; Dilmanian, F.A.; Slatkin, D.N. Gold nanoparticle imaging and radiotherapy of brain tumors in mice. *Nanomedicine* **2013**, *8*, 1601–1609. [CrossRef]

52. He, H.; Xie, C.; Ren, J. Nonbleaching fluorescence of gold nanoparticles and its applications in cancer cell imaging. *Anal. Chem.* **2008**, *80*, 5951–5957. [CrossRef] [PubMed]
53. Moser, F.; Hildenbrand, G.; Müller, P.; Al Saroori, A.; Biswas, A.; Bach, M.; Wenz, F.; Cremer, C.; Burger, N.; Veldwijk, M.R.; et al. Cellular Uptake of Gold Nanoparticles and Their Behavior as Labels for Localization Microscopy. *Biophys. J.* **2016**, *110*, 947–953. [CrossRef]
54. Lacombe, S.; Porcel, E.; Scifoni, E. Particle therapy and nanomedicine: State of art and research perspectives. *Cancer Nanotechnol.* **2017**, *8*, 9. [CrossRef]
55. Stefančíková, L.; Porcel, E.; Eustache, P.; Li, S.; Salado, D.; Marco, S.; Guerquin-Kern, J.-L.; Réfrégiers, M.; Tillement, O.; Lux, F.; et al. Cell localisation of gadolinium-based nanoparticles and related radiosensitising efficacy in glioblastoma cells. *Cancer Nanotechnol.* **2014**, *5*, 6. [CrossRef] [PubMed]
56. Yameen, B.; Choi, W.I.; Vilos, C.; Swami, A.; Shi, J.; Farokhzad, O.C. Insight into nanoparticle cellular uptake and intracellular targeting. *J. Control. Release* **2014**, *190*, 485–499. [CrossRef] [PubMed]
57. Fernando, L.P.; Kandel, P.K.; Yu, J.; McNeill, J.; Ackroyd, P.C.; Christensen, K.A. Mechanism of cellular uptake of highly fluorescent conjugated polymer nanoparticles. *Biomacromolecules* **2010**, *11*, 2675–2682. [CrossRef] [PubMed]
58. Cartiera, M.S.; Johnson, K.M.; Rajendran, V.; Caplan, M.J.; Saltzman, W.M. The uptake and intracellular fate of PLGA nanoparticles in epithelial cells. *Biomaterials* **2009**, *30*, 2790–2798. [CrossRef]
59. Fröhlich, E. Cellular targets and mechanisms in the cytotoxic action of non-biodegradable engineered nanoparticles. *Curr. Drug Metab.* **2013**, *14*, 976–988. [CrossRef]
60. Lemmer, P.; Gunkel, M.; Baddeley, D.; Kaufmann, R.; Urich, A.; Weiland, Y.; Reymann, J.; Müller, P.; Hausmann, M.; Cremer, C. SPDM: Light microscopy with single-molecule resolution at the nanoscale. *Appl. Phys. B* **2008**, *93*, 1–12. [CrossRef]
61. Hausmann, M.; Wagner, E.; Lee, J.-H.; Schrock, G.; Schaufler, W.; Krufczik, M.; Papenfuß, F.; Port, M.; Bestvater, F.; Scherthan, H. Super-resolution localization microscopy of radiation-induced histone H2AX-phosphorylation in relation to H3K9-trimethylation in HeLa cells. *Nanoscale* **2018**, *10*, 4320–4331. [CrossRef] [PubMed]
62. Depes, D.; Lee, J.-H.; Bobkova, E.; Jezkova, L.; Falkova, I.; Bestvater, F.; Pagacova, E.; Kopecna, O.; Zadneprianetc, M.; Bacikova, A.; et al. Single-molecule localization microscopy as a promising tool for γH2AX/53BP1 foci exploration. *Eur. Phys. J. D* **2018**, *72*. [CrossRef]
63. Reindl, J.; Girst, S.; Walsh, D.W.M.; Greubel, C.; Schwarz, B.; Siebenwirth, C.; Drexler, G.A.; Friedl, A.A.; Dollinger, G. Chromatin organization revealed by nanostructure of irradiation induced γH2AX, 53BP1 and Rad51 foci. *Sci. Rep.* **2017**, *7*, 40616. [CrossRef] [PubMed]
64. Sun, H.; Jia, J.; Jiang, C.; Zhai, S. Gold Nanoparticle-Induced Cell Death and Potential Applications in Nanomedicine. *Int. J. Mol. Sci.* **2018**, *19*, 754. [CrossRef] [PubMed]
65. Duve, C. Lysosomes revisited. *Eur. J. Biochem.* **1983**, *137*, 391–397. [CrossRef] [PubMed]
66. Wattiaux, R.; Coninck, S.W.-D.; Jadot, M.; Hamer, I.; Bielande, V.; Beauloye, V. Lysosomes as Suicide Bags. In *Endocytosis*; Courtoy, P.J., Ed.; Springer: Berlin/Heidelberg, Germany, 1992; pp. 433–437, ISBN 978-3-642-84297-9.
67. Zhang, R.; Piao, M.J.; Kim, K.C.; Kim, A.D.; Choi, J.-Y.; Choi, J.; Hyun, J.W. Endoplasmic reticulum stress signaling is involved in silver nanoparticles-induced apoptosis. *Int. J. Biochem. Cell Biol.* **2012**, *44*, 224–232. [CrossRef] [PubMed]
68. Szegezdi, E.; Logue, S.E.; Gorman, A.M.; Samali, A. Mediators of endoplasmic reticulum stress-induced apoptosis. *EMBO Rep.* **2006**, *7*, 880–885. [CrossRef]
69. Zhang, F.; Zhu, X.; Gong, J.; Sun, Y.; Chen, D.; Wang, J.; Wang, Y.; Guo, M.; Li, W. Lysosome—Mitochondria-mediated apoptosis specifically evoked in cancer cells induced by gold nanorods. *Nanomedicine* **2016**, *11*, 1993–2006. [CrossRef]
70. Dahmen, V.; Kriehuber, R. Cytotoxic effects and specific gene expression alterations induced by I-125-labeled triplex-forming oligonucleotides. *Int. J. Radiat. Biol.* **2012**, *88*, 972–979. [CrossRef]
71. Hausmann, M.; Winkler, R.; Hildenbrand, G.; Finsterle, J.; Weisel, A.; Rapp, A.; Schmitt, E.; Janz, S.; Cremer, C. COMBO-FISH: Specific labeling of nondenatured chromatin targets by computer-selected DNA oligonucleotide probe combinations. *BioTechniques* **2003**, *35*, 564–577. [CrossRef]

72. Krufczik, M.; Sievers, A.; Hausmann, A.; Lee, J.-H.; Hildenbrand, G.; Schaufler, W.; Hausmann, M. Combining Low Temperature Fluorescence DNA-Hybridization, Immunostaining, and Super-Resolution Localization Microscopy for Nano-Structure Analysis of ALU Elements and Their Influence on Chromatin Structure. *Int. J. Mol. Sci.* **2017**, *18*, 1005. [CrossRef]
73. Müller, P.; Schmitt, E.; Jacob, A.; Hoheisel, J.; Kaufmann, R.; Cremer, C.; Hausmann, M. COMBO-FISH enables high precision localization microscopy as a prerequisite for nanostructure analysis of genome loci. *Int. J. Mol. Sci.* **2010**, *11*, 4094–4105. [CrossRef] [PubMed]
74. Zanta, M.A.; Belguise-Valladier, P.; Behr, J.P. Gene delivery: A single nuclear localization signal peptide is sufficient to carry DNA to the cell nucleus. *Proc. Natl. Acad. Sci. USA* **1999**, *96*, 91–96. [CrossRef] [PubMed]
75. Chithrani, B.D.; Ghazani, A.A.; Chan, W.C.W. Determining the size and shape dependence of gold nanoparticle uptake into mammalian cells. *Nano Lett.* **2006**, *6*, 662–668. [CrossRef] [PubMed]
76. Falk, M.; Lukášová, E.; Štefančíková, L.; Baranová, E.; Falková, I.; Ježková, L.; Davídková, M.; Bačíková, A.; Vachelová, J.; Michaelidesová, A.; et al. Heterochromatinization associated with cell differentiation as a model to study DNA double strand break induction and repair in the context of higher-order chromatin structure. *Appl. Radiat. Isot.* **2014**, *83*, 177–185. [CrossRef] [PubMed]
77. Ježková, L.; Falk, M.; Falková, I.; Davídková, M.; Bačíková, A.; Štefančíková, L.; Vachelová, J.; Michaelidesová, A.; Lukášová, E.; Boreyko, A.; et al. Function of chromatin structure and dynamics in DNA damage, repair and misrepair: γ-rays and protons in action. *Appl. Radiat. Isot.* **2014**, *83*, 128–136. [CrossRef] [PubMed]
78. Sevcik, J.; Falk, M.; Macurek, L.; Kleiblova, P.; Lhota, F.; Hojny, J.; Stefancikova, L.; Janatova, M.; Bartek, J.; Stribrna, J.; et al. Expression of human BRCA1Δ17-19 alternative splicing variant with a truncated BRCT domain in MCF-7 cells results in impaired assembly of DNA repair complexes and aberrant DNA damage response. *Cell. Signal.* **2013**, *25*, 1186–1193. [CrossRef]
79. Kozubek, M.; Kozubek, S.; Lukásová, E.; Bártová, E.; Skalníková, M.; Matula, P.; Matula, P.; Jirsová, P.; Cafourková, A.; Koutná, I. Combined confocal and wide-field high-resolution cytometry of fluorescent in situ hybridization-stained cells. *Cytometry* **2001**, *45*, 1–12. [CrossRef]
80. Matula, P.; Maška, M.; Daněk, O.; Matula, P.; Kozubek, M. Acquiarium: Free Software for the Acquisition and Analysis of 3D Images of Cells in Fluorescence Microscopy. In Proceedings of the IEEE International Symposium on Biomedical Imaging, Boston, MA, USA, 28 June–1 July 2009; pp. 1138–1141, ISBN 978-1-4244-3932-4.
81. Eryilmaz, M.; Schmitt, E.; Krufczik, M.; Theda, F.; Lee, J.-H.; Cremer, C.; Bestvater, F.; Schaufler, W.; Hausmann, M.; Hildenbrand, G. Localization Microscopy Analyses of MRE11 Clusters in 3D-Conserved Cell Nuclei of Different Cell Lines. *Cancers* **2018**, *10*, 25. [CrossRef]

Commentary

Nanodiamonds and nanoparticles as tumor cell radiosensitizers—promising results but an obscure mechanism of action

Martin Falk

Department of Cell Biology and Radiobiology, Institute of Biophysics, Czech Academy of Sciences, Brno, Czech Republic

Correspondence to: Martin Falk, PhD. Department of Cell Biology and Radiobiology, Institute of Biophysics, Czech Academy of Sciences, Kralovopolska 135, 612 65 Brno, Czech Republic. Email: falk@ibp.cz.

Provenance: This is a Guest Commentary commissioned by Section Editor Hongcheng Zhu, MD, PhD (Department of Radiation Oncology, The First Affiliated Hospital of Nanjing Medical University, Nanjing, China).

Comment on: Grall R, Girard H, Saad L, *et al.* Impairing the radioresistance of cancer cells by hydrogenated nanodiamonds. Biomaterials 2015;61:290-8.

Submitted Nov 18, 2016. Accepted for publication Nov 23, 2016.

doi: 10.21037/atm.2016.12.62

View this article at: http://dx.doi.org/10.21037/atm.2016.12.62

While cancer still represents one of the most serious threats to human health, a boom of nanoparticle applications has been experienced in medicine in the last decade, in the fields of both diagnostics and therapy [reviewed in (1-5)]. Hence, it is not surprising that in order to fight malignant diseases a veritable 'ZOO' of nanoparticles is being investigated (6).

Currently, the most efficient ways to eradicate tumors, or at least limit tumor growth, are radiotherapy and chemotherapy (R&CH). Both these methods are based on damaging the DNA molecules in cancer cells, which are more sensitive to this damage compared to slower dividing normal cells. There are many different types of DNA lesions introduced by radiotherapy and some kinds of chemotherapy, of which double strand breaks (DSBs) [reviewed in (7)] represent the most deleterious lesions and are mostly responsible for the cell-killing effect of these therapeutic approaches. In many cases, such as in head and neck cancers, R&CH are preferred over primary surgery since they are less mutilating for the patients (8). However, both these approaches are burdensome and risky. Radiotherapy, the main focus of this article, results in limited clinical outcomes due to frequently insufficient tumor responses. If radiotherapy fails, salvage surgery on irradiated tissue and tissue healing are complicated by the radiation damage (8). Moreover, incomplete eradication of the tumor supports selection of even more radioresistant tumor cell clones. Further risks of radiotherapy arise from potential patient hypersensitivity to ionizing radiation and the damage caused to normal tissue adjacent to the tumor. While hypersensitivity may produce acute life-threatening side effects, the latter phenomenon may initiate the development of secondary (therapy-induced) cancers. Radiotherapy thus urgently calls for new improvements reducing these limitations.

In principle, several strategies exist for making radiotherapy more efficient and safer: first, γ-rays or X-rays, mostly used in current medicine, could be replaced by other types of ionizing radiation with more suitable physical characteristics in indicated cases [reviewed in (9)]. Accelerated protons (10) and ions (11,12) are generating significant improvements in radiotherapy due to their preferable dose deposition course (Bragg peak) and better tumor targeting. Accelerated ions also offer higher linear energy transfer (LET) and thus higher radiobiological effectiveness (RBE). Due to these characteristics, even some tumors resistant to conventional (photon) radiotherapy can be successfully controlled by accelerated ions. However, while proton therapy is quickly spreading all over the world, ion therapy remains expensive, technically demanding, and is still an experimental method (12). A different approach to improving radiotherapy is to radiosensitize tumor cells (5,13-16) and/or radioprotect normal cells surrounding the tumor (17). This strategy can also be combined with the above-described ion beam irradiation to maximize the final effect of radiotherapy. This combined strategy will be further discussed in this article.

As already mentioned, a plethora of nanoparticles is currently being studied for various medical applications,

including usage as tumor cell radiosensitizers in radiotherapy. Even in the mid-1970s, several studies revealed enhanced radiation damage of chromosomal DNA in patients undergoing iodine angiography; this was accompanied by enhanced lymphocyte death (18). Consequently, the findings were confirmed *in vitro* (19) and the radiosensitizing effects of numerous nanoparticle types have been well described in terms of physics. However, the biological mechanisms of nanoparticle-mediated radiosensitization (N-MR) remain more obscure (16).

One type of promising versatile nanotool in medicine is hydrogenated nanodiamonds (HD), which were proposed as radiosensitizers in the recently published study by Grall *et al*. (15). The size of nanodiamonds can range from 5 to 100 nm and their surfaces can be modified in various ways to achieve a broad scale of specific physical and chemical characteristics [see (15) and literature therein for more details]. This means that nanodiamonds can be applied to a plenitude of possible situations with significantly improved effects; for instance, current imaging/diagnostics, targeted drug delivery, and/or enhance drug/therapy effects.

Physically, HD exhibit a negative electron affinity together with a positive charge in aqueous solutions (15). These characteristics ensure their high reactivity with oxygen species and allow them to emit secondary electrons upon 'activation' by ionizing radiation. On the bases of these effects, it could be expected that HD can radiosensitize (tumor) cells primarily through locally enhancing the nuclear DNA damage caused by ionizing radiation. This is shown in Grall *et al*. (15). Similarly, a greater efficiency of cell killing was also correlated with an increased induction of DNA DSB in irradiated cells preincubated with some kinds of metal nanoparticles (i.e., nanoparticles composed of high-Z atoms) (20-22).

From these results, the mechanism of N-MR seems to be simple: the main target for ionizing radiation is nuclear DNA and nanoparticles escalate the attack of radiation on this molecule. In support of this conclusion, there is a general consensus in the literature on increased DSB induction by irradiated nanoparticles *in vitro* (23). However, many reports failed to demonstrate augmented nanoparticle-mediated DSB damage in irradiated cells, though a significant radiosensitizing effect had occurred (16). Importantly, the discrepancy between results also exists for nanoparticles of the same or very similar physico-chemical parameters [e.g., (23) *vs.* (16)] pointing to fundamental roles of nanoparticle-cell interactions and biological behavior of nanoparticles in the mechanism of N-MR.

Reactive radicals and secondary electrons produced by irradiated nanoparticles are short living and can only travel for a limited range. Therefore, upon irradiation, these damaging agents only concentrate themselves to high levels in tight shells around the ND/nanoparticle clusters. The primary cellular (biological) targets for ND/N-MR could thus be searched for in close proximity to ND/nanoparticle intracellular distribution hotspots. This opens an unresolved paradox: while the main target for ionizing radiation is undoubtedly the nuclear DNA, most reports show that ND/nanoparticles, efficiently amplifying the effect of radiation, remain localized in the cytoplasm without penetrating into the cell nucleus [e.g., (16)].

Though some secondary electrons or radicals produced by ND/nanoparticles can occasionally reach the nucleus and damage the DNA, it is still unclear whether this damage can sufficiently explain the increase in radiation-induced cell death by ND/nanoparticles. Moreover, as already noted, many studies failed to detect additional DNA damage due to nanoparticles present in irradiated cells (16). Therefore, at least for some nanoparticles, an alternative target to the nuclear DNA might exist.

Logically, a potential cytoplasmic target for ND/nanoparticles could be mitochondria since, in addition to the nucleus, they also contain DNA and exert irreplaceable functions in cell metabolism. However, recent reports showed that nanoparticles in the cytoplasm colocalize with lysosomes instead of mitochondria [(16) and citations therein]. Until recently, lysosomes have been only considered as cellular trash liquidators. However, a growing body of evidence suggests that these organelles are also involved in cell signaling pathways that regulate cell survival (24). Therefore, though more experiments are needed, extensive damage to lysosomes can potentially result in altered acido-basic cell homeostasis, release of proteolytic enzymes into the cytoplasm, and/or deregulation of cell signaling (16). All these processes, or their combinations, might in principle mediate the radiosensitizing effect of nanoparticles.

To summarize, the mechanism of N-MR still represents a subject of intensive disputations. The lack of conclusive information reflects differences among the studied cell types and, especially, nanoparticle diversity (material, composition, size, surface modifications, etc.). ND/nanoparticles have huge potential for physical modifications, which in turn can change many aspects of their biological behavior. This is extremely promising for future ND/nanoparticle design and therefore for clinical applications.

For instance, though nanoparticles are preferentially internalized by tumor cells, even passively due to the EPR effect, their tumor targeting and therapeutic effectivity can be further stimulated by nanoparticle association with specific antibodies and/or therapeutic agents. For instance, triplex-forming oligonucleotides (TFO) tagging seems to potentiate transport and accumulation of nanoparticles in proximity/inside the cell nucleus (25,26), which not only allows the nuclear DNA damage to be more efficient (25), but also enables simultaneous silencing of mutated or otherwise altered genes in cancer cells (26), such as *BRCA1* in breast cancer (27,28). Moreover, some ND/nanoparticles, such as hydrogenated ND, described in Grall *et al*. (15), can even be active by themselves; they can release free radicals even in absence of irradiation (15).

On the other hand, the variability of ND/nanoparticles largely complicates research into their effects. Data on direct nanoparticle cytotoxicity differs with each type of nanoparticle, but many types have been shown to be non-toxic or only slightly toxic. Therefore, direct cytotoxicity does not seem to significantly contribute to the nanoparticle-mediated radiosensitizing effect. Results on nuclear DNA involvement in the radiosensitizing mechanism are contradictory and alternative targets for N-MR, such as lysosomes, have been proposed on the basis of intracellular nanoparticle localization. However, future work is necessary to determine the organelle-specific effects of ND/nanoparticles and to further comprehension of the whole topic.

Acknowledgements

Funding: Cited research of the author was supported by the Czech Science Foundation (projects 16-12454S, P302/12/G157), Ministry of Health of the Czech Republic (16-29835A) and MEYS CR (project of the Czech Plenipotentiary 2016, the 3+3 Project for 2016–2018).

Footnote

Conflicts of Interest: The author has no conflicts of interest to declare.

References

1. Murthy SK. Nanoparticles in modern medicine: state of the art and future challenges. Int J Nanomedicine 2007;2:129-41.
2. Biffi S, Voltan R, Rampazzo E, et al. Applications of nanoparticles in cancer medicine and beyond: optical and multimodal in vivo imaging, tissue targeting and drug delivery. Expert Opin Drug Deliv 2015;12:1837-49.
3. Lin W. Introduction: Nanoparticles in Medicine. Chem Rev 2015;115:10407-9.
4. Luque-Michel E, Imbuluzqueta E, Sebastián V, et al. Clinical advances of nanocarrier-based cancer therapy and diagnostics. Expert Opin Drug Deliv 2017;14:75-92.
5. Babaei M, Ganjalikhani M. The potential effectiveness of nanoparticles as radio sensitizers for radiotherapy. Bioimpacts 2014;4:15-20.
6. Falk M. Nanoscopy and Nanoparticles Hand-in-Hand to Fight Cancer: An Exciting Entrée into the Rising NANOworld. Biophys J 2016;110:872-3.
7. Falk M, Lukasova E, Kozubek S. Higher-order chromatin structure in DSB induction, repair and misrepair. Mutat Res 2010;704:88-100.
8. Falková I, Falk M, Horáková Z, et al. DNA repair in the head and neck cancers and their radiosensitivity – the dilemma of the first therapy. Health and Social Work 2016;11:19-25.
9. Jiang GL. Particle therapy for cancers: a new weapon in radiation therapy. Front Med 2012;6:165-72.
10. Ježková L, Falk M, Falková I, et al. Function of chromatin structure and dynamics in DNA damage, repair and misrepair: γ-rays and protons in action. Appl Radiat Isot 2014;83 Pt B:128-36.
11. Marx V. Cancer treatment: Sharp shooters. Nature 2014;508:133-8.
12. Kamada T, Tsujii H, Blakely EA, et al. Carbon ion radiotherapy in Japan: an assessment of 20 years of clinical experience. Lancet Oncol 2015;16:e93-e100.
13. Kwatra D, Venugopal A, Anant S. Nanoparticles in radiation therapy: a summary of various approaches to enhance radiosensitization in cancer. Transl Cancer Res 2013;2:330-42.
14. Belz JE, Ngwa W, Korideck H, et al. Multifunctional nanoparticles in radiation oncology: an emerging paradigm. In: Harper-Leatherman AS, Solbrig CM. editors. The science and function of nanomaterials: from synthesis to application. Washington, DC: American Chemical Society, 2014:75-106.
15. Grall R, Girard H, Saad L, et al. Impairing the radioresistance of cancer cells by hydrogenated nanodiamonds. Biomaterials 2015;61:290-8.
16. Štefančíková L, Lacombe S, Salado D, et al. Effect of gadolinium-based nanoparticles on nuclear DNA

damage and repair in glioblastoma tumor cells. J Nanobiotechnology 2016;14:63.
17. Hofer M, Falk M, Komůrková D, et al. Two New Faces of Amifostine: Protector from DNA Damage in Normal Cells and Inhibitor of DNA Repair in Cancer Cells. J Med Chem 2016;59:3003-17.
18. Adams FH, Norman A, Mello RS, et al. Effect of radiation and contrast media on chromosomes. Preliminary report. Radiology 1977;124:823-6.
19. Matsudaira H, Ueno AM, Furuno I. Iodine contrast medium sensitizes cultured mammalian cells to X rays but not to gamma rays. Radiat Res 1980;84:144-8.
20. Watson C, Ge J, Cohen J, et al. High-throughput screening platform for engineered nanoparticle-mediated genotoxicity using CometChip technology. ACS Nano 2014;8:2118-33.
21. Mowat P, Mignot A, Rima W, et al. In vitro radiosensitizing effects of ultrasmall gadolinium based particles on tumour cells. J Nanosci Nanotechnol 2011;11:7833-9.
22. Miladi I, Aloy MT, Armandy E, et al. Combining ultrasmall gadolinium-based nanoparticles with photon irradiation overcomes radioresistance of head and neck squamous cell carcinoma. Nanomedicine 2015;11:247-57.
23. Porcel E, Liehn S, Remita H, et al. Platinum nanoparticles: a promising material for future cancer therapy? Nanotechnology 2010;21:85103.
24. Turk B, Turk V. Lysosomes as "suicide bags" in cell death: myth or reality? J Biol Chem 2009;284:21783-7.
25. Moser F, Hildenbrand G, Müller P, et al. Cellular Uptake of Gold Nanoparticles and Their Behavior as Labels for Localization Microscopy. Biophys J 2016;110:947-53.
26. Huo S, Jin S, Ma X, et al. Ultrasmall gold nanoparticles as carriers for nucleus-based gene therapy due to size-dependent nuclear entry. ACS Nano 2014;8:5852-62.
27. Sevcik J, Falk M, Kleiblova P, et al. The BRCA1 alternative splicing variant Δ14-15 with an in-frame deletion of part of the regulatory serine-containing domain (SCD) impairs the DNA repair capacity in MCF-7 cells. Cell Signal 2012;24:1023-30.
28. Sevcik J, Falk M, Macurek L, et al. Expression of human BRCA1Δ17-19 alternative splicing variant with a truncated BRCT domain in MCF-7 cells results in impaired assembly of DNA repair complexes and aberrant DNA damage response. Cell Signal 2013;25:1186-93.

Cite this article as: Falk M. Nanodiamonds and nanoparticles as tumor cell radiosensitizers—promising results but an obscure mechanism of action. Ann Transl Med 2017;5(1):18. doi: 10.21037/atm.2016.12.62

Štefančíková et al. J Nanobiotechnol (2016) 14:63
DOI 10.1186/s12951-016-0215-8

Journal of Nanobiotechnology

RESEARCH

Open Access

Effect of gadolinium-based nanoparticles on nuclear DNA damage and repair in glioblastoma tumor cells

Lenka Štefančíková[1,2*], Sandrine Lacombe[2], Daniela Salado[2], Erika Porcel[2], Eva Pagáčová[1], Olivier Tillement[3], François Lux[3], Daniel Depeš[1], Stanislav Kozubek[1] and Martin Falk[1*]

Abstract

Background: Tumor targeting of radiotherapy represents a great challenge. The addition of multimodal nanoparticles, such as 3 nm gadolinium-based nanoparticles (GdBNs), has been proposed as a promising strategy to amplify the effects of radiation in tumors and improve diagnostics using the same agents. This singular property named theranostic is a unique advantage of GdBNs. It has been established that the amplification of radiation effects by GdBNs appears due to fast electronic processes. However, the influence of these nanoparticles on cells is not yet understood. In particular, it remains dubious how nanoparticles activated by ionizing radiation interact with cells and their constituents. A crucial question remains open of whether damage to the nucleus is necessary for the radiosensitization exerted by GdBNs (and other nanoparticles).

Methods: We studied the effect of GdBNs on the induction and repair of DNA double-strand breaks (DSBs) in the nuclear DNA of U87 tumor cells irradiated with γ-rays. For this purpose, we used currently the most sensitive method of DSBs detection based on high-resolution confocal fluorescence microscopy coupled with immunodetection of two independent DSBs markers.

Results: We show that, in the conditions where GdBNs amplify radiation effects, they remain localized in the cytoplasm, i.e. do not penetrate into the nucleus. In addition, the presence of GdBNs in the cytoplasm neither increases induction of DSBs by γ-rays in the nuclear DNA nor affects their consequent repair.

Conclusions: Our results suggest that the radiosensitization mediated by GdBNs is a cytoplasmic event that is independent of the nuclear DNA breakage, a phenomenon commonly accepted as the explanation of biological radiation effects. Considering our earlier recognized colocalization of GdBNs with the lysosomes and endosomes, we revolutionary hypothesize here about these organelles as potential targets for (some) nanoparticles. If confirmed, this finding of cytoplasmically determined radiosensitization opens new perspectives of using nano-radioenhancers to improve radiotherapy without escalating the risk of pathologies related to genetic damage.

Keywords: Radiosensitization, Nanomedicine, Gadolinium, Nanoparticles, DNA double-strand breaks, DNA repair, Radiotherapy, Theranostic

*Correspondence: lenka.stefancikova@u-psud.fr; falk@ibp.cz
[1] Department of Cell Biology and Radiobiology, Institute of Biophysics of ASCR, Brno, Czech Republic
[2] Institute des Sciences Moléculaires d'Orsay (ISMO), Université Paris Sud 11, CNRS, Université Paris Saclay, Bât 351, 91405 Orsay Cedex, France
Full list of author information is available at the end of the article

Background

Radiation-based therapies are used to treat half of cancer patients. Most common treatments based on highly penetrating MeV photons (X-rays and γ-rays) have the advantage of being non-invasive and applicable on inoperable tumors. However, the photon radiotherapy suffers from a serious disadvantage—it lacks tumor specificity. Photons induce damage all along their tracks, inflicting thus severe side effects in the healthy tissue. On the other hand, some tumors are resistant to high-energy photons. Therefore, a simultaneous enhancement of tumor selectivity and biological effectiveness of radiations is a long-lasting objective of cancer radiotherapy.

Nanoparticles (NPs) composed of high-Z atoms have been proposed as new nanodrugs able to improve both these desired aspects of radiation-based therapies (specificity and efficiency). Results obtained with various NPs showed that they can specifically increase radiosensitivity of tumor cells [1–4]. The use of nano-size agents that preferentially accumulate in the tumor (even passively due to the enhanced permeability and retention effect, EPR) [5, 6] may achieve the paradigm of local treatment of solid tumors. Among metal-based NPs, gold NPs have been widely used for diagnostics as contrast agents, and for therapy as nano-enhancers of radiation effects [7–11]. Gold NPs potentiate the effects of different photon beams, both in vivo and in vitro [1–4, 10, 12–14]. More recently, we have found [15, 16] that also platinum NPs enhance the effects of radiations, γ-rays as well as fast medical ions. Likewise, metal oxide nanoparticles are already on the market, currently evaluated in oncology clinical trials as compounds for tumor diagnostic and cancer treatment [17, 18].

An important step forward has been the development of gadolinium-based nanoparticles (GdBNs), which can act as multimodal agents and improve not only the therapeutic index of the treatment but also MRI performance (theranostics) [19, 20]. Due to its atomic mass ($Z = 64$), gadolinium is a good electron emitter, which is the property required to enhance the radiation effects. When applied in combination with both low and high-energy X-rays, γ-rays [21, 22], or fast ions [23], GdBNs significantly amplify radiation-induced cell killing, even in the case of U87 glioblastoma cells derived from a highly aggressive and radio-resistant human tumor [24, 25]. Concomitantly, GdBNs can serve as good contrast agents [19, 26] while they are rapidly eliminated from the organism by the kidneys, with no evidence of toxicity [24, 27–30].

GdBNs exert strong radiosensitizing effect on tumors [22–24, 31–33] when combined with several types of radiation of different energies (≥keV). For γ-rays used in this work, the radiosensitization appears due to prominent physical processes, namely the photoelectric and Compton effects, in dependence of the photon beam energy. The cascade of GdBNs-mediated processes resulting to cell radiosensitization starts with electron 'showers' emitted from nanoparticles upon irradiation and continues with water radiolysis producing free reactive oxygen species (ROS) [34, 35]. As these ROS are concentrated in nano-clusters, they induce complex nanosized bio-damages that are lethal for the cells [36, 37]. NPs thus increase the ionizing density (and damage) at the nanoscale, without influencing the macroscopic dose deposition [36, 38–40]. In accordance with this hypothesis, Burger and co-workers [41] showed that a high focal concentration of NPs is required to ensure an increased cellular inactivation by irradiated NPs. Also the local effect model (LEM) simulations suggested that the nanosized character of dose amplification is the key aspect of the 'nanosensitization' [38, 39].

Though the radio-enhancing effect of GdBNs has been clearly proved and explained in terms of physics, the structures and processes targeted by these (and other) nanoparticles in cells remain a subject to controversy. The nuclear DNA is logically the first suspect: it represents a critical cell structure and its damage by double strand breaks (DSBs) is commonly considered as the cause of radiation-induced cell death [42, 43]. Hence, it has been proposed that nanoparticles radiosensitize cells through amplifying the DSBs damage. However, several in vitro studies demonstrated [12, 13, 23, 32, 44, 45] that the radiosensitizers (metal complexes or NPs) are located in the cell cytoplasm. Stated in other words, NPs seem to amplify cell killing without entering the nucleus. As discussed below, these results open the question of whether secondary electrons only produced in close vicinity of cytoplasmically localized NPs may reach and damage to a sufficient extent the cell nucleus or whether cytoplasmic structures in closer proximity to NPs represent another (or even a more important) target for NPs-mediated radiosensitization.

Jones et al. [46] showed that also the dose enhancement mediated by NPs can spread as far as several micrometers. Leung et al. [47] reported that electrons can travel up to 3 μm or even 1 mm when activated by a 50 kVp and 6 MV source, respectively; this flying range is sufficient to reach the nuclear DNA. Thus, at least some electrons from NP-mediated electron showers might directly damage the nuclear DNA [41]. Whether this is sufficient to enhance cell killing remains a question.

Important evidence that the cytoplasmic damage may strongly influence the cell nucleus emerged from recent microbeam experiments. The group of Kevin Prise demonstrated that also cytoplasmically micro-irradiated cells develop 53BP1 protein foci—the markers of DNA

DSBs—dispersed in the nucleus [48]. Moreover, these experiments revealed that the radiation damage to the cytoplasm can elicit 53BP1 foci formation both in directly exposed and bystander cells, independently of the dose and number of cells targeted. Hence, we can conclude that the cytoplasmic injury might also be followed by DNA damage with a corresponding biological response, though its kinetics for the pan-cellular and cytoplasmic irradiations differs.

The expansion of radiation damage from the cytoplasm to the nucleus is thus probably mediated by ROS [49]. In accordance, we can hypothesize that NPs might enhance the nuclear DNA damage by amplifying ROS production in the cytoplasm. In addition, disruption to protein transport and synthesis in the cytoplasm upon high radiation doses may slow down or even preclude DNA repair and further contribute to the cell killing by irradiated NPs. However, the information on the damage exerted by NPs to the nuclear DNA remains very limited and conflicting as available studies feature huge heterogeneity precluding the combination of results. This situation calls for further comprehensive analyses comparing the impact of physico-biological properties of various NPs and different treatment protocols on the radiosensitization processes.

In this work, together with providing a detailed information on the intracellular localization of GdBNs, we evaluated by currently the most sensitive method to detect DSBs how these nanoparticles influence the radiation damage introduced to the genomic DNA and how these lesions are consequently repaired during a long period of time post-irradiation (PI) in radioresistant U87 human glioblastoma cells. Our results represent new, direct and surprising evidence on the radiosensitizing mechanism of GdBNs: We demonstrate that this mechanism does not rely on the amplification of DSBs damage in the genomic DNA. Rather, based on our previous findings, we suppose that injury to the endosomes and lysosomes play a crucial role. These results may change the current dogma suspecting the nuclear DNA and/or mitochondria as the key targets for the nanoparticle-mediated radiosensitization.

Methods

Gadolinium-based nanoparticles (GdBNs) were synthesised by the group of O. Tillement (LPCML, Lyon, France). Briefly, the GdBN consist of a polysiloxane core surrounded by gadolinium chelates covalently grafted on the inorganic matrix. The procedure of synthesis is detailed in Morlieras et al. [50] and Mignot et al. [27]. Briefly, the diameter of GdBNs was 3.0 ± 1.0 nm and their molecular mass 8.5 ± 1 kDa. These nanoparticles are stable, so they can be lyophilized and stored at 4 °C. For the analysis of DNA DSBs, label-free GdBNs were used. For the localization experiments by confocal microscopy, GdBNs were fluorescently labeled with Cyanine 5.5 (GdBNs-Cy5.5) as described elsewhere [50]. We have demonstrated earlier, by using different microscopy techniques [including synchrotron radiation deep ultraviolet microscopy (SR-DUV), transmission electron microscopy, and confocal microscopy], that labeling of GdBNs with cyanine 5.5 does not influence the nanoparticle localization [31].

Cell culture

U87 cells grew (37 °C, 5 % CO_2) in Dulbecco's modified essential medium (Life Technologies) supplemented with 10 % heat-inactivated fetal calf serum (PAA), 100 U/ml penicillin (PAA), 100 µg/ml streptomycin (PAA), and 1 % NEAA (Life Technologies).

Cell irradiation with γ-rays

U87 cells grown on microscopic slides (for DNA damage detection experiment) or in culture flasks (for the clonogenic survival experiment) were irradiated in culture medium at room temperature (RT) with 1 or 4 Gy of γ-rays (1 Gy/min), delivered by a ^{60}Co irradiator (Chisostat, Chirana). During irradiation, the samples were kept in thermo-isolating boxes to prevent sample infection and temperature changes, and then immediately returned to the incubator (37 °C, 5 % CO_2).

Quantification of GdBN-mediated cell radiosensitization by clonogenic assay

Part of U87 cells followed incubation with 1 mM GdBNs for 1 h and consequently some samples were irradiated with 1 or 4 Gy of γ-rays as described above. The survival of cells was quantified by clonogenic assay and compared for non-irradiated and irradiated cells, in both cases either incubated or not incubated with GdBNs. After irradiation, cells were trypsinized and plated into 60 mm Petri dishes (Falcon 3002) at a density of 100 surviving cells per dish. The plating efficiency was 13 %. After 14 days of incubation, the colonies were fixed with 50 % methanol and stained with 1 % methylene blue. The colonies were counted manually by an experience examiner to determine the cell surviving fractions.

Confocal microscopy studies of GdBNs localization

U87 cells were incubated with GdBNs labeled with Cy5.5 (GdBNs-Cy5.5) (1 mM) for 1, 6, and 16 h, respectively. Afterward, the cells were rinsed three times with 1× PBS and maintained in HBSS medium during the time of observation. The localization of GdBNs by confocal microscopy was performed with a LEICA SP5 confocal system, under constant temperature and CO_2 levels (37 °C and 5 % CO_2), at the Centre de Photonique

Bio-Medical (CPBM), University Paris Sud, Orsay, France. GdBNs-Cy5.5 fluorescence was excited at 633 nm and the emission was detected in the 650–750 nm range. Images were recorded for three different z-positions (0.2 µm-thick confocal slices) for each cell. Transmission imaging was performed to visualize the size and shape of the cells and to discriminate between the nucleus and the cytoplasm. The fluorescence images obtained were merged with the transmission images by ImageJ software (Rasband, W.S., ImageJ, U. S. National Institutes of Health, Bethesda, Maryland, USA, http://www.imagej.nih.gov/ij/, 1997–2011) to determine the intracellular localization of GdBNs-Cy5.5. The same settings were used to perform fluorescence spectroscopy. The spectra for different cell compartments were registered together with random background (out-of-cell) values.

Immunostaining of nuclear DSBs and their visualization by confocal microscopy

DSBs were detected in spatially (3D) fixed cells using a high-resolution confocal microscopy; the procedure was optimized by Falk et al. [51]. To maximize the sensitivity and fidelity of DSBs analyses, we took advantage of a dual fluorescence immunostaining to simultaneously visualize γH2AX and 53BP1 repair foci, the independent markers of nuclear DSBs [52, 53].

U87 cells were incubated with 1 mM GdBNs for 1, 6, and 24 h, respectively, and consequently some samples were irradiated with 1 or 4 Gy of γ-rays (1 Gy/min) as described. At the times post-irradiation (PI) of 5, 15, 30 min, 1, 2, 4, 8, and 24 h, the cells were spatially (3D) fixed with 4 % formaldehyde in 1X PBS for 10 min/RT, washed 3 times for 5 min each in 1X PBS, permeabilized with 0.2 % Triton X 100/PBS for 15 min/RT, and again washed 3 times for 5 min each in 1X PBS. Before the incubation with the primary antibodies (10 min RT and then overnight at 4 °C), the cells were blocked with 7 % inactivated fetal bovine serum +2 % bovine serum albumin/PBS for 30 min at RT.

Antibodies from two different hosts were used to simultaneously detect two DSBs markers in the same nuclei: anti-phospho-H2AX (serine 139) (mouse, monoclonal, dilution 1:500, Upstate Biotechnology) and anti-53BP1 (rabbit, polyclonal, dilution 1:500, Cell Signalling). Secondary antibodies, affinity purified FITC-conjugated donkey anti-mouse (diluted 1:200) and Cy3-conjugated donkey anti-rabbit (diluted 1:100) (both from Jackson Laboratory), were applied for 1 h in the dark at RT after the pre-incubation of slides with 5.5 % donkey serum/PBS for 30 min at RT. After washing 3 times for 5 min each in 1X PBS, cells were counterstained with 1 µM TOPRO-3 (Molecular Probes) in saline sodium citrate (2× SSC). Vectashield medium (Vector Laboratories) was used for the final mounting of slides.

Forty *z*-stacks, acquired at 0.2 µm steps, were recorded (at IBP ASCR Brno, CR) in three separate spectral channels by the confocal microscope Leica SP5 (Leica Microsystems) and an automated Leica DM RXA fluorescence microscope equipped with a Nipkow disk (Jokogawa, Japan) for confocal imaging (in detail described in Kozubek et al. [54, 55]). The visualization and analysis of the 3D images were performed using the *Aquarium software* [56], *3D image viewer* [56], and *ImageJ software* (Rasband, W.S., ImageJ, U. S. National Institutes of Health, Bethesda, MD, USA, http://www.imagej.nih.gov/ij/, 1997–2011). Fifty to 100 cells were analyzed for each treatment and period of time PI. This approach allowed us to analyze (a) the initial induction of DSBs immediately after the irradiation (5 min PI), (b) the repair kinetics of these lesions during a long period of time post-irradiation (up to 24 h), and (c) the persistence of unrepaired DSBs at late times PI (8 and 24 h). The representative maximum images composed of 40 confocal 0.2 µm thick slices are shown in Figs. 3, 4, 5 and 6.

Data analysis

The SigmaPlot 12.5 (Systat Software Inc.) has been used for data analysis. The Mann–Whitney Rank Sum Test was employed to compare at all the particular periods of time PI the distributions of DSBs (γH2AX/53BP1 foci) numbers per nucleus in untreated control cells and cells incubated with 1 mM GdBNs for 1 h. The relevant P values are indicated in Tables 1 and 2. Around 100 nuclei were quantified in each single experiment. To mutually compare the distributions of DSBs for untreated controls and cells incubated with GdBNs for 1, 6, and 24 h, respectively, the Kruskal–Wallis One Way Analysis of Variance on Ranks (a non-parametric equivalent of the one-way analysis of variance, ANOVA) was applied; the corresponding P values are shown in Table 3.

In Figs. 3, 4 and 5, the data are displayed in the form of box graphs showing the distributions of DSBs foci per nucleus. The boxes include 50 % of the values (25th to 75th percentile) centred on the median (the horizontal line through the box). The mean values are represented by the squares within the boxes. The vertical lines begin at the 5th percentile and end at the 95th percentile. Representative nuclei for each time point PI are shown above the respective box.

Results

Uptake and localization of GdBNs in U87 cells

First, we analyzed by confocal microscopy the cellular uptake and localization of 1 mM GdBNs in U87 cells during 16 h-long period of observation. Figure 1a shows exclusively cytoplasmic localization of GdBNs (labelled with Cy5.5) as demonstrated by 'correlative' transmission

Table 1 Effect of GdBNs on DSBs quantity in irradiated (1 Gy) U87 cells

	NI	5 min	15 min	30 min	1 h	2 h	4 h	8 h
U87	1.4	18.1	21.1	19.7	14.9	8.7	5.5	3.1
U87 + GdBNs	1.2	16.7	19.3	17.5	15.7	8.6	5.0	2.9
P	0.533	0.111	0.083	0.096	0.379	0.970	0.485	0.241

Table 2 Effect of GdBNs on DSBs quantity in irradiated (4 Gy) U87 cells

	NI	1 h	4 h	8 h	24 h
U87	1.9	42.4	20.6	12.2	5.0
U87 + GdBNs	2.0	42.9	20.1	12.3	4.9
P	0.059	0.731	0.916	0.350	0.686

Table 3 Effect of incubation times with GdBNs on DSBs quantity in irradiated (1 Gy) U87 cells

	NI	5 min	1 h	4 h	24 h
U87	1.6	12.7	12.3	4.9	2.2
U87 + GdBNs 1 h	1.6	14.4	12.7	5.8	
U87 + GdBNs 6 h	1.5	11.3	12.5	5.1	1.8
U87 + GdBNs 24 h		12.3	11.9	6.0	2.0
P	0.433	0.091	0.647	0.328	0.699

light images and confocal fluorescence images. To further probe the intracellular distribution of GdBNs, we completed confocal microscopy by fluorescence spectroscopy (Fig. 1b) of the regions of interest located in (a) the nucleus, (b) the cytoplasm, and (c) the extracellular space (plain medium). The spectra measured in the cytoplasm displayed an intensive peak at $\lambda = 688$ nm, which corresponds to the fluorescence of GdBNs labelled with Cyanine 5.5. This peak was clearly absent in the spectra obtained inside the nucleus or outside the cells. Both microscopy and spectrometry thus confirmed absence of GdBNs in the cell nucleus.

Next, we compared the uptake and localization of GdBNs in U87 cells also for two shorter incubation periods: 1 and 6 h. As demonstrated by Fig. 2, GdBNs were already internalized after 1 h incubation and longer incubation times of 6 and 16 h (see also Fig. 1) had no influence on GdBNs uptake efficacy. For all the periods of time studied, GdBNs were localized in the cytoplasm of U87 cells without penetrating into the nucleus. In contrast to the situation described for SQ20B cells by Miladi and coworkers [33], we observed no clustering of NPs on the cytoplasmic membrane.

Effect of GdBNs on nuclear DNA damage in U87 cells

We investigated whether GdBNs alone or in combination with irradiation cause the nuclear DNA damage and/or

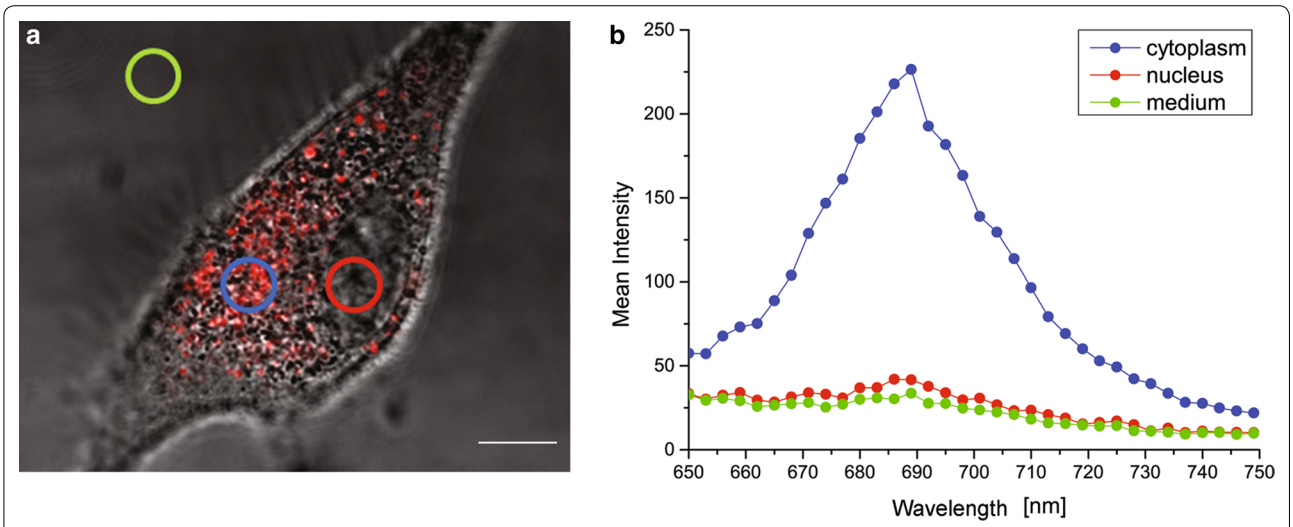

Fig. 1 Localization of GdBNs-Cy5.5 nanoparticles in U87 cell. **a** Correlative fluorescence confocal image and transmission light image of U87 cell with internalized GdBNs-Cy5.5 (*red*) at the end of 16 h-long observation. The *scale bar* equals to 10 μm. The *circles* represent the regions of fluorescence spectroscopy measurements, cytoplasm (*blue*), nucleus (*red*), and plain medium (*green*). **b** Fluorescence emission spectra of the three regions

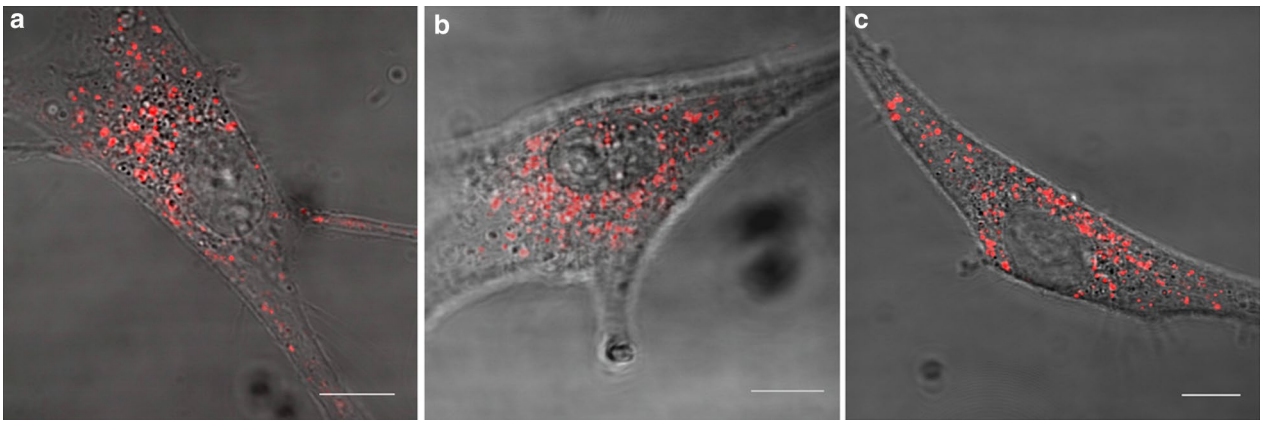

Fig. 2 Localization of GdBNs-Cy5.5 nanoparticles in U87 cells as a function of the incubation time. Correlative fluorescence confocal images and transmission light images of U87 cells incubated with 1 mM GdBNs-Cy5.5 (*red*) for three different incubation times: **a**—1 h, **b**—6 h and **c**—16 h. *Scale bars* equal to 10 µm

influence repair of these lesions. We focused on the DNA double strand breaks (DSBs; visualized as γH2AX foci co-localizing with 53BP1 foci) that represent the most important type of DNA damage.

Effect of GdBNs on nuclear DNA in non-irradiated cells (nanoparticle genotoxicity)

Biological toxicity of nanoparticles represents a critical issue in therapy. We demonstrated earlier [31] that GdBNs used in this study are not toxic and neither the survival nor the division of cells. However, several authors reported that the silver [57–59] and gold nanoparticles enhance the levels of γH2AX [60] and the oxidative stress [61], both in normal and cancer cells. Hence, we further investigated the effect of our GdBNs on the DNA integrity in U87 cells without irradiation.

Figure 3 compares the distribution of γH2AX/53BP1 (DSBs) foci numbers in U87 cells never incubated with GdBNs (control cells) and incubated with 1 mM GdBNs for 1 and 6 h, respectively. For both the periods of time, without irradiation, the cell treatment with GdBNs had no effect on the number of DSBs detected. The average values from two independent experiments were 1.6 DSBs/nucleus for untreated cells, 1.5 DSBs/nucleus for cells incubated with GdBNs for 1 h, and 1.6 DSBs/nucleus for cells incubated with GdBNs for 6 h. Hence, GdBNs of parameters used in this work are not genotoxic by themselves.

Effect of GdBNs on nuclear DNA DSBs induction and repair in irradiated U87 cells

In the next step, we studied how cytoplasmic GdBNs influence the extent and reparability of DSBs introduced to the nuclear DNA by irradiation with two

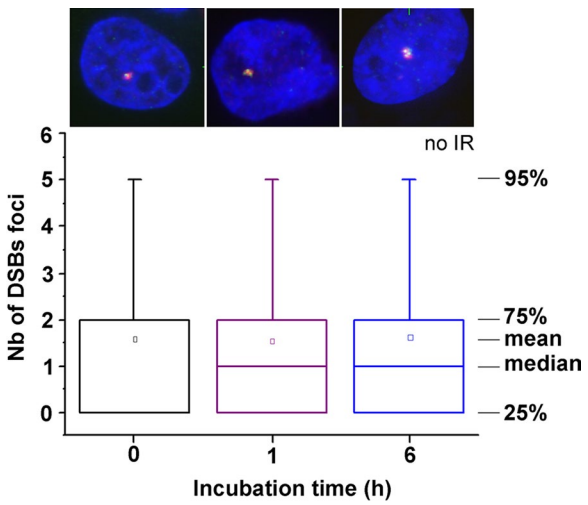

Fig. 3 Effect of GdBNs on DSBs formation in non-irradiated U87 cells. Distribution of DSBs foci numbers are compared for non-irradiated U87 cells never incubated with GdBNs (*black*) and incubated with 1 mM GdBNs for 1 h (*purple*) and 6 h (*blue*). The respective cell nuclei are shown as the maximum images (composed of 40 confocal slices 0.2 µm-thick) with 3D projections; γH2AX—*green*, 53BP1—*red*, chromatin—artificially *blue*

different doses of γ-rays, 1 and 4 Gy, respectively. The application of high resolution confocal immuno-fluorescence microscopy with two independent DSBs markers (γH2AX and 53BP1) allowed us to precisely analyze the extent of DSBs induction in intact cells as early as 5 min post-irradiation (PI). Consequently, we evaluated the repair of DSBs in terns of γH2AX/53BP1 foci disappearance over 8 h-long period of time PI; this period is sufficient to repair the majority of DSBs and allows considering effects of the two main DSBs repair pathways,

NHEJ—non-homologous end-joining, and HR—homologous recombination. To follow both the kinetics and the final efficiency of DSBs repair, we scored γH2AX/53BP1 foci in 7 time points PI. The results for U87 cells irradiated with 1 Gy of γ-rays and incubated or not incubated with 1 mM GdBNs for 1 h are summarized in Fig. 4 and Table 1.

Average numbers of DSBs foci per nucleus at indicated periods of time PI are compared for U87 cells irradiated with 1 Gy of γ-rays in absence or presence of 1 mM GdBNs (1 h incubation). Non-irradiated control cells (NI) are included. P values indicate the significance of differences between cells untreated and treated with GdBNs, respectively.

For all the periods of time PI, we observed comparable mean/median numbers of γH2AX/53BP1 foci per nucleus between the U87 cells incubated with GdBNs and the untreated controls. These results show that both the extent of DSBs induction measured at 5 min PI and the kinetics of DSBs repair between 5 min PI and 8 h PI are not affected by GdBNs present in the cytoplasm of irradiated U87 cells.

To check whether these conclusions hold also for higher radiation doses, we repeated the above described experiments also with 4 Gy irradiation. This dose also ensures more extensive DNA damage which in turn allows recognition of smaller differences between the compared samples. U87 cells were again incubated with 1 mM GdBNs for 1 h; however, this time we have focused on less time-points (1, 4, 8 and 24 h) but dispersed along a period of time extended up to 24 h PI. Indicated time-points were selected as they allowed us to estimate: (1) the extent of DSBs induction (since the numbers of γH2AX/53BP1 foci at 1 h PI still approach the maximum values), (2) the efficiency of NHEJ and HR repair pathways (4/8 h PI, respectively), and (3) also the extent of DSBs that are repaired only with difficulty (and persist in nuclei 24 h PI, when the repair process are usually accomplished even for 4 Gy and higher dose γ-irradiations). The results are summarized in Fig. 5 and Table 2. As for 1 Gy, we found only insignificant differences between the mean/median γH2AX/53BP1 (DSBs) foci numbers in cells incubated or not incubated with GdBNs.

Altogether, these results indicate that our GdBNs (1 mM)—alone or in combination with irradiation—do not affect nuclear DNA. GdBNs of defined parameters influenced neither the induction of DSBs nor the kinetics and efficiency of their repair. Based on these results, we conclude that GdBNs may amplify radiation-induced cell killing through effects independent on the nuclear DNA.

Average numbers of DSBs foci per nucleus at different periods of time PI are compared for U87 cells irradiated with 4 Gy of γ-rays in absence or presence of 1 mM GdBNs (1 h incubation). Non-irradiated control cells (NI) are also included. P values indicate the significance of differences between cells treated and untreated with GdBNs.

Influence of the incubation time with GdBNs on DSBs foci induction by γ-rays and their repair

As reviewed in Sancey et al. [24], available studies on GdBNs used different nanoparticle incubation times. At the same time, several reports with gold [62] and gadolinium [32] NPs demonstrated that this experimental parameter has a significant effect on NPs concentration and distribution in the cells. This makes comparisons and interpretations of results problematic. Thus, we investigated how different times of incubation with our GdBNs influence the induction of DSBs by γ-rays and repair of these lesions.

As in the previous experiments, we quantified γH2AX/53BP1 (DSBs) foci in U87 cells incubated with 1 mM GdBNs and exposed to 1 Gy of γ-rays. The results for 0, 1, 6, or 24 h-long incubations followed by DSBs quantification at 5 min, 1, 4, and 24 h PI, respectively, are presented in Fig. 6 and Table 3. Evidently, the prolonged incubations increased neither the induction of DSBs lesions nor delayed their repair. These results thus agree with our observation presented in Fig. 2 that GdBNs do not penetrate in the nucleus even at longer incubation times.

Average numbers of DSBs foci per nucleus in different periods of time PI are compared for U87 cells irradiated with 1 Gy of γ-rays in absence or presence of GdBNs, applied for 1, 6 or 24 h prior to irradiation. Non-irradiated control cells (NI) are also included. P values indicate the significance of differences between samples for each period of time PI.

Radiosensitizing effect exerted by irradiated GdBNs

Recently, we have shown that GdBNs of the parameters and concentration used in this work (1 mM) exert a substantial radiosensitizing effect in CHO cells irradiated with He2+ or C6+ high energy ions [23]. In our previous work, we have also confirmed the radiosensitizing effect of these GdBNs in U87 cells irradiated with γ-rays [31]. However, a controversy exists in the literature on the radiosensitizing efficiency of higher (about >1 mM) GdBN concentrations. Hence, we confirmed here by clonogenic assay the effects of 1 mM GdBNs on the cell vitality and proliferation potential. Figure 7 shows significantly lower clonogenic survival of U87 cells in presence of GdBNs at doses 1 and 4 Gy, respectively; the non-irradiated controls are also included. Though the

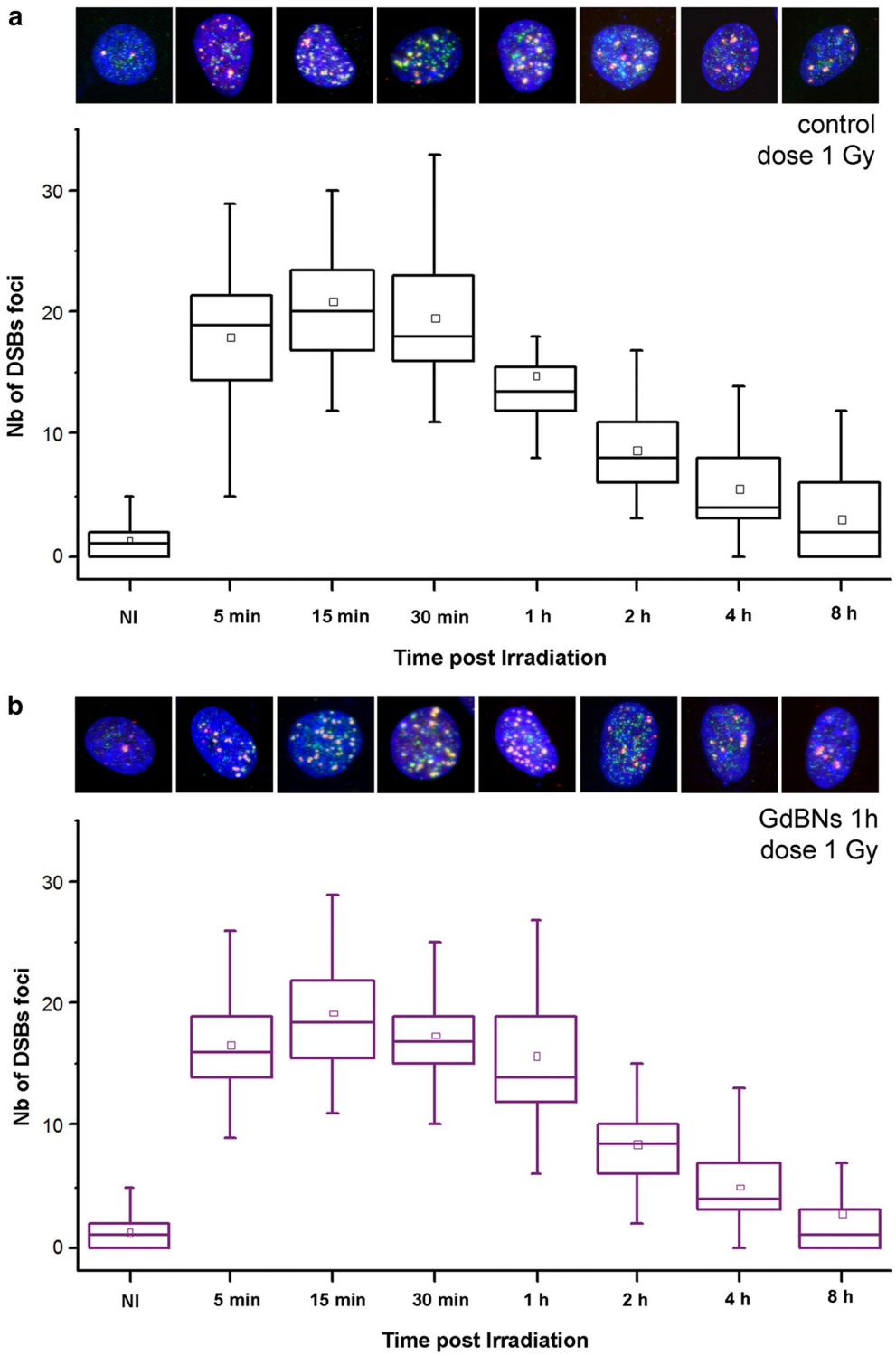

Fig. 4 Effect of GdBNs on DSBs formation and repair in irradiated (1 Gy) U87 cells. Distribution of DSBs foci numbers are compared for irradiated U87 cells **a** never incubated with GdBNs and **b** incubated with 1 mM GdBNs for 1 h. Non-irradiated controls are indicated as NI. The respective maximum images of representative nuclei for each period of time PI are shown above: γH2AX—*green*, 53BP1—*red*, chromatin—artificially *blue*

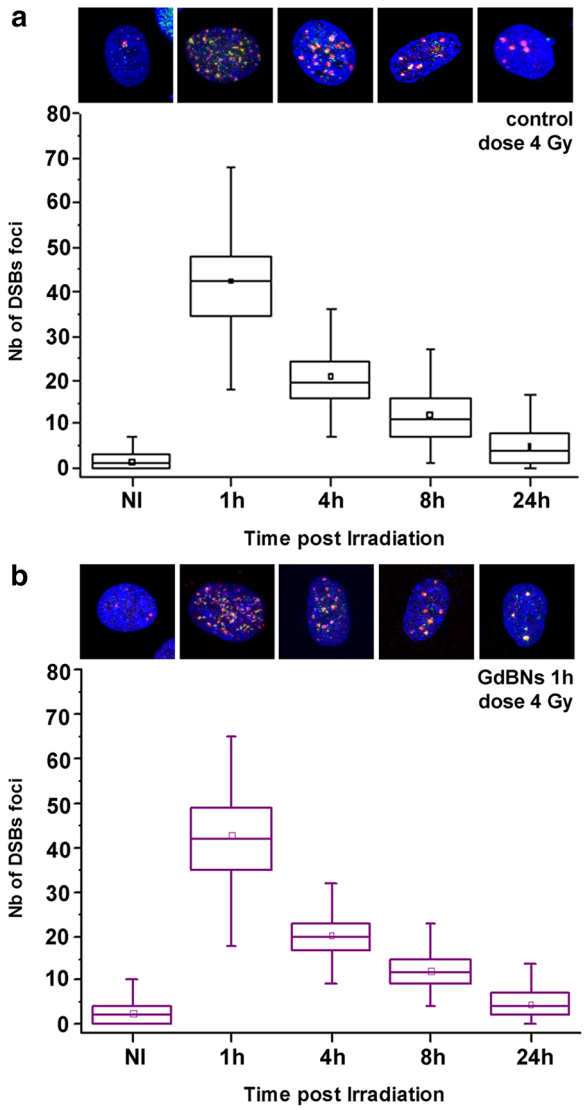

Fig. 5 Effect of GdBNs on DSBs formation and repair in irradiated (4 Gy) U87 cells. Distribution of DSBs foci in U87 cells never incubated with GdBNs (**a**) and incubated with 1 mM GdBNs for 1 h (**b**). Non-irradiated controls (NI) are also compared. The respective maximum images of representative nuclei for each period of time PI are shown above: γH2AX—*green*, 53BP1—*red*, chromatin—artificially *blue*

NP-mediated radiosensitization is less prominent at 4 Gy as compared with 1 Gy dose (see Discussion), these results unequivocally confirm the presence of the radiosensitizing effect upon the conditions used in this work. Therefore, missing effects of GdBNs on nuclear DNA damage and repair support the idea of cell radiosensitization by GdBNs that originates in the cytoplasm, instead of reflecting the absence of the radiosensitizing effect.

Discussion

To our best knowledge, there are only few other reports on the effects of nanoparticles on DSBs formation and/or repair upon irradiation. In this work, we show that nanoparticles irradiated in the cytoplasm can potentiate radiation-induced cell killing without a need to penetrate into the cell nucleus and damage DNA. This conclusion might be surprising concerning the fact that the nuclear DNA is undoubtedly the most important and, at the same time, fragile structure in the cell. For a long time, a direct damage to DNA has been assumed as the key event starting the cascade of reactions mediating the cell response to irradiation [63]. However, microbeam irradiations only restricted to specific cellular subcompartments [49, 63, 64] clearly demonstrated that DNA can be damaged even without being directly hit; the cytoplasmic and also the extracellular irradiation triggered similar DNA damage and associated important cellular pathways as the dose deposited in the nucleus [65–67]. Moreover, several studies suggested that damage to the mitochondria or cell membrane markedly contribute to the cytotoxic effect of radiations [68]. Therefore, the whole cell, rather than DNA only, should be considered a sensor of radiation exposure [64].

The only cytoplasmic organelles containing DNA in human cells are the mitochondria. As the 'energy generators', the mitochondria are vital for the cell. However, our previous colocalization studies [31] excluded the possibility that GdBNs localize into (or close to) these organelles. On the other hand, we have revealed that GdBNs of parameters used in this work colocalize with the lysosomes in U87 cells [31]. In the light of our further findings presented here, i.e. that NPs affect neither the damage nor the repair of the nuclear DNA, we propose a provoking hypothesis that the radiosensitization mediated by our GdBNs is triggered by damage to the lysosomes and endosomes and potentially other cytoplasmic organelles in their proximity.

Several reports [69–72] revealed only recently that the lysosomes, these still mysterious organelles, play an important role in the initiation of the cell death signalling (reviewed e.g. in [72, 73]), regulation of the cell cycle [73] and energy metabolism (reviewed e.g. in [74]). Already a moderate lysosomal rupture forces the cell to apoptosis while more pronounced lysosomal leak results in necrosis without caspases activation [72, 73, 75]. Though we currently run experiments on this topic, we cannot provide a direct evidence for the lysosome damage mediated by our GdBNs (since these NPs are no more available). Nevertheless, Heid et al. [76] recently demonstrated that release of mitochondrial ROS subsequently leads to the

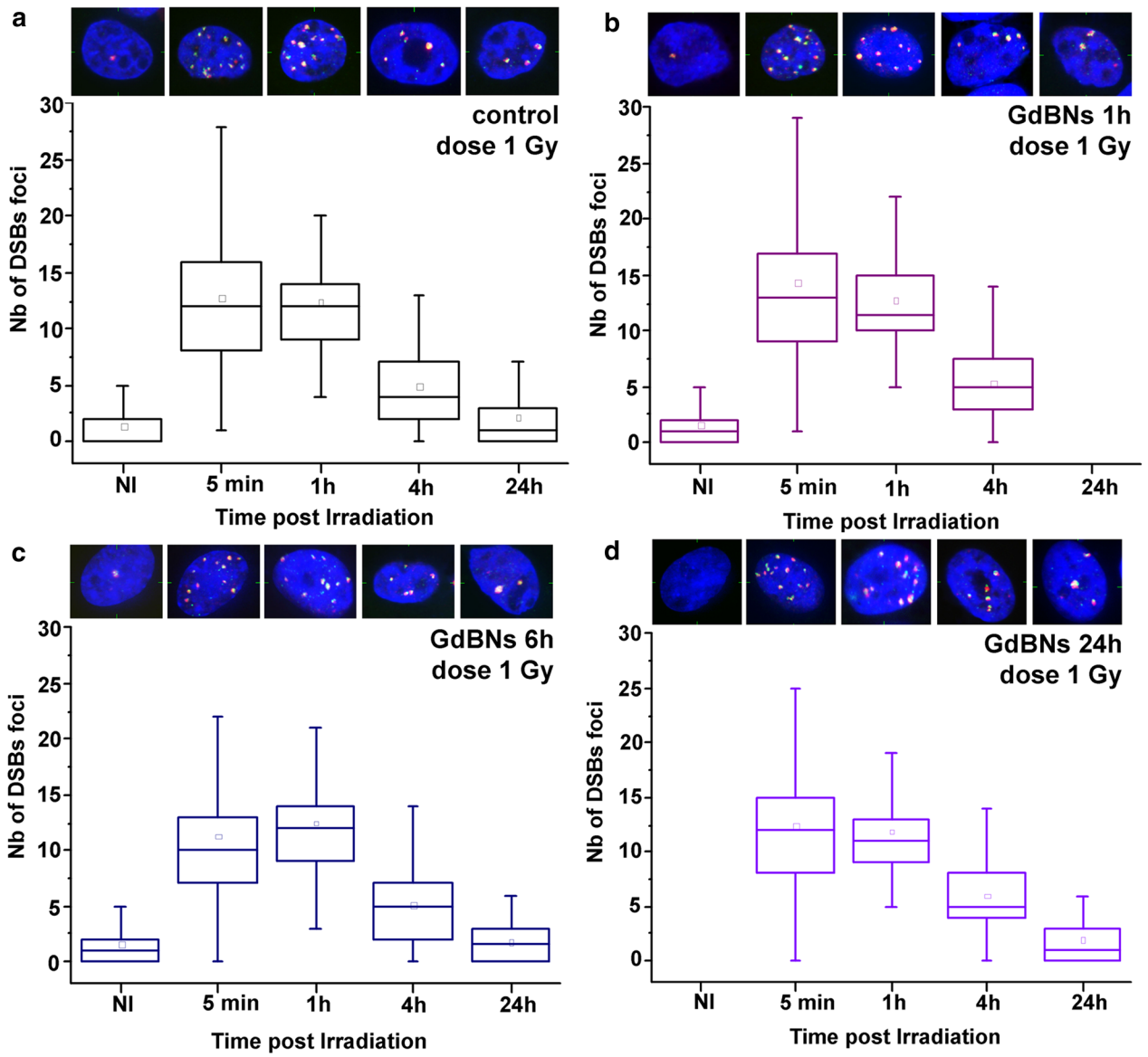

Fig. 6 Effect of incubation times with GdBNs on DSBs formation and repair in irradiated U87 cells. Distributions of DSBs foci numbers are compared for U87 cells irradiated with 1 Gy of γ-rays and never incubated with GdBNs (**a**) or incubated with 1 mM GdBNs for 1 h (**b**), 6 h (**c**) and 24 h (**d**). Non-irradiated controls (NI) are also compared. The respective maximum images of representative nuclei are shown above: γH2AX—*green*, 53BP1—*red*, chromatin—*blue*

lysosomal membrane permeabilization (LMP). Hence, we can legitimately suppose that huge amounts of ROS produced by irradiated NPs in the lysosomes can easily disintegrate the membranes in their substantial fraction, with the already described consequences for the cell.

In accordance with fundamental changes in the long-accepted paradigm on the role of the cytoplasm in the cell response to radiation, our results seem to disclose new important features of the mechanism by which GdBNs exert their radiosensitizing effect; however, the details and complexity of NPs-mediated cellular radiosensitization still remain a mystery. We speculate here about new molecular targets for NPs, other than the nuclear or mitochondrial DNA; this offers a broad scale of new opportunities for much safer therapeutic attacks on cancer cells. Indeed, many survival attributes of neoplastic cells are determined by extra-nuclear structures and processes, including mitochondrial and lysosomal proteins involved in (anti)apoptotic, cell cycle, and cell damage signaling pathways.

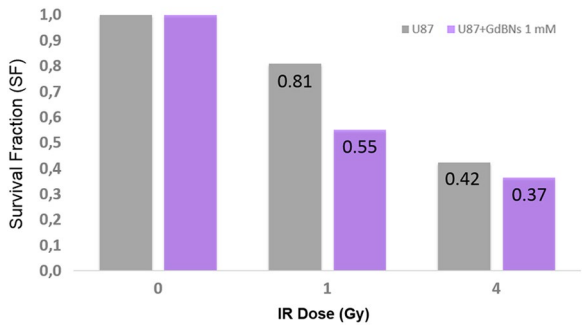

Fig. 7 Effect of GdBNs on clonogenic survival fraction of U87 cells. Surviving fractions of U87 cells never incubated with GdBNs (*grey*) or in the U87 incubated with 1 mM GdBNs for 1 h (*purple*) and irradiated by 1 and 4 Gy of γ-rays (^{60}Co), respectively. Non-irradiated controls (dose 0) were normalized to 1

Our preliminary experiments (results not shown) with other cell types and nanoparticle types of the similar size as GdBNs used in this work suggest that the conclusions (the cytoplasm damage-based radiosensitization, no escalation of DNA damage and no DNA repair inhibition), postulated in the above paragraphs for U87 cells and GdBNs, could be more generally valid.

As discussed later in more detail, many key factors may determine intracellular localization and distribution of NPs and, in turn, the extent and the mechanism of radiosensitization. It is, for instance, the size of NPs, which also dictates the effectivity of NPs intake and exclusion by the cells (e.g. Moser et al. [77]). The NPs concentration and composition as well have been reported to influence distribution of NPs in cells [32, 33] with a significant impact on the radiosensitization intensity and, perhaps, its mechanism (see later). Finally, as also demonstrated by our results, the radiation dose seems to be unimportant concerning the mechanism of NP-mediated cell radiosensitization (physical processes of NPs activation and damage introduction to biomolecules are still the same) but the contribution of NP-mediated effects to cell killing by irradiation depends on the dose (see Fig. 7). As soon as the radiation dose is high enough to activate NPs to an extent sufficient for damaging cytoplasmic organelles (lysosomes or other) in NPs proximity, additional dose escalation could not be expected to further increase the radiosensitization (while radiation damage to DNA still grows with the dose). Hence, for higher doses, the additional value of radiosensitization to therapy relatively decreases (see Fig. 7). These results may also explain why some authors, working with higher radiation doses, did not observed radiosensitizing effect of 1 mM GdBNs [22]. To conclude, our results are not limited to the cell type, nanoparticle type and conditions used herein; however, they should be generalized only with caution since our understanding to biological processes that take place in cells after the cytoplasmic irradiation, especially if NPs are present, is still very limited. Systematic studies in living cells are also necessary to understand how the key physical and biological factors mutually interact in providing the final radiosensitizing effect.

In addition to the efficiency, the genotoxicity of NPs represents another crucial issue in the context of therapy. It has been already demonstrated for cells loaded with silver NPs [58, 59] that even cytoplasmically localized NPs can induce DSBs without being irradiated. Preferentially sequestered in tumors though, NPs thus seem to undesirably damage also normal cells. By contrast, we showed here by currently the most sensitive method to detect DSBs that GdBNs of our parameters and under conditions used in this work are not genotoxic. This points to the importance of careful studies on the genotoxicity of each particular NPs type. Taken together, our results open new optimistic horizons for further development of efficient but safe NPs-based therapies of malignant and also non-malignant diseases; however each individual NPs type should be carefully characterized before being used in clinical practice, both in terms of its physical properties and biological activity.

There are only few studies our results can be compared with. In agreement with the present work, Jain et al. [2] demonstrated that 1.9 nm gold NPs neither enhance radiation-induced DSBs formation nor inhibit DNA repair in MDA-MB-231 breast cancer cells irradiated with MV electrons. On the other hand, Chithrani et al. [3] observed an increase of DSBs induction in HeLa cells incubated with 50 nm citrate-coated gold NPs irradiated with 6 MV photons. Similarly, Berbeco and co-workers [78] described a significant increase in DNA damage for 50 nm gold NPs in HeLa cells when activated by clinical MV photon beams. Finally, Zhu and co-workers [79] showed augmentation of DNA damage for megavoltage X-rays (6 MeV) and gold NPs in the size range of 20–74 nm (HepG2 cells). Taken together, it seems that bigger gold NPs enhance the DNA damage while the smaller NPs do not. Contradictory effects of NPs on DNA might be thus, at least partially, explained by their size. Indeed, for physical reasons, nanoparticles of 50 nm in diameter provide stronger radioenhancing effect than their smaller variants [3, 41]. However, Mowat et al. [22] and Miladi et al. [33] evidenced a significant rise in the nuclear DNA damage when they irradiated U87 or SQ20B cells in presence of GdBNs as small as 3 nm.

In the context of present article, Mowat's work [22] is particularly interesting since the authors used similar

experimental design (U87 cells, gadolinium-based NPs, and γ-ray irradiation) but came to different conclusions. The difference between our results and those of Mowat and coauthors [22] might reflect several factual and/or experimental factors:

1. Nanoparticles design: The design of GdBNs used in the present and Mowat's work [22] is different. We cannot exclude that differently designed NPs (gadolinium oxide core surrounded by polysiloxane shell vs. polysiloxane core surrounded by gadolinium chelates covalently grafted on the inorganic matrix), though composed of the same material, behave differently in cells and increase cell killing by various biological mechanisms.
2. Nanoparticles concentration and intracellular localization: Rima et al. [32] revealed by transmission electron microscopy that the number per cell of vacuoles containing GdBNs as well as the average size of these vacuoles increase with GdBNs concentration up to 0.6 mM; however, for concentrations up to 2 mM the average vacuole size still increases but their number per cell decreases. Confirming a functional importance of these findings, another work demonstrated that the size of NPs clusters is more relevant parameter determining the radiosensitizing effect of NPs than their intracellular concentration as the whole [32]. The concentration effects were also mentioned in a recent article of Miladi et al. [33] where GdBNs (labelled with Cy5.5) started to cluster on the membrane of SQ20B cells when higher (≥0.8 mM) NP concentrations were used. By contrast, with 1 mM GdBNs, we observed an intensive nanoparticle uptake by U87 cells without any signs of their accumulation on the membrane. This strictly cytoplasmic residence of 1 mM GdBNs agrees with our previous results in CHO cells [23] obtained with NPs of the same parameters.
   Along with influencing the NPs intracellular distribution, the concentration of NPs seems to affect the mechanism of radiosensitization and the final radiosensitizing effect. The experiments have been performed particularly using low gadolinium concentrations ranging from 0.1 to 1 mM (see Table 3 in the review paper [24]). In two different cancer cell lines, U87 (glioblastoma cell line) and SQ20B (squamous cell carcinoma cell line), the moderate gadolinium concentrations (0.4–0.7 mM) potentiated the effects of radiation most efficiently in in vitro conditions [22, 28]. Mowat and co-workers [22] showed that while 0.5 mM GdBNs substantially enhance radiation-induced DSBs foci formation as quantified by comet assay, this effect is absent or only minor for higher (1 and 2 mM) GdBNs concentrations. In other studies [22, 29], enhanced DNA damage as monitored by γH2AX levels appeared for the concentrations between 0.4 and 0.6 mM but not for the concentration of 2 mM [22]. In accordance, Rima et al. [32] found that the quantity of gadolinium in U87 cells and SQ20B cells increases almost linearly with the GdBNs concentration but the cell killing by irradiation peaks at the concentration of 0.6 mM and almost disappears at 1 mM. In contrary to the above mentioned studies, Porcel et al. [23] demonstrated significant radiosensitization of CHO cells exposed to He2+ and C6+ high energy ions, respectively, in presence of 1 mM GdBNs of the same parameters as used in the present work. The extent of U87 cell radiosensitization by 1 mM GdBNs after irradiation with 1 or 4 Gy of gamma rays is quantified in Fig. 7 and is obvious. Even small differences in the GdBNs concentration (in combination with other factors) may thus dramatically change the radiosensitizing effect; the concentrations around 1 mM seem to be most controversial in this respect. Hence, by choosing 1 mM GdBNs, we aimed to complete the mentioned studies and make another step towards our better understanding of the radiosensitization mediated by these NPs.
3. Nanoparticle surface modifications and labeling: Mowat et al. [22] used GdBNs conjugated with FITC for their DSBs studies. While we have proved consistently that the intracellular behavior of free GdBNs and GdBNs labeled with Cy5.5 does not differ [31], it is possible that FITC influences the uptake, distribution, and intracellular localization of NPs. This becomes evident when one compares the localization of GdBNs conjugated with Cy5.5 [31] and those with FITC [22]. Considering this risk of experimental artifacts, we deliberately used GdBNs without any fluorescent marker in our present study on the DSBs induction and repair, as well as in our earlier works on the cell survival [23, 31].
4. Methodology used to monitor DSBs damage induction and repair: detection of DSBs repair foci by confocal immunofluorescence microscopy currently represents the most sensitive method to detect DSBs and monitor their repair. However, one should keep in mind some limitations of this method. Recent evidence suggests that γH2AX (histone H2AX phosphorylation on Ser139) alone may not always correspond with DSBs. In addition to ATM-mediated phosphorylation, H2AX can be phosphorylated also by ATR kinase in response to single-stranded DNA formation [60–62], such as during the replication stress caused by the replication fork arrest. Further, DNA-PK mediates phosphorylation of H2AX in cells

during the apoptotic DNA fragmentation [52, 80]. Finally, γH2AX staining independent of DNA DSBs formation but related to nucleotide excision repair has previously been observed with primary human fibroblasts after UV irradiation [81]. In addition, it may be sometimes difficult to discriminate between true γH2AX foci and the background noise, especially in short periods of time post-irradiation (about 2–15 min PI) that are most relevant when DSBs induction is concerned [82]. Hence, we used independent immunolabelling of two DSBs markers—γH2AX and 53BP1—in combination with high-resolution confocal microscopy [82]. According to our best knowledge, this approach increases the accuracy of the DSBs recognition [83–86], and has not been used in earlier studies.

Further experimental incompatibility between studies follow from the fact that some authors analyzed the DSBs foci induction early PI [22] but the others [10, 46] rather followed the repair process, assuming that only the unrepaired DNA damage would lead to cell death or at least prevent further cell division. Here, we studied both the formation of DSBs immediately (5 min) PI and the removal of these lesions in several periods of time PI, up to 24 h PI. Therefore, we significantly extend the DSBs experiments performed by Mowat et al. [22] and Miladi et al. [33] in several aspects.

Conclusions

We demonstrate that GdBNs of parameters defined in this study are localized in the cell cytoplasm and are not genotoxic. In conditions where these NPs exert significant radioenhancing effect they affect neither the induction of DNA double strand breaks nor their repair kinetics and efficiency. While further studies are needed to shed more light on processes forcing the cells to die after the cytoplasmic damage, and on the role of NPs in these processes, we can reasonably hypothesize on the basis of our results that electron showers and ROS emitted by irradiated NPs accumulated in lysosomes can disintegrate these organelles. This could be accompanied by a massive release of degradation enzymes into the cytoplasm and consequently auto-digestion and death of the cell. New super-resolution 'nanoscopy' techniques [77, 87] open opportunities to test our hypothesis directly in future.

Authors' contributions

LS cooperated substantially in designing of the study, performed the irradiation and microscopy experiments, image acquisitions and analyses of images and data, proposed the interpretation of data and the manuscript draft. SL participated substantially in study design and drafting of the manuscript and revising it critically. DS was involved in microscopy image acquisitions. EPo was engaged in study design and the data interpretation. EPa participated in microscopy image acquisition. OT and FL designed and prepared GdBNs. DD helped with part of image analysis. SK took care of microscopy systems and participated in statistical evaluation of the data. MF contributed substantially on study design and drafting of the manuscript and in statistical evaluation of the data and their interpretation. All authors read and approved the final manuscript.

Author details

[1] Department of Cell Biology and Radiobiology, Institute of Biophysics of ASCR, Brno, Czech Republic. [2] Institute des Sciences Moléculaires d'Orsay (ISMO), Université Paris Sud 11, CNRS, Université Paris Saclay, Bât 351, 91405 Orsay Cedex, France. [3] Institut Lumière Matière, Université Claude Bernard Lyon 1, CNRS, 69622 Villeurbanne Cedex, France.

Acknowledgements

The work was supported by the following projects: the Ministry of Health of CR (16-29835A), The Ministry of Education, Youth and Sports of CR (OPVK CZ.1.07/2.3.00/30.0030), the Czech Science Foundation (P302/12/G157 and 16-12454S), EU COST MP1002 Nano-IBCT, and the Czech contribution to JINR Dubna 2015/2016–2018. The research leading to these results has received funding from the People Programme (Marie Curie Actions) of the European Union's Seventh Framework Programme (FP7/2007–2013) under REA Grant Agreement No [624370].

Competing interests

Authors have read and understood BioMed Central's guidance on competing interests and declare no competing interests in this manuscript.

Received: 13 May 2016 Accepted: 18 July 2016
Published online: 28 July 2016

References

1. Hainfeld JF, Slatkin DN, Smilowitz HM. The use of gold nanoparticles to enhance radiotherapy in mice. Phys Med Biol. 2004;49:N309–15.
2. Jain S, Coulter JA, Hounsell AR, Butterworth KT, McMahon SJ, Hyland WB, et al. Cell-specific radiosensitization by gold nanoparticles at megavoltage radiation energies. Int J Radiat Oncol Biol Phys. 2011;79:531–9.
3. Chithrani DB, Jelveh S, Jalali F, van Prooijen M, Allen C, Bristow RG, et al. Gold nanoparticles as radiation sensitizers in cancer therapy. Radiat Res. 2010;173:719–28.
4. Hainfeld JF, Dilmanian FA, Slatkin DN, Smilowitz HM. Radiotherapy enhancement with gold nanoparticles. J Pharm Pharmacol. 2008;60:977–85.
5. Matsumura Y, Maeda H. A new concept for macromolecular therapeutics in cancer chemotherapy: mechanism of tumoritropic accumulation of proteins and the antitumor agent smancs. Cancer Res. 1986;46:6387–92.
6. Noguchi Y, Wu J, Duncan R, Strohalm J, Ulbrich K, Akaike T, et al. Early phase tumor accumulation of macromolecules: a great difference in clearance rate between tumor and normal tissues. Jpn J Cancer Res. 1998;89:307–14.
7. Powell AC, Paciotti GF, Libutti SK. Colloidal gold: a novel nanoparticle for targeted cancer therapeutics. Methods Mol Biol. 2010;624:375–84.
8. Lim Z-ZJ, Li J-EJ, Ng C-T, Yung L-YL, Bay B-H. Gold nanoparticles in cancer therapy. Acta Pharmacol Sin. 2011;32:983–90.
9. Hainfeld JF, Slatkin DN, Focella TM, Smilowitz HM. Gold nanoparticles: a new X-ray contrast agent. Br J Radiol. 2006;79:248–53.
10. Chattopadhyay N, Cai Z, Kwon YL, Lechtman E, Pignol J-P, Reilly RM. Molecularly targeted gold nanoparticles enhance the radiation response of breast cancer cells and tumor xenografts to X-radiation. Breast Cancer Res Treat. 2013;137:81–91.
11. Mieszawska AJ, Mulder WJM, Fayad ZA, Cormode DP. Multifunctional gold nanoparticles for diagnosis and therapy of disease. Mol Pharm. 2013;10:831–47.
12. Chang M-Y, Shiau A-L, Chen Y-H, Chang C-J, Chen HH-W, Wu C-L. Increased apoptotic potential and dose-enhancing effect of gold nanoparticles in combination with single-dose clinical electron beams on tumor-bearing mice. Cancer Sci. 2008;99:1479–84.

13. Zhang X, Xing JZ, Chen J, Ko L, Amanie J, Gulavita S, et al. Enhanced radiation sensitivity in prostate cancer by gold-nanoparticles. Clin Investig Med Médecine Clin Exp. 2008;31:E160–7.
14. Zheng Y, Hunting DJ, Ayotte P, Sanche L. Radiosensitization of DNA by gold nanoparticles irradiated with high-energy electrons. Radiat Res. 2008;169:19–27.
15. Porcel E, Kobayashi K, Usami N, Remita H, Le Sech C, Lacombe S. Photosensitization of plasmid-DNA loaded with platinum nano-particles and irradiated by low energy X-rays. J Phys Conf Ser. 2011;261:12004.
16. Porcel E, Li S, Usami N, Remita H, Furusawa Y, Kobayashi K, et al. Nano-Sensitization under gamma rays and fast ion radiation. J Phys Conf Ser. 2012;373:12006.
17. Maier-Hauff K, Ulrich F, Nestler D, Niehoff H, Wust P, Thiesen B, et al. Efficacy and safety of intratumoral thermotherapy using magnetic iron-oxide nanoparticles combined with external beam radiotherapy on patients with recurrent glioblastoma multiforme. J Neurooncol. 2011;103:317–24.
18. Bradbury MS, Phillips E, Montero PH, Cheal SM, Stambuk H, Durack JC, et al. Clinically-translated silica nanoparticles as dual-modality cancer-targeted probes for image-guided surgery and interventions. Integr Biol. 2013;5:74–86.
19. Sharma P, Brown SC, Walter G, Santra S, Scott E, Ichikawa H, et al. Gd nanoparticulates: from magnetic resonance imaging to neutron capture therapy. Adv Powder Technol. 2007;18:663–98.
20. Tillement O, Roux S, Perriat P, Leduc G, Mandon C, Mutelet B, et al. Utilisation de nanoparticules a base de lanthanides comme agents radiosensibilisants; 2008. http://www.google.com/patents/EP2200659A2?cl=fr. Accessed 23 Jul 2015.
21. Le Duc G, Miladi I, Alric C, Mowat P, Bräuer-Krisch E, Bouchet A, et al. Toward an image-guided microbeam radiation therapy using gadolinium-based nanoparticles. ACS Nano. 2011;5:9566–74.
22. Mowat P, Mignot A, Rima W, Lux F, Tillement O, Roulin C, et al. In vitro radiosensitizing effects of ultrasmall gadolinium based particles on tumour cells. J Nanosci Nanotechnol. 2011;11:7833–9.
23. Porcel E, Tillement O, Lux F, Mowat P, Usami N, Kobayashi K, et al. Gadolinium-based nanoparticles to improve the hadrontherapy performances. Nanomed Nanotechnol Biol Med. 2014;10:1601–8.
24. Sancey L, Lux F, Kotb S, Roux S, Dufort S, Bianchi A, et al. The use of theranostic gadolinium-based nanoprobes to improve radiotherapy efficacy. Br J Radiol. 2014;87:20140134.
25. Louis DN, Ohgaki H, Wiestler OD, Cavenee WK, Burger PC, Jouvet A, et al. The 2007 WHO Classification of Tumours of the Central Nervous System. Acta Neuropathol (Berl.). 2007;2007(114):97–109.
26. Bridot J-L, Faure A-C, Laurent S, Rivière C, Billotey C, Hiba B, et al. Hybrid gadolinium oxide nanoparticles: multimodal contrast agents for in vivo imaging. J Am Chem Soc. 2007;129:5076–84.
27. Mignot A, Truillet C, Lux F, Sancey L, Louis C, Denat F, et al. A top-down synthesis route to ultrasmall multifunctional Gd-based Silica nanoparticles for theranostic applications. Chem Eur J. 2013;19:6122–36.
28. Lux F, Mignot A, Mowat P, Louis C, Dufort S, Bernhard C, et al. Ultrasmall rigid particles as multimodal probes for medical applications. Angew Chem Int Ed. 2011;50:12299–303.
29. Roux S, Tillement O, Billotey C, Coll JL, Duc GL, Marquette CA, et al. Multifunctional nanoparticles: from the detection of biomolecules to the therapy. Int J Nanotechnol. 2010;7:781.
30. Bianchi A, Dufort S, Lux F, Courtois A, Tillement O, Coll J-L, et al. Quantitative biodistribution and pharmacokinetics of multimodal gadolinium-based nanoparticles for lungs using ultrashort TE MRI. Magn Reson Mater Phys Biol Med. 2014;27:303–16.
31. Štefančíková L, Porcel E, Eustache P, Li S, Salado D, Marco S, et al. Cell localisation of gadolinium-based nanoparticles and related radiosensitising efficacy in glioblastoma cells. Cancer Nanotechnol. 2014;5:1–15.
32. Rima W, Sancey L, Aloy M-T, Armandy E, Alcantara GB, Epicier T, et al. Internalization pathways into cancer cells of gadolinium-based radiosensitizing nanoparticles. Biomaterials. 2013;34:181–95.
33. Miladi I, Aloy M-T, Armandy E, Mowat P, Kryza D, Magné N, et al. Combining ultrasmall gadolinium-based nanoparticles with photon irradiation overcomes radioresistance of head and neck squamous cell carcinoma. Nanomed Nanotechnol Biol Med. 2015;11:247–57.
34. Butterworth KT, McMahon SJ, Taggart LE, Prise KM. Radiosensitization by gold nanoparticles: effective at megavoltage energies and potential role of oxidative stress. Transl Cancer Res. 2013;2:269–79.
35. Misawa M, Takahashi J. Generation of reactive oxygen species induced by gold nanoparticles under x-ray and UV Irradiations. Nanomed Nanotechnol Biol Med. 2011;7:604–14.
36. Porcel E, Liehn S, Remita H, Usami N, Kobayashi K, Furusawa Y, et al. Platinum nanoparticles: a promising material for future cancer therapy? Nanotechnology. 2010;21:85103.
37. Krpetić Ž, Nativo P, Sée V, Prior IA, Brust M, Volk M. Inflicting controlled nonthermal damage to subcellular structures by laser-activated gold nanoparticles. Nano Lett. 2010;10:4549–54.
38. McMahon SJ, Hyland WB, Muir MF, Coulter JA, Jain S, Butterworth KT, et al. Nanodosimetric effects of gold nanoparticles in megavoltage radiation therapy. Radiother Oncol. 2011;100:412–6.
39. McMahon SJ, Hyland WB, Muir MF, Coulter JA, Jain S, Butterworth KT, et al. Biological consequences of nanoscale energy deposition near irradiated heavy atom nanoparticles. Sci Rep. 2011;1. http://www.nature.com/srep/2011/110620/srep00018/full/srep00018.html. Accessed 22 Jul 2015.
40. Lechtman E, Mashouf S, Chattopadhyay N, Keller BM, Lai P, Cai Z, et al. A Monte Carlo-based model of gold nanoparticle radiosensitization accounting for increased radiobiological effectiveness. Phys Med Biol. 2013;58:3075–87.
41. Burger N, Biswas A, Barzan D, Kirchner A, Hosser H, Hausmann M, et al. A method for the efficient cellular uptake and retention of small modified gold nanoparticles for the radiosensitization of cells. Nanomed Nanotechnol Biol Med. 2014;10:1365–73.
42. Kassis AI, Adelstein SJ. Radiobiologic principles in radionuclide therapy. J Nucl Med Off. Publ Soc Nucl Med. 2005;46(Suppl 1):4S–12S.
43. Belli M, Sapora O, Tabocchini MA. Molecular targets in cellular response to ionizing radiation and implications in space radiation protection. J Radiat Res. 2002;43(Suppl):S13–9.
44. Usami N, Furusawa Y, Kobayashi K, Lacombe S, Reynaud-Angelin A, Sage E, et al. Mammalian cells loaded with platinum-containing molecules are sensitized to fast atomic ions. Int J Radiat Biol. 2008;84:603–11.
45. Kong T, Zeng J, Wang X, Yang X, Yang J, McQuarrie S, et al. Enhancement of radiation cytotoxicity in breast-cancer cells by localized attachment of gold nanoparticles. Small. 2008;4:1537–43.
46. Jones BL, Krishnan S, Cho SH. Estimation of microscopic dose enhancement factor around gold nanoparticles by Monte Carlo calculations. Med Phys. 2010;37:3809.
47. Leung MKK, Chow JCL, Chithrani BD, Lee MJG, Oms B, Jaffray DA. Irradiation of gold nanoparticles by X-rays: Monte Carlo simulation of dose enhancements and the spatial properties of the secondary electrons production. Med Phys. 2011;38:624–31.
48. Tartier L, Gilchrist S, Burdak-Rothkamm S, Folkard M, Prise KM. Cytoplasmic irradiation induces mitochondrial-dependent 53BP1 protein relocalization in irradiated and bystander cells. Cancer Res. 2007;67:5872–9.
49. Wu L-J, Randers-Pehrson G, Xu A, Waldren CA, Geard CR, Yu Z, et al. Targeted cytoplasmic irradiation with alpha particles induces mutations in mammalian cells. Proc Natl Acad Sci. 1999;96:4959–64.
50. Morlieras J, Chezal J-M, Miot-Noirault E, Roux A, Heinrich-Balard L, Cohen R, et al. Development of gadolinium based nanoparticles having an affinity towards melanin. Nanoscale. 2013;5:1603–15.
51. Falk M, Lukasova E, Gabrielova B, Ondrej V, Kozubek S. Chromatin dynamics during DSB repair. Biochim Biophys Acta. 2007;1773:1534–45.
52. Rogakou EP, Pilch DR, Orr AH, Ivanova VS, Bonner WM. DNA double-stranded breaks induce histone H2AX phosphorylation on serine 139. J Biol Chem. 1998;273:5858–68.
53. Bakkenist CJ, Kastan MB. DNA damage activates ATM through intermolecular autophosphorylation and dimer dissociation. Nature. 2003;421:499–506.
54. Kozubek M, Kozubek S, Lukásová E, Marecková A, Bártová E, Skalníková M, et al. High-resolution cytometry of FISH dots in interphase cell nuclei. Cytometry. 1999;36:279–93.
55. Kozubek M, Kozubek S, Lukásová E, Bártová E, Skalníková M, Matula P, et al. Combined confocal and wide-field high-resolution cytometry of fluorescent in situ hybridization-stained cells. Cytometry. 2001;45:1–12.
56. Matula P, Maska M, Danek O, Matula P, Kozubek M. Acquiarium: free software for the acquisition and analysis of 3D images of cells in fluorescence microscopy. In: IEEE International Symposium on Biomedical Imaging: from Nano to Macro 2009 ISBI 09; 2009. p. 1138–41.

57. Kim S, Choi JE, Choi J, Chung K-H, Park K, Yi J, et al. Oxidative stress-dependent toxicity of silver nanoparticles in human hepatoma cells. Toxicol In Vitro. 2009;23:1076–84.
58. Ahamed M, Karns M, Goodson M, Rowe J, Hussain SM, Schlager JJ, et al. DNA damage response to different surface chemistry of silver nanoparticles in mammalian cells. Toxicol Appl Pharmacol. 2008;233:404–10.
59. Zheng Q, Yang H, Wei J, Tong J, Shu Y. The role and mechanisms of nanoparticles to enhance radiosensitivity in hepatocellular cell. Biomed Pharmacother. 2013;67:569–75.
60. Kang B, Mackey MA, El-Sayed MA. Nuclear targeting of gold nanoparticles in cancer cells induces DNA damage, causing cytokinesis arrest and apoptosis. J Am Chem Soc. 2010;132:1517–9.
61. Li JJ, Zou L, Hartono D, Ong C-N, Bay B-H, Lanry Yung L-Y. Gold nanoparticles induce oxidative damage in lung fibroblasts in vitro. Adv Mater. 2008;20:138–42.
62. Trono JD, Mizuno K, Yusa N, Matsukawa T, Yokoyama K, Uesaka M. Size, concentration and incubation time dependence of gold nanoparticle uptake into pancreas cancer cells and its future application to X-ray drug delivery system. J Radiat Res. 2011;52:103–9.
63. Prise KM, Folkard M, Kuosaite V, Tartier L, Zyuzikov N, Shao C. What role for DNA damage and repair in the bystander response? Mutat Res (Tokyo). 2006;597:1–4.
64. Zhou H, Hong M, Chai Y, Hei TK. Consequences of cytoplasmic irradiation: studies from microbeam. J Radiat Res (Tokyo). 2009;50(Suppl A):A59–65.
65. Morgan WF. Non-targeted and delayed effects of exposure to ionizing radiation: I. Radiation-induced genomic instability and bystander effects in vitro. Radiat Res. 2003;159:567–80.
66. Morgan WF. Non-targeted and delayed effects of exposure to ionizing radiation: II. Radiation-induced genomic instability and bystander effects in vivo, clastogenic factors and transgenerational effects. Radiat Res. 2003;159:581–96.
67. Mothersill C, Seymour CB. Radiation-induced bystander effects—implications for cancer. Nat Rev Cancer. 2004;4:158–64.
68. Prise KM, Schettino G, Folkard M, Held KD. New insights on cell death from radiation exposure. Lancet Oncol. 2005;6:520–8.
69. Cuervo AM, Dice JF. Lysosomes, a meeting point of proteins, chaperones, and proteases. J Mol Med. 1998;76:6–12.
70. Eskelinen E-L, Tanaka Y, Saftig P. At the acidic edge: emerging functions for lysosomal membrane proteins. Trends Cell Biol. 2003;13:137–45.
71. Luzio JP, Pryor PR, Bright NA. Lysosomes: fusion and function. Nat Rev Mol Cell Biol. 2007;8:622–32.
72. Turk B, Turk V. Lysosomes as "suicide bags" in cell death: myth or reality? J Biol Chem. 2009;284:21783–7.
73. Boya P, Kroemer G. Lysosomal membrane permeabilization in cell death. Oncogene. 2008;27:6434–51.
74. Settembre C, Fraldi A, Medina DL, Ballabio A. Signals for the lysosome: a control center for cellular clearance and energy metabolism. Nat Rev Mol Cell Biol. 2013;14:283–96.
75. Kurz T, Terman A, Gustafsson B, Brunk UT. Lysosomes in iron metabolism, ageing and apoptosis. Histochem Cell Biol. 2008;129:389–406.
76. Heid ME, Keyel PA, Kamga C, Shiva S, Watkins SC, Salter RD. Mitochondrial reactive oxygen species induces NLRP3-dependent lysosomal damage and inflammasome activation. J Immunol. 2013;191:5230–8.
77. Moser F, Hildenbrand G, Müller P, Al Saroori A, Biswas A, Bach M, et al. Cellular uptake of gold nanoparticles and their behavior as labels for localization microscopy. Biophys J. 2016;110:947–53.
78. Berbeco RI, Korideck H, Ngwa W, Kumar R, Patel J, Sridhar S, et al. DNA damage enhancement from gold nanoparticles for clinical MV photon beams. Radiat Res. 2012;178:604–8.
79. Zhu C, Zheng Q, Wang L, Xu H-F, Tong J, Zhang Q, et al. Synthesis of novel galactose functionalized gold nanoparticles and its radiosensitizing mechanism. J Nanobiotechnol. 2015;13. http://www.jnanobiotechnology.com/content/13/1/67. Accessed 30 Mar 2016.
80. Mukherjee B, Kessinger C, Kobayashi J, Chen BPC, Chen DJ, Chatterjee A, et al. DNA-PK phosphorylates histone H2AX during apoptotic DNA fragmentation in mammalian cells. DNA Repair. 2006;5:575–90.
81. Marti TM, Hefner E, Feeney L, Natale V, Cleaver JE. H2AX phosphorylation within the G1 phase after UV irradiation depends on nucleotide excision repair and not DNA double-strand breaks. Proc Natl Acad Sci USA. 2006;103:9891–6.
82. Hofer M, Falk M, Komůrková D, Falková I, Bačíková A, Klejdus B, et al. Two new faces of amifostine: protector from DNA damage in normal cells and inhibitor of DNA repair in cancer cells. J Med Chem. 2016;59:3003–17.
83. Falk M, Lukasova E, Falkova I, Stefancikova L, Jezkova L, Bacikova A, et al. Chromatin differentiation of white blood cells decreases DSB damage induction, prevents functional assembly of repair foci, but has no influence on protrusion of heterochromatic DSBs into the low-dense chromatin. J Radiat Res (Tokyo). 2014;55:i81–2.
84. Ježková L, Falk M, Falková I, Davídková M, Bačíková A, Štefančíková L, et al. Function of chromatin structure and dynamics in DNA damage, repair and misrepair: γ-rays and protons in action. Appl Radiat Isot. 2014;83:128–36.
85. de Feraudy S, Revet I, Bezrookove V, Feeney L, Cleaver JE. A minority of foci or pan-nuclear apoptotic staining of γH2AX in the S phase after UV damage contain DNA double-strand breaks. Proc Natl Acad Sci USA. 2010;107:6870–5.
86. Wakasugi M, Sasaki T, Matsumoto M, Nagaoka M, Inoue K, Inobe M, et al. Nucleotide Excision Repair-dependent DNA Double-strand Break Formation and ATM Signaling Activation in Mammalian Quiescent Cells. J Biol Chem. 2014. doi:10.1074/jbc.M114.589747.
87. Falk M. Nanoscopy and nanoparticles hand-in-hand to fight cancer: an exciting entrée into the rising NANOworld. Biophys J. 2016;110:872–3.

New and Notable

Nanoscopy and Nanoparticles Hand-in-Hand to Fight Cancer: An Exciting Entrée into the Rising NANOworld

Martin Falk[1,*]
[1]Department of Cell Biology and Radiobiology, Institute of Biophysics, Czech Academy of Sciences, Brno, Czech Republic

Two words with the prefix "NANO"—nanoparticles and nanoscopy—appear in the title of Moser's article published in this issue of the *Biophysical Journal* (1), although the latter one remains hidden behind the term "localization microscopy". What is so exciting about this title (and Moser's article) is that it describes how two nanotechnologies are used to fight cancer and further amend each other. The article thus unequivocally demonstrates that both biological sciences and medical research have definitely left the micro-dimensions and dives head-first into the rising NANOworld.

Nanoparticles might represent new versatile weapons in the war on cancer. Among numerous applications, gold (GNPs) and other metal nanoparticles (composed of high-*Z* atoms) were proposed as selective tumor cell radiosensitizers (2). In animal experiments, GNPs were preferentially sequestered by tumors and, upon irradiation, locally enhanced the dose by emitting showers of Auger electrons. Metal nanoparticles thus promise to increase the radiotherapy efficiency while reducing its side effects. Although the radioactivation of nanoparticles is well described in terms of physics, practical development of these new nanodrugs depends on our better understanding of the fate of nanoparticles in cells.

Submitted December 22, 2015, and accepted for publication January 11, 2016.

*Correspondence: mfalk@seznam.cz

Editor: Paul Wiseman.

0006-3495/16/02/0001/2

In their work, Moser et al. (1) study intracellular uptake, distribution, and persistence of GNPs differing in diameter by means of spectral position determination microscopy (SPDM) with previously unprecedented resolution. This represents a breakthrough innovation over earlier studies. Although modern applications of classical optical microscopy (like 4D live-cell fluorescence confocal microscopy, FRAP, FLIM, etc.) are among the most fruitful methods of biological research in the past decade and brought about many important discoveries of the principal features of cell architecture and function (e.g., Falk et al. (3)), the restriction of optical resolution determined by Abbe criterion to ~0.2 micrometers could hardly be circumvented. Already developed optical single-molecule localization techniques have allowed us to determine intracellular nanoparticle location (in low-density limits where single fluorochrome molecule localization is possible), but not to quantify more densely arranged particle clusters, which is necessary for making more precise structural and mechanistic interpretations. A number of electron microscopy studies recently appeared taking advantage of electron-beam contrast qualities of gold nanoparticles to analyze their uptake by cells under physiological conditions (4,5). However, usability of electron microscopy for intact/living cell applications is rather exceptional. Microscopy limitations thus largely complicate identification of intracellular targets and processes influenced by GNPs and other nanoparticles.

The situation has dramatically changed with the discovery of superresolution methods like localization microscopy, which SPDM variant has been employed in Moser's work (1). Recognizing this milestone, superresolution microscopy has been published in *Nature Methods* (6) as the Method of the Year for 2008 and in 2014, Eric Betzig, William Moerner, and Stefan Hell were awarded the Nobel Prize in Chemistry for converting the microscope into the nanoscope. Although several other ways for circumventing the Abbe criterion have also been proposed and transferred into practice, SPDM—originally published in Esa et al. (7) and substantially elaborated by teams of Christoph Cremer and Michael Hausmann (both coauthoring the article) (reviewed in Cremer et al. (8))—offers an important advantage over many of the other techniques. While ensuring effective optical resolution of ~10 nm, the method allows working with numerous conventional dyes and is naturally compatible with spatial (3D) cell fixation and even living cell observation. The trick of SPDM consists in optical isolation of individual fluorochrome molecules/nanoparticles and their position determination with nanometer precision via their time-dependent blinking. Thus, for instance, spatial arrangements of individual nanoparticles or nanostructures of organelles, membranes, or chromatin can be studied under truly physiological conditions of the cell.

Despite tremendous progress, SPDM is still in its infancy. Similar to standard fluorescence microscopy, one of substantial problems with SPDM may appear with permanent bleaching of conventional blinking dyes. While originally aiming to improve cancer radiotherapy by exploring intracellular behavior of GNPs, Moser et al. (1) also recognized their stable blinking. Because the effect followed from plasmon resonance and not from reversible photobleaching as for dyes, the blinking lasted for a sufficiently long time to preclude current problems with conventional fluorochromes and facilitate usage of GNPs as preferable tags for various labeling strategies associated with SPDM. Importantly, spectral fluorescence of GNPs depended on their size and environment; this opens doors to simultaneous nanoimaging of multiple

http://dx.doi.org/10.1016/j.bpj.2016.01.005

cellular targets and promises broad experimental possibilities.

In considering future perspectives of SPDM, Moser et al. (1) performed their observations on spatially (3D) fixed cells in two colors. Although multicolor and 3D SPDM applications have been already reported (frequently by M. Hausmann and C. Cremer coauthoring Moser's work) (9), practical mastering of this technique still represents a challenge contrasting with its simple principle. Thousands of images must be registered and analyzed for each color and each optical section to obtain the desired resolution. A future dream thus remains 3D time-lapse (4D) SPDM in living cells, where whole image mega-sets have to be taken continuously with time intervals of minutes, seconds, or perhaps milliseconds. New nonbleachable blinking labels, as discussed, might avoid the problem with permanent bleaching of intensively and repeatedly illuminated samples. Future attempts must also discover a method, equivalent to GFP-tagging of proteins, to label specific DNA loci in vivo. Combinatorial oligonucleotide fluorescence in situ hybridization (COMBO FISH), proposed by M. Hausmann (for review, see Burger et al. (10)), might point the direction to this Holy Grail of cell biology (11).

With the exciting SPDM technology at hand, Moser et al. (1) quantify cell internalization of experimentally more (25 nm) and less (10 nm) therapeutically efficient gold nanoparticles, for the first time simultaneously under physiological conditions and in terms of absolute numbers. This attempt is important to understand the biological mechanism of nanoparticle-mediated radiosensitization, quantitative and dynamic modeling of this effect, and therapy planning in future. For instance, it is not clear on the basis of literature review and our unpublished data whether the radiosensitization always relies on enhancing the DNA damage or the cytoplasmic events (like mitochondria or lysosomes disruption) might be involved. Evidently, SPDMs have strong potential to substantially participate in answering this and other fundamental questions associated with nanoparticle research: In addition to providing superresolution under physiological conditions, the method also enables spectroscopic resolution of nanoparticles of different sizes, as nanoparticles optically blink at a size-dependent wavelength (demonstrated for GNPs in Moser's work). Finally, Stuhlmüller and Hausmann (11) recently proposed new technology of how to deliver and retain therapeutically more efficient bigger gold nanoparticles in cells; GNPs were tagged with modified DNA oligonucleotides and conveyed into the cells by transfection. In Moser's work (1), the authors demonstrate, using SPDM, that this strategy allows enhanced and stable cellular internalization of these nanoparticles.

REFERENCES

1. Moser, F., G. Hildenbrand, …, M. Hausmann. 2015. Cellular uptake of gold nanoparticles and their environment-dependent behavior as labels for localization microscopy. *Biophys. J.* 110:■■■–■■■.

2. Retif, P., S. Pinel, …, M. Barberi-Heyob. 2015. Nanoparticles for radiation therapy enhancement: the key parameters. *Theranostics.* 5:1030–1044.

3. Falk, M., E. Lukasova, and S. Kozubek. 2010. Higher-order chromatin structure in DSB induction, repair and misrepair. *Mutat. Res.* 704:88–100.

4. Peckys, D. B., and N. de Jonge. 2011. Visualizing gold nanoparticle uptake in live cells with liquid scanning transmission electron microscopy. *Nano Lett.* 11:1733–1738.

5. Peckys, D. B., and N. de Jonge. 2014. Gold nanoparticle uptake in whole cells in liquid examined by environmental scanning electron microscopy. *Microsc. Microanal.* 20:189–197.

6. Editorial. 2009. Method of the Year 2008. *Nature Methods.* 6:1.

7. Esa, A., P. Edelmann, …, C. Cremer. 2000. Three-dimensional spectral precision distance microscopy of chromatin nanostructures after triple-colour DNA labelling: a study of the BCR region on chromosome 22 and the Philadelphia chromosome. *J. Microsc.* 199:96–105.

8. Cremer, C., R. Kaufmann, …, M. Hausmann. 2011. Superresolution imaging of biological nanostructures by spectral precision distance microscopy. *Biotechnol. J.* 6:1037–1051.

9. Kaufmann, R., P. Müller, …, C. Cremer. 2011. Analysis of Her2/neu membrane protein clusters in different types of breast cancer cells using localization microscopy. *J. Microsc.* 242:46–54.

10. Burger, N., A. Biswas, …, M. R. Veldwijk. 2014. A method for the efficient cellular uptake and retention of small modified gold nanoparticles for the radiosensitization of cells. *Nanomedicine (Lond.).* 10:1365–1373.

11. Stuhlmüller, M., and M. Hausmann. 2015. Selection of COMBO-FISH probes for multi-purpose applications. *J. Theor. Comput. Sci.* 2:131–132.

Gold Nanoparticle Enhanced Radiosensitivity of Cells: Considerations and Contradictions from Model Systems and Basic Investigations of Cell Damaging for Radiation Therapy

Martin Falk[1], Michael Wolinsky[2,3], Marlon R. Veldwijk[2], Georg Hildenbrand[2,3], Michael Hausmann[3]

[1]Institute of Biophysics, Czech Academy of Sciences, Brno; [2]Dept. Radiation Oncology, Universitätsmedizin Mannheim; [3]Kirchhoff-Institute for Physics, Heidelberg University

Most cancer patients are currently treated with radiotherapy [#Atun2015] and/or chemotherapy, which so far are besides surgery very effective and successful therapy approaches for many types of cancer. The primary precondition for successful radiotherapy (and/or chemotherapy) [#Wenz2001] is a higher sensitivity of cancer cells than normal cells to DNA damage by radiation and their lower DNA repair capacity. This is fulfilled in many cases. For instance, due to improper cell cycle checkpoints or deficient repair pathways [#Loeffler2007], cancer cells become genetically instable and accumulate genomic alterations making tumors more and more vulnerable to DNA damaging agents compared to non-cancer cells. Damage tolerance is of relevance here as well and most likely quite in favor for the tumor cells. Cancer cells often become radioresistant since genomic instability accelerates their evolution and overgrow of aggressive cell clones. Highly radioresistant tumors are difficult to be eradicated without seriously damaging also the normal tissue and organs in tumor surroundings [#Tomita2018/ #Lahm2018/ #Gu2018]. In these cases, a crucial question for improved cancer treatment therefore is, how to enhance the radiation treatment effects in the (radioresistant) tumor cells while preserve the normal, non-tumorous tissues around as much as possible. This issue also becomes of fundamental importance for tumors located in very close proximity of organs with central vital functions. In the worst situation, the radioresistance and problematic location appear in combination, as for instance in the case of the most aggressive and highly radioresistant tumor [#Zhou2007] starting in the brain know as glioblastoma multiforme [#Davies2016]. Investigations of such tumors require the developments of special model systems [#Struve2015]. SkBr3 cells [#Engel1978] as used in the data presented here in detail were involved as a model for breast cancer with Her2/neu up-regulation, on which the radiation effects are studied in combination with antibody and/or chemo-treatment [#Lacroix2004].

Many promising strategies are under development to improve radiotherapy. Spatial dose fractionation, time dose fractionation, micro/mini-beam irradiation, heavy-ion irradiation [#Durante2017/ #González2018 /#Jánváry2018 /#Zhang2018 /#Sammer2017 /#Prezado2009/ #Jezkova2018/ #Girst2016], and application of normal cell radio-protectants [#Hofer2017a/ #Hofer2017b] and/or tumor cell radio-sensitizers [#Hofer2016] are already being used and combined in practice. One of the radio-sensitizing approaches often discussed is to selectively potentiate radiation toxicity only in tumor cells by incorporation of metal nanoparticles either into the tumor tissue or even into the tumor cells [#Štefančiková2016/ #Ngwa2017/ #Hildenbrand2018/ #Ngwa2014/ #Kuncik2018/ #Lux2018/ #Li2017/ #Sancey2014/ #Pagácová2019]. Due to high electron content and photoelectric absorption cross-section, metal (high-Z material; Z = atomic number of the element) nanoparticles emit showers of secondary electrons upon irradiation [#Nikjoo20087/

#Hossain2012]. Launched electrons then generate clouds of highly dense ionization processes, enhancing radiation-induced cell damage followed by cell death [#Zygmanki2013].

Even under physiological conditions the DNA in the cell nucleus is sensitive to many environmental stressing conditions [#Falk2014a/ #Falk2014b/ #Rittich2004/ #Freneau2018] and can be considerably damaged even with relatively low doses of ionizing radiation [#Falk2010/ #Hausmann2017]. As serious damaging effects of ionizing radiation on (cancer) cells are mostly mediated through fragmentation of nuclear chromatin by inserting single strand (SSB) and double strand (DSBs) DNA breaks [#Schipler2013], nanoparticle radio-sensitizing effects have been ascribed to an increase of DSBs generated with the same radiation dose in presence of nanoparticles [#Hildenbrand2018]. Clustered and thus complex DSBs can hardly be repaired without any remaining damage consequences [#Jezkova2018/ #Bobkova2018/ #Mladenov2016/ #Mladenov2013] and are known as the main factor responsible for the enhanced radiobiological efficiency (RBE) of densely ionizing high LET radiation. According to this hypothesis, at a given dose of a given radiation type, nanoparticles boost cell killing by locally amplifying the dose within the cell volume [#Porcel2010], which is followed by additional DNA damage processes. Indeed, an increase of SSBs and DSBs has been reported relative to untreated samples (i.e. without nanoparticle incorporation) in nuclear DNA of cells irradiated in presence of various metal nanoparticles [#Porcel2010].

In general, nanoparticles are preferentially internalized by and enriched in tumor tissue due to the phenomenon known as Enhanced Permeability and Retention (EPR). This enhancement effect reasons that, in radiotherapy, nanoparticles may be selectively targeted to tumor cells [#Maeda2010/ #Maeda2011/ #Fang2011/ #Prabhakar2013/ #Bertrand2014/ #Chitrani2010a/ #Chitrani2010b]. Furthermore several types of nanoparticles can simultaneously be used as imaging contrast agents in theranostics [#Hainfeld2013]. Nanoparticles can be also functionalized to better select and infiltrate tumor cells (only) or to target cellular organelles specifically [#Hildenbrand2018/ #Bertrand2014]. Such surface modifications include attachment of antibodies, drugs, labelling with purposefully designed oligonucleotide sequences etc. Another advantage especially for microscopic driven research may be that nanoparticles can also be used as imaging tags, thereby avoiding photo-bleaching [#He2008/ #Moser2016] experienced with classic fluorochromes (see also the chapter “Imaging with Nanoparticles” in this book).

The aforementioned properties of nanoparticles and the nanoparticle-mediated radio-sensitization were experimentally confirmed both in cells [#Burger2014/ #Hildenbrand2018/ #Pagáčová2019] and animal models [#Hainfeld2013]. Increased cell death compared to non-incubated controls was also observed in several studies when nanoparticles were added to cell cultures prior to irradiation [#Štefančiková2016/ #Porcel2010/ #Lacombe2017]. In parallel, experiments with isolated DNA showed higher radiation-induced fragmentation of the DNA molecule in presence of various nanoparticles [#Porcel2010]. However, efforts to repeat these findings for cell systems only provided contradictory results, as is further discussed for gold nanoparticles. Among many high-Z materials, gold nanoparticles have attracted scientific attention due to their unique characteristics, including good biocompatibility, advantageous physical and chemical properties (e.g., chemical stability, simple synthesis, and ability to locally amplify radiation dose, to serve as contrast agents, and to blink after laser excitation [Figure XX], etc.). It should also be noted that gold nanoparticles of less than 12 nm in diameter can penetrate the blood–brain barrier [#Oberdorster2004/ #Sarin2008/ #Sonavane2008] and those smaller than about 50 nm can be easily internalized by cells [#Conner2003/ #Chitrani2006], although larger ones are in general not excluded from incorporation. More

important, there seems to be an optimum for retention around 50 nm. Much smaller will be taken up readily, yet can leave the cell also way more efficiently. As such, gold nanoparticles promise potentially wide applicability in research and medicine. Many different studies demonstrated that gold nanoparticles open new opportunities for improvement in treatment of cancer and various non-malignant diseases, i.e. for radiotherapy or drug delivery, diagnostics, chemical sensing, biological imaging, etc. [#Alkilany2010]. However, the research on the relationship between physical and chemical properties of gold nanoparticles and their biological effects is still in the beginning. This is mostly due to the fact that, in the nano-range of about 1 – 100 nm, the physico-chemical properties (electronic, magnetic, optical, mechanical, etc.) and biological interactions of nanoparticles extremely depend on their size, shape, and surface modification which complicates systematic research.

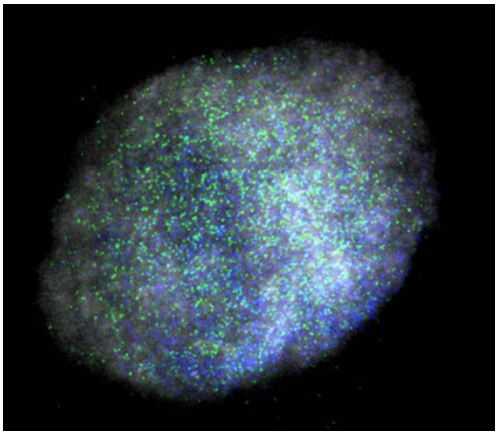

Figure XX: Example of a SkBr3 cell after treatment with gold nanoparticles. The image shows an overlay of a widefield image of the cell and a localization microscopy image of 10 nm gold nanoparticles (blue-green points). By means of high laser illumination power, surface plasmons are induced leading the gold nanoparticles to blink. The on-off of particle fluorescence allows the precise nano-scaled localization of each particle. For details about the imaging mechanisms of localization microscopy see the chapter "Imaging with Nanoparticles" in this book.

It is in fact not so easy to understand the nanoparticle-mediated radio-sensitization and radio-response of cells and a lot of open questions are under debate [#Pagáčová2019]. Another shortcoming with respect to DNA damaging followed from *in situ*/*in vivo* experiments: Nanoparticles of all sizes up to about 50 nm are able to cross the cell membrane and penetrate the cellular cytosol; however, even those of very small dimensions, e.g., of 2 – 3 nm in diameter, do not pervade the cell nucleus [#Štefančiková2014/ #Štefančiková2016/ #Hildenbrand2018/ #Moser2016] unless they are specifically modified and treated according to a certain transfection protocol for this purpose. Nevertheless even there the nanoparticles were primarily perinuclear [#Burger2014]. Nanoparticles of different materials and sizes enter cells by pinocytosis (reviewed in [#Yameen2014]) and remain retained inside the cytoplasm. There they can accumulate not only in particle aggregates but also in endoplasmic vesicles (endosomes) and lysosomes [#Štefančiková2014/ #Štefančiková2016/ #Fernando2010]. In some cases, nanoparticles may also be found to co-localize preferentially with/in the endoplasmic reticulum [#Hildenbrand2018/ #Cartiera2009] and/or Golgi apparatus (reviewed in

[#Yameen2014]). Mitochondria, however, the only organelles in human cells that contain their own DNA except of the nucleus, are not primary targets for nanoparticles or nanoparticle aggregates.

These sometime contradicting findings occurring under certain experimental conditions only put into play a plethora of cellular and biophysical processes that could potentially participate in nanoparticle-mediated tumor cell radio-sensitization. It is therefore not excluded that different types and sizes of nanoparticles do not follow a common mode of action, both in terms of the type of cell damage and its potentially underlying mechanism (reviewed in [#Fröhlich2013]). Contradictories on the radio-sensitization mediated by (various) gold nanoparticles and the mechanism of this phenomenon, as they follow from the comparison of irradiated cell viability (Clonogenic Assay) and their DNA integrity (Super-Resolution Microscopic Analysis of γH2AX Foci), are in detail discussed below.

Cell viability upon cell irradiation in presence of nanoparticles – Colony formation assay (CFA)

Irrespectively of the mechanism behind, some types of nanoparticles added to culture medium significantly reduce clonogenic survival of cells either by themselves (cytotoxicity) or upon irradiation (radio-sensitization). After cell irradiation with doses known to be high for a given cell type, irradiated cells can die immediately by necrosis or apoptosis due to irreparable DNA damage and extensive harm to all cellular structures (membranes, organelles). However, the majority of irradiated cells is usually surviving the initial period after irradiation and enters senescence or dies later because of their inability to accomplish mitosis. These cells can continue to live for some period of time but cannot multiply – they are clonogenically inactivated, i.e., “mitotically dead”. Conclusions based simply on cell viability measurements other than CFA after irradiation can be therefore misleading. The assay that can discriminate between surviving cells capable of producing progeny and mitotically dead cells and quantify their fractions has been proposed by Puck and Marcus already in 1956 [#Puck1956] and is currently accepted as the gold standard method in (radio)biology. Referred to as clonogenic assay or colony formation assay (CFA), this method is often used as primary approach to follow survival of irradiated cells (or anyhow treated cells) and also to confirm results of other tests of cell viability, like flow cytometric quantification of annexin V/propidium iodide positivity (apoptosis induction), methyl-thiazol-tetrazolium [MTT-] test, or trypan blue exclusion test. Before discussing the results of clonogenic assay relevant for nanoparticle radiosensitization, a brief introduction of the method will be provided:

The data of clonogenic assays are usually represented as the so called survival curves, showing the fraction of cells that are able to generate a colony (perform at least 5-6 division) in dependence on radiation dose. An example of such curves is provided in Figure XY. Typically, the survival curves follow the linear-quadratic dependence, described by the equation

$$SF = \exp(-\alpha D - \beta D^2)$$

where SF is the survival fraction of cells and α and β are the linear and quadratic parameters, respectively. D is the radiation dose.

Many individual studies reported different effects of various gold nanoparticles on clonogenic survival of cells, leading to contradictory conclusions on their cytotoxicity [#Pan2007/ #Alkilany2010/ #Coulter2012/ #Soenen2012/ #Youkhana2017/ #Benton2018/ #Martínez-Torres2018/ #Yang2018/ #Patil2019]; and the same holds true for nanoparticle-mediated radio-sensitization by gold (and

other types of) nanoparticles [#Herold2000/ #Jain2011/ #Coulter2012/ #Chen2015/ #Taggart2016/ #Paro2017/ #Kim2017/ #Yang2018]. Hence, we are still far from understanding the structure function relationship between the physical and chemical properties of nanoparticles and consequently their interactions with cells and organisms.

Challenges with interpretation of results on nanoparticle-mediated cell radio-sensitization can be illustratively demonstrated on our experimental dataset for SkBr3 cells, as presented below. Clonogenic assay (Figure XY) indicated the contradictions between investigations of radiation-sensitizing effects due to gold nanoparticle incorporation. We found no significant difference between the survival curves for cells irradiated with or without pure gold nanoparticle (10 nm) incorporation. This well agrees with the findings on HeLa cells after application of unmodified 10 nm gold nanoparticles recently published by Burger et al. [#Burger2014] but is the opposite of some other cell survival studies [#Wolfe2015/ #Paro2017/ #Kim2017] in also different sizes were used. Interestingly, our experiments also in some way contrast the results of Hildenbrand et al. [#Hildenbrand2018] for the same cell line, where the counting of γH2AX foci (accepted as the most sensitive surrogate DSB marker, see below next chapter) revealed a small additional increase in DSB numbers in cells that were incubated with gold nanoparticles prior to irradiation with different X-rays doses. This contradiction motivated us to analyze γH2AX foci on single cell level, too. If tumor cells are either tolerant toward DNA damage or effective enough in DNA (strand break) repair, clonogenic survival would not be altered even if gold nanoparticles enhanced DNA damage by ionizing radiation.

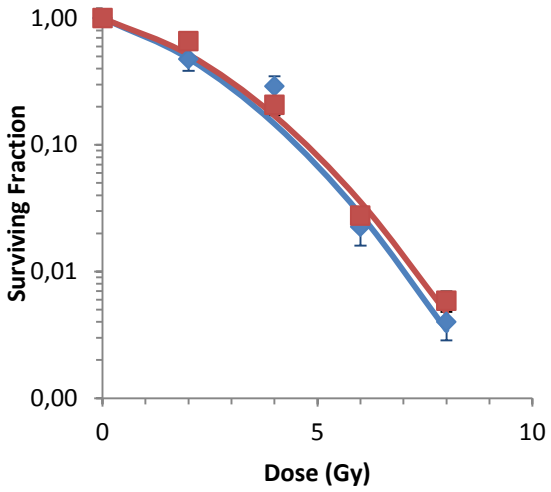

without gold nanoparticles(control)	
α = 0.02518	α/β = 4.4088
β = 0.0571	
with gold nanoparticles(NG)	
α = 0.2170	α/β = 3.8362
β = 0.0566	

Figure XY: Clonogenic survival of SkBr3 cells after irradiation with indicated doses of 6 MV X-rays in presence (■) and absence (◆) of 10 nm gold nanoparticles, respectively. A semi-logarithmic plot of cell survival is shown. Red corresponds to SkBr3 cells, treated with gold nanoparticles and irradiated. Blue corresponds to SkBr3 cells, irradiated, but not treated with gold nanoparticles. Error bars are the standard deviation of surviving fractions across three replicates. No differences in the survival fractions were found with and without gold nanoparticle incorporation. The table shows the α and β values are coefficients of the fit curve $SF = \exp(-\alpha D - \beta D^2)$.

DNA damage upon cell irradiation in presence of nanoparticles – Super-Resolution Microscopic Analysis of γH2AX Foci

The phosphorylation of the histone variant H2AX [#Turinetto2015] is a key factor highlighting double stranded DNA breaks after cell exposure to ionizing radiation. In minutes after irradiation, H2AX becomes phosphorylated on serine 139 (then called γH2AX) [#Rogakou1998] in a vicinity of about 1 Mb around a DNA double strand break. With this tagging also other repair proteins are accumulated at the damaged side. Importantly, labelling of γH2AX by fluorescent antibodies allows visualization of DSBs as microscopically visible repair foci. Since this γH2AX focus formation is a sensitive and early indicator of DSBs both *in vitro* and *in vivo* [#Kuo2008], it has been proven useful as a measure for this most serious type of DNA damage [#Loebrich2010], also in cases of low doses where other established methods as for instance pulse-field gel electrophoresis (PFGE) or comet assay lose their accuracy [#Banath2004/ #Loebrich2017]. Since the relationship between DSBs and γH2AX foci is close to 1:1, the counting of γH2AX foci has been established as a potent method in biological dosimetry [#Loebrich2010].

At a dose of about 1 Gy about 1-2 % of H2AX histone protein molecules become phosphorylated leading in the formation of hundreds to thousands γH2AX molecules at repair foci. It has been shown that different cell types have different background levels of γH2AX [#Dikomey1998], which results in different γH2AX focus responses. The relative dose-dependency of focus numbers after DNA damage induction does not seem to be influenced by different radiation sensitivity of cells whereas the intensity of the single foci (= number of antibody-labelled γH2AX molecules) differs in different cell lines [#MacPhail2003]. Recently, it has been shown that that the counting of single fluorescently labelled γH2AX molecules by super-resolution light microscopy can bring about deeper insights into DNA damage induction and focus formation [#Natale2017/ #Hausmann2018]. The number of γH2AX labelling tags increases with dose and decreases during repair in a compatible way to γH2AX foci. However, the analysis of distances between the labelling points indicates focus sub-structures (clusters) that seem to be characteristic for individual breaks and their chromatin surroundings [#Hofmann2018].

In the example presented here, γH2AX was specifically labelled in cell nuclei using fluorescent antibodies and the fluorescence was detected by single molecule localization microscopy (see the chapter “Imaging with Nanoparticles” in this book), which is a technique of super-resolution fluorescence light microscopy [#Cremer2013] that circumvents the Abbe-Rayleigh boundary conditions of diffraction and offers effective optical resolution down to the order of 10 nm. The fundamental concept of the technique is optical isolation of molecular objects (for instance individual fluorophores of antibodies). Switching the fluorophores between two different spectral states, e.g., on and off [#Thompson2002], allows a temporal isolation and thus a spatial separation of single (molecule) signals. From a reversible dark state, fluorescent molecules can randomly return to the emission state and emit their photons when they are irradiated by laser light [#Lemmer2008/ #Lemmer2009/ #Kaufmann2009]. Each of the emitting fluorophores is represented by an Airy disc in the microscopic image. The barycentre of such an Airy disc approximates the location of the emitting single molecule. This allows the precise determination of spatial object positions and the calculation of spatial distances between single molecules with a precision and thus optical resolution in the 10 nm regime [#Deschout2014]. All coordinates of fluorescent molecules can be merged into a matrix and visualized in a “pointillist”, super-resolution image (Figure XZ) [#Hausmann2017].

A 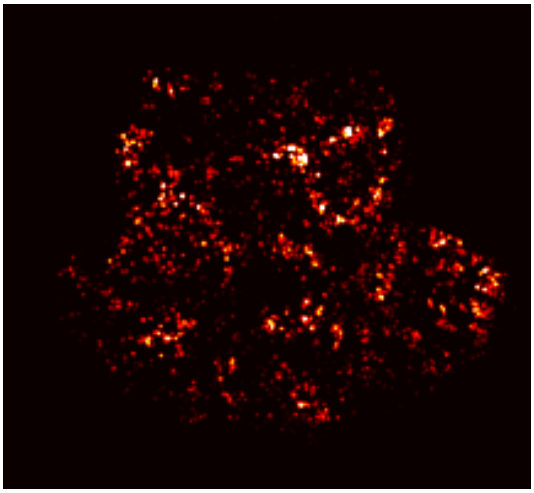 B 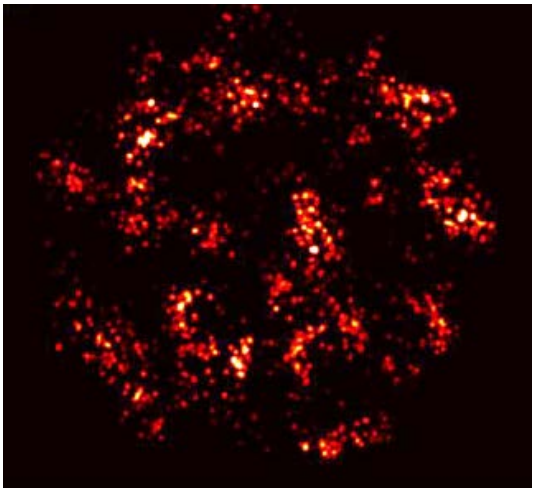

Figure XZ: Example of a SkBr3 cell nucleus after (A) irradiation with a dose of 4 Gy of 6 MV X-rays and (B) treatment with 10 nm gold nanoparticles and irradiation with a dose of 4 Gy of 6 MV X-rays. The figure shows a localization microscopy image of γH2AX fluorescent labeling points obtained after visualization with the specific antibody. The intensity of signals encodes the relative number of next neighbors. For details about the imaging mechanisms of localization microscopy see the chapter "Imaging with Nanoparticles" in this book.

Thirty minutes after irradiation with 2 Gy and 4 Gy X-rays, the SkBr3 cells were fixed, labelled with specific fluorescent antibodies against γH2AX, and the labelling points were counted in relation to the non-irradiated control. The data were compared also for cells with and without gold nanoparticle incorporation. For each type of the six different treatments, 35 to 40 cell nuclei of stained cells were visualized and their composite images analyzed (see Materials and Methods). The position of the fluorescent label was precisely determined and the coordinates were transferred into a density image where the intensity of each point refers to the numbers of its next neighbors [Figure XZ].

The results show that the numbers of γH2AX signals in irradiated cell nuclei grow with radiation dose [Figure YX]. It is also evident that the incorporation of gold nanoparticles by themselves increases the numbers of γH2AX signals, i.e. even without irradiation. This may be due to a toxicity effect of the particles or a cell stress provoked by particle load in the cytoplasm. Hence, it is not surprising that this effect seems to synergistically work with radiation stress so that in all cases the number of γH2AX molecules was higher for cells with gold nanoparticles than for those without. If one would subtract this 0 Gy nanogold effect from the data of the nanogold treated and irradiated cells, no difference would occur any longer between the irradiated specimens with and without gold nanoparticle incorporation. This means that the results based on the amount of single labelling tags of γH2AX molecules did not reveal any significant difference between irradiated specimens treated and not-treated with gold nanoparticles.

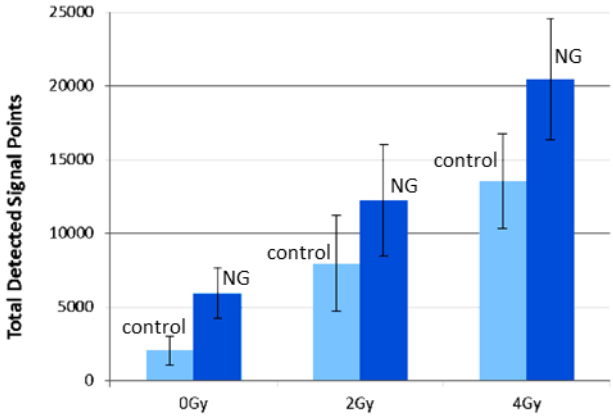

Figure YX: Numbers of γH2AX signal points detected in cells for indicated treatments, i.e. exposures to different doses of 6 MV X-rays (dose rate 6.67 Gy/min) combined or not combined with 10 nm gold nanoparticle incubation. The columns represent the mean γH2AX signal detected in cell nuclei 30 min after irradiation. Light blue columns are the mean signal points in cells not treated with gold nanoparticles ("control"). The dark blue columns are the mean signal points from cells incubated with gold nanoparticles ("NG"). Error bars show the standard deviation of signal numbers.

In the next step, we analyzed whether presence of gold nanoparticles influences clustering of γH2AX signals. γH2AX clusters were analyzed as described in [#Krufczik2017/ #Hausmann2018]. Clusters were interactively determined and defined by presence of at least 45 signal points within a circular region of 200 nm radius around any point (Figure YY). The counting of γH2AX clusters in each cell (Figure YZ) revealed that their number grows with radiation dose. An additional (although not significant) increase of γH2AX cluster numbers was observed in irradiated cells treated with gold nanoparticles as compared to irradiated but untreated controls. This points to more serious damage introduced to the (nuclear) DNA by the combined action of radiation and nanoparticles.

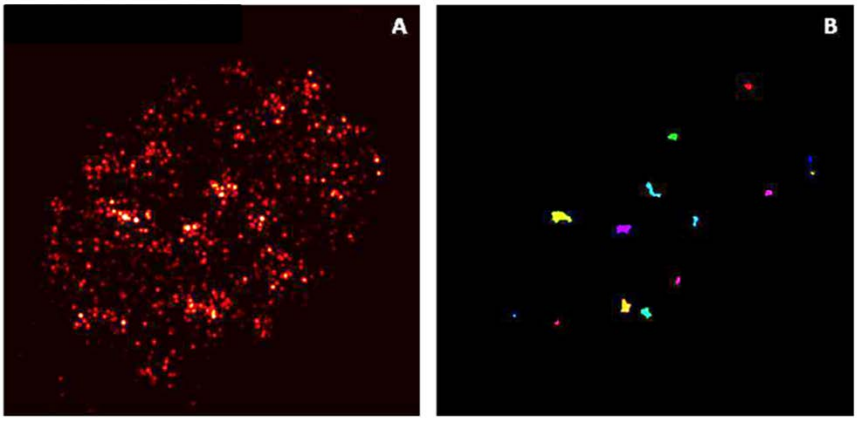

Figure YY: Determination of clusters: A) Signal density image of γH2AX labelling tags in a SkBr3 cell nucleus irradiated with 2 Gy of X-rays but not treated with gold nano-particles. B) Clusters highlighted by contiguous areas of different colors. The cluster parameters of minimum 45 points in a radius of 200 nm around a labeling tag were interactively determined.

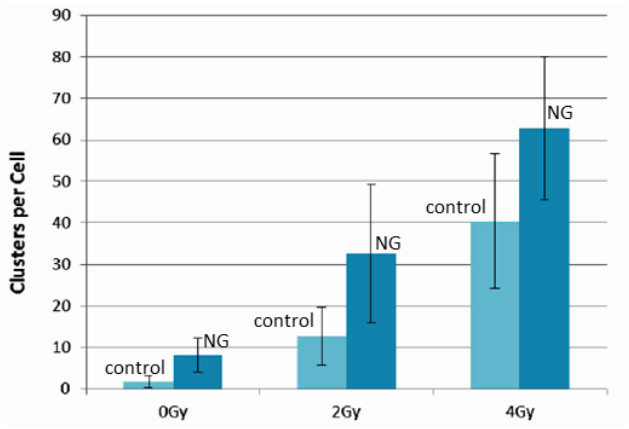

Figure YZ: Numbers of γH2AX clusters in SkBr3 cell nuclei observed for indicated treatments. The columns represent the mean numbers of γH2AX signal clusters per cell nucleus obtained from 35 to 40 cell nuclei analyzed for each treatment. The light blue columns show the mean number of clusters in cell nuclei not treated with gold nanoparticles ("control"). The dark blue columns show the mean number of clusters in cell nuclei treated with gold nanoparticles ("NG"). Error bars show the standard deviation of cluster numbers per cell.

To summarize, the mechanisms of radiation interaction with nanoparticles, specifically gold nanoparticles, and the radiation response of differently radio-sensitive cells remain to be elusive. Standard procedures such as clonogenic assay provide the crucial information on survival of nanoparticle-treated cells upon irradiation but do not consider initial DNA damage unless it forces them to die. Hence, with the "survival" approaches, the results on DNA damage induction may be more influenced by damage tolerance or improved repair capacity of various cancer cells than presence or absence of nanoparticles. The counting of γH2AX foci may help to directly access radiation-induced nanoparticle-enhanced damage of chromatin since it can be performed just after damage induction on the single cell level. These approaches could be supported by the application of novel super-resolution light microscopy techniques which offer a more detailed view on the damaging process and DNA lesion complexity. New super-resolution microscopy techniques thus significantly broaden our experimental opportunities and bring about new chances to better understand the mechanisms of radiation effect enhancement by nanoparticles in tumor cells and to allow methodological translation of this knowledge into cancer radiation therapy.

Beyond the aforementioned nanoparticle damaging effects, another open question has for instance to be accessed: How could nanoparticles be modified to directly access the cell nucleus or even target tumor-related genome sites? So far, only an unspecific transfer into the cell nucleus has been reported. It seemed to result in an additional decrease of cell survival after irradiation as compared to cells irradiated with nanoparticles in the cytosol only [#Aliru2017]. This may be due to short-range Auger electrons inducing additional damaging effects. But for 6 MV X-rays, it does not seem to be very relevant as short-ranged Auger electrons in gold are irrelevant at those energies. On the other hand, if nanoparticles would not easily pass the nuclear membrane, other organelles relevant for cell survival could be preferentially targeted and damaged [#Hildenbrand2018] as discussed in the following paragraph. The final and rather "philosophical" question therefore is, if we really want to target nanoparticles to the nucleus. Would be the increase in tumor cell dying given by the ability of

nanoparticles to penetrate the cell nucleus sufficient to compensate the increased risk of genome damage in normal cells, also to some extent infiltrated by nanoparticles?

Nanoparticle-mediated radio-sensitization of tumor cells independent of nuclear DNA damage

Radio-sensitizing effects of nanoparticles that are not dependent on amplified DNA damage in cells irradiated in presence of nanoparticles remain mostly unexplored as holds true also for cytoplasmic effects of irradiation only. The first extra-nuclear target one can think of in the relation to nanoparticle mediated radio-sensitization are mitochondria, since they are the only cytoplasmic organelles in human cells that contain DNA and produce energy for cell processes. Thus, the same physical mechanism as that already proposed to damage the cell nucleus (nuclear DNA) – based on electron showers emission and local dose amplification by scattering – can also harm mitochondria. However, most studies did not observe co-localization of randomly non-targetedly incorporated nanoparticles with this organelle, leaving the mitochondria-based hypothesis rather theoretical; hence, damage to mitochondria would be probably overweighed by effects on the nucleus or other cellular targets. Moreover, incorporation into mitochondria would require that the gold nanoparticles pass two additional membranes. Nevertheless, mitochondria damage was considered as an important aspect of nanoparticle-mediated tumor cell radio-sensitization for instance by Taggart et al. (2014) or Ghita et al. (2017) [#Taggart2014/ #Ghita2017/]

Endoplasmic reticulum is another important cytoplasmic organelle potentially affected by nanoparticles. Similar to mitochondria though, studies localizing nanoparticles to this space are rather exceptional; nevertheless, induction of endoplasmic reticulum stress by nanoparticles has been described in several studies [#Chen2014/ #Noël2015/ #Gunduz2017/].

In addition, targeting of modified targeting nanogold probes tagged with multiple DNA oligonucleotides or PNA chains that are aiming for against RNAs of genes that are up-regulated in tumor cells and accumulated in the endoplasmic reticulum could represent a new therapeutic approach. In these cases, RNA tagging would lead to a preferred accumulation of gold nanoparticles in the endoplasmatic reticulum and damage the protein synthesizing machinaery. The SmartFlare probes [#Seferos2007/ #Prigodich2012], based on this design, were originally proposed for RNA targeting and visualization (the gold core serves just as a carrier for the dye). However, SmartFlare binding to a gene product in the endoplasmic reticulum would also concentrate nanoparticles in this organelle and around the cell nucleus. Thus, in tumor cell types where certain genes are considerably upregulated, targeting of nanoparticles to over-transcribed RNAs of these genes could ensure nanoparticle accumulation in the tumor cells only. Upon irradiation, this will selectively reduce the radioresistance of cancer cells as compared to normal counterparts without extra-ordinary gene up-regulation.

In contrast to mitochondria and endoplasmatic reticulum, frequent studies localized nanoparticles to lysosomes that represent the place of their final destination in the cells. Colocalization studies showed that lysosomes accumulate substantial amounts of nanoparticles as compared to other cellular compartments. Nanoparticles appear also in the free cytoplasm, with some of them forming a sort of rim around the cell nucleus, and in endosomes (before being released into lysosomes). Several groups showed that nanoparticles internalized in lysosomes can increase cell dying upon irradiation independently of the nuclear DNA damage enhancement [#Boya2008/ #Serrano-Puebla2018]. This finding, confirmed also by clonogenic assay that still represents the gold standard method in radiobiology for this purpose, was quite surprising as scientists originally only considered

lysosomes as cellular thresh bins clearing the cells from extracellular agents and redundant or damaged cellular components (autophagy). However, as discovered later, lysosomes also participate in important regulatory cell pathways, most importantly cell death initiation [#Boya2008/ #Serrano-Puebla2018].

Hence, in principle two ways, though still hypothetical, could explain activation of cell death by nanoparticles irradiated inside lysosomes. Lysosomes contain many different hydrolytic enzymes, including proteases, nucleases, phosphatases, phospholipases, glycosidases and sulfatases [#Boya2008/ #Serrano-Puebla2018]. Massive disintegration of many lysosomes – for instance by harmful free radicals generated by irradiated nanoparticles, can therefore release large amounts these enzymes into the cytoplasm and its direct damage. Although aggressive lysosomal enzymes usually work at low pH that is actively being maintained only in lysosomes, if the leakage is extensive enough, the cytoplasm cannot further buffer its pH, becomes acidified, and digested together with all the organelles contained. This leads to fast death of the cell by necrosis.

Less extensive disruption of lysosomes by irradiated nanoparticles may then contribute to dying of irradiated cells indirectly. Under these circumstances, only limited amounts of proteases enter the cytoplasm. Among them, cathepsin B, cathepsin D and cathepsin L remain active at neutral pH and activate proapoptotic effectors, such as caspases, and mitochondria. This pathway can thus translate local effects of short-live secondary electrons and reactive oxygen species produced by irradiated nanoparticles into global cell signaling and finally cell death by apoptosis [#Boya2008]. In fact, some nanoparticles produce ROS even without irradiation, which may also result to lysosome damage, in turn manifested as cytotoxicity. Production of free radicals by nanoparticles [#Soenen2012/ #Martínez-Torres2018/] and lysosome-mediated nanoparticle-enhanced cell death by both the direct and the indirect mechanisms upon irradiation have already been proposed in the literature [#Štefančíková2016]; however, their experimental confirmation remains a matter of future research. Just to emphasize the importance of lysosomes – the former trash bins – for the cell life, a hypothesis was proposed [#Settembre2012] based on data that lysosomes sense the physiological and nutritional condition of the cells and signal this information to the nucleus, where it is used to coordinate gene expression programs. Altogether, a compelling evidence indicates that lysosomes have much broader role than previously thought – they play a key role in maintaining cell homeostasis by regulating cellular clearance, energy production [#Settembre2012/ #Lim2016/], and cell death signaling associated with apoptosis and/or autophagy [#Boya2008/ #Settembre2013/ #Lim2016/]. Lysosomes thus serve as regulating nots interconnecting several important pathways of the cell signaling network and their damage can have far-reaching consequences even upon relatively mild stimuli.

Conclusions

To conclude, contradictions remain on the mechanism of nanoparticle-mediated tumor cell radio-sensitization as well as on the relationship between their physical and chemical properties and biological effects, including cytotoxicity. This is not much surprising concerning the variability of nanoparticles (material, size, shape, composition, surface modifications and functionalization) and biological systems used in experiments. Nevertheless, it becomes evident that functional structuralization of cells and their biological behavior play an important role in process initiated by nanoparticles in cells prior to and after irradiation. Super-resolution optical microscopy methods, as

also demonstrated in the present contribution, thus represent new experimental approaches that promise new important discoveries in the field which could support so far well-established techniques in biological dosimetry as clonogenic assay or others. Since clonogenic growth is the most important result for the clinical outcome, a better understanding of DNA damage might support methods to modify cell treatment towards further reduction of tumor cell survival.

Materials and Methods

Cell Culture, Gold Nanoparticle Incorporation, and Specimen Irradiation

SkBr3 human breast adenocarcinoma cells, obtained from ATCC (American Type Culture Collection, Manassas, VA, USA), were cultivated in flat-bottom T75 flasks in McCoy's Medium supplemented with 10% FBS without any antibiotics. Cells were incubated in a chamber at 37 °C and 95% air / 5 % CO_2. Every three to four days the cells were harvested and reseeded 1:10 in flasks: The cells were washed with PBS and incubated in 2 ml of a solution of 3x Trypsin / EDTA at 37 °C for 5 min. Once all cells were detached from the bottom of the flask, fresh media was added and the cell suspension was homogenized by pipette. Upon reaching approximately 70-90% visible confluence of cells, they again were harvested, counted, and diluted to obtain 10^4 cells / ml in each well of a 6-well culture plate, and incubated overnight, allowing cells to adhere to the bottom of each well.

Then the medium was removed from each well, and cells were washed with PBS. Each well received 2.5 ml of fresh McCoy's Medium containing no FBS. Each well for gold nanoparticle incorporation received 8 µl colloidal gold nanoparticle (10 nm diameter, $5 \cdot 10^{12}$ particles/ml) suspension ("NG") in 2.5 ml of FBS-free media. Untreated control wells only received FBS-free media. Cells were then incubated in these well-plates for 18 h at 37 °C.

In addition, SkBr3 cells were also grown on clean coverslips in well-plates according to same protocol. After 18 h incubation, cells adhered to coverslips were washed with PBS, and fresh McCoy's medium containing 10% FBS was added.

Each well-plate was irradiated at room temperature by 6 MV X-rays (dose: 2 Gy, 4 Gy) delivered from a clinical linear accelerator (LINAC, Synergy, Elekta AB, Stockholm, Sweden; dose rate 6.67 Gy/min). During irradiation, the well-plates were positioned in such a way that the surface of the media in each well was about 100 cm distant from the radiation source. Each well-plate was put on top of eight 1 cm thick RW3 phantom plates with one 1 cm thick PMMA plate placed on top to homogenize backscatter effects (Figure ZX).

Following irradiation, cells were incubated at 37 °C for 30 min, after which the media was removed from all wells in all plates and replaced with PBS for 5 min at room temperature. Then the cells were fixed in 3.7% formaldehyde (prepared from paraformaldehyde) for 30 min at room temperature. After fixation, cells were washed three times with PBS and stored in PBS containing 0.05% Sodium Azide for further processing.

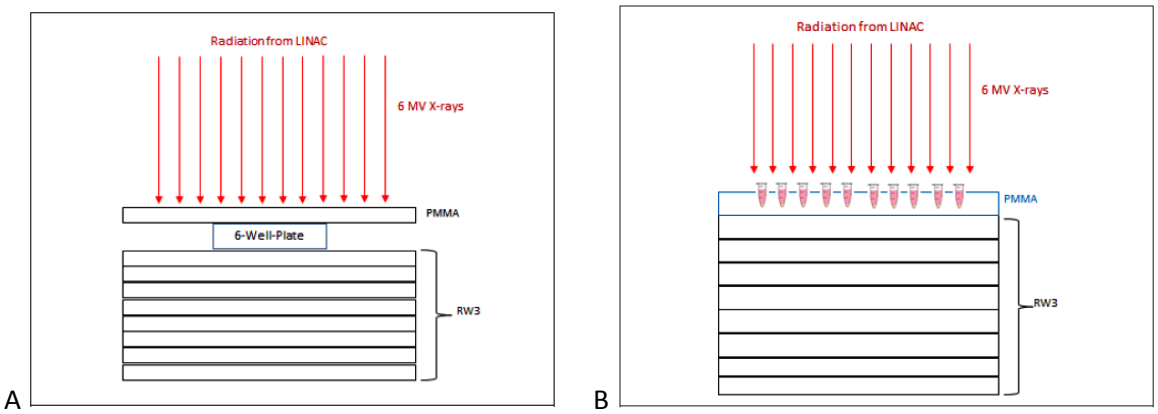

Figure ZX: Schematic representation of the setup for cell irradiation in the clinical linear accelerator. A) Set-up for the localization microscopy experiments. B) Set-up for clonogenic assays.

Clonogenic Assay (Colony Forming Assay)

The following Clonogenic Assay (also known as Colony Forming Assay; CFA) procedure was adapted from a protocol described in Burger et al. [#Burger2014]. SkBr3 cells were grown in well plates as described above. After 18 h incubation, medium was removed from each well and cells were washed with PBS. Cells were then incubated in 1 ml 3x Trypsin/EDTA per well at 37 °C for 5 min. Once all cells were detached from the bottom of the wells, 2 ml of fresh McCoy's Medium with 10% FBS were added to each well and the cell suspension was homogenized by pipette. From each well the cell suspension was transferred to two separate 15 ml tubes, one for untreated cells ("control") and the other for cells treated with gold nanoparticles (NG). The number of cells in each tube was counted with a hemo-cytometer viewed under the microscope.

The content of each 15 ml tube was diluted with a specific volume of fresh McCoy's medium with 10% FBS calculated to achieve the desired cell number in 400 µl, the volume consequently transferred into a single micro-centrifuge tube for each radiation dose. This process created 10 micro-centrifuge tubes, each containing 400 µl of liquid, where five tubes contained cells treated with gold nanoparticles and five tubes untreated cells, one for each radiation dose.

All 10 micro-centrifuge tubes were sealed and centrifuged at 290 g for 5 min. The cells were irradiated in the closed micro-centrifuge tubes by 6MV X-rays delivered from a linear accelerator (LINAC, Synergy, Elekta AB, Stockholm, Sweden; dose rate 6.67 Gy/min) at room temperature. During irradiation, the tubes were positioned in such a way that the surface of the media in each well was about 100 cm distant from the radiation source. The tubes were put on top of eight 1 cm thick RW3 phantom plates (Figure ZX).

After irradiation, cell pellets were thoroughly re-suspended by pipette to ensure homogeneity and individual dispersal of cells within each tube. 100 µl was then transferred from each tube into one of three corresponding T25 flasks. Assuming homogenous resuspension, each flask received one quarter of the cells seeded into each micro-centrifuge tube. 5 ml of fresh McCoy's Medium with 10% FBS was then added to each flask.

Cells were incubated at 37 °C and 95% air/ 5% CO_2 for 14 days to allow sufficient colony growth. After the two weeks of incubation, the medium was removed from the flasks; the cells were washed with PBS and fixed with 3.7% formaldehyde (prepared from paraformaldehyde), followed by 70% ethanol fixation for 10 min each. For visualization of colonies, adherent cells were then stained with Coomassie dye for 40 seconds, rinsed with cold water, and subsequently dyed with Giemsa solution for 40 min. Stained colonies, of at least 50 cells, were visualized under the microscope and counted. The surviving fraction of cells in each flask was determined by dividing the number of colonies per cells seed by the plating efficiency of the cells. Plating Efficiency (PE) of the SkBr3 cell line used in these experiments had already been determined by growing the cells (without treatment or radiation) in McCoy's Medium with 10% FBS at various densities and counting the colonies that formed after two weeks. Surviving fractions (SF) were plotted for each treatment at each dose (D) and survival curves fitted using the linear-quadratic model ($SF = e^{-(\alpha D+\beta D^2)}$).

γH2AX Immunostaining

Immunostaining of γH2AX was performed according to the protocol described recently [#Krufczik2017]. Coverslips containing fixed cells were washed with 1x PBS + Mg/Ca to remove residual Sodium Azide. The coverslips, each within the well of a 6-well plate, were submerged in 2 ml of permeabilisation solution (0.2% Triton-X in 1x PBS + Mg/Ca) and the plate was shaken for 3 min at room temperature. Cells were then washed three times with 1x PBS + Mg/Ca for 5 min each before being incubated in blocking solution (2% BSA in 1x PBS + Mg/Ca) for 30 min. Cells were then incubated with 100 µl of primary mouse-anti-phospho-histone H2AX (Ser139) antibody solution (clone JBW301, Merck Chemicals GmbH, Darmstadt, Germany; 1:500 in 2 % BSA in 1 x PBS + Mg/Ca) for 18 h at 4 °C in a humidified chamber. After incubation, cells were washed three times with 1x PBS + Mg/Ca for 5 min each, and then incubated with 100 µl of the secondary Alexa Fluor® 647 labelled goat-anti-mouse IgG antibody solution (Merck Chemicals GmbH, Darmstadt, Germany; 1:500 in 2 % BSA (in 1x PBS + Mg/Ca)for 30 min in a 37 °C humidified chamber. Cells were then washed three times with 1x PBS + Mg/Ca for 5 min before being fixed in 2% formaldehyde (freshly prepared from paraformalsdehyde) at 37 °C for 10 min. The cells were incubated for 21 h in a 37 °C humidified chamber. The cells were washed three times in 2x SSC at 37 °C for 10 min each. Coverslips were then soaked in 1x PBS + Mg/Ca and the cells allowed to equilibrate for 5 min. The cells were then incubated in 100 µl 4',6-Diamidino-2-Phenylindole (DAPI) solution (100–500 ng/ml in 1x PBS) for 5 min at room temperature in the dark. After DAPI staining, coverslips were again washed with 1x PBS + Mg/Ca before being placed cell side down onto 20 µl of ProlongGold (ThermoFischer, Massachusetts, USA, ProLong® Gold Antifade Mountant, P36930) on a microscope slide. Coverslips were sealed on slides and stored in darkness at 4 °C until being used for localization microscopy.

Single Molecule Localization Microscopy

Single Molecule Localization Microscopy (SMLM) was used to count γH2AX labelling tags and to determine the frequency distributions of γH2AX foci/clusters within SkBr3 cell nuclei. For data acquisition, the setup from the light microscopy facility of the German Cancer Research Centre (DKFZ) was used (in detail described elsewhere [#Krufczik2017/ #Hausmann2017/ #Hausmann2018/ #Eryilmaz2018]). The microscope has an oil-objective (100x / NA 1.46) and four lasers 405 nm / 491 nm / 561 nm / 642 nm with maximal laser powers of 120 mW / 200 mW / 200 mW / 140 mW, respectively. An in-built electron multiplier (EM-gain) enhances signals detected by the EmCCD camera (80 nm / px). In order to minimize drifts, the microscope was installed on a Smart-Table,

compensating for vibrations, and provided with a water-cooling system to keep constant temperature.

Cells in this experiment were imaged using the 405 nm and 642 nm lasers to visualize DAPI and γH2AX stains, respectively. At least 35 cells from each treatment were imaged. Individual cell nuclei were selected by uniform shape as visualized by DAPI staining (using the 405 nm laser). Images were cropped to isolate and encompass an entire cell nucleus. 2,000 image frames were acquired at each wavelength with an exposure time of 100 ms per image.

Super-resolution signal coordinates were calculated using a Matlab-based in-house software as described elsewhere [#Hausmann2017/ #Krufczik2017/ #Pilarczyk2017/ #Stuhlmüller2015/ #Kaufmann2009]. Background levels were multiplied by threshold factors for more rigorous background subtraction. The intensity bary center determined the x-, y-coordinates of a signal point with a certain localization error. For quantitative super-resolution data analyses, the total number of signal points and all-to-all point distances between signal points were calculated. Resulting single-cell data were summarized for each experimental setup for further statistical analysis. Cluster analysis was performed according to interactively determined parameters. (Figure YY): Pixel size = 10 nm, radius = 20 pixels, maximum distance for all distances = 200 nm, maximum distance for next neighbors = 200 nm. The minimal neighbor value (N) was determined to N=45. The mean number of clusters per cell was calculated.

Acknowledgement

The authors thank PD. Dr. Carsten Herskind, Dept. Radiation Oncology, Mannheim, for using his laboratory for cell culture work and Dr. Felix Bestvater, German Cancer Research Center, Heidelberg, for using the localization microscope setup. The authors also thank Adriana Grbenicek, Miriam Bierbaum, Philipp Metzler and Jin-Ho Lee for their support and discussions. The work was supported by the Heidelberg University Mobility Grant for International Research Cooperation within the excellence initiative II of the Deutsche Forschungsgemeinschaft (DFG) to M.H., and by the Mobility project DAAD-19-03 to M.H. and M.F.

Literature

[#Aliru2017] Aliru, M.L.; Aziz, K.; Bodd, M.; Sanders, K.; Mahadevan, L.S.K.; Sahoo, N.; Tailor, R.C.; and Krishnan, S. Targeted Gold Nanoparticles Enhance RadiationEffects in Pancreatic Tumor Models. *Int. J. Radiat. Oncol. Biol. Phys*. **2017**, 99(2), E574-E575.

[#Alkilany2010] Alkilany, A.M.; Murphy, C.J. Toxicity and cellular uptake of gold nanoparticles: what we have learned so far? *J. Nanopart. Res.* **2010**, 12,2313–2333.

[#Atun2015] Atun, R.; Jaffray, D.A.; Barton, M.B.; Bray, F.; Baumann, M.; Vikram, B.; Hanna, T.P.; Knaul, F.M.; Lievens, Y.; Lui, T.Y.M.; et al. Expanding global access to radiotherapy. *Lancet Oncol.* **2015**, *16*, 1153–1186, doi:10.1016/S1470-2045(15)00222-3.

[#Banath2004] Banath, J.P.; MacPhail, S.H.; Olive, P.L. Radiation sensitivity, H2AX phosphorylation, and kinetics of repair of DNA strand breaks in irradiated cervical cancer cell lines. *Cancer Res* **2004**, *64,* 7144-7149.

[#Benton2018] Benton, J.Z.; Williams, R.J.; Patel, A.; Meichner, K.; Tarigo, J.; Nagata, K.; Pethel, T.D.; Gogal, R.M. Jr. Gold nanoparticles enhance radiation sensitization and suppress colony formation in a feline injection site sarcoma cell line, in vitro. *Res. Vet. Sci*. **2018**, 117, 104-110, doi: 10.1016/j.rvsc.2017.11.018.

[#Bertrand2014] Bertrand, N.; Wu, J.; Xu, X.; Kamaly, N.; Farokhzad, O.C. Cancer nanotechnology: The impact of passive and active targeting in the era of modern cancer biology. *Adv. Drug Deliv. Rev.* **2014**, *66*, 2–25, doi:10.1016/j.addr.2013.11.009.

[#Bobkova2018] Bobkova, E.; Depes, D.; Lee, J.-H.; Jezkova, L.; Falkova, I.; Pagacova, E.; Kopecna, O.; Zadneprianetc, M.; Bacikova, A.; Kulikova, E.; Smirnova, E.; Bulanova, T.; Boreyko, A.; Krasavin, E.; Wenz, F.; Bestvater, F.; Hildenbrand, G.; Hausmann, M.; Falk, M. Recruitment of 53BP1 proteins for DNA repair and persistence of repair clusters differ for cell types as detected by single molecule localization microscopy. *Int. J. Molec. Sci.* **2018**, *19*, 3713. doi:10.3390/ijms19123713

[#Boya2008] Boya, P.; Kroemer, G. Lysosomal membrane permeabilization in cell death. *Oncogene*. **2008**, 27(50), 6434-6451, doi:10.1038/onc.2008.310.

[#Burger2014] Burger, N.; Biswas, A.; Barzan, D.; Kirchner, A.; Hosser, H.; Hausmann, M.; Hildenbrand, G.; Herskind, C.; Wenz, F.; Veldwijk, M.R. A method for the efficient cellular uptake and retention of small modified gold nanoparticles for the radiosensitization of cells. *Nanomed. Nanotechnol. Biol. Med.* **2014**, *10*, 1365–1373, doi:10.1016/j.nano.2014.03.011.

[#Cartiera2009] Cartiera, M.S.; Johnson, K.M.; Rajendran, V.; Caplan, M.J.; Saltzman, W.M. The uptake and intracellular fate of PLGA nanoparticles in epithelial cells. *Biomaterials* **2009**, *30*, 2790–2798, doi:10.1016/j.biomaterials.2009.01.057.

[#Chen2014] Chen, R.; Huo, L.; Shi, X.; Bai, R.; Zhang, Z.; Zhao, Y.; Chang, Y.; Chen, C. Endoplasmic reticulum stress induced by zinc oxide nanoparticles is an earlier biomarker for nanotoxicological evaluation. *ACS Nano*. **2014**, 8(3), 2562-74, doi:10.1021/nn406184r.

[#Chen2015] Chen, F.; Zhang, X.H.; Hu, X.D.; Zhang, W.; Lou, Z.C.; Xie, L.H.; Liu, P.D.; Zhang, H.Q. Enhancement of radiotherapy by ceria nanoparticles modified with neogambogic acid in breast cancer cells. Int J *Nanomedicine*. **2015**, 10, 4957-69, doi:10.2147/IJN.S82980.

[#Chithrani2006] Chithrani, B.D.; Ghazani, A.A.; Chan, W.C. Determining the size and shape dependence of gold nanoparticle uptake into mammalian cells. *Nano Lett*. **2006**, 6(4), 662-668.

[#Chitrani2010a] Chithrani, D.B. Nanoparticles for improved therapeutics and imaging in cancer therapy. *Recent Pat. Nanotechnol.* **2010**, *4*, 171–180.

[#Chitrani2010b] Chithrani, D.B.; Jelveh, S.; Jalali, F.; van Prooijen, M.; Allen, C.; Bristow, R.G.; Hill, R.P.; Jaffray, D.A. Gold nanoparticles as radiation sensitizers in cancer therapy. *Radiat. Res.* **2010**, *173*, 719–728, doi:10.1667/RR1984.1.

[#Conner2003] Conner, S.D.;, Schmid, S.L. Regulated portals of entry into the cell. *Nature*. **2003**, 422(6927), 37-44.

[#Coulter2012] Coulter, J.A.; Jain, S.; Butterworth, K.T.; Taggart, L.E.; Dickson, G.R.; McMahon, S.J.; Hyland, W.B.; Muir, M.F.; Trainor, C.; Hounsell, A.R.; O'Sullivan, J.M.; Schettino, G.; Currell, F.J.; Hirst,

D.G.; Prise, K.M. Cell type-dependent uptake, localization, and cytotoxicity of 1.9 nm gold nanoparticles. *Int. J. Nanomedicine*. **2012**, 7, 2673-2685, doi:10.2147/IJN.S31751.

[#Cremer2013] Cremer, C.; Masters, B.R. Resolution enhancement techniques in microscopy. *Eur Phys J H* **2013**, *38,* 281-344.

[#Davis2016] Davis, M.E. Glioblastoma: Overview of disease and treatment. *Clin. J. Oncol. Nurs.* **2016,** *20,* S2-S8. doi:10.1188/16.CJON.S1.2-8.

[#Deschout2014] Deschout, H.; Cella Zanacchi, F.; Mlodzianoski, M.; Diaspro, A.; Bewersdorf, J.; Hess, S.T.; Braeckmans, K. Precisely and accurately localizing single emitters in fluorescent microscopy. *Nat. Methods* **2014**, *11*, 253–266.

[#Dikomey1998] Dikomey, E.; Dahm-Daphi, J.; Brammer, I.; Martensen, R.; Kaina, B. Correlation between cellular radiosensitivity and non-repaired double-strand breaks studied in nine mammalian cell lines. *Int J Radiat Biol* **1998**, *73***,** 269-278.

[#Durante2017] Durante, M.; Orecchia, R.; Loeffler, J.S. Charged-particle therapy in cancer: Clinical uses and future perspectives. *Nat. Rev. Clin. Oncol.* **2017**, *14*, 483–495, doi:10.1038/nrclinonc.2017.30.

[#Engel1978] Engel, L.W.; Young, N.A. Human breast carcinoma cells in continuous culture: A review. *Cancer Res.* **1978**, *38*, 4327–4339.

[#Eryilmaz2018] Eryilmaz, M.; Schmitt, E.; Krufczik, M.; Theda, F.; Lee, J.-H.; Cremer, C.; Bestvater, F.; Schaufler, W.; Hausmann, M.; Hildenbrand, G. Localization microscopy analyses of MRE11 clusters in 3D-conserved cell nuclei of different cell lines. *Cancers* **2018,** *10*, 25; doi:10.3390/cancers10010025

[#Falk2014a] Falk, M.; Hausmann, M.; Lukášová, E.; Biswas, A.; Hildenbrand, G.; Davídková, M.; Krasavin, E.; Kleibl, Z.; Falková, I.; Ježková, L.; Štefančíková, L.; Ševčík, J.; Hofer, M.; Bačíková, A.; Matula, P.; Boreyko, A.; Vachelová, J.; Michaelidisová, A.; Kozubek, S. Determining Omics spatiotemporal dimensions using exciting new nanoscopy techniques to assess complex cell responses to DNA damage: Part A—Radiomics. *Crit. Rev. Eukaryot. Gene Expr.* **2014**, *24*, 205–223.

[#Falk2014b] Falk, M.; Hausmann, M.; Lukášová, E.; Biswas, A.; Hildenbrand, G.; Davídková, M.; Krasavin, E.; Kleibl, Z.; Falková, I.; Ježková, L.; Štefančíková, L.; Ševčík, J.; Hofer, M.; Bačíková, A.; Matula, P.; Boreyko, A.; Vachelová, J.; Michaelidisová, A.; Kozubek, S. Determining Omics spatiotemporal dimensions using exciting new nanoscopy techniques to assess complex cell responses to DNA damage: Part B—Structuromics. *Crit. Rev. Eukaryot. Gene Expr.* **2014**, *24*, 225–247.

[#Falk2010] Falk, M.; Lukasova, E.; Kozubek, S. Higher-order chromatin structure in DSB induction, repair and misrepair. *Mutat. Res.* **2010**, *704*, 88–100, doi:10.1016/j.mrrev.2010.01.013.

[#Fang2011] Fang, J.; Nakamura, H.; Maeda, H. The EPR effect: Unique features of tumor blood vessels for drug delivery, factors involved, and limitations and augmentation of the effect. *Adv. Drug Deliv. Rev.* **2011**, *63*, 136–151, doi:10.1016/j.addr.2010.04.009.

[#Fernando2010] Fernando, L.P.; Kandel, P.K.; Yu, J.; McNeill, J.; Ackroyd, P.C.; Christensen, K.A. Mechanism of cellular uptake of highly fluorescent conjugated polymer nanoparticles. *Biomacromolecules* **2010**, *11*, 2675–2682, doi:10.1021/bm1007103.

[#Freneau2018] Freneau, A.; Dos Santos, M.; Voisin, P.; Tang, N.; Bueno Vizcarra, M.; Villagrasa, C.; Roy, L.; Vaurijoux, A.; Gruel, G. Relation between DNA double-strand breaks and energy spectra of secondary electrons produced by different X-ray energies. *Int. J. Radiat. Biol.* **2018**, 1–10, doi:10.1080/09553002.2018.1518612.

[#Fröhlich2013] Fröhlich, E. Cellular targets and mechanisms in the cytotoxic action of non-biodegradable engineered nanoparticles. *Curr. Drug Metab.* **2013**, *14*, 976–988.

[#Ghita2017] Ghita, M.; McMahon, S.J.; Taggart, L.E.; Butterworth, K.T.; Schettino, G.; Prise, K.M. A mechanistic study of gold nanoparticle radiosensitisation using targeted microbeam irradiation. *Sci Rep*. **2017**, 7, 44752, doi:10.1038/srep44752.

[#Girst2016] Girst, S.; Greubel, C.; Reindl, J.; Siebenwirth, C.; Zlobinskaya, O.; Walsh, D.W.M.; Ilicic, K.; Aichler, M.; Walch, A.; Wilkens, J.J.; , Multhoff, G.; Dollinger, G.; Schmid, T.E. Proton minibeam radiation therapy reduces side effects in an in vivo mouse ear model. *Int. J. Radiat. Oncol.* **2016**, *95*, 234–241, doi:10.1016/j.ijrobp.2015.10.020.

[#Gonzalez2018] González, W.; Prezado, Y. Spatial fractionation of the dose in heavy ions therapy: An optimization study. *Med. Phys.* **2018**, *45*, 2620–2627, doi:10.1002/mp.12902.

[#Gu2018] Gu, H.; Huang, T.; Shen, Y.; Liu, Y.; Zhou, F.; Jin, Y.; Sattar, H.; Wei, Y. Reactive oxygen species-mediated tumor microenvironment transformation: The mechanism of radioresistant gastric cancer. *Oxid. Med. Cell. Longev.* **2018**, *2018*, 5801209, doi:10.1155/2018/5801209.

[#Gunduz2017] Gunduz, N.; Ceylan, H.; Guler, M.O.; Tekinay, A.B. Intracellular Accumulation of Gold Nanoparticles Leads to Inhibition of Macropinocytosis to Reduce the Endoplasmic Reticulum Stress. *Sci. Rep*. **2017**, 7, 40493, doi:10.1038/srep40493.

[#Hainfeld2013] Hainfeld, J.F.; Smilowitz, H.M.; O'Connor, M.J.; Dilmanian, F.A.; Slatkin, D.N. Gold nanoparticle imaging and radiotherapy of brain tumors in mice. *Nanomedicine* **2013**, *8*, 1601–1609, doi:10.2217/nnm.12.165.

[#Hausmann2017] Hausmann, M.; Ilić, N.; Pilarczyk, G.; Lee, J.-H.; Logeswaran, A.; Borroni, A.; Krufczik, M.; Theda, F.; Waltrich, N.; Bestvater, F.; Hildenbrand, G.; Cremer, C.; Blank, M. Challenges for Super-Resolution Localization Microscopy and Biomolecular Fluorescent Nano-Probing in Cancer Research. *Int. J. Mol. Sci.* **2017**, *18*, 2066, doi:10.3390/ijms18102066.

[#Hausmann2018] Hausmann, M.; Wagner, E.; Lee, J.-H.; Schrock, G.; Schaufler, W.; Krufczik, M.; Papenfuß, F.; Port, M.; Bestvater, F.; Scherthan, H. Super-resolution localization microscopy of radiation-induced histone H2AX-phosphorylation in relation to H3K9-trimethylation in HeLa cells. *Nanoscale* **2018**, *10*, 4320–4331, doi:10.1039/c7nr08145f.

[#He2008] He, H.; Xie, C.; Ren, J. Nonbleaching fluorescence of gold nanoparticles and its applications in cancer cell imaging. *Anal. Chem.* **2008**, *80*, 5951–5957, doi:10.1021/ac8005796.

[#Herold2000] Herold, D.M.; Das, I.J.; Stobbe, C.C.; Iyer, R.V.; Chapman, J.D. Gold microspheres: a selective technique for producing biologically effective dose enhancement. *Int. J. Radiat. Biol.* **2000**, *76*, 1357-1364.

[#Hildenbrand2018] Hildenbrand, G.; Metzler, P.; Pilarczyk, G.; Bobu, V.; Kriz, W.; Hosser, H.; Fleckenstein, J.; Krufczik, M.; Bestvater, F.; Wenz, F.; et al. Dose enhancement effects of gold nanoparticles specifically targeting RNA in breast cancer cells. *PLoS ONE* **2018**, *13*, e0190183, doi:10.1371/journal.pone.0190183.

[#Hofer2016] Hofer, M.; Falk, M.; Komůrková, D.; Falková, I.; Bačíková, A.; Klejdus, B.; Pagáčová, E.; Štefančíková, L.; Weiterová, L.; Angelis, K.J.; et al. Two New Faces of Amifostine: Protector from DNA Damage in Normal Cells and Inhibitor of DNA Repair in Cancer Cells. *J. Med. Chem.* **2016**, *59*, 3003–3017, doi:10.1021/acs.jmedchem.5b01628.

[#Hofer2017a] Hofer, M.; Hoferová, Z.; Depeš, D.; Falk, M. Combining Pharmacological Countermeasures to Attenuate the Acute Radiation Syndrome-A Concise Review. *Molecules* **2017**, *22*, 834, doi:10.3390/molecules22050834.

[#Hofer2017b] Hofer, M.; Hoferová, Z.; Falk, M. Pharmacological Modulation of Radiation Damage. Does It Exist a Chance for Other Substances than Hematopoietic Growth Factors and Cytokines? *Int. J. Mol. Sci.* **2017**, *18*, 1385, doi:10.3390/ijms18071385.

[#Hofmann2018] Hofmann, A.; Krufczik, M.; Heermann, D.W.; Hausmann, M. Using persistent homology as a new approach for super-resolution localization microscopy data analysis and classification of γH2AX foci/clusters. *Int. J. Mol. Sci.* **2018**, *19*, 2263; doi:10.3390/ijms19082263

[#Hossain2012] Hossain, M.; Su, M. Nanoparticle location and material dependent dose enhancement in X-ray radiation therapy. *J. Phys. Chem. C Nanomater. Interfaces* **2012**, *116*, 23047–23052, doi:10.1021/jp306543q.

[#Jain2011] Jain, S.; Coulter, J.A.; Hounsell, A.R.; Butterworth, K.T.; McMahon, S.J.; Hyland, W.B.; Muir, M.F.; Dickson, G.R.; Prise, K.M.; Currell, F.J.; O'Sullivan, J.M.; Hirst, D.G. Cell-specific radiosensitization by gold nanoparticles at megavoltage radiation energies. *Int. J. Radiat. Oncol. Biol. Phys*. **2011**, 79(2), 531-539, doi:10.1016/j.ijrobp.2010.08.044.

[#Janvary2018] Jánváry, L.Z.; Ferenczi, Ö.; Takácsi-Nagy, Z.; Bajcsay, A.; Polgár, C. [Application of CyberKnife stereotactic radiosurgery in the treatment of head and neck cancer]. *Magy. Onkol.* **2018**, *62*, 180–185.

[#Jezkova2018] Jezkova, L.; Zadneprianetc, M.; Kulikova, E.; Smirnova, E.; Bulanova, T.; Depes, D.; Falkova, I.; Boreyko, A.; Krasavin, E.; Davidkova, M.; Kozubek, S.; Valentova, O.; Falk, M. Particles with similar LET values generate DNA breaks of different complexity and reparability: a high-resolution microscopy analysis of γH2AX/53BP1 foci. *Nanoscale* **2018,** *10*, 1162-1179.

[#Kaufmann2009] Kaufmann, R.; Lemmer, P.; Gunkel, M.; Weiland, Y.; Müller, P.; Hausmann, M.; Baddeley, D.; Amberger, R.; Cremer, C. SPDM – Single molecule superresolution of cellular nanostructures. *Proc. SPIE* **2009,** *7185*, 71850J1-71850J19

[#Kim2017] Kim, E.H.; Kim, M.S.; Song, H.S.; Yoo, S.H.; Sai, S.; Chung, K.; Sung, J.; Jeong, Y.K.; Jo, Y.; Yoon, M. Gold nanoparticles as a potent radiosensitizer in neutron therapy. *Oncotarget*. **2017**, 8(68), 112390-112400, doi:10.18632/oncotarget.19837.

[#Krufczik2017] Krufczik, M.; Sievers, A.; Hausmann, A.; Lee, J.-H.; Hildenbrand, G.; Schaufler, W.; Hausmann, M. Combining low temperature fluorescence DNA-hybridization, immunostaining, and super-resolution localization microscopy for nano-structure analysis of ALU elements and their influence on chromatin structure. *Int. J. Mol. Sci.* 2017, *18*, 1005; doi:10.3390/ijms18051005

[#Kuncic2008] Kuncic, Z.; Lacombe, S. Nanoparticle radio-enhancement: Principles, progress and application to cancer treatment. *Phys. Med. Biol.* **2018**, *63*, 02TR01, doi:10.1088/1361-6560/aa99ce.

[#Kuo2008] Kuo LJ, Yang LX. γ-H2AX – a novel biomarker for DNA double-strand breaks. *In vivo* **2008**, *22***,** 305-310.

[#Lacombe2017] Lacombe, S.; Porcel, E.; Scifoni, E. Particle therapy and nanomedicine: State of art and research perspectives. *Cancer Nanotechnol.* **2017**, *8*, 9, doi:10.1186/s12645-017-0029-x.

[#Lacroix2004] Lacroix, M.; Leclercq, G. Relevance of breast cancer cell lines as models for breast tumours: An update. *Breast Cancer Res. Treat.* **2004**, *83*, 249–289, doi:10.1023/B:BREA.0000014042.54925.cc.

[#Lam2018] Lam, W.W.; Oakden, W.; Murray, L.; Klein, J.; Iorio, C.; Screaton, R.A.; Koletar, M.M.; Chu, W.; Liu, S.K.; Stanisz, G.J. Differentiation of Normal and Radioresistant Prostate Cancer Xenografts Using Magnetization Transfer-Prepared MRI. *Sci. Rep.* **2018**, *8*, 10447, doi:10.1038/s41598-018-28731-0.

[#Lemmer2008] Lemmer, P.; Gunkel, M.; Baddeley, D.; Kaufmann, R.; Urich, A.; Weiland, Y.; Reymann, J.; Müller, P.; Hausmann, M.; Cremer, C. SPDM: Light microscopy with single-molecule resolution at the nanoscale. *Appl. Phys. B* **2008**, *93*, 1–12, doi:10.1007/s00340-008-3152-x.

[#Lemmer2009] Lemmer, P.; Gunkel, M.; Weiland, Y.; Müller, P.; Baddeley, D.; Kaufmann, R.; Urich, A.; Eipel, H.; Amberger, R.; Hausmann, M.; Cremer, C. Using conventional fluorescent markers for far-field fluorescence localization nanoscopy allows resolution in the 10 nm range. *J. Microsc.* **2009**, *235*, 163–171.

[#Li2017] Li, S.; Porcel, E.; Remita, H.; Marco, S.; Réfrégiers, M.; Dutertre, M.; Confalonieri, F.; Lacombe, S. Platinum nanoparticles: An exquisite tool to overcome radioresistance. *Cancer Nanotechnol.* **2017**, *8*, 4, doi:10.1186/s12645-017-0028-y.

[#Lim2016] Lim, C.Y.; Zoncu, R. The lysosome as a command-and-control center for cellular metabolism. *J. Cell. Biol*. **2016**, 214(6), 653-64, doi:10.1083/jcb.201607005.

[#Loebrich2017] Löbrich, M.; Jeggo, P.A. A process of resection-dependent non-homologous end joining involving the goddess artemis. *Trends Biol. Sci.* **2017**, *42*, 690–701

[#Loebrich2010] Löbrich, M.; Shibata, A.; Beucher, A.; Fisher, A.; Ensminger, M.; Goodarzi, A.A.; Barton, O.; Jeggo, P.A. γ-H2AX foci analysis for monitoring DNA double-strand repair: Strengths, limitations and optimization. *Cell Cycle* **2010**, *9*, 662–669.

[#Loeffler2007] Löffler, H.; Bochtler, T.; Fritz, B.; Tews, B.; Ho, A.D.; Lukas, J.; Bartek, J.; Krämer, A. DNA Damage-Induced Accumulation of Centrosomal Chk1 Contributes to its Checkpoint Function. *Cell Cycle* **2007**, *6*, 2541–2548, doi:10.4161/cc.6.20.4810.

[#Lux2018] Lux, F.; Tran, V.L.; Thomas, E.; Dufort, S.; Rossetti, F.; Martini, M.; Truillet, C.; Doussineau, T.; Bort, G.; Denat, F.; et al. AGuIX® from bench to bedside-Transfer of an ultrasmall theranostic gadolinium-based nanoparticle to clinical medicine. *Br. J. Radiol.* **2018**, doi:10.1259/bjr.20180365.

[#MacPhail2010] MacPhail SH, Banath JP, Yu TY, et al. Expression of phosphorylated histone H2AX in cultured cell line following exposure to x-rays. *Int J Radiat Biol* 2003; **79:** 351-358.

[#Maeda2010] Maeda, H. Tumor-selective delivery of macromolecular drugs via the EPR effect: Background and future prospects. *Bioconjug. Chem.* **2010**, *21*, 797–802, doi:10.1021/bc100070g.

[#Maesa2011] Maeda, H.; Matsumura, Y. EPR effect based drug design and clinical outlook for enhanced cancer chemotherapy. *Adv. Drug Deliv. Rev.* **2011**, *63*, 129–130, doi:10.1016/j.addr.2010.05.001.

[#Martínez-Torres2018] Martínez-Torres, A.C.; Zarate-Triviño, D.G.; Lorenzo-Anota, H.Y.; Ávila-Ávila, A.; Rodríguez-Abrego, C.; Rodríguez-Padilla, C. Chitosan gold nanoparticles induce cell death in HeLa and MCF-7 cells through reactive oxygen species production. *Int. J. Nanomedicine*. **2018**, 13, 3235-3250, doi: 10.2147/IJN.S165289.

[#Mladenov2013] Mladenov, E.; Magin, S.; Soni, A.; Iliakis, G. DNA double-strand break repair as determinant of cellular radiosensitivity to killing and target in radiation therapy. *Front. Oncol.* **2013**, *3*, 113, doi:10.3389/fonc.2013.00113.

[#Mladenov2016] Mladenov, E.; Magin, S.; Soni, A.; Iliakis, G. DNA double-strand-break repair in higher eukaryotes and its role in genomic instability and cancer: Cell cycle and proliferation-dependent regulation. *Semin. Cancer Biol.* **2016**, *37–38*, 51–64, doi:10.1016/j.semcancer.2016.03.003.

[#Moser2016] Moser, F.; Hildenbrand, G.; Müller, P.; Al Saroori, A.; Biswas, A.; Bach, M.; Wenz, F.; Cremer, C.; Burger, N.; Veldwijk, M.R.; et al. Cellular Uptake of Gold Nanoparticles and Their Behavior as Labels for Localization Microscopy. *Biophys. J.* **2016**, *110*, 947–953, doi:10.1016/j.bpj.2016.01.004.

[#Natale2017] Natale, F.; Rapp, A.; Yu, W.; Maiser, A.; Harz, H.; Schall, A.; Grulich, S.; Anton, T.; Hörl, D.; Chen, W.; Durante, M.; Taucher-Scholz, G.; Leonhardt, H.; Cardoso, C. Identification of the elementary structural units of the DNA damage response. *Nat. Commun.* **2017**, *8*, 15760, doi:10.1038/ncomms15760

[#Ngwa2017] Ngwa, W.; Boateng, F.; Kumar, R.; Irvine, D.J.; Formenti, S.; Ngoma, T.; Herskind, C.; Veldwijk, M.R.; Hildenbrand, G.L.; Hausmann, M.; Wenz, F.; Hesser, J. Smart Radiation Therapy Biomaterials. *Int. J. Radiat. Oncol. Biol. Phys.* **2017**, *97*, 624–637, doi:10.1016/j.ijrobp.2016.10.034.

[#Ngwa2014] Ngwa, W.; Kumar, R.; Sridhar, S.; Korideck, H.; Zygmanski, P.; Cormack, R.A.; Berbeco, R.; Makrigiorgos, G.M. Targeted radiotherapy with gold nanoparticles: Current status and future perspectives. *Nanomedicine* **2014**, *9*, 1063–1082, doi:10.2217/nnm.14.55.

[#Nijkoo2010] Nikjoo, H.; Uehara, S.; Emfietzoglou, D.; Brahme, A. Heavy charged particles in radiation biology and biophysics. *New J. Phys.* **2008**, *10*, 075006, doi:10.1088/1367-2630/10/7/075006.

[#Noël2016] Noël, C.; Simard, J.C.; Girard, D. Gold nanoparticles induce apoptosis, endoplasmic reticulum stress events and cleavage of cytoskeletal proteins in human neutrophils. *Toxicol. In Vitro*. **2016**, 12-22, doi:10.1016/j.tiv.2015.11.003.

[#Oberdorster2004] Oberdorster, G.; Sharp, Z.; Atudorei, V.; et al. Translocation of inhaled ultrafine particles to the brain. *Inhal. Toxicol*. **2004**, 16, 437–445, doi:10.1080/08958370490439597.

[#Pan2007] Pan, Y.; Neuss, S.; Leifert, A.; Fischler, M.; Wen, F.; Simon, U.; Schmid, G.; Brandau, W., Jahnen-Dechent, W. Size-Dependent Cytotoxicity of Gold Nanoparticles. *Small*. **2007**, 3(11), 1941–1949.

[#Paro2017] Paro, A.D.; Shanmugam. I.; van de Ven, A.L. Nanoparticle-Mediated X-Ray Radiation Enhancement for Cancer Therapy. *Methods. Mol. Biol*. **2017**, 1530, 391-401, doi:10.1007/978-1-4939-6646-2_25.

[#Patil2019] Patil, Y.M.; Rajpathak, S.N.; Deobagkar, D.D. Characterization and DNA methylation modulatory activity of gold nanoparticles synthesized by Pseudoalteromonas strain. *J. Biosci*. **2019**, 44(1), pii:15.

[#Pegácová2019] Pagáčová, E.; Štefančíková, L.; Schmidt-Kaler, F.; Hildenbrand, G.; Vičar, T.; Depeš, D.; Lee, J.-H.; Bestvater, F.; Lacombe, S.; Wenz, F.; Kopečná, O.; Falková, I.; Hausmann, M.; Falk, M. Challenges and contradictions of metal nano-particle applications for radio-sensitivity enhancement in cancer therapy. *Int. J. Molec. Sci.* **2019**, *20*, 588. doi:10.3390/ijms20030588

[#Pilarczyk2017] Pilarczyk, G.; Nesnidal, I.; Gunkel, M.; Bach, M.; Bestvater, F.; Hausmann, M. Localisation microscopy of breast epithelial ErbB-2 receptors and gap junctions: Trafficking after gamma-irradiation, Neuregulin-1b and Herceptin application. *Int. J. Mol. Sci.* **2017,** *18*, 362

[#Porcel2010] Porcel, E.; Liehn, S.; Remita, H.; Usami, N.; Kobayashi, K.; Furusawa, Y.; Le Sech, C.; Lacombe, S. Platinum nanoparticles: A promising material for future cancer therapy? *Nanotechnology* **2010**, *21*, 85103, doi:10.1088/0957-4484/21/8/085103.

[#Prabhakar2013] Prabhakar, U.; Maeda, H.; Jain, R.K.; Sevick-Muraca, E.M.; Zamboni, W.; Farokhzad, O.C.; Barry, S.T.; Gabizon, A.; Grodzinski, P.; Blakey, D.C. Challenges and key considerations of the enhanced permeability and retention effect for nanomedicine drug delivery in oncology. *Cancer Res.* **2013**, *73*, 2412–2417, doi:10.1158/0008-5472.CAN-12-4561.

[#Prezado2009] Prezado, Y.; Renier, M.; Bravin, A. A new method of creating minibeam patterns for synchrotron radiation therapy: A feasibility study. *J. Synchrotron Radiat.* **2009**, *16*, 582–586, doi:10.1107/S0909049509012503.

[#Prigodich2012] Prigodich, A.E.; Randeria, P.S.; Briley, W.E.; Kim, N.J.; Daniel, W.L.; Giljohann, D.A.; Mirkin, C.A. Multiplexed nanoflares: mRNA detection in live cells. *Anal Chem* **2012**, *84*, 2062–2066.

[#Puck1956] Puck, T.T.; Markus, P.I. Action of X-rays on mammalian cells. *J. Exp. Med*. **1956**, 103, 653–666.

[#Rittich2004] Rittich, B.; Spanová, A.; Falk, M.; Benes, M.J.; Hrubý, M. Cleavage of double stranded plasmid DNA by lanthanide complexes. *J. Chromatogr. B Analyt. Technol. Biomed. Life Sci.* **2004**, *800*, 169–173.

[#Rogakou1998] Rogakou, E.P.; Pilch, D.R.; Orr, A.H.; Ivanova, V.S.; Bonner, W.M. DNA double-starnd breaks induce histone H2AX phosphorylation on serine 139. *J. Biol. Chem.* **1998**, *273*, 5858–5868.

[#Sammer2017] Sammer, M.; Greubel, C.; Girst, S.; Dollinger, G. Optimization of beam arrangements in proton minibeam radiotherapy by cell survival simulations. *Med. Phys.* **2017**, *44*, 6096–6104, doi:10.1002/mp.12566.

[#Sancey2014] Sancey, L.; Lux, F.; Kotb, S.; Roux, S.; Dufort, S.; Bianchi, A.; Crémillieux, Y.; Fries, P.; Coll, J.-L.; Rodriguez-Lafrasse, C.; et al. The use of theranostic gadolinium-based nanoprobes to improve radiotherapy efficacy. *Br. J. Radiol.* **2014**, *87*, doi:10.1259/bjr.20140134.

[#Sarin2008] Sarin, H.; Kanevsky, A.S.; Wu, H.T.; et al. Effective transvascular delivery of nanoparticles across the blood-brain tumor barrier into malignant glioma cells. *J. Transl. Med*. **2008**, 6, 1–15, doi:10.1186/1479-5876-6-80.

[#Schipler2013] Schipler, A.; Iliakis, G. DNA double-strand-break complexity levels and their possible contributions to the probability for error-prone processing and repair pathway choice. *Nucleic Acids Res.* **2013**, *41*, 7589–7605, doi:10.1093/nar/gkt556.

[#Seferos2007] Seferos, D.S.; Giljohann, D.A.; Hill, H.D.; Prigodich, A.E.; Mirkin, C.A. Nano-Flares: Probes for transfection and mRNA detection in living cells. *J. Am. Chem. Soc.* **2007**, *129*, 15477-15479.

[#Serrano-Puebla2018] Serrano-Puebla, A.; Boya, P. Lysosomal membrane permeabilization as a cell death mechanism in cancer cells. *Biochem. Soc. Trans*. **2018**, 46(2), 207-215, doi:10.1042/BST20170130.

[#Settembre2012] Settembre, C.; Zoncu, R.; Medina, D.L.; Vetrini, F.; Erdin, S.; Erdin, S.; Huynh, T.; Ferron, M.; Karsenty, G.; Vellard, M.C.; Facchinetti, V.; Sabatini, D.M.; Ballabio, A. A lysosome-to-nucleus signalling mechanism senses and regulates the lysosome via mTOR and TFEB. *EMBO J*. **2012**, 31(5), 1095-108, doi:10.1038/emboj.2012.32.

[#Settembre2013] Settembre, C.; Fraldi, A.; Medina, D.L.; Ballabio A. Signals for the lysosome: a control center for cellular clearance and energy metabolism. *Nat. Rev. Mol. Cell. Biol*. **2013**, 14(5), 283–296.

[#Soenen2012] Soenen, S.J.; Manshian, B.; Montenegro, J.M.; Amin, F.; Meermann, B.; Thiron, T.; Cornelissen, M.; Vanhaecke, F.; Doak, S.; Parak, W.J.; De Smedt, S.; Braeckmans, K. Cytotoxic effects of gold nanoparticles: a multiparametric study. *ACS Nano*. **2012**, 6(7), 5767-5783, doi:10.1021/nn301714n.

[#Sonavane2008] Sonavane, G.; Tomoda, K.; Makino, K. Biodistribution of colloidal gold nanoparticles after intravenous administration: effect of particle size. *Colloids Surf B Biointerfaces*. **2008**, 66(2), 274-80, doi:10.1016/j.colsurfb.2008.07.004.

[#Štefančíková2016] Štefančíková, L.; Lacombe, S.; Salado, D.; Porcel, E.; Pagáčová, E.; Tillement, O.; Lux, F.; Depeš, D.; Kozubek, S.; Falk, M. Effect of gadolinium-based nanoparticles on nuclear DNA damage and repair in glioblastoma tumor cells. *J. Nanobiotechnol.* **2016**, *14*, 63, doi:10.1186/s12951-016-0215-8.

[#Štefančíková2014] Stefančíková, L.; Porcel, E.; Eustache, P.; Li, S.; Salado, D.; Marco, S.; Guerquin-Kern, J.-L.; Réfrégiers, M.; Tillement, O.; Lux, F.; et al. Cell localisation of gadolinium-based nanoparticles and related radiosensitising efficacy in glioblastoma cells. *Cancer Nanotechnol.* **2014**, *5*, 6, doi:10.1186/s12645-014-0006-6.

[#Struwe2015] Struve, N.; Riedel, M.; Schulte, A.; Rieckmann, T.; Grob, T.J.; Gal, A.; Rothkamm, K.; Lamszus, K.; Petersen, C.; Dikomey, E.; Kriegs, M. EGFRvIII does not affect radiosensitivity with or without gefitinib treatment in glioblastoma cells. *Oncotarget* **2015**, *20*, 33867-33877.

[#Stuhlmüller2015] Stuhlmüller, M.; Schwarz-Finsterle, J.; Fey, E.; Lux, J.; Bach, M.; Cremer, C.; Hinderhofer, K.; Hausmann, M.; Hildenbrand, G. In situ optical sequencing and nano-structure analysis of a trinucleotide expansion region by localization microscopy after specific COMBO-FISH labelling. *Nanoscale* **2015**, *7*, 17938-17946.

[#Taggart2014] Taggart, L.E.; McMahon, S.J.; Currell, F.J.; Prise, K.M.; Butterworth, K.T. The role of mitochondrial function in gold nanoparticle mediated radiosensitisation. *Cancer Nanotechnol*. **2014**, 5(1), 5.

[#Taggart2016] Taggart, L.E.; McMahon, S.J.; Butterworth, K.T.; Currell, F.J.; Schettino, G.; Prise, K.M. Protein disulphide isomerase as a target for nanoparticle-mediated sensitisation of cancer cells to radiation. *Nanotechnology*. **2016**, 27(21), 215101. doi:10.1088/0957-4484/27/21/215101.

[#Thompson2002] Thompson RE, Larson DR, Webb WW. Precise nanometer localization analysis for individual fluorescent probes. *Biophys J* 2002; **82:** 2775-2783.

[#Tomita2018] Tomita, K.; Kuwahara, Y.; Takashi, Y.; Igarashi, K.; Nagasawa, T.; Nabika, H.; Kurimasa, A.; Fukumoto, M.; Nishitani, Y.; Sato, T. Clinically relevant radioresistant cells exhibit resistance to H_2O_2 by decreasing internal H_2O_2 and lipid peroxidation. *Tumour Biol.* **2018**, *40*, doi:10.1177/1010428318799250.

[#Turinetto2015] Turinetto, V.; Giachino, C. Multiple facets of histon variant H2AX: a DNA double-strand-break marker with several biological functions. *Nucl. Acids Res.* **2015**, *43***,** 2489-2498.

[#Wenz2001] Wenz, F.; Tiefenbacher, U.; Willeke, F.; Weber, K.-J. Auf der Suche nach der *Therapeutischen breite* in der Radioonkologie. *Oncol. Res. Treat.* **2001**, *24*, 51–55, doi:10.1159/000055187.

[#Wolfe2015] Wolfe, T.; Chatterjee, D.; Lee, J.; Grant, J.D.; Bhattarai, S.; Tailor, R.; Goodrich, G.; Nicolucci, P.; Krishnan, S. Targeted gold nanoparticles enhance sensitization of prostate tumors to megavoltage radiation therapy *in vivo*. *Nanotechnology, Biology, and Medicine* **2015**, *11*, 1277–1283.

[#Yang2018] Yang, C.; Bromma, K.; Sung, W.; Schuemann, J.; Chithrani, D. Determining the Radiation Enhancement Effects of Gold Nanoparticles in Cells in a Combined Treatment with Cisplatin and Radiation at Therapeutic Megavoltage Energies. *Cancers* (Basel). **2018**, 10(5), pii: E150, doi:10.3390/cancers10050150.

[#Yameen2014] Yameen, B.; Choi, W.I.; Vilos, C.; Swami, A.; Shi, J.; Farokhzad, O.C. Insight into nanoparticle cellular uptake and intracellular targeting. *J. Control. Release* **2014**, *190*, 485–499, doi:10.1016/j.jconrel.2014.06.038.

[#Youkhana2017] Youkhana, E.Q.; Feltis, B.; Blencowe, A.; Geso, M. Titanium Dioxide Nanoparticles as Radiosensitisers: An In vitro and Phantom-Based Study. *Int. J. Med. Sci*. **2017**, 14(6), 602-614, doi:10.7150/ijms.19058.

[#Zhang2018] Zhang, H.; Wan, C.; Huang, J.; Yang, C.; Qin, Y.; Lu, Y.; Ma, J.; Wu, B.; Xu, S.; Wu, G.; et al. In Vitro Radiobiological Advantages of Hypofractionation Compared with Conventional Fractionation: Early-Passage NSCLC Cells are Less Aggressive after Hypofractionation. *Radiat. Res.* **2018**, doi:10.1667/RR14951.1.

[#Zhou2007] Zhou, H.; Miki, R.; Eeva, M.; Fike, F.M.; Seligson, D.; Yang, L.; Yoshimura, A.; Teitell, M.A.; Jamieson, C.A.M.; Cacalano, N.A. Reciprocal Regulation of SOCS1 and SOCS3 Enhances Resistance to Ionizing Radiation in Glioblastoma Multiforme. *Clin. Cancer Res.* **2007**, *13*, 2344–2353, doi:10.1158/1078-0432.CCR-06-2303.

[#Zygmanski2013] Zygmanski, P.; Liu, B.; Tsiamas, P.; Cifter, F.; Petersheim, M.; Hesser, J.; Sajo, E. Dependence of Monte Carlo microdosimetric computations on the simulation geometry of gold nanoparticles. *Phys. Med. Biol.* **2013**, *58*, 7961–7977, doi:10.1088/0031-9155/58/22/7961.

Changes in Cryopreserved Cell Nuclei Serve as Indicators of Processes during Freezing and Thawing

Article *in* Langmuir · October 2018

DOI: 10.1021/acs.langmuir.8b02742

10 authors, including:

Irena Kratochvılová
Institute of Physics ASCR
91 PUBLICATIONS **841** CITATIONS
SEE PROFILE

Olga Kopecna
Institute of Biophysics ASCR
7 PUBLICATIONS **1** CITATION
SEE PROFILE

Eva Pagacova
Institute of Biophysics ASCR
20 PUBLICATIONS **156** CITATIONS
SEE PROFILE

Iva Falkova
Institute of Biophysics ASCR
35 PUBLICATIONS **167** CITATIONS
SEE PROFILE

LANGMUIR Article
Cite This: Langmuir XXXX, XXX, XXX−XXX
pubs.acs.org/Langmuir

Changes in Cryopreserved Cell Nuclei Serve as Indicators of Processes during Freezing and Thawing

Irena Kratochvílová,[†] Olga Kopečná,[‡] Alena Bačíková,[‡] Eva Pagáčová,[‡] Iva Falková,[‡] Shelby E. Follett,[§] K.Wade Elliott,[∥] Krisztina Varga,[∥] Martin Golan,[†] and Martin Falk*[,‡]

[†]Institute of Physics, v.v.i., Czech Academy of Sciences, Na Slovance 2, CZ-182 21 Prague 8, Czech Republic
[‡]Institute of Biophysics, v.v.i., Czech Academy of Sciences, Královopolská 135, CZ-612 65 Brno, Czech Republic
[§]Department of Chemistry, University of Wyoming, 1000 E. University Avenue, Laramie, Wyoming 82071, United States
[∥]Department of Molecular, Cellular, and Biomedical Sciences, University of New Hampshire, 46 College Road, Durham, New Hampshire 03824, United States

ABSTRACT: The mechanisms underlying cell protection from cryoinjury are not yet fully understood. Recent biological studies have addressed cryopreserved cell survival but have not correlated the cryoprotection effectiveness with the impact of cryoprotectants on the most important cell structure, the nucleus, and the freeze/thaw process. We identified changes of cell nuclei states caused by different types of cryoprotectants and associate them with alterations of the freeze/thaw process in cells. Namely, we investigated both higher-order chromatin structure and nuclear envelope integrity as possible markers of freezing and thawing processes. Moreover, we analyzed in detail the relationship between nuclear envelope integrity, chromatin condensation, freeze/thaw processes in cells, and cryopreservation efficiency for dimethyl sulfoxide, glycerol, trehalose, and antifreeze protein. Our interdisciplinary study reveals how changes in cell nuclei induced by cryoprotectants affect the ability of cells to withstand freezing and thawing and how nuclei changes correlate with processes during freezing and thawing. Our results contribute to the deeper fundamental understanding of the freezing processes, notably in the cell nucleus, which will expand the applications and lead to the rational design of cryoprotective materials and protocols.

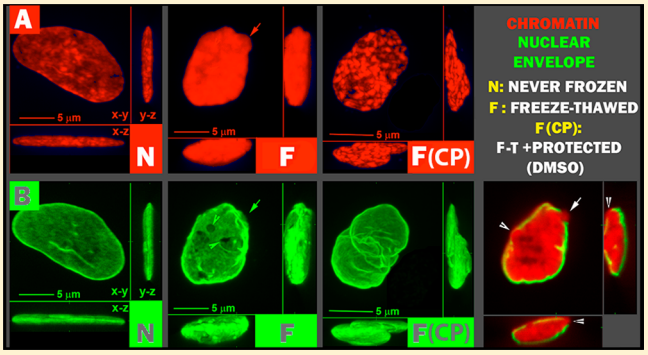

INTRODUCTION

Cryopreservation of living cells and tissues became fundamental in biotechnology, plant programmes, and modern medicine.[1−4] Increasing problems associated with human reproduction put techniques of assisted reproduction, including in vitro fertilization (IVF), to the center of human medicine. In the frame of IVF, embryos and sperm are deeply frozen prior to being mutually coupled, cultured, checked for possible defects, and implanted. The effects of the freeze−thaw cycle on cells and especially their genomes have been studied only insufficiently. The need of such a research appears to be even more urgent than previously thought, especially in the light of recent discoveries showing that epigenetic alterations—which can appear even easier and in the absence of genetic damage—could have serious impacts on the cell health as genetic damage.[5] Indeed, several reports revealed effects of IVF on (e.g., insulin) gene[6−9] epigenetic status and expression. Accordingly, it has been proposed that epigenetic modifications that may occur in cells during cryopreservation can be one of the factors responsible for defects in live births after in vitro fertilization.[10−12] Except for rare reports, recent biological research on cryopreserved cell genetic and epigenetic defects has remained limited.

The effectiveness of cryoprotection thus remains to be examined in the context of freeze/thaw mechanisms and the complex cell/cell nuclei states during the freezing/thawing process. This is not only necessary to comprehend the mechanisms of the freeze/thaw cycle per se but also to reveal the potential (health) risks associated with cryopreservation and to rationally design new, more efficient cryoprotective materials and protocols.[13,14] It should be empasized that the importance of the research on processes induced in cells by freezing/thawing reaches far beyond human medicine. In veterinary medicine, improvement breeding, and species preservation, usage of frozen gametes represents a gold standard.

Special Issue: Interfaces and Biology 1: Mechanobiology and Cryobiology

Received: August 11, 2018
Revised: October 17, 2018
Published: October 19, 2018

DOI: 10.1021/acs.langmuir.8b02742
Langmuir XXXX, XXX, XXX−XXX

The difficulty in cryopreservation is that ice crystallization, which appears mainly throughout the slow freezing process, can significantly damage the cells and cause the loss of viability after the cells are thawed. The ice crystallization starts in the extracellular space, where the concentration of macromolecules and solvents is lower than inside the cell. Freezing of the extracellular solution effectively leads to an increase in the concentration of solvents in the part that remains liquid. That brings an osmotic imbalance, which results in a net flow of water from the inside of cells out. This dehydration was one of the first consequences identified in cell cryobiology,[2] later shown to cause a number of damaging events including changes in ultrastructure of cell membranes, loss or fusion of membrane bilayers, and organelle disruption. Moreover, when the concentration of ions and other solvents increases beyond physiological concentrations, the following stress may be toxic for cells. The second major damaging event recognized during cell freezing was the propagation of intracellular and extracellular ice crystals.[15] The mechanisms of cell damage from intracellular and extracellular ice include physical destruction of membranes and organelle disruption.[15]

Fortunately, the freezing process in cells is strongly affected by velocity of the freezing/cooling and the cryoprotective additives, due to which a multitude of cells from prokaryotic and eukaryotic organisms can be recovered from temperatures as low as almost 200 °C below freezing point when the cryoprotectants are present.[10,16] The mechanism of action of the cryoprotectants is complex; however, they appear to act primarily within the cells or in their immediate surroundings. Recent biological studies have addressed survival of cryopreserved cells but have not correlated the efficiency of cryoprotection with description of cell states and the freezing mechanism.[2,10,14,16−18] To rationally design new cryoprotective materials and protocols, a much better fundamental understanding of both the physical and biological aspects of the cryoprotection process is necessary.[19,20]

In the present work, we identified subcellular changes during freezing and thawing processes associated with the nuclei of normal cryopreserved human skin fibroblasts (NHDF), namely, higher-order chromatin[9] structure and nuclear envelope integrity. By using high-resolution confocal fluorescent microscopy and flow cytometry, we simultaneously evaluated the impact of cryoprotectants on chromatin domain condensation and degradation and the nuclear envelope quality, as well as the viability of untreated versus cryopreserved cells after freeze/thaw. Subcellular changes were characterized in both nonfrozen and frozen/thawed cells prior to and after the cryoprotectant treatment. We utilized materials that change the thermodynamic properties of the freezing process or block ice formation and/or growth, such as dimethyl sulfoxide (DMSO),[21] trehalose, and the antifreeze fusion protein TrxA-ApAFP752 (AFP).[22,24] These cryoprotectants affect intra and extracellular space of nonfrozen cells and consequently the whole freezing/thawing process.[23,24]

Our interdisciplinary study reveals how changes in cell nuclei induced by cryoprotectants affect the ability of cells to withstand freezing and thawing and how nuclei changes correlate with processes during freezing and thawing. We investigated both higher-order chromatin structure and nuclear envelope integrity as possible end points of freezing and thawing processes.[25,26] This effort resulted in identification of important cell markers that can be applied as indicators of processes during freezing and thawing and predictors of the frozen/thawed cells' viability. The results of our interdisciplinary work thus enhance the fundamental understanding of the freezing process, which will move the field of cryobiology forward and lead to the rational design of cryoprotective materials and processes.[14,27−29]

EXPERIMENTAL SECTION

Cryoprotectants. 10% (w/w) DMSO, 10% (w/w) glycerol, 100 mM (3.2% w/w) trehalose, or 10% DMSO + 100 mM trehalose were added to cell cultures prior to freezing. Because of slow penetration into the cells, trehalose was applied 24 h before freezing/thawing, and the cells were returned back to the cell incubator, until they were submitted to the freeze procedure. To minimize cytotoxicity of DMSO, DMSO was only added to precooled (4 °C) cell cultures, 2 min prior to freezing. Samples containing glycerol were also treated for 2 min with the cryoprotectant. In the case of combined cryopreservation (trehalose + DMSO), cells treated with trehalose were cooled to 4 °C and supplied with DMSO as described. See Table 1 for cryoprotectant treatments.

Table 1. Cryoprotectants Used for Cell Experiments

sample	referred to as	composition
DMSO	DMSO	DMSO 10% (w/w) in DMEM (cell culture) medium
glycerol	G	glycerol 10% (w/w) in DMEM (cell culture) medium
DMSO + trehalose	DMSO+T	DMSO 10% (w/w) +100 mM trehalose 3.2% (w/w) in DMEM (cell culture) medium
AFP	AFP	0.5 mg·ml^{-3} in DMEM (cell culture) medium
trehalose	T	3.2% (w/w) (100 mM) trehalose in DMEM (cell culture) medium

We also prepared 1% (w/w) solution of the fusion protein TrxA-ApAFP752 in phosphate-buffered saline (PBS) or deionized (DI) water (AFP solution). The recombinant plasmid pET32b-*Apafp752* was transformed into *Escherichia coli* Rosetta-gami 2(DE3) (Novagen) or BL21 (DE3)pLysS competent cells (Promega). Detailed way of AFP preparation is described in Ceelen et al.

Cells and Cell Culturing. The certified normal human skin fibroblasts (NHDF) obtained from CLS Cell Line Service GmbH were used and grown at 37 °C in humidified atmosphere with 5% CO_2 in Dulbecco's Modified Eagle Medium (DMEM; PAN Biotech, catalog No. P03-0710) supplemented with 10% fetal calf serum (FCS; PAA Laboratories GmbH) and standard antibiotics (1% penicillin + streptomycin; stock solution mixture containing 10 000 U/mL penicillin and 10 mg/mL streptomycin (PAN Biotech, catalog No. P06-07100). The cells obtained at passage 2 were multiplied and freeze aliquoted on liquid nitrogen, and the "young" passages (5−8) used for experiments to exclude possible differences in higher-order chromatin structure among experiments.

Freeze/Thaw Procedure. Untreated cells in standard DMEM medium (1 mL) or cells in standard medium treated with AFP or trehalose were cooled to 4 °C and eventually supplied with DMSO or glycerol. Precooled obtained samples—untreated controls and samples treated with AFP, trehalose, DMSO, glycerol, or a combination of trehalose + DMSO—were consequently frozen by slow cooling to the final temperature of −80 °C, using a gradient of −1 °C/min. Frozen cells were kept at this temperature overnight (18 h) before thawing, performed as follows: Frozen cells were warmed in a water bath (37 °C) for 1 min. To remove toxic DMSO and AFP protein debris, DMSO- and AFP-treated thawed cell suspensions (1 mL) were immediately diluted with 9 mL of fresh culture medium (preheated to 37 °C) and gently centrifuged. Pelleted cells were again diluted in new medium and transferred into the cell incubator (5% CO_2, 37 °C) until processed. Samples treated with trehalose (+trehalose or +trehalose+DMSO) were handled adequately, but

DOI: 10.1021/acs.langmuir.8b02742
Langmuir XXXX, XXX, XXX−XXX

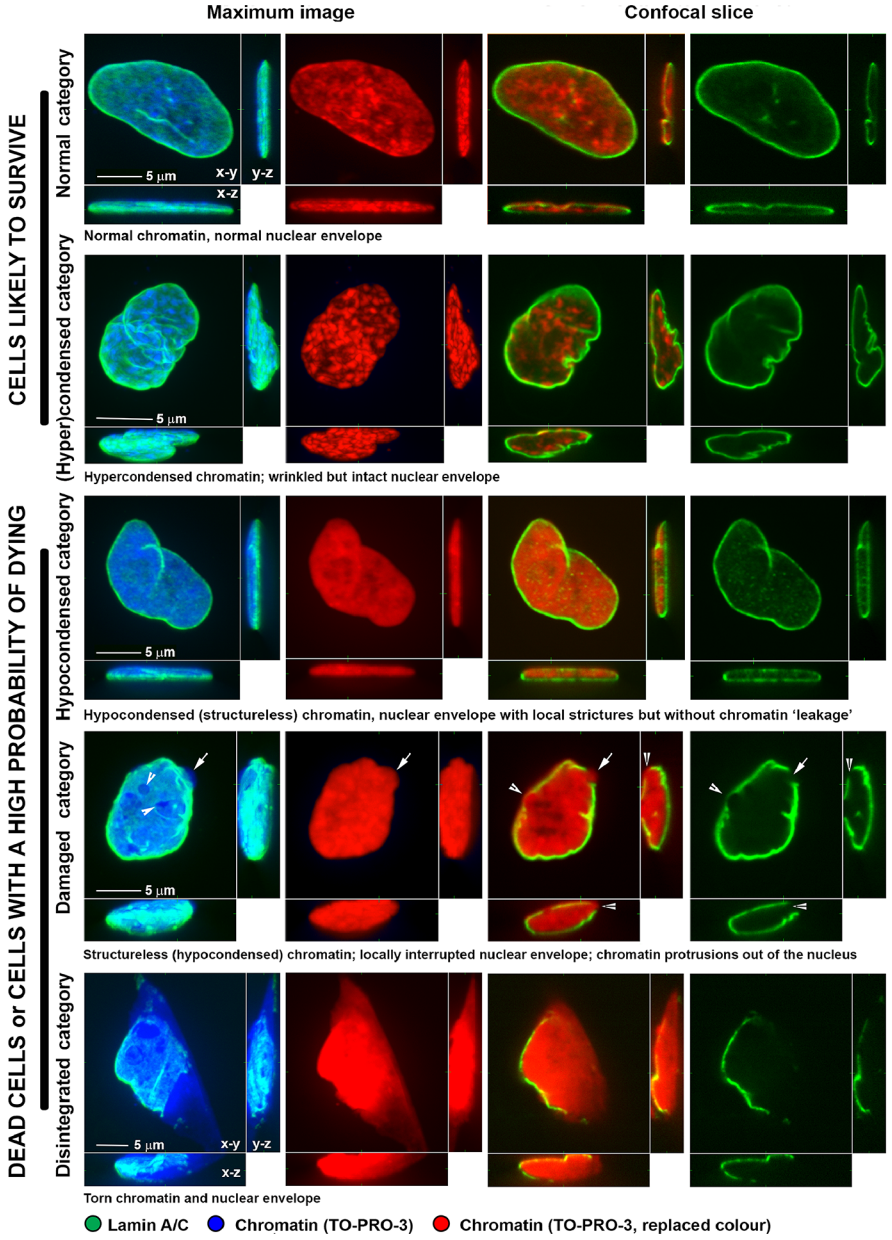

Figure 1. Human fibroblasts were categorized into two groups based on the appearance of their nuclei after a freeze/thaw cycle. (top two rows) Cells with a high probability of surviving had normal appearance or hypercondensed chromatin and an intact or wrinkled/shrunken nuclear envelope. (bottom three rows) Cells with a low probability of surviving had damaged nuclei with hypocondensed chromatin and a nuclear envelope with or without local interruptions and chromatin leakage (minimal or no probability of surviving), or a disintegrating nucleus showing leaking chromatin that lacked any structure (no probability of surviving). (two right columns) "Maximum images" that are composed of 40 superimposed 0.2 μm thick confocal slices; central nuclear confocal slices (0.2 μm thick) are provided in two left columns; *x-y*, *x-z*, and *y-z* projections are displayed for each image. Nuclear envelopes were visualized using lamin A/C antibody (green), and the chromatin was counterstained with TO-PRO-3 (blue or red to better visualize the chromatin structure). Holes in the nuclear membranes are indicated by white arrows.

culture medium supplemented with 3.2% (w/w) (100 mM) trehalose was used in all steps during and after thawing. This prevented cells from a hypotonic shock, since trehalose accumulated (to some extent) in cells can only slowly diffuse to extracellular space after thawing. Concerning a long (24 h) incubation time of cells with trehalose prior to freezing, this modification could not be expected to influence results substantially compared to DMSO- and AFP-treated samples. In the concentration used, glycerol is only slightly toxic to the cells but is known to induce strong osmotic changes during thawing. Therefore, after they were warmed in a water bath, the cell suspensions with glycerol were transferred to new culture media and incubator without glycerol removing.

Immunostaining. The nuclear envelope was stained with antilamin A/C monoclonal mouse antibody (No. SAB4200236; dilution 1:1000; Sigma-Aldrich) using the procedure described earlier.[30] Counterstaining of nuclear chromatin[31,32] was performed with 1 μM TO-PRO-3 (Molecular Probes) diluted in 2× saline sodium citrate (SSC) prepared afresh from stock. After the cells were washed with 2× SSC, the samples were mounted on slides (using Vectashield medium from Vector Laboratories).

Quantification of Changes in Higher-Order Chromatin Structure and Nuclear Envelope Integrity. Changes in the higher-order structure of chromatin (e.g., condensation) after a freeze/thaw cycle were evaluated using the intensity profiles using the "RGB Profile Plot" and "Surface Plot" plugins for ImageJ 1.52a

DOI: 10.1021/acs.langmuir.8b02742
Langmuir XXXX, XXX, XXX−XXX

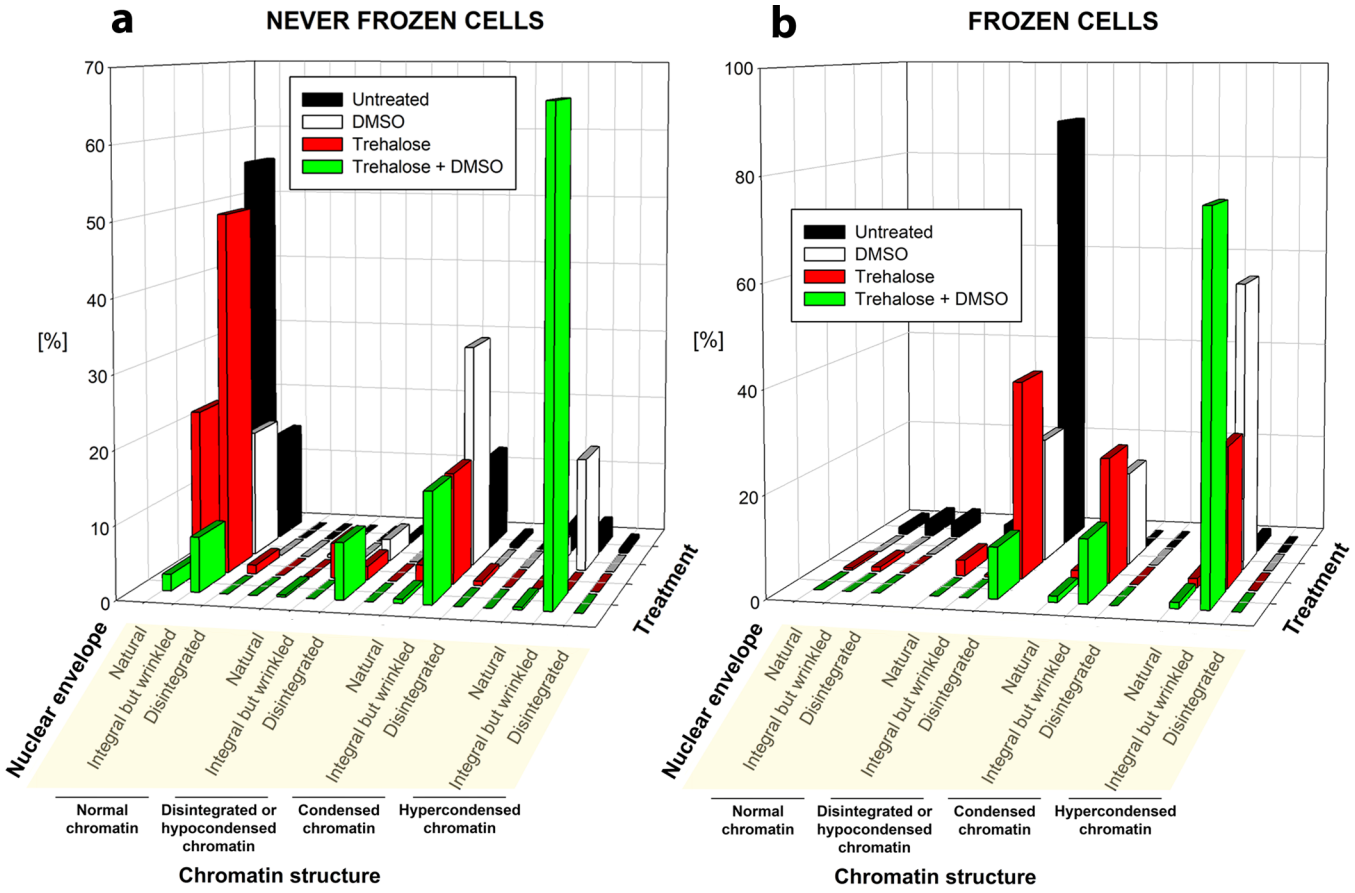

Figure 2. Proportions of particular (a) never frozen or (b) frozen/thawed human skin fibroblast (NHDF) categories determined for each cryoprotectant according to defined states of chromatin condensation and nuclear envelope condition. (a) In never frozen cells, all cryoprotectants induced nuclear envelope shrinkage to different extents, but only DMSO provoked chromatin condensation in a higher proportion of cells. (b) For frozen/thawed cells, the levels of nuclear envelope shrinkage and chromatin condensation correlated with the protective effects of cryoprotectants. Normal chromatin condensation mostly associated with low level of nuclear envelope shrinkage and vice versa. On the one hand, a high level of both chromatin condensation and, at the same time, nuclear envelope shrinkage appeared especially in DMSO-treated samples (DMSO and DMSO+trehalose). On the other hand, untreated controls mostly had structureless chromatin and disintegrated nuclear envelopes.

software (Wayne Rasband, http://imagej.nih.gov/ij). Furthermore, visual inspection of three-dimensional (3D) microscopic images of nuclei and their confocal slices was performed in all three planes. Also, fluorescence intensity profiles along line segments marked over 0.2 μm thick confocal slices of nuclei were created and analyzed.[31] The path of each line was chosen so as to cover substantial and representative parts of the nuclei. High variation and steep changes of staining intensity along the line segments indicate functionally and structurally distinct chromatin domains that are well-preserved following the freeze/thaw procedure. On the contrary, the absence of such large changes in staining intensity along the line segment (i.e., only gradual changes and/or changes with low amplitude are present) indicate extensive degradation of the native higher-order chromatin structure. Disruptions or narrowing in the nuclear lamina (visualized by lamin A/C antibody) plus chromatin (stained by TO-PRO-3) leakage out of the nucleus were taken as a sign indicating damage to the nuclear envelope.

Cell Survival and Apoptosis. To quantify survival and apoptosis in cells that were frozen either with or without cryoprotectants, flow cytometry was used. The cells were analyzed on a Muse Cell Analyzer (Merck Millipore). To discriminate between live, early apoptotic, late apoptotic, and dead cells, fluorescent staining with Muse Annexin V & Dead Cell Assay Kit (MCH100105, Millipore) was used according to the manufacturer's instructions as described earlier.[33] The cell condition was analyzed 24 h after thawing of the cells.

Confocal Microscopy and Data Analysis. An Ar/Kr-laser (Innova 70C Spectrum, Coherent) was used for fluorescence excitation. The confocal microscope used was an automated Leica DM RXA fluorescence microscope (Leica) equipped with an oil immersion Plan Fluotar objective (100×/NA1.3) and a CSU 10a Nipkow disc (Yokogawa). Sample images were acquired with a CoolSnap HQ CCD-camera (Photometrix).[34] Setting of the exposure time, image quality control, and other procedures were done in Acquiarium software.[35] The exposure time and the dynamic range of the camera in the red, green, and blue channels (R-G-B) were set to the same values for all slides to ensure that the obtained images are quantitatively comparable. For each viewed cell, 40 serial optical sections (0.2 μm thick) were captured.

■ RESULTS AND DISCUSSION

To thoroughly probe the state of cell nuclei during the freeze/thaw cycle, we simultaneously investigated higher-order chromatin structure (chromatin domains, condensation, and degradation) and nuclear envelope quality in human skin fibroblasts (NHDF) cultured and frozen in standard medium and in medium with cryoprotectants added prior to freezing and thawing. Five main categories of nuclei, as documented in Figure 1, appeared according to the chromatin and nuclear envelope[19,36] state.

On the basis of these results and on our previous findings,[37,38] we classified these categories in two main groups of cells concerning their probability to survive the freeze/thaw

DOI: 10.1021/acs.langmuir.8b02742
Langmuir XXXX, XXX, XXX−XXX

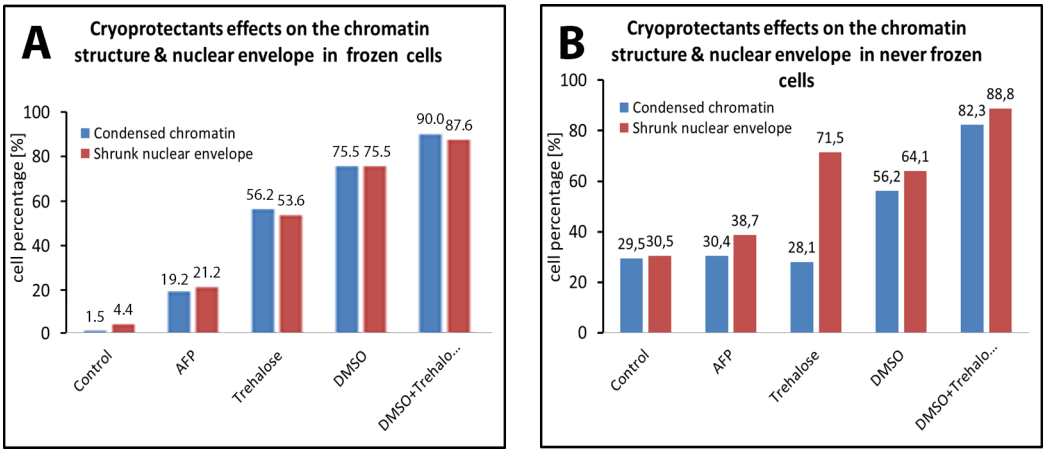

Figure 3. :Effects of cryoprotectants on the NHDF cell nuclei states—their chromatin and envelope structure—during prefreezing incubation (a) and after a freeze/thaw cycle (b). Between 50 and 150 cells were analyzed for each sample (deviations were less than 7% of the presented values). For frozen/thawed cells, the levels of nuclear envelope shrinkage and chromatin condensation correlated with the cryoprotective effects of cryoprotectants.

cycle (Figure 1). (1) Cells with a high probability of surviving ("surviving cells") had normal physiological chromatin structure or condensed chromatin plus a normal (smooth) or shrunken nuclear envelope after labeling with lamin A/C antibody (Figure 1; top two rows). (2) Cells with a low probability of surviving ("dead cells") had either mostly dispersed chromatin that lacked any structure or totally disintegrated chromatin; in these cells, the nuclear envelope quality did not matter, and in some cases the nuclear envelope seemed to be disintegrating (Figure 1, bottom three rows).

First, we quantified and statistically cross-compared the changes induced by individual cryoprotectants in the chromatin and nuclear envelope structure during the prefreezing treatment (Figures 2a and 3a) and later on in frozen cells upon thawing (Figures 2b and 3b). The individual cryoprotectants influenced the chromatin and nuclear envelope structure of both never frozen and frozen/thaw cells to various extents. As quantified in Figure 2a and summarized in Figure 3a, nonfrozen cells incubated with trehalose showed relatively strong shrinkage of nuclear envelopes but only a very slightly condensed nuclear chromatin. DMSO application, on the other hand, led to the nuclear envelope shrinkage associated with strong chromatin condensation. Finally, addition of AFP to the culture medium of nonfrozen cells had only minor effects on both these parameters.

The influence of individual cryoprotectants on the NHDF cell nuclei upon freezing down to −80 °C using a gradient of −1 °C/min and thawing is summarized in Figure 2b. On the basis of the level of chromatin condensation (evaluated by intensity profiles as shown in Figure 4) and the state of the nuclear envelope, three main categories can be distinguished concerning the cryoprotectants' effects: (1) surviving cells that were frozen/thawed with trehalose mostly display chromatin structure somewhat more condensed than in nonfrozen cells and have shrunken nuclear envelopes; this is also the case for AFP-treated cells, although the effects appear to a lesser extent (Figure 3b); (2) cells frozen/thawed with DMSO or DMSO +trehalose show highly condensed chromatin (especially the DMSO+trehalose-treated cells) (Figure 4) and have shrunken nuclear envelopes similar to cells in (1) (Figures 2b and 3b); (3) a few cells with an integral nucleus that were frozen/thawed in the absence of cryoprotectants (Figures 2b and 3b)

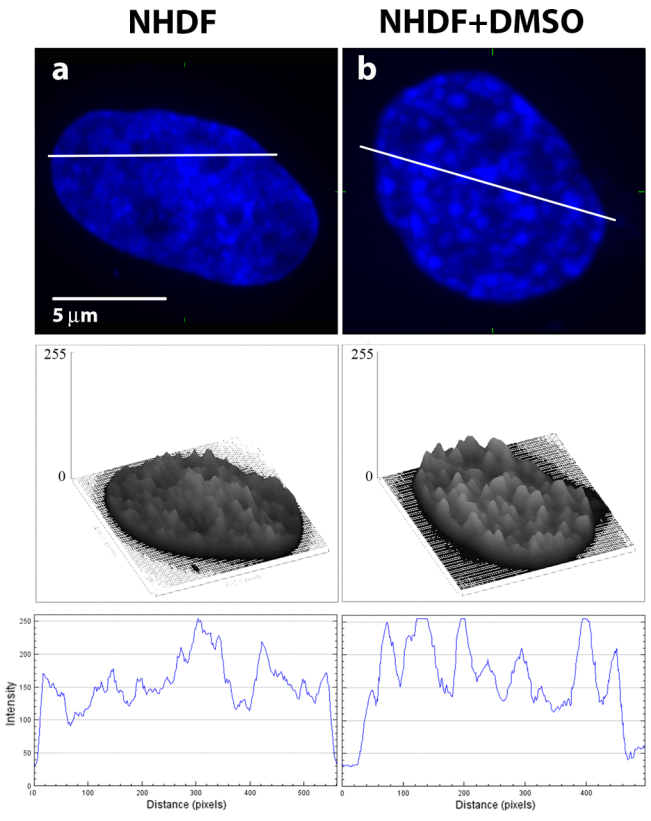

Figure 4. Chromatin condensation in (a) NHDF fibroblasts and (b) NHDF fibroblast treated with 10% DMSO for 2 min (at 4 °C). (top) The maximum images of cell nuclei composed of superimposed individual confocal slices (each 0.2 μm wide) and stained with TO-PRO-3. (middle) The surface profiles of nuclei based on relative fluorescence intensity [RFU, 0-255]. (bottom) Intensity profiles in the blue color channel along the white lines indicated at the top two images. All right images clearly demonstrate formation of condensed chromatin clumps as compared to left images.

show hypocondensed (structureless) chromatin, contrasting with cells in (2). The nuclear envelopes of these cells (if not totally disintegrated) are frequently thin, with numerous constricted sites indicative of the envelope damage or even interruption (Figure 1). Untreated (no cryoprotectants were

DOI: 10.1021/acs.langmuir.8b02742
Langmuir XXXX, XXX, XXX−XXX

applied) nonfrozen cells are included (Figure 3a) to illustrate proportions of cells with particular chromatin and nuclear envelope states under physiological conditions. Normal-looking nuclear envelopes and normal chromatin structure are shown in Figure 4.

To summarize (Figure 3b), unlike in never frozen NHDF cells (Figure 3a), states of chromatin structure correlated with nuclear envelope shrinkage for all cryoprotectants in frozen/thawed cells. Cells with normal chromatin condensation practically disappeared, while the vast majority of cells had either structureless (hypocondensed) or condensed chromatin. Frozen/thawed cells with condensed chromatin typically had shrunken envelopes. On the one hand, this picture was characteristic for the vast majority of cells in samples containing DMSO (DMSO and DMSO+trehalose). On the other hand, frozen/thawed cells with disintegrated chromatin predominantly showed disrupted nuclear envelopes. Rare cells with normal chromatin, irrespectively of nuclear envelope structure (normal or shrunken) practically appeared only in unprotected frozen/thawed cells. Proportions of cells with particular chromatin and nuclear envelope states were thus strongly dependent on the cryoprotectant used.

On the basis of NHDF nuclear envelope and chromatin states, by using the categories described in Figure 1, we also established (30 min after treatment/thawing) the cell survival probability ("the structure-based cell survival") for each particular treatment (Figure 5a,b). In parallel, we determined the real cell viability for all samples by flow cytometry (Figure 5c,d). To allow the cells to enter apoptosis, flow cytometry measurements were performed 24 h after the cryoprotectant treatment (in the case of nonfrozen cells) or after thawing (in the case of frozen cells). As shown in (Figure 5c), none of the cryoprotectants had a profound negative impact on viability of nonfrozen cells.

For frozen/thawed cells (Figure 3b), we found that more than 75% of DMSO (2 min incubation) treated cells and 92% of DMSO+trehalose (24 h + 2 min incubation) treated cells and less than 5% of untreated cells had shrunken envelopes and condensed chromatin. Correspondingly, 80.7% of DMSO-treated cells, 85.6% of DMSO+trehalose-treated, and 7.3% of untreated cells survived 24 h after thawing as determined by flow cytometry (Figure 5d). The effect of 24 h trehalose treatment on the nucleus of frozen cells was less prominent (less than 60% of cells had condensed chromatin, and less than 60% of them had shrunken envelope) and again correlated with the real cell survival (58.5%) determined 24 h after thawing. AFP exerted the smallest effects among the cryoprotectants studied: of AFP-treated frozen/thawed cells, only ~20% of nuclei showed structural changes, and only 32.3% of cells survived 24 h after thawing.

Taken together, our microscopic classification of cell viability upon freezing/thawing, based on the two structural parameters we identified (the chromatin structure and the nuclear envelope structure), correlates perfectly with the cytometric data (Figure 5d). Hence, we can summarize that chromatin and nuclear envelope states can be used as markers predictive of the cell condition upon freeze/thaw.

To challenge the relationship between the ability of a given cryoprotectant to penetrate cells and cell nuclei, condense chromatin, and improve cell viability, we tried to estimate how cryoprotective effects correlate with chromatin condensation also for another widely used cryoprotectant—glycerol—that is known to easily diffuse through biological membranes[39] and

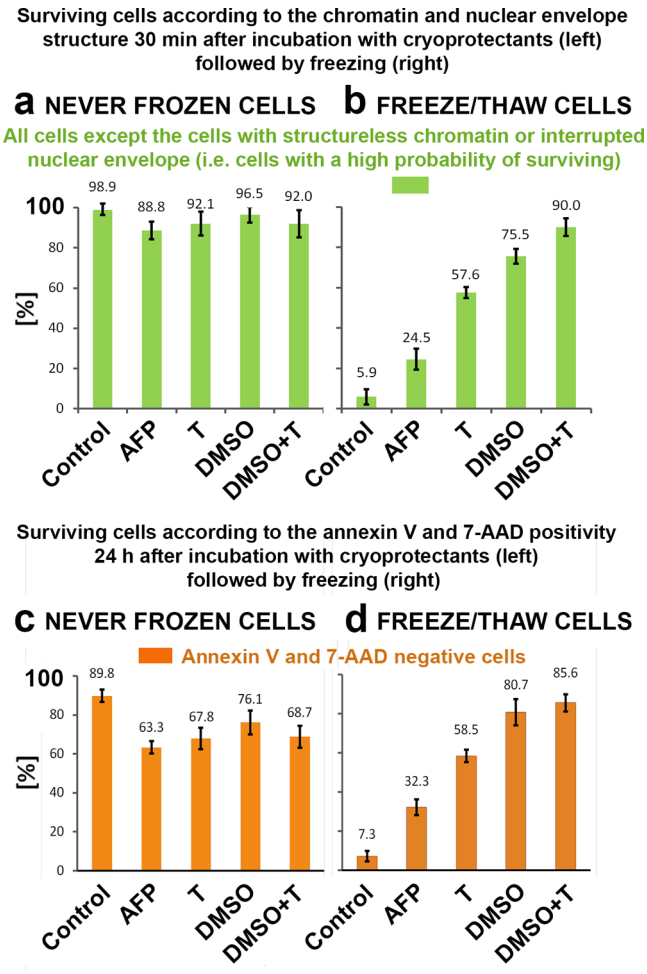

Figure 5. Effects of cryoprotectants on the viability of nonfrozen (a, c) and frozen/thawed (b, d) cells. (top) Cell viability estimated (30 min after the treatment/thawing) on the basis of microscopic analysis of two structural parameters of cell nuclei—the structure of chromatin and the structure of nuclear envelope (identified in this work as important in the context of cryopreservation). The cells were designated as "surviving" or "dead" using the categories defined in Figure 1. Between 50 and 150 cells were analyzed for each sample. (bottom) Real cell viability measured (24 h after the treatment/thawing) by flow cytometry (Annexin V/7-AAD staining). Error bars indicate SE from three analyses. Microscopic cell nuclei classification (structured chromatin and noninterrupted nuclear envelope) correlates perfectly with the cytometric data on cell survival. Deviations were less than 7% of the presented values.

induce strong osmotic changes in cells.[40,41] Glycerol could be thus awaited to efficiently condense chromatin, similarly to DMSO. But ~35% survived freezing/thawing in the presence of various glycerol concentrations, 5−30% as observed in Feng et al.[42]

As demonstrated in Figures 6 and 7, cell-penetrating glycerol strongly condensed chromatin (Figure 6B) in a high proportion of cells (comparable to DMSO; Figure 7) already prior to freezing, and this proportion further increased at 30 min after freezing/thawing. Chromatin condensation in frozen/thawed cells was also stronger than before freezing. This trend is consistent with what we saw for DMSO (Figures 1−5, Figure 6A). However, as could be noticed in Figure 7A,B, only ~20% of cells survived freezing/thawing with glycerol as measured at the same period of time by flow-cytometry

DOI: 10.1021/acs.langmuir.8b02742
Langmuir XXXX, XXX, XXX−XXX

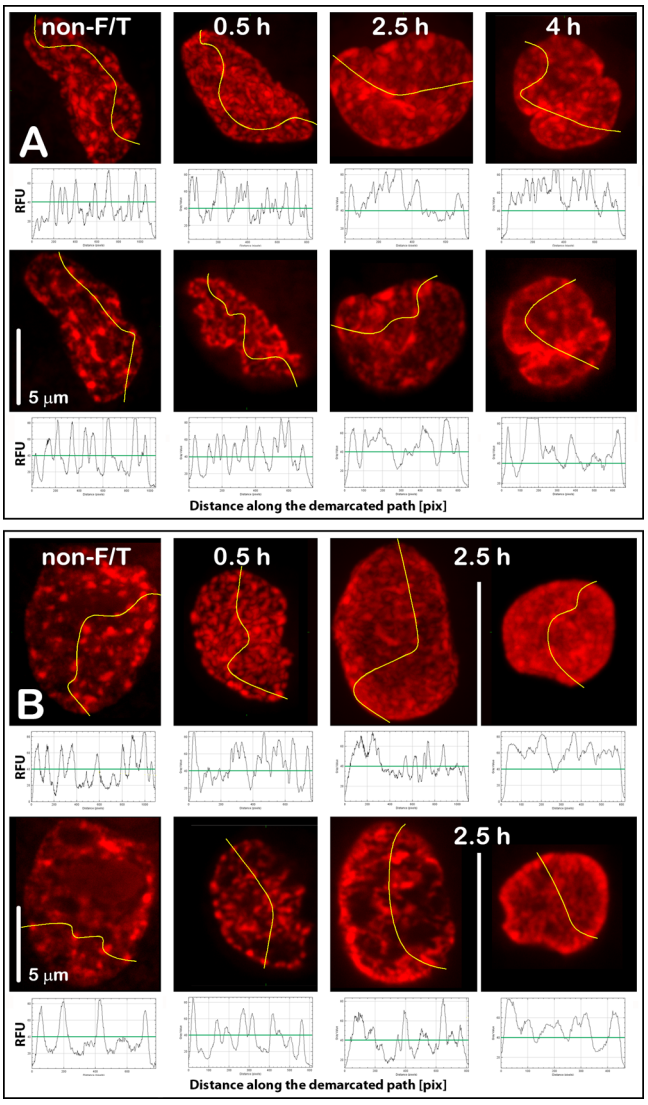

Figure 6. Changes of higher-order chromatin structure compared for NHDF cells treated with DMSO (A) and glycerol (B). Chromatin texture is shown for cells treated with the particular cryoprotectant (10% for 2 min in both cases) before freezing/thawing and in different periods of time (0.5, 2.5, and 4 h) after a freeze−thaw cycle. Examples of nuclei with normal (physiological) chromatin structure are provided for comparison in Figures 1 and 4. In the present figure, the upper line images represent "maximum images" that are composed of 40 superimposed 0.3 μm thick confocal slices. The bottom line images show central nuclear confocal slices (0.3 μm thick). Nuclear chromatin was counterstained with TO-PRO-3 (displayed in red to better visualize the chromatin structure). The fluorescence intensity profile graphs qualitatively describe chromatin density along the yellow lines indicated at the corresponding images of nuclei. The lines were demarcated in such a way that they include both the most condensed and sparse chromatin domains in a given nucleus. The green lines, corresponding to 40 RFU (relative fluorescence units), are provided for easier comparisons between plots with different RFU maxima (vertical axes). It can be seen from the images that both DMSO and glycerol condense chromatin already prior to freezing/thawing. This condensation further increases at 30 min after freezing/thawing. Later, as measured at 2.5 and 4 h post-F/T, chromatin condensation progressively decreases but still remains visible in many cell nuclei, especially in samples treated with DMSO. In the case of glycerol, chromatin decondensation is accompanied by strong erosion of chromatin structure in most cells, as demonstrated in the right image for 2.5 h post-F/T.

(Annexin V/PI positivity scoring) (Figure 7C). The proportion of cells with condensed (Figure 7A) or viable (i.e., physiological + condensed) chromatin (Figure 7B) dropped dramatically in glycerol-treated cells later (2.5 h) after thawing, and this proportion well-correlated with the proportion of surviving cells measured by flow-cytometry immediately (at 30 min) after thawing (Figure 7). At 2.5 h post-thawing, the majority of cells that were frozen/thawed with glycerol showed either relicts of chromatin domains with still-condensed centers but dissolving border regions or completely structureless chromatin (Figure 6B). This type of chromatin markedly contrasted with condensed, well-structuralized chromatin visible at the same period of time after thawing in cells cryopreserved by DMSO (Figure 6A). Many of glycerol-treated cells (2.5 h post-thawing) rather showed chromatin structure similar to untreated frozen/thawed cells or cells frozen/thawed with AFP or trehalose (Figure 6B); however, unlike these cells, chromatin damage did not immediately accompany the occurrence of flow-cytometric death markers (Annexin V/PI double-positivity; Figure 7).

Figure 7D shows that, in the case of DMSO, the proportion of frozen/thawed cells with condensed chromatin and also the level of chromatin condensation in these cells decrease with time post-thawing, while the proportion of cells with viable (i.e., normal + condensed) chromatin remains practically unchanged. On the one hand, condensed chromatin structure therefore gradually decondenses in DMSO-treated cells, giving rise to cells with normal (physiological) chromatin. In samples cryoprotected with glycerol,[43] on the other hand, both proportions of cells with condensed chromatin and cells with viable chromatin have fallen dramatically at 2.5 h after thawing, suggesting death of most cells. This proportion of cells that persisted with condensed chromatin at 2.5 h post-thawing well-correlated with the percentage of viable cells as measured by flow-cytometry (Annexin V/PI positivity at 0.5 h post-thawing).

CONCLUSIONS

The cell nucleus and DNA represent critical targets for various stressors,[44−46] including the freeze/thaw cycle. In this work we analyzed in detail the relationship between nuclear envelope integrity, chromatin condensation, freeze/thaw processes in cells, and cryopreservation efficiency for DMSO, glycerol, trehalose, and AFP. We showed how selected cryoprotectants affect nuclear envelope integrity and chromatin structure and how these changes point to specific processes initiated in NHDF cells by freezing and thawing.

In our experiments we cooled the samples with a gradient of −1 °C/min. Under these circumstances, as ice crystals grow first in the extracellular medium, there is an effective osmotic stress causing the "freeze-dehydration" of cells. Typically, low-temperature freezing of untreated cells strongly damages the nuclear envelope and disrupts the chromatin structure (hypocondensed or even structureless chromatin appeared due to osmotic shock). Consequently, freezing in standard medium (without cryoprotectants) resulted in death of most cells after thawing.

Remarkably, the efficiency of AFP, trehalose, DMSO, and glycerol, determined in terms of frozen/thawed cell viability, tightly correlated with the cryoprotectants' ability to prevent damages to cell nuclei as discussed below. On the basis of these results, we propose the combined chromatin and nuclear

DOI: 10.1021/acs.langmuir.8b02742
Langmuir XXXX, XXX, XXX−XXX

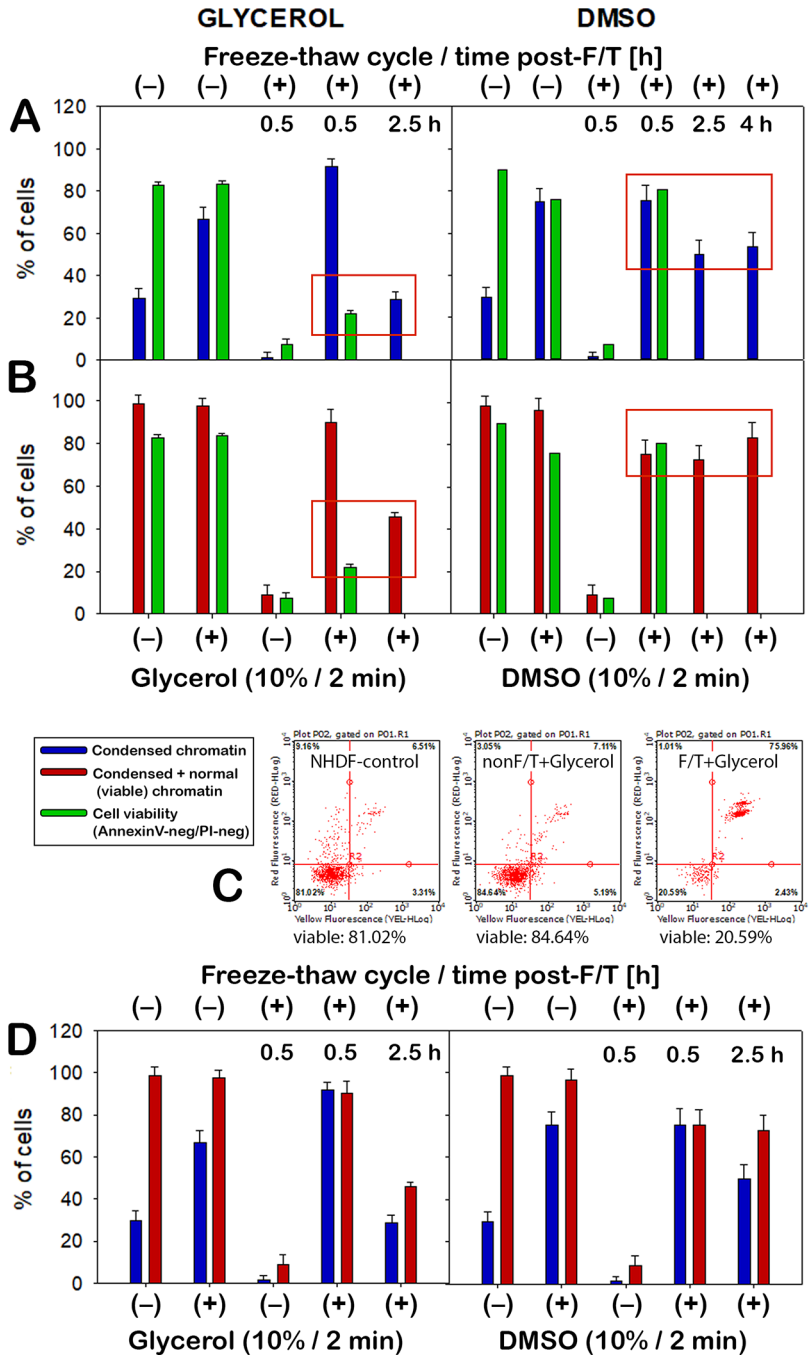

Figure 7. The cell viability and higher-order chromatin structure in NHDF fibroblasts cryopresereved by DMSO and glycerol, respectively. The parameters are qualitatively evaluated for NHDF cells after the cryoprotectant application (i.e., prior to freezing) and in different periods of time after freezing/thawing in the presence of the cryoprotectant. (A) The proportion of cells with condensed chromatin structure (blue) compared to the proportion of viable cells (Annexin V-neg/PI-neg cells) (green). (B) The proportion of cells with "viable" (i.e., normal + condensed) chromatin (red) compared to the proportion of viable cells (Annexin V-neg/PI-neg cells) (green). Red frames in plots (A, B) highlight correlations between the proportions of cells with condensed and/or viable chromatin and the cell viability measured by flow-cytometry. (C) Flow cytograms demonstrating the viability of control NHDF cells (no cryoprotectant, no freezing/thawing; left), never-frozen NHDF cells treated with 10% glycerol for 2 min (middle), and NHDF cells frozen/thawed in the presence of 10% glycerol, as measured 0.5 h post-thawing (right). The percentages of viable cells are indicated below each particular flowcytogram. Horizontal axis: Annexin V fluorescence intensity, vertical axis: propidium iodide (PI) fluorescence intensity; lower left quadrant: Annexin V(−)/PI(−) (viable cells), lower right quadrant: Annexin V(+)/PI(−), upper left quadrant: Annexin V(−)/PI(+), upper right quadrant: Annexin V(+)/PI(+). (D) The proportion of NHDF cells with condensed chromatin (blue) compared to the proportion of NHDF cells with viable chromatin (i.e., normal + condensed chromatin) (red) for untreated controls and cells treated (2 min) with 10% DMSO or 10% glycerol prior to freezing/thawing and during a period of time after freezing/thawing.

envelope states as important markers predictive of the cell condition upon freeze/thaw.

For nontreated cells, freezing/thawing causes unregulated water influx and further (hypotonic) chromatin and nuclear membrane damage; most cells (90%) die. On the one hand,

DOI: 10.1021/acs.langmuir.8b02742
Langmuir XXXX, XXX, XXX−XXX

AFP to negligible extent, trehalose to medium extent, and DMSO or glycerol to highest extent increased chromatin condensation and nuclear envelope shrinkage in frozen/thawed cells; however, only DMSO also had these effects in nonfrozen cells. On the other hand, AFP and trehalose markedly raised nuclear envelope shrinkage prior to freezing but without chromatin condensation. Importantly, for all the studied cryoprotectants, the levels of chromatin condensation and envelope shrinkage in frozen/thawed cells precisely correlated with each other and with cell viability. Hence, it is tempting to hypothesize that these cryoprotectants counteract the erosive effects of the freeze/thaw process by stabilizing the chromatin and/or nuclear envelope structure. However, the situation is complex and requires separate explanation for the individual cryoprotectants.

The addition of AFP to standard medium shrunk the nuclear envelopes, but it had only a small effect on chromatin condensation of unfrozen cells. 32.3% of AFP-treated cells survived the freeze/thaw treatment. This could be explained by the fact that, due to its large molecular weight, AFP does not penetrate into the cells, acts mainly in the extracellular space (affecting phospholipid membranes), and in frozen/thawed cells induces relatively slight chromatin condensation and nuclear envelope shrinkage. It has also been proposed that at least some AFPs can interact with cell membranes and provide partial protection during freeze/thaw by plugging holes in the membrane.[47]

While trehalose treatment of nonfrozen cells had only a minor effect on chromatin condensation, it caused shrinkage of the nuclear envelope.[48−53] In contrast, in addition to shrunken envelopes, the frozen/thawed trehalose-treated cells also displayed condensed chromatin. The high chromatin condensation and envelope shrinkage correlated with the relatively high viability of frozen/thawed trehalose-treated cells (58% of trehalose-treated cells survived the freeze/thaw). Trehalose can act as a natural osmolyte (osmoprotectant), which stabilizes phospholipid membranes and the tertiary structure of proteins in consequence of dehydration.[48−52] Addition of trehalose to the standard medium changed the osmotic pressure between the extracellular space, cell cytoplasm, and nucleus and caused dehydration of the nuclei and shrinkage of nonfrozen cells nuclear envelope.[29] These findings well agree with a limited but measurable[20,22] internalization of trehalose by cells. Trehalose is able to penetrate into cells by pinocytosis; however, spontaneous uptake by fluid-phase endocytosis is very limited.[20,22] Under standard conditions trehalose is practically not able to enter cell nuclei, so, when applied as cryoprotectant, it affects freeze/thaw processes in cells mainly from the cytoplasm[20] and extracellular space. In contrast, larger AFP molecules only remain in the extracellular space, so their osmotic effect on the cell nucleus (envelope and chromatin) is less intensive compared with trehalose.

During freezing, the dehydration of nuclei due to ice formation is mediated by AFP- and trehalose-affected osmotic gradient between the extracellular space/cytoplasm and the cell nucleus. Trehalose and AFP applied as cell cryoprotectants change/slow the dynamics of dehydration of the cell nucleus during freezing, which enables the chromatin to get into a condensed state during freezing in a more cultivated way compared to unprotected cells and avoid the loss of the chromatin structure leading to death. As we showed in our previous work, both AFP and trehalose influence the process of ice formation and growth.[22] Also, the dynamics of ice formation in cryoprotectant-containing solutions affect cell dehydration and chromatin condensation by freezing processes; that is, cryoprotectants strongly affect cell viability even if they are present in the extracellular space only.

Small DMSO molecules penetrated and accumulated both in the cell cytoplasm and the nucleus, as confirmed by Jinping Dong et al.[29] DMSO caused considerable chromatin condensation and nuclear envelope shrinkage even in the case of nonfrozen cells. 81% of DMSO-treated cells survived the freeze/thaw processes. The additive effects of DMSO and trehalose ensured even more efficient chromatin condensation and cell envelope shrinkage, further increasing cell survival to ∼90%. We propose that DMSO can prevent cell damage to frozen/thawed cells at least in three ways. First, DMSO present in the intracellular and extracellular space is able to induce important changes in the ice crystallization process.[11] Second, DMSO directly causes chromatin condensation before freezing, which then becomes less prone to ice-mediated damage. Irianto et al. (2013)[54] showed that condensed chromatin was more resistant to frost damage. Third, chromatin condensation mediated by DMSO stabilizes chromatin structure during a freeze/thaw cycle and reduces strong osmotic effects on chromatin during thawing. Also, as we demonstrated earlier,[38] artificially induced chromatin hypocondensation is less reversible and more threatening for the consequent cell survival than chromatin hypercondensation. It is therefore easier for the cells to revert chromatin condensation (stimulated by cryoprotectants) than to deal with a potential loss of chromatin structure frequently observed in unprotected frozen/thawed cells (with disrupted nuclear envelope).

We suggest that chromatin condensation and nuclear envelope shrinkage we observed in nonfrozen cells treated with DMSO are primarily caused by interactions between DMSO and other molecules and molecular complexes inside the cells. These interactions of intracellular DMSO result in chromatin reorganization and structural changes. As DMSO possesses both hydrophobic and hydrophilic moieties it affects the content of cell nuclei simultaneously in several ways. DMSO can favorably interact with water by forming hydrogen bonds (hydrophilic groups), while, in contrast, hydrophobic groups force water out and tend to self-aggregate by breaking the water structure ("hydrophobic hydration"). Concerning the interactions of DMSO with molecular complexes in cells, it has been reported[2,55] that DMSO displaces the hydration layer of proteins and binds with nucleic acids.[56] Moreover, the interaction of DMSO with DNA can distort hydrogen bonds in DNA base pairs.[57] In the present study, chromatin condensation provoked by DMSO appeared even prior to freezing/thawing (when DMSO was present) and persisted at least 30 min after thawing and DMSO removal. On the basis of these results, we suppose that chromatin structure changes in frozen/thawed cells, together with alterations of other conditions inside the cells treated with DMSO, are so extensive that chromatin recovery to the original status requires some time.

The hypothesis on the relationship between the chromatin structure (condensation) and cell survival upon freeze/thaw, introduced in the text above, was further tested with another widely used cryoprotectant—glycerol. As assumed, cell-penetrating glycerol strongly condensed chromatin in a high proportion of cells already prior to freezing, and this condensation further increased early (0.5 h) after freezing/

DOI: 10.1021/acs.langmuir.8b02742
Langmuir XXXX, XXX, XXX−XXX

thawing. This trend is consistent with what we saw for DMSO. However, in accordance with some reports,[42] only ∼20% of cells survived freezing/thawing with glycerol as measured by flow-cytometry (Annexin V/PI positivity) at the same period of time. Explaining this effect we showed that the proportion of cells with condensed or viable (i.e., physiological + condensed) chromatin dropped dramatically in glycerol-treated cells later (2.5 h) after thawing. This proportion of cells with condensed chromatin well-correlated with the proportion of surviving cells as measured by flow-cytometry (0.5 h post-freeze/thaw (F/T)). At 2.5 h post-thawing, most cells frozen/thawed with glycerol had either structureless chromatin or showed relicts of persisting condensed chromatin domains but with signs of extensive structure erosion. Some cells survived with condensed chromatin. This picture was well-compatible with consequences of cell nucleus disruption and osmotic chromatin damage during thawing, as discussed later. Indeed, the cryoprotective efficiency of glycerol strongly depends on the cell type and thawing procedure.[42,43] Survival upon freeze/thaw of cells cryopreserved by glycerol would be thus substantially higher if osmotic shocks during thawing have been better prevented.[43] High level of DMSO-treated cells viability and chromatin condensation measured at long periods after thawing was shown in our previous work.[20]

Altogether, these observations suggest that glycerol (preliminary results) evokes chromatin condensation that efficiently protects chromatin (and cells) against damage by the freeze processes, as it is predicted by the outlined hypothesis. However, osmotic changes in thawing cells, which are strongly intensified by glycerol but not DMSO (because of different effects on the cell membranes[58−61]), interrupt the cells and cell nuclei membranes, which consequently leads to unregulated water influx into the cell nucleus and chromatin swelling that cannot be further compensated by chromatin condensation. Finally, the cells die due to a combined (envelopes, chromatin) injury.

In untreated frozen/thawed cells and cells frozen/thawed with AFP or trehalose, chromatin structure changes coincided with appearance of flow-cytometric death markers (Annexin V/PI). A delayed manifestation of chromatin structure changes in glycerol-treated cells relative to the emergence of the flow-cytometric markers could be explained by a different nature of chromatin damage in cells frozen/thawed with glycerol compared to other studied cryoprotectants. In untreated frozen/thawed cells or cells frozen/thawed with AFP or trehalose the chromatin and nuclear envelope defects arise simultaneously due to ice crystal formation and/or other freeze/thaw processes. In contrast, chromatin in glycerol-treated cells is much better protected against a direct freeze damage by its condensation (like in the DMSO-treated cells) but the nuclear envelope disintegration occurs later due to an osmotic shock during thawing. This also leads to a disturbance of chromatin structure but only with some delay. Though osmotic gradients can change rapidly, the restoration of physiological chromatin structure requires some time. This can be observed also in surviving frozen/thawed cells with condensed chromatin, where reversion of chromatin to physiological structure lasts several hours. Only gradual character of chromatin structure changes is also supported by the observation that isolated nuclear envelope breakage is not always immediately transferred into the pan-nuclear loss of chromatin structure. As we have demonstrated recently,[20] a single nuclear envelope rupture first resulted in chromatin leakage from the nucleus, though structural damage to chromatin remained only local. Here we propose that chromatin, stabilized by various proteins, attachments to the nuclear scaffold, and a strong condensation in the case of DMSO- or glycerol-treated cells has initially some structural inertia, reducing the speed of chromatin decondensation during thawing. Indeed, as already discussed, we consider this effect as one of the important protective ways of cryoprotection mediated by DMSO and glycerol (i.e., chromatin condensing cryoprotectants) (Figure 8).

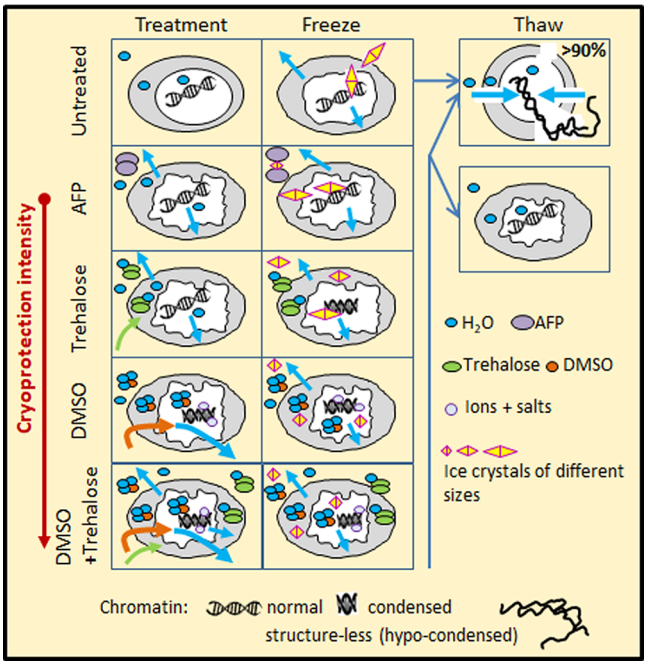

Figure 8. Biological and physical processes occurring in the cells during freezing and thawing. The image shows a schematic summary of untreated cells (top) and cells treated with individual cryoprotectants. Probable localization of the cryoprotective molecules within the cell is shown as well as the effect on ice crystal size, chromatin condensation, and nuclear envelope shape. Without treatment (top line): disruption of chromatin structure, integrity loss of the nuclear envelope. Defrosting causes unregulated water influx and further (hypotonic) chromatin and nuclear membrane damage; most cells (90%) die. AFP: AFP in extracellular space binds to ice crystals; the effect on chromatin condensation and intracellular ice formation is very small. Approximately 30% of cells survive. Trehalose: Trehalose penetrates into the cell cytoplasm but not the nucleus, and trehalose treatment leads to nuclear envelope shrinkage without chromatin condensation 58% of trehalose-treated cells survived the freeze/thaw. DMSO: DMSO penetrates also into the nucleus, condenses chromatin, and shrinks the nuclear envelope. The cell is protected in parallel by chromatin condensation and formation of small ice with 80% survival. DMSO+trehalose: The additive effects of DMSO and trehalose ensure even more efficient chromatin condensation and envelope shrinkage, further increasing cell survival to ∼90%.

The experiments with glycerol thus confirm a correlation of chromatin condensation and nuclear envelope integrity with the cryoprotective efficiency of a given cryoprotectant. However, at the same time, our results emphasize the complexity of the cryopreservation processes and importance of their kinetic aspects. Both identified markers—the chromatin condensation and the nuclear envelope integrity—

DOI: 10.1021/acs.langmuir.8b02742
Langmuir XXXX, XXX, XXX−XXX

should be thus studied in parallel and in different periods of time after thawing to provide more comprehensive results. We do not propose the structural markers described here to replace the direct and methodologically easier cell viability measurements in the search for new cryoprotectants; nevertheless, these markers allow us to identify and better understand the effects responsible for efficient cryoprotection.

Chromatin condensation is a hallmark of apoptosis that may be initiated in frozen/thawed cells and cells incubated with cryoprotectants; hence, chromatin condensation observed in the present study may rather reflect toxic than protective effects of DMSO and glycerol on cells. Apoptosis may be also activated by freeze/thaw damage. However, though DMSO and glycerol condense chromatin in similar proportions of cells, the toxicity of glycerol is much lower compared to DMSO. Also, a short time needed for chromatin condensation in the present study after DMSO or glycerol addition does not support this alternative, because, as reported for various stressors and cell types,[62] apoptosis usually proceeds with much slower kinetics (in order of hours or days). Moreover, while the fraction of frozen/thawed cells with condensed chromatin would be expected to increase with time post-thawing if it was caused by apoptosis, we noticed the opposite trend, that is, a progressive decrease with time after thawing. In addition, DMSO is an efficient cryoprotectant, known for its ability to save most cells from dying upon freezing/thawing. The majority of DMSO-treated cells (showing condensed chromatin structure) survived freezing/thawing also in the current study as measured by Annexin V/7-AAD positivity. Glycerol induced strong chromatin condensation at 0.5 h post-thawing, but the proportion of cells with condensed chromatin decreased dramatically 2 h later—and this value corresponded to the cell survival as measured by flow cytometry. The observed correlation between the fractions of surviving cells and cells with condensed chromatin (both prior to and after freezing/thawing) thus provides strong indication that condensed chromatin appears predominantly in Annexin V/7-AAD double-negative cells. This alternative is also supported by our earlier findings,[38] showing a picture of chromatin condensation similar to that observed here also in viable cells exposed to hypertonic conditions. Finally, both DMSO-treated and apoptotic cell nuclei are known to have their envelopes shrunken; however, in apoptotic cells, formation of easily distinguishable apoptotic bodies should appear at least in a fraction of nuclei that have already reached the final stage of apoptosis. These bodies were not present in our data in a noticeable extent.

To summarize, in contrast to AFP and trehalose, DMSO affecting the ice crystallization process (i.e., having a long-range effect on water dynamics)[11] penetrates even the cell nucleus and causes strong chromatin condensation and nuclear envelope shrinkage due to its direct contact with chromatin and extensive change in the intracellular osmotic pressure.[19] Glycerol induced strong chromatin condensation early after thawing, but the proportion of cells with condensed chromatin decreased dramatically 2 h later—and this value corresponded to the cell survival as measured by flow cytometry. Glycerol efficiently protects chromatin against damage by the freeze processes, but osmotic changes in thawing cells (that are strongly dependent on the cell type and thawing conditions) lead to unregulated water influx into the cell nucleus and chromatin swelling that cannot be further compensated by chromatin condensation. On the one hand, reported cryoprotective efficiency of glycerol therefore differs in the literature. Trehalose and AFP, on the other hand, affect the ice crystallization process mainly in the extracellular space.[11] As these agents practically do not penetrate into the cell nucleus, both trehalose and AFP stimulate nuclear membrane shrinkage in nonfrozen and frozen cells but have negligible effect on chromatin condensation in nonfrozen cells. We hypothesize that the nuclear envelope shrinkage appears due to induced difference between the osmotic pressure in the cytoplasm and cell nucleus. This effect is stronger for trehalose than for AFP, because trehalose penetrates the cells,[20] and its presence in the cytoplasm influences the dynamics of the osmotic dehydration more intensively than extracellular-only AFP. The envelope shrinkage is followed by chromatin condensation during freezing/thawing. Ice formation dynamics in cryoprotectant-containing solutions affect the cell dehydration and chromatin condensation; that is, cryoprotectants improve the frozen/thawed cells' viability even if only present in the extracellular space.

Cryoprotectants affect a wide range of cell parameters, which support the ability of cells to survive freezing and thawing. In the present study, we showed that the chromatin condensation and nuclear envelope shrinkage reflect processes in cells that are important for cell cryopreservation. Our microscopic classification of cell viability upon freezing/thawing, based on chromatin structure and the nuclear envelope integrity, correlates with the cytometric data on cell viability (Table 2). We outlined possible causes of the changes in cell nucleus parameters during freezing/thawing, their relation to the cryoprotective efficiency, and a possible way of effective cryoprotection. These findings shed a new light on the mechanisms of different cryoprotectant action.

Table 2. Specific Biological Effects of Chromatin Condensation, Nuclear Envelope Shrinkage, and Viability of AFP, Trehalose, and DMSO on Treated Never Frozen and Frozen/Thawed Cells

property	AFP	trehalose	DMSO
chromatin condensation (prefreezing)	medium	medium	high
chromatin condensation (post-freezing/thawing)	low	medium	high
shrunk nuclear envelope (prefreezing)	medium	medium	high
shrunk nuclear envelope (post-freezing)	low	medium	high
cell viability (post-freezing/thawing)	low	medium	high

AUTHOR INFORMATION

Corresponding Author

*E-mail: falk@ibp.cz. (M.F.)

ORCID

Irena Kratochvílová: 0000-0002-6633-9432

Notes

The authors declare no competing financial interest.

ACKNOWLEDGMENTS

This work was supported by the Ministry of Education, Youth and Sports of the Czech Republic (MEYS OPVVV SAFMAT CZ.02.1.01/0.0/0.0/16_013/0001406, MEYS:LO1409, SOLID21 CZ.02.1.01/0.0/0.0/16019/0000760; by the Czech Science Foundation (15-05095S, 16-12454S); by the Ministry of Health of the Czech Republic (16-29835A); by Czech contribution to JINR Dubna (Project of Czech Plenipotentiary

DOI: 10.1021/acs.langmuir.8b02742
Langmuir XXXX, XXX, XXX−XXX

and Project 3-Plus-3, 2015-18); by the National Science Foundation (CHE-1740399 and DGE-0948027); and by the National Institute of General Medical Sciences at the National Institutes of Health (P20GM103432).

REFERENCES

(1) Matsumura, K.; Jain, M.; Rajan, R. *Cell and Materials Interface in Cryobiology and Cryoprotection;* CRC Press-Taylor & Francis Group: Boca Raton, FL, 2016; Vol. *52*, pp 163−186.
(2) Fuller, B. J. Cryoprotectants: The essential antifreezes to protect life in the frozen state. *Cryoletters* **2004**, *25* (6), 375−388.
(3) Piehowski, P. D.; Kurczy, M. E.; Willingham, D.; Parry, S.; Heien, M. L.; Winograd, N.; Ewing, A. G. Freeze-etching and vapor matrix deposition for ToF-SIMS imaging of single cells. *Langmuir* **2008**, *24* (15), 7906−7911.
(4) Ahmed, S.; Miyawaki, O.; Matsumura, K. Enhanced Adsorption of a Protein-Nanocarrier Complex onto Cell Membranes through a High Freeze Concentration by a Polyampholyte Cryoprotectant. *Langmuir* **2018**, *34* (6), 2352−2362.
(5) Kantidze, O. L.; Velichko, A. K.; Luzhin, A. V.; Razin, S. V. Heat Stress-Induced DNA Damage. *Acta Naturae* **2016**, *8* (2), 75−78.
(6) Chatterjee, A.; Saha, D.; Glasmacher, B.; Hofmann, N. Chilling without regrets Deciphering the effects of cryopreservation on the epigenetic properties of frozen cells will benefit the applications of cryo-technology. *EMBO Rep.* **2016**, *17* (3), 292−295.
(7) Shaw, L.; Sneddon, S. F.; Brison, D. R.; Kimber, S. J. Comparison of gene expression in fresh and frozen-thawed human preimplantation embryos. *Reproduction* **2012**, *144* (5), 569−582.
(8) Ghosh, J.; Coutifaris, C.; Sapienza, C.; Mainigi, M. Global DNA methylation levels are altered by modifiable clinical manipulations in assisted reproductive technologies. *Clin. Epigenet.* **2017**, *9*. DOI: 10.1186/s13148-017-0318-6
(9) Urrego, R.; Rodriguez-Osorio, N.; Niemann, H. Epigenetic disorders and altered gene expression after use of Assisted Reproductive Technologies in domestic cattle. *Epigenetics* **2014**, *9* (6), 803−815.
(10) Han, B.; Bischof, J. C. Thermodynamic nonequilibrium phase change behavior and thermal properties of biological solutions for cryobiology applications. *J. Biomech. Eng.* **2004**, *126* (2), 196−203.
(11) Ceelen, M.; van Weissenbruch, M. M.; Vermeiden, J. P. W.; van Leeuwen, F. E.; Delemarre-van de Waal, H. A. Growth and development of children born after in vitro fertilization. *Fertil. Steril.* **2008**, *90* (5), 1662−1673.
(12) Kopeika, J.; Thornhill, A.; Khalaf, Y. The effect of cryopreservation on the genome of gametes and embryos: principles of cryobiology and critical appraisal of the evidence. *Hum. Reprod. Update* **2015**, *21* (2), 209−227.
(13) Deller, R. C.; Vatish, M.; Mitchell, D. A.; Gibson, M. I. Synthetic polymers enable non-vitreous cellular cryopreservation by reducing ice crystal growth during thawing. *Nat. Commun.* **2014**, *5*. DOI: 10.1038/ncomms4244
(14) Stokich, B.; Osgood, Q.; Grimm, D.; Moorthy, S.; Chakraborty, N.; Menze, M. A. Cryopreservation of hepatocyte (HepG2) cell monolayers: Impact of trehalose. *Cryobiology* **2014**, *69* (2), 281−290.
(15) Nandi, S.; Parui, S.; Halder, R.; Jana, B.; Bhattacharyya, K. Interaction of proteins with ionic liquid, alcohol and DMSO and in situ generation of gold nano-clusters in a cell. *Biophys. Rev.* **2018**, *10* (3), 757−768.
(16) Dluska, E.; Cui, Z. F.; Markowska-Radomska, A.; Metera, A.; Kosicki, K. Cryoprotection and banking of living cells in a 3D multiple emulsion-based carrier. *Biotechnol. J.* **2017**, *12* (8), 9.
(17) Paasch, U.; Sharma, R. K.; Gupta, A. K.; Grunewald, S.; Mascha, E. J.; Thomas, A. J.; Glander, H. J.; Agarwal, A. Cryopreservation and thawing is associated with varying extent of activation of apoptotic machinery in subsets of ejaculated human spermatozoal. *Biol. Reprod.* **2004**, *71* (6), 1828−1837.
(18) Hubalek, Z. Protectants used in the cryopreservation of microorganisms. *Cryobiology* **2003**, *46* (3), 205−229.
(19) Golan, M.; Jelinkova, S.; Kratochvilova, I.; Skladal, P.; Pesl, M.; Rotrekl, V.; Pribyl, J. AFM Monitoring the Influence o f Selected Cryoprotectants on Regeneration of Cryopreserved Cells Mechanical Properties. *Front. Physiol.* **2018**, *9*, 10.
(20) Falk, M.; Pagáčová, E.; Kopečná, O.; Bačíková, A.; Šimek, D.; Golan, M.; Kozubek, S.; Pekarová, M.; Follett, S. E.; Klejdus, B.; Elliott, K. W.; Varga, K.; Teplá, O.; Kratochvílová, I. Critical defects in cryopreserved cell nuclei: DNA structure changes. *Sci. Rep.* **2018**, *8*, 14694.
(21) Krasteva, N.; Vollhardt, D.; Brezesinski, G.; Mohwald, H. Effect of sugars and dimethyl sulfoxide on the structure and phase behavior of DPPC monolayers. *Langmuir* **2001**, *17* (4), 1209−1214.
(22) Kratochvilova, I.; Golan, M.; Pomeisl, K.; Richter, J.; Sedlakova, S.; Sebera, J.; Micova, J.; Falk, M.; Falkova, I.; Reha, D.; Elliott, K. W.; Varga, K.; Follett, S. E.; Simek, D. Theoretical and experimental study of the antifreeze protein AFP752, trehalose and dimethyl sulfoxide cryoprotection mechanism: correlation with cryopreserved cell viability. *RSC Adv.* **2017**, *7* (1), 352−360.
(23) Venketesh, S.; Dayananda, C. Properties, potentials, and prospects of antifreeze proteins. *Crit. Rev. Biotechnol.* **2008**, *28* (1), 57−82.
(24) Liu, Z.; Li, H.; Pang, H.; Ma, J.; Mao, X. Enhancement effect of solutes of low molecular mass on the insect antifreeze protein ApAFP752 from Anatolica polita. *J. Therm. Anal. Calorim.* **2015**, *120* (1), 307−315.
(25) Velichko, A. K.; Petrova, N. V.; Razin, S. V.; Kantidze, O. L. Mechanism of heat stress-induced cellular senescence elucidates the exclusive vulnerability of early S-phase cells to mild genotoxic stress. *Nucleic Acids Res.* **2015**, *43* (13), 6309−6320.
(26) Petrova, N. V.; Velichko, A. K.; Razin, S. V.; Kantidze, O. L. Early S-phase cell hypersensitivity to heat stress. *Cell Cycle* **2016**, *15* (3), 337−344.
(27) Ruan, R. Q.; Zou, L. L.; Sun, S. J.; Liu, J.; Wen, L. P.; Gao, D. Y.; Ding, W. P. Cell Blebbing upon Addition of Cryoprotectants: A Self-Protection Mechanism. *PLoS One* **2015**, *10* (4), 14.
(28) Sharp, D. M. C.; Picken, A.; Morris, T. J.; Hewitt, C. J.; Coopman, K.; Slater, N. K. H. Amphipathic polymer-mediated uptake of trehalose for dimethyl sulfoxide-free human cell cryopreservation. *Cryobiology* **2013**, *67* (3), 305−311.
(29) Dong, J.; Malsam, J.; Bischof, J. C.; Hubel, A.; Aksan, A. Spatial Distribution of the State of Water in Frozen Mammalian Cells. *Biophys. J.* **2010**, *99* (8), 2453−2459.
(30) Lukasova, E.; Kovarik, A.; Bacikova, A.; Falk, M.; Kozubek, S. Loss of lamin B receptor is necessary to induce cellular senescence. *Biochem. J.* **2017**, *474*, 281−300.
(31) Jezkova, L.; Falk, M.; Falkova, I.; Davidkova, M.; Bacikova, A.; Stefancikova, L.; Vachelova, J.; Michaelidesova, A.; Lukasova, E.; Boreyko, A.; Krasavin, E.; Kozubek, S. Function of chromatin structure and dynamics in DNA damage, repair and misrepair: gamma-rays and protons in action. *Appl. Radiat. Isot.* **2014**, *83*, 128−136.
(32) Falk, M.; Lukasova, E.; Stefancikova, L.; Baranova, E.; Falkova, I.; Jezkova, L.; Davidkova, M.; Bacikova, A.; Vachelova, J.; Michaelidesova, A.; Kozubek, S. Heterochromatinization associated with cell differentiation as a model to study DNA double strand break induction and repair in the context of higher-order chromatin structure. *Appl. Radiat. Isot.* **2014**, *83*, 177−185.
(33) Hofer, M.; Falk, M.; Komurkova, D.; Falkova, I.; Bacikova, A.; Klejdus, B.; Pagacova, E.; Stefancikova, L.; Weiterova, L.; Angelis, K. J.; Kozubek, S.; Dusek, L.; Galbavy, S. Two New Faces of Amifostine: Protector from DNA Damage in Normal Cells and Inhibitor of DNA Repair in Cancer Cells. *J. Med. Chem.* **2016**, *59* (7), 3003−3017.
(34) Kozubek, M.; Kozubek, S.; Lukasova, E.; Bartova, E.; Skalnikova, M.; Matula, P.; Matula, P.; Jirsova, P.; Cafourkova, A.; Koutna, I. Combined confocal and wide-field high-resolution cytometry of fluorescent in situ hybridization-stained cells. *Cytometry* **2001**, *45* (1), 1−12.
(35) Matula, P.; Maska, M.; Danek, O.; Matula, P.; Kozubek, M. *IEEE, Acquiarium: Free Software for the Acquisition and Analysis of 3D*

DOI: 10.1021/acs.langmuir.8b02742
Langmuir XXXX, XXX, XXX−XXX

Images of Cells in Fluorescence Microscopy; IEEE: New York, 2009; pp 1138−1141.
(36) Masek, J.; Bartheldyova, E.; Korvasova, Z.; Skrabalova, M.; Koudelka, S.; Kulich, P.; Kratochvilova, I.; Miller, A. D.; Ledvina, M.; Raska, M.; Turanek, J. Immobilization of histidine-tagged proteins on monodisperse metallochelation liposomes: Preparation and study of their structure. *Anal. Biochem.* **2011**, *408* (1), 95−104.
(37) Kratochvilova, I.; Nesprek, S.; Sebera, J.; Zalis, S.; Pavelka, M.; Wang, G.; Sworakowski, J. New organic FET-like photoactive device, experiments and DFT modeling. *Eur. Phys. J. E: Soft Matter Biol. Phys.* **2008**, *25* (3), 299−307.
(38) Falk, M.; Lukasova, E.; Kozubek, S. Chromatin structure influences the sensitivity of DNA to gamma-radiation. *Biochim. Biophys. Acta, Mol. Cell Res.* **2008**, *1783* (12), 2398−2414.
(39) Si, W.; Zheng, P.; Li, Y. H.; Dinnyes, A.; Ji, W. Z. Effect of glycerol and dimethyl sulfoxide on cryopreservation of rhesus monkey (Macaca mulatta) sperm. *Am. J. Primatol.* **2004**, *62* (4), 301−306.
(40) Armitage, W. J.; Mazur, P. TOXIC AND OSMOTIC EFFECTS OF GLYCEROL ON HUMAN-GRANULOCYTES. *Am. J. Physiol.* **1984**, *247* (5), C382−C389.
(41) Awad, M. M. Effect of some permeating cryoprotectants on CASA motility results in cryopreserved bull spermatozoa. *Anim. Reprod. Sci.* **2011**, *123* (3−4), 157−162.
(42) Feng, H. Y.; Wu, L. J.; Xu, A.; Hu, B. R.; Hei, T. K.; Yu, Z. L. Survival of mammalian cells under high vacuum condition for ion bombardment. *Cryobiology* **2004**, *49* (3), 241−249.
(43) Rakha, B. A.; Ansari, M. S.; Akhter, S.; Blesbois, E. Cryoprotective effect of glycerol concentrations on Indian Red Jungle Fowl (Gallus gallus murghi) spermatozoa. *Avian Biology Research* **2018**, *11* (2), 80−88.
(44) Jezkova, L.; Zadneprianetc, M.; Kulikova, E.; Smirnova, E.; Bulanova, T.; Depes, D.; Falkova, I.; Boreyko, A.; Krasavin, E.; Davidkova, M.; Kozubek, S.; Valentova, O.; Falk, M. Particles with similar LET values generate DNA breaks of different complexity and reparability: a high-resolution microscopy analysis of gamma H2AX/53BP1 foci. *Nanoscale* **2018**, *10* (3), 1162−1179.
(45) Rittich, B.; Spanova, A.; Falk, M.; Benes, M. J.; Hruby, M. Cleavage of double stranded plasmid DNA by lanthanide complexes. *J. Chromatogr. B: Anal. Technol. Biomed. Life Sci.* **2004**, *800* (1−2), 169−173.
(46) Kratochvilova, I.; Golan, M.; Vala, M.; Sperova, M.; Weiter, M.; Pav, O.; Sebera, J.; Rosenberg, I.; Sychrovsky, V.; Tanaka, Y.; Bickelhaupt, F. M. Theoretical and Experimental Study of Charge Transfer through DNA: Impact of Mercury Mediated T-Hg-T Base Pair. *J. Phys. Chem. B* **2014**, *118* (20), 5374−5381.
(47) Garner, J.; Inglis, S. R.; Hook, J.; Separovic, F.; Harding, M. M. A solid-state NMR study of the interaction of fish antifreeze proteins with phospholipid membranes. *Eur. Biophys. J.* **2008**, *37* (6), 1031−1038.
(48) Wolkers, W. F.; Walker, N. J.; Tablin, F.; Crowe, J. H. Human platelets loaded with trehalose survive freeze-drying. *Cryobiology* **2001**, *42* (2), 79−87.
(49) Wang, G. M.; Haymet, A. D. J. Trehalose and other sugar solutions at low temperature: Modulated differential scanning calorimetry (MDSC). *J. Phys. Chem. B* **1998**, *102* (27), 5341−5347.
(50) Kadekar, D.; Rangole, S.; Kale, V.; Limaye, L. Conditioned Medium from Placental Mesenchymal Stem Cells Reduces Oxidative Stress during the Cryopreservation of Ex Vivo Expanded Umbilical Cord Blood Cells. *PLoS One* **2016**, *11* (10), 21.
(51) Stefanic, M.; Ward, K.; Tawfik, H.; Seemann, R.; Baulin, V.; Guo, Y. C.; Fleury, J. B.; Drouet, C. Apatite nanoparticles strongly improve red blood cell cryopreservation by mediating trehalose delivery via enhanced membrane permeation. *Biomaterials* **2017**, *140*, 138−149.
(52) Takeuchi, K.; Nakazawa, M.; Ebina, Y.; Sato, K.; Metoki, T.; Miyagawa, Y.; Ito, T. Inhibitory effects of trehalose on fibroblast proliferation and implications for ocular surgery. *Exp. Eye Res.* **2010**, *91* (5), 567−577.
(53) Zalis, S.; Kratochvilova, I.; Zambova, A.; Mbindyo, J.; Mallouk, T.; Mayer, T. Combined experimental and theoretical DFT study of molecular nanowires negative differential resistance and interaction with gold clusters. *Eur. Phys. J. E: Soft Matter Biol. Phys.* **2005**, *18* (2), 201−206.
(54) Irianto, J.; Swift, J.; Martins, R. P.; McPhail, G. D.; Knight, M. M.; Discher, D. E.; Lee, D. A. Osmotic Challenge Drives Rapid and Reversible Chromatin Condensation in Chondrocytes. *Biophys. J.* **2013**, *104* (4), 759−769.
(55) Li, R.; Yu, G. L.; Azarin, S. M.; Hubel, A. Freezing Responses in DMSO-Based Cryopreservation of Human iPS Cells: Aggregates Versus Single Cells. *Tissue Eng., Part C* **2018**, *24* (5), 289−299.
(56) Zeltovsky, N. V.; Samoilenko, S. A.; Kolomiets, I. N.; Kondratyuk, I. V. INTERACTION BETWEEN NUCLEOTIDE BASES AND THE AMINE ACID CARBOXYLIC GROUP IN DMSO - A MODEL OF POINT PROTEIN-NUCLEIC CONTACTS. *Dopovidi Akademii Nauk Ukrainskoi Rsr Seriya B-Geologichni Khimichni Ta Biologichni Nauki* **1988**, No. 8, 68−71.
(57) Pathania, S. K.; Sharma, V.; Thakur, R. C.; Kumar, A.; Sharma, S. A Comparative Study of Interactions between Protein (Lysozyme) and Ionic Surfactants (SDS, CTAB) in Aqueous Rich Mixtures of Dmso At Different Temperatures. *Research Journal of Pharmaceutical Biological and Chemical Sciences* **2015**, *6* (1), 721−729.
(58) Gurtovenko, A. A.; Anwar, J. Modulating the structure and properties of cell membranes: The molecular mechanism of action of dimethyl sulfoxide. *J. Phys. Chem. B* **2007**, *111* (35), 10453−10460.
(59) de Menorval, M.-A.; Mir, L. M.; Fernandez, M. L.; Reigada, R. Effects of Dimethyl Sulfoxide in Cholesterol-Containing Lipid Membranes: A Comparative Study of Experiments In Silico and with Cells. *PLoS One* **2012**, *7* (7), e41733.
(60) Cheng, C.-Y.; Song, J.; Pas, J.; Meijer, L. H. H.; Han, S. DMSO Induces Dehydration near Lipid Membrane Surfaces. *Biophys. J.* **2015**, *109* (2), 330−339.
(61) Notman, R.; Noro, M.; O'Malley, B.; Anwar, J. Molecular basis for dimethylsulfoxide (DMSO) action on lipid membranes. *J. Am. Chem. Soc.* **2006**, *128* (43), 13982−13983.
(62) Wolbers, F.; Buijtenhuijs, P.; Haanen, C.; Vermes, I. Apoptotic cell death kinetics in vitro depend on the cell types and the inducers used. *Apoptosis* **2004**, *9* (3), 385−392.

DOI: 10.1021/acs.langmuir.8b02742
Langmuir XXXX, XXX, XXX−XXX

Cryopreserved Cells Regeneration Monitored by Atomic Force Microscopy and Correlated With State of Cytoskeleton and Nuclear Membrane

Martin Golan, Jan Přibyl, Martin Pesl, Sarka Jelinkova, Ivana Acimovic, Josef Jaroš, Vladimir Rotrekl, Martin Falk, Luděk Šefc, Petr Skládal, and Irena Kratochvílová

***Abstract*— Atomic force microscopy (AFM) helps to describe and explain the mechanobiological properties of living cells on the nanoscale level under physiological conditions. The stiffness of cells is an important parameter reflecting cell physiology. Here, we have provided the first study of the stiffness of cryopreserved cells during post-thawing regeneration using AFM combined with confocal fluorescence microscopy. We demonstrated that the nonfrozen cell stiffness decreased proportionally to the cryoprotectant concentration in the medium. AFM allowed us to map cell surface reconstitution in real time after a freeze/thaw cycle and to monitor the regeneration processes at different depths of the cell and even different parts of the cell surface (nucleus and edge). Fluorescence microscopy showed that the cytoskeleton in fibroblasts, though damaged by the freeze/thaw cycle, is reconstructed after long-term plating. Confocal microscopy confirmed that structural changes affect the nuclear envelopes in cryopreserved cells. AFM nanoindentation analysis could be used as a noninvasive method to identify cells that have regenerated their surface mechanical properties with the proper dynamics and to a sufficient degree. This identification can be important particularly in the field of *in vitro* fertilization and in future cell-based regeneration strategies.**

***Index Terms*— Atomic force microscopy, cell surface stiffness, cryopreservation, cryopreserved cells reconstruction.**

Manuscript received March 1, 2018; revised May 17, 2018 and August 17, 2018; accepted September 27, 2018. Date of publication October 11, 2018; date of current version November 16, 2018. This work was supported in part by the CIISB Research Infrastructure Project through MEYS CR under Grant LM2015043 (Core Facility Nanobiotechnology), in part by the Ministry of Education, Youth and Sports of the Czech Republic under Grant FUNBIO CZ.2.16/3.1.00/21568, Grant SAFMAT LM 2015088, and Grant SOLID21CZ.02.1.01 0.0/0.0/16_019/0000760, in part by the frame of the COST CA15107 under Grant LTC17083, in part by the National Program of Sustainability II CEITEC 2020 under Grant LQ1601, Grant FNUSA-ICRC (LQ1605), and Grant GA MŠk LO1409, and in part by the Czech Science Foundation under Grant P302/12/G157. *(Corresponding authors: Jan Přibyl; Irena Kratochvílová.)*

M. Golan is with the Institute of Physics, Czech Academy of Sciences, 18221 Prague, Czech Republic, and also with the Faculty of Mathematics and Physics, Charles University, 12116 Prague, Czech Republic.

J. Přibyl and P. Skládal are with CEITEC, Masaryk University, 62500 Brno, Czech Republic (e-mail: pribyl@nanobio.cz).

M. Pesl is with the Department of Biology, Faculty of Medicine, Masaryk University, 62500 Brno, Czech Republic, also with the International Clinical Research Center, St. Anne's University Hospital Brno, 65691 Brno, Czech Republic, and also with the First Department of Internal Medicine/Cardioangiology, Masaryk University, 65691 Brno, Czech Republic.

S. Jelinkova and V. Rotrekl are with the Department of Biology, Faculty of Medicine, Masaryk University, 62500 Brno, Czech Republic, and also with the International Clinical Research Center, St. Anne's University Hospital, 65691 Brno, Czech Republic.

I. Acimovic is with the Department of Biology, Faculty of Medicine, Masaryk University, 62500 Brno, Czech Republic.

J. Jaroš is with the International Clinical Research Center, St. Anne's University Hospital, 65691 Brno, Czech Republic, and also with the Department of Histology and Embryology, Faculty of Medicine, Masaryk University, 62500 Brno, Czech Republic.

M. Falk is with the Institute of Biophysics, Czech Academy of Sciences, 61265 Brno, Czech Republic.

L. Šefc is with the Center of Advanced Preclinical Imaging, First Faculty of Medicine, Charles University, 12000 Prague, Czech Republic.

I. Kratochvílová is with the Institute of Physics, Czech Academy of Sciences, 182 21 Prague, Czech Republic (e-mail: krat@fzu.cz).

This paper has supplementary downloadable material available at http://ieeexplore.ieee.org, provided by the author. The material is 1200 kB in size.

Digital Object Identifier 10.1109/TNB.2018.2873425

I. Introduction

MONITORING the mechanical stiffness of living cells surface is one way to detect cell physiology [1]–[3]. More importantly, changes in cell mechanical properties are also often found to be closely associated with various disease conditions [4]. Cell mechanics are largely dependent on the cytoskeletal architecture, especially the networks of actin and intermediate filaments and other associated proteins [5]. The stiffness of living cells is regarded as an index of the cytoskeletal assembly, myosin activity and other cellular processes. The structure of actin filaments is being intensively investigated [6], [7] as a basic marker of cell development and adhesion properties [4], [8]. Additionally, cell stiffness, which is related to cytoskeletal dynamics, has been shown to act as a sensor and mediator of apoptosis [9], [10]. Studies of embryo and oocyte stiffness have suggested a link between their mechanical properties and viability [11].

In the case of cryopreserved cells specifically [12]–[14], the frozen liquid around the cell membrane and cytoskeleton affects the cell mechanical properties and stiffness and further disrupts the structures of the membrane blebs and microvilli, leading to irreversible damage to the cell structure [15], [16]. The freezing process can be strongly affected by cryoprotective additives, and frozen cells [17] can be recovered when appropriate cryoprotectants are applied [19], [20]. In our

previous work [21], we showed how cryoprotectants changed the constitution of ice during freezing and how the ice constitution influences the states of frozen and thawed cells.

Atomic force microscopy (AFM) [14], [22]–[28] is a very sensitive, noninvasive surface method that is able to provide insight into cells' mechanical parameters [29]–[35]. AFM allows the use of surface cellular stiffness as an indicator of multiple cellular processes, including stem cell differentiation, hepatocyte cirrhosis [36], tissue-level tension in epithelial monolayers, and the biomechanical properties of living cardiomyocytes [37], [38]. We are the first to study the surface stiffness of cryopreserved cells during the post-thawing growth and regeneration process using atomic force microscopy (AFM) [39] combined with confocal fluorescence microscopy. This method allowed us to map cell stiffness in time and space under physiological conditions (i.e., in culture medium and at elevated temperature) [40]–[42]. In AFM force spectroscopy mode, cells are indented at many sites, and their complete elastic responses are recorded, enabling the construction of a stiffness map [43]. We measured the surface stiffness and cell attachment of frozen cells immediately after thawing (i.e., 30 min. after thawing); then, we observed the dynamics of the development of the cell surface stiffness in detail. We also found differences in the development of stiffness in different parts of cryopreserved cells (nuclei, edges). We combined AFM with standard fluorescence-based methods [44], [45], which demonstrated that cell cytoskeleton regeneration occurs after freezing/thawing. Confocal microscopy showed defects in the nuclear envelopes of cryopreserved cells (shrinkage and ruptures). This strategy was successfully used to correlate the cell surface mechanical properties with the dynamics of actin filament structures [46], [47] after cell exposure to cryogenic temperatures [48].

II. Experimental

A. Cell Treatment

Both non-irradiated (non-IR) and irradiated (IR) mouse embryonic fibroblasts (MEFs) (CF-1 mouse strain) were propagated till passage 3 (P3). IR fibroblasts were mitotically inactivated by gamma irradiation at 50 Gy delivered in 30 min (^{137}Cs; irradiator OGL from VF a.s. Cerna Hora, Czech Republic). Suspension of MEFs P3 was frozen in the amount of one million of cells per 2 ml cryo tube (TPP, Trasadingen, Switzerland). Freezing was done by addition of 0.8 ml of ice-cold freezing medium drop by drop into 0.8 ml of MEF suspension in MEF medium consisting of Knockout Dulbecco's modified Eagle's medium (KO-DMEM; Gibco), 10% heat-inactivated fetal bovine serum (FBS; Invitrogen), 1% L-glutamine (Gibco), 1% non-essential amino acids (PAA), 1% penicillin-streptomycin (PAA), and 0.1 mM β-mercaptoethanol (Sigma). Composition of freezing medium was KO-DMEM : FBS : DMSO = 3 : 1 : 1 (v/v/v); Dimethyl sulfoxide (DMSO), Hybri-Max™(Sigma). For more details, see Suppl. Materials.

After the thawing procedure was finished, the Petri dish containing cells was incubated in standard CO_2 incubator for only 30 minutes in order to initialize the adhesion process. Then the dish was taken out of the incubator, installed in the AFM dish holder preheated during the calibration process. The whole internal volume of the dish was filled with 2 ml of the fresh, preheated MEF medium and after the AFM instrument adjustment, the force mapping measurement was immediately started. The scheme representing all the experiments of the presented manuscript is shown in Fig. 1. All the measurements were done on samples/cells which were more than 30 minutes adhered on the surface. So we have been monitoring the development of cells that have overcome the transient state [49], [50] of adhesion. Longer periods of time would reduce immediate effects of the freeze/thaw procedure on the cells.

B. Young's Modulus Mapping by Atomic Force Microscopy

A standard BioAFM microscope (JPK NanoWizard 3; JPK, Berlin, Germany) was used to perform force mapping procedure. The scanning probe head (maximal visualization range 100-100-15 μm on the X-Y-Z axes) of the AFM system was placed on an Olympus IX-81 inverted optical microscope, and a 10× objective was used to find the appropriate area covered with cells and to place the cantilever in the proper position for the force mapping procedure. A plastic Petri dish with either distilled water for instrument calibration or the fibroblast culture was placed inside the Petri dish heater (JPK) preheated to 37 °C.

An uncoated silicon nitride AFM cantilever (Hydra 2R-100N; AppNano, Mountain View, CA, USA) equipped with a pyramidal silicon tip (tip length 6 μm) was used for all experiments. The probe was calibrated prior to every experiment. The calibration procedure was done in double-distilled water after the entire setup had been preheated with a Petri dish heater to 37 °C for 30 minutes. Then, the laser reflection sum was maximized, followed by centering of the laser detector. The AFM probe was brought into contact with the surface during a standard landing process. Calibration of the cantilever sensitivity was calculated as the slope of the Force-Distant (FD) curve indentation. The FDC curve was recorded during the interaction of the tip with the Petri dish surface. The set point was 2.0 V, the time per curve was 1.0 s, and the Z length was 5.0 μm. The typical sensitivity value was found to be between 11.3 and 14.3 nm/V. Cantilever stiffness was then calibrated by the measurement of its thermal noise, which ranged between 17.34 and 19.19 nN/μm on the different experiment days.

The BioAFM settings were identical for all the force mapping procedures. The set point value was 1.0 nN (relative to the baseline value), time per curve 0.45 s, Z-length 15.0 μm, speed of curve recording 33.3 μm/s. The force-distance curves were recorded with a data sampling rate of 2 kHz. The force mapping procedure was performed as step-by-step recording of force-distance curves in the network of 64 × 64 points on 55×55 μm area covering a single fibroblast cell. One mapping procedure takes usually 40 - 45 minutes. The experimental parameters (64 × 64 points) were found as optimal to capture enough details to show real status of the cell during its live.

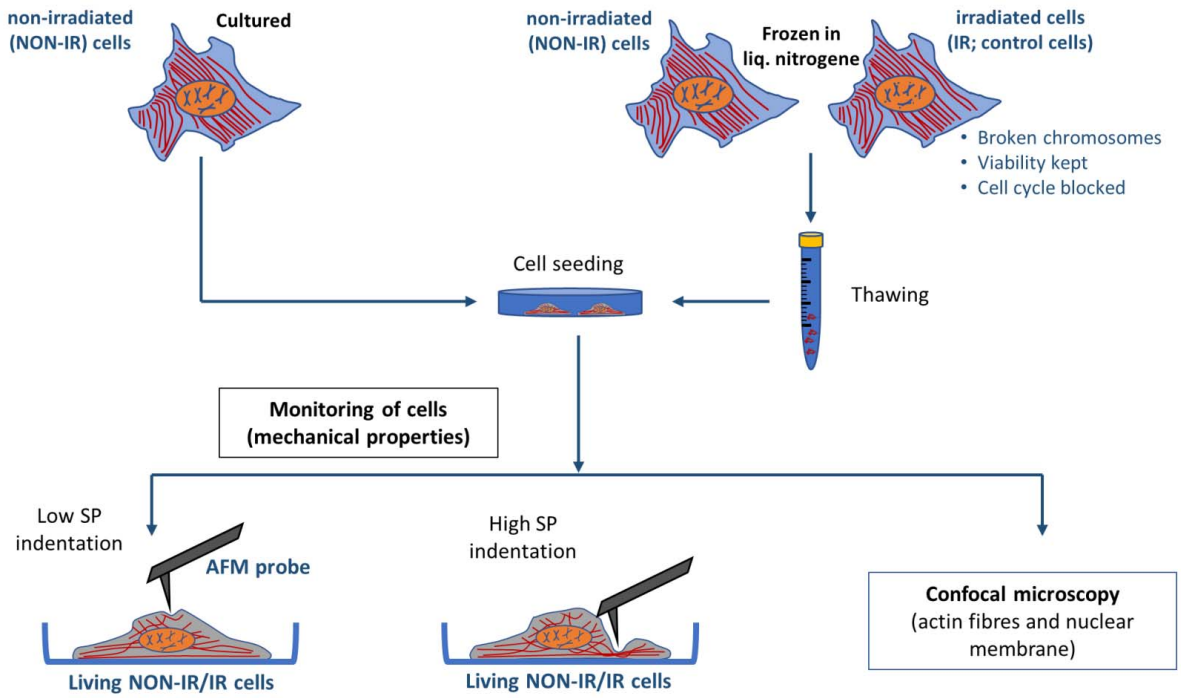

Fig. 1. Overall schematic view of the experiments. Irradiated cells (IR cells) are prepared by exposing the non irradiated cells (NON IR) to gamma radiation (50 Gy). Irradiation affects cell ability to proceed the cell cycle, cell viability is however kept unchanged. Both cell types are frozen in liquid nitrogen to be subsequently thawed by a standard protocol. Mechanical properties of the cells during the post thawing period and cultured (never frozen cells) are subsequently monitored by AFM based nano-indentation method. Finally, structure of the actin fibers of polyformaldehyde fixed cells as well as the living cell nucleus was checked by confocal microscopy.

As the cell cycle of fibroblast takes typically 24 hours, a single step of such duration should be long enough to distinguish the monitored process.

Images of the cells during the AFM stiffness mapping are shown in the Supplementary data section as Fig. S1. Cells taken during different stages of the mapping process are shown – i.e. at the beginning and at the end of the time-lapsed process, force mapping with the AFM probe over the monolayer of so-called never frozen cells is shown as well.

Standard, Fetal Bovine Serum based, medium was used, as it has been tested in many cases and projects, especially when the irradiated fibroblast cells were cultured. To avoid significant loss of the CO_2 content in the measuring chamber, the whole volume of the Petri dish was exchange between recordings of each force map, i.e. roughly each 40-45 minutes. No AFM instrument adjustment was involved during the repeated mapping procedure [51], [52] thanks to use of uncoated cantilevers.

Place-to-place reproducibility was studied by performing identical force mapping experiments sequentially on two different, randomly identified sites on the Petri dish surface covered with fibroblasts. The effect of the set point value on the measured stiffness of the cells and the effects of different set point values and set point height profiles, together with stiffness maps, are shown in Fig. S2.

Before the measured AFM data were further processed and interpreted, all parts of each sample corresponding to the plastic dish were algorithmically removed using Gwyddion [53] or Mathematica software [54].

C. Long Term Monitoring of Cell Growth

Surface stiffness of the fibroblasts cultured on a Petri dish shortly (30 minutes) after thawing process was monitored during overnight nanomechanical mapping of the fibroblast cell. Petri dish containing freshly thawed suspension of cells was for a short period pre-incubated in a standard CO_2 incubator (see chapter Short term incubation). When first cells started to adhere (30 min after thawing), culturing medium in the dish was completely exchanged and force mapping process was started immediately. AFM measurement was performed during continuous experiment of repeated force mapping process on identical place. Parameters identical to other mapping processes were used also in this case. Neither medium exchange nor AFM instrument adjustment was involved during the repeated mapping procedure.

D. Effects of DMSO or Glycerol in the Culture Media on the Stiffness of the Cells

The effects of DMSO and glycerol application (both from Penta, Prague, Czech Republic) on cell stiffness were tested during subsequent measurement of force maps in the presence of 5%, 10%, 15% and 20% solvent in standard MEF culture medium. DMSO is a strong polar solvent having specific electrical properties [55]. First, a Petri dish with cultured

fibroblasts was filled with MEF medium with no solvent, and a force map was recorded to obtain baseline values of cell stiffness under standard conditions. The whole volume of medium in the Petri dish was then depleted by using a standard medical syringe connected with the inner space of the dish via stainless steel tubing fixed inside the Petri dish heater; the AFM cantilever was kept in contact with the sample surface. The Petri dish was immediately filled with preheated MEF medium containing the appropriate amount of the solvent, and after 3 min of temperature adjustment, the force mapping of the same area was started. After 45 min, when the nanomechanical mapping process was finished, the inner volume of the dish was completely exchanged with MEF medium containing a higher concentration of the solvent, in the following sequence: 5%, 10%, 15% and 20% solvent.

When the stiffness of a single cell is investigated by the AFM indentation method over a large area, typically, not only the cell but also the surrounding plastic surfaceis captured. However, the stiffness of plastic (polystyrene dish) is approximately three orders of magnitude higher than that of the cell. It was therefore possible to identify the parts of each AFM image corresponding to the plastic surface by setting a YM threshold. Points exceeding the threshold were masked from further analysis using the Gwyddion software [53].

E. Statistical Evaluation of Data

Quantitative Young's modulus data were calculated as the mean ± standard error of the mean from experiments at the time points where the force-mapping procedure was finished simultaneously (the duration depended on cell topography). In all cases, the standard error was less than 7%. When YM values within a certain time interval were compared, the normality of the data distribution was evaluated by the Shapiro–Wilk method, thus proving the data normality at the 0.05 level.

F. Viability of Cells Determination

The viability of the cells tested by AFM testing was checked at the timepoints from 30 min (0 hours) to 6 hours 30 min (6 hours) to correspond to force mapping procedures. The cells were washed to exclude floating cells, trypsinized and collected into tubes. Cell suspension was then incubated in 0,5% TrypanBlue solution (1:1) for 2 min and viable cell ratio was counted on hematocytometer.

G. Data Processing

The force mapping process provides a grid of force-distance curves (FDC, dependency of the tip-sample interaction force on tip height above the surface), or so-called force maps (FM). The absolute value of the Young's modulus was determined by fitting the FDC using Equation 1 (pyramidal indentation model by Bilodeau [56]).

$$F(\delta) = \frac{1.4906\ E\ tan\alpha}{2\left(1-\upsilon^2\right)}\delta^2 \tag{1}$$

where F is the measured force, E is the Young's modulus, ν is the Poisson ratio (0.5 for incompressible materials), δ is the tip-sample separation (obtained by correction of the cantilever height to its bending), and α is the half-angle to the face of pyramidal tip, in this case, 18° (reflects the tip geometry).

Relative value of Young's modulus was calculated as ratio of the actual stiffness value relativized to initial value of stiffness in the first time point of time dependency:

$$E_{rel} = \frac{E_t}{E_{in}}\,[100\%] \tag{2}$$

where E_{rel} is the relative value of the Young's modulus, E_t is its value at time point t and E_{in} is the value of the YM at the initial time point.

The fitting of the FDC by Equation 1 was performed in the software AtomicJ [57], with the contact point position estimated by an incorporated robust exhaustive algorithm and best fit found by the Robust HLTA algorithm. The Poisson ratio was set to 0.5. In all cases, the fitting was performed on the approach curve. The resulting Young's modulus maps were exported for processing in Wolfram Mathematica (Figs. S3, S4).

After the fitting, some points were removed from the YM maps based on the values of various parameters of the corresponding fit. First, a threshold of 50 kPa was introduced for the YM value in order to exclude all curves measured over the dish surface or over very thin cell regions. Furthermore, all fits yielding indentation greater than 2.5 μm were filtered out as such a large indentation always meant a faulty contact point estimation. In rare cases typically in high and soft parts of the cells it was not possible to precisely detect contact point.

In our case, indentation was defined as the difference in indentation depth between the shallowest (i.e., contact) point and the deepest point of the fitted part of the FDC. The height of the cells was determined directly from the contact point position. The optimization of the contact point position was part of the force-curve fitting. The resulting contact point position therefore corresponded best to the measured data (given the chosen indentation model). In the case of curves that passed through filtering and were used for further analysis, any uncertainty in the position of the contact points was approximately 2 orders of magnitude smaller than the measured cell height. This is corroborated by the apparent smoothness of the AFM height maps.

Additionally, when the indentation force at the deepest point of the fitted region was less than 80% of the total set point, the corresponding curve was removed. Thus, FDCs whose fitted region was too small were not taken into consideration.

We excluded force curves that could not be well described by the Bilodeau model with a single E value (typically containing a significantly stiffened region at greater depths). Such curves were typically located in the border regions of the measured cells. In the remaining curves, it was therefore not necessary to employ modified indentation models incorporating, e.g., bottom effect cone correction.

Finally, the adequacy of the Bilodeau model was checked. In the curves kept for final statistical analysis, the root-mean-square deviation of the model from the actual data points was always smaller than 5% of the maximum set point, and the maximum deviation of the model values from the

measured data was always smaller than 7% of the maximum set point. Of all the models used, including the Bilodeau, Sneddon, Power, Blunt Pyramid and Cone Sneddon models, the deviations were smallest for the Bilodeau model (Figs. S3-S5).

After applying all filters, 70 – 80% of curves and corresponding YM values remained for statistical analysis. Measurements were made for 3 sets of cell samples, each of which contained 2-3 cells.

Additionally, minimal deviations between calculated results and the measured data (least squares method) were taken into consideration. Curves in which the maximum deviation of the measured data from the model values was smaller than 7% of the measured data at each point were considered.

H. Confocal Microscopy and Data Analysis

Effects of the treatments were directly analyzed on the microscopic slides under the microscope (about 500 – 2000 cells) and/or on acquired 3D images (>50 cells). Two specimens of microscopic slides for each sample were directly evaluated by two experienced scientists. The following equipment was used for confocal microscopy and image acquisition: an automated Leica DM RXA fluorescence microscope (Leica, Wetzlar, Germany) equipped with an oil immersion Plan Fluotar objective (100×/NA1.3) and a CSU 10a Nipkow disc (Yokogawa, Japan); a CoolSnap HQ CCD-camera (Photometrix, Tuscon, AZ, USA); and an Ar/Kr-laser (Innova 70C Spectrum, Coherent, Santa Clara, CA, USA). Automated exposure, image quality control and other procedures were performed using Acquarium software [17]. The exposure time and the dynamic range of the camera in the red, green and blue channels (R-G-B) were adjusted to the same values for all slides to obtain quantitatively comparable images. Forty serial optical sections were captured at 0.2-μm intervals along the z-axis. Controls and frozen/thawed cells were observed 30 min after transferring to microscopic slides. Longer periods of time would reduce immediate effects of the freeze/thaw procedure on the cells. Nevertheless, as described in **Results**, structural changes of the nuclear envelope only appeared in frozen/thawed cells (and not control cells).

I. Immunostaining of Nuclear Envelope for Confocal Microscopy

Nuclear envelopes were visualized by high-resolution confocal microscopy using a mouse monoclonal antibody against lamin A/C (dilution 1:1000; Sigma-Aldrich). The secondary antibody, namely, affinity-purified donkey anti-mouse-FITC-conjugated antibody (dilution 1:100; ImmunoResearch Laboratories, West Grove, PA), was used to visualize the primary antibody. The immunostaining procedure was performed as described in [58] with minor modifications. The nuclear envelope was stained with anti-lamin A/C monoclonal mouse antibody (dilution 1:1000; Sigma-Aldrich). After the cells were briefly washed in 2× SSC, the samples were mounted using Vectashield medium (Vector Laboratories, Burlingame, CA, USA).

III. Results and Discussion

A. AFM Nanoindentation

AFM microscopy allowed us to evaluate the elastic properties of cryopreserved cells in different cell parts and times after thawing. First, we measured the stiffness of cultured (never frozen) murine fibroblasts incubated with different cryoprotectants (DMSO and glycerol). Then, we measured the development of mouse fibroblast surface stiffness after freezing/thawing. For this case, cells mitotically inactivated by 50 Gy of γ irradiation (IR cells) and frozen/thawed with DMSO were used as a negative control for which cell stiffness changes were not expected after freezing/thawing (IR frozen/thawed cells were compared to non-IR frozen/thawed cells) (Fig. 1).

To properly interpret the AFM results, we compared various models of the cell surface response to AFM tip pressure, specifically the equations containing the material parameter of stiffness – the Young's modulus (YM) E, see Equation 1 [51]. We used a pyramidal sharp tip, as this indenter shape ensured sufficiently high resolution in horizontal direction, which was necessary for a proper description of cryopreserved cells after thawing. In support of this choice, a number of studies have reported that cell stiffness can be reliably measured using "sharp" probes and that the values obtained are similar to those found with spherical probes, as well as observing no detrimental effects due to persistent probing of individual cells with a pyramidal tip [59]–[61]. The membrane as well as the whole fibroblast cell is one of the most robust cells, as it is an important part of the body covering skin (see i.e. [62]). Statistical adhesion data are presented in Fig. S6.

The advantage of the sharp tip we used was the possibility to simultaneously combine high resolution mapping of the cell topography with measurements of mechanical and spreading properties of the cell, without a necessity to change the tips during experiments. For a given amount of applied force, the sharper probes can penetrate deeper into the probed sample – which was important for our purposes. The force indentation relationships were formulated in a variety of ways, specifically, with the neo-Hookean [63], [64], one/two-term reduced polynomial [65], single-term Ogden [66], Fung [67], van der Waals [68]–[71] and Bilodeau models [56]. The Bilodeau model (Equation 1) gave by far the best agreement between our data (obtained with a sharp tip) and the calculated force indentation relationships (AtomicJ software [57])-Figs. S3, S4. We compared application of the Bilodeau model with Sneddon, Power, Blunt Pyramid and Cone Sneddon models on the same data set–see Fig. S5.

When only a small area of the surface of a fibroblast is studied, a lower set point (SP) value (i.e., under 0.5 nN) can be used, which allows both cell stiffness close to the membrane and submembrane structures to be studied. It should be noted that in the border regions of the cell, the contribution of the cytoskeleton can play a role; we address this by selecting an appropriate region of the cell for our measurement. In our measurement, we chose to use a set point of 0.4 nN because the signal-to-noise ratio was not satisfactory when smaller values were used. Using a larger SP (1 nN) value and area

(100×100 μm^2) provides information about the overall cell stiffness, i.e., the inner cell structure dynamics.

First, we investigated the correlation between the cell membrane stiffness and cell spreading in never frozen murine embryonic fibroblasts incubated with the DMSO or glycerol (cultured cells). Their stiffness changes were identical for both cryoprotectants (DMSO, glycerol) at the corresponding concentrations within the tested concentration range. The relative stiffness in the presence of 5% DMSO or glycerol decreased to 84% of the initial value. Increasing the concentrations of these cryoprotective compounds in the culture media (i.e., to 10%, 15% and 20%) further decreased the relative stiffness (i.e., to 70%, below 50% and below 15%, respectively) Fig. 2. Such membrane stiffness changes (i.e., decreases in Young's modulus) presumably correspond to change in the membrane organization composition caused by DMSO or glycerol [72], [73]. Stiffness maps and height profiles of fibroblasts treated with various percentages of cryoprotectants are shown in Fig. 3. It is generally accepted that as the cell spreading increases, the cell profile height decreases [74]. We correlated cell height and stiffness maps. The far-left column (DMSO Height) in Fig. 3 presents the height maps. The increasing height together with the decreasing stiffness observed in the corresponding Young's modulus map suggests that DMSO-treated cells exhibit lower surface spreading and that the surface spreading decreases as the DMSO concentration in the medium increases, causing cells to lose their spreading and form higher and softer structures. The glycerol-treated cells, which are shown in the two columns of images on the right side of Fig. 3, exhibit a decrease in average cell stiffness (i.e., cell surface softening). Glycerol did not induce an increase in the cell height within the tested glycerol concentration range, suggesting that better spreading of the cells on the surface occurs in the presence of glycerol than in the presence of DMSO. It was shown that DMSO creates membrane pores [72] and inhibits the cytoskeleton dynamics that affect proteins, such as Rho-kinase [75], whereas glycerol may strengthen the cohesive forces in the membrane bilayer and render it more flexible [76]. Fig. 2 shows a trend where the glycerol-induced softness change is weaker than the DMSO-induced and it becomes more and more obvious with the dosage increasing, however, for the 20% case, the situation changes. The reason is probably based on the chemical properties of the cryoprotecting solvents, e.g. DMSO as a strong polar solvent can remove phospholipids from cellular structures, mostly from the membranes.

Small areas (Fig. 4a) 10×10 μm, low SP (0.4 nN) of never frozen standard cells are mapped under conditions that guarantee that the interaction between the AFM probe and sample surface is not interrupted during the long period of the measurement. Masking the area surrounding the cell (plastic support with a surface stiffness approximately 3 orders of magnitude greater than that of the cell) is an essential procedure when single cells grown on plastic surface are mapped by the AFM nanoindentation process. The average Young's modulus value is shown below the processed map in Fig. 4b; the masked regions of the plastic surface are indicated. Fig. 4b clearly shows the obvious differences between

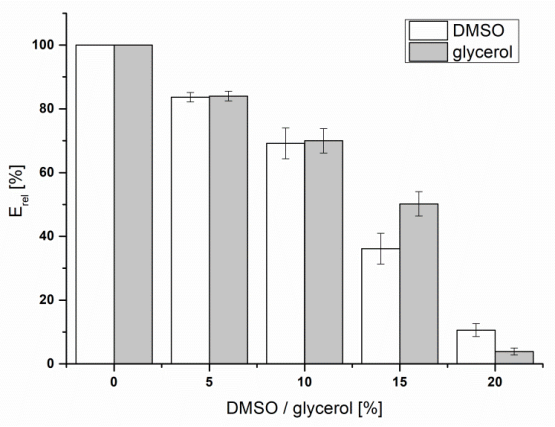

Fig. 2. Immediate effects of the cryoprotectant content (DMSO or glycerol) in the culture media on the relative stiffness of non-frozen and non IR cells determined by measuring the change in the relative stiffness (relative value of Young's modulus - E_{rel}). Increasing the concentrations of DMSO/glycerol in the culture media further decreased the relative stiffness. Such membrane stiffness changes (i.e., decreases in Young's modulus) presumably correspond to changes in the membrane compositions caused by DMSO or glycerol.

processed and unprocessed maps containing a single fibroblast. The average stiffness is 1.08 MPa for the unprocessed maps and 22.2 kPa for the processed maps.

Next, we investigated the development of the fibroblast surface stiffness and heights above the dish surface over time after thawing and at different positions in the cell. The results obtained from frozen/thawed fibroblasts were compared to the results obtained from the same type of cells that were mitotically inactivated (i.e., irradiated with 50 Gy of γ-rays prior to freezing/thawing; IR cells/fibroblasts).

When measurements of small areas (10×10 μm^2) were performed (with a low-SP of 0.4 nN), their position was selected in the space between the cell nucleus and filopodia, thus avoiding the influence of the nuclear region or cell edge on the measurements (i.e., a too deep indentation in the border area of the cell). Each point in Fig. 5 represents statistics measured in a 10×10 μm^2 region of each cell. A mapping area of 10×10 μm^2 was selected because for frozen/thawed fibroblasts, it was always possible to locate an area of such size distinct both from the nucleus and the cell edge. The average indentation depth was 570 nm (i.e., the cell stiffness was investigated to 6% of the total cell depth). For each curve, the deviation of the measured data from the modeled values was smaller than 7% of the measurement value. As low-SP measurements were performed over a relatively small cell area, the values of E were quite uniform across the area (maximum deviation from median was 28%); error bars are shown in Fig. 5. The measured region was located halfway between the nucleus and the cell edge. The elastic response of the cell in the measured region was predominantly determined by its membrane and submembrane structures. Up to 2.7 hours after adhesion initiation, the elasticity of the frozen/thawed non-IR fibroblasts oscillated by approximately 40% of the initialization value. At 2.7 hours after the initiation of adhesion, the fibroblast membrane and submembrane structures'

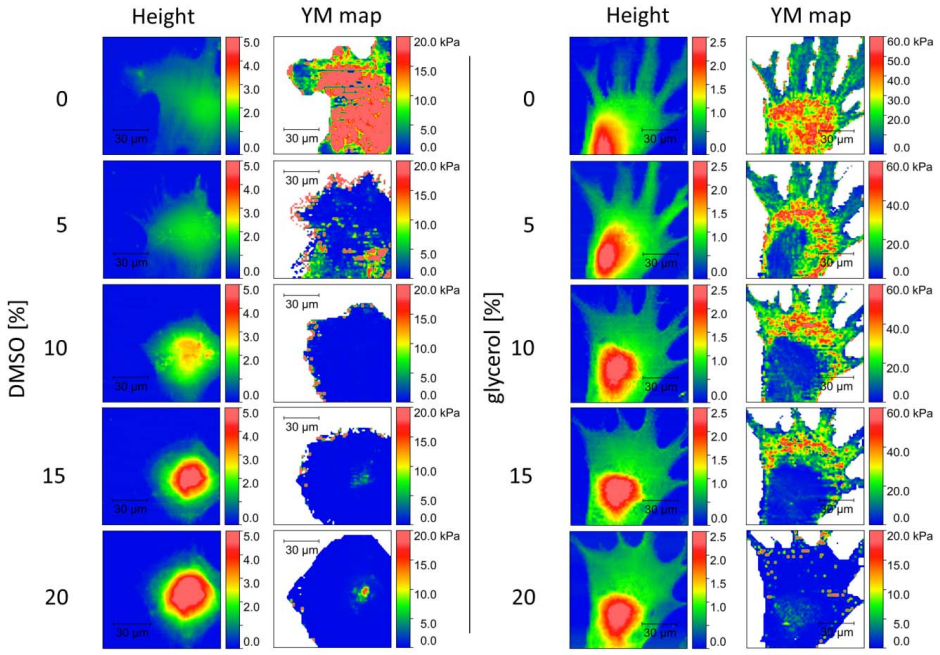

Fig. 3. Height profile images and corresponding stiffness maps taken during the force mapping of non-IR fibroblast cells exposed to different concentrations of cryoprotectant compound (a – DMSO, b - glycerol). The concentration of the cryoprotective compound in the culture medium is shown on the left side of both panels, and a high set point (SP) measured height and stiffness maps are presented for each concentration. The displayed area is 100 × 100 μm^2.

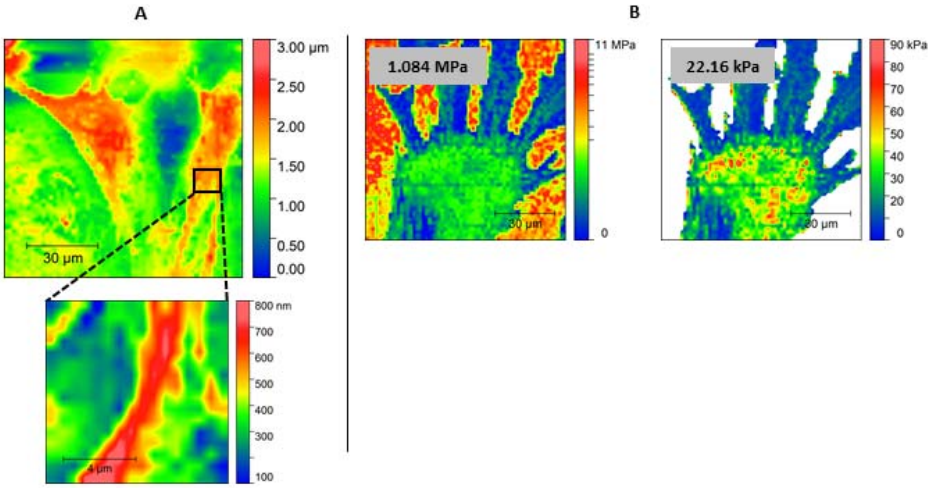

Fig. 4. Two approaches were used to study cell stiffness by AFM in force mapping mode (demonstrated on the cell as shown in Fig.3). A) Large area (100 × 100 μm^2) containing one or more cells can be monitored by a nano-indentation process when higher SP values are used (upper image). The image below schematically shows the selection of a small area on the cell surface (10 × 10 μm^2), which facilitates applying a faster nano-indentation process with a low set point value(0.4 nN) for the maximum loading force. B) Masking the surrounding area of the cell. The average value of Young's modulus is shown below the appropriate image (left, unprocessed map; right, map with masked regions of plastic surface).

stiffness began to increase continually (Fig. 5). IR fibroblast stiffness (median of YM over the measured area) did not change significantly during the measured period of time. Irradiation affects cells' ability to proceed the cell cycle. Cell viability, however, remained unchanged. Therefore, in Fig. 5, we show that in the case of non-IR cells only, cell stiffness regeneration connected with internal cells processes is taking place.

The application of a higher SP value (1.0 nN) and a large mapping area (100 × 100 μm^2) of frozen/thawed cells facilitated the observation of the inner cell structure, which is important for cell survival and the development of the whole cell state. The average value of the indentation depth was 2.5 μm (i.e., the cell stiffness was investigated to 30% of the total cell depth). The dynamics of changes in high-SP-measured fibroblast elasticity obtained from stiffness measurements after thawing and plating is shown in Fig. 6. Due to fibroblast inhomogeneity, we divided the sample surface into 3 basal regions: the high region, middle region and low region, comprising sample heights of 80-95%, 30-80% and 15-30%

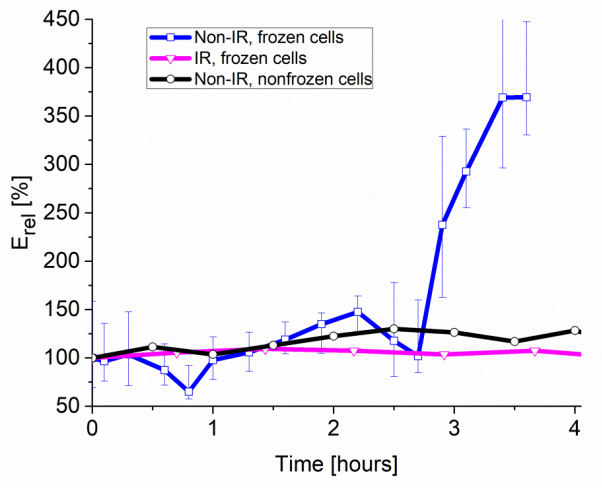

Fig. 5. Time development of non-IR non frozen/cultured cells, non-IR frozen/thawed cells and IR frozen/thawed fibroblasts relative value of surface elasticity (Young's modulus E_{rel}) measured by AFM nano-indentation method after thawing. Low SP value of 0.4 nN was used to scan over a small cell-covered region ($10 \times 10\ \mu m^2$). For each curve for IR frozen cells and non-IR non-frozen cells the deviation of the measured data from the modelled values was smaller than 7% of the measured data. Maximum deviation of E from median was 28% across the measured area - error bars span values between the 1st and 3rd quartile. All values are relative to the first data points in each respective series. Controls and frozen/thawed cells were observed by fluorescence microscopy 30 min after transferring to microscopic slides. Longer periods of time would reduce immediate effects of the freeze/thaw procedure on the cells. Measurements were made on 3 sets of cell samples, each set contained 2-3 cells.

of the maximum height above the dish surface, respectively. We correlated the cell height and stiffness maps. At 1 hour after plating, the stiffness of all regions of the sample begins decreasing. Compared to cultured (nonfrozen) DMSO-treated fibroblasts, the surface stiffness of cryopreserved fibroblasts is remarkably lower at all parts. For each curve, the deviation of the data from the modeled/calculated values did not exceed 7% of the measured value

Of all the basal regions, the middle region (30-80%) had the smallest deviation from median E, less than 35%. Such deviation corresponds to the relatively broad distributions of E values (even within each of the basal regions) measured with a sharp tip, which is able to distinguish even minor spatial inhomogeneity in the cell.

The stiffness of the high region of non-IR fibroblasts is remarkably lower than the stiffness of the low and middle regions of the sample (Fig. 6). This reflects the changes in the nuclear envelope, which may correspond to the nuclear envelope shrinkage of the frozen/thawed cells indicated by confocal microscopy. The stiffness of the surface in the high area of the sample begins to increase more than 5 hours after plating.

In all three cell regions, the stiffness gradually decreased in the first 5 hours after plating, after which it began to increase. Throughout the measurement, the highest cell region was the area with the lowest stiffness.

Fig. 6c shows that the region of the non-IR cells with the maximum median E (YM) gradually shifts from the higher parts of the cells to the lower parts. At the same time,

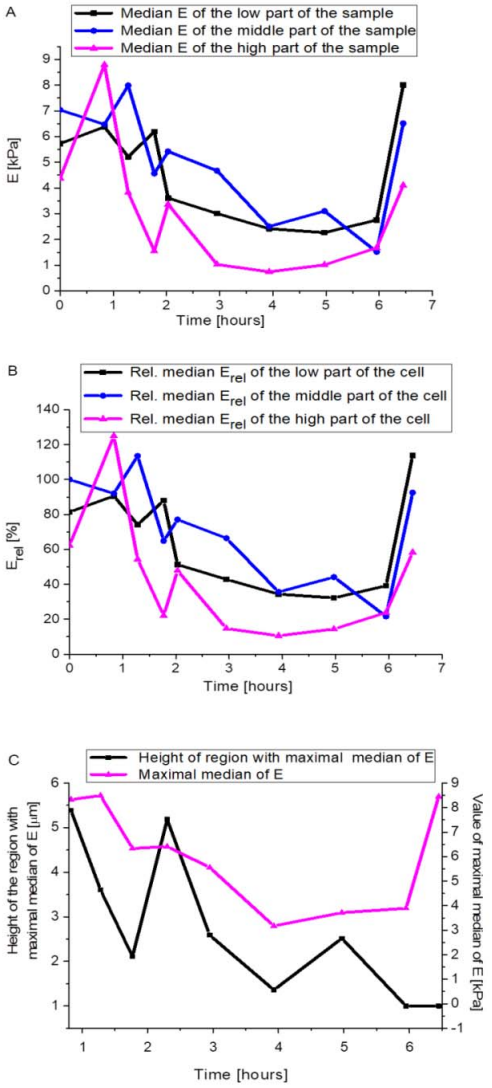

Fig. 6. Time development of non-IR fibroblasts surface elasticity (Young's modulus E) after thawing. High SP AFM nano-indentation was used to scan over a large cell-covered region ($100 \times 100\ \mu m^2$). A) Median of elasticity change in time (Young's modulus E) in low, middle and high part of cell B) Median of relative values of elasticity change in time (relative values of Young's modulus E_{rel}) in low part, middle and high part of the cell. C) Time development of the height of the region with maximal Young's modulus (E) and median of values of Young's modulus at the regions with maximal Young's modulus In this case, cell was divided to parts of 0.5 μm in height. For each curve the deviation of the measured data from the modelled values was smaller than 7% of the measured data. In the middle part (30-80%) we found the biggest continuous areas where the deviation from median E of the middle region was smaller than 35%. Measurements were made on 3 sets of cell samples, each set contained 2-3 cells.

the median E itself also decreases. However, this decrease is less pronounced in the lower parts of the cell, which may reflect an ongoing reconstruction of the cell interior. Non-IR cells immediately after thawing and cell attachment (i.e., 30 min. after thawing) had the highest elevation and stiffness. After 1.5 hours, the interaction of the cell with the substrate gradually built, and cell stiffness and height significantly decreased. The height of the sample decreased from the initial plating and after 6 hours was at 65% of its initial value. Rapid increasing of the non-IR cell stiffness after 6 hours (Fig. 6) is

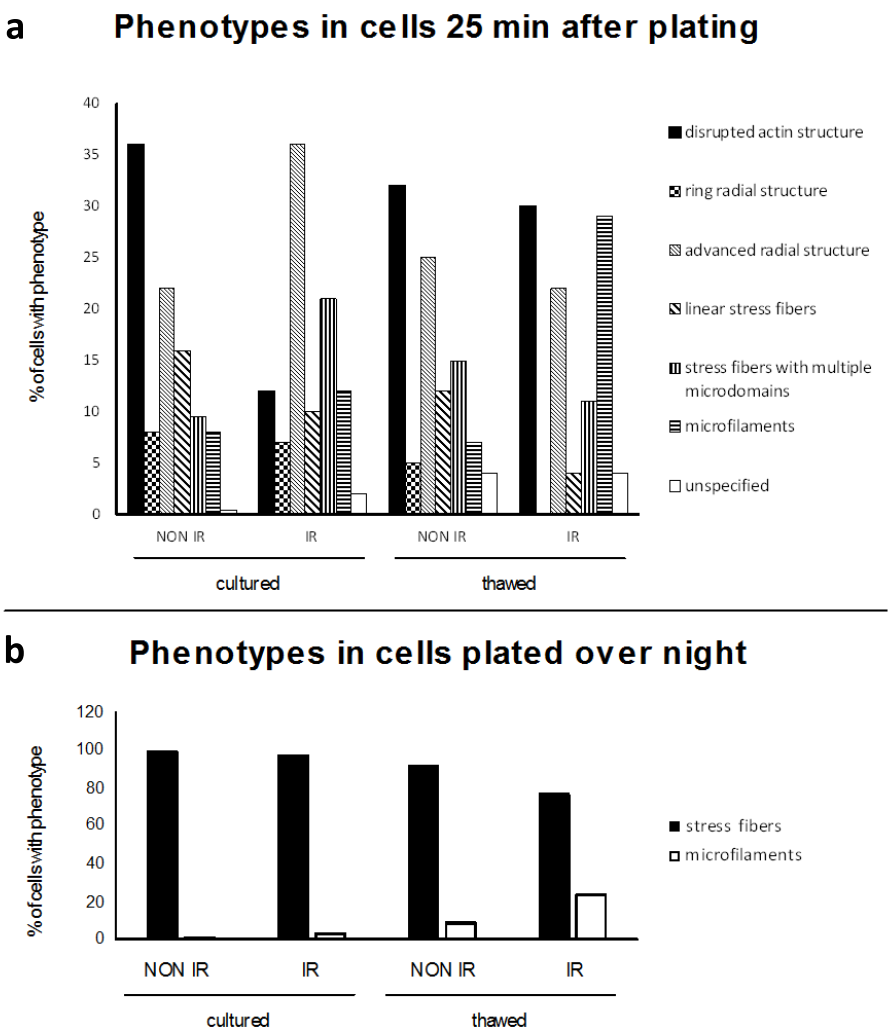

Fig. 7. Statistics of cytoskeletal features after thawing. a - The percentage (%) of phenotypes of the skeletons of IR and non-IR cultured and frozen/thawed fibroblasts in the cell population plated for 30 minutes. b - The percentage (%) of phenotypes of the cytoskeletons of IR and non-IR cultured and frozen/thawed fibroblasts in the cell population plated overnight. Up to 4% of cells analyzed 25 min after plating presenting indistinguishable phenotypes were described as “unspecified”. Fuorescence microscopy were made on a set of cells per group, each set contained 48-56 of evaluated cells.

an interesting phenomenon, if this fact is compared with values shown in Fig. 5 for irradiated cells. As the cell cycle of IR cells is affected by disrupted chromosomal content, the regeneration of cell is affected as well.

Compared to non-IR fibroblasts, the repairs of the inner and surface parts of the IR cells were not significant at any of the 3 basal regions. The results obtained by low-SP AFM on IR fibroblasts indicated that extensive remodeling did not occur (Fig. 5). After a decrease in the high-SP-measured stiffness in IR fibroblasts from 2.5 to 5 hours, the flat profile of the elasticity demonstrates the absence of potential for inner cell structure remodeling in IR fibroblasts in this period after thawing. The possible inner cell repairs begin 6 hours after culturing in the case of non-IR fibroblasts and, to a much lesser extent, of IR fibroblasts. Never frozen/cultured fibroblasts stiffness was slightly growing immediately after plating and oscillated around 115-128% of the initial low SP E value 4 hours after plating (Fig. 5). The viability of the cells probed by AFM measurements was checked at time points up to 6 hours in a way corresponding to the force mapping procedures. It was shown that the viability of AFM-tested cells was more than 90% (Fig. S7).

B. Fluorescence Microscopy of the Cytoskeletons of Cultured and Frozen/Thawed Fibroblasts

Fluorescence microscopy of the cytoskeleton in IR and non-IR (standard) cultured and frozen/thawed fibroblast was conducted. The cytoskeleton develops during attachment after plating the cells. The key role in cytoskeleton and cell elasticity plays actin and its filamentous architecture and the disruption of actin filaments always lead to decrease in Young’s modulus [62], while destabilization of microtubule dynamics results in increased stiffness only in cancer cells [77]. Control fibroblasts, which were neither subjected to IR nor frozen/thawed, presented patterns and phenotypes corresponding to the progression of actin structure development from early attachment until late complex structure formation (non-IR, cultured). The actin structure exhibited different patterns and phenotypes as the cytoskeleton

developed after plating of the cells (Figs. 7, 8). Shortly after plating (25 min), we observed actin assembly in a dense radial structure around the nucleus, which subsequently dissolved into a looser, advanced radial structure as linear fibers began to form across the cell. Surprisingly, this dense structure was not observable in IR cells undergoing the freeze/thaw cycle, likely because it underwent quick dissolution into loose structures or because advanced radial structures were formed from the beginning. Thick stress fibers were more observable after irradiation of cultured cells and were less frequent in cultured non-IR cells. A distinct linear structure was less frequently observed in IR cells undergoing the freeze/thaw cycle. Finally, cells with disrupted actin filaments were found in every sample but were most frequent in cultured and plated cells, and their ratio decreased after irradiation and the freeze/thaw cycle. Up to 4% of cells analyzed 25 min after plating presented indistinct phenotypes and were described as "unspecified". In cells plated overnight, the freeze/thaw cycle resulted in smaller cells with assembled stress fibers (Fig. 8). The irradiation led to a further decrease in the proportion of cells containing assembled stress fibers and enrichment in cells containing microfilaments (Fig. 7) suggesting that IR, but not freezing/thawing, affects actin remodeling.

Only minor differences in the early, naive structures (such as ring and advanced radial structures) were induced by irradiation and/or the freeze/thaw cycle (Figs. 7, 8). While the freeze/thaw cycle induced only minor changes in non-IR fibroblasts soon after thawing (Fig. 7a), it significantly affected the spreading of the structure that occurred 24 hours after seeding (Fig. 7b). Irradiation treatment allowed even cells that underwent the freeze/thaw cycle to reach a size similar to that of the cryopreserved cells, but their linear fibers were markedly thinner. This observation is in good agreement with the AFM data, which showed an increasing high-SP stiffness in frozen/thawed fibroblasts, which presented thick stress fibers in the cytoplasm (Fig. 7). Additionally, the lack of change in stiffness in the same set of IR fibroblasts prior to the freeze/thaw cycle corresponded to the similar stress fiber content and composition in treated and control cells. The *de novo* synthesis and massive remodeling of actin fibers were shown to be associated with an elevated level of visibly disrupted fibers [78], which corresponds to our observations in nonirradiated cultured cells (Fig. 7). The IR-mediated disruption of synthesis and/or remodeling of actin corresponds to a decrease in the quantity of disrupted fibers in IR cells that did not undergo the freeze/thaw cycle (Fig. 7). Based on these data, we suggest that the thinner linear stress fibers in the frozen/thawed and IR cells [79] are a result of the lack of massive *de novo* stress fiber synthesis and actin remodeling in IR cells; this suggestion is supported by the reduction of disrupted fibers.

We compared the ratio of linear fibers in cultured cells to those in frozen/thawed cells 25 minutes after plating and the ratio of linear fibers in cultured cells to those in frozen/thawed cells plated overnight. We found that after 24 hours, the number of linear fibers in frozen cells was closer (20%) to that in never-frozen cells than was the number in cultured cells compared to frozen/thawed cells plated for

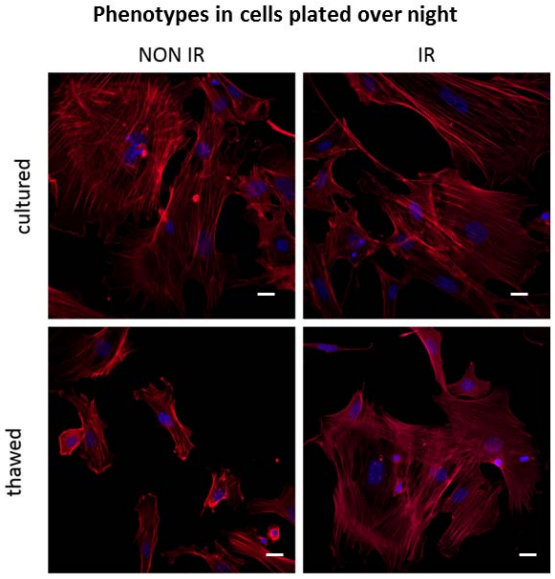

Fig. 8. Fluorescence microscopy of the cytoskeletons of IR and non-IR cultured and frozen/thawed fibroblasts plated overnight. The actin structure (red) shows different patterns and phenotypes as the cytoskeleton develops after plating/freezing the cells (DAPI stained nuclei in blue).

25 minutes (Figs. 7 a, b). Regarding stress fibers, their numbers were much higher in cells that had been irradiated and then plated for 25 minutes than in non-IR cells. The fibroblasts contained a lower percentage of linear fibers 25 minutes after irradiation. This effect of IR on linear stress fibers is recapitulated in frozen/thawed cells. Additionally, cells that had undergone a freeze/thaw cycle displayed more microfilament structures, and this increase was further accented by IR treatment (Fig. 7 and 8). Such microfilaments are considered to be the building units for the thicker stress fibers during actin remodeling [80]. Both of these differences suggest that IR cells remodel their actin fibers to support strong attachment and spreading/movement (microfilamentous structures), while non-IR fibroblasts seem to form small and rigid structures, which presumably support cell proliferation.

Both the frozen/thawed cultured and IR fibroblasts remodeled their cytoskeletons after initial attachment (at least 2 hours; Figs. 8, S8), resulting in ring radial structures and, eventually, disrupted structure/filopodia formation. The initial increase in stiffness at 30 minutes might be attributed to cell spreading, consistent with the published data [81], accompanied by strong cytoskeleton remodeling and actin depolymerization/turnover. By contrast, the absence of the initial stiffness increase in IR cells might be explained by the spreading of these cells under modulated actin metabolism due to DNA damage caused by irradiation [82]. Indeed, DNA damage has been demonstrated to induce stress fiber formation, and G2/M arrest can induce cofilin phosphorylation, which induces a lower rate of actin depolymerization [83].

Comparing AFM and fluorescence microscopy data, we showed that the cytoskeletons of non-IR fibroblasts damaged by a freeze/thaw cycle and reconstructed after long-term plating is accompanied by the restoration of the cell

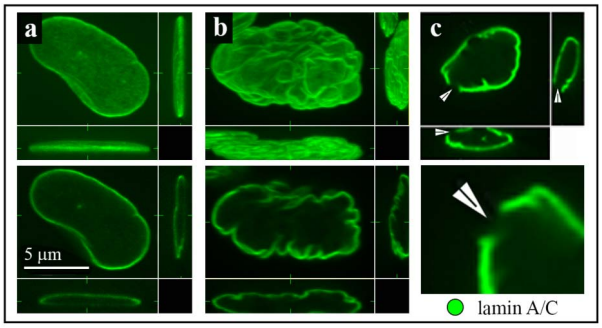

Fig. 9. Nuclear envelope states compared, by means of immunofluorescence confocal microscopy (lamin A/C antibody, green), for a) untreated non-frozen fibroblasts and b) the same cells frozen in presence of 10% DMSO (2 min incubation at 4 °C prior freezing) and visualized 30 min after thawing. Structural changes of the nuclear envelope only appeared in frozen/thawed cells (and not control cells). Top line: maximum images composed of 30 superimposed confocal slices (0.2 μm-wide); bottom line: an illustrative single confocal slice. Nuclear envelopes were markedly shrunken (b; about 80% of cells) or eventually disrupted (c; about 15% of cells). Envelope disruptions are indicated by white arrows and a magnified view of one of disruptions is shown in the bottom line, panel c. Measurements were made on 20 cells.

mechanical properties that had been decreased after freezing/thawing.

C. Confocal Microscopy of the Nuclear Envelope Shrinkage

To further study the effects of cryoprotectants before and after freezing/thawing on nuclear envelope states, we immunostained the cells with lamin A/C antibody (green). Confocal microscopy images of nuclear envelopes in untreated nonfrozen mouse skin fibroblasts and frozen/thawed mouse skin fibroblasts in the presence of 10% DMSO are compared in Fig. 9. Nuclear cell envelopes were evidently shrunken in approximately 80% of cryopreserved cells at 30 min after thawing. A small proportion (less than 15%) of thawed cells had ruptured nuclear envelopes. These results could be interpreted as a reflection of increased nuclear envelope fluidity in cryopreserved frozen/thawed cells within short periods of time after thawing, thus supporting the conclusions derived from AFM. All cells (controls and treated + frozen/thawed cells) were observed 30 min after transferring to microscope slides.

IV. Conclusions

The mechanical and elastic properties of cells are closely related to their functions. Monitoring the mechanical stiffness of living cells can therefore provide a novel means of monitoring cell physiology, detecting and diagnosing diseases, and evaluating the effectiveness of drug treatments. We are the first to study the stiffness regeneration process of cryopreserved cells using atomic force microscopy (AFM) nanoindentation combined with confocal fluorescence microscopy.

First, surface stiffness of never-frozen fibroblasts was studied by AFM upon the application of cryoprotectants. We found that higher concentrations of glycerol/DMSO decreased the fibroblast stiffness, with similar changes in the average stiffness values (i.e., cell surface softening) induced by both cryoprotectants. However, DMSO caused less surface spreading of the cells than did glycerol.

After that, AFM nanoindentation was used to map cellular reconstitution in real time after freezing/thawing cycle and to differentiate the regeneration processes at the different depths of the cell and even at different parts of the cell surface. Two AFM approaches were used to study the stiffness of cryopreserved cells (nonirradiated and IR fibroblasts) after freezing/thawing: 1. A higher SP value (i.e., 1 nN, 100 $\times$ 100 μm^{2}area) provided information about the inner parts of the cell, and 2. A low SP value (i.e., 0.4 nN, 10 $\times$ 10 μm^{2}area) allowed us to study the cell stiffness close to the membrane.

The increase in stiffness measured by low-SP AFM, which was related to regeneration of the membrane and submembrane structures, began 2.7 hours after cell plating. Applying high-SP AFM to a 100 $\times$ 100 μm^{2}area, we found that the stiffness of the high sample regions decreased after thawing, reaching remarkably lower stiffness values than the low and middle regions of the sample. Since the high region contained the cell nucleus, this observation most likely reflected changes in the state of this part, in addition to the states of the cytoskeleton and membrane. This was supported by the nuclear envelope shrinkage recognized in $\sim$80% of the frozen/thawed cells by confocal microscopy. After 1.5 hours, the interaction of cell with the substrate was gradually built, and cell stiffness and height significantly decreased. Six hours after plating, the reconstruction of the inner parts of the cell probably began, as the cell height decreased and cell stiffness significantly increased. The change in frozen/thawed cell stiffness (measured by both high- and low-SP AFM) was much less pronounced in mitotically inactivated IR fibroblasts. This observation can be explained by an only marginal regeneration of the membrane, submembrane and inner parts of IR cells.

The cytoskeletons of never-frozen fibroblasts and frozen/thawed fibroblasts, both nonirradiated and irradiated, were observed by fluorescence microscopy, and the results were compared to the AFM results. Cell mechanical stiffness is determined by the cytoskeleton, particularly the networks of actin and intermediate filaments and their associated proteins [62], [84]. Fluorescence microscopy confirmed that the cytoskeletons of non-IR fibroblasts damaged by a freeze/thaw cycle are reconstructed after long-term plating. The *de novo* synthesis and massive remodeling of actin fibers were shown to be associated with elevated levels of disrupted fibers. This finding was confirmed by the decreased number of disrupted fibers in IR cells that did not undergo a freeze/thaw cycle. The thinner ventral stress fibers in the frozen/thawed IR cells may be explained by a lack of massive *de novo* synthesis and actin remodeling in IR cells, which is supported by the near absence of disrupted fibers.

To summarize, AFM nanoindentation allowed us to resolve the mechanical properties at different depths of cryopreserved cells (membrane, submembrane and inner parts) following a freeze/thaw cycle in both time and space. Fluorescence microscopy revealed that the substantial change in the cell membrane stiffness after freezing and thawing correlated with

the damage to the cytoskeleton in these cells, which was subsequently repaired. Using immunofluorescence confocal microscopy, we demonstrated post-thawing changes in the cell nucleus, showing shrinkage of the nuclear membrane, consistent with the decreased stiffness in the area of the cell nucleus. Applying the methods described here improves our understanding of the regeneration processes in frozen and thawed cells.

We also demonstrated that AFM can be used as a non-invasive method to find cells that have regenerated their mechanical properties with the proper dynamics and to the proper degree after thawing. This can be important in the area of assisted reproduction and in vitro fertilization processes (e.g., oocytes regeneration after freezing/thawing), as well as in proposed cell-based regeneration strategies that would require off-the-shelf availability of stock cells for prompt utilization. These stock cells will need to withstand long storage periods, typically in liquid nitrogen or similar media, after which their functional and structural properties will need to be tested.

REFERENCES

[1] K. Hayashi and M. Iwata, "Stiffness of cancer cells measured with an AFM indentation method," *J. Mech. Behav. Biomed. Mater.*, vol. 49, pp. 105–111, Sep. 2015.

[2] Y. Ding, G.-K. Xu, and G.-F. Wang, "On the determination of elastic moduli of cells by AFM based indentation," *Sci. Rep.*, vol. 7, Apr. 2017, Art. no. 45575.

[3] N. Guz, M. Dokukin, V. Kalaparthi, and I. Sokolov, "If cell mechanics can be described by elastic modulus: Study of different models and probes used in indentation experiments," *Biophys. J.*, vol. 107, no. 3, pp. 564–575, Aug. 2014.

[4] R. S. Fischer, K. A. Myers, M. L. Gardel, and C. M. Waterman, "Stiffness-controlled three-dimensional extracellular matrices for high-resolution imaging of cell behavior," *Nature Protocols*, vol. 7, no. 11, pp. 2056–2066, Nov. 2012.

[5] M. L. Gardel, K. E. Kasza, C. P. Brangwynne, J. Liu, and D. A. Weitz, "Chapter 19: Mechanical response of cytoskeletal networks," *Methods Cell Biol.*, vol. 89, pp. 487–519, Feb. 2008.

[6] X. Cai, X. Xing, J. Cai, Q. Chen, S. Wu, and F. Huang, "Connection between biomechanics and cytoskeleton structure of lymphocyte and Jurkat cells: An AFM study," *Micron*, vol. 41, no. 3, pp. 257–262, Apr. 2010.

[7] M. Golan *et al.*, "AFM monitoring the influence o f selected cryoprotectants on regeneration of cryopreserved cells mechanical properties," *Frontiers Physiol.*, vol. 9, p. 804, Jun. 2018.

[8] W. Xu, R. Mezencev, B. Kim, L. Wang, J. McDonald, and T. Sulchek, "Cell stiffness is a biomarker of the metastatic potential of ovarian cancer cells," *PLoS ONE*, vol. 7, no. 10, p. e46609, Oct. 2012.

[9] M. Desouza, P. W. Gunning, and J. R. Stehn, "The actin cytoskeleton as a sensor and mediator of apoptosis," *Bioarchitecture*, vol. 2, no. 3, pp. 75–87, 2012.

[10] A. Calzado-Martín, M. Encinar, J. Tamayo, M. Calleja, and A. S. Paulo, "Effect of actin organization on the stiffness of living breast cancer cells revealed by peak-force modulation atomic force microscopy," *ACS Nano*, vol. 10, no. 3, pp. 3365–3374, 2016.

[11] L. Z. Yanez, J. Han, B. B. Behr, R. A. R. Pera, and D. B. Camarillo, "Human oocyte developmental potential is predicted by mechanical properties within hours after fertilization," *Nature Commun.*, vol. 7, Feb. 2016, Art. no. 10809.

[12] B. J. Fuller, A. Y. Petrenko, J. V. Rodriguez, A. Y. Somov, C. L. Balaban, and E. E. Guibert, "Biopreservation of hepatocytes: Current concepts on hypothermic preservation, cryopreservation, and vitrification," *CryoLetters*, vol. 34, no. 4, pp. 432–452, Jul./Aug. 2013.

[13] P. Roca-Cusachs, V. Conte, and X. Trepat, "Quantifying forces in cell biology," *Nature Cell Biol.*, vol. 19, no. 7, pp. 742–751, Jul. 2017.

[14] Y. F. Dufrêne *et al.*, "Imaging modes of atomic force microscopy for application in molecular and cell biology," *Nature Nanotechnol.*, vol. 12, no. 4, pp. 295–307, Apr. 2017.

[15] S. Vahabi, B. N. Salman, and A. Javanmard, "Atomic force microscopy application in biological research: A review study," *Iranian J. Med. Sci.*, vol. 38, no. 2, pp. 76–83, 2013.

[16] B. G. Hosu, S. F. Mullen, J. K. Critser, and G. Forgacs, "Reversible disassembly of the actin cytoskeleton improves the survival rate and developmental competence of cryopreserved mouse oocytes," *PLoS ONE*, vol. 3, no. 7, p. e2787, Jul. 2008.

[17] G. Thomas, N. A. Burnham, T. A. Camesano, and Q. Wen, "Measuring the mechanical properties of living cells using atomic force microscopy," *J. Visualized Exp.*, vol. 76, p. 50497, Jun. 2013.

[18] A. X. Cartagena-Rivera, W.-H. Wang, R. L. Geahlen, and A. Raman, "Fast, multi-frequency, and quantitative nanomechanical mapping of live cells using the atomic force microscope," *Sci. Rep.*, vol. 5, Jun. 2015, Art. no. 11692.

[19] N. I. Nikolaev, T. Müller, D. J. Williams, and Y. Liu, "Changes in the stiffness of human mesenchymal stem cells with the progress of cell death as measured by atomic force microscopy," *J. Biomech.*, vol. 47, no. 3, pp. 625–630, Feb. 2014.

[20] R. Q. Ruan *et al.*, "Cell blebbing upon addition of cryoprotectants: A self-protection mechanism," *PLoS ONE*, vol. 10, no. 4, p. e0125746, Apr. 2015.

[21] I. Kratochvílová *et al.*, "Theoretical and experimental study of the antifreeze protein AFP752, trehalose and dimethyl sulfoxide cryoprotection mechanism: Correlation with cryopreserved cell viability," *RSC Adv.*, vol. 7, no. 1, pp. 352–360, 2017.

[22] D. Alsteens, V. Dupres, G. Andre, and Y. F. Dufrêne, "Frontiers in microbial nanoscopy," *Nanomedicine*, vol. 6, no. 2, pp. 395–403, Feb. 2011.

[23] L. Fekete, K. Kůsová, V. Petrák, and I. Kratochvílová, "AFM topographies of densely packed nanoparticles: A quick way to determine the lateral size distribution by autocorrelation function analysis," *J. Nanoparticle Res.*, vol. 14, no. 8, p. 1062, Aug. 2012.

[24] S. W. Chen *et al.*, "Nanoscale structural features determined by AFM for single virus particles," *Nanoscale*, vol. 5, no. 22, pp. 10877–10886, 2013.

[25] G. Ofek, D. C. Wiltz, and K. A. Athanasiou, "Contribution of the cytoskeleton to the compressive properties and recovery behavior of single cells," *Biophys. J.*, vol. 97, no. 7, pp. 1873–1882, Oct. 2009.

[26] K. D. Webster, A. Crow, and D. A. Fletcher, "An AFM-based stiffness clamp for dynamic control of rigidity," *PLoS ONE*, vol. 6, no. 3, p. e17807, Mar. 2011.

[27] M. Li, L. Liu, N. Xi, Y. Wang, X. Xiao, and W. Zhang, "Quantitative analysis of drug-induced complement-mediated cytotoxic effect on single tumor cells using atomic force microscopy and fluorescence microscopy," *IEEE Trans. Nanobiosci.*, vol. 14, no. 1, pp. 84–94, Jan. 2015.

[28] J. Mašek *et al.*, "Immobilization of histidine-tagged proteins on monodisperse metallochelation liposomes: Preparation and study of their structure," *Anal. Biochem.*, vol. 408, no. 1, pp. 95–104, Jan. 2011.

[29] N. C. Santos and M. A. R. B. Castanho, "An overview of the biophysical applications of atomic force microscopy," *Biophys. Chem.*, vol. 107, no. 2, pp. 133–149, Feb. 2004.

[30] A. Alessandrini and P. Facci, "AFM: A versatile tool in biophysics," *Meas. Sci. Technol.*, vol. 16, no. 6, pp. R65–R92, Jun. 2005.

[31] I. Kratochvílová *et al.*, "Theoretical and experimental study of charge transfer through DNA: Impact of mercury mediated T-Hg-T base pair," *J. Phys. Chem. B*, vol. 118, no. 20, pp. 5374–5381, May 2014.

[32] A. Touhami, B. Nysten, and Y. F. Dufrene, "Nanoscale mapping of the elasticity of microbial cells by atomic force microscopy," *Langmuir*, vol. 19, pp. 4539–4543, May 2003.

[33] D. J. Müller, J. Helenius, D. Alsteens, and Y. F. Dufrene, "Force probing surfaces of living cells to molecular resolution," *Nature Chem. Biol.*, vol. 5, no. 6, pp. 383–390, Jun. 2009.

[34] M. E. Dokukin, N. V. Guz, and I. Sokolov, "Quantitative study of the elastic modulus of loosely attached cells in AFM indentation experiments," *Biophys. J.*, vol. 104, no. 10, pp. 2123–2131, May 2013.

[35] I. Sokolov, M. E. Dokukin, and N. V. Guz, "Method for quantitative measurements of the elastic modulus of biological cells in AFM indentation experiments," *Methods*, vol. 60, no. 2, pp. 202–213, 2013.

[36] S. Sun, Z. Song, S. J. Cotler, and M. Cho, "Biomechanics and functionality of hepatocytes in liver cirrhosis," *J. Biomech.*, vol. 47, no. 9, pp. 2205–2210, Jun. 2014.

[37] M. Pesl *et al.*, "Forced aggregation and defined factors allow highly uniform-sized embryoid bodies and functional cardiomyocytes from human embryonic and induced pluripotent stem cells," *Heart Vessels*, vol. 29, no. 6, pp. 834–846, Nov. 2014.

[38] T. Bongiorno *et al.*, "Mechanical stiffness as an improved single-cell indicator of osteoblastic human mesenchymal stem cell differentiation," *J. Biomech.*, vol. 47, no. 9, pp. 2197–2204, Jun. 2014.

[39] C. Marlière and S. Dhahri, "An *in vivo* study of electrical charge distribution on the bacterial cell wall by atomic force microscopy in vibrating force mode," *Nanoscale*, vol. 7, no. 19, pp. 8843–8857, 2015.

[40] K. A. Melzak and J. L. Toca-Herrera, "Atomic force microscopy and cells: Indentation profiles around the AFM tip, cell shape changes, and other examples of experimental factors affecting modeling," *Microscopy Res. Techn.*, vol. 78, no. 7, pp. 626–632, Jul. 2015.

[41] J. L. Alonso and W. H. Goldmann, "Feeling the forces: Atomic force microscopy in cell biology," *Life Sci.*, vol. 72, no. 23, pp. 2553–2560, 2003.

[42] E. Henderson, P. G. Haydon, and D. S. Sakaguchi, "Actin filament dynamics in living glial cells imaged by atomic force microscopy," *Science*, vol. 257, no. 5078, pp. 1944–1946, Sep. 1992.

[43] J. Wang *et al.*, "Atomic force microscope study of tumor cell membranes following treatment with anti-cancer drugs," *Biosensors Bioelectron.*, vol. 25, no. 4, pp. 721–727, Dec. 2009.

[44] H. Oldenhof *et al.*, "Osmotic stress and membrane phase changes during freezing of stallion sperm: Mode of action of cryoprotective agents," *Biol. Reproduction*, vol. 88, no. 3, pp. 1–11, Mar. 2013.

[45] G. Benga *et al.*, "Comparative NMR studies of diffusional water permeability of red blood cells from different species: XVI Dingo (Canis familiaris dingo) and dog (Canis familiaris)," *Cell Biol. Int.*, vol. 34, no. 4, pp. 373–378, Apr. 2010.

[46] S. E. Cross, Y. S. Jin, J. Rao, and J. K. Gimzewski, "Nanomechanical analysis of cells from cancer patients," *Nature Nanotechnol.*, vol. 2, no. 12, pp. 780–783, Dec. 2007.

[47] K. Haase and A. E. Pelling, "Investigating cell mechanics with atomic force microscopy," *J. Roy. Soc. Interface*, vol. 12, no. 104, p. 20140970, Mar. 2015.

[48] J. B. Mandumpal, C. A. Kreck, and R. L. Mancera, "A molecular mechanism of solvent cryoprotection in aqueous DMSO solutions," *Phys. Chem. Chem. Phys.*, vol. 13, no. 9, pp. 3839–3842, 2011.

[49] A. Pietuch and A. Janshoff, "Mechanics of spreading cells probed by atomic force microscopy," *Open Biol.*, vol. 3, no. 7, p. 130084, Jul. 2013.

[50] D. H. Kim, B. Li, F. Si, J. M. Phillip, D. Wirtz, and S. X. Sun, "Volume regulation and shape bifurcation in the cell nucleus," *J. Cell Sci.*, vol. 128, no. 18, pp. 3375–3385, Sep. 2015.

[51] E. K. Dimitriadis, F. Horkay, J. Maresca, B. Kachar, and R. S. Chadwick, "Determination of elastic moduli of thin layers of soft material using the atomic force microscope," *Biophys. J.*, vol. 82, no. 5, pp. 2798–2810, 2002.

[52] N. Gavara and R. S. Chadwick, "Determination of the elastic moduli of thin samples and adherent cells using conical atomic force microscope tips," *Nature Nanotechnol.*, vol. 7, no. 11, pp. 733–736, Nov. 2012.

[53] D. Necas and P. Klapetek, "Gwyddion: An open-source software for SPM data analysis," *Central Eur. J. Phys.*, vol. 10, no. 1, pp. 181–188, 2012.

[54] *Mathematica*, Wolfram Res., Inc., Champaign, IL, USA, 2017.

[55] J. Šebera, S. Nešpurek, I. Kratochvílová, S. Záliš, G. Chaidogiannos, and N. Glezos, "Charge carrier mobility in sulphonated and non-sulphonated Ni phthalocyanines: Experiment and quantum chemical calculations," *Eur. Phys. J. B*, vol. 72, no. 3, pp. 385–395, Dec. 2009.

[56] G. G. Bilodeau, "Regular pyramid punch problem," *J. Appl. Mech.-Trans. Asme*, vol. 59, no. 3, pp. 519–523, Sep. 1992.

[57] P. Hermanowicz, M. Sarna, K. Burda, and H. Gabryś, "AtomicJ: An open source software for analysis of force curves," *Rev. Sci. Instrum.*, vol. 85, no. 6, p. 063703, Jun. 2014.

[58] M. Falk, E. Lukášová, and S. Kozubek, "Chromatin structure influences the sensitivity of DNA to γ-radiation," *Biochim. Biophys. Acta-Mol. Cell Res.*, vol. 1783, no. 12, pp. 2398–2414, Dec. 2008.

[59] F. Rico, P. Roca-Cusachs, N. Gavara, R. Farré, M. Rotger, and D. Navajas, "Probing mechanical properties of living cells by atomic force microscopy with blunted pyramidal cantilever tips," *Phys. Rev. E, Stat. Phys. Plasmas Fluids Relat. Interdiscip. Top.*, vol. 72, no. 2, p. 021914, Aug. 2005.

[60] N. Gavara and R. S. Chadwick, "Relationship between cell stiffness and stress fiber amount, assessed by simultaneous atomic force microscopy and live-cell fluorescence imaging," *Biomech. Model. Mechanobiol.*, vol. 15, no. 3, pp. 511–523, Jun. 2016.

[61] P. G. Haydon, R. Lartius, V. Parpura, and S. P. Marchese-Ragona, "Membrane deformation of living glial cells using atomic force microscopy," *J. Microscopy*, vol. 182, no. 2, pp. 114–120, May 1996.

[62] C. Rotsch and M. Radmacher, "Drug-induced changes of cytoskeletal structure and mechanics in fibroblasts: An atomic force microscopy study," *Biophys. J.*, vol. 78, pp. 520–535, Jan. 2000.

[63] K. Urayama, "An experimentalist's view of the physics of rubber elasticity," *J. Polymer Sci. B, Polymer Phys.*, vol. 44, no. 24, pp. 3440–3444, Dec. 2006.

[64] L. R. G. Treloar, *The Physics of Rubber Elasticity*. London, U.K.: Oxford Univ. Press, 1975.

[65] M. Mooney, "A theory of large elastic deformation," *J. Appl. Phys.*, vol. 11, no. 9, p. 582, 1940.

[66] R. W. Ogden, "Large deformation isotropic elasticity: On the correlation of theory and experiment for compressible rubberlike solids," *Proc. Roy. Soc. London A, Math. Phys. Eng. Sci.*, vol. 328, no. 1575, pp. 565–584, 1972.

[67] Y. C. B. Fung, "Elasticity of soft tissues in simple elongation," *Amer. J. Physiol.*, vol. 213, no. 6, pp. 1532–1544, 1967.

[68] H.-G. Kilian, K. Unseld, E. Jaeger, J. Müller, and B. Jungnickel, "Characterization of polyethylene networks based on the jointed description of melting, swelling and deformation," *Colloid Polymer Sci.*, vol. 263, no. 8, pp. 607–619, 1985.

[69] L. A. Mihai, L. Chin, P. A. Janmey, and A. Goriely, "A comparison of hyperelastic constitutive models applicable to brain and fat tissues," *J. Roy. Soc. Interface*, vol. 12, no. 110, p. 20150486, Sep. 2015.

[70] D. C. Lin, E. K. Dimitriadis, and F. Horkay, "Elasticity of rubber-like materials measured by AFM nanoindentation," *Express Polymer Lett.*, vol. 1, no. 9, pp. 576–584, Sep. 2007.

[71] D. Maugis, "Adhesion of spheres: The JKR-DMT transition using a dugdale model," *J. Colloid Interface Sci.*, vol. 150, no. 1, pp. 243–269, Apr. 1992.

[72] R. Notman, M. Noro, B. O'Malley, and J. Anwar, "Molecular basis for dimethylsulfoxide (DMSO) action on lipid membranes," *J. Amer. Chem. Soc.*, vol. 43, no. 128, pp. 13982–13983, Nov. 2006.

[73] A. A. Gurtovenko and J. Anwar, "Modulating the structure and properties of cell membranes: The molecular mechanism of action of dimethyl sulfoxide," *J. Phys. Chem. B*, vol. 111, no. 35, pp. 10453–10460, Sep. 2007.

[74] A. Janshoff, A. Kunze, S. Michaelis, V. Heitmann, B. Reiss, and J. Wegener, "Cell adhesion monitoring using substrate-integrated sensors," *J. Adhes. Sci. Technol.*, vol. 24, nos. 13–14, pp. 2079–2104, 2010.

[75] T. Kaneda, N. Sasaki, N. Urakawa, and K. Shimizu, "Endothelium-dependent and-independent vasodilator effects of dimethyl sulfoxide in rat aorta," *Pharmacology*, vol. 97, nos. 3–4, pp. 171–176, 2016.

[76] J. H. Buckingham and L. A. Staehelin, "The effect of glycerol on the structure of lecithin membranes; a study by freeze-etching and X-ray diffraction," *J. Microscopy*, vol. 90, pp. 83–106, Oct. 1969.

[77] M. E. Grady, R. J. Composto, and D. M. Eckmann, "Cell elasticity with altered cytoskeletal architectures across multiple cell types," *J. Mech. Behav. Biomed. Mater.*, vol. 61, pp. 197–207, Aug. 2016.

[78] Y.-W. Heng and C.-G. Koh, "Actin cytoskeleton dynamics and the cell division cycle," *Int. J. Biochem. Cell Biol.*, vol. 42, no. 10, pp. 1622–1633, Oct. 2010.

[79] R. Veselská and R. Janisch, "The effect of uv irradiation on changes in cytoskeleton and viability of mouse fibroblasts L929 cell line," *Scripta Med.*, vol. 73, no. 6, pp. 393–408, 2000.

[80] S. Pellegrin and H. Mellor, "Actin stress fibres," *J. Cell Sci.*, vol. 120, pp. 3491–3499, Oct. 2007.

[81] K. Bhadriraju and L. K. Hansen, "Extracellular matrix- and cytoskeleton-dependent changes in cell shape and stiffness," *Exp. Cell Res.*, vol. 278, no. 1, pp. 92–100, Aug. 2002.

[82] H. Chen and R. Han, "Characterization of actin filament dynamics during mitosis in wheat protoplasts under UV-B radiation," *Sci. Rep.*, vol. 6, Jan. 2016, Art. no. 20115.

[83] C.-Y. Chang, J.-D. Leu, and Y.-J. Lee, "The actin depolymerizing factor (ADF)/cofilin signaling pathway and DNA damage responses in cancer," *Int. J. Mol. Sci.*, vol. 16, no. 2, pp. 4095–4120, Feb. 2015.

[84] A. N. Ketene, P. C. Roberts, A. A. Shea, E. M. Schmelz, and M. Agah, "Actin filaments play a primary role for structural integrity and viscoelastic response in cells," *Integrative Biol.*, vol. 4, no. 5, pp. 540–549, 2012.

SCIENTIFIC REPORTS

OPEN

Chromatin architecture changes and DNA replication fork collapse are critical features in cryopreserved cells that are differentially controlled by cryoprotectants

Received: 17 April 2018
Accepted: 17 September 2018
Published online: 02 October 2018

Martin Falk[1], Iva Falková[1], Olga Kopečná[1], Alena Bačíková[1], Eva Pagáčová[1], Daniel Šimek[2], Martin Golan[2,3], Stanislav Kozubek[1], Michaela Pekarová[1], Shelby E. Follett[4], Bořivoj Klejdus[5,6], K. Wade Elliott[7], Krisztina Varga[7], Olga Teplá[8,9] & Irena Kratochvílová[2]

In this work, we shed new light on the highly debated issue of chromatin fragmentation in cryopreserved cells. Moreover, for the first time, we describe replicating cell-specific DNA damage and higher-order chromatin alterations after freezing and thawing. We identified DNA structural changes associated with the freeze-thaw process and correlated them with the viability of frozen and thawed cells. We simultaneously evaluated DNA defects and the higher-order chromatin structure of frozen and thawed cells with and without cryoprotectant treatment. We found that in replicating (S phase) cells, DNA was preferentially damaged by replication fork collapse, potentially leading to DNA double strand breaks (DSBs), which represent an important source of both genome instability and defects in epigenome maintenance. This induction of DNA defects by the freeze-thaw process was not prevented by any cryoprotectant studied. Both in replicating and non-replicating cells, freezing and thawing altered the chromatin structure in a cryoprotectant-dependent manner. Interestingly, cells with condensed chromatin, which was strongly stimulated by dimethyl sulfoxide (DMSO) prior to freezing had the highest rate of survival after thawing. Our results will facilitate the design of compounds and procedures to decrease injury to cryopreserved cells.

Application of cryopreservation to living cells and tissues has revolutionized biotechnology and modern medicine[1,2]. However, extensive damage occurs to a percentage of frozen and thawed cells and tissues. Though the freeze-thaw process can be greatly affected by the use of cryoprotective additives to improve cell viability[3,4], the effects of freezing and cryoprotectants *per se* on the complex status of cell nuclei (and the genetic information contained therein) remain controversial[4–7]. Contradictory results in the literature have prevented a consensus on the fundamental question of the extent of DNA and chromatin fragmentation that occurs during freezing and

[1]The Czech Academy of Sciences, Institute of Biophysics, Královopolská 135, CZ-612 65, Brno, Czech Republic. [2]The Czech Academy of Sciences, Institute of Physics, Na Slovance 2, CZ-182 21, Prague 8, Czech Republic. [3]Faculty of Mathematics and Physics, Charles University in Prague, Ke Karlovu 5, Prague 2, CZ-121 16, Czech Republic. [4]Department of Chemistry, University of Wyoming, 1000 E. University Ave, WY 82071, Laramie, USA. [5]Institute of Chemistry and Biochemistry, Faculty of Agronomy, Mendel University in Brno, Zemědělská 1, CZ-613 00, Czech Republic. [6]CEITEC-Central European Institute of Technology, Mendel University in Brno, Zemědělská 1, CZ-613 00, Brno, Czech Republic. [7]Department of Molecular, Cellular, and Biomedical Sciences, University of New Hampshire, 46 College Road, Durham, NH, 03824, USA. [8]ISCARE IVF a.s, Jankovcova 1692, CZ-160 00, Praha 6, Czech Republic. [9]VFN Gynekologicko-porodnická klinika, Apolinářská 18, CZ-120 00, Czech Republic. Correspondence and requests for materials should be addressed to M.F. (email: falk@ibp.cz) or I.K. (email: krat@fzu.cz)

thawing[8–11]. Moreover, even subtle changes to the chromatin structure can be expected to affect the viability and/or genetic information of freeze-thawed cells.

Concerning practical applications, it is very important to know which factors associated with freezing and thawing are responsible for the observed increase in the incidence of defects in live births resulting from *in vitro* fertilization[4,12–15]. Additionally, developments in the field of cryosurgery have the promise of positive therapeutic outcomes with few side effects in the treatment of certain cancers (e.g., skin, breast and liver)[16]. However, regarding the sensitivity of different cancer cells to low temperatures[17], there is a lack of deep understanding of the mechanisms underlying this phenomenon as few studies have sought to compare the responses of normal somatic cells and cancer cells to freezing and thawing. Normal (non-transformed) cells largely differ in their resistance to freezing and thawing; for example, oocytes are extremely cryosensitive[18]. The condition and status of chromatin are critical for cell survival and functioning as well as for the preservation of unchanged genetic information. Therefore, varying sensitivities of chromatin to cryodamage may be an important factor as to why different cells respond differently to the freeze-thaw process. This topic, however, requires further exploration.

In our previous work[3], we focused on the formation of ice during freezing as an important parameter that strongly influences cellular destruction and examined specific properties of selected cryoprotectant solutions during freezing, including dimethyl sulfoxide (DMSO), trehalose and a recombinant antifreeze fusion protein (AFP) that was originally isolated from the *Anatolica polita* desert beetle[2,3]. Building on this knowledge, here, we used these cryoprotectants to investigate the importance and extent of chromatin damage in freeze-thawed cells, specifically fragmentation and structural changes of chromatin. We described the post-freeze-thaw status of cells from two major perspectives: (i) the widely debated damage to DNA integrity, which can directly lead to death or genetic defects in cryopreserved cells, and (ii) the previously unexplored, less prominent alterations in the functional status of the higher-order chromatin structure and its impact on the viability of freeze-thawed cells.

In the present study, we correlate cell viability with freeze-thawed DNA integrity and chromatin states as explored by high-resolution confocal fluorescence microscopy and flow cytometry[19–23], and we are the first to identify novel critical attributes of chromatin damage, shedding new light on the mechanisms of freeze-thaw-induced chromatin alteration, consequent cell survival, and cryoprotection. DNA double strand breaks (DSBs) represent the most serious DNA lesions[20,21,24,25], but their induction through the freeze-thaw process remains controversial[26–29]. We have shown that freezing and thawing preferentially damage replicating (S-phase) cells by causing the collapse of replication forks, eventually leading to DSBs, thereby making rapidly dividing cells more sensitive to freeze damage. Excepting S-phase cells, in contrast to many earlier reports, we found that the freeze-thaw process does not directly induce DSBs; instead, it alters cells' higher-order chromatin structure. The results of the present study, which was performed on normal human skin fibroblasts (NHDFs) and mammary carcinoma cells (MCF7s), significantly enhance our understanding of the freezing process and its impacts on normal and cancer cells, which can contribute to the future rational design of cryofunctional materials and cryotherapy. NHDF and MCF7 cells were chosen as they 1) allow to compare behavior of normal and cancer cells, 2) differ in higher-order chromatin architecture[2] (which is relevant in the context of the present work) and 3) skin and breast cancers are often mentioned in literature as two of the preferred candidates for cryoablation[16].

Results

DNA integrity, double-strand break induction, and replication fork collapse in cryopreserved cells.

There is no consensus in the literature[6,30] regarding DNA double strand break (DSB) induction (chromatin fragmentation) in cells that have undergone freezing and thawing. We identified a new type of DNA lesion that is associated with freezing and thawing, that specifically appears in replicating (S-phase) cells and that can be labelled with γH2AX and 53BP1 antibodies. Nuclear patterns of γH2AX/53BP1 foci in affected cells co-localize with collapsed replication forks, which can be converted to DSBs. We also found extensive alterations of higher-order chromatin structure, even in non-S-phase freeze-thawed cells. However, non-S-phase cells did not suffer from increased DSB induction.

Using high-resolution immunofluorescence confocal microscopy to detect γH2AX and 53BP1 signals[31], which are the two accepted markers of DSBs, we compared DSB induction in frozen and thawed cells that had been cultured in standard medium (untreated cells) or in standard medium supplemented with cryoprotectants of different classes (AFP, trehalose, DMSO or trehalose + DMSO; Methods), which have different abilities to penetrate cells (or even the cell nuclei) and influence the chromatin status. Since γH2AX foci can be formed in the absence of DSBs[32], in parallel, we co-stained cells with an additional DSB marker, the protein 53BP1[33]. We also irradiated MCF7 and NHDF cells with 1 Gy or 2 Gy of γ-rays as a DSB positive control. This process resulted in the rapid development of relatively large γH2AX foci co-localized with the 53BP1 repair protein 30 min post-irradiation, showing extensive formation of γH2AX/53BP1 (DSB) foci with approximately 23 DSB/Gy/nucleus (Figs 1 and 2 and S1).

The cryoprotectants had minor effects on the viability of non-frozen cells (Table S1, Data 1, 2) and did not lead to increased DSB induction (Figs 3A and S1). As expected, the highest decrease in viability was found for trehalose or trehalose plus DMSO-treated (24 h incubation in trehalose + 5 min DMSO) MCF7 cells as they were also more sensitive to negative cryoprotectant viability effects than NHDF cells (Table S1, Data 1 and 2).

After freezing and thawing (−80 °C; rate of −1 °C/min), we identified important DNA defects that were associated with this process in both NHDF and MCF7 cells. A significant proportion (Table 1) of freeze-thawed cells exhibited a dramatically enhanced number of γH2AX/53BP1 foci (>30 to >100 foci/nucleus; Figs 1–3, S1). The nuclear patterns (number plus spatial distributions) of the γH2AX/53BP1 foci in cells with >30 to >100 γH2AX/53BP1 foci/nucleus were clearly different from the other freeze-damaged cells (Figs 1 and 2) and from cells exposed to γ-radiation (Figs 1 and S1). A careful inspection of images in 3D-space allowed us to sort cells with high numbers of γH2AX/53BP1 foci into three categories, as presented in Figs 2 and S2. Nuclei belonging to the first category contain approximately 100 or more small γH2AX/53BP1 foci dispersed throughout the nucleus. Nuclei in the second category have similar numbers of small γH2AX/53BP1 foci, but these foci are

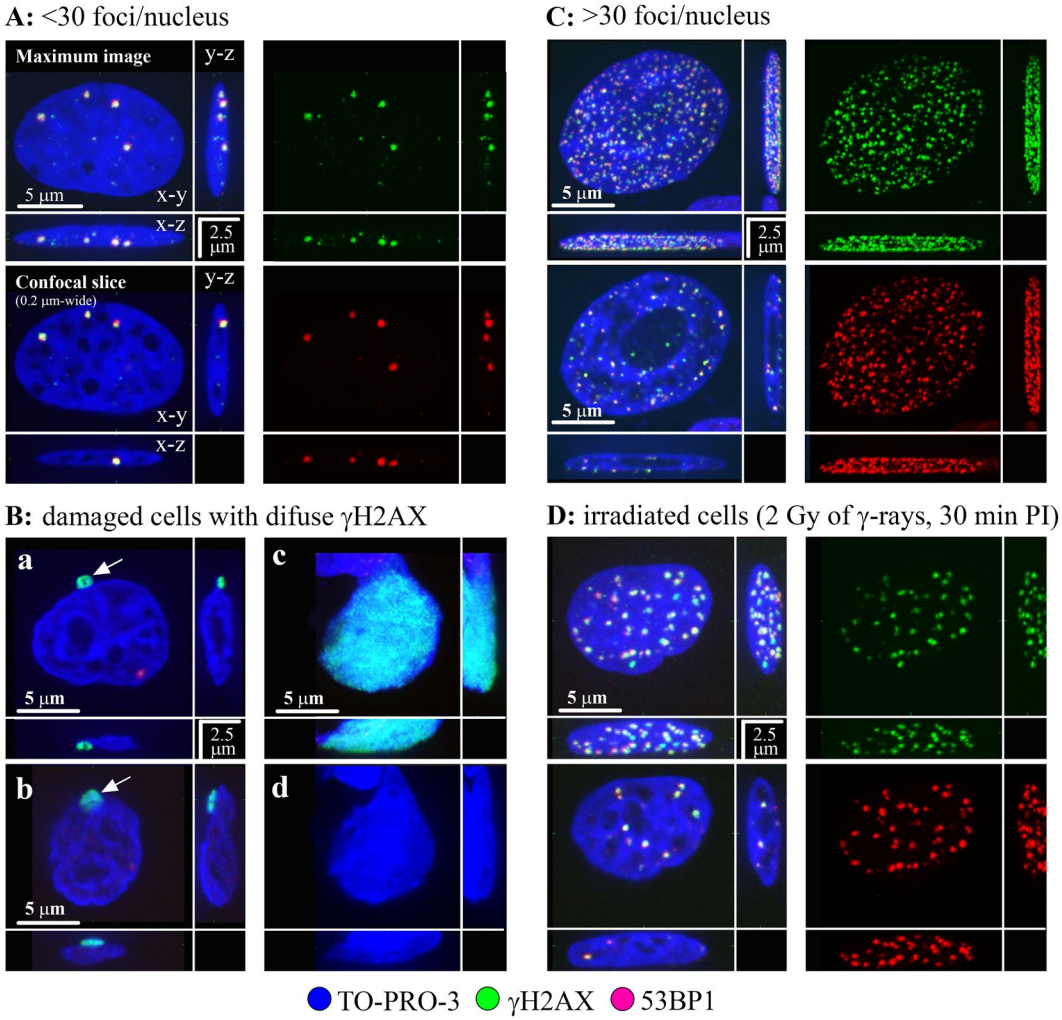

Figure 1. Three main categories (**A–C**) of MCF7 cells according to their γH2AX signal upon freezing/thawing. (**A**) The majority of cells remained unaffected by freezing/thawing in terms of DSB induction (category A, <30 γH2AX/53BP1 foci); the cells of this category were typical for DMSO-treated samples since in unprotected ones or those incubated with trehalose, a majority/substantial proportion of cells had damaged nuclei (**B**). In category (**B**) nuclei were stained with diffuse, localized (a,b) or pan-nuclear (c) γH2AX signals that did not colocalize with 53BP1. Cells with localized intense γH2AX signals largely preserved chromatin structure but with localized structure less chromatin protrusion(s) from the cell nucleus (white arrow). The chromatin structure of cells with pan-nuclear γH2AX was frequently altered (d), typically decondensed with complete loss of structure (panel d only shows chromatin staining). (**C**) A fraction of cells showed, for all cryoprotectant treatments, extremely high numbers of tiny γH2AX foci (green) that colocalized with 53BP1 protein foci (red) (category C, >30 γH2AX/53BP1 foci). The overall chromatin structure of these cells remained preserved, especially in cryopreserved samples. Preservation of higher-order chromatin structure for cells A and C is demonstrated in 3D confocal (0.3 μm-thick) images. (**D**) Formation of γH2AX/53BP1 foci at sites of DNA double strand breaks (DSBs) in MCF7 cells irradiated with 2 Gy of γ-rays (^{60}Co, 1 Gy/min) and visualized 30 min post-irradiation. γH2AX – green, 53BP1 – red, TO-PRO-3 (chromatin) – blue.

concentrated along the nuclear rim. Finally, nuclei in the third category show a mixture of 30 to 100 of both small and large γH2AX/53BP1 foci distributed along the nucleolus and irregularly throughout the rest of the nucleus. The γH2AX/53BP1 foci patterns in categories 1, 2 and 3 perfectly corresponded to those observed in early-, mid-, and late-S-phase (replicating) cells with collapsed (e.g., by camptothecin or topotecan) replication forks[34,35]. Our results thus show that the γH2AX foci (cells in categories 1–3) represent replication forks in S-phase cells that had collapsed upon freeze-thaw.

For never frozen and freeze-thawed cells, we directly compared the proportions of cells with >30 γH2AX /53BP1 foci/nucleus with the proportions of replicating (S-phase) cells, as determined by flow cytometry (PI staining) (Table 1, Fig. 4, and Data 3, 4). The number of never frozen S-phase cells was higher for faster-propagating MCF7 cells (approximately 13%) than for NHDF fibroblasts (approximately 8%) and remained nearly the same before and immediately (30 min) after freezing and thawing (Table 1, Fig. 4). Importantly, the S-phase cell fractions corresponded to the percentage of cells with >30 γH2AX/53BP1 foci in freeze-thawed cell populations. By

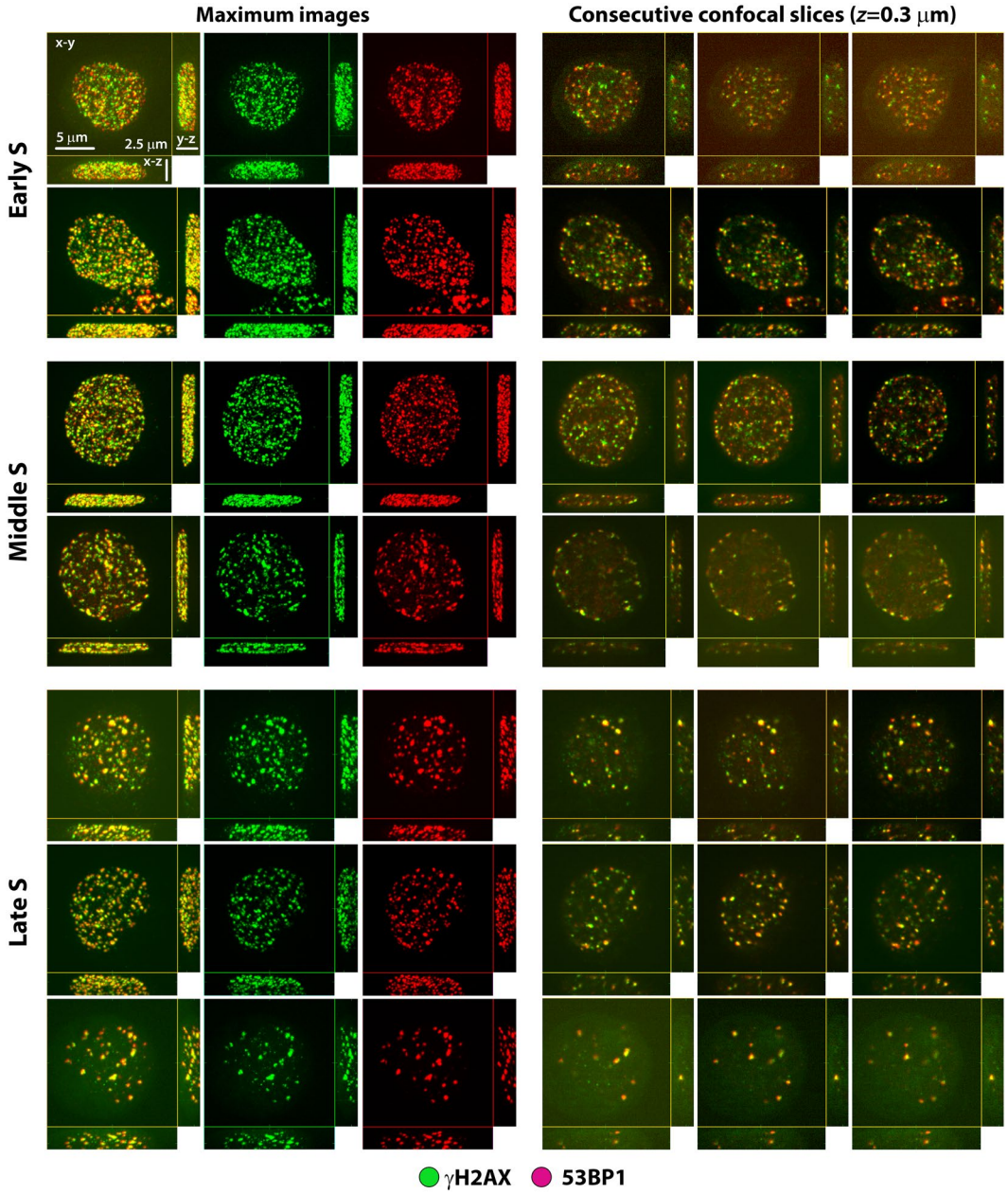

Figure 2. Three subcategories of MCF7 cells with increased numbers of γH2AX/53BP1 foci/nucleus after freezing/thawing, as determined using immunofluorescence confocal microscopy. Category 1 (top): nuclei with about >100 small γH2AX/53BP1 foci dispersed throughout the nucleus. Category 2 (middle): nuclei with >100 small γH2AX/53BP1 foci but distributed largely along the nuclear rim. Category 3 (bottom): nuclei with approximately 30 to 100 both small and large γH2AX/53BP1 foci distributed along the nucleolus and irregularly throughout the rest of the nucleus. There is evident similarity between the described γH2AX patterns (numbers and distribution) and the patterns of early (top), mid (middle), and late (bottom) S-phase replication (left captions). γH2AX foci (cells of category 1–3) thus seem to represent replication forks in S-phase cells collapsed upon freeze/thaw. 3D projections (x-y, x-z and y-z) of representative nuclei are shown for the composed of 40 confocal slices, each 0.3 μm thick (left column) and three consecutive single confocal slices, 0.3 μm thick (remaining columns). For maximum images, γH2AX (green) and 53BP1 (red) signals are also shown separately to demonstrate their mutual colocalization. Chromatin staining suppressed to improve the visibility of γH2AX/53BP1 foci.

contrast, the fraction of cells containing more than 30 γH2AX/53BP1 foci/nucleus was very rare (<1%) among never frozen MCF7 and NHDF cells, either treated or untreated with cryoprotectants (Table 1, Fig. 4). The substantial fraction of freeze-thawed cells with >30 γH2AX/53BP1 foci per nucleus, therefore, likely corresponds to S-phase cells with collapsed replication forks.

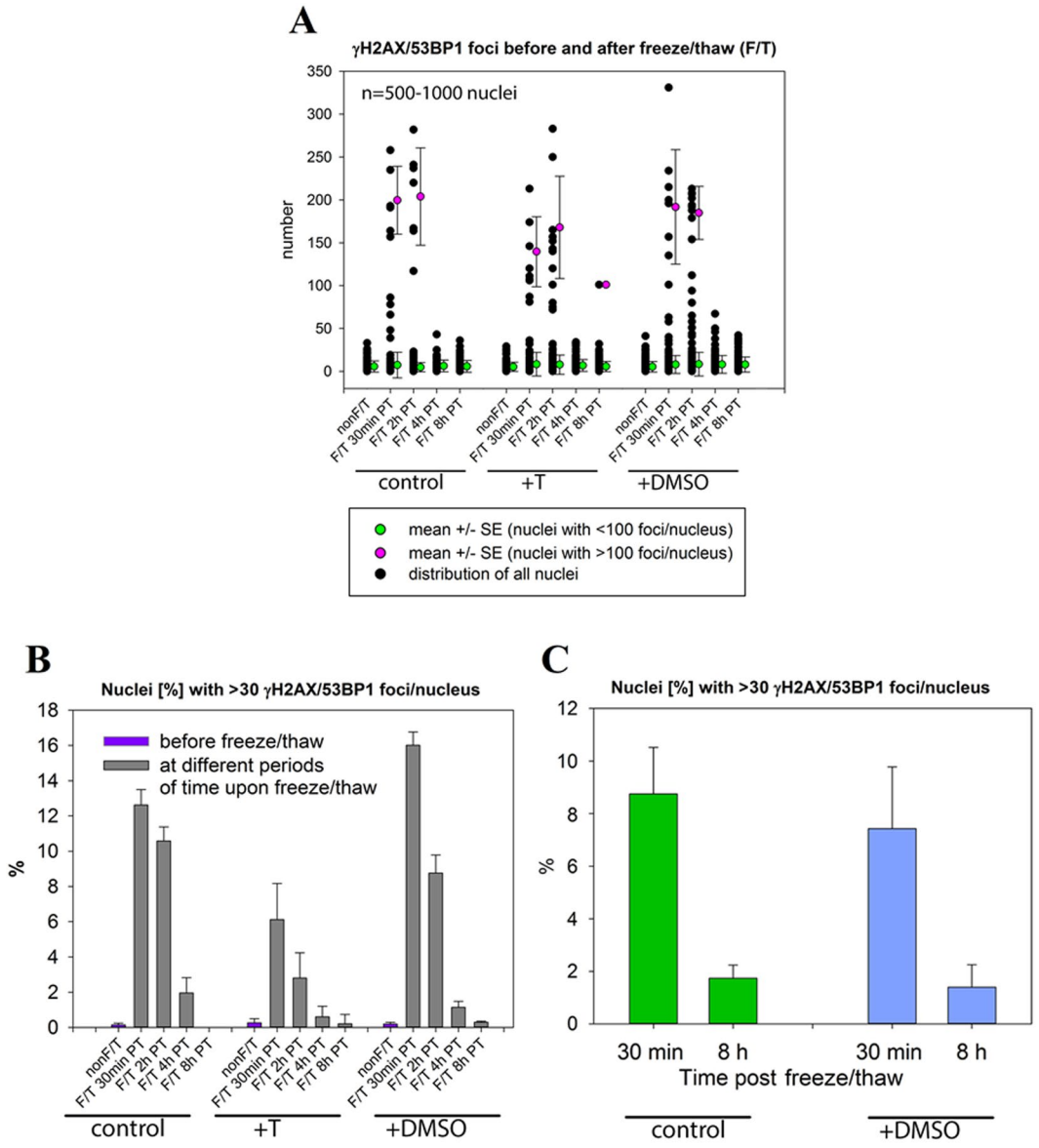

Figure 3. Distributions of γH2AX/53BP1 focus numbers per nucleus and proportions of cells with >30 γH2AX/53BP1 foci/nucleus in never frozen MCF7 cell samples and samples that were freeze-thawed with or without cryoprotectants. (**A**) Distributions of γH2AX/53BP1 focus numbers per nucleus before and in different periods of time after freezing/thawing. To emphasize presence of cells with "extreme" focus values (>100), the average numbers of γH2AX/53BP1 foci and their SDs were separately calculated for nuclei with <100 foci/nucleus (green circles) and >100 foci/nucleus (purple circles). For cells with <100 or <30 foci there is no statistically significant difference between the distributions of γH2AX/53BP1 foci/nucleus before and after freezing/thawing, irrespective of the cryoprotectant used (Kruskal-Wallis one way analysis of variance on ranks + Mann-Whitney rank sum test, $p < 0.05$ considered as significant). The fractions of cells with <100 or <30 foci/nucleus represented vastly dominant cell populations (i.e., approximately 93% or 86% of all cells), even in freeze-thawed cultures. Samples evaluated 30 min and 2 h post-freezing/thawing, which contain maximum numbers of cells with >100 foci/nucleus, were used for these calculations. Proportion [%] of MCF7 (**B**) and NHDF (**C**) cells with >30 γH2AX/53BP1 foci/nucleus determined prior to and in different periods of time after freezing/thawing. Results are compared for cells incubated or non-incubated with the indicated cryoprotectants. Horizontal axis – hours after the freeze/thaw cycle; N – never-frozen cells).

The γH2AX foci in cells with >30 γH2AX/53BP1 foci per nucleus colocalized with 53BP1 (Figs 1, 2, and S2), and in a parallel experiment, they also colocalized with proliferating cell nuclear antigen (PCNA) (Fig. 5), a key factor in DNA replication that is localized in the replication fork. These results confirmed the identification of γH2AX/53BP1 foci with collapsed replication forks in cells with >30 γH2AX/53BP1 foci. The proliferative status of these cells was further supported by immunofluorescence microscopy images of freeze-thawed MCF7 cells that were stained with anti-γH2AX and anti-Ki67 antibodies, which revealed preferential nucleolar Ki67-staining, as is typical of S-phase, in the majority of the cells with >30 γH2AX foci (Fig. 5).

Treatment	NHDF cells				MCF7 cells			
	Non-frozen		Freeze/thawed (30 min after F/T)		Non-frozen		Freeze/thawed (30 min after F/T)	
	Cells with > 30 foci (CM)	S-phase cells (FC)	Cells with > 30 foci (CM)	S-phase cells (FC)	Cells with > 30 foci (CM)	S-phase cells (FC)	Cells with > 30 foci (CM)	S-phase cells (FC)
Untreated	0.5 ± 0.2	8.2 ± 2.5	9.0 ± 0.5	7.7 ± 2.5	0.5 ± 0.2	13.4 ± 0.2	13.8 ± 2.1	14.3 ± 0.4
Trehalose	0.5 ± 0.2	5.5 ± 1.5	3.8 ± 0.2	4.4 ± 0.6	0.5 ± 0.2	8.0 ± 0.5	6.2 ± 2.2	9.5 ± 0.6
DMSO	0.5 ± 0.2	6.9 ± 1.7	5.2 ± 0.4	8.3 ± 1.6	0.5 ± 0.2	14.7 ± 1.2	16.0 ± 2.0	15.8 ± 0.3
DMSO + trehalose	0.5 ± 0.2	5.3 ± 2.2	4.0 ± 0.2	5.3 ± 1.5	0.5 ± 0.2	7.3 ± 0.5	7.3 ± 2.3	10.2 ± 0.6

Table 1. Fractions [%] of NHDF and MCF7 cells with >30 γH2AX/53BP1 foci before freezing and after freezing/thawing compared to the fraction [%] of S-phase cells. Results for the indicated cryoprotectant treatments are shown. The fractions of cells with >30 γH2AX/53BP1 foci were determined using immunofluorescence confocal microscopy (CM) prior to and 30 min after freezing/thawing. S-phase cells were quantified at the corresponding times by flow cytometry with propidium iodide (PI) staining. Values represent the means and standard errors.

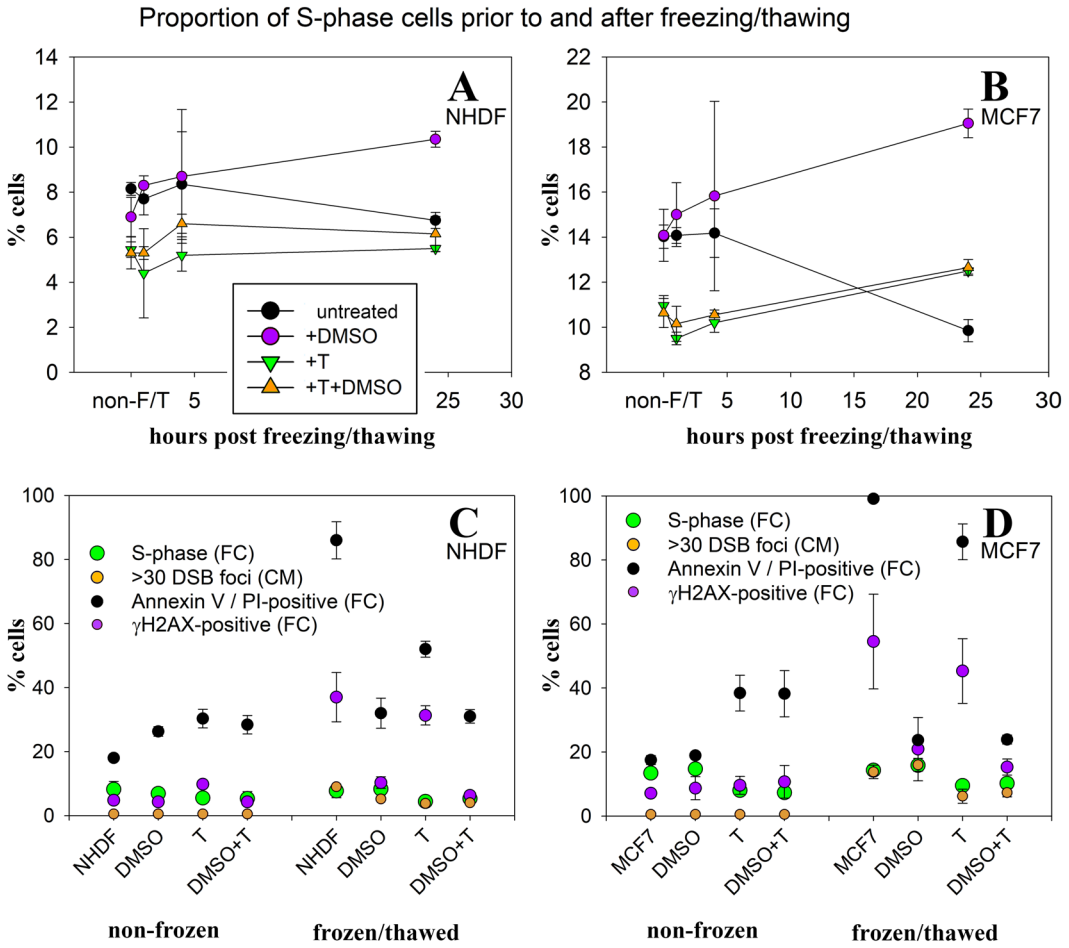

Figure 4. Fractions [%] of S-phase NHDF **(A)** and MCF7 **(B)** cells before freezing and at different time periods after freezing/thawing, determined by flow cytometry (PI staining), for the indicated cryoprotectant treatments. Dish-attached cells and cells released into culture media were included into the analyses. Fractions [%] of NHDF **(C)** and MCF7 **(D)** cells with >30 γH2AX/53BP1 foci, determined using immunofluorescence confocal microscopy (CM) prior to and 30 min after freezing/thawing (F/T), are compared to flow cytometric fractions of S-phase cells, γH2AX-positive cells and Annexin V/PI-positive cells quantified using flow cytometry (FC) prior to and 30 min after F/T. S-phase cells were identified using propidium iodide (PI) staining to show DNA content. Values represent the means and standard errors (see Table S1 for all the values).

Cryoprotectants added to the cell cultures prior to freezing and thawing did not influence the susceptibility of cells to replication fork collapse (Fig. 3, Table S1). Only trehalose reduced the proportion of freeze-thawed cells with >30 γH2AX/53BP1 foci; however, this cryoprotectant exerted the same effect on the total number of S-phase cells, both in never frozen and freeze-thawed cells (Fig. 4).

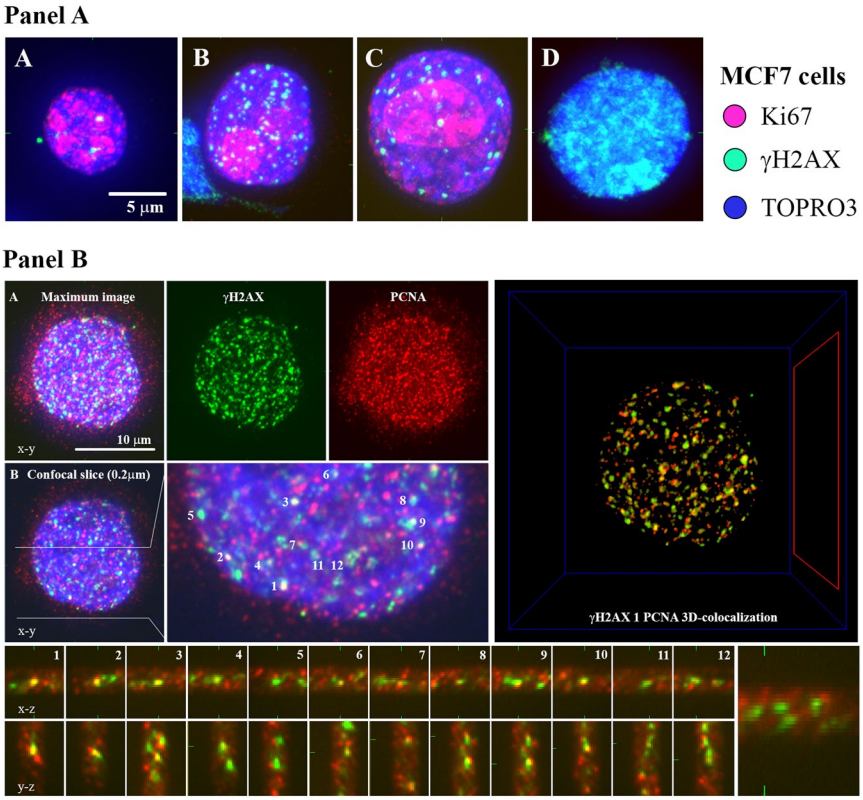

Figure 5. Cells with >30 γH2AX/53BP1 foci are S-phase cells with collapsed replication forks. Panel (A) Immunofluorescence microscopy of freeze-thawed MCF7 cells, stained with anti-γH2AX (green) and anti-Ki67 (red) antibodies, demonstrates the S-phase status of the cells with >30 γH2AX foci. (**A**) Cell nuclei with <30 γH2AX foci mostly showed jaguar-like patterns of Ki67 distribution typical of G1-phase or nucleolar staining with nucleoplasmic staining typical of G2-phase. (**B**,**C**) Cell nuclei with >30 γH2AX foci predominantly showed intense nucleolar Ki67-staining as typical for S-phase cells. (**D**) Most nuclei with pan-nuclear γH2AX staining (apoptotic or disintegrated nuclei) showed no Ki67 signal. Maximum projection images composed of approximately 40 confocal slices, each 0.3 μm thick, are displayed. Chromatin was counterstained with TO-PRO-3 (artificially colored blue). Panel (B) Immunofluorescence microscopy of frozen/thaw MCF7 cells, stained with anti-γH2AX (green) and PCNA (red) antibodies, demonstrates the colocalization of γH2AX foci with replication forks (PCNA) in cells containing >30 γH2AX foci. (**A**) Maximum projection images (composed of approximately 40 confocal slices, each 0.3 μm thick), showing patterns for anti-γH2AX and anti-PCNA antibodies, merged and separately. (**B**) Same as (A) but only showing the central confocal slice. The right panel displays an enlarged view of the colocalization of γH2AX and PCNA signals in the x-y plane. Detailed 3D colocalization for twelve γH2AX foci indicated in (panel B, bottom). Software-generated 3D-colocalization for all γH2AX and PCNA foci (panel B, right; Acquiarium software). Chromatin was counterstained (where relevant) with TO-PRO-3 (artificially colored blue).

Regardless of the cryoprotectant used, the number of cells exhibiting >30 γH2AX/53BP1 foci/nucleus decreased at 8 h after freezing and thawing (Fig. 3), indicating that a proportion of S-phase cells with collapsed replication forks either repaired their lesions (with potential consequences to genetic information due to misrepair) or died due to extensive damage (Fig. 4). During the post-thaw period, damaged S-phase cells were replaced by new cells entering the S-phase. In the post-thaw period, the portion of S-phase cells decreased only in the untreated control (Fig. 4). Unprotected cells, therefore, suffer from other (or additional, in case of S-phase cells) types of serious (chromatin) damage.

In addition to immunofluorescence microscopy (Fig. 4, Table S1), we quantified γH2AX-fluorescence using flow cytometry, which provided us with a broad view of chromatin defects in a statistically relevant number of cells. All freeze-thawed samples showed higher fractions of cells with increased γH2AX-fluorescence compared to never frozen cells, for both normal human skin fibroblasts and MCF7 mammary carcinoma cells. The highest increase (up to approximately 40%, 30 min after thawing) appeared in unprotected controls; these values were lower in trehalose-treated samples and were lowest in cells treated with DMSO or a combination of trehalose + DMSO. Flow cytograms of cells stained for γH2AX are shown in Data 5 and 6.

A comparison of the confocal microscopy and flow cytometry provided some interesting results. The relative number of S-phase cells with >30 γH2AX/53BP1 foci/nucleus was strongly correlated with the relative number of all γH2AX-positive cells, as determined by flow cytometry of cells frozen and thawed with DMSO (Fig. 4, Table S1). By contrast, the proportion of (damaged) replicating cells with >30 γH2AX/53BP1 foci was much

lower than the proportion of all cells positive for γH2AX (by flow cytometry) in cells frozen and thawed with no cryoprotectant or with trehalose. In these cultures, microscopy revealed numerous cells with higher-order alterations in chromatin structure (TO-PRO-3 staining), chromatin protrusions (stained with γH2AX but not 53BP1) (Figs 1 and S3), or completely disintegrated chromatin, eventually manifested as pan-nuclear γH2AX fluorescence (Figs 1 and S4).

In summary, S-phase cells exhibited collapsed replication forks after freezing and thawing, which could not be prevented by any of the cryoprotectants studied. Collapsed replication forks thus represent the dominant type of damage in cryopreserved cells (DMSO or trehalose + DMSO), in which other effects of the freeze-thaw process on chromatin are minimized, as described in the following chapter. Hence, larger proportions of rapidly dividing cell populations, such as embryos and cancer cells, are more prone to freeze-thaw-induced DNA damage and eventual death compared to more slowly dividing cells[36–38]. However, a small fraction of damaged S-phase cells can survive the freeze-thaw process with collapsed replication forks. This condition, potentially more frequent in cancer cells for several reasons (e.g., higher proliferation, resistance to cell death, genomic instability), threatens the quality of the genome, even if these errors are not converted into DSBs[36,37,39].

Higher-order chromatin structure in cryopreserved cells. Next, we examined other important sources of defects that affect genetic information maintenance in cryopreserved cells — higher-order chromatin structure changes. The higher-order chromatin structure plays an important role in the regulation and maintenance of fundamental cellular processes, such as DNA transcription, replication and repair. It can also be considered to be a summarized representation of the epigenetic cell status. We compared chromatin texture (degradation of chromatin domains) and chromatin condensation before and after freezing and thawing (−80 °C; rate of −1 °C/min) in cells cultured in standard medium or in media containing cryoprotectants (AFP, DMSO, trehalose, and trehalose + DMSO; Methods).

To clarify the relationship between the chromatin state (Figs 6 and S5) and viability of cells upon freezing and thawing, we statistically quantified the changes in chromatin for each cryoprotectant and compared them with cell viability (Table S2, Fig. 7), as assessed by flow cytometry (Fig. S6, Data 1, 2). We performed these measurements at 30 min and 24 h (Table S2, Fig. 7) post-thaw to evaluate immediate cell damage resulting from freezing and thawing (disintegration, necrosis, etc.) and to potentially observe additional cell dying from delayed apoptosis, respectively. In the present study, all the viability values were obtained with a new software (Guava InCyte, Methods) allowing us more precise analyses. First, we used the same gates in all experiments, and second, in all cases, we excluded cell debris more precisely (as compared to RSC Adv.)[3]. The same gating and the same style of debris exclusion is extremely important to correctly evaluate viability of freeze-thawed cells because many of these cells are more or less fragmented. With the software used in RSC Adv[3]. (MUSE machine original software) this was not feasible.

First, we analyzed the effects of the cryoprotectants on never frozen cells (Fig. 7, Table S2). As quantified for NHDF fibroblasts, never frozen cells incubated with trehalose or AFP exhibited an uninfluenced chromatin structure with the proportion of cells with condensed nuclear chromatin (~20–25%) similar to that of the untreated control, i.e., never frozen cells without cryoprotectants (~17%).

By contrast, application of DMSO to never frozen NHDF cells caused extensive chromatin condensation in approximately 57% of cells, which was a 40% increase compared to the control.

The quantitative effects of freezing and thawing on the nuclei of untreated and cryoprotectant-treated NHDF and MCF7 cells are summarized in Fig. 7 and Table S2. Freezing and thawing of untreated cells caused serious chromatin damage (largely decondensed, disrupted chromatin structure) that was detrimental to cell survival–roughly 14% of untreated cells survived the freeze-thaw process (Figs S6 and S7 Data 1, 2).

To objectively quantify the level and statistical occurrence of chromatin structure and condensation among the observed cell nuclei, in addition to performing visual inspections of chromatin in large sets of cells, we calculated a 2D Fourier transform (Suppl. Info.) in polar coordinates from a single (central) 2D section of the 3D image z-stack. To discriminate nuclei with condensed chromatin, the best criterion appeared to be the first momentum of the middle frequency of the Fourier-transformed data component (Fig. S8). The discrimination criterion was 7.5×10^{-6} (where unity is the zero frequency maximum). Typical trehalose- and AFP-treated condensed chromatin cells were close to the boundary defined by the first momentum of the middle frequency of the Fourier-transformed data between condensed and standard or disintegrated chromatin, while typical DMSO-treated cells were farther from this condensation border.

Cryoprotectants had a significant effect on the chromatin structure and cell survival upon freezing and thawing (Fig. 7, Table S2). First, we describe the results for NHDF fibroblasts. AFP exerted the smallest effect on chromatin condensation and NHDF cell survival (approximately 35%) among the cryoprotectants studied. Due to its large molecular size, the effect of AFP is restricted to the extracellular space, where it binds to ice crystals, thus mitigating cell damage caused during the freezing process. AFP was studied only with NHDF fibroblasts due to a lack of this unique material.

Regarding DMSO, the freeze-thaw process further increased chromatin condensation that was already induced by this compound prior to freezing. The proportion of cells with condensed chromatin was 73% of DMSO-treated cells and increased to 83% of cells when DMSO was applied in combination with trehalose. Importantly, these values correlated well with the viability (i.e., the annexin V/PI negativity) of cells 30 min and 24 h after thawing. Approximately 68% of DMSO-treated cells survived freezing and thawing, while only 14% of untreated cells survived.

The high cryoprotective efficiency of DMSO could be, to a large extent, attributed to the ability of the small DMSO molecules to penetrate into cells and nuclei. Therefore, unlike many other cryoprotectants, DMSO can affect the freeze-thaw process directly in the cell nucleus and efficiently protect this vital organelle and chromatin (Table S2).

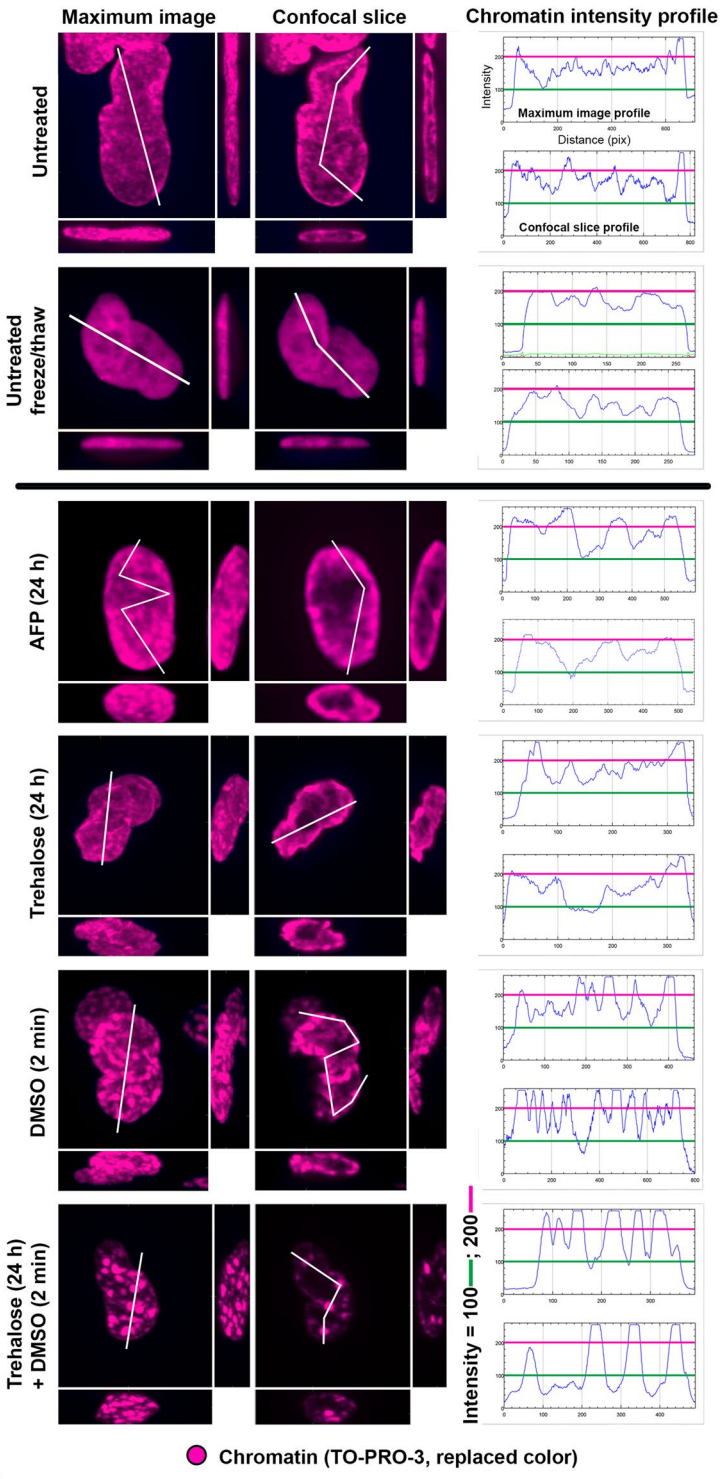

Figure 6. Effects of a freeze/thaw cycle on the higher-order chromatin structure of NHDF fibroblasts in the presence of cryoprotectants. Top row: untreated control cells that were not frozen. Other rows: cells frozen in the presence of the indicated cryoprotectant. 'Maximum images' are composed of 40 superimposed 0.3-μm thick confocal slices and are shown with x-z and y-z projections (left columns). The left columns present single confocal slices (0.3-μm thick) through the central nuclear plane with x-z and y-z projections. Chromatin was counterstained with TO-PRO-3 (blue or violet to better visualize the chromatin structure). Right column: intensity profiles of the violet (chromatin) channel along the demarcated paths (white lines) drawn above the maximum images and confocal slices of the cell nuclei. Each profile path was chosen to include nuclear areas with the maximum and minimum chromatin (violet) intensity. The intensity profiles show differences in the nuclear chromatin 'texture' and chromatin condensation; RFU [0–255] indicates relative fluorescence. Violet and green lines, which correspond to RFU = 100 and RFU = 200, respectively, are shown to facilitate comparisons. Images were acquired 30 min after thawing.

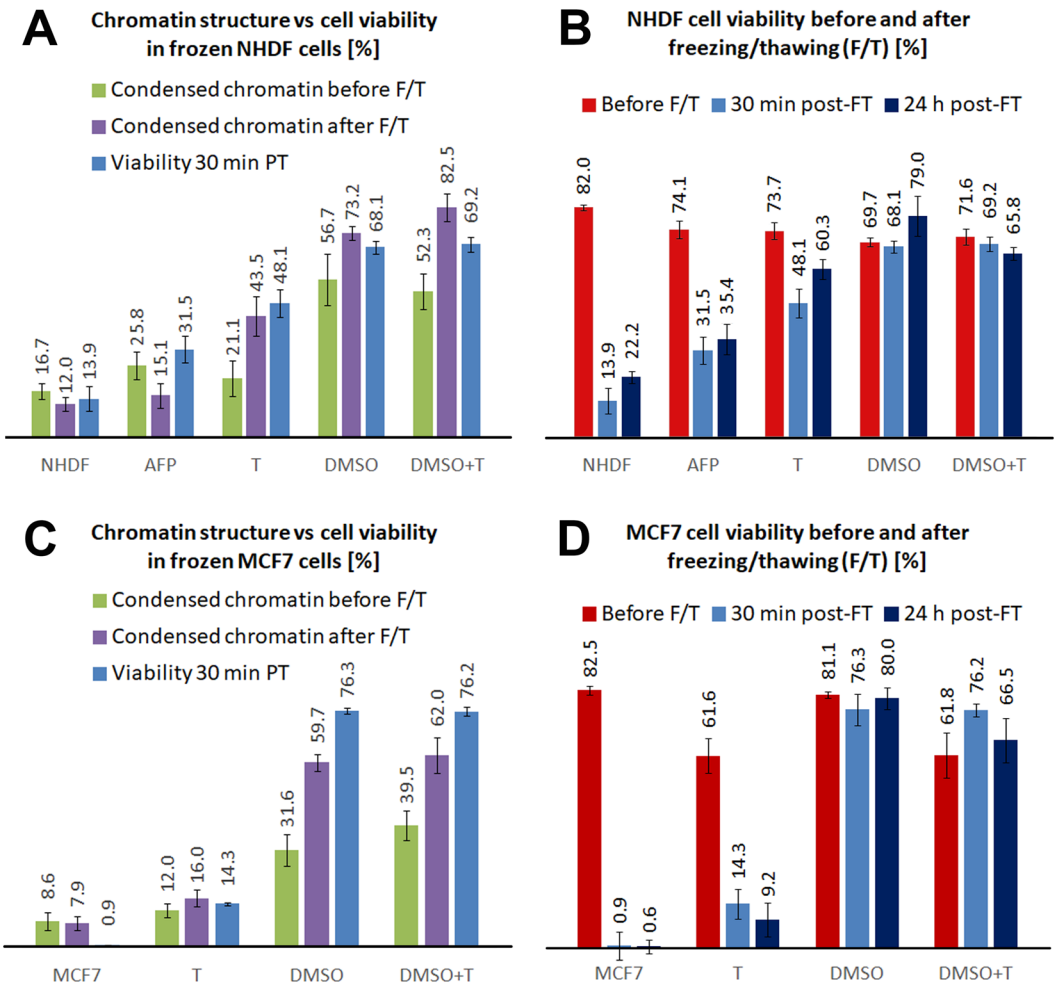

Figure 7. Effects of cryoprotectants on the chromatin structure of NHDF fibroblasts (**A**) and MCF7 cells (**C**) after a freeze/thaw (F/T) cycle. For freeze-thawed cells, the levels of chromatin condensation were correlated with the cryoprotective effects of cryoprotectants, quantified as the proportion of surviving (24 h after thawing) cells identified by flow cytometry (Annexin V/7-AAD staining). (**B**,**D**) Survival of NHDF fibroblasts (**B**) and MCF7 cells (**D**) compared for 30 min and 24 h after freezing/thawing. AFP was only used with fibroblasts due to the lack of this unique material.

Finally, trehalose had an intermediate effect on freeze-thawed NHDF cells, inducing chromatin condensation in 44% of cells. This value was again close to the 30 min post-thaw cell survival rate of 48% in trehalose-treated cells. Importantly, when trehalose was applied for shorter periods of time (4 or 6 h), the freeze-thawed cell survival remained practically unaffected. The survival of NHDF cells was improved only when trehalose was applied for 24 h. This observation indicates that trehalose penetrates cells, but does so slowly. To further support this hypothesis, we analyzed the phenomenon using several mass spectrometry techniques (LC-MS/MS, DART and DESI). The LC-MS/MS results, which demonstrate and quantify the presence of trehalose in the filtered lysates of both cell types under study, are summarized in Fig. S9. DART successfully confirmed the identity of the trehalose peaks detected by LC-MS/MS. We further demonstrated the penetration of trehalose into intact cells using DESI with NHDF fibroblasts and two of the trehalose concentrations in the culture medium, as illustrated in Fig. S10. Trehalose in the cell cytoplasm affects the osmolarity in different cellular subcompartments, such as the nucleus, and therefore also affects the chromatin structure, which is in contrast to the solely extracellular effect of AFP.

In parallel, we performed the same set of experiments with MCF7 cells (Fig. 7, Table S2). Untreated MCF7 cells showed chromatin condensation at approximately half the rate of untreated NHDF fibroblasts (8.6% vs. 16.7%, respectively) before freezing and thawing. In accordance with the results for NHDF fibroblasts, only DMSO induced chromatin condensation in never frozen MCF7 cells. Among freeze-thawed MCF7 cells, we found about 60% of DMSO-treated cells and less than 8% of untreated cells had condensed chromatin. According to the annexin V/PI positivity results (Fig. 7 and Table S2), approximately 76% and 80% of DMSO-treated MCF7 cells survived for 30 min and 24 hours, respectively, after freezing and thawing, which markedly contrasted with the less than 1% survival rate of untreated MCF7 cells. Trehalose exerted an insignificant effect on chromatin condensation in MCF7 cells upon freezing and thawing. Chromatin condensation in these cells appeared only in ~16% of cells (44% in NHDF cells) and was less visually obvious than in NHDF fibroblasts treated with the same cryoprotectant

(compare Figs 6 and S5). According to the annexin V/PI positivity results, trehalose-treated MCF7 cells had 14% survival at 30 min after freezing and thawing, which slightly decreased 24 hours later (Fig. 7). Unlike in NHDF fibroblasts, the combined treatment of DMSO and trehalose did not further increase either chromatin condensation (62%) (Fig. 7) or cell survival (76% and 67% at 30 min and 24 h post-thaw, respectively) (Figs S6 and S7) compared with the DMSO-only treatment (Table S2). MCF7 cell nuclei condensation upon cell incubation with cryoprotectants (studied before and after freeze/thaw) is shown in Fig. S11. DMSO was the treatment leading to highest nucleus condensation and smallest damage.

In contrast to surviving cells that had condensed chromatin, cells with decondensed chromatin were frequently stained, locally or pan-nuclearly, with a diffuse γH2AX fluorescence that was not colocalized with 53BP1 signal (Fig. 1) and indicated cell death. Cells with this type of γH2AX signal increased in number with the post-thawing time, except for the DMSO-treated sample, which had a consistently low percentage of these cells (Fig. S4). To evaluate the effects of chromatin condensation on thawed cell survival from the other effects of the cryoprotectants, we investigated the impact of a short pre-freezing incubation on the higher-order chromatin structure and cell viability using cells in media with different osmolarities (hypertonic, hypotonic and isotonic) (Fig. S12). Freeze-thawed cells treated with hypertonic medium showed the strongest chromatin condensation and the highest (approximately 40%) cell viability compared to the other osmolarities. On the other hand, the hypotonic pretreatment of non-frozen cells induced slight chromatin hypocondensation compared to the isotonic pretreatment. Upon freezing and thawing, the viability of hypotonic-treated cells was similar to that (below 10%) of cells frozen and thawed in normal (isotonic) medium. This further supports our assumption that chromatin condensation plays a positive role in improving cell survival during cryopreservation.

We conclude that the viability of NHDF and MCF7 cells upon freezing and thawing is strongly positively correlated with condensation of chromatin structure. Chromatin condensation is influenced by cryoprotective compounds to varying extents.

Altogether, non-replicating and replicating (S-phase) cells both suffer from non-DSB chromatin damage, i.e., more or less obvious changes in the higher-order chromatin structure, which can be efficiently reduced by DMSO and, to a lesser extent, by trehalose. Viability measurements at later periods of time after freezing and thawing (24 h) support the inference that chromatin condensation, provoked by cryoprotectants and protective of cells during freezing and thawing, does not negatively influence cell survival over the long term. S-phase cells, in addition, face replication fork collapse, potentially leading to the induction of multiple DSBs. However, further study is required regarding the influence of both DSB damage and non-DSB chromatin damage on genetic and epigenetic information.

Discussion

Chromatin represents a critical target for cryodamage and cryoprotection. Recent progress in our understanding of chromatin biology has revealed that this material not only preserves genetic information but also plays important roles in the regulation and maintenance of fundamental cellular processes, such as DNA transcription, replication and repair. In this respect, the chromatin structure is of the utmost importance since it represents a unified manifestation of the epigenetic cell status and directly or indirectly influences the interactions of DNA and proteins. The status of cryopreserved freeze-thawed cells can be evaluated from two basic viewpoints: a) susceptibility of chromatin to the induction of DSBs, which can lead to genetic defects in freeze-thawed cells or to chromatin fragmentation (cell death), and b) susceptibility of chromatin to (epigenetic) alterations of its structure, with potential consequences on the expression of genetic information.

The relationship between an altered chromatin structure and carcinogenesis has been described in our earlier work, which revealed the presence of alterations in the higher-order chromatin structure in histologically normal tissue that was adjacent to the tumor[40]. Additionally, Leffak[41] linked the amplification of repetitive sequences, which is the mechanism responsible for the development of numerous neurodegenerative diseases, to the repair of collapsed replication forks.

In the present study, we shed new light on the highly debated chromatin fragmentation of cryopreserved cells. Rather than the expected extensive induction of DSBs in the majority of cells undergoing the freeze-thaw processes[11,29], we identified alterations in the higher-order chromatin structure, the extent of which was cryoprotectant-dependent. Moreover, for the first time, we described a new type of chromatin damage associated with freezing and thawing that is specific to S-phase cells and could not be mitigated by any of the cryoprotectants used in this study. The damage consists of extensive collapse of the replication forks, which could be potentially converted into DSBs[42–44]. Taken together, these findings may help explain why some studies have identified extensive chromatin disintegration upon freezing and thawing[11] while others report only conditional chromatin fragmentation (e.g., in defective sperm)[7] or the complete absence of DSB formation[8,9,45] (reviewed in[5,10]). Furthermore, by identifying new fundamental attributes of cryodamage in NHDF and MCF7 cells, we describe important implications for cell cryoprotection and cryoablation.

With regard to DNA double strand breaks, we found that only approximately 14% of MCF7 and 9% of NDHF freeze-thawed cells exhibited an enhanced number of γH2AX/53BP1 foci, which is in contrast to numerous studies[42–44,46–48]. Importantly, these cells contained a minimum of 30 γH2AX/53BP1 foci/nucleus, but they typically had more than 100. The pattern of γH2AX/53BP1 foci in freeze-thawed cell nuclei corresponds to the patterns of the replication sites in S-phase cells, suggesting that cells with >30 γH2AX/53BP1 foci per nucleus represent replicating (S-phase) cells with collapsed replication forks, potentially leading to DSBs and genetic defects, as previously mentioned. The S-phase status of affected cells was further confirmed by the Ki67 patterns that are characteristic of the S-phase that were expressed by a majority of these cells and, more specifically, by the colocalization of γH2AX foci with the PCNA antigen (localized to replication sites). The total size of the S-phase subpopulations did not significantly change before and after the freeze-thaw process. Notably, MCF7 and NHDF cells that had >30 γH2AX/53BP1 foci/nucleus before freezing and thawing represented less than 0.5% of cells.

These results suggest that S-phase cells are intact before freezing, but almost all experience a massive collapse of replication forks when they are freeze-thawed. Localization of 53BP1 to sites of stalled or broken replication forks, as observed in the present study, has been previously reported[49].

The proportion of freeze-thawed NHDF and MCF7 cells with >30 γH2AX/53BP1 foci/nucleus was analyzed for various cryoprotectant treatments. DMSO treatment did not have a significant effect either on the proportion of total S-phase cells or on the number of S-phase cells with >30 γH2AX/53BP1 foci/nucleus. By contrast, in agreement with previous studies[50,51], long (24 h) trehalose treatment somewhat inhibited cell division, i.e. decreased the total fraction of S-phase cells compared with that of untreated or DMSO-cryopreserved NHDF and MCF7 cell samples, even prior to freezing. To a comparable extent, trehalose also reduced the number of cells with >30 γH2AX/53BP1 foci/nucleus after freezing and thawing. This observation further confirms that cells with >30 γH2AX/53BP1 foci/nucleus were in the S-phase and suggests that the collapse of replication forks during freezing and thawing could not be prevented by any of the cryoprotectants studied.

The reduced incidence of cells with >30 γH2AX/53BP1 foci/nucleus among normal NHDF fibroblasts after the freeze-thaw process likely reflects their lower replication activity relative to cancerous MCF7 cells. As freezing and thawing preferentially and more seriously damages S-phase cells, rapidly dividing cells, such as tumors and embryos, are likely to be more sensitive to DNA cryodamage. To the best of our knowledge, this finding has not yet been reported. Replication-induced DSBs may extensively accumulate especially in cancer cells that frequently exhibit defects in DNA repair, particularly in homologous recombination[42,52].

Next, we investigated changes in the epigenetic chromatin structure as another potential form of DNA damage in NHDF and MCF7 cells that had undergone a freeze-thaw cycle. Cells in standard culture medium with no added cryoprotectants exhibited chromatin structure alterations similar to cells in hypotonic medium when exposed to a freeze-thaw cycle. The majority of chromatin decondensed to varying extents, which frequently correlated with damage of the nuclear envelope (preliminary results). By contrast, DMSO stimulated chromatin condensation in never frozen NHDF and MCF7 cells, and chromatin remained condensed after thawing. Accordingly, cells of both types incubated with DMSO had the highest viabilities after thawing. The lower tendency of MCF7 cells to form condensed chromatin compared to NHDF fibroblasts may be explained by the differing levels of native chromatin condensation in untreated, never frozen NHDF and MCF7 cells[2]. It should be noted that chromatin condensation naturally appears in prometaphase cells along with mitotic chromosomes formation. Hence, unwanted cell synchronization induced by freeze/thaw processes or the cryoprotectants *per se* can theoretically increase the fraction of prometaphase cells with highly condensed chromatin. Nevertheless, except of the already described decrease of S-phase cells, we did not recognize any significant change in the cell cycle distribution after freezing/thawing. Moreover, our measurements of chromatin condensation were performed at 30 minutes after thawing, which is, in any case, very short period of time to experience manifestation of any alterations of the cell cycle. Therefore, chromatin condensation provoked in the present study by freezing/thawing can be attributed to cryoprotectant- and freeze/thaw-invoked processes independent of the cell cycle, as described below.

AFP and trehalose had only minor impacts on chromatin condensation prior to freezing and thawing. Trehalose molecules do not penetrate into the nucleus, and large AFP molecules protect cells only from the extracellular space[53]. Compared to the DMSO treatment, lower amounts of AFP- and trehalose-treated freeze-thawed cells had condensed chromatin and survived the freeze-thaw cycle. These results thus suggest that chromatin condensation is very important for protecting cells against damage during the freeze-thaw processes.

To test the importance of chromatin condensation on the viability of freeze-thawed cells separately from any additional effects of cryoprotectants (e.g., nuclear envelope stabilization, ROS sequestration, etc.), we treated NHDF cells with hypertonic and hypotonic media prior to freezing and thawing. The hypertonic treatment, which condensed chromatin, significantly reduced the adverse effects of freezing and thawing on NHDF cells compared to the hypotonic treatment, which decondensed chromatin. Moreover, cryoprotectant-induced chromatin condensation that protected cells during freezing and thawing did not have negative effects on the long-term (24 h) survival of these cells. Based on these results, we propose that chromatin condensation provoked prior to freezing is less destructive to higher-order chromatin structure than the abrupt condensation that takes place as a consequence of cellular dehydration during freezing. The condensed chromatin state reduces damage to the chromatin structure during freezing and prevents the loosening and dispersion of chromatin during the hypotonic shock induced by cell rehydration after thawing. Further chromatin condensation that occurs as a consequence of freezing *per se* is related to dehydration of the nucleus and chromatin, which leads to an increase in the intracellular concentration of ions. This condition, in turn, likely further stabilizes the condensed chromatin state and higher-order chromatin structure during freezing and thawing. Since condensed chromatin is largely surrounded by neighboring chromatin molecules and chromatin-bound proteins, it is better protected from the destructive effects of ice formation, and thus its integrity is preserved. Nevertheless, the possible effects of chromatin structure changes on the epigenetic cell status remain to be determined.

Based on these results, we propose two hypotheses as a possible mechanism of freeze-thaw-induced replication fork collapse: 1. The freeze-thaw process generates large amounts of reactive oxygen species (ROS) that extensively induce single-strand DNA breaks[54]. When the replication fork encounters this lesion, its progression is stopped and the fork may collapse and eventually be converted into a DSB. 2. Replication forks, which are sensitive to mechanical stress, may also be directly damaged by chromatin structure changes provoked by the freeze-thaw cycle. This latter explanation appears to be more probable (or more important) since DMSO, an efficient ROS scavenger[55], does not reduce the number of collapsed replication forks. Indeed, in some experiments, the number of γH2AX/53BP1 foci that were colocalized with replication forks was higher in samples freeze-thawed with DMSO than in unprotected controls. This may suggest that chromatin condensation, provoked by the freeze-thaw process and further stimulated by DMSO, is harmful to the replication forks.

The literature provides differing conclusions regarding cell survival upon extensive replication fork damage[42–44,46–48]; therefore, it is difficult to predict the fate of freeze-thawed cells affected by this damage, particularly if the cells suffer from additional types of chromatin alterations. For instance, Dixon and colleagues described[56] impaired DNA damage signaling and repair in cells exposed to hyperosmolar microenvironments, which caused chromatin condensation. Chromatin condensation, as observed in the present study after cell freezing and thawing, can therefore potentially decrease the efficiency of collapsed replication fork repair and increase the induction of mutations or cell death. In any case, it is reasonable to propose that a fraction of damaged S-phase cells can survive the freeze-thaw cycle, even with collapsed replication forks. Current evidence suggests that multiple mechanisms are used to repair replication damage, yet these mechanisms can have deleterious consequences on genome integrity[57]. This worsens the condition of the genetic information, even if these aberrations are not converted into DSBs. Mechanisms of how stalling DNA replication forks can promote either epigenetic or genetic changes were recently reviewed by Rowlands *et al.*[58] and Leffak[41], respectively.

In summary, the present study is the first to show that replicating (S-phase) cells are strongly affected by the collapse of replication forks during freezing and thawing. These collapsed forks may develop into DSBs. Rapidly dividing cell populations, such as tumors and embryos, may thus be more sensitive to this type of damage. The collapse of replication forks in S-phase cells was not prevented by any cryoprotectant studied. In addition to replication fork collapse, both replicating and non-replicating cells suffered from non-DSB chromatin damage, i.e., freeze-thaw-induced alterations of the chromatin structure and/or secondary chromatin fragmentation in cells with disintegrated or apoptotic nuclei, which could be efficiently reduced by DMSO and, to a lesser extent, by trehalose. Cells with strongly condensed chromatin prior to freezing had the highest rate of survival after freezing.

Cryoprotectants added to the culture media before freezing and thawing stabilized the nuclear integrity to varying extents and ensured sufficient cell amounts surviving the freeze-thaw process, but none of these factors protected S-phase cells from freeze-thaw-induced collapse of the replication forks.

Both collapsed replication forks and epigenetic structural chromatin damage may affect genetic information[39,59] and can lead to defects in live births after *in vitro* fertilization. Taken together, these results provide a deeper understanding of the freezing process in cells, particularly its effect on cell nuclei, revealing potential risks associated with cell freezing but also facilitating the rational design of cryofunctional compounds and cryoprotective procedures.

Methods and Materials

Cells and cell culture. Certified normal human foreskin fibroblasts (NHDF) and human breast adenocarcinoma cells (MCF7) were obtained from CLS Cell Lines Service GmbH (Eppelheim, Germany), cultivated in DMEM medium (PAN Biotech, Aidenbach, Germany, cat. no: P03–0710), supplemented with 10% fetal calf serum (PAA Laboratories GmbH, Pasching, Austria) and 1% penicillin + streptomycin (stock solution mixture 10 000 U/mL penicillin + 10 mg/mL streptomycin; PAN Biotech, cat. no.: P06–07100), at 37 °C in a humidified atmosphere of 5% CO_2. The cells obtained (at passage 2) were freshly defrost, multiplied, and used for experiments in low passages (about 5–7) to prevent possible effects of senescence on chromatin structure and cell functions.

Cryoprotectants and cells freezing. Human fibroblasts and MCF7 cells were frozen down to −80 °C using a gradient of −1 °C/min in culture media (unprotected controls) or in culture media supplemented with particular cryoprotectant. The following concentrations of cryoprotectants were used in indicated concentrations: DMSO −10% (w/w), trehalose −3.2% (w/w) (i.e. 100 mM), DMSO + trehalose −10% (w/w) +3.2% (w/w) (i.e. 100 mM), and AFP (TrxA-ApAFP752) −0.5 $mg.ml^{-1}$. D-(+)-trehalose dihydrate and DMSO were purchased from Sigma-Aldrich, AFP protein was prepared as described below. Cryoprotectants were injected to culture media of cryopreserved cells 24 h (AFP, trehalose) or 2 min (DMSO) prior to freezing. To prevent cytotoxicity of DMSO, DMSO-containing samples (DMSO and DMSO + trehalose) were cooled to 4 °C before adding DMSO to cells; also the remaining samples were precooled in the same way and then submitted to the freezing procedure. For the indicated treatments, the cryoprotectants had only minor effects on the viability of non-frozen cells as described in Results.

Expression and purification of recombinant TrxA-ApAFP752 fusion protein. The recombinant plasmid pET32b-*Apafp752* was transformed into *Escherichia coli* Rosetta-gami 2(DE3) or BL21 (DE3)pLysS competent cells (Novagen). A single transformed colony was used to inoculate 25 mL of Luria-Bertani (LB) medium containing 0.3 mM ampicillin and cultured overnight at 37 °C and shaken at 225 rpm. 4 mL of the overnight culture was transferred into 1 L of fresh LB medium with 0.3 mM ampicillin and grown at 37 °C and 225 rpm until the optical density at 600 nm (OD_{600}) reached 0.6–0.7. The culture was induced with 1 mL of 400 mM isopropanol -1-thio-β-D-galactopyranoside (IPTG), to cause over-expression of TrxA-ApAFP752, for 8 hours at 25 °C. The cells were harvested by centrifugation (20 minutes, 8700 g, 4 °C) and stored at −80 °C until purification.

The cell pellet was resuspended with ice-cold binding buffer (EDTA-free Halt™ protease inhibitor cocktail (Fisher), 50 mM sodium phosphate, 150 mM NaCl, 20 mM imidazole and Benzonase nuclease (Millipore) at pH 8.0) and lysed using a French press (1300 psi). The lysate was collected and centrifuged (20 minutes, 27200 g, 4 °C) to remove the cell debris. The supernatant was filtered through a 0.22 μm syringe-driven filter (Millipore) and concentrated to 5 mL before being purified by Fast Protein Liquid Chromatography (FPLC; GE Healthcare ÄKTA purifier 900) equipped with a HisTrap HP Ni-NTA column (GE Healthcare). The sample was loaded into the Ni-NTA column, washed with washing buffer (50 mM sodium phosphate, 150 mM NaCl, 20 mM imidazole at pH 8.0), and eluted with the same buffer containing 500 mM imidazole through a gradient elution. The fractions were pooled and dialysed in sodium phosphate buffer (50 mM sodium phosphate, 150 mM NaCl at pH 8.0) for 2 hours, then switched to fresh buffer and left overnight. The purity of the sample was analysed by 12.5% SDS-PAGE and

stained with Coomassie blue; TrxA-ApAFP752 has a molecular weight of 27 kDa and was compared to a stained protein ladder (BioRad). Additional purification steps were taken to obtain a pure sample and SDS-PAGE was used after each step to analyse the purity. The sample was divided into three fractions that were each concentrated to 1 mL and run through a Superdex 75 10/300 GL size exclusion column (GE Healthcare) equilibrated with sodium phosphate buffer. Fractions that were still not pure were run through a Ni-NTA column and dialysed for a second time. Once the desired purity was obtained, the sample was buffer exchanged into a $K_xH_YPO_4$ buffer (50 mM potassium phosphate, 20 mM NaCl, and 1 mM NaN_3 at pH 8.0). The concentration was estimated using UV-Visible spectrophotometry at 280 nm with the calculated extinction coefficient of 19,575 $M^{-1}cm^{-1}$. The sample was concentrated to 1 mL and lyophilized overnight. For further experiments, the protein was rehydrated as needed and buffer exchanged.

Irradiation. Cells were irradiated in the culture medium at 37 °C from a ^{60}Co source (Chisostat, Chirana, Prague, Czech Republic) with a dose of 1 Gy or 2 Gy (γH2AX/53BP1 foci immunofluorescence) or 5 Gy (flow cytometry); the dose rate was 1.0 Gy/min. During the irradiation, the cells were kept in a thermostable box, ensuring a constant temperature and prevention from infection during the whole procedure. After irradiation, the cells were immediately placed back into the incubator (37 °C/5% CO_2) until the fixation.

γH2AX phosphorylation by flow cytometry. Flow cytometry was used to quantify γH2AX phosphorylation in cells that were frozen with or without cryoprotectants. The Muse Cell Analyser (Merck Millipore) and Muse H2A.X Activation Dual Detection Kit (MCH200101, Merck Millipore), which discriminate between H2AX (−)/γH2AX (−) vs. H2AX (+)/γH2AX (−) vs. H2AX (−)/γH2AX (+) and H2AX (+)/γH2AX (+) cells, were used according to the manufacturer's instructions. The cell state was analysed 1 h and 4 h after the cells were thawed.

Cell cycle by flow cytometry. The Muse Cell Analyser (Merck Millipore) and Muse Cell Cycle Assay Kit (MCH100106) were used according to the manufacturer's instructions (download at http://www.merckmillipore.com/CZ/cs/product/Muse-Cell-Cycle-Assay-Kit,MM_NF-MCH100106#anchor_DS). In the present study, all the viability values were obtained with new software (Guava InCyte soft. 3.1.1., Millipore) allowing us more precise analyses. We used the same gates in all experiments and, in all cases, we excluded more precisely cell debris (compared to RSC Adv.)[3]. The same gating and the same style of debris exclusion is extremely important to correctly evaluate viability of freeze-thawed cells because many of these cells are more or less fragmented. With the software used in RSC Adv[3]. (MUSE machine original software) this was not possible.

Immunostaining. DSBs were quantified by high-resolution confocal microscopy as foci showing dual co-localization of γH2AX and 53BP1; together, these proteins are generally accepted as DSB markers[14]. The proteins were visualized using a mouse monoclonal antibody against H2AX phosphorylated at serine 139 (γH2AX) (dilution 1:500; Upstate) and with a rabbit polyclonal antibody against 53BP1 (dilution 1:500; Upstate). The maximum DSB signals typically appeared about 30 min post-DSB induction[21]. Hence, after complete thawing, the cells were maintained for an additional 30 min in the incubator (37 °C, 5% CO_2) in fresh pre-heated (37 °C) DMEM medium supplemented with 10% FCS to allow full development of the foci. Secondary antibodies, namely, affinity-purified donkey anti-mouse-FITC-conjugated antibody (dilution 1:100) and affinity-purified donkey anti-rabbit-Cy3-conjugated antibody (dilution 1:200) (ImmunoResearch Laboratories, West Grove, PA), were used to visualize the primary antibodies. The immunostaining procedure was performed as described in *et al.*[19] and Sevcik *et al.*[60] with minor modifications. The nuclear envelope (Fig. S5) was stained with anti-lamin A/C monoclonal mouse antibody (dilution 1:1000; Sigma-Aldrich). Nuclear chromatin was counterstained with 1 μM TO-PRO-3 (Molecular Probes, Eugene, USA) in 2 × saline sodium citrate (SSC) prepared fresh from a stock solution. After the cells were briefly washed in 2 × SSC, the samples were mounted using Vectashield medium (Vector Laboratories, Burlingame, CA, USA).

Cell survival (flow cytometry and Trypan blue exclusion assay). Flow cytometry was used to quantify survival and apoptosis in cells that were frozen with or without cryoprotectants. The Muse Cell Analyser (Merck Millipore) and Muse Annexin V & Dead Cell Assay Kit (MCH100105, Merck Millipore), which discriminate between Annexin V (+)/Propidium Iodide (+) (live) vs. Annexin V (+)/Propidium Iodide (−) vs. Annexin V (−)/Propidium Iodide (+) and Annexin V (−)/Propidium Iodide (−) cells, were used according to the manufacturer's instructions. The cell state was analysed 30 min or 24 h after the cells were thawed. Trypan blue exclusion assay was used according to standard protocol as an alternative method to determine the cell survival. TC20 Automated Cell Counter was used.

Confocal microscopy and data analysis. Effects of the treatments were directly analysed on the microscopic slides under the microscope (about 500–2000 cells) and/or on acquired 3D images (>50 cells) (below). Two replicas of microscopic slides for each sample were directly evaluated by two experienced scientists. The following equipment was used for confocal microscopy and image acquisition: an automated Leica DM RXA fluorescence microscope (Leica, Wetzlar, Germany) equipped with an oil immersion Plan Fluotar objective (100×/NA1.3) and a CSU 10a Nipkow disc (Yokogawa, Japan); a CoolSnap HQ CCD-camera (Photometrix, Tuscon, AZ, USA); and an Ar/Kr-laser (Innova 70 C Spectrum, Coherent, Santa Clara, CA, USA)[23]. Automated exposure, image quality control and other procedures were performed using Acquarium software[24]. The exposure time and the dynamic range of the camera in the red, green and blue channels (R-G-B) were adjusted to the same values for all slides to obtain quantitatively comparable images. Forty serial optical sections were captured at 0.3-μm intervals along the z-axis.

Chromatin condensation quantification by the 2D Fourier transform. In addition to analyses using the intensity profiles from the red, green and blue (R-G-B) channels (R: 53BP1; G: γH2AX; B: TO-PRO3, chromatin) described in the previous paragraph, chromatin condensation was also evaluated by the 2D Fourier transform. From a single 2D section (from a 2D projection) of chromatin (blue channel) observed in the confocal microscope, the 2D Fourier transform in polar coordinates was calculated. Results (correlation coefficients) calculated from confocal microscopy data for DMSO + trehalose, DMSO, trehalose, AFP and untreated were used as criterion for chromatin condensation (sufficiently strong and sharp middle frequency component of the signal). Further details see Suppl. Inf.

Quantification of DSB induction, changes in higher-order chromatin structure and nuclear envelope integrity. The presence and number of γH2AX/53BP1 foci and other γH2AX signals, as well as co-localization of γH2AX and 53BP1 in the nuclei, was determined visually. Changes in higher-order chromatin structure (condensation) after a freeze/thaw cycle were quantified using the intensity profiles from the red, green and blue (R-G-B) channels (R: 53BP1; G: γH2AX; B: TO-PRO3, chromatin) using the 'RGB Profile Plot' plugin for ImageJ 1.47 v software (Wayne Rasband, NIH USA, http://imagej.nih.gov/ij) in addition to visual inspection of 3D microscopic images of nuclei and their confocal slices in all three planes. Intensity profiles along line segments demarcated over 0.2-m thick confocal slices of nuclei were determined separately for the R-G-B channels. Each line segment was designed to cover a substantial part of the nucleus and to include nuclear areas showing maximum and minimum chromatin staining. Sharp changes in high amplitude chromatin staining intensity along the line segment indicate structurally and functionally distinct chromatin domains that are well preserved after the freeze/thaw procedure. By contrast, the absence of these changes in chromatin intensity along the line segment (i.e., only slight and slow changes) indicates extensive erosion in the higher-order chromatin structure. Intensive G-peaks (γH2AX) that co-localized with R-peaks (53BP1) mark DSBs. A continuous γH2AX signal that is more constant in intensity and that is not accompanied by a 53BP1 signal indicates apoptotic/necrotic DNA damage. Evaluation of the shape of cell nuclei (maximum area, roundness factor) was determined using the 'selection' and 'analysis' tools in Adobe Photoshop CS6. Narrowing or disruptions in the nuclear lamina, as visualized using a lamin A/C antibody, plus chromatin (TO-PRO3) leakage out of the nucleus was interpreted as indicating damage to the nuclear envelope.

Formation of medium with different osmolarities and cells treatments. All procedures have been described in[19]. The osmolarity of standard culture medium is 290 mOsm. To induce reversible artificial chromatin condensation, the cells were incubated for 12 min in hyperosmotic (570 mOsm) medium. Hyperosmotic (hypertonic) medium was prepared by addition of 1 ml 20 × PBS (2.8 M NaCl, 54 mM KCl, 130 mM Na_2PO_4, 30 mM KH_2PO_4, pH 7.4) to 19 ml DMEM containing 10% FCS. Hypocondensed chromatin in cells was obtained by cell treatment (12 min) in hypoosmotic (hypotonic) medium. Hypoosmotic medium of about 140 mOsm was obtained by diluting standard DMEM medium with an equal quantity of sterile ddH2O. Since chromatin condensation and decondensation started within seconds, washing in physiological salt solution before cell fixation (immuno-fluorescence microscopy) was strictly avoided. For flow cytometry analyses of cell viability, a post-treatment (hypertonic or hypotonic) cultivation of cells in normal (isotonic) medium (30 min or 24 h) was added to allow cell recovery and/or apoptosis induction. Up to about 15 min the hyperosmotic/hypoosmotic treatment has no/minor effect on cell viability and all changes in chromatin structure and cellular processes were reversible.

Cells preparation for DART-Orbitrap and LC-MS/MS analyses and DESI. Twenty-four hours prior to the measurements, the cells in culture flasks were provided with fresh DMEM medium (37 °C, pH 7.1) supplemented with 100 mM or 200 mM trehalose (Sigma). Consequently, the cells were thoroughly washed (4 × 1 min) in fresh DMEM without trehalose (as proved by LC-MS/MS), harvested by scratching, resuspended in 1 mL of DMEM (1xPBS for DESI), disintegrated by shaking with glass bead tubes 0.5 mm (MO BIO Laboratories, Carlsbad, CA), with microtube homogenizer (BeadBug microtube homogenizer D 1030-E, Benchmark Scientific, Edison, NJ), 3 min, 4000 rpm, all extracts were centrifuged (6000 rpm/15 min, HERMLE Z326K, Germany) to remove cells debris and glass pellets, and 100× diluted for the measurements. Filtered (Nylon filter Mini-UniPrep 0.45 μm pore size, Whatman, UK) cell supernatants were used for DART and LC-MS/MS. For DESI-MS the cells were cultivated the same way as for DART. Cell culture was rinsed and centrifuged. The pellet was loaded onto a nylon membrane Nylon 66, 0.2 μm (Supelco, Bellefonte, PA). 2 μL of cell suspense were loaded using the MICROMAN pipette (Gilson, Villiers-le-Bel, France). Nylon membrane was fixed to the glass slides (Prosolia, Indianapolis, IN) by the means of double-site tape.

DART-Orbitrap analysis. DART-Standardized Voltage and Pressure Adjustable (SVPA) ion source with tweezer holder module (IonSense, Saugus, MA) was coupled to Orbitrap Elite mass spectrometer (Thermo Fischer Scientific, Bremen, Germany) through the interface evacuated by the diaphragm pump. The DART ion source was operated in the negative ion mode with helium ionizing gas at the pressure 0.55 MPa. The beam was heated to 400 °C, the grid electrode voltage was set to 350 V. The parameters of the mass spectrometer were tuned as follows: capillary voltage 50 V, tube lens voltage 100 V, skimmer voltage 18 V and capillary temperature 300 °C. The acquisition rate was set to 2 spectra/s with mass resolving power of 120,000 FWHM. All DART mass spectra were acquired over a mass range of *m/z* 50–600. Xcalibur software (Thermo Fischer Scientific, Germany) with DART web-based module was used for the instrument operation, data acquisition and processing.

LC-MS/MS. An Agilent 1200 Series Rapid Resolution LC System (Agilent Technologies, Waldbronn, Germany) consisted of an on-line degasser, a binary pump, a high performance SL autosampler, a thermostated

column compartment, a photodiode array UV-vis detector. The system was coupled on-line to an MS detector Agilent Technologies 6460 Triple Quadrupole LC/MS with Agilent Jet Stream. MassHunter (Agilent Technologies, Germany) software was used for the instrument operation, data acquisition and processing. The Unison UK-Amino 250 mm × 3.0 mm, 3μm particle size (Imtakt, Portland, OR) for trehalose separation under isocratic elution was used. The mobile phase consisted of 70% (acetonitrile) and 30% (0.1% acetic acid (v/v)). The flow rate was 0.7 mL/min and column temperature was 60 °C. The column effluent was directly introduced into triple quadrupole mass detector operated in a negative ESI mode. Samples were analyzed by fast chromatography-MS/MS in the multiple reaction monitoring (MRM) mode to maximize sensitivity. Characteristic transition for trehalose was *m/z* 341 → 89.

DESI-MS imaging experiments. DESI imaging analysis was performed using a Orbitrap Elite (Thermo Fischer Scientific, Bremen, Germany) with a DESI-2D ion source (Prosolia, Indianapolis, IN). Imaging experiments were performed by continuously scanning the surface in the x-direction and stepping in the y-direction (moving opposite to the direction of the spray) at the end of each line. The DESI ion source geometry was as follows: sprayer-to-sample surface distance of 0.5–1.0 mm, sprayer-to-MS inlet distance of 1.0–1.5 mm, spray impact angle of 58° was used, and collection angle of 10°. Solvent MeOH was sprayed at flow rate 3 μL/min in conventional DESI imaging. Typically, a cells slice (10 × 6 mm) was imaged using 55 lines and step size of 100 μm in the y-direction. The lines were scanned at a constant velocity of 72 μm/s. Full scan mass spectra were acquired in negative ion mode over the range of *m/z* 50–450. The total time to record this image was 63 min. BioMap software was used to process the mass spectral data to generate two-dimensional ion images. The optimized MS instrumental parameters used were 6 bar nebulizer (N_2) pressure, 380 °C heated capillary temperature, 4 kV spray voltage, 60 V tube lens voltage. The ion injection time was 800 ms, and one microscans were averaged for each pixel in the images. DESI-MSI analysis was performed in negative ion mode for trehalose (*m/z* 341.108).

Statistical analyses. The results were analysed statistically using the Kruskal-Wallis One Way Analysis of Variance on Ranks with $p = < 0.05$ considered as statistically significant. Positive cases were re-evaluated by the Mann−Whitney Rank Sum test. Number of samples depended on the analysis (about 50 to 2000 cells/sample in 2 or 3 replicas), as indicated.

Data Availability

The authors declare that all data supporting the findings of this study are available within the paper and its Supplementary Information files. In addition, all relevant data are available from the authors per request.

References

1. Fuller, B. J. Cryoprotectants: The essential antifreezes to protect life in the frozen state. *Cryoletters* **25**, 375–388 (2004).
2. Liu, X. S., Little, J. B. & Yuan, Z. M. Glycolytic metabolism influences global chromatin structure. *Oncotarget* **6**, 4214–4225 (2015).
3. Kratochvilova, I. *et al*. Theoretical and experimental study of the antifreeze protein AFP752, trehalose and dimethyl sulfoxide cryoprotection mechanism: correlation with cryopreserved cell viability. *Rsc Advances* **7**, 352–360 (2017).
4. Ceelen, M., van Weissenbruch, M. M., Vermeiden, J. P. W., van Leeuwen, F. E. & Delemarre-van de Waal, H. A. Growth and development of children born after *in vitro* fertilization. *Fertility and Sterility* **90**, 1662–1673 (2008).
5. Di Santo, M., Nadalini, T. N. & Borini, M. A Human Sperm Cryopreservation: Update on Techniques, Effect on DNA Integrity, and Implications for ART. *Adv Urol.* **2012**, 12 (2012).
6. Matsumura, K., Jain, M. & Rajan, R. Cell and Materials Interface in Cryobiology and Cryoprotection, Vol. 52. (Crc Press-Taylor & Francis Group, Boca Raton; 2016).
7. Donnelly, E. T., McClure, N. & Lewis, S. E. M. Cryopreservation of human semen and prepared sperm: effects on motility parameters and DNA integrity. *Fertility and Sterility* **76**, 892–900 (2001).
8. Duru, N. K., Morshedi, M. S., Schuffner, A. & Oehninger, S. Cryopreservation-thawing of fractionated human spermatozoa is associated with membrane phosphatidylserine externalization and not DNA fragmentation. *Journal of Andrology* **22**, 646–651 (2001).
9. Paasch, U. *et al*. Cryopreservation and thawing is associated with varying extent of activation of apoptotic machinery in subsets of ejaculated human spermatozoal. *Biology of Reproduction* **71**, 1828–1837 (2004).
10. Fraser, L., Strzezek, J. & Kordan, W. Effect of Freezing on Sperm Nuclear DNA. *Reprod. Domest. Anim.* **46**, 14–17 (2011).
11. de Paula, T. S. *et al*. Effect of cryopreservation on sperm apoptotic deoxyribonucleic acid fragmentation in patients with oligozoospermia. *Fertility and Sterility* **86**, 597–600 (2006).
12. Kopeika, J., Thornhill, A. & Khalaf, Y. The effect of cryopreservation on the genome of gametes and embryos: principles of cryobiology and critical appraisal of the evidence. *Human Reproduction Update* **21**, 209–227 (2015).
13. https://www.medicalnewstoday.com/articles/251768.php New Orleans (2012).
14. Stokich, B. *et al*. Cryopreservation of hepatocyte (HepG2) cell monolayers: Impact of trehalose. *Cryobiology* **69**, 281–290 (2014).
15. Masek, J. *et al*. Metallochelating liposomes with associated lipophilised norAbuMDP as biocompatible platform for construction of vaccines with recombinant His-tagged antigens: Preparation, structural study and immune response towards rHsp90. *J. Control. Release* **151**, 193–201 (2011).
16. Tarkowski, R. & Rzaca, M. Cryosurgery in the treatment of women with breast cancer-a review. *Gland surgery* **3**, 88–93 (2014).
17. Theodorescu, D. Cancer cryotherapy: evolution and biology. *Reviews in urology* **6**(Suppl 4), S9–S19 (2004).
18. Konc, J., Kanyo, K., Kriston, R., Somoskoi, B. & Cseh, S. Cryopreservation of Embryos and Oocytes in Human AssistedReproduction. *Biomed Research International* (2014).
19. Falk, M., Lukasova, E. & Kozubek, S. Chromatin structure influences the sensitivity of DNA to gamma-radiation. *Biochimica Et Biophysica Acta-Molecular Cell Research* **1783**, 2398–2414 (2008).
20. Falk, M., Lukasova, E., Gabrielova, B., Ondrej, V. & Kozubek, S. Chromatin dynamics during DSB repair. *Biochimica Et Biophysica Acta-Molecular Cell Research* **1773**, 1534–1545 (2007).
21. Kozubek, M. *et al*. Combined confocal and wide-field high-resolution cytometry of fluorescent *in situ* hybridization-stained cells. *Cytometry* **45**, 1–12 (2001).
22. Wolkers, W. F., Walker, N. J., Tablin, F. & Crowe, J. H. Human platelets loaded with trehalose survive freeze-drying. *Cryobiology* **42**, 79–87 (2001).
23. Simons, M. *et al*. Directly interrogating single quantum dot labelled UvrA(2) molecules on DNA tightropes using an optically trapped nanoprobe. *Scientific Reports* **5**, 29 (2015).

24. Ventham, N. T. *et al*. Integrative epigenome-wide analysis demonstrates that DNA methylation may mediate genetic risk in inflammatory bowel disease. *Nat. Commun.* **7**, 14 (2016).
25. Kad, N. M. & Van Houten, B. DNA REPAIR Clamping down on copy errors. *Nature* **539**, 498–499 (2016).
26. Ismail, I. H., Wadhra, T. I. & Hammarsten, O. An optimized method for detecting gamma-H2AX in blood cells reveals a significant interindividual variation in the gamma-H2AX response among humans. *Nucleic Acids Res.* **35**, 10 (2007).
27. Wiss, T. *et al*. Properties of the high burnup structure in nuclear light water reactor fuel. *Radiochim. Acta* **105**, 893–906 (2017).
28. Noda, M. *et al*. Protective effect of DMSO on DNA double-strand break among different lesions: gamma-ray, photo-induced active oxygen and freezing. *Molecular Biology of the Cell* **27** (2016).
29. Noda, M. *et al*. A single-molecule assessment of the protective effect of DMSO against DNA double-strand breaks induced by photo- and gamma-ray-irradiation, and freezing. *Scientific Reports* **7** (2017).
30. Soleimani, R. *et al*. Oxidative-Stress Induces Double Strand Dna Breaks During Ovarian Tissue Storage And Cryopreservation For Fertility Preservation. *Fertility and Sterility* **96**, S77–S77 (2011).
31. Hofer, M. *et al*. Two New Faces of Amifostine: Protector from DNA Damage in Normal Cells and Inhibitor of DNA Repair in Cancer Cells. *Journal of Medicinal Chemistry* **59**, 3003–3017 (2016).
32. Loebrich, M. *et al*. gamma H2AX foci analysis for monitoring DNA double-strand break repair Strengths, limitations and optimization. *Cell Cycle* **9**, 662–669 (2010).
33. Schultz, L. B., Chehab, N. H., Malikzay, A. & Halazonetis, T. D. p53 Binding protein 1 (53BP1) is an early participant in the cellular response to DNA double-strand breaks. *Journal of Cell Biology* **151**, 1381–1390 (2000).
34. Berniak, K. *et al*. Relationship Between DNA Damage Response, Initiated by Camptothecin or Oxidative Stress, and DNA Replication, Analyzed by Quantitative 3D Image Analysis. *Cytometry Part A* **83**, 913–924 (2013).
35. Zhao, H., Rybak, P., Dobrucki, J., Traganos, F. & Darzynkiewicz, Z. Relationship of DNA damage signaling to DNA replication following treatment with DNA topoisomerase inhibitors camptothecin/topotecan, mitoxantrone, or etoposide. *Cytometry Part A* **81A**, 45–51 (2012).
36. Maya-Mendoza, A. *et al*. Immortalised breast epithelia survive prolonged DNA replication stress and return to cycle from a senescent-like state. *Cell Death Dis.* **5**, 13 (2014).
37. Fugger, K. *et al*. FBH1 Catalyzes Regression of Stalled Replication Forks. *Cell Reports* **10**, 1749–1757 (2015).
38. Yingjie Zhu, A.B., Benjamin Pardo, Romain Forey, Norbert Dojer, Raziyeh Yousefi, Jules Berlin, Nde Kengne, Bernard Fongang, Abhishek Mitra, Ji Li, Magdalena Skrzypczak, Andrzej Kudlicki, Philippe Pasero, Krzysztof Ginalski, Maga Rowicka in bioRxiv (2017).
39. Sarni, D. & Kerem, B. Oncogene-Induced Replication Stress Drives Genome Instability and Tumorigenesis. *International Journal of Molecular Sciences* **18** (2017).
40. Lukasova, E. *et al*. Topography of genetic loci in the nuclei of cells of colorectal carcinoma and adjacent tissue of colonic epithelium. *Chromosoma* **112**, 221–230 (2004).
41. Leffak, M. Break- induced replication links microsatellite expansion to complex genome rearrangements. *Bioessays* **39** (2017).
42. Jones, R. M. & Petermann, E. Replication fork dynamics and the DNA damage response. *Biochemical Journal* **443**, 13–26 (2012).
43. Berti, M. & Vindigni, A. Replication stress: getting back on track. *Nature Structural & Molecular Biology* **23**, 103–109 (2016).
44. Techer, H., Koundrioukoff, S., Nicolas, A. & Debatisse, M. The impact of replication stress on replication dynamics and DNA damage in vertebrate cells. *Nature Reviews Genetics* **18**, 535–550 (2017).
45. Isachenko, E. *et al*. DNA integrity and motility of human spermatozoa after standard slow freezing versus cryoprotectant-free vitrification. *Human Reproduction* **19**, 932–939 (2004).
46. Pellicioli, A. & Foiani, M. Recombination at collapsed replication forks: the payoff for survival. *Mol Cell* **18**, 614–615 (2005).
47. Petermann, E., Orta, M. L., Issaeva, N., Schultz, N. & Helleday, T. Hydroxyurea-Stalled Replication Forks Become Progressively Inactivated and Require Two Different RAD51-Mediated Pathways for Restart and Repair. *Mol Cell* **37**, 492–502 (2010).
48. Cortez, D. Preventing replication fork collapse to maintain genome integrity. *DNA Repair* **32**, 149–157 (2015).
49. Morales, J. C. *et al*. Role for the BRCA1 C-terminal repeats (BRCT) protein 53BP1 in maintaining genomic stability. *J Biol Chem* **278**, 14971–14977 (2003).
50. Takeuchi, K. *et al*. Inhibitory effects of trehalose on fibroblast proliferation and implications for ocular surgery. *Exp. Eye Res.* **91**, 567–577 (2010).
51. Kudo, T., Takeuchi, K., Ebina, Y. & Nakazawa, M. Inhibitory effects of trehalose on malignant melanoma cell growth: implications for a novel topical anticancer agent on the ocular surface. *ISRN ophthalmology* **2012**, 968493 (2012).
52. Kim, T. M., Son, M. Y., Dodds, S., Hu, L. & Hasty, P. Deletion of BRCA2 exon 27 causes defects in response to both stalled and collapsed replication forks. *Mutation research* **766-767**, 66–72 (2014).
53. Khurana, S. & Oberdoerffer, P. Replication Stress: A Lifetime of Epigenetic Change. *Genes* **6**, 858–877 (2015).
54. Kwang-Hyun Baek, D.Z.S. Production of reactive oxygen species by freezing stress and the protective roles of antioxidant enzymes in plants. *Journal of Agricultural Chemistry and Environment* (2012).
55. Noda, M. *et al*. A single-molecule assessment of the protective effect of DMSO against DNA double-strand breaks induced by photo- and gamma-ray-irradiation, and freezing. *Sci Rep* **7**, 8557 (2017).
56. Dixon, B. P., Chu, A., Henry, J., Kim, R. & Bissler, J. J. Increased cancer risk of augmentation cystoplasty: possible role for hyperosmolal microenvironment on DNA damage recognition. *Mutation research* **670**, 88–95 (2009).
57. Alexander, J. L. & Orr-Weaver, T. L. Replication fork instability and the consequences of fork collisions from rereplication. *Gene Dev* **30**, 2241–2252 (2016).
58. Rowlands, H., Dhavarasa, P., Cheng, A. & Yankulov, K. Forks on the Run: Can the Stalling of DNA Replication Promote Epigenetic Changes. *Frontiers in genetics* **8**, 86 (2017).
59. Burrell, R. A. *et al*. Replication stress links structural and numerical cancer chromosomal instability. *Nature* **494**, 492–496 (2013).
60. Sevcik, J. *et al*. The BRCA1 alternative splicing variant Delta 14-15 with an in-frame deletion of part of the regulatory serine-containing domain (SCD) impairs the DNA repair capacity in MCF-7 cells. *Cellular Signalling* **24**, 1023–1030 (2012).

Acknowledgements

This work was supported by the Ministry of Health of the Czech Republic (16–29835 A); by the Ministry of Education, Youth and Sports of the Czech Republic (FUNBIO CZ.2.16/3.1.00/21568 and MEYS:LO1409); by the Czech Science Foundation (16–12454 S); by Czech contribution to JINR Dubna (Project of Czech Plenipotentiary and Project 3-Plus-3, 2016/18); by the National Science Foundation (CHE-1740399 and DGE-0948027); by the National Institute of General Medical Sciences at the National Institutes of Health (P20GM103432); and by the CEITEC 2020 (LQ1601) project with financial contributions from the Ministry of Education, Youths and Sports of the Czech Republic and special support paid from the National Programme for Sustainability II funds.

Author Contributions

Martin Falk - leading experiment manager, data interpretation, manuscript writing. Iva Falková - confocal microscopy, data interpretation. Eva Pagáčová - immunostaining experiments, cell cryopreservation. Olga Kopečná – flow cytometry experiments. Alena Bačíková - immunostaining experiments, confocal microscopy. Daniel Šimek – quantification of chromatin condensation, data analysis. Martin Golan – data interpretation. Stanislav Kozubek – management of experimental devices, senior scientific consultations. Michaela Pekarová – cell cryopreservation, image preparation. Shelby E. Follett - antifreeze protein preparation. Bořivoj Klejdus - LC-MS/MS, DART and DESI experiments. K. Wade Elliott - antifreeze protein preparation. Krisztina Varga – leading antifreeze protein preparation. Olga Teplá – scientific consultation, manuscript redaction. Irena Kratochvílová - project initiation and leadership, manuscript writing.

Additional Information

Supplementary information accompanies this paper at https://doi.org/10.1038/s41598-018-32939-5.

Competing Interests: The authors declare no competing interests.

Publisher's note: Springer Nature remains neutral with regard to jurisdictional claims in published maps and institutional affiliations.

Chromatin architecture changes and DNA replication fork collapse are critical features in cryopreserved cells that are differentially controlled by cryoprotectants

SUPPLEMENTARY INFORMATION

Martin Falk[1*], Iva Falková[1], Olga Kopečná[1], Alena Bačíková[1], Eva Pagáčová[1], Daniel Šimek[2], Martin Golan[2,3], Stanislav Kozubek[1], Michaela Pekarová[1], Shelby E. Follett[4], Bořivoj Klejdus[5,6], K. Wade Elliott[7], Krisztina Varga[7], Olga Teplá[8,9] and Irena Kratochvílová[2*]

[1]The Czech Academy of Sciences, Institute of Biophysics, Královopolská 135, CZ-612 65 Brno, Czech Republic
[2]The Czech Academy of Sciences, Institute of Physics, Na Slovance 2, CZ-182 21, Prague 8, Czech Republic
[3]Faculty of Mathematics and Physics, Charles University in Prague, Ke Karlovu 5, CZ-121 16 Prague 2, Czech Republic
[4]Department of Chemistry, University of Wyoming, 1000 E. University Ave, Laramie, WY 82071, USA
[5]Institute of Chemistry and Biochemistry, Faculty of Agronomy, Mendel University in Brno, Zemědělská 1, CZ-613 00
[6]CEITEC-Central European Institute of Technology, Mendel University in Brno, Zemědělská 1, CZ-613 00 Brno, Czech Republic
[7]Department of Molecular, Cellular, and Biomedical Sciences, University of New Hampshire, 46 College Road, Durham, NH 03824, USA
[8]ISCARE IVF a.s. Jankovcova 1692, CZ-160 00 Praha 6
[9]VFN Gynekologicko-porodnická klinika, Apolinářská 18, CZ-120 00, Czech Republic

*Corresponding authors: falk@ibp.cz; krat@fzu.cz

Table S1 | Proportions [%] of NHDF and MCF7 cells with >30 γH2AX/53BP1 foci/nucleus (confocal microscopy) compared to proportions of S-phase cells (flow cytometry), γH2AX-positive cells (flow cytometry) and Annexin V/PI-positive cells (flow cytometry) γH2AX-positive and S-phase cells were quantified by flow cytometry (FC) using γH2AX/H2AX and Propidium iodide (PI, DNA content) staining, respectively. Experiments were performed 30 min after cryoprotectant treatment and/or freezing/thawing (F/T). Immunofluorescence confocal microscopy (CM). The values are the means with standard errors.

treatment		Cells (30 min post-treatment and/or freezing/thawing)			
		with >30 γH2AX/53BP1 foci (CM)	in S-phase (PI staining; FC)	γH2AX-positive (FC)	annexin V/PI positive (FC)
NHDF cells					
non frozen	untreated	<0.5	8.2 ± 2.5	4.8 ± 1.1	18.0 ± 1.0
	T	<0.5	5.5 ± 1.5	9.8 ± 0.4	26.3 ± 2.9
	DMSO	<0.5	6.9 ± 1.7	4.3 ± 0.8	30.3 ± 1.5
	DMSO+T	<0.5	5.3 ± 2.2	4.3 ± 0.4	28.4 ± 2.9
post F/T	untreated	9.0 ± 0.5	7.7 ± 2.1	37.0 ± 7.7	86.1 ± 4.4
	T	3.8 ± 0.2	4.4 ± 0.6	31.3 ± 3.0	51.9 ± 5.0
	DMSO	5.2 ± 0.4	8.3 ± 1.8	10.3 ± 1.8	31.9 ± 2.2
	DMSO+T	4.0 ± 0.2	5.3 ± 1.5	6.3 ± 0.7	30.8 ± 2.5
MCF7 cells					
non frozen	untreated	<0.5	13.4 ± 0.2	7.1 ± 0.7	17.5 ± 1.4
	T	<0.5	8.0 ± 0.5	9.6 ± 2.8	38.4 ± 5.6
	DMSO	<0.5	14.7 ± 1.3	8.7 ± 3.6	18.9 ± 1.1
	DMSO+T	<0.5	7.3 ± 0.5	10.7 ± 5.1	38.2 ± 7.2
post F/T	untreated	13.8 ± 2.1	14.3 ± 0.4	54.5 ± 14.8	99.1 ± 0.2
	T	6.2 ± 2.2	9.5 ± 0.2	45.3 ± 10.1	85.7 ± 1.0
	DMSO	16.0 ± 2.0	15.8 ± 0.3	20.9 ± 9.9	23.7 ± 1.0
	DMSO+T	7.3 ± 1.3	10.2 ± 0.6	15.3 ± 2.5	23.9 ± 1.5

Table S2 | Correlation between condensed chromatin, determined by confocal fluorescence microscopy (TO-PRO-3 staining) in combination with image 2D Fourier transform, and cell survival quantified by flow cytometry (Annexin V + PI positivity) before freezing and at 30 min and 24 h after thawing. Upper table – NHDF cells; bottom table – MCF7 cells.

Note: In our previous work[3] (PMC5602551), only the data on the viability of fibroblasts 24 h post treatment were studied. In the present study, we have evaluated cell viability for NHDF fibroblasts and MCF7 cells at two time points post freezing/thawing (30 min and 24 h); this is important to obtain more detailed image about the freezing/thawing effects. In the present study, all the viability values were obtained with new software (Guava InCyte soft. 3.1.1., Millipore) allowing us more precise analyses. First, we used the same gates in all experiments, and second, in all cases, we excluded cell debris more precisely (as compared to RSC Adv.)[3]. The same gating and the same style of debris exclusion is extremely important in viability evaluation of frozen/thawed cells because many thawed cells are more or less fragmented. With the software used in RSC Adv. (MUSE machine original software) this was not feasible.

	Condensed chromatin [% of cells]		Viable cells [%] (flow-cytometry)	
treatment:	before freezing/thawing	30 min after freezing/thawing	30 min after freezing/thawing	24 h after freezing/thawing
NHDF cells				
untreated	16.7 ± 2.9	12.0 ± 2.5	13.9 ± 4.4	22.2 ± 2.1
AFP	25.8 ± 5.1	15.1 ± 4.6	31.5 ± 4.8	35.4 ± 5.3
trehalose	21.1 ± 6.4	43.5 ± 6.9	48.1 ± 5.1	60.3 ± 3.5
DMSO	56.7 ± 9.2	73.2 ± 2.5	68.1 ± 2.2	79.0 ± 7.0
DMSO + trehalose	52.3 ± 6.4	82.5 ± 5.0	69.2 ± 2.5	65.8 ± 2.2
MCF7 cells				
untreated	8.6 ± 2.8	7.9 ± 2.3	0.9 ± 0.2	0.6 ± 0.8
trehalose	12.0 ± 2.2	16.0 ± 2.8	14.3 ± 0.5	9.2 ± 1.0
DMSO	31.6 ± 5.1	59.7 ± 2.8	76.3 ± 1.0	80.0 ± 0.5
DMSO + trehalose	39.5 ± 4.7	62.0 ± 5.8	76.2 ± 1.5	66.5 ± 1.0

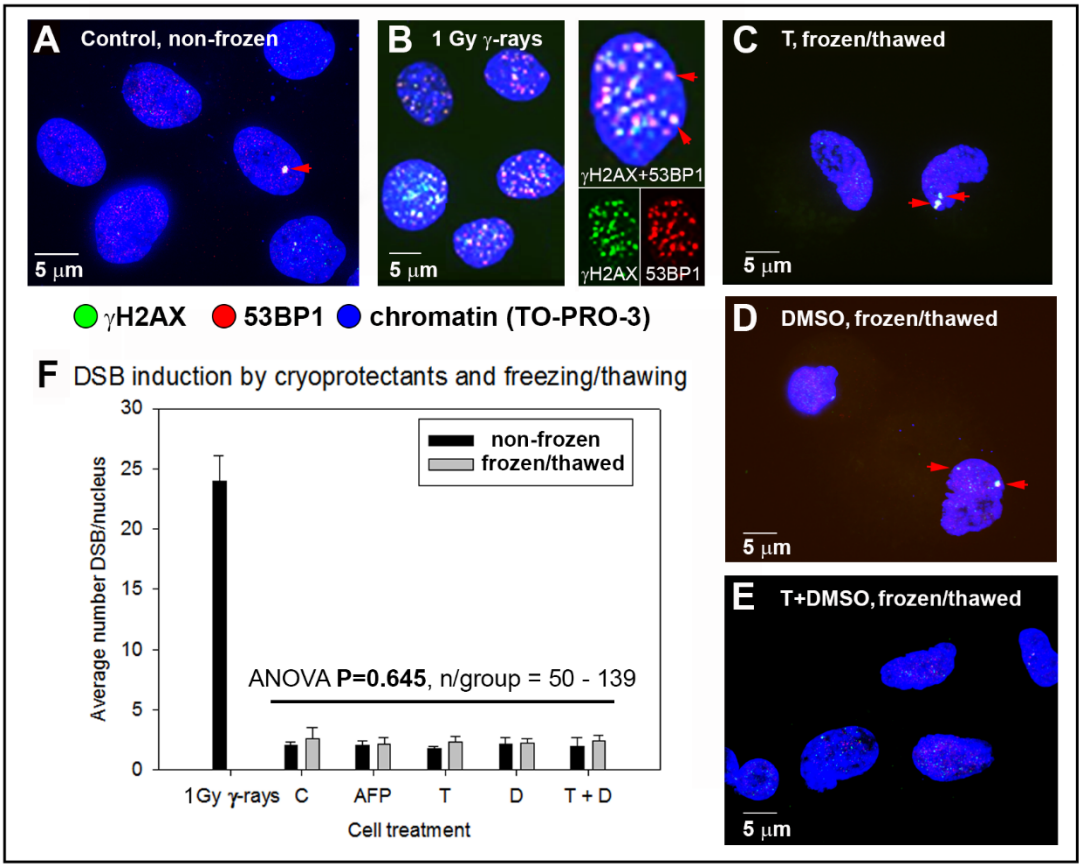

Fig. S1 | DSB induction in a sub-fraction of frozen/thaw NHDF cells with <30 DSB that were treated or not treated with the indicated cryoprotectants. Images show 40 superimposed 0.2-μm thick confocal slices. DSBs are marked by γH2AX (green) colocalizing with 53BP1 (red). **A.** positive control cells were irradiated with 1 Gy of γ-rays and were not frozen; the right panel shows a detail of γH2AX foci and 53BP1 foci co-localization, marking the DSB lesions. **B.** Negative controls were not frozen; **C-D.** Cells were frozen/thawed in the presence of the cryoprotectants (**C**, trehalose; **D,** DMSO; **E,** trehalose+DMSO). Chromatin is counterstained with TO-PRO3 (blue). **F.** Average DSB foci numbers per nucleus determined 30 min PT for cells treated or not treated with cryoprotectants and submitted to freezing/thawing. Average numbers of DSB foci and their standard deviations were calculated only for nuclei with <30 foci/nucleus in order to compare DSB induction in predominate fractions of cells before and after freezing/thawing. In unfrozen and frozen/thawed states, these fractions corresponded to about 99 % and 91 % of the cell population, respectively. The *P* value was obtained using the Kruskal-Wallis One Way Analysis of Variance on Ranks for all samples except for the γ-ray irradiated sample (n = 50–139 nuclei).

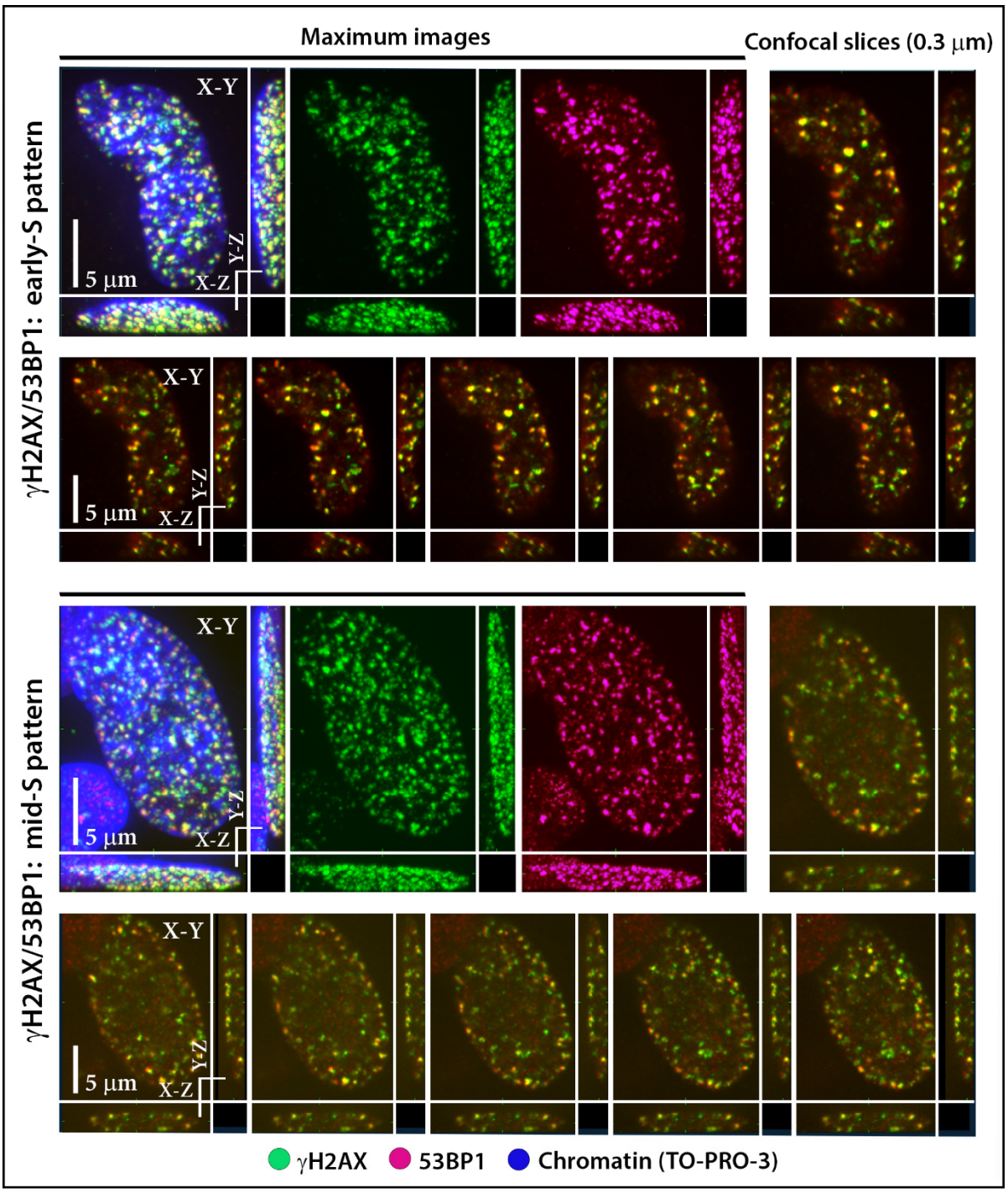

Fig. S2 | Immunofluorescence confocal images of NHDF cells with >30 γH2AX/53BP1 foci/nucleus that emerged after freezing/thawing. Top panel: A nucleus with >100 small DSB foci dispersed throughout the nucleus in a pattern resembling that of replication sites in the early S-phase. Lower panel: A nucleus, again with >100 small DSB foci, but distributed especially along the nuclear rim (i.e. in a pattern resembling that of replication sites in the mid S-phase). Upper lines of images: 3D projections (x-y, x-z and y-z) of maximum images composed of 40 confocal slices, each 0.3 μm-thick (left column), plus an enlarged confocal slice plus (the rightmost images). Lower lines of images: five consecutive single confocal slices, 0.3 μm-thick (remaining columns). γH2AX – green, 53BP1 – purple, blue – chromatin staining (TO-PRO3).

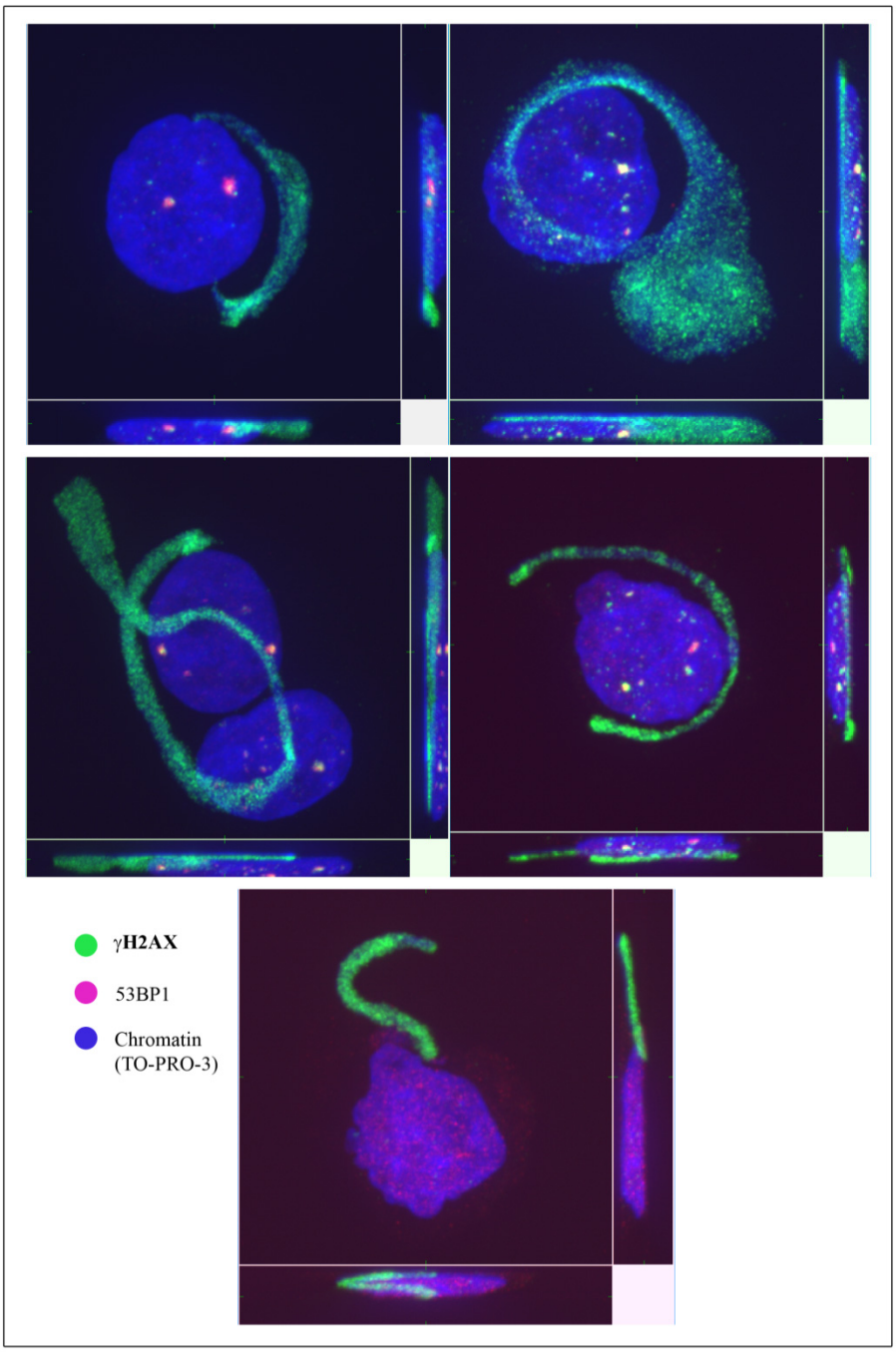

Fig. S3 | Chromatin perturbations (out of interrupted nuclei) caused by freeze/thaw processes and marked by γH2AX. Visible is also altered (decondensed) higher-order chromatin structure (blue, TO-PRO3) while DSBs (colocalized γH2AX and 53BP1 signal, green + red) are detected in the extent corresponding to never frozen cells. Images consist of 40 superimposed 0.2-μm thick confocal slices; magnification 100×).

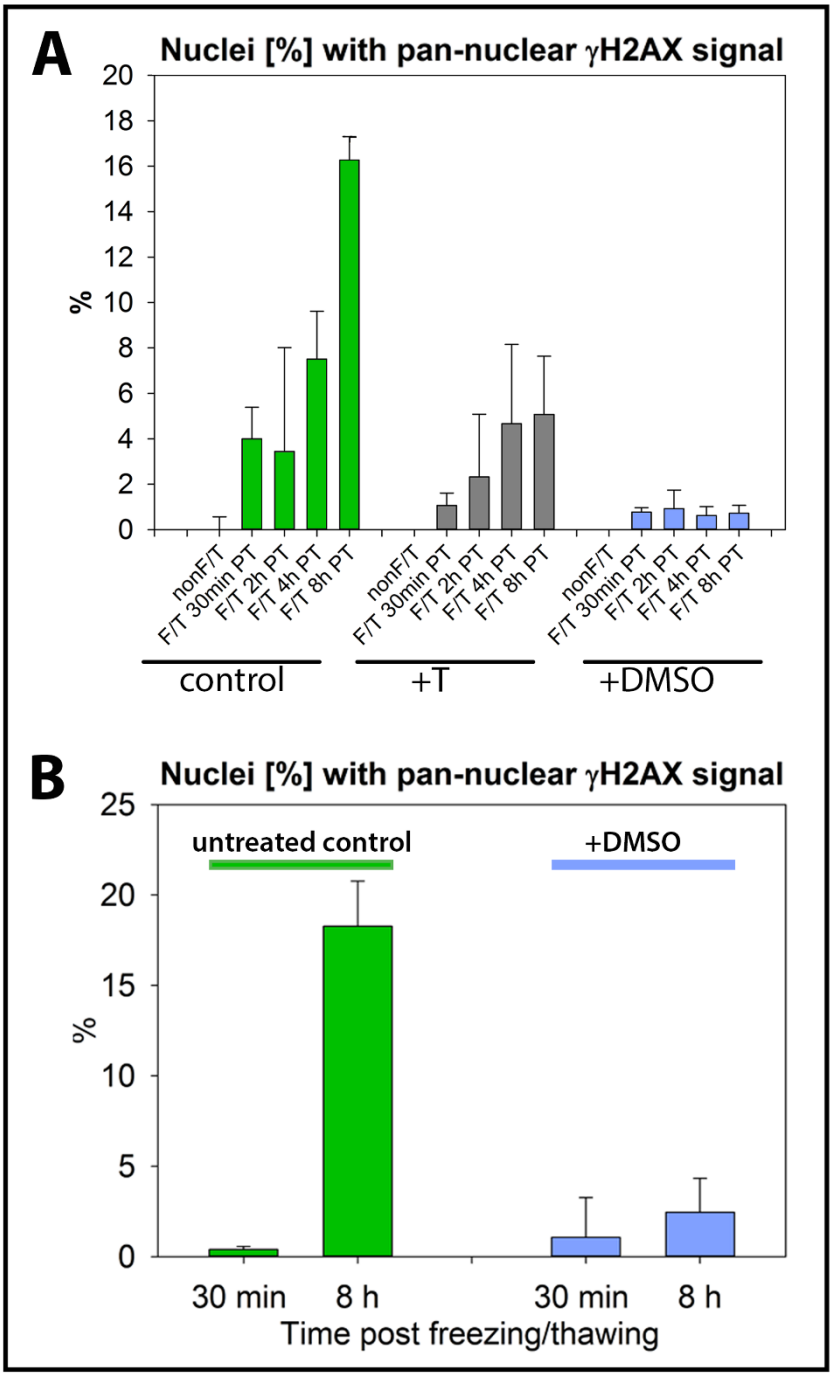

Fig. S4 | Proportion [%] of MCF (A) NHDF (B) cells with pan-nuclear γH2AX staining prior to freezing/thawing and at the indicated periods of time after thawing for cells incubated or not incubated with the cryoprotectants.

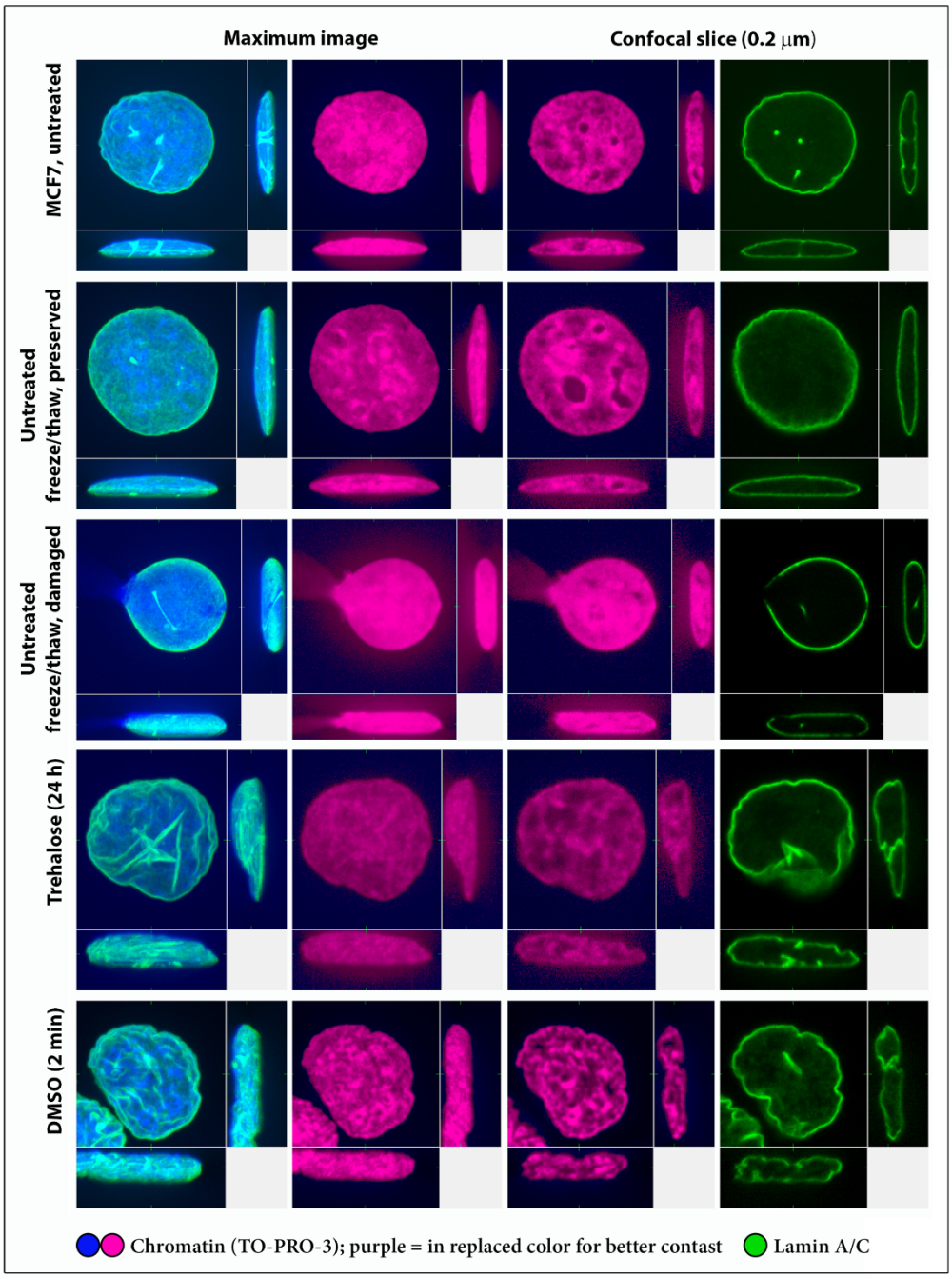

Fig. S5 | The effects of a freeze/thaw cycle on the higher-order chromatin structure and nuclear envelope in mammary carcinoma MCF7 cells in the presence of cryoprotectants. Top row: untreated control cells that were not frozen. Other rows: cells frozen in the presence of the indicated cryoprotectant. 'Maximum images' are composed of 40 superimposed 0.2-μm thick confocal slices and shown together with x-z and y-z projections (left columns). Left columns present single confocal slices (0.2-μm thick) through the cell nucleus (performed at the central nuclear plane) with their x-z and y-z projections. Nuclear envelopes were visualized using lamin A/C antibody (green), and the chromatin was counterstained with TO-PRO3 (blue or violet to better visualize the chromatin structure).

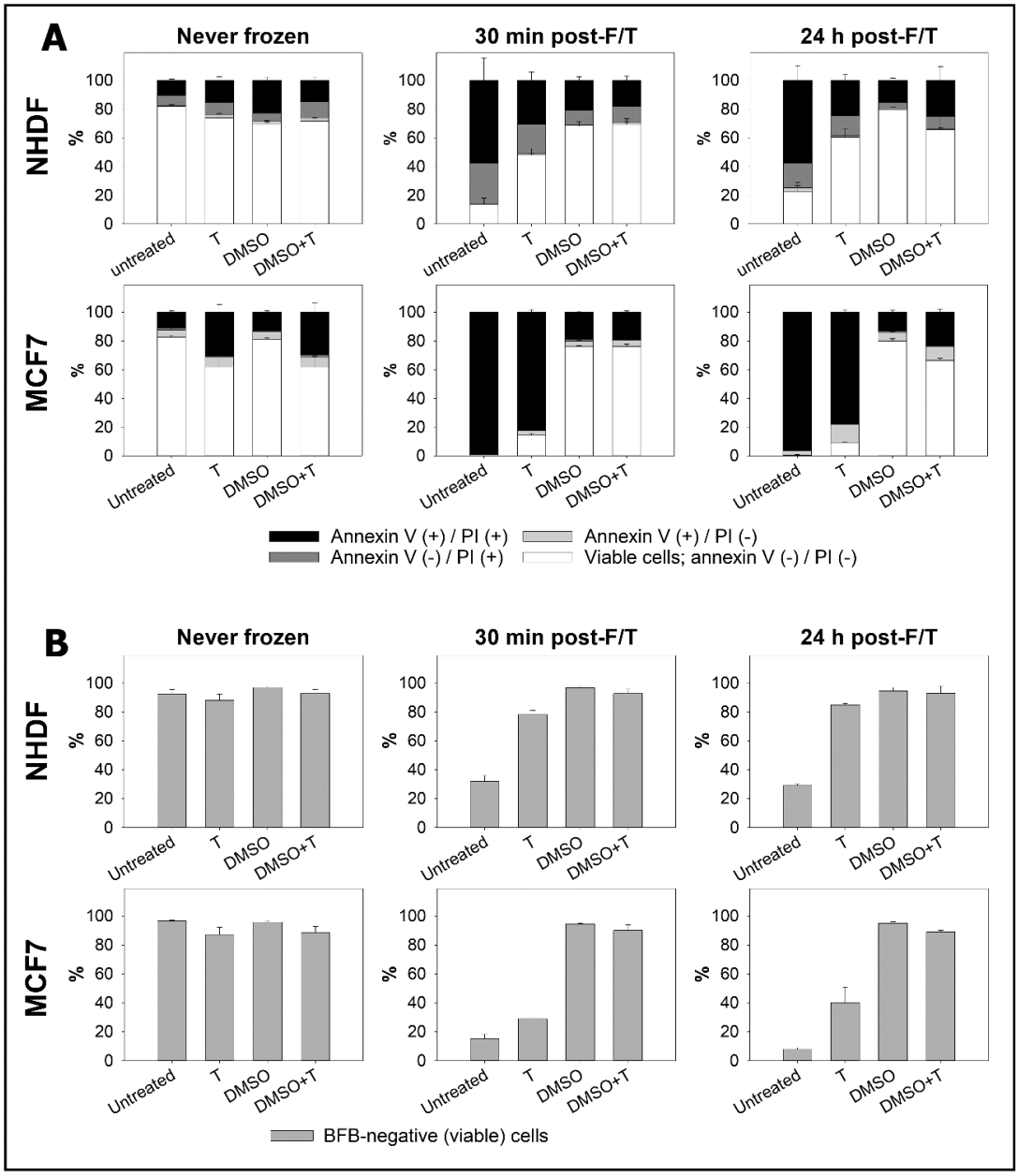

Fig. S6 | Detailed analyses of NHDF cells' dying upon freezing/thawing in presence or absence of trehalose, DMSO or combination of both cryoprotectants. A. Flow cytometry with Annexin V + Propidium iodide (PI), 24 h post-thawing. B. Viability of untreated and DMSO, trehalose, DMSO+trehalose treated never frozen and frozen/thawed MCF7 and NHDF cells. Note: In our previous work[3] (PMC5602551), only the data on the viability of fibroblasts 24 h post treatment were studied. In the present study, we have evaluated cell viability for NHDF fibroblasts and MCF7 cells at two time points post freezing/thawing (30 min and 24 h); this is important to obtain more detailed image about the freezing/thawing effects. In the present study, all the viability values were obtained with a new software (Guava InCyte soft. 3.1.1., Millipore) allowing us more precise analyses. First, we used the same gates in all experiments, and second, in all cases, we excluded cell debris more precisely (as compared to RSC Adv.)[3]. The same gating and the same style of debris exclusion is extremely important in viability evaluation of frozen/thawed cells because many thawed cells are more or less fragmented. With the software used in RSC Adv. (MUSE machine original software) this was not feasible.

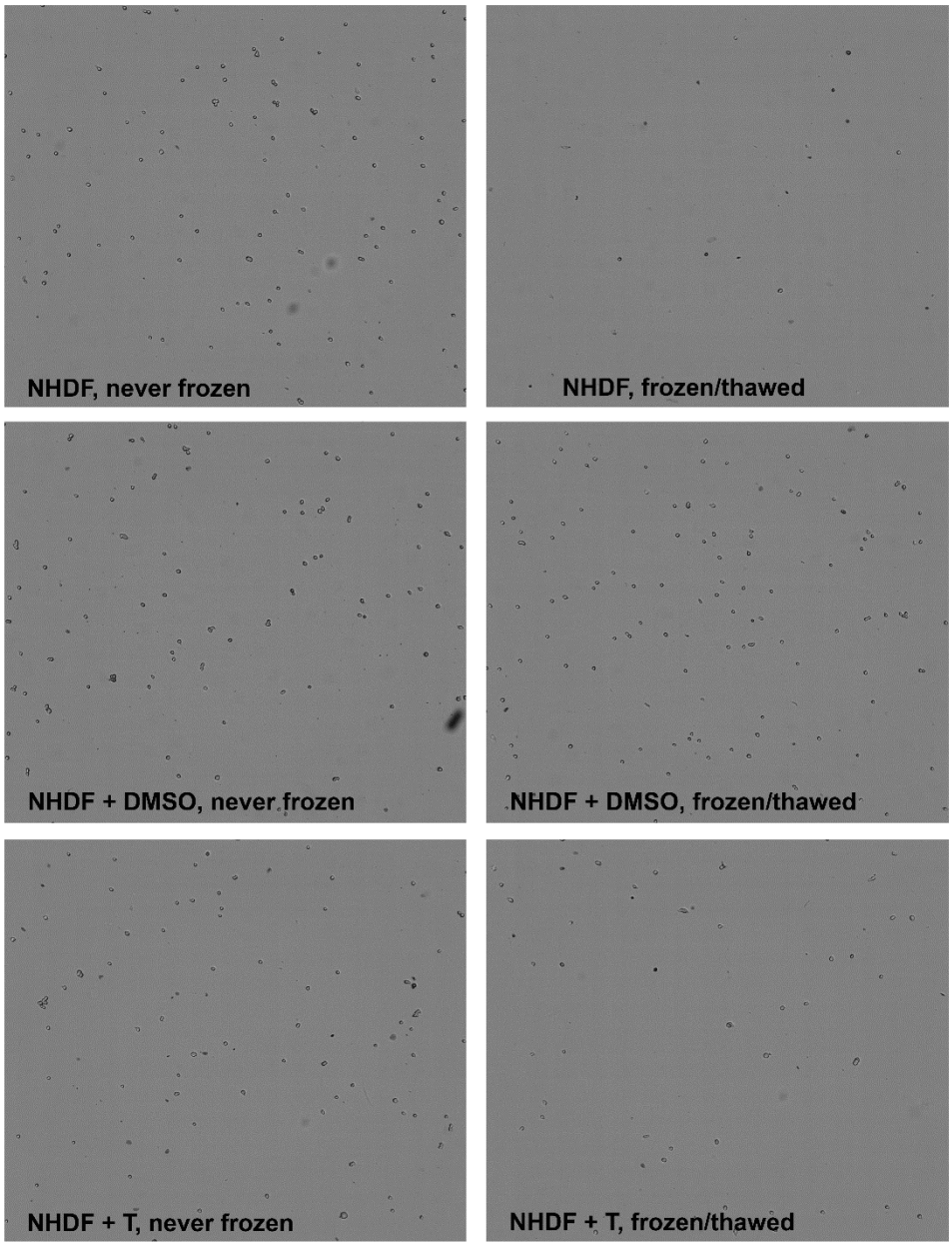

Fig. S7 | Detailed analyses of NHDF cells' dying upon freezing/thawing in presence or absence of trehalose, DMSO or combination of both cryoprotectants. Flow cytometry (Fig. S6) with criterion (7.5×10^{-6}, when unity is the zero frequency maximum), which assured 90% of nuclei in testing samples being properly qualified in accordance with the experienced staff judgment.

Chromatin condensation quantification

Fourier transform composes from a three basic components: i) the zero and low spatial frequency component coming from the rotationally averaged size of the whole nucleus, ii) the middle frequency component coming from the condensed chromatin, and iii) the broad frequency background coming mostly from the noise recorded. From a single 2d section (from a 2d projection) of chromatin (blue channel) observed in the confocal microscope, the 2d Fourier transform in polar coordinates was calculated.

$$c(\rho,\beta)=\int_0^{2\pi}\int_0^{R_{\max}} b(r,\alpha)e^{i2\pi\rho r\cos(\alpha-\beta)}r\,dr\,d\alpha\ ,$$

where *b*(r,α) represents the luminosity of blue channel in polar coordinates. Only the radial part of *c*(ρ,α) was considered, while the phase of the Fourier transform was forgotten and the function was normalized have maximum equal to one:

$$y(\rho)=\frac{c(\rho)}{c(0)};\quad c(\rho)=\tfrac{1}{2\pi}\int_0^{2\pi}\left|c(\rho,\beta)\right|d\beta\ .$$

The resulting radial part of F.T. *y*(ρ) then composes from a three basic components: i) the zero and low spatial frequency component coming from the rotationally averaged size of the whole nucleus, ii) the middle frequency component coming from the condensed chromatin, and iii) the broad frequency background coming mostly from the noise recorded. The low frequency peak has always its maximum for zero frequency (ρ=0), while the middle frequency component, if a dominant condensation length L_c occurs, can show a peak for a frequency inversely proportional to the condensation length $\rho_m=1/L_c$. We fit the whole radial part of the spectrum by these three components represented by 8 parameters:

$$y_{calc}(\rho)=k_l\left(1+\frac{\rho^2}{w_l^2}\right)^{-h_l}+k_m\left(1+\frac{(\rho-\rho_m)^2}{w_m^2}\right)^{-h_m}+k_b\ .$$

It is the sum of two Pearson VII functions plus c constant background, the interesting middle-frequency component being the second term. The examples of three different nuclei, classified as those with condensed chromatin, normal chromatin and damaged (after freezing-thawing) nucleus are shown in Figure S11. As obvious, the middle frequency component (black dots) is the strongest for nucleus with condensed chromatin.

For discrimination of nuclei with condensed chromatin, the best criterion appears to look for the first momentum of the middle frequency component:

$$m_{1m}=\frac{\int_0^{\rho_{\max}} y_{MF}(\rho)\rho d\rho}{\sqrt{\int_0^{\rho_{\max}}\rho^2 d\rho}}\ ,$$

Where the y_{MF} represents either the calculated middle-frequency component from the refinement or the difference of the experimental profile from the other components (i.e. black dots in Fig. S8). The best results gave the product of both these. With all the images of the same magnification, a threshold value of the first momentum gave a good discrimination criterion (7.5×10^{-6}, when unity is the zero frequency maximum), which assured 90% of nuclei in testing samples being properly qualified in accordance with the experienced staff judgment.

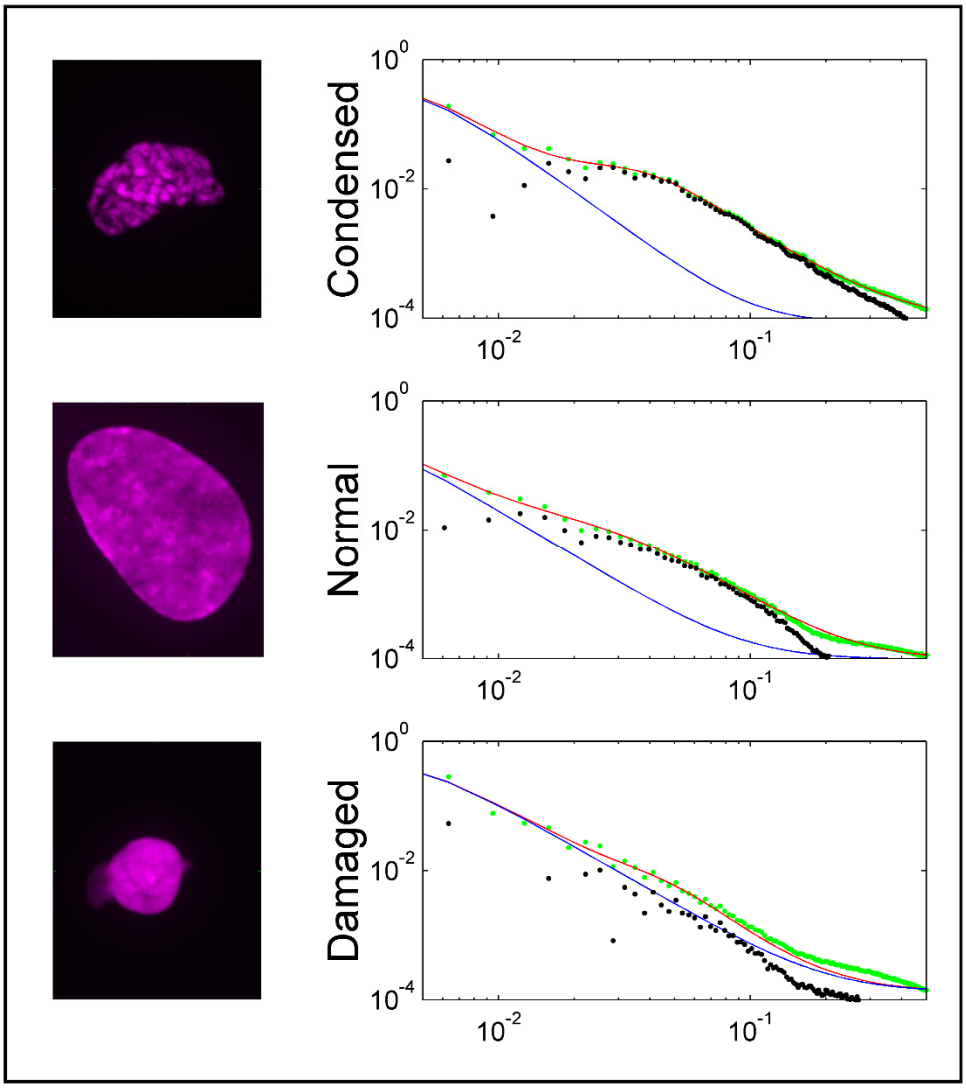

Fig. S8 | Examples of nuclei (left) with (top to bottom) condensed, normal, and damaged/structureless chromatin with corresponding radial profile of Fourier transform intensity in log-log scale (right). Green dots are data calculated from the pictures, blue line represents the low-frequency component and the background, red line includes also a middle frequency component. Black dots show the difference of measured data from the blue line.

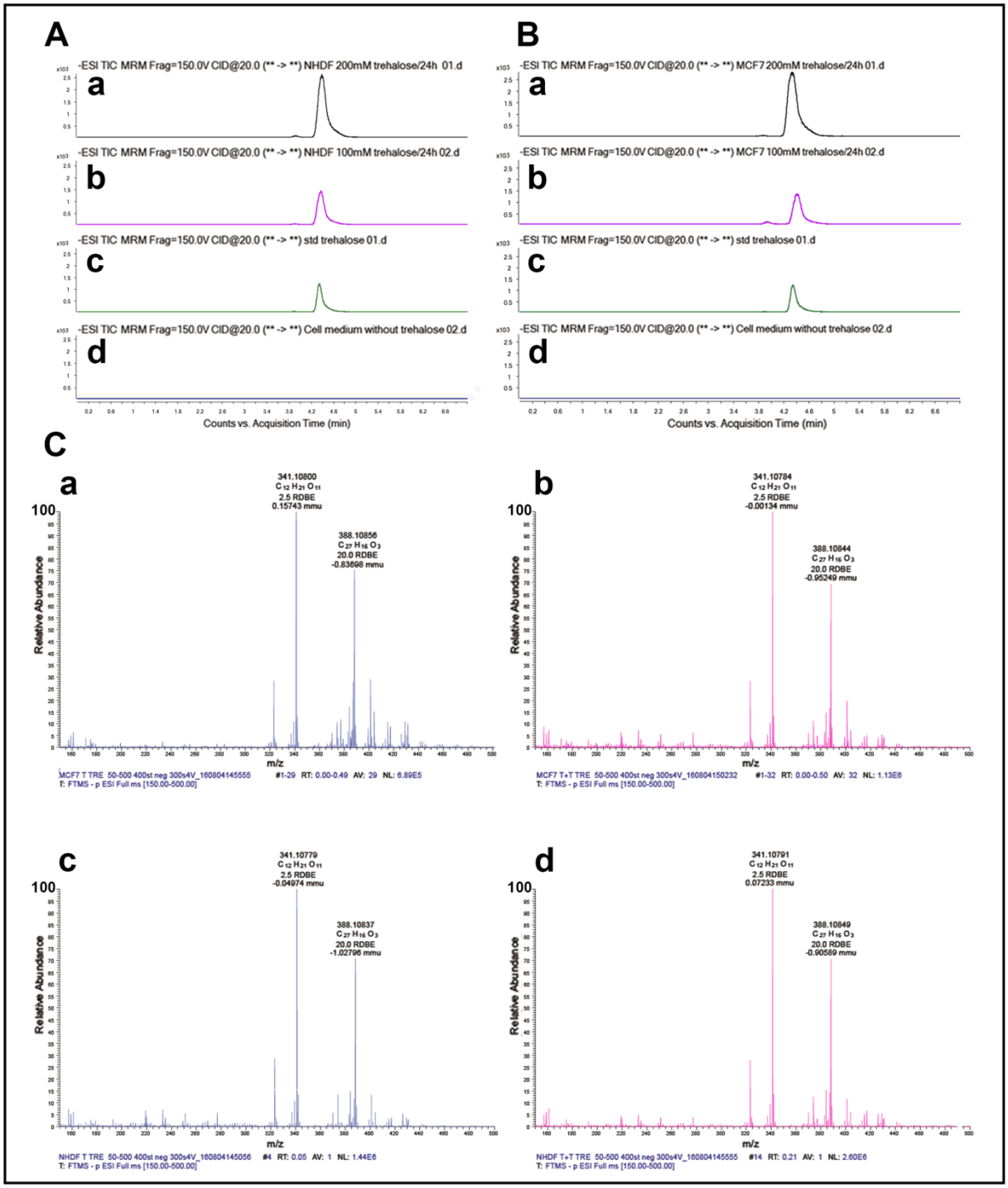

Fig. S9 | LC MS/MS + DART-Orbitrap analysis of trehalose in NHDF and MCF7 cells. A + **B**: Negative ion mode of MRM chromatograms: **a**. NHDF cells with 200 mM trehalose/24 h; **b**. NHDF cells with 100 mM trehalose/24 h; **c**. standard of trehalose; **d**. Cells medium without trehalose **B**. MCF7 cells (a-d as for A). **C**. DART: **a**. MCF7 cells incubated with 100 mM trehalose for 24 h; **b**. MCF7 cells incubated with 200 mM trehalose for 24 h; **c**. NHDF cells incubated with 100 mM trehalose for 24 h; d. NHDF cells incubated with 200 mM trehalose for 24 h.

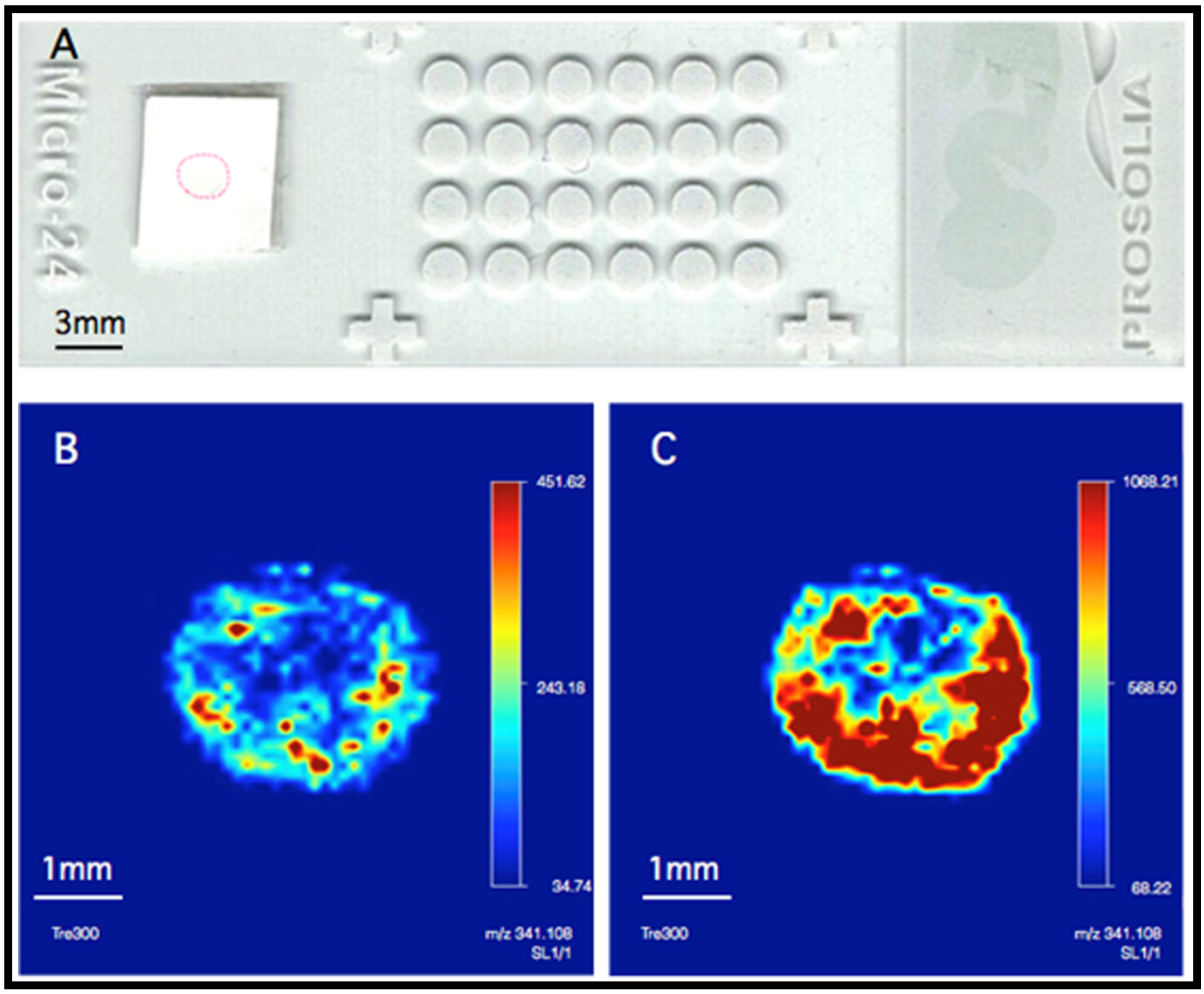

Fig. S10 | DESI-MS images showing the cell absorption and relative ion intensity of trehalose (m/z 341.108) by/in NHDF cells. Displayed are spots of cells incubated for 24 h with **A:** Cell culture loaded onto a nylon membrane, fixed to the glass slide by the means of double-site tape**.** Displayed are spots of cells incubated for 24 h with: **B –** 100 mM trehalose; or **C –** 200 mM trehalose. Trehalose is being absorbed by cells in the time course of our experiments; blue-to-red scale indicates increasing concentrations of trehalose in cells. See Fig. S9 for LC-MS/MS and DART results.

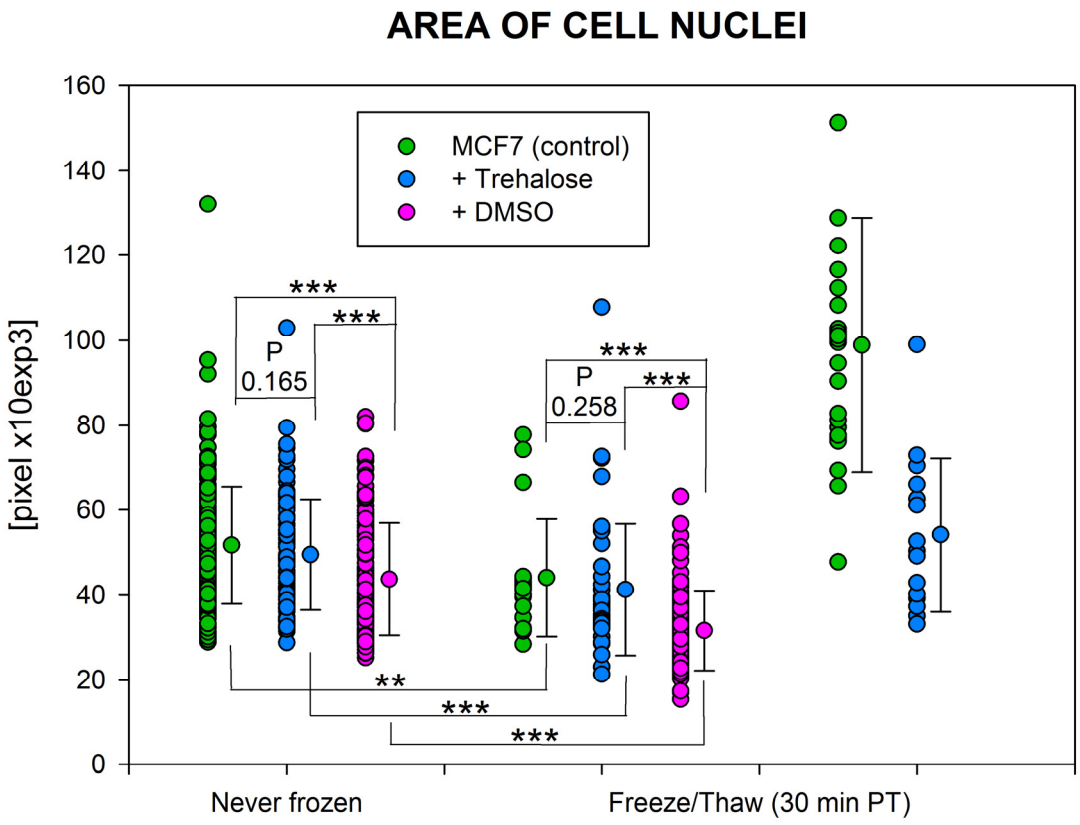

Fig. S 11 | MCF7 cell nuclei condensation upon cell incubation with cryoprotectants studied, before and after freeze/thaw. Nuclear areas [pixels $.10^3$]) on maximum images are displayed for all cell nuclei together with means ± SE. Two rightmost data distributions are for cells with highly damaged cell nuclei (that are almost absent for DMSO treatment and therefore not displayed) while remaining distributions are for preserved nuclei (*) = P<0.05; (**) = P<0.01; (***) = P<0.001; Mann-Whitney Rank Sum Test.

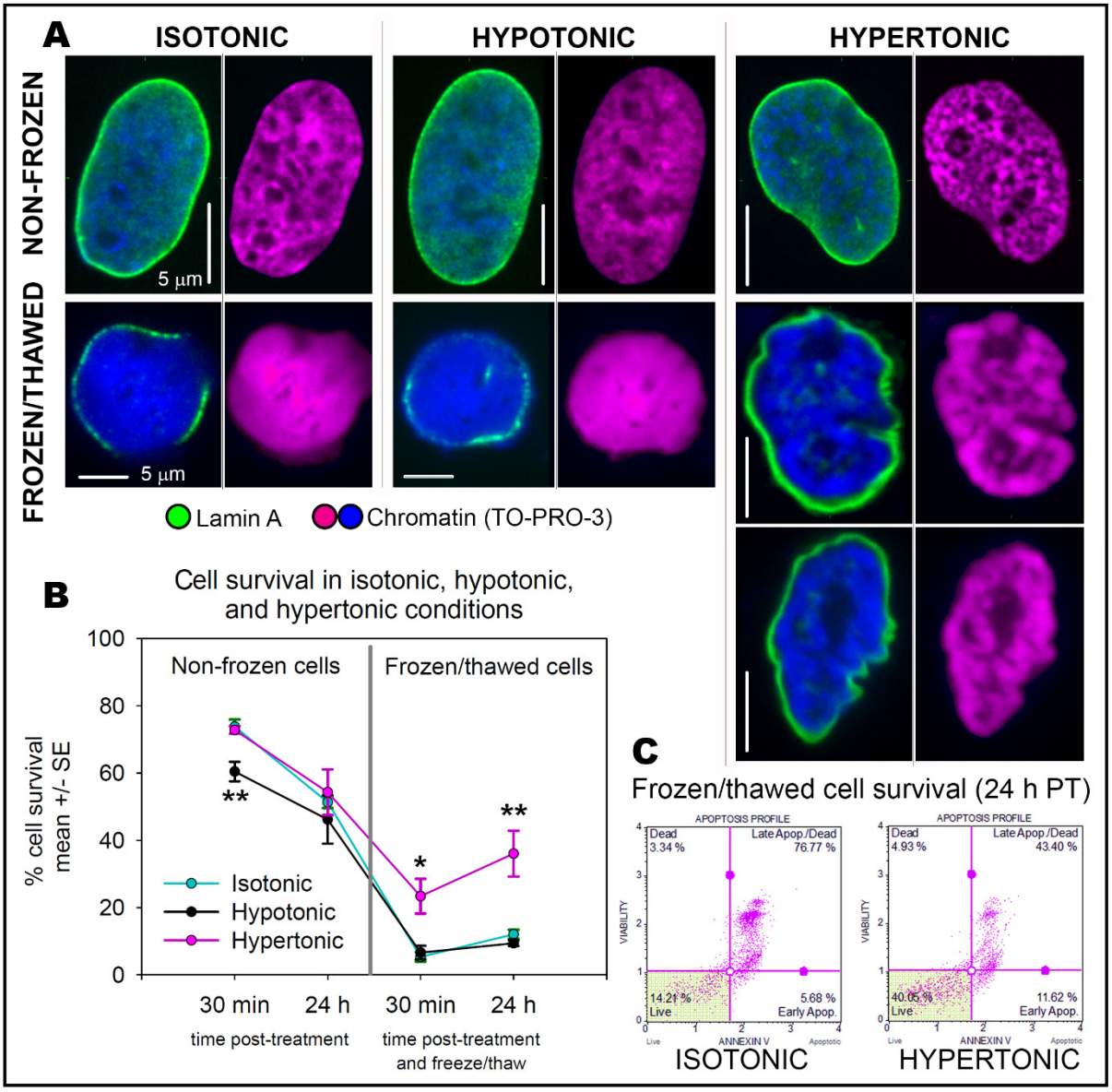

Fig. S12 | Impact of short pre-freeze incubation of NHDF cells in media with different osmolarities on higher-order chromatin structure, nuclear envelope quality and cell viability. Before freezing, cells were incubated for 12 min in hypertonic (570 mOsm), hypotonic (140 mOsm), or normal culture medium (isotonic control, 290 mOsm). (A) Higher-order chromatin structure and nuclear envelope quality of non-frozen (top line) and frozen/thawed skin fibroblasts (NHDF), determined by high-resolution confocal immunofluorescence microscopy immediately (without changing the media) after the incubation or after the incubation and freezing/thawing. Nuclear envelopes were visualized using lamin A/C antibodies (green), and the chromatin was counterstained with TO-PRO-3 (blue or purple to better visualize the chromatin structure). (B) Viability of control NHDF (isotonic medium) and NHDF pre-incubated for 12 min in hypotonic or hypertonic medium before and after a freeze/thaw cycle as determined by flow cytometry (see C). After freezing/thawing, cells were transferred to normal (isotonic) medium and cultured for 30 min or 24 h before viability was assessed. Error bars correspond to the SE; statistically significant (unpaired two-tailed t-test) differences relative to control (isotonic) cells are indicated by asterisks (*, $P < 0.05$; **, $P < 0.01$; ***, $P < 0.001$). (C) Representative flow cytograms for NHDF cells that were frozen/thawed in isotonic (left) and hypertonic (right) medium. Horizontal axis: Annexin V staining, vertical axis: 7-AAD staining (bottom-left corner contains viable cells).

Chromatin architecture changes and DNA replication fork collapse are critical features in cryopreserved cells that are differentially controlled by cryoprotectants

RAW DATA

Martin Falk[1*], Iva Falková[1], Olga Kopečná[1], Alena Bačíková[1], Eva Pagáčová[1], Daniel Šimek[2], Martin Golan[2,3], Stanislav Kozubek[1], Michaela Pekarová[1], Shelby E. Follett[4], Bořivoj Klejdus[5,6], K. Wade Elliott[7], Krisztina Varga[7], Olga Teplá[8,9] and Irena Kratochvílová[2*]

[1] The Czech Academy of Sciences, Institute of Biophysics, Královopolská 135, CZ-612 65 Brno, Czech Republic

[2] The Czech Academy of Sciences, Institute of Physics, Na Slovance 2, CZ-182 21, Prague 8, Czech Republic

[3] Faculty of Mathematics and Physics, Charles University in Prague, Ke Karlovu 5, CZ-121 16 Prague 2, Czech Republic

[4] Department of Chemistry, University of Wyoming, 1000 E. University Ave, Laramie, WY 82071, USA

[5] Institute of Chemistry and Biochemistry, Faculty of Agronomy, Mendel University in Brno, Zemědělská 1, CZ-613 00

[6] CEITEC-Central European Institute of Technology, Mendel University in Brno, Zemědělská 1, CZ-613 00 Brno, Czech Republic

[7] Department of Molecular, Cellular, and Biomedical Sciences, University of New Hampshire, 46 College Road, Durham, NH 03824, USA

[8] ISCARE IVF a.s. Jankovcova 1692, CZ-160 00 Praha 6

[9] VFN Gynekologicko-porodnická klinika, Apolinářská 18, CZ-120 00, Czech Republic

*Corresponding authors: falk@ibp.cz; krat@fzu.cz

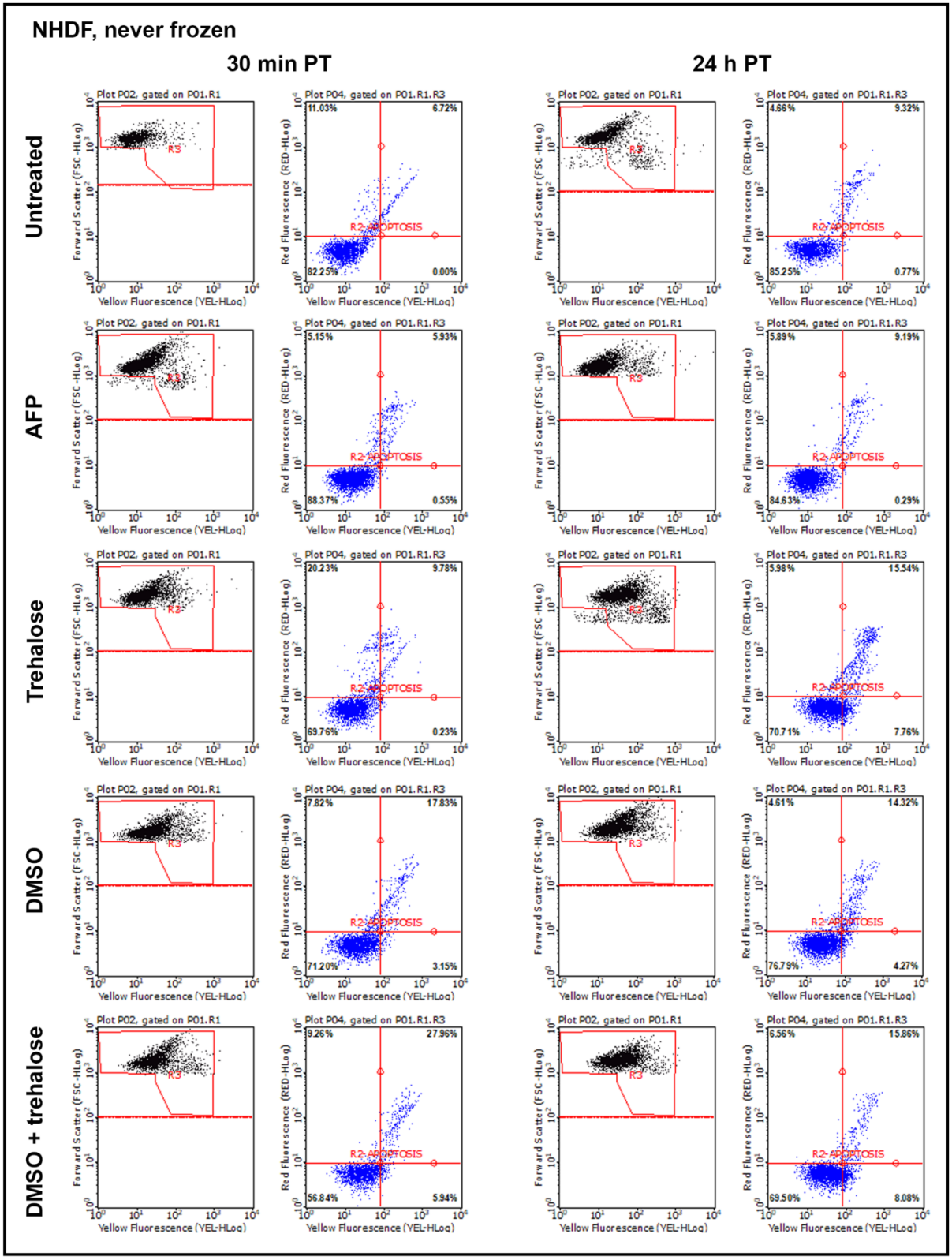

Data 1A: Flowcytograms (Annexin V vs. Propidium iodide, PI) obtained for never frozen NHDF cells before (untreated) and 30 min or 24 h after their treatments (post-treatment, PT) with cryoprotectants (AFP, trehalose, DMSO or combination of trehalose + DMSO). Left columns: FSC vs. Annexin V (YEL-HLog, horizontal axis) plots showing fractions of gated cells; right plots: Annexin V (YEL-HLog, horizontal axis) vs. Propidium iodide (PI, RED-HLog, vertical axis) showing cell viability. The percentage of cells is indicated for each Annexin V/PI category.

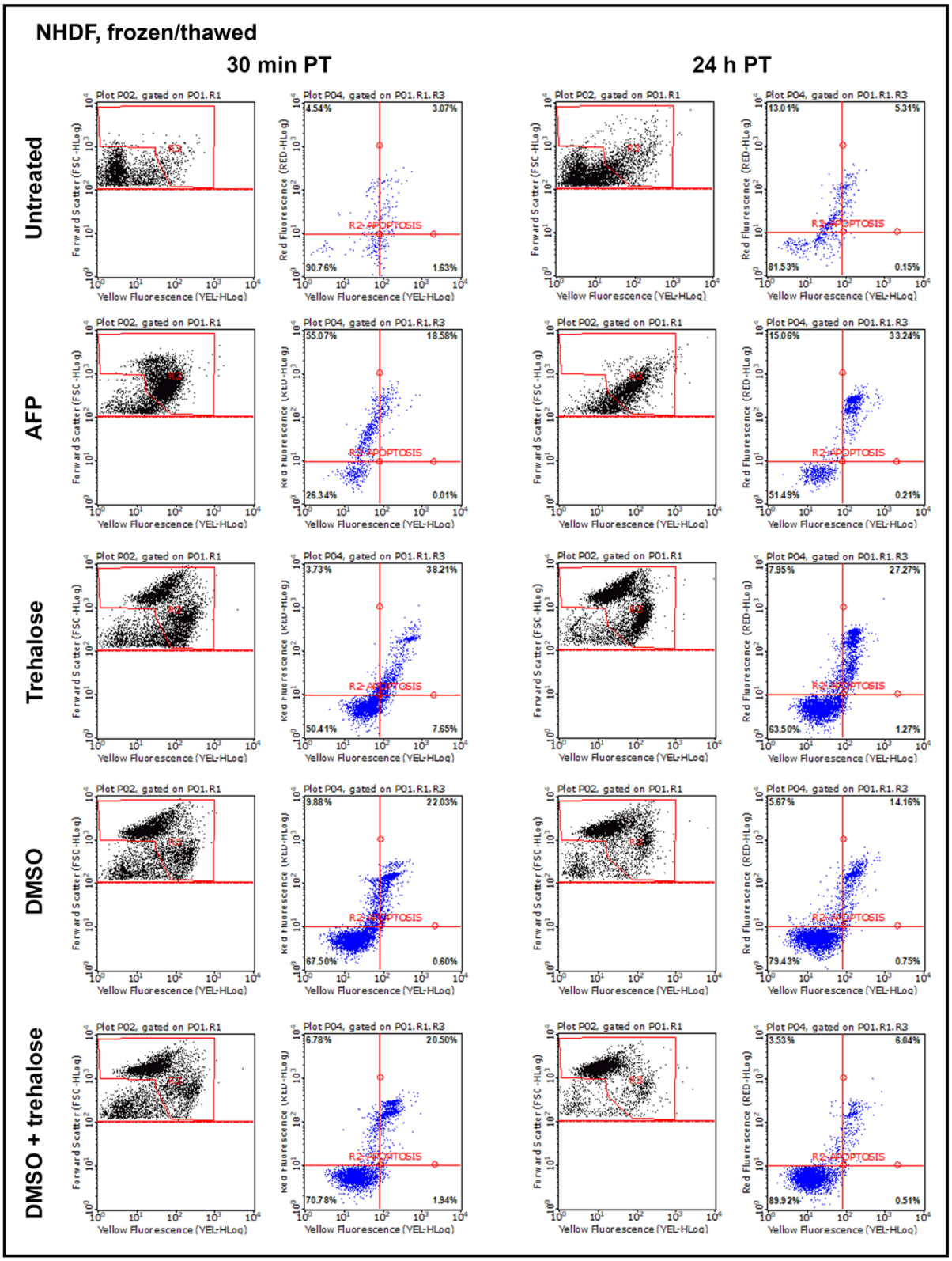

Data 1B: Flowcytograms (Annexin V vs. Propidium iodide, PI) obtained for frozen/thawed NHDF cells immediately (30 min) and 24 h after their treatments with cryoprotectants (AFP, trehalose, DMSO or combination of trehalose + DMSO) and freezing/thawing. Left columns: FSC vs. Annexin V (YEL-HLog, horizontal axis) plots showing fractions of gated cells; right plots: Annexin V (YEL-HLog, horizontal axis) vs. Propidium iodide (PI, RED-HLog, vertical axis) showing cell viability. The percentage of cells is indicated for each Annexin V/PI category.

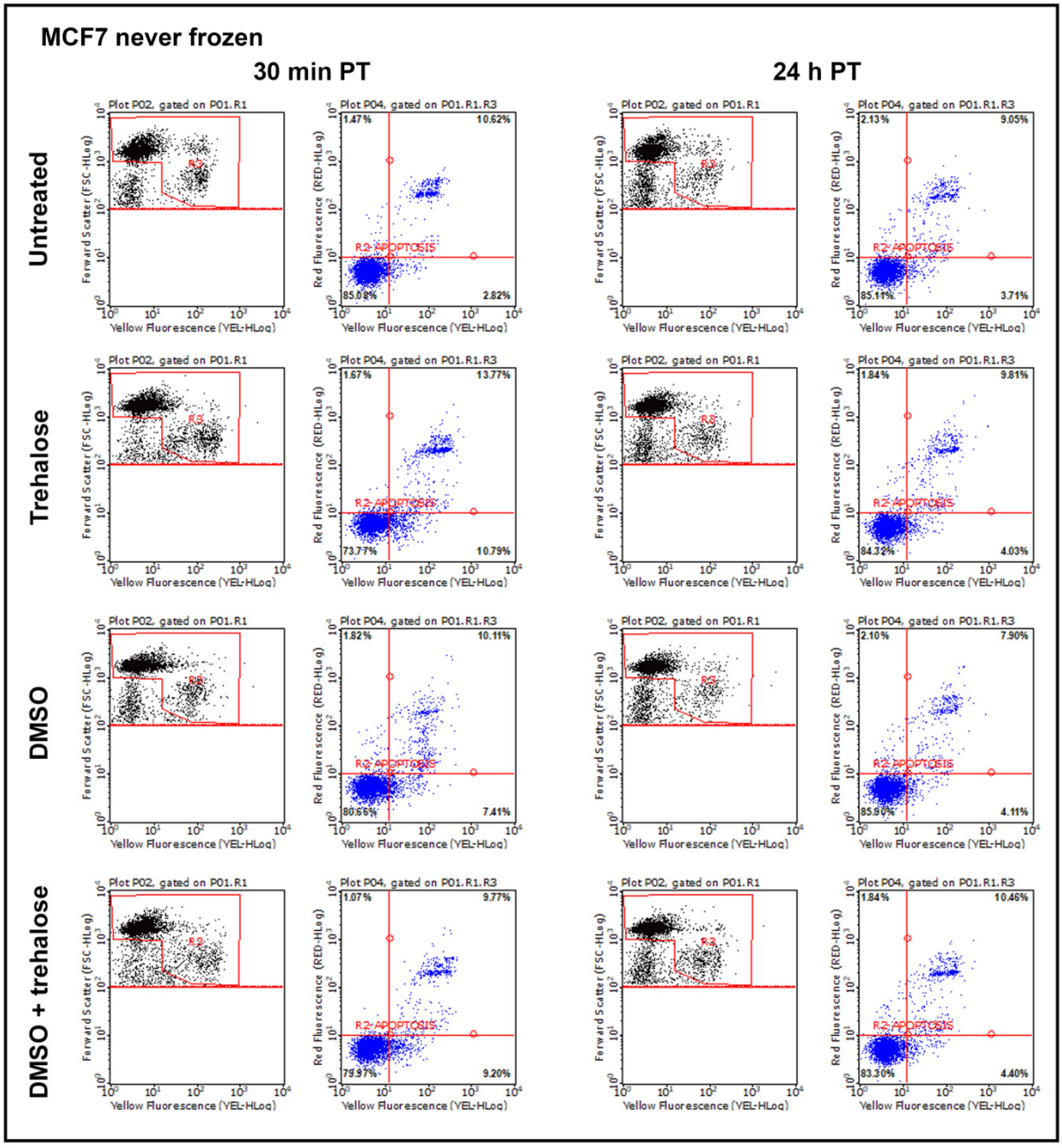

Data 1C: Flowcytograms (Annexin V vs. Propidium iodide, PI) obtained for never frozen MCF7 cells before (untreated) and 30 min or 24 h after their treatments (post-treatment, PT) with cryoprotectants (AFP, trehalose, DMSO or combination of trehalose + DMSO). Left columns: FSC vs. Annexin V (YEL-HLog, horizontal axis) plots showing fractions of gated cells; right plots: Annexin V (YEL-HLog, horizontal axis) vs. Propidium iodide (PI, RED-HLog, vertical axis) showing cell viability. The percentage of cells is indicated for each Annexin V/PI category.

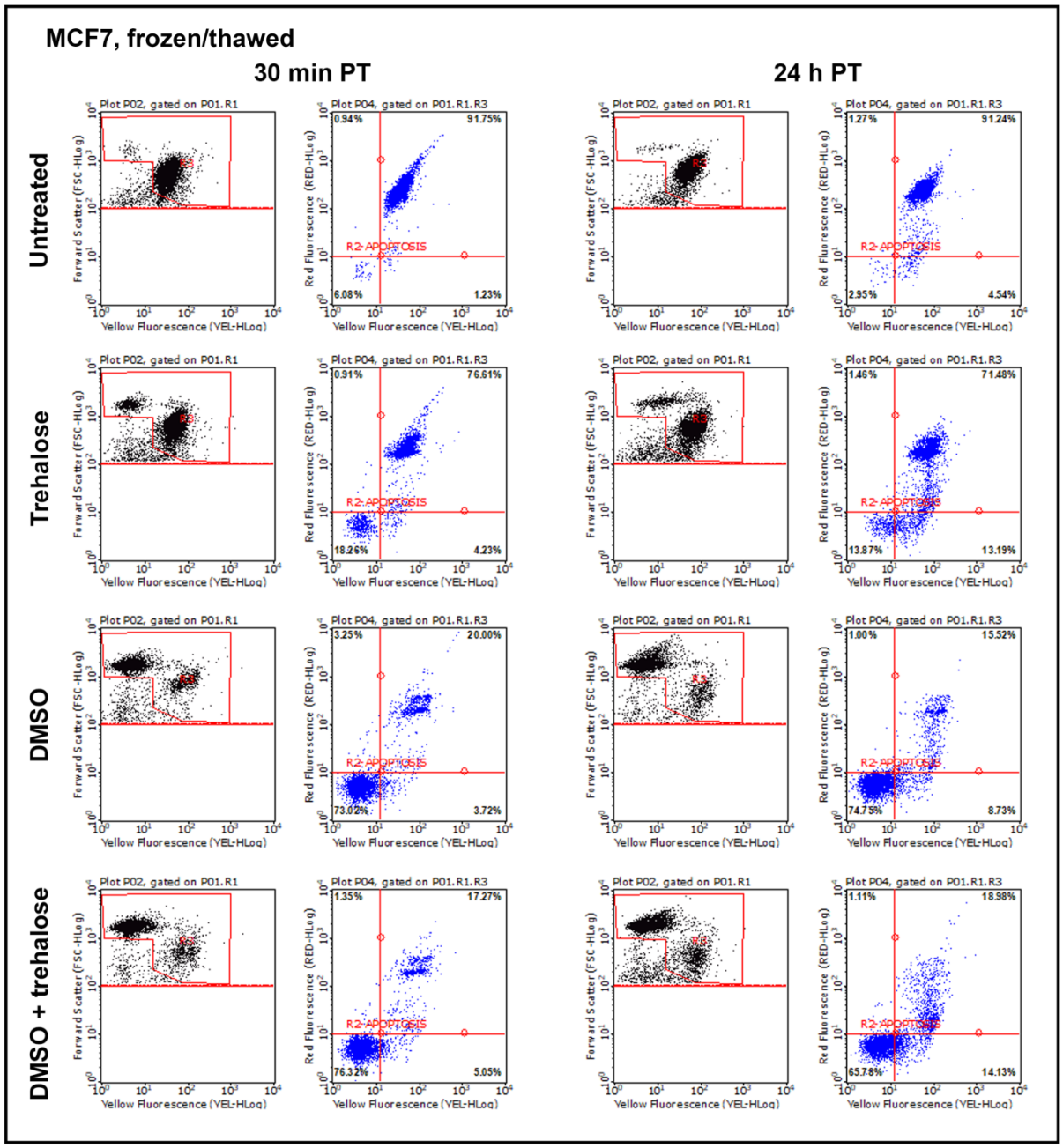

Data 1D: Flowcytograms (Annexin V vs. Propidium iodide, PI) obtained for frozen/thawed MCF7 cells immediately (30 min) and 24 h after their treatments with cryoprotectants (AFP, trehalose, DMSO or combination of trehalose + DMSO) and freezing/thawing. Left columns: FSC vs. Annexin V (YEL-HLog, horizontal axis) plots showing fractions of gated cells; right plots: Annexin V (YEL-HLog, horizontal axis) vs. Propidium iodide (PI, RED-HLog, vertical axis) showing cell viability. The percentage of cells is indicated for each Annexin V/PI category.

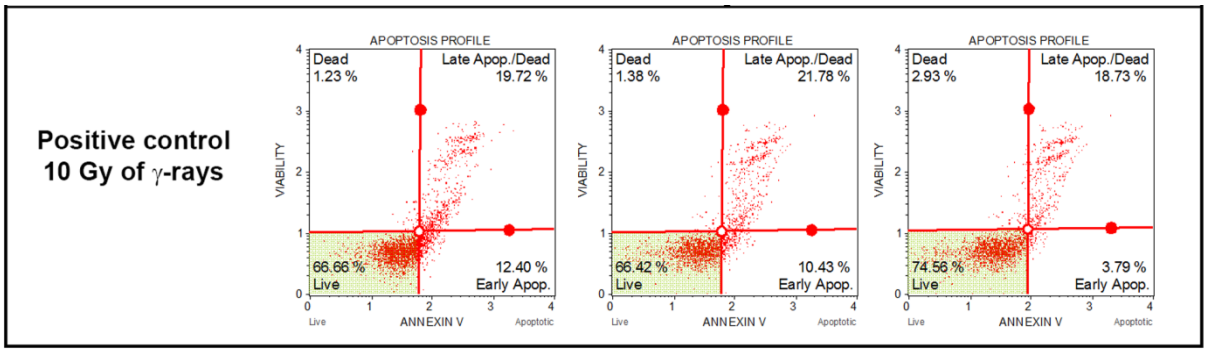

Data 2: Flowcytograms (Annexin V vs. Propidium iodide, PI) obtained for positive controls – NHDF cells irradiated with 10 Gy of γ-rays, 24 h after their irradiation. Annexin V (YEL-HLog, horizontal axis) vs. Propidium iodide (PI, RED-HLog, vertical axis) plots show cell viability. The percentage of cells is indicated for each Annexin V/PI category.

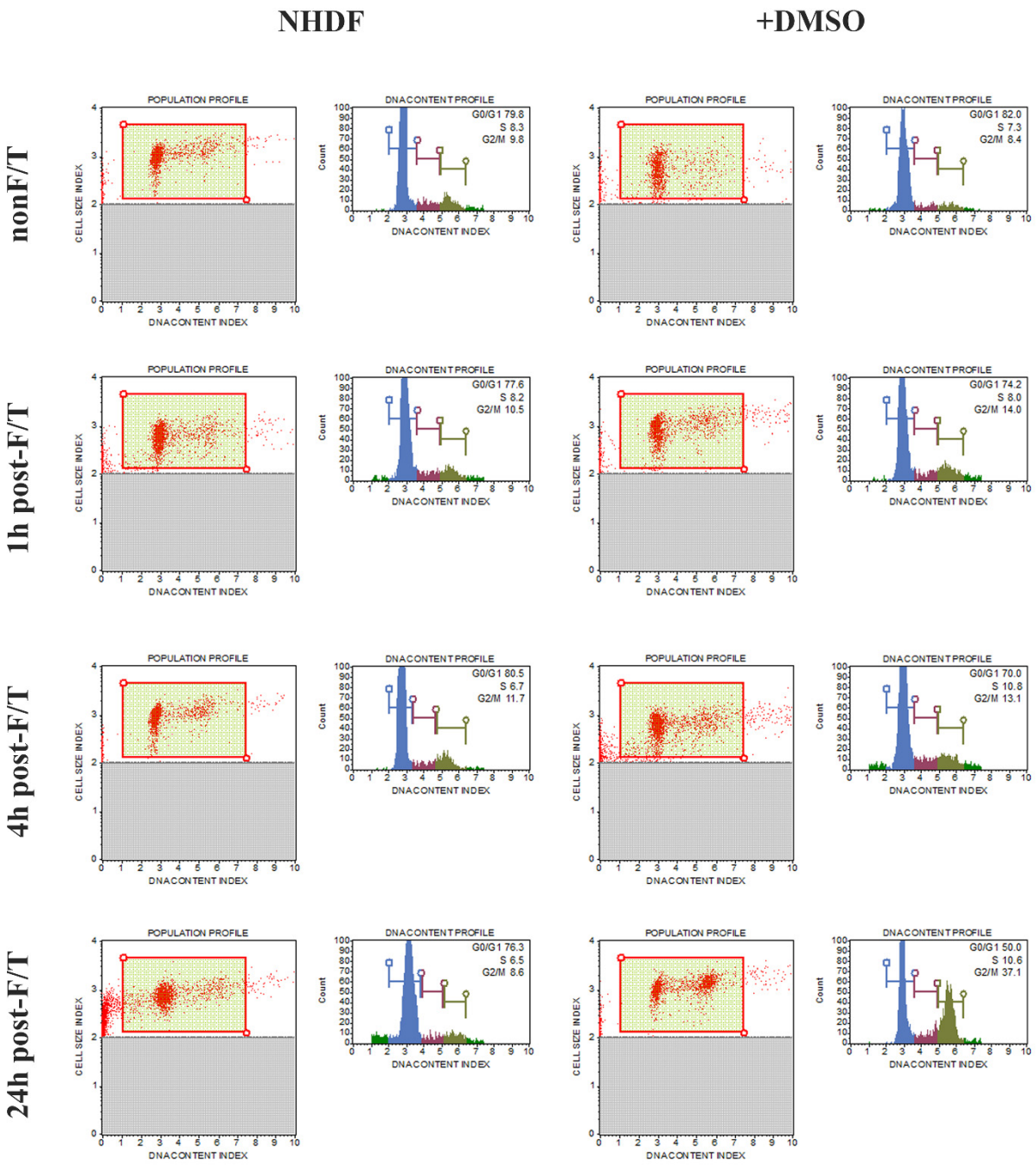

Data 3 (part 1): Cell cycle distributions before and after freeing/thawing – flowcytograms for NHDF fibroblasts. All cells harvested from cell cultures (including cells floating in the media) were scored according to DNA content before freezing (nonF/T) and 1, 4, and 24 hours after freezing/thawing (F/T).

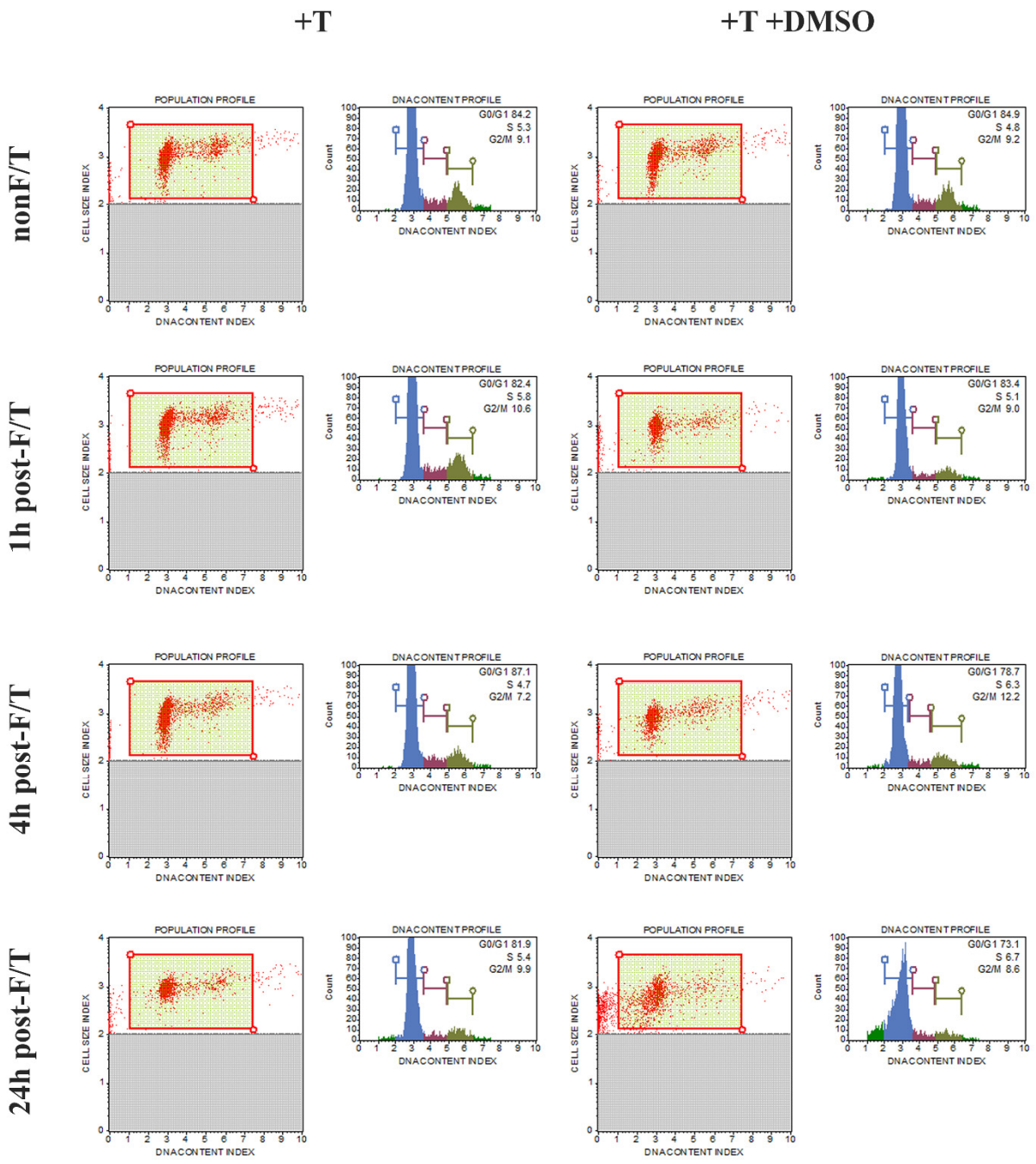

Data 3 (part 2): Cell cycle distributions before and after freeing/thawing – flowcytograms for NHDF fibroblasts. All cells harvested from cell cultures (including cells floating in the media) were scored according to DNA content before freezing (nonF/T) and 1, 4, and 24 hours after freezing/thawing (F/T).

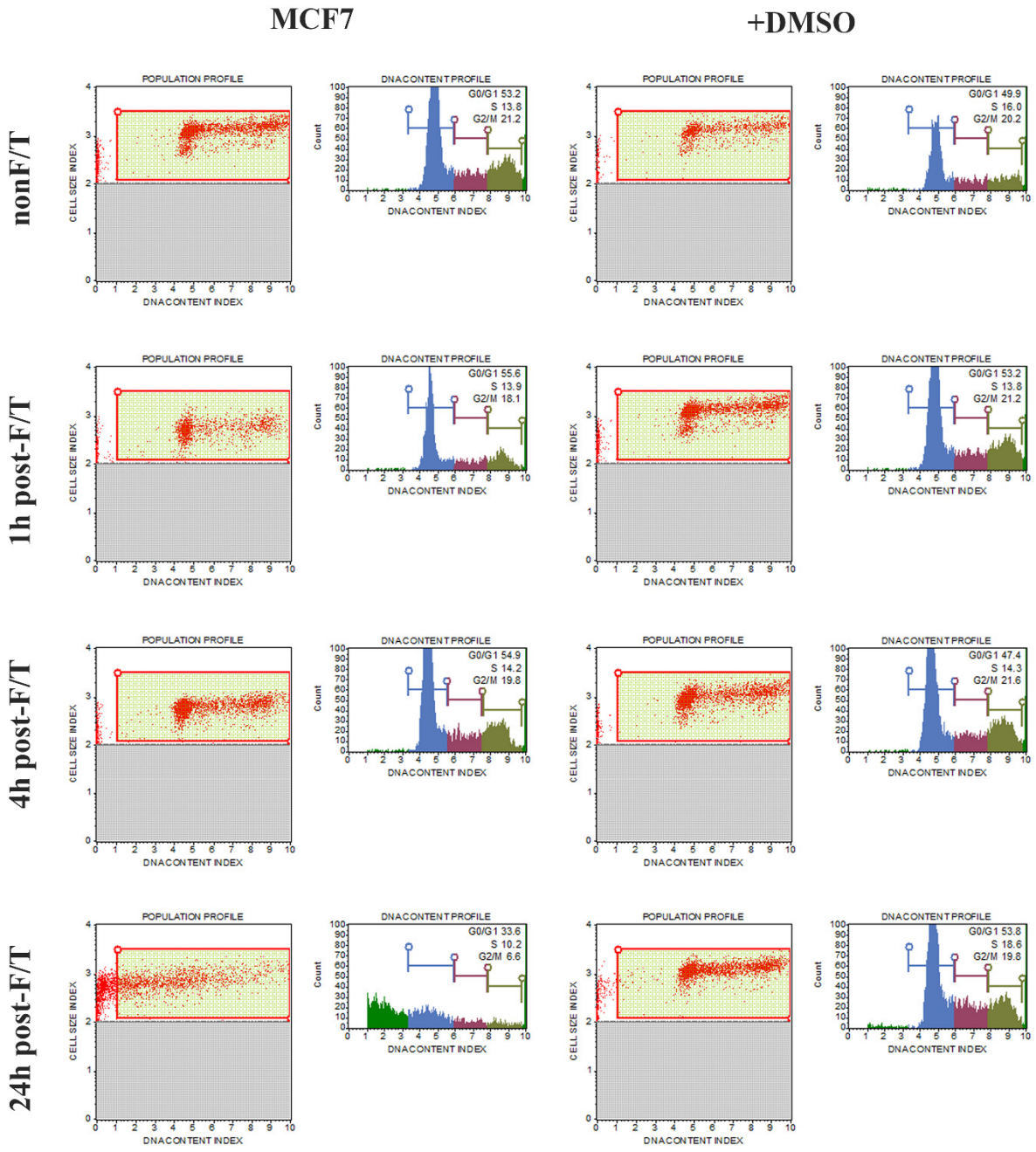

Data 4 (part 1): Cell cycle distributions before and after freeing/thawing – flowcytograms for MCF7 cells. All cells harvested from cell cultures (including cells floating in the media) were scored according to DNA content before freezing (nonF/T) and 1, 4, and 24 hours after freezing/thawing (F/T).

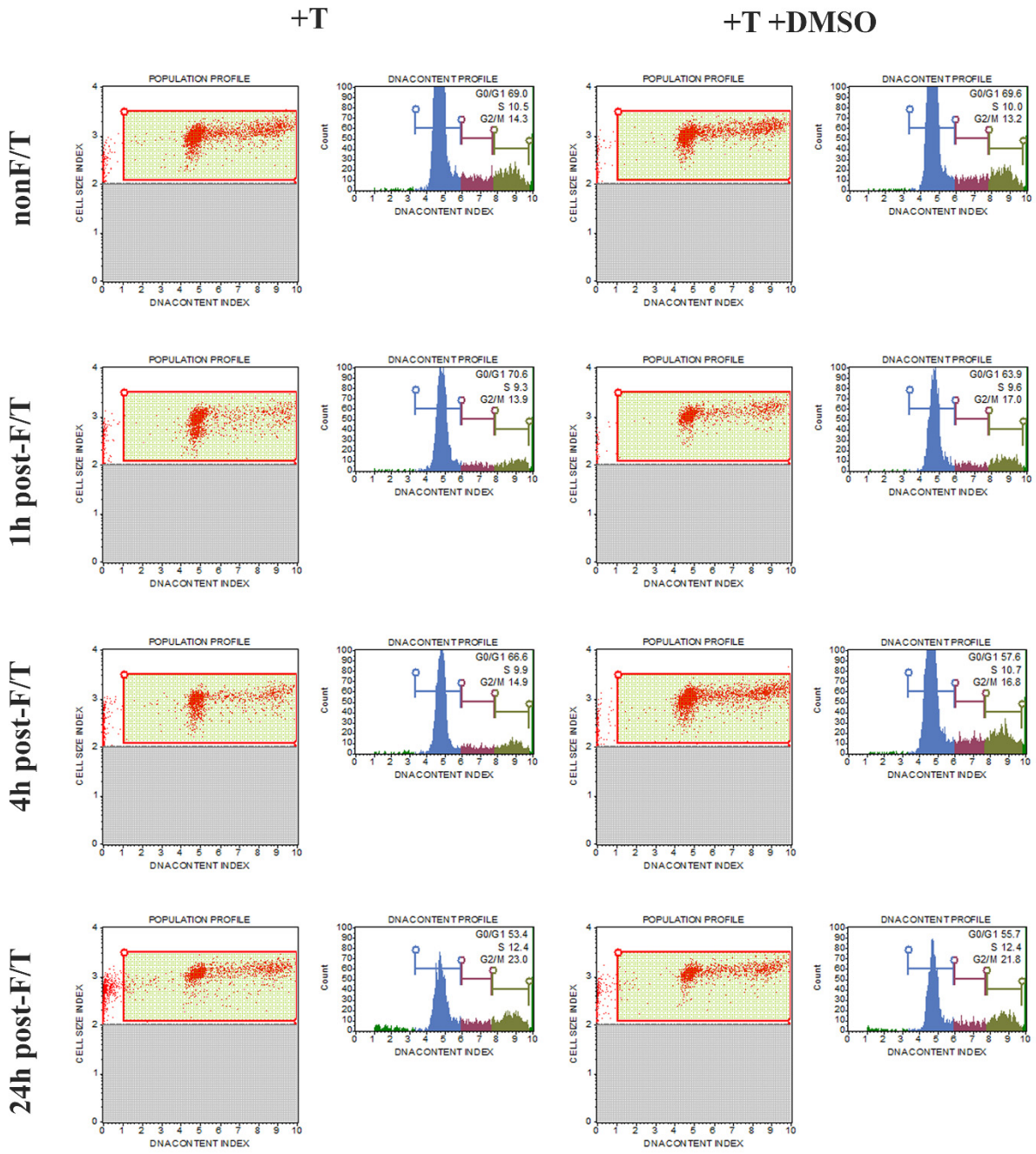

Data 4 (part 2): Cell cycle distributions before and after freeing/thawing – flowcytograms for MCF7 cells. All cells harvested from cell cultures (including cells floating in the media) were scored according to DNA content before freezing (nonF/T) and 1, 4, and 24 hours after freezing/thawing (F/T).

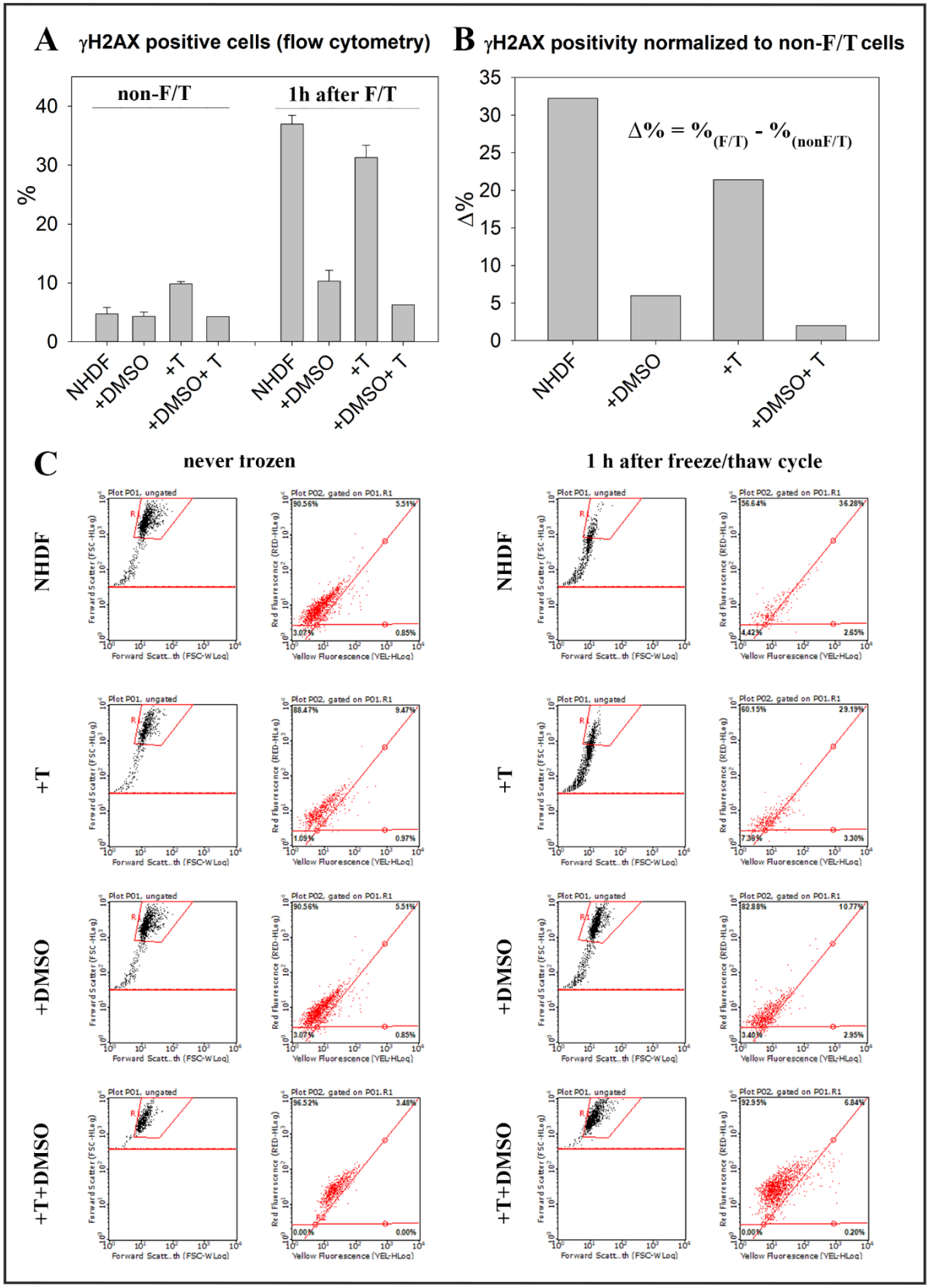

Data 5: H2AX phosphorylation at Ser139 (γH2AX) quantified by flow cytometry in never frozen and frozen/thawed NHDF cells treated or not treated with cryoprotectants of different classes – trehalose, DMSO and their combination. A. Proportions [%] of γH2AX-positive cells; **B.** Increase of γH2AX-positivity upon the freeze/thaw cycle, normalized to background values in non-frozen cells (calculated as $\Delta\% = \%_{(F/T)} - \%_{(nonF/T)}$). **C.** Illustrative flowcytograms for all treatments; left: cell gating; right: flowcytograms showing γH2AX (YEL-HLog, horizontal axis) vs. H2AX (RED-HLog, vertical axis) cell staining intensity; the percentage of γH2AX positive cells is indicated (upper right corner).

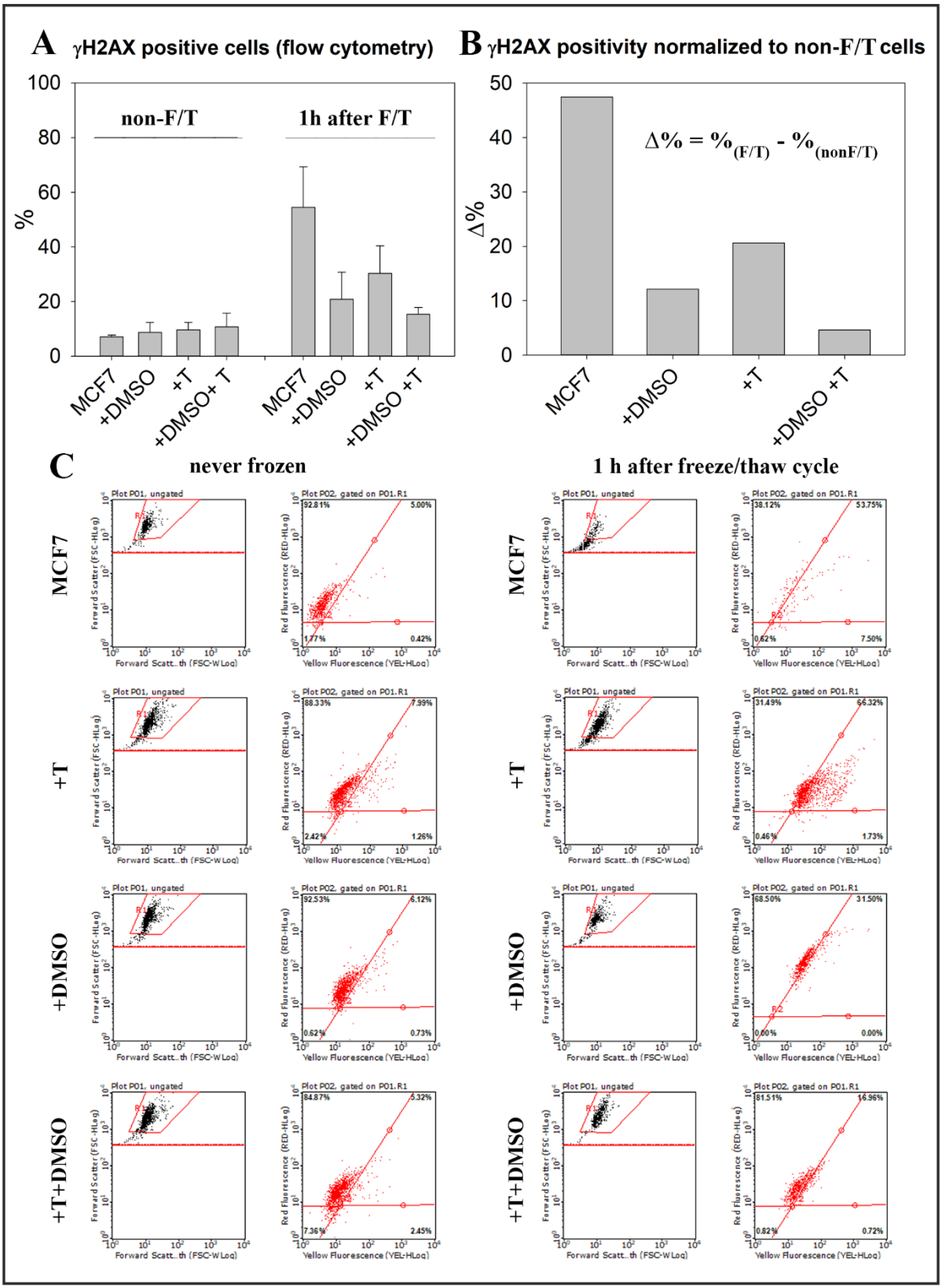

Data 6: H2AX phosphorylation at Ser139 (γH2AX) quantified by flow cytometry in never frozen and frozen/thawed MCF7 cells treated or not treated with cryoprotectants of different classes – trehalose, DMSO and their combination. A. Proportions [%] of γH2AX-positive cells; **B.** Increase of γH2AX-possitivity upon the freeze/thaw cycle, normalized to background values in non-frozen cells (calculated as $\Delta\% = \%_{(F/T)} - \%_{(nonF/T)}$). **C.** Illustrative flowcytograms for all treatments; left: cell gating; right: flowcytograms showing γH2AX (YEL-HLog, horizontal axis) vs. H2AX (RED-HLog, vertical axis) cell staining intensity; the percentage of γH2AX positive cells is indicated (upper right corner).

RSC Advances

PAPER

View Article Online
View Journal | View Issue

Cite this: *RSC Adv.*, 2017, **7**, 352

Theoretical and experimental study of the antifreeze protein AFP752, trehalose and dimethyl sulfoxide cryoprotection mechanism: correlation with cryopreserved cell viability†

Irena Kratochvílová,*[a] Martin Golan,[af] Karel Pomeisl,[a] Jan Richter,[a] Silvia Sedláková,[a] Jakub Šebera,[a] Júlia Mičová,[ag] Martin Falk,[b] Iva Falková,[b] David Řeha,[ch] K. Wade Elliott,[d] Krisztina Varga,[d] Shelby E. Follett[e] and Daniel Šimek[a]

Received 12th October 2016
Accepted 30th November 2016

DOI: 10.1039/c6ra25095e

www.rsc.org/advances

In this work the physico-chemical properties of selected cryoprotectants (antifreeze protein TrxA-AFP752, trehalose and dimethyl sulfoxide) were correlated with their impact on the constitution of ice and influence on frozen/thawed cell viability. The freezing processes and states of investigated materials solutions were described and explained from a fundamental point of view using *ab initio* modelling (molecular dynamics, DFT), Raman spectroscopy, differential scanning calorimetry and X-ray diffraction. For the first time, in this work we correlated the microscopic view (modelling) with the description of the frozen solution states and put these results in the context of human skin fibroblast viability after freezing and thawing. DMSO and AFP had different impacts on their solution's freezing process but in both cases the ice crystallinity size was considerably reduced. DMSO and AFP treatment in different ways improved the viability of frozen/thawed cells.

1. Introduction

Effective cryopreservation is an important practical problem not only in medicine, but also in the pharmaceutical and food industries. A major drawback of cryopreservation is that ice crystallization during the freezing process can significantly damage the cells which then lose viability after thawing.[1–4] The freezing process is very complex, and the behaviour of water in both its liquid and frozen states is strongly affected by added substances.[2–4]

In the presence of cryoprotectants, cells can be recovered from temperatures at almost two hundred degrees below the freezing point of water due to application of specific materials – cryoprotectants. Cryoprotectants affect many processes which take place outside and inside frozen and thawed cells at various levels.[1–4] Recent studies have addressed cell survival after cryopreservation but have not correlated the effectiveness of cryoprotection with the freezing mechanism. In this work we focused on frozen/thawed cell protection induced by altering the freezing/thawing conditions and processes resulting namely in different sizes of frozen solution ice crystals.[5–10]

From thermodynamic point of view there are two classes of substances that can modify the water freezing. Compounds from the first class (dimethyl sulfoxide, trehalose) affect the thermodynamics of the freezing process. Materials from the second category (antifreeze proteins) block ice formation based on the kinetic factors.[1–3]

In this work we explored the difference in ice crystal formation and cells viability when different cryoprotectants were applied. We examined properties of frozen/thawed dimethyl sulfoxide (DMSO), trehalose, the antifreeze protein TrxA-ApAFP752 (AFP) and DMSO + trehalose solutions both experimentally and theoretically using X-ray diffraction (XRD), Raman spectroscopy, differential scanning calorimetry (DSC), molecular dynamics and *ab initio* modelling.[4,11–29] For the first time, in this work we correlated the microscopic view (modelling) with the description of the frozen solution states (XRD,

[a]*Institute of Physics, Academy of Sciences of the Czech Republic, v.v.i., Na Slovance 2, CZ-182 21, Prague 8, Czech Republic. E-mail: krat@fzu.cz*
[b]*Institute of Biophysics, Academy of Sciences of the Czech Republic, v.v.i., Kralovopolska 135, CZ-612 65 Brno, Czech Republic*
[c]*Institute of Microbiology, Academy of Sciences of the Czech Republic, v.v.i., Zámek 136, CZ-373 33 Nové Hrady, Czech Republic*
[d]*Deparment of Molecular, Cellular, and Biomedical Sciences, University of New Hampshire, 46 College Road, Durham, NH, 03824, USA*
[e]*Department of Chemistry, University of Wyoming, 1000 E. University Ave, Laramie, WY, 82071, USA*
[f]*Faculty of Mathematics and Physics, Charles University in Prague, Ke Karlovu 5, CZ-121 16 Prague 2, Czech Republic*
[g]*Institute of Chemistry, Slovak Academy of Sciences, Dubravska cesta 9, 845 38 Bratislava 4, Slovak Republic*
[h]*Faculty of Sciences, University of South Bohemia in Ceske Budejovice, Zamek 136, 373 33 Nove Hrady, Czech Republic*

† Electronic supplementary information (ESI) available. See DOI: 10.1039/c6ra25095e

Raman spectroscopy, DSC)[27] and put these results in the context of human skin fibroblasts viability after freezing and thawing.[28,29] Correlating cell viability and the influence of cryoprotectants on the ice constitution, we identified important characteristics of materials that induce cell cryoprotection. Results of this interdisciplinary theoretical and experimental work lead to deeper understanding of the complex freezing/thawing processes, which will contribute to the rational design of cryofunctional materials.[30]

2. Materials and methods

2.1 Cryoprotectant solutions, cells processing

Cryoprotection experiments in live cells were performed on certified normal human skin fibroblasts (NHDF) obtained from CLS Cell Line Service GmbH (Eppelheim, Germany). Cells were grown at 37 °C in humidified atmosphere with 5% CO_2 in DMEM medium (PAN Biotech, Aidenbach, Germany, cat. no.: P03-0710) supplemented with 10% foetal calf serum (FCS; PAA Laboratories GmbH, Pasching, Austria) and standard antibiotics (1% penicillin + streptomycin; stock solution mixture 10 000 U mL^{-1} penicillin + 10 mg mL^{-1} streptomycin; PAN Biotech, cat. no.: P06-07100). The cells obtained (at passage 2) were multiplied and frozen, and the "young" passages 5 and 6 used for experiments to prevent possible accumulation of chromosomal aberrations and mutations and their potential effects on results.

Flow cytometry was used to quantify survival and apoptosis in cells that were frozen with or without cryoprotectants. The Muse® Cell Analyser (Merck Millipore) and Muse® Annexin V & Dead Cell Assay Kit (MCH100105, Millipore), which can discriminate between live, early apoptotic, late apoptotic/necrotic and dead cells, were used according to Hofer *et al.*[25] To allow the cells to enter apoptosis, flow cytometry measurements were performed 24 h after the cryoprotectant treatment (in the case of non-frozen cells) or after thawing (in the case of frozen cells).

Cells were frozen by cooling to −80 °C using a gradient of −1 °C min^{-1} in standard medium (untreated cells). Cryoprotectant treated cells were incubated prior to cooling (to −80 °C using a gradient of −1 °C min^{-1}) in standard medium containing either trehalose for 24 h, in DMSO for 2 min or in AFP for 2 h (Table 1). Details of expression and purification of recombinant TrxA-ApAFP752 (AFP) fusion protein are in the ESI section.†

Table 1 Cryoprotectants solutions used for flow cytometry

Sample	Composition
DMSO	DMSO 10% (w/w) in DMEM (cell culture) medium
DMSO + trehalose	DMSO 10% (w/w) + 100 mM trehalose 3.2% (w/w) in DMEM (cell culture) medium
AFP	0.5 mg mL^{-1} in DMEM (cell culture) medium
Trehalose	3.2% (w/w) (100 mM trehalose in DMEM (cell culture) medium

For XRD and Raman spectroscopy experiments, aqueous solutions of DMSO and trehalose or DMSO and trehalose PBS solutions containing 50 mM sodium phosphate and 50 mM NaCl in DI water at pH 8.0 (phosphate buffered saline, PBS) were used – Table 2. We also measured the fusion TrxA-ApAFP752 antifreeze protein: 6.85 μM TrxA-ApAFP752 with PBS dissolved in DI water (AFP solution). The D-(+)-trehalose dihydrate and the dimethyl sulfoxide (DMSO) were purchased from Sigma-Aldrich. Deionized water for preparation of solutions was purified by Milli Q Plus system (Millipore), having a resistivity 18.2 MΩ cm (25 °C).

2.2 X-ray diffraction

The X-ray diffraction (XRD) measurements were performed using a DCS 350 dome-type temperature chamber from Anton-Paar mounted on a Bruker D8 horizontal diffractometer equipped with a 12 kW copper rotating-anode. Each liquid specimen was inserted in an aluminium cuvette, covered with 5 μm Mylar foil and sealed by tightening a steel ring over the foil. The incident beam was collimated using a Goebel mirror with a divergence of around 0.02° in the horizontal direction and around 4° in the vertical direction. For all specimens, ω–χ mapping was performed using the 110 reflection of hexagonal ice. The detector was kept at a 2θ angle of 39.85°, leading to an effective integration angle of ±0.15° in 2θ. The angle of incidence (horizontal tilt) varied from 5° to 35° (by 0.02° steps), and the vertical inclination was varied from −4° to +16° (by 2° steps). The whole map covers a solid angle of 0.12 sr. Since the two nearest (110) crystallographic planes are inclined 60°, none of the diffracting crystals can be recorded twice in the range of the map, and the probability of any randomly-oriented ice crystal being recorded in the map trough of one of its six equivalent {110} planes is about 5.8%. The quality of the statistics was thus affected by the number of observed crystallites, and it should be kept in mind that they represent only 1/17 of the entire statistical ensemble. Each map was acquired over 90 min at a constant temperature.

Concerning the size of the ice crystals in frozen solutions, we performed a specimen-to-specimen relative comparison using the diffraction intensity distribution.[31,32]

Based on the assumption that the angular profile of the intensity of diffracting crystal is normal (Gaussian), we can deconvolute the diffracting volume distribution from the distribution of levels of equal intensity to the expected number of peaks that created such a distribution. The theoretical distribution of levels of equal intensity for non-overlapping Gaussian peaks with the same peak intensity is a step-function on a logarithmical x-scale (*i.e.*, equal to one below the peak intensity value and zero above it if only a single crystal size was observed), which was shown using a simulation of a hundred random Gaussian peaks with a maximum intensity of 3×10^5 cps and random noise of 1000 cps. The deconvolution represents decomposing the observed intensity histograms into a set of such step-functions, which represent the distribution of peak intensities. The simulated data proceeding through this deconvolution procedure exhibit the maximum distribution at

Table 2 Composition of samples for XRD and Raman spectroscopy

Sample	Composition
DMSO solution/DMSO PBS solution	DMSO 10% (w/w) in DI water/PBS
DMSO + trehalose solution/DMSO + trehalose PBS solution	DMSO 10% (w/w) + 100 mM trehalose 3.2% (w/w) in DI water/PBS
AFP solution	0.05–1% (w/w) TrxA-ApAFP752, phosphate + NaCl in DI water, molar concentration of TrxA-ApAFP752: (71.34 μM TrxA-ApAFP752 in 50 mM $Na_xH_yPO_4$ buffer containing 50 mM NaCl)
Trehalose solution/trehalose PBS solution	3.2–41% (w/w) trehalose in DI water/PBS

the expected peak intensity level, being smeared by the effect of peak overlapping and added noise (the distribution therefore does not show only a single peak). The same procedure was applied on the experimental data to estimate the volume distribution of diffracting ice crystals.[31]

2.3 Theoretical modelling

In order to investigate the antifreeze activity of the selected cryoprotectants (DMSO, trehalose and ApAFP752) in aqueous solution, molecular dynamics simulations were performed using the GROMACS 4.5.5 software package[13] and the AMBER99SB-ILDN force field.[14] All molecular dynamics simulations were performed in explicit SPC/E water and under periodic boundary conditions. Long-range electrostatic interactions were calculated using the particle mesh Ewald method.[15] The Berendsen thermostat was used in all simulations with a thermostat relaxation time of 0.1 ps at both room temperature (27 °C) and low temperature (−8 °C). After energy minimization and an equilibration phase of 100 ps, a production run of 10 ns was performed for each simulated system. The trehalose and DMSO residues, for which the parameters were not available in the Amber99SB-ILDN force field, were parameterized using the standard RESP procedure with charges derived from an HF/6-31G* calculation.[16] In order to evaluate the strength of the interactions between individual components, the interaction energies between water molecules, DMSO molecules, trehalose molecules, trehalose/water molecules and DMSO/water molecules were also calculated. The 3D structure of ApAFP752 protein is not known, and we therefore used the 3D-JIGSAW (version 2.0) – online structure prediction program.[17] The 3D geometry of ApAFP752 protein was created on the basis of homology modelling using a known 3D structure of *Tenebrio molitor* AFP named TmAFP (PDB ID: 1EZG),[18] which has a 69% sequence homology to the ApAFP752 protein. The model refinement was performed using the YASARA program.[19] Hydrogens were added automatically in GROMACS except for one amino acid (histidine), where the correct orientations and protonation patterns were derived from the chemical environment and the hydrogen bonding capabilities using an algorithm embedded in YASARA that is based on optimization of hydrogen bond networks combined with pK_a estimation. The initial geometry of trehalose was derived on the basis of the crystal structure prepared and measured by H. Nagase *et al.*[20] The crystal structure of trehalose was gradient optimized by the DFT method using B3LYP-D3/6-31G*. The molecular dynamics simulations were done for the following cases: (i) one trehalose sugar in a cubic simulation box with 500 water molecules, (ii) 56 DMSO molecules in a cubic simulation box with 2000 water molecules, (iii) four trehalose sugars and 56 DMSO molecules in a cubic simulation box with 2000 water molecules, (iv) ApAFP752 protein and two Cl^- ions were covered by a water layer (9043 molecules) in a cubic simulation box. The concentration of trehalose, DMSO, and mixture of trehalose and DMSO correspond to our experimental concentrations.

Hydrogen bonding facilitates cryoprotectant–water and water–water interactions in solution, and the dynamics and H-bonding characterize the freezing process of the cryoprotective solutions. The analysis of this behaviour includes the study of the hydrogen bond lifetime. The geometrical criterion that determines the existence of a hydrogen bond is specified as $r \leq r_{HB}$ 0.35 nm and $\alpha \leq \alpha_{HB} = 30°$, where r_{HB} indicates the maximum distance between a donor and acceptor pair for a hydrogen bond within the maximum angle of 30°. The lifetime of the hydrogen bond is calculated from the H-bond time autocorrelation function of the existence criterion.

$$C_{HB}(t) = \frac{\langle s_i(t_0)s_i(t)\rangle}{\langle {s_i}^2(t_0)\rangle} \quad (1)$$

with $s_i(t) = (0,1)$ for a hydrogen bond i at time t. The hydrogen bond forward lifetime τ_{HB} can then be calculated by

$$\tau_{HB} = \int_0^\infty C_{HB}(t)\mathrm{d}t \quad (2)$$

which allows us to yield an estimate for the average existence time.[21,22] In order to evaluate H-bond time autocorrelation function correctly, at every 0.1 ps we recorded the trajectory in our simulations.

In order to estimate the interaction potential between individual molecules included in our study we computed the interaction energy ΔE_{int} (BSSE) with inclusion of the basis set superposition error (BSSE) using the following equation:

$$\Delta E_{int}\,(\mathrm{BSSE}) = E_{dimer} - (E_{monomer1} + E_{monomer2}) + E_{BSSE} \quad (3)$$

where E_{dimer} is an electronic energy of a dimer system, $E_{monomer}$ is an electronic energy of monomer units and E_{BSSE} is a BSSE correction. The basis set superposition error was calculated using counterpoise corrections. Our computational procedure consisted of several steps: (1) gradient optimization of individual monomers with the B3LYP + D3/6-31G(d,p) method using the PCM model, which describes implicit water

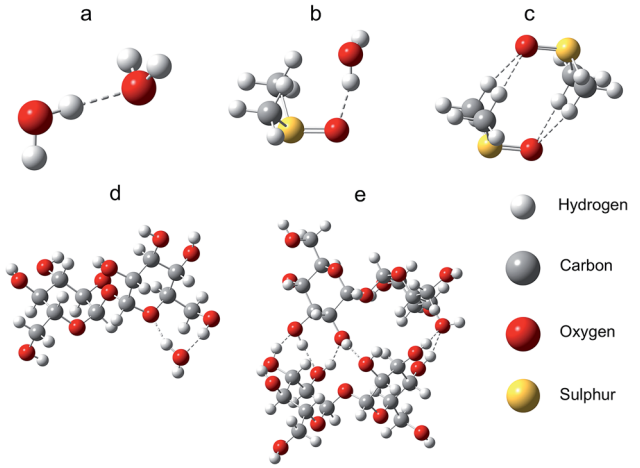

Fig. 1 The geometry-optimized structures. (a) Water dimer, (b) DMSO/water system, (c) DMSO dimer, (d) trehalose/water system, (e) trehalose dimer. Dashed lines indicate intermolecular noncovalent interactions.

environment, (2) geometry optimization of a few possible dimers of all investigated systems with the B3LYP + D3/6-31G(d,p) method using the PCM model, (3) single point calculations directly performed on the optimized geometries of monomers and dimers with large basis set 6-311++G(d,p), (4) calculations of the basis set superposition correction with large basis set 6-311++G(d,p) *in vacuo*, (5) applications of eqn (1). Geometry-optimized dimers are depicted in Fig. 1.

2.4 Raman spectroscopy

Raman spectra can reveal chemical and phase composition of the sample as well as interactions of its constituents.[28] Specifically, they can be used for detection of a irregularity of the ice lattice and so-called eutectic phase. Euthetic phase is a shared crystal lattice formed by constituents mixed in a fixed ratio.[27–29]

All data was acquired by a Renishaw RM1000 spectrometer equipped with a Leica DMLP microscope with a Leica PL FLUOTAR L 50×/0.55 objective. The excitation wavelength was 488 nm. The temperature during the course of the data acquisition was controlled by a Linkam LNP95 cooling stage. The stage operates with 0.01 °C precision and can reach temperatures as low as −196 °C.

Samples (50 μL) were held on the stage in PerkinElmer aluminium pans. After freezing, the samples became almost opaque, data was therefore collected from a surface layer of estimated thickness around 5 μm. The spectra were normalized at 3165 cm^{-1}.

For each sample, multiple spectra were measured. The spectra shown are those that exhibit all the observed spectral features of a given specimen and are thus characteristic of it.

2.5 Differential scanning calorimetry

Calorimetry, which is a universal method for investigating transition processes associated with the generation or consumption of heat, was used to evaluate the transformation temperatures (melting T_m, T_1) of the aqueous solutions of DMSO, trehalose disaccharide, and TrxA-ApAFP752.[3] Differential scanning calorimetry was performed in a Linkam optical differential scanning calorimeter DSC600 (single cell) system equipped with the LNP95 cooling system; this can reach temperatures as low as −196 °C. The experimental procedure for all investigated samples consisted of two rounds of calorimetric measurements performed in the cooling/heating mode at the same rates starting with the liquid sample at room temperature. The first round involved monitoring of the initial reversible transformation behaviour and determination of the freezing temperature, T_f, and the melting temperature, T_m. The cooling rate was −5 °C per minute down to −80 °C; stabilization for 5 minutes; then heating back to room temperature. The second round involved cycling between the T_f and T_m temperatures at a rate of 1 °C per minute with 10 minutes of stabilization. Cycling all of the measurements at one rate produced practically the same results (±1 °C shift).

3. Results

3.1 Cryopreserved cells viability

Using flow cytometry, we first checked whether the application of cryoprotectants and their combinations affected cell viability (Table 3). Next, we measured cell viability for cells after freeze/thaw experiments (Fig. 2). Without cryoprotectants, almost all frozen cells died after being thawed; only <7.5% survived 24 h post-thawing. The highest cryoprotective effect was brought about by DMSO (>80% survival 24 h post-thawing), especially when it was combined with trehalose (trehalose for 24 h followed by DMSO for 2 min); in that case, about 85% of cells survived 24 h after thawing. The improvement of cell viability by trehalose only (24 h-incubation) was also relatively large: 58.5% of cells survived 24 h after thawing. However, the cryoprotective effect of trehalose strongly depended on the incubation time and was only observable for incubations ≥24 h (4 h and 6 h incubations had no effect). AFP[10] exerted the smallest effect among the cryoprotectants studied with only 32.3% cell survival. Based on these results, we hypothesize that trehalose during 24 h of incubation enters the cells *via* pinocytosis. Small DMSO penetration and accumulation both in the cell cytoplasm and the nucleus was confirmed by Jinping Dong and colleagues.[28]

3.2 X-ray diffraction

X-ray diffraction measurements were performed on frozen samples, and the crystal angular distribution was measured and

Table 3 Cell viability of unfrozen cells detected 24 h after incubation by flow cytometry (Annexin V/7-AAD staining)

Cryoprotectant	Cell viability of unfrozen cells [%] (24 hours after incubation)
Control	89.8
AFP	63.3
Trehalose	67.8
DMSO	76.1
DMSO + trehalose	68.7

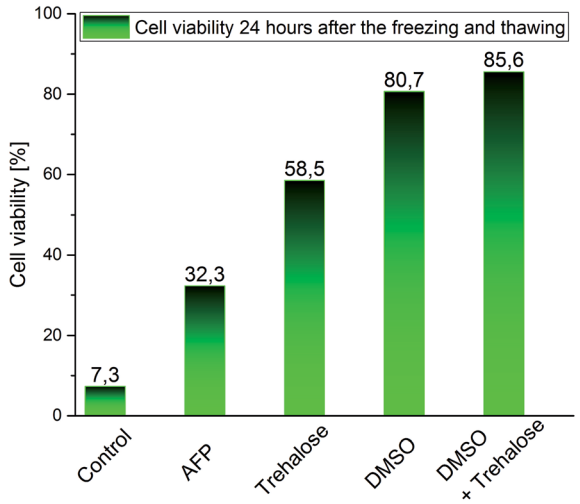

Fig. 2 Cell viability measured 24 h after freezing/thawing by flow cytometry (Annexin V/7-AAD staining).

compared for the studied materials (Table 2). Pure water had just a few very large crystals and the strongest diffraction intensity. An aqueous trehalose (41% (w/w)) solution showed crystal aggregates with similar orientations. This indicated that a crystal grew on one nucleus and that the growth was accompanied by precipitation of another phase, leading to curved crystals with needle/platelet/dendrite shapes. Trehalose in solution supports such aggregation of crystals in frozen samples. The rest of the samples, which contained AFP, DMSO and DMSO + trehalose, showed random crystal nucleation and growth. Fig. 4a shows histograms counting the data-points whose diffraction intensities lay in the particular ranges for each of the plots from Fig. 3 (from top to bottom correspondingly). Using a deconvolution procedure, equivalent histograms of the distribution of Gaussian peaks with maximum intensity in particular ranges are shown in Fig. 4b. The maps shown within each figure use the same logarithmical scale in order to be obvious, how the diffraction intensities differ among the maps. The same maps as in Fig. 3 can be found more contrasting in corresponding figures in ESI,† where it corresponds to a particular map at −20 °C (here the figures are sorted according to the cryoprotectant concentration).

In all cases, except for pure water, the results showed a decrease in the distribution for the strongest observed peaks (greatest x-values), which means that the distribution median lay in the range of smaller crystallites than would correspond to the maximum on the x-scale.

According to the kinematical theory of XRD, the diffraction intensity of crystallites (x-axis in Fig. 4b) is proportional to their volume. The histograms in Fig. 4b count the relative sample volume occupied by crystals with particular ranges of diffraction magnitude (proportional to crystal volume).[31,32] The linear dimension (diameter) of the ice crystals, being roughly the third root of the diffracting volume, was the greatest for frozen pure water. The thinnest distribution was observed for 41%(w/w) trehalose solution. Their crystal volumes were at least ten times smaller than ice crystals from pure water (where the true distribution maximum is expected to lie beyond the chart upper limit). 0.05% AFP solution crystal volumes were more than twice those of 41% (w/w) trehalose, while in frozen 1%(w/w) AFP

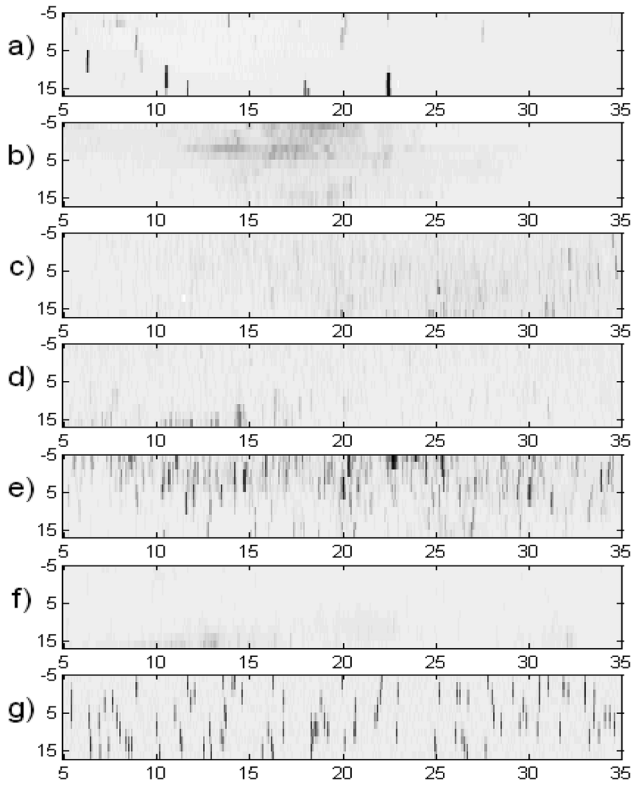

Fig. 3 Diffraction intensity maps in angular coordinates. A comparison of frozen specimens of (a) water, (b) 41% (w/w) trehalose, (c) 10% (w/w) DMSO, (d) 10% (w/w) DMSO + 3.2% (w/w) trehalose, (e) 0.05% (w/w) AFP, (f) 1% (w/w) AFP, (g) simulated peaks. Horizontal axis, angle ω (horizontal tilt); vertical axis, angle χ (vertical inclination); the grey scale is logarithmic and is the same for all plots.

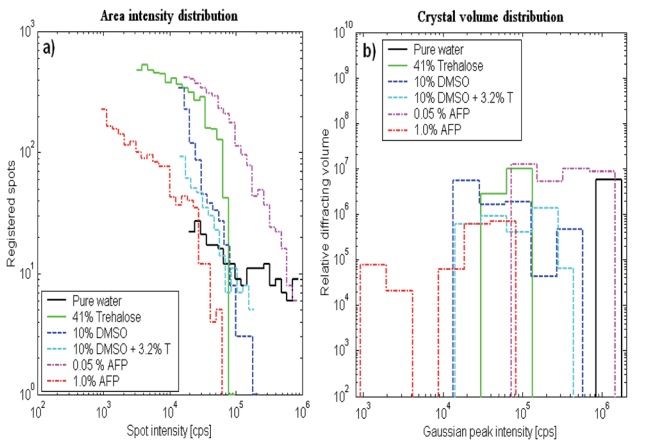

Fig. 4 Histograms of the (a) area intensity distribution and (b) crystal volume distribution. The range (horizontal axis) scales start at intensity levels that are safely over the noise level. The vertical scale is either the number of data points with the specified intensity (a) or the relative volume of diffracting crystals with particular maximum intensity (b).

solutions ice crystals were less than half the volume of 41% (w/w) trehalose. The mean crystal sizes of 41% (w/w) trehalose solution were roughly comparable to both samples with 10% (w/w) DMSO (with or without 3.2% trehalose).

Concerning the melting procedure, the samples differ significantly. The 41% (w/w) trehalose solution exhibited a gradual shift of the distribution of crystal volumes to smaller values maintaining its relatively narrow distribution range. This means that the larger crystals were melting continuously to small crystals (the number of small crystals became relatively higher). In the pure solution of PBS, this effect was not observed (the melting mode was similar to DMSO). DMSO-rich solutions exhibited a continuous decrease of the size crystal distribution, but the mean volume and the ratio of smaller-to-larger crystals were conserved (compared to the frozen solution). This indicates that once an ice crystal starts to thaw, it will complete the process of melting completely, while some others remain stable at certain temperature level, regardless of their size. The 1% (w/w) AFP sample exhibited the melting mode similar to 41% (w/w) trehalose (ESI section S1–S6†).

3.3 Theoretical modelling

Our calculations showed that the studied cryoprotectants in water influenced the water dynamics (hydrogen bond lifetime). The calculated lifetimes reflect the influence of cryoprotectants on water dynamics and subsequently the crystallization process (Table 4). DMSO affected the largest amount of water molecules in the solution of all the studied cryoprotectants. In addition, water molecules near the methyl groups of a DMSO molecule cannot form an alternative H-bond, which changes both their interactions with other water molecules and ice formation. DMSO also affected the water dynamics due to the negative charge of the oxygen atom (greater than the charge on oxygens in trehalose or in water) increasing the strength of the H-bond with water. Adding 3.2% (w/w) trehalose to 10% (w/w) DMSO aqueous solution did not significantly change the water/water and DMSO/water hydrogen bond lifetimes (compared to 10% (w/w) DMSO).

Table 4 Hydrogen bond lifetimes (τ_{HB}) between water/water molecules and cryoprotectant/water molecules calculated at 25 °C and at −8 °C for the tested solutions

Molecules used for the hydrogen bond lifetime calculations	τ_{HB} (ps) at 25 °C/τ_{HB} (ps) at −8 °C
Water	
Water/water	3.02/7.93
ApAFP752 in water	
ApAFP752/water	16.90/50.64
Surrounding water/water	3.02/7.95
Trehalose in water	
Trehalose/water	4.92/15.16
Surrounding water/water	3.12/8.08
DMSO in water	
DMSO/water	5.36/13.39
Surrounding water/water	3.71/10.14
Trehalose and DMSO in water	
Trehalose/water	6.81/21.41
DMSO/water	5.19/13.45
Surrounding water/water	3.76/10.34

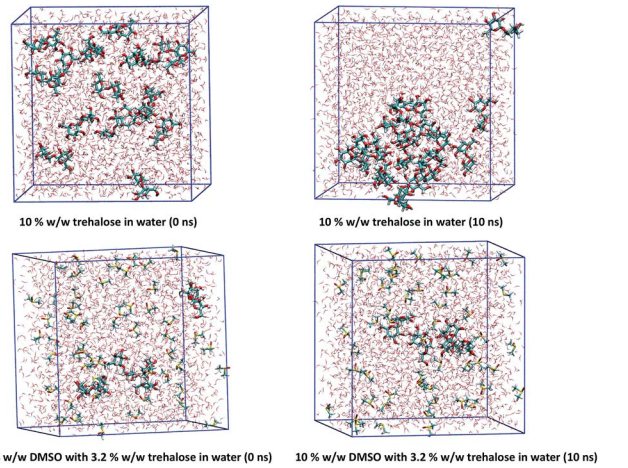

Fig. 5 10% (w/w) trehalose in the solvation box (top), and 10% (w/w) DMSO with 3.2% (w/w) trehalose in the solvation box (bottom). The start (0 ns) of the molecular dynamics simulation is on the left, and the end (10 ns) of the molecular dynamics simulation is on the right. The simulations were performed at room temperature.

The hydrogen bond lifetime calculated for AFP/water was longer than the DMSO/water and trehalose/water lifetimes. The reduction of surrounding water mobility when AFP is present may be related to the large size of the AFP molecule and ice-binding surface (mainly through the hydroxyl groups).[6,18] The AFP does not significantly influence free water but strongly influences the solvation shell around it. Under these conditions, AFP bound to the surface of ice crystals can inhibit their growth.

The electric dipole moments of DMSO and trehalose molecules in water were DFT calculated: 2.1 D for trehalose in water, 6.0 D for DMSO in water, and 2.5 D for water in water environment. The large electric dipole moment of DMSO, caused mainly by the strong negative charge of the oxygen atom and the strong positive charge of the sulphur atom, affected water molecules in the solutions. Mainly due to the prevalence of hydroxyl groups (high trehalose/trehalose interaction energy) and creation of multiple hydrogen bonds, trehalose easily forms clusters in water solutions (Table 4, Fig. 5 and Table S1†). The ratio of solvent 3(water) to the cryoprotectant atoms in modelled systems corresponded to the measured sample values.

Due to a relatively strong negative charge on the oxygen, DMSO can attract the positive part of a water molecule. DMSO does not form clusters – due to homogeneous distribution of DMSO molecules in solution, its large dipole moment affects material with high permittivity in the whole volume.

3.4 Raman spectroscopy

For PBS and AFP solutions frozen at −170 °C (Fig. 6), the mode at 3420 cm^{-1} (related to the 'eutectic' phase – in this case

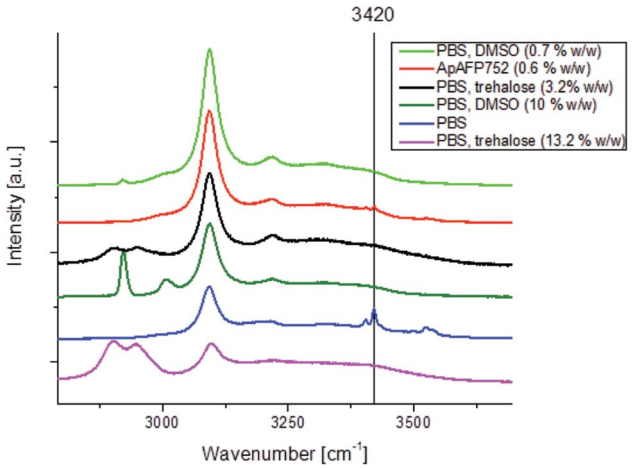

Fig. 6 Raman spectra of solutions frozen at −170 °C. The samples are: AFP, PBS (50 mM phosphate and 50 mM NaCl in DI water), trehalose in PBS, DMSO in PBS. The mode at 3420 cm^{-1} (related to the 'eutectic' phase – in this case hydrohalite – originating from PBS) can be clearly seen in the case of PBS and AFP solutions.

hydrohalite – originating from PBS) can be clearly seen (even at high AFP concentrations). 3420 cm^{-1} peak was not observed for 10% (w/w) DMSO + PBS solution and also for 0.7% (w/w) DMSO + PBS solutions frozen at −170 °C. In trehalose with PBS containing solutions frozen at −170 °C the 3420 cm^{-1} peak was not observed both for 13.2 (w/w)% + PBS and for 3.2 (w/w)% + PBS solutions (Fig. 6). It is therefore likely that DMSO and trehalose prevent water from forming a eutectic phase with other substances (such as NaCl), while AFP does not. That is in accord with their assumed mechanisms of action: during freezing, DMSO and trehalose concentrate in pockets of unfrozen solution which would otherwise form a eutectic, blocking its formation. On the other hand, AFP molecules associate with the surface of emerging ice crystals and don't therefore affect the rest of the sample.

3.5 Differential scanning calorimetry

DSC curves of DI water, AFP solution, aqueous solutions of trehalose and mixture of DMSO with trehalose were measured. In all studied cryoprotectant-containing solutions, the melting/freezing points were shifted to lower values (compared to deionized (pure) water/ice) – Table 5. The great shift of the melting/freezing point (related to the concentration of cryoprotectant in the solution) was observed in 10% (w/w) DMSO containing solutions. This correlates with change in the DMSO solution crystallinity (XRD). The glass phase transition temperature for the trehalose/water solution was found to be $T_1 = -38$ °C. Strong interactions between AFP and the first shell of solvation water led to disruption of the structure providing protection against ice growth and induced the highest freezing–melting ice hysteresis (14 °C). This hysteresis increased with AFP concentration. In accordance with the results of Raman spectroscopy the eutectic (hydrohalite) phase was also observed by DSC in ApAFP752 solutions and PBS solutions. DSC (peaks at −23, −31 °C in PBS solution and at −22, −27 °C in ApAFP solution). Temperatures of both ice and hydrohalite melting points were changed when ApAFP752 was added to the PBS solution. No eutectic phase was observed in 10% (w/w) DMSO PBS containing solutions and 3.2% (w/w) trehalose and PBS contacting solutions. Even if we worked with pure (deionized) water all the cryoprotectants (possible ice nucleation centres) reduced freezing and melting temperatures – ice construction was deformed.

Table 5 Melting temperatures measured by DSC

Sample	T_m [°C]
DI water	0
1% (w/w) AFP + DI water	−2
100 mM (3.2% w/w) trehalose + DI water	−1
10% w/w DMSO + 100 mM (3.2% w/w) trehalose + DI water	−10
10% w/w DMSO + DI water	−10
41% w/w trehalose + DI water	−13
15% w/w trehalose + DI water	−3

4. Discussion

In this work, theoretical and experimental studies of antifreeze protein AFP752, trehalose and dimethyl sulfoxide influence on the ice constitution were correlated with post freeze/thaw cell viability. The motivation was to identify attributes of investigated materials which are important for functional cryoprotection of cells.

The diameter of ice crystallites was greatest in frozen water (without cryoprotectants) so all cryoprotectants in this study more or less efficiently prevented the ice growth (XRD). The mean crystal sizes in frozen 10% (w/w) DMSO solution (with or without 3.2% (w/w) trehalose) were ten times smaller than ice in frozen water. The smallest diameter of ice crystallites was detected in frozen 1% (w/w) AFP – ice crystals were less than the volume of ice in 10% (w/w) DMSO. Ice crystals in frozen 3.2% (w/w) trehalose solutions were biggest from all cryoprotectants frozen solutions (half in size compared to frozen water). DMSO and trehalose in PBS solutions prevented water from forming 'eutectic' (hydrohalite) phase. In frozen AFP solutions the eutectic phase/hydrohalite was constituted (Raman spectroscopy, DSC).

During the melting process of the frozen solutions, in 1% (w/w) AFP and trehalose (41% (w/w)) frozen solutions larger crystals were melted continuously to small crystals (the number of small crystals became relatively higher). The reason for the melting mode of crystals with trehalose could be a gradient composition (crystals and glassy state).[3,33] In frozen AFP solutions gradient ice crystals composition with a pure ice core and increasing concentration of defects or solvents in the outer shells was constituted. In DMSO-rich solutions the mean volume and the ratio of smaller-to-larger crystals was conserved.

We showed (DSC) that the presence of studied additives in the solution generally leads to changes in freezing process. Even if the DSC measurements were made using pure (deionized) water all cryoprotectants (possible ice nucleation centres)

reduced freezing and melting temperatures of solutions – ice construction process was deformed by cryoprotectants.

The modelling studies showed that DMSO, which has an oxygen atom with a strong negative charge and a sulphur atom with a strong positive charge/high dipole moment, influences the high permittivity water strongly affecting the water freezing process. In addition, water molecules near the DMSO methyl groups cannot form alternative hydrogen bonds with DMSO, which affects their interactions with other water molecules and also ice formation. DMSO molecules with high dipole moments homogeneously distributed in solution (practically forming no clusters) have a long-range effect on water dynamics affecting the thermodynamics of the solution. In other words, DMSO molecules strongly change the conditions for water freezing in the entire volume which results in the formation of small ice crystals.

Trehalose, due to its high inter-molecular interaction potential can easily form cluster structure which can contain also glass phase[3,20,28] and just moderately impact neighbouring and remote water molecules. Trehalose supports aggregation of crystals in frozen samples. In solutions in which trehalose concentrations were relevant for biological applications (3.2% (w/w)) ice crystal sizes were biggest from all cryoprotectants solutions.

AFP (noncolligative material)[22] had the strongest influence on the neighbouring water molecules hydrogen bond dynamics (short-range effect). Strong interactions between AFP and the first shell of solvation water induce the highest freezing–melting ice hysteresis (measured by DSC). The strong interaction with water is mainly caused by the fact that AFP is a large and less mobile molecule with hydroxyl groups on the surface. AFP, attached to the ice surface reduces ice crystal size mainly if the ice nucleus growing is blocked. This results in smallest ice crystals in 1%(w/w) AFP solutions.

In our case the cells were so slowly frozen (using a gradient of $-1\ ^{\circ}C\ min^{-1}$) that they loose water (dehydrate) rapidly enough to eliminate critical supercooling. According to[34,35] in such dehydrated cells intracellular freezing is not crucial. As cryoprotectants affect the volume of ice crystals, they influence the direct damage of cell membranes and the viability of the frozen/thawed cells. Small DMSO molecules enter intracellular space, effectively decrease ice size and strongly improve cell viability after freezing/thawing (81% of DMSO-treated cells survived the freezing/thawing treatment). The protective effect of large ice-blocking AFP molecules was smaller compared to DMSO, as only 32% of AFP-treated cells survived the freezing/thawing treatment. The effects of trehalose treatment were observable only after 24 h of incubation: 58% of trehalose-treated cells survived freezing/thawing. Of all cryoprotectants under study, trehalose has the smallest impact on ice crystal size and when used as cryoprotectants. Thus trehalose probably acts mainly as a natural osmolyte (osmoprotectant), which then stabilizes phospholipid membranes and the tertiary structure of proteins.[36,37] The highest cell viability was observed when a mixture of DMSO + trehalose was applied: 86% of DMSO + trehalose-treated cells survived the freeze/thaw.

5. Conclusions

Altering the physical conditions of the liquid/solid phase transition within the cells or immediately surrounding them is important attribute of materials that induce cell cryoprotection. One important reason for death of frozen cells is due to the direct membrane damage caused by the ice crystals volume. This work is the first example where ice crystal size in frozen solutions was quantified (XRD) and correlated with theoretical models (DFT, MD) and cryopreserved cell viability. The results were complemented by Raman spectroscopy and DSC studies. Influence of cryoprotectants on the ice constitution was correlated with viability of so slowly frozen cryopreserved cells that critical supercooling was according to ref. 34 and 35 eliminated.

From our results we can conclude that the presence of additives in the solution generally leads to the irregularity and worse ordering of the ice lattice. DMSO and AFP have such impact on their solutions freezing process that ice crystallinity size is considerably reduced. This contributes to parameters that affect viability of cryopreserved frozen/thawed cells.[9] DMSO is homogeneously distributed in solution (practically no clusters) and has a long-range effect on bulk water dynamics. DMSO molecules are able to enter both extra and intracellular space,[28] effectively change the condition for freezing and strongly improve frozen/thaw cells viability. AFP even at low concentration inhibits standard crystallization process from ice nuclei. Consequently, specific gradient composition with a pure ice core and increasing concentration of defects in the outer parts is developed. All these aspects support the fact that AFP molecules, even practically without entering the cells have cryoprotective effect. The best viability results were obtained when combination of DMSO strongly changing freezing process also in cells and trehalose stabilizing phospholipid membranes and the tertiary structure of proteins were applied.

Acknowledgements

This work was supported by the Ministry of Education, Youth and Sports of the Czech Republic (FUNBIO CZ.2.16/3.1.00/21568 and MEYS: LO1409); by the Czech Science Foundation (14-10279S, 15-05095S, 16-12454S and P302/12/G157); by the Ministry of Health of the Czech Republic (16-29835A); by Czech contribution to JINR Dubna (Project of Czech Plenipotentiary and Project 3-Plus-3, 2015/16); by the National Science Foundation (CHE-1413696 and DGE-0948027); and by the National Institute of General Medical Sciences at the National Institutes of Health (P20GM103432).

References

1 B. J. Fuller, *CryoLetters*, 2004, **25**, 375.
2 Y. Yeh and R. E. Feeney, *Chem. Rev.*, 1996, **96**, 601.
3 G. M. Wang and A. D. J. Haymet, *J. Phys. Chem. B*, 1998, **102**, 5341.
4 J. B. Mandumpal, C. A. Kreck and R. L. Mancera, *Phys. Chem. Chem. Phys.*, 2011, **13**, 3839.
5 B. Kirchner and M. Reiher, *J. Am. Chem. Soc.*, 2002, **124**, 6206.

6 D. R. Nutt and J. C. Smith, *J. Am. Chem. Soc.*, 2008, **130**, 13066.
7 B. Han and J. C. Bischof, *J. Biomech. Eng.*, 2004, **126**, 196.
8 S. Venketesh and C. Dayananda, *Crit. Rev. Biotechnol.*, 2008, **28**, 57.
9 R. C. Deller, M. Vatish, D. A. Mitchell and M. I. Gibson, *Nat. Commun.*, 2014, **5**, 3244.
10 X. Mao, Z. Liu, J. Ma, H. Pang and F. Zhang, *Cryobiology*, 2011, **62**, 91.
11 J. J. Towey, A. K. Soper and L. Dougan, *Faraday Discuss.*, 2013, **167**, 159.
12 J. Sebera, S. Nespurek, I. Kratochvilova, S. Zalis, G. Chaidogiannos and N. Glezos, *Eur. Phys. J. B*, 2009, **72**, 385.
13 H. J. C. Berendsen, D. van der Spoel and R. van Drunen, *Comput. Phys. Commun.*, 1995, **91**, 43.
14 K. Lindorff-Larsen, S. Piana, K. Palmo, P. Maragakis, J. L. Klepeis, R. O. Dror and D. E. Shaw, *Proteins*, 2010, **78**, 1950.
15 T. Darden, D. York and L. Pedersen, *J. Chem. Phys.*, 1993, **98**, 10089.
16 M. J. Frisch, G. W. Trucks, H. B. Schlegel, G. E. Scuseria, M. A. Robb, J. R. Cheeseman and J. A. Pople, *GAUSSIAN 09 (Revision B.01)*, Gaussian, Wallingford, 2010.
17 P. A. Bates and M. J. E. Sternberg, *Proteins: Struct., Funct., Genet.*, 1999, (3), 47.
18 Y. C. Liou, A. Tocilj, P. L. Davies and Z. Jia, *Nature*, 2000, **406**, 322.
19 E. Krieger and G. Vriend, *Bioinformatics*, 2014, **30**, 2981.
20 H. Nagase, N. Ogawa, T. Endo, M. Shiro, H. Ueda and M. Sakurai, *J. Phys. Chem. B*, 2008, **112**, 9105.
21 J. Smiatek, R. K. Harishchandra, H.-J. Galla and A. Heuer, *Biophys. Chem.*, 2013, **180–181**, 102.
22 A. Narayanan Krishnamoorthy, C. Holm and J. Smiatek, *J. Phys. Chem. B*, 2014, **118**, 11613.
23 B. Contreras-Moreira and P. A. Bates, *Bioinformatics*, 2002, **18**, 1141.
24 S. Záliš, I. Kratochvílová, A. Zambová, J. Mbindyo, T. E. Mallouk and T. S. Mayer, *Eur. Phys. J. E*, 2005, **18**, 201.
25 M. Hofer, M. Falk, D. Komůrková, I. Falková, A. Bačíková, B. Klejdus, E. Pagáčová, L. Štefančíková, L. Weiterová, K. J. Angelis, S. Kozubek, L. Dušek and Š. Galbavý, *J. Med. Chem.*, 2016, **59**, 3003.
26 A. Luzar and D. Chandler, *J. Chem. Phys.*, 1993, **98**, 8160.
27 A. Kreiner-Møller, F. Stracke and H. Zimmermann, *CryoLetters*, 2013, **34**, 248.
28 J. Dong, J. Malsam, J. C. Bischof, A. Hubel and A. Aksan, *Biophys. J.*, 2010, **99**, 2453.
29 C. Branca, S. Magazu, G. Maisano and P. Migliardoa, *J. Chem. Phys.*, 1999, **111**, 281.
30 R. L. Suttont, *J. Chem. Soc., Faraday Trans.*, 1991, **87**, 3747.
31 D. Simek, D. Rafaja, M. Motylenko, V. Klemm, G. Schreiber, A. Brethfeld and G. Lehmann, *Steel Res. Int.*, 2008, **79**, 800.
32 Z. Matej, L. Matejova and R. Kuzel, *Powder Diffr.*, 2013, **28**, S161.
33 L. Weng and G. D. Elliott, *Phys. Chem. Chem. Phys.*, 2014, **16**, 11555.
34 P. Mazur, *Cryobiology*, 1977, **14**, 251.
35 P. Mazur and C. Koshimoto, *Biol. Reprod.*, 2002, **66**, 1485.
36 N. Krasteva, D. Vollhardt, G. Brezesinski and H. Möhwald, *Langmuir*, 2001, **17**, 1209.
37 W. B. Yu, T. Jiang, D. M. Lan, J. H. Lu, Z. Y. Yue, J. Wang and P. Zhou, *Arch. Biochem. Biophys.*, 2012, **523**, 144.

Journal of Medicinal Chemistry

Article

pubs.acs.org/jmc

Two New Faces of Amifostine: Protector from DNA Damage in Normal Cells and Inhibitor of DNA Repair in Cancer Cells

Michal Hofer,[†] Martin Falk,[*,†] Denisa Komůrková,[†] Iva Falková,[†,‡] Alena Bačíková,[†] Bořivoj Klejdus,[§,∥] Eva Pagáčová,[†] Lenka Štefančíková,[†] Lenka Weiterová,[†] Karel J. Angelis,[⊥] Stanislav Kozubek,[†] Ladislav Dušek,[#] and Štefan Galbavý[‡]

[†]Department of Cell Biology and Radiobiology, Institute of Biophysics, v.v.i., Czech Academy of Sciences, Královopolská 135, CZ-612 65 Brno, Czech Republic

[‡]Department of Medical Technology, St. Elisabeth University of Health and Social Sciences, Palackého 1, SK-810 00 Bratislava, Slovak Republic

[§]Institute of Chemistry and Biochemistry, Faculty of Agronomy, and [∥]CEITEC-Central European Institute of Technology, Mendel University in Brno, Zemědělská 1, CZ-613 00 Brno, Czech Republic

[⊥]Institute of Experimental Botany, v.v.i., Czech Academy of Sciences, Na Karlovce 1, CZ-160 00 Prague 6, Czech Republic

[#]Institute of Biostatistics and Analyses, Masaryk University, Kamenice 126/3, CZ-625 00 Brno, Czech Republic

Supporting Information

ABSTRACT: Amifostine protects normal cells from DNA damage induction by ionizing radiation or chemotherapeutics, whereas cancer cells typically remain uninfluenced. While confirming this phenomenon, we have revealed by comet assay and currently the most sensitive method of DNA double strand break (DSB) quantification (based on γH2AX/53BP1 high-resolution immunofluorescence microscopy) that amifostine treatment supports DSB repair in γ-irradiated normal NHDF fibroblasts but alters it in MCF7 carcinoma cells. These effects follow from the significantly lower activity of alkaline phosphatase measured in MCF7 cells and their supernatants as compared with NHDF fibroblasts. Liquid chromatography−mass spectrometry confirmed that the amifostine conversion to WR-1065 was significantly more intensive in normal NHDF cells than in tumor MCF cells. In conclusion, due to common differences between normal and cancer cells in their abilities to convert amifostine to its active metabolite WR-1065, amifostine may not only protect in multiple ways normal cells from radiation-induced DNA damage but also make cancer cells suffer from DSB repair alteration.

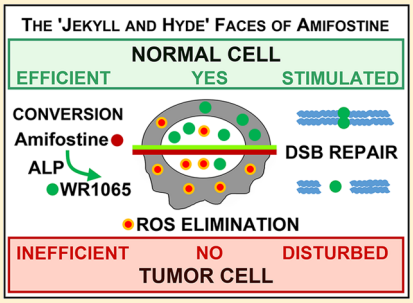

1. INTRODUCTION

Amifostine (ethanethiol, 2-[(3-aminopropyl)amino]dihydrogen phosphate), also known as WR-2721, is an organic thiophosphate agent; it is rapidly dephosphorylated by alkaline phosphatase (ALP) at the cell surface of healthy tissues, giving rise to its clinically active metabolite, WR-1065.[1−3] When activated, amifostine protects cells from radiation- and chemotherapy-induced DNA damage, mostly by competing with oxygens and preventing their interactions with DNA radicals and donating hydrogen to repair the already existing DNA damage.[4,5] Currently, amifostine is the only radioprotective drug approved for clinical use.

Concerning the practical application of amifostine in human medicine, a key role has been ascribed to its differential effect on cancer and normal cells, respectively: Whereas in normal cells or tissues amifostine clearly acts as a radio- and chemoprotective agent, this property of the drug is lost in cancer cells.[6−12] This cell type-specific behavior of amifostine has been largely attributed to low levels of ALP in cancer cells as compared with normal cells;[13] however, the situation is still not that clear because a variety of human cancers ectopically express high levels of ALP, thus leading some scientists to the (opposite) suggestion that ALP might be critically involved in tumor development.[14−16] Indeed, a comprehensive comparison of ALP mRNA and protein expression and activity in cancer cells in the literature is missing. This uncertainty points to the caution with which each model of disease (e.g., different cell types) should be tested.

In addition, it is still not obvious how the four main classes of ALP (tissue nonspecific TNAP, intestinal IAP, placental PLAP, and placental-like GCAP)[15] participate in amifostine conversion in various normal and especially cancer cells where expression of ALP isoenzymes may be altered.[17] ALP genes are also highly inducible by many agents.[15] Finally, though covalently anchored to the outer surface of the plasma membrane,[16] ALP can be released into the serum (or extracellular medium) by the GPI-dependent phospholipase D under stress and some medical conditions, such as cancer. While previous reports showed that the membrane-bound ALP

Received: October 16, 2015
Published: March 15, 2016

DOI: 10.1021/acs.jmedchem.5b01628
J. Med. Chem. 2016, 59, 3003−3017

has different enzymatic kinetics and molecular properties as compared to the soluble enzyme,[16,18] the question remains of how this finding is reflected in amifostine metabolism in normal and cancer tissues.

The most serious radiation-induced DNA damage is the double strand break (DSB) that causes a loss of the DNA molecule integrity. As DSB formation is also modulated by amifostine,[19,20] DSBs represent the most relevant type of DNA lesions in the context of amifostine-mediated cell radioprotection and radiosensitization. Molecular events following the ionizing radiation-induced DNA breakage include an immediate phosphorylation of histone H2AX (ser139),[21,22] which can be nowadays used to immunologically visualize the extent of DSB damage induction in intact cells as the so-called γH2AX foci within minutes after the DSB induction.[23−25] On the other hand, assessment of γH2AX foci disappearance during the postirradiation (PI) time allows monitoring of DSB repair.

In this work, we advantageously employ this method, combined with a high-resolution confocal microscopy, to quantify currently with the maximum sensitivity the induction and processing of DSBs in intact (3D-preserved) cells (Figure 1)[21,26] irradiated with γ-rays in the presence or absence of amifostine or WR-1065. To further increase the fidelity of DSB evaluation, we simultaneously detect γH2AX together with 53BP1 DSB repair protein that colocalizes with γH2AX foci both in very early and late periods of time PI.[27−30] To our best knowledge, this study is the first to use this approach for exploring the effects of amifostine on the DSB damage induction and repair.

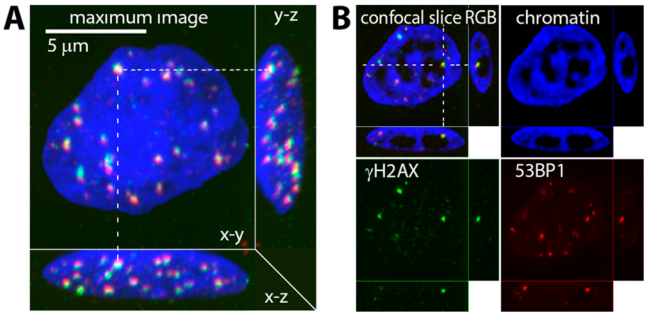

Figure 1. Precise detection of γH2AX/53BP1 DSB repair foci in spatially (3D) fixed cells by dual immunochemistry combined with high-resolution confocal fluorescence microscopy. A. A maximum image of an MCF7 cell in $x-y$, $x-z$, and $y-z$ planes. The image consists of 40 superimposed individual confocal slices 0.2 μm thick. Dotted lines indicate the position in all three planes of a selected γH2AX focus (green) that colocalizes with 53BP1 repair protein and represents a DSB. γH2AX/53BP1 foci detection at 60 min PI; chromatin counterstaining with TO-PRO-3 (artificial blue). B. Images showing a single confocal $x-y$ slice (0.2 μm thick) through the nucleus displayed at image A; $x-z$ and $y-z$ projections were obtained by image reconstruction in the Acquiarium 2.0 software. Top left: all R-G-B channels together; top right: chromatin only (B-channel); bottom left: γH2AX only (G-channel); bottom right: 53BP1 only (R-channel).

We compare the effects of amifostine and its clinically active metabolite WR-1065 in two human cell lines, normal dermal fibroblasts (NHDF) and breast adenocarcinoma cells (MCF7). MCF7 cells were selected due to a high prevalence of breast cancer while NHDFs were chosen because of their inevitable direct irradiation during the classical radiotherapy (especially with γ- or X-rays).

To explore whether different cellular and/or extracellular levels of ALP in fibroblasts and MCF7 cells may explain the cell type-specific effects of amifostine on DSB induction and repair, as observed in this work, we compared the levels of ALP mRNA and ALP protein in the supernatant and cell fraction of these cell lines.

2. RESULTS

2.1. Codetection of γH2AX and 53BP1 Foci by Immunofluorescence High-Resolution Confocal Microscopy in Spatially (3D) Preserved Cells To Monitor DSB Induction and Repair. The response of normal and cancer cells to amifostine and WR-1065 was analyzed by various approaches in the past, usually in terms of DNA damage formation; however, the repair of DNA lesions has not been systematically studied yet. In this work, we used currently the most sensitive method to detect DNA double strand breaks (DSBs) and monitored their induction and consequent repair during the postirradiation (PI) time in γ-irradiated normal NHDF fibroblasts and cancer MCF7 cells treated with amifostine and WR-1065 radioprotective drugs, respectively. The results of our approach are demonstrated in Figure 1. γH2AX and 53BP1 foci, markers of DSBs, were immunodetected in the cell nuclei of spatially fixed cells (i.e., cells with the structure of nuclei preserved in 3D space by paraformaldehyde[27,31]) (MCF7 in Figure 1) and visualized for scoring by high-resolution confocal microscopy. Figure 1A shows the maximum images of an illustrative nucleus computationally reconstructed from forty 0.2 μm-thick confocal slices in all three planes. Figure 1B then displays a single confocal slice through the same nucleus in $x-y$, $x-z$, and $y-z$ planes (indicated by dashed lines); γH2AX, 53BP1, and chromatin stainings are presented overlaid (top-left image) and separately for each of these signals (remaining images). It is evident from the panels A and B that almost all individual γH2AX/53BP1 foci can be easily distinguished in space and precisely identified. For the analyses, we considered as DSB only γH2AX foci colocalizing with 53BP1 and fulfilling the criterion of a minimum size, arbitrarily determined separately for each period of time PI. Immediately after irradiation (5 min PI), we obtained the average numbers of DSBs per nucleus per Gray (Figures 2 and 3) that were comparable with the already reported results obtained in a research context different from that followed in this study with a similar method of DSB foci detection.[24,27,28,32] Our earlier results demonstrated, both for NHDF[29,30] and MCF7[27,28] cells studied in this work, that a 5 min period after irradiation is sufficient to develop 53BP1 foci and their colocalization with γH2AX, detectable by high-resolution confocal microscopy. This is in agreement also with several other reports.[33−36]

2.2. Immediate Radioprotection by Amifostine and Its Effect on DSB Repair in Irradiated Normal NHDF Fibroblasts and MCF7 Cancer Cells. Figure 2 summarizes the median numbers of colocalizing γH2AX and 53BP1 foci per nucleus in normal NHDF fibroblasts and MCF7 cancer cells irradiated with a dose of 1 Gy of γ-rays and treated or not treated with 4 mM amifostine 15 min before irradiation. In both cell types, material samplings were performed 5, 60, and 120 min PI. The first time interval reflected the extent of the radiation-induced damage "immediately" after the irradiation, and the other two allowed us to quantify the efficiency and kinetics of DSB repair processes. Panel A in Figure 2 shows the maximum images (see Experimental Section) of illustrative

DOI: 10.1021/acs.jmedchem.5b01628
J. Med. Chem. 2016, 59, 3003−3017

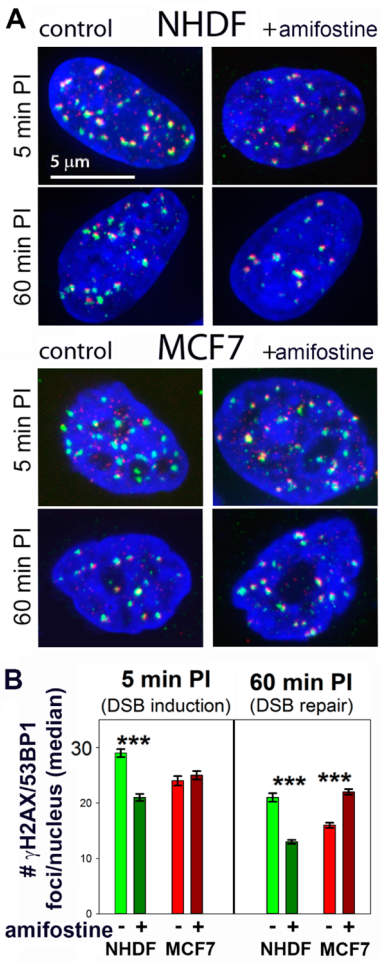

Figure 2. Numbers of ionizing radiation-induced repair foci (γH2AX, green; 53BP1, red) demonstrating the effects of amifostine on the extent of DSB induction (5 min PI) and efficiency of DSB repair (60 min PI) in normal human skin fibroblasts (NHDF) and mammary carcinoma cells (MCF7). A. Maximum images composed of 40 confocal slices (0.2 μm thick) through spatially (3D) fixed cells by paraformaldehyde are shown; chromatin counterstaining with TO-PRO-3 (artificial blue). B. Median DSB values with standard errors; statistical significance determined by the Mann–Whitney U test is indicated (*, $P < 0.05$; **, $P < 0.01$; ***, $P < 0.001$).

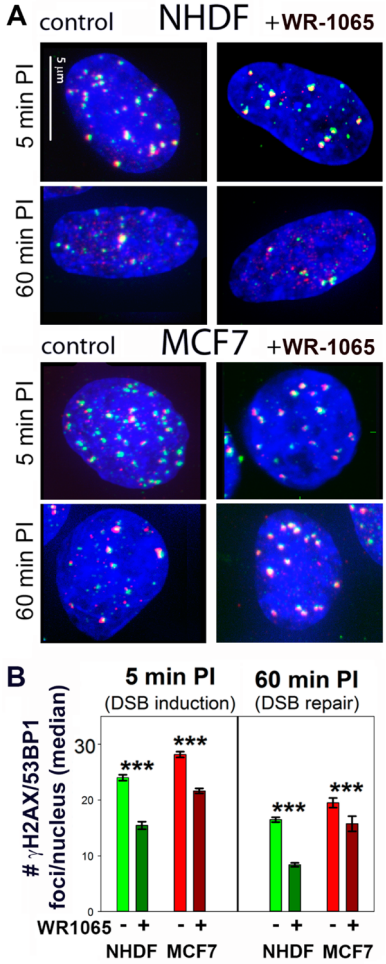

Figure 3. Numbers of ionizing radiation-induced repair foci (γH2AX, green; 53BP1, red) demonstrating the effects of WR1065 on the extent of DSB induction (5 min PI) and efficiency of DSB repair (60 min PI) in normal human skin fibroblasts (NHDF) and mammary carcinoma cells (MCF7). A. Maximum images composed of 40 confocal slices (0.2 μm thick) through spatially (3D) fixed cells by paraformaldehyde are shown; chromatin counterstaining with TO-PRO-3 (artificial blue). B. Median DSB values with standard errors; statistical significance determined by the Mann–Whitney U test is indicated (*, $P < 0.05$; **, $P < 0.01$; ***, $P < 0.001$).

nuclei of NHDF and MCF7 cells for each treatment and the first two periods of time PI analyzed (data for 120 min PI are presented and discussed in more detail later in section 2.3, Figure 5). In normal NHDF fibroblasts, amifostine induced a significant ($P < 0.001$) decrease in the median numbers of γH2AX/53BP1 foci per nucleus in all the time intervals, for 5 and 60 min PI, namely up to 75.8% and 61.9% of the values in untreated cells, respectively. The repair efficiency determined as the difference between the median DSB values at 5 and 60 min PI (Figure 4) corresponded to 7 DSBs in cells irradiated in the plain medium and 8 DSBs in cells irradiated in the medium supplemented with amifostine. This result reflects an ongoing DSB repair slightly accelerated (about 10%) by amifostine (and/or its active metabolite WR-1065, discussed later; see Figure 4).

On the other hand, cancer MCF7 cells provided a totally different picture as compared with normal fibroblasts. Amifostine did not significantly decrease the median numbers of γH2AX/53BP1 foci per nucleus in MCF7 cells at 5 min PI

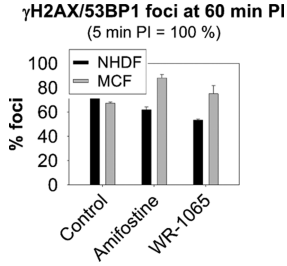

Figure 4. Kinetics of DSB repair in irradiated (1 Gy of γ-rays; 1 Gy/min) NHDF and MCF7 cells treated or not with 4 mM amifostine or WR-1065 for 15 min prior to irradiation. The graph shows average fractions of γH2AX/53BP1 foci persisting in cells at 60 min PI, determined as % of corresponding values measured at 5 min PI. Mean values with SEM are shown.

(Figure 2). In addition, as we report here for the first time for γ-irradiated intact cells, a significantly ($P < 0.001$) higher number of the foci (137.5% of the value in untreated cells) surprisingly

DOI: 10.1021/acs.jmedchem.5b01628
J. Med. Chem. 2016, 59, 3003−3017

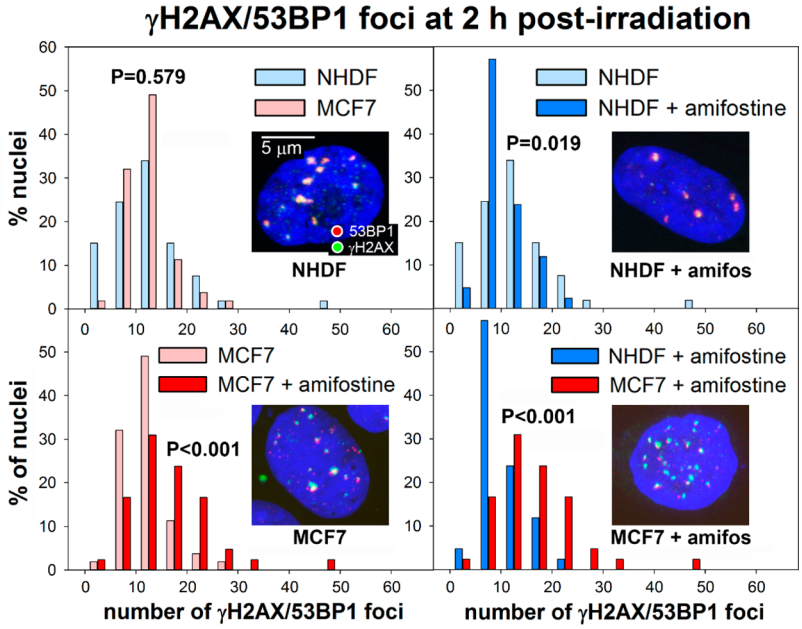

Figure 5. Distributions of the numbers of ionizing radiation-induced repair foci (γH2AX, green; 53BP1, red) persisting 2 h postirradiation in nuclei of NHDF and MCF7 cells, respectively, exposed to 1 Gy of γ-rays and treated or not treated with amifostine. Illustrative images of nuclei are inserted. Chromatin counterstaining with TO-PRO-3. *P*-values indicate the results of the Mann−Whitney U test.

persisted in amifostine-treated MCF7 cells at 60 min PI (Figures 2 and 4) and 120 min PI (Figure 5; discussed later). Hence, amifostine treatment not only selectively protected normal cells from DSB damage but it also markedly slowed down the repair of lesions already induced by irradiation in cancer cells (Figures 2 and 4).

2.3. Immediate and Later Effects of Amifostine Metabolite WR-1065 in Irradiated Normal NHDF Fibroblasts and MCF7 Cancer Cells. In the next step, we used the same experimental approach to reveal the effects of an isomolar concentration of WR-1065 (Figure 3), an amifostine metabolite that is supposed to mediate the radioprotective effects of amifostine. Unlike in cells treated with amifostine, WR-1065 in the cultures reduced the numbers of γH2AX/53BP1 foci per nucleus in both normal and cancer cell types and both the time intervals of 5 and 60 min PI. The percentage decreases produced by WR-1065 for MCF7 cells amounted to 75.0% ($P < 0.001$) and 82.9% ($P < 0.05$) at 5 min PI and 60 min PI, respectively; for NHDF fibroblasts, these values corresponded to 65.2% ($P < 0.05$) and 50.0% ($P < 0.001$) at 5 min PI and 60 min PI, respectively.

Altogether, the immediate (5 min PI) and late (60 min PI) response to the irradiation was comparable for normal NHDF and cancer MCF7 cells only in cultures incubated with WR-1065 (Figure 3). For amifostine, the response basically depended on the normal or cancer cell status. Though amifostine at 5 min PI induced a response similar to that of WR-1065 (radioprotection) in the case of NHDF fibroblasts, we observed no effect of this prodrug in MCF7 cells (Figure 2). At 60 min PI, as compared with the averaged value for untreated irradiated controls, we observed a small acceleration (about 9%) of DSB repair in NHDF fibroblasts incubated with amifostine (Figure 4). On the other hand, the speed of repair markedly decreased (−20.7%) in cancer MCF7 cells relative to the average control. WR-1065 then also speeded up (17.7%) DSB repair in NHDF fibroblasts relative to the averaged untreated control but exerted slightly opposite (−7.7%) changes in MCF7 cells.

Figure 5 shows how DSB foci continued until 120 min PI in NHDF and MCF7 cells irradiated with 1 Gy of γ-rays and treated or not treated with amifostine, as described previously. As follows from both the inserted images and graphs showing the distributions of γH2AX/53BP1 foci per nucleus, amifostine supported DSB repair in normal NHDF fibroblasts while it had the opposite influence on cancer MCF7 cells. The differences from the untreated cells were statistically significant in both cell types though the enhancement of DSB repair in NHDF fibroblasts was less prominent ($P = 0.019$) than its deceleration in MCF7 cells ($P < 0.001$). The repair of untreated NHDF and MCF7 cells proceeded with similar efficiency ($P = 0.579$).

2.4. DSB Induction and Repair Analyzed by Comet Assay. To verify our results obtained above with γH2AX/53BP1 foci immunostaining, we quantified DSB induction and repair in irradiated normal NHDF and cancer MCF7 cells treated or not treated with amifostine or WR-1065 also by the comet assay, the method accepted in radiobiology as a "gold standard" for this purpose. While the comet assay provides a more direct view on DNA breakage and rejoining than γH2AX/53BP1 foci immunodetection, it suffers from lower sensitivity. Therefore, we irradiated the cells with 6 Gy of γ-rays (1 Gy/min) instead of 1.0 Gy used in the immunodetection experiments.

As demonstrated by Figure 6 and Figures S1-A and S1-B in Supporting Information, the measurements of comet tail moments (TM = $L_{(T)} \times IF_{(T)}/100$, where $L_{(T)}$ = length of the tail and $IF_{(T)}$ = the fluorescence intensity of the tail given as a percentage; Figure 6B) well correlated at all the periods of time postirradiation with the results that followed from γH2AX/53BP1 foci immunodetection. Shortly (5 min) after irradiation, WR-1065 markedly decreased DSB induction in NHDF ($p < 0.01$) and MCF7 ($p < 0.001$) cells but amifostine only protected the first cells ($p < 0.01$ for NHDF vs $p = 0.553$ for MCF7). In later periods of time PI (60 and 120 min PI)

DOI: 10.1021/acs.jmedchem.5b01628
J. Med. Chem. 2016, 59, 3003−3017

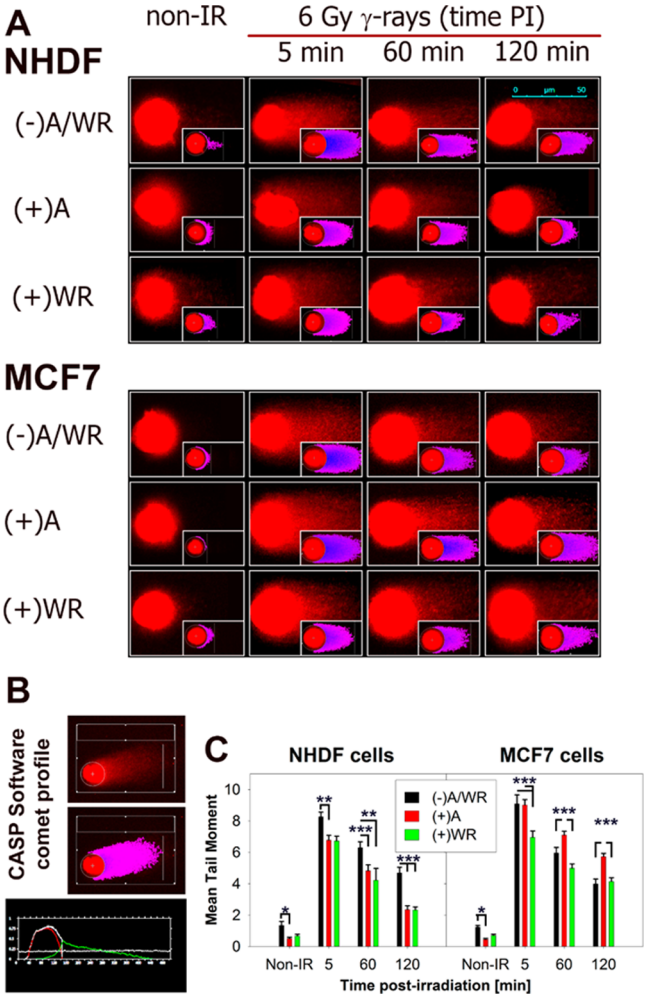

Figure 6. DSB induction and repair quantified by the neutral comet assay. A. Illustrative DNA comets of NHDF and MCF7 cells treated or not treated for 15 min with 4 mM amifostine or WR-1065 prior to irradiation with 6 Gy of γ-rays (1 Gy/min). Detailed DNA comets at 5, 60, and 120 min PI are shown as the maximum images obtained by superimposition of 30−50 individual confocal slices taken with a *z*-step of 0.3 μm using the 63× oil-immersion lens. Inserted comet images show the comet tails and amounts of DNA in these tails (the purple to blue gradient reflects increasing DNA staining) as detected by the CASP Lab Software (see Experimental Section). B. Comet analysis by the CASP Lab Software. Top image: an example of DNA comet stained with Gel Red and obtained by superimposition of a confocal 3D *z*-stack (described in A). Middle image: the comet head and tail as detected by the CASP software. Bottom image: red fluorescence (606−708 nm) profiles quantifying DNA amounts in the comet head (red line) and tail (green line); white line indicates the cell nucleus. C. Average comet tail moments with standard errors calculated for particular cells and cell treatments (described in A); statistical significance of differences between the samples was determined by the Mann−Whitney U test (*, $P < 0.05$; **, $P < 0.01$; ***, $P < 0.001$). For wide-field microscopic images of comets see Figures S1-A and S1-B.

amifostine and WR1065 supported DSB repair in normal NHDF cells ($p < 0.001$ for amifostine, $p < 0.01$ for WR-1065) but decreased the kinetics of this process in MCF7 cancer cells. When compared as a difference between the average tail moments of untreated irradiated controls and cells treated with amifostine or WR-1065, the delay of DSB repair was significant ($p < 0.001$) for amifostine in both periods of time but insignificant ($P = 0.722$, 60 min PI; $P = 0.063$, 120 min PI) for WR-1065. This lack of significance in case of WR-1065 in MCF7 cells clearly follows from the "averaging" of the two opposite effects observed with this drug in this cell type: the slower repair kinetics and the (already described) lower induction of DSBs at 5 min PI ($p < 0.001$) in MCF7 cells treated with WR-1065 but not amifostine (Figure 6). Hence, the repair in MCF7 cells treated with WR-1065 proceeds with a similarly slower kinetics to that observed for cell cultures with amifostine. The obtained results agreed well with both analytical strategies used in this work (see Experimental Section, section 4.6.2): the high-throughput analysis of "low-resolution" comets (Figures S1-A and S1-B) and the comparison of detailed comets acquired with a high resolution (63× oil immersion lens; Figure 6A).

Our results coming from DNA comet measurements and γH2AX/53BP1 foci counting thus correspondingly support the hypothesis that while amifostine administration protects normal cells from radiation damage through its metabolite WR-1065, it is rather toxic for cancer cells, where it negatively influences DSB repair. Moreover, WR-1065 in normal cells has a double-positive effect; it protects them from radiation-induced DSB lesions and consequently supports their repair.

2.5. Activity of ALP in Cell Lysates of Normal NHDF Fibroblasts and MCF7 Cancer Cells and in Their Extracellular Environment. To confirm that our observations described above correlate with the metabolic conversion of amifostine to WR-1065, we determined the activity of alkaline phosphatase (ALP) in NHDF and MCF7 cells. To reveal a potential importance of ALP localization, we compared the enzyme activity in both the cells themselves (the membrane-bound ALP) and in the supernatants of their cultures (excreted ALP). This approach was used because of uncertainty in the literature about some data showing that rather extracellular ALP is responsible for the conversion of amifostine to WR-1065 in in vivo conditions.[37] The results are summarized in Figure 7. It is evident that when we measured

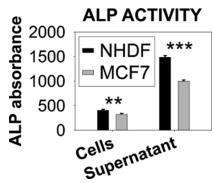

Figure 7. Alkaline phosphatase (ALP) activity in tumor MCF7 cells, normal NHDF cells, and their supernatants as determined by colorimetric conversion of the ALP substrate, 4-*p*-nitrophenyl phosphate. Mean values with standard errors are shown. Statistical significance of differences between the samples (*, $P < 0.05$; **, $P < 0.01$; ***, $P < 0.001$) was determined by the two-sample *t* test performed on the data of merged experiments after standardization using *z*-score; all analyses were repeated six times.

the ALP activity in the cells themselves, its value in the normal NHDF cells was 124.8% of that in the tumor MCF7 cells ($P < 0.01$); when determining its values in the supernatants, the ALP activity in NHDF cells was 148.9% of that in MCF7 cells ($P < 0.001$).

Next, we addressed (ALP-mediated) conversion of amifostine to WR-1065 in NHDF and MCF7 cells directly by quantifying the ratio of these compounds in cells and cell supernatants by liquid chromatography−mass spectrometry (LC-MS/MS). Figure 8A proves a high percentage (>90%) of

DOI: 10.1021/acs.jmedchem.5b01628
J. Med. Chem. 2016, 59, 3003−3017

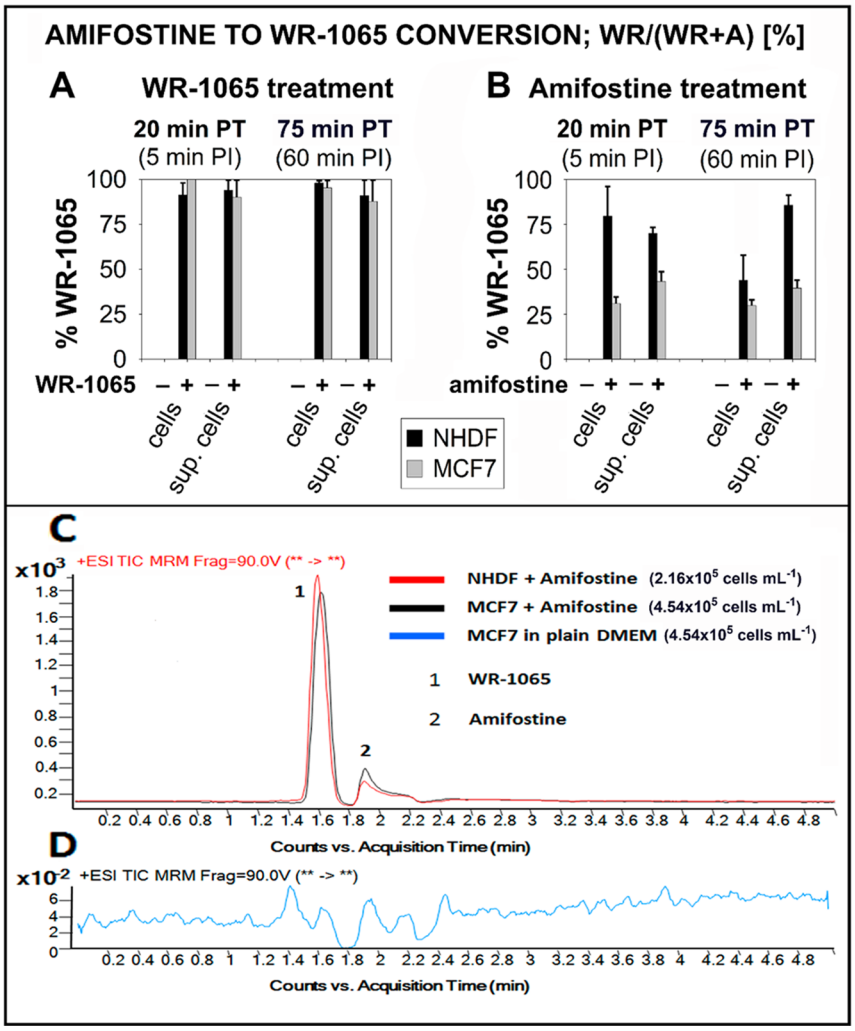

Figure 8. Relative amifostine and WR-1065 amounts in tumor MCF7 cells, normal NHDF cells, and their supernatants as determined by LC-MS/MS at 20 and 75 min after the treatment (PT, post-treatment) with these compounds. Mean values with standard errors are shown; 4 mM drug concentration, incubation at 37 °C, pH 7.1 (A, B). C, D. LC-MS/MS chromatograms of amifostine and WR-1065 in NHDF and MCF7 cells (NHDF: 2.16 × 10^5 cells mL^{-1}, MCF7:4.54 × 10^5 cells mL^{-1}). Total-ion compound chromatogram of amifostine and WR-1065 in NHDF and MCF7 cells after 20 min incubation (C); total-ion chromatogram of MCF7 cells in plain DMEM medium (D).

WR-1065 in both NHDF and MCF7 cells directly treated with this compound (4 mM, 37 °C, pH 7.1, at the beginning of incubation) and at both periods of time studied, i.e. at 20 and 75 min after the drug administration. Figure 8B then compares percentages of WR-1065 in cell cultures incubated with 4 mM amifostine under the same experimental conditions. It is evident from the figure that the levels of WR-1065, the amifostine metabolite, are substantially higher in normal NHDF fibroblasts and their culture supernatants than in MCF7 cells and their culture supernatants, both at 20 min (2.56× for the cells; 1.62× for the supernatants) and 75 min (1.47× for the cells; 2.17× for the supernatants) of incubation. Twenty and 75 min drug incubations used here correspond to 5 and 60 min time periods in γH2AX/53BP1 immunodetection and comet assay experiments (15 min drug preincubation + 5 or 60 min postirradiation time).

Figure 8C shows illustrative LC-MS/MS total-ion compound chromatograms for amifostine and WR-1065 in NHDF and MCF7 cells after 20 min incubation. It should be noted that the chromatograms show the raw data before their correction for cell concentrations and vitalities. As determined by flow cytometry, the concentration of MCF cells was 2.1 times higher as compared with NHDF fibroblasts, and this ratio was 1.8 when only nonapoptotic cells were considered (the later conversion factor was used to obtain Figure 8A,B). The total-ion chromatogram of MCF7 cells in plain DMEM medium shown in Figure 8D (with *x*-axis resolution increased by several orders of magnitude as compared with Figure 8C) revealed no signals in amifostine and WR-1065 positions.

The LC-MS/MS results thus correlate with our colorimetric measurements on ALP activity (Figure 7) and directly prove conversion of amifostine to WR-1065, which is high in NHDF cells and their supernatants and substantially lower (but still measurable) in MCF7 cells and their supernatants. The lower level of WR-1065 in NHDF cells observed for the 75 min treatment as compared with the 20 min treatment probably reflects WR-1065 decomposition into its metabolites (see Discussion).

2.6. Transcription Levels of ALP Isoenzyme Genes in Normal NHDF Fibroblasts and MCF7 Cancer Cells. At least four main classes of ALP, namely tissue nonspecific ALP (TNAP), intestinal ALP (IAP), placental ALP (PLAP), and

DOI: 10.1021/acs.jmedchem.5b01628
J. Med. Chem. 2016, 59, 3003−3017

placental-like ALP (GCAP), have been distinguished,[15] but their involvement in amifostine conversion in normal and cancer cells remains to be systematically studied. The expression patterns of ALP isoenzymes may be altered in cancer cells,[17] and ALP genes are highly inducible by a variety of agents.[15] Hence, in addition to the overall ALP activity and WR-1065 levels in cells and supernatants of their cultures, we also determined mRNA expression for individual ALP isoenzymes in both the tumor MCF7 and normal NHDF cells. The values for TNAP, IAP, and PLAP are shown in Figure 9; the GCAP isoenzyme mRNA expression was too low to allow for quantification. Unexpectedly and in contrary to the ALP activity, the mRNA expression levels of all three quantifiable isoenzymes including IAP, which has been suggested as predominantly responsible for the conversion of amifostine to WR-1065,[38] were always higher in MCF7 cells than in NHDF cells, the differences being significant ($P < 0.05$) in the case of the TNAP and IAP isoenzymes.

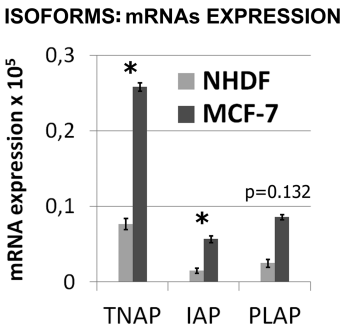

Figure 9. Expression of mRNA for various types of alkaline phosphatase (ALP) isoenzymes in tumor MCF7 and normal NHDF cells. Mean values with standard errors are shown. Statistical significance of differences between the samples (*, $P < 0.05$; **, $P < 0.01$; ***, $P < 0.001$) was determined by the two-sample t test performed on the data of merged experiments after standardization using z-score; all measurements were performed in biological triplicates. PLAP (placental ALP); IAP (intestinal ALP); TNAP (tissue nonspecific ALP).

3. DISCUSSION AND CONCLUSIONS

3.1. Mysterious Amifostine as a Still Controversial Paradigm in Radiotherapy and Radioprotection. Cancer therapy always balances on a sharp edge between the killing of the tumor and the survival of (critically important) adjacent normal tissues. Chemical compounds specifically interacting with altered biochemical and genetic processes in cancer cells in the way they support cancer cell eradication while leaving normal cells uninfluenced or even protected may thus significantly shift therapeutic outcomes to benefits. However, there is still only one radioprotectant fulfilling these criteria that has been approved for clinical use: amifostine[6−12,39,40] (see ref 41 for a comprehensive review).

Not surprisingly, amifostine is the best characterized radioprotective agent; however, reassessment of its mechanism of action by newly emerged molecular-genetic methods brought about interesting findings, showing that biological effects of amifostine are more complex and difficult to explain than previously thought. This is documented by a number of conclusions published in the literature on various aspects of amifostine and WR-1065 and on the activities of their metabolites (e.g., ref 42 and citations therein; comprehensively reviewed in ref 41). Hence, our better understanding of the amifostine paradigm may pave the way for a more efficient search of new selective radiomodifiers, so needed in light of the still increasing incidence of cancers. Current reports and also our results discussed here suggest that amifostine could be (at least) in some therapeutic circumstances more advantageous than it seemed previously. On the other hand, some discoveries warn that the clinical use of amifostine might also be counterproductive. For instance, Andreassen et al.[43] demonstrated undesirable radioprotection of some tumors upon amifostine treatment. Thus, what remains unclear is the phenomenon of why amifostine selectively protects non-transformed and some transformed cells while it does not eliminate the cytotoxicity delivered by ionizing radiation to other cancer cells.

3.2. Radioprotection versus Radiosensitization by Amifostine in Normal and Cancer Cells. With the use of two independent methods, the comet assay and γH2AX/53BP1 foci immunofluorescence microscopy, we systematically compared under the same conditions the effects of amifostine and its active metabolite WR-1065 on the induction and repair of DNA double strand breaks (DSBs) in normal human skin fibroblasts and mammary carcinoma MCF7 cells irradiated with γ-rays.

It follows from our results obtained by both the methods (the first representing a gold standard in radiobiology and the second the most sensitive method of DSB detection at present) that, in contrast to the earlier opinion simply considering (activated) amifostine as a selective radioprotector of normal cells,[6−12] the drug has also pronounced negative effects on irradiated cancer (MCF7) cells. We have also found that both amifostine and WR-1065, its metabolite, not only protect normal (NHDF) cells from acute radiation damage but also significantly support DSB repair in these cells. Because the DSB repair-supporting effects were higher for WR-1065 than for amifostine, it could be supposed that amifostine was not completely converted to WR-1065 even in normal cells, though the "equilibrium" was largely shifted to WR-1065. These assumptions have been confirmed in our study by a direct assessment of the amifostine-to-WR-1065 conversion by LC-MS/MS in the two cell lines (see Figure 8).

Contrary to normal cells, the radioprotective effect of amifostine on DSB induction (5 min PI) was absent in cancer MCF7 cells as detected by comet assay (see Figure 6) as well as by γH2AX/53BP1 foci immunodetection (see Figure 2). Even more, the addition of the drug increased the persistence of DSBs in the nuclei at 60 and 120 min PI (Figures 2 and 6). Therefore, amifostine (or its metabolites) not only missed its radioprotective effect in cancer (MCF7) cells, it even altered the DSB repair process and acted in a *radiosensitizing* manner.

The lower DSB induction measured at 5 min PI in normal cells incubated with amifostine prior to their irradiation (relative to untreated cells) can be easily explained by the radical scavenging ability of the metabolized drug (reviewed in ref 44). However, the necessity of converting amifostine into its active thiolic form (WR1065) can account (at least partially, Mitchell et al.[45,46]) for the absence of the amifostine-mediated radioprotection in cancer cells; the activation is mediated by alkaline phosphatase which is in low abundance in the majority of cancer cells[3] including the MCF7 cells, as we also show in this study.

3.3. What is the Mechanism of How Amifostine Exerts Its Negative Effects on DSB Repair in Cancer Cells?

DOI: 10.1021/acs.jmedchem.5b01628
J. Med. Chem. 2016, 59, 3003−3017

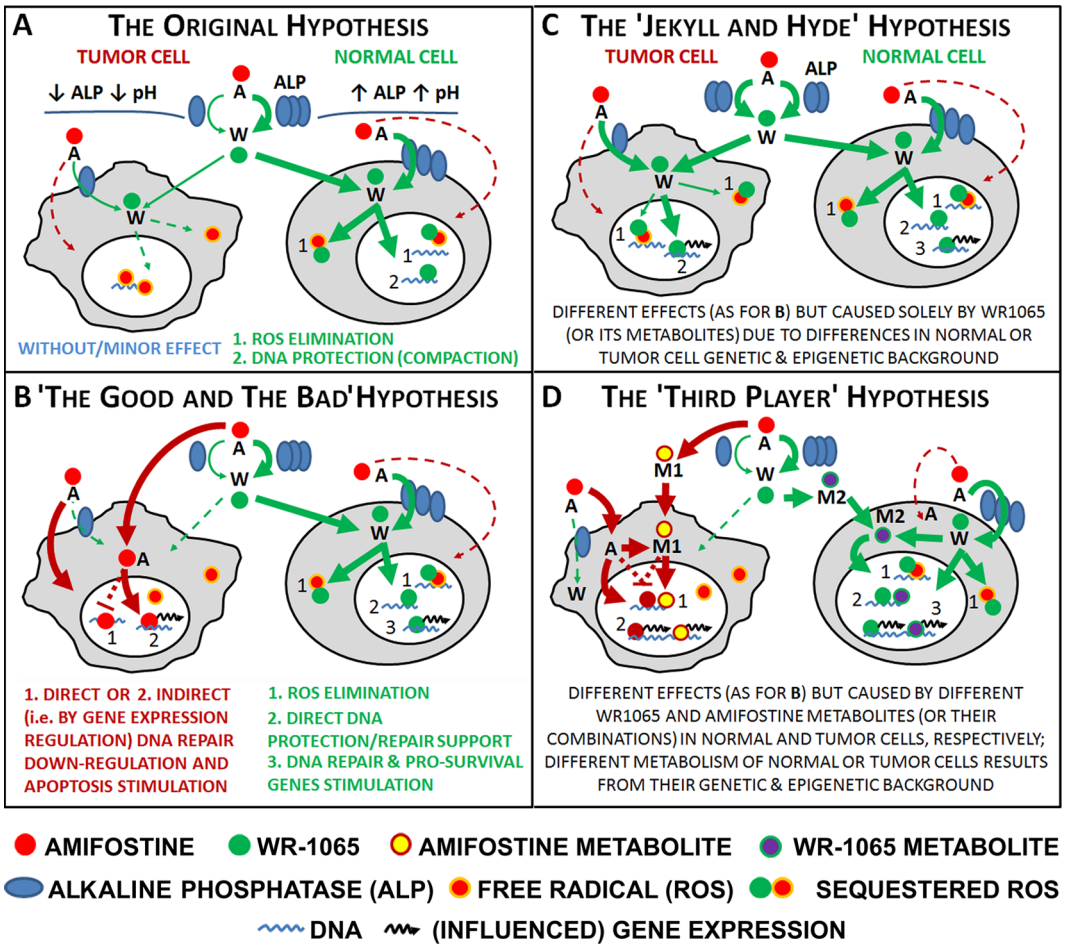

Figure 10. The original hypothesis (A) and the current "Good and Bad" (B), "Jekyll and Hyde" (C), and "Third Player" (D) hypotheses on amifostine effects in normal and cancer cells. B: In cancer cells, amifostine is almost not converted to WR-1065 (because of low levels of ALP and acidic pH) and behaves as "Bad". While amifostine was considered as biologically inactive in previous works (panel A), some authors[55,86] show that this prodrug per se is rather toxic, with direct and/or indirect negative effects on DSB repair and cell survival. On the other hand, amifostine in normal cells is converted to WR-1065, its "Good" active metabolite. WR-1065 primarily ensures protection of normal cells against immediate cytoplasmic and DNA radiation-induced damage by scavenging free radicals (ROS). However, as also shown here, it supports the repair of DSBs too, directly by (physicochemical) interactions with damaged DNA and/or indirectly by modifying gene expression and biochemical cell regulatory pathways (see main text for more detailed discussion). C: As for (B) but the negative effect on cancer cells is exerted by WR-1065 (instead of amifostine). Low amounts of WR-1065 in cancer cells cannot protect these cells from DSB induction but are sufficient to negatively influence their DSB repair (and potentially other functions). The opposite effects of WR-1065 on DSB repair in normal and cancer cells follow from different WR-1065 levels and/or genetic backgrounds of these cells. WR-1065 thus only shows its "Mr. Hyde" face in cancer cells but "Mr. Jekyll" face in normal cells. D: As for B and C but varying mixtures of amifostine, WR-1065 and their metabolites are produced in normal and cancer cells, respectively; these mixtures interact with processes in normal and cancer cells in specific ways.

However, how amifostine exerts its negative effect on DSB repair in cancer cells remains disputable (Figure 10). We suppose that amifostine and/or its metabolites interfere in malignant cells in some detrimental way with the processes of DNA repair, having no significant influence on the process of the radiation-induced formation of DSBs itself. Some authors reported that only the active metabolite of amifostine, WR1065, was taken up into the cells.[37] This finding opens up a paradox: Nonmetabolized amifostine, if considered responsible for the alteration of DSB repair, cannot penetrate into the cells; WR-1065, when suspect, is not produced in cancer cells in larger amounts.

Theoretically, low amounts of amifostine itself might enter the cells, which could be enough to exert negative effects of this drug on DSB repair in cancer cells. Inside the cells, amifostine may influence the repair directly or indirectly by interfering with vital cell processes. Differences in signaling pathways in normal and cancer cells, and their cell type-specific interactions with amifostine, can explain how the negative influence on DSB repair is mediated in cancer cells. Because the benefits for normal cells, the immediate radioprotection and improvement of DSB repair, are exerted by amifostine metabolites, we termed this scenario *The Good and the Bad Hypothesis* (Figure 10B).

Though this mechanism might be supported by our LC-MS/MS data (see Figure 8) revealing non negligible concentrations of amifostine also inside the cells, the sensitivity of the method does not exclude the possibility that amifostine contained in the cell medium contributed to the values measured, despite our careful cell washing. In any case, because we observed the alteration of DSB repair also in MCF7 cells directly incubated with WR-1065 and a reverse conversion of this metabolite back to amifostine has not been described, we consider as more probable *The Jekyll and Hyde Hypothesis*, where WR-1065 supports DSB repair in normal cells but disturbs it in cancer

DOI: 10.1021/acs.jmedchem.5b01628
J. Med. Chem. 2016, 59, 3003−3017

cells (Figure 10C). Only low amounts of WR-1065 produced in cancer cells, which does not allow for efficient radioprotection, are probably sufficient to modify the expression of genes that alter directly or indirectly DSB repair.

Alternatively, other metabolites of amifostine or WR-1065 might cooperate in a plethora of different effects, including the deceleration of DSB repair observed in this work (*The Third-Player Effect Hypothesis*; Figure 10D). In support of this hypothesis, McKibbin et al.[47] showed that amifostine and WR-1065 are rapidly metabolized and distributed in the tissues, whereas the excretion of their metabolic products is very slow. WR1065 could be eliminated by several pathways[47] and, in turn, the metabolites might interact with various cellular compounds and processes in their specific ways. In vitro studies showed that oxidation of WR-1065 to its polyamine-like disulfide metabolite (WR-33278) is followed by a rapid consumption of oxygen in the culture medium; through this hypoxia, WR-33278 may up-regulate the expression of a variety of proteins participating in DNA repair and apoptosis, such as Bcl-2 and the hypoxia-inducible factor-1α.[48−50] Bcl-2 may then initiate or inhibit apoptosis depending on its cell type- and cell status-specific interactions (reviewed in refs 51 and 52). Similar dual effects might thus also influence DSB repair.

Concerning all the presented hypotheses, the different response of normal (NHDF) and cancer (MCF7) cells to amifostine treatment most probably and primarily reflects (1) a different rate of ALP-mediated conversion of amifostine to WR-1065 (and consequently other metabolites), resulting in qualitatively and quantitatively varying "mixtures" of biologically active compounds influencing the cells, and (2) a different genetic background of the cells that is responsible for cell type- and cell status-specific interactions of cells with these mixtures. In in vivo conditions, physiological parameters (hypoxia, pH, etc.) play an additional important role (reviewed in ref 41).

3.4. What is the Mechanism of How Amifostine Exerts Its Positive Effect on DSB Repair in Normal Cells? A further question remains, namely how amifostine metabolites stimulate DSB repair in normal cells. As already discussed in the previous paragraphs, (metabolized) amifostine influences normal cells via multiple pathways. It has been known that amifostine/WR-1065 can directly support DNA repair (Figure 10) by donating hydrogen atoms and depleting oxygen to a singlet state.[53] Further, Almeida et al.[20] revealed that the protection by amifostine against radiation-induced genotoxicity in *Escherichia coli* cells depends on the functional *recN* gene that is essential for the SOS response and repair of DSBs by homologous recombination. Dziegielewski et al.[54] showed that WR-1065 prevents delayed genomic instability though, contrary to Almeida et al.,[20] these authors suppose that WR-1065 disrupts homologous recombination and prevents its dangerous hyperstimulation by ionizing radiation. In any case, direct interactions of the drug with p53, NFκB, ATM, and Tip60 (Xu et al.[55]), together with the modified expression of genes involved in DNA repair, cell cycle regulation, and apoptosis[56−58] confirm a more general influence of amifostine (and its metabolites) on DSB repair. In amifostine-treated cells, this influence is also evidenced by a reduced frequency of chromosomal aberrations[59,60] which represent late effects of ionizing radiation.

Multiple direct and indirect mechanisms therefore seem to cooperate on the final positive effect of WR1065 on DSB repair in normal cells (Figure 10). However, it remains yet undisclosed how individual processes interconnected in this amifostine response network interplay in providing the final effect. For instance, because cancer cells are usually resistant to cell-cycle checkpoint arrests, only normal cells can profit from prolonged times available for DSBs repair (reviewed in ref 61). At the same time, DSB repair can be stimulated directly[54] and by initiating other (still unknown) processes. The more pronounced effect on DSB repair observed in this work at 60 min PI for WR-1065 as compared with amifostine (Figures 2−4) could be explained by an incomplete amifostine metabolic conversion, though in normal cells.

3.6. Do Amifostine Effects Correlate with Extracellular and Cellular Activity of Alkaline Phosphatase in Normal NHDF Fibroblasts and MCF7 Cancer Cells? How extracellular amifostine is converted into its active metabolites and how these metabolites are transported into the cells are intensely disputed questions. Our findings revealed a significantly higher ALP activity in the normal NHDF fibroblasts compared to cancer MCF7 cells. By LC-MS/MS in cells treated with amifostine, we also directly measured substantially higher levels of WR-1065 in normal NHDF fibroblasts and their culture supernatants than in cancer MCF7 cells and their supernatants. In accordance with our data discussed above, these observations support the concept by which ALP is necessary to metabolize amifostine to WR-1065 in order to attain radioprotective effectiveness (Figure 10).[3,13,44,62] However, the differences in ALP activity between normal and cancer cells were only about 25% for the cell mass and 50% for cell supernatants. The quantification of WR-1065 in cells incubated with amifostine for 20 min by LC-MS/MS then revealed a more efficient amifostine conversion and WR-1065 accumulation in normal NHDF cells by the factor 2.6 when compared to cancer MCF7 cells. Higher though than in the case of ALP activity measurements, this difference still leaves open the question of why the radioprotective effect at the level of DNA damage is totally absent in MCF7 cells. An explanation could consist of the fact that we only quantified WR-1065 levels in total cell lysates and not solely in the cell nuclei. Moreover, our measurements were limited to the free thiolic form of amifostine, WR-1065. While WR-1065 has been broadly studied and known to passively diffuse in cells, the still mysterious disulfide form of amifostine, WR-33278, which also exerts potent radioprotective properties,[63] is transported actively via the polyamine transport system.[45,46] Therefore, we could not exclude that yet other mechanisms, such as the polyamine transport system, regulate the cellular intake or exclusion of amifostine and its metabolites.[45,46,64] Indeed, Quiñones et al.[63] demonstrated that selective exclusion of amifostine derivatives by this system could account for differential radio- or chemoprotection in normal versus cancer tissues. Furthermore, intracellular redox-mediated reactions, dependent on the cell type and condition, can significantly affect the interconversion between the thiol and disulfide forms of amifostine[64] where the disulfide form can concentrate itself over 10-fold within the nucleus as the consequence of its active sequestration by this organelle.[64,65] Our LC-MS/MS data also support earlier findings[66] that WR-1065 is quite fast decomposed into its metabolites, in our hands only by the cells themselves and not the supernatants of their cultures (see Figure 8). The different extent and kinetics of WR-1065 conversion in NHDF and MCF7 cells might suggest that this phenomenon further contributes to selective effects of the amifostine prodrug, as presupposed by *The Third-Player Effect*

DOI: 10.1021/acs.jmedchem.5b01628
J. Med. Chem. 2016, 59, 3003−3017

Hypothesis discussed in section 3.3. Taken together, the levels of active radioprotective compounds in the cell nucleus might be much higher in normal (NHDF) cells and much lower in cancer (MCF7) cells than indicated by our ALP-activity and LC-MS/MS measurements, in accordance with the pronounced radioprotective effect in NHDF fibroblasts but its absence in MCF7 cells.

The measurement of ALP activity (and WR-1065 levels) also in the culture supernatants and the finding of high ALP levels also in the cell milieu suggest that the conversion of amifostine to WR-1065 can, in principle, take place both extracellularly and during the passage through the cell membrane (Figure 10).

Of interest is also the observation that whereas the ALP activity is significantly higher in normal cells compared with cancer cells, the opposite is true for the levels of ALP mRNAs. The finding of a high ALP mRNA concentration in the cancer MCF cells suggests that some malfunction of the translation of ALP mRNA into the respective functional protein exists in these cells, which unsuccessfully try to compensate for it by an increased mRNA production. This is in good agreement with the fact that ALP is suspected to play an important role in carcinogenesis, because some tumors showed a strong activity of alkaline phosphatase.[67] ALP ensures the cellular absorption of complex molecules, regulates the activity of other enzymes, and provides phosphate groups for various cellular functions. Cancer cells would be expected to preferentially suffer from ALP insufficiency because they are fast proliferating and have a high metabolic activity. In our study, the mRNA levels of tissue nonspecific ALP (TNAP) were the highest and 1 order higher in cancer MCF7 cells than in normal fibroblasts. Nevertheless, further studies are needed to understand the role of individual ALP isoenzymes in amifostine processing and in carcinogenesis.

3.7. Reassessment of Old Problems with New Tools. Methodological Progress in the Research of Radioprotective Agents and Novelty of This Work. Concerning our methodology, we followed DSB damage induction and repair in intact normal and cancer cells treated with amifostine or WR-1065 by double immunodetection of DSB repair foci in combination with high-resolution fluorescence microscopy. To our best knowledge, the only similar work was published by Kataoka et al.[68] (discussed in ref 69) who, however, used flow cytometry to quantify fractions of cells positive for DSB damage at 1 h PI. Instead, we scored individual γH2AX and 53BP1 foci (Figure 1) at 3D-high resolution microscopic images immediately (5 min) postirradiation and then at 1 and 2 h PI. This allowed us to separately evaluate the effect of amifostine or WR-1065 on DSB induction and repair. Our method also currently provides the highest sensitivity of DSB detection (in principle down to a single lesion)[69,70] and, in combination with confocal microscopy, the ability to directly score DSBs in situ. The combined immunolabeling of γH2AX and 53BP1 foci allowed us to further increase the fidelity of DSB detection and to distinguish unrepaired DSBs from the background or "relicts" of already rejoined lesions.

DSB induction in amifostine-treated cells was already evaluated by a number of techniques, including neutral comet assay[71] also employed in this work, pulsed-field gel electrophoresis (PFGE),[11] counting of chromosomal aberrations,[72] measuring of apoptosis activation,[73] cytokinesis-blocked micronucleus assay,[74] or methods assessing genomic instability.[54] All these methods have their benefits but also suffer from some underlying limits. The immunofluorescence microscopy that we used here allowed us to quantify DSBs from minutes up to hours postirradiation, in intact cells, with the maximum sensitivity, and upon the (relatively low) radiation doses typically used in radiotherapy[30,75] (reviewed in ref 76). Comet assay enabled us to study DSB repair more directly, though higher doses (6 Gy of γ-rays) were required to obtain more prominent differences between the samples. The results of both methods well correlated; nevertheless, our results still have to be generalized only with caution: Kataoka et al.[68] found that while an increased γH2AX signal corresponded with a subsequent cell survival in the case of WR-1065, this was not true for some other radioprotectors included in their study. Leaving thus the detection of γH2AX as a method of searching for novel radioprotectors as disputable, these findings indicate that amifostine/WR-1065 influences more aspects of the cellular response to irradiation than only DSB induction; this is retrospectively in accordance with our results.

3.8. Conclusions. Taken altogether, our results put amifostine in an entirely new light. In the treatment of some malignancies, this drug can not only selectively protect normal tissues but can also act as a radiosensitizer which in parallel improves the killing of the cancer cells by disrupting DNA DSB repair. This finding highlights separated effects of amifostine on DSB induction and repair. Nevertheless, the complexity of cellular processes potentially specifically influenced by amifostine and its metabolites in various normal and cancer cells prevents a simple extension of our results to normal and cancer cells in general. Hence, the action of amifostine and other radiomodifiers should be studied carefully for each particular cell type. The rapidly growing repertoire of new molecular-genetic, genomic, and other "omic" methods[77,78] now opens new dimensions of further research on radiomodifying drugs and the mechanisms of their action.

4. EXPERIMENTAL SECTION

All materials were obtained from common commercial suppliers and used without further purification. Amifostine and WR-1065, the compounds studied in this article, were of ≥97% purity determined by TLC and ≥98% purity determined by HPLC, respectively.

4.1. Cell Lines and Their Cultivation. Certified normal human dermal fibroblasts (NHDF) and human breast adenocarcinoma cells (MCF7) were obtained from CLS Cell Lines Service GmbH (Eppelheim, Germany), cultivated in DMEM medium (PAN Biotech, Aidenbach, Germany, cat. no: P03-0710), supplemented with 10% fetal calf serum (PAA Laboratories GmbH, Pasching, Austria) and 1% penicillin + streptomycin (stock solution mixture 10 000 U/mL penicillin + 10 mg/mL streptomycin; PAN Biotech, cat. no.: P06-07100), at 37 °C in a humidified atmosphere of 5% CO_2. The cells obtained (at passage 2) were multiplied and frozen, and the "young" passages 5 and 6 used for experiments to prevent possible accumulation of chromosomal aberrations and mutations and their potential effects on results.

4.2. Amifostine and WR-1065. Amifostine (Sigma, St. Louis, MO, product no.: A5922) was added to the cell cultures 15 min before irradiation. The concentration of amifostine in the cultures was 4 mM. This concentration was chosen as the most effective on the basis of literature data.[12,14] WR-1065 (Tocris, Abingdon, UK, catalogue no.: 3356) was used in an isomolar concentration and applied in the same time interval as amifostine.

4.3. Irradiation. The cells were irradiated in the culture medium at 37 °C from a ^{60}Co source (Chisostat, Chirana, Prague, Czech Republic) with a dose of 1 Gy (γH2AX/53BP1 foci immunofluorescence) or 6 Gy (comet assay); the dose rates were 0.5 Gy/min and 1.0 Gy/min, respectively. During the irradiation, the cells were kept in a thermostable box, ensuring a constant temperature and prevention from infection during the whole procedure. After irradiation, the cells

DOI: 10.1021/acs.jmedchem.5b01628
J. Med. Chem. 2016, 59, 3003−3017

were immediately placed back into the incubator (37 °C/5% CO_2) until the fixation.

4.4. γH2AX and 53BP1 Foci Immunostaining. Nonirradiated cells (0 min PI) and cells irradiated with 1 Gy of γ-rays (^{60}Co; 0.5 Gy/min) were washed in PBS, spatially (3D) fixed with 4% paraformaldehyde (10 min, room temperature (RT)) in early and later time intervals PI (5 and 60 min PI), permeabilized in 0.2% Triton X-100/PBS (14 min, RT), and immunoassayed as described in refs 26 and 75. The primary mouse antibodies, antiphospho-H2AX (serine 139) (Upstate Biotechnology, Lake Placid, NY, cat. no.: 05-636) and rabbit anti-53BP1 (Cell Signaling Technology, Danvers, MA, cat. no.: 4937), were used simultaneously to detect the γH2AX and 53BP1 ionizing radiation-induced DSB-repair foci (IRIFs). The antibodies bound were visualized with the secondary FITC-conjugated donkey antimouse and Cy3-conjugated donkey antirabbit antibodies (both Jackson Laboratory, West Grove, PA, cat. no.: 715-095-150 and 711-165-152); nuclear chromatin was counterstained with 1 μM TO-PRO-3 (Molecular Probes, Eugene, OR) in 2× saline sodium citrate (SSC) prepared fresh from a stock solution. After brief washing in 2× SSC, Vectashield medium (Vector Laboratories, Burlington, Canada) was used for the final mounting of the samples.

4.5. Evaluation of DNA Double Strand Break (DSB) Damage and Repair by Comet Assay. Cell cultures were washed with fresh DMEM medium (described in section 4.1) to remove dead cells and supplemented with new medium containing or not 4 mM amifostine (Sigma) or 4 mM WR1065 (Tocris), both prepared fresh from 100 mM stock solution. After 15 min treatment with these compounds in an incubator (37 °C, 5% CO_2), cells were irradiated as described (section 4.3) and immediately harvested (5 min PI) or allowed to repair their DNA for next 60 or 120 min. For the comet assay, cells were deprived of medium and scratched (by cell scrapers, Biotech) in 800 μL of 1× PBS. The cell suspension (100 μL) was mixed with 400 μL of melted 0.7% LMT-agarose (Ultra Pure Low Melting Point Agarose, ThermoFisher Scientific) at 40 °C, and 80 μL of this suspension was immediately spread over preheated microscopic slides (cut edges, frosted ends slides from P-lab) coated with 0.5% LMT-agarose. The slides were covered by coverslips and placed on ice for 2 min. Then coverslips were removed and slides submersed in lysis buffer[79] for 90 min, equilibrated in TA buffer for 5 min, and subjected to electrophoresis for 15 min at 25 V (1.06 V/cm), 6 °C, in darkness. For fluorescence microscopy, DNA comets were stained with Gel Red Nucleic Acid Stain (Biotium). The detailed procedure was described previously.[79]

4.6. Confocal Microscopy and Image Analysis. *4.6.1. Imaging and Quantification of γH2AX and 53BP1 Foci.* An automated high-resolution confocal fluorescence microscopic system Leica DM RXA,[73] equipped with a CSU10a Nipkow disc (Yokogawa, Tokyo, Japan), an oil immersion Plan Fluotar objective (100×/NA1.3), a CoolSnap HQ CCD camera (Photometrix, Tucson, AZ), and an Ar/Kr laser (Innova 70C Spectrum, Coherent, Santa Clara, CA), was used for image acquisition.[80] Forty serial optical sections were captured at 0.2 μm intervals along the *z*-axis to reconstruct 3D images of the nuclei,[81] at a constant temperature of 26 °C. The maximal images represent computational superimpositions of individual confocal slices. The exposure time and the dynamic range of the camera in the red, green, and blue channels were adjusted to the same values for all slides to obtain quantitatively comparable images. Automated exposure, image quality control, and other procedures were performed using Acquiarium software.[82]

4.6.2. Imaging and Quantification of DNA Comets (comet assay). A Leica SP5 microscopy system equipped with UV-lasers (355 and 405 nm), a white laser, and sensitive hybrid detectors (Leica) was used for acquisition[29] of comet images stained with Gel Red Nucleic Acid Stain (Biotium). Two kinds of confocal image *z*-stacks (3D images) were acquired to ensure the maximum sensitivity and fidelity of comet analyses: (1) "Low-magnification" images were obtained with the N PLAN 10× 0.25 DRY lens and (2) "high-magnification" images (1 to 5 comets per slide) using the HCX PL APO lambda blue 63× 1.4 OIL lens. One hundred to 200 confocal slices with a *z*-step of 1.01 μm (low-magnification images) or 30−50 confocal slices with a *z*-step of 0.3 μm (detailed comets) were captured and superimposed to maximum images for consequent analyses. The same conditions were kept for all slides (image size 1024 × 1024, scanning frequency 400 Hz in bidirectional mode, pinhole 208.01 μm for low-magnification images and 95 μm for high-magnification images, constant laser power, and hybrid detector acquisition range 606−708 nm). Two hundred to 1000 comets per sample and about 50 comets per sample were used for the "high-throughput" and the "detailed" comets analyses, respectively.

Maximum images were computed and converted to TIFF files by Leica LAS AF software (ver. 2.6.0, Leica Microsystems). CASP Lab software (ver. 1.2.3beta1, Comet Assay Software Project Lab; Krzysztof Końca, 2003)[83] was consequently used to quantify comets parameters with the same settings for all samples compared. The slides were prepared and analyzed in duplicates. The data were analyzed in Sigma Plot Scientific Software (SPSS, ver. 12.5, Systat Software); statistical significance of tail moment differences was determined using the Mann−Whitney U test.

4.7. Flow Cytometry. Flow cytometry was used to quantify cell concentrations and vitality prior to LC-MS/MS and colorimetric measurements. The Muse Cell Analyzer (Merck Millipore) and Muse Annexin V & Dead Cell Assay Kit (MCH100105, Millipore) were used according to the manufacturer's instructions. The status of the cells was analyzed in three measurements.

4.8. Alkaline Phosphatase (ALP) Activity. The ALP activity in NHDF and MCF7 cells was determined in a lysate of sonicated cells (5×10^5 per sample) and cell supernatants, respectively, after incubation with the ALP substrate (4-*p*-nitrophenyl phosphate, Fluka, Buchs, Switzerland). The incubation took place in a 96-well plate at 37 °C for 30 min, as described previously.[84] The optical densities were measured at 405 nm (DigiScan Reader). The same approach was used for the measurement of ALP activity in the cell lysates and supernatants of the cell cultures.

4.9. Liquid Chromatography−Mass Spectrometry (LC-MS/MS). Preparation of cells and cell supernatants: The cells in culture flasks were provided with fresh DMEM medium (section 4.1) supplemented (37 °C, pH 7.1 at the beginning of incubation) with 4 mM amifostine (Sigma) or 4 mM WR1065 (Tocris) prepared fresh from 100 mM stock solution. The cells treated were placed into a cell incubator (37 °C) for 20 or 75 min until harvested for the measurement (i.e., scratched, resuspended in 800 μL of 1× PBS, and disintegrated by sonication (2 min) and 3× repeated freezing in liquid nitrogen. Filtered suspension with disintegrated cells was used for LC-MS/MS.

LC-MS/MS instrumentation and conditions: The analyses were performed on an Agilent 1200 series (Agilent, Waldbronn, Germany) equipped with a G1312B binary pump, a G1367D-HiPALS SL autosampler, and a G1316B column oven. The sample was separated using a Zorbax Poroshell 120 EC 18 column (I.D. 3.0 mm × 50 mm, 2.7 μm particle size; Agilent, Santa Clara, CA) and the column temperature was 25 °C. Isocratic elution was applied with 0.2% acetic acid and methanol (2:98, v/v). The flow rate was 0.60 mL min^{-1}, and the injection volume was 1 μL.

Determination was performed using an Agilent Technologies 6460 Triple Quadrupole LC/MS system with Jet Stream Technologies with electrospray ionization (ESI). The compounds were ionized in the positive ion polarity mode. The ionization source conditions were as follows: capillary voltage 400 V, gas temperature 350 °C, gas flow 12 L min^{-1}, nebulizer pressure 50 psi, sheath gas temperature 350 °C, sheath gas flow 12 L min^{-1}. Quantification was performed using multiple reaction (MRM) modes. Precursor ion → product ion, fragmentor voltage and collision energy were selected for each compound individually for amifostine: 215 → 135, 90 V, 8 eV; for WR 1065: 135 → 58, 90 V, 16 eV.

4.10. Quantitative Real-Time Reverse Transcription-PCR (qRT-PCR) analyses. cDNA was prepared using the Transcriptor First Strand cDNA Synthesis Kit (Roche Diagnostics, Mannheim, Germany). One microgram of RNA was used per each reverse transcription. The mRNA levels of selected genes (four isotypes of ALP) were measured by a real-time reverse-transcription-polymerase

DOI: 10.1021/acs.jmedchem.5b01628
J. Med. Chem. 2016, 59, 3003−3017

chain reaction (qRT-PCR) in triplicates on a RotorGene 6000 cycler (Cobett Research, Sydney, Australia) using the FastStart SYBR Green Master (Rox) (Roche Diagnostics, Mannheim, Germany). The final reaction volume (20 μL) included 10 μL of FastStart SYBR Green Master (Rox), 2 μL of cDNA, and 100 nM concentration of each primer. The primer sequences (see Table S1, Supporting Information) were obtained from Schär et al.[85] The initial reaction cycle carried out at 95 °C for 10 min was followed by 40 cycles, each consisting of 15 s denaturation at 95 °C, 20 s annealing at 60 °C, and 20 s extension at 72 °C. To determine the relative gene expression levels, we used the delta−delta Ct method based on the difference of the threshold cycles (Ct) of the target gene and β-actin housekeeping.

4.11. Statistics. For the testing of statistical significance of the differences in the numbers of γH2AX foci between pairs of experimental groups, the Mann−Whitney U test was used. For the testing of statistical significance of the differences in the ALP activity or the mRNA expression of the individual ALP isoenzymes, the two-sample *t* test was used; these analyses were performed on data of merged experiments after standardization using *z*-score. All the statistical analyses were performed using the IBM SPSS Statistics 19 for Windows software (Release 19.0.1, IBM Corporation 2010).

■ ASSOCIATED CONTENT

Supporting Information

The Supporting Information is available free of charge on the ACS Publications website at DOI: 10.1021/acs.jmedchem.5b01628.

Sequence of primers used in RT-PCR for amplifying alkaline phosphatase (ALP) isoenzyme mRNAs; DSB induction and repair quantified by the neutral comet assay−wide-field images (extending Figure 6); HPLC-MS/MS fragmentation spectra of WR-1065 and amifostine (for Figure 8) (PDF)

■ AUTHOR INFORMATION

Corresponding Author

*E-mail: falk@ibp.cz. Phone: +420-541517116 (work), +420-728084060 (mobile).

Author Contributions

Michal Hofer and Martin Falk contributed equally. They designed the experiments, analyzed data, and prepared the manuscript. Martin Falk summarized and proposed the hypotheses on amifostine action displayed in Figure 5. Martin Falk also participated in confocal microscopy. Denisa Komůrková, Lenka Weiterová, and Lenka Štefančíková performed γH2AX/53BP1 foci immunostaining, quantification, and confocal microscopy; Denisa Komůrková also analyzed the ALP activity and mRNA levels. Iva Falková, Alena Bačíková, and Bořivoj Klejdus determined amifostine conversion to WR-1065 by LC-MS/MS. Iva Falková, Alena Bačíková, Karel Angelis, and Štefan Galbavý performed comet assay experiments, confocal image acquisition, and data analyses. IF also contributed to manuscript preparation. Eva Pagáčová took part in immunofluorescence experiments and image acquisition and analyses; she also maintained cell cultures. Stanislav Kozubek participated in confocal microscopy, data acquisition and analyses, and in manuscript preparation. Ladislav Dušek performed statistical evaluations.

Notes

The authors declare no competing financial interest.

■ ACKNOWLEDGMENTS

This work was supported by the Czech Science Foundation (projects 16-12454S, P302/12/G157, and 16-01137S), Ministry of Health of the Czech Republic, AZV grant no. 16-29835A (all rights reserved) and from the Czech Republic contribution to the Joint Institute for Nuclear Research, Dubna (Project of the Czech Plenipotentiary and the 3 + 3 Project for 2015, 2016). LC-MS/MS experiments were realized in CEITEC-Central European Institute of Technology with research infrastructure supported by the project CZ.1.05./1.1.00/02.0068 financed from European Regional Development Fund.

■ ABBREVIATIONS USED

ALP, alkaline phosphatase; DSB, DNA double strand breaks; GCAP, placental-like ALP; IAP, intestinal ALP; IR, ionizing radiation; MCF7, human mammary carcinoma cell line; NHDF, normal human dermal fibroblasts; PI, postirradiation; PLAP, placental ALP; TNAP, tissue nonspecific ALP

■ REFERENCES

(1) Calabro-Jones, P. M.; Fahey, R. C.; Smoluk, G. D.; Ward, J. F. Alkaline Phosphatase Promotes Radioprotection and Accumulation of WR-1065 in V79−171 Cells Incubated in Medium Containing WR-2721. *Int. J. Radiat. Biol. Relat. Stud. Phys., Chem. Med.* **1985**, *47*, 23−27.

(2) Calabro-Jones, P. M.; Aguilera, J. A.; Ward, J. F.; Smoluk, G. D.; Fahey, R. C. Uptake of WR-2721 Derivatives by Cells in Culture: Identification of the Transported Form of the Drug. *Cancer Res.* **1988**, *48*, 3634−3640.

(3) Levi, M.; Knol, J. A.; Ensminger, W. D.; DeRemer, S. J.; Dou, C.; Lunte, S. M.; Bonner, H. S.; Shaw, L. M.; Smith, D. E. Regional Pharmacokinetics of Amifostine in Anesthetized Dogs: Role of the Liver, Gastrointestinal Tract, Lungs, and Kidneys. *Drug Metab. Dispos.* **2002**, *30*, 1425−1430.

(4) Tahsildar, H. I.; Biaglow, J. E.; Kligerman, M. M.; Varnes, M. E. Factors Influencing the Oxidation of Radioprotector WR-1065. *Radiat. Res.* **1988**, *113*, 243−251.

(5) Durand, R. E.; Olive, P. L. Radiosensitisation and Radioprotection by BSO and WR-2721: the Role of Oxygenation. *Br. J. Cancer* **1989**, *60*, 517−522.

(6) Taylor, C. W.; Wang, L. M.; List, A. F.; Fernandes, D.; Paine-Murrieta, G. D.; Johnson, C. S.; Capizzi, R. L. Amifostine Protects Normal Tissues from Paclitaxel Toxicity While Cytotoxicity against Tumour Cells Is Maintained. *Eur. J. Cancer* **1997**, *33*, 1693−1698.

(7) Kurbacher, C. M.; Mallmann, P. K. Chemoprotection in Anticancer Therapy: The Emerging Role of Amifostine (WR-2721). *Anticancer Res.* **1998**, *18*, 2203−2210.

(8) Orditura, M.; de Vita, F.; Roscigno, A.; Infusino, S.; Auriemma, A.; Iodice, P.; Ciaramella, F.; Abbate, G.; Catalano, G. Amifostine: a Selective Cytoprotective Agent of Normal Tissues from Chemo-Radiotherapy Induced Toxicity (Review). *Oncol. Rep.* **1999**, *6*, 1357−1362.

(9) Buschini, A.; Aneschi, E.; Carlo-Stella, C.; Regazzi, E.; Rizzoli, V.; Poli, P.; Rossi, C. Amifostine (WR-2721) Selective Protection against Melphalan Toxicity. *Leukemia* **2000**, *14*, 1642−1651.

(10) Buschini, A.; Aneschi, E.; Carlo-Stella, C.; Regazzi, E.; Rizzoli, V.; Poli, P.; Rossi, C. Bleomycin Genotoxicity and Amifostine (WR-2721) Cell Protection in Normal Leukocytes vs. K562 Tumoral Cells. *Biochem. Pharmacol.* **2002**, *63*, 967−975.

(11) Majsterek, I.; Gloc, E.; Blasiak, J.; Reiter, R. J. A Comparison of the Action of Amifostine and Melatonin on DNA-Damaging Effects and Apoptosis Induced by Idarubicin in Normal and Cancer Cells. *J. Pineal Res.* **2005**, *38*, 254−263.

(12) Margulies, B. S.; Damron, T. A.; Allen, M. J. The Differential Effects of the Radioprotectant Drugs Amifostine and Sodium Selenite Treatment in Combination with Radiation Therapy on Constituent Bone Cells, Ewing's Sarcoma or Bone Tumor Cells, and Rhabdomyosarcoma Tumor Cells in Vitro. *J. Orthop. Res.* **2008**, *26*, 1512−1519.

DOI: 10.1021/acs.jmedchem.5b01628
J. Med. Chem. 2016, 59, 3003−3017

(13) Eisbruch, A. Amifostine in the Treatment of Head and Neck Cancer: Intravenous Administration, Subcutaneous Administration, or None of the Above. *J. Clin. Oncol.* **2011**, *29*, 119−121.
(14) Brenner, B.; Wasserman, L.; Beery, E.; Nordenberg, J.; Schlechter, J.; Gutman, H.; Fenig, E. Variable Cytotoxicity of Amifostine in Malignant and Non-Malignant Cell Lines. *Oncol. Rep.* **2003**, *10*, 1609−1613.
(15) Tsai, L. C.; Hung, M. W.; Chen, Y. H.; Su, W. C.; Chang, G. G.; Chang, T. C. Expression and Regulation of Alkaline Phosphatases in Human Breast Cancer MCF-7 Cells. *Eur. J. Biochem.* **2000**, *267*, 1330−1339.
(16) Sadeghirizi, A.; Yazdanparast, R. Plasma Membrane Homing of Tissue Nonspecific Alkaline Phosphatase under the Influence of 3-Hydrogenkwadaphnin, an Antiproliferative Agent from Dendrostellera lessertii. *Acta Biochim. Polym.* **2007**, *54*, 323−329.
(17) Chang, T. C.; Wang, J. K.; Hung, M. W.; Chiao, C. H.; Tsai, L. C.; Chang, G. G. Regulation of the Expression of Alkaline Phosphatase in a Human Breast-Cancer Cell Line. *Biochem. J.* **1994**, *303*, 199−205.
(18) Chan, J. R.; Stinson, R. A. Dephosphorylation of Phosphoproteins of Human Liver Plasma Membranes by Endogenous and Purified Liver Alkaline Phosphatases. *J. Biol. Chem.* **1986**, *261*, 7635−7639.
(19) Muller, A. C.; Pigorsch, S. U.; Dunst, J. Radioprotection with Activated Amifostine via Trans-Dominant Inhibition of PARP: DSB-Misrejoining and Chromosome Aberrations. *Strahlenther. Onkol.* **2003**, *179*, 657−657.
(20) Almeida, E.; Fuentes, J. L.; Cuetara, E.; Prieto, E.; Llagostera, M. Amifostine Protection against Induced DNA Damage in Gamma-Irradiated Escherichia coli Cells Depend on recN DNA Repair Gene Product Activity. *Environ. Toxicol.* **2010**, *25*, 130−136.
(21) Rogakou, E. P.; Pilch, D. R.; Orr, A. H.; Ivanova, V. S.; Bonner, W. M. DNA Double Strand Breaks Induce Histone H2AX Phosphorylation on Serine 139. *J. Biol. Chem.* **1998**, *273*, 5858−5868.
(22) Turinetto, V.; Giachino, C. Multiple Facets of Histone Variant H2AX: a DNA Double-Strand-Break Marker with Several Biological Functions. *Nucleic Acids Res.* **2015**, *43*, 2489−2498.
(23) Ivashkevich, A.; Redon, C. E.; Nakamura, A. J.; Martin, R. F.; Martin, O. A. Use of the γ-H2AX Assay to Monitor DNA Damage and Repair in Translational Cancer Research. *Cancer Lett.* **2012**, *327*, 123−133.
(24) Mariotti, L. G.; Pirovano, G.; Savage, K. I.; Ghita, M.; Ottolenghi, A.; Prise, K. M.; Schettino, G. Use of the γ-H2AX Assay to Investigate DNA Repair Dynamics Following Multiple Radiation Exposures. *PLoS One* **2013**, *8*, e79541.
(25) Cornelissen, B.; Kersemans, V.; Darbar, S.; Thompson, J.; Shah, K.; Sleeth, K.; Hill, M. A.; Vallis, K. A. Imaging DNA Damage in Vivo Using GammaH2AX-Targeted Immunoconjugates. *Cancer Res.* **2011**, *71*, 4539−4549.
(26) Falk, M.; Lukasova, E.; Gabrielova, B.; Ondrej, V.; Kozubek, S. Chromatin Dynamics during DSB Repair. *Biochim. Biophys. Acta, Mol. Cell Res.* **2007**, *1773*, 1534−1545.
(27) Sevcik, J.; Falk, M.; Kleiblova, P.; Lhota, F.; Stefancikova, L.; Janatova, M.; Weiterova, L.; Lukasova, E.; Kozubek, S.; Pohlreich, P.; Kleibl, Z. The BRCA1 Alternative Splicing Variant Δ14−15 with an In-Frame Deletion of Part of the Regulatory Serine-Containing Domain (SCD) Impairs the DNA Repair Capacity in MCF-7 Cells. *Cell. Signalling* **2012**, *24*, 1023−1030.
(28) Sevcik, J.; Falk, M.; Macurek, L.; Kleiblova, P.; Lhota, F.; Hojny, J.; Stefancikova, L.; Janatova, M.; Bartek, J.; Stribrna, J.; Hodny, Z.; Jezkova, L.; Pohlreich, P.; Kleibl, Z. Expression of Human BRCA1Δ17−19 Alternative Splicing Variant with a Truncated BRCT Domain in MCF-7 Cells Results in Impaired Assembly of DNA Repair Complexes and Aberrant DNA Damage Response. *Cell. Signalling* **2013**, *25*, 1186−1193.
(29) Falk, M.; Lukášová, E.; Štefančíková, L.; Baranová, E.; Falková, I.; Ježková, L.; Davídková, M.; Bačíková, A.; Vachelová, J.; Michaelidesová, A.; Kozubek, S. Heterochromatinization Associated with Cell Differentiation As a Model to Study DNA Double Strand Induction and Repair in the Context of Higher-Order Chromatin Structure. *Appl. Radiat. Isot.* **2014**, *83*, 177−185.
(30) Ježková, L.; Falk, M.; Falková, I.; Davídková, M.; Bačíková, A.; Štefančíková, L.; Vachelová, J.; Michaelidesová, A.; Lukášová, E.; Boreyko, A.; Krasavin, E.; Kozubek, S. Function of Chromatin Structure and Dynamics in DNA Damage, Repair and Misrepair: γ-Rays and Protons in Action. *Appl. Radiat. Isot.* **2014**, *83*, 128−136.
(31) Kozubek, S.; Lukásová, E.; Amrichová, J.; Kozubek, M.; Lisková, A.; Slotová, J. Influence of Cell Fixation on Chromatin Topography. *Anal. Biochem.* **2000**, *282*, 29−38.
(32) Vasireddy, R. S.; Sprung, C. N.; Cempaka, N. L.; Chao, M.; McKay, M. J. H2AX Phosphorylation Screen of Cells from Radiosensitive Cancer Patients Reveals a Novel DNA Double-Strand Break Repair Cellular Phenotype. *Br. J. Cancer* **2010**, *102*, 1511−1518.
(33) Rappold, I.; Iwabuchi, K.; Date, K.; Chen, J. Tumor Suppressor p53 Binding Protein 1 (53BP1) Is Involved in DNA Damage-Signaling Pathways. *J. Cell Biol.* **2001**, *153*, 613−620; *J. Cell Biol.* **2001**, *154*, 469 (erratum).
(34) Fernandez-Capetillo, O.; Chen, H. T.; Celeste, A.; Ward, I.; Romanienko, P. J.; Morales, J. C.; Naka, K.; Xia, Z.; Camerini-Otero, R. D.; Motoyama, N.; Carpenter, P. B.; Bonner, W. M.; Chen, J.; Nussenzweig, A. DNA Damage-Induced G2-M Checkpoint Activation by Histone H2AX and 53BP1. *Nat. Cell Biol.* **2002**, *4*, 993−997.
(35) Liu, B.; Wang, J.; Chan, K. M.; Tjia, W. M.; Deng, W.; Guan, X.; Huang, J. D.; Li, K. M.; Chau, P. Y.; Chen, D. J.; Pei, D.; Pendas, A. M.; Cadiñanos, J.; López-Otín, C.; Tse, H. F.; Hutchison, C.; Chen, J.; Cao, Y.; Cheah, K. S.; Tryggvason, K.; Zhou, Z. Genomic Instability in Laminopathy-Based Premature Aging. *Nat. Med.* **2005**, *11*, 780−785.
(36) Chronis, F.; Rogakou, E. P. Interplay Between gH2 and 53BP1 Pathways in DNA Double-Strand Break Repair Processes. In *Cancer Drug Discovery And Development Apoptosis, Senescence and Cancer*; Gevirtz, D. A., Holt, S. E., Grant, S., Eds.; Humana Press: Totowa, NJ, 2007; p 253.
(37) Capizzi, R. L. The Preclinical Basis for Broad-Spectrum Selective Cytoprotection of Normal Tissues from Cytotoxic Therapies by Amifostine. *Semin. Oncol.* **1999**, *26*, 3−21.
(38) Giatromanolaki, A.; Sivridis, E.; Maltezos, E.; Koukourakis, M. I. Down-Regulation of Intestinal-Type Alkaline Phosphatase in the Tumor Vasculature and Stroma Provides a Strong Basis for Explaining Amifostine Selectivity. *Semin. Oncol.* **2002**, *29*, 14−21.
(39) Seed, T. M.; Inal, C. E.; Singh, V. K. Radioprotection of Hematopoietic Progenitors by Low Dose Amifostine Prophylaxis. *Int. J. Radiat. Biol.* **2014**, *90*, 594−604.
(40) Brizel, D. M.; Overgaard, J. Does Amifostine Have a Role in Chemoradiation Treatment? *Lancet Oncol.* **2003**, *4*, 378−381.
(41) Grochová, D.; Šmardová, J. The Antimutagenic and Cytoprotective Effects of Amifostine: the Role of p53. *J. Appl. Biomed.* **2007**, *5*, 171−178.
(42) Meier, T.; Issels, R. D. Degradation of 2-(3-aminopropylamino)-ethanethiol (WR-1065) by Cu-Dependent Amine Oxidases and Influence on Glutathione Status of Chinese Hamster Ovary Cells. *Biochem. Pharmacol.* **1995**, *50*, 489−496.
(43) Andreassen, C. N.; Grau, C.; Lindegaard, J. C. Chemical Radioprotection: A Critical Review of Amifostine as a Cytoprotector in Radiotherapy. *Semin. Radiat. Oncol.* **2003**, *13*, 62−72.
(44) Kouvaris, J. R.; Kouloulias, V. E.; Vlahos, L. J. Amifostine: The First Selective Target and Broad-Spectrum Radioprotector. *Oncologist* **2007**, *12*, 738−747.
(45) Mitchell, J. L.; Judd, G. G.; Diveley, R. R.; Choe, C. Y., Jr.; Leyser, A. Involvement of the Polyamide Transport System in Cellular Uptake of the Radioprotectants WR-1065 and WR-33278. *Carcinogenesis* **1995**, *16*, 3063−3068.
(46) Mitchell, J. L.; Rupert, J.; Leyser, A.; Judd, G. G. Mammalian Cell Polyamine Homeostasis is Altered by the Radioprotector WR1065. *Biochem. J.* **1998**, *335*, 329−334.
(47) McKibbin, T.; Panetta, J. C.; Fouladi, M.; Gajjar, A.; Bai, F.; Okcu, M. F.; Stewart, C. F. Clinical Pharmacokinetics of Amifostine and WR 1065 in Pediatric Patients with Medulloblastoma. *Clin. Cancer Res.* **2010**, *16*, 1049−1057.
(48) Carmeliet, P.; Dor, Y.; Herbert, J. M.; Fukumura, D.; Brusselmans, K.; Dewerchin, M.; Neeman, M.; Bono, F.;

DOI: 10.1021/acs.jmedchem.5b01628
J. Med. Chem. 2016, 59, 3003−3017

Abramovitch, R.; Maxwell, P.; Koch, C. J.; Ratcliffe, P.; Moons, L.; Jain, R. K.; Collen, D.; Keshet, E. Role of HIF-1α in Hypoxia-Mediated Apoptosis, Cell Proliferation and Tumour Angiogenesis. *Nature* **1998**, *394*, 485−490.
(49) Kajstura, J.; Cheng, W.; Reiss, K.; Clark, W. A.; Sonneblick, E. H.; Krajewski, S.; Reed, J. C.; Olivetti, G.; Anversa, P. Apoptotic and Necrotic Myocyte Cell Deaths Are Independent Contributing Variables of Infarct Size in Rats. *Lab. Invest.* **1996**, *74*, 86−107.
(50) Shimizu, S.; Eguchi, Y.; Kamiike, W.; Itoh, Y.; Hasegawa, J.; Yamabe, K.; Otsuki, Y.; Matsuda, H.; Tsujimoto, Y. Induction of Apoptosis As Well As Necrosis by Hypoxia Are Predominant Prevention of Apoptosis by Bcl-2 and Bcl-XL. *Cancer Res.* **1996**, *56*, 2161−2166.
(51) Akl, H.; Vervloessem, T.; Kiviluoto, S.; Bittremieux, M.; Parys, J. B.; De Smedt, H.; Bultynck, G. A Dual Role for the Anti-Apoptotic Bcl-2 Protein in Cancer: Mitochondria versus Endoplasmic Reticulum. *Biochim. Biophys. Acta, Mol. Cell Res.* **2014**, *1843*, 2240−2252.
(52) Weyhenmeyer, B.; Murphy, A. C.; Prehn, J. H.; Murphy, B. M. Targeting the Anti-Apoptotic Bcl-2 Family Members for the Treatment of Cancer. *Exp. Oncol.* **2012**, *34*, 192−199.
(53) Grdina, D. J.; Kataoka, Y.; Murley, J. S. Amifostine: Mechanisms Underlying Cytoprotection and Chemoprevention. *Drug Metab. Drug Interact.* **2000**, *16*, 237−279.
(54) Dziegielewski, J.; Goetz, W.; Murley, J. S.; Grdina, D. J.; Morgan, W. F.; Baulch, J. E. Amifostine Metabolite WR-1065 Disrupts Homologous Recombination in Mammalian Cells. *Radiat. Res.* **2010**, *173*, 175−183.
(55) Xu, Y.; Parmar, K.; Du, F.; Price, B. D.; Sun, Y. The Radioprotective Agent WR1065 Protects Cells from Radiation Damage by Regulating the Activity of the Tip60 Acetyltransferase. *J. Biochem. Mol. Biol.* **2011**, *2*, 295−302.
(56) Wozniak, K.; Gloc, E.; Morawiec, Z.; Blasiak, J. Amifostine Can Differentially Modulate DNA Double-Strand Breaks and Apoptosis Induced by Idarubicin in Normal and Cancer Cells. *Exp. Oncol.* **2008**, *30*, 22−28.
(57) Khodarev, N. N.; Kataoka, Y.; Murley, J. S.; Weichselbaum, R. R.; Grdina, D. J. Interaction of Amifostine and Ionizing Radiation on Transcriptional Patterns of Apoptotic Genes Expressed in Human Microvascular Endothelial Cells (HMEC). *Int. J. Radiat. Oncol., Biol., Phys.* **2004**, *60*, 553−563.
(58) North, S.; Pluquet, O.; Maurici, D.; El-Ghissassi, F.; Hainaut, P. Restoration of Wild-Type Conformation and Activity of a Temperature-Sensitive Mutant of p53 (p53(V272M)) by the Cytoprotective Aminothiol WR1065 in the Esophageal Cancer Cell Line TE-1. *Mol. Carcinog.* **2002**, *33*, 181−188.
(59) Hoffmann, G. R.; Sayer, A. M.; Littlefield, L. G. Potentiation by Bleomycin by the Aminothiol WR-1065 in Assays for Chromosomal Damage in G0 Human Lymphocytes. *Mutat. Res., Fundam. Mol. Mech. Mutagen.* **1994**, *307*, 273−283.
(60) Camelo, R. M.; Kehdy, F. S.; Salas, C. E.; Lopes, M. T. Amifostine Protection Against Mitomycin-Induced Chromosomal Breakage in Fanconi Anaemia Lymphocytes. *Molecules* **2008**, *13*, 1759−1772.
(61) Kastan, M. B.; Bartek, J. Cell-Cycle Checkpoints and Cancer. *Nature* **2004**, *432*, 316−323.
(62) Koukourakis, M. I. Amifostine in Clinical Oncology: Current Use and Future Applications. *Anti-Cancer Drugs* **2002**, *13*, 181−209.
(63) Quiñones, H. I.; List, A. F.; Gerner, A. W. Selective Exclusion by the Polyamine Transporter as a Mechanism for Differential Radioprotection of Amifostine Derivatives. *Clin. Cancer Res.* **2002**, *8*, 1295−1300.
(64) Murley, J. S.; Kataoka, Y.; and Grdina, D. J. Amifostine and the Endogenous Cellular Antioxidant Enzyme Manganese Superoxide Dismutase in Radioprotection. In *Oxidative Stress in Cancer Biology and Therapy; Oxidative Stress in Applied Research and Clinical Practice*; Spitz, D. R., Dornfeld, K. J., Krishnan, K., Gius, D., Eds.; Springer Science & Business Media: New York, 2011; p 152.
(65) Newton, G. L.; Aguilera, J. A.; Ward, J. F.; Fahey, R. C. Binding of Radioprotective Thiols and Disulfides in Chinese Hamster V79 Cell Nuclei. *Radiat. Res.* **1996**, *146*, 298−305.
(66) Meier, T.; Issels, R. D. Degradation of 2-(3-aminopropylamino)-ethanethiol (WR-1065) by Cu-Dependent Amine Oxidases and Influence on Glutathione Status of Chinese Hamster Ovary Cells. *Biochem. Pharmacol.* **1995**, *50*, 489−496.
(67) Zhang, Z.; Zhou, Y.; Qian, H.; Shao, G.; Lu, X.; Chen, Q.; Sun, X.; Chen, D.; Yin, R.; Zhu, H.; Shao, Q.; Xu, W. Stemness and Inducing Differentiation of Small Cell Lung Cancer NCi-H446 cells. *Cell Death Dis.* **2013**, *4*, e633.
(68) Kataoka, Y.; Murley, J. S.; Baker, K. L.; Grdina, D. J. Relationship Between Phosphorylated Histone H2AX Formation and Cell Survival in Human Microvascular Endothelial Cells (HMEC) As a Function of Ionizing Radiation Exposure in the Presence or Absence of Thiol-Containing Drugs. *Radiat. Res.* **2007**, *168*, 106−114.
(69) Mah, L. J.; Orlowski, C.; Ververis, K.; Vasireddy, R. S.; El-Osta, A.; Karagiannis, T. C. Evaluation of the Efficacy of Radiation-Modifying Compounds Using γH2AX As a Molecular Marker of DNA Double-Strand Breaks. *Genome Integr.* **2011**, *2*, 3.
(70) Rothkamm, K.; Löbrich, M. Evidence for a Lack of DNA Double-Strand Break Repair in Human Cells Exposed to Very Low X-Ray Doses. *Proc. Natl. Acad. Sci. U. S. A.* **2003**, *100*, 5057−5062.
(71) Littlefield, L. G.; Joiner, E. E.; Colyer, S. P.; Sallam, F.; Frome, L. Concentration-Dependent Protection Against X-Ray-Induced Chromosome Aberrations in Human Lymphocytes by the Aminothiol WR-1065. *Radiat. Res.* **1993**, *133*, 88−93.
(72) Petrovecki, M.; Prager, A.; Terry, N. H. A.; Murray, D. Relationships between DNA Damage and the Survival of Murine Bone Marrow Cells Irradiated In Situ. *Radiat. Res.* **1994**, *138*, 443−450.
(73) Mazur, L.; Augustynek, A.; Halicka, H. D.; Deptala, A. Induction of Apoptosis in Bone Marrow Cells After Treatment of Mice with WR-2721 and Gamma-Rays: Relationship to the Cell Cycle. *Cell Biol. Toxicol.* **2003**, *19*, 13−27.
(74) Mozdarani, H.; Taheri, A.; Haeri, S. A. Assessment of Radioprotective Effects of Amifostine on Human Lymphocytes Irradiated in Vitro by Gamma-Rays Using Cytokinesis-Blocked Micronucleus Assay. *Iran. J. Radiat. Res.* **2007**, *5*, 9−16.
(75) Falk, M.; Lukasova, E.; Kozubek, S. Chromatin Structure Influences the Sensitivity of DNA to γ-Radiation. *Biochim. Biophys. Acta, Mol. Cell Res.* **2008**, *1783*, 2398−2414.
(76) Falk, M.; Lukasova, E.; Kozubek, S. Higher-Order Chromatin Structures in DSB Induction, Repair and Misrepair. *Mutat. Res., Rev. Mutat. Res.* **2010**, *704*, 88−100.
(77) Falk, M.; Hausmann, M.; Lukášová, E.; Biswas, A.; Hildebrand, G.; Davídková, M.; Krasavin, E.; Kleibl, Z.; Ježková, L.; Štefančíková, L.; Ševčík, J.; Hofer, M.; Bačíková, A.; Matula, P.; Boreyko, A.; Vachelová, J.; Michaelidisová, A.; Kozubek, S. Determining Omics Spatiotemporal Dimensions Using Exciting New Nanoscopy Techniques to Assess Complex Cell Responses to DNA Damage. Part A − Radiomic. *Crit. Rev. Eukaryotic Gene Expression* **2014**, *24*, 205−223.
(78) Falk, M.; Hausmann, M.; Lukášová, E.; Biswas, A.; Hildebrand, G.; Davídková, M.; Krasavin, E.; Kleibl, Z.; Ježková, L.; Štefančíková, L.; Ševčík, J.; Hofer, M.; Bačíková, A.; Matula, P.; Boreyko, A.; Vachelová, J.; Michaelidisová, A.; Kozubek, S. Determining Omics Spatiotemporal Dimensions Using Exciting New Nanoscopy Techniques to Assess Complex Cell Responses to DNA Damage. Part B − Structuromics. *Crit. Rev. Eukaryotic Gene Expression* **2014**, *24*, 225−247.
(79) Holá, M.; Vágnerová, R.; Angelis, K. J. Mutagenesis During Plant Responses to UVB Radiation. *Plant Physiol. Biochem.* **2015**, *93*, 29−33.
(80) Kozubek, M.; Kozubek, S.; Lukasova, E.; Bartova, E.; Skalnikova, M.; Matula, P.; Matula, P.; Jirsova, P.; Cafourkova, A.; Koutna, I. Combined Confocal and Wide-Field High Resolution Cytometry of Fluorescent In Situ Hybridization-Stained Cells. *Cytometry* **2001**, *45*, 1−12.

DOI: 10.1021/acs.jmedchem.5b01628
J. Med. Chem. 2016, 59, 3003−3017

(81) Falk, M.; Lukasova, E.; Gabrielova, B.; Ondrej, V.; Kozubek, S. Local changes of higher-order chromatin structure during DSB-repair. *JPCS* **2008**, *101*, 12018−12035.
(82) Matula, P.; Maška, M.; Daněk, O.; Matula, P.; Kozubek, M. Acquiarium: Free Software for the Acquisition and Analysis of 3D Images of Cells in Fluorescence Microscopy; IEEE International Symposium on Biomedical Imaging, Boston, MA, June 28−July 1, 2009; IEEE: Picataway, NJ, 2009, pp 1138−1141.
(83) Końca, K.; Lankoff, A.; Banasik, A.; Lisowska, H.; Kuszewski, T.; Góźdź, S.; Koza, T.; Wojcik, A. A. Cross-Platform Public Domain PC Image-Analysis Program for the Comet Assay. *Mutat. Res., Genet. Toxicol. Environ. Mutagen.* **2003**, *534*, 15−20.
(84) Fajkus, J.; Borský, M.; Kunička, Z.; Kovaříková, M. Changes in Telomerase Activity, Expression and Splicing in Response to Differentiation of Normal and Carcinoma Colon Cells. *Anticancer Res.* **2003**, *23*, 1605−1612.
(85) Schär, B. K.; Otto, V. I.; Hänseler, E. Simultaneous Detection of Four Alkaline Phosphatase Isoenzymes in Human Germ Cell Tumors Using Reverse Transcription-PCR. *Cancer Res.* **1997**, *57*, 3841−3846.
(86) Gloc, E.; Warszawski, M.; Mlynarski, W.; Stolarska, M.; Hoser, G.; Skorski, T.; Blasiak, J. TEL/JA2 Tyrosine Kinase Inhibits DNA Repair in the Presence of Amifostine. *Biochim. Polym.* **2002**, *49*, 121−128.

DOI: 10.1021/acs.jmedchem.5b01628
J. Med. Chem. 2016, 59, 3003−3017

International Journal of
Molecular Sciences

MDPI

Review

Pharmacological Modulation of Radiation Damage. Does It Exist a Chance for Other Substances than Hematopoietic Growth Factors and Cytokines?

Michal Hofer *, Zuzana Hoferová and Martin Falk

Department of Cell Biology and Radiobiology, Institute of Biophysics, v.v.i., Czech Academy of Sciences, Královopolská 135, 61265 Brno, Czech Republic; hoferovaz@centrum.cz (Z.H.); falk@ibp.cz (M.F.)
* Correspondence: hofer@ibp.cz; Tel.: +420-541-517-171; Fax: +420-541-211-293

Received: 5 June 2017; Accepted: 26 June 2017; Published: 28 June 2017

Abstract: In recent times, cytokines and hematopoietic growth factors have been at the center of attention for many researchers trying to establish pharmacological therapeutic procedures for the treatment of radiation accident victims. Two granulocyte colony-stimulating factor-based radiation countermeasures have been approved for the treatment of the hematopoietic acute radiation syndrome. However, at the same time, many different substances with varying effects have been tested in animal studies as potential radioprotectors and mitigators of radiation damage. A wide spectrum of these substances has been studied, comprising various immunomodulators, prostaglandins, inhibitors of prostaglandin synthesis, agonists of adenosine cell receptors, herbal extracts, flavonoids, vitamins, and others. These agents are often effective, relatively non-toxic, and cheap. This review summarizes the results of animal experiments, which show the potential for some of these untraditional or new radiation countermeasures to become a part of therapeutic procedures applicable in patients with the acute radiation syndrome. The authors consider β-glucan, 5-AED (5-androstenediol), meloxicam, γ-tocotrienol, genistein, IB-MECA (N^6-(3-iodobezyl)adenosine-5′-*N*-methyluronamide), Ex-RAD (4-carboxystyryl-4-chlorobenzylsulfone), and entolimod the most promising agents, with regards to their contingent use in clinical practice.

Keywords: acute radiation syndrome; radioprotectors; radiomitigators; hematopoiesis

1. Introduction

Radiation accidents, as well as contingent terrorist attacks using ionizing radiation sources, can result in serious health damage whose manifestations are designated as the acute radiation syndrome (ARS). Depending on the absorbed radiation dose, the manifestation of ARS takes place in different organ systems as individual organ syndromes, namely hematopoietic, gastrointestinal, cutaneous, and neurovascular [1]. Not surprisingly, both the topics of "radioprotectors for use prior to irradiation" and "therapeutic agents for post-exposure treatments" (radiomitigators) enjoy top priority among the research areas for radiological nuclear threat countermeasures [2]. Although endeavors aimed at developing medically effective radiation countermeasures (including both the radioprotectors and radiomitigators) were initiated more than fifty years ago, only two radiation countermeasures, namely Neupogen® and Neulasta®, have been recently approved by the United States Food and Drug Administration (FDA) as radiomitigators [3,4].

Hematopoietic growth factors are proteins that regulate growth and differentiation of red and white blood cells. Cytokines are proteins of low molecular weight that exert a stimulating or inhibiting influence on the proliferation, differentiation, and function of cells of the immune system. Both Neupogen® and Neulasta® are granulocyte colony-stimulating factor (G-CSF)-based drugs, made to improve the pharmacokinetic properties of G-CSF [5]. G-CSF belongs to hematopoietic growth

factors which, together with cytokines, have been intensively tested and evaluated for modulation of the acute radiation damage e.g., [6,7], and have also been used for the treatment of radiation accident victims [8]. Nevertheless, comparable attention has also been paid by radiation researchers to substances not counted among hematopoietic growth factors or cytokines and/or their derivatives. As shown mostly in animal studies, there exists a wide spectrum of such substances which are often effective in modulating ARS, as well as being relatively non-toxic and cheap. This review summarizes important pieces of information on these agents and emphasizes their potential for incorporation into the treatment schemes of patients with ARS.

2. Immunomodulators

Immunotherapy is defined as "treatment of disease by inducing, enhancing, or suppressing an immune response". A number of immunomodulators inducing and/or enhancing the immune response, which are represented by an array of various preparations, have been tested with the aim of modulating ARS.

2.1. β-Glucan

Glucans, especially β-glucan, belong to the most studied immunomodulators both generally, and in the field of the pharmacological modulation of radiation damage. β-glucans are known as cell wall constituents of bacteria [9], yeast [10], fungi [11], and plants [12]. Early hematological studies have revealed that β-glucan stimulates proliferation of non-irradiated mouse pluripotent stem cells, as well as of several hematopoietic progenitor cell lineages, namely those of granulocytes, granulocytes/macrophages, macrophages, and erythrocytes e.g., [13]. Several studies performed, especially by Patchen and McVittie (Bethesda, MD, USA) and Hofer and Pospíšil (Brno, Czech Republic), have shown that the hematopoiesis-stimulating effects of β-glucan can be successfully employed in treating hematopoietic ARS in mice. An important feature of the use of β-glucan in irradiated experimental was the possibility of its profitable administration both prior to and after irradiation, i.e., as radioprotector or radiomitigator [14–25]. The use of β-glucan in combined-treatment regimen has also turned out to be successful—mutually potentiating effects of β-glucan have been observed following its combined administration with the chemical radioprotectors cystamine or WR-2721 [26,27]. A three-drug combination treatment of β-glucan, WR-2721, and selenium has shown a positive outcome as well [28]. β-glucan has also been successfully combined with G-CSF [29] or diclofenac, a cyclooxygenase inhibitor [30,31]. Many details concerning the experiments summarized in this paragraph, including information about the enhancement of survival of lethally irradiated experimental animals by β-glucan in some of these studies, can be found in a separate detailed review [32].

Later studies have added new understanding and have confirmed the above-mentioned ability of β-glucan to stimulate hematopoiesis and enhance survival in radiation-exposed animals. In 2006, Cramer et al. [33] revealed the role of complement in mediating the hematopoietic recovery after radiation-induced injury. In 2011, Salama [34] emphasized the possibility to administer, with a positive outcome, β-glucan to irradiated rats orally. In their thorough study from 2013, Pillai and Devi [35] examined the effects of pre-irradiation β-glucan administration, in which cytological and biochemical parameters were included, besides post-irradiation survival and hematopoiesis. Further, apart from their promising findings, they also examined the non-toxicity of β-glucan. In their review from 2009 on the biological activities of β-glucan, Rondanelli et al. [36] stressed the contingent use of β-glucan both as a prophylactic and as a therapy in cases of nuclear emergencies.

2.2. 5-Androstenediol (5-AED)

5-androstenediol (5-AED) is a natural adrenocortical steroid hormone. AED has been found to stimulate the innate immune system and, therefore, it is counted among immunomodulators. The first report on the hematopoietic and immune system stimulation observed in γ-irradiated mice is from 2000—both pre- and post-irradiation administration of 5-AED has produced stimulation of myelopoiesis and enhancement of resistance to infection in irradiated animals [37]. In the following

study, a stimulation of cells of the immune system, like monocytes, natural killer cells, eosinophils, and basophils, has been observed following administration of 5-AED [38]. Further experiments have revealed that 5-AED is effective at both subcutaneous and oral administration routes, and that the radioprotective efficacy of the drug is accompanied by low toxicity [39]. As one of the mechanisms of the hematopoiesis-stimulating effects of 5-AED, an induction of amplified production of G-CSF (when 5-AED was administered either as a radioprotector or as a radiomitigator) has been reported [40]. Comparative experiments have shown that the radioprotective efficacy of 5-AED is unique among ten selected different steroids [41]. Subsequently, studies on mice have been supplemented by experiments on non-human primates—a multilineage stimulation of hematopoiesis in irradiated rhesus monkeys has been found [42]. This knowledge has been obtained even when the irradiated monkeys were otherwise clinically unsupported [43]. An induction of nuclear factor-κB activation has been found as the mechanism of enhanced survival of irradiated human hematopoietic progenitors in the presence of 5-AED [44]. To further elucidate the mechanisms of hematopoiesis-stimulating effects of 5-AED, expression of a number of hematopoietic growth factors and cytokines in 5-AED-treated mice has been evaluated. An increased expression following the injection of 5-AED has been referred to as granulocyte-macrophage colony-stimulating factor (GM-CSF), interleukin-2 (IL-2), interleukin-3 (IL-3), interleukin-6 (IL-6), and interleukin-10 (IL-10) in the spleen, as well as to G-CSF, GM-CSF, interferon-γ (IFN-γ), thrombopoietin (TPO), IL-2, IL-3, IL-6, IL-10, and interleukin-12 (IL-12) in the bone marrow [45]. The significant role of G-CSF in mediating the effects of 5-AED has been confirmed by a study in which G-CSF antibody was used for abrogating the radioprotective efficacy of 5-AED [46]. A synergistic action of 5-AED and TPO has been shown in mice suffering from hematopoietic ARS [47]—in this study, a 20.1-fold increase in the life-saving short-term repopulating cells in the bone marrow has been observed in the 5-AED + TPO-treated mice [47]. A sequential injection of 5-AED, comprising one pre-irradiation administration and twice weekly injections for three weeks post-irradiation, have been reported to be very successful in treating the radiation-induced myelosuppression [48]. The authors have stated that "5-AED can be a significant therapeutic candidate for the management of ARS, particularly in a mass casualty scenario where rapid and economic intervention is important [47]". 5-AED is now in advanced development and has been granted FDA investigational new drug (FDA IND) status [49]. First positive clinical observations on the safety, tolerability, and hematologic activity of 5-AED in healthy adults have been already reported as well [50].

2.3. Other Immunomodulators

This paragraph summarizes data on another immunomodulators tested from the point of view of their abilities to modulate ARS.

Perhaps the oldest immunomodulator studied as a radioprotector is endotoxin, a bacterial lipopolysaccharide. As early as 1958, a report on decreased X-ray mortality in endotoxin-treated mice was published [51]. As an important manifestation of its radioprotective action, an increased number of spleen colony-forming units (used for expression of numbers of hematopoietic stem cells) in endotoxin-pre-treated irradiated mice has been reported [52]. A large amount of literature has been published on the endotoxin's radioprotective properties. However, because of its severe side effects [53], endotoxin has been gradually abandoned as a potentially usable drug in irradiated humans. On the contrary, reduction of endotoxemia has been considered a desirable effect of drugs used for the treatment of ARS, e.g., with antibiotics [54].

Broncho-Vaxom® is a bacterial lysate. It has been shown to significantly enhance post-irradiation survival in several mouse strains [55]. Subsequent studies have revealed positive hematological effects of Broncho-Vaxom® in sublethally irradiated mice [56–58]. Broncho-Vaxom® has been also tested with success in its combined administration with the chemical radioprotector WR-2721 (amifostine) [59,60]. Broncho-Vaxom® has been found to act radioprotectively when administered pre-irradiation [55–60], as well as a radiomitigator following its post-irradiation administration [60]. In a later study, Broncho-Vaxom® has been administered to rats in repeated injections comprising one pre-irradiation

dose and repeated post-irradiation doses in the course of a three-week period of fractionated irradiation. The drug has been reported to enhance the antioxidant system and to increase the serum γ-globulin content [61].

Trehalose dimycolate is a glycolipid molecule found in the cell wall of *Mycobacterium tuberculosis*. It has been reported to enhance resistance to infection in irradiated neutropenic mice [62]. A synthetic derivative of trehalose dimycolate (trehalose dicornomycolate) has been tested with success in mice with sepsis following irradiation and trauma [63].

An interesting radioprotective combination is that of the oligoelements selenium, zinc, and manganese administered concomitantly with *Lachesis muta* venom. This combination is called "immunomodulator" by the authors and has been tested in both mice [64] and rats [65].

Peptidoglycan is a bacteria cell wall polymer consisting of sugars and amino acids. In a recent study, peptidoglycan was observed to promote survival, as well as to ameliorate intestinal and bone marrow damage in irradiated mice when injected after irradiation [66]. These parameters have been found to be synergistically promoted when the mice were given the chemical radioprotectant WR-2721 pre-irradiation and peptidoglycan post-irradiation [66]. Apart from radioprotection of the hematopoietic and gastrointestinal tissues, a complete prevention of permanent submandibular gland radiation-induced alterations has been reported, following the administration of this radiomodifying mixture of compounds [66].

Other recent studies have been concerned with *Sipunculus nudus* (a species of unsegmented marine worms) polysaccharide. *Sipunculus nudus* polysaccharide, consisting of mannose, rhamnose, galacturonic acid, glucose, arabinose, and fucose, administered before irradiation, has been found to significantly increase survival of irradiated mice [67]. When the substance was tested in Beagle dogs, *Sipunculus nudus* polysaccharide-treated animals have shown, among others, an improved blood picture and an improved hematopoietic activity in the bone marrow [68]. Synergistic effects have been reported for the radioprotective combination of the *Sipunculus nudus* polysaccharide, WR-2721, recombinant human interleukin-11 (rhIL-11), and recombinant human G-CSF (rhG-CSF) in radiation-injured mice [69]. Marked antioxidant effects of *Sipunculus nudus* polysaccharide [67], and its efficacy following its oral administration [68], have been emphasized.

3. Prostaglandins and Inhibitors of Prostaglandin Production

Quite surprisingly, both prostaglandins, especially prostaglandin E_2 (PGE_2), and inhibitors of prostaglandin production (cyclooxygenase (COX) inhibitors), have been successfully tested regarding their abilities to support recovery of experimental animals from ARS. Therefore, both groups of substances are dealt with in the same section.

Several studies from the 1980s showed radioprotective effects of prostaglandins, particularly PGE_2 and a synthetic derivative of prostaglandin E_1, misoprostol, on irradiated gastrointestinal tracts [70–72]. These effects might be ascribed to the subsequently confirmed protective action of prostaglandins on the gastrointestinal tissues [73,74]. However, at the approximately same time, articles showing that PGE_2 stimulates and/or protects erythroid and multilineage hematopoietic progenitor cells [75–77] also appeared. Nevertheless, findings on inhibition of myelopoiesis in vivo by PGE_2 were also published at that time [78,79].

The results mentioned [78,79] help to justify the findings obtained when the action of inhibitors of prostaglandin production (COX inhibitors, non-steroidal anti-inflammatory drugs) in irradiated experimental animals was evaluated. In earlier studies, the radiomodifying effects of non-selective COX inhibitors, inhibiting the synthesis of both cyclooxygenase-1 (COX-1), expressed constitutively in a variety of tissues including the gastrointestinal tract, and cyclooxygenase-2 (COX-2), was tested. This is inducible and responsible for the production of prostaglandins during inflammatory states [80]. In sublethally irradiated experimental animals, hematopoiesis-stimulating effects of non-selective COX inhibitors have been observed when they were administered pre- or post-irradiation, or in the course of the fractionated radiation regimen [81–90]. However, administration of non-selective COX inhibitors

has also been connected to the occurrence of a rather high incidence and intensity of undesirable side effects, especially on the gastrointestinal tissues [90], and a reduced survival of lethally irradiated animals [91,92]. Numerous details on the effects of non-selective COX inhibitors in irradiated animals can be found in an earlier detailed review [93].

Later investigations on the radiomodifying action of COX inhibitors have used a representative of selective COX-2 inhibitors, meloxicam, whose administration preserves the activity of COX-1 and maintains the protective action of prostaglandins in the gastrointestinal tissues [73,74]. Meloxicam has been shown not only to support hematopoiesis in irradiated mice [94,95], but also to enhance the post-irradiation survival of the animals, namely when administered in a mere single dose 1 h after a lethal irradiation [96]. Thus, favorableness of the use of selective COX-2 inhibitors as radiomitigators has been confirmed.

In a recent study, Hoggatt re-opened investigations on hematological and radiomodifying effects of pharmacological interventions into the metabolism of PGE_2. They stated that PGE_2 enhances hematopoietic stem cell homing, survival, and proliferation [97]. Taking into account all of the available knowledge on the modulation of PGE_2 signaling post-irradiation, as well as their own experimental results, Hoggatt et al. found that an increased survival and stimulation of hematopoiesis in irradiated mice can be obtained both by an administration of PGE_2, and following the treatment with the selective COX-2 inhibitor meloxicam, but that the effectiveness of the therapies depends on the timing of the injections [98].

4. Herbal Extracts

Herbal extracts tested for radioprotective and radiomitigating properties comprise preparations from a number of plants. Their action is complex and comprises their antiemetic activity, anti-inflammatory activity, antimicrobial activity, antioxidant activity, hematopoietic stimulation, immunostimulant activity, metal chelation activity, and wound healing activity [99]. In a thorough review from 2005, radioprotective/radiomodifying effects of the extracts from the following plants are summarized with a number of citations: *Acanthopanax senticosus*, *Aegle marmelos*, *Ageratum conyzoides*, *Allium cepa*, *Allium sativum*, *Aloe arborescens*, *Amaranthus paniculatus*, *Angelica sinensis*, *Archangelica officinalis*, *Centella asiatica*, *Curcuma longa*, *Gingko biloba*, *Glycyrhizza glabra*, *Hipophae rhamnoides*, *Hypericum perforatum*, *Lycium chinense*, *Mentha arvensis*, *Mentha piperita*, *Moringa oleifera*, *Ocimum sanctum*, *Panax ginseng*, *Podophyllum hexandrum*, and *Tinospora cordifolia* [99]. Generally, herbal extracts are considered successful in treating symptoms of ARS, and their research has continued until the present time. e.g., an extract from *Cordyceps sinensis* has been observed to protect against both the bone marrow and intestinal radiation-induced injuries [100]. Pre-irradiation administration of an extract from *Podophyllum hexandrum* has shown radioprotective efficacy, which has been further enhanced by post-irradiation application of an extract from *Picrorhizza kurroa* [101]. A semi-purified fraction of *Podophyllum hexandrum*, REC-2001, has been shown to significantly enhance survival of lethally irradiated mice [102]. Stimulatory effects in both the immune tissues in irradiated mice have been reported following the administration of the extract from *Vernonia cinerea* [103]. Recently, a potent radioprotective effect of a herbal drug prepared from *Rosa canina*, *Urtica dioica*, and *Tanacetum vulgare*, has been observed [104].

5. Amifostine

Amifostine (WR-2721) will be dealt with here briefly. Amifostine has been the most exhaustively studied classical chemical radioprotector from the point of view of its ability to protect against ARS because of its high radioprotective efficacy, as summarized in many reviews e.g., [105–107]. For interested readers, we refer them to a rich literature on amifostine and other chemical radioprotectors. Despite the comprehensive number of studies, amifostine has not been approved for the treatment of ARS in humans because of its undesirable side effects, and has found its use in radiation oncology [108,109]. These issues are, however, outside the topic of this review. Nevertheless, attention is still paid to amifostine

from the point of view of its contingent use in treating of ARS—successful attempts have been made recently when administering mice with low doses of amifostine (30 or 50 μg/kg) plus γ-tocotrienol in a combined prophylactic modality [110]. Combined approaches using low amifostine doses might enable the use of this radioprotector in humans in the treatment of ARS.

6. Antioxidants

A rather wide spectrum of substances, mostly naturally occurring ones, will be addressed in this section Their common feature their ability to protect against or to treat radiation damage by scavenging radiation-induced free radicals. These natural antioxidants are generally less effective radioprotectors in comparison with amifostine and other classical chemical radioprotectors, but may provide a longer window of protection [111] and are often non-toxic.

6.1. Vitamin E Family Members

Vitamin E represents a family of compounds that is divided into two subgroups called tocopherols and tocotrienols; both function as important antioxidants [112]. They differ chemically in that tocotrienols contain three double bonds in their isoprenoid side chain, while tocopherols do not [113]. Tocotrienols have superior antioxidant activity compared with tocopherols [114]. There exist ample literature on the radioprotective and radiomitigating action of vitamin E family members, whose detailed summarization exceeds the extent of this review. Therefore, for each subgroup, selected examples of experimental findings will be shown and, finally, further research literature will be recommended.

Concerning tocopherols, three compounds have been tested for their contingent modulating effects on ARS. α-tocopherol has been found to enhance both survival and ARS symptoms when administered both pre- and post-irradiation [115–117]. As the mechanism of the α-tocopherol's radiomitigative effect, an enhancement of cell-mediated immunity has been proposed [118]. α-tocopherol-mono-glucoside is a water-soluble glycosylated derivative of α-tocopherol. When administered post-irradiation, α-tocopherol-mono-glucoside has been demonstrated to increase survival [119] and to stimulate hematopoiesis in mice [120,121]. Attention has also been paid to α-tocopherol succinate, the hemisuccinate ester derivative of α-tocopherol. α-tocopherol succinate has been observed to enhance survival of irradiated mice, including mice irradiated with doses causing the gastrointestinal ARS [122,123]. As for hematopoiesis-modulating action of α-tocopherol succinate, it has been reported that its radioprotective efficacy is mediated through the induction of G-CSF production [124].

Regarding tocotrienols, two vitamin E family members have been investigated from the point of view of their abilities to influence ARS, namely δ-tocotrienol and γ-tocotrienol. δ-tocotrienol possess very high antioxidant activity [125], and has been also shown to protect hematopoiesis and increase survival of irradiated mice [126,127]. In recent years, attention has been paid especially to γ-tocotrienol, another vitamin E derivative with a high antioxidant ability [128]. From the perspective of its contingent use in treating ARS, the hematopoiesis-stimulating [129] and survival-enhancing efficacy of γ-tocotrienol [130] should be emphasized. An important role of G-CSF in mediating the radioprotective effects of γ-tocotrienol has been shown when using G-CSF antibodies [131]. Recently, the radioprotective efficacy of γ-tocotrienol has also been confirmed in non-human primates [132].

Many more details and literature on the radiobiological properties of tocopherols and tocotrienols can be found in a 2013 review [133]. A recent separate detailed review has been devoted to γ-tocotrienol [134]. It has been stated that a single administration of γ-tocotrienol without any supportive care was equivalent, in terms of improving hematopoietic recovery, to multiple doses of Neupogen and Neulasta (both G-CSF-based drugs) with full supportive care (including blood products) in the non-human primate model [summarized in 134]. γ-tocotrienol has been categorized by Singh et al. among "promising molecules at advanced stages of development" [49].

6.2. Selenium-Containing Compounds

Several selenium derivatives have been investigated for their radioprotective effects; perhaps the most intensively studied selenium compounds have been sodium selenite and selenomethionine. Selenomethionine, which is a naturally occurring derivative of low toxicity, can be found in soy, grains, and legumes [135]. Expressive and significant survival benefits in irradiated mice have been obtained when either sodium selenite or selenomethionine were administered to mice 24 h or one hour before, or 15 min after, irradiation [136]. Concerning the mechanisms of the radiomitigating effects of the post-irradiation administration of selenium, an enhancement of functions of immunocompetent cells has been proposed [137]. There exists a great amount of research on the ability of selenium compounds to modulate radiation damage where many details can be found [138,139]. Recent findings showing that selenium protects intestinal tissue against ionizing radiation [140] suggest the usefulness of selenium administration in the intestinal ARS.

6.3. Other Antioxidative Compounds

Many antioxidative compounds have been tested for their radiomodifying properties. This paragraph gives examples of some of them. Their common characteristics are mostly very low toxicity, as well as the possibility of their peroral administration.

Vitamin C (ascorbic acid) has been reported to improve the bone marrow status and survival of irradiated mice [141]. Further, mice given peroral vitamin A or its precursor, β-carotene, have shown reduced morbidity and mortality [142]. Recently, protective effects of α-lipoic acid on radiation-induced small intestine injury has been found in mice [143], suggesting the potential use of this antioxidative compound in the treatment of the intestinal ARS.

An interesting contribution to the topic of the combined pharmacological approach to the modulation of radiation damage has been provided by Wambi et al. who tested the efficacy of a dietary supplement consisting of L-selenomethionine, vitamin C, vitamin E succinate, α-lipoic acid, and *N*-acetyl-cysteine. This supplement positively influenced hematopoiesis and survival of irradiated mice when given either before or after their irradiation with X-rays [144], or when administered after exposure of the animals to proton irradiation [145].

Antioxidant nutrients are considered in more detail in a review [146].

7. Other Compounds Tested as Radioprotectors or Radiomitigators

7.1. Genistein

Genistein is a soy isoflavone. Its effects in an irradiated organism are probably complex, including antioxidative [147] and hematopoiesis-stimulating actions [148].

In a report from 2003, genistein has been shown to significantly increase survival of mice when administered in a single preirradiation subcutaneous injection [149]. A complex enhancement of a wide spectrum of bone marrow and blood parameters has been reported when genistein was administered once daily for seven consecutive days before a whole-body irradiation [148]. Hematopoiesis-stimulating effects of genistein have also been confirmed following its single pre-irradiation dose [150]. Details on the radiomodifying actions of genistein are summarized in a separate review [151].

Genistein, administered pre-irradiation has also been successfully combined with captopril, an angiotensin converting enzyme, given to mice in their drinking water on days 1 to 30 after irradiation, as shown by stimulated hematopoiesis and increased survival of mice. For example, whereas the whole-body dose of 8.25 Gy resulted in 0% survival in untreated mice, administration of genistein, captopril, or genistein + captopril increased survival to 72%, 55%, and 95%, respectively [152]. To overcome genistein's low water solubility, a nanoparticle suspension of genistein has been formulated. This form of genistein has also shown protection of hematopoietic system in irradiated mice [153]. Genistein has been granted FDA IND status [49].

7.2. Adenosine Receptor Agonists

The combination of dipyridamole (DP), a drug inhibiting the cellular uptake of adenosine [154], and adenosine monophosphate (AMP), an adenosine prodrug [155], has been used in an attempt to enhance the receptor action of adenosine in a series of studies on irradiated mice. The results of these studies have clearly shown that the pre-irradiation combination of DP and AMP stimulates hematopoiesis and increases survival under conditions of single [156–159], as well as fractionated irradiation [159,160].

Adenosine receptors, activated non-selectively in the experiments mentioned [155–160], exist in four subtypes. Further experimentation, using agonists selected for the individual subtypes, has been aimed at finding out whether stimulation of one of the four subtypes is responsible for the previously observed hematopoiesis-stimulating and radioprotective effects. These experiments are described in detail in a separate review [161]. It follows from the findings that IB-MECA (N^6-(3-iodobenzyl)adenosine-5′-*N*-methyluronamide) stimulates the cycling of hematopoietic progenitor cells [162]. Subsequently, IB-MECA has been shown to support hematopoiesis, as well as the hematopoiesis-stimulating effects of G-CSF in sublethally irradiated mice [163]. Mutually potentiating effects on hematologic parametrs in irradiated mice have been also observed following a concommitant administration of IB-MECA and meloxicam, a cyclooxygenase-2 inhibitor, in a post-irradiation treatment regimen [164]. This series of studies has been completed with the finding that IB-MECA and meloxicam, given in the same therapeutical treatment regimen to lethally irradiated mice, enhance the survival of the exposed animals, each alone or in a combination [165].

7.3. More Selected Compounds

Ex-RAD (ON 01210.Na, 4-carboxystyryl-4-chlorobenzylsulfone), is a rather new chemical entity, reported to possess significant radioprotective effects in terms of survival following either subcutaneous [166] or peroral administration routes [167], as well as of ameliorating hematopoietic and gastrointestinal damage [168]. The mechanisms of the radioprotective effects of Ex-RAD involve prevention of p53-dependent and independent radiation-induced apoptosis [162], as well as attenuation of the DNA damage response [169] and the up-regulation of PI3-Kinase/AKT pathways in cells exposed to radiation [170]. Ex-RAD possesses the FDA IND status [49].

Metformin is a biguanide drug used in the treatment of type II diabetes. Recently metformin's radiomitigating effects when administered 24 h after irradiation alone or in pharmacological combinations [171]. Metformin is approved by FDA for human use and has a well characterized human safety profile [171].

Toll-like receptor 5 (CBLB502, entolimod) is a polypeptide drug derived from salmonella flagellin [172]. It has been shown to enhance survival and protect against hematopoietic and gastrointestinal ARS when administered either before or after irradiation [172,173]. Entolimod has been found to increase the clonogenic potential of the bone marrow cells and to reduce apoptosis in the intestinal crypts [173]. Entolimod has found its use also in mitigation of radiation-induced epithelial damage in a mouse model of fractionated head and neck irradiation [174]. It has been also demonstrated that G-CSF and IL-6 may serve as efficacy biomarkers for this agent [175]. This is an important observation since such biomarkers may be helpful for dose conversion from animal to human, especially in view of the fact that entolimod also possesses the FDA IND status [49].

FGF-2 peptide, a peptide derived from the binding domain of fibroblast growth factor, has been reported to rescue a significant fraction of four strains of mice with the gastrointestinal ARS. Use of FGF-2 peptide has improved crypt survival and repopulation, partially preserved or restored GI function, and has reduced radiation-induced increased plasma endotoxin and pro-inflammatory cytokine levels [176].

Octadecenyl thiophosphate, a small molecule mimic of the growth factor-like mediator lysophosphatidic acid, has been shown to either protect from or mitigate both the hematopoietic and gastrointestinal ARS [177]. Besides direct effects on the gastrointestinal and hematopoietic tissues, octadecenyl thiophosphate has also been found to reduce endotoxin seepage into blood [177].

The gastrointestinal ARS has also been the target of the radioprotective and radiomitigating pharmacological approach using inhibitors of prolyl hydroxylase domain-containing enzymes (PHDs), whose administration has resulted in stabilization of hypoxia-inducible factors (HIFs) protecting important cellular compartments from radiation-induced damage [178]. The role of the PHD/HIF axis in the radiation-induced gastrointestinal toxicity has been recently reviewed and the procedures using PHDs resulting in stabilization of HIFs have been proposed as new class of radioprotectors [179].

8. Remarks to Cutaneous Syndrome of Acute Radiation Syndrome (ARS)

Although the cutaneous syndrome of ARS is clinically relevant both for both the radiation victims and radiotherapy-exposed oncological patients, it will be briefly considered separately. In patients with the cutaneous syndrome, pharmacological therapy applying topical or systemic steroids [180,181], or combined pentoxifylline and vitamin E [182] (for the treatment of late consequences of the radiation damage to the skin) has been used. However, current approaches for the treatment of the cutaneous syndrome consist of, among others, non-pharmacological methods like local injections of bone marrow mesenchymal stem cells [183,184] or adipose tissue-derived stromal/stem cells [185]. A more detailed consideration of therapeutical approaches aimed at treatment of the cutaneous syndrome lies outside of the scope of this article.

Agents mentioned in this review which have been used in attempts to modify the course of the acute radiation syndrome (ARS) (not including hematopoietic growth factors and cytokines) are summarized in Table 1.

Table 1. Summary of agents (not including hematopoietic growth factors and cytokines) used in attempts to modify the course of the acute radiation syndrome (ARS).

Agent or Group of Agents	Predominant Radiomodifying Effect(s)	Reference Number(s)
4-carboxystyryl-4-chlorobenzylsulfone (Ex-RAD)	Prevention of apoptosis	[49,166–170]
5-androstenediol (5-AED)	Immunomodulator, stimulator of hematopoiesis	[37–50]
Adenosine monophosphate (AMP)	Stimulator of proliferation of hematopoietic progenitor cells	[155–160]
α-Lipoic acid	Antioxidant	[143,145]
Amifostine (WR-2721)	Free radical scavenger	[59,60,66,69,105–110]
β-Glucan	Immunomodulator, stimulator of hematopoiesis	[9–36]
Broncho-Vaxom	Immunomodulator, stimulator of hematopoiesis	[55–61]
Captopril	Vasodilator	[152]
Dipyridamole	Enhances adenosine receptor action, stimulator of proliferation of hematopoietic progenitor cells	[154,156–160]
Endotoxin	Immunomodulator, stimulator of hematopoiesis	[51–54]
FGF-2 peptide	Improvement of regeneration of radiation-induced gastrointestinal damage, reduction of endotoxemia	[176]
Genistein	Antioxidant	[49,147–153]
Inhibitors of prolyl hydroxylase domain- containing enzymes	Antioxidants	[178,179]
Lachesis muta venom	Immunomodulator	[64,65]
Manganese-containing compounds	Antioxidants	[64,65]
Meloxicam, selective cyclooxygenase-2 inhibitor	Inhibitor of prostaglandin production, stimulator of myelopoiesis	[94–98]
Metformin	Antioxidant, modulator of cell renewal	[171]
N^6-(3-iodobenzyl)adenosine-5′-*N*- methyuronamide (IB-MECA)	Stimulator of hematopoietic cell proliferation through adenosine receptor action	[161–165]
N-acetyl-cysteine	Antioxidant	[144,145]

Table 1. *Cont.*

Agent or Group of Agents	Predominant Radiomodifying Effect(s)	Reference Number(s)
Non-selective cyclooxygenase inhibitors (non-selective non-steroidal anti-inflammatory drugs)	Inhibitors of prostaglandin production, stimulators of myelopoiesis	[81–93]
Octadecenyl thiophosphate	Stimulation of hematopoiesis, reduction of endotoxemia	[177]
Pentoxifylline	Improvement of blood flow properties	[182]
Peptidoglycan	Immunomodulator, ameliorates bone marrow and intestinal radiation-induced damage	[66]
Prostaglandins E and their derivatives	Hematopoietic modulators, radioprotectants of intestinal tissues	[70–79]
Selenium-containing compounds	Antioxidants	[64,65,135–140]
Sipunculus nudus polysaccharide	Immunomodulator, antioxidant	[67–69]
Steroids	Antiinflammatory action	[180,181]
Toll-like receptor 5 (CBLB502, entolimod)	Stimulation of proliferation of hematopoietic cells, prevention of apoptosis	[49,172–175]
Trehalose dimycolate and its derivatives	Immunomodulators	[62,63]
Vitamin C (ascorbic acid)	Antioxidant	[141]
Vitamin A and its precursor	Antioxidant	[142]
Vitamin E and its derivatives	Antioxidants	[49,112–134]
Zinc-containing compounds	Antioxidants	[64,65]

9. Discussion and Conclusions

Though rather rich in content, this review cannot address all publications dealing with the topic of non-hematopoietic growth factor- and non-cytokine-based treatment of ARS. However, it hopefully gives a suitable overview of important pharmacological approaches aimed and protecting from, or mitigating the consequences of, acute radiation doses inducing ARS.

It can be inferred from the literature summarized here that the topic of pharmacological modulation of radiation damage not only has a long history, but is still alive and active. Many compounds seem to be promising from the point of view of their contingent future incorporation into medical procedures aimed at mitigating or protecting from ARS. In the authors' opinion, β-glucan, 5-AED, meloxicam, γ-tocotrienol, genistein, IB-MECA, Ex-RAD, and entolimod can find their place among the most promising agents, apart from other hopeful compounds recently or currently tested.

An important aspect in considering the contingent use of the individual compounds in human clinical practice is the fact that many of them are non-toxic (or possess only low toxicity), that they are available (or can be made available readily), and that they are often cheap to prepare in even large quantities.

Therefore, the answer to the question from the title of this review, namely is there is a chance for other compounds than hematopoietic growth factors or cytokines in the pharmacological modulation of radiation damage, is "yes, there is a good chance".

Acknowledgments: This work was supported by the Czech Science Foundation project 16-12454S, Ministry of Health of the Czech Republic (AZV grant no. 16-29835A; all rights reserved) and from the Czech Republic contribution to the Joint Institute for Nuclear Research, Dubna (project of the Czech Plenipotentiary and the 3 + 3 Project for 2015, 2016).

Author Contributions: Michal Hofer designed the manuscript and significantly participated in its writing. Zuzana Hoferová contributed to writing of Part 3 (Prostaglandins and inhibitors of prostaglandin production) and Part 7 (Other compounds tested as radioprotectors or radiomitigators). Martin Falk contributed to writng of Part 5 (Amifostine) and Part 6 (Antioxidants).

Conflicts of Interest: The authors declare no conflict of interest.

References

1. Dörr, H.; Meineke, V. Acute radiation syndrome caused by accidental radiation exposure—Therapeutic principles. *BMC Med.* **2011**, *9*, 1–6. [CrossRef] [PubMed]
2. Pellmar, T.C.; Rockwell, S. Priority list of research areas for radiological nuclear threat countermeasures. *Radiat. Res.* **2005**, *163*, 115–123. [CrossRef] [PubMed]
3. Singh, V.K.; Romaine, P.L.P.; Newman, V.L.; Seed, T.M. Medical countermeasures for unwanted CBRN exposures: Part II radiological and nuclear threats with review of recent countermeasure patents. *Expert Opin. Ther. Pat.* **2016**, *26*, 1399–1408. [CrossRef] [PubMed]
4. Singh, V.K.; Romaine, P.L.P.; Seed, T.M. Medical countermeasures for radiation exposure and related injuries: Charcaterization of medicines, FDA-approval status and inclusion into the strategic national stockpile. *Health Phys.* **2015**, *108*, 607–630. [CrossRef] [PubMed]
5. Strohl, W.R. Fusion proteins for half-life extension of biologics as a strategy to make biobetters. *BioDrugs* **2015**, *29*, 215–239. [CrossRef] [PubMed]
6. Hérodin, F.; Roy, L.; Grenier, N.; Delaunay, C.; Bauge, S.; Vaurijoux, A.; Gregoire, E.; Martin, C.; Alonso, A.; Mayol, L.F.; et al. Antiapoptotic cytokines in combination with pegfilgrastim soon after irradiation mitigate myelosuppression in nonhuman primates exposed to high radiation dose. *Exp. Hematol.* **2007**, *35*, 1172–1181. [CrossRef] [PubMed]
7. Hirouchi, T.; Ito, K.; Nakano, M.; Monzen, S.; Yoshino, H.; Chiba, M.; Hazawa, M.; Nakano, A.; Ishikawa, J.; Yamaguchi, M.; et al. Mitigative effects of a combination of multiple pharmaceutical drugs on the survival of mice exposed to lethal ionizing radiation. *Curr. Pharm. Biotechnol.* **2016**, *17*, 190–199. [CrossRef]
8. Singh, V.K.; Newman, V.L.; Seed, T.M. Colony-stimulating factors for the treatment of the hematopoietic compartment of the acute radiation syndrome (H-ARS): A review. *Cytokine* **2015**, *71*, 22–37. [CrossRef] [PubMed]
9. Dunlap, J.; Minami, E.; Bhagwat, A.A.; Keister, D.L.; Stacey, G. Nodule development induced by mutants of Bradyrhizobium japonicum defective in cyclic β-glucan synthesis. *Mol. Plant Microbe Interact.* **1996**, *9*, 546–555. [CrossRef] [PubMed]
10. Magnani, M.; Castro-Gomez, R.H.; Aoki, M.N.; Gregorio, E.P.; Libos, F.; Watanabe, M.A.E. Effects of carboxymethyl-glucan from *Saccharomyces cerevisiae* on the peripheral blood of patients with advanced prostate cancer. *Exp. Ther. Med.* **2010**, *5*, 859–862. [CrossRef]
11. Ohno, N.; Miura, N.N.; Nakajima, M.; Yadomae, T. Antitumor 1,3-β-glucan from cultured fruit body of *Sparassis crispa*. *Biol Pharm. Bull.* **2000**, *23*, 866–872. [CrossRef] [PubMed]
12. Chang, R. Bioactive polysaccharides from traditional Chinese medicine herbs as anticancer adjuvants. *J. Altern. Complement. Med.* **2002**, *8*, 559–565. [CrossRef] [PubMed]
13. Patchen, M.L.; MacVittie, T.J. Dose-dependent responses of murine pluripotent stem cells and myeloid and erythroid progenitor cells following administration of the immunomodulating agent glucan. *Immunopharmacology* **1983**, *5*, 303–313. [CrossRef]
14. Pospíšil, M.; Jarý, J.; Netíková, J.; Marek, M. Glucan-induced enhancement of hemopoietic recovery in γ-irradiated mice. *Experientia* **1982**, *38*, 1232–1234. [CrossRef] [PubMed]
15. Pospíšil, M.; Šandula, J.; Pipalová, I.; Hofer, M.; Viklická, Š. Hemopoiesis stimulating and radioprotective effects of carboxymethylglucan. *Physiol. Res.* **1991**, *40*, 377–380. [PubMed]
16. Hofer, M.; Pospíšil, M.; Viklická, Š.; Pipalová, I.; Holá, J.; Šandula, J. Effects of postirradiation carboxymethylglucan administration in mice. *Int. J. Immunopharmacol.* **1995**, *17*, 167–174. [CrossRef]
17. Hofer, M.; Pospíšil, M.; Pipalová, I.; Holá, J.; Šandula, J. Haemopoiesis-enhancing effects of repeatedly administered carboxymethylglucan in mice exposed to fractionated irradiation. *Folia Biol.* **1995**, *41*, 249–256.
18. Hofer, M.; Pospíšil, M. Glucan as stimulator of hematopoiesis in normal and γ-irradiated mice. A survey of the authors' own results. *Int. J. Immunopharmacol.* **1997**, *19*, 607–609. [CrossRef]
19. Patchen, M.L.; MacVittie, T.J. *Macrophages and Natural Killer Cells*; Borman, J.J., Sorkin, E., Eds.; Plenum Publishing Corporation: New York, NY, USA, 1982; pp. 267–272.
20. Patchen, M.L.; MacVittie, T.J. Stimulated hemopoiesis and enhanced survival following glucan treatment in sublethally and lethally irradiated mice. *Int. J. Immunopharmacol.* **1985**, *7*, 923–932. [CrossRef]

21. Patchen, M.L.; MacVittie, T.J.; Wathen, L.M. Effects of pre- and post-irradiation glucan treatment on pluripotent stem cells, granulocyte, macrophage and erythroid progenitor cells, and hemopoietic stromal cells. *Experientia* **1984**, *40*, 1240–1244. [CrossRef] [PubMed]
22. Patchen, M.L.; MacVittie, T.J.; Brook, I. Glucan-induced hemopoietic and immune stimulation: Therapeutic effects in sublethally and lethally irradiated mice. *Meth. Find. Exp. Clin. Pharmacol.* **1986**, *8*, 151–155.
23. Patchen, M.L.; D'Alesandro, M.M.; Brook, I.; Blakely, W.F.; MacVittie, T.J. Glucan: Mechanisms involved in its "radioprotective" effect. *J. Leukoc. Biol.* **1987**, *42*, 95–105. [PubMed]
24. Patchen, M.L.; DiLuzio, N.R.; Jacques, P.; MacVittie, T.J. Soluble polyglycans enhance recovery from cobalt-60-induced hemopoietic injury. *J. Biol. Response Mod.* **1984**, *3*, 627–633. [PubMed]
25. Patchen, M.L.; Brook, I.; Elliott, T.B.; Jackson, W.E. Adverse effects of pefloxacin in irradiated C3H/HeN mice: Correction with glucan therapy. *Antimicrob. Agents Chemother.* **1993**, *37*, 1882–1889. [CrossRef] [PubMed]
26. Pospíšil, M.; Netíková, J.; Pipalová, I.; Jarý, J. Combined radioprotection by preirradiation peroral cystamine and postirradiation glucan administration. *Folia Biol.* **1991**, *37*, 117–124.
27. Patchen, M.L.; D'Alesandro, M.M.; Chirigos, M.A.; Weiss, J.F. Radioprotection by biological response modifiers alone and in combination with WR-2721. *Pharmacol. Ther.* **1988**, *39*, 247–254. [CrossRef]
28. Patchen, M.L.; MacVittie, T.J.; Weiss, J.F. Combined modality radioprotection: The use of glucan and selenium with WR-2721. *Int. J. Radiat. Oncol. Biol. Phys.* **1990**, *18*, 1069–1075. [CrossRef]
29. Patchen, M.L.; MacVittie, T.J.; Solberg, B.D.; Souza, L.M. Survival enhancement and hemopoietic regeneration following radiation exposure: Therapeutic approach using glucan and granulocyte colony-stimulating factor. *Exp. Hematol.* **1990**, *18*, 1042–1048. [PubMed]
30. Pospíšil, M.; Hofer, M.; Pipalová, I.; Viklická, Š.; Netíková, J.; Šandula, J. Enhancement of hematopoietic recovery in γ-irradiated mice by the joint use of diclofenac, an inhibitor of prostaglandin synthesis, and glucan, a macrophage activator. *Exp. Hematol.* **1992**, *20*, 891–896. [PubMed]
31. Hofer, M.; Pospíšil, M.; Viklická, Š.; Vacek, A.; Pipalová, I.; Bartoníčková, A. Hematopoietic recovery in repeatedly irradiated mice can be enhanced by a repeatedly administered combination of diclofenac and glucan. *J. Leukoc. Biol.* **1993**, *53*, 185–189. [PubMed]
32. Hofer, M.; Pospíšil, M. Modulation of animal and human hematopoiesis by β-glucans: A review. *Molecules* **2011**, *16*, 7969–7979. [CrossRef] [PubMed]
33. Cramer, D.E.; Allendorf, D.J.; Baran, J.T.; Hansen, R.; Marroquin, J.; Li, B.; Ratajcza, J.; Ratajczak, M.Z. β-glucan enhances complement-mediated hematopoietic recovery after bone marrow injury. *Blood* **2006**, *107*, 835–840. [CrossRef] [PubMed]
34. Salama, S.F. β-glucan ameliorates γ-rays induced oxidative in jury in male Swiss albino rats. *Pak. J. Zool.* **2011**, *43*, 933–939.
35. Pillai, T.G.; Devi, P.U. Mushroom β glucan: Potential candidate for post irradiation protection. *Mutat. Res. Genet. Toxicol. Environ. Mutagen.* **2013**, *751*, 109–115. [CrossRef] [PubMed]
36. Rondanelli, M.; Opizzi, A.; Monteferrario, F. The biological activity of β-glucans. *Minerva Med.* **2009**, *3*, 237–245.
37. Whitnall, M.H.; Elliott, T.B.; Harding, R.A.; Inal, C.E.; Landauer, M.R.; Wilhelmsen, C.L.; McKinney, L.; Miner, V.L.; Jackson, W.E.; Loria, R.M.; et al. Androstenediol stimulates myelopoiesis and enhances resistance to infection in γ-irradiated mice. *Int. J. Immunopharmacol.* **2000**, *22*, 1–14. [CrossRef]
38. Whitnall, M.H.; Inal, C.E.; Jackson, W.E.; Miner, V.L.; Villa, V.; Seed, T.M. In vivo radioprotection by 5-androstenediol: Stimulation of the innate immune system. *Radiat. Res.* **2001**, *156*, 283–293. [CrossRef]
39. Whitnall, M.H.; Wilhelmsen, C.L.; McKinney, L.; Miner, V.; Seed, T.M.; Jackson, W.E. Radioprotective efficacy and acute toxicity of 5-androstenediol after subcutaneous or oral administration in mice. *Immunopharmacol. Immunotoxicol.* **2002**, *24*, 595–626. [CrossRef] [PubMed]
40. Singh, V.K.; Shafran, R.L.; Inal, C.E.; Jackson, W.E.; Whitnal, M.H. Effects of whole-body γ irradiation and 5-androstenediol administration on serum G-CSF. *Immunopharmacol. Immunotoxicol.* **2005**, *27*, 521–534. [CrossRef] [PubMed]
41. Whitnall, M.H.; Villa, V.; Seed, T.M.; Banjack, J.; Miner, V.; Lewbart, M.L.; Dowding, C.A.; Jackson, W.E. Molecular specificity of 5-androstenediol as a systemic radioprotectant in mice. *Immunopharmacol. Immunotoxicol.* **2005**, *27*, 15–32. [CrossRef] [PubMed]

42. Stickney, D.R.; Dowding, C.; Garsd, A.; Ahlem, C.; Whitnall, M.; McKeon, M.; Reading, C.; Frincke, J. 5-androstenediol stimulates multilineage hematopoiesis in rhesus monkeys with radiation-induced myelosuppression. *Int. Immunopharmacol.* **2006**, *6*, 1706–1713. [CrossRef] [PubMed]
43. Stickney, D.R.; Dowding, C.; Authier, S.; Garsd, A.; Onizuka-Handa, N.; Reading, C.; Frincke, J.M. 5-androstenediol improves survival in clinically unsupported rhesus monkeys with radiation-induced myelosuppression. *Int. Immunopharmacol.* **2007**, *7*, 500–505. [CrossRef] [PubMed]
44. Xiao, M.; Inal, C.E.; Parekh, V.I.; Chang, C.M.; Whitnall, M.H. 5-androstenediol promotes survival of γ-irradiated human hematopoietic progenitors through induction of nuclear factor-κB activation and granulocyte colony-stimulating factor expression. *Mol. Pharmacol.* **2007**, *72*, 370–379. [CrossRef] [PubMed]
45. Singh, V.K.; Grace, M.B.; Jacobsen, K.O.; Chang, C.M.; Parekh, V.L.; Inal, C.E.; Shafran, R.L.; Whitnall, A.D.; Kao, T.C.; Jackson, W.E.; et al. Administration of 5-androstenediol to mice: Pharmacokinetics and cytokine gene expression. *Exp. Mol. Pathol.* **2008**, *84*, 178–188. [CrossRef] [PubMed]
46. Grace, M.B.; Singh, V.K.; Rhee, J.G.; Jackson, W.E.; Kao, T.C.; Whitnall, M.H. 5-AED enhances survival of irradiated mice in a G-CSF-dependent manner, stimulates innate immune cell function, reduces radiation-induced DNA damage and induces genes that modulate cell cycle progression and apoptosis. *J. Radiat. Res.* **2012**, *53*, 840–853. [CrossRef] [PubMed]
47. Arts-Kaya, F.S.F.; Visser, T.P.; Arshad, S.; Frincke, J.; Stickney, D.R.; Reading, C.L.; Wagemaker, G. 5-androstene-3β,17β-diol promotes recovery of immature hematopoietic cells following myelosuppressive radiation and synergizes with thrombopoietin. *Int. J. Radiat. Oncol. Biol. Phys.* **2012**, *84*, E401–E407. [CrossRef] [PubMed]
48. Kim, J.S.; Jang, W.S.; Lee, S.; Son, Y.; Park, S.; Lee, S.S. A study of the effects of sequential injection of 5-androstenediol on radiation-induced myelosuppression in mice. *Arch. Pharm. Res.* **2015**, *38*, 1213–1222. [CrossRef] [PubMed]
49. Singh, V.K.; Newman, V.L.; Romaine, P.L.P.; Wise, S.Y.; Seed, T.M. Radiation countermeasure agents: An update (2011–2014). *Exp. Opin. Ther. Pat.* **2014**, *24*, 1229–1255. [CrossRef] [PubMed]
50. Stickney, D.R.; Groothuis, J.R.; Ahlem, C.; Kennedy, M.; Miller, B.S.; Onizuka-Handa, N.; Schlangen, K.M.; Destiche, D.; Reading, C.; Garsd, A.; et al. Preliminary clinical findings on Nemunne as a potential treatment for acute radiation syndrome. *J. Radiol. Prot.* **2010**, *30*, 687–698. [CrossRef] [PubMed]
51. Ainsworth, E.J.; Hatch, M.H. Decreased X-ray mortality in endotoxin-treated mice. *Radiat. Res.* **1957**, *9*, 84.
52. Hanks, G.E.; Ainsworth, E.J. Endotoxin protection and colony-forming units. *Radiat. Res.* **1967**, *32*, 367–382. [CrossRef] [PubMed]
53. Opal, S.M. Endotoxins and other sepsis triggers. *Contrib. Nephrol.* **2010**, *67*, 14–24.
54. Bertok, L.; Sztanyik, L.B.; Bertok, L. The effect of kanamycin treatment of rats on the development of gastrointestinal syndrome of radiation disease. *Acta Microbiol. Hung.* **1992**, *39*, 155–158. [PubMed]
55. Fedoročko, P.; Brezáni, P. Radioprotection of mice by the bacterial extract Broncho-Vaxom—Comparison of survival 5 inbred mouse strains. *Int. J. Immunother.* **1992**, *8*, 185–190.
56. Fedoročko, P.; Brezáni, P.; Macková, N.O. Radioprotection of mice by the bacterial extract Broncho-Vaxom®—Hematopoietic stem-cells and survival enhancement. *Int. J. Radiat. Biol.* **1992**, *61*, 511–518. [CrossRef] [PubMed]
57. Macková, N.O.; Fedoročko, P. Preirradiation hematological effects of the bacterial extract Broncho-Vaxom® and postirradiation acceleration recovery from radiation-induced hematopoietic depression. *Drug Exp. Clin. Res.* **1993**, *19*, 143–150.
58. Fedoročko, P.; Macková, N.O.; Kopka, M. Administration of the bacterial extract Broncho-Vaxom® enhances radiation recovery and myelopoietic regeneration. *Immunopharmacology* **1994**, *28*, 163–170. [CrossRef]
59. Fedorocko, P.; Brezani, P.; Mackova, N.O. Radioprotective effects of WR-2721, Broncho-Vaxom® and their combinations—Survival, myelopoietic restoration and induction of colony-stimulating activity in mice. *Int. J. Immunopharmacol.* **1994**, *16*, 177–184. [CrossRef]
60. Macková, N.O.; Fedoročko, P. Combined radioprotective effect of Broncho-Vaxom® and WR-2721 on hematopoiesis and circulating blood cells. *Neoplasma* **1995**, *42*, 25–30. [PubMed]
61. Saada, H.N.; Azab, K.S.; Zahran, A.M. Post-irradiation effect of Broncho-Vaxom, OM-85 BV, and its relationship to anti-oxidant activities. *Pharmazie* **2001**, *56*, 654–656. [PubMed]

62. Madonna, G.S.; Ledney, G.D.; Elliott, T.B.; Brook, I.; Ulrich, J.T.; Myers, K.R.; Patchen, M.L.; Walker, R.I. Trehalose dimycolate enhances resistence to infection in neutropenic animals. *Infect. Immun.* **1989**, *57*, 2495–2501. [PubMed]
63. Madonna, G.S.; Ledney, G.D.; Moore, M.M.; Elliott, T.B.; Brook, I. Treatment of mice with sepsis following irradiation and trauma with antibiotics and synthetic trehalose dicornomycolate (S-TDCM). *J. Trauma* **1991**, *31*, 316–325. [CrossRef] [PubMed]
64. Crescenti, E.; Croci, M.; Medina, V.; Sambucco, L.; Bergoc, R.; Rivera, E. Radioprotective potential of a novel therapeutic formulation of oligoelements Se, Zn, Mn plus *Lachesis muta* venom. *J. Radiat. Res.* **2009**, *50*, 537–544. [CrossRef] [PubMed]
65. Crescenti, E.J.V.; Medina, V.A.; Croci, M.; Sambuco, L.A.; Prestifilippo, J.P.; Elverdin, J.C.; Bergoc, R.M.; Rivera, E.S. Radioprotection of sensitive rat tissues by oligoelements Se, Zn, Mn plus *Lachesis muta* venom. *J. Radiat. Res.* **2011**, *52*, 557–567. [CrossRef] [PubMed]
66. Liu, W.; Chen, Q.; Wu, S.; Xia, X.C.; Wu, A.Q.; Cui, F.M.; Gu, Y.P.; Zhang, X.G.; Cao, J.P. Radioprotector WR-2721 and mitigating peptidoglycan synergistically promote mouse survival through the amelioration of intestinal and bone marrow damage. *J. Radiat. Res.* **2015**, *56*, 278–286. [CrossRef] [PubMed]
67. Li, N.; Shen, X.R.; Liu, Y.M.; Zhang, J.L.; He, Y.; Liu, Q.; Jiang, D.W.; Zong, J.; Li, J.M.; Hou, D.Y.; et al. Isolation, characterization, and radiation protection of *Sipunculus nudus* L. polysaccharide. *Int. J. Biol. Macromol.* **2016**, *83*, 288–296. [CrossRef] [PubMed]
68. Cui, F.M.; Li, M.; Chen, Y.J.; Liu, Y.M.; He, Y.; Jiang, D.W.; Tong, J.; Li, J.X.; Shen, X.R. Protective effects of polysaccharides from *Sipunculus nudus* on beagle dogs exposed to γ-radiation. *PLoS ONE* **2014**, *9*, e104299. [CrossRef] [PubMed]
69. Jiang, S.Q.; Shen, X.R.; Liu, Y.M.; He, Y.; Jiang, D.W.; Chen, W. Radioprotective effects of *Sipunculus nudus* L. polysaccharide combined with WR-2721, rhIL-11 and rhG-CSF on radiation-injured mice. *J. Radiat. Res.* **2015**, *56*, 515–522. [CrossRef] [PubMed]
70. Hanson, W.R.; Thomas, C. 16,16-dimethyl prostaglandin-E_2 increases survival of murine intestinal stem-cells when given before photon radiation. *Radiat. Res.* **1983**, *96*, 393–398. [CrossRef] [PubMed]
71. Hanson, W.R. Radiation protection of murine intestine by WR-2721, 16,16-dimethyl prostaglandin-E_2, and the combination of both agents. *Radiat. Res.* **1987**, *111*, 361–373. [CrossRef] [PubMed]
72. Hanson, W.R.; Houseman, K.A.; Nelson, A.K.; Collins, P.W. Radiation protection of the murine intestine by misoprostol, a prostaglandin-E_1 analog, given alone or with WR-2721, is stereospecific. *Prostagl. Leukot. Essent. Fatty Acids* **1988**, *32*, 101–105.
73. Satoh, H.; Amagase, K.; Ebara, S.; Akiba, Y.; Takeuchi, K. Cyclooxygenase (COX)-1 and COX-2 both play an important role in the protection of the duodenal mucosa in cats. *J. Pharmacol. Exp. Ther.* **2013**, *344*, 189–195. [CrossRef] [PubMed]
74. Mahmud, T.; Scott, D.-L.; Bjarnason, I. A unifying hypothesis for the mechanism of NSAID related gastrointestinal toxicity. *Ann. Rheum. Dis.* **1996**, *55*, 211–231. [CrossRef] [PubMed]
75. Hanson, W.R.; Ainsworth, E.J. 16,16-dimethyl prostaglandin E_2 induces radioprotection in murine intestinal and hematopoietic stem-cells. *Radiat. Res.* **1985**, *103*, 196–203. [CrossRef] [PubMed]
76. Lu, L.; Pelus, L.M.; Broxmeyer, H.E. Modulation of the expression of HLA-DR (Ia) antigens and the proliferation of human erythroid (BFU-E) and multipotential (CFU-GEMM) progenitor cells by prostaglandin E_2. *Exp. Hematol.* **1984**, *12*, 741–748. [PubMed]
77. Lu, L.; Pelus, L.M.; Piacibello, W.; Moore, M.A.S.; Hu, W.; Broxmeyer, H.E. Prostaglandin E acts at two levels to enhance colony formation in vitro by erythroid (BFU-E) progenitor cells. *Exp. Hematol.* **1987**, *15*, 765–771. [PubMed]
78. Kurland, J.; Moore, M.A.S. Modulation of hemopoiesis by prostaglandins. *Exp. Hematol.* **1977**, *7*, 119–126.
79. Gentile, P.; Byer, D.; Pelus, L.M. In vivo modulation of murine myelopoiesis following intravenous administration of prostaglandin E_2. *Blood* **1983**, *62*, 1100–1107. [PubMed]
80. Frölich, J.C. A classification of NSAIDs according to the relative inhibition of cyclooxygenase isoenzymes. *Trends Pharmacol. Sci.* **1997**, *18*, 30–34. [CrossRef]
81. Furuta, Y.; Hunter, N.; Barkley, T.; Hall, E.; Milas, L. Increase in radioresponse of murine tumors by treatment with indomethacin. *Radiat. Res.* **1988**, *48*, 3008–3013.

82. Kozubík, A.; Pospíšil, M.; Netíková, J. The stimulatory effect of single-dose pre-irradiation administration of indomethacin and dicofenac on hematopoietic recovery in the spleen of γ-irradiated mice. *Studia Biophys.* **1989**, *131*, 93–101.
83. Nishiguchi, I.; Furuta, Y.; Hunter, N.; Murray, D.; Milas, L. Radioprotection of haematopoietic tissue by indomethacin. *Radiat. Res.* **1990**, *122*, 188–192. [CrossRef] [PubMed]
84. Kozubík, A.; Hofmanová, J.; Holá, J.; Netíková, J. The effect of nordihydroguairetic acid, an inhibitor of prostaglandin and leukotriene biosynthesis, on hematopoiesis of γ-irradiated mice. *Exp. Hematol.* **1993**, *21*, 138–142. [PubMed]
85. Pospíšil, M.; Netíková, J.; Kozubík, A. Enhancement of haemopoietic recovery by indomethacin after sublethal whole-body γ irradiation. *Acta Radiol. Oncol.* **1986**, *25*, 195–198. [CrossRef] [PubMed]
86. Pospíšil, M.; Netíková, J.; Kozubík, A.; Pipalová, I. Effect of indomethacin, diclofenac sodium and sodium salicylate on peripheral blood cell counts in sublethally γ-irradiated mice. *Strahlenther. Onkol.* **1989**, *165*, 627–631. [PubMed]
87. Serushago, B.A.; Tanaka, K.; Koga, Y.; Taniguchi, K.; Nomoto, K. Positive effects of indomethacin on restoration of splenic nucleated cell population in mice given sublethal irradiation. *Immunopharmacology* **1987**, *14*, 21–26. [PubMed]
88. Sklobovskaya, I.E.; Zhavoronkov, L.P.; Dubovik, R.V. Haemostimulating efficiency of prostaglandin biosynthesis inhibitors in conditions of fractionated irradiation. *Radiobiologiya* **1986**, *26*, 185–188.
89. Hofer, M.; Pospíšil, M.; Pipalová, I. Radioprotective effects of flurbiprofen. *Folia Biol.* **1996**, *42*, 267–269.
90. Hofer, M.; Pospíšil, M.; Pipalová, I.; Holá, J. Modulation of haemopoietic radiation response of mice by diclofenac in fractionated treatment. *Physiol. Res.* **1996**, *45*, 213–220. [PubMed]
91. Hofer, M.; Pospíšil, M.; Tkadleček, L.; Viklická, Š.; Pipalová, I. Low survival of mice following lethal γ-irradiation after administration of inhibitors of prostaglandin synthesis. *Physiol. Res.* **1992**, *41*, 157–161. [PubMed]
92. Floersheim, G.L. Allopurinol, indomethacin and riboflavin enhance radiation lethality in mice. *Radiat. Res.* **1994**, *139*, 240–247. [CrossRef] [PubMed]
93. Hofer, M.; Pospíšil, M.; Hoferová, Z.; Weiterová, L.; Komůrková, D. Stimulatory action of cyclooxygenase inhibitors on hematopoiesis. A review. *Molecules* **2012**, *17*, 5615–5625. [CrossRef] [PubMed]
94. Hofer, M.; Pospíšil, M.; Znojil, V.; Holá, J.; Vacek, A.; Weiterová, L.; Štreitová, D.; Kozubík, A. Meloxicam, a cyclooxygenase-2 inhibitor, supports hematopoietic recovery in γ-irradiated mice. *Radiat. Res.* **2006**, *166*, 556–560. [CrossRef] [PubMed]
95. Hofer, M.; Pospíšil, M.; Znojil, V.; Holá, J.; Vacek, A.; Štreitová, D. Meloxicam, an inhibitor of cyclooxygenase-2, increases the level of G-CSF and might be usable as an auxiliary means in G-CSF therapy. *Physiol. Res.* **2008**, *57*, 307–310. [PubMed]
96. Hofer, M.; Pospíšil, M.; Dušek, L.; Hoferová, Z.; Weiterová, L. A single dose of an inhibitor of cyclooxygenase 2, meloxicam, administered shortly after irradiation increases survival of lethally irradiated mice. *Radiat. Res.* **2011**, *176*, 269–272. [CrossRef] [PubMed]
97. Hoggatt, J.; Singh, P.; Sampath, J.; Pelus, L.M. Prostaglandin E_2 enhances hematopoietic stem cell homing, survival, and proliferation. *Blood* **2009**, *113*, 5444–5455. [CrossRef] [PubMed]
98. Hoggatt, J.; Singh, P.; Stilger, K.N.; Plett, P.A.; Sampson, C.H.; Chua, H.L.; Orschell, C.M.; Pelus, L.M. Recovery from hematopoietic injury by modulating prostaglandin E_2 signaling post-irradiation. *Blood Cells Mol. Dis.* **2013**, *50*, 147–153. [CrossRef] [PubMed]
99. Arora, R.; Gupta, D.; Chawla, R.; Sagar, R.; Sharma, A.; Kumar, R.; Prasad, J.; Singh, S.; Samanta, N.; Sharma, R.K. Radioprotection by plant products: Present status and future prospects. *Phytother. Res.* **2005**, *19*, 1–22. [CrossRef] [PubMed]
100. Liu, W.C.; Wang, S.C.; Tsai, M.L.; Chen, M.C.; Wang, Y.C.; Hong, J.H.; McBride, W.H.; Chiang, C.S. Protection against radiation-induced bone marrow and intestinal injuries by *Cordyceps sinensis*, a Chinese herbal medicine. *Radiat. Res.* **2006**, *166*, 900–907. [CrossRef] [PubMed]
101. Gupta, M.L.; Sankwar, S.; Verma, S.; Devi, M.; Samanta, N.; Agarwala, P.K.; Kumar, R.; Singh, P.K. Whole-body protection to lethally irradiated mice by oral administration of semipurified fraction of *Podophyllum hexandrum* and post irradiation treatment with *Picrorhizza kurroa*. *Tokai J. Exp. Clin. Med.* **2008**, *33*, 6–12. [PubMed]

102. Lata, M.; Prasad, J.; Singh, S.; Kumar, R.; Singh, L.; Chaudhary, P.; Arora, R.; Chawla, R.; Tyagi, S.; Soni, N.L.; et al. Whoe body protection against lethal ionizing radiation in mice by REC-2001: A semi-purified fraction of *Podophyllum hexandrum*. *Phytomedicine* **2009**, *16*, 47–55. [CrossRef] [PubMed]
103. Pratheeshkumar, P.; Kuttan, G. Protective role of *Vernonia cinerea* L. against γ radiation-induced immunosuppression and oxidative stress in mice. *Hum. Exp. Toxicol.* **2011**, *30*, 1022–1038. [CrossRef] [PubMed]
104. Shakeri-Boroujeni, A.; Mozdaravi, H.; Mahmmoudzadeh, M.; Faeghi, F. Potent radioprotective effect of herbal immunomodulator drug (IMOD) on mouse bone marrow erythrocytes as assayed by the micronucleus test. *Int. J. Radiat. Res.* **2016**, *14*, 221–228. [CrossRef]
105. Wasserman, T.H.; Brizel, D.M. The role of amifostine as a radioprotector. *Oncolohy N. Y.* **2001**, *15*, 1349–1354.
106. Upadhyay, S.N.; Dwarakanath, B.S.; Ravindranath, T.; Mathew, T.L. Chemical radioprotectors. *Def. Sci. J.* **2005**, *55*, 402–425. [CrossRef]
107. Upadhay, S.N.; Ghose, A. Radioprotection by chemical means with the help of combined regimen radio-protectors—A short review. *J. Ind. Chem. Soc.* **2017**, *94*, 321–325.
108. Mell, L.K.; Movsas, B. Pharmacologic normal tissue protection in clinical radiation oncology: Focus on amifostine. *Expert Opin. Drug Met.* **2008**, *4*, 1341–1350. [CrossRef] [PubMed]
109. Gu, J.D.; Zhu, S.W.; Li, X.B.; Wu, H.; Li, Y.; Hua, F. Effects of amifostine in head and neck cancer patients treated with radiotherapy: A systematic review and meta-analysis based on randomized controlled trials. *PLoS ONE* **2014**, *9*, e95968. [CrossRef] [PubMed]
110. Singh, V.K.; Fatanami, O.O.; Wise, S.Y.; Newman, V.L.; Romaine, L.P.; Seed, T.M. The potentiation of the radioprotective efficacy of two medical countermeasures, γ-tocotrienol and amifostine, by a combination prophylactic modality. *Radiat. Prot. Dosim.* **2016**, *172*, 302–310. [CrossRef] [PubMed]
111. Weiss, J.F.; Landauer, M.R. Radioprotection by antioxidants. *Ann. N. Y. Acad. Sci.* **1998**, *899*, 44–60. [CrossRef]
112. Palozza, P.; Simone, R.; Picci, N.; Buzzoni, L.; Ciliberti, N.; Natangelo, A.; Manfredini, S.; Vertuani, S. Design, synthesis, and antioxidant potency of novel α-tocopherol analogues in isolated membranes and intact cells. *Free Radic. Biol. Med.* **2008**, *44*, 1452–1454. [CrossRef] [PubMed]
113. Sen, C.K.; Khanna, S.; Roy, S.; Packer, L. Molecular basis of vitamin E action tocotrienol potently inhibits glutamate-induced pp60$^{c\text{-}Src}$ kinase activation and death of HT4 neuronal cells. *J. Biol. Chem.* **2000**, *275*, 13049–13055. [CrossRef] [PubMed]
114. Kamal-Eldin, A.; Appelqist, L.A. The chemistry and antioxidant properties of tocopherols and tocotrienols. *Lipids* **1996**, *31*, 671–701. [CrossRef] [PubMed]
115. Bichay, T.J.; Roy, R.M. Modification of survival and hematopoiesis in mice by tocopherol injection following irradiation. *Strahlenther. Onkol.* **1986**, *162*, 391–399. [PubMed]
116. Srinivasan, V.; Weiss, J.F. Radioprotection by vitamin E: Injectable vitamin E administered alone or with WR-3689 enhances survival in irradiated mice. *Int. J. Radiat. Oncol. Biol. Phys.* **1992**, *23*, 841–845. [CrossRef]
117. Kumar, K.S.; Srinivasan, V.; Toles, R. Nutritional approaches to radioprotection. Vitamin E. *Mil. Med.* **2002**, *167*, 57–59. [PubMed]
118. Roy, R.M.; Petrella, M.; Shateri, H. Effects of administering tocopherol after irradiation on survival and proliferation of murine lymphocytes. *Pharmacol. Ther.* **1988**, *39*, 393–395. [CrossRef]
119. Satyamitra, M.; Uma Devi, P.; Murase, H.; Kagiya, V.T. In vivo postirradiation protection by a vitamin E analog, α-TMG. *Radiat. Res.* **2003**, *160*, 655–661. [CrossRef] [PubMed]
120. Cherdyntseva, N.; Shishkina, A.; Butorin, I.; Murase, H.; Gervas, P.; Kagiya, T.V. Effect of tocopherol-monoglucoside (TMG), a water-soluble glycosylated derivate of vitamin E, on hematopoietic recovery in irradiated mice. *J. Radiat. Res.* **2005**, *46*, 37–41. [CrossRef] [PubMed]
121. Ueno, M.; Inano, H.; Onoda, M.; Murase, H.; Ikota, N.; Kagiya, T.V.; Anzai, K. Modification of mortality and tumorigenesis by tocopherol-mono-glucoside (TMG) administered after irradiation in mice and rats. *Radiat. Res.* **2009**, *172*, 519–524. [CrossRef] [PubMed]
122. Singh, V.K.; Brown, D.S.; Kao, T.C. Tocopherol succinate: A promising radiation countermeasure. *Int. Immunopharmacol.* **2009**, *9*, 1423–1430. [CrossRef] [PubMed]
123. Singh, P.K.; Wise, S.Y.; Ducey, E.J.; Fatanmi, O.O.; Elliott, T.B.; Singh, V.K. α-tocopherol succinate protects mice against radiation-induced intestinal injury. *Radiat. Res.* **2012**, *177*, 133–145. [CrossRef] [PubMed]
124. Singh, P.K.; Wise, S.Y.; Ducey, E.J.; Brown, D.S.; Singh, V.K. Radioprotective efficacy of α-tocopherol succinate is mediated through granulocyte-colony stimulating factor. *Cytokine* **2011**, *56*, 411–421. [CrossRef] [PubMed]

125. Palozza, P.; Verdecchia, S.; Avanzi, L.; Vartuani, S.; Serini, S.; Manfredini, S. Comparative antioxidant activity of tocotrienols and the novel chromanyl-polyisoprenyl molecule PeAox-6 in isoleted membranes and intact cells. *Mol. Cell Biochem.* **2006**, *287*, 21–32. [CrossRef] [PubMed]
126. Li, X.H.; Fu, D.D.; Latif, N.H.; Mullaney, C.P.; Ney, P.H.; Mog, S.R.; Whitnall, M.H.; Srinivasan, V.; Xiao, M. δ-tocotrienol protects mouse and human hematopoietic progenitors from γ-irradiation through extracellular signal-regulated kinase/mammalian target of rapamycin signaling. *Haematologica* **2010**, *95*, 1996–2004. [CrossRef] [PubMed]
127. Satyamitra, M.; Kulkarni, S.; Ghosh, S.P.; Mullaney, C.P.; Condliffe, D.; Srinivasan, V. Hematopoietic recovery and amelioration of radiation-induced lethality by the vitamin E isoform, δ-tocotrienol. *Radiat. Res.* **2011**, *175*, 736–745. [CrossRef] [PubMed]
128. Baliarsingh, S.; Beg, Z.H.; Ahmad, J. The therapeutic impacts of tocotrienols in type 2 diabetic patients with hyprlipidemia. *Atherosclerosis* **2005**, *182*, 367–374. [CrossRef] [PubMed]
129. Kulkarni, S.S.; Ghosh, S.P.; Satyamitra, M.; Mog, S.; Hieber, K.; Romanyukha, L.; Gambles, K.; Toles, R.; Kao, T.C.; Hauer-Jensen, M.; et al. γ-tocotrienol protects hematopoietic stem and progenitor cells in mice after total-body irradiation. *Radiat. Res.* **2010**, *173*, 738–747. [CrossRef] [PubMed]
130. Ghosh, S.P.; Kulkarni, S.; Hieber, K.; Toles, R.; Romayukha, L.; Kao, T.C.; Hauer-Jensen, M.; Kumar, K.S. γ-tocotrienol, a tocol antioxidant as a potent radioprotector. *Int. J. Radiat. Biol.* **2009**, *85*, 598–606. [CrossRef] [PubMed]
131. Kulkarni, S.; Singh, P.K.; Ghosh, S.P.; Posarac, A.; Singh, V.K. Granulocyte colony-stimulating factor antibody abrogates radioprotective efficacy of γ-tocotrienol, a promising radiation countermeasure. *Cytokine* **2013**, *62*, 278–285. [CrossRef] [PubMed]
132. Singh, V.K.; Kulkarni, S.; Fatanmi, O.O.; Wise, S.Y.; Newman, V.L.; Romaine, P.L.P.; Hendrickson, H.; Gulani, J.; Ghosh, S.P.; Kumar, K.S.; et al. Radioprotective efficacy of γ-tocotrienol in nonhuman primates. *Radiat. Res.* **2016**, *185*, 285–298. [CrossRef] [PubMed]
133. Singh, V.K.; Beattie, L.A.; Seed, T.M. Vitamin E: Tocopherols and tocotrienols as potential radiation countermeasures. *J. Radiat. Res.* **2013**, *54*, 973–988. [CrossRef] [PubMed]
134. Singh, V.K.; Hauer-Jensen, M. γ-tocotrienol as a promising countermeasure for acute radiation syndrome: Current status. *Int. J. Mol. Sci.* **2016**, *17*, 663. [CrossRef] [PubMed]
135. Whanger, P.D. Selenocompounds in plants and animals and their biological significance. *J. Am. Coll. Nutr.* **2002**, *21*, 223–232. [CrossRef] [PubMed]
136. Weiss, J.F.; Srinivasan, V.; Kumar, K.S.; Landauer, M.R. Radioprotection by metals: Selenium. *Adv. Space Res.* **1992**, *12*, 223–231. [CrossRef]
137. Kiremidjian-Schumacher, L.; Stotzky, G. Selenium and immune responses. *Environ. Res.* **1987**, *42*, 227–303. [CrossRef]
138. Weiss, J.F.; Srinivasan, V.; Kumar, K.S.; Landauer, M.R.; Patchen, M.L. Radioprotection by selenium compounds. In *Trace Elements and Free Radicals in Oxidative Diseases*; Favier, A.E., Neve, J., Fauve, P., Eds.; AOCS Press: Champain, IL, USA, 1994; pp. 211–222.
139. Weiss, J.F.; Landauer, M.R. Protection against ionizing radiation by antioxidant nutrients and phytochemicals. *Toxicology* **2003**, *189*, 1–20. [CrossRef]
140. Karabulut-Bulan, O.; Bolkent, S.; Kizir, A.; Yanardag, R. Protective effects of vitamin E and selenium administration on small intestinal damage prior to abdominal radiation. *Pak. J. Zool.* **2016**, *48*, 1225–1232.
141. Okunieff, P. Interactions between ascorbic acid and the radiation of bone marrow, skin, and tumor. *Am. J. Clin. Nutr.* **1991**, *54*, 1281S–1283S. [PubMed]
142. Seifter, E.; Rettura, G.; Padawar, J.; Stratford, F.; Weinzweig, J.; Demetriou, A.A.; Levenson, S.M. Morbidity and mortality reduction by supplemental vitamin A or β-carotene in CBA mice given total-body-irradiation. *J. Natl. Cancer Inst.* **1984**, *73*, 1167–1177. [PubMed]
143. Jeong, B.K.; Song, J.H.; Jeong, H.; Choi, H.S.; Jung, J.H.; Hahm, J.R.; Woo, S.H.; Jung, M.H.; Choi, B.H.; Kim, J.H.; et al. Effect of α-lipoic acid on radiation-induced small intestine injury in mice. *Oncotarget* **2016**, *7*, 15105–15117. [PubMed]
144. Wambi, C.; Sanzari, J.; Wan, X.S.; Nuth, M.; Davis, J.; Ko, Y.H.; Sayers, C.M.; Baran, M.; Ware, J.H.; Kennedy, A.R. Dietary antioxidants protect hematopoietic cells and improve survival after total-body irradiation. *Radiat. Res.* **2008**, *169*, 384–396. [CrossRef] [PubMed]

145. Wambi, C.O.; Sanzari, J.K.; Sayers, C.M.; Nuth, M.; Zhou, Z.Z.; Davis, J.; Finnberg, N.; Lewis-Wambi, J.S.; Ware, J.H.; El-Deiry, W.S.; et al. Protective effects of dietary antioxidants on proton total-body irradiation-mediated hematopoietic cell and animal survival. *Radiat. Res.* **2009**, *172*, 175–186. [CrossRef] [PubMed]
146. Weiss, J.F.; Landauer, M.R. History and development of radiation-protective agents. *Int. J. Radiat. Biol.* **2009**, *85*, 539–573. [CrossRef] [PubMed]
147. Han, R.M.; Tian, Y.X.; Liu, Y.; Chen, C.H.; Ai, X.C.; Zhang, J.P.; Skibsted, L.H. Comparison of flavonoinds and isoflavonoids as antioxidants. *J. Agric. Food Chem.* **2009**, *57*, 3780–3785.
148. Zhou, Y.; Mi, M.T. Genistein stimulates hematopoiesis and increases survioval in irradiated mice. *J. Radiat. Res.* **2005**, *46*, 425–433. [CrossRef] [PubMed]
149. Landauer, M.R.; Srinivasan, V.; Seed, T.M. Genistein protects mice from ionizing radiation injury. *J. Appl. Toxicol.* **2003**, *23*, 379–385. [CrossRef] [PubMed]
150. Davis, T.A.; Clarke, T.K.; Mog, S.R.; Landauer, M.R. Subcutaneous administration of genistein prior to lethal irradiation suports multilineage, hematopoietic progenitor cell recovery and survival. *Int. J. Radiat. Biol.* **2007**, *83*, 141–151. [CrossRef] [PubMed]
151. Landauer, M.R. Radioprotection by the soy isoflavone genistein. In *Herbal Radiomodulators: Applications in Medicine, Homeland Defence and Space*; Arora, R., Ed.; Cabi Publishing: Wallingford, UK, 2008; pp. 163–173.
152. Day, R.M.; Davis, T.A.; Barshishat-Kupper, M.; McCart, E.A.; Tipton, A.J.; Landauer, M.R. Enhanced hematopoietic protection from radiation by the combination of genistein and captopril. *Int. Immunopharmacol.* **2013**, *15*, 348–356. [CrossRef] [PubMed]
153. Ha, C.T.; Li, X.H.; Fu, D.D.; Xiao, N.; Landauer, M.R. Genistein nanoparticles protect mouse hematopoietic system and prevent proinflammatory factors after γ irradiation. *Radiat. Res.* **2013**, *180*, 316–325. [CrossRef] [PubMed]
154. Thorn, J.A.; Jarvis, S.M. Adenosine transporters. *Gen. Pharmacol.* **1996**, *27*, 613–620. [CrossRef]
155. Gordon, E.L.; Pearson, J.D.; Dickinson, E.S.; Moreau, D.; Slakey, L.L. The hydrolysis of extracellular adenine nucleotides by arterial smooth muscle cells—Regulation of adenosine production at the cell surface. *J. Biol. Chem.* **1989**, *264*, 18986–18992. [PubMed]
156. Pospíšil, M.; Hofer, M.; Netíková, J.; Viklická, Š.; Pipalová, I.; Bartoníčková, A. Effect of dipyridamole and adenosine monophosphate on cell proliferation in the hemopoietic tissue of normal and γ-irradiated mice. *Experientia* **1992**, *48*, 253–257.
157. Pospíšil, M.; Hofer, M.; Netíková, J.; Pipalová, I.; Vacek, A.; Bartoníčková, A.; Volenec, K. Elevation of extracellular adenosine induces radioprotective effects in mice. *Radiat. Res.* **1993**, *134*, 323–330. [CrossRef] [PubMed]
158. Hofer, M.; Pospíšil, M.; Netíková, J.; Znojil, V.; Vácha, J. Enhancement of of haemopoietic spleen colony formation by drugs elevating extracellular adenosine: Effects of repeated in vivo treatment. *Physiol. Res.* **1997**, *46*, 285–290. [PubMed]
159. Pospíšil, M.; Hofer, M.; Znojil, V.; Vácha, J.; Netíková, J.; Holá, J. Radioprotection of mouse hemopoiesis by dipyridamole and adenosine monophosphate in fractionated treatment. *Radiat. Res.* **1995**, *142*, 16–22. [CrossRef] [PubMed]
160. Hofer, M.; Pospíšil, M.; Netíková, J.; Znojil, V.; Vácha, J.; Holá, J. Radioprotective efficacy of dipyridamole and AMP combination in fractionated radiation regimen, and its dependence on the time of administration of the drugs prior to irradiation. *Physiol. Res.* **1995**, *44*, 93–98. [PubMed]
161. Hofer, M.; Pospisil, M.; Weiterova, L.; Hoferova, Z. The role of adenosine receptor agonists in regulation of hematopoiesis. *Molecules* **2011**, *16*, 675–685. [CrossRef] [PubMed]
162. Hofer, M.; Pospíšil, M.; Znojil, V.; Holá, J.; Vacek, A.; Štreitová, D. Adenosine A_3 receptor agonist acts as a homeostatic regulator of bone marrow hematopoiesis. *Biomed. Pharmacother.* **2007**, *61*, 356–359. [CrossRef] [PubMed]
163. Hofer, M.; Pospíšil, M.; Šefc, L.; Dušek, L.; Vacek, A.; Holá, J.; Hoferová, Z.; Šteritová, D. Activation of adenosine A_3 receptors supports hematopoiesis-stimulating effects of granulocyte colony-stimulating factor in sublethally irradiated mice. *Int. J. Radiat. Biol.* **2010**, *86*, 649–656. [CrossRef] [PubMed]
164. Hofer, M.; Pospíšil, M.; Dušek, L.; Hoferová, Z.; Weiterová, L. Inhibition of cyclooxygenase-2 promotes the stimulatory action of adenosine A_3 receptor agonist on hematopoiesis in sublethally γ-irradiated mice. *Biomed. Pharmacother.* **2011**, *65*, 427–431. [CrossRef] [PubMed]

165. Hofer, M.; Pospíšil, M.; Dušek, L.; Hoferová, Z.; Komůrková, D. Agonist of the adenosine A_3 receptor, IB-MECA, and inhibitor of cyclooxygenase-2, meloxicam, given alone or in a combination early after total body irradiation enhance survival of γ-irradiated mice. *Radiat. Environ. Biophys.* **2014**, *53*, 211–215. [CrossRef] [PubMed]
166. Ghosh, S.P.; Perkins, M.W.; Hieber, K.; Kulkarni, S.; Kao, T.C.; Reddy, E.P.; Reddy, M.V.R.; Maniar, M.; Seed, T.M.; Kumar, K.S. Radiation protection by a new chemical entity, Ex-Rad™: Efficacy and mechanisms. *Radiat. Res.* **2009**, *171*, 173–179. [CrossRef] [PubMed]
167. Suman, S.; Datta, K.; Doiron, K.; Ren, C.; Kumar, R.; Taft, D.R.; Fornace, A.J.; Maniar, M. Radioprotective effects of ON 01210.Na upon oral administration. *J. Radiat. Res.* **2012**, *53*, 368–376. [CrossRef] [PubMed]
168. Ghosh, S.P.; Kulkarni, S.; Perkins, M.W.; Hieber, K.; Pessu, R.L.; Gambles, K.; Maniar, M.; Kao, T.C.; Seed, T.M.; Kumar, K.S. Amelioration of radiation-induced hematopoietic and gastrointestinal damage by Ex-RAD® in mice. *J. Radiat. Res.* **2012**, *53*, 526–536. [CrossRef] [PubMed]
169. Suman, S.; Maniar, M.; Fornace, A.J.; Datta, K. Administration of ON 01210.Na after exposure to ionizing radiation protects bone marrow cells by attenuating DNA damage response. *Radiat. Oncol.* **2012**, *7*, 6. [CrossRef] [PubMed]
170. Kang, A.D.; Coscenza, S.C.; Bonagura, M.; Manair, M.; Reddy, M.V.R.; Reddy, E.P. ON01210.Na (Ex-RAD®) mitigates radiation damage through activation of the AKT pathway. *PLoS ONE* **2013**, *8*, e58355. [CrossRef] [PubMed]
171. Miller, R.C.; Murley, J.S.; Grdina, D.J. Metformin exhibits radiation countermeasures efficacy when used alone or in combination with sulfhydryl containing drugs. *Radiat. Res.* **2014**, *181*, 464–470. [CrossRef] [PubMed]
172. Burdelya, L.G.; Krivokrysenko, V.I.; Tallant, T.C.; Strom, E.; Gleiberman, A.S.; Gupta, D.; Kurnasov, O.V.; Fort, F.L.; Osterman, A.L.; DiDonato, J.A.; et al. An agonist of toll-like receptor 5 has radioprotective activity in mouse and primate models. *Science* **2008**, *320*, 226–230. [CrossRef] [PubMed]
173. Krivokrysenko, V.I.; Toshkov, I.A.; Gleiberman, A.S.; Krasnov, P.; Shyshynova, I.; Bespalov, I.; Maitra, R.K.; Narizhneva, N.V.; Singh, V.K.; Whitnall, M.H.; et al. The toll-like receptor 5 agonist entolimod mitigates lethal acute radiation syndrome in no-human primates. *PLoS ONE* **2015**, *10*, e0135388. [CrossRef] [PubMed]
174. Toshkov, I.A.; Gleiberman, A.S.; Mett, V.L.; Hutson, A.D.; Singh, A.K.; Gudkov, A.V.; Burdelya, L.G. Mitigation of radiation-induced epithelial damage by the TLR5 agonist entolimod in a mouse model of fractionated head and neck irradiation. *Radiat. Res.* **2017**, *187*, 570–580. [CrossRef] [PubMed]
175. Krivokrysenko, V.I.; Shakhov, A.N.; Singh, V.K.; Bone, F.; Kononov, Y.; Shyshynova, I.; Cheney, A.; Maitra, R.K.; Purmal, A.; Whitnall, M.H.; et al. Identification of granulocyte colony-stimulating factor and interleukin-6 as candidate biomarkers of CBLB502 efficacy as a medical radiation countermeasure. *J. Pharmacol. Exp. Ther.* **2012**, *343*, 497–508. [CrossRef] [PubMed]
176. Zhang, L.R.; Sun, W.M.; Wang, J.J.; Zhank, M.; Yang, S.M.; Tian, Y.P.; Vidyasagar, S.; Pena, L.A.; Zhang, K.Z.; Cao, Y.B.; et al. Mitigation effect of an FGF-2 peptide on acute gastrointestinal syndrome after high-dose ionizing radiation. *Int. J. Radiat. Oncol. Biol. Phys.* **2010**, *77*, 261–268. [CrossRef] [PubMed]
177. Deng, W.L.; Kimura, Y.; Gududuru, V.; Wu, W.J.; Balogh, A.; Szabo, E.; Thompson, K.E.; Yates, C.R.; Balasz, L.; Johnson, L.R.; et al. Mitigation of the hematopoietic and gastrointestinal acute radiation syndrome by octadecenyl thiophosphate, a small molecule mimic of lysophosphatidic acid. *Radiat. Res.* **2015**, *183*, 465–475. [CrossRef] [PubMed]
178. Taniguchi, C.M.; Miao, Y.R.; Diep, A.N.; Wu, C.; Rankin, E.B.; Atwood, T.F.; Xing, L.; Giaccia, A.J. PHD inhibition mitigates and protects against radiation-induced gastrointestinal toxicity via HIF2. *Sci. Transl. Med.* **2014**, *6*, 236ra64. [CrossRef] [PubMed]
179. Olcina, M.M. Reducing radiation-induced gastrointestinal toxicity—The role of the PHD/HIF axis. *J. Clin. Investig.* **2016**, *126*, 3708–3715. [CrossRef] [PubMed]
180. Dainiak, N.; Gent, R.N.; Carr, Z.; Schneider, R.; Bader, J.; Buglova, E.; Chao, N.; Coleman, C.N.; Ganser, A.; Gorin, C.; et al. Literature review and global consensus on management of acute radiation syndrome affecting non-hematopoietic organ systems. *Disaster Med. Public Health Prep.* **2011**, *5*, 183–201. [CrossRef] [PubMed]
181. Hirama, T.; Tanosaki, S.; Kandatsu, S.; Kuroiwa, N.; Kamada, T.; Tsuji, H.; Yamada, S.; Katoh, H.; Yamamoto, N.; Tsuji, H.; et al. Initial medical management of patients severely irradiated in the Tokai-mura criticality accident. *Br. J. Radiol.* **2003**, *76*, 246–352. [CrossRef] [PubMed]

182. Delanian, S.; Porcher, R.; Balla-Mekias, S.; Lefaix, J.L. Randomize, placebo-controlled trial of combined petoxifylline and tocopherol for regression of superficial radiation-induced fibrosis. *J. Clin. Oncol.* **2003**, *13*, 2545–2550. [CrossRef] [PubMed]
183. Bey, E.; Prat, M.; Duhamel, P.; Benderitter, M.; Brachet, M.; Trompier, F.; Battaglini, P.; Emou, I.; Boutin, L.; Gourven, M.; et al. Emerging therapy for improving wound repair of severe radiation burns using local bone marrow-derived stem cell administrations. *Wound Repair Regen.* **2010**, *18*, 50–58. [CrossRef] [PubMed]
184. Agay, D.; Scherthan, H.; Forcheron, F.; Grenier, N.; Herodin, F.; Meineke, V.; Drouet, M. Multipotent mesenchymal stem cell grafting to treat cutaneous radiation syndrome: Development of a new minipig model. *Exp. Hematol.* **2010**, *38*, 945–956. [CrossRef] [PubMed]
185. Riccobono, D.; Agay, D.; Francois, S.; Scherthan, H.; Drouet, M.; Forcheron, F. Contribution of intramuscular autologous adipose tissue-derived stem cell injection to treat cutaneous radiation syndrome: Preliminary results. *Health Phys.* **2016**, *111*, 117–126. [CrossRef] [PubMed]

molecules

MDPI

Review

Combining Pharmacological Countermeasures to Attenuate the Acute Radiation Syndrome—A Concise Review

Michal Hofer *, Zuzana Hoferová, Daniel Depeš and Martin Falk

Department of Cell Biology and Radiobiology, Institute of Biophysics, v.v.i., Czech Academy of Sciences, Královopolská 135, 61265 Brno, Czech Republic; hoferovaz@centrum.cz (Z.H.); blackburn@ibp.cz (D.D.); falk@ibp.cz (M.F.)

* Correspondence: hofer@ibp.cz; Tel.: +420-541-517-171; Fax: +420-541-211-293

Academic Editor: Diego Muñoz-Torrero

Received: 28 March 2017; Accepted: 16 May 2017; Published: 19 May 2017

Abstract: The goal of combined pharmacological approaches in the treatment of the acute radiation syndrome (ARS) is to obtain an effective therapy producing a minimum of undesirable side effects. This review summarizes important data from studies evaluating the efficacy of combining radioprotective agents developed for administration prior to irradiation and therapeutic agents administered in a post-irradiation treatment regimen. Many of the evaluated results show additivity, or even synergism, of the combined treatments in comparison with the effects of the individual component administrations. It can be deduced from these findings that the research in which combined treatments with radioprotectors/radiomitigators are explored, tested, and evaluated is well-founded. The requirement for studies highly emphasizing the need to minimize undesirable side effects of the radioprotective/radiomitigating therapies is stressed.

Keywords: acute radiation syndrome; radioprotectors; radiomitigators; combined treatment; cytokines

1. Introduction

Although the search for suitable radiation countermeasures for radiation-associated injuries was initiated more than half a century ago, very few safe and effective radiation countermeasures for the most severe of these injuries, namely acute radiation syndrome (ARS), defined as 'an acute illness caused by irradiation of the entire body (or most of the body) by a high dose of penetrating ionizing radiation in a very short period of time (usually a matter of minutes) [1], have been approved. This exception is represented by two granulocyte colony-stimulating factor (G-CSF)-based radiation countermeasures (Neupogen® and Neulasta®) which have recently been approved by the United States Food and Drug administration (US FDA) for treatment of the hematopoietic ARS; both of these agents are radiomitigators for use after radiation exposure [1,2]. Not surprisingly both of the topics of "radioprotectors for use prior to exposure" and "therapeutic agents for post-exposure treatment" possess top priority among the research areas for radiological nuclear threat countermeasures [3].

It is well known that most of the agents tested for their abilities to protect from accidental radiation exposure or mitigate its health consequences, including the most effective ones, exhibit toxicities that can limit their usefulness. Therefore, various approaches have been used to decrease their undesirable side effects. One of the approaches is to combine two or more agents with the aim to reduce their toxicities while preserving, or even enhancing, the overall therapeutic outcome (e.g., [4,5]). This concise review deals with some of the most studied and promising experimental combinatory pharmacological interventions in ARS. The aim of the review is to emphasize the advantages of the approach of combined pharmacological treatment with radioprotectors/radiomitigators in patients with ARS.

2. Combinations Including Amifostine (WR-2721)

Amifostine (WR-2721), the most important representative of thiol radioprotectors, is a powerful radioprotective agent (a drug for use prior to irradiation); it acts on the principle of chemical radioprotection, i.e., predominantly by decreasing the levels of reactive oxygen species and hydrogen peroxide (e.g., [5]). Amifostine has been reported to reduce the effect of a radiation dose by a factor of up to 2.7 (the highest dose reduction factor (DRF) seen in a mouse 30-day survival model) [6]. However, due to its rather high toxicity, amifostine has not been approved for the treatment of ARS; nevertheless, it has found its use in radio- and/or chemotherapy-treated oncological patients (especially in head-and-neck cancer) as a selective protector of normal cells (e.g., [7,8]). Ongoing studies on amifostine using modern methods have confirmed its advantageous therapeutic qualities (e.g., [9]) and, therefore, the research on the combined use of amifostine with other agents in the treatment of ARS is worth mentioning.

Much work has been done on evaluation of combined effects of amifostine and antioxidative salts of various metals, like copper, zinc, or selenium (summarized by Weiss et al. [10]), both administered in the pre-irradiation regimen. It is noteworthy that the radioprotective efficacy of the metal-containing compounds themselves has been found to be low, whereas they have been found to significantly enhance the protective effects of amifostine and other thiol radioprotectors and reduce the thiol toxicity (e.g., [10,11]). Several hypotheses have been proposed explaining how metal salts positively influence the metabolism of amifostine; e.g., alkaline phosphatase activity in bone marrow cells has been shown to be significantly depressed after treatment with selenium, suggesting that a retardation of conversion of amifostine to its active free sulfhydryl form through the action of alkaline phosphatase might be responsible for the effects of selenium [10]; selenium has also been reported to induce glutathione peroxidase activity [12]. These findings and considerations have been reflected in later clinical attempts combining selenium and amifostine to attenuate undesirable effects of oncological radio/chemotherapy [13,14].

Another naturally-occurring antioxidant studied for the treatment of ARS in a combination with amifostine is vitamin E, a less effective radioprotector than synthetic thiols, like amifostine, but providing a longer window of protection against lethality (summarized by Weiss and Landauer [15]). In a 30-day survival experiment, WR-3689 (a thiol drug related to amifostine) and its combination with vitamin E (both administered pre-irradiation) have shown their DRFs of 1.35 and 1.49, respectively [16]. Later studies on rats' whole bodies irradiated with a dose producing ARS have revealed mutually potentiating action of amifostine and vitamin E on radiation-damaged liver [17]. Recent findings have confirmed and extended the data from previous studies: an important observation has been obtained regarding the possibility to use low, non-toxic doses of amifostine and γ-tocotrienol, a vitamin E family member, for obtaining a high level of radioprotection [18].

In a pre-radiation administration setting, amifostine has also been experimentally combined with prostaglandin E_2 (PGE_2) or its synthetic analog, misoprostol. In a 30-day survival study, the DRF of amifostine alone, PGE_2 alone, and amifostine + PGE_2 in combination has been found to be 1.9, 1.45, and 2.15, respectively [19]. Prostaglandins have been found to stimulate erythroid and multilineage progenitor cells [20], as well as to enhance homing of hematopoietic stem cells through upregulation of the chemokine receptor CXCR4 and to stimulate hematopoietic stem cell survival by upregulation of apoptosis protein Survivin [21]. Both PGE_2 and misoprostol have been reported to also be effective in the intestinal radiation syndrome [22]. Much later findings on the protective role of amifostine in preventing gastric damage produced by the prostaglandin synthesis inhibitor indomethacin have confirmed a positive influence of amifostine on the metabolism of prostaglandins [23].

Immunomodulators represent a wide group of substances stimulating the immune/hematopoietic system. Many of them, e.g., β-glucan and Broncho-Vaxom, shown here as examples of immunomodulators suitable for combined administration with amifostine for the treatment of ARS, possess no, or low, toxicity and are often commercially available. Their mechanism of action enables them to be administered in both protective and therapeutic regimens. Beta-glucan,

a polyglucose, has been isolated from various sources. Thus, β-glucan from *Saccharomyces cerevisiae*, administered post-radiation, has been shown to significantly enhance the radioprotective effects of pre-irradiation-administered amifostine, their DRFs in a survival study being 1.37, 1.08, and 1.52 for amifostine alone, β-glucan alone, and amifostine + β-glucan, respectively [24]. The triple combination of pre-irradiation-administered amifostine, selenium, and β-glucan has been also reported as a very successful multiple-agent radioprotector [25]. In 2013, Pillai and Devi [26] followed up these studies with their experiments using β-glucan from the mushroom *Ganoderma lucidum*; they have reported a 100% mortality in untreated mice, but a 66% survival rate after 8 Gy exposure and post-irradiation administration of β-glucan, and even higher survival (83%) following the combination of pre-irradiation amifostine and post-irradiation β-glucan [26]. The authors stress that β-glucan is not toxic at the radioprotective dose [26]. For details on hematologic and radioprotective efficacy of β-glucan, see [27]. Broncho-Vaxom, a bacterial lysate, has been shown to potentiate in both protective and therapeutic administration settings the radioprotective effects of pre-irradiation amifostine [28,29]. The values of DRF in a survival study have been reported to be 1.92, 1.17, and 2.07 for amifostine alone, Broncho-Vaxom alone, and amifostine + Broncho-Vaxom, respectively, if both the drugs were applied pre-irradiation [29]. Recent studies on immunomodulators as components of drug combinations tested for their potential radioprotection/radiomitigation comprise polysaccharide from *Sipunculus nudus* and peptidoglycan. Polysaccharide from *Sipunculus nudus*, which is a species of unsegmented marine worms, administered post-irradiation jointly with interleukin-11 (IL-11) and G-CSF, has been reported to enhance the radioprotective action of pre-irradiation amifostine, as shown when parameters of hematopoietic, immune, and reproductive tissues in irradiated mice were evaluated [30]. Pre-irradiation amifostine and post-irradiation peptidoglycan, a polymer from the bacterial cell wall consisting of sugars and amino acids, have been found to synergistically promote the survival of irradiated mice through the amelioration of intestinal and bone marrow damage [31].

Granulocyte colony-stimulating factor (G-CSF) is a hematopoietic growth factor especially stimulating the production of neutrophils [32] and also showing antiapoptotic qualities [33]. For the detailed summary of its use in the treatment of ARS, see [34]. The combination of amifostine and G-CSF for the treatment of ARS has been aimed especially at evaluating the efficacy of the combined pre-irradiation amifostine and post-irradiation G-CSF therapy. In animal studies, this combination has been shown to be very effective [35,36], e.g., in a 30-day survival study, the LD50/30 values (radiation doses killing 50% of the experimental animals by day 30 after irradiation) for mice administered saline, G-CSF, amifostine, and amifostine + G-CSF have been reported to be 7.85 Gy, 8.30 Gy, 11.30 Gy, and 12.85 Gy, respectively [35]. In later publications dealing with the use of the amifostine + G-CSF combination in oncological patients, this approach has been thoroughly discussed in connection with both chemotherapy [37] and radiotherapy [38].

Metformin, a biguanide drug used in the treatment of type II diabetes, administered in a single dose 24 h after irradiation, has been found to significantly potentiate the radioprotective effects of amifostine in several cell types [39]. Metformin has been proposed to reduce endogenous reactive oxygen species and/or to slow down cell renewal progression and, as a result, to increase the time for repair; it has been suggested as a potentially useful agent for radiation countermeasures use [39].

The chemical structures of the selected substances explored in Section 2, namely amifostine, vitamin E, WR-3689, prostaglandin E_2, misoprostol, and metformin, are summarized in Figure 1.

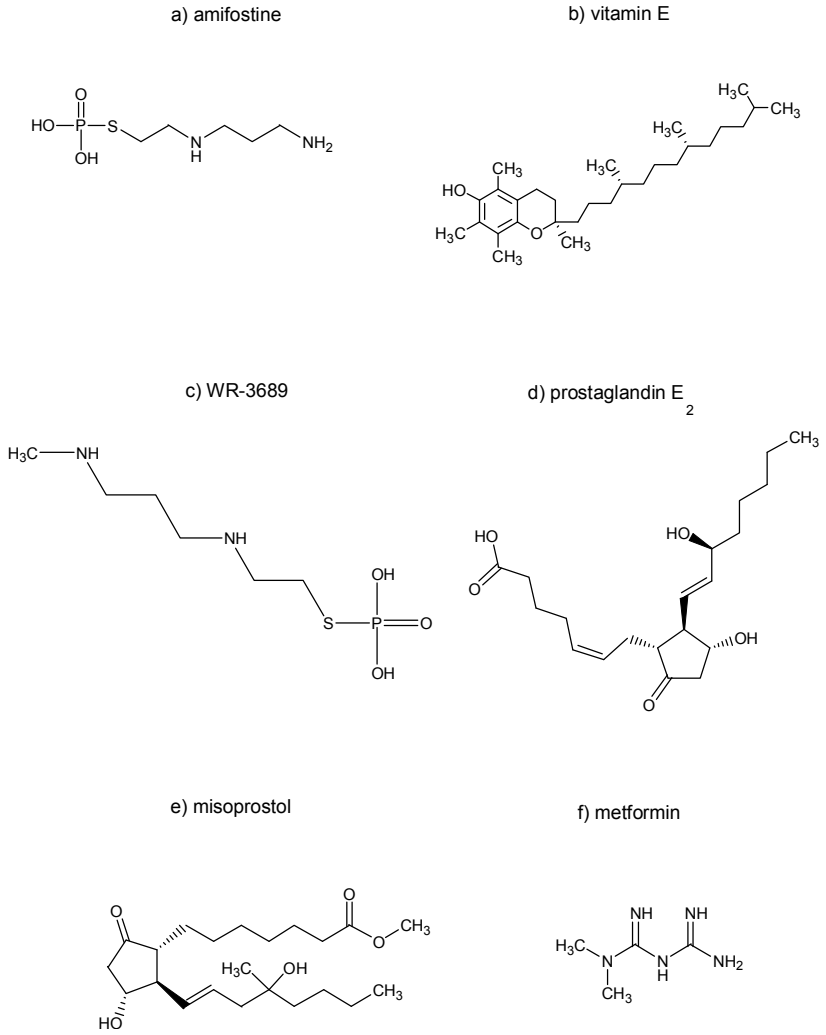

Figure 1. Chemical structures of selected substances explored in Section 2.

3. Combinations without Amifostine or Other Thiol Radioprotectors

Whereas amifostine and related substances act in ARS mostly on the principle of chemical radiprotection (scavenging of free radicals), the combinations addressed in this paragraph include mostly agents functioning by influencing various metabolic and regulatory pathways in the mammalian organism. The latter agents have been often classified under the term "biological response modifiers" [40]. Their advantage is the possibility of both pre- and post-irradiation administration.

It has been found that the receptor action of extracellular adenosine acts radioprotectively in mice by the mechanisms of hypoxia induction due to the effects of the treatment on the cardiovascular system and enhanced regeneration of hematopoiesis; elevation of extracellular adenosine has been produced by combined administration of dipyridamole, a drug inhibiting the cellular uptake of adenosine, and adenosine monophosphate, an adenosine prodrug [41]. These findings and considerations have been confirmed in several studies and are summarized in a review [42]. Though not done on irradiated mice, the key for this topic were the results of a study describing the synergistic effects of combining dipyridamole + adenosine monophosphate with G-CSF on the production of neutrophils [43]; the effectiveness of this drug combination has been confirmed also under the conditions of ARS [44]. Later is was found that a selective stimulation of adenosine A_3 receptors, e.g., by N^6-(3-iodobenzyl)adenosine-5′-*N*-methyluronamide (IB-MECA), is responsible for the radioprotective and hematopoiesis-stimulating effects, previously observed after non-selective adenosine receptor

activation, by the combination of dipyridamole and adenosine monophosphate [45]. Further experiments have shown that IB-MECA supports hematopoiesis-stimulating effects of G-CSF in sub-lethally irradiated mice when the two drugs are administered in a combination [46].

Cyclooxygenase inhibitors have been long studied for their ability to enhance hematopoiesis in an irradiated mammalian organism. With respect to their mechanism of action, they have been reported to remove, by inhibiting synthesis of PGE_2, the negative feedback control of myelopoiesis played by PGE_2 (for a detailed review, see [47]). Combined administration of diclofenac, a non-selective cyclooxygenase-1 and cyclooxygenase-2 inhibitor, and β-glucan, an immunomodulator, in single doses before irradiation of mice with a single sublethal dose of γ-rays, has been found to produce significantly better restoration of hematopoiesis in comparison with the mice administered with each of the drugs alone [48]. The same has become true when the two agents have been applied to mice before each of several repeated radiation doses [49]. When selective cyclooxygenase-2 inhibitors appeared, retaining the hematopoiesis-stimulating efficacy of non-selective cyclooxygenase inhibitors and producing less undesirable side effects, their representative, meloxicam, has been tested in a combined administration with IB-MECA, an adenosine A_3 receptor agonist, in a post-irradiation regimen for the treatment of ARS. The combination of meloxicam + IB-MECA has been reported to be effective both when hematopoiesis was evaluated following a sub-lethal radiation dose [50] and when the survival of mice served as an outcome after a lethal radiation dose [51]. Meloxicam has also been found to stimulate endogenous production of G-CSF in irradiated mice [52] and to be able to substitute G-CSF in the treatment of ARS [53].

The abovementioned experimental combinatory ARS treatments including G-CSF represent only a part of the studies on the combined use of hematopoietic growth factors and cytokines in the treatment of the acute radiation disease. There exists a rather high number of papers on this topic already from the 1980s and 1980s. Some examples of these papers follow. As reported by Patchen et al., treatment of irradiated mice with the combination of β-glucan and G-CSF in a post-irradiation setting has been found to positively influence hematopoietic regeneration and survival of mice [54]. Enhanced radioprotection of mice has also been observed for the combinations of interleukin-1 (IL-1) and tumor necrosis factor [55] in a pre-irradiation therapeutic approach, IL-6 and G-CSF [56] administered after irradiation, or the triple combination of mast cell growth factor (C-kit ligand) + granulocyte-macrophage colony-stimulating factor (GM-CFC) + interleukin-3 (IL-3) also given post-irradiation [57]. Combination therapy of ARS using post-irradiation administration of G-CSF and synthokine SC-55494 (a synthetic high-affinity IL-3 ligand [58]) has been reported to be effective against post-irradiation neutropenia and thrombocytopenia in rhesus monkeys [59]. These experimental animals have also been used to evaluate the effects of the post-irradiation combinations of thrombopoietin (TPO), GM-CSF, and G-CSF; it has been stated that TPO significantly improves the performance of GM-CSF and G-CSF in alleviating severe neutropenia [60]. Significantly enhanced multilineage hematopoietic recovery in non-human primates has been observed following combined administration of megakaryocyte growth and development factor (MGDF) and G-CSF [61]. Intense attention has been paid to the topic of the post-irradiation administration of cytokine and growth factor combinations by the group of Hérodin and coworkers. Their experiments in mice have shown that the combinations of stem cell factor (SCF), Flt3-ligand, TPO, interleukin-3 (IL-3), and stromal-derived factor-1, administered 2 and 24 h after irradiation, significantly improved both short-term and long-term survival of the animals [62]. These findings have also been confirmed in subsequent studies on non-human primates where heavily irradiated (a whole-body dose of 7 Gy) monkeys were reported to be successfully treated from a severe bone marrow radiation syndrome when administered one-time combinations of SCF + glycosylated erythropoietin (EPO) + pegylated G-CSF [31] or pegylated G-CSF + SCF + Flt3-ligand + TPO + IL-3 [63] very early (2 h) after irradiation. The authors propose, as the main therapeutic mechanism of these cytokine cocktails, their anti-apoptotic action and emphasize the necessity of the early post-irradiation application of the drugs ("the sooner the better" [64]). Studies on the combined pharmaceutical modulation of ARS manifestation by pharmacological combinations

comprising hematopoietic growth factors and cytokines still continue: a recent study has evaluated the efficacy of the joint administration of EPO, G-CSF, c-mpl receptor agonist romiplostim (a fusion protein analog of TPO), and nandrolone decanoate (a synthetic androgen) in mice following either a single post-irradiation dose within 2 h after irradiation, or five doses in five days following irradiation, as the most efficacious combination of EPO, G-CSF, and romiplostim that has been appraised [65].

Combinations of hematopoietic growth factors and cytokines have already found their use in the treatment of radiological accident victims. Various combinations of G-CSF, GM-CSF, EPO, SCF, and IL-3 have been administered to victims of accidents in Soreq (Israel, 1990), Neshviz (Belarus, 1992), Henan Province (China, 1999), Tokaimura (Japan, 1999), Prakan (Thailand, 2000), Fleurus (Belgium, 2006), and Dakar (Senegal, 2006) (summarized in [66]). Differing outcomes of the individual treatments are difficult to evaluate due to differing radiation sources, exposure doses, and other circumstances of the accidents.

Various natural antioxidants also play a role in radioprotective/radiomitigating combinations, e.g., mutual potentiation of the effects of post-irradiation administration of quercetin, an antioxidative flavonoid, and indralin, an adrenomimetic, in mice has been reported [67]. Enhanced hematopoietic protection has been obtained by combined pre-irradiation administration of the isoflavone genistein, an antioxidant and protein kinase inhibitor modulating signal transduction pathways, and captopril, an angiotensin-converting enzyme and vasodilator [68]. The combination of tocopherol succinate (a hemisuccinate ester of α-tocopherol belonging to the vitamin E family), an antioxidant, and AMD3100, an antagonist of chemokine receptor CXCR 4, enabling the displacement of hematopoietic stem cells and their subsequent migration to the peripheral blood, has been found to stimulate hematopoiesis in supralethally-irradiated mice [69]. Combined pre-irradiation administration of α-tocopherol acetate (an agent from the vitamin E family) and ascorbic acid (vitamin C), both antioxidants, has been reported to produce radioprotective properties, as shown by reduction of the numbers of chromosome aberrations in the bone marrow of rats [70]. A mixture of dietary antioxidants, including L-selenomethionine (an aminoacid), vitamin C, vitamin E succinate, α-lipoic acid (an organosulphur compound derived from octanoic acid), combined with *N*-acetyl-cysteine (an antioxidative drug and dietary supplement) has been found to protect hematopoietic cells and improve survival after its pre- or post-irradiation administration to X-irradiated mice [71] or post-irradiation administration to proton-irradiated mice [72].

Attention has also been paid to combinations of herbal extracts, e.g., Gupta and coworkers have shown potentiating effects of post-irradiation treatment with *Picrorrhiza kurroa* extract on pre-irradiation radioprotective efficacy of *Podophyllum hexandrum* extract [73]. Both the herbs are considered antioxidants, and *Podophyllum hexandrum* is also known for its anticancer effects.

An interesting report concerning radioprotective properties of the combination of selenium, zinc, and manganese with *Lachesis muta* (a pit viper species) venom in whole-body irradiated rats has been published by Crescenti and coworkers [74]. The authors call the combination an immunomodulator which positively affects radiosensitive tissues, including those of the gastrointestinal and hematopoietic systems [74].

Of additional interest are recent studies on pharmacological reduction of radiation-induced gastrointestinal toxicity by inhibitors of prolyl hydroxylase domain-containing enzymes (PHDs) whose administration has resulted in the stabilization of hypoxia-inducible factors (HIFs) protecting important cellular compartments from radiation-induced damage [75]. Combined administration of PHDs with glycogen synthase kinase-3 (GSK-3) inhibitors, decreasing the induction of p53-upregulated modulator of apoptosis (PUMA), has been proposed for radioprotection [76].

Chemical structures of selected substances explored in Section 3, namely dipyridamole, adenosine monophosphate, N^6-(3-iodobenzyl)adenosine-5′-*N*-methyluronamide, diclofenac, meloxicam, nandrolone decanoate, quercetin, indralin, genistein, captopril, tocopherol succinate, AMD3100, α-tocopherol acetate, ascorbic acid, L-selenomethionine, α-lipoic acid, and *N*-acetylcysteine, are summarized in Figure 2.

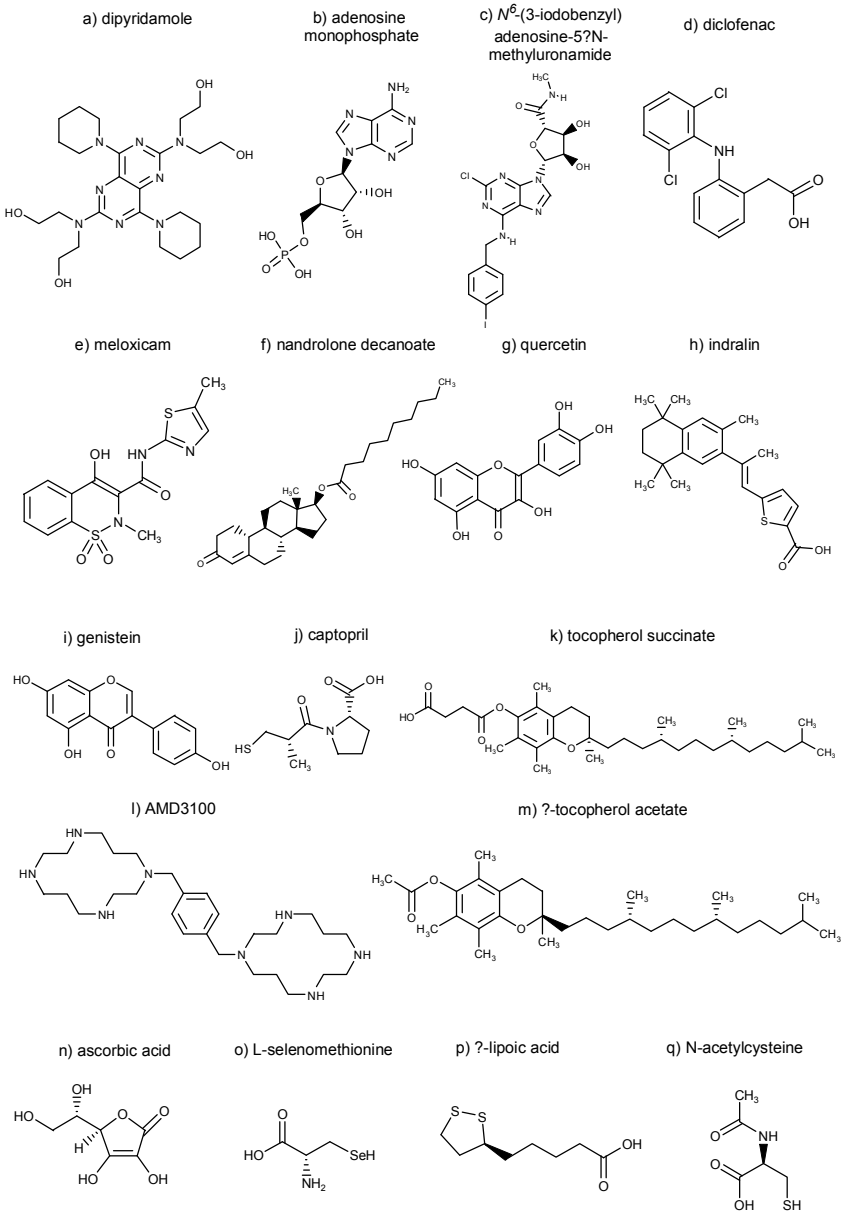

Figure 2. Chemical structures of selected substances explored in Section 3.

Agents mentioned in this review that have been used in pharmacological combinations in attempts to modify the course of ARS are summarized in Table 1.

Table 1. Summary of agents tested in pharmacological combinations in attempts to modify the course of the acute radiation syndrome (ARS).

Agent or Group of Agents	Predominant Radiomodifying Effect(s)	Reference Number(s)
Adenosine monophosphate	Stimulator of hematopoietic cell proliferation through adenosine receptor action	[41–44]
Alpha-lipoic acid	Antioxidant	[71,72]
AMD3100	Influences migration and homing of hematopoietic stem cells	[60]
Amifostine	Free radical scavenger	[5–39]
Ascorbic acid (vitamin C)	Antioxidant	[70–72]
Beta-glucan	Immunomodulator, stimulator of hematopoiesis	[24–27,54]

Table 1. *Cont.*

Agent or Group of Agents	Predominant Radiomodifying Effect(s)	Reference Number(s)
Broncho-Vaxom	Immunomodulator, stimulator of hematopoiesis	[28,29]
Captopril	Vasodilator	[68]
Diclofenac	Inhibitor of prostaglandin synthesis, stimulator of myelopoiesis	[47–49]
Dipyridamole	Enhances adenosine receptor action, stimulator of proliferation of hematopoietic cells	[41–44]
Erythropoietin (EPO)	Hematopoietic growth factor, stimulator of erythropoiesis	[31,65,66]
Flt3-ligand	Hematopoietic growth factor, stimulator of hematopoiesis	[62,63]
Genistein	Antioxidant	[68]
Glycogen synthase kinase-3 (GSK-3) inhibitor	Regulator of apoptosis	[76]
Granulocyte colony-stimulating factor (G-CSF)	Hematopoietic growth factor, stimulator of hematopoiesis	[30–38,52–54,56,58, 61,63,65,66]
Granulocyte-macrophage colony-stimulating factor (GM-CSF)	Hematopoietic growth factor, stimulator of hematopoiesis	[57,60,66]
Indralin	Adrenomimetic	[67]
Inhibitors of prolyl hydroxylase domain-containing enzymes (PHDs)	Antioxidants	[75,76]
Interleukin-1 (IL-1)	Cytokine, regulator of immune response, inflammation, and hematopoiesis	[55]
Interleukin-3 (IL-3)	Cytokine, regulator of production of granulocytes and macrophages	[57,63,66]
Interleukin-6 (IL-6)	Cytokine, stimulator of myelopoiesis	[56]
Interleukin-11 (IL-11)	Cytokine, stimulator of hematopoiesis and lymphopoiesis	[30]
Lachesis muta venom	Immunomodulator (?)	[74]
Megakaryocyte growth and development factor (MGDF)	Hematopoietic growth factor, stimulator of thrombopoiesis	[61]
Meloxicam	Inhibitor of prostaglandin synthesis, stimulator of myelopoiesis	[50–53]
Metformin	Antioxidant, modulator of cell renewal	[39]
N^6-(3-iodobenzyl)adenosine-5′-*N*-methyluronamide (IB-MECA)	Stimulator of hematopoietic cell proliferation through adenosine receptor action	[45,46,50,51]
N-acetyl-cysteine	Antioxidant	[71,72]
Nandrolone decanoate	Anabolic effects	[65]
Peptidoglycan	Immunomodulator, stimulator of hematopoiesis	[31]
Picrorhiza kuroa extract	Antioxidant	[73]
Podophyllum hexandrum extract	Antioxidant	[73]
Polysaccharide from Sipunculus nudus	Immunomodulator, stimulator of hematopoiesis	[30]
Prostaglandin E_2 and prostaglandin family members (misoprotol)	Modulators of proliferation of hematopoietic cells, protectors of intestinal tissue	[19–23]
Quercetin	Antioxidant	[67]
Romiplostim	Hematopoietic growth factor, stimulator of hematopoiesis	[65]
Salts of various metals (copper, manganese, selenium, zinc)	Antioxidants	[10–14,71,72,74]
Stem cell factor (SCF) (c-kit ligand, mast cell growth factor)	Hematopoietic growth factor, stimulator of hematopoiesis	[31,57,62,63,66]
Stromal-derived factor-1 (SDF-1)	Chemokine, influences migration of hematopoietic cells	[62]
Synthokine SC-55494	Cytokine, stimulator of hematopoiesis	[58,59]
Thrombopoietin (TPO)	Hematopoietic growth factor, stimulator of thrombopoiesis	[60,62]
Tumor necrosis factor (TNF)	Modulator of inflammation	[55]
Vitamin E and its family members	Antioxidants	[15–18,69–72]

4. Discussion and Conclusions

As follows from the above summary of the findings on pharmacological modulation of ARS by combined drug treatment, this topic has required long-term attention. It can be deduced from the literature that, whereas in the years of the Cold War researchers focused their studies predominantly on the evaluation of "true radioprotectors", i.e., chemical radioprotectors effective at pre-irradiation administration, current efforts are concentrated especially on compounds usable in therapeutic post-irradiation treatment approaches. Summaries of therapeutic principles for post-irradiation approaches to the treatment of ARS due to radiation accidents or contingent terrorist attacks can be found in several publications (e.g., [77,78]).

ARS is connected with multi-organ involvement, or even multi-organ failure [78]. Therefore, its general medical management is complex in essence and can comprise, e.g., administration of antibiotic, antimycotic, and antiviral substances (e.g., [79]), drugs for maintaining homeostasis through supporting renal function (e.g., [80]), transplantation of hematopoietic stem cells (e.g., [81]), or drugs modulating the course of the cutaneous radiation damage (e.g., [82]). These aspects of the treatment of the acute radiation disease exceed the thematic extent of this review and should be studied from other sources. This article has focused on pharmacological approaches directly influencing the radiation damage and those aimed preferentially at the hematopoietic radiation syndrome which represents the primary challenge in the case of whole-body acute exposure over 2 Gy [83].

As documented by the rich literature data, the aim of achieving a high efficacy of pharmacological reduction of the acute radiation damage in connection with a low toxicity of the therapy by means of combining suitable drugs has represented a challenge for a number of researchers over a long period. Many of the treatment schemes confirm the correctness of the idea; the values of important parameters after combined treatment are often additive or synergistic when compared to those following administration of the individual components of the combinations studied. According to the opinion of the authors of this review, the future of the research consists especially in studies on post-irradiation approaches which correspond more to the current dangers and demands in comparison with classical chemical radioprotectors set for pre-irradiation protective administration. Cytokines will undoubtedly remain the most efficacious component of the combined therapies of ARS. However, supplementation of the cytokine cocktails with some of the other drugs mentioned in this review would be worthy of study. Moreover, it should be taken into consideration that the most effective drug combination utilizing high doses of its individual components do not always represent the optimum general outcome. Development of effective combinations of radioprotectors/radiomitigators using doses of their components that are as low as possible, which would, thus, show the lowest possible intensities and incidences of their undesirable effects, might be the goal of some of the future studies on this topic. In this way, the aim of obtaining pharmacological approaches, which would be well tolerated in patients with ARS, could be achieved.

Acknowledgments: This work was supported by the Czech Science Foundation project 16-12454S, Ministry of Health of the Czech Republic (AZV grant no. 16-29835A; all rights reserved) and from the Czech Republic contribution to the Joint Institute for Nuclear Research, Dubna (Project of the Czech Plenipotentiary and the 3 + 3 Project for 2015, 2016).

Author Contributions: M.H. designed the manuscript and significantly participated in its writing; Z.H. contributed to writing of Section 3 (Combinations without Amifostine); D.D. was significantly engaged in looking up and drawing chemical structures of selected radiomodifying substances; and M.F. contributed to writing of Section 2 (Combinations including Amifostine).

Conflicts of Interest: The authors declare no conflict of interest.

References

1. Singh, V.K.; Romaine, P.L.P.; Newman, V.L.; Seed, T.M. Medical countermeasures for unwanted CBRN exposures. Part II radiological and nuclear threats with review of recent countermeasure patents. *Expert Opin. Ther. Pat.* **2016**, *26*, 1399–1408. [CrossRef] [PubMed]

2. Singh, V.K.; Romaine, P.L.P.; Seed, T.M. Medical countermeasures for radiation exposure and related injuries: Characterization of medicines, FDA-approval status and inclusion into the strategic national stockpile. *Health Phys.* **2015**, *108*, 607–630. [CrossRef] [PubMed]
3. Pellmar, T.C.; Rockwell, S. The Radiological/Nuclear Threat Countermeasures Working Group. Priority list of research areas for radiological nuclear threat countermeasures. *Radiat. Res.* **2005**, *163*, 115–123. [CrossRef] [PubMed]
4. Weiss, J.F.; Kumar, K.S.; Walden, T.L.; Neta, R.; Landauer, M.R.; Clark, E.P. Advances in radioprotection through the use of combined agent regimens. *Int. J. Radiat. Biol.* **1990**, *57*, 709–722. [CrossRef] [PubMed]
5. Hosseinimehr, S.A. Trends in development of radioprotective agents. *Drug Discov. Today* **2007**, *12*, 794–805. [CrossRef] [PubMed]
6. Brown, D.G.; Pittock, J.W.; Rubinstein, J.S. Early results of the screening program for radioprotectors. *J. Radiat. Oncol. Biol. Phys.* **1982**, *8*, 565–570. [CrossRef]
7. Buschini, A.; Aneschi, E.; Carlo-Stella, C.; Regazzi, E.; Rizzoli, V.; Poli, P.; Rossi, C. Amifostine (WR-2721) selective protection against melphalan toxicity. *Leukemia* **2000**, *14*, 1642–1651. [CrossRef] [PubMed]
8. Buschini, A.; Aneschi, E.; Carlo-Stella, C.; Regazzi, E.; Rizzoli, V.; Poli, P.; Rossi, C. Bleomycin genotoxicity and amifostine (WR-2721) cell protection in normal leukocytes vs. K562 tumoral cells. *Biochem. Pharmacol.* **2002**, *63*, 967–975. [CrossRef]
9. Hofer, M.; Falk, M.; Komůrková, D.; Falková, I.; Bačíková, A.; Klejdus, B.; Pagáčová, E.; Štefančíková, L.; Weiterová, L.; Angelis, K.J.; et al. Two new faces of amifostine: Protector from DNA damage in normal cells and inhibitor of DNA repair in cancer cells. *J. Med. Chem.* **2016**, *59*, 3003–3017. [CrossRef] [PubMed]
10. Weiss, J.F.; Hoover, R.L.; Kumar, K.S. Selenium pretreatment enhances the radioprotective effect and reduces the lethal toxicity of WR-2721. *Free Radic. Res. Commun.* **1987**, *3*, 33–38. [CrossRef] [PubMed]
11. Brown, D.Q.; Graham, W.J.; MacKenzie, L.J.; Pittock, J.W.; Shaw, L.M. Can WR-2721 be improved upon? *Pharmacol. Ther.* **1988**, *39*, 157–168. [CrossRef]
12. Kumar, K.S.; Vaishnav, Y.N.; Weiss, J.F. Radioprotection by antioxidant enzymes and enzyme mimetics. *Pharmacol. Ther.* **1988**, *39*, 301–309. [CrossRef]
13. Buntzel, J.; Micke, O.; Mucke, R.; Glatzel, M.; Schonekaes, K.G.; Schafer, U.; Kisters, K.; Bruns, F. Amifostine and selenium during simultaneous radiochemotherapy in head and neck cancer—Redox status data. *Trace Elem. Electrol.* **2005**, *22*, 211–2015. [CrossRef]
14. Ali, B.H.; Al Moundhri, M.S. Agents ameliorating or augmenting the nephrotoxicity of cisplatin and other platinum compounds: A review of some recent research. *Food Chem. Toxicol.* **2006**, *44*, 1173–1183. [CrossRef] [PubMed]
15. Weiss, J.F.; Landauer, M.R. Radioprotection by antioxidants. *Ann. N. Y. Acad. Sci.* **2000**, *899*, 44–60. [CrossRef] [PubMed]
16. Srinivasan, V.; Weiss, J.F. Radioprotection by vitamin-E–injectable vitamin-E administered alone or with WR-3689 enhances survival of irradiated mice. *Int. J. Radiat. Oncol. Biol. Phys.* **1992**, *23*, 841–845. [CrossRef]
17. Kaplan, B.; Orhan, O.; Yazici, C.; Karahacioglu, E. Radioprotective effects of amifostine (WR 2721) and vitamin E on whole-body-irradiated rat liver. *Turk. Klin. Tip Bilim. Derg.* **2009**, *29*, 1055–1062.
18. Singh, V.K.; Fatanmi, O.O.; Wise, S.Y.; Newman, V.L.; Romaine, P.L.; Seed, T.M. Potentiation of the radioprotective efficacy of two medical countermeasures, gamma-tocotrienol and amifostine, by a combination prophylactic modality. *Radiat. Prot. Dosim.* **2016**, *172*, 302–310. [CrossRef] [PubMed]
19. Hanson, W.R. Radioprotection of murine intestine by WR-2721, 16,16-dimethyl-prostaglandin E_2 and the combination of both agents. *Radiat. Res.* **1987**, *111*, 361–373. [CrossRef] [PubMed]
20. Lu, L.; Pelus, L.M.; Broxmeyer, H.E. Modulation of expression of HLA-DR (Ia) antigens and the proliferation of human erythroid (BFU-E) and multipotential (CFU-GEMM) progenitor cells by prostaglandin E. *Exp. Hematol.* **1984**, *12*, 741–748. [PubMed]
21. Hoggatt, J.; Singh, P.; Sampath, J.; Pelus, L.M. Prostaglandin E_2 enhances hematopoietic stem cell homing, survival, and proliferation. *Blood* **2009**, *113*, 5444–5455. [CrossRef] [PubMed]
22. Hanson, W.R.; Houseman, K.A.; Collins, P.W. Radiation protection in vivo by prostaglandins and related compounds of the arachidonic acid cascade. *Pharmacol. Ther.* **1988**, *39*, 347–356. [CrossRef]

23. Mota, J.M.S.C.; Soares, P.M.G.; Menezes, A.A.J.; Lemos, H.P.; Cunha, F.Q.; Brito, G.A.C.; Ribeiro, R.A.; de Souza, M.H.L.P. Amifostine (Wr-2721) prevents indomethacin-induced gastric damage in rats: Role of non-protein sulfhydryl groups and leukocyte adherence. *Dig. Dis. Sci.* **2007**, *52*, 119–125. [CrossRef] [PubMed]
24. Patchen, M.L.; MacVittie, T.J.; Jackson, W.E. Postirradiation glucan administration enhances the radioprotective effects of WR-2721. *Radiat. Res.* **1989**, *117*, 59–69. [CrossRef] [PubMed]
25. Patchen, M.L.; MacVittie, T.J.; Weiss, J.F. Combined modality radioprotection: The use of glucan and selenium with WR-2721. *Int. J. Radiat. Oncol. Biol. Phys.* **1990**, *18*, 1069–1075. [CrossRef]
26. Pillai, T.G.; Devi, P.U. Mushroom beta glucan: Potential candidate for post irradiation protection. *Mutat. Res. Genet. Toxicol. Environ.* **2013**, *751*, 109–115. [CrossRef] [PubMed]
27. Hofer, M.; Pospíšil, M. Modulation of animal and human hematopoiesis by β-glucans. A review. *Molecules* **2011**, *16*, 7969–7979. [CrossRef] [PubMed]
28. Macková, N.O.; Fedoročko, P. Combined radioprotective effect of Broncho-Vaxom® and WR-2721 on hematopoiesis and circulating blood-cells. *Neoplasma* **1995**, *42*, 25–30. [PubMed]
29. Fedoročko, P.; Brezáni, P.; Macková, N.P. Radioprotective effects of WR-2721, Broncho-Vaxom® and their combinations—Survival, myelopoietic restoration and induction of colony-stimulating activity in mice. *Int. J. Immunopharmacol.* **1994**, *16*, 177–184. [CrossRef]
30. Jiang, S.Q.; Shen, X.R.; Liu, Y.M.; He, Y.; Jiang, D.W.; Chen, W. Radioprotective effects of Sinpulus nudus L. polysaccharide combined with WR-2721, rhIL-11 and rhG-CSF on radiation-injured mice. *J. Radiat. Res.* **2015**, *56*, 515–522. [CrossRef] [PubMed]
31. Liu, W.; Chen, Q.; Wu, S.; Xia, X.C.; Wu, A.Q.; Cui, F.M.; Gu, Y.P.; Zhang, X.G.; Cao, J.P. Radioprotector WR-2721 and mitigating peptidoglycan synergistically promote mouse survival through the amelioration of intestinal and bone marrow damage. *J. Radiat. Res.* **2015**, *56*, 278–286. [CrossRef] [PubMed]
32. Nagata, S. *The Cytokine Handbook*; Thomson, A., Ed.; Academic Press: New York, NY, USA, 1994; p. 371.
33. Drouet, M.; Delaunay, C.; Grenier, N.; Garrigou, P.; Mayol, J.F.; Hérodin, F. Cytokines in combination to treat radiation-induced myelosuppression: Evaluation of SCF + glycosylated EPO + pegylated G-CSF as an emergency treatment in highly irradiated monkeys. *Haematol. Hematol. J.* **2008**, *93*, 465–466. [CrossRef] [PubMed]
34. Hofer, M.; Pospíšil, M.; Komůrková, D.; Hoferová, Z. Granulocyte colony-stimulating factor in the treatment of acute radiation syndrome: A concise review. *Molecules* **2014**, *19*, 4770–4778. [CrossRef] [PubMed]
35. Patchen, M.L.; MacVittie, T.J.; Souza, L.M. Postirradiation treatment with granulocyte colony-stimulating factor and preirradiation WR-2721 administration synergize to enhance hematopoietic recostitution and increase survival. *Int. J. Radiat. Oncol. Biol. Phys.* **1992**, *22*, 773–779. [CrossRef]
36. Patchen, M.L. Amifostine plus granulocyte colony-stimulating factor therapy enhances recovery from supralethal radiation exposures—Preclinical experience in animal-models. *Eur. J. Cancer* **1995**, *31A*, S17–S21. [CrossRef]
37. Neumeister, P.; Jaeger, G.; Eibl, M.; Sormann, S.; Zinke, W.; Linkesch, W. Amifostine in combination with erythropoietin and G-CSF promotes multilineage hematopoiesis in patients with myelodysplastic syndrome. *Leuk. Lymphoma* **2001**, *40*, 345–349. [CrossRef] [PubMed]
38. Winczura, P.; Jassem, J. Combined treatment with cytoprotective agents and radiotherapy. *Cancer Treat. Rev.* **2010**, *36*, 268–275. [CrossRef] [PubMed]
39. Miller, R.C.; Murley, J.S.; Grdina, D.J. Metformin exhibits radiation countermeasures efficacy when used alone or in combination with sulfhydryl containing drugs. *Radiat. Res.* **2014**, *181*, 464–470. [CrossRef] [PubMed]
40. Zucali, J.R. Mechanisms of protection of hematopoietic stem-cells from irradiation. *Leuk. Lymphoma* **1994**, *13*, 27–32. [CrossRef] [PubMed]
41. Pospíšil, M.; Hofer, M.; Netíková, J.; Pipalová, I.; Vacek, A.; Bartoníčková, A.; Volenec, K. Elevation of extracellular adenosine induces radioprotective effects in mice. *Radiat. Res.* **1995**, *134*, 323–330. [CrossRef]
42. Hofer, M.; Pospisil, M.; Weiterova, L.; Hoferova, Z. The role of adenosine receptor agonists in regulation of hematopoiesis. *Molecules* **2011**, *16*, 675–685. [CrossRef] [PubMed]
43. Pospíšil, M.; Hofer, M.; Znojil, V.; Vácha, J.; Netíková, J.; Holá, J. Synergistic effect of granulocyte colony-stimulating factor and drugs elevating extracellular adenosine on neutrophil production in mice. *Blood* **1995**, *86*, 3692–3697. [PubMed]

44. Pospíšil, M.; Hofer, M.; Znojil, V.; Netíková, J.; Vácha, J.; Holá, J.; Vacek, A. Granulocyte colony-stimulating factor and drugs elevating extracellular adenosine synergize to enhance the haemopoietic reconstitution in irradiated mice. *Eur. J. Haematol.* **1998**, *60*, 172–180. [CrossRef] [PubMed]
45. Bar-Yehuda, S.; Madi, L.; Barak, D.; Mittelman, M.; Ardon, E.; Ochaion, A.; Cohn, S.; Fishman, P. Agonists to the A_3 adenosine receptor induce G-CSF production via NF-kappa B activation: A new class of myeloprotective agents. *Exp. Hematol.* **2002**, *30*, 1390–1398. [CrossRef]
46. Hofer, M.; Pospíšil, M.; Šefc, L.; Dušek, L.; Vacek, A.; Holá, J.; Hoferová, Z.; Štreitová, D. Activation of adenosine A_3 receptors supports hematopoiesis-stimulating effects of granulocyte colony-stimulating factor in sublethally irradiated mice. *Int. J. Radiat. Biol.* **2010**, *86*, 649–656. [CrossRef] [PubMed]
47. Hofer, M.; Pospíšil, M.; Hoferová, Z.; Weiterová, L.; Komůrková, D. Stimulatory action of cyclooxygenase inhibitors on hematopoiesis. A review. *Molecules* **2012**, *17*, 5615–5625. [CrossRef] [PubMed]
48. Pospíšil, M.; Hofer, M.; Pipalová, I.; Viklická, Š. Enhancement of hematopoietic recovery in gamma-irradiated mice by the joint use of diclofenac, an inhibitor of prostaglandin production, and glucan, a macrophage activator. *Exp. Hematol.* **1992**, *20*, 891–895. [PubMed]
49. Hofer, M.; Pospíšil, M.; Viklická, Š.; Vacek, A.; Pipalová, I.; Bartoníčková, A. Hematopoietic recovery in repeatedly irradiated mice can be enhanced by a repeatedly administered combination of diclofenac and glucan. *J. Leukoc. Biol.* **1993**, *53*, 185–189. [PubMed]
50. Hofer, M.; Pospíšil, M.; Dušek, L.; Hoferová, Z.; Weiterová, L. Inhibition of cyclooxygenase-2 promotes the stimulatory action of adenosine A_3 receptor agonist on hematopoiesis in sublethally γ-irradiated mice. *Biomed. Pharmacother.* **2011**, *65*, 427–431. [CrossRef] [PubMed]
51. Hofer, M.; Pospíšil, M.; Dušek, L.; Hoferová, Z.; Komůrková, D. Agonist of the adenosine A_3 receptor, IB-MECA, and inhibitor of cyclooxygenase-2, meloxicam, given alone or in a combination early after total body irradiation, enhance survival of γ-irradiated mice. *Radiat. Environ. Biophys.* **2014**, *53*, 211–215. [CrossRef] [PubMed]
52. Hofer, M.; Pospíšil, M.; Holá, J.; Vacek, A.; Štreitová, D.; Znojil, V. Inhibition of cyclooxygenase 2 in mice increases production of G-CSF and induces radioprotection. *Radiat. Res.* **2008**, *170*, 566–571. [CrossRef] [PubMed]
53. Hofer, M.; Pospíšil, M.; Znojil, V.; Holá, J.; Vacek, A.; Štreitová, D. Meloxicam, a cyclooxygenase-2 inhibitor, increases the level of serum G-CSF and might be usable as an auxiliary means in G-CSF therapy. *Physiol. Res.* **2008**, *57*, 307–310. [PubMed]
54. Patchen, M.L.; MacVittie, T.J.; Solberg, B.D.; Souza, L.M. Survival enhancement and hemopoietic regeneration following radiation exposure: Therapeutic approach using glucan and granulocyte colony-stimulating factor. *Exp. Hematol.* **1990**, *18*, 1042–1048. [PubMed]
55. Neta, R.; Oppenheim, J.J.; Douches, S.D. Interdependence of the radioprotective effects of human recombinant interleukin 1α, tumor necrosis factor α, granulocyte colony-stimulating factor, and murine recombinant granulocy-macrophage colony-stimulating factor. *J. Immunol.* **1988**, *140*, 108–111. [PubMed]
56. Patchen, M.L.; Fischer, R.; MacVittie, T.J. Effects of combined administration of interleukin-6 and granulocyte colony-stimulating factor on recovery from radiation-induced hemopoietic aplasia. *Exp. Hematol.* **1993**, *21*, 338–344. [PubMed]
57. Patchen, M.L.; Fischer, R.; MacVittie, T.J.; Seiler, F.R.; Williams, D.E. Mast cell growth factor (C-kit ligand) in combination with granulocyte-macrophage colony-stimulating factor and interleukin-3: In vivo hemopoietic effects in irradiated mice compared to in vitro effects. *Biotherapy* **1993**, *7*, 13–26. [CrossRef] [PubMed]
58. Farese, A.M.; Hérodin, F.; McKearn, J.P.; Baum, C.; Burton, E.; MacVittie, T.J. Acceleration of hematopoietic reconstitution with a synthetic cytokine (SC-55494) after radiation-induced bone marrow aplasia. *Blood* **1996**, *87*, 581–591. [PubMed]
59. MacVittie, T.J.; Farese, A.M.; Hérodin, F.; Grab, L.B.; Baum, C.M.; McKearn, J.P. Combination therapy for radiation-induced bone marrow aplasia in nonhuman primates using synthokine SC-55494 and recombinant human granulocyte colony-stimulating factor. *Blood* **1996**, *87*, 4129–4135. [PubMed]
60. Neelis, K.J.; Hartong, S.C.; Egeland, T.; Thomas, G.R.; Eaton, D.L.; Wagemaker, G. The efficacy of single-dose administeration of thrombopoietin with coadministration of either granulocyte/macrophage colony-stimulating factor or granulocyte colony-stimulating factor in myelosuppressed rhesus monkeys. *Blood* **1997**, *90*, 2565–2573. [PubMed]

61. Farese, A.M.; Hunt, P.; Grab, L.B.; MacVittie, T.J. Combined administration of recombinant human megakaryocyte growth and development factor and granulocyte colony-stimulating factor enhances multilineage hematopoietic reconstitution in nonhuman primates after radiation-induced marrow aplasia. *J. Clin. Investig.* **1996**, *97*, 2145–2151. [CrossRef] [PubMed]
62. Hérodin, F.; Bourin, P.; Mayol, J.F.; Lataillade, J.J.; Drouet, M. Short-term injection of antiapoptotic cytokine combinations soon after lethal gamma-irradiation promotes survival. *Blood* **2003**, *101*, 2609–2616. [CrossRef] [PubMed]
63. Hérodin, F.; Roy, L.; Grenier, N.; Delaunay, C.; Bauge, S.; Vaurijoux, A.; Gregoire, E.; Martin, C.; Alonso, A.; Mayol, L.F.; et al. Antiapoptotic cytokines in combination with pegfilgrastim soon after irradiation mitigate myelosuppression in nonhuman primates exposed to high radiation dose. *Exp. Hematol.* **2007**, *35*, 1172–1181. [CrossRef] [PubMed]
64. Hérodin, F.; Drouet, M. Myeloprotection following cytotoxic damage: The sooner the better. *Exp. Hematol.* **2008**, *36*, 769–770. [CrossRef] [PubMed]
65. Hirouchi, T.; Ito, K.; Nakano, M.; Monzen, S.; Yoshino, H.; Chiba, M.; Hazawa, M.; Nakano, A.; Ishikawa, J.; Yamaguchi, M.; et al. Mitigative effects of a combination of multiple pharmaceutical drugs on the survival of mice exposed to lethal ionizing radiation. *Curr. Pharm. Biotechnol.* **2016**, *17*, 190–199. [CrossRef]
66. Singh, V.K.; Newman, V.L.; Seed, T.M. Colony-stimulating factors for the treatment of the hematopoietic compartment of the acute radiation syndrome (H-ARS): A review. *Cytokine* **2015**, *71*, 22–37. [CrossRef] [PubMed]
67. Vasin, M.V.; Ushakov, I.B.; Kovtun, V.I.; Komarova, S.N.; Semenova, L.A.; Koroleva, L.V.; Galkin, A.A. The influence of combined application of quercetin and indralin on post-irradiation repair of hematopoiesis in acute radiation injury. *Radiat. Biol. Radioecol.* **2011**, *51*, 247–251. (in Russian)
68. Day, R.M.; Davis, T.A.; Barshishat-Kupper, M.; McCart, E.A.; Tipton, A.S.; Landauer, M.R. Enhanced hematopoietic protection from radiation by the combination of genistein and captopril. *Int. Immunopharmac.* **2013**, *15*, 348–356. [CrossRef] [PubMed]
69. Singh, V.K.; Wise, S.Y.; Fatanmi, O.O.; Beattie, L.A.; Ducey, E.J.; Seed, T.M. Alpha tocopherol succinate- and AMD3100-mobilized progenitors mitigate radiation combined injury in mice. *J. Radiat. Res.* **2014**, *55*, 41–53. [CrossRef] [PubMed]
70. Vasil'eva, I.N.; Bespalov, V.G.; Baranenko, D.A. Radioprotective and apoptotic properties of a combination of alpha-tocopherol acetate and ascorbic acid. *Bull. Exp. Biol. Med.* **2016**, *161*, 248–251. [CrossRef] [PubMed]
71. Wambi, C.; Sanzari, J.; Wan, X.S.; Nuth, M.; Davis, J.; Ko, Y.H.; Sayers, C.M.; Baran, M.; Ware, J.H.; Kennedy, A.R. Dietary antioxidants protect hematopoietic cells and improve animal survival after total-body irradiation. *Radiat. Res.* **2008**, *169*, 384–396. [CrossRef] [PubMed]
72. Wambi, C.O.; Sanzari, J.K.; Sayers, C.M.; Nuth, M.; Zhou, Z.Z.; Davis, J.; Finnberg, N.; Lewis-Wambi, J.S.; Ware, J.H.; El-Deiry, W.S.; et al. Protective effects of dietary antioxidants on proton total-body irradiation-mediated hematopoietic cell and animal survival. *Radiat. Res.* **2009**, *172*, 175–186. [CrossRef] [PubMed]
73. Gupta, M.L; Sankwar, S.; Verma, S.; Devi, M.; Samanta, N.; Agarwala, P.K.; Kumar, R.; Singh, P.K. Whole-body protection to lethally irradiated mice by oral administration of semipurified fraction of *Podophyllum hexandrum* and post irradiation treatment with Picorrhiza kurroa. *Tokai J. Exp. Clin. Med.* **2008**, *33*, 6–12. [PubMed]
74. Crescenti, E.J.V.; Medina, V.A.; Croci, M.; Sambuco, L.A.; Prestifilippo, J.P.; Elverdin, J.C.; Bergoc, R.M.; Rivera, E.S. Radioprotection of sensitive rat tissues by oligoelements Se, Zn, Mn plus *Lachesis muta* venom. *J. Radiat. Res.* **2011**, *52*, 557–567. [CrossRef] [PubMed]
75. Taniguchi, C.M.; Miao, Y.R.; Diep, A.N.; Wu, C.; Rankin, E.B.; Atwood, T.F.; Xing, L.; Giaccia, A.J. PHD inhibition mitigates and protects against radiation-induced gastrointestinal toxicity via HIF2. *Sci. Transl. Med.* **2014**, *6*, 236ra64. [CrossRef] [PubMed]
76. Olcina, M.M.; Giaccia, A.J. Reducing radiation-induced gastrointestinal toxicity – the role of the PHD/HIF axis. *J. Clin. Investig.* **2016**, *126*, 3708–3715. [CrossRef] [PubMed]
77. Moulder, J.E. Post-irradiation approaches to treatment of radiation injuries in the context of radiological terrorism and radiation accidents. *Int. J. Radiat. Biol.* **2004**, *80*, 3–10. [CrossRef] [PubMed]
78. Dörr, H.; Meineke, V. Acute radiation syndrome caused by accidental radiation exposure—Therapeutic principles. *BMC Med.* **2011**, *9*, 126. [CrossRef] [PubMed]

79. Waselenko, J.K.; MacVittie, TJ.; Blakely, W.F.; Pesik, N.; Wiley, A.L.; Dickerson, W.E.; Tsu, H.; Confer, D.L.; Coleman, C.N.; Seed, T.; et al. Strategic National Stockpile Radiation Working Group: Medical management of the acute radiation syndrome: Recommendations of the Strategic National Stockpile Radiation Working Group. *Ann. Intern. Med.* **2004**, *140*, 1037–1051. [CrossRef] [PubMed]
80. Moulder, J.E.; Cohen, E.P. Radiation-induced multi-organ involvement and failure: The contribution of radiation effects on the renal system. *Br. J. Radiol.* **2005**, *27* (Suppl. 2005), 82–88. [CrossRef]
81. Dainiak, N.; Ricks, R.C. The evolving role of haematopoietic stem cell transplantation in radiation injury: Potentials and limitations. *Br. J. Radiol.* **2005**, *27* (Suppl. 2005), 169–174. [CrossRef]
82. Dainiak, N.; Gent, R.N.; Carr, Z.; Schneider, R.; Bader, R.; Buglova, E.; Chao, N.; Coleman, C.N.; Ganser, A.; Gorin, C.; et al. Literature review and global consensus on management of acute radiation syndrome affecting non-hematopoietic organs systems. *Disaster Med. Public Health Prep.* **2011**, *5*, 183–201. [CrossRef] [PubMed]
83. Drouet, M.; Hérodin, F. Radiation victim management and the haematologist in the future: Time to revisit therapeutic guidelines? *Int. J. Radiat. Biol.* **2010**, *86*, 636–648. [CrossRef] [PubMed]